Cell Physiology Sourcebook

Fourth Edition

Essentials of Membrane Biophysics

Edited by Nicholas Sperelakis

Cell Physiology Sourcebook

Essentials of Membrane Biophysics

This page intentionally left blank

Cell Physiology Sourcebook

Essentials of Membrane Biophysics

Fourth Edition

Nicholas Sperelakis
Department of Physiology and Biophysics,
College of Medicine, University of Cincinnati,
Cincinnati, Ohio

ELSEVIER

AMSTERDAM • BOSTON • HEIDELBERG • LONDON • NEW YORK • OXFORD • PARIS
SAN DIEGO • SAN FRANCISCO • SINGAPORE • SYDNEY • TOKYO

Academic Press is an Imprint of Elsevier

Academic Press is an Imprint of Elsevier
32 Jamestown Road, London NW1 7BY, UK
225 Wyman Street, Waltham, MA 02451, USA
525 B Street, Suite 1800, San Diego, CA 92101-4495, USA

First edition 1995
Second edition 1998
Third edition 2001
Fourth edition 2012

British Library Cataloguing-in-Publication Data
A catalogue record for this book is available from the British Library

Library of Congress Cataloging-in-Publication Data
A catalog record for this book is available from the Library of Congress

ISBN: 978-0-12-387738-3

Typeset by TNQ Books and Journals Pvt Ltd.
www.tnq.co.in

Printed and bound in Canada

12 13 14 15 16 10 9 8 7 6 5 4 3 2 1

Dedication

This book is dedicated to Planet Earth and to all those organizations that are working tirelessly to save and protect the environment, to stop pollution of our oceans, lakes, rivers, drinking water, air, and soil, to preserve the farmlands, to stabilize world population, to protect and preserve wildlife, to promote animal welfare, and to fight for human rights around the globe.

I also want to acknowledge the love and support of my family: my wife Dolores and children Mark Demitri (deceased), Christine M., Sophia A., Thomas A., and Anthony J., daughter-in-law Sherri, and grandchildren Demetra, Gregory and Nina-Nicole.

A special thanks to David Magnuson, M.D., Chairman of Pediatric Surgery at Cleveland Clinic, for his great dedication, skills, wisdom and humanity. Efharisto para poli, aka "Εύχαριστω παρά πολύ".

This page intentionally left blank

Contents

This page intentionally left blank

In Memoriam

Dr Hugo Gonzalez-Serratos passed away on April 1, 2011. Hugo was Professor of Physiology at the University of Maryland in Baltimore. He was a graduate student of Professor Andrew F. Huxley, Nobel laureate, at University College London in the mid-1960s. Dr Gonzalez-Serratos achieved great recognition as a top scientist in the field of muscle physiology. He will be greatly missed by all of us. Professor Gonzalez-Serratos was a contributing author to this book. May his memory be eternal!

This page intentionally left blank

Contributors

Francisco J. Alvarez-Leefmans MD, PhD, Professor, Department of Pharmacology and Toxicology, Boonshoft School of Medicine, Wright State University, Dayton, Ohio, USA

Clive M. Baumgarten, Professor of Physiology and Biophysics, Biomedical Engineering and Medicine (Cardiology), School of Medicine, Virginia Commonwealth University, Richmond

Kenneth M. Blumenthal, Professor and Chairman, SUNY Department of Biochemistry, School of Medicine and Biomedical Sciences, Buffalo, New York, USA

John H.B. Bridge, Research Professor of Medicine, Division of Cardiology, University of Utah Health Sciences Center, Nora Eccles Harrison Cardiovascular Research and Training Institute, University of Utah, CVRTI, Salt Lake City, Utah, USA

Bruce A. Carlson, Washington University, St Louis, Missouri, USA

Laura Conforti, Department of Internal Medicine, University of Cincinnati, Cincinnati, Ohio, USA

John R. Dedman, Professor and Ohio Eminent Scholar, Department of Cancer & Cell Biology, Department of Molecular and Cell Biology, University of Cincinnati, Cincinnati, Ohio, USA

Neil D. Detweiler, Department of Pharmacology and Toxicology, University of Arkansas for Medical Sciences, Little Rock, Arkansas, USA

Istvan Edes, Institute of Cardiology, University of Debrecen, Debrecen, Hungary

Robert A. Farley PhD, Professor Physiology and Biophysics, Biochemistry and Molecular Biology, Departments of Physiology and Biophysics, and Biochemistry and Molecular Biology, Keck School of Medicine, University of Southern California, Los Angeles, California, USA

Joseph J. Feher PhD, Professor of Physiology and Biophysics, School of Medicine, Virginia Commonwealth University, Richmond, Virginia, USA

Darrell Fleischman, Adjunct Associate Professor, Department of Biochemistry and Molecular Biology, Boonshoft School of Medicine, Wright State University, Dayton, Ohio, USA

Michael S. Forbes Ph.D., Department of Pediatrics, University of Virginia School of Medicine, Charlottesville, Virginia, USA

Kenneth W. Foster, Professor, Physics Department, Syracuse University, Syracuse, New York, USA

Jeffrey C. Freedman, Associate Professor, Neuroscience and Physiology, SUNY Upstate Medical University, Syracuse, New York, USA

Andrew S. French, Professor of Physiology and Biophysics, Department of Physiology and Biophysics, Halifax, Nova Scotia, Canada

Nicole Gallo-Payet, Professor and Research Chair of the Faculty of Medicine and Health Sciences, Departments of Endocrinology, and Medicine, University of Sherbrooke, Sherbrooke, Quebec, Canada

Hugo Gonzalez-Serratos, Professor, Physiology, University of Maryland, School of Medicine, Baltimore, Maryland, USA

Anthony L. Gotter, Division of Human Genetics, The Children's Hospital of Philadelphia and the Joseph Stokes Jr Research Institute, Philadelphia, Pennsylvania, USA

Michael S. Grace, Associate Professor, Biological Sciences Department, College of Science, Florida Institute of Technology, Melbourne, Florida, USA

Steven M. Grassl, Associate Professor, Pharmacology, State University of NY Upstate Medical University, Syracuse, New York, USA

Dennis W. Grogan, Professor, Department of Biological Sciences, University, College of Arts and Sciences, University of Cincinnati, Cincinnati, Ohio, USA

J. Woodland Hastings, Professor of Natural Sciences, Department of Molecular and Cellular Biology, Harvard University, Cambridge, Massachusetts, USA

Judith Heiny, Associate Professor, Department of Molecular and Cellular Physiology, University of Cincinnati, Cincinnati, Ohio, USA

Aldebaran M. Hofer, Associate Professor of Surgery & Research Health Scientist, VA Boston Healthcare System and the Department of Surgery, Brigham and Women's Hospital and Harvard Medical School, Massachusetts, USA

Atsushi Inanobe, Department of Pharmacology, Graduate School of Medicine and The Center for Advanced Medical Engineering and Informatics, Osaka University, Osaka, Japan

Marcia A. Kaetzel, Department of Cancer and Cell Biology, University of Cincinnati, Cincinnati, Ohio, USA

Robert S. Kass, Alumni and David Hosack Professor of Pharmacology and Chair, Columbia University College of Physicians and Surgeons, New York, USA

Sujay V. Kharade, Department of Pharmacology and Toxicology, University of Arkansas for Medical Sciences, Little Rock, Arkansas, USA

Takeshi Kobayashi, Assistant Professor, Department of Cellular Physiology and Signal Transduction, Sapporo Medical University School of Medicine, Sapporo, Japan

Evangelia G. Kranias, Chair, Department of Pharmacology & Cell Biophysics, Distinguished University Professor, Co-Director, Cardiovascular Center of Excellence, Department of Pharmacology and Cell Biophysics, University of Cincinnati, Cincinnati, Ohio, USA

Yoshihisa Kurachi, Department of Pharmacology, Graduate School of Medicine and The Center for Advanced Medical Engineering and Informatics, Osaka University, Osaka, Japan

Stephen Lambert, Associate Professor of Medicine, College of Medicine, University of Central Florida, Health Sciences Campus at Lake Nona, Orlando, Florida, USA

Michael Levandowsky, Research Scientist, Adjunct Professor of Biology, Haskins Laboratories, Pace University, New York, USA

Simon Rock Levinson, Professor, Department of Physiology and Biophysics, University of Colorado School of Medicine, Aurora, Colorado, USA

Daniel C. Marcus, Program Director, KSU COBRE grant; Professor, Anatomy and Physiology, College of Veterinary Medicine, Kansas State University, Manhattan, Kansas, USA

Gerhard Meissner, Professor, Departments of Cell and Molecular Physiology, and Biochemistry and Biophysics, The University of North Carolina at Chapel Hill School of Medicine, Chapel Hill, North Carolina, USA

Stan Misler, Associate Professor, Internal Medicine, Cell Biology and Physiology, Washington University in St Louis School of Medicine, St Louis, Missouri, USA

Catherine E. Morris, Senior Scientist, Neuroscience, Ottawa Hospital Research Institute; Professor, Department of Medicine, Division of Neurology, University of Ottawa, Ottawa, Ontario, Canada

Michela Ottolia, Department of Physiology, Cardiovascular Research Laboratories, David Geffen School of Medicine at UCLA, Los Angeles, California, USA

Richard J. Paul, Professor, Director, PhD Program in Systems Biology and Physiology, Department of Molecular and Cellular Physiology, College of Medicine, University of Cincinnati, Cincinnati, Ohio, USA

Asif R. Pathan, Department of Pharmacology and Toxicology, University of Arkansas for Medical Sciences, Little Rock, Arkansas, USA

Marcel Daniel Payet, Professor, Department of Physiology and Biophysics, Faculté de Médecine, Université de Sherbrooke, Sherbrooke, Quebec, Canada

Matthew Pincus, Professor, Clinical Pathology, SUNY Downstate Medical Center in Brooklyn; Chief, Department of Pathology & Laboratory Medicine, New York Harbor VA Medical Center, Brooklyn, New York, USA

Tracy J. Pritchard, Department of Pharmacology and Cell Biophysics, University of Cincinnati, Cincinnati, Ohio, USA

Robert W. Putnam, Professor, Department of Neuroscience, Cell Biology and Physiology, Boonshoft School of Medicine, Wright State University, Datyton, Ohio, USA

Seth Robey, Department of Pharmacology, College of Physicians and Surgeons, Columbia University, NY, New York, USA

Stephen D. Roper, Professor, Department of Physiology and Biophysics, University of Miami Miller School of Medicine, Miami, Florida, USA

Nancy J. Rusch, Professor and Chair, Department of Pharmacology and Toxicology, University of Arkansas

College of Medicine, University of Arkansas for Medical Sciences, Little Rock, Arkansas, USA

Kevin J. Sampson, Department of Pharmacology, College of Physicians and Surgeons, Columbia University, NY, New York, USA

William A. Sather, Associate Professor, Department of Pharmacology, University of Colorado Denver, Aurora, Colorado, USA

Nicholas Sperelakis, Department of Physiology and Biophysics, College of Medicine, University of Cincinnati, Cincinnati, Ohio, USA

Anup K. Srivastava, Department of Pharmacology and Toxicology, University of Arkansas for Medical Sciences, Little Rock, Arkansas, USA

Janusz B. Suszkiw, Professor, Department of Molecular and Cellular Physiology, University of Cincinnati, Cincinnati, Ohio, USA

Timothy C. Tricas, Professor, Department of Zoology & Hawaii Institute of Marine Biology, University of Hawaii at Manoa, Honolulu, Hawaii, USA

Noritsugu Tohse, Professor, Department of Cellular Physiology and Signal Transduction, Sapporo Medical University School of Medicine, Sapporo, Japan

Päivi H. Torkkeli, Professor of Physiology and Biophysics, Department of Physiology and Biophysics, Dalhousie University, Halifax, Nova Scotia, Canada

Natalia S. Torres, Nora Eccles Harrison Cardiovascular Research and Training Institute, University of Utah, Salt Lake City, Utah, USA

Kenneth R. Tovar, Vollum Institute, Oregon Health and Science University, Portland, Oregon, USA

Richard D. Veenstra, Department of Pharmacology, SUNY Upstate Medical University, Syracuse, New York, USA

Gordon M. Wahler, Professor, Physiology, Midwestern University, Downers Grove, Illinois, USA

Gary L. Westbrook, Senior Scientist and Co-Director, Vollum Institute Dixon, Professor of Neurology Oregon Health and Science University Portland, OR USA

Hisashi Yokoshiki, Associate Professor, Department of Cardiovascular Medicine, Hokkaido University Graduate School of Medicine, Sapporo, Japan

Anita L. Zimmerman, Professor and Vice Chair, Molecular Pharmacology, Physiology and Biotechnology, Brown University, Providence, Rhode Island, USA

This page intentionally left blank

Foreword to the First Edition

It was kind and generous of my friend Nicholas Sperelakis to relate this excellent book so closely to my own, *A Textbook of General Physiology*. In the preface to the first edition of my book, I had expressed the hope that it might be compared with Bayliss' *Principles of General Physiology*. If this comparison is valid, it is very appropriate that the present book be organized and partly written by one who is, along with Sir William Bayliss and myself, associated with University College London (Professor Sperelakis having spent a sabbatical year there). It is a pleasure to recall that it was there that I first met Nicholas, and I remember discussing his pioneering study on the potentials across the crystalline lens of the eye.

For reasons that I think bear no relation to its scope, this book has a different title; I presume it is because the distinction between "ordinary" and "general" physiology has become sufficiently blurred to demand something more appropriate. The definition of general physiology that I had proposed in the preface to the first edition of my textbook was "the study of those aspects of living material that show some immediate prospect of being described in terms of the known laws of physics and chemistry." Later, I had misgivings as to the narrowness of this definition, and I then suggested that it might be replaced by "the study of those features of life that appear to be common to all forms." Whatever definition we choose, however, it is of immense satisfaction to me that this new book, essentially, has been fitted into the same sectional headings that I employed in my own book.

If I may be permitted to reminisce further, I have wondered frequently how a single scientist, actively engaged in research, could write a new book of such wide scope. The answer is that I wrote the book during the 2 years immediately following the end of World War II. Thus, for several years — in Great Britain for as many as 10 years — very little original academic physiology and new research had been published. This made it possible to survey the original literature of a lengthy period without being overwhelmed by a rapid succession of new discoveries that would have rendered my task nearly impossible, a fate similar to that of Sisyphus. Today, this task would be impossible, and it only surprises me that Nicholas has been able to produce this magnificent book with so few collaborators.

Hugh Davson
1995

This page intentionally left blank

Foreword

Foreword to the Second Edition

In his Foreword to the first edition of the *Cell Physiology Sourcebook*, Hugh Davson established it as the lineal descendent of his own well-known and highly respected work *The Textbook of General Physiology*. The second edition of the *Cell Physiology Sourcebook,* again edited by Nicholas Sperelakis, continues in this same tradition. Although the first edition was enthusiastically received by the cell physiology community because of its depth and breadth of coverage, considerable important progress has been made in this rapidly developing area since its publication. The second edition deals with these new developments by a thorough reworking of topics and by the inclusion of new chapters in all sections covered in the first edition. The new topics introduced into the various sections include lipid structure, mitochondrial physiology, cell responses to hormones, red blood cell transport, neuron physiology, developmental changes in ion channels, sonotransduction, excitation-contraction coupling, and electroplax cells. In addition, the scope of the new edition has been valuably broadened by the inclusion of two entirely new sections. One titled *Protozoa and Bacteria* covers the physiology of these organisms in two chapters. In the other, *Cell Division and Programmed Cell Death*, there are chapters on the regulation of cell division, the cancer cell, apoptosis, and the effects of ionizing radiation. The extensive revisions and the new material in the second edition raise it to a new level.

Cell physiology, an area of central importance in biology, has grown out of a number of more traditional fields, and as a result, the literature continues to be widely dispersed. The great value of the *Cell Physiology Sourcebook* is that it gathers together under a single cover a broad range of up-to-date chapters that, taken together, define the field. The various chapters exhibit a uniformity of style and level of presentation that are a credit to the editor. Because of this and the scope and clarity of the presentations, this book can serve exceptionally well as an advanced undergraduate or graduate level text for cell physiology courses. The broad coverage of this second edition also makes it very attractive for use in cell biophysics, membrane biology, and biomedical engineering courses. It can serve equally well as a textbook for introductory courses in ion channel structure and physiology.

I was pleased, and indeed proud, to be asked by my colleague Nicholas Sperelakis to contribute the Foreword to the second edition of the *Cell Physiology Sourcebook*. This book clearly sets a new standard of excellence.

Thomas E. Thompson
1997

This page intentionally left blank

Foreword

Foreword to the Third Edition

When Nicholas Sperelakis kindly invited me to write this foreword, I wondered how I could possibly follow in the footsteps of Hugh Davson. I studied physiology at University College London (UCL) at the time when his monumental *Textbook of General Physiology* was published. UCL was an extraordinary place in which to be a student at that time. Not only was Hugh Davson laying his particular cornerstone of the subject, but Leonard Bayliss was also reworking his father's famous *Principles of General Physiology*. These were the books that convinced me to become a research physiologist and that cell physiology was the place to begin. Between them, Davson and Bayliss were responsible for seducing generations of medical students to discover the challenge and delights of physiological research. Later, as a young lecturer at UCL, I remember asking Hugh Davson why he didn't lecture very much to the students. He simply replied: "Denis, I've written it all. Tell them to read!" Actually, that remark inspired me to reread his books. My copies are still in my library, and they are well and truly thumbed.

It will be the greatest tribute to the work of Nicholas Sperelakis and his colleagues that the pages of their book will also become the well-thumbed bible of a new generation of physiologists. They will be entering the discipline at an exciting time, for cell physiology is the base on which our understanding of all aspects of integrative and systems physiology must rest. This book, therefore, will be an essential source for all of us who aspire to understand the "logic of life," which is, after all, the meaning and origin of the word "physiology." Life has no single "logic," of course. Unraveling the physicochemical mechanisms that nature has discovered, fashioned, combined, and interwoven into the tangled skein of processes that form the function of even the simplest cell is a process full of surprises as we discover with awe the audacity with which nature's molecular mechanisms are reused again and again in different contexts. One might call this audacity the "dance of the genes" were it not for the inanimate and unthinking nature of these bits of code that transmit the logic from one generation to another. The logic is physiological, not genetic. The molecular biologist Sydney Brenner put the point succinctly when he wrote recently (in a Novartis symposium titled The Limits of Reductionism in Biology) that "Genes can only specify the properties of the proteins they code for, and any integrative properties of the system must be 'computed' by their interactions." We are approaching the point at which our understanding of those interactions is deep enough for physiology to aspire to become the quantitative analytical discipline it needs to be to solve the problems it tackles. Brenner went on to remark, significantly, "This provides a framework for analysis by simulation." It is a sign of the maturity of our science that simulation is indeed also becoming an essential tool of analysis.

It is further such a sign that the scope of cell physiology is now so wide. The breadth of this book is therefore one of its greatest strengths. The chapters encompass the great majority of important molecular and cell systems, so that it does indeed justify its title as a *sourcebook*.

Denis Noble

This page intentionally left blank

Foreword to the Fourth Edition

It is my pleasure to write a Foreword for the fourth edition of this textbook, entitled *Cell Physiology Sourcebook*. Professor Hugh Davson did not continue after the fourth edition of his monumental *A Textbook of General Physiology*. Perhaps he realized that the knowledge of physiology had become too broad for him to continue to cover the entire field alone, as he had done for his highly respected textbook.

So what permitted Professor Nicholas Sperelakis to write a noteworthy successor to Davson's formidable textbook? He decided to call upon an increasing number of specialists, and these prestigious specialists accepted to collaborate with him because they highly respected him as one of the major role models in Cell Physiology. Instead of really retiring when he closed his laboratory in 2002, Professor Sperelakis continued to publish articles, generally in collaboration with Dr L. Ramasamy from the Department of Electrical and Computer Engineering of the University of Cincinnati. Professor Sperelakis took the time to familiarize himself with the techniques used in PSpice, an electrical engineering software program (for circuit design and analysis), in which one substitutes electronic equivalents (e.g. resistances, capacitances, etc.) for physiological parameters. He was very excited while learning this new methodology. They have published about 10 articles using the PSpice simulations primarily in Theor Biol & Med Modelling and BioMed Eng Online. Since the first article summarizes the main ideas, I shall give complete reference only to this one, namely *N. Sperelakis and L. Ramasamy, Propagation in Cardiac Muscle and Smooth Muscle Based on Electric Field Transmission at Cell Junctions: An Analysis by PSpice. IEEE-EMB* **21**, *177-190, 2002.*

Professor Nicholas Sperelakis had some rather controversial research findings in the 1960s. In 1977, he reported with his mathematician collaborator, James E. Mann, that the transmission from one cell to the next one can occur in the myocardium by the development of an intense electric field in the narrow clefts of the intercalated disks. They stated, therefore, that propagation in myocardium can occur without the need of any gap-junction channels connecting the myocardial cells. They demonstrated that the density of fast Na^+ channels is greater in the intercalated-disk membrane than in the surface sarcolemma, which means that the excitability is likewise greater at the intercalated disks. I am glad to find that Professor Sperelakis is no longer alone in his Electric Field Hypothesis ever since that hypothesis was independently confirmed in the article by a Japanese group, namely *K. Tsumoto, T. Ashihara, R. Haraguchi, K. Nagazawa, and Y. Kurachi, Role of Subcellular Na Channel Distributions in the Mechanism of Cardiac Conduction. Biophysical Journal* **100**, *554-563, 2011.*

The third edition is packed with important information about the various aspects of the field of cell physiology and membrane biophysics. Most notably, I am impressed by the exceptional quality of the contributors relating to my field of expertise, namely the contractile mechanism and excitation–contraction coupling. Since the first edition of the *Cell Physiology Sourcebook*, new contributors were added for the subsequent editions, and I am certain that such will be the case for the fourth edition. It is always a pleasure to receive a telephone call from Professor Nicholas Sperelakis. He is so excited about his research, so vibrant with his passion for discovery. This enthusiasm is just one of the reasons why we respect him so much. Perhaps it is this passion to which his wife Dolores refers when she says that he is still as youthful and intellectually active as the young man she married 51 years ago. According to Professor Diomedes Logothetis, Chairman of our department at the Medical College of Virginia, the exceptionally good students are being hyperexcited by the "virus" of physiology, and I think that this happens also to established scientists such as Professor Sperelakis.

Professor Nicholas Sperelakis is celebrating his 81st birthday as I write this Foreword. For such a special anniversary, many Greeks add a "chronia polla" exclamation, which loosely translated is "many more years" or "with many happy returns". We wish that blessing, not only to Professor Sperelakis personally, but also for the new edition of his *Cell Physiology Sourcebook*.

Alexandre Fabiato
Richmond, VA
March 8, 2011

This page intentionally left blank

Preface to the Fourth Edition

Once upon a time, an 80-year-old retired university professor was leading a quiet and secluded life. Then one day in the spring of 2010, out of a clear blue sky, he was contacted by Janice Audet, Senior Acquisitions Editor for Academic Press. She said that a number of colleges were still using our third edition of *Cell Physiology Sourcebook* as the textbook for their courses in cell physiology, even though the third edition came out long ago, namely, in 2001.

In fact, I was aware of the use of the third edition in a number of colleges. About 2 years earlier, I was contacted by a graduate student from Georgia State University saying that they were using my book as the textbook for their class on cell physiology, but that he could not buy a copy because it was out of print. He asked me to send him my personal copy of the book. He said he would treat it well and return it to me at the end of the course. He even offered to drive to my home in Cincinnati to pick it up. This student was obviously desperate, so I talked to Noelle Gracy, my former editor, about the problem. She arranged for the class to have access to the e-book version of the textbook. Problem solved!

Janice wanted to know if I was interested in doing a fourth edition. Before I could give her a definitive answer, I wanted her to sample a number of course directors around the country to learn what they liked and what they didn't like about the third edition of the book. The consensus was that our book, in general, was pitched at too high a level for beginning graduate students (or senior undergraduates) taking a course in cell physiology. Some other suggestions were that we should eliminate some chapters/topics that are well-covered in the three textbooks available on cell biology, such as cell division, apoptosis, etc; we should improve the figures by using color; we should add a summary section at the beginning of each chapter; and, although difficult to achieve with so many contributing authors, we should try to make the various chapters more uniform in style.

I agreed to work on the fourth edition, and focused on incorporating the suggestions into the new edition. Some of the changes made to this edition include the omission of approximately 14 chapters, combining a few chapters, and asking contributors to try to pitch their chapters at the graduate student level. About 10 new contributors were recruited for specific expertise in the subject area. I believe that the final slate of contributors is top-notch, and I am extremely grateful for their participation.

So why did I agree to carry out this project that would require tremendous effort on my part, while in precarious health at that? Was it fortune/money? Absolutely not! That is miniscule. Was it fame/recognition? No, I'm too old to benefit from that now. Besides, I already edited three editions of the very same book. Was it dedication to teaching? Yes, that's what it was! I have dedicated my life to teaching, and I believe that I have the unique ability to present difficult concepts in an easily understandable way. For example, during my student days at the University of Illinois, four of us were studying together for an exam in genetics the next day. I was answering questions that the group had when one of them said, "Nick, you should be the one teaching this class." In the course of my career, I had also received multiple "golden apple" awards from graduate students in the Department of Physiology at the University of Cincinnati for the best teaching in our graduate courses.

One final example is worth mentioning. Michael Palmer, a best-selling author of medical mysteries, used my last name in one of his novels, "The Second Opinion", which came out in 2009. My son, Thomas, asked Dr Palmer how he came up with the name "Sperelakis", which is very uncommon in persons of Greek heritage. Dr Palmer replied that he was a medical student at Case-Western Reserve University in the mid-1960s, and he took my lectures on electrophysiology of nerve and muscle. He said that I was the favorite instructor in basic science of his entire class, and that they gave me the nickname of "Spike" which is jargon for a nerve action potential. Can you believe that Dr Palmer would remember me and my nickname after about 45 years? Dedication to teaching! My dedication to teaching is more amazing because I was a severe stutterer throughout my life, beginning at age 10 and continuing to the present (although now much less severe).

Before the first edition of this book was published, I saw a real need for a good, authoritative textbook in the area of cell physiology and membrane biophysics. The days when a single individual, like my friend Professor Hugh Davson, could cover such a broad area are gone. To cover the wide-ranging expertise necessary for an authoritative textbook, there seems to be no alternative other than arranging a multi-authored textbook by assembling a group of experts in the various topics to be covered. We used this principle in all four editions. The first edition, second edition, and third edition of this textbook came out in 1995, 1998, and 2001. The first and second editions received awards from the American Library Association for being outstanding, namely receiving their "Choice Award".

The Foreword to the first edition was written by Professor Hugh Davson of University College London (UCL). Professor Davson became very famous because of his textbook on cell physiology. It was indeed the "Bible" for all graduate students for a number of years. I first met Hugh when I was there on sabbatical leave in 1965−66. He was an amazing guy and we struck up an immediate friendship. In those days, UCL was quite the place. A.F. Huxley, Nobel Laureate, was head of the Physiology Department, and Bernard Katz, future Nobel Laureate, was head of the Biophysics Department. A.V. Hill, Nobel Laureate, was still coming to his office in the Biophysics Department about once or twice a week at age 90! Unbelievable! Incidentally, UCL is also where I first met Hugo Gonzalez-Serratos, a contributor to this book.

The Foreword for the second edition was written by Thomas E. Thompson. Tom was head of the Biochemistry Department at the University of Virginia while I was there. He was a leading investigator in the area of planar and spherical lipid bilayer membranes. Tom was an excellent teacher, and I had him participate in my graduate courses. Tom served as President of the Biophysical Society.

The Foreword for the third edition was written by Denis Noble of Oxford University. Denis became a leading investigator and theorist in the field of cardiac electrophysiology. One time, he asked me to give a lecture at a meeting being held at Oxford, and Sir Alan Hodgkin, Nobel Laureate, was chairing the session. I was shaking in my boots!

I decided to ask a long-time good friend, Professor Alexandre Fabiato of the Medical College of Virginia, to write the Foreword for this fourth edition. Alex is an outstanding scientist working on cardiac muscle. He is very well known and highly cited for his Ca-induced Ca release mechanism (CICR). He received the very prestigious Research Achievement Award from the national American Heart Association in 1989. Alex was trained as a cardiologist in France, and he was a graduate student with Professor Edouard Corabouef (University of Paris, Orsay, France) and Professor Silvio Weidmann (University of Bern, Switzerland), both leading pioneers and giants in the field of electrophysiology of cardiac muscle. I am proud and pleased that Alex agreed to do it.

The roadway along the book preparation trail was not without some large bumps and, at times, seemingly insurmountable roadblocks. Dedication to teaching, along with the great need for this textbook, kept me inspired to finish it. In addition, I felt a strong obligation to the Contributors, some of whom already had spent time and effort in beginning their revision. Again, I cannot stress how much I appreciate their efforts and how proud I am that they contributed to this book. We all hope that this textbook will be well received and highly successful.

Nicholas Sperelakis
May 2011

Section I

Biophysical Chemistry, Metabolism, Second Messengers, and Ultrastructure

This page intentionally left blank

Chapter 1

Biophysical Chemistry of Physiological Solutions

Jeffrey C. Freedman

Chapter Outline

I. SUMMARY

This chapter describes the hydrogen-bonded structure of liquid water and its dipolar and dielectric properties. In salt solutions, water exhibits three regions of structure: oriented dipoles near ions; an intermediate structure-breaking region; and flickering clusters with short-range order characteristic of ice. Electrostatic interactions between ions and water based on Coulomb's law account for the enthalpy of hydration, as well as for the sequence of ionic mobilities of the hydrated alkali cations. Salts and non-electrolytes dissolve in cell water with nearly the same solubility and activity as in extracellular water; even the viscosities are similar. Protons in solution are hydrogen-bonded to water to form H_3O^+, which is further hydrated due to electrostatic forces. Protons migrate through water by a Grotthus chain mechanism; in contrast, other hydrated ions migrate through water as hard spheres that interact with water dipoles according to the ionic radius and charge. Non-specific ion−ion interactions reduce the activity coefficients of ions, as described by the Debye−Hückel theory, which conceptualizes a central ion surrounded by a cloud of counterions with smeared charge. Selective interactions of ions with sites on enzymes or on channel proteins occur in certain predictable specific patterns (Eisenman sequences) that depend on the energy of interaction between the ions and water dipoles, relative to that between ions and their binding sites.

All of the solutes in a cell contribute to the free energy of the intracellular solution. The Gibbs equation, which is derived in the Appendix by combining the first and second laws of thermodynamics, enables estimation of the changes in free energy when solutes cross cell membranes. The change in free energy is zero at equilibrium and negative for spontaneous processes. Solutes will redistribute until the electrochemical potential is the same in every compartment to which that solute has access. The Nernst equation (see Appendix), which follows from the Gibbs equation, relates the ratio of intracellular to extracellular ion concentrations at equilibrium to the membrane potential, and can be used to test whether a solute is in electrochemical equilibrium across a cell membrane.

II. INTRODUCTION

All living cells contain proteins, salts and water enclosed in membrane-bounded compartments. These biochemical and ionic cellular constituents, along with a set of genes, enzymes, substrates, and metabolic intermediates, function to maintain cellular homeostasis and enable cells to replicate and to perform chemical, mechanical and electrical work. *Homeostasis*, a term introduced by the physiologist Walter Cannon in *The Wisdom of the Body* (1932), means that certain parameters, including cellular volume, intracellular pH, the transmembrane electrical potential and intracellular concentrations of salts are maintained relatively constant in

Cell Physiology Sourcebook. DOI: 10.1016/B978-0-12-387738-3.00001-9

resting cells. Cellular homeostasis depends on a relative constancy of the extracellular fluids that bathe cells. The extracellular fluid compartment was termed the *milieu intérieur,* or internal environment, by Claude Bernard, who recognized around 1865 that "*La fixité du milieu intérieur est la condition de la vie libre*", that the constancy of the internal environment is the condition for independent life. In *An Introduction to the Study of Experimental Medicine* (see 1949 translation), Bernard wrote that "only in the physico-chemical conditions of the inner environment can we find the causation of the external phenomena of life". The development of cell physiology has been greatly influenced by the Bernard–Cannon theory of physical-chemical homeostasis.

Biophysical chemistry concerns the application of the concepts and methods of physical chemistry to the study of biological systems. Physical chemistry includes such physiologically relevant subjects as thermodynamics, chemical equilibria and reaction kinetics, solutions and electrochemistry, properties and kinetic theory of gases, transport processes, surface phenomena and molecular structure and spectroscopy. Throughout this book, it is seen that many cellular physiological phenomena are best understood with a rigorous and comprehensive understanding of physical chemistry. During the past 65 years, outstanding monographs on biophysical chemistry have been available: Höber (1945), Edsall and Wyman (1958), Tanford (1961), Cantor and Schimmel (1980), Silver (1985), Bergethon and Simons (1990), and Weiss (1996). To help the reader begin to understand how cellular homeostasis is achieved, this chapter will introduce some of the conceptual underpinnings of cell physiology by describing certain physicochemical properties of water and electrolytes that are relevant for understanding living cells.

III. STRUCTURE AND PROPERTIES OF WATER

Biological cells contain a large amount of water, ranging from 0.66 g H_2O/g cells in human red blood cells to around 0.8 g H_2O/g tissue in skeletal muscle. The amount of water in cells is determined by osmosis. Liquid water is a highly polar solvent, with a structure stabilized by extensive intermolecular *hydrogen bonds* (Fig. 1.1). The hydrogen bonds between adjacent water molecules are linear (O–H···O) but are able to bend by about 10°. From x-ray diffraction studies of ice crystals, it is known that each of the two covalent O–H bonds in water is 1 Å in length, that each of the two hydrogen bonds is about 1.8 Å in length and that these occur around each oxygen atom at angles of 104°30′ in a tetrahedral array.

The energy required to break hydrogen bonds in liquid water is 5 to 7 kcal/mol, much less than the 109.7 kcal/mol required to break the covalent O–H bond. A calorie is

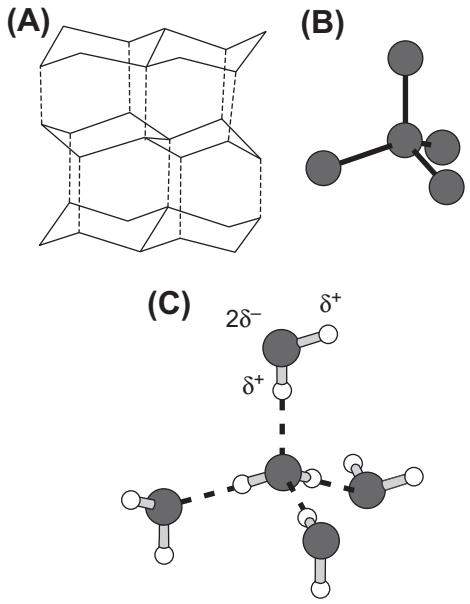

FIGURE 1.1 Hydrogen bonds in ice and liquid water. (A) Crystal structure of ice, showing the puckered hexagonal rings of oxygen atoms. (B) Each oxygen atom is connected to four others in a tetrahedron. (C) The linear hydrogen bonds are indicated by dotted lines between adjacent water molecules (O–H O). Two covalent bonds (O–H), indicated by solid lines, and two hydrogen bonds occur around each oxygen atom in a tetrahedral array. The partial charge separation of the O–H dipoles is indicated on the upper water molecule.

a unit of work equal to 4.18 J in the SI system of units, where 1 joule (J) equals 1 Newton·meter. The newton ($N = k \cdot gm/s^2$) is the unit of force in the International System of Units (SI); the dyne ($dyn = g \cdot cm/s^2$) is the corresponding unit of force in the older cgs system ($1\ N = 10^5$ dyn). Recall that, according to Newton's first law, the force (F) is mass times acceleration and that work is defined as force times distance. Because of the strength of hydrogen bonds, liquid water has unique physicochemical properties, including a high boiling point (100°C), a high *molar heat capacity* (18 cal/mol·K), a high *molar heat of vaporization* (9.7 kcal/mol at 1 atm) and a high *surface tension* (72.75 dyn/cm). As discussed by Bergethon and Simons (1990), all of these thermodynamic parameters are considerably higher for H_2O than for the analogous compound H_2S, which boils at −59.6°C. The outer electrons of the S atom shield its nuclear charge and reduce its electronegativity, making the S–H bond weaker, longer and less polar than the O–H bond. Also, the bond angle of H_2S is only 92°20′, an angle that does not form a tetrahedral array and thus H_2S does not form a hydrogen bonded network like water.

The extensive intermolecular association in liquid water is due to the geometry of the water molecule and also to its strong permanent *dipole moment*. Water molecules have no net charge, yet possess permanent charge separation along each of the two O–H bonds. Since oxygen is more *electronegative* than hydrogen, its electron density is preferentially

greater. Oxygen thus acquires a partial negative charge (δ^-), leaving the hydrogens with a partial positive charge (δ^+) (see Fig. 1.1C). The magnitude of the dipole moment (μ) of a chemical bond is computed as the product of the separated charge (q) at either end, and the distance (d) between the centers of separated charge ($\mu = qd$). The dipole moment of a molecule is the vector sum of the dipole moments of each bond. For water in the gaseous phase, the dipole moment is 1.85 debye, where 1 debye $= 10^{-18}$ esu·cm. One esu (electrostatic unit), or stat-coulomb, equals 3.336×10^{-10} C, the coulomb (C) being a unit of electric charge. In liquid water, the dipole moment becomes even larger (2.5 debye) due to association with other water molecules. In comparison, the linear molecule carbon dioxide (O=C=O) also has a separation of charge, with a partial negative charge on each oxygen atom and a partial positive charge on the carbon atom. In this case, the oppositely directed dipole moments of the two C=O bonds sum to a zero dipole moment for the CO_2 molecule. In H_2S, the S−H bond has a smaller dipole moment (1.1 debye) than the O−H bond in water because sulfur is less electronegative than oxygen. Electrostatic attractions between opposite charges in adjacent water dipoles stabilize the hydrogen-bonded structure of liquid water.

Water strongly affects the forces between ions in solution by virtue of its high *dielectric constant*. The dielectric constant (ε) of a medium known as a *dielectric* is defined as the ratio of the coulombic force (F_{coul}) between two charges in a vacuum to the actual force (F) between the same two charges in the dielectric medium.

$$\epsilon = \frac{F_{coul}}{F}$$

In a vacuum, the coulombic force, Fcoul (newtons, N), between two ions with charges q^+ and q^- (C) separated by a distance d (meters, m) is given by Coulomb's law:

$$F_{coul} = \frac{q^+ q^-}{4\pi\epsilon_0 d^2}$$

where ε_0 is the permittivity constant ($8.854 \times 10^{-12} C^2/N\,m^2$). Coulomb's law states that the force between two point charges is directly proportional to the magnitude of each charge and inversely proportional to the square of the distance between the charges. Substituting F_{coul} into the above expression and rearranging yields the following:

$$F = \frac{q^+ q^-}{4\pi\epsilon_0 \epsilon d^2}$$

The dielectric constant of a vacuum is unity and that of air is close to unity ($\varepsilon_{air} = 1.00054$). Increasing the dielectric constant of the solvent decreases the attractive force between oppositely charged ions. The force felt by a distant ion is reduced in a dielectric medium, such as water, as compared with a vacuum, because part of the interaction energy is spent aligning the intervening water dipoles and distorting their polarizable electron clouds. The dielectric constant of water at 25°C is 78.5, much greater than methanol ($\varepsilon = 32.6$), ethanol (24.0) or methane (1.7). In liquid water, the high dielectric constant weakens the coulombic attractive forces between oppositely charged particles and thus promotes dissociation and ionization of salts.

Although the thermodynamic properties of liquid water are explicable in terms of extensive hydrogen-bonding, the actual structure of water is complex. In the flickering cluster model, groups of 50−70 water molecules, resembling a slightly expanded broken piece of the ice lattice (icebergs), are continuously associating and dissociating on a picosecond time scale. This dynamic model contrasts with the extended order of solid ice. At a given instant, some water molecules are unattached to the clusters and are located in the interstitial regions of the network, but may attach and detach as the clusters continuously form and break down. Other theories treat water as a mixture of distinct states, or as a continuum of states, with considerable short-range order, characteristic of the crystalline lattice of ice.

Despite these uncertainties regarding the structure of liquid water and the influence of macromolecules on its properties in cells, the ability of water to act as a solvent inside cells closely resembles that of extracellular water. Thus, a variety of permeant, hydrophilic, non-metabolized non-electrolytes distribute at equilibrium across human red blood cell membranes with ratios of intracellular to extracellular concentrations that deviate from unity by less than 10% (Gary-Bobo, 1967). In mouse diaphragm muscle, Miller (1974) found that several alcohols, diols and monosaccharides exhibit distribution ratios within 2% of unity, whereas certain other sugars appear to be excluded from membrane-bounded intracellular compartments. The amount of solute that dissolves at equilibrium is also nearly normal in water that is constrained in gels, which are cross-linked networks of fibrous macromolecules. The diffusion of solutes within gels, however, may be hindered by collisions and interactions with the macromolecules and by the tortuosity of the diffusion paths.

Viscosity, another property of water, contributes to the resistance to flow. A fluid with a greater viscosity exhibits less flow under the influence of a given pressure gradient than a fluid with a lesser viscosity. For example, molasses, a concentrated sugar solution, is much more viscous than pure water. During *laminar flow*, a frictional force develops between adjacent layers (laminae) in the fluid and this force impedes the sliding of one lamina past its neighbor. In a *Newtonian fluid*, the frictional force per unit area, or shear stress (τ, dyn/cm^2), is proportional to the velocity gradient, or rate of strain (dv/dy, s^{-1}) between laminae,

$$\tau = \eta \cdot (dv/dy)$$

where the viscosity (η) is the proportionality constant with units of poise (=1 dyn s/cm^2), named after Poiseuille. The viscosity of H_2O at 20.3°C is 0.01 poise, or 1 centipoise (cp). In cultured fibroblasts, the fluid-phase cytoplasmic viscosity, as determined from rotational motions of fluorescent probes on a picosecond time scale, is only 1.2−1.4 times that of pure water (Fushimi and Verkman, 1991). Fluorescence studies also show that the viscosity is the same in the cytoplasm and nucleoplasm and is unaffected by large decreases in cell volume or by disruption of the cytoskeleton with cytochalasin B. The fluid-phase viscosity, as determined from fluorophore rotational motions, is not nearly as affected by macromolecules as is the bulk viscosity and it thus provides a more accurate view of the physical state of the aqueous domain of the cytoplasm. These and other studies (e.g. Schwan and Foster, 1977; Horowitz and Miller, 1984) set limits on the extent to which the physicochemical properties of intracellular water differ from those of extracellular water.

IV. INTERACTIONS BETWEEN WATER AND IONS

Ions in solution behave as charged, hard spheres that interact with and orient water dipoles. When crystals of sodium chloride are dissolved in water, the electrostatic attractive forces between water dipoles and ions in the crystal lattice overcome the inter-ionic attractive forces between oppositely charged ions in the crystal. The dissociated ions then acquire the freedom of translational motion as they diffuse into the solution accompanied by a layer of tightly associated *hydration water* (Fig. 1.2). *Ion* is the Greek word for "wanderer". The strength of the attraction between ions and water dipoles depends to a large extent on the ionic charge and radius. For the alkali metal cations, the force of attraction and the energy of interaction of ions with water, decreases according to the following series: $Li^+ > Na^+ > K^+ > Rb^+ > Cs^+$.

Li^+, being the smallest of the alkali metal cations, has the strongest interaction with water because its positively charged nucleus can approach most closely to the negative side of neighboring water dipoles. As the ionic radius increases with increasing atomic number in the alkali metal series, the filled outer shells of electrons effectively shield the cationic charge and reduce the distance of closest approach to water molecules. The smallest ion thus acquires the greatest degree of hydration and has the largest hydrated ionic radius.

According to Frank and Wen (1957), the orienting influence of ions on water dipoles results in three regions of water structure (Fig. 1.3). The electric field of an ion is sufficiently strong to remove water dipoles from the bulk water clusters and to attract to itself the oppositely charged ends of from one to five water dipoles. A certain number of these water dipoles, called the *hydration number*, then become trapped and oriented in the ion's electric field. The inner hydration shell includes water molecules that are aligned by the force field and in direct contact with the ion, 5 ± 1 for Li^+, 4 ± 1 for Na^+, 3 ± 2 for K^+ and Rb^+, 4 ± 1 for F^-, 2 ± 1 for Cl^- and Br^- and 1 ± 1 for I^-. Thus, in physiological saline at 0.15 M NaCl in water (55.5 M), about 1.6% (=100 × 0.15 × 6/55.5) of the water is located in the inner hydration shells of Na^+ and of Cl^-. Water in the inner hydration shells of Na^+, K^+ and Ca^{2+} rapidly exchanges with bulk water on a nanosecond time scale but, in contrast, the smaller divalent cation Mg^{2+}, with its high

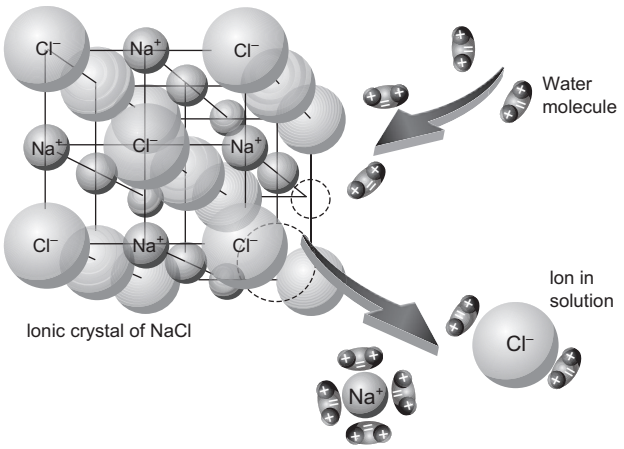

FIGURE 1.2 Dissociation of NaCl in water into hydrated Na^+ and Cl^- ions.

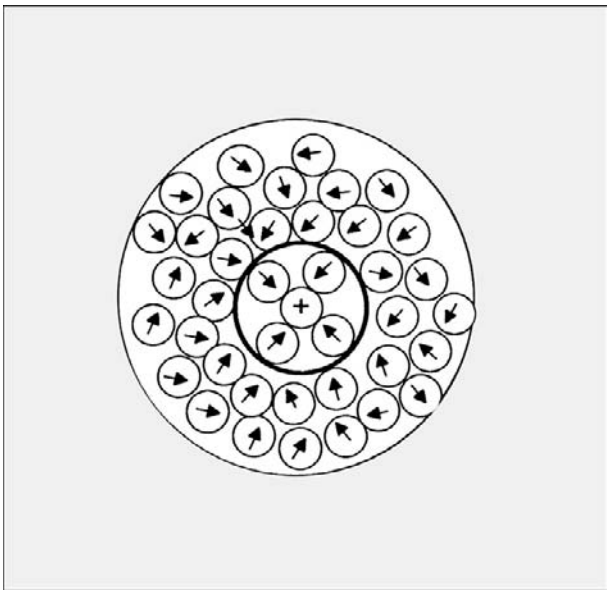

FIGURE 1.3 Three regions of water structure near an ion. A central cation is shown with a primary hydration shell of four oriented water dipoles, surrounded by a partially oriented secondary sheath. The gray region indicates the hydrogen-bonded structure of the bulk water.

charge density, is some four orders of magnitude slower in exchanging its inner hydration water. The inner hydration sheath of water molecules moves together with the ion as a distinct and single kinetic entity.

The mobilities of the alkali cations in water decrease as the non-hydrated ionic radius decreases, but as the hydrated ionic radius increases (Table 1.1; for discussion, see Hille, 2001). The ionic *mobility* (u) is defined as the proportionality constant that relates the velocity (v) of ionic migration to the force exerted by an external electric field E ($v = u \cdot E$); in other words, mobility is the velocity per unit electric field. Farther away from the ion, where the ion's electric field falls towards zero, water retains the structure of bulk water. In the region between the inner hydration sheath and the bulk water, the orienting influences of the ion and the bulk water network tend to compete and to disrupt the structure of water. In this intermediate structure-breaking region, the water dipoles are partially oriented toward the central ion, yet do not migrate with the ion, and they join only infrequently with the hydrogen-bonded clusters of the bulk water. If the net effect of an ion is to disorganize more water in the intermediate region than is found in the primary hydration shell, then the ion is termed a *structure-breaker*. Conversely, water may form a variety of hydrogen-bonded clathrate structures around apolar protein side chains, whose action resembles that of the class of solutes termed *structure-makers* (see Klotz, 1970, for review).

TABLE 1.1 Radii, Enthalpies of Hydration and Mobilities of Selected Ions

Ion	Non-hydrated Radius[a] (Å)	$\Delta H^0_{\text{hydration}}$[b] (kcal/mol)	Mobility[c] $10^{-4}\frac{\text{cm/s}}{\text{V/cm}}$
H^+	—	−269	36.25
Li^+	0.60	−131	4.01
Na^+	0.95	−105	5.19
K^+	1.33	−85	7.62
Rb^+	1.48	−79	8.06
Cs^+	1.69	−71	8.01
Mg^{2+}	0.65	−476	2.75
Ca^{2+}	0.99	−397	3.08
Sr^{2+}	1.13	−362	3.08
Ba^{2+}	1.35	−328	3.30
Cl−	1.81	−82	7.92

[a] *Radii are from Pauling (1960).*
[b] *Standard enthalpies of hydration at 25°C are from Edsall and McKenzie (1978).*
[c] *Mobilities in water at 25°C are from Hille (2001, p. 317).*

The *enthalpy of hydration* of an ion is a measure of the strength of the interaction between ions and water and is defined as the increase in enthalpy when one mole of free ion in a vacuum is dissolved in a large quantity of water. The enthalpy of hydration may be estimated from the heat released upon dissolving salts in water, usually less than 10 kcal/mol, taking into account the energy needed to dissociate the salt crystal and then to hydrate the ions. The enthalpy of hydration may be calculated using electrostatic theory. Accurate results are obtained if water is considered to be an electric quadrupole with four centers of charge, two partial positive charges near the hydrogen nuclei and two partial negative charges on the non-bonded electron orbitals near the oxygen nucleus. A further improvement in the calculated enthalpy of hydration is obtained when the polarizability (α) of the water dipole by the ion is taken into account. The electric field of the ion distorts the electron cloud of the hydration water along its permanent dipole axis, thus inducing an additional increment of charge separation and increasing the dipole moment. For small fields, this *induced dipole moment* (μ_{ind}) is proportional to the electric field strength (E) and the constant of proportionality is the *polarizability* ($\mu_{\text{ind}} = \alpha \cdot E$). In Fig. 1.4, the measured enthalpies of hydration for alkali metal cations and halides are compared with calculated values; the impressive agreement demonstrates the primary importance of electrostatic forces in determining the solvation of ions in water. The enthalpy of hydration for the smallest alkali metal cation Li^+ is quite large at −131 kcal/mol. With increasing ionic radius, the enthalpy falls progressively for Na^+, K^+ and Rb^+, reaching −71 kcal/mol for Cs^+, the largest non-hydrated but smallest hydrated ion in the series (see Table 1.1). For the divalent, alkaline earth

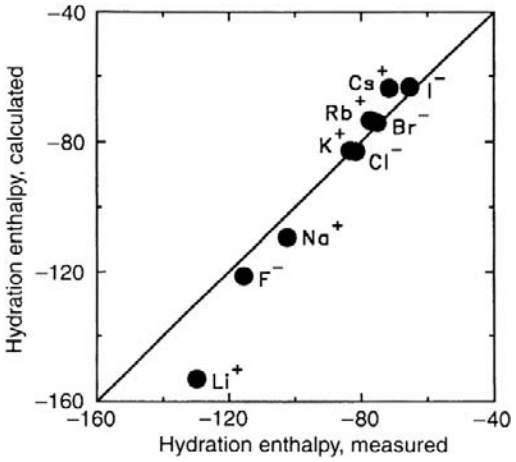

FIGURE 1.4 Comparison of measured enthalpies of hydration of alkali metal cations and halides in water (abscissa), with those calculated (ordinate) taking into account the Born charging energy, ion-dipole interactions, ion-quadrupole interactions and ion-induced dipole interactions *(data from Bockris and Reddy, 1970, p. 107).*

metal ions Mg^{2+} and Ca^{2+}, the enthalpies of hydration also follow the ionic radius but are considerably larger at −476 kcal/mol and −397 kcal/mol, respectively. As pointed out by Hille (2001), the magnitude of ionic hydration enthalpies approximates the cohesive strength of the ionic bonds in a crystalline salt lattice.

Physical chemical analyses show that, in small spaces that restrict the formation of tetrahedral water clusters, the dielectric constant will be reduced and electrostatic forces between ions will then be correspondingly increased. In the primary hydration shell of ions, the oriented water is polarizable but cannot be reoriented by applied fields and so the dielectric constant is reduced from its bulk value of 78 to a value of about 6, with intermediate values in the partially oriented structure-breaking region between the primary hydration shell and the bulk water. For this reason, the dielectric constant of a solution decreases with increasing salt concentration but, in protein-free solutions at physiological salt concentrations, the extent of the decrease is small due to the small fraction of hydration water.

V. PROTONS IN SOLUTION

The hydrogen-bonded structure of liquid water also contributes to high proton mobility by a mechanism that differs fundamentally from the migration of other hydrated ions. The proton is a highly reactive, positively-charged hydrogen nucleus, devoid of electrons. Whereas ions with electron shells typically have diameters in angstroms, the diameter of the proton is only about 10^{-5} Å. With such a small size, the proton has a strong attraction to electrons, as indicated by the high *ionization energy* of 323 kcal/mol needed to remove an electron from a hydrogen atom to form a proton. By comparison, the ionization energies for the alkali cations decrease with increasing atomic number in the series as follows:

$$\begin{aligned} \text{Li} + (124\ \text{kcal/mol}) &> \text{Na} + (118\ \text{kcal/mol}) \\ &> \text{K} + (100\ \text{kcal/mol}) \\ &> \text{Rb} + (96\ \text{kcal/mol}) \\ &> \text{Cs} + (90\ \text{kcal/mol}) \end{aligned}$$

As more filled electron shells separate and shield the outer shell from the positively charged atomic nucleus, it becomes easier to form a cation by removing an electron. The high affinity of the proton for electrons, and its small size, explain its tendency to form hydrogen bonds with the unshared electrons of oxygen in water. Infrared spectra indicate that protons in solution exist predominantly in the form of hydronium ions H_3O^+. Nuclear magnetic resonance (NMR) data are consistent with a flattened trigonal pyramidal structure, with O—H bond lengths of 1.02 Å and H—O—H bond angles of 115°, a structure resembling that of NH_3 but with a radius similar to that of K^+. The free energy of formation of H_3O^+ from H_2O and H^+ is about −170 kcal/mol, which corresponds to a hypothetical concentration of free protons in solution at room temperature of about 10^{-150} M — "about as zero as one can get" say Bockris and Reddy (1970). The heat of hydration of H_3O^+ is an additional −90 kcal/mol. The change in the density of water with temperature is consistent with the hydration of H_3O^+ with an additional three water molecules, forming the tetrahedral cluster $H_9O_4^+$ (Bockris and Reddy, 1970). The proton mobility in water is 36×10^{-4} $cm^2/s\cdot V$, much slower than expected on the basis of hydrodynamic theory if free protons were to carry the current, but curiously about seven times as fast as expected if H_3O^+ migrates like K^+. The abnormally high proton mobility in water (and also in ice) is consistent with a *Grotthus chain mechanism* (Fig. 1.5) in which the successive breakage and formation of hydrogen bonds, accompanied by proton jumps between neighboring water molecules, effectively results in the passage of H_3O^+ along a chain. This transport process is rate-limited by the time needed for each successive acceptor water molecule to rotate and reorient its non-bonded orbital into a suitable position to accept the donated proton. The Grotthus mechanism accounts for about 80% of proton mobility, with the remaining 20% due to H_3O^+ itself, as a single kinetic entity, undergoing a translational migratory movement through the solvent like other ions.

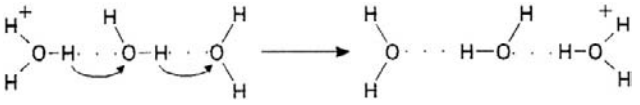

FIGURE 1.5 Grotthus chain mechanism for proton mobility in water.

VI. INTERACTIONS BETWEEN IONS

Interactions between ions may be weak or highly selective. Ions in solution attract ions of the opposite charge, in accordance with Coulomb's law. Since the long-range attractive forces are inversely proportional to the square of the distance between charges, the interaction energies are greater in more concentrated solutions. In a uni-univalent salt solution, defined as having monovalent cations and anions, of concentration c (mol/L), the average distance (d, angstroms or Å) between any two ions is given by:

$$d = (10^{27}/2N_A c)^{1/3}$$

where N_A is Avogadro's number (6.023×10^{23}). The factor 2 is included because the anions and cations are both counted and the factor 10^{27} is $Å^3$/L. For 0.15 M NaCl, the average distance between Na^+ and the nearest Cl^- is 17.7 Å, at which range coulombic forces are highly significant. At pH 7.4, where the concentration of "protons" (really

hydronium ions) is only 40 nM, the average distance between "protons" is 0.28 μm.

Attractive ion−ion interactions are stabilizing and they lower the chemical potential of an ion from its value in an ideal, infinitely-dilute solution. The *activity* (a) of an ion is defined in terms of its *chemical potential* (μ) as follows:

$$\mu = \mu^0(T,P) + RT \ \text{In}\ a$$

where $\mu^0(T, P)$ is the *standard-state chemical potential*, or the chemical potential when the activity is 1. Increases in chemical activity increase the chemical potential. The chemical potential of a solute in an ideal dilute solution, where the activity equals the chemical concentration (c), is:

$$\mu_{\text{ideal}} = \mu^0(T,P) + RT \ \text{In}\ c$$

In order to describe the properties of more concentrated non-ideal solutions, G.N. Lewis introduced the *activity coefficient* (γ), such that the activity is the product of the concentration (c) and the activity coefficient ($a = \gamma \cdot c$). The chemical potential of an ion in a non-ideal solution is:

$$\mu = \mu^0(T,P) + RT \ \text{In}\ c + RT \ \text{In}\ \gamma$$

where the term RT ln γ includes the effect of ion−ion interactions on the chemical potential.

When a salt (c_+c_-) is added to water, the cations and anions, at concentrations c_+ and c_- respectively, both contribute to the free energy of the solution. The chemical potentials of the cations and anions (μ_+ and μ_-, respectively) are given by:

$$\mu_+ = \mu_+^0 + RT \ \text{In}\ c_+ + RT \ \text{In}\ \gamma_+$$

$$\mu_- = \mu_-^0 + RT \ \text{In}\ c_- + RT \ \text{In}\ \gamma_-$$

Adding these two expressions and taking the average, gives:

$$\frac{\mu_+ + \mu_-}{2} = \frac{\mu_+^0 + \mu_-^0}{2} + RT \ \text{In}\ (c_+ \ c_-)^{1/2} + RT \ \text{In}\ (\gamma_+ \ \gamma_-)^{1/2}$$

The mean ionic activity coefficient $\gamma\pm$ is defined as:

$$\gamma_\pm = (\gamma_+ \ \gamma_-)^{1/2}$$

Mean ionic activity coefficients of salts have been estimated theoretically by the *Debye−Hückel theory*, which supposes that central ions attract oppositely-charged ions (or *counterions*) in a diffuse and structureless ion cloud (or atmosphere). The forces of coulombic attraction between the central ion and its cloud of counterions are opposed by the randomizing influence of the thermal motion of the ions. In dilute solutions, in which the theory treats central ions as point charges relative to the size of the ion cloud, the mean ionic activity coefficient ($\gamma\pm$) for salt ions with charges z_+ and z_-, is given by the limiting law as follows:

$$\log \ \gamma_\pm = -A|z_+ \ z_-|I^{1/2}$$

where I is the *ionic strength*, defined as:

$$I = \frac{1}{2}\sum_i c_i z_i^2$$

The constant A, which equals 0.5108 $\text{kg}^{1/2}\cdot\text{mol}^{-1/2}$ is given in terms of B, which equals 0.3287×10^8 $\text{kg}^{1/2}\cdot\text{mol}^{-1/2}\cdot\text{cm}^{-1}$, both at 25°C, as follows:

$$A = \frac{1}{2.303}\frac{N_A e_0^2}{2\epsilon RT}B$$

$$B = \sqrt{\frac{8\pi N_A e_0^2}{1000\epsilon kT}}$$

where N_A is Avogadro's number (6.023×10^{23} ions/mol), e_0 is the charge on an electron (4.80×10^{-10} statcoul $= 1.60 \times 10^{-19}$ C), ε is the dielectric constant, R is the gas constant (8.32 J/mol·K), T is the absolute temperature (K) and k ($=R/N_A$) is Boltzmann's constant (1.38×10^{-23} J/K).

The derivation of the Debye−Hückel limiting law (see Bockris and Reddy, 1970) computes the spherically symmetric electric field around an ion, leading to an expression relating the charge density (ρ_r) of the ionic cloud to the electrostatic potential (ψ_r) at a distance r from the central point charge. The counterions, at concentration n_i for ionic species i at a distance r from the central ion, are considered to distribute in the electric field according to a *Boltzmann distribution*:

$$n_i = n_i^0 e^{-z_i e_0 \psi_r / kT}$$

where n_i^0 is the bulk ion concentration (ions/L). By linearizing the Boltzmann equation, using a Taylor series expansion and retaining only the first two terms, which assumes that $z_i e_0 \psi_r \ll kT$, a resulting expression shows how the electrostatic potential ψ decreases as a function of distance (r) from the central ion (Fig. 1.6A):

$$\psi_r = \frac{z_i e_0}{\epsilon}\frac{e^{-\kappa r}}{r}$$

where κ is given by:

$$\kappa = \sqrt{\frac{4\pi}{\epsilon kT}\sum_i n_i^0 z_i^2 e_0^2}$$

The charge density (ρ_r) of the ionic cloud also decreases with increasing distance from the central ion (see Fig. 1.6B) according to:

$$\rho_r = -\frac{r_i e_0}{4\pi}\kappa^2\frac{e^{-\kappa r}}{r}$$

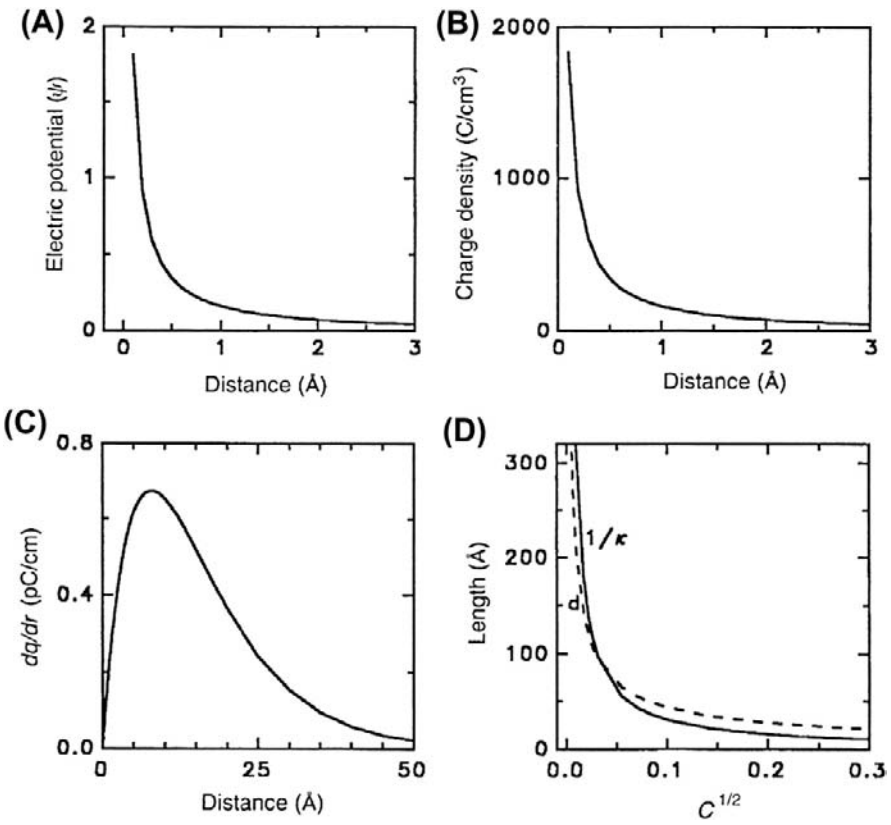

FIGURE 1.6 Debye–Hückel theory. (A) Electrostatic potential (ψ), (B) charge density (ρ) of the counterion cloud and (C) the charge (dq) enclosed in a spherical shell of thickness (dr), each calculated and plotted versus distance d from the central ion. (D) Debye length κ^{-1} (solid line) and average distance d between ions (dashed line) versus square root of ion concentration.

The amount of charge dq contained in a concentric spherical shell of thickness dr located at a distance r from the central ion (see Fig. 1.6C) is given by:

$$dq = -z_i e_0 e^{-\kappa r} \kappa^2 r dr$$

Furthermore, the maximum amount of charge contained in such a spherical shell occurs at a distance κ^{-1}, known as the *Debye length*, which defines the effective radius of the counterion atmosphere. It can also be shown that the Debye length is the distance away from the central ion where an ion of equal and opposite charge would contribute to the electrostatic field by an amount equivalent to that of the dispersed cloud of counterions (Bockris and Reddy, 1970). The Debye length decreases as the ionic concentration increases (see Fig. 1.6D).

The Debye–Hückel limiting law predicts activity coefficients accurately only to concentrations of about 0.01 M. In more concentrated solutions, the finite radius (a, in cm) of the ion is taken into account in the *extended Debye–Hückel equation*, given by:

$$\log \gamma_{\pm} = \frac{A|z_+ z_-| I^{1/2}}{1 + Ba\ I^{1/2}}$$

where the constants A and B are still $0.5108\ \mathrm{kg}^{1/2}\,\mathrm{mol}^{-1/2}$ and $0.3287 \times 10^8\ \mathrm{kg}^{1/2}\,\mathrm{mol}^{-1/2}\,\mathrm{cm}^{-1}$, respectively, for water at 25°C. The ion-size parameter (a) is adjustable, but reasonable values extend the range of concentrations for which the Debye–Hückel theory accurately predicts ionic activity coefficients (Fig. 1.7).

At still higher salt concentrations above about 0.7 M, the activity coefficient stops decreasing and instead begins to increase with increasing salt concentration. This

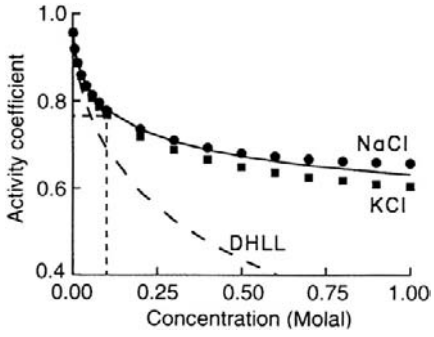

FIGURE 1.7 Activity coefficients of NaCl (circles) and KCl (squares). (*Data are from Robinson and Stokes (1959).*) The dashed curve represents the prediction of the Debye–Hückel limiting law. The solid line represents the prediction of the extended Debye–Hückel equation with an ion size parameter a of 4.7 Å. The dashed vertical line indicates that at 0.1 M, the activity coefficients of NaCl and KCl are 0.77 and 0.76, respectively.

behavior has been explained by the increasing fraction of hydration water, which both reduces the amount of free water in the solution and raises the effective concentration and, therefore, the activity, of the dissolved ions. Corrections for hydration enable prediction of the activity coefficient as a function of salt concentration over the full range of salt concentrations reaching to several molar. A related effect is that, in concentrated protein solutions, a certain shell of volume known as *excluded volume* around each protein is unavailable for solutes because the center of the solutes with their own finite size can only approach to within one solute radius of the protein surface. The fraction of excluded volume increases with increasing protein concentration and with increasing radius of the solutes which themselves may be proteins with enzymatic or regulatory activities. Such *macromolecular crowding* can dramatically increase activities of proteins in concentrated solutions.

The activity coefficients calculated by the Debye−Hückel theory indicate that the forces between ions in dilute solutions are weak and non-selective. The predicted activity coefficients depend on the ionic charge and the ionic strength of the solution and they are largely independent of the specific ion within, say, the alkali metal series. A very small degree of selectivity is introduced with the ion size parameter. The mean ionic activity coefficients for NaCl and KCl as a function of salt concentration are shown in Fig. 1.7. At 0.1 M concentrations, the activity coefficient of Na^+ is 0.77, whereas those of K^+ and Cl^- are both 0.76. These relatively high activity coefficients correspond to ion−ion interaction energies of only about −0.3 kcal/mol (see Hille, 2001).

Agreement between theory and data, such as seen in Fig. 1.7 for the Debye−Hückel theory, does not necessarily imply the correctness of the theory, or of the model on which the theory is based. A fundamental criticism of the Debye−Hückel theory concerns the smeared charge model for the cloud of counterions (Frank and Thompson, 1960). Below a concentration of about 0.001 M, the Debye length κ^{-1} is greater than the average distance between ions in the solution (see Fig. 1.6D), in which case the counterions could reasonably appear as a cloud of smeared charge from the vantage point of the central ion. Above 0.001 M, however, the Debye length incongruously falls below the average distance between ions in the solution. Moreover, at only 0.01 M, just one ion is needed to account for 50% of the effect of the counterion cloud on the central ion, yet this ion must be smeared around the central ion in a cloud of spherically symmetric charge distribution located only 25 Å away from the central ion (Bockris and Reddy, 1970). Thus, well below physiological salt concentrations, the assumption of smeared charge in the Debye−Hückel theory is not in accord with the coarse-grained structure of salt solutions, despite the impressive ability of the theory to predict activity coefficients. A quasi-lattice approach to salt solutions minimizing the free energy using modern computational power would seem to be a preferable alternative (see Horvath, 1985, for references).

Intracellular solutions may be quite concentrated. The red-cell membrane and associated cytoskeleton enclose a viscous cytoplasmic solution of the oxygen-binding pigment *hemoglobin* at a concentration of 34 g/100 mL cells, corresponding to 5.2 mM, 7.3 millimolal, or 44 g Hb/100 g cell water. This concentration is near the threshold for gelation, but hemoglobin is one of the most soluble of all proteins and constitutes more than 98% of red-cell protein by mass. The hemoglobin $\alpha_2\beta_2$ tetrameters have a molecular weight of 64 373 Da and are approximately spheroidal with dimensions of 65 × 55 Å×50 Å. In the interior of red blood cells, hemoglobin is nearly close-packed, with the distance between the surfaces of neighboring proteins averaging only about 20 Å. With the 86 carboxylates of aspartic and glutamic acids and with the 98 basic amino and amine groups of arginine, lysine and histidine per hemoglobin tetramer, the total cellular concentration of the titratable amino acids of human hemoglobin is around 0.9 M. Thus, hemoglobin contributes significantly, depending on intracellular pH, to a high intracellular ionic strength. Since the charged amino acids are located on the surface of hemoglobin and taking the radius of hemoglobin to be 28 Å, the average distance between charged sites is only about 7 Å. About 7600 water molecules per hemoglobin tetramer occupy the narrow interstices between the protein molecules. The hydration of hemoglobin in dilute solution is 0.2−0.3 g water/g Hb, representing about 15% of the intracellular water. When the tortuosity of the surface of soluble proteins is taken into account, as much as 30% of red-cell water could reside in the first monolayer around the protein surface.

To determine the *mean ionic activities* of the intracellular KCl and NaCl in the concentrated charged environment of human red blood cells, studies were conducted in which the red-cell membrane was rendered permeable to cations by exposure of the cells to the channel-forming antibiotic nystatin, thus allowing K^+, Na^+ and Cl^- to reach *Gibbs−Donnan equilibrium*. In these experiments, sufficient extracellular sucrose was added to prevent cell swelling by balancing the colloid osmotic pressure of hemoglobin and other impermeant cell solutes. The *mean ionic activity coefficient* of KCl and NaCl in the concentrated intracellular hemoglobin solution was found to be within 2% of that in the extracellular solution (Freedman and Hoffman, 1979a). In view of the high intracellular ionic strength and the high volume fraction of cell water in direct contact with hemoglobin, it is both curious and remarkable that intracellular salts and non-electrolytes appear to behave as if in dilute solution. Either the intracellular solution is indeed like a dilute solution or, alternatively, the

expected effect of protein–solvent interactions in altering the activity of intracellular solutes is offset by the effect of interactions between proteins and the solutes themselves.

Specific effects of small anions on the solubility, aggregation or denaturation of proteins often follow the *Hofmeister (lyotropic) series* in the following order of effectiveness:

$$F^- < PO_4^{3-} < SO_4^{2-} < CH_3COO^- < Cl^- < Br^- < NO_3^- < I^- < SCN^-$$

The ions to the right of Cl^- are referred to as *chaotropic*, since they tend to destabilize proteins (for review, see Collins and Washabaugh, 1985). Ions may also associate with sites on proteins, as exemplified by the binding to albumin of Ca^{2+} (Katz and Klotz, 1953), and of Cl^- (Scatchard et al., 1957; see ch. 8 in Tanford, 1961). Certain enzymes, ion channels and membrane transport proteins interact with the alkali cations with a high degree of *ionic selectivity*. Considering the five alkali metal cations, there are 5! (=120) possible orders of selectivity that might arise. However, only 11 cationic selectivity orders commonly occur in chemical and biological systems, as listed in Table 1.2. Eisenman (1967) predicted these selectivity orders by calculating the ion-site interaction energies. If the field strength of a negatively-charged site is weak, then an associated ion remains hydrated. In this case, Cs^+, having the smallest hydrated ionic radius, is favored (Sequence I) because it can approach most closely to the site and thus has the strongest coulombic force of attraction. If the field strength of the site is strong and the interaction energy between the ion and the site is stronger than the energy between the ion and water dipoles, then the ion is stripped of its associated water and becomes dehydrated. In this case, Li^+, having the smallest non-hydrated ionic radius, becomes favored (sequence XI). With intermediate field strengths, ions partially dehydrate, giving rise to the intervening selectivity sequences. For example, K^+ functions as a co-factor for the glycolytic enzyme pyruvate kinase, with the maximal catalytic velocity following Eisenman sequence IV. During in vitro protein synthesis, K^+ maintains an active conformation of 50S ribosomal subunits that catalyze peptide bond formation following Eisenman sequence III. Other sequences are possible when the sites are assumed to be polarizable (for review, see Eisenman and Horn, 1983).

TABLE 1.2 Eisenman's Selectivity Sequences for Binding of Alkali Cations to Negatively Charged Sites

Highest field strength of site	
Li > Na > K > Rb > Cs	Sequence XI
Na > Li > K > Rb > Cs	Sequence X
Na > K > Li > Rb > Cs	Sequence IX
Na > K > Rb > Li > Cs	Sequence VIII
Na > K > Rb > Cs > Li	Sequence VII
K > Na > Rb > Cs > Li	Sequence VI
K > Rb > Na > Cs > Li	Sequence V
K > Rb > Cs > Na > Li	Sequence IV
Rb > K > Cs > Na > Li	Sequence III
Rb > Cs > K > Na > Li	Sequence II
Cs > Rb > K > Na > Li	Sequence I
Lowest field strength of site	

VII. SOLUTE TRANSPORT: BASIC DEFINITIONS

In the intracellular or extracellular solutions, a solute is said to be at *equilibrium* when its concentration is constant in time without requiring the continuous input of energy from metabolism or other sources. In human red blood cells, for example, Cl^-, HCO_3^- and H^+ are at thermodynamic equilibrium, i.e. they are passively distributed. A solute is said to be at *steady-state* when its concentration is constant in time, but is dependent on the continuous input of energy from metabolism or other sources. *Active transport* utilizes energy and results in steady-state distributions that represent a deviation from equilibrium. In biological cells, the concentrations of Na^+, K^+ and Ca^{2+} are at a steady-state. Their concentrations are constant in time, but are dependent on the continuous hydrolysis of ATP by the Na^+-K^+ pump (for review, see Glynn, 1985) and the Ca^{2+} pump. With isolated red cell membranes ("ghosts"), active transport of Na^+ and K^+ against their respective concentration gradients has been observed directly by measurements of net fluxes (Freedman, 1976). The active production and maintenance of ion concentration gradients by membrane pumps, such as the Na^+, K^+-ATPase and the Ca^{2+}-ATPase, represent *chemical work* and *electrical work* done by the cell. The energy required for continuous pumping of Na^+ by resting frog sartorius muscles has been estimated to represent some 14–20% of the energy available from the hydrolysis of ATP and the value is similar in red blood cells.

Passive transport is the movement of solutes toward a state of equilibrium. Passive transport of *hydrophobic* substances across cell membranes usually occurs directly by diffusion across the lipid bilayer. Passive transport of *hydrophilic* substances is usually mediated by specific membrane proteins via a process known as *facilitated diffusion*. Passive ion transport may occur through pores or ion channels under the influence of concentration gradients and electrical forces by a process known as

electrodiffusion. The passive flow of ionic currents down their concentration gradients through specific ion channel proteins constitutes negative work done by the cell. The changes in free energy associated with ion transport and the Nernst equilibrium equation are described in the Appendix.

VIII. MEASUREMENT OF ELECTROLYTES AND MEMBRANE POTENTIAL

Ion concentrations in biological fluids may be expressed as millimoles per liter of solution (millimolar, or mM), or as millimoles per kilogram of water (millimolal). When a solution containing metallic ions is aspirated into a flame, each type of ion burns with a characteristic color, Na^+ giving a yellow flame, K^+ giving a violet flame and Ca^{2+} giving a red flame. In the technique of *flame photometry*, the intensity of the emitted light, in comparison with that produced by solutions containing known concentrations of ions, provides a convenient measure of ion concentration in extracellular fluids and in acid extracts of cells. With a uniform rate of aspiration, a flame photometer accurately measures the intensity of the emitted light, which is related linearly to the cation concentrations in suitably diluted standards and unknowns (see e.g. Funder and Wieth, 1966). *Atomic absorption spectroscopy* is an alternative technique that measures the light absorbed by ions during electronic excitation in a flame. Flame photometry and atomic absorption spectroscopy both measure total ionic concentrations in cell extracts irrespective of any intracellular compartmentation and they are sensitive in the millimolar range of cellular concentrations. K^+, Na^+, Ca^{2+} and other elements in single cells, or even in single cell organelles, may be measured by *electron probe microanalysis*, a technique that utilizes an electron beam to excite the emission of x-rays with energies characteristic of the various elements in cells.

The development of *ion-specific glass microelectrodes* by Eisenman (1967) and then of selective *liquid ion exchange microelectrodes*, made possible the direct determination of intracellular cation activities. Palmer and Civan (1977) found that for Na^+, K^+ and Cl^- of *Chironomus* salivary gland cells, the ion activities are the same in the nuclear and cytoplasmic compartments. In a related study, Palmer et al. (1978) found that during development of frog oocytes, the ratio of the cytoplasmic concentration of Na^+ to K^+ increases, while the corresponding ratio of ion activities decreases. This observation could reflect the development of yolk platelets and intracellular vesicles that contain ions at differing concentrations and activities than does the bulk cytoplasm. In frog skeletal muscle, the sarcoplasmic reticulum contains a solution enriched in calcium, whereas the ionic composition of the solution in the t-tubules is extracellular. The extracellular space, however, consists of the interstitial space between the muscle fibers as well as the vascular space; solutes leave these two extracellular compartments with differing rate constants, thus considerably complicating the interpretation of experiments that assess the rate of membrane transport with radioactive isotopes of Na^+, K^+ and other solutes (Neville, 1979; Neville and White, 1979).

To measure transient changes of intracellular Ca^{2+} in the micromolar and submicromolar range, *fluorescent chelator dyes* such as Quin-2, Fura-2, Indo-1 and Fluo-3 have been developed (Tsien, 1988). Quin-2, Fura-2, and Indo-1 are fluorescent analogs of ethylenediaminetetraacetic acid (EDTA), which contains four carboxylate groups that specifically bind two divalent cations. EGTA is a non-fluorescent analog with a higher binding affinity for Ca^{2+} as compared with its affinity for Mg^{2+} and it is thus quite useful in experiments where the extracellular concentration of Ca^{2+} is systematically varied. Fluo-3 is a tetracarboxylate fluorescein analog that exhibits a shift in the emission spectrum upon binding Ca^{2+}; in contrast, Fura-2 undergoes a shift in its excitation spectrum. By measuring the ratio of Fura-2 fluorescence upon excitation at two exciting wavelengths, changes in the concentration of Ca^{2+} may be monitored. The cells are incubated with a permeant ester form of the dye to enable the dye to permeate into cells; intracellular esterases then release the Ca^{2+}-sensitive chromophore. With video microscopy of cells stained with fluorescent Ca^{2+} indicators, it is also possible to obtain time-resolved and spatially-resolved light microscopic images of the changes in intracellular Ca^{2+}. Another fluorescent probe (SPQ), developed by Helsey and Verkman (1987), has been used to measure intracellular Cl^- and to study its transport across cell membranes.

The transmembrane electrical potential is usually measured by means of open-tipped microelectrodes such as those developed and used by Ling and Gerard (1949) to obtain accurate and stable measurements of the membrane potential of frog skeletal muscle. With human red blood cells, stable potentials have not been achieved with microelectrodes. As an alternative technique, Hoffman and Laris (1974) utilized fluorescent cyanine dyes to monitor and measure red cell membrane potentials. Fluorescent cyanines, merocyanines, oxonols, sytryls, rhodamines and other dyes have since been used in numerous electrophysiological studies of red blood cells, neutrophils, platelets and other non-excitable cells and organelles that are too small for the use of microelectrodes (for review, see Freedman and Novak, 1989a). The equilibrium distribution of permeant, lipophilic, radioactively labeled ions such as triphenylmethylphosphonium ($TPMP^+$) may also be used to assess the membrane potential using the Nernst equilibrium equation (see Freedman and Novak, 1989b).

APPENDIX: THERMODYNAMICS OF MEMBRANE TRANSPORT

AI. FREE ENERGY

When ions cross cell membranes, changes in free energy are involved. Consider a membrane permeable only to cations separating two solutions of KCl of differing concentrations, c_i and c_o, where the subscripts i and o represent the intracellular and extracellular compartments, respectively (Fig. 1A.1). If the intracellular concentration (c_i) is greater than the extracellular concentration (c_o), then potassium will tend to diffuse out of the cell down its concentration gradient. When only a very slight amount of potassium crosses the membrane (which for this example is assumed to be impermeable to chloride), the separation of charge creates a transmembrane electrical potential (E_m) that is negative inside, relative to outside. The resultant electrical force retards further efflux of potassium. An equilibrium is reached when the diffusion force favoring efflux of potassium exactly balances the electrical force, preventing efflux of potassium.

Prior to the attainment of equilibrium, the process of moving dn moles of K^+ ions out of the cell from compartment i to compartment o involves a change in *free energy* (dG) of the system. According to the laws of thermodynamics, the process will occur spontaneously only if $dG < 0$ and the system will be at equilibrium if $dG = 0$. Thus, in order to compute the change in free energy (dG), we need to review certain basic thermodynamic principles.

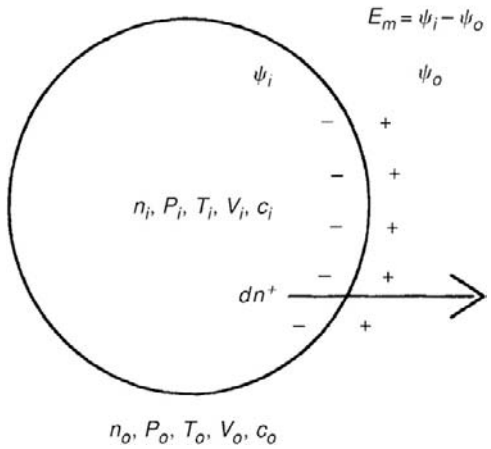

FIGURE 1A.1 Free energy of ion transport. A cell membrane separates the intracellular (subscript i) and the extracellular (subscript o). Each compartment is at pressure P and temperature T, has volume V and electrical potential ψ and contains solutes at concentration c. A free energy change is involved when dn^+ moles of cation leave the cell. The membrane potential E_m is $\psi_i - \psi_o$.

The *first law of thermodynamics*, also known as the law of conservation of energy, states that for any system, the increase in *energy* (dE) is the gain in *heat* (dQ) minus the *work* (dW) done by the system:

$$dE = dQ - dW$$

For reversible processes, the second law of thermodynamics defines the change in entropy (dS) of a system in terms of the heat gained (dQ) and the absolute temperature (T) as follows:

$$dS = \frac{dQ}{T}$$

Combining the first and second laws gives:

$$dE = TdS - dW$$

Since the difference in pressure (dP) between the internal and external solutions of animal cells is negligible, the work (dW) done by the system includes pressure−volume work, PdV, and electrical work, $zF\in_m dn$, summed as follows:

$$dW = PdV + zF\in_m dn$$

where P is the pressure, V is the total volume of the system, z is the ionic valence (eq/mol), F is the Faraday constant (=96 490 C/eq) and dn is the number of moles of solute crossing the membrane and leaving the cell. The transmembrane electrical potential ($\in_m$) is the difference in electrical potential (ψ, in volts or J/C), between the two compartments:

$$\in_m = \psi_i - \psi_0$$

The electrical potential (ψ) represents the work done in moving a unit positive test charge from infinity to a point in the solution. Note that when the transmembrane electrical potential ($\in_m$) is negative inside, the electrical work done by the system is negative whenever Na^+ or K^+ leave the cell, but positive when K^+ or Na^+ enter the cell, irrespective of the mechanism of transport.

According to the first and second laws, the change in energy (dE) of the system is:

$$dE = TdS - PdV - zF\in_m dn$$

For systems of variable chemical composition, the free energy (G) is by definition:

$$G = H - TS + \sum \mu_j n_j$$

where the enthalpy (H) is defined as;

$$H = E + PV$$

The *chemical potential* μ_j of the jth solute in the system at constant T, P, and n_k is defined by:

$$\mu_j = (\partial G/\partial n_j)_{T,P,n_k}$$

where n_j and n_k are the number of moles of the jth and kth solutes, respectively. The chemical potential, also called the *partial molar free energy*, represents the incremental addition of free energy to the system upon incremental addition of a solute. All solutes contribute to the free energy of a solution. While the free energy itself is a parameter of state for the whole system, the chemical potential refers to a particular solute. The free energy is thus given by:

$$G = E + PV - TS + \sum \mu_j n_j$$

Differentiating yields:

$$dG = dE + PdV + Vdp - TdS - SdT + \sum \mu_j dn_j$$

Substituting the expression for dE given previously and simplifying yields a form of the *Gibbs equation*,

$$dG = -SdT + VdP - zF\in_m dn + \sum \mu_j dn_j$$

which states that the free energy of a system of variable chemical composition is a function of the temperature, the pressure and the number of moles of each component in the mixture, or $G = G(T, P, n_j)$. For processes that occur at constant temperature and pressure, where $dT = dP = 0$, the Gibbs equation simplifies to:

$$dG = -zF\in_m dn + \sum \mu_j dn_j$$

which states that the increase in free energy of a system is equal to the sum of the electrical work done on the system plus the total change in free energy due to changes in chemical composition. Furthermore, when the system is at equilibrium, dG must equal zero. The second law of thermodynamics also implies that the change in free energy (dG) is negative for all spontaneous processes. Thus, the first and second laws of thermodynamics, when combined with the definitions of free energy and enthalpy, result in the Gibbs equation, which is the fundamental equation for the estimation of free energy changes when water, ions, or other solutes cross cell membranes.

AII. NERNST EQUILIBRIUM

The *Nernst equation* describes the relationship between voltage across a semipermeable membrane and the ion concentrations at equilibrium in the compartments adjacent to the membrane. The Nernst equation provides a simple method of testing whether or not a particular solute is at equilibrium.

Considering the example described in the previous section and using the Gibbs equation, the change in the free energy of the system that occurs when dn moles of K^+ ions move from compartment i containing K^+ at activity a_i to compartment o containing K^+ at activity a_o is given by:

$$dG = -zF\in_m dn + \mu_i dn_i + \mu_o dn_o$$

where the change in free energy has been summed for the two compartments. For this process, the decrease in the number of moles of solute inside the cell ($-dn_i$) equals the increase outside the cell (dn_o), so that both may be represented by dn:

$$-dn_i = dn_o = dn$$

and therefore

$$dG = [-zF\in_m - (\mu_i - \mu_o)]dn$$

The chemical potential in each solution is:

$$\mu_i = \mu_i^0 + RT\ln a_i$$

$$\mu_o = \mu_o^0 + RT\ln a_o$$

For the system under consideration, the intracellular and extracellular standard-state chemical potentials are assumed to be identical:

$$\mu_i^0 = \mu_o^0$$

and thus:

$$dG = [-zF\in_m - RT\ln\ (a_i/a_o)]dn$$

At equilibrium, $dG = 0$ and, since, $dn \neq 0$ therefore

$$-zF\in_m - RT\ln\ (a_i/a_o) = 0$$

Rearranging yields the Nernst equation for a cationic concentration cell,

$$\in_m = -\frac{RT}{zF}\ln\frac{a_i}{a_o}$$

Converting the natural logarithm to base 10 yields:

$$\in_m = -2.303\frac{RT}{zF}\log\frac{a_i}{a_o}$$

The value of $2.303RT/F$ is 58.7 mV at 23°C and 61.5 mV at 37°C.

For charged solutes, the *electrochemical potential* ($\mu_j = dG/dn_j$) of the *jth* solute is defined as the sum of a chemical and an electrical component. The electrical contribution to the electrochemical potential is $zF\psi$ and the chemical contribution is $RT\ln a$.

$$\mu_j = \mu_j^0(T, P) + RT\ln a_j + zF\psi$$

Note that a fundamental condition of equilibrium is that the difference in electrochemical potential between compartments i and o is zero. The electrochemical potential of the solute is the same in each compartment to which that solute has access.

The Nernst equation is independent of the mechanism of transport and is often used for ascertaining whether or not an intracellular ion is at electrochemical equilibrium. If so, then:

$$a_i = a_o e^{-zF\in_m/RT}$$

Another way of understanding the Nernst equation is that, at equilibrium, ions distribute across the membrane electric field in accordance with a Boltzmann distribution.

If $z = 0$, as for non-electrolytes, then $a_i = a_o$, and the activities of the solutes will be the same at equilibrium on both sides of the membrane, as was found to be nearly the case for the distribution of non-electrolytes across the membranes of human red blood cells (Gary Bobo, 1967). If $z \neq 0$, as for electrolytes then, at equilibrium, each permeant monovalent ion will reach the same ratio of intracellular to extracellular activity. Such is the case for the passive distribution of Cl^-, HCO_3^- and H^+ in human red blood cells.

$$r = \frac{[Cl^-]_i}{[Cl^-]_o} = \frac{[HCO_3^-]_i}{[HCO_3^-]_o} = \frac{[H^+]_o}{[H^+]_i} = e^{F\in_m/RT}$$

In red blood cells, Na^+, K^+ and Ca^{2+} deviate from this ratio due to the action of the Na^+-K^+ pump and Ca^{2+} pump. In skeletal muscle, K^+ and Cl^- have Nernst equilibrium potentials that are close to the actual measured resting potential, while Na^+ is far from equilibrium. In squid axons, the Nernst equilibrium potential for K^+ is closest to the resting potential, Cl^- is somewhat removed and, as in muscle and red blood cells, Na^+ is far from equilibrium.

BIBLIOGRAPHY

Bergethon, P. R., & Simons, E. R. (1990). *Biophysical Chemistry. Molecules to Membranes*. New York: Springer-Verlag.

Bernard, C. (1949). *An Introduction to the Study of Experimental Medicine*. (H.C. Green, translator). New York: Schuman.

Bockris, J. O'M., & Reddy, A. K. N. (1970). *Modern Electrochemistry,* Vol. (1). New York: Plenum Press.

Cannon, W. B. (1932). *The Wisdom of the Body*. New York: Norton.

Cantor, C. R., & Schimmel, P. R. (1980). *Biophysical Chemistry*. Parts I, II, III. San Francisco: W.H. Freeman.

Collins, K. D., & Washabaugh, M. W. (1985). The Hofmeister effect and the behavior of water at interfaces. *Q Rev Biophys, 18*, 323–422.

Cooke, R., & Kuntz, I. D. (1975). The properties of water in biological systems. *Ann Rev Biophys Bioeng, 3*, 95–126.

Debye, P. (1929). *Polar Molecules*. New York: Dover Publications.

Dick, D. A. T. (1959). Osmotic properties of living cells. *Internatl Rev Cytol, 8*, 387–448.

Edsall, J. T., & McKenzie, H. A. (1978). Water and proteins. I. The significance and structure of water; its interaction with electrolytes and nonelectrolytes. *Adv Biophys, 10*, 137–207.

Edsall, J. T., & Wyman, J. (1958). *Physical Biochemistry*. New York: Academic Press.

Eisenberg, D., & Kauzmann, W. (1969). *The Structure and Properties of Water*. Oxford: Oxford University Press.

Eisenman, G. (1967). *Glass Electrodes for Hydrogen and other Cations*. New York: M. Dekker.

Eisenman, G., & Horn, R. (1983). Ionic selectivity revisited: the role of kinetic and equilibrium processes in ion permeation through channels. *J Membr Biol, 76*, 197–225.

Frank, H. S., & Thompson, P. T. (1960). A point of view on ion clouds. In W. J. Hamer (Ed.), *The Structure of Electrolyte Solutions* (pp. 113–134). New York: John Wiley & Sons.

Frank, H. S., & Wen, W.-Y. (1957). Structural aspects of ion-solvent interaction in aqueous solutions: a suggested picture of water structure. *Disc Faraday Soc, 24*, 133–140.

Freedman, J. C. (1976). Partial restoration of sodium and potassium gradients by human erythrocyte membranes. *Biochim Biophys Acta, 455*, 989–992.

Freedman, J. C., & Hoffman, J. F. (1979a). Ionic and osmotic equilibria of human red blood cells treated with nystatin. *J Gen Physiol, 74*, 157–185.

Freedman, J. C., & Novak, T. S. (1989a). Optical measurement of membrane potentials of cells, organelles, and vesicles. *Meth Enzymol, 172*, 102–122.

Freedman, J. C., & Novak, T. S. (1989b). Use of triphenylmethylphosphonium to measure membrane potentials in red blood cells. *Meth Enzymol, 173*, 94–100.

Funder, J., & Wieth, J. O. (1966). Determination of sodium, potassium, and water in human red blood cells. Elimination of sources of error in the development of a flame photometric method. *Scand J Clin Lab Invest, 18*, 151–166.

Fushimi, K., & Verkman, A. S. (1991). Low viscosity in the aqueous domain of cell cytoplasm measured by picosecond polarization microfluorimetry. *J Cell Biol, 112*, 719–725.

Gary-Bobo, C. M. (1967). Nonsolvent water in human erythrocytes and hemoglobin solutions. *J Gen Physiol, 50*, 2547–2564.

Glynn, I. M. (1985). The Na^+, K^+-transporting adenosine triphosphatase. In A. N. Martonosi (Ed.) (2nd edn).*The Enzymes of Biological Membranes, Vol. 3* (pp. 35–114). New York: Plenum Press.

Heilbrunn, L. V. (1956). *The Dynamics of Living Protoplasm*. New York: Academic Press.

Helsey, N. P., & Verkman, A. S. (1987). Membrane chloride transport measured using a chloride-sensitive fluorescent probe. *Biochemistry, 26*, 1215–1219.

Hille, B. (2001). *Ion Channels of Excitable Membranes* (3rd ed.). Sunderland, MA: Sinauer Associates.

Höber, R. (1945). *Physical Chemistry of Cells and Tissues*. Philadelphia: The Blakiston Company.

Hoffman, J. F., & Laris, P. C. (1974). Determination of membrane potentials in human and Amphiuma red blood cells by means of a fluorescent probe. *J Physiol (London), 239*, 519–552.

Horowitz, S. B., & Miller, D. S. (1984). Solvent properties of ground substance studied by cryomicrodissection and intracellular reference-phase techniques. *J Cell Biol, 99*, 172s–179s.

Horvath, A. L. (1985). *Handbook of Aqueous Electrolyte Solutions. Physical Properties, Estimation and Correlation Methods*. New York: John Wiley and Sons.

Katz, S., & Klotz, I. M. (1953). Interactions of calcium with serum albumin. *Arch Biochem, 44*, 351–361.

Klotz, I. M. (1970). Water: its fitness as a molecular environment. In E. E. Bittar (Ed.), *Membranes and Ion Transport, Vol. 1* (pp. 93–122). New York: Wiley.

Läuger, P. (1991). *Electrogenic Ion Pumps*. Sunderland, MA: Sinauer Associates.

Ling, G. N., & Gerard, R. W. (1949). The normal membrane potential of frog sartorius fibers. *J Cell Comp Physiol, 34*, 383–396.

Miller, C. (1974). Nonelectrolyte distribution in mouse diaphragm muscle. I. The pattern of nonelectrolyte distribution and reversal of the insulin effect. *Biochim Biophys Acta, 339*, 71–84.

Neville, M. C. (1979). The extracellular compartments of frog skeletal muscle. *J Physiol, 288*, 45–70.

Neville, M. C., & White, S. (1979). Extracellular space of frog skeletal muscle in vivo and in vitro: relation to proton magnetic resonance relaxation times. *J Physiol, 288*, 71−83.

Palmer, L. G., & Civan, M. M. (1977). Distribution of Na^+, K^+, and Cl^- between nucleus and cytoplasm in Chironomus salivary gland cells. *J Membr Biol, 33*, 41−61.

Palmer, L. G., Century, T. J., & Civan, M. M. (1978). Activity coefficients of intracellular Na^+ and K^+ during development of frog oocytes. *J Membr Biol, 40*, 25−38.

Pauling, L. (1960). *The Nature of the Chemical Bond and the Structure of Molecules and Crystals; an Introduction to Modern Structural Chemistry* (3rd ed.). Ithaca, NY: Cornell University Press.

Robinson, R. A., & Stokes, R. H. (1959). *Electrolyte Solutions* (2nd ed.). London: Butterworths.

Scatchard, G., Coleman, J. S., & Shen, A. L. (1957). Physical chemistry of protein solutions. VII. The binding of some small anions to serum albumin. *J Am Chem Soc, 79*, 12−20.

Schwan, H. P., & Foster, K. R. (1977). Microwave dielectric properties of tissue. Some comments on the rotational mobility of tissue water. *Biophys J, 17*, 193−197.

Silver, B. L. (1985). *The Physical Chemistry of Membranes*. Boston: Allen and Unwin.

Tanford, C. (1961). *Physical Chemistry of Macromolecules*. New York: Wiley.

Tsien, R. Y. (1988). Fluorescence measurement and photochemical manipulation of cytosolic free calcium. *Trends Neurosci, 11*, 419−424.

Weiss, T. F. (1996). *Cellular Biophysics, Vol. 1: Transport, Vol. 2: Electrical Properties*. Cambridge, MA: The MIT Press.

This page intentionally left blank

Chapter 2

Physiological Structure and Function of Proteins

Matthew R. Pincus

Chapter Outline

I. SUMMARY

We see in this chapter that the three-dimensional structures of proteins are dictated by their linear sequences of amino acids. A protein's structure is the one of lowest free energy for the given polypeptide chain, the detailed conformation of which is determined by the dihedral angles of the backbone and side chains. Proteins are structured in such a way that their polar amino acids tend to be directed towards the aqueous solvent while the non-polar or hydrophobic residues tend to point towards the interior of the protein. The three-dimensional structures of proteins can be determined by a variety of techniques, which include circular dichroism (for regular structure), x-ray crystallography, two-dimensional nuclear magnetic resonance spectroscopy (NMR) and theoretical techniques.

The three-dimensional structures of proteins determine bulk properties of these proteins, such as their behavior towards titration with acids or bases, their isoionic points and their migration in electric fields, as in electrophoresis. The ionization of charged groups on the surfaces of proteins can be treated, and thus their titration curves can be predicted using ligand-binding theory combined with electrostatic

Cell Physiology Sourcebook. DOI: 10.1016/B978-0-12-387738-3.00002-0

field theory (using the Debye-Hückel formulation) or using more explicit models based on the actual three-dimensional structure of the protein surrounded by water dipoles.

The structure of a protein and its functioning have a well-defined relationship. Membrane proteins, for example, tend to fold into α-helices. This structure is of critical importance to the functioning of leader peptides that allow for proteins to be secreted both within the cell and outside of the cell. The ability of melittin to intercalate into cell membranes and to cause cell lysis depends on its ability to adopt an α-helical conformation and to change the angle of these helices. Membrane active peptides, like PNC-27, fold into membrane-active helix-loop-helix amphipathic structures and bind to unique protein targets in the membranes of cancer cells allowing them to kill the cancer cells but not affect normal cells making them potentially effective anti-cancer agents.

Certain large proteins, like *neu*/HER-2, contain major transmembrane domains which can adopt several different conformations, some of which allow them to dimerize and thus initiate cellular signal transduction. This process is especially critical for oncogene-encoded proteins that are involved in mitogenic signal transduction to the nucleus, causing cell division. We have begun to understand the structural basis for this process using conformational analysis as described in this chapter. In this regard, conformational analysis has now been extended to the identification of the regions of oncogenic proteins involved in activation of downstream target proteins and has opened new possibilities in the field of drug design. Voltage-dependent conformational changes in the transmembrane domains of ion channel proteins are vital to their regulated functioning. The basic functioning of cells is therefore controlled by the proper folding and functioning of cellular proteins, making vital the understanding of protein structure.

II. MOLECULAR STRUCTURE OF PROTEINS

Proteins are biopolymers that are essential for all plant and animal life. All antibodies, enzymes and cell receptors are proteins. The basis for all connective tissue is the fibrous proteins, such as elastin and collagen. The entire genetic apparatus of every cell, regardless of how simple or complex its functions, is dedicated to the synthesis of proteins. The building blocks for proteins are α-amino acids that are linked to one another by peptide (or amide) bonds. The twenty naturally occurring amino acids (Fig. 2.1) all have the same *backbone* structure, the N−C^{α}−C=O unit, but differ from one another in that they have different side chains attached to the α-carbon, as shown in Fig. 2.1. Also, all of these amino acids are chiral − optically active and in the L-configuration − except for the simplest amino acid, glycine, which has two H atoms attached to the α-carbon. Note that cysteine has a sulfhydryl group, giving it the capacity to form disulfide bonds (Fig. 2.1). Disulfide bonds are important in stabilizing the three-dimensional structures of proteins, as discussed in Section IIC.

Topographically, proteins are divided into the *fibrous proteins*, which are long repeating helical proteins and the *globular proteins*, which tend to fold up into spherical or ellipsoidal shapes. As we will show, how proteins fold is governed uniquely by their linear sequences of amino acids.

IIA. Primary Amino Acid Structure

All proteins are composed of linear sequences of amino acids that are unique to each protein and are covalently bound to one another by peptide bonds (Fig. 2.2). This peptide bond is almost always arranged so that the C^{α} atoms of two successive residues are *trans* to one another and the atoms attached to the C′ and N of the peptide all lie in the same plane since the C′−N bond has double-bond character, namely, the *trans*-planar peptide bond described long ago by Linus Pauling. The linear sequence of amino acids is called the *primary structure*.

Note that the amino acids in Fig. 2.1 are classified as *polar*, *non-polar* and *neutral* depending on the nature of the side chain. Thus, for example, leucine and valine are non-polar amino acids with aliphatic side chains that are hydrophobic, or non-miscible with water and other polar solvents. Amino acids like lysine and glutamic acid, on the other hand, contain charged side chains that are highly soluble in water and are completely miscible in polar solvents. Amino acids such as glycine and alanine do not contain groups that predispose them to be classified as either polar or non-polar, so they are referred to as neutral.

IIB. Regular or Secondary Structure in Proteins

The three-dimensional structures of over 300 proteins have been determined by x-ray crystallography. One striking feature in all of these proteins is the presence of recurrent regular structures, in particular, α-helices, β-sheets and reverse turns (Fig. 2.3). The existence of the first two of these structural types was predicted by Linus Pauling in the early 1950s on the basis of x-ray diffraction patterns of model poly-α-amino acids.

Note that in the α-helix in Fig. 2.3A, the residues form a spiral such that at every 3.6 residues, the spiral or helix makes one complete turn. The repeat distance of this helix is 5.4 Å. This structural motif is observed in virtually all proteins and, some proteins like myoglobin, are virtually completely α-helical. One very important interaction for stabilizing helices is the *i*-to-*i*+4 hydrogen-bonding

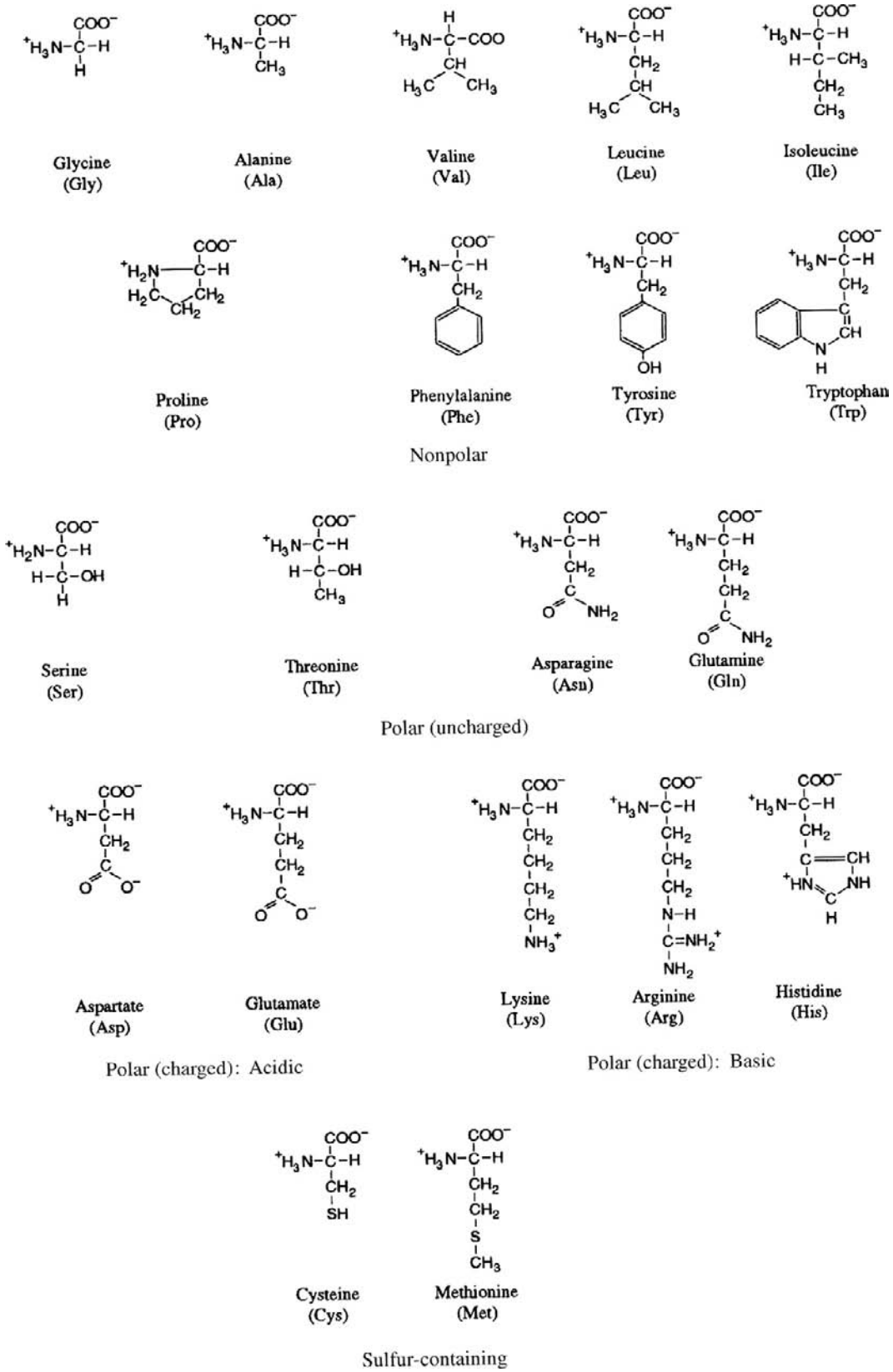

FIGURE 2.1 The 20 naturally occurring amino acids grouped by type. Note that Cys residues can form disulfide bonds in the following reaction: R−SH + R−SH → R−S−S−R, where R is the backbone atoms of Cys + the side chain CH_2 group.

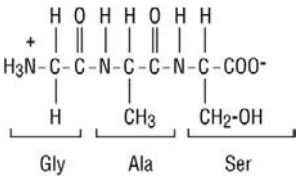

FIGURE 2.2 A typical tripeptide, Gly-Ala-Ser, showing the CO—NH peptide bond linkage.

scheme shown in Fig. 2.3A. The C=O of the *i*th residue accepts a hydrogen bond from the N—H of the *i*+4th residue. The hydrogen bond can provide up to 3 kcal/mol in stabilization energy. For an amino acid residue in the middle of an α-helix, two hydrogen bonds form to its N—H and C=O groups. This occurrence tends to cause helices to propagate because the more such double hydrogen bonds form, the greater the stabilization energy provided. Two other long-range factors stabilize α-helices. The first is the presence of negatively charged amino acid residues on the amino terminal end of a helix and positively charged amino acids on the carboxyl terminal end of the helix. This stabilization results from the backbone dipole moment of an α-helix, where the center of positive charge is on the amino terminus of the helix and the center of negative charge is on the carboxyl terminus of the helix. The presence of the oppositely charged amino acids stabilizes the helical dipole.

The second stabilizing factor is *amphipathicity*. This refers to the *i*-to-*i*+4 side chain—side chain interactions such that non-polar or hydrophobic amino acids contact one another on one face of the helix while other polar *i*-to-*i*+4 interactions occur on the opposite side of the helix. This segregation of polar and non-polar faces allows for hydrophobic clustering to occur on one face and hydrogen bonding and charge neutralization to occur on the opposite face. This motif is vital in stabilizing α-helices in membrane proteins such as ion channel proteins.

α-Helices are extremely important in membrane proteins, in the transmembrane domains of cellular receptors and in ion channel proteins, as we discuss in Section V.

In contrast, the β-sheet is composed of alternating residues of amino acids that are "flipped" 180° with respect to their nearest neighbors, as shown in Fig. 2.3B. We may regard the structure of single strands in these sheets as a flat helix whose repeat is every two residues. Note that within each strand of a β-sheet are minimal interactions between the backbone atoms of different amino acid residues. The hydrogen-bonding stabilization comes from other strands that lie in proximity to one another. As shown in Fig. 2.3B, the arrangement of the strands is either *parallel* or *antiparallel*. Regardless of the arrangement of the two interacting strands, it should be noted from Fig. 2.3B that two hydrogen bonds between the backbone atoms form for *alternate* residues; every other residue forms no hydrogen bond to the neighboring strand. Thus there is twice the number of hydrogen bonds in long α-helices as in long β-sheets. Evidently, other interactions are important in stabilizing β-sheets besides backbone—backbone hydrogen bonding.

Another type of regular structure is the *reverse turn*, the prototype of which is shown in Fig. 2.3C. In this structure, the polypeptide chain reverses its direction. A minimum of two amino acids is needed to form a reverse or hairpin turn, which is also called a β-bend. Usually, three amino acids are involved, however, because the C=O of the first residue can form an *i*-to-*i*+3 hydrogen bond with the N—H of the *i*+3rd residue, as shown in Fig. 2.3.

Of the three regular structures described, α-helices tend to propagate most strongly due to the double hydrogen bonding of the NH and C=O groups of central residues in the helix discussed above and illustrated in Fig. 2.3D. This type of "medium-range" interaction is not present for the two other types of regular structures.

The specific sequences of amino acids in proteins will adopt specific structures such as the three basic regular structures just described. Thus the amino acid sequences of proteins determine their respective three-dimensional structures. This conclusion has been verified as we now describe.

IIC. Tertiary or Three-Dimensional Structure of Proteins

IIC1. The Amino Acid Sequences of Proteins Determine their Three-Dimensional Structures

In a classic series of experiments, Christian Anfinsen and his coworkers at the National Institutes of Health showed in the early 1960s that the primary structure (linear sequence of amino acids) of a protein determines its unique three-dimensional structure (Anfinsen et al., 1961). These investigators took the protein ribonuclease A, which hydrolyzes RNA and whose amino acid sequence had just been determined and was known to contain four disulfide bonds, and denatured it in the denaturing agent 6 M guanidine hydrochloride. This agent and 8 M urea are both known to disrupt the hydrogen bonds in proteins and destroy their three-dimensional structures. In addition, using β-mercaptoethanol, they reduced the four disulfides to eight sulfhydryl (SH) groups, thereby destroying all of the major determinants of the three-dimensional structure. The denatured protein was completely inactive towards RNA hydrolysis and possessed spectral properties that differed greatly from those of the native protein. They then allowed the sulfhydryl groups to reoxidize to disulfides and dialyzed the 6 M guanidine hydrochloride. Within 2 hours, virtually all of the native enzymatic activity returned and the spectral properties of the refolded protein were identical to those of the undenatured protein. In addition, all of the disulfides were paired exactly as they were in the native protein.

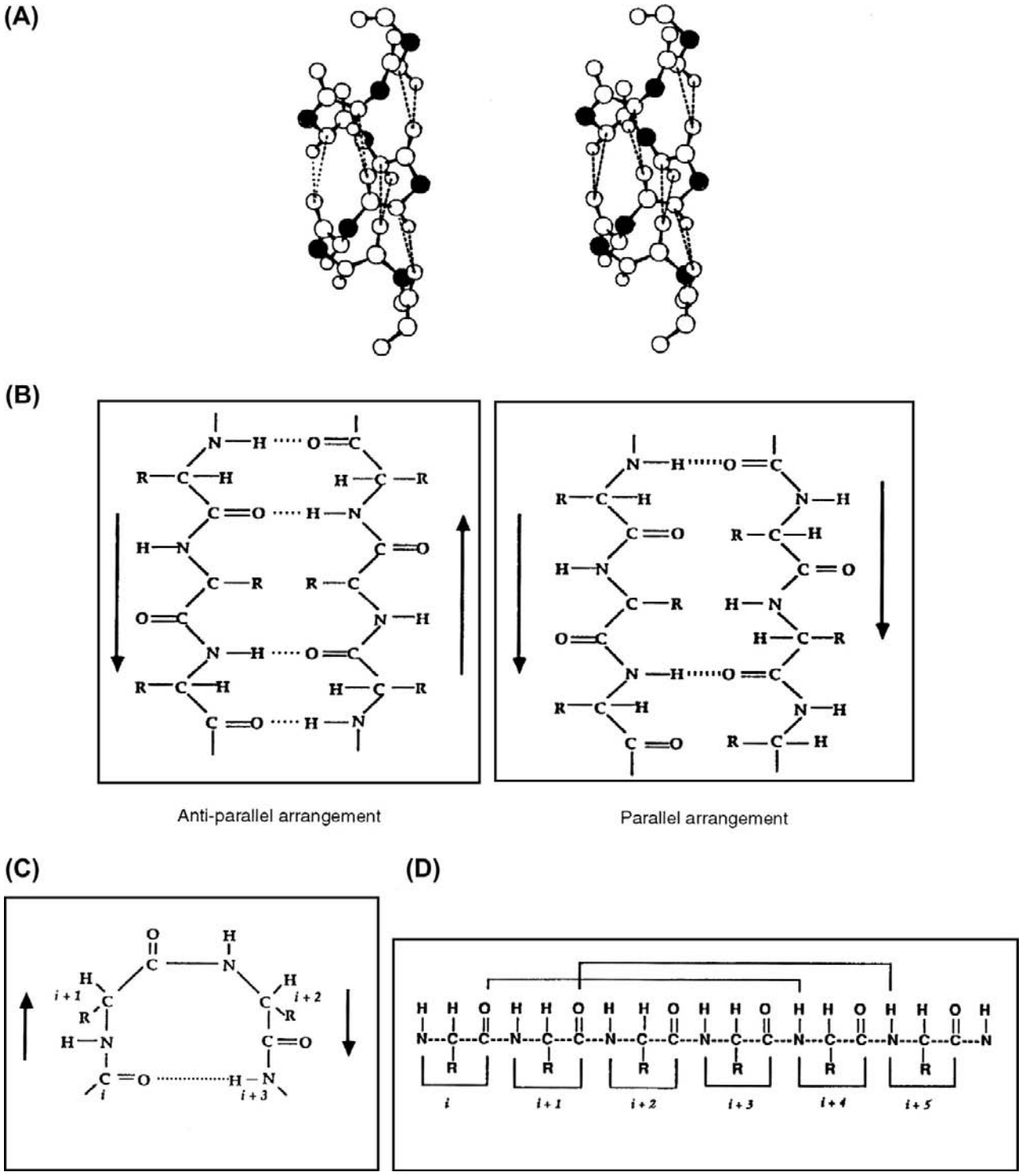

FIGURE 2.3 Three types of regular (secondary) structure. (A) Stereo view of an α-helix for a polypeptide backbone showing the *i*-to-*i*+4 hydrogen bond. The filled circles are α-carbons; double dashed lines are drawn from C=O to NH (shorter dashed line) and from C=O to N (longer dashed line). (B) Two types of β-sheets. The left side shows the antiparallel arrangement while the right side shows the parallel arrangement, as indicated by the arrows in both figures. (C) The arrangement of backbone atoms in a β-bend showing how an *i*-to-*i*+3 hydrogen bond stabilizes the reverse turn structure. (D) Illustration of an extended α-helical chain showing how internal residues have both their NH and CO groups involved in hydrogen bonds. Residue *i*+4 would have its NH and C=O both hydrogen-bonded if 2 more residues were added to the carboxyl terminal end.

This experiment illustrated that the primary sequence of amino acids in a protein determines its three-dimensional structure. Further, it demonstrated that the interactions that govern the correct folding of a protein must be highly specific and strong because, of the vast number of possible structures that the polypeptide could have adopted, only one such structure actually ultimately formed. This conclusion is reinforced by the following consideration. Once the protein is reduced to the eight-sulfhydryl state, there are many ways in which these eight sulfhydryls can pair to give four disulfides. In particular, there are seven ways in which the first disulfide can form, five for the second, three for the third and one for the fourth, or $7 \times 5 \times 3 \times 1 = 105$ possible ways. Of this total, only one pairing scheme, the native pairing, ultimately was found to form in this experiment.

Similar results have been obtained for a number of different proteins. In every case, the native structure is regenerated. Such dramatic results imply that, given the amino acid sequence, it should be possible to infer the three-dimensional structure of the protein.

Indeed, methods have been and are continuing to be developed that allow us to predict the three-dimensional structure of a polypeptide or a protein from its amino acid sequence. At present, it is possible to compute the three-dimensional structures of polypeptides from their amino acid sequences for polypeptides and proteins containing more than 100 amino acid residues. As might be imagined, the field of structure prediction is a burgeoning one that is developing rapidly. All of the methods used to predict protein structure are based on the physicochemical principle that the observed structure of a molecule is the one with the lowest free energy. If we can compute the energies for the possible conformations of a protein, we can pick out the structure of lowest energy, which is the structure that the protein is most likely to adopt. In order to perform this task, we must understand the types of energetic interactions within a polypeptide chain that must be optimized for the protein to fold correctly.

IID. Possible Interactions Between Amino Acids in a Protein Chain

As might be expected from the differing nature of the side chains of the naturally occurring amino acids, a vast number of possible interactions between different side chains and backbone are possible for given amino acid sequences. These types of interactions include *electrostatic interactions* (given by the Coulombic potential q_1q_2/DR_{12}, where the qs are the charges on two different interacting atoms, R is the distance between them, and D is the dielectric constant of the medium) between positive and negative charges of oppositely charged side chains, such as the $-COO^-$ group of glutamic acid and the $-NH_3^+$ group of lysine as well as the interactions between the partial charges on all of the atoms of the protein; *non-bonded* interactions between the individual atoms, explained below; *hydrogen-bonding interactions* between polar atoms with H atoms and other polar atoms; and a *solvation energy* for most proteins.

This solvation energy is such that the non-polar side chains of non-polar amino acids tend to avoid water and therefore "bury" themselves in the core of the protein, while the side chains of polar amino acids tend to interact strongly with water and become solvated. This favorable solvation energy is due to water dipole interactions with charged residues such that the charges on the side-chain atoms are reduced by favorable interactions with the water dipoles. It is also due to hydrogen bonding between water molecules and the polar atoms of the exposed polar side chains.

IID1. Specific Interactions: Hydrogen-Bonding, Non-Bonded and Hydrophobic Interactions

In the preceding paragraph, we noted that hydrogen-bonding interactions between polar atoms in a protein can greatly stabilize the structure of a protein. These interactions are due to the sharing of a hydrogen atom between the donor atom to which the H atom is covalently linked and the receptor polar atom as in Fig. 2.4. This interaction stabilizes the distribution of charges over the three atoms involved in the hydrogen bonding system (Fig. 2.4). For a given protein sequence, hydrogen bonding patterns can be arranged in many possible ways. However, in every protein whose three-dimensional structure is known, only one or a few hydrogen-bonding schemes are observed, many of these occurring between backbone atoms (NH—O=C) and others occurring between the polar atoms of side chains.

In addition to the hydrogen-bonding interactions between the atoms of a protein, all pairs of atoms in a protein interact with one another so as to attract each other weakly until they become sufficiently close that their electron clouds repel one another. The weak attractive interactions between a pair of atoms are due to the polarization of charges in each atom between the negatively charged electrons and the positively charged nucleus that is induced by the other interacting atom. This induced-dipole−induced-dipole interaction is attractive because the positive end of

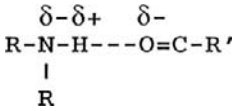

FIGURE 2.4 Illustration of how hydrogen bonds are stabilized by partial sharing of a polar H atom between two polar heavy atoms (N and O in this case).

the dipole of the first atom interacts attractively with the negative end of the dipole of the other atom of the pair and vice versa. The overall attractive energy for this interaction can be simply expressed as $-B_{ij}/R_{ij}^6$, where B_{ij} represents a constant that characterizes the magnitude of the attractive energy between any two interacting atoms and R_{ij} is the distance between the two interacting atoms. As shown in Fig. 2.5, as two interacting atoms approach one another, the attractive energy becomes progressively stronger until the electrons in the outer shells repel one another. This repulsive energy increases rapidly as the internuclear distance between the atoms decreases.

Most proteins fold in an aqueous environment. Changing the solvent, such as by adding non-polar solvents to water, is known to denature proteins so that they cannot function properly. Evidently, water provides important interactions with proteins, such that they fold correctly to their native conformations.

The three-dimensional structures of over 300 proteins have been determined mostly by the technique of x-ray crystallography (see Section III.B). In all of these proteins, the non-polar amino acid residues tend to "pack" in the interior of the protein, while the polar residues tend to interact with water on the surface of the protein. Avoidance of interaction of the non-polar residues with water is due to the *hydrophobic (water-avoiding) effect*. This behavior is caused predominantly by an entropy effect. Water molecules tend to become highly ordered around the side chains of non-polar or hydrophobic amino acid residues. On the other hand, water molecules can interact in a large number of low-energy complexes with polar side chains and so are less constricted structurally. This ordering of water molecules by non-polar residues causes the latter to "pack" into the interior of the protein, allowing the water to be more disordered on the outside of the protein.

If one measures the free energy of transfer, ΔG, of non-polar compounds (such as benzene or *n*-hexane) from non-polar to polar solvents, it is found that the enthalpy of transfer, ΔH, is small whereas the entropy of transfer, ΔS, is a large negative value. From the Gibbs free energy expression,

$$\Delta G = \Delta H - T\Delta S \tag{2.1}$$

it can be seen that a large negative entropy makes the overall process unfavorable; in other words ΔG becomes more positive. This effect can be attributed to the water structure effect (see Scheraga, 1984).

All of the above interactions have been taken into account in a variety of computer programs that generate the conformations of polypeptides and proteins and calculate their conformational energies. One such program is ECEPP (Empirical Conformational Energies of Peptides Program) developed in the laboratory of Professor Harold A. Scheraga of Cornell University. The energy parameters, such as the constants for the non-bonded interaction energies, have been determined experimentally. This program has been used to compute the structures of many polypeptides and proteins with excellent agreement between predicted and experimentally determined structures (Scheraga, 1984). We give examples below of how these methods have been used to predict protein structure and provide insight into the relationship between the structure of a protein and its function. First, we describe the properties of the structures of proteins.

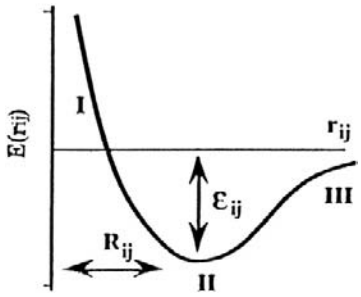

FIGURE 2.5 Interatomic van der Waals energy as a function of distance. Notice that two atoms can approach one another with decreasing energy (regions II and III) until the energy reaches a minimum (ε_{ij}) at a distance of R_{ij}. If the atoms become closer, they then repel one another so that the energy rises steeply (region I).

IIE. Properties of the Structures of Proteins

IIE1. Geometry and Dihedral Angles

Among the many protein structures that have been determined by crystallography, each of the amino acid residues that compose the protein have geometries that are remarkably constant throughout the protein and when compared between any two proteins. Remarkably, this geometry is essentially the same as that found in single crystals of the individual amino acids. Geometry refers to the bond lengths and bond angles of the individual amino acid. An example of the geometry of an amino acid is illustrated for glycine in Fig. 2.6. The basic variables that allow for changes in chain conformation are the dihedral angles, defined as the angle made between two overlapping planes. For example, in Fig. 2.7, the angle between the planes determined by the N−Cα−C′ atom and the Cα−C′−N atoms of the two amino acid residues shown is a dihedral angle. These angles are generated by rotation around single bonds. As shown in Fig. 2.7, for the backbone of a single amino acid residue, three dihedral angles exist:Φ, ψ and ω.

The dihedral angle Φ is determined by the angle between the planes of C′−N−Cα and N−Cα−C′, whereas the dihedral angle ψ is determined by the angle between the planes of N−Cα−C′ and Cα−C′−N. To determine Φ, one merely has to look down the N−Cα axis using the C′-N

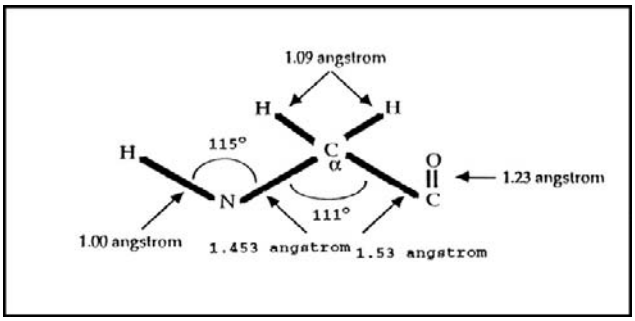

FIGURE 2.6 The geometry of a glycine residue showing typical bond lengths and bond angles.

bond as a reference and determine the angle made between the C′−N bond and the Cα−C′ bond as shown in Fig. 2.7. To determine ψ, one uses the N−Cα bond as a reference and measures its angle with the C′−N bond. The dihedral angle ω is the interpeptide dihedral angle, which is determined by rotation around the C′−N bond shown in Fig. 2.7. It can be measured by determining the angle made between the Cα−C′ bond and the N−Cα bond when sighting down the C′−N bond. This angle is almost always close to 180°, the trans-planar peptide conformation.

Given the geometry and a complete set of dihedral angles for a given sequence of amino acids in a polypeptide, a unique three-dimensional structure can be generated, called the conformation of the protein. All regular structures described above have repeating values for Φ and ψ from residue to residue. All α-helices have values for Φ and ψ that are close to −60° while, for the individual extended chains of β-sheets, the values for both of these dihedral angles lie close to 180°.

In fact, the α-helical or A and extended or E conformations are minimum-energy conformations for all of the

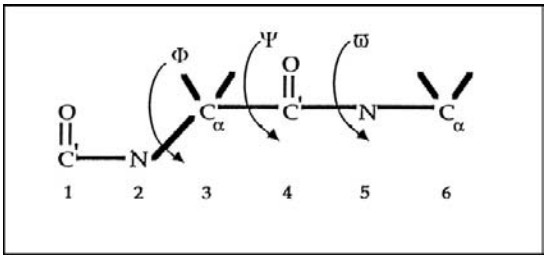

FIGURE 2.7 Dihedral angles, Φ, ψ and ω, for the backbone of an amino acid. Φ is determined by atoms 1, 2, 3, and 4. Clockwise rotations of the 3−4 bond relative to the 1−2 bond are considered positive while counterclockwise rotations are considered negative. 0° is the conformation in which the 3−4 bond is eclipsed relative to the 1−2 bond, while 180° is the conformation in which the two bonds are *trans* relative to one another. Ψ is determined by the 4−5 bond relative to the 2−3 bond. The same considerations apply to this dihedral angle as to those for Φ. ω is determined by the angle between the 5−6 bond and the 3−4 bond. This dihedral angle is almost always very close to 180° (i.e. the 5−6 bond is *trans* to the 3−4 bond).

naturally occurring amino acids. Using conformational energy calculations based on ECEPP, all of the low-energy minimum conformations for the 20 naturally occurring amino acids have been computed as a function of the dihedral angles Φ and ψ. In Fig. 2.8, these energies are plotted as isoenergetic contours in the same way that different elevations are plotted on contour maps. All of the amino acids have at least seven basic low-energy minima as indicated by the dots in Fig. 2.8.

Note in this figure that large regions of the map are energetically forbidden and that the allowed (low-energy) regions of the map are relatively restricted (see Fig. 2.8). Analysis of the conformations of the individual amino acids in proteins whose three-dimensional structures are known reveals that virtually all of these amino acids adopt one of these eight basic conformational states, consistent with the results of the energy calculations.

IIE2. Computation of the Structures of Polypeptides and Proteins

Using programs such as ECEPP, systematic methods, reviewed extensively in Vasquez et al. (1994), have been developed that generate representative sets of the low-energy structures for a given polypeptide chain. These methods include the chain build-up procedure (Pincus, 1988), molecular dynamics (Karplus and McCammon, 1986), Monte Carlo procedures, and more specialized methods that allow for "jumping" potential energy barriers

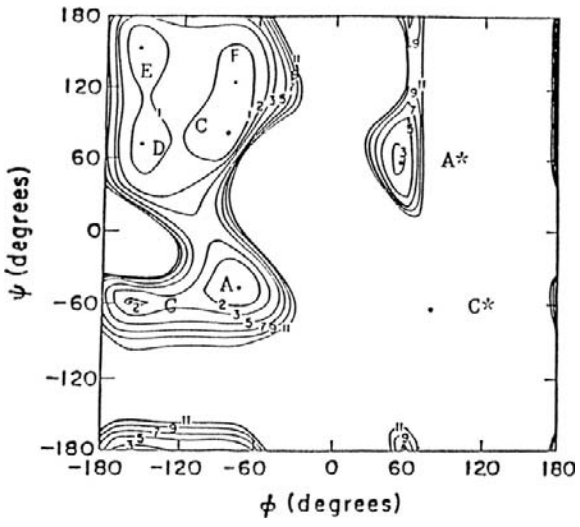

FIGURE 2.8 Contour map for Φ and ψ for N-acetyl-alanine-N′-methyl amide as computed by ECEPP (Scheraga, 1984). Note that the actual energy minima are denoted by dots on the energy contour map. Seven low-energy minima are shown: A (α-helical), C, D (both of which are seen in bends), G, E, and F (which are seen in β-sheets), A* (left-handed α-helix), and C*, which is energetically forbidden for all L-amino acids except glycine. Note also that some of these regions are "split" (i.e. more than one minimum can exist for a given conformational region).

between different conformations of the given polypeptide chain (Scheraga, 1989). All of these methods take advantage of the energy map shown in Fig. 2.8, since the backbone of each amino acid is constricted to adopting one of the low-energy states shown in this figure. Once the low-energy conformations for a given polypeptide are generated and their energies computed, the lowest energy structure is selected and this structure is the one that should be observed experimentally.

Successful ECEPP computations of the three-dimensional structures of a number of polypeptides and proteins have been performed. Examples are shown in Fig. 2.9 for the cyclic decapeptide gramicidin A, collagen and melittin (Pincus and Scheraga, 1985). There is close agreement between these computed structures and the experimentally determined ones. Excellent agreement between theory and experiment has also been achieved for other proteins, such as avian pancreatic polypeptide and bovine pancreatic trypsin inhibitor (Scheraga, 1989) and a 100-residue segment of human leukocyte interferon (Gibson et al., 1986). The experimental structures of these polypeptides and proteins have been determined by specific methods, namely, x-ray crystallography, two-dimensional NMR, or circular dichroism.

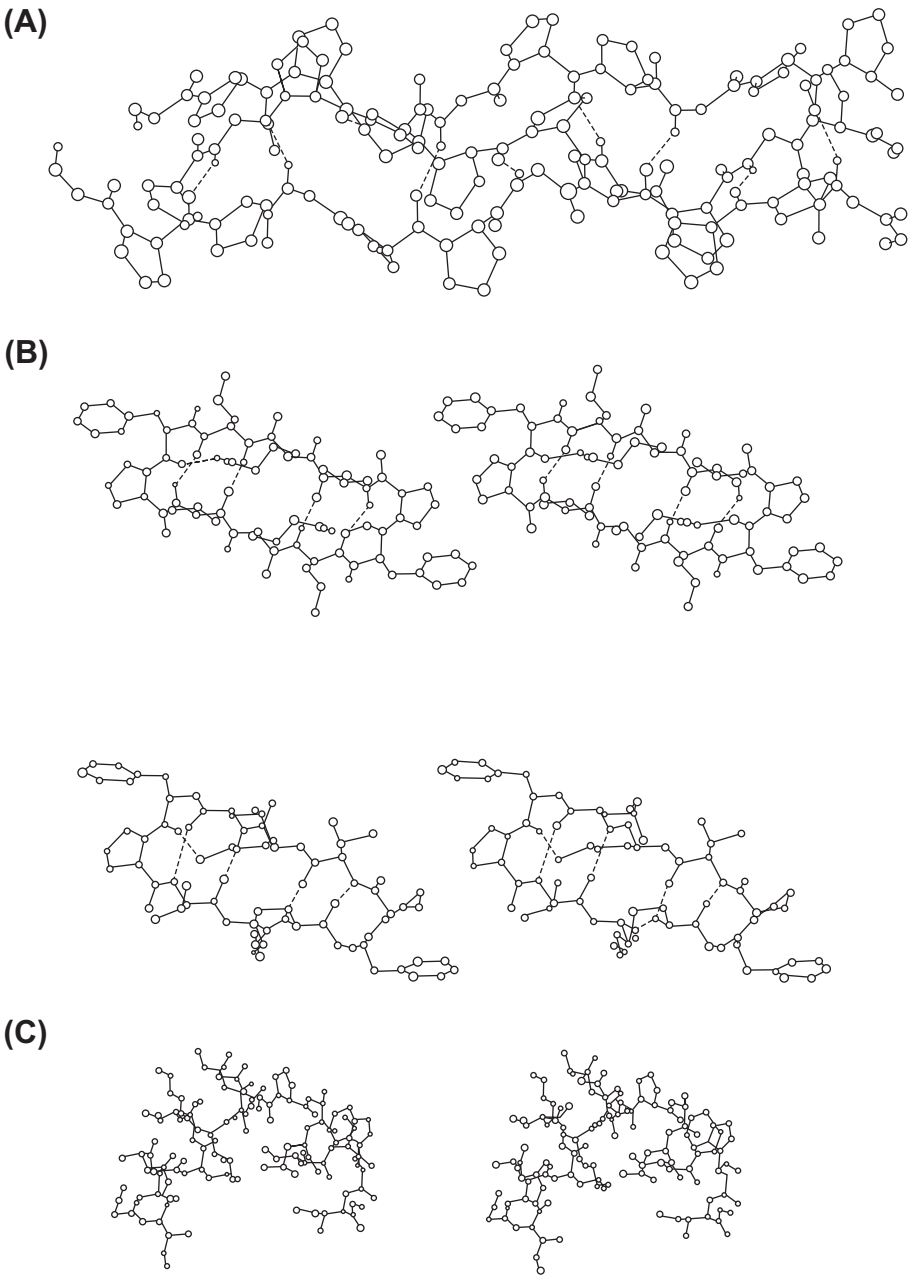

FIGURE 2.9 Views of computed structures. (A) The structure of a section of collagen model polypeptide, $(Gly\text{-}Pro\text{-}Pro)_{20}$, (Miller and Scheraga, 1976), which was directly confirmed by single-crystal x-ray crystallographic studies subsequent to the computations of the structure of this molecule. (B) The computed structure for the cyclic decapeptide gramicidin A (upper part) and the x-ray structure of the same polypeptide (lower part) show the close agreement between the predicted structure and the x-ray crystal structure (Dygert et al., 1975). (C) The computed structure for the membrane-active protein melittin, which consists of two α-helical rods, separated by a bend in the middle of the chain (Pincus et al., 1982). These features have been described in the x-ray crystal structure of this protein. Each polypeptide represents a type of structure seen in many proteins, viz., the collagen helix (A) in fibrous proteins, β-sheets with reverse turns (B) and α-helices (C). (See Pincus and Scheraga, 1985, for a further description of these structures.)

More recently, methods have been developed that allow for the computation of the lowest energy structures of larger proteins. In one of these, called UNRES (Scheraga et al., 2004), a virtual protein chain represents a given sequence. This chain consists of Cα atoms attached to centroids inside ellipsoids representing side chains of the individual amino acids. Peptide centroids along each Cα-Cα bond are inserted. These centroids represent the backbone peptide (amide) groups. The conformational energies are then computed as the sum of backbone centroid−backbone centroid, side-chain−side chain, backbone centroid−side chain and torsion terms for rotations around the virtual bonds and the side-chain centroids. This simplified polypeptide chain greatly reduces the complexity of the calculation of conformational energies.

Search procedures for low energy conformations are then carried out on this virtual chain. These include molecular dynamics, genetic algorithms and a technique called the electrostatically-driven-Monte Carlo method (EDMC) technique. In this latter approach, the electric field for a given energy minimum structure is searched for the backbone dipole moment(s) that is (are) the least optimally aligned with the field. The backbone dihedral angles are changed such that the alignment is optimized. The resulting structure is then subjected to energy minimization and the process is repeated.

If the same energy minima are repeated frequently in the search, the chain is randomly perturbed via the Monte Carlo procedure and the new chain is subjected to energy minimization and then the procedure described above. Once low energy conformations are computed, they are classified into different structure types. Then for each structure, the full atom representation of the chain is generated and the search is repeated for each of these structures. The lowest energy structures from this search are then determined. This approach has been used to compute the low energy structures for proteins of 140 amino acids or more using supercomputers that can perform the computations in a little over an hour. The lowest energy structures are in good agreement with the experimentally determined ones. A good case in point is the agreement between the computed structure for the first 75 residues of bovine calbindin and the x-ray crystal structure of this protein, the root-mean square deviation being 3.9 Å (Scheraga, 2004).

III. TECHNIQUES FOR THE DETERMINATION OF THE STRUCTURES OF PROTEINS

IIIA. Regular (Secondary) Structure: Circular Dichroism

One of the most widely used techniques for determining regular structure is circular dichroism, which is based on the principle that molecules with asymmetric structures absorb light asymmetrically. Light is electromagnetic radiation which can be plane-polarized to the right or to the left. Normally light consists of both types of plane-polarized waves. When a molecule with an asymmetric structure absorbs light, it preferentially absorbs either the left- or right-polarized light wave. The amount of light absorbed, A, is equal to E×C, where E is the molar extinction coefficient and C is the concentration of the molecules. For molecules with asymmetric structures, the E values for left- and right-plane-polarized light differ. The difference EL−ER depends on the wavelength of the incident light. A plot of EL−ER (called the molar ellipticity) versus wavelength is referred to as the circular dichroism or CD spectrum. Regular structures in proteins are asymmetric both because the amino acids in these structures are themselves asymmetric and because these structures have a handedness or a twist-sense as in the case of the α-helix, which is right-handed (see van Holde, 1985, for a complete treatment of circular dichroism). Since the peptide bond has strong absorption in the far-UV wavelengths from 230 nm down to about 190 nm, CD spectra for each different type of regular structure should be unique in this range of wavelengths. The patterns in the CD spectra found for each structure type are shown in Fig. 2.10. In this figure, the term random coil is a misnomer: the term refers collectively to all structures that are not α-helices or β-sheets, but these other structures are unique, not random.

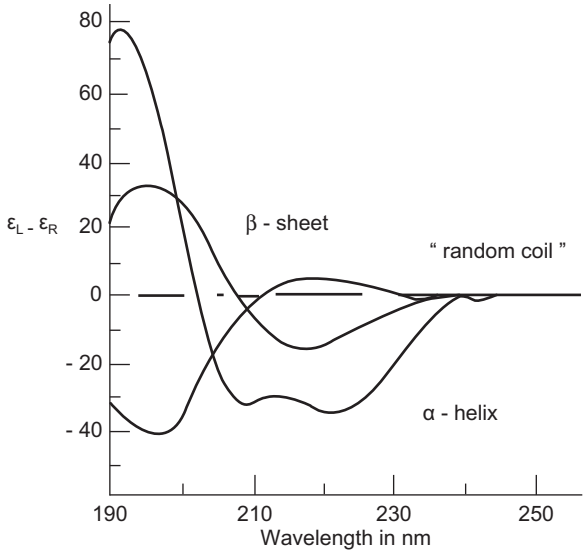

FIGURE 2.10 CD spectra for regular structures: α-helix, β-sheet, and so-called random coil. Note that α-helices have a characteristic "dip" in the region around 210 nm. For a given protein, one can compute the amount of each such structure from its CD spectrum by curve-fitting, using different amounts of each structure type and assuming that the resulting spectrum is the sum of the individual spectra for each structure type.

For proteins of unknown three-dimensional structures, a knowledge of the contents of regular structures (α-helices and β-pleated sheets) can be obtained by taking their CD spectra. Since patterns for α-helix, β-sheet and random coil structures are known, these patterns may be combined to reproduce the observed CD spectrum of a particular protein by curve-fitting. The combination of regular structure that best fits the observed CD curve is the one most likely to exist in the protein. This methodology has been tested on proteins of known three-dimensional structures (so that the percentage of regular structures can be determined) and found to reproduce the regular structure quite satisfactorily.

IIIB. Three-Dimensional Structure of Proteins: X-Ray Crystallography

This technique is based on the principle that the electron clouds around atoms diffract incident light in a predictable way. If the atoms are parts of an oriented molecule, in other words, the protein molecules are all oriented in a crystal, the same atoms of different molecules diffract the light in the same way. The closer two atoms are in the molecule, the farther apart the diffraction pattern will be. Conversely, the farther away two atoms are in the molecule, the closer the diffraction patterns from each atom will be. Thus, the diffraction pattern is the reciprocal of the atomic pattern. The diffraction pattern can be analyzed with respect to the amplitude of diffraction and the relative positions of the scattering pattern. The light diffracted must be x-rays because the wavelength of light used must be of the order of single bond lengths, around 1.5−2.0 Å. Only x-rays have this range of wavelengths.

Once a diffraction pattern has been obtained, the problem is to relate the positions of the atoms to one another from the diffraction pattern. The relative positions of two atoms can be computed from their (diffraction) amplitudes and a phase factor that is related to the angular displacement of one atom relative to the other. This phase factor cannot be determined from the diffraction pattern. Since the position of at least one atom is required, in the x-ray diffraction of proteins, a heavy atom bound to the protein is used in the so-called heavy atom replacement method. Once the phase factor is determined, the individual atomic positions can be computed from the diffraction pattern as a Fourier transform that converts from reciprocal (diffraction) space to real (three-dimensional) space.

IIIC. Two-Dimensional High-Resolution NMR

In one of the most exciting developments in protein chemistry, this technique is being applied to solving the structure of proteins in solution without requiring them to be oriented in a crystal. NMR is based on the principle that most nuclei of atoms have spins. If a magnetic field is applied to the atom, the nuclei tend to align their spins with the field. The energy difference between the spins in the absence and the presence of the field is proportional to the magnetic field strength and is given as:

$$\Delta E = h\nu = g\beta H \tag{2.2}$$

where ΔE is the energy difference, h is the Planck constant, ν is the resonance frequency corresponding to the energy absorbed by the spinning nuclei, gβ is a constant and H is the magnetic field strength. Nuclei like hydrogen exist in a protein in different environments so that some are more shielded by electrons than others, thereby requiring higher ν values or field strengths to excite them. The frequencies corresponding to the transitions of the spins of individual nuclei to align themselves with the field is in the radio-frequency range. Because different H atoms absorb at different field strengths or values, one can obtain an absorption spectrum for a given compound or protein, where, for a given field strength, H, different radio frequencies excite the nuclei to change their spins to orient with the field. When two H atoms from different parts of a protein approach one another, their spins either add to or subtract from one another and affect the intensity of each other's absorption in a phenomenon known as the nuclear Overhauser effect or NOE. This change in intensity is inversely proportional to the sixth power of the distance between the two H atoms. If the individual resonant frequencies for the two interacting H atoms are known, the distance between them can be calculated.

The specific H atoms that give rise to different NOE values in a protein can be identified by an elegant technique called two-dimensional NMR (2D-NMR) (Wuthrich, 1986). By irradiating the nuclei at two different frequencies, it is possible to construct a correlation map between the different interacting atoms. A large number of inter-H distances allows us to fit well-defined structures that have these distances so that a class of structures can be directly determined for the given polypeptide or protein.

Once a protein has adopted its final folded form, it possesses a unique size and shape that confer on it certain bulk properties, among the most important of which are electrical properties, which we now discuss.

IV. BULK PROPERTIES OF PROTEINS: PROTEINS AS POLYELECTROLYTES

Folded proteins will, in general, have different shapes and sizes depending on their specific sequences of amino acids. Virtually all folded proteins have their non-polar groups buried in the interior of the protein as a result of hydrophobic interactions and their polar and charged groups on the surface of the protein interacting with the

solvent. This distribution of charged groups on the surfaces of proteins strongly affects the manner in which these proteins will be oriented and migrate in electric fields that are either applied in electrophoresis experiments or that result from the transmembrane potential in cells. Proteins with net charges also contribute to the fixed charge inside cells. How proteins migrate in electric fields gives much information about their sizes, shapes and molecular masses. We must therefore consider the properties of proteins as polyelectrolytes dissolved in solution.

IVA. Acid–Base Properties of Amino Acids

All amino acids have free α-amino (NH_2) groups and carboxyl (COOH) groups. Amino groups are *basic*, i.e. *take up* hydrogen ions (H^+), while carboxyl groups are *acidic*, i.e. *give up* hydrogen ions. Using glycine as an example, at neutral pH (7.0), the only form to exist is the dipolar, or zwitterionic, form, $^+H_3N{-}CH_2{-}COO^-$. Figure 2.11 shows a prototypical titration curve for a dibasic acid such as glycine over the pH range of 1–10. In this figure, note that there are two regions of the titration curve where the change in pH is minimal for added base: at pH of around 2.0 and 9.0, the pK_a values for the COOH and NH_2 groups, respectively. At pH 2.0, the buffering capacity of the COOH group is maximal, while at pH 9.0, the buffering of the NH_2 is maximal. The buffering capacity is governed by the Henderson–Hasselbalch equation:

$$\mathrm{pH} = \mathrm{p}K_a + \log \frac{[\text{conjugate base form}]}{[\text{acid form}]} \tag{2.3}$$

where the pK_a is the negative logarithm of the proton dissociation constant for the acid. For the acid segment of the titration curve in Fig. 2.11, these two forms are $H_3N^+{-}CH_2{-}COO^-$ and $H_3N^+{-}CH_2{-}COOH$, respectively; for the high-pH portion of the curve, these forms are $H_2N{-}CH_2{-}COO^-$ and $H_3N^+{-}CH_2{-}COO^-$, respectively. Note also that the following equilibria exist over this range:

$$\begin{aligned} &H_3N^+ - CH_2 - COOH \rightleftharpoons H_3N^+ - CH_2 - COO^- + H^+ \\ &H_3N^+ - CH_2 - COO^- \rightleftharpoons H_2N - CH_2 - COO^- + H^+ \end{aligned} \tag{2.4}$$

We can write two separate sets of equilibrium conditions for the two reactions in Equation 2.4 as follows:

$$K_1 = \frac{[H_3N^+ - CH_2 - COO^-]\ [H^+]}{[H_3N^+ - CH_2 - COOH]}$$

$$K_2 = \frac{[H_2N - CH_2 - COO^-]\ [H^+]}{[H_3N^+ - CH_2 - COO^-]} \tag{2.5}$$

Solving both of these equations for the common zwitterionic species, $H_3N^+{-}CH_2{-}COO^-$, we obtain the expression:

$$K_1K_2 = \frac{[H_3N^+ - CH_2 - COOH]}{[H_2N - CH_2 - COO^-]} \times [H^+]^2 \tag{2.6}$$

Taking the negative logarithms of both sides of Equation. 2.6, we obtain the expression:

$$\mathrm{pH} = \frac{\mathrm{p}K_1 + \mathrm{p}K_2}{2} + \frac{1}{2} \log \frac{[H_2N - CH_2 - COO^-]}{[H_3N^+ - CH_2 - COOH]} \tag{2.7}$$

where pK_1 and pK_2 are the negative logarithms of K_1 and K_2. This equation is the same as the Henderson–Hasselbalch equation for any acid–base equilibrium except, in this case, it is written for two equilibria. The *isoelectric point*, pI, is defined as the pH at which the total negative charge of the molecule is equal to its total positive charge (i.e. where only the zwitterionic species exists). In terms of Equation 2.7, this condition is met if the numerator and denominator are equal. In this case:

$$\mathrm{pH} = \frac{\mathrm{p}K_1 + \mathrm{p}K_2}{2} \tag{2.8}$$

For amino acids with charged side chains, the isoelectric point is easily shown to be that pH equal to $(pK_1 + pK_2 + pK_3)/3$. In general, for multiple prototropic dissociations for a whole protein, the isoelectric point of the protein is simply that point on the titration curve for the whole protein where:

$$\mathrm{pH} = \sum \mathrm{p}K_i/N \tag{2.9}$$

where the sum is taken over all proton-dissociating groups, and N is the number of these groups in the protein.

IVB. Protein Charge and Solubility

Since all proteins are charged because of charged side chains and the α-NH_3^+ group and the $-COO^-$ carboxyl terminal group, there is generally a *net* charge on the protein. These net charges tend to be solvated and interact with counterions in solution. The solvation of these charges makes the protein soluble in H_2O. However, interactions of the charged side chains of the protein with surrounding ions and aqueous solvent become minimal at the isoelectric point, where the charges on the protein exactly balance one another. At its isoelectric point, the solubility of the protein in water is minimal and it will tend to precipitate from solution. Different proteins have different sequences and different charges and isoelectric points so that their tendencies to precipitate will differ from one another and

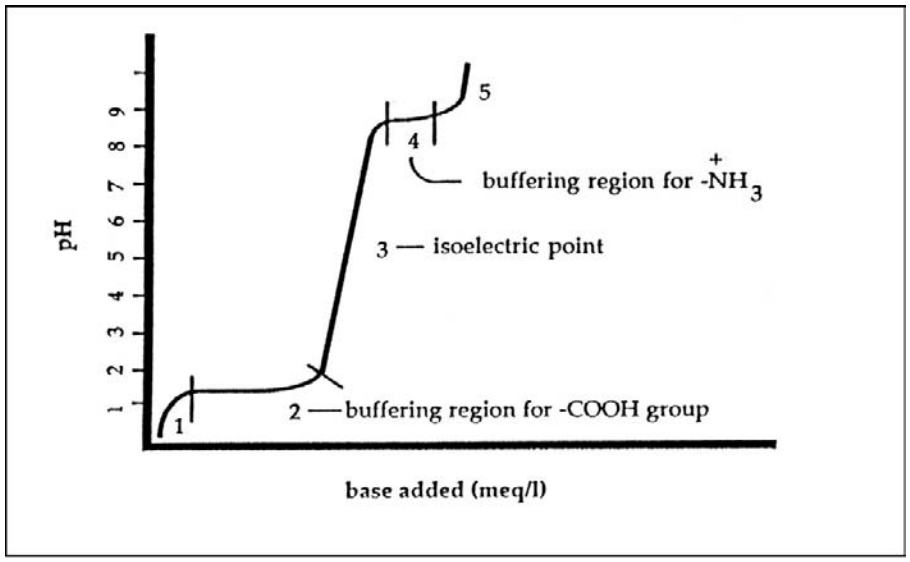

FIGURE 2.11 Titration curve for a dibasic acid like glycine to show the two buffering regions for the $COOH^-$ and NH_3^+ groups and the isoelectric point that can be computed as $(pK_{a1} + pK_{a2})/2$. A protein has multiple buffering regions, characteristic of each residue type that is involved in a prototropic dissociation.

1) $H_3\overset{+}{N}\text{-}CH_2\text{-}COOH$

2) $H_3\overset{+}{N}\text{-}CH_2\text{-}COOH \longleftrightarrow H_3\overset{+}{N}\text{-}CH_2\text{-}COO^-$

3) $H_3\overset{+}{N}\text{-}CH_2\text{-}COO^-$

4) $H_3\overset{+}{N}\text{-}CH_2\text{-}COO^- \longleftrightarrow H_2N\text{-}CH_2\text{-}COO^-$

5) $H_2N\text{-}CH_2\text{-}COO^-$

depend on the pH of the solution. Thus, by changing the pH of protein solutions, it is possible to effect differential precipitation of these proteins. A more sophisticated version of isolation of proteins based on their isoelectric points is *isoelectric focusing*, an electrophoretic method discussed in Section IVD.

IVB1. Isoionic Point

This term is used when proteins are dissolved in aqueous solutions where the only counterions are H^+ and OH^-; in other words, the counterion for the anionic groups is H^+, and the counterion for the cationic groups is OH^-. Since the total number of positive charges for the system must equal the total number of negative charges for the system:

$$(H^+) + (\text{total positive charges on protein}) = (OH^-) + (\text{total negative charges on protein}) \quad (2.10)$$

From Equation 2.10, if the isoionic point of a protein is at pH 7 (i.e. $H^+ = OH^-$), *the isoelectric point is the same as the isoionic point* since from Equation 2.10, if $H^+ = OH^-$, then total positive charges on the protein equal total negative charges on the protein.

IVC. Titration of Proteins

Because of their large number of exposed acidic and basic groups, proteins behave as buffers. Generally, the pH of the buffering region will depend on the relative numbers of acidic and basic groups on the protein surface. Binding of protons to proteins may be considered to be formally the same as the binding of ligands (small molecules) to proteins. To understand the behavior of proteins as buffers, it is important to understand ligand-binding theory.

IVC1. Ligand-Binding Theory

Suppose a protein has n equivalent sites for binding to a ligand and each site is completely independent of any other site. The equilibrium for the binding of a ligand, A, to any one site of the protein can be written as:

$$A + P \rightleftharpoons AP \quad (2.11)$$

where A is the free ligand, P is the unbound protein and AP is the ligand bound to protein. The equilibrium association constant, K, for this process is:

$$K = \frac{[AP]}{[A][P]} \quad (2.12)$$

where [A] is the free ligand concentration, [P] is the concentration of unbound protein and [AP] is the concentration of ligand bound to protein. If there are n equivalent binding sites per protein molecule, then the total concentration of sites is $n[P]_o$, where $[P]_o$ is the concentration of total protein and is equal to the sum of the concentrations of free and bound protein:

$$[P]_o = [P] + [AP] \tag{2.13}$$

Combining Equations 2.12 and 2.13, we find that:

$$[P]_o = [P] + K[A][P] \tag{2.14}$$

Solving for [P], we obtain:

$$[P] = \frac{[P]_o}{1 + K[A]} \tag{2.15}$$

Since from Equation 2.12, $[AP] = K[A][P]$, the ratio of bound protein to total protein is:

$$\frac{[AP]}{[P]_o} = \frac{K[A]}{1 + K[A]} \tag{2.16}$$

If there are n equivalent binding sites per protein molecule, the fraction of sites bound from Equation 2.15 is:

$$\frac{[AP]}{n[P]_o} = \frac{K[A]}{1 + K[A]} \tag{2.17}$$

This equation can be linearized. Defining $R = [AP]/[P]_o$:

$$R/[A] = nK - KR \tag{2.18}$$

Plots of $R/[A]$ versus R (called *Scatchard plots*) should give a straight line whose slope is K and whose intercept is nK. Thus both K and n are readily determined.

For n equivalent proton binding sites on a protein, we can write Equation 2.16 as:

$$R = \frac{K[H^+]}{1 + K[H^+]} \tag{2.19}$$

In this case, $R = [PH^+]/n\ [P]_o$. If we use the dissociation constant $K' = 1/K$, Equation 2.19 may be recast as:

$$[PH^+]\ K' = (n\ [P]_o - [PH^+])\ [H^+] \tag{2.20}$$

Rearranging and taking logs of both sides of Equation 2.20, we obtain the equation:

$$pH = pK_a + \log \frac{n[P]_o - [PH^+]}{[PH^+]} \tag{2.21}$$

where pK_a is $-\log\ (K')$. Note that Equation 2.21 is the Henderson–Hasselbalch equation for multiple dissociations. The denominator in the logarithmic term in Equation 2.21 represents the concentration of H^+-bound protein while the numerator represents non-proton-bound protein. This equation is useful for titration of proteins provided that the pK_a of each group is independent of that of any other group for a given set of groups, such as the carboxyl groups of Glu and Asp.

For proteins, it is not generally correct to assume that the above condition holds because, as each carboxyl group dissociates from a protein, the protein becomes progressively negatively charged, so that it becomes progressively difficult for the next proton to dissociate. In fact, the protein behaves as a polyelectrolyte wherein proton dissociations are strongly dependent on the electric field of the protein.

IVC2. The Electrostatic Field Effect (Bull, 1943)

To account for the electrostatic field effect of the charged protein on the dissociation process, we note that the free energy of dissociation per mole of acid group, ΔG, can be written as:

$$\Delta G = \Delta G_i + \Delta G_e \tag{2.22}$$

where ΔG_i is the intrinsic dissociation free energy for the group and ΔG_e is the electrostatic free energy for dissociating a proton from the acid group in the presence of the field of the protein. From electrostatic theory:

$$\Delta G_e = eU \tag{2.23}$$

where $e = 1$ electrostatic charge unit and U is the electrical potential from the protein. Since the standard free change for dissociation, ΔG, equals $-2.303 \times RT \log K$ and ΔG_i equals $-2.303 \times RT \log K_i$ (where R is the gas constant and T is the temperature in K), from Equation 2.22, we obtain the relation:

$$pK = pK_i + eU/2.303RT \tag{2.24}$$

From Equation 2.21, we have:

$$pH - \log \frac{n[P]_o - [PH^+]}{[PH^+]} = pK_i + eU/2.303RT \tag{2.25}$$

It is of obvious importance to obtain an explicit expression for U since it strongly influences the dissociation of protons from proteins.

IVC3. Computation of the Electrical Potential

To compute the electrical potential U, it is necessary to use a model for the interaction of protein charges with those of small ions. The simplest model is to assume that the protein is a charged sphere and that the counterions surrounding it, like protons, form a spherical shell around

the central charged protein sphere as represented in Fig. 2.12. The overall arrangement is that of two concentric spheres of radii R_1 and R_2, the first term being the distance from the center of the protein to its surface, and the second term being the distance from the center of the protein to the center of mass of the ions surrounding the protein. It is clear from this figure that the interactions of protons, and/or any ions, with the central, charged protein molecule depend on the distance of the centers of these ions from the center of the protein ion. The distribution of ions around the central charged protein ion is given by the Boltzmann distribution:

$$\psi = \sum en_iZ_i \exp - (en_iZ_iU/RT) \tag{2.26}$$

where Z_i is the valence of the ith ion. We can expand the exponential term in a Taylor series as follows:

$$\begin{aligned}\psi = {} & \sum n_iZ_ie - \sum n_iZ_ie(eZ_iU/RT) \\ & +(\sum n_iZ_ie/2)(Z_ieU/RT)^2 + \cdots\end{aligned} \tag{2.27}$$

We make the assumption that the eZU term is much less in value than RT, and that electrical neutrality must be preserved (i.e. the first sum on the right of Equation 2.27 is 0). Then:

$$\psi \approx - \sum n_iZ_i^2e^2U/RT \tag{2.28}$$

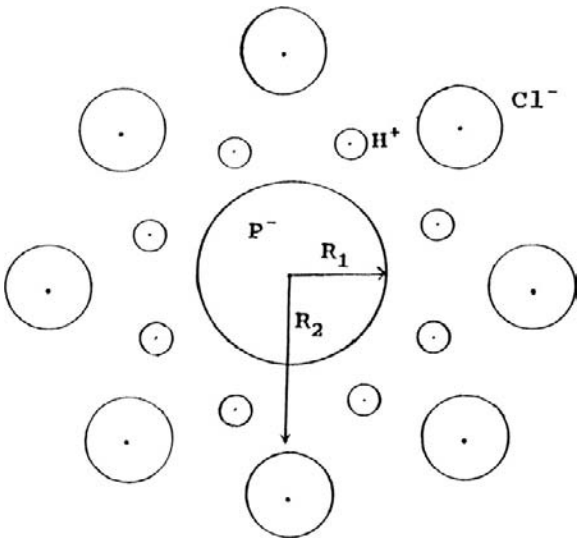

FIGURE 2.12 The model for the effect of the charge on a protein (p^-) on the dissociation of protons from groups on the protein involved in prototropic dissociations. R_1 is the radius of the protein, assuming that it has a spherical shape. R_2 is the distance from the center of the protein sphere to the mean center of the ions surrounding the protein. In this figure, H^+ ions are shown as the positive ions and Cl^- as the negative ions. Their distributions around the protein will depend upon the charge on the protein and the Boltzmann factors for each surrounding ion type. R_2 is therefore a mean distance from the center of the protein to the mean center of the surrounding ions.

This charge distribution must satisfy the Poisson charge distribution equation:

$$\nabla^2U = -4\pi\psi/D \tag{2.29}$$

where ∇^2U is the second derivative of the potential with respect to the sum of the coordinates of the system, ψ is the charge distribution and D is the dielectric constant of the medium, water. Combining Equations 2.28 and 2.29, we obtain:

$$\nabla^2U = (4\pi e^2)/(DRT) \times \sum n_iZ_i^2U \tag{2.30}$$

Solution of this equation for U as a function of the coordinates of the system constitutes the Debye-Hückel theory and it depends on the assumed configuration of small ions around the central large protein ion, assumed here to be spherical in shape as in Fig. 2.12.

Solution of Equation 2.30 for this circumstance at R_1 gives:

$$U = Ze(R_2 - R_1)/DR_1R_2$$

where $Z = \sum n_iZ_i$. Letting $1/\chi = R_2 - R_1$,

$$U = \frac{Ze}{DR_1(\chi R_1 + 1)} \tag{2.31}$$

Combining Equations 2.24 and 2.31, we obtain:

$$pK = pK_i + \frac{Ze^2}{2.303RTD} \times \frac{1}{R_1(\chi R_1 + 1)} \tag{2.32}$$

Setting:

$$W = \frac{e^2}{2.303RTD} \times \frac{1}{R_1(\chi R_1 + 1)} \tag{2.33}$$

Equation 2.25 may now be written as:

$$pH - \log\frac{n[P]_o - [PH^+]}{[PH^+]} = pK_i + 0.868\ \ WZ \tag{2.34}$$

This equation now takes into account the field effect of protein and surrounding ion charges provided that the system conforms to the assumptions made for this model: that $U<<RT$, that the protein is spherical in shape and that the ions around the protein form a spherical shell around it. Plots of the left side of Equation 2.34 versus Z, the overall protein charge, should yield a straight line whose slope is $0.868W$. This term may be regarded as a structure term that depends on the radius of the protein and the position of the center of mass of the surrounding ion cloud.

IVC4. More Explicit Models Based on Protein Structures

The above theoretical expression is based on several critical assumptions that do not always apply to proteins, namely, that the charge distribution around the protein is uniform

and spherical and that its electrical potential is such that the ZU term $<<$RT. We know from the many x-ray crystallographically determined protein structures that protein surfaces are far from spherical and that the charge distributions are not uniform. Thus, to understand the effects of protein charge and the effect of the medium on proton dissociations from the protein, more explicit and detailed models are needed. One treatment is based on conformational energy calculations on proteins surrounded explicitly by solvent molecules. These calculations have thus far been aimed at determination of the intrinsic pK_as of specific groups on protein surfaces.

In this approach (Russell and Warshel, 1985), the energy of dissociation of a particular acid group, AH, is computed for the whole protein surrounded by water molecules placed on a grid around the protein. The energy of interaction of the atoms of the protein with one another is computed using energy functions similar to those discussed in Section IID. Included in this energy is the effect of the permanent dipoles of the atoms of the protein that induce dipoles on the other atoms of the protein. The magnitude of this energy depends on the polarizability of the interacting atoms. Further account is taken of the effect of the interaction of the dipoles of the atoms of the protein with water molecules which themselves are represented as dipoles. The calculations are then applied to the dissociation of a proton from a particular group, e.g. Asp 3 and Glu 7 in bovine pancreatic trypsin inhibitor (BPTI) whose structure has been determined at high resolution by x-ray crystallography (see Section IIIB).

In this procedure, a thermodynamic cycle is employed in which the free energy difference of the system is computed for the acid group in the AH form in the protein and for the AH group dissolved in water (process 1). The group is then allowed to dissociate in water at a given pH (process 2). The free energy difference between AH and A^- in water is known (for Asp residues, this would be the free energy of the dissociation of acetic acid in water at a given pH) and is equal to $2.303RT(pK_a - pH)$. Finally, the free energy difference between solvated A^- in water and A^- in the protein (process 3) is computed. The overall free energy for dissociation is then computed as the difference between the free energy for process 1 and the free energy for process 3 plus a constant (free energy for dissociation of AH in water).

These calculations have been carried out on a supercomputer using molecular dynamics and iterative procedures (for the polarization energies) and have reproduced ionization constants satisfactorily. The method, which is computer intensive, includes the effects of both solvent and the atoms of the whole protein on the ionization process. Thus the approach appears to be a fruitful one in the investigation of prototropic dissociations in proteins.

IVD. Protein Charge and Electrophoresis

Different proteins have different net charges as discussed above. If these proteins are placed in an electric field, positively charged proteins migrate towards the negatively charged pole, the cathode, while negatively charged proteins migrate to the positively charged pole, the anode. If a protein is present at a pH equal to its isoelectric point, it will generally not move toward either pole. The electrostatic force on a protein present in an electric field is equal to ZeU, where U is the electric field, e is the charge of an electron (or a proton), and Z is the number of charges present. There is a drag force on the proteins that is proportional to the velocity at which they move towards either pole, fv, where v is the velocity of the protein moving in the electric field and f is a proportionality constant. This force balances the electrostatic force so that:

$$ZeU = fv \tag{2.35}$$

and

$$v = ZeU/f \tag{2.36}$$

The value of f generally increases with increasing size and molecular weight so that, for proteins of similar charge but different molecular weights, the higher molecular weight proteins move more slowly than the lower molecular weight proteins.

There are several types of electrophoresis, all of which are extremely effective not only in separating proteins but in directly determining their molecular weights.

IVD1. Slab Gel Electrophoresis

Proteins are separated on gels made up of such polymers as starch, polyacrylamide and agarose. The separation is based mainly on charge, and, to an extent, on size.

IVD2. Sodium Dodecylsulfate (SDS) Electrophoresis

SDS is a detergent that contains a long aliphatic chain and a sulfate group. This detergent interacts with denatured proteins to form a strongly negatively charged complex (the negative charge arising from the SO_4^{2-} groups of SDS). The proteins are first denatured by heat and then the SDS is added in large excess. The SDS–protein complexes all contain about the same negative charge because the SDS swamps out all of the protein charges. Since the charges are all the same, the proteins all separate from one another strictly on the basis of their sizes. From Equation 2.36, the larger polypeptide chains of higher molecular weight migrate the most slowly while the lower molecular weight proteins migrate more rapidly towards the anode. Proteins of known molecular weight can be subjected to this procedure and used as "markers". A plot of the molecular weights versus the log of the distance traveled from the

point of application yields a straight line. The log of the distance of migration of a protein of unknown molecular weight can then be plotted on this line and the molecular weight directly determined.

IVD3. Isoelectric Focusing

In this elegant technique, a polymer is used in which acidic and basic groups change in density from one end of the polymer to the other. When this polymer is placed in solution, a continuous pH gradient is established along the polymer. A mixture of proteins is then applied to the polymer in a weak buffer. When the proteins migrate in the electric field, they experience local differences in pH on the polymer and eventually reach a local pH equal to their individual pIs. At the pI, the protein no longer migrates in the electric field. This method of separation depends only on the presence of proteins with different pI values.

IVD4. Two-Dimensional Gel Electrophoresis

Proteins can be separated from one another in one lane as described in the preceding three sections; however, these approaches may not meet the conditions for separating all of the proteins. For example, on agarose gel electrophoresis, two proteins may not separate well at the pH of the buffer used. A buffer of different pH may then be added and the electrophoresis carried out at right angles to the original direction of migration to allow further separation of the proteins.

IVD5. Western Blots (Immunoblots)

All proteins are antigens and can provoke the production of antibodies against them when injected into animals. The antibodies are immunoglobulins which are proteins that bind very specifically to and with high affinity for specific antigens. Antibodies and, in fact, all proteins can be conjugated covalently to fluorescent dyes or to enzymes. If we wish to identify a particular protein on an electrophoretogram, we can use a "tagged" antibody to the protein and reveal its presence on the electrophoretic gel. The antibody is "tagged" with a covalently labeled enzyme that catalyzes a reaction that produces a chromophoric (colored) reaction product. For example, alkaline phosphatase catalyzes the hydrolysis of *p*-nitrophenol phosphate, which is colorless, to *p*-nitrophenol (more accurately, *p*-nitrophenoxide anion), which is bright yellow. Since antibody cannot be added directly to the gel from electrophoresis, the gel itself is blotted onto nitrocellulose or another suitable membrane that contains all of the separated bands of proteins as they were on the original electrophoretic gel. This nitrocellulose strip is then incubated in a solution containing the antibody. The antibody itself may be conjugated to an enzyme like alkaline phosphatase, and the band can be identified, or antibodies to the primary antibodies, such as goat anti-rabbit IgG, are conjugated to the enzyme and the blot is incubated with these secondary antibodies after being treated with the primary antibody. The secondary antibodies are then markers for the desired protein band.

V. RELATIONSHIP OF PROTEIN STRUCTURE TO FUNCTION

In this section, we discuss some of the relationships of the conformations of proteins to their functions. This is a vast field and so we concentrate on one aspect of fundamental importance to cell physiology, membrane polypeptides and proteins.

VA. Membrane Polypeptides and Proteins

Membrane proteins have exceptional physiological importance in a number of different ways. Virtually all extracellular receptors have a transmembrane domain that is essential to the functioning of the receptor protein. Other membrane polypeptides are vital in the transport of secreted proteins across cell membranes. Still other membrane proteins, such as the components of the complement system, are involved in intercalating into the cell membrane, causing cell lysis. Yet other membrane proteins form ion channels which allow for selective entry or exit of specific ions to and from the cell. In this section, we discuss the relationship of the structures of some of these membrane proteins to their functions. It should be emphasized that this entire field of structure—function relationships of membrane proteins is quite new. Most of our knowledge in this field comes from experimental cell biological data on specific proteins and from the results of computations on membrane and membrane-associated protein structure.

VA1. Structure and Function of Leader Peptides

Each protein, after it is synthesized on the ribosome, must be transported across the rough endoplasmic reticulum (RER) membranes. If the protein is to be secreted from the cell, or to intercalate into the cell membrane, it must undergo transport across and/or into the cell membrane. For virtually every protein that is synthesized in the cell, there is a polypeptide segment beginning at the N-terminal methionine residue that consists of about 20—30 amino acid residues. Typically, these sequences consist of several hydrophilic amino acids followed by a long stretch of hydrophobic amino acids. When the protein is secreted across the RER membrane, this *leader sequence* is cleaved off, presumably by intracellular proteases. Absence of these leader sequences results in the inability of the protein to traverse the RER membrane, resulting in ultimate intracellular degradation of the protein. Thus, these leader sequences are of vital importance to cellular protein function in general.

The regulation of transmembrane transport of newly-synthesized proteins is delicate. It has been shown in in vitro systems that newly synthesized proteins that are secreted across reticulocyte membranes do not undergo leader sequence cleavage. These proteins are non-functional because they do not fold correctly. Thus, leader sequences must be attached to the polypeptide chain to enable protein secretion, but must be cleaved off to allow correct protein folding.

To explain how proteins are secreted across membranes, Engelman and Steitz (1981) proposed the so-called *helical hairpin hypothesis* in which the leader sequence adopts an α-helical conformation. At the end of this segment there is a hairpin turn followed by another α-helix involving 30—40 residues of the protein itself. Both the amino terminal end of the leader sequence and the carboxyl terminal end of the growing polypeptide chain lie on the same side of the membrane while the hairpin turn lies on the opposite side of the membrane. Because the leader sequence helix and the succeeding helical sequence are both independently stable, they interact minimally with one another so that the growing polypeptide chain can slide past the hydrophobic leader sequence in the membrane. As the nascent polypeptide chain pushes through the membrane, anchored by the leader sequence, it begins to fold in the aqueous environment of the cytoplasm on the opposite side of the RER membrane. The leader sequence, however, remains in the membrane because of its hydrophobic character. The hairpin connection between the two helices is a signal for intracellular proteases that ultimately results in cleavage of the leader sequence.

Pincus and Klausner (1982), using ECEPP, have computed the low energy structures for the leader sequence of the κ-light chain immunoglobulin. This sequence, which contains 16 amino acids, is Asp-Thr-Glu-Thr-Leu-Leu-Leu-Trp-Val-Leu-Leu-Leu-Trp-Val-Pro-Gly. These investigators found that the first four polar residues tend to adopt an extended conformation followed by a long α-helix that ends in a hairpin turn at the carboxyl terminal Val-Pro-Gly sequence. This structure was lower in energy than any other competing structure by at least 10 kcal/mol. Thus, these calculations support the essential features of the Engelman—Steitz hypothesis and have been further corroborated experimentally. For example, the CD spectrum of synthetically prepared leader sequences shows high α-helical content when the sequence is dissolved in hexafluoroisopropanol, a non-polar solvent that simulates the low dielectric medium of the membrane (Rosenblatt et al., 1980).

In site-specific mutagenesis experiments, Thomas Silhavy and his coworkers, then at the National Cancer Institute, have placed proline residues in the middle of the hydrophobic transmembrane domain of a bacterial leader sequence (Emr and Silhavy, 1982). Proline residues tend to disrupt α-helices. These investigators found that if they introduced two proline residues close together in the sequence, the protein to which the leader sequence was attached was no longer secreted. This result strongly corroborates the conclusion that leader sequences must adopt α-helices in the membrane.

In a series of elegant experiments, Blobel and his coworkers (1979) have shown that specific sequences in proteins will insert into membranes but will not lead to cleavage of the inserted sequence from the rest of the protein. These specific sequences contain what are referred to as "stop signals" that do not permit cleavage. Because the transmembrane domain is hydrophobic, it remains inserted in the membrane and there is no impetus for it to move through the membrane, resulting in secretion. This mechanism is extremely important for the function of receptor proteins, as will be discussed in Section VA3.

VA2. Membrane-Active Peptides: Melittin and Magainin

These are peptides that insert into cell membranes and induce lysis of these membranes, by forming pores.

Melittin

Melittin is one of the smallest proteins known to fold spontaneously. Unlike most proteins, it folds in non-polar media and is denatured in aqueous solutions and consists of 26 amino acids, i.e. $^{+}$H-Gly-Ile-Gly-Ala-Val-Leu-Lys-Val-Leu-Thr-Thr-Gly-Leu-Pro-Ala-Leu-Ile-Ser-Trp-Ile-Lys-Arg-Lys-Arg-Gln-Gln-NH_2. As the major component by mass of bee venom, it specifically induces lysis of red blood cell membranes. Note that this peptide contains six positive charges and *no* negative charges. Also note that most of the positively charged residues occur at the carboxyl terminal end of the molecule. As discussed in Section IIB above, α-helices are stabilized by the presence of positively charged residues on their carboxyl terminal ends as is present in this sequence.

As noted in Section IIE above, the structure of melittin has been computed (see Fig. 2.9) and determined by x-ray crystallography (Terwiliger, 1982). Overall, the structure of this protein may be thought of as a bent α-helical rod with α-helices from Gly 1 to Thr 10, a reverse turn at Thr 11 to Gly 12, followed by another α-helix from Pro 14 to Gln 26. Leu 13 can adopt an energetically favorable conformation, a D state (see Fig. 2.8) that results in a compact structure for the monomeric state. In the x-ray structure of tetrameric melittin, this residue adopts an energetically less favorable α-helical conformation, causing it to adopt a more open, "straight" structure. In both structures, melittin forms an amphipathic helix in which the non-polar groups contact one another on the inside of the structure while the polar groups protrude out towards the solvent.

Inspection of the structure for the tetrameric protein reveals that packing between the monomeric units is such that the positive charges of each lie as far away from one another as possible while the hydrophobic cores pack as tightly as possible with one another. This can be accomplished if the monomeric units become slightly less compact by allowing Leu 13 to adopt the α-helical conformation. The sacrifice in conformational energy is about 3 kcal/mol (Kempf et al., 1982).

Magainin

This 23-residue peptide intercalates into the cell membranes of bacteria and some fungi and induces lysis of these membranes, but has low activity in lysing red blood cell membranes. The sequence of magainin is H-Gly-Ile-Gly-Lys-Phe-Leu-His-Ser-Ala-Lys-Lys-Phe-Gly-Lys-Ala-Phe-Val-Gly-Glu-Ile-Met-Asn-Ser-OH. As with melittin, this sequence contains a preponderance of positive charges (6 Lys, 1 His [positive at pHs below 7] and one amino terminal positive charge vs two negative charges, one Glu and carboxyl terminal carboxylate). Unlike melittin, magainin has the positively charged residues closer to the amino terminal domain of the peptide. This peptide has been found to adopt an α-helical structure.

Multiple theories about the mechanism by which melittin and magainin cause cell lysis have been proposed. Most recently, studies with artificial membranes using 1,2-dioleoyl-*sn*-glycero-3-phosphatidylcholine (DOPC) and 1,2-dioleoyl-*sn*-glycero-3-phosphatidylglycerol (DOPG) indicate that melittin interacts strongly with DOPG which is negatively charged in two ways: flat, i.e. in the plane of the membrane and perpendicular to the plane of the membrane. In the latter manner, melittin can form channels that disrupt the membrane while molecules in the former mode of binding block channel formation (Bogaart et al., 2008). Deductions about the arrangement of melittin molecules in artificial membranes using fluorescence quenching of the Trp 19 and use of Raman spectroscopy suggest that melittin forms terameric pores through the membrane (Vogel and Jahnig, 1986). These pores would allow extrusion of the intracellular contents resulting in cell death.

The structure of magainin in artificial membranes has been determined using neutron diffraction of magainin in membranes containing 1,2-dimyristoyl-sn-glycero-3-phosphatidylcholine (DMPC) and 1,2-dimyristoyl-sn-glycero-3-phosphatidylglycerol (DMPG). It appears to form hexagonal pores that are stacked across the membrane that can explain membrane lysis (Yang et al., 2000). The pores appear to have variable sizes over time that are also dependent on the concentration of magainin (Tamba et al., 2010). Thus far it is not clear what causes the selectivity of each peptide for specific cell membranes, i.e. melittin for red blood cell membranes and magainin for bacterial and fungal membranes.

Other theories include the possibility that melittin and magainin have detergent actions because they are both amphipathic, containing both polar positively charged groups and hydrophobic groups, which allows them to interact favorably with water and the hydrophobic membrane lipid bilayer, respectively, resulting in solubilization of the membrane causing its breakdown. This theory does not account for the fact that virtually all biological membranes contain lysolecithins and like fatty acid derivatives that contain non-polar and positively charged headgroups that actually stabilize membrane structure.

A third theory (Kempf et al., 1982), based on evidence that formation of melittin channels depends on the transmembrane potential, proposes that melittin undergoes a conformational change in the presence of a transmembrane electric field such that it adopts a less compact structure and becomes a more rigid rod-like structure that spans the whole membrane and disrupts the lipids in the lipid bilayer. In this theory, monomeric melittin would form pores or channels. Evidence for this theory comes from experimental work in which melittin was added to artificial bilayers. Proteolytic enzymes (pronase) were added to the aqueous phase under the bilayer. If the transmembrane potential was 0 or such that the outside was negative relative to the inside of the bilayer, no proteolysis of melittin occurred. However, if the inside of the membrane was made negative with respect to the outside such that the transmembrane potential was -60 mV or less, proteolysis of melittin occurred. A potential of -60 mV, found in most resting cells, corresponds to an energy of 2$-$3 kcal/mol, sufficient to convert compact monomeric melittin to a straightened structure that then spans the membrane and encounters the proteolytic enzymes. This example illustrates the great biological relevance of the relationship of charges on the protein surface to their interactions with electric fields, as in electrophoresis, and to the effects of an electric field on the conformations of proteins. This relationship is vital in understanding the functioning of ion channel proteins as described in Section VA4.

New Membrane-Active Anti-Cancer Peptides Kill Cancer Cells (Yazdi et al., 2010)

Recently, peptides derived from the p53 protein have been developed that kill cancer cells but not normal cells. p53 is an anti-oncogenic protein that slows down or blocks cell division and induces apoptosis of cancer cells. Its lifetime is shortened when it binds to another important protein in the cell, the double-minute-binding protein of human (H) or mouse (M) origin, and called H(M)DM-2 (called HDM-2 in this section). HDM-2 induces the addition of a 76 amino acid protein, called ubiquitin, onto p53, targeting p53 for proteolysis. p53 binds to HDM-2 using its amino terminal amino acid residues 12$-$26 in the human sequence.

Originally, this p53 peptide was to be introduced into cancer cells to block the binding of p53 to ubiquitin, resulting in increasing the half-life of p53. In order to get the p53 12−26 peptide into cancer cells, it had to be attached to a transmembrane carrier. There is a group of peptides, called penetratins, that are highly positively charged and include the TAT sequence of HIV, that cause the transport of proteins across cell membranes, much in the same manner as leader sequences, discussed in Section VA1 above. Since the structure of the HDM-2-binding domain of p53 is largely α-helical when bound to HDM-2 (Kussie et al., 1996), the positively charged transmembrane-penetrating sequence (or membrane residency peptide or MRP) was added to the carboxyl terminal end of the p53 12−26 peptide using the principal that α-helices are stabilized by positive charges on their carboxyl terminal ends. When the p53 12−26-MRP, called PNC-27, was incubated with cancer cells, it killed them within 1 hour. Surprisingly, it killed p53-defective cells just as rapidly. On the other hand, it had no effect on the growth or viability of normal cells. Electron micrographs of cancer cells killed by PNC-27 and a shorter analog consisting of p53 residues 17−26-MRP, called PNC-28, showed that transmembrane pores formed. The two-dimensional NMR structure of PNC-27 showed that it had the classical α-helix-loop-α-helix structure as shown in Fig. 2.13 (Rosale et al., 2004). This structure was highly amphipathic. Thus PNC-27 and PNC-28 kill cancer cells selectively by forming pores in their membranes as membrane-active peptides.

The question, as with melittin and magainin, was why these peptides were selective for one cell type, in this case, cancer cells. Recent work has shown that cancer cells express HDM-2 in their cell membranes while normal cells do not. The reason is thought to be that HDM-2 in the cell membrane binds to cadherin, a cell-to-cell adhesion protein. When it binds to cadherin, it targets its catabolism so that the cells do not stick together and therefore undergo contact-inhibited cell growth. Thus PNC-27 and PNC-28, which adopt a membrane-active amphipathic helix-loop-helix structure, bind to and are held by HDM-2 in the cell membrane. In this conformation, they form transmembrane pores, resulting in cell lysis. Thus it is possible that membrane-active peptides can become effective agents in the treatment of cancer.

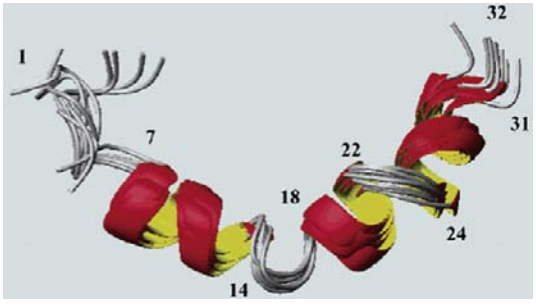

FIGURE 2.13 Ribbon structure for PNC-27, an anti-cancer, amphipathic, helix-loop-helix peptide structure that binds to membrane-bound HDM-2 that holds it in the membrane allowing it to form transmembrane pores. The two α-helical domains are shown as the spiral ribbons.

VA3. The Function of Transmembrane Proteins

Currently, there appear to be three classes of transmembrane proteins: intercellular adhesion molecules, receptor proteins and ion channel proteins. Studies on the first category of these proteins are incipient whereas the second and third categories of proteins have been better studied. Generally, receptor proteins contain three specific domains: an extracellular domain (ECD), an intramembrane domain and an intracytoplasmic domain which often contains a tyrosine kinase. This motif has been found to exist for several growth factor receptors and for the T-cell receptor. The x-ray crystal structures of several growth factor receptors (mostly their extracellular domains) have been determined (see, for example, Cho et al., 2003). Mutagenesis experiments and these x-ray structures have elucidated critical features concerning their functioning. A seemingly constant feature of growth factor receptor proteins is that, when the growth factor, which is often a polypeptide, binds to its transmembrane receptor, the receptor dimerizes. This dimerization induces the activation of the intracellular tyrosine kinase that results in activation of critical cellular processes in a so-called signal transduction pathway.

One of the critical growth factor receptors involved in mitogenic signaling is the epidermal growth factor receptor (EGFR). The x-ray crystal structure of the ECD of EGFR has been determined. In its unbound state, the ECD is folded such that it cannot dimerize spontaneously. When EGF binds to the ECD, however, the internal interactions in the native state are disrupted such that the dimerization domains are exposed and able to interact with one another (Ferguson et al., 2003). Thus binding of the growth factor EGF to EGFR ECD results in critical changes in the structure of EGFR allowing for dimerization and activation of this protein.

As another example, the sequence for the growth factor receptor called *neu* or *her-2,* which is a protein of molecular weight 185 kDa, or p185, is known (Padhy et al., 1982). This growth factor receptor is extremely important in the control of mitogenesis in epithelial cells (Padhy et al., 1982). Defects in this receptor protein can result in unregulated cell division and have been found to be highly associated with breast cancer (King et al., 1985; Slamon et al., 1987). It is known that activation of this protein requires that its growth factor bind simultaneously to two receptors (Ben-Levy et al., 1992), thus cross-linking them.

As a result of this cross-linking process, tyrosine kinases become activated, as noted above, resulting in phosphorylation of critical target proteins in a mitogenic signal transduction pathway (Bargmann and Weinberg, 1988).

It is known that substitution of single amino acids within the transmembrane domain of this protein activates the protein, presumably by facilitating dimerization in the membrane (Bargmann and Weinberg, 1988). The essential segment of the transmembrane domain contains the sequence (residues 650−683) -Glu-Gln-Arg-Ala-Ser-Pro-Val-Thr-Phe-Ile-Ile-Ala-Thr-Val-XXX-Gly-Val-Leu-Leu-Phe-Leu-Ile-Leu-Val-Val-Val-Val-Gly-Ile-Leu-Ile-Lys-Arg-Arg-. The XXX amino acid residue can be Val, His, Tyr, Lys or Gly for normal proteins and Gln or Glu for transforming proteins.

Calculations (Brandt-Rauf et al., 1989) on the structure of the transmembrane domain of the *neu* protein indicate that the entire transmembrane domain, most of which is hydrophobic, can exist in two states, as shown schematically in Fig. 2.14. The normal non-mutated transmembrane domain is a bent α-helix in which two helices are separated by a β-turn at residues 664−665. (These conformations are defined in Section II above.) In the "off" state for the normal protein, not bound to ligand, the α-helices are bent and are not favorably disposed to interact with one another. Amino acid substitutions at critical positions around where the bend occurs that obliterate the bend between the helices result in the formation of two regular α-helices that can easily associate with one another.

A complete analysis (Brandt-Rauf et al., 1990) of the Boltzmann distribution of the low-energy conformations of the p185 protein shows that 90% of the protein is in the bent helical state while 10% is in the all-helical state for all normal proteins. For the transforming proteins with Gln or Glu at position 664, this distribution reverses so that 90% of the protein is in the all-helical conformation while 10% is in the bent-helical conformation. These results predict therefore that if the normal protein is overexpressed by about a factor of 10, then sufficient all-helical forms would be present in the cell to cause cell transformation. This computed result has been confirmed in experiments where overexpression of the normal protein by factors of 1−4 causes no effect on the cell (Hudziac et al., 1987) while 10-fold overexpression of the normal protein has been found to cause cell transformation (DiFiore et al., 1987). They have been further directly confirmed in ligand-binding experiments using Scatchard plots (see Section IVC1) (Ben-Levy et al., 1992), in which it was found that, for the normal cellular protein with Val at position 664, 90% of the protein was in a low-affinity state for the cross-linking ligand and only about 10% of the protein was in a high-affinity state. However, with Glu at position 664, a transforming substitution, the reverse was found: over 90% of the receptors were in the high-affinity state, or readily cross-linked.

Thus a change in conformation from a bent to a straight helix may cause major changes in the functioning of a transmembrane protein, much like the proposed change in structure of melittin in the presence of an electric field. It is clear from the above examples that to understand cell function it is necessary to understand the conformational properties of proteins, the basis of which have been presented in this chapter.

VA4. Ion Channels (Caterall, 1995)

As discussed in the preceding section on melittin and as explained in detail in several later chapters of this textbook, cell membranes are polarized, resulting in a voltage change across them as a result of the fact that the inside of the cell is negative with respect to the outside. Furthermore, in the resting state of most cells, the extracellular sodium ion concentration is much higher than the intracellular sodium, while the reverse is true for potassium ions. During action potentials in electrically excitable cells, such as neurons and myocytes, the membrane becomes depolarized. During this period, there is a large influx of sodium ions, followed during repolarization by an almost equivalent efflux of potassium ions. These fluxes are then rapidly reversed, during which time the cell becomes refractory to further excitation.

The change in the permeability of the cell to sodium and potassium ions is caused by changes in voltage across the cell membrane. Thus the motion of these ions across the membrane is said to be *voltage dependent*. During action potentials, there is a voltage-dependent increase in the conductance of the membrane to sodium, followed by a rapid and then a slower inactivation of sodium conductance.

All of these changes in conductance and permeability-selectivity of the membrane are mediated by sodium, potassium and calcium channel proteins, all of which have been cloned, purified and expressed in different cell lines and in artificial lipid bilayers (Caterall, 1995). More recently, x-ray crystallographic structures of the potassium channel protein have been determined (see, for example, Long et al., 2005). All of these channel proteins have remarkably similar linear amino acid sequences with differences that cause each to bind selectively to different ions.

All of the channel proteins are composed of an α-subunit of molecular mass between 240−250 kDa that is heavily glycosylated. Sequencing of the gene for this protein reveals four domains that contain six repeating sequences (called S1−S6). These repeats are characterized by regular spacing in the sequence between hydrophobic amino acid residues and positively charged residues. As with leader sequences, melittin and the transmembrane domain of the *neu/her*-2 protein, the six repeat sequences are highly hydrophobic. Therefore, they are thought to be transmembrane domains and have been

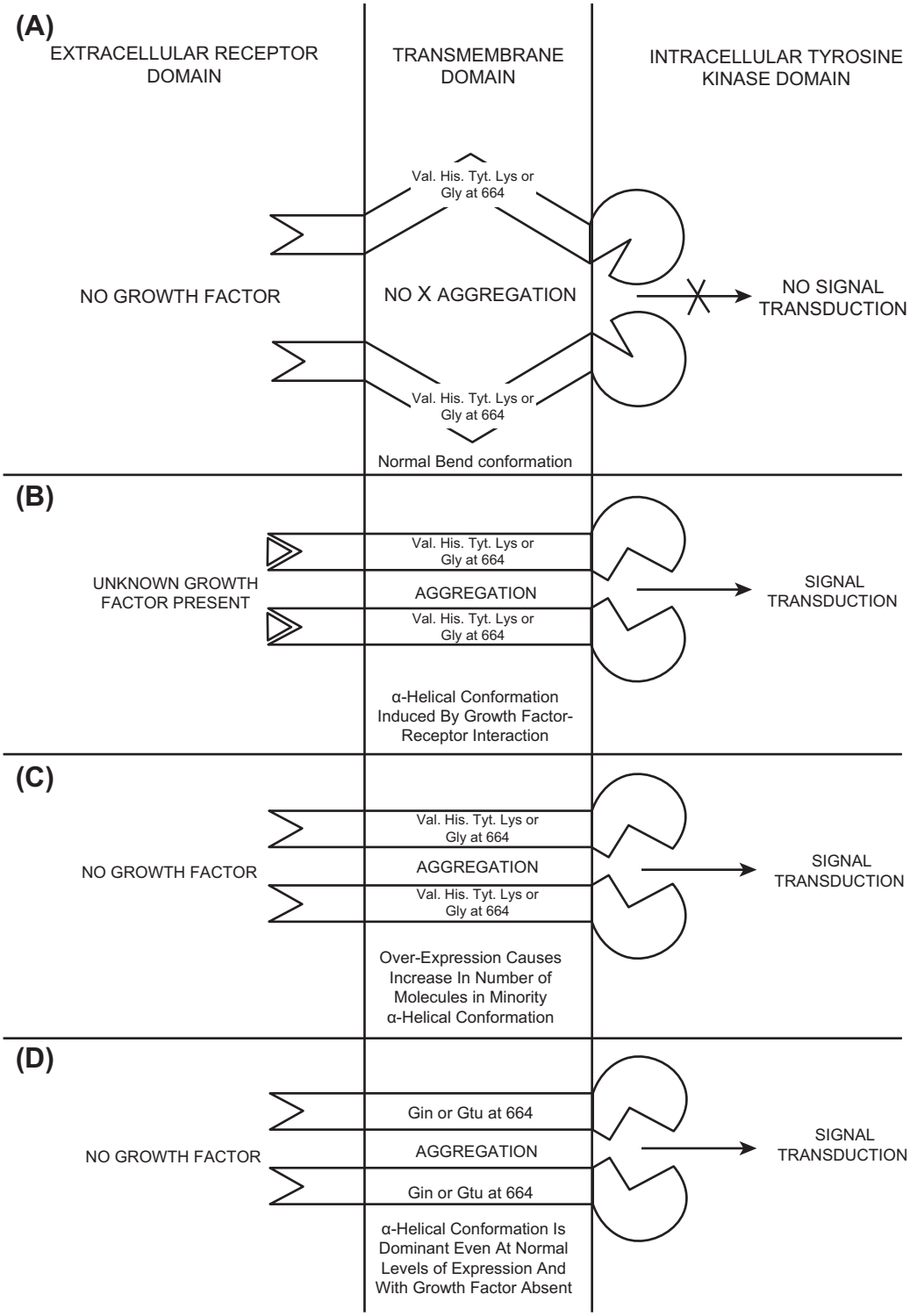

FIGURE 2.14 The effects of transmembrane domain structure of transmembrane proteins on their function. The *neu*-oncogene-encoded p185 protein is a transmembrane protein that has three distinct domains: an extracellular ligand-binding domain (left), a transmembrane domain (middle) and an intracellular signaling domain (right). To get signal transduction of a mitogenic signal to the nucleus, two p185 molecules must associate by the binding of their transmembrane domains to one another. This can be accomplished in a variety of ways as shown in this figure. (Modified from Brandt-Rauf et al., 1990.) (A) The normal protein has Val, His, Tyr, Lys, or Gly at position 664 in the amino acid sequence for the normal protein. The structure of the transmembrane domain is a bent α-helix, preventing the two domains from associating with one another. (B) When a growth factor binds to the extracellular domain of the protein, the bend is removed from the middle of the helix, allowing two straight helices to associate. This dimerization allows for activation of mitogenic signaling elements via the intracellular domain in the pathway ending in the nucleus. (C) From the calculations of the

postulated to be α-helical. The basic arrangement of the four domains is shown schematically in Fig. 2.15. In three dimensions, these four domains would be arranged in a cylindrical fashion and would surround a pore. The α subunit in the sodium channel protein is non-covalently linked to a heavily glycosylated β-1 subunit of molecular mass 36 kDa and by a disulfide link to a β-2 subunit.

Voltage Activation

The actual voltage at which activation of the sodium channel occurs has recently been shown to depend on positively-charged and hydrophobic amino acid residues in the S4 amphipathic helical segment of each transmembrane domain. As shown schematically in Fig. 2.16, seven critical positively-charged Arg and Lys residues are interspersed among many hydrophobic residues. Each of these positive charges must interact with a negative charge from an Asp or Glu residue from another subunit.

In site-specific mutagenesis experiments, each of the positively-charged residues has been replaced with neutral amino acid residues. Neutralization of positively-charged residues 1, 3, 5 and 7 results in shifting the activation transmembrane potential to more positive values so that the influx of sodium ions begins to occur at more depolarized states. Neutralization of charged residues 2 and 4 produces the opposite effect. Thus residues 1, 3, 5 and 7 are involved with activation of sodium influx while residues 2 and 4 are involved with pore closing and inactivation of sodium influx.

To explain how the S4 segment causes activation of sodium influx, it has been hypothesized that at a certain level of depolarization, the S4 helix rotates such that positive charges on the helix change negatively charged partners in an upward spiral from the inner to the outer membrane, resulting in effective transfer of a positive charge to the outside of the membrane. Since, as indicated in the above discussion, not all positive charges perform the same function, this hypothesis may be oversimplified.

Another explanation for charge transfer across the membrane is that, at a critical transmembrane voltage, the S4 helix unfolds into a fully extended conformation, allowing for the shifting of positive charges towards the outer membrane surface. One problem with this explanation is that the energy required to convert an all-helical protein into an all-extended form requires the disruption of a large number of hydrogen bonds, each about 1−2 kcal/mol in energy. Unless the fully extended form can make hydrogen bonds with other segments in a β-pleated sheet arrangement, the energy barriers for this conformational transition would be very high.

Nonetheless, it is clear that the change in the transmembrane potential causes a change in the conformation of the S4 helix, resulting in the opening or closing of the sodium channel. This effect is strongly analogous to the proposed effect of the transmembrane potential on the conformation and function of melittin discussed above. Pore formation is clearly influenced by transmembrane voltage and results from a conformational change in the transmembrane protein.

Permeability-Selectivity

Neural toxins, such as from snake venom, have long been known to bind with high affinity for and selectivity to specific ion channels. The toxin tetrodotoxin is known to bind to the sodium channel pore at its outermost surface. Localization of the tetrodotoxin (and sodium channel pore) binding site has recently been accomplished. Between the S5 and S6 helical segments are two short segments, named short segments 1 and 2 (SS1 and SS2), shown in Fig. 2.15. In SS2, neutralization of Glu 387 by site-specific mutagenesis results in a 10 000-fold decrease in the binding of tetrodotoxin to the mutated sodium channel. In similar experiments, it has further been found that additional residues are vital to perm-selectivity of the sodium ion channel. These include negatively charged residues in domains 1 and 2, a positively-charged amino acid residue in domain 3, and a neutral amino acid in domain 4.

Position 385 is also a vital amino acid residue in SS2. In brain and skeletal muscle sodium channels, this residue is Phe or Tyr; in cardiac muscle, it contains the non-conservative substitution, Cys. The cardiac muscle sodium channel has a several hundred-fold lower affinity for tetrodotoxin than does brain or skeletal muscle channel protein. If the Cys residue of cardiac muscle channel protein is changed to Tyr or Phe, the high affinity for tetrodotoxin is restored. Thus Tyr/Phe 385 appears to be vital in tetrodotoxin binding and ion selectivity.

Sodium and calcium channel structure are similar to one another. However, calcium ions bind with only about one-tenth the affinity to the sodium channel protein as that for sodium ions. However, mutation of Lys 1422 and Ala 1714 to Glu residues completely reverses the order of affinity of these two ions to the mutated sodium channel protein. These two residues are therefore implicated as being present at the mouth of the pore of the sodium channel.

distribution of conformations for the normal transmembrane domain (Brandt-Rauf et al., 1990) of p185, 90% of the molecules exist in the bent helix state, while 10% are straight helices. Overexpression of the normal protein by a factor of 10 was therefore predicted to produce sufficient straight helices to cause mitogenic cell signaling, leading to cell transformation. (D) Finally, substitution of Glu or Gln at position 664 reverses the distribution of bent and straight helices directly so that 90% of the molecules are straight helices while only 10% are bent helices. This results in significant levels of dimerization, resulting in permanent mitogenic cell signaling and oncogenic transformation of the cells.

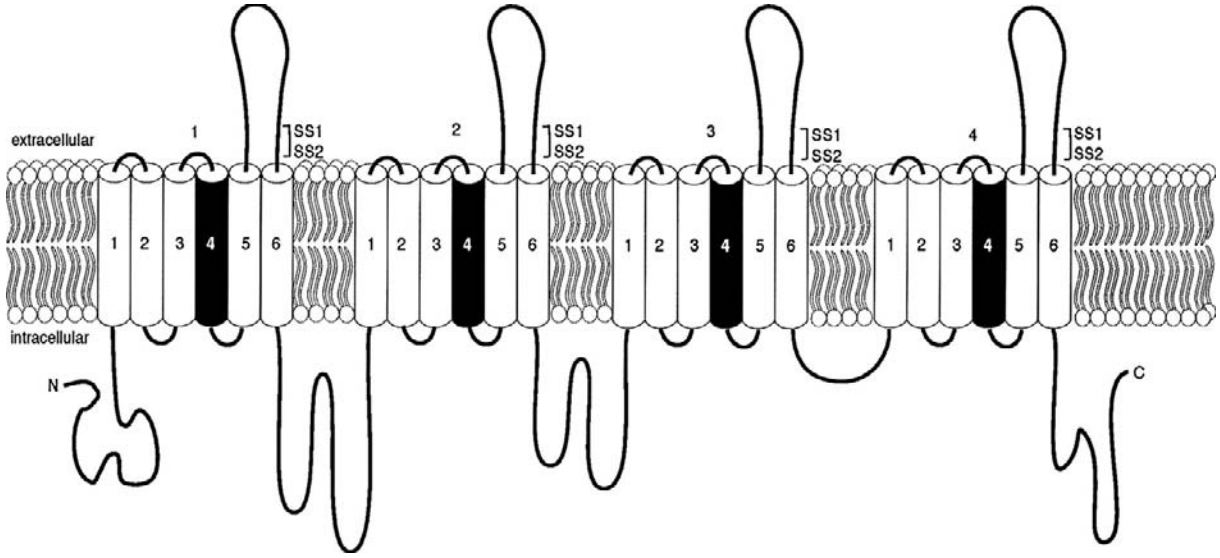

FIGURE 2.15 Model for the arrangement of the domains in the α-subunit of the sodium ion channel protein. The four domains are labeled 1−4. Each domain is shown to contain six transmembrane helical segments labeled 1−6. Subdomain 4 is highlighted in each domain because it contains the critical residues for voltage-dependent gating. The short segments 1 and 2 that are critical for ion selectivity are labeled SS1 and SS2, respectively. This region contains the critical residues Glu 387 and Phe/Tyr or Cys 385. *(This model is modified from Hall, 1992, p. 109.)*

Inactivation

Normally, after the voltage-gated increase in sodium ion permeability, there is a rapid inactivation of the sodium conductance. This inactivation process can be blocked by treatment of the intracellular domain of the sodium channel protein with proteases and by a monoclonal antibody directed against a segment of the protein connecting domains 3 and 4. Further studies involving site-specific mutagenesis have identified three critical amino acid residues as being vital to the inactivation process: residues 1488−1490, the sequence of which is Ile-Phe-Met, all hydrophobic amino acid residues. Mutation of Phe 1489 to Gln completely blocks inactivation of sodium channel conductance.

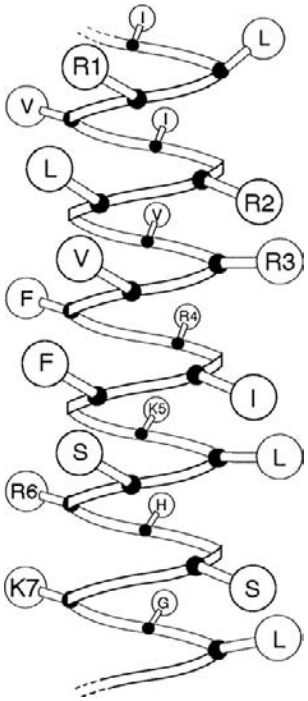

FIGURE 2.16 Helical model for the critical segment of the S4 subdomain of the sodium channel. The critical positively charged residues are labeled in numerical order. *(Modified from Caterall, 1995, Fig. 3, p. 515.)*

To explain the inactivation process, the three-residue segment has been proposed to constitute a "hinged lid" which moves to form a block in the sodium conductance channel after the conformational changes occur that increase sodium ion conductance. Phe 1489 would bind to another as yet unidentified pocket in the protein, blocking further movement of sodium ions.

Similar experiments on the potassium channel protein have identified a completely different segment of this protein involved in the inactivation of potassium conductance. This constitutes the amino terminal domain consisting of hydrophobic (especially Leu 7) and hydrophilic amino acid residues.

The model for inactivation for the potassium channel protein is the "ball and chain" model in which the amino terminal arm of the protein swings into the pore, blocking further potassium conductance. Convincing evidence for this model has been provided by experiments in which native amino terminal peptides hybridized with mutant potassium channel proteins, which do not inactivate potassium ion conductance, completely restore their abilities to inactivate

potassium ion conductance. These results compared with those for the sodium channel suggest that inactivation of sodium channels occurs on the intracellular surface whereas that for the potassium channels occurs on the extracellular surface.

Our knowledge of the functioning of ion channels is incipient but has been greatly advanced by the cloning of the sodium, potassium and calcium channel proteins and the site-specific mutagenesis work. The x-ray structures of the potassium channel are also providing more insights. These studies all suggest that the functioning of all of these proteins is based on the principles discussed earlier in this chapter. Selective binding of ions is caused by specific ionic (electrostatic) interactions; changes in conductance of the channel proteins is caused by changes in the three-dimensional structure of the proteins induced by changes in the electric field across the cell membrane as proposed for the simpler melittin protein. The basic structure of the channel protein consists of a series of amphipathic α-helices containing large numbers of hydrophobic amino acid residues. As found for the transmembrane domain of the *neu/her*-2 receptor protein, the interaction of the helices with one another is responsible for the functioning of the channel protein.

VA5. Effects of Amino Acid Substitutions on the ras-p21 Protein

One of the most striking discoveries over the past three decades has been the finding that a single base change at codon 12 in the human *ras* gene, which encodes a protein of Mr 21 kDa called the p21 protein (with 189 amino acids in its sequence), results in the malignant transformation of quiescent (NIH 3T3) cells in culture. The encoded p21 protein contains a Val in place of the normally occurring Gly at position 12 in its amino acid sequence. Transfection of the oncogene, but not its normal counterpart proto-oncogene, into NIH 3T3 cells in culture results in their malignant transformation (Barbacid, 1987).

Microinjection of cloned, purified oncogene-encoded (Val 12-containing) p21 protein, but not its normal counterpart protein, into NIH 3T3 cells also causes these cells to undergo cell transformation. Thus the transforming agent is the *ras*-gene-encoded p21 protein itself. Similarly, oncogenic but not normal p21 induces maturation (meiotic division) of frog *(Xenopus laevis)* oocytes. The biochemical changes induced by oncogenic p21 in all of these cells are very similar, suggesting that *ras*-p21 induces stereotypical events in each cell line. Incredibly, oncogenic *ras* genes have been identified overall in about one out of three common human cancers, in over 90% of human pancreatic and 70% of human colon cancers (Almoguerra et al., 1988). Oncogenic p21 protein has also been found to occur at elevated concentrations in the sera of patients with specific types of malignant neoplasms (Pincus et al., 2006).

There are other critical positions in the polypeptide chain of p21, such as at Gly 13, Ala 59 and Gln 61, where single amino acid substitutions result in a transforming protein. By far the most common site for oncogenic substitution is Gly 12. Since 18 out of 20 amino acids that occur at position 12 cause the protein to become oncogenic, it seems reasonable to conclude that these substitutions induce changes in the three-dimensional structure of the protein, resulting in its being permanently activated.

Activation of *ras*-p21 (Pincus et al., 2000)

ras-p21 is a *G protein* that becomes activated when GDP, bound to the protein in its inactive state, is exchanged for GTP. This process of activation is set in motion when a specific growth factor, such as epidermal growth factor (EGF), itself a polypeptide, binds to its receptor. As discussed under the *neu/her*-2 growth factor receptor section (Section VA3), the transmembrane receptor contains an extracellular growth factor binding domain, a transmembrane domain and an intracytoplasmic domain which, for *neu* and EGF receptors, contains a tyrosine kinase domain. This kinase becomes activated when the growth factor receptor dimerizes as a consequence of the binding of the growth factor to it.

As a result, the intracytoplasmic domain binds to an "adapter" molecule, called *grb*-2, which simultaneously binds to a protein called SOS that, in turn, binds to p21, promoting the exchange of GDP for GTP. Modulating the effect of GTP on activation of p21 is the GTPase activating protein (GAP), which binds to activated p21 and induces the hydrolysis of GTP to GDP, thereby resulting in the inactivation of *ras*-p21.

All of these events occur in or near the inner cell membrane. *ras*-p21 is attached to the inner cell membrane by a covalent link at Cys 186 (Willumsen et al., 1984) in which its sulfur atom is in thioether link to the farnesyl moiety, a lipophilic hydrocarbon that intercalates in the lipid medium of the cell membrane. Thus, like melittin, *ras*-p21 is active as a membrane-associated protein.

Thioether synthesis is catalyzed by the enzyme farnesyl transferase. In site-specific mutagenesis experiments, if Cys 186 is replaced by a Ser residue, *ras*-p21 not only is inactive, even if it contains oncogenic amino acid substitutions, but it competes with its cell-membrane associated counterpart protein so as to *inhibit* mitogenesis. The double inactive mutant of p21 with the Val-for-Gly 12 and Ser-for-Cys 186 substitutions, is therefore called a dominant negative mutant of *ras*-p21. A number of farnesyl transferase inhibitors have been synthesized that block insertion of p21 into the membrane and allow the cytosolic p21 to compete with its membrane-bound counterpart protein, resulting in the slowing down or halting of mitogenesis in *ras*-induced cancers (James et al., 1993; Downward, 2003).

Signal transduction induced by G proteins is a generalized phenomenon that explains the action of many hormones and external stimuli. For example, polypeptide hormones, such as ACTH, growth hormone, calcitonin, cholecystokinin and insulin, all activate G proteins that stimulate phosphorylation cascades. Light induces electrical signals on the retina; conversion of light to electrical signals traveling to the brain is performed by the G protein transducin in the retina. Much pharmacotherapy is currently aimed at interfering with the signal transduction events that occur after the hormone has bound to its receptor.

Function of *ras*-p21

A natural question that arises from the foregoing discussion is that, if *ras*-p21 is membrane bound, what is the mechanism by which it induces mitosis, when the latter process occurs in the nucleus? The answer to this question appears to be that activated *ras*-p21 induces a number of phosphorylation cascades in the cytosol in which successive proteins become activated until one or more of these proteins directly activates nuclear proteins that are intimately involved in DNA synthesis. These successive activation cascades are referred to as signal transduction pathways.

Activated *ras*-p21 binds directly to a protein called *raf*-p74 (Mr, 74 kDa). When activated by *ras* or other intracellular proteins, *raf* binds to and phosphorylates an extracellular *mitogen-stimulated kinase* called MEK which, in turn, binds to and phosphorylates a vital protein, MAP kinase (mitogen-activated protein kinase) or ERK. This protein is critical in catalyzing cytoskeletal rearrangements in mitosis and in activating the highly important nuclear transcriptional activating factor, *fos*. To be active, *fos* forms a heterodimeric complex with another protein, *jun*. Together, these two activated proteins bind to promoter regions of the genome and induce the transcription of mRNA for a number of mitogenesis-promoting proteins such as the cyclins. The factor *jun* is activated by another pathway in which it is activated by the critical kinase, *jun* kinase (JNK). Further, oncogenic (Val 12-containing) *ras*-p21 interacts preferentially with both JNK and *jun* proteins, providing a "short circuit" pathway for activating direct nuclear transcription.

Remarkably, the above-described cascades occur in a wide variety of different cells with differing effects depending on the cell type. Thus, for example, in frog oocytes, oncogenic *ras*-p21 induces meiosis and cell *maturation*, not malignant transformation. In cardiac muscle that has suffered injury, infarction or hypertrophy, the above cascades also become activated.

Relationship of Structure to Function of *ras*-p21

The fact that arbitrary amino acid substitutions at critical positions in the polypeptide chain cause the *ras*-p21 protein to become oncogenic suggests that critical changes in its three-dimensional structure occur in response to these substitutions. Another point of view is that these substitutions affect the ability of GAP to induce an increase in the GTPase activity of p21. There is an excellent correlation of the abilities of some oncogenic p21 proteins to induce cell transformation with their diminished levels of GAP-induced GTPase activities and with their binding affinities to GAP. On the other hand, there are striking exceptions to this correlation. For example, a Glu-for-Asp 38−substituted p21 protein binds tightly to GAP and has low GTPase activity but does *not* transform cells. Some substituted proteins efficiently hydrolyze GTP to GDP but transform cells. Also there are triply substituted forms of p21 that do not bind at all to any nucleotide but are permanently activated and strongly induce cell transformation. Thus it appears that for many substituted oncogenic p21 proteins, permanent activation is related to structural changes induced by the oncogenic amino acid substitutions themselves.

The x-ray structures of wild-type and oncogenic forms of p21 bound to GDP and GTP and of wild-type p21 bound to the *ras*-binding domain of *raf*, to SOS and to GAP proteins have all been determined. Comparison of oncogenic and normal unbound p21 structures reveals some conformational changes in an effector loop from residues Tyr 32-Asp 47, which is involved in the binding of p21 to GAP, *raf* and SOS. Because the protein occurs in a crystal lattice, wherein interactions between protein molecules limit conformational flexibility, the x-ray structures may not identify other regions that undergo conformational changes.

Use of Conformational Energy Calculations to Identify Effector Domains of p21

To identify other regions of the protein that may change conformation when the oncogenic form is compared with that of the wild-type protein, calculations of the low-energy conformations of these proteins have been carried out. These calculations are based on the principle, discussed in Section IIE1, that the observed structure of a protein is the one of lowest energy; there may be a group of lowest energy structures for a protein that have the same overall chain fold but which differ from one another in the conformation of local regions.

In these calculations, using sampling methods such as molecular dynamics (discussed in Section IIE1), the x-ray crystal structure is subjected to energy minimization and then allowed to move so that all of the low-energy structures that lie close to this structure, but which may differ from it regionally, are sampled. The average structure is the average of these low-energy structures. If oncogenic amino acid substitutions induce permanent, regional conformational changes in the three-dimensional structure

of the protein, these will be reflected in differences in the average structures for the oncogenic proteins compared with that of the normal (wild-type) protein. We might expect that synthetic segments of p21 corresponding to these regions may inhibit the functioning of the oncogenic protein.

Results of these calculations on the wild-type protein bound to GDP and GTP and of the Val 12- and Leu 61-substituted proteins bound to GTP (Monaco et al., 1995; Pincus et al., 2007) show that the overall fold of the proteins is virtually identical, but local regions differ in conformation between oncogenic and the inactive (GDP-bound) protein. There are six such regions: residues 4−20, 35−47, 55−71, 81−93, 96−110 and 115−126. Peptides corresponding to each of these regions have been synthesized and tested for their abilities to alter the ability of *ras*-p21 to induce mitogenesis.

Test Cell System for Identification of Functional Domains of *ras*-p21

As it happens, a very convenient cell system for measuring the abilities of agents to inhibit *ras*-p21 is oocytes. Oocyte maturation induced by a particular agent, such as oncogenic *ras*-p21, is easy to evaluate because of the large structural changes, like disappearance of the brown-colored animal pole, that each matured oocyte undergoes. Maturation of all oocytes in a given experiment occurs in a relatively short time, within 1−2 days after injection or treatment of the oocytes with a maturation-promoting agent. Finally, oocytes contain an abundance of insulin receptors; insulin is a growth factor that induces oocyte maturation by activating normal cellular *ras*-p21.

Proof that insulin acts through *ras*-p21 was provided by the finding that if oocytes are first injected with an inactivating antibody against *ras*-p21 and then incubated in insulin, they do not undergo maturation. Prior injection of other, unrelated antibodies has no effect; insulin induces maturation in these oocytes. Thus oocytes are ideal for studying the specificity of anti-*ras*-p21 agents to study whether they have a preferential effect on the oncogenic form versus the normal form of p21 by either co-injecting the agent with oncogenic p21 or by injecting the agent into oocytes that are then incubated with insulin.

Effects of p21 Peptides from Effector Domains Identified by Conformational Analysis (Pincus et al., 2000, 2007)

Microinjection into oocytes of each of the synthesized peptides from the *ras*-p21 domains identified from the conformational energy calculations mentioned above, either together with oncogenic *ras*-p21 or into oocytes subsequently incubated with insulin, has been performed. Three peptides, 35−47 (PNC-7) from the previously identified effector domain, 96−110 (PNC-2), and 115−126 (PNC-1), all strongly block the ability of oncogenic p21 to induce oocyte maturation. Significantly, these peptides, especially peptides corresponding to residues 96−110 and 115−126, only minimally affected the ability of insulin, hence activated normal p21, to induce maturation. This finding suggests that oncogenic and normal p21 induce mitogenesis by differing signal transduction pathways. As it happens, the latter two peptides have been found to interfere in the interaction of oncogenic p21 with JNK and *jun* proteins; their abilities to inhibit oncogenic p21-induced oocyte maturation strongly correlate with their abilities to inhibit this interaction.

The above results suggest that activated normal and oncogenic *ras*-p21 stimulate different pathways; the oncogenic form can preferentially activate JNK and *jun* directly, leading to unregulated nuclear transcriptional processes. By breaking this "short circuit" with effector peptides, selective inhibition of oncogenic *ras*-p21 can be achieved. This result has important implications for the design of new selective chemotherapeutic agents.

The Two *ras* Peptides, PNC-2 and PNC-7, Block Cancer Cell but not Normal Cell Growth (Pincus et al., 2007)

Two *ras*-p21 peptides, PNC-2 and PNC-7, attached to the transmembrane-penetrating sequence discussed above, were used to treat ras-transformed cancer cells. It was found that a ras-transformed rodent pancreatic cancer cell line called TUC-3, when incubated with either peptide but not a control peptide, are induced to revert to the untransformed phenotype. These cells, unlike their untreated or control peptide-treated cancer cells, do not grow when transplanted into nude mice. Neither PNC-2 nor PNC-7 has any effect on the growth of normal cells such as the untransformed counterpart cells to TUC-3, called BMRPA1. Both peptides likewise exert the same effect on ras-transformed HT1080 human fibrosarcoma cells and have cytotoxic effects on other cancer cell lines. It seems, therefore, that these *ras*-p21 peptides have potential for treating cancers.

Thus, use of the methods of conformational analysis based on the principles of protein structure described in this chapter has resulted in our being able to identify critical residues of an oncogenic protein that are vital to their function, to design peptides that selectively inhibit oncogenic *ras*-p21, and to detect differences in signal transduction pathways induced by oncogenic and normal p21 protein.

BIBLIOGRAPHY

Almoguerra, C., Shibata, D., Forrester, K., Martin, J., Arnheim, M., & Perucho, M. (1988). Most human carcinomas of the endocrine pancreas contain mutant c-K-*ras* genes. *Cell, 53*, 813−815.

Anfinsen, C. B., Haber, E., Sela, M., & White, F. H., Jr. (1961). The kinetics of formation of native ribonuclease during oxidation of the reduced polypeptide chain. *Proc Natl Acad Sci USA, 47*, 1309−1314.

Barbacid, M. (1987). ras genes. *Ann Rev Biochem, 56*, 779−827.

Bargmann, C. I., & Weinberg, R. A. (1988). Oncogenic activation of the neu-encoded receptor protein by point mutation and deletion. *EMBO J, 7*, 2043−2052.

Ben-Levy, R., Peles, E., Goldman-Michael, R., & Yarden, Y. (1992). An oncogenic point mutation confers high affinity ligand binding to the neu receptor. *J Biol Chem, 267*, 17304−17313.

Blobel, G., Walter, P., Chang, C. N., Goldman, B. M., Erickson, A. H., & Lingappa, R. (1979). Translocation of proteins across membranes: the signal hypothesis and beyond. *Symp Soc Exp Biol, 33*, 9−37.

Bogaart, G. V. D., Guzman, J. V., Mica, J. T., & Poolman, B. (2008). On the mechanism of pore formation by melittin. *J Biol Chem, 283*, 33854−33857.

Brandt-Rauf, P. W., Pincus, M. R., & Chen, J. M. (1989). Conformational changes induced by the transforming amino acid substitution in the transmembrane domain of the neu-oncogene-encoded p185 protein. *J Protein Chem, 8*, 749−755.

Brandt-Rauf, P. W., Rackovsky, S., & Pincus, M. R. (1990). Correlation of the transmembrane domain of the neu-oncogene-encoded p185 protein with its function. *Proc Natl Acad Sci USA, 87*, 8660−8664.

Bull, H. B. (1943). *Physical Biochemistry.* London: John Wiley and Sons.

Caterall, W. A. (1995). Structure and function of voltage-gated ion channels. *Annu Rev Biochem, 64*, 493−531.

Cho, H. S., Mason, K., Ramyar, K. X., et al. (2003). Structure of the extracellular region of HER2 alone and in complex with the Herceptin Fab. *Nature, 421*, 756−760.

Di Fiore, P. P., Pierce, J. H., Kraus, M. H., Segatto, O. S., King, R., & Aaronson, S. A. (1987). erbB-2 is a potent oncogene when overexpressed in NIH/3T3 cells. *Science, 237*, 178−182.

Downward, J. (2003). Targeting the Ras signalling pathway in cancer therapy. *Nat Rev Cancer, 3*, 11−22.

Dygert, M., Go, N., & Scheraga, H. A. (1975). Use of a symmetry condition to compute the conformation of gramicidin S. *Macromolecules, 8*, 750−761.

Emr, S. D., & Silhavy, T. J. (1982). Molecular components of the signal sequence that function in the initiation of protein export. *J Cell Biol, 95*, 689−696.

Engelman, A. M., & Steitz, T. A. (1981). The spontaneous insertion of proteins into and across membranes: the helical hairpin hypothesis. *Cell, 23*, 411−422.

Ferguson, K. M., Berger, M. B., Mendrola, J. M., Cho, H., Leahy, D. J., & Lemmon, M. A. (2003). EGF activates its receptor by removing interactions that autoinhibit ectodomain dimerization. *Mol Cell, 11*, 507−517.

Gibson, K., Chin, S., Pincus, M. R., Clementi, E., & Scheraga, H. A. (1986). Parallelism in conformational energy calculations on proteins: partial structure of interferon. In M. Dupuis (Ed.), *Montreal Symposium on Supercomputer Simulation in Chemistry. Lecture Notes in Chemistry, Vol. 44* (pp. 198−213).

Hall, Z. W. (1992). Ion channels. In Z. W. Hall (Ed.), *An Introduction to Molecular Neurobiology* (pp. 81−118). Sunderland: Sinauer Associates, Inc.

Hudziak, R. M., Schlessinger, J., & Ullrich, A. (1987). Increased expression of the putative growth factor reception $p185^{HER2}$ causes transformation and tumorigenesis of NIH/3T3 cells. *Proc Natl Acad Sci USA, 84*, 7159−7163.

James, G. L., Goldstein, G. L., Brown, M. S., et al. (1993). Benzodiazepine peptidomimetics: potent inhibitors of ras farnesylation in animal cells. *Science, 260*, 1937−1942.

King, C. F., Kraus, M. H., & Aaronson, S. A. (1985). Amplification of a novel v-erbB-related gene in a human mammary carcinoma. *Science, 229*, 974−976.

Karplus, M., & McCammon. (1986). The dynamics of proteins. *Sci Am, 254*, 42−52.

Kempf, C., Klausner, R. D., Weinstein, J. N., van Renswoude, J., Pincus, M. R., & Blumenthal, R. (1982). Voltage-dependent transbilayer orientation of melittin. *J Biol Chem, 257*, 2469−2475.

Kussie, P. H., Gorina, S., Marechal, V., et al. (1996). Structure of the MDM2 oncoprotein bound to the p53 tumor suppressor transactivation domain. *Science, 274*, 921−922.

Long, S. B., Campbell, E. B., & MacKinnon, R. (2005). Crystal structure of a mammalian voltage-dependent shaker family K^+ channel. *Science, 309*, 897−903.

Miller, M. H., & Scheraga, H. A. (1976). Calculation of the structure of collagen models. Role of interchain interactions in determining the triple helical coiled coil conformation. *J Polymer Sci, 54*, 171−200.

Monaco, R., Chen, J. M., Friedman, F. K., Brandt-Rauf, P. W., & Pincus, M. R. (1995). Structural effects of the binding of GTP to the wild-type and oncogenic forms of the ras-gene-encoded p21 proteins. *J Protein Chem, 14*, 721−730.

Padhy, L. C., Shih, C., Cowing, D., Finkelstein, R., & Weinberg, R. A. (1982). Identification of a phosphoprotein specifically induced by the transforming DNA of rat neuroblastomas. *Cell, 28*, 865−871.

Pincus, M. R. (1988). The chain build-up procedure in computing the structures of biologically active polypeptides and proteins. *Int J Quant Chem: Quant Biol Symp, 15*, 209−220.

Pincus, M. R., & Klausner, R. D. (1982). Prediction of the three-dimensional structure of the leader sequence of murine pre-kappa light chain, a hexadecapeptide. *Proc Natl Acad Sci, USA, 79*, 3413−3417.

Pincus, M. R., & Scheraga, H. A. (1985). Conformational analysis of biologically active polypeptides, with application to oncogenesis. *Accnt Chem Res, 18*, 372−379.

Pincus, M. R., Klausner, R. D., & Scheraga, H. A. (1982). Calculation of the three-dimensional structure of the membrane-bound portion of melittin from its amino acid sequence. *Proc Natl Acad Sci, USA, 79*, 5107−5110.

Pincus, M. R., Brandt-Rauf, P. W., Michl, J., & Friedman, F. K. (2000). ras-p21-induced cell transformation: unique signal transduction pathways and implications for the design of new chemotherapeutic agents. *Cancer Invest, 18*, 39−50.

Pincus, M. R., Brandt-Rauf, P. W., & Bluth, M. (2006). Oncoproteins and early tumor detection. In R. McPherson, & M. R. Pincus (Eds.), *Henry's Clinical Diagnosis and Management by Laboratory Methods* (21st ed.). (pp. 1367−1380) Philadelphia: Elsevier.

Pincus, M. R., Michl, J., Bowne, W., & Zenilman, M. (2007). Anti-cancer peptides from the ras-p21 and p53 proteins. In R. M. Mohan (Ed.), *Research Advances in Cancer* (pp. 65−90). Kerala, India: Global Research Network Publishers.

Rosale, R., Pincus, M. R., Brandt-Rauf, P. W., Fine, R. L., Michl, J., & Wang, H. (2004). NMR solution structure of a peptide from the mdm-2 binding domain of the p53 protein that is selectively cytotoxic to cancer cells. *Biochemistry, 43*, 1754−1861.

Rosenblatt, M., Beaudette, N. V., & Fasman, G. D. (1980). Conformational studies of the synthetic precursor-specific region of preproparathyroid hormone. *Proc Natl Acad Sci USA, 77*, 3983−3987.

Russell, S. T., & Warshel, A. (1985). Calculations of electrostatic energies in proteins. The energetics of ionized groups in bovine pancreatic trypsin inhibitor. *J Mol Biol, 185*, 389−404.

Sarafraz-Yazdi, E., Bowne, W. B., Adler, V., et al. (2010). Anticancer peptide PNC-27 adopts an HDM-2-binding conformation and kills cancer cells by binding to HDM-2 in their membranes. *Proc Natl Acad Sci USA, 107*, 1918−1923.

Scheraga, H. A. (1984). Protein structure and function, from a colloidal to a molecular point of view. *Carlsberg Res Commun, 49*, 1−55.

Scheraga, H. A. (1989). Calculations of stable conformations of polypeptides, proteins, and protein complexes. *Chim Scripta, 29A*, 3−13.

Scheraga, H. A., Liwo, A., Oldziej, S., et al. (2004). The protein folding problem:global optimization of force fields. *Front Biosci, 9*, 3296−3323.

Slamon, D. J., Clark, G. M., Wong, S. G., Levin, W. J., Ullrich, A., & McGuire, W. L. (1987). Human breast cancer: correlation of relapse and survival with amplification of the her-2/neu oncogene. *Science, 235*, 177−182.

Tamba, Y., Arivama, H., Levadny, V., & Yamazaki, M. (2010). Kinetic pathway of antimicrobial peptide magainin 2-induced pore formation in lipid membranes. *J Phys Chem B, 114*, 2018−2026.

Terwilliger, T. C., Weissman, L., & Eisenberg, D. (1982). The structure of melittin in the form I crystals and its implication for melittin's lytic and surface activities. *Biophys J, 37*, 353−361.

van Holde, K. E. (1985). *Physical Biochemistry*. Englewood Cliffs: Prentice Hall, Inc.

Vasquez, M., Nemethy, G., & Scheraga, H. A. (1994). Conformational energy calculations on polypeptides and proteins. *Chem Rev, 94*, 2183−2239.

Vogel, H., & Jahnig, F. (1986). *The structure of melittin in membranes Biophys J, 50*, 573−582.

Willumsen, B. M., Christensen, A., Humbert, N. L., Papageorge, A. G., & Lowy, D. R. (1984). The p21 ras C-terminus is required for transformation and membrane association. *Nature, 310*, 583−586.

Wuthrich, K. (1986). *NMR of Proteins and Nucleic Acids*. New York: John Wiley and Sons.

Yang, L., Weiss, T. M., Lehrer, R. I., & Huang, H. W. (2000). Crystallization of antimicrobial pores in membranes: magainin and protegrin. *Biophys J, 79*, 2002−2009.

This page intentionally left blank

Chapter 3

Cell Membranes

Jeffrey C. Freedman

Chapter Outline

I. SUMMARY

This chapter reviews some basic biochemical properties of membrane lipids and describes the experimental evidence for models of the structure of cell membranes, starting with the Gorter and Grendel bimolecular phospholipid leaflet and proceeding through the Davson–Danielli paucimolecular model and the Singer–Nicholson fluid mosaic model. Extensions of the fluid mosaic model include heterogeneous lipid phases, lateral domains of cholesterol-poor and cholesterol-rich pools, annular lipids whose properties differ from bulk lipids, phospholipid asymmetry and membrane microdomains known as rafts. The much-studied red blood cell membrane is considered throughout this chapter as a paradigm applicable to other plasma membranes.

II. THE BIMOLECULAR LIPID MEMBRANE

The term *plasma membrane* derives from the German *Plasmamembran,* a word coined by Karl Wilhelm Nägeli (1817–1891) to describe the firm film that forms when the proteinaceous sap of an injured cell comes into contact with water. The physiologist L.V. Heilbrunn referred to this and similar phenomena as the "surface precipitation reaction", as described in his book *The Dynamics of Living Protoplasm* (1956). "Protoplasm" was the old term for the substance inside cells and was in general use before the techniques of electron microscopy and differential centrifugation helped to elucidate the detailed structures and specific functions of discrete cell organelles. The involvement of what we know today as the cell membrane and the biochemistry of the formation of a surface film in response to cell injury have not subsequently been explained. The original usage of the term "plasma membrane," therefore, has an obscure relationship to its current meaning.

Much knowledge concerning membrane structure and function derives from studies of red blood cells, as depicted in the scanning electron photomicrograph in Fig. 3.1. Red cells are highly differentiated and are specialized for the transport of oxygen and carbon dioxide in the blood. They consist essentially of a plasma membrane surrounding a concentrated solution of hemoglobin and lack a nucleus, mitochondria, endoplasmic reticulum, ribosomes, Golgi apparatus and lysosomes. Over 100 years ago, extensive osmotic and permeability studies of red cells by Hamburger,

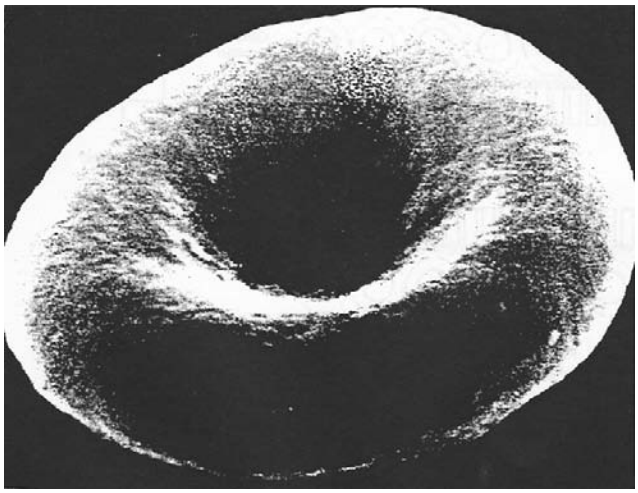

FIGURE 3.1 Scanning electron photomicrograph of human red blood cells. The biconcave discoid cells are 8 μm in diameter and 2.4 μm thick at the rim and 1.0 μm thick at the center. *(From Bessis, M. 1974. Corpuscles. Atlas of Red Blood Cell Shapes. Springer-Verlag, New York, Fig. 1, with permission.)*

Cell Physiology Sourcebook. DOI: 10.1016/B978-0-12-387738-3.00003-2

of plant cells by de Vries and of many living cells by Overton provided evidence that a lipoid membrane surrounds cells. Fat-soluble substances that are lipophilic and easily dissolve in lipids enter cells easily, whereas water-soluble substances enter cells more slowly, if at all. Overton recognized a correlation between the oil−water partition coefficient and membrane permeability; nevertheless, in none of these early studies was a membrane postulated as a distinct structural entity to explain the findings (see Jacobs, 1962).

In 1925, Gorter and Grendel used acetone to extract lipids from a known quantity of red blood cells and, after evaporating the solvent, measured the area that the extracted lipids occupied as a monomolecular film at an air−water interface using a Langmuir trough. From the area of the film of extracted lipids and from the surface area of the red cells as estimated by light microscopy, they concluded that: "It is clear that all our results fit in well with the supposition that the chromocytes are covered by a layer of fatty substances that is two molecules thick" (Gorter and Grendel, 1925, p. 443). Some 40 years later, however, it was pointed out that the red blood cell surface area is actually 50% greater; also, the acetone extraction had left about 30% of the lipid remaining in the ghosts. Fortunately, these two errors tended to offset each other (Bar et al., 1966), showing that on infrequent occasions in science, you can be right for the wrong reasons. The bimolecular lipid leaflet, 75−100 Å thick, first proposed by Gorter and Grendel as a model for the cell membrane (Fig. 3.2), still forms the basis for contemporary thinking about the structure of cell membranes. The essence of this model is that membrane phospholipids are arranged in parallel sheets forming two hemileaflets with their polar head-groups facing the aqueous intracellular and extracellular solutions and their non-polar fatty acid chains interacting laterally within the hydrophobic core of the membrane.

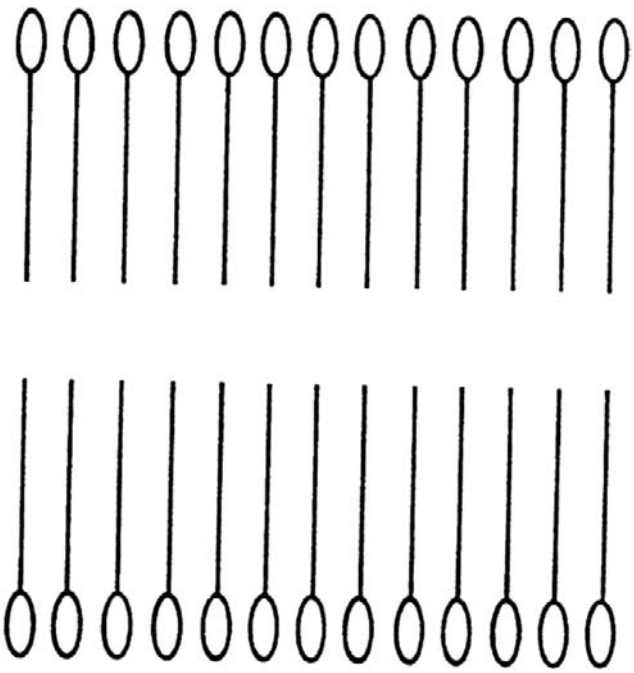

FIGURE 3.2 Model of bimolecular phospholipid membrane as proposed by Gorter and Grendel (1925).

For pure lipids, the expected *surface tension*, as measured in a Langmuir trough, is about 9 dyn/cm, but the surface tension of marine eggs and other types of cells is about 50−100 times less at only 0.1−0.2 dyn/cm. The surface tension can be visualized as the force necessary to close a slit in the surface of the membrane. Danielli and Harvey found that egg protein can lower the surface tension of an oil−water interface to about 0.6 dyn/cm, leading Davson and Danielli (1943) to postulate the presence of two films of protein associated with the polar head groups at each side of the bimolecular lipid leaflet, a model that became known as the *Davson−Danielli paucimolecular membrane* (Fig. 3.3). Presumably, the protein functioned to strengthen and stabilize the thin lipid film. *Paucimolecular* means that this model included just a few molecules: a bimolecular lipid leaflet with adhering protein films on the inner and outer surfaces.

Using electrophysiological techniques, the electrical resistance of cell membranes was measured and found to be very high, a finding that was also consistent with the proposal of an insulating lipid membrane surrounding cells. In other studies of membranes their *birefringence* was determined. Birefringence is an optical property of certain oriented materials that can be determined by placing a specimen between two crossed Polaroids on a microscope stage. A Polaroid film only passes light that has its electric vector parallel with the axis of the Polaroid film; two Polaroid films, crossed at right angles and held up to a light, appear black. But, if a crystal, or some other substance in which the molecules themselves are oriented, is placed between the crossed Polaroids, the transmitted light is circularly polarized, and the specimen looks brilliantly bright. A specimen that appears bright when placed between crossed Polaroids is said to be birefringent. *Intrinsic birefringence* is due to the oriented nature of individual molecules, such as filamentous proteins, whereas *form birefringence* is due to the oriented arrangement of molecules in an array, such as occurs with the parallel packing of actin and myosin filaments in muscle sarcomeres. When red cell membranes were viewed with a polarization microscope, the lipids contributed to birefringence, as did the underlying cytoskeleton, in a fashion consistent with the paucimolecular model of membrane structure.

High-resolution electron micrographs of the *unit membrane* also supported the Davson−Danielli paucimolecular model. The term *unit membrane* refers to the ubiquitous trilaminar structure, 75−100 Å thick, seen in

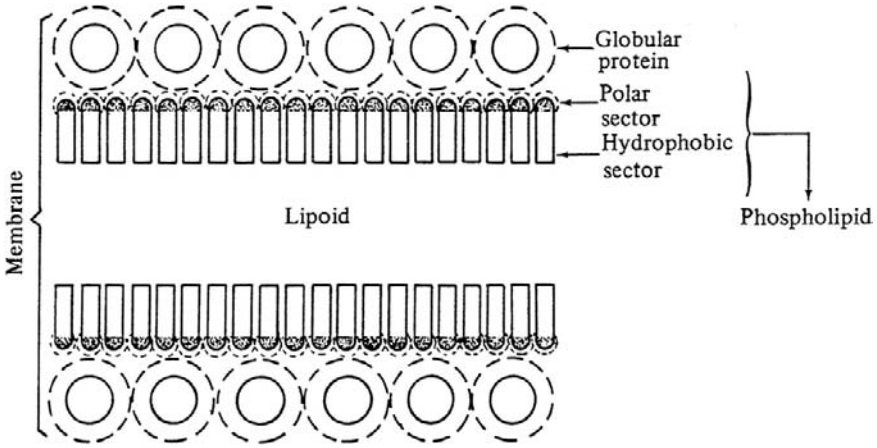

FIGURE 3.3 Paucimolecular model of membrane structure. *(From Danielli, J.F. and Davson, H.A. (1935). A contribution to the theory of permeability of thin films. J Cell Comp Physiol. 5, 495–508, p. 498, reprinted by permission of Wiley-Liss, Inc., a subsidiary of John Wiley and Sons, Inc.)*

electron micrographs of thin sections of cells and organelles. The image appears as two dark lines, each about 25–30 Å thick, sandwiching a lighter zone, and is especially well-resolved in samples fixed with potassium permanganate. A thin section electron micrograph of the human red blood cell plasma membrane is shown in Fig. 3.4. Virtually the same trilaminar structure was seen not only at the surface of red cells but also in muscle cells, nerve cells, epithelial cells, plant cells, bacterial cells and in just about every membranous cell organelle that was examined. In situations where two cells were tightly apposed, two trilaminar structures constituted a *double membrane*. In the myelin sheath that surrounds nerve cells, a series of trilaminar structures was seen in a spiral arrangement, consistent with the envelopment of nerve axons by the membrane of Schwann cells, as shown in Fig. 3.5A. Since the detailed chemical reactions of potassium permanganate with tissue are not entirely understood, some uncertainty remained concerning the basis of the image that was observed in thin sections. The universal occurrence of the unit membrane, however, was taken as strong evidence in support of the Davson–Danielli paucimolecular model. Further studies of the multilamellar myelin sheath of nerve axons by x-ray diffraction of centrifuged unfixed and unstained membranes yielded electron density profiles that were also consistent with the Davson–Danielli paucimolecular model (Worthington and McIntosh, 1973). As seen in Fig. 3.5B, the electron density is low in the hydrophobic core of the membrane and high in the polar regions of the phosphate groups. Moreover, the thickness of the membrane, as determined from these computed electron density profiles of unstained myelin sheath, quantitatively agrees with that seen as the unit membrane in thin sections fixed with potassium permanganate – an observation constituting compelling evidence supporting the proposal of a bimolecular phospholipid leaflet as the backbone structure of cell membranes. Thus, the evidence for the paucimolecular membrane model consisted of studies of permeability, electrical resistance and microscopic observations of birefringence with the light microscope, as well as high-resolution images of both stained and unstained cells with the electron microscope. These convincing arguments were summarized in the classic monograph entitled *The Permeability of Natural Membranes* written by Davson and Danielli (1943), a book that greatly influenced subsequent development of cellular and membrane physiology.

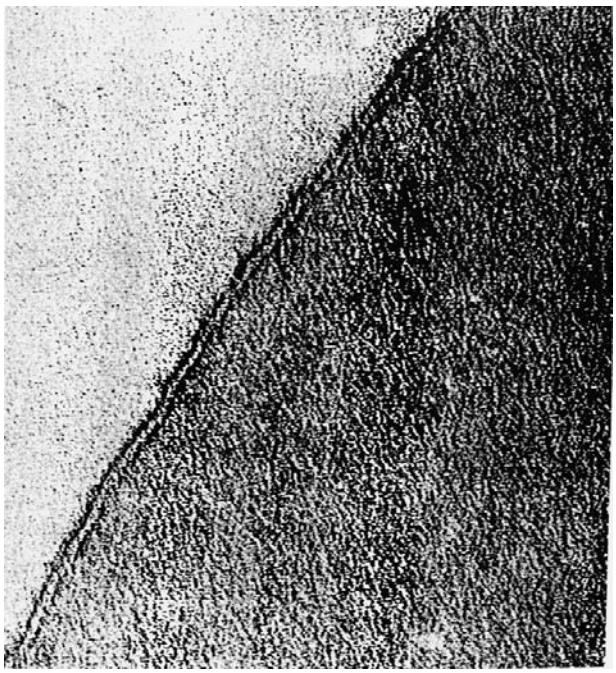

FIGURE 3.4 Thin-section electron micrograph of the unit membrane of a red blood cell. *(Photomicrograph by J.D. Robertson from Dyson, R.D. (1974). Cell Biology. A Molecular Approach. Allyn and Bacon, Boston, with permission.)*

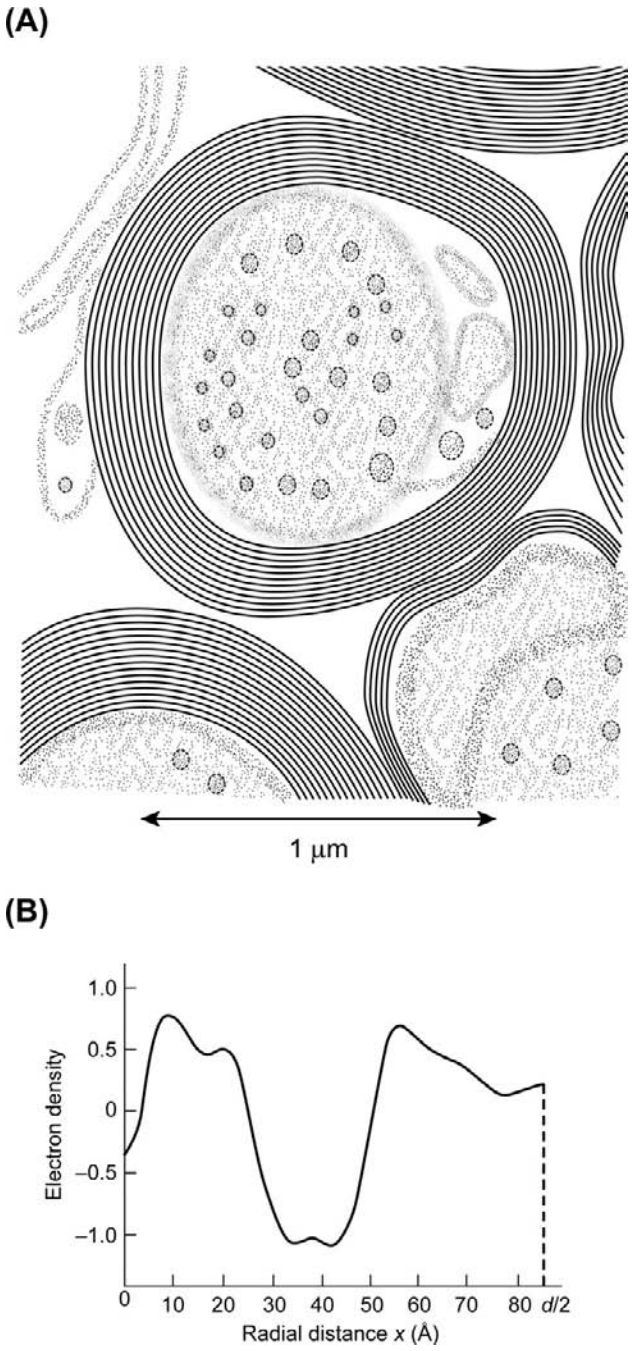

FIGURE 3.5 (A) Myelin sheath of spinal cord axon (courtesy of Dr Cedric Raine.) (B) Electron density profile of frog sciatic nerve. *(From Worthington, C.R. and McIntosh, T.J. (1973). Direct determination of the electron density profile of nerve myelin. Nature-New Biology. 245, 97–99, p. 99. Reprinted by permission from* Nature *copyright 1973 Macmillan Magazines Ltd.)*

III. MEMBRANE LIPIDS AND PROTEINS

The ability to separate intact red blood cell membranes from the rest of the cell by hypotonic hemolysis (Dodge et al., 1963) was further evidence for the existence of a distinct membrane and enabled detailed studies of the chemical composition of cell membranes. After centrifugation of red blood cells, followed by resuspension in distilled water, the water enters the cells by *osmosis* and then the cells swell and hemolyze. Following centrifugation and washing of the pellet by further resuspension and centrifugation at the optimal pH and ionic strength to remove adherent hemoglobin, the resultant pellet is pure white. When these isolated washed membranes are examined by the technique of negative staining with an electron microscope (a negative stain is excluded from biological structures in contrast with positive stains, which bind more or less specifically to various structures), the image resembles an empty bag, as seen in Fig. 3.6. In red cell physiology, the isolated membranes are known as *ghosts*, which can be either pink or white depending on the extent and conditions of washing. Red blood cell membranes were the first to be isolated and remain the best characterized.

The mass ratio of protein to lipid ranges from about 1:4 to 4:1 in various membranes. Myelin, which electrically insulates nerve axons from the extracellular solution, has only 18% protein by mass. In contrast, the energy-transducing inner membranes of mitochondria and chloroplasts, where ATP is synthesized by oxidative or photo phosphorylation, respectively, are densely packed with

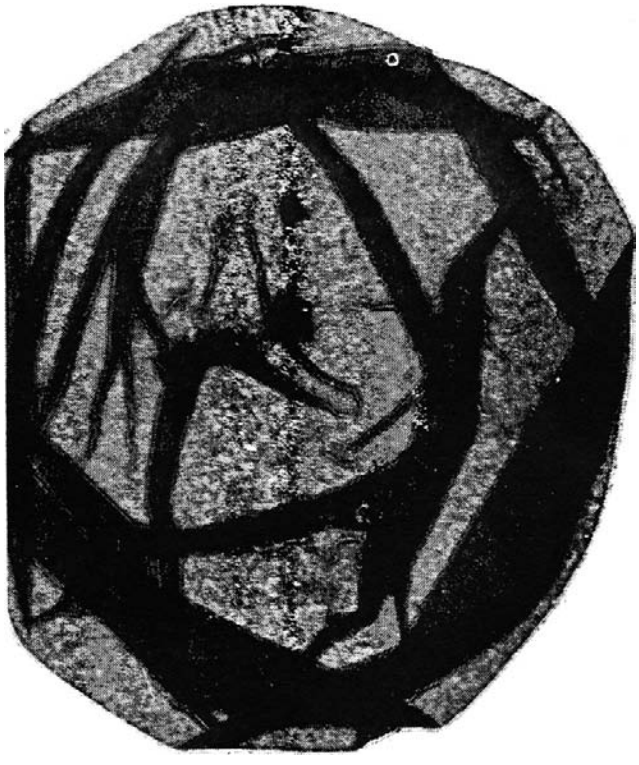

FIGURE 3.6 Isolated red cell membrane negatively stained with phosphotungstic acid. *(From McMillan, P.N. and Luftig, R.B. (1973). Preservation of erythrocyte ghost ultrastructure achieved by various fixatives. Proc Natl Acad Sci USA. 70, 3060–3064, p. 3061, with permission.)*

TABLE 3.1 Composition of Red Blood Cell Ghosts

Substance	Mass Percent
Protein	49
Phospholipid	33
Cholesterol	11
Lipid (total)	44
Carbohydrate (total)	7

Adapted from Rosenberg, S.A. and Guidotti, G.J. (1968). The protein of human erythrocyte membranes. I. Preparation, solubilization, & partial characterization. J Biol Chem. 243, 1985–1992.

75% protein. The chemical composition of isolated red cell membranes is summarized in Table 3.1, which indicates that these membranes, like many other membranes, are about half protein and half lipid by mass, with an additional fraction of carbohydrate. The carbohydrate exists as sugars on glycoproteins, glycolipids and on sialic acid; the sugars always protrude from the outer membrane surface. Due to sialic acids on *glycophorin*, an integral membrane glycoprotein, the external surface of red cells is negatively charged. The external surface of the red cell membrane is also coated with adsorbed albumin and also with some plasma globulins.

The three major classes of membrane lipids are phospholipids, glycolipids and cholesterol. *Phospholipids* are derived either from glycerol, a 3-carbon alcohol, or from sphingosine, a more complex amino alcohol with a long unsaturated carbon chain. Phosphoric acid esterified to diacylglycerol forms phosphatidate, from which the major glycero-phospholipids are formed. The chemical structures of a fatty acid, cholesterol and a diglyceride are shown in Fig. 3.7A, along with the structures of some phospholipids in Fig. 3.7B. Membrane lipids are *amphipathic* molecules comprised of a polar (hydrophilic) headgroup, an interfacial region and a non-polar (hydrophobic) tail. Phospholipids can be neutral (e.g. phosphatidylcholine, PC, also known as lecithin; phosphatidylethanolamine, PE; sphingomyelin, SM) or carry a net negative charge (e.g. phosphatidylserine, PS; phosphatidylinositol, PI). *Diacylphospholipids* are the major components of the plasma membrane of mammalian cells and usually occur as mixed-chain lipids such that two different fatty acids are linked to the glycerol backbone. The two esterified fatty acids have a different even number of carbon atoms ranging from 14 to 24. The sn-1 acyl chain esterified at the end carbon position is often saturated and assumes the all-*trans* conformation, whereas the sn-2 acyl chain esterified at the middle carbon position is predominantly unsaturated. The

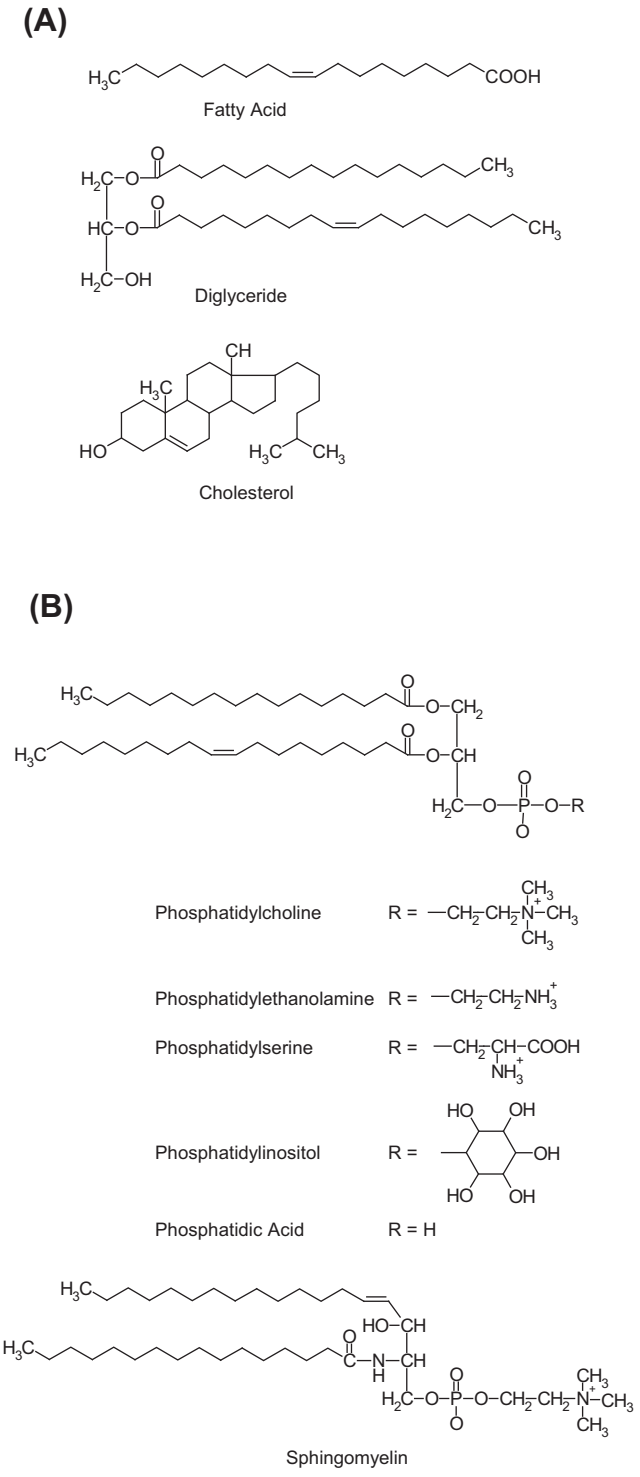

FIGURE 3.7 (A) Chemical structure of fatty acid, cholesterol, diglyceride. (B) Structures of phospholipids. *(Structures drawn by T.B. Freedman.)*

conformation of double bonds in unsaturated fatty acids is nearly always *cis*, which produces a bend along the chain where the double bond occurs. POPC, or 1-palmitoyl-2-oleoyl-phosphatidylcholine, is one of the most abundant

membrane lipids found in animal cell membranes. PE is often the principal phospholipid of microorganisms and is also abundant in rod outer segments of photoreceptor cells. PI typically comprises 2−8% of the phospholipid in animal cells and can be phosphorylated to participate in intracellular signaling pathways. Diphosphatidylglycerol, or cardiolipin, is abundant in mitochondrial membranes. PS is an important constituent of brain cell membranes and it activates protein kinase C in signaling pathways. Over one thousand distinct species of phospholipids exist in eukaryotic membranes.

The space-filling model of C(14):C(14) PC obtained by x-ray diffraction of single crystals shown in Fig. 3.8 agrees closely with the conformation calculated by minimizing the free energy of the structure. Even-numbered saturated fatty acids have a bend at the second carbon of the sn-2 chain, known as the h-shaped geometry, resulting in effectively uneven lengths of the two chains. These uneven lengths of the two acyl chains can interact across the bilayer to further stabilize the bimolecular phospholipid membrane.

Since the mole ratio of phospholipid to cholesterol is 0.8 in red cells, the paucimolecular model needed modification to include cholesterols interspersed among the phospholipid fatty acyl chains in parallel with the phospholipids. The plasma membranes of eukaryotic cells are rich in cholesterol, whereas organelle membranes have less of this neutral lipid.

The proportions of phospholipids found in human red blood cell membranes are shown in Table 3.2. The fatty acyl chains in the phospholipids usually contain an even number of carbons between 14 and 24; the 16- and 18-carbon fatty acids are the most common. In red cells, the major fatty acids are palmitic (16:0), oleic (18:1), linoleic (18:2), stearic (18:0) and arachidonic (20:4) (Table 3.3), which together account for some 92% of the total fatty acid content. Different membranes differ in their *lipid signature*, a term that refers to the characteristic pattern of phospholipids, cholesterol and fatty acids that comprise the plasma membranes of different cells and of specific organelles. Lipid composition and content are usually measured by chromatographic methods and have been measured and cataloged for many different membranes (Ansell et al., 1973). The functional significance, however, of the different lipid signatures that occur in various specialized cells and organelles is largely not understood.

With two hydrophobic acyl chains, individual phospholipids have very low solubility in water, but form micelles at a critical micelle concentration of about 10^{-10} M. A *micelle* is a globular structure, usually less than 200 Å in diameter, with the polar head groups on the outside and the hydrophobic fatty acyl chains buried in the interior. Salts of fatty acids readily form micelles, whereas phospholipids tend to form bilayers. The *self-association* of phospholipids to form a bimolecular leaflet depends on the *hydrophobic effect*: the release of structured water molecules from around the hydrocarbon tails of the fatty acids results in an overall gain of entropy that serves as the driving force for self-assembly of phospholipids into bimolecular membranes. The membrane is further

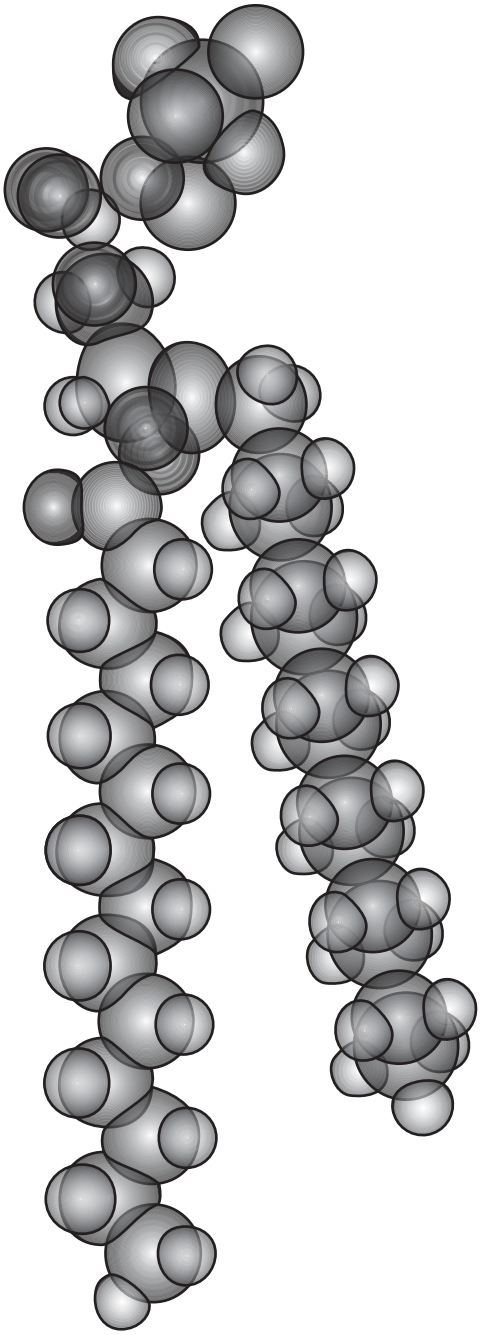

FIGURE 3.8 The x-ray single crystal structure of C(14):C14) PC shown as a space-filling model. *(Adapted from Huang, C.-H. (1998). Membrane lipid structure and organization. In Cell Physiology Sourcebook, 2nd edn, Chapter 3, p. 44, Academic Press, New York.)*

TABLE 3.2 Approximate Proportions of Phospholipids in Human Red Blood Cells

Phospholipid	Abbreviation	Mass Percent
Phosphatidylcholine (lecithin)	PC	35
Lysolecithin	Lyso-PC	2
Sphingomyelin	SM	23
Phosphatidylethanolamine	PE	30
Phosphatidylserine + phosphatidylinositol	PS + PI	10

Adapted from van Deenen, L.L.M. and de Gier, J. (1964). Chemical composition and metabolism of lipids in red blood cells of various animal species. In (C. Bishop and D.M. Surgenor, eds), The Red Blood Cell, a Comprehensive Treatise, p. 266. Academic Press, New York.

stabilized by lateral van der Waals attractive forces between the fatty acyl chains, by electrostatic forces and by hydrogen bonding between adjacent polar headgroups. Depending on the method of preparation, membranes can form as planar bilayers, multilamellar vesicles (MLVs) and as small (200−500 Å) or large (0.1−1 μm) unilamellar vesicles (SUVs and LUVs), as illustrated in Fig. 3.9. In each structure, the polar, or hydrophilic, headgroups have an affinity for water whereas the non-polar, or hydrophobic, fatty acyl chains avoid water.

TABLE 3.3 Fatty Acids in the Membrane Phospholipids of Human Red Blood Cells

Fatty Acid	X:Y[a]	Mass Percent
Lauric	12:0	0.3
Myristic	14:0	1.0
	15:0	0.3
Palmitic	16:0	27.1
	16:1	3.4
	17:0	0.6
Stearic	18:0	9.4
Oleic	18:1	19.5
Linoleic	18:2	16.5
	18:3	0.5
	20:0	0.2
	20:3	1.4
Arachidonic	20:4	19.5

[a]*In X:Y,X refers to the number of C atoms in the acyl chain and Y refers to the number of double bonds.*
Data from de Gier, J., van Deenen, L.L.M., Verloop, M.C. & van Gastel, C. (1964). Phospholipid and fatty acic characteristics of erythrocytes in some cases of anaemia. Brit J Haematol. 10, 251.

When isolated red cell membranes are solubilized in the detergent sodium dodecyl sulfate (SDS), then subjected to electrophoresis on polyacrylamide gels containing SDS, followed by staining with the dye Coomassie blue, seven major bands are found (Fig. 3.10 and Table 3.4). In addition, stains for carbohydrate reveal glycophorin and other glycoproteins. Actually, more than 10 bands can be counted and many more spots are seen when two-dimensional chromatography is employed. Specific proteins mediate the distinctive functions of membranes; e.g. membrane proteins serve as ion channels, pumps, receptors, energy transducers and enzymes. Membranes with different functions show different banding patterns of proteins on SDS gels. Whereas the membrane lipids form a permeability barrier to most polar molecules and also form closed compartments around and within cells, specific proteins mediate most other membrane functions.

When a cell membrane, such as the human red blood cell, is rapidly frozen in liquid nitrogen and then fractured with the sudden impact of a microtome blade, the cleavage plane can pass along the outer surface of the cell, then slice through the hydrophobic core of the membrane and then continue along the inner surface of the membrane. *Freeze-fracture electron micrographs* provide a view of the unfixed interior of the membrane. After shadowing with carbon and platinum, a replica of the membrane interior is obtained. A variation of this technique is *freeze-etching*, in which some of the ice is sublimed away before the shadowing. With this technique, globular intramembranous particles (75 Å) are seen to lie in the plane of the membrane (Fig. 3.11). In red cells, the surface density of these particles (10^6 per cell) approximately corresponds to the number of copies of the major membrane protein variously known as band 3, capnophorin, or AE1, the anion exchange protein. In contrast, freeze-etch images of myelin are relatively poor in intramembranous particles and images of pure lipid membranes are devoid of such particles.

IV. THE FLUID MOSAIC MODEL OF CELL MEMBRANES

Spectroscopic studies provided evidence that lipids and proteins have some degree of rotational and translational mobility in the plane of the membrane. Subsequently, the review article entitled "The fluid mosaic model of the structure of cell membranes" (Singer and Nicholson, 1972) popularized the view that the overall structure of the membrane is a two-dimensional solution of globular proteins embedded in a fluid lipid matrix, as shown in Fig. 3.12. *Integral proteins* span the membrane and can be extracted only with detergents or organic solvents;

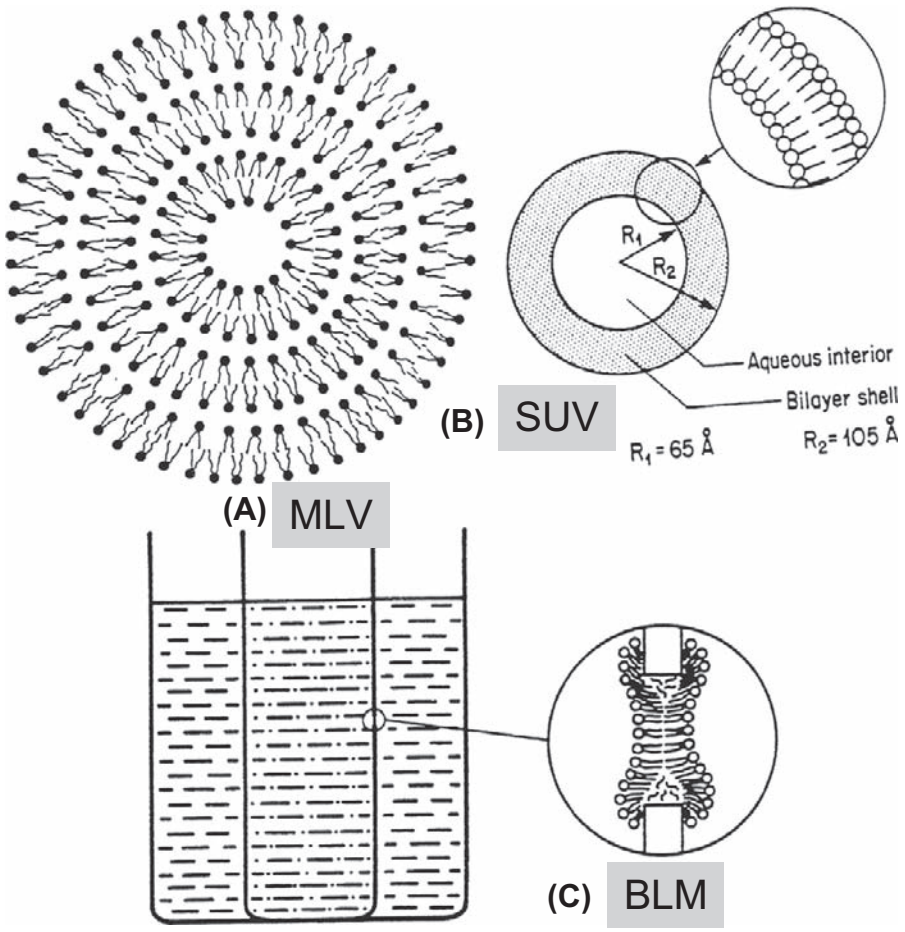

FIGURE 3.9 Model membranes: (A) liposomes; (B) vesicles; (C) planar bilayers. *(From Yeagle, P.L. (1993). The Membranes of Cells, 2nd edn, pp. 48, 52, and 54, Academic Press, New York, with permission.)*

peripheral proteins are attached more loosely to the surface of the membrane and are more easily extracted by more mild chemical treatments, such as by changing the pH or by exposure to high ionic strength solutions (e.g. 1 M NaCl). Peripheral proteins interact with the membrane by electrostatic or hydrogen-bonding interactions; integral proteins have transmembrane hydrophobic domains that interact extensively with the hydrophobic core of the membrane. The *fluid mosaic model* constituted an important extension of the Davson–Danielli paucimolecular model, especially with regard to the fluid state of the lipids and the location of integral membrane proteins. Further refinement of the fluid mosaic model incorporates lipid heterogeneities, such as annular phospholipid microdomains around integral membrane proteins, transbilayer phospholipid asymmetry, lipid phase separations and lateral microdomains of cholesterol-rich and cholesterol-poor pools.

Lipid molecules and some proteins diffuse rapidly in the plane of the membrane, but rarely flip across the membrane from one hemileaflet to the other. The diffusion coefficient of lipids in a variety of membranes is about 10^{-8} cm^2/s, corresponding to a distance traveled of about 2 μm in 1 s. From the diffusion coefficient it is estimated that the viscosity of the membrane lipids is about 100 times that of water, similar to olive oil. Cell fusion experiments first demonstrated that fluorescent labeled antibodies attached to human and mouse cell surface proteins could diffuse a distance of several microns in approximately 1 min (Frye and Edidin, 1970). Another way of measuring the lateral translational mobility of membrane lipids and proteins is the technique of fluorescence recovery after photobleaching (FRAP). In human red blood cells, FRAP studies showed that a portion of band 3 protein is slowly mobile, whereas another fraction is immobile due to attachments to the cytoskeletal protein matrix adjacent to the inner surface of the membrane. Proteins in different cells, and different proteins in a single cell, vary markedly in their *lateral mobility*, Bloom and Webb (1983).

Attachments between integral membrane proteins and the cytoskeleton represent another refinement of the fluid mosaic model of membrane structure. In red cells, the

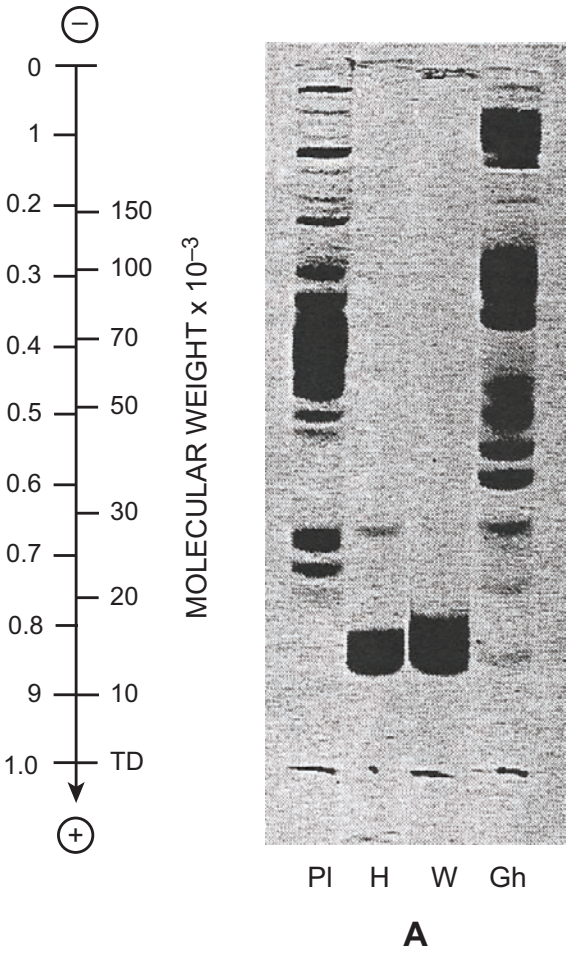

FIGURE 3.10 SDS gel of red blood cell membrane proteins. *(From Steck, P.L. and Yu, J. (1973). Selective solubilization of proteins from red blood cell membranes by protein perturbants. J Supramolec Struct. 1, 220–232, p. 223, Copyright © 1973. Reprinted by permission of Wiley-Liss, Inc., a subsidiary of John Wiley & Sons, Inc.)*

cytoskeleton is an organized polygonal fibrous network, about 60 nm thick containing spectrin and actin. Sides of the regular five- or six-sided polygons are formed by *spectrin*, a flexible filamentous protein 200 nm in length. Vertices of the polygons are formed by β-*actin* protofilaments 30–40 nm in length consisting of 12–14 actin monomers; both grooves of the actin filaments contain *tropomyosin*, which binds to *tropomodulin* at junctional complexes. At the mid-region of the spectrin filaments, a junctional ternary complex formed by *ankyrin* and band 4.2 protein links spectrin to the membrane-spanning integral band 3 protein. At the ends of the spectrin filaments, an additional linkage site to band 3 and to *glycophorin C* may be provided by protein 4.1. Spectrin–actin junctional complexes also contain the actin-bundling protein *dematin* (band 4.9) and the calmodulin-binding protein *adducin*, which functions to cap and to regulate the length of the actin filaments and which may be involved in Ca^{2+}-dependent alterations in cytoskeletal structure. A small amount of *myosin* is also found in the red-cell cytoskeleton, but whether active tension is generated or regulated in mature red cells is not known. Presumably, the cytoskeleton is actively involved during *enucleation* in developing red cells and during *diapedesis*, or egress of red cells from the bone marrow to the peripheral circulation.

Rotational molecular motions in membranes may be studied by the technique of *fluorescence polarization*, also called *fluorescence anisotropy*. A hydrophobic fluorescent probe, such as diphenylhexatriene (DPH), is first added to the membrane. The fluorescence is excited by light that is polarized, say in the vertical direction. Vertical exciting light only excites those probe molecules that are oriented in the same direction as the polarized excitation beam, a phenomenon known as *selective excitation*. If the probe molecule is immobilized during the time interval between excitation and emission, all of the emitted light would remain polarized in the vertical direction. However, if the probe molecule can rotate before light is emitted, then the emitted light will no longer be vertically polarized, but instead will contain a mixture of light that is polarized in all directions. By detecting and measuring the intensity of the emitted light that is polarized in the vertical and horizontal planes, one obtains a measure of the rotational mobility of the probe. By using the equations of motion, one further obtains a measure of the *microviscosity* of the fluid membrane. The inverse of microviscosity is termed *fluidity* and many studies have been performed to attempt to elucidate the determinants of membrane fluidity. Lipid composition, the length and degree of unsaturation of fatty acyl chains, the cholesterol content and the temperature all have profound effects on membrane lipid fluidity.

Deeper insight into the structure of pure lipid membranes has been obtained using the technique of *differential scanning calorimetry* (DSC). When liposomes are enclosed in a calorimeter and the temperature is slowly and continuously raised, the membranes absorb heat at particular temperatures corresponding to the occurrence of structural rearrangements, or *phase transitions*. In a plot of excess heat capacity versus temperature, the peaks in the DSC scans occur at the phase transition temperature, Tm, and the area under the peak corresponds to the transition enthalpy. The main transition is often called the gel-to-liquid crystalline phase transition. Below Tm the lipid is a gel with the fatty acyl chains in an ordered rigid state. Above Tm the lipid melts into a more disordered fluid-like liquid crystalline phase. A liquid crystal is a substance that flows like a liquid but has more short range order than a typical liquid. In the rigid gel state, the C-C bonds of the fatty acyl chains are all in the *trans* conformation. In the more disordered fluid state, some have rotated

TABLE 3.4 Protein Composition of Human Red Blood Cell Membrane

Band	MW	%	Position[a]	Name
Band 1	240 000	15	P	Dimeric spectrin
Band 2	215 000	15	P	Monomeric spectrin, myosin
Band 3	101 700	24	I	Capnophorin, Na^+,K^+-ATPase
Band 4.1	78 000	4.2	P	Junctional protein
Band 4.2	72 000	5.0	P	Junctional protein
Band 4.9	50 000			Dematin (actin-bundling protein)
Band 5	43 000	4.5	P	Actin
Band 6	35 000	5.5	P	Glyceraldehyde-3-phosphate dehydrogenase
Band 7	29 000	3.4		

[a]*P refers to a peripheral, and I to an integral, membrane protein.*
Data from Stack, T.L. (1974). The organization of proteins in the human red blood cell membrane. A review. J Cell Biol. 62, 1–19, Table 1, p. 4.

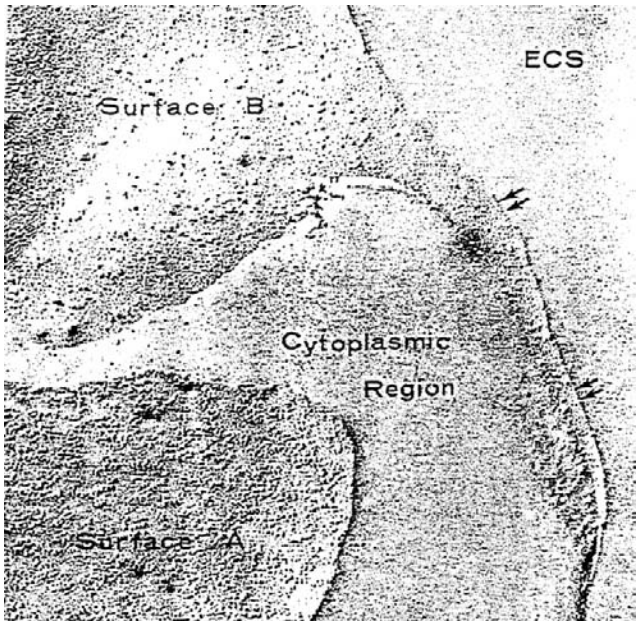

FIGURE 3.11 Freeze-etch image of red cell membrane showing intramembranous particles. *(From Weinstein, R.S. (1969). Electron microscopy of surfaces of red cell membranes. In (G.A. Jamieson and T.J. Greenwalt, eds), Red Cell Membrane. Structure and Function, p. 54. J.B. Lippincott Company, Philadelphia, with permission.)*

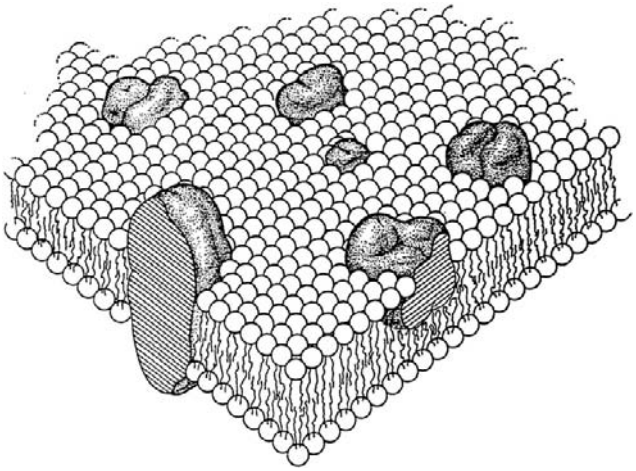

FIGURE 3.12 Fluid mosaic model of the structure of cell membranes.

120° clockwise or counterclockwise about the C-C bonds into the gauche conformation. Tm depends on the length of the fatty acyl chains and on their degree of unsaturation. Saturated fatty acids promote the gel state, whereas the presence of double bonds produces a bend in the carbon chain that disorders the lipid and lowers Tm. Longer carbon chains have higher melting points due to the stronger lateral interactions with neighboring chains.

Cholesterol is heterogeneously distributed in the membrane, with some regions being cholesterol-poor and other regions cholesterol-rich. In cholesterol-rich lateral domains, known as cholesterol pools, cholesterol located between phospholipids prevents crystallization, thereby abolishing phase transitions; it also sterically interferes with large motions of fatty acyl chains and thereby promotes order and reduces membrane fluidity. In cholesterol-poor regions, cholesterol is randomly distributed in a highly fluid phospholipid domain.

In mixtures of lipids, Tm may be experimentally determined by DSC as a function of systematic variation of the mole fraction of the components of the mixture. At elevated temperature, both lipids are melted in the liquid state, whereas at low temperature both lipids are solidified in the gel state. At intermediate temperatures and depending on the composition of the mixture, the lipid with the lower Tm is in the liquid state in equilibrium with the gelled lipid that has the higher Tm. Thus, depending on the temperature, different lipid phases may coexist in a cell membrane, thereby extending the concept of the fluid mosaic model of cell membranes, which assumed that membrane lipid is a homogeneous fluid. More recently, membrane microdomains enriched in sphingolipids and cholesterol, denoted as *rafts* in the ordered liquid phase, have been associated with various cellular functions including protein sorting, signal transduction, calcium

homeostasis, endocytosis, internalization of toxins, bacteria and viruses and cholesterol transport.

The lipids that directly surround integral membrane proteins differ in conformation and mobility from the bulk membrane lipids due to interactions with the protein. The *annular lipid* may either be more ordered or more disordered. In the case of the Ca-ATPase, which spans the bilayer, 15 annular phospholipid molecules in each of the two hemileaflets are in contact with the protein. If less than 30 molecules of lipid are associated with the protein, then activity is lost, showing that the annulus lipid is essential for the function of this particular protein. In a mixture of membrane lipids, the Ca-ATPase specifically attracts to itself and segregates into its annulus those particular lipids that optimize its activity.

In contrast to the rapid movement of lipids in the plane of the membrane, their spontaneous movement from one hemileaflet to the other, known as *flip-flop*, is slow. A typical phospholipid molecule flip-flops once every several hours, as measured by electron spin resonance spectroscopy. Thus, it takes about 10^9 times as long to flip-flop across the membrane as it does to diffuse along the equivalent distance of 50 Å in the plane of the membrane. Flip-flop of membrane proteins has not been detected and is unlikely because of the energetic barrier against moving the polar protein surface through the hydrophobic core of the membrane. The phospholipids in the red cell membrane and in many other cells as well are asymmetrically distributed, with the electrically neutral PC and SM preferentially located in the outer hemileaflet and the negatively-charged PS and PI preferentially located in the inner hemileaflet along with the neutral PE. Experiments with phospholipases added to the inside or outside of cells have experimentally established this phospholipid asymmetry. Cholesterol is located in both hemileaflets of the plasma membrane. The phospholipid asymmetry is maintained in part by the action of an aminophospholipid translocase, or "flippase", which catalyzes the inward translocation of PS or PE. This enzyme utilizes ATP, is stereospecific in the transport of L isomers and is inhibited by intracellular calcium or by sulfhydryl reagents.

BIBLIOGRAPHY

Ansell, G. B., Hawthorne, J. N., & Dawson, R. M. C. (1973). *Form and Function of Phospholipids*. New York: Elsevier Scientific Publishing Company.

Bar, R. S., Deamer, D. W., & Cornwell, D. G. (1966). Surface area of human erythrocyte lipids: reinvestigation of experiments on plasma membrane. *Science, 153*, 1010–1012.

Bloom, J. A., & Webb, W. E. (1983). Lipid diffusibility in the intact erythrocyte membrane. *Biophys J, 42*, 295–305.

Davson, H., & Danielli, J. F. (1943). *The Permeability of Natural Membranes*. Darien, CT: Hafner Publishing Company.

Dodge, J. T., Mitchell, C., & Hanahan, D. J. (1963). The preparation and chemical characteristics of hemoglobin-free ghosts of human erythrocytes. *Arch Biochem Biophys, 100*, 119–130.

Frye, C. D., & Edidin, M. (1970). The rapid intermixing of cell surface antigens after formation of mouse-human heterokaryons. *J Cell Sci, 7*, 319–335.

Gorter, E., & Grendel, F. (1925). On bimolecular layers of lipoids on the chromocytes of the blood. *J Exp Med, 41*, 439–443.

Heilbrunn, L. V. (1956). *The Dynamics of Living Protoplasm*. New York: Academic Press.

Jacobs, M. H. (1962). Early osmotic history of the plasma membrane. In Symposium on the Plasma Membrane, New York Heart Association, Inc. *Circulation, 26*, 1013–1021.

Luckey, M. (2008). *Membrane Structural Biology: with Biochemical and Biophysical Foundations*. New York: Cambridge University Press.

McMillan, P. N., & Luftig, R. B. (1973). Preservation of erythrocyte ghost ultrastructure achieved by various fixatives. *Proc Natl Acad Sci USA, 70*, 3060–3064.

Singer, S. J., & Nicholson, G. L. (1972). The fluid mosaic model of the structure of cell membranes. *Science, 175*, 720–731.

Weinstein, R. S. (1969). Electron microscopy of surfaces of red cell membranes. In G. A. Jamieson, & T. J. Greenwalt (Eds.), *Red Cell Membrane. Structure and Function*. Philadelphia: J. B. Lippincott Company.

Worthington, C. R., & McIntosh, T. J. (1973). Direct determination of the electron density profile of nerve myelin. *Nat New Biol, 245*, 97–99.

Yeagle, P. L. (2005). *The Structure of Biological Membranes* (2nd ed.). Boca Raton: CRC Press.

This page intentionally left blank

Chapter 4

Ionophores in Planar Lipid Bilayers

Jeffrey C. Freedman

Chapter Outline

I. SUMMARY

Planar lipid bilayers made from synthetic lipids and incorporating ionophores such as valinomycin or gramicidin, provide a useful tool for the study of membrane transport. Fusion of vesicles from native cell membranes into planar lipid bilayers provides information concerning ion channels that complements what is available from patch-clamp studies. Selective ion channels in planar lipid bilayers display high transport rates and low temperature coefficients, characteristics that distinguish ion channels from other modes of mediated transport. Finally, the features of cation transport by gramicidin in planar lipid bilayers are summarized. Detailed kinetic studies have shown that transport of cations and water through gramicidin occurs by means of single-file diffusion in which the ions and the waters cannot pass each other in the narrow part of the pore. The cation binds at a site near either end of the pore and then is driven over an energy barrier in the pore by the electrochemical gradient. The rate-limiting step, however, is the dissociation of the ion from the channel.

II. IONOPHORES

Ionophores are a class of compounds that form complexes with specific ions and facilitate their transport across cell membranes. An ionophore typically has a hydrophilic pocket (or hole) that forms a binding site specific for a particular ion. The exterior surface of an ionophore is hydrophobic, allowing the complexed ion in its pocket to cross the hydrophobic membrane. A list of ionophores showing the ion specificity of each is given in Table 4.1. Ionophores are useful tools in cell physiology experiments. *Nystatin* forms a channel in membranes for monovalent cations and anions and has proven useful for altering the cation composition of cells. *Gramicidin* forms dimeric channels specific to monovalent cations. *Valinomycin* carries K^+ across membranes with a high selectivity and has been used extensively to impose a high K^+ permeability on cell membranes. *Monensin* is a carrier with specificity for Na^+. *Hemisodium* is a synthetic Na^+ ionophore with an even greater degree of selectivity for Na^+. The *Ca^{2+} ionophore A23187* has been used extensively to permit entry of Ca^{2+} into cells, which normally have a low native permeability to Ca^{2+}, and thereby to activate a variety of cellular processes that are regulated by Ca^{2+}. *Nigericin* exchanges K^+ for protons and has been used in many studies of mitochondrial bioenergetics to alter electrical and chemical gradients for

TABLE 4.1 Ionophores and their Ion Selectivities

Conductive Carriers	
Valinomycin	K^+
Hemisodium	Na^+
FCCP, CCCP	H^+
Electroneutral Exchangers	
A23187	Ca^{2+}/Mg^{2+}; $Ca^{2+}/2H^+$
Nigericin	K^+/H^+
Channels	
Gramicidin	$H^+ > Cs^+ \approx Rb^+ > K^+ > Na^+ > Li^+$
Nystatin	Monovalent cations and anions

Cell Physiology Sourcebook. DOI: 10.1016/B978-0-12-387738-3.00004-4

protons. Ionophores such as *FCCP* and *CCCP* are specific for protons. Study of the mechanism of membrane transport mediated by ionophores has provided important conceptual insights relevant to the understanding of ion transport mediated by native transport proteins.

III. PLANAR LIPID BILAYERS

Planar lipid bilayers, also called *black lipid membranes* (BLMs), were first described in 1963 by Mueller and colleagues using the painting technique. A small aperture of about 1 mm diameter in a Teflon or polyethylene septum separating two aqueous salt solutions is coated by means of a beveled Teflon rod with a solution of pure lipids that are usually dissolved in decane. The thick lipid film covering the aperture then spontaneously thins to a bimolecular lipid leaflet surrounded by a thicker annular torus (Fig. 4.1A). The bimolecular portion of the film appears black because light reflected from the front surface undergoes a phase shift of 180° and destructively interferes with light reflected from the back surface. The film thickness of about 100 Å is small compared to the wavelength of visible light (3800−7600 Å). The lipids used to make the film are usually commercially purchased phospholipids − phosphatidylethanolamine (PE), phosphatidylcholine (PC), phosphatidylserine (PS), cardiolipin − and are sometimes supplemented with cholesterol for added stability. The proportions of the various lipids in the bilayer are set by dissolving the pure lipids in chloroform/methanol, mixing in desired proportions, evaporating the solvent with a stream of nitrogen and then re-dissolving the mixed lipids in decane.

The first attempts at reconstituting native ion channels into planar lipid bilayers were made by adding cell membrane extracts or partially purified membrane proteins into the aqueous solutions. Increases in electrical conductance were noted, often followed by breakage of the membrane; these effects were often due to adsorption of protein onto the bilayer and a generalized non-specific disruption of the membrane associated with increased leakage of current. Some success was achieved by adding membranes, membrane proteins or membrane extracts directly to the lipid-forming solution. Subsequently, techniques were developed for fusing vesicles, either native vesicles isolated from cell membranes or, alternatively, vesicles reconstituted with specific ion channels, into the planar lipid bilayer (see Miller, 1986, 1987). Tip-dipping is an alternative technique involving dipping the tip of a micropipette into a pure lipid film twice to form a bilayer covering the tip of the pipette so as to form a tight electrical seal, with a resistance of 1−5 GΩ (1 GΩ = 10^{15} Ω). Tip-dipping improves the time resolution and reduces noise due to the smaller area of membrane that is being examined; this technique allows the study of asymmetric bilayers and does not require solvents if the monolayers are formed from dried lipids (Coronado and Latorre, 1983).

The planar lipid bilayer technique is an excellent method for studying the transport kinetics of lipid-soluble ionophores. With planar lipid bilayers, one can easily vary the membrane lipid composition and also change the solutions or add reagents on either side of the membrane. Purified membrane channels may be studied apart from the regulatory mechanisms of intact cells and the resultant information should complement that obtained from

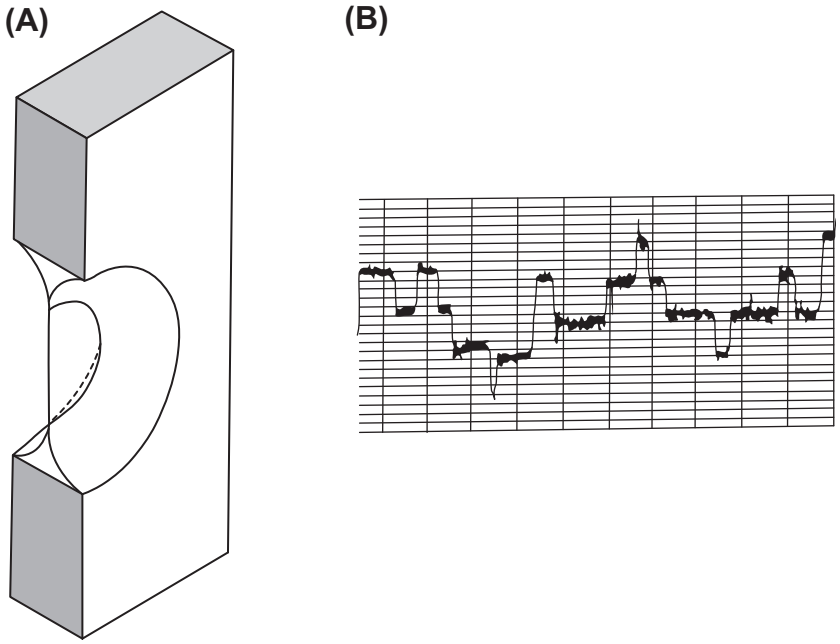

FIGURE 4.1 (A) Septum with planar lipid bilayer. (B) Traces showing currents through four dimeric gramicidin channels associating and dissociating in a black lipid membrane, as determined in the author's laboratory.

patch-clamp studies of intact cells. Planar lipid bilayers can also be used as an assay for channel purification. The planar lipid bilayer technique has several disadvantages. One is that the membranes tend to break. Once observed, the channels may disappear during the period of observation by diffusing into the thick annulus around the bilayer. The organic solvent, when present, may alter the properties of ion channels. The increases in conductance that are detected may not necessarily be physiologically relevant because the conductance properties may change during isolation of the vesicles or during purification of the channels and the conductances themselves may originate from small amounts of impurities or from contaminating cells. Some channels incorporate into bilayers more easily than others, so there may be long periods of time when nothing happens and the channel ultimately studied may not be the channel that was desired to be studied.

IV. ION CHANNEL PROPERTIES IN PLANAR LIPID BILAYERS

Studies of ion transport through channels in planar lipid bilayers revealed that ion channels are characterized by high transport rates and low temperature coefficients. Observations of single ion channels show that the current passing through a channel is on the order of picoamps (10^{-12} A). In order to convert 1 pA to the flux J in ions/s, note that the flux through a channel can be estimated from the single channel current i (C/s), using Avogadro's number N_A (ions/mol), the Faraday constant F (C/eq) and the ionic valence z (eq/mole).

$$J = \frac{iN_A}{Fz}$$

So for 1 pA of current carried by a univalent ion, we have:

$$J(ions/s) = \frac{(10^{-12}\text{C/s})(6 \times 10^{23}\ \text{ions/mol})}{(9.6 \times 10^{4}\ \text{C/eq})(1\ \text{eq/mol})} = 6 \times 10^{6}\ \text{ions/s}$$

or 6 million ions/s. By comparison, enzymes and membrane transporters that are not ion channels have turnover rates that are less than 10^5/s. For example, the Na^+,K^+-ATPase pumps at a maximal rate of about 100 ions/s. The fastest non-channel transporter is the Cl^--HCO^{3-} exchanger of red blood cells, which has an exchange rate of 10^4 ions/s at 25°C. The enzymes carbonic anhydrase and acetylcholinesterase have turnover rates of about 10^5/s. Thus, ion channels typically show high transport rates, one to several orders of magnitude faster than the fastest enzymes or non-channel transporters.

Ion channels were also found to have low temperature coefficients. Q_{10} is defined to be the change in the rate of a reaction when the temperature is increased by 10°C. Hodgkin and Huxley found that Q_{10} for Na^+ and K^+ currents in squid axon is 1.2−1.4, which is comparable to that for unrestricted diffusion of ions in free solution, a finding consistent with these ions moving through ion channels in nerve membranes. From thermodynamics, the Q_{10} is related to the enthalpy of activation for the reaction. The Q_{10} for Na^+ and K^+ currents in squid axon corresponds to an enthalpy of activation of only 5 kcal/mol. Enzymes and non-channel transporters have a Q_{10} of 3−4 or higher, corresponding to higher enthalpies of activation.

V. GRAMICIDIN

One of the best-studied ion channels in planar lipid bilayers is gramicidin, an antibiotic synthesized by *Bacillus brevis* against Gram-positive bacteria (hence the name). Gramicidin is commercially used as a topical bacteriostatic agent. The primary sequence of gramicidin A is a linear pentadecapeptide consisting of 15 alternating D- and L-amino acids. Natural sequence variations occur at position 11 with substitution of Trp with Phe (gramicidin B) or Tyr (gramicidin C). The natural mixture is termed gramicidin D and contains about 80% gramicidin A. All of the amino acids in gramicidin are hydrophobic with no free charges. Gramicidin is thus virtually insoluble in water. Both end groups are blocked: the N-terminal valine (the head) is blocked by a formyl group; the C-terminal tryptophan (the tail) is blocked by an ethanolamine. In membranes, the peptide chain is wound in a β-helix with a pore right down the central core of the molecule (Fig. 4.2). Carbonyl and imino

FIGURE 4.2 Space-filling model of gramicidin. *(From Urry, D.W. (1972) A molecular theory of ion-conducting channels: a field-dependent transition between conducting and nonconducting conformations. Proc Natl Acad Sci USA, 69, 1610-1614, with permission.)*

groups of the peptide bonds line the pore. All amino acid side chains extend away from the pore into the membrane lipid. The β-helix is stabilized by −NH ··· O− hydrogen bonds extending parallel to the pore axis. The aqueous pore is about 25 Å long and 4 Å in diameter. Gramicidin assumes different conformations in organic solvents; the double helical structure deduced from spectroscopic studies does not pertain to the channel conformation in membranes. The conducting pore is formed by a head-to-head dimer linked transiently by six hydrogen bonds. Evidence for a head-to-head dimer is that chemical modifications at the N-terminus (the head) drastically affect channel formation, whereas similar modifications at the C-terminus (the tail) do not. With fluorescent analogs of gramicidin, it was possible to measure simultaneously the conductance and the concentration of gramicidin in the membrane. The conductance was proportional to the square of the gramicidin concentration, and the equilibrium constant for dimerization was determined (Veatch et al., 1975). Since gramicidin is synthesized non-ribosomally in vivo and contains D-amino acids that are not normally genetically coded, site-directed mutagenesis using recombinant DNA methods is not possible. Chemical synthesis has permitted alterations of the primary sequence for studies relating chemical structure to ion transport function.

Hladky and Haydon (1972) first observed single-channel conductances with gramicidin in planar lipid bilayers (see Fig. 4.1B for an example). The channel lifetimes are on the order of a second (compared to ms for Na^+ channels). With symmetrical 0.1 M NaCl, the single-channel current is 1.0 pA at 200 mV, corresponding to a single-channel conductance of 5 pS and a flux of 6.3×10^6 ions/s. The high flux is consistent with a channel mechanism. The highest conductance so far reported is 107 pS at 23°C with 3 M RbCl solutions in a neutral membrane made from glycerylmonooleate-hexadecane mixtures. The mean single-channel lifetime depends on lipid dynamics. For example, channels in thicker membranes, where pinching of the membrane may be required for dimer formation, have shorter lifetimes. Greater interfacial tension shortens channel lifetime.

Despite the absence of fixed negative charges in the pore, the gramicidin channels are cation selective (Myers and Haydon, 1972). The permeability ratios are determined from bi-ionic potentials, whereas the conductance ratios are determined in symmetrical salt solutions. The channels are ideally selective to cations. With a gradient of monovalent chloride salt, the reversal potential equals the Nernst potential for the cation, implying that the permeability to Cl^- is negligible. The channel is also impermeant to divalent cations. The selectivity order corresponds to Eisenman's sequence I, indicative of a weak field strength interaction between the pore and the ions.

The selectivity for K^+:Na^+ is only about 4:1 − much less than that of the delayed rectifier K^+ channel (20:1 to 100:1), which is primarily responsible for resetting the resting potential of nerve and muscle following activation, and very much less than that of the carrier valinomycin (more than 1000:1).

The gramicidin channel is blocked by divalent cations (e.g. Ca^{2+}, Ba^{2+} and, to a lesser extent, Mg^{2+} and Zn^{2+}). These ions probably block by binding near the channel mouth and occluding entrance into the channel. Flicker block may be observed with iminium ions; this transient block is thought to result from transient association of these ions with the channel wall during permeation.

Passage of ions or water through gramicidin is by means of *single-file transport*. The high proton conductance, and the known geometrical dimensions of the pore, suggest that the pore is filled with a continuous column of hydrogen-bonded water molecules (2.8 Å). The diffusive water permeability through gramicidin in bilayers has been measured with tracers and is about 10^8 water molecules per second at low ionic strength. Water permeation is probably by means of a Grotthus, or "hopping" mechanism (see Chapter 1). The pore diameter is too small to permit passage of urea (5 Å diameter) or larger non-electrolytes. Consequently, a *streaming potential* develops when non-electrolyte is added to the salt solution on one side of the bilayer to make an osmotic gradient. In another type of study, an *electro-osmotic* volume flow occurs when an ionic current is passed across the membrane. For single file transport, the number N of water molecules in the channel is obtained by dividing the water flux ϕ_w (molecules/s) by the ion flux J (ions/s):

$$N = \frac{\phi_w}{J}$$

For gramicidin channels, the number N of water molecules in the pore is 5−6. Quantitative analysis of streaming potentials and electro-osmosis indicates that an ion passing through a gramicidin channel drags with it a column of about six water molecules in single file.

The channel is too narrow for water molecules to slip past each other; nor can ions and water molecules pass each other in the single-file part of the channel. However, sodium ion occupancy does not depress water permeability. The water permeability of a channel at high [Na^+], when the channel always contains a sodium ion, is essentially the same as that of a channel at low [Na^+], when the channel never contains a sodium ion. Thus, water can pass the sodium ion somewhere in the channel, presumably near an ion-binding site at the end of the channel.

The single-channel conductance for sodium increases as a function of Na^+ concentration, but then saturates at around 1 M NaCl. Half-maximal conductance is reached at 0.31 M NaCl, at which concentration half the channels have

one Na^+ ion and half are empty. The curve of conductance g versus $[Na^+]$ fits a single-ion occupancy model, given by:

$$g_{Na} = \frac{g_{max}[Na^+]}{C_{1/2} + [Na^+]}$$

where $C_{1/2}$ is the concentration of Na^+ that gives half-maximal conductance. The single-ion occupancy model indicates that an ion-binding site, or energy well, exists near the end of the channel. Since the dimeric structure is symmetrical, there must be two binding sites, one at each end, but only one at a time is occupied by sodium. Additional compelling evidence for single-ion occupancy for sodium is that the flux ratio equation is satisfied at all sodium concentrations ranging from 0.1 to 5 M. Given that single-file transport occurs, a net flux in one direction would inhibit the unidirectional flux in the opposite direction, thus producing deviations from the flux ratio equation if the two Na^+ binding sites were simultaneously occupied. Consequently, double occupancy must not occur for Na^+. These two lines of evidence imply that there is never more than one sodium ion at a time in the gramicidin channel (Sandblom et al., 1977).

The dehydration energy for ions is of the order of 100 kcal/mol; the selectivity sequence indicating a weak field strength interaction with the pore suggests that ions do not dehydrate during passage through the gramicidin pore. The hydration shell of water around the permeating ions is partially replaced by hydrophilic groups lining the channel wall. The dielectric constant is lower in the middle of the pore than near the ends of the pore. Thus, the electrostatic energy of the ion in the middle of the pore is greater than at either end of the pore. The actual flux of Na^+ at high $[Na^+]$ is within a factor of 5 of the maximal possible flux of Na^+, given the water permeability of an ion-free channel. This means that there is no significant electrostatic energy barrier to Na^+ movement through the channel. The rate of Na^+ transport is largely determined by the necessity for six water molecules to be moved along with the ion. Thus, two energy wells near the ends of the channel are separated by a low-energy barrier (or a series of small barriers) in the middle of the channel. Strict single filing of water and ions occurs between the two wells, whereas water can pass a sodium ion sitting in either well. The kinetic equations describing single-file transport are complex and beyond the scope of this text (see Finkelstein and Anderson, 1981).

Cation transport through gramicidin also involves channel motions, subconductance states and channel flickering. The gramicidin channel is not rigid but, instead, motion of the peptide appears to be essential to its function. Solid-state nuclear magnetic resonance (NMR) measurements of ^{15}N-labeled Ala 3 and Leu 4 indicate rocking motions of $\pm 8^\circ$ and $\pm 15^\circ$, respectively, for these sites in the absence of ions. Molecular dynamics simulations confirm local distortions in gramicidin structure during ion transport. Peptide rotation is not necessary for function since the channel is active in gel-phase lipid. Subconductance states, or "mini-channels", are frequently observed as an intermediate in the opening and closing of normal channels. These may constitute from 5 to 40% of the channel events in a single-channel recording, with lifetimes similar to those of normal gramicidin channels. The low-conductance state may correspond to less common side-chain conformations with altered coordinating ability in the conducting pore. Channel flickering to a low-conductance state with lifetimes ranging from 20 μs to about 1 ms is also observed. Rapid flickering may correspond to a state in which the dimer is partially dissociated. An increase in membrane thickness increases the frequency of these low-conductance states. This rather detailed analysis of ion channel permeation through gramicidin channels in planar lipid bilayers provides some basis for understanding ion permeation through native ion channel proteins in cell membranes.

BIBLIOGRAPHY

Coronado, R., & Latorre, R. (1983). Phospholipid bilayers made from monolayers on patch-clamp pipettes. *Biophys J, 43*, 231–236.

Ehrlich, B. (1992). Planar lipid bilayers on patch pipettes: bilayer formation and ion channel incorporation. *Meth Enzymol, 207*, 463–470.

Finkelstein, A. (1974). Bilayers: formation, measurements, and incorporation of components. *Meth Enzymol, 32B*, 489–501.

Finkelstein, A., & Andersen, O. S. (1981). The gramicidin A channel: a review of its permeability characteristics with special reference to the single-file aspect of transport. *J Memb Biol., 59*, 155–171.

Hille, B. (2001). *Ion Channels of Excitable Membranes* (3rd ed.). Sunderland, MA: Sinauer Associates Inc.

Hladky, S. B., & Haydon, D. A. (1972). Ion transfer across lipid membranes in the presence of gramicidin A. I. Studies of the unit conductance channel. *Biochim Biophys Acta, 274*, 294–312.

Labarca, P., & Latorre, R. (1992). Insertion of ion channels into planar lipid bilayers by vesicle fusion. *Meth Enzymol, 207*, 447–463.

Miller, C. (1986). *Ion Channel Reconstitution*. New York: Plenum Press.

Miller, C. (1987). How ion channel proteins work. In L. K. Kaczmarek, & I. B. Levitan (Eds.), *Neuromodulation. The Biochemical Control of Neuronal Excitability* (pp. 39–63). New York: Oxford University Press.

Montal, M., & Mueller, P. (1972). Formation of bimolecular membranes from lipid monolayers and a study of their electrical properties. *Proc Natl Acad Sci USA, 69*, 3561–3566.

Mueller, P., Rudin, D. O., Ti Tien, H., & Wescott, W. C. (1963). Methods for the formation of single bimolecular lipid membranes in aqueous solution. *J Phys Chem, 67*, 534–535.

Myers, V. B., & Haydon, D. A. (1972). Ion transfer across lipid membranes in the presence of gramicidin A. II. The ion selectivity. *Biochim Biophys Acta, 274*, 313–322.

Sandblom, J., Eisenman, G., & Neher, E. (1977). Ionic selectivity, saturation and block in gramicidin A channels: I. Theory for the

electrical properties of ion selective channels having two pairs of binding sites and multiple conductance states. *J Memb Biol, 31*, 383−417.

Veatch, W. R., Mathies, R., Eisenberg, M., & Stryer, L. (1975). Simultaneous fluorescence and conductance studies of planar bilayer membranes containing a highly active and fluorescent analog of Gramicidin A. *J Mol Biol, 99*, 75−92.

Woodbury, D. J., & Hall, J. E. (1988). Role of channels in the fusion of vesicles with a planar bilayer. *Biophys J, 54*, 1053−1063.

Woodbury, D. J., & Miller, C. (1990). Nystatin-induced liposome fusion. A versatile approach to ion channel reconstitution into planar bilayers. *Biophys J, 58*, 833−839.

Wooley, G. A., & Wallace, B. A. (1992). Model ion channels: gramicidin and alamethicin. *J Memb Biol, 129*, 109−136.

Chapter 5

Cell Structure

Michael S. Forbes

Chapter Outline

I. INTRODUCTION

Vertebrate cells (and to a degree, cells of any type) are variations on basic themes, namely the classes of substructures of which the cells are composed. While certain disciplines of biomedicine can be engaged in without recourse to cell structure, others such as pathology are vitally dependent upon this knowledge. Though this chapter, formerly entitled "Ultrastructure of Cells", has appeared in several versions of this book, the editor and publishers have made their wishes clear, that the book is now – rather than being a "Sourcebook" – intended rather to serve as a *textbook*. Because of this, I have broadened the title to "Cell Structure" so as to provide a more useful context. Cell structure cannot be considered in practical terms without considering the various techniques that belong to *microscopy*. Since the student involved in biomedical study and practice is far more likely to have access to the so-called light (as opposed to electron) microscopes and, since the electron microscope – in addition to its cost, availability and difficulty of operation – has some severe limitations, I have included pictures of cells obtained from both sources. Since examples of many of the different cell components are present in pictures throughout the chapter (see, e.g. Fig. 5.7), only a minimal attempt has been made to make a close correlation of plates of figures with the individual sections on Nucleus, Mitochondria, etc.

II. TECHNIQUES

What follows is intended to acquaint the reader with just how structure can be documented. The potential investigator will benefit wherever possible by availing him/herself of the opportunity of actually observing and, when possible, performing the procedures described below, in order to understand the process, all the better to interpret the results.

First some basic facts: light microscopes depend on a beam of light, passing through a specimen, to form an image. Depending on the source of light and other mechanical features, light microscopes include instruments known variously as "bright-field", fluorescent, differential-interference-contrast (a.k.a. "Nomarski") and confocal scanning microscopes, among others. Since the beam of light contains a range of wavelengths, different stains interact with the light to generate images that have different colors which correspond to different cell types and intracellular structures. Transmission-type electron microscopes use a beam of electrons that pass through the specimen, which is kept in a vacuum, to generate what amounts to a "shadowgram", since more dense regions deflect the electrons and less dense ones allow the electrons to pass through. This results in a grayscale image, since by and large the beam of electrons has a limited wavelength and thus does not generate colors (micrographs – which is the

Cell Physiology Sourcebook. DOI: 10.1016/B978-0-12-387738-3.00005-6

term for pictures made with a microscope – from electron microscopes that appear in color in some magazines have been artificially colored). Those with some experience with microscopes will note that I have ignored the so-called "dissecting" microscope which, although it uses light as illumination only shows the surface of, say, an insect or an isolated organ; so too I have not spoken of the scanning electron microscope, or SEM, which produces much the same sort of picture as the dissecting light microscope (albeit, again, in shades of black and gray), since it either bounces electrons off a surface or, more commonly, generates secondary electrons just below the surface to form an image.

All that established, let us compare only microscopes that use a transmitted beam (i.e. one that passes through a specimen). It turns out that the preparation techniques for light microscopes (LMs) and transmission electron microscopes (TEMs) have a great deal in common. Though in science there are always exceptions (a phrase you commonly hear is "*It's not that simple, though*"), *in general*, to view something in a microscope one has to: (1) *preserve it* (the term "fix" is usually used, implying immobilization by techniques such as freezing, immersing in chemicals, or even heat-inactivating ["cooking" for lack of a better term]); (2) *dehydrate it* so as to make it compatible with anhydrous materials such as paraffin or plastic; and (3) *infiltrate it* ("embed") with those media. This last step is to stabilize the specimen (for our purposes, let us say a piece of brain, liver or kidney) so that it can be cut ("sectioned") into thin slices ("sections"). Such sections range from one micrometer (abbreviated as "μm" and equivalent to roughly four one hundred-thousandths of an inch) in thickness up to 50 μm or so for LM examination, and generally in the range of 0.05–0.1 μm (known as *ultrathin* sections) for the TEM. Obviously, the μm to inch conversion is unwieldy; one can readily estimate sizes in microscopic images by using a couple of rules of thumb: (1) in the LM, the practical limit of resolution (meaning essentially what one can clearly distinguish as a separate structure) is about 1 μm; (2) mitochondria, when they can be resolved, are usually on the order of 1–2 μm in size (see Figs. 5.2, 5.4A, 5.5A, 5.6C, 5.7, 5.9, 5.12); also, the contractile units ("sarcomeres": see Figs. 5.6C, 5.10) in skeletal and cardiac muscle are around 2 μm in length.

The purpose of having sections is…? …Simply to have the specimen thin enough so that the imaging beam can pass through it! This necessity leads to a basic limitation of microscopy: only a sample, a mere slice of a specimen is being examined, which can lead to erroneous conclusions about three-dimensional relationships. Also, while on the subject, interpretation of microscopic images should be recognized as an exercise in "making dynamic conclusions from static entities". In any event, for LM specimens, paraffin – similar to the stuff some of our grandmothers and great-grandmothers may have used to seal their jars of home-made jam and jelly – is used. Specimens embedded in paraffin can be readily sectioned with a razorblade, though usually dedicated "knives" are used, designed to fit into a cutting machine – a "microtome" – that can be adjusted to cut sections of consistent thickness. These sections are floated onto glass microscope slides, usually about 1"×3" (2.54×7.62 cm) in size. To process the sections further, however, the paraffin in them must be removed with some organic solvent such as xylene, and then gradually *rehydrated* – brought back to water – to stain them. This deparaffinization and rehydration serves two purposes: it removes the paraffin, which would interfere with the passage of the LM's light beam, and it renders the sectioned material – the liver, heart, kidney, whatever – compatible with a wide variety of stains (including immunohistochemical reagents), which are prepared as aqueous solutions and would not react with the material if it were still in paraffin.

TEM specimens also are cut into extremely thin slices with some sort of sharp blade, but in order to have a hard enough embedment, some sort of plastic is used to infiltrate the specimen. Most often this is an epoxy-type plastic, somewhat similar to the two-component glue (resin and catalyst) that one uses in "civilian" life. Here there is seen a substantial difference between LM and TEM preparation, though: for the TEM, the embedding plastic is *not* removed from the specimen, since the section – which is cut either with a knife edge made of glass or diamond, and affixed onto a 3-mm circular piece of metallic mesh known as a *grid* – has to withstand imaging within a vacuum chamber, through which there passes an electron beam of perhaps 100 000 volts in penetrating/imaging power. The "ultrathin" sections on their grids, rather than being stained with colored dyes, instead are contrasted with heavy metals (including osmium, uranium and lead), which enhance details of the shadowgram spoken of earlier, in particular their unit membranes (see below). The electrons are deflected or let pass at various angles, depending on the density of the parts of the section, and expose an image either on a piece of film in the microscope or, more commonly these days, the electron pattern is converted into a digital image (as also is now routinely the case with the LM).

So as a result of these processes, we can visualize either *structure* as seen through the LM on a glass slide, or *ultrastructure* (meaning literally "beyond structure"; an unfortunate term, but one that has nevertheless become firmly embedded in the literature) in the TEM, on a specimen grid. Structure and ultrastructure remain compatible, though, with limitations at both ends of the spectrum: the images in Fig. 5.1 are of the same type of structure (rat kidney glomerulus) and the specialized nature and specific appearance of the various cells can be appreciated in one

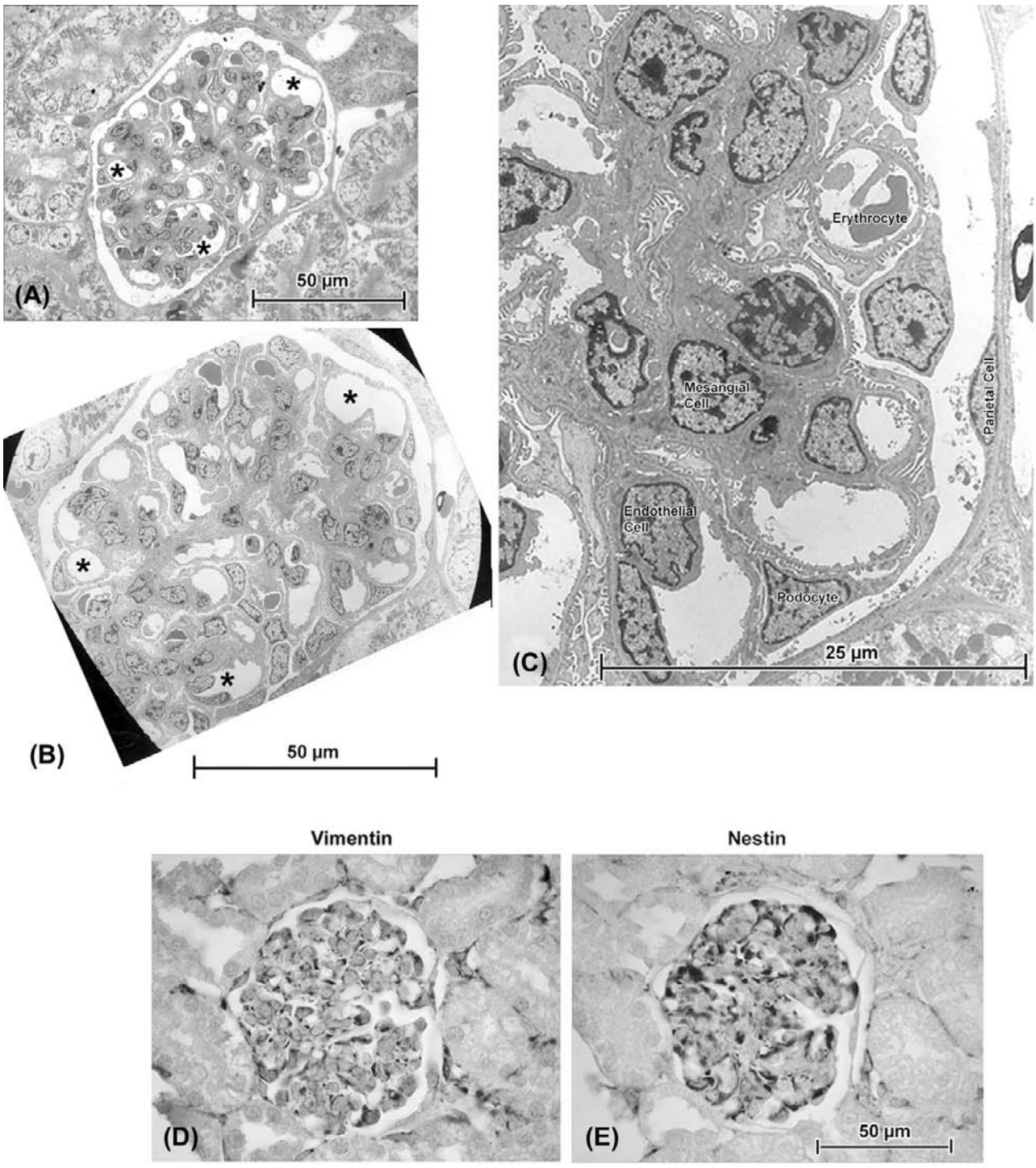

FIGURE 5.1 (A) and (B) are consecutive serial sections, taken with a diamond knife on an ultramicrotome, of a glomerulus in rat kidney. The semithin section ((A): ca. 0.25 µm thick) was cut immediately before the ultrathin section ((B): ca. 900 Å, i.e. 0.09 µm thick) and there is close correlation between such features as the pattern of capillaries (* in both micrographs). An enlarged view of the electron micrograph (C) identifies examples of the various cell types found in glomeruli. For most purposes, the ultrathin section – which required considerably more effort to document than the semithin – does not provide any special advantage to the investigator unless high-resolution details such as podocyte processes, endothelial fenestrations, cytoskeletal filaments or intercellular junctions are specific subjects of interest. (D) and (E) are serial consecutive paraffin sections in which immunohistochemical staining is readily accomplished: here the podocytes show reactivity (dark staining) for both vimentin, a structural protein, and nestin, a protein which under normal conditions is restricted to these cells.

way or another in each micrograph, regardless of its origin. By combining the techniques (plastic embedding and serial sectioning with a diamond-edge for both LM and TEM: Figs. 5.1A and B, respectively) bring the two microscopic images into even closer correlation. An important thing to note is that, at the enlargements (magnifications) shown, which are low for a TEM but high for an LM, the LM gives just about as much general information as the TEM! Kidney structure, which I have been studying for the past couple of decades, can be fantastically complicated when viewed in a TEM, since the various cylindrical structures, including epithelial tubules and blood vessels that make up the majority of the organ, weave in and out of section, and particularly so in ultrathin sections (Fig. 5.2). I have found that so-called "semithin" plastic sections – on the order of a quarter of a micrometer in thickness – bridge the gap between the LM and TEM nicely (Fig. 5.1). It is somewhat ironic, however, to remember that many kidney ailments depend absolutely on the TEM and thin sections for their diagnosis, since structures such as immune deposits are best appreciated there. Certainly, one must choose one's goals carefully when choosing to do electron microscopy, but this is necessitated by the presence of many features of cells that are either poorly resolved or are practically invisible with light microscopy (Fig. 5.8 demonstrates an example of the former situation, where the TEM is required to make positive identification of autophagic bodies).

Even though I have described microscopy largely in terms of slices of tissue, it has been necessary to diverge from this in several figures (Figs. 5.4B, 5.4C, 5.5B, and 5.11B,C) to illustrate an important concept of unit membrane structure by means of the procedure known as "freeze-fracture", in which a cutting action is retained in terms of breaking a specimen at low temperature and under vacuum, with subsequent deposition of a carbon and metal film to make a replica that demonstrates the different sides ("faces") of these membranes that in large part define and limit many cell components (including the plasmalemma, nuclear membrane, Golgi and endoplasmic reticulum, mitochondria and lysosomes).

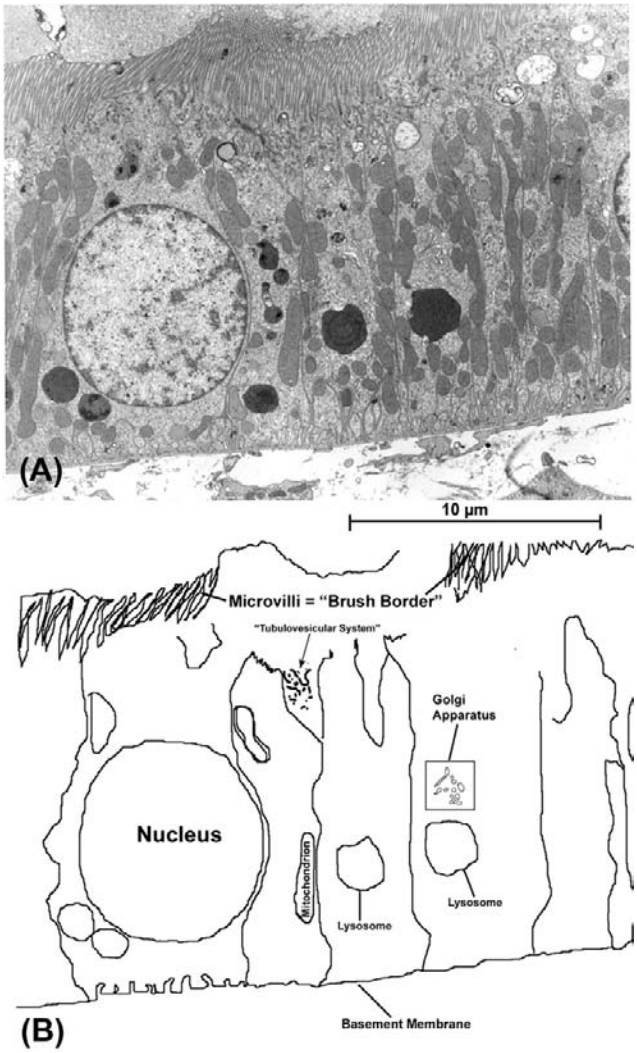

FIGURE 5.2 (A) Though a "typical" cell exists only in idealized diagrams, one type that is often used to illustrate general structural features is the epithelial cell of kidney tubules (here shown in a rat proximal tubule). In (B), a tracing of some of the cells and their organelles is shown. These cells exhibit the "polarity" that is a consistent feature of epithelial cell layers, with apical specializations ("brush border", consisting of tightly-packed thin cell-membrane extensions known as microvilli) that provide the cell tip with a greatly enlarged surface area for absorption and release and a basal reinforcing layer of extracellular material on which the cells sit ("basement membrane").

III. CELL THEORY

The appreciation of the very existence of individual cells did not come about in the form of a linear, smooth progression. Despite Robert Hooke's often-cited observations (ca. 1665) of individual units (actually cell walls; the living cells were long gone) in thin sheets of cork, aided by one of the earliest microscopes (he likened the units to cubicles [L. "cellula: small rooms"] occupied by monks or other sorts of prisoners, thence the term "cells"), centuries later the cellular nature of some tissues was still questioned. Though in the late 1830s Matthias Schleiden and Theodor Schwann had proposed that most tissues were composed of individual cells, toward the end of the 19th century the *reticular theory* of Joseph von Gerlach and Camillo Golgi came to stand as an exception. This posited that nervous tissue was a *syncytium*, i.e. a system possessing multiple nuclei but having its cell substance continuous through its entire network. Opposed to reticular theory was the *neuronal theory* of Santiago Ramon y Cahal, whose exquisite staining techniques and careful microscopic renderings demonstrated neurons to be individual entities (the accuracy of his drawings has in fact been confirmed in modern times, by examination of his original preparations

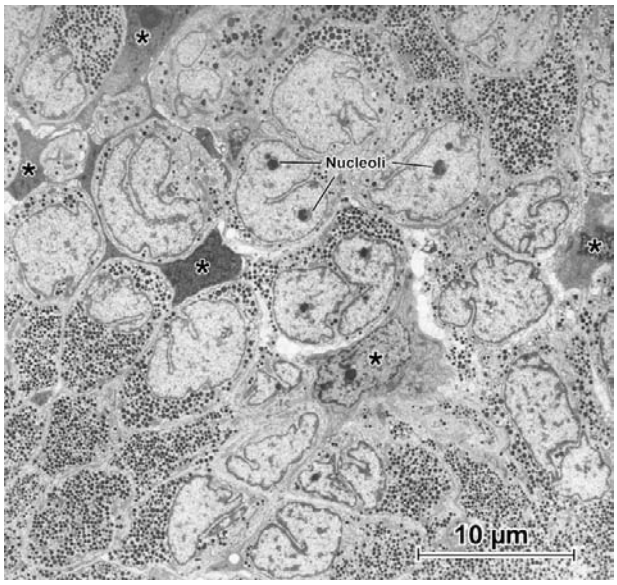

FIGURE 5.3 Pituitary gland. Low magnification ("survey") transmission electron micrograph shows the dense concentrations of granules that contain the hormones produced by the secretory cells. Note the elaborate profiles of the nuclei (several nucleoli are indicated by Nuc). A supporting framework of "stellate" cells (examples at *) is recognizable because of their extended cell processes. It is instructive to point out what this picture does not show. Though the glial-like stellate cells are evident because of their opaque cytoplasm and lack of secretory granules, on the basis of their ultrastructure, the granulated cells themselves cannot be identified as to their specific hormonal content; for this, additional coordinated approaches are needed, including additional characterization and measurements of the granules at higher magnification, correlation of precise location of these cells within the whole gland and histo- and immunocytochemical staining both at the LM and TEM levels, in addition to biochemical analysis to confirm the presence of the hormones in question.

and three-dimensional reconstruction from them by the confocal scanning light microscope).

While the battle over nerve structure was carried out in Europe, an international controversy developed in the case of the heart, with cellular theory being espoused by the camp of Zimmerman in Germany (among others) and the contrasting view – namely that heart muscle was a true syncytium – being defended by Harvey Ernest Jordan in America (Jordan, incidentally, was the first dean of the University of Virginia School of Medicine, where this review is being written). In truth, both nervous tissue and cardiac muscle *behave* as if they were true syncytia, with impulses being passed from cell to cell; in the case of nerve this most often happens through the intercellular contacts known as *synapses* (see Fig. 5.12C), whereas in heart, the muscle cells are held together via elaborate arrays of intercellular connections known collectively as *intercalated disks*, components of which are the basis of cell-to-cell transmission (see Fig. 5.11D).

Ultimately refinements to microscopic equipment – in particular the invention of electron microscopes – carried the day for the establishment of cell theory as valid for both brain and heart, since the actual separations between adjacent cells could finally be visualized. This did not happen until the 1950s, however, and even in the face of definitive electron microscopic evidence, some clung to the syncytial theory of heart organization into the following decade (for further review of this, see Forbes and Sperelakis, 1985).

IV. THE PLASMA MEMBRANE AS THE BASIS OF CELLULARITY

To understand the fundamental mechanisms that constitute the normal activities of any organism, it is essential to consider the structural correlates that underlie these activities. Once cell theory was established, there arose another important question which revolved around the nature of the barriers that separate cells from one another and from the surrounding environment. A major breakthrough in resolving this question was made independently by Gorter and Grendel in the 1920s and Davson and Danielli in the 1930s. The latter authors examined the behavior of phospholipids in aqueous environments and determined that the most favorable energetic configuration was a bilayer having the hydrophilic polar headgroups located at the water interface and the hydrophobic non-polar tails apposed to each other. Such a cell membrane ("plasmalemma"), formed by a phospholipid bilayer, would be impermeable to fluids and charged species, such as ions. Thus it would isolate the cell contents from the extracellular environment. It should be understood that those cell contents, specifically organelles including the Golgi complex, mitochondria and endoplasmic reticulum, are themselves composed in large part of similarly-constructed unit membranes.

Proteins were recognized as being closely associated with the phospholipid bilayer and early models proposed that they form a layer on either side of the membrane (i.e. a protein–lipid sandwich). This model remained hypothetical until the introduction and refinement of the transmission electron microscope (TEM) in the 1930s and 1940s; in the TEM, resolution was so much improved that, in properly-prepared "ultrathin" sections, all cells were bounded by a trilaminar membrane, 70 Å (=7 nm) thick that to some observers resembled a "railroad track" consisting of two darker lines separated by a relatively clear inner region (Fig. 5.4A). This structure was termed the unit membrane by J.D. Robertson in the early 1950s. It had already been recognized by Davson and Danielli that many of the proteins associated with the cell membrane were tightly attached, since they were not extracted by changing the ionic strength of the bathing solutions or even by mild detergent treatment. Thus, the notion of a phospholipid bilayer with a coating of protein had evolved, by the 1960s, into a "fluid mosaic" model proposed by Singer and Nicholson. In this model, there were both peripheral

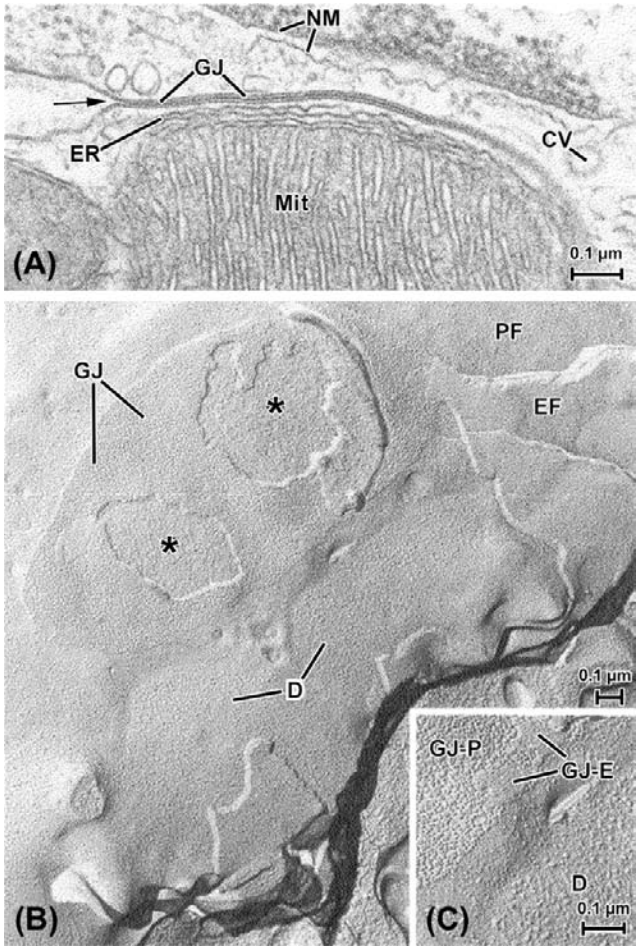

FIGURE 5.4 Unit membranes of cells. (A) Cell border formed by two cardiac muscle cells. Unit membranes are the basis of most of the structures shown here, including the double membrane of the nucleus (NM), the outer envelope and inner membrane shelves (cristae) of a mitochondrion (Mit) and several vesicular bodies, including a coated vesicle at the right of the picture (CV). The membrane-based, multilayered structure that dominates this view is a specialized adhesion known as a gap junction (GJ), formed between the two cells where the outer faces of the two cells' plasmalemmata come into close apposition. At the arrow, the relatively unspecialized cell surface membranes are clearly continuous with the membranes that form the gap junction. Note the membrane-based tubule of endoplasmic reticulum (ER) sandwiched between the mitochondrion and the gap junction. (B) and (C) show cardiac cell membranes as revealed by the technique of freeze-fracture, in which tissue is quickly frozen and broken and a thin (ca. 2−3 nm) coating of metal is evaporated onto the specimen and stabilized with a thicker carbon film (similar techniques were used to produce the replicas depicted in Figs. 5.5B, 5.11B,C). The tissue is then digested away, leaving only the metal−carbon replica of the fractured surfaces. The fracturing process specifically cleaves unit membranes to expose their inner "faces", thus showing the intramembranous particles (IMPs) that correspond to a variety of functionally important proteins. This also demonstrates the characteristic asymmetry inherent within a unit membrane; typically there is a greater density of larger particles on the P face, the face adjacent to the protoplasm (cytoplasm), whereas the E face (that closest to the "ectoplasm", i.e. the extracellular space) is characteristically smoother. Compare, for example, the regions labeled PF and EF at the upper right corner of (B). This region shows the relatively unspecialized plasmalemmas of two apposed cells (cf. the cell surface membranes in (A)). The large oval body is a gap junction between the two muscle cells, broken away in two regions (*) to expose underlying intracellular structures, probably mitochondria (a similar association is shown in the thin section in (A)). The detail shown in panel (C) shows that though this gap junction replica consists mainly of large P-face particles (GJ−P), in some areas, small regions of the junction's E face (labeled GJ−E) have adhered, which are characterized by a finer topography of pit-like depressions, into which the P-face particles fit in the intact gap junction. In (B), two smaller ovoid membrane regions (D) appear which correspond to another type of intercellular junction, the desmosome (see also Fig. 5.11). The P-face particles belonging to desmosomes (also shown at higher magnification in (C)) are larger and more coarse-appearing than those of either the gap junction or the unspecialized plasmalemma.

(or extrinsic) and integral (or intrinsic) membrane proteins. Peripheral proteins are associated with the inner and outer surfaces of the membrane, but are not anchored in it. Integral membrane proteins are actually embedded in at least one leaflet of the phospholipid bilayer (Figs. 5.4B,C) and some traverse the entire thickness of the membrane.

The fluid mosaic model was more consistent with functional studies, which clearly demonstrated that cell membranes were not totally impermeable, but rather were semipermeable. The integral membrane proteins included ion channels that acted as low-resistance pores, as well as energy-dependent pumps. This model better accounted for the establishment of ionic gradients and the influx or efflux of ions under various conditions.

As mentioned, the extrinsic proteins are membrane-associated rather than actually embedded in the lipid bilayer. The extracellular matrix exists on the outer cell surface as a layer of varying thickness, known as the basement membrane or *basal lamina*, depending on the cell type (see Figs. 5.2 and 5.7). Historically, this coating was considered to be an inert structural framework composed of collagen and elastic fibrils. Not only can the extracellular matrix act as a filtration device but, in addition, recent evidence points to a more dynamic role, with proteins such as fibronectin and laminin active in stimulating a number of cellular activities. These functions are likely mediated through interactions with intrinsic membrane proteins which, in turn, are connected to and exert influences on the extrinsic membrane proteins that form subplasmalemmal networks on the inner (cytoplasmic) surface of the cell membrane. Ultimately, signals from outside the cell may be communicated deep within the cell via the interior membrane systems and elements of the cytoskeleton and may even influence gene activity in the nucleus. In this sense, the unit membranes can be considered to represent the "nervous system" of the cell.

The contents of the cell enclosed by the plasmalemma are collectively known as the cytoplasm. The cytoplasm is not an amorphous soup, but in fact contains a number of distinct structural elements known as organelles

(by analogy to the different organs of the body). Figure 5.2A is an electron micrograph of kidney tubule epithelial cells, often considered to be a characteristic type of animal cell, with a diagrammatic representation of the same micrograph in Fig. 5.2B, where some of the organelles are shown; these serve to compartmentalize different activities of the cell, just as the organs perform different functions within the body.

V. NUCLEUS

The most prominent organelle within the cell is readily visible in the light microscope and, since it is most often located at the cell center, it came to be called the *nucleus*. The nucleus contains most of the cell's DNA and its genetic apparatus as well. Because it is the locus of the genetic programming that directs cytoplasmic synthetic activity, as well as the site at which cell division is initiated, the nucleus can be considered as the organelle that corresponds in the cell in part to the reproductive system of the body.

In most cells, the nucleus is an ovoid body, but it can assume a variety of shapes and sizes (see Figs. 5.1, 5.2, 5.3 and 5.5). Multiple nuclei are characteristic of certain cell types (e.g. skeletal myocytes). Early EM observations discovered the nucleus to be bounded by the *nuclear envelope*, essentially a double unit membrane (see Fig. 5.4A) and noted as well a dense intranuclear body, the *nucleolus* (see Figs 5.3, 5.5). The nucleus was characterized in addition by darker material (*heterochromatin*), found interspersed with the lighter euchromatin (see Fig. 5.2). Beyond these initial descriptions, the regional specializations of the nucleoplasm remain rather poorly understood. Recent studies with antibody localization of nuclear-specific proteins demonstrate the presence of domains within the nucleoplasm; these are not readily apparent even with ultrastructural inspection, but appear to be organized through attachment to the filamentous proteins of the nuclear matrix. On the basis of compartmentation of DNA polymerases and RNA splicing factors, it has been suggested that discrete domains are involved in different processes, such as transcription and translation of the genetic material.

As noted earlier, the nuclear envelope is a double bilayer. The outer membrane, often decorated with spherical RNA-containing particles called *ribosomes*, is often continuous in places with a network of cytoplasmic membranes known collectively as the endoplasmic reticulum (ER) (e.g. Fig. 5.6B). The nuclear envelope has a proteinaceous lamina at its inner surface, which is composed of cytoskeletal proteins called lamins; the major portion of the envelope is the prominent double membrane itself (see Fig. 5.4A), which is interrupted at periodic intervals by circular discontinuities, the *nuclear pore complexes* (see Fig. 5.5B,C). Detailed studies have

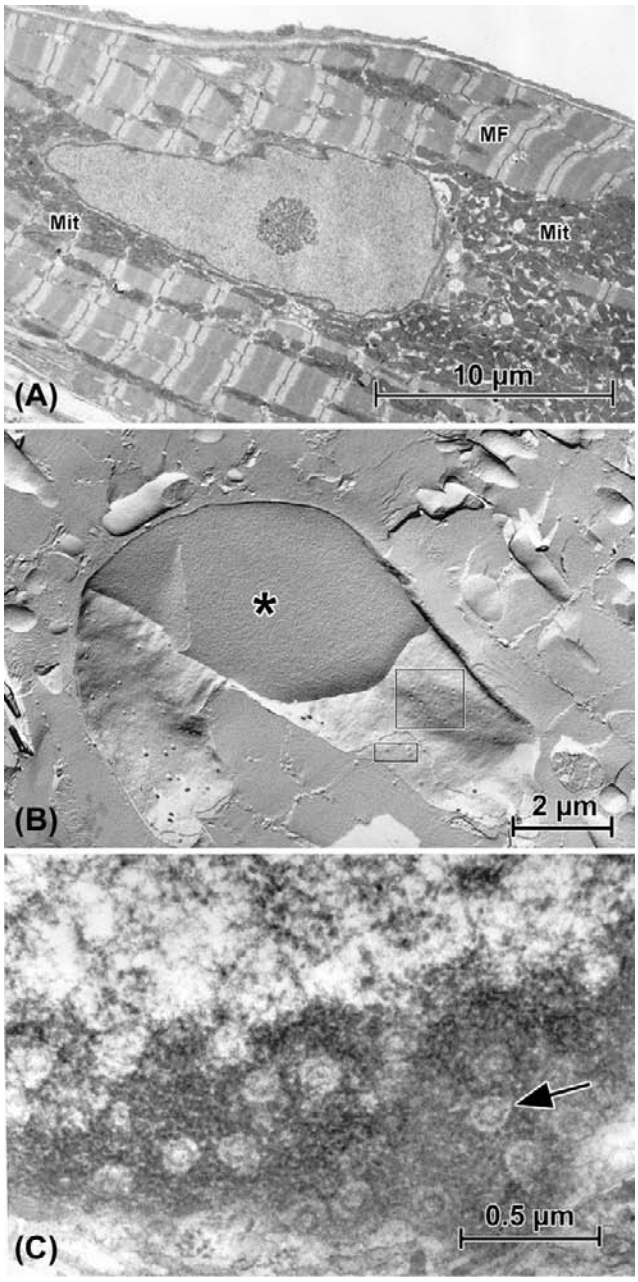

FIGURE 5.5 Aspects of nuclear structure as seen in cardiac muscle cells ("cardiomyocytes"). (A) The nucleolus is prominent within this nuclear profile. Additional characteristics of the cardiomyocyte are the interspersed arrays of myofibrils (MF) and mitochondria (Mit). (B) Freeze-fracture replica of a nucleus. The plane of fracture reveals cytoplasmic myofibrils and mitochondria (see panel (A)) and breaks through the nucleus to show the homogeneous nucleoplasm (*), then passes into the outer nuclear membrane leaflet (larger rectangle) to show nuclear pores as depressions, then into the inner nuclear membrane (small rectangle), where the pores appear as corresponding protuberances. (C) Grazing thin section of nucleus, passing through the peripheral dark heterochromatin to reveal the complex nuclear pores' substructure (arrow).

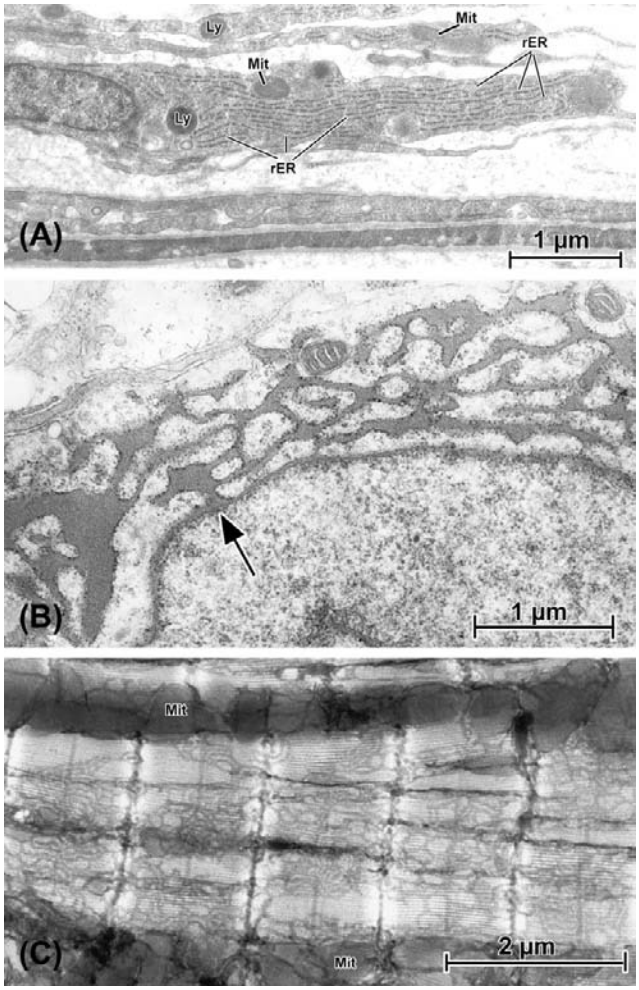

FIGURE 5.6 The variable appearances of endoplasmic reticulum ("ER"). (A) Fibroblastic cells that form the capsule layer of kidney. Each of these elongated cells is characterized by a corresponding flattened nucleus, along with limited numbers of lysosomes (Ly) and mitochondria (Mit). Filling the cytoplasm of these collagen-producing cells are parallel arrays of rough ER (rER). (B) Pituitary cell (thyrotroph) in which synthetic activity has been stimulated by removal of the thyroid gland. This induces a dramatic increase in production of thyroid-stimulating hormone (TSH) and, instead of generating storage granules (see Fig. 5.3), the rough ER expands into interconnected networks of dilated tubules and cisternae filled with freshly-synthesized hormone. Note (at arrow) the connection between the nuclear envelope and rER. (C) Atrial tissue from mouse in which the smooth endoplasmic reticulum (known as "SR" in muscle, is specifically stained by an osmium impregnation technique related to those used by Golgi and Cajal (see Cell Theory section) to contrast neurons. In this application, only the SR is darkened; by cutting relatively thick (ca. 2 µm) plastic sections for the TEM, the extent, distribution and elaborate patterning of the SR where it enwraps the banded myofibrils can be appreciated. Linear masses of mitochondria (Mit) are seen running between some myofibrils.

demonstrated that the nuclear pore complexes are complicated structures indeed, incorporating an eight-subunit annular structure centered around an aqueous channel that allows passive diffusion of small molecules and ions. The nuclear envelope is not a complete barrier, because it is necessary for RNA, proteins and ions to pass in and out of the nucleus; the system of nuclear pores regulates the trafficking of these substances.

VI. ENDOPLASMIC RETICULUM

The ER was originally described by light microscopists in the late 1800s, who used special preparative procedures that selectively infiltrated this organelle system with a variety of staining moieties (see Fig. 5.6C). Understanding of the structure of the ER was greatly advanced in the late 1940s and early 1950s by the elegant EM work of Porter and Palade, who demonstrated that the ER was an extensive network of interconnecting tubules and cisterns.

Ribosomes are compact rounded particles, approximately 300 nm in diameter, that dissociate in the presence of low Mg^{2+} into two smaller units. They consist in large part of ribosomal RNA but, in eukaryotes, as much as 50% of the ribosomal mass can be composed of associated proteins. Ribosomes are often found organized into strands or rosettes called polyribosomes or simply "polysomes" (Fig. 5.7). These are aggregations of ribosomes active in the messenger RNA-directed linkage of amino acids to form peptide chains. Protein synthesis is initiated on ribosomes, which may be free in the cytoplasm or bound to the ER to form a complex known as rough endoplasmic reticulum

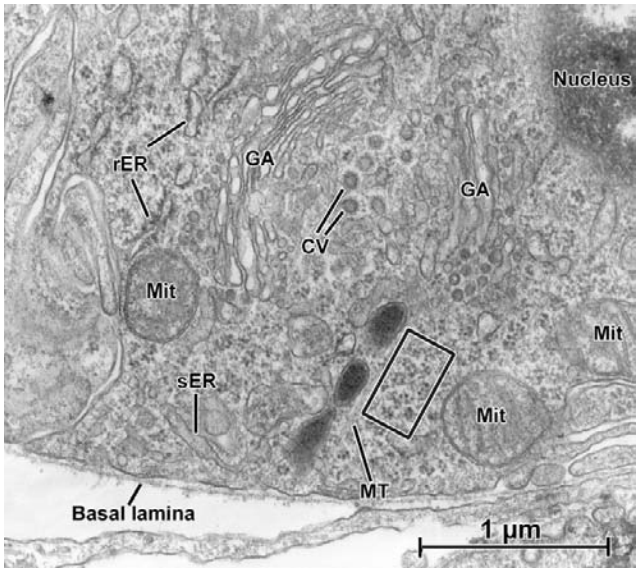

FIGURE 5.7 Transmission electron micrograph of a "juxtaglomerular cell" in kidney blood vessel. In this limited area, examples of many of the organelles described in this chapter are seen in close proximity to one another. In particular, the saccules, cisternae and vesicles that make up the Golgi system (GA) are clearly defined. In this cell, which is the source of the vasoactive hormone renin, polyribosomes are abundant (examples within the rectangle), along with smooth ER (sER), rough ER (rER), mitochondria (Mit), and a microtubule (MT).

(see Figs. 5.6A,B, 5.7). The rough ER is presumed to be involved virtually exclusively in protein synthesis. In contrast, ER that does not have attached ribosomes is known as smooth endoplasmic reticulum (see Figs. 5.6C, 5.7) and has been implicated in a number of different functions depending on the particular cell type. In steroid hormone-secreting cells, for example, smooth ER is associated with the production of secretory products. In liver cells, the smooth ER has been shown to be active in glycogen metabolism. In cardiac, skeletal and smooth muscle, the smooth ER is better known as the *sarcoplasmic reticulum* (SR) (see Fig. 5.6C); SR membrane proteins are responsible for the uptake, sequestration, and release of Ca^{2+} during the cycles of excitation–contraction coupling and relaxation. ER in non-muscle cells may also be involved in Ca^{2+} metabolism.

VII. GOLGI APPARATUS

Synthesis of membrane proteins and secretory products is completed in another organelle, which is at least functionally connected with the ER and is called the *Golgi apparatus* (see Fig. 5.7). This organelle was named for Camillo Golgi, a 19th-century microscopist-histologist who developed numerous staining techniques and described many of the light-microscopic features of cells. In the electron microscope, this organelle was found to be composed of flattened disk- or saucer-shaped membranous elements known as cisternae. In each Golgi apparatus, numbers of these cisternae are organized into stacks, with individual cisternae interconnected through tubular channels. As secretory products pass through the Golgi apparatus, they undergo chemical modifications such as glycosylation, proteolytic cleavage, phosphorylation and sulfation. Other functions performed by the Golgi apparatus include carbohydrate metabolism, targeting of plasmalemmal proteins (pumps, channels and receptors) and the condensation of secretory materials into opaque "secretory granules" (see Fig. 5.3).

Although a variety of terminologies has been used to identify different regions of the Golgi apparatus, four morphological subsections are generally recognized. The cisternae are slightly dished in conformation, which confers both concave and convex faces to the Golgi complexes. The convex or *cis* face is also known as the forming or immature face, since it is at this level that newly synthesized proteins enter the Golgi. The medial or intermediate region comprises the varying numbers of cisternae in the middle of the stack. The concave or *trans* face is also called the mature or secretory face, since it is the site from which large secretory vesicles bud off after their contents have been modified for export. The trans-Golgi network is a reticulum of tubules emanating from the *trans* face and is thought to be associated with the lysosomal system.

This general scheme is applicable to all Golgi complexes and transport within the Golgi is generally vectorial, going from the *cis* to the *trans* face. However, more recent evidence suggests that maturation and pinching off is not totally restricted to the *trans* face. There is likely much more intra-Golgi shuttling back and forth of material than was originally believed. The numerous vesicles of various shapes and sizes in the immediate vicinity of the Golgi complex (see Fig. 5.7) may be transporting proteins along the pathway during maturation and processing. There is also evidence for some retrograde transport from the Golgi apparatus to the ER.

VIII. LYSOSOMES

In addition to packaging and modifying secretory products, the Golgi apparatus plays a role in the formation of another important cellular organelle, the *lysosome* (see Figs. 5.2, 5.6A, 5.8A,B). In fact, the functional continuity of the ER, the Golgi apparatus and the lysosomes has led to the

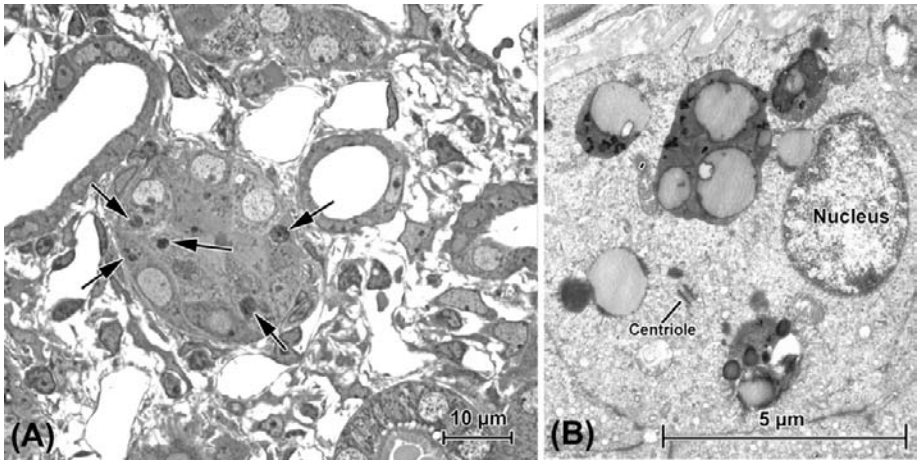

FIGURE 5.8 Autophagy in kidney proximal tubules following obstruction of the ureter. (A) "Semithin" (ca. 0.25 µm) section of tissue embedded in plastic. Use of such sections allows survey viewing in the light microscope for selection of areas to be more closely examined in the TEM, as seen in (B). In this case, the structures of interest are the dark bodies indicated in (A) by arrows; for all practical purposes, their substructure is below the resolution of the light microscope and it is only in the TEM that they are revealed to be autolysosomes, the complex products of a multistep process (described in text) that isolates defunct or excess cell contents for digestion. Nuclei in cells undergoing autophagy often appear normal; a centriole is also present in one cell.

concept of the GERL (Golgi—endoplasmic reticulum—lysosome) system. Lysosomes are a heterogeneous population of membrane-limited vesicles, differing in size and density, that were identified and characterized by De Duve in the mid-1950s. Lysosomes contain hydrolytic enzymes that can break down virtually every form of biological material and thus these organelles act, in part, as the cell's digestive system. Many of the lysosomal enzymes are more effective at low pH and the lumen of the lysosome accordingly is more acidic than the cytoplasm. The lysosome acts to break down and recycle intracellular components such as cytoskeletal proteins and defunct organelles, such as mitochondria (by a process known as *autophagy*), as well as to digest extracellular material that has been trapped in phagocytic vesicles formed by internalized plasmalemma (heterophagy). Viewed in the electron microscope, newly formed "primary" lysosomes are more uniform in size, with an amorphous electron-opaque content. After fusing with phagocytic vesicles or other cell contents, they form "secondary" lysosomes, whose size and internal density is more variable (Fig. 5.8). Lysosomes containing indigestible material often remain in the cytoplasm as residual bodies, also variously known as aging pigment or *lipofuscin*.

Cell death mechanisms are now of particular interest. *necrosis*, in which the semipermeable properties of the plasmalemma are compromised, has been well known for many decades and the term *apoptosis* (a.k.a. "type I programmed cell death") was coined in the 1970s (apoptosis is discussed further in the section on Mitochondria). More recently, however, autophagy has attracted special interest. Though lysosomes were well-established as fundamental cellular organelles, their role in autophagy (literally "self-eating"; also known as type II programmed cell death) is only now being detailed. The sequestration of cellular materials into lysosomes to form secondary lysosomes has now been found, largely on the basis of electron microscopic studies, to be more complex. Autophagy is now considered to be initiated by the formation of a double-membrane structure, the "isolation membrane" (likely derived from the ER, but this is still not completely clear), which develops into a body known as an *autophagosome* (or autophagic vacuole), which is the entity that envelops the target organelle or substance. The autophagosome with its contents then joins ("docks and fuses") with the lysosome proper, forming the secondary lysosome, now known as the *autolysosome*. Autophagy is not entirely an ineluctable path to cell death, however, and in some cases — such as starvation — promotes cell survival.

Peroxisomes, while similar in overall appearance to lysosomes, are considered to be a separate class of organelle. These bodies are abundant in liver, kidney and heart (among others) and contain both peroxidase and catalase, through the action of which fatty acids are broken down and the resulting, potentially harmful hydrogen peroxidase is dissociated into water and oxygen. Endogenous peroxidatic activity is of technical interest when one is performing immunohistochemistry; peroxisomes and erythrocytes (which also have peroxidatic activity) require "quenching" with hydrogen peroxidase to neutralize endogenous peroxidase, since certain steps of standard immunohistochemical procedures utilize exogenous peroxidase in generating the colored compounds (chromogens) that mark the sites of antigens (see Fig. 5.1D,E).

IX. MITOCHONDRIA

Aside from the nucleus, the most obvious feature of the majority of cells is the collection of organelles called mitochondria (Fig. 5.9). The term "mitochondrion" (literally "thread-grain") was introduced at the turn of the 20th century based on the appearance of these bodies, under the light microscope, as elongated granules. In the TEM, each mitochondrion is seen to be bounded by a double bilayer membrane (see Fig. 5.4A). The outer bilayer is smooth in contour and forms the boundary around the entire mitochondrion. The inner membrane has a variable number of infoldings, called *cristae*, which increase the internal surface area substantially (see Figs. 5.4A, 5.9).

It is now clear that the mitochondria are sites of cellular respiration and thus are the center of energy production in the cell. The inner mitochondrial membrane contains abundant transport proteins responsible for establishing a proton gradient between the intermembrane space and the matrix. The proton motive force created by this gradient is essential for driving many of the reactions of oxidative phosphorylation, a fundamental metabolic process occurring within the inner compartment of the mitochondrion. Oxidative phosphorylation generates much of the cell's adenosine triphosphate (ATP), the high-energy compound that is the source of energy for most cellular activities. The enzymes responsible for the tricarboxylic acid cycle, one component of oxidative phosphorylation, are located in the mitochondrial matrix and the enzymes involved in electron transport, another major function of the oxidative phosphorylation process, are associated with the inner mitochondrial membrane.

As would be expected, mitochondria concentrate at sites within the cell that require high energy utilization, as well as being more abundant in cells that exhibit a high degree of metabolic activity. For example, heart muscle tissue has one of the higher measured metabolic rates; accordingly, in myocardial cells, mitochondria constitute up to 40% of the total cell volume, and are sandwiched in between the collections of contractile proteins (myofibrils) (see Figs. 5.5A, 5.6C).

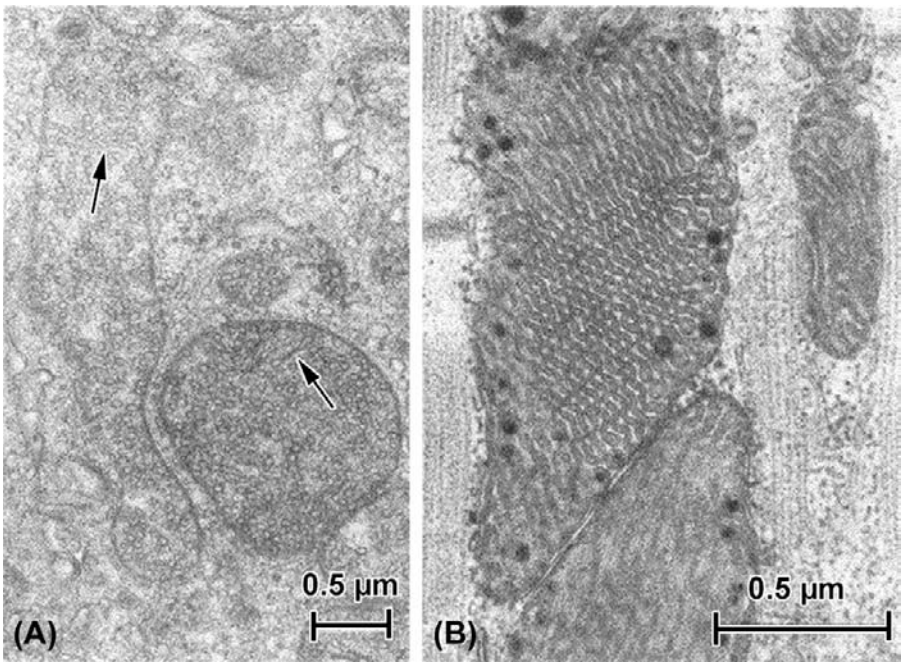

FIGURE 5.9 Mitochondria. (A) Mitochondria in cell from adrenal cortex. Steroid-secreting cells often are characterized by spheroidal or elongate mitochondria packed with internal membranes (cristae) that take the form of fine tubules (arrows) or chains of tiny vesicles. (B) Mitochondria in cardiac muscle. In addition to being tightly sandwiched between the myofibrils (collections of contractile filaments; see also Figs 5.6C, 5.10A), cardiac mitochondria are often densely populated with elaborate pleated shelves of internal cristae. Opaque granules often are present within the mitochondrial matrix.

Apoptosis, as mentioned earlier, is a mechanism of "programmed cell death". Morphologically, it is most clearly evident in changes in nuclear appearance (condensed chromatin, nuclear fragmentation). However, the impetus for the apoptotic process is found in the mitochondrion where, under certain circumstances, there is a change in its membrane permeability and thence its electrical potential. "Apoptogenic factors" such as cytochrome c and proteases are then released from the mitochondria and lead to the so-called "caspase cascade" and eventually to the nuclear alterations that are obvious in the microscope. Like autophagy, however, apoptosis can serve beneficial purposes. Apoptosis is a necessary process, particularly in development; e.g. it is thought to bring about the establishment of microvessel lumina in kidney glomeruli (Fierlbeck et al., 2003).

X. CYTOSKELETON

The cytoplasm is not just a watery bag in which organelles move about at will. In fact, cell contents are to one degree or another compartmentalized, with certain cytoplasmic regions specialized to subserve particular functions. Underlying this compartmentalization is the framework of fibrillar structures that make up the cytoskeleton of each cell. Normally, 20–35% of the total protein of a cell is tied up in the cytoskeleton, although this proportion can vary, being considerably greater in muscle, where cytoskeletal proteins also form part of the extensive contractile apparatus. In all cells, cytoskeletal elements are involved in intracellular motility (such as migration of chromosomes during mitosis, translocation of organelles and cytoplasmic streaming), cell locomotion, and maintenance of cell shape. More specialized functions, such as muscle contraction and ciliary/flagellar movement, also are supported by cytoskeletal elements.

XA. Filaments

Filaments are composed of backbones of single proteins, polymerized to form long, slender fibrillar structures. Such filaments are both helical and polar and frequently interact with one another. There are three general filament categories in cells: *microfilaments*, often called "thin filaments", which are primarily composed of the protein actin and ranging from 6 to 8 nm in diameter; *thick filaments*, consisting mainly of myosin and 12–15 nm in average diameter; and *intermediate filaments*, so called because their customary 10 nm average diameter is intermediate between that of thin and thick filaments (thus also known as 100 Å or 10 nm filaments). Intermediate filaments may be composed of a variety of related proteins, depending on cell type.

XA1. Microfilaments

As noted above, the backbone of microfilaments is composed of the cytoskeletal protein actin; in most cell types, however, additional regulatory proteins (e.g. troponin) and structural proteins (e.g. tropomyosin) are intimately associated with the actin filaments. G (globular)-actin polymerizes to form filaments and in this form is

known as F (filamentous)-actin. A number of associated proteins may regulate initiation and growth of a filament, as well as its final length. Tropomyosin, for example, stabilizes thin filaments of muscle cells.

In different cells, and in different tissues, thin filaments are associated with a variety of recognizable intracellular formations. Bundles of filaments, all having the same polarity, form the cores of microvilli in epithelial cells; actin filaments are also evident in smooth muscle and striated muscle cells as intrinsic parts of the contractile apparatus (Fig. 5.10). Bundles of thin filaments having opposite polarities are also found, located on opposing sides of the Z disks in skeletal and cardiac muscle, across from one another at dense bodies in smooth muscle, and within the stress fibers of non-muscle cells. Three-dimensional networks of filaments are found in subplasmalemmal (cortical) arrays in many cells.

XA2. Thick Filaments

The most detailed structural information regarding myosin-containing filaments comes from the study of striated muscle thick filaments (see Fig. 5.10A,B). Smooth muscle cells clearly contain thick filaments (see Fig. 5.10C), but the exact organization of the molecules within the filaments is still controversial. It is likely that non-muscle cells also contain thick filaments, but that they are shorter and less ultrastructurally obvious.

It is generally accepted that thick filaments are required for movement and motility, which are carried out through interactions with actin-containing thin filaments.

XA3. Intermediate Filaments

Intermediate filaments (IFs) actually comprise a related family of proteins found in virtually all cell types; lamins are IF proteins that form the internal lamina of cell nuclei, for example. However, there are also tissue-specific IF proteins. Vimentin is found in mesenchymal tissue (connective tissue, bone, blood, cartilage); desmin is localized in muscle; neurofilament protein, or neurofilamin (NF), is found in neurons; GFAP (for "glial fibrillar acidic protein") is found in glial cells of the nervous system. Finally, keratins are IF proteins that are abundant in epithelial cells. Additional IF proteins do not form filaments (e.g. nestin: see Fig. 5.1E), but help to stabilize the filamentous forms.

IFs are often observed as loose three-dimensional networks, intermixed with other cellular components (see Fig. 5.10C), but in astrocytes and other cells can form dense skeins that consist primarily of 10 nm filaments. As pointed out above, IFs form the framework of the inner nuclear membrane, the nuclear lamina. IFs are also associated with subplasmalemmal plaques adjacent to the plasma membrane at specialized cell–cell contacts (desmosomes)

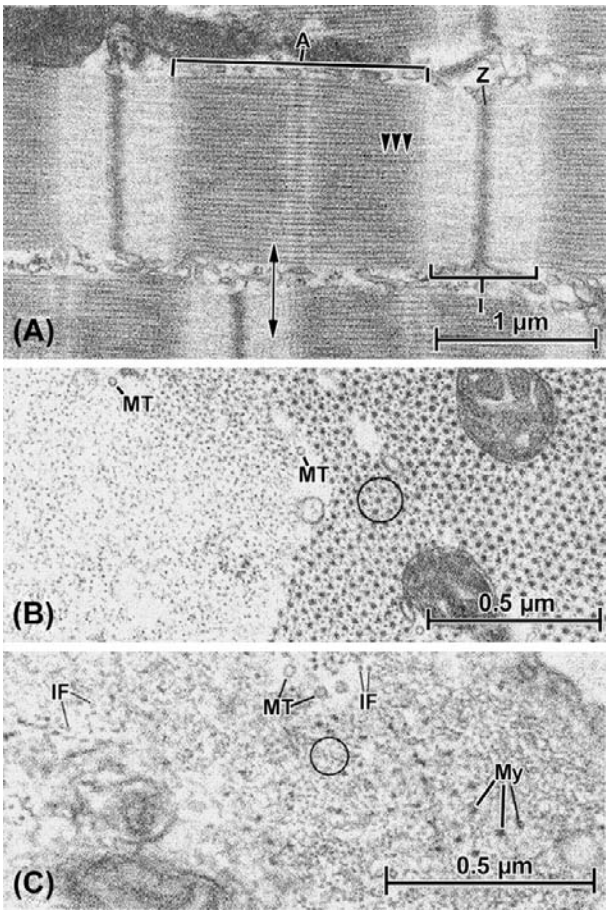

FIGURE 5.10 Fibrillar elements in muscle cells. (A) Longitudinal section through a cardiac muscle cell, showing the characteristic banded pattern of the ordered masses of contractile filaments known as myofibrils. Between myofibrils, other cell organelles, such as mitochondria and endoplasmic (sarcoplasmic) reticulum, are sandwiched. The units of the banding pattern are known as sarcomeres and the major filament categories that contribute to their formation are thin (actin) filaments and thick (myosin) filaments. The so-called A band (A) is a composite of interdigitated actin and myosin and the subtle cross-hatching pattern derives from portions of the myosin filaments that form cross-bridges (several shown by arrowheads) with the adjacent actin filaments. The I band (I) is occupied only by thin filaments, which insert into the dense material of the Z bands (Z), which are primarily composed of the protein α-actinin. Adjacent Z bands define a sarcomere unit, each of which covers a distance of ca. 2.2 μm in heart. Note in this panel that adjacent myofibrils are not always aligned with one another in terms of the levels of their sarcomere patterns. (B) A transverse section through two cardiac myofibrils, its plane of sectioning corresponding to the double-headed arrow in (A). At the left of the picture, the section passes through the I-band region and therefore reveals only actin filaments, whereas at the right the A band is cut, showing the characteristic hexagonally arrayed myosin filaments, each surrounded by actin filaments, usually in the "six-around-one" pattern circled. Mitochondria are enmeshed by the filaments in one myofibril, and additional fibrillar components, namely microtubules (MT), appear in the same orientation as the muscle filaments. (C) Cross-section through a vascular smooth muscle cell in the wall of a coronary artery. Like the cardiac muscle shown in the other panels, the smooth muscle contains examples of actin (circled) and myosin (My), but a geometric arrangement similar to that of cardiac or skeletal muscle is not evident. Cytoskeletal fibrils, including microtubules (MT) and intermediate filaments (IF), also are present in the same orientation as the contractile actin and myosin.

(see Fig. 5.11D, F) and are disposed in muscle in transverse meshworks that link and align myofibrils to one another, to the sarcolemma, and perhaps also to the nucleus. Thus, IFs are an internal scaffolding that can form networks to link peripheral and central components of the cell as a mechanically integrated complex.

XB. Microtubules

Microtubules are elongate, hollow cylinders of notably larger diameter (ca. 25 nm) than other cytoskeletal fibrils (see Figs. 5.7, 5.10B,C) and are composed of the protein tubulin. The walls of the microtubules are formed from protofilaments aligned parallel to the long axis of the microtubule. The number of protofilaments that make up the microtubule cross-section varies, but 13 is the most common complement. The protofilaments are polar structures and are assembled so that they confer polarity to the microtubule.

There are several different microtubule-associated proteins (MAPs), including MAPI, MAP2 and tau (aberrant formations composed of tau are responsible for the formation of "tangles" within neurons in Alzheimer's disease). The MAPs serve to stabilize the microtubules and are the targets of regulatory signals. One of the most functionally important MAPs is dynein, which forms side arms on the microtubules found in the cores of cilia and flagella. These side arms enable microtubules to slide past one another, allowing bending of the whole structure and accounting for their basic motility. In addition to being the fibrillar component of cilia and flagella, microtubules are the basis of the so-called MTOCs (microtubule-organizing centers). Microtubules are involved in movement of chromosomes during cell division and perform a role in translocation of organelles within the cytoplasm. In some cases, microtubules also can form the framework on which some of the cell compartments are organized and it has even been shown that the orientation of IFs depends, in some instances, upon the integrity of the microtubules in the same cell.

XI. CELL JUNCTIONS

Where they are located in tissues and organs, cells do not exist in isolation, but rather exert multiple influences on one another. When they reside in different parts of the organism, the influences are usually realized through an intermediary milieu such as the bloodstream, but where neighboring cells come into contact with one another, specialized structures known as *intermembranous junctions* connect them. The electron microscope has proven a particularly apt tool for detecting such connections, since they usually incorporate some form of modification of the apposed cell plasmalemmas that is best visualized in the TEM.

Four types of intercellular junctions are commonly encountered in vertebrate tissue: (1) tight junctions; (2) gap junctions; (3) intermediate or adherens junctions; and (4) desmosomes. Epithelial layers such as seen in small intestine display a rather stylized "junctional complex" that consists of the four junctional types arranged in a sequence from the luminal surface down to the basal surface; in order, the complex goes tight junction/adherens junction/desmosome/gap junction.

Because of the extreme thinness of sections used in the electron microscope, the views of cells and their constituents are essentially two-dimensional; in such views, the casual observer can easily fail to appreciate the true shape and extent of any particular profile. This is certainly the case for specialized intercellular junctions. More stringent observations, including examination of multiple sections of cells in various orientations, as well as use of serial sections, has shown, in epithelium as well as other tissues, that some categories of junctions occupy continuous bands of plasmalemma (zonulae) that form rings about the lateral cell surface. Other junctions are more strictly delimited, in three dimensions occupying round, ovoid, or sometimes irregular patches of plasmalemma in each of the joined cells (see Fig. 5.4B).

Tight junctions, viewed in thin sections, are identified, as the name would imply, by plasmalemmal appositions that come into such close contact as to obliterate the intercellular space between cells. Often multiple points of leaflet fusion are visible along short stretches of apposed membranes (Fig. 5.11A). Replication of membrane surfaces by freeze-fracture techniques (Figs. 5.11B,C) has revealed that tight junctions actually are composed of intramembranous particles arranged to form networks of "tongue-and-groove" interdigitations, which provide a barrier largely impenetrable to most particles and fluids. Tight junctional arrays prevent direct diffusion of various products through the extracellular fluid space, thus forcing their passage "through proper channels," so to speak, namely via mechanisms such as vesicular transport through the cytoplasm. Tight junctions are also found in abundance in pancreatic acini, as well as between endothelial cells in certain segments of blood vessels. To some degree, tight junctions are likely responsible for maintenance of the blood−brain barrier.

Gap junctions, also known as nexuses or *maculae communicantes*, were in early studies mistaken for tight junctions, but it was realized, through the use of special staining procedures and particle tracer techniques, that these complexes were different in their overall thickness and, furthermore, allowed particles below a certain size to penetrate the extracellular space at their level. Gap junctions appear in thin EM sections to be composed of seven layers (see Figs. 5.4A, 5.11D), the middle one appearing as a 2−4 nm "gap", explaining the common name for this type

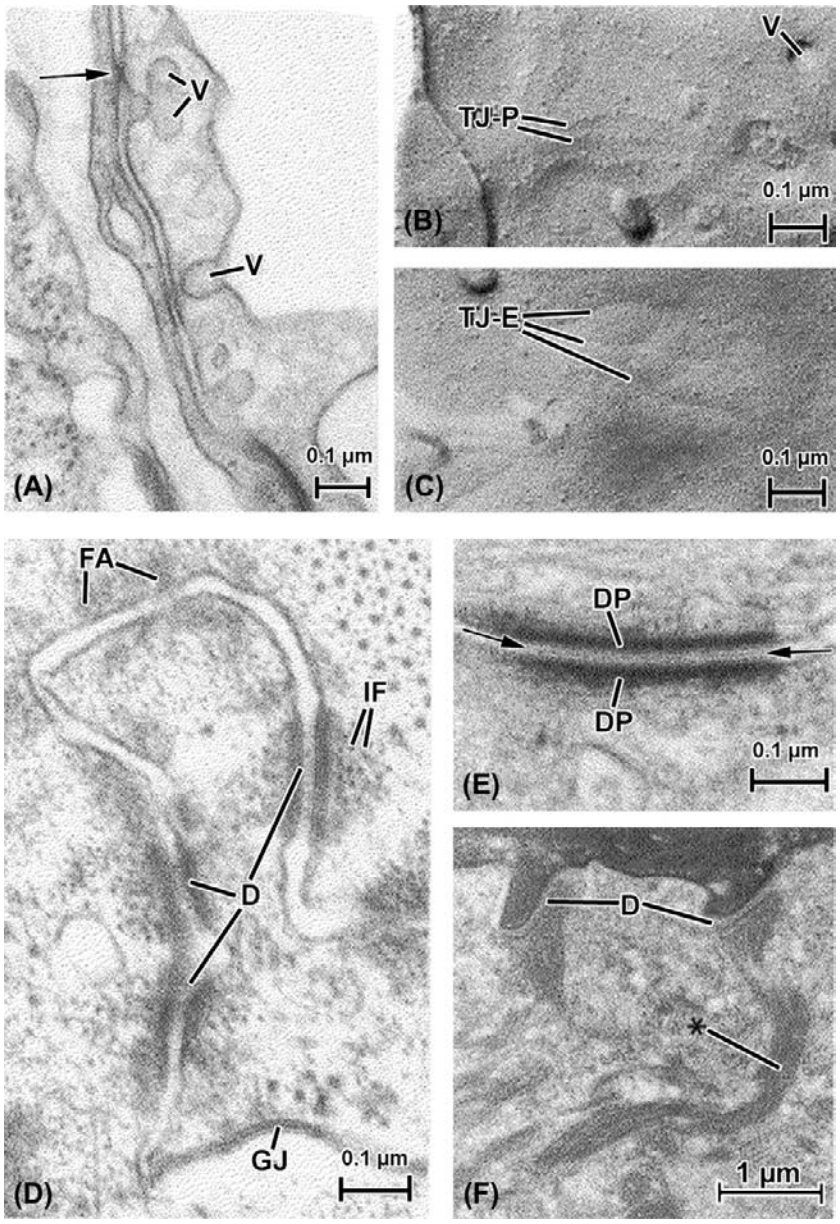

FIGURE 5.11 Cell-to-cell appositions, also called intercellular junctions. (A), (B) and (C) show endocardium (the endothelial lining of the heart) both in thin section (A) and freeze-fracture replicas (B) and (C). (A) The plane of section passes vertically through two overlapping endocardial cells, whose plasmalemmas bear cytoplasmic vesicles (V) that support transport of materials in and out of these cells. The plasma membranes of the two endocardial cells come into close proximity at several points, at one appearing to touch or fuse (arrow). Such junctions are known generally as "tight junctions" and form barriers to the penetration of certain materials past them in the intercellular spaces. (B) A freeze-fracture replica of the endocardial membrane's P face (see Fig. 5.4B) shows vesicular openings (V) as well as linear arrays of particles that correspond to the tight junction (TJ-P). (C) These correspond in replicas of the E face to linear indentations (TJ—E) into which the corresponding P-face particles fit to form an interlocking junctional barrier. (D) and (E) show junctions from the myocardial cell-to-cell junctional complex (the "intercalated disk"), which consists of interdigitated muscle cell tips that bear a variety of interspersed types of junctions, including gap junctions (GJ, see also Fig. 5.4). (D) At the top of the micrograph there appears a zone of fascia adherens (FA), the points at which thin actin filaments of the myofibrils insert into the intercalated disk. The adherens-type junctions are characterized primarily by accumulations of intracellular dense material that face one another across the intercellular space, but which incorporate no particular extracellular specializations. In contrast, the adhesive junctions known as desmosomes (three of which appear in this picture, D) not only bear intensely opaque intracellular densities closely associated with intermediate filaments (IF), but also contain a distinct component located in the extracellular space (see also (E)). (E) A desmosome is shown at high magnification. The intracellular material is concentrated into desmosomal "plaques" (DP) which, together with the associated plasmalemmal unit membranes, are arranged in a striking parallel array. The extracellular material, known as a "central lamella" (between arrows), is likely responsible for maintaining the register of the apposed membranes, having toothed projections from a center linear component that anchor in the adjacent plasma membrane leaflets. (F) Keratinocytes in the epithelium of skin. Here the major filament type is keratin, considered to be one of the family of intermediate filaments. Keratin is concentrated into fibrous cords (*) that insert onto the intracellular plaque material of the numerous desmosomes (D) that connect the cells of this layer of the skin.

of junction. Closer examination has revealed that the gap junction is an assemblage of hexagonally packed "connexons" (as their individual intramembranous particles are called; see Fig. 5.4B,C), each of which contains a tiny pore at its center. It is thought that such pores are aligned to form thin channels, allowing intracytoplasmic passage of ions (e.g. Ca^{2+}) and other substances (such as ATP and amino acids) directly from the cytoplasm of one cell into the interior of the other, a distance calculated to be only about 2.5 nm. In this way, it is postulated, neighboring cells can be "coupled" both electrically and metabolically.

Adherens junctions, though often descriptively linked with desmosomes, can be distinguished from them structurally on the basis of the adherens junctions being more diffuse-appearing and more widely distributed than desmosomes (see Fig. 5.11D). In addition to this morphological disparity are fundamental differences in the species of proteins associated with and composing the two types of junctions.

Adherens junctions are frequently associated with microfilaments, whereas desmosomes instead are accompanied by intermediate filaments. A well-described example of this dichotomy is found in cardiac muscle in the intercalated disks, the zones of extensive junctional attachment between adjacent cardiac muscle cells (see Fig. 5.11D,E). Here at the cell tips, the actin filaments of the myofibrils terminate in the amorphous dense zones of the fascia adherens portion of the disk. In contrast, myofibrils do not come into contact with desmosomes. Furthermore, desmosomes exhibit a far more distinct and layered ultrastructure (see Fig. 5.11E), including a central lamella lying in the extracellular space between cells and intensely opaque intracellular, subplasmalemmal plaques, within whose substance profiles of intermediate filaments can often be detected. In epithelial cells, both desmosomes and hemidesmosomes — which are essentially "half" desmosomes confined to the cells' basal regions — contain subplasmalemmal plaques that are the insertion points for cords of keratin-type intermediate filaments (see Fig. 5.11F). As mentioned, distinctly different types of proteins are specific to each type of junction, and so, according to the philosophy of form following function, their structural resemblance to one another is related largely to their similar adhesive roles in cells.

XII. SPECIAL TISSUES, SPECIALIZED ULTRASTRUCTURE

Although a chapter such as this one necessarily deals in generalities, in reality few researchers work on generic "cells". Instead, certain types of cells, for one or many reasons, are of special interest to individual investigators. It is therefore useful to view cell ultrastructure as it is specifically arranged to form a cell type that is particularly appealing to physiologists: the nerve cell or neuron. This cell type not only generates and transfers electrochemical signals, it is also heavily devoted to synthetic activity. Though neurons vary considerably in size and shape in their various locations in the central, peripheral and enteric nervous systems, as a group they are characterized by their ability to exercise their functions at points far removed from the central cell region that contains the nucleus. This action-at-a-distance ability can be directly correlated with ultrastructural features of neurons. The cell body or *soma*, which contains a single prominent nucleus, also houses the bulk of the synthetic machinery of the cell (Fig. 5.12A), including extensive, often multiple Golgi apparatus and groupings of rough endoplasmic reticulum cisternal profiles, known collectively as "Nissl substance", because of the staining properties of their ribonucleoprotein. "Free" ribosomes (i.e. not attached to membranes) and polysomes abound as well within the neuronal soma.

It is the cytoplasmic processes of neurons, their dendrites and axons, that most effectively attest to their specialized functions. While dendrites, which generally bring signals toward the cell body, are usually limited to no more than several micrometers in length, the points at which the axons terminate may be located several millimeters away (or even farther, depending upon such factors as the size of the animal, type of neuron and its particular location in the body). Both dendrites and axons, as would be expected, are well endowed with cytoskeletal elements, oriented preferentially along the processes in a configuration that best supports their attenuated shapes. Electron microscopic observation demonstrates that microtubules and intermediate filaments are the most prominent constituents of axons (see Fig. 5.12B).

As pointed out, neurons, though organized along certain unified architectural lines, can vary markedly in their ultrastructure. Nowhere is this more pronounced than at their most distal portions, the tips of the axons, or axon terminals. These termini may have as their target other neurons, or may abut contractile cells, such as smooth muscle (both in viscera and blood vessels), cardiac muscle cells or skeletal myocytes. Axon terminals are usually characterized by concentrations of vesicles of one type or another. Where these axon terminals occur, they may lack any specialized structure that attaches them to the target cell. Often, though, where neurons terminate on one another, a distinct appositional complex known as the synapse is found.

The axon terminal (also known as a "bouton") constitutes the presynaptic element, and may terminate on a neuronal soma or another axon but, in the central nervous system (CNS), more often is found in contact with a dendrite (see Fig. 5.12C). In addition to the neurosecretory vesicles that fill the axonal bouton, there is a prominent synaptic density whose function appears similar to that of an adherens or desmosomal type of adhesive junction. The

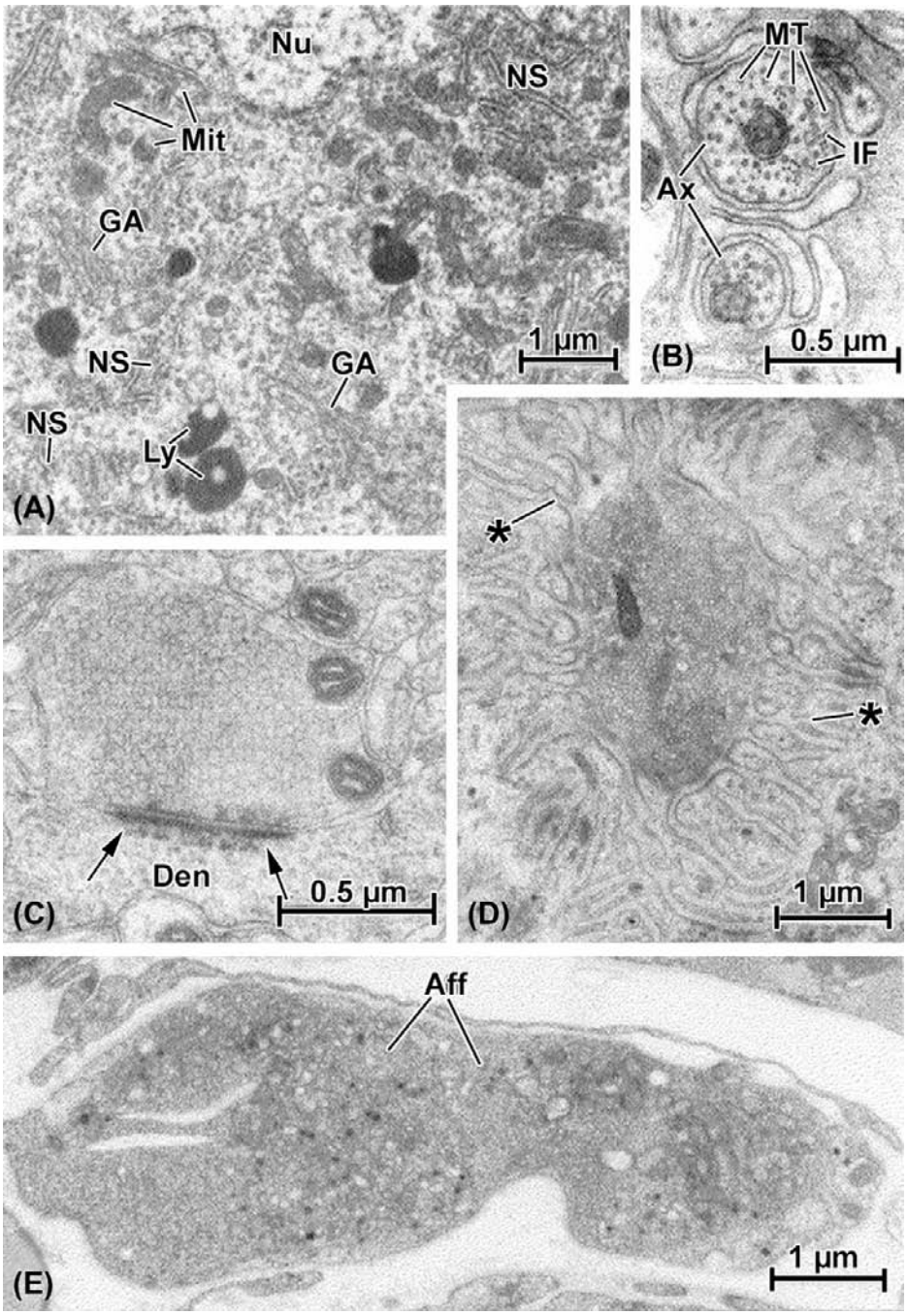

FIGURE 5.12 Electron micrographs illustrating specialized ultrastructure of neurons. (A) A portion of the cell body, or soma, that contains the nucleus (Nu). The cytoplasm in this region is filled with membrane-based synthetic organelles, including multiple profiles of the Golgi apparatus (GA) and cytoplasmic islands of rough endoplasmic reticulum and polyribosomes (known collectively as "Nissl substance," NS). Numerous small mitochondria are scattered throughout the soma and other examples of typical cell organelles such as lysosomes (Ly) are represented as well. (B) High-magnification view of axons (Ax), the elongated cytoplasmic processes of neurons. These are cut transversely and contain individual mitochondria (Mi) and numerous cross-sectioned cytoskeletal elements, including both microtubules (MT) and intermediate filaments (IF). (C) Axodendritic synapse (i.e. a nerve-to-nerve contact made by an axon with a dendrite, Den). The presynaptic axon terminal is packed with neurosecretory vesicles and also contains mitochondria. The hallmark of this complex is the synaptic density (arrows) which both attaches the two apposed nerve elements and delineates the region in which transfer of neurotransmitter will occur. (D) Motor end-plate, a contact made by an axon terminal of the peripheral nervous system with a skeletal muscle fiber. Although much larger than the CNS terminal (see scale bars in (B), (C), (D) and (E)), like it, the end-plate terminal is filled with vesicles; instead of a dense plaque at the point of contact, however, there is a deep depression in the skeletal muscle into which the terminal nestles, together with elaborate secondary folds formed by the muscle cell membrane (*). (E) An afferent or sensory nerve terminal (Aff) in heart. This axon termination is considerably larger than most efferent terminals (see (C) and (D)) and contains a variety of inclusions such as mitochondria, clear and dense vesicles and other structures.

synapse functions through a process of vesicle fusion with the presynaptic membrane, with subsequent exocytosis of the transmitter chemical substance (which can be either excitatory or inhibitory) into the synaptic cleft, where it acts on the postsynaptic membrane side of the complex (i.e. the dendritic membrane in Fig. 5.12C), changing its electrical potential and thus generating a signal (thence the term "chemoelectric" for such an event). Where no synapse is formed, as for example in axon terminations near blood vessel walls, diffusion of neurotransmitter is sufficient to modulate the contractile activity of the vascular smooth muscle cells there.

In the case of vertebrate motor neuron axons, which terminate on skeletal muscle fibers, considerable specialization characterizes both the axon terminal and the adjacent muscle cell. This sort of "synapse" is better known as a *motor end-plate* (see Fig. 5.12D). The axon tip here is considerably larger than the typical boutons

found in the CNS and, accordingly, contains a considerably greater number of neurosecretory vesicles. The underlying muscle cell plasmalemma ("sarcolemma"), furthermore, has itself become specialized, containing concentrations of membrane-associated receptors (usually for acetylcholine) and forming both a large depression into which the axon fits (the synaptic "gutter") and numerous secondary infoldings that increase the amount of excitable muscle membrane available to the released neurotransmitter.

The terminal axons discussed thus far are efferent, i.e. they convey outbound signals from the nerve cell body to its distant target. Also found are afferent, or sensory, terminals, which function to send stimuli such as pressure or pain back to the soma. The contents of such terminals usually greatly vary, including not only vesicles of different shapes and sizes, but also numerous mitochondria, granules, and whorled membranous bodies (see Fig. 5.12E).

ACKNOWLEDGMENTS

Over a 40-year career in microscopy, I have been privileged to have trained by and collaborated with many excellent scientists, among them Professors James Norman Dent, W. Gerald Robison, Nick Sperelakis and Lennart Heimer. During this time, my research projects were greatly aided by Ms Jan Redick, Miss Barbara Ann Plantholt, Ms Susan Purdy-Ramos, Mr Lawrence A. Hawkey, Ms Ellen van Niel and Ms Barbara Thornhill and many others too numerous to list. Special thanks goes to Dr Robert L. Chevalier, in whose laboratory I have worked for the past decade, and in which this latest version of the present chapter was prepared.

BIBLIOGRAPHY

Andre, J. (1994). Mitochondria. *Biol Cell, 80*, 103–106.

Bershadsky, A. D., & Vasiliev, J. M. (1988). *Cytoskeleton*. New York: Plenum Press.

Clermont, Y., Rambourg, A., & Hermo, L. (1995). Trans-Golgi network (TGN) of different cell types: three-dimensional structural characteristics and variability. *Anat Rec, 24*, 289–301.

Davis, L. I. (1995). The nuclear pore complex. *Annu Rev Biochem, 64*, 865–896.

Dessev, G. N. (1992). Nuclear envelope structure. *Curr Opin Cell Biol, 4*, 430–435.

Di Fiore, M. S. H. (1974). *Atlas of Normal Histology* (6th ed.). Philadelphia: Lea and Febiger.

Fawcett, D. W. (1981). *The Cell* (2nd ed.). Philadelphia: W.B. Saunders.

Fawcett, D. W. (1997). *Bloom and Fawcett: A Textbook of Histology* (12th ed.). New York: Hodder Arnold.

Fierlbeck, W., Liu, A., Coyle, R., & Ballermann, B. J. (2003). Endothelial cell apoptosis during glomerular capillary lumen formation in vivo. *J Am Soc Nephrol, 14*, 1349–1354.

Forbes, M. S., & Sperelakis, N. (1985). Intercalated discs of mammalian heart: a review of structure and function. *Tissue Cell, 17*, 605–648.

Gerace, L. (1992). Molecular trafficking across the nuclear pore complex. *Curr Opin Cell Biol, 4*, 637–645.

Gonatas, N. K. (1994). Contributions to the physiology and pathology of the Golgi apparatus. *Am J Pathol, 145*, 751–761.

Hayat, M. A. (1989). *Principles and Techniques of Electron Microscopy* (3rd ed.). Boca Raton: CRC Press.

Hotchkiss, R. S., Strasser, A., McDunn, J. E., & Swanson, P. E. (2009). Cell death. *New Engl J Med, 361*, 1570–1583.

Lodish, H., Berk, A., Kaiser, C. A., et al. (2007). *Molecular Cell Biology* (6th ed.). New York: W.H. Freeman.

Novikoff, A. B. (1976). The endoplasmic reticulum: a cytochemist's view. *Proc Natl Acad Sci USA, 73*, 2781–2786.

Nunnari, J., & Walter, P. (1992). Protein targeting to and translocation across the membrane of the endoplasmic reticulum. *Curr Opin Cell Biol, 4*, 573–580.

Palade, G. E. (1956). The endoplasmic reticulum. *J Biophys Biochem Cytol, 2*, 85–98.

Pante, N., & Aebi, U. (1996). Molecular dissection of the nuclear pore complex. *Crit Rev Biochem Mol Biol, 31*, 153–199.

Peters, A., Palay, S. L., & Webster, H.deF. (1991). *The Fine Structure of the Nervous System. Neurons and their Supporting Cells* (3rd ed.). New York: Oxford University Press.

Porter, K. R., & Bonneville, M. A. (1973). *Fine Structure of Cells and Tissue*. Philadelphia: Lea and Febiger.

Rhodin, J. A. G. (1974). *Histology. A Text and Atlas*. New York: Oxford University Press.

Shay, J. W. (1986). *Cell and Molecular Biology of the Cytoskeleton*. New York: Plenum Press.

This page intentionally left blank

Chapter 6

Signal Transduction and Second Messengers

Aldebaran M. Hofer

Chapter Outline

I. WHAT IS SIGNAL TRANSDUCTION?

Primeval unicellular organisms undoubtedly possessed rudimentary detection systems to sense nutrient and temperature gradients, to react to variations in light and to avoid noxious stimuli in their extracellular environments. With the advent of multicellularity, eukaryotic organisms required progressively more sophisticated means to respond to an ever larger array of external cues and to coordinate activities between different cells. Increasingly complex signal transduction networks evolved in higher organisms to control intricate physiological processes such as cellular differentiation, embryonic development, memory and learning.

Classically defined, signal transduction is usually regarded as a process of information transfer mediated by soluble extracellular chemical stimuli (e.g. hormones, neurotransmitters, cytokines) that bind to transmembrane receptors at the cell surface. This initiates intracellular signaling events (e.g. phosphorylation by a kinase) that culminate in a change in a physiological process. Second messengers refer to small molecule chemical mediators, such as calcium ions, cAMP, cGMP, diacylglycerol (DAG) or inositol trisphosphate ($InsP_3$), the concentration of which is rapidly and transiently increased inside the cell following receptor activation.

In recent years, additional modes of intracellular communication have begun to be recognized. Signal transduction has therefore become more broadly defined to encompass any type of signaling circuit used by cells to monitor external and internal states in order to effect a change in cellular activity. Most of these pathways do not require the generation of soluble second messenger molecules and they do not even necessarily involve the detection of a soluble extracellular ligand. Moreover, many

Cell Physiology Sourcebook. DOI: 10.1016/B978-0-12-387738-3.00006-8

seemingly specialized signaling pathways, e.g. those formerly of interest principally to developmental biologists such as Wnt, Hedgehog and Notch pathways, are now receiving attention from physiologists as well, as these highly conserved signaling mechanisms continue to exert homeostatic effects on the organism throughout its lifetime. Knowledge about the details of signaling circuits and their elaborate interrelationships is continually evolving. In this chapter, we will survey this complex topic in order to provide a general framework for understanding signaling as it relates to the study of physiology.

II. GENERAL PRINCIPLES

The human genome consists of about 23−25 000 protein-coding genes, but there are actually far more biological processes than unique proteins (including splice variants), indicating that many proteins are "recycled" for multiple purposes. Proteins dedicated to signal transduction are highly represented in the human genome. It has been estimated that there are 1543 genes for receptors, 518 protein kinases and 150 different protein phosphatases. Signals are used to control rapidly cellular functions such as ion channel activity, secretion or motility, but most signaling cascades ultimately converge on transcription factors (of which there are at least 1850) to execute programs of gene expression that result in long-term changes in cellular and organismal physiology (Papin et al., 2005). Differentiated cells (of which there are about 200 different types in humans) express a particular repertoire of signaling components (this has sometimes been referred to as the "signalsome") that allow them to respond appropriately to some types of stimuli while ignoring others.

A number of factors contribute to the enormous diversification that is a hallmark of signaling circuits. First, nearly all types of signaling proteins exist as a multiplicity of distinct *isoforms*. For example, there are 10 isoforms of the adenylyl cyclases, the enzymes that catalyze the production of cAMP, and 12 protein kinase C (PKC) family members. While at first glance this may seem redundant, the presence of specific isoforms for receptors, effectors (the proteins mediating the signal) and final target proteins that have varying affinities for their ligands actually permits further "tuning" of responses, as it allows the pathway to discriminate between small- and large-amplitude stimulus strength. Moreover, individual isoforms of signaling proteins receive *customized inputs* from other signaling circuits of the signalsome to regulate differentially their activity.

Second, while there is great diversity in the individual constituents of signaling cascades, there is also some degree of *redundancy* coming from the fact that multiple signaling pathways frequently converge on the same target to give a similar physiological outcome. An example of this is in transcription factors, which are generally the target of multiple parallel signaling inputs.

A third factor that generates both diversity and specificity among signaling circuits is their *spatial organization*. Scaffolding molecules increase the efficiency of the process by helping to assemble *signaling platforms*. These large multiprotein complexes provide physically coupled activation−deactivation cycles of kinases, their phosphatases, upstream activators and downstream effectors. It is important to remember that the enzymatic reactions taking place in these large immobilized aggregates may not necessarily obey simple models of enzymes kinetics. Messages can also be *temporally encoded*, i.e. some effectors are tuned to respond to short-lived signals, while other processes require sustained signaling to exert an effect. Thus the "*spatiotemporal*" features of a message, even highly diffusible second messengers like Ca^{2+} and cAMP, can dictate the physiological response to that signal.

Subtle *remodeling* of signaling properties takes place throughout the lifetime of a cell due to changes in expression levels of elements within a cascade. This can give rise to a certain degree of heterogeneity even among cells of the same type. Remodeling has been considered to be a key feature in the progression of certain disease states (e.g. cancer, cardiovascular disease).

Finally, there is an incredible degree of *interconnectivity* among the various signaling pathways, which are also subject to complex feedback and feed-forward regulation. The signalsome of any given cell would therefore be more realistically represented as a *non-linear network of interacting circuits*, although generally depicted (as they are in this chapter) as simplified linear sequences of biochemical events.

III. GENERAL TYPES OF SIGNAL TRANSDUCTION CASCADES AND THEIR COMPONENTS

Sir Michael Berridge has categorized the major intracellular signal transduction cascades into ≈19 different groups (Berridge, 2009). Most of these pathways (Fig. 6.1) are highly conserved across animal and even plant species and many are initiated following engagement of two general types of cell surface receptors: G-protein coupled receptors (GPCRs) or receptor tyrosine kinases (RTKs). Signals are often transduced and amplified through cycles of reversible covalent modification of target proteins, catalyzed by an activator and deactivator. For example, protein kinases phosphorylate protein targets and their activity is terminated through the action of phosphatases. Another general class of transducer is the small GTP-binding proteins, whose action is accelerated by guanine-nucleotide exchange factors (GEFs) and terminated by GTPase-activating proteins (GAPs).

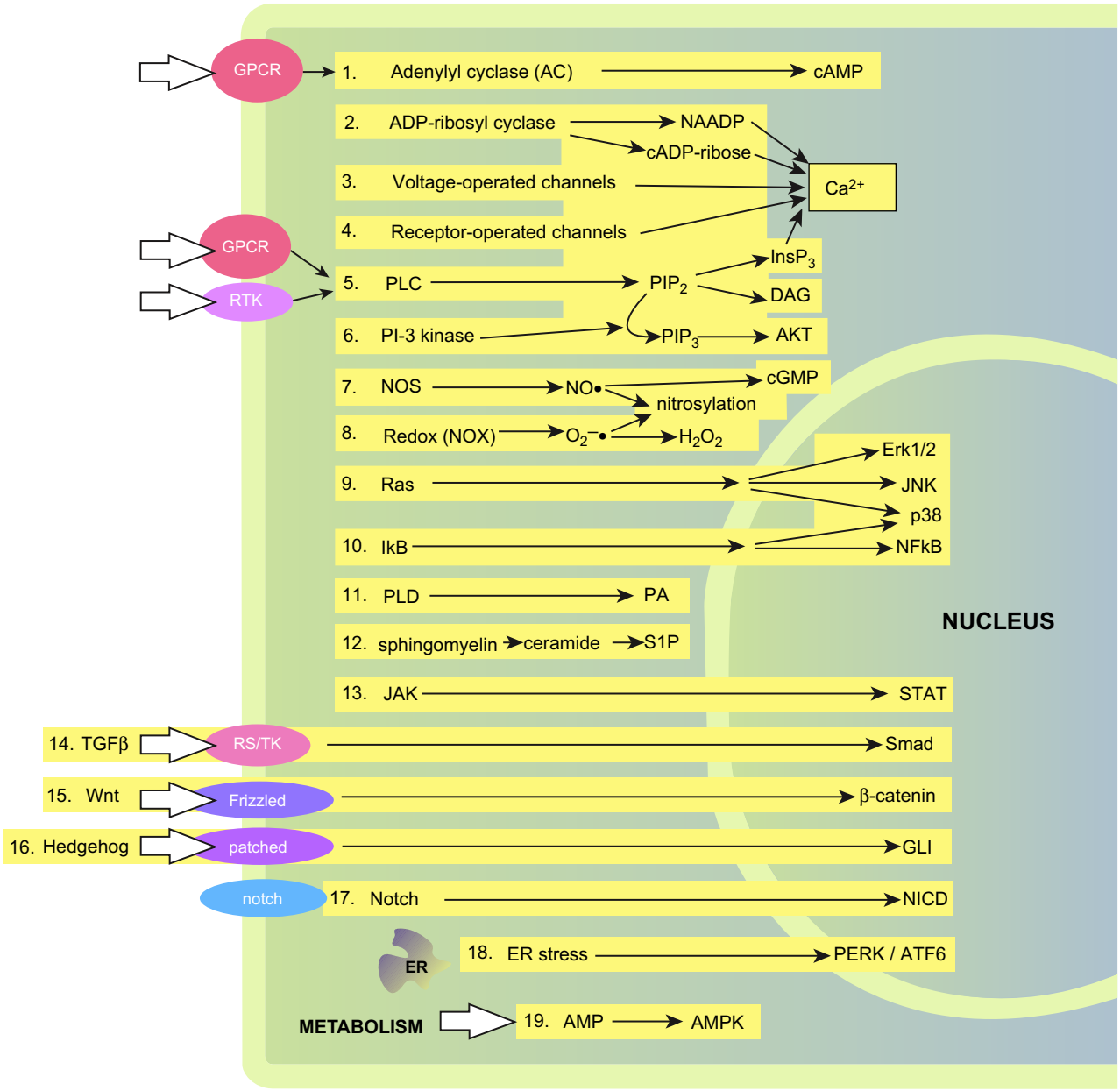

FIGURE 6.1 Inventory of major intracellular signaling pathways. 1. Cyclic AMP signaling pathway; 2. cyclic ADP-ribose and nicotinic acid-adenine dinucleotide phosphate (NAADP); 3. voltage-operated channels (VOCs); 4. receptor-operated channels (ROCs); 5. phospholipase C-dependent hydrolysis of PtdIns4,5P_2 (PIP_2); 6. PtdIns 3-kinase signaling (phosphorylation of PIP_2 to form PIP_3); 7. nitric oxide (NO)/cyclic GMP signaling pathway; 8. redox signaling: NADPH oxidase (NOX)→ reactive oxygen species (ROS); 9. mitogen-activated protein kinase (MAPK) signaling; 10. nuclear factor κB (NF-κB) signaling pathway; 11. phospholipase D pathway: phosphatidylcholine→phosphatidic acid (PA); 12. sphingomyelin signaling pathway: formation of ceramide and sphingosine 1-phosphate (S1P); 13. Janus kinase (JAK)/signal transducer and activator of transcription (STATs); 14. Smad signaling pathway: TGFβ→ Smad transcription factors; 15. Wnt signaling pathway; 16. hedgehog signaling: generation of the transcription factor GLI; 17. Notch signaling: generation of the transcription factor NICD (Notch intracellular domain); 18. endoplasmic reticulum stress signaling: information transfer from the ER to the nucleus; 19. AMP signaling: metabolic sensor. *(Adapted from Berridge (2009). See http://www.cellsignallingbiology.org for further details.)*

Transcription factors are frequently the ultimate target for many of these inputs (Brivanlou and Darnell, 2002). These can be resident in the nucleus, shuttle between nucleus and cytosol or require activation in the cytosol in order to gain access to the nucleus (Table 6.1). We will begin our discussion by briefly introducing some of the common players in signal transduction and then address each pathway separately.

TABLE 6.1 Examples of Signal-Dependent Transcription Factors

Most transcription factors are regulated by multiple signaling inputs; a classic example is CREB (cAMP response element binding), which is phosphorylated by both PKA and Ca^{2+}/calmodulin-dependent kinase IV (CaMKIV).
Nuclear receptors (e.g. steroid hormone receptors) GR, ER, PR, TR, RARs, RXRs, PPARs
Regulated by internal states (e.g. ER stress, DNA damage, hypoxia) SREBP, ATF6, p53, HIF
Regulated by signals generated at the cell surface:
Resident in nucleus CREB, E2F1, ETS, ATMs, SRF, FOS-JUN, MEF2, Myc, MeCP2 Shuttle between nucleus and cytosol DREAM, FOXO Become activated in the cytosol, translocate to nucleus STATs, SMADs, NFκB, β-catenin, NFAT, Tubby, GLI, MITF
From Brivanlou and Darnell, 2002.

IIIA. GPCRs and Classical Second Messenger Signaling

GPCRs comprise an enormous family represented by over 800 genes in the human genome. They have a common structure characterized by seven transmembrane-spanning domains. While a significant percentage of these genes encode receptors for odorants, there are ≈200 distinct GPCRs that recognize a remarkably diverse assortment of known non-odorant ligands. They serve as detectors for neurotransmitters, hormones, peptides, photons, bile acids, amino acids, Ca^{2+} ions and tastants (including bitter, sweet and umami taste). There are also ≈150 orphan receptors for which the natural ligand remains unidentified. As of 2009, eight Nobel prizes have been awarded for contributions in the field of signal transduction via G proteins and second messengers. GPCRs are also targets (directly or indirectly) for at least 30% of all currently prescribed drugs, further attesting to the physiological and medical importance of this class of proteins (Pierce et al., 2002).

G-protein coupled receptors are so-named because they interact with a class of proteins known as *heterotrimeric G-proteins* (Oldham and Hamm, 2008), consisting of a G_α subunit (represented by 16 genes) and fused G_β and G_γ subunits (six and 12 genes, respectively). *Lipid modifications* (e.g. palmitoylation, prenylation) keep the various subunits anchored to the plasma membrane where they interact with GPCRs.

Most of the specificity of the signal derives from the G_α subunit, which is allowed to couple to an effector when the receptor is engaged by its ligand. The major types of Gα subunits are:

- $G_{\alpha s}$ – couples to adenylyl cyclases (AC1–AC9) to generate the second messenger, cAMP
- $G_{\alpha i/o}$ – inhibits the activity of most adenylyl cyclases
- $G_{\alpha q/11}$ – couples to phospholipase C and the Ca^{2+}-phopshoinositide pathway
- $G_{\alpha 12/13}$ – ultimately engages the small GTP-binding protein Rho A, to alter the cytoskeleton.

Engagement of the GPCR with its ligand results in exchange of a GDP for GTP on the G_α subunit and dissociation of the heterotrimeric complex into free G_α and $G_{\beta\gamma}$ dimers. This permits the GTP-bound G_α subunit to couple with its effectors (e.g. adenylyl cyclases or phospholipase C; see below). The $G_{\beta\gamma}$ subunits also have biological activities that include interactions with ion channels, monomeric G-proteins (e.g. Rac, Cdc42) and PI 3-kinase. GPCRs can also interact (via heterotrimeric G proteins) with ion channels, e.g. the GIRK channels (G protein-coupled inwardly rectifying potassium channels).

Figure 6.2 illustrates some of the more common stimuli and biological outputs of this signaling system (Neves et al., 2002). There are a few things worth pointing out. First, because of GPCR isoform diversity, a single type of extracellular ligand can activate multiple kinds of intracellular signaling pathways. It is also the case that certain GPCRs are promiscuous, i.e. it is possible for particular GPCRs to couple to more than one type of G_α subunit in order simultaneously to activate multiple pathways (Hofer and Brown, 2003). It is also noteworthy that communication via the vast majority of GPCR ligands ultimately converges on just two second messenger systems: the Ca^{2+}/phosphoinositide (via $G_{\alpha q/11}$) and cAMP signaling systems (via $G_{\alpha s}$ and $G_{\alpha i/o}$). How these simple messengers manage to control so many biological functions is an exciting area of continuing investigation.

IIIB. Receptor Tyrosine Kinases and Receptor Serine/Threonine Kinases

Numerous growth factors, survival factors and hormones, such as insulin, exert their actions through receptor tyrosine kinases (RTKs). These are single-membrane spanning proteins that are represented by ≈20 different subfamilies. They generally form *dimers* upon engagement with their ligand (an exception is the insulin receptor, which is already in a dimeric configuration in the absence of insulin), causing tyrosine residues in a cytoplasmic domain of the receptor to become autophosphorylated. The RTK then assumes an active conformation that permits it to interface with several types of downstream signaling transducers. RTKs are also linked to scaffolding proteins

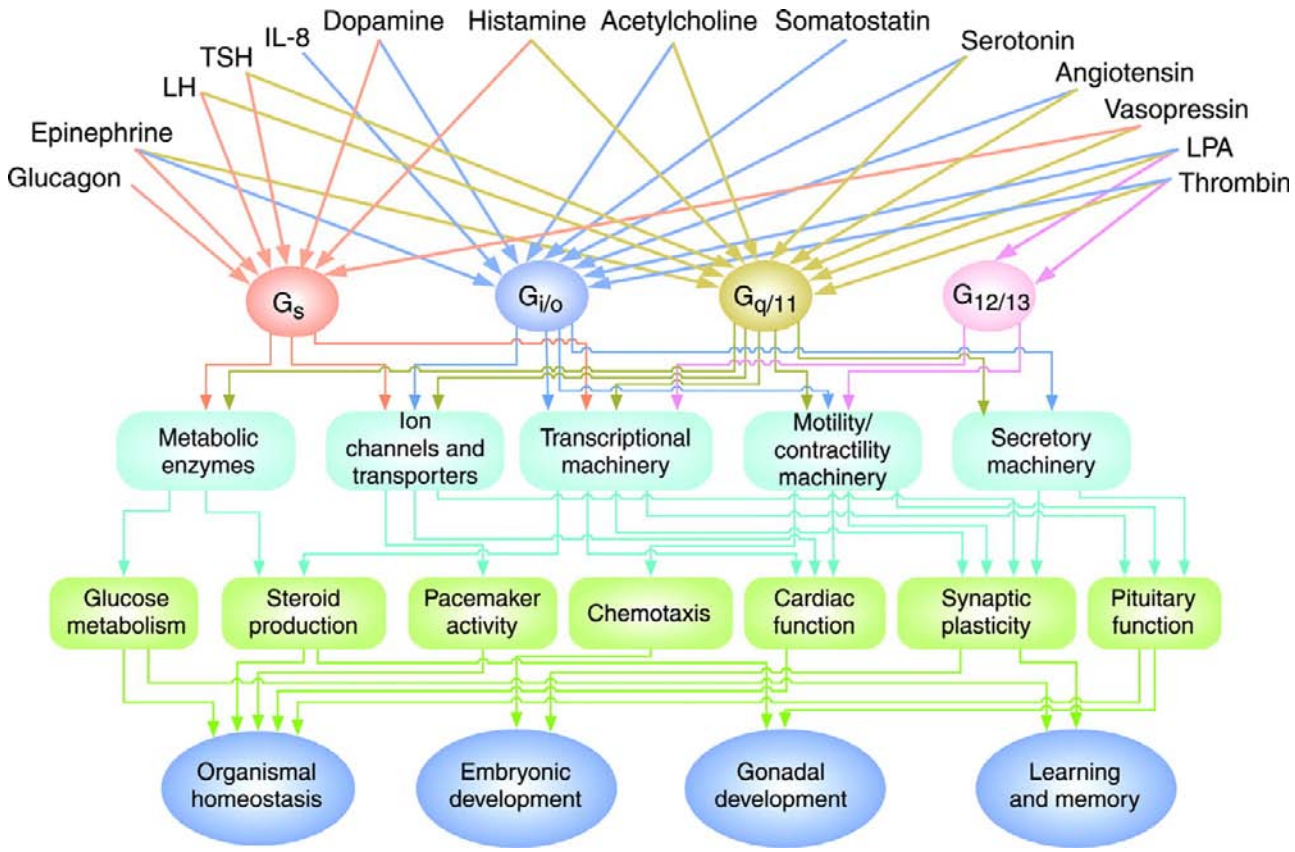

FIGURE 6.2 Regulation of biological functions through heterotrimeric G-protein pathways. Examples of regulatory networks that control functions via the four major classes of heterotrimeric G proteins are depicted. See text for further details. *(Taken from Neves et al. (2002). Science. 296, 1636–1639, AAAS Publishers.)*

that facilitate these processes. Major intracellular pathways that are turned on by RTK stimulation include:

1. Ras – the activated RTK is linked via adaptors proteins (Grb2 and SOS) to the small G protein ras which, in turn, activates another monomeric G protein known as raf. Raf is important in turning on the MAP kinase cascade (e.g. ERK1/2; see below)
2. PLCγ – activation of phospholipase Cγ generates $InsP_3/Ca^{2+}$ and DAG (see Ca^{2+}-phosphoinositide pathway below)
3. PI-3kinase – generates the lipid PIP_3 to activate Akt (protein kinase B; see below)
4. Src family kinases – these are part of a large family of non-receptor tyrosine kinases. They work by both helping to assemble signaling complexes and to phosphorylate tyrosine residues on targets within the complex.

The receptor serine/threonine kinases (RS/TKs) of the transforming growth factor β (TGFβ) superfamily are also single-membrane spanning receptors. RS/TKs are detectors for certain growth stimuli, including bone morphogenetic protein (BMP) and TGFβ (Moustakas et al., 2001). These receptors generally form *tetramers* and couple to the Smad signaling pathway (discussed below).

IIIC. Small GTP-Binding Proteins

As the name suggests, these are small monomeric proteins that bind GTP, which results in the G protein assuming an "on" state. This reaction is generally catalyzed by a large assortment of guanine nucleotide exchange factors (GEFs). When GTP is hydrolyzed to GDP, the G proteins are in the "off" state. GTPase activating proteins (GAPs) accelerate this process (Bos et al., 2007).

Monomeric G proteins (≈150 different ones) are important intermediaries in numerous types of signal transduction systems and can be subdivided into five general families: Ras, Rho, Rab, Ran and Arf. Ras proteins (36 genes) are control points for multiple types of signaling pathways (e.g. MAP kinase and PI-3 kinase pathways; see below). Many of the other G proteins (e.g. Rho family members) have key roles in the control of the cytoskeleton, while others (e.g. Rab, Arf) are involved in membrane trafficking. Ran is involved in nuclear transport.

IV. PHOSPHORYLATION BY KINASES AND OTHER POST-TRANSLATIONAL MODIFICATIONS

The most common motif for altering the activity of a target is through reversible *phosphorylation* of specific amino acid residues by a protein kinase (Pearce et al., 2010). These are usually serine or threonine residues or, in the case of tyrosine kinase family members, a tyrosine residue. Protein kinases have regulatory roles in all aspects of eukaryotic cell function and provide tremendous *signal amplification*. The domains of some of the more common kinases with similarity to the classical protein kinases A, C and G (PKA, PKC, PKG) are illustrated in Fig. 6.3. *Phosphatases* accelerate the removal of phosphate groups on phosphorylated proteins to terminate the signal.

Other types of reversible modifications to amino acid residues are also used (albeit less commonly than

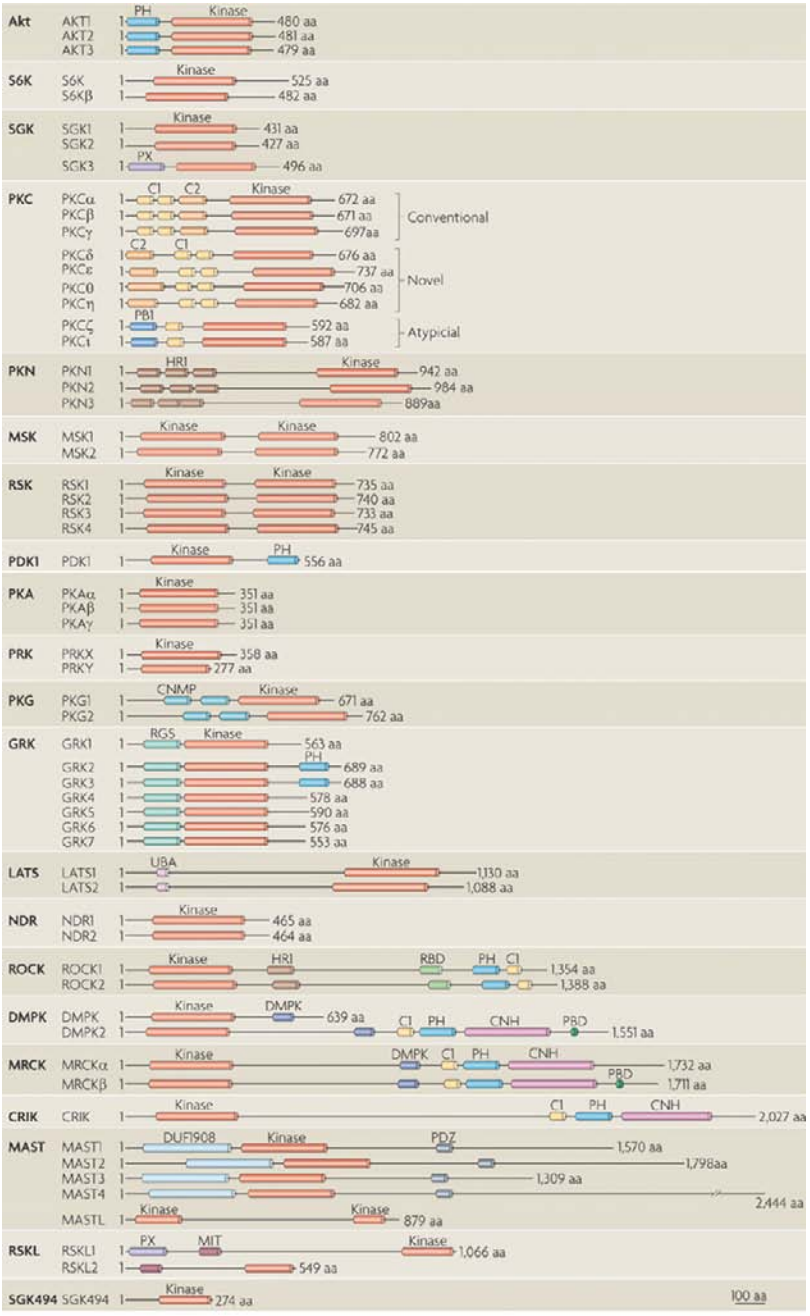

Nature Reviews | Molecular Cell Biology

FIGURE 6.3 Examples of kinases with structural similarities to protein kinase A (PKA), protein kinase G (PKG) and protein kinase C (PKC). *(From Pearce, L.R., Komander, D. & Alessi, D.R. (2010). The nuts and bolts of AGC protein kinases. Nat Rev Mol Cell Biol, 11, 9–22.)*

phosphorylation) to control the activity of intermediates and final targets in signaling cascades. These include:

- oxidation of cysteine residues by the redox signaling pathway (see NADPH oxidase pathway below)
- nitrosylation (from nitric oxide pathway; see below)
- sumoylation
- acetylation
- protein methylation
- ubiquitination.

V. INTRACELLULAR SIGNAL TRANSDUCTION PATHWAYS

VA. Cyclic AMP Pathway

The foundations of the second messenger concept were established nearly half a century ago when Sutherland and Rall identified a small heat stable factor that mediated the intracellular actions of the hormones glucagon and epinephrine on glycogen metabolism in the liver. The mysterious factor turned out to be cAMP, a discovery that earned Sutherland the 1971 Nobel Prize in Physiology or Medicine (Rehmann et al, 2007).

This small highly diffusible second messenger is produced mostly through the activation of GPCRs that are coupled via $G_{\alpha s}$ to adenylyl cyclases (ACs; Fig. 6.4). The conventional ACs are a family of nine membrane spanning proteins (AC1−AC9) that are regulated differentially by other signaling pathways (e.g. Ca^{2+}). A given cell type may express several different isoforms of AC. Apart from the conventional ACs, there is also another route to cAMP production via a so-called "soluble" adenylyl cyclase (sAC or AC10). This AC is not a transmembrane protein, but it can nevertheless be localized to discrete regions of the cell (e.g. organelles) to provide localized cAMP signals. Because sAC is activated mainly by HCO_3^-/CO_2 (it is also regulated by Ca^{2+}) it has been considered to function as a metabolic sensor.

Once cAMP is generated, it can bind to and alter the activity of three general types of effector proteins:

- protein kinase A (PKA)
- cyclic nucleotide-gated channels (see Chapter 35)
- epac (exchange protein activated by cAMP; see below).

PKA is without question the most important target of the cAMP signal. At rest, PKA exists as a four-protein complex known as a heterotetramer because it consists of two catalytic subunits and two regulatory subunits. When cAMP binds the regulatory subunits, it releases the catalytic subunits, which are then free to phosphorylate other proteins within the cell. Important PKA targets include ion channels (e.g. CFTR, AMPA receptors), metabolic enzymes (e.g. lipase) and cAMP-dependent transcription factors such as the prototypical CREB (cAMP response element binding) protein. Inputs from other signaling cascades, including Ca^{2+} and MAP kinase pathways, also converge on CREB to regulate its function.

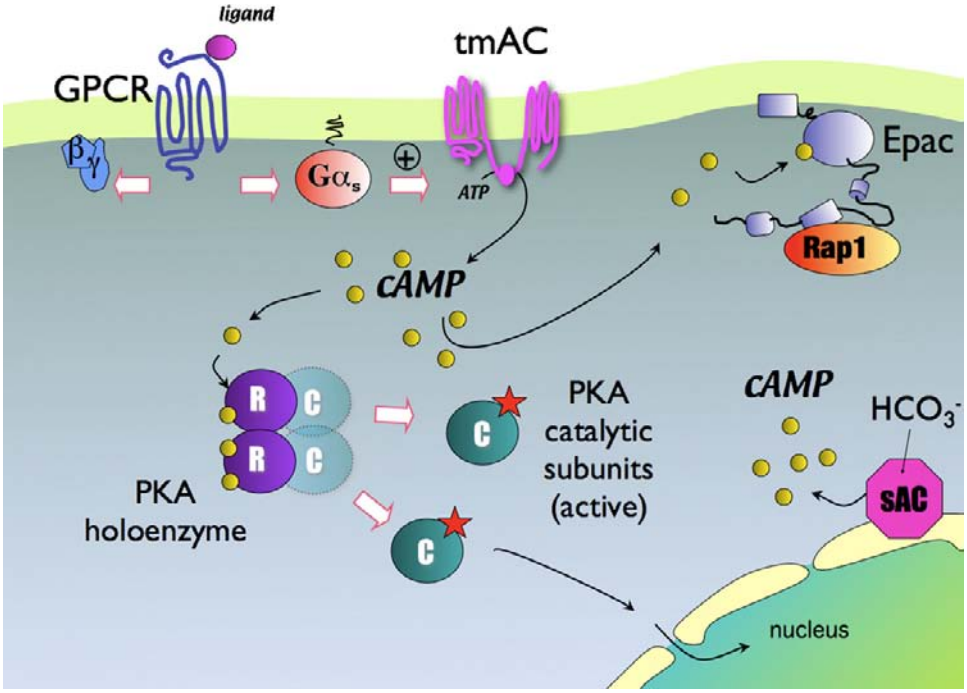

FIGURE 6.4 Basic features of the cyclic AMP signaling cascade.

Epac (exchange protein activated by cAMP) is a more recently identified effector of the cAMP signal for which there are two isoforms, Epac1 and Epac2. The best understood action of Epac is to enhance the GTP-ase activity of the small G proteins of the Ras superfamily, Rap1 and Rap2.

The cAMP signal is terminated by phosphodiesterases (PDEs), a complex family of enzymes with more than 20 members. Some of these isoforms of PDE also preferentially metabolize cyclic GMP (see below). PDEs are of major interest for drug development. Because the various isoforms can have tissue-specific distributions (e.g. in airway and cardiovascular systems), they may provide an avenue for controlling particular tissue functions using isoform-selective drugs.

VB. Calcium Signaling Pathway: VOCs, ROCs, SMOCs, SOCs and Store Release

Calcium is a major second messenger used by virtually all cells. It is at the same time the simplest messenger, since no enzymes are needed to create or destroy this ubiquitous signal, and one of the most versatile, since it can convey information in many different compartments within the cell (e.g. local events within cytosol, mitochondria, ER lumen and extracellular space) (Hofer and Brown, 2003; Berridge et al., 2003). Moreover, signaling targets can respond differentially to specific types of signals. For example, many Ca^{2+} signals are oscillatory in nature and this pattern may preferentially activate one kind of target (e.g. an ion channel) while a sustained elevation in Ca^{2+} may ultimately activate another (e.g. a transcriptional cascade). As details of this system are covered in several other chapters in this volume (e.g. Chapters 13, 14, 42), we will present only a general overview of the Ca^{2+} signaling pathway here.

Ca^{2+} is normally maintained at very low levels in the cytosol ($\approx$50 nM – this is very low if you consider that distilled water contains about 5–10 μM free Ca^{2+}!) but it can rapidly become elevated as much as 10–20-fold through any number of different mechanisms:

1. VOCs: voltage-operated Ca^{2+} entry pathways (in excitable cells; see Chapter 21)
2. ROCs: receptor operated Ca^{2+} channels, activated by extracellular ligands such as glutamate or ATP (see Chapter 36)
3. SMOCs: second messenger-gated channels are opened by ligands generated inside the cell (cAMP, cGMP, DAG, arachidonic acid)
4. release from intracellular Ca^{2+} stores, especially the ER, following activation of intracellular Ca^{2+} release channels. These are Ca^{2+} selective channels typically located on the ER or SR membrane, and include $InsP_3R$, release channels activated via cADPR, and RyR (see Chapter 42). These pathways are discussed below.
5. SOCs: store-operated Ca^{2+} entry channels are activated when the free concentration of Ca^{2+} in the ER lumen is reduced, for example following agonist/$InsP_3$-induced release described in the next section.

VC. The Ca^{2+}-Phosphoinositide Pathway

GPCRs and RTKs elicit Ca^{2+} signals via the Ca^{2+}-phosphoinositide pathway, a ubiquitous mechanism found in nearly all cell types (including excitable cells). Receptor engagement results in increased turnover by phospholipases (PLCβ for GPCRS and PLCγ for RTKs) that hydrolyze the plasma membrane lipid PIP_2 to produce DAG (which remains associated with the bilayer) and a small diffusible hydrophilic molecule, $InsP_3$. While DAG works to stimulate certain PKC isoforms, $InsP_3$ is able to bind to a Ca^{2+} release channel on the ER membrane known as the $InsP_3$ receptor. The ER continually sequesters Ca^{2+} via a pump known as the SERCA (sarcoendoplasmic Ca^{2+}-ATPase; see Chapter 13) so that the free resting [Ca^{2+}] is $\approx$500 μM in the ER lumen. Once the $InsP_3$ receptor is opened, the cation floods out of the ER into the cytoplasm, generating a spike in cytosolic Ca^{2+} that subsides as the stores become emptied.

There is then a second and very interesting phase of the signal. The reduction in free [Ca^{2+}] within the ER lumen is sensed by the luminal domain of a recently identified ER transmembrane protein known as STIM1. The decreased [Ca^{2+}] causes STIM1 to aggregate in discrete zones of ER just under the plasma membrane and this leads to the activation of Ca^{2+} selective channels (mostly of the family of channels known as Orai channels) in the plasma membrane. Entry of Ca^{2+} through these channels typically generates a sustained phase of the Ca^{2+} signal that serves both as a source of Ca^{2+} for refilling the ER stores and as a signal for cellular targets that require a more persistent elevation for their activation. When the initiating stimulus is removed and $InsP_3$ production ceases, the stores refill through the action of the SERCAs.

VD. Cyclic ADP-Ribose and NAADP Pathways

Cyclic ADP-ribose (cADPR) and nicotinic acid-adenine dinucleotide phosphate (NAADP) are related Ca^{2+}-mobilizing messengers that are synthesized by a single enzyme (ADP ribosyl cyclase) from NAD^+ and NADP, respectively. Curiously, the same synthetic enzyme also degrades cADPR. While cADPR is established to release Ca^{2+} from the ER, the physiological role of cADPR as a messenger has been somewhat controversial. The stimuli

leading up to its production and the precise mechanisms by which it releases Ca^{2+} are, however, an active area of investigation.

NAADP is an extremely potent releaser of intracellular Ca^{2+} stores. The "two-pore channels" (TPC1 and TPC2) that reside in acidic endolysosomal compartments, were recently identified as *bona fide* targets of NAADP (Zhu et al., 2010). Since other intracellular Ca^{2+} release channels on the ER/SR ($InsP_3R$ and RyR) increase their open probability with increasing levels of cytosolic [Ca^{2+}], a small spurt of Ca^{2+} from these acidic compartments may serve to "prime" the $InsP_3R$ and/or RyR, resulting in the generation of global Ca^{2+} signals.

VE. PtdIns 3-Kinase Signaling

The membrane lipid constituent PIP_2 has many biological functions that include regulation of ion channels and exocytosis. It is also an important precursor for other biologically active lipids (Wymann and Schneiter, 2008). As noted above, stimulation of GPCRs and RTKs can lead to activation of phospholipases (PLCβ or PLCγ, respectively) that metabolize PIP_2 into $InsP_3$ and DAG. Following receptor engagement, another parallel arm of these reactions can also be set in motion that involves phosphorylation of PIP_2 by the enzyme phosphatidyl inositol 3-kinase (PI3-kinase). A major target of the newly generated lipid species, PIP_3, is another kinase, protein kinase B (PKB), more commonly known as AKT.

AKT is in effect recruited to the inner leaflet of the plasma membrane by the freshly generated PIP_3 because it contains a domain known as the Pleckstrin Homology (PH) domain, a common lipid-binding motif found in many lipid-dependent signaling proteins. Another player in this cascade, that also has a PH-domain, is PDK1 (phosphoinositide-dependent protein kinase 1). When AKT and PDK1 are both recruited to the plasma membrane at the same time, PDK1 can phosphorylate and turn on AKT. Once activated, AKT phosphorylates or interacts with a wide range of targets (e.g. the kinase mTOR) to govern processes such as growth, protein, lipid and glycogen synthesis and apoptosis and proliferation.

PI3K/AKT signaling is arrested when PIP_3 in the membrane becomes metabolized. This occurs through a specific enzyme known as PTEN. PTEN is a phosphoinositide phosphatase, i.e. an enzyme capable of removing phosphate groups from PIP_3. The timely termination of the signal by PTEN is crucial. For example, during growth factor stimulation, the absence of PTEN leads to overstimulation of this pathway and inappropriate entry into the cell cycle even after the initiating stimulus has been removed. In fact, PTEN is defined as a tumor suppressor gene and PTEN mutations and deficiencies are prevalent in many types of human cancers. PTEN and other elements of the PI3K pathway are actively being investigated as targets for anticancer drugs.

VF. Nitric Oxide (NO)/Cyclic GMP Signaling Pathway

Nitric oxide (NO) is a highly reactive, membrane permeable gaseous transmitter that is produced from the amino acid L-arginine by three different nitric oxide synthase (NOS) enzymes: eNOS (endothelial NOS), nNOS (neuronal NOS) and iNOS (inducible NOS) (Pacher et al., 2007). The nNOS and eNOS isoforms were named for the tissues in which they were originally identified and iNOS was so named because its expression could be induced in macrophages during inflammation, however, all three enzymes are actually widely distributed across different cell types.

NO is generated by eNOS and nNOS following an elevation in intracellular Ca^{2+}. The iNOS enzyme, on the other hand, appears to be constitutively active (although regulated by other signaling molecules, particularly calmodulin) and can produce large amounts of NO for prolonged periods.

Once synthesized, the NO molecule has two major jobs. The first is to activate the so-called "soluble" guanylyl cyclase (sGC), which catalyzes the formation of cGMP (Rehmann et al., 2007) (which is more stable than NO) from GTP. Cyclic GMP in turn activates a cGMP-dependent protein kinase (PKG) that can phosphorylate numerous downstream targets. The cyclic nucleotide can also activate channels in the plasma membrane (see Chapter 35).

Note that there is also a nitric oxide-*independent* route to cGMP production that occurs when certain peptide hormones, such as atrial natriuretic factor (ANP) and guanylin, bind to the transmembrane receptor known as particulate guanylyl cyclase (pGC). In addition to stimulating the formation of cGMP, the other major action of NO is to cause S-nitrosylation of the thiol-side chains of cysteine residues within protein targets, thereby altering their activity.

Ferid Murad, Louis Ignarro, and Robert Furchgott were awarded the 1998 Nobel prize for their discovery of NO, underscoring the physiological and clinical importance of this messenger. NO (originally known as EDRF or endothelial-derived relaxing factor) regulates smooth muscle relaxation and hence controls vasodilatation, bladder function, penile erection and gastrointestinal motility, to name but a few of its functions. Nitric oxide is also used by fireflies to elicit flashes of light and by plants to evade pathogens. Other endogenous "gasotransmitters" have recently been described, including carbon monoxide (CO) and hydrogen sulfide (H_2S) gas.

VG. Redox Signaling through NADPH Oxidase (NOX)

It has long been appreciated that immune cells, such as neutrophils, take advantage of the regulated production of reactive oxygen species (ROS) via NADPH oxidases (Nox) in order to neutralize invading pathogens. It is now known that nearly all cell types utilize Nox (of which there are five isoforms, Nox1−Nox5) and the related dual-oxidase enzymes, Duox (represented by two isoforms, Duox1 and Duox2), to generate reactive oxygen species and peroxide (H_2O_2) metabolites that, in effect, serve as short-lived second messengers to regulate a wide variety of cell functions.

One route to the activation of NADPH oxidases occurs at the plasma membrane after stimulation of receptors for hormones, growth factors or cytokines linked to PI3-K. This enzyme converts PIP_2 into PIP_3 (see above) and the resulting PIP_3 stimulates Nox, producing superoxides that can inactivate many protein targets (e.g. transcription factors, tyrosine phosphatases, PTEN) in the localized microdomain surrounding the Nox complex. It should be noted that substantial amounts of ROS can also be generated as a by-product of mitochondrial respiration.

VH. Mitogen-Activated Protein Kinase (MAPK) Signaling

The MAPK pathway is a major multikinase signaling circuit that is often thought of in the context of growth factor stimulation (e.g. gene expression leading to growth and proliferation). In fact, it controls a multitude of cellular functions including metabolism, motility, apoptosis and long-term memory, to name a few. It receives inputs from multiple signaling systems, including GPCRs, RTKs, Toll receptors and integrins, and can also transduce the effects of environmental stresses (e.g. osmotic stress, UV radiation).

There are three major types of MAPK cascades named after their major transducers:

1. extracellular-signal-related kinase (ERK)
2. c-Jun N-terminal kinase (JNK)
3. p38.

As shown in Fig. 6.5, the general scheme of this pathway involves the initial activation of a MAPKKK, which phosphorylates a MAPKK which, in turn, phosphorylates ERK, JNK or p38 (the MAPK). Although counterintuitive, it is thought that this arrangement of having three kinases in a row may actually conduct the signal faster than systems employing fewer numbers of kinases. Once phosphorylated, ERK, JNK and p38 frequently translocate to the nucleus to regulate gene expression.

VI. Nuclear Factor κB (NF-κB) Signaling Pathway

The NF-κB/Rel family (NF-κB1, NF-κB2, NF-κB3, RelB, and cRel) consists of a group of master transcription factors that remain latent in the cytoplasm until activated (Hayden et al., 2006; Perkins, 2007). It is commonly regarded as

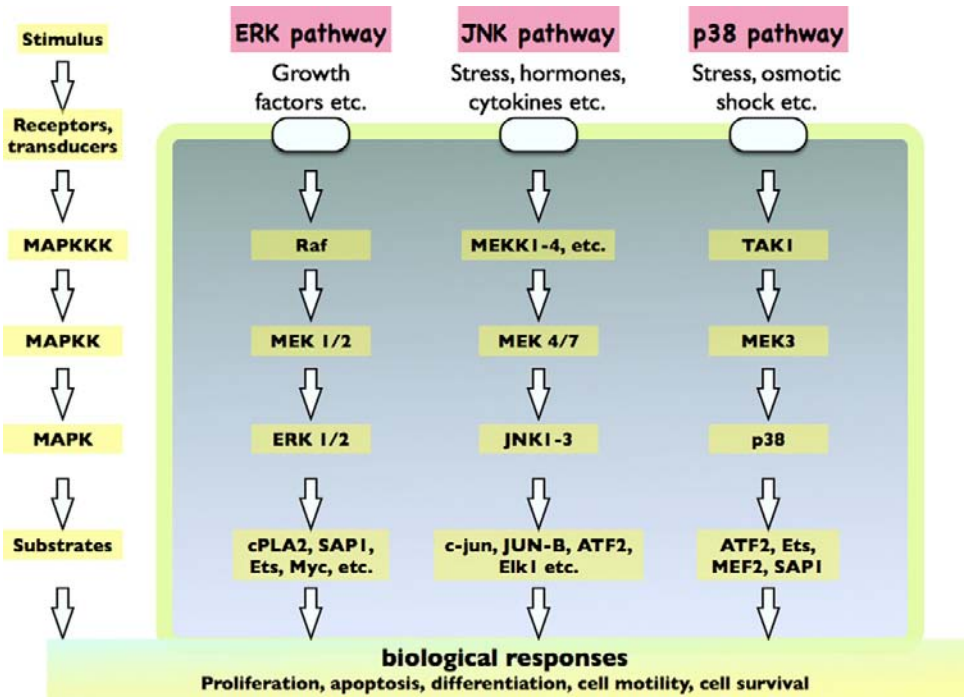

FIGURE 6.5 MAP kinase cascades.

a "first responder" to a large, diverse, panel of stress-induced stimuli that include cytokines (e.g. tumor necrosis factor, TNFα), lymphokines, mitogens, hormones, carcinogens, inflammatory agents, tumor promoters, drugs, UV light, oxidative stress and certain growth factors. There are at least 150 types of extracellular stimuli known to activate this signaling system, which is present in nearly all cells. It also is involved in the control of osteoclastogenesis through the RANKL receptor and activation of receptors, known as Toll-like receptors, whose job it is to recognize pathogens and inflammatory cytokines. Each of these types of inputs requires a complex cast of players (not detailed here) that ultimately converge on the NF-κB pathway according to the following general scheme.

At rest, NF-κB is retained in the cytoplasm (and is therefore kept inactive) by "IκB" (inhibitor of NF-κB). IκB is a cytosolic resident that belongs to a family of six proteins responsible for masking the nuclear localization signal of NF-κB. However, in response to diverse stimuli, a kinase known as "IKK" (inhibitor of NF-κB kinase) becomes activated. There are three forms of IKK (IKKα, IKKβ and "NEMO", a regulatory protein also known as IKKγ), which phosphorylate IκB, thereby tagging it for degradation by the proteasome. Liberated from IκB, NF-κB is now free to enter the nucleus, where it can bind to DNA and turn on expression of large gene sets, e.g. those involved in innate immune and stress responses. The NF-κB pathway also receives inputs from numerous other signaling systems to modulate its activity and is an important object of drug discovery efforts.

VJ. Phospholipase D Pathway

There are more than 1000 types of biological lipids. Phospholipase D enzymes (two isoforms: PLD1 and PLD2) hydrolyze phoshatidylcholine, a ubiquitous lipid constituent of the bilayer, to generate the bioactive lipid, phosphatidic acid (PA). PLD1 is located principally on intracellular membranes (the ER, Golgi and endosomal membranes) and in caveolae of the plasma membrane. PLD1 becomes activated by elements downstream of GPCR or RTK stimulation (e.g. via PKC). PLD2 appears to *not* be activated by these stimuli and is mainly localized to the plasma membrane. Once synthesized, PA acts as a second messenger to regulate a number of enzymes, including protein phosphatases, mTOR and other targets that control budding and fusion, secretion, changes in cytoskeleton and proliferation (Cazzolli et al., 2006).

VK. Sphingomyelin/Ceramide Signaling Pathway

Ceramides are bioactive lipids that can be generated enzymatically in response to stressful stimuli that include TNFα, radiation, chemotherapy drugs and through the activation of "death receptors" by a transmembrane protein known as Fas ligand on a neighboring cell. There are two routes to its formation: (1) from the breakdown of sphingomyelin (a constituent of the lipid bilayer, particularly the plasma membrane); or (2) through de novo synthesis (Hannun and Obeid, 2008).

Ceramide has several protein targets, including the protease cathepsin D, a particular isoform of PKC (PKCξ) and ceramide-activated phosphatases. However, its action does not stop there. Ceramide is further converted to the lipid messenger sphingosine, which activates certain kinases. Like ceramide, sphingosine can drive apoptosis (programmed cell death) and cell cycle arrest.

This cascade continues even further, however, since sphingosine is the precursor for another potent bioactive lipid, sphingosine 1-phosphate (S1P). S1P is generated when sphingosine kinase becomes activated by diverse stimuli that include growth factors (PDGF, IGF, VEGF), cytokines (IL-1, TNF), hypoxia and oxidized LDL to name a few (Wymann and Schneiter, 2008). S1P can act as a local extracellular messenger to stimulate GPCRs of the "EDG" family (specifically EDG1, 3, 5, 6 and 8) on the same cell or on neighboring cells. EDG receptors are coupled to the Ca^{2+}-phosphoinositide signaling pathways.

VL. Janus Kinase (JAK)/Signal Transducer and Activator of Transcription (STATs)

This relatively simple pathway mediates the actions of more than 30 different hormones and cytokines, including numerous interleukins (e.g. IL-2), interferons, growth hormone, erythropoietin and prolactin. It is frequently referred to as a "fast-track" for signaling because there are so few components between the initial activation of the receptor (RTK, GPCR, cytokine receptor etc.) and the translocation of activated STATs to the nucleus, where they bind the promoter region of responsive genes. There are four JAK family members (JAK1−JAK3 and TYK1) and seven STATs.

Typically, JAKs "prime" the ligand-bound cytokine receptor for its interaction with the STATs by phosphorylating specific tyrosine residues on the dimerized receptor. STATs dock onto the phosphorylated receptor and then themselves become phosphorylated by JAKs (which remain associated with the receptor). At this point the activated STATs disengage from the receptor and form dimers, rendering them competent to enter into the nucleus to complete their work as transcription factors.

VM. Smad Signaling Pathway

Instructions from the TGF-β super-family of growth factors, including bone morphogenetic proteins (BMPs),

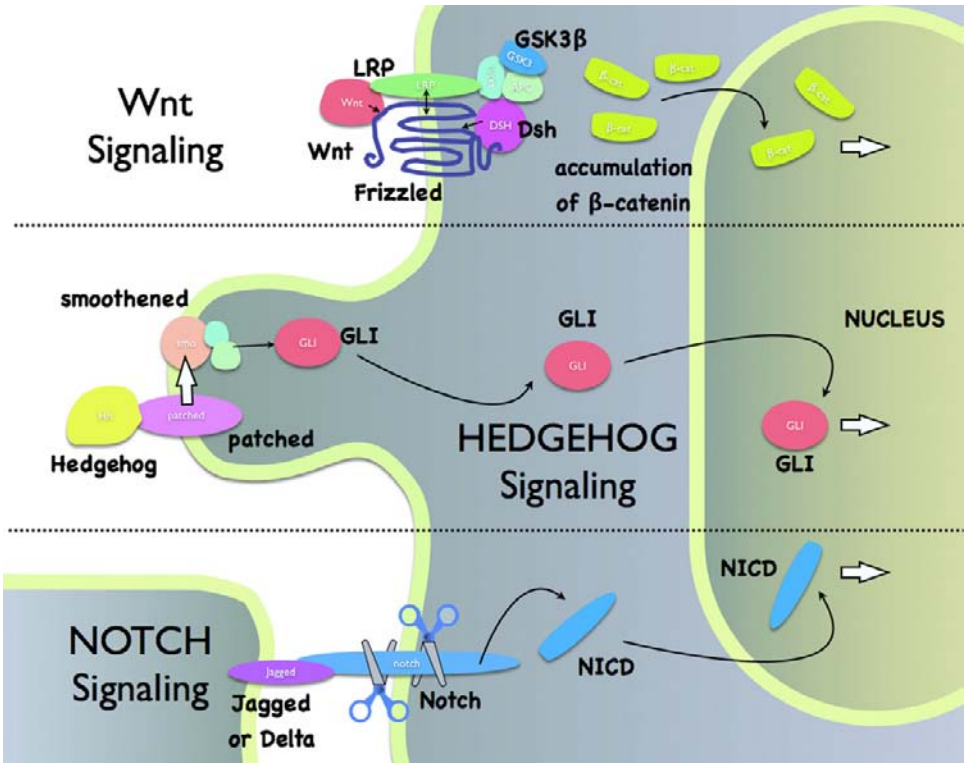

FIGURE 6.6 Wnt, Hedgehog and Notch pathways.

are funneled via their serine-threonine kinase receptors on the cell surface into an intracellular system of transcription factors and regulators known as Smads (Moustakas et al., 2001). Smads exist as three different types: R-Smads, co-Smad and I-Smads. The R-Smads are receptor-regulated and become directly phosphorylated when TGF-β binds its receptor (through a multistep process), activating the R-Smads, Smad2 or Smad3. Alternatively, agonists of the BMP-type bind to their cognate receptors to activate Smad1, Smad5, or Smad8. Smad4 is known as a co-Smad, which serves to facilitate signaling by forming dimers with R-Smads that then translocate to the nucleus to elicit expression of target genes. I-Smads (Smad6, 7) compete with Smad4 to inhibit this process.

In addition to controlling developmental processes, these systems maintain important physiological functions in the adult. For example, BMP is involved in skeletal remodeling and controlling proliferation of cells within the intestinal stem cell niche. TGF-β also directs differentiation of maturing cells within the intestinal villus, a structure characterized by extremely rapid cell turnover.

VN. Wnt Signaling Pathway

Wnt, Notch and Hedgehog (along with the TGF-β and receptor tyrosine kinase systems described above) are the major signaling pathways controlling early development throughout the animal kingdom. These pathways (Fig. 6.6) also exert important homeostatic and remodeling functions in adult organisms and are being increasingly indicted in the genesis of disease states, including tumorigenesis.

Wnts are extracellular lipoprotein growth factors that are encoded by 19 different genes in humans (Gordon and Nusse, 2006). Wnt binds to a receptor known as "Frizzled" (of which there are 10 types) that resembles the seven membrane-spanning receptors of the GPCR family. In the "canonical" (i.e. orthodox) Wnt/β-catenin pathway, Wnt also binds to a co-receptor of the LRP family and these proteins then form a complex with an intracellular protein known as disheveled. The Wnt pathway is somewhat unusual in that ligand binding leads to downstream steps that turn off constitutive degradation of the transcription factor β-catenin by a destruction complex formed by Axin, adenomatous polyposis coli (APC) protein and glycogen synthase kinase 3β (GSK-3). This allows β-catenin to accumulate to high levels and act as a transcription factor in the nucleus. There also exist β-catenin-independent modes of Wnt/Frizzled signaling. Among its many functions, the Wnt pathway is known to turn on proliferation of intestinal stem cells. It is noteworthy that mutations in members of this pathway are frequently observed in colon cancer cells.

VO. Hedgehog Signaling

The hedgehog gene was so named following the discovery of a *Drosophila* mutant possessing anterior-posterior patterning defects. This animal also presented a spiky hedgehog-like appearance due to the condensed solid lawn of denticles (cuticular extensions) on the body surface. The hedgehog protein (of which there are three in vertebrates, Indian hedgehog, desert hedgehog and sonic hedgehog) is a secreted morphogen that has recently emerged as an important target for anticancer drugs, with several compounds in clinical trials. This pathway is active in adult hematopoietic stem cells and hair follicles, where it signals the transition to the growth phase. Components of this pathway are frequently mutated in skin cancer cells.

Hedgehog (often abbreviated Hh) is secreted from cells by an unusual pathway (Chen et al., 2007). The cytosolic protein first acquires certain unique lipid modifications that allow it to be recognized and exported from the cell by a transmembrane enzyme known as dispatched. Carrier proteins in the extracellular milieu facilitate the delivery of Hh to target cells, where it binds a receptor called patched. At rest, the function of patched is to repress another transmembrane protein, smoothened. The job of smoothened is to keep transcription factors of the GLI family (three in mammals: GLI1−GLI3) in a dormant state. Binding of Hh to patched therefore effectively allows for the activation of GLI. An interesting feature of the preceding steps is that they take place almost entirely on the primary cilium of the target cell, a specialized surface projection present in virtually every vertebrate cell type. Once GLI is generated, it translocates to the nucleus where it controls transcription of genes involved in proliferation.

VP. Notch Signaling

Notch is a cell surface receptor that is an integral component of a relatively simple signaling pathway used extensively throughout the animal kingdom for controlling development (Bray, 2006). It takes its name from a notched wing phenotype in *Drosophila* first identified in genetic studies performed nearly a century ago. Flies with the notch mutation have increased numbers of neurons but less epidermal tissue.

There are four human Notch receptors (Notch1−4). Notch is unusual because most of its ligands are transmembrane proteins, therefore it becomes activated only when there is contact between receptor and ligand on a neighboring cell. This pathway is also very straightforward in that it signals without any amplification. The cascade starts when the Notch receptor encounters a transmembrane ligand on the communicating cell. One such ligand is known as Jagged and another is known as Delta. This interaction initiates two proteolytic cleavage events (not detailed here) that ultimately liberate an intracellular fragment of the Notch receptor called NICD (Notch intracellular domain). NICD works as a transcription factor that then translocates to the nucleus to alter gene expression. The signal is terminated via proteolytic degradation of NICD.

It is possible to envision how this arrangement permits one cell to influence gene expression in another and thereby allow an organism to assemble complex multicellular structures with similar or dissimilar phenotypes. In adult organisms, Notch signaling is involved in structural homeostasis, response to injury and repair. For example, this can take the form of influencing of the fate of intestinal cells destined for either secretory or absorptive lineages, and during angiogenesis.

VQ. Endoplasmic Reticulum Stress Signaling

This pathway provides a route for transmitting information from the ER to the nucleus (Ron and Walter, 2007). The ER stress response starts when polypeptides that are being processed in the ER lumen lose their tertiary structure or there is an overload of ER proteins. This can occur physiologically, e.g. if there is a sudden upregulation of protein production so that the protein-folding machinery in the ER becomes overwhelmed, and during viral infections. It also occurs when there is a persistent loss of Ca^{2+} from the ER lumen, causing Ca^{2+}-dependent chaperones to allow unfolding of the proteins they are escorting (note that this underscores the overall importance of reliable ER Ca^{2+} homeostasis, apart from its signaling function).

The presence of unfolded polypeptides in the lumen is sensed by several different systems (Lai et al., 2007). For example, this condition elicits processing and release of an ER-resident transcription factor ATF6, which ultimately travels to the nucleus, where it induces the expression of more chaperone proteins. Another attempt to correct the problem is mediated by the ER kinase PERK, which ultimately turns off protein synthesis. Persistent unfolded protein responses result in apoptosis through other ER stress sensors.

VR. AMPK Signaling: Metabolic Sensors

Cells need a way to communicate and adapt to changes in energetic status. When ATP levels are low, AMP is increased and this is detected by a fuel-sensing kinase, AMPK (AMP-activated protein kinase) (Steinberg and Kemp, 2009). AMPK directs processes that allow the cell to correct its energy deficit by turning on ATP-generating processes (glycolysis, fatty acid oxidation and

mitochondrial biogenesis) while inhibiting activities that use up ATP (gluconeogenesis, glycogen, fatty acid and protein synthesis). It also directly influences appetite-regulation in the hypothalamus.

AMPK is interesting in that it not only senses local AMP concentrations, but it also integrates the actions of hormones involved in energy balance such as leptin, ghrelin, adiponectin, glucocorticoids, insulin, as well as cannabinoids. It has generated recent excitement due to its apparent role in mediating the longevity-producing effects of calorie restriction.

VI. CONCLUSIONS

The preceding provides a brief and highly simplified snapshot of the major signaling pathways involved in the control of physiological processes. It highlights their beautiful diversity but also hints at their overwhelming intricacy. For the physiologist, the interconnected nature of these signaling networks means that perturbation of any one component may result in unforeseen alterations in other aspects of a cell's function. Systems biology approaches and new methods for monitoring signaling molecules with high spatiotemporal resolution (e.g. fluorescence- and GFP-based sensors) are among the tools that are currently being used to help unravel this complexity. The good news for those of us studying the regulation of physiological function is that each cell type and organ system will present us with diverse and exciting challenges for a long time to come.

BIBLIOGRAPHY

Berridge, M. (2009). Cell Signalling Pathways. In www.cellsignallingbiology.org ed.). Portland Press Limited.

Berridge, M. J., Bootman, M. D., & Roderick, H. L. (2003). Calcium signalling: dynamics, homeostasis and remodelling. *Nat Rev Mol Cell Biol, 4*, 517–529.

Bos, J. L., Rehmann, H., & Wittinghofer, A. (2007). GEFs and GAPs: critical elements in the control of small G proteins. *Cell, 129*, 865–877.

Bray, S. J. (2006). Notch signalling: a simple pathway becomes complex. *Nat Rev Mol Cell Biol, 7*, 678–689.

Brivanlou, A. H., & Darnell, J. E., Jr. (2002). Signal transduction and the control of gene expression. *Science, 295*, 813–818.

Cazzolli, R., Shemon, A. N., Fang, M. Q., & Hughes, W. E. (2006). Phospholipid signalling through phospholipase D and phosphatidic acid. *IUBMB Life, 58*, 457–461.

Chen, M. H., Wilson, C. W., & Chuang, P. T. (2007). SnapShot: hedgehog signaling pathway. *Cell, 130*, 386.

Gordon, M. D., & Nusse, R. (2006). Wnt signaling: multiple pathways, multiple receptors, and multiple transcription factors. *J Biol Chem, 281*, 22429–22433.

Hannun, Y. A., & Obeid, L. M. (2008). Principles of bioactive lipid signalling: lessons from sphingolipids. *Nat Rev Mol Cell Biol, 9*, 139–150.

Hayden, M. S., West, A. P., & Ghosh, S. (2006). SnapShot: NF-kappaB signaling pathways. *Cell, 127*, 1286–1287.

Hofer, A. M., & Brown, E. M. (2003). Extracellular calcium sensing and signalling. *Nat Rev Mol Cell Biol, 4*, 530–538.

Lai, E., Teodoro, T., & Volchuk, A. (2007). Endoplasmic reticulum stress: signaling the unfolded protein response. *Physiology (Bethesda), 22*, 193–201.

Moustakas, A., Souchelnytskyi, S., & Heldin, C. H. (2001). Smad regulation in TGF-beta signal transduction. *J Cell Sci, 114*, 4359–4369.

Neves, S. R., Ram, P. T., & Iyengar, R. (2002). G protein pathways. *Science, 296*, 1636–1639.

Oldham, W. M., & Hamm, H. E. (2008). Heterotrimeric G protein activation by G-protein-coupled receptors. *Nat Rev Mol Cell Biol, 9*, 60–71.

Pacher, P., Beckman, J. S., & Liaudet, L. (2007). Nitric oxide and peroxynitrite in health and disease. *Physiol Rev, 87*, 315–424.

Papin, J. A., Hunter, T., Palsson, B. O., & Subramaniam, S. (2005). Reconstruction of cellular signalling networks and analysis of their properties. *Nat Rev Mol Cell Biol, 6*, 99–111.

Pearce, L. R., Komander, D., & Alessi, D. R. (2010). The nuts and bolts of AGC protein kinases. *Nat Rev Mol Cell Biol, 11*, 9–22.

Perkins, N. D. (2007). Integrating cell-signalling pathways with NF-kappaB and IKK function. *Nat Rev Mol Cell Biol, 8*, 49–62.

Pierce, K. L., Premont, R. T., & Lefkowitz, R. J. (2002). Seven-transmembrane receptors. *Nat Rev Mol Cell Biol, 3*, 639–650.

Rehmann, H., Wittinghofer, A., & Bos, J. L. (2007). Capturing cyclic nucleotides in action: snapshots from crystallographic studies. *Nat Rev Mol Cell Biol, 8*, 63–73.

Ron, D., & Walter, P. (2007). Signal integration in the endoplasmic reticulum unfolded protein response. *Nat Rev Mol Cell Biol, 8*, 519–529.

Steinberg, G. R., & Kemp, B. E. (2009). AMPK in health and disease. *Physiol Rev, 89*, 1025–1078.

Wymann, M. P., & Schneiter, R. (2008). Lipid signalling in disease. *Nat Rev Mol Cell Biol, 9*, 162–176.

Zhu, M. X., Ma, J., Parrington, J., Galione, A., & Evans, A. M. (2010). TPCs: Endolysosomal channels for Ca2+ mobilization from acidic organelles triggered by NAADP. *FEBS Lett, 584*, 1966–1974.

Chapter 7

Calcium as an Intracellular Second Messenger: Mediation by Calcium-Binding Proteins

John R. Dedman and Marcia A. Kaetzel

Chapter Outline

I. INTRODUCTION

Sidney Ringer provided the first report relating tissue and cellular function with Ca^{2+} in 1883. He demonstrated that Ca^{2+} was necessary for normal regular contractions of the isolated frog heart. Following this landmark study, Ca^{2+} became an essential component of physiological saline solutions. There have been numerous studies relating Ca^{2+} and cell functions including fertilization, development, differentiation, adhesion, growth, division, movement, contraction and secretion. This evidence demonstrates a primary regulatory role for ionized Ca^{2+} in biological systems. Ca^{2+} has also been associated with a number of diseases, particularly those of the muscular and nervous systems, in which this ion plays an important role in contraction and neurotransmitter release.

Understanding the mechanism of Ca^{2+} action has required approaches and expertise from distinct fields. Ca^{2+} is unique compared with other second messengers, which are formed as metabolic intermediates, such as cyclic nucleotides, inositol phosphates and diacylglycerol. Ca^{2+} is a divalent elemental metal and is not converted to any other form as a part of its cellular regulatory properties. Ca^{2+} is unlike other metal ions, such as K^+ and Na^+, which are involved in membrane potentials and excitability, or Mg^{2+} and Zn^{2+}, which act as enzyme cofactors involved in the catalysis of metabolic intermediates. The fact that Ca^{2+} has been associated with a wide variety of cellular functions brings attention to the fact that the blocking of one Ca^{2+}-regulated function could very likely affect interdependent secondary and tertiary functions.

II. DETERMINATION OF CA^{2+} INVOLVEMENT IN PHYSIOLOGICAL PROCESSES

The most direct approach to understanding the involvement of Ca^{2+} in a given physiological activity has been to follow the tradition of Ringer, i.e. through the reduction of extracellular Ca^{2+}. For example, the reduction of $[Ca^{2+}]_o$ from 1 to 0.1 mM markedly alters cell growth, adhesion, secretion and motility. A second approach has been to use various pharmacological agents. As discussed in other chapters, Ca^{2+} channel modulators have also proven useful in probing cellular systems. These distinct chemicals act by binding to the membrane Ca^{2+} channel, thereby blocking (Ca^{2+} channel agonist) the influx of extracellular Ca^{2+}. The

Cell Physiology Sourcebook. DOI: 10.1016/B978-0-12-387738-3.00007-X

antibiotic A23187 has been shown to cage divalent metal ions such as Ca^{2+} and thereby to act as an ionophore to facilitate their movement across biological membranes (Fig. 7.1). The A23187 ionophore binds Ca^{2+}, Mn^{2+} and Mg^{2+} with respective affinities of 210:2:1. Under specified conditions, A23187 can provide evidence for a role for Ca^{2+} in a given biological response. The ionophore elevates intracellular Ca^{2+} and, for example, can induce the activation of lymphocytes, platelets and sea urchin egg development.

III. CA^{2+} AS AN INTRACELLULAR SIGNAL

The total intracellular Ca^{2+} concentration has been estimated to be approximately 1 mM, a value similar to extracellular Ca^{2+} values. Early studies used model systems such as the skinned muscle fiber, in which the sarcolemma was physically removed. In such a system, the Ca^{2+} ion concentration can be regulated in the bathing solution, while contraction and glycogenolysis are monitored. This approach demonstrated that Ca^{2+} was active at micromolar levels, and that it was rapidly sequestered from the cytosol. Conclusions drawn from such studies indicated that contraction and metabolism are regulated at micromolecular Ca^{2+} levels. It was suspected that Ca^{2+} acted by moving from one cellular compartment to another, that is, into and out of the cytosol. Ca^{2+} channels and pumps were identified using isolated intact vesicles through which the uptake of $^{45}Ca^{2+}$ was monitored. Convincing evidence for the movement of Ca^{2+} into and out of cellular compartments using isotopic methods in intact tissues proved difficult, since the ion was in a dynamic state of flux between the various intracellular organelles, the cytoplasm, and the extracellular fluids.

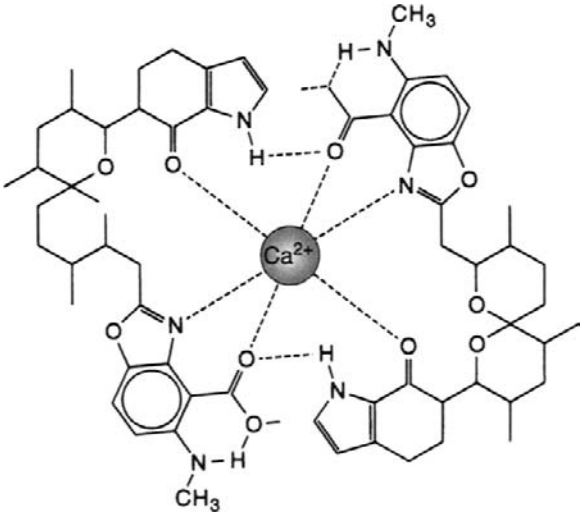

FIGURE 7.1 Molecular structure of A23187. The charged Ca^{2+} ions are extremely impermeable to the plasma membrane. Two molecules of ionophore A23187 form a molecular cage around the charged Ca^{2+} ion. The complex is membrane soluble and dissociates in the cytosol. Intracellular Ca^{2+} is then elevated.

During the past 20 years, however, several generations of Ca^{2+} indicators have been developed. Many coelenterates have the ability to glow by using Ca^{2+}-activated luminescent proteins. Aequorin was the first photoprotein to be used to measure intracellular free Ca^{2+}. Photoproteins can be used to measure free Ca^{2+} levels within the range of 0.1−10 μM. The use of aequorin, however, is limited since it is a relatively large molecule, with a molecular weight of approximately 20 000, and hence must be injected into cells. Early studies with aequorin required the use of large cells for microinjections. For example, the permeability of gap junctions to Ca^{2+} ions into large dipteran salivary glands was determined using aequorin luminescence with image intensification techniques. Under these conditions, nanograms of aequorin can be injected into a cell, which gives the cytosol the capacity to produce 10^4 to 10^8 photons per second. At these levels, the blue light luminescent output is readily measurable with sensitive photomultipliers.

More recently, a series of fluorescent indicator dyes that bind Ca^{2+} with high affinity and selectivity has been developed. The most commonly used is Fura-2. Since the free acids of these fluorescent indicators are not membrane permeable, the carboxyl acid groups are esterified during their chemical synthesis to make them permeable to the plasma membrane. Intact cells are loaded with the permeable form of the dye and the ester groups are then hydrolyzed in the cytoplasm by cellular esterases, thereby trapping the fluorescent probe within the cells. Fura-2 has been used in many biological systems. The use of Fura-2, in combination with high-resolution fluorescence video microscopy and computer-assisted image analysis systems, has provided valuable insight into understanding the intracellular Ca^{2+} signal (Berridge, 1990):

1. the resting intracellular ionized Ca^{2+} level is approximately 0.1 μM. Ca^{2+} ions not complexed to counterions or proteins are frequently referred to as being *free*. Cell stimulation by a variety of agents causes a transient rise in intracellular free Ca^{2+}; the increase is variable, lasting for a fraction of one second to minutes. The amplitude of the Ca^{2+} spike also varies from tissue to tissue
2. the elevation in Ca^{2+} may be uniform throughout a cell or group of cells or highly localized to specific regions of individual cells
3. in many cellular systems, the Ca^{2+} signal occurs as a wave, beginning at a discrete initiation site and then moving across the cell. Fertilization is a cellular process that displays this Ca^{2+} wave phenomenon. The Ca^{2+} influx is initiated at the point of sperm−egg contact,

from where it spreads as a propagated wave toward the opposite pole. This Ca^{2+} signal initiates cellular reactions to prevent polyspermy (penetration of the ovum by more than one sperm)

4. in many cell systems, the intracellular level of Ca^{2+} oscillates. The frequency depends on several factors, including the cell type and cellular effectors such as hormones, neurotransmitters, growth factors and cytokines. Most oscillations occur at a periodicity of 20−60 s when the cell is at "rest". When the cell is stimulated with a hormonal agonist, the frequency can increase to less than 5 s or result in a sustained elevation of up to 100 s. The oscillation frequency in Ca^{2+} may represent a periodic code, which can distinguish extracellular effector type and concentration.

IV. CREATION OF THE CA^{2+} SIGNAL

Cells are able to maintain a resting level of Ca^{2+} of less than 0.1 μM in an environment where the extracellular Ca^{2+} is 1 mM or greater. This gradient is achieved because the plasma membrane is relatively impermeable to Ca^{2+} and also contains ATP-driven Ca^{2+} pumps and Na^{+}-Ca^{2+} exchangers. In addition, the endoplasmic reticulum sequesters cytosolic Ca^{2+}, also by ATP-driven pumps. When $[Ca^{2+}]_i$ increases to above 1 μM, mitochondria will internalize Ca^{2+}. Mitochondria that are heavily loaded with Ca^{2+} reflect a distressed cellular state: under such conditions, the mitochondria develop dense granules containing complexed Ca^{2+}. Collectively, these pump and exchanger systems maintain a resting $[Ca^{2+}]_i$ of less than 0.1 μM.

Initiation of the calcium signal is achieved from two primary sources, the extracellular fluid and sequestered internal stores. The plasma membrane can contain multiple species of Ca^{2+}-specific channels as determined by electrophysiological or pharmacological methods. In general, there are three channel types: voltage-dependent, ligand-gated and mechanical (i.e. stretch-activated). The opening of these channels allows a rush of Ca^{2+} to enter the cytoplasm, producing a localized increase in intracellular Ca^{2+}. The mechanism of Ca^{2+} release from intracellular stores evaded elucidation for many decades. It was shown that inositol 1,4,5-trisphosphate (IP_3) causes Ca^{2+} mobilization from internal vesicular stores, primarily the endoplasmic reticulum (Berridge, 1993). IP_3 is a phospholipase C (PLC) hydrolysis product of phosphatidylinositol 4,5-bisphosphate (PIP_2), which is induced during cell stimulation. Recent evidence indicates that not all of the endoplasmic reticulum-sequestered Ca^{2+} is IP_3 sensitive and release is prompted by cyclic ADP-ribose (Lee, 1993). A second product of PLC hydrolysis of PIP_2 is diacylglycerol (DAG).

Stimulation of the membrane phospholipase C is through receptor binding by agonists and is G-protein regulated. $GTP_\gamma S$, a non-metabolizable analog of GTP, can artificially activate PLC production of IP_3 and DAG. G proteins also appear to regulate several processes, including the exchange of Ca^{2+} from IP_3-insensitive to IP_3-sensitive pools, the gating properties of plasma membrane Ca^{2+} channels, and the generation of cyclic AMP. The microinjection of $GTP_\gamma S$ causes a marked increase in Ca^{2+} oscillation frequency and amplitude and stimulation of many cellular processes.

V. MEDIATION OF THE CA^{2+} SIGNAL

Intracellular Ca^{2+}, like cyclic AMP, acts as a second messenger. Cyclic AMP is mediated by a limited number of receptor proteins, leading to the activation of specific protein kinases. There are, however, numerous intracellular Ca^{2+}-binding proteins; therefore, the intracellular Ca^{2+} signal has many possible bifurcations of action. A simple example is found in skeletal muscle, where elevated Ca^{2+} binds to troponin C to cause myofibrillar contraction at the expense of ATP. An independent, simultaneous Ca^{2+} pathway is mediated by a second Ca^{2+} receptor protein, calmodulin, which activates phosphorylase kinase. This activation initiates glycogenolysis, which leads to the regeneration of expended ATP (Fig. 7.2).

The most completely described family of intracellular Ca^{2+}-binding proteins to date is characterized by a protein structure known as the EF hand. The binding site is achieved through side-chain coordination of Ca^{2+} within a helix-loop-helix composed of precisely spaced amino acids (Fig. 7.3). This EF hand is found in a number of proteins as determined from the primary amino acid sequence and, in a few cases, has been confirmed by direct Ca^{2+} binding. The sequence data for the Ca^{2+}-dependent protease calpain suggest that it may have resulted from the fusion of a gene encoding four EF hand domains with a thiol protease gene (Ohno et al., 1984). Likewise, α-actinin may have resulted from the fusion of a gene encoding an actin-binding protein with a gene for a single EF hand domain (Noegel et al., 1987). In many cases, the EF hand is non-functional. For example, the Ca^{2+} insensitivity of the muscle form of α-actinin is due to the imprecise positioning of the amino acids shown in Fig. 7.3. The identification of a number of putative Ca^{2+}-binding proteins is based on sequence similarity to members of the troponin C/calmodulin superfamily. For example, cell cycle yeast mutants which carry the temperature-sensitive allele of *CDC31* are blocked in spindle-pole body duplication (Baum et al., 1986). This gene has 42% sequence similarity with human calmodulin and may contain functional EF hands. A second cell division cycle gene, *CDC24*, is required for bud formation. Sequence analysis of *CDC24* indicates two potential Ca^{2+}-binding EF hands (Miyamoto et al., 1987).

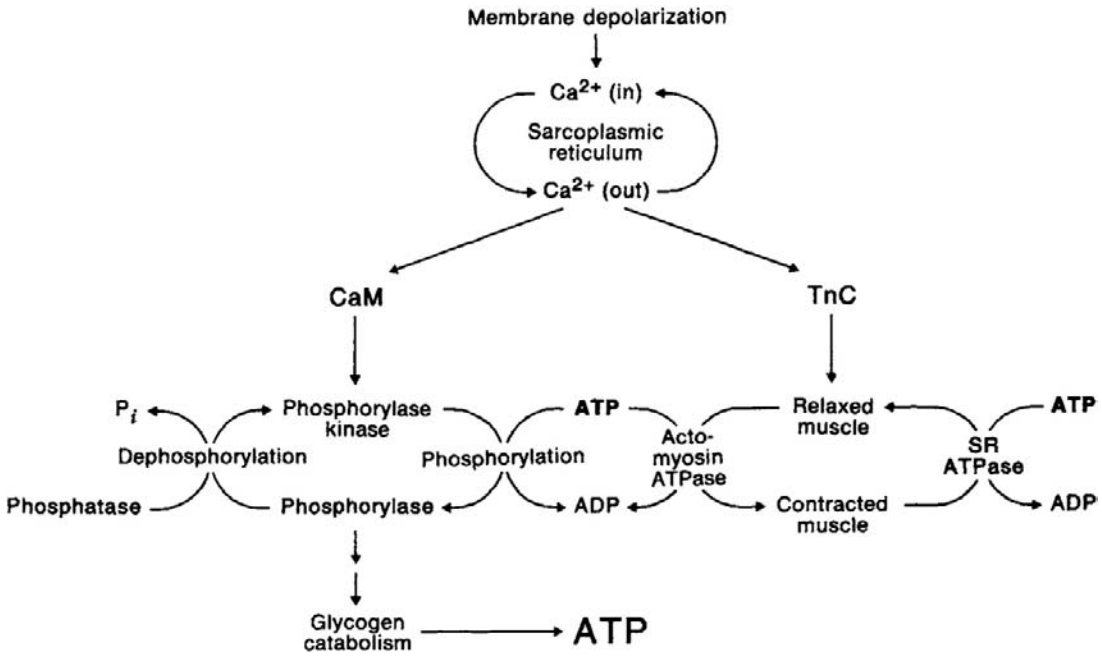

FIGURE 7.2 Independent pathways of Ca^{2+} regulation in skeletal muscle. Depolarization of the sarcolemma causes release of Ca^{2+} stored in the sarcoplasmic reticulum. This elevated Ca^{2+} level triggers contraction, an ATP-consuming process. The same signal Ca^{2+} also binds calmodulin (CaM), which initiates glycogenolysis, an ATP-producing process. This parallelism allows for metabolic coordination.

Troponin C is present only in skeletal and cardiac muscle; calmodulin is present in all cells. The binding of four Ca^{2+} ions causes conformational changes with the formation of an active state. Ca^{2+}-bound calmodulin has very high affinity for its target proteins, which act as additional steps in mediating the original Ca^{2+} signal. The calmodulin target proteins include protein kinases, protein phosphatases, hydrolases, nitric oxide synthetase and ion channels.

Sequence analysis and site-directed mutagenesis studies have provided a general model for calmodulin regulation of its target proteins (Fig. 7.4). The target protein contains a pseudosubstrate attached to a flexible region of the polypeptide chain. This sequence acts as an endogenous inhibitor of the enzyme. Ca^{2+}-activated calmodulin clamps around an adjacent target site and physically displaces the pseudosubstrate from the active site, causing a derepression or activation of the enzyme. This process is reversed by the reduction of intracellular Ca^{2+} levels, which reduces the affinity of calmodulin for the target site and autoinhibition of the enzyme occurs. A smooth muscle contraction is a paradigm for calmodulin mediation of the Ca^{2+} signal (Fig. 7.5).

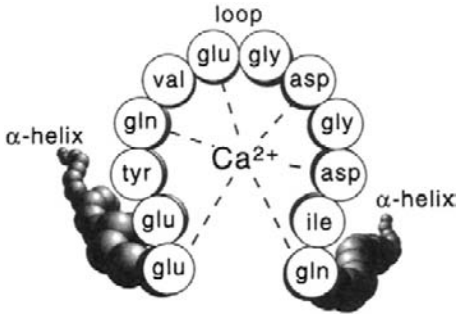

FIGURE 7.3 The EF hand Ca^{2+} binding pocket. Many intracellular Ca^{2+}-receptor proteins contain precisely positioned amino acids in a loop between highly structured α-helical coil. The Ca^{2+} ion is coordinated in this loop, which alters the overall structure of the protein and, in turn, its cellular activity.

One approach to understanding the cellular role of a protein is to correlate subcellular localization with function. This information can be effectively obtained through the use of antibodies that are monospecific for the targeted protein. As shown in Fig. 7.6, when affinity-purified antibodies were used to localize calmodulin during mitosis, the spindle poles were stained most brightly. This result suggested that calmodulin is involved in mitotic function. Indeed, microtubules depolymerize in the presence of Ca^{2+}-bound calmodulin both in vitro and in microinjected cells (Dedman et al., 1982). Many other cellular functions have been assigned to calmodulin through a combination of localization, biochemical and genetic approaches (Davis, 1992).

VI. CA^{2+}-CALMODULIN DEPENDENT PROTEIN KINASE II

Many of the calmodulin-regulated kinases, including phosphorylase kinase (see Fig. 7.2) and myosin light chain

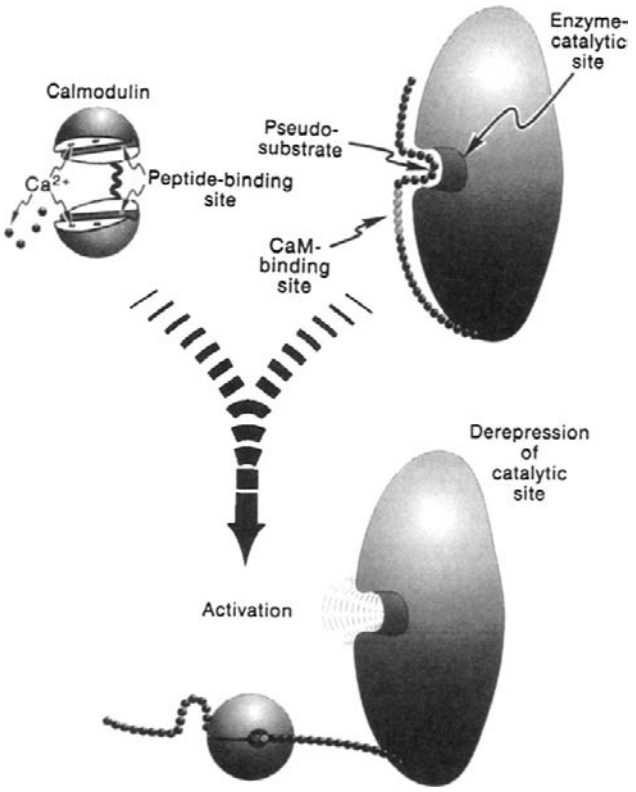

FIGURE 7.4 Mechanism of action of calmodulin regulation of target proteins. Calmodulin is molecularly structured as two opposing lobes containing Ca^{2+}-binding sites connected by a flexible peptide hinge. Ca^{2+} binding causes the formation of complementary grooves on each, which then allows binding to specific regulatory sites on target proteins. Ca^{2+}-dependent binding causes derepression of the enzyme active site by displacing an endogenous inhibitory pseudosubstrate.

kinase (see Fig. 7.5), directly reflect the changes in free cytosolic Ca^{2+} through the phosphorylation of their respective specific protein substrates. Ca^{2+}-calmodulin dependent protein kinase II (CaM kinase II) is distinct in that it is multifunctional, having numerous substrates, and can develop many active states including Ca^{2+}-CaM autonomy (Braun and Schulman, 1999). The individual subunits of CaM kinase II assemble through their association domains to form a flower-like structure of 8–12 "petals" (Fig. 7.7). In low cytosolic free Ca^{2+}, the naive enzyme is inactive. When levels are elevated, free intracellular Ca^{2+} binds CaM which, in turn, binds to the regulatory domain of the CaM kinase II subunits and derepresses the active site. "Autophosphorylation" of adjacent CaM-bound subunits occurs at threonine-286 (pT286) during this activation period. Autophosphorylation renders the individual catalytic sites constitutively active and independent from Ca^{2+}-CaM regulation. A second "wave" of elevated Ca^{2+} allows additional sites to be activated by Ca^{2+}-CaM and provides a further opportunity for transphosphorylation of adjacent pT286. After a series of Ca^{2+} waves, the enzyme complex becomes increasingly autonomous from Ca^{2+}-CaM regulation. In addition, pT286 phosphorylation produces a 1000-fold increase in affinity for CaM and effectively "traps" CaM, making the Ca^{2+} mediator protein temporally unavailable for other target proteins. When Ca^{2+} levels are reduced and calmodulin is released, the regulatory domain may be "capped" by phosphorylation of T305 and/or T306 in the CaM binding domain. Rebinding of CaM in the event of subsequent Ca^{2+} increases is prevented until pT305 and pT306 are dephosphorylated; pT286 autonomy is not affected. Autonomy and capping are reversed by protein phosphatases that are regulated by cAMP. The subunits are

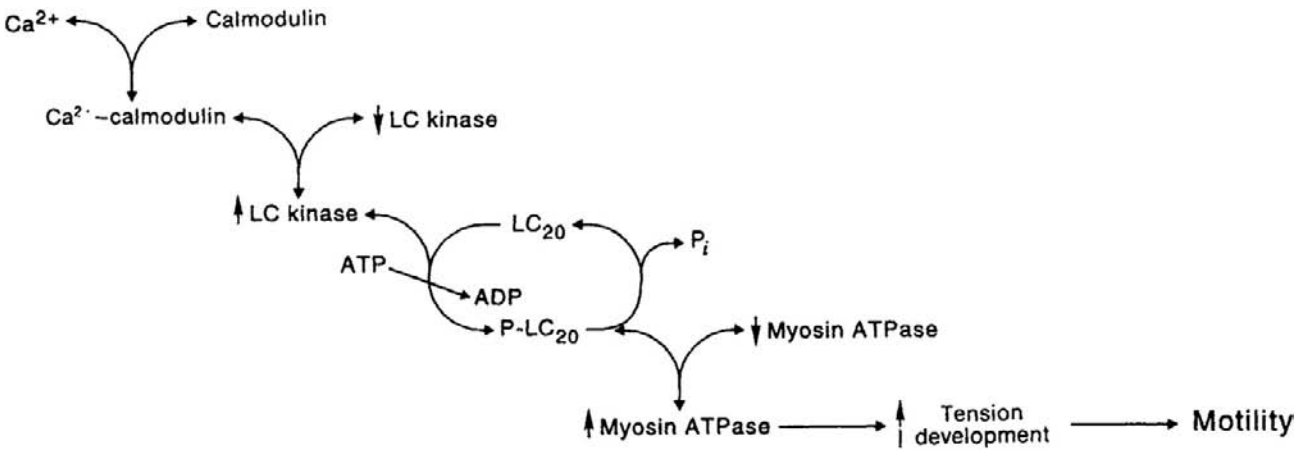

FIGURE 7.5 Calmodulin regulation of non-striated muscle contraction. An increase in intracellular Ca^{2+} binds to calmodulin, causing its increased affinity for the target protein myosin light chain kinase (LC kinase). The activated kinase specifically phosphorylates one of the myosin light chains which, in turn, increases the activity of myosin and its affinity for actin. Cross-bridge formation develops contraction. This process is reversed after cytosolic reduction in Ca^{2+}.

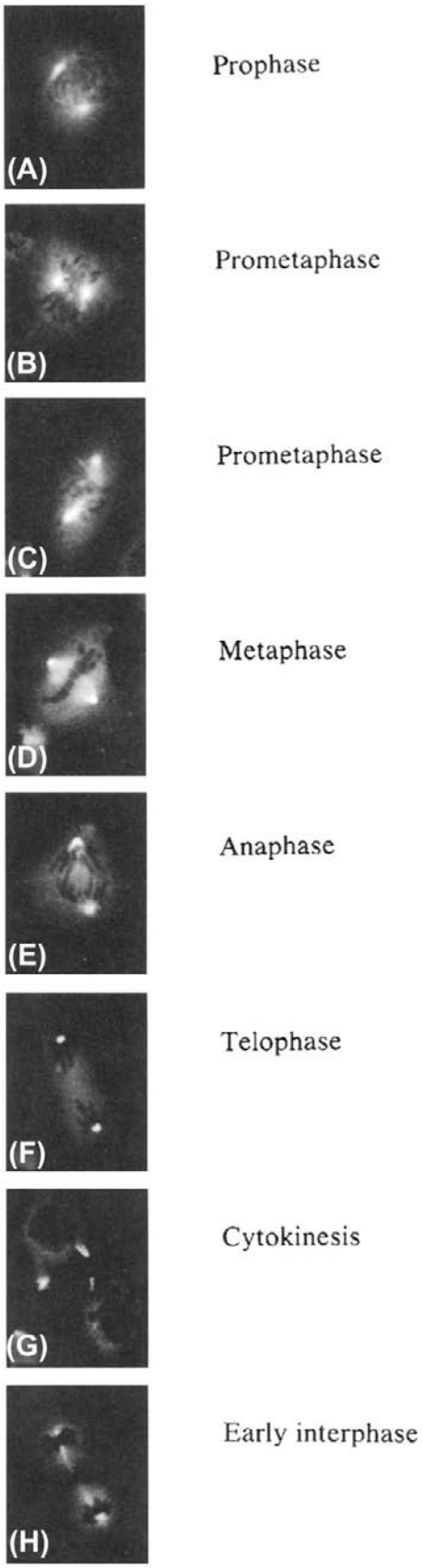

resensitized to Ca^{2+}-CaM following dephosphorylation of T305 and T306.

The metabolic sculpturing of CaM KII reflects the changes in free Ca^{2+} levels, the availability of CaM, autophosphorylation and protein phosphatase activities. These events allow CaM KII to develop numerous active states reflecting the physiologic state of the cell. Dynamic changes in second messenger levels, amplitude and frequency of Ca^{2+} oscillations and cAMP levels are decoded by CaM KII which, in turn, phosphorylates and modifies the activity of numerous enzymes including Ca^{2+}-channels, Ca^{2+}-pumps, synaptic proteins and components of the nuclear envelope. In summary, CaM KII is a molecular microprocessor that integrates and stores cellular signals.

VII. ANNEXINS: CALCIUM-DEPENDENT PHOSPHOLIPID-BINDING PROTEINS

A number of laboratories with distinct experimental goals have identified a family of Ca^{2+}-dependent phospholipid-binding proteins. These proteins have the common property of binding (annexing) membranes (Crumpton and Dedman, 1990). Sequence data indicate that there are 10 unique mammalian annexins. Annexins are also present in the slime mold *Dictyostelium*, in the sponge, in the coelenterate *Hydra*, in the insect *Drosophila* and in the mollusk *Aplysia*, as well as in higher plants.

The sequence organization of the family is highly conserved (Fig. 7.8). All except annexin VI are composed of a core of four repeated domains: annexin VI is composed of eight domains. Each domain is approximately 70 amino acids in length. The sequence conservation for each ranges between 40 and 60% when individual annexins are compared. The amino terminus of each protein is unique, suggesting that this region may confer functional differences to the proteins. This property has been confirmed with annexin II, in that the amino terminus binds a subunit, p11, and forms an actin-binding heterotetramer. Calcium-dependent phospholipid binding is a property of the four-domain core of each protein. In vitro functions of annexins — which include membrane binding and fusion, ion channel activity, modulation of ion channel activity, inhibition of phospholipase A_2 and inhibition of blood coagulation — all require this property. The core does not contain the classic EF hand calcium-binding motif. Coordination of Ca^{2+} is accomplished through a unique, discontinuous binding loop. Chemical cross-linking data indicate that monomeric annexin in solution self-associates into trimers, which then

FIGURE 7.6 Subcellular localization of calmodulin in mitotic cells. Monospecific antibody and immunofluorescence identifies calmodulin to be concentrated at the poles of the spindle apparatus.

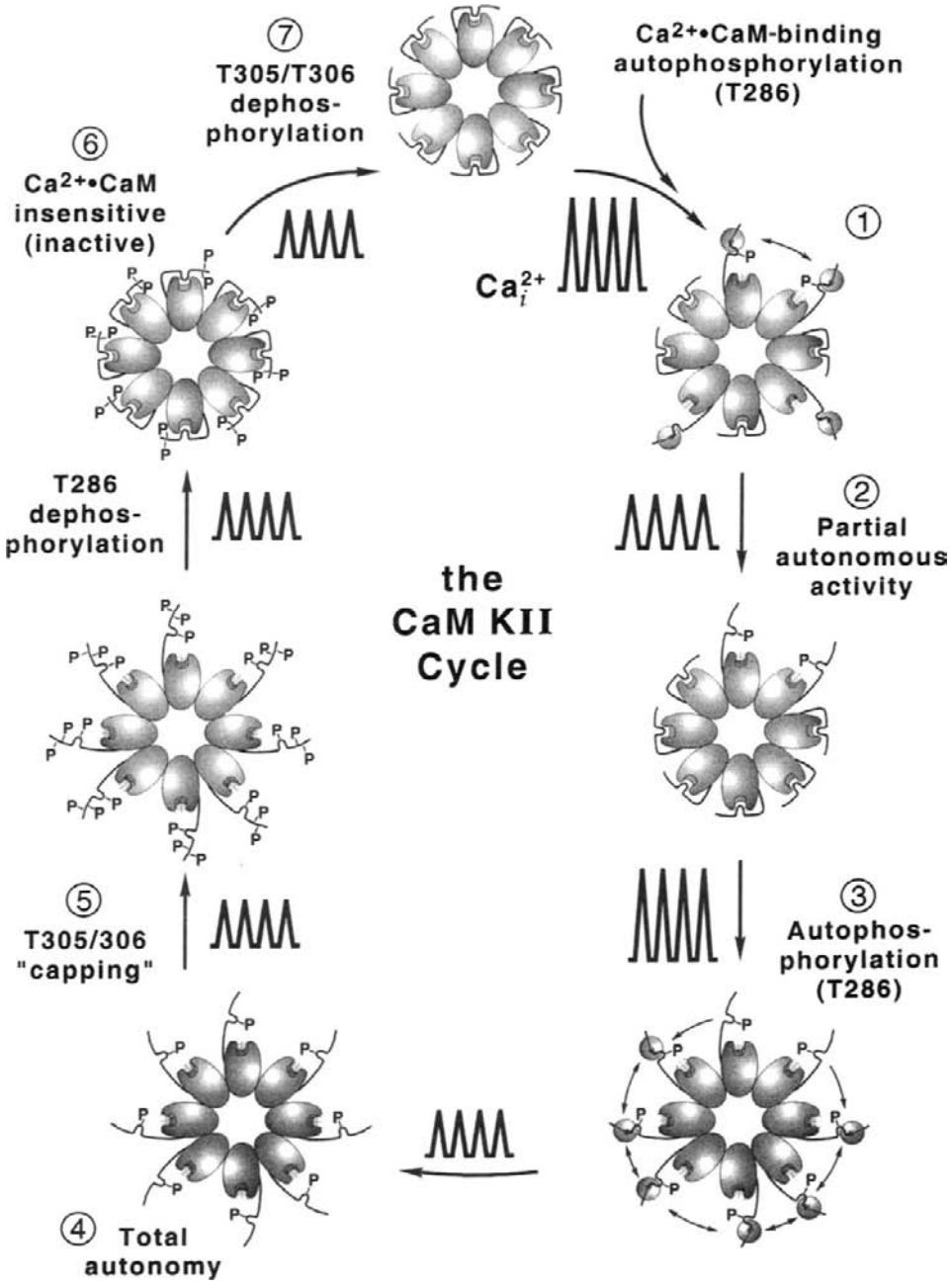

FIGURE 7.7 Ca^{2+}-CaM-dependent kinase II. (1) The active site of each subunit is repressed by an autoregulatory domain. (2–5) Ca^{2+}-CaM binds to this domain and adjacent subunits are transphosphorylated at threonine-286 (T286). These autophosphorylated subunits are active and autonomous from Ca^{2+}-CaM regulation. (6) The regulatory domain can be further phosphorylated at threonine-305 and/or 306 (T305/T306), modifications which inhibit CaM binding. (7) Dephosphorylation of T286 renders the enzyme inactive and insensitive to Ca^{2+}-CaM. (1) Dephosphorylation of T305 and T306 returns the enzyme to its Ca^{2+}-CaM-dependent state.

form higher aggregates when bound to phospholipid vesicles. This observation is consistent with the diffraction pattern obtained from two-dimensional crystals.

Collectively, protein structural data, biophysical reconstitution studies and subcellular localization results allowed development of the following model to describe the cellular function of the annexins. In the resting cell when free Ca^{2+} concentrations are low, the annexin exists as a soluble monomer. During cell stimulation, free Ca^{2+} concentrations subjacent to the cell membrane rise to micromolar levels (Llinas et al., 1992). The annexin would bind to target proteins associated with a phospholipid surface, then organize into trimers, hexamers and higher aggregates, ultimately forming an extended hexagonal

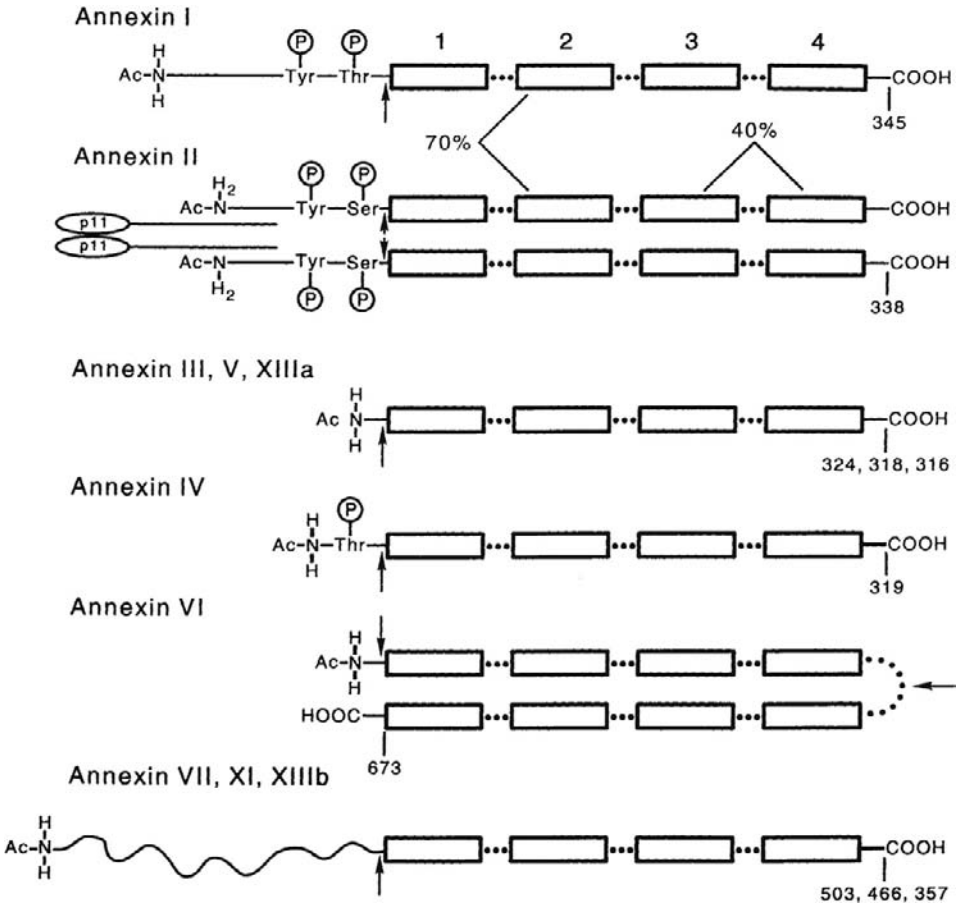

FIGURE 7.8 Structural similarities among the annexins. The boxed regions represent the ordered 70-amino-acid repeat domains. The numbers indicate the relative sequence similarities between repeat domains. The arrows indicate highly sensitive sites of proteolysis. The repeat regions form a highly structured, protease resistant, Ca^{2+}-phospholipid binding core. The amino terminal "tails" are highly variable in length, sequence, and structure and provide individually to each annexin family member.

array around the target protein (Andree et al., 1992; Concha et al., 1992). The immunofluorescent localization studies of annexins support this model. A sheet of annexin multimers lining the inner membrane leaflet would locally alter membrane properties, such as fluidity and sequestration of specific phospholipids. Changes in membrane properties have been shown to modify specific membrane protein function (Bennett, 1985; Sweet and Schroeder, 1988). Such a submembranous scaffolding maintains and stabilizes the membrane. For example, dystrophin is localized to the inner surface of the sarcolemma in normal skeletal muscle. When absent, as in Duchenne muscular dystrophy, the plasma membrane is unstable and the fibers rapidly turn over (Koenig et al., 1988). In addition, the Ca^{2+}-dependent lining of the membrane would sterically block the translocation of phospholipid-binding proteins, such as protein kinase C and cellular phospholipases. The Ca^{2+}-dependent self-association on membrane surfaces represents a novel mechanism of second-messenger coupled cell regulation. This may be the regulatory mechanism by which annexins modify the gating activity of the channels.

Immunolocalization studies have proved valuable in providing insight into evaluating cellular function of the annexins. The individual annexins are associated with secretory granules, the endoplasmic/sarcoplasmic reticulum, actin bundles and the plasma membrane. Annexin IV, for example, is expressed in many epithelia and is concentrated along the apical membrane, subjacent to the lumen of the organ (Fig. 7.9) (Kaetzel et al., 1994). This region is the cellular site of fluid secretion into the lumen. Recent studies indicate that this annexin regulates chloride-ion efflux, which produces an electrochemical gradient to draw sodium ions transcellularly across the epithelium. This salt causes water to follow because of hyperosmotic pressure. The luminal fluid is required for normal tissue function. Abnormal fluid secretion is involved in the pathologies of cholera and cystic fibrosis.

VIII. PROTEIN KINASE C

The protein kinase C family is a third mediation pathway of intracellular Ca^{2+} action. One class of protein kinase C

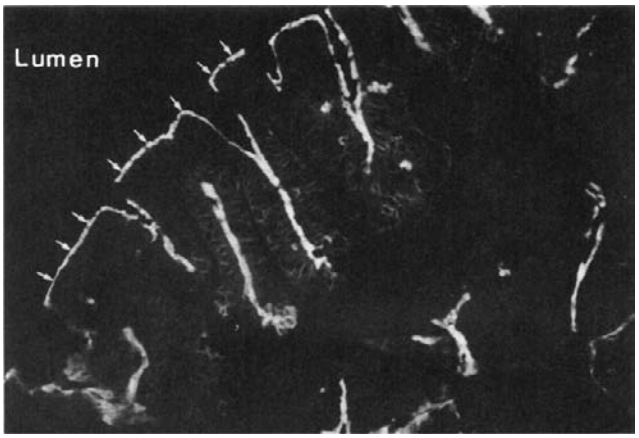

FIGURE 7.9 Localization of annexin IV in the rat fallopian tube. Monospecific antibody identifies annexin IV as concentrated along the membrane bordering the lumen of the oviduct of the ciliated, columnar epithelia (arrows). This region is the cellular site of fluid secretion.

isozymes is activated by Ca^{2+}, which increases the affinity of the enzyme for phosphatidylserine. This ligand binding targets the translocation of protein kinase C to the plasma membrane. Once bound to the membrane surface, the enzyme can be further stimulated by DAG (Fig. 7.10). This latter metabolite is a product of G-protein-activated phospholipase C hydrolysis of membrane PIP_2. Protein kinase C stimulates DNA synthesis and is the cellular mechanism by which many tumor promoters act (Nishizuka, 1992). A major widely distributed cellular substrate for protein kinase C is MARCKS, myristoylated alanine-rich C-kinase substrate (Aderem, 1992). This protein binds to the plasma membrane, calmodulin and actin and has been associated with secretion, motility, vesicle trafficking and transformation through the rearrangement of the actin cytoskeleton. Actin filament bundling by MARCKS is regulated by Ca^{2+}-dependent calmodulin binding which is, in turn, regulated by protein kinase C phosphorylation. The kinase has numerous protein substrates in the cell; however, the precise mechanism of cellular regulation is not fully understood.

There are additional distinct intracellular Ca^{2+} -binding proteins that have been well characterized in biochemical terms (see Smith et al., 1990). Ca^{2+} has the responsibility of regulating a large number of unrelated cellular activities such as cell growth, secretion, motility and transport. The ubiquitous Ca^{2+} signal is discriminated through the individual Ca^{2+}-mediator proteins (Fig. 7.11).

IX. CURRENT PERSPECTIVES

Scientific progress is not restricted by effort, but is dependent on insight and advances in technology. Technical progress in protein chemistry in the late 1960s and early 1970s led to the identification and characterization of

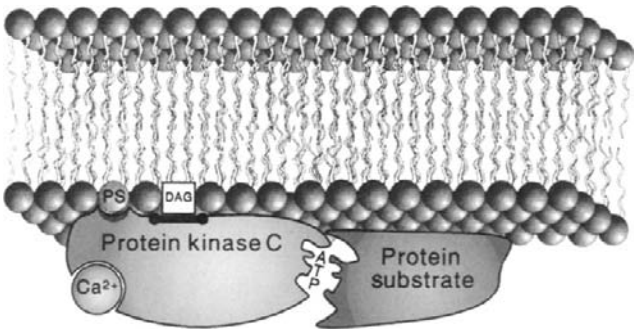

FIGURE 7.10 Regulation of protein kinase C. Elevations in intracellular Ca^{2+} cause translocation of PKC to the plasma membrane where phosphatidylserine (PS) and diacylglycerol (DAG) further activate the enzyme.

the Ca^{2+} receptors, troponin C and calmodulin. Development of recombinant DNA technology in the mid-1970s provided precise knowledge of the molecular evolution and structural conservation of these proteins. In the early 1980s, Ca^{2+}-sensitive dyes and computer-assisted image processing allowed visualization of transient spatial changes in intracellular Ca^{2+}. Detailed information is being obtained on the cellular components that are essential for maintaining these levels, including Ca^{2+} channels, Na^{+}-Ca^{2+} exchangers and Ca^{2+}-ATPases. The original observations of Hokin and Hokin (1953) concerning the turnover of

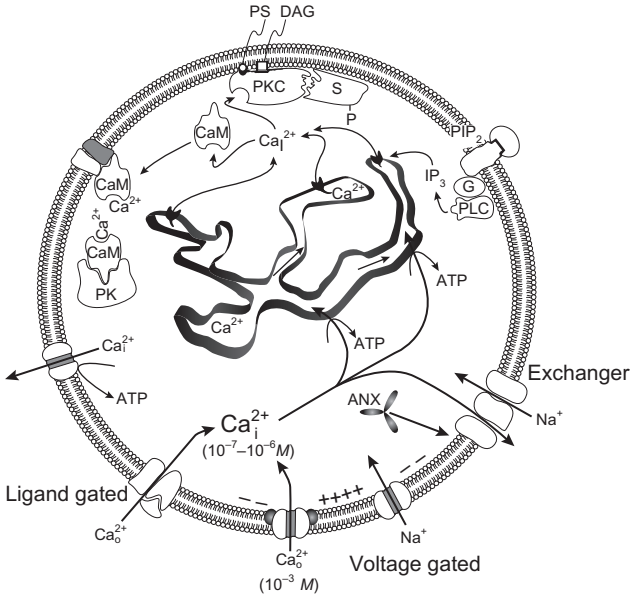

FIGURE 7.11 Interplay of cellular components involved in creating and mediating the intracellular Ca^{2+} signal. Low intracellular Ca^{2+} levels are the result of pumps and ion exchangers. Ca^{2+} transients develop from influx through voltage and ligand-gated channels on the plasmalemma and from IP_3-gated channels located in the endoplasmic/sarcoplasmic reticulum. IP_3 is generated from extracellular stimuli through a G protein (G)-regulated phospholipase C (PLC). The intracellular Ca^{2+} signal is mediated by three primary pathways: calmodulin (CaM), annexins (ANX), and protein kinase C (PKC).

membrane phosphatidylinositols were finally appreciated some 20 years later. New insights in second-messenger action revealed that the hydrolysis of PIP_2 to form IP_3 and DAG could coordinate, respectively, the release of intracellular Ca^{2+} from the endoplasmic reticulum and the activation of protein kinase C. Although the mechanisms involved in maintaining intracellular Ca^{2+} homeostasis are being defined, understanding the events that couple stimuli to specific cellular responses has resisted biochemical definition. The elucidation of physiological regulation by Ca^{2+} through specific Ca^{2+} mediator proteins is not a trivial undertaking. Initial implications of function can be explored by cellular microinjection of inhibitor peptides, antibodies and anti-sense RNA or by in vitro reconstitution. Information obtained from these inhibition experiments, however, is limited because it does not fully reflect the intact organism. For example, although our knowledge of the molecular aspects and regulatory properties of calmodulin in vitro is impressive, little is known of the functional role of calmodulin in the living cell or the whole animal, other than by inference. An attractive approach to obtaining this information is genetic manipulation. Fungi, such as yeast, are powerful models for the introduction and study of site-directed and temperature-sensitive mutations and fundamental questions regarding the regulatory role Ca^{2+} in growth, division and secretion have been addressed (see Davis, 1992). The usefulness of such haploid systems, however, is limited to genes that are expressed in these organisms and to non-lethal mutations in these genes.

The cellular function of the diverse Ca^{2+}-binding proteins that are expressed in highly differentiated cells remains elusive. The respective pathways can be manipulated at many levels. Synthetic genes can be introduced into cultured cells and the resulting phenotypic changes monitored. In addition, specific genes can be deleted or "knocked out" in whole animals using homologous recombination of genes in mouse embryonic stem cells (see Frohmen and Martin, 1989).

Interpretation of targeted gene "knockout" studies is, however, complicated by the fact that the animal lacks the gene in its genome throughout its development. Phenotypic consequences within individual cell types resulting from gene disruptions may be due to defects that occur during embryonic development or inadequate communication with other defective cell types.

An alternative approach to understanding the precise role of proteins associated with the intracellular Ca^{2+} signal is to design and construct dominant-negative genes that, when expressed, neutralize the function of specific proteins. For example, peptides consisting of the calmodulin-binding site on target proteins (see Fig. 7.4) are extremely potent inhibitors of calmodulin. Wang et al. (1995, 1996) constructed a synthetic gene that produced a string of these calmodulin-binding peptides. This peptide inhibitor was targeted to the nucleus of mouse-lung epithelial cells. By neutralizing the activity of nuclear calmodulin, it was shown that the cells did not synthesize DNA and the embryonic lung did not develop. Dominant-positive genes can also be designed to elucidate Ca^{2+}-regulated cellular systems. The amino acid sequence of the pseudosubstrate domain on calmodulin target proteins (see Fig. 7.4) can be altered to abolish inhibition of the catalytic site. This mutated enzyme becomes autonomous from Ca^{2+}-calmodulin regulation and remains active even during periods of low intracellular Ca^{2+}. Mayford et al. (1996) have shown, for example, that expression of an autonomously active CaM kinase II in mouse brain causes deficits in memory.

The understanding of Ca^{2+}-coupled stimulus responses has advanced through direct visualization of Ca^{2+} transients, the identification of Ca^{2+}-binding proteins, determination of their subcellular localization and their biochemical role through reconstitution of a cellular function, and genetic manipulation of intact cells. Although many candidates for Ca^{2+} mediator proteins are currently under investigation, it is anticipated that more Ca^{2+}-binding proteins will be identified as further research continues to solve the stimulus–response coupling puzzle.

X. SUMMARY

Ca^{2+} is a ubiquitous intracellular regulator of cellular function. Levels of Ca^{2+} are controlled by a variety of channels, exchangers and pumps found in the plasmalemma and internal membranes. Cell stimulation causes the intracellular Ca^{2+} to increase transiently. This second-messenger signal is then mediated by Ca^{2+}-binding proteins. There are three primary molecular mechanisms of transmitting the signal: calmodulin, annexins and protein kinase C. Each of these pathways intersects and can be cross-regulatory. Ca^{2+}-calmodulin binds to specific sites on target proteins and activates enzymes by derepressing the active site. In the presence of Ca^{2+}, the annexins have a strong affinity for phospholipids. Annexins can form an interlocking network along membrane surfaces and alter membrane fluidity. Annexins are important in regulating membrane ion conductances. Protein kinase C is regulated by Ca^{2+}, phospholipid and diacylglycerol. Cellular studies using specific activators and inhibitors of protein kinase C have shown this Ca^{2+} pathway to be involved in cell growth, differentiation and development of tumors. Physiological, cellular and molecular techniques are being used in combination to define the precise cellular roles of Ca^{2+}-binding proteins.

BIBLIOGRAPHY

Aderem, A. (1992). The MARCKS brothers: a family of protein kinase C substrates. *Cell, 71*, 713–716.

Andree, H. A. M., Stuart, M. C. A., Hermens, W. T., et al. (1992). Clustering of lipid-bound annexin V may explain its anticoagulant effect. *J Biol Chem, 267*, 17907−17912.

Baum, P., Furlong, C., & Byers, B. (1986). Yeast gene required for spindle pole body duplication: homology of its product with Ca^{2+}-binding proteins. *Proc Natl Acad Sci, USA, 83*, 5512−5516.

Bennett, V. (1985). The membrane skeleton of human erythrocytes and its implications for more complex cells. *Annu Rev Biochem, 54*, 273−304.

Berridge, M. J. (1990). Calcium oscillations. *J Biol Chem, 264*, 9583−9586.

Berridge, M. J. (1993). Inositol trisphosphate and calcium signaling. *Nature, 361*, 315−361.

Braun, A. P., & Schulman, H. (1999). Structural examination of autoregulation of multifunctional calcium/calmodulin-dependent protein kinase II. *J Biol Chem, 274*, 26199−26208.

Concha, N. O., Head, J. F., Kaetzel, M. A., Dedman, J. R., & Seaton, B. A. (1992). Annexin V forms calcium-dependent trimeric units on phospholipid vesicles. *FEBS Lett, 314*, 159−162.

Crumpton, M. J., & Dedman, J. R. (1990). Protein terminology tangle. *Nature, 345*, 212.

Davis, T. N. (1992). What's new with calcium? *Cell, 71*, 557−564.

Dedman, J. R., Welsh, M. J., Kaetzel, M. A., Pardue, R. L., & Brinkley, B. R. (1982). Localization of calmodulin in tissue culture cells. In W. Y. Cheung (Ed.), *Calcium and Cell Function, Vol. 3*. New York: Academic Press.

Frohman, M. A., & Martin, G. R. (1989). Cut, paste, and save: new approaches to altering specific genes in mice. *Cell, 56*, 145−147.

Heizmann, C. W., & Hunziker, W. (1991). Intracellular calcium-binding proteins: more sites than insights. *Trends Biochem Sci, 16*, 98−103.

Hodgkin, A. L., & Keynes, R. D. (1957). Movements of labeled calcium in squid giant axons. *J Physiol, 138*, 253−281.

Hokin, M. R., & Hokin, L. E. (1953). Enzyme secretion and the incorporation of ^{32}P into phospholipids of pancreas slices. *J Biol Chem, 203*, 967−977.

Kaetzel, M. A., Cahn, H. C., Dubinsky, W. P., Dedman, J. R., & Nelson, D. J. (1994). A role for annexin IV in epithelial cell function: Inhibition of calcium-activated chloride conductance. *J Biol Chem, 269*, 5297−5302.

Kaetzel, M. A., Hazarika, P., & Dedman, J. R. (1989). Differential tissue expression of three 35−kDa annexin calcium-dependent phospholipid-binding proteins. *J Biol Chem, 264*, 14463−14470.

Koenig, M., Monaco, A. P., & Kunkel, L. M. (1988). The complete sequence of dystrophin predicts a rod-shaped cytoskeletal protein. *Cell, 53*, 219−228.

Lee, H. C. (1993). Potential of calcium- and caffeine-induced calcium release by cyclic ADP-ribrose. *J Biol Chem, 268*, 293−299.

Llinas, R., Sugimori, M., & Silver, R. B. (1992). Microdomains of high calcium concentration in a presynaptic terminal. *Science, 256*, 677−679.

Mayford, M., Bach, M. E., Huang, Y. Y., Wang, L., Hawkins, R. D., & Kandel, E. R. (1996). Control of memory formation through related expression of a CaMKII transgene. *Science, 274*, 1678−1683.

Meers, P., Daleke, D., Hong, K., & Papahadjopoulos, D. (1991). Interactions of annexins with membrane phospholipids. *Biochemistry, 30*, 2903−2908.

Miyamoto, S., Ohya, Y., Ohsumi, Y., & Anraku, Y. (1987). Nucleotide sequence of the CLS4 (CDC24) gene of *Saccharomyces cerevisiae*. *Gene, 54*, 125−132.

Nishizuka, Y. (1992). Intracellular signaling by hydrolysis of phospholipids and activation of protein kinase C. *Science, 258*, 607−614.

Noegel, A., Witke, W., & Schleicher, M. (1987). Calcium-sensitive nonmuscle α-actinin contains EF-hand structures and highly conserved regions. *FEBS Lett, 221*, 391−396.

Ohno, S., Emori, Y., Imajoh, S., Kawaskai, H., Kisaragi, M., & Suzuki, K. (1984). Evolutionary origin of a calcium-dependent protease by fusion of genes for a thiol protease and a calcium-binding. *Nature, 312*, 566−570.

Ringer, S. (1883). A further contribution regarding the influence of the different constituents of the blood of the contraction of the heart. *J Physiol, 4*, 29−43.

Smith, V. L., Kaetzel, M. A., & Dedman, J. R. (1990). Stimulus-response coupling: the search for intracellular calcium mediator proteins. *Cell Regul, 1*, 165−172.

Sweet, W. D., & Schroeder, F. (1988). *Lipid Domains and the Relationship to Membrane Function*. New York: R. Liss. p. 1742.

Wang, J., Campos, B., Jamieson, A., Kaetzel, M., & Dedman, J. (1995). Functional elimination of calmodulin with the nucleus by targeted expression of an inhibitor peptide. *J Biol Chem, 270*, 30245−30248.

Wang, J., Moreira, K., Campos, B., Kaetzel, M., & Dedman, J. (1996). Targeted neutralization of calmodulin in the nucleus blocks DNA synthesis and cell cycle progression. *Biochim Biophys Acta, 1313*, 223−228.

This page intentionally left blank

Section II

Membrane Potential, Transport Physiology, Pumps, and Exchangers

This page intentionally left blank

Chapter 8

Diffusion and Permeability

Nicholas Sperelakis and Jeffrey C. Freedman

Chapter Outline

I. SUMMARY

This chapter describes diffusion of uncharged particles and charged ions across membranes with and without partitioning and provides the relevant equations that govern such diffusion. The relationship between the diffusion coefficient (D) and the permeability coefficient (P) is presented, as well as the factors that determine these coefficients. The dependence of P on the mobility of an ion through the membrane under a voltage gradient is also described. Electrochemical potential is defined and the interconversion between flux and current is presented. Finally, the Ussing flux ratio equation is presented and examples of its significance are given. Relating to this, the concept of potential energy wells and barriers is presented, describing the movement of an ion through an ion channel.

II. INTRODUCTION

In order to understand the fundamentals of membrane transport, as well as the mechanisms for development of the electrical resting potential (RP) of cells, it is first necessary to consider the basic processes of *diffusion* and membrane *permeability*. Therefore, this chapter discusses fundamental principles that are utilized in subsequent chapters in this book.

Molecules of gases and liquids and dissolved solutes are continuously in motion. The velocities of individual molecules vary tremendously, as do their kinetic energies (in accordance with the Maxwell−Boltzmann distribution). Diffusion is the process whereby particles in a gas or liquid tend to intermingle due to their spontaneous motion caused by thermal agitation. Any diffusing substance tends to move from *regions of higher concentration* to *regions of lower concentration*, until the substance is uniformly distributed at *equilibrium*. The molecules continue to move at equilibrium, but the *net movement* is zero. In the absence of *convection*, which refers to bulk flow of solvent, such as that caused by stirring, the movement of the molecules is by diffusion only. Diffusion occurs because of the *random thermal motions* of the molecules. Particles flow from a region of high concentration to one of low concentration. If a solution of high solute concentration is adjacent to one of low concentration, but separated by an imaginary plane, it is probable that more molecules per unit of time will be crossing the plane from the side of higher concentration to the side of lower concentration than in the opposite direction. There are *fluxes* (movements of molecules) in both directions (the *unidirectional fluxes*), but the *net flux* is from the side of higher concentration to the side of lower concentration.

Now, if the imaginary plane were replaced with a thin membrane permeable to the molecules, then the same situation would apply; the particles would diffuse from the side of higher concentration to the side of lower concentration across the membrane. In a living cell, it is usually assumed that the bulk solutions are relatively well mixed and diffusion of most substances through the cell membrane is much slower than that through a free solution. Therefore, diffusion through the membrane is the *rate-limiting* step. For simplicity, we assume that the solutions on either side are well stirred (although there may actually

Cell Physiology Sourcebook. DOI: 10.1016/B978-0-12-387738-3.00008-1

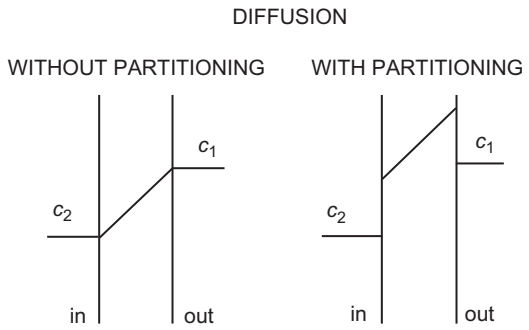

FIGURE 8.1 Concentration gradients across the membrane during diffusion without partitioning (left) and with partitioning (right).

be unstirred layers near the membrane). We confine ourselves here to the diffusion of small molecules or ions across the cell membrane.

For thin membranes, we first consider the case of diffusion without partitioning, as illustrated in Fig. 8.1 (left), in which the diffusing molecule can freely enter the membrane. We will then introduce the effect of partitioning into the membrane, a process that involves a change of chemical potential upon entrance into the membrane phase, as illustrated in Fig. 8.1 (right). We disregard possible structural obstacles that may be a series of *potential energy barriers* within the membrane (Danielli, 1943).

III. FICK'S LAW OF DIFFUSION

The fundamental law describing diffusion was enunciated by Adolph E. Fick in 1855, who noted a similarity between diffusion of solutes and Fourier's law describing the flow of heat in solids. *Fick's law of diffusion* was deduced theoretically in 1860 by James C. Maxwell from the kinetic theory of gases. The derivation of Fick's law includes the following assumptions: (1) statistical laws apply; (2) the average duration of a collision is short compared to the average time between collisions, a condition pertaining to dilute solutions; (3) the particles move independently; (4) classical mechanics can be used to describe molecular collisions; (5) energy, momentum and mass are conserved in every collision; and (6) the diffusing solute particles are much larger than the solvent molecules of the liquid.

IV. DIFFUSION COEFFICIENT

Consider two compartments, separated by a membrane of thickness Δx, in which a substance diffuses from inside a cell (denoted as compartment i with high concentration c_i) across the cell membrane into the outside medium (denoted as compartment o with low concentration c_o). It is assumed that the temperature and pressure are the same in both compartments. For such a system, *Fick's first law of diffusion* states that the *flux density* (J, mol/s-cm^2) is directly proportional to the concentration gradient dc/dx (mol/cm^3/cm) across the membrane.

$$J = \frac{dN}{Adt} = -D\frac{dc}{dx} \tag{8.1}$$

where dN/Adt (mol/(cm$^2\cdot$s) is the number (dN) of moles that diffuse across a unit area (A, cm^2) of the membrane during an interval of time (dt, s). The diffusion coefficient D (cm^2/s).indicates how much flux will occur for a given concentration gradient.

The concentration gradient in the steady state is equal to the difference in the concentration ($\Delta c = c_o - c_i$) of the solute on both sides of the membrane divided by the thickness of the membrane (Δx), so that:

$$J = -D\frac{\Delta c}{\Delta x} \tag{8.2}$$

$$\frac{mol}{\sec\cdot cm^2} = \frac{cm^2}{\sec}\frac{mol/cm^3}{cm}$$

It is assumed that the concentration gradient through the thin membrane is linear over its thickness (Δx).

The time required for diffusion to become 50, 63 or 90% complete varies directly with the square of the distance and inversely with the diffusion coefficient. Thus, diffusion is extremely fast over short distances (e.g. 10−1000 nm), but is exceedingly slow over long distances (e.g. 1 cm). For a small particle like K^+ or acetylcholine (ACh^+), with a D value of about 1×10^{-5} cm^2/s, the time required for 90% equilibration to be reached over a distance of 1 μm is about 1 ms. Table 8.1 shows how the time required changes as a function of distance. The chef knows that the time

TABLE 8.1 Calculations of Time Required for Diffusion to Become 90% Complete

Distance d	Time t
100 Å	0.1 μs
0.1 μm	0.01 ms
1 μm	1 ms
10 μm	100 ms
100 μm	10 s
1 mm	16.7 min
1 cm	28 h

Diffusion time varies inversely with square of diffusion distance. These approximate values are for a substance having a diffusion coefficient (D) of about 1×10^{-5} cm^2/s in free solution. Einstein's approximation equation is $d = \sqrt{Dt}$, where d is the mean displacement.

TABLE 8.2 Physicochemical Properties of Selected Ions

Ion	Limiting Equivalent Conductivity ($cm^2/S \cdot eq$)	Activity Coefficient[a]	Crystallographic Radius (Å)	Singly-hydrated Radius[b] (Å)	Hydrated Volume[c] ($Å^3$)	Heat of Hydration (kcal/g ion)	Number of Water Molecules[c]
Na^+	50.10	0.778	0.96	3.67	150	−115	(4−6)
K^+	73.50	0.770	1.33	4.05	(150)	−90	(3−6)
Cl^-	76.35	–	1.81	3.92	90	−59	(0−6)
Mg^{2+}	53.05	0.528	0.65	3.60	360	−501	12
Ca^{2+}	59.50	0.518	0.99	3.70	310	−428	10
Sr^{2+}	59.45	0.515	1.13	3.85	310	−381	10
Ba^{2+}	63.63	0.508	1.35	4.08	290	−347	9−10

[a]*Activity coefficient for each cation given for the Cl^- salt at 0.1 M and at 25°C.*
[b]*Singly-hydrated radius equals crystallographic radius plus 2.72 Å (diameter of water molecule) for cations having crystal radii between 0.9 and 1.7 Å, and crystal radius plus 2.23 Å for anions. Values for singly-hydrated radii taken from Mullins (1961).*
[c]*Values in parentheses are estimated.*
Values taken from R.A. Robinson and R.H. Stokes, *Electrolyte Solutions*, London, Butterworth & Co. (Publishers), Ltd., 1959 and from J.O.M. Bockris and B.E. Conway, *Modern Aspects of Electrochemistry*, London, Butterworth & Co. (Publishers), Ltd., 1954.

required for a meat roast to cook in the middle is dependent on the thickness of the roast and the physiologist knows that there is a critical thickness (e.g. 0.5−1.0 mm) of a muscle bundle in an incubation bath that allows adequate diffusion of oxygen to the core of the strip, no matter how vigorously the bath is oxygenated.

The *diffusion coefficient (D)* is a constant for a given substance and membrane under a given set of conditions. The diffusion coefficient of substances in free solution is dependent upon molecular size (and shape, for large molecules). For ions, the smaller the *crystal (unhydrated) radius*, the greater the *charge density*, which means that more water molecules are held in the *hydration shells*, thus giving a larger *hydrated radius*. The larger water shell causes diffusion to be slower. The hydrated and unhydrated radii of some relevant ions are given in Table 8.2. Thus, although Na^+ has a lower atomic weight than K^+, Na^+ attracts and holds a larger hydration shell because of its greater charge density (same charge as K^+, but smaller unhydrated ion size) and, therefore, Na^+ diffuses in water considerably slower than does K^+ (ratio of about 1: 2).

The diffusion coefficient is inversely related to the resistance to free diffusion and, therefore, is very much lower in water than in a gas. *Graham's law* states that the diffusion coefficient of a gas is inversely proportional to the square root of the molecular weight:

$$DM^{1/2} = \text{constant} \tag{8.3}$$

Graham's law was originally discovered by experiment and was later derived theoretically by Maxwell. The *random molecular motions* due to *thermal energy* are opposed by *intermolecular attractive forces* but, in dilute gases, these attractive forces are small because the molecules are relatively far apart.

The *Einstein−Stokes equation* applies to diffusion in liquids when spherical solute molecules are much larger than the solvent molecules, e.g. of colloidal size. The diffusion coefficient of the solute is related to the viscosity (η) of the solvent and the radius (r) of the solute particle:

$$D = \frac{RT}{6\pi\eta r N_A} \tag{8.4}$$

where R is the *gas constant*, T is the absolute temperature and N_A is Avogadro's number.

Temperature also affects the rate of diffusion. The relative increase in the diffusion coefficient when the temperature (T) is raised by 10°C is known as Q_{10}. For dilute solutions, the Q_{10} value should be the same for all molecules and is 1.03 (between 25 and 35°C). A Q_{10} value of 2 or 3 indicates that some process other than diffusion is probably responsible for transport.

In liquids, the solute and solvent molecules are close together. Hence, for any solute particle to move, it must first break away from its surrounding solvent molecules. Diffusion in liquids consequently occurs in a discontinuous manner. A solute molecule is able to move only when it has acquired sufficient energy by collision to break away from its solvent neighbors. Thus, the molecule diffuses in a series of jumps, each jump requiring a critical *activation energy*.

When the attractive forces between solvent molecules are weak, diffusion is more rapid.

The Q_{10} for diffusion of a substance in water depends on the activation energy necessary for a jump. If a large amount of energy is required (high Q_{10}), only a few molecules have the necessary energy to diffuse at any moment. Raising the temperature increases the number of molecules with the required energy and thereby appreciably speeds up the rate of diffusion. If only a small activation energy is required (low Q_{10}), a greater fraction of the molecules possesses this minimal energy at any moment and so raising the temperature has less of an effect. The Q_{10} for diffusion of Na^+ or K^+ in water is only about 1.22.

The cell membrane constitutes a barrier to diffusion. In penetrating through the lipid bilayer matrix, a non-charged small solute molecule must move as follows: (1) detach itself from its surrounding solvent molecules and jump into the membrane phase; (2) move through the thickness of the membrane, perhaps by a series of small jumps over energy barriers; and (3) detach itself from the membrane and jump into the solvent phase on the opposite side of the membrane. The permeability of the membrane to the solute depends greatly on the activation energy required for the molecule to jump into and out of the membrane. If the activation energy is high, the Q_{10} is high and the permeability is low; if the activation energy is low, then the Q_{10} is low and the permeability is high.

V. DIFFUSION ACROSS A MEMBRANE WITH PARTITIONING

When a solute partitions into the membrane, the concentration gradient across the membrane itself differs from that calculated from the internal and external concentrations in the bulk solutions. For example, if a solute is at 10 mM in the internal solution and at 1 mM in the external solution, the concentration gradient would be $c_i - c_o = 10 - 1 = 9$ mM. Now suppose that the solute dissolves into the membrane phase such that the concentration just within the membrane at the internal boundary is 10-fold greater than in the internal solution and the same 10-fold partitioning occurs at the external boundary. With such partitioning, the concentrations in the membrane would be 100 mM at the internal boundary and 10 mM at the external boundary, constituting a gradient of $100 - 10 = 90$ mM, or a 10-fold higher concentration gradient within the membrane. The *partition coefficient* (β) relates the concentration just within the membrane at the boundary to the external or internal concentrations. β is assumed to be equal at the internal and external boundaries of the cell membrane.

The diffusion coefficient across cell membranes for various substances is generally greater when the molecular size of the substance is small and when the lipid solubility is high; i.e. small molecules of high lipid solubility (i.e. less polar and non-polar molecules) penetrate most quickly through the membrane.

The above paragraphs present the basis for Overton's classical rule that the rate of diffusion of many substances across cell membranes correlates with the *oil/water partition coefficient*. The rate of permeation of a water-soluble substance is primarily determined by how easily the substance passes from water to lipid; its oil/water partition coefficient is a measure of this ease. The more a substance dissolves in the membrane, the greater its concentration gradient within the membrane and the faster the rate of diffusion across the membrane. The data for permeation of non-electrolytes, including alcohols, into cells are an example of this mechanism.

VI. PERMEABILITY COEFFICIENT

The *permeability coefficient* (P, cm/s) is the product of the partition coefficient (β) and the diffusion coefficient (D) divided by the thickness (Δx), of the membrane:

$$P = \frac{\beta D}{\Delta x} \qquad \text{cm/s} = \text{cm}^2/\text{s/cm} \tag{8.5}$$

Note that permeability coefficients apply only to membranes, whereas diffusion coefficients apply to both membranes and solutions. Equation 8.5 indicates that, the higher the diffusion coefficient for movement of a substance across a membrane, the higher the permeability coefficient.

The flux density *(J)* across the membrane is given by:

$$J = -P(c_O - c_I) \tag{8.6}$$

$$\frac{mol}{sec \cdot cm^2} = \frac{cm}{sec}\frac{mol}{cm^3}$$

Hence the net flux density of a non-electrolyte across a membrane is equal to the permeability coefficient *(P)* times the difference in concentration across the membrane. The permeability coefficient for K^+ (P_K) across resting skeletal muscle membrane is about 1×10^{-6} cm/s. Some values for P_K (in cm/s) are given in Table 8.3 for some cardiac tissues. The *unidirectional influx* (J_i) and *efflux* (J_o) are defined by:

$$J_i = -Pc_O \tag{8.7a}$$

$$J_o = -Pc_I \tag{8.7b}$$

The *net flux* is defined as the difference between the efflux and influx. Thus,

$$J = J_o - J_i = -P(c_O - c_I) \tag{8.8}$$

TABLE 8.3 Summary of Internal K^+ and Na^+ Concentrations and Permeabilities for Some Selected Heart Tissues

Preparation	Resting Potential (mV)	P_K (cm/s×10^{-7})	P_{Na}(cm/s×10^{-7})	P_{Na}/P_K	$[K^+]_i$(mM)	$[Na^+]_i$(mM)	Reference
Chick embryo 19 days old	—	3.10	0.053	0.017	122	15	Carmeliet et al. (1976)
Rabbit papillary muscle	−77.5	—	—	—	135	32.7	Lee and Fozzard (1975)
					82.6[a]	5.7[a]	
Rabbit papillary muscle	−86	—	—	—	119[b]	—	Akiyama and Fozzard (1975)
Rabbit ventricle	−76	—	—	—	83.1[a]	—	Fozzard and Lee (1976)
Cow Purkinje	−75	1.66	—	—	—	—	Carmeliet and Verdonck (1977)
Sheep Purkinje	—	—	—	—	160	—	Carmeliet and Bosteels (1969)

Unless otherwise specified, all ion concentrations are based on total tissue analyses, and all permeability coefficients are for tissues bathed in normal Ringer's solution.
[a]*Measured with ion-selective microelectrodes.*
[b]*Calculated from the internal K^+ concentration and activity coefficient.*

which is the same as Equation 8.6. Equations 8.7a and 8.7b show that the influx of a substance is equal to its permeability coefficient times the external concentration (c_o), whereas the efflux (or outflux) is equal to the permeability coefficient times the internal concentration (c_I). Algebraic manipulation shows that the permeability coefficient is equal to the ratio of flux to concentration (influx to c_O and efflux to c_i).

The electrical current (i, in amp) carried by Na^+ is equal to the flux (J' in mol/s) times zF *(coul/mol or coul/equiv , if univalent)*, or

$$i = J' zF \tag{8.9a}$$

Converting to current density:

$$I = JzF \tag{8.9b}$$

$$\frac{\text{amp}}{\text{cm}^2} = \frac{\text{mol}}{\text{sec}\cdot\text{cm}^2}\frac{\text{coul}}{\text{mol}}$$

where I is the current density in amp/cm^2, and J is the flux density in mol/cm^{2}-s.

VII. ELECTRODIFFUSION

Fick's law of diffusion (Equation 8.1) applies only to uncharged molecules. If there is a net charge on the molecule, then the unidirectional fluxes are also determined by any electrical field that may exist across the membrane. The equation for the net flux is then:

$$J = Pf(E_m)(c_1 - c_2 e^{E_m F/RT}) \tag{8.10}$$

where $f(E_m)$ is some function of the *electrical potential difference* (p.d.) across the membrane and F, R and T are the Faraday constant, gas constant and absolute temperature, respectively. Note the similarity of Equation 8.10 to Equations 8.6 and 8.8, except for the membrane potential terms. The electrical p.d. across the membrane (E_m) equals $\psi_I - \psi_O$,where ψ_I is the inside potential and ψ_O is the outside potential. When $f(E_m)$ is equal to E_mF/RT, this term is dimensionless (E_mF is the electrical energy, whereas RT is the thermal energy); $RT/F = 0.026$ V at 25°C. Similarly, the term $e^{E_mF/RT}$ is dimensionless; therefore, the units for flux are the same as those given in Equation 8.6.

For a monovalent cation, *Einstein's law of diffusion* states that:

$$D = U\,kT = U\frac{RT}{F} \tag{8.11}$$

where U is the *electrophoretic mobility* of the ion through the membrane and has units of a velocity per unit driving voltage gradient (cm/s per V/cm) and k is the Boltzmann constant (R/F).

Substituting Equation 8.11 into the definition of the permeability coefficient (Equation 8.5) gives:

$$P = U\frac{\beta}{\Delta x}\frac{RT}{F} \tag{8.12}$$

$$\frac{\text{cm}}{\text{sec}} = \frac{\text{cm/sec}}{\text{V/cm}}\frac{1}{\text{cm}}\frac{\text{V}}{1}$$

where β is the partition coefficient (dimensionless) for the ion between the bulk solution and the edge of the membrane and Δx is the membrane thickness (cm). Equation 8.12 indicates that the permeability coefficient of an ion is directly related to the electrophoretic mobility of the ion through the membrane.

The *Nernst–Planck equation* states that the total flux density, J_i (mol/cm^2·s), of an ion species (i) across the membrane is the sum of the flux density due to diffusion and the flux density due to the electrical potential:

$$J_i = J_{i(\text{diff})} + J_{i(\text{elec})} \tag{8.13}$$

The net outward flux due to diffusion, given by *Fick's law*, is proportional to the concentration gradient, dc_i/dx:

$$J_{O(\text{diff})} = -D_i\frac{dc_i}{dx} \tag{8.14}$$

where D_i (cm^2/s) is the diffusion coefficient of the *ion* species.

The flux of an ion is proportional to the gradient of *electrochemical potential* ($\overline{\mu}$) for that ion. The net flux is from the side of greater electrochemical potential to the side of lesser electrochemical potential. $\overline{\mu}$ is a measure of the useful energy and its units are in joules/mole (just as voltage is in joules/coulomb). Electrochemical potential is composed of a chemical part (μ_c) and an electrical part (μ_e), that is,

$$\overline{\mu} = \mu_c + \mu_e \tag{8.15}$$

The chemical part (μ_c) is given by:

$$\mu_c = \mu_c^0 + RT\ln a \tag{8.16a}$$

where μ_c^0 is the chemical potential at standard temperature and pressure and a is the activity (activity coefficient, γ, times the concentration). The electrical part (μ_e) is given by

$$\mu_e = zF\psi \tag{8.16b}$$

The difference in electrochemical potential for Na^+, for example, between inside and outside ($\Delta\overline{\mu} = \overline{\mu}_2 - \overline{\mu}_1$) is:

$$\Delta\overline{\mu}_{\text{Na}} = RT\ln\frac{[\text{Na}^+]_2}{[\text{Na}^+]_1} + zF\Delta\psi \tag{8.17}$$

where $\Delta\psi = \psi_2 - \psi_1$ and is the same as E_m. The activity coefficients cancel out, assuming $\gamma_2 = \gamma_1$.

VIII. SPECIAL TRANSPORT PROCESSES

Most non-polar molecules pass directly through the lipid bilayer matrix of the membrane, i.e. not through special sites (e.g. water-filled pores or channels). Small charged ions (e.g. Na^+, K^+, Cl^-, Ca^{2+}) pass through water-filled channels, some of which have a voltage-dependent gating mechanism. These channels can exhibit a high degree of selectivity for specific ions, with the selectivity orders not being based solely on the hydrated or unhydrated sizes of the ions. One type of ionophore, valinomycin, forms a hydrophobic cage around K^+. This K^+-ionophore complex is lipid soluble and passes rapidly through the lipid bilayer matrix.

Special *transport proteins* are normally present in the cell membrane for net uptake of nutrients, such as glucose and amino acids. Some of these are for *downhill transport* only, i.e. down the electrochemical gradient. One type of protein-mediated transport in cells (e.g. for glucose) is known as *facilitated diffusion*, a type of transport that contrasts with *simple diffusion* across the cell membrane. Another type of mediated transport is known as *exchange diffusion*, in which one molecule of substance (or ion) inside the cell is exchanged for one molecule outside the cell, in which case there is no net movement. In either type of mediated transport, the *rate of downhill movement* of the substance across the membrane is enhanced by the transport protein.

Mediated transport systems differ from simple diffusion in that they exhibit *saturation kinetics*. That is, the rate of transport increases with an increase in the substrate concentration up to a maximum, after which the rate levels off due to a finite number of available transport sites. Other characteristics of mediated transport systems include *competitive inhibition*, in which an inhibitor substance competes at the same site for binding to the transporter. In *non-competitive inhibition*, the *inhibitor* (non-transported) substance binds to the transporter at a site different from the transport site, but still alters or prevents binding of the usual substrate. Mediated transport exhibits greater *specificity* than simple diffusion; e.g. the rate of mediated transport of D-glucose is greater than for L-glucose. Because mediated transport resembles an enzymatic process involving protein conformational changes, the temperature coefficient (Q_{10}) is also higher than for simple diffusion.

IX. USSING FLUX RATIO EQUATION

As pointed out in Equations 8.7a and 8.7b, the unidirectional fluxes are determined also by the permeability coefficient. Ussing (1949) developed the so-called *flux ratio equation*, in which the *ratio of influx to efflux* is used

(permeability cancels out). Specifically, for the ratio of Na^+ fluxes (by simple electrodiffusion), the following applies:

$$\frac{J_i^{Na}}{J_o^{Na}} = \frac{[Na^+]o}{[Na^+]i}\, e^{-E_m F/RT} \tag{8.18}$$

Thus, the ratio of influx:efflux (or outflux) (passive) in a resting membrane (assuming a RP of −80 mV) is

$$\frac{J_i^{Na}}{J_o^{Na}} = \frac{150\ \text{mM}}{15\ \text{mM}}\, e^{+80\text{mV}/26\text{mV}} = (10)e^{3.08} = 217 \tag{8.19a}$$

Thus, the passive influx of Na^+ should be 217 times greater than the passive efflux, because of the large electrochemical gradient directed inward.

The flux ratio for K^+ would be

$$\frac{J_i^{K}}{J_o^{K}} = \frac{4\ \text{mM}}{150\ \text{mM}}\, e^{+80\ \text{mV}/26\ \text{mV}} = (1/37.5)e^{3.07} = 0.574 \tag{8.19b}$$

Thus, the passive influx should be 0.574 times the passive efflux. The K^+ equilibrium potential (E_K) is only slightly greater (more negative by about 14 mV) than the RP and so the passive flux ratio should be close to one.

A modified form of Equation 8.18 can be obtained by substituting the ratio of ions with $e^{E_i F/RT}$ (derived from the Nernst equation), giving

$$\frac{J_i^i}{J_o^i} = e^{-(E_m - E_i)F/RT} \tag{8.20a}$$

where E_i is the *equilibrium potential* for the cation in question, and J_i^i and J_o^i are the inward and outward fluxes, respectively, for ion i. The sign convention refers inside solution to outside solution. Thus, for Na^+ we have

$$\frac{J_i^{Na}}{J_o^{Na}} = e^{-[-80\ \text{mV}-(+60\ \text{mV})]/26\ \text{mV}} = 217 \tag{8.20b}$$

This value of 217 obtained for the flux ratio is identical to that obtained from Equation 8.19a. One advantage of Equation 8.20a is that it is obvious at a glance that when $E_i = E_m$, the flux ratio is exactly 1.0, because $e^0 = 1$, where e is the base (2.717) for the natural logarithm. Thus, if Cl^- is passively distributed so that $E_{Cl} = E_m$, its flux ratio should be 1.0; i.e. influx equals efflux, so there is no net flux. The larger the difference between E_i and E_m, i.e. the farther the ion is from equilibrium, the greater the flux ratio.

Sometimes Equations 8.20a and 8.20b do not fit the experimental facts. The data are better fitted if the exponential term contains another factor *(n),* which is an empirical factor:

$$\frac{J_i^i}{J_o^i} = e^{-n(E_m - E_i)F/RT} \tag{8.21}$$

The best fit of the data is when n has a value of 2.5 to 4.0, depending on the membrane under investigation. One interpretation given to n is that if the length of the water-filled pore that the ion must traverse to cross the membrane is much longer than the ion diameter, as is likely, then for so-called *single-file diffusion*, n hits on the same side are required for the ion to complete its journey across the membrane. One could consider, for example, that there are three potential energy wells, or a chain of reactive sites, along the length of the pore, and the only way for the ion to escape the well is to receive a kinetic bump from an adjacent ion in the file. Complete permeation of an ion through the pore is more likely to happen if the ion is moving in the same direction as the majority of ions, i.e. down the electrochemical gradient. Therefore, this factor (Equation 8.21) makes the flux ratio much greater than would otherwise be predicted.

BIBLIOGRAPHY

Akiyama, T., & Fozzard, H. A. (1975). Influence of potassium ions and osmolality on the resting membrane potential of rabbit ventricular papillary muscle with estimation of activity and the activity coefficient of internal potassium. *Circ Res, 37*, 621–629.

Bockris, J. O'M., & Conway, B. E. (1954). *Modern Aspects of Electrochemistry.* London: Butterworths.

Carmeliet, E., & Bosteels, S. (1969). Coupling between Cl flux and Na or K flux in cardiac Purkinje fibers: influence of pH. Arch Int Physio. *Biochim, 77*, 57–72.

Carmeliet, E., & Verdonck, F. (1977). Reduction of potassium permeability by chloride substitution in cardiac cells. *J Physiol (London), 265*, 193–206.

Carmeliet, E. E., Horres, C. R., Lieberman, M., & Vereecke, J. S. (1976). Developmental aspects of potassium flux and permeability of the embryonic chick heart. *J Physiol (London), 254*, 673–692.

Crank, J. (1956). *Mathematics of Diffusion*. New York: Oxford University Press.

Danielli, J. (1943). The theory of penetration of a thin membrane: Appendix. In D. F. Danielli (Ed.), *The Permeability of Natural Membranes*. London: Cambridge University Press.

Einstein, A., & A.D. Cowper, Transl. (1926). Investigations on the Theory of Brownian Movement. In R. Furth (Ed.), *Methuen*. London: reprinted by Dover Publications, Inc. 1956.

Fozzard, H. A., & Lee, C. O. (1976). Influence of changes in external potassium and chloride ions on membrane potential and intracellular potassium ion activity in rabbit ventricular muscle. *J Physiol (London), 256*, 663–689.

Hodgkin, A. L., & Huxley, A. F. (1952). Currents carried by sodium and potassium ions through the membrane of the giant axon of Loligo. *J Physiol (London), 116*, 449–472.

Jacobs, M. H. (1967). *Diffusion Processes*. New York: Springer-Verlag.

Jost, W. (1960). *Diffusion in Solids, Liquids, Gases*. New York: Academic Press.

Lee, C. O., & Fozzard, H. A. (1975). Activities of potassium and sodium ions in rabbit heart muscle. *J Gen Physiol, 65*, 695–708.

Mullins, L. J. (1961). The macromolecular properties of excitable membranes. *Ann NY Acad Sci, 94*, 390–404.

Robinson, R. A., & Stokes, R. H. (1959). *Electrolyte Solutions*. London: Butterworths.

Ussing, H. H. (1949). Distinction by means of tracers between active transport and diffusion. The transfer of iodide across isolated frog skin. *Acta Physiol Scand, 19*, 43–56.

Chapter 9

Origin of Resting Membrane Potentials

Nicholas Sperelakis

Chapter Outline

I. SUMMARY

Most of the factors that determine or influence the resting E_m of cells are discussed in this chapter. The structural and chemical composition of the cell membrane is briefly examined and correlated with the resistive and capacitative properties of the membrane. The factors that determine the intracellular ion concentrations in cells are examined. These factors include the *Na^+-K^+-coupled pump*, the *Ca^{2+}-Na^+ exchange* reaction and the sarcolemmal *Ca^{2+} pump*. The Na^+-K^+ pump enzyme, Na^+,K^+-ATPase, requires both Na^+ and K^+ for activity and transports three Na^+ ions outward and usually two K^+ ions inward per ATP hydrolyzed. Cardiac glycosides are specific blockers of this transport ATPase. The Na^+-K^+ pump, if electroneutral, is not directly related to excitability, but only indirectly related by its role in maintaining the Na^+ and K^+ concentration gradients.

The carrier-mediated Ca^{2+}-Na^+ exchange reaction is driven by the Na^+ electrochemical gradient; i.e. the energy for transporting out internal Ca^{2+} by this mechanism comes from the Na^+,K^+-ATPase. The Ca^{2+}-Na^+ exchange reaction exchanges one internal Ca^{2+} ion for three external Na^+ ions when working in the *forward mode* in cells at rest. In myocardial cells, during the action potential (AP) plateau depolarization, the energetics cause the Ca^{2+}-Na^+ exchanger to operate in *reverse mode*, allowing Ca^{2+} influx.

The mechanism whereby the *ionic distributions* give rise to diffusion potentials is discussed, as are the factors that determine the magnitude and polarity of each ionic *equilibrium potential*. The equilibrium potential for any ion and the transmembrane potential determine the total *electrochemical driving force* for that ion and the product of this driving force and membrane conductance for that ion

Cell Physiology Sourcebook. DOI: 10.1016/B978-0-12-387738-3.00009-3

determines the net ionic current. The direction of the net ionic movement, inward or outward, depends on the direction of the electrochemical gradient.

The key factor that determines the resting E_m is the *relative permeability* of the various ions, particularly of K^+ and Na^+, i.e. the P_{Na}/P_K ratio (or g_{Na}/g_K ratio), as calculated from the constant-field equation. The major physiologic ions that have some effect on the resting E_m or on the APs are K^+, Na^+, Ca^{2+} and Cl^-. The Ca^{2+} electrochemical gradient has only a small direct effect on the resting E_m, although low external Ca^{2+} can affect the permeabilities and conductances for the other ions, such as Na^+ and K^+. Elevation of internal Ca^{2+} can increase the permeability to K^+ by activating Ca^{2+}-operated K^+-selective $I_{K(Ca)}$ channels.

Cl^- is usually *passively distributed* according to the membrane potential, i.e. not actively transported. However, there is some evidence indicating that, in some smooth muscle cells, $[Cl^-]_i$ may be about twice as high as that predicted from E_m. If so, this would give an E_{Cl} value about 18 mV less negative than the resting E_m. Before one can conclude that there is a Cl^- pump directed inward, however, the calculated E_{Cl} must be significantly more positive than the mean resting E_m averaged over time; i.e. any spontaneous APs must be taken into account. If Cl^- is passively distributed, it cannot determine the resting E_m. However, transient net movements of Cl^- ions, e.g. during the AP, do affect the E_m, particularly when g_{Cl} is high.

Elevation of $[K^+]_o$ to more than the normal concentration of about 4.5 mM decreases the K^+ equilibrium potential (E_K), as predicted from the Nernst equation ($[K^+]_i$ constant) and depolarization is produced.

Not only is the resting E_m the *potential energy storehouse* that is drawn upon for production and propagation of the APs but, because the membrane voltage-dependent cationic channels are inactivated with sustained depolarization, the rate of rise of the AP, and hence propagation velocity, is critically dependent on the level of the resting E_m. For example, a relatively small elevation of K^+ concentration in the blood has dire consequences for functioning of the heart.

The contribution of the Na^+-K^+ pump to the resting E_m depends on: (1) the coupling ratio of Na^+ pumped out to K^+ pumped in; (2) the turnover rate of the pump; (3) the number of pumps; and (4) the magnitude of the membrane resistance. The *electrogenic pump potential* is in parallel to the net ionic diffusion potential (E_{diff}), determined by the ionic equilibrium potentials and relative permeabilities. The contribution of the electrogenic pump potential to the measured resting E_m of cells varies from 2 to 16 mV, depending on the type of cell. The immediate depolarization produced by complete Na^+-K^+ pump stoppage with cardiac glycosides is only a few millivolts in cells like myocardial cells. Of course, long-term pump inhibition produces a larger and larger depolarization as the ionic gradients are dissipated. The rate of Na^+-K^+ pumping, and hence the magnitude of the electrogenic pump contribution to E_m, is controlled primarily by $[Na^+]_i$ and by $[K^+]_o$. The electrogenic pump potential might be physiologically important to various tissues, particularly the heart, under certain conditions that tend to depolarize the cells, such as transient ischemia or hypoxia. In such cases, the actual depolarization produced may be less because of a relatively constant pump potential in parallel with a diminishing E_{diff}. The electrogenic pump potential may also affect *automaticity* of the nodal cells of the heart, as well as other cells that exhibit automaticity.

II. INTRODUCTION

The cell membrane exerts tight control over the electrical activity and the contractile machinery during the process of excitation–contraction (electromechanical) coupling. Some drugs and toxins exert primary or secondary effects on the electrical properties of the cell membrane and thereby exert effects, for example, on automaticity, arrhythmias and force of contraction of the heart. Therefore, for an understanding of the mode of action of therapeutic drugs, toxic agents, neurotransmitters, hormones and plasma electrolytes on the electrical activity of nerve and muscle, it is necessary to understand the electrical properties and behavior of the cell membrane at rest and during excitation. The first step in gaining such an understanding is to examine the electrical properties of nerve and muscle cells at rest, including the origin of the resting membrane potential (E_m). The resting E_m and action potential result from properties of the cell membrane and the ion distributions across it.

III. PASSIVE ELECTRICAL PROPERTIES

IIIA. Membrane Structure and Composition

As discussed in previous chapters, the cell membrane is composed of a bimolecular leaflet of phospholipid molecules with protein molecules floating in the lipid bilayer. The non-polar hydrophobic ends of the phospholipid molecules project toward the middle of the membrane and the polar hydrophilic ends project toward the edges of the membrane bordering on the water phases (Fig. 9.1). This orientation is thermodynamically favorable. The lipid bilayer membrane is about 50–70 Å thick and the phospholipid molecules are about the right length (30–40 Å) to stretch across half of the membrane thickness. *Cholesterol* molecules are in high concentration in the cell membrane (of animal cells) and are inserted between the phospholipid molecules, giving a phospholipid/cholesterol ratio of about 1.0. Some of the large protein molecules, called *integral membrane proteins*, protrude through the entire membrane thickness; e.g. the Na^+, K^+-ATPase, Ca^{2+}-ATPase and the

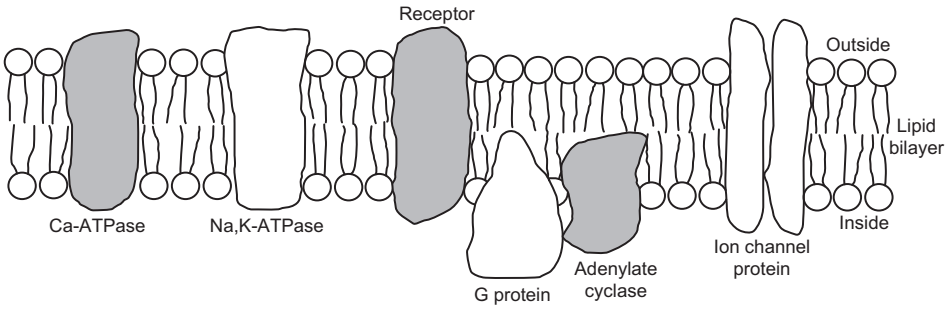

FIGURE 9.1 Diagrammatic illustration of cell membrane substructure showing the lipid bilayer. Non-polar hydrophobic tail ends of the phospholipid molecules project toward the middle of the membrane and polar hydrophilic heads border on the water phase at each side of the membrane. Lipid bilayer is about 50−70 Å thick. For simplicity, the cholesterol molecules are not shown. Large protein molecules protrude through entire membrane thickness or are inserted into one leaflet only, as depicted. These proteins include various enzymes associated with the cell membrane as well as membrane ionic channels. Membrane has fluidity so that the protein and lipid molecules can move around in the plane of the membrane.

various ion channel proteins (i.e., protrude through both leaflets), whereas other proteins are inserted into one leaflet (inner or outer) only. These proteins "float" in the lipid bilayer matrix and the membrane has *fluidity* (reciprocal of microviscosity), such that the protein molecules can move around laterally in the plane of the membrane. Some ion channels, e.g. fast Na^+ channels of the node of Ranvier of myelinated neurons, are tethered in place to the cytoskeleton by *anchoring proteins*, such as ankyrin.

The outer surface of the cell membrane is lined with strands of mucopolysaccharides (the *cell coat* or glycocalyx) that endow the cell with immunochemical properties. The cell coat is highly charged negatively and therefore can bind cations, such as Ca^{2+}. Treatment with neuraminidase to remove sialic acid residues destroys the cell coat.

IIIB. Membrane Capacitance and Resistivity

Lipid bilayer membranes made artificially have a specific *membrane capacitance* (C_m) of 0.4−1.0 μF/cm^2, which is close to the value for biological membranes. The capacitance of biological cell membranes is due to this *lipid bilayer matrix*. A capacitor consists of two parallel plate conductors separated by a *dielectric material* of high resistance (e.g. oil). The factors that determine the value of the capacitance of a membrane are given in the equation:

$$C_m = \frac{\in A_m}{\delta}\frac{1}{4\pi k} \qquad (9.1)$$

where A_m is the membrane area (in cm^2) and k is a constant (9.0×10^{11} cm/F). Calculation of membrane thickness (δ) from Equation 9.1, assuming a measured membrane capacitance (C_m) of 0.7 μF/cm^2 and a dieletric constant (ε) of 5, gives 63 Å. Most oils have dielectric constants of 3−5. The more dipolar the material, the greater the dielectric constant. For example, water, which is very dipolar, has a value of 81, compared with a value of 1.000 for a vacuum (air is nearly equal to that of vacuum).

The artificial lipid bilayer membrane, on the other hand, has an exceedingly high specific resistance (R_m) of 10^6−10^9 Ω•cm^2, which is several orders of magnitude higher than that of the biological cell membrane (about 10^3 Ω•cm^2). R_m is greatly lowered, however, when the bilayer is doped with certain proteins or substances, such as macrocyclic polypeptide antibiotics (ionophores). The added ionophores may be of the ion-carrier type, such as valinomycin, or of the channel-former type, such as gramicidin. Therefore, the presence of proteins that span across the thickness of the cell membrane must account for the relatively low resistance (high conductance) of the cell membrane. These proteins include those constituting the voltage-dependent gated ion channels of the cell membrane. In summary, the capacitance is due to the lipid bilayer matrix and the conductance is due to proteins inserted in the lipid bilayer.

The dielectric property of the cell membrane is very good. For a resting E_m of −80 mV and a thickness of 60 Å, the voltage gradient sustained across the membrane is 133 000 V/cm. Thus, the cell membrane tolerates an enormous voltage gradient.

IIIC. Membrane Fluidity

The electrical properties and the ion transport properties of the cell membrane are determined by the molecular composition of the membrane. The lipid bilayer matrix even influences the function of the membrane proteins; e.g. the Na^+, K^+-ATPase activity is affected by the surrounding lipid. A high cholesterol content lowers the fluidity of the membrane. The polar portion of cholesterol lodges in the hydrophilic part of the membrane and the nonpolar part of the planar cholesterol molecule is wedged between the fatty acid tails, thus restricting their motion and lowering fluidity. A high degree of unsaturation and branching of the tails of the phospholipid molecules raises the fluidity; phospholipids with unsaturated and branched-chain fatty acids cannot be packed tightly because of steric

hindrance. Chain length of the lipids also affects fluidity. Low temperature decreases membrane fluidity, as expected. Ca^{2+} and Mg^{2+} may diminish the charge repulsion between the phospholipid headgroups; this allows the bilayer molecules to pack together more closely, thereby constraining the motion of the tails and reducing fluidity. Each phospholipid tail occupies about 20−30 $Å^2$ and each headgroup about 60 $Å^2$ (Jain, 1972). Membrane fluidity changes occur in muscle development and in certain disease states, such as cancer, muscular dystrophy (Duchenne type) and myotonic dystrophy.

The hydrophobic portion of local anesthetic molecules may interpose between the lipid molecules. This separates the acyl chain tails of the phospholipid molecules further, reducing the van der Waals forces of interaction between adjacent tails and thus increasing the membrane fluidity. Local anesthetics depress the resting conductance of the membrane and the voltage-dependent changes in gNa, gK and gCa. That is, the local anesthetics produce a non-selective depression of all ionic conductances of the membrane. At the concentration of a local anesthetic required to completely block excitability, its estimated concentration in the lipid bilayer is more than 100 000/μm^2. This should be compared with a density of fast Na^+ channels of about 20−100/μm^2, and even less for K^+ channels and Ca^{2+} channels. Local anesthetics depress Na^+,K^+-ATPase activity also. Additional information on fluidity is given in several preceding chapters.

IIID. Potential Profile across Membrane

The cell membrane has fixed negative charges on its outer and inner surfaces. The charges are presumably due to acidic phospholipids in the bilayer and to protein molecules either embedded in the membrane (islands floating in the lipid bilayer matrix) or tightly adsorbed to the surface of the membrane. Most proteins have an acid isoelectric point, so at a pH near 7.0 they possess a net negative charge. The charge at the outer surface of the cell membrane, with respect to the solution bathing the cell, is known as the *zeta potential*. This charge is responsible for the electrophoresis of cells in an electric field, the cells moving toward the anode (positive electrode) because unlike charges attract. This surface charge affects the true potential difference (PD) across the membrane, as shown in Fig. 9.2A. At each surface, the fixed charge produces an electric field that extends a short distance into the solution and causes each surface of the membrane to be slightly more negative (by a few millivolts) than the extracellular and intracellular solutions. The potential theoretically recorded by an ideal tiny electrode, as the electrode is driven through the solution perpendicular to the membrane surface, should become negative as the electrode approaches within a few angstroms of the surface. The potential difference between the membrane surface and the solution declines exponentially as a function of distance from the surface. Its length constant is a function of the ionic strength (or resistivity) of the solution: the lower the ionic strength, the greater the length constant. The magnitude of the PD depends on the density of the charge sites (number of chemical groups per unit of membrane area). The number of ionized charge groups is affected by the pH and ionic strength.

The membrane potential (E_m) measured by an intracellular microelectrode is the potential of the inner solution (ψ_i) minus the potential of the outer solution (ψ_o); i.e.:

$$E_m = \psi_i - \psi_o \tag{9.2}$$

The true PD across the membrane (E'_m), however, is really that PD directly across the membrane, as shown in Fig. 9.2A. If the *surface charges* at each surface of the membrane are equal, then $E'_m = E_m$. If the outer surface charge is decreased to zero by extra binding of protons or cations (such as Ca^{2+}), then the membrane becomes slightly hyperpolarized ($E'_m > E_m$), although this is not measurable by the intracellular microelectrode (see Fig. 9.2B). Conversely, if the inner surface charge were neutralized and the outer surface charge restored, then the membrane would become slightly depolarized ($E'_m < E_m$). Again, this change is not measurable by the microelectrode, which can only measure the PD between the two solutions.

Because the membrane ionic conductances are controlled by the PD directly across the membrane (i.e. by E'_m and not by E_m), changes in the surface charges (e.g. by drugs, ionic strength or pH) can lead to apparent shifts in the electrical threshold potential, mechanical threshold potential (the E_m value at which contraction of muscle just begins), activation curve and inactivation curve (discussed in subsequent chapters). For example, elevation of extracellular Ca^{2+} concentration ($[Ca^{2+}]_o$) is known to raise the threshold potential (i.e. the critical depolarization required to reach electrical threshold), as expected from the small increase in E'_m that occurs.

IV. MAINTENANCE OF ION DISTRIBUTIONS

IVA. Resting Potentials and Ion Distributions

The transmembrane potential in resting nerve and muscle cells varies with the type of cell. In myocardial cells, it is about −80 mV (Table 9.1). The resting E_m or maximum diastolic potential in cardiac Purkinje fibers is somewhat greater (about −90 mV), whereas that in the nodal cells of the heart is lower (about −60 mV). In nerve cells, the RP is about −70 mV, whereas in mammalian skeletal muscle fibers the value is close to −80 mV. In most smooth muscle cells, the resting E_m is about −55 mV.

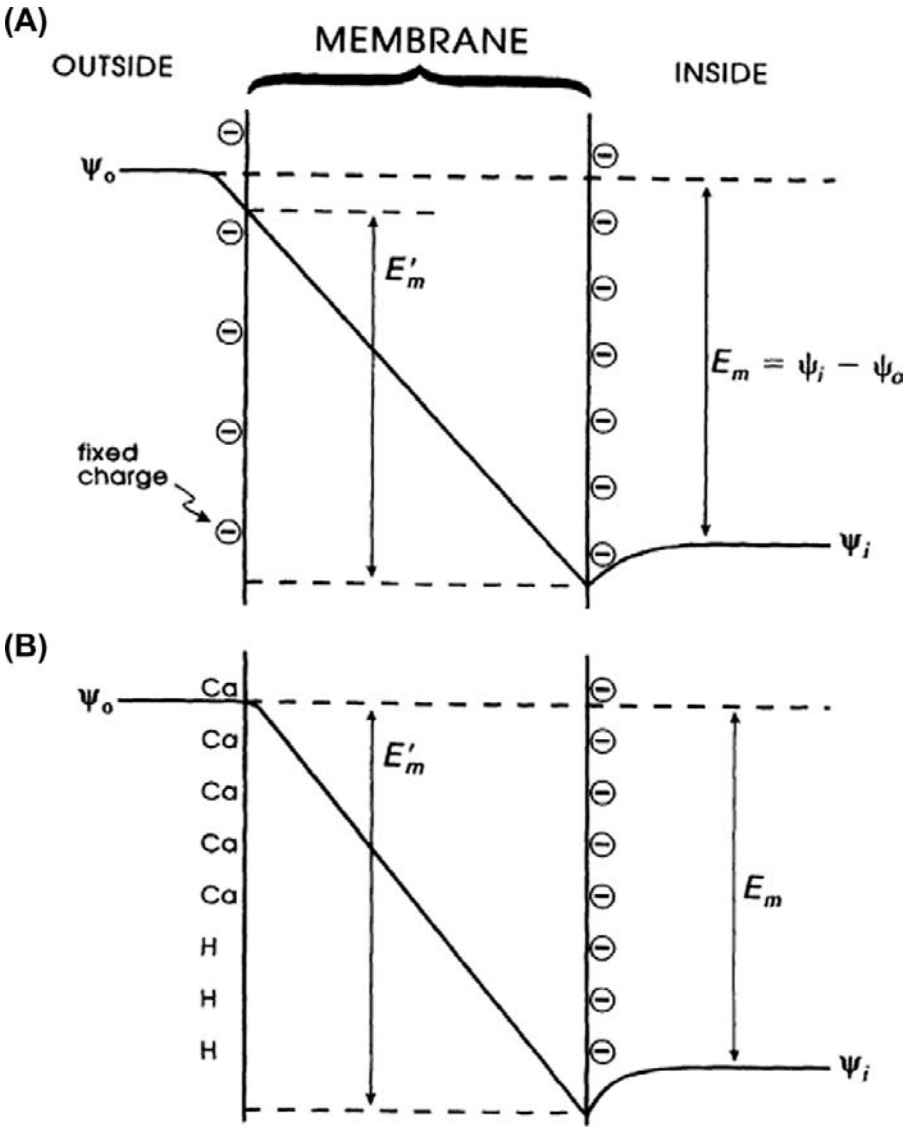

FIGURE 9.2 Potential profile across the cell membrane. (A) Because of fixed negative charges (at pH 7.4) at outer and inner surfaces of the membrane, there is a negative potential that extends from the edge of the membrane into the solutions on both sides. This surface potential falls off exponentially with distance into the solution. Magnitude of the surface potential is a function of the charge density. ψ_o is the electrical potential of the outside solution, ψ_i. is that of the inside solution and membrane potential (E_m) is the difference ($\psi_i - \psi_o$). E_m is determined by the equilibrium potentials and relative conductances. Profile of the potential through the membrane is shown as linear (the constant-field assumption), although this need not be true for the present purpose. If the outer surface potential is exactly equal to that in the inner surface, then the true transmembrane potential (E'_m) is exactly equal to the (microelectrode) measured membrane potential (E_m). (B) If the outer surface potential is different from the inner potential, e.g. by increasing the extracellular Ca^{2+} concentration or decreasing the pH to bind Ca^{2+} or H^+ to more of the negative charges, then the E'_m is greater than the measured E_m. Diminution of the inner surface charge decreases E'_m. The membrane ion channels are controlled by E'_m.

TABLE 9.1 Comparison of the Resting Potentials in Different Types of Cells

Cell Type	Resting Potential (mV)
Neuron	−70
Skeletal muscle (mammalian)	−80
Skeletal muscle (frog)	−90
Cardiac muscle (atrial and ventricular)	−80
Cardiac Purkinje fiber	−90
Atrioventricular nodal cell	−65
Sinoatrial nodal cell	−55
Smooth muscle cell	−55

The ionic composition of the extracellular fluid bathing the muscle cells is similar to that of the blood. It is high in Na^+ (about 145 mM) and Cl^- (about 100 mM), but low in K^+ (about 4.5 mM). The Ca^{2+} concentration is about 2 mM, but about half is bound to serum proteins. In contrast, the intracellular fluid has a low concentration of Na^+ (about 15 mM or less) and Cl^- (about 6−8 mM), but a high concentration of K^+ (about 150−170 mM). These ion distributions are listed in Table 9.2. The free intracellular Ca^{2+} concentration $[Ca^{2+}]_i$ is about 10^{-7} M or less, but during contraction it may rise as high as 10^{-5} M. The total intracellular Ca^{2+} is much higher (about 2 mM/kg), but most of this is bound to molecules, such as proteins, or is sequestered into compartments, such as mitochondria and the sarcoplasmic reticulum (SR). Most of the intracellular K^+ is free and it has a diffusion coefficient only

TABLE 9.2 Summary of the Ion Distributions in Most Types of Cells and the Equilibrium Potentials Calculated from the Nernst Equation

Ion	Extracellular Distribution (mM)	Intracellular Distribution (mM)	Equilibrium Potential (mV)
Na^+	145	15	+60
Cl^-	100	5[a]	−80
K^+	4.5	150	−94
Ca^{2+}	1.8	0.0001	+130
H^+	0.0001	0.0002	−18

[a]*Assuming Cl^- is passively distributed and resting E_m is −80 mV. The extracellular H^+ concentration is given for pH 7; it would be 40 nM at pH 7.4.*

slightly less than that of K^+ in free solution. Thus, under normal conditions, the cell maintains an internal ion concentration markedly different from that in the medium bathing the cells and it is these ion concentration differences that underlie the RP and excitability. The existence of the RP enables APs to be produced in those types of cells that have excitability. The ion distributions and related pumps and exchange reactions are depicted in Fig. 9.3.

Inhibition of the Na^+-K^+ pump (e.g. by cardiac glycosides such as digitalis) causes the ion concentration gradients gradually to run down or dissipate. The cells lose K^+ and gain Na^+, Cl^- and water. Therefore, the K^+ and Na^+ equilibrium potentials (E_K and E_{Na}) become smaller and the cells become depolarized. The depolarization causes the cells to gain Cl^-, and therefore also to gain water because of the resultant gain in osmotic strength, causing the cells to swell.

Although the topic of Na^+,K^+-ATPase and the Na^+-K^+ pump is discussed in detail in a subsequent chapter, a brief description is given here.

IVB. Na^+ and K^+ Distribution and the Na^+-K^+ Pump

The intracellular ion concentrations are maintained differently from those in the extracellular fluid by active ion transport mechanisms that expend metabolic energy to transport specific ions against their concentration (or electrochemical) gradients. These ion pumps are located in the cell membrane at the cell surface and probably also in

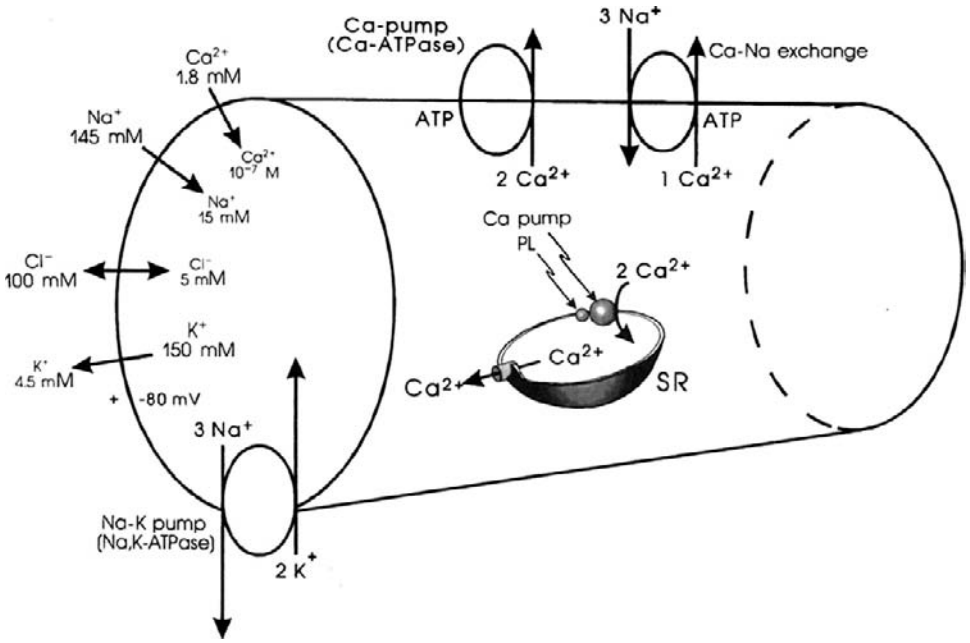

FIGURE 9.3 Intracellular and extracellular ion distributions in a skeletal muscle fiber. Also given are polarity and magnitude of the RP. Arrows give direction of the net electrochemical gradient. Na^+-K^+ pump is located in the cell surface and the T-tubule membranes. A Ca^{2+}-ATPase/Ca^{2+} pump, similar to that in the SR, is located in the cell membrane. A Ca^{2+}-Na^+ exchange carrier is located in the cell membrane.

the transverse tubular membrane of striated muscle cells. The major ion pump is the Na^+-K^+-linked pump, which pumps Na^+ out of the cell against its electrochemical gradient, while simultaneously pumping K^+ in against its electrochemical gradient (see Fig. 9.3). The coupling between Na^+ and K^+ pumping is obligatory, since in zero $[K^+]_o$, the Na^+ can no longer be pumped out. That is, a *coupling ratio* of three Na^+:0 K^+ is not possible. The coupling ratio of Na^+ pumped out to K^+ pumped in is generally 3:2. The Na^+-K^+ pump is half-inhibited (K_i value) when $[K^+]_o$ is lowered to about 2 mM.

If the ratio were 3:3, the pump would be electrically neutral or non-electrogenic. A PD across the membrane would not be produced directly, because the pump would pull in three positive charges (K^+) for every three positive charges (Na^+) it pushed out. When the ratio is 3:2, the pump is electrogenic and directly produces a PD that causes E_m to be greater (more negative) than it would be otherwise, based solely on the ion concentration gradients and relative permeabilities or *net diffusion potential* (E_{diff}). A coupling ratio of 3 Na^+:1 K^+ would produce a greater electrogenic pump potential (V_p). Under normal steady-state conditions, the contribution of the Na^+-K^+ electrogenic pump potential to E_m (ΔV_p) is only a few millivolts in myocardial cells; the contribution is greater in smooth muscle cells (6–8 mV) and mammalian skeletal muscle fibers (12–16 mV).

The driving mechanism for the Na^+-K^+ pump is a membrane ATPase, the *Na^+,K^+-ATPase*, which spans the membrane and requires both Na^+ and K^+ ions for activation. This enzyme requires Mg^{2+} for activity. ATP, Mg^{2+} and Na^+ are required at the inner surface of the membrane and K^+ is required at the outer surface. A *phosphorylated intermediate* of the Na^+,K^+-ATPase occurs in the transport cycle, its phosphorylation being Na^+-dependent and its dephosphorylation being K^+-dependent (for references, see Sperelakis, 1979). The pump enzyme usually drives three Na^+ ions out and two K^+ ions in for each ATP molecule hydrolyzed. The Na^+,K^+-ATPase is specifically inhibited by the *cardiac glycosides* (digitalis drugs) acting on the outer surface. The pump enzyme is also inhibited by vanadate ion and by sulfhydryl (SH) reagents (such as N-ethylmaleimide [NEM], mercurial diuretics and ethacrynic acid), thus indicating that the SH groups are crucial for activity.

Blockade of the Na^+-K^+ pump produces only a small immediate effect on the resting E_m: a small depolarization of about 2–16 mV, depending on cell type, representing the contribution of V_p to E_m (ΔV_p). Because excitability and generation of APs are almost unaffected at short times, excitability is independent of active ion transport. However, over many minutes, depending on the *ratio of surface area to volume* of the cell, the resting E_m slowly declines because of gradual dissipation of the ionic gradients. The progressive depolarization depresses the rate of rise of the AP, and hence the propagation velocity and eventually all excitability is lost. Thus, a large RP and excitability, although not immediately dependent on the Na^+-K^+ pump, are ultimately dependent on it.

The rate of Na^+-K^+ pumping in excitable cells must change with the amount of electrical activity to maintain relatively constant intracellular ion concentrations. A higher frequency of APs results in a greater overall movement of ions down their electrochemical gradients and these ions must be repumped to maintain the ion distributions. For example, the cells tend to gain Na^+, Cl^- and Ca^{2+} and to lose K^+. The factors that control the rate of Na^+-K^+ pumping include $[Na^+]_i$ and $[K^+]_o$. In cells that have a large surface area to volume ratio (such as small-diameter non-myelinated axons), $[Na^+]_i$ may increase by a relatively large percentage during a train of APs and this would stimulate the pumping rate. Likewise, an accumulation of K^+ externally occurs and this also stimulates the pump. The K_m value for K^+, i.e. the concentration for half-maximal rate, is about 2 mM. It has been shown that $[K^+]_o$ is significantly increased during the long AP plateau in cardiac muscle.

IVC. Cl^- Distribution

In many nerve and muscle cells, Cl^- ion does not appear to be actively transported; i.e. there is no Cl^- ion pump. In such cases, *Cl^- distributes itself passively* (no energy used) in accordance with E_m. Consequently, E_{Cl} is equal to E_m in a resting cell. For example, in mammalian myocardial cells, Cl^- seems to be close to passive distribution, because $[Cl^-]_i$. is at, or only slightly above, the value predicted by the Nernst equation from the resting E_m (for references, see Sperelakis, 1979). When passively distributed, $[Cl^-]_i$ is low because the negative potential inside the cell (the RP) pushes out the negatively-charged Cl ion (*like charges repel*) until the Cl^- distribution is at equilibrium with the resting E_m. Hence, for a resting E_m of −80 mV and taking $[Cl^-]_o$ to be 100 mM, $[Cl^-]_i$ calculated from the Nernst equation would be 4.9 mM.

$$
\begin{aligned}
E_{\text{Cl}} &= E_m \\
E_m &= +61\ \text{mV} \log \frac{[Cl^-]_i}{[Cl^-]_o} \\
&= -61\ \text{mV} \log \frac{[Cl^-]_0}{[Cl^-]_i} \\
\frac{-80\ \text{mV}}{-61\ \text{mV}} &= \log \frac{100\ \text{mM}}{[Cl^-]_i} \\
\frac{100\ \text{mM}}{[Cl^-]_i} &= \text{antilog} \frac{-80\ \text{mV}}{-61\ \text{mV}} = \text{antilog}\ 1.31 = 20.5 \\
[Cl^-]_i &= \frac{100\ \text{mM}}{20.5} = 4.88\ \text{mM}
\end{aligned}
\tag{9.3}
$$

During the AP, the inside of the cell goes in a positive direction and a net Cl^- influx (outward Cl^- current, I_{Cl}) will occur and thus increase $[Cl^-]_i$. The magnitude of the Cl^- influx depends on the Cl^- conductance (g_{Cl}) of the membrane:

$$I_{Cl} = g_{Cl}(E_m - E_{Cl}) \tag{9.4}$$

The average level of $[Cl^-]_i$ in excitable cells should depend on the frequency and duration of the AP, i.e. the mean E_m averaged over many AP cycles.

In some smooth muscles, $[Cl^-]_i$ is much higher (e.g. 30 mM) than the value of 12.5 mM predicted from passive distribution:

$$E_{Cl} = E_m = -55 \text{ mV}$$

$$[Cl^-]_i = \frac{[Cl^-]_o}{\text{antilog}\dfrac{E_m}{-61 \text{ mV}}}$$

$$= \frac{100 \text{ mM}}{\text{antilog}\dfrac{-55 \text{ mV}}{-61 \text{ mV}}}$$

$$= \frac{100}{7.973}$$

$$= 12.5 \text{ mM}$$

The elevated $[Cl^-]_i$ in smooth muscle could be due to an exchange carrier (e.g. Cl^-—HCO_3^- exchange) or to a co-transporter (e.g. Na^+-K^+-Cl^- transport).

IVD. Ca^{2+} Distribution

IVD1. Need for Calcium Pumps

For the positively-charged Ca^{2+} ion, there must be some mechanism for removing it from the cytoplasm. Otherwise, the cell would continue to gain Ca^{2+} until there was no electrochemical gradient for net influx of Ca^{2+}. Ca^{2+} loading would occur until the free $[Ca^{2+}]_i$ in the cytoplasm was even greater than that outside (ca. 2 mM) because of the negative potential inside the cell. Therefore, there must be one or more Ca^{2+} pumps in operation. The SR (or ER) membrane contains a *Ca^{2+}-activated ATPase* (which requires Mg^{2+} for activity) that actively pumps two Ca^{2+} ions from the cytoplasm into the SR lumen at the expense of one ATP. This pump ATPase is capable of pumping down the Ca^{2+} to less than 10^{-7} M. The Ca^{2+}-ATPase of the SR is regulated by an associated low-molecular-weight protein, *phospholamban*. Phospholamban is phosphorylated by *cyclic-AMP-dependent protein kinase* and, when phosphorylated, stimulates the Ca^{2+}-ATPase and Ca^{2+} pumping (by a derepression process). The sequestration of Ca^{2+} by the SR is essential for muscle relaxation. The mitochondria also can actively take up Ca^{2+} almost to the same degree as the SR, but this Ca^{2+} pool probably does not play an important role in normal excitation—contraction coupling.

The resting Ca^{2+} influx and the extra Ca^{2+} influx that enters with each AP must be returned to the interstitial fluid. Two mechanisms have been proposed for this: (1) a Ca^{2+}-ATPase, similar to that in the SR, is present in the sarcolemma; and (2) a *Ca^{2+}-Na^+ exchange* occurs across the cell membrane. It has been reported that there is a Ca^{2+}-ATPase in the sarcolemma of myocardial cells (Dhalla et al., 1977; Jones et al., 1980) and smooth muscle (Daniel et al., 1977) that actively transports two Ca^{2+} outward against an electrochemical gradient, using one ATP in the process.

IVD2. Ca_i - Na_o Exchange Reaction

The Ca_i - Na_o exchange reaction exchanges one internal Ca^{2+} ion for three external Na^+ ions via a membrane carrier molecule (see Fig. 9.3). This reaction is facilitated by ATP, but ATP is not hydrolyzed (consumed) in this reaction. Instead, the energy for the transport of Ca^{2+} against its large electrochemical gradient comes from the Na^+ electrochemical gradient. That is, the uphill transport of Ca^{2+} is coupled to the downhill movement of Na^+. Effectively, the energy required for this Ca^{2+} movement is derived from the Na^+,K^+-ATPase. Thus, the Na^+- K^+ pump, which uses ATP to maintain the Na^+ electrochemical gradient, indirectly helps to maintain the Ca^{2+} electrochemical gradient. Hence, the inward Na^+ leak is greater than it would be otherwise. A complete discussion of Ca^{2+}-Na^+ exchange is given in a subsequent chapter.

The *energy cost* (ΔG_{Ca}, in joules/mole) for pumping out Ca^{2+} ion is directly proportional to its electrochemical gradient. These energetic equations are as follows (where ΔG is the change in free energy, z is the valence, and F is the Faraday constant):

$$\Delta G_{Ca} = zF(E_m - E_{Ca}) \tag{9.5}$$

The energy available from the Na^+ distribution is directly proportional to its electrochemical gradient.

$$\Delta G_{Na} = zF(E_m - E_{Na}) \tag{9.6}$$

Depending on the exact values of $[Na^+]_i$ and $[Ca^{2+}]_i$ in a muscle cell at rest, the energetics would be about adequate for an exchange ratio of 3 Na^+:1 Ca^{2+}. An exchange ratio of 3:1 would produce a small depolarization due to a net inward flow of current (3 Na^+ in to 1 Ca^{2+} out) via this electrogenic Ca_i^{2+}-Na_o^+ exchanger. That is, there is a net positive charge moving inward for every cycle of the exchanger. This *net exchanger current* can be measured in whole-cell voltage-clamp studies when all ionic currents and Na^+-K^+ pump currents are blocked.

The exchange reaction depends on relative concentrations of Ca^{2+} and Na^+ on each side of the membrane and on

relative affinities of the binding sites to Ca^{2+} and Na^{+}. Because of this exchange reaction, whenever the cell gains Na^{+}, it will also gain Ca^{2+}, because the Na^{+} electrochemical gradient is reduced and the exchange reaction becomes slowed. The Ca_i^{2+}- Na_o^{+} exchange process has been proposed as the mechanism of the *positive inotropic action* (i.e. more forceful contraction) in the heart resulting from cardiac glycoside inhibition of the Na^{+}-K^{+} pump.

In addition, when the myocardial cell membrane is depolarized during the AP plateau, the exchange carriers will exchange the ions in reverse, namely, internal Na^{+} for external Ca^{2+} and thus increase Ca^{2+} influx. The net effect of this mechanism is to elevate $[Ca^{2+}]_i$. Such *reversed* Ca_o^{2+}-Na_i^{+} *exchange* appears to be a significant source of Ca^{2+} for contraction in cardiac muscle of some species.

V. EQUILIBRIUM POTENTIALS

VA. Equivalent Electrical Circuit

The electrical equivalent circuit of the cell membrane at rest is depicted in Fig. 9.4. In Fig. 9.4A, the membrane is indicated as a parallel resistance (R_m) and capacitance (C_m). The capacitance results from the lipid bilayer matrix of the membrane and the resistance or conductance (G_m) results from the protein ion channels floating in the lipid bilayer and spanning across it. The RP is depicted as a battery in series with R_m, with the negative pole facing inside the cell.

In Fig. 9.4B, the equivalent circuit for the resting membrane is shown further expanded, by breaking up the membrane conductance (G_m) into its four component parts, one for each ion of major importance electrophysiologically, namely K^{+}, Cl^{-}, Na^{+} and Ca^{2+}. The respective conductances are g_K, g_{Cl}, g_{Na}, and g_{Ca}. The equilibrium potential (E) for each ion is placed in series with the conductance pathway for that ion, as depicted. The polarity of each battery is as shown; namely, the pole facing inwards is negative for K^{+} and Cl^{-} and positive for Na^{+} and Ca^{2+}. These polarities are based on the directions of the concentration gradients and charge on the ions.

VB. Nernst Equation

For each ionic species distributed unequally across the cell membrane, an equilibrium potential (E_i) or battery can be calculated for that ion from the Nernst equation (for 37°C),

$$E_i = \frac{-RT}{zF} \ln \frac{C_i}{C_o} \tag{9.7a}$$

$$E_i = \frac{-2.303\,RT}{zF} \log \frac{C_i}{C_o} \tag{9.7b}$$

$$E_i = \frac{-61\ \text{mV}}{z} \log \frac{C_i}{C_o} \tag{9.7c}$$

where C_i is the internal concentration of the ion, C_o is the extracellular concentration, R is the gas constant (8.3 J/mol/K), T is the absolute temperature in Kelvins (K = 273+°C), F is the Faraday constant (96 500 Coul/eq), and z is the valence (with sign). Thus, zF = Coul/mol. Taking the RT/F constants and the factor of 2.303 for conversion of natural log (ln), or log to the base of e (2.717), to log to the base of 10 ($\log_{10}$) gives:

$$\frac{-RT}{F} \ln N = \frac{-2.303\,RT}{F} \log N = -61\ \text{mV} \log N \tag{9.7d}$$

Therefore, the Nernst equation (Equation 9.7a) becomes

$$E_i = \frac{-2.303\,RT}{zF} \log \frac{C_i}{C_o} \tag{9.7e}$$

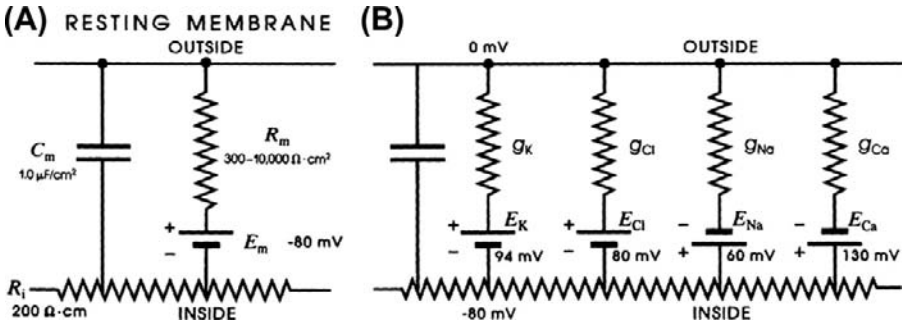

FIGURE 9.4 Electrical equivalent circuits for a cell membrane at rest. (A) Membrane as a parallel resistance-capacitance circuit, the membrane resistance (R_m) being in parallel with the membrane capacitance (C_m). Resting E_m is represented by a −80 mV battery in series with the membrane resistance, the negative pole facing inward. (B) Membrane resistance is divided into its four component parts, one for each of the four major ions of importance: K^{+}, Cl^{-}, Na^{+} and Ca^{2+}. Resistances for these ions (R_K, R_{Cl}, R_{Na} and R_{Ca}) are parallel to one another and represent totally separate and independent pathways for permeation of each ion through the resting membrane. These ion resistances are depicted as their reciprocals, namely, ion conductances (g_K, g_{Cl}, g_{Na}, g_{Ca}). Equilibrium potential for each ion (e.g. E_K), determined solely by the ion distribution in the steady state and calculated from the Nernst equation, is shown in series with the conductance path for that ion. RP of −80 mV is determined by the equilibrium potentials and by the relative conductances.

$$E_i = \frac{-61\ \text{mV}}{z} \log \frac{C_i}{C_o} \tag{9.7f}$$

The −61 mV constant (2.303 *RT/F*) becomes −59mV at 22°C. A derivation of the Nernst equation is given in the Appendix to this chapter. The Nernst equation gives the *potential difference (PD) (electrical force) that would exactly oppose the concentration gradient (diffusion force)*.

Only very small charge separation (*Q*, in coulombs) is required to build a very large PD.

$$E_m = \frac{Q}{C_\text{m}} \tag{9.8}$$

where C_m is the membrane capacitance. This is further discussed in the next section.

For the ion distributions given previously (see Table 9.2), the approximate equilibrium potentials are:

$E_{Na} = +60$ mV
$E_{Ca} = +130$ mV
$E_K = -93$ mV
$E_{Cl} = -80$ mV

The sign of the equilibrium potential represents the inside of the cell with reference to the outside (see Fig. 9.4). Because Na^+ is higher outside (ca. 145 mM) than inside (ca. 15 mM), the positive pole of the Na^+ battery (E_{Na}) is inside the cell. The concentration gradient for Ca^{2+} is in the same direction as for Na^+ (1.8 mM $[Ca^{2+}]_o$ and about 1×10^{-7} M $[Ca^{2+}]_i$,) and so the positive pole of E_{Ca} is inside. K^+ is higher inside (ca. 150 mM) than outside (ca. 4.5 mM) and so the negative pole is inside. Because Cl^- is higher outside (ca. 100 mM) than inside (ca. 5 mM), the negative pole is inside. Voltages are, by convention, given for the inside with respect to the outside.

VC. Concentration Cell

In a concentration cell (essentially a two-compartment system separated by a membrane), the *side of higher concentration becomes negative for cations* (positive ions) and *positive for anions* (negative ions). Any ion whose equilibrium potential is different from the RP (e.g. −80 mV for a myocardial cell or skeletal muscle fiber) is off equilibrium and therefore must effectively be pumped at the expense of energy. In many cell types, only Cl^- ion appears to be at or near equilibrium, whereas Na^+, Ca^{2+} and K^+ are actively transported. Even H^+ ion is off equilibrium, E_H being closer to zero potential (see Table 9.2). If H^+ were passively distributed, the negative intracellular potential would pull in more H^+ ions, causing $[H^+]_i$ to increase, making the cell interior more acidic.

The mechanism for development of the *equilibrium potential* is depicted in Fig. 9.5. To show the development of an equilibrium potential, we can use an artificial membrane (e.g. one made of celloidin) to separate two solutions, i.e. to form a concentration cell. This membrane contains negatively-charged pores, which therefore allows cations (like K^+) to pass through, but prevents anions (like Cl^-) from passing. This is because like charges repel one another and unlike charges attract one another. Therefore, in this particular membrane, K^+ is permeant and Cl^- is impermeant. If one side (side 1) contains a salt like KCl at a concentration higher (e.g. 0.10 M) than that in the other side (side 2) (e.g. 0.01 M), then a steady PD is very quickly built up across the membrane. As calculated from the Nernst equation, for a 10-fold difference in concentration of the permeant monovalent cation (K^+), the PD would be −61 mV at 37°C (or −59 mV at a room temperature of 22°C).

This PD is between the two solutions and expressed across the membrane. Side 1 (side of highest K^+ concentration) becomes negative with respect to side 2. The PD is developed because of the tendency for diffusion (diffusion force) from high concentration to low concentration. This is based on the *random thermal motion* of the ions (particles), somewhat related to *Brownian motion* of larger particles. That is, the side of higher concentration has a *greater probability* of K^+ ions moving from side 1 to side 2 than in the reverse direction, based on the greater number of particles, all moving in random directions. Therefore, there will be a loss of positive charges (K^+ ions) from side 1 and a gain of positive charges in side 2.

Because negative charges (Cl^- ion) cannot accompany the positive charges, as the membrane was made impermeable to anions, a *charge separation* is built up across the membrane. It can now be readily understood why side 1, the side of higher cation concentration, becomes negatively charged (due to loss of positive charges) and why side 2, the side of lower cation concentration, becomes positively charged (due to gain of positive charges). The charge separation is very tiny and they stay plastered very close to the membrane. That is, for the example depicted in Fig. 9.5, side 1 will have the small excess of Cl^- ions held very close to the membrane and side 2 will have the small excess of K^+ ions held very close to the membrane. The force holding them there is called the electrostatic or Coulombic force, based on the attraction between unlike charges. This is related to Coulomb's law and the nature of capacitors.

In the two bulk solutions, the *law of electroneutrality* is upheld; i.e. for every cation (K^+) there is a nearby anion (Cl^-). Thus, the *charge separation* occurs only directly across the membrane and is very tiny with respect to the total number of charges in the two solutions. In fact, after equilibrium is reached (within a few seconds), the most sensitive chemical analyses would fail to detect the very slight decrease in K^+ in side 1 or gain of K^+ on side 2.

Thus, the system comes to equilibrium quickly and with very little charge (K^+ and Cl^-) separation. That is, K^+ does

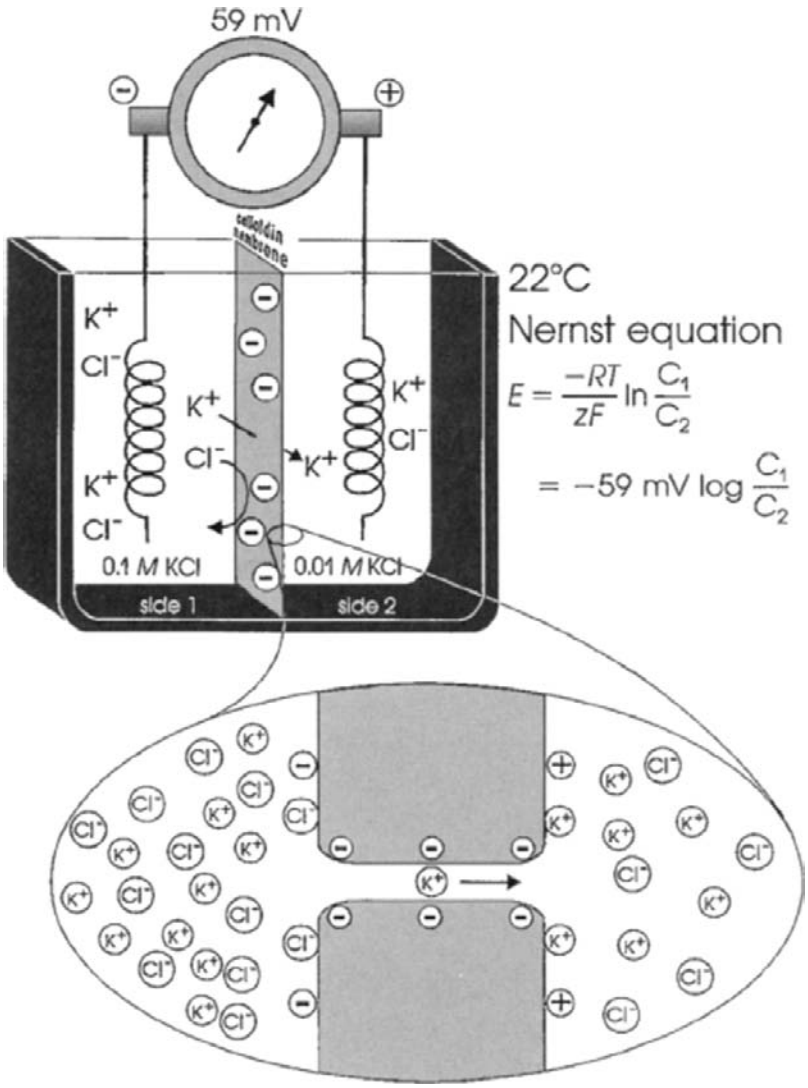

FIGURE 9.5 Upper diagram: concentration cell diffusion potential developed across artificial membrane containing negatively-charged pores. The membrane is impermeable to Cl^- ions, but permeable to cations such as K^+. Concentration gradient for K^+ causes a potential to be generated, the side of higher K^+ concentration becoming negative. Lower diagram: expanded diagram of water-filled pore in the membrane, showing the permeability to K^+ ions, but lack of penetration of Cl^- ions. Potential difference is generated by charge separation, a slight excess of K^+ ions being held close to the right-hand surface of the membrane; a slight excess of Cl^- ions is aggregated close to the left surface.

not continue to have a net movement from side 1 to side 2 until the concentrations become equal. Why not? The answer is that the *small charge separation produces a large PD* across the membrane and this PD is in such a polarity that it antagonizes further net movement of K^+ from side 1 to side 2. That is, the positive voltage that is developing on side 2 repels the positively-charged K^+ ions because like charges repel. At equilibrium, these two forces become equal and opposite and there is no further net movement of ions. Unidirectional fluxes of K^+ ions would still occur (because of their random thermal motion), but these would be equal and opposite and so no further *net flux* would occur.

In the example selected, KCl was used. However, any salt, such as NaCl, $CaCl_2$ or Na_2SO_4, could have been illustrated. If a divalent cation like Ca^{2+} were used, then from the Nernst equation, the same 10-fold concentration gradient would develop a potential of only half, namely 30.5 mV (37°C) or 29.5 mV (22°C). The reason that this factor is half, rather than double as one might guess from the fact that the charge is double, is that the Nernst equation gives the PD that exactly opposes the diffusion force due to the concentration gradient, as stated in the paragraph above. Therefore, because the charge is double, only half the voltage is necessary to oppose effectively the concentration force. If the cation in question were trivalent, such as La^{3+}, then the 2.303 *RT*/*zF* factor would be one-third of 61 mV, or about 20.3 mV. It is for this reason that it is convenient to give the Nernst equation in the form shown in Equation 9.7c, namely with the factor (at 37°C) being $-61 \text{ mV}/z$. This allows easy calculation of the equilibrium potential for an ion of any charge and sign (polarity).

That is, the sign and charge should be used, for example, +1 for K^+ or Na^+, +2 for Ca^{2+} and −1 for Cl^-. When the ion in question is an anion like Cl^-, then $-1/-1$ gives a plus (+). Because $[Cl^-]_o > [Cl^-]_i$, this concentration ratio can be

inverted by changing the sign of the 2.30 *RT/zF* factor back to negative (−). That is, changing the sign of the factor in front of a log ratio simply inverts the ratio.

Finally, if the concentration cell depicted in Fig. 9.5 were made with a membrane that had positively-charged pores, then everything would be reversed. The membrane would be permeable to Cl^- and impermeable to K^+ and E_{Cl} would be +59 mV (at 22°C) and +61 mV (at 37°C). Again, the voltage is given for side 1 with respect to side 2. Thus, in dealing with an anion, the side of higher concentration becomes positive (due to a small loss of Cl^-) and the side of lower concentration becomes negative (due to a small gain of Cl^-). The separated charges again are plastered very close to the membrane: K^+ ions on side 1 and Cl^- ions on side 2.

VD. Activity Coefficient

Thus, an equilibrium potential can be calculated for any species of ion that is distributed unequally across a membrane. All that one needs to know are the concentrations in the two solutions and the charge (and temperature). Actually, we should use the *activity* (*a*) of the ion in question in the two solutions, instead of concentration. Thus, the Nernst equation given in Equation 9.7c becomes (for K^+, for example):

$$E_K = \frac{-61\text{ mV}}{+1}\log\frac{a_K^i}{a_K^o}$$

The activity of an ion (in molar) can be obtained by multiplying the concentration of the ion (in molar) by the activity coefficient (γ) for the ion:

$$a = c \cdot \gamma \tag{9.9}$$

In the biological case, the activity coefficients are relatively close to 1.0 (e.g. 0.7−0.9) for Na^+, K^+ and Cl^- in *both* the extracellular and intracellular solutions. Therefore, in these cases, using the concentrations gives a good approximation. However, in the case of Ca^{2+}, the activity coefficient in the intracellular solution especially is substantially lower and so this would affect the calculated value of E_{Ca}.

VE. Nernst−Planck Equation

The basic Nernst equation has been modified in several ways for special situations. For example, in the concentration cell depicted in Fig. 9.5, a cell in which a single salt (both ions of same valence) is distributed across the membrane at two different concentrations, the PD developed across the membrane (E_m) can be calculated from the equation:

$$E_m = \frac{U_c - U_a}{U_c + U_a}\frac{-61\text{ mV}}{z}\log\frac{[\text{salt}]_1}{[\text{salt}]_2} \tag{9.10}$$

where $[salt]_1$ and $[salt]_2$ are the concentrations of the salt on side 1 and side 2 and U_c and U_a are the *mobilities* of the cations and anions, respectively, through the membrane. Thus, when the mobilities (or permeabilities) of the cation and anion are equal ($U_c = U_a$), E_m is zero, regardless of the equilibrium potentials. When the anion is impermeable ($U_a = 0$), the mobility fraction in Equation 9.10 becomes 1.0 and the equation reduces to the simple Nernst equation. When the cation is impermeable ($U_c = 0$), the fraction becomes −1.0 and the same numerical value of E_m is produced, but of opposite sign. Equation 9.10 can be used to calculate E_m for any combination of U_a and U_c. For example, if $U_a = 0.5\ U_c$, then for the problem illustrated in Fig. 9.5, E_m would be about −20 mV (side 1 negative). Thus, the membrane potential is related to the relative mobilities.

VF. Energy Wells

Ions do not just "fall" through a water-filled pore in the membrane (protein ion channel) down an electrochemical gradient. Instead, an ion may bind to several charged sites on its journey through the channel pore. The K^+ ion depicted in the bottom of Fig. 9.5, for example, is shown as binding to three negatively-charged sites within the pore. These may be considered energy wells and the ion must gain kinetic energy to become dislodged from this energy well to pass over the next *energy barrier* and into the next energy well. This energy comes from the ion being hit by another ion just entering the pore, producing a billiard-ball effect. Some evidence for this model was presented in Chapter 8, which discusses the Ussing flux ratio equation.

From the measured value of the conductance of single ion channels (e.g. 20 pS, range of 10−300 pS), how many ions that pass through a single channel per second can be estimated. This number is about 6 000 000 ions/s. Therefore, the average transit time for a single ion to cross the membrane (50−70 Å thick) is about 0.17 μs.

VI. ELECTROCHEMICAL DRIVING FORCES AND MEMBRANE IONIC CURRENTS

VIA. Electrochemical Driving Forces

The electrochemical driving force for each species of ion is the algebraic difference between its equilibrium potential, E_i, and the membrane potential, E_m. The total driving force is the sum of two forces: an electrical force (the negative potential in a cell at rest tends to pull in positively-charged ions, because unlike charges attract) and a diffusion force (based on the concentration gradient) (Fig. 9.6); i.e.:

$$\text{driving force} = E_m - E_i \tag{9.11a}$$

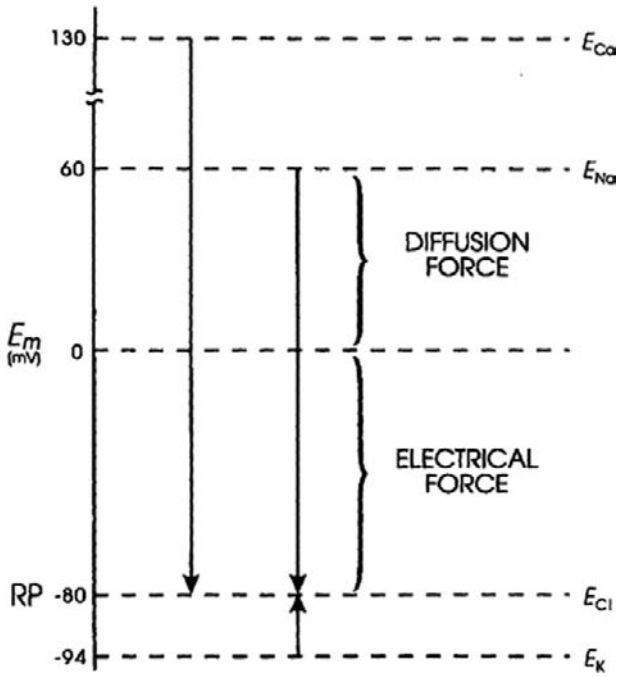

FIGURE 9.6 Representation of the electrochemical driving forces for Na^+, Ca^{2+}, K^+, and Cl^-. Equilibrium potentials for each ion (e.g. E_{Na}) (calculated from the Nernst equation for their extracellular and intracellular concentrations) are positioned vertically according to their magnitude and sign. Measured RP is assumed to be −80 mV. Electrochemical driving force for an ion is the difference between its equilibrium potential (E_i) and the membrane potential (E_m), i.e. (E_m−E_i). Thus, at rest, the driving force for Na^+ is the difference between E_{Na} and the resting E_m. If E_{Na} is +60 mV and resting E_m is −80 mV, the driving force is 140 mV. That is, the driving force is the algebraic sum of the diffusion force and the electrical force and is represented by the length of the arrows in the diagram. Driving force for Ca^{2+} (about 210 mV) is even greater than that for Na^+, whereas that for K^+ is much less (about 14 mV). Direction of the arrows indicates the direction of the net electrochemical driving force, namely, the direction for K^+ is outward, whereas that for Na^+ and Ca^{2+} is inward. If Cl^- is passively distributed, then its distribution across the cell membrane is determined by the net membrane potential. For a cell sitting a long time at rest, $E_{Cl} = E_m$ and there is no net driving force.

Thus, in a resting cell, the driving force for Na^+ is:

$$(E - E_{Na}) = -80\ \text{mV} - (+60\ \text{mV}) = -140\ \text{mV} \tag{9.11b}$$

The negative sign means that the driving force is directed to bring about net movement of Na^+ inward. The driving force for Ca^{2+} is very large and is directed inward:

$$(E_m - E_{Ca}) = -80\ \text{mV} - +129\ \text{mV}) = -209\ \text{mV} \tag{9.11c}$$

The driving force for K^+ is:

$$(E_m - E_K) = -80\ \text{mV} - (-94\ \text{mV}) = +14\ \text{mV} \tag{9.11d}$$

Hence, the driving force for K^+ is small and directed outward. The driving force for Cl^- is nearly zero for a cell at rest in which Cl^- is passively distributed (e.g. neuron, myocardial cell, skeletal muscle fiber); i.e.:

$$(E_m - E_{Cl}) = -80\ mV - (-80\ \text{mV}) = 0 \tag{9.12}$$

However, during the AP, when E_m is changing, the driving force for Cl^- becomes large and there is a net driving force for inward Cl^- movement (Cl^- influx is an outward Cl^- current). Similarly, the driving force for K^+ outward movement increases during the AP, whereas those for Na^+ and Ca^{2+} decrease.

VIB. Membrane Ionic Currents

The net current for each ionic species (I_i) is equal to its *driving force* times its *conductance* (g_i, reciprocal of the resistance) through the membrane. This is essentially Ohm's law:

$$I = \frac{V}{R} = g \cdot V \tag{9.13}$$

Ohm's law must be modified to reflect the fact that, in an electrolytic system, the total force tending to drive net movement of a charged particle must take into account both the electrical force and the concentration (or chemical) force. Thus, for the four ions, the net current can be expressed as:

$$I_{Na} = g_{Na}(E_m - E_{Na}) \tag{9.14}$$

$$I_{Ca} = g_{Ca}(E_m - E_{Ca}) \tag{9.15}$$

$$I_K = g_K(E_m - E_K) \tag{9.16}$$

$$I_{Cl} = g_{Cl}(E_m - E_{Cl}) \tag{9.17}$$

In a resting cell, Cl^- and Ca^{2+} can be neglected and the Na^+ current (inward) must be equal and opposite to the K^+ current (outward) to maintain a steady resting potential:

$$I_K = -I_{Na} \tag{9.18a}$$

$$g_K(E_m - E_K) = -g_{Na}(E_m - E_{Na}) \tag{9.18b}$$

Thus, although in the resting membrane the driving force for Na^+ is much greater than that for K^+, g_K is much larger than g_{Na}, so the currents are equal. Hence, there is a continuous leakage of Na^+ inward and K^+ outward, even in a resting cell, and the system would run down if active pumping were blocked. Because the ratio of the Na^+ to K^+ driving forces (−140 mV/−14 mV) is 10, the ratio of conductances (g_{Na}/g_K) will be about 1:10. The fact that g_K is much greater than g_{Na} accounts for the RP being close to E_K and far from E_{Na}.

VII. DETERMINATION OF RESTING POTENTIAL AND NET DIFFUSION POTENTIAL (E_{diff})

VIIA. Determining Factors

For given ion distributions, which normally remain nearly constant under usual steady-state conditions, the resting potential (RP) is determined by the *relative membrane conductances (g)* or *permeabilities (P)* for Na^+ and K^+ ions. That is, the RP (of about −80 mV in cardiac muscle or skeletal muscle) is close to E_K (about −94 mV) because $g_K >> g_{Na}$ or $P_K >> P_{Na}$. There is a direct proportionality between P and g at constant E_m and concentrations. From simple circuit analysis (using Ohm's law and Kirchhoff's laws), one can prove that the membrane potential will always be closer to the battery (equilibrium potential) having the lowest resistance (highest conductance) in series with it (see Figs. 9.4 and 9.6). In the resting membrane, this battery is E_K, whereas in the excited membrane it will be E_{Na} (or E_{Ca}), because there is a large increase in g_{Na} and/or g_{Ca} during the AP.

Any ion that is passively distributed cannot determine the RP; instead, the RP determines the distribution of that ion. Therefore, Cl^- is not considered for myocardial cells, skeletal muscle fibers and neurons because it seems to be passively distributed. However, transient net movements of Cl^- across the membrane do influence E_m; e.g. washout of Cl^- (in Cl^--free solution) produces a transient depolarization and reintroduction of Cl^- produces a transient hyperpolarization. Cl^- movement is also involved in the production of inhibitory postsynaptic potentials (IPSPs) (see chapter on synaptic transmission).

Because of its relatively low concentration, coupled with its relatively low resting conductance, the Ca^{2+} distribution has only a relatively small effect on the resting E_m and can be ignored.

VIIB. Constant-Field Equation

A simplified, but most useful, version of the Goldman–Hodgkin–Katz constant-field equation can be given (for 37°C):

$$E_m = -61 \text{ mV} \log \frac{[K^+]_i + \frac{P_{Na}}{P_K}[Na^+]_i}{[K^+]_o + \frac{P_{Na}}{P_K}[Na^+]_o} \qquad (9.19)$$

This equation shows that for a given ion distribution, the resting E_m is determined by the P_{Na}/P_K ratio, the *relative permeability* of the membrane to Na^+ and K^+. For myocardial cells and skeletal muscle fibers, the P_{Na}/P_K ratio is about 0.04, whereas for nodal cells of the heart and smooth muscle cells, this ratio is closer to 0.10 or 0.20.

Inspection of the constant-field equation shows that the numerator of the log term will be dominated by the $[K^+]$ term [since the (P_{Na}/P_K) $[Na^+]_i$ term will be very small], whereas the denominator will be affected by both the $[K^+]_o$ and (P_{Na}/P_K) $[Na^+]_o$ terms. This relationship thus accounts for the deviation of the E_m versus log $[K^+]_o$ curve from a straight line (having a slope of 61 mV/decade) in normal Ringer solution (Fig. 9.7). When $[K^+]_o$ is elevated ($[Na^+]_o$ being reduced by an equimolar amount), the denominator becomes more and more dominated by the $[K^+]_o$ term and less and less by the (P_{Na}/P_K) $[Na^+]_o$ term. Therefore, in bathing solution containing high K^+, the constant-field equation approaches the simple Nernst equation for K^+ and E_m approaches E_K. As $[K^+]_o$ is raised stepwise, E_K becomes correspondingly reduced, because $[K^+]_i$ stays relatively constant; therefore, the membrane becomes more and more depolarized (see Fig. 9.7). Sometimes, however, some hyperpolarization is produced at a $[K^+]_o$ level between 5 and 9 mM. In addition, lowering $[K^+]_o$ to 0.1 mM often produces a prominent depolarization. These effects are usually explained on the basis that: (1) P_K is reduced in low $[K^+]_o$; and (2) an electrogenic Na^+-K^+ pump potential is inhibited at a low $[K^+]_o$ (K_m of about 2 mM).

A more detailed discussion of the constant-field equation is given in the Appendix to this chapter.

When $[K^+]_o$ is elevated (e.g. to 8 mM) in some types of cells, a hyperpolarization of up to about 10 mV may be produced. Such behavior is often observed in cells with a high P_{Na}/P_K ratio (due to low P_K) and therefore a low resting E_m, such as in young embryonic chick hearts. This hyperpolarization could be explained by several factors: (1) stimulation of the electrogenic Na^+ pump current (I_p); (2) an increase in P_K (and therefore g_K) due to $[K^+]_o$ effect on P_K; and (3) an increase in g_K (but not P_K) due to the concentration effect. A similar explanation may apply to the fall-over in the E_m versus log $[K^+]_o$ curve when $[K_o]$ is lowered to 1 mM and less, hence depolarizing the cells. This effect is prominent in rat skeletal muscle, for example (see Fig. 7 of chapter on skeletal muscle excitability).

VIIC. Chord Conductance Equation

An alternative method of approximating the membrane resting potential (E_m) is the chord conductance equation. The word *chord* means a straight line connecting two points on a curve, and here specifically refers to the *average slope* of a non-linear steady-state voltage–current curve, i.e. a straight line from any point on the curve through the origin (zero applied current). (In contrast, slope conductance is the tangent at any point on the curve.) Thus:

$$E_m = \frac{g_K}{\sum g} E_K + \frac{g_{Na}}{\sum g} E_{Na} + \frac{g_{Cl}}{\sum g} E_{Cl} + \frac{g_{Ca}}{\sum g} E_{Ca} \qquad (9.20a)$$

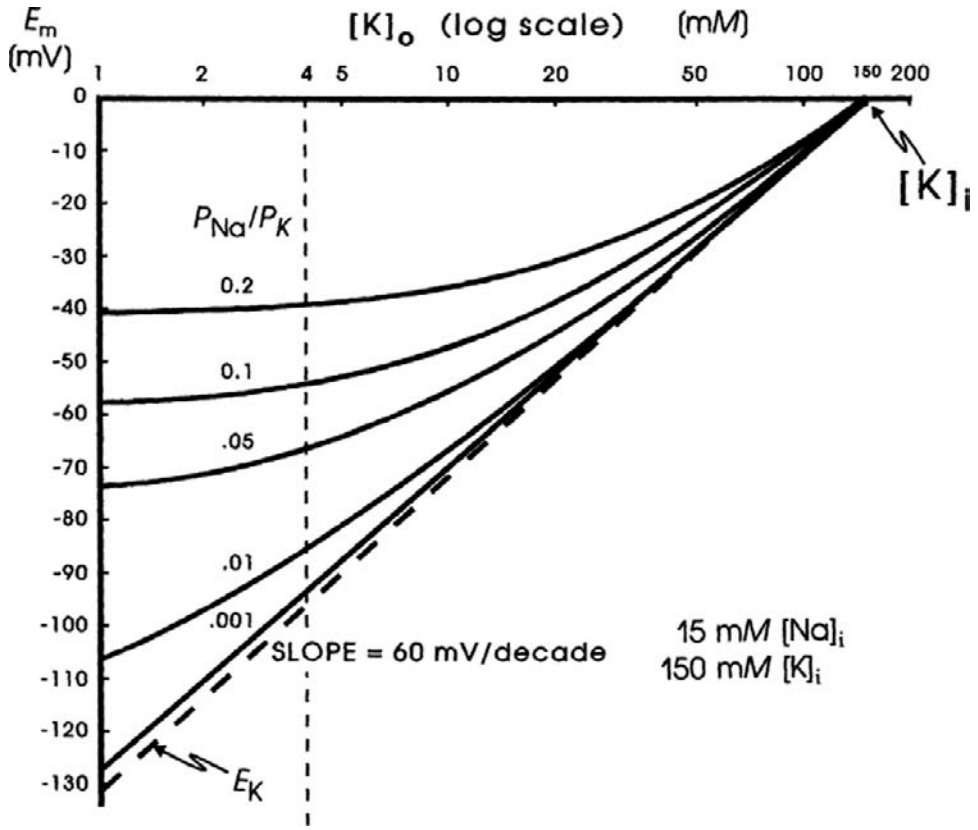

FIGURE 9.7 Theoretical curves calculated from the Goldman constant-field equation for RP (E_m) as a function of $[K^+]_o$. Family of curves is given for various P_{Na}/P_K ratios (0.001, 0.01, 0.05, 0.1 and 0.2). K^+ equilibrium potential (E_K) calculated from the Nernst equation (broken straight line). Curves calculated for a $[K^+]_i$ of 150 mM and a $[Na^+]_i$ of 15 mM. Calculations made holding $[K^+]_o + [Na^+]_o$ constant at 154 mM; i.e. as $[K^+]_o$ was elevated, $[Na^+]_o$ was lowered by an equimolar amount. Possible change in P_K as a function of $[K^+]_o$ was ignored. Point at which E_m is zero gives $[K^+]_i$. The potential reverses in sign when $[K^+]_o$ exceeds $[K^+]_i$.

where g_K, g_{Na}, g_{Cl}, and g_{Ca} are the membrane conductances for K^+, Na^+, Cl^-, and Ca^{2+}, respectively, and Σg is the total conductance (sum of all ionic partial conductances). The ratio of $g_K/\Sigma g$, for example, is the *relative* or *fractional conductance* for K^+.

The chord conductance equation can conveniently take into account all ions, including divalent cations, that are distributed unequally across the membrane. The ions important to membrane potentials (including APs, postsynaptic potentials and receptor potentials) are K^+, Na^+, Cl^- and Ca^{2+}. As discussed previously, Cl^- cannot help in determining the RP if it is passively distributed. Thus, Equation 9.20a can be rewritten, omitting the Cl^- term, as:

$$E_m = \frac{g_K}{\sum g} E_K + \frac{g_{Na}}{\sum g} E_{Na} + \frac{g_{Ca}}{\sum g} E_{Ca} \qquad (9.20b)$$

For simplicity, we can ignore the Ca^{2+} term also, giving:

$$E_m = \frac{g_K}{g_K + g_{Na}} E_K + \frac{g_{Na}}{g_K + g_{Na}} E_{Na} \qquad (9.20c)$$

where Σg is now equal to $g_K + g_{Na}$.

The chord conductance equation can be derived simply from Ohm's law and from circuit analysis for the condition when net current is zero ($I_{Na} + I_K = 0$). (See the Appendix to this chapter for the derivation.) The equation holds true whenever the net current across the membrane is zero, as for the RP.

The chord conductance equation is useful for giving the membrane potential when the ion conductances and distributions are known. For example, at the neuromuscular junction, the neurotransmitter acetylcholine opens the gates of many ionic channels that allow both Na^+ and K^+ to pass through equally well (i.e. $g_{Na} = g_K$). Hence, the potential that the postsynaptic membrane tends to seek when maximally activated (i.e. the equilibrium potential or so-called *reversal potential* for the end-plate potential, EPP) is:

$$E_{EPP} = \frac{1}{2}(-94\text{ mV}) + \frac{1}{2}(+60\text{ mV}) = -17\text{ mV} \qquad (9.20d)$$

A disadvantage of the chord conductance equation is that it gives nearly a straight line for the E_m versus log

$[K^+]_o$ plot (actually a slight bend in the opposite direction at low $[K^+]_o$). In contrast, the constant-field equation gives the complete bending of the curves (for different P_{Na}/P_K ratios).

The chord conductance equation again illustrates the important fact that the g_K/g_{Na} ratio determines the RP. When $g_K \gg g_{Na}$, then E_m is close to E_K; conversely, when $g_{Na} \gg g_K$ (as during the spike part of the AP), E_m shifts to close to E_{Na} or to E_{Ca} (in the case of smooth muscle cells).

The chord conductance equation can be rewritten using resistances instead of conductances and may then be called the *chord resistance equation*:

$$E_m = \frac{R_K}{R_K + R_{Na}} E_{Na} + \frac{R_{Na}}{R_K + R_{Na}} E_K \qquad (9.20e)$$

where R_K and R_{Na} are the K^+ and Na^+ resistances, which are the reciprocals of the conductances. Note that, in this equation, the positions of the two batteries are interchanged. This equation can be derived by simply substituting the two reciprocals into the chord conductance equation. It can also be derived by circuit analysis, as discussed in the Appendix to this chapter. This Appendix section also shows how circuit analysis can be used to determine what the RP should be, without using either the Goldman constant-field equation or the chord conductance equation.

VIID. Net Diffusion Potential, E_{diff}

In the presence of ouabain (short-term exposure only) to inhibit the Na^+-K^+ pump and V_p, the RP that remains reflects the net diffusion potential, E_{diff}. E_{diff} is determined by the ion concentration gradients for K^+ and Na^+ and by the relative permeability for K^+ and Na^+. When the Na^+-K^+ pump is operating, there is normally a small additional contribution of V_p to the resting E_m of about 2−16 mV, depending on cell type (discussed in the following section).

Inhibition of the Na^+-K^+ pump for long periods will gradually run down the ion concentration gradients. The cells lose K^+ and gain Na^+ and therefore E_K and E_{Na} become smaller. The cells thus become depolarized (even if the relative permeabilities were unaffected), which causes them to gain Cl^- (because $[Cl]_i$ was held low by the large resting potential), and therefore, to also gain water (cells swell).

VIII. ELECTROGENIC SODIUM PUMP POTENTIALS

A brief summary of the previous principles is as follows: the Na^+−K^+ pump is responsible for maintaining the cation concentration gradients. The equilibrium potentials for K^+ (E_K) and Na^+ (E_{Na}) are about −94 mV and +60 mV, respectively. The RP value is usually near E_K, because the K^+ permeability (P_K) is much greater than P_{Na} in a resting membrane. The exact resting membrane potential (E_m) depends on the P_{Na}/P_K ratio, myocardial cells and skeletal muscle fibers having P_{Na}/P_K ratios of 0.01−0.05, whereas smooth muscle or nodal cells of the heart have a ratio closer to 0.10−0.15. In the various types of cells, the resting E_m has a smaller magnitude (i.e. is less negative) than E_K by 10−40 mV. If there were no *electrogenic pump potential* contribution to the RP (i.e. as though the Na^+-K^+ pump was only indirectly responsible for the RP by its role in producing the ionic gradients), E_m would equal E_{diff}.

However, a direct contribution of the pump to the resting E_m can be demonstrated. For example, if the Na^+-K^+ pump is blocked by the addition of ouabain, there usually is an immediate depolarization of 2−16 mV, depending on the type of cell. Thus, the direct contribution of the electrogenic Na^+-K^+ pump to the measured resting E_m is small under physiologic conditions (but very important).

However, under conditions in which the pump is stimulated to pump at a high rate (e.g. when $[Na^+]_i$ or $[K^+]_o$ is abnormally high), the direct electrogenic contribution of the pump to the RP can be much greater and E_m can actually exceed E_K by as much as 20 mV or more. For example, if the ionic concentration gradients are allowed to run down (e.g. by storing the tissues in zero $[K^+]_o$ and at low temperatures for several hours), then after the tissues are allowed to restart pumping, the measured E_m can exceed the calculated E_K (e.g. by 10−20 mV) for a time (Fig. 9.8). The Na^+ loading of the cells is facilitated by placing them in cold low or zero $[K^+]_o$ solutions, because external K^+ is necessary for the Na^+-K^+-linked pump to operate; K_m of the Na^+,K^+-ATPase for K^+ is about 2 mM. After several hours in such a solution, the internal concentrations of Na^+, K^+ and Cl^- approach the concentrations in the bathing Ringer solution and the RP is very low (<−30 mV).

The cells are then transferred to a pumping solution, which is the appropriate Ringer solution containing normal K^+ and at normal temperature. Under such conditions, the pump turns over at a maximal rate, because the major control over pump rate is $[Na^+]_i$ and $[K^+]_o$. The low initial E_m also stimulates the pump rate, because the energy required to pump out Na^+ is less. The measured E_m of such Na^+ preloaded cells increases rapidly and more rapidly than E_K, as shown in Fig. 9.8. After this transient phase, however, a crossover of the two curves occurs, so that E_K again exceeds E_m, as in the physiologic condition. Cardiac glycosides prevent or reverse the transient hyperpolarization beyond E_K. The possibility that ionic conductance changes (e.g. an increase in g_K or a decrease in g_{Na}) can account for the observed hyperpolarization, can be ruled out whenever E_m exceeds (is more negative than) E_K.

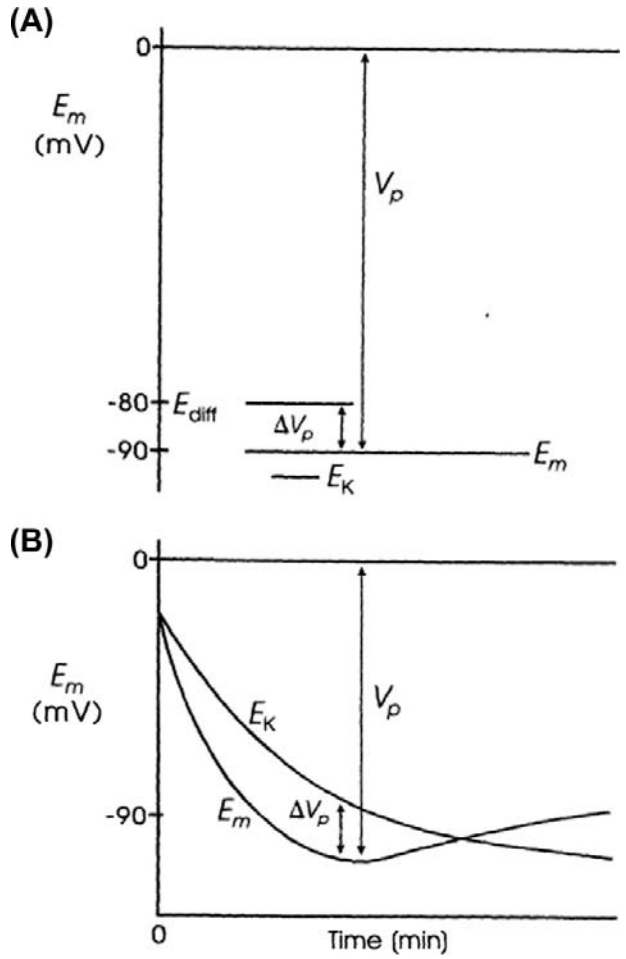

FIGURE 9.8 Diagrammatic representation of an electrogenic sodium pump potential. (A) Muscle fiber in which the net ionic diffusion potential (E_{diff}, function of ion equilibrium potentials and relative conductances) is −80 mV, yet exhibits a measured RP (E_m) that is greater. Difference between E_m and E_{diff} represents the contribution of the electrogenic pump to the RP. The electrogenic pump potential must be equal to V_p. The contribution of the electrogenic pump potential to the RP ($E_m - E_{diff}$) is equal to ΔV_p. (B) Fiber that was run down (Na^+ loaded, K^+ depleted) over several hours by inhibition of Na^+-K^+ pumping, resulting in a low RP. Returning the fiber to a pumping solution allows the resting E_m to rebuild as a function of time. Buildup in E_m occurs faster than buildup in E_K, as illustrated.

Rewarming cells previously cooled leads to the rapid restoration of the normal RP (within 10 min), whereas recovery of the intracellular Na^+ and K^+ concentrations is slower. During prolonged hypoxia, the RP of cardiac muscle decreases much less than E_K decreases (a difference of about 25 mV). This is because the electrogenic pump attempts to hold the RP constant, despite dissipating ionic gradients.

Another method used to demonstrate that the pump is electrogenic is to inject Na^+ ions into the cell through a micropipette. This procedure rapidly produces a small transient hyperpolarization, which is prevented by ouabain. The *pump current* and the rate of Na^+ extrusion increase in proportion to the amount of Na^+ injected. To prove that the pump is electrogenic, it must be demonstrated that the hyperpolarization produced in an intact muscle is not the result of enhanced pumping of an electroneutral pump. This could cause depletion of external K^+ in a restricted diffusion space just outside the cell membrane, leading to a larger E_K and thereby to hyperpolarization. Depletion could occur if the Na^+-K^+ pump pumped in K^+ faster than it could be replenished by diffusion from the bulk interstitial fluid.

The electrogenic Na^+ pump is influenced by the membrane potential. From energetic considerations, depolarization should enhance the electrogenic Na^+ pumping, whereas hyperpolarization should inhibit it. This is because depolarization reduces the electrochemical gradient (and hence the energy requirements) against which Na^+ must be extruded, whereas hyperpolarization increases the gradient. Thus, there should be a distinct potential, more negative than E_K, at which Na^+ pumping is prevented (e.g. a *pump equilibrium potential*). A value close to −140 mV was reported for cardiac cells and rat skeletal muscle fibers.

Any method used to increase membrane resistance increases the contribution of the pump to the RP (Fig. 9.9). That is, the electrogenic Na^+ pump contribution is augmented under conditions that increase membrane resistance. The contribution of the pump potential to the measured E_m is the difference in E_m when the pump is operating versus that immediately after the pump has been stopped by the addition of ouabain or zero $[K^+]_o$. Consequently, it appears as though the contribution from the electrogenic pump potential (ΔV_p) is in series with the net cationic diffusion potential (E_{diff}):

$$E_m = E_{diff} + R_m I_p = E_{diff} + \Delta V_p \qquad (9.21)$$

where I_p is the electrogenic component of the pump current and E_{diff} is the E_m that would exist solely on the basis of the ionic gradients and relative permeabilities in the absence of an electrogenic pump potential. Equation 9.21 states that E_m is the sum of E_{diff} and a voltage (IR) drop produced by the electrogenic pump current across R_m. The electrogenic pump potential (V_p) can be considered to be in parallel with E_{diff} (see Fig. 9.9). Because the *density of pump sites* is more than a 1000-fold greater than that of Na^+ and K^+ channels in resting membrane, there is no relation between the pump pathway (the active flux path) and R_m (the passive flux paths); i.e. the pump path and the passive conductance paths are in parallel. The pump potential should be considered the full potential between zero and the maximum negative pump potential (V_p) while the pump is pumping (see Fig. 9.8).

One possible equivalent circuit for an electrogenic Na^+ pump that takes into account some of the known facts is

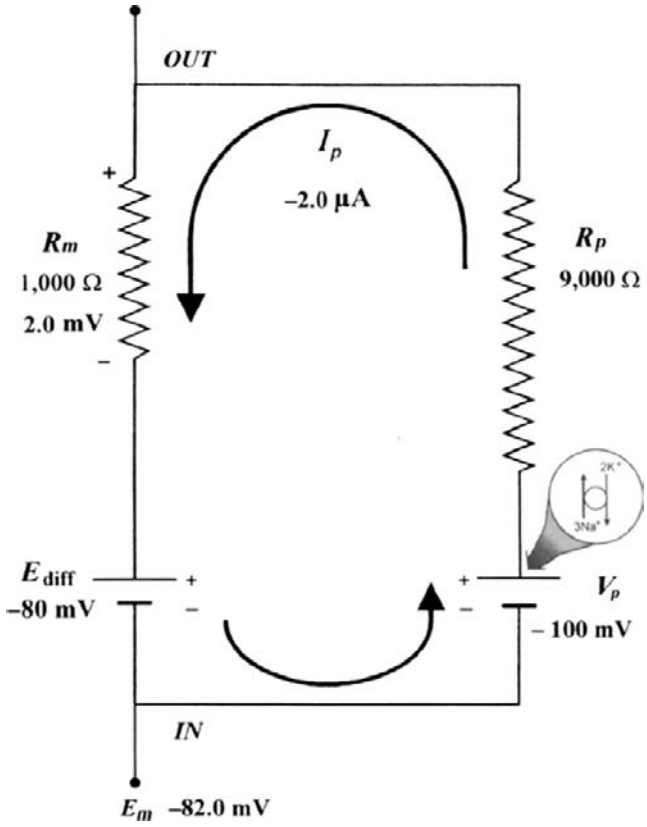

FIGURE 9.9 Hypothetical electrical equivalent circuit for electrogenic sodium pump. Model consists of a pump pathway in parallel with the membrane resistance (R_m) pathway. This model fits the evidence that the pump proteins and channel proteins are embedded in the lipid bilayer as parallel elements. Net diffusion potential (E_{diff}, determined by the ion equilibrium potentials and relative permeabilities) of −80 mV is depicted in series with R_m. Pump leg is assumed to consist of a battery in series with a fixed resistor (pump resistance, R_p) that does not change with changes in R_m and whose value is about ninefold higher than R_m. Pump battery is charged up to some voltage (e.g. V_p of −100 mV) by a pump current generator. Net electrogenic pump current is developed by the pumping in of only two K^+ ions for every three Na^+ ions pumped out. For the values given in the figure (namely, R_m of 1000 Ω, E_{diff} of −80 mV, R_p of 9000 Ω, and V_p of −100 mV), circuit analysis shows that the measured membrane potential (E_m) is −82.0 mV: i.e. the direct electrogenic pump potential contribution to the RP is −2.0 mV. The calculated pump current (I_p) is −2.0 µA.

given in Fig. 9.9. The pump pathway is in parallel with the resistance pathways. The pump resistance (R_p) is estimated to be about ninefold higher than R_m. If so, the pump resistance acts to minimize a short-circuit path to E_{diff} when the pump potential is low or zero (pump inhibited). The pump potential contribution to E_m (ΔV_p) is a function of membrane resistance (R_m); the higher the R_m (R_p constant), the more nearly E_m approaches V_p. The pump battery is charged to some voltage by a pump current generator. If the pump is stopped by ouabain, V_p goes to zero. Using circuit analysis for the values of the parameters given in Fig. 9.9, E_m would be −82.0 mV, moderately close to E_{diff} (−80 mV) (Table 9.3). If R_m is raised twofold (to 2000 Ω), E_m would be −83.6 mV. Thus, this circuit clearly gives a pump potential contribution to E_m that is dependent on R_m. The higher R_m is relative to R_p, the more E_m reflects V_p. If E_{diff} is made smaller (e.g. in smooth muscle cells having a higher P_{Na}/P_K ratio), then the relative contribution of the pump potential to E_m becomes greater (see Table 9.3).

In general, Cl^- ions are known to have a "short-circuiting" effect on the electrogenic Na^+ pump potential. For example, if the external Cl^- is replaced by less permeant anions, the magnitude of the hyperpolarization produced by the electrogenic Na^+ pump is substantially increased. This Cl^- effect could be caused by the lowering of membrane resistance in the presence of Cl^-. The greater the R_m, the greater the contribution of the electrogenic pump potential to resting E_m (see Fig. 9.9 and Table 9.3).

The density of Na^+-K^+ pump sites, estimated by specific binding of [^{3}H]ouabain, is usually about 700−1000/µm^2. The turnover rate of the pump is generally estimated to be 20−100/s. The *pump current* (I_p) has been estimated as:

$$I_p = \frac{\Delta V_p}{R_m} \tag{9.22}$$

where ΔV_p is the pump potential contribution. Values of about 20 pmol/(cm^2/s) were obtained. A density of 1000 sites/µm^2 (10^{11} sites/cm^2) times a turnover rate of 40/s gives 4×10^{12} turnovers/(cm^2/s). If three Na^+ are pumped with each turnover, this gives 12×10^{12} Na^+ ions/(cm^2/s); dividing by Avogadro's number (6.02×10^{23} ions/mol) yields 20×10^{-12} mol/(cm^2/s), which is the same value as the 20 pmol/(cm^2/s) measured. The net pump current would be less, depending on the amount of K^+ pumped in the opposite direction, i.e. depending on the coupling ratio (e.g. 3 Na^+:2 K^+). Whenever the Na^+-K^+ pump is stimulated to turn over faster, e.g. by increasing $[Na^+]_i$ or $[K^+]_o$, the electrogenic pump current is increased.

Ion flux (J) can be converted to current (I) by the relationship:

$$I = J \cdot zF$$
$$\frac{\text{A}}{\text{cm}^2} = \frac{\text{mol}}{\text{s}\cdot\text{cm}^2}\,\frac{\text{C}}{\text{mol}} \tag{9.23}$$

Thus, a flux of 20 pmol/(cm^2/s) is equal to approximately 2 µA/cm^2 (20×10^{-12} mol/(s/cm^2)$\times0.965\times10^5$ coul/mol). Since $\Delta V_p = I_p \times R_m$, if R_m were 1000 Ω/cm^2 and I_p were 2 µA/cm^2, the electrogenic pump contribution to E_m would be 2 mV ($E_m = E_{diff} + I_p R_m$).

Two K^+ ions are usually carried in for every three Na^+ ions moved out. Because the pump is electrogenic, i.e. produces a net current (and hence potential) across the membrane, then the amount of K^+ pumped in must be less

TABLE 9.3 Summary of Calculations of Resting Potential (E_m) for a Model Having an Electrogenic Pump Potential (V_p) in Parallel with Net Diffusion Potential (E_{diff}), as Depicted in Figure 9.9

E_{diff} mV	R_m Ω	V_p mV	I_p μA	V_{rev} mV	ΔV_p mV	RP mV
−80	1000	−100	−2.0	+18	−2.0	−82
−80	2000	−100	−1.82	−16.4	−3.64	−83.6
−80	1000	0	+8.0	−72	+8.0	−72
−50	1000	−100	−5.0	+45	−5.0	−55
−50	2000	−100	−4.55	+40.9	−9.1	−59.1
−50	1000	0	+5.0	−45	+5.0	−45

Pump resistance, R_p, was assumed to have constant value of 9000 Ω. R_m, membrane resistance; ΔV_p contribution of V_p to the measured E_m. E_m was calculated from the equation $E_m = \left(\frac{R_m}{R_m + R_p}\right) V_p + \left(\frac{R_p}{R_m + R_p}\right) E_{diff}$.

than the amount of Na^+ pumped out; e.g. the Na^+/K^+ coupling ratio must be 3:2 (or 3:1). The coupling ratio cannot be 3:0, because of the well-known fact that external K^+ must be present for the pump to operate. The coupling ratio might be increased under some conditions, e.g. when $[Na^+]_i$ is elevated. If the coupling ratio were to increase (e.g. to 3:1), the pump potential contribution would become larger, for a constant pumping rate.

The pump current may be stimulated by increasing the *turnover rate* of each pump site or by increasing the *number of pump sites*. In skeletal muscle, insulin has been reported to increase the number of Na^+-K^+ pump sites in the sarcolemma by increasing the rate of translocation from an internal pool, thereby increasing the pump current. β-Adrenergic agonists, like isoproterenol, stimulate the pump current by cyclic AMP/protein kinase-A phosphorylation of the pump.

The electrogenic pump potential has *physiologic importance* in cells. Although small, the electrogenic pump potential contribution to the RP could have significant effects on the level of inactivation of the fast Na^+ channels and hence on propagation velocity. Further, an electrogenic pump potential could act to delay depolarization under adverse conditions (e.g. ischemia and hypoxia) and would act to speed repolarization of the normal RP during recovery from the adverse conditions. It is crucial that the excitable cell maintain its normal RP as much as possible, because of the effect of small depolarizations on the AP rate of rise and conduction velocity and the complete loss of excitability with larger depolarizations. For example, the rate of firing of pacemaker nodal cells of the heart is affected significantly by very small potential changes.

In cells in which there are lower RPs (e.g. smooth muscle cells and cardiac nodal cells), the electrogenic pump potential contribution can be larger (see Table 9.3). *Sinusoidal oscillations in the Na^+-K^+ pumping rate* could produce oscillations in E_m, which could exert important control over the spontaneous firing of the cell. The period of enhanced pumping hyperpolarizes the cell and suppresses automaticity, whereas slowing of the pump leads to depolarization and consequently to triggering of APs. Oscillation of the pump rate would be brought about by oscillating changes in $[Na^+]_i$. For example, the firing of several APs should raise $[Na^+]_i$ (these cells have a small volume to surface area ratio) and stimulate the electrogenic pump. The increased pumping rate, in turn, hyperpolarizes and suppresses firing, thus allowing $[Na^+]_i$ to decrease again and removing the stimulation of the pump; the latter condition depolarizes and triggers spikes and the cycle is repeated. In rabbit sinoatrial nodal cells, it was concluded that the electrogenic Na^+ pump is one factor that modulates the heart rate under physiologic conditions. When stimulated at a high rate, cardiac Purkinje fibers and nodal cells undergo a transient period of inhibition of automaticity after cessation of the stimulation, known as *overdrive suppression of automaticity*. Stimulation of the electrogenic pump due to elevation in $[Na^+]_i$ is the major cause of this phenomenon.

APPENDIX

AI. MORE DETAILS ON Ca^{2+}-Na^+ EXCHANGER

The ratio of free energy changes for Na^+ to Ca^{2+} was calculated for a coupling ratio of 3 Na^+:1 Ca^{2+} ($3\,\Delta G_{Na}/\Delta G_{Ca}$) and a $[Na^+]_i$ of 15 mM, and plotted as a function of membrane potential, for different $[Ca^{2+}]_i$ levels

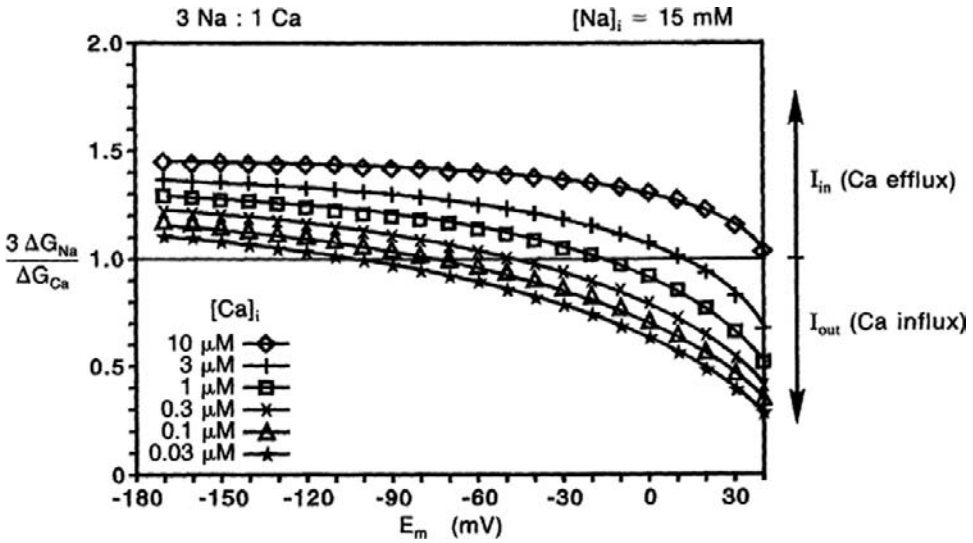

FIGURE 9A.1 Electrogenic Na^+-Ca^{2+} exchange for $[Na^+]_i$ of 15 mM for a coupling ratio of 3 Na^+:1 Ca^{2+}. Calculated ratio of the free energies for Na^+ versus Ca^{2+} ($3\,\Delta G_{Na}/\Delta G_{Ca}$) plotted as a function of membrane potentials (E_m) for six different intracellular Ca^{2+} concentrations ($[Ca^{2+}]_i$). At a ratio of 1.0, $3\,\Delta G_{Na} = -\Delta G_{Na}$ and the sum equals zero: $3\,\Delta G_{Na} + \Delta G_{Ca} = 0$. Therefore, the exchange would be at equilibrium at the E_m value at which each curve crosses the ratio of 1.0 line; i.e. this gives the value of the exchanger equilibrium potential, $E_{Na\text{-}Ca}$. At ΔG ratios >1.0, there is a net inward current carried by Na^+ ion, coupled with net Ca^{2+} efflux from the cell. This represents the forward mode of operation of the exchanger. At ΔG ratios <1.0, there is a net outward current carried by Na^+ ion, coupled with net Ca^{2+} influx into the cell. This reflects the reverse mode of operation of the exchanger.

(Fig. 9A.1). This plot allows an assessment of how the directionality of the exchanger is affected by E_m, i.e. *forward mode* versus *reverse mode* of operation, and how the reversal potential of the exchanger is shifted by $[Ca^{2+}]_i$. When the ratio is 1.0, $3\Delta G_{Na} = -\Delta G_{Ca}$ and the sum equals zero: $3\,\Delta G_{Na} + -\Delta G_{Ca} = 0$. Therefore, the exchanger would be at equilibrium. For ΔG ratios >1.0, there is a net inward current carried by Na^+ ion, coupled with net Ca^{2+} efflux from the cell. This represents forward mode of operation of the exchanger. For ΔG ratios <1.0, there is a net outward current carried by Na^+ ion, coupled to a net Ca^{2+} influx into the cell. This represents reverse mode of operation of the exchanger.

The *equilibrium potential* or *reversal potential* for the Ca^{2+}-Na^+ exchanger ($E_{Na\text{-}Ca}$), for an exchange ratio of 3 Na^+:1 Ca^{2+} is:

$$E_{Na-Ca} = 3E_{Na} - 2E_{Ca} \qquad (9A.1)$$

where E_{Na} and E_{Ca} are the equilibrium potentials for Na^+ and Ca^{2+}, respectively, as calculated from the Nernst equation. Thus, the $E_{Na\text{-}Ca}$ varies during changes in the $[Ca^{2+}]_i$ level that occurs with contraction.

Therefore, when a myocardial cell changes from the RP (ca. −80 mV) to the AP plateau (ca. +20 mV), simultaneous with $[Ca^{2+}]_i$ being elevated from about 0.1 to 3 μM, the exchanger switches to reverse mode of operation, with Ca^{2+} influx. As stated previously, this Ca^{2+} influx can be a significant source of the total Ca^{2+} influx during excitation−contraction coupling.

AII. DERIVATION OF NERNST EQUATION

The Nernst equation may be derived from the general equation for the free energy change (ΔG_c) resulting from both osmotic work and electrical work for transporting 1 mole of cation (c^+) across a membrane. Thus:

$$\Delta G_c = RT \ln \frac{[c^+]_i}{[c^+]_o} + zFE_m \qquad (9A.2)$$

where R is the gas constant (8.3 joule/mole-°K); T is absolute temperature (°K = 273+°C); $[c^+]_i$ and $[c^+]_o$ are the internal and external c^+ concentrations, respectively; z is the valence (equiv/mol); F is the Faraday constant (96 500 coul/equiv); and E_m is membrane potential. The first term on the right side of this equation, RT ln ($[c+]_i/[c+]_o$), gives the osmotic work for transporting one mole of particles across the membrane against a concentration gradient. The second term, zFE_m, gives the electrical work for transporting one mole of charged particles across the membrane against an electrical gradient. The sum of these two terms then gives the total work required. At equilibrium, the change in free energy for moving one or only a few particles across the membrane must be zero ($\Delta G = 0$). Therefore:

$$0 = RT \ln \frac{[c^+]_i}{[c^+]_o} + zFE_m \qquad (9A.3a)$$

and

$$zFE_m = -RT \ln \frac{[c^+]_i}{[c^+]_o} \qquad (9A.3b)$$

or

$$E_m = \left(\frac{-RT}{zF}\right) \ln \frac{[c^+]_i}{[c^+]_o} \qquad (9A.3c)$$

which is the Nernst equation.

Since the Faraday constant (F) is equal to the charge on an electron (e, in coulombs) times Avogadro's number (N_A, number of ions per mole), then:

$$\frac{RT}{F} = \frac{RT}{N_A Q_e} = \frac{kT}{Q_e} \qquad (9A.4)$$

where k (the Boltzmann constant) is equal to the gas constant (R) divided by Avogadro's number (N_A), i.e. the energy (in joules) of an ion per °kelvin; and Q_e is the charge (in coulombs) on an electron (namely, 1.6×10^{-19} coul/e$^-$).

AIII. HALF-CELL POTENTIALS

In measuring biological potentials, care must be taken not to introduce artifacts, such as half-cell potentials. This section will give a brief description of electrode half-cell potentials. For example, if two beakers containing NaCl at 0.1 and 0.01 M were joined by a salt bridge (agar-NaCl) and if an Ag-AgCl half-cell electrode were placed in each beaker, then a PD of 59 mV would be recorded between the two electrodes, because the potential of each half-cell, reversible to Cl^- ions, would be different (Fig. 9A.2). In this example, the beaker containing the higher Cl^- concentration would be negative and the one with the lower Cl^- concentration would be positive. The AgCl coat of the electrode immersed in the lower Cl^- concentration would have the greater tendency to solubilize and ionize, leaving this electrode positive. Conversely, the AgCl coat of the electrode immersed in the higher Cl^- concentration would have the lower tendency to solubilize and actually would tend to deposit more AgCl, stealing a positive charge from the wire and thus leaving that electrode negatively charged. A positive potential is applied to electroplate the Ag wires with AgCl by electrophoresing Cl^- to the Ag wire, as shown in Fig. 9.A2.

Note that the RP recorded in biological cells by an intracellular microelectrode is not a function of the half-cell potentials (i.e. an artifact), because the solutions bathing the half-cells (e.g. Ag-AgCl wires or calomel half-cells) remain constant; i.e. the half-cell potentials stay the same whether the microelectrode is inside or outside the cell. The two half-cell potentials are nearly equal in magnitude and so cancel each other. Any small amount of difference between the two half-cell potentials (e.g. a few millivolts) when the two electrodes are in the same Ringer's solution is arbitrarily called the zero potential. (In practice, with the microelectrode in position, any small microelectrode tip potential, e.g. up to 5 mV, would be included in the zeroing procedure.) The RP of the cell is added in series with the half-cell potential, and thus the recording system gives the true transmembrane RP.

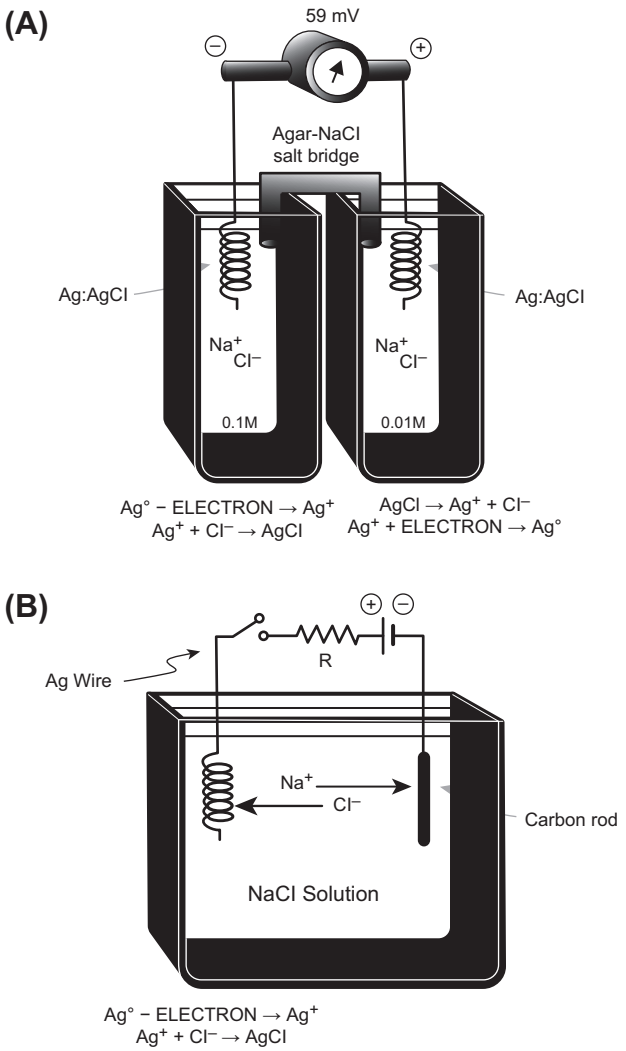

FIGURE 9A.2 Reversible half-cell electrode potentials. (A) Two Ag-AgCl half-cell electrodes are bathed in two different solutions containing Cl^- ion at different concentrations (0.1 and 0.01 M). The Ag-AgCl half-cells are reversible to Cl^- and therefore the half-cell potential depends on the Cl^- concentration in which the electrode is bathed. Therefore, the two half-cell potentials are not equal to one another and their potentials do not cancel out, as is normally true. There is a net PD produced by the two unequal half-cell potentials, the electrode in the higher Cl^- concentration being negative and the electrode in the lower Cl^- concentration being positive. The two solutions are connected by an agar salt bridge to complete the circuit. (B) For electroplating a silver wire electrode with AgCl, the silver wire must be made positive so that Cl^- ions can be electrophoresed through the solution to react with silver atoms to plate AgCl.

AIV. CONSTANT-FIELD EQUATION DETAILS

An important modification of the Nernst equation in common use for calculating the membrane potential, or for

determining the P_{Na}/P_K ratio, is the Goldman–Hodgkin–Katz constant-field equation (Goldman, 1943; Hodgkin and Katz, 1949):

$$E_m = \frac{-RT}{F} \ln \frac{P_K[K^+]_i + P_{Na}[Na^+]_i + P_{Cl}[Cl^-]_o}{P_K[K^+]_o + P_{Na}[Na^+]_o + P_{Cl}[Cl^+]_i} \quad (9A.5a)$$

where P_K, P_{Na} and P_{Cl} are the membrane permeabilities for K^+, Na^+ and Cl^-, respectively. The $P_K\,[K^+]_i$ product, for example, is given in the units of a flux (mol/s per cm^2), but the entire right-hand term (fraction) is dimensionless. Plugging in the numerical values for the constants and converting from natural logarithm (ln) to logarithm to the base 10 (log): ln N=2.303 log N gives:

$$E_m = -61 \text{ mV} \log \frac{P_K[K^+]_i + P_{Na}[Na^+]_i + P_{Cl}[Cl^-]_o}{P_K[K^+]_o + P_{Na}[Na^+]_o + P_{Cl}[Cl^+]_i} \quad (9A.5b)$$

and E_m is expressed in mV. Dividing the right-hand term by P_K gives:

$$E_m = -61 \text{ mV} \log \frac{[K^+]_i + \frac{P_{Na}}{P_K}[Na^+]_i + \frac{P_{Cl}}{P_K}[Cl^-]_o}{[K^+]_o + \frac{P_{Na}}{P_K}[Na^+]_o + \frac{P_{Cl}}{P_K}[Cl^-]_i} \quad (9A.6)$$

Again, the right-hand term (fraction) is dimensionless. Any ion that is passively distributed, i.e. not actively pumped, however, cannot determine the RP, because the distribution of that ion must follow the RP. Therefore, when Cl^- is passively distributed, it is not considered because RP cannot be determined by Cl^-. As a result, Equation 9A.6 can be reduced to:

$$E_m = -61 \text{ mV} \log \frac{[K^+]_i + \frac{P_{Na}}{P_K}[Na^+]_i}{[K^+]_o + \frac{P_{Na}}{P_K}[Na^+]_o} \quad (9A.7)$$

Equation 9A.7 is one of the most useful forms of the constant-field equation, because if E_m is measured and if the internal and external ion concentrations are known, the P_{Na}/P_K ratio can be calculated. Thus, for given ionic gradients, the RP is determined by the P_{Na}/P_K ratio (i.e. the relative permeabilities of the cell membrane to Na^+ and K^+) and not by the absolute permeabilities. For simplicity, Ca^{2+} is ignored here as a factor contributing to the RP. The relationship between the permeability coefficient for an ion (P_i) and the membrane conductance for that ion (g_i) is complex, involving several terms including membrane potential.

Figure 9.8 gives the expected RP as a function of the P_{Na}/P_K ratio for a muscle fiber (having a $[K^+]_i$ of 150 mM) bathed in normal Ringer's solution ($[K^+]_o$ of 4.5 mM, $[Na^+]_o$ of 150 mM), assuming an $[Na^+]_i$ value of 15 mM. As can be seen, a P_{Na}/P_K ratio of 0.1 gives a RP close to −60 mV, whereas a ratio of 0.01 gives a potential close to −85 mV. Some muscle cells (e.g. smooth muscle and young embryonic chick myocardial cells) have a low RP of about −55 mV, because of a high P_{Na}/P_K ratio of about 0.15 (rather than smaller ionic gradients). The P_{Na}/P_K ratio can be high because of either a high P_{Na} or a low P_K, or both; in most cases the main reason is a low P_K.

One advantage the constant-field equation has over the chord-conductance equation is that it nicely accounts for the bend at low $[K^+]_o$ in the E_m versus log $[K^+]_o$ curves (see Fig. 9.8). As can be seen in Fig. 9.8, which presents theoretical curves calculated from Equation 9A.7, the higher the P_{Na}/P_K ratio, the greater the deviation from a straight line as $[K^+]_o$ is lowered. As mentioned previously, from this equation one can deduce that as $[K^+]_o$ is lowered and $[Na^+]_o$ is concomitantly elevated, the denominator of the right-hand term becomes more and more dominated by the Na^+ term, for any given P_{Na}/P_K ratio. Because the numerator is relatively fixed, E_m is more influenced by E_{Na} as $[K^+]_o$ is lowered more and more. Thus, this relationship accounts for the deviation from the straight line for E_K.

Although the $P_{Na}/P_K = 0.05$ curve is almost linear at high $[K^+]_o$ with a slope of 60 mV/decade, the membrane does not become "purely K^+-selective" as is often stated in textbooks because, for these theoretical calculations, the P_{Na}/P_K ratio was held constant over the entire $[K^+]_o$ range. There is some evidence, however, that P_K itself increases as $[K^+]_o$ increases, but this effect was not taken into consideration in Fig. 9.8. g_K is a function of $[K^+]_o$, namely, $g_K \propto P_K\,[K^+]_o$. Finally, the increased bending for the higher P_{Na}/P_K ratios can again be seen from Equation 9A.7; at a given $[K^+]_o$ (e.g. 4 mM), the denominator is more and more dominated by the Na^+ term as the P_{Na}/P_K ratio is increased more and more.

The order of selectivity of the resting membrane for the alkali metal ions generally is in the following sequence, from the highest permeability to the lowest: $K^+ > Rb^+ > Cs^+ > Na^+ > Li^+$. For example, the relative permeabilities (assigning $P_K = 1$) in squid giant axon (Baker et al., 1968) are:

$$\begin{array}{ccccccccc} P_K & > & P_{Rb} & > & P_{Cs} & > & P_{Na} & > & P_{Li} \\ 1.0 & & 0.69 & & 0.19 & & 0.17 & & 0.12 \end{array} \quad (9A.8)$$

In frog sartorius (Mullins, 1961) the values are:

$$\begin{array}{ccccccc} P_K & > & P_{Rb} & > & P_{Cs} & > & P_{Na} \\ 1.0 & & 0.54 & & 0.11 & & 0.04 \end{array} \quad (9A.9)$$

So far in our discussion, Ca^{2+} has been ignored. It can be demonstrated that Ca^{2+} has only a negligible effect on the RP, regardless of its P value. This is because of the relatively low extracellular and intracellular concentration of free Ca^{2+} ion compared with K^+ and Na^+ ions.

A modified version of the Goldman constant-field equation, which includes a Ca^{2+} term, is:

$$E_m = -60\,\text{mV}\log\frac{(B-A)+\sqrt{y}}{2(A-4P_{Ca}[Ca^{2+}]_i)} \qquad (9A.10)$$

(This equation was kindly provided by Professor D.E. Goldman.)
where

$$A = P_K[K^+]_i + P_{Na}[Na^+]_i$$

$$B = P_K[K^+]_o + P_{Na}[Na^+]_o$$

$$y = (B-A)^2 + 4\,(A + 4P_{Ca}[Ca^{2+}]_i)(B + 4P_{Ca}[Ca^{2+}]_o)$$

For simplification, the analogous Cl^- terms in the definition of A and B have been omitted, assuming Cl^- to be passively distributed.

Calculations made from Equation 9A.10 demonstrate some interesting points: (1) for the same permeabilities ($P_{Ca} = P_{Na}$), Ca^{2+} has much less effect on E_m than does Na^+, because of the lower Ca^{2+} concentrations and because of the square root function for the Ca^{2+} concentrations. For example, the depolarization produced by taking into account the Ca^{2+} ion is only +0.4 mV for a P_{Na}/P_K ratio of 0.1. (2) Even when P_{Ca} is set to 10 times P_{Na}, the effect of Ca^{2+} on the RP is still relatively small (e.g.+3.5 mV for a P_{Na}/P_K ratio of 0.01 and +8.0 mV for a P_{Na}/P_K ratio of 0.1). (3) The effect of Ca^{2+} is somewhat greater when the P_{Na}/P_K ratio is higher (as in cardiac nodal cells or smooth muscle). (4) The effect of Ca^{2+} is considerably less at high $[K^+]_o$ values.

Thus, these calculations indicate that Ca^{2+} can be virtually ignored in discussion of the ionic basis of the RP. This agrees with the well-known fact that variation in $[Ca^{2+}]$ throughout a relatively wide range has a negligible effect on the RP (see Sperelakis, 1972). Further, these facts have implications about the relative importance of Na^+ versus Ca^{2+} background currents (inward) during genesis of the pacemaker potential (concomitant with the decrease in g_K and I_K). Finally, it should be emphasized that, for example, if $P_{Ca} = P_K$, then g_{Ca} does not equal g_K, because of the concentration differences. To calculate g_K from a given P_K, one must use the appropriate equation that takes into account the concentrations and membrane potential.

AV. DERIVATION OF CHORD CONDUCTANCE EQUATION

Ohm's law states that the current (I) is equal to the voltage (E) either divided by the resistance (R) or multiplied by the conductance (g = 1/R):

$$I = \frac{E}{R} = gE \qquad (9A.11)$$

When dealing with solutions, the voltage or driving force must take into account both the concentration force and the electrical force. In this case, the ionic current (I_i) is a product of the conductance for a given ion times the total driving force on that ion ($E_m - E_i$) and so may be expressed as:

$$I_i = g_i(E_m - E_i) \qquad (9A.12)$$

In a resting cell membrane (stable RP), the total ionic current must be zero; otherwise, the membrane potential would change. Therefore, the K^+ current in the outward direction (I_K) must be equal and opposite to the Na^+ current (I_{Na}) entering the cell (neglecting Ca^{2+}, Cl^- and minor ions) expressed as:

$$I_K = -I_{Na} \qquad (9A.13a)$$

Therefore,

$$I_K + I_{Na} = 0 \qquad (9A.13b)$$

Substituting the equations for ionic currents from Equation 9A.12,

$$g_K(E_m - E_K) + g_{Na}(E_m - E_{Na}) = 0 \qquad (9A.14)$$

Algebraic manipulations give:

$$\begin{aligned} 0 &= g_K E_m - g_K E_K + g_{Na} E_m - g_{Na} E_{Na} \\ g_K E_m + g_{Na} E_m &= g_K E_K - g_{Na} E_{Na} \\ E_m(g_K + g_{Na}) &= g_K E_K + g_{Na} E_{Na} \end{aligned} \qquad (9A.15)$$

Rearrangement gives

$$E_m = \frac{g_K}{g_K + g_{Na}} E_K + \frac{g_{Na}}{g_K + g_{Na}} E_{Na} \qquad (9A.16)$$

Equation 9A.16 is the chord conductance equation. The ratios $g_K/(g_K+g_{Na})$ and $g_{Na}/(g_K+g_{Na})$ are the *fractional conductances* (relative) and are dimensionless.

If Cl^- were to be included, one would get:

$$E_m = \frac{g_K}{\sum g} E_K + \frac{g_{Na}}{\sum g} E_{Na} + \frac{g_{Cl}}{\sum g} E_{Cl} \qquad (9A.17)$$

where $\Sigma g = g_K + g_{Na} + g_{Cl}$. However, if Cl^- is passively distributed (in equilibrium at the resting E_m), then Cl^- cannot be involved in determining the RP. (However, transient movements of Cl^- do affect the membrane potential when Cl^- is shifted off equilibrium during an AP or postsynaptic potential.)

On the other hand, the Ca^{2+} ion is actively transported and is off equilibrium, so its conductance influences the RP. The chord conductance equation containing the Ca^{2+} term is:

$$E_m = \frac{g_K}{\sum g} E_K + \frac{g_{Na}}{\sum g} E_{Na} + \frac{g_{Ca}}{\sum g} E_{Ca} \qquad (9A.18)$$

where $\sum g = g_K + g_{Na} + g_{Ca}$

The chord conductance equation, of course, can be written using resistances rather than conductances. For Equation 9A.16 using only K^+ and Na^+ terms, substitution of $R = 1/g$ in the equation and algebraic manipulation gives the equation:

$$E_m = \frac{R_K}{R_K + R_{Na}} E_{Na} + \frac{R_{Na}}{R_K + R_{Na}} E_K \qquad (9A.19)$$

Note that the E_{Na} and E_K terms are interchanged from the chord conductance equation. This form of the equation is the *chord resistance equation*.

The chord conductance equation applies only to those situations in which the net ionic current is zero, such as when the membrane is at rest. This equation is derived simply from Ohm's law and one advantage it has over the constant-field equation is that it can more easily include divalent cations such as Ca^{2+}.

AVI. CIRCUIT ANALYSIS APPLICABLE TO CELL MEMBRANE

Using Ohm's and Kirchhoff's laws and logic, it is possible to see why in the nerve or muscle cell, the K^+ battery dominates the RP, whereas the Na^+ or Ca^{2+} batteries dominate the peak of the AP. The circuit in Fig. 9A.3 will be used to show that the battery having the lowest resistance in series with it is the battery that is the most expressed across the network. Before analyzing the circuit rigorously, we can consider three conditions and make some qualitative judgments: (1) If the left resistor (R_1) equals the right resistor (R_2) (regardless of their absolute values), the PD across the network is +150 V (upper terminal positive with respect to the lower terminal), i.e. halfway between both batteries because both should be equally expressed. (2) If R_2 is made infinite (e.g. open circuit in branch 2) and R_1 is finite, then the PD is exactly +100 V, since the right battery (E_2) cannot be expressed at all. (3) If R_1 is much less than R_2, then the PD approaches +100 V, because E_1 is dominant.

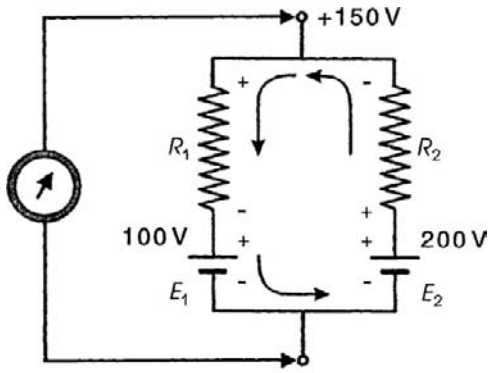

FIGURE 9A.3 Circuit diagram of the circuit analysis applicable to the cell membrane, showing why the RP of a cell is determined by the relative permeabilities (or conductances). Battery having the lowest resistance in series with it is the battery most expressed across such a network.

The circuit in Fig. 9A.3 can also be analyzed quantitatively. For example, if $R_1 = 10\,\Omega$ and $R_2 = 990\,\Omega$, the exact PD may be obtained from the following analysis. The current (I) has one magnitude; i.e. it is constant throughout this closed circuit, but the current flows upward in branch 2 and downward in branch 1. This occurs because the right battery (E_2) is larger than E_1, and so the net driving force for the net current is in the direction as indicated in Fig. 9A.3. Therefore, the voltage drops produced across R_1 and R_2 are in opposite polarities, as shown. The voltage drop across R_1 adds to E_1 to make a greater PD across branch 1, like two batteries in series (+ −, + −). In contrast, the voltage drop across R_2 subtracts from E_2 to make a smaller PD, like two batteries back to back (− +, + −). Therefore, the following two equations can be written for the PD across branch 1 (PD_1) and across branch 2 (PD_2):

$$(PD)_1 = E_1 - IR_1 \qquad (9A.20)$$

$$(PD)_2 = E_2 - IR_2 \qquad (9A.21)$$

To solve these equations, we must first calculate the current (I). The net driving force for I is equal to $E_2 - E_1$; hence from Ohm's law, the net current is equal to ($E_2 - E_1$) divided by the total resistance ($R_1 + R_2$):

$$I = \frac{E_2 - E_1}{R_2 + R_1}$$

$$I = \frac{200\text{ V} - 100\text{ V}}{990\,\Omega + 10\,\Omega} \qquad (9A.22)$$

$$= \frac{100\text{ V}}{1000\,\Omega} = 0.1\text{ A}$$

Now we can enter this value for I into Equation 9A.20

$$(PD)_1 = E_1 - IR_1$$

$$= 100\text{ V} - (-0.1\text{ A})\,(10\,\Omega)$$

$$= 100\text{ V} - (-1\text{ V})$$

$$= 100\text{ V} + 1\text{ V}$$

$$= 101\text{ V}$$

The negative sign in the current is because the current in branch 1 produces a voltage drop that adds to E_1. Because

the two branches are connected by zero resistances, they are effectively the same point and:

$$(\mathrm{PD})_1 = (\mathrm{PD})_2 \tag{9A.23}$$

Therefore, we can also calculate the PD by substituting into Equation 9A.21.

$$\begin{aligned}(\mathrm{PD})_2 &= E_2 - IR_2\\ &= 200\ \mathrm{V} - (+0.1\mathrm{A})(990\ \Omega)\\ &= 200\ \mathrm{V} - (99\ \mathrm{V})\\ &= 101\ \mathrm{V}\end{aligned}$$

Thus, the two methods check.

To summarize, it has been quantitatively demonstrated that the battery with the lowest series resistance is the battery most expressed across this network. This analysis holds true regardless of the absolute values of the resistances or batteries or the polarity of each battery. Other methods of circuit analysis can be used to calculate the PD across such a network, but this method is one of the simplest.

The following chord resistance equation can also be used to calculate the PD across the network:

$$\begin{aligned}\mathrm{PD} &= \frac{R_1}{R_1+R_2}E_2 + \frac{R_2}{R_1+R_2}E_1\\ &= \frac{10\ \Omega}{10\ \Omega + 990\ \Omega}200\ \mathrm{V} + \frac{990\ \Omega}{10\ \Omega + 990\ \Omega}100\ \mathrm{V}\\ &= \frac{10}{1000}200\ \mathrm{V} + \frac{990}{1000}100\ \mathrm{V}\\ &= 2\ \mathrm{V} + 99\ \mathrm{V}\\ &= 101\ \mathrm{V}\end{aligned} \tag{9A.24}$$

This equation again emphasizes the point that it is the relative resistances that determine which battery is most expressed.

BIBLIOGRAPHY

Baker, P. F. (1968). Nervous conduction: some properties of the ion selective channels which appear during the action potential. *Br Med Bull, 24*, 179–182.

Daniel, E. E., Kwan, C. Y., Matlib, M. A., Crankshaw, D., & Kidwai, A. (1977). Characterization and Ca^{2+}-accumulation by membrane fractions from myometrium and artery. In R. Casteels, T. Godfraind, & J. C. Ruegg (Eds.), *Excitation-Contraction Coupling in Smooth Muscle* (pp. 181–188). Amsterdam: Elsevier-North-Holland.

Dhalla, N. S., Ziegelhoffer, A., & Hazzow, J. A. (1977). Regulatory role of membrane systems in heart function. *Can J Physiol Pharmacol. 55*, 1211–1234.

Goldman, D. E. (1943). Potential, impedance, and rectification in membranes. *J Gen Physiol, 27*, 37–60.

Hodgkin, A. L., & Katz, B. (1949). The effect on sodium ions in electrical activity of the giant axon of the squid. *J Physiol (London), 108*, 37–77.

Jain, M. K. (1972). *The Bimolecular Lipid Membrane: a System*. New York: Van Nostrand.

Jones, I. R., Maddock, S. W., & Besch, H. R., Jr. (1980). Unmasking effect of alamethicin on the (Na^+, K^+)-ATPase, beta-adrenergic receptor-coupled adenylate cyclase, and cAMP-dependent protein kinase activities of cardiac sarcolemmal vesicles. *J Biol Chem, 255*, 9971–9980.

Mullins, L. J. (1961). The macromolecular properties of excitable membranes. *Ann NY Acad Sci, 94*, 390–404.

Sperelakis, N. (1972). (Na^+, K^+)-ATPase activity of embryonic chick heart and skeletal muscles as a function of age. *Biochim Biophys Acta, 266*, 230–237.

Sperelakis, N. (1979). Origin of the cardiac resting potential. In R. M. Berne, & N. Sperelakis (Eds.), *Handbook of Physiology, Vol. 1, the Cardiovascular System* (pp. 187–267). Bethesda, MD: American Physiological Society.

This page intentionally left blank

Chapter 10

Gibbs–Donnan Equilibrium Potentials

Nicholas Sperelakis

Chapter Outline

I. SUMMARY

A Gibbs–Donnan (G-D) equilibrium becomes established and a G-D potential is developed across the cell membrane of cells under conditions in which metabolism and energy production have been inhibited or the Na^+-K^+ pump has been inhibited by digitalis. The G-D equilibrium occurs because of the large impermeant charged macromolecules, such as proteins, inside the cell. The G-D equilibrium does not require energy for its establishment, i.e. it is passive. This contrasts with the normal resting potential (RP) of the cell, which requires active ion transport and use of metabolic energy to establish large ionic electrochemical gradients.

The G-D potential is usually less than −20 mV, whereas the RP is considerably greater. In the G-D equilibrium, all permeable ions are in equilibrium across the membrane, whereas this is not true for the normal RP. The equilibrium potentials for all permeant ions (e.g. E_K, E_{Cl}) are of equal magnitude and polarity. The G-D potential is developed even if the cell membrane had equal permeability or conductance for all small ions, whereas the normal RP requires different permeabilities for Na^+ and K^+, namely a low P_{Na}/P_K ratio. In the G-D equilibrium, the osmolarity of the cell becomes higher than the interstitial fluid bathing the cell and so the cell tends to gain water and swell (unless prevented from doing so by a rigid cell wall, such as in plant cells).

When equilibrium is established, the product of the concentrations of the permeant ions inside the cell is equal to that outside the cell. The gains in cations and anions inside the cell also must be equal to each other. From these required conditions, an equation can be solved to give the final concentrations at equilibrium and, from this, the calculated potential difference across the membrane.

II. INTRODUCTION

Because intracellular cytoplasm contains many colloids, including large non-diffusible polyvalent electrolytes, a *Donnan equilibrium* can be established across the cell membrane with an accompanying transmembrane *Gibbs–Donnan (G-D) potential*. The resting potential (RP) of most cells in the body, including nerve and muscle cells, however, is not due to a Donnan equilibrium and the normal RP is not a Gibbs–Donnan potential, as is erroneously stated in some textbooks (Sperelakis, 1995; Sperelakis, 2001). In the true Donnan equilibrium, all diffusible ions are in equilibrium across the membrane. But many ions, like Na^+, K^+, Ca^{2+} and H^+, in nerve and muscle cells are not in equilibrium; i.e.

$$E_{Na} \neq E_m$$
$$E_K \neq E_m$$
$$E_{Ca} \neq E_m$$

and

$$E_H \neq E_m$$

On the other hand, Cl^- is at equilibrium (i.e. passively distributed) in many vertebrate cells; namely,

$$E_{Cl} = E_m$$

In addition, a large internal pressure and concomitant swelling of animal cells would occur if a Donnan

Cell Physiology Sourcebook. DOI: 10.1016/B978-0-12-387738-3.00010-X

equilibrium were allowed to become established. The action of two types of cation pumps keeps the Donnan osmotic pressure from developing and keeps certain cations out of equilibrium. Thus, a second important function of the Na^+-K^+ pump is the *regulation of cell volume*. The Na^+-K^+ pump actively pumps three Na^+ ions out (to two K^+ ions pumped in) with each cycle. The pump action decreases the osmotic pressure of the cytoplasm and prevents cell swelling. Inhibition of active ion transport by any means leads to osmotic swelling because of the establishment of the Donnan equilibrium. Under such conditions, the cells gain Na^+, Cl^-, Ca^{2+} and H_2O and they lose K^+.

Thus, the G-D potential is *passive*; i.e. energy is not necessary to its establishment. In contrast, the RP is actively generated (indirectly or directly) by the action of the Na^+-K^+ pump. The G-D potential is usually less than -20 mV, whereas the RP is -40 to -100 mV, depending on the cell type (and its ratio of P_{Na} to P_K).

III. MECHANISM FOR DEVELOPMENT OF THE GIBBS–DONNAN POTENTIAL

In the Gibbs–Donnan equilibrium, a small membrane potential is established even though the biological membrane involved, or the artificial membrane used in a laboratory experiment, may be equally permeable to the small diffusible ions used. For the example illustrated in Fig. 10.1, where aqueous solutions of 0.1 M $(Na^+)_n$-proteinate^{n-} (side 1) and 0.1 M NaCl (side 2) are initially placed on the two sides of a two-compartment chamber separated by a membrane and, if $g_{Na} = g_{Cl}$ in this membrane then, at equilibrium, $E_{Na} = E_{Cl} = -18$ mV. The side containing the protein anion becomes negative with respect to the other side. Thus, because both diffusion potentials have the same polarity (as well as magnitude), a potential difference (PD) occurs across the membrane, even though conductances for Na^+ and Cl^- across the membrane may be equal. The osmotic pressure of the

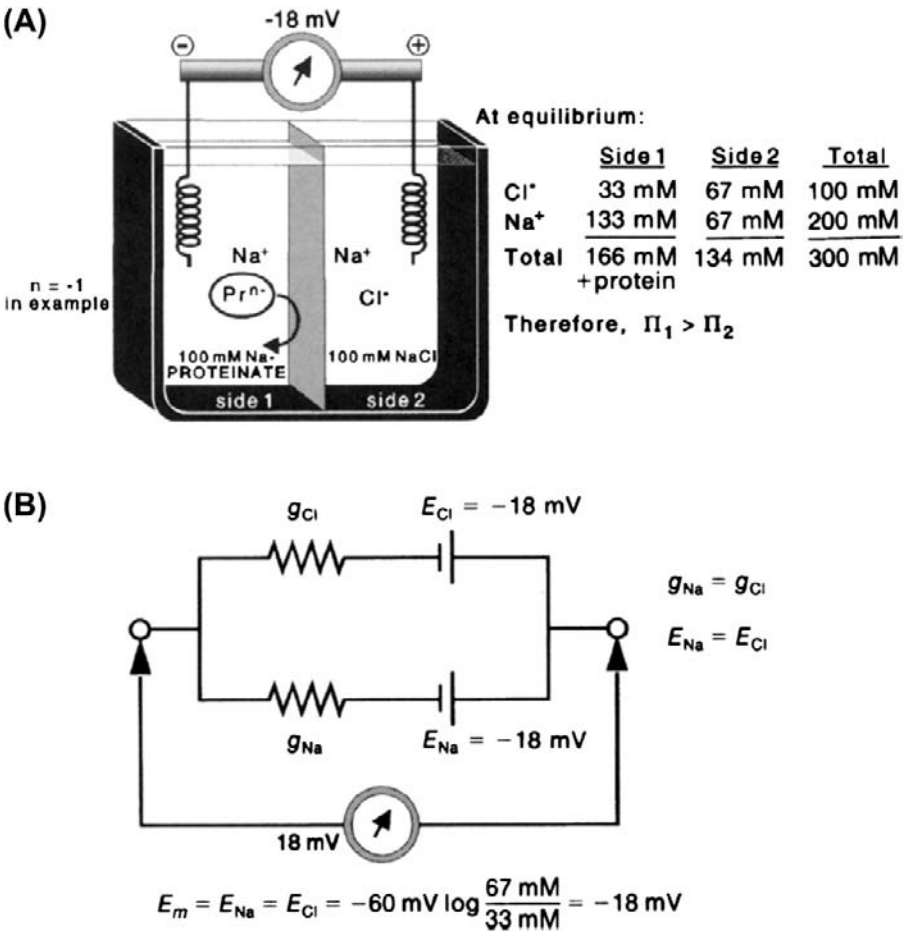

FIGURE 10.1 Gibbs–Donnan potential. (A) Gibbs–Donnan experiment. Diagram depicts the experimental arrangement for obtaining G-D potential. A membrane freely permeable to all small ions, but impermeable to the large protein molecules, is used to separate two solutions, only one of which (side 1) contains protein. Side containing the protein becomes negative, with respect to the other side, by a small voltage (−18 mV in example). This membrane potential (E_m) does not depend on active ion transport or on selective permeability properties of the membrane, as normal cell RP does. The diffusible ions (Na^+ and Cl^- in example), however, become unequally distributed across the membrane and it is their diffusion potentials ($E_{Na} = E_{Cl}$) that produce the G-D potential. (B) Equivalent circuit for experiment depicted in panel A, demonstrating that $E_m = E_{Na} = E_{Cl}$. The Na^+ and Cl^- batteries are of equal magnitude and of the same sign. Therefore, the relative conductances of the membrane to Na^+ and Cl^-, whether equal or not, are irrelevant to the potential (g_{Cl} and g_{Na} are conductances for Cl^- and Na^+, respectively).

solution on side 1 containing the non-permeant protein is greater than that on side 2. In the G-D equilibrium, all permeant ions are in electrochemical equilibrium across the membrane, i.e. they are passively distributed and there is no net electrochemical driving force:

$$(E_m - E_{Na}) = 0$$

$$(E_m - E_{Cl}) = 0$$

A more complete explanation for the development of the G-D potential follows. The G-D potential (which is an equilibrium PD) does not depend on metabolic energy. Therefore, this discussion applies to a cell that either has no ATP for pumping ions against electrochemical gradients or has had its Na^+-K^+ pump completely blocked by either ouabain or another agent. The G-D potential is passively produced by the concentration gradients for diffusible electrolytes (e.g. Na^+ and Cl^-) across a membrane. These ion gradients are caused by the presence of one or more large non-diffusible (with respect to the membrane) polyvalent electrolytes (e.g. *negatively-charged proteins*) on one side of the membrane, as is present in all biological cells. In essence, the negatively-charged protein molecules (at pH 7) inside the cell attract cations (e.g. Na^+ or K^+) and repel anions (e.g. Cl^-). Therefore, in the G-D situation, the inside of the cell has a higher concentration of Na^+ (or K^+) and a lower concentration of Cl^- than has the solution bathing the cell. The equilibrium potentials for Na^+ (E_{Na}) and for Cl^- (E_{Cl}) are equal in magnitude and are of the same sign, thereby producing a PD across the membrane. The PD is negative on the inside (side containing the protein) and usually is about −20 mV or less.

IV. GIBBS–DONNAN EQUILIBRIUM

To quantitate the ion distributions produced at equilibrium and the PD developed, let us examine the artificial system shown in Fig. 10.1A. In this system, a chamber is separated into two compartments by a collodion membrane, which has small uncharged pores that allow Na^+ and Cl^- ions, but not large protein molecules, to diffuse through. A 100 mM solution of Na^+ proteinate is added to one side (compartment 1) and a 100 mM solution of NaCl to the other side (compartment 2). An electrode is positioned on each side so that the PD across the membrane can be recorded (37°C). Let us assume that the Na^+ proteinate is completely ionized and, for simplicity, that the protein has a net negative charge of only one.

Thus, there is, at the first instant, no diffusion force for Na^+, but there is diffusion force for Cl^-, because Cl^- is 100 mM in compartment 2 and 0 mM in compartment 1. Na^+ must accompany the diffusion of Cl^- from side 2 to side 1, because the *principle of electroneutrality* in the bulk solution cannot be violated (i.e. there must be an equal number of cations and anions). So one relation that must be true when the system comes to equilibrium is that:

$$[Na^+]_2 = [Cl^-]_2 \tag{10.1}$$

In actuality, there is a small charge separation directly across the membrane to account for the PD; i.e. side 2 of the membrane has a small excess of Na^+ ions and side 1 has a small excess of Cl^- ions. Such a charge separation is very small, but is necessary to develop a PD across the membrane ($V = Q/C$) and is discussed in the preceding chapter on the RP generation.

The principle of electroneutrality also requires that the increase in Na^+ on side 1 must be exactly equal to the increase in Cl^- on side 1. Thus, the concentration difference of Na^+ that is built up at equilibrium must be exactly equal to the final concentration difference for Cl^-. This is because the large initial gradient for Cl^- is what drives the Na^+ to make its gradient. Therefore, it must also be true that:

$$\frac{[Na^+]_1}{[Na^+]_2} = \frac{[Cl^-]_2}{[Cl^-]_1} \tag{10.2}$$

Cross-multiplying gives:

$$[Na^+]_1[Cl^-]_1 = [Na^+]_2[Cl^-]_2 \tag{10.3}$$

Another way of considering this is that E_{Na} must equal E_{Cl} and, therefore, using the respective Nernst equations (see Chapter 9), we can write:

$$E_{Na} = E_{Cl} \tag{10.4}$$

$$\begin{aligned}\frac{-61\text{ mV}}{+1}\log\frac{[Na^+]_1}{[Na^+]_2} &= \frac{-61\text{ mV}}{-1}\log\frac{[Cl^-]_1}{[Cl^-]_2}\\ &= \frac{-61\text{ mV}}{+1}\log\frac{[Cl^-]_2}{[Cl^-]_1}\end{aligned} \tag{10.5}$$

Dividing both sides by −61 mV and removing the log gives Equation 10.2:

$$\frac{[Na^+]_1}{[Na^+]_2} = \frac{[Cl^-]_2}{[Cl^-]_1}$$

Equation 10.3 indicates that, at equilibrium, the product of the diffusible ions on side 1 must be equal to the product of the diffusible ions on side 2. From the Nernst equation, the relationships

$$E_{Na} = \frac{-RT}{zF}\ln\frac{[Na^+]_1}{[Na^+]_2} \tag{10.6}$$

$$= \frac{-61\text{ mV}}{+1}\log\frac{[Na^+]_1}{[Na^+]_2} \tag{10.7}$$

and

$$E_{Cl} = \frac{-61\text{ mV}}{-1}\log\frac{[Cl^-]_1}{[Cl^-]_2} \tag{10.8}$$

can be given because Cl^- is negative ($z = -1$), whereas Na^+ is positive ($z = +1$). Equation 10.8 is the same as (note that a negative sign in front of a log inverts the ratio)

$$E_{Cl} = -61 \text{ mV} \log \frac{[Cl^-]_2}{[Cl^-]_1} \quad (10.9)$$

because $[Na^+]_1/[Na^+]_2 = [Cl^-]_2/[Cl^-]_1$, as Equation 10.2 indicates and, from Equations 10.7 and 10.9, one obtains Equation 10.4: $E_{Na} = E_{Cl}$.

V. QUANTITATION OF THE GIBBS–DONNAN POTENTIAL

For quantitation, let us use x to indicate the amount (in mM) of Cl^- or Na^+ that shifted from side 2 to side 1 at equilibrium. Then the amount of Na^+ on side 2 is (100 mM$-x$) (the original amount minus the amount lost); Cl^- on side 2 is also (100 mM$-x$), because $[Na^+]_2 = [Cl^-]_2$. The Na^+ on side 1 at equilibrium is (100 mM$+x$) (the original amount plus the amount gained) and the Cl^- on side 1 is simply x. These parameters may be listed as follows:

$$[Na^+]_2 = 100 \text{ mM} - x$$
$$[Cl^-]_2 = 100 \text{ mM} - x$$
$$[Na^+]_1 = 100 \text{ mM} + x$$
$$[Cl^-]_1 = x$$

The value for x can be obtained by substituting these values into Equation 10.3:

$$[Na^+]_1 [Cl^-]_1 = [Na^+]_2 [Cl^-]_2 \quad (10.3)$$

$$(100 + x)x = (100 - x)(100 - x)$$

$$100x + x^2 = 10\,000 - 200x + x^2$$

$$300x = 10\,000$$

$$x = 33.3$$

Thus, at equilibrium

$$[Cl^-]_1 = 33 \text{ mM}$$
$$[Na^+]_1 = (100 + 33) = 133 \text{ mM}$$
$$[Cl^-]_2 = (100 - 33) = 67 \text{ mM}$$
$$[Na^+]_2 = (100 - 33) = 67 \text{ mM}$$

These values are also given in Fig. 10.1A. Note that all the equations and conditions are obeyed. The G-D potential produced then may be calculated by substituting into Equations 10.7 and 10.8:

$$E_{Na} = \frac{-61 \text{ mV}}{+1} \log \frac{133 \text{ mM}}{67 \text{ mM}} = -18 \text{ mV} \quad (10.10)$$

and

$$E_{Cl} = -\frac{-61 \text{ mV}}{-1} \log \frac{33 \text{ mM}}{67 \text{ mM}} = -18 \text{ mV} \quad (10.11)$$

Hence, $E_{Na} = E_{Cl}$ (Equation 10.4). That is, the two diffusion potentials are equal in magnitude and of the same sign. The PD across the membrane is −18 mV; side 1 containing the protein is negative. Therefore, relative permeability of the membrane to Na^+ and Cl^- is irrelevant. The equivalent circuit for this example at equilibrium is given in Fig. 10.1B.

VI. OSMOTIC CONSIDERATIONS

We should note that, at equilibrium, the sum of Na^+ and Cl^- on side 1 (166 mM) is greater than that on side 2 (134 mM). In addition, there is 100 mM protein on side 1. Thus, the total osmotic concentration on side 1 is 266 mOsm (milliosmolar), compared to 134 mOsm on side 2. Therefore, there is a large osmotic gradient between the two sides. Water moves from side 2 to side 1 (i.e. water accompanies the net movement of Na^+ and Cl^-) until the hydrostatic pressure head buildup is sufficient to oppose further net movement of water. As expected, the biological cell swells when a G-D equilibrium is allowed to develop following a blockade of active ion transport for long periods.

The total osmotic concentration, [osm], on each side, at equilibrium, may be summarized as follows:

$$[\text{osm}]_1 = [Na^+]_1 + [Cl^-]_1 + [\text{protein}]_1 \quad (10.12)$$

$$[\text{osm}]_2 = [Na^+]_2 + [Cl^-]_2 \quad (10.13)$$

Substitution gives:

$$[\text{osm}]_1 = 133 \text{ mM} + 33 \text{ mM} + 100 \text{ mM} = 266 \text{ mM}$$
$$[\text{osm}]_2 = 67 \text{ mM} + 67 \text{ mM} = 134 \text{ mM}$$

The osmotic pressure (Π, in atm) of each solution is equal to the osmotic concentration in osmol/L (C) times the osmotic coefficient (i) times the gas constant (R, 0.082 L·atm/mol·K) times the absolute temperature (T, in °K)

$$\Pi = iCRT \quad (10.14)$$

where C is the number of osmoles per liter of solution. In the example depicted in Fig. 10.1, a hydrostatic pressure of 3.17 atm would need to be applied to side 1 to prevent this compartment from gaining water from side 2 (at 20°C and assuming $i = 1.0$)

$$\begin{aligned}\Pi &= i\Delta CRT \\ &= (1.0)(266\ \text{mM} - 134\ \text{mM})\left(0.082\frac{\text{L}\cdot\text{atm}}{\text{mol}\cdot\text{K}}\right) \\ &\quad \times (273 + 20)\ \text{K} \\ &= \left(0.132\frac{\text{mol}}{\text{L}}\right)\left(0.082\frac{\text{L}\cdot\text{atm}}{\text{mol}\cdot\text{K}}\right)(293\ \text{K}) \\ &= 3.17\ \text{atm}\end{aligned} \tag{10.15}$$

The situation illustrated in Fig. 10.1 is actually more complex because the net water movement into side 1 acts to dilute the ion concentrations building up there and, therefore, a true G-D equilibrium can become established only if the net water movement is stopped, i.e. by allowing an osmotic pressure gradient to develop by making side 1 a closed, or rigid, system. Otherwise, theoretically all of the water and NaCl eventually would move out of side 2.

The example of a G-D equilibrium in Fig. 10.1 could have been illustrated using another salt, such as KCl, instead of NaCl, or two or more salts.

The extra osmotic pressure in side 1 (or inside a cell) produced by the presence of the negatively-charged proteins and other impermeant large charged molecules is known as the *colloid osmotic pressure* (COP). The COP is also important for water movement across the capillary wall, which separates the blood plasma (containing impermeant proteins) and the interstitial fluid (ISF). At the arterial end of the capillary, the intracapillary hydrostatic blood pressure exceeds the COP, so water moves out of the capillary into ISF space. At the venous end, the COP exceeds the capillary hydrostatic pressure, so water moves into the capillary. In the mid-region of the capillary, the two pressures are about equal and there is no net water flow. Thus, there is a circulation of fluid distributed along the length of the capillary and this idea is generally known as the *Starling hypothesis* (Davson, 1964; Sperelakis, 2001).

BIBLIOGRAPHY

Davson, H. (1964). *A Textbook of General Physiology* (3rd ed.). Boston: Little, Brown.

Sperelakis, N. (1995). *Electrogenesis of Biopotentials*. New York: Kluwer Publishing Co.

Sperelakis, N. (2001). Gibbs–Donnan equilibrium potentials. In *Cell Physiology Sourcebook* (3rd ed.). San Diego: Chapt 15. Academic Press.

This page intentionally left blank

Chapter 11

Mechanisms of Carrier-Mediated Transport: Facilitated Diffusion, Cotransport and Countertransport

Steven M. Grassl

Chapter Outline

I. SUMMARY

This chapter describes the functional properties of carrier-mediated transport mechanisms present in the cellular plasma membrane. The functional properties defining facilitated diffusion, cotransport and countertransport are considered with regard to the thermodynamic constraints imposed by primary and secondary active transport as well as passive transport. A stepwise kinetic model is described for each mechanism illustrating the substrate concentration dependence of the rate of transport and differences in the rate limiting steps accounting for transport. The functional properties of facilitated diffusion, cotransport and countertransport are further considered with regard to competitive and non-competitive inhibition, stoichiometric coupling and electrogenic transport. The structure–function relationship of prototypical membrane proteins mediating facilitated diffusion, cotransport and countertransport is briefly considered.

II. INTRODUCTION

The selective and regulated passage of ions and non-electrolytes across the cell membrane is an essential component of cellular homeostasis. The maintenance of cell pH and volume and the accumulation of nutrients for protein synthesis and cell metabolism are physiological processes that depend on membrane transport for cells to thrive. Cell membranes are composed of phospholipids organized as a bilayer (5 nm) of two closely opposed leaflets separating the intracellular from the extracellular space. The hydrophobic properties of phospholipids make the cell membrane an impermeable barrier excluding the transfer of hydrophilic solutes that are either charged (anions and cations) or uncharged (non-electrolytes). The selective passage of hydrophilic solutes across the hydrophobic barrier, a physiological property known as *membrane permeability*, is mediated by the presence of membrane transport proteins that span the phospholipid bilayer. Transport proteins may be functionally subdivided into channels, pumps and carriers according to differences in the mechanism mediating ion and non-electrolyte transport. This chapter describes the mechanisms of *carrier-mediated transport*, which include *facilitated diffusion*, *cotransport* and *countertransport*.

III. ELECTROCHEMICAL POTENTIAL

Transport mechanisms may be distinguished thermodynamically according to their ability to mediate active or passive transport. *Active transport* is defined as movement of a solute from a region of low electrochemical potential on one side of the cell membrane to a region of higher electrochemical potential on the opposite side. *Passive*

Cell Physiology Sourcebook. DOI: 10.1016/B978-0-12-387738-3.00011-1

transport is defined as movement of a solute from a region of high electrochemical potential on one side of the cell membrane to a region of lower electrochemical potential on the opposite side. The *electrochemical potential* of a solute is the partial molar free energy of the solute or the potential to do work when a difference in electrochemical potential exists across the cell membrane. The electrochemical potential of a solute on either side of the cell membrane is a function of the solute activity (or concentration in dilute solution), the solute charge and valence and the electrical potential. The difference in electrochemical potential, therefore, reflects the magnitude of the difference in transmembrane solute concentration and the difference in transmembrane voltage factored by the charge and valence of the solute. Notably, for solutes without charge, such as non-electrolytes, solute free energy is neither increased nor decreased by electrical potential and only the chemical potential of the solute is considered. Thus, the electrochemical or chemical potential difference of a solute across the cell membrane may be considered a driving force acting on solute transport. In the absence of an electrochemical potential difference or a driving force for solute transport, transport mechanisms that are passive mediate equal solute transport in the forward and reverse direction across the membrane resulting in no net transport. For anions and cations, this would occur when the chemical and electrical driving forces acting on solute transport are equal and opposite in direction across the membrane such that the net driving force is zero. For non-electrolytes, this would occur in the absence of a solute concentration gradient where transmembrane solute concentrations are equal. In both instances where no net transport occurs, the ion and non-electrolyte are at electrochemical equilibrium with the driving forces acting on the transported solutes. Where an electrochemical potential difference for a solute exists across the cell membrane, the direction of net solute transport by a passive transport mechanism will depend on the direction and magnitude of the chemical and/or electrical driving forces acting on the solute. The chemical and electrical potential difference of a charged solute or ion may occur as opposing driving forces of unequal magnitude, with the direction of net solute transport determined by the direction of the larger driving force. In no instance would a passive transport mechanism mediate net transport of a charged solute in a direction across the cell membrane that opposed both the chemical and electrical driving forces acting on the ion. The same limitation holds for net transport of non-electrolytes in a direction that opposes the chemical driving force acting on the solute.

Active transport mechanisms may be distinguished from passive transport mechanisms by the ability to generate and maintain an electrochemical or chemical potential difference for ions and non-electrolytes across the cell membrane. This requires net transfer of ions or non-electrolytes across the membrane in a direction that is opposed by the prevailing electrical gradient and/or chemical concentration gradients as driving forces acting on the transported solutes. To perform the work of moving solutes "uphill" against an electrical gradient and/or a chemical concentration gradient, active transport mechanisms require energy. The source of energy driving active transport is the hydrolysis of ATP. The direct or indirect coupling of active transport to ATP hydrolysis distinguishes *primary* active transport from *secondary* active transport. Primary active transport mechanisms, such as the ion translocating ATPases or pumps, are directly coupled to ATP hydrolysis and thermodynamically transduce the energy released upon ATP hydrolysis to the energy stored in the formation of an ion electrochemical potential difference. Secondary active transport mechanisms, such as *cotransporters* and *countertransporters*, are indirectly coupled to ATP hydrolysis and thermodynamically transduce the energy from one solute electrochemical potential difference to the energy stored in the formation of a second solute electrochemical potential difference. The indirect coupling of secondary active transport to ATP hydrolysis arises from the intermediate formation and ATP dependence of the solute electrochemical potential difference that drives secondary active transport.

IV. CARRIER-MEDIATED TRANSPORT MECHANISMS

IVA. Facilitated Diffusion

Facilitated diffusion or *uniport* is the simplest form of carrier-mediated transport and results in the transfer of large hydrophilic molecules (sugars, amino acids, nucleotides and organic acids and bases) across the cell membrane. Transport by facilitated diffusion is passive and reversible, with the direction of net transport into or out of the cell determined by the direction of the electrochemical potential difference of the transported solute. Net transport by facilitated diffusion may continue in either direction until the solute is at equilibrium with the electrical and/or chemical driving forces acting on the solute. At equilibrium, facilitated diffusion of a solute occurs equally in both directions resulting in no net transport. The transport mechanism mediating facilitated diffusion may be modeled as shown in Fig. 11.1. The two main features of the transport mechanism are an association and dissociation of the transported solute with the transport protein and a change in the conformation of the transport protein which makes the occupied or unoccupied site of solute interaction accessible from either side of the membrane (Fig. 11.1A). The transport mechanism may be considered in greater detail as a four-step process (Fig. 11.1B). First, solute S associates with the transport protein C facing side

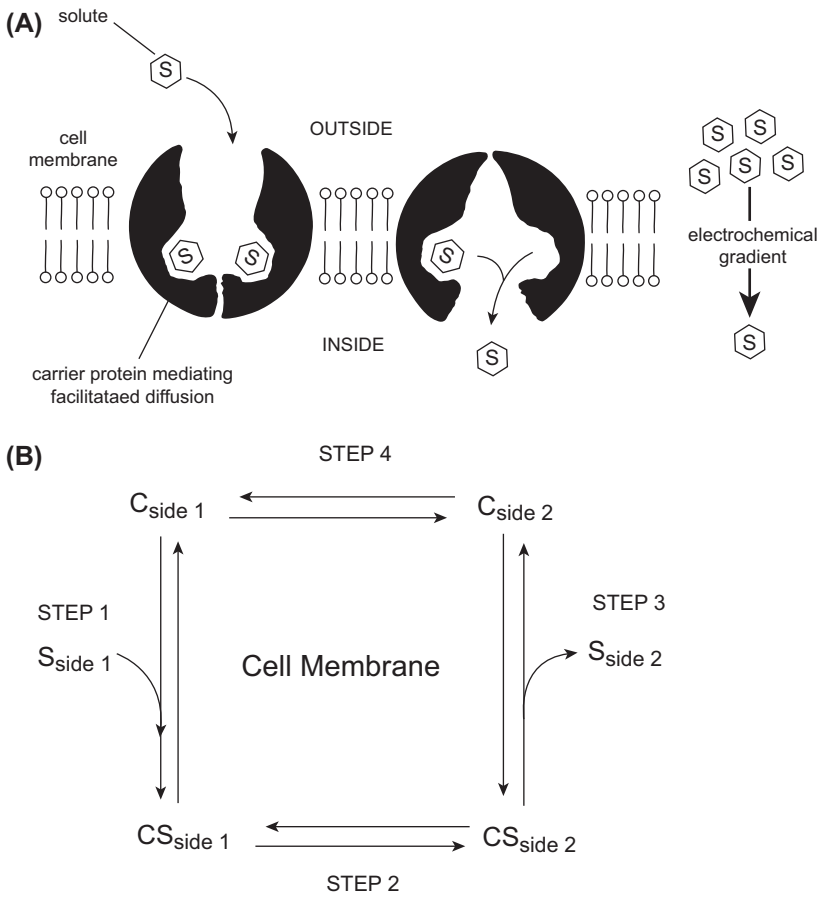

FIGURE 11.1 Conceptual and kinetic model of facilitated diffusion.

1 (labeled "outside" in the figure) to form a solute–carrier complex SC. Second, the solute–carrier complex undergoes a conformational change that reorients the solute–carrier complex to face side 2 (labeled "inside" in the figure). Third, the solute dissociates with the transport protein on side 2. Fourth, the unoccupied carrier undergoes a second conformational change to reorient the solute association site to face side 1. Net solute transport from side 1 to side 2 occurs when an unoccupied solute association site is reoriented from side 2 to side 1. However, as the solute concentration on side 2 increases, net solute transport from side 1 to side 2 decreases because a greater proportion of the unoccupied carrier becomes associated with solute on side 2 and undergoes reorientation moving solute to side 1. When the solute concentrations on side 1 and side 2 are equal, no net solute transport will occur because the occupancy and reorientation of the carrier will be equal at both sides of the membrane. A principal feature of facilitated diffusion illustrated by the model is the interaction with solutes exclusively at one side of the membrane or the other but never at both sides simultaneously. This functional property of facilitated diffusion invokes the need for a conformational change in the protein, alternately orienting the solute association site from side to side across the membrane. Each step in the process is reversible and is linked to the preceding and succeeding step by rate constants defining the rate of solute association and dissociation on either side of the membrane and the rate of conformational change for transporter reorientation in either direction when associated with or without solute. In general, the rate of solute association and dissociation with the transporter occurs more rapidly than the rates of conformational change. Furthermore, the conformational change reorienting the sidedness of the transporter occurs at a faster rate for the solute-occupied transporter than for the solute-unoccupied transporter. The relative slowness of the rate constant for the conformational change reorienting the solute-unoccupied transporter (step 4) makes it the rate-limiting step in the process of facilitated diffusion.

The *unidirectional rate* of solute transport across the cell membrane mediated by facilitated diffusion is dependent on the solute concentration at the side where transport originates. This is analogous to the substrate concentration

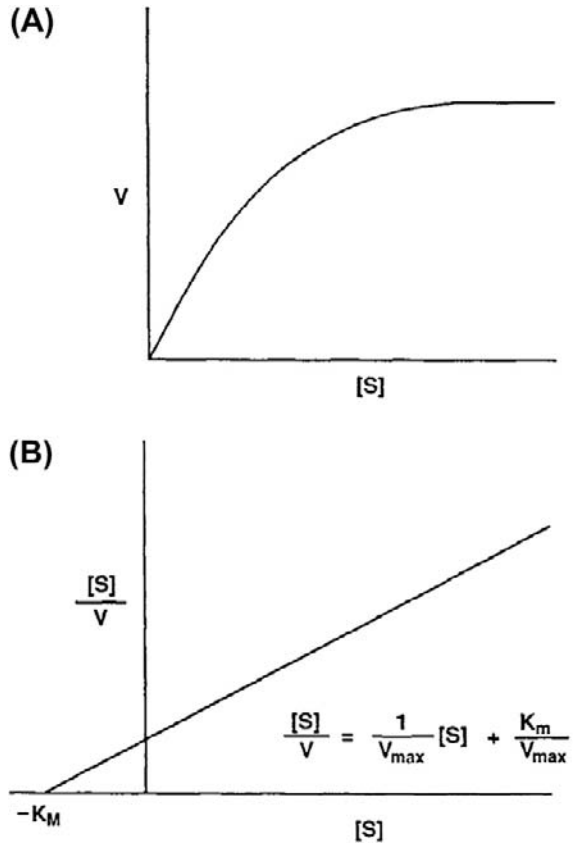

FIGURE 11.2 Relationship of solute transport rate (V) to solute concentration [S].

dependence of the rate of product formation mediated by an enzyme. As shown in Fig. 11.2, at low solute concentrations the rate of solute transport increases linearly with solute concentration and, as solute concentration increases further, the rate of solute transport increases less and less as it approaches a maximum value at high solute concentrations (Fig. 11.2A). The relationship of the unidirectional solute transport rate to solute concentration shown in Fig. 11.2 is described mathematically by an equation analogous to the Michaelis−Menten equation from enzyme kinetics:

$$V = \frac{[S]V_{max}}{K_m + [S]} \tag{11.1}$$

where V is determined experimentally as the initial rate of solute transport, [S] is the solute concentration, V_{max} is the maximal rate of solute transport and K_m is a constant described by the solute concentration where V is one-half the V_{max}. The validity of using the Michaelis−Menten equation in a kinetic analysis of facilitated diffusion requires experimental conditions in which the rate of solute transport reflects solute transport only in one direction. Accordingly, initial rates of solute transport across the cell membrane are measured in the absence of a significant solute concentration on one side of the membrane. The Michaelis−Menten equation may be rearranged to obtain a linear relation as shown in Fig. 11.2B, where the kinetic parameters K_m and V_{max} are the x-intercept and 1/slope, respectively. The kinetic parameters of solute transport are functional properties that characterize different facilitated diffusion mechanisms as well as transport of different solutes by the same facilitated diffusion mechanism. The K_m value characterizes the affinity of solute association−dissociation with the transporter such that a lower or higher K_m value reflects a greater or lesser affinity, respectively. The accuracy of the K_m value as a measure of solute affinity is further dependent on initial rate determinations performed at solute concentrations both above and below the K_m value. The V_{max} value is a measure of the number of transporters present in the membrane and the time required for a transporter to undergo one complete transport cycle or turnover. The maximum velocity of transport occurs when solute association and dissociation with the transporter are not rate-limiting steps in the transport process or when the transporter is saturated. Under these conditions, the maximal velocity of solute transport is only as fast as the rate-limiting step in the transport process, which is the conformational change of the solute dissociated transporter.

The facilitated diffusion of a solute may be inhibited in the presence of other solutes that interact with, but are not necessarily transported by, the same transporter. The nature of interaction of the inhibitor with the transporter may be assessed by observing the effect of the inhibitor on the kinetic parameters characterizing the transport mechanism. An effect of the inhibitor to decrease the maximal velocity of solute transport, without an effect on the K_m value of the solute, characterizes non-competitive inhibition. Non-competitive inhibition is not reversed by increasing the concentration of the transported solute and therefore results from an interaction of the inhibitor with both the solute-associated and -dissociated transporter at a second site that does not interact with the transported solute. An effect of the inhibitor to increase the apparent K_m value of the solute, without an effect on the maximal velocity of transport, characterizes competitive inhibition. Competitive inhibition is reversed by increasing the concentration of the transported solute and, therefore, results from an interaction of the inhibitor with only the solute-dissociated transporter at the same site that interacts with the transported solute.

The same facilitated diffusion mechanism may mediate the transport of multiple solutes that share common chemical and physical determinants, such as negatively-charged carboxyl groups or positively-charged amino groups. The nature of these chemical determinants and their spatial position in the solute molecule permits recognition

and interaction with the solute association site of the transport protein. The solute specificity of a facilitated diffusion mechanism is a functional property of the transporter characterized by solute-specific differences in the kinetic parameters of solute transport. A rank order of the relative affinity of the transporter for different solutes may be compiled by determination of the K_m values for multiple solutes transported by the same mechanism. The transporter is more highly specific for solutes with the lowest K_m values and less specific for solutes with the highest K_m values. However, solutes with higher affinity for the transporter do not necessarily have a greater maximal velocity of transport than solutes with a lower affinity. A comparison of the relative affinities and maximal velocities of solute transport determined experimentally further suggests which solutes are most likely to be transported in a physiological setting where multiple solutes are present at different concentrations.

The kinetic parameters characterizing solute transport by facilitated diffusion may differ depending on the direction of unidirectional solute transport. The K_m value as a measure of solute affinity for transport may be larger or smaller for solute transport mediated in one direction across the cell membrane when compared to the K_m value for solute transport in the reverse direction. However, the kinetic asymmetry of facilitated diffusion is subject to a thermodynamic limitation which requires the product of all the rate constants associated with the stepwise transport in the inward and outward direction be equal. Accordingly, a directional asymmetry in the K_m value of solute transport must be matched by a corresponding asymmetry in the maximal velocity of transport such that the ratio of V_{max} to K_m for transport in either direction is equal. Thus, a kinetic asymmetry of solute transport results from an increase or decrease of both kinetic parameters where an increased or decreased affinity for solute is matched by a corresponding decrease or increase in maximal velocity of transport, respectively.

In contrast to non-electrolytes, the facilitated diffusion of charged solutes, such as organic anions and cations, is *electrogenic* and results in the net transfer of charge in the direction of net solute transport across the membrane. As a consequence of mediating net charge transfer across the membrane, the facilitated diffusion of charged solutes will increase or decrease the electrical potential difference across the membrane depending on the sign and magnitude of the solute charge and on the direction of net transport. As a further consequence of mediating net charge transfer, the rate and direction of electrogenic solute transport by facilitated diffusion is sensitive to membrane potential, which must be considered as an additional driving force acting on electrogenic solute transport. This results from the voltage sensitivity of at least one step in the transport process mediating the facilitated diffusion of charged solutes. A voltage-dependent increase or decrease in the kinetic parameters of electrogenic solute transport may indicate an effect of voltage on the affinity of the transporter for the charged solute (K_m) and/or on the conformational change reorienting the solute-associated or -dissociated transporter (V_{max}).

Facilitated diffusion mechanisms are present in the membranes of all cells and many different mechanisms exist in the same membrane of a single cell. The common features of these different facilitated diffusion mechanisms include: (1) their presence as integral membrane proteins spanning the lipid bilayer; (2) a broad or narrow range of substrate specificity; (3) inhibition by physiological and non-physiological solute analogs; (4) solute saturation conforming to Michaelis–Menten kinetics; and (5) evidence of an alternate side-to-side reorientation of the solute association site. Whereas solute transport via channels and facilitated diffusion are both mediated and passive, sharing the common functional properties of inhibition and saturation, other functional criteria distinguish these two forms of transport. In contrast to solute transport by facilitated diffusion, most channels mediate transport of inorganic anions or cations and have a solute specificity limited by the physical size of the ion. Channels are accessible for solute association from both sides of the membrane simultaneously and mediate transport at a rate orders of magnitude faster than facilitated diffusion, which is rate limited by the relatively slow conformational changes reorienting the sidedness of the carrier. In further contrast to solute transport mediated by facilitated diffusion, the rate-limiting step in ion transport mediated by channels is the association and dissociation of an ion with the channel, not the actual ion translocation through the channel.

The functional properties of solute transport mediated by facilitated diffusion have been characterized in detail for many different cell- and solute-specific transport mechanisms. A major question remaining in the study of facilitated diffusion is the structure–function relationship of the transport protein. This requires the identification of individual membrane proteins as the structural correlates of transport activities of different facilitated diffusion mechanisms present in the cell membrane. A limited number of transport proteins have been identified by a difficult biochemical process involving detergent solubilization of the cell membrane, affinity purification of the protein and functional reconstitution of transport activity to prove its identity. The identification of many more transport proteins has been recently achieved using the techniques of molecular biology to clone the genes coding for these membrane proteins. The molecular cloning of a transporter gene begins with the preparation of mRNA from a tissue rich in a functionally well-characterized transporter activity. A high transporter activity suggests an abundance of transporter protein as well as transporter mRNA from

which the protein is translated. The total mRNA is reverse transcribed to complementary DNA and individual cDNA molecules are inserted into plasmids or minichromosomes used to transform *Escherichia coli* bacterial cells. The transformed *E. coli* are grown to form a library of thousands of colonies or clones each reproducing a different cDNA plasmid. The library serves to renew and amplify a continuous source of cDNA plasmids which may be screened for possible hybridization with short DNA sequences thought to code for various regions of the transporter gene. To assess the function of the putative transporter gene, mRNA may be reverse transcribed from the plasmid cDNA of positively identified clones and injected into frog oocytes for translation or expression of the corresponding protein. The identity of the transporter gene is proven by the mRNA-dependent expression of a transport activity with functional properties similar to those characterizing transport activity in the tissue of origin. The transporter gene may also be identified without prescreening the library for hybridization by systematically preparing mRNA from the entire cDNA library and assessing functional expression of transport activity. The cDNA plasmid coding for the transporter gene may be sequenced to obtain the deduced amino acid sequence, or primary structure, and molecular weight of the transport protein. The deduced amino acid sequence of the transport protein may be further analyzed for the presence and concentration of hydrophobic amino acids at multiple sites along the peptide chain. Typically, 10−12 regions of relative hydrophobicity may be identified in the transporter amino acid sequence and are thought to represent the putative transmembrane domains of the transport protein. The location of the transmembrane domains further suggests the size and topological location of intracellular and extracellular peptide loops between the transmembrane domains as well as the amino and carboxy termini of the transport protein. A topological model depicting the putative secondary protein structure of a mammalian facilitated diffusion transporter for glucose is shown in Fig. 11.3. Further analysis of the amino acid sequence for the presence of asparagine in the extracellular peptide loops may suggest potential sites for N-linked glycosylation of the transport protein. Likewise, the presence of serine, threonine and tyrosine in consensus phosphorylation sites in intracellular peptide loops suggests that the phosphorylation state of the transporter may regulate its activity.

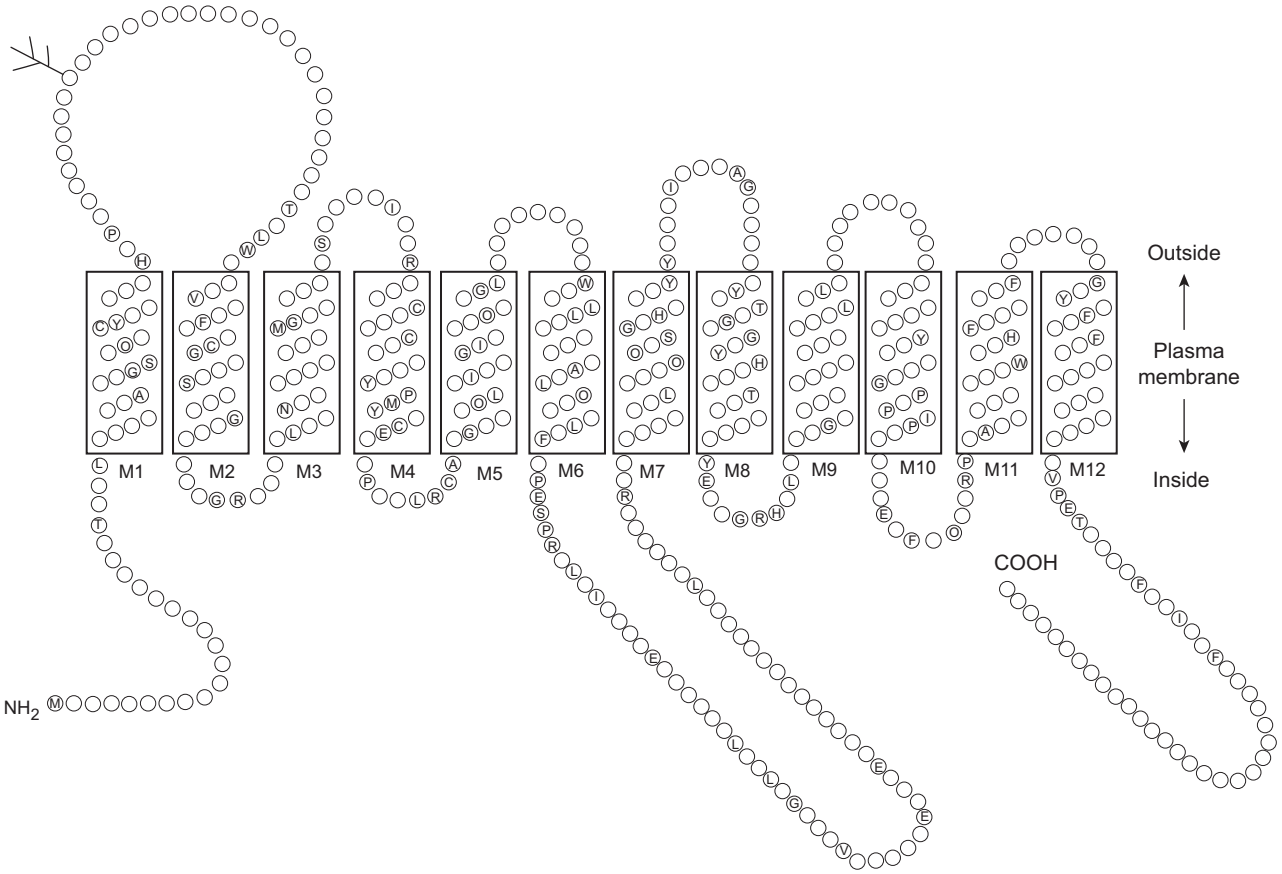

FIGURE 11.3 Consensus structure of the mammalian D-glucose carriers. *(Reprinted with permission from Bell, G.I. (1991). Molecular defects in diabetes mellitus. Diabetes. 40, 413−422. Copyright © 1991 American Diabetes Association.)*

The structure–function relationship of the protein mediating facilitated diffusion may be investigated upon identification of the primary structure or amino acid sequence of the protein. Mutant transport proteins may be engineered with single or multiple amino acid deletions, or with substitutions in the transmembrane domains, the intra- and extracellular peptide loops between transmembrane domains and in the amino and carboxy termini. The functional properties of the engineered transport proteins may be assessed by heterologous expression in frog oocytes or cell cultures and compared to the native protein. Thus, the individual amino acids or amino acid sequences important for solute recognition by, and interaction with, the transport protein may be identified as well as those involved in the conformational change reorienting the solute-associated and -dissociated transporter. The mutational analysis of transporter function is limited by null mutations which result in the expression of non-functional transport proteins or in the absence of expression.

The information obtained from identifying and cloning the gene coding for a facilitated diffusion mechanism may be used to survey the distribution of the same or related transport proteins in different tissues and in different cells within the same tissue. Oligonucleotide probes may be made from short sequences of the transporter gene and used to detect the presence of complementary transporter sequences in cDNA from tissue libraries, in mRNA prepared from multiple tissues, or by in situ hybridization of mRNA in thin tissue slices. The positively identified mRNA or cDNA may be isolated and sequenced for comparison with the deduced amino acid sequences present in different tissues. Such a comparison will indicate either complete sequence identity, suggesting the presence of the same transport protein in different tissues, or will indicate minor tissue-specific differences in sequence, suggesting that different isoforms of the same protein exist in different tissues. Thus, the facilitated diffusion of glucose in different tissues is mediated by at least five different isoforms of the same transport protein as shown in Table 11.1. The high degree of sequence conservation among different isoforms of the same transport protein is consistent with a common solute specificity and mechanism of solute translocation across the membrane. The minor tissue-specific differences in sequence distinguishing isoforms of the same protein presumably reflect a unique variation in the functional properties and/or regulation of the transporter serving the specialized physiology of the tissue.

TABLE 11.1 D–glucose Carrier Isoforms

Designation	Function
GLUT1	Basal uptake in placenta, brain, kidney, colon
GLUT2	Primarily found in transport in liver cells
GLUT3	Basal uptake in the brain
GLUT4	Insulin-stimulated uptake in the skeletal muscle, cardiac muscle and adipose tissue
GLUT5	Absorption in small intestines

IVB. Cotransport

Cotransport, or *symport*, is a form of secondary active transport that mediates net transfer of a solute across the cell membrane from a place of low solute electrochemical potential to a place of higher solute electrochemical potential. The source of energy driving secondary active transport of a solute against its electrochemical potential difference arises from a coupling to the transport of a second solute from a place of higher electrochemical potential to a place of lower electrochemical potential. The coupling of the driving solute to the driven solute results in the cotransport of both solutes in the same direction across the cell membrane. Cotransport mechanisms are reversible and will mediate net transport either into or out of the cell until the opposing electrochemical potential differences of the driven solute and the driving solute become equal across the cell membrane. The direction of net transport mediated by a cotransport mechanism may be determined by either solute, depending on which solute has the larger driving force and by the direction of the larger driving force across the membrane. The mechanism mediating cotransport may be modeled as a six-step process as shown in Fig. 11.4: (1) an association of solutes S and (2) A with the carrier facing side 1 to form the SCA solute-carrier complex; (3) a conformational change reorienting the SCA carrier complex to face side 2; (4) dissociation of A and (5) S with the carrier facing side 2; and (6) a second conformational change reorienting the solute-free carrier to face side 1. The cotransport mechanism may be further modeled in three different variations depending on the solute interaction with the carrier. Solute interaction with the carrier may be r*andom*, with either solute associating and dissociating first with the carrier, or solute association–dissociation may be *ordered*, in which either one of the solutes must associate or dissociate first with the carrier before the second solute may associate or dissociate. Note, as shown in Fig. 11.4 for an ordered interaction of solute with the carrier, the second solute associating with the carrier at one side of the membrane is the first solute to dissociate with the carrier at the opposite side. Neither form of the partially associated carrier SC or AC may undergo a conformational change reorienting the sidedness of the partially associated carrier and therefore the cotransport mechanism mediates only the coupled transport of both solutes but does not mediate the uncoupled transport of

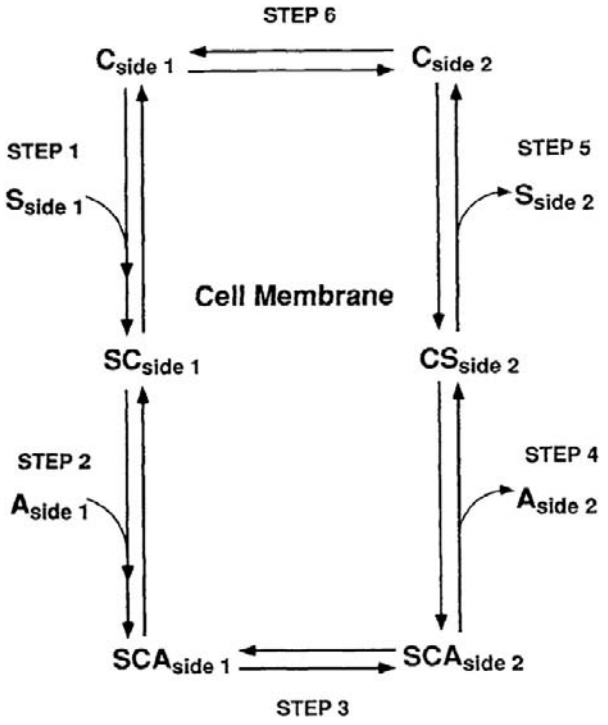

FIGURE 11.4 Kinetic model of cotransport.

either solute. Each step in the cotransport process is reversible and is linked to the preceding and succeeding step by rate constants defining the rate of solute association and dissociation on either side of the membrane and by the rate of conformational change for carrier reorientation in either direction when associated with or without both solutes. Similar to facilitated diffusion, solute association–dissociation with the carrier occurs faster than the conformational change reorienting the sidedness of the carrier and the rate-limiting step in the cotransport process is the conformational change reorienting the solute-dissociated carrier.

The unidirectional rate of solute transport across the cell membrane mediated by a cotransporter is dependent on the concentration of both solutes at the side where cotransport originates. When either solute concentration is constant, the cotransport rate of the second solute will approach a maximum value with increasing solute concentration and the saturation kinetics of the cotransport process may be analyzed using the Michaelis–Menten equation to describe the kinetic parameters K_m and V_{max} for each solute. The random or ordered association of cotransported solutes with the transporter may be determined from the mutual dependence of kinetic parameters on cotransported solute concentrations. As shown in Fig. 11.4, where the association of solutes S and A with the cotransporter at side 1 is ordered and S associates first, solute A will have the same maximal rate of transport (V_{max}) when determined at different concentrations of solute S. However, the K_m value for solute A will decrease when determined at increasing concentrations of solute S, indicating the initial association of S with the cotransporter effectively increases its affinity for association with solute A. In contrast, the V_{max} and K_m values characterizing transport of solute S, the first solute to associate with the cotransporter, will both vary when determined at different solute A concentrations. An increase in solute A concentration will increase the maximal rate of solute S through the cotransport mechanism and will also effectively increase its affinity for solute S as reflected by a decreased K_m value. The effect of solute A on the maximal rate of solute S transport arises from its ordered association, as the second solute, to form the SCA solute–carrier complex, which may then transfer both solutes across the membrane. Thus, where a mutual solute concentration dependence of the kinetic parameters characterizing the transport of both solutes is determined for a cotransport mechanism, an ordered association–dissociation of solutes with the cotransporter may be indicated and a random association–dissociation of solutes may be excluded.

The cotransport of a solute may be inhibited by the presence of other solutes that interact with, but are not necessarily transported by, the same cotransport mechanism. Similar to facilitated diffusion, the competitive or noncompetitive nature of inhibitor interaction with the cotransport mechanism may be assessed by determining the effect of the inhibitor on the kinetic parameters characterizing transport of both solutes by the cotransport mechanism.

The same cotransport mechanism may mediate transport of multiple solutes that share common chemical and physical determinants. Similar to facilitated diffusion, the solute specificity of a cotransport mechanism may be characterized by determining the kinetic parameters of different solutes transported by the same cotransport mechanism. A comparison of the relative affinities and maximal velocities of solute transport determined experimentally will suggest the relative magnitudes of solute transport mediated by the cotransporter in vivo.

The cotransport mechanism modeled in Fig. 11.4 will be at a steady state and mediate equal transport of S and A in both directions across the membrane when the driving forces acting on the cotransported solutes are equal and opposite. This would occur when the transmembrane concentration difference or gradient of S in one direction is equal to the transmembrane concentration difference or gradient of A in the opposition direction. At the steady state, where no net solute transport occurs, the solute driving forces will be in thermodynamic equilibrium with each other and the transmembrane concentration ratios of S and A may be described by:

$$\frac{S_1}{S_2} = \frac{A_2}{A_1} \tag{11.2}$$

Thus, in the presence of a 10-fold concentration gradient of S, a cotransport mechanism coupling the transport of S and A across the membrane may generate up to, but not exceeding, a 10-fold concentration gradient of A. Because the cotransport mechanism effectively transduces the energy stored in the concentration gradient of S to the energy stored in the concentration gradient of A, it would be thermodynamically impossible for the cotransport mechanism to generate more than a 10-fold concentration gradient of A.

The cotransport process modeled in Fig. 11.4 describes the coupled transport of one molecule of S together with one molecule of A, or an S to A *coupling ratio* of 1:1. However, the stoichiometric coupling of solutes mediated by a cotransport mechanism may exceed unity, resulting in cotransport of unequal amounts of solute. This may be modeled kinetically as an extension of Fig. 11.4 to include an extra step of solute association on side 1 prior to carrier reorientation to face side 2 and an extra step of solute dissociation on side 2 prior to carrier reorientation to face side 1. The kinetic parameter (K_m) characterizing the solute affinity of a cotransport mechanism must account for each additional solute association or dissociation at mutually exclusive sites in the cotransport protein. The thermodynamic equilibrium of solute driving forces defining the steady state, where no net solute transport occurs, is profoundly affected by the stoichiometric coupling of solutes by the cotransport mechanism. Where the stoichiometric coupling is other than 1:1, the solute driving forces will be in thermodynamic equilibrium at transmembrane solute concentration ratios raised to the power of their respective coupling coefficient as shown.

$$\left(\frac{S_1}{S_2}\right)^s = \left(\frac{A_2}{A_1}\right)^a \tag{11.3}$$

The coupling coefficients s and a are the number of S and A molecules that must associate with the carrier before a conformational change may occur reorienting the sidedness of the solute−carrier complex. The stoichiometric coupling of solutes by a cotransport mechanism is significant because, in the presence of a 10-fold concentration gradient of S, a cotransport mechanism coupling the transport of two molecules of S to one molecule of A may generate a 100-fold concentration gradient of A.

Similar to the facilitated diffusion of charged solutes, cotransport mechanisms may also be electrogenic and mediate net charge transfer across the membrane in the direction of net solute transport. In general, the electrogenicity of cotransport mechanisms arises from the transport of the inorganic cation sodium coupled to the transport of organic and inorganic anions and cations, such as negatively-charged amino acids, mono- and dicarboxylic acids, sulfate and phosphate or positively-charged amino acids and amines as well as non-electrolytes, such as sugars. In most instances, the coupled transport of charged or uncharged solutes with the transport of sodium results in the net transfer of positive charge in the direction of net solute transport into the cell. The positive electrogenicity of solute transport mediated by a sodium-coupled cotransport mechanism will tend to depolarize the cell membrane potential difference and results from at least one voltage-sensitive step in the process accounting for electrogenic cotransport. A voltage-dependent increase or decrease in the kinetic parameters characterizing an electrogenic cotransport mechanism may indicate an effect of voltage on the affinity of the cotransporter for either or both solutes (K_m) and/or on the conformational change reorienting the solute-associated or -dissociated transporter (V_{max}). However, because the rate-limiting step in the process accounting for cotransport is the conformational change reorienting the solute-dissociated transporter, a voltage-dependent increase in the rate of cotransport must result from the voltage sensitivity and acceleration of at least this step in the cotransport process. The voltage sensitivity of an electrogenic cotransport mechanism makes the voltage difference across the cell membrane a driving force acting on solute cotransport. Thus, the rate, magnitude and direction of solute transport mediated by an electrogenic sodium cotransport mechanism is determined by two driving forces including the transmembrane voltage difference as well as the transmembrane sodium and solute concentration gradients. An electrogenic cotransport mechanism will be at steady state and mediate equal solute transport in both directions across the membrane when the electrical and chemical forces driving cotransport are at equilibrium across the membrane. For an uncharged solute S, and a charged solute A, the driving forces may be related by:

$$RT \ln\left(\frac{S_1}{S_2}\right) = -RT \ln\left(\frac{A_2}{A_1}\right) + zF(\psi_2 - \psi_1) \tag{11.4}$$

where R is the universal gas constant, T is absolute temperature, z is the valence of A, F is the Faraday constant, and $(\psi_2-\psi_1)$ is the transmembrane voltage difference. Thus, in the presence of a 10-fold sodium concentration gradient and a transmembrane voltage difference of 60 mV, a cotransport mechanism mediating 1:1 Na-to-solute transport may generate a 100-fold uncharged solute gradient.

The functional properties of solute transport mediated by sodium-dependent cotransport mechanisms have been characterized in detail for many different cell- and solute-specific cotransporters. Like facilitated diffusion, a major question remaining in the study of sodium-dependent cotransport mechanisms is the structure−function relationship of the cotransport protein. Several sodium-dependent

cotransport proteins been identified using a molecular biological approach to clone the genes coding for these membrane proteins. The primary structure of sodium-dependent cotransport proteins suggests topological features similar to membrane proteins mediating facilitated diffusion. These include the presence of 10–12 putative transmembrane domains, the location of extracellular N-linked glycosylation sites and the location of intracellular phosphorylation sites. The structure–function relationship of the sodium–glucose cotransport protein SGLT1 has been investigated in mutagenesis studies of the cotransport protein. Intestinal glucose–galactose malabsorption is a genetic disorder resulting from multiple mutations localized in two putative transmembrane domains of SGLT1. Individual functional analysis of the different mutant SGLT1 proteins suggested the identity and location of specific amino acids that participate in the association of glucose and the inhibitor phloridzin with the cotransport protein as well as the amino acids involved in the conformational changes reorienting the solute-dissociated cotransporter. In addition to identifying the amino acids affecting the functional properties of the cotransport protein, mutagenesis studies of SGLT1 further suggest the identity and location of amino acids that participate in the membrane trafficking of cotransport proteins from its site of synthesis in the cell interior to the cell surface.

Three isoforms of the sodium–glucose cotransporter have been identified (SGLT1, SGLT2, SGLT3) and are distinguished by a high (SGLT1) or low (SGLT2, SGLT3) affinity for glucose, by differences in substrate specificity and by tissue distribution in small intestine (SGLT1) and/or renal proximal tubule (SGLT1, SGLT2). The structural basis for isoform-specific differences in function may be assessed by functional studies of *chimeric proteins* composed of different peptide sequence combinations from different isoforms. Thus, the chimera composed of the amino terminus including the initial seven transmembrane domains of SGLT3 and the final five transmembrane domains including the carboxy terminus of SGLT1 is observed to have the substrate specificity of the SGLT1 isoform. Accordingly, this finding indicates that the topological location of the glucose association site in the sodium–glucose cotransport protein is in a region of the peptide sequence extending from the eighth transmembrane domain to the carboxy terminus.

IVC. Countertransport

Countertransport, or *antiport*, is a form of secondary active transport which, like cotransport, may also mediate net transfer of a solute across the cell membrane in a direction against the electrochemical potential gradient of the solute. The energy driving countertransport of a solute against its electrochemical potential difference arises from a coupling to the transport of a second solute moving across the cell membrane from a place of higher electrochemical potential to a place of lower electrochemical potential. In contrast to cotransport, the coupling of the driving solute to the driven solute in countertransport results in transport of solutes in the opposite direction across the cell membrane. Thus, countertransporters mediate the exchange of intracellular and extracellular solutes across the cell membrane. Countertransport mechanisms are reversible and will mediate net transport either into or out of the cell until the opposing electrochemical potential differences of the driven solute and the driving solute become equal across the cell membrane. The direction of net transport mediated by a countertransport mechanism may be determined by either solute, depending on which solute has the larger driving force and the direction of the larger driving force across the membrane. The mechanism mediating countertransport may be modeled as a six-step process as shown in Fig. 11.5. The principal features of the countertransport mechanism are (1, 4) a mutually exclusive association of either solute S or A with the carrier facing side 1 or side 2 to form the SC or AC carrier complex, (2, 5) a conformational change reorienting the sidedness of the solute–carrier complex and (3, 6) a dissociation of solute with carrier on the opposite side of the membrane. In contrast to the process of facilitated diffusion or cotransport, the solute-free carrier does not undergo a conformational change in countertransport and only the SC or AC carrier complex may undergo

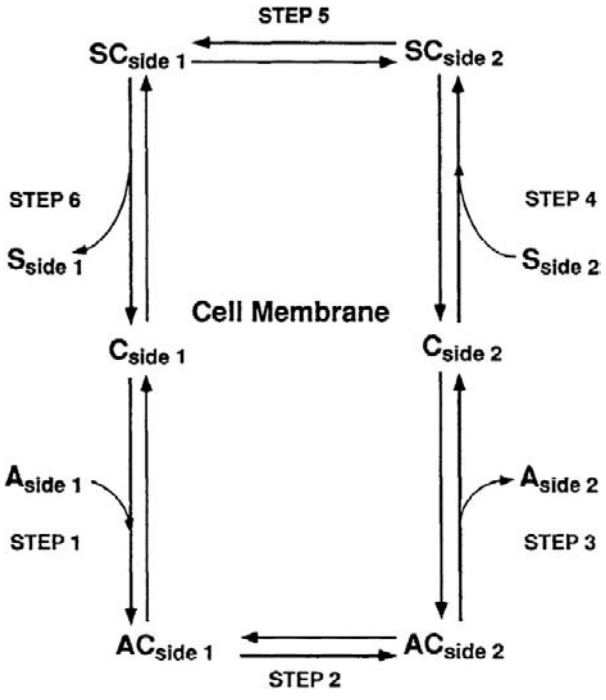

FIGURE 11.5 Kinetic model of countertransport.

a conformational change reorienting the sided access of carrier to solute. It is the absence of a conformational change reorienting the sidedness of the solute-free carrier that explicitly distinguishes countertransport from facilitated diffusion and confers the ability to mediate net solute transport against an electrochemical potential difference. Countertransport mechanisms may mediate the exchange of the same solutes (*homoexchange*) or different solutes (*heteroexchange*) and will mediate net solute transport only when exchanging different solutes. Each step describing the process of countertransport is reversible and is linked to the preceding and succeeding step by rate constants defining the rate of solute association and dissociation on either side of the membrane and by the rate of conformational change reorienting the sidedness of the solute-associated carrier. The conformational change reorienting the sidedness of the solute-associated carrier occurs more slowly than solute association−dissociation with the carrier and is considered the rate-limiting step in the countertransport process.

The unidirectional rate of solute transport across the cell membrane mediated by a countertransport mechanism depends on the concentration of both solutes at opposite sides of the membrane. When either solute concentration is constant, the countertransport rate of the second solute will approach a maximum value with increasing solute concentration and the saturation kinetics of the countertransport process may be analyzed using the Michaelis−Menten equation to obtain the kinetic parameters K_m and V_{max} for each of the exchanged solutes. The solute concentration dependence of the rate of solute transport by countertransport may be different for transport occurring into or out of the cell. A kinetic asymmetry of solute transport mediated by countertransport results from a difference in the apparent affinity (K_m) for solute at either side of the membrane and not from a difference in the maximal rate of transport (V_{max}). This limitation in kinetic asymmetry is a unique property of countertransport arising from the inability of the solute-dissociated carrier to reorient across the membrane. While kinetic asymmetry is not a property of all countertransport mechanisms, the asymmetry in solute transport mediated by a countertransporter is observed to occur for all possible combinations of solutes exchanged by the countertransport mechanism.

The countertransport of a solute may be inhibited by the presence of other solutes that interact with, but are not necessarily transported by, the same countertransport mechanism. The competitive or non-competitive nature of interaction of the inhibitor with the countertransport mechanism may be assessed by determining the effect of the inhibitor on the kinetic parameters characterizing transport of exchanged solutes by the countertransport mechanism. The same countertransport mechanism may mediate the exchange of multiple pairs of solutes that share common chemical and physical determinants. Countertransport mechanisms may be broadly categorized as either anion or cation exchange mechanisms, such as the chloride−bicarbonate countertransporter present in kidney, intestine and red blood cells or the ubiquitous pH-regulating sodium−proton countertransporter. The solute specificity of a countertransport mechanism may be characterized by determining the kinetic parameters of different solutes proven to be countertransported by the same mechanism. A comparison of the relative affinities and maximal velocities of solute transport determined experimentally will suggest the relative magnitudes of solute transport mediated by the countertransporter in vivo.

The countertransport mechanism modeled in Fig. 11.5 will be at a steady state and mediate equal transport of S and A from side 1 to side 2 and from side 2 to side 1, when the driving forces acting on solutes S and A are equal. For countertransport, this will occur when the transmembrane concentration differences of S and A are equal and in the same direction across the cell membrane. At the steady state, where no net solute transport occurs, the solute driving forces will be in thermodynamic equilibrium with each other and the transmembrane concentration ratios of S and A resulting from countertransport may be described by:

$$\frac{S_1}{S_2} = \frac{A_1}{A_2} \tag{11.5}$$

Thus, in the presence of a 10-fold concentration gradient of S, a countertransport mechanism coupling exchange of S for A may generate up to, but not exceeding, a 10-fold concentration gradient of A. Because the countertransport mechanism effectively transduces the energy stored in a 10-fold concentration gradient of S to the energy stored in a concentration gradient of A, it would be thermodynamically impossible for the countertransport mechanism to generate more than a 10-fold concentration gradient of A. The important difference distinguishing cotransport and countertransport at the steady state is the sidedness or direction of solute concentration gradients across the membrane. Cotransport is at steady state when solute concentration gradients are of equal magnitude but in opposite direction across the membrane, whereas countertransport is at steady state when solute concentration gradients are of equal magnitude and in the same direction across the membrane.

The countertransport process modeled in Fig. 11.5 describes the coupled exchange of one molecule of S for one molecule of A, or an S-to-A coupling ratio of 1:1. Whereas most countertransport mechanisms mediate the coupled exchange of single solutes, the stoichiometric coupling of solutes may exceed unity, resulting in unequal amounts of solute transported to opposite sides of the membrane. This may be modeled kinetically as an extension of Fig. 11.5 to include an extra step of solute

association on side 1 prior to carrier reorientation to face side 2 and by an extra step of solute dissociation on side 2. The kinetic parameter (K_m) characterizing the solute affinity of a countertransport mechanism must account for each additional solute association–dissociation at mutually exclusive sites in the countertransport protein. Similar to cotransport, the thermodynamic equilibrium of solute driving forces coupled by the countertransport mechanism and defining the steady state is profoundly affected by the stoichiometric coupling of solutes. Where the stoichiometric coupling of solutes by a countertransport mechanism is other than 1:1, the solute driving force will be in thermodynamic equilibrium at transmembrane solute concentration ratios raised to the power of their respective coupling coefficient as shown.

$$\left(\frac{S_1}{S_2}\right)^s = \left(\frac{A_1}{A_2}\right)^a \tag{11.6}$$

Thus, in the presence of a 10-fold concentration gradient of S, a countertransport mechanism coupling the exchange of two molecules of S for one molecule of A may generate a 100-fold concentration gradient of A in the same direction across the membrane.

Most countertransport mechanisms mediate the coupled exchange of single solutes with the same positive or negative charge and same valence and are therefore electroneutral and do not mediate net charge transfer across the membrane. However, when countertransport mechanisms mediate the coupled exchange of solutes of the same charge but different valence or mediate an unequal stoichiometric coupling of solutes of the same charge, a net charge transfer will occur across the cell membrane. Thus, the countertransport mechanism mediating sodium–calcium exchange across the cell membrane couples the influx of three sodium ions to the efflux of one calcium ion, resulting in a net transfer of positive charge into the cell. The positive electrogenicity of the sodium–calcium countertransport mechanism will tend to depolarize the cell membrane potential and results from the voltage sensitivity of at least one step in the process describing a complete sodium–calcium countertransport cycle. A voltage-dependent increase or decrease in the kinetic parameters characterizing an electrogenic countertransport mechanism would suggest an effect of membrane potential on the solute affinities of the countertransporter (K_m) and/or on the conformational change reorienting the sidedness of the solute-associated countertransporter (V_{max}). Because the conformational change reorienting the countertransporter is the rate-limiting step in the process accounting for electrogenic countertransport, a voltage-dependent increase in the rate of countertransport must result from an acceleration of at least this step. The voltage sensitivity of an electrogenic countertransport mechanism makes the cell membrane potential difference a driving force acting on solute countertransport. Thus, the rate, magnitude and direction of electrogenic countertransport of solutes across the membrane is determined by the transmembrane voltage difference in addition to the transmembrane differences in solute concentration for both solutes coupled by the countertransport mechanism. An electrogenic countertransport mechanism will be at steady state and mediate equal solute transport in both directions across the membrane when the electrical and chemical forces driving countertransport are at equilibrium. For the 1:1 exchange of charged solutes S and A with valences z_S and z_A, respectively, the driving forces may be related by:

$$RT \ln\left(\frac{S_1}{S_2}\right) = -RT \ln\left(\frac{A_1}{A_2}\right) + (z_S - z_A)F(\psi_2 - \psi_1) \tag{11.7}$$

The electrogenicity of a countertransport mechanism may arise from the exchange of solutes with the same charge and valence but with an unequal stoichiometric coupling. In this instance the driving forces acting on electrogenic countertransport must be factored by the stoichiometric coupling coefficients s and a for solutes S and A, respectively, and may be related by:

$$RT \ln\left(\frac{S_1}{S_2}\right)^s = -RT \ln\left(\frac{A_1}{A_2}\right)^a + (sz_S - sz_A)F(\psi_2 - \psi_1) \tag{11.8}$$

Thus, in the presence of a 10-fold sodium concentration gradient and a transmembrane voltage difference of 60 mV, an electrogenic countertransport mechanism mediating the 3:1 exchange of sodium and calcium ions, respectively, may generate a maximum calcium concentration gradient of 10 000-fold across the cell membrane.

The functional properties of solute transport mediated by countertransport mechanisms have been characterized in detail for many different cell- and solute-specific countertransporters. Like facilitated diffusion and cotransport, the structure–function relation of membrane proteins mediating countertransport continues to be an important question under study. The techniques of modern molecular biology have resulted in the cloning of several genes coding for countertransport proteins. Analysis of the deduced amino acid sequences of countertransport proteins suggests topological features similar to membrane proteins mediating facilitated diffusion and cotransport, including the presence of 10–12 putative transmembrane domains, the location of extracellular N-linked glycosylation sites and the location of intracellular phosphorylation sites. Low-resolution electron density maps of the red blood cell chloride–bicarbonate exchange protein have been obtained from two-dimensional crystals of the countertransport protein studied by electron microscopy. The membrane

domain of the countertransport protein exists as a dimeric structure with three electron-dense regions in each monomer. Within each monomer, the configuration of electron densities suggests two closely apposed peptide structures which are spatially separated from a third structure by a peptide domain existing in two different conformations.

The structure–function relationship of the anion exchange protein AE1 has been investigated in mutagenesis studies of the countertransport protein. The functional significance of single amino acids or domains of multiple amino acids on the interaction with transport inhibitors at the extracellular side of AE1 has been studied to determine the nature and topological location of amino acids involved in substrate interaction and translocation. These mutagenesis studies involving both the deletion and substitution of amino acids indicate several positively charged lysines at the surface of AE1 influence, and are necessary for, substrate recognition by the countertransport protein. The genes coding for three anion exchange proteins (AE1, AE2, AE3) have been identified and their gene products may be functionally distinguished by differences in inhibitor sensitivity and by the intracellular pH dependence of anion exchange activity. Multiple species-specific isoforms of the AE1 gene have been identified and the predominant sites of expression are the erythropoietic tissues and the acid-secreting cells of the renal cortical collecting duct. In contrast, AE2 gene expression occurs more widely in epithelial and non-epithelial tissues and AE3 gene expression is predominant in brain and heart. The putative transmembrane amino acid sequences of AE1, AE2 and AE3 are approximately 70% identical. The aligning portion of the N-terminal cytoplasmic domains of AE1 and AE2 are only 30% identical, with little or no corresponding sequence identity among AE1, AE2 or AE3 at the N-terminus. The observed amino acid sequence identity in the putative transmembrane domains of AE1, AE2 and AE3 is consistent with the common functional properties of the three anion exchange proteins. The divergent amino acid sequences noted in the N-terminal regions suggest possible cell- and tissue-specific differences in the regulation of anion exchange activity and/or in the intracellular sorting and membrane targeting of anion exchange proteins. Mutations in the human AE1 gene in the form of nucleotide deletions, insertions and substitutions result in inheritable diseases of the red blood cell which manifest multiple clinical phenotypes ranging from mild to severe. The single amino acid substitution characterizing mutant AE1 in Band 3 Memphis has essentially no effect on red blood cell anion exchange activity. However, the nine-amino-acid deletion characterizing AE1 in Southeast Asian ovalocytosis (SAO) results in a heterozygous genetic disorder of red blood cells with only half the normal complement of functional anion exchangers. Interestingly, the red blood cell membrane of SAO patients is more resistant to plasmodial invasion, a property that may confer a selective survival advantage against malarial infection and thereby perpetuate this genetic disorder.

BIBLIOGRAPHY

Alper, S. L. (1994). The band 3-related AE anion exchanger gene family. *Cell Physiol Biochem, 4*, 265–281.

Aronson, P. S. (1981). Identifying secondary active solute transport in epithelia. *Am J Physiol, 240*, F1–F11.

Heinz, E. (1978). *Mechanics and Energetics of Biological Transport*. New York: Springer-Verlag.

Heinz, E. (1981). *Electrical Potentials in Biological Membrane Transport*. New York: Springer-Verlag.

Naftalin, R. J. (2010). Reassessment of models of facilitated transport and cotransport. *J Membrane Biol, 234*, 75–112.

Neame, K. D., & Richards, T. G. (1972). *Elementary Kinetics of Membrane Carrier Transport*. Oxford: Blackwell Scientific.

Steel, A., & Hediger, M. (1998). The molecular physiology of sodium- and proton-coupled solute transporters. *News Physiol Sci, 13*, 123–131.

Stein, W. D. (1990). *Channels, Carriers and Pumps*. New York: Academic Press.

This page intentionally left blank

Chapter 12

Active Ion Transport by ATP-Driven Ion Pumps

Robert A. Farley

Chapter Outline

I. SUMMARY

P-type ATPases are the largest and most diverse of the ATP-dependent ion transporters in biology. They transport many different ions, metals and other substrates and are characterized by a similar structure and transport mechanism. Specific inhibitors of certain P-type ATPases are of clinical importance and the activity of the P-type ATPases is regulated at different levels by hormones and other physiologically important ligands and proteins. The crystal structures of several P-type ATPases have been determined and provide insight into many of the biochemical and pharmacological properties of this important class of transport proteins.

II. INTRODUCTION

Living cells are separated from their surroundings by lipid bilayers that limit the passive diffusion of water-soluble solutes and ions between the cytoplasm and the extracellular environment. In most instances, the concentrations of the solutes and ions are different inside and outside the cell and these concentration differences serve as thermodynamic driving forces that encourage movement of the solutes and ions across the lipid plasma membrane toward equilibrium distributions. Movement of the water-soluble solutes and ions across the impermeable lipid barrier is facilitated by membrane transport proteins that are embedded in the lipid membrane and which provide an aqueous pathway for these molecules to cross the barrier. It is often necessary for cells to maintain or establish concentration differences of ions or solutes across the cell membranes in order to sustain cellular life and this process necessarily involves moving the solutes or ions against the thermodynamic driving forces that favor equilibrium distributions. Movement of matter across cell membranes against electrochemical driving forces is called active transport and is facilitated by specialized membrane proteins that couple the thermodynamically unfavorable movement of the solute or ion to a chemical reaction that releases energy that can be captured by the transport protein. As long as the net change in free energy of the coupled reactions is negative, the active transport protein is able to catalyze the movement of the solutes and ions against their thermodynamic driving forces.

There are two broad classes of active transport proteins: primary active transport proteins and secondary active transport proteins. Primary active transport proteins are distinguished from secondary active transport proteins by the utilization of primary energy sources, such as light or chemical reactions, to drive solute or ion movement across cell membranes. The primary active transporters use energy from these sources by incorporating catalytic mechanisms driven by these energy sources into their structures.

Cell Physiology Sourcebook. DOI: 10.1016/B978-0-12-387738-3.00012-3

Secondary active transporters do not derive energy for transport from these primary energy sources but instead rely on energy stored in ion gradients established by primary active transporters to translocate solutes and ions. Most primary active transport proteins have been found to transport ions rather than water-soluble solutes and, therefore, these proteins are often called ion pumps. Although several different energy sources for ion pumps have been identified in the plant and animal kingdoms (Läuger, 1991), the most abundant and most diverse class of ion pumps utilize energy derived from the hydrolysis of ATP. This chapter is concerned with these ATP-driven ion pumps. Since these proteins derive energy for ion transport from ATP hydrolysis, they are also called ion-transporting ATPases.

III. CLASSES OF ATP-DRIVEN ION PUMPS

There are three main types of ATP-driven ion pumps: the F-type, the V-type and the P-type. The prototypical F-type ion pump is the mitochondrial F_0-F_1-ATP synthase. These proteins are multisubunit complexes containing an F_0 part, which serves as a proton transporter, and an F_1 part, which is associated with ATP hydrolysis or synthesis (Abrahams et al., 1994; Stock et al., 1999). In addition to being located in the inner mitochondrial membrane, F-type ion pumps are found in chloroplasts and bacteria. In mitochondria and chloroplasts, these proteins seem to function exclusively to synthesize ATP from ADP and P_i, with the energy for bond formation being provided by the dissipation of an H^+ gradient across the membrane through the F_0 part of the complex. Bacterial F-type ion pumps, however, can also operate in the reverse direction in which the hydrolysis of ATP releases energy that is utilized by the protein to create a proton gradient. V-type ATPases are found primarily in the membranes of intracellular vacuoles, but are also located in the plasma membranes of certain mammalian cells such as the osteoclasts and intercalated cells of the renal tubules. V-type ion pumps are structurally similar but not identical to the F-type pumps and they also actively transport protons using energy derived from ATP hydrolysis (Toei et al., 2010). The mechanism of both F-type and V-type ATPases is a rotary catalytic mechanism in which the F_0 part of the complex rotates with respect to the F_1 part, thereby coupling H^+ transport to ATP hydrolysis or synthesis. This mechanism has been the subject of several excellent reviews (Boyer, 1997; Nakamoto et al., 2008). The P-type ATPases differ from the F-type and the V-type in both structure and catalytic mechanism (Morth et al., 2011). P-type ATPases derive their names from the fact that during the catalytic cycle the γ phosphate from ATP is transferred to a conserved aspartate residue on the proteins to form a phosphoenzyme intermediate. P-type pumps are also structurally much less complex than the F-type or the V-type ATPases in that most of them are composed of a single polypeptide subunit. Two members of the P-type ATPase family, the Na^+,K^+-ATPase and the H^+,K^+-ATPase, however, also contain a second glycoprotein subunit. As shown in Fig. 12.1, the P-type ATPases are widely distributed throughout the plant and animal kingdoms, in both plasma membranes and intracellular membranes, and they catalyze the transport of many different monovalent or divalent cations, heavy metals, or phospholipids (Axelsen and Palmgren, 1998). Because of their critical importance in maintaining cell viability, the rest of this chapter will focus on P-type ion pump structures and transport mechanisms.

IV. THE ALBERS–POST MECHANISM OF ION TRANSPORT BY P-TYPE ION PUMPS

The Na^+,K^+-ATPase was the first P-type ATPase to be sufficiently well-characterized that a complete catalytic mechanism could be proposed. Although ATP hydrolysis was known for many years to be required for sodium transport out of mammalian cells, Jens Christian Skou was the first person to recognize that both of these activities were located on the same enzyme. For this and for his early contributions to characterize the mechanism of ATP-coupled ion transport by this enzyme, he shared the Nobel Prize in Chemistry in 1997 (Skou, 1998). Many investigators contributed to the elucidation of the mechanism of Na,K-ATPase (Glynn and Karlish, 1975) and the catalytic cycle that represents this mechanism is called the Albers–Post scheme in recognition of the important contributions of R. Wayne Albers and Robert Post. The Albers–Post scheme for Na^+,K^+-ATPase is shown in Fig. 12.2. A detailed account of the kinetic mechanism of the Na^+,K^+-ATPase has been published by Cantley (1981). Except for the identity of the transported ions, the Albers–Post scheme for Na,K-ATPase is generally accepted to represent the mechanism of ATP-coupled ion transport by all P-type ATPases.

In the Albers–Post scheme, the enzyme exists in two major conformations, E1 and E2. In the E1 conformation, the ion and ATP binding sites are accessible from the cytoplasmic side of the cell membrane and, in the E2 conformation, the ion binding sites are accessible from the non-cytoplasmic side of the membrane. Vectorial transport occurs as the ion binding sites are alternately exposed to the different sides of the membrane (alternating access mechanism) as the transporter undergoes conformational changes. ATP binds with high affinity ($K_d \approx 0.1–2\ \mu M$) to the E1 conformation. Cytoplasmic Na^+ also binds to the E1 conformation and activates ATP-dependent phosphorylation of the Na^+,K^+-ATPase hyperbolically with a K_M of approximately 8 mM. Phosphoenzyme formation from ATP in the presence of Na^+ also requires cytoplasmic Mg^{2+}. Na^+ is released to the outside of the cell from the E2

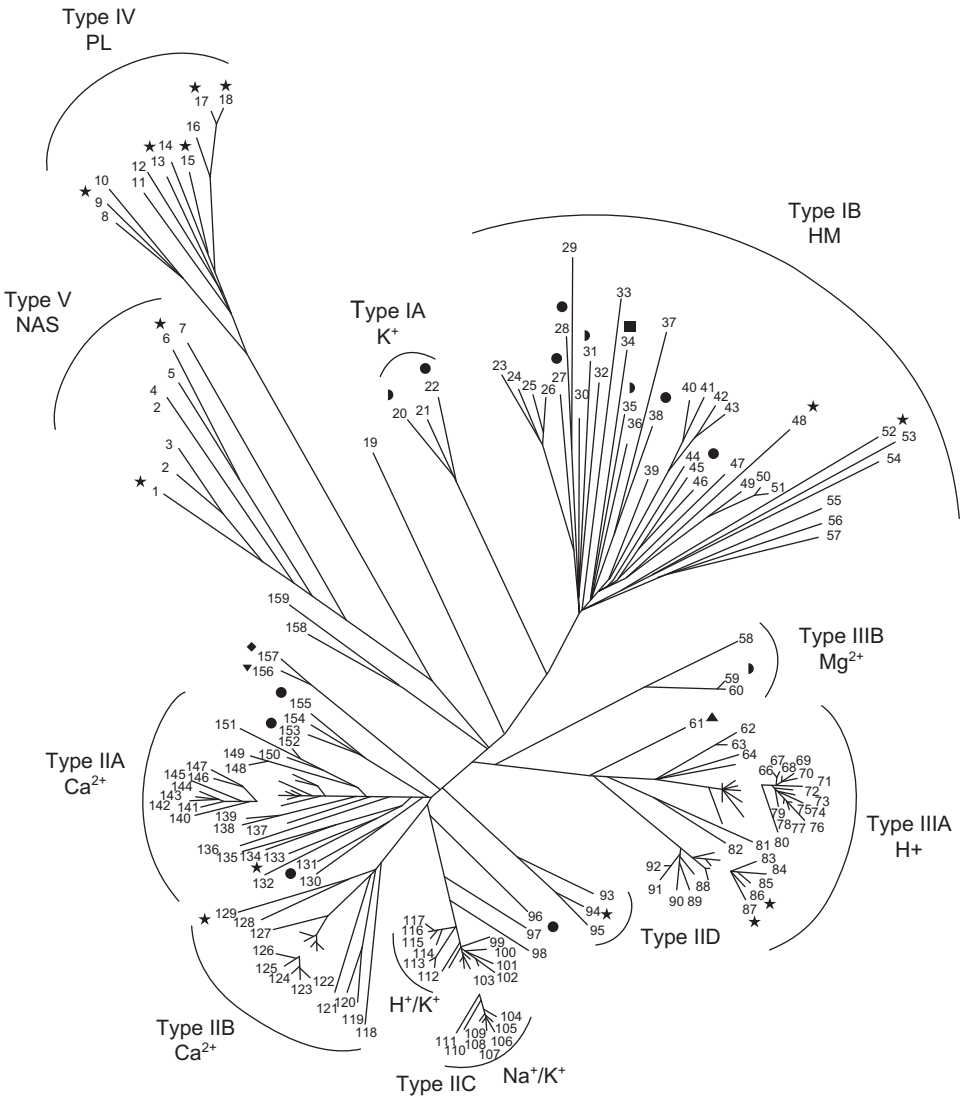

FIGURE 12.1 Phylogenetic tree for P-type ATPases. Based on 159 core amino acid sequences of P-type ATPases, the different transporters are grouped according to the substrates that are transported: *HM*, heavy metal substrates; *PL*, phospholipid substrates; *NAS*, no substrate yet determined. Type IIA and Type IIB Ca^{2+}-ATPases are PMCA and SERCA/SPCA types (see text for details). Numbers refer to the sequences used to construct the tree (Axelsen and Palmgren, 1998). *(Reproduced from Axelsen and Palmgren, 1998, with permission.)*

conformation, which has a low affinity for Na^+. Extracellular potassium binds with high affinity ($K_M \approx 0.1$ mM in the absence of sodium) to the same sites on E2 from which sodium was released and is released into the cytoplasm from the E1 conformation, which binds K^+ with low affinity. The ion binding sites on E1 are very specific for Na^+ and only Li^+ will substitute for Na^+ to catalyze some enzymatic reactions, whereas the ion binding sites on E2 will bind a number of monovalent cations in addition to K^+, including Rb^+, NH_4^+ and Cs^+, in a catalytically competent manner.

Transport of the different ions is sequential, with Na^+ being transported out of the cell before K^+ is transported into the cell. One molecule of ATP is hydrolyzed during a single turnover of the catalytic cycle and is coupled to the transport of three Na^+ ions out of the cell and two K^+ ions into the cell. This difference in charge transport stoichiometry generates an electrical potential difference across the cell membrane as three positive charges are moved to the outside of the cell and two positive charges are moved to the cytoplasm (De Weer et al., 1988). Measurement of ionic current carried by the Na^+,K^+-ATPase under different experimental conditions showed that current is associated with the movement of Na^+, but that transport of K^+ is electroneutral. This observation suggests that there is the equivalent of two negative charges in the ion binding sites of Na^+,K^+-ATPase and that these charges are neutralized by the binding of two monovalent cations.

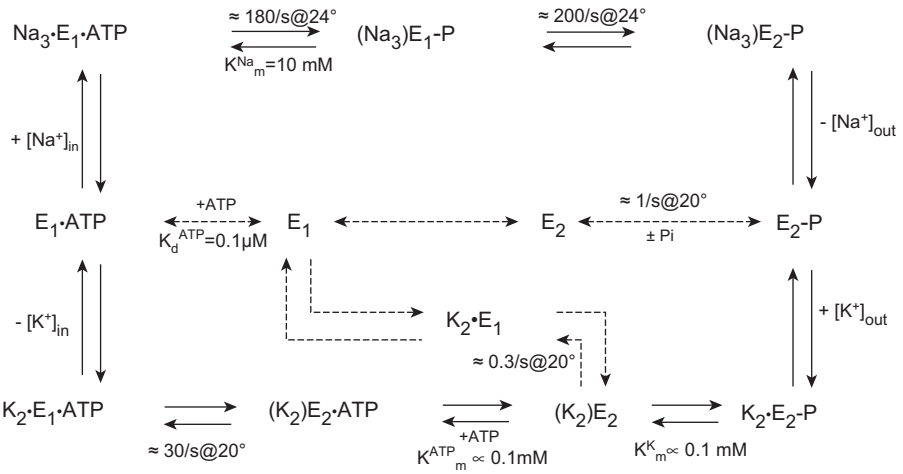

FIGURE 12.2 The Albers–Post scheme for ATP-dependent ion transport by the Na^+,K^+-ATPase. Solid arrows represent forward and reverse transitions between states of the enzyme that are populated under physiological conditions of turnover. Dashed arrows represent transitions between states that are not present under normal physiological conditions but which can be shown to exist under defined experimental conditions. Rate constants and K_d or K_m values are from Cantley (1981). Positive (+) and negative (−) signs correspond to binding and dissociation of ions from the protein. See text for a discussion of the mechanism.

During the transition between the E1 and the E2 conformational states, the transported ions are occluded within the structure of the protein. In the occluded state, the bound ions are not exchangeable with similar ions in either the cytoplasmic or non-cytoplasmic solutions. Occluded transported cations in P-type ATPases, representing an intermediate step during the transition between E1 and E2 states, were first suggested by Glynn and Hoffman, and by Robert Post and his coworkers, and were experimentally measured in Na^+,K^+-ATPase by Ian Glynn and Luis Beauge (Glynn and Karlish, (1990). Recently, crystal structures for several solute transporters have confirmed the existence of occluded states in all types of alternating access transport proteins (Shimamura et al., 2010; Weyand et al., 2010).

When cytoplasmic ATP, Mg^{2+} and Na^+ are bound, the γ phosphate of ATP is transferred from the bound nucleotide to an aspartate residue on the Na^+,K^+-ATPase, forming a covalent phosphoenzyme intermediate, and ADP is released into the cytoplasm. This aspartate residue is conserved in all P-type ATPases. The binding of K^+ to the E2 form of the enzyme catalyzes the hydrolysis of the phosphoenzyme intermediate, with the concurrent release of P_i and Mg^{2+} to the cytoplasm. Upon hydrolysis of the phosphoenzyme, potassium ions become occluded and the enzyme conformation changes from E2 to E1. This transition is very slow in the absence of cytoplasmic ATP ($k \approx 0.2–0.3\ s^{-1}$), but is accelerated more than a 100-fold by the binding of ATP with low affinity to the E2 conformation of the protein ($K_M > 1$ mM). Since normal cytoplasmic ATP concentrations are 2–5 mM, this transition is usually fast under physiological conditions.

In P-type ATPases other than Na^+,K^+-ATPase, the identity of the transported cations is different, but the essential catalytic mechanism is the same. For Ca^{2+}-ATPases, the transport stoichiometry is different for the different subfamilies (see below), with one or two Ca^{2+} ions transported out of the cytoplasm in exchange for one or two protons. In Ca^{2+} pumps where it has been measured, the transport stoichiometry is electrogenic and generates a voltage difference across the membrane. In the gastric H^+,K^+-ATPase, one proton is transported from the cytoplasm of the parietal cell and one K^+ is transported into the cell. In this protein, net transport is electroneutral.

Measurements of individual reaction steps in the Albers–Post cycle have been made under conditions that prevent progression of the pumps through the complete cycle. These partial reactions of the pumps have been very useful for the characterization of individual rates of the reaction steps and the interaction of different ions and ligands with the pumps. In vitro measurements like these have shown that every step in the mechanism is reversible, however, under physiological conditions of ion and ligand concentrations and pH, the pumps progress around the cycle shown in Fig. 12.2 in a clockwise direction. The thermodynamic basis for this directionality was provided by Pickart and Jencks (1984) for the sarcoplasmic reticulum Ca^{2+}-ATPase. After measuring all but one of the microscopic equilibrium constants in the Albers–Post scheme for the Ca^{2+}-pump, these investigators used the equilibrium constants to construct free energy diagrams for the Ca^{2+} transport cycle under standard conditions of 1 M reactant concentrations and under physiological conditions. Under physiological conditions in which active Ca^{2+} transport takes place, the Gibbs free energy changes (ΔG) are favorable for calcium binding from the cytoplasm and dissociation into the lumen of the sarcloplasmic reticulum, while ΔG for the other steps in the cycle are either balanced or slightly negative as the enzyme progresses in a clockwise direction through the cycle shown in Fig. 12.2.

V. STRUCTURES OF P-TYPE ION PUMPS

The nucleotide sequences of complete cDNA clones of both the sarcoplasmic Ca^{2+}-ATPase and the Na^+,K^+-ATPase were published in 1985 by the laboratories of Numa, MacLennan, and Lingrel. Soon thereafter, cDNA sequences of several P-type pumps from different organisms were published. Considerable effort prior to these accomplishments was made by many investigators using protein chemical methods and chemical modification of the proteins to identify amino acids that are important to the catalytic or transport functions of the different pumps, or are located in functionally important sites of the proteins. Photochemical, immunological and biochemical approaches were also used to determine the folding of the pump polypeptides through the cell membrane. After the amino acid sequences of the proteins were deduced from the cDNA sequences, these results could be mapped on the complete sequences of the different pumps and it was found that all P-type pumps contain several highly conserved amino acid sequences that are located in functionally important sites. Particularly highly conserved amino acids are found in the ATP binding sites of these proteins (Aravind et al., 1998) and, perhaps surprisingly given that different pumps transport different cations, many of the same amino acids are found at the ion binding sites in the different proteins (Morth et al., 2011). Extensive site-directed mutagenesis of Ca^{2+}-ATPase and Na^+,K^+-ATPase, together with heterologous expression of the mutant pumps in Xenopus oocytes, yeast or mammalian cells, confirmed the importance of many amino acids previously identified using protein chemical methods and identified additional amino acids that are important for ATP-coupled ion transport by these proteins. Amino acids that are important for specific functions of the pumps, such as ATP binding or hydrolysis, are often found in widely separated sequences of the polypeptides, indicating that the folding of the polypeptides is complex, bringing together these widely separated amino acids into specific functional sites.

The structural basis for active ion transport by the P-type ATPases was elevated to a new level in 2000 when the laboratory of Chikashi Toyoshima published the first atomic resolution structure of the sarcoplasmic reticulum Ca^{2+}-ATPase (Toyoshima et al., 2000). Since that time, crystal structures of the Ca^{2+}-ATPase in conformations that correspond to most of the catalytic intermediates in the Albers–Post cycle have been determined by several investigators. These structures provide an unprecedented opportunity to look into the structural basis for the activity of this ion pump (Moller et al., 2010). The Na^+,K^+-ATPase has also been crystallized and the overall three-dimensional structure of the catalytic α subunit of Na^+,K^+-ATPase is almost identical to that of the Ca^{2+}-ATPase, consistent with the expectation that all P-type ion pumps are composed of a similarly folded catalytic polypeptide (Morth et al., 2007; Shinoda et al., 2009). The structures of the Ca^{2+}-ATPase in the E1 conformation with bound Ca^{2+} ions and the Na^+,K^+-ATPase with bound K^+ ions are shown in Fig. 12.3.

The catalytic polypeptides of the P-type pumps are folded into both a membrane-embedded domain and three separate structural domains that are located in the cytoplasm of the cell. The N domain binds ATP, the P domain contains the conserved aspartate residue that is phosphorylated by ATP and the A domain contains a conserved TGES sequence that is involved in dephosphorylation of the phosphoenzyme. During ATP-coupled ion transport by the P-type ATPases, large rigid body movements of the N, P and A domains occur as ATP bound to the N domain is brought into position for transfer of the γ-phosphate to the aspartate residue in the P domain and the phosphoenzyme is subsequently hydrolyzed in a reaction that requires the TGES residues in the A domain. The movements of the cytoplasmic domains are transmitted to the transmembrane domain and shift the affinity of the ion binding sites located there between high affinity and low affinity to favor ion binding or release. Only a small amount of protein mass of the catalytic subunits is located on the non-cytoplasmic side of the membrane. In contrast, most of the mass of the β subunit of the Na^+,K^+-ATPase and H^+,K^+-ATPase is located on the extracellular side of the plasma membrane of cells in which these proteins are found. The transmembrane domains of the P-type pumps that have been crystallized consists of a bundle of 10 α–helices that are connected to the cytoplasmic domains of the proteins primarily through two long transmembrane α–helices that merge into the cytoplasmic domains. These connections between the membrane-embedded domain and the cytoplasmic domains provide the basis for the mechanical coupling of ATP hydrolysis to changes in the affinity of the ion binding sites for the transported cations. Amino acid sequence comparisons suggest that some members of the P-type ATPase family may contain fewer than 10 transmembrane helices. The structure of the Ca^{2+}-ATPase, shown in Fig. 12.3A, contains two Ca^{2+} ions bound near the middle of the transmembrane domain. In the crystal structure of Na^+,K^+-ATPase, shown in Fig. 12.3B, two bound K^+ ions are bound in the analogous location on the α subunit. The two K^+ ions presumably bind to the same sites where three Na^+ ions bind during sodium transport by the Na^+,K^+-ATPase, but the location of the third Na^+ site remains ambiguous. In both Ca^{2+}-ATPase and Na^+,K^+-ATPase, the bound cations are coordinated by both main chain carbonyl oxygen atoms and by amino acid side chains that contain oxygen atoms. Despite differences in the identity and charge of the bound cations, several of the amino acid side chains that coordinate the cations are identical in both Ca^{2+}-ATPase

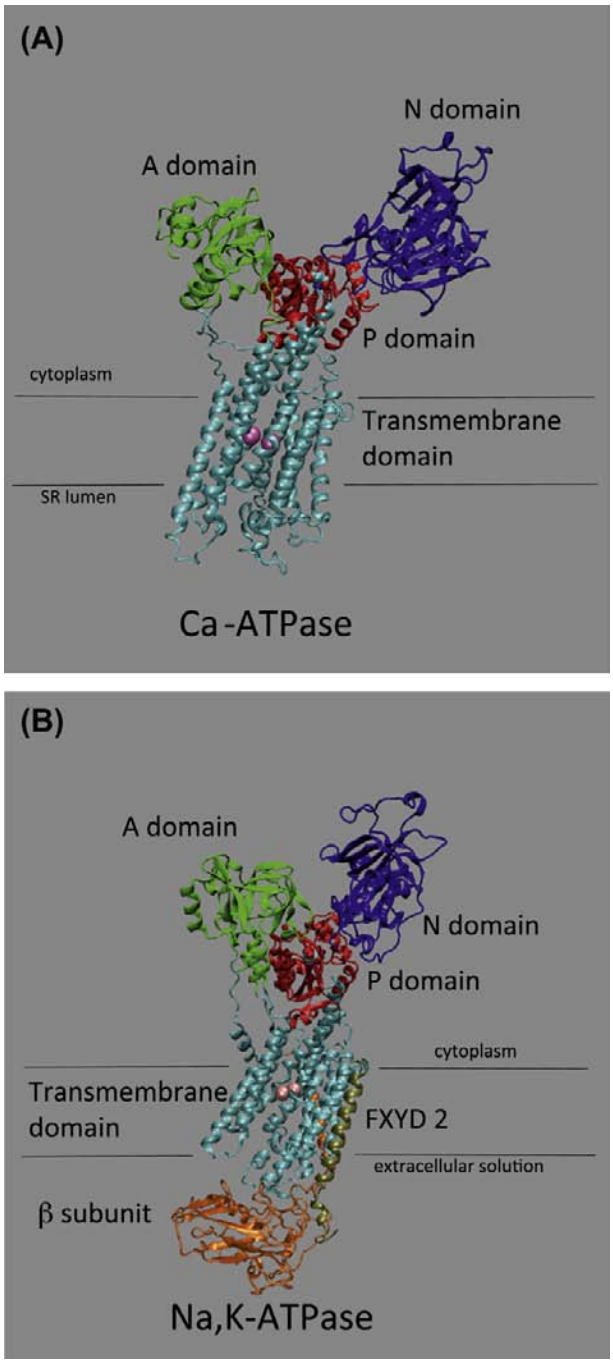

FIGURE 12.3 Molecular structures for sarcoplasmic reticulum Ca^{2+}-ATPase (A) and Na^+,K^+-ATPase (B). In both structures, the approximate locations of the cytoplasmic and non-cytoplasmic membrane surfaces are indicated by black lines. The N domain, the P domain and the A domain of each structure are located on the cytoplasmic side of the membrane, which is at the top of each panel. The transmembrane domain, consisting of 10 transmembrane helices, is colored cyan in both structures. In (A), two Ca^{2+} ions bound within the transmembrane domain are shown as magenta spheres and in (B), two K^+ ions in similar locations in Na^+,K^+-ATPase are also shown. In each structure, the aspartate residue in the P domain that is phosphorylated by ATP is shown in space-filling representation. In (B), the β subunit of Na^+,K^+-ATPase is shown in orange and the FXYD2 protein is shown in gold. Most of the mass of the β subunit is exposed to the non-cytoplasmic side of the membrane at the bottom of the panel. Protein Data Bank files are 1SU4 for panel A and 2ZXE for panel B. Structures were drawn using VMD.

and Na^+,K^+-ATPase. In several of the crystal structures, no clear water-filled access pathway to the ion binding sites from either the cytoplasm or the non-cytoplasmic side of the membrane is obvious, suggesting that some of these structures contain occluded cations.

VI. BETA SUBUNITS

Only the Na^+,K^+-ATPase and the H^+,K^+-ATPase are known to require a second (β) subunit for their activity (McDonough et al., 1990). A requirement for the β subunit was demonstrated for Na^+,K^+-ATPase by showing that yeast cells, which are one of the few eukaryotic cells that do not contain an endogenous Na^+,K^+-ATPase, would express functional Na^+,K^+-ATPase pumps only when cDNA for both α and β subunits was transfected into the cells (Horowitz et al., 1990). Transfection of cDNA for either the α subunit or the β subunit alone did not result in any functional Na^+,K^+-ATPase pumps. As shown in Fig. 12.3B, the β subunits of P-type pumps are integral membrane proteins with a single transmembrane α helix. Most of the mass of these polypeptides is located on the non-cytoplasmic side of the membrane and only a small N-terminal region is found in the cytoplasm. The extracellular domain of the β subunits contains several N-linked oligosaccharide chains, the number of which is different for the different β subunits. Since all of the functionally important amino acids of the P-type pumps are associated with the α subunit, the role of the β subunit in the activity of these pumps was unclear for many years. Early data indicated that the β subunit assembled with the α subunit early in the process of protein synthesis and maturation and it was found that in the absence of the β subunit, the α subunit was not delivered to the plasma membrane and was rapidly degraded. Association of the β subunit with the α subunit facilitates the correct folding of the α subunit (Geering, 1990). Chimeric constructs in which the extracellular domains of the Na^+,K^+-ATPase and gastric or colon H^+,K^+-ATPase β subunits were exchanged onto the other protein's transmembrane domain and proteolytic cleaveage of the β subunits, showed that the structure of the β subunit extracellular domain also influenced the affinity of the α subunits for extracellular K^+ ions. The structural basis for these observations was revealed in the crystal structure of the Na^+,K^+-ATPase (see Fig. 12.3B) where the extracellular domain of β is seen to interact with the α subunit near the site where extracellular K^+ binds to

the protein (Shinoda et al., 2009). Although it is now apparent that the β subunits of Na^+,K^+-ATPase and H^+,K^+-ATPase influence both protein folding and assembly and the interaction of K^+ with the pumps, it is not known why only these two members of the P-type ATPase family require the β subunit. It is also unknown how, in cells that contain both of these ion pumps, such as gastric parietal cells, the correct β subunit assembles with each α subunit, since it has been shown in heterologous expression systems that either α subunit will assemble with the β subunit of the other pump. In colon and kidney, there is immunological evidence that the H^+,K^+-ATPase α subunits assemble into functional pumps with the Na^+,K^+-ATPase β1 subunit.

VII. ISOFORMS OF PUMP SUBUNITS AND SUBFAMILIES OF P-TYPE PUMPS

Multiple isoforms of both α subunits and β subunits of Na^+,K^+-ATPase have been identified (Lingrel, 1992; Woo et al., 1999). These isoforms are encoded by different genes, have >80% identical amino acid sequences and may be located in different cells throughout the organism in which they are found. Four isoforms of the α subunit (α1−α4) of Na^+,K^+-ATPase, for example, and three isoforms of the β subunit (β1−β3) of this pump are present in humans. α1 is widely distributed in many tissues of the body and is usually the isoform found in cells that contain only one isoform of the Na^+,K^+-ATPase. α2 and α3 are found primarily in muscle and neuronal cells and α4 is restricted to testis. More than one isoform of the α subunit may be present in a single cell. The different isoforms of the α subunit have slightly different affinities for Na^+ and K^+ that appear to enable different cells to transport these ions optimally under different conditions. In some cells, such as rat mesenteric artery myocytes and cortical astrocytes, the α2 or α3 subunit of Na^+,K^+-ATPase is confined to microdomains of the plasma membrane located close to the sites of Ca^{2+} release from the sarcoplasmic/endoplasmic reticulum and to the plasma membrane Na^+/Ca^{2+} exchanger. This juxtaposition of the Na^+,K^+-ATPase and proteins involved in calcium homeostasis provides an explanation for how cardiac glycosides, which bind only to Na^+,K^+-ATPase, can influence local $[Ca^{2+}]_{in}$ and cellular processes that depend on mobilization of Ca^{2+} from intracellular stores (Golovina et al., 2003).

Based on cellular location, sensitivity to inhibitors and amino acid sequence, the Ca^{2+}-ATPases can be divided into three subfamilies: those that are located in the plasma membrane of cells (PMCA); those that are located in the sarcoplasmic reticulum of muscle or the endoplasmic reticulum (SERCA); and those that are located in organelles of the secretory pathway (SPCA), such as the Golgi (although these may have a post-Golgi distribution in some cells). Although there are some biochemical differences in the kinetics of these different types of Ca^{2+} pumps, the primary functional difference is that the Ca^{2+} pumps that are located in the plasma membranes are regulated by interaction with the Ca^{2+}-binding protein calmodulin and the pumps located in intracellular membranes do not interact with calmodulin. Plasma membrane Ca^{2+} pumps are autoinhibitory and, when intracellular Ca^{2+} levels rise, Ca^{2+}-calmodulin binds to these pumps, releases the inhibition, and increases Ca^{2+} efflux from the cell. Although these different forms of the Ca^{2+}-ATPases represent different subfamilies of this pump that actively transport Ca^{2+} using the Albers−Post mechanism, within each subfamily different isoforms have been identified (Brini and Carafoli, 2009). There are three isoforms for the SERCA pumps, four isoforms for the PMCA pumps and two isoforms for the SPCA pumps in mammals. For the H^+,K^+-ATPases, there are two subfamilies of pumps, the gastric type and the non-gastric type (Shin et al., 2009; Gumz et al., 2010). Gastric type H^+,K^+-ATPase is found only in the gastric parietal cells and in the renal collecting duct, whereas the non-gastric type has a much wider tissue distribution that includes kidney, prostate, uterus, placenta, skin, brain and colon. In the stomach, the gastric H^+,K^+-ATPase is responsible for the secretion of acid and the inhibition of this enzyme is an effective treatment for symptoms of peptic ulcer. The physiological role of the non-gastric H^+,K^+-ATPases seems to be primarily as a mechanism for the conservation of potassium during states of potassium deprivation.

VIII. FXYD PROTEINS

In some preparations of Na^+,K^+-ATPase, a small polypeptide is found to be associated with the pump in addition to the α and β subunits. It was initially suggested by some investigators that this polypeptide was a third (γ) subunit of the pump, however, it was subsequently shown that sodium pumps do not require the γ polypeptide for their function and so this is not a true subunit of the enzyme. Nevertheless, measurement of the ion dependence of Na^+,K^+-ATPase activity in cells either containing this polypeptide or not, demonstrated that the $K_{½}$ values for activation of pump activity by Na^+ or K^+ were different in the presence of the γ polypeptide and in its absence. The magnitude of the differences is small, but is possibly significant for ionic homeostasis in different tissues. It is now known that there is a small family of proteins containing the conserved amino acid sequence FXYD that modulate the activity of Na^+,K^+-ATPase in different cells (Sweadner and Rael, 2000). These different proteins are listed in Table 12.1.

TABLE 12.1 FXYD Protein Tissue Expression and Functional Effects on Na^+,K^+-ATPase

Family Designation	Common Name	Tissue Expression	Functional Effects on Na^+,K^+-ATPase
FXYD 1	Phospholemman	Heart, liver, skeletal muscle	↑ $K_{½}$ K^+ ↑ $K_{½}$ Na^+
FXYD 2	γ-subunit	Kidney, heart, stomach	↑ $K_{½}$ Na^+
FXYD 3	MAT-8	Colon, stomach, uterus	↑ $K_{½}$ K^+ ↑ $K_{½}$ Na^+
FXYD 4	CHIF	Distal colon, kidney collecting duct	↑ $K_{½}$ K^+ ↓ $K_{½}$ Na^+
FXYD 5	RIC	Heart, brain, spleen, lung, skeletal muscle, kidney, testis	Not determined
FXYD 6	-	Brain, kidney	Not determined
FXYD 7	-	Brain	↑ $K_{½}$ K^+

FXYD proteins have a single transmembrane helix and are expressed in a tissue-specific pattern. The crystal structure of Na^+,K^+-ATPase shows that the FXYD proteins bind to transmembrane helices of the α subunit and also interact with the α subunit and the β subunit near the extracellular surface of the membrane (see Fig. 12.3B) (Shinoda et al., 2009). Based on the crystal structure, it has been suggested that the FXYD proteins exert their effects on ion binding to the α subunit through contacts between amino acids located in the transmembrane helices of each polypeptide. Alterations in either the expression or the function of different FXYD proteins have been implicated in several disease states including acute cardiac ischemia, renal hypomagnesemia, malignancies and ventricular remodeling following myocardial infarction, but the mechanism whereby these changes in FXYD expression or function are involved is not known. One FXYD protein, phospholemman, is a substrate for protein kinase A and protein kinase C in the heart and is involved in the regulation of cardiac contractility (Bers and Despa, 2009). There is some evidence that phospholemman interacts with the cardiac Na^+/Ca^{2+} exchanger in addition to the Na^+,K^+-ATPase and may exert its regulatory effect through interactions with the exchanger.

IX. REGULATION OF P-TYPE ATPase ACTIVITY

In order to survive under different environmental conditions, cells need to increase or decrease their transport of ions and solutes appropriately as the need to take up or excrete these substances changes. The transport capacity of cells for any transported solute can be changed either by increasing or decreasing the abundance of functional transport proteins in the cell membranes or by changing the intrinsic transport activity of the individual transporters. Changes in the number of functional transport proteins in cell membranes can be accomplished by changes in translational and transcriptional rates of transporter genes or by inserting or removing transporters from the cell membranes. Changes in the intrinsic activity of transport proteins can accompany post-transcriptional modification of the transport proteins, changes in the concentration of transported substrates and ions and interaction of the transporters with regulatory proteins or small molecule regulators. All of these mechanisms are known to occur for the regulation of different P-type ATPases and, in several instances, multiple types of regulation are observed. For the Na^+,K^+-ATPase, for example, aldosterone markedly increases transepithelial sodium absorption in the distal nephron by increasing apical Na^+ influx. The increase in $[Na^+]_{in}$ increases Na^+,K^+-ATPase activity because maximal pump activity is achieved at $[Na^+]_{in}$ levels considerably above those found in resting cells (see below). Prolonged aldosterone secretion, however, also induces increases in mRNA levels for both α and β subunits of the sodium pump and an increase in the abundance of the pump protein in the cell membrane. Thyroid hormone also increases mRNA levels for Na^+,K^+-ATPase subunits, leading to an increase in the number of active sodium pumps in the cell membrane. The increase in energy consumption associated with increased sodium pump activity plays an important role in the calorigenic action of thyroid hormone.

Insulin has been shown to increase the number of functional sodium pumps in the plasma membrane of insulin-sensitive cells, such as skeletal muscle, by increasing the movement of intracellular vesicles

containing the pump to the plasma membrane, just as insulin increases GLUT 4 transporter abundance in the plasma membrane and increases glucose uptake in these tissues (Benziane and Chibalin, 2008). The intracellular vesicles containing GLUT4 are different, however, from the vesicles that contain the Na^+,K^+-ATPase. In the stomach, gastric parietal cells are stimulated by histamine that is released from enterochromaffin-like cells after a meal, in response to vagal stimulation and the release of acetylcholine and gastrin. Histamine binds to H2 receptors on the parietal cell and results in an increase in cAMP in the cell. Several targets of cAMP-dependent kinase that bind actin have been identified and, through a mechanisms that is not completely understood, a cytoskeletal rearrangement occurs in the parietal cells that facilitates fusion of intracellular tubulovesicles containing the gastric H^+,K^+-ATPase with the plasma membrane of the cell at the secretory canaliculus (Forte and Zhu, 2010). Delivery of the H^+,K^+-ATPase to the plasma membrane increase the capacity of the cell to secrete acid as it increases the surface area of the canalicular membrane of the cell 50−100-fold. When the stimulus is withdrawn, the H^+,K^+-ATPase is withdrawn and the tubulovesicles are reformed.

The K_M for intracellular Na^+ activation of the sodium pump is near the intracellular concentration of Na^+ for most mammalian cells (5−10 mM) and even small changes in $[Na^+]_{in}$ will have significant effects on pump activity due to the sigmoid relationship between $[Na^+]_{in}$ and pump activity. The dependence of sodium pump activity on $[Na^+]_{in}$ is the primary mechanism for the minute-to-minute regulation of cytoplasmic Na^+ concentrations. Under physiological conditions, the concentration of extracellular potassium is generally close to the saturation concentration for stimulation of Na^+,K^+-ATPase activity and changes in extracellular K^+ do not normally have significant effects on sodium pump activity.

Several hormones and neurotransmitters that bind to receptors at the extracellular surface of the cell membrane activate cascades of protein kinases and protein phosphatases and there are many reports of either activation or inhibition of P-type ATPase activity by these signaling molecules. Although it is possible to recover phosphoryated P-type pump polypeptides from in vitro assays that contain protein kinase A or protein kinase C, it has been difficult to demonstrate a direct relationship between pump phosphorylation and changes in activity in vivo. At this time, there is no conclusive evidence for sodium pump activity being affected by direct phosphorylation of the α or β subunits by protein kinases, despite many reports that the α subunit can be phosphorylated by these enzymes in vitro. One of the best examples of regulation of P-type ATPase activity by direct protein kinase phosphorylation is the response of the fungal plasma membrane H^+-ATPase activity in carbon-starved yeast cells to the addition of glucose (Lecchi et al., 2007). In the yeast Pma1 H^+-ATPase, there are two adjacent serine and threonine amino acids in the cytoplasmic carboxy-terminal tail of the protein that are phosphorylated. T912 is constitutively phosphorylated and is the major site of phosphorylation on the protein in cells that have been starved for carbon and in which the H^+-ATPase activity is low. Addition of glucose to these cells leads to a threefold reduction of phosphorylation at T912, an 11-fold increase in phosphorylation at S911 and a 5−10-fold increase in ATPase activity in the cells. The increase in ATPase activity is due to a several-fold increase in the affinity of the proton pump for ATP that occurs when the phosphorylation status of these two amino acids changes in response to glucose addition.

Regulation of P-type ATPase activity by interaction with other regulatory proteins has been shown for Na^+,K^+-ATPase and the FXYD proteins, as discussed above, and for the SERCA pumps and phospholamban. Phospholamban is an endogenous inhibitor of the SERCA pumps that binds to the pumps and reduces their affinity for Ca^{2+} without affecting the maximum transport rate, especially at low $[Ca^{2+}]$. In response to adrenergic stimulation in the heart, phospholamban is phosphorylated by protein kinase A on a serine residue, and dissociates from the ATPase. Without associated phospholamban, the SERCA pumps have higher affinity for Ca^{2+} and pump activity is increased. Recent data indicate that the FXYD protein phospholemman affects Na^+,K^+-ATPase activity in the same way (Bers and Despa, 2009). Unphosphorylated phospholemman binds to the pump and reduces the affinity of the pump for cytoplasmic Na^+, but when phospholemman is phosphorylated, the affinity of the sodium pump for sodium increases.

X. PHARMACOLOGICAL INHIBITORS OF P-TYPE ATPases

Much of the information that has been obtained for some of the P-type ATPases is a result of the unique inhibition of those pumps by small molecules, several of which are of clinical or physiological importance. The most well-known example is the inhibition of Na^+,K^+-ATPase by cardiac glycosides, such as digoxin, digitalis and ouabain, whose only known receptor is the Na^+,K^+-ATPase. Cardiac glycosides have been used for many years to treat patients with congestive heart failure and these drugs exert their effects on the heart through a mechanism that couples inhibition of a fraction of the total cardiomyocyte sodium pump activity to activation of the Na^+/Ca^{2+} exchanger. Increases in $[Na^+]_{in}$ localized near the exchanger lead to a reduced influx of extracellular Na^+ and efflux of cytoplasmic Ca^{2+}. This results in an increase in sarcoplasmic reticulum Ca^{2+} levels that are available for release when

the cardiomyocyte is stimulated. Increased release of Ca^{2+} from the SR leads to an increase in the force of contraction. Although cardiac glycosides are found abundantly in certain plants, it has been shown recently that an endogenous ouabain is found in many mammals (Schoner and Scheiner-Bobis, 2007). Endogenous ouabain at concentrations significantly lower than those that inhibit the Na^+,K^+-ATPase catalytic activity binds to the sodium pump and activates several signaling pathways in cells that affect protein kinase activity, $[Ca^{2+}]_{in}$ and gene expression. Na^+,K^+-ATPase is also inhibited by very low concentrations of the marine toxin palytoxin. Palytoxin is made by marine corals of the genus *Palythoa* and is one of the most potent animal toxins known, with an LD_{50} of approximately 0.15 μg/kg in mice. When palytoxin binds to animal cells, it causes a non-specific leak of cations across the plasma membrane. Palytoxin-induced K^+ efflux from cells can be antagonized by ouabain, indicating that Na^+,K^+-ATPase is involved in the mechanism of palytoxin toxicity. Expression of mammalian Na^+,K^+-ATPase in yeast showed that palytoxin binds directly to the Na^+,K^+-ATPase and converts the active ion pump into an ion channel (Scheiner-Bobis et al., 1994).

A clinically relevant inhibitor of the gastric H^+,K^+-ATPase is omeprazole. Omeprazole is a benzimidazole that, in its activated form, reacts with sulfhydryl groups on proteins. As such is not specific for the gastric H^+,K^+-ATPase, but because it must be activated by acidic conditions, such as those found in the stomach, it is inactive in most tissues of the body. When activated by the low pH found in the stomach, omeprazole reacts with a specific cysteine residue in the gastric H^+,K^+-ATPase and inhibits gastric acid secretion (Sachs and Wallmark, 1989). The drug is effective for the treatment of the symptoms of hyperacidity and peptic ulcers and is one of the best selling drugs in the world. Because of the clinical and financial benefits of treating these symptoms, much effort has been made to find additional specific gastric H^+,K^+-ATPase inhibitors and several, including the imidazopyridines such as SCH28080, have been identified that inhibit the pump by different mechanisms.

SERCA pumps are uniquely inhibited by thapsigargin, a sesquiterpene lactone from the plant *Thapsia garganica*. Thapsigargin is a component of a root extract from this plant that was used in ancient times for the treatment of muscle and joint inflammations, but which caused skin irritation. This irritation is now known to be due to the effects of thapsigargin on intracellular Ca^{2+} pools and the release of histamine. Thapsigargin inhibits SERCA pumps at subnanomolar concentrations in what appears to be a stoichiometric interaction with the pumps by binding to the SERCA pumps in the transmembrane domain and locking the enzyme in the E2 conformation (Inesi and Sagara, 1992). This interferes with the conformational changes that are needed for the active pumping of Ca^{2+} (Toyoshima and Nomura, 2002).

BIBLIOGRAPHY

Abrahams, J. P., Leslie, A. G. W., Lutter, R., & Walker, J. E. (1994). Structure at 2.8Å resolution of F1-ATPase from bovine heart mitochondria. *Nature, 370*, 621–628.

Aravind, L., Galperin, M. Y., & Koonin, E. V. (1998). The catalytic domain of the P-type ATPase has the haloacid dehalogenase fold. *Trends Biochem Sci, 23*, 127–129.

Axelsen, K. B., & Palmgren, M. G. (1998). Evolution of substrate specificities in the P-type ATPase superfamily. *J Mol Evol, 46*, 84–101.

Benziane, B., & Chibalin, A. V. (2008). Frontiers: skeletal muscle sodium pump regulation: a translocation paradigm. *Am J Endocrinol Metab, 295*, E553–E558.

Bers, D. M., & Despa, S. (2009). Na/K-ATPase – an integral player in the adrenergic fight-of-flight response. *Trends Cardiovasc Med, 19*, 111–118.

Boyer, P. D. (1997). The ATP synthase – a splendid molecular machine. *Annu Rev Biochem, 66*, 717–749.

Brini, M., & Carafoli, E. (2009). Calcium pumps in health and disease. *Physiol Rev, 89*, 1341–1378.

Cantley, L. C. (1981). Structure and mechanism of the (Na, K)-ATPase. *Curr Topics Bioenerget, 11*, 201–237.

De Weer, P., Gadsby, D. C., & Rakowski, R. F. (1988). *Ann Rev Physiol, 50*, 225–241.

Forte, J. G., & Zhu, L. (2010). Apical recycling of the gastric parietal cell H, K-ATPase. *Ann Rev Physiol, 72*, 273–296.

Geering, K. (1990). Subunit assembly and functional maturation of Na, K-ATPase. *J Membr Biol, 115*, 109–121.

Glynn, I. M., & Karlish, S. J. D. (1975). The sodium pump. *Ann Rev Physiol, 37*, 13–55.

Glynn, I. M., & Karlish, S. J. D. (1990). Occluded cations in active transport. *Ann Rev Biochem, 59*, 171–205.

Golovina, V. A., Song, H., James, P. F., Lingrel, J. B., & Blaustein, M. P. (2003). Na^+ pump α2-subunit expression modulates Ca^{2+} signaling. *Am J Physiol Cell Physiol, 284*, C475–C486.

Gumz, M. L., Lynch, I. J., Greenlee, M. M., Cain, B. D., & Wingo, C. S. (2010). The renal H^+, K^+-ATPases: physiology, regulation, and structure. *Am J Physiol Renal Physiol, 298*, F12–F21.

Horowitz, B., Eakle, K. A., Scheiner-Bobis, G., et al. (1990). Synthesis and assembly of functional mammalian Na, K-ATPase in yeast. *J Biol Chem, 265*, 4189–4192.

Inesi, G., & Sagara, Y. (1992). Thapsigargin, a high affinity and global inhibitor of intracellular Ca^{2+} transport ATPases. *Arch Biochem Biophys, 298*, 313–317.

Läuger, P. (1991). *Electrogenic Ion Pumps*. Sunderland, MA: Sinauer Associates, Inc.

Lecchi, S., Nelson, C. J., Allen, K. E., et al. (2007). Tandem phosphorylation of Ser-911 and Thr-912 at the C terminus of yeast plasma membrane H^+-ATPase leads to glucose-dependent activation. *J Biol Chem, 282,* 35471–35381.

Lingrel, J. B. (1992). Na, K-ATPase: isoform structure, function, and expression. *J Bioenerg Biomembr, 24*, 263–270.

McDonough, A. A., Geering, K., & Farley, R. A. (1990). The sodium pump needs its β subunit. *FASEB J, 4*, 1598–1605.

Moller, J. V., Olesen, C., Winther, A. M., & Nissen, P. (2010). The sarcoplasmic Ca^{2+}-ATPase: design of a perfect chemi-osmotic pump. *Q Rev Biophys, 43*, 501–566.

Morth, J. P., Pedersen, B. P., Buch-Pedersen, M. J., et al. (2011). A structural overview of the plasma membrane Na^+, K^+-ATPase and H^+-ATPase ion pumps. *Nat Rev Mol Cell Biol, 12*, 60–70.

Morth, J. P., Pedersen, B. P., Toustrup-Jensen, M. S., et al. (2007). Crystal structure of the sodium-potassium pump. *Nature, 450*, 1043–1050.

Nakamoto, R. K., Baylis Scanlon, J. A., & Al-Shawi, M. K. (2008). The rotary mechanism of the ATP synthase. *Arch Biochem Biophys, 476*, 43–50.

Pickart, C. M., & Jencks, W. P. (1984). Energetics of the calcium-transporting ATPase. *J Biol Chem, 259*, 1629–1643.

Sachs, G., & Wallmark, B. (1989). Biological basis of omeprazole therapy. *J Gastroenterol Hepatol, 4*(Suppl 2), 7–18.

Scheiner-Bobis, G., Zu Heringdorf, D. M., Christ, M., & Habermann, E. (1994). Palytoxin induces K^+ efflux from yeast cells expressing the mammalian sodium pump. *Mol Pharmacol, 45*, 1132–1136.

Schoner, W., & Scheiner-Bobis, G. (2007). Endogenous and exogenous cardiac glycosides: their roles in hypertension, salt metabolism, and cell growth. *Am J Cell Physiol, 293*, C509–C536.

Shimamura, T., Weyand, S., Beckstein, O., et al. (2010). Molecular basis of alternating access membrane transport by the sodium-hydantoin transporter Mhp1. *Science, 328*, 470–473.

Shin, J. M., Munson, K., Vagin, O., & Sachs, G. (2009). The gastric HK-ATPase: structure, function, and inhibition. *Pflügers Arch Eur J Physiol, 457*, 609–622.

Shinoda, T., Ogawa, H., Cornelius, F., & Toyoshima, C. (2009). Crystal structure of the sodium-potassium pump at 2.4Å resolution. *Nature, 459*, 446–451.

Skou, J. C. (1998). Nobel lecture: identification of the sodium pump. *Biosci Rep, 18*, 155–169.

Stock, D., Leslie, A. G. W., & Walker, J. E. (1999). Molecular architecture of the rotary motor in ATP synthase. *Science, 286*, 1700–1705.

Sweadner, K. J., & Rael, E. (2000). The FXYD gene family of small ion transport regulators or channels: cDNA sequence, protein signature sequence, and expression. *Genomics, 68*, 41–56.

Toei, M., Saum, R., & Forgac, M. (2010). Regulation and isoform function of the V-ATPases. *Biochemistry, 49*, 4715–4723.

Toyoshima, C., & Nomura, H. (2002). Structural changes in the calcium pump accompanying the dissociation of calcium. *Nature, 418*, 605–611.

Toyoshima, C., Nakasako, M., Nomura, H., & Ogawa, H. (2000). Crystal structure of the calcium pump of sarcoplasmic reticulum at 2.6Å resolution. *Nature, 405*, 647–655.

Weyand, S., Shimamura, T., Yajima, S., et al. (2010). Structure and molecular mechanism of a nucleobase-cation-symport-1 family transporter. *Science, 322*, 709–713.

Woo, A. L., James, P. F., & Lingrel, J. B. (1999). Characterization of the fourth alpha isoform of the Na, K-ATPase. *J Membr Biol, 169*, 39–44.

This page intentionally left blank

Chapter 13

Ca^{2+}-ATPases

Tracy J. Pritchard, Istvan Edes and Evangelia G. Kranias

Chapter Outline

I. INTRODUCTION

During the cardiac action potential, Ca^{2+} enters the cell via Ca^{2+} channels, which also act as dihydropyridine receptors (Fig. 13.1). This Ca^{2+} can either activate the myofilaments directly or produce the release of additional Ca^{2+} from the sarcoplasmic reticulum (SR). The SR Ca^{2+}-release channel in cardiac and skeletal muscle also acts as a ryanodine receptor and spans the gap between the transverse tubule and the SR ("foot" protein). Furthermore, it has been shown that the outer cell membrane Ca^{2+} channel is located close to the SR Ca^{2+} channel. Thus, the excitation–contraction coupling apparently involves the sarcolemmal Ca^{2+} channel and the SR Ca^{2+}-release channel with the Ca^{2+} current through the sarcolemmal channel being responsible for the initiation of Ca^{2+} release from the SR (Fig. 13.1). In skeletal muscle, the sarcolemmal membrane depolarization itself apparently is responsible for the induction of SR Ca^{2+} release. The relative importance of release from the SR in activation of the cardiac muscle contraction varies from preparation to preparation but, in the heart of mammals, it usually accounts for 40–70% of the Ca^{2+} required (Bers, 2008).

The rising cytosolic Ca^{2+} concentration induces contraction through binding to troponin C, which activates a chain of conformational changes, allowing the thin and thick filaments to interact. Subsequently, Ca^{2+} is dissociated from troponin C and is rapidly removed from the cytosol by various systems, resulting in relaxation. At least three processes are responsible for the removal of Ca^{2+} to end contraction (see Fig. 13.1): (1) the SR Ca^{2+} pump, which actively translocates Ca^{2+} at the cost of ATP into the SR system – this is thought to be the most important process in mediating relaxation; (2) the Na^{+}-Ca^{2+} exchanger, which transports Ca^{2+} out of the cell during diastole; and (3) the sarcolemmal Ca^{2+}-ATPase, which also extrudes Ca^{2+} from the cell.

The SR is a tubular network which serves as a sink for Ca^{2+} ions during relaxation and as a Ca^{2+} source during contraction. In cardiac muscle, about 60–70% of the intracellular Ca^{2+} released during systole is taken up by the SR (Bers, 2008) and the remaining amount is extruded from the cell by the Na^{+}-Ca^{2+} exchanger and the sarcolemmal Ca^{2+}-ATPase. The SR in both skeletal and cardiac muscles contains an acidic protein, calsequestrin (see Fig.13.1),

Cell Physiology Sourcebook. DOI: 10.1016/B978-0-12-387738-3.00013-5

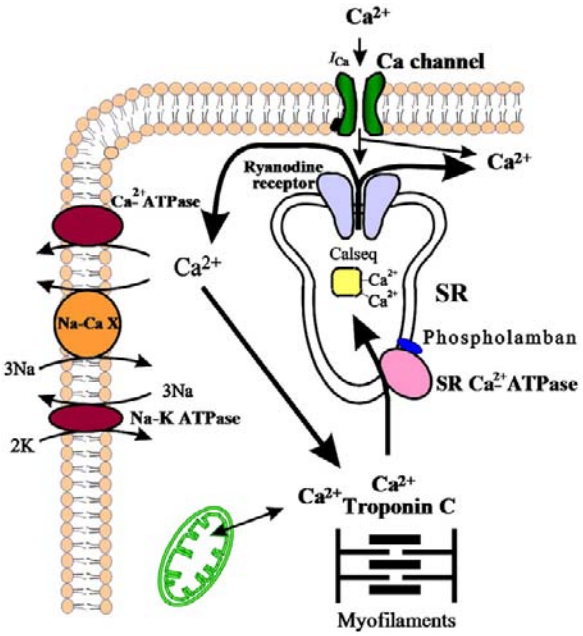

FIGURE 13.1 Schematic diagram of Ca^{2+} fluxes in the cardiac cell. Na-CaX, Na^{+}-Ca^{2+} exchanger; Calseq., calsequestrin; I_{Ca}, slow inward Ca^{2+} current; SR, sarcoplasmic reticulum.

which binds 40–50 mol of Ca^{2+} per mol of protein (MacLennan et al., 2002). The binding and release of Ca^{2+} by calsequestrin is believed to be an integral step of excitation–contraction coupling, but the details of this process are still not fully understood. Mitochondria can also accumulate large amounts of Ca^{2+} under pathological conditions (ischemia, Ca^{2+} overload, etc.) (Bers, 2008).

II. SARCOPLASMIC RETICULAR (SR) Ca^{2+}-ATPase

IIA. Properties of SR Ca^{2+}-ATPase

The major protein in the SR membrane is the Ca^{2+}-ATPase (M_r 100 000), representing about 40% of the total protein in cardiac SR. The cardiac SR Ca^{2+}-ATPase can create intraluminal Ca^{2+} concentrations of 5–10 mM. The SR or endoplasmic reticulum (ER) Ca^{2+}-ATPase family (SERCA) is the product of at least three alternatively spliced genes, producing a minimum of 11 different proteins (Dally et al., 2010) (Table 13.1). SERCA1 is expressed in fast skeletal muscle and alternative splicing of the 3′ end of the primary transcript gives rise to two mRNA forms (SERCA1a and SERCA1b), which are expressed at different stages of development (Brini and Carafoli, 2009). Alternatively, spliced forms of SERCA2 have been detected in cardiac muscle and slow skeletal muscle (SERCA2a) and in adult smooth muscle and non-muscle tissues (SERCA2b). A third isoform of

TABLE 13.1 Structure and Distribution of the Sarcoplasmic Reticular Ca^{2+}-ATPase (SERCA) Isoforms

Gene	Splice	Tissue
SERCA1[a]	a[b]	Adult fast skeletal muscle
SERCA1	b	Neonatal fast skeletal muscle
SERCA2	a	Cardiac/slow skeletal muscle
SERCA2	b	Smooth muscle/non-muscle
SERCA2	c	Cardiac/non-muscle
SERCA3	a–f	Various tissues

[a]*The SERCA numbers identify different gene products.*
[b]*The letters a and b indicate spliced isoforms.*

SERCA2 (SERCA2c) is found in cardiac muscle as well as non-muscle tissue including epithelial, mesenchymal and hematopoietic cells (Gianni et al., 2005). SERCA3 is expressed in a selective manner, with the highest mRNA levels in intestine, spleen, lung, uterus and brain. The human SERCA2 gene is localized on chromosome 12 and maps to position 12q23-q24.1. SERCA2 is about 85% identical to SERCAl, whereas SERCA3 is about 75% identical to either SERCA1 or SERCA2. The SERCA isoforms have different rates of transport, affinities for Ca^{2+} and subcellular compartmentalization.

The proposed general model of the enzyme has three cytoplasmic domains joined to a set of 10 transmembrane helices by a narrow extramembrane pentahelical stalk (MacLennan et al., 2002). The cytoplasmic region includes a nucleotide-binding site, or a domain to which the MgATP substrate binds, and a phosphorylation domain (Fig. 13.2). The third cytoplasmic domain is the actuator domain, which may be involved in conformational changes. In skeletal muscle, 2 mol of Ca^{2+} is transported per mole of ATP hydrolyzed. In cardiac muscle, a similar stoichiometry is expected, but this ratio has been generally found to be lower (0.4–1.0 mol Ca^{2+}/mol ATP). Ca^{2+} has been shown to bind to a region involving several of the membrane-spanning α-helices (M4, M5, M6 and M8) on the cytoplasmic side (MacLennan et al., 2002). During the Ca^{2+} transport cycle, the enzyme undergoes a transition from a high-affinity state to a low-affinity state for Ca^{2+} and the ions are translocated from the binding sites into the lumen of the SR (Fig. 13.2). This reaction pathway is characterized by the covalent phosphorylated Ca^{2+}-ATPase form (E_1~P), when the energy of ATP is transferred to an acylphosphoprotein intermediate (Fig. 13.3). E_1~P rapidly becomes E_2–P when the energy contained originally in the acylphosphoprotein is transduced into the translocation of bound Ca^{2+} into the SR ("marionette" model, see Fig. 13.2)

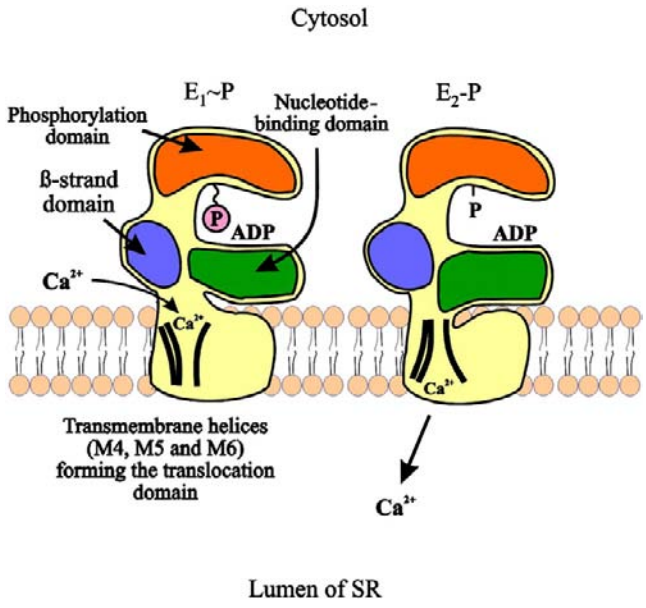

FIGURE 13.2 Model illustrating Ca^{2+} translocation by SERCA-type Ca^{2+} pumps. In E_1~P conformation, Ca^{2+} binds to the high-affinity binding sites in the cytosol. The energy of the hydrolyzed ATP triggers a series of conformational changes and transforms the E_1~P intermediate to the E_2—P intermediate. These conformational changes are directly coupled to alterations in the orientation of the transmembrane regions, leading to Ca^{2+} release into the lumen of the sarcoplasmic reticulum.

in exchange for two to three protons from the lumen of the SR to the cytosol. Subsequently, the acid-labile intermediate (E_2—P) decomposes to enzyme (E_2) and inorganic phosphate (Møller et al., 2005).

The Ca^{2+}-free form of the enzyme exists in two different conformational states: one with low affinity for Ca^{2+} (E_2) and one with high affinity for Ca^{2+} (E_1) (see Fig. 13.3). The conversion of E_2 to E_1 is proposed to be the rate-limiting step in the cycle. Thapsigargin (a plant sesquiterpene lactone) has been shown to interact specifically with the M3 transmembrane segment of the E_2 form of all members of the SR Ca^{2+}-ATPase family and to inhibit enzyme activity even at subnanomolar concentrations (Brini and Carafoli, 2009). It has been shown that the cardiac SR Ca^{2+}-ATPase (SERCA2) can be phosphorylated by the Ca^{2+}/CAM-dependent protein kinase at Ser 38 (Toyofuku et al., 1994). However, the physiological role of this phosphorylation is still not fully understood.

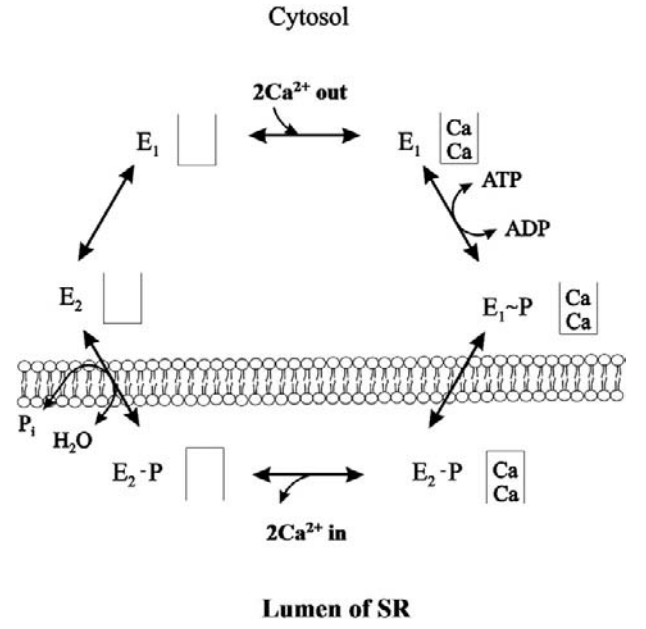

FIGURE 13.3 Reaction scheme of sarcoplasmic reticular Ca^{2+}-ATPase.

IIB. Genetic Models to Elucidate SERCA Function In Vivo

Human mutations in both SERCA1 and SERCA2 genes have been identified and linked to disease. Brody myopathy, an autosomal recessive disorder, can be caused by mutations in SERCA1 and results in defective muscle relaxation contributing to cramping and stiffness with exercise (Odermatt et al., 1996). Another genetic disease presenting as a skin disorder, Darier disease, is caused by a mutation in the SERCA2 gene (Sakuntabhai et al., 1999) and results in decreased SERCA2 protein expression.

SERCA isoform gene-targeted mouse models have also been designed to elucidate further the function of the Ca^{2+}-ATPase in physiological and pathophysiological conditions. Ablation of the SERCA1 gene was not embryonically lethal in mice. However, these mice had respiratory malfunction, likely due to reduced Ca^{2+} uptake by the diaphragm, resulting in death soon after birth (Pan et al., 2003). Consistent with Brody myopathy, the SERCA1 knockout mice had impaired limb movement and cramping (Pan et al., 2003). In the case of SERCA2, mice lacking one copy of the SERCA2 gene had decreased myocyte contractility and SR Ca^{2+} load, compared to wild-type (WT) mice (Ji et al., 2000). Moreover, mean arterial blood pressure and cardiac function was depressed in vivo in SERCA2 heterozygous mice (Periasamy et al., 1999). Interestingly, these mice did not develop heart failure spontaneously, but exhibited reduced function and increased susceptibility to heart failure development upon aortic constriction (Schultz et al., 2003). Similar to Darier disease in humans, which is associated with SERCA2 mutations, mice lacking one copy of SERCA2 have defects in keratinocytes and develop squamous cell tumors (Liu et al., 2001). To determine further the function of the major cardiac isoform of SERCA2, SERCA2a, another model was generated with SERCA2a ablation. There were cardiac malformations observed in this mouse and SERCA2b was upregulated. SERCA2a null mice developed cardiac hypertrophy and had decreased cardiac contractility and impaired relaxation (Ver Heyen et al., 2001). Gene ablation of SERCA3 in mice did not result in any gross phenotypes or

lethality. Ca^{2+} handling in endothelial cells and endothelium-dependent smooth muscle relaxation was impaired in SERCA3 null mice (Liu et al., 1997). Conversely, overexpression of SERCA1a or SERCA2a in the heart in transgenic mice increased Ca^{2+} transport by the pump. This translated to improved cardiac function with increases in cardiac contraction and relaxation (Baker et al., 1998; Loukianov et al., 1998). Together these studies indicate SERCA is important in maintaining proper Ca^{2+} cycling in the cell. Loss of SERCA impairs calcium uptake which can result in altered tissue function and disease phenotypes while overexpression of SERCA1a or 2a improves cardiac function.

IIC. Regulation of SR Ca^{2+}-ATPase by Phospholamban

IIC1. Structure of Phospholamban

In cardiac muscle, slow-twitch skeletal muscle and smooth muscle, SERCA2a can be regulated by a low-molecular-weight protein, phospholamban, which can be phosphorylated by various protein kinases. In the dephosphorylated form, a substantial fraction of phospholamban monomers (20%) exists and this has been proposed to be the active species of phospholamban that binds SERCA2 and inhibits it. Upon phosphorylation, phospholamban appears to form mainly pentamers, which is due to changes in the isoelectric point (from 10 to 6.7) of the protein (Simmerman and Jones, 1998).

The complete amino acid sequence of phospholamban has been determined for various tissues and species. There is currently no evidence for the existence of any isoforms for this protein and the phospholamban gene has been mapped to human chromosome 6 (Fujii et al., 1991). The calculated molecular weight of phospholamban is 6080 Da and the protein has been proposed to contain two major domains (Fig. 13.4): a hydrophilic domain (domain I) with three unique phosphorylatable sites (Ser 10, Ser 16 and Thr 17), and a hydrophobic C-terminal domain (domain II) anchored into the SR membrane. The hydrophilic domain (amino acids 1−30) has been further divided into two subdomains: domain Ia (amino acids 1−20) and Ib (amino acids 21−30). Domain Ia has a net positive charge in the dephosphorylated form and consists of an α-helix followed by a Pro residue at position 21 (stalk region). Domain Ib has been suggested to be relatively unstructured (MacLennan et al., 1998, 2002). The hydrophobic domain (amino acids 31−52) forms an α-helix in the SR membrane (Fig. 13.4).

Phospholamban migrates as a 24- to 28-kDa pentamer on sodium dodecyl sulfate (SDS) gels and dissociates into dimers and monomers upon boiling in SDS before electrophoresis. Spontaneous aggregation of phospholamban into pentamers was also observed upon expression of this protein in bacteria or in mammalian cells. Site-specific

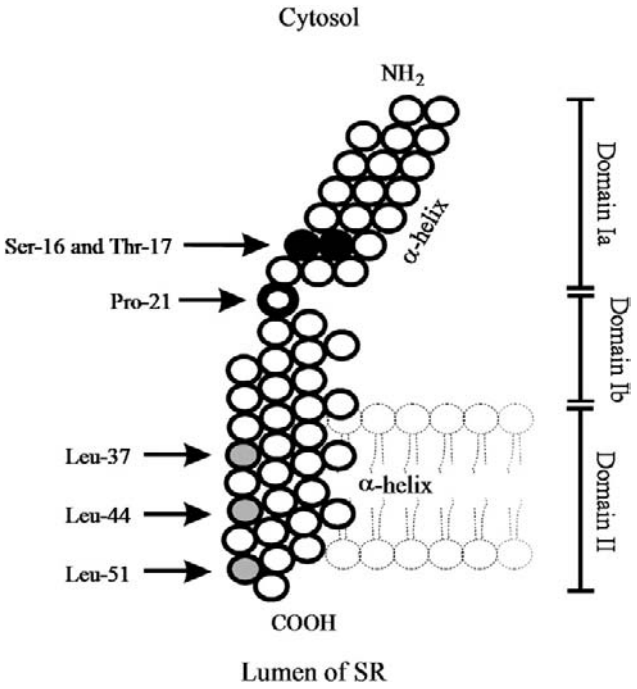

FIGURE 13.4 Molecular model of the structure of phospholamban. The cytoplasmic α-helix (domain Ia, residues 8−20) is interrupted by Pro 21 (heavy circle). Residues 22−32 (domain Ib) are relatively unstructured and may interconvert between transient conformations; residues 33−52 constitute the transmembrane domain II (α-helix). Ser 16 and Thr 17 (black circles) are the adjacent phosphorylation sites. The shaded circles indicate the leucines (Leu 37, Leu 44 and Leu 51), which are important for the phospholamban subunit interactions (pentamer formation).

mutagenesis experiments identified Cys (Cys 36, Cys 41 and Cys 46), Leu (Leu 37, Leu 44 and Leu 51), and Ile (Ile 40 and Ile 47) residues in the hydrophobic transmembrane domain as essential amino acids for phospholamban pentamer formation (reviewed in MacLennan et al., 1998). The leucine and isoleucine amino acids are suggested to form five zippers in the membrane that stabilize the pentameric form of the protein with a central pore (Fig. 13.5), defined by the surface of the hydrophobic amino acids (Simmerman and Jones, 1998).

Monoclonal antibodies raised against phospholamban stimulate SR Ca^{2+} uptake in vitro (Morris et al., 1991). Furthermore, removal of phospholamban from the SR or uncoupling phospholamban from the Ca^{2+}-ATPase (using detergents, high-ionic-strength solutions or polyanions such as heparin sulfate) markedly increases the affinity of the SR Ca^{2+} pump for Ca^{2+}. These findings suggest that the dephosphorylated form of phospholamban is an inhibitor of the SR Ca^{2+}-ATPase. This "depression hypothesis" has been confirmed by studies using purified Ca^{2+}-ATPase and purified or recombinant phospholamban in reconstituted systems. Inclusion of phospholamban resulted in inhibition of the SR Ca^{2+}-ATPase activity in reconstituted vesicles or cells (Kim et al., 1990; Reddy et al., 1996). Cyclic AMP

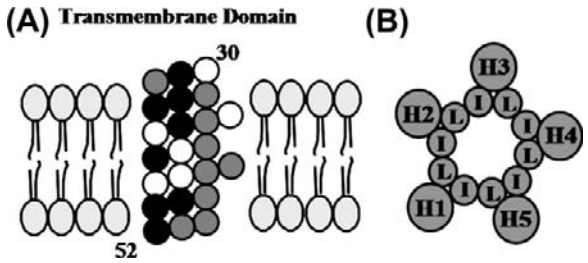

FIGURE 13.5 Model of the transmembrane domain of phospholamban monomer (A) and pentamer (B). (A) Residues 31−52 of monomeric phospholamban are configured as a 3.5 residues/360° turn helix. Darkly shaded circles represent mutations that enhance the inhibitory function of phospholamban by enhanced monomer formation (destabilization of pentamer structure). Lightly shaded circles represent mutations that reduce inhibitory function. (B) The phospholamban pentamer model shows the interaction between the monomer transmembrane domains (H1−H5) at Leu (L) and Ile (I) residues constituting zippers.

phosphorylation of phospholamban reversed its inhibitory effect on the Ca^{2+} pump. The inhibitory role of phospholamban on SR and cardiac function has been directly confirmed using transgenic animal models. Overexpression of the protein (phospholamban-overexpressing mice) was associated with inhibition of SR Ca^{2+} transport, Ca^{2+} transient and depression of basal left ventricular function (Kadambi et al., 1996). On the other hand, partial (phospholamban-heterozygous mice) or complete ablation of the protein (phospholamban-deficient mice) in mouse models was associated with increases in SR Ca^{2+} transport and cardiac function (Luo et al., 1994, 1996; Hoit et al., 1995). Actually, a close linear correlation between the levels of phospholamban and cardiac contractile parameters was observed (Lorenz and Kranias, 1997), indicating that phospholamban is a prominent regulator of myocardial contractility. These findings suggest that changes in the level of this protein will result in parallel changes in SR function and cardiac contractility.

The region of phospholamban interacting with the Ca^{2+}-ATPase may involve amino acids 2−18 (reviewed in MacLennan et al., 1998). Based on these reports, the simplest model for the interaction between the phospholamban cytoplasmic domain and the SR Ca^{2+}-ATPase is one in which the highly positively-charged region of phospholamban (residues 7−16) interacts directly with a negatively-charged region on the surface of the Ca^{2+}-ATPase (Lys-Asp-Asp-Lys-Pro-Val 402) to modulate the inhibitory interactions between the two proteins (Fig. 13.6) (reviewed in MacLennan et al., 1998). This association is disrupted by phosphorylation of Ser 10, Ser 16 or Thr 17 (phosphorylated by protein kinase C, cAMP-dependent and Ca^{2+}-calmodulin dependent protein kinase, respectively) in phospholamban, because the positive charges of the phospholamban cytosolic domain are partially neutralized by the phosphate moiety in this vicinity. Phosphorylation of phospholamban by the cAMP-dependent protein kinase at Ser 16 is associated with local unwinding of the α-helix at position 12−16 resulting in conformational changes in the recognition unit of the protein (Mortishire-Smith et al., 1995).

Interestingly, phospholamban peptides, corresponding to the hydrophobic membrane-spanning domain, also affect Ca^{2+}-ATPase activity by lowering its affinity for Ca^{2+} (reviewed in MacLennan et al., 1998). The importance of the membrane-spanning region of phospholamban in inhibiting SR Ca^{2+}-ATPase activity was demonstrated through mutagenesis studies (reviewed in MacLennan et al., 1998). It was shown that substitution of the pentamer-stabilizing residues (Leu 37, Leu 44, Leu 51, Ile 40 and Ile 47) in the membrane-spanning region (domain II) by Ala resulted in monomeric mutants, which were more effective inhibitors of the SR Ca^{2+}-ATPase activity than wild-type phospholamban. These phospholamban monomeric mutants were called "supershifters" because they decreased the apparent affinity of SR Ca^{2+}-ATPase more

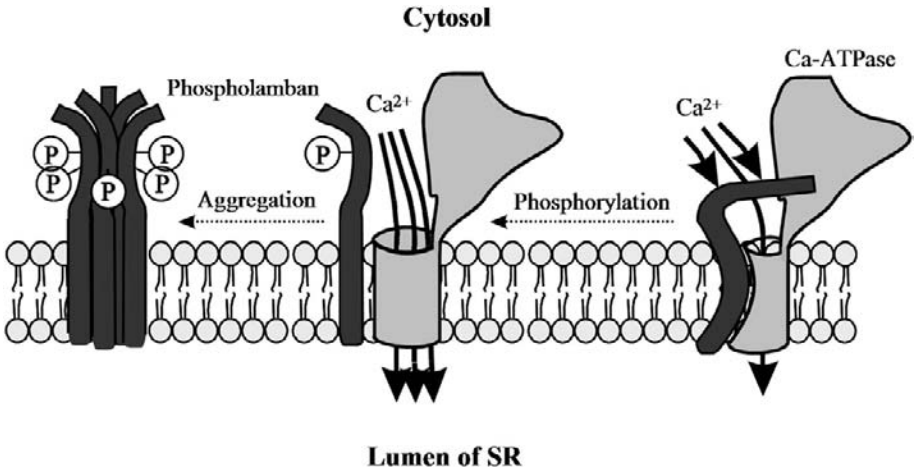

FIGURE 13.6 Model for regulation of SR Ca^{2+}-ATPase by phosphorylated and non-phosphorylated phospholamban. Phosphorylation of phospholamban disrupts the interaction between the two proteins so that the inhibition of the Ca^{2+}-ATPase is relieved. Note that both the cytosolic domain and the membrane-spanning region of phospholamban are involved in the phosphorylation-mediated conformational change to relieve the inhibition. Phosphorylation of phospholamban monomers promotes association into inactive phosphorylated pentamers.

effectively than wild-type phospholamban. Thus, it was proposed that monomeric phospholamban is the active form, which is involved in the interaction with SR Ca^{2+}-ATPase. Furthermore, scanning alanine-mutagenesis studies have identified the amino acid residues in the transmembrane domain of phospholamban (Leu 31, Asn 34, Phe 35, Ile 38, Leu 42, Ile 48, Val 49 and Leu 52), which are associated with loss of function (reviewed in MacLennan et al., 1998). These amino acids are located on the exterior face of each helix in the pentameric assembly of phospholamban (opposite from the pentamer-stabilizing face) (see Fig. 13.5). The importance of these transmembrane domain residues of phospholamban to SR Ca^{2+}-ATPase function has been demonstrated in vivo using several transgenic models. N27A phospholamban can act as a superinhibitor, where hearts have depressed Ca^{2+}-ATPase activity and cardiac function, that cannot be recovered completely by β-adrenergic stimulation and progressed to heart failure (Zhai et al., 2000; Schmidt et al., 2002). Mice expressing the V49G variant in the phospholamban transmembrane domain exhibited diminished cardiac function and hypertrophy which progressed to dilated cardiomyopathy (Haghighi et al., 2001). Moreover, L37A and I40A phospholamban transgenic mice showed similar decreased function and pathology (Zvaritch et al., 2000).

A schematic representation of interaction of phospholamban with SR Ca^{2+}-ATPase is shown in Fig. 13.6. It has been proposed that the phospholamban monomer is the active species for interaction with the SR Ca^{2+}-ATPase and the pentamers are regarded as functionally inactive forms of phospholamban (MacLennan et al., 1998). Phosphorylation of phospholamban monomers promotes association into inactive pentamers. Thus, two important steps for SR Ca^{2+}-ATPase inhibition have been suggested: (1) dissociation of monomeric phospholamban from dephosphorylated pentamers (K_{d1}); and (2) binding of phospholamban monomers to the SR Ca^{2+}-ATPase (K_{d2}). These dissociation constants (K_{d1} and K_{d2}) will control both the concentration of phospholamban monomers and the concentration of units in which monomers are associated with the SR Ca^{2+}-ATPase (MacLennan et al., 1998). There are at least two interaction sites between phospholamban and the SR Ca^{2+}-ATPase (see Fig. 13.6): one in the cytoplasmic domains of the two proteins and another one within the transmembrane sequences. The interaction between the hydrophobic membrane-spanning regions is associated with inhibition of the apparent affinity of SR Ca^{2+}-ATPase for Ca^{2+} (K_{Ca}). The interaction between the cytosolic phospholamban domain Ia and the SR Ca^{2+}-ATPase modulates the inhibitory interaction in the transmembrane region (domain II) through long-range coupling. Disruption of the cytosolic interactions (domain Ia) by phosphorylation of phospholamban or binding of a phospholamban antibody results in disruption of the inhibitory intramembrane interactions. However, resolution of the exact molecular mechanism by which phospholamban inhibits the SR Ca^{2+}-ATPase Ca^{2+} affinity and the concomitant regulation of SR Ca^{2+} transport will have to await the development of a new methodology that allows detection of protein−protein interactions in a membrane environment.

IIC2. In Vitro Studies on Regulation of SR Ca^{2+}-ATPase

In the early 1970s, it was suggested that the effects of various catecholamines on cardiac function may be partly attributed to phosphorylation of the SR by cAMP-dependent protein kinase(s). It soon became clear that the substrate for the protein kinase (PK) was not the SR Ca^{2+}-ATPase but phospholamban. Various other high- and low-molecular-weight SR proteins were also identified as minor substrates for cAMP-dependent PK, but only the changes in the phosphorylation of phospholamban were associated with functional alterations of the cardiac SR.

cAMP-dependent and Ca^{2+}-CaM-dependent PKs have been shown to phosphorylate phospholamban independently of each other (reviewed in Mattiazzi et al., 2005). Phosphorylation by cAMP-dependent PK occurred on Ser 16, whereas Ca^{2+}-CaM-dependent PK catalyzed exclusively the phosphorylation of Thr 17 (reviewed in Mattiazzi et al., 2005). Phosphorylation by either kinase was shown to result in stimulation of the SR Ca^{2+}-ATPase activity and the initial rates of SR Ca^{2+} transport. Stimulation was associated with an increase in the apparent affinity of the SR Ca^{2+}-ATPase for Ca^{2+} (K_{Ca}).

In vitro, phospholamban is phosphorylated by two additional PKs: PK-C and a cGMP-dependent PK. Protein kinase C (Ca^{2+}/phospholipids-dependent PK) phosphorylated the protein at a site distinct (Ser 10) from those phosphorylated by either cAMP-dependent PK or Ca^{2+}-CaM-dependent PK (reviewed in Mattiazzi et al., 2005). Phosphorylation stimulated the SR Ca^{2+}-ATPase activity and it was postulated that this activity played a role in the action of agents known to stimulate phosphoinositide (PI) hydrolysis, since one product of PI hydrolysis, diacylglycerol, is an activator of PK-C. Cyclic GMP-dependent PK was shown to phosphorylate phospholamban on the same residue (Ser 16) as that phosphorylated by cAMP-dependent PK (reviewed in Mattiazzi et al., 2005). This phosphorylation stimulated cardiac SR Ca^{2+} transport, similar to the effects of cAMP-dependent PK. Furthermore, the stimulatory effects on Ca^{2+} transport, mediated by cGMP-dependent phosphorylation of phospholamban, were also observed in smooth muscle and this may be of particular interest because some vasodilators act by increasing cGMP levels in vascular smooth muscle.

IIC3. In Vivo Studies on Regulation of SR Ca^{2+}-ATPase

The phosphorylation of SR proteins and their regulatory effects on the SR Ca^{2+}-ATPase activity have been studied in perfused hearts from various animal species whose ATP pool was labeled with [^{32}P]orthophosphate. Microsomal fractions enriched in SR were prepared from hearts freeze-clamped during stimulation with different agonists (catecholamines, forskolin, phosphodiesterase inhibitors, phorbol esters) and analyzed by gel electrophoresis and autoradiography for ^{32}P incorporation. β-Adrenergic agonist (isoproterenol) stimulation of the perfused hearts produced an increase in ^{32}P incorporation into phospholamban (Kranias and Solaro, 1982; Lindemann et al., 1983). The stimulation of ^{32}P incorporation into phospholamban was associated with an increased rate of Ca^{2+} uptake into SR membrane vesicles and an increased SR Ca^{2+}-ATPase activity (Lindemann et al., 1983; Kranias et al., 1985).

These biochemical changes were associated with increases in left ventricular functional parameters (contractility and relaxation). The in vivo phosphorylation of phospholamban was specific only for inotropic agents that increased the cAMP content of the myocardium (β-adrenergic agonists, forskolin and phosphodiesterase inhibitors). On the other hand, positive inotropic interventions, which increased the intracellular Ca^{2+} level by cAMP-independent mechanisms (α-adrenergic agonists, ouabain and elevated [Ca^{2+}]), failed to stimulate phospholamban phosphorylation and relaxation. Calmodulin inhibitors (fluphenazine) attenuated the isoproterenol-induced phosphorylation of phospholamban (Lindemann and Watanabe, 1985a) and it was shown that at steady-state isoproterenol exposure, phospholamban contains equimolar amounts of phosphoserine (pSer 16) and phosphothreonine (pThr 17). Phosphorylation of Ser 16, however, correlated most closely with changes in cardiac function in beating hearts (Talosi et al., 1993). Based on these results and findings in transgenic animals (Luo et al., 1998), it is proposed that: (1) prevention of Ser 16 phosphorylation (Ser 16 → Ala mutation) results in attenuation of the β-adrenergic response in mammalian hearts; and (2) that phosphorylation of Ser 16 is a prerequisite for Thr 17 phosphorylation. Indeed, in mice containing an alanine substitution for Ser 16, there were diminished responses to the β-adrenergic stimulation. Also, in these animals there was no phosphorylation at Thr 17 (Luo et al., 1998). Conversely, substituting alanine for Thr 17 did not interfere with phosphorylation of Ser 16, and hearts were responsive to β-adrenergic stimulation (Chu et al., 2000). Moreover, overexpression of a non-phosphorylatable form of phospholamban (both Ser 16 and Thr 17 sites mutated to Ala) resulted in maximum inhibition of the SR Ca^{2+}-ATPase calcium affinity (Brittsan et al., 2000). It should be noted that, in some conditions, Thr 17 has been shown to be phosphorylated independently of Ser 16, such as increased frequency stimulation of the heart, elevated intracellular Ca^{2+}, ischemia-reperfusion injury and acidosis (Zhao et al., 2004; Mattiazzi et al., 2005).

The muscarinic agonist acetylcholine attenuated the increases in cAMP levels, phosphorylation of phospholamban and the SR Ca^{2+}-ATPase activity produced either by β-adrenergic stimulation or by phosphodiesterase inhibition (using isobutylmethylxanthine) (Lindemann and Watanabe, 1985b). Protein kinase C and cGMP-dependent PK, which have been shown to phosphorylate phospholamban in vitro, failed to demonstrate similar effects in beating guinea pig hearts in response to stimuli that activate PK-C or elevate the cGMP levels (Huggins et al., 1989; Edes and Kranias, 1990). Thus, the physiological relevance of PK-C and PK-G in beating hearts is not clear at present.

The functional alterations in the SR Ca^{2+}-ATPase activity may explain, at least partly, the activating and relaxing effects of β-adrenergic agents in cardiac muscle (Figs. 13.7 and 13.8). The cAMP-dependent phosphorylation of phospholamban under either in vitro or in vivo conditions increases the rate of SR Ca^{2+} transport and SR Ca^{2+}-ATPase activity. Such an increase in Ca^{2+} transport is expected to contribute primarily to the relaxing effects of

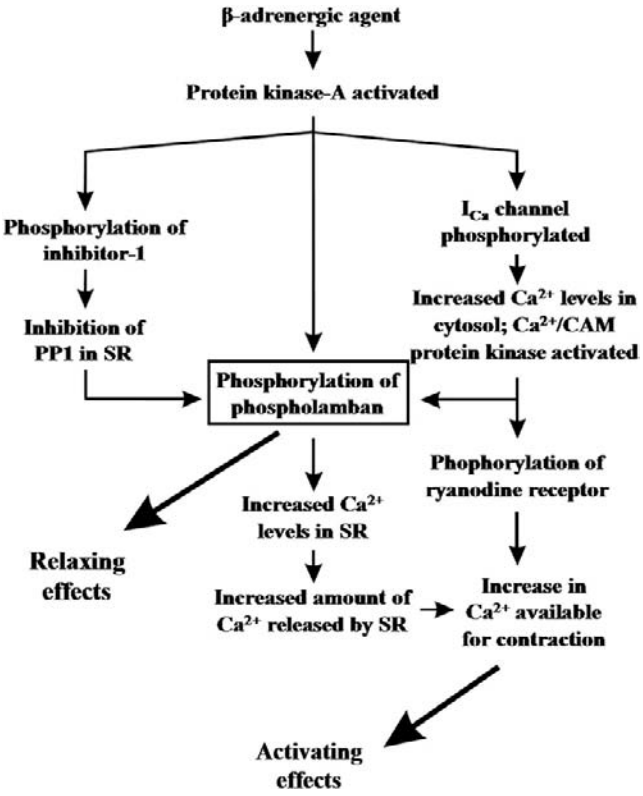

FIGURE 13.7 Schematic diagram of possible relaxing and activating effects of β-adrenergic agents in the heart. PP1, protein phosphatase 1.

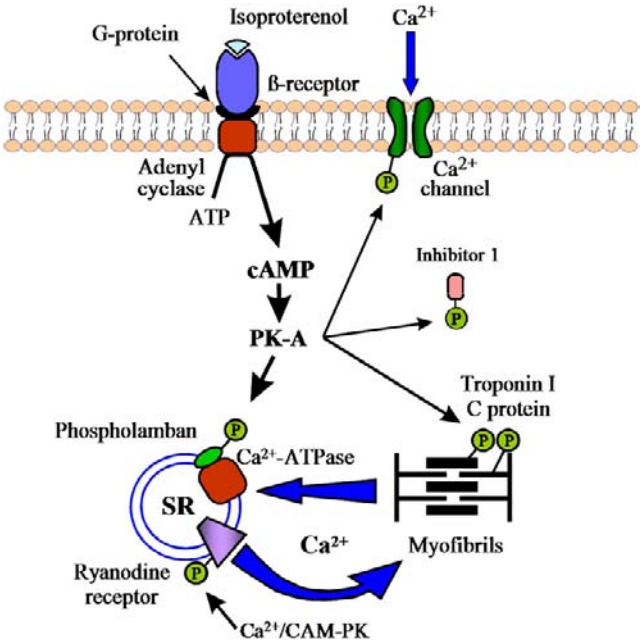

FIGURE 13.8 Effects of β-adrenergic agents on protein phosphorylation in cardiac cells. Increased intracellular cAMP levels activate the cAMP-dependent protein kinase(s), which phosphorylates various proteins (phospholamban, inhibitor-1, Ca^{2+}-channel and myofibrillar proteins) and increases the rates of SR Ca^{2+} uptake and release.

catecholamines (Fig. 13.7). An additional mechanism which contributes to the increased phosphorylation of phospholamban upon β-adrenergic stimulation is the phosphorylation of the phosphatase inhibitor protein by the stimulated cAMP-dependent kinase. This phosphorylation results in inactivation of protein phosphatase 1 and, thus, inhibition of dephosphorylation of phospholamban during the action of catecholamines (Fig. 13.7). The increased phosphorylation of phospholamban and the increased Ca^{2+} levels accumulated by the SR would lead to the availability of higher levels of Ca^{2+} to be subsequently released for binding to the contractile proteins (Fig. 13.7). The critical and prominent role of phospholamban in the mediation of β-adrenergic functional responses was also confirmed in transgenic animal studies. Cardiac myocytes or work-performing heart preparations from phospholamban-deficient mice exhibited largely attenuated responses to β-adrenergic agonist stimulation (Luo et al., 1996; Wolska et al., 1996), indicating that phospholamban is a key phosphoprotein in the heart's responses to β-adrenergic agonists.

Phosphorylation of other myocardial phosphoproteins has also been suggested to be involved in the mediation of positive inotropic and lusitropic effects of β-adrenergic agonists. Cyclic AMP-dependent protein kinase-mediated phosphorylation of the α_1 subunit of the Ca^{2+} channel (see Fig. 13.8) is associated with an increase in the voltage-dependent Ca^{2+} current (I_{Ca}), which enhances the Ca^{2+} levels available in the cytosol during β-adrenergic agonist stimulation. Phosphorylation of troponin I has been shown to decrease the sensitivity of myofilaments for Ca^{2+} both in intact myocardium and skinned fibers (Kranias et al., 1985). The desensitization of myofibrils is accompanied by an increased off-rate of Ca^{2+} from troponin C, which could contribute to faster relaxation (see Fig. 13.8). In addition, phosphorylation of the SR Ca^{2+}-release channel (ryanodine receptor) by Ca^{2+}-CaM-dependent protein kinase may stimulate Ca^{2+} release from the SR vesicles and contribute to the elevation of intracellular Ca^{2+} levels during systole. Thus, the enhanced Ca^{2+} influx across the sarcolemma, together with the increased Ca^{2+} levels to be released from the SR, may result in an elevation of the Ca^{2+} available for the contractile machinery, leading to an increase in the amplitude of contraction (see Fig. 13.8).

In recent years, several human mutations in the phospholamban gene have been identified and additional insights into phospholamban regulation of SERCA2 have been obtained. The first mutation discovered encoded Arg 9 Cys, which is included in the PKA phosphorylation consensus sequence of phospholamban. This mutation reduced the phosphorylation of phospholamban in vitro and in vivo using a gene-targeted mouse model (Schmitt et al., 2003). Two human mutations, Leu 39 stop and Arg 14 del, in phospholamban interfered with targeting of the protein to the endoplasmic reticulum. The Leu 39 stop mutation produces a truncated phospholamban protein that, when introduced in HEK 293 cells, resulted in an unstable protein that was misrouted to other membranes. Cardiac explants from human carriers of Leu 39 stop had no detectable phospholamban in the endoplasmic reticulum (Haghighi et al., 2003). Deletion of Arg 14 also interfered with targeting of phospholamban to the endoplasmic reticulum (Sharma et al., 2010). Mice expressing the Arg 14 del mutation had ventricular dilation and fibrosis accompanied by increased mortality with death as early as two weeks (Haghighi et al., 2006). These naturally occurring mutations in phospholamban have revealed the importance of the balance of phosphorylated and unphosphorylated phospholamban and its localization in the heart.

IID. Other Regulators of the SR Ca^{2+}-ATPase

While phospholamban is the primary regulator of SR Ca^{2+}-ATPase activity, several other proteins have been identified that modulate the SR Ca^{2+} pump (Fig. 13.9). For example, sarcolipin, a homolog of phospholamban, has been shown to inhibit SERCA1a and SERCA2a; however, sarcolipin is expressed more abundantly in atria unlike phospholamban which is predominantly in the ventricle of the heart (Bhupathy et al., 2007). Overexpression of sarcolipin in mice resulted in reduced Ca^{2+} affinity of SERCA2a as well as decreased cardiac function which was improved by

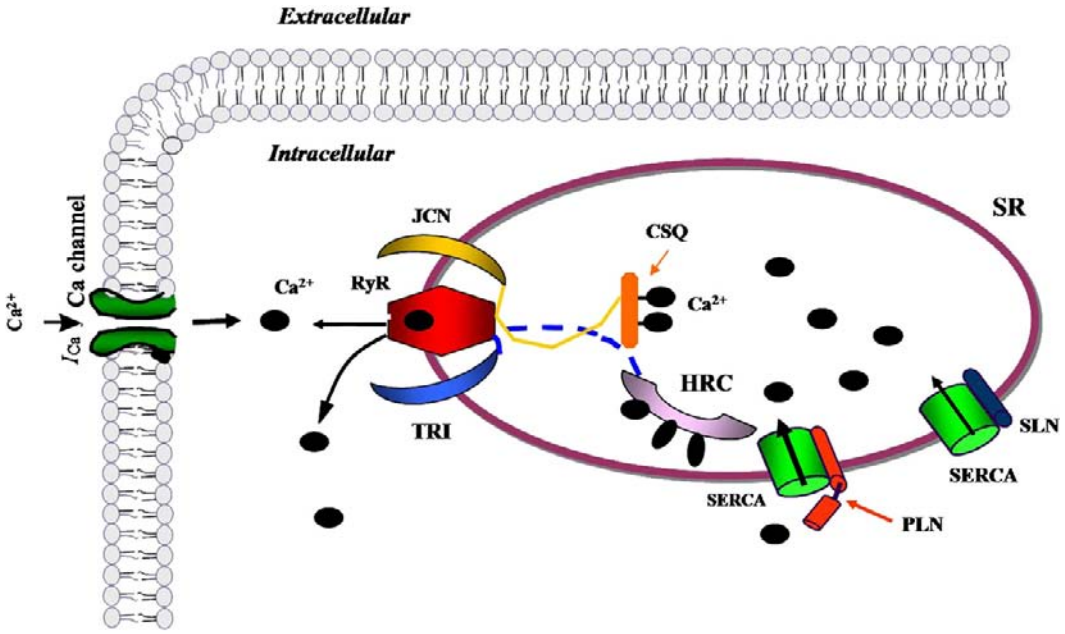

FIGURE 13.9 Schematic of regulators of SR Ca^{2+}-ATPase (SERCA) function. Phospholamban (PLN) is the primary regulator of the SR Ca^{2+} pump. Sarcolipin (SLN), a homolog of PLN, can also modulate SERCA activity and may be important to Ca^{2+} cycling in the atria where it is abundant. Histidine-rich Ca^{2+}-binding protein (HRC) is an SR lumen protein that binds Ca^{2+} and has been shown to interact with SERCA and affect Ca uptake. HRC also interacts with triadin, a protein that is part of the Ca^{2+} release quaternary complex including the ryanodine receptor (RyR) and junctin (JCN).

β-adrenergic stimulation in vivo (Bhupathy et al., 2007). Conversely, ablation of sarcolipin in mice resulted in elevated SR Ca^{2+} uptake and faster relaxation of the atria (Babu et al., 2007). The histidine-rich calcium binding protein (HRC), located in the SR, was shown to interact with SERCA2a in vitro in a Ca^{2+} sensitive manner with maximal binding occurring at low Ca^{2+} concentrations (Arvanitis et al., 2007). HRC also interacts with triadin, a protein that is part of the Ca^{2+} release quaternary complex; therefore, HRC can regulate both Ca^{2+} release uptake and release making it an interesting new molecule in SR Ca^{2+} handling. Indeed, acute overexpression of HRC decreased Ca^{2+} release and contractility in vitro while chronic overexpression reduced SR Ca^{2+} uptake and contractility in vivo (Fan et al., 2004; Gregory et al., 2006). Moreover, HRC transgenic mice exhibited cardiac remodeling with aging (Gregory et al., 2006).

IIE. SR Ca^{2+}-ATPase in Cardiac Diseases

The complex regulation of the SR function clearly indicates that even small disturbances in SR Ca^{2+} handling may result in profound changes and deterioration of normal myocardial function. The fast removal of Ca^{2+} by the SR Ca^{2+}-ATPase during diastole and the subsequent rapid release through the SR Ca^{2+} channel (ryanodine receptor) at the beginning of contraction are prerequisites for normal diastolic and systolic function. We briefly outline in the next section the alterations in the SR Ca^{2+}-ATPase in the major cardiac diseases.

IIE1. SR Ca^{2+}-ATPase in Hyperthyroidism and Hypothyroidism

Thyroid hormones are important regulators of myocardial contractility and relaxation. Chronic increases in thyroid hormone levels lead to cardiac hypertrophy, with increases in the heart rate and cardiac output as well as left ventricular contractility and velocity of relaxation. On the other hand, opposite effects are associated with a hypothyroid condition. The mechanisms underlying these changes have been the subject of numerous investigations. It is assumed that in hypo- and hyperthyroid hearts the altered gene expression of the cardiac SR proteins and, hence, the changes in the intracellular Ca^{2+} transients, is the most important determinant of the altered myocardial function. It was shown that the velocity of ATP-dependent Ca^{2+} transport and the Ca^{2+}-ATPase activity are specifically increased in SR vesicle preparations from hyperthyroid compared with euthyroid hearts (Beekman et al., 1989). Opposite changes were noted for hypothyroid animals compared with euthyroid ones (Beekman et al., 1989).

Examination of the steady-state mRNA levels of the cardiac SR Ca^{2+}-ATPase and the ryanodine receptor revealed a significant increase (140−190%) in hyperthyroid and a marked decline (40−50%) in hypothyroid

animals (Arai et al., 1991). The changes in mRNA levels for the Ca^{2+}-ATPase in hypothyroid and hyperthyroid conditions also reflected changes in the protein amounts of the enzyme in these hearts (Kiss et al., 1994, 1998). Interestingly, in the case of phospholamban, the regulator of the Ca^{2+}-ATPase, and calsequestrin, there was no coordinated regulation with respect to the Ca^{2+}-ATPase. In fact, both the relative mRNA level and the protein content of phospholamban were reported to decrease in hyperthyroid animals, whereas there was no change noted in the calsequestrin mRNA level upon L-thyroxine treatment. In hypothyroid hearts, an opposite trend was noted since the protein amount of phospholamban was found to be increased as compared to the euthyroid or hyperthyroid animals (Kiss et al., 1994, 1998). Consequently, the phospholamban-Ca^{2+}-ATPase protein ratio was highest in the hypothyroid animals, followed by euthyroid and hyperthyroid animals. These changes in the phospholamban-Ca^{2+}-ATPase ratio were associated with coordinate alterations in the SR Ca^{2+} uptake, affinity of the SERCA2 for Ca^{2+} and myocardial function (Kiss et al., 1994; Kimura et al., 1994).

These changes indicate that the SR proteins responsible for Ca^{2+} uptake and release (Ca^{2+}-ATPase and ryanodine receptor) are coordinately regulated in hypothyroid and hyperthyroid hearts and provide a simple explanation for the altered Ca^{2+} release and reuptake capacity and hence the myocardial function under these conditions.

IIE2. SR Ca^{2+}-ATPase in Cardiomyopathies

Dilated cardiomyopathy is a frequent form of cardiac muscle disease and is characterized by an impaired systolic function and dilatation of both ventricles (systolic pump failure). In various animal models of primary and secondary dilated cardiomyopathy, it was shown that both SR Ca^{2+} binding capacity and uptake were depressed because of the decreased activity and protein level of the SR Ca^{2+}-ATPase (Edes et al., 1991). In some studies of human idiopathic dilated cardiomyopathy, decreases were noted for both SR Ca^{2+} uptake rates and Ca^{2+}-ATPase activity (Limas et al., 1987; Unverferth et al., 1988) as well as myocardial Ca^{2+} handling (Gwathmey et al., 1987; Beuckelmann et al., 1992). Examination of the mRNA levels in left ventricular biopsies from patients with dilated cardiomyopathy revealed a significant decrease in mRNA content for the SR Ca^{2+}-ATPase relative to other mRNA forms (Mercadier et al., 1990; Arai et al., 1993). In contrast, other authors were unable to detect a decrease in SR Ca^{2+} uptake activity (Movsesian et al., 1989) or the immunodetectable levels of the SR Ca^{2+}-ATPase protein (Schwinger et al., 1995) in the left ventricular myocardium from patients with idiopathic dilated cardiomyopathy. Furthermore, the gating mechanism of the SR Ca^{2+}-release channel was reported to be abnormal in dilated cardiomyopathy (D'Agnolo et al., 1992; Sen et al., 2000), and it was suggested that defective excitation–contraction coupling is involved in the pathogenesis of this disease.

Another type of cardiomyopathy, hypertrophic cardiomyopathy, has only been recognized in clinical practice for the last four decades. The characteristics of this disease are asymmetric interventricular septal hypertrophy and narrowing of the left ventricular outflow tract, with or without outflow obstruction (outflow tract pressure gradient). In the familial form of hypertrophic cardiomyopathy, which accounts for about 45–70% of all cases, mutations in myofibrillar protein genes (β-myosin heavy chain, troponin T, troponin I, α-tropomyosin and C protein among others) are associated with the disease (Ho, 2010). Additionally, prolongation of the Ca^{2+} transient, abnormal Ca^{2+} handling and a decline in SR Ca^{2+}-ATPase mRNA levels are reported to be characteristic for human hypertrophic cardiomyopathy (Lipskaia et al., 2009), which may explain the diastolic function impairment in this disease.

In chronic heart failure due to hemodynamic overload, irrespective of the specific etiology (valvular heart disease, cardiomyopathy, chronic ischemic heart disease or hypertension), a reduction was observed in both the number and the activity of the SR Ca^{2+} pump (Limas et al., 1987; Unverferth et al., 1988). Furthermore, a close correlation was obtained between the SR Ca^{2+}-ATPase mRNA or protein levels and the myocardial function (Gregory and Kranias, 2006). In addition, total phospholamban protein levels are unchanged in heart failure, but phosphorylated phospholamban levels are decreased further compounding reduced SR Ca^{2+}-ATPase activity (Gregory and Kranias, 2006). Interestingly, the Na^{+}-Ca^{2+} exchanger gene expression is increased in failing human hearts and it is hypothesized that the upregulation of this protein may compensate for the depressed SR function (Bers and Despa, 2006).

IIE3. SR Ca^{2+}-ATPase in Ischemia

A brief period of ischemia (10–20 min) induces reversible tissue damage in cardiac muscle, resulting in a "stunned" myocardium. This condition is characterized by regional contractile abnormalities (declines in both systolic and diastolic function) that persist for several hours despite the absence of necrosis. These hemodynamic changes are associated with a reduction in SR Ca^{2+} transport (Krause et al., 1989; Limbruno et al., 1989). The maximal activity of the SR Ca^{2+}-ATPase was found to be depressed and the Ca^{2+} sensitivity of this enzyme was decreased (Krause et al., 1989). Furthermore, a decrease in the coupling ratio (mol Ca^{2+}/mol ATP) was observed in the SR membranes isolated from the stunned

myocardium, which was suggested to be the result of an increase in the Ca^{2+} permeability of the SR membrane. The SR Ca^{2+}-release process was also found to be impaired in the stunned myocardium due to a reduction of the number of ryanodine receptors (Zucchi et al., 1994). These data suggest that complex modifications of the SR function occur in the stunned myocardium, which are at least partly responsible for the contractile impairment found in this condition.

In long-lasting myocardial ischemia, gradual declines in both SR Ca^{2+}-ATPase activity and Ca^{2+} uptake were found, which may be due to decreased SR Ca^{2+}-ATPase protein (Talukder et al., 2009). Increasing SERCA2a via gene transfer or transgenic overexpression is cardioprotective against ischemia/reperfusion injury. Ischemia was also shown to result in variable changes in the phosphorylation of phospholamban (Talukder et al., 2009). Thus, the role of phospholamban regulation of sarcoplasmic reticulum Ca^{2+}-ATPase in ischemia is not resolved. A combination of various pathogenic factors has been suggested to be responsible for the reduced SR function and the final tissue necrosis in the ischemic myocardium. These pathological factors include pH reduction (acidosis), activation of intracellular proteolytic enzymes, and increased generation of free radicals.

IIE4. SR Ca^{2+}-ATPase as a Target for Heart Failure Treatment

Given the central importance of the SR Ca^{2+}-ATPase to proper SR Ca^{2+} cycling, excitation–contraction coupling and thus cardiac function, SERCA2 has been a focus of potential gene-targeted therapy for heart failure, especially since pump activity is depressed in failing hearts. SERCA2a gene transfer in animal models and human failing cardiomyocytes has shown beneficial effects, including improved contractility and energetics as well as prevention of arrhythmias and hypertrophy. For example, adenoviral delivery of SERCA2a to human failing cardiomyocytes rescued the depressed contractility and Ca^{2+} transients (reviewed in Lipskaia et al., 2010). Adenovirus-mediated gene transfer also improved function and survival in rat failing hearts. Additionally, SERCA2a delivery suppressed arrhythmias as well as infarct size in a rat model of ischemia/reperfusion injury (reviewed in Lipskaia et al., 2010). These beneficial effects in heart failure have also been demonstrated in large animals (reviewed in Lipskaia et al., 2010).

III. OTHER ATPases

The Ca^{2+} regulation in eukaryotic cells involves a complex mechanism that maintains a low background Ca^{2+} concentration (usually 0.1–0.2 μM) in the cell interior. Eukaryotic cells generally satisfy their Ca^{2+} demands by extracting Ca^{2+} from their own internal stores, but it is also evident that the long-term regulation of the Ca^{2+} gradient across the plasma membrane is a result of the concerted operation of the importing (Ca^{2+} channel) and exporting (SR Ca^{2+} pump; Na^{+}-Ca^{2+}exchanger and Ca^{2+} pump of the surface membrane) Ca^{2+} systems. The plasma membrane Ca^{2+}-ATPase is a low-capacity system possessing a very high Ca^{2+} affinity, which enables the enzyme to interact with Ca^{2+} at low intracellular concentrations. Consequently, its function is continuous and presumably satisfies the fine tuning of Ca^{2+} homeostasis.

IIIA. General Properties of Plasma Membrane Ca^{2+}-ATPase(s)

The plasma membrane Ca^{2+}-ATPase (molecular mass of 140 kDa) general kinetic mechanism follows the pattern of the SR Ca^{2+}-ATPase. ATP phosphorylates an Asp residue to yield an acid-stable phosphorylated intermediate. The elementary steps of the cycle are probably similar in both SR and plasma membrane Ca^{2+}-ATPases (Schatzmann, 1989). The stoichiometry between transported Ca^{2+} and hydrolyzed ATP is only 1.0 for the plasma membrane Ca^{2+} pump. The administration of La^{3+} under various experimental conditions has been associated with an increase in the steady-state phosphoenzyme level of the plasma membrane Ca^{2+}-ATPase and this increase possibly results from stabilization of the aspartyl phosphate (inhibition of hydrolysis of the phosphate group). The other classic inhibitor of Ca^{2+} pumps, vanadate, has been found to be a potent inhibitor of the plasma membrane Ca^{2+}-ATPase (Brini and Carafoli, 2009).

Calmodulin stimulates the plasma membrane Ca^{2+}-ATPase by direct interaction with the enzyme. It has been shown that the stimulation results from a combined effect on the affinity for Ca^{2+} (K_m) and the maximal transport rate (V_{max}) (Brini and Carafoli, 2009). The calmodulin-binding domain of the Ca^{2+} pump has been suggested to function as a repressor of the enzymatic activity (autoinhibitory function) and calmodulin may relieve this inhibition (Brini and Carafoli, 2009). A common mechanism in the autoinhibition of plasma membrane Ca^{2+}-ATPase and phospholamban inhibition of SR Ca^{2+}-ATPase has been suggested. In both proteins, the interacting sites are amphiphilic and located in the cytoplasmic region. The interaction occurs with homologous regions in the SR and plasma membrane Ca^{2+}-ATPases close to the phosphorylation sites. In the absence of calmodulin, the plasma membrane Ca^{2+} pump can be activated by several other compounds. Polyunsaturated fatty acids and acidic phospholipids (phosphatidylinositol, phosphatidylinositol 4-phosphate and phosphatidylinositol 4,5-diphosphate) have been reported to be good activators

and, since they are present in the plasma membrane, they may be important regulators of the Ca^{2+}-ATPase under in vivo conditions (Brini and Carafoli, 2009). Phosphorylation of the enzyme by cAMP-dependent PK or PK-C has also been reported to stimulate plasma membrane Ca^{2+}-ATPase activity. The cAMP-dependent phosphorylation occurs C-terminally to the calmodulin-binding domain and the phosphorylation-mediated activation may likewise be significant in vivo. The PK-C phosphorylation occurs in the calmodulin-binding domain, inhibiting the binding of calmodulin to the plasma membrane Ca^{2+}-ATPase and lowering the autoinhibitory potential of this domain (Brini and Carafoli, 2009). Cyclic GMP—dependent PK has also been reported to stimulate the plasma membrane Ca^{2+} pump in vascular smooth muscle, but the Ca^{2+}-ATPase enzyme was not found to be the substrate for this kinase.

IIIB. Primary Structure and Topography of Plasma Membrane Ca^{2+}-ATPase(s)

The complete amino acid sequence of the plasma membrane Ca^{2+} pump has been deduced from rat and human cells (Shull and Greeb, 1988; Verma et al., 1988). It appears that four plasma membrane Ca^{2+}-ATPase (PMCA 1—4) isoforms are encoded by a multigene family and additional variability is produced by alternative RNA splicing of each gene transcript (Table 13.2). The regions important for the catalytic function and the transmembrane domains are highly conserved, with no observed diversity. The isoform diversity seems to alter primarily the regulatory characteristics of the enzyme and it can be regarded as an adaptation to tissue specificity.

The secondary structure of the plasma membrane Ca^{2+}-ATPase is similar to that of the SR Ca^{2+}-ATPase (Shull and Greeb, 1988). The enzyme contains 10 putative transmembrane helices, which are connected on the outside of the plasma membrane by short loops. Three primary domains (about 80% of the pump protein) protrude into the cytoplasm. The first domain corresponds to the transducing unit, which couples ATP hydrolysis to Ca^{2+} translocation. The second protruding domain contains the aspartyl phosphate site (phosphorylation domain). The C-terminal portion of this domain can also be labeled by ATP analogs and contains a "hinge" region that permits the movement of aspartyl phosphate and the ATP-binding site. The third C-terminal protruding domain contains the calmodulin-binding sequence and the phosphorylation sites for protein kinase C and cAMP-dependent protein kinase. The latter is not present in all isoforms. As in the SR Ca^{2+}-ATPase, selective mutations in the M4 and M6 transmembrane segments in the plasma membrane Ca^{2+}-ATPase have been associated with loss of its ability to form the ATP- and Ca^{2+}-dependent phosphorylated intermediate and to transport Ca^{2+} (Guerini et al., 1998).

IIIC. Isoform-Specific Function of the Plasma Membrane Ca^{2+}-ATPase

While there is no specific inhibitor of the plasma membrane Ca^{2+}-ATPase (PMCA), the use of gene-altered mouse models has provided insights into the function of specific isoforms of the pump. Ablation of the PMCA1 gene in mice is lethal, suggesting its importance in a housekeeping function (Okunade et al., 2004). However, ablation of PMCA2 does not result in lethality, but mice have a reduction in spinal cord motor neurons, hearing loss and abnormalities in balance control. The deafness in PMCA2 null mice is related to a loss of otoconia and pathology of the auditory system. The PMCA2 isoform is also involved in lactation as PMCA2 null mice had a decrease in the Ca^{2+} levels in the milk (reviewed in Brini and Carafoli, 2009). PMCA4 homozygous null mice are also viable, but male mice are infertile due to reduced sperm motility (Okunade et al., 2004). No mouse model of PMCA3 ablation has been generated yet, thus the functional importance of this isoform is not currently clear. These studies indicate that the plasma membrane Ca^{2+}-ATPase is essential for maintaining various processes in a variety of cell types and there are different functional roles for the various isoforms.

TABLE 13.2 Distribution of the Human Plasma Membrane Ca^{2+}-ATPase (PMCA) Isoforms

Gene	Tissue Distribution	Level of Expression	Inhibition by Calmodulin
PMCA1[a]	Ubiquitous	High	Medium sensitive
PMCA2	Restricted (brain high)	High	Highly sensitive
PMCA3	Restricted (brain low)	Low	N/A[b]
PMCA4	Ubiquitous	Medium	Medium sensitive

[a] *PMCA numbers identify different gene products.*
[b] *N/A = data not available.*

IV. OVERVIEW

The Ca^{2+} levels in muscle are primarily regulated by the sarcoplasmic reticulum (SR) network, which serves as a sink for Ca^{2+} ions during relaxation and as a Ca^{2+} source during contraction. In cardiac muscle, most of the intracellular Ca^{2+} released during systole is taken up by the SR through its Ca^{2+}-ATPase. This translocation of Ca^{2+} from the cytosol into the SR lumen uses ATP as the energy source, and is characterized by the formation of a phosphorylated intermediate (E_1~P) for the Ca^{2+}-ATPase.

In cardiac muscle, slow-twitch skeletal muscle and smooth muscle, the Ca^{2+}-ATPase is regulated by a low-molecular-weight phosphoprotein called phospholamban. In its dephosphorylated form, phospholamban is an inhibitor of the Ca^{2+}-ATPase and phosphorylation relieves this inhibition. Phosphorylation of phospholamban occurs by cAMP-dependent, cGMP-dependent, Ca^{2+}-calmodulin-dependent, and Ca^{2+}-phospholipid-dependent protein kinases in vitro. However, in vivo studies have indicated that phospholamban is phosphorylated only by cAMP-dependent and Ca^{2+}-calmodulin-dependent protein kinases in intact beating hearts. A phospholamban phosphatase activity has been reported to be present in SR membranes, which can dephosphorylate this regulatory protein and reverse its stimulatory effects on the Ca^{2+}-ATPase.

Alterations in the SR Ca^{2+}-ATPase activity and its regulation by phospholamban have been shown to occur in cardiac diseases such as hypothyroidism, hyperthyroidism, hypertrophy, heart failure and ischemia. In most instances, alterations in Ca^{2+}-ATPase activity correlated with alterations in its mRNA levels and ventricular function. Recent studies have supported the targeting of the SR Ca^{2+}-ATPase as a therapeutic modality in cardiomyopathy and heart failure.

Another Ca^{2+}-ATPase, which is also important for maintaining Ca^{2+} homeostasis in muscle, is the plasma membrane Ca^{2+}-ATPase. This enzyme transports Ca^{2+} to the extracellular space and uses ATP as its energy source, similar to the SR Ca^{2+}-ATPase. The plasmalemmal Ca^{2+}-ATPase may be distinguished from the SR Ca^{2+}-ATPase primarily by its distinct sensitivity to La^{3+}, vanadate and calmodulin.

The primary structure of the various Ca^{2+} pumps has been elucidated and efforts are underway to further understanding the structural–functional relationships of these enzymes under pathological conditions. Furthermore, there is a growing interest in uncovering the mechanisms underlying regulation of the Ca^{2+}-ATPases by key endogenous proteins.

ACKNOWLEDGMENTS

The authors' research discussed in this chapter was supported by National Institutes of Health Grants HL-26057, HL-64018 and HL007382 training grant. This article was published in *Cell Physiology Sourcebook* 3rd edn, I. Edes and E.G. Kranias, eds (2001), Ch. 18, Ca^{2+}-ATPases, pp. 271-282. Copyright Elsevier, Inc.

BIBLIOGRAPHY

Arai, M., Alpert, N. R., MacLennan, D. H., Barton, P., & Periasamy, M. (1993). Alterations in sarcoplasmic reticulum gene expression in human heart failure. A possible mechanism for alterations in systolic and diastolic properties of the failing myocardium. *Circ Res, 72*, 463–469.

Arai, M., Otsu, K., MacLennan, D. H., Alpert, N. R., & Periasamy, M. (1991). Effect of thyroid hormone on the expression of mRNA encoding sarcoplasmic reticular proteins. *Circ Res, 69*, 266–276.

Arvanitis, D. A., Vafiadaki, E., Fan, G. C., et al. (2007). Histidine-rich Ca-binding protein interacts with sarcoplasmic reticulum Ca-ATPase. *Am J Physiol Heart Circ Physiol, 293*, H1581–H1589.

Babu, G. J., Bhupathy, P., Timofeyev, V., et al. (2007). Ablation of sarcolipin enhances sarcoplasmic reticulum calcium transport and atrial contractility. *Proc Natl Acad Sci USA, 104*, 17867–17872.

Baker, D. L., Hashimoto, K., Grupp, I. L., et al. (1998). Targeted overexpression of the sarcoplasmic reticulum Ca^{2+}-ATPase increases cardiac contractility in transgenic mouse hearts. *Circ Res, 83*, 1205–1214.

Beekman, R. E., van Hardeveld, C., & Simonides, W. S. (1989). On the mechanism of the reduction by thyroid hormone of β-adrenergic relaxation rate stimulation in rat heart. *Biochem J, 259*, 229–236.

Bers, D. M. (2008). Calcium cycling and signaling in cardiac myocytes. *Annu Rev Physiol, 70*, 23–49.

Bers, D. M., & Despa, S. (2006). Cardiac myocytes Ca^{2+} and Na^{+} regulation in normal and failing hearts. *J Pharmacol Sci, 100*, 315–322.

Beuckelmann, D. J., Nabauer, M., & Erdmann, E. (1992). Intracellular calcium handling in isolated ventricular myocytes from patients with terminal heart failure. *Circulation, 85*, 1046–1055.

Bhupathy, P., Babu, G. J., & Periasamy, M. (2007). Sarcolipin and phospholamban as regulators of cardiac sarcoplasmic reticulum Ca^{2+} ATPase. *J Mol Cell Cardiol, 42*, 903–911.

Brini, M., & Carafoli, E. (2009). Calcium pumps in health and disease. *Physiol Rev, 89*, 1341–1378.

Brittsan, A. G., Carr, A. N., Schmidt, A. G., & Kranias, E. G. (2000). Maximal inhibition of SERCA2 Ca^{2+} affinity by phospholamban in transgenic hearts overexpressing a non-phosphorylatable form of phospholamban. *J Biol Chem, 275*, 12129–12135.

Chu, G., Lester, J. W., Young, K. B., Luo, W., Zhai, J., & Kranias, E. G. (2000). A single site (Ser^{16}) phosphorylation in phospholamban is sufficient in mediating its maximal cardiac responses to β-agonists. *J Biol Chem, 275*, 38938–38943.

D'Agnolo, A., Luciani, G. B., Mazzucco, A., Gallucci, V., & Salviati, G. (1992). Contractile properties and Ca^{2+} release activity of the sarcoplasmic reticulum in dilated cardiomyopathy. *Circulation, 85*, 518–525.

Dally, S., Corvazier, E., Bredoux, R., Bobe, R., & Enouf, J. (2010). Multiple and diverse coexpression, location, and regulation of additional SERCA2 and SERCA3 isoforms in nonfailing and failing human heart. *J Mol Cell Cardiol, 48*, 633–644.

Edes, I., & Kranias, E. G. (1990). Phospholamban and troponin I are substrates for protein kinase C in vitro but not in intact beating guinea pig hearts. *Circ Res, 67*, 394–400.

Edes, I., Talosi, L., & Kranias, E. (1991). Sarcoplasmic reticulum function in normal heart and in cardiac disease. *Heart Failure, 6*, 221−237.

Fan, G. C., Gregory, K. N., Zhao, W., Park, W. J., & Kranias, E. G. (2004). Regulation of myocardial function by histidine-rich, calcium-binding protein. *Am J Physiol Heart Circ Physiol, 287*, H1705−H1711.

Fujii, J., Zarain-Herzberg, A., Willard, H. F., Tada, M., & MacLennan, D. H. (1991). Structure of the rabbit phospholamban gene, cloning of the human cDNA, and assignment of the gene to human chromosome 6. *J Biol Chem, 266*, 11669−11675.

Gianni, D., Chan, J., Gwathmey, J. K., del Monte, F., & Hajjar, R. J. (2005). SERCA2a in heart failure: role and therapeutic prospects. *J Bioenerg Biomembr, 37*, 375−380.

Gregory, K. N., & Kranias, E. G. (2006). Targeting sarcoplasmic reticulum calcium handling proteins as therapy for cardiac disease. *Hellenic J Cardiol, 47*, 132−143.

Gregory, K. N., Ginsburg, K. S., Bodi, I., et al. (2006). Histidine-rich Ca binding protein: a regulator of sarcoplasmic reticulum calcium sequestration and cardiac function. *J Mol Cell Cardiol, 40*, 653−665.

Guerini, D., Garcia-Martin, E., Zecca, A., Guidi, F., & Carafoli, E. (1998). The calcium pump of the plasma membrane: membrane targeting, calcium binding sites, tissue-specific isoform expression. *Acta Physiol Scand Suppl, 643*, 265−273.

Gwathmey, J. K., Copelas, L., MacKinnon, R., et al. (1987). Abnormal intracellular calcium handling in myocardium from patients with end-stage heart failure. *Circ Res, 61*, 70−76.

Haghighi, K., Kolokathis, F., Gramolini, A. O., et al. (2006). A mutation in the human phospholamban gene, deleting arginine 14, results in lethal, hereditary cardiomyopathy. *Proc Natl Acad Sci USA, 103*, 1388−1393.

Haghighi, K., Kolokathis, F., Pater, L., et al. (2003). Human phospholamban null results in lethal dilated cardiomyopathy revealing a critical difference between mouse and human. *J Clin Invest, 111*, 869−876.

Haghighi, K., Schmidt, A. G., Hoit, B. D., et al. (2001). Superinhibition of sarcoplasmic reticulum function by phospholamban induces cardiac contractile failure. *J Biol Chem, 276*, 24145−24152.

Ho, C. Y. (2010). Hypertrophic cardiomyopathy. *Heart Fail Clin, 6*, 141−159.

Hoit, B. D., Khoury, S. F., Kranias, E. G., Ball, N., & Walsh, R. A. (1995). In vivo echocardiographic detection of enhanced left ventricular function in gene-targeted mice with phospholamban deficiency. *Circ Res, 77*, 632−637.

Huggins, J. P., Cook, E. A., Piggott, J. R., Mattinsley, T. J., & England, P. J. (1989). Phospholamban is a good substrate for cyclic GMP-dependent protein kinase in vitro, but not in intact cardiac or smooth muscle. *Biochem J, 260*, 829−835.

Ji, Y., Lalli, M. J., Babu, G. J., et al. (2000). Disruption of a single copy of the SERCA2 gene results in altered Ca^{2+} homeostasis and cardiomyocyte function. *J Biol Chem, 275*, 38073−38080.

Kadambi, V. J., Ponniah, S., Harrer, J. M., et al. (1996). Cardiac-specific overexpression of phospholamban alters calcium kinetics and resultant cardiomyocyte mechanics in transgenic mice. *J Clin Invest, 97*, 533−539.

Kim, H. W., Steenaart, N. A., Ferguson, D. G., & Kranias, E. G. (1990). Functional reconstitution of the cardiac sarcoplasmic reticulum Ca^{2+}-ATPase with phospholamban in phospholipid vesicles. *J Biol Chem, 265*, 1702−1709.

Kimura, Y., Otsu, K., Nishida, K., Kuzuya, T., & Tada, M. (1994). Thyroid hormone enhances Ca^{2+} pumping activity of the cardiac sarcoplasmic reticulum by increasing Ca^{2+} ATPase and decreasing phospholamban expression. *J Mol Cell Cardiol, 26*, 1145−1154.

Kiss, E., Brittsan, A. G., Edes, I., Grupp, I. L., & Kranias, E. G. (1998). Thyroid hormone-induced alterations in phospholamban-deficient mouse hearts. *Circ Res, 83*, 608−613.

Kiss, E., Jakab, G., Kranias, E. G., & Edes, I. (1994). Thyroid hormone-induced alterations in phospholamban protein expression. regulatory effects on sarcoplasmic reticulum Ca^{2+} transport and myocardial relaxation. *Circ Res, 75*, 245−251.

Kranias, E. G., & Solaro, R. J. (1982). Phosphorylation of troponin I and phospholamban during catecholamine stimulation of rabbit heart. *Nature, 298*, 182−184.

Kranias, E. G., Garvey, J. L., Srivastava, R. D., & Solaro, R. J. (1985). Phosphorylation and functional modifications of sarcoplasmic reticulum and myofibrils in isolated rabbit hearts stimulated with isoprenaline. *Biochem J, 226*, 113−121.

Krause, S. M., Jacobus, W. E., & Becker, L. C. (1989). Alterations in cardiac sarcoplasmic reticulum calcium transport in the postischemic "stunned" myocardium. *Circ Res, 65*, 526−530.

Limas, C. J., Olivari, M. T., Goldenberg, I. F., Levine, T. B., Benditt, D. G., & Simon, A. (1987). Calcium uptake by cardiac sarcoplasmic reticulum in human dilated cardiomyopathy. *Cardiovasc Res, 21*, 601−605.

Limbruno, U., Zucchi, R., Ronca-Testoni, S., Galbani, P., Ronca, G., & Mariani, M. (1989). Sarcoplasmic reticulum function in the "stunned" myocardium. *J Mol Cell Cardiol, 21*, 1063−1072.

Lindemann, J. P., & Watanabe, A. M. (1985). Muscarinic cholinergic inhibition of β-adrenergic stimulation of phospholamban phosphorylation and Ca^{2+} transport in guinea pig ventricles. *J Biol Chem, 260*, 122−133.

Lindemann, J. P., & Watanabe, A. M. (1985). Phosphorylation of phospholamban in intact myocardium. Role of Ca^{2+}-calmodulin-dependent mechanisms. *J Biol Chem, 260*, 4516−4525.

Lindemann, J. P., Jones, L. R., Hathaway, D. R., Henry, B. G., & Watanabe, A. M. (1983). β-adrenergic stimulation of phospholamban phosphorylation and Ca^{2+}-ATPase activity in guinea pig ventricles. *J Biol Chem, 258*, 464−471.

Lipskaia, L., Chemaly, E. R., Hadri, L., Lompre, A., & Hajjar, R. J. (2010). Sarcoplasmic reticulum Ca^{2+} ATPase as a therapeutic target for heart failure. *Expert Opin Biol Ther, 10*, 29−41.

Lipskaia, L., Hulot, J. S., & Lompre, A. M. (2009). Role of sarco/endoplasmic reticulum calcium content and calcium ATPase activity in the control of cell growth and proliferation. *Pflugers Arch, 457*, 673−685.

Liu, L. H., Boivin, G. P., Prasad, V., Prasad, V., Periasamy, M., & Shull, G. E. (2001). Squamous cell tumors in mice heterozygous for a null allele of Atp2a2, encoding the sarco(endo)plasmic reticulum Ca^{2+}-ATPase isoform 2 Ca^{2+} pump. *J Biol Chem, 276*, 26737−26740.

Liu, L. H., Paul, R. J., Sutliff, R. L., et al. (1997). Defective endothelium-dependent relaxation of vascular smooth muscle and endothelial cell Ca^{2+} signaling in mice lacking sarco(endo)plasmic reticulum Ca^{2+}-ATPase isoform 3. *J Biol Chem, 272*, 30538−30545.

Lorenz, J. N., & Kranias, E. G. (1997). Regulatory effects of phospholamban on cardiac function in intact mice. *Am J Physiol, 273*, H2826−H2831.

Loukianov, E., Ji, Y., Grupp, I. L., et al. (1998). Enhanced myocardial contractility and increased Ca^{2+} transport function in transgenic hearts expressing the fast-twitch skeletal muscle sarcoplasmic reticulum Ca^{2+}-ATPase. *Circ Res, 83*, 889–897.

Luo, W., Chu, G., Sato, Y., Zhou, Z., Kadambi, V. J., & Kranias, E. G. (1998). Transgenic approaches to define the functional role of dual site phospholamban phosphorylation. *J Biol Chem, 273*, 4734–4739.

Luo, W., Grupp, I. L., Harrer, J., et al. (1994). Targeted ablation of the phospholamban gene is associated with markedly enhanced myocardial contractility and loss of β-agonist stimulation. *Circ Res, 75*, 401–409.

Luo, W., Wolska, B. M., Grupp, I. L., et al. (1996). Phospholamban gene dosage effects in the mammalian heart. *Circ Res, 78*, 839–847.

MacLennan, D. H., Abu-Abed, M., & Kang, C. (2002). Structure–function relationships in Ca^{2+} cycling proteins. *J Mol Cell Cardiol, 34*, 897–918.

MacLennan, D. H., Kimura, Y., & Toyofuku, T. (1998). Sites of regulatory interaction between calcium ATPases and phospholamban. *Ann NY Acad Sci, 853*, 31–42.

Mattiazzi, A., Mundina-Weilenmann, C., Guoxiang, C., Vittone, L., & Kranias, E. G. (2005). Role of phospholamban phosphorylation on Thr17 in cardiac physiological and pathological conditions. *Cardiovasc Res, 68*, 366–375.

Mercadier, J. J., Lompre, A. M., Duc, P., et al. (1990). Altered sarcoplasmic reticulum Ca^{2+}-ATPase gene expression in the human ventricle during end-stage heart failure. *J Clin Invest, 85*, 305–309.

Møller, J. V., Nissen, P., Sorensen, T. L., & le Maire, M. (2005). Transport mechanism of the sarcoplasmic reticulum Ca^{2+} -ATPase pump. *Curr Opin Struct Biol, 15*, 387–393.

Morris, G. L., Cheng, H. C., Colyer, J., & Wang, J. H. (1991). Phospholamban regulation of cardiac sarcoplasmic reticulum (Ca^{2+}-Mg^{2+})-ATPase. Mechanism of regulation and site of monoclonal antibody interaction. *J Biol Chem, 266*, 11270–11275.

Mortishire-Smith, R. J., Pitzenberger, S. M., Burke, C. J., Middaugh, C. R., Garsky, V. M., & Johnson, R. G. (1995). Solution structure of the cytoplasmic domain of phopholamban: phosphorylation leads to a local perturbation in secondary structure. *Biochemistry, 34*, 7603–7613.

Movsesian, M. A., Bristow, M. R., & Krall, J. (1989). Ca^{2+} uptake by cardiac sarcoplasmic reticulum from patients with idiopathic dilated cardiomyopathy. *Circ Res, 65*, 1141–1144.

Odermatt, A., Taschner, P. E., Khanna, V. K., et al. (1996). Mutations in the gene-encoding SERCA1, the fast-twitch skeletal muscle sarcoplasmic reticulum Ca^{2+} ATPase, are associated with Brody disease. *Nat Genet, 14*, 191–194.

Okunade, G. W., Miller, M. L., Pyne, G. J., et al. (2004). Targeted ablation of plasma membrane Ca^{2+}-ATPase (PMCA) 1 and 4 indicates a major housekeeping function for PMCA1 and a critical role in hyperactivated sperm motility and male fertility for PMCA4. *J Biol Chem, 279*, 33742–33750.

Pan, Y., Zvaritch, E., Tupling, A. R., et al. (2003). Targeted disruption of the ATP2A1 gene encoding the sarco(endo)plasmic reticulum Ca^{2+} ATPase isoform 1 (SERCA1) impairs diaphragm function and is lethal in neonatal mice. *J Biol Chem, 278*, 13367–13375.

Periasamy, M., Reed, T. D., Liu, L. H., et al. (1999). Impaired cardiac performance in heterozygous mice with a null mutation in the sarco(endo)plasmic reticulum Ca^{2+}-ATPase isoform 2 (SERCA2) gene. *J Biol Chem, 274*, 2556–2562.

Reddy, L. G., Jones, L. R., Pace, R. C., & Stokes, D. L. (1996). Purified, reconstituted cardiac Ca^{2+}-ATPase is regulated by phospholamban but not by direct phosphorylation with Ca^{2+}/calmodulin-dependent protein kinase. *J Biol Chem, 271*, 14964–14970.

Sakuntabhai, A., Ruiz-Perez, V., Carter, S., et al. (1999). Mutations in ATP2A2, encoding a Ca^{2+} pump, cause Darier disease. *Nat Genet, 21*, 271–277.

Schatzmann, H. J. (1989). The calcium pump of the surface membrane and of the sarcoplasmic reticulum. *Annu Rev Physiol, 51*, 473–485.

Schmidt, A. G., Zhai, J., Carr, A. N., et al. (2002). Structural and functional implications of the phospholamban hinge domain: impaired SR Ca^{2+} uptake as a primary cause of heart failure. *Cardiovasc Res, 56*, 248–259.

Schmitt, J. P., Kamisago, M., Asahi, M., et al. (2003). Dilated cardiomyopathy and heart failure caused by a mutation in phospholamban. *Science, 299*, 1410–1413.

Schultz, Jel. J., Glascock, B. J., Witt, S. A., et al. (2003). Accelerated onset of heart failure in mice during pressure overload with chronically decreased SERCA2 calcium pump activity. *Am J Physiol Heart Circ Physiol, 286*, H1146–H1153.

Schwinger, R. H., Bohm, M., Schmidt, U., et al. (1995). Unchanged protein levels of SERCA II and phospholamban but reduced Ca^{2+} uptake and Ca^{2+}-ATPase activity of cardiac sarcoplasmic reticulum from dilated cardiomyopathy patients compared with patients with nonfailing hearts. *Circulation, 92*, 3220–3228.

Sen, L., Cui, G., Fonarow, G. C., & Laks, H. (2000). Differences in mechanisms of SR dysfunction in ischemic vs. idiopathic dilated cardiomyopathy. *Am J Physiol Heart Circ Physiol, 279*, H709–H718.

Sharma, P., Ignatchenko, V., Grace, K., Ursprung, C., Kislinger, T., & Gramolini, A. O. (2010). Endoplasmic reticulum protein targeting of phospholamban: a common role for an N-terminal di-arginine motif in ER retention? *PLoS One, 5*, e11496.

Shull, G. E., & Greeb, J. (1988). Molecular cloning of two isoforms of the plasma membrane Ca^{2+}-transporting ATPase from rat brain. Structural and functional domains exhibit similarity to Na^+, K^+- and other cation transport ATPases. *J Biol Chem, 263*, 8646–8657.

Simmerman, H. K., & Jones, L. R. (1998). Phospholamban: protein structure, mechanism of action, and role in cardiac function. *Physiol Rev, 78*, 921–947.

Talosi, L., Edes, I., & Kranias, E. G. (1993). Intracellular mechanisms mediating reversal of β-adrenergic stimulation in intact beating hearts. *Am J Physiol, 264*, H791–H797.

Talukder, M. A., Zweier, J. L., & Periasamy, M. (2009). Targeting calcium transport in ischaemic heart disease. *Cardiovasc Res, 84*, 345–352.

Toyofuku, T., Curotto Kurzydlowski, K., Narayanan, N., & MacLennan, D. H. (1994). Identification of Ser^{38} as the site in cardiac sarcoplasmic reticulum Ca^{2+}-ATPase that is phosphorylated by Ca^{2+}/calmodulin-dependent protein kinase. *J Biol Chem, 269*, 26492–26496.

Unverferth, D. V., Lee, S. W., & Wallick, E. T. (1988). Human myocardial adenosine triphosphatase activities in health and heart failure. *Am Heart J, 115*, 139–146.

Ver Heyen, M., Heymans, S., Antoons, G., et al. (2001). Replacement of the muscle-specific sarcoplasmic reticulum Ca^{2+}-ATPase isoform SERCA2a by the nonmuscle SERCA2b homologue causes mild concentric hypertrophy and impairs contraction–relaxation of the heart. *Circ Res, 89*, 838–846.

Verma, A. K., Filoteo, A. G., Stanford, D. R., et al. (1988). Complete primary structure of a human plasma membrane Ca^{2+} pump. *J Biol Chem, 263*, 14152−14159.

Wolska, B. M., Stojanovic, M. O., Luo, W., Kranias, E. G., & Solaro, R. J. (1996). Effect of ablation of phospholamban on dynamics of cardiac myocyte contraction and intracellular Ca^{2+}. *Am J Physiol, 271*, C391−C397.

Zhai, J., Schmidt, A. G., Hoit, B. D., Kimura, Y., MacLennan, D. H., & Kranias, E. G. (2000). Cardiac-specific overexpression of a super-inhibitory pentameric phospholamban mutant enhances inhibition of cardiac function in vivo. *J Biol Chem, 275*, 10538−10544.

Zhao, W., Uehara, Y., Chu, G., et al. (2004). Threonine-17 phosphorylation of phospholamban: a key determinant of frequency-dependent increase of cardiac contractility. *J Mol Cell Cardiol, 37*, 607−612.

Zucchi, R., Ronca-Testoni, S., Yu, G., Galbani, P., Ronca, G., & Mariani, M. (1994). Effect of ischemia and reperfusion on cardiac ryanodine receptors−sarcoplasmic reticulum Ca^{2+} channels. *Circ Res, 74*, 271−280.

Zvaritch, E., Backx, P. H., Jirik, F., et al. (2000). The transgenic expression of highly inhibitory monomeric forms of phospholamban in mouse heart impairs cardiac contractility. *J Biol Chem, 275*, 14985−14991.

Chapter 14

Na^+-Ca^{2+} Exchange Currents

John H.B. Bridge, Natalia S. Torres and Michela Ottolia

Chapter Outline

I. SUMMARY

At first, study of the Na^+-Ca^{2+} exchange current was impeded because multicellular preparations did not permit adequate control of the driving forces producing exchange. However, methods for isolating single cells, together with the patch-clamp technique, made it possible to isolate exchange current and to provide reliable measurements of its properties. Now that the exchange molecule has been cloned, it is possible to express the mammalian exchanger in other cell types including frog oocytes. Currents may now be measured in these cell types with the giant patch technique or with the whole-cell patch-clamp method. These preparations and methods introduce the possibility of studying mutated forms of the exchanger with a view to understanding the relationship between structure and function.

Studies with isolated giant patches have resulted in significant advances in our understanding of both the regulation and mechanism of exchange activity. The phenomenon of Na^+-dependent inactivation of exchange was first identified in isolated patches and our understanding of secondary Ca^{2+} regulation, as well as regulation by phosphatidylinositol-4,5-bisphosphate (PIP_2) and phosphorylation, have been significantly advanced by this technique. Advances in the molecular biology of the Na^+-Ca^{2+} exchanger – which include the elucidation of the primary structure of the exchange molecule together with the development of recombinant DNAs coding for the Na^+-Ca^{2+} exchanger, their expression in systems suitable for current measurement and, finally, the production of various mutations – have already resulted in extensive studies of the relationship between structure and function which we have discussed in this chapter.

Measurements of both whole-cell currents as well as currents in giant patches have produced evidence in favor of the idea that a consecutive mechanism can explain exchange activity. Moreover, at least two laboratories have claimed to have isolated currents associated with partial reactions of the exchanger consistent with the idea that a consecutive (ping-pong) reaction scheme is operative. Preliminary results seem to suggest that much of the voltage dependence of the exchange resides in rate-limiting steps associated with Na^+ translocation in NCX1, although not with NCX-SQ1, in which voltage dependence appears to be associated with Ca^{2+} translocation. With the availability of the techniques of modern molecular biology, it

Cell Physiology Sourcebook. DOI: 10.1016/B978-0-12-387738-3.00014-7

seems likely that we may expect further progress in the study of the relationship between the structure and function of the exchange molecule. Elegant measurements of whole-cell currents have resulted in a plausible model of the behavior of the Na^+-Ca^{2+} exchange during the cardiac cycle. The way that the Na^+-Ca^{2+} exchange contributes to excitation coupling is not completely understood but is an active area of research. The advent of peptide inhibitors like XIP, together with methods for rapidly changing extracellular solutions, suggest that we may soon gain more insight into the contribution of both inward and outward exchange currents to the events of excitation–contraction coupling.

II. INTRODUCTION

The existence of Na^+-Ca^{2+} exchange was first postulated in 1964 by both Repke (1964) and Langer (1964) as a consequence of their studies on the contractility of heart muscle. Three years later, Baker and his colleagues (Baker et al., 1967) provided the first report documenting Na^+-Ca^{2+} exchange in giant squid axons. Shortly after this, Reuter and Seitz (1968) presented the first complete study describing Na^+-Ca^{2+} countertransport in heart. Based on studies of isotopic fluxes, these authors proposed that two Na^+ ions were coupled to the extrusion of a single Ca^{2+} ion in a modified exchange diffusion process. Blaustein and Hodgkin (1969) then published the results of their studies on squid axons. They recognized that the distribution of free Ca^{2+} could not be predicted on simple electrochemical principles. However, cyanide (which was expected to block metabolic processes) failed to prevent the efflux of ^{45}Ca, so that it seemed unlikely that a metabolic pump was involved in Ca^{2+} extrusion. However, this efflux of Ca^{2+} was (among other things) dependent upon external Na^+. Blaustein and Hodgkin therefore concluded that, in unpoisoned axons, some or possibly all of the energy for extruding Ca^{2+} ions came from the inward movement of Na^+ down its electrochemical gradient.

These early studies were seminal and provided impetus for an enormous number of subsequent investigations that have led not only to a study of Na^+-Ca^{2+} exchange currents, but to the molecular cloning and elucidation of the structure of the exchanger molecule itself. This, in turn, introduced the possibility of studying the relationship between molecular structure and function.

This chapter provides a brief description of current knowledge of Na^+-Ca^{2+} exchange currents. The ease with which heart cells can be patch-clamped, together with the presence of a vigorous exchange activity, doubtless explains the fact that most of our information on exchange current comes from this tissue. Na^+-Ca^{2+} exchange currents have been measured in other cell types including the squid giant axon (Matsuoka et al., 1997). Although measurements of exchange current are difficult in many tissues, it is now possible to express Na^+-Ca^{2+} exchangers in other cell types, for example frog oocytes. This, together with the development of giant excised patches that can be voltage-clamped, has made studies of the relationship between structure of the exchanger and function much easier.

III. ENERGETICS OF Na^+-Ca^{2+} EXCHANGE

Reuter and Seitz in their classic study (Reuter and Seitz, 1968) proposed that two Na^+ ions exchanged for a single Ca^{2+} ion in a modified exchange diffusion process. Based upon this proposal, one would not expect steady-state exchange activity to produce a measurable electric current. However, the existence of exchange currents is a well-established fact and one that can be appreciated by consideration of the energetic and stoichiometric properties of the exchange as they are currently understood. It is convenient (but not necessarily correct) to represent the transmembranous exchange reaction as a sequential (simultaneous) process:

$$n\mathrm{Na}_i^+ + \mathrm{Ca}_o^{2+} \leftrightarrow n\mathrm{Na}_o^+ + \mathrm{Ca}_i^{2+}$$

where n is the stoichiometric coefficient of the exchange reaction. If the forward and reverse reaction rates are equal, the exchange reaction is at equilibrium. Even if n is greater than 2, there can be no net charge movement and, hence, no electric current generated at equilibrium. An electric current can only be measured when the exchange is displaced from equilibrium. While the net reaction rate at equilibrium is zero, the unidirectional rates might be substantial (Axelsen and Bridge, 1985). As soon as the forward and reverse exchange rates differ from one another, net ion translocation takes place; provided that the stoichiometric coefficient is appropriate (i.e. n greater than 2) and no ions of opposite charge are co-transported, one can expect to measure an electric current as a consequence of exchange.

If electrochemical forces solely determine net movement of ions through the Na^+-Ca^{2+} exchanger, classical thermodynamics may be used to calculate both the direction of exchange and the conditions under which we may expect equilibrium to occur. Having the capacity to do this is of enormous value when designing experiments to measure exchange currents. The electrochemical potential difference or driving force ($n\Delta\tilde{\mu}$) producing exchange is the difference between n times the electrochemical potential difference or force producing sodium movement ($n\Delta\tilde{\mu}_{Na}$) and calcium movement ($\Delta\tilde{\mu}_{Ca}$). Driving force can be expressed in terms of membrane potential (Em), Na^+ equilibrium potential (ENa) and Ca^{2+} equilibrium potential (ECa). Thus, we may write:

$$\Delta\tilde{\mu} = n\Delta\tilde{\mu}_{Na} - \Delta\tilde{\mu}_{Ca} \qquad (14.1)$$

At equilibrium, $\Delta\tilde{\mu} = 0$, so that:

$$n\Delta\tilde{\mu}_{Na} - \Delta\tilde{\mu}_{Ca} = 0 \quad (14.2)$$

$$\Delta\tilde{\mu}_{Na}(mV) = \frac{RT}{F}\ln\frac{[Na^+]_o}{[Na^+]_i} + E_m = E_{Na} + E_m \quad (14.3)$$

$$\Delta\tilde{\mu}_{Ca}(mV) = \frac{RT}{F}\ln\frac{[Ca^{2+}]_o}{[Ca^{2+}]_i} + 2E_m = 2E_{Ca} + 2E_m \quad (14.4)$$

Substitution yields:

$$nE_{Na} - 2E_{Ca} - (n-2)E_m = 0 \quad (14.5)$$

The exponential form of Equation 14.5 is:

$$\frac{[Ca^{2+}]_o}{[Ca^{2+}]_i} = \left(\frac{[Na^+]_o}{[Na^+]_i}\right)^n \exp\left(-(n-2)\frac{E_m F}{RT}\right) \quad (14.6)$$

The driving force $\Delta\tilde{\mu}$ on exchange is given as:

$$\Delta\tilde{\mu} = 3ENa - 2ECa - Em \quad (14.7)$$

These are the equations that can be used to predict the equilibrium conditions of the exchanger. Before doing so, one needs to know the stoichiometric coefficient (n) of the exchanger. This issue has been the subject of a lengthy debate and numerous investigations. However, there now appears to be broad agreement that three Na^+ ions are exchanged for a single Ca^{2+} ion in most mammalian systems studied (Bridge and Bassingthwaighte, 1983; Reeves and Hale, 1984; Kimura et al., 1987; Bridge et al., 1990; Crespo et al., 1990). There is also good evidence that exchange stoichiometry is 3:1 in barnacle fibers (Rasgado-Flores and Blaustein, 1987).

Besides predicting equilibrium conditions we can, with sufficient information, predict the direction of exchange. Consider a heart cell at rest (or during diastole). If we assume the internal Na^+ concentration is 5 mM and Ca^{2+} is at 100 nM while external Ca^{2+} is 2 mM and Na^+ is 140 mM and, finally, the membrane potential is −80 mV, we can use Equation 14.7 to predict the direction of exchange if we assume n to be three (Fig. 14.1A). Thus the driving force on exchange is 18 mV which produces a net extrusion of Ca^{2+}. The exchange is said to be operating in its forward mode and there is net inward charge movement or a net inward current. If the cell is depolarized to +50 mV, the quantity $\Delta\tilde{\mu}$ becomes −112 mV and there is net Ca^{2+} influx through the exchange (see Fig. 14.1C). The exchange is then said to be operating in reverse mode and there is net outward current. Finally, equilibrium will occur at −62 mV for these ionic concentrations (see Fig. 14.1B). It should be noted that, in a cell like a heart cell, which has a small surface to volume ratio, ion movements through the exchange may alter the intracellular concentrations so that the quantities that we have just calculated will change. For a description of the way that the exchange changes during the phases of a cardiac action potential, we refer the reader to Bers (2001).

An elegant (though somewhat indirect) demonstration of exchange stoichiometry was provided by Reeves and Hale (Reeves and Hale, 1984). This demonstration employed the foregoing principles and equations. Their study not only produced a value for the exchange stoichiometry, but provided an excellent example of the way that the foregoing energetic principles may guide experimental design. These authors took advantage of the fact that exchange equilibrium can be achieved simply by appropriate adjustment of the Na^+ and Ca^{2+} electrochemical gradients. Bovine sarcolemmal vesicles containing Na^+-Ca^{2+} exchanger were equilibrated with solutions of both Na^+ and ^{45}Ca. Under these circumstances, the equilibrium may be described by Equation 14.5. After treating the membrane with valinomycin in the presence of KCl, known membrane potentials were established that caused disequilibrium of the exchanger and either Ca^{2+} entry or exit. By adjusting the Na^+ gradient, it was possible to null precisely the tendency of membrane potential to produce Ca^{2+} movement. Thus, if any of the quantities E_m, E_{Na}, and E_{Ca} are held constant, the relationship between the other two may be found. The point at which Ca^{2+} movement was nulled by Na^+ gradient is given by:

$$E_{rev} = 3E_{Na} - 2E_{Ca} = -50\ mV \quad (14.8)$$

By nulling Ca^{2+} movement over a range of membrane potentials, the value for n that these authors obtained was 2.97 ± 0.03, which is close to the currently accepted value of 3.0.

IV. METHODS AND PROBLEMS ASSOCIATED WITH THE MEASUREMENT OF Na^+-Ca^{2+} EXCHANGE CURRENT

Several recent techniques have greatly facilitated the isolation of exchange current. First, the *whole-cell ruptured patch voltage clamp* in conjunction with intracellular dialysis (Hamill et al., 1981) has probably contributed most to the initial isolation of exchange currents. To record whole-cell current with the ruptured patch technique, a microelectrode or patch pipette is pressed onto the cell membrane and suction is applied, usually with a syringe or directly by the experimentalist. This often results in a high-resistance seal that forms between the pipette and the cell membrane. The resistance of this seal is ideally $>10^{10}$ ohms and it is therefore referred to as a gigaseal. This is usually accompanied by the formation of an Ω structure as the membrane is pulled into the pipette (see Chapter 20). Continued suction ruptures the Ω, and this creates continuity between the cell interior and the pipette solution. By

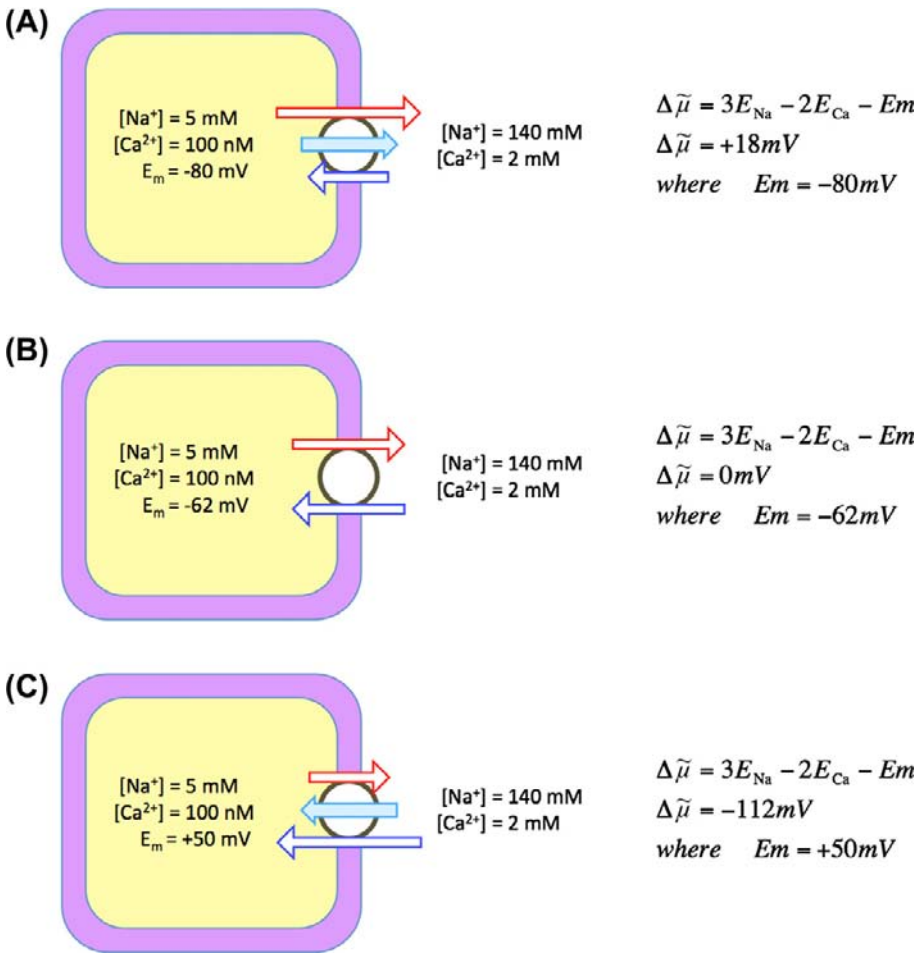

FIGURE 14.1 (A) The red arrow represents the rate of the forward exchange reaction which exceeds the rate of the reverse reaction represented by the blue arrow (see the reaction described in section II). This results in net extrusion of Ca^{2+} and a net inward current (light blue arrow). This is usually referred to as the forward mode of the exchange. The calculations to the right of all figures simply indicate the magnitude and direction of the driving force producing net exchange. (B) The red and blue arrows have the same significance as in (A). In this case, the forward and reverse reactions occur at the same rate so that there is no net reaction and therefore no net current. The exchange is at equilibrium, as the calculation to the right indicates, i.e. there is not net driving force on the exchange. (C) Again red and blue arrows retain their significance. However, the rate of the reverse reaction exceeds the rate of the forward reaction. This results in net influx of Ca^{2+} accompanied by an outward current. The calculation to the right indicates both the magnitude and direction of the driving force.

pulling the sealed pipette from the cell one may isolate an outside-out patch. It is also possible with the methods illustrated in Chapter 20 to create an inside-out patch. Hilgemann has refined this technique so that very large membrane patches can be isolated from appropriately treated cell membranes (Hilgemann, 1989).

A simplified arrangement for voltage-clamping heart cells and recording exchange current through a ruptured patch is depicted in Fig. 14.2. Essentially the same arrangement applies to the voltage-clamping of an isolated patch. The micropipette attached to the cell is connected via a (non-polarizable) electrode to the front end of a high-gain amplifier known as a current-to-voltage converter. The most significant feature of this high amplifier is the feedback loop R_f and its branch point (the summing junction). In operational amplifiers (of which this current-to-voltage converter is an example), this branch point has special significance. Negative feedback through the feedback loop tends to cancel the input signal at S. A command potential V_c is applied to the non-inverting input (+). A property of this amplifier is that, as a result of negative feedback through R_f, current always flows so that the voltage at the summing junction is identical to the voltage V_c (the command potential). The potential difference between the summing junction and ground is therefore ideally equal to V_c. This potential difference therefore falls across the electrode resistance (and any other resistances in series with the membrane resistance R_m). Provided that the product of this series resistance (R_s) and the exchange current $I_{Na\text{-}Ca}$ ($R_s I_{Na\text{-}Ca}$) is small, most of the potential difference V_c occurs across the membrane. Feedback through R_f always compensates varying input at the summing junction, thus ensuring that the voltage across the membrane is held constant (i.e. is clamped). Exchange current $I_{Na\text{-}Ca}$ passing across the membrane produces a potential difference across the membrane. As this potential difference causes the membrane potential to depart from V_c, current (equal in magnitude to the exchange current) flows into the summing junction. In reality, additional circuitry is required to reduce noise in the recording system while increasing its fidelity. This is dealt with in greater detail in Chapter 20.

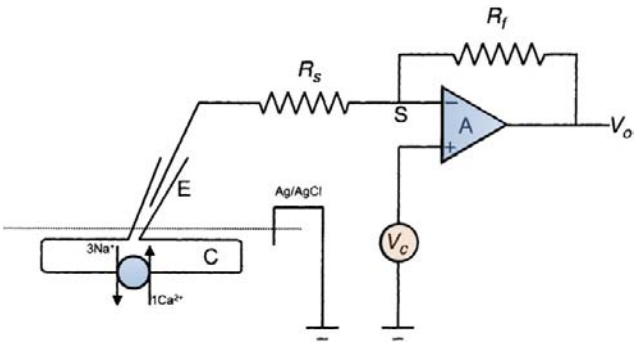

FIGURE 14.2 An arrangement suitable for measuring Na^+-Ca^{2+} exchange current in a ventricular heart cell. Under these circumstances, the exchanger is producing a net outward current across the cell membrane by exchanging three internal Na^+ ions with a single external Ca^{2+} ion. This produces outward movement of one net charge. The voltage-clamp circuit consists of a high-gain amplifier A. Any deviations from the command potential V_c produced by the exchanger are compensated by feedback from the output through the feedback resistor R_f. The amplifier is connected to the cell through the electrode E, which is sealed to a ruptured patch. The output of this amplifier is proportional to the current flowing through the feedback resistor R_f and hence the cell C. The success of this method depends upon minimizing voltage drops across the series resistance R_s. The bath in which the cell is maintained is grounded by an Ag/AgCl electrode connected to a salt bridge (not shown).

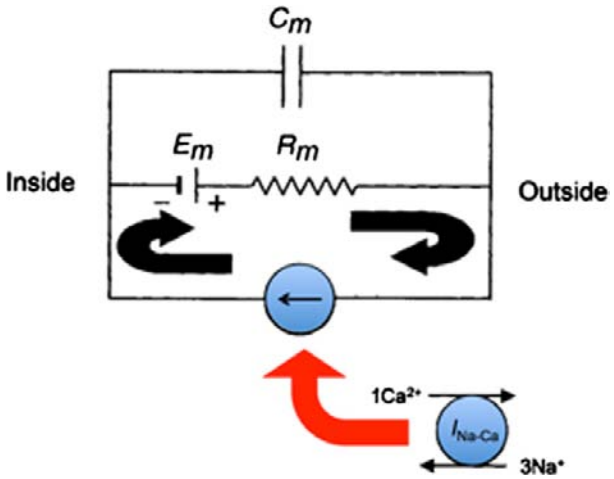

FIGURE 14.3 A simple equivalent circuit for a resting heart cell. The resting membrane potential E_m is typically about −80 mV. This resting membrane potential is modeled as a battery in series with an internal resistance of about 50 MΩ. The membrane capacitance is in series with the battery. The Na^+-Ca^{2+} exchanger may be considered to be a current generator in parallel with the battery and membrane resistance (symbolized by an open circle containing an arrow). At rest, with the exchanger steadily extruding Ca^{2+}, a small depolarizing current $I_{Na\text{-}Ca}$ causes a small voltage drop across the membrane resistance R_m. The solid arrows indicate the direction of current. The circle containing an arrow indicates a current generator (the Na^+-Ca^{2+} exchange). Thus, for each cycle of the exchanger a single net charge is conveyed from the cell exterior to its interior.

The current flowing through a heart cell membrane, I_m, consists of two components: a capacity current and an ionic current I_i. The capacity current $I_C = CdV/dt$ and the membrane current is denoted I_m. Therefore:

$$I_m = C\frac{dV}{dt} + I_i + I_{Na-Ca} \tag{14.9}$$

The ionic current consists of ions flowing through ion channels as well as those translocated by ion exchange mechanisms (principally the Na^+-Ca^{2+} exchange and the Na^+ pump). For purposes of illustration, the exchange current has been separated from the ionic current in Equation 14.9. Under voltage-clamp $dV/dt = 0$,

$$I_m = I_i + I_{Na-Ca} \tag{14.10}$$

If one can remove or minimize I_i (which includes the Na^+ pump current and all contaminating channel currents) without affecting exchange current $I_{Na\text{-}Ca}$, one may measure a membrane current that is comprised mainly of $I_{Na\text{-}Ca}$.

How will the activity of an electrogenic Na^+-Ca^{2+} exchange affect membrane potential? A convenient equivalent circuit to explain this is depicted in Fig. 14.3. This simplified equivalent resting membrane circuit consists of a membrane capacitance that is in parallel with a battery E_m, which is largely responsible for producing the membrane potential. The membrane resistance R_m is modeled as the internal resistance of this battery. Under resting conditions, the reversal potential for the Na^+-Ca^{2+} exchange in heart is approximately −40 mV. At −80 mV the exchange will produce a net inward current, which can be modeled as a current generator that is in parallel with the membrane battery and capacitance (Fig. 14.3). At the steady state, when the resting membrane potential is not changing, $C\,dV/dt = 0$. Thus, the net membrane potential is composed of contributions from ionic currents (mainly through K^+ channels), exchange currents and the Na^+ pump current (Equation 14.10). The exchange will produce an IR drop across the membrane resistance so that the contribution of Na^+-Ca^{2+} current to the membrane potential ($V_{Na\text{-}Ca}$) at rest is given by:

$$V_{Na-Ca} = R_m I_{Na-Ca} \tag{14.11}$$

A large inward exchange current produced by elevated intracellular [Ca^{2+}] may be of the order 200 pA. If we assume that the resting exchange current is one-tenth of this value and given a resting R_m of 50 mΩ, the exchange will contribute about 1 mV to the resting membrane potential. In reality, the value is likely to be less than this but cannot be specified with certainty because reliable measurements of resting current are not available.

The first observations of exchange current were not published until nearly 20 years after Reuter and Seitz originally reported Na^+-Ca^{2+} exchange activity in heart tissue. It is worth considering some of the problems associated with the measurement of exchange current that might account for this lengthy hiatus.

To stimulate exchange so that it can be measured, one can either change electrochemical gradients (and hence the exchange driving forces) by using a voltage-clamp step or one can abruptly change external ion composition with a rapid switching device. In the case of the voltage-clamp step, the experimentalist must have a complete understanding of what interfering currents will be activated, as well as some means of inhibiting them. If exchange is to be activated by changing ionic gradients, then these changes must be sufficiently rapid that they are not immediately dissipated by the exchange activity. It is difficult rapidly to change or control extracellular ionic composition in multicellular preparations because diffusion distances are large and diffusion may be hindered by a surface structure. In multicellular preparations, voltage-clamp is usually established with small microelectrodes, which are unsuitable for cell dialysis. It is, therefore, very difficult to control the intracellular ionic composition. This doubtless contributed to the difficulty of isolating exchange currents in multicellular preparations. Despite these difficulties, a measurement of exchange currents has been reported in multicellular preparations (Horackova and Vassort, 1979).

Recently, it has proved feasible to use the patch-clamp technique in conjunction with wide-tipped microelectrodes (10-μm diameter) to obtain an isolated patch whose surface area is approximately 75 μm^2 (see Fig. 14.2). A conventional isolated patch is of the order 2−3 μm^2. These *giant patches* are sufficiently large to permit the detection of exchange currents (Hilgemann, 1989). Their great virtue is that they permit relatively easy access to either side of the membrane. Thus, solution adjacent to the external surface of the sarcolemma can be changed by changing the pipette solution. The internal surface of the sarcolemma can be changed rapidly by changing the bathing solution. Clearly, this method of voltage-clamp allows the experimentalist considerable control over the forces that drive exchange.

Several other techniques have recently become available that improve exchange current isolation. For example, forward exchange current in intact cells can be activated by abruptly elevating intracellular Ca^{2+}, which is then transported to the cell exterior. This has been accomplished in an elegant fashion by Niggli and Lederer (Niggli and Lederer, 1991). These workers used the compound DM-dinitrophen that is commonly referred to as *caged* Ca^{2+}. This can be introduced into the cell interior through a patch pipette. Upon appropriate irradiation with UV light, Ca^{2+} is released from the caged Ca^{2+} with extremely rapid kinetics. This abruptly elevates cytosolic Ca^{2+} and transiently stimulates forward Na^+-Ca^{2+} exchange as the released Ca^{2+} is pumped to the cell exterior.

As we have indicated, to activate exchange it is desirable to change external ionic composition (and the electrochemical gradients driving exchange) extremely rapidly in comparison with the time required for the exchange to dissipate these changes. It is now possible to change external solutions surrounding heart cells or isolated patches with a half-time of about 20 ms (this includes exchange of the unstirred layer). One method consists of placing a cell with attached microelectrodes in one of two adjacent microstreams of solution (Spitzer and Bridge, 1989). The boundary separating these streams is abruptly moved across the cell so that it is placed in the adjacent stream. This rapid switching method has proved valuable in stimulating both inward and outward exchange currents (Chin et al., 1993).

V. ISOLATION OF Na^+-Ca^{2+} EXCHANGE CURRENT

VA. Whole-Cell Patch-Clamp Studies

The first clear evidence that an electric current was generated by Na^+-Ca^{2+} exchange was provided simultaneously by Kimura and coworkers (Kimura et al., 1986) and by Mechmann and Pott (Mechmann and Pott, 1986). Given the probable stoichiometry of the exchange, electrophysiologists expected to be able to measure a current generated by the exchange. By using the whole-cell patch-clamp technique together with intracellular dialysis, Junko Kimura and her associates were able to isolate the Na^+-Ca^{2+} exchange current. These investigators voltage-clamped guinea pig ventricular myocytes with single microelectrodes. The pipette contained a dialyzing solution completely deficient in Na^+ and in which Ca^{2+} was buffered to a value of 73 nM with EGTA. The superfusing external solution contained no Ca^{2+}. Under these circumstances, no exchange could take place. Very little change in current was observed when external Ca^{2+} was reapplied and subsequently removed. However, an outward current was generated after changing the pipette solution for one containing 30 mM Na^+ and then applying 1.0 mM external Ca^{2+}. Under these circumstances, Ca^{2+} entered the cell in exchange for internal Na^+, which was extruded. This current (Fig. 14.4) is clearly attributable to the operation of electrogenic Na^+-Ca^{2+} exchange. This conclusion was strengthened by several additional observations. Upon removal of external Ca^{2+}, the current was turned off. The current was reduced when lower concentrations of dialyzing Na^+ were used and enlarged by increasing external Ca^{2+}. Thus, the current exhibited the expected dependency on both Na^+ and Ca^{2+}. The current was blocked by La^{3+}, which is known to block Na^+-Ca^{2+} exchange. The current also exhibited *voltage dependence* (see Section XI). One might have expected sustained current under these circumstances, but this was not observed (see Fig. 14.4) and the current exhibited a tendency to decay. One plausible explanation for this is that excessive Ca^{2+} entry displaces protons when it is

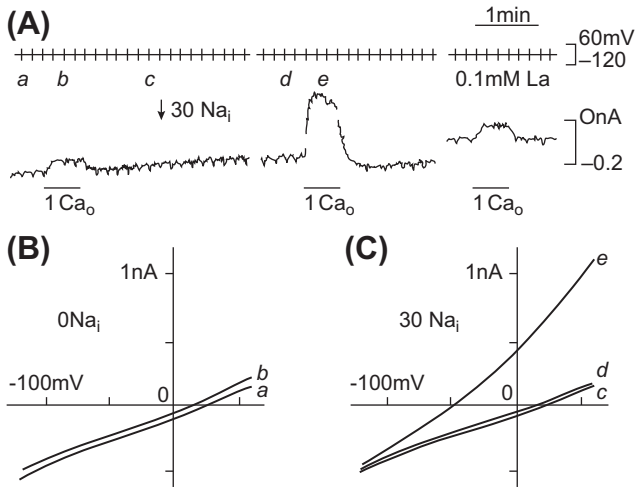

FIGURE 14.4 (A) Voltage-clamp record from a single myocyte showing voltage (upper trace) and current (lower trace). A ramp pulse from +60 mV to −120 mV was given from a holding potential of −30 mV every 10 s at a ramp speed of about 0.2 V/s. Current−voltage relationships were then constructed. An application of 1 mM Ca^{2+} in the absence of intracellular Na^+ (zero pipette Na^+) produced a small outward current. To exchange the pipette solution, a piece of tapered polyethylene tube was inserted into the pipette. The arrow indicates when the solution change was started. The holding current shifted outward slightly on loading Na^+. The middle current record shows 1 mM Ca^{2+} superfusion in the presence of 30 mM pipette Na^+. The Ca^{2+}-induced outward current appears to decay after reaching a peak. Current undershoot is seen after washing off Ca^{2+}. These phenomena may be due to Ca^{2+} accumulation immediately below the membrane of acid induced by binding of Ca^{2+} to EGTA. (B) I-*V* relations measured before (a) and during (b) 1 mM Ca^{2+} superfusion in the absence of Na_i^+. (C) I-V curves before (c) and after (d) loading Na_i^+ and during subsequent 1 mM Ca_o^{2+} application (e). *(Reprinted from Kimura et al. (1986) with kind permission of the authors and* Journal of Physiology.*)*

buffered by the dialyzing EGTA. The resulting acidification in the vicinity of the exchanger should inhibit exchange activity. An alternative possibility is that EGTA fails to buffer incoming Ca^{2+}, which accumulates in the vicinity of the exchanger. The resulting collapse of the Ca^{2+} gradient would also slow exchange.

Kimura and colleagues reported the measurement of an outward current corresponding to the entry of Ca^{2+} and extrusion of Na^+ from the cell. Mechmann and Pott demonstrated the existence of an inward exchange current corresponding to Ca^{2+} extrusion and Na^+ entry into a cardiac cell (Mechmann and Pott, 1986). In one experiment, these authors voltage-clamped spherical atrial cells from an adult guinea pig. Transient inward current occurred spontaneously in this preparation. These transient inward currents seemed to depend on intracellular Ca^{2+} because they were abolished if the cell was dialyzed with 1.0 mM EGTA. Moreover, they could not be elicited in the presence of caffeine, which depletes the SR of Ca^{2+}. Presumably, the transient release of SR Ca^{2+} activated these currents. The currents also showed a dependence on extracellular Na^+ and voltage as expected of a Na^+-Ca^{2+} exchange current. The more negative the voltage, the larger the inward current. This is reasonable and simply indicates that, at more negative potentials, the exchange rate is greater so that Ca^{2+} released from the SR is removed rapidly from the cell.

Shortly after these early demonstrations of exchange current, Hume and Uehara were able to demonstrate Na^+-Ca^{2+} exchange currents in isolated frog atrial cells by using the whole-cell patch-clamp technique in combination with intracellular dialysis (Hume and Uehara, 1986a,b). It is fair to say that since this time measurement of exchange current has become both reliable and routine. An example of an inward exchange current measured in a ventricular cell is displayed in Fig. 14.5.

The development of the giant patch technique has also facilitated measurement of the exchange current produced by the squid exchanger NCX−SQ1 (He et al., 1998).

VB. Na^+-Ca^{2+} Exchange Current Reversal Potential

It is desirable when studying any ionic current to be able to demonstrate a *reversal potential* for that current. The existence of reversal potentials is a thermodynamic necessity and provides one of the least ambiguous ways of identifying an ionic current. However, it is not always a straightforward matter to demonstrate reversal potentials. For example, if exchange current were extremely small

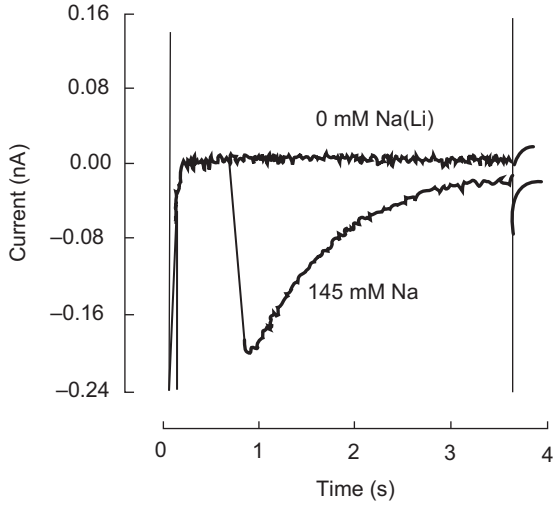

FIGURE 14.5 Transient inward Na^+-Ca^{2+} exchange. To activate this current, a guinea pig ventricular cell was tetanized with voltage-clamp pulses in the presence of ryanodine and in the absence of external Na^+. This resulted in an elevation of cytosolic Ca^{2+} and a sustained contraction (not shown). Abrupt application of 145 mM extracellular Na^+ while the cell was held at −40 mV produced mechanical relaxation and activated a transient inward Na^+-Ca^{2+} exchange current. As intracellular Ca^{2+} declined, the current decayed.

over a large voltage range in the vicinity of the reversal potential, then the precise potential at which zero current occurred could be extremely difficult to specify. Moreover, subsarcolemmal spaces from which diffusion is restricted can produce changes in ionic concentration that confound measurement of the exchange reversal potential. For the Na^+-Ca^{2+} exchange in heart, the reversal potential is given by Equation 14.8. For the conditions of their experiment, Kimura and coworkers (see Fig. 14.4) calculated that the reversal potential of exchange ought to be −131 mV (Kimura et al., 1986). Their results indicate that exchange current becomes zero at a potential close to this value. Ehara and colleagues extended studies of the exchange reversal potential (Ehara et al., 1989). With the fairly specific exchange inhibitor Ni^{2+}, these authors were able to show that, over a wide range of external Na^+ values, the measured exchange reversal potential conformed to theoretical expectation. Moreover, in view of the wide range over which the reversal potential remains constant, the stoichiometry is unlikely to vary.

VI. IONIC DEPENDENCIES OF Na^+-Ca^{2+} EXCHANGE CURRENT

It is of considerable physiological significance that the Na^+-Ca^{2+} exchange current is extremely sensitive to internal Na^+. There are two aspects of this sensitivity to consider, one purely thermodynamic and the other kinetic. If we assume that a resting heart cell contains 100 nM free cytosolic Ca^{2+} and is bathed in 2.0 mM Ca^{2+} and 140 mM Na^+, we can use Equation 14.8 to calculate the way the exchange reversal potential varies with internal Na^+. The results are displayed in Fig. 14.6.

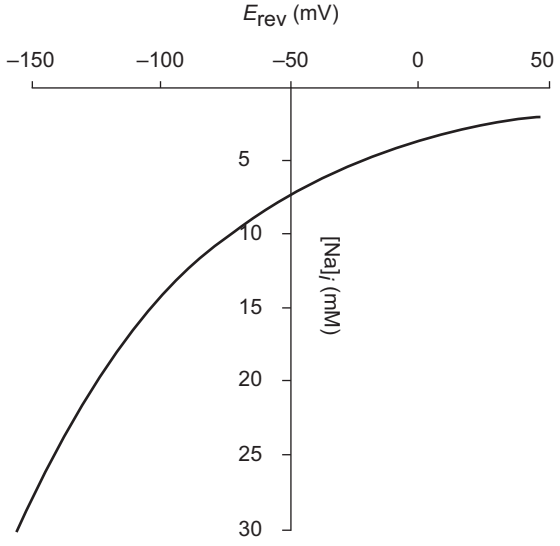

FIGURE 14.6 Calculated variation of exchange reversal potential with intracellular Na^+. Intracellular Ca^{2+} was set at 100 nM and extracellular Ca^{2+} was 2.0 mM. Extracellular Na^+ was 140 mM.

It is apparent that with 7 mM intracellular Na^+, 140 mM extracellular Na^+, and 100 nM intracellular free Ca^{2+}, the reversal potential for exchange is approximately −50 mV. Since the resting membrane potential is at least 30 mV negative to this, at rest the exchanger will extrude Ca^{2+}. However, a modest increase in intracellular Na^+ to 12 mM would change the reversal potential by 14 mV to −64 mV. Were the Na^+ to accumulate to 15 mM, then the reversal potential would be −80 mV. Since the resting potential is likely to be close to this value, the exchange would be close to, or at equilibrium and would be incapable of extruding intracellular Ca^{2+}. Further Na^+ accumulation would cause the exchange to reverse and transmit Ca^{2+} into the cell. Na^+ accumulation will tend to bring the exchange closer to its equilibrium potential and, therefore, increase the likelihood of Ca^{2+} entry via the exchanger upon membrane depolarization. Cardiac glycosides which, depending on dose, partially or completely block the sodium pump, tend to produce an accumulation of intracellular Na^+ (Sheu and Fozzard, 1982). Part of the basis of their inotropic effect resides in their shifting the reversal potential of the Na^+-Ca^{2+} exchange to more negative values. In extreme cases, this will prevent Ca^{2+} extrusion which, in the face of continued Ca^{2+} leak, will lead to Ca^{2+} accumulation.

The Na^+-Ca^{2+} exchange current also exhibits a physiologically important kinetic dependence upon internal Na^+. This issue has been investigated directly by Miura and Kimura, who studied outward exchange current in guinea pig ventricular cells under voltage-clamp (Miura and Kimura, 1989). Intracellular Ca^{2+} was buffered to 100 nM and intracellular Na^+ was varied by varying the pipette Na^+ concentration. External Na^+ was reduced to zero and a unidirectional exchange reaction was activated by applying 0.2 mM Ca^{2+} as rapidly as possible to the cell exterior. The results demonstrate that exchange current density exhibits a steep and somewhat sigmoid dependence on internal Na^+. The K_m for this dependency is approximately 20 mM and Hill plots reveal a Hill coefficient of 1.9. It is notable that an application of rate theory revealed that the voltage dependence of the exchange did not depend on intracellular Na^+ (see Section XI). It is clear from these results that at least Ca^{2+} influx on the exchange will be extremely sensitive to fluctuations in intracellular Na^+ produced, for example, by increases in stimulation rate or cardiac glycosides. It is unfortunate that we have no information on the intracellular Na^+ dependence of inward exchange current which corresponds to Ca^{2+} efflux. However, studies with isotopic fluxes reveal that Na^+ and Ca^{2+} compete for transport on the exchanger. For example, Na^+ on the same side of the cardiac sarcolemmal membrane as Ca^{2+} inhibits Ca^{2+} flux through the exchanger with a K_i of about 15 mM (Reeves and Sutko, 1983). Finally, the net inward exchange current

does depend on external Na^+. This has been investigated by Kimura and coworkers, who showed that inward current exhibited a sigmoidal dependence on external Na^+ with a $K_{1/2}$ of 87.5 mM and a Hill coefficient of 2.9 (Kimura et al., 1986).

Net inward exchange current (i.e. Ca^{2+} extrusion in exchange for Na^+ entry) is also dependent on intracellular Ca^{2+}. The relationship between Ca^{2+} concentration and current has been measured in two different ways. Miura and Kimura used whole-cell patch-clamp on guinea pig myocytes to determine K_m (Ca^{2+}) (Miura and Kimura, 1989). They controlled intracellular Ca^{2+} by dialyzing the cell with various EGTA-buffered solutions and determined a K_m (Ca^{2+}) to be 0.6 μM. With a different approach, Barcenas-Ruiz and colleagues used guinea pig ventricular myocytes to measure exchange current and intracellular Ca^{2+} simultaneously (Barcenas-Ruiz et al., 1987). Intracellular Ca^{2+} was measured with the Ca^{2+}-sensitive indicator Fura−2, introduced through the dialyzing pipette used to voltage-clamp the cells. Heart cells can be tetanized or caused to go into contracture in the presence of ryanodine. Various clamp pulses up to 120 mV in amplitude (holding potential of −80 mV) produced slow and sustained increases in Ca^{2+}. This Ca^{2+} declined upon repolarization and the decline was accompanied by a Na^+-Ca^{2+} exchange current tail. Plots of current against $[Ca^{2+}]_i$ revealed a linear relationship and no sign of saturation (Fig. 14.7). It is not possible to extract a K_m value from these data since the relationship between Ca^{2+} and current does not saturate. However, it is reasonable to conclude that the K_m value is well above the 0.6 μM obtained by Kimura and colleagues. Discrepancies of this nature are not easy to resolve. It is, however, worth noting that EGTA has the rather curious effect of increasing the affinity of the exchanger for Ca^{2+} (Trosper and Philipson, 1984).

VII. REGULATION OF Na^+-Ca^{2+} EXCHANGE CURRENT

The regulation of Na^+-Ca^{2+} exchange current has largely been studied in NCX1. We will consider five types of regulation. First, intracellular Ca^{2+} regulates the exchange current. The exchange current also exhibits a regulatory phenomenon known as Na^+-dependent inactivation. Thus, the exchanger not only transports Na^+ and Ca^{2+}, but these ions are capable of regulating its function as well. Exchange current is also known to be regulated by phosphatidylinositol-4,5-bisphosphate (PIP_2), phosphorylation and, finally, the XIP region of the exchanger in the cytosolic loop appears to be involved in the regulation of the NCX (see Section VIII). In addition, a great deal has been learned about regulatory function and its relationship to the structure of the exchanger.

VIIA. Regulation by Na^+ and Ca^{2+}

There are two Ca^{2+}-binding sites on the cytoplasmic loop of NCX (see Section VIII). It is now apparent that Ca^{2+} influx in exchange for internal Na^+ cannot occur if intracellular Ca^{2+} is reduced below a certain critical level. Dipolo provided the first evidence that Ca^{2+} was required to activate NCX (DiPolo and Beauge, 1987b). However, in

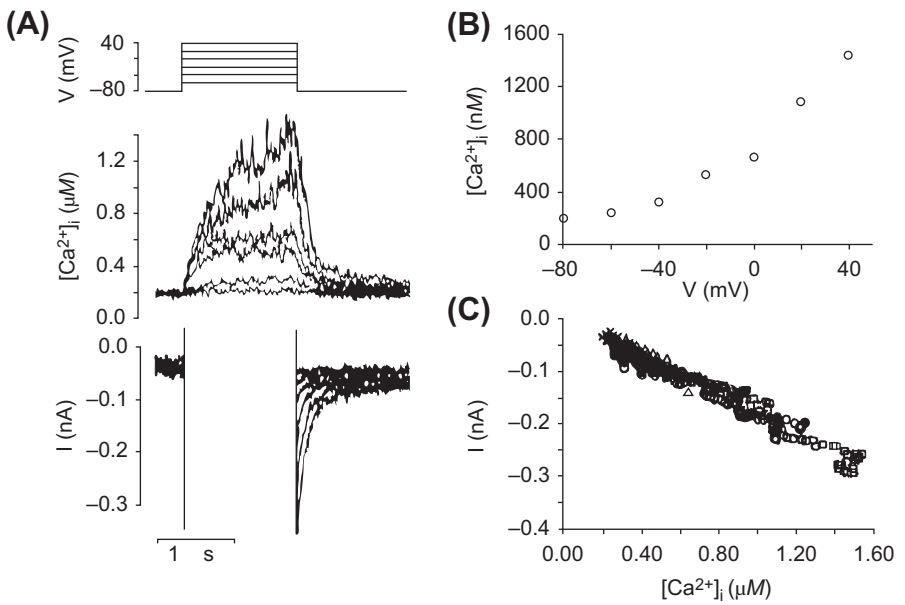

FIGURE 14.7 Changes in $[Ca^{2+}]_i$ and membrane current attributed to Na^+-Ca^{2+} exchange in a single guinea pig ventricular myocyte under voltage-clamp. Micropipette $[Na^+]$ was 7.5 mM. (A) Simultaneous recordings of $[Ca^{2+}]_i$ and membrane current. The holding potential was −80 mV, and depolarizing pulses lasting for 1.5 s were given from −60 mV to +40 mV. Outward currents during the depolarizing pulse are off-scale. (B) Voltage dependence of the change in $[Ca^{2+}]_i$. Values plotted are average $[Ca^{2+}]_i$ over the last 200 ms of the depolarizing pulse. (C) The relationship between $[Ca^{2+}]_i$ and membrane current after repolarization. The current, *I*, has been plotted as a function of $[Ca^{2+}]_i$ at 2 ms intervals during the first second after repolarization from +40 mV (circles), 0 mV (triangles), −20 mV (diamonds), and −40 mV (crosses). *(Reprinted with permission from Barcenas-Ruiz, L., Beuckelmann, D.J. and Wier, W.G. (1987). Sodium-calcium exchange in heart: membrane currents and changes in $(Ca^{2+})_i$. Science. 238, 1720−1722. Copyright 1987 American Association for the Advancement of Science).*

isolated patches from cardiac cells, the K_D appears to be from 0.1 to 0.3 μM (Hilgemann et al., 1992b; Matsuoka et al., 1995). This is reasonable because Ca^{2+} in junctional regions is thought to rise by as much as 15 μM (Acsai et al., 2011). The possible physiological significance of Ca^{2+} regulation will be discussed in a later section. Moreover, regions of the NCX molecule involved in Ca^{2+} regulation are now understood (see section VIII). Na^+-dependent inactivation of exchange current is a rather curious regulatory phenomenon first described by Hilgemann and coworkers (Hilgemann et al., 1992b). Outward Na^+-Ca^{2+} exchange currents were activated in giant sarcolemmal patches by increasing Na^+ on the cytoplasmic side of the patch. Ca^{2+} was then transported from the pipette to the cytoplasmic side of the patch in exchange for Na^+. This outward current declined with a time constant of approximately 1 s. This decay rate is far too low to represent an initial turnover of exchangers and it appears to be a true regulatory phenomenon. An example of this sort of behavior is displayed in Fig. 14.8. Here, application of 100 mM Na^+ to the cytoplasmic surface activated a transient outward current. It is believed that the XIP region of the exchange molecule (see Section VII) is involved in this process.

VIIB. PIP_2

Hilgemann has been able to show that outward exchange current in isolated giant sarcolemmal patches is stimulated by MgATP (Hilgemann, 1990). With this preparation, it is possible to control MgATP on the cytoplasmic side of the cell membrane. This stimulation by MgATP appears to be a different process than that described in squid axon. For example, it does not appear to involve a protein-dependent kinase (Collins et al., 1992). Hilgemann has also shown that brief treatment of membrane patches with chymotrypsin abolished modulation of exchange current by MgATP. However, recent evidence has been obtained for a mechanism that seems likely to explain regulation by ATP (Hilgemann and Ball, 1996). It now appears that phosphatidylinositol-4,5-bisphosphate (PIP_2) can strongly activate the cardiac Na^+-Ca^{2+} exchanger. Apparently ATP generates PIP_2 from phosphatidylinositol (PI). A number of observations suggest that the generation of PIP_2 can explain the regulation of Na^+-Ca^{2+} exchange by ATP: (1) PI-specific phospholipase C can abolish the action of ATP which can, in turn, be restored by the addition of exogenous PI. (2) The effect of ATP can be reversed by a PIP_2-specific phospholipase C. However, the stimulatory effect of ATP can be mimicked by exogenous PIP_2. (3) Aluminum, which binds with high affinity to PIP_2, reverses the effect of ATP on the exchanger. It therefore appears that the generation of PIP_2 is an important regulator of Na^+-Ca^{2+} exchange activity in heart. A possible mechanism for this is explained in Section VIII.

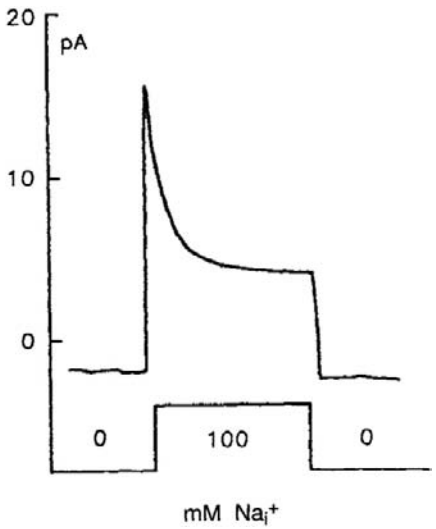

FIGURE 14.8 Secondary modulation of outward Na^+-Ca^{2+} exchange current in giant excised inside-out patches (37°C, 0 mV). Current transients activated with 100 mM Na^+ (substituted for 100 mM Cs^+). *(This figure was kindly provided by Dr Donald Hilgemann.)*

VIIC. Phosphorylation

It has been known for some time that exchange activity in squid giant axons could be regulated by ATP. The main effect of ATP is to increase the affinity of the exchanger for its substrates Na^+ and Ca^{2+}. Moreover, recent evidence suggests the involvement of a Ca^{2+}-dependent protein kinase. It appears that, at least in the squid, Na^+-Ca^{2+} exchange that is stimulated by ATP requires intracellular Ca^{2+} and can be mimicked by hydrolyzable ATP analogs (DiPolo and Beauge, 1987a,b).

It has been difficult to demonstrate regulatory effects of ATP in cardiac tissues. The whole-cell isolated patch technique does not lend itself to studies of this nature because it is extremely difficult, if not impossible, to control intracellular ATP concentrations. However, recent evidence suggests that the molecule may be phosphorylated and regulated by two mechanisms. One which remains controversial is that phophorylation can take place by β-adrenergic/PKA activation. There appears to be stronger evidence that PKC mediated signaling can regulate NCX phosphorylation. We refer the interested reader to the review by Zhang and Hancox (Zhang and Hancox, 2009).

VIID. Regulation by the XIP region of the exchanger

The XIP region of the exchanger refers to a stretch of amino acid (Li et al., 1991; Matsuoka et al., 1997) modeled at the N-terminus of the large cytoplasmic loop. This domain,

which is well conserved among the exchangers, is autoinhibitory and involved in Na^+-dependent inactivation and PIP_2 regulation. The mechanisms of action of XIP are unknown. A possible model is that the autoinhibition is accomplished when the site interacts with some other undisclosed region of the exchanger molecule: Na^+-dependent inactivation could be explained if high concentrations of Na^+ promoted this interaction (Reeves and Condrescu, 2008). PIP_2, instead, could exert its effect by interacting with the XIP sequence preventing it to block the exchanger (He et al., 2000). The properties of the XIP region are further discussed in the next section.

VIII. STRUCTURE OF NCX AND ITS RELATIONSHIP TO FUNCTION

The cardiac Na-Ca exchanger (NCX1) has been cloned and isolated (Philipson et al., 1988; Nicoll et al., 1990). Besides revealing its primary structure, this has lead to considerable understanding of its regulation and the relationship between its structure and function. These issues will be the focus of this section.

Our current knowledge of the exchanger's structure principally arises from cysteine accessibility mutagenesis (Nicoll et al., 1999; Iwamoto et al., 2000), epitope mapping (Porzig et al., 1993) and cross-linking studies (Philipson et al., 2002). Although these studies were conducted using the cardiac exchanger isoform, their results are likely to be true for all other isoforms of the exchanger.

The 938 amino acids comprising the primary structure of the exchanger are organized into three regions. The N-terminal region, composed of five transmembrane segments (TMS), a large cytoplasmic loop and a C-terminal group of four TMSs. A schematic drawing of NCX1 is displayed in Fig. 14.9.

At present, there are no structural data on the exchanger TMSs organization. Nevertheless, extensive disulfide cross-linking studies (Qiu et al., 2001; Ren et al., 2006, 2008, 2010) have provided information on the exchanger TMS packing arrangement. This has enabled Ren and her colleagues to generate a model describing the exchanger TMSs organization (Fig. 14.10).

TMSs 2, 3, 7 and 8 (Qiu et al., 2001) are in close proximity and this is of considerable interest. Within these TMSs are found the α repeats (see Fig. 14.9). These are two stretches of about 40 amino acids each with a similar sequence which are highly conserved among the exchanger family (Schwarz and Benzer, 1997). The α repeats are modeled as spanning TMSs 2 and 3 (α1 repeat) and parts of TMS 7 and the following cytoplasmic loop (α2 repeat). The hydrophilic portions of the α repeats appear to form re-entrant loops (Iwamoto et al., 1999; Nicoll et al., 1999; Shigekawa et al., 2002), similar to P-loops found in ion channels (Hille et al., 1999). This suggests that they are

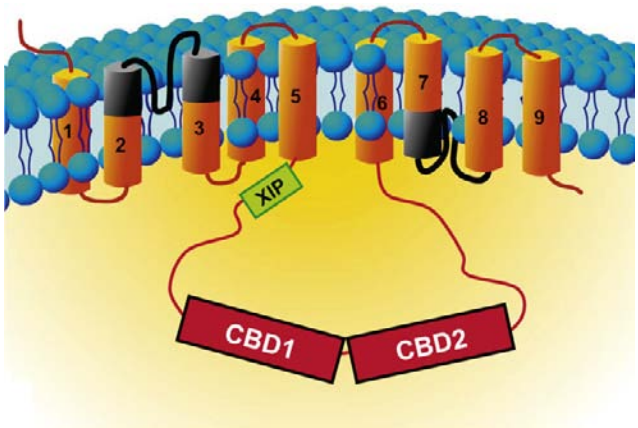

FIGURE 14.9 Secondary structure of the cardiac Na^+-Ca^{2+} exchanger. The exchanger is organized into nine transmembrane segments and a large intracellular loop between TMS5 and 6. The α repeats, which are involved in ion translocation, are indicated in black. The large intracellular loop is involved in NCX regulation. The XIP region, shown in green, is a stretch of residues that controls the Na^+-dependent inactivation and the modulation of NCX by lipids. CBD1 and CBD2 are the Ca^{2+}-binding domains. Calcium bound to these sites is not transported but activates the exchanger and rescues it from the Na^+-dependent inactivation.

involved in ion translocation. This suggestion has been supported by studying mutations at these sites, which have been shown to affect ion transport (Nicoll et al., 1996; Iwamoto et al., 2000; Ottolia et al., 2005). This provides the first information on regions of NCX that may be crucial for ion translocation. For example, several residues within the hydrophilic region of the α repeats set the sensitivity of NCX for extracellular Ca^{2+}, while two residues within TMS3 (Ala^{140} and Ile^{147}) of the α1 repeat influence the cytoplasmic affinity of NCX for the transported Na^+. To date, the residues that directly coordinate the binding of transported Na^+ or Ca^{2+} have not been found, so that additional studies in this area are required.

Our understanding of the modes of operation of the exchanger has been clouded by new evidence indicating that this secondary transporter exists as a dimer in the plasma membrane. First, cross-linking studies showed that cysteines at position 122 (TMS2) in adjacent exchangers form disulfide bonds (Ren et al., 2008). Similar results were obtained for cysteines introduced at position 40 of TMS1, indicating that NCX exists as oligomers in the plasma membrane. This was then confirmed by fluorescence resonance energy transfer (FRET) studies, which demonstrated the dimeric organization of NCX (John et al., 2011). We will provide a short explanation of this technique shortly. However, how dimerization of NCX affects either its transport or regulatory properties is still unknown.

While transport functions are associated with the transmembrane segments of NCX, the large cytoplasmic loop between TMS 5 and 6 is involved in regulatory

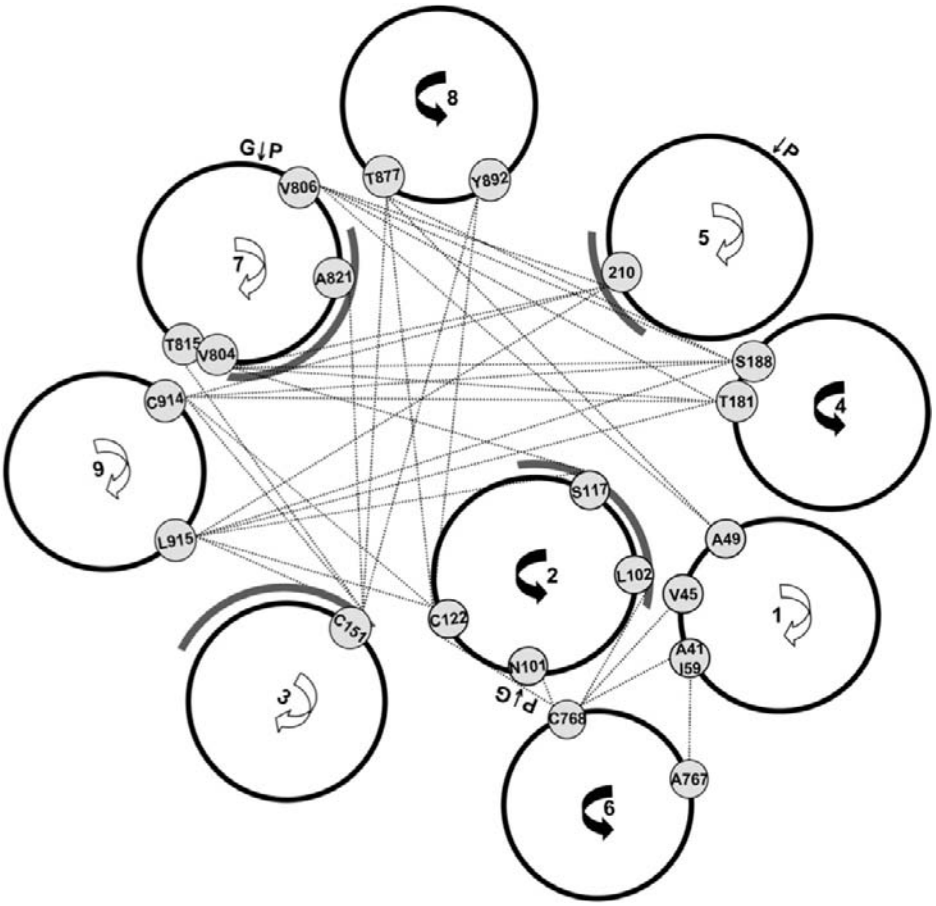

FIGURE 14.10 Computer-generated model of NCX1 helix packing. Pairs of residues that demonstrated cross-linking are indicated with lines. The faces of TMSs that contain residues that have altered activity upon mutagenesis are indicated with gray arcs. *(Reprinted from Ren et al. with kind permission of the authors and* Biochemistry.*)*

mechanisms. This is confirmed by the fact that a mutant lacking this loop still transport Na^+ and Ca^{2+} (Matsuoka et al., 1993). Within this portion of NCX there are several regions of interest. For example, the XIP region is found at the N-terminal side of the loop. This is a stretch of hydrophobic and positive residues (amino acids 219−238) named after a synthetic peptide (exchanger inhibitory peptide) with an identical sequence which potently blocks NCX transport activity (Hilgemann et al., 1991a). This site is mainly known to regulate the Na^+-dependent inactivation (see Section VI; Matsuoka et al., 1997) since mutations within it either eliminate this secondary regulation or alter its properties. Also exogenous regulators such as lipids interact with this region to modulate exchanger activity by affecting the Na^+-dependent inactivation (He et al., 2000; Riedel et al., 2006).

Two Ca^{2+}-binding domains are downstream of the XIP region (see Figs 14.9 and 14.11). These are indicated as Ca^{2+}-binding domains 1 and 2 (CBD1 and CBD2). In the cardiac exchanger isoform NCX1, CBD1 encompasses residues 371 to 501, CBD2 consists of residues 501−689. Cytoplasmic Ca^{2+} that binds to these sites is not transported (thereby indicated as regulatory Ca^{2+}) but activates the exchanger and rescues it from Na^+-dependent inactivation (Hilgemann et al., 1992a,b).

Both CBD1 and CBD2 are organized into seven-stranded antiparallel β-sandwiches with Ca^{2+} ions bound at

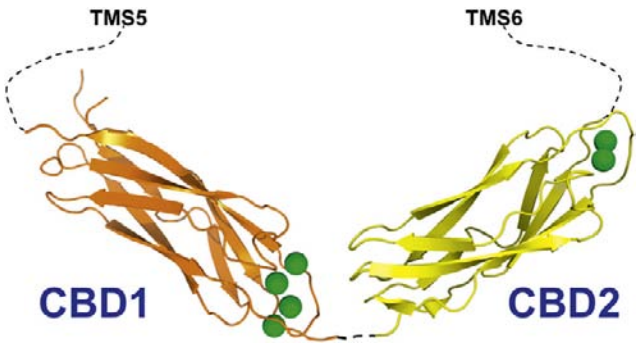

FIGURE 14.11 Structure of the cardiac Na^+-Ca^{2+} exchanger Ca^{2+}-binding domains. Shown is the crystal structure of the first and second Ca^{2+}-binding domains (CBD1 and CBD2). The orientation between the two domains is arbitrary since there is no information about their structure as conjunct domains. CBD1 spans residues 371 to 501, while CBD2 consists of residues 501 to 689 (cardiac isoform, NCX1.1). Calcium ions are shown as green spheres.

one end of the β-barrel (Hilge et al., 2006, 2009; Besserer et al., 2007; Johnson et al., 2008; Chaptal et al., 2009; Wu et al., 2009a,b). The structure of the conjunct CBDs is currently unknown. CBD1 binds four Ca^{2+} ions, however, mutagenesis studies indicate that only the occupancy of sites 3 and 4 is important for Ca^{2+} regulation (Ottolia et al., 2009). CBD2 coordinates two Ca^{2+} ions and removal of the primary Ca^{2+} completely abolishes the sensitivity of NCX to cytoplasmic Ca^{2+} (Besserer et al., 2007).

While CBD1 does not drastically vary among the exchanger isoforms, CBD2 contains a region of diversity that is the result of alternative exon splicing. Six exons exist within CBD2 which are indicated A to F. While A and B are mutually exclusive, the remaining can mix in different combinations. As a result, CBD2s of different lengths and Ca^{2+}-binding properties are created providing unique biophysical properties to the various NCX products. Generally, exon A-containing exchangers (such as the cardiac NCX) can alleviate the Na^+-dependent inactivation at high Ca^{2+} concentrations while exchangers with exon B (such as NCX1.3, kidney) lack this capability (Dyck et al., 1999; Hilge et al., 2009).

The molecular mechanisms underlying Ca^{2+} regulation of the exchanger are unexplained. It is reasonable to speculate that the Ca^{2+}-binding domains undergo conformational changes upon Ca^{2+} binding. This is based on isolated individual and conjoined CBD studies which show the loss of structure of CBD1 in absence of Ca^{2+} (Hilge et al., 2006). In addition, FRET studies show Ca^{2+}-dependent movements within the isolated CBDs (Ottolia et al., 2004; Xie et al., 2008; John et al., 2011) and the full length exchanger (John et al., 2011).

It has also been proposed that electrostatic interactions occur between CBD1 and CBD2 and that these interactions are disrupted by Ca^{2+} binding to CBD1 thereby reorienting CBD in respect to CBD2 (Hilge et al., 2009). This model is supported by recent evidence showing that either the orientation or the proximity of CBD1 and CBD2 is important for NCX Ca^{2+} regulation as is demonstrated by inserting seven alanines between the two CBDs and showing that the resulting ionic currents were less sensitive to cytoplasmic Ca^{2+} (Ottolia et al., 2010). Subsequently, the kinetic properties of a peptide consisting of the conjunct CBD1 and CBD2 were found profoundly altered by the insertion of the seven alanines (Giladi et al., 2010), consistent with the electrophysiological data.

These results suggest that the two Ca^{2+}-binding domains do not act as separate entities but somehow act synergistically to regulate exchanger activity. Indeed, the apparent affinity of the conjunct Ca^{2+}-binding domains for cytoplasmic Ca^{2+} (John et al., 2011) and its kinetics (Giladi et al., 2010) are different from those of CBD1 or CBD2. Although synergism between the CBDs has been demonstrated, two puzzles remain. How do the two CBDs interact mechanistically with each other upon Ca^{2+} binding/unbinding; and, how does this combined entity of CBD1 and CBD2 transmit its information to the remainder of NCX?

Since FRET studies have been useful in detecting movements of these subunits, it is perhaps worth providing a brief description of this technique. Fluorescence resonance energy transfer is the non-radiative transfer of energy from a fluorescent donor to another excitable moiety which can be attached to, for example, different regions of the same molecule (in this case NCX) or to two closely apposed molecules. In FRET, a donor fluorophore in an excited electronic state can transfer its excitation energy to an acceptor chromophore. Although the process does not involve photon emission, usually the donor and the acceptor molecules are fluorescent. Energy transfer quenches donor fluorescence and there is an increase in acceptor fluorescence emission. The efficiency of energy transfer varies in proportion to the inverse sixth power of the distance separating donor and acceptor molecules. Donor and acceptor molecules can be on the same molecules, e.g. NCX, or different molecules. There are two requirements for FRET to occur: first, the emission spectrum of the donor has to overlap the excitation spectrum of the acceptor and, second, the two moieties have to be in close proximity (10 nm). Since the efficiency of energy transfer is strongly dependent on this distance, FRET therefore is a powerful technique to measure the proximity of molecules or their changes in conformation. Labeling the protein, e.g. NCX, can be achieved either chemically, by attaching a fluorophore to the protein, such as maleimide fluorophores dyes, or by molecular biology techniques. Examples of the latter are the cyan (CFP) and yellow (YFP) variants of the green fluorescent protein (GFP), which are popular FRET pairs.

The methods for measuring FRET are several; however, the ratiometric and photobleaching approaches are the mostly widely used. The ratiometric method involves the recording of both acceptor and donor emissions either sequentially or simultaneously. This is because, when FRET occurs, excitation of the donor causes acceptor emission at the expense of donor emission. Hence, the acceptor/donor fluorescence intensity ratio is an estimate of the amount of energy transfer. FRET recording in this manner has the advantage that it can monitor changes in real time. To measure FRET efficiency, which can give estimates of actual distance between fluorescent moieties, the alternative method acceptor photobleaching approach is used. This method relies on the concept that when FRET occurs part of the energy of excited donor is transferred to the acceptor resulting in decreased donor emission. This energy transfer is eliminated by bleaching of YFP and leads to an increase in CFP emission. A cartoon describing the

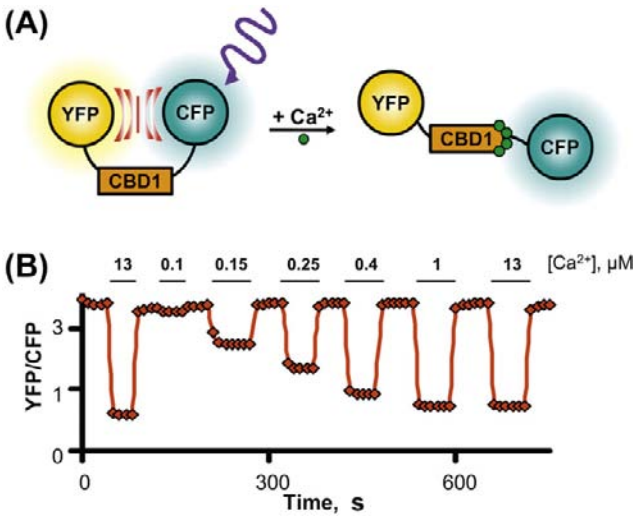

FIGURE 14.12 Example of FRET between CFP and YFP. The yellow and cyan variants of the green fluorescent protein were fused to the N and C termini of the first Ca^{2+}-binding domain (CBD1) of the cardiac Na^+-Ca^{2+} exchanger (A). In absence of cytoplasmic Ca^{2+}, excitation of the CFP caused YFP emission since the two fluorophores are in close proximity. However, as shown in plot (B), addition of cytoplasmic Ca^{2+} moved the fluorophores apart causing a decrease in FRET (measured as YFP/CFP ratio). For this experiment, the fluorescent CBD1 was anchored to the plasma membrane by fusing to its C terminus a short plasma membrane targeting sequence. The construct was then expressed into *Xenopus laevis* oocytes to isolated portion of its plasma membrane onto coverslip. This technique allows accessibility to the cytoplasmic surface of the membrane which now are perfused with different Ca^{2+} concentrations, indicated above the trace. *(Reprinted from John et al. with kind permission of the authors and* PNAS*).*

way that this technique can be use to detect the CBD movements is displayed in Fig. 14.12.

IX. THE PHYLOGENY OF THE Na^+-Ca^{2+} EXCHANGER

The number of proteins belonging to the exchanger family is increasing. These proteins are defined by the presence of the signature sequence α repeats (see previous sections) and a membrane topology of two clusters of transmembrane segments separated by a cytoplasmic loop of different length. Recent analysis indicates five families of exchangers, which constitute a "superfamily". This is explained in some detail in the review by Lytton (Lytton, 2007). Among them is the *NCX family.* These are all mammalian exchangers and include NCX1, the first exchanger to be isolated, as well as NCX2 and NCX3. These exchangers are ubiquitous with NCX1 found in the heart, brain and kidney, NCX2 in the brain and NCX3 in the brain and skeletal muscle. NCX1 is particularly abundant in the heart and it has been the subject of intensive investigations. It is on NCX1 that most studies of currents that are generated by exchange have been performed.

Other exchangers in the NCX family are found, for example, in the nematode *C. elegans* and also in the fruit fly *Drosophila.* The NCX family is found in a wide variety of mammalian species including human, dog, rabbit, cow, rat and guinea pig as well as in various non-mammalian species.

The other four members of the Ca^{2+}/cation antiporter gene superfamily are: bacterial exchangers, Ca^{2+}/anion exchanger, Ca^{2+}/cation exchanger and the NCKX family. Discussion of the first three families of exchangers is outside the scope of this chapter. Here we will briefly described the NCKX family.

NCKX are plasma membrane proteins that, at difference from NCX, require K^+ for transport exchanging four Na^+ for one Ca^{2+} and one K^+ during each cycle. The first member of this family, NCKX1, was cloned from retinal tissue. Here, NCKX1 is associated to the cGMP-gated channel which opens in the dark allowing Ca^{2+} to enter the cell. As Ca^{2+} extrusion mechanism, NCKX counterbalance this Ca^{2+} influx maintaining resting levels of intracellular Ca^{2+}. The physiological impact of the remaining NCKX is less understood but evidence suggests an important role of NCKX2, 3 and 4 in neuronal Ca^{2+} signaling. The fifth member of this family NCKX 5 is, instead, found in skin and retinal epithelia but its function has yet to be explained. Excellent reviews are available to the reader (Cuomo et al., 2007; Lytton, 2007).

X. ISOFORMS OF THE Na^+-Ca^{2+} EXCHANGER

The large intracellular loop of NCX1 can be spliced in different ways to produce a variety of splice variants. The region of alternative splicing is found in the second Ca^{2+}-binding domains (CBD2) (see Section VIII). Six small exons are used in different combinations to produce CBD2 with different properties (Hilge et al., 2006, 2009; Besserer et al., 2007). The resulting exchanger isoforms are tissue-specific (Quednau et al., 1997; Hryshko, 2002) and have different properties such as the ability to overcome Na^+-dependent inactivation (Dyck et al., 1999), altered stimulatory effects of Ca^{2+} (Hilge et al., 2009) and, in the case of the *Drosophila* NCX (CalX), negative regulation by cytoplasmic Ca^{2+} (Hryshko et al., 1996). Still, the physiological significance of tissue-specific isoforms is unclear. Presumably they evolved to perform functions required only by those tissues in which they are found.

XI. CURRENT–VOLTAGE RELATIONSHIPS AND VOLTAGE DEPENDENCE OF Na^+-Ca^{2+} EXCHANGE CURRENT

The origin of the voltage dependence of Na^+-Ca^{2+} exchange has yet to be explained. However, current–voltage

relationships obtained under a variety of ionic conditions can provide a great deal of information that forms a basis for discussing possible mechanisms of voltage dependence. Here we will try to show what can and cannot be concluded about voltage-dependent mechanisms from available current−voltage data. Before interpreting current−voltage relationships, the experimentalist should be confident that he or she is dealing with a pure current. Thus, considerable care in eliminating contaminating currents with appropriate inhibitors and an understanding of which currents (besides exchange current) are activated over the voltage range of interest is essential.

Most Na^+-Ca^{2+} exchange current−voltage relationships that have been measured so far do not show a region of negative slope. This is consistent with the idea that only a single rate-limiting charge translocation step exists in the reaction pathway. Were a second voltage-dependent step to exist in which charge moved in the opposite direction, then one might expect a region of slight negative slope. This is because the increasing voltages that stimulated forward exchange would necessarily begin to retard the movement of exchange in the opposite direction, with resulting decline in net transport and hence current. However, conditions under which a region of negative slope in an exchange current−voltage relationship have been detected. Using the giant patch technique, Hilgemann and coworkers have measured outward exchange current−voltage relationships as a function of extracellular Ca^{2+} (Fig. 14.13) (Hilgemann et al., 1991b). When extracellular Ca^{2+} is 0.1 mM, voltage dependence is diminished and, at extreme depolarization, the slope of the current−voltage relationship becomes discernibly negative. It is currently believed that most of the exchange voltage dependence is associated with Na^+ translocation. Hilgemann has suggested that the negative slope could be explained if Ca^{2+} passes through a small fraction of the membrane field before binding to the carrier. This would constitute a second voltage-dependent step associated with Ca^{2+} translocation in the transport pathway.

A second property expected of current−voltage relationships for electrogenic exchange reactions is that they should saturate at extreme voltages. This is because reaction steps whose rate increases with voltage should become sufficiently rapid that they cease to be rate limiting for the entire reaction sequence. The reaction may then be rate limited by a voltage-independent step, at which point reaction rate will cease to be responsive to voltage. Many current−voltage relationships do show clear evidence of saturation. For example, the measurements of outward current depicted in Fig. 14.13 clearly exhibit saturation. Though not so obvious, measurements of inward current by Bridge and colleagues and by Miura and Kimura also show signs of saturation at extremely negative voltages (Miura and Kimura, 1989; Bridge et al., 1991). In contrast,

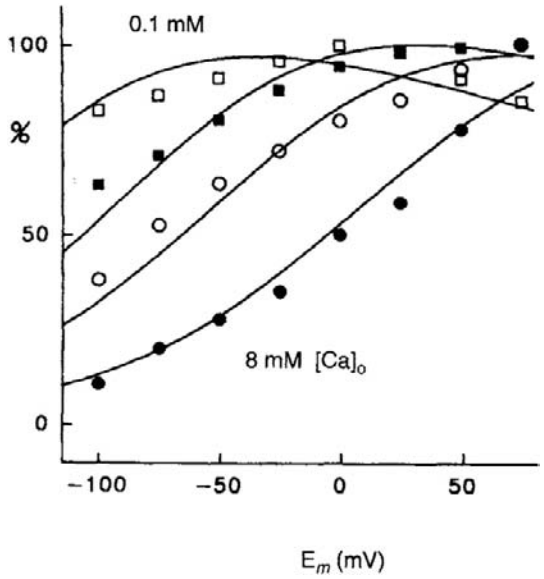

FIGURE 14.13 Ion and voltage dependencies of cardiac Na^+-Ca^{2+} exchange current conform to consecutive exchange model with voltage dependencies at extracellular Na^+ release and binding. Flattening and saturation of outward $I_{Na\text{-}Ca}$-voltage relations as extracellular $[Ca^{2+}]$ is lowered from 8 mM (closed circles) to 2 mM (open circles) to 0.4 mM (closed squares) to 0.1 mM (open squares). All results are normalized to the largest current occurring in the current−voltage relation. Note the negative slope with strong depolarization at 0.1 mM. *(Reprinted with kind permission of the author and* Nature.*)*

results (from giant patches) under zero *trans* conditions suggest little saturation of inward exchange current at very negative potentials (Matsuoka and Hilgemann, 1992). The origin of these discrepancies is not clear, but may be related to whether or not net or unidirectional exchange is producing the inward current. Moreover, current−voltage relationships obtained in whole cells may be complicated by other partial reactions (e.g. Ca^{2+} dissociation from intracellular buffers) not present in the giant patch experiments.

The way that exchange current−voltage relationships depend on ionic conditions can also yield information about voltage-dependent steps in the reaction sequence that leads to exchange. With voltage-clamped giant patches under zero *trans* conditions − i.e. Ca^{2+} in the pipette (extracellular) side and Na^+ in the bath solution − that superfuse the cytoplasmic surface, outward current-voltage relationships showed a striking dependence on pipette (extracellular) Ca^{2+} (see Fig. 14.13). However, when the extracellular (pipette) Ca^{2+} is reduced to very low values, voltage dependence tends to disappear. An attractive explanation for this result is that as extracellular Ca^{2+} is reduced, a voltage-independent step or a step with very modest voltage dependence (presumably associated with Ca^{2+} translocation) starts to become rate limiting, with the result that exchange loses its voltage dependence. However,

Ca^{2+} translocation is not independent of voltage in all species. In the squid Na^+-Ca^{2+} exchanger NCX-SQ1, charge movement accompanies Ca^{2+} translocation rather than Na^+ translocation, as has been shown rather elegantly by He and coworkers (He et al., 1998). These authors examined giant patches from oocytes expressing either NCX1 or NCX1-SQ1. Na^+ and Ca^{2+} were respectively inside the pipette. This forced Na^+- and Ca^{2+}-binding sites to the intracellular surface. Rapid application of Na^+ or Ca^{2+} to the intracellular (outside) surface of the patch produces a transient half-reaction which, in turn, was expected to produce a transient charge movement if the half-reaction is electrogenic. It appears that, in NCX1, transient current is produced by application of Na^+ but, in the case of NCX1-SQ1, application of Ca^{2+} produces an electrogenic half-reaction. Thus, it seems that, in the squid, Ca^{2+} translocation is electrogenic (Fig. 14.14).

The dependence of outward current–voltage relationships on Na^+ is also interesting. Hilgemann and colleagues, using the giant patch technique, have measured outward current–voltage relationships when extracellular Na^+ was 100 and 400 mM (Fig. 14.15). At 400 mM, there was a pronounced flattening of the current–voltage relationship (Hilgemann et al., 1991b). There are two possible (and not necessarily unrelated) explanations for this. If we assume that some step in the Na^+ translocation pathway is both rate limiting and voltage dependent, it is possible that, as extracellular Na^+ increases, this step ceases to be rate limiting because it is accelerated. Were some other voltage-independent step to become rate limiting, one would expect a flattening of the current–voltage relationship as it became dominated by the voltage-independent step, as is in fact observed. Alternatively, if Na^+ binding to some external site were voltage dependent, one would expect voltage dependence of this binding to be lost as the site becomes saturated (Lagnado and McNaughton, 1990).

These results seem to suggest that, somewhere in the Na^+ translocation pathway, a voltage-dependent (charge translocation) step may be involved. In this regard, the data obtained with giant patches, where ideal zero *trans* conditions are most likely to be achieved, are particularly compelling.

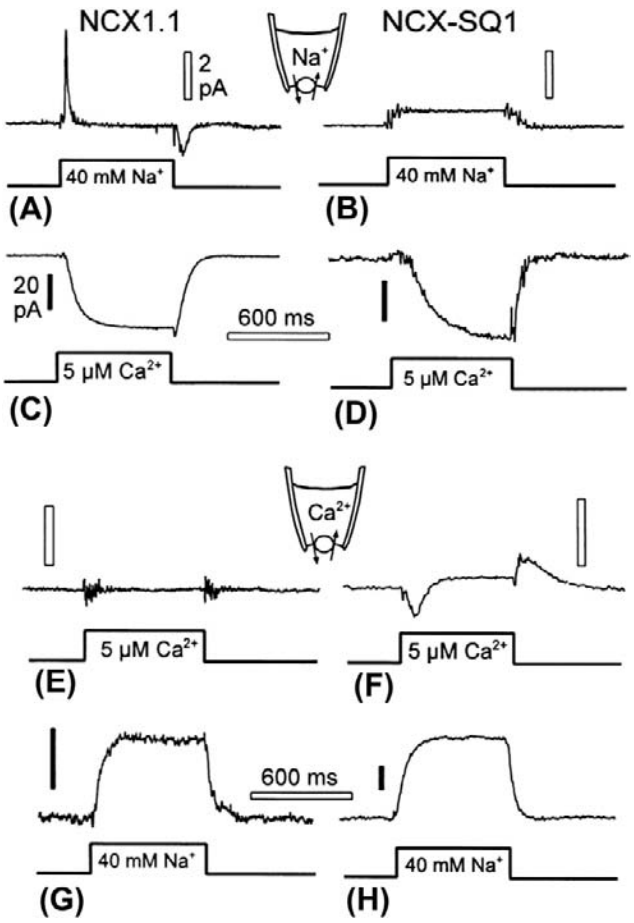

FIGURE 14.14 Identification of electrogenic reactions of NCX1 and NCX-SQ1 using concentration jumps. (A) Current transients recorded from NCX1-expressing patch when 40 mM cytoplasmic Na^+ is applied and removed in the presence of 20 mM extracellular Na^+. (B) Typical lack of current transients recorded from NCX-SQ1-expressing patch when 40 mM cytoplasmic Na^+ is applied and removed in the presence of 20 mM extracellular Na^+. (C) Inward NCX1 current activated when a solution with 5 μM free Ca^{2+} is applied as in (A). (D) Inward NCX-SQ1 current activated when a solution with 5 μM free Ca^{2+} is applied as in (B). (E) Typical lack of current transients for a Ca^{2+} jump to 5 μM free Ca^{2+} in NCX1- expressing patch; 50 μM extracellular Ca^{2+}. (F) Current transients recorded from NCX-SQ1-expressing patch when a solution with 5 μM free Ca^{2+} is applied and removed in the presence of 50 μM extracellular Ca^{2+}. (G) Outward current activated by applying 40 mM Na^+ to an NCX1 patch with 50 μM extracellular Ca^{2+}. (H) Outward current activated by applying 40 mM Na^+ to an NCX1 patch with 50 μM extracellular Ca^{2+}. *(Reprinted from He et al. (1998) with kind permission from the* Journal of General Physiology.*)*

XII. MECHANISM OF Na^+-Ca^{2+} EXCHANGE

A discussion of the evidence for and against various kinetic schemes to account for Na^+-Ca^{2+} exchange is beyond the scope of this chapter. The interested reader is referred to Khananshvili (Khananshvili, 1991). Here we will simply show the way in which measurement of exchange current can be used to infer mechanism. It should, however, be clearly understood that the measurement of isotopic fluxes and rapid mixing techniques provide indispensable tools to investigate mechanism but will not be discussed here.

For the Na^+-Ca^{2+} exchange, two different basic mechanisms for ion translocation can be considered: the *ping-pong* or *consecutive mechanism* and the *sequential* or *simultaneous mechanism*. Although it has been difficult to distinguish between these mechanisms, recent data using the patch-clamp technique provide strong evidence in favor

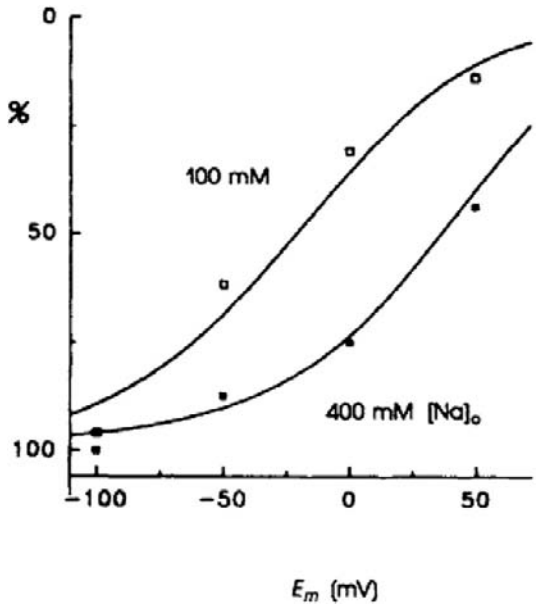

FIGURE 14.15 Flattening and saturation of inward $I_{Na\text{-}Ca}$-voltage relationships when extracellular [Na^+] is increased from 100 mM to 400 mM. Na^+-MES was replaced by Ca^{2+}-MES in the pipette, as osmolarity for all extracellular solutions was equal. 20 μM free [Ca^{2+}] on the cytoplasmic side. $I_{Na\text{-}Ca}$ magnitudes in each current−voltage relationship were normalized to values at −100 mV. *(Reprinted from Hilgemann et al. (1991) with kind permission from the* Journal of General Physiology.*)*

of the ping-pong mechanism, diagrammed in its simplest form in Fig. 14.16. There is only one set of binding sites that binds either Ca^{2+} or Na^+ and the translocation of Na^+ and Ca^{2+} are separate events. For example, Ca^{2+} binds to the carrier E′ at the inner (cytoplasmic) surface and is translocated to the exterior, where it is released. The carrier E″ then can either bind Na^+ or Ca^{2+} at the external face, which is then transported to the internal surface where it is in turn released. A basic property of the ping-pong mechanism is that Na^+-Na^+ and Ca^{2+}-Ca^{2+} exchange are

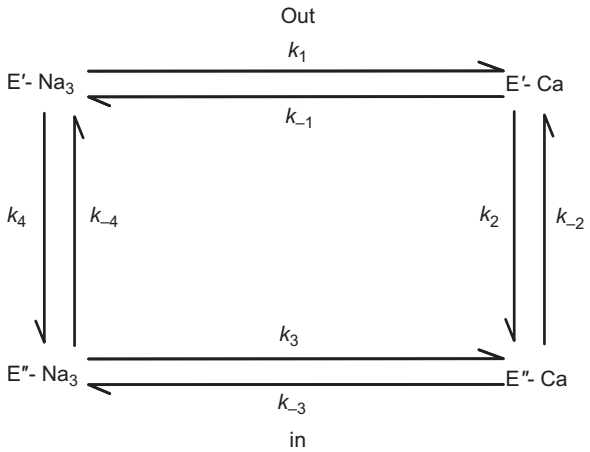

FIGURE 14.16 Diagram of the ping-pong mechanism of ion translocation.

reversible partial reactions of the exchange. As such, it should be possible to isolate them (see Fig. 14.14). These partial reactions do not exist as elementary steps in the simultaneous mechanism.

Partial reactions of the exchanger have been observed (Hilgemann, 1991a). Using giant sarcolemmal patches, rapid application of Na^+ to the intracellular surface caused binding and translocation of intracellular Na^+ to the pipette side. This produced a transient current which could be blocked by exchange blockers including the exchanger inhibitory peptide (XIP) (Li et al., 1991). Similar currents were measured in giant oocyte patches in which the cloned exchanger had been expressed. Control oocytes did not exhibit this current. It appears that charge translocation is associated with Na^+ translocation and that the Na^+ translocation step can be isolated, consistent with the idea that a ping-pong mechanism is operative.

Further support for a consecutive model of exchange comes from work by Niggli and Lederer. These authors measured very small transient Ca^{2+} currents induced by the photo release of caged Ca^{2+} DM-dinitrophen (Niggli and Lederer, 1991). Insofar as these currents could be inhibited by known blockers of the Na^+-Ca^{2+} exchange, they appear to be associated with exchange. Since they are unaffected by Na^+, they are presumably associated with a partial reaction of the exchange. These authors have speculated that this current represents a charge movement associated with Ca^{2+} binding and the associated conformational change of the exchange molecule. This suggests that (as we have already seen) a voltage-dependent step might be associated in some way with the partial reactions leading to Ca^{2+} translocation. It is becoming clear that we as yet do not know exactly how many charge-translocating steps are actually in the exchange pathway. However, evidence is accruing that the mechanism is consecutive in nature.

Two additional pieces of evidence suggest that a consecutive mechanism could account for Na^+-Ca^{2+} exchange. First, Hilgemann and colleagues have demonstrated that the apparent affinity of one ion for the exchanger is a function of the concentration of the other (Hilgemann et al., 1991a). This is a requirement of a sequential reaction scheme. Moreover, Kimura has employed classic enzyme kinetics to outward exchange currents under assumed zero *trans* conditions. Her results suggest that while it is difficult to discriminate between a simultaneous and consecutive reaction, the available evidence favors a consecutive reaction (Li and Kimura, 1991).

XIII. Na^+-Ca^{2+} EXCHANGE CURRENTS DURING THE CARDIAC ACTION POTENTIAL

During every action potential, a Ca^{2+} current is activated and a modest quantity of Ca^{2+} enters the cell. As we shall discuss, it now seems likely that reverse exchange takes

place, which also causes some Ca^{2+} entry. During a steady-state train of action potentials, this continual Ca^{2+} entry must in some way be compensated. It is therefore likely that forward exchange during the repolarizing phase of the action potential extrudes the Ca^{2+} entering during the initial phase of the action potential and thus maintains a beat-to-beat homeostasis. Direct evidence that Ca^{2+} entering the cell through Ca^{2+} channels can be extruded by the Na^+-Ca^{2+} exchange has been obtained by Bridge et al. (Bridge et al., 1990). Guinea pig ventricular cells treated with caffeine can be tetanized in the absence of extracellular Na^+ with a voltage-clamp pulse from −40 mV to +10 mV. During this clamp, an inward Ca^{2+} current can be measured (Fig. 14.17). Although the SR is depleted by caffeine, the enlarged Ca^{2+} current can apparently produce sufficient Ca^{2+} entry to cause contractures. It should be

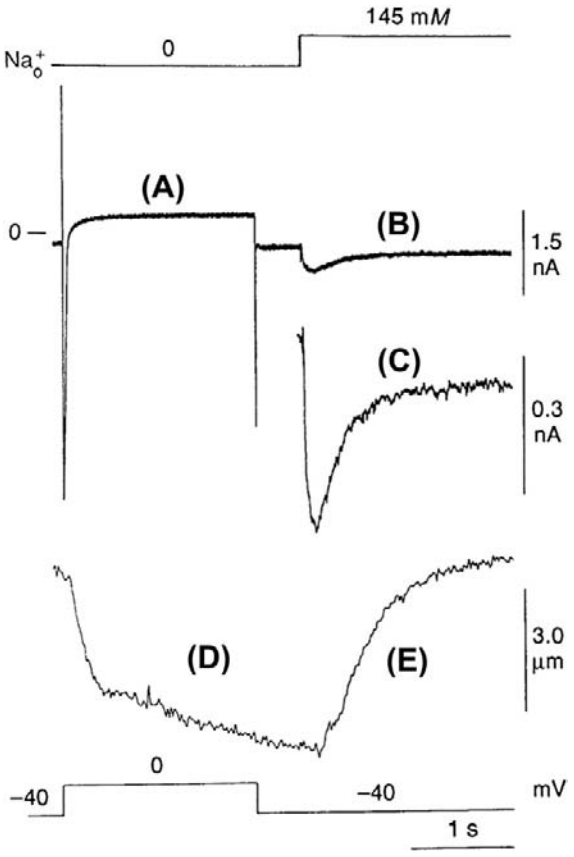

FIGURE 14.17 Two-second voltage-clamp pulses in the absence of Na^+_o and presence of 10.0 mM caffeine cause contraction. Rapid application of Na^+_o 500 ms after repolarization causes relaxation. (A) I_{Ca} elicited by membrane depolarization. (B) The application of Na^+ produces putative transient inward $I_{Na\text{-}Ca}$. (C) This current is displayed on an expanded scale. (D) Contraction (cell shortening) activated by I_{Ca} recorded in (A). (E) After repolarization to −40 mV, relaxation does not occur until 500 ms after the clamp pulse when Na^+ is suddenly applied. *(Reprinted with permission from Bridge, J.H.B., Smolley, J.R. and Spitzer, K.W. (1990). The relationship between charge movements associated with/Ca and INa-Cain cardiac myocytes.* Science. *248, 376-378. Copyright 1990 American Association for the Advancement of Science.)*

emphasized that in these experiments the pipette contained no Na^+ so that in the absence of extracellular Na^+, Ca^{2+} entry by reverse exchange was unlikely. At the peak of the contracture, rapid application of extracellular Na^+ produced prompt mechanical relaxation and activated an inward transient current. This current was most likely due to forward Na^+-Ca^{2+} exchange because it could not be activated when intracellular Ca^{2+} was buffered with EGTA. If the Na^+-Ca^{2+} exchange current extruded all the entering Ca^{2+} and, if we further assume that three Na^+ ions exchange with a single Ca^{2+} ion, it follows that the integral of the exchange current is one-half that of the Ca^{2+} current. The relationship between the integrals of exchange current and Na^+-Ca^{2+} exchange current was best explained by assuming that three Na^+ ions exchange with a single Ca^{2+} ion and that the exchange extruded all the entering Ca^{2+}. It seems therefore that the Na^+-Ca^{2+} exchange does have the capacity to extrude all Ca^{2+} entering during the duty cycle.

It now seems likely that the activity of Na^+-Ca^{2+} exchange is profoundly modified by the cardiac action potential. It is also likely that the exchange current in part determines the duration of the cardiac action potential. The first comprehensive discussion of this topic was made by Mullins (Mullins, 1979). We will consider the behavior of the Na^+-Ca^{2+} exchange during the ventricular action potential. The guinea pig ventricular action potential is approximately 300 ms in duration. During the initial part of this action potential Ca^{2+} is released from the sarcoplasmic reticulum and this causes a rise of Ca^{2+} in the cytosol. Peak values for cytosolic free Ca^{2+} are probably 1−2 µM. The Ca^{2+} transient rises to a peak in approximately 50 ms, whereas the peak of the upstroke of the action potential occurs in approximately 2 ms. After the upstroke of the action potential, but before intracellular Ca^{2+} has risen appreciably, the membrane potential becomes positive to the exchange reversal potential, which is about −50 mV. Therefore, an outward exchange current is generated and this will be accompanied by Ca^{2+} entry and Na^+ exit. This current has been implicated in the "triggering" of SR Ca^{2+} release (Leblanc and Hume, 1990). As the Ca^{2+} released from the SR begins to rise and the membrane begins to repolarize, the membrane potential will become negative to the reversal potential, the exchange current will reverse its direction and Ca^{2+} will be extruded in exchange for Na^+. As the intracellular Ca^{2+} begins to decline, inward exchange current will also decline to resting values. The same principles presumably govern the behavior of the atrial cell. Earm and Noble have modeled the time course of Ca^{2+} current, Na^+-Ca^{2+} exchange current, and the Ca^{2+} transient during the rabbit atrial action potential (Fig. 14.18) (Earm and Noble, 1990). Other more recent models seek to explain the way exchange current behaves during action potencials (Luo and Rudy, 1994; Iyer et al., 2004). The Na^+-Ca^{2+} exchange current is the main

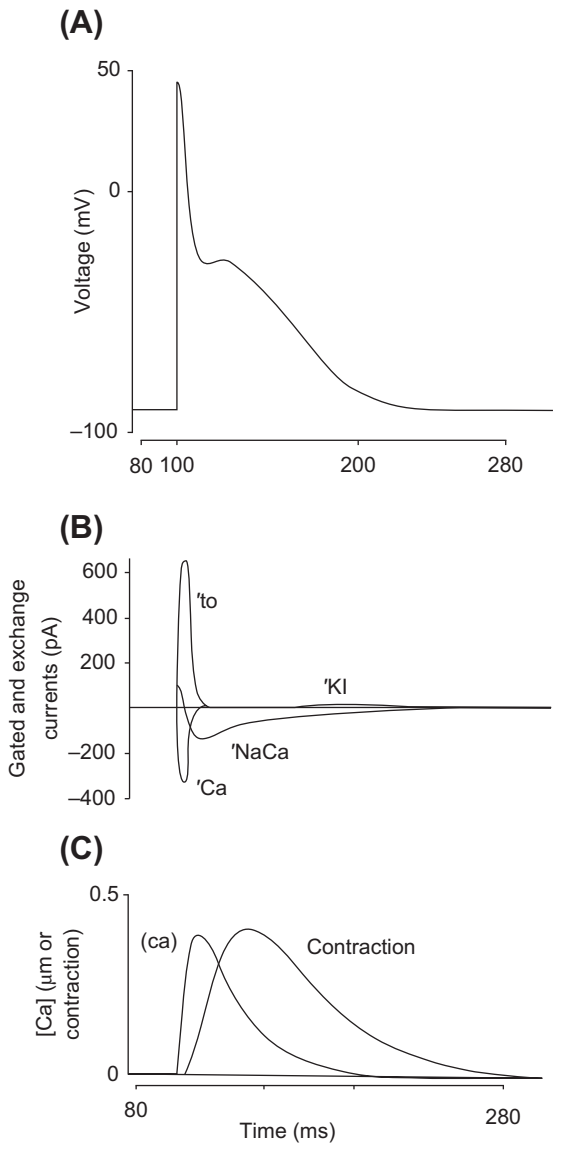

FIGURE 14.18 The Earm–Noble model of the single rabbit atrial cell, based on the multicellular model of Hilgemann and Noble (1987). (A) Computed action potential. (B) Computed currents. (C) $[Ca^{2+}]_i$ and contraction (Earm and Noble, 1990). *(Reprinted with kind permission of the author and the Royal Society.)*

depolarizing current during the plateau. Moreover, the exchange activity required to maintain the late plateau is precisely sufficient to balance Ca^{2+} influx (Ca^{2+} current + Na^+-Ca^{2+} exchange) during the early part of the action potential. It should be appreciated that, regardless of the value of intracellular Ca^{2+}, membrane repolarization will tend to stimulate inward exchange current. On the other hand, the decline of the Ca^{2+} transient will tend to reduce exchange current. Therefore, the relationship between the Ca^{2+} transient and membrane repolarization will largely determine the time course of inward exchange current and therefore the pattern of Ca^{2+} extrusion.

XIV. Na^+-Ca^{2+} EXCHANGE CURRENTS AND EXCITATION–CONTRACTION COUPLING

Contractions occur in heart cells when Ca^{2+} released from intracellular stores known as the sarcoplasmic reticulum (SR) activates the contractile elements (for a more detailed account of excitation–contraction the reader is referred to Bers (2001)). This release is coupled to electrical excitation at the surface membrane and the whole process is often referred to as *excitation–contraction coupling*. The pioneering studies on skinned fibers by Alexander Fabiato led to at least two fundamental findings (for a discussion of these see Stern and Lakatta, 1992). The first was that Ca^{2+} can be released from the SR when the concentration of Ca^{2+} in the vicinity of the SR is abruptly increased. This small increase in the concentration of Ca^{2+} leads to a much larger release of SR Ca^{2+}, so the system is one of inherently high gain. This process is usually referred to as *Ca^{2+}-induced Ca^{2+} release* or CICR. A second and important property of CICR is that, under voltage clamp, the release is graded with the size of the Ca^{2+} increase that induces the release. A priori such a system might be expected to be regenerative since the Ca^{2+} that is released from the SR ought to stimulate further release. A discussion of why SR Ca^{2+} release in heart is not normally regenerative is beyond the scope of this chapter. Nevertheless, will discuss some of the evidence that suggests that Na^+-Ca^{2+} exchange currents are involved in CICR.

It is now known that large tetrameric Ca^{2+}-release channels (usually referred to as ryanodine receptors) are embedded in the sarcoplasmic reticulum (Saito et al., 1988). These apparently respond to elevations of Ca^{2+} in their vicinity by gating the release of Ca^{2+} from the SR (Stern and Lakatta, 1992). Therefore, a molecular basis for the early observations by Fabiato has been established. A central question for those studying excitation–contraction in heart is, what in intact cells produces the rise in intracellular Ca^{2+} that gates the SR release channel and triggers SR Ca^{2+} release?

It is now well established that the L-type Ca^{2+} current is principally involved in triggering SR Ca^{2+} release in mammalian ventricular cells (London and Krueger, 1986; Beuckelmann and Wier, 1988; Cheng et al., 1993; Lopez-Lopez et al., 1994). Because Fabiato showed SR Ca^{2+} release is graded with the size of the increase in Ca^{2+} concentration that induces the release, it follows that if L-type Ca^{2+} channels trigger or induce the release of Ca^{2+}, the extent of SR Ca^{2+} release also should be graded with the size of the L-type Ca^{2+} current. Since the size of the Ca^{2+} current has a bell-shaped dependence on voltage, the finding that the rate or extent of SR Ca^{2+} release (or the magnitude of triggered contractions) is (under appropriate conditions) also bell-shaped lends strong support to

the idea that the Ca^{2+} current is a trigger for SR Ca^{2+} release. For example, a detailed study by Beuckelmann and Wier has clearly established the bell-shaped relationship between triggered Ca^{2+} transients and voltage (Beuckelmann and Wier, 1988).

However, a number of studies in ventricular cells have revealed that, under certain circumstances, a more complex relationship between the voltage dependence of triggered contractions and Ca^{2+} current (Nuss and Houser, 1992; Vornanen et al., 1994; Litwin et al., 1998). In particular, tension measurements did not follow a simple bell-shaped relationship with voltage but rather showed a sigmoid relationship. At positive potentials, shortening did not decline steeply with voltage. The studies by Litwin et al. on guinea pig cells under voltage-clamp and dialyzed with various Na^+ solutions indicate that while the shape of the Ca^{2+} current/voltage relationship was independent of pipette Na^+, the triggered shortening-voltage relationship showed a striking dependence on pipette Na^+ (Fig. 14.19) (Litwin et al., 1998). At positive potentials the shortening-voltage relationship departed from a simple bell shape and the extent of this departure depended on the concentration of dialyzing Na^+.

If L-type Ca^{2+} current is blocked extremely rapidly, triggered contractions are reduced but not abolished (Levi et al., 1996). Thus, if Ca^{2+} currents are elicited under voltage-clamp, it is possible to record what could be a triggered contraction or a triggered Ca^{2+} transient. It therefore seems likely that another process besides the Ca^{2+} current is involved, triggering the release of SR Ca^{2+}. The most likely process is in fact the Na^+-Ca^{2+} exchange. Grantham and Cannell used voltage-clamp pulses shaped like an action potential to infer the magnitude and trajectory of Na^+-Ca^{2+} exchange currents during the initial part of an action potential. They found that the magnitude of the exchange current was somewhat less than 30% of the magnitude of the Ca^{2+} current that occurred during the initial part of the action potential (Fig. 14.20) (Grantham and Cannell, 1996). As the authors point out, this is not a negligible current and is consistent with the idea that at least some of the triggered SR Ca^{2+} release could be due to the activity of the Na^+-Ca^{2+} exchange. It is worth mentioning that if the Na^+-Ca^{2+} exchange is capable of contributing part of the trigger for SR Ca^{2+} release, then this component of the trigger will be extremely sensitive to intracellular Na^+. In this regard, it has been proposed that the initial Na^+ current might provide enough Na^+ accumulation (provided the accumulation takes place in a restricted space) in the vicinity of the Na^+-Ca^{2+} exchangers to enhance triggering by reverse Na^+-Ca^{2+} exchange current (Leblanc and Hume, 1990; Lipp and Niggli, 1994). A difficulty with the idea that exchange can under physiological circumstances trigger significant Ca^{2+} release is that it is extremely small (Sipido et al., 1997).

Litwin et al. have suggested, for example, that the exchange may sum its effects with the Ca^{2+} current in a highly non-linear way to augment triggering by Ca^{2+} current (Litwin et al., 1998). It is possible that one function of the exchange is to increase the probability with which a Ca^{2+} current triggers exchange in a highly non-linear system. It is therefore not yet clear what contribution Na^+-Ca^{2+} exchange currents make to triggering SR Ca^{2+} release under physiological circumstances. However, since the exchanger is regulated by intracellular Na^+, Ca^{2+} and voltage, it seems likely that its contribution to triggering (either direct or indirect) will be both complex and variable. Recently, the idea that NCX is involved in CICR has been significantly strengthened (Sobie et al., 2008). In both mouse and rabbit cells (Larbig et al., 2010; Torres et al., 2010), inactivation of Na^+ currents while applying action potential shaped voltage clamps abolished a significant fraction of the SR Ca release. Between 27 and 34% of the release was eliminated in rabbits and as much as 50% in mice. When this experiment was repeated in mice lacking NCX (mouse NCX knockout), inactivation of the Na^+ current had no effect on SR Ca^{2+} release, which provides additional strong support for the idea that the effect of Na^+ current on triggering is mediated by NCX.

A report by Maier et al. indicated that a brain or neuronal type Na^+ channel is involved in excitation contraction coupling in heart (Maier et al., 2002). Both neuronal (brain) and skeletal muscle Na^+ channels are thought to exist in heart (Sills et al., 1989; Dhar Malhotra et al., 2001; Huang et al., 2001; Maier et al., 2002; Pereon et al., 2003; Haufe et al., 2005a,b; Marionneau et al., 2005; Gershome et al., 2011). These channels are sensitive to

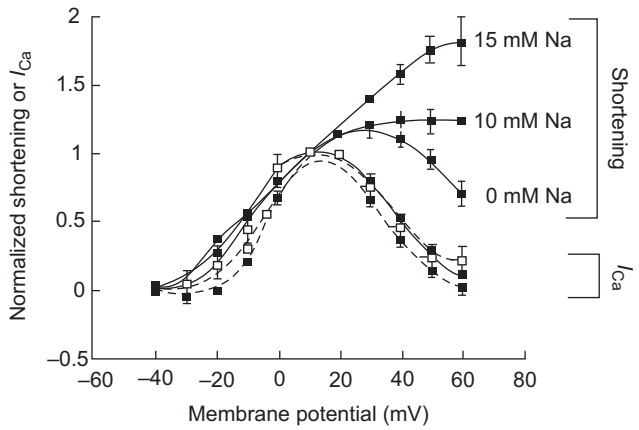

FIGURE 14.19 The relationship between voltage and I_{Ca} is bell-shaped regardless of dialyzing Na^+ concentration. However, the relationship between triggered shortening and voltage depends upon the concentration of dialyzing Na^+. When dialyzing Na^+ is nominally zero mM, the relationship between voltage and the extent of shortening approaches a bell shape. *(Reprinted with permission of the* Proceeding of the New York Academy of Sciences.*)*

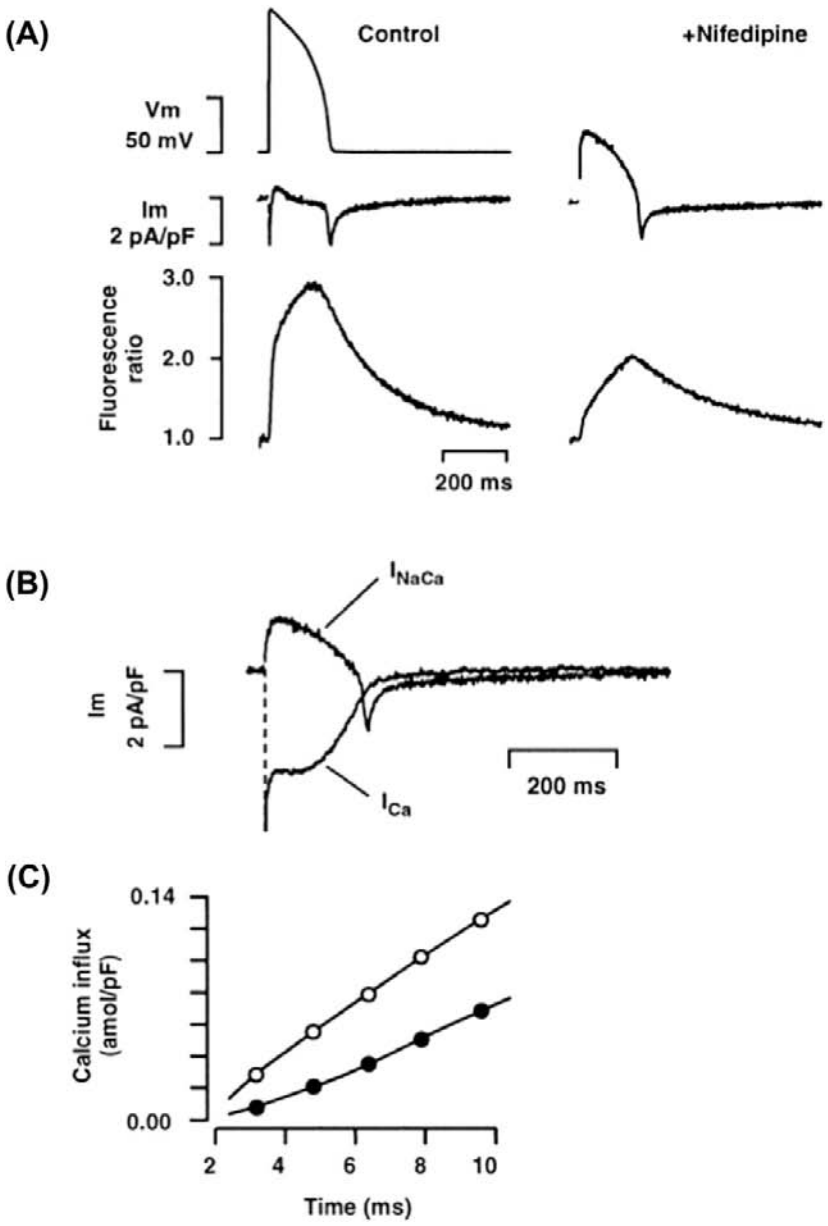

FIGURE 14.20 Membrane currents and Ca^{2+} influx in a myocyte with intact Na^+-Ca^{2+} exchange and SR release in response to an action potential (AP). The myocyte was at steady state, having been stimulated continuously at 0.2 Hz with a train of at least 20 APs. (A) Top, AP command; middle, membrane current; and bottom, [Ca^{2+}] transient time course in the absence of nifedipine or, on the right, immediately after blockade of I_{Ca} by 10 μmol/L nifedipine. (B) Time course of AP-evoked nifedipine-sensitive current (I_{Ca}) and calculated $I_{Na\text{-}Ca}$. (C) Cumulative Ca^{2+} influx via I_{Ca} (open circles) and the calculated $I_{Na\text{-}Ca}$ (closed circles) at the beginning of the AP. Cell capacitance, 150 pF. Similar results were obtained in at least four other cells. *(Reprinted with permission of* Circulation Research *from Grantham and Cannell, 1996.)*

TTX, i.e. they are blocked by relative low doses of TTX (100 nM TTX), whereas the cardiac Na^+ channel Nav 1.5 is blocked by much higher concentrations of this drug (in the order of micromolar). Torres et al. obtained clear evidence that very low doses of TTX (100 nM) eliminated as much as 27% of the release flux (Torres et al., 2010). This is similar to the effect of voltage dependent inactivation of the Na^+ current. It is therefore possible that a rapidly activating TTX-sensitive Na^+ current could significantly increase Na^+ concentration in junctional regions between the sarcolemma and the sarcoplasmic reticular membranes. This, in turn, could cause the reverse of exchange prior to activation of Ca^{2+} currents and prime the junction with Ca^{2+}, although the process might not in itself produce much triggering. However, with a primed junction, Ca^{2+} currents might trigger SR Ca^{2+} release much more efficiently since they would not first have to fill the junctional regions with Ca^{2+}. In the absence of intracellular Na^+, the efficiency of release is extremely low at positive potential (when one would expect it to be high). A process of the type that we have just described might increase triggering efficiently when it is most needed and, in effect, set the efficiency of EC coupling. Such a process is likely to be inherently non-linear and account for the non-linear summation of NCX and Ca currents proposed by Litwin et al. (Litwin et al., 1998).

BIBLIOGRAPHY

Acsai, K., Antoons, G., Livshitz, L., Rudy, Y., & Sipido, K. R. (2011). Microdomain [Ca2+] near ryanodine receptors as reported by L-type Ca2+ and Na+/Ca2+ exchange currents. *J Physiol, 589*, 2569−2583.

Axelsen, P. H., & Bridge, J. H. B. (1985). Electrochemical ion gradients and the Na/Ca exchange stoichiometry. Measurements of these gradients are thermodynamically consistent with a stoichiometric coefficient >3. *J Gen Physiol, 85*, 471−478.

Baker, P. F., Blaustein, M. P., Hodgkin, A. L., & Steinhardt, R. A. (1967). Effect of sodium concentration on calcium movements in giant axons of loligo forbesi. *J Physiol (Lond), 192*, 43−44.

Barcenas-Ruiz, L., Beuckelmann, D. J., & Wier, W. G. (1987). Sodium-calcium exchange in heart: membrane currents and changes in $(Ca2+)_i$. *Science, 238*, 1720−1722.

Bers, D. M. (2001). *Excitation-contraction Coupling and Cardiac Contractile Force*. Dordrecht: Kluwer Academic Publishers.

Besserer, G. M., Ottolia, M., Nicoll, D. A., et al. (2007). The second Ca2+-binding domain of the Na+ Ca2+ exchanger is essential for regulation: crystal structures and mutational analysis. *Proc Natl Acad Sci USA, 104*, 18467−18472.

Beuckelmann, D. J., & Wier, W. G. (1988). Mechanism of release of calcium from sarcoplasmic reticulum of guinea- pig cardiac cells. *J Physiol (Lond), 405*, 233−255.

Blaustein, M. P., & Hodgkin, A. L. (1969). The effect of cyanide on the efflux of calcium from squid axons. *J Physiol, 200*, 497−527.

Bridge, J. H. B., & Bassingthwaighte, J. B. (1983). Uphill sodium transport driven by an inward calcium gradient in heart muscle. *Science, 219*, 178−180.

Bridge, J. H. B., Smolley, J., Spitzer, K. W., & Chin, T. K. (1991). Voltage dependence of sodium-calcium exchange and the control of Ca extrusion in the heart. *Ann NY Acad Sci, 639*, 34−47.

Bridge, J. H. B., Smolley, J. R., & Spitzer, K. W. (1990). The relationship between charge movements associated with I_{Ca} and $I_{Na\text{-}Ca}$ in cardiac myocytes. *Science, 248*, 376−378.

Chaptal, V., Ottolia, M., Mercado-Besserer, G., Nicoll, D. A., Philipson, K. D., & Abramson, J. (2009). Structure and functional analysis of a Ca2+ sensor mutant of the Na+/Ca2+ exchanger. *J Biol Chem, 284*, 14688−14692.

Cheng, H., Lederer, W. J., & Cannell, M. B. (1993). Calcium sparks: elementary events underlying excitation-contraction coupling in heart muscle. *Science, 262*, 740−744.

Chin, T. K., Spitzer, K. W., Philipson, K. D., & Bridge, J. H. B. (1993). The effect of exchanger inhibitory peptide (XIP) on sodium-calcium exchange current in guinea pig ventricular cells. *Circ Res, 72*, 497−503.

Collins, A., Somlyo, A. V., & Hilgemann, D. W. (1992). The giant cardiac membrane patch method: stimulation of outward Na^+-Ca^{2+} exchange current by MgATP. *J Physiol, 454*, 27−57.

Crespo, L. M., Grantham, C. J., & Cannell, M. B. (1990). Kenetics, stoichiometry and role of the Na-Ca exchange mechanism in isoleted cardiac myocytes. *Nature, 345*, 618−621.

Cuomo, O., Pignataro, G., Gala, R., et al. (2007). Involvement of the potassium-dependent sodium/calcium exchanger gene product NCKX2 in the brain insult induced by permanent focal cerebral ischemia. *Ann NY Acad Sci, 1099*, 486−489.

Dhar Malhotra, J., Chen, C., Rivolta, I., et al. (2001). Characterization of sodium channel alpha- and beta-subunits in rat and mouse cardiac myocytes. *Circulation, 103*, 1303−1310.

DiPolo, R., & Beauge, L. (1987a). Characterization of the reverse Na/Ca exchange in squid axons and its modulation by Cai and ATP. Cai-dependent Nai/Cao and Nai/Nao exchange modes. *J Gen Physiol, 90*, 505−525.

DiPolo, R., & Beauge, L. (1987b). In squid axons ATP modulates Na+-Ca2+ exchange by a Ca2+i dependent phosphorylation. *Biochim Biophys Acta, 897*, 347−354.

Dyck, C., Omelchenko, A., Elias, C. L., et al. (1999). Ionic regulatory properties of brain and kidney splice variants of the NCX1 Na(+)-Ca(2+) exchanger. *J Gen Physiol, 114*, 701−711.

Earm, Y. E., & Noble, D. (1990). A model of the single atrial cell: relation between calcium current and calcium release. *Proc R Soc Lond B, 240*, 83−96.

Ehara, T., Matsuoka, S., & Noma, A. (1989). Measurement of reversal potential of Na^+-Ca^{2+} exchange current in single guinea-pig ventricular cells. *J Physiol, 410*, 227−249.

Gershome, C., Lin, E., Kashihara, H., Hove-Madsen, L., & Tibbits, G. F. (2011). Colocalization of voltage-gated Na+ channels with the Na+/Ca2+ exchanger in rabbit cardiomyocytes during development. *Am J Physiol Heart Circ Physiol, 300*, H300−311.

Giladi, M., Boyman, L., Mikhasenko, H., Hiller, R., & Khananshvili, D. (2010). Essential role of the CBD1-CBD2 linker in slow dissociation of Ca2+ from the regulatory two-domain tandem of NCX1. *J Biol Chem, 285*, 28117−28125.

Grantham, C. J., & Cannell, M. B. (1996). Ca2+ influx during the cardiac action potential in guinea pig ventricular myocytes. *Circ Res, 79*, 194−200.

Hamill, O. P., Marty, E., Neher, E., Sakmann, B., & Sigworth, F. (1981). Improved patch-clamp techniques for high resolution current recording from cells and cell-free membrane patches. *Pflügers Arch, 391*, 85−100.

Haufe, V., Camacho, J. A., Dumaine, R., et al. (2005a). Expression pattern of neuronal and skeletal muscle voltage-gated Na+ channels in the developing mouse heart. *J Physiol, 564*, 683−696.

Haufe, V., Cordeiro, J. M., Zimmer, T., et al. (2005b). Contribution of neuronal sodium channels to the cardiac fast sodium current INa is greater in dog heart Purkinje fibers than in ventricles. *Cardiovasc Res, 65*, 117−127.

He, Z., Feng, S., Tong, Q., Hilgemann, D. W., & Philipson, K. D. (2000). Interaction of PIP(2) with the XIP region of the cardiac Na/Ca exchanger. *Am J Physiol Cell Physiol, 278*, C661−666.

He, Z., Tong, Q., Quednau, B. D., Philipson, K. D., & Hilgemann, D. W. (1998). Cloning, expression, and characterization of the squid Na+-Ca2+ exchanger (NCX-SQ1). *J Gen Physiol, 111*, 857−873.

Hilge, M., Aelen, J., Foarce, A., Perrakis, A., & Vuister, G. W. (2009). Ca2+ regulation in the Na+/Ca2+ exchanger features a dual electrostatic switch mechanism. *Proc Natl Acad Sci USA, 106*, 14333−14338.

Hilge, M., Aelen, J., & Vuister, G. W. (2006). Ca2+ regulation in the Na+/Ca2+ exchanger involves two markedly different Ca2+ sensors. *Mol Cell, 22*, 15−25.

Hilgemann, D. W. (1989). Giant excised cardiac sarcolemmal membrane patches: Sodium and sodium-calcium exchange currents. *Pflügers Arch, 415*, 1−3.

Hilgemann, D. W. (1990). Regulation and deregulation of cardiac Na^+-Ca^{2+} exchange in giant excised sarcolemmal membrane patches. *Nature, 344*, 242−245.

Hilgemann, D. W., & Ball, R. (1996). Regulation of cardiac Na+-Ca2+ exchange and K_{ATP} potassium channels by PIP_2. *Science, 273*, 956−959.

Hilgemann, D. W., Collins, A., Cash, D. P., & Nagel, G. A. (1991a). Cardiac Na^+-Ca^{2+} exchange system in giant membrane patches. *Ann NY Acad Sci, 639*, 126−139.

Hilgemann, D. W., Collins, A., & Matsuoka, S. (1992a). Steady-state and dynamic properties of cardiac sodium-calcium exchange. Secondary modulation by cytoplasmic calcium and ATP. *J Gen Physiol, 100*, 933−961.

Hilgemann, D. W., Matsuoka, S., Nagel, G. A., & Collins, A. (1992b). Steady-state and dynamic properties of cardiac sodium-calcium exchange. Sodium-dependent inactivation. *J Gen Physiol, 100*, 905−932.

Hilgemann, D. W., Nicoll, D. A., & Philipson, K. D. (1991b). Charge movement during Na^+ translocation by native and cloned cardiac Na^+/Ca^{2+} exchanger. *Nature, 352*, 715−718.

Hille, B., Armstrong, C. M., & MacKinnon, R. (1999). Ion channels: from idea to reality. *Nat Med, 5*, 1105−1109.

Horackova, M., & Vassort, G. (1979). Sodium-Calcium exchange in regulation of cardiac contractility. Evidence for an electrogenic, voltage-dependent mechanism. *J Gen Physiol, 73*, 403−424.

Hryshko, L. V. (2002). Tissue-specific modes of Na/Ca exchanger regulation. *Ann NY Acad Sci, 976*, 166−175.

Hryshko, L. V., Matsuoka, S., Nicoll, D. A., et al. (1996). Anomalous regulation of the Drosophila Na(+)-Ca2+ exchanger by Ca2+. *J Gen Physiol, 108*, 67−74.

Huang, B., El-Sherif, T., Gidh-Jain, M., Qin, D., & El-Sherif, N. (2001). Alterations of sodium channel kinetics and gene expression in the postinfarction remodeled myocardium. *J Cardiovasc Electrophysiol, 12*, 218−225.

Hume, J. R., & Uehara, A. (1986a). "Creep currents" in single frog atrial cells may be generated by electrogenic Na-Ca exchange. *J Gen Physiol, 87*, 857−884.

Hume, J. R., & Uehara, A. (1986b). Properties of "creep currents" in single frog atrial cells. *J Gen Physiol, 87*, 833−855.

Iwamoto, T., Nakamura, T. Y., Pan, Y., Uehara, A., Imanaga, I., & Shigekawa, M. (1999). Unique topology of the internal repeats in the cardiac Na+/Ca2+ exchanger. *Febs Lett, 446*, 264−268.

Iwamoto, T., Uehara, A., Imanaga, I., & Shigekawa, M. (2000). The Na+/Ca2+ exchanger NCX1 has oppositely oriented reentrant loop domains that contain conserved aspartic acids whose mutation alters its apparent Ca2+ affinity. *J Biol Chem, 275*, 38571−38580.

Iyer, V., Mazhari, R., & Winslow, R. L. (2004). A computational model of the human left-ventricular epicardial myocyte. *Biophys J, 87*, 1507−1525.

John, S. A., Ribalet, B., Weiss, J. N., Philipson, K. D., & Ottolia, M. (2011). Ca2+-dependent structural rearrangements within Na+-Ca2+ exchanger dimers. *Proc Natl Acad Sci, USA*.

Johnson, E., Bruschweiler-Li, L., Showalter, S. A., Vuister, G. W., Zhang, F., & Bruschweiler, R. (2008). Structure and dynamics of Ca2+-binding domain 1 of the Na+/Ca2+ exchanger in the presence and in the absence of Ca2+. *J Mol Biol, 377*, 945−955.

Khananshvili, D. (1991). Mechanism of partial reactions in the cardiac Na-Ca exchange system. *Ann NY Acad Sci., 639*, 85−95.

Kimura, J., Miyamae, S., & Noma, A. (1987). Identification of sodium-calcium exchange currents in single ventricular cells of guinea-pig. *J Physiol, 384*, 199−222.

Kimura, J., Noma, A., & Irisawa, H. (1986). Na-Ca exchange current in mammalian heart cells. *Nature, 319*, 596−599.

Lagnado, L., & McNaughton, P. A. (1990). Electrogenic properties of the Na: Ca exchange. *J Memb Biol, 113*, 177−191.

Langer, G. A. (1964). Kinetic studies of calcium distribution in ventricular muscle of the dog. *Circ Res, 15*, 393−405.

Larbig, R., Torres, N., Bridge, J. H., Goldhaber, J. I., & Philipson, K. D. (2010). Activation of reverse Na+-Ca2+ exchange by the Na+ current augments the cardiac Ca2+ transient: evidence from NCX knockout mice. *J Physiol, 588*, 3267−3276.

Leblanc, N., & Hume, J. R. (1990). Sodium current-induced release of calcium from cardiac sarcoplasmic reticulum. *Science, 248*, 372−376.

Levi, A. J., Li, J., Spitzer, K. W., & Bridge, J. H. B. (1996). Effect on the Indo-1 transient of applying Ca2+ channel blocker for a single beat in voltage-clamped guinea-pig cardiac myocytes. *J Physiol (Lond), 494.3*, 653−673.

Li, J. M., & Kimura, J. (1991). Translocation mechanism of cardiac Na-Ca exchange. *Ann NY Acad Sci, 639*, 48−60.

Li, Z., Nicoll, D. A., Collins, A., et al. (1991). Identification of a peptide inhibitor of the cardiac sarcolemmal Na(+)-Ca2+ exchanger. *J Biol Chem, 266*, 1014−1020.

Lipp, P., & Niggli, E. (1994). Modulation of Ca^{2+} release in cultured neonatal rat cardiac myocytes: insight from subcellular release patterns revealed by confocal microscopy. *Circ Res, 74*, 979−990.

Litwin, S. E., Li, J., & Bridge, J. H. (1998). Na-Ca exchange and the trigger for sarcoplasmic reticulum Ca release: studies in adult rabbit ventricular myocytes. *Biophys J, 75*, 359−371.

London, B., & Krueger, J. W. (1986). Contraction in voltage-clamped, internally perfused single heart cells. *J Gen Physiol, 88*, 475−505.

Lopez-Lopez, J. R., Shacklock, P. S., Balke, C. W., & Wier, W. G. (1994). Local, stochastic release of Ca2+ in voltage-clamped rat heart cells: visualization with confocal microscopy. *J Physiol (Lond), 480*, 21−29.

Luo, C. H., & Rudy, Y. (1994). A dynamic model of the cardiac ventricular action potential. I. Simulations of ionic currents and concentration changes. *Circ Res, 74*, 1071−1096.

Lytton, J. (2007). Na+/Ca2+ exchangers: three mammalian gene families control Ca2+ transport. *Biochem J, 406*, 365−382.

Maier, S. K., Westenbroek, R. E., Schenkman, K. A., Feigl, E. O., Scheuer, T., & Catterall, W. A. (2002). An unexpected role for brain-type sodium channels in coupling of cell surface depolarization to contraction in the heart. *Proc Natl Acad Sci USA, 99*, 4073−4078.

Marionneau, C., Couette, B., Liu, J., et al. (2005). Specific pattern of ionic channel gene expression associated with pacemaker activity in the mouse heart. *J Physiol, 562*, 223−234.

Matsuoka, S., & Hilgemann, D. W. (1992). Steady-state and dynamic properties of cardiac sodium-calcium exchange. Ion and voltage dependencies of the transport cycle. *J Gen Physiol, 100*, 963−1001.

Matsuoka, S., Nicoll, D. A., He, Z., & Philipson, K. D. (1997). Regulation of cardiac Na(+)-Ca2+ exchanger by the endogenous XIP region. *J Gen Physiol, 109*, 273−286.

Matsuoka, S., Nicoll, D. A., Hryshko, L. V., Levitsky, D. O., Weiss, J. N., & Philipson, K. D. (1995). Regulation of the cardiac Na(+)-Ca2+ exchanger by Ca2+. Mutational analysis of the Ca(2+)-binding domain. *J Gen Physiol, 105*, 403−420.

Matsuoka, S., Nicoll, D. A., Reilly, R. F., Hilgemann, D. W., & Philipson, K. D. (1993). Initial localization of regulatory regions of the cardiac sarcolemmal Na(+)-Ca2+ exchanger. *Proc Natl Acad Sci, USA, 90*, 3870−3874.

Mechmann, S., & Pott, L. (1986). Indentification of Na-Ca exchange current in single cardiac myocytes. *Nature, 319*, 597−599.

Miura, Y., & Kimura, J. (1989). Sodium-calcium exchange current. *J Gen Physiol, 93*, 1129−1145.

Mullins, L. J. (1979). The generation of electric currents in cardiac fibers by Na/Ca exchange. *Am J Physiol, 236*, C103−C110.

Nicoll, D. A., Hryshko, L. V., Matsuoka, S., Frank, J. S., & Philipson, K. D. (1996). Mutation of amino acid residues in the putative transmembrane segments of the cardiac sarcolemmal Na+-Ca2+ exchanger. *J Biol Chem, 271*, 13385−13391.

Nicoll, D. A., Longoni, S., & Philipson, K. D. (1990). Molecular cloning and functional expression of the cardiac sarcolemmal Na(+)-Ca2+ exchanger. *Science, 250*, 562−565.

Nicoll, D. A., Ottolia, M., Lu, L., Lu, Y., & Philipson, K. D. (1999). A new topological model of the cardiac sarcolemmal Na+-Ca2+ exchanger. *J Biol Chem, 274*, 910−917.

Niggli, E., & Lederer, W. J. (1991). Photorelease of Ca2+ produces Na-Ca exchange currents and Na-Ca exchange "gating" currents. *Ann NY Acad Sci, 639*, 61−70.

Nuss, H. B., & Houser, S. R. (1992). Sodium-calcium exchange-mediated contractions in feline ventricular myocytes. *Am J Physiol Heart Circ Physiol, 263*, H1161−H1169.

Ottolia, M., Nicoll, D. A., John, S., & Philipson, K. D. (2010). Interactions between Ca(2+) binding domains of the Na(+)-Ca(2+) exchanger and secondary regulation. *Channels (Austin)* 4.

Ottolia, M., Nicoll, D. A., & Philipson, K. D. (2005). Mutational analysis of the alpha-1 repeat of the cardiac Na(+)-Ca2+ exchanger. *J Biol Chem, 280*, 1061−1069.

Ottolia, M., Nicoll, D. A., & Philipson, K. D. (2009). Roles of two Ca2+-binding domains in regulation of the cardiac Na+-Ca2+ exchanger. *J Biol Chem*.

Ottolia, M., Philipson, K. D., & John, S. (2004). Conformational changes of the Ca(2+) regulatory site of the Na(+)-Ca(2+) exchanger detected by FRET. *Biophys J, 87*, 899−906.

Pereon, Y., Lande, G., Demolombe, S., et al. (2003). Paramyotonia congenita with an SCN4A mutation affecting cardiac repolarization. *Neurology, 60*, 340−342.

Philipson, K. D., Longoni, S., & Ward, R. (1988). Purification of the cardiac Na+-Ca2+ exchange protein. *Biochim Biophys Acta, 945*, 298−306.

Philipson, K. D., Nicoll, D. A., Ottolia, M., et al. (2002). The Na+/Ca2+ exchange molecule: an overview. *Ann NY Acad Sci, 976*, 1−10.

Porzig, H., Li, Z., Nicoll, D. A., & Philipson, K. D. (1993). Mapping of the cardiac sodium-calcium exchanger with monoclonal antibodies. *Am J Physiol, 265*, C748−756.

Qiu, Z., Nicoll, D. A., & Philipson, K. D. (2001). Helix packing of functionally important regions of the cardiac Na(+)-Ca(2+) exchanger. *J Biol Chem, 276*, 194−199.

Quednau, B. D., Nicoll, D. A., & Philipson, K. D. (1997). Tissue specificity and alternative splicing of the Na+/Ca2+ exchanger isoforms NCX1, NCX2, and NCX3 in rat. *Am J Physiol, 272*, C1250−1261.

Rasgado-Flores, H., & Blaustei, M. P. (1987). Na/Ca exchange in barnacle muscle cells has a stoichiometry of 3 Na+/1 Ca+. *Am J Physiol Cell Physiol, 252*, C499−C504.

Reeves, J. P., & Condrescu, M. (2008). Ionic regulation of the cardiac sodium-calcium exchanger. *Channels (Austin), 2*, 322−328.

Reeves, J. P., & Hale, C. C. (1984). The stoichiometry of the cardiac sodium-calcium exchange system. *J Biol Chem, 259*, 7733−7739.

Reeves, J. P., & Sutko, J. L. (1983). Competitive interactions of sodium and calcium with the sodium-calcium exchange system of cardiac sarcolemmal vesicles. *J Biol Chem, 258*, 3178−3182.

Ren, X., Nicoll, D. A., Galang, G., & Philipson, K. D. (2008). Intermolecular cross-linking of Na+-Ca2+ exchanger proteins: evidence for dimer formation. *Biochemistry, 47*, 6081−6087.

Ren, X., Nicoll, D. A., & Philipson, K. D. (2006). Helix packing of the cardiac Na+-Ca2+ exchanger: proximity of transmembrane segments 1, 2, and 6. *J Biol Chem, 281*, 22808−22814.

Ren, X., Nicoll, D. A., Xu, L., Qu, Z., & Philipson, K. D. (2010). Transmembrane segment packing of the Na(+)/Ca(2+) exchanger investigated with chemical cross-linkers. *Biochemistry*.

Repke, K. (1964). Ubersichten uber den biochemischen wirkungsmodus von digitalis [On the Biochemical Mode of Action of Digitalis]. *Klin Wochenschr, 42*, 157−165.

Reuter, H., & Seitz, N. (1968). The dependence of calcium efflux from cardiac muscle on temperature and external ion composition. *J Physiol, 195*, 451−470.

Riedel, M. J., Baczko, I., Searle, G. J., et al. (2006). Metabolic regulation of sodium-calcium exchange by intracellular acyl CoAs. *EMBO J, 25*, 4605−4614.

Saito, A., Inui, M., Radermacher, M., Frank, J., & Fleischer, S. (1988). Ultrastructure of the calcium release channel of sarcoplasmic reticulum. *J Cell Biol, 107*, 211−219.

Schwarz, E. M., & Benzer, S. (1997). Calx, a Na-Ca exchanger gene of Drosophila melanogaster. *Proc Natl Acad Sci, USA, 94*, 10249−10254.

Sheu, S. S., & Fozzard, H. A. (1982). Transmembrane Na+ and Ca2+ electrochemical gradients in cardiac muscle and their relationship to force development. *J Gen Physiol, 80*, 325−351.

Shigekawa, M., Iwamoto, T., Uehara, A., & Kita, S. (2002). Probing ion binding sites in the Na+/Ca2+ exchanger. *Ann NY Acad Sci, 976*, 19−30.

Sills, M. N., Xu, Y. C., Baracchini, E., et al. (1989). Expression of diverse Na+ channel messenger RNAs in rat myocardium. Evidence for a cardiac-specific Na+ channel. *J Clin Invest, 84*, 331−336.

Sipido, K. R., Maes, M., & Van de Werf, F. (1997). Low efficiency of Ca2+ entry through the Na(+)-Ca2+ exchanger as trigger for Ca2+ release from the sarcoplasmic reticulum. A comparison between L-type Ca2+ current and reverse-mode Na(+)-Ca2+ exchange. *Circ Res, 81*, 1034−1044.

Sobie, E. A., Cannell, M. B., & Bridge, J. H. (2008). Allosteric activation of Na+-Ca2+ exchange by L-type Ca2+ current augments the trigger flux for SR Ca2+ release in ventricular myocytes. *Biophys J, 94*, L54−56.

Spitzer, K. W., & Bridge, J. H. B. (1989). A simple device for rapidly exchanging solution surrounding a single cardiac cell. *Am J Physiol Cell Physiol, 256*, C441−C447.

Stern, M. D., & Lakatta, E. G. (1992). Excitation-contraction coupling in the heart: the state of the question. *FASEB J, 6*, 3092−3100.

Torres, N. S., Larbig, R., Rock, A., Goldhaber, J. I., & Bridge, J. H. (2010). Na+ currents are required for efficient excitation-contraction coupling in rabbit ventricular myocytes: a possible contribution of neuronal Na+ channels. *J Physiol, 588*, 4249−4260.

Trosper, T. L., & Philipson, K. D. (1984). Stimulatory effect of calcium chelators on Na-Ca exchange in cardiac sarcolemmal vessicles. *Cell Calcium, 5*, 211−222.

Vornanen, M., Shepherd, N., & Isenberg, G. (1994). Tension-voltage relations of single myocytes reflect Ca release triggered by Na/Ca

exchange at 35 degrees C but not 23 degrees C. *Am J Physiol, 267*, C623−632.

Wu, M., Le, H. D., Wang, M., et al. (2009a). Crystal structures of progressive Ca2+ binding states of the Ca2+ sensor Ca2+ binding domain 1 (CBD1) from the CALX Na+/Ca2+ exchanger reveal incremental conformational transitions. *J Biol Chem, 285*, 2554−2561.

Wu, M., Wang, M., Nix, J., Hryshko, L. V., & Zheng, L. (2009b). Crystal structure of CBD2 from the Drosophila Na(+)/Ca(2+) exchanger: diversity of Ca(2+) regulation and its alternative splicing modification. *J Mol Biol, 387*, 104−112.

Xie, Y., Ottolia, M., John, S. A., Chen, J. N., & Philipson, K. D. (2008). Conformational changes of a Ca2+-binding domain of the Na+/Ca2+ exchanger monitored by FRET in transgenic zebrafish heart. *Am J Physiol Cell Physiol, 295*, C388−393.

Zhang, Y. H., & Hancox, J. C. (2009). Regulation of cardiac Na+-Ca2+ exchanger activity by protein kinase phosphorylation − -still a paradox? *Cell Calcium, 45*, 1−10.

This page intentionally left blank

Chapter 15

Intracellular Chloride Regulation

Francisco J. Alvarez-Leefmans

Chapter Outline

I. INTRODUCTION

The importance of chloride ions in cell physiology has not been fully recognized until relatively recently. This is in spite of the fact that chloride (Cl^-), together with bicarbonate (HCO_3^-), is the most abundant free anion in living animal cells and, as will be seen in this chapter, it performs or determines fundamental biological functions in virtually all tissues. For decades it was thought that Cl^- moved through plasma membranes by a purely electrodiffusive mechanism, i.e. a passive mechanism in which membrane permeation of a given ion is driven by both its electrical and concentration gradients. According to this view, Cl^- was distributed passively across the plasma membrane, in thermodynamic equilibrium as defined by Equation 15.2 (see Section III, below), and from a functional perspective it was necessary just to maintain electroneutrality of intra- and extracellular fluids and for keeping the cell osmotic balance. The notion that Cl^- was passively distributed implied that it was not actively transported, nor could it provide energy for transport of other substances. Moreover, if passively distributed, Cl^- was unlikely to play any role in cell signaling functions. Research carried out during the last two decades has led to a revolutionary change in this simplistic view. It is now well established that Cl^- plays vital roles in cell physiology and that most animal cell types exhibit a non-equilibrium distribution of Cl^- across their plasma membranes (Alvarez-Leefmans and Delpire, 2009b; Hartzell, 2009). Far from being passively distributed across the plasma membrane in accordance with the membrane potential (E_m), we now know that Cl^- is actively transported and tightly regulated. Some cells actively extrude Cl^-, others actively accumulate it, but few cells ignore it. The intracellular Cl^- concentration, $[Cl^-]_i$, is determined by the relative contribution of various anion

Cell Physiology Sourcebook. DOI: 10.1016/B978-0-12-387738-3.00015-9

transporting proteins expressed in cell membranes. These transport proteins include several types of Cl^- channels as well as numerous transporters that work mostly as cotransporters (symporters) or as exchangers (antiporters). During the last two decades, the molecular structure and function of these specialized Cl^- transport proteins have been elucidated. The three-dimensional crystal structure of some prokaryotic homologous and, more recently, that of eukaryotes is beginning to emerge, providing insights into the working mechanisms of these proteins at the atomic and molecular levels (Warmuth et al., 2009; Feng et al., 2010).

By virtue of being distributed out of electrochemical equilibrium, Cl^- serves as a key player in a variety of cellular functions, such as pH_i regulation, cell volume regulation, transepithelial salt and water transport and membrane potential stabilization. In addition to these functions, in the nervous system, Cl^- gradients are fundamental in synaptic signaling mediated by the neurotransmitters GABA (γ-aminobutyric acid) and glycine. This signaling results from ionic currents flowing through ligand-gated anion channels primarily permeable to Cl^-. The signals can be in the depolarizing and hyperpolarizing directions thereby determining mechanisms such as presynaptic and postsynaptic inhibition, or the GABA-mediated depolarizing excitation observed in immature neurons. In some cell types, the "ligand" that opens Cl^- channels, instead of being a neurotransmitter, is ionized calcium (Ca^{2+}). Cl^- gradients also play key roles in neuronal growth and development, cell migration, extracellular K^+ scavenging, neurotransmitter reuptake and vesicular storage, and sensory transduction including olfaction and nociception (Alvarez-Leefmans and Delpire, 2009a). In this chapter, some examples are presented to illustrate how Cl^- is regulated and involved in some of these processes.

II. ORIGIN OF THE PASSIVE Cl^- DISTRIBUTION ASSUMPTION

The notion that Cl^- is non-passively distributed and actively transported across cell membranes may sound obvious nowadays. When dealing with the Goldman–Hodgkin–Katz equation for resting membrane potential, Cl^- is still often omitted. One of the usual arguments for this omission is that any ion that is passively distributed cannot determine the resting membrane potential (E_m); instead, E_m determines the distribution of that ion across the membrane. Another argument is that P_{Cl}, the membrane permeability to Cl^-, is negligible. However, neither of these arguments is applicable to all cell types. The question arises as to how and why basic facts such as the non-equilbrium distribution of Cl^- across the plasma membranes, the transport mechanisms that make it possible and its functional significance were missed, neglected and even denied for decades. The passive Cl^- distribution assumption exemplifies how scientific knowledge often advances by learning from our mistakes.

The notion that Cl^- was passively distributed in all cells emerged from three key experimental observations made in squid axons, skeletal muscle cells and red blood cells between the 1940s and the 1960s. First, in the early 1940s an influential paper reported that in freshly dissected squid axons, still one of the best animal cell models to study ion transport, the average $[Cl^-]_i$ was 36 mmol/kg axoplasm (Steinbach, 1941). Taking the water content of squid axoplasm as 880 g/kg, this corresponded to 41 mM, a value close to what would be expected if Cl^- was in electrochemical equilibrium across the axolemma of this seawater animal. However, in 1963, the British physiologist Richard Keynes (1919–2010) published a landmark paper entitled "chloride in squid giant axons" in which he reanalyzed the chloride content of extruded axoplasm from *Loligo forbesi*, and Steinbach's low values for $[Cl^-]_i$ could not be confirmed (Keynes, 1963). The average $[Cl^-]_i$ measured by Keynes in squid axoplasm was 108 ± 2 mM, a concentration "…well over twice that expected for a simple passive distribution…" Thus, E_{Cl}, the Nernst equilibrium potential for Cl^- as defined by Equation 15.1 (see below, Section III), was less than -40 mV, which was different to the resting E_m of -60 to -70 mV typically measured in squid axons. Based on these findings and measurements of Cl^- fluxes, Keynes suggested that Cl^- was "…being transported inwards against the electrochemical gradient by some form of active transport mechanism…" The nature of the transport mechanism in squid axons was elucidated nearly 20 years later by the biophysicist John M. Russell. The active Cl^- uptake mechanism turned out to be an electroneutral Na^+-K^+-Cl^- cotransporter (Russell, 2000) similar to that described in 1980 by P. Geck, E. Heinz and coworkers in Ehrlich cells, a mammalian cell line (Geck et al., 1980; Geck and Heinz, 1986). The difference between the squid and the mammalian Na^+-K^+-Cl^- is in the stoichiometry which is $2Na^+$:$1K^+$:$3Cl^-$ in the squid and $1Na^+$:$1K^+$:$2Cl^-$ in most mammalian cells, probably reflecting some hitherto unknown differences in the protein structure.

The second set of observations that gave rise to the "passive distribution assumption" came from work on frog skeletal muscle done in the late 1950s and early 1960s, that showed that the resting membrane Cl^- conductance was twice as large as that for K^+ (Hodgkin and Horowicz, 1959; Hutter and Noble, 1960). Further, measured $[Cl^-]_i$ was consistent with a distribution of Cl^- determined by a purely passive mechanism (Adrian, 1961). Thus, E_{Cl} was found to be close or equal to E_m. Direct, real-time measurements of $[Cl^-]_i$ and E_m in skeletal muscle by means of Cl^--sensitive microelectrodes demonstrated that, indeed, in skeletal

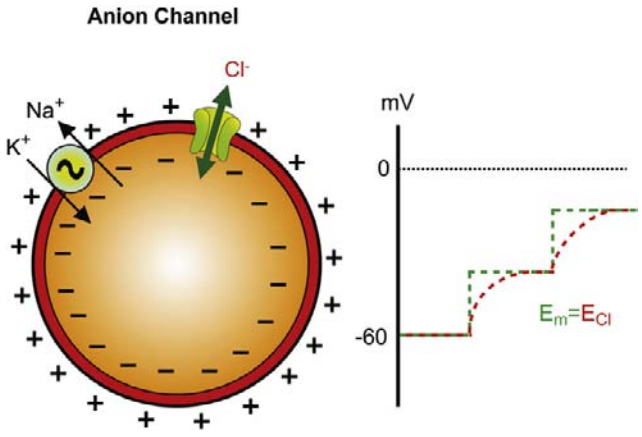

FIGURE 15.1 Passive Cl^- distribution across the cell membrane of an idealized cell having only Cl^- channels and a Na^+/K^+ ATPase (left). The resting membrane potential (E_m) is −60 mV. Right: E_m is changed in steps of ≈20 mV, from the initial resting membrane potential. Chloride redistributes passively, following E_m. At each steady state $E_m = E_{Cl}$. *(Reproduced with permission from Alvarez-Leefmans and Delpire, 2009b.)*

muscle, E_{Cl} closely follows E_m (Vaughan-Jones, 1982). This is due to the relatively high P_{Cl} characteristic of the sarcolemma, as illustrated schematically in Fig. 15.1. We now know that this exceptionally high resting P_{Cl} of skeletal muscle fibers is due to the expression of CLC-1 chloride channels. CLC-1 is a member of the CLC family of chloride channels and transporter proteins (Jentsch, 2008). The functional significance of this high P_{Cl} is that it stabilizes the membrane potential of skeletal muscle fibers. Thus, for all practical purposes, Cl^- appears passively distributed across the sarcolemma. Nevertheless, the fact that $E_m = E_{Cl}$ does not preclude the existence of carrier-mediated active transport of Cl^- in skeletal muscle cells or in any cell type. In fact, there is compelling evidence for an inward active transport of Cl^- in skeletal muscle (Aickin, 1990). This inward transport of Cl^- is mediated primarily by one of the two isoforms of the Na^+-K^+-$2Cl^-$ cotransporters, NKCC1, a member of the electroneutral cation-coupled chloride cotransporter protein family encoded by the *SLC12* gene family (Wong et al., 2001; Gosmanov et al., 2003; Jurkat-Rott et al., 2006; Kristensen and Juel, 2010). However, as shown in Fig. 15.2, the relatively high P_{Cl} mediated by CLC-1 masks any effects that the operation of this inward transport system may have on $[Cl^-]_i$. Accordingly, reducing P_{Cl} by pharmacological blockage of CLC-1 with 9-anthracene carboxylic acid (9-AC) unmasks the active Cl^- uptake mediated by NKCC1.

The third set of observations that led to the generalization of the "passive distribution assumption" came from red blood cells in which $[Cl^-]_i$ was also found to be close to that predicted for electrochemical equilibrium. Several Cl^- transport studies in red blood cells were consistent with the

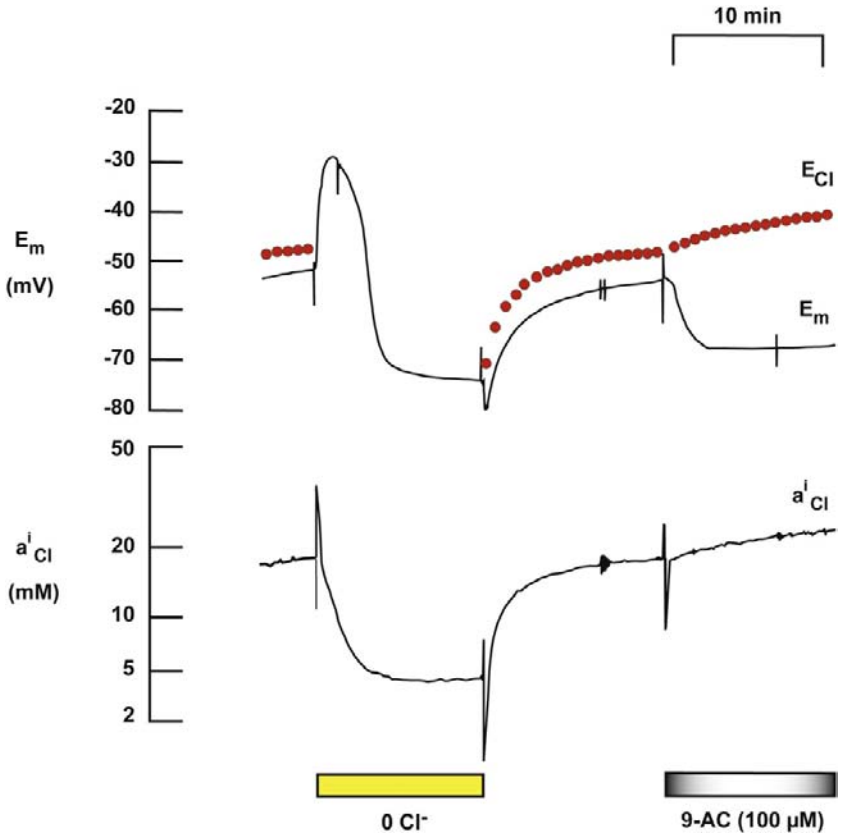

FIGURE 15.2 Active accumulation of Cl^- in rat skeletal muscle unmasked by reducing the resting Cl^- conductance mediated by Cl^- channels. Membrane potential (E_m) and the intracellular Cl^- activity (a^i_{Cl}) were measured simultaneously in a rat lumbrical muscle during the removal and readdition of external Cl^- and the inhibition of the resting Cl^- conductance by application of 9-anthracene carboxylic acid (9-AC). The Cl^- equilibrium potential (E_{Cl}), calculated from the recorded a^i_{Cl} and a^o_{Cl}, using Equation 15.1 has been plotted as red filled circles above the recording of E_m. Note that E_{Cl} was slightly positive with respect to E_m, indicating that a^i_{Cl} was maintained just above equilibrium. Upon reduction of the Cl^- conductance a^i_{Cl} began to increase, and the difference between E_m and E_{Cl} became significantly larger. The recording was made with a double-barreled microelectrode, one barrel sensing E_m and the other the a^i_{Cl}. The preparation was maintained in the nominal absence of CO_2 in solutions equilibrated with 100% O_2. The mechanism responsible for the uphill accumulation of Cl^- is a Na^+-K^+-Cl^- cotransporter. *(Modified from Aickin, 1990.)*

view that the Cl^- transmembrane distribution was thermodynamically passive and, in addition, showed that Cl^- crossed the membrane extremely rapidly. This latter finding, erroneously interpreted for a long time as being only the result of high passive P_{Cl}, made it quite likely that Cl^- could remain at thermodynamic equilibrium. In fact, it was later found that the high P_{Cl} of erythrocytes was primarily due to expression of an anion exchanger transport protein, the Cl^-/HCO_3^- exchanger originally identified as "Band 3" because of its relative migration position in SDS-PAGE (Sodium dodecyl sulfate polyacrylamide gel electrophoresis) gels. "Band 3" is now known as "anion exchanger 1" (AE1) and it is one of 10 members of the SLC4 gene and protein family of anion transporters (Alper, 2009).

The three sets of experimental observations that we have considered above were generalized so that virtually all cells were thought to have a very high P_{Cl} and a thermodynamically passive Cl^- transmembrane distribution, implying that Cl^- was not actively transported. Moreover, to make things worse for the case of Cl^-, cations claimed center stage during this period with attention focused on the Na^+ and Ca^{2+} action potentials, the K^+ channels and the Na^+/K^+ pump. Thus, the belief that Cl^- played no major role in membrane physiology and the attention directed to the study of cations combined to cause research on Cl^- transport to be largely neglected for many years.

III. PASSIVE AND NON-PASSIVE Cl^- DISTRIBUTION ACROSS THE PLASMA MEMBRANE

The Cl^- equilibrium potential, E_{Cl}, is defined by the Nernst equation:

$$E_{Cl} = \frac{RT}{zF} \ln \frac{[Cl^-]_i}{[Cl^-]_o} \tag{15.1}$$

where $[Cl^-]_i$ and $[Cl^-]_o$ are the intracellular and extracellular Cl^- concentrations, R is the gas constant, T is absolute temperature, F is the Faraday's constant and z the valence ($=-1$). If Cl^- is passively distributed, E_m will have the same value as E_{Cl} and therefore:

$$E_m = \frac{RT}{zF} \ln \frac{[Cl^-]_i}{[Cl^-]_o} \tag{15.2}$$

From Equation 15.2, the predicted $[Cl^-]_i$ at electrochemical equilibrium, $[Cl^-]_i^{eq}$, is given by:

$$[Cl^-]_i^{eq} = [Cl^-]_o e^{E_m F/RT} \tag{15.3}$$

Thus, Equation 15.3 predicts the value that $[Cl^-]_i$ will reach when Cl^- is passively distributed across the plasma membrane. Evidently, this value will change with E_m, as illustrated in Fig. 15.1. For example, if $[Cl^-]_o$ is 113 mM and E_m is constant at -60 mV, *RT/F* at 37°C will be 26.73 mV and $[Cl^-]_i^{eq} \approx 12$ mM. Clearly, both E_m and E_{Cl} are -60 mV. If the cell is depolarized, say by 20 mV, to -40 mV, Cl^- redistributes across the membrane until reaching equilibrium which, for the example considered, will occur when $[Cl^-]_i^{eq} = 25.3$ mM, and thus $E_{Cl} = -40$ mV.

Another way of arriving at Equation 15.2 and grasping its meaning is to consider once more the idealized cell shown in Fig. 15.1 that has only anion channels and Na^+ pumps, but no active (uphill) Cl^- transporters. In this cell, Cl^- distributes passively following E_m. The Cl^- flux through the anion channel is driven by the electrochemical potential gradient for Cl^-, $\Delta\mu_{Cl}$, which is the sum of a chemical and an electrical component. This is formally defined by Equation 15.4:

$$\Delta\mu_{Cl} = RT \ln \frac{[Cl^-]_i}{[Cl^-]_o} + zFE_m \tag{15.4}$$

Since the cell is negative inside with respect to the outside (in the model shown $E_m = -60$ mV and z, the Cl^- valence is -1), the electrical potential gradient will tend to drive Cl^- out of the cell. However, the chemical potential gradient is inward; $[Cl^-]_o$ is higher than $[Cl^-]_i$. Consequently, the chemical gradient will drive Cl^- towards the cell interior. When the two forces cancel each other (they are equal and opposite), the system reaches equilibrium. At that point $\Delta\mu_{Cl} = 0$. When this condition is met, we can readily derive Equation 15.2 from Equation 15.4. That is, when Cl^- is passively distributed, E_m will have the same value as E_{Cl}.

If Cl^- is non-passively distributed it means that it is actively transported and this implies energy consumption. Active Cl^- transport (i.e. transport against Cl^- electrochemical equilibrium or "uphill" transport) requires demonstrating that $[Cl^-]_i$ is maintained at a level different from that predicted by Equation 15.3 and this implies that E_{Cl} and E_m will have different values. In most cells, $[Cl^-]_i$ is maintained at a value different from that predicted from Equation 15.3. However, as mentioned above, *equal values of E_m and E_{Cl} do not preclude the presence of carrier-mediated active Cl^- transport*. A clear example illustrating this notion is the case of skeletal muscle cells which, as mentioned above (Section II) and shown in Fig. 15.2, have a substantial channel-mediated (electrodiffusional) Cl^- permeability that masks the effects of an inwardly directed active Cl^- transport mechanism (Harris and Betz, 1987; Aickin, 1990).

In most cell types of both vertebrates and invertebrates, in which Cl^- is not in electrochemical equilibrium, the $[Cl^-]_i$ is maintained at a higher value than that predicted for a passive distribution across the plasma membrane, i.e. E_{Cl} has a more depolarized (less negative) value than E_m. This implies the presence of transport mechanisms that actively accumulate Cl^- often referred to as "Cl^- loaders". Examples of mammalian cells in which $[Cl^-]_i$ is maintained

above equilibrium include primary sensory neurons, sympathetic ganglion cells, immature central nervous system neurons, epithelial cells, leukocytes and both smooth and cardiac muscle cells (Fig. 15.3). In contrast, in some cells, mature cortical neurons in particular, $[Cl^-]_i$ is maintained at a value lower than that predicted for a passive Cl^- distribution across the plasma membrane due to the presence of active Cl^- extrusion mechanisms (i.e. Cl^- extruders). In this case, E_{Cl} has a more hyperpolarized (more negative) value than E_m. This lower than passive Cl^- distribution in adult neurons in the CNS constitutes the basis for hyperpolarizing synaptic inhibition mediated by neurotransmitters such as GABA and glycine. A prototypical case is the hyperpolarizing inhibition produced by GABA acting via $GABA_A$ receptors thereby opening Cl^- channels with consequent hyperpolarizing Cl^- influx that results in an increase in neuronal firing threshold (i.e. decreased excitability). By controlling neuronal excitability, Cl^--mediated postsynaptic inhibition shapes the firing pattern of individual neurons and entire neuronal networks and thus this mechanism plays a key role in the processing of information in the nervous system. The carrier protein that actively extrudes Cl^- in mature CNS neurons, making possible hyperpolarizing inhibition, is one of four isoforms of the K^+-Cl^- cotransporters, KCC2, a member of the electroneutral cation-coupled chloride cotransporter protein family encoded by the SLC12A gene family, as discussed below (see Section VI).

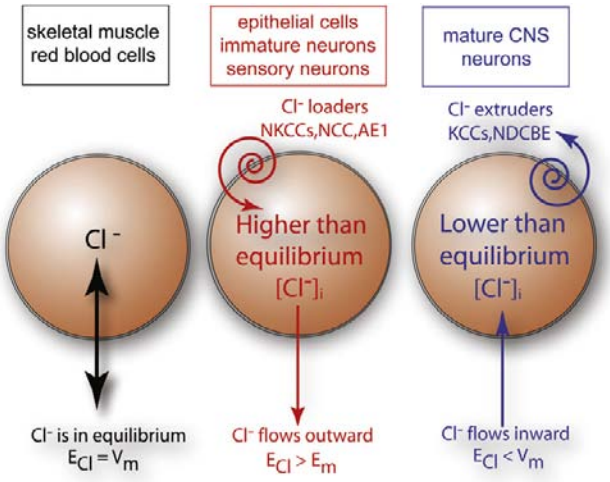

FIGURE 15.3 Control of cytosolic Cl^- in different cell types. In skeletal muscle and erythrocytes, Cl^- appears to be in electrochemical equilibrium because there is a large resting Cl^- conductance that masks active Cl^- transport. In epithelial cells, immature neurons and adult sensory neurons, Cl^- loaders establish a higher than electrochemical equilibrium intracellular Cl^- concentration. In mature neurons, Cl^- extruders establish a lower than electrochemical equilibrium intracellular Cl^- concentration. Examples of Cl^- loaders are: the Na^+, K^+, $2Cl^-$ cotransporters (NKCCs), the Na^+-Cl^- cotransporter (NCC), and the anion exchanger 1(AE1). Examples of Cl^- extruders are some K^+-Cl^- cotransporters (KCCs) and the Na^+-driven Cl^-/HCO_3 exchanger (NDCBE). *(Modified from Hartzell, 2009.)*

IV. ACTIVE TRANSPORT MECHANISMS FOR Cl^-

Intracellular Cl^- levels are determined by the relative contributions of the various Cl^- transport mechanisms expressed in the plasma membrane of a given cell type. A variety of mechanisms capable of transporting Cl^- across the plasma membrane have been identified in vertebrate and invertebrate cells. They include various types of Cl^- channels that behave as *passive leak pathways*, and a series of specialized *carriers that mediate "active" Cl^- transport*. All Cl^- carrier proteins known in animal cells are secondary active transport mechanisms and all of them are encoded by members of the solute carrier (SLC) gene superfamily (see http://ghr.nlm.nih.gov/geneFamily/slc). As we will see, secondary active transport does not directly utilize ATP hydrolysis to drive "uphill" solute transport. In animal cells, there is no firm evidence for the existence of an active Cl^- pump, i.e. a primary active transport mechanism *directly* energized by ATP. Chloride channels are the subject of other chapters of this book and therefore they will only be briefly mentioned here. The carrier protein molecules that actively transport Cl^- include but are not limited to (1) *anion exchangers* (AEs) and (2) the *electroneutral cation-chloride cotransporters*. The latter are the main focus of this chapter. *Neurotransmitter transporters* encoded by the SLC6 gene family (Na^+- and Cl^--dependent neurotransmitter transporter family) cotransport Cl^-. An example is the GABA transporter GAT1 (SLC6A1). The ion-substrate stoichiometry of GABA transporters has been determined to be $2Na^+$:$1Cl^-$:1GABA. The role of Cl^- in the transport process is not understood and it is unclear whether this Cl^- cotransport impacts $[Cl^-]_i$ or Cl^- is merely used as a cofactor (Wu et al., 2007). For this reason, neurotransmitter transport proteins are not considered further in the present chapter.

IVA. Anion Exchangers

Anion exchangers are encoded by two evolutionarily unrelated mammalian gene families, SLC4 and SLC26 (Alper, 2009; Romero et al., 2009). Plasmalemmal Cl^-/HCO_3^- exchangers are ubiquitously expressed in various cell types. Their primary function is the regulation of intracellular pH, but they also play key roles in the regulation of $[Cl^-]_i$ and cell volume. The Cl^-/HCO_3^- exchangers of polarized epithelial cells contribute to transepithelial secretion and reabsorption of acid–base equivalents and Cl^-. The mammalian SLC4 gene and protein family includes three Na^+-independent Cl^-/HCO_3^- exchangers (AE1, AE2 and AE3) that couple the electroneutral movement of 1 Cl^- in exchange for 1 HCO_3^- across plasma membranes. Under physiological conditions, most AEs of the SLC4 family behave as cell Cl^- loaders; they couple the

inward movement of 1 Cl^- with the outward movement of 1 HCO_3^-. However, *reversibility is a key thermodynamic feature of carrier-mediated transport* proteins and thus solutes can be transported in either inward or outward direction under physiological conditions; these proteins use the chemical gradient of either one of the transported ions to move the other. The transport process of AE1, AE2 and AE3 is *electroneutral*. This means that the transport process occurs without net charge transfer across the membrane and without being affected by the membrane potential (see below). This is in contrast with *electrogenic* transport, in which the driving force for the transport process is the sum of the chemical and electrical gradients of the transported ions and thus the transport process is affected by the membrane potential and it generates a current across the membrane, i.e. it transfers net charge across the membrane. An example of carrier electrogenicity and reversibility is the Cl^-/HCO_3^- exchanger SLC26A6. This carrier protein mediates the coupled exchange of Cl^- and HCO_3^- with a transport stoichiometry of $1Cl^-:2HCO_3^-$ (Fig. 15.4).

One of the best examples of transport reversibility of an electroneutral transporter under physiological conditions is the erythroid Cl^-/HCO_3^- exchanger (AE1), a carrier that is essential for removing CO_2 produced by tissue metabolism and transporting it to the lungs where the gas can be expelled from the body. AE1 operates near equilibrium (see below) so that a relatively small variation in the chemical gradients of Cl^- or HCO_3^- across the plasma membrane of red blood cells (RBCs) alters the direction of transport. This feature permits HCO_3^- formed from CO_2 in the systemic capillaries by the intracellular enzyme carbonic anhydrase (CA) to leave the RBCs in exchange for Cl^-, thus effectively storing CO_2 in the blood in the form of plasma HCO_3^-, greatly increasing the CO_2 carrying capacity of the blood. In the lungs, the process is reversed to regenerate CO_2 that is then exhaled. In other words, the relatively high external concentration of CO_2 generated by metabolism in tissues drives CO_2 entry into RBCs. CO_2 is then hydrated inside RBCs, a forward reaction catalyzed by the enzyme CA ($CO_2 + H_2O \rightarrow H_2CO_3 \rightarrow H^+ + HCO_3^-$). The resulting increase in $[HCO_3^-]_i$ drives the Cl^-/HCO_3^- exchanger to operate in the bicarbonate-out-chloride-in mode. In the alveolar capillaries, the CO_2 concentration gradient is reversed because of the relatively low CO_2 concentration in the alveolar space, thereby driving CO_2 from the RBCs into the alveolus. This process is possible because the reactions catalyzed by CA are also reversible, so CA now catalyzes the net dehydration of H_2CO_3 ($H^+ + HCO_3^- \rightarrow H_2CO_3 \rightarrow H_2O + CO_2$). The consequent decrease in $[HCO_3^-]_i$ drives the Cl^-/HCO_3^- exchanger to operate in the bicarbonate-in-chloride-out mode.

Heart muscle cells are an interesting example in which $[Cl^-]_i$ is determined by the presence of electrogenic anion exchangers working in parallel with the electroneutral Cl^- loader NKCC1. Early studies using intracellular ion-selective microelectrodes demonstrated that $[Cl^-]_i$ is maintained at a *higher* value than that predicted for a passive distribution across the sarcolemma of cardiac muscle cells (Vaughan-Jones, 1982). It is now known that a variety of sarcolemmal AEs, in conjunction with the Na^+-K^+-$2Cl^-$ cotransporter NKCC1, serve as uphill Cl^- accumulating mechanisms in cardiac cells. The anion exchangers predominantly expressed in adult heart muscle are AE3 (SLC4A3), SLC26A3 and particularly SLC26A6, all of which play a central role in the regulation of pH_i in cardiomyocytes (Alvarez et al., 2004). Both SLC26A3 and SLC26A6 function as dual Cl^-/OH^- and Cl^-/HCO_3^- exchangers. The transport stoichiometry of SLC26A6 is $2HCO_3^-:1Cl^-$, whereas that of SLC26A3 is $1HCO_3^-:2Cl^-$ (Shcheynikov et al., 2006). These stoichiometries mean that both these SLC26 transporters are *electrogenic*; on each cycle they transport net charge across the plasma

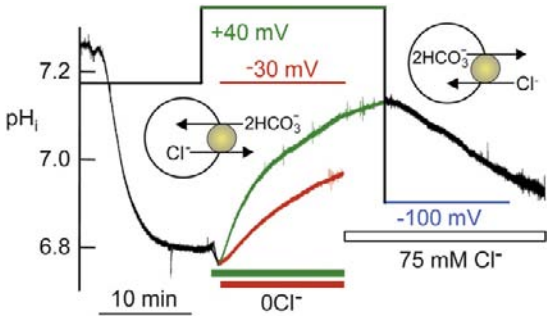

FIGURE 15.4 Electrogenicity and flux reversibility of the Cl^-/HCO_3^- exchanger SLC26A6 heterologously expressed in *Xenopus* oocytes. The membrane potential of transfected *Xenopus* oocytes was controlled by voltage clamp as indicated. Intracellular pH (pH_i) changes were measured with pH_i-sensitive microelectrodes. Changes in $[Cl^-]_i$ were also measured (not shown) using Cl^--sensitive microelectrodes. The experiment shows the effect of membrane potential and external $[Cl^-]$ on HCO_3^- transport by SLC26A6. The HCO_3^- fluxes are inferred from the pH_i changes reflecting net H^+ fluxes. Accordingly, when HCO_3^- enters the cell in exchange for Cl^-, the cell interior is alkalinized (green and red traces) and when HCO_3^- exits the cell in exchange for Cl^-, the cell is acidified (black trace following green trace). The reversibility and direction of transport occurring during the experiment are illustrated in the inset diagrams. In this experiment, the *Xenopus* oocyte expressing SLC26A6 was bathed in HCO_3^-- buffered media. After the stabilization of pH_i, the membrane potential was clamped at −30 mV (red pH_i trace) or +40 mV (green pH_i trace) before exposing the oocyte to Cl^--free medium (0 Cl^-). Note the effect of membrane potential on HCO_3^- influx upon removal of eternal Cl^- (green trace at +40 mV and red trace at −30 mV). At the time indicated by the white bar, external $[Cl^-]$ (75 mM) was restored and, after an additional period of 5 min, the membrane potential was switched from +40 mV to −100 mV. This resulted in intracellular acidification (black trace) due to HCO_3^- efflux. SLC26A6 mediates the coupled exchange of Cl^- and HCO_3^- with a transport stoichiometry of $1Cl^-/2HCO_3^-$. Accordingly, holding the membrane potential at +40 (green pH_i trace) and −100 mV (black trace) accelerated and inhibited, respectively, Cl^--mediated HCO_3^- influx and holding the membrane potential at −100 mV increased HCO_3^--mediated Cl^- influx. *(Modified from Shcheynikov et al., 2006.)*

membrane thereby producing a change in membrane potential (Romero et al., 2009). Thus, their operation is also affected by the membrane potential (see Fig. 15.4). The "opposite" stoichiometry of SLC26A6 and SLC26A3 transporters means that their relative transport activity will vary with the membrane potential; SLC26A6 will operate to cause efflux of HCO_3^- at resting membrane potential (≈ -80 mV), while SLC26A3 will become active in the HCO_3^- efflux mode as the cell moves to more positive potential during the cardiac action potential.

All these AEs (SLC4A3, SLC26A3 and SLC26A6) play key roles in the regulation of pH_i in cardiac myocytes. Further, the outward Cl^- gradient of cardiac myocytes that is generated and maintained by the above mentioned AEs in conjunction with the operation of NKCC1 is of high functional significance, as revealed by studies using double knockout mice in which both AE3 (SLC4A3) and NKCC1 (SLC12A2) are genetically deleted resulting in impaired cardiac contractility (Prasad et al., 2008). Numerous Cl^- channels are expressed in cardiac muscle (Duan, 2009). Their activation produces significant effects on cardiac action potential characteristics and pacemaker activity. The repertoire of cardiac Cl^- channels include the cystic fibrosis transmembrane conductance regulator (CFTR), which is a member of the ATP-binding cassette (ABC) transporter superfamily and may be responsible for the Cl^- currents activated by protein kinase A (PKA), ClC-2, ClC-3 and the Ca^{2+}activated Cl^- channel TMEM16A. The resting E_m of cardiac myocytes is -80 to -90 mV and during an action potential the overshoot and plateau phases can be several millivolts positive. Given that E_{Cl} remains fairly constant, E_m can be either more positive or more negative than E_{Cl} during the normal cardiac action potential cycle. Thus, cardiac Cl^- channels can generate both outward and inward currents and cause both depolarization and repolarization during the action potential.

Anion exchangers, in parallel with NKCC1, also appear to play a role in intracellular Cl^- homeostasis in developing neurons in some CNS areas. For instance, in developing rat auditory brainstem neurons (Becker et al., 2003) and in embryonic chick motoneurons (Gonzalez-Islas et al., 2009), AEs contribute to the maintenance of $[Cl^-]_i$ at *higher* values than predicted for a passive distribution across the plasma membrane. The resulting outward Cl^- gradient underlies the *depolarizing* action of glycine and GABA, which is important in these and other central neurons in promoting neurogenesis, migration and differentiation (Reynolds et al., 2008; Wang and Kriegstein, 2009).

How much Cl^- can a cell accumulate through electroneutral anion exchangers like AE1, AE2 or AE3? It depends on *thermodynamic equilibrium conditions of the AEs*, on kinetic constraints dictated by mechanisms regulating ion translocation, as well as on the presence of other transporters and channels expressed in the same cell. For understanding the $[Cl^-]_i$ that would be reached when an anion exchanger attains thermodynamic equilibrium consider the cell model shown in Fig. 15.5. Let us assume that the cell expresses only an electroneutral Cl^-/HCO_3^- exchanger with a stoichiometry of $1Cl^-:1HCO_3^-$ per cycle, that there are no kinetic constraints and that the only passive leak pathway is a GABA-gated Cl^- channel. Since AEs are secondary active transporters, the driving force for anion transport will be determined by the overall net free energy (ΔG) of the system, which in this case is the sum of the *chemical* potential gradients of the anions involved. Because the anions are transported in opposite directions, the combined chemical gradient ($\Delta\mu_{Cl/HCO_3}$) is given by the *difference* of the Cl^- and HCO_3^- chemical potential gradients $\Delta\mu_{Cl}$ and $\Delta\mu_{HCO_3}$, respectively:

$$\Delta G = \Delta\mu_{Cl/HCO_3} = \Delta\mu_{Cl} - \Delta\mu_{HCO_3} \tag{15.5}$$

Hence,

$$\Delta G = \Delta\mu_{Cl/HCO_3} = RT \ln \frac{[Cl^-]_i}{[Cl^-]_o} - RT \ln \frac{[HCO_3^-]_i}{[HCO_3^-]_o} \tag{15.6}$$

The transport process reaches thermodynamic equilibrium when $\Delta G = \Delta\mu_{Cl/HCO_3} = 0$, and Equation 15.6 becomes:

$$\frac{[Cl^-]_i}{[Cl^-]_o} = \frac{[HCO_3^-]_i}{[HCO_3^-]_o} \tag{15.7}$$

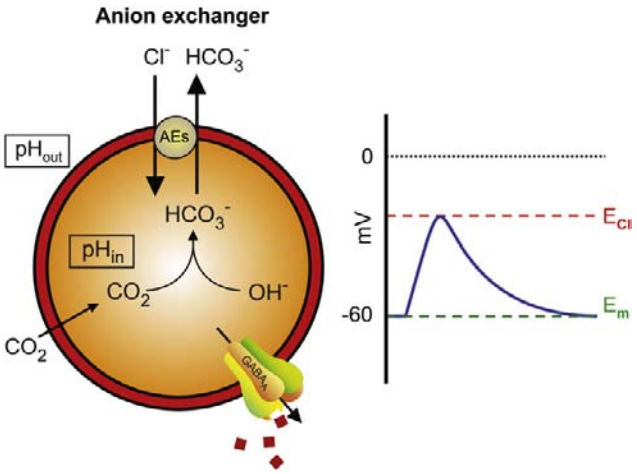

FIGURE 15.5 Model of a cell (e.g. a neuron) expressing only anion exchangers (AEs), Na^+/K^+ ATPase (not shown) and a ligand-gated anion channels ($GABA_A$ receptor-channels). The ΔpH across the plasma membrane ($pH_{in}-pH_{out}$) is constant. Resting $E_m = -60$ mV. The AEs mediate active accumulation of Cl^- in exchange for HCO_3^-. Intracellular $[Cl^-]$ is maintained at higher than passive levels. Consequently, E_{Cl} is more positive than E_m. Opening GABA-gated anion channels produces a depolarization mediated by electrodiffusional Cl^- efflux. The red squares represent GABA molecules acting on the $GABA_A$ receptor-channel. *(Reproduced from Alvarez-Leefmans and Delpire, 2009b.)*

Equation 15.7 relates the intracellular and extracellular Cl^- and HCO_3^- concentrations when the Cl^-/HCO_3^- exchange mechanism has reached equilibrium, i.e. when no further net movement of Cl^- and HCO_3^- can occur across the membrane. For the model shown in Fig. 15.5, pH_o=7.3 and $pH_i = 7.1$ (i.e. $\Delta pH = 0.2$) and $[HCO_3^-]_o$ is taken as 22 mM, the concentration measured in mammalian arterial plasma. In the presence of a CO_2/HCO_3^--buffered solution, the distribution of Cl^- will be determined by the distribution of HCO_3^- across the membrane. This is because CO_2 is freely permeable through the membrane and, at constant PCO_2 ($[CO_2]_i = [CO_2]_o$), the ratio of intracellular and extracellular $[HCO_3^-]$ is determined by ΔpH. Under these conditions E_H, the equilibrium potential for H^+, is equal to $E_{HCO_3^-}$, the equilibrium potential for bicarbonate (Bevensee and Boron, 1998). In the model considered here, the cell possesses only an anion exchanger (see Fig. 15.5). Thus, the $[Cl^-]_i$ when the anion exchanger reaches equilibrium can be predicted by knowing the $[Cl^-]_o$ and the ΔpH. Since we know ΔpH we can calculate E_H, which is given by the Nernst equation:

$$E_H = \frac{RT}{F} \ln (pH_i - pH_o) \tag{15.8}$$

At 37°C, and taking $pH_o = 7.3$ and $pH_i = 7.1$, $E_H = -12.3$ mV. Since $E_H = E_{HCO_3}$, we can now calculate the $[HCO_3^-]_i$ at equilibrium using the following expression:

$$[HCO_3^-]_i = [HCO_3^-]_o \exp\left(\frac{E_{HCO_3} F}{RT}\right) \tag{15.9a}$$

Hence,

$$[HCO_3^-]_i = 22 \text{ mM} \exp\left(\frac{-12.3 \text{ mV} F}{RT}\right) = 13.9 \text{ mM} \tag{15.9b}$$

We can now calculate $[Cl^-]_i$ when the Cl^-/HCO_3^- reaches equilibrium, using Equation 15.10, which is derived from Equation 15.7. For $[Cl^-]_o = 113$ mM,

$$[Cl^-]_i = \frac{[HCO_3^-]_i \ [Cl^-]_o}{[HCO_3^-]_o} = \frac{13.9 \times 113}{22} = 71.4 \text{ mM} \tag{15.10}$$

Thus, the maximal possible $[Cl^-]_i$ due to the AE under the conditions considered here would be 71.4 mM. Obviously, in a cell endowed with AEs, activation of $GABA_A$ receptors would produce a depolarizing Cl^- efflux (see Fig. 15.5). For thermodynamic equilibrium conditions of other anion exchangers the interested reader should consult the excellent review by Romero and colleagues (Romero et al., 2009). It is important to mention that AEs may be kinetically inhibited at different set points for $[Cl^-]_i$ and thus these "kinetic brakes" may prevent the exchanger from reaching thermodynamic equilibrium under physiological conditions (Alper et al., 2002; Kurschat et al., 2006). A key kinetic brake is pH itself (Alper et al., 2002; Alper, 2009). However, the discussion of regulatory mechanisms of AEs is beyond the scope of the present chapter.

AE1, AE2 and AE3 are often referred to as "Na^+-independent SLC4 anion exchangers" to distinguish them from the *Na^+-driven Cl^-/HCO_3^- exchanger NDCBE*, also an electroneutral transporter of the SLC4 family (SLC4A8) that, under physiological conditions, mediates the uptake of $1Na^+$ and $2HCO_3^-$ in exchange for $1Cl^-$. Thus, NDCBE normally behaves as a Cl^- extruder and, because of its capacity to transport HCO_3^- inwardly, it is a major acid extruder. Although NDCBE mediates a large Cl^- efflux that can potentially affect $[Cl^-]_i$, its role in intracellular Cl^- regulation is little known (see below); instead, NDCBE appears to be a major pH_i regulator in several types of CNS neurons (Chen et al., 2008). In fact, NDCBE was the first transporter shown to be involved in pH_i regulation, a discovery made in the mid-1970s in squid giant axons by Walter Boron, Paul De Weer and John Russell, and by Roger C. Thomas working independently in snail neurons (for references see Thomas, 1984; Romero et al., 2004). Human NDCBE was cloned by Boron's group (Grichtchenko et al., 2001). The possible role of NDCBE in the regulation of $[Cl^-]_i$ has been recently addressed in certain type of mammalian neurons, the cartwheel cells of the dorsal cochlear nucleus. These neurons exhibit activity-dependent intracellular acidification that is offset by activation of NDCBE with a consequent hyperpolarizing shift in E_{Cl} due to a decrease in $[Cl^-]_i$ mediated by NDCBE (Kim and Trussell, 2009). More recently, work on neurons of the nematode *Caenorhabditis elegans* shows that NDCBEs function with KCCs in generating the neuronal inward Cl^- gradient necessary for the hyperpolarizing action of GABA, and suggests a mechanism for the close tie between pH and excitability in the brain (Bellemer et al., 2011).

IVB. The Electroneutral Cation-Chloride Cotransporter Family

The electroneutral cation-chloride cotransporter family (SLC12A), which is the main focus of this chapter, comprises the major proteins responsible for intracellular Cl^- regulation (Gamba, 2005; Di Fulvio and Alvarez-Leefmans, 2009; Garbarini and Delpire, 2009; Payne, 2009). The SLC12A gene/protein family encompasses nine members: SLC12A3 (the thiazide-sensitive Na^+-Cl^- cotransporter NCC), SLC12A2 (the Na^+-K^+-$2Cl^-$ cotransporter NKCC1), SLC12A1 (the Na^+-K^+-$2Cl^-$ cotransporter NKCC2) and four Na^+-independent K^+-Cl^- cotransporters, namely SCLC12A4 (KCC1), SCLC12A5 (KCC2), SLC12A6 (KCC3), SLC12A7 (KCC4) and two orphan members named SLC12A9 (CIP) and SLC12A8 (CCC9) that do not

appear to transport ions and whose function is little understood. Thus only seven of the nine members of the SCL12A family have been established to function as cation-coupled Cl^- cotransporters. NKCC1, NKCC2 and NCC normally work as active Cl^- loaders, whereas the four KCCs (1–4) normally work as Cl^- extruders (see Fig. 15.3).

As mentioned above, all of these cation-coupled Cl^- cotransporters, as well as the Cl^-/HCO_3^- exchangers, are secondary active transport mechanisms. In this kind of transport, the translocation of the substrate is coupled to the translocation of another substrate that uses the same carrier, whether in the opposite direction (countertransport, antiport or exchanger) or in the same direction (cotransport or symport). The energy consumed in this type of transport process comes secondarily or indirectly from ATP. In other words, in these transporters, the flow of the substrate that is being translocated up its electrochemical gradient is coupled to the flow of a second substrate down its electrochemical gradient; the gradient of this second substrate is maintained by a primary active transport mechanism, i.e. one that consumes metabolic energy directly derived from the hydrolysis of ATP. In the case of cation-coupled Cl^- cotransporters, the primary active transport mechanism that generates and maintains the Na^+ and K^+ gradients is the Na^+/K^+ pump, also known as the Na^+/K^+ATPase. For example, let us consider the Na^+-Cl^- cotransporter (NCC). The uphill movement of Cl^- carried out by this electroneutral cotransporter system is driven primarily by the energy stored in the Na^+ chemical potential gradient which, in turn, is maintained by the ATP-requiring Na^+/K^+ pump. The Na^+ that enters the cell is pumped back out by the Na^+/K^+ pump. Hence there is no net gain of intracellular Na^+. In essence, energy is directly invested into a primary active transport mechanism (the Na^+/K^+ pump) that is responsible for extruding Na^+ from the cell (in exchange for K^+) and thereby maintaining a low and constant intracellular Na^+ concentration that results in a steep Na^+ inward gradient. The Na^+-Cl^- cotransport mechanism can then convey the uphill movement of Cl^- energized by the downhill flow of Na^+.

V. ELECTRONEUTRAL Na^+-K^+-Cl^- COTRANSPORTERS

VA. Isoforms and Splice Variants: An Overview of their Functional Roles

The Na^+-K^+-Cl^- cotransporters (NKCCs) are a class of membrane proteins that mediate the coupled, electrically neutral movement of Na^+, K^+ and Cl^- ions across the membrane of many animal cells, in most cases with a stoichiometry of $1Na^+$:$1K^+$:$2Cl^-$ (Russell, 2000). Under normal physiological conditions, NKCCs work as active ("uphill") transport mechanisms for accumulating Cl^- in cells. NKCCs maintain $[Cl^-]_i$ at levels above the predicted electrochemical equilibrium, generating an outward Cl^- gradient across the plasma membranes of many cell types. The higher than equilibrium $[Cl^-]_i$ is used in multifarious functions, depending on the cell type in which NKCCs are expressed. Some examples of these functions are given below and in Section VE.

Two distinct but highly homologous isoforms of the Na^+-K^+-Cl^- cotransporter proteins (NKCC1 and NKCC2) have been identified by cDNA cloning and functional expression (Delpire et al., 1994; Gamba et al., 1994; Payne and Forbush, 1994, 1995; Xu et al., 1994). The two genes encoding Na^+-K^+-Cl^- cotransporter are members of the SLC12A family and are known as SLC12A1 and SLC12A2. The SLC12A1 gene encodes NKCC2, often referred to as "the renal Na^+-K^+-Cl^- cotransporter" because it is predominantly expressed in the apical membrane of the epithelial cells that form the thick ascending limb of Henle's loop (TALH) and the macula densa. The SLC12A2 gene encodes the ubiquitously expressed NKCC1, a cotransporter that is found in nearly all cell types, whether epithelial or not. In the vast majority of secretory epithelial cells, NKCC1 expression is restricted to the basolateral membrane, together with the Na^+/K^+-ATPase (Haas and Forbush, 2000), as shown in Fig. 15.14A. So far the definitive exception is the choroid plexus epithelium where both NKCC1 and the Na^+/K^+ ATPase reside in the apical membrane (Wu et al., 1998), as depicted in Fig. 15.17. A similar case appears to be that of the retinal pigment epithelium, where the Na^+/K^+-ATPase is also located in the apical membrane (Gundersen et al., 1991) together with a Na^+, K^+, $2Cl^-$ mechanism that most likely is NKCC1 (Strauss, 2005). However, the evidence comes from functional studies and the molecular identity and exact location of this NKCC have not been established.

The high $[Cl^-]_i$ maintained by NKCC1 is used in polarized epithelial cells to promote net salt and water transport (Haas and Forbush, 2000). For instance, in salivary glands, NKCC1 is the major Cl^- uptake mechanism across the basolateral membrane of acinar cells and is critical for driving saliva secretion in vivo. Mice with targeted disruption of the *Slc12a2* gene encoding NKCC1 exhibit a dramatic reduction (>60%) in the volume of saliva secreted in response to a muscarinic agonist, the primary in situ salivation signal (Evans et al., 2000).

Besides epithelial cells, NKCC1 is expressed in many non-polarized cells, such as neurons. By virtue of the outward Cl^- gradient that NKCC1 generates and maintains, it makes possible the depolarizing action of neurotransmitters that open Cl^- channels, such as GABA and glycine, or second messengers such as Ca^{2+}, that open Ca^{2+}-activated Cl^- channels. For instance, the GABA-induced depolarizations made possible by NKCC1 in the

intraspinal terminals of primary sensory neurons constitute the basis for the phenomenon of presynaptic inhibition in the spinal cord (Alvarez-Leefmans et al., 1998; Alvarez-Leefmans, 2009), as illustrated in Fig. 15.15 and discussed below in more detail (Section VE). This GABAergic presynaptic control is a crucial mechanism in the gating of afferent flow of information of various sensory modalities, including proprioception and pain, into the spinal cord (Rudomin and Schmidt, 1999; Willis, 1999, 2006). NKCC1 is also involved in sensory transduction. Two well documented examples that are discussed below (Section VE) are the inner ear and the olfactory sensory neurons.

NKCCs play key roles in cell volume regulation and maintenance. There is evidence that in some cell types NKCCs function to offset osmotically induced cell shrinkage by mediating the net influx of ions and water (Russell, 2009). In addition, recent evidence demonstrates that NKCC1 serves to maintain cell volume under euvolemic conditions (Rocha-Gonzalez et al., 2008) and that, in addition to ions, it cotransports water (Hamann et al., 2010). NKCC1 function is also important in cell cycle and cell division (Russell, 2009). Overexpression of the NKCC1 cotransporter gene has been shown to induce cell proliferation and phenotypic transformation in mouse fibroblasts (Panet et al., 2000). NKCC1 also functions as a K^+ uptake mechanism, thereby contributing to the maintenance of $[K^+]_i$ at constant levels. It has also been proposed that NKCC1 works as an extracellular K^+ buffer, keeping $[K^+]_o$ constant, thereby preventing K^+ accumulation in the extracellular space (Walz, 1992; Wu et al., 1998; Alvarez-Leefmans et al., 2001; Lytle, 2003; Kristensen and Juel, 2010).

The introduction of knockout mice models in biomedical research has greatly advanced our understanding of the function of cation-chloride-cotransporters and many other proteins. Knockout mice are transgenic animals that contain a modification in a specific gene that makes the gene product (i.e. the protein) non-functional. The functional roles of various members of the SLC12A gene/protein family have been studied using knockout mice models (Garbarini and Delpire, 2009) or animals or humans with mutations in specific SLC12A genes. NKCC1 knockout mice exhibit several abnormalities. The most salient are: deafness, imbalance, hypotension, increased nociceptive threshold suggesting NKCC1 involvement in pain perception, severe salivation impairment and male infertility (Delpire et al., 1999; Flagella et al., 1999; Evans et al., 2000). So far there are no known human phenotypes of NKCC1 gene abnormalities.

The SLC12A1 gene encodes NKCC2 which, as mentioned above, is predominantly expressed in kidney, specifically in the apical membrane and in subapical vesicles of the epithelial cells of both the thick ascending limb of the loop of Henle (TALH) and the macula densa (Nielsen et al., 1998). NKCC2-dependent salt transport constitutes the major apical entry pathway for transepithelial salt reabsorption in the TALH; 80% of the NaCl uptake across the apical membrane of TALH cells is mediated by NKCC2 (Castrop and Schnermann, 2008). To achieve net salt absorption, electroneutral cotransport of Na^+, K^+ and $2Cl^-$ via NKCC2 is complemented by recycling of K^+ via apical K^+ channels (the so called ROMK), efflux of Cl^- via basolateral Cl^- channels and basolateral extrusion of Na^+ by the Na^+/K^+-ATPase which, in addition, generates the inward Na^+ gradient necessary to energize the cotransport (see Fig. 15.14B). Pharmacological blockade of NKCC2 by loop diuretics like bumetanide results in marked natriuresis, diuresis and decrease in blood pressure. This is the rationale for using loop diuretics in the treatment of high blood pressure.

Besides effecting transcellular absorption of Na^+ and Cl^- by the medullary and cortical TALH, NKCC2 plays a secondary role in the paracellular transport of Na^+, Ca^{2+} and Mg^{2+} by this nephron segment (Gamba and Friedman, 2009). The TALH also functions in renal acid secretion given that NH_4^+ competes with K^+ at its binding site on the NKCC2 (Good, 1994; Weiner and Verlander, 2011). The NH_4^+ generated by the renal proximal tubule is thus reabsorbed from the tubule lumen in the TALH and excreted from the renal interstitium by more distal nephron segments.

Besides its function in TALH salt retrieval, NKCC2-mediated transport constitutes the first step in the tubulovascular signaling pathway between macula densa cells in the juxtaglomerular region with the afferent arteriole. NKCC2 is located in the apical membrane of macula densa cells, a specialized group of tubular cells situated at the point of apposition of renal tubules with their parent glomeruli. Macula densa cells are modified epithelial cells that sense luminal Na^+ and Cl^- concentrations and generate paracrine chemical signals to the glomerular vascular elements. Thus, these cells control two important physiological processes: tubuloglomerular feedback and tubular regulation of renin release. The tubuloglomerular feedback mechanism plays a crucial role in regulating glomerular filtration rate and blood flow. An increase in luminal Na^+ and Cl^- concentrations at the macula densa decreases glomerular filtration by inducing constriction of the afferent renal arteriole. Increases in luminal Na^+ and Cl^- concentration at the macula densa also inhibit renin release from juxtaglomerular cells in the afferent arteriole. Thus NKCC2 plays a central role in the regulation of body fluid volume and osmolarity (Bell et al., 2009; Peti-Peterdi and Harris, 2010).

Although NKCC2 is encoded by a single gene, differential splicing results in the generation of several alternative transcripts. Specifically, three full length NKCC2 splice variants (NKCC2A, NKCC2B and NKCC2F) and three variants with truncated carboxyl termini have been described. They differ in their location along the TALH and the macula densa, and have different kinetic properties.

Analysis of the molecular and functional properties of individual splice variants is beyond the scope of this chapter. References on this subject can be found in excellent reviews (Gamba, 2005, 2009a; Gamba and Friedman, 2009) and in studies reported by Castrop's group (Oppermann et al., 2006, 2007; Castrop and Schnermann, 2008; Carota et al., 2010).

Inactivating homozygous mutations of the human NKCC2 gene product are the cause of Bartter's disease. The characteristic clinical picture includes a salt-wasting state with hypotension, metabolic alkalosis with hypokalemia, hypercalciuria and secondary aldosteronism. The vital function of NKCC2 proteins is also manifest in various knockout mice models. Targeted disruption of the promoter and the first three exons of mouse NKCC2 gene results in a full NKCC2 knockout with a phenotype sharing many similarities to Bartter's syndrome (Takahashi et al., 2000).

VB. Basic Functional Features of the Na^+-K^+-Cl^- Cotransporters

Four functional features define the NKCCs:

1. Ion translocation by the NKCCs requires the simultaneous presence of all three ions (Na^+, K^+ and Cl^-) on the same side of the membrane
2. The cotransport process is electroneutral; in vertebrate cells the stoichiometry is $1Na^+$:$1K^+$:$2Cl^-$ in nearly all cases (Lytle, 2003)
3. The transporter can work in forward and backward modes, i.e. net transport may occur into or out of the cells, the magnitude and direction of this transport being determined by the sum of the chemical potential gradients of the transported ions (Lytle et al., 1998)
4. Transport is inhibited by the so-called loop diuretics derived from 5-sulfamoyl benzoic acid, which include furosemide, bumetanide, and benzmetanide, as shown in Fig. 15.11 (O'Grady et al., 1987b; Hannaert et al., 2002).

VB1. Absolute Requirement for All Three Ions on the Same Side of the Membrane

NKCC-mediated fluxes of all three ions require the presence of the other two ions on the side of the membrane from which the flux originates (termed the *cis*-side). This property has been definitely proved by measuring individual fluxes of Na^+, K^+ and Cl^- and looking at their interdependence. Perhaps the most stringent test for this coupling of ion fluxes has been carried out in internally dialyzed squid giant axons. This preparation has the unique advantage of permitting the simultaneous control of the composition of the intracellular as well as the extracellular milieu while measuring unidirectional fluxes. Using this preparation Russell and his coworkers have demonstrated the absolute requirement for the *cis*-side presence of all three ions both for unidirectional influx and efflux (Russell, 2000). Each of the three co-ions was systematically removed while measuring the bumetanide-sensitive influx of the other two, using a double-label flux approach. This is illustrated in Fig. 15.6A, which shows the effects on ^{36}Cl (yellow dots) and ^{24}Na (green squares) influx when an axon was sequentially superfused with external solutions without K^+ (0 K^+), with K^+ (10 mM) and, finally, with K^+ (10 mM) plus bumetanide (10 μM). Clearly, the presence of extracellular K^+ increased the influx of both Cl^- (by $\approx 21\ pmol \cdot cm^{-2}\ s^{-1}$) and Na^+ (by $\approx 14\ pmol \cdot cm^{-2}\ s^{-1}$) and these increases were reversed by blocking the cotransporter with bumetanide. Figure 15.6 shows a similar protocol applied to examine the external Na^+ (Fig. 15.6B) and Cl^- (Fig. 15.6C) requirement. Note that in each case, the increase in the influx of the two co-ions caused by supplying the third one is reversed by bumetanide treatment.

The absolute requirement for the *cis*-side presence of Na^+, K^+ and Cl^- for the uphill accumulation of Cl^- mediated by NKCC was first demonstrated in vertebrate cells using different methodologies. Examples include Ehrlich ascites tumor cells (Geck et al., 1980), Madin-Darby canine kidney (MDCK) cell line (McRoberts et al., 1982), duck red cells (Haas et al., 1982), frog and rat dorsal root ganglion (DRG) neurons (Alvarez-Leefmans et al., 1988; Rocha-Gonzalez et al., 2008), immature rat neocortical neurons (Achilles et al., 2007) and other cell types (Russell, 2000). In frog sensory neurons, measurements were made using Cl^--selective intracellular microelectrodes. Measurements of changes in intracellular Cl^- activity (a^i_{Cl}) with intracellular microelectrodes reflect net Cl^- fluxes occurring through the plasma membrane. Figure 15.7 shows an example of one experiment in which the cell body of a single neuron was penetrated with a double-barreled microelectrode (inset), one barrel containing a liquid anion exchanger (the Cl^--sensitive barrel) and the other a reference electrolyte to measure E_m. The advantages of this method are obvious; it is possible to measure simultaneously intracellular a^i_{Cl} and E_m in single cells. Moreover, in contrast with methods that measure total $[Cl^-]_i$, which includes free-plus-bound or sequestered Cl^-, the microelectrodes give a measurement of free Cl^- in the cytosolic space (Alvarez-Leefmans et al., 1990). The dependence on extracellular Na^+ and K^+ of the bumetanide-sensitive active accumulation of Cl^- was explored in these cells. To this end, the effects of Na^+- or K^+-free isosmotic solutions on a^i_{Cl} were studied in the steady state and during the active Cl^- reaccumulation following exposure to Cl^--free solutions. A typical result showing the effects of external Na^+ removal on a^i_{Cl} is shown in Fig. 15.7. The basal a^i_{Cl} (upper trace) and E_m (lower trace) were recorded in the standard frog Ringer's

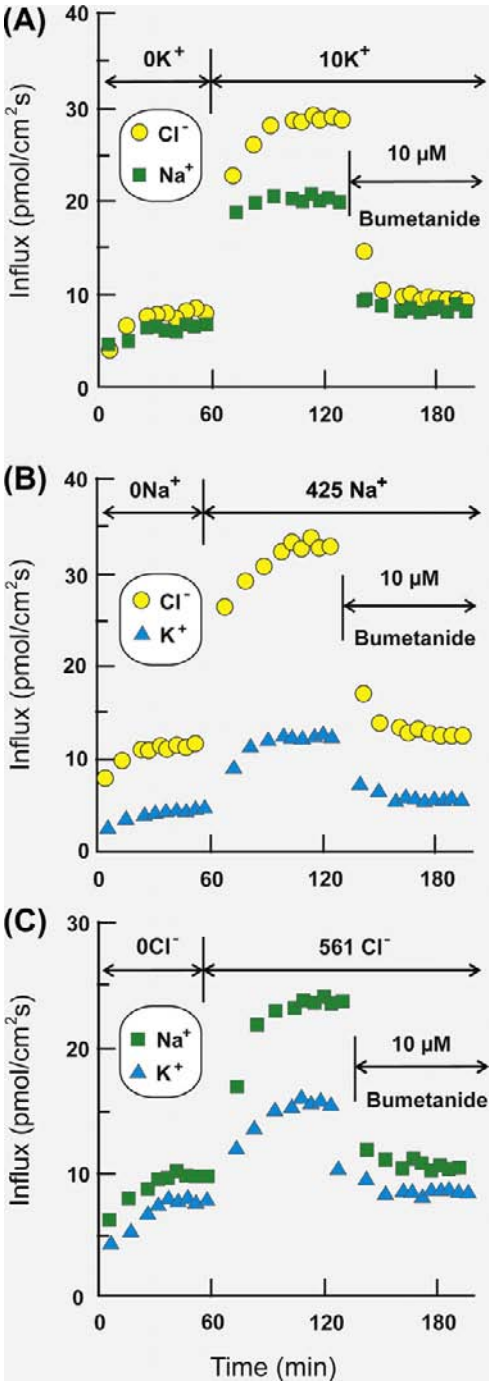

FIGURE 15.6 Dependence of cotransporter influxes of Na^+, K^+ and Cl^- on simultaneous presence of all three ions in external fluid. Experiments were carried out on internally dialyzed squid axons. Internal fluid in all cases contained the following (in mM): 400 K^+, 0 Na^+, 0 Cl^-, 8 Mg^{2+} and 4 ATP. Ouabain and tetrodotoxin were present to block the Na^+/K^+ pump and Na^+ channels, respectively. (A) Effect of external K^+ on $^{24}Na^+$ and $^{36}Cl^-$ influxes. After a control period (0 K^+) in which the external K^+ was replaced with N-methyl-D-glucammonium (NMDG), 10 mM K^+ was applied and influxes of both $^{24}Na^+$ (green squares) and $^{36}Cl^-$ (yellow circles) increased. Finally, bumetanide (10 µM) was added and both influxes decreased to levels similar to those seen in the absence of external K^+. (B) Effect of external Na^+ on $^{42}K^+$ (blue triangles) and $^{36}Cl^-$ (yellow circles) influxes. After a control period in which the external Na^+ was removed and replaced with NMDG (0 Na^+), 425 mM Na^+ was applied, leading to increases in both $^{42}K^+$ and $^{36}Cl^-$ influxes. Subsequent application of bumetanide caused influxes to decrease to values close to those observed in 0 Na^+. (C) Effect of external Cl^- on $^{42}K^+$ (blue triangles) and $^{24}Na^+$ (green squares) influxes. In the control condition (0 Cl^-), gluconate substituted for Cl^-. Note that upon admission of the external solution containing 561 mM Cl^-, both $^{42}K^+$ and $^{24}Na^+$ increased. Subsequent application of bumetanide caused influxes to decrease to levels near those observed in the absence of external Cl^-. *(Adapted from Russell, 2000.)*

solution (FR) for about 3 min after impalement. The initial E_m was ≈ -50 mV and a^i_{Cl} was 25 mM. The latter value was twice the a^i_{Cl} predicted for an equilibrium distribution according to Equation 15.3. It is important to mention that the measured a^i_{Cl} is equivalent to an intracellular [Cl^-] of $\approx$33 mM, considering 0.76 as the intracellular activity coefficient. Then, the cell was exposed for about 3.5 min to a solution in which Na^+ was eliminated (0 Na^+) and replaced mole by mole with the impermeant cation N-methyl-D-glucammonium, keeping a^o_{Cl} at the same level as in the FR solution. This resulted in an immediate decrease in a^i_{Cl} accompanied by a membrane hyperpolarization. The latter was due to suppression of a resting Na^+ conductance. Both E_m and a^i_{Cl} returned to control levels upon readmission of FR solution to the bath. Observations like these indicate that external Na^+ is required to maintain internal Cl^- above electrochemical equilibrium in the resting state.

To explore if external Na^+ is required for the active reaccumulation of Cl^- after intracellular Cl^- depletion, external Cl^- was removed (0 Cl^-) and replaced mole by mole with the impermeant anion gluconate, keeping the other ions as in control FR. This also resulted in a decrease in a^i_{Cl}. The reaccumulation of Cl^- was then observed in the Na^+-free solution containing normal Cl^- (0 Na^+) and, finally, in standard FR. It was found that the rate of Cl^- reaccumulation in the Na^+-free solution was slowed to about 15% of its value in standard FR solution.

These observations indicate that extracellular Na^+ is required for active reaccumulation of Cl^- following cell Cl^- depletion. The concurrent changes in E_m and calculated values for E_{Cl} in the same experiment are shown in Fig. 15.8A, which illustrates more clearly the effects of external Na^+ on the distribution of Cl^- across the cell membrane. External Na^+ removal reduced the basal intracellular accumulation of Cl^-, as reflected by the reduction in the difference between E_m (blue filled circles) and E_{Cl} (red filled circles). In addition, Na^+ removal after Cl^- depletion impeded the reaccumulation of Cl^- even though E_{Cl} was now more negative than E_m, a situation in which the direction of the Cl^- gradient was reversed, favoring Cl^- influx. Therefore, it can be concluded that external Na^+ is required to accumulate Cl^- above equilibrium and for keeping it out of equilibrium in basal conditions.

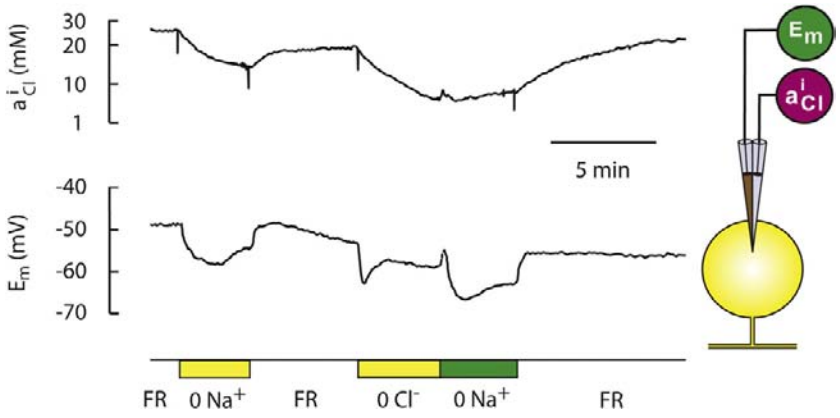

FIGURE 15.7 Effect of external Na^+ removal on intracellular Cl^- activity (a^i_{Cl}) and on membrane potential (E_m) in a frog dorsal root ganglion neuron. The recording was made with a double-barreled microelectrode, one barrel sensing E_m and the other a^i_{Cl}. Inset (right), diagram of a double-barreled electrode where a^i_{Cl} denotes the Cl^--selective barrel filled with a liquid anion exchanger which senses a^i_{Cl}. When the microelectrode is inside the cell, the a^i_{Cl} barrel records the sum of a potential proportional to a^i_{Cl} plus E_m. To obtain a^i_{Cl}, the potential on the E_m barrel is subtracted from that recorded by the Cl^--sensitive barrel giving a differential voltage signal that is proportional to a^i_{Cl} (top trace). During the times indicated by the bottom bars, the bathing solution was changed from frog Ringer (FR) to a Na^+-free solution (0 Na^+), in which external Na^+ was replaced with N-methyl-D-glucammonium, and back to FR. Note that removal of external Na^+ led to a decrease in a^i_{Cl}. The cell was then exposed to Cl^--free solution (0 Cl^-), which also produced a decrease in a^i_{Cl}. Then the reaccumulation of internal Cl^- was monitored in the absence of external Na^+ (0 Na^+) and in FR, i.e. in the presence of external Na^+. Note that in the absence of external Na^+, active Cl^- uptake was inhibited. *(Modified from Alvarez-Leefmans et al., 1988.)*

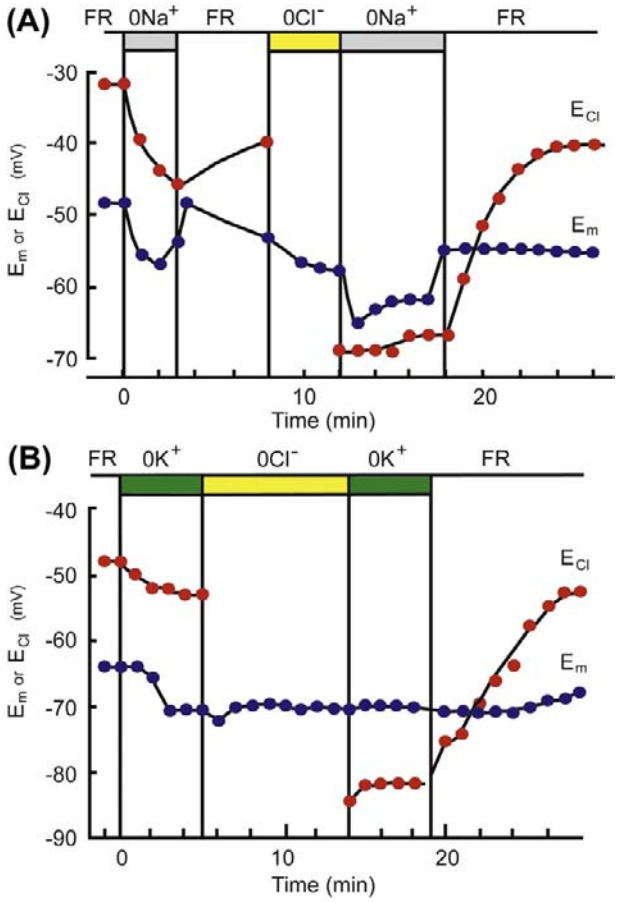

FIGURE 15.8 (A) Effects of external Na^+ on the intracellular accumulation of Cl^-. Membrane potential (E_m, blue dots) and the calculated Cl^- equilibrium potential (E_{Cl}, red dots) from measured a^i_{Cl} and a^o_{Cl} are plotted on the same time scale using data from the experiment illustrated in Fig. 15.7. (B) Effects of external K^+ on the intracellular accumulation of Cl^-. Symbols as in (A). Data were obtained from an experiment similar to that shown in Fig. 15.7 but in which external K^+ was removed instead of external Na^+. *(Modified from Alvarez-Leefmans et al., 1988.)*

The effects of extracellular K^+ on a^i_{Cl} were similar to those observed for Na^+. Figure 15.8B shows a plot of E_m and E_{Cl} from an experiment similar to that shown in Fig. 15.7 but in which external K^+, instead of external Na^+, was removed during the periods indicated. Removal of external K^+ was accompanied by an immediate reduction in a^i_{Cl} revealed in the graph by the changes in E_{Cl} toward more negative values. In the absence of extracellular K^+ the reaccumulation of Cl^- in standard FR solution was impeded. Summarizing, the steady-state a^i_{Cl} levels in DRG cells depend on the simultaneous presence of extracellular Na^+ and K^+. Similarly, the active reaccumulation of Cl^- after intracellular Cl^- depletion requires the simultaneous presence of Na^+ and K^+ in the extracellular medium.

Similar results to those described above for frog sensory neurons have been recently obtained in rat DRG neurons, which are also characteristically endowed with NKCC1. Mammalian neurons are too delicate to stand penetration with microelectrodes and thus a non-invasive procedure to measure changes in $[Cl^-]_i$ is needed. These non-invasive procedures to measure changes in $[Cl^-]_i$ use various types of fluorescent indicators, some of which are genetically engineered (Berglund et al., 2009; Verkman, 2009; Waseem et al., 2010). The strategy used in rat DRG neurons was to study the external ion requirements of native NKCC1 by measuring changes in $[Cl^-]_i$ using the fluorescent dye MQAE (Rocha-Gonzalez et al., 2008).

VB2. Electroneutral Cotransport Process: Stoichiometry of 1Na^+:1K^+:2Cl^-

Geck and coworkers (Geck et al., 1980; Geck and Heinz, 1986), working with Ehrlich ascites tumor cells, provided the first comprehensive evidence for the existence of the electrically neutral cotransport of Na^+, K^+ and Cl^- ions,

with a stoichiometry of $1Na^+:1K^+:2Cl^-$. A solidly documented exception is the squid axon cotransporter which has a stoichiometry of $2Na^+:1K^+:3Cl^-$ (Russell, 2000). This different stoichiometry probably reflects differences in molecular structure with respect to the vertebrate isoforms. Unfortunately, the squid isoform has not yet been cloned, so it is impossible to know what determines the difference. The $1Na^+:1K^+:2Cl^-$ stoichiometry has been found in many vertebrate cells (O'Grady et al., 1987a; Russell, 2000; Hoffmann, 2001; Lytle, 2003; Flatman, 2004; Gamba, 2005). However, some "atypical" stoichiometries have also been described in some vertebrate cells, as recently discussed (Delpire and Gagnon, 2011).

There is general agreement that the NKCC is electrically silent, which means that the overall transport process of Na^+, K^+ and Cl^- via the cotransporter is not driven by the transmembrane voltage, nor does the transport process directly generate a membrane current that may affect the transmembrane voltage. As pointed out by Russell (2000), the electrical silence of the NKCC is now well accepted by workers in the field, yet direct evidence for the assertion is surprisingly sparse. Electrical silence is often inferred from the apparent stoichiometry of the cotransport process, but arriving at this conclusion involves a somewhat circular argument.

Conclusive proof of electrical silence requires direct and simultaneous measurement of transmembrane potential and cotransporter mediated ion fluxes. There are only two reports in the literature fulfilling these requirements, one for the squid axon NKCC cotransporter (Russell, 1984) and one for amphibian dorsal root ganglion neurons (Alvarez-Leefmans et al., 1988). The latter is, so far, the only existing direct evidence for the electroneutrality of Cl^- transport through NKCC in a vertebrate cell. Figure 15.9 shows an example of one of these experiments in which a frog DRG cell was penetrated with a double-barreled microelectrode (inset). At the time indicated by the downward orange arrow, the cell was penetrated with the microelectrode and E_m stabilized at about −55 mV. The deflection in the differential signal (upper trace) at this time corresponded to an *apparent* intracellular Cl^- activity $(a^i_{Cl})_{app}$ of about 40 mM, which, after correction for background intracellular interference produced by other native intracellular anions on microelectrode response (Alvarez-Leefmans, 1990), gave an a^i_{Cl} of 30 mM. If Cl^- were passively distributed, a^i_{Cl} as predicted from Equation 15.3 should be only 10.2 mM. It is worth mentioning here that the ion-selective electrodes measure a^i_{Cl} and not $[Cl^-]_i$. Thus, for an activity coefficient of 0.76, the basal a^i_{Cl} of 30 mM is equivalent to a basal $[Cl^-]_i$ of ≈40 mM. Clearly, *intracellular Cl^- was almost three times the value expected for an equilibrium distribution*. E_{Cl} was −27 mV and the driving force for Cl^-, $(E_m - E_{Cl})$, was 28 mV. The red filled circles superimposed on the E_m trace (lower record in Fig. 15.9) correspond to the point by point values of E_{Cl} calculated using Equation 15.1. Removal of external Cl^- and its replacement with an impermeant anion (gluconate) led to a rapid decrease in $(a^i_{Cl})_{app}$, reaching a final steady-state level of ≈10 mM in about 10 min. The recovery of intracellular Cl^- started immediately after external Cl^- was restored. Note that the net Cl^- movements occurred without changes in E_m, i.e. they were electroneutral (Fig. 15.9 large gray arrow). The small rapid changes that can be observed in the E_m trace upon removal and readmission of external Cl^- were due to liquid junction potentials at the reference (bath) electrode. Subtraction of this liquid junction potential yielded the

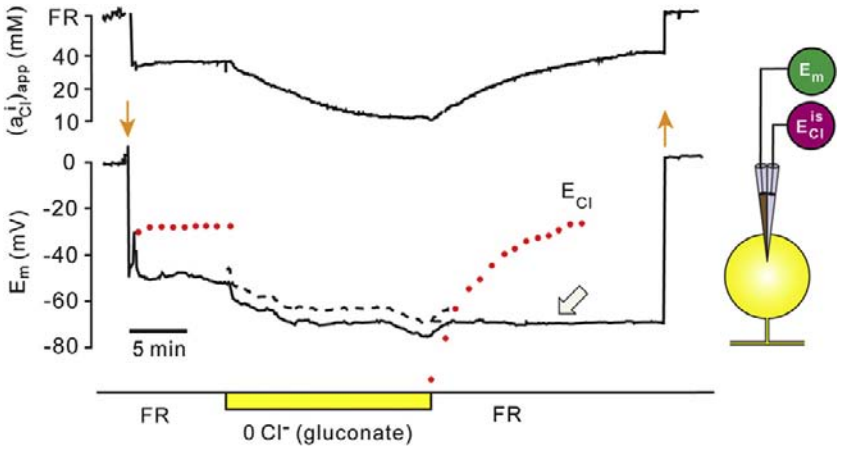

FIGURE 15.9 Electrically silent transmembrane movements of Cl^- mediated through Na^+,K^+,Cl^- cotransport in a frog dorsal root ganglion (DRG) neuron. The intracellular Cl^- activity, a^i_{Cl}, was measured with a double-barrel Cl^--selective microelectrode in the neuronal cell body (scheme on the right). After obtaining steady-state readings, the effects of removing and re-adding external Cl^- on a^i_{Cl} and E_m were recorded. The upper trace shows the differential signal $(E_m - E^{is}_{Cl})$, where E^{is}_{Cl} is the potential recorded through the ion-sensitive barrel. The differential signal indicates $(a^i_{Cl})_{app}$, the apparent intracellular Cl^- activity. The lower trace is the membrane potential (E_m). The dashed trace above a segment of the recorded E_m trace is the E_m value after subtraction of liquid junction potentials. At the periods indicated by the yellow bar at the bottom, the bathing solution was changed from standard frog Ringer (FR) to a Cl^--free solution in which Cl^- was replaced with gluconate. The red filled circles superimposed on the E_m trace are the estimated E_{Cl} calculated from measured a^o_{Cl} and a^i_{Cl}. Large gray arrow indicates that the "uphill" accumulation of Cl^- following Cl^- depletion occurred without changes in E_m. Small orange arrows indicate electrode penetration and withdrawal from the cell. *(Modified from Alvarez-Leefmans et al., 1988 and reproduced from Alvarez-Leefmans and Delpire, 2009b.)*

dashed trace superimposed on the recorded E_m trace. If Cl^- movements had occurred through an electrodiffusional pathway (i.e. channel-mediated) or through an electrogenic "carrier," E_m should have changed both upon Cl^- efflux and upon Cl^- influx. Clearly, that was not the case. Since the cell membrane of DRG neurons has a relatively low resting Cl^- permeability, the movements of Cl^- should have occurred through a non-electrodiffusional pathway, i.e. an electroneutral carrier mechanism. As already mentioned, the red circles superimposed on the E_m trace in Fig. 15.9 correspond to the calculated values of E_{Cl}. Note that on exposure to the Cl^--free Ringer's solution, the cell was depleted of Cl^- and, immediately after restoring the external Cl^-, E_{Cl} was transiently below E_m. However, during the recovery period in Ringer's solution, the movement of Cl^- occurred against its electrochemical potential difference across the cell membrane, i.e. uphill, without changes in E_m. Since the Cl^- fluxes were bumetanide-sensitive and required the simultaneous presence of external Na^+ and K^+, this was direct functional evidence for the presence of an active process for accumulation of Cl^- in DRG cells through an electroneutral membrane transport mechanism, i.e. an Na^+-$1K^+$-$2Cl^-$ cotransporter. The presence of NKCC protein in frog DRG cells was corroborated later on using immunolabeling and Western blot analyses (Alvarez-Leefmans et al., 2001). NKCC was also found in DRG cells of cat, rat and mouse (Plotkin et al., 1997; Sung et al., 2000; Alvarez-Leefmans et al., 2001).

VB3. The Magnitude and Direction of the Cotransport Process are Determined by the Sum of the Chemical Potential Gradients of the Transported Ions

We have seen that the transport process carried out by NKCC is electrically neutral and thus net cotransport neither affects nor is affected by the membrane potential. Consequently, the magnitude and direction of the driving force for net ion movement must be calculated from the *chemical*, rather than the *electrochemical* potential gradients of all the transported ions.

The NKCC is a secondary active transport mechanism and hence it is reversible, i.e. it mediates ion fluxes into or out of the cell, the net direction of cotransport depending on the overall net free energy (ΔG) of the system. If ΔG is negative, it means that the direction of the cotransport will be inward, i.e. favoring uptake. If ΔG is zero, the system is at equilibrium. Since NKCC is electroneutral and has a $1Na^+$:$1K^+$:$2Cl^-$ stoichiometry, ΔG is given by the following equation:

$$\Delta G = \Delta\mu_{Na,K,Cl} = \Delta\mu_{Na} + \Delta\mu_K + 2\Delta\mu_{Cl} \qquad (15.11)$$

In other words, the driving force for the electroneutral $1Na^+$,$1K^+$,$2Cl^-$ cotransport ($\Delta\mu_{Na,K,Cl}$) is the sum of the chemical potential differences of Na^+ ($\Delta\mu_{Na}$) and K^+ ($\Delta\mu_K$) plus twice the Cl^- potential difference ($\Delta\mu_{Cl}$), since two Cl^- ions are translocated per cycle. From the definition of chemical potential for each of the ions involved, it follows:

$$\begin{aligned}\Delta G &= \Delta\mu_{Na,K,Cl} \\ &= RT\ln\frac{[Na^+]_i}{[Na^+]_o} + RT\ln\frac{[K^+]_i}{[K^+]_o} + 2RT\ln\frac{[Cl^-]_i}{[Cl^-]_o}\end{aligned} \qquad (15.12)$$

Hence,

$$\Delta G = \Delta\mu_{Na,K,Cl} = RT\ln\frac{[Na^+]_i\,[K^+]_i\,[Cl^-]_i^2}{[Na^+]_o[K^+]_o[Cl^-]_o^2} \qquad (15.13)$$

In most vertebrate cells, under physiological conditions and for a stoichiometry $1Na^+$:$1K^+$:$2Cl^-$, ΔG is always negative, therefore favoring net ion uptake. Russell has computed ΔG for a variety of vertebrate cells; it ranges from -0.71 KJ/mol in bovine aortic endothelial cells up to -8.86 KJ/mol in rabbit ventricular myocytes (Russell, 2000). ΔG has been estimated to be -1.29 KJ/mol and -2.8 KJ/mol in rat and frog DRG neurons, respectively (Russell, 2000; Rocha-Gonzalez et al., 2008). As pointed out by Lytle (2003), the rare exception may be red blood cells which, as discussed above, have an usually high $[Cl^-]_i$ (75−100 mM) reflecting their high anion permeability mediated by the anion exchanger protein AE1, which has translocation rates and characteristics similar to channels (Alper et al., 2008). The consequence of this high $[Cl^-]_i$ is that $\Delta\mu_{Na,K,Cl}$ is nearly 0. Indeed, in human, duck and ferret red blood cells under physiological conditions, $\Delta\mu_{Na,K,Cl}$ is nearly 0, leaving little if any driving force to run the cotransporter under basal conditions (Lytle, 2003). This means that relatively small variations in the chemical gradients of any of the transported ions can alter the direction of transport in these red blood cells.

The NKCC cotransport mechanism reaches thermodynamic equilibrium when $\Delta G = \Delta\mu_{Na,K,Cl} = 0$, i.e. when the product of the concentrations of Na^+ and K^+ times the square of the Cl^- concentration on one side of the membrane is matched by the product of these ions in the *trans* side:

$$[Na^+]_i\,[K^+]_i\,[Cl^-]_i^2 = [Na^+]_o\,[K^+]_o\,[Cl^-]_o^2 \qquad (15.14)$$

Since the cotransporter is electroneutral, thermodynamic equilibrium will not be affected by E_m. Assuming for the sake of argument that Na^+,K^+,Cl^- cotransport is the only Cl^- transport system operating at steady state in a cell, that it has a $1Na^+$:$1K^+$:$2Cl^-$ stoichiometry and that there are no kinetic constraints, the predicted $[Cl^-]_i$ when the

cotransport reaches thermodynamic equilibrium is given by the following equation derived from Equation 15.14:

$$[Cl^-]_i = \sqrt{\frac{[Na^+]_o\,[K^+]_o\,[Cl^-]_o^2}{[Na^+]_i[K^+]_i}} \qquad (15.15)$$

For example, consider the model cell shown in Fig. 15.10, an idealized neuron in which NKCC is the sole mechanism for active Cl^- transport. The $[Na^+]_i$ and $[K^+]_i$ are maintained at constant levels by the operation of the Na^+/K^+ pump. The cell has a resting E_m of −60 mV and relevant physiological ion concentrations (in mM) are: $[Na^+]_o = 132$; $[K^+]_o = 3$; $[Cl^-]_o = 113$; $[Na^+]_i = 10$ and $[K^+]_i = 120$. Under these conditions, when the cotransporter reaches thermodynamic equilibrium, *without any kinetic constraints* (e.g. phosphorylation or dephosphorylation of the cotransporter), the $[Cl^-]_i$ will be ≈65 mM and this would be the *maximal possible* $[Cl^-]_i$ under these conditions. Thus, we can conclude from the examples considered in Figs. 15.1 and 15.10 that if Cl^- were in electrochemical equilibrium, $[Cl^-]_i$ calculated from Equation 15.3 would be 12 mM, but if we add NKCC to the same cell (Fig. 15.10), assuming that the resting channel-mediated permeability to Cl^- is negligible, the $[Cl^-]_i$ can increase up to about five times above its equilibrium level, and E_{Cl} would now be ≈ −12 mV. Since E_m is kept constant, at −60 mV, opening of Cl^- channels, for example $GABA_A$-receptor-channels in the example considered, will produce an efflux of Cl^-. Since Cl^- is negatively charged, its electrodiffusional efflux produces an inward (depolarizing) current. However, most vertebrate cells endowed with NKCC do not have the high intracellular Cl^- level of the cell considered in this example (i.e. ≈65 mM). Why is that? Are there parallel mechanisms that prevent the NKCC from achieving thermodynamic equilibrium? The answer is yes. The first point to be considered is that, besides NKCC, other Cl^- transport systems, such as Cl^- channels, anion exchangers (Cl^-/HCO_3^-) and KCl cotransporters (KCCs) could and in fact do coexist in the same cell with NKCC. The final $[Cl^-]_i$ will be determined by the coordinated functional interaction between the various transporter systems present in the cell. For instance, in skeletal muscle, active Cl^- uptake via NKCC is "shunted" by a large Cl^- conductance, as shown in Fig. 15.2. In this case, the $[Cl^-]_i$ will be determined by a balance between the net Cl^- influx mediated by NKCC and the net Cl^- efflux occurring through Cl^- channels. Since the Cl^- leak through channels is larger than the net Cl^- influx brought up by NKCC, $[Cl^-]_i$ in skeletal muscle is very low, so low that E_{Cl} is close to E_m as discussed above in Section II. In addition to Cl^- channels, in most cells, NKCC coexists with KCC. Under physiological conditions, KCCs mediate net efflux of K^+ and Cl^- from cells, thus functioning as active Cl^- extruders (see Fig. 15.3). Hence NKCCs and KCCs have opposing roles; the former are Cl^- loaders and the latter are Cl^- extruders. Thus, KCCs may influence the levels of intracellular Cl^- just by counteracting Cl^--uptake mechanisms and vice versa. This interaction between two cotransporters working in opposite directions is ideally suited for achieving tight regulation of an intracellular ion, in this case Cl^- (and K^+). However, the result of these interactions is not just the simple algebraic sum of two fluxes having opposite direction; cotransporters are *kinetically* regulated by several mechanisms, notably by phosphorylation/dephosphorylation via a complex system of kinases, some of which are sensitive to $[Cl^-]$ (Flatman, 2004; Delpire and Gagnon, 2008; Gamba et al., 2009; Kahle et al., 2010).

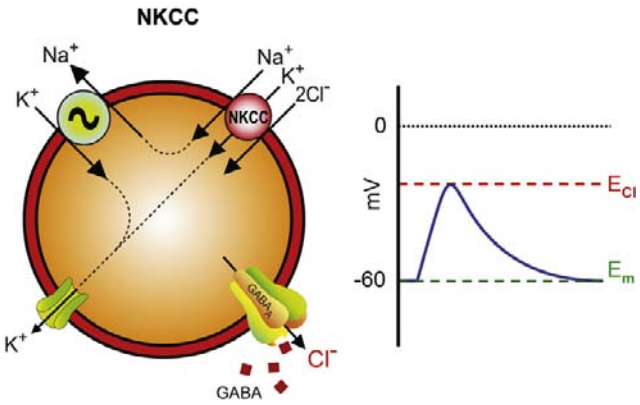

FIGURE 15.10 Model of a cell expressing Na^+,K^+,$2Cl^-$cotransport (NKCC) and a $GABA_A$-gated anion channel. The energy stored mainly in the inward Na^+ chemical gradient maintained by the Na^+/K^+ ATPase is used by NKCC for the active Cl^- uptake process. The Na^+/K^+ ATPase expels the Na^+ entering through NKCC. The K^+ entering through NKCC diffuses out of the cell via K^+ channels. Cl^- is accumulated above electrochemical equilibrium, shifting E_{Cl} to values more positive than E_m. Opening of GABA-gated anion channels produces a membrane depolarization (blue trace) due to Cl^- efflux.

The consequences of functional interactions between KCCs and NKCCs have been experimentally addressed using human embryonic kidney cells (HEK-293), an epithelial cell line in which the ubiquitous isoform of the KCCs, KCC1, was overexpressed by transfection (Gillen and Forbush, 1999). Overexpression of KCC1 not only led to a decrease in $[Cl^-]_i$ but also to a significant increase in endogenous NKCC activity. Indeed, the reduction of $[Cl^-]_i$ produced by KCC1 was responsible for NKCC activation. A steep relationship between cell Cl^- and NKCC activity was found over the physiological ranges supporting a primary role for $[Cl^-]_i$ in activation of NKCC. This means that *NKCC activity is determined not only by the thermodynamic driving force but also by kinetic constraints.* In this case, internal Cl^- acts as a "kinetic brake" on the ion translocating capacity of NKCC. Thus, kinetic constraints can inactivate the cotransporter, even in the presence of a substantial thermodynamic driving force. The experimental results of Gillen and Forbush in transfected HEK-293 cells, are in agreement with previous observations showing that lowering $[Cl^-]_i$ activates NKCC, and increasing $[Cl^-]_i$ inhibits its activity. In other words, intracellular Cl^- acts as

a negative feedback signal controlling the transport activity of NKCC. It was the Danish physiologist Hans Ussing (1911−2000) who first proposed that NKCC might be activated by a fall in $[Cl^-]_i$. Working with frog skin epithelium, Ussing realized that when the cells lose Cl^- NKCC restores it back to its initial higher than equilibrium level, but that the cotransporter "…seems to be virtually dormant unless the cells have lost chloride" (Ussing, 1982). The definitive proof came from studies in the internally dialyzed squid axon preparation, in which it was shown that elevation of $[Cl^-]_i$ inhibits bumetanide-sensitive unidirectional fluxes of all three cotransported ions in both the influx and efflux direction (Russell, 2000, 2009). The negative-feedback system in which intracellular Cl^- regulates its own influx via NKCC has been recently demonstrated for the endogenous NKCC1 protein of a mammalian cell, namely rat DRG neurons (Rocha-Gonzalez et al., 2008). As mentioned above, the mechanisms by which intracellular Cl^- regulate NKCCs involve a complex system of kinases (see below). Regulation of NKCCs and other members of the SLC12A family is an extensive topic that is beyond the scope of the present chapter.

VB4. Loop Diuretics Derived From 5-sulfamoylbenzoic Acid Inhibit NKCCs

Diuretics derived from 5-sulfamoylbenzoic acid are organic anions that reversibly inhibit NKCCs in a variety of preparations by a concentration-dependent mechanism, with a half inhibitory constant (IC_{50}) ranging from ≈0.1 μM to 8.7 μM in mammalian cells (Russell, 2000). These compounds are members of the so-called *loop diuretics* because they inhibit Na^+ and Cl^- reabsorption by the thick ascending limb of the loop of Henle (TALH) by blocking the NKCC isoform located in the apical membrane of these epithelial cells, i.e. NKCC2, thereby promoting diuresis (increased formation and excretion of urine). However, 5-sulfamoylbenzoic acid derivatives also block NKCC1. Native NKCC2 is a very active transport mechanism under basal conditions, permanently reabsorbing Na^+ and Cl^-. In contrast, basal activity of native NKCC1 of extra-renal non-epithelial cells is relatively small; the cotransporter is "dormant" which means that *net* ion fluxes in basal conditions are negligible. NKCC1 can be activated by either cell shrinkage produced by exposure to hypertonic solutions ("anisosmotic shrinkage") and or by decreases in $[Cl^-]_i$. For instance, decreases in $[Cl^-]_i$ leading to activation of NKCC1 can be accompanied by "isosmotic shrinkage," like that produced by removal of external Cl^- in isosmotic media. Intracellular $[Cl^-]$ can also decrease by activation of Cl^- conductances, producing relatively small changes in cell volume, e.g. the decrease in $[Cl^-]_i$ produced by secretagogues in several epithelia. When measuring the inhibitory effect of 5-sulfamoylbenzoic acid derivatives like bumetanide, piretanide and furosemide on the native NKCC proteins, *activated* NKCC1 has the same sensitivity to these compounds as *basal* NKCC2 (Hannaert et al., 2002).

The relative efficacy (IC_{50} values) and order of potency for blocking NKCC1 was systematically investigated in the intestinal epithelium of winter flounder (O'Grady et al., 1987b). As shown in Fig. 15.11B, the order of potency of 5-sulfamoylbenzoic acid derivatives to block NKCC1 was: benzmetanide > bumetanide > piretanide >furosemide > amino-piretanide. This order of potency is similar to that determined for NKCC2 in TALH from rabbit kidney (Schlatter et al., 1983) and in other mammalian cells like human fibroblasts and dog trachea that express NKCC1 (O'Grady et al., 1987b).

Bumetanide and furosemide are among the most commonly prescribed drugs worldwide. They are clinically used to treat moderate hypertension and edema associated with congestive heart failure, hepatic and renal disease, including nephrotic syndrome (Shankar and Brater, 2003). Research during the last decade shows that NKCC1 is involved in many more functions and pathologies than previously thought, depending on the tissues in which it is expressed. Thus it is not surprising that NKCC1 has emerged as a potential therapeutic drug target for bumetanide and other loop diuretics in conditions as diverse as inflammatory pain given its analgesic effects (Granados-Soto et al., 2005), neonatal seizures given that it blocks this abnormal brain electrical activity (Kahle and Staley, 2008; Dzhala et al., 2010), idiopathic intracranial hypertension (Dzhala et al., 2010), ischemic brain edema (Kahle et al., 2009) and glioma cell invasion (Haas and Sontheimer, 2010), to mention the most salient.

Besides their clinical importance, loop diuretics, particularly bumetanide, have played a crucial role in the identification of the NKCC proteins and in their subsequent cloning and functional characterization. Bumetanide is by far the most commonly used loop diuretic for research on NKCCs. As mentioned above, bumetanide is not a specific blocker of NKCC1; it also blocks NKCC2 at similar concentrations under physiological conditions in endogenous/native cotransporters. Bumetanide inhibits *basal* NKCC2 activity in medullary TALH tubules isolated from rat kidney with a half inhibitory constant (IC_{50}) of 0.33 μM and, with the same IC_{50}, it inhibits *activated* NKCC1 from either rat erythrocytes or rat thymocytes (Hannaert et al., 2002). In these experiments, NKCC1 was activated by exposing the cells to hypertonic solutions. An increase in NKCC2/NKCC1 selectivity was found when comparing diuretic sensitivity of *basal* NKCC2 versus *basal* NKCC1. For the specific case of bumetanide, the IC_{50} for *basal* NKCC1 goes up from 0.33 μM (activated state) to 2.5 μM in rat erythrocytes and 2.2 μM in rat thymocytes. In other mammalian cells expressing native/endogenous NKCC1, bumetanide inhibits the cotransporter with an IC_{50} ranging from 0.1 μM in human fibroblasts (HSWP) to

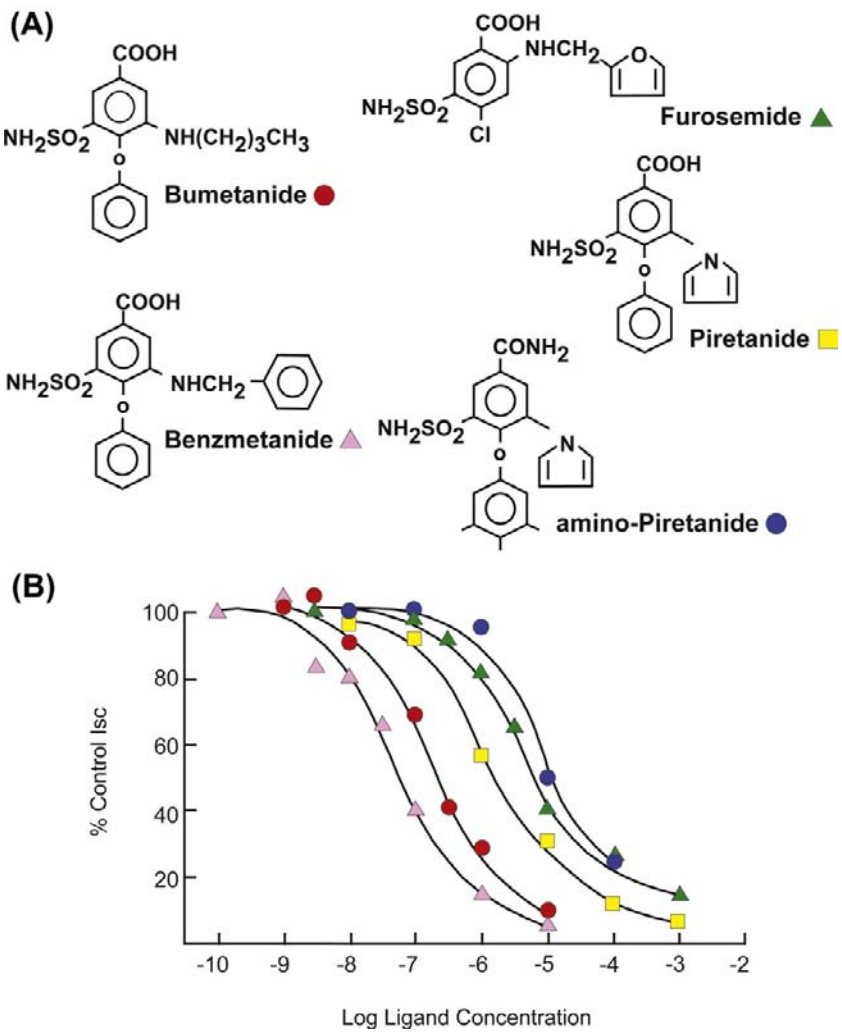

FIGURE 15.11 (A) Structures of several 5-sulfamoyl benzoic acid derivatives that affect NKCC in flounder intestine. (B) Dose–response curves for these derivatives on epithelial short-circuit current (Isc) measured in flounder intestine. Order of potency is benzmetanide (5×10^{-8} M; $n = 4$), bumetanide (3×10^{-7} M; $n = 7$), piretanide (3×10^{-6} M; $n = 4$), furosemide (7×10^{-6} M; $n = 4$), amino-piretanide (1×10^{-5} M; $n = 4$). *(Modified from O'Grady et al., 1987b.)*

8.7 μM in Ehrlich ascites tumor cells, the cells in which NKCC was first discovered (Hoffmann et al., 1986). The bumetanide IC_{50} of *activated* NKCC1 in rat DRG neurons is 5.7 μM, slightly lower than that reported for Ehrlich ascites tumor cells (Rocha-Gonzalez et al., 2008). In DRG neurons, NKCC1 was activated by cell Cl^- depletion, which also led to isosmotic cell shrinkage, and the effect of bumetanide was tested on the Na^+ dependent re-accumulation of Cl^-. Bumetanide sensitivity has also been measured in NKCC1 expressed in HEK-293 cells. Bumetanide inhibits human NKCC1 expressed in HEK-293 cells with an IC_{50} of 0.16 ± 0.03 μM (Payne et al., 1995), whereas it inhibits rat NKCC1 expressed in HEK-293 cells with an IC_{50} of 2.4 ± 0.7 μM. Interestingly, mutating alanine 483 with cysteine (A483C) of rat NKCC1 shifts the bumetanide dose-response curve to the left, i.e. this point mutation renders NKCC1 more sensitive to bumetanide, shifting the IC_{50} from 2.4 ± 0.7 μM (wild-type) to 0.37 ± 0.02 μM for the A483C mutant (Dehaye et al., 2003). Clearly, at least for mammalian NKCC1, bumetanide sensitivity (IC_{50}) varies almost two orders of magnitude; it appears to be dependent on animal species, cell type, activation state of NKCC1 and whether measurements are done in native/endogenous NKCC1 or in heterologous expression systems. *Based on bumetanide sensitivity, it is impossible to discriminate between NKCC1 and NKCC2.* However, in many recent publications, it is often mistakenly stated that bumetanide is a "specific NKCC1 blocker".

The sensitivity to bumetanide of the three full-length spliced variants of NKCC2 has been studied in the *Xenopus* oocyte heterologous expression system. When mouse NKCC2s are expressed in *Xenopus* oocytes, the IC_{50} values for bumetanide are 3.4 μM for NKCC2F, 2.0 μM for NKCC2A, and 0.6 μM for NKCC2B (Plata et al., 2002). The IC_{50} values for bumetanide inhibition of the human NKCC2 full-length splice variants expressed in *Xenopus* oocytes are 0.16 μM for NKCC2F, 0.54 μM for NKCC2A and 0.22 μM for NKCC2B (Carota et al., 2010). Thus,

the human NKCC2A variant is the least sensitive to bumetanide, whereas in mouse, the least sensitive variant is NKCC2F. The reasons for these discrepancies between mouse and human NKCC2 variants remain to be elucidated. However, we can conclude that *it is impossible to discriminate between NKCC2 splice variants based on bumetanide sensitivity.*

The overall conclusion is that sensitivity of NKCCs to bumetanide varies over two orders of magnitude; it depends on whether it is assessed under basal conditions or upon activation of the cotransporters (Hannaert et al., 2002), on degree of glycosylation (Paredes et al., 2006), on animal species, on cell type and on whether these proteins are in their native cell (endogenous) or expressed in heterologous systems like *Xenopus* oocytes or HEK-293 cells. Moreover, used alone and/or in relatively high concentrations (e.g. >50 μM), not even bumetanide can provide positive proof that a given function is mediated by the NKCCs. This is because bumetanide also blocks KCCs, although at significantly higher concentrations than those needed to block NKCCs. As discussed below, bumetanide blocks KCCs with IC_{50} values of ≈60−180 μM for KCC1 (Gillen et al., 1996; Mercado et al., 2000); 55−80 μM for KCC2 (Payne, 1997; Song et al., 2002), although values as high as 655 μM have been reported for KCC2 measuring net fluxes with a new fluorescence-based assay (Delpire et al., 2009); 100 μM for KCC3 (Mount et al., 1999; Race et al., 1999) and 900 μM for KCC4 (Mercado et al., 2000). Clearly, bumetanide is a less effective inhibitor of the KCCs than of the NKCCs. Thus, *bumetanide sensitivity can be used to differentiate between NKCCs and KCCs activity in functional assays.*

Finally, it is necessary to keep in mind that 5-sulfamoylbenzoic acid derivatives can inhibit channels or other carriers, although at considerably higher concentrations than those with which they inhibit NKCCs or KCCs. For instance, bumetanide blocks native CFTR Cl^- channels in sweat ducts with an IC_{50} of 300 μM (Reddy and Quinton, 1999). Furosemide blocks NMDA-induced currents in cultured spinal neurons but with an IC_{50} of 1.2 mM. Likewise, piretanide (5 mM) and bumetanide (2 mM) partially block NMDA-induced currents at millimolar concentrations (Lerma and Martin del Rio, 1992). Bumetanide and furosemide, also at very high concentrations (400 μM and 1 mM, respectively), partially block Ca^{2+}-activated Cl^- channels in rat lacrimal glands (Evans et al., 1986). Bumetanide and furosemide block vesicular glutamate uptake with an IC_{50} of 230 and 250 μM, respectively (Roseth et al., 1995). More recently, it has been suggested that bumetanide reduces aquaporin 4 osmotic water flow at concentrations well above 100 μM (Migliati et al., 2009). However, a possible direct effect of bumetanide on NKCC1 could not be ruled out. This is important because there is strong evidence supporting the notion that NKCC1 cotransports water and ions (Hamann et al., 2005, 2010). These observations are also significant from a "translational research" perspective local (Yan et al., 2003) as well as intravenous administration of bumetanide (O'Donnell et al., 2004) attenuate brain edema associated with transient as well as permanent experimental focal cerebral ischemia. The overall conclusion based on the data discussed above is that bumetanide at or below 20 μM concentrations can be used as a "selective" inhibitor of NKCCs.

Loop diuretics are anionic at physiological pH range, with very high lipid solubility, and hence can cross cell membranes (Alvarez-Leefmans et al., 1990). This raises the question of their site of action. It has long been suggested that bumetanide binds exclusively to the external face of NKCCs (Haas, 1994). Work from Forbush, Isenring and colleagues suggests that the central hydrophobic domain of NKCC1 determines its apparent affinities for Na^+, K^+ and Cl^- as well as for bumetanide, and that the cytosolic N- and C-termini have little effect on these properties and are mainly involved in the regulation of transport activity (Isenring and Forbush, 2001).

VC. Molecular Structure and Distribution of Na^+-K^+-Cl^- Cotransport Proteins

VC1. The Na^+-K^+-$2Cl^-$ Cotransporter 1 (NKCC1)

As already mentioned, two distinct Na^+-K^+-Cl^- cotransporter isoforms encoded by the SLC12A2 and the SLC12A1 genes have been identified by cDNA cloning and expression, NKCC1 and NKCC2 respectively. NKCC1 is still often referred to as BSC2 (bumetanide-sensitive cotransporter 2) or as "the basolateral bumetanide-sensitive Na-K-2Cl cotransporter" or as "the secretory isoform". Fortunately, these confusing and inappropriate nomenclatures are being superseded; NKCC1 is not sensitive to bumetanide only, neither is it exclusively located in the basolateral membrane of epithelial cells, nor is it expressed exclusively in epithelial cells, nor is it always "secretory." Thus, the nomenclature used by the GenBank (National Center for Biotechnology Information) is recommended.

A cDNA encoding NKCC1 was first cloned from the shark rectal gland (Xu et al., 1994), a well-characterized secretory epithelium that has been used as a model to study Cl^- secretion in epithelial cells. More important, shark rectal gland has a high density of Na^+-K^+-Cl^- cotransporters located in the basolateral membrane of the epithelial cells (Silva et al., 1996). Subsequently, cDNAs encoding NKCC1 were cloned from other secretory epithelia, including T84 cells, a human colonic epithelial cell line (Payne et al., 1995) and cultured inner medullary collecting duct cells (mIMCD-3) from mouse kidney (Delpire et al., 1994). Both of these mammalian NKCC1 proteins share a high degree of homology with the shark NKCC1 (71−74%) and even

higher identity with each other (91%). Later on, a cDNA encoding for the bovine aortic endothelial cell NKCC1 was also cloned and it was found that the predicted protein exhibits ≈95% amino acid identity with the T84 cell cotransporter amino acid sequence (Yerby et al., 1997).

There is evidence for the existence in rodents of an NKCC1 splice variant lacking exon 21. This shorter NKCC1 was first detected by partial cloning in mouse brain tissue (Randall et al., 1997). Exon 21 encodes 16 amino acid residues from the carboxyl terminus of the NKCC1 protein (Fig. 15.12). The function of this shorter NKCC1 splice variant is unknown. The absence of exon 21 predicts the loss of a protein kinase A (PKA) consensus site of the cotransporter protein. This suggests that the short NKCC1 could be subjected to different regulation than the full-length NKCC1. The absence of exon 21 does not appear to affect NKCC1 transport function, as suggested from experiments in MDCK (Madin Darby Canine Kidney) epithelial cells transfected with constructs of this short NKCC1 (Carmosino et al., 2008). Further, NKCC1 phosphorylation related to cotransport activation is carried out by the kinases SPAK (STE20/SPS1-related proline/alanine-rich kinase) and OSR1 (oxidative stress-responsive kinase 1) at specific threonine residues located in the N-terminus of the cotransporter (Delpire and Gagnon, 2008; Gamba et al., 2009; Kahle et al., 2010), as discussed below. Little is known about whether PKA phosphorylation plays a direct role in NKCC1 activation. Interestingly, the sequence encoded by exon 21 contains a conserve dileucine motif that appears to be involved in sorting of NKCC1 in polarized epithelial cells (Carmosino et al., 2008).

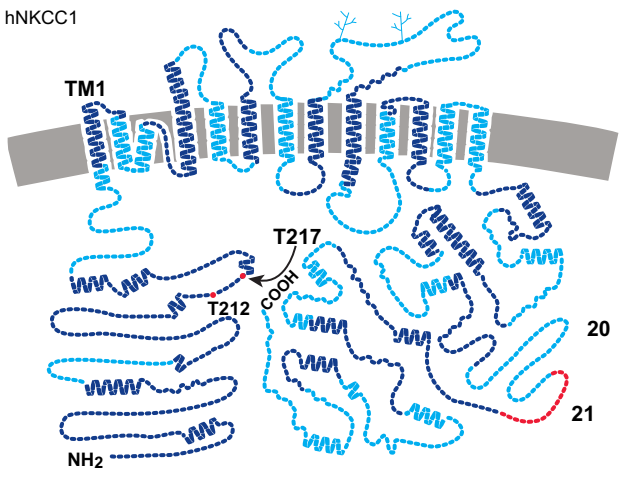

FIGURE 15.12 Hypothetical structural model of the human Na^+-K^+-$2Cl^-$ cotransporter protein NKCC1 (hNKCC1) showing the boundaries betwen amino acid sequences encoded by each exon (highlighted in light and dark blue, except for exon 21 highlighted in red). Each link symbolizes a single amino acid residue. "NH_2" and "COOH" indicate amino- and carboxy-termini, respectively. The branched lines in the long extracellular loop formed between putative transmembrane (TM) segments 7 and 8 indicate potential N-linked glycosylation sites. Biochemically identified phosphorylated threonine (T) residues (positions T212 and T217) are indicated by red dots. The proposed secondary structure of this protein with 12 TM helices and large intracellular amino- and carboxy-terminal domains is shared by other members of the cation-chloride cotransporter family. TM1 indicates the position of transmembrane segment 1. The residues encoded by exons 20 and 21 in the carboxyl terminus are indicated. *(Adapted from Carmosino et al., 2008.)*

Full-length NKCC1 comprises ≈1200 amino acids and has a molecular weight of 130−132 kDa. The predicted two-dimensional topology of NKCC1 from shark rectal gland shows 12 α-helical transmembrane (TM) domains and hydrophilic amino- and carboxyl-terminal regions (NH_2 and COOH) flanking a central hydrophobic domain. Whereas the amino (N) terminus displays considerable variability, the large carboxyl (C) terminus is well conserved among the different NKCC proteins. This predicted two-dimensional topology appears to be preserved in mammals and is similar to that predicted for NKCC2 and NCC (Gamba, 2009a) and the KCCs (see below). So far, NKCC1 is the only member of the SLC12A family for which the proposed topology is supported by experimental data (Gerelsaikhan and Turner, 2000a,b; Gerelsaikhan et al., 2006). Fig. 15.12 shows the predicted two-dimensional topology of human NKCC1.

NKCCs are glycoproteins and therefore possess consensus sites for N-linked glycosylation (*sequons*) within the large hydrophilic (extracellular) loop between TM segments 7 and 8, as shown in Fig. 15.12 (Haas and Forbush, 1998). A *sequon* is a sequence of three consecutive amino acids in a protein that can serve as the attachment site to a polysaccharide (sugar) called an N-linked-glycan. N-linked protein glycosylation occurs at asparagines (N) of the NXS/T *sequon*, where X is any amino acid except proline, S is serine and T threonine (Ben-Dor et al., 2004). There are two conserved extracellular N-glycosylation *sequons* which correspond to asparagines 547 and 556 (N^{547} and N^{556}) in mouse NKCC1 and N^{544} and N^{553} in rat NKCC1 (Gerelsaikhan et al., 2006). Evidence that NKCC1s are N-glycosylated in vivo comes from Western blot analyses of various tissues from animals of various species including shark, frog, duck, rat, cat, rabbit and human. These analyses show proteins with molecular weight higher than predicted for the core protein (≈160 KDa). Upon enzymatic deglycosylation, the molecular weight decreases to ≈130 kDa, the core molecular weight (reviewed in Di Fulvio and Alvarez-Leefmans, 2009). The impact of N-glycosylation on NKCC1 function has not been studied. The protein in its physiological plasma membrane environment is glycosylated. It is believed that glycosylation enhances cell-surface expression of these proteins.

NKCC1 has several potential phosphorylation sites within the predicted amino- and carboxy-terminal domains. As already mentioned, phosphorylation of NKCC1 plays a critical role in regulating its transport activity. Activation of NKCC1 by intracellular Cl^- depletion is associated with

increased phosphorylation of the cotransporter at conserved threonine (T) residues located within the N-terminal domain. The pioneering studies of Lytle and Forbush in the shark rectal gland epithelium yielded the first evidence suggesting that activation of NKCC1 was associated with phosphorylation of a threonine (T) residue (Lytle and Forbush, 1992). Later studies demonstrated that the phosphoacceptor amino acid sites within the cotransporter N-terminal domain corresponded to the threonines located at positions 184, 189 and 202 of shark NKCC1. Of these residues, T189 was found to be absolutely necessary for NKCC1 to be functional. Forbush and colleagues carried out studies in vivo using an antiphospho-NKCC1 antibody raised against a synthetic peptide of the amino terminal domain containing T212 and T217 of human NKCC1, which correspond to T184 and T189 of shark NKCC1 (Darman and Forbush, 2002; Flemmer et al., 2002) and demonstrated that activation of NKCC1 was associated with phosphorylation of these threonines (see Fig. 15.12).

Immunofluorescence studies using anticotransporter antibodies have shown that in secretory epithelia, NKCC1 protein is localized in the basolateral membrane (Lytle et al., 1995; Evans et al., 2000; Shillingford et al., 2002; McDaniel et al., 2005; Nejsum et al., 2005; Chou et al., 2008). As mentioned above, the only exception documented by functional and molecular methods is the choroid plexus (CP) where NKCC1 is located in the apical membrane (Plotkin et al., 1997; Wu et al., 1998). Another possible exception are the cells of the retinal pigment epithelium (RPE); there is abundant functional evidence for the apical location of an NKCC mechanism together with the Na^+/K^+ATPase, but the molecular identity of this NKCC has not been determined. The NKCC1 cotransporters that are localized in the basolateral membrane mediate net salt influx into the cells and, in doing so, act in concert with apical Cl^- channels and basolateral K^+ channels to produce net salt and fluid secretion in these epithelia. The location of NKCC1 in the apical membrane of CP argues against its involvement in ion secretion into cerebrospinal fluid. It has been proposed that the CP cotransporter is constitutively active and that it functions to reabsorb K^+ from cerebrospinal fluid to blood (Wu et al., 1998). The location of NKCC in the paranodal region of the Schwann cells suggests a similar role in K^+ uptake from the peri-axonal space, thereby preventing extracellular K^+ accumulation which could produce abnormal changes in axonal excitability (Alvarez-Leefmans et al., 2001).

VC2. The Na^+-K^+-2Cl^- Cotransporter 2 (NKCC2)

NKCC2 has thus far been identified exclusively in the kidney (Gamba, 2009a; Gamba and Friedman, 2009) where, as already mentioned, it is located in the apical membrane of the TALH epithelial cells. For this reason, NKCC2 is still often referred to as "the apical bumetanide-sensitive Na^+-K^+-2Cl^- cotransporter", as "BSC1" (bumetanide-sensitive cotransporter 1) or as "the absorptive isoform." As with NKCC1, these nomenclatures are not recommended, among other reasons because NKCC1 can also be located in the apical membrane of some epithelial cells, because NKCC2 is sensitive to other loop diuretics besides bumetanide and because the possible expression of NKCC2 in extrarenal locations has not been excluded.

NKCC2 shares only ≈60% amino acid sequence identity with NKCC1. In fact, these two proteins are the products of independent genes; SLC12A1 located on human chromosome 15 encodes NKCC2, whereas SLC12A2 located on human chromosome 5 encodes NKCC1 (Gamba and Friedman, 2009). As already mentioned, the gene encoding for NKCC2, gives rise to different NKCC2 transcripts derived from alternative splicing events. These splicing events yield three full-length NKCC2 variants: NKCC2A, NKCC2B and NKKC2F, all of which are differentially distributed in different regions of the TALH, have different transport kinetics characteristics and have been found in different species including humans (Carota et al., 2010). In addition to these three full-length variants, there are shorter variants with truncated carboxyl-terminal ends. The meaning of this differential splicing is that it contributes to the diversity of proteins encoded by a limited number of genes in the genome. Discussion about the possible function of each of these variants is beyond the scope of the present chapter. The interested reader should consult recent reviews by the groups of Gamba, Castrop and Schnermann (Castrop and Schnermann, 2008; Gamba, 2009a; Gamba and Friedman, 2009; Carota et al., 2010).

Full-length NKCC2 proteins are smaller than NKCC1, with a deduced amino acid sequence of ≈1095−1099 residues and a core molecular mass of ≈110−120 kDa. Like NKCC1, NKCC2 is N-glycosylated at two sites located in the long extracellular loop between TM7 and TM8, which is consistent with the size of ≈150−160 kDa of the glycosylated cotransporter. N-glycosylation has been shown to impact NKCC2F function when expressed in oocytes (Gamba, 2005). Protein N-glycosylation is a co- and post-translational modification crucial for folding, trafficking, insertion and function of many proteins (for references see Di Fulvio and Alvarez-Leefmans, 2009). Prevention of N-glycosylation in rat NKCC2F by site directed mutagenesis produces a protein with reduced transport activity and decreased bumetanide sensitivity (Paredes et al., 2006). The predicted topology of NKCC2 is very similar to that of NKCC1 featuring a central hydrophobic domain made up of 12 putative transmembrane (TM) spanning regions. The difference between the two isoforms can be accounted for almost entirely by the additional amino acids at the amino

terminus of NKCC1. In fact, the amino terminus is the most divergent region of the entire protein, both between the two isoforms and when comparing the same isoform between species (Haas and Forbush, 1998).

VD. A Kinetic Model of Na^+-K^+-$2Cl^-$ Cotransport

Normal operation of NKCC requires the binding to the cotransporter of all the ions involved (i.e. $1Na^+$, $1K^+$ and $2Cl^-$) on the same side of the membrane before ion translocation occurs. The order of binding of the cotransported ions does not seem to occur at random. Evidence shows a preferred order of ion binding resulting from an allosteric effect such that the binding of one ion increases the apparent affinity of a binding site for the next ion. The best-tested model to date is still the one based on a systematic study of ion dependencies of self-exchange fluxes mediated by the cotransporter in duck and human red blood cells (Lytle et al., 1998; Lytle, 2003). Two partial reactions of the cotransporter cycle have been revealed: K^+-K^+ exchange in normal high-K^+ cells and Na^+-Na^+ exchange in high-Na^+ cells. The internal and external ion requirements of each mode can be explained by a reaction cycle based on ordered binding and glide symmetry. The latter means that the first ion to bind on one side of the "carrier" will be the first ion to be released on the other.

Figure 15.13 shows the cotransport model based on ordered ion binding and glide symmetry. Net cotransport influx would require that the ions bind to the cotransporter in the order shown. In the initial loading of the empty carrier at the outer face of the membrane, binding of a Na^+ in the pocket (reaction 2) induces formation of a Cl^- site, and binding of that Cl^- (reaction 3) creates a site that can bind K^+, and so forth. All four ions are occluded momentarily in a transitional state (E_4) without access to either side of the membrane. Reaction 5 represents a conformational change of the NKCC such that the binding sites are now accessible from the intracellular compartment, and reactions 6 to 9 represent the ordered release of ions. Reaction 10 leads to a conformational change that involves the reorientation of the totally unloaded cotransporter to an outwardly facing conformation. The model has been quantitatively tested using simulations based on flux data from duck red blood cells, HeLa cells and epithelial cells (Benjamin and Johnson, 1997). Russell (2000) and more recently Delpire and Gagnon (2011) have offered stimulating critiques of this model showing its weaknesses and strengths. Also recently, a mathematical model of NKCC2 has been proposed (Marcano et al., 2009). This model basically adopts the kinetic scheme proposed by

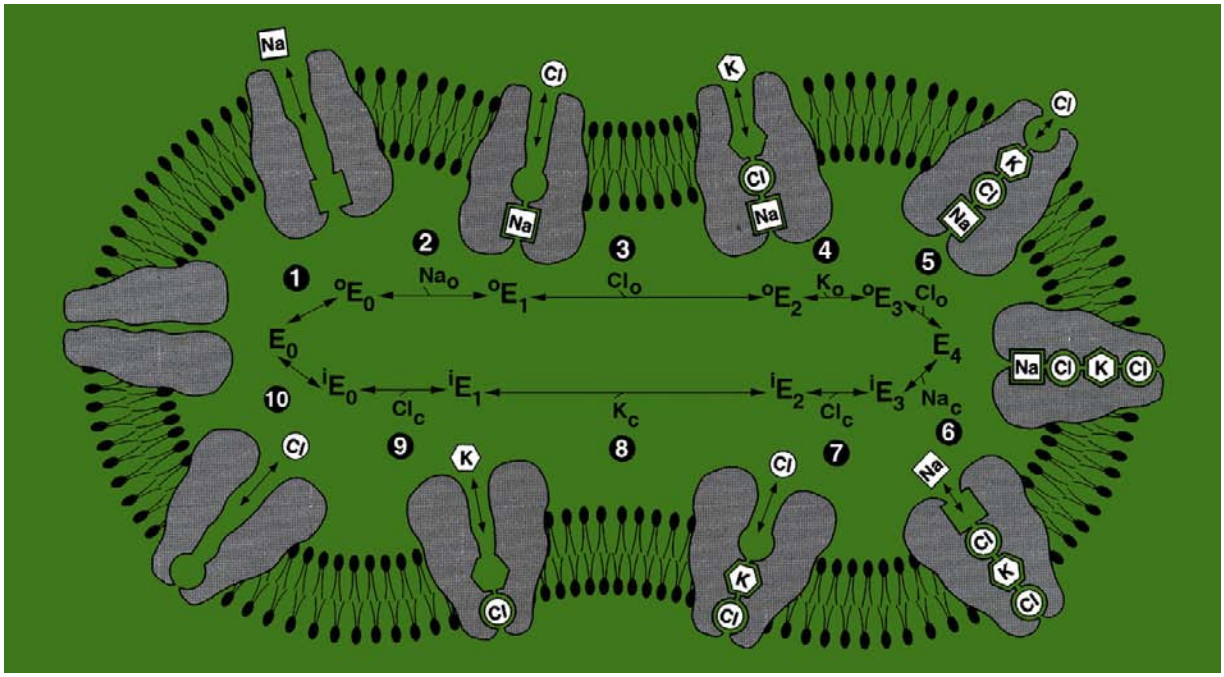

FIGURE 15.13 Hypothetical model of transport cycle of Na^+-K^+-$2Cl^-$ cotransport by ordered ion binding with glide symmetry. Ten intermediate states of the transporter are depicted. The model assumes that cotransport is completely reversible and that only fully loaded (E_4) and completely unloaded (E_0) forms of cotransporter protein are capable of changing orientation from inward- to outward-facing (and vice versa). The idea is that when all sites are occupied (E_4), a major conformational change occurs, allowing bound ions to unload on the opposite side of the membrane in the order they were bound (first on, first off). When the carrier is completely unloaded (E_0), the empty form can also undergo a major conformational change, allowing it to begin reloading ions at the opposite side of the membrane, thus facilitating net cotransport. Numbers refer to order of binding, reorientation and release for one complete influx cycle. *(Modified from Lytle et al., 1998.)*

Lytle and colleagues, but uses kinetic data reported for each splice variant of NKCC2. The authors conclude that the three long splice variants of NKCC2 differ only in ion-binding affinities, a result that is consistent with published mutagenesis analysis and differences in $^{86}Rb^+$ uptake among the A, B and F variants. NKCC2 cotransporter models will facilitate the development of larger scale models of ion transport by TALH cells. One problem in studying the partial reactions of the transport cycle of NKCCs is that they are electroneutral transporters. Thus, it is not possible, as with electrogenic transporters, to measure the partial reactions by electrophysiological means (Garcia-Celma et al., 2010). Future molecular dynamics studies will be potentiated when the crystal structure of NKCCs becomes available.

VE. Functions of Na^+-K^+-2 Cl^- Cotransport

The coupled electroneutral cotransport of Na^+, K^+ and Cl^- mediated by NKCCs serves multiple functions depending on the cell type expressing these proteins. Some examples of NKCCs functions are discussed below in this section. Some of them have been mentioned in Section VA and can be summarized as follows:

1. NKCCs maintain $[Cl^-]_i$ at levels above those predicted for electrochemical equilibrium. The resulting outward Cl^- gradient is used by epithelial cells to promote transepithelial ion and water transport. In neurons, the outward Cl^- gradient generated and maintained by NKCC1 provides the driving force for the depolarizing efflux of Cl^- through ligand-gated Cl^- channels activated by neurotransmitters like GABA or glycine, or second messengers like intracellular Ca^{2+}. The ensuing depolarizations play important roles in central and peripheral neurons
2. Another major function of NKCCs is their participation in cell volume regulation, particularly in cell volume recovery in response to cell shrinkage
3. NKCCs contribute to extracellular K^+ buffering in various cell types
4. NKCCs have been implicated in cell cycle and cell division.

NKCCs are key players in transepithelial Cl^- transport. In most cases, Cl^- transporting epithelia are *secretory* (e.g. exocrine glands such as salivary, pancreatic, eccrine, lacrimal, airway epithelium, intestinal crypts and corneal epithelium) and, in a few instances, they are *absorptive* (e.g. TALH). In cells of Cl^--absorptive and Cl^--secretory epithelia, NKCCs serve as the major Cl^- entry pathway and functions in concert with three other transport proteins, namely Cl^- and K^+ channels and the Na^+/K^+pump, to carry out net transepithelial movements of salt (Fig. 15.14). The impact of the Na^+/K^+ pump in the operation of NKCCs in all cell types, whether epithelial or not, cannot be overstated; it is the primary active transport mechanism that generates and maintains the inward Na^+ gradient that, in turn, provides a substantial part of the driving force that energizes the NKCCs (see Section VB3 above). Thus, the net Cl^- flux in epithelia depends on the Na^+ chemical gradient developed and maintained by primary active transport. In fact, as expected, active transepithelial Cl^- transport is abolished by Na^+ removal or by dissipating the Na^+ gradient between the extracellular fluid and the cell interior (Silva et al., 1977).

In *secretory epithelia* (see Fig. 15.14A), the essential components for active transepithelial Cl^- transport are a Cl^- channel in the apical membrane and a three-component mechanism located in the basolateral membrane causing

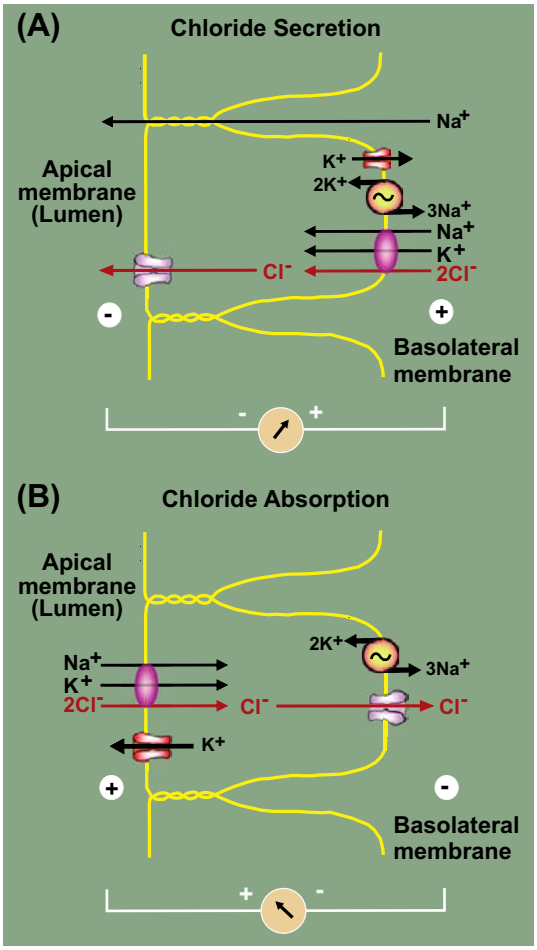

FIGURE 15.14 Mechanisms for active Cl^- absorption and secretion in Cl^- transporting epithelia. (A) Transport model for exocrine gland Cl^--secreting epithelium (e.g. salivary glands or tracheal epithelium). Intracellular $[Cl^-]$ is maintained above electrochemical equilibrium by NKCC1 across the basolateral membrane. Na^+ influx is balanced by efflux via Na^+/K^+-ATPase; K^+ influxes are balanced by efflux via K^+ channels. Transepithelial secretion is induced by activation of apical-membrane Cl^- channels. (B) Model of Cl^- transport in thick ascending limb of Henle's loop, a Cl^--absorptive epithelium. Cl^- entry across the apical membrane is mediated by NKCC2. Most basolateral Na^+ and Cl^- efflux proceeds through the Na^+/K^+-ATPase and Cl^- channels, respectively.

active Cl^- influx across this membrane. The three components that operate in concert to cause net Cl^- uptake across the basolateral membrane are NKCC1, the Na^+/K^+pump and a K^+ channel. NKCC1 maintains $[Cl^-]_i$ above electrochemical equilibrium and transepithelial secretion is produced by activation of apical Cl^- channels. The Na^+ that enters through NKCC1 is balanced by efflux through the Na^+/K^+-pump. The K^+ influx mediated by NKCC and the Na^+/K^+ pump is balanced by efflux via K^+ channels. The end result is that transcellular transport involves only Cl^-; both Na^+ and K^+ recycle across the basolateral membrane via the Na^+/K^+ pump and the K^+ channels, respectively. In Cl^- secretory epithelia, there is an apical negative transepithelial voltage which acts as a driving force for paracellular Na^+ transport towards the lumen. The net result is NaCl secretion which, in turn, results in net fluid secretion. The mechanisms and the pathways of epithelial fluid transport remain unsolved. There is evidence for water being transported through both transcellular (through the cells) and paracellular (intercellular, through tight junctions in series with lateral intercellular spaces) pathways (Reuss, 1997; Tradtrantip et al., 2009; Fischbarg, 2010). Whether fluid transport occurs *purely* by osmotic water flow through aquaporins is also controversial. There is evidence suggesting that cotransporters including NKCC1 and KCCs cotransport water and ions and thus they may contribute to transcellular fluid transport (MacAulay et al., 2009; Hamann et al., 2010; Zeuthen, 2010).

The transport mechanisms in Cl^--*absorptive epithelia*, like the one lining the thick ascending limb of the loop of Henle (TALH), are illustrated in Fig. 15.14B. In this case, the Cl^- channels (ClC-Kb) are located in the basolateral membrane and the NKCC (NKCC2 in TALH) is characteristically located in the apical membrane together with K^+ channels (ROMK2). However, the Na^+/K^+ pump is located at the basolateral membrane, so that Na^+ entering the cell via NKCC2 is not recycled, but instead undergoes transcellular transport. The same occurs with Cl^-; it enters through the apical NKCC2 and exits though basolateral Cl^- channels. Thus, NKCC2 contributes to net Na^+ and Cl^- reabsorption. Most of the K^+ taken up by NKCC2 recycles across the apical membrane via inward rectifier K^+ channels ROMK2. In the TALH, Cl^- absorption is entirely transcellular, whereas Na^+ absorption is partly transcellular and partly paracellular (Gamba and Friedman, 2009). The paracellular Na^+ flux is driven by the transepithelial voltage, which in contrast with Cl^--secreting epithelia is lumen positive.

Primary sensory neurons (PSNs) convey virtually all somatic and visceral information to the spinal cord and brainstem, including nociceptive signals, i.e. incoming signals arising from nociceptors. The latter are sensory receptors capable of transducing and encoding noxious stimuli. NKCC1 maintains $[Cl^-]_i$ of PSNs above electrochemical equilibrium throughout adulthood. In this case, the Na^+ and K^+ entering the cell via NKCC1 recycle through the Na^+/K^+ ATPase and K^+ channels respectively (Fig. 15.15). Thus, $[Na^+]_i$ and $[K^+]_i$ are maintained at a constant level by the Na^+/K^+ ATPase. The outward Cl^- gradient generated by NKCC1 is maintained throughout the entire cell surface, including the soma (located in DRG ganglia) and the central and peripheral processes. This Cl^- gradient is of high functional significance; at the peripheral endings, it is thought to contribute to excitation of nociceptors produced by chemical mediators of pain released upon tissue damage, whereas at the central terminals, it makes possible the GABA-mediated depolarizing Cl^- efflux underlying presynaptic inhibition, a key mechanism in gating the flow of somatosensory information of various sensory modalities to the spinal cord and brainstem (Alvarez-Leefmans, 2009). The mechanisms that make possible presynatic inhibition in the spinal cord are depicted in Fig. 15.15. The prevailing notion is that GABA released from dorsal horn interneurons depolarizes primary afferent fibers via axoaxonic synapses. This primary afferent depolarization (PAD) inactivates Na^+ channels thereby reducing the amplitude of the action potential as it invades the primary afferent terminals, resulting in a reduction in neurotransmitter release from these terminals (Rudomin and Schmidt, 1999; Willis, 2006). The depolarizing inward current results from opening of $GABA_A$-gated Cl^- channels expressed in intraspinal terminals of primary afferent fibers. Opening of these GABA-gated channels results in efflux of Cl^- which transiently drives the transmembrane potential toward the E_{Cl}. This peculiar depolarizing action of a traditionally hyperpolarizing inhibitory transmitter like GABA is possible because the $[Cl^-]$ inside the nerve terminals of primary sensory neurons is maintained at a level higher than predicted from a passive distribution, thereby providing the necessary driving force for electrodiffusional (i.e. channel-mediated) Cl^- efflux. An example of how this mechanism can impact nociceptive signaling is the antihyperalgesic action of diazepam, a $GABA_A$ receptor modulator that enhances PAD by increasing the open probability of Cl^- channels activated by GABA. By potentiating PAD and presynaptic inhibition on nociceptive primary afferents, diazepam has been found to have an antihyperalgesic action against inflammatory hyperalgesia in vivo (Witschi et al., 2011). It is worth remembering here that hyperalgesia is defined as increased pain sensitivity.

NKCC1 is involved in sensory transduction. Two well documented examples are the *inner ear* and the *olfactory sensory neurons.* The mechanisms of acoustic transduction are discussed in detail in Chapter 37 in this book. Here we briefly examine the role of NKCC1 as an important component of the sensory transduction machinery in the inner ear. Hearing critically depends on the ion composition

of the cochlear endolymph, the fluid surrounding the upper surface of mechanosensitive hair cells. These cells carry out mechano-transduction, the conversion of a mechanical stimulus (sound-induced vibration of hair cells cilia) into an electrical response that is then processed by the central nervous system. Endolymph has a high K^+ concentration (157 mM) and low Na^+ (1.3 mM) and Ca^{2+} ($\approx$20 μM) concentrations. Thus, the ion composition of the endolymph resembles intracellular fluid. This ionic composition depends on active transport processes in the stria vascularis, a specialized epithelium at the lateral cochlear wall. NKCC1 is located at the basolateral membrane of the strial marginal cells, together with the Na^+/K^+ ATPase and Cl^- channels (ClC-Ka/barttin and ClC-Kb/barttin), whereas the apical membrane, facing the "lumen" which in this case is the endolymph-filled scala media, expresses outwardly conducting K^+ channels (KCNQ1/KCNE1). Clearly, strial marginal cells form a *K^+-secreting epithelium;* Na^+ and Cl^- entering the cells via NKCC1 recycle though the Na^+/K^+ pump and the Cl^- channels, whereas K^+ entering though NKCC1 and the Na^+/K^+ pump exits though the apical K^+ channels. Thus, transcellular transport in these cells involves only K^+. The unique composition of the endolymph is needed because the apical mechanosensitive channels of sensory hair cells function as K^+ channels (they are in fact mechanosensitive non-selective cation channels). Sound-induced movement of the basilar and tectorial membranes deflects the cilia of sensory hair cells and opens these mechanosensitive channels through which K^+ enters. The resulting K^+ influx depolarizes the hair cells and triggers a complex cascade of events that culminate in exocytosis of synaptic vesicles at their basal pole. K^+ leaves outer hair cells through KCNQ4 K^+ channels and is recycled through a complex mechanism that involves other members of the SLC12A family of cation-coupled cotransporters (Hubner and Rust, 2007; Mistrik and Ashmore, 2009; Zdebik et al., 2009). The important role played by SLC12A members for inner ear ion homeostasis and endolymph secretion may explain the well-known ototoxic effects of loop diuretics (Ikeda et al., 1997) and the deafness exhibited by gene disruption of some members of the SLC12A family in knockout mouse models.

In *olfactory sensory neurons,* the transduction strategy is different from that of inner hair cells in the cochlea, but the mechanism is also critically dependent on NKCC1 function (Frings, 2009). Mammalian olfactory receptor neurons (ORNs) present to the air a tuft of sensory cilia expressing odorant receptors. Upon contact with odorants, these receptors trigger a cascade of events that culminates with the firing of action potentials. The cascade of events begins with the activation of odorant receptors, resulting in a rise of the second messengers cAMP and Ca^{2+} inside the cilia, a process that involves cAMP-gated-Ca^{2+} channels. The resulting Ca^{2+} influx opens Cl^- channels (TMEM16B). ORNs accumulate Cl^- through NKCC1 and maintain a higher than equilibrium $[Cl^-]_i$ thereby setting an outward Cl^- gradient. Thus, opening of Ca^{2+}-activated Cl^- channels (TMEM16B) leads to a depolarizing Cl^- efflux from the cilia, a mechanism that amplifies the receptor potential approximately 10-fold, thus helping to excite the neuron even when stimulation is weak. Accordingly, disruption of the NKCC1 gene, as well as the pharmacologic suppression of Cl^- accumulation or blocking the Cl^- efflux, strongly inhibits the sensory response of ORNs. Experiments with NKCC1 knockout mice have shown that NKCC1 is not the only Cl^- transporter active in ORNs. In fact, NKCC1 knockout mice retain the ability to smell, a finding that suggests the existence of an additional Cl^--uptake mechanism. The latter turned out to be the AE1, i.e. SLC4A1 (Hengl et al., 2010).

The role of NKCCs in *cell volume regulation* has also been mentioned. In many cells, NKCC is involved in regulatory volume increase in response to hypertonic cell shrinkage, by promoting net gain of K^+, Cl^- and osmotically obliged water. For detailed accounts on this subject the reader should consult the reviews by Russell (2000, 2009) and Hoffmann and colleagues (Hoffmann et al., 2009). In the cell bodies of primary sensory neurons (i.e. DRG neurons) known to express NKCC1, it has been possible to measure changes in cell water volume that reflect solute and water fluxes and $[Cl^-]_i$. The results demonstrate a tight link between Na^+,K^+,$2Cl^-$ cotransporter activity, water fluxes, steady-state $[Cl^-]_i$ and cell water volume (Rocha-Gonzalez et al., 2008). Isosmotic removal of external Cl^- results in intracellular Cl^- depletion and immediate cell shrinkage. The extent of cell shrinkage is accounted for in terms of measured Cl^- depletion. Upon readmission of the isosmotic control solution, water influx takes place in *isosmotic* media. This water influx requires the presence of external Na^+ and K^+ and is abolished by 10 μM bumetanide. Thus, net water flux is tightly linked to NKCC1 transport activity. In DRG neurons, NKCC1 determines not only the higher than passive $[Cl^-]_i$ characteristic of these neurons but also the cell volume set point, through a negative feedback system in which intracellular Cl^- regulates water and Cl^- influx, thereby maintaining intracellular Cl^- concentration and cell volume constant (Alvarez-Leefmans, 2009). Moreover, due to their small volume/surface ratio, presynaptic nerve terminals of primary sensory neurons are expected to be partially depleted of solutes (Cl^- and K^+) and water upon repetitive GABA action. It has been proposed that NKCC1 is capable of restoring ionic gradients and osmotic balance altered as a consequence of neurotransmitter action (see Fig. 15.15).

As mentioned above, NKCC exhibits some of the features required for an efficient extracellular K^+ buffer;

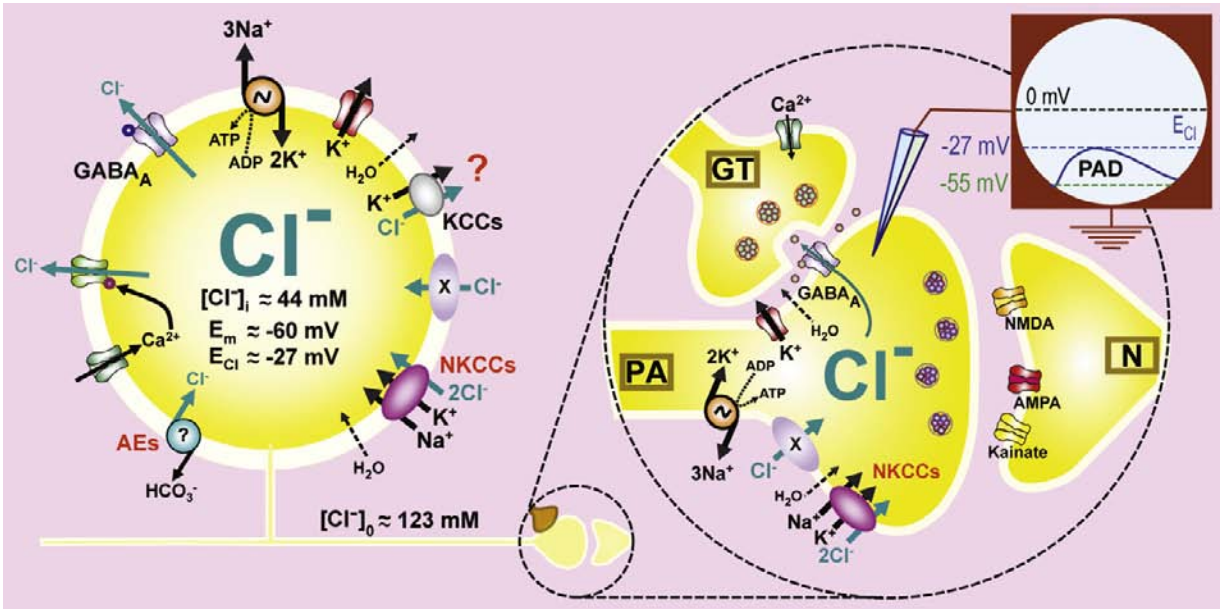

FIGURE 15.15 Schematic diagram depicting the known and hypothetical transporters and channels involved in intracellular Cl^- regulation in primary sensory neurons and proposed mode of generation of primary afferent depolarization (PAD) and presynaptic inhibition in the intraspinal terminals of these neurons. The left circle represents a mammalian DRG neuron showing measured values of intracellular Cl^- concentration, $[Cl^-]_i$; membrane potential (E_m) and Cl^--equilibrium potential, E_{Cl}. The Na^+/K^+ ATPase maintains the Na^+ and K^+ gradients across the membrane. AEs, anion exchangers; NKCCs, Na^+,K^+,$2Cl^-$ cotransporters; KCCs are K^+-Cl^- cotransporters 1,3 or 4. The contribution of KCCs to intracellular Cl^- regulation in these neurons under euvolemic conditions is not clear. KCC2 is not expressed in primary sensory neurons. X represents other yet to be identified active Cl^--uptake transporters. The right diagram encircled by a dashed line represents a magnified intraspinal primary afferent terminal from which an intracellular micropipette connected to an oscilloscope monitors E_m. PA, primary afferent; GT, GABAergic terminal from an interneuron; N, postsynaptic terminal with glutamate receptor-channels. Note that PAD (blue trace in the oscilloscope screen) blocks the release of neurotransmitter from the PA terminal. *(Reproduced from Alvarez-Leefmans, 2009.)*

i.e. it has a strong net inwardly directed driving force and a high affinity for external K^+ (Payne and Forbush, 1995). There is some evidence for its role as a K^+-uptake mechanism that contributes to buffering and regulation of extracellular K^+ in some tissues. For instance, NKCC1 is present in the apical membrane of mammalian choroid plexus and, in concert with other transport systems coexisting in these polarized cells, may play an important role in the reabsorption of K^+ from the cerebrospinal fluid to the blood, thereby contributing to the buffering and regulation of brain interstitial $[K^+]$, as illustrated in Fig. 15.17 (Wu et al., 1998). NKCC is also prominently located in the paranodal region of Schwann cells of myelinated axons, a region prone to extracellular K^+ accumulation resulting from axonal impulse activity. This suggests the possible involvement of NKCC in K^+ uptake from the periaxonal space, thereby regulating the external $[K^+]$ and maintaining the axonal excitability in this critical location (Alvarez-Leefmans, 2009).

VI. ELECTRONEUTRAL K^+-Cl^- COTRANSPORTERS

K^+-Cl^- cotransporters (KCCs) are carrier proteins that mediate the coupled, electroneutral movement of K^+ and Cl^- across the plasma membrane. This coupled transport is obligatory as it absolutely requires the simultaneous presence of both K^+ and Cl^- on the same side of the membrane for net transport to proceed. As other electroneutral secondary active transport mechanisms, the direction of the net movement of K^+ and Cl^- by KCCs is determined solely by the sum of the chemical potential gradients of the two cotransported ions. Under normal physiological conditions, the outwardly directed K^+-chemical potential gradient maintained by the Na^+/K^+ pump drives the uphill movement of Cl^- against its chemical potential gradient. Hence, under normal conditions, KCCs are efflux pathways for K^+ and Cl^-. However, the cotransporters are bidirectional and can mediate net ion efflux or influx, depending upon the prevailing K^+- and Cl^--chemical potential gradients. In neurons, this is crucial because KCC2, the neuronal-specific isoform, might work near its thermodynamic equilibrium and, therefore, it would have the potential to mediate Cl^- fluxes in both directions (Payne, 2009). The stoichiometry of KCCs is $1K^+$:$1Cl^-$, as determined in rabbit red blood cells (Jennings and Adame, 2001). This means that the transport process involves one-for-one movement of K^+ with Cl^-. Thus, the overall transport process of K^+ and Cl^- via the cotransporter is not driven by the transmembrane voltage, nor does the

transport process directly generate a membrane current that may change the transmembrane voltage (Kaji, 1993).

This transport mechanism has been implicated in regulatory volume decrease in response to hyposmotic cell swelling, by promoting net efflux of K^+ and Cl^- and osmotically obliged water (Hoffmann et al., 2009). All four main isoforms of the cotransporter can be activated by significant hypotonic challenges. However, the fact that they are volume sensitive does not necessarily mean that the physiological function of these cotransporters is to regulate cell volume. As lucidly stated by Payne (2009): "…a transporter should be considered volume regulatory only after it has been demonstrated that the transport rate is a graded function of the stimulus and that the net ion transport is large enough to restore cell volume to normal. In the absence of such measurements, it is best to refer to the transporter as volume sensitive until more extensive experimentation is conducted." Besides its possible function in cell volume regulation, K^+-Cl^- cotransport plays important roles in the vectorial movement of salt and water across some epithelia (Reuss, 1997; Velazquez and Silva, 2003; Gamba, 2005). A crucial function of an isoform of the K^+-Cl^- cotransporters, KCC2, has been clearly demonstrated in neurons, where by effecting active extrusion of Cl^- it keeps E_{Cl} at more negative values than E_m, making possible the hyperpolarizing action of inhibitory neurotransmitters like GABA and glycine in the adult central nervous system (Payne et al., 2003; Payne, 2009). A brief account of what is known about the function and distribution of KCCs is presented below.

VIA. Basic Features of the K^+-Cl^- Cotransporters

The basic functional characteristics of KCCs have been summarized in a recent review (Gibson et al., 2009). A defining feature of KCCs is that the transport process is Na^+ independent. Another key feature of KCCs is that the thiol-alkylating reagent N-ethylmaleimide (NEM) stimulates transport (Lauf and Theg, 1980). The cotransporters can also be activated by osmotic cell swelling (Ellory and Dunham, 1980). Reducing $[Mg^{2+}]_i$ stimulates the cotransporter, presumably via effects on regulatory kinases (Delpire and Lauf, 1991). Likewise, KCC is stimulated by the protein kinase inhibitor staurosporine (Bize and Dunham, 1994). Unlike either the NKCC or the NCC, KCCs can be inhibited by disulfonic acid stilbenes such as DIDS (Delpire and Lauf, 1992). KCCs are also inhibited by loop diuretics but, in general, the sensitivity for furosemide>>bumetanide, as discussed above in Section VB4. They can also be inhibited by dihydroindenyloxyalkanoic acid (DIOA), which is often erroneously used as if it were a "specific" KCC inhibitor. More recently, a new series of KCC2 inhibitors such as *N*-(4-methylthiazol-2-yl)-2-(6-phenylpyridazin-3-ylthio) acetamide has been reported (Delpire et al., 2009). The new inhibitors are more potent than furosemide and DIOA. Another series of KCC2 inhibitors has also been recently described (Pégurier et al., 2010). Future experiments will reveal if these new compounds are specific for KCCs. Activity of all KCCs can be influenced by intracellular pH (pH_i), with KCC1 and KCC3 exhibiting lower activity at pH_i <7.0 or >7.5, KCC2 at <7.5 and KCC4 at >7.5.

VIB. Molecular Structure, Distribution and Functions of K^+-Cl^- Cotransport Proteins

Four distinct isoforms and several splice variants of these members of the cation-coupled Cl^- cotransporter family (SLC12A) have been identified. The isoforms are KCC1, KCC2, KCC3 and KCC4. They are encoded by the genes *SLC12A4, SLC12A5, SLC12A6* and *SLC12A7,* respectively. In vertebrates, all of these genes code for proteins over 1000 amino acids with core molecular weights of 120−128 kDa (Payne, 2009). The four KCCs exhibit alternative exon splicing and the use of alternative promoters and first exons, leading to even greater protein diversity. The four KCC proteins are 69−75% identical when comparing their full length sequences. The most variable segment of these proteins is the N-terminal domain, defined as the portion that extends from the first methionine to the beginning of TM1. Identity of the N-terminal domain sequence among KCCs varies between 38 and 50% (Gamba, 2005). It is important to mention that in the original cloning report of Mount and coworkers (1999), the isoform KCC3 (Hiki et al., 1999) was misleadingly named KCC4 and the latter was named KCC3. This was clarified in subsequent work. In the present chapter, the corrected nomenclature has been followed.

NKCC1, NKCC2, NCC and the four KCCs share a predicted basic membrane topology consisting of a central core of 12 TM domains flanked by hydrophilic amino- and carboxy-terminal domains that have a cytoplasmic orientation. The carboxy-termini of KCCs make up nearly half the size of these proteins (Fig. 15.16). When compared over their entire length, KCC proteins are 25−30% identical to NCC and NKCCs. A major structural difference between the KCCs and the NKCCs is the position of a large glycosylated extracellular loop, predicted to occur between TM5 and TM6 in the KCCs and between TM7 and TM8 in the NKCCs and the NCC (Mount et al., 1999). This can be appreciated by comparing Fig. 15.12 with Fig. 15.16.

KCC1 was the first isoform of the KCCs to be cloned and functionally characterized by heterologous expression in HEK 293 cells (Gillen et al., 1996). The gene for human KCC1 is at chromosomal location 16q22.1. KCC1 has a deglycosylated molecular mass of ≈120 kDa and it is widely expressed in mammalian tissues (brain, kidney, heart, lung, liver, stomach, colon, spleen and placenta). This ubiquitous tissue distribution suggests that KCC1 may

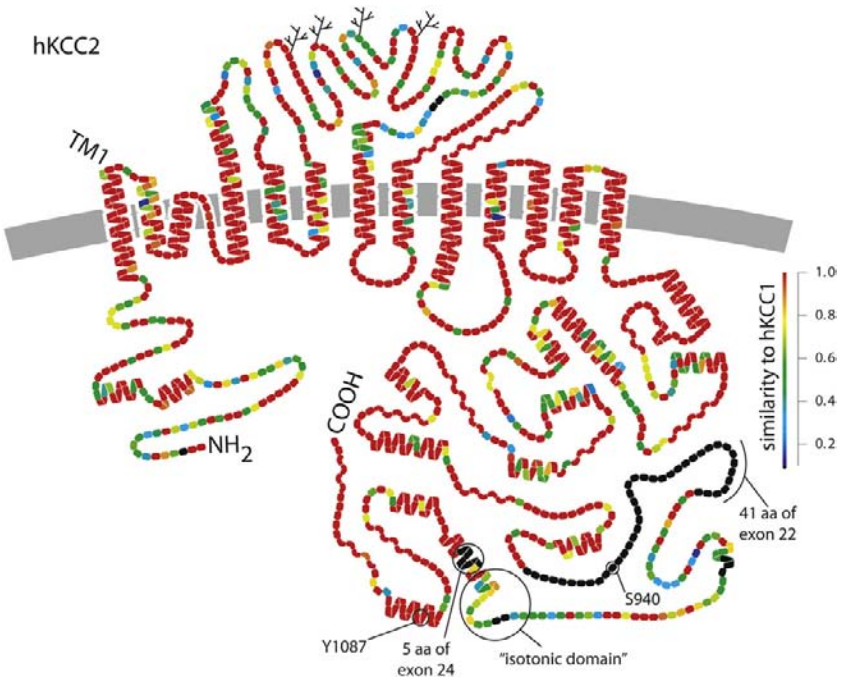

FIGURE 15.16 Hypothetical structural model of the K^+-Cl^- cotransporter. Human KCC2 (hKCC2) and human KCC1 (hKCC1) are compared to one another by colors that indicate the degree of similarity on a per residue basis: red residues are identical and black residues are absent from hKCC1 (alignment performed using CLUSTAL X ver. 1.8). The branched lines in black are potential N-linked glycosylation sites between putative transmembrane segments (TM) 5 and 6. Predicted secondary structural elements are shown as helices for predicted α-helix and wavy lines for predicted β-sheet. A reentrant loop between putative TM segments 2 and 3 has also been predicted for NKCC2 and is shown for KCC2. The 15 amino acid region required for constitutive "isotonic" activity of KCC2 is encircled. Serine-940 (S940) is also encircled. Protein kinase C directly phosphorylates S940 of KCC2. S940 phosphorylation is required for activation of KCC2 by protein kinase C (Payne, 2009). KCC2 has a large region in the carboxy-terminus (COOH), exhibiting little identity with the other KCCs. This unique region of KCC2 is coded by two extra exons (exons 22 and 24) which are apparently absent from the other KCC genes. Exon 22 of KCC2 codes for 41 amino acids and exon 24 of KCC2 codes for five amino acids. Exon 23 of the KCC2 gene is conserved among the KCC genes, however, the identity of the predicted amino acids in exon 23 of KCC2 is low when compared to the other KCCs. A consensus tyrosine protein kinase phosphorylation site is also shown (Y1087). Mutation of this tyrosine residue (Y1087D) inhibits constitutive "isotonic" activity as well as swelling-induced activity in heterologously expressed KCC2 (see Payne, 2009 for references). *(This figure was kindly provided by John Payne and Bliss Forbush. It was generated using DNAPLOT.)*

represent a "housekeeping" isoform responsible for cell volume regulation and maintenance, and for the regulation of $[Cl^-]_i$. However, this "housekeeping" role is difficult to reconcile with the fact that disruption of KCC1 gene does not produce any obvious phenotype even in vertebrate red blood cells where KCC1 was thought to be the key player in cell volume control. In fact, KCC1 knockout are indistinguishable from wild-type animals (Rust et al., 2007). It is now known that red blood cells express KCC1, KCC3 and KCC4, but that the volume-sensitive K^+-Cl^- cotransporter activity in mouse and human red blood cells is mostly mediated by KCC3 (Rust et al., 2007; Pan et al., 2011). Heterologous expression of KCC1 in HEK-293 cells showed that the cotransporter is little active in isosmotic media but that its activity can be stimulated by cell swelling ($\approx$twofold) and N-ethylmaleimide, and inhibited by furosemide (K_i of $\approx 40\,\mu M$) and by bumetanide (K_i of $\approx 60\,\mu M$). When KCC1 is expressed in *Xenopus* oocytes, it also shows minimal transport activity in isosmotic media. However, when exposed to hyposmotic solutions, its activity increases by 20-fold (Mercado et al., 2000). The cotransporter in the *Xenopus* expression system is inhibited by bumetanide and furosemide with a K_i of $180\,\mu M$. Clearly, the sensitivity to loop diuretics of KCC1 varies between expression systems but, in all cases, is significantly different than that of NKCCs. The latter are in general more sensitive to bumetanide than furosemide; the K_i for bumetanide is at least an order of magnitude lower. Even though the expression of human KCC1 has been found in every cell and tissue tested so far, its specific physiological function remains unclear. The fact that K^+-Cl^- cotransport activity in red blood cells is undiminished in KCC1 knockout mice suggests that this protein has other hitherto unknown functions.

KCC2 is a neuron-specific isoform of the K^+-Cl^- cotransporters. It was first cloned and characterized by Payne and colleagues (Payne et al., 1996; Payne, 1997). KCC2 is present in the plasma membrane of cell bodies and dendrites of various types of CNS neurons, but appears to be absent in axons and glial cells (Williams et al., 1999; Stil et al., 2009; reviewed in Blaesse et al., 2009; Payne, 2009; Viemari et al., 2011). As originally proposed by Payne and colleagues, KCC2 is the isoform that actively extrudes Cl^- from nerve cells, rendering E_{Cl} more negative than E_m and thus setting an inwardly directed electrochemical gradient for Cl^-, making possible hyperpolarizing inhibition mediated by GABA- or glycine-gated Cl^- channels in mature CNS neurons. The cloning and molecular characterization of KCC2 has been a highly significant discovery in the field of Cl^- transport; although it had long been suspected that the mechanism of active Cl^- extrusion in CNS neurons was a K^+-Cl^- cotransporter (Alvarez-Leefmans, 1990), its

molecular identity and its functional and kinetic features had remained elusive. However, as discussed below, KCC2 might not be the only candidate for such an important function; in some neurons KCC3 appears to have a significant role in setting the inward Cl^- gradient needed for hyperpolarizing inhibition (Boettger et al., 2003). Finally, KCC2 expression in the CNS increases with development and becomes functionally dominant over NKCC1. This explains why GABA and glycine responses, which are depolarizing in embryonic or early postnatal nerve cells, become hyperpolarizing in the adult brain (Rivera et al., 1999).

The mammalian KCC2 gene (SLC12A5) generates two variants of KCC2, named KCC2a and KCC2b, with different N-termini (Uvarov et al., 2007). This N-termini heterogeneity is due to the use of alternative promoters and alternative first exons. Exon 1a encodes 40 N-terminal amino acid residues giving rise to KCC2a, and exon 1b encodes 17 amino acids giving rise to KCC2b, the variant originally described by Payne and coworkers (1996). The function of KCC2a is not known. Both variants are exclusively expressed in CNS neurons, but they differ in timing, level and site of expression. During postnatal development, KCC2b is steeply upregulated whereas KCC2a is not. KCC2b is more abundant in the cortex whereas KCC2a appears more abundant in brainstem and spinal cord. Interestingly, full KCC2 knockout mice die immediately after birth due to respiratory failure and other motor disturbances (Hubner et al., 2001), whereas mice lacking KCC2b retaining normal levels of KCC2a, survive for up to 2 weeks, although they exhibit abnormal posture and gait, and generalized seizures (Woo et al., 2002). So far, there is no KCC2a knockout model. However, the observations mentioned above in available knockout mice suggest that KCC2a may to a certain extent compensate for the lack of KCC2b in brainstem and spinal cord, making possible the survival of these animals for up to postnatal day 17. Expression of either KCC2a or KCC2b in HEK 293 cells demonstrated that both variants exhibit comparable cotransport activity. Further, both variants exhibit constitutive activity in isosmotic media, a functional characteristic that makes KCC2 suitable for the control of $[Cl^-]_i$ (Payne, 2009). Since most published data reflect expression of both KCC2a and KCC2b, "KCC2" will be used here to refer to both splice variants.

Human KCC2 has a predicted core molecular mass of 123.5 kDa (Payne, 2009), close to that predicted for mouse and rat KCC2 (123.6 kDa). Western blots of membranes isolated from rat brain show that the glycosylated molecular mass of KCC2 is $\approx$140 kDa and, upon deglycosylation, the protein migrates to near $\approx$125 kDa, which is close to the predicted molecular mass (Williams et al., 1999). Similarly, human KCC2 has a glycosylated molecular mass of $\approx$140 kDa and, upon deglycosylation, the protein migrates to a broad band centered around 120 kDa (Munoz et al., 2007). KCC2 expressed in HEK 293 is also stimulated by NEM and inhibited by furosemide (K_i of $\approx$25 μM), bumetanide (K_i of $\approx$55 μM), DIDS and DIOA. The main functional difference from other KCC isoforms is that KCC2 is not stimulated by osmotic swelling when expressed in HEK 293 cells. However, when expressed in *Xenopus* oocytes its activity increases 3.5−20-fold by hyposmotic swelling (Gamba, 2005; Payne, 2009). These and other discrepancies (e.g. bumetanide sensitivity in HEK versus *Xenopus*) highlight the limitations of studying transporters in heterologous expression systems. A key feature of KCC2 is that it exhibits significant basal constitutive activity, i.e. it is active in isotonic media, a functional property shared with KCC3a (see below). This constitutive activity makes these KCCs ideal, from the functional perspective, to establish the steady state $[Cl^-]_i$ of adult CNS neurons. The segment of the KCC2 protein conferring constitutive "isotonic" activity, known as the "isotonic domain", comprises 15 amino acids coded by exon 23 (see Fig. 15.16).

Like NKCC1, KCC2 exhibits all the features required for an efficient $[K^+]_o$ buffer: (1) it is reversible and the direction of net transport is sensitive to subtle changes in $[K^+]_o$; (2) the affinity of the cotransporter for external K^+ is compatible with the range of the observed $[K^+]_o$ (3−10 mM), allowing a high rate of cotransport activity. These requirements seem to be a feature of both KCC2 (K_m $\approx$5.2 mM) and KCC3 (K_m $\approx$10 mM). Hence, it has been postulated that KCC2 could also act as a $[K^+]_o$ buffer (Payne, 1997). However, external $[K^+]$ in CNS interstitial fluid is tightly regulated and, under normal physiological conditions, never exceeds 3 mM. Only during extreme seizure activity does $[K^+]_o$ exceed 3 mM and can reach up to 12 mM, the so-called *ceiling* level (Somjen, 2004). Thus, most likely KCC2 normally works in the efflux mode.

KCC3 was first identified by three groups simultaneously (Hiki et al., 1999; Mount et al., 1999; Race et al., 1999). The KCC3 gene (SLC12A6) gives rise to two major splice variants, KCC3a and KCC3b. The KCC3 cDNA cloned by Hiki et al. (1999) predicted a protein of 1099 amino acids, whereas the cDNA cloned by Race et al. (1999) and Mount et al. (1999) predicted a protein of 1150 amino acids. These two KCC3 variants are termed KCC3a (1150 aa) and KCC3b (1099 aa). They are identical except for their N-termini. Both variants come from the same gene which, in humans, is located in chromosome 15 (15q13). KCC3 proteins have deglycosylated molecular mass of $\approx$120 to 128 kDa. Subsequent studies showed that the mammalian KCC3 gene has the potential to produce more than two alternative splice variants giving rise to proteins with considerable N-termini heterogeneity (Mercado et al., 2005). To date, six different KCC3 transcripts coding for

five different KCC3 variants are known to exist. They are termed KCC3a, KCC3a−x2M (KCC3a minus exon 2), KCC3a-S (encodes a protein 60 amino acids shorter than KCC3a), KCC3b and KCC3b−x2M (KCC3b minus exon 2). Exon 2 encodes 15 amino acid residues. When expressed in *Xenopus* oocytes all five variants function as K^+-Cl^- cotransporters (Mercado et al., 2005). It is not clear how the N-termini heterogeneity impacts KCC3 function. When expressed in HEK 293 cells, human KCC3a is not active in isotonic media and is activated by cell swelling, staurosporine and prominently by NEM. However, recent work shows that the activity of KCC3a in isosmotic media depends upon the phosphorylation state of the protein, suggesting that dephosphorylation increases KCC3's intrinsic transport activity (Rinehart et al., 2009). Human KCC3a expressed in HEK cells is inhibited by bumetanide (K_i ≈100 μM), furosemide (K_i ≈103 μM) and DIOA (K_i ≈9.3 μM). Hence, the most potent inhibitor of KCC3a is DIOA (Race et al., 1999). When expressed in HEK 293 cells, human KCC3b is active in isotonic media but its activity does not increase upon hypotonic swelling. KCC3b is inhibited by bumetanide (K_i ≈40 μM) and furosemide (K_i ≈10 μM). Thus, the emerging picture is that KCC3a in neurons may play functions similar to those that are carried out by KCC2.

KCC3s have different distribution patterns; KCC3a is expressed predominantly but not exclusively in various brain regions, in the basolateral membrane of choroid plexus epithelial cells (Fig. 15.17), in heart and skeletal muscle, lung, liver and pancreas (Pearson et al., 2001). A recent study using in situ hybridization and immunohistochemical techniques demonstrated that KCC3a is mainly expressed in neurons and, to a much lesser extent, in some glial cells, whereas KCC3b is not expressed in brain tissue (Shekarabi et al., 2011). In human red blood cells, KCC3a is the functionally dominant isoform (Pan et al., 2011), whereas KCC3b is abundantly expressed in kidney, localized in the basolateral membranes of proximal tubule epithelial cells where it may contribute to proximal tubular cell volume regulation (Lang et al., 2007).

Mutations in the human gene SLC12A6, which encodes KCC3s, lead to a rare neurological illness known as Andermann's syndrome (Howard et al., 2002). This syndrome is characterized by a progressive sensorimotor neuropathy associated with complete or partial absence of corpus callosum, mental retardation, progressive physical disability and an average life expectancy of 33 years. Death is usually caused by respiratory complications (Dupre et al., 2003). Full KCC3 knockout mice models not only display peripheral neuropathy, but reduced seizure threshold and deafness. The latter is due to inner ear defects in K^+ transport in the cochlea, where some of the cells involved in K^+ recirculation slowly degenerate, as do sensory hair cells (Boettger et al., 2003). KCC3 knockout mice also show hypertension of neurogenic origin due to elevated sympathetic tone (Rust et al., 2006). Further, full KCC3 knockout mice exhibit axonal and Schwann cell swelling of sciatic nerves that ultimately results in neurodegeneration (Byun and Delpire, 2007). This suggests that KCC3 may play a role in cell water volume maintenance in sensorimotor axons and that this mechanism is critical for peripheral nerve integrity and function. In sum, KCC3s appear to have significant roles in transepithelial transport and in the regulation of cell volume and $[Cl^-]_i$. While KCC2 may be the key regulator of neuronal $[Cl^-]_i$, data suggest that KCC3a may have a similar role.

KCC4 was first cloned and functionally characterized by Mount and coworkers (1999). The KCC4 gene is located on chromosome 5, at 5p15, and encodes for a protein product of 1083 amino acids that shares high identity (≈75%) with KCC2. However, unlike KCC2 (and KCC3), KCC4 does not mediate constitutive K^+-Cl^- cotransport under isotonic conditions, but cotransport is activated by osmotic cell swelling. Indeed, when expressed in *Xenopus* oocytes, KCC4 does not mediate K^+-Cl^- cotransport activity in isotonic media. However, its activity increases 200-fold when exposed to hypotonic solutions (Mercado et al., 2000). Using this heterologous expression system, it has been possible to establish functional comparisons between KCC1 and KCC4. Although cell swelling activates both cotransporters, KCC4 is one order of magnitude more sensitive to hypotonic activation than KCC1. Another distinctive feature of KCC4 is its relatively poor sensitivity to both furosemide (K_i ≈900 μM) and bumetanide (K_i ≈900 μM), and its sensitivity to barium and high concentrations of thiazides. Among the four KCC isoforms, KCC4 is the least sensitive to furosemide as corroborated using the HEK 293 expression system, in which KCC2 properties were compared with KCC4 (Hartmann et al., 2010). KCC2 was more sensitive to furosemide (K_i ≈185 μM) than KCC4 (K_i ≈550 μM).

KCC4 is prominently expressed in several epithelia including the apical membrane of choroid plexus cells (Karadsheh et al., 2004), the basolateral membrane of α-intercalated cells of the cortical collecting duct in kidney (Boettger et al., 2002) and the apical membrane of gastric parietal cells (Fujii et al., 2009). In the apical membrane of the choroid plexus, KCC4 is thought to be involved in K^+ recycling, working in parallel with the Na^+/K^+ pump and NKCC1 (Karadsheh et al., 2004) and in Cl^- recycling working in parallel with NKCC1. However, given its high volume sensitivity and its lack of constitutive activity, it is conceivable that KCC4 works to regulate cell volume in choroidal epithelial cells. In the basolateral membrane of α-intercalated cells in cortical collecting ducts in kidney, KCC4 is involved in the regulation of acid secretion working in parallel with the basolateral AE1 and the apical

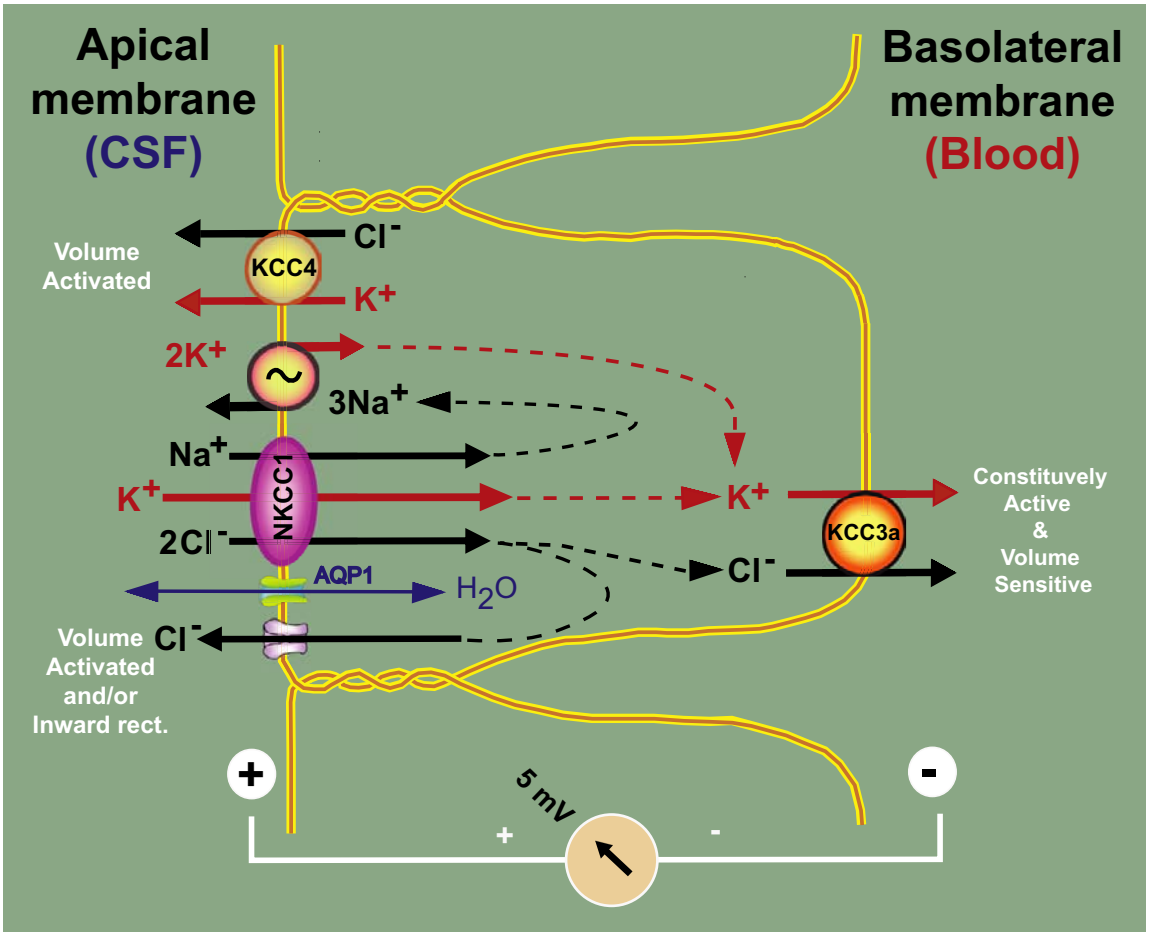

FIGURE 15.17 Model of Na^+-K^+-$2Cl^-$cotransporter function in choroid plexus (CP) epithelial cells. The Na^+-K^+-$2Cl^-$ cotransporter (NKCC1) and the Na^+/K^+-ATPase are localized in the apical membrane facing cerebrospinal fluid (CSF). K^+ is taken up into CP cells via the Na^+-K^+-$2Cl^-$ cotransporter NKCC1 and it exits via K^+-Cl^- cotransporter KCC3 in the basolateral membrane (facing blood). Na^+ is recycled by the apical Na^+/K^+-ATPase. Cl^- is partly recycled via Cl^- channels in the apical membrane. It is proposed that NKCC1 plays a central role in the reabsorption of K^+ from CSF to the blood and in the buffering and regulation of brain interstitial K^+ concentration.

proton pump. The apical proton pump secretes H^+ into the lumen of the collecting duct. At the basolateral membrane, acid equivalents are transported by the AE1. Basolateral HCO_3^- efflux is coupled to Cl^- uptake, which is recycled by KCC4. Interestingly, KCC4 knockout mice exhibit renal tubular acidosis that probably results from an impairment of Cl^- recycling across the basolateral membrane of acid-secreting α-intercalated cells (Boettger et al., 2002). In the apical membrane of gastric parietal cells, the K^+/H^+-ATPase (i.e. the proton pump) working in parallel with KCC4 is the main mechanism for basal HCl secretion in the apical canalicular membrane of parietal cells (Fujii et al., 2009). KCC4 is also expressed in the Deiter's cells of the inner ear where it participates in the K^+ recycling mechanism (Boettger et al., 2002). KCC4 knockout mice are deaf due to hair cell degeneration after the beginning of hearing (Boettger et al., 2002). KCC4 is also expressed in some areas of the nervous system (the suprachiasmatic nucleus of the hypothalamus, cranial nerves, spinal cord and peripheral nerves), but its function in nervous tissue is unknown (Karadsheh et al., 2004; Le Rouzic et al., 2006). KCC4 is also expressed in red blood cells, but its functional role there is also unknown. More exciting is the emerging role of KCC4 in cancer cell invasiveness and tumor metastasis. It has been found that epidermal-growth factor (EGF) and insulin-like growth factor 1 (IGF-1) stimulate the membrane recruitment of KCC4 at lamellipodia through myosin Va-actin trafficking route. KCC4 functions as a membrane scaffold for the assembly of signal complexes via the association with the actin-binding protein ezrin. Further, molecular studies of surgical specimens suggest that the expression of KCC3, KCC4 and their stimulators, EGF or IGF-1, exhibit a close association with the clinical outcome of cancer patients. It has been proposed that KCC4 may be used as a biomarker to predict cancer patient outcome (Chen et al., 2010).

VIC. Thermodynamics of K^+-Cl^- Cotransport

Let us now turn our attention to the thermodynamic aspects of K^+-Cl^- cotransport. Consider the example shown in Fig. 15.18 which depicts a model of a neuron expressing a KCC, a Na^+/K^+ pump, a voltage-gated Cl^- leak channel and a GABA-gated Cl^- channel. Assuming that the K^+-Cl^- cotransport is the sole system transporting Cl^- (channels are closed) and that $[K^+]_i$ is held constant by the Na^+/K^+ pump, the driving force for the cotransport $\Delta\mu_{K,Cl}$ is the sum of the chemical potential differences of K^+ and Cl^-, as expressed in the following equation:

$$\Delta\mu_{K,Cl} = \Delta\mu_K + \Delta\mu_{Cl} \tag{15.16}$$

It follows that

$$\Delta G = \Delta\mu_{K,Cl} = RT\ln\frac{[K^+]_i}{[K^+]_o} + RT\ln\frac{[Cl^-]_i}{[Cl^-]_o} \tag{15.17}$$

This system attains thermodynamic equilibrium when

$$\Delta G = \Delta\mu_{K,Cl} = 0 \tag{15.18}$$

and, therefore, for a 1:1 stoichiometry,

$$\frac{[K^+]_o}{[K^+]_i} = \frac{[Cl^-]_i}{[Cl^-]_o} \tag{15.19}$$

and hence the $[Cl^-]_i$ when the cotransporter reaches thermodynamic equilibrium will be

$$[Cl^-]_i = \frac{[K^+]_o[Cl^-]_o}{[K^+]_i} \tag{15.20}$$

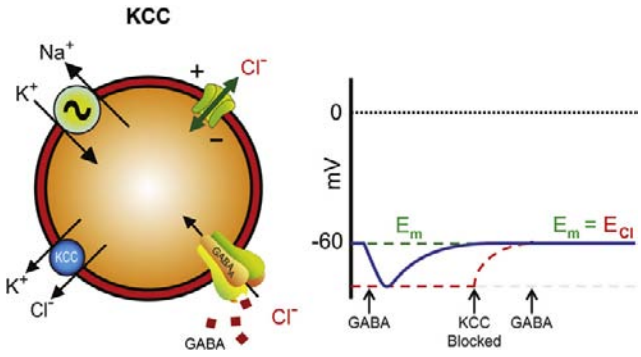

FIGURE 15.18 Model of a neuron expressing only K^+-Cl^- cotransporter, Na^+/K^+ ATPase, voltage-gated anion channels and GABA-gated anion channels. KCC actively extrudes Cl^- from the cell shifting E_{Cl} (red dashed line) to a more negative value than E_m (green dashed line). Right: A puff of GABA produces a hyperpolarizing IPSP (blue trace). When KCC is blocked, $[Cl^-]_i$ raises until reaching passive equilibrium ($E_m = E_{Cl}$). A second GABA application under these conditions does not produce a change in E_m but an increase in membrane conductance which is the basis of "shunting synaptic inhibition". *(Reproduced from Alvarez-Leefmans and Delpire, 2009b.)*

From Equation 15.20 one can readily calculate the $[K^+]_o$ at which the flux reverses from outward to inward or vice versa (flux reversal point or FRP):

$$\text{FRP} = [K^+]_o = \frac{[K^+]_i[Cl^-]_i}{[Cl^-]_o} \tag{15.21}$$

The FRP is an important parameter. At the FRP, the driving force for net K^+-Cl^- cotransport is zero ($\Delta\mu_{K,Cl} = 0$). For instance, in a cortical neuron having typical intracellular K^+ and Cl^- concentrations of 120 mM and 10 mM respectively, and $[Cl^-]_o = 113$ mM, the KCC2 mediated flux will reverse from efflux to influx when $[K^+]_o = 10.6$ mM.

VII. ELECTRONEUTRAL Na^+-Cl^- COTRANSPORTER

The Na^+-Cl^- cotransporter (NCC) was the first member of the SLC12A gene family to be identified at the molecular level. It was initially cloned from epithelial cells of the urinary bladder of the winter flounder (*Pseudopleuronectes americanus*) by Steve Hebert and colleagues (Gamba et al., 1993). NCC is also known as CC3 or TSC (thiazide-sensitive sodium chloride cotransporter), but the preferred nomenclature is NCC or SLC12A3. Its mammalian homolog was isolated from rat renal cortex (Gamba, 2009b). NCC is expressed predominantly in kidney, but is also expressed in osteoblasts and intestine. In mammalian kidney, NCC is located in the apical membrane of the epithelial cells of the distal convoluted tubule (DCT), where it functions as the major salt reabsorption pathway. The DCT mediates reabsorption of 5−15% of glomerular filtrate. The Na^+ gradient that drives transport from the lumen to the interstitium is generated and maintained by the Na^+/K^+ ATPase located in the basolateral membrane of DCT epithelial cells. A distinctive feature of NCC is its sensitivity to thiazides. The natriuretic effect of the thiazide diuretics underlies their therapeutic effect in edema states and hypertension. In addition, luminal thiazide in the DCT has a hypocalciuric effect, implicating NCC in the fine-tuning of Ca^{2+} excretion.

In humans, SLC12A3 is a 55-kb gene containing 26 exons. NCC is a membrane protein of 1002 to 1028 amino acid residues with a predicted topology typical of all the members of the SLC12A family. It exhibits a central hydrophobic domain made up of 12 putative transmembrane (TM) spanning regions. A hydrophilic loop connects TMs 7 and 8 and contains two glycosylation sites. The hydrophobic domain is flanked by a short amino-terminal domain and a long carboxy-terminal domain that are located inside the cell. Functional expression of this cotransporter in *Xenopus laevis* oocytes demonstrated the known characteristics of the cotransporter in native

tissue: sensitivity to thiazide diuretics (metolazone > cyclothiazide > hydrochlorothiazide > chlorothiazide), insensitivity to amiloride and loop diuretics, K^+ independence, lower affinity for Cl^- than for Na^+ and a $1Na^+$:$1Cl^-$ stoichiometry; hence, it is an electroneutral transporter. The molecular mass of the core (deglycosylated) protein is ≈110 kDa. It has ≈45% amino acid identity with NKCC1; 45–48% with NKCC2 and ≈25% with KCC1 and KCC2 (Gamba, 2005, 2009b).

ACKNOWLEDGMENTS

This chapter is dedicated to the memory of Professor Richard D. Keynes (1919–2010), who revolutionized our thinking about chloride transport across cell membranes. The author thanks Professor Eric Delpire for enriching discussions and for reading the manuscript, Professor Shmuel Muallem for providing the original data used in Fig. 15.4 and Professors John Payne and Bliss Forbush for providing Fig. 15.16. Likewise, the author thanks Ms Jeannine Crum for reading the manuscript. The work done by the author has been supported by The National Institute of Neurological Disorders and Stroke Grant NS29227 and by Wright State University Boonshoft School of Medicine Research Challenge and Seed Grant Programs.

BIBLIOGRAPHY

Achilles, K., Okabe, A., Ikeda, M., et al. (2007). Kinetic properties of Cl uptake mediated by Na^+-dependent K^+-$2Cl^-$ cotransport in immature rat neocortical neurons. *J Neurosci, 27*, 8616–8627.

Adrian, R. H. (1961). Internal chloride concentration and chloride efflux of frog muscle. *J Physiol, 156*, 623–632.

Aickin, C. C. (1990). Chloride transport across the sarcolemma of vertebrate smooth and sketal. In F. J. Alvarez-Leefmans, & J. M. Russell (Eds.), *Chloride Channels and Carriers in Nerve, Muscle, and Glial Cells* (pp. 209–249). New York: Plenum Press.

Alper, S. L. (2009). Molecular physiology and genetics of Na^+-independent SLC4 anion exchangers. *J Exp Biol, 212*, 1672–1683.

Alper, S. L., Chernova, M. N., & Stewart, A. K. (2002). How pH regulates a pH regulator: a regulatory hot spot in the N-terminal cytoplasmic domain of the AE2 anion exchanger. *Cell Biochem Biophys, 36*, 123–136.

Alper, S. L., Vandorpe, D. H., Peters, L. L., & Brugnara, C. (2008). Reduced DIDS-sensitive chloride conductance in Ae1-/- mouse erythrocytes. *Blood Cells Mol Dis, 41*, 22–34.

Alvarez, B. V., Kieller, D. M., Quon, A. L., Markovich, D., & Casey, J. R. (2004). Slc26a6: a cardiac chloride-hydroxyl exchanger and predominant chloride-bicarbonate exchanger of the mouse heart. *J Physiol, 561*, 721–734.

Alvarez-Leefmans, F. J. (1990). Intracellular Cl^- regulation and synaptic inhibition in vertebrate and invertebrate neurons. In F. J. Alvarez-Leefmans, & J. M. Russell (Eds.), *Chloride Channels and Carriers in Nerve, Muscle, and Glial Cells* (pp. 109–158). New York: Plenum Press.

Alvarez-Leefmans, F. J. (2009). Chloride transporters in presynaptic inhibition, pain and neurogenic inflammation. In F. J. Alvarez-Leefmans, & E. Delpire (Eds.), *Physiology and Pathology of Chloride Transporters and Channels in the Nervous System* (pp. 439–470). Amsterdam: Academic Press-Elsevier.

Alvarez-Leefmans, F. J., & Delpire, E. (2009a). *Physiology and Pathology of Chloride Transporters and Channels in the Nervous System: from Molecules to Diseases*. Amsterdam: Academic Press-Elsevier.

Alvarez-Leefmans, F. J., & Delpire, E. (2009b). Thermodynamics and kinetics of chloride transport in neurons: an outline. In F. J. Alvarez-Leefmans, & E. Delpire (Eds.), *Physiology and Pathology of Chloride Transporters and Channels in the Nervous System* (pp. 81–108). Amsterdam: Academic Press-Elsevier.

Alvarez-Leefmans, F. J., Gamino, S. M., Giraldez, F., & Nogueron, I. (1988). Intracellular chloride regulation in amphibian dorsal root ganglion neurones studied with ion-selective microelectrodes. *J Physiol, 406*, 225–246.

Alvarez-Leefmans, F. J., Giraldez, F., & Russell, J. M. (1990). Methods for measuring chloride transport across nerve, muscle, and glial cells. In F. J. Alvarez-Leefmans, & J. M. Russell (Eds.), *Chloride Channels and Carriers in Nerve, Muscle, and Glial Cells* (pp. 3–66). New York: Plenum Press.

Alvarez-Leefmans, F. J., Leon-Olea, M., Mendoza-Sotelo, J., Alvarez, F. J., Anton, B., & Garduno, R. (2001). Immunolocalization of the Na^+-K^+-$2Cl^-$ cotransporter in peripheral nervous tissue of vertebrates. *Neuroscience, 104*, 569–582.

Alvarez-Leefmans, F. J., Nani, A., & Márquez, S. (1998). Chloride transport, osmotic balance, and presynaptic inhibition. In P. Rudomin, R. Romo, & L. M. Mendell (Eds.), *Presynaptic Inhibition and Neural Control* (pp. 50–79). New York: Oxford University Press.

Becker, M., Nothwang, H. G., & Friauf, E. (2003). Differential expression pattern of chloride transporters NCC, NKCC2, KCC1, KCC3, KCC4, and AE3 in the developing rat auditory brainstem. *Cell Tissue Res, 312*, 155–165.

Bell, P. D., Komlosi, P., & Zhang, Z. R. (2009). ATP as a mediator of macula densa cell signalling. *Purinergic Signal, 5*, 461–471.

Bellemer, A., Hirata, T., Romero, M. F., & Koelle, M. R. (2011). Two types of chloride transporters are required for $GABA_A$ receptor-mediated inhibition in C. elegans. *Embo J, 30*, 1852–1863.

Ben-Dor, S., Esterman, N., Rubin, E., & Sharon, N. (2004). Biases and complex patterns in the residues flanking protein N-glycosylation sites. *Glycobiology, 14*, 95–101.

Benjamin, B. A., & Johnson, E. A. (1997). A quantitative description of the Na-K-2Cl cotransporter and its conformity to experimental data. *Am J Physiol, 273*, F473–482.

Berglund, K., Kuner, T., & Augustine, G. J. (2009). Clomeleon, a genetically encoded chloride indicator. In F. J. Alvarez-Leefmans, & E. Delpire (Eds.), *Physiology and Pathology of Chloride Transporters and Channels in the Nervous System* (pp. 125–139). Amsterdam: Academic Press-Elsevier.

Bevensee, M. O., & Boron, W. F. (1998). Thermodynamics and physiology of cellular pH regulation. In K. Kaila, & B. R. Ransom (Eds.), *pH and Brain Function* (pp. 173–194). New York: Wiley-Liss.

Bize, I., & Dunham, P. B. (1994). Staurosporine, a protein kinase inhibitor, activates K-Cl cotransport in LK sheep erythrocytes. *Am J Physiol, 266*, C759–770.

Blaesse, P., Airaksinen, M. S., Rivera, C., & Kaila, K. (2009). Cation-chloride cotransporters and neuronal function. *Neuron, 61*, 820–838.

Boettger, T., Hubner, C. A., Maier, H., Rust, M. B., Beck, F. X., & Jentsch, T. J. (2002). Deafness and renal tubular acidosis in mice lacking the K-Cl cotransporter Kcc4. *Nature, 416*, 874–878.

Boettger, T., Rust, M. B., Maier, H., et al. (2003). Loss of K-Cl cotransporter KCC3 causes deafness, neurodegeneration and reduced seizure threshold. *Embo J, 22*, 5422–5434.

Byun, N., & Delpire, E. (2007). Axonal and periaxonal swelling precede peripheral neurodegeneration in KCC3 knockout mice. *Neurobiol Dis, 28*, 39−51.

Carmosino, M., Gimenez, I., Caplan, M., & Forbush, B. (2008). Exon loss accounts for differential sorting of Na-K-Cl cotransporters in polarized epithelial cells. *Mol Biol Cell, 19*, 4341−4351.

Carota, I., Theilig, F., Oppermann, M., et al. (2010). Localization and functional characterization of the human NKCC2 isoforms. *Acta Physiol (Oxf), 199*, 327−338.

Castrop, H., & Schnermann, J. (2008). Isoforms of renal Na-K-2Cl cotransporter NKCC2: expression and functional significance. *Am J Physiol Renal Physiol, 295*, F859−866.

Chen, L. M., Kelly, M. L., Parker, M. D., et al. (2008). Expression and localization of Na-driven $Cl^-HCO_3^-$ exchanger (SLC4A8) in rodent CNS. *Neuroscience, 153*, 162−174.

Chen, Y. F., Chou, C. Y., Ellory, J. C., & Shen, M. R. (2010). The emerging role of KCl cotransport in tumor biology. *Am J Transl Res, 2*, 345−355.

Chou, C. L., Yu, M. J., Kassai, E. M., et al. (2008). Roles of basolateral solute uptake via NKCC1 and of myosin II in vasopressin-induced cell swelling in inner medullary collecting duct. *Am J Physiol Renal Physiol, 295*, F192−201.

Darman, R. B., & Forbush, B. (2002). A regulatory locus of phosphorylation in the N terminus of the Na-K-Cl cotransporter, NKCC1. *J Biol Chem, 277*, 37542−37550.

Dehaye, J. P., Nagy, A., Premkumar, A., & Turner, R. J. (2003). Identification of a functionally important conformation-sensitive region of the secretory Na^+-K^+-$2Cl^-$ cotransporter (NKCC1). *J Biol Chem, 278*, 11811−11817.

Delpire, E., & Gagnon, K. B. (2008). SPAK and OSR1: STE20 kinases involved in the regulation of ion homoeostasis and volume control in mammalian cells. *Biochem J, 409*, 321−331.

Delpire, E., & Gagnon, K. B. (2011). Kinetics of hyperosmotically-stimulated Na-K-2Cl cotransporter in Xenopus laevis oocytes. *Am J Physiol Cell Physiol*.

Delpire, E., & Lauf, P. K. (1991). Magnesium and ATP dependence of K-Cl cotransport in low K^+ sheep red blood cells. *J Physiol, 441*, 219−231.

Delpire, E., & Lauf, P. K. (1992). Kinetics of DIDS inhibition of swelling-activated K-Cl cotransport in low K sheep erythrocytes. *J Membr Biol, 126*, 89−96.

Delpire, E., Days, E., Lewis, L. M., et al. (2009). Small-molecule screen identifies inhibitors of the neuronal K-Cl cotransporter KCC2. *Proc Natl Acad Sci, USA, 106*, 5383−5388.

Delpire, E., Lu, J., England, R., Dull, C., & Thorne, T. (1999). Deafness and imbalance associated with inactivation of the secretory Na-K-2Cl cotransporter. *Nat Genet, 22*, 192−195.

Delpire, E., Rauchman, M. I., Beier, D. R., Hebert, S. C., & Gullans, S. R. (1994). Molecular cloning and chromosome localization of a putative basolateral Na^+-K^+-$2Cl^-$ cotransporter from mouse inner medullary collecting duct (mIMCD-3) cells. *J Biol Chem, 269*, 25677−25683.

Di Fulvio, M., & Alvarez-Leefmans, F. J. (2009). The NKCC and NCC genes: an in silico view. In F. J. Alvarez-Leefmans, & E. Delpire (Eds.), *Physiology and Pathology of Chloride Transporters and Channels in the Nervous System: from Molecules to Diseases* (pp. 169−208). Amsterdam: Academic Press-Elsevier.

Duan, D. (2009). Phenomics of cardiac chloride channels: the systematic study of chloride channel function in the heart. *J Physiol, 587*, 2163−2177.

Dupre, N., Howard, H. C., Mathieu, J., et al. (2003). Hereditary motor and sensory neuropathy with agenesis of the corpus callosum. *Ann Neurol, 54*, 9−18.

Dzhala, V. I., Kuchibhotla, K. V., Glykys, J. C., et al. (2010). Progressive NKCC1-dependent neuronal chloride accumulation during neonatal seizures. *J Neurosci, 30*, 11745−11761.

Ellory, J. C., & Dunham, P. B. (1980). Volume-dependent passive potassium transport in LK LK sheep red cells. In U. V. Lassen, H. H. Ussing, & J. O. Wieth (Eds.), *Membrane Transport in Erythrocytes, Alfred Benzon Symposium, Vol. 14* (pp. 409−427). Munksgaard.

Evans, M. G., Marty, A., Tan, Y. P., & Trautmann, A. (1986). Blockage of Ca-activated Cl conductance by furosemide in rat lacrimal glands. *Pflügers Arch, 406*, 65−68.

Evans, R. L., Park, K., Turner, R. J., et al. (2000). Severe impairment of salivation in $Na^+/K^+/2Cl^-$ cotransporter (NKCC1)-deficient mice. *J Biol Chem, 275*, 26720−26726.

Feng, L., Campbell, E. B., Hsiung, Y., & MacKinnon, R. (2010). Structure of a eukaryotic CLC transporter defines an intermediate state in the transport cycle. *Science, 330*, 635−641.

Fischbarg, J. (2010). Fluid transport across leaky epithelia: central role of the tight junction and supporting role of aquaporins. *Physiol Rev, 90*, 1271−1290.

Flagella, M., Clarke, L. L., Miller, M. L., et al. (1999). Mice lacking the basolateral Na-K-2Cl cotransporter have impaired epithelial chloride secretion and are profoundly deaf. *J Biol Chem, 274*, 26946−26955.

Flatman, P. W. (2004). Regulation of Na-K-2Cl cotransport in red cells. *Adv Exp Med Biol, 559*, 77−88.

Flemmer, A. W., Gimenez, I., Dowd, B. F., Darman, R. B., & Forbush, B. (2002). Activation of the Na-K-Cl cotransporter NKCC1 detected with a phospho-specific antibody. *J Biol Chem, 277*, 37551−37558.

Frings, S. (2009). Chloride-based signal amplification in olfactory sensory neurons. In F. J. Alvarez-Leefmans, & E. Delpire (Eds.), *Physiology and Pathology of Chloride Transporters and Channels in the Nervous System* (pp. 413−424). Amsterdam: Academic Press-Elsevier.

Fujii, T., Takahashi, Y., Ikari, A., et al. (2009). Functional association between K^+-Cl^- cotransporter-4 and H^+, K^+-ATPase in the apical canalicular membrane of gastric parietal cells. *J Biol Chem, 284*, 619−629.

Gamba, G. (2005). Molecular physiology and pathophysiology of electroneutral cation-chloride cotransporters. *Physiol Rev, 85*, 423−493.

Gamba, G. (2009a). The sodium-dependent chloride cotransporters. In F. J. Alvarez-Leefmans, & E. Delpire (Eds.), *Physiology and Pathology of Chloride Transporters and Channels in the Nervous System: from Molecules to Diseases* (pp. 307−331). Amsterdam: Academic Press-Elsevier.

Gamba, G. (2009b). The thiazide-sensitive Na^+-Cl^- cotransporter: molecular biology, functional properties, and regulation by WNKs. *Am J Physiol Renal Physiol, 297*, F838−F848.

Gamba, G., & Friedman, P. A. (2009). Thick ascending limb: the Na^+:K^+:$2Cl^-$ cotransporter, NKCC2, and the calcium-sensing receptor, CaSR. *Pflügers Arch, 458*, 61−76.

Gamba, G., Garbarini, N., & Delpire, E. (2009). Regulation of cation-chloride cotransporters. In F. J. Alvarez-Leefmans, & E. Delpire (Eds.), *Physiology and Pathology of Chloride Transporters and Channels in the Nervous System: from Molecules to Diseases* (pp. 357−381). Amsterdam: Academic Press-Elsevier.

Gamba, G., Miyanoshita, A., Lombardi, M., et al. (1994). Molecular cloning, primary structure, and characterization of two members of the mammalian electroneutral sodium-(potassium)-chloride cotransporter family expressed in kidney. *J Biol Chem, 269*, 17713–17722.

Gamba, G., Saltzberg, S. N., Lombardi, M., et al. (1993). Primary structure and functional expression of a cDNA encoding the thiazide-sensitive, electroneutral sodium-chloride cotransporter. *Proc Natl Acad Sci, USA, 90*, 2749–2753.

Garbarini, N., & Delpire, E. (2009). Kockout models of cation-chloride cotransporters. In F. J. Alvarez-Leefmans, & E. Delpire (Eds.), *Physiology and Pathology of Chloride Transporters and Channels in the Nervous System: from Molecules to Diseases* (pp. 159–166). Amsterdam: Academic Press-Elsevier.

Garcia-Celma, J. J., Ploch, J., Smirnova, I., Kaback, H. R., & Fendler, K. (2010). Delineating electrogenic reactions during lactose/H^+ symport. *Biochemistry, 49*, 6115–6121.

Geck, P., & Heinz, E. (1986). The Na-K-2Cl cotransport system. *J Membr Biol, 91*, 97–105.

Geck, P., Pietrzyk, C., Burckhardt, B. C., Pfeiffer, B., & Heinz, E. (1980). Electrically silent cotransport on Na^+, K^+ and Cl^- in Ehrlich cells. *Biochim Biophys Acta, 600*, 432–447.

Gerelsaikhan, T., Parvin, M. N., & Turner, R. J. (2006). Biogenesis and topology of the secretory Na^+-K^+-$2Cl^-$ cotransporter (NKCC1) studied in intact mammalian cells. *Biochemistry, 45*, 12060–12067.

Gerelsaikhan, T., & Turner, R. J. (2000a). Membrane topology and function of the secretory Na^+-K^+-$2Cl^-$ cotransporter (NKCC1). *J Korean Med Sci.*(15 Suppl), S3–S4.

Gerelsaikhan, T., & Turner, R. J. (2000b). Transmembrane topology of the secretory Na^+-K^+-$2Cl^-$ cotransporter NKCC1 studied by in vitro translation. *J Biol Chem, 275*, 40471–40477.

Gibson, J. S., Ellory, J. C., Adragna, N. C., & Lauf, P. K. (2009). Pathophysiology of the K^+-Cl^-cotransporters: paths to discovery and overview. In F. J. Alvarez-Leefmans, & E. Delpire (Eds.), *Physiology and Pathology of Chloride Transporters and Channels in the Nervous System* (pp. 27–42). Amsterdam: Academic Press-Elsevier.

Gillen, C. M., & Forbush, B., 3rd. (1999). Functional interaction of the K-Cl cotransporter (KCC1) with the Na-K-Cl cotransporter in HEK-293 cells. *Am J Physiol, 276*, C328–336.

Gillen, C. M., Brill, S., Payne, J. A., & Forbush, B., 3rd. (1996). Molecular cloning and functional expression of the K-Cl cotransporter from rabbit, rat, and human. A new member of the cation-chloride cotransporter family. *J Biol Chem, 271*, 16237–16244.

Gonzalez-Islas, C., Chub, N., & Wenner, P. (2009). NKCC1 and AE3 appear to accumulate chloride in embryonic motoneurons. *J Neurophysiol, 101*, 507–518.

Good, D. W. (1994). Ammonium transport by the thick ascending limb of Henle's loop. *Annu Rev Physiol, 56*, 623–647.

Gosmanov, A. R., Schneider, E. G., & Thomason, D. B. (2003). NKCC activity restores muscle water during hyperosmotic challenge independent of insulin, ERK, and p38 MAPK. *Am J Physiol Regul Integr Comp Physiol, 284*, R655–665.

Granados-Soto, V., Arguelles, C. F., & Alvarez-Leefmans, F. J. (2005). Peripheral and central antinociceptive action of Na^+-K^+-$2Cl^-$ cotransporter blockers on formalin-induced nociception in rats. *Pain, 114*, 231–238.

Grichtchenko, I. I., Choi, I., Zhong, X., Bray-Ward, P., Russell, J. M., & Boron, W. F. (2001). Cloning, characterization, and chromosomal mapping of a human electroneutral Na^+-driven Cl^-HCO_3 exchanger. *J Biol Chem, 276*, 8358–8363.

Gundersen, D., Orlowski, J., & Rodriguez-Boulan, E. (1991). Apical polarity of Na, K-ATPase in retinal pigment epithelium is linked to a reversal of the ankyrin-fodrin submembrane cytoskeleton. *J Cell Biol, 112*, 863–872.

Haas, B. R., & Sontheimer, H. (2010). Inhibition of the sodium-potassium-chloride cotransporter isoform-1 reduces glioma invasion. *Cancer Res, 70*, 5597–5606.

Haas, M. (1994). The Na-K-Cl cotransporters. *Am J Physiol, 267*, C869–885.

Haas, M., & Forbush, B., 3rd. (1998). The Na-K-Cl cotransporters. *J Bioenerg Biomembr, 30*, 161–172.

Haas, M., & Forbush, B., 3rd. (2000). The Na-K-Cl cotransporter of secretory epithelia. *Annu Rev Physiol, 62*, 515–534.

Haas, M., Schmidt, W. F., 3rd, & McManus, T. J. (1982). Catecholamine-stimulated ion transport in duck red cells. Gradient effects in electrically neutral [Na^+ K^+ $2Cl^-$] Cotransport. *J Gen Physiol, 80*, 125–147.

Hamann, S., Herrera-Perez, J. J., Bundgaard, M., Alvarez-Leefmans, F. J., & Zeuthen, T. (2005). Water permeability of Na^+-K^+-$2Cl^-$ cotransporters in mammalian epithelial cells. *J Physiol, 568*, 123–135.

Hamann, S., Herrera-Perez, J. J., Zeuthen, T., & Alvarez-Leefmans, F. J. (2010). Cotransport of water by the Na^+-K^+-$2Cl^-$ cotransporter NKCC1 in mammalian epithelial cells. *J Physiol, 588*, 4089–4101.

Hannaert, P., Alvarez-Guerra, M., Pirot, D., Nazaret, C., & Garay, R. P. (2002). Rat NKCC2/NKCC1 cotransporter selectivity for loop diuretic drugs. *Naunyn Schmiedebergs Arch Pharmacol, 365*, 193–199.

Harris, G. L., & Betz, W. J. (1987). Evidence for active chloride accumulation in normal and denervated rat lumbrical muscle. *J Gen Physiol, 90*, 127–144.

Hartmann, A. M., Wenz, M., Mercado, A., et al. (2010). Differences in the large extracellular loop between the K^+-Cl^- cotransporters KCC2 and KCC4. *J Biol Chem, 285*, 23994–24002.

Hartzell, H. C. (2009). Chloride channels: an historical perspective. In F. J. Alvarez-Leefmans, & E. Delipre (Eds.), *Physiology and Pathology of Chloride Transporters and Channels in the Nervous System: from Molecules to Diseases* (pp. 3–15). Amsterdam: Academic Press-Elsevier.

Hengl, T., Kaneko, H., Dauner, K., Vocke, K., Frings, S., & Mohrlen, F. (2010). Molecular components of signal amplification in olfactory sensory cilia. *Proc Natl Acad Sci, USA, 107*, 6052–6057.

Hiki, K., D'Andrea, R. J., Furze, J., et al. (1999). Cloning, characterization, and chromosomal location of a novel human K^+-Cl^- cotransporter. *J Biol Chem, 274*, 10661–10667.

Hodgkin, A. L., & Horowicz, P. (1959). The influence of potassium and chloride ions on the membrane potential of single muscle fibres. *J Physiol, 148*, 127–160.

Hoffmann, E. K. (2001). The pump and leak steady-state concept with a variety of regulated leak pathways. *J Membr Biol, 184*, 321–330.

Hoffmann, E. K., Lambert, I. H., & Pedersen, S. F. (2009). Physiology of cell volume regulation in vertebrates. *Physiol Rev, 89*, 193–277.

Hoffmann, E. K., Schiodt, M., & Dunham, P. (1986). The number of chloride-cation cotransport sites on Ehrlich ascites cells measured with [3H]bumetanide. *Am J Physiol, 250*, C688–693.

Howard, H. C., Mount, D. B., Rochefort, D., et al. (2002). The K-Cl cotransporter KCC3 is mutant in a severe peripheral neuropathy

associated with agenesis of the corpus callosum. *Nat Genet, 32*, 384−392.

Hubner, C. A., & Rust, M. B. (2007). Physiology of cation-chloride cotransporters. In M. Pusch (Ed.), *Chloride Movements across Cellular Membranes, Vol. 38* (pp. 241−277). Amsterdam: Elsevier.

Hubner, C. A., Stein, V., Hermans-Borgmeyer, I., Meyer, T., Ballanyi, K., & Jentsch, T. J. (2001). Disruption of KCC2 reveals an essential role of K-Cl cotransport already in early synaptic inhibition. *Neuron, 30*, 515−524.

Hutter, O. F., & Noble, D. (1960). The chloride conductance of frog skeletal muscle. *J Physiol, 151*, 89−102.

Ikeda, K., Oshima, T., Hidaka, H., & Takasaka, T. (1997). Molecular and clinical implications of loop diuretic ototoxicity. *Hear Res, 107*, 1−8.

Isenring, P., & Forbush, B. (2001). Ion transport and ligand binding by the Na-K-Cl cotransporter, structure-function studies. *Comp Biochem Physiol A Mol Integr Physiol, 130*, 487−497.

Jennings, M. L., & Adame, M. F. (2001). Direct estimate of 1:1 stoichiometry of K^+-Cl^- cotransport in rabbit erythrocytes. *Am J Physiol Cell Physiol, 281*, C825−832.

Jentsch, T. J. (2008). CLC chloride channels and transporters: from genes to protein structure, pathology and physiology. *Crit Rev Biochem Mol Biol, 43*, 3−36.

Jurkat-Rott, K., Fauler, M., & Lehmann-Horn, F. (2006). Ion channels and ion transporters of the transverse tubular system of skeletal muscle. *J Muscle Res Cell Motil, 27*, 275−290.

Kahle, K. T., Rinehart, J., & Lifton, R. P. (2010). Phosphoregulation of the Na-K-2Cl and K-Cl cotransporters by the WNK kinases. *Biochim Biophys Acta, 1802*, 1150−1158.

Kahle, K. T., Simard, J. M., Staley, K. J., Nahed, B. V., Jones, P. S., & Sun, D. (2009). Molecular mechanisms of ischemic cerebral edema: role of electroneutral ion transport. *Physiology (Bethesda), 24*, 257−265.

Kahle, K. T., & Staley, K. J. (2008). The bumetanide-sensitive Na-K-2Cl cotransporter NKCC1 as a potential target of a novel mechanism-based treatment strategy for neonatal seizures. *Neurosurg Focus, 25*, E22.

Kaji, D. M. (1993). Effect of membrane potential on K-Cl transport in human erythrocytes. *Am J Physiol, 264*, C376−382.

Karadsheh, M. F., Byun, N., Mount, D. B., & Delpire, E. (2004). Localization of the KCC4 potassium-chloride cotransporter in the nervous system. *Neuroscience, 123*, 381−391.

Keynes, R. D. (1963). Chloride in the squid giant axon. *J Physiol, 169*, 690−705.

Kim, Y., & Trussell, L. O. (2009). Negative shift in the glycine reversal potential mediated by a Ca^{2+}- and pH-dependent mechanism in interneurons. *J Neurosci, 29*, 11495−11510.

Kristensen, M., & Juel, C. (2010). Potassium-transporting proteins in skeletal muscle: cellular location and fibre-type differences. *Acta Physiol (Oxf), 198*, 105−123.

Kurschat, C. E., Shmukler, B. E., Jiang, L., et al. (2006). Alkaline-shifted pHo sensitivity of AE2c1-mediated anion exchange reveals novel regulatory determinants in the AE2 N-terminal cytoplasmic domain. *J Biol Chem, 281*, 1885−1896.

Lang, F., Vallon, V., Knipper, M., & Wangemann, P. (2007). Functional significance of channels and transporters expressed in the inner ear and kidney. *Am J Physiol Cell Physiol, 293*, C1187−1208.

Lauf, P. K., & Theg, B. E. (1980). A chloride dependent K^+ flux induced by N-ethylmaleimide in genetically low K^+ sheep and goat erythrocytes. *Biochem Biophys Res Commun, 92*, 1422−1428.

Le Rouzic, P., Ivanov, T. R., Stanley, P. J., et al. (2006). KCC3 and KCC4 expression in rat adult forebrain. *Brain Res., 1110*, 39−45.

Lerma, J., & Martin del Rio, R. (1992). Chloride transport blockers prevent N-methyl-D-aspartate receptor-channel complex activation. *Mol Pharmacol, 41*, 217−222.

Lytle, C. (2003). Na^+-K^+-$2Cl^-$ cotransport. In I. Bernhardt, & J. C. Ellory (Eds.), *Red Cell Membrane Transport in Health and Disease* (pp. 173−195). Berlin ; New York: Springer.

Lytle, C., & Forbush, B., 3rd. (1992). The Na-K-Cl cotransport protein of shark rectal gland. II. Regulation by direct phosphorylation. *J Biol Chem., 267*, 25438−25443.

Lytle, C., McManus, T. J., & Haas, M. (1998). A model of Na-K-2Cl cotransport based on ordered ion binding and glide symmetry. *Am J Physiol, 274*, C299−309.

Lytle, C., Xu, J. C., Biemesderfer, D., & Forbush, B., 3rd. (1995). Distribution and diversity of Na-K-Cl cotransport proteins: a study with monoclonal antibodies. *Am J Physiol, 269*, C1496−1505.

MacAulay, N., Hamann, S., & Zeuthen, T. (2009). Chloride transporters as water pumps: elements in a new model of epithelial water transport. In F. J. Alvarez-Leefmans, & E. Delpire (Eds.), *Physiology and Pathology of Chloride Transporters and Channels in the Nervous System* (pp. 547−568). Amsterdam: Academic Press-Elsevier.

Marcano, M., Yang, H. M., Nieves-Gonzalez, A., Clausen, C., & Moore, L. C. (2009). Parameter estimation for mathematical models of NKCC2 cotransporter isoforms. *Am J Physiol Renal Physiol, 296*, F369−381.

McDaniel, N., Pace, A. J., Spiegel, S., et al. (2005). Role of Na-K-2Cl cotransporter-1 in gastric secretion of nonacidic fluid and pepsinogen. *Am J Physiol Gastrointest Liver Physiol, 289*, G550−560.

McRoberts, J. A., Erlinger, S., Rindler, M. J., & Saier, M. H., Jr. (1982). Furosemide-sensitive salt transport in the Madin-Darby canine kidney cell line. Evidence for the cotransport of Na^+, K^+, and Cl. *J Biol Chem, 257*, 2260−2266.

Mercado, A., Song, L., Vazquez, N., Mount, D. B., & Gamba, G. (2000). Functional comparison of the K^+-Cl^- cotransporters KCC1 and KCC4. *J Biol Chem, 275*, 30326−30334.

Mercado, A., Vazquez, N., Song, L., et al. (2005). NH2-terminal heterogeneity in the KCC3 K^+-Cl^- cotransporter. *Am J Physiol Renal Physiol, 289*, F1246−1261.

Migliati, E., Meurice, N., DuBois, P., et al. (2009). Inhibition of aquaporin-1 and aquaporin-4 water permeability by a derivative of the loop diuretic bumetanide acting at an internal pore-occluding binding site. *Mol Pharmacol, 76*, 105−112.

Mistrik, P., & Ashmore, J. (2009). The role of potassium recirculation in cochlear amplification. *Curr Opin Otolaryngol Head Neck Surg, 17*, 394−399.

Mount, D. B., Mercado, A., Song, L., et al. (1999). Cloning and characterization of KCC3 and KCC4, new members of the cation-chloride cotransporter gene family. *J Biol Chem, 274*, 16355−16362.

Munoz, A., Mendez, P., DeFelipe, J., & Alvarez-Leefmans, F. J. (2007). Cation-chloride cotransporters and GABA-ergic innervation in the human epileptic hippocampus. *Epilepsia, 48*, 663−673.

Nejsum, L. N., Praetorius, J., & Nielsen, S. (2005). NKCC1 and NHE1 are abundantly expressed in the basolateral plasma membrane of secretory coil cells in rat, mouse, and human sweat glands. *Am J Physiol Cell Physiol, 289*, C333−340.

Nielsen, S., Maunsbach, A. B., Ecelbarger, C. A., & Knepper, M. A. (1998). Ultrastructural localization of Na-K-2Cl cotransporter in thick ascending limb and macula densa of rat kidney. *Am J Physiol, 275*, F885−893.

O'Donnell, M. E., Tran, L., Lam, T. I., Liu, X. B., & Anderson, S. E. (2004). Bumetanide inhibition of the blood-brain barrier Na-K-Cl cotransporter reduces edema formation in the rat middle cerebral artery occlusion model of stroke. *J Cereb Blood Flow Metab, 24*, 1046–1056.

O'Grady, S. M., Palfrey, H. C., & Field, M. (1987a). Characteristics and functions of Na-K-Cl cotransport in epithelial tissues. *Am J Physiol, 253*, C177–192.

O'Grady, S. M., Palfrey, H. C., & Field, M. (1987b). Na-K-2Cl cotransport in winter flounder intestine and bovine kidney outer medulla: [3H] bumetanide binding and effects of furosemide analogues. *J Membr Biol, 96*, 11–18.

Oppermann, M., Mizel, D., Huang, G., et al. (2006). Macula densa control of renin secretion and preglomerular resistance in mice with selective deletion of the B isoform of the Na, K,2Cl cotransporter. *J Am Soc Nephrol, 17*, 2143–2152.

Oppermann, M., Mizel, D., Kim, S. M., et al. (2007). Renal function in mice with targeted disruption of the A isoform of the Na-K-2Cl cotransporter. *J Am Soc Nephrol, 18*, 440–448.

Pan, D., Kalfa, T. A., Wang, D., et al. (2011). KCl cotransporter gene expression during human and murine erythroid differentiation. *J Biol Chem*.

Panet, R., Marcus, M., & Atlan, H. (2000). Overexpression of the $Na^{+/}K^{+}/Cl^{-}$ cotransporter gene induces cell proliferation and phenotypic transformation in mouse fibroblasts. *J Cell Physiol, 182*, 109–118.

Paredes, A., Plata, C., Rivera, M., et al. (2006). Activity of the renal Na^{+}-K^{+}-$2Cl^{-}$ cotransporter is reduced by mutagenesis of N-glycosylation sites: role for protein surface charge in Cl^{-} transport. *Am J Physiol Renal Physiol, 290*, F1094–1102.

Payne, J. A. (1997). Functional characterization of the neuronal-specific K-Cl cotransporter: implications for $[K^{+}]_o$ regulation. *Am J Physiol, 273*, C1516–1525.

Payne, J. A. (2009). The potasium-chloride cotransporters: from cloning to structure and function. In F. J. Alvarez-Leefmans, & E. Delpire (Eds.), *Physiology and Pathology of Chloride Transporters and Channels in the Nervous System: from Molecules to Diseases* (pp. 333–356). Amsterdam: Academic Press-Elsevier.

Payne, J. A., & Forbush, B., 3rd. (1994). Alternatively spliced isoforms of the putative renal Na-K-Cl cotransporter are differentially distributed within the rabbit kidney. *Proc Natl Acad Sci USA, 91*, 4544–4548.

Payne, J. A., & Forbush, B., 3rd. (1995). Molecular characterization of the epithelial Na-K-Cl cotransporter isoforms. *Curr Opin Cell Biol, 7*, 493–503.

Payne, J. A., Rivera, C., Voipio, J., & Kaila, K. (2003). Cation-chloride cotransporters in neuronal communication, development and trauma. *Trends Neurosci, 26*, 199–206.

Payne, J. A., Stevenson, T. J., & Donaldson, L. F. (1996). Molecular characterization of a putative K-Cl cotransporter in rat brain. A neuronal-specific isoform. *J Biol Chem, 271*, 16245–16252.

Payne, J. A., Xu, J. C., Haas, M., Lytle, C. Y., Ward, D., & Forbush, B., 3rd. (1995). Primary structure, functional expression, and chromosomal localization of the bumetanide-sensitive Na-K-Cl cotransporter in human colon. *J Biol Chem, 270*, 17977–17985.

Pearson, M. M., Lu, J., Mount, D. B., & Delpire, E. (2001). Localization of the K^{+}-Cl^{-} cotransporter, KCC3, in the central and peripheral nervous systems: expression in the choroid plexus, large neurons and white matter tracts. *Neuroscience, 103*, 481–491.

Pégurier, C., Bosman, N., Collart, P., Delporte, M. L., Leclercq, K., Lengelé, S., Kanduluru, A. K., Meunier, S., Pacico, N., Vadali, L. R., Wagner, A., Wolff, C., & Provins, L. (2010). Benzyl prolinate derivatives as novel selective KCC2 blockers. *Bioorg Med Chem Lett, 20*, 2542–2545.

Peti-Peterdi, J., & Harris, R. C. (2010). Macula densa sensing and signaling mechanisms of renin release. *J Am Soc Nephrol, 21*, 1093–1096.

Plata, C., Meade, P., Vazquez, N., Hebert, S. C., & Gamba, G. (2002). Functional properties of the apical Na^{+}-K^{+}-$2Cl^{-}$ cotransporter isoforms. *J Biol Chem, 277*, 11004–11012.

Plotkin, M. D., Kaplan, M. R., Peterson, L. N., Gullans, S. R., Hebert, S. C., & Delpire, E. (1997). Expression of the Na^{+}-K^{+}-$2Cl^{-}$ cotransporter BSC2 in the nervous system. *Am J Physiol, 272*, C173–183.

Prasad, V., Bodi, I., Meyer, J. W., et al. (2008). Impaired cardiac contractility in mice lacking both the AE3 Cl^{-}/HCO_3^{-} exchanger and the NKCC1 Na^{+}-K^{+}-$2Cl^{-}$ cotransporter: effects on Ca2+ handling and protein phosphatases. *J Biol Chem, 283*, 31303–31314.

Race, J. E., Makhlouf, F. N., Logue, P. J., Wilson, F. H., Dunham, P. B., & Holtzman, E. J. (1999). Molecular cloning and functional characterization of KCC3, a new K-Cl cotransporter. *Am J Physiol, 277*, C1210–1219.

Randall, J., Thorne, T., & Delpire, E. (1997). Partial cloning and characterization of Slc12a2: the gene encoding the secretory Na^{+}-K^{+}-$2Cl^{-}$ cotransporter. *Am J Physiol, 273*, C1267–1277.

Reddy, M. M., & Quinton, P. M. (1999). Bumetanide blocks CFTR GCl in the native sweat duct. *Am J Physiol, 276*, C231–237.

Reuss, L. (1997). Epithelial transport. In J. P. Hoffman, & J. D. Jamieson (Eds.), *Handbook of Physiology. Section 14: Cell Physiology* (pp. 309–388). New York: Oxford University Press.

Reynolds, A., Brustein, E., Liao, M., et al. (2008). Neurogenic role of the depolarizing chloride gradient revealed by global overexpression of KCC2 from the onset of development. *J Neurosci, 28*, 1588–1597.

Rinehart, J., Maksimova, Y. D., Tanis, J. E., et al. (2009). Sites of regulated phosphorylation that control K-Cl cotransporter activity. *Cell., 138*, 525–536.

Rivera, C., Voipio, J., Payne, J. A., et al. (1999). The K^{+}/Cl^{-} cotransporter KCC2 renders GABA hyperpolarizing during neuronal maturation. *Nature, 397*, 251–255.

Rocha-Gonzalez, H. I., Mao, S., & Alvarez-Leefmans, F. J. (2008). Na^{+}, K^{+},$2Cl^{-}$ cotransport and intracellular chloride regulation in rat primary sensory neurons: thermodynamic and kinetic aspects. *J Neurophysiol, 100*, 169–184.

Romero, M. F., Chang, M.-H., & Mount, D. (2009). From cloning to structure, function, and regulation of chloride-dependent and independent bicarbonate transporters. In F. J. Alvarez-Leefmans, & E. Delipre (Eds.), *Physiology and Pathology of Chloride Transporters and Channels in the Nervous System: from Molecules to Diseases* (pp. 43–79). Amsterdam: Academic Press-Elsevier.

Romero, M. F., Fulton, C. M., & Boron, W. F. (2004). The SLC4 family of HCO_3^{-} transporters. *Pflügers Arch, 447*, 495–509.

Roseth, S., Fykse, E. M., & Fonnum, F. (1995). Uptake of L-glutamate into rat brain synaptic vesicles: effect of inhibitors that bind specifically to the glutamate transporter. *J Neurochem, 65*, 96–103.

Rudomin, P., & Schmidt, R. F. (1999). Presynaptic inhibition in the vertebrate spinal cord revisited. *Exp Brain Res, 129*, 1–37.

Russell, J. M. (1984). Chloride in the squid giant axon. *Curr Top Membr Transp, 22*, 177−193.

Russell, J. M. (2000). Sodium-potassium-chloride cotransport. *Physiol Rev, 80*, 211−276.

Russell, J. M. (2009). Sodium-coupled chloride cotransporters: discovery and newly emerging concepts. In F. J. Alvarez-Leefmans, & E. Delpire (Eds.), *Physiology and Pathology of Chloride Transporters and Channels in the Nervous System* (pp. 17−26). Amsterdam: Academic Press-Elsevier.

Rust, M. B., Alper, S. L., Rudhard, Y., et al. (2007). Disruption of erythroid K-Cl cotransporters alters erythrocyte volume and partially rescues erythrocyte dehydration in SAD mice. *J Clin Invest, 117*, 1708−1717.

Rust, M. B., Faulhaber, J., Budack, M. K., et al. (2006). Neurogenic mechanisms contribute to hypertension in mice with disruption of the K-Cl cotransporter KCC3. *Circ Res, 98*, 549−556.

Schlatter, E., Greger, R., & Weidtke, C. (1983). Effect of "high ceiling" diuretics on active salt transport in the cortical thick ascending limb of Henle's loop of rabbit kidney. Correlation of chemical structure and inhibitory potency. *Pflügers Arch, 396*, 210−217.

Shankar, S. S., & Brater, D. C. (2003). Loop diuretics: from the Na-K-2Cl transporter to clinical use. *Am J Physiol Renal Physiol, 284*, F11−21.

Shcheynikov, N., Wang, Y., Park, M., et al. (2006). Coupling modes and stoichiometry of Cl^-/HCO_3^- exchange by slc26a3 and slc26a6. *J Gen Physiol, 127*, 511−524.

Shekarabi, M., Salin-Cantegrel, A., Laganiere, J., Gaudet, R., Dion, P., & Rouleau, G. A. (2011). Cellular expression of the K^+-Cl^- cotransporter KCC3 in the central nervous system of mouse. *Brain Res, 1374*, 15−26.

Shillingford, J. M., Miyoshi, K., Flagella, M., Shull, G. E., & Hennighausen, L. (2002). Mouse mammary epithelial cells express the Na-K-Cl cotransporter, NKCC1: characterization, localization, and involvement in ductal development and morphogenesis. *Mol Endocrinol, 16*, 1309−1321.

Silva, P., Solomon, R. J., & Epstein, F. H. (1996). The rectal gland of Squalus acanthias: a model for the transport of chloride. *Kidney Int, 49*, 1552−1556.

Silva, P., Stoff, J., Field, M., Fine, L., Forrest, J. N., & Epstein, F. H. (1977). Mechanism of active chloride secretion by shark rectal gland: role of Na-K-ATPase in chloride transport. *Am J Physiol, 233*, F298−306.

Somjen, G. S. (2004). *Ions in the Brain*. New York: Oxford University Press.

Song, L., Mercado, A., Vazquez, N., et al. (2002). Molecular, functional, and genomic characterization of human KCC2, the neuronal K-Cl cotransporter. *Brain Res Mol Brain Res, 103*, 91−105.

Steinbach, H. B. (1941). Chloride in the giant axons of the squid. *J Cell Comp Physiol, 17*, 57−64.

Stil, A., Liabeuf, S., Jean-Xavier, C., Brocard, C., Viemari, J. C., & Vinay, L. (2009). Developmental up-regulation of the potassium-chloride cotransporter type 2 in the rat lumbar spinal cord. *Neuroscience, 164*, 809−821.

Strauss, O. (2005). The retinal pigment epithelium in visual function. *Physiol Rev, 85*, 845−881.

Sung, K. W., Kirby, M., McDonald, M. P., Lovinger, D. M., & Delpire, E. (2000). Abnormal $GABA_A$ receptor-mediated currents in dorsal root ganglion neurons isolated from Na-K-2Cl cotransporter null mice. *J Neurosci, 20*, 7531−7538.

Takahashi, N., Chernavvsky, D. R., Gomez, R. A., Igarashi, P., Gitelman, H. J., & Smithies, O. (2000). Uncompensated polyuria in a mouse model of Bartter's syndrome. *Proc Natl Acad Sci USA, 97*, 5434−5439.

Thomas, R. C. (1984). Experimental displacement of intracellular pH and the mechanism of its subsequent recovery. *J Physiol, 354*, 3P−22P.

Tradtrantip, L., Tajima, M., Li, L., & Verkman, A. S. (2009). Aquaporin water channels in transepithelial fluid transport. *J Med Invest* (56 Suppl), 179−184.

Ussing, H. H. (1982). Volume regulation of frog skin epithelium. *Acta Physiol Scand, 114*, 363−369.

Uvarov, P., Ludwig, A., Markkanen, M., et al. (2007). A novel N-terminal isoform of the neuron-specific K-Cl cotransporter KCC2. *J Biol Chem, 282*, 30570−30576.

Vaughan-Jones, R. D. (1982). Chloride activity and its control in skeletal and cardiac muscle. *Philos Trans R Soc Lond B Biol Sci., 299*, 537−548.

Velazquez, H., & Silva, T. (2003). Cloning and localization of KCC4 in rabbit kidney: expression in distal convoluted tubule. *Am J Physiol Renal Physiol, 285*, F49−58.

Verkman, A. S. (2009). Chemical and GFP-based fluorescent chloride indicators. In F. J. Alvarez-Leefmans, & E. Delipre (Eds.), *Physiology and Pathology of Chloride Transporters and Channels in the Nervous System: from Molecules to Diseases* (pp. 111−123). Amsterdam: Academic Press-Elsevier.

Viemari, J. C., Bos, R., Boulenguez, P., et al. (2011). Importance of chloride homeostasis in the operation of rhythmic motor networks. *Prog Brain Res, 188*, 3−14.

Walz, W. (1992). Role of Na/K/Cl cotransport in astrocytes. *Can J Physiol Pharmacol,* (70 Suppl), S260−262.

Wang, D. D., & Kriegstein, A. R. (2009). Defining the role of GABA in cortical development. *J Physiol, 587*, 1873−1879.

Warmuth, S., Zimmermann, I., & Dutzler, R. (2009). X-ray structure of the C-terminal domain of a prokaryotic cation-chloride cotransporter. *Structure, 17*, 538−546.

Waseem, T., Mukhtarov, M., Buldakova, S., Medina, I., & Bregestovski, P. (2010). Genetically encoded Cl-sensor as a tool for monitoring of Cl-dependent processes in small neuronal compartments. *J Neurosci Meth, 193*, 14−23.

Weiner, I. D., & Verlander, J. W. (2011). Role of NH_3 and NH_4^+ transporters in renal acid-base transport. *Am J Physiol Renal Physiol, 300*, F11−23.

Williams, J. R., Sharp, J. W., Kumari, V. G., Wilson, M., & Payne, J. A. (1999). The neuron-specific K-Cl cotransporter, KCC2. Antibody development and initial characterization of the protein. *J Biol Chem, 274*, 12656−12664.

Willis, W. D. (2006). John Eccles' studies of spinal cord presynaptic inhibition. *Prog Neurobiol, 78*, 189−214.

Willis, W. D., Jr. (1999). Dorsal root potentials and dorsal root reflexes: a double-edged sword. *Exp Brain Res, 124*, 395−421.

Witschi, R., Punnakkal, P., Paul, J., et al. (2011). Presynaptic alpha2-$GABA_A$ receptors in primary afferent depolarization and spinal pain control. *J Neurosci, 31*, 8134−8142.

Wong, J. A., Gosmanov, A. R., Schneider, E. G., & Thomason, D. B. (2001). Insulin-independent, MAPK-dependent stimulation of NKCC activity in skeletal muscle. *Am J Physiol Regul Integr Comp Physiol, 281*, R561−571.

Woo, N. S., Lu, J., England, R., et al. (2002). Hyperexcitability and epilepsy associated with disruption of the mouse neuronal-specific K-Cl cotransporter gene. *Hippocampus, 12*, 258–268.

Wu, Q., Delpire, E., Hebert, S. C., & Strange, K. (1998). Functional demonstration of Na^+-K^+-$2Cl^-$ cotransporter activity in isolated, polarized choroid plexus cells. *Am J Physiol, 275*, C1565–1572.

Wu, Y., Wang, W., Diez-Sampedro, A., & Richerson, G. B. (2007). Nonvesicular inhibitory neurotransmission via reversal of the GABA transporter GAT-1. *Neuron, 56*, 851–865.

Xu, J. C., Lytle, C., Zhu, T. T., Payne, J. A., Benz, E., Jr., & Forbush, B., 3rd. (1994). Molecular cloning and functional expression of the bumetanide-sensitive Na-K-Cl cotransporter. *Proc Natl Acad Sci USA, 91*, 2201–2205.

Yan, Y., Dempsey, R. J., Flemmer, A., Forbush, B., & Sun, D. (2003). Inhibition of Na^+-K^+-Cl^- cotransporter during focal cerebral ischemia decreases edema and neuronal damage. *Brain Res, 961*, 22–31.

Yerby, T. R., Vibat, C. R., Sun, D., Payne, J. A., & O'Donnell, M. E. (1997). Molecular characterization of the Na-K-Cl cotransporter of bovine aortic endothelial cells. *Am J Physiol, 273*, C188–197.

Zdebik, A. A., Wangemann, P., & Jentsch, T. J. (2009). Potassium ion movement in the inner ear: insights from genetic disease and mouse models. *Physiology (Bethesda), 24*, 307–316.

Zeuthen, T. (2010). Water-transporting proteins. *J Membr Biol, 234*, 57–73.

This page intentionally left blank

Chapter 16

Osmosis and Regulation of Cell Volume

Clive M. Baumgarten and Joseph J. Feher

Chapter Outline

I. SUMMARY

The study of mechanisms underlying osmosis and the regulation of cell volume under both isosmotic and anisosmotic conditions has been fruitful. We understand in substantial detail how water and ions cross the membrane. Where do we go from here? Many directions are possible and as many details are missing as are known. For example, the identification and cloning of water channels raise several important questions. What is it about the protein structure that makes this a water

Cell Physiology Sourcebook. DOI: 10.1016/B978-0-12-387738-3.00016-0

channel? How does water interact with the channel? From a theoretical perspective, how is osmotic pressure sensed and how does osmosis occur through a channel structure that is different in important ways from the well-explored hydrodynamic models? From the perspective of regulation of ion transport, much remains to be understood about how cells sense swelling and shrinking and how a cell decides on its optimal volume. There are also unanswered questions concerning the regulation of volume regulatory ion transporters by cellular messengers, metabolic demands and pathological states. In short, we can look forward to many more fruitful years of research on these topics.

II. INTRODUCTION

In whole blood, erythrocytes are biconcave disks about 7 μm in diameter and 2 μm thick. When diluted in a solution of 0.9% NaCl (w/v), erythrocytes retain this shape. When diluted with higher concentrations of salt, the erythrocytes shrink, appearing as spheres with spikes all over their surface. These cells are described as *crenated*. If erythrocytes are diluted with a markedly lower concentration of salt, the cells swell. They first become spherical and then, if the solution is sufficiently low in salt, the cells burst and release their contents. These simple observations give rise to the concept of tonicity. *Tonicity* is operationally defined as the ability of a solution to shrink or swell specified cells. Thus, an *isotonic* solution induces no volume change when placed in contact with the cells. The tonicity of the solution is equal to the tonicity of the cell's contents. *Hypertonic* solutions shrink cells, whereas *hypotonic* solutions increase cell volume. A solution that is isotonic for one type of cell may or may not be isotonic for others.

All animal cells shrink or swell on exposure to *anisotonic* solutions. Figure 16.1 shows the volume response of single isolated heart cells on exposure to hypertonic or hypotonic solutions. In hypotonic solution, myocytes swelled to more than 1.5 times their initial volume. The swelling was complete within 2 min, the new volume was stable and volume returned to normal upon return of the isotonic solution. In hypertonic solution, cell volume decreased to about 0.65 times normal and the original volume was restored upon return of the isotonic solution.

The data in Fig. 16.1 show that volume changes in anisotonic media are very rapid. What is moving when the cells swell or shrink? What routes do these substances take? Are there homeostatic mechanisms that limit swelling and shrinking? If so, how are the compensatory mechanisms engaged? The answers to these questions are not yet complete. The purpose of this chapter is to provide the basis for understanding regulation of cell volume through the exchange of water and solutes across the plasma membrane.

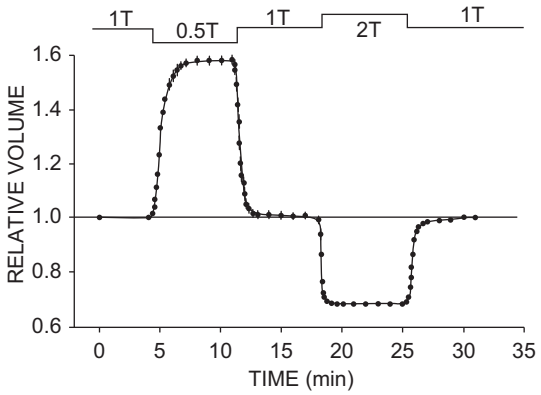

FIGURE 16.1 Response of isolated rabbit ventricular myocytes to osmotic stress. Cell volume was initially measured in isotonic solution (1T). Myocytes rapidly swelled 58% in a hypotonic solution with an osmolarity 0.5 times that of 1T and rapidly shrank 33% in a hypertonic solution with an osmolarity two times that of 1T. Cell volume was stable for the duration of perfusion with either hypotonic or hypertonic media and rapidly returned to its control value when 1T solution was readmitted. Volume was measured by digital video microscopy, and relative volume was calculated as $volume_{test}/volume_{1T}$. Solution osmolarity was adjusted by varying the concentration of mannitol. (From Suleymanian and Baumgarten (1996). *Reproduced from The Journal of General Physiology, 1996, 107, 503–514, by copyright permission of The Rockefeller University Press.)*

III. WATER MOVEMENT ACROSS MODEL MEMBRANES

IIIA. Definition of Osmosis

Osmosis refers to the movement of fluid across a membrane in response to differing concentrations of solutes on the two sides of the membrane. Osmosis has been used since antiquity to preserve foods by dehydration with salt or sugar. The removal of water from a tissue by salt was referred to as imbibition. This description comes from the notion that these solutes attracted water from material they touched. In 1748, J.A. Nollet used an animal bladder to separate chambers containing water and wine. He noted that the volume in the wine chamber increased and, if this chamber was closed, a pressure developed. He named the phenomenon osmosis from the Greek ωσμος, meaning thrust or impulse.

Pfeffer (1877) provided early quantitative observations on osmosis. He made an artificial membrane in the walls of an unglazed porcelain vessel by reacting copper salts with potassium ferrocyanide to form a copper ferrocyanide precipitation membrane on the surface of the vessel. He used this membrane to separate a sucrose solution inside the vessel from water outside and found a volume flow from the water side to the sucrose side. Pfeffer observed that the flow was proportional to the sucrose concentration. Further, a pressure applied inside the vessel produced a filtration flow proportional to the pressure. He found that a closed

vessel containing a sucrose solution would develop a pressure proportional to the concentration of sucrose. He recognized this as an equilibrium state in which the pressure balanced the osmosis caused by the sucrose solution. Pfeffer's original data for the osmotic pressure of sucrose solutions are plotted in Fig. 16.2. He defined *osmotic pressure* as the hydrostatic pressure necessary to stop osmotic flow across a barrier (e.g. a membrane) that is impermeable to the solute. This concept is illustrated in Fig. 16.3. Osmotic pressure is a property intrinsic to the solution and is measured at equilibrium, when the pressure-driven flow exactly balances the osmotic-driven flow. By defining osmotic pressure in this way, we assign a positive value to an apparent reduction in pressure brought about by dissolving the solute. Thus, fluid movement occurs from the solution of low osmotic pressure (water) to the solution of high osmotic pressure, opposite in direction to the hydraulic flow of water from high to low hydrostatic pressure.

An ideal *semipermeable* membrane is required for determining osmotic pressure. These membranes are permeable to water but absolutely impermeable to solute. The concept of osmotic pressure differs from tonicity in that tonicity compares two solutions separated by a specific non-ideal membrane. If the membrane is highly permeable to solute as well as to water, no water flow will occur and, therefore, the externally applied pressure required to stop osmosis is zero. This observation makes it plain that the *effective* osmotic pressure, which is measured with a real membrane, must be due to some interaction of the membrane with the solute because pressure depends on both the specific solute and the specific membrane.

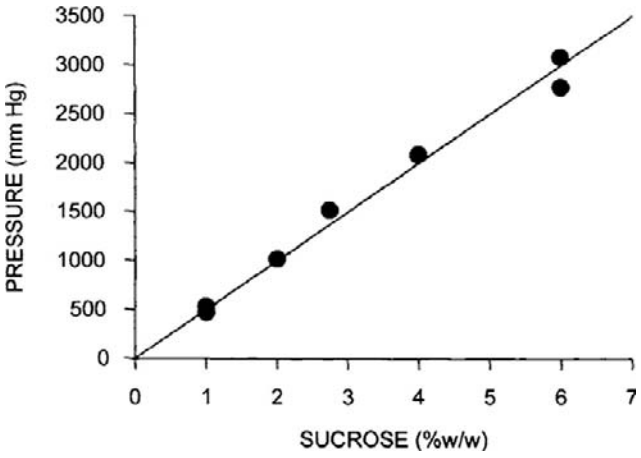

FIGURE 16.2 Plot of data from Pfeffer (1877) for the osmotic pressure of sucrose solutions. A copper ferrocyanide precipitation membrane was formed in the walls of an unglazed porcelain cup. The membrane separated a sucrose solution in the inner chamber from water in the outer chamber. The inner chamber was then attached to a manometer and sealed. The linear relation between the pressure measured with this device and the sucrose concentration were the experimental impetus for deriving van't Hoff's law.

IIIB. van't Hoff's Law

From Pfeffer's data and thought experiments considering gases in equilibrium with water, van't Hoff (1887) argued that the osmotic pressure should be given by:

$$\pi = RT\,\Sigma C_s \tag{16.1}$$

where π is the usual symbol for osmotic pressure, R is the gas constant, T is the temperature in kelvins, and C_s is the concentration of solute particles in solution. This equation is known as van't Hoff's law. Table 16.1 lists common units for osmotic pressure along with the values and units of R and C_s needed to make the calculation.

The concentration used in van't Hoff's law, ΣC_s, refers to the number of osmotically active particles that are formed upon dissolution of the solute. For example, organic compounds such as glucose ideally yield one particle, whereas strong salts such as NaCl or $CaCl_2$ ideally yield two (Na^+ and Cl^-) or three (Ca^{2+} and two Cl^-) particles. The osmolarity of a solution equals ΣC_s and is expressed in osmol per liter to indicate that we are referring to the number of osmotically active particles, termed osmolytes, rather than the concentration of the solute. An alternative scale, osmolality, defines ΣC_s per kilogram of solvent. Although the osmolal scale better describes the osmotic pressure in van't Hoff's equation, the osmolar scale is more generally used in physiological studies. As we shall see, van't Hoff's law is a limiting law that is true only for dilute solutions. In this limit of dilute solutions, both osmolal and osmolar concentration scales converge to the same results.

To illustrate the magnitude of osmotic pressure, ideal solutions of 10 mM glucose or 5 mM NaCl, which dissociates into two particles, both have an osmolarity of 10 mosmol L^{-1} and an osmotic pressure at 37°C of $0.082\,L\cdot atm\cdot moL^{-1}\cdot K^{-1} \times 310\ K \times 0.01\,mol\cdot L^{-1} = 0.254$ atm or 193 mmHg. Thus, the osmotic pressure of even dilute solutions are large in comparison to normal hydrostatic pressures in physiological systems.

IIIC. Thermodynamic Derivation of van't Hoff's Law

One of the conclusions of chemistry is that all spontaneous processes are accompanied by a decrease in free energy. The total free energy of a solution can be divided among its components. This parceling out of the Gibbs free energy, G, is embodied in the concept of chemical potential:

$$\mu_i = \left[\frac{\partial G}{\partial n_i}\right]_{T,P,n_k} \tag{16.2}$$

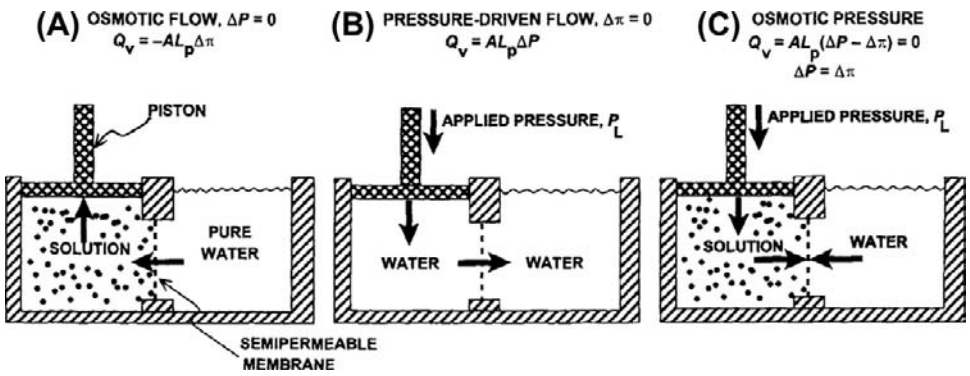

FIGURE 16.3 Equivalence of hydrostatic and osmotic pressures in driving fluid flow across a membrane. (A) An ideal, semipermeable membrane is freely permeable to water, but is impermeable to solute. When the membrane separates pure water on the right from solution on the left, water moves to the solution side. This water flow is *osmosis*. The flow, Q_v, in $cm^3 \cdot s^{-1}$, is linearly related to the difference in osmotic pressure, $\Delta\pi$, by the area of the membrane, A, and the hydraulic conductivity, L_p. Positive Q_v is taken as flow to the right. The flow causes expansion of the left compartment and movement of the piston (which is assumed to be weightless). (B) Application of a pressure, P_L, to the left compartment forces water out of this compartment, across the semipermeable membrane. The flow is linearly related to the pressure difference between the two compartments. (C) Application of a P_L so that $\Delta P = \Delta\pi$ results in no net flow across the membrane. The osmotic pressure of a solution is defined as the pressure necessary to stop water movement when the ideal, semipermeable membrane separates water from the solution.

where μ_i is the chemical potential of component i, n_i is the number of moles of component i and $i \neq k$. The chemical potential of a component of a solution consists of three terms: a standard potential, which refers to the chemical energy involved in the formation of the material from standard states; a compositional term, which depends on the presence of other constituents; and a work term, encompassing other work required (per mole) to bring additional material into the solution. The work term in the chemical potential of water is $\int d(\overline{V}_w P)$, where $\overline{V}_w$ is the volume of water per mole and P is the pressure. The electrochemical potential of ions in solution requires the inclusion of an electrical work term, $\int z_i F \, d\psi$, where z_i is the ion's valence, F is Faraday's constant, and ψ is voltage.

In the case of a solution separated from pure water by an ideal semipermeable membrane, water movement will occur when there is a difference in the chemical potential of water on the two sides of the membrane, such that water movement will result in a decrease in free energy. When the pressure applied to the solution is equal to the osmotic pressure, equilibrium is established and the chemical potential of water is equal on both sides of the membrane; no net water movement occurs. This equality of chemical potential is written as:

$$\mu^0 + \overline{V}_w \; P_L + RT \; \ln \; a_{w,\,L} = \mu^0 + \overline{V}_w P_R + RT \; \ln \; a_{w,\,R} \qquad (16.3)$$

where the subscripts L and R refer to the left and right sides of the semipermeable membrane, μ^0 is the chemical potential of liquid water in its standard state (pure water at 1 atm pressure) and a_w is the activity of water. For an ideal solution, the activity of water can be replaced by its *mole fraction*, X_w

$$a_w = X_w = \frac{n_w}{n_w + n_s} \qquad (16.4)$$

TABLE 16.1 Units for Calculation of Osmotic Pressure

Pressure Units	1 atm Equivalent	Gas Constant (R)	Solute Osmolyte Concentration, ΣC_s
atm	1	0.082 $L \cdot atm \cdot moL^{-1} \cdot K^{-1}$	$mol \cdot L^{-1}$
mmHg	760	62.36 $L \cdot mm\ Hg \cdot moL^{-1} \cdot K^{-1}$	$mol \cdot L^{-1}$
$Pa = N \cdot m^{-2}$	1.013×10^5	8.314 $N \cdot m \cdot moL^{-1} \cdot K^{-1}$	$Mol \cdot m^{-3} = mol \cdot (1000\,L)^{-1}$
$dyn \cdot cm^{-2}$	1.013×10^6	8.314×10^7 $dyn \cdot cm \cdot moL^{-1} \cdot K^{-1}$	$Mol \cdot cm^{-3}$

Osmolarity ($osmol \cdot L^{-1}$) is defined as the concentration of osmotically active particles, osmolytes, in $mol \cdot L^{-1}$. Therefore, the units osmoles and moles cancel in the calculation of osmotic pressure.

where n_w and n_s are the moles of water and solute, respectively. The balance of the chemical potential can be written as:

$$\mu^0 + \overline{V}_w P_L + RT \ln X_{w,L} = \mu^0 + \overline{V}_w P_R + RT \ln X_{w,R} \tag{16.5}$$

Consider the situation in Fig. 16.3, where pure water is on the right side of the membrane and a solution is on the left. $X_{w,R} = 1.0$ and thus, $\ln X_{w,R} = 0$. Rearranging we find:

$$\overline{V}_w(P_L - P_R) = -RT \ln X_{w,L} \tag{16.6}$$

The mole fractions of water and solute in a solution must sum to 1.0. This is expressed as:

$$\begin{aligned} X_{w,L} + X_{s,L} &= 1 \\ \ln X_{w,L} &= \ln(1 - X_{s,L}) \end{aligned} \tag{16.7}$$

where $X_{s,L}$ is the mole fraction of solute in the solution on the left. In dilute solutions, $X_{s,L} << 1.0$, and thus, $\ln(1 - X_{S,L}) \approx -X_{S,L}$. Substitution of this approximation in Equation 16.6 gives:

$$P_L - P_R = \frac{RT}{\overline{V}_w} X_{s,L} \tag{16.8}$$

The left-hand side of Equation 16.8 is just the osmotic pressure, π, which is equal to the extra pressure that must be applied to the solution on the left side in order to establish equality of the chemical potential of water on the two sides of the membrane. For physiological studies, it is convenient to express π in terms of concentration. From the definition of mole fraction and the assumption of dilute solutions ($n_s << n_w$), we get:

$$\begin{aligned} \pi &= \frac{RT}{\overline{V}_w} X_{s,L} = \frac{RT}{\overline{V}_w} \frac{n_s}{n_s + n_w} \approx \frac{RTn_s}{n_s \overline{V}_w} \\ &= RT \frac{n_s}{V} = RTC_s \end{aligned} \tag{16.9}$$

where $n_w \overline{V}_w \approx V$, is the total volume of solution and C_s is the concentration of impermeable solute on the solution side of the membrane. This last expression is the van't Hoff equation for the osmotic pressure, Equation 16.1. The thermodynamic derivation entails two assumptions: (1) the solution is sufficiently dilute as to approach ideality; and (2) the solution is incompressible so that $\int d(\overline{V}_w P) = \overline{V}_w \Delta P$. It is important to recognize that Equation 16.9 is not exact for physiological solutions. Rather, it is an approximation that is strictly true only for dilute ideal solutions.

The van't Hoff equation is based on thermodynamics and, as such, it tells us nothing about the rate of osmosis or the mechanism by which it occurs. Conceivably, the semipermeable membrane could be like a sieve that allows water to pass freely while blocking solute movement. Alternatively, solvent could dissolve in the membrane, whereas solute is insoluble. Both of these models would exhibit osmotic flow from the region of low osmotic pressure (pure water) to that of high osmotic pressure (impermeant solute solution). The mechanism by which osmosis occurs must be determined by methods of chemical kinetics, and must be determined for every membrane-solvent pair.

IIID. Other Colligative Properties of Solutions

The thermodynamic derivation given previously indicates that osmotic pressure (and osmotic flow) originates in the lowering of the chemical potential of water by the amount $\approx RTX_s$ when solute is dissolved. Several other properties of solutions also are a consequence of the lowered chemical potential of water because of dissolution of solutes. Together, these are called the *colligative* properties (from the Latin, *ligare,* meaning to bind) and include *osmotic pressure*, *vapor pressure depression*, *boiling point elevation* and *freezing point depression*. Consider two open compartments enclosed in a chamber. One compartment contains pure water and the other a solution of a non-volatile solute. The vapor pressure above a solution is defined as the partial pressure of water vapor in equilibrium with the solution. Since the vapor pressure of pure water is higher than that of the solution, water vapor above pure water will be at a higher pressure than that above the solution. As a result, water vapor will diffuse from the water side to the solution side. At the surface of the solution, water vapor will condense because the vapor pressure there will be higher than the equilibrium vapor pressure for the solution. Thus, water will move from the pure water to the solution side. In short, "osmosis" would occur through the "semipermeable membrane" represented by the surfaces of the two fluids and the intervening air. This illustrates the strong connection among the colligative properties of solutions. Laboratory osmometers typically use either vapor pressure depression or freezing point depression to determine the total solute concentration in an aqueous solution.

IIIE. Osmotic Pressure of Non-ideal Solutions

As discussed above, the van't Hoff equation is an approximation that adequately describes the osmotic pressure for dilute solutions. Its derivation requires the assumptions that the solutions are dilute and that the solutions are ideal. Here, *ideal* means that Raoult's law (vapor pressure is proportional to mole fraction of solvent) is valid for the solution (Hildebrand, 1955; Kiil, 1989).

Because the behavior of real solutions is not ideal, the van't Hoff equation must be modified to include a correction term, the osmotic coefficient (ϕ_s):

$$\pi = RT \sum \phi_s C_s \tag{16.10}$$

At physiological concentrations, the osmotic coefficients for NaCl and $CaCl_2$ are 0.93 and 0.85, respectively. This means the osmolarity of 150 mM NaCl is $0.93 \times 2 \times 150 = 279$ mosmol L^{-1} and the osmolarity of 150 mM $CaCl_2$ is $0.85 \times 3 \times 150 = 382.5$ mosmol L^{-1}. The osmotic coefficients for electrolytes vary with temperature, concentration and the chemical nature of the electrolyte. For most electrolytes, $\phi < 1.0$ for dilute solutions, due to weak attraction of the ions. At higher concentrations, ϕ increases to exceed 1.0. Values for the osmotic coefficients for electrolytes can be found in Robinson and Stokes (1959) or can be calculated from the parameters tabulated by Pitzer and Mayorga (1973). These osmotic coefficients are corrections to van't Hoff's law due to interactions only for the particular solute. When more than one solute is present, interactions could occur that are not accounted for by the osmotic coefficients. Therefore, calculations of the osmotic pressure of a mixture of solutes, even when osmotic coefficients are used, are only approximations.

Non-electrolytes and polyelectrolytes, especially proteins, also show marked departure from van't Hoff's law with increasing concentration. According to Equation 16.10, the osmotic coefficient for a single solute can be calculated as:

$$\phi_s = \frac{\pi_{\text{observed}}}{\pi_{\text{calculated}}} = \frac{\pi_{\text{observed}}}{RTC_s} \tag{16.11}$$

The osmotic coefficient for sucrose is plotted against sucrose concentration in Fig. 16.4. The osmotic coefficient is nearly 1.0 in dilute solutions, but approaches 3 in saturated sucrose solutions. Thus, the van't Hoff equation successfully describes the osmotic pressure of dilute solutions, but fails at high solute concentrations. The failure of the van't Hoff equation for highly concentrated solutions is due to deviation of reality from the assumptions used to derive the equation, that solutions are dilute and ideal. The osmotic coefficient accounts for these deviations.

For high solute concentrations, we can calculate the osmotic pressure from the mole fraction of water without assuming a dilute solution by identifying $\pi = P_L - P_R$ in Equation 16.6:

$$\pi = -\frac{RT}{\overline{V}_w} \ln X_w \tag{16.12}$$

This equation still requires the assumption of ideal solution behavior: the activity of water is equal to its mole fraction.

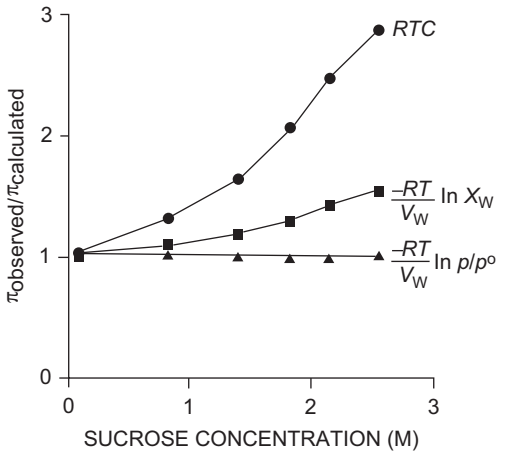

FIGURE 16.4 Osmotic coefficients as a function of sucrose concentration. Plotted are the molar osmotic coefficient, defined as ϕ_s in Equation 16.11 (●), obtained by dividing the observed osmotic pressure by *RTC;* the rational osmotic coefficient, g, defined in Equation 16.15 (■), obtained by dividing the observed osmotic pressure by $(-RT/\overline{V}_w) \ln X_w$; and the observed osmotic pressure divided by that predicted by vapor pressure measurements $(-RT/\overline{V}_w) \ln p/p^0$ according to Equation 16.13 (▲). Deviation of the molar osmotic coefficient from 1.0 means that the van't Hoff law fails to describe adequately the osmotic pressure at high concentrations, but is accurate for dilute solutions. The van't Hoff law requires the assumption of dilute solution and ideal behavior. Deviation of the rational osmotic coefficient from 1.0 means that the solution is not ideal, as the equation requires this assumption. The nearly perfect agreement between the theoretical osmotic pressure predicted from vapor pressure measurements illustrates the connection between these two colligative properties. *Data from Glasstone (1946).*

The expression for osmotic pressure without assuming a dilute solution or ideality is given by:

$$\pi = -\frac{RT}{\overline{V}_w} \ln a_w = -\frac{RT}{\overline{V}_w} \ln \frac{p}{p^0} \tag{16.13}$$

where p and p^0 are the vapor pressures of the solution and pure water, respectively.

The rational osmotic coefficient, g, accounts for non-ideal behavior and is defined as:

$$\ln a_w = g \ln X_w \tag{16.14}$$

Then, from Equations 16.12–16.14, we find that:

$$g = \frac{\pi_{\text{observed}}}{\pi_{\text{calculated}}} = \frac{\pi_{\text{observed}}}{-\frac{RT}{\overline{V}_w} \ln X_w} \tag{16.15}$$

The rational osmotic coefficient is closer to 1.0, but still deviates significantly at higher sucrose concentrations where solution behavior is further from ideal (see Fig. 16.4). In contrast, the ratio of the observed osmotic pressure to the theoretical osmotic pressure calculated from vapor pressure measurements, according to Equation 16.13, is very close to 1.0 throughout the entire concentration range. This shows the validity of Equation 16.13 and the

absolute correlation between vapor pressure depression and osmotic pressure as different measures of the same phenomenon, the lowering of the activity of solvent water by the dissolution of solute. Equation 16.12 does not adequately describe the variation of π with C_s because it requires ideal adherence to Raoult's law (vapor pressure is proportional to X_w); van't Hoff's limiting law further deviates from a linear relationship between π and C_s because it requires the additional approximation of dilute solutions. Despite these limitations in the high concentration domain, van't Hoff's law remains a good approximation for electrolyte solutions in the physiological range.

Because of their importance in physiological systems, the non-ideality of the osmotic pressure of protein solutions requires special comment. Adair (1928) found that the observed osmotic pressure increased faster than the concentration in hemoglobin solutions, as shown in Fig. 16.5. Part of the osmotic pressure was due to the unequal distribution of ions across the semipermeable membrane caused by electric charge on the immobile protein molecules. This is the Gibbs–Donnan equilibrium, discussed in more depth later. The contribution of the Gibbs–Donnan distribution to osmotic pressure is small, however, and nearly all of the non-linearity between π and C_s is due to the protein itself. From the data obtained by Adair (1928), $\phi_{Hb} = 4.03$ at the concentration of hemoglobin within erythrocytes (34.4 g hemoglobin per 100 ml of solution).

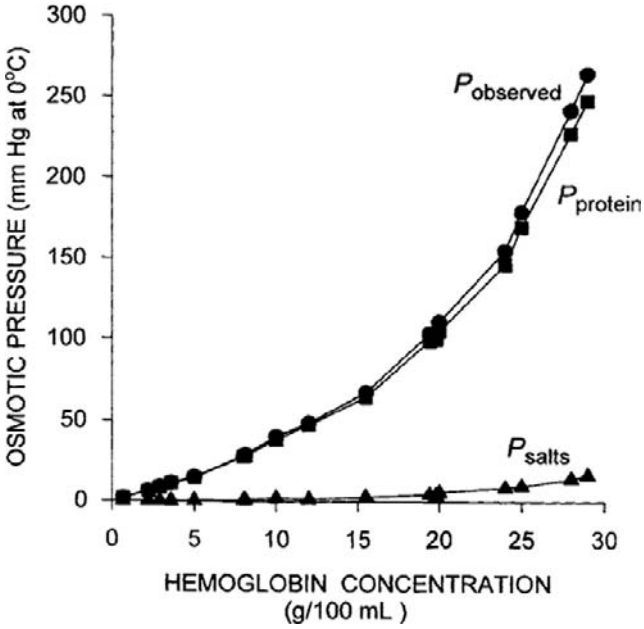

FIGURE 16.5 Dependence of the observed osmotic pressure on hemoglobin concentrations. $P_{observed}$ is the observed osmotic pressure (●). P_{salts} is the contribution of the salts to the osmotic pressure as calculated from the Gibbs–Donnan distribution and the van't Hoff equation (▲). Protein is the contribution of the protein itself to the observed osmotic pressure, calculated as $P_{observed} - P_{salts}$ (■). *Data from Adair (1928).*

The observed osmotic pressure of solutions of plasma proteins also increases more rapidly than concentration, but the degree of deviation from linearity is different for different proteins. Thus, serum albumin shows marked deviation, whereas γ-globulins are more nearly linear. The empirical fits to the concentration-dependence of osmotic pressure are given by Landis and Pappenheimer (1963) as:

$$\begin{aligned} \pi_{\text{albumin}} &= 2.8C + 0.18C^2 + 0.012C^3 \\ \pi_{\text{globulins}} &= 1.6C + 0.15C^2 + 0.006C^3 \\ \pi_{\text{plasma proteins}} &= 2.1C + 0.16C^2 + 0.009C^3 \end{aligned} \tag{16.16}$$

In each of these three equations, the first term represents the limiting law of van't Hoff.

The rather large ϕ_s for proteins and polymers is due in part to *excluded volume effects*. That is, proteins and polymers exclude solvent from a larger volume than inorganic ions. The lowering of the free energy of solvent water upon dissolution of solute, which gives rise to osmosis, can be calculated from the increase of entropy on mixing. This entropy of mixing depends on the volume occupied by the solute. From considerations of the excluded volume, it can be shown (Tanford, 1961) that the expected osmotic pressure is given as:

$$\pi = RTC\left(1 + \frac{\overline{V}_s}{\overline{V}_w}C\right) \tag{16.17}$$

IIIF. Equivalence of Osmotic and Hydrostatic Pressure

As mentioned earlier, Pfeffer originally observed a linear relationship between the flow rate and the concentration of solute. This is expressed as:

$$J_v = -L_p(\pi_L - \pi_R) = -L_p\ \Delta\pi \tag{16.18}$$

where J_v is the volume flux in $\text{cm}^3 \cdot \text{s}^{-1}$ per unit area of membrane, L_p is variously called the *filtration coefficient*, *hydraulic conductivity*, or *hydraulic permeability* and $\Delta\pi$ is the osmotic pressure difference. A positive J_v in Equation 16.18 represents flux from the left to the right compartment and this is the order in which the osmotic pressure difference is taken. The minus sign before L_p indicates flux is from the region of low osmotic pressure to the region of high osmotic pressure. In Fig. 16.3A, $\pi_L > \pi_R$, $\Delta\pi > 0$, and J_v is negative. This means that the flux is from the right to the left compartment. The flow across an extent of membrane is just the flux times the area exposed to the driving forces, expressed as:

$$Q_v = -AL_p\ \Delta\pi \tag{16.19}$$

where A is the area of the membrane and Q_v is the flow in units of $\text{cm}^3 \cdot \text{s}^{-1}$.

In the absence of solute, the volume flow across Pfeffer's artificial membrane was also linearly related to the hydrostatic pressure:

$$\begin{aligned} J_v &= L_p(P_L - P_R) = L_p\ \Delta P \\ Q_v &= AL_p\ \Delta P \end{aligned} \tag{16.20}$$

In a study on collodion membranes, Meschia and Setnikar (1958) found that the proportionality constant for hydrostatic pressure-driven filtration was the same as the constant relating flow and osmotic pressure. That means that the L_p in Equation 16.19 is the same as the L_p in Equation 16.20. Thus, not only can the osmotic flow be nulled by opposing osmotic pressure with an equal but opposite hydrostatic pressure, but the equivalent proportionality implies that the mechanism of volume flow is also identical for osmotic and hydraulic flow. The equivalence of osmotic and hydrostatic pressures allows us to write:

$$\begin{aligned} Q_v &= AL_p[(P_L - P_R) - (\pi_L - \pi_R)] \\ &= AL_p(\Delta P - \Delta\pi) \end{aligned} \tag{16.21}$$

This equation describes the net flow that would be observed in the presence of both hydrostatic and osmotic pressure differences across a semipermeable membrane.

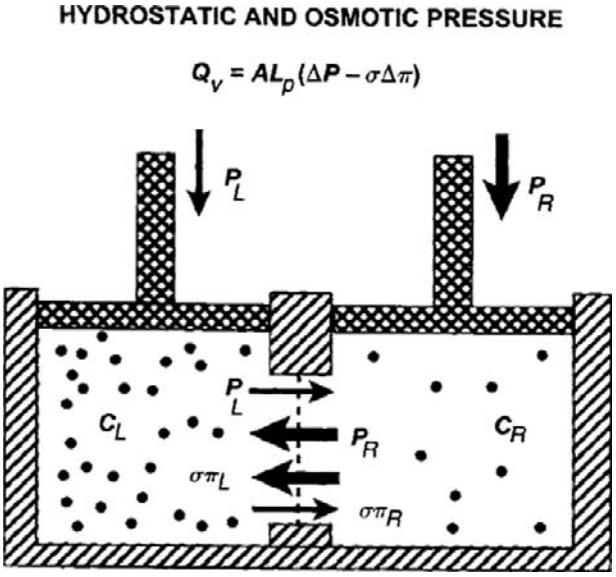

FIGURE 16.6 Net flow in the presence of osmotic and hydrostatic pressures. For a real membrane, the effective osmotic pressure on the left, $\sigma\pi_L$, causes flow toward the left, while the applied hydrostatic pressure, P_L, drives flow to the right. A similar situation occurs on the right. The *net* flow is driven by the balance of the forces, $\Delta P - \sigma\Delta\pi$, and is proportional to the area, A, and the hydraulic conductivity, L_p.

IIIG. Reflection Coefficient

Equation 16.1, van't Hoff's law, describes the relation between osmotic pressure and concentration when a solution is separated from water by an ideal semipermeable membrane. Recall that a semipermeable membrane is defined as absolutely impermeable to the solute. Real membranes may not fit this ideal; they may be somewhat permeable to the solute. When membranes are permeable to the solute, the measured osmotic pressure is actually less than that predicted by van't Hoff s law. This phenomenon has led to a second membrane parameter, σ, the *reflection coefficient* which is defined as:

$$\sigma = \frac{\pi_{\text{observed}}}{\pi_{\text{theoretical}}} = \frac{\pi_{\text{observed}}}{\phi_s\ RTC_s} \tag{16.22}$$

The reflection coefficient derives its name from the idea that all of the collisions of solute with a semipermeable membrane will result in the solute being reflected back into the solution. The reflection coefficient for an ideal membrane is 1.0. For a permeable solute, some fraction of the collisions with the membrane will result in permeation of the membrane, so that $\sigma < 1.0$ and the observed osmotic pressure will be less than that predicted by van't Hoff s law. The value of σ is not simply the fraction of collisions that penetrate the membrane. It involves discrimination by the membrane between solvent and solute. Thus, σ is a parameter that is different for every membrane-solute pair. A vapor pressure osmometer or a freezing-point osmometer would still register the proper osmolarity of the solution, however (for non-volatile solutes). A molecular interpretation of the origin of the reflection coefficient is given later.

Permeation of the solute should reduce osmotic flow along with osmotic pressure. In the presence of both hydrostatic pressure differences and concentration differences across a membrane, the resulting volume flow is given by:

$$Q_v = AL_p\left[(P_L - P_R) - \left(\sum_i \sigma_i\ \pi_{i,L} - \sum_i \sigma_i\ \pi_{i,R}\right)\right] \tag{16.23}$$

where σ_i is the reflection coefficient of solute i, and $\pi_{i,L}$ and $\pi_{i,R}$ are the osmotic pressures of solute i on the left and right sides of the membrane, respectively. The π_i in this equation is that given by van't Hoff's law; its multiplication by the reflection coefficient, σ, gives the effective osmotic pressure. The consequence of a combination of hydrostatic and osmotic pressures on the flow across a membrane is shown in Fig. 16.6.

IV. MECHANISMS OF OSMOSIS

The ultimate cause of osmosis is the reduction of the chemical potential of water in a solution. This thermodynamic statement and equations derived from it tell us nothing about the rate of osmosis or its mechanism. Several

possible mechanisms have been investigated. As will be developed, classes of models can be distinguished by comparing the proportionality between applied force, which is either a pressure or concentration gradient, and water flow.

IVA. Microporous Membranes

IVA1. Osmotic and Pressure-Driven Flow through Porous Membranes

The equivalence of L_p for osmotic and pressure-driven flow suggests a common mechanism. At least three different models have been proposed to explain flow across membranes: (1) hydrodynamic flow through a porous membrane; (2) diffusion through the membrane; and (3) non-hydrodynamic flow through narrow pores. As we shall see, it is likely that biological membranes are not modeled well by any one of these. Despite this, we shall consider these model membranes because investigators have relied heavily on them to clarify their thinking.

First, we consider a porous membrane as a model for understanding osmotic and hydrostatic pressure-driven flow and derive L_p, the proportionality constant relating pressure and flow. We assume the membrane is a flat, thin sheet of thickness δ. We imagine that the membrane is pierced by right-cylindrical pores of radius r, and the number of pores, N, per unit area is $n = N/A$. The membrane separates two compartments of water that are at different hydrostatic pressures. If we assume that the pores are large enough for laminar flow to occur, then the filtration flow will be given by the Poiseuille equation:

$$q_v = \frac{\pi r^4}{8\eta\delta}\Delta P \tag{16.24}$$

where q_v is the flow per pore in $\mathrm{cm}^3 \cdot \mathrm{s}^{-1}$, η is the viscosity of the fluid, δ is the thickness of the membrane (equal to the length of the pore), and ΔP is the pressure difference across the pore. The π in this equation is the geometric ratio, 3.14…, and should not be confused with the symbol for osmotic pressure. Since the flow through N pores is just Nq_v, the observed macroscopic flux and flow are:

$$\begin{aligned} J_v &= \frac{Nq_v}{A} = nq_v = \frac{n\pi r^4}{8\eta\delta}\Delta P \\ Q_v &= AJ_v = Nq_v = \frac{N\pi r^4}{8\eta\delta}\Delta P \end{aligned} \tag{16.25}$$

Recall here that J_v is the flux, or flow per unit area of membrane and Q_v is the flow in units of volume per unit time.

Equation 16.25 describes the steady-state flow of water across the membrane. Because at steady-state there is no buildup or depletion of water, there is no difference in the flow of water at any two points in the pore. Consequently, pressure changes linearly with distance through the pore, and the gradient of pressure, $\Delta P/\delta$, is constant.

A comparison of Equation 16.25 with Equation 16.20 indicates that the hydraulic conductivity is:

$$L_p = \frac{n\pi r^4}{8\eta\delta} \tag{16.26}$$

Thus, L_p is a parameter determined by the viscosity of the fluid and by membrane characteristics including the number of pores per unit area, n, the pore radius, and the membrane thickness.

IVA2. Diffusional Permeability of Porous Membranes: P_d

In the absence of a pressure gradient, solute and water cross a porous membrane by diffusion through the pores. If we assume that the membrane is impermeable at all other points, the permeability is given by Fick's first and second law of diffusion:

$$\begin{aligned} j_s &= -D\frac{\partial C}{\partial x} \\ \frac{\partial C}{\partial t} &= D\frac{\partial^2 C}{\partial x^2} \end{aligned} \tag{16.27}$$

where j_s is the flux of solute through one pore. The second expression describes the time dependence of the concentration profile over distance, x, within the pore. At steady-state, the concentration profile no longer changes. This means that $\partial C/\partial t = \partial^2 C/\partial x^2 = 0$; the concentration gradient is linear; and $\delta C/\delta x = (C_L - C_R)/(0 - \delta) = -\Delta C/\delta$, where δ is the thickness of the membrane. Total solute flux across the entire membrane, J_s, is:

$$J_s = \frac{n\pi r^2 D}{\delta}\Delta C \tag{16.28}$$

where n is the number of pores per unit area of membrane. According to this equation, the observed macroscopic flux of solute across a porous membrane is linearly related to the concentration difference by a coefficient that includes properties of the solute (diffusion coefficient) and the membrane (thickness, pore density and pore cross-sectional area). The *permeability* of the membrane to solute, p_s, includes several parameters in Equation 16.28 that are difficult to obtain experimentally; p_s relates solute flux, J_s, to the difference in concentration across the membrane:

$$J_s = p_s\ \Delta C \tag{16.29}$$

From Equations 16.28 and 16.29, p_s is defined as:

$$p_s = \frac{n\pi\, r^2 D}{\delta} \tag{16.30}$$

Isotopic water on one side of a porous membrane is distinguishable from ordinary water and may be viewed as a solute. Thus, water itself will obey these equations. This allows us to define the diffusional permeability of water, P_d, for a porous membrane:

$$P_d = \frac{n\pi r^2 D_w}{\delta} \tag{16.31}$$

where D_w is the diffusion coefficient of water. The units of P_d are $cm \cdot s^{-1}$. Note that multiplication of a permeability by a concentration, as in Equation 16.29, gives a flux with units of $mol \cdot cm^{-2}\ s^{-1}$.

IVA3. Evidence for Pores: P_f/P_d Ratio

In the absence of a concentration gradient, pressure-driven water flow gives rise to a second permeability constant termed the *filtration permeability* or *osmotic permeability*, P_f, which has units of $cm \cdot s^{-1}$. Mauro (1957) realized that the proportionality constants relating pressure and concentration-gradient-driven water flow, P_f and P_d, provide evidence for the mechanism of transport. The ratio P_f/P_d should be 1.0 if water crosses by a dissolution-diffusion process. Mauro (1957) recognized that the flux of water in response to a pressure gradient could be partitioned into two components, diffusional and non-diffusional (e.g. bulk flow) and that the diffusional component of water flux, J_w, would obey the Nernst–Planck equation:

$$J_w = -\frac{n\pi r^2 D_w}{RT} C_w \frac{d\mu_w}{dx} \tag{16.32}$$

where C_w is the concentration of water. In the case where only a hydrostatic pressure is applied, $d\mu_w = \overline{V}_w dP$, and $C_w \overline{V}_w = 1$. Assuming steady-state flows and a uniform membrane, $dP/dx = -\Delta P/\delta$, and Equation 16.32 becomes:

$$J_w = -\frac{n\pi r^2 D_w}{RT\delta} \Delta P \tag{16.33}$$

This flow of water is in units of moles of water per second per cm^2 of membrane. It can be converted to units of volume per second per cm^2 (the units of J_v) by multiplying by the volume of water per mole, or $\overline{V}_w$:

$$J_v = \overline{V}_w J_w = \frac{\overline{V}_w n\pi r^2 D_w}{RT\delta} \Delta P \tag{16.34}$$

This equation relates the volume flux to the pressure difference across the membrane.

The total volume flux was earlier given as $J_v = L_p \Delta P$ (see Equation 16.20). If diffusional flux is the only component of volume flux, Equations 16.20 and 16.34 may be combined to give:

$$L_p = \frac{\overline{V}_w n\,\pi\, r^2 D_w}{RT\delta} \tag{16.35}$$

Part of this expression for L_p incorporates P_d. Insertion of Equation 16.31 into Equation 16.35 gives:

$$P_f = \frac{L_p\ RT}{\overline{V}_w} = \frac{n\,\pi\, r^2\, D_w}{\delta} = P_d \tag{16.36}$$

This definition of P_f converts L_p into a parameter having the same units as P_d, thereby allowing direct comparison of filtration and diffusional permeabilities. The equality of P_f and P_d obtained in Equation 16.36 is dependent on the condition that the flow of water in response to a hydrostatic pressure difference is due only to diffusional processes. Thus, for a purely diffusional process, $P_f/P_d = 1$. In contrast, Mauro (1957) found that P_f/P_d was 727 in collodion membranes. That is to say, pressure-driven water movement was much greater than expected from a diffusional process. From this he concluded that pressure-driven and osmotic flow across these membranes was predominately non-diffusional.

IVA4. Physical Origin of Osmotic Pressure

If a porous membrane separates a solution containing only impermeant solutes from pure water, we observe experimentally that water flows through the membrane from the pure water to the solution side. The flow is proportional to the osmotic pressure of the solution times L_p (see Equation 16.20). The question is, what causes this water movement? Because the membrane is impermeable to solute, solute cannot enter the pores and the fluid in the pore is pure water. Consider a water molecule in the middle of the pore. How does the water "know" to move toward the solution side? It appears there are only two possible answers to this question. Either there is a concentration gradient of water within the pore, or there is a pressure gradient within the pore. These two possibilities are not mutually exclusive, but diffusion-driven water flow and pressure-driven water flow are often thought of as separate mechanisms. The dichotomy reflects the notion that water is an incompressible fluid. Water is not absolutely incompressible, however. The coefficient of compressibility is given as:

$$\beta = -\frac{1}{V}\left(\frac{\partial V}{\partial P}\right)_T \tag{16.37}$$

and the value of β for water is $4.53 \times 10^{-5}\ atm^{-1}$. The equation for the volume of water is:

$$V = V^0\,(1 - \beta P) \tag{16.38}$$

where V^0 is the volume at a standard temperature and pressure (1 atm), and P is the pressure in excess of 1 atm. The coefficient of compressibility is virtually constant in the range −500 to +1000 atm. Equation 16.38 indicates that application of a negative pressure of 2.5 atm would expand a pure water solution by 0.01%, which corresponds to a change in the concentration of water of about 5 mM.

Looked at the other way, an expansion of water of only 0.01% would induce a negative pressure of 2.5 atm, equal to the osmotic pressure of a 0.1 molal solution at 37°C.

Dainty (1965) proposed a model in which he considered the density of water immediately within the pore opening on the solution side. As solute molecules cannot enter the pore, Dainty reasoned that the concentration of water within the pore must be higher than in the solution. Because of this difference in concentration, he argued that water would diffuse into the solution side faster than water could diffuse into the pore. The resulting net movement of water toward the solution side would lower the density of water in the pore, thereby creating a reduced pressure. Bulk movement of water down its pressure gradient would follow.

This explanation of the origin of osmotic pressure supposes that the driving force is actually water diffusing down its concentration gradient. The data in Fig. 16.7 show, however, that the concentration of water cannot be the major determinant of the colligative properties of solutions. In Fig. 16.7A, the water concentration in solutions of sucrose and glucose are plotted against the concentration of the solute. The water concentration is indeed decreased by dissolving solute, but sucrose, being almost twice as large as glucose, displaces almost twice as much solvent. As shown in Fig. 16.7B, however, the colligative properties, represented here by the freezing point depression, depend *only* on the concentration of solute. Solutions with equal solute concentrations but different water concentrations have the same freezing point.

An alternative view of the physical origin of the osmotic pressure begins with the notion of pressure as a force divided by an area. The macroscopic concept of pressure relies on the averaging over time of the myriad of collisions that produce the pressure. By Newton's law, force is the time derivative of momentum. An elastic collision of a solvent or solute molecule with the walls of the vessel results in a momentum change of $2mv$, where m is the mass of the molecule and v is its velocity, which contributes to the pressure against the vessel wall. At the entrance to the pore, however, solute molecules cannot transfer their momentum to the interior of the pore because they collide with the rim of the pore and are reflected back into the solution. Thus, the water molecules immediately inside the pore experience a momentum deficit that is equal to the component of pressure contributed by the solute molecules in the bulk phase.

Figure 16.8 shows the one-dimensional concentration profile of solute molecules near a pore opening. Because there is a steep solute gradient, there should be a diffusion of solute toward the pore opening. However, the actual steady-state flux of solute in this direction is zero because of the force exerted on the solute molecules by the membrane. The equation that describes the solute flux, J_s, in units of mol $cm^{-2}s^{-1}$, is:

$$J_s = -D\frac{\partial C(x)}{\partial x} + \frac{D}{RT} f\, C(x) \qquad (16.39)$$

where $C(x)$ is the concentration of solute at position x, D is the solute diffusion coefficient in units of $cm^2 \cdot s^{-1}$, f is the force per solute molecule and R and T have their usual meanings.

Villars and Benedek (1974) derived an equation for the drop in pressure immediately inside the pore on the solution side by setting the flux in Equation 16.39 to zero and analyzing the net force on a plug of volume near the pore. Under steady-state conditions with zero J_s through the pore, Equation 16.39 gives:

$$f\ C(x) = RT\frac{\partial C(x)}{\partial x} \qquad (16.40)$$

where $f\,C(x)$ is the force per molecule times the number of molecules per unit volume, or the force per unit volume. Figure 16.9 shows a volume element near the opening of

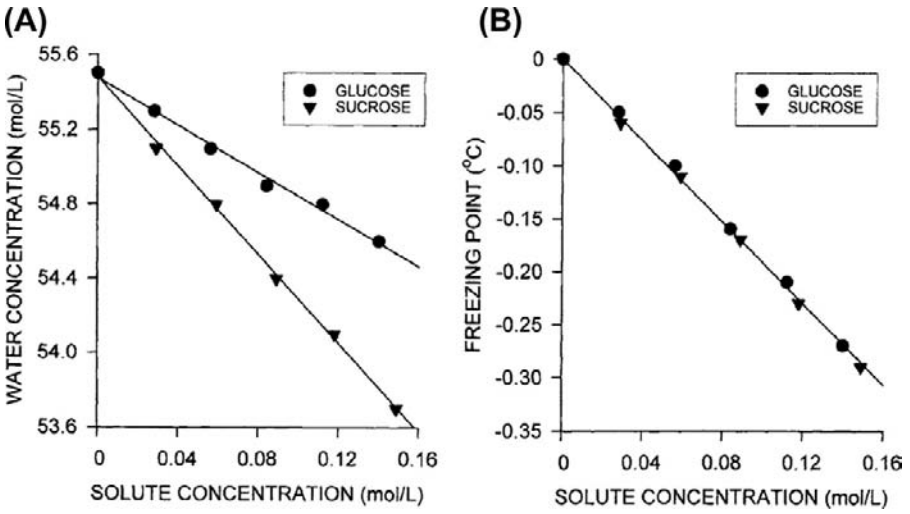

FIGURE 16.7 Effect of solute concentration on water concentration and freezing point depression in glucose and sucrose solutions. (A) Because solute displaces water, the water concentration decreases with increasing solute concentration. Sucrose is nearly twice the size of glucose. Consequently, there is less water in a sucrose solution having the same molarity as a glucose solution. (B) The freezing point depression, however, is dependent only on the solute concentration. It is the *mole fraction* of water that determines the colligative properties of solutions (the osmotic pressure, vapor pressure depression, boiling point elevation, and freezing point depression). *(Data from The Handbook of Chemistry and Physics, Chemical Rubber Company, Cleveland, OH, 1965.)*

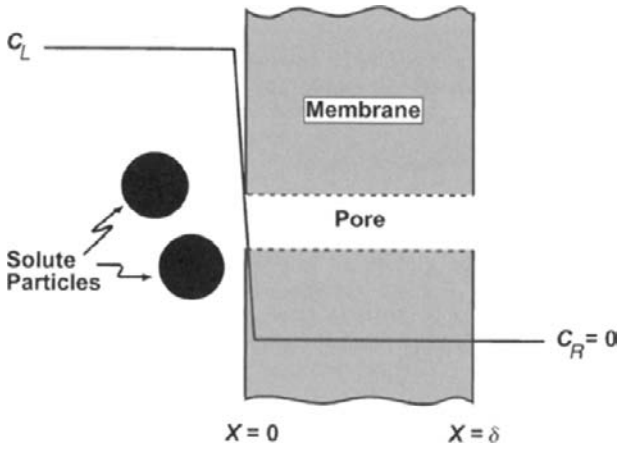

FIGURE 16.8 Concentration profile in the vicinity of a pore in a microporous membrane. The membrane is impermeable at all places except the pores, where water may penetrate but solute particles (solid circles) are too large to enter the pore. The concentration of solute in the bulk solution (C_L) must fall to zero upon entering the pore. The steep concentration gradient is accompanied by diffusion towards the pore that is balanced by reflection of solute by collision with the membrane.

the pore on the solution side. We consider the forces acting on the element of fluid with an area A from a point x well within the bulk solution to a point $x + \Delta x$ just inside the pore. We assume that this element is in mechanical equilibrium; although it may be moving, it is not accelerated or decelerated. The forces acting on the volume are contact forces on the edges of the volume and additional forces acting on the solute molecules alone to counteract the diffusive flux. At mechanical equilibrium the sum of the forces must be zero. This is written as:

$$F_s + F_c = 0 \tag{16.41}$$

where F_s is the total force acting on the solutes in the volume and F_c is the net contact force due to the pressure from the adjacent volume elements. The net contact forces are the result of pressure acting over an area:

$$F_c = AP(x) - AP(x + \Delta x) \tag{16.42}$$

The forces acting on the volume due to the solute particles is given by integrating Equation 16.40:

$$F_s = \int_x^{x+\Delta x} f\, C(x)\, dV \tag{16.43}$$

Inserting the volume element $dV = A\ dx$ and $fC(x) = RT\partial C(x)/\partial x$ from Equation 16.40, we obtain:

$$\begin{aligned} F_s &= ART \int_x^{x+\Delta x} \frac{\partial C(x)}{\partial x} dx \\ &= ART\ [C(x + \Delta x) - C(x)] \end{aligned} \tag{16.44}$$

Since $C(x + \Delta x) = 0$ because solute particles are not in the pore, this becomes:

$$F_s = -ART\, C(x) \tag{16.45}$$

where the negative sign indicates that F_s is directed to the left. Inserting Equations 16.42 and 16.45 into Equation 16.41, we have:

$$AP(x) - AP(x + \Delta x) = ART\, C(x) \tag{16.46}$$

or

$$P(x + \Delta x) = P(x) - RTC_L \tag{16.47}$$

This last equation indicates that the pressure experienced by the volume of fluid immediately inside the pore is less than the bulk pressure, $P(x)$, by the amount RTC_L, where C_L is the concentration of impermeant solute in the solution on the left of the membrane. This analysis is consistent with the intuitive idea that water movement from the water side to the solution side of a semipermeable membrane must be due to a real force, which appears in this analysis to be due to the momentum deficit, and thus pressure deficit, within the pore on the solution side.

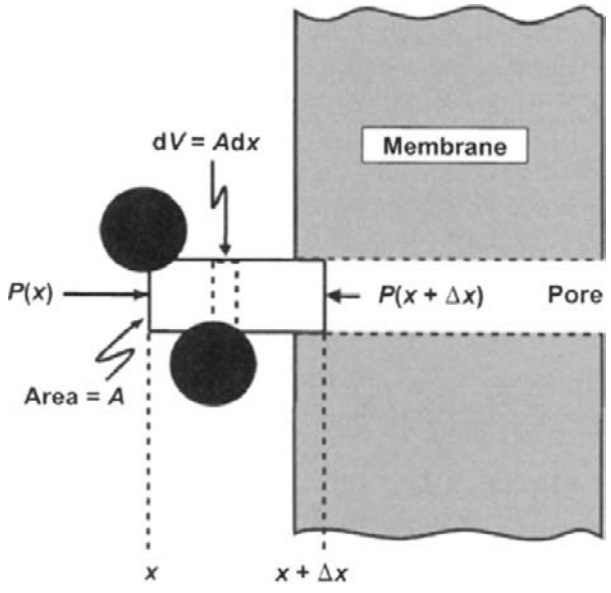

FIGURE 16.9 Forces acting on a volume element immediately adjacent to a pore opening. The ideal, porous, semipermeable membrane separates pure water on the right from solution of impermeant solute on the left. The volume element has an area, A, equal to the cross-sectional area of the pore. The pressure in the bulk phase at position x is $P(x)$. The pressure at position $x + \Delta x$, just within the pore, is $P(x + \Delta x)$. The net force on the element is the sum of the forces at both ends plus the forces acting only on the solute particles (solid circles) within the element.

IVA5. Physical Interpretation of the Reflection Coefficient, σ

The microporous semipermeable membrane presented previously distinguishes between solvent water and solute on the basis of pore and solute size. That is, the solute is too

large to enter the pore and so cannot cross the membrane. If the pores were somewhat larger or the solute molecules smaller, the solute could enter the pore, but with a lower probability than water because of the tight fit. In this case, rather than the solute being absolutely impermeant, the membrane would allow its slow passage. How does this affect the situation? Let us suppose that solute molecules that hit the rim of the pore before entry are reflected back into the bulk solution. This is shown diagrammatically in Fig. 16.10, looking down the axis of the pore perpendicular to the surface of the membrane. The area of the pore that is accessible to solute is:

$$A_s = \pi(r-a)^2 = \pi r^2\left(1-\frac{a}{r}\right)^2 \tag{16.48}$$

where a is the radius of the solute molecule. Assuming that the radius of water molecules (0.75 Å) is negligible compared to the pore's radius, the ratio of areas available to solute and solvent water is:

$$\frac{A_s}{A} = \frac{\pi r^2\left(1-\frac{a}{r}\right)^2}{\pi r^2} = \left(1-\frac{a}{r}\right)^2 \tag{16.49}$$

The fraction of collisions of solute molecules with the pore opening that are reflected back, compared with those of water, is approximated by the ratio of the area of the gray annulus in Fig. 16.10 to the cross-sectional area of the pore. This is identified with the reflection coefficient:

$$\sigma = \frac{A-A_s}{A} = 1-\frac{A_s}{A}$$
$$\sigma = 1-\left(1-\frac{a}{r}\right)^2 \tag{16.50}$$

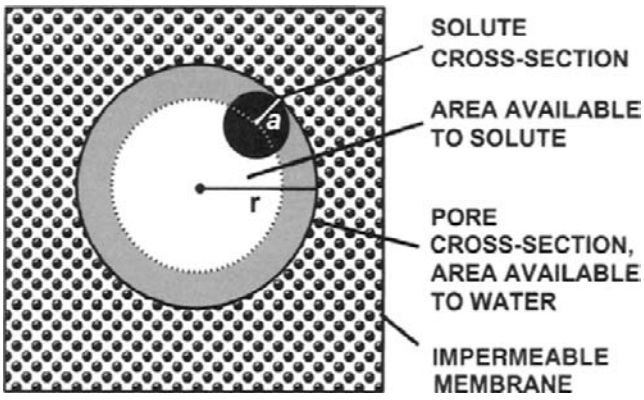

FIGURE 16.10 A physical interpretation of the reflection coefficient, σ, for a solute and a porous membrane. The view is down the pore in a direction perpendicular to the membrane. The pore is modeled as a right circular cylinder of radius r. The model assumes that any contact of the membrane with a solute particle of radius a (solid circle) will result in reflection of the particle back into the solution. The area available to solute is indicated in white. The total area of the pore, white plus gray annulus, is available for water movement.

According to this view, the concentration of solute immediately within the pore would not be zero, as in the case when the solute was impermeant, but instead would be $(1-\sigma)C$ and the excluded concentration would be σC. Thus, the momentum deficit inside the pore would be due only to the excluded solute and would be equal to σRTC, which is equal to $\sigma\pi$.

In addition to entrance effects, the concentration profile within the pore will be influenced by the combination of diffusion through the pore, solvent drag due to movement of fluid in response to pressure gradients and interaction of the solutes with the non-linear velocity profile within the pore. Laminar flow through long pores is characterized by a parabolic velocity profile, with a motionless layer of fluid adjacent to the pore walls and most rapid flow in the center. Large solute molecules will span several layers of velocity, thereby distorting the velocity profile and changing the solute molecule's velocity. Various equations have been derived to relax the assumption of negligible water radius and to relate the effective filtration area of the solute to the geometric radius of the pore (Renkin, 1954; Villars and Benedek, 1974; Hobbie, 1978). Although models assuming hydrodynamic flow through pores have been useful, their applicability to osmotic flow across biological membranes remains an open question.

IVB. Lipid Bilayer Membranes: the Dissolution–Diffusion Model

There are two types of lipid bilayer membranes that are useful models of membranes: the lipid vesicle and the planar bilayer membrane. The lipid vesicle is a small spherical shell of lipid usually produced by sonicating a dispersion of lipid in water. Planar bilayer membranes consist of a thin film of phospholipids formed over a small hole in a partition between two aqueous compartments. The film is formed by "painting" the hole with a non-polar solvent containing the lipids, which then spontaneously form a bilayer to separate fully the two solutions. This arrangement allows measurement of electrical and permeability properties of the bilayer. In the case of the liposome, the inner compartment is exceedingly small and experimentally inaccessible. In both cases, there are no components of the membranes other than the lipid.

IVB1. Osmotic and Pressure-Driven Flow for the Dissolution-Diffusion Model: P_f

One model of water permeation through the lipid bilayer supposes that the water dissolves in the lipid phase and crosses the membrane by simple diffusion. In this model, the solution in contact with the membrane is one phase, while the hydrophobic core of the membrane is a second phase. Equilibrium of water in the solution phase with

water in the membrane phase is described by equating the chemical potential of water in the two phases:

$$\mu^0_{w(\text{solution})} + RT\ \ln\ X_{w(\text{solution})} + P\overline{V}_{w(\text{solution})} = \mu^0_{w(\text{membrane})} + RT\ \ln\ X_{w(\text{membrane})} + P\overline{V}_{w(\text{membrane})} \tag{16.51}$$

where $X_{w\ (\text{solution})}$ and $X_{w\ (\text{membrane})}$ are the mole fractions of water in the solution in equilibrium with the membrane and in the membrane phase, respectively. The partition coefficient is defined as:

$$K_w = \frac{X_{w(\text{membrane})}}{X_{w(\text{solution})}} = \exp\frac{\mu^0_{w(\text{solution})} - \mu^0_{w(\text{membrane})} + \Delta P\overline{V}_w}{RT} \tag{16.52}$$

Consider the case where only osmotic pressure drives water flow and hydrostatic pressure across the membrane, ΔP, is 0. Since water generally partitions poorly into hydrocarbon solvents, we may assume that the mole fraction of water in the membrane phase is low. That is, the water concentration is dilute, and we may replace the mole fraction of water with its concentration:

$$C_{w(\text{membrane})} \simeq \frac{X_{w(\text{membrane})}}{\overline{V}_{\text{lipid}}} \tag{16.53}$$

where $\overline{\text{V}}_{\text{lipid}}$ is the partial molar volume of lipid in the membrane. If the concentration of water immediately inside the membrane is in equilibrium with the solution in contact with the membrane, we combine Equations 16.52 and 16.53 to get:

$$C_{w(\text{membrane})} \simeq K_w \frac{X_{w(\text{solution})}}{\overline{V}_{\text{lipid}}} \tag{16.54}$$

For dilute solutions, this is approximated by:

$$C_{w(\text{membrane})} \simeq K_w \frac{(1 - \overline{V}_w\ C_s)}{\overline{V}_{\text{lipid}}} \tag{16.55}$$

where C_s is the solute concentration. The concentration of water immediately inside the left side of the membrane, $C_{w,L}$, is given by Equation 16.55 where C_s is the concentration of solute in the solution on the left side of the membrane. A similar expression pertains to the concentration of water immediately inside the membrane on the right side ($C_{w,R}$). From the concentrations of water at both faces of the membrane, its diffusion across the membrane is given by Fick's law:

$$J_w = -D^m_w \frac{(C_{w,L} - C_{w,R})}{(0 - \delta)} \tag{16.56}$$

where D^m_w is the diffusion coefficient of water in the membrane phase. Substitution from Equation 16.55 into Equation 16.56 gives:

$$J_w = -\frac{D^m_w\ K_w\ \overline{V}_w(C_{s,L} - C_{s,R})}{\overline{V}_{\text{lipid}}\delta} = -\frac{D^m_w\ K_w\ \overline{V}_w\Delta C_s}{\overline{V}_{\text{lipid}}\delta} \tag{16.57}$$

The flux of water, J_w, is in units of moles of water per second per cm^2 of membrane. It is converted to units of volume flow by multiplying by V_w, as in Equation 16.34, to obtain:

$$J_v = \overline{V}_w J_w = -\frac{D^m_w\ K_w\ \overline{V}^2_w\Delta C_s}{\overline{V}_{\text{lipid}}\delta} = -\frac{D^m_w\ K_w\ \overline{V}^2_w}{\overline{V}_{\text{lipid}}RT\delta}RT\Delta C_s \tag{16.58}$$

The last term on the right is the osmotic pressure difference, $\Delta\pi$. This equation relates the volume flux to the osmotic pressure difference when the mechanism of water flow is dissolution and diffusion. Comparison to the earlier description of osmotic flow by Equation 16.18 allows us to identify L_p as:

$$L_p = \frac{D^m_w\ K_w\overline{V}^2_w}{\overline{V}_{\text{lipid}}RT\delta} \tag{16.59}$$

From the definition, $P_f = L_pRT/\overline{V}_w$, we get the expression for P_f as:

$$P_f = \frac{D^m_w\ K_w\overline{V}_w}{\overline{V}_{\text{lipid}}\delta} \tag{16.60}$$

Equation 16.58 was derived for an osmotic gradient ($\Delta C_s > 0$) in the absence of a hydrostatic gradient ($\Delta P = 0$). The expression relating volume flux and pressure when $\Delta C_s = 0$ can be derived by returning to Equation 16.51 and setting the mole fractions of water on the two sides of the membrane equal, while the pressures differ. The result is that exactly the same L_p is derived for pressure-driven flow as for osmotic flow when the mechanism is by rapid dissolution of water followed by slow diffusion through the lipid membrane phase (Finkelstein, 1987).

IVB2. Diffusional Water Permeability through Lipid Membranes: P_d

The permeability of lipid membranes to a diffusional water flux is expressed as:

$$J_w = P_d\ \Delta C_w \tag{16.61}$$

where P_d is the diffusional permeability and ΔC_w is the difference in water concentration across the

membrane. The overall permeation of the membrane by water is a consequence of three steps: dissolution into the membrane phase at the left interface; diffusion across the membrane phase; and reversal of dissolution at the right interface. If we assume, as we did in the derivation of P_f, that the rate-limiting step is diffusion through the membrane phase, then Equation 16.61 may be written as:

$$J_w = D_w^m \frac{\Delta C_{w(\text{membrane})}}{\delta} \tag{16.62}$$

From Equation 16.54, this is:

$$J_w = \frac{D_w^m \; K_w}{\overline{V}_{\text{lipid}}} \frac{\Delta X_{w(\text{solution})}}{\delta} \tag{16.63}$$

Because $\Delta X_w = \overline{V}_w \Delta C_w$, this becomes:

$$J_w = \frac{D_w^m K_w \overline{V}_w}{\overline{V}_{\text{lipid}} \delta} \Delta C_w \tag{16.64}$$

P_d can be identified by comparing Equations 16.64 and 16.61:

$$P_d = \frac{D_w^m K_w \overline{V}_w}{\overline{V}_{\text{lipid}} \delta} \tag{16.65}$$

IVB3. P_f/P_d Ratio for the Dissolution–Diffusion Model

The expressions for P_f in Equation 16.60 and P_d in Equation 16.65 derived for a lipid membrane under identical assumptions (equilibrium at the interfaces with relatively slow diffusion across the membrane), indicate that the P_f/P_d ratio for diffusive flow of water across lipid membranes should be 1.0. Cass and Finkelstein (1967) measured the osmotic and diffusive permeability of planar lipid bilayers and found that, within experimental uncertainty, the ratio was indeed 1.0. The uncertainty arose mainly in the determination of P_d because of the presence of unstirred layers adjacent to the planar lipid bilayer. These unstirred layers are an additional diffusional barrier that affects the experimental determination of P_d much more than P_f. In the flux equations, permeability appears as a conductance relating a flux (J_w or J_s) to a driving force (ΔC_w or ΔC_s). Thus, the inverse of permeability is like a resistance. For a membrane in series with unstirred layers, the total resistance is the inverse of the observed permeability, which is the sum of the resistances offered by the individual barriers, the membrane and the unstirred layers. We write this as:

$$\frac{1}{P_{d(\text{obs})}} = \frac{1}{P_d} + \frac{1}{P_u} \tag{16.66}$$

From this equation, it is plain that if P_u, the combined permeability of the unstirred layers on both sides of the membrane, is less than infinity, the observed P_d will be less than the actual P_d of the membrane alone. Since diffusion of water through the unstirred layer is given by Fick's law, Equation 16.66 may be rewritten as:

$$\frac{1}{P_{d(\text{obs})}} = \frac{1}{P_d} + \frac{\delta_L + \delta_R}{D_w} \tag{16.67}$$

where δ_L and δ_R are the equivalent unstirred layer thickness on the left and right sides of the membrane.

Unstirred layers also can affect measurement of the coefficients for pressure gradient-driven flow, P_f and L_p, but the error introduced is much less than for concentration gradient-driven flow, P_d (Barry and Diamond, 1984; Finkelstein, 1987), and was safely ignored in evaluating the P_f/P_d ratio (e.g. Cass and Finkelstein, 1967). The osmotic flow sweeps solute toward the membrane on the side with lower osmolarity and away from the membrane on the other side. As long as convection is faster than diffusion, this diminishes the transmembrane osmotic gradient, reducing J_v for the apparent $\Delta\pi$ and causing underestimation of P_f and L_p. The observed P_f, $P_{f\,(\text{obs})}$, is given as:

$$P_{f(\text{obs})} = P_{f(\text{membrane})} \exp(-J_v \; \delta / D_s) \tag{16.68}$$

where $P_{f(\text{membrane})}$ is the true membrane parameter, δ is the unstirred layer thickness, J_v is the volume flux and D_s is the diffusion coefficient of the osmolyte. The error can be minimized by determining P_f with a small $\Delta\pi$ so that J_v is small. Because P_f and L_p are proportional (Equation 16.36), the errors are also proportional.

The value of P_d and P_f varies with the lipid composition of the membrane and ranges from 1×10^{-5} cm·s^{-1} to 5×10^{-3} cm·s^{-1} (Deamer and Bramhall, 1986). Cholesterol, which generally reduces the fluidity of lipid bilayers, reduces P_d and P_f progressively with increasing cholesterol content (Finkelstein and Cass, 1968). The *unidirectional* flux across a lipid membrane equals $P_d \times C_w$. Using a typical P_d of 1×10^{-3} cm·s^{-1} and a C of 55 mol·L^{-1}, the unidirectional flux across a membrane is 5.5×10^{-5} mol·cm^{-2}·s^{-1}. By comparison, the unidirectional flux of water across a distance $\delta = 5$ nm (approximately the thickness of the lipid bilayer) can be calculated as $(D_w \times C_w)/\delta$. Using 3×10^{-5} cm^2·s^{-1} for D_w, the unidirectional flux of water in water is 3.3 mol·cm^{-2}·s^{-1}. Thus, water flux through the membrane is about 60 000 times slower than that through water. Nevertheless, the water flux is still enormous. Taking 0.7 nm^2 as the average area of a typical phospholipid in the bilayer, the unidirectional water flux corresponds to about 2.2×10^5 water molecules passing each phospholipid molecule each second.

IVC. Flow through Narrow Pores: P_f/P_d Ratio

The equations derived earlier for P_f for a porous membrane required the assumption that the pores were large enough to allow laminar flow as described by the Poiseuille equation. Suppose that the pores are so narrow that water passes through the pores in single file. It is clear that laminar flow cannot occur here and the Poiseuille equation does not apply. As shown in Fig. 16.11, the narrow pore restricts free diffusion in the pore because diffusion of one water molecule from one position in the pore to the next requires its neighbor to move away to provide a vacancy. In this way, diffusion within the restricted geometry of the pore becomes a collective property of all of the molecules in the pore. The likelihood that a tracer molecule will diffuse all the way through the pore will depend on the number of water molecules in the pore, as movement of tracer water (solid circle) through the pore requires the movement of a vacancy (×) all the way through the pore.

Suppose that there are N water molecules in a pore. We may assume that the length of the pore, δ, is proportional to N, and that the water molecules reside in more or less specific positions separated by δ/N. In the free diffusion of liquid water in the bulk solution, according to Fick's first law of diffusion, the flux of water is proportional to $1/\delta$ or $1/N$. In the case of a single-file diffusion through a narrow pore, the diffusion of a vacancy through the water within the pore looks exactly like the diffusion of water through a series of vacancies in free diffusion. Thus, the flux of the vacancy also is proportional to $1/N$. The movement of tracer from one position to the next in the pore requires the diffusion of a vacancy all the way through the pore, so that the flux of tracer one step is proportional to $1/N$. In order to diffuse all the way through the pore, the tracer must make N such jumps. The unidirectional flux of tracer over N steps of equal flux is given by Stein (1976):

$$J_{0\rightarrow N} = \frac{J_{ij}^{N}}{N\ J_{ij}^{N-1}} = \frac{1}{N} J_{ij} \tag{16.69}$$

where $J_{0\rightarrow N}$ is the unidirectional flux of tracer across N steps (all the way through the membrane) and J_{ij} is the unidirectional flux of tracer over one step. Since J_{ij} requires diffusion of a vacancy all the way through the pore, it is proportional to $1/N$. The unidirectional diffusional flux of tracer through a single-file pore is thus proportional to $1/N^2$, rather than $1/N$. Pressure-driven flow, on the other hand, remains inversely proportional to pore length. The theoretical analysis of both pressure-driven flow and diffusive flow through a single-file pore has led to the conclusion that the proportionality constants relating P_f to $1/N$ and P_d to $1/N^2$ are identical. The result, for a single-file pore, is:

$$\frac{P_f}{P_d} = N \tag{16.70}$$

where N is the number of water "binding sites" within the pore (Finkelstein, 1987). A more recent theoretical analysis suggests that this result is true near equilibrium, but the ratio of osmotic to diffusive permeability may exceed N for a membrane far from equilibrium (Hernandez and Fischbarg, 1992).

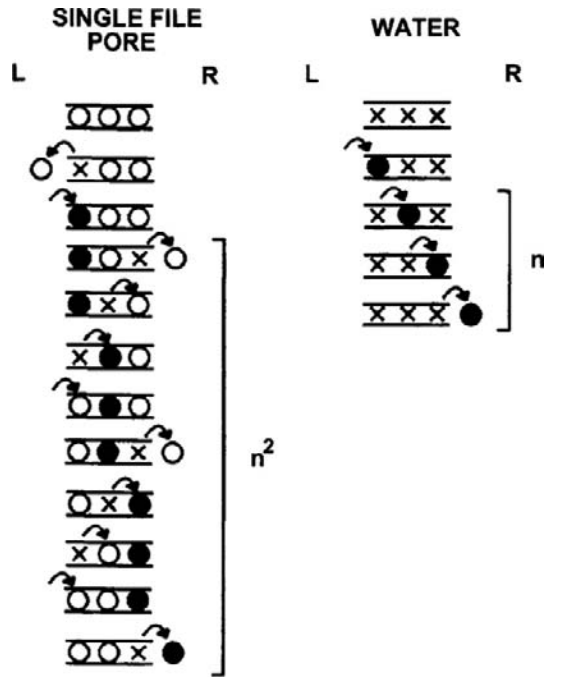

FIGURE 16.11 Jumping model of diffusion of water through a narrow pore. In the model of free water diffusion (right), tracer water (solid circles) makes successive jumps from one vacancy (×) to another. In order to move three places, it must make three jumps. In a narrow pore (left), tracer water cannot move to the next position in the pore unless a vacancy is present because unlabeled water (open circles) cannot move out of the way. Movement of tracer water from one site to the next in the pore requires a vacancy to diffuse all the way through the pore. Since the vacancy requires three steps to diffuse through the pore, tracer water diffusion through three steps in a narrow pore requires nine jumps. The result is that single-file diffusion becomes a collective property of the single file and is slower than free water diffusion.

IVD. Mechanism of Water Transport across Lipid Bilayer Membranes

The previous discussion suggests that water transport across lipid bilayer membranes occurs by rapid dissolution at the membrane interface followed by diffusion across a hydrocarbon-like interior. Three observations strongly support this mechanism: (1) the P_f/P_d ratio, after correction for unstirred layers, appears to be close to 1.0 (Cass and Finkelstein, 1967; Andreoli and Troutman, 1971); (2) insertion of pore-forming antibiotics such as nystatin, amphotericin B or gramicidin A increases the P_f/P_d ratio to small values of N (between 3 and 5) (Holz and

Finkelstein, 1970; Rosenberg and Finkelstein, 1978); and (3) the activation energy for water transport, typically 10–20 kcal·moL^{-1}, is larger than the activation energy for free water diffusion, ≈4 kcal·moL^{-1}, which should apply if water moves through a pore (Solomon, 1972; Fettiplace and Haydon, 1980). However, experimental studies of water permeation across liposomes appear to give a different answer. The P_f of liposomes, measured by turbidimetric methods, is not affected by the chain length of the lipids or the degree of saturation (Carruthers and Melchior, 1983; Jansen and Blume, 1995), whereas water solubility in hydrocarbons is affected by chain length (Schatzberg, 1963). Further, the activation energy of P_f in liposomes is only 3.2 kcal·moL^{-1} (Carruthers and Melchior, 1983), similar to the activation energy for free water diffusion. The P_f of liposomes is discontinuous near phase transitions of the lipid and P_f/P_d ratios from 7 to 23 have been reported (Jansen and Blume, 1995). From these observations, it appears that liposomes do not behave as planar lipid bilayers, perhaps because of membrane defects induced by the marked curvature of the membrane in these small structures. The activation energy has been taken as diagnostic of whether water traverses the membrane through pores or by diffusion through the lipid itself (Finkelstein, 1987; Verkman, 1993). Low activation energies of water transport are associated with a high P_f or L_p in membranes containing water channels or pores, whereas high activation energies are associated with a low P_f or L_p, indicating diffusional water transport in membranes without pores or when pores are blocked by mercurials (Table 16.2).

In the dissolution–diffusion mechanism, water encounters a minimum of three sequential barriers: dissolution on one side of the membrane; transport across the hydrocarbon-like interior; and then removal from the membrane on the opposite side. Assuming rapid equilibration at the interfacial regions is equivalent to assuming that the barriers there are insignificant compared to the barrier of diffusion, but there is no a priori reason to make this assumption. The alternate view proposes that the rate-limiting step is lateral movement of the phospholipid head groups that creates a transient defect required for penetration of water into the interfacial region of the membrane (Trauble, 1971; Haines, 1994). Water transport through the hydrophobic core requires vacancies within the bilayer that form when hydrocarbon chains make *gauche-trans-gauche* kinks caused by the rotation of carbon–carbon bonds in the hydrocarbon tails. Kinks in the hydrocarbon tails propagate rapidly down acyl chains and provide sufficient space for water. Experimental support for this model comes from studies showing addition of cardiolipin to phosphatidylcholine liposomes decreases P_f without changing bilayer fluidity by stabilizing head group interactions (Shibata et al., 1994). These two models make very different assumptions, and the detailed mechanism of water permeation through lipid bilayers remains uncertain.

TABLE 16.2 Hydraulic Conductivity and its Apparent Activation Energy

Tissue	Lp 10^{-10} L·N^{-1}·s^{-1}	E_a kcal·moL^{-1}
Water channels		
RBC, human	18.0	3.9
RBC, beef	18.2	4.0
RBC, dog	23.0	4.3
Prox. tubule BLM-V, rabbit	21.9	2.5
Liposomes + AQP1	30.8	3.1
Water channels + mercurials		
RBC, human + PCMBS	1.3	11.6
Prox. tubule BLM-V, rabbit + Hg	4.4	8.2
Diffusional		
RBC, chicken	0.6	11.4
Intestinal brush border, rat	0.9	9.8
Ventricle, rabbit	1.2	10.5
Liposomes	1.9	16.0
PC bilayer	1.6	13.0
PC/chol bilayer	0.4	12.7
Water self-diffusion	—	4.2

Hydraulic conductivity, L_p, and activation energy, E_a, are characteristic of the mechanism of water transport. High L_p and low E_a are typical of membranes containing functioning water channels, whereas low L_p and high E_a indicate diffusional water transport. Note that 10^{-10} L·N^{-1}·s^{-1} (SI units)=10^{-12}·cm^3·dyn^{-1}·s^{-1} (cgs units). RBC, red blood cell; BLM-V, basolateral membrane vesicles; AQP1, aquaporin-1; PCMBS, *p*-chloromercuribenzene sulfonate; PC, phosphatidylcholine; chol, cholesterol. For references, see Suleymanian and Baumgarten (1996).

V. WATER MOVEMENT ACROSS CELL MEMBRANES

In the prior sections, we considered osmotic- or pressure-driven flow and diffusive flow of water across membranes that were characterized as: (1) porous membranes with pores large enough to allow laminar flow; (2) lipid membranes with no pores, but allowing water permeation by a dissolution–diffusion mechanism; and (3) membranes containing narrow pores. We found expressions for the osmotic permeability, P_f, and the diffusive permeability,

P_d, for each and found that the membranes could be distinguished in principle by the ratio P_f/P_d: large values of P_f/P_d indicate a porous membrane, $P_f/P_d = 1$ signifies a diffusive mechanism and small values of $P_f/P_d > 1$ are characteristic of narrow pores. What are the permeabilities of real biological membranes, and what do these permeabilities tell us about the routes of water transport through membranes?

VA. Rate of Water Exchange: Experimental Measure of P_d

Paganelli and Solomon (1957) measured the diffusional exchange of water across erythrocyte membranes by rapidly mixing a suspension of the cells with an isotonic buffer with added tracer ^3H_2O. The mixture was forced down a tube and samples of the extracellular water were obtained by filtration at various distances, corresponding to various times of exchange. Paganelli and Solomon found that the half-time for exchange of ^3H_2O was 4.2 ms at room temperature. This means that 90% of all of the water within an erythrocyte is exchanged with extracellular water every 14 ms. This is an extraordinarily rapid rate of exchange. Erythrocytes are sufficiently small that the presence of an unstirred layer within the cells does not appreciably affect the determination of P_d (i.e. $(\delta_L + \delta_R)/D_w << 1/P_d$; see Equation 16.67).

Diffusional exchange of water across erythrocyte membranes also can be measured by nuclear magnetic resonance (NMR) spectroscopy. Relaxation of the nuclear spin states of hydrogen is much slower inside a cell than outside when a relatively impermeant paramagnetic ion like Mn^{2+} is added to the extracellular solution. This allows calculation of P_d because the relaxation of the spin states is then effectively limited by permeation through the membrane. The values of P_d for the erythrocyte determined by isotopic or NMR methods cluster around $4\times10^{-3}\,\mathrm{cm\cdot s^{-1}}$ (Solomon, 1989).

VB. Rate of Osmotic Flow: Experimental Measure of P_f and L_p

According to Equation 16.23, the hydraulic conductivity, L_p, can be determined experimentally as:

$$L_p = \left(\frac{-Q_v}{A\sigma\Delta\pi}\right)_{\Delta P=0} \tag{16.71}$$

The osmotic permeability, P_f, can then be calculated as $P_f = L_p RT/\overline{V}_w$ (Equation 16.36). The experimentally determined values reflect the rate of water flow, Q_v, in the presence of a known osmotic pressure difference, $\Delta\pi$, produced by a solution with a known reflection coefficient, $\sigma \approx 1.0$, over a known surface area, A.

The rate of water movement into or out of erythrocytes in response to mixing with hypertonic or hypotonic media has been measured by using light scattering as an index of erythrocyte volume. The experiments are similar to those used to determine P_d; a suspension of erythrocytes is mixed with media of defined osmolality and the mixture then flows down a tube passing through an observation cell. Light scattering is monitored at known distances down the tube and cell volume changes are calculated from changes in light scattering. This and other methods give values for L_p that cluster around $1.8\times10^{-11}\,\mathrm{cm^3\cdot dyn^{-1}\cdot s^{-1}}$ (Solomon, 1989). Using $R = 8.314\times10^7\,\mathrm{dyn\cdot cm\cdot mol^{-1}\cdot K^{-1}}$, $\overline{V}_w = 18\,\mathrm{cm^3\cdot mol^{-1}}$ and $T = 298\,\mathrm{K}$, this average value of L_p corresponds to a P_f of about $2.5\times10^{-2}\,\mathrm{cm\cdot s^{-1}}$.

VC. Water Channels in Biological Membranes

The ratio of P_f/P_d for the erythrocyte membrane described earlier is about 5. Although there is some uncertainty in this ratio, it is clearly in excess of the value of 1.0 predicted for a diffusive mechanism. This suggests that there are pores in the erythrocyte membrane. The actual value of P_f/P_d for the pore alone cannot be obtained from just this information, however, because the erythrocyte membrane is actually a mosaic of lipid bilayer and pores; water moves through both in parallel, so the permeabilities of the components add. Experiments that block the pore suggest that the P_f/P_d ratio for the pore alone is about 10 and that 90% of water flux is via the pore, whereas 10% crosses the lipid bilayer (Macey, 1979; Finkelstein, 1987).

Two distinct means of inhibiting water transport provide additional evidence for proteinaceous pores. Mercurial sulfhydryl reagents, such as $HgCl_2$, *p*-chloromercuribenzoate (PCMB) and *p*-chloromercuribenzene sulfonate (PCMBS), decrease the erythrocyte P_f by a factor of 10 and P_d by less than a factor of 2 and the osmotic and diffusional permeabilities become equal (Macey and Farmer, 1970; Macey et al., 1972). Concurrently, the activation energy for permeation is increased from about $4\,\mathrm{kcal\cdot mol^{-1}}$ expected for water-filled pores to $>10\,\mathrm{kcal\cdot mol^{-1}}$, a value typical of artificial lipid bilayers (see Table 16.2). Mercurials inhibit water transport primarily by targeting protein SH groups because their effect is fully and rapidly reversed by cysteine. The second inhibitor is radiation. High doses of radiation inhibit water transport in both erythrocytes (van Hoek et al., 1992) and renal brush-border membrane vesicles (van Hoek et al., 1991). The characteristics of radiation inactivation suggest that the target is the size of a 30-kDa protein and are inconsistent with the entire membrane or transient defects serving as the major water pathway.

Although these studies and others, especially in epithelia (e.g. Verkman, 1993), made it clear that water pores or channels must exist, until recently, their identity and characteristics remained mysterious. Are what we call "water channels" simply water moving through open ion channels or through an ion exchanger or ion co-transporter? Are water channels specific, admitting water but excluding ions? These questions have been answered with the cloning and expression of a family of water channels called aquaporins (Agre et al., 1993; King and Agre, 1996; Verkman et al., 1996; Heymann et al., 1998; Nielsen et al., 1999).

VC1. Aquaporins

Water channels are related to the membrane integral protein (MIP) family (20−40% homology). The first water channel identified was cloned from a human bone marrow library by Preston and Agre (1991) based on the sequence of a purified protein of uncertain function. Initially called CHIP28 (channel-forming integral protein, 28 kDa), this protein was later redesignated aquaporin-1 (AQP1) and MIP-1 is referred to as AQP0. Ten mammalian aquaporins are known and more than 100 related proteins have been found in amphibians, *Drosophila*, plants, *Escherichia coli* and yeast, but not all of these conduct water (Heyman et al., 1998; Nielsen et al., 1999; Heymann and Engel, 1999).

The cloned AQP protein exhibits all of the characteristics of a water channel. AQP1 expressed in *Xenopus* oocytes induces up to 30-fold increases in P_f that is blocked by $HgCl_2$ (Preston et al., 1992). Reconstitution of purified AQP1 protein in liposomes verified that AQP1 itself, rather than modulation of an endogenous oocyte membrane protein, was responsible for mercurial-sensitive water permeation (Zeidel et al., 1992). Furthermore, incorporation of AQP1 into liposomes reduced the activation energy of P_f from 16.1 kcal·mol^{-1}, characteristic of permeation through the bilayer, to 3.1 kcal·mol^{-1}, characteristic of water passing through water-filled pores. Moreover, AQP1 appears to be active and highly selective for water without requiring regulatory subunits or cofactors (Preston et al., 1992; Zhang et al., 1993).

There are about 2×10^5 AQP1 molecules per erythrocyte (Zeidel et al., 1992). Taking the erythrocyte's membrane area as 1.35×10^{-6} cm^2 (Solomon, 1989), this corresponds to a density of about 1.5×10^{11} AQP1 cm^{-2} or 1500 AQP1 μm^{-2}. Despite this remarkable density of pores, the water permeability of a human erythrocyte is only ≈10 to 50 times greater than that of a phosphatidylcholine/cholesterol bilayer (Fettiplace and Haydon, 1980). Thus, 30−150 aquaporin channels are needed to equal the permeability of 1 μm^2 of bilayer.

AQP1 contains 269 amino acid residues and was postulated to have six membrane-spanning domains based on an analysis of hydrophilicity (Preston and Agre, 1991) and selective proteolysis of protein loops that face the intra- or extracellular side (Preston et al., 1994). The topology for the AQP1 and the other members of the AQP family is shown in Fig. 16.12. Mercurial-inhibition, N-glycosylation and PKA phosphorylation sites have been identified. There is an internal homology between the halves of AQP designated repeat-1 and -2. The greatest homology among AQPs is in the segments surrounding asparagine-proline-alanine (NPA) motifs in loops B and E. These loops are thought to be arranged antiparallel and are postulated to dip back into the membrane to form an hourglass-shaped pore represented in the cartoon in Fig. 16.12 (Jung et al., 1994).

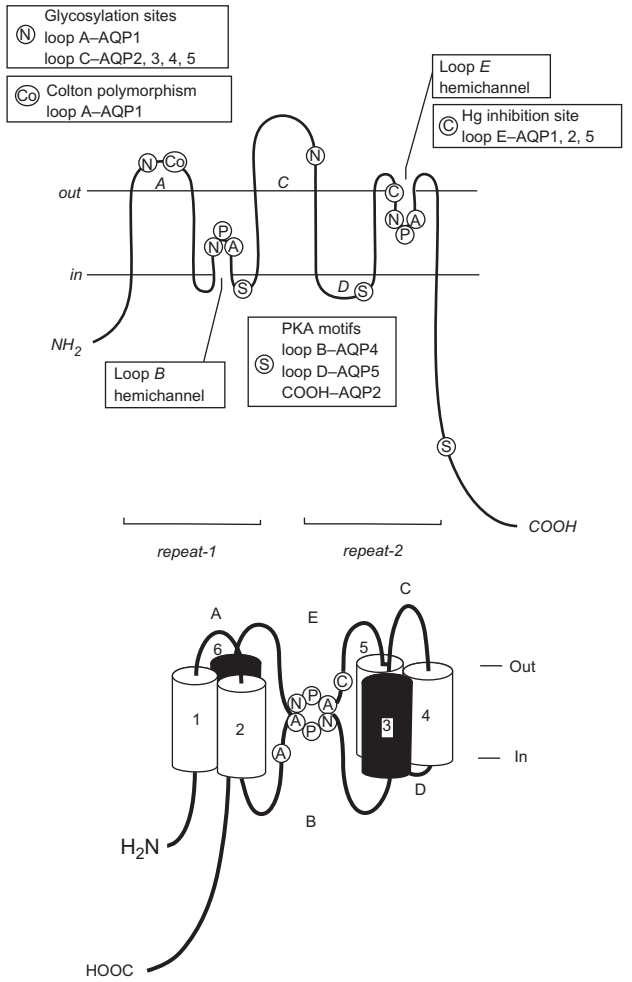

FIGURE 16.12 AQP family portrait. Cartoon illustrating the postulated topology of AQP as a structure with six membrane spanning α-helices (top). Cysteine (C) responsible for inhibition by mercurials and consensus PKA phosphorylation (S) and glycosylation (N) sites are also shown. Loops B and E are envisioned to dip into the membrane with the two NPA motifs forming the narrow neck of an hourglass-shaped, water-filled pore (bottom). Single letter codes are standard amino acid abbreviations. The position of the Colton polymorphic blood group antigen (Co) is noted. *(Reproduced from King and Agre (1996) with permission, from the Annual Review of Physiology, volume 58, © 1996, by Annual Reviews, Inc. and from Jung et al. (1994) with permission.)*

It is hypothesized that four highly conserved polar residues, E17, N76, N192, E142, comprise a critical portion of the water permeation pathway (Heymann et al., 1998).

The biochemical behavior of solubilized erythrocyte AQP1 suggested that it is a non-covalently-linked tetrameric structure and electron microscopy of negatively stained AQP1 confirmed this (Walz et al., 1994). Co-expression of Hg-sensitive and -insensitive recombinant proteins indicates that each AQP monomer forms an independent functioning pore, however (Preston et al., 1993). An exception to the tetrameric design of AQPs is AQP4. AQP4 forms large multimeric square arrays in the end-feet of astrocytes that surround capillaries (Rash et al., 1998). X-ray diffraction patterns at 3.5- and 6-Å resolution have been obtained from two-dimensional crystalline AQP1 arrays (Jap and Li, 1995; Walz et al., 1997). Electron density contour maps confirmed a tetrameric arrangement of monomers and each monomer appeared to have a central low density core, presumably the permeation pathway, surrounded by six tilted high density regions thought to represent membrane-spanning α-helicies.

Immunohistochemistry, Western blot (protein determination) and Northern and in situ hybridization and RNase protection assays (mRNA determinations) have identified broad but only partially overlapping distributions of AQP homologs in regions where water permeability is high (Hasegawa et al., 1993; Nielsen et al., 1993, 1999; Zhang et al., 1993; Umenishi et al., 1996; Ma and Verkman, 1999). For example, AQP1 is located in erythrocytes, renal proximal tubules and the descending thin limb of the loop of Henle (but not in the collecting duct, where water permeability is controlled by vasopressin), the choroid plexus, the iris, ciliary and lens epithelia and corneal endothelium of the eye, lung alveolar capillaries and epithelium, red splenic pulp (with erythrocyte precursors), colonic crypt epithelium and non-fenestrated capillary and lymphatic endothelium in a number of organs including cardiac, skeletal and smooth muscle. The exception with regard to broad distribution is AQP2. AQP2 underlies the vasopressin-regulated water permeation pathway of the renal collecting duct apical membrane that maintains water balance (Nielsen et al., 1995, 1999). Mutation of AQP2 is responsible for inherited nephrogenic diabetes insipidus and targeting and expression defects may cause acquired forms of this disease. On the other hand, AQP2 expression is upregulated in pregnancy and congestive heart failure, states associated with enhanced water retention (Nielsen et al., 1999).

Several cautions are warranted when drawing physiological interpretations from the localization of AQP. For example, AQP1 mRNA is higher in cardiac homogenate than in homogenate from any other organ (Umenishi et al., 1996), but functionally, the story is different. In isolated myocytes, L_p is very low and the activation energy is high, about 10 kcal·mol^{-1} (Suleymanian and Baumgarten, 1996) (see Table 16.2). Thus, AQPs do not significantly contribute to water transport across the myocyte membrane.

Organs comprise cells with diverse functions and often different requirements for water transport. Because of its localization in vascular tissue, AQP detected in homogenates should not be attributed to the principal cells of the organ without confirmation. Even careful immunohistochemistry and in situ hybridization may lead the physiologist astray. The problem is the high density of AQP necessary to significantly affect P_f. If, for example, the density of AQP1 in the erythrocyte membrane was 10 AQP1 μm^{-2} rather than 1500 AQP1 μm^{-2}, AQP1 would still be detected by modern techniques, but it would make a physiologically insignificant contribution to P_f.

VC2. Other Channels and Transporters

The identification of specific water channels does not exclude the possibility that water flux through ion channels or transporters significantly contributes to the water permeability of the membrane. One interesting example is the cystic fibrosis conductance regulator (CFTR). CFTR functions as a cAMP-regulated Cl^- channel. Hasegawa et al. (1992) recently found that CFTR expressed in oocytes also acts as a water channel with an estimated single channel P_f comparable to that of AQP1. Both P_f and Cl^- conductance were increased by cAMP. The effect of the CFTR channel on P_f is large but not unique. Pore-forming antibiotics such as gramicidin, nystatin and amphotericin, are reported to induce a more modest P_f. Transporters also may contribute to P_f. Fischbarg et al. (1990) found that expression of Na^+-independent glucose transporters in oocytes increases water permeability and Solomon et al. (1983) suggested that some of the water permeability of erythrocytes was contributed by the Cl^--HCO^-_3 exchanger. However, water flux mediated by these transporters does not account for the macroscopic properties of water transport.

VI. REGULATION OF CELL VOLUME UNDER ISOSMOTIC CONDITIONS

VIA. Gibbs–Donnan Equilibrium

Because ions exert an effective osmotic pressure, the distribution of ions affects water flow across the cell membrane and thus cell volume. The starting point for understanding these effects is the theoretical ideas of Gibbs that were first demonstrated experimentally by Donnan. The phenomenon is now called *Gibbs–Donnan equilibrium* or simply *Donnan equilibrium*. Macknight and Leaf (1977) elegantly describe the history of how these ideas were applied to cell volume regulation and Overbeek

(1956) provides a detailed derivation and considers non-ideal solution behavior.

In a Donnan system, the membrane permits the movement of small charged solutes (e.g. K^+ and Cl^-) between two compartments but restricts the movement of large charged species, such as proteins, which are usually polyvalent and negatively charged at intracellular pH. It is the inability of one (or more) charged species to distribute freely between the compartments that profoundly influences the distribution of the mobile ions and, consequently, water. For a cell, it is the cell membrane that restricts the movement of large ions. A membrane is not required to establish a Donnan equilibrium, however. All that is needed is a means of restricting one charged species to a single compartment. Donnan equilibria can arise in gels consisting of charged structural components (e.g. an ion-exchange column) because the charges on the gels are fixed in place. Donnan equilibria can also arise in cells after their membranes have been removed, leaving a cytoplasmic "gel" consisting of interconnected cellular proteins. A Donnan system represents a true equilibrium, although as we will see, an equilibrium is not attained under the usual biological conditions.

There are three important characteristics in a Donnan equilibrium system: (1) an unequal distribution of ions; (2) a potential difference between the compartments; and (3) an osmotic pressure. These characteristics can be understood from the application of a basic thermodynamic principle to the system. Species that can cross the membrane, including both mobile ions and water, will distribute themselves so that their electrochemical potential (μ_i) is the same in both compartments.

To understand how a Donnan equilibrium develops, imagine starting an experiment by "filling" the cell and the extracellular space with solutions of concentrations indicated in Fig. 16.13A. Since ions move down their electrochemical gradients, the first question is: what are the electrochemical gradients? Initially, there is no potential difference across the membrane because both internal and external solutions start with an equal number of positive and negative charges. There is no concentration gradient for K^+ because the amount of K^+ is the same on both sides of the membrane. Due to the presence of impermeant anions inside the cell, however, $[Cl^-]_o$ must be greater than $[Cl^-]_i$. Consequently, Cl^- will enter the cell, moving down its electrochemical gradient, which is initially just the concentration gradient. Inward movement of Cl^- makes the inside of the cell negative with respect to the outside. The developing inside negative potential has two consequences. First, it slows the rate of further influx of Cl^-. Second, the electrical gradient causes the accumulation of K^+ inside the cell. As K^+ moves down its

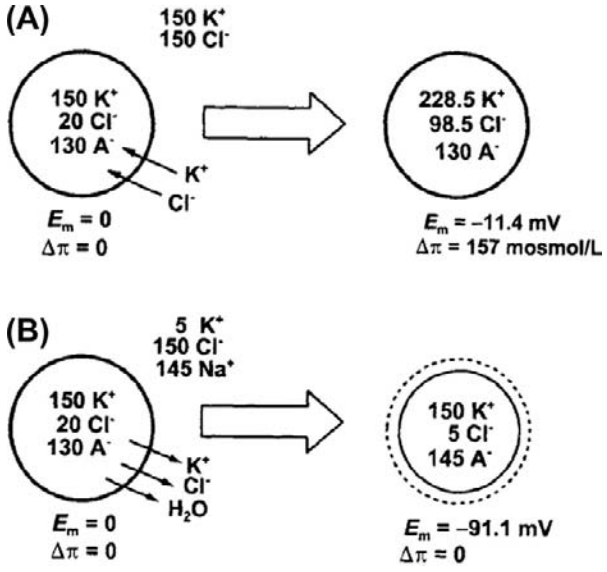

FIGURE 16.13 Development of a Donnan equilibrium. (A) Cell bathed in 150 mM KCl is "filled" with 150 mM K^+, 20 mM Cl^-, and 130 mM A^-. Initially, there is no potential or osmotic gradient (left). K^+ and Cl^- enter the cell until $[K^+]_o \cdot [Cl^-]_o = [K^+]_i \cdot [Cl^-]_i$ and the ionic fluxes establish a potential and osmotic gradient (right). An equilibrium is achieved only if the membrane is rigid and cell volume is constant. With a biological membrane, however, water enters the cell, cell volume increases and $[K^+]_i \cdot [Cl^-]_i$ decreases. This causes further entry of solute and solvent and the cycle repeats until the cell bursts. (B) Double-Donnan system. Part of the extracellular K^+ is replaced by Na^+, which is assumed to be impermeant. With impermeant ions on both sides of a membrane (left), equilibrium is attained (right) without an osmotic pressure gradient. In this case, K^+, Cl^-, and water leave the cell, until at equilibrium $[K^+]_o \cdot [Cl^-]_o = [K^+]_i \cdot [Cl^-]_i$. The amount of A^- in the cell is fixed, and thus, the decrease in cell volume increases $[A^-]_i$.

electrochemical gradient in the direction set by the potential gradient, an opposing concentration gradient is created. Finally, an equilibrium is reached when the electrical and concentration gradients for both K^+ and Cl^- are equal in magnitude and opposite in direction. This satisfies the requirement that μ_K and μ_{Cl}, the electrochemical potential for K^+ and Cl^-, respectively, are the same in both compartments.

During the evolution of the equilibrium, the influx of K^+ and Cl^- are equal on a macroscopic scale and are said to be coupled by the requirement for macroscopic electroneutrality. This is simply a shorthand for the idea that any difference in rates of anion and cation transmembrane flux (a separation of charge) gives rise to a potential that equalizes the fluxes (e.g. if the influx of K^+ was greater than that of Cl^-, an inside positive potential would develop, slowing K^+ influx and accelerating Cl^- influx until the rates matched exactly). In the example in Fig. 16.13A, both $[K^+]_i$ and $[Cl^-]_i$ increased by $\approx$78.5 mM. The total entry of K^+ and Cl^- cannot be precisely equal, however, because establishing a potential

difference implies that a separation of charge, albeit quite small, must have taken place. If this were a spherical cell with a radius of 20 µm, an inequality of the K^+ and Cl^- fluxes of less than 1 ion per 100 000 would cause a potential difference of 100 mV.[1]

The basis for Donnan equilibrium can be expressed in terms of the electrochemical potentials[2] of ions that cross the membrane, here K^+ and Cl^-. For ideal solutions, μ is given by:

$$\begin{aligned} \mu_{Ko} &= \mu^0 + RT\ \ln\ [K^+]_o + z_K\, F\psi_o \\ \mu_{K_i} &= \mu^0 + RT\ \ln\ [K^+]_i + z_K F\psi_i \end{aligned} \tag{16.72a}$$

and

$$\begin{aligned} \mu_{Cli} &= \mu^0 + RT\ \ln\ [Cl^-]_o + z_{Cl}\, F\psi_o \\ \mu_{Cli} &= \mu^0 + RT\ \ln\ [Cl^-]_i + z_{Cl}\, F\psi_i \end{aligned} \tag{16.72b}$$

where the subscripts o and i represent the outside and inside of a cell, μ^0 is the chemical potential of the standard state, ψ is the potential of the compartment, z_i is the valence of species i and R, T and F have their usual meanings. At equilibrium, each permeant species distributes so that μ is identical inside and outside the cell. Equating the expressions for μ and simplifying gives:

$$\begin{aligned} RT\ \ln\ [K^+]_o + z_K\, F\psi_o &= RT\ \ln\ [K^+]_i + z_K F\psi_i \\ RT\ \ln\ [Cl^-]_o + z_{Cl}\, F\psi_o &= RT\ \ln\ [Cl^-]_i + z_{Cl} F\psi_i \end{aligned} \tag{16.73}$$

Membrane potential, E_m, is measured as $\psi_i - \psi_o$. Rearranging and substituting in for E_m and z gives:

$$\begin{aligned} E_m &= E_K = \frac{RT}{F} \ln \frac{[K^+]_i}{[K^+]_o} \\ E_m &= E_{Cl} = \frac{RT}{F} \ln \frac{[Cl^-]_o}{[Cl^-]_i} \end{aligned} \tag{16.74}$$

These expressions are the *Nernst equilibrium potentials* for K^+ (E_K) and Cl^- (E_{Cl}). Thus, when the mobile ions attain their equilibrium distribution in a Donnan system, the potential between the compartments, E_m, simultaneously equals both E_K and E_{Cl}. Equating the Nernst potentials and simplifying gives the ratio of intra and extracellular ions predicted by Donnan equilibrium:

$$\frac{[K^+]_i}{[K^+]_o} = \frac{[Cl^-]_o}{[Cl^-]_i} \tag{16.75}$$

or expressed another way:

$$[K^+]_i \cdot [Cl^-]_i = [K^+]_o \cdot [Cl^-]_o \tag{16.76}$$

In a Donnan equilibrium, the KCl product inside a cell equals the KCl product outside.

This simple rule implies that increasing extracellular K^+ (e.g. by replacing Na^+) will cause a cell obeying Donnan equilibrium to take up K^+ and Cl^- and swell. Ion movements in a number of tissues appear to follow Donnan equilibrium, at least for some conditions. Boyle and Conway (1941) made careful measurements of $[K^+]_i$, $[Cl^-]_i$ and cell water in frog sartorius muscles while varying extracellular KCl. For $[K^+]_o$ greater than 6 mM, the experimental ratio of the KCl products, $([K^+]_o \cdot [Cl^-]_o)/([K^+]_i \cdot [Cl^-]_i)$, was very nearly 1.0, as predicted by Equation 16.76. The deviation at low $[K^+]_o$ occurs because Na^+ influx causes E_m to deviate from E_K. Accompanying changes in cell water in these experiments and in separate experiments in which K^+ replaced Na^+ also agreed with theory.

The expectations for a Donnan equilibrium are calculated for the system shown in Fig. 16.13A. When the intracellular and extracellular KCl products are equal, $E_m = E_K = E_{Cl} = -11.4$ mV. In addition, because the number of ions inside the cell is much greater than that outside, the

---

[1] The amount of charge, q, necessary to establish a potential difference, E_m, is related to the specific capacitance of the membrane, C_m, and its area, A, by:

$$q = C_m\, AE_m$$

Assuming a specific membrane capacitance of 1 µF/cm^2, as is typical of most biological membranes, the amount of charge necessary to develop a potential of 100 mV in a spherical cell with a radius of 20 µm is:

$$q = \left(1 \times 10^{-6}\ \text{F/cm}^2\right)\left[4\pi\left(20 \times 10^{-4}\ \text{cm}\right)^2\right]\left(0.1\ \text{V}\right)\left(\frac{C/V}{F}\right)$$

$$q = 5.0 \times 10^{-12}\text{C}$$

This can be converted to a change in the concentration, ΔC, of ions in the cell:

$$\Delta C = (q/F)/\vartheta$$

where F is Faraday's constant, and ϑ is used for the volume of the cell here to distinguish it from voltage. For the same 20-µm-radius cell:

$$\Delta C = \left(5.0 \times 10^{-12}\ C/96\,500\ C/\text{mol}\right) \Big/ \left[\frac{4}{3}\pi\left(20 \times 10^{-4}\text{cm}\right)^3\left(\frac{1\text{L}}{1000\ \text{cm}^3}\right)\right]$$

$$\Delta C = 1.5 \times 10^{-6}\ \text{mol/L}$$

Thus, a potential gradient of 100 mV would develop if ion influx were to increase $[K^+]_i$ by only 1.5 µM more than it increased $[Cl^-]_i$.

[2] Formally, as presented previously in Equation 16.3 for the chemical potential of a neutral species, μ_i should be defined in terms of the mole fraction rather than the concentration of a component and an additional term, $P\overline{V}$, representing the pressure times the partial molar volume, should be added. For dilute solutions, the mole fraction of a solute closely approximates its concentration (see Equations 16.5 and 16.9). The $P\overline{V}$ terms are ignored in the derivation of the ion distribution for a Donnan equilibrium because to simplify we initially assume the membrane is rigid (see Fig. 16.13A) and then we consider a situation without a pressure gradient where the $P\overline{V}$ terms cancel (see Fig. 16.13B). Derivations of Donnan equilibrium retaining the mole fraction and the pressure-volume terms can be found in Overbeek (1956) and Lakshminarayanaiah (1984).

Donnan system has established a significant osmotic gradient. Assuming ideal behavior, the osmolarity inside the cell, $\approx 457\,\text{mosmol}\cdot\text{L}^{-1}$, is about 1.5 times that outside, $300\,\text{mosmol}\cdot\text{L}^{-1}$. The resulting osmotic pressure can be calculated as follows:

$$\begin{aligned}\Delta\pi &= RT\,\Delta C \\ &= (0.082\ \text{L}\cdot\text{atm}\cdot\text{K}^{-1}\cdot\text{mol}^{-1})(310\ \text{K}) \\ &\quad \times (0.457 - 0.300\ \text{mol}\cdot\text{L}^{-1}) \\ &= 3.99\ \text{atm}\end{aligned} \tag{16.77}$$

Because most cells are readily permeable to water, the osmotic pressure generated here would cause water to enter the cell. This influx of water dilutes the intracellular ion content and the product $[K^+]_i\cdot[Cl^-]_i$ must fall below $[K^+]_o\cdot[Cl^-]_o$. As a result, more KCl would enter the cell, followed again by more water, in an endless cycle that would lead to destruction of the cell. That is to say, the simple Donnan system described in Fig. 16.13A fails to reach equilibrium when typical cell membrane properties are assumed.

VIB. Double-Donnan or Pump-Leak Hypothesis

How can we reconcile the failure of the simple Donnan equilibrium model (see Fig. 16.13A) and the experimental studies demonstrating behavior consistent with Donnan equilibrium? The Donnan system can be stabilized in two ways. A hydrostatic pressure could be applied to balance the osmotic pressure and arrest transmembrane water movement. In view of the enormous pressures required, this is not a realistic solution for animal cells. Alternatively, equilibrium can be attained by restricting an ionic species to the extracellular compartment just as one is restricted to the intracellular compartment. This arrangement is referred to as a *double-Donnan* (Leaf, 1959) or *pump-leak system* (Tosteson and Hoffman, 1960) and is illustrated diagrammatically in Fig. 16.13B. Assume that both Na^+ and macromolecular anions, A^-, are restricted to the extracellular and intracellular compartments, respectively. Filling the cell with the same concentrations of K^+, Cl^- and A^- as before, we find now that $[K^+]_i\cdot[Cl^-]_i > [K^+]_o\cdot[Cl^-]_o$ and thus KCl must leave the cell to establish Donnan equilibrium. In the process, water follows the KCl, adjusting cell volume until the KCl, products are equal. A consequence of water flow is that the concentration of the impermeant intracellular ion exactly equals the concentration of the impermeant extracellular ion. At equilibrium, $E_m = E_K = E_{Cl} = -91.1$ mV. In contrast to the simple Donnan system, the osmotic pressure developed by intracellular macromolecules and their counterions (sometimes referred to as *colloid osmotic pressure*) is exactly balanced in the double-Donnan system by the osmotic pressure developed by ions restricted to the extracellular fluid and their counterions. As a consequence, there is no net osmotic pressure across the membrane, and the system is stable.

Another approach for considering the volume change expected in the system in Fig. 16.13B is to calculate the effective osmotic pressure of each compartment. We can suppose that the reflection coefficients, σ, are 1.0 for both A^- and Na^+ because they are impermeant and that the reflection coefficients are 0 for both K^+ and Cl^- because they freely pass the membrane. Extracellular and intracellular osmotic pressures are given by:

$$\begin{aligned}\pi &= \sum_n \sigma_n C_n \\ \pi_o &= 1\cdot[Na^+]_o + 0\cdot[K^+]_o + 0\cdot[Cl^-]_o \\ \pi &= 1\cdot[A^-]_i + 0\cdot[K^+]_i + 0\cdot[Cl^-]_i\end{aligned} \tag{16.78}$$

Because only the impermeant species contribute to osmotic pressure, the only way for the cell to reach osmotic equilibrium, $\pi_o = \pi_i$, is to alter cell volume until $[Na^+]_o = [A^-]_i$. As a result, the ratio of $\text{volume}_{t=\infty}/\text{volume}_{t=0}$ must equal $[A^-]_i/[Na^+]_o$.

It is important to realize that an ion does not need to be impermeant to be *effectively* restricted to the extracellular space and thus counterbalance the osmotic pressure developed by intracellular macromolecules. Na^+ is permeant, but it adequately plays this role anyway. As long as the leak of Na^+ down its electrochemical gradient into the cell is matched by its transport back out, cell volume will remain stable. Consequently, the existence of a pump that actively extruded Na^+ against its concentration gradient was postulated to explain cell volume (Leaf, 1956) and, subsequently, the Na^+, K^+-ATPase, which extrudes three Na^+ while taking up two K^+ at the cost of ATP hydrolysis, was identified. Because energy is consumed to extrude Na^+, the cell is in a *steady state* rather than a true equilibrium.

VIC. Modulation of the Na^+-K^+ Pump

One implication of the double-Donnan or pump-leak model is that the Na^+-K^+ pump is ultimately responsible for cell volume regulation. Perturbations that alter passive Na^+ entry must lead to offsetting changes in the rate of Na^+ extrusion by the Na^+-K^+ pump, or cell volume will change. Because the K_m of the Na^+-K^+ pump, for intracellular Na^+ is close to the physiological $[Na^+]_i$, alterations in Na^+ influx automatically give rise to a compensatory modulation of Na^+ efflux. Nevertheless, metabolic or pharmacologic inhibition of the Na^+-K^+ pump should lead to a net gain of Na^+ and anions coupled by macroscopic electroneutrality and result in a swelling of the cell.

The effect of pump inhibition has been examined extensively (Macknight and Leaf, 1977; Macknight, 1988). The predicted cell swelling has been reported in many tissues, including brain slices, kidney slices, renal tubules, hepatocytes and sheep erythrocytes, when the Na^+-K^+ pump is inhibited by cardiac glycosides (e.g. ouabain) or by depleting ATP. It is equally clear, however, that swelling after pump inhibition in renal cortex, liver slices, various muscle preparations, lymphocytes and human erythrocytes is very slow or even absent, perhaps reflecting a low Na^+ permeability.

Several processes may affect the response of cell volume to Na^+-K^+ pump inhibition and the outcome in some tissues depends on the experimental conditions. Rather than accumulating Cl^- with Na^+, cells might instead lose K^+ to satisfy macroscopic electroneutrality. An equivalent gain of Na^+ and loss of K^+ replaces one osmotically active particle with another, causing no change in cell volume. Closer consideration of this mechanism indicates that it can only be a holding action, however. The loss of intracellular K^+ eventually must lead to a reduction of the K^+ gradient and a less negative E_m. This will lead to accumulation of Cl^- with Na^+ and cell swelling. Nevertheless, a loss of K^+ must slow the swelling that otherwise would have occurred and this would explain the absence of swelling in cells with appropriate Na^+ and K^+ permeabilities over the time course of experiments.

The possibility that a mechanism other than the Na^+-K^+ pump can extrude Na^+ has been considered. Although controversial, a cardiac glycoside-insensitive but metabolically dependent volume regulation mechanism in kidney that does not incorporate the Na^+-K^+ pump has been described (for review, see Macknight and Leaf, 1977). In addition, circulating erythrocytes from a number of carnivores, including dog, cat, bear and ferret, lack a functioning Na^+-K^+ pump and must regulate their volume by a different mechanism (Sarkadi and Parker, 1991). In these cells, Na^+ efflux must depend on the gradient of other ions.

VID. Isosmotic Volume Regulation

Although principles of the pump-leak or double-Donnan model are correct and still relevant to the regulation of cell volume, it has become apparent that neither the leak nor the pump is constant. Not only is the control of these fluxes more complex than originally envisioned, but a myriad of other transport processes also contribute to cell volume regulation. Stated simply, constant cell volume under isosmotic conditions implies an equality of intra- and extracellular osmolarity that is perpetuated by a continuous balance of the efflux and influx of osmolytes. The transport processes involved include, but are not limited to: (1) ion and organic osmolyte channels; (2) the Na^+-K^+ pump; (3) the Na^+-K^+-$2Cl^-$, K^+-Cl^- and Na^+-Cl^- co-transporters, which transport the specified ions in one direction; (4) Na^+-dependent sugar and amino acid co-transport; (5) Na^+-Ca^{2+}; exchange, which exchanges three Na^+ for one Ca^{2+}; and (6) osmotically neutral exchangers that indirectly provide a net solute flux. For example, Na^+-H^+ exchange allows the cell to accumulate Na^+, but the H^+ removed is replaced by dissociation of H^+ from intracellular buffers. Cl^--HCO_3^- and Na^+-H^+ exchange can operate in parallel to mediate a net influx of Na^+ and Cl^- in exchange for H^+ and HCO_3^-, which are converted to CO_2 and H_2O by the action of carbonic anhydrase. It should be noted that CO_2 freely crosses the cell membrane ($\sigma = 0$) and does not directly contribute to solution tonicity. Also, the direct extrusion of water by these two parallel exchangers is negligible compared to the osmotic water gain caused by the accumulation of Na^+ and Cl^-.

Of the number of transporters that participate in volume regulation in any given type of cell, which are most important in regulating cell volume under isosmotic conditions? No simple answer can be offered. The importance of each process to cell volume regulation depends critically upon the tissue and species under consideration as well as the conditions. Moreover, transporters and channels are modulated by multiple signaling pathways and they extensively interact by altering membrane potential or the concentration of the transported species. If the rates of ion transport are not correctly matched, cells will inappropriately shrink or swell. The precise maintenance of cell volume exemplifies the need for sensitive and complex regulatory mechanisms. Attempts to integrate mathematically the fluxes and study their interaction have been made based on the cell's requirement for macroscopic electroneutrality and osmotic equilibrium and the equations governing ion fluxes (Jakobsson, 1980). For erythrocytes, the non-ideal behavior of hemoglobin has been added (Bookchin et al., 1989). Although these simplified models correctly predict a number of observations, they fail to explain others. In short, we remain a long way from a complete quantitative description of the processes underlying cell volume regulation. In the following sections, we will discuss three examples of isosmotic regulation of cell volume that illustrate some of the underlying principles.

VID1. Na^+-K^+-$2Cl^-$ Co-transport in Heart

Recent findings indicate that the Na^+-K^+-$2Cl^-$ co-transporter plays a critical role in regulating cardiac myocyte cell volume under isosmotic conditions. As in other tissues, Na^+-K^+-$2Cl^-$ co-transport conveys osmolytes into cardiac cells under physiological conditions. Because *net* transmembrane fluxes control cell volume, a decreased osmolyte influx is equivalent to increased efflux. Therefore, inhibition of the Na^+-K^+-$2Cl^-$ co-transport by bumetanide, for

example, favors a reduction of cell volume. Consistent with this idea, bumetanide decreases the volume of atrial and ventricular myocytes by about 10% in less than 5 min and myocyte volume is stable at this new level (Drewnowska and Baumgarten, 1991). The Na^+-K^+-$2Cl^-$ co-transporter cannot operate without Na^+ and Cl^- in the extracellular fluid and removing either ion renders bumetanide ineffective. These data imply that ion uptake by Na^+-K^+-$2Cl^-$ co-transport in the heart must be responsible for a significant osmolyte flux under isosmotic conditions and that other transport processes are incapable of fully compensating when this flux is removed. In contrast, myocyte volume was unchanged after inhibiting the Na^+-K^+ pump with 10 µM ouabain (Drewnowska and Baumgarten, 1991) or by cooling to 9°C (Drewnowska et al., 1991) for 20 min. At least in the short term, cardiac cell volume in isosmotic solution is influenced more by Na^+-K^+-$2Cl^-$ co-transport than by the Na^+-K^+ pump.

Modulation of Na^+-K^+-$2Cl^-$ co-transport by intracellular messengers, such as cGMP, may provide a physiological means of modulating cell volume in heart tissue. Figure 16.14 shows the effects of elevating intracellular cGMP in three ways: (1) by adding 8-Br-cGMP, a membrane-permeant analog of cGMP; (2) by adding atrial natriuretic factor (ANF), a natriuretic, diuretic and vasodilatory hormone released by the heart that elevates cGMP by activating guanylate cyclase; and (3) by adding sodium nitroprusside (SNP), a vasodilator, that also activates guanylate cyclase. In each case, cell volume decreased. Furthermore, blocking cGMP-specific phosphodiesterase with zaprinast (M&B22948) augmented the effect of ANF. Based on its sensitivity to bumetanide and the requirement for ions transported by Na^+-K^+-$2Cl^-$ co-transport, cGMP-dependent volume decreases were shown to be due to an inhibition of Na^+-K^+-$2Cl^-$ co-transport by cGMP (Clemo et al., 1992; Clemo and Baumgarten, 1995). Interestingly, *lowering* cGMP levels by inhibiting guanylate cyclase with LY83583 resulted in a small amount of cell swelling. Thus, changing cGMP from its physiological level in either direction altered cell volume. The mechanism and evidence for isosmotic regulation of cell volume in the heart are summarized in Fig. 16.15.

Does the same mechanism regulate cell volume under isosmotic conditions in other tissues? Perhaps it does in some cells, such as vascular endothelium, in which cGMP inhibits Na^+-K^+-$2Cl^-$ co-transport. In other cells, Na^+-K^+-$2Cl^-$ co-transport is stimulated by cAMP, cGMP or a PKC-dependent pathway, and perhaps by a number of other signaling pathways (Palfrey and O'Donnell, 1992; Palfrey, 1994). This diversity in the control of Na^+-K^+-$2Cl^-$ co-transport may be related to the variety of transporter isoforms that have been identified and cloned (Haas, 1994; Kaplan et al., 1996). Although the physiological significance of this diversity in the control of ion transport is not well understood, it must lead to diversity in the regulation of cell volume.

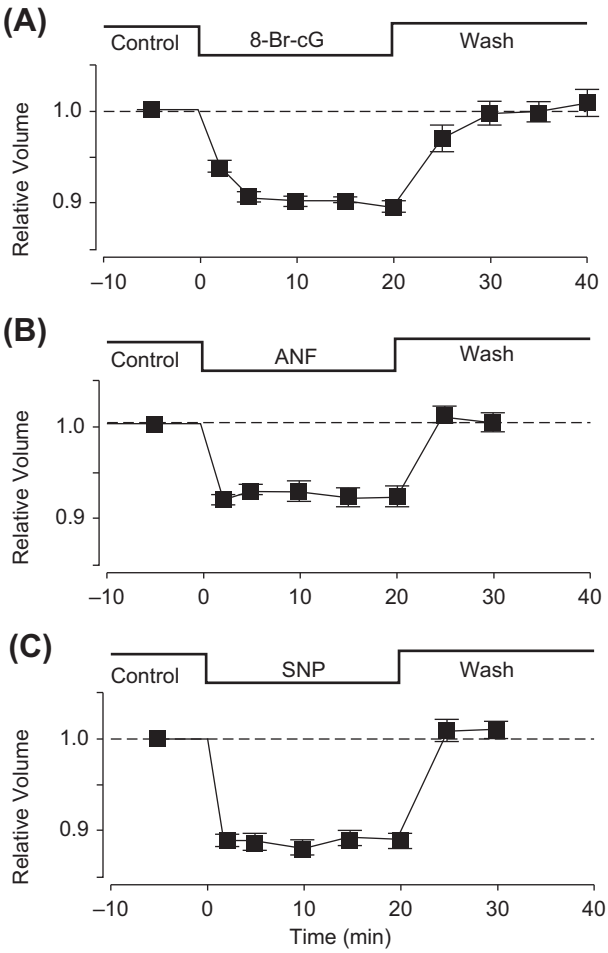

FIGURE 16.14 Changes in the volume of isolated ventricular myocytes during a 20-min exposure to: (A) 10 µM 8-Br-cGMP (8-Br-cG), a permeable cGMP analog; (B) 1 µM atrial natriuretic factor (ANF); and (C) 100 µM sodium nitroprusside (SNP). These agents reversibly decreased cell volume 11%, 8% and 11%, respectively (n=5 for each time point). The decreases in cell volume were caused by inhibition of Na^+-K^+-$2Cl^-$ co-transport by cGMP. Relative cell volume was measured and calculated as described in the legend of Fig. 16.1. *(From Clemo et al. (1992). Reproduced from The Journal of General Physiology, 1992, 100, 89–114, by copyright permission of The Rockefeller University Press.)*

VID2. Hormones and Substrate Transport in Liver

Another interesting example of isosmotic volume regulation is found in hepatocytes. An impressive number of hormones induce either cell swelling or cell shrinkage at physiological concentrations and these actions are related to their control of liver metabolism (Häussinger and Lang, 1991; Häussinger et al., 1994; Agius et al., 1994; Häussinger, 1998). Na^+-H^+ exchange, Na^+-K^+-$2Cl^-$

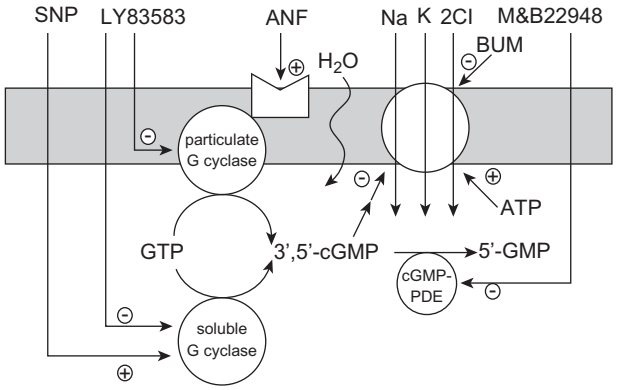

FIGURE 16.15 Schematic diagram of the action of atrial natriuretic factor (ANF) and cGMP on cardiac cell volume. Binding of ANF activates guanylate cyclase and increases intracellular cGMP levels. By one or more steps, cGMP inhibits Na^+-K^+-$2Cl^-$ co-transport. Reducing ion influx by this means is equivalent to increasing *net* ion efflux and cell shrinkage ensues. LY83583 inhibits guanylate cyclase, thereby blocking the effect of ANF and zaprinast (M&B22948) potentiates the effect of ANF by inhibiting cGMP-specific phosphodiesterase (PDE). Sodium nitroprusside (SNP) also increases cGMP levels, and bumetanide (BUM) directly inhibits the co-transporter; both cause cell shrinkage. *(From Clemo et al. (1992) Reproduced from The Journal of General Physiology, 1992, 100, 89–114, by copyright permission of The Rockefeller University Press.)*

co-transport and the Na^+-K^+ pump are stimulated in rat liver cells by insulin. The net effect is that insulin increases $[K^+]_i$, $[Na^+]_i$ and $[Cl^-]_i$ and causes cells to swell by about 12%. This swelling is prevented by bumetanide, a blocker of Na^+-K^+-$2Cl^-$ co-transport, or by amiloride, a blocker of Na^+-H^+ exchange. In contrast, glucagon shrinks hepatocytes by about 14%. Instead of directly opposing the action of insulin, glucagon reduces cell volume by increasing K^+ and Cl^- efflux through ion channels. Other agents that swell hepatocytes include bradykinin and phenylephrine. Shrinking is initiated by adenosine, 5-HT, vasopressin and cAMP.

Hepatocytes also swell as a result of Na^+-dependent amino acid co-transport in isosmotic media (Häussinger and Lang, 1991; Boyer et al., 1992; Häussinger et al., 1994; Häussinger, 1998). Exposure to amino acids that are accumulated with Na^+ (e.g. alanine, glutamine, glycine, hydroxyproline, phenylalanine, proline and serine) causes cell swelling. These effects occur at amino acid levels found physiologically in the portal vein. For example, glutamine provokes up to a 10% swelling with a half-maximal effect at approximately 0.7 mM. Amino acid co-transport gives rise to an inward current and Cl^- enters to maintain macroscopic electroneutrality. Instead of loading the cell, Na^+ is pumped out, mainly by the Na^+-K^+ pump, leaving an accumulation of K^+ and Cl^-. In contrast to these amino acids, substances not accumulated by the liver, such as glucose and leucine, do not affect hepatocyte volume. Cell swelling caused by Na^+-dependent amino acid co-transport has also been observed in intestine and renal proximal tubule.

VID3. Na^+-Ca^{2+} Exchange in Carnivore Erythrocytes

The Na^+-K^+ pump in erythrocytes from dogs, cats, ferrets and bears ceases to function as cells mature. As a result, $[K^+]_i$ and $[Na^+]_i$ are similar to $[K^+]_o$ and $[Na^+]_o$. This poses a special problem for cell volume regulation. How can these cells offset the osmotic pressure generated by impermeant intracellular molecules and avoid swelling without an Na^+-K^+ pump to make Na^+ effectively impermeant? Carnivore erythrocytes solve this dilemma by extruding three Na^+ in exchange for one Ca^{2+} via the Na^+-Ca^{2+} exchanger (Parker, 1973; Sarkadi and Parker, 1991). In most cells, the electrochemical gradients for Na^+ and Ca^{2+} favor the efflux of Ca^{2+}. In these erythrocytes, however, the gradients favor Ca^{2+} entry because the Na^+ gradient is reduced and Na^+-Ca^{2+} exchange operates in what is called the *reverse mode*. To stabilize their volume, carnivore erythrocytes also must have a means of maintaining the Ca^{2+} gradient (i.e. low $[Ca^{2+}]_i$). This is accomplished by an ATP-dependent Ca^{2+} pump in the plasma membrane. Thus, as in other cells, maintaining cell volume in the face of impermeant intracellular colloids requires the expenditure of energy in a pump-leak mechanism. In this case, ATP is expended by a plasma membrane Ca^{2+} pump rather than by the Na^+-K^+ pump.

VII. REGULATION OF CELL VOLUME UNDER ANISOSMOTIC CONDITIONS

VIIA. Osmometric Behavior of Cells

Because the permeability of most cell membranes to water is much greater than that to solutes, cells swell or shrink when placed in an environment that is hyposmotic or hyperosmotic, respectively. Water rapidly flows to equalize its chemical potential, μ_w, inside and outside the cell. The initial volume response is often close to that predicted for an ideal osmometer from van't Hoff's law. An example is shown in Fig. 16.16, which illustrates the response of rabbit ventricular myocytes to solutions with osmolarities ranging from 195 to 825 mosmol/L (0.60 to 2.55 times isotonic). Relative cell volume (V), calculated as $V_{test}/V_{isosmotic}$, is plotted against the inverse of relative osmolality, $\pi_{isosmotic}/\pi_{test}$, and the data are fit to

$$V = (1 - V_b)\,(\pi_{isosmotic}/\pi_{test}) + V_b \qquad (16.79)$$

By definition, relative volume is 1.0 at a relative osmolarity of 1.0. Two conclusions can be reached from the data in Fig. 16.16. First, as expected from van't Hoff's law, the relationship between relative cell volume and the inverse of

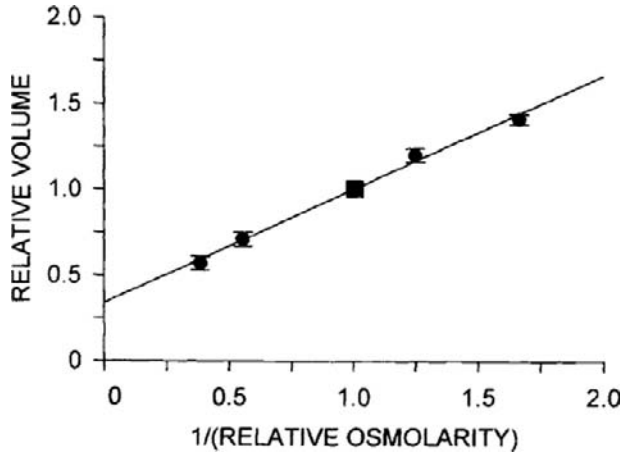

FIGURE 16.16 Relationship between relative cell volume and the inverse of relative osmolarity in cardiac ventricular myocytes. Data from 38 measurements of relative cell volume in anisosmotic solutions (0.6T, 0.8T, 1.8T and 2.6T) were fit to a least squares regression line constrained to pass through (1, 1) (square) because relative cell volume is 1 in isotonic solution by definition. The extrapolated intercept on the relative volume axis, 0.34, represents the fraction of cell volume that is osmotically inactive (see Equation 16.79). Volume measurements, calculation of relative cell volume, and means of adjusting osmolarity are as described for Fig. 16.1. *(Reproduced from Drewnowska and Baumgarten, 1991.)*

relative osmolarity is linear. Second, the intercept of the relationship on the volume axis, V_b, is 0.34, which is significantly different from 0. This is interpreted as meaning that a fraction of cell volume is *osmotically inactive*, i.e. it apparently does not participate in the response to anisosmotic solutions.

Several arguments can be made to justify the observation of an osmotically inactive volume. The expectation from the simplest model is that *cell water* should vary in proportion to osmolarity. However, not all of cell volume is water. The volume of non-aqueous components, such as small solutes and proteins, which represent 25−30% of the cell on a weight/weight basis, is unaffected by water movements. Even measurements of cell water show non-ideal behavior, however (Macknight and Leaf, 1977; Solomon, 1989), so additional explanations are necessary. One suggestion is that a fraction of cell water is intimately associated with cell proteins or membranes and thereby is *bound* or *structured* and unavailable as solvent (e.g. LeNeveu et al., 1976; Hinke, 1980). Although the state of water molecules adjacent to proteins and membranes must be different from that in the bulk phase of the cytoplasm, in light of NMR, intracellular ion activity, and other data, most investigators believe that virtually all water (≈95%) is available as solvent (Shporer and Civan, 1977; Hladky and Rink, 1978). Another possibility is that the behavior of intracellular macromolecules is concentration dependent. For example, the osmotic coefficient and charge on hemoglobin increase with its concentration as red cells shrink and anions are drawn in to maintain electroneutrality. These phenomena are important in explaining water movement in red cells (Freedman and Hoffman, 1979), but their importance in other tissues remains uncertain. A third possibility is that intracellular compartments, such as mitochondria, nuclei, endoplasmic reticulum and sarcoplasmic reticulum of muscle cells, may undergo volume changes that are not proportional to those of the whole cell. Differential responses to an osmotic challenge are expected because the plasmalemma and intracellular membranes possess distinct arrays of transporters and ion channels and each sees a unique environment. Most methods for determining cell water or cell volume fail to distinguish between cytoplasmic and total cell water or volume (for a method that does distinguish these, see Reuss, 1985).

A crucial assumption made in determining osmotically inactive volume also may affect the value obtained for V_b in Equation 16.79. The analysis assumes that only water has moved at the time volume is measured. That is to say, transmembrane ionic fluxes can be ignored. Although the permeability of the cell membrane to water is many times greater than the permeability to ions, the net fluxes of both water and ions start at the instant extracellular osmolarity is changed. If ion fluxes significantly affect intracellular osmolarity at the time of measurement, the extrapolated osmotically inactive volume will be imprecise. If, in addition, the ion fluxes depend on the direction or magnitude of the osmotic gradient, the plot of relative volume versus $\pi_{isosmotic}/\pi_{test}$ can become non-linear (e.g. Grinstein et al., 1984).

VIIB. Compensatory Regulation of Cell Volume

Although an osmotic gradient initiates cell swelling or shrinkage, the initial volume response is not maintained in a wide variety of cells. Cell swelling activates compensatory processes that lead to an efflux of osmolytes and a reduction of cell volume. This is called a *regulatory volume decrease* (RVD). Similarly, cell shrinking activates an influx of osmolytes in some cells, leading to a compensatory swelling referred to as a *regulatory volume increase* (RVI). RVD and RVI nearly restore the original cell volume in some cells, are far less complete in others and are absent in a few types of cells.

Regulatory volume effects are thought to be adaptive and were first identified in nucleated duck erythrocytes (for a review, see Kregenow, 1981). Examples of an RVD and RVI taken from work by Grinstein et al. (1983) are shown in Fig. 16.17. Exposure of human peripheral blood lymphocytes to a solution made hypotonic by 50% dilution with water leads to a rapid, 1.6-fold increase in cell volume (Fig. 16.17B). Then, over about 10 min, an RVD returned cell volume almost completely to its initial value. On

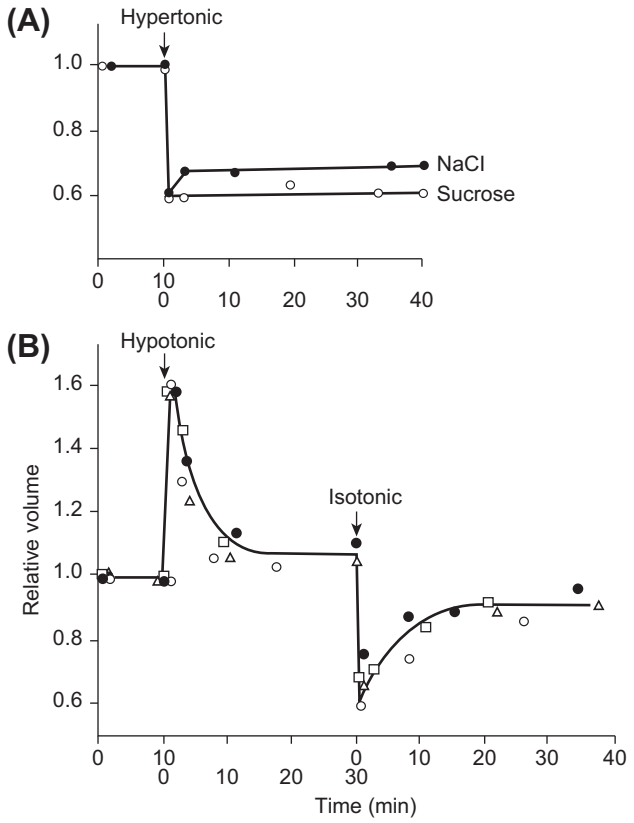

FIGURE 16.17 (A) Effect of hypertonic solution (2T) on relative cell volume of human peripheral blood mononuclear lymphocytes. Solution osmolarity was increased by adding 300 mosmol·L^{-1} of NaCl or sucrose. Cells shrank 40% in hypertonic solution and a small regulatory volume increase (RVI) was observed in the NaCl solution. Points are representative of four experiments. (B) Response to hypotonic solution (0.5T). After swelling by nearly 60%, a regulatory volume decrease (RVD) virtually restored cell volume to its initial value in 10 min. On returning to isotonic solution, cell volume decreased below its control value, and an RVI lead to full recovery. Different symbols represent separate experiments selected from over 40. Cell volume was measured with a Coulter counter that determines volume from the change in electrical resistance of a column of solution as cells pass through an aperture. *(From Grinstein et al. (1983). Reproduced from The Journal of General Physiology, 1983, 82, 619–638, by copyright permission of The Rockefeller University Press.)*

switching back to isotonic solution, cell volume shrank to less than the control value and then was restored by an RVI. RVDs and RVIs may differ in magnitude, however. A much less complete RVI was observed when lymphocytes in isotonic solution were shrunk in media made hyperosmotic by adding of 300 mosmol·L^{-1} of NaCl and the RVI was absent when the lymphocytes were challenged with 300 mosmol·L^{-1} of sucrose instead of NaCl (Fig. 16.17A). The RVD also could be eliminated, for example, by cooling lymphocytes to 4°C (Grinstein et al., 1984). Thus, regulation of cell volume following an osmotic challenge depends on the particulars of the perturbation as well as the cell under study (compare Figs. 16.1 and 16.17).

VIIC. Transport Processes Responsible for RVD and RVI

How do cells gain or lose osmotic equivalents in anisosmotic media? The mechanisms underlying RVDs and RVIs have been extensively characterized in a variety of cell types and exhaustively reviewed (Hoffmann and Simonsen, 1989; Chamberlin and Strange, 1989; Grinstein and Foskett, 1990; Sarkadi and Parker, 1991; Häussinger and Lang, 1991; McCarty and O'Neil, 1992; Strange, 1994; Hoffmann and Dunham, 1995; Lang et al., 1998; O'Neil, 1999). In general, cells undergo RVD or RVI by translocating Na^+, K^+, and Cl^- and a variety of channels, exchangers, co-transporters and pumps can participate. In some cases, organic osmolytes (e.g. taurine, betaine, sorbitol, and urea) are transported instead of, or in addition to, inorganic ions. Table 16.3 lists processes that are activated by altering the volume of various cells and Fig. 16.18 illustrates some of the mechanisms diagrammatically. The compensatory mechanisms invoked vary with the tissue, species and conditions under which osmotic stress is applied.

The primary mechanism of RVD in a number of cell types is activation of conductive pathways and this process will be discussed in more detail. Cell swelling, acting directly or via a messenger, opens ion channels that allow increased efflux of K^+ and Cl^- and H_2O follows. Although the openings of cation and anion channels are independent events, K^+ and Cl^- efflux are tightly coupled by the need to maintain macroscopic electroneutrality. If only the anion or cation channel were to open, the resulting change in E_m would rapidly make ion efflux self-limiting and arrest volume regulation. The effect of this coupling of K^+ and Cl^- fluxes is illustrated in Fig. 16.19A, which shows RVDs in Ehrlich ascites cells (Hoffmann et al., 1986; Hoffmann and Dunham, 1995). At time zero, cells were switched from 300 to 150 mosmol·L^{-1} media. Cells rapidly swelled to about 1.9 times their initial volume and then underwent an RVD that returned relative cell volume to about 1.3 within 5 min. When K^+ conductance was increased by pretreating cells with 0.5 µM gramicidin, a K^+ ionophore, the compensation by the RVD was more rapid and larger in magnitude, returning cell volume to nearly its control level in 2 min. When K^+ channels were blocked with 1 µM quinine, however, only a feeble RVD took place. These data argue that conductive K^+ efflux cannot keep up with Cl^- efflux in control cells and limits the rate of RVD (Hoffmann et al., 1986). Thus, cell swelling must increase Cl^- conductance more than K^+ conductance, leading to greater efflux of Cl^- than of K^+. Consistent with this idea, a depolarization is observed during the RVD. The activation of Cl^- conductance by swelling is only transient, however. The ability of gramicidin to induce RVD decays with time, as shown in Fig. 16.19B. In contrast to the high

TABLE 16.3 Ionic Mechanisms of Regulatory Responses to Anisosmotic Solutions

Transport Mechanism Activated	Cell Types
Cell swelling-induced regulatory volume decrease	
K^+ and Cl^- conductances	Frog urinary bladder
	Chinese hamster ovary cells
	Ehrlich ascites tumor cells
	Frog skin
	HeLa carcinoma cells
	Human platelets
	Human granulocytes
	Human lymphocytes
	Intestinal 407 cells
	Madin-Darby canine kidney (MDCK) cells
	Necturus enterocytes
	Necturus gallbladder
	Rabbit renal proximal convoluted tubule
	Rat hepatocytes
K^+-Cl^- co-transport	Avian, dog, fish, human, rabbit, and low-K^+ sheep erythrocytes
	Ehrlich ascites tumor cells (Ca^{2+} depleted)
	Necturus gallbladder
Coupled K^+-H^+ and Cl^--HCO_3^- exchange	*Amphiuma* erythrocytes
Na^+-Ca^{2+} exchange	Dog and ferret erythrocytes
Organic osmolyte efflux	Crustacean muscle and myocardium
	Ehrlich ascites tumor cells
	Elasmobranch and molluscan erythrocytes
Cell shrinkage-induced regulatory volume increase	
Na^+-K^+-$2Cl^-$ co-transport	Astrocytes
	C6 glioma cells
	Duck, fish, rat, and human erythrocytes
	Ehrlich ascites tumor cells
	Frog skin
	HeLa cells
	Rat kidney medullary thick ascending limb
	3T3 cells
Coupled Na^+-H^+ and Cl^--HCO_3^- exchange	Amphibian gallbladder
	Dog and amphibian erythrocytes
	Human lymphocytes
	Mouse medullary thick ascending limb
	Rabbit renal proximal straight tubule

(*Continued*)

TABLE 16.3 Ionic Mechanisms of Regulatory Responses to Anisosmotic Solutions—cont'd

Transport Mechanism Activated	Cell Types
	Ehrlich ascites tumor cells
Na^+-Cl^- co-transport	Ehrlich ascites tumor cells
	Necturus gallbladder
K^+ and Cl^- conductances, inhibited	Madin-Darby canine kidney (MDCK) cells
Organic osmolyte influx	Many animal and plant cells, bacteria and fungi

For references, see Yancey et al. (1982), Hoffmann and Simonsen (1989), Chamberlin and Strange (1989), Grinstein and Foskett (1990), Wolff and Balaban (1990), Sarkadi and Parker (1991), Häussinger and Lang (1991), McCarty and O'Neil (1992), Boyer et al. (1992), Strange (1994), Hoffmann and Dunham (1995), Lang et al. (1998) and O'Neil (1999).

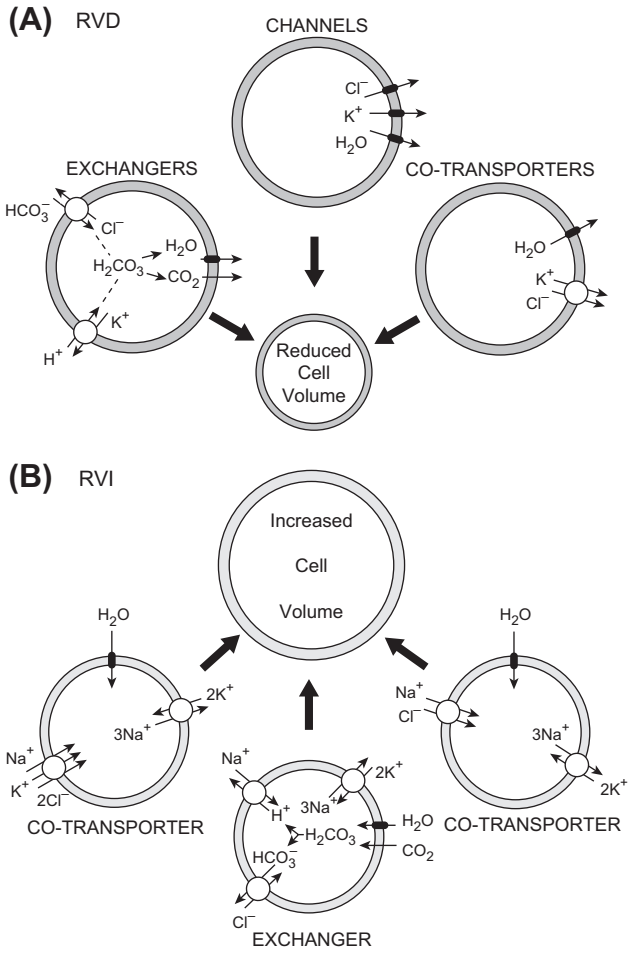

FIGURE 16.18 Schematic diagrams of the transport processes involved in (A) regulatory volume decrease (RVD) and (B) regulatory volume increase (RVI). Following cell swelling, a compensatory reduction in cell volume (RVD) may result from increased K^+ and Cl^- conductance (channels), activation of functionally coupled Cl^--HCO_3^- and K^+-H^+ exchange (exchangers) or activation of K^+-Cl^- co-transport (co-transporters). Following cell shrinking, a compensatory increase in cell volume (RVI) may result from activation of the Na^+-K^+-$2Cl^-$ or Na^+-Cl^- co-transporters (co-transporters) or activation of functionally coupled Cl^--HCO^-_3) and Na^+-H^+ exchange (exchangers). The Na^+-K^+ pump extrudes the Na^+ that enters during RVI, so that cells gain K^+ and Cl^-.

selectivity of Cl^--dependent co-transporters, RVD is also supported by Br^-, NO_3^- and SCN, suggesting the Cl^- channel responsible for RVD poorly discriminates among these anions. Furthermore, RVD can be suppressed by Cl^- channel blockers such as inacrinone (MK-196) and diphenylamine-2-carboxylate (DPC), but not by the co-transport inhibitors. Taken together, the data in Ehrlich ascites cells provide strong evidence that two independent channels are responsible for RVD instead of, for example, activation of a single K^+-Cl^- co-transporter. Organic osmolytes also permeate a class of swelling-activated Cl^- channels referred to as volume-sensitive organic osmolyte-anion channels (VSOAC) and are released by a number of cells to regulate volume (Jackson et al., 1994). VSOAC have a high permeability to taurine ($P_{taurine}/P_{Cl} = 0.75$) and glutamate ($P_{glutamate}/P_{Cl} = 0.20$) and other amino acids and small organic molecules are permeant (Bandarali and Roy, 1992).

Whereas many types of cells exhibit extensive RVDs, fewer cells exhibit robust RVIs. RVIs are usually due to an accumulation of Na^+, Cl^- and, in some cases, K^+, which occurs over minutes. The primary mechanisms underlying RVIs are acceleration of Na^+-K^+-$2Cl^-$ or Na^+-Cl^- co-transport and coupled Na^+-H^+ and Cl^--HCO_3^- exchange. Volume recovery can be blocked by application of appropriate inhibitors such as bumetanide for Na^+-K^+-$2Cl^-$ co-transport, amiloride for Na^+-H^+ exchange and SITS (4-acetamido-4′-isothiocyano-stilbene-2,2′-disulfonic acid) for Cl^--HCO_3^- exchange. RVI in most cells is readily observed when simple salt solutions bathe the cells, but in renal cortical collecting duct and proximal tubules, butyrate, acetate or other metabolizable fatty acids must be in the perfusate to support RVI. Substrate metabolism may provide H^+ and HCO_3^- to support Na^+-H^+ and Cl^--HCO_3^- exchange in these cells (for a review, see McCarty and O'Neil, 1992).

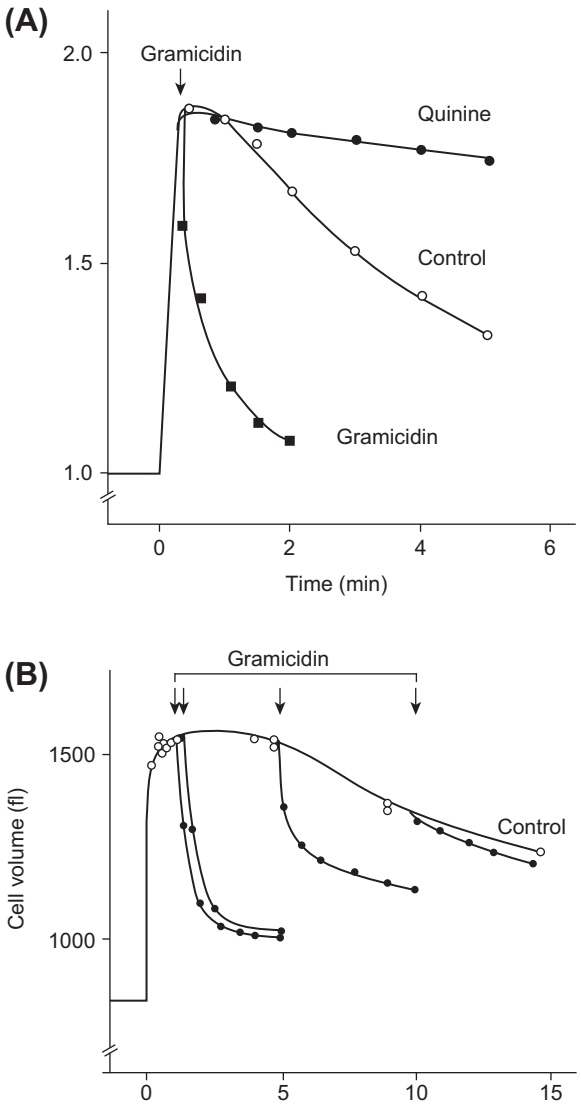

FIGURE 16.19 (A) Effects of quinidine (1 mM) and gramicidin (5 µM) on regulatory volume decrease (RVD) in Ehrlich ascites cells suspended in a Na^+-free choline medium with 1 mM Ca^{2+}. Swelling was induced by diluting the medium to 0.5T. Quinidine blocks Ca^{2+}-activated K^+ channels, and gramicidin increases cation conductance (K^+ conductance in the absence of Na^+). The data indicate that K^+ permeability is rate-limiting during the RVD. (B) The swelling-induced increase in Cl^- conductance is transient. Same protocol as in (A), except that quinidine (1 mM) was added to the hypotonic media to reduce K^+ conductance (control). At selected times, 0.5 µM gramicidin was added to increase cation permeability. The ability of gramicidin to induce an RVD follows the time-course of the swelling-induced Cl^- conductance. Relative cell volumes measured with a Coulter counter, as described for Fig. 16.17. *(Reproduced with permission from Hoffmann et al., 1986.)*

VIID. Organic Osmolytes

Adaptation to hyperosmolarity over a longer term also occurs in some cells and is mediated by an accumulation of organic osmolytes, including amino acids, polyols, and urea (Yancey et al., 1982; Chamberlin and Strange, 1989; Wolff and Balaban, 1990; Garcia and Berg, 1991; Yancey, 1994; Berg, 1995). Three of these organic osmolytes, taurine, betaine, and inositol, are taken up by Na^+-dependent or Na^+- and Cl^--dependent co-transporters. The taurine and betaine transporters have been cloned and belong to the same family as the Na^+- and Cl^--dependent norepinephrine, γ-aminobutyric acid (GABA), dopamine, serotonin and proline transporters (Uchida, 1992). The taurine transporter is found in a variety of cell types. The distribution of mRNA levels is kidney>ileum>brain>liver>heart (Berg, 1995). This sequence for taurine transporter mRNA is surprising because heart has the highest intracellular taurine concentration among these tissues. The mRNA level for the betaine transporter is also highest in the kidney (Yamauchi et al., 1992). A different family of transporters is responsible for Na^+-dependent inositol uptake. The inositol transporter is related to those for glucose and nucleosides and is highly expressed in renal medulla (Kwon et al., 1992). A common feature of all three osmolyte transporters is that gene transcription is upregulated by hypertonic stress. Cells cultured under hypertonic conditions slowly increase their maximum rates of transport and intracellular concentrations rise. For example, betaine transporter mRNA levels in MDCK cells peak about 16 h after the osmotic challenge, and the transport rate peaks at about 24 h (Uchida et al., 1993).

Another mechanism for accumulating organic osmolytes while adapting to hypertonicity and cell shrinkage is to modulate their synthesis. For example, renal medullary cells, which experience osmolarities of more than 1200 mosmol·L^{-1} during antidiuresis, accumulate sorbitol and inositol to regulate their volume (Wolff and Balaban, 1990; Garcia and Berg, 1991; Sands, 1994). Sorbitol levels rise 12–24 h after osmotically challenging cultured renal medullary cells and accumulation depends on the induction of aldose reductase by enhanced transcription. Aldose reductase converts exogenous glucose to sorbitol. Sorbitol is synthesized from stored glycogen in other tissues. This requires coordinated upregulation of glycogen phosphorylase and hexosekinase to produce glucose 6-phosphate, an intermediate for sorbitol production, and the downregulation of phosphofructokinase to prevent consumption of substrates for sorbitol production.

Inhibition of degradation is another mechanism for accumulating organic osmolytes when cells are challenged by hypertonicity. This is the main mechanism by which MDCK and medullary collecting duct accumulate glycerophosphocholine (GPC) (Berg, 1995). In response to hypertonicity or elevated urea, GPC-choline phosphodiesterase is inhibited. Under some conditions, synthesis of GPC by phospholipase also may be enhanced.

The accumulation of organic osmolytes is metabolically expensive, especially considering that many cells dump

organic osmolytes to respond acutely to swelling (Chamberlin and Strange, 1989; Rasmusson et al., 1993; Jackson et al., 1994, Hoffmann and Dunham, 1995). Why does the cell expend extra energy to use organic compounds rather than inorganic ions? Apparently the reason is that accumulation of inorganic ions may perturb protein structure within cells. The Hofmeister series, first described more than 100 years ago, lists inorganic ions according to their ability to alter the solubility and conformation of proteins. Non-specific effects of inorganic salts include changes in V_{max}, K_m, tertiary structure and subunit assembly of enzymes (Yancey et al., 1982; Somero, 1986; Yancey, 1994). Why are some organic compounds accumulated rather than others? Yancey et al. (1982) categorized osmolytes as non-perturbing (stabilizing) or perturbing (destabilizing). Elevated concentrations of non-perturbing osmolytes are compatible with normal enzyme function, whereas high concentrations of perturbing osmolytes are not. This distinction could be due either to direct interaction of osmolytes with enzymes or substrates or to effects on hydration, solubility or charge interactions of proteins. Organic solutes that are non-perturbing generally are uncharged [e.g. trimethylamine N-oxide (TMAO), glycerol] or zwitterionic (e.g. betaine, taurine), although negatively-charged octopine is used by some cells. In contrast, most perturbing organic osmolytes are positively charged (e.g. arginine, guanidinium). Neutral urea, however, perturbs proteins. Finally, non-perturbing osmolytes can counteract the destabilizing effects of perturbing osmolytes. Several organisms accumulate perturbing osmolytes, such as urea, in fixed ratios with non-perturbing osmolytes.

VIIE. Signaling Pathways Underlying RVD and RVI

How do cells detect alterations in their volume and activate the transport processes underlying compensatory volume regulation? Do the transporters themselves sense cell volume and respond by changing their activity? Alternatively, does water movement simply change the concentration of a critical regulatory substance? Answers to these questions are just beginning to emerge. It appears that the signaling pathways modulated by cell volume are as diverse as the transporters that respond.

VIIE1. Anisosmotic Media

An obvious candidate for signaling a change in cell volume is the composition of the anisosmotic media itself, i.e. the ionic strength or concentrations of ions in the bathing media might initiate a regulatory volume response. Changing concentration or ionic strength must affect various ion transport processes and transmembrane ion fluxes to some degree. Nevertheless, these factors seem relatively unimportant in volume regulation because comparable responses are observed when non-electrolytes, such as mannitol or sucrose, replace a large fraction of the electrolytes in the bathing media. RVDs also are initiated in isosmotic solutions after swelling caused by sugar or amino acid uptake. Thus, it appears that regulation is initiated by the volume change itself rather than the composition of the bathing media.

VIIE2. Membrane Potential

Another possibility is that regulatory volume responses are initiated by dilution or concentration of intracellular K^+ via an effect on E_m. A two-fold change in volume without compensatory K^+ fluxes would alter $[K^+]_i$ and cause an 18 mV change in E_m in a cell that conforms to the Nernst equation. Fluxes through K^+ and Cl^- channels are voltage dependent, reflecting both the electrochemical driving force and the voltage-dependent conductance. For many K^+ channels, the current–voltage relationship is highly non-linear. Furthermore, the Na^+-K^+ pump and Na^+-Ca^{2+} exchange are both voltage dependent because they mediate a net movement of charge across the membrane. Despite this, it is unlikely that changes in E_m are the primary cause of RVDs or RVIs in most cells. Regulatory responses have been observed with changes in cell volume of $<5\%$ (Hoffmann and Simonsen, 1989), which would directly alter E_m by only ≈ 1 mV. This is too small to have a significant effect. Nevertheless, it is clear that E_m can modulate RVDs due to activation of K^+ and Cl^- channels. In most instances, the increase in Cl^- conductance is greater than that for K^+ (Hoffmann and Simonsen, 1989; Grinstein and Foskett, 1990). This leads to a significant depolarization during the RVD due to a greater passive efflux of Cl^- than K^+ and the depolarization equalizes the anion and cation fluxes (due to macroscopic electroneutrality). Depolarization may have additional effects that support the RVD. The sensitivity of certain K^+ channels to intracellular Ca^{2+} (i.e. Ca^{2+}-activated K^+ channels) is increased by depolarization, and other K^+ channels are directly opened by depolarization.

VIIE3. Cytoskeleton

The cytoskeleton consists of three main elements: actin filaments (F-actin), which are microfilaments 5–7 nm in diameter that are double-stranded α-helical polymers of globular actin (G-actin); microtubules, which are hollow tubes 25 nm in diameter that are made from tubulin monomers arranged in 13 threads; and intermediate filaments (IF), which are 10-nm diameter strands composed of tissue-specific proteins, such as keratin in epithelial cells and desmin in muscle cells (Bershadsky and Vasiliev, 1988; Luna and Hitt, 1992; Mills et al., 1994). In non-muscle cells, the majority of actin filaments are associated with the

cell membrane. F-actin is tied together to integral membrane proteins by ankyrin, spectrin, MARKS (myristolated acid-rich C-kinase substrate) and other binding proteins to form a structural unit. This scaffolding undergoes constant reorganization as G-actin polymerizes and depolymerizes in response to various stimuli. The main role of microtubules in mature cells is thought to be the transport of vesicles within the cell using specific microtubule-associated proteins (MAPs) to attach to kinesin and dynein, which act as molecular motors. The functions of IF are not fully understood. Because IF binds to ankyrin and to desmosomal plaques, it is thought that these filaments have a structural role and link organelles to the membrane or cytoskeleton. Intermediate filaments are phosphorylated and dephosphorylated by protein kinases and phosphatases and it is likely that their phosphorylation state regulates function.

Alterations in cell volume lead to deformation or reorganization of the cytoskeleton, and ideas of how these effects may be linked to cell volume regulation have been proposed (Chamberlin and Strange, 1989; Sachs, 1989; Sarkadi and Parker, 1991; Mills et al., 1994; Hoffmann and Dunham, 1995; Henson, 1999). One possibility is that the cytoskeleton might mechanically resist cell swelling, but the evidence for this is inconclusive.[3] Ion channels, exchangers and co-transporters are structurally anchored in the membrane by specific components of the cytoskeleton (Luna and Hitt, 1992) and their interaction may help regulate cell volume. Agents that disrupt the microfilaments, such as the cytochalasins, modify the regulatory responses to both hypotonic and hypertonic stress by inhibiting K^+ and Cl^- channels that promote RVD and stimulating Na^+-K^+-$2Cl^-$ co-transport responsible for RVI (Chamberlin and Strange, 1989; Mills et al., 1994; Hoffmann and Dunham, 1995). In a few cases, cell volume under isosmotic conditions is affected (McCarty and O'Neil, 1992). Microtubules also may be involved in some cell lines. Colchicine, which prevents microtubule polymerization, decreases macrophage volume by 20% (Mills et al., 1994). The shrinkage is inhibited by SITS, suggesting that either Cl^--HCO_3^- exchange or Cl^- channels are involved. Additionally, water and ion channels are inserted reversibly into the membrane in response to volume perturbations in a process that can be blocked by cytochalasin B (Lewis and de Moura, 1982). Furthermore, mechanical deformation of the membrane and supporting structures can modulate biochemical signaling systems such as the cAMP and protein kinase C cascades (Richter et al., 1987; Watson, 1991). Emerging evidence suggests that protein kinases and phosphatases may be specifically localized by cytoskeletal binding proteins to sites adjacent to their target transport proteins. Moreover, the extracellular matrix is coupled to the cytoskeleton by integrins which regulate complex signaling cascades including focal adhesion kinase (FAK) and extracellular signal regulated kinases (ERK/MAPK) (Boudreau and Jones, 1999). These developments are important because it remains obscure how the cytoskeleton exerts its regulatory effect on ion transporters and whether or not constraints imposed by three-dimensional tissues in situ affect cell volume.

Another role for the cytoskeleton involves widely distributed mechanosensitive and volume-sensitive ion channels (Sachs, 1989; Morris, 1990; Hu and Sachs, 1997; Vandenberg et al., 1996; Wright and Rees, 1998). The probability of channel opening is increased by osmotic stretch or mechanical deformation. It has been proposed that mechanical forces detected by a cytoskeletal protein, spectrin, can directly affect cation channel gating, whereas the gating of volume-sensitive anion channels is regulated by their phosphorylation state. Most stretch-activated channels poorly discriminate between permeant species (e.g. the stretch-activated cation channel admits Na^+, K^+, and Ca^{2+}), but some are highly selective for K^+. There are also reports of mechanosensitive channels that are inactivated by stretch (Sachs, 1989; Morris, 1990). Mechanosensitive channels are potentially important in cell volume regulation as both sensors and effectors. The evidence that they are opened by osmotic stretch is convincing and they carry substantial currents, which might directly or indirectly lead to volume regulation. For example, it has been argued that K^+-selective stretch-activated channels in molluscan heart cells pass sufficient current to alter $[K^+]_i$ by 1% in 1 s when the cell is voltage-clamped away from E_K (Brezden et al., 1986) and that poorly selective cation stretch-activated channels in *Necturus* choroid epithelium raise Ca^{2+} sufficiently in 100 s to open Ca^{2+}-activated K^+ channels and initiate an RVD (Christensen, 1987). Such calculations must be regarded as estimates, however,

[3] For eukaryotic cells, it is generally assumed that the osmotic gradient across a membrane is negligible. This view arises because the thin bilayer membrane is too fragile to resist the substantial forces developed by even small differences in osmotic pressure. A tension of $\approx 10\,\text{dyn}\cdot\text{cm}^{-2}$ is sufficient to rupture erythrocyte (Evans et al., 1976), protoplast (Wolfe et al., 1986), or lipid bilayer (Needham and Nunn, 1990) membranes. The relationship between tension on the membrane and transmembrane pressure is given by the law of Laplace. For a thin-walled spherical cell $P = 2T/r$ where P is pressure, T is tension and r is the cell's radius. If we assume a radius of 10 µm, a lytic tension is developed by a pressure of 2×10^4 dyn cm^{-2}, which equals ≈15mmHg. This is the osmotic pressure developed by only ≈ 0.0008 osmol L^{-1}. Hence, the membrane cannot support a sufficient hydrostatic pressure to offset an osmotic gradient.

Before accepting this conclusion, it is necessary to consider the effective radius of the cell in view of the geometry of the cytoskeleton (Jacobson, 1983). For example, there are $\approx 10^5$ copies of ankyrin per erythrocyte. If all these attach integral membrane proteins to the cytoskeleton and are evenly distributed, the membrane is strengthened by load-bearing cytoskeletal elements at ≈40 nm intervals. Even if we assume an effective radius of 100 nm, lytic tension now requires a pressure of 2×10^6 dyn cm^{-2}, which equals ≈1500 mmHg or nearly 2 atm. This is equivalent to the osmotic pressure generated by 0.078 osmol L^{-1}.

because they do not reflect E_m under the relevant conditions. Nevertheless, Ca^{2+} entry via stretch-activated channels has been implicated in volume regulation in several types of cells (Foskett, 1994) and arguments favoring the idea that stretch-activated channels participate in cell volume regulation are accumulating (Sackin, 1994). It has been found that Gd^{3+}, a blocker of non-selective stretch-activated cation channels, reduced swelling of both intact (i.e. unclamped) and voltage-clamped cardiac myocytes in hypoosmotic solutions and that 9-anthracene carboxylic acid (9-AC), a blocker of stretch-activated anion channels, increased swelling in the same solutions (Suleymanian et al., 1995; Clemo and Baumgarten, 1997; Clemo et al., 1998, 1999). Opposite effects of the two blockers are expected because anions and cations travel in opposite directions under these conditions. In contrast, Gd^{3+} and 9-AC have negligible effects on myocyte volume in isosmotic solution when stretch-activated channels are expected to be closed. Interestingly, the same volume-sensitive cation and anion channels became persistently activated and modulated cell volume under isosmotic conditions in a canine model of congestive heart failure (Clemo et al., 1998, 1999).

VIIE4. Calcium

A role for Ca^{2+} in cell volume regulation has been recognized for many years (Pierce and Politis, 1990; McCarty and O'Neil, 1992; Foskett, 1994; Hoffmann and Dunham, 1995). RVD is blocked by removing extracellular Ca^{2+} in *Amphiuma* erythrocytes, *Necturus* gallbladder, proximal convoluted and straight tubule, intestine 407 and osteosarcoma cells. Extracellular Ca^{2+} is not a requirement for RVD in lymphocytes and Ehrlich ascites cells, but RVD is more rapid in Ehrlich ascites cells when Ca^{2+} is present. In some tissues, it appears that the Ca^{2+} involved in RVD enters, at least in part, through dihydropyridine-sensitive, L-type Ca^{2+} channels. Significant Ca^{2+} entry can also occur via non-selective stretch-activated cation channels. Block of RVD by lanthanides and disruption of the cytoskeleton, both of which affect stretch-activated cation channels, is consistent with this possibility. Instead of the entry of extracellular Ca^{2+}, release of Ca^{2+} from intracellular stores is critical for RVD in a variety of cells, including lymphocytes, Ehrlich ascites, intestine 407 and opossum kidney cells. Depletion of internal Ca^{2+} stores eliminates RVD in these cells; it is restored by extracellular Ca^{2+} and the Ca^{2+} ionophore, A23187. $[Ca^{2+}]_i$ has been shown to increase during swelling of *Amphiuma* erythrocytes using arsenazo III as a Ca^{2+} indicator. More recently, fluorescent Ca^{2+} indicators, quin-2 and fura-2, have been used to demonstrate increases in $[Ca^{2+}]_i$ that accompany cell swelling in urinary bladder, osteosarcoma, lymphoma and proximal and straight convoluted tubule cells. On the other hand, $[Ca^{2+}]_i$ remains unchanged during volume changes in some cells, including human lymphocytes. More evidence for elevated Ca^{2+} comes from patch-clamp studies. In a number of tissues, recordings of single channel activity established that Ca^{2+}-activated K^+ channels open more frequently during RVD than under isotonic conditions. This suggests an increase in $[Ca^{2+}]_i$ because the probability that these channels open increases as $[Ca^{2+}]_i$ increases. Although studied in less detail, a decrease in $[Ca^{2+}]_i$ has been implicated in RVI in *Amphiuma* erythrocytes, Ehrlich ascites cells and lymphocytes.

The mechanism by which Ca^{2+} modulates cell volume appears to vary (Table 16.4). Ca^{2+} has direct effects on ion channels, but additional signaling mechanisms may be involved. For example, calmodulin inhibitors can block the increased K^+ conductance in lymphocytes, Ehrlich ascites cells and *Necturus* gallbladder; the increased Cl^- conductance in Ehrlich ascites cells; and increased K^+-H^+ exchange in *Amphiuma* erythrocytes. In other cells, modulation of protein kinase C and leukotriene synthesis by Ca^{2+} have been proposed as signals in volume regulation.

VIIE5. Phosphorylation

The activities of many of the transporters discussed here are modified by phosphorylation (Parker, 1992; McCarty and O'Neil, 1992; Palfrey, 1994; Hoffmann and Dunham, 1995). This raises the possibility that cell volume alterations initiate an RVD or RVI by either increasing or decreasing the fraction of transporters in the phosphorylated state. Until recently, supporting data have been lacking. Over the last few years, however, strong evidence for this idea has come from studies in several tissues. We will discuss some of these data from erythrocytes in detail.

Pewitt et al. (1990) studied RVI in duck erythrocytes and determined that activation of Na^+-K^+-$2Cl^-$ co-transport on shrinking is caused by phosphorylation. Both cAMP-dependent and cAMP-independent protein kinase phosphorylate the Na^+-K^+-$2Cl^-$ co-transporter (or possibly a regulatory protein), but cAMP levels in duck erythrocytes are not affected by osmotic stress. Pewitt et al. (1990) found that the protein kinase inhibitors K252a and H-9 prevent transporter activation on shrinking. Conversely, an inhibitor of serine and threonine protein-phosphatases, okadaic acid, which slows protein dephosphorylation, stimulates Na^+-K^+-$2Cl^-$ co-transport under isotonic conditions. These changes in the activity of the transporter with phosphorylation and with shrinking apparently result largely from a modulation of the number of functioning transporters, as detected by bumetanide binding, rather than from a modulation of their turnover rate. At about the same time, Jennings and

TABLE 16. 4 Intracellular Signaling Pathways for RVD and RVI

Signal	Effector	Cell Type
Ca^{2+}	K^+ conductance	*Necturus* gallbladder Frog urinary bladder Ehrlich ascites cells Human lymphocytes
	Cl^- conductance	Ehrlich ascites cells
	Taurine efflux Na^+-H^+ exchange K^+-H^+ exchange	Elasmobranch and molluscan erythrocytes Human lymphocytes *Amphiuma* erythrocytes
Phosphorylation	Na^+-H^+ exchange Taurine efflux Na^+-K^+-$2Cl^-$ co-transport K^+-Cl^- co-transport	Human lymphocytes Elasmobranch erythrocytes Duck erythrocytes Duck, rabbit, and dog erythrocytes
Leukotrienes	K^+ conductance Cl^- conductance	Ehrlich ascites cells Ehrlich ascites cells
cAMP	Na^+-H^+ exchange Cl^--HCO_3^- exchange Na^+-Cl^- co-transport	Mouse thick ascending limb of Henle (mTALH) cells Mouse thick ascending limb of Henle (mTALH) cells *Necturus* gallbladder
G proteins	Na^+-H^+ exchange	Barnacle skeletal muscle
Voltage	K^+ channels	Human lymphocytes

For references, see Chamberlin and Strange (1989), Sarkadi and Parker (1991), McCarty and O'Neil (1992), Strange (1994), Hoffmann and Dunham (1995), Lang et al. (1998), O'Neil (1999), Häussinger and Schliess (1999).

al-Rohil (1990) and Jennings and Schulz (1991) developed evidence that K^+-Cl^- co-transport in rabbit erythrocytes, which is responsible for RVD, is activated by a dephosphorylation. They discovered that swelling inhibits a protein kinase distinct from protein kinases A and C. An RVD occurred only after a slow dephosphorylation, now identified as due to a type 1 protein phosphatase (PP1) that is blocked by calyculin A (Starke and Jennings, 1993). Parker et al. (1991) obtained similar results in dog erythrocytes.

Parker et al. (1991) also recognized the important reciprocal coordination of K^+-Cl^- co-transport and Na^+-H^+ exchange by phosphorylation and dephosphorylation during both RVDs and RVIs in mammalian erythrocytes. This strategy is illustrated in Fig. 16.20 and can be summarized as follows: (1) shrinking activates and swelling inhibits a protein kinase. (2) On shrinking, activated protein kinase rapidly phosphorylates regulatory sites associated with the K^+-Cl^- co-transporter and the Na^+-H^+ exchanger (or the Na^+-K^+-$2Cl^-$ co-transporter in duck erythrocytes). (3) Phosphorylation inhibits the K^+-Cl^- co-transporter, reducing osmolyte efflux, but stimulates the Na^+-H^+ exchanger or Na^+-K^+-$2Cl^-$ co-transporter, stimulating osmolyte uptake and leading to an RVI. (4) Conversely, slow dephosphorylation on swelling stimulates K^+-Cl^- co-transport and inhibits Na^+-H^+ exchange or Na^+-K^+-$2Cl^-$ co-transport, leading to an RVD. Thus, the transporters underlying ion influx and efflux are regulated reciprocally by the activity of a protein kinase that reflects cell volume.

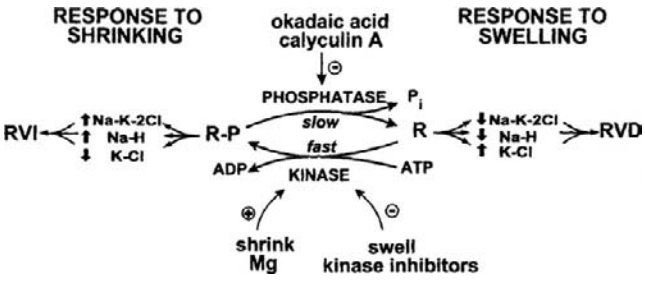

FIGURE 16.20 Schematic diagram of the mechanism of coordination of Na^+-K^+-$2Cl^-$ co-transport and Na^+-H^+ and Na^+-K^+ exchange during cell swelling and shrinking. R-P and R represent phosphorylated and dephosphorylated regulatory sites that modulate the activity of transporters leading to a regulatory volume decrease (RVD) or regulatory volume increase (RVI). Changes in cell volume affect protein kinase activity. Several interventions that inhibit or stimulate the protein kinase and phosphatase are indicated.

How does cell volume govern the activity of a protein kinase? Several possible detectors have been considered: cell shape or cytoskeletal deformation; the concentration of an impermeant intracellular co-factor such as Mg^{2+}; and a concept referred to as macromolecular crowding. The first possibility was already discussed, but experimental evidence suggests cell shape does not regulate phosphorylation of the relevant transport proteins, at least in erythrocytes. The last two possibilities will be considered next.

VIIE6. Mass Action Model

Increasing intracellular Mg^{2+} activates Na^+-H^+ exchange and inhibits K^+-Cl^- co-transport and it has been suggested that Mg^{2+} might act by activating a kinase. Before accepting the idea that Mg^{2+} or another intracellular ion is the volume sensor, it is necessary to explain the steep dependence of ion transport on cell volume. Jennings and Schulz (1990) illustrated one possible answer for K^+-Cl^- co-transport with a theoretical mass action model. They assumed: (1) the volume sensor (e.g. Mg^{2+}) is an impermeant intracellular species; (2) the kinase and phosphatase are soluble enzymes; and (3) the sensor inhibits dephosphorylation. They then described the model in terms of three first-order Michaelis–Menten expressions. Taking into account that the concentrations of sensor, kinase and phosphatase vary inversely with volume, they were able to reproduce the steep volume dependence of experimental K^+ influx data. As the authors emphasized, however, a good fit of the experimental data does not prove that the model is correct. Rather, it illustrates only that a simple dilution mechanism can give rise to a steep volume dependence of transport if dilution has different effects on the activity of enzymes that regulate the transporter (e.g. Fig. 16.20).

VIIE7. Macromolecular Crowding

The concept of *macromolecular crowding* comes from the idea that proteins do not behave ideally in solution at concentrations in the physiological range. We have already mentioned that the osmotic coefficient for hemoglobin and other proteins increases steeply with concentration and that Freedman and Hoffman (1979) used this fact to explain water movement in red cells. Non-ideal behavior is thought to be a more general phenomenon, however. Minton (1983, 1990, 1994) has argued that the kinetics and equilibria of enzymes (macromolecules) are markedly altered by the presence of inert macromolecules that occupy more than a few percent of the total solution volume. Just as one hemoglobin molecule affects another, macromolecules that are neither substrate nor product affect the behavior of their macromolecular neighbors in solution. This results because crowding reduces the solution volume accessible to a macromolecule by excluded-volume effects illustrated in Fig. 16.21. An excluded volume means that solution behavior is non-ideal and the chemical potential, μ_i, and activity, a_i, of a macromolecule is increased by crowding. Consequently, reaction rates are affected. On the other hand, small solutes (e.g. ions) are unaffected by the same concentration of macromolecules. Several examples are worth noting. Minton (1983) showed that the specific activity of glyceraldehyde-3-phosphate dehydrogenase decreased dramatically as the concentration of bovine serum albumin, β-lactoglobulin, polyethylene glycol (PEG) or ribonuclease in the reaction medium was increased. This

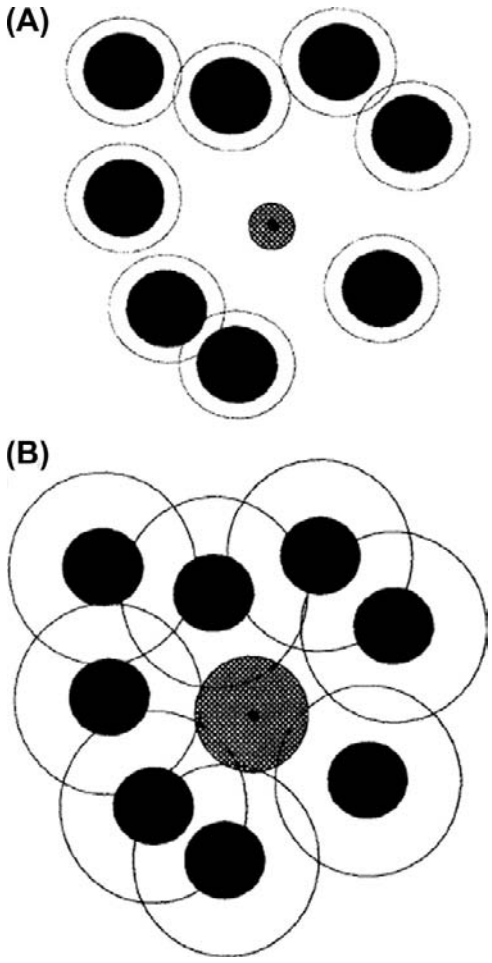

FIGURE 16.21 Diagram of macromolecular crowding. Background macromolecules (solid) in solution differentially affect the behavior of small molecules, such as ions (A) and other macromolecules (B). A test molecule (cross-hatched) cannot enter the excluded volume represented by a circle with a radius equal to the sum of the radii of the test molecule and the background macromolecule. The excluded volume is much greater for a test macromolecule (B) than for a test small molecule (A). Restricting the volume that a test molecule can enter increases its activity, *a*, and chemical potential, μ. Consequently, both reaction rates and equilibria are altered. *(Reproduced with permission from Minton (1994). Copyright CRC Press, Boca Raton, Florida.)*

was explained by suggesting that crowding favored the formation of tetramers of the enzyme that possess a lower catalytic specific activity than monomers. Similarly, the cohesion of complementary ends of λ DNA can be increased up to 2000-fold by albumin, Ficoll 70 or PEG (Zimmerman and Harrison, 1985) and the activity of T4 polynucleotide kinase is augmented by PEG (Harrison and Zimmerman, 1986). Protein concentrations within cells are sufficient to give significant excluded-volume effects (Zimmerman and Trach, 1991).

How does macromolecular crowding relate to cell volume regulation? Perhaps the activity of the kinase governing the phosphorylation state of transporters decreases as macromolecular crowding is lessened during cell swelling. This would, for example, activate K^+-Cl^- co-transport and inactivate Na^+-H^+ exchange (see Fig. 16.20) and an RVD would ensue. Colclasure and Parker (1991, 1992) provided experimental support for this hypothesis (see also Sarkadi and Parker, 1991; Parker, 1992). They osmotically ruptured dog erythrocytes and then allowed the "ghosts" to reseal in a hypotonic medium. This gave resealed ghosts with about 1/4 normal volume but with a normal protein (hemoglobin or hemoglobin plus albumin) concentration. During osmotic challenge, K^+-Cl^- co-transport and Na^+-H^+ exchange were regulated at about the same protein concentration as in normal erythrocytes even though the volumes of the resealed ghosts were vastly different. This hypothesis is also consistent with studies on the kinetics of volume regulation by Jennings and al-Rohil (1990) who concluded that the swelling-sensitive step was a decrease in the rate of phosphorylation rather than an increase in the rate of dephosphorylation.

The new insight that macromolecular crowding may be a mechanism for volume transduction is an interesting possibility. Minton et al. (1992) have presented a model quantitatively accounting for volume-dependent stimulation of ion fluxes on this basis. It is important to recognize that operation of the scheme depends on the components having appropriate sensitivity. In erythrocytes, for example, the activities of both the kinase and the phosphatase should be reduced by swelling. Consequently, as the rate of protein phosphorylation falls, so does the rate of protein dephosphorylation. Whether this leads to an increase or decrease in the fraction of transporters in the phosphorylated state must depend both on the relative effects of macromolecular crowding and the amount of substrate available for each enzyme. With injudicious choices for the parameters (e.g. pathological interventions), this mechanism might lead to an inappropriate RVI rather than an RVD.

ACKNOWLEDGMENTS

We thank J. Maghirang for preparing numerous figures. Supported by National Institutes of Health grants HL-24847, HL-46764, and NS-19235, and Grants-in-Aid from the American Heart Association and its Mid-Atlantic Affiliate.

BIBLIOGRAPHY

Adair, G. S. (1928). A theory of partial osmotic pressures and membrane equilibrium with special reference to the application of Dalton's law to haemoglobin solutions in the presence of salts. *Proc Roy Soc London, 120A*, 573–603.

Agius, L., Peak, M., Beresford, G., al-Habori, M., & Thomas, T. (1994). The role of ion content and cell volume in insulin action. *Biochem Soc Trans, 22*, 518–522.

Agre, P., Preston, G. M., Smith, B. L., et al. (1993). Aquaporin CHIP: the archetypal molecular water channel. *Am J Physiol, 265*, F463–F476.

Andreoli, T. E., & Troutman, S. L. (1971). An analysis of unstirred layers in series with "tight" and "porous" lipid bilayer membranes. *J Gen Physiol, 57*, 464–478.

Bandarali, U., & Roy, G. (1992). Anion channels for amino acids in MDCK cells. *Am J Physiol, 263*, C1200–C1207.

Barry, P. H., & Diamond, J. M. (1984). Effects of unstirred layers on membrane phenomena. *Physiol Rev, 64*, 763–873.

Berg, M. B. (1995). Molecular basis of osmolyte regulation. *Am J Physiol, 268*, F983–F996.

Bershadsky, A. D., & Vasiliev, J. M. (1988). *Cytoskeleton*. New York: Plenum Press.

Bookchin, R. M., Ortiz, O. E., Freeman, C. J., & Lew, V. L. (1989). Predictions and tests of a new integrated reticulocyte model: implications for dehydration of sickle cells. In *The Red Cell: Seventh Annual Ann Arbor Conference* (pp. 615–625). New York: Alan R. Liss Publishers.

Boudreau, N. J., & Jones, P. L. (1999). Extracellular matrix and integrin signalling: the shape of things to come. *Biochem J, 339*, 481–488.

Boyer, J. L., Graf, J., & Meier, P. J. (1992). Hepatic transport systems regulating pH_i, cell volume, and bile secretion. *Annu Rev Physiol, 54*, 415–438.

Boyle, P. J., & Conway, E. J. (1941). Potassium accumulation in muscle and associated changes. *J Physiol, 100*, 1–63.

Brezden, B. L., Gardner, D. R., & Morris, C. E. (1986). A potassium-selective channel in isolated Lymnaea stagnalis heart muscle cells. *J Exp Biol, 123*, 175–190.

Carruthers, A., & Melchior, D. L. (1983). Studies of the relationship between bilayer water permeability and bilayer physical state. *Biochemistry, 22*, 5797–5807.

Cass, A., & Finkelstein, A. (1967). Water permeability of thin lipid membranes. *J Gen Physiol, 20*, 1765–1784.

Chamberlin, M. E., & Strange, K. (1989). Anisosmotic cell volume regulation: a comparative view. *Am J Physiol, 257*, C159–C173.

Christensen, O. (1987). Mediation of cell volume regulation by Ca^{2+} influx through stretch-activated channels. *Nature, 330*, 66–68.

Clemo, H. F., & Baumgarten, C. M. (1995). cGMP and atrial natriuretic factor regulate cell volume of rabbit atrial myocytes. *Circ Res, 77*, 741–749.

Clemo, H. F., & Baumgarten, C. M. (1997). Swelling-activated Gd^{3+}-sensitive cation current and cell volume regulation in rabbit ventricular myocytes. *J Gen Physiol, 110*, 297–312.

Clemo, H. F., Feher, J. J., & Baumgarten, C. M. (1992). Modulation of rabbit ventricular cell volume and $Na^+/K^+/2Cl^-$ cotransport by cGMP and atrial natriuretic factor. *J Gen Physiol, 100*, 89–114.

Clemo, H. F., Stambler, B. S., & Baumgarten, C. M. (1998). Persistent activation of a swelling-activated cation current in ventricular myocytes from dogs with tachycardia-induced congestive heart failure. *Circ Res, 83*, 147−157.

Clemo, H. F., Stambler, B. S., & Baumgarten, C. M. (1999). Swelling-activated chloride current is persistently activated in ventricular myocytes from dogs with tachycardia-induced congestive heart failure. *Circ Res, 84*, 157−165.

Colclasure, C. G., & Parker, J. C. (1991). Cytosolic protein concentration is the primary volume signal in dog red cells. *J Gen Physiol, 98*, 881−892.

Colclasure, C. G., & Parker, J. C. (1992). Cytosolic protein concentration is the primary volume signal for swelling-induced [KCl] cotransport in dog red cells. *J Gen Physiol, 100*, 1−10.

Dainty, J. (1965). Osmotic flow. *Symp Soc Exptl Biol, 19*, 75−85.

Deamer, D. D., & Bramhall, J. (1986). Permeability of lipid bilayers to water and ionic solutes. *Chem Phys Lipids, 40*, 167−188.

Drewnowska, K., & Baumgarten, C. M. (1991). Regulation of cellular volume in rabbit ventricular myocytes: bumetanide, chlorothiazide, and ouabain. *Am J Physiol, 260*, C122−C131.

Drewnowska, K., Clemo, H. F., & Baumgarten, C. M. (1991). Prevention of myocardial intracellular edema induced by St Thomas' Hospital cardioplegic solution. *J Molec Cell Cardiol, 23*, 1215−1221.

Evans, E., Waugh, R., & Melnik, L. (1976). Elastic area compressibility modulus of red cell membrane. *Biophys J, 16*, 585−595.

Fettiplace, R., & Haydon, D. A. (1980). Water permeability of lipid membranes. *Physiol Rev, 60*, 510−550.

Finkelstein, A. (1987). Water Movement Through Lipid Bilayers, Pores, and Plasma Membranes. *Theory and Reality.* New York: Wiley-Interscience.

Finkelstein, A., & Cass, A. (1968). Permeability and electrical properties of thin lipid membranes. *J Gen Physiol, 52*, 145s−172s.

Fischbarg, J., Kuang, K., Vera, J. C., et al. (1990). Glucose transporters serve as water channels. *Proc Natl Acad Sci USA, 87*, 3244−3247.

Foskett, J. K. (1994). The role of calcium in the control of volume-regulatory pathways. In K. Strange (Ed.), *Cellular and Molecular Physiology of Cell Volume Regulation* (pp. 259−277). Boca Raton: CRC Press.

Freedman, J. C., & Hoffman, J. F. (1979). Ionic and osmotic equilibria of human red blood cells treated with nystatin. *J Gen Physiol, 74*, 157−185.

Garcia, A., & Berg, M. B. (1991). Role of organic osmolytes in adaption of renal cells to high osmolarity. *J Memb Biol, 119*, 1−13.

Glasstone, S. (1946). *Textbook of Physical Chemistry.* Princeton: Van Nostrand.

Grinstein, S., & Foskett, J. K. (1990). Ionic mechanisms of cell volume regulation in leukocytes. *Annu Rev Physiol, 52*, 399−414.

Grinstein, S., Clarke, C. A., & Rothstein, A. (1983). Activation of Na^+/H^+ exchange in lymphocytes by osmotically-induced volume changes and by cytoplasmic acidification. *J Gen Physiol, 82*, 619−638.

Grinstein, S., Rothstein, A., Sarkadi, B., & Gelfand, E. W. (1984). Responses of lymphocytes to anisotonic media: volume-regulating behavior. *Am J Physiol, 246*, C204−C215.

Haas, M. (1994). The Na-KCl cotransporters. *Am J Physiol, 267*, C869−C885.

Haines, T. H. (1994). Water transport across biological membranes. *FEBS Lett, 346*, 115−122.

Harrison, B., & Zimmerman, S. B. (1986). T4 polynucleotide kinase: macromolecular crowding increases the efficiency of reaction at DNA termini. *Anal Biochem, 158*, 307−315.

Hasegawa, H., Skach, W., Baker, W., Calayag, M. C., Lingappa, V., & Verkman, A. S. (1992). A multifunctional aqueous channel formed by CFTR. *Science, 258*, 1477−1479.

Hasegawa, H., Zhang, R., Dohrman, A., & Verkman, A. S. (1993). Tissue-specific expression of mRNA encoding rat kidney water channel CHIP28k by in situ hybridization. *Am J Physiol, 264*, C237−C245.

Häussinger, D. (1998). Osmoregulation of liver cell function: signalling, osmolytes and cell heterogeneity. *Contrib Nephrol, 123*, 185−204.

Häussinger, D., & Lang, F. (1991). Cell volume in the regulation of hepatic function: a mechanism for metabolic control. *Biochim Biophys Acta, 1071*, 331−350.

Häussinger, D., & Schliess, F. (1999). Osmotic induction of signaling cascades: role in regulation of cell function. *Biochem Biophys Res Commun, 255*, 551−555.

Häussinger, D., Lang, F., & Gerok, W. (1994). Regulation of cell function by the cellular hydration state. *Am J Physiol, 267*, E343−E355.

Henson, J. H. (1999). Relationships between the actin cytoskeleton and cell volume regulation. *Microsc Res Tech, 47*, 155−162.

Hernandez, J. A., & Fischbarg, J. (1992). Kinetic analysis of water transport through a single-file pore. *J Gen. Physiol, 99*, 645−662.

Heymann, J. B., & Engel, A. (1999). Aquaporins: phylogeny, structure, and physiology of water channels. *News Physiol Sci, 14*, 187−193.

Heymann, J. B., Agre, P., & Engel, A. (1998). Progress on the structure and function of aquaporin 1. *J Struct Biol, 121*, 191−206.

Hildebrand, J. H. (1955). Osmotic pressure. *Science, 121*, 116−119.

Hinke, J. A. M. (1980). Water and electrolyte content of the myofilament phase in the chemically skinned barnacle fiber. *J Gen Physiol, 75*, 531−551.

Hladky, S. B., & Rink, T. J. (1978). Osmotic behaviour of human red blood cells: an interpretation in terms of negative intracellular fluid pressure. *J Physiol, 274*, 437−446.

Hobbie, R. K. (1978). *Intermediate Physics for Medicine and Biology, pp. 126−132*. New York: John Wiley.

Hoffmann, E. K., & Dunham, P. B. (1995). Membrane mechanisms and intracellular signalling in cell volume regulation. *Int Rev Cytol, 161*, 173−262.

Hoffmann, E. K., & Simonsen, L. O. (1989). Membrane mechanisms in volume and pH regulation in vertebrate cells. *Physiol Rev, 69*, 315−382.

Hoffmann, E. K., Lambert, I. H., & Simonsen, L. O. (1986). Separate, Ca^{2+}-activated K^+ and Cl^- transport pathways in Ehrlich ascites tumor cells. *J Memb Biol, 91*, 227−244.

Holz, R., & Finkelstein, A. (1970). The water and nonelectrolyte permeability induced in thin lipid membranes by the polyene antibiotics nystatin and amphotericin B. *J Gen Physiol, 56*, 125−145.

Hu, H., & Sachs, F. (1997). Stretch-activated ion channels in the heart. *J Mol Cell Cardiol, 29*, 1511−1523.

Jackson, P. S., Morrison, R., & Strange, K. (1994). The volumesensitive organic osmolyte-anion channel VSOAC is regulated by non-hydrolytic ATP binding. *Am J Physiol, 267*, C1203−C1209.

Jacobson, B. S. (1983). Interaction of the plasma membrane with the cytoskeleton: an overview. *Tissue Cell, 15*, 829−852.

Jakobsson, E. (1980). Interactions of cell volume, membrane potential, and membrane transport parameters. *Am J Physiol, 238*, C196−C206.

Jansen, M., & Blume, A. (1995). A comparative study of diffusive and osmotic water permeation across bilayers composed of phospholipids with different head groups and fatty acyl chains. *Biophys J, 68*, 997−1008.

Jap, B. K., & Li, H. (1995). Structure of the osmo-regulated H_2O^- channel, AQP-CHIP, in projection at 3.5 Å resolution. *J Mol Biol, 251*, 413−420.

Jennings, M. L., & al-Rohil, N. (1990). Kinetics of activation and inactivation of swelling-stimulated K^+/Cl^- transport. The volume sensitive parameter is the rate constant for inactivation. *J Gen Physiol, 95*, 1021−1040.

Jennings, M. L., & Schulz, R. K. (1990). Swelling-activated KCl cotransport in rabbit red cells: flux is determined mainly by cell volume rather than shape. *Am. J. Physiol, 259*, C960−C967.

Jennings, M. L., & Schulz, R. K. (1991). Okadaic acid inhibition of KCl cotransport. Evidence that protein dephosphorylation is necessary for activation of transport by either cell swelling or N-ethylmaleimide. *J Gen Physiol, 97*, 799−817.

Jung, J. A., Preston, G. M., Smith, B. L., Guggino, W. B., & Agre, P. (1994). Molecular structure of the water channel through aquaporin CHIP: the hourglass model. *J Biol Chem, 269*, 14648−14654.

Kaplan, M. R., Mount, D. B., & Delpire, E. (1996). Molecular mechanisms of NaCl cotransport. *Annu Rev Physiol, 58*, 649−668.

Kiil, F. (1989). Molecular mechanisms of osmosis. *Am J Physiol, 256*, R801−R808.

King, L. S., & Agre, P. (1996). Pathophysiology of the aquaporin water channels. *Annu Rev Physiol, 58*, 619−648.

Kregenow, F. M. (1981). Osmoregulatory salt transporting mechanisms: control of cell volume in anisotonic media. *Annu Rev Physiol, 43*, 493−505.

Kwon, H. M., Yamauchi, A., Uchida, S., et al. (1992). Cloning of a Na^+/myo-inositol cotransporter, a hypertonicity stress protein. *J Biol Chem, 267*, 6229−6301.

Lakshminarayanaiah, N. (1984). *Equations of Membrane Biophysics, pp. 107−118*. Orlando: Academic Press.

Landis, E. M., & Pappenheimer, J. R. (1963). *Exchange of substances through the capillary walls*. In: *Handbook of Physiology, Vol. 2*. Washington, DC: American Physiological Society. Sec. 2, 961−1034.

Lang, F., Busch, G. L., & Volkl, H. (1998). The diversity of volume regulatory mechanisms. *Cell Physiol Biochem, 8*, 1−45.

Leaf, A. (1956). On the mechanism of fluid exchange of tissues in vitro. *Biochem J, 62*, 241−248.

Leaf, A. (1959). Maintenance of concentration gradients and regulation of cell volume. *Ann NY Acad Sci, 72*, 396−404.

LeNeveu, D. M., Rand, R. P., & Parsegian, V. A. (1976). Measurement of forces between lecithin bilayers. *Nature, 259*, 601−603.

Lewis, S. A., & de Moura, J. L. (1982). Incorporation of cytoplasmic vesicles into apical membrane of mammalian urinary bladder epithelium. *Nature, 297*, 685−688.

Luna, E. J., & Hitt, A. L. (1992). Cytoskeleton-plasma membrane interactions. *Science, 258*, 955−964.

Ma, T., & Verkman, A. S. (1999). Aquaporin water channels in gastrointestinal physiology. *Am J Physiol, 517*, 317−326.

Macknight, A. D. C. (1988). Principles of cell volume regulation. *Renal Physiol Biochem, 3−5*, 114−141.

Macknight, A. D. C., & Leaf, A. (1977). Regulation of cellular volume. *Physiol Rev, 57*, 510−573.

Macey, R. I. (1979). Transport of water and nonelectrolytes across red cell membranes. In G. Giebisch, D. C. Tosteson, & H. H. Ussing (Eds.), *Membrane Transport in Biology, Vol. II Transport Across Single Biological Membranes* (pp. 1−57). Berlin: Springer Verlag.

Macey, R. I., & Farmer, R. E. L. (1970). Inhibition of water and solute permeability in human red cells. *Biochim Biophys Acta, 211*, 104−106.

Macey, R. I., Karan, D. M., & Farmer, R. E. L. (1972). Properties of water channels in human red cells. In F. Kreuzer, & J. F. G. Slegers (Eds.), *Biomembranes, Vol. 3, Passive Permeability of Cell Membranes* (pp. 331−340). New York: Plenum Press.

Mauro, A. (1957). Nature of solvent transfer in osmosis. *Science, 126*, 252−253.

McCarty, N. A., & O'Neil, R. G. (1992). Calcium signaling in cell volume regulation. *Physiol Rev, 72*, 1037−1061.

Meschia, G., & Setnikar, I. (1958). Experimental study of osmosis through a collodion membrane. *J Gen Physiol, 42*, 429−444.

Mills, J. W., Schweibert, E. M., & Stanton, B. A. (1994). The cytoskeleton and cell volume regulation. In K. Strange (Ed.), *Cellular and Molecular Physiology of Cell Volume Regulation* (pp. 241−258). Boca Raton: CRC Press.

Minton, A. P. (1983). The effect of volume occupancy upon the thermodynamic activity of proteins: some biochemical consequences. *Molec Cell Biochem, 55*, 119−140.

Minton, A. P. (1990). In *Holobiochemistry: the effect of local environment upon equilibria and rates of biochemical reactions*. *Int J Biochem, 22* (pp. 1063−1067).

Minton, A. P. (1994). Influence of macromolecular crowding on intracellular association reactions: possible role in volume regulation. In K. Strange (Ed.), *Cellular and Molecular Physiology of Cell Volume Regulation* (pp. 181−190). New York: Academic Press.

Minton, A. P., Colclasure, G. C., & Parker, J. C. (1992). Model for the role of macromolecular crowding in regulation of cellular volume. *Proc Natl Acad Sci USA, 89*, 10504−10506.

Morris, C. E. (1990). Mechanosensitive ion channels. *J Memb Biol, 113*, 93−107.

Needham, D., & Nunn, R. S. (1990). Elastic deformation and failure of lipid bilayer membranes containing cholesterol. *Biophys J, 58*, 997−1009.

Nielsen, S., Smith, B. L., Christensen, E. I., Knepper, M. A., & Agre, P. (1993). CHIP28 water channels are localized in constitutively wateRPermeable segments of the nephron. *J Cell Biol, 120*, 371−383.

Nielsen, S., Chou, C. L., Marples, D., Christensen, E. I., Kishore, B. K., & Knepper, M. A. (1995). Vasopressin increases water permeability of kidney collecting duct by inducing translocation of aquaporin-CD water channels in rat kidney inner medulla. *Proc Natl Acad Sci USA, 92*, 1013−1017.

Nielsen, S., Kwon, T. H., Christensen, B. M., Pomeneur, D., Frokiaer, J., & Marples, D. (1999). Physiology and pathophysiology of renal aquaporins. *J Am Soc Nephrol, 10*, 647−663.

O'Neil, W. C. (1999). Physiological significance of volume regulatory transporters. *Am J Physiol, 276*, C995−C1011.

Overbeek, J. T. G. (1956). The Donnan equilibrium. *Prog Biophys Biophys Chem, 3*, 57−84.

Paganelli, C. V., & Solomon, A. K. (1957). The rate of exchange of tritiated water across the human red cell membrane. *J Gen Physiol, 41*, 259−277.

Palfrey, H. C. (1994). Protein phosphorylation control in the activity of volume-sensitive transport systems. In K. Strange (Ed.), *Cellular and Molecular Physiology of Cell Volume Regulation* (pp. 201−214). Boca Raton: CRC Press.

Palfrey, H. C., & O'Donnell, M. E. (1992). Characteristics and regulation of the Na/K/2Cl cotransporter. *Cell Physiol Biochem, 2*, 293−307.

Parker, J. C. (1973). Dog red blood cells. Adjustment of density in vitro. *J Gen Physiol, 62*, 147–156.

Parker, J. C. (1992). Volume-activated cation transport in dog red cells: detection and transduction of the volume stimulus. *Comp Biochem Physiol, 102A*, 615–618.

Parker, J. C., Colclasure, G. C., & McManus, T. J. (1991). Coordinated regulation of shrinkage-induced Na/H exchange and swelling-induced [K-Cl] cotransport in dog red cells. Further evidence from activation kinetics and phosphatase inhibition. *J Gen Physiol, 98*, 869–880.

Pewitt, E. B., Hegde, R. S., Haas, M., & Palfrey, H. C. (1990). The regulation of Na/K/2Cl cotransport and bumetanide binding in avian erythrocytes by protein phosphorylation and dephosphorylation: effects of kinase inhibitors and okadaic acid. *J Biol Chem, 265*, 20747–20756.

Pfeffer, W. (1877). *Osmotische Untersuchungen. Studien zur Zellmechanik. Wilhelm Engelmann, Leipzig. [Translated by G.R. Kepner and E.J. Tadelmann (1985). Osmotic investigations. Studies on cell membranes*. New York: Van Nostrand Reinhold.

Pierce, S. K., & Politis, A. D. (1990). Ca^{2+}-activated cell volume recovery mechanisms. *Annu Rev Physiol, 52*, 27–42.

Pitzer, K. S., & Mayorga, G. (1973). Thermodynamics of electrolytes. II. Activity and osmotic coefficients for strong electrolytes with one or both ions univalent. *J Phys Chem, 77*, 2300–2308.

Preston, G. M., & Agre, P. (1991). Isolation of the cDNA for erythrocyte integral membrane protein of 28 kilodaltons member of an ancient channel family. *Proc Natl Acad Sci USA, 88*, 11110–11114.

Preston, G. M., Carroll, T. P., Guggino, W. B., & Agre, P. (1992). Appearance of water channels in Xenopus oocytes expressing red cell CHIP28 protein. *Science, 256*, 385–387.

Preston, G. M., Jung, J. S., Guggino, W. B., & Agre, P. (1993). The mercury-sensitive residue at cysteine-189 in the CHIP28 water channel. *J Biol Chem, 268*, 17–20.

Preston, G. M., Jung, J. S., Guggino, W. B., & Agre, P. (1994). Membrane topology of aquaporin CHIP: analysis of functional epitope scanning mutants by vectorial proteolysis. *J Biol Chem, 269*, 1668–1673.

Rash, J. E., Yasumura, T., Hudson, C. S., Agre, P., & Nielsen, S. (1998). Direct immunogold labeling of aquaporin-4 in square arrays of astrocyte and ependymocyte plasma membranes in rat brain and spinal chord. *Proc Natl Acad Sci USA, 95*, 11981–11986.

Rasmusson, R. L., Davis, D. G., & Lieberman, M. (1993). Amino acid loss during volume regulatory decrease in cultured chick heart cells. *Am J Physiol, 264*, C136–C145.

Renkin, E. M. (1954). Filtration, diffusion, and molecular sieving through porous cellulose membranes. *J Gen Physiol, 38*, 225–243.

Reuss, L. (1985). Changes in cell volume measured with an electrophysiological technique. *Proc Natl Acad Sci USA, 82*, 6014–6018.

Richter, E. A., Cleland, P. J. F., Rattigan, S., & Clark, M. G. (1987). Contraction-associated translocation of protein kinase C. *FEBS Lett, 217*, 232–236.

Robinson, R. A., & Stokes, R. H. (1959). *Electrolyte Solutions, pp. 480–490*. London: Butterworth.

Rosenberg, P. A., & Finkelstein, A. (1978). Water permeability of gramicidin A-treated lipid bilayer membranes. *J Gen Physiol, 72*, 341–350.

Sachs, F. (1989). Ion channels as mechanical transducers. In W. D. Stein, & F. Bronner (Eds.), *Cell Shape: Determinants, Regulation, and Regulatory Role* (pp. 63–92). San Diego: Academic Press.

Sackin, H. (1994). Stretch-activated ion channels. In K. Strange (Ed.), *Cellular and Molecular Physiology of Cell Volume Regulation* (pp. 215–240). Boca Raton: CRC Press.

Sands, J. M. (1994). Regulation of intracellular polyols and sugars in response to osmotic stress. In K. Strange (Ed.), *Cellular and Molecular Physiology of Cell Volume Regulation* (pp. 133–144). Boca Raton: CRC Press.

Sarkadi, B., & Parker, J. C. (1991). Activation of ion transport pathways by changes in cell volume. *Biochim Biophys Acta, 1071*, 407–427.

Schatzberg, P. (1963). Solubilities of water in several normal alkanes from C_7 to C_{16}. *J Phys Chem, 67*, 776–779.

Shibata, A., Ikawa, K., Shimooka, T., & Terada, H. (1994). Significant stabilization of the phosphatidylcholine bilayer structure by incorporation of small amounts of cardiolipin. *Biochim Biophys Acta, 1192*, 71–78.

Shporer, M., & Civan, M. M. (1977). The state of water and alkali cations within the intracellular fluids: the contribution of NMR spectroscopy. *Curr Top Membr Transport, 9*, 1–69.

Solomon, A. K. (1972). Properties of water in red cells and synthetic membranes. In F. Kreuzer, & J. F. G. Slegers (Eds.), *Biomembranes, Vol. 3, Passive Permeability of Cell Membranes* (pp. 299–330). New York: Plenum Press.

Solomon, A. K. (1989). Water channels across the red blood cell and other biological membranes. *Meth Enzymol, 173*, 192–222.

Solomon, A. K., Chasan, B., Dix, J. A., Lukacovic, M. F., Toon, M. R., & Verkman, A. S. (1983). The aqueous pore in the red cell membrane: band 3 as a channel for anions, cations, nonelectrolytes, and water. *Ann NY Acad Sci, 414*, 97–124.

Somero, G. N. (1986). Protons, osmolytes, and fitness of internal milieu for protein function. *Am J Physiol, 251*, R197–R213.

Starke, L. C., & Jennings, M. L. (1993). K-Cl cotransport in rabbit red cells: further evidence for regulation by protein phosphatase type 1. *Am J Physiol, 264*, C118–C124.

Stein, W. D. (1976). An algorithm for writing down flux equations for carrier kinetics, and its application to co-transport. *J Theor Biol, 62*, 467–478.

Strange, K. (1994). *Cellular and Molecular Physiology of Cell Volume Regulation*. Boca Raton: CRC Press.

Suleymanian, M. A., & Baumgarten, C. M. (1996). Osmotic gradient-induced water permeation across the sarcolemma of rabbit ventricular myocytes. *J Gen Physiol, 107*, 503–514.

Suleymanian, M. A., Clemo, H. F., Cohen, N. M., & Baumgarten, C. M. (1995). Stretch-activated channel blockers modulate cell volume in cardiac ventricular myocytes. *J Mol Cell Cardiol, 27*, 721–728.

Tanford, C. (1961). *Physical Chemistry of Macromolecules*. New York: John Wiley.

Tosteson, D. C., & Hoffman, J. F. (1960). Regulation of cell volume by active cation transport in high and low potassium sheep red cells. *J Gen Physiol, 44*, 169–194.

Trauble, H. (1971). The movement of molecules across lipid membranes: a molecular theory. *J Memb Biol, 4*, 193–208.

Uchida, S., Kwon, H., Yamauchi, A., Preston, A., Marumo, F., & Handler, J. (1992). Molecular cloning of the cDNA for an MDCK cell Na^+ and Cl^--dependent taurine transporter that is regulated by hypertonicity. *Proc Natl Acad Sci USA, 89*, 8230–8234.

Uchida, S., Kwon, H., Yamauchi, A., Preston, A., Kwon, H., & Handler, J. (1993). Medium tonicity regulates expression of the Na^+- and

Cl^--dependent betaine transporter in Madin-Darby canine kidney cells by increasing transcription of the transporter gene. *J Clin Invest, 91*, 1604−1607.

Umenishi, F., Verkman, A. S., & Gropper, M. A. (1996). Quantitative analysis of aquaporin mRNA expression in rat tissues by RNase protection assay. *DNA Cell Biol, 15*, 475−480.

Vandenberg, J. I., Rees, S. A., Wright, A. R., & Powell, T. (1996). Cell swelling and ion transport pathways in cardiac myocytes. *Cardiovasc Res, 32*, 85−97.

van Hoek, A. N., Hom, M. L., Luthjens, L. H., de Jong, M. D., Dempster, J. A., & van Os, C. H. (1991). Functional unit of 30 kDa for proximal tubule water channel as revealed by radiation inactivation. *J Biol Chem, 266*, 16633−16635.

van Hoek, A. N., Luthjens, L. H., Hom, M. L., van Os, C. H., & Dempster, J. A. (1992). A 30 kDa functional size for the erythrocyte water channel determined by in situ radiation inactivation. *Biochem Biophys Res Commun, 184*, 1331−1338.

van't Hoff, J.H. (1887). Die Rolle des osmotischen Druckes in der Analogie zwischen Lösungen und Gasen. Z. Physik. Chemie. 1, 481−493 [Translated by G.L. Blackshear (1979). In (G.R. Kepner, ed.) Cell Membrane Permeability and Transport. Dowden, Hutchinson and Ross, Stroudsburg, PA.]

Verkman, A. S. (1993). *Water Channels*. Austin: R. G. Landis Co.

Verkman, A. S., van Hoek, A. N., Ma, T., et al. (1996). Water transport across mammalian cell membranes. *Am J Physiol, 270*, C11−C30.

Villars, F. M., & Benedek, G. B. (1974) *Physics with Illustrative Examples from Medicine and Biology. Statistical Physics, Vol. 2*. Reading: Addison-Wesley.

Walz, T., Smith, B. L., Agre, P., & Engel, A. (1994). The three-dimensional structure of human erythrocyte aquaporin CHIP. *EMBO J, 13*, 2985−2993.

Walz, T., Hirai, T., Murata, K., et al. (1997). The three-dimensional structure of aquaporin-1. *Nature, 387*, 624−627.

Watson, P. A. (1991). Function follows form: generation of intracellular signals by cell deformation. *FASEB J, 5*, 2013−2019.

Wolfe, J., Dowgert, M. F., & Steponkus, P. L. (1986). Mechanical study of the deformation and rupture of the plasma membranes of protoplasts during osmotic expansions. *J Memb Biol, 93*, 63−74.

Wolff, S. D., & Balaban, R. S. (1990). Regulation of the predominant renal medullary organic solutes in vivo. *Annu Rev Physiol, 52*, 727−746.

Wright, A. R., & Rees, S. A. (1998). Cardiac cell volume: crystal clear or murky waters? A comparison with other cell types. *Pharmacol Ther, 80*, 89−121.

Yamauchi, A., Uchida, S., Kwon, H., et al. (1992). Cloning of a Na^+ and Cl^- dependent betaine transporter that is regulated by hypertonicity. *J Biol Chem, 267*, 649−652.

Yancey, P. H. (1994). Compatible and counteracting solutes. In K. Strange (Ed.), *Cellular and Molecular Physiology of Cell Volume Regulation* (pp. 81−177). Boca Raton: CRC Press.

Yancey, P. H., Clark, M. E., Hand, S. C., Bowlus, R. D., & Somero, G. N. (1982). Living with water stress: evolution of osmolyte systems. *Science, 217*, 1214−1222.

Zeidel, M. L., Ambudkar, S. V., Smith, B. L., & Agre, P. (1992). Reconstitution of functional water channels in liposomes containing purified red cell CHIP28 protein. *Biochemistry, 31*, 7436−7440.

Zhang, R., Skach, W., Hasegawa, H., van Hoek, A. N., & Verkman, A. S. (1993). Cloning, functional analysis and cell localization of a kidney proximal tubule water transporter homologous to CHIP28. *J Cell Biol, 120*, 359−369.

Zimmermann, S. B., & Harrison, B. (1985). Macromolecular crowding accelerates the cohesion of DNA fragments with complementary termini. *Nucl Acids Res, 13*, 2241−2249.

Zimmerman, S. B., & Trach, S. (1991). Estimation of macromolecular concentrations and excluded volume effects for the cytoplasm of Escherichia coli. *Mol Biol, 222*, 599−620.

This page intentionally left blank

Chapter 17

Intracellular pH Regulation

Robert W. Putnam

Chapter Outline

I. SUMMARY

Virtually all of the H^+ ions within a cell are buffered by reversible binding to weak acids and bases, resulting in a low free H^+ ion activity. Therefore, the activity of free H^+ ions within the cytoplasm is usually expressed as cytoplasmic pH (pH_i), defined as $pH = -\log(a_H)$, which is a more convenient scale for molecules at low activities.

Cytoplasmic pH is an important aspect of the intracellular milieu and can affect nearly all aspects of cell function. In most cells, pH_i is maintained at a value of about 7.0, well alkaline with respect to the equilibrium pH_i, calculated on the assumption that H^+ ions are at equilibrium across the membrane. The fact that pH_i is alkaline to its equilibrium value creates a passive acidifying influx of H^+. In fact, most cells face a continuous acid load due not only to this acidifying influx but to metabolic acid production and leakage from internal acidic compartments as well. Such challenges to a stable pH_i can be blunted by cellular buffers, but the only way to regulate pH_i fully is through the activity of membrane-bound transporters. These transporters fall into five categories: (1) cation-H^+ exchangers, such as the alkalinizing Na^+-H^+ exchanger and the acidifying K^+-H^+ exchanger; (2) HCO_3^--dependent transporters, such as the (Na^+ + HCO_3^-)-Cl^- and the Cl^--HCO_3^- exchangers and Na^+-HCO_3^- co-transporters; (3) H^+-ATPases or proton pumps; (4) Na^+-organic anion co-transporters; and (5) Cl^--organic anion exchangers.

Changes in pH_i can affect many cellular functions. Cell metabolism can be affected by changes in pH, predominantly because of pH-sensitive metabolic enzymes, such as phosphofructokinase. Changes of pH_i have also been shown to affect the cross-linking and polymerization of cytoskeletal elements such as actin and tubulin. The loss of the ability of muscle cells to generate tension (muscle fatigue) has been correlated with a decrease of pH_i. Cell pH is also believed to have a modulatory role in gap junctions and many ion-selective channels. Further, changes of pH_i,

Cell Physiology Sourcebook. DOI: 10.1016/B978-0-12-387738-3.00017-2

mediated by activation of the Na^+-H^+ exchanger, may serve as an intracellular signal for the promotion of cell growth and proliferation. It is significant that changes in pH_i can affect other intracellular signals, such as cellular Ca^{2+} and cAMP levels, suggesting a complex interaction among cellular signaling systems.

Many pH-regulating transporters move an osmotically active ion, such as Na^+ or Cl^-, in exchange for a buffered (and thus osmotically "invisible") ion like H^+ or HCO_3^- and thereby mediate the net movement of solute into or out of the cell. This net movement of solute will be accompanied by a net water flow and result in a change in cell volume. Thus, many pH-regulating transporters, in addition to contributing to pH_i regulation, can mediate the regulation of cell volume.

The pH of certain organellar compartments can differ from the value of pH_i and these differences in pH are important for organellar function. For example, mitochondria maintain an internal pH of 7.5, about 0.5 unit more alkaline than pH_i. This pH gradient across the mitochondrial membrane is essential for the major function of mitochondria, the production of ATP. Further, several intracellular organelles in the vacuolar system (e.g. endosomes, lysosomes and storage granules) maintain an internal pH of 5–6, well below pH_i. These organelles contribute to the movement of membranes, membrane-bound proteins and soluble proteins around the cell and their acidic pH is essential for this function.

Given the importance of pH to so many cellular functions, it is not surprising that cells have elaborated highly regulated mechanisms to control pH_i.

II. INTRODUCTION

Intracellular pH is an important aspect of the intracellular environment. Changes in intracellular pH can potentially affect virtually all cellular processes, including metabolism, membrane potential, cell growth, movement of substances across the surface membrane, state of polymerization of the cytoskeleton and ability to contract in muscle cells. Changes of intracellular pH are also often one of the responses of cells to externally applied agents, including growth factors, hormones and neurotransmitters. Further, many organelles, such as lysosomes, mitochondria and endosomal vesicles, maintain an organellar pH that is different from the cytoplasmic pH (pH_i) and these pH differences have important functional consequences for those organelles. It is thus not surprising to find that cells have elaborated a variety of mechanisms that enable them to regulate their intracellular pH. In this chapter, we will discuss the pH level in the cytoplasm and various compartments of a cell, the variety of mechanisms available to a cell to regulate its pH_i and the functional consequences of changes in pH_i.

III. pH AND BUFFERING POWER

The concept of pH was first introduced in 1909 by Sörenson and defined as $-\log [H^+]$. This term was a more convenient way to express the concentration of an ion that is present at very low concentrations. Incorporating the concept of activity, pH is defined as:

$$\mathrm{pH} = -\log\ (a_\mathrm{H}) = -\log(\gamma_\mathrm{H}[H^+]) \qquad (17.1)$$

where a_H is the activity of H^+ and γ_H is the activity coefficient of H^+. At normal intracellular ionic strength, γ_H is about 0.83.

Protons tend to bind to macromolecules and thus are usually present at very low concentrations in biological solutions. This property is the basis for buffering power. A variety of weak acids and bases can bind H^+ through reversible equilibrium binding reactions. Thus, a weak acid in solution obeys the equilibrium reaction:

$$\mathrm{HA}\{=\}\mathrm{H}^+ + \mathrm{A}^- \qquad (17.2)$$

where HA is the weak acid (e.g. lactic acid) and A^- is the conjugate weak base (e.g. lactate). This equilibrium is described by an apparent equilibrium constant, K'_a, as:

$$K'_a = a_\mathrm{H} \cdot \frac{[\mathrm{A}^-]}{[\mathrm{HA}]} \qquad (17.3)$$

This equation is more familiar in its logarithmically transformed expression,

$$\mathrm{pH} = \mathrm{p}K'_a\ \log \frac{[\mathrm{A}^-]}{[\mathrm{HA}]} \qquad (17.4)$$

where pK'_a is $-\log\ K'_a$. This equation, better known as the Henderson–Hasselbalch equation, describes the thermodynamic equilibrium that holds for a weak acid in a solution of constant pH. The Henderson–Hasselbalch equation is most commonly used in its specialized form for the total reaction of the hydration of CO_2 and the dissociation of the resulting carbonic acid into H^+ and bicarbonate as:

$$\mathrm{pH} = \mathrm{p}K'_a + \log \frac{[\mathrm{HCO}_3^-]}{\alpha \cdot P_{\mathrm{CO}_2}} \qquad (17.5)$$

where a is the solubility coefficient of CO_2 in a given solution and P_{CO_2} is the partial pressure of CO_2 in that solution. Two important facts can be deduced from the Henderson–Hasselbalch equation. First, in any weak acid solution, there will be a finite amount of both A^- and HA. For example, if HCO_3^- is added to a solution, CO_2 will be generated and thus be present. Conversely, if CO_2 is bubbled through a solution, HCO_3^- will be produced. Second, this equation can be used to calculate any of the variable parameters if the other three are known. For instance, if a solution is equilibrated with a gas of known P_{CO_2}, the HCO_3^- in that solution can be calculated from

Equation 17.5 once the pH has reached a stable value (values for pK'_a are readily available).

On addition of H^+ (or OH^-) to a solution, the pH will change. However, if the solution contains weak acids (or bases), many of the added protons (or hydroxyl ions) will be bound up, thus minimizing the change in the concentration of free H^+ and thereby minimizing the change in pH. Since these substances minimize the change in pH upon addition of acid or base, weak acids and bases are referred to as buffers. The definition of the buffering power (β) of a solution is:

$$\beta = \frac{d[\mathrm{B}]}{d\mathrm{pH}} \tag{17.6}$$

where d[B] is the amount of base added to the solution and dpH is the change in pH of the solution due to that base addition. The addition of acid to the solution is equivalent to a negative addition of base, $-d$[B]. The units of β are mM/pH unit.

An example will indicate the importance of buffering power to maintaining the pH of a solution. If 1 mM NaCl is added to a solution, [Na^+] and [Cl^-] increase by 1 mM (for simplicity, the effects of the non-ideal activity coefficients will be ignored). However, the addition of 1 mM HCl to a solution that has a pH of 7.0 and a buffering power of 10 mM/pH unit will cause that [Cl^-] to increase by 1 mM, but will cause the pH to decrease by only about 0.28 pH unit, to 6.72. Thus, of the added 1 mM of H^+, only 0.091% remain free, i.e. only 1 out of every 11 000 added H ions remains free. The rest are bound to the weak acid buffers. If the buffers had not been present, the same addition of 1 mM HCl would have changed the solution pH by about 4 units to pH 3. This clearly demonstrates that the presence of buffers in a solution markedly blunts the effects of added acid or base.

A buffer can act as either a *closed buffer* or an *open buffer*. A closed buffer is one in which the total buffer concentration remains constant. Most of the commonly used laboratory buffers, such as Hepes or Tris, operate as closed buffers in solution. If a buffer is a weak acid (HA {=}A^-+H^+), then it operates as a closed buffer when the concentration of the total acid ($[A]_T$ = [HA]+[A^-]) remains constant. Such a buffer can become protonated or deprotonated, but the total amount of buffer does not change. The following is a mathematical expression for the buffering power of a weak acid acting as a closed buffer:

$$\beta_{\mathrm{closed}} = \frac{2.303[\mathrm{A}]_T \; K'_a a_H}{(K'_a + a_H)^2} \tag{17.7}$$

where K'_a is the apparent dissociation constant of the weak acid. Several conclusions can be derived from this equation. When pH is very high ($a_H \rightarrow 0$) or very low ($a_H \rightarrow \infty$), β_{closed} approaches 0. β_{closed} reaches a maximum when $a_H = K'_a$ (i.e. when pH = pK'_a) and = 0.58$[A]_T$. The relationship between pH and β_{closed} for a theoretical closed buffer is shown in Fig. 17.1.

In contrast to the conditions for a closed buffer, if the protonated (or uncharged) form of a buffer remains constant (i.e. [HA] = constant), then the buffer operates as an open buffer. The most common example of an open buffer in solution is CO_2/ HCO_3^-. Such a solution contains HCO_3^- and is equilibrated with gaseous CO_2 (usually by bubbling). If acid is added to such a solution, H^+ combines with HCO_3^- and forms additional CO_2. Since the solution is in equilibrium with a fixed P_{CO_2}, the additional CO_2 diffuses from the solution and is removed. Thus, under these conditions, the amount of the uncharged form of the buffer (CO_2) remains constant, whereas the total buffer amount goes down because the HCO_3^- has decreased. The buffering power of an open buffer is given by:

$$\beta_{\mathrm{open}} = 2.303\ [\mathrm{A}^-] \tag{17.8}$$

where [A^-] = HCO_3^- for the open buffering power of CO_2/HCO_3^-. The relationship between pH and β_{open} for a theoretical open buffer is shown in Fig. 17.1.

Open buffers differ from closed buffers in two important respects. First, unlike closed buffers, the buffering power of open buffers is not maximal at their pK'_a values. In fact, open buffers become better buffers at the more extreme values of pH (see Fig. 17.1). β_{open} becomes larger with alkalinization for weak acids and with acidification for weak bases. Second, open buffers have a much higher buffering power than closed buffers under similar conditions (see Fig. 17.1). Note, however, that neither Equation 17.7 nor Equation 17.8 includes any indication of the nature of the buffer. Thus, all closed buffers are equally potent when the pH is at their pK'_a and all open buffers are equally potent when they have the same [A^-].

Since most uncharged substances are substantially more permeant through cell membranes than charged species, *almost all weak acids and bases can act as open buffers in cells*. For example, a weak acid that has a pK'_a of 4.0 acts like a closed buffer in solution and, since its pK'_a is 4.0, it would be a poor buffer at pH 7.0. However, inside a cell at pH 7.0, this weak acid acts like an open buffer. Any added H^+ will bind to the anionic form of the buffer. The uncharged buffer molecule formed will readily diffuse from the cell and be removed by the blood. Thus, although this weak acid is a poor buffer in the medium, it can contribute substantially to the buffering power inside a cell if present at sufficient concentration.

Complex solutions, like cytoplasm, contain multiple buffers. The *total buffering power* (β_{total}) of such solutions

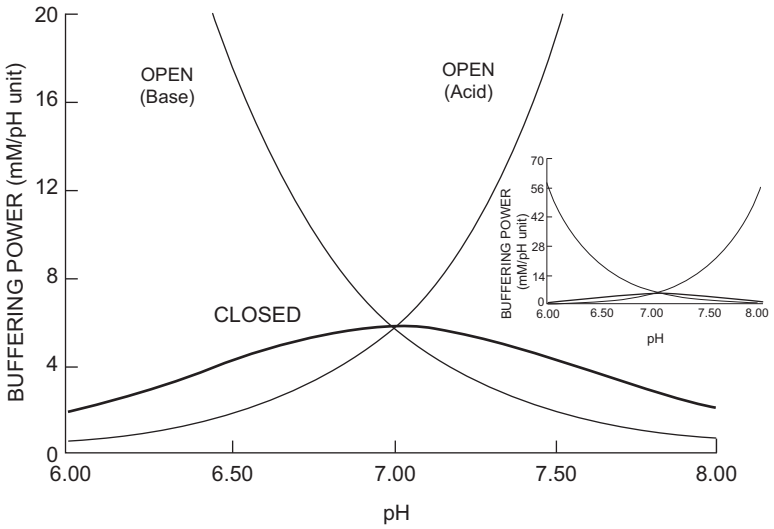

FIGURE 17.1 The pH dependence of a buffer operating as a closed or open buffer. The buffering powers for both a weak acid buffer (H^++A^-{ReversReact}HA) and weak base buffer (H^++B{ReversReact}BH^+) are plotted. The buffers are assumed to have a pK'_a of 7.0 and to have the same buffering power at pH 7.0 whether operating as an open or closed buffer. Note that while closed buffers have maximal buffering power when pH= pK'_a, the buffering power for an open buffer is higher at pH values higher than pK'_a (for weak acid buffers) or at pH values lower than pK'_a (for weak base buffers). Inset: the same plot with a different scale for the ordinate. Note how much higher the open buffering power is compared with the closed buffering power at pH values well above (weak acid) or below (weak base) the value of pK'_a.

will be the sum of the various buffers; i.e. buffers operate independently in solution. Thus,

$$\beta_{\text{total}} = \sum \beta_{\text{closed}} + \sum \beta_{\text{open}} \qquad (17.9)$$

Finally, it is inherent in the definition of buffering power (Equation 17.6) that buffering power is a coefficient that can be used to convert a change of pH into a change in the amount of proton equivalents moved. This relationship has practical application. For instance, in the study of the regulation of intracellular pH, the activity of a transporter that moves H^+ across the surface membrane (such as the Na^+-H^+ exchanger, see Section VIIA) is determined by measuring the rate of change of pH_i (dpH_i/dt). The movement of H^+ on this transporter is accompanied by Na^+, whose movement is measured as a radioisotopic flux (amount of Na^+ influx per unit time). To compare the flux of Na^+ with the flux of H^+, the rate of change of pH_i needs to be converted to the amount of H^+ moved per unit time. This is accomplished by the following equation:

$$J_{\text{H}} = \frac{dp\text{H}}{dt} \cdot \beta_{\text{total}} \qquad (17.10)$$

where J_H is the flux of protons and has units of mM H^+ per unit time. Using this equation, the flux of H^+, calculated from the measured rate of pH change, can be directly compared to the flux of another ion determined with radioisotopes.

IV. INTRACELLULAR pH

Protons are just like any other cation, except for three distinguishing characteristics: (1) H ions are a dissociation product of water molecules (H_2O{=}H^++OH^-) and thus are always present in aqueous solutions; (2) H ions are present at very low concentrations in most solutions; and (3) H ions have much higher mobility than other cations. However, the equilibrium distribution and movement of H^+ across biological membranes are governed by the same principles that govern the movement of all other ions across biological membranes.

Originally, protons were assumed to be at equilibrium across biological membranes because of their very high mobility. Assuming an extracellular pH (pH_o) of 7.4, a V_m of −60 mV (inside negative) and assuming that H ions are passively distributed across the membrane (i.e. at equilibrium), pH_i would be 6.4 (calculated from the Nernst equation). However, at such an intracellular pH, metabolism and a variety of other cellular functions would be impaired. With the advent of modern reliable techniques for measuring intracellular pH, including *pH-sensitive glass microelectrodes* and *pH-sensitive fluorescent dyes*, it was shown that, in the majority of cells, pH_i was between 6.8 and 7.2, well above the calculated value for equilibrium pH. It is now clear that for most cells (with the notable exception of red blood cells), pH_i is considerably more alkaline than it would be if protons were at passive equilibrium across the cell membrane.

The question still remains how pH_i can be well above its equilibrium value, since H^+ should be highly permeant to most cell membranes. In fact, the *permeability of* H^+ across biological membranes has been estimated to be between 10^{-4} and 10^{-2} cm/s, about four orders of magnitude higher than typical K^+ permeability. However, it is the conductance and not the permeability of H^+ that is crucial. *Conductance* is a measure of ion flux and is a function of both the permeability and the free concentration of an ion. H ions have low conductance across biological membranes despite their high permeability, because they are present in such low concentrations (10^{-7} M free concentration for H^+

versus 10^{-1} M free concentration for K^+). Thus, the acidifying influx of H ions (down their electrochemical gradient) will be small and these H ions can easily be removed from the cell by membrane transport systems (see Section VII).

In summary, most cells have a cytoplasmic pH that is more alkaline than the value calculated assuming equilibrium of H^+ across the cell membrane, and pH_i for most cells is about 6.8−7.2.

V. ORGANELLAR pH

Several intracellular organelles independently control their internal pH, which differs from the cytoplasmic pH (Fig. 17.2). These organelles include *mitochondria* and *acidic intracellular organelles*.

VA. Mitochondria

One of the major roles of mitochondria is the production of ATP. A proton gradient across the inner mitochondrial membrane is required for the production of ATP. The electron transport chain translocates protons from the mitochondrion to the cytoplasm across the inner mitochondrial membrane. This proton extrusion creates an electrical and chemical gradient for proton influx into the mitochondrion. This H^+ influx occurs through a membrane-bound ATPase that produces ATP upon passive proton flux back into the mitochondrion. This is known as the *chemiosmotic hypothesis*.

The extrusion of H^+ to establish a proton gradient renders mitochondria alkaline relative to the cytoplasm by about 0.3−0.5 pH unit. Thus, intramitochondrial pH can be between 7.5 and 8.0. In addition, this pH gradient is maintained in the face of considerable acid loads, indicating that mitochondria may well be able to regulate their internal pH independently of cytoplasmic pH.

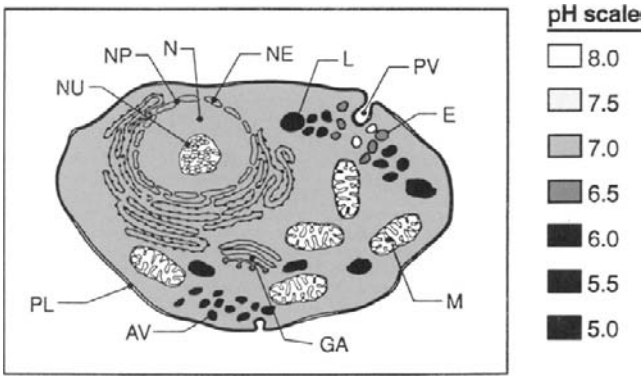

FIGURE 17.2 A diagram of an idealized cell with the gray scale representing different values of pH (note calibration scale on the right). The cytoplasm has a fairly uniform pH of about 7.0, but note the alkaline mitochondria, the increasing acidification in the Golgi apparatus and in the endosomes and the very acidic lysosomes. AV: acidic vesicles; E: endosomes; GA: Golgi apparatus; L: lysosomes; M: mitochondria; N: nucleus; NE: nuclear envelope; NP: nuclear pore; NU: nucleolus; PL: plasmalemma; PV: pinocytotic vesicle.

VB. Acidic Intracellular Organelles

Organelles with a markedly acidic interior are those involved in either the endocytic pathway or the secretory pathway. The acidic organelles involved in endocytosis include *coated pits*, *endosomes* (i.e. prelysosomal endocytic vesicles) and *lysosomes*. Acidic vesicles in the secretory pathway include the *Golgi apparatus* (or at least part of it) and *storage granules* for amines (e.g. chromaffin granules involved in catecholamine secretion) and peptides (e.g. secretory granules in the endocrine pancreas). The pH is not known for all of these compartments, but can be as low as 4.5−5.0 in lysosomes and 5.0−5.7 in endosomes and secretory granules. The pH in the Golgi apparatus seems to fall the farther the compartment is from the nucleus, with values of 6.2−6.4 in the medial Golgi and values as low as 5.9 in the trans Golgi network (TGN).

The acidic internal environment of these various organelles is believed to be necessary for their function. For example, the primary function of lysosomes is the biochemical degradation of macromolecules and these organelles contain a large number of hydrolytic enzymes whose pH optima are about pH 5.0. This serves as protection for the cell. If the lysosomes should leak, the hydrolytic enzymes would be inactivated by the high cytoplasmic pH, thus preventing the indiscriminate degradation of important macromolecules. Receptor-mediated endocytosis involves the internalization of ligand-receptor complexes in endocytic vesicles, or endosomes. Acidification of these vesicles is essential for the dissociation of the ligand from the receptor within the endosome. Once the ligand has dissociated, the internalized receptor is recycled to the surface membrane, while the ligand is delivered to the lysosome. Finally, secretory granules (and perhaps part of the Golgi) serve to accumulate macromolecules to be secreted and often mediate processing or modification of these substances. The maintenance of an acidic environment in these granules can be crucial to both of these functions. There is evidence that the large outward H^+ gradient is used to accumulate biogenic amines in amine secretory granules. This accumulation may be mediated by an H^+-amine exchanger in the granule membrane. These accumulated substances can be biochemically modified into their final form and the enzymes responsible for these modifications often have low pH optima or depend on the availability of organic compounds that will accumulate only in acidic compartments. For all of these acidic compartments, then, it is clear that their proper functioning depends on the maintenance of a low internal pH.

VC. Nucleus

The nucleus is separated from the cytoplasm by a double membrane system that has large nuclear pores. Large macromolecules (up to 5 kDa) readily permeate the nuclear pores and rapidly come to equilibrium between the nucleus and cytoplasm. Given this high degree of permeability of the nuclear membrane, it was believed that nuclear pH could not differ much from cytoplasmic pH. However, measurements clearly show that nuclear pH is from 0.1 to 0.5 pH unit more alkaline than cytoplasmic pH. This is consistent with the findings that the nuclear envelope contains Na^+-H^+ exchangers, indicating active pH regulation across the nuclear membrane.

VI. MAINTENANCE OF A STEADY-STATE pH_i

If a cell is maintaining a *steady-state* pH_i (i.e. the pH of the cytoplasm is constant over time), the rate of acid loading must be equal to the rate of acid extrusion from the cell (in these terms it is exactly equivalent if an acid molecule moves in one direction or a base molecule moves in the opposite direction) (Fig. 17.3). Several processes can contribute to acid loading of a cell, including metabolic production of acid, passive influx of H^+ across the cell membrane, leakage of H^+ from acidic internal compartments, pumping of H^+ from alkaline internal compartments and active influx of H^+ or active extrusion of base. Conversely, acid extrusion includes metabolic consumption of H^+, sequestration of H^+ in internal compartments, and active extrusion of acid or active influx of base.

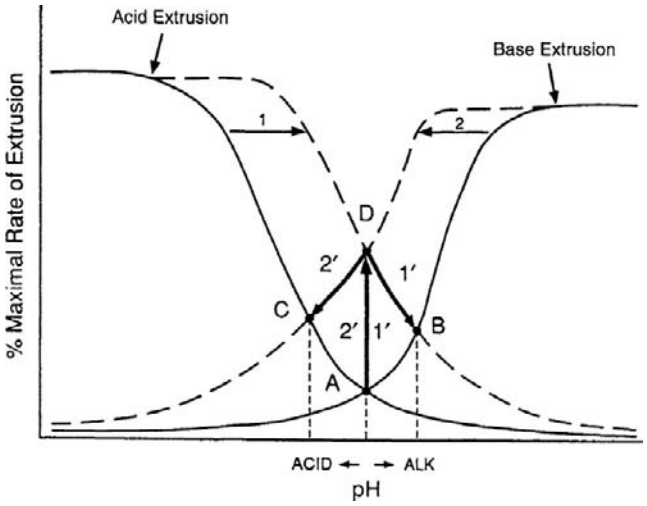

FIGURE 17.3 A model for the regulation of steady-state pH_i. In the cell, steady-state pH_i is determined as the point where acid-extruding processes are balanced by base-extruding (or acid influx) pathways (point A). If acid-extruding processes are activated (arrow 1 — represented as a shift to the right of the pH versus % maximal rate curve), as occurs when growth factors activate Na^+-H^+ exchange, the rate of acid extrusion exceeds the rate of base extrusion and the cell alkalinizes (arrows 1′). Eventually, the cell alkalinizes to the point where acid and base extrusion are again equal and a new alkaline steady state pH_i is reached (point B). In contrast, if base extrusion is activated (arrow 2 — represented as a shift to the left of the pH versus % maximal rate curve), as occurs with an increase in the activity of Cl^--HCO_3^- exchange, the rate of base extrusion exceeds acid extrusion and the cell will acidify (arrows 2′). Eventually, the cell acidifies to the point where acid and base extrusion are again equal and a new acidic steady-state pH_i is reached (point C). If acid and base extrusion are activated to the same extent, the steady state pH_i will remain unchanged (point D).

VIA. Metabolic Production and Consumption of Acids

Several metabolic reactions involve the production of H^+ (Table 17.1). These processes include the production of CO_2, glycolysis (through the generation of lactic and pyruvic acids), formation of creatine phosphate, ATP hydrolysis, lipolysis, triglyceride hydrolysis, the generation of superoxide and the operation of the hexose monophosphate shunt. Obviously, when these reactions run in the opposite direction (e.g. creatine phosphate hydrolysis, ATP formation or consumption of CO_2), there is a net consumption of H^+ and the cell will alkalinize.

When the cell is at steady state, these reactions must be balanced and thus the levels of cellular metabolites such as ATP, creatine phosphate, CO_2 and lactate will also be at steady state. However, during transient periods, these metabolic reactions can result in net changes in metabolite concentrations and thus contribute markedly to changes in pH_i. For instance, during periods of ischemia, cellular lactate and CO_2 may accumulate while ATP will be

TABLE 17.1 Examples of Various Metabolic Reactions that Involve the Generation or Consumption of H^+

Glycolysis[a]	$Glucose + 2MgADP^- + 2P_i^{2-} \rightarrow 2(lactate)^- + 2MgATP^{2-} 2MgATP^{2-} \rightarrow 2MgADP^- + 2P_i^{2-} + 2H^+$
Glycogenolysis[b]	$Glycogen + 3P_i^{2-} + 3MgADP^- + \rightarrow 3MgATP^{2-} + 2(lactate)^- + glycogen$
Creatine phosphate hydrolysis	$H^+ + creatine\ phosphate^{2-} + MgADP^- \rightarrow MgATP^{2-} + creatine$
Lipolysis	$Triglyceride \rightarrow 3(palmitate)^- + 3H^+ 3(palmitate)^- + 3MgATP^{2-} + 3CoA^{4-} \rightarrow 3(palmitoyl\ CoA)^{4-} + 3AMP^{2-} + 6P_i^{2-} + 3H^+ + 3Mg^{2+}$
Superoxide formation	$NADPH + 2O_2 \rightarrow 2O^- + NADP^+ + H^+$
Hexose-monophosphate shunt	$G6P^- + 12NADP^+ + 6H_2O \rightarrow NADPH + P^- + 12H^+ + 6CO_2$

[a] *At pH 7.2 and high $[Mg^{2+}]$, $2H^+$ are always generated but the balance of H^+ produced by the two reactions varies with pH and Mg.*
[b] *Net H^+ production when hydrolysis of the 3MgATP is taken into account.*

hydrolyzed. All of these reactions can contribute to the observed cellular acidification. The hydrolysis of creatine phosphate during ischemia consumes H^+ and will blunt the cellular acidification. Another example of a transient effect of metabolism on cellular pH is the initial acidification seen upon activation of neutrophils with phorbol esters. In this case, stimulation of the production of superoxide and activation of the hexose monophosphate shunt results in increased production of H^+.

VIB. Passive Transmembrane Flux of H^+

Although the H^+ permeability of most biological membranes is quite high ($P_H \approx 10^{-3}$ cm/s), the actual H^+ flux across the membrane is quite low because of the low free H^+ concentration. For example, the putative H^+ flux across a frog muscle fiber can be calculated. Assuming a constant electric field across the membrane, $P_H = 10^{-3}$ cm/s, $V_m = -90$ mV, $pH_i = 7.2$, $pH_o = 7.35$ and $\beta_{otal} = 26$ mM, passive H^+ influx would result in a cellular acidification of only 0.02 pH unit/hour. Although negligible, this does represent a continued acid load on the cell and, if mechanisms do not exist to remove these H ions, the cell will eventually acidify toward its equilibrium pH_i value.

H^+ currents associated with *proton channels* have been reported in several cells, such as snail neurons, salamander oocytes and a number of mammalian cells, including neutrophils, B cells, spermatozoa and airway epithelial cells. All of these channels are activated by depolarization and the resulting H^+ currents alkalinize the cell. Other characteristics of these channels include inhibition by divalent cations (such as Zn^{2+} and Cd^{2+}), gating by both intracellular and extracellular pH and low single-channel conductance. These channels are also purely selective for H ions and they have a very high temperature dependence, both rare features for an ion channel. The proton channel has recently been cloned and shown to contain four transmembrane domains, a large N terminal and a somewhat smaller C terminal domain. The channel often functions as a dimer. These channels have been implicated in the regulation of NADPH oxidase activity during phagocytosis, the facilitation of histamine release from basophils, the activation of sperm and the regulation of pH in airway epithelia. Proton channels may also contribute to the maintenance of pH in restricted submembrane spaces within the cell or contribute to pH_i regulation in cells undergoing prolonged depolarization, such as the prolonged depolarizing fertilization potential in oocytes.

VIC. Internal Compartments

If the pH values of intracellular compartments, such as mitochondria and lysosomes, are at steady state, then they should have no impact on cytoplasmic pH. However, under pathological conditions where mitochondria or acidic intracellular compartments are rendered leaky or mitochondria take up cytoplasmic Ca^{2+} in exchange for H^+, these compartments could influence pH_i. Under normal conditions, though, these compartments should contribute little to the maintenance of a steady-state pH_i, especially owing to their relatively small volume compared with total cell volume.

It is clear that, at the very least, cells face a continual acid load from passive H^+ influx. In addition, under many conditions of metabolic stress, cells also experience a metabolic acid load. Thus, cells must possess active extrusion mechanisms to maintain a steady-state pH_i well above the equilibrium value for pH_i.

VII. ACTIVE MEMBRANE TRANSPORT OF ACIDS AND BASES

To study the ability of cells to actively extrude acid or base from the cell, techniques must be available to alter intracellular pH experimentally. In some large cells, this has been achieved directly by injecting acid into cells, by passing current through microelectrodes, or by internal dialysis through tubing threaded through the cytoplasm of the cell. Changes in pH_i have been accomplished by internal perfusion of cells using whole-cell patch-clamp electrodes. However, the most commonly used experimental method to modify pH_i is by external exposure of cells to weak acids or bases. One of the most popular of such techniques is the *NH_4Cl prepulse technique*. Cells are exposed to an external solution containing NH_4Cl. External NH_3, being uncharged, enters the cell (arrow 1 in Fig. 17.4A) far more rapidly than external NH_4^+. In the cell, the NH_3 combines with an H ion to form NH_4^+ (arrow 2 in Fig. 17.4A), thereby alkalinizing the cell. This alkalinization will continue until the internal and external concentrations of NH_3 are the same, at which time no more NH_3 will enter and the pH_i will reach a new steady-state value alkaline relative to the original pH_i. If NH_4^+ is unable to enter the cell, no further change in pH_i will occur until external NH_4Cl is removed, at which time cytoplasmic NH_4^+ will dissociate to NH_3 and H^+ and all the NH_3 will diffuse from the cell, returning pH_i back to its original value (top pH trace in Fig. 17.4A). However, if NH_4^+ has some membrane permeability, it will enter the cell (arrow 3 in Fig. 17.4A), largely driven by the negative internal membrane potential. The NH_4^+ that enters will dissociate into NH_3 and H^+. The newly formed NH_3 will diffuse from the cell, leaving H^+ in the cell. Thus, a shuttle is established whereby NH_4^+ enters the cell and NH_3 leaves the cell (arrows 3, 2, 1 and 4 in Fig. 17.4A). For each cycle of the shuttle, an H ion is added to the cell and so the cell slowly acidifies in the maintained presence of external NH_4Cl

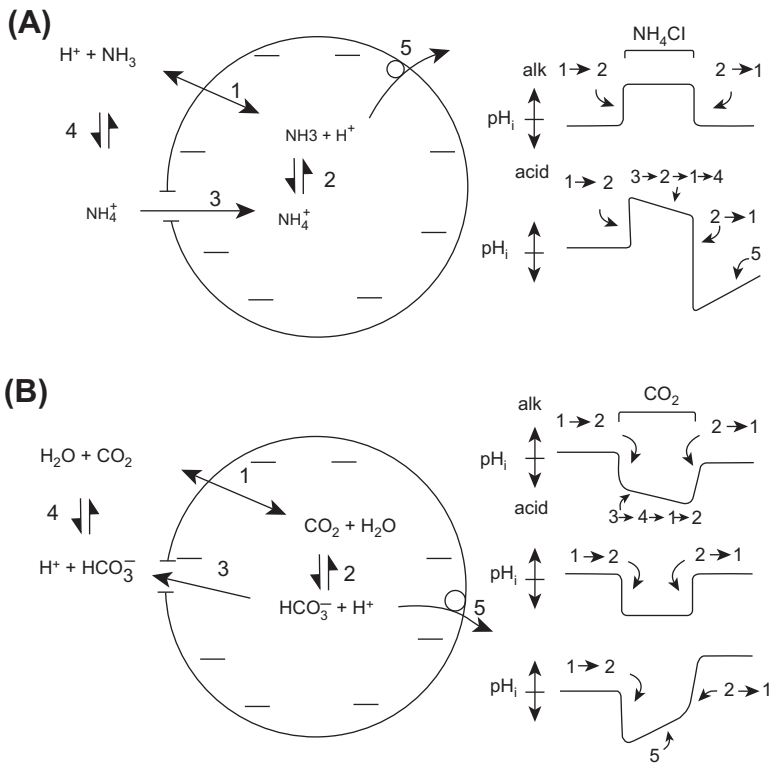

FIGURE 17.4 (A) A diagram of the effects on intracellular pH of a transient exposure of a cell to external NH_4Cl. (B) A diagram of the effects on intracellular pH of a transient exposure of a cell to external CO_2 and HCO_3^-. The meaning of the various numbers and the pH traces to the right are given in the text.

(termed *plateau acidification*). Upon removal of external NH_4Cl, all the original NH_4^+ formed upon exposure will dissociate and regenerate NH_3 (which diffuses from the cell) and H^+. However, the cell will contain extra H^+ due to the operation of the shuttle and thus pH_i will undershoot its initial value, achieving a more acid pH_i than it had before the NH_4Cl exposure. The degree of this undershoot is dependent on the amount of NH_4Cl initially added, the membrane permeability to NH_4^+ and the duration of exposure to NH_4Cl. The net effect of an NH_4Cl prepulse is to acidify the cell and it is entirely analogous to an injection of acid. If a cell possesses membrane transport systems for active H^+ extrusion (arrow 5 in Fig. 17.4A), pH_i will return toward its initial pH value, a process termed *pH recovery* (lower pH trace in Fig. 17.4A).

The other common way to alter pH_i is by exposure of cells to weak acids. The most common weak acid is carbonic acid, in the form of CO_2. This process is analogous to the NH_4Cl prepulse. Upon exposure to a solution containing CO_2 and HCO_3^-, CO_2 rapidly enters the cell (arrow 1 in Fig. 17.4B), hydrates and dissociates to form internal HCO_3^- and H^+ (arrow 2 in Fig. 17.4B). The addition of H^+ internally acidifies the cell. The cell will continue to acidify until internal and external CO_2 are equal. At this point, if HCO_3^- is impermeant, no further change in pH will occur, and pH will return to its initial value upon removal of extracellular CO_2 (middle pH trace in Fig. 17.4B). However, if HCO_3^- can move across the membrane, a shuttle will be established. HCO_3^- will leave the cell (arrow 3 in Fig. 17.4B), mostly driven by the negative membrane potential, internal CO_2 will hydrate and dissociate, and more CO_2 will enter the cell. Thus, HCO_3^- will leave the cell and CO_2 will enter the cell, adding an internal H^+ for every cycle of the shuttle (arrows 3, 4, 1 and 2 in Fig. 17.4B). The cell will slowly acidify (top pH trace in Fig. 17.4B). If, however, the cell possesses transmembrane H^+ extrusion mechanisms (arrow 5 in Fig. 17.4B), pH will recover back toward the initial pH_i value because of active extrusion of internal H^+ even in the maintained presence of CO_2. If external CO_2 is removed after recovery, the H^+ initially formed upon CO_2 exposure will recombine with HCO_3^- and leave the cell as H_2O and CO_2, thereby alkalinizing the cell. However, the cell pH will overshoot, reaching an alkaline value of pH (bottom pH trace in Fig. 17.4B), because of the removal of internal H^+ during pH recovery. Thus, exposure to or removal of weak acids can induce cellular acidification or alkalinization, respectively.

Several integral proteins within the surface membrane of cells are specialized for the active transport of acids and bases across the membrane. Because of their importance to cellular pH regulation, these transport pathways have been extensively studied and can be divided into five groups: (1) those that move H^+ directly in exchange for another

cation; (2) those that move HCO_3^- or an associated species like CO_3^{2-}; (3) H^+-ATPases (proton pumps) that use energy from ATP hydrolysis to transport H^+; (4) those that co-transport anionic weak bases with Na^+; and (5) those that transport anionic weak bases in exchange for Cl^-. Many of the pH-regulating transporters can be derived from genes from one of three gene superfamilies. Na^+/H^+ exchangers (group 1) belong to the SLC9 (solute carrier) gene family, while HCO_3^--dependent transporters belong mainly to the SLC4 superfamily (anion exchanger like Cl^-/HCO_3^- exchangers and Na^+-HCO_3^- co-transporters).

VIIA. Cation-H^+ Exchangers

The best characterized of the cation-H^+ exchangers is the *Na^+-H^+ exchanger (NHE)* (model 1 in Fig. 17.5A). This exchanger responds to cellular acidification by extruding one H^+ in exchange for the influx of one Na^+ (1:1 stoichiometry means that the exchanger is *electroneutral*, i.e. it does not involve net charge movement). There are now known to be at least eight isoforms of the Na^+-H^+ exchanger in mammalian cells. NHE-1 is found in virtually all cells, is inhibited by the loop diuretic amiloride and its analogs, can be activated by a variety of agents and has a molecular weight of 91 000. NHE-2, which has only 50% amino acid homology with NHE-1, is found predominantly in the gastrointestinal tract (GI tract), kidney and skeletal muscle, is much less sensitive to inhibition by amiloride analogs than NHE-1 and has a molecular weight of about 91 000. NHE-3 has about 40% amino acid homology with NHE-1, has a molecular weight of 93 000, is expressed largely in the GI tract and kidney and is not readily inhibited by amiloride. NHE-4 also has about 40% amino acid homology with NHE-1, is the smallest NHE isoform with a molecular weight of 81 000, is largely expressed in the GI tract (with some expression in the uterus, brain, and kidney) and is not very sensitive to inhibition by amiloride. NHE-5 is most similar to NHE-3 ($\approx$53% amino acid homology), but has a larger molecular weight, 99 000, than any of the other NHE isoforms. This isoform is not very sensitive to inhibition by amiloride analogs. NHE-5 is largely expressed in the brain, especially in neuronal cell bodies. Other NHE isoforms undoubtedly exist in mammalian cells. Isoforms NHE-6 and -7 are highly homologous and differ considerably ($\approx$25% homology) from NHE-1. NHE-6 are largely associated with recycling endosomes and NHE-7 are largely associated with the trans-Golgi network. NHE-7 has a high affinity for K^+ and may function largely as a K^+/H^+ exchanger. NHE-8 is at most 25% homologous with the other NHEs and is therefore the most distinct. Its distribution is uncertain, some studies suggesting that it resides mostly on the surface membrane while others indicate a largely intracellular localization.

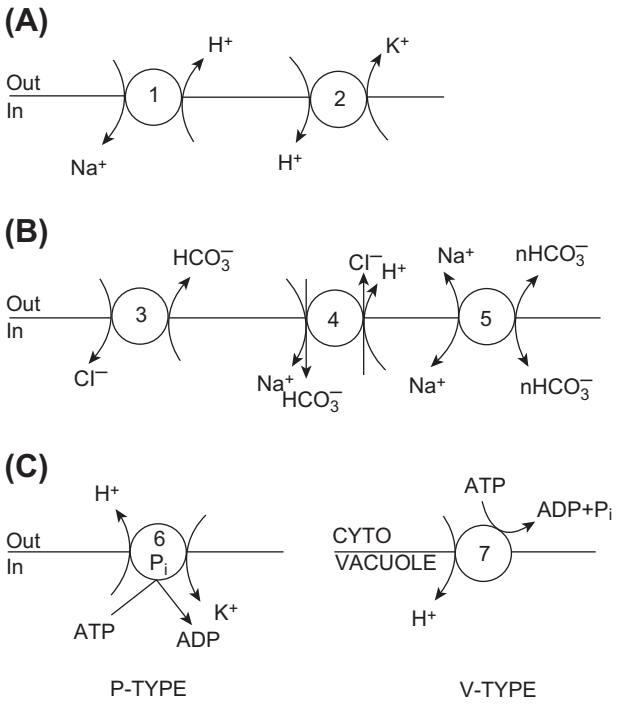

FIGURE 17.5 Models of several different types of pH-regulating transporters. (A) Cation-H^+ exchangers. Included in this group are the alkalinizing Na^+-H^+ exchanger (1) and the acidifying K^+-H^+ exchanger (2). (B) HCO_3^--dependent transporters. This group includes the Cl^--HCO_3^- exchanger (band 3 from red blood cells) (3). Another transporter in this group is the (Na^++HCO_3^-)-Cl^- exchanger (4). Shown here is merely one possible model for this exchanger. This transporter could involve the influx of two HCO_3^- instead of the influx of one HCO_3^- and the efflux of an H^+. Alternatively, one CO_3^{2-} or two $NaCO_3^-$ could be transported in. These four different variants have the same effect on pH, but can be partially distinguished kinetically. The Na^+-HCO_3^- co-transporter is shown as model 5. This transporter is electrogenic, mediating the movement of *n* HCO_3^- for each Na^+ and is thus sensitive to membrane potential (V_m). The direction of co-transport depends on the value of V_m. (C) Two different types of H^+-ATPases. The P-type H^+-ATPase (6), typified by the electroneutral gastric H^+, K^+-ATPase, involves a phosphorylated intermediate. The V-type H^+-ATPase (7), typified by the vacuolar H^+-ATPase, does not produce a phosphorylated intermediate.

Other NHE isoforms also exist in cells from lower vertebrates, invertebrates, plants and bacteria. For instance, an unusual isoform, β-NHE, that is 50–75% homologous to NHE-1 and is activated by cAMP (unlike NHE-1) has been described in trout red blood cells. The significance of these different isoforms is still largely unclear, but given the variety of functions performed by NHE in cells, it is not surprising that multiple forms have arisen.

The basic structure of the mammalian plasma membrane NHE isoforms is similar (Fig. 17.6A), containing two major domains, a transmembrane domain and a cytoplasmic domain. In NHE-1 the transmembrane domain (N-terminal $\approx$500 amino acids) is believed to have 12 membrane-spanning regions with an N-linked glycosylation site on the first external loop. This means that NHE

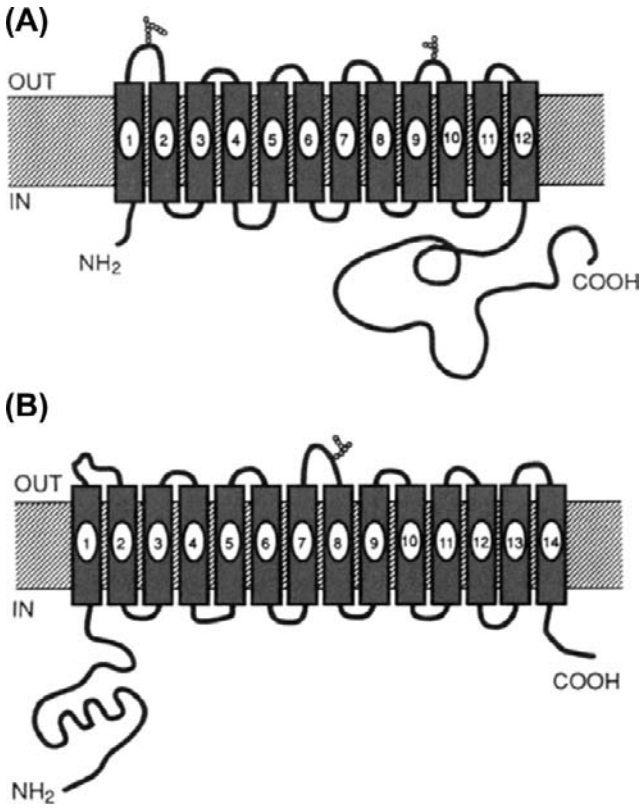

FIGURE 17.6 Models of (A) the structure of the Na^+-H^+ exchanger (NHE-1) and (B) the Cl^--HCO_3^- exchanger (AE 1). The Na^+-H^+ exchanger is believed to have 12 membrane-spanning regions with a large cytoplasmic domain at the C-terminal end. This cytoplasmic domain contains several potential phosphorylation sites that are important to the regulation of the Na^+-H^+ exchanger. The N-terminal end is also cytoplasmic. Two potential glycosylation sites are shown. The Cl^--HCO_3^- exchanger is believed to have 14 membrane-spanning regions and both terminal ends are cytoplasmic. The large cytoplasmic domain is on the N-terminal end in the Cl^--HCO_3^- exchanger. This cytoplasmic domain (in red blood cells at least) contains many binding sites, including those for the cytoskeletal element ankyrin, for hemoglobin, and for some glycolytic enzymes.

is a glycoprotein. The cytoplasmic domain (C-terminal $\approx$300 amino acids) represents a large cytoplasmic region with available serine phosphorylation sites. Both the N- and C-terminal ends of NHE are cytoplasmic. It is believed that the cytoplasmic C-terminal end is involved in the regulation of NHE while the membrane-spanning regions are responsible for Na^+ and H^+ transport. This is borne out by the expression of NHE mutants that lack the C-terminal end in fibroblasts that do not have NHE. In these cells, Na^+-H^+ exchange activity is seen, but can no longer be activated by growth factors. Some variation in this basic structure is seen in other isoforms but the main pattern is the same.

A wide variety of substances have been shown to activate NHE, including hormones, neurotransmitters, growth factors and the extracellular matrix. Many of these factors are believed to activate the NHE by phosphorylating residues on the C-terminal end. These factors may also affect the NHE through the binding of a regulatory protein with the exchanger and/or by binding of a Ca^{2+}—calmodulin complex to a putative autoinhibitory domain on the exchanger. Activation often involves an increase in the affinity of the exchanger's internal binding site for cytoplasmic H^+ (see arrow 1, Fig. 17.3). In some cases, activation of NHE may also involve interaction between the exchanger and the cell cytoskeleton. There is accumulating evidence that NHE isoforms may function best as homodimers. The functional significance of dimerization is unclear. Cell acidification also dramatically activates NHE. This activation is due to an internal allosteric H^+-binding site on NHE (distinct from the H^+ transport site) that increases exchange when occupied. Finally, decreased cell volume (cell shrinkage) also activates NHE. This activation does not involve phosphorylation of NHE and appears to be mediated by a unique activation pathway.

Many signaling pathways can activate NHE, depending on the stimulus. For example, growth factor activation of NHE is usually mediated by an elevation of intracellular Ca^{2+} and/or by an increased activity of protein kinase C. These pathways commonly involve phosphoinositide breakdown. Activation of NHE by cell shrinkage appears to involve ATP- and GTP-dependent pathways.

Much progress has been made to correlate NHE function with structure. As stated above, the transmembrane domain contains the Na^+ and H^+ transport sites. In addition, this domain contains the external amiloride binding site and the internal H^+ allosteric binding site, although the p*K* for this latter site is markedly acid in the absence of the C-terminal cytoplasmic domain. The C-terminal cytoplasmic domain contains several putative phosphorylation sites and is involved in the regulation of NHE. This region also contains the autoinhibitory domain, the calmodulin binding site, and a possible binding site for the putative cytoplasmic regulatory factor. The C-terminal domain may also contain sites able to interact with cytoskeletal proteins.

Transgenic mice now exist that lack various NHE isoforms such as NHE-1, NHE-2 and NHE-3. All three types of mice are viable, but mice lacking NHE-1 have slowed postnatal development and by 14 days exhibit neurologic symptoms (primarily gait problems and seizures). These mice usually die before weaning. In contrast, high levels of NHE-1 activity, as seen with transient ischemia, result in excessive cellular Na^+ levels and increased intracellular Ca^{2+} which is especially damaging for cardiac and neural cells. Mice lacking NHE-2 are apparently normal, but show long-term gastric changes, including a small decrease in acid secretion and degeneration of parietal cells. Mice lacking NHE-3 also have long-term viability but exhibit gastrointestinal (GI) and renal defects. These defects cause diarrhea, mild acidosis and lowered blood pressure. These symptoms are consistent with a role for NHE-3 in GI and

renal HCO_3^- and fluid absorption. The use of transgenic mice should be helpful in further defining the role of various other NHE isoforms.

The other major cation-H^+ exchanger is the *K^+-H^+ exchanger* (see model 2 in Fig. 17.5A). This transporter exchanges intracellular K^+ for extracellular H^+ and results in cellular acidification. K^+-H^+ exchange has been found in nucleated red blood cells and mediates solute efflux during regulatory volume decrease (see Section VIIIH). It has also been observed in retinal pigment epithelial cells, where it enables the cell to regulate pH_i in the face of an alkaline load.

VIIB. HCO_3^--Dependent Transporters

These transporters are actually a superfamily of related transport proteins (SLC4) that affect pH_i and are characterized by their ability to transport HCO_3^- (or a related species like CO_3^-) and by the ability of disulfonic stilbene derivatives to inhibit them. The three major types of HCO_3^--dependent transporters are Cl^--HCO_3^- exchangers (band 3 from red blood cells, termed AE for anion exchanger), (Na^++HCO_3^-)-Cl^- exchangers (often termed NDCBE for Na^+-dependent or Na^+-driven Cl^--HCO_3^- exchange) and Na^+-HCO_3^- co-transporters (termed NBC for Na^+ bicarbonate co-transport), both electrogenic (NBCe) and electroneutral (NBCn).

The operation of *Cl^--HCO_3^- exchange* (AE) (see model 3 in Fig. 17.5B) has been studied most extensively in red blood cells. This electroneutral transporter involves a 1:1 exchange of Cl^- for HCO_3^- (although many other ions, such as $SO4^-$, can also be transported under specific conditions). As with the Na^+-H^+ exchanger, the Cl^--HCO_3^- exchanger has several isoforms, denoted AE 1, 2 and 3. These various isoforms have about 80–90% homology. AE 1 is widely distributed and is best known as the band 3 transporter from red blood cells. It is the smallest isoform ($M_r = 115\,000$). This protein has as many as 14 (or 13 with a re-entrant loop) membrane-spanning domains (helices) and a large N-terminal cytoplasmic domain that contains various binding sites, including one for ankyrin (see Fig. 17.6B). AE 2 and 3 are larger ($M_r = 145\,000$–$165\,000$). AE 2 appears to be the housekeeping anion exchanger and is the most widely distributed, but is especially prevalent in the choroid plexus and throughout the GI tract. It is activated by cellular alkalinization and returns pH_i to normal by extruding base (HCO_3^-) and thereby re-acidifying the cell. This exchanger may also possess an internal allosteric regulatory site that activates the exchanger at *alkaline* values of pH_i (see the base extrusion curve in Fig. 17.3). In addition to its role in the regulation of pH_i, Cl^--HCO_3^- exchange may also play a role in regulating intracellular Cl^-. The function of AE 3 is not yet clear but it has a far more restricted distribution than AE 2, being found largely in the heart and the central nervous system.

The *(Na^++HCO_3^-)-Cl^- exchanger* (see model 4 in Fig. 17.5B) was originally described as the pH-regulating transport system in invertebrate nerve and muscle preparations, but has since been found in a wide variety of cells. Because it transports Na^+, it operates in the opposite way than Na^+-independent Cl^--HCO_3^- exchange (i.e. the anion exchangers described above). Thus, the (Na^++HCO_3^-)-Cl^- exchanger exchanges one external Na^+ for one internal Cl^- and neutralizes the equivalent of two internal protons. As such, this exchanger is electroneutral and mediates the alkalinization of the cell in response to an acid load. The ability of this exchanger to neutralize two acid equivalents could be achieved by the influx of two HCO_3^-, the influx of one HCO_3^- in exchange for the efflux of one H^+, the influx of one CO_3^{2-}, or the influx of an ion pair ($NaCO_3^-$). In squid axon, this exchanger has been suggested to involve $NaCO_3^-Cl^-$exchange whereas, in barnacle muscle fibers, it must be another variant, suggesting that this exchanger also has at least two isoforms.

The *Na^+-HCO_3^- co-transporter* (NBC) (see model 5 in Fig. 17.5B) was originally identified in renal epithelial cells but has since been found in a number of other cell types as well. It mediates the movement of one Na^+ with one, two or three HCO_3^-, depending on the cell type in which the transporter is located, and can thus be either electroneutral (NBCe) or electrogenic (NBCn). This transporter differs from the other HCO_3^--dependent transporters in that it does not require Cl^- and, in the case where the stoichiometry is 1:2 or 1:3, it is electrogenic. In proximal tubule epithelial cells, NBC is involved in HCO_3^- reabsorption by mediating HCO_3^- efflux across the basolateral membrane. In other cells, the co-transporter is proposed to mediate HCO_3^- influx and contribute to the regulation of intracellular pH in the face of an acid load. The renal co-transporter (1:3 stoichiometry) has been suggested to involve the co-transport of one Na^+ with one HCO_3^- and one CO_3^{2-}. NBCn transporters are widely expressed and play a role in maintaining pH_i and in the secretion of cerebrospinal fluid.

The NBC and several of its variants have been cloned. The first mammalian NBC to be cloned is from rat kidney (rkNBC). This is a glycoprotein consisting of 1035 amino acids ($M_r \approx 130\,000$). Its structure is similar to other members of the Na^+-HCO_3^--coupled transporters (NCBT: NBCs and NDCBE), includes 12–14 membrane-spanning domains, a large extracellular loop between membrane-spanning segments 5 and 6 that can be glycosylated and large cytoplasmic domains (one each at the N- and C-terminal ends), with the N-terminus domain being the largest. These cytoplasmic domains are probably the site of co-transport regulation and contain putative phosphorylation sites for protein kinases A and C, casein kinase II and tyrosine kinase. A human kidney clone (hkNBC), with 97%

homology to rkNBC, has also been described. These kidney NBCs are electrogenic, with a stoichiometry of one Na^+ transported for every three HCO_3^- ions.

An NBC from human heart (hhNBC) has been described. This clone (along with an identical one from human pancreas) is identical to rkNBC, except that hhNBC has a longer N-terminus (by 44 amino acids); hhNBC is also electrogenic, but with a stoichiometry of 1:2. A similar clone has been isolated from rat brain (rbNBC). This clone has longer C- and N-terminal ends, a stoichiometry of 1:2 and is predominantly localized to cortical neurons but not astrocytes. Finally, a novel clone has been isolated from vascular smooth muscle cells (also found in testis and spleen cells). This clone (NBCn1) has a very large N-terminus, is electroneutral (stoichiometry of 1:1) and is apparently not inhibited by DIDS. These NBC clones are about 30–35% identical to AE transport proteins, indicating that these transporters are indeed part of the SLC4 superfamily.

VIIC. H^+-ATPases (Proton Pumps)

There are at least three known varieties of *H^+-ATPases*: (1) F_0-F_1-type ATPase; (2) E_1-E_2 or P-type ATPase; and (3) vacuolar or V-type ATPase. The *F_0-F_1-type ATPase* is found in mitochondria. This ATPase has also been called the ATP synthase, since it functions to produce ATP when H^+ moves down its electrochemical gradient. F_0-F_1-type ATPase has a lollipop shape and a membrane-spanning region, F_0, that forms the putative H^+ pore through the membrane as well as an extrinsic head region, F_1, that contains the ATPase activity. The F_0 subunit is quite large, with five subunits and a molecular weight of about 380 000. The F_1 region has four subunits and a molecular weight of about 100 000. These two regions are connected by a stalk that contains several subunits, one of which confers sensitivity to oligomycin. The F_0-F_1-type ATPase can be inhibited by azide and N, N'-dicyclohexylcarbodiimide (DCCD) in addition to oligomycin.

The *P-type ATPases* (see model 6 in Fig. 17.5C) are characterized by forming a phosphorylated intermediate upon ATP hydrolysis. The classic example of such an ATPase is the Na^+, K^+-ATPase. An example of a P-type H^+-ATPase is the H^+, K^+-ATPase, best characterized from the apical membrane of gastric glands, where it is responsible for acid secretion into the stomach. This ATPase has also been implicated in the acidification of the urine and reabsorption of K^+ by the kidney and in the establishment of an H^+ gradient across yeast plasma membrane. In contrast to the F_0-F_1-ATPase, the H^+, K^+-ATPase exchanges one K^+ for one H^+ and is thus electroneutral. The H^+, K^+-ATPase has a molecular weight of about 110 000 and has a structure similar to those of other membrane-bound ATPases with several membrane-spanning regions and a large cytoplasmic domain containing the ATP hydrolysis site. Inhibition by vanadate is characteristic for P-type ATPases.

The third type of H^+-ATPase is the vacuolar, or V-type, ATPase (see model 7 in Fig. 17.5C) which is found in yeast and plant vacuoles as well as in several eukaryotic cells (e.g. kidney cells, osteoclasts and macrophages) and organelles (e.g. endosomes, lysosomes, secretory granules and Golgi apparatuses). *V-type ATPases* are more like the F_0-F_1-type ATPase than the P-type ATPase in that they do not form phosphorylated intermediates, are quite large (>400 kDa), assume a lollipop shape and are electrogenic. The major function of V-type ATPases is the acidification of intracellular organelles (see Section VB), which is important for proper protein targeting and handling. These ATPases are characterized by their lack of sensitivity to vanadate and oligomycin and by their inhibition by N-ethylmaleimide (NEM), DCCD and bafilomycin. While P- and F_0-F_1-type ATPases are found in both prokaryotes and eukaryotes, the V-type ATPases are only found in eukaryotes and, therefore, presumably evolved more recently.

VIID. Na^+-Organic Anion Co-transport

In a variety of organisms, renal proximal tubule cells have been shown to have *Na^+-organic anion co-transporters* (model 1 in Fig. 17.7). These co-transporters mediate the influx of a Na^+ with the conjugate base of an organic weak acid, such as lactate or acetate. Such co-transport would cause cellular alkalinization due to the entry of base. The base would bind a proton upon entry and alkalinize the cell. These transport systems are likely to be part of a mechanism designed for the transepithelial movement of organic molecules and should be considered to *affect* pH_i rather than *regulate* it.

VIIE. Chloride-Organic Anion Exchange

Another class of organic anion transporters has been described in renal proximal tubule cells. These transporters involve the exchange of organic anions for inorganic anions such as Cl^- or OH^-. For example, as part of the mechanism for NaCl reabsorption, an exchanger that mediates Cl^- influx (from the lumen) in exchange for formate efflux resides in the apical membrane of proximal tubule epithelia. This *Cl^--formate exchanger* (model 2 in Fig. 17.7) can be inhibited by disulfonic stilbene derivatives and is functionally similar to the Cl^--HCO_3^- exchanger. However, the Cl^--formate exchanger is distinct from the Cl^--HCO_3^- exchanger. The operation of this transporter during NaCl reabsorption should result in epithelial cell acidification. Other transporters involve the movement of organic anions including urate and oxalate. When these

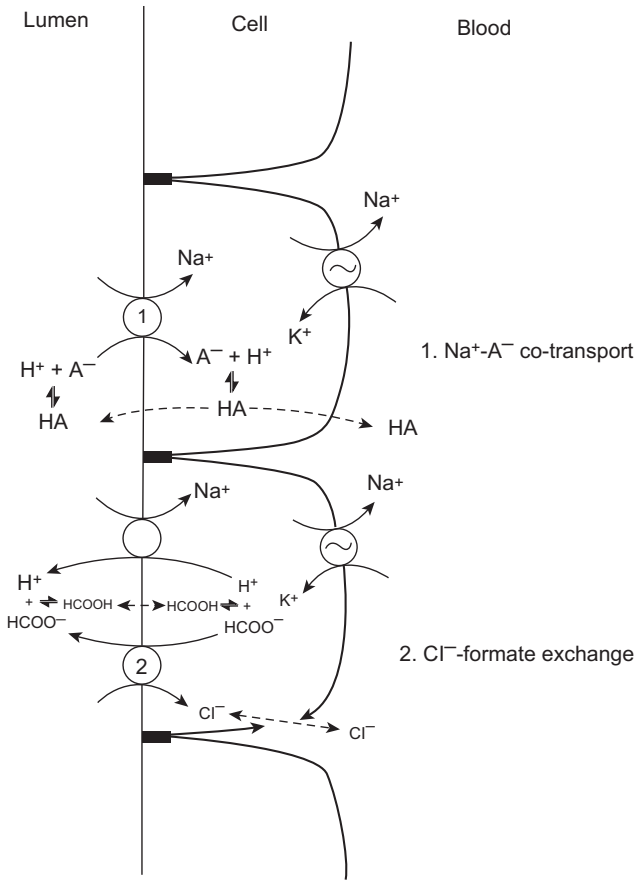

FIGURE 17.7 A model of anionic weak base fluxes in the renal proximal tubule mediated by either co-transport with Na^+ (1) or in exchange for Cl^- (2). An example of 1 is the Na^+-acetate co-transporter. The Cl^--formate exchanger is depicted by 2. These transporters are apparently involved in the luminal entry of Na^+ or Clin NaCl-reabsorbing epithelia like the renal proximal tubule. Solid lines represent ion fluxes mediated by membrane transporters. Dotted lines represent passive diffusion of molecules across the membrane. Cl^- movements across the basolateral membrane are mediated by an ion-selective Cl^- channel.

anions are transported into the cell, they will result in cellular alkalinization.

VIII. CELLULAR FUNCTIONS AFFECTED BY INTRACELLULAR pH

A wide variety of cellular processes and properties are affected by intracellular pH and perhaps in some way all cell functions are influenced by the level of pH_i. It is impossible to discuss all of the various effects, but many of the most important will be highlighted in the following sections (Fig. 17.8).

VIIIA. Cellular Metabolism

The fact that cellular metabolism can affect pH_i was discussed previously (see Section VIA). It has been appreciated for many years that the converse is also true; i.e. changes of pH_i can affect cellular metabolism. Theoretically, because pH will affect the charge on ionizable groups in proteins, it would be anticipated that changes in pH_i could change the configuration of proteins and affect their activity. Such an effect of pH_i has been well documented for two key metabolic enzymes. Phosphofructokinase, a key glycolytic enzyme that converts fructose 6-phosphate (F6P) to fructose 1,6-diphosphate (FDP), has an exquisite pH sensitivity in the physiological range (6.5−7.5), its activity decreasing with a decrease of pH_i. The actual pH sensitivity is dependent on the cellular levels of F6P and 5′-AMP. Similarly, the conversion of phosphorylase (which catalyzes the metabolism of glycogen) from its inactive to active form is inhibited by a decrease in pH_i.

Two observations can be made from these findings. First, the pH dependence of enzyme activity is often affected by the concentrations of other factors, including substrates and other effectors. Thus, caution must be exercised in relating the in vitro pH profile of an enzyme to cellular conditions. Second, the general reaction of metabolic enzymes to a decrease in pH is a reduction in activity. This suggests that a decrease in pH_i could be used to prevent growth or to put a cell in a dormant state, as has been observed for many cells (see Section VIIIG).

VIIIB. Cytoskeleton

Changes in pH_i have been shown to affect the cytoskeleton, which can lead to changes in cell shape or motility. One example of such an effect on the cytoskeleton is the pH dependence of *actin filament* cross-linking to form gels. This cross-linking is mediated by actin-binding proteins whose ability to interact with actin is pH dependent. In some cases, cell alkalinization increases the actin cross-linking to form a gel state in the cytoplasm or to form networks of microfilament bundles. In other cells, alkalinization reduces the cross-linking of actin filaments. The cell-specific responses of cytoskeletal cross-linking are probably due to different pH profiles of actin-binding proteins from different cells.

Changes in cellular pH can also affect the polymerization of cytoskeletal elements, such as *tubulin*. It has been shown that, in some cells, alkalinization can cause depolymerization of tubulin and disaggregation of microtubules within the cell. There are probably many other pH-dependent components to cytoskeletal assembly and function. It should be pointed out, however, that the conditions that lead to a change in pH_i are often accompanied by changes in intracellular calcium concentration and by phosphorylation of the cytoskeleton and it is not always clear which is the predominant effector of cytoskeletal changes. Nevertheless, it is clear that changes in

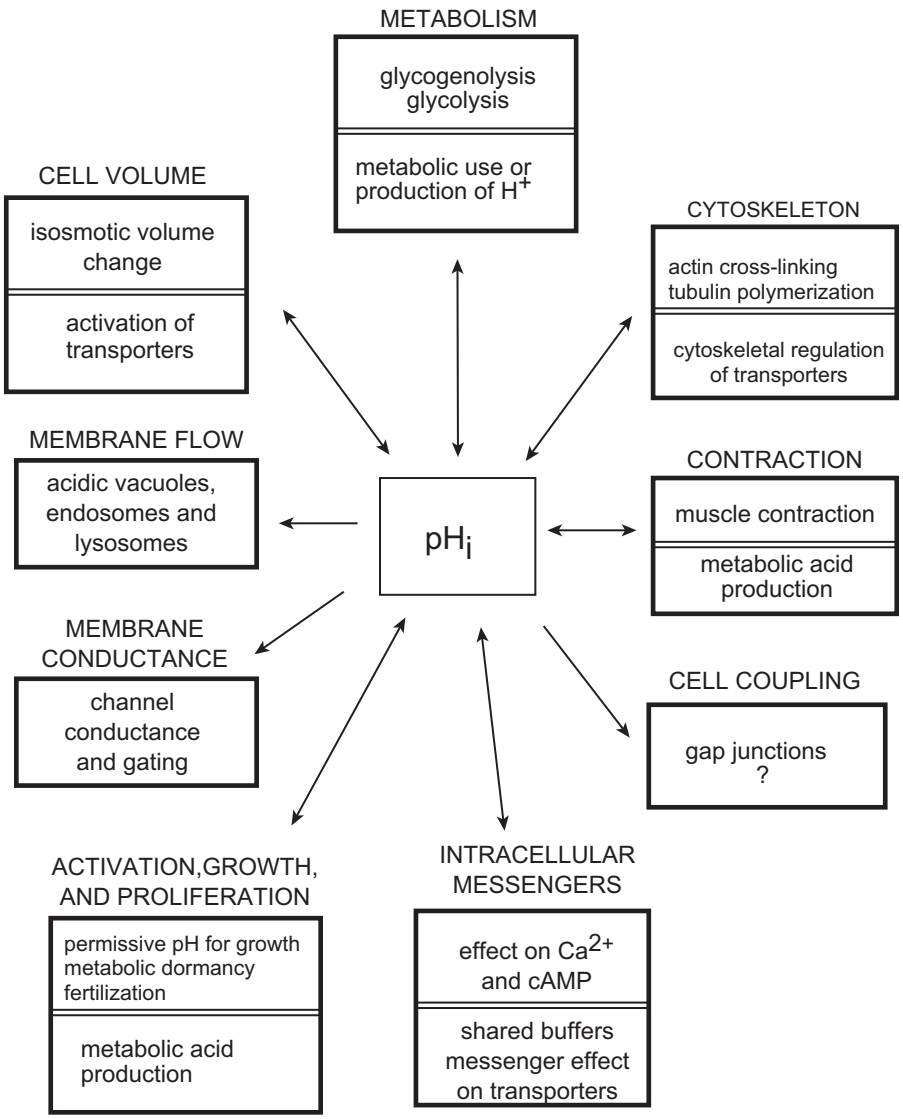

FIGURE 17.8 A summary of the cellular processes affected by intracellular pH. Each box represents a different cellular process. A two-headed arrow indicates that pH_i affects the process and that the process can also affect pH_i. Single-headed arrows suggest that pH affects that cellular function but that the cellular process probably does not have a major impact on pH_i. Within a box, the top half indicates the cellular processes affected by pH_i, while the bottom half indicates the mechanisms by which the process can affect pH_i.

pH_i can play a major modulatory role in at least some alterations of the cytoskeleton.

VIIIC. Muscle Contraction

Intracellular acidification is known to reduce the ability of contractile cells to generate tension. This effect is particularly marked in cardiac muscle, but skeletal muscle also shows a reduced contractility at acidic values of pH_i. There are several possible ways by which cellular acidification could influence contractility: changes in surface channels could reduce cellular excitability, low pH could prevent calcium release from the sarcoplasmic reticulum through the calcium release channel, protons could compete with calcium for binding to the regulatory protein troponin, protons could inhibit the myofibrillar ATPase, or acidification could impair the ability of the cell to generate ATP. The effect of pH on muscle contraction could also be indirect. For example, during intense muscle activity, inorganic phosphate (P_i) accumulates in the cell. A reduced pH will increase the diprotonated form of P_i ($H_2PO_4^-$), which has been shown to be particularly effective in inhibiting muscle force development during muscle fatigue.

VIIID. Cell–Cell Coupling

The coupling of cells through *gap junctions* is apparently affected by intracellular pH. Several studies have suggested that a fall in pH_i uncouples gap junctions, thereby eliminating cell–cell coupling. The direct role of pH_i in the uncoupling process has been questioned and it appears that

changes in intracellular Ca^{2+} levels are responsible for uncoupling in some cells. The control of gap junction conductance may differ from cell to cell, but even in cells where Ca^{2+} is the primary regulator, changes in pH_i probably still have a modulatory effect on gap junction conductance.

VIIIE. Membrane Conductance

Ion-selective channels require the presence of charges within the channel proteins for proper ion conduction and channel gating. If these charges have p*K* values within the physiological range, these channels could well be affected by changes in pH. Indeed, the conductances of many channels are affected by changes in either pH_o or pH_i, including the tetrodotoxin-sensitive Na^+ channel, the delayed-rectifying and inward-rectifying K^+ channels and Cl^- channels. Through the effect on conductance of membrane channels, changes in pH can affect the excitability of nerve and muscle cells and alter the membrane potential in all cells.

One interesting pH-sensitive K^+ channel has been described, the TASK channel (for TWIK-related acid-sensitive K^+ channel). The TASK channel exhibits rectification in asymmetric K^+ solutions that is consistent with the Goldman–Hodgkin–Katz equation, is non-inactivating, is not voltage sensitive and is highly sensitive to changes in *external* pH, with channel conductance falling with decreased pH_o. This type of leak channel is believed to be partly responsible for the resting membrane potential (especially in pancreas, placenta and brain cells) and could explain the relationship between changes of pH_o and membrane potential in these cells.

VIIIF. Intracellular Messengers

Changes in pH_i can affect the levels of important intracellular signaling molecules, such as Ca^{2+} and cAMP. There are several possible ways by which pH can affect intracellular Ca^{2+}. An elevation of cytoplasmic H^+ can activate mitochondrial Ca^{2+}-H^+ exchange, resulting in a sequestering of H^+ within the mitochondria and an elevation of cytoplasmic $[Ca^{2+}]$. A decreased pH_i can reduce Ca^{2+} entry across the plasmalemma. The most direct interaction between cytoplasmic H^+ and Ca^{2+} ions, however, results from shared buffers. Many molecules that buffer H^+ will also bind, and thus buffer, Ca^{2+}. Depending on the relative affinities, an elevation of cytoplasmic $[H^+]$ can elevate intracellular $[Ca^{2+}]$ by displacing Ca^{2+} ions from intracellular buffer sites.

The interaction between changes of pH_i and $[Ca^{2+}]_i$ can also be indirect. An example of such an interaction is the pH-dependence of the binding of Ca^{2+} to calmodulin. Under certain conditions, a decrease in pH can be shown to reduce the binding of Ca^{2+} to calmodulin. Another example of the interaction between pH and Ca^{2+} is the pH-dependence of the interaction of the Ca^{2+}–calmodulin complex with other proteins, the direction of which depends on the protein being considered. Thus, the potential exists for changes of pH_i to alter the effect of Ca^{2+} on cellular function.

Changes of pH_i could affect another important intracellular signaling pathway as well, that involving cAMP. The proposed effects of pH_i on cAMP are based on the pH dependence of adenylyl cyclase (AC – the enzyme that synthesizes cAMP) and the cyclic nucleotide phosphodiesterase (PDE – the enzyme that hydrolyzes cAMP). In most cells, PDE apparently has a rather constant activity over the physiological range of pH (6.5–7.5). However, depending on the cell, an increase in pH can either markedly increase or decrease AC activity. Thus, alkalinization can result in either an increase or a decrease in cellular cAMP levels.

Given the pervasive effect of changes of pH_i on proteins, it is likely that pH_i effects on other signaling pathways, such as those mediated by cGMP or phosphoinositide metabolism, also exist. It should be noted, however, that the physiological significance of these pH_i effects on signaling pathways is often not clear, especially for cells that normally should see only small fluctuations of pH_i.

Some cells in the body function to sense changes in external pH, either in direct response to external acid (acid-sensing taste bud cells) or to elevated external CO_2 (glomus cells of the carotid body and central chemosensitive neurons). In these cells, extracellular acidification results in a *maintained* intracellular acidification, with pH recovery mechanisms being inhibited (most likely by decreased pH_o). It is believed that this decrease in pH_i inhibits K^+ channels, resulting in cell depolarization and increased generation of action potentials. Thus, in these chemosensitive cells, a decrease in pH_i apparently acts as an intracellular signal.

VIIIG. Cell Activation, Growth and Proliferation

One of the most active areas of research on the role of intracellular pH in cell function has been the study of the role of changes of pH_i early in cell proliferation. These studies grew out of early observations that, shortly after fertilization of sea urchin eggs, egg pH increased markedly (roughly 0.4 pH unit) and this rise in pH was necessary for the initiation of growth by fertilization. These observations were followed by others on mammalian cells showing that a variety of growth-promoting agents, including epidermal growth factor (EGF), platelet-derived growth factor (PDGF), insulin, vasopressin and serum albumin, similarly

induced a cellular alkalinization (of about 0.1−0.2 pH unit) shortly after exposure. All of these alkalinizing effects are mediated by activation of Na^+-H^+ exchange. These growth-promoting agents activate the exchanger by activating cellular signaling pathways, which increase the affinity of the exchanger for internal H^+ ions and increase its activity, thereby alkalinizing the cell (see arrow 1 in Fig. 17.3).

It was initially hypothesized that the growth factor-induced increase in pH was part of a suite of early signals that are required for initiation of cell growth and proliferation. Cellular alkalinization was believed to contribute to the initiation of growth by activating key cellular enzymes that were then either direct effectors of growth (e.g. metabolic enzymes) or activators of other systems.

The direct signaling role of increases of pH_i in cell activation has been questioned. Changes in pH_i by themselves do not promote cell growth or division. Further, it has been shown that a number of cells have a higher pH_i in the presence of 5% CO_2 than in its absence. However, most of the initial experiments on the pH_i responses to growth factors had been done in the absence of CO_2. Upon repeating a number of these experiments under conditions more similar to physiological conditions (presence of 5% CO_2), the initial alkalinization upon exposure to stimulatory factors was not always seen and, in some cells, the initial response was indeed an *acidification*. Thus, the current view of the role of pH_i in cell activation, growth and proliferation is that pH_i plays a permissive role. That is, cells will only grow and proliferate if pH_i is above a certain critical value, regardless of how that value is obtained. If a cell had a pH_i above the critical value before exposure to a stimulatory agent, no change in pH_i would be required for cell growth. In fact, the cell could acidify and still grow as long as its pH_i stays above the critical value.

In reality, the role of pH_i as a signal to initiate cell growth may depend on the cell and the activating agent. It is likely that a rapid and marked rise in pH_i is one of the critical early steps necessary for the initiation of growth in fertilized sea urchin eggs. Even more dramatic is the nearly 1-pH-unit increase of pH_i in *Artemia* (brine shrimp) embryos upon arousal from anaerobic dormancy by exposure to oxygen. Undoubtedly, this large rise in pH_i is crucial for the transition from metabolic dormancy in these organisms. On the other hand, in many mammalian cells, the rather modest increase in pH_i on exposure to an activating agent is probably of limited physiological significance, especially given the variability in the degree and direction of pH changes observed in different experimental conditions.

Finally, even under conditions where a change of pH_i is not observed in response to a stimulatory agent, pH-regulating transport systems can still be shown to be activated. It has been hypothesized that, although a change of pH_i may not be crucial for the stimulation of cell growth, the initiation of this growth may confront the cell with an acid or alkaline load. In this regard, activation of the pH-regulating transport systems by growth-promoting agents could be viewed as preparatory, enabling the cell better to maintain a constant pH_i during a period of high metabolic activity.

VIIIH. Cell Volume Regulation

Most pH-regulating transporters move ions such as Na^+ and Cl^- in exchange for a proton equivalent (H^+ or HCO_3^-). Because the transported proton equivalents are buffered (H^+ by HCO_3^- and protein buffers and HCO_3^- by formation of CO_2), they are osmotically "invisible". For example, virtually all of the H^+ transported by the Na^+-H^+ exchanger derive from internal buffers and upon efflux from the cell are buffered by external buffers. Thus, the Na^+-H^+ exchanger mediates the net import of one osmotically active particle (Na^+) and this import of osmolytes will be accompanied by the influx of water and cell swelling. Therefore, the Na^+-H^+ exchanger, in addition to contributing to pH_i regulation, can mediate the regulation of cell volume.

Other pH-regulating transporters can similarly mediate cell volume changes. For example, the Cl^-- HCO_3^- exchanger transports Cl^- into the cell. The HCO_3^- that leaves combines with an H^+ and is removed as CO_2. Thus, like Na^+-H^+ exchange, Cl^--HCO_3^- exchange contributes to cell swelling. In fact, these two exchangers often act in concert to result in the net influx of NaCl (and therefore water) into the cell. The Na^+-HCO_3^- and Na^+-anionic weak base co-transporters would be ideally suited to mediate net solute transfer and therefore cell volume change. Finally, the (Na^++HCO_3^-)-Cl^- exchanger should not contribute to cell volume regulation because it mediates the entry of one osmotically active ion (Na^+) for the efflux of another (Cl^-).

Cell volume can be rapidly changed by exposure to anisosmotic media, with hypertonic media causing cell shrinkage and hypotonic media causing cell swelling. Many cells respond to shrinkage with a *regulatory volume increase* (RVI) that involves the net uptake of solutes, and therefore water, so that cells swell back toward the initial cell volume (Fig. 17.9). In several different types of cells, RVI has been shown to involve an activation of Na^+-H^+ exchange. This exchanger, often in association with the Cl^--HCO_3^- exchanger, results in NaCl influx and a regulatory volume increase. The mechanism by which cell shrinkage activates the Na^+-H^+ exchanger is not fully understood but, interestingly, unlike most other activation pathways, cell shrinkage apparently does not result in phosphorylation of the exchanger. It is possible that the cell cytoskeleton is involved in activating the Na^+-H^+ exchanger upon cell shrinkage.

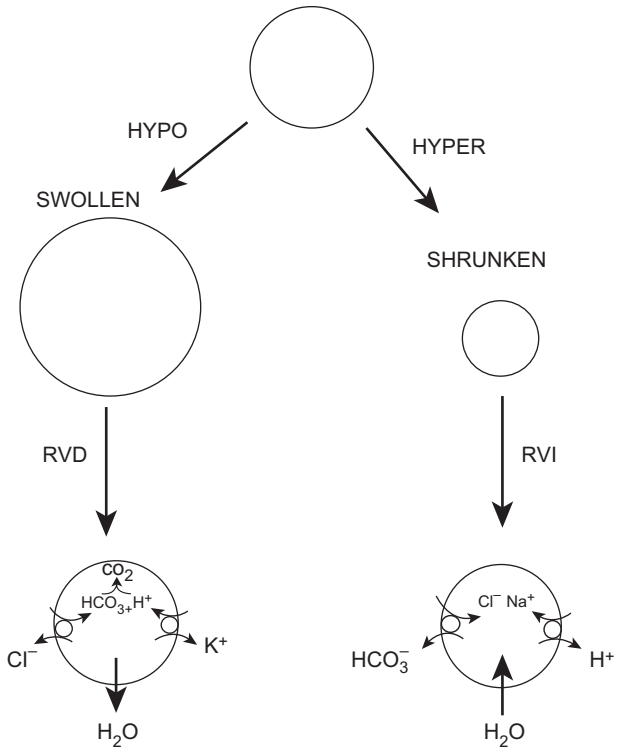

FIGURE 17.9 The role of pH-regulating transporters in cellular volume regulation. Upon cell swelling in hypotonic media, KCl has been shown to be removed from nucleated red blood cells by functionally coupled operation of the K^+-H^+ and the Cl^--HCO_3^- exchangers. The removal of KCl from the cell causes a loss of water from the cell and thus cell shrinkage in a process called regulatory volume decrease (RVD). Upon cell shrinkage in hypertonic media, NaCl enters the cell by parallel operation of Na^+-H^+ and Cl^--HCO_3^- exchangers. The NaCl entry results in water influx and cell swelling in a process called regulatory volume increase (RVI).

Recently, it has been shown that shrinkage can also activate (Na^++ HCO_3^-)-Cl^- exchange in some cells. This observation is interesting since, as stated previously, this exchanger does not mediate any net solute movement and thus should not directly contribute to cell volume regulation. This activation of (Na^++HCO_3^-)-Cl^- exchange by cell shrinkage suggests that pH-regulating transporters may be activated by shrinkage to alkalinize the cell regardless of whether they contribute to volume regulation. It is not clear what benefit a shrunken cell derives from becoming alkaline, but it may involve pH-dependent cytoskeletal rearrangements (see Section VIIIB).

In response to swelling, most cells exhibit a *regulatory volume decrease* (RVD). RVD involves the efflux of solutes accompanied by water and therefore cell shrinkage back toward the initial cell volume (see Fig. 17.9). In at least one cell type, the nucleated red blood cell, RVD has been shown to be mediated by K^+-H^+ exchange (K^+ efflux and H^+ influx) in association with Cl^--HCO_3^- exchange (Cl^- efflux and HCO_3^- influx).

Cell volume can also be altered under isosmotic conditions by an imbalance of solute influx and efflux. For instance, during periods of active pH recovery from acidification, the Na^+ influx mediated by the Na^+-H^+ exchanger could result in cell swelling. Thus, changes in pH_i and the response to them could result in an alteration of cell volume.

It is clear that the regulation of intracellular volume and intracellular pH are highly linked in most cells. This linkage is due in part to the use of many of the same membrane transport systems for the regulation of cell pH and volume. In any given cell type, these transporters may respond predominantly either to changes in pH_i or to changes in cell volume.

VIIII. Intracellular Membrane Flow

The intracellular flow of membranes is affected by changes of pH within acidic vacuolar compartments. In cells, these vacuolar compartments are often involved in the movement of membranes, membrane-bound proteins and soluble proteins around the cell. In addition, components of the vacuolar system are involved in the synthesis, processing and degradation of various proteins. This system includes the endoplasmic reticulum, the Golgi apparatus, lysosomes and endosomes. Movement of materials through this system can be divided into the endocytic and exocytic pathways. The endocytic pathway is involved in the uptake of external macromolecules, the degradation or delivery to the cell of these macromolecules and the downregulation of surface proteins; it includes coated pits, endosomes and lysosomes. The exocytic pathway delivers newly-synthesized proteins to a variety of sites, including the surface membrane or extracellular space. Many of the compartments within this vacuolar system are acidic (see Section VB) and the maintenance of an acidic interior is critical for the functioning of these compartments. This criticality has been shown by the marked disturbance of endocytic and exocytic pathways by a number of agents, such as chloroquine and ammonia, which alkalinize these compartments. In addition, inhibition of vacuolar H^+-ATPase results in alkalinization of the acidic compartments and can lead to inhibition of endocytosis and exocytosis. Thus, the maintenance of a proper pH in acidic intracellular compartments is crucial for continued and proper intracellular membrane flow.

BIBLIOGRAPHY

Al-Awqati, Q. (1986). Proton-translocating ATPases. *Annu Rev Cell Biol, 2*, 179–199.

Alper, S. L. (2009). Molecular physiology and genetics of Na^+-independent SLC4 anion exchangers. *J Exp Biol, 212*, 1672–1683.

Ammann, D., Lanter, F., Steiner, R. A., Schulthess, P., Shijo, Y., & Simon, W. (1981). Neutral carrier based hydrogen ion selective

microelectrode for extra- and intracellular studies. *Anal Chem, 53*, 2267−2269.

Aronson, P. S. (1989). The renal proximal tubule: a model for diversity of anion exchangers and stilbene-sensitive anion transporters. *Annu Rev Physiol, 51*, 419−441.

Aronson, P. S., & Boron, W. F. (Eds.), (1986). *Na^+-H^+ Exchange, Intracellular pH, and Cell Function, Vol. 26 in Current Topics in Membranes and Transport*. New York: Academic Press.

Aronson, P. S., Nee, J., & Suhm, M. A. (1982). Modifier role of internal H^+ in activating the Na^+-H^+ exchanger in renal microvillus membrane vesicles. *Nature, 299*, 161−163.

Attaphitaya, S., Park, K., & Melvin, J. E. (1999). Molecular cloning and functional expression of a rat Na^+/H^+ exchanger (NHE5) highly expressed in brain. *J Biol Chem, 274*, 4383−4388.

Baird, N. R., Orlowski, H., Szabo, E. Z., et al. (1999). Molecular cloning, genomic organization, and functional expression of Na^+/H^+ exchanger isoform 5 (NHE5) from human brain. *J Biol Chem, 274*, 4377−4382.

Bell, S. M., Schreiner, C. M., Schultheis, P. J., et al. (1999). Targeted disruption of the murine Nhe1 locus induces ataxia, growth retardation, and seizures. *Am J Physiol, 276*, C788−C795.

Bidani, A., & Brown, S. E. S. (1990). ATP-dependent recovery in lung macrophages: evidence for a plasma membrane H^+-ATPase. *Am J Physiol, 259*, C586−C598.

Bock, G., & Marsh, J. (1988). *Proton Passage across Cell Membranes. Ciba Foundation Symposium 139*. New York: Wiley.

Boron, W. F. (1986). Special topic: acid/base physiology. *Annu Rev Physiol, 48*, 347−413.

Boron, W. F., & Boulpaep, E. L. (1983). Intracellular pH regulation in the renal proximal tubule of the salamander. Basolateral H cotransport. *J Gen Physiol, 81*, 53−94.

Boron, W. F., & De Weer, P. (1976). Intracellular pH transients in squid giant axons caused by CO_2, NH_3, and metabolic inhibitors. *J Gen Physiol, 67*, 91−112.

Boron, W. F., Chen, L., & Painter, M. D. (2009). Modular structure of sodium-coupled bicarbonate transporters. *J Exp Biol, 212*, 1697−1706.

Busa, W. B., & Nuccitelli, R. (1984). Metabolic regulation via intracellular pH. *Am J Physiol, 246*, R409−R438.

Cala, P. M. (1980). Volume regulation by Amphiuma red blood cells. The membrane potential and its implications regarding the nature of the ion-flux pathways. *J Gen Physiol, 76*, 683−708.

Capasso, M., DeCoursey, T. E., & Dyer, M. J. S. (2011). pH regulation and beyond: unanticipated functions for the voltage-gated proton channel, HVCN1. *Trends Cell Biol, 21*, 20−28.

Chamberlin, M. E., & Strange, K. (1989). Anisosmotic cell volume regulation: a comparative view. *Am J Physiol, 257*, C159−C173.

Chesler, M. (2003). Regulation and modulation of pH in the brain. *Physiol Rev, 83*, 1183−1221.

Counillon, L., & Pouysségur, J. (1995). Structure-function studies and molecular regulation of the growth factor activatable sodium-hydrogen exchanger (NHE-1). *Cardiovasc Res, 29*, 147−154.

DeCoursey, T. E., & Cherney, V. V. (1994). Voltage-activated hydrogen ion currents. *J Membr Biol, 141*, 1994.

Duprat, F., Lessage, F., Fink, M., Reyes, R., Heurteaux, C., & Lazdunski, M. (1997). TASK, a human background K^+ channel to sense external pH variations near physiological pH. *EMBO J, 16*, 5464−5471.

Durham, J. H., & Hardy, M. A. (Eds.), (1989). *Bicarbonate, Chloride, and Proton Transport Systems, Vol. 574*. New York: New York Academy of Sciences.

Edmonds, B. T., Murray, J., & Condeelis, J. (1995). pH regulation of the F-actin binding properties of Dictyostelium elongation factor 1a. *J Biol Chem, 270*, 15222−15230.

Gevers, W. (1977). Generation of protons by metabolic processes in heart cells. *J Molec Cell Cardiol, 9*, 867−874.

Grinstein, S. (1996). Non-invasive measurement of the luminal pH of compartments of the secretory pathway. *Physiologist, 39*, 144.

Grinstein, S. (Ed.), (1988). *Na^+/H^+ Exchange*. Boca Raton: CRC Press.

Grinstein, S., & Rothstein, A. (1986). Mechanisms of regulation of the Na^+/H^+ exchanger. *J Membr Biol, 90*, 1−12.

Häussinger, D. (Ed.), (1988). *pH Homeostasis. Mechanisms and Control*. New York: Academic Press.

Hille, B. (1992). *Ionic Channels of Excitable Membranes*. Sunderland, MA: Sinauer Associates.

Hochachka, P. W., & Mommsen, T. P. (1983). Protons and anaerobiosis. *Science, 219*, 1391−1397.

Hoffmann, E. K., & Simonsen, L. O. (1989). Membrane mechanisms in volume and pH regulation in vertebrate cells. *Physiol Rev, 69*, 315−382.

Karniski, L. P., & Aronson, P. S. (1985). Chloride/formate exchange with formic acid recycling: a mechanism of active chloride transport across epithelial membranes. *Proc Natl Acad Sci USA, 82*, 6362−6365.

Kopito, R. R., & Lodish, H. F. (1985). Primary structure and transmembrane orientation of the murine anion exchange protein. *Nature, 316*, 234−238.

Kotyk, A., & Slavik, J. (1989). *Intracellular pH and Its Measurement*. Boca Raton: CRC Press.

Llopis, J., McCaffery, J. M., Miyawaki, A., Farquhar, M. G., & Tsien, R. Y. (1998). Measurement of cytosolic, mitochondrial, and Golgi pH in single living cells with green fluorescent proteins. *Proc Natl Acad Sci USA, 95*, 6803−6808.

Lowe, A. G., & Lambert, A. (1983). Chloride-bicarbonate exchange and related transport processes. *Biochim Biophys Acta, 694*, 353−374.

Madshus, I. H. (1988). Regulation of intracellular pH in eukaryotic cells. *Biochem J, 250*, 1−8.

Masuda, A., Oyamada, M., Nagaoka, T., Tateishi, N., & Takamatsu, T. (1998). Regulation of cytosol-nucleus pH gradients by K^+/H^+ exchange mechanism in the nuclear envelope of neonatal rat astrocytes. *Brain Res, 807*, 70−77.

Murer, H., Hopfer, U., & Kinne, R. (1976). Sodium/proton antiport in brush-border membranes isolated from rat small intestine and kidney. *Biochem J, 154*, 597−604.

Noël, J., & Pouysségur, J. (1995). Hormonal regulation, pharmacology, and membrane sorting of vertebrate Na^+/H^+ exchanger isoforms. *Am J Physiol, 268*, C283−C296.

Nosek, T. M., Fender, K. Y., & Godt, R. E. (1987). It is diprotonated inorganic phosphate that depresses force in skinned skeletal muscle fibers. *Science, 236*, 191−193.

Nuccitelli, R., & Deamer, D. W. (Eds.), (1981). *Intracellular pH: its Measurement, Regulation, and Utilization in Cellular Function*. New York: A. R. Liss.

Orlowski, J., & Grinstein, S. (2004). Diversity of the mammalian sodium/proton exchanger SLC9 gene family. *Pflügers Arch, 447*, 549−565.

Palokangas, H., Metsikkö, K., & Väänänen, K. (1994). Active vacuolar H^+ ATPase is required for both endocytic and exocytic processes during viral infection of BHK-21 cells. *J Biol Chem, 269*, 17577−17585.

Pouysségur, J., Sardet, C., Franchi, A., L'Allemain, G., & Paris, S. (1984). A specific mutation abolishing Na^+/H^+ antiport activity in hamster fibroblasts precludes growth at neutral and acidic pH. Proc Natl. *Acad Sci USA, 81*, 4833−4837.

Putnam, R. W. (2010). CO_2 chemoreception in cardiorespiratory control. *J Appl Physiol, 108*, 1796−1802.

Putnam, R. W., Filosa, J. A., & Ritucci, N. A. (2004). Cellular mechanisms involved in CO_2 and acid signaling in chemosensitive neurons. *Am J Physiol Cell Physiol, 287*, C1493−C1526.

Reusch, H. P., Lowe, J., & Ives, H. E. (1995). Osmotic activation of a Na^+-dependent Cl^-/HCO_3^- exchanger. *Am J Physiol, 268*, C147−C153.

Rink, T. J., Tsien, R. Y., & Pozzan, T. (1982). Cytoplasmic pH and free Mg^{2+} in lymphocytes. *J Cell Biol, 95*, 189−196.

Ritucci, N. A., Chambers-Kersh, L., Dean, J. B., & Putnam, R. W. (1998). Intracellular pH regulation in neurons from chemosensitive and nonchemosensitive areas of the medulla. *Am J Physiol, 275*, R1152−R1163.

Ritucci, N. A., Dean, J. B., & Putnam, R. W. (1997). Intracellular pH response to hypercapnia in neurons from chemosensitive areas of the medulla. *Am J Physiol, 273*, R433−R441.

Romero, M. F., & Boron, W. F. (1999). Electrogenic Na^+/HCO_3^- cotransporters: cloning and physiology. *Annu Rev Physiol, 61*, 699−723.

Roos, A., & Boron, W. F. (1980). The buffer value of weak acids and bases: origin of the concept, and first mathematical derivation and application to physicochemical systems. The work of M. Koppel and K. Spiro (1914). *Respir Physiol, 40*, 1−32.

Roos, A., & Boron, W. F. (1981). Intracellular pH. *Physiol Rev, 61*, 296−434.

Sardet, C., Counillon, L., Franchi, A., & Pouysségur, A. (1990). Growth factors induce phosphorylation of the Na^+/H^+ antiporter, a glycoprotein of 110 kD. *Science, 247*, 723−726.

Sardet, C., Franchi, A., & Pouysségur, J. (1989). Molecular cloning, primary structure, and expression of the human growth factor-activatable Na^+/H^+ antiporter. *Cell, 56*, 271−280.

Schultheis, P. J., Clarke, L. L., Meneton, P., Nieman, M. L., Riddle, T. M., Flagella, M., Duffey, J. J., Doetschman, T., Miller, M. L., & Shull, G. E. (1998). Renal and intestinal absorptive defects in mice lacking the NHE3 Na^+/H^+ exchanger. *Nat Genet, 19*, 282−285.

Schultheis, P. J., Clarke, L. L., Meneton, P., Harline, M., Boiven, G. P., Stemmermann, G., Duffey, J. J., Doetschman, T., Miller, M. L., & Shull, G. E. (1998). Targeted disruption of the murine Na^+/H^+ exchanger isoform 2 gene causes reduced viability of gastric parietal cells and loss of net acid secretion. *J Clin Invest, 101*, 1243−1253.

Seksek, O., & Bolard, J. (1996). Nuclear pH gradient in mammalian cells revealed by laser microspectrofluorimetry. *J Cell Sci, 109*, 257−262.

Seksek, O., Biwersi, J., & Verkman, A. S. (1995). Direct measurement of trans-Golgi pH in living cells and regulation by second messengers. *J Biol Chem, 270*, 4967−4970.

Soleimani, M., & Aronson, P. S. (1989). Ionic mechanism of Na^+-HCO_3^- cotransport in rabbit renal basolateral membrane vesicles. *J Biol Chem, 264*, 18302−18308.

Svichar, N., Esquenazi, S., Chen, H. Y., & Chesler, M. (2011). Preemptive regulation of intracellular pH in hippocampal neurons by a dual mechanism of depolarization-induced alkalinization. *J Neurosci, 31*, 6997−7004.

Thomas, J. A., Buchsbaum, R. N., Zimniak, A., & Racker, E. (1979). Intracellular pH measurements in Ehrlich ascites tumor cells utilizing spectroscopic probes generated in situ. *Biochemistry, 18*, 2210−2218.

Thomas, R. C. (1974). Intracellular pH of snail neurones measured with a new pH-sensitive glass micro-electrode. *J Physiol (London), 238*, 159−180.

Thomas, R. C. (1978). *Ion-sensitive Intracellular Microelectrodes. How to Make and Use Them*. New York: Academic Press.

Trivedi, B., & Danforth, W. H. (1966). Effect of pH on the kinetics of frog muscle phosphofructokinase. *J Biol Chem, 241*, 4110−4111.

Wakabayashi, S., Ikeda, T., Iwamoto, T., Pouysségur, J., & Shigekawa, M. (1997). Calmodulin-binding autoinhibitory domain controls "pH-sensing" in the Na^+/H^+ exchanger NHE1 through sequence-specific interaction. *Biochemistry, 36*, 12854−12861.

Wakabayashi, S., Shigekawa, M., & Pouysségur, J. (1997). Molecular physiology of vertebrate Na^+/H^+ exchangers. *Physiol Rev, 77*, 51−74.

Yun, C. H. C., Tse, C.-M., Nath, S. K., Levine, S. A., Brant, S. R., & Donowitz, M. (1995). Mammalian Na^+/H^+ exchanger gene family: structure and function studies. *Am J Physiol, 269*, G1−G11.

This page intentionally left blank

Section III

Membrane Excitability and Ion Channels

This page intentionally left blank

Chapter 18

Cable Properties and Propagation of Action Potentials

Nicholas Sperelakis

Chapter Outline

I. SUMMARY

Although the *biological cable* (i.e. nerve fiber or skeletal muscle fiber) is the best possible, it is a relatively poor cable with a short *length constant* and relatively long *time constant*. Therefore, for faithful and rapid signal transmission over long distances, energy must be put into the system at each point along the way. The system evolved is that of action potential (AP) generation, which are *all-or-none signals* of constant amplitude and constant propagation velocity, in addition to having refractory periods and sharp thresholds. This is a *frequency-modulated* system, in which increasing strength of sensation or motor response follows from an increase in frequency of the AP signals.

AP propagation occurs by means of *local-circuit currents*. The transmembrane current has three phases: outward, inward and outward. The internal and external longitudinal currents have two phases: forward and backward (for internal) or backward and forward (for external). The external currents use the path of least resistance, enabling *electrograms* (e.g. ECG, EMG) to be recorded from the body surface. The compound AP is graded in amplitude, reflecting the summation of the external currents generated from each fiber that is activated; i.e. the more fibers simultaneously activated, the greater the amplitude of the electrogram signal.

Propagation velocity is faster when (1) the diameter of the fiber is larger, (2) the length constant is longer, and (3) the time constant and capacitance are lower. The *myelin sheath* evolved by vertebrates enables much faster propagation velocity and at a lower energy cost. Myelination raises the effective membrane resistance and lowers the effective capacitance. Excitability occurs only at the short *nodes of Ranvier* that periodically interrupt the myelin sheath. Therefore, the AP signal jumps from node to node in a saltatory pattern of conduction.

Cell Physiology Sourcebook. DOI: 10.1016/B978-0-12-387738-3.00018-4

II. INTRODUCTION

The resting potential (RP) of cells enables the electrogenesis of *action potentials* and excitability. In this chapter, we examine the mechanism for propagation of the APs and excitability from one part of a neuron or muscle to a distal part.

It is imperative that the body be able to transmit a signal from one point to another very rapidly. The only way that this can be accomplished is by an electrical mechanism. Blood flow and diffusion and signaling molecules are much too slow to allow rapid signaling. In contrast, electricity flows very quickly, at the speed of light (3×10^8 m/s) in a copper wire or about one-ninth the speed of light in a water solution (like the composition of the body). (The velocity of electricity in solution is equal to the velocity of light (c) divided by the square root of the dielectric constant of water [which is 81].) Therefore, the body makes use of electricity for rapid signaling in the nervous system, skeletal muscle, heart and smooth muscles. Propagation velocity is about 120 m/s in our fastest nerve fibers, about 6 m/s in skeletal muscle, about 0.5 m/s in heart and about 0.05 m/s in smooth muscle (Table 18.1).

One example of the need for very fast communication or signaling is the process of walking. Very rapid signals must travel from the motor cortex of the brain, down to the lower spinal cord region and out the motor axons to the skeletal muscles of the lower extremities (Fig. 18.1). In this process, the signal crosses one or more *synapses*, which are regions in which one neuron ends and the next one begins and in which a special chemical neurotransmitter signal is involved (Fig. 18.2). At the termination of each branch of a motor nerve axon on the skeletal muscle fiber, there is another synapse, known as the *neuromuscular junction* or *motor end-plate* (see Fig. 18.1). The signal crosses the neuromuscular junction and gives rise to an AP in the muscle fiber that propagates in both directions from the motor end-plate. The muscle AP elicits contraction. Receptors in the muscles (e.g. stretch receptors) transmit information (in the form of propagating APs) back into the central nervous system (CNS). Thus, in walking, there is a continuous rapid flow of information and instructions to the muscles in both directions: out of the CNS and into the CNS. Therefore, even a relatively simple skeletal activity such as walking would not be possible without a very rapid signaling system. To illustrate, in various demyelinating diseases (e.g. caused by some viruses, heavy metals, autoimmune reactions), loss of the myelin sheath around the myelinated nerve fibers causes propagation to become slowed and impaired in the affected nerve fibers, with associated incoordination and partial paralysis.

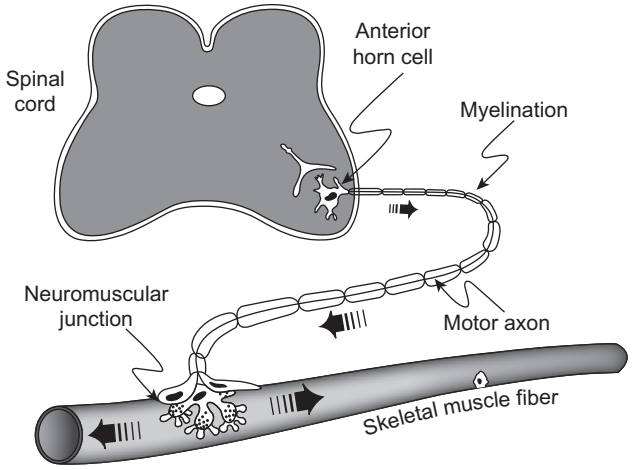

FIGURE 18.1 Schematic diagram of a motor axon, with the cell body (soma) in the anterior horn of the spinal cord and its terminal branches ending on skeletal muscle fibers (only one muscle fiber depicted) to form the neuromuscular junctions (motor end-plates). Each motor axon with its attached skeletal muscle fibers is known as the motor unit. The motor axons are of large diameter (e.g. 20 μm) and are myelinated and therefore propagate at fast velocities (e.g. 120 m/s). As a consequence of the chemical synaptic transmission process at the neuromuscular junction, an AP is initiated in the muscle fiber and propagates in both directions, bringing about contraction.

TABLE 18.1 Conduction Velocity as a Function of Fiber Diameter in Nerve Axons and Muscle Fibers

Fiber Type	Fiber Diameter (μm)	Propagation Velocity (m/s)	Velocity/ Diameter (m/s/μm)
Myelinated axons	20	120	6.0
	12	70	5.8
	5	30	6.0
Non-myelinated axons	1.5	2.0	1.3
	1.0	1.3	1.3
Squid giant axons (20°C)	500	25	0.05
Skeletal muscle fibers	50	6	0.12
Cardiac muscle fibers	15	0.5	0.03
Smooth muscle fibers	5	0.05	0.01

III. FREQUENCY-MODULATED SIGNALS

Because propagating all-or-none APs are all very similar to each other (in shape, duration, amplitude, rate of rise and propagation velocity), to make the signal stronger or weaker,

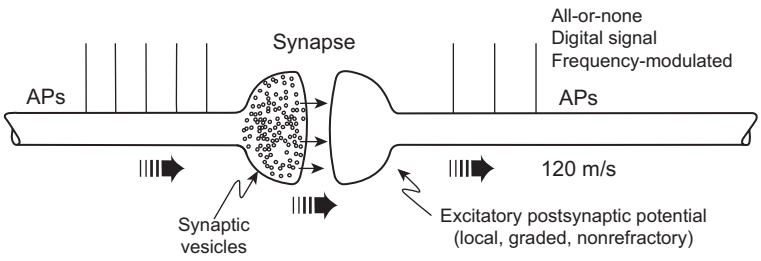

FIGURE 18.2 Diagram of a chemical excitatory synapse between two nerve fibers. An AP in the presynaptic fiber (left) brings about the release of the neurotransmitter at its nerve terminal. The transmitter molecules rapidly diffuse the short distance (e.g. 0.1 μm) across the synaptic cleft, bind to receptor sites on the postsynaptic membrane and open the associated non-selective ion channels (Na^+, K^+ mixed conductance) complexed to the receptor (i.e. these are ligand-gated ion channels). The associated synaptic current depolarizes the postsynaptic membrane, producing the excitatory postsynaptic potential (EPSP); this depolarization spreads passively into the adjacent conductile membrane (excitable) because of cable properties, thereby triggering one or more APs in the postsynaptic axon. The EPSPs are local, graded in amplitude and non-refractory whereas the APs are all-or-none (maximal), refractory and propagated actively. Thus, the AM synaptic process gives rise to an FM or digital signal. The strength of a biological response (e.g. contraction, secretion, sensation) is a function of the frequency of the signal. That is, higher AP frequency corresponds to stronger contraction or stronger sensation.

the body increases or decreases, respectively, the frequency of the APs. That is, the body uses a *frequency-modulated (FM) system*, rather than an amplitude-modulated (AM) system (see Fig. 18.2). It is a digital system composed of on-off identical signals. At each synapse, the signal becomes graded in amplitude rather than all-or-none: the greater the amplitude and duration of the local *postsynaptic potential*, the higher the frequency of APs triggered. The same is true of the local graded *receptor potential* generated at some sensory organs/receptors. Stronger signals translate into a higher frequency of impulses, and weaker signals correspond to a lower frequency of impulses.

IV. CABLE PROPERTIES

IVA. Biological Fiber as a Cable

An *electrical cable* consists of two parallel conductors separated by insulation material, e.g. two copper wires separated by rubber. Usually one of the conductors is arranged as a tubular sleeve surrounding a central solid rod (wire), as depicted in Fig. 18.3A. The equivalent electrical circuit for a cable is shown in Fig. 18.3B: two parallel conductors (wires) separated by a transverse resistance (R) shown distributed along the length of the cable. The resistance of the conductors is so small, compared with the transverse insulation resistance, that it is assumed to be zero. In the case of the *biological cable* (a long narrow nerve fiber or skeletal muscle fiber), one parallel conductor is the inside fluid (cytoplasm) and the second parallel conductor is the outside fluid surrounding (bathing) the cell (the interstitial fluid). Because the conductivity of biological fluid is much less (i.e. much higher resistance) than that of copper wire and because the cross-sectional area of the cell is so small, the inside longitudinal resistance is high and cannot be ignored (Fig. 18.3C). The outside longitudinal resistance is relatively small, as compared with the inside, because of the larger volume (cross-sectional area) of fluid available to carry the outside current, and therefore is assumed to be negligible (Taylor, 1963).

In addition, there is a *stray capacitance* distributed along the length of the cable (see Fig. 18.3D), because a capacitance occurs when two parallel conductors ("plates") are separated by a high-resistance dielectric material. The dielectric constant of materials is related to vacuum, which is assigned a value of 1.0000; air has a value very close to vacuum, oils have a value of 3−6 and that of pure water is 81. The biological membrane, which has a matrix of phospholipid molecules, has a dielectric constant of about 5, typical of oils. The higher the dielectric constant, the higher the capacitance. The closer the parallel plates, the higher the capacitance. Because the biological membrane is so thin (approx.70 Å or 7 nm), its capacitance is relatively high. All cell membranes have a membrane capacitance (C_m) of about 0.7−1.0 μF/cm^2 (where F stands for *farads* (Cole KC, 1965)).

IVB. Length Constant

In the electric cable depicted in Fig. 18.3A and B, a voltage (or signal) applied at one end would be transmitted to the distant end with little or no *decrement* (diminution or attenuation) and the so-called *length constant* would be very long or nearly infinite. In the biological cable (see Fig. 18.3C and D), however, a signal applied at one end rapidly falls off (decays) in amplitude as a function of distance, with a relatively short length constant (λ). This decay in voltage is exponential (Fig. 18.4A). An exponential process gives a straight line on a semilogarithmic plot (log V versus distance) (Fig. 18.4B). In a cable, the relationship between the voltage at any distance (x) from the applied voltage (V_0) is:

$$\mathrm{V_x} = \mathrm{V_o}\, \mathrm{e}^{-\mathrm{x}/\lambda} \tag{18.1}$$

Thus, when $\mathrm{x} = \lambda$

$$\begin{aligned} V_x &= V_o \frac{1}{e} \\ &= V_o \frac{1}{2.718} \\ &= 0.368\, V_o \end{aligned} \tag{18.2a}$$

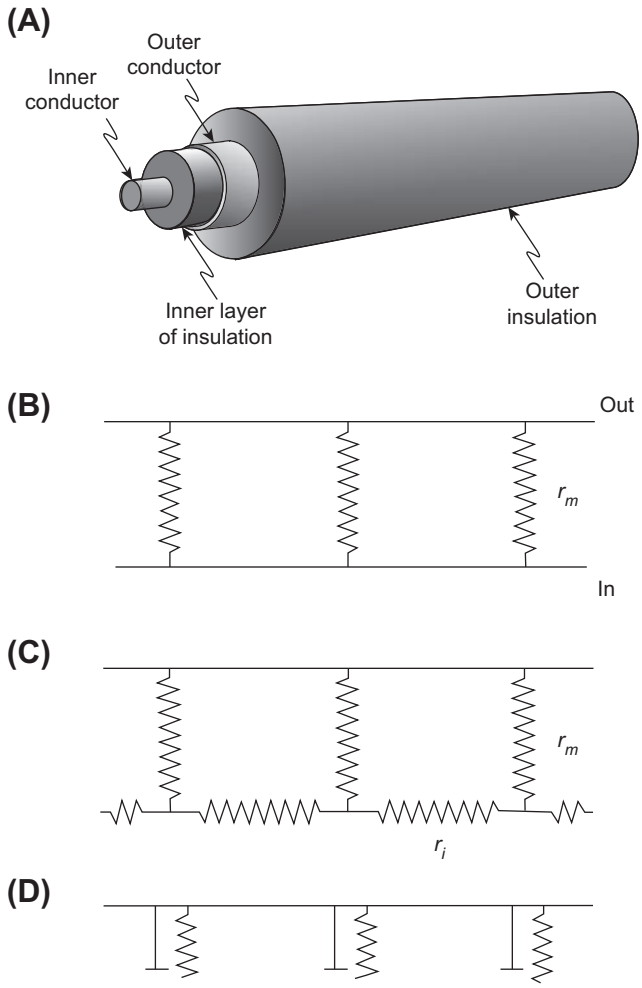

FIGURE 18.3 A coaxial cable and associated electrical equivalent circuit (A, B) and the electrical equivalent circuit for a biological cable (C, D). (A) The coaxial cable consists of an inner conductor (e.g. copper wire) and an outer concentric conductor separated by a layer of insulation (e.g. rubber). (B) The equivalent circuit for a coaxial cable. The inner and outer conductors are depicted as having nearly zero resistances and the transmembrane insulation resistance is shown distributed along the length of the cable. (C) In the biological cable, the inner conductor is the cytoplasm (axoplasm or myoplasm), which is not of negligible resistivity and therefore is depicted as r_i distributed along the length of the fiber. The transverse insulation resistance is the cell membrane resistance (r_m). (D) Addition of the capacitance elements to the biological cable (c_m), which arise due to the lipid bilayer matrix of the cell membrane.

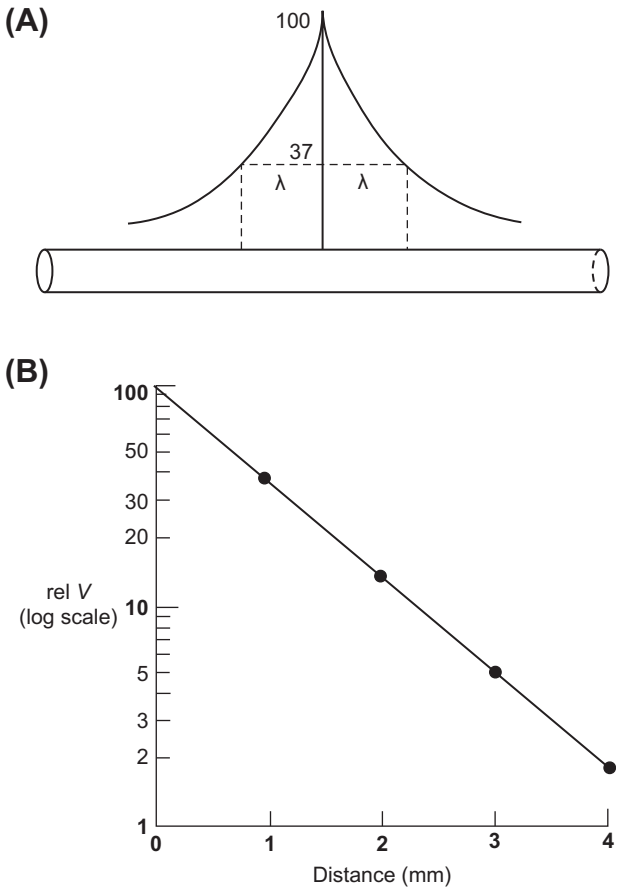

FIGURE 18.4 Length constant of the biological cable (fiber). (A) The exponential decay of voltage on both sides of an applied current (voltage) as a function of distance is diagrammed. The distance at which the voltage falls to 1/e or 36.8% of initial voltage (at x = 0), gives the λ value. (B) When the voltage is plotted on a log scale against distance, a straight line is obtained.

The mathematical solution to Equation 18.1 is:

$$V_x = \text{antiln}\left(\ln V_o - \frac{x}{\lambda}\right) \qquad (18.2b)$$

$$V_x = \text{antilog}\frac{2.303 \log V_o - (x/\lambda)}{2.303} \qquad (18.2c)$$

Hence, the distance at which the voltage decays to 36.8% of the initial value gives the length constant, λ. In nerve fibers and skeletal muscle fibers, λ has a value of only about 1−3 mm.

Therefore, the relatively short λ, compared with the length of the neuron (e.g. over 1.0 m for a lumbar anterior horn cell motor neuron) or skeletal muscle fiber, means that a signal applied at one end (or midpoint) would fall off very quickly with distance along the fiber (Fig. 18.5). If the length constant were 1.0 mm, then at 4 mm, the signal would become negligibly small. Hence, the electrical signal cannot be conducted passively in the biological cable, because it would decrement and disappear over relatively short distances. The AP (signal) is amplified to a constant value at each point (or each node) in the membrane, as discussed in the following chapter. That is, conduction is active, not passive, with energy being put into the signal at each point to prevent any decay of the signal.

The parameters that determine the length constant of a cable are the square root of the ratio of the transverse

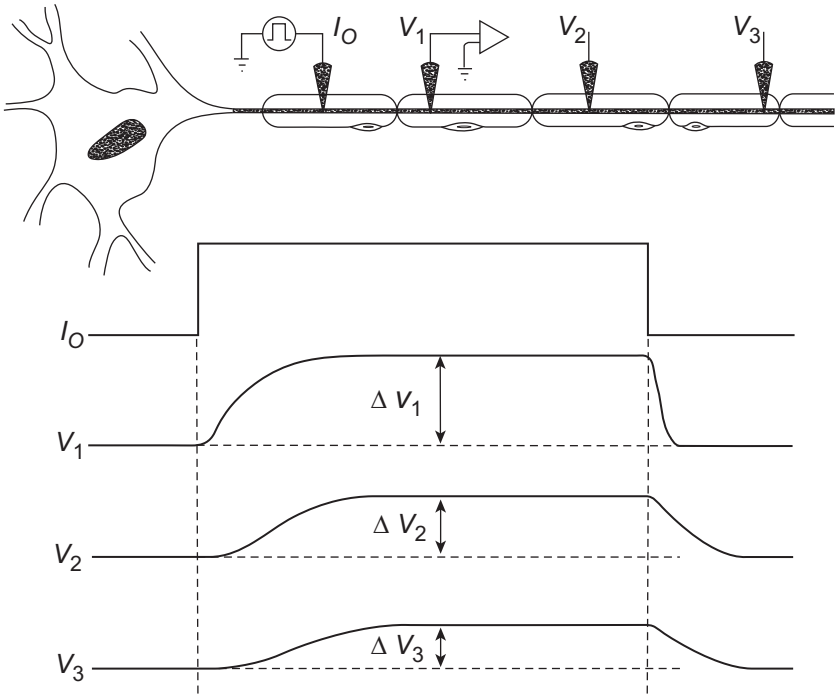

FIGURE 18.5 Diagram of a motor axon and how the voltage signal would decay with distance if the neuron were only a passive cable (non-excitable). The voltage traces illustrate the voltage signals that would be simultaneously recorded at three different points along the axon (V_1, V_2, and V_3) from the site of injection of a rectangular current pulse (I_o). As depicted, the amplitude of the steady-state voltage pulse rapidly falls off with distance, because the length constant (λ) of the biological cable is short (e.g. 1 mm) compared with the length of the axon (e.g. 1000 mm). Therefore, an active response of the cell membrane at each point is required faithfully to propagate the signal. The voltage recorded at point V_1 (ΔV_1) also illustrates that the membrane potential changes in an exponential manner, both at the beginning of an applied rectangular current pulse and at the end. This exponential change results from the capacitance of the cell membrane, the time constant (τ) being a product of the resistance and capacitance (R_mC_m). The time it takes for the voltage to decay to $1/e$ (36.8%) of the initial (maximal) value at the end of the pulse, or to build up to 63.2% (1−1/e) of the maximal value at the beginning of the pulse, gives the τ value.

resistance (r_m) to the sum of the inside (r_i) and outside (r_o) longitudinal resistances:

$$\lambda = \sqrt{\frac{r_m}{r_i + r_o}} \tag{18.3}$$

$$\text{cm} = \sqrt{\frac{\Omega \cdot \text{cm}}{\frac{\Omega}{\text{cm}} + \frac{\Omega}{\text{cm}}}} = \text{cm}$$

where r_m, r_i and r_o are the resistances normalized for a unit length (1.0 cm) of fiber.

For surface fibers of a nerve or a muscle bundle bathed in a large volume conductor, r_o is negligibly small and Equation 18.3 reduces to:

$$\lambda = \sqrt{\frac{r_m}{r_i}} \tag{18.4a}$$

Equation 18.4a is the same as:

$$\lambda = \sqrt{\frac{R_m}{R_i}\frac{a}{2}} \tag{18.4b}$$

$$\text{cm} = \sqrt{\frac{\Omega \cdot \text{cm}^2 \cdot \text{cm}}{\Omega \cdot \text{cm}}} = \text{cm}$$

where a is the fiber radius and R_m and R_i are the membrane resistance and longitudinal cytoplasmic resistance, respectively, normalized for both length (1.0 cm) and cell diameter. Thus, the greater the membrane resistance and the smaller the internal longitudinal resistance (larger cell diameter), the greater the λ value. We will see later that the propagation velocity is a function of λ; i.e. larger diameter fibers propagate faster. We will also see that myelination increases the effective membrane resistance (R_m) and lowers the effective capacitance, thereby increasing propagation velocity.

IVC. Time Constant

Because of the high capacitance of the cell membrane (C_m), the membrane potential (E_m) cannot change instantaneously upon application of a step current pulse. Instead, E_m changes in an exponential (negative) manner (see Fig. 18.5) on both the charge and the discharge. The *membrane time constant* (τ_m) is a product of the resistance (R_m) and capacitance of the membrane and can be expressed as:

$$\tau_m = r_m c_m \tag{18.5a}$$

$$= R_m C_m$$
$$\text{s} = \Omega \cdot \text{F} \tag{18.5b}$$

where R_m is the resistance in ohms (Ω-cm^2), and C_m is the capacitance in farads (F/cm^2).

The discharge of the membrane (parallel *RC* network) is given by:

$$V_t = V_{\max}\, e^{-t/\tau} \tag{18.6}$$

where V_t is the voltage at any time t (at the site of current injection) and V_{max} is the final maximum voltage attained during the pulse. When $t = \tau$,

$$V_t = V_{max} \frac{1}{e} \tag{18.7a}$$

$$= V_{max} \frac{1}{2.718}$$

$$= 0.368\ V_{max}$$

Hence, the time at which the voltage decays to 36.8% of the initial (maximal) value gives the *time constant*, τ (see Fig. 18.5). In nerve fibers and skeletal muscle fibers, τ_m has a value of about 1.0 ms.

When the membrane is charging, there is a similar *exponential (negative) process*, with the identical time constant (see Fig. 18.5). The corresponding relationship is given by:

$$V_t = V_{max}\ (1 - e^{-t/\tau}) \tag{18.7b}$$

The time it takes for the voltage to build up to 63.2% of its final value gives the time constant. When $t = \tau$,

$$V_t = \left(1 - \frac{1}{e}\right) V_{max} \tag{18.7c}$$

$$= (1 - 0.368)\ V_{max}$$

$$= 0.632\ V_{max}$$

Thus, the time constant can be measured on the build-up of the pulse (time to reach 63.2% of the final voltage) or on the decay (time to decay to 36.8% of the initial voltage).

IVD. Input Resistance

The *input resistance* (R_{in}) of a muscle or nerve fiber is essentially the resistance that an intracellular microelectrode "looks" into when a small current (DC pulse) is injected. Thus, R_{in} is determined by the change in membrane potential (V_o or $V_{x=0}$) at steady-state produced at the site of injection ($x = 0$) by the injection of a known (measured) amount of current (I_o or $I_{x=0}$), based on *Ohm's law.*

$$R_{in} = \frac{V_o}{I_o} \tag{18.8}$$

If the microelectrode is near the middle of a very long fiber (or "infinite" cable), then R_{in} is related to the other cable parameters (e.g. to the internal longitudinal resistance r_i and the DC length constant λ_{DC}):

$$R_{in} = 0.5\ r_i\ \lambda_{DC}$$

$$\Omega = \frac{\Omega}{cm} \cdot cm \tag{18.9}$$

The factor of 0.5 is present because current flows in both directions from the microelectrode. If the microelectrode is at one end of the long fiber, then the factor of 0.5 is removed. Equation 18.9 indicates that the R_{in} is greater when r_i and/or λ_{DC} are greater. Combining Equations 18.8 and 18.9 gives:

$$\frac{V_a}{I_o} = 0.5\ r_i\ \lambda_{DC} \tag{18.10a}$$

or

$$V_o = I_o 0.5\ r_i\ \lambda_{DC} \tag{18.10b}$$

This equation indicates that the change in membrane potential at $x = 0$ is equal to the applied current (I_0) times the input resistance.

To obtain the change in membrane potential at any point x along the fiber cable (V_x), then an exponential term ($e^{-x/\lambda}$) must be added to account for the exponential decay of voltage over distance:

$$V_x = I_o\ 0.5\ r_i\ \lambda_{DC}\ e^{-x/\lambda} \tag{18.11}$$

This equation is identical to Equation 18.1, because the I_o 0.5 r_i λ_{DC} term is equal to V_o (Equation 18.10b):

$$V_x = V_o\ e^{-x/\lambda}$$

Further discussion is given in Appendix 18.1.

IVE. Local Potentials

In contrast to the active propagation of APs, *synaptic potentials* and sensory *receptor potentials* are not actively propagated. Such potentials decay exponentially (from their source of initiation) along the fiber cable, as described previously. Therefore, postsynaptic potentials and receptor potentials are *local potentials*. When local potentials are in the depolarizing direction, they can give rise to APs, which are propagated; when hyperpolarizing, they act to inhibit production of APs. These local potentials are similar to the *local excitatory response* (see following chapter), in that both are confined to a local region; however, the electrogenesis of the two is different. As stated before, the neuromuscular junction is an excitatory type of chemical synapse and produces *excitatory postsynaptic potentials* (EPSPs), also known as *end-plate potentials* (EPPs).

Most synaptic potentials are *graded*, i.e. they can add on to one another, both in time and in space (*temporal summation* and *spatial summation*), to produce larger responses. Larger synaptic potentials exert a greater stimulatory or inhibitory effect on the production of APs.

V. CONDUCTION OF ACTION POTENTIALS

VA. Local-Circuit Currents

The generation of APs is described in the subsequent chapter. This section examines the mechanism for their rapid propagation (conduction). *Propagation* occurs by means of the *local-circuit currents* that accompany the propagating APs, as depicted in Fig. 18.6. Such currents exist because, when two points are at a different potential (voltage) in a conducting medium, current (I) will flow between the two points, as governed by Ohm's law ($I = V/R$).

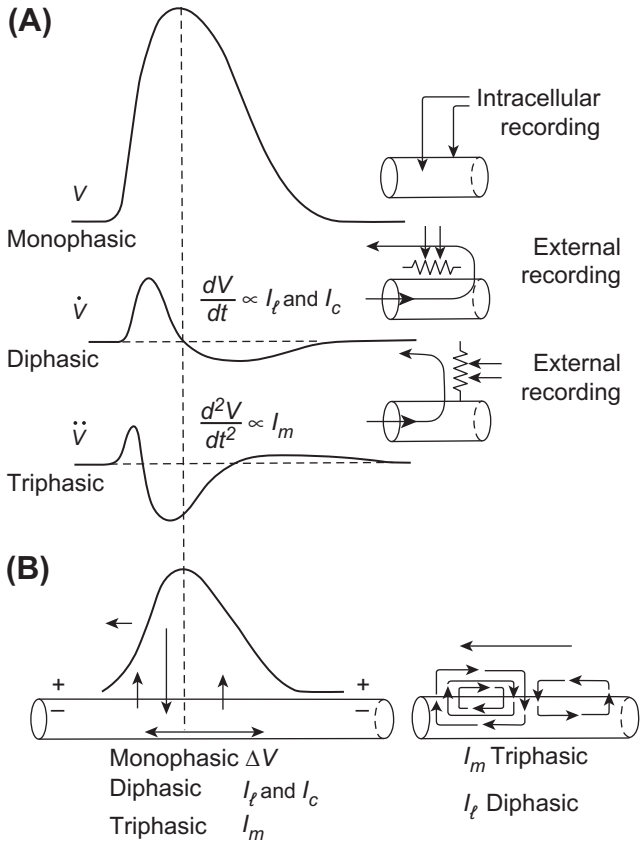

FIGURE 18.6 (A) Schematic representation of the first ($\dot{V}$) and second ($\ddot{V}$) time derivatives of the AP spike and the longitudinal and radial currents associated with the propagating spike. The first derivative (dV/dt or $\dot{V}$) is proportional to the capacitive current ($I_c = C_m\, dV/dt$) and to the longitudinal (axial) current and is *diphasic*, having an intense forward phase and a less intense backward phase, as depicted in the diagram at the lower right. The second derivative (d^2V/dt^2 or $\ddot{V}$) is proportional to the radial transmembrane current (I_m), and is *triphasic*, having a moderately intense initial outward phase, then a very intense inward phase (the "current sink"), followed by a least intense second outward phase, as depicted in the lower diagrams. (B) The arrows at the lower left also depict the three phases of the membrane current and the two phases of the axial current. dV/dt can be recorded externally by a pair of closely-spaced (relative to the spike wavelength) electrodes arranged parallel to the fiber axis, as illustrated. d^2V/dt^2 can be recorded by a pair of electrodes arranged perpendicular to the fiber axis, as depicted. The vertical dashed line indicates that when the slope of the spike goes to zero at the peak of the spike, dV/dt is zero; dV/dt is maximum at about the middle of the rising phase of the spike.

At the peak of the AP in one region of the fiber, the inside of the membrane at that region becomes positive with respect to the outside. The inside is also positive with respect to the inside cytoplasm at a region downstream from the active region. Therefore, current flows through the cytoplasm from the active region (*current source*) to the adjacent inactive region, then out of the fiber across the cell membrane, then through the interstitial fluid back to the active region (current "sink") and, finally, through the membrane of the active region. This completes the *closed loop* for the current.

The outward current through the membrane of the inactive region produces an IR voltage drop (Ohm's law), positive inside to negative outside. This acts to depolarize this region, because the polarity of the voltage drop is opposite to that of the RP (negative inside, positive outside). When the depolarization exceeds the *threshold potential*, an AP is triggered. Thus, the inactive region becomes converted to an active region. This process is repeated in each segment of fiber, thus resulting in movement (propagation) of the impulse sequentially down the fiber.

If we examine a propagating AP in the middle region of a fiber (see Fig. 18.6), we see that there is also a small backflow of current internally, coupled with a corresponding small forward flow externally, associated with the repolarizing phase of the AP. Thus, as the AP propagates down the fiber, from right to left, there is a simultaneous double flow of local-circuit current: clockwise flow associated with the rising phase of the AP and counterclockwise flow associated with the repolarizing phase of the AP.

The internal longitudinal current, sweeping past a transverse plane of the fiber, has two phases, first forward (right to left) and then reverse (left to right). The external longitudinal current also has two phases: first left to right and then right to left.

The transverse membrane current, flowing outward in a plane perpendicular to the membrane, has three consecutive phases: first outward (still passive membrane), then inward (active membrane) and, finally, outward again (still active membrane).

It is the local-circuit current flow that enables the *electrocardiogram* (ECG), *electromyogram* (EMG), *electroencephalogram* (EEG) and *electroretinogram* (ERG) to be recorded from the body surface over the tissue of interest (heart, skeletal muscle, brain and eye). The internal longitudinal current is confined to the cytoplasm of the fiber, but the external current can use whatever conducting fluid is available (e.g. the entire torso *volume conductor*) because of the principle that parallel resistors give a lower total resistance (or current takes the path of least

resistance). Thus, this external local-circuit current causes the skin to be at different potentials, and these differences can be recorded (as the ECG, etc.).

VB. Propagation Velocity Determinants

The factors that determine active velocity of propagation (θ) include: (1) fiber diameter, (2) length constant (λ), (3) time constant (τ_m), (4) local-circuit current intensity, (5) threshold potential and (6) temperature. Some of these factors are interrelated, such as fiber diameter and length constant (since λ is proportional to the square root of the radius) and length constant and time constant (since both have a dependence on R_m). Propagation velocity is directly proportional to length constant and inversely proportional to time constant as:

$$\theta \propto \frac{\lambda}{\tau_m} \tag{18.12a}$$

By substituting Equation 18.4a for λ and Equation 18.5a for τ_m, we have:

$$\theta \propto \frac{1}{C_m}\sqrt{\frac{a}{R_m R_i}} \tag{18.12b}$$

Thus, propagation velocity is directly proportional to the square root of fiber diameter or radius (a) and inversely proportional to *membrane capacitance* (C_m). The larger the fiber diameter, the lower the absolute longitudinal resistance of the intracellular cytoplasm (principle of resistors in parallel) and therefore the greater the amount of local-circuit current flowing longitudinally and the greater the length constant. For example, it is well known that the larger the diameter of nerve fibers, the faster they propagate (see Table 18.1). Equation 18.12b shows that if C_m can be reduced (by myelination), then θ should increase in proportion. This is discussed in Section IVC.

In addition, θ depends on the intensity of the local-circuit current, and hence on the rate of rise of the AP. The greater the AP rate of rise (max *dV/dt*), the greater the longitudinal current and the transmembrane *capacitive current* (I_c). Therefore, all other factors being constant, faster-rising APs propagate faster. The AP rate of rise depends on the density of the fast Na^+ channels that carry inward current, on C_m and on temperature. Max *dV/dt* decreases with increased C_m, with cooling and with partial depolarization (due to the h_∞ versus E_m relationship discussed in the following chapter). Cooling slows the rate of all chemical reactions, particularly those with a high Q_{10} (activation energy), such as the ion conductance changes in activated membrane.

Finally, the *threshold potential* (V_{th}) affects propagation velocity. If the threshold were to be shifted to a more positive voltage (more depolarized), then it would take longer for a given point in the membrane to reach threshold (and explode) during propagation of an AP from upstream. A greater *critical depolarization* (difference between RP and V_{th}) would be required to bring the membrane to threshold. Therefore, propagation velocity would be slowed.

As stated earlier, some of these factors are interrelated and some actually exert opposing effects.

The foregoing discussion applies to non-myelinated nerve axons and skeletal muscle fibers. An electron micrograph of small bundles of non-myelinated nerve fibers enveloped by *Schwann cells* is shown in Fig. 18.7. In myelinated nerve fibers, propagation velocity is greatly increased by the *myelin sheath*, as discussed in the following section.

VC. Saltatory Conduction

The nerve cable has been vastly improved by the evolutionary development of *myelination* in vertebrates. An electron micrograph of a myelinated nerve fiber is shown in Fig. 18.8. The *myelin sheath* improves the cable by increasing the effective R_m by about 100-fold and decreasing the effective C_m by about 100-fold. This increases the length constant, λ. Although τ_m tends to increase with the increase in effective R_m (due to the myelin sheath), the decrease in C_m counteracts this effect, thus acting to hold τ_m almost constant. Thus, Equations 18.12a and 18.12b predict that propagation velocity should increase with myelination.

One consequence of myelination, therefore, is that propagation velocity is greatly increased (see Table 18.1). Another consequence is that the *energy cost of signaling* is

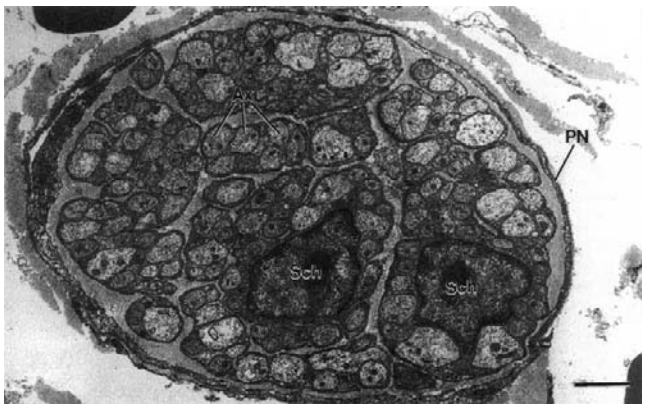

FIGURE 18.7 Electron micrograph of an autonomic nerve of mouse heart cut in transverse section. The unmyelinated axons (Ax) are arranged in small groups (bundles) that are engulfed by the cytoplasm of a Schwann cell. That is, the non-myelinated axons are embedded in, and surrounded by, a Schwann cell. Two Schwann cell nuclei (Sch) can be seen. The axon bundles are separated and surrounded by a collagenous matrix. The entire nerve is surrounded by a perineurial sheath (PN). The scale bar at lower right equals 2 µm. *(Micrograph courtesy of Dr Mike Forbes, University of Virginia.)*

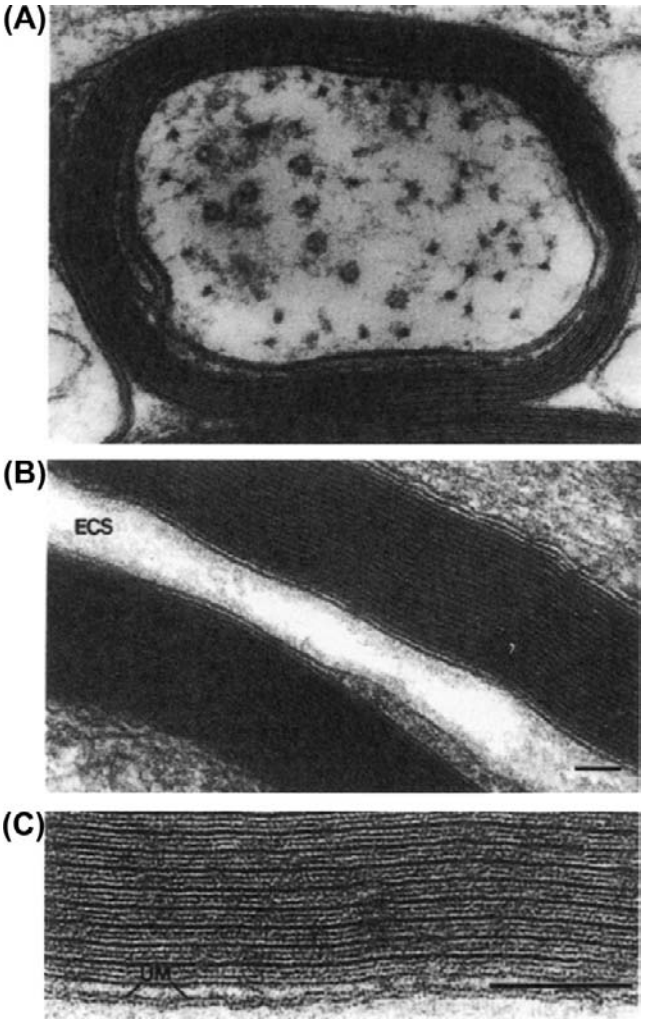

FIGURE 18.8 Myelin sheath of myelinated nerve fibers. (A) Myelinated nerve fiber in spinal cord of rat cut in cross-section. There are about seven wrappings of the Schwann cell around the axon, thus giving about 14 membranes in series with the cell membrane of the axon (axolemma). The internal *mesaxon* is visible at the left side (lower) of the axon and represents the beginning of the spiraling of the Schwann cell membranes (cytoplasm squeezed out) to form the myelin sheath surrounding the axon. On the upper left side, a process of an oligodendrocyte abuts on the myelin sheath. The axon shown is closely plastered up against the myelin sheath of a neighboring axon (bottom of figure). *Microtubules* and *neurofilaments* are visible in the cytoplasm of the axon. Magnification of 168 000×. (From J. Rhodin, An Atlas of Histology, Oxford University Press, New York, 1975.) (B) Higher magnification of two adjacent nerves fibers (in phrenic nerve of rat) cut in longitudinal section to illustrate an axon with a thicker myelin sheath (approx. 23 wrappings=46 membranes). Note that between the thicker (dense) lines are two thinner lines, which can be seen more clearly in (C). The extracellular space (ECS) between the two axons is labeled. The calibration bar at the lower right equals 0.1 μm. (C) Still higher magnification of a portion of one of the myelin sheaths shown in the middle panel better to illustrate the periodicity of the myelin membranes. The dense lines alternate with a pair of thin lines. The space in between the pair of thin lines is extracellular space. The dense lines represent the intracellular (cytoplasmic) region of the Schwann cell process, with the cytoplasm extruded, thus allowing the inner (cytoplasmic face) leaflets of the cell membrane of the Schwann cell to come into close contact. The outer (extracellular face) leaflets of the Schwann cell membrane are seen as the thin lines. Thus, each cell membrane has the appearance of a double line, representing the hydrophilic surfaces of the cell membrane; the hydrophobic region of the membrane is the clear region between the dense line and the contiguous thin line on either side. UM; unit cell membrane. The scale bar on the lower right represents 0.1 μm. *(Micrographs (B) and (C) courtesy of Dr Mike Forbes, University of Virginia.)*

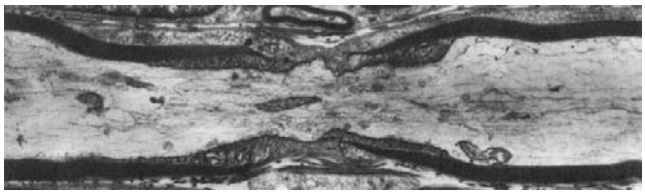

FIGURE 18.9 Electron micrograph of one node of Ranvier in a single myelinated nerve axon of rat sciatic nerve cut in longitudinal section. Dark myelin bordering the axon on each side is interrupted near the middle of the micrograph, leaving the neuronal cell membrane nude of myelin at the node region. However, cytoplasmic processes of the Schwann cells cover the nodal membrane. Collagenous fibrils of the endoneurium are visible at the region of the node. The myelin tapers and thins as it approaches the node and there is a frayed appearance caused by the successive laminae of the myelin sheath terminating as cytoplasmic swellings. The axoplasm contains neurofilaments and microtubules. Magnification of 9000×. *(From J. Rhodin, An Atlas of Histology, Oxford University Press, New York, 1975.)*

greatly decreased, because passive ion leaks are limited and active current losses are restricted to the small nodes of Ranvier, which are spaced relatively far apart. An electron micrograph of a node of Ranvier is shown in Fig. 18.9. At each node, the length of exposed (naked) cell membrane is very short. The node forms an annulus around the entire perimeter of the fiber. The *internodal distance* is about 0.5−2.0 mm (depending on fiber diameter) and the width (length) of each node is only about 0.5−3 μm. Therefore, the degree of energy-requiring active ion transport (Na^+-K^+ and Ca^{2+}) required to maintain the steady-state ion distributions and to hold the system in a state of high potential energy is greatly reduced. For example, the amount of Na^+ gained and K^+ lost per impulse is reduced as a result of myelination. The low rate of oxidative metabolism in myelinated fibers reflects this lowered energy requirement.

The *myelin sheath* is produced by the wrapping of the Schwann cell repeatedly around the nerve fiber in a spiral, forming 20−200 wrappings, depending on axon diameter. That is, the larger axons have a thicker myelin sheath. For the purpose of our discussion, we will assume an average of 100 wrappings. The myelin sheath covers the nerve axon as a coat sleeve and is interrupted at each node. The cytoplasm of the Schwann cell in the region of the myelin sheath is nearly completely extruded during its formation, so that the sheath consists essentially of 100 cell membranes stacked in series. Because resistors in series are added to calculate the total resistance, the effective transmembrane resistance

is increased 100-fold, but the effective capacitance is reduced 100-fold (because the total capacitance of capacitors in series is calculated like resistors in parallel). Since λ is directly proportional to $\sqrt{R_m}$, λ is increased accordingly. The greater λ and lowered C_m increase θ.

Myelinated nerves usually have an *optimal amount of myelin*, which is an amount such that the ratio of diameter of axon cylinder (naked axon) to total fiber (including myelin sheath) is about 0.6−0.8. Assuming a maximal total diameter feasible (the body must pack many circuits within a limited space, e.g. sciatic nerve bundle), a greater fraction of myelin, by infringing on the diameter of the axis cylinder, would raise r_i too high, causing θ to decrease. Thus, there are two opposing factors in determining the degree of optimal thickness of the myelin sheath. The more the myelin, the greater the decrease in C_m and increase in effective R_m, but then the smaller diameter of the axis cylinder causes a higher r_i.

In *saltatory conduction* (Latin *saltare*, to jump), the impulse jumps from one node to the next. The internodal membrane *does not fire* an AP. This is due to two reasons: (1) the internodal membrane is much less excitable (e.g. much fewer fast Na^+ channels); and (2) the depolarization of the neuron cell membrane at the internodal region is only about 1/100th of that at the node. The latter occurs because the *IR* voltage drop across the internodal cell membrane is only 1/100th of that across the entire series resistance network (neuron cell membrane plus 100 layers of Schwann cell membrane) (*Kirchhoff's laws* dealing with voltage drops across resistors in series). Even though the internal potential in the internodal region swings positive (e.g. to +30 mV) when the adjacent nodes fire, the potential at the outer surface of the internodal membrane also swings nearly as positive (e.g. to +29 mV). Therefore, the depolarization of the neuronal membrane at the internode is only about 1 mV, which is well below threshold and so the internodal membrane does not fire. The potential that controls the membrane conductances (activates the voltage-dependent ion channels) is the pd (potential difference) directly across the membrane and not the absolute potential on either side.

As stated previously, the internodal membrane has only a few fast Na^+ channels, whereas the nodal membrane has a very high density. Since the cell membrane is fluid and proteins can diffuse (float) laterally in the lipid bilayer matrix, what keeps the fast Na^+ channel proteins confined (at high density) in the nodal region? There are *special anchoring proteins* (e.g. *ankyrin*) that anchor the ion channel proteins to the cytoskeletal framework, thus preventing their lateral movement into the internodal membrane.

The effect of myelin and saltatory propagation is to make propagation much faster. For example, a 20-μm-diameter myelinated nerve fiber conducts even faster than a 700-μm (0.7 mm) diameter non-myelinated nerve fiber (e.g. the *giant axon* in squid, lobster, earthworm): 120 m/s versus 25−50 m/s. Thus, invertebrates, to achieve fast conduction in some essential circuits, must resort to *giant neurons*, resulting in a lower r_i and hence fast conduction. Because of space/size limitations, only a few critical neurons can be made giant in diameter. In vertebrates, on the other hand, a large fraction of the nerve fibers in the peripheral nerves are myelinated for fast propagation.

We saw earlier that, in non-myelinated axons and skeletal muscle fibers, θ should vary with the square root of the cell diameter or radius ($a^{0.5}$). In myelinated axons, θ varies with the first power of the cell radius (a^1) because θ varies with λ^2 as indicated by:

$$\theta \propto \frac{\lambda^2}{\tau_m} = \frac{a}{2R_iC_m} \tag{18.13}$$

The dependence of conduction velocity on diameter of nerve fibers is summarized in Table 18.1.

VD. Wavelength of the Impulse

We can calculate the wavelength of the AP, which is the length of the axon simultaneously undergoing some portion of the AP. The wavelength is equal to propagation velocity (θ) times the duration of the AP (APD100); thus,

$$\text{wavelength} = \theta \times \text{APD}_{100} \tag{18.14}$$

$$\text{cm} = (\text{cm/s}) \times \text{s}$$

$$\text{distance} = \text{velocity} \times \text{time}$$

Note the similarity of this relationship to that for the wavelength of an electromagnetic radiation: wavelength = velocity of light/frequency of the radiation. The reciprocal of frequency is the period (duration of one cycle). The wavelength in a large myelinated nerve axon is about 12 cm: 120 m/s × 1.0 ms. In a skeletal muscle fiber, it is about 1.8 cm (6 m/s × 3.0 ms). In a smooth muscle bundle, the wavelength is only about 1.5 mm (5 cm/s×30 ms).

VI. EXTERNAL RECORDING OF ACTION POTENTIALS

VIA. Monophasic, Diphasic and Triphasic Recording

As discussed previously, local-circuit currents accompany the propagating AP in each fiber. The intracellular and extracellular longitudinal currents are diphasic; i.e. initially they travel in the forward direction intracellularly and then in the reverse direction. The forward direction current is intense (high current density) and the reverse direction

current is weak (low current density). The transmembrane radial currents are triphasic; i.e. the first phase is outward (moderate intensity), the second phase is inward (high intensity) and the third phase is outward (low intensity). The first phase (outward) gives rise to the passive exponential foot of the AP and is due to the passive cable spread of voltage and current. The second phase (inward) corresponds to the large inward fast Na^+ current, which occurs during the later portion of the rising phase and peak of the AP. The third phase (outward) corresponds to the net outward current (K^+), which occurs during the repolarizing phase.

These longitudinal and radial currents can be recorded by suitably-placed external electrodes. The extracellular longitudinal currents can be recorded by two electrodes (bipolar) placed close together along the length of the fiber. If the interelectrode distance is short (relative to the wavelength), an approximate first (time) derivative of the AP is obtained (see Figs. 18.6 and 18.10C). The extracellular radial currents can be recorded by two electrodes placed close together in a plane perpendicular to the fiber axis. This gives an approximation of the second (time) derivative of the AP (see Fig. 18.6).

The internal axial currents are confined to the cytoplasm, whereas the external longitudinal currents can use the entire interstitial fluid space of the nerve bundle or muscle or even the entire torso (volume conductor), since current takes the path of least resistance (resistors in parallel). As mentioned in Section IVA, this allows the recording of the ECG from the body surface and the EMG from the skin overlaying an activated skeletal muscle. The ECG and EMG consist essentially of diphasic potentials, reflecting the external longitudinal currents during propagation of APs.

When the two external electrodes are placed far apart (with respect to the wavelength) along a nerve or muscle fiber, the diphasic recording has two phases that are about equal (Fig. 18.10A). The proximal electrode records the wave of negativity (associated with the propagating AP) first and then returns to isopotential. When the wave reaches the second electrode, the wave is recorded by it in reversed polarity (because current flow through the voltmeter is reversed). If the AP were now prevented from reaching the second (distal) electrode by crushing this region of the fiber or elevating $[K^+]_o$ to depolarize it, then a monophasic recording would be obtained (Fig. 18.10B). This monophasic recording would most resemble the true AP recorded by a microelectrode impaled into a fiber to record the transmembrane potential, but would be much smaller in amplitude.

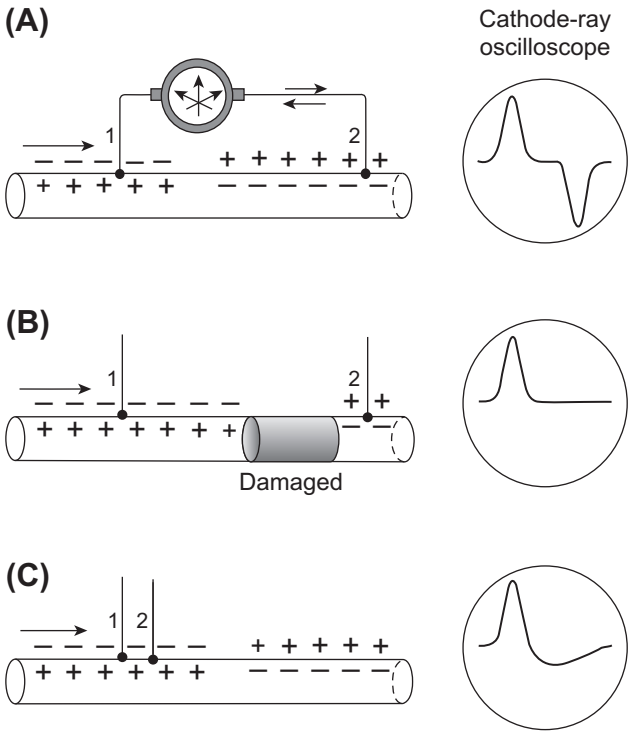

FIGURE 18.10 Diagram of the waveforms that would be recorded externally during propagation of an AP in a single fiber. (A) When the two electrodes are far apart (relative to the AP wavelength), a diphasic recording is obtained, with the two phases being symmetrical and separated by an isopotential segment. The two phases are due to the current flow through the voltmeter recorder being first in one direction and then in the opposite direction. (B) If the fiber between these two electrodes is damaged (e.g. by crushing) or depolarized (by elevated $[K^+]_o$), so the AP cannot sweep past the second electrode (2), then this second phase is prevented and the recording is monophasic. (C) If the two electrodes depicted in (A) are brought progressively closer, then the isopotential segment would shorten and disappear. If electrode 2 is brought very close to electrode 1, so that the interelectrode distance is short relative to the wavelength, then the second phase is smaller than the first phase, and the record resembles the first derivative of the true AP.

VIB. Compound Action Potential

When one records the APs externally, the records are graded and not all-or-none. (In contrast, in the case of the true APs recorded intracellularly from single fibers [see following chapter], the APs are all-or-none.) That is, the signal recorded becomes larger and larger, up to a maximum amplitude as the intensity of stimulation is increased. This is the so-called compound action potential. It is graded because, as a greater and greater fraction of the fibers are activated, the external longitudinal currents associated with the all-or-none AP in each fiber cut across the recording electrodes, thereby producing a larger signal. The AP in each individual fiber is always all-or-none. The amplitude of the signal is determined by the resistance between the electrodes multiplied by the amount of current flowing through this resistance ($V = IR$). The recording of compound action potentials is diagrammed in Fig. 18.11.

The compound action potentials can be demonstrated by recording the EMG from a human subject when one

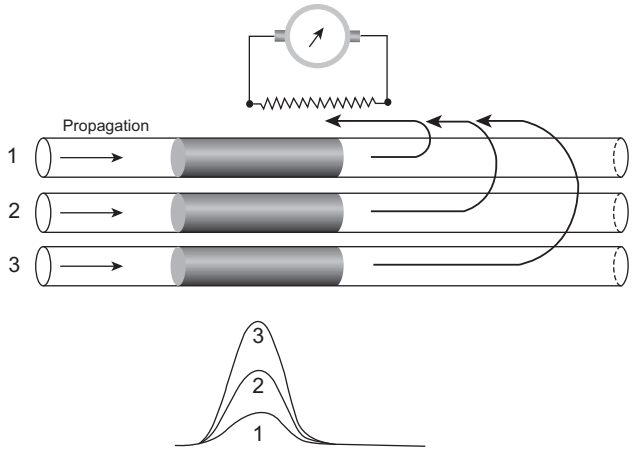

FIGURE 18.11 Diagram of a compound action potential in an isolated nerve trunk, such as the frog sciatic nerve, recorded externally by a pair of longitudinal electrodes. The voltmeter (oscilloscope) records the voltage (*IR*) drop across the resistance (fluid) between the two electrodes. If only fiber 1 is activated, the current passing between the electrodes is small and the voltage recorded is small. If fiber 2 is simultaneously activated with fiber 1, then the amount of current is doubled and the voltage is doubled. When all three fibers are simultaneously activated, the current is tripled, and the voltage is tripled. Therefore, the externally recorded compound action potential is graded because it reflects the electrical activity of numerous fibers, each of which produces an all-or-none AP.

electrode is placed on the skin of the ventral forearm and the other (reference) electrode on the wrist of the same arm. Then, as the subject voluntarily produces stronger and stronger contraction to flex the hand, the electrical signals picked up become greater and greater in amplitude and frequency. The amplitude becomes larger because more muscle fibers are simultaneously activated. This is known as **fiber recruitment**. The frequency also increases, because the motor nerves fire at a higher frequency, causing the muscle fibers to fire at a higher frequency and thus producing a more powerful tetanic contraction.

APPENDIX 1 ADDITIONAL DISCUSSION OF INPUT RESISTANCE AND IMPEDANCE

Because: $\lambda_{DC} = \sqrt{r_m/r_i}$ (Equation 18.4a), Equation 18.9 can be given as:

$$R_{in} = 0.5\, r_i \sqrt{\frac{r_m}{r_i}} = 0.5\sqrt{r_m r_i} \qquad (18A.1)$$

and Equation 18.11 can also be given as:

$$V_x = I_o 0.5\sqrt{r_m r_i}\, e^{-x/\lambda} \qquad (18A.2)$$

Thus, input resistance is proportional to $\sqrt{r_m r_i}$. This indicates that the higher the longitudinal resistance of the fiber's axoplasm (or myoplasm), which is a function of the resistivity of the axoplasm and fiber diameter, and the higher the membrane resistance, the higher the input resistance. The input resistance also can be calculated from the electrical equivalent circuit for a cable.

The input impedance can also be given in terms of R_m and R_i, the specific resistance of the cell membrane and resistivity of the axoplasm, respectively. Since $R_m = 2\pi a r_m$ and $R_i = \pi a 2 r_i$, then Equation 18.12 can be converted to:

$$R_{in} = 0.5\sqrt{\frac{R_m}{2\pi a}\frac{R_i}{\pi a^2}} \qquad (18A.3a)$$

$$= 0.5\sqrt{\frac{R_m R_i}{2\pi^2 a^3}} \qquad (18A.3b)$$

Thus, the input resistance is directly proportional to the square root of the membrane specific resistance and the resistivity of the axoplasm and inversely proportional to the square root of the fiber radius raised to the third power.

Calculation of the input impedance (Z_{in}) is more complicated because it also depends on the membrane capacitance (C_m) and on the frequency (f) of the alternating current (AC) used. According to Katz (1966), the input impedance of a long fiber (current injected at one end) is given by:

$$Z_{in} = \sqrt{\frac{R_m R_i}{2\pi^2 a^3 \sqrt{1 + 4\pi^2 f^2 R_m^2 C_m^2}}} \qquad (18A.4)$$

$$\Omega = \sqrt{\frac{(\Omega\cdot\mathrm{cm}^2)(\Omega\cdot\mathrm{cm})}{\mathrm{cm}^3\sqrt{(\mathrm{s}^{-2})(\mathrm{s}^2)}}}$$

A discussion of the AC length constant (λ_{AC}) is beyond the scope of this chapter.

APPENDIX 2 PROPAGATION IN CARDIAC MUSCLE AND SMOOTH MUSCLES

A1. BACKGROUND

Chapter 18 discusses propagation in cells that are long cables, such as nerve fibers and skeletal muscle fibers. Propagation is more complex in tissues composed of assemblies of short cells, such as cardiac muscle and visceral smooth muscles. These short cells may be considered to be short or truncated cables. In such a truncated cable cell, its true length constant λ is much longer than the cell's length. Therefore, there is relatively little voltage fall-off (decay) over the length of each cell. It follows that the entire cell undergoes an action potential (AP) nearly simultaneously. Yet propagation velocity θ is much slower in cardiac muscle (ca. 0.5 m/s) and smooth muscles (ca. 0.05 m/s) than in skeletal muscle (ca. 5–6 m/s) or non-myelinated nerve fibers

(ca. 2 m/s). Part of the reason for the slower θ concerns fiber diameter (i.e. diameter of cardiac muscle fiber is about 15 μm compared to about 60 μm for skeletal muscle fibers). Equation 16b in Chapter 18 indicates that in a simple cable, θ is a function of $\sqrt{a}$ (where a is the fiber radius). The fact that skeletal muscle also has a much higher max *dV/dt* (rising phase of the AP) than cardiac muscle and smooth muscle is another factor that contributes to the lower than expected θ in cardiac muscle and smooth muscle. The max *dV/dt* in cardiac muscle is ca. 200 V/s and in smooth muscle ca. 5 V/s, as compared with skeletal muscle ca. 600 V/s. In addition, the higher the extracellular resistance, which depends on the tightness of packing of the fibers in the muscle tissue, the slower the velocity.

Another factor that determines velocity in cardiac muscle and smooth muscle is the high resistance of the junctional membranes (the intercalated disk membranes in the case of cardiac muscle). It is still controversial as to exactly how high the junctional resistance is. When gap junctions are present, the gap junction channels span the intercellular junction, and so serve to lower the cell-to-cell resistance (see chapter on gap junctions). However, the hearts of lower vertebrates (e.g. fish, amphibians, reptiles) either have no gap junctions or they are very sparse and tiny. In addition, even parts of mammalian hearts and some visceral smooth muscles (e.g. longitudinal muscle layer of intestine) do not appear to contain gap junctions. If so, another mechanism may be involved for cell-to-cell propagation in those muscles in which there is a virtual absence of gap junctions. One of the mechanisms proposed is known as the *electric field model* (Sperelakis and Mann, 1977; Sperelakis et al., 1979). This mechanism is discussed in this appendix.

Since the short cardiac muscle cell shows no voltage decay, the entire length of the cell should undergo the AP nearly simultaneously (i.e. nearly infinite propagation velocity within each cell). Yet, the overall propagation velocity in the tissue is relatively slow. Clearly, a large time delay must occur at each cell junction. In fact, most of the propagation time is consumed at the cell junctions. This has been demonstrated experimentally. Propagation in cardiac muscle has been shown to be actually *discontinuous* or *saltatory* in nature (Spach et al., 1981; Cole et al.,1988; Sperelakis et al., 1983). Therefore, the presence of a few gap-junction channels is insufficient to reduce the junctional resistance enough to allow a chain of cells to behave as a simple cable. This relatively high junctional resistance may have relevance to heart block and fibrillation.

AII. SOME EXPERIMENTAL FACTS

Some of the key experimental facts relevant to the transmission of excitation from one cell to the next in cardiac muscle and visceral smooth muscle can be summarized as follows. These tissues can be enzymatically separated into their individual cells and the individual single cells are viable and functional. Gap junctions are absent in the hearts of lower vertebrates and in some regions of mammalian hearts, as well as in some visceral smooth muscles, as stated previously. The length constant λ of cardiac muscle and smooth muscle tissues, when measured properly, is relatively short, i.e. less than 0.3 mm (i.e. not much more than about one cell length). The input resistance (R_{in}) of cardiac muscle and smooth muscle, when measured properly, is relatively high, about 5−40 MΩ. The short λ and high R_{in} suggest that the cells are not profusely connected by low-resistance pathways (e.g. by gap-junction channels). Thus, even when gap junctions are present, the junctional membranes still constitute a substantial barrier to current flow from one cell to the next (Tarr & Sperelakis, 1964).

As stated above, there is almost no voltage decay in a single cell and the entire cell fires an AP nearly simultaneously. Therefore, most of the propagation time is consumed at the cell junctions and propagation in these tissues is a discontinuous process. Propagation velocity in cardiac muscle and smooth muscle is slower than what can be accounted for by the smaller fiber diameter and lower max *dV/dt*. The cell-to-cell transmission process is quite labile, somewhat like that in synaptic transmission.

Considerable data have been published concerning the degree of spread of electrotonic current between neighboring cells in cardiac muscle and visceral smooth muscles. Only one example is presented here for frog cardiac (ventricular) muscle. In these experiments, electrode 1 was used to record voltage and to inject current (using a Wheatstone bridge circuit), whereas electrode 2 recorded voltage only. As illustrated in Fig. 18A.1, using a pair of microelectrodes whose tips were spaced 11 μm apart, in some double impalements there was no electrotonic current spread between the two electrodes (e.g. panel A in Fig. 18A.1), whereas in other impalements there was substantial spread of current (e.g. panel B). In one unusual case (panels C, D), the double impalement first showed good spread (i.e. interaction) between the electrodes (C), but then due to muscle contraction, one electrode left that cell and impaled a neighboring cell having a normal RP (right portion of panel C); then there was no significant interaction between the two electrodes residing in neighboring cells (D). In the impalements in which there was substantial interaction between the electrodes (e.g. panels B, C), it was proposed that the two electrodes had impaled the same cell (e.g. both electrodes recorded low RPs (perhaps due to damage caused by the two electrodes impaling one cell). In the impalements in which there was little or no interaction (e.g. panels A, D), it was proposed that the electrodes had impaled neighboring cells. This interpretation is most clear in panel D, in which the two

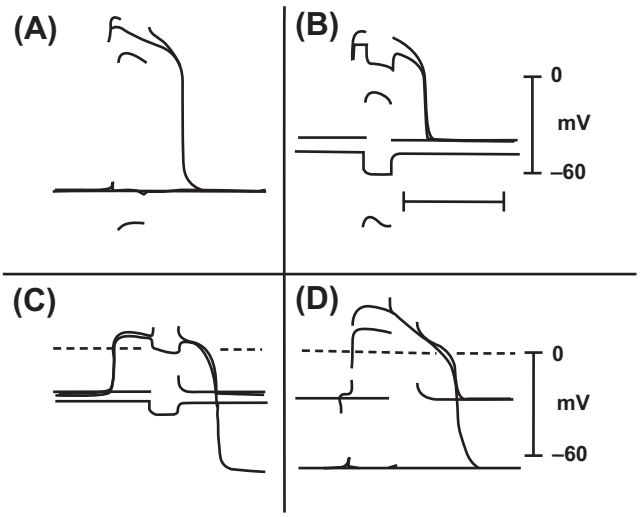

FIGURE 18A.1 Three typical experiments (A, B and C, D) measuring the spread of electrotonic current between two closely spaced intracellular microelectrodes in intact frog ventricular trabeculae at rest and during the plateau of the action potential. The interelectrode distance was 11 µm. Rectangular hyperpolarizing current pulses (approx. 150 ms in duration) were applied. Two successive sweeps of the oscilloscope are superimposed in each panel. (A) Interaction at rest and during the plateau was nearly 0%. Capacitive transients are only seen on the trace from electrode 2, whereas a large maintained hyperpolarization occurred at electrode 1. (B) In another impalement in which the cell was injured by the two electrodes, the resting potential was low and the degree of interaction was high. (C, D) In another impalement in which the cell was damaged, the resting potential was low and the degree of interaction was high (electrode I deflection not shown because of bridge imbalance). The contraction accompanying the action potential caused one of the electrodes to become dislodged from that cell and penetrate into a neighboring cell that had a normal resting potential; the degree of interaction then became nearly zero. *(Reproduced with permission from Tarr, M. and Sperelakis, N. (1964). Am J Physiol. 207, 691-700.)*

electrodes recorded markedly different RPs. Thus, there appears to be little or no spread of current between neighboring cells in frog cardiac muscle. If so, then propagation of excitation must occur by some other means.

AIII. ELECTRIC FIELD MODEL

AIIIA. Electric Field Effect

Sperelakis and colleagues developed an electric field (EF) hypothesis for propagation of APs in cardiac muscle for situations in which there were no functioning gap junction channels. A computer simulation model for cell-to-cell propagation in cardiac muscle was developed and progressively improved since the mid-1970s (Sperelakis and Mann, 1977; Sperelakis et al., 1983; Sperelakis, 1987; Picone et al., 1991). The model allows electrical transmission to occur between adjacent excitable cells by means of the EF effect in the very narrow junctional cleft between the contiguous cells (Sperelakis and Mann, 1977). This EF model does not require low-resistance channels (gap junctions) between cells. The major requirements of the model are that the pre- and post-junctional membranes (pre-JM and post-JM) be ordinary excitable membranes and that these membranes be very closely apposed to one another (i.e. the junctional cleft be very narrow, about 10 nm). When the pre-JM fires, the cleft between the cells becomes negative with respect to ground (the interstitial fluid surrounding the cells) and this negative cleft potential (about −40 mV) acts to depolarize the post-JM by an equal amount (namely, 40 mV) and brings it to threshold. (The inner surface of the post-JM remains at nearly constant potential with respect to ground.) This, in turn, brings the surface membrane of the post-junctional cell to threshold.

Figure 18A.2A illustrates propagation of an AP along a chain of 10 cells by the EF effect. In this computer simulation of cardiac muscle, propagation of overshooting APs occurred at a constant velocity of 32 cm/s and the maximum rate of rise of the AP averaged 209 V/s. As can be seen, the upstroke of each AP exhibited a *break* or *step*, reflecting the junctional transmission process.

In the model, a plot of propagation time as a function of distance along a chain of cells has a **staircase shape**, indicating that almost all propagation time is consumed at the cell junctions and that excitation of each cell is virtually instantaneous (Picone et al., 1991; Sperelakis et al., 1983) (see Fig. 18A.2B). In this figure, it can also be seen that the prejunctional membrane fires a fraction of a millisecond *before* the surface membrane of the same cell, as required by the EF model. Propagation was found to be strongly dependent on radial cleft resistance (R_{jc}) and the junctional membrane properties. There was an optimal R_{jc} for maximum propagation velocity under any given conditions. This model is consistent with many experimental facts about propagation in cardiac muscle, and provides an alternative mechanism for AP propagation that does not require low-resistance pathways to transfer excitation directly between adjacent cells. The EF model can also account for the fact that propagation in cardiac muscle is actually discontinuous or saltatory in nature (Spach et al., 1981).

AIIIB. High Density of Fast Na^+ Channels at Intercalated Disks

For this mechanism to work efficiently, there is a requirement for the prejunctional membrane to fire an AP a fraction of a millisecond before the contiguous surface membrane (Sperelakis and Mann, 1977). That is, the prejunctional membrane should be more excitable than the surface membrane, which would cause it to reach threshold first. This situation would be achieved if there were a greater density of fast Na^+ channels in the junctional membranes (intercalated disks, IDs) than in the contiguous

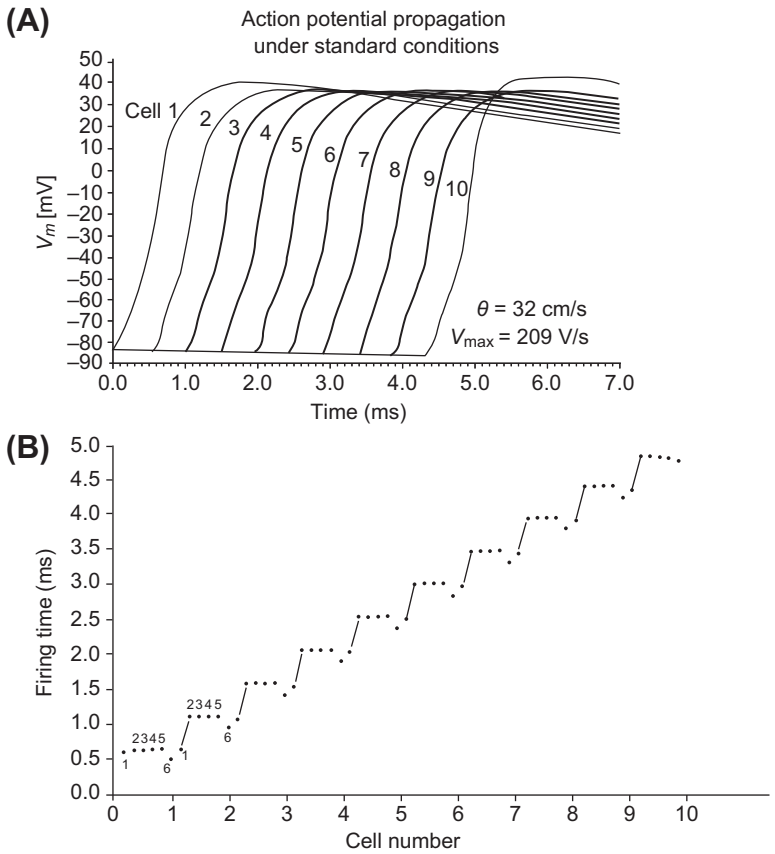

FIGURE 18A.2 Electric field model for propagation in cardiac muscle using a computer simulation. (A) Successful propagation of an AP at constant velocity along a chain of 10 cells under standard conditions. Propagation velocity was 32 cm/s; max *dV/dt* was 209 V/s. Note the small step, or prepotential, on the AP upstroke. (B) Plot illustrating that junctional delays occupy most of the propagation time. Firing time for an AP to spread along the chain of 10 cells under standard conditions (corresponding to part A) is plotted against distance. Within each cell, the units are numbered 1 through 6 from left to right, 1 corresponding to the post-JM (input), 2–5 the surface membrane and 6 the pre-JM (output). The AP travels along the surface membrane at a high velocity. At the junctions between cells, there is a significant conduction delay as the AP "jumps" across the cleft. This clearly demonstrates the discontinuous nature of AP propagation. *(Adapted with permission from Figs. 2 and 3 of Sperelakis, N., Ortiz-Zuazaga, H. and Picone, J.B. (1991). Innov Tech Biol Med. 12, 404-414.)*

surface membranes (Sperelakis and Mann, 1977). This would make the IDs more excitable and give them a lower threshold than the surface membrane. To examine this possibility, a polyclonal antibody raised against fast Na^+ channels (from rat brain) was used to immunolocalize the fast Na^+ channels in rat atrial and ventricular tissues. In immunofluorescence examination, intense labeling was observed associated with the IDs of both atrial and ventricular cells (Ferguson, D., Sperelakis, N., and Angelides, K. J., 1991 (unpublished) (Fig. 18A.3). This fluorescence was more intense than that of the cell surface membrane. These findings are in agreement with results reported by Cohen and Levitt (1993).

Therefore, it is likely that, not only are fast Na^+ channels present at the ID membranes, they are present in a higher concentration (density) than in the surface cell membrane. A higher density of fast Na^+ channels in the junctional membrane would cause it to have a lower threshold than the surface membrane and so it would reach threshold and discharge first. This would be analogous to the initial segment of the axon of the anterior horn neuron having a lower threshold and therefore discharging before the soma or proximal dendrites (where the excitatory synapses are actually located). Consistent with these

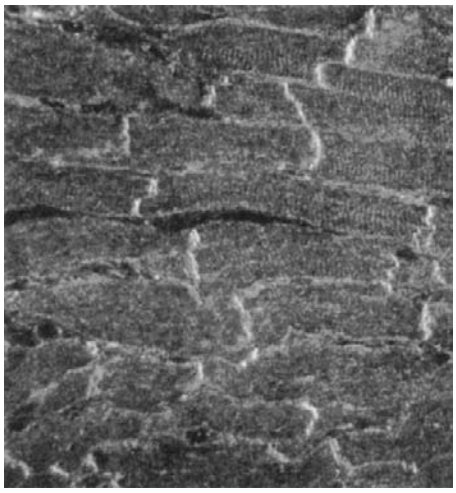

FIGURE 18A.3 Immunofluorescence localization of Na^+ channels in adult rat cardiac muscle (ventricle) using polyclonal antibody to the fast Na^+ channels of rat brain. The antibody is most densely localized at the cell junctions (intercalated disks), but also stained the surface cell membrane. These results suggest that the intercalated disks are highly excitable membranes, even more excitable than the surface cell membrane, consistent with the requirement of the electric field model for propagation between cells not connected by low-resistance tunnels (gap junction connectons). *(From Ferguson, D., Sperelakis, N. and Angelides, K.J., unpublished observations.)*

findings, it was reported that K^+ channels are also localized at the IDs (Mays et al., 1995). Therefore, the EF model is a plausible mechanism for cell-to-cell transmission of excitability in cardiac muscle and in visceral smooth muscle. EF effects may also occur between closely spaced contiguous neurons in the central nervous system.

AIV. ELECTRONIC MODEL FOR SIMULATION OF PROPAGATION

Sperelakis and colleagues (1990) constructed an electronic model to simulate an excitable membrane and this model was used to examine propagation. Four such circuits were successfully made to interact with one another through capacitive coupling to simulate propagation over four cells. Adjustment of one parameter either slightly depolarized and caused repetitive spontaneous APs, or hyperpolarized slightly and depressed excitability, causing partial block (e.g. 2:1, 3:1, 4:1) or complete block of propagation from cell to cell at the cell junctions. When four such cells were connected head to tail in a closed loop, re-entry of excitation occurred and could keep going for many seconds before dying out (due to failure at one of the labile junctions).

In a subsequent study (Ge et al., 1993), 12 such units were arranged to model two adjacent cells: four units for each surface membrane and one for each junctional membrane. The first unit was stimulated to threshold and AP propagation spread over the two cells was recorded (Fig. 18A.4). In this example, the first cell was set to be spontaneously active and fire a spontaneous cardiac-like AP. All four surface-membrane units in cell 1 (U2, 3, 4, 5) fired an AP nearly simultaneously. However, there was a short delay (e.g. ca. 0.5 ms) in the firing of the unit (U6) representing the prejunctional membrane (at the ID). Firing of U6 led to the firing of all units (U7, 8, 9, 10,11, 12) of cell 2 after a junctional delay of about 2 ms. The firing of the pre-junctional membrane (U6) drove inward hyperpolarizing current through the post-junctional membrane (U7) and outward depolarizing current through the other units (U8, 9, 10, 11, 12) of cell 2 due to current flow (prior to triggering an AP). The time delay was 1−2 ms at the junction. Raising the effective coupling resistance (R_c) between the two cells *and lowering* C_j increased the conduction delay. Propagation was blocked when R_{jc}, the radial shunt resistance at the cell junction, was below 10 KΩ. The post-JM (unit 7) only fired an AP when unit 6 was active, reflecting the EF effect across the junction. Both local-circuit current and the EF effect play roles in the transfer of excitation in this model.

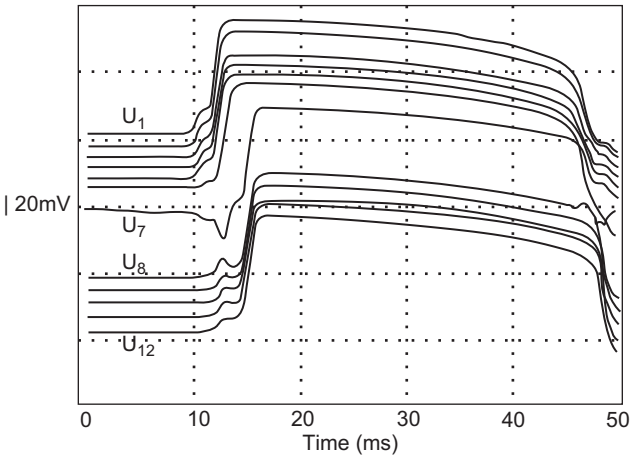

FIGURE 18A.4 Action potentials produced in an electronic model of two heart cells with a cell junction between them. There were six excitable-circuit units in each cell: four representing the surface cell membrane (U2, 3, 4, 5 and U8, 9, 10, 11) and one for each junctional membrane (U1, 6 and U7, 12). The parameters in the first cell (cell 1) were adjusted so that it fired spontaneously in response to pacemaker potential depolarization. Note the nearly simultaneous firing of all units in cell 1 and, after a slight junctional delay time, the nearly simultaneous firing of all units of cell 2. *(Reproduced with permission from Fig. 5A of Ge, J., Sperelakis, N. and Ortiz-Zuazaga, H. (1993). Innov Tech Biol Med. 14, 404-420.)*

AV. PSPICE MODEL FOR SIMULATION OF PROPAGATION

PSpice is an electrical engineering software program for circuit design and analysis. The appropriate differential equations are built into PSpice. We recently modeled propagation of APs of cardiac muscle using the PSpice program (Sperelakis and Ramasamy, 2002). Like the mathematical simulation and the electronic model, we found that the EF developed in the junctional clefts (negative V_{JC}) was large and sufficient to allow transfer of excitation to the contiguous cell, without the requirement of gap-junction (gj) channels. In the absence of gj channels, transmission of excitation from one cell to the next occurs by means of the intense EF that develops in the narrow junctional cleft (IDs) when the pre-junctional membrane fires an AP. This cleft potential is negative (with respect to ground (interstitial fluid bathing the cells)), and thus acts to depolarize the post-junctional membrane to its threshold potential. This causes the surface sarcolemma of the post-junctional cell to fire an AP and the process is repeated at the next junction. For this EF mechanism to work, the pre-junctional membrane must fire slightly before the surface sarcolemma of the pre-junctional cell (Sperelakis and Mann, 1977). The fact that the density of fast Na^+ channels is greater at the ID membranes than in the surface sarcolemma (Sperelakis N., 1995; Cohen SA and Levitt LK, 1993) means that the excitability of the junctional membranes should be greater than that of the surface sarcolemma.

The myocardial cells were assumed to be cylindrical in shape, 150 μm in length and 16 μm in diameter. The cleft width of the cell junctions (IDs) was assumed to be 100 Å.

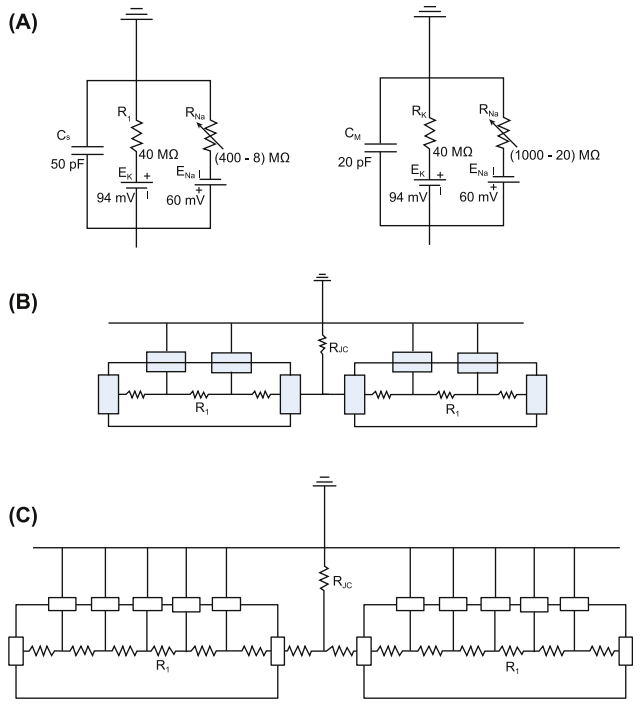

FIGURE 18A.5 (A) Depiction of the basic circuit components in the PSpice model representing a patch of surface membrane of a myocardial cell and a patch of junctional membrane. (B) Four units/cell, two in surface membrane and one in each of the two junctional membranes at the ends of the cell. (C) Seven units/cell.

Each cell was simulated by four basic circuit units; two for the surface sarcolemma and one for each junctional membrane at the two ends of the cell (Fig. 18A.5). The cell junctions contained a transverse resistance, the radial resistance of the junctional cleft (R_{JC}). The standard value used for R_{JC} was 25 MΩ (two 50 MΩ resistors in parallel). The basic units were connected internally by the intracellular longitudinal resistance (r_i) and externally by the extracellular resistance (R_O). The chain of cells was assumed to be bathed in a large volume of Ringer solution connected to ground. The values of the capacitive and the resistive elements in each basic unit were set to reflect an input resistance of 20 MΩ and input capacitance of 100 pF for the individual cells and the junctional units were prorated, based on relative areas represented. At rest, the resistance of K^+ compared to Na^+ was set to give RPs of −80 mV. During excitation, the APs overshot to +34 mV.

To make the circuit as simple as possible, all other types of ion channels were not entered. We focused only on those channels that set the RP and predominate during the rising phase of the AP. That is, we only wanted to inscribe the rising phase of the APs in a chain of cells to study the mechanism of longitudinal propagation. The longitudinal resistance in each junctional cleft was calculated to be 14 Ω (see Fig. 18A.5C). Increasing the longitudinal cleft resistance over a very wide range had no effect on propagation velocity, because there is almost no local-circuit current across the cell junctions. A shunt resistance (R_{gj}, resistance of the gap junction channels) was placed across each cell junction, i.e. from one cell interior to the next (Fig. 18A.6). It was assumed that each gj-channel had a conductance of 100 pS, so R_{gj} was 100 MΩ when 100 gj-channels were inserted. The possibility that the gj-channels are rectifying was ignored for the present purposes. In the current presentation, the data with variation in R_{gj} are not given.

A stimulating current pulse was applied to the inside of unit 1 of cell 1. The values for the rectangular current pulse were 0.50 ms duration and 0.5 nA amplitude. The longitudinal average propagation velocity (θ) was calculated from the measured total propagation time (TPT), assuming a cell length of 150 μm.

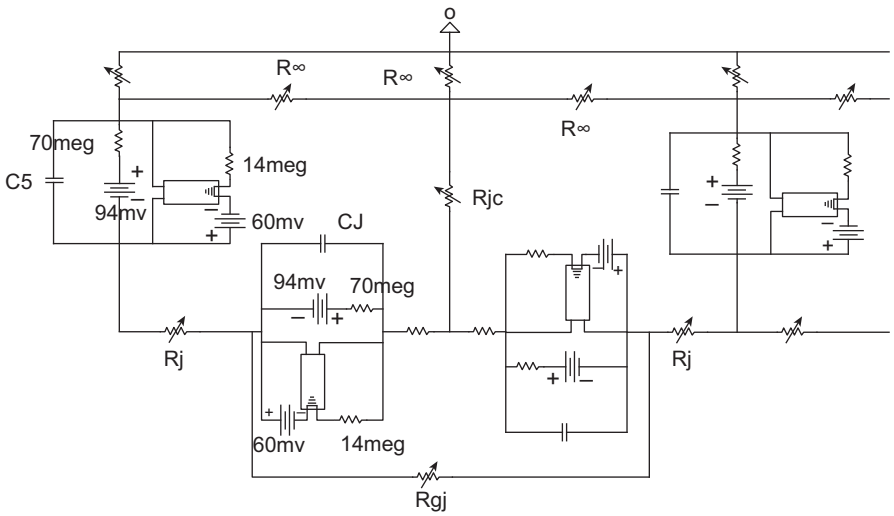

FIGURE 18A.6 A typical cell junction of circuit used for PSpice simulation of propagation of action potentials. A gap-junction shunt resistance (R_{gj}) is inserted across the cell junction and is in parallel with the electric field (EF) mechanism.

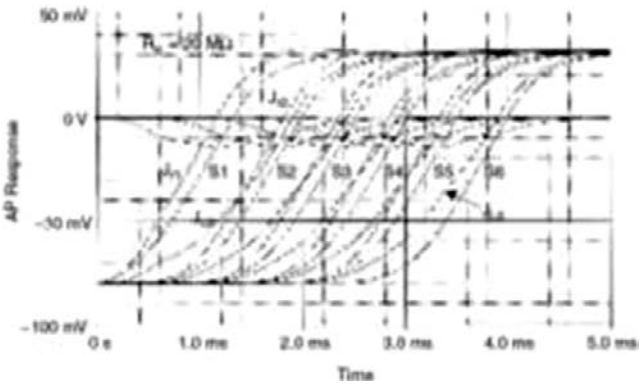

FIGURE 18A.7 Staircase propagation and firing sequences. Absence of gap junctions. Graph plots total propagation time (TPT) as a function of distance along the six-cell chain in membrane units. Total of 42 units: 7 U/cell × 6 cells. Each cell is assumed to be 150 µm long. The surface membrane of each cell is represented by five units and the two junctional membranes by one unit each. The units were numbered consecutively: 1–7 (cell 1), 8–14 (cell 2), 15–21 (cell 3), 22–28 (cell 4), 29–35 (cell 5) and 36–42 (cell 6). The junctional units fired before the surface units. *Taken from Sperelakis and Ramasamy, 2002.*

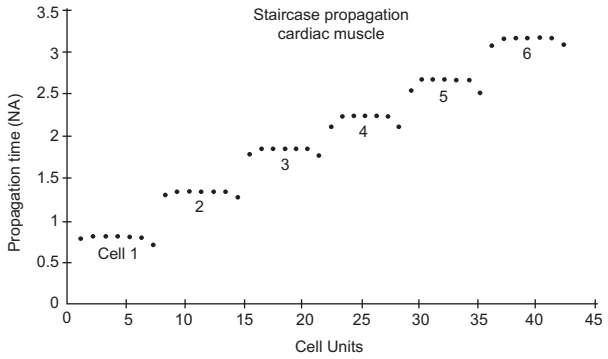

FIGURE 18A.8 Action potential (AP) responses of the six-cell chain of myocardial cells. Absence of gap junctions. At −50 mV, the first trace (of each group of three) is the post-JM (left end of cells), whereas at −10 mV, the leading trace is the pre-JM (right end of cells); i.e. the first two traces criss-cross between −40 and −20 mV). Thus, the post-JM starts to depolarize first because of the cleft potential, but the pre-JM on the far end of the cell reaches the overshoot potential first. The surface membrane units (S1–S6) fire last. *Taken from Sperelakis and Ramasamy, 2002.*

The basic response of the circuit for the six-cell chain under standard conditions is illustrated in Fig. 18A.7. In this experiment, a rectangular current pulse was applied to interior of cell 1 at 0 time. The voltages directly across each of the 42 units (7 U/cell × 6 cells) and the voltage across R_{JC} (the cleft potential) were measured.

The rising phase of the AP response in each of the six cells can be seen. Because the five surface units in each cell fired virtually simultaneously, only three voltage traces can be seen for each cell: (a) post-JM, (b) pre-JM and (c) surface membrane. The RP of the cells was −80 mV and the AP overshoot potential was +34 mV (see Fig. 18A.7), thus giving an AP amplitude of 114 mV. The cleft potential went from 0 mV at rest to a peak of about −12 mV during excitation of the pre-JM in each cell (see Fig. 18A.7). The maximum rate of rise of the APs (max *dV/dt*) was about 110 V/s, the junctional delay time was about 0.3–0.6 ms and propagation velocity (θ) was about 30 cm/s. In general, the transmission delay was reduced when R_{JC} and the cleft potential were increased and when C_j and C_s were decreased. Total propagation time (TPT) was measured between when the APs of the first cell and last cell crossed a V_m of −20 mV.

The firing sequence of the seven units of each cell is shown in Fig. 18A.8. As can be seen, in cell 1, the pre-JM (unit 7) fired before the post-JM (unit 1), which fired before the surface units (units 2–6). As stated earlier, all surface units fired virtually simultaneously. The lead time of the pre-JM became less and less in cells 2–6. This behavior pattern of the pre-JM (right end of cell) firing slightly before the post-JM (left end of cell) was also observed in the mathematical model (Picone et al., 1991). The graphic plot of propagation time as a function of distance along the chain of six cells also illustrates the *staircase propagation* (Fig. 18A.8). That is, the shape of the plot is like a *staircase*. The flat part of each step represents the long surface membrane of each cell. The sharp rise of each step represents the very short (e.g. 100 Å) cell junction gap. The overall propagation time consists almost entirely of the junctional delay times summed. That is, almost all of the propagation time is due to the junctional transmission process. The surface sarcolemma along the cell's entire length fires simultaneously.

The cleft potential occurs during the rising phase of the AP in the pre-JM. The shape of the cleft potential is an approximation of the first time derivative of the AP upstroke (see Fig. 18A.5). In general, the cleft potential is larger when R_{JC} is increased and when C_j and C_s are decreased. When R_{JC} was increased from the standard 20 MΩ to 50 MΩ and 100 MΩ, the cleft potential increased from −12 mV to −27 mV and to −47 mV. The cleft potential instantly depolarizes the post-JM by an equal amount because of its patch-clamp-like action. The amplitude of the depolarization (step) on the rising phase of the AP of the post-JM is proportional to the amplitude of the cleft potential. The value of R_{JC} for minimum junctional delay, and hence maximal propagation velocity, had a broad optimum of 20–30 MΩ. The value of R_{JC} reflects the degree of closeness of the two junctional membranes.

In summary, it was found that propagation of excitation can occur by the EF mechanism alone, even when the excitability of the cells was low. Therefore, the EF mechanism alone can account for propagation of excitation in cardiac muscles that do not possess gap junctions. In those cases in which gap junctions do exist and are functioning, the EF mechanism would act in parallel and thereby increase the safety factor for conduction.

BIBLIOGRAPHY

Cohen, S. A., & Levitt, L. K. (1993). Partial characterization of the rHl sodium channel protein from rat heart using subtype-specific antibodies. *Circ Res, 73*, 735–742.

Cole, K. S. (1968). *Membranes, Ions and Impulses: a Chapter of Classical Biophysics*. Berkeley: University of California Press.

Cole, W. C., Picone, J. B., & Sperelakis, N. (1988). Gap junction uncoupling and discontinuous propagation in the heart: a comparison of experimental data with computer simulations. *Biophys J, 53*, 809–818.

Ge, J., Sperelakis, N., & Ortiz-Zuazaga, H. (1993). Simulation of action potential propagation with electronic circuits. *Innov Tech Biol Med, 14*, 404–420.

Katz, B. (1966). *Nerve, Muscle, and Synapse*. New York: McGraw-Hill.

Mann, J. E., Jr., Sperelakis, N., & Ruffner, J. A. (1981). Alterations in sodium channel gate kinetics of the Hodgkin-Huxley equations on an electric field model for interaction between excitable cells. *IEEE Trans Biomed Eng, 28*, 655–661.

Mays, D. J., Foose, J. M., Philipson, L. H., & Tamkun, M. M. (1995). Localization of the Kv1.5K^+ channel protein in explanted cardiac tissue. *J Clin Invest, 96*, 282–292.

Picone, J. B., Sperelakis, N., & Mann, J. E., Jr. (1991). Expanded model of the electric field hypothesis for propagation in cardiac muscle. *Math Comp Mod, 15*, 17–35.

Rail, W. (1977). In J. M. Brookhart, & V. B. Mounteastle (Eds.), *Handbook of Physiology, Vol. 1* (pp. 39–97). Bethesda: American Physiological Society.

Spach, M. S., Miller, W. T., III, Geselowitz, D. B., Barr, R. C., Kootsey, J. M., & Johnson, E. A. (1981). The discontinuous nature of propagation in normal canine cardiac muscle. Evidence for recurrent discontinuity of intracellular resistance that affects the membrane currents. *Circ Res, 48*, 39–54.

Sperelakis, N. (1987). Electrical field model for electric interactions between myocardial cells. In S. Sideman, & R. Beyar (Eds.), *Activation, Metabolism, and Perfusion of the Heart – Simulation and Experimental Models* (pp. 77–113). Dordrecht: Martinus Nijhoff.

Sperelakis, N. (1992). Cable properties and propagation mechanisms. In N. Sperelakis, & R. O. Banks (Eds.), *Essentials of Physiology* (pp. 83–97). Boston: Little, Brown.

Sperelakis, N. (2001). Cable properties and propagation of action potentials. In *Cell Physiology Sourcebook*, (3rd ed., chapt 24). San Diego: Academic Press.

Sperelakis, N. (2002). Editorial: An electric field mechanism for transmission of excitation between myocardial cells. *Circ Res., 91*, 985–987.

Sperelakis, N., & Mann, J. E., Jr. (1977). Evaluation of electric field changes in the cleft between excitable cells. *J Theor Biol, 64*, 71–96.

Sperelakis, N., & Ramasamy, L. (2002). Modeling electric field transfer of excitation at cell junctions. *IEEE Eng Med Biol, 22*, 130–143.

Sperelakis, N., Marschall, R., & Mann, J. E. (1983). Propagation down a chain of excitable cells by electric field interactions in the junctional clefts: effect of variation in extracellular resistances, including a "sucrose gap" simulation. *IEEE Trans Biomed Eng, 30*, 658–664.

Sperelakis, N., Rollins, C., & Bryant, S. H. (1990). An electronic analog simulation for cardiac arrhythmias and reentry. *J Cardiovasc Electrophysiol, 1*, 294–302.

Tarr, M., & Sperelakis, N. (1964). Weak electronic interaction between contiguous cardiac cells. *Am J Physiol, 207*, 691–700.

Taylor, R. E. (1963). Cable theory. In W. L. Nastuk (Ed.), *Physical Techniques in Biological Research, Vol. 6* (pp. 219–262). New York: Academic Press.

This page intentionally left blank

Chapter 19

Electrogenesis of Membrane Excitability

Nicholas Sperelakis

Chapter Outline

I. SUMMARY

Membrane excitability is a fundamental property of nerve and muscle cells (skeletal, cardiac and smooth), as well as certain other cell types, such as some endocrine cells. An excitable cell is one that, in response to certain environmental stimuli (electrical, chemical or mechanical), generates an all-or-none electrical signal or *action potential* (AP). The AP is sometimes called an "impulse", e.g. a *nerve impulse*. The AP is triggered by a depolarization of the membrane, which is produced by the applied stimulus. The depolarization initiates an increase in the membrane permeability to Na^+ ions, which then flow into the cell, causing a transient reversal in the membrane potential (i.e. the *spike*). A slower increase in the permeability of the membrane to K^+ ions contributes to the repolarization of the membrane, in addition to the spontaneous inactivation of the Na^+ channels. Some cells display the property of *automaticity*; i.e. they produce APs spontaneously without any externally-applied stimulus.

In some excitable cell types (such as cardiac), a slow inward Ca^{2+} current contributes to the long plateau of the AP and, in others (such as smooth muscle), the Ca^{2+} current itself generates the upstroke. The membrane currents that contribute to the AP can be studied by the *voltage-clamp method*, which allows isolation and characterization of each membrane current as a function of membrane potential and time. Ionic currents flow across the membrane by means of numerous ion-specific protein channels. Each channel molecule has a region that senses the transmembrane potential and acts as a gate to open or close the channel to ion passage through its *central water-filled pore*.

Some types of channels (i.e. Na^+ channels) have a *second gating system* that closes (or inactivates) the

Cell Physiology Sourcebook. DOI: 10.1016/B978-0-12-387738-3.00019-6

channel during a maintained depolarization. The pattern of minute currents that flow through individual voltage-dependent ion channels can be studied using the patch-clamp method. *Single-channel current measurement* and structural information have given a greater understanding of the molecular basis of membrane excitability.

The APs in vertebrate nerve fibers consist of a spike followed by a hyperpolarizing afterpotential. A large fast inward Na^+ current, passing through *fast Na^+ channels*, is responsible for electrogenesis of the spike, which rises rapidly (ca 1000 V/s). Subsequently, a small inward Ca^{2+} current, passing through kinetically-slower channels, is involved in *excitation–secretion coupling* at the nerve terminals. The nerve cell membrane has voltage-dependent K^+ channels which allow K^+ ions to pass readily outward down the electrochemical gradient for K^+. This is responsible for repolarization. This K^+ channel, which opens more slowly than g_{Na} upon depolarization, is called the *delayed rectifier*. The activation of this channel produces the large increase in total g_K that terminates the AP.

The nerve AP amplitude is about 110 mV, from a resting potential (RP) of −70 mV to a peak overshoot potential of about +40 mV. The duration of the AP (at 50% repolarization) ranges between 0.5 and 1 ms, depending on the species and temperature. The threshold potential (V_{th}) for triggering of the fast Na^+ channels is about −55 mV; a critical depolarization of about 15 mV is required to reach V_{th}. The turn-on of the fast Na^+ conductance is very rapid (within 0.2 ms) and E_m is brought rapidly toward E_{Na}. There is an explosive (positive exponential initially) increase in g_{Na} caused by a *positive-feedback relationship between g_{Na} and E_m*.

In certain nerve cells, as well as muscle cells, as E_m depolarizes it crosses V_{th} (about −35 mV) for the slow Ca^{2+} channels. Turn-on of the slow Ca^{2+} conductance (g_{Ca}) and I_{Ca} is slow and tends to bring E_m toward E_{Ca}. The peak I_{Ca} is considerably smaller than the peak fast I_{Na}. The currents decrease at more depolarized E_m levels because of the diminution in electrochemical driving force, even though the conductance remains high. At the reversal potential (E_{rev}) for the current, the driving force goes to zero and reverses direction with greater depolarization. In some smooth muscle cells, the slow Ca^{2+} current itself is sufficient to depolarize the membrane and generate a regenerative slowly-rising AP in the absence of any fast Na^+ current.

II. INTRODUCTION

Excitability is an intrinsic membrane property that allows a cell to generate an electrical signal or AP in response to stimuli of sufficient magnitude. The elongated nerve axon serves to transmit information in the form of APs over long distances. The AP mechanism is required to propagate a uniform signal in a non-decremental manner. In muscle cells, the AP serves to spread excitation over the entire cell surface and is involved in triggering cell contraction.

The energy source for the generation of the AP is stored in the excitable cell itself. An initial depolarization is produced by a stimulus and triggers the intrinsic AP mechanism. The immediate source of energy for the AP comes from the transmembrane ionic gradients for K^+ and Na^+, which act like a battery. The K^+ ion concentration gradient is mainly responsible for the generation of the resting potential (RP), which causes an excess of negative charge to build up on the inner surface of the membrane. Upon depolarization to threshold, the Na^+ ion electrochemical driving force, which is directed inward, causes a large and rapid inward Na^+ current that generates the AP upstroke. Over a longer time frame, the Na^+-K^+ pump is responsible for the generation of the Na^+ and K^+ ionic gradients and for their maintenance and restoration after repetitive AP activity. The Na^+-K^+ pump derives chemical energy from the hydrolysis of ATP. The bases of the RP and active ion transport have been discussed in earlier chapters.

Important technological improvements have led to significant advances in the understanding of the basis of membrane excitability. In the early 1900s, several theories were proposed to explain the mechanism that produces the AP. Julius Bernstein (1902, 1912) proposed that the excitable cell membrane, at rest, was selectively permeable to K^+ ions (producing the RP) and that during excitation the membrane became permeable to all ions (producing the AP). About the same time, Overton (1902) had demonstrated that Na^+ ions were essential for excitability.

By the 1940s, improvements had been achieved in electronic instrumentation, especially in the high-input impedance amplifiers necessary to record bioelectric phenomena using tiny intracellular microelectrodes. In addition, biophysicists began to study the squid giant axon (500–1000 μm in diameter), which permitted insertion of relatively large intracellular electrodes, yielding the first measurements of the true transmembrane potential. The transmembrane potential is recorded as the difference between an intracellular and an extracellular electrode (Fig. 19.1). The findings from the squid giant axon were successfully applied to the smaller diameter (1–20 μm) neurons found in the vertebrate nervous system (Fig. 19.2).

III. ACTION POTENTIAL CHARACTERISTICS

APs in a given fiber (e.g. myelinated nerve fiber) have the properties of being *all-or-none*, and they have a *sharp threshold* and a *refractory period*. All impulses look alike, being very similar in shape, amplitude and duration. Thus, they constitute a *digital system*. Strength of the signal is conveyed by changing the frequency of the impulses, as discussed in the preceding chapter on propagation. The all-or-none property means that the single signal is not

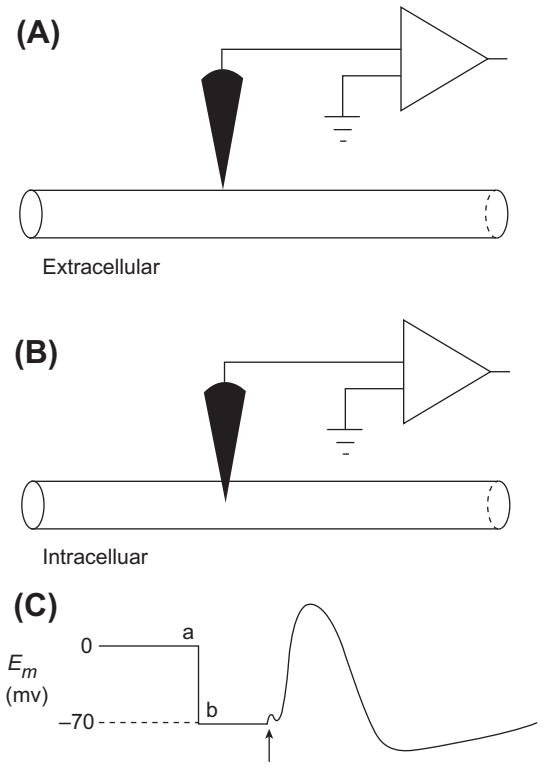

FIGURE 19.1 Recording the transmembrane potential of a squid giant nerve axon. The transmembrane potential is measured as the potential difference between the intracellular and extracellular electrodes. (A) The microelectrode is outside the axon and measures 0 mV (segment a in panel C). (B) As the electrode is advanced and crosses the membrane, the RP of −70 mV is measured (segment b in C). The cell membrane makes a tight seal around the glass electrode. (C) The membrane potential (E_m) is depicted. Stimulation (at arrow) elicits an AP.

graded in amplitude (i.e. not an amplitude-modulated system) and that the signal is either zero ("off" or "no") or maximum ("on" or "yes"). These characteristics of the AP are discussed in the next sections.

IIIA. Local-Circuit Currents

During propagation of an AP down a nerve fiber, current flow accompanies the propagating change in membrane voltage. This current is called the *local-circuit current* and has both longitudinal and radial (transverse) components that make a complete circuit (Fig. 19.3A,B). Propagation and local-circuit currents have been thoroughly discussed in the preceding chapter. For our purpose here, we focus on the longitudinal component. The intracellular and the extracellular (external) longitudinal current are exactly equal in amplitude, but flow in opposite directions (Fig. 19.3A,B). The intracellular current is, of course, confined to the cross-sectional area of the nerve fiber (neuroplasm), whereas the extracellular current can use the entire extracellular volume (so-called *volume conductor*). If a single nerve fiber or nerve bundle is mounted in air, then the extracellular action current is confined to the surface film of fluid adhering to the single fiber or the interstitial fluid space between fibers in the bundle.

To illustrate the principles involved, let us record externally with a pair of electrodes from a single nerve fiber (e.g. squid giant axon) bathed in air (see Fig. 19.3C). The fluid between the two electrodes constitutes a resistance (R) and longitudinal current (I) flowing through this resistance produces an IR voltage drop (Ohm's law: $V = IR$). As the AP moves from left to right past the pair of recording electrodes, the first electrode becomes negative with respect to the second electrode. Therefore, the voltmeter swings in one direction (an upward deflection is defined as negative in extracellular recording) due to the potential difference (pd). When the wave moves to a position between the two electrodes, the voltmeter will record almost zero voltage. When the AP reaches the second electrode, the voltmeter will swing in the opposite direction, because the second electrode is now negative with respect to the first. Thus, the electrodes will record a biphasic change in voltage as the AP sweeps past. When recording externally, the AP is a *wave of negativity* sweeping down the fiber; when recording internally, the AP is a wave of positivity.

Propagation velocity is a function of axon diameter and myelination, such that the larger the diameter, the greater the velocity. *Myelinated axons* conduct much faster than *non-myelinated axons*. The factors that determine propagation velocity and the mechanism of saltatory conduction were discussed in the preceding chapter.

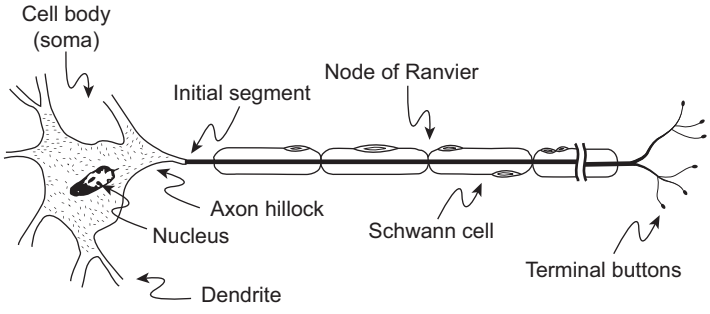

FIGURE 19.2 Diagram of a motor neuron with a myelinated axon. The major structural elements are diagrammed, including the cell body, initial segment, Schwann cell and node of Ranvier.

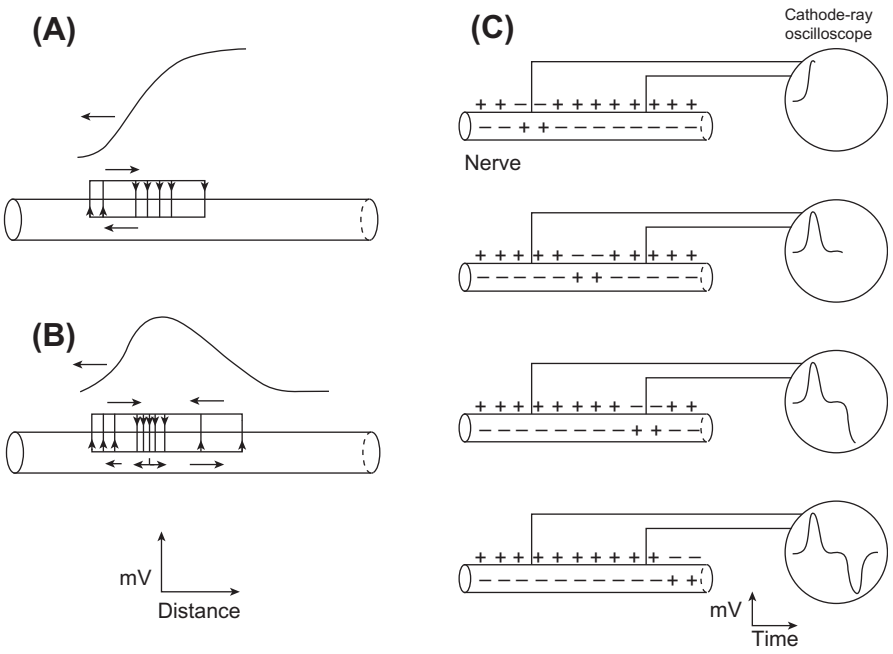

FIGURE 19.3 Diagram of the local-circuit current in a nerve fiber during an AP. (A) The current during the rising phase. (B) The current during the entire AP. The AP is depicted as propagating from right to left. (C) The actual registration of the signal is depicted for an AP propagating from left to right past a pair of electrodes spaced relatively far apart.

IIIB. Threshold and All-or-None Property

Nerve membrane responses near the site of application of brief current pulses vary depending on the magnitude and direction of the pulses (Fig. 19.4). Anodal (inward) currents produce hyperpolarization and cathodal (outward) currents produce depolarization. Hyperpolarizing and subthreshold depolarizing responses are graded in magnitude according to the stimulus current. However, as can be seen, a somewhat higher intensity outward current produces a depolarizing response with a different waveform and a longer duration. This condition is referred to as the *local excitatory state* (Fig. 19.4A, B). It occurs when a small area of the membrane near the stimulus electrode comes close to threshold, but it does not generate an AP. This local membrane activity is not propagated and decays with distance along the axon. A slightly stronger stimulus is, however, sufficient to bring the membrane potential of a large enough membrane area to the *threshold potential*, thereby initiating an all-or-none AP. At the threshold potential, a large inward (depolarizing) current is initiated and the membrane continues to depolarize.

In regard to the applied stimulus, outward current depolarizes the resting membrane (*IR* drop across the membrane is positive inside, negative outside), whereas inward current hyperpolarizes (*IR* drop is negative inside). In contrast, for the active membrane, inward currents are depolarizing (bringing positive charge inside the cell) and outward currents are hyperpolarizing. That is, when the membrane is behaving passively, applied inward current is hyperpolarizing and outward current is depolarizing; this is equivalent to a circuit external to a battery. In contrast, when the membrane is behaving actively, inward current generated is depolarizing and outward current is hyperpolarizing; this is equivalent to the internal current within a battery. This difference is because current flows from positive to negative in the external circuit and from negative to positive within the battery itself.

A subthreshold depolarization is defined as one that does not reach threshold to elicit an AP. It is proportional to the applied stimulus and it decrements with distance along the nerve axon cable. If a stimulus current is of sufficient magnitude, then the resulting membrane depolarization reaches a critical value, called the *threshold potential*, at which an AP is initiated (see Fig. 19.4).

The AP parameters, including overshoot, duration and rate of rise, are characteristic for each type of excitable cell. For example, the duration of the AP of the squid giant axon is about 1 ms, whereas the cardiac AP lasts over a hundred milliseconds. These differences in the APs subserve the functions performed by the different excitable tissues. The overshoot and a hyperpolarizing afterpotential (following the spike) are illustrated in Fig. 19.4C.

IIIC. Refractoriness

Once an AP is initiated, a finite and characteristic time must elapse before a second AP can be generated. This time interval is called the *refractory period* and its value depends on the type of excitable cell. Cells with long-duration APs (e.g. myocardial cells) have long refractory periods; cells

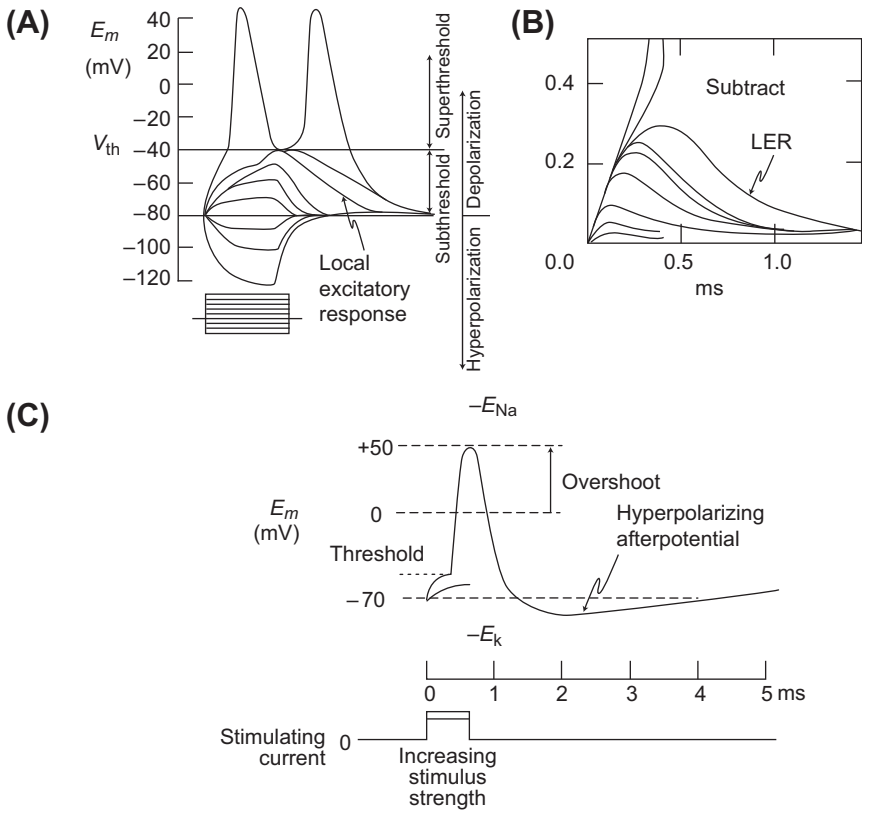

FIGURE 19.4 Diagrammatic sketches depicting initiation of the nerve impulse by membrane depolarization. (A) Membrane responses to depolarizing and hyperpolarizing current pulses are shown. The non-linear local excitatory response (LER) occurs just below the threshold for the all-or-none AP. (B) Illustration of the LER obtained by subtraction of the membrane responses to hyperpolarizing current pulses (passive only) from the responses to depolarizing pulses (passive plus active). (C) A nerve AP is depicted, illustrating the sharp threshold, overshoot and hyperpolarizing afterpotential.

with brief APs (e.g. neurons) have short refractory periods. That is, the refractory periods are related to the AP duration.

Two types of refractory periods are usually defined: an *absolute refractory period* and a *relative refractory period* (Fig. 19.5). The absolute refractory period denotes the interval during which a second AP cannot be elicited, regardless of the intensity of the applied stimulus. During the relative refractory period, a second AP may be elicited, provided that a greater than normal stimulus is applied. The second AP often is subnormal in amplitude and rate of rise. Therefore, the physiologically important refractory period is the *functional (effective) refractory period*, which is defined by the highest frequency of APs that the excitable cell can propagate. For example, if a myelinated nerve axon can propagate impulses up to 1000/s, then the functional refractory period is 1.0 ms. Since the triggering of a second impulse at a given point (or node of Ranvier) is limited by the amount of action current available from an active point (or node) upstream, the functional refractory period encompasses all of the absolute refractory period and part of the relative refractory period.

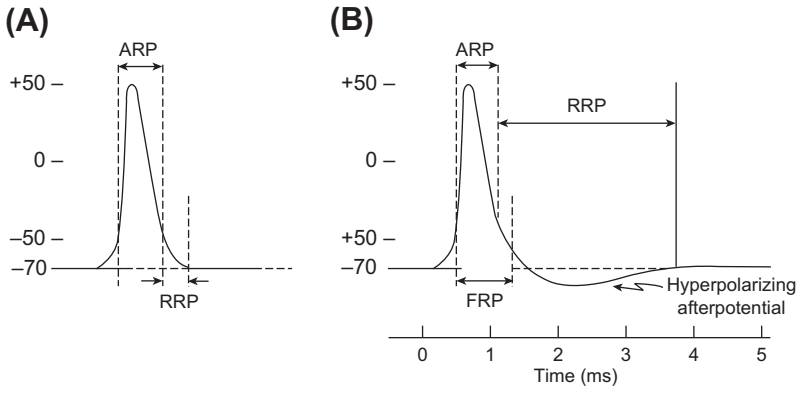

FIGURE 19.5 Refractory periods of nerve APs, both without (A) and with (B) a hyperpolarizing afterpotential. The absolute (ARP), relative (RRP) and functional (FRP) refractory periods are labeled.

The absolute refractory period extends from when threshold (V_{th}) is reached at the initial portion of the rising phase of the AP to when repolarization has reached a level of about −50 mV. During further repolarization beyond −50 mV (e.g. to −70 mV), a larger and larger fraction of the fast Na^+ channels recovers from inactivation and so more fast channels are again available to be reactivated to produce another AP. This is the period that inscribes the relative refractory period. The greater the degree of repolarization (toward the RP), the larger the subsequent AP.

In addition to voltage, time is a factor in the recovery of the ion channels. Therefore, the absolute and relative refractory periods persist briefly beyond the theoretical voltages and the relative refractory period actually slightly exceeds the AP duration.

Membrane excitability is greatly altered during the refractory periods. Excitability is zero during the absolute refractory period and is depressed during the relative refractory period, becoming less and less depressed as the membrane repolarizes back towards the RP.

The afterpotentials that many cells exhibit also affect membrane excitability: hyperpolarizing afterpotentials depress excitability (greater critical depolarization required to reach V_{th}) and depolarizing afterpotentials enhance excitability. A depolarizing afterpotential produces a *supernormal period of excitability*. In contrast, a hyperpolarizing afterpotential blends into and extends the relative refractory period. Thus, for example, since neurons usually exhibit hyperpolarizing afterpotentials, the functional refractory period actually includes part of the afterpotential.

Propagation velocity is slowed during the relative refractory period, achieving the normal value at the end of the relative refractory period. Propagation velocity is slightly faster than normal during the supernormal period of excitability.

IIID. Strength−Duration Curve

Whether the threshold potential is reached depends on the amount of charge transferred across the membrane. Figure 19.6 shows that the total charge transfer across the membrane required to produce excitation is approximately constant ($k = xy$ or $Q = IT$). It is an approximate rectangular hyperbola ($xy = k$) over the sharply-bending region of the curve. The strength−duration (S-D) curve can be derived from the equation for the exponential charge of the membrane capacitance.

The S-D curve deals only with the stimulus parameters (i.e. strength and duration of the applied current pulses) necessary to bring the membrane to threshold. It shows that the greater the duration of the applied pulse, the smaller the current intensity required to just excite the fiber. The asymptote parallel to the *x*-axis is the *rheobase*, which is the lowest intensity of current capable of producing excitation, even when the current is applied for infinite time (practically, >10 ms for myelinated nerve fibers). The asymptote parallel to the y-axis is the *minimal stimulation time*, which is the shortest duration of stimulation capable of producing excitation, even when huge currents are applied.

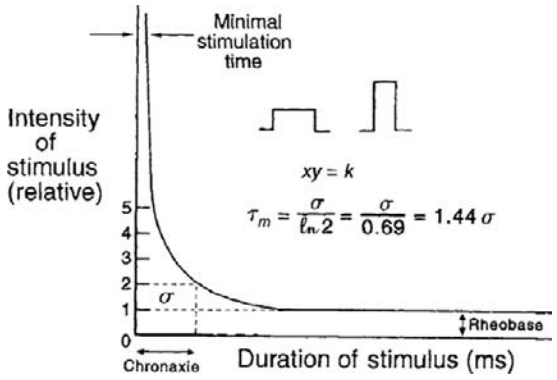

FIGURE 19.6 Strength−duration curve for AP initiation in excitable membranes. The intensity of rectangular stimulating pulses is plotted against their duration for stimuli that are just sufficient to elicit an AP. The rheobase current and chronaxie (σ) are indicated.

The usefulness of the rheobase is limited when comparing the excitability of one nerve with another because only the relative current intensity is meaningful. Furthermore, it is difficult to measure the stimulation time of a current with the intensity of the rheobase because it is an asymptote. Thus, a graphic measurement is made of the time during which a stimulus of double the rheobasic strength must act in order to reach threshold. This time is the *chronaxie*. Chronaxie values tend to remain constant regardless of geometry of the stimulating electrodes. The shorter the chronaxie, the more excitable the fiber. The chronaxie value for normal myelinated nerve fibers is about 0.7 ms. Some nerve pathologies in humans can be detected early by changes in their chronaxies.

Measurement of chronaxie in the laboratory is also valuable because it provides an easy method for measuring the value of the membrane time constant τ_m (see Chapter 18). In brief, the relationship between chronaxie (σ) and time constant (τ_m) is:

$$\tau_m = \frac{\sigma}{\ln 2} = \frac{\sigma}{0.69} = 1.44\sigma \qquad (19.1)$$

Thus, τ_m is 1.44 times the value of σ. Therefore, σ is analogous to a half-time for a first-order reaction, whose rate constant is the reciprocal of the τ_m ($k = 1/\tau_m$).

The S-D curve indicates that current pulses of very short duration (e.g. <0.1 ms) are less effective for stimulation. Thus, sinusoidal alternating current (AC) at frequencies above 10 000 Hz is less capable of stimulation. Another way to view this is that, because the membrane impedance decreases greatly at high frequencies (since the cell

membrane is a parallel RC network), the pd that can be produced across the membrane by current flow across it (IR or IX drops) is very small. Hence, AC of very high frequency has less tendency to electrocute and the energy of such currents can be dissipated as heat in body tissues and thus may be used in diathermy for therapeutic warming of injured tissues.

IIIE. Accommodation

Accommodation, in electrophysiology, refers to the loss of sensitivity of a cell to an applied stimulus. Sensory organs exhibit the property of accommodation, as do many neurons and other excitable membranes, such as skeletal muscle fibers. When a rectangular (square-wave) current pulse is used to depolarize a quiescent motor neuron (step depolarization) from the RP (e.g. −70 mV) to the threshold potential (V_{th}) or beyond, the neuron quickly responds with an all-or-none AP. However, if the applied pulse is ramp-shaped (triangular), the neuron may or may not respond, even if the normal V_{th} is exceeded, depending on the slope of the ramp. If the slope of the ramp is steep, the neuron will respond, but at a higher V_{th} level (more critical depolarization is required). If the slope is shallow, the neuron will fail to fire an AP, regardless of the level to which it is depolarized. This is accommodation. That is, when the membrane is depolarized gradually, the stimulus is ineffective in producing an AP response (Fig. 19.7A).

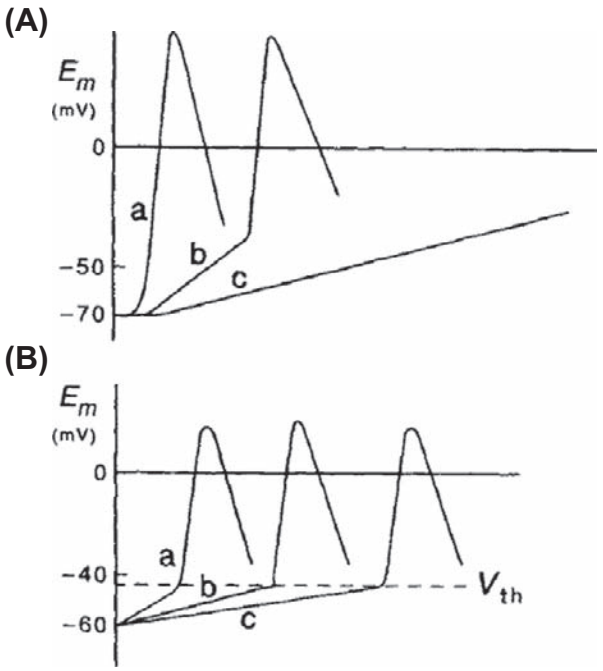

FIGURE 19.7 Sketches of accommodation and non-accommodation. (A) Accommodation in response to a ramp stimulus in a motor neuron and (B) lack of accommodation in a nodal pacemaker cell from the heart. In (A), as the slope of the ramp stimulus is decreased (from a to c), the AP response is delayed (b) and then fails completely (c). V_{th}, threshold potential.

This is not true of pacemaker cells (see Fig. 19.7B). Automatic (spontaneously-discharging) cells (e.g. nodal pacemaker cells of the heart and some sensory neurons) do not exhibit accommodation. Such cells will discharge an AP no matter how gradually the membrane is brought to the V_{th} point. In fact, the pacemaker potential in cardiac nodal cells is of the ramp type, producing depolarization to V_{th} over a period of about 200−800 ms.

The explanation for the phenomenon of accommodation is as follows. As the membrane is slowly depolarized toward V_{th}, the positive feedback cycle between E_m, Na^+ conductance (g_{Na}) and I_{Na} begins to operate (beginning at about 80% of the critical depolarization). Therefore, some of the fast Na^+ channels are turned on (activated), only to inactivate spontaneously (I-gates close) within 1−2 ms. If a critical number (critical mass) of fast Na^+ channels are not activated simultaneously, then the positive feedback cycle does not become explosive and a regenerative AP is not produced. That is, the slow depolarization does not allow a critical number of fast Na^+ channels to be simultaneously in the open conducting state. The channels that opened and spontaneously inactivated cannot be reactivated until they return to the resting state, which requires repolarization to near the RP. Hence, they are lost from the pool of available channels.

Added to this is the fact that K^+ channels (delayed rectifier type) will open during the slow depolarization, thus increasing K^+ conductance (g_K). Whenever g_K is increased, excitability becomes depressed, because it tends to repolarize and keep the membrane from depolarizing (to produce an AP). The g_K increase lowers R_m and so lowers the effectiveness of the depolarizing current.

Therefore, accommodation to low-slope stimuli occurs for two reasons: (1) spontaneous inactivation of fast Na^+ channels that have been activated, and therefore lack of a simultaneously-open critical mass, and (2) increase in g_K, which depresses excitability.

The lack of accommodation in automatic cells (e.g. SA nodal cells of the heart) then may be due to (1) less spontaneous ion channel inactivation and (2) less g_K increase during the applied ramp stimulus or natural ramp pacemaker potential. Both of these conditions apparently apply to cardiac nodal cells. The inward current responsible for the rising phase of the AP is not a fast Na^+ current, but rather a slow Ca^{2+} current, which inactivates very slowly and the kinetics of the turn-on of the delayed-rectifier K^+ current is also very slow.

As stated previously, accommodation also occurs in sensory organs. For example, some stretch receptors accommodate to a sustained stretch. When the stretch is first applied, there is a burst of APs. But the bursting frequency of discharge gradually slows down and then stops, even though the stretch is maintained.

IIIF. Anodal-Break Excitation

Excitation occurs on the make (the beginning) of a square-wave depolarizing stimulus. If the applied stimulus duration is very long (relative to the AP duration), repetitive firing of APs will occur if the membrane is of the non-accommodating type. If the membrane is of the accommodating type, then only the initial AP is produced, because accommodation occurs.

If the cathode (negative) and anode (positive) electrodes are placed directly on an isolated single nerve axon (e.g. squid giant axon), then an AP will be triggered at the cathode region on the make of the square-wave stimulus. This happens because, as depicted in Fig. 19.8A, depolarization occurs under the cathode, whereas hyperpolarization occurs under the anode. However, something unexpected occurs under the anode on the break of the stimulating pulse; namely, an AP is triggered from this hyperpolarized region of the axon (Fig. 19.8B). The explanation for this is that ion channel changes occur during the hyperpolarization, such that the excitability of that membrane is transiently increased (lower V_{th} point) immediately following cessation of the applied pulse.

The increase in excitability is due to two factors: (1) there is an increase in h_∞ during the hyperpolarization, reflecting that almost 100% of the fast Na^+ channels have their I-gates open, and hence are capable of conducting (open state) when the membrane is depolarized on cessation of the hyperpolarizing pulse ($g_{Na} = \max g_{Na}\, m^3 h$); and (2) there is a decrease in n during the hyperpolarization, hence decreasing g_K ($g_K = \max g_K\, n^4$). These equations are discussed in the following section. The changes in the h and n parameters persist for a short period after termination of the applied pulse and hence increase membrane excitability during this brief period and trigger an AP. This is called *anodal-break excitation* and post-anodal enhancement of excitability (due to the post-anodal depolarization).

In contrast, under the cathode, after termination of the applied pulse, an opposite change occurs in E_m and excitability. The membrane is hyperpolarized transiently and excitability is depressed. This is known as post-cathodal hyperpolarization and *post-cathodal depression of excitability*. In Hodgkin–Huxley terms, this phenomenon also is due to two factors: (1) decrease in h_∞ during the depolarization, reflecting a smaller fraction of fast Na^+ channels having their I-gates open and hence incapable of conducting and thereby decreasing g_{Na}; and (2) increase in n_∞, hence increasing g_K. The increased g_K and decreased g_{Na} produce hyperpolarization (refer to Chapter 9), and thereby depress excitability.

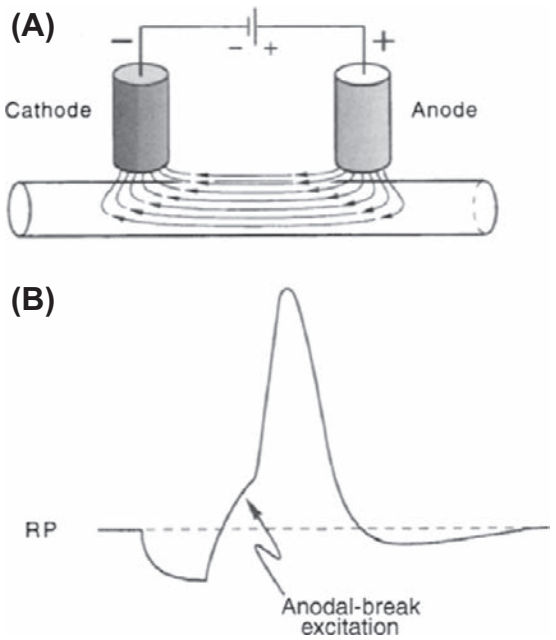

FIGURE 19.8 Current flow under the anode and cathode during extracellular stimulation (A) and anodal-break stimulation of an AP (B). (A) Excitation occurs under the cathode on the make of a current pulse and under the anode at the break of the rectangular pulse. (B) An intracellularly-applied hyperpolarizing current pulse produces an anodal-break response. RP, resting potential.

IV. ELECTROGENESIS OF ACTION POTENTIALS

Early experimentation in electrophysiology focused on determining the mechanism for the generation of the AP. One important finding by Cole and Curtis (1939) was that during the AP, the membrane resistance (but not the capacitance) changed dramatically (Fig. 19.9). The large reduction in membrane resistance during the AP supported the hypothesis that the AP resulted from a large increase in the ionic permeability of the membrane.

To determine which ionic species might be involved in generating the AP, subsequent experimentation was directed toward varying the concentrations of the different ions bathing the axon. When the concentration of Na^+ ions bathing the squid axon was lowered, it was found that the overshoot and the rate of rise of the AP were reduced. This result was the first indirect demonstration that the AP resulted from an increase in the membrane permeability to Na^+ ions. Several years later, this hypothesis was confirmed directly by the voltage-clamp method, as discussed in the next section.

IVA. Voltage-Clamp Method

The membrane current (I_M) that generates the AP is composed of ionic current (Ii) and capacitive current (Ic) according to the relationship:

$$I_M = Ii + Ic \qquad (19.2)$$

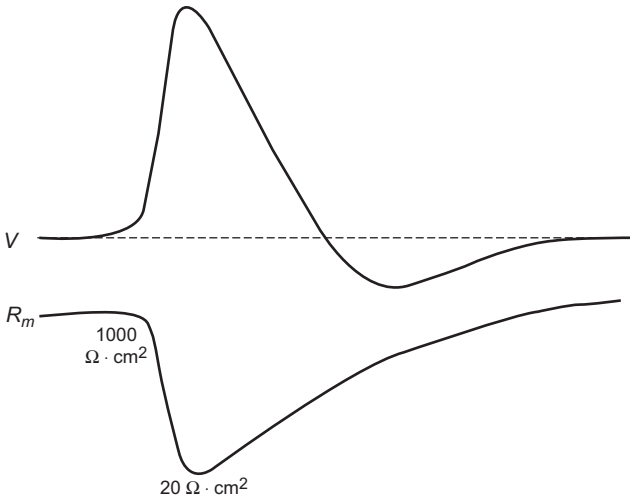

FIGURE 19.9 Time course for the decrease in membrane resistance (R_m) to the passage of current measured during the AP (V) in a nerve axon. R_m falls from about 1000 Ω·cm^2 at rest to about 20 Ω·cm^2 near the peak of the AP. *(Adapted from Cole, K.S. and Curtis, H.J. (1939). J Gen Physiol. 22, 649–687.)*

The flow of ionic currents across their respective resistive membrane pathways (or channels) causes a change in the membrane potential (from Ohm's law: $V = IR$). The change in membrane voltage causes an I_C also to flow as:

$$I_C = C_m \, dV/dt \qquad (19.3)$$

where dV/dt is the rate of change of the AP. Substituting Equation 19.3 into Equation 19.2 yields:

$$I_M = I_i + C_m \, dV/dt \qquad (19.4)$$

Since the membrane potential during an AP is constantly changing, it is difficult to separate the contributions of these ionic and capacitive components. In addition, the total ionic current is composed of multiple individual currents carried by specific ions. To analyze and separate the membrane currents into their capacitive and ionic components, a revolutionary method, called voltage clamping, was introduced in the early 1950s by Cole and then by Hodgkin and Huxley. A diagram of the voltage-clamp method is shown in Fig. 19.10. During a voltage-clamp experiment, the membrane potential is held constant (clamped) by a negative-feedback amplifier and the amount of current that is necessary to perform this task is recorded. Since the membrane potential (V_m) is held constant, the capacitive current is equal to zero. However, at the very beginning of the depolarizing clamp pulse, there is a large transient capacitive current that occurs and again at the "off" of the pulse; these can be electronically subtracted and thus removed by a special procedure. Since V_m is constant during the clamp pulse,

$$dV/dt = 0$$

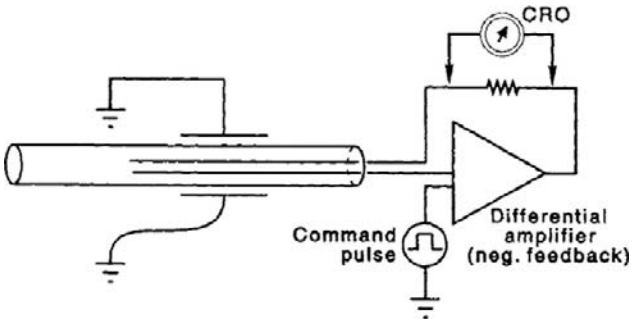

FIGURE 19.10 The voltage-clamp method used in a squid giant axon. The two wires inserted into the axon are used to measure membrane potential (V) and to pass current (I). The high-gain negative-feedback amplifier compares the command pulse with the membrane potential and outputs the amount of current necessary to hold the membrane potential constant (clamped). The magnitude of the feedback current can be measured as the IR voltage drop across a resistor and displayed on a cathode-ray oscilloscope (CRO).

and

$$I_c = 0$$

Therefore,

$$I_M = I_i$$

The voltage-clamp experiment gives the magnitude and time course of the ionic currents at a given clamp potential. By clamping the membrane to many different potentials, information about the flow of ionic currents and the underlying conductance changes during the AP is obtained.

IVB. Voltage-Clamp Analysis

In the voltage-clamp experiments, the various ion currents (such as Na^+, Ca^{2+} or K^+ currents) can be isolated from the total ionic current and analyzed individually. For example, in the squid axon experiments, the total ionic current consists of an early inward current followed by a delayed outward current (Fig. 19.11). By varying $[Na^+]_o$, the early inward current can be shown to be carried by Na^+ ions. Similarly, by changing $[K^+]_o$, the delayed outward current can be shown to be carried by K^+ ions. The Na^+ and K^+ currents can also be separated by blocking their pathways through the membrane. Na^+ channels can be blocked with *tetrodotoxin* (TTX), derived from the ovaries of Japanese puffer fish. K^+ channels can be blocked by several inorganic ions and organic compounds, including tetraethylammonium ions (TEA^+) and 4-aminopyridine (4-AP). The current remaining can then be subtracted from the total ionic current to reveal the time course for the current that was blocked.

The *current–voltage relationship* is obtained from measurements of the peak inward Na^+ current and peak outward K^+ current during a series of voltage clamp steps

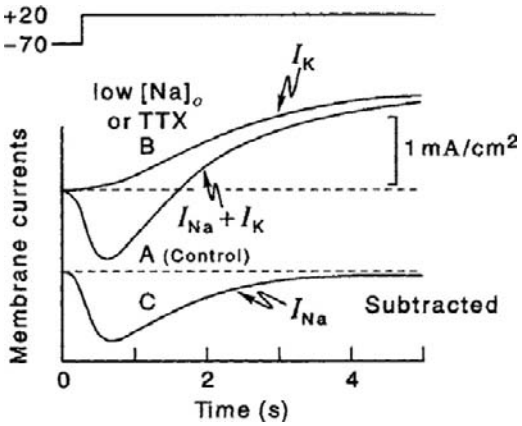

FIGURE 19.11 The ionic currents that flow when a squid giant axon is clamped from its RP (−70 mV) to a transmembrane potential of +20 mV. Trace A shows the net inward Na^+ current (I_{Na}) and outward K^+ current (I_K) in normal medium. Trace B shows the net ionic current when the axon is placed in artificial seawater with most of the Na^+ replaced by $choline^+$ (an impermeant cation), so that the intracellular and extracellular Na^+ concentrations are now equal. This current is due to K^+ only. TTX also can be used to block I_{Na}. Trace C shows the difference between curves A and B, which represents I_{Na}. *(Redrawn from Hodgkin, A.L. and Huxley, A.F. (1952a). J Physiol (London). 116, 449.)*

(Fig. 19.12). Depolarizing voltage steps to just above the RP first produce a small outward current. In this voltage region, the membrane behaves in an ohmic fashion. With greater depolarization, the inward I_{Na} is activated and the *I-V* relationship displays a negative slope or *negative resistance* region. At potentials above the peak current of the *I-V* curve, a positive slope is seen and the current magnitude decreases as E_{Na} is approached (and actually

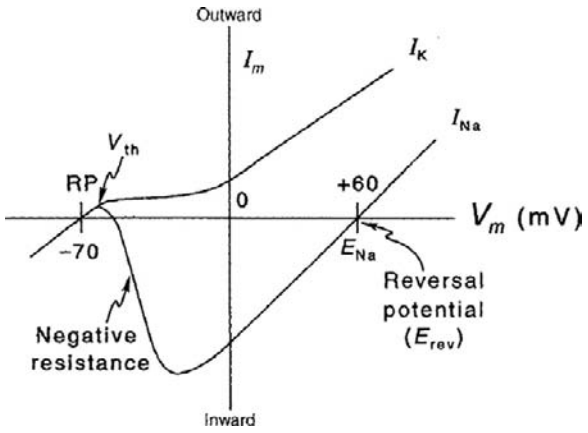

FIGURE 19.12 Current-voltage relationship for the peak early inward current and delayed outward current obtained from a squid axon under voltage-clamp. The inward current is carried by Na^+ (I_{Na}), the outward current by K^+ (I_K). The reversal potential for I_{Na} is the voltage at which the current changes from inward to outward. The region of the I_{Na} curve that has a negative slope is known as negative resistance. RP, resting potential; V_{th}, threshold; E_{Na}, Na^+ equilibrium potential; I_m, total membrane current; V_m, membrane potential. *(Redrawn from Hodgkin, 1964.)*

becomes outward at voltages above E_{Na}). The voltage at which the current reverses in direction is the *reversal potential*. The reason that the current diminishes and reverses at potentials approaching E_{Na} and beyond is that the net electrochemical driving force for Na^+ ions first becomes smaller and smaller and then outwardly directed, whereas the conductance for Na^+ ions remains constant and high over this entire voltage range, as indicated by:

$$I_{Na} = g_{Na} (E_m - E_{Na}) \quad (19.5)$$

The outward K^+ current activates above about −40 mV (in squid axon) and increases with further depolarization as:

$$I_K = g_K (E_m - E_K) \quad (19.6)$$

The voltage-clamp experiments have revealed the most fundamental property of the ionic conductances of excitable membrane: namely, that they are both voltage dependent and time dependent (Fig. 19.13). Both g_{Na} and g_K activate with depolarization, but with different time courses (Figs. 19.13 and 19.14). With time, g_{Na} spontaneously turns off, or inactivates. That is, the I_{Na} current shuts off within 1−2 ms.

A number of biological toxins that act on specific ion channels have been discovered. For example, TTX, mentioned previously, has a very high affinity for the fast Na^+ channel of nerve and some types of muscle cells. It

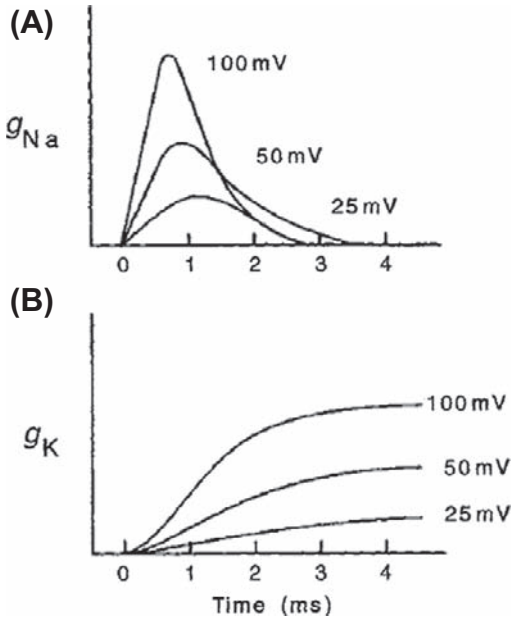

FIGURE 19.13 Voltage dependence and time dependence of the changes in Na^+ conductance (g_{Na}) and K^+ conductance (g_K) during voltage-clamp of the squid giant axon. The numbers refer to the magnitude of depolarization (in mV) from the RP. (A) g_{Na} turns on rapidly and then spontaneously declines over a brief time period. (B) g_K turns on more slowly and is sustained in amplitude during the entire clamp pulse. *(Redrawn from Hodgkin, 1964).*

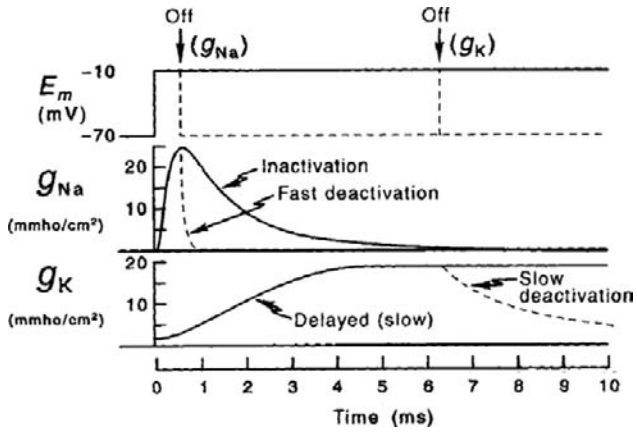

FIGURE 19.14 Na^+ conductance (g_{Na}) and K^+ conductance (g_K) changes are shown in response to voltage-clamp of the squid giant axon from the RP to a membrane potential (E_m) of −10 mV. g_{Na} inactivates after a short time, even when the voltage-clamp is maintained. In contrast, g_K remains elevated until the clamp is released. When the clamp pulse is terminated early, the g_{Na} increase is quickly turned off (deactivated); the turn-off of g_K is considerably slower. *(Redrawn from Hodgkin, A.L. (1958). Proc R Soc London (Biol). B148, 1.)*

binds to the fast Na^+ channel and blocks the passage of Na^+ ions through the channel. Several different types of toxins, including *batrachotoxin* (BTX), inhibit the inactivation process of the Na^+ channel, so that the Na^+ currents are greatly prolonged once activated. Such toxins have proven to be valuable tools in analyzing voltage-clamp currents and understanding ion channel function. The ion channel toxins are discussed in great detail in a later chapter.

IVC. Whole-Cell Voltage-Clamp

A newer electrophysiological method, the whole-cell voltage-clamp technique, has enabled researchers to examine the basis of excitability at the single cell level, e.g. in single myocardial cells or smooth muscle cells. The method allows the recording of the macroscopic currents that flow through the assembly of ion channels in the cell membrane. More information is given in Appendix III to this chapter. In addition, the details of this method are given in the following chapter.

IVD. Overview of Action Potential Generation

The increase in g_{Na} and resulting increase in inward I_{Na} cause the regenerative depolarization of the AP. The depolarization is limited by the approach of the membrane potential toward E_{Na} and by the Na inactivation process. As the membrane is depolarized, both g_K and the driving force for I_K increase and the outward I_K repolarizes the membrane. The increase in g_K is *self-limiting*; i.e. the increase in g_K produces repolarization which, in turn, shuts off the increase in g_K.

The slow kinetics of the turn-off of g_K result in a transient hyperpolarization, the *hyperpolarizing afterpotential*. During the hyperpolarizing afterpotential, the membrane potential is brought closer to E_K than at rest.

The membrane conductance changes that occur during the nerve AP are shown in Fig. 19.15 and the time course for the resultant ionic currents is shown in Fig. 19.16. The total ionic current (I_i) is separated into its two major components, I_{Na} and I_K. Since I_K is slower to activate than I_{Na}, the inward I_{Na} predominates initially, giving rise to the fast upstroke of the AP. Later, I_K dominates, causing a net outward current that repolarizes the membrane, i.e. it is partly responsible for the downstroke of the AP.

As stated in Equations 19.5 and 19.6, the specific ionic currents are a product of the membrane conductance for the ionic species and the electrochemical driving force exerted on the ion. Thus, the driving forces on Na^+ and K^+ ions continually change during the time course of the AP, as diagrammed in Fig. 19.17. At the RP, there is a large driving force for Na^+ to flow into the cell, since (E_m−E_{Na}) is large. Conversely, at the peak of the AP, (E_m−E_{Na}) is at its lowest value and the driving force for Na^+ entry is small. In contrast, the driving force for K^+ efflux is largest at the peak of the AP, when (E_m−E_K) is maximal. It is important to remember that ionic current flow depends on both conductance and driving force. There is no net current if only one, but not the other, is present.

The biological elements of the excitable membrane may be represented in terms of an electrical equivalent circuit model, as shown in Fig. 19.18. Currents flow through the individual conductance pathways for each type of ion. The

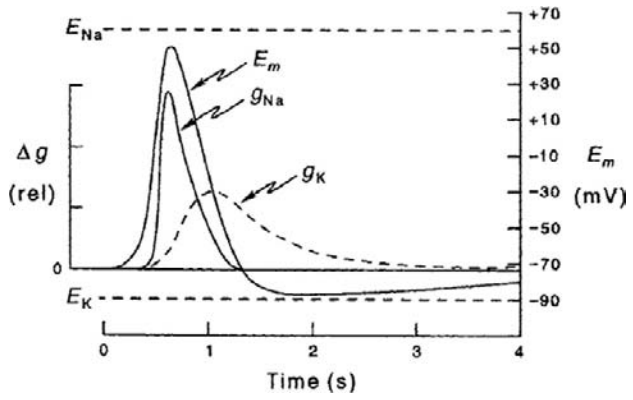

FIGURE 19.15 The relative conductance for Na^+ (g_{Na}) and K^+ (g_K) during an AP in a nerve fiber. The rising phase of the AP is caused by an increase in g_{Na}. The falling phase is due to the rise of g_K (delayed rectification) and to the decrease in g_{Na} (Na^+ inactivation). The hyperpolarizing afterpotential is explained by g_K remaining elevated for a short time following repolarization, tending to hold the membrane potential (E_m) near E_K. Δg, change in conductance. *(Redrawn from Hodgkin, A.L. and Huxley, A.F. (1952d). J Physiol. 117, 500–544.)*

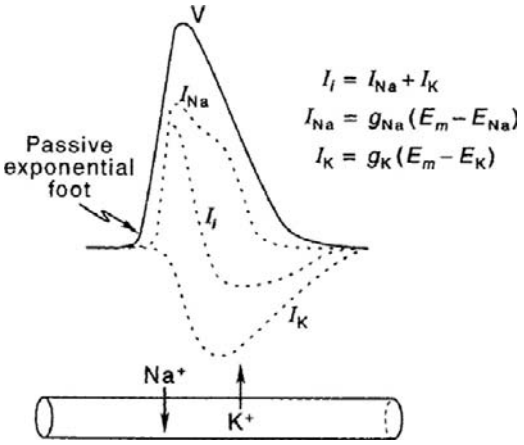

FIGURE 19.16 Ionic currents that flow during the nerve AP. The total current (I_i) is separated into an inward Na^+ current (I_{Na}) and an outward K^+ current (I_K). I_i is the algebraic sum of I_{Na} and I_K. The appropriate equations for I_i, I_{Na} and I_K are given. Also depicted is the fact that a net inward Na^+ flux occurs during the rising phase of the AP and a net K^+ efflux occurs during the repolarizing phase. *(Redrawn from Hodgkin and Huxley, 1952a.)*

conductances for Na^+ and K^+ ions are variable and depend on the transmembrane potential and time. Batteries (positive pole directed inwardly for Na^+ ions and outwardly for K^+ ions) provide the driving forces for current flow. A passive leak conductance for Cl^- ions is also included in the model. If the correct values for the elements are incorporated and varied over time, the model circuit will generate an AP.

IVE. Fast Na^+ Channel Activation

During an AP, the increase in g_{Na} is related to the membrane potential E_m in a *positive-feedback* fashion, or "vicious cycle" (Fig. 19.19A). That is, a small depolarization leads to an increase in g_{Na}, which allows a larger inward I_{Na}, which causes further depolarization. This

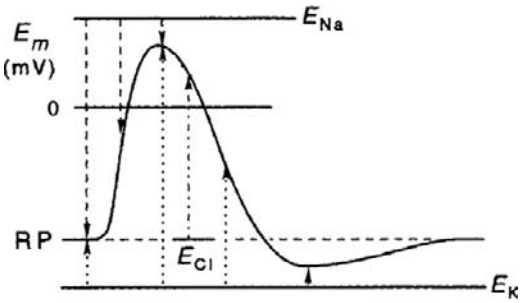

FIGURE 19.17 Driving forces for Na^+ and K^+ currents during the AP. The total electrochemical driving force is equal to membrane potential (E_m) minus the equilibrium potential for the ion (E_i):($E_m - E_i$). As depicted, the driving force for the Na^+ current decreases during the AP, whereas that for K^+ increases. Even when Cl^- is passively distributed, a net driving force for Cl^- influx (outward Cl^- current) occurs during the AP.

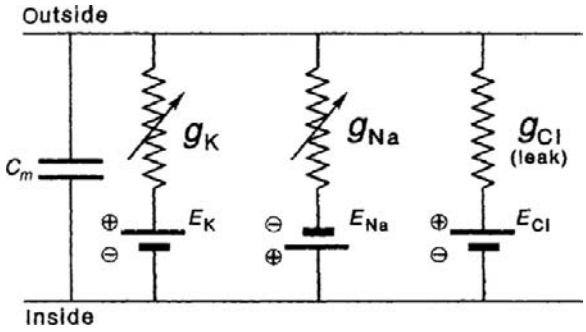

FIGURE 19.18 Hodgkin–Huxley electrical equivalent circuit for the squid giant nerve axon. The K^+ conductance (g_K) is in series with E_K and g_{Na} is in series with E_{Na}. The arrows indicate that g_{Na} and g_K vary with voltage and time. The low conductance for Cl^- (g_{Cl}) was termed the leak conductance. C_m, membrane capacitance. *(Redrawn with permission from Hodgkin, A.L. (1964). The Conduction of the Nervous Impulse. Charles C. Thomas, Springfield.)*

greater depolarization produces a greater increase in g_{Na}. This positive feedback process is "explosive," with a sharp trigger point (threshold) resulting from the exponential relationship (initially positive) between g_{Na} and E_m (Fig. 19.19B). It is this positive-feedback relationship that accounts for the *negative resistance* (slope) in the current–voltage curve (see Fig. 19.12). As Fig. 19.19B shows, g_{Na} reaches a maximum (saturates) at positive potentials that gives maximal activation of the population of fast Na^+ channels.

The fast Na^+ channels (and the slow Ca^{2+} channels) have a double gating mechanism: an inactivation gate (I-gate) and an activation gate (A-gate) (Fig. 19.20). For a channel to be conducting, both the A-gate and the I-gate must be open; if either one is closed, the channel is nonconducting. The A-gate is located somewhere near the middle of the channel; it is not at the outer surface because even TTX does not prevent the movement of this gate and it is not at the inner surface because proteases perfused internally do not affect it. The A-gate is closed at the resting E_m and opens rapidly on depolarization; in contrast, the I-gate is open at the resting E_m and closes slowly on depolarization.

In the Hodgkin–Huxley (1952) analysis, the opening of the A-gate requires simultaneous occupation of three negatively-charged sites by three positively-charged (m^+) particles. The activation variable, m, is the probability of one site being occupied and m^3 is the probability that all three sites are occupied; therefore,

$$g_{Na} = \overline{g}_{Na} m^3 h \qquad (19.7)$$

where h is the inactivation variable and $\overline{g}_{Na}$ is the maximum conductance.

Hodgkin and Huxley found that, in squid giant axon, there was an e-fold increase in g_{Na} per 4–6 mV of depolarization. To convert to ln from $\log_{10}$, the 2.303 RT/zF

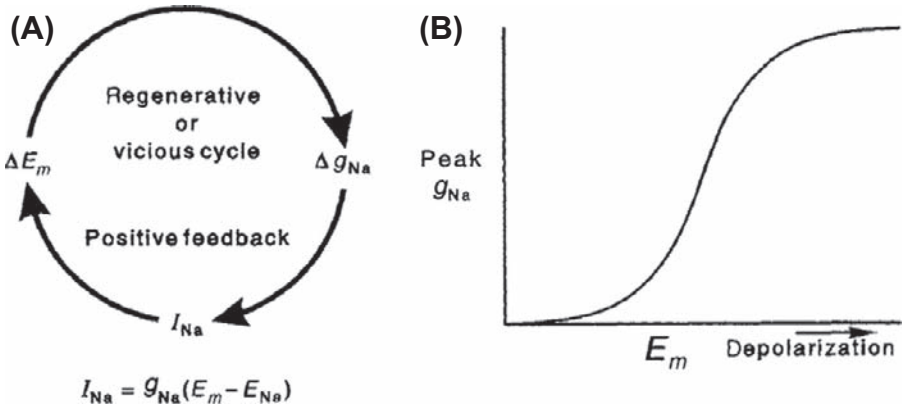

FIGURE 19.19 The positive-feedback relationship between Na^+ conductance (g_{Na}) and membrane potential E_m, leading to the all-or-none AP. (A) The increase in g_{Na} allows an increase in the inward Na^+ current, $I_{Na} = g_{Na}(E_m - E_{Na})$, which is depolarizing and so triggers a further increase in g_{Na}. This explosive feedback cycle is caused by the voltage dependency of the gated fast Na^+ channels. (B) Plot of g_{Na} versus depolarization, showing the initial exponential (positive) increase in g_{Na} as a function of voltage, followed by saturation at greater depolarization, thus giving a sigmoidal relationship. *(Adapted from Hodgkin, A.L. (1964). The Conduction of the Nerve Impulse. Charles C. Thomas, Springfield.)*

factor of 58 mV (at 20°C) becomes 58 mV/2.303, or 25.2 mV. Therefore, they concluded that the voltage-sensitive activation gate must have about 4 to 6 unitary charges (25/6 to 25/4).

IVF. Gating Current

Since the gating of the ionic channels is voltage dependent, a part of the channel protein contains a charged group or dipole that can sense the electric field across the membrane and move in response to a change in transmembrane voltage. When the gating region moves, it causes a shift in the overall conformation of the channel, which allows it to conduct ions. A *gating current* (I_g) that corresponds to the movement of the charged m^+ particles (or rotation of an equivalent dipole) has been measured. The gating current is very small in intensity and is measured by subtracting the linear capacitive current (from a hyperpolarizing clamp step) from the total capacitive current (linear plus non-linear) that occurs with a depolarizing clamp step beyond threshold. The outward I_g precedes the inward I_{Na}. Tetrodotoxin does not block I_g, although it does block I_{Na}. Thus, the gating current is a non-linear outward capacitive current (not an ionic current) obtained during depolarizing clamps that reflects movement of the A-gates from the closed to the open configuration, i.e. the charge movement associated with the A-gates. The linear capacitive current results mainly from the lipid bilayer matrix.

Specific charged residues are located along the primary sequence of amino acids that comprise the channel polypeptide and they can "sense" the transmembrane electric field and move in response to changes in it. The movement of these voltage-sensing or gating residues initiates a conformational change in the channel structure, which then permits ions to flow through the central pore region of the alpha subunit of the channel. Gating currents have been recorded from several types of ion channels.

IVG. Na^+ Inactivation

The fast I_{Na} lasts only for 1−2 ms because of the spontaneous inactivation of the fast Na^+ channels. That is, the fast Na^+ channels inactivate quickly, even if the membrane

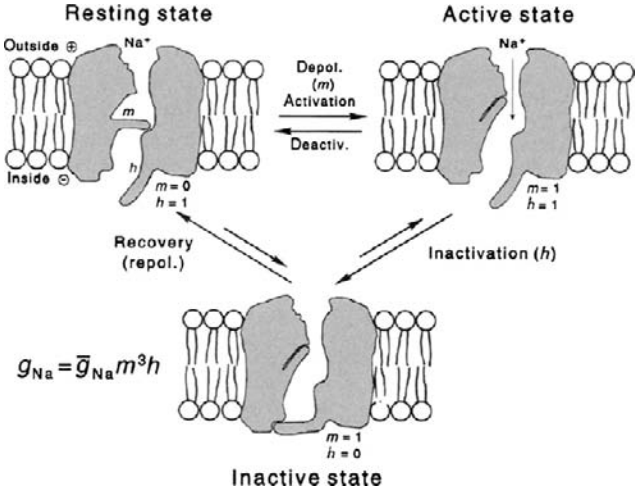

FIGURE 19.20 The three hypothetical states of the fast Na^+ channel, based on the Hodgkin−Huxley model. In the resting state, the activation gate (A or *m)* is closed and the inactivation gate (I or *h)* is open: $m = 0$, $h = 1$. Depolarization to the threshold or beyond activates the channel to the active state, the A-gate opening rapidly and the I-gate still being open: $m = 1$, $h = 1$. The activated channel spontaneously inactivates to the inactive state because of delayed closure of the I-gate: $m = 1$, $h = 0$. The recovery process on repolarization returns the channel from the inactive state to the resting state, thus making the channel again available for reactivation. Na^+ is depicted as being bound to the outer mouth of the channel and poised for entry down its electrochemical gradient when both gates are open (active state of channel). The reaction between resting state and the active states is reversible, whereas the other reactions may be less reversible. The Ca^{2+} slow channels pass through similar states.

were to remain depolarized. (In contrast, the slow Ca^{2+} channels inactivate slowly.) Inactivation is produced in the fast Na^+ channels (and in the slow Ca^{2+} channels) by the voltage-sensitive slow closing of the inactivation gate (I-gate) (see Fig. 19.20). The I-gate is located near the inner surface of the membrane, as evidenced by the fact that addition of proteolytic enzyme to the inside of a perfused giant axon chops off the I-gate and eliminates inactivation. (Protease added outside does not have this effect.) The I-gate is presumably charged positively to allow it to move with changes in the membrane potential. During depolarization, the inside of the membrane becomes less negative or more positive and this causes the I-gate to close. At the normal RP, the I-gate is open (but the A-gate is closed).

The voltage dependency of inactivation is given by the h_∞ versus E_m curve (Fig. 19.21). The inactivation variable h (probability function) varies between 0 and 1.0, perhaps reflecting occupation of a negatively-charged site by a positively-charged h particle; h_∞ is the value of h at infinite time (>10 ms) or at steady state. When $h = 1.0$, the I-gates of all of the fast Na^+ channels are in the open configuration; conversely, when $h = 0$, all the I-gates are closed. Since g_{Na} at any time is equal to the maximal value ($\overline{g}_{Na}$) times m^3h (see Equation 19.7), when $h = 0$, $g_{Na} = 0$. When $h = 1.0$, $g_{Na} = \overline{g}_{Na}$ (if $m = 1.0$). At the normal RP, h_∞ is nearly 1.0 and it diminishes with depolarization, becoming zero at about −30 mV in squid axon (Fig. 19.21A). The maximal rate of rise of the AP (max dV/dt) is directly proportional to the net inward I_{Na}, which is directly proportional to g_{Na}. The decrease in h_∞ is the cause of decrease in g_{Na}. Therefore, depolarization by any means (e.g. elevated $[K^+]_o$ or applied depolarizing current) decreases g_{Na} and excitability disappears at about −50 mV (Fig. 19.21B). The AP disappears at −50 mV (rather than −30 mV) because of a minimum current density requirement for a regenerative and propagating response.

A plot of the inactivation curve along with the activation curve is given in Fig. 19.21C to illustrate the overlap in these curves, giving rise to a so-called *window current* (or steady-state inward current) over a certain voltage region. The presence of the window current means that, over the voltage range of about −50 to −30 mV, there is a steady inward Na^+ current passing through about 10−20% of the fast Na^+ channels that are open (on a rotating population basis).

The slow Ca^{2+} channels behave much the same way as the fast Na^+ channels with respect to activation and inactivation, with one main difference being the voltage range over which the slow channels operate. For example, inactivation occurs between −50 and 0 mV for the slow channels, compared with between −100 and −30 mV for the fast Na^+ channels. Another major difference is that slow channels inactivate much more slowly than the fast channels; i.e. they have a long inactivation time constant (τ_{inact}). In myocardial cells, the h variable for the slow channel is referred to as the f variable and the m variable as the d variable and the exponent is 2.0:

$$g_{Ca} = \overline{g}_{Ca} d^2 f \qquad (19.8)$$

The amino acid sequences of Na^+ and Ca^{2+} channels are known, as well as their putative tertiary structure (Fig. 19.22). Na^+ and Ca^{2+} channels consist of several subunits, one of which contains the water-filled pore through which the ions pass. Ion channels have one or more sites that can be phosphorylated, and phosphorylation alters

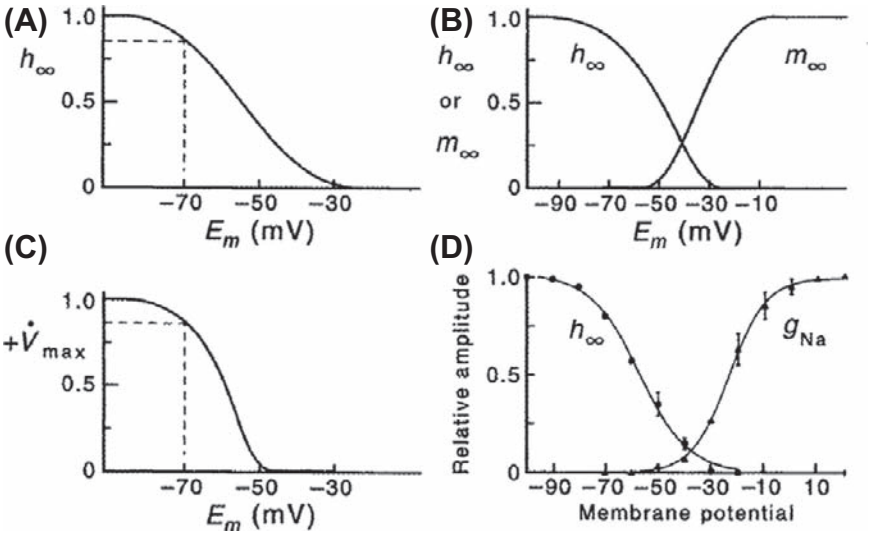

FIGURE 19.21 Voltage inactivation of the fast Na^+ channels as a function of the membrane potential (E_m). (A) h_∞ plotted against E_m, where h is the inactivation factor of Hodgkin−Huxley. The h_∞ represents h at infinite time or steady state. This graph illustrates that fast Na^+ channels begin to inactivate at about −75 mV and nearly complete inactivation occurs at about −30 mV. (B) Maximal rate of rise of the AP (max dV/dt) as a function of resting E_m. Max dV/dt is a measure of the inward current intensity, which is dependent on the number of channels available for activation. Therefore, max dV/dt decreases as h_∞ decreases. (C) Plot of both steady-state inactivation (h_∞) and activation (m_∞) against E_m to illustrate the overlap of the two curves, depicting the window current region. (D) Steady-state activation and inactivation curves for the fast Na^+ current ($I_{Na(f)}$) recorded, using the whole-cell voltage-clamp technique, from uterine smooth muscle cells isolated from late-pregnant (18-day) rats. Note the overlap between the activation and inactivation curves, resulting in a steady-state window current between about −50 and −30 mV. *(Data from Y. Inoue and N. Sperelakis, unpublished observations.)*

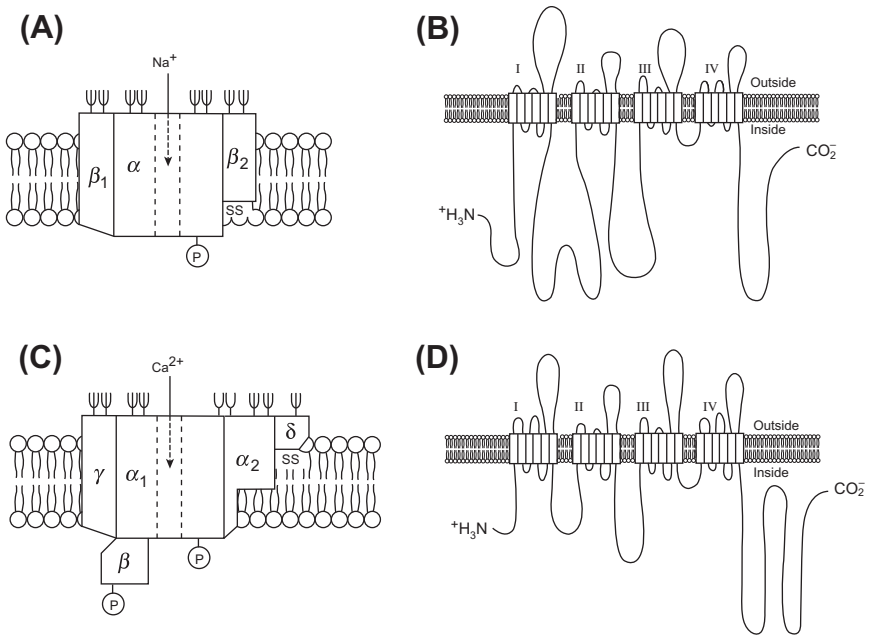

FIGURE 19.22 Models of the fast Na^+ channel and the slow Ca^{2+} channel proteins. (A) The Na^+ channel has multiple protein subunits, labeled α, β_1 and β_2. The α subunit is the one that contains the water-filled pore through which Na^+ passes. One site that can be phosphorylated by cyclic AMP–dependent protein kinase (cAMP-PK) is present on the α subunit which contains the pore. The β_2 subunit has a disulfide bond (SS). (B) In the α subunit, there are four homologous intramembrane polypeptide repeat domains, connected by intracellular polypeptide segments or loops, arranged into a circular structure within the plane of the membrane to form a channel. Each domain consists of six units that span the membrane, as depicted. (C) The Ca^{2+} channel also is composed of several subunits: α_1, α_2, β, γ and δ. The α_1 subunit contains the pore pathway. Two sites can be phosphorylated by the cAMP-PK, one on the α_1 subunit and the other on the β subunit. The β and δ subunits do not span the lipid bilayer and the δ subunit possesses a disulfide bond. (D) The polypeptide structure of the α_1 subunit of the Ca^{2+} channel is similar to that for the fast Na^+ channel, with four repeat membrane-spanning domains connected by intracellular and extracellular loops. *(Reprinted with permission from Catterall, W. (1988). Science. 242, 50–61.)*

their behavior. For example, in cardiac muscle, the slow Ca^{2+} channel activity is increased by epinephrine (adrenaline), a hormone that increases the cyclic AMP level and leads to Ca^{2+} channel phosphorylation (see subsequent chapter). The molecular structure of ion channels is discussed in more detail in a later chapter.

IVH. Recovery

Any Na^+ or Ca^{2+} channel that has been activated and then spontaneously inactivated must go through a recovery process before it can return to the resting state from which it can be reactivated (see Fig. 19.20). The recovery process is dependent on voltage and time. The membrane must be repolarized beyond about −50 mV before the recovery process can begin. At any given E_m, time is necessary for the recovery process to occur, namely, the time required for the charged A-gates and I-gates to move back to their resting configuration (A-gate closed, I-gate open) with the electric field. The recovery process is rapid for fast Na^+ channels (e.g. 1–10 ms) and less rapid for the slow Ca^{2+} channels. The recovery process of the slow channels is slowed by organic calcium antagonist drugs.

IVI. K^+ Activation

The K^+ channel (outward-going delayed rectifier) is generally believed to have only an A-gate, because it does not inactivate. This gate is thought to be located near the inner surface of the membrane, because TEA^+ blocks the K^+ channel more readily from the inner surface. The block is *use dependent* or *frequency dependent*: as the A-gate opens, the TEA^+ molecule can bind in the channel behind the gate. The A-gate is believed to be positively charged and depolarization (inside going positive) opens the gate. In the Hodgkin–Huxley analysis of squid giant axon, the A-gate opens when four positively-charged n^+ particles simultaneously occupy four negatively-charged sites. If n is the probability that one site is occupied, then n^4 is the probability that all four sites are occupied; therefore,

$$g_K = \bar{g}_K n^4 \tag{19.9}$$

The power to which n is raised varies in different tissues.

IVJ. Types of K^+ Channels

The cell membrane of some cells (e.g. myocardial cells) has at least five separate K^+ channels. Some information on these K^+ channels is given in Appendix II to this chapter.

IVK. Model for Activation and Inactivation of Na^+ and K^+ Channels

As stated previously, in the Hodgkin–Huxley analysis, the Na^+ conductance g_{Na} is controlled by three charged activating m particles and one blocking h particle, which move with changes in the electric field across the membrane either to occupy or unoccupy certain sites on the Na^+ channel protein. If m is the probability of one favorable site

being occupied, then $m \times m \times m$ or m^3 is the probability that all three sites are occupied simultaneously. The A-gate cannot be fully opened unless all three sites are occupied. A simplistic variant is to consider that the A-gate actually consists of three separate subgates or subdoors, as illustrated in Fig. 19.23. For an Na^+ ion to pass through the channel, all three subdoors must be open.

The value of h is the probability of one favorable site being occupied that opens the I-gate and this site is already occupied at the normal RP (I-gate open) and becomes unoccupied with depolarization. Therefore, g_{Na} is given by Equation 19.7.

The K^+ conductance g_K is controlled by four charged activating n particles which move with depolarization to occupy four sites on the K^+ channel protein. If n is the probability of one favorable site being occupied, then $n \times n \times n \times n$ or n^4 is the probability that all four sites will be occupied simultaneously. There is no inactivation variable for the K^+ channel, because g_K does not exhibit a major decrease during a short depolarizing voltage-clamp pulse (e.g. 20 ms). Therefore, g_K is given by Equation 19.9. Additional details of the Hodgkin–Huxley analysis are given in Appendix I to this chapter.

IVL. Mechanisms of Repolarization

The AP is terminated primarily by the turn-on of g_K, the *delayed rectification*. It is called the delayed rectifier because its turn-on is slower and delayed with respect to the turn-on of the fast Na^+ channels. The increase in g_K acts to bring E_m toward E_K (about −90 mV), since the membrane potential at any time is determined mainly by the ratio of g_{Na}/g_K (see Chapter 9). This type of g_K channel is activated by depolarization and turned off by repolarization. Therefore, this g_K channel is *self-limiting*, in that it turns itself off as the membrane is repolarized by its action.

In addition to the g_K turn-on, there is also some turn-off of g_{Na}, which contributes to repolarization. Two reasons for g_{Na} turnoff are (1) spontaneous inactivation of fast Na^+ channels that had been activated, i.e. closing of their I-gate (inactivation τ of 1–3 ms); and (2) a reversible shifting of activated channels directly back to the resting state because of the rapid repolarization occurring due to the g_K mechanism. Theoretically, it would be possible to have an AP that would repolarize (but more slowly) even if there were no g_K mechanism, because the g_{Na} channels would spontaneously inactivate and so the g_{Na}/g_K ratio and E_m would slowly be restored to their original resting values. Turn-on of g_K acts to sharpen repolarization of the AP and allows higher frequency of impulses.

IVM. Skeletal Muscle Repolarization

The two mechanisms for sharp repolarization of the AP discussed previously for neurons also apply to skeletal muscle. But there is an important *third factor* involved in repolarization of the skeletal muscle AP, the *Cl^- current*. The Cl^- permeability (P_{Cl}) and conductance (g_{Cl}) are very high in skeletal muscle. In fact, P_{Cl} of the surface membrane is much higher than P_K, the P_{Cl}/P_K ratio being about 3–7. However, as discussed in Chapter 9, the Cl^- ion is passively distributed, or nearly so, and thus cannot determine the RP. However, net Cl^- movements inward (hyperpolarizing) or outward (depolarizing) can and do affect E_m transiently until re-equilibration occurs. There is

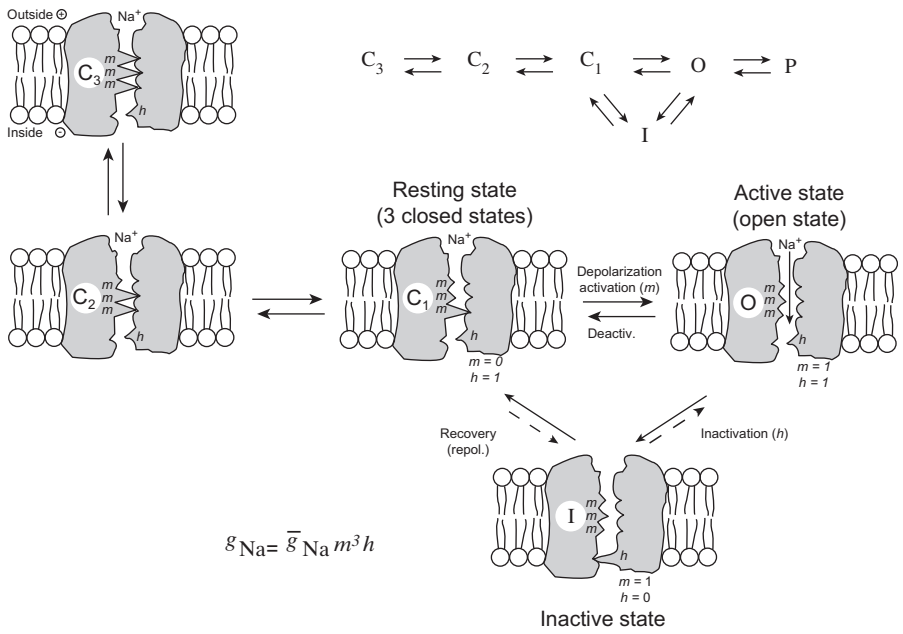

FIGURE 19.23 Diagram depicting the modified Hodgkin–Huxley view of the three states of the fast Na^+ channel. As shown, there is evidence for the existence of three closed states of the channel (C_3, C_2 and C_1). The activation gate (A-gate) is depicted as consisting of three parts, each one being controlled by one m^+ particle. For the A-gate to be open to allow Na^+ ions to pass, all three subgates must be open and therefore all m sites must be occupied. The C_3 closed state is depicted as having all three subgates closed, the C_2 closed state with two subgates closed (one open) and the C_1 closed state with one subgate closed (two open). For the open state (O), all three subgates must be open. P, plugged channel; I, inactive.

no net electrochemical driving force for Cl^- current (I_{Cl}) at the RP, since:

$$E_m = E_{Cl} \quad (19.10a)$$

and

$$(E_m - E_{Cl}) = 0 \quad (19.10b)$$

However, during AP depolarization, there is a larger and larger driving force for outward I_{Cl} (i.e. Cl^- influx), since:

$$I_{Cl} = g_{Cl}(E_m - E_{Cl}) \quad (19.11)$$

where E_{Cl} is the Cl^- equilibrium potential calculated from the Nernst equation (see Fig. 19.17). In other words, the large electric field that was keeping Cl^- out (i.e. $[Cl^-]_i << [Cl^-]_o$) is diminishing during the AP and so Cl^- ions enter the fiber. This Cl^- entry is hyperpolarizing and, therefore, tends to repolarize the membrane more quickly than would otherwise occur. That is, repolarization of the AP is sharpened by the Cl^- mechanism. The higher the g_{Cl}, the greater this effect.

To illustrate some of the above points, if skeletal muscle fibers are placed into Cl^--free Ringer's solution (e.g. methanesulfonate substitution), depolarization and spontaneous APs and twitches occur for a few minutes until most or all of the Cl^- is washed out. After equilibration, the resting E_m then returns to the original value (ca. −90 mV for frog muscle), clearly indicating that Cl^- does not determine the RP and that net Cl^- efflux produces depolarization. Re-addition of Cl^- to the bath produces a rapid large hyperpolarization (e.g. to −120 mV) due to net Cl^- influx and E_m then slowly returns to the original value (−90 mV) as Cl^- re-equilibrates (i.e. redistributes itself passively). These same effects would occur in cardiac muscle, smooth muscle and nerve, but to a lesser extent, because P_{Cl} is much lower in these tissues.

V. EFFECT OF RESTING POTENTIAL ON ACTION POTENTIAL

Any agent that affects the RP has important repercussions on the AP. Depolarization reduces the rate of rise of the AP and thereby also slows its velocity of propagation. A slow spread of excitation throughout the nerve or muscle will interfere with its ability to act efficiently. This effect is progressive as a function of the degree of depolarization. If nerve, skeletal muscle fibers or cardiac muscle cells are depolarized to about −50 mV by any means, then all excitability is lost.

Hyperpolarization usually produces only a small increase in the rate of rise. Larger hyperpolarization may actually slow the velocity of propagation, because the critical depolarization required to bring the membrane to its threshold potential is increased and it can cause propagation block.

The explanation for the effect of resting E_m (or take-off potential) on maximum rate of rise (max *dV/dt*) of the AP is based on the sigmoidal h_∞ versus E_m curve (see Fig. 19.21A). The I (*h*)-gates are open in a resting membrane and close with depolarization. As discussed previously, *h*, the inactivation variable for the fast Na^+ conductance, is a probability factor that deals with the open ($h = 1.0$) versus closed ($h = 0$) positions of the inactivation gate of the channel (see Fig. 19.20). At the RP of −80 mV, h_∞ is 0.9−1.0 and diminishes with depolarization, becoming nearly zero at about −30 mV.

The RP also affects the duration of the AP. With use of polarizing current, depolarization lengthens the AP, whereas hyperpolarization shortens it. This occurs because of anomalous rectification (i.e. g_K decreases with depolarization and increases with hyperpolarization). In contrast, when elevated $[K^+]_o$ levels are used to depolarize the cells, the AP is shortened. One important determinant of the AP duration is g_K. Agents or conditions that increase g_K, such as elevation of $[K^+]_o$, tend to shorten the duration. In contrast, agents that decrease g_K or slow its activation, such as Ba^{2+} ion or TEA^+, tend to lengthen the AP duration. Other factors are also important in determining the AP duration. For example, agents that slow the closing of the I-gates of the fast Na^+ channels, such as veratridine, prolong the AP.

VI. ELECTROGENESIS OF AFTERPOTENTIALS

The APs of nerve and muscle cells usually consist of two components: an initial spike followed by an *early afterpotential* (Fig. 19.24A, B). The early afterpotentials may be of two types: *depolarizing* or *hyperpolarizing*. In addition, *late afterpotentials*, both depolarizing or hyperpolarizing, may appear following a brief train of spikes (Fig. 19.24C, D). The electrogenesis of the early and late afterpotentials is different. The early afterpotentials are due to a conductance change, whereas the late afterpotentials may be due to K^+ accumulation or depletion in restricted diffusion spaces and to electrogenic pump stimulation.

VIA. Early Depolarizing Afterpotentials

The AP spike in skeletal muscle fibers is immediately followed by a prominent depolarizing afterpotential (also called a negative afterpotential, based on the terminology used in external recording) (see Fig. 19.24A). The early depolarizing afterpotential of frog skeletal fibers is about 25 mV (immediately after the spike component) and gradually decays to the RP within 10−20 ms. It results from the fact that the delayed rectifier K^+ channel that opens during depolarization to terminate the spike is less selective

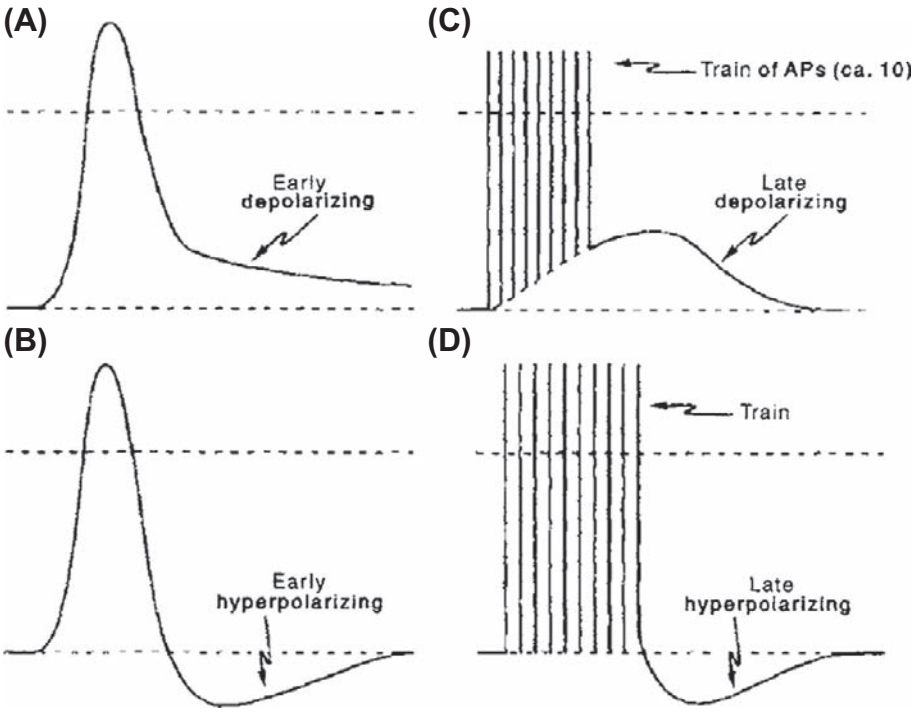

FIGURE 19.24 Examples of the different types of afterpotentials. (A) Early depolarizing (negative) afterpotential recorded after a single AP in a skeletal muscle fiber. (B) Early hyperpolarizing (positive) afterpotential recorded after a single AP in a nerve fiber. (C) Late depolarizing afterpotential recorded after a train (e.g. 10) of APs in a skeletal muscle fiber. (D) Late hyperpolarizing afterpotential recorded following a train of APs in a nerve terminal.

for K^+ (ca. 30:1, K^+:Na^+) than is the K^+ channel in the resting membrane (ca. 100:1, K^+:Na^+). Therefore, from the constant-field equation (see Chapter 9), one can predict that the membrane should be partly depolarized when the membrane is dominated by this delayed rectifier K^+ conductance. Thus, the early depolarizing afterpotential is due to the persistence of, and slow decay of, this less selective K^+ conductance.

VIB. Early Hyperpolarizing Afterpotentials

Neurons, heart pacemaker cells and vascular smooth muscle cells often exhibit early hyperpolarizing (positive) afterpotentials (see Fig. 19.24B). These are due to the delayed rectifier K^+ conductance increase (which terminates the spike) persisting after the spike, thereby bringing E_m closer to E_K. The maximum amplitude possible for the afterpotential is the difference between E_K and the normal RP. The time course of this afterpotential is determined by the decay of the K^+ conductance increase.

VIC. Late Depolarizing Afterpotentials

The *late depolarizing afterpotential* of skeletal muscle fibers results from *accumulation of K^+ ions in the transverse (T) tubules* (see Fig. 19.24C). During the AP depolarization and turn-on of the g_K (delayed rectifier), there is a large driving force for K^+ efflux from the myoplasm coupled with a large K^+ conductance, resulting in a large outward K^+ current ($I_K = g_K\ (E_m - E_K)$) across all surfaces of the fiber, namely, the surface sarcolemma and T-tubule walls. The K^+ efflux at the fiber surface membrane can rapidly diffuse away and mix with the relatively large interstitial fluid (ISF) volume, whereas the K^+ efflux into the T-tubules is trapped in this *restricted diffusion space*. The resulting high $[K^+]_{TT}$ decreases E_K across the T-tubule membrane and thereby depolarizes this membrane. Because of cable properties, part of this depolarization is transmitted to the surface sarcolemma and is recorded by an intracellular microelectrode. The K^+ accumulation in the T-tubules can only be dissipated relatively slowly by diffusion out of the mouth of the T-tubules and by active pumping back into the myoplasm across the T-tubule wall. Thus, the decay of the late afterpotential will be a function of these two processes.

The amplitude and duration of the late depolarizing afterpotential of frog skeletal fibers are functions of the number of spikes in the train and their frequency. That is, the greater the spike activity, the greater the amplitude and duration of the late depolarizing afterpotential. If the

train consists of 20 spikes at a frequency of 50/s, a typical value for the amplitude of the afterpotential is about 20 mV. When the diameter of the T-tubules is increased by placing the fibers in hypertonic solutions, the amplitude of the afterpotential decreases, as expected, because of the greater dilution of the K^+ ions accumulating in the T-tubule lumen. When the T-tubular system is disrupted and disconnected from the surface membrane by the glycerol osmotic shock method, the late depolarizing afterpotential disappears (whereas the early depolarizing afterpotential persists).

VID. Late Hyperpolarizing Afterpotentials

Some cells, such as non-myelinated neurons, exhibit *late hyperpolarizing afterpotentials* following a train of spikes (see Fig. 19.24D). These hyperpolarizing afterpotentials are due to the Na^+-K^+ pump, because inhibition of the pump by any means (such as ouabain) abolishes them. Two mechanisms have been proposed for the hyperpolarization. (1) Hyperpolarization occurs because there is an increased *electrogenic Na^+ pump potential* (V_p), stimulated both by an increase in the $[Na^+]_i$ (since these neurons are small in diameter, and hence have a large surface area/volume ratio) and by an increase in $[K^+]_o$ (since these axons are surrounded by Schwann cells and hence have a narrow intercellular cleft and restricted diffusion space). (2) Hyperpolarization occurs due to an increased E_K caused by K^+ depletion in the intercellular cleft because of the stimulated Na^+-K^+ pump overpumping the K^+ back in. It is generally believed that the first mechanism is the most probable.

VIE. Importance of Afterpotentials

All afterpotentials have physiological importance because they alter the excitability and propagation velocity of the cell. A depolarizing afterpotential enhances excitability (lower threshold) and a hyperpolarizing afterpotential depresses excitability to a subsequent AP. This is because the critical depolarization required to reach the threshold potential would be decreased or increased, respectively. A large late depolarizing afterpotential, such as that due to K^+ accumulation in the T-tubules, can trigger repetitive APs under certain pathological conditions.

The effect of afterpotentials on velocity of propagation is complex because there are two opposing factors: (1) the change in critical depolarization required and (2) the change in maximal rate of rise of the AP, which is a function of the takeoff potential (h_∞ versus E_m curve). For example, during a depolarizing afterpotential in skeletal muscle fibers, the critical depolarization required is decreased, but the maximal rate of rise of the AP is also decreased. Therefore, these two factors exert opposing effects.

APPENDIX

AI. ADDITIONAL HODGKIN–HUXLEY ANALYSIS

Based on the preceding analysis, Hodgkin and Huxley (1952a,b,c) then gave the differential equations that govern the values of n, m and h using a pair of rate constants, α and β, for the forward reaction and reverse reaction, respectively. The subscripts for the α and β rate constants identify which variable they pertain to (i.e. n, m or h). The α and β rate constants depend only on membrane potential (at constant temperature and $[Ca^{2+}]_o$). A schematic model is given in Fig. 19A.1 and the corresponding equations are:

$$\frac{dn}{dt} = \alpha_n(1-n) - \beta_n n \qquad (19A.1)$$

$$\frac{dm}{dt} = \alpha_m(1-m) - \beta_m m \qquad (19A.2)$$

$$\frac{dh}{dt} = \alpha_h(1-h) - \beta_h h \qquad (19A.3)$$

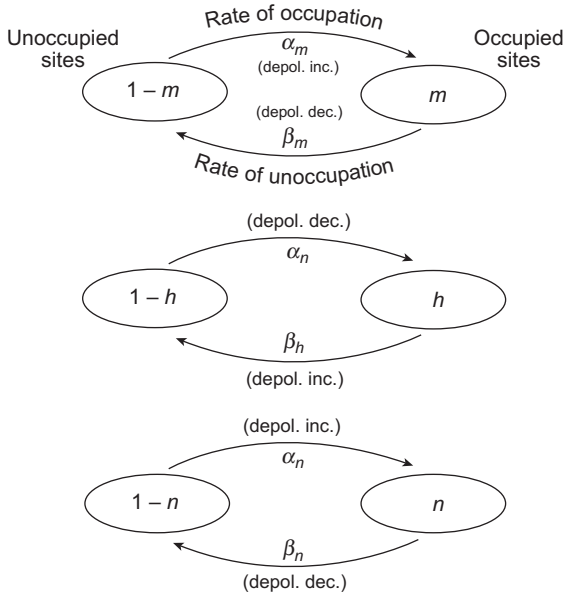

FIGURE 19A.1 Schematic diagram based on the Hodgkin–Huxley model for activation and inactivation of Na^+ channels and K^+ channels. α and β are the rate constants for occupation and unoccupation, respectively, of sites on the channel protein by the m^+, h^+ and n^+ particles. See text for further explanation.

where n is the fraction of sites occupied and, therefore, $(1-n)$ is the fraction of sites unoccupied. Therefore,

$$\text{rate of occupation} = \alpha\,(1-n) \tag{19A.4}$$

$$\text{rate of unoccupation} = \beta_n n \tag{19A.5}$$

$$\text{rate of change of } n = \text{rate of occupation} - \text{rate of unoccupation} \tag{19A.6}$$

which is the same as Equation 19A.1.

The same analysis can be applied to the m and h factors. The effect of making the inside of the fiber more positive (i.e. depolarizing) is to increase α_n, α_m and β_h and to decrease β_n, β_m and α_h. One must remember that the h particles occupy the favorable site at the RP (I-gate open) and this site becomes unoccupied with depolarization (I-gate closes). This is opposite to the situation for the m and n particles (and A-gate).

In voltage-clamp experiments, at a given clamp step, the membrane potential is fixed and the differential equations (Equations 19A.1, 19A.2 and 19A.3) lead to exponential expressions for n, m and h, and the K^+ and Na^+ conductances can then be calculated. When this was done, there was a good fit of the calculated curves with the experimental data points for the changes in g_{Na} and g_K with time at various clamp steps (see Fig. 19.13).

AII. ADDITIONAL INFORMATION ON K^+ CHANNELS

As discussed previously, one type of voltage-dependent K^+ channel is the usual K^+ channel found in many types of excitable membranes. This channel slowly opens (increasing total g_K) on depolarization and is the so-called *delayed rectifier* [I_K or $I_{K(del)}$]. This channel allows K^+ to pass readily outward down the usual electrochemical gradient for K^+ and so is also known as the *outward-going rectifier*. This delayed rectifier channel in myocardial cells turns on much more slowly than in nerve, skeletal muscle or smooth muscle and, therefore, accounts for the long duration of the AP. The activation of this channel produces the increase in total g_K that terminates the cardiac AP plateau (so-called phase 3 repolarization) (see chapter on cardiac AP).

A second type, known as the I_{K1} channel, allows K^+ ion to pass more readily inward than outward, the so-called *inward-going rectifier* or *anomalous rectification*.[1] This kinetically fast channel is responsible for the rapid decrease in K^+ conductance on depolarization (and increase in conductance with repolarization), helps to set the RP and helps bring about the terminal repolarization of the cardiac AP (phase 3). The I_{K1} channel was found to appear at a certain stage of heart development.

A third type of K^+ channel is activated by elevation of $[Ca^{2+}]_i$ and is therefore known as the *Ca^{2+}-activated K^+ channel* or $I_{K(Ca)}$. With Ca^{2+} influx and internal release of Ca^{2+} during the AP and contraction, these channels are activated and help the $I_{K(del)}$ channels to repolarize the AP, i.e. to bring the membrane back to the RP. The presence of this type of K^+ channel has been reported for many types of excitable cells. In actuality, two subtypes of $I_{K(Ca)}$ channel have been found: one that has a high conductance of about 400 pS (big or maxi-K channel) and one that has a lower conductance of about 120 pS (small or mini-K channel).

A fourth type of K^+ channel present in some types of cells, such as myocardial cells, is kinetically fast (compared to $I_{K(del)}$) and provides a rapid outward K^+ current that produces a small amount of initial repolarization, known as phase 1 repolarization in cardiac cells. This occurs immediately following the rapidly-rising spike portion of the AP and is known as the *transient outward current* (I_{to}) in myocardial cells and I_A in neurons. There is some evidence that Cl^- current may contribute to I_{to} (Cl^- influx provides an outward I_{Cl}, which is repolarizing).

A fifth type of K^+ channel is sensitive to ATP, the *K_{ATP} channel* and provides a current known as $I_{K(ATP)}$. This channel is regulated by ATP such that, in normal myocardial cells, this K^+ channel is inhibited (masked or silent). However, in ischemic or hypoxic conditions, when the ATP level is lowered, the $I_{K(ATP)}$ channels become unmasked and provide a large outward I_K that prematurely shortens the cardiac AP. This channel provides a protection mechanism for the heart; namely, the ischemic region of the heart develops very-abbreviated APs and hence contraction is greatly depressed. This effect acts to conserve ATP in the affected cells, enabling full recovery when the blood flow returns to normal after a short time period.

AIII. WHOLE-CELL VOLTAGE CLAMP

To record the whole-cell current, a small-tipped glass pipette, known as a *patch pipette*, is pressed against the cell membrane and negative pressure is applied to the interior of the pipette to draw a small patch of membrane into its tip. A *high-resistance seal* (e.g. $10^{10}\,\Omega$) spontaneously forms (Fig. 19A.2). Then, strong suction is applied to the patch pipette to blow out the membrane patch and allow the lumen of the pipette to be continuous with the lumen of the cell. This technique allows recording of the *whole-cell current* and a complete voltage-clamp analysis can be done for small cells. This technique also allows some control over the intracellular content of the cell; e.g. a substance can be introduced into the cell by diffusion from the patch pipette solution.

[1] It is anomalous in the sense that this channel turns off with depolarization and turns on with hyperpolarization.

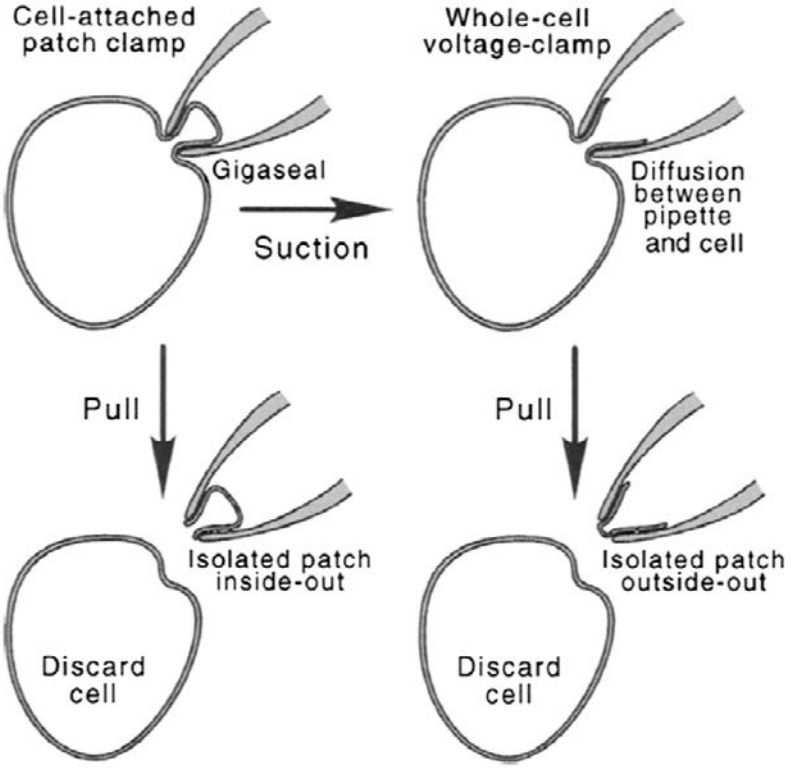

FIGURE 19A.2 The whole-cell voltage-clamp technique in isolated single cells to record the macroscopic current (e.g. I_{Na}, I_{Ca} or I_K) from the entire cell membrane. (Upper left) Cell-attached patch mode, produced by applying light suction to the patch pipette to produce a gigaseal (10^9 Ω). This mode is used to record the microscopic currents from only one channel or from a few channels. (Upper right) Whole-cell clamp mode produced by applying strong suction to the patch pipette to blow out the membrane patch and allowing the lumen of the pipette to be continuous with the lumen of the cell. This mode is used to record the macroscopic currents from the entire complement of ion channels in the cell membrane. (Bottom) Preparation of isolated membrane patches. *(Reprinted with permission from Hamill, O.P. and Sakmann, B. (1981). Nature. 294, 462–464.)*

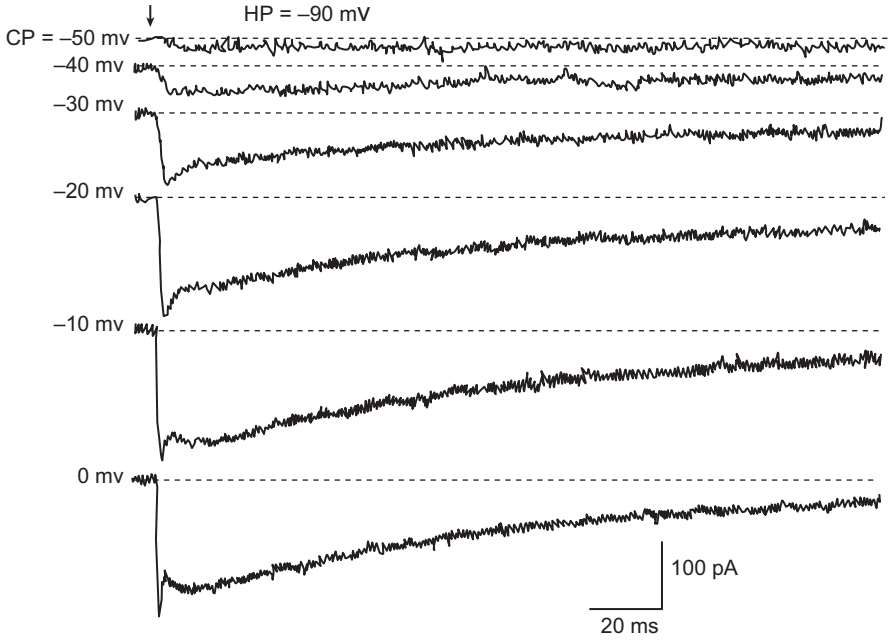

FIGURE 19A.3 Two types of inward current recorded from isolated single myometrial cells from pregnant rat using whole-cell voltage-clamp with a patch-pipette technique. Depolarizing potential steps (−50 to 0 mV) were applied from a holding potential (HP) of −90 mV. The arrow indicates the beginning of a voltage step that continues to the end of the trace. The bath contained K^+-free solution with 150 mM Na^+ and 2 mM Ca^{2+}. The pipette solution contained high Cs^+. Cell capacitance was 80 pF. CP, command potential. *(Reproduced with permission from Ohya, Y. and Sperelakis, N. (1989). Am J Physiol. 257, C408–C412.)*

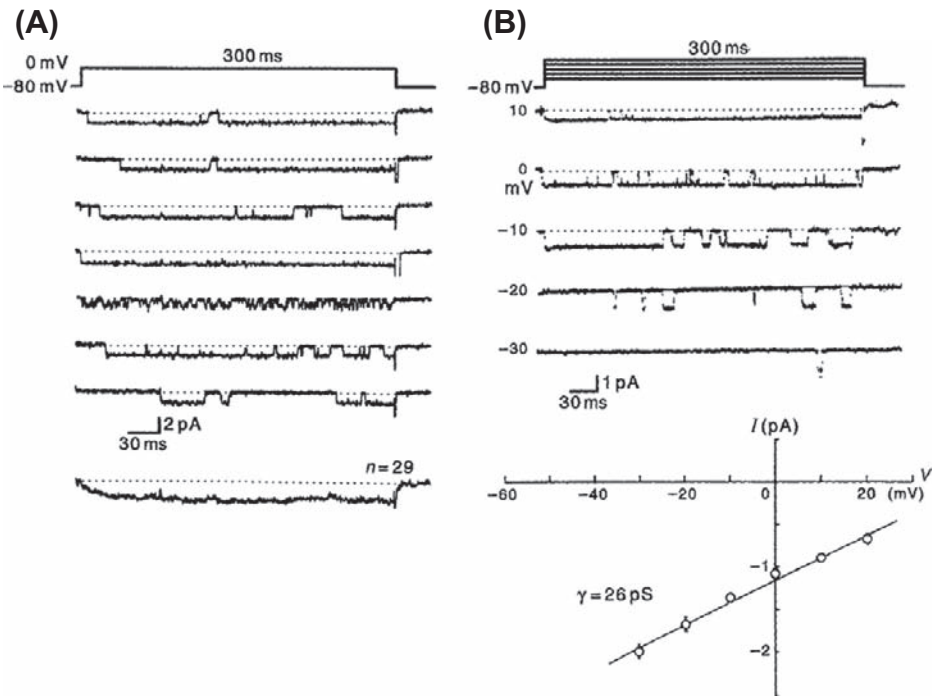

FIGURE 19A.4 Single-channel currents recorded from a slow (L-type) Ca^{2+} channel, using the cell-attached patch-clamp technique, in a single cardiomyocyte isolated from a young (3-day-old) embryonic chick heart. These Ca^{2+} channels in young embryonic/fetal chick and rat heart cells exhibit a high incidence of long openings. Recordings in a cell illustrating the inward currents recorded at five different command step potentials (−30, −20, −10, 0 and +10 mV) from an HP of −80 mV. Note the presence of numerous long openings. The amplitude of the unitary current became smaller at the higher (more positive) command potentials. The current amplitudes are plotted below in the current−voltage curve (each point being the mean ± SE of 5−10 experiments). The data points were fitted by a straight line giving a slope conductance of 26 pS for the single-channel conductance. *(Modified from Tohse, N. and Sperelakis, N. (1990). Am J Physiol. 259, H639−H642.)*

Whole-cell voltage-clamp records obtained from isolated single uterine smooth muscle cells (18-day pregnant rat) are illustrated in Fig. 19A.3. The outward K^+ currents were blocked (by high Cs^+ concentration in the patch pipette) and any inward currents carried by Ca^{2+} or Na^+ ions can be recorded. As shown, there are two inward currents: an initial fast current and a later slow current. The *initial fast current is carried by Na^+ ion*, and this Na^+ current is blocked by TTX; the later slow current is carried by Ca^{2+} ions. The presence of functional fast Na^+ channels is unusual for most smooth muscles and it was discovered that such channels developed during pregnancy and reached their maximum density close to term.

The information gained from such whole-cell voltage-clamp experiments, performed on a variety of excitable cell types, has greatly increased our knowledge of the properties and regulation of the many types of ionic currents. The macroscopic or whole-cell current (I) is the product of the number of functional channels in the cell membrane (N) times the probability that the "average" channel is open during the clamp step (p_o) times the single-channel current (i), giving:

$$I = i\,N\,p_o \qquad (19A.7)$$

The single-channel current (in pA), open probability (p_o) and single-channel conductance (γ) are obtained from patch-clamp experiments, in which the activity of a single channel (or a few channels) can be monitored in a small patch of membrane (e.g. 1−10 μm^2) that is electrically isolated from the rest of the cell membrane (cell-attached patch) or excised (isolated patch). Opening and closing of the gates of the single channel reflect conformational changes in the channel protein. This sophisticated technique, which earned the Nobel Prize in physiology and medicine in 1991 for E. Neher and B. Sakmann, allows the biophysical study of the behavior of a single protein molecule and thus represents electrophysiology at the molecular level. An illustration of actual records, obtained from young embryonic chick heart cells, is given in Fig. 19A.4. This patch-clamp technique and analysis is discussed in detail in the following chapter.

BIBLIOGRAPHY

Bernstein, J. (1902). Untersuchengen zür Thermodynamik der bioelektrischen Ströme. *Pflügers Arch, 92*, 521.

Bernstein, J. (1912). *Elektrobiologie*. Braunschweig: Vieweg.

Catterall, W. A. (1988). Structure and function of voltage-sensitive ion channels. *Science, 242*, 50−61.

Cole, K. S. (1949). Dynamic electrical characteristics of the squid axon membrane. *Arch Sci Physiol, 3*, 253−258.

Cole, K. S., & Curtis, H. J. (1939). Electric impedance of the squid giant axon during activity. *J Gen Physiol, 22*, 649−687.

Hamill, O. P., & Sakmann, B. (1981). Multiple conductance states of single acetylcholine receptor channels in embryonic muscle cells. *Nature, 294*, 462−464.

Hamill, O. P., Marty, A., Neher, E., Sakmann, B., & Sigworth, F. J. (1981). Improved patch-clamp technique for high resolution current recording from cells and cell-free membrane patches. *Pflügers Arch, 391*, 85−100.

Hille, B. (1984). *Ionic Channels of Excitable Membrane*. Sunderland: Sinauer Associates.

Hodgkin, A. L. (1964). *The Conduction of the Nervous Impulse*. Liverpool: Liverpool University Press.

Hodgkin, A. L., & Huxley, A. F. (1952a). Currents carried by sodium and potassium ions through the membrane of the giant axon of *Loligo*. *J Physiol (London), 116*, 449−472.

Hodgkin, A. L., & Huxley, A. F. (1952c). The dual effect of membrane potential on sodium conductance in the giant axon of *Loligo*. *J Physiol (London), 116*, 497−506.

Hodgkin, A. L., & Huxley, A. F. (1952d). A quantitative description of membrane current and its application to conduction and excitation in nerve. *J Physiol (London), 117*, 500−544.

Hodgkin, A. L., & Huxley, A. F. (1952b). The components of membrane conductance in the giant axon of *Loligo*. *J Physiol (London), 116*, 473−496.

Hodgkin, A. L., & Katz, B. (1949). The effect of sodium ions on the electrical activity of the giant axon of the squid. *J Physiol (London), 108*, 37−77.

Hodgkin, A. L. (1958). Ionic movements and electrical activity in giant nerve fibres. *Proc Roy Soc B, 148*, 1.

Katz, B. (1966). *Nerve, Muscle and Synapse*. New York: McGraw-Hill.

Ohya, Y., & Sperelakis, N. (1989). Fast Na^{+} and slow Ca^{2+} channels in single uterine muscle cells from pregnant rat. *Am J Physiol Cell., 257*, C408−C412.

Overton, E. (1902). Beiträge zur allgemeinen Muskel- und Nervenphysiologie. *Pflügers Arch., 92*, 346.

Tohse, N., & Sperelakis, N. (1990). Long-lasting openings of single slow (L-type) Ca^{2+} channels in chick embryonic heart cells. *Am J Physiol, 259*, H639−H642.

Tohse, N., & Sperelakis, N. (1991). cGMP inhibits the activity of single calcium channels in embryonic chick heart cells. *Circ Res, 69*, 325−331.

This page intentionally left blank

Chapter 20

Patch-Clamp Techniques

Laura Conforti

Chapter Outline

I. INTRODUCTION

The patch-clamp technique allows the electrophysiological measurements of currents through ion channels in the cell membrane. Developed in 1976, it has been the technique of choice for measurements of ion-channel activities in cells with resolution up to a single channel (Neher and Sakmann, 1976; Sakmann and Neher, 1984). This technique has wide applications ranging from the recording of the activity of native channels in their natural environment to recombinant channels expressed in heterologous cells.

Historically the patch-clamp technique was based on the work of Alan Hodgkin and Andrew Huxley who, in the 1950s, conducted a series of elegant voltage-clamp experiments that allowed the recording of macroscopic currents in the squid giant axon by controlling the voltage of the membrane (Hodgkin and Huxley, 1952). These studies established the physiological importance of ion fluxes through ion channels in the activity of cells and set the foundation for much of the subsequent work in electrophysiology. In 1963, Hodgkin and Huxley were awarded the Nobel Prize in Physiology or Medicine for this work. A limitation of the technique developed by Hodgkin and Huxley was that it did not have the resolution to measure the current through a single channel. This was made possible in 1976 by Neher and Sackman, who developed the patch-clamp technique. Using this new technique, they succeeded in recording from a tiny area (a patch) of the plasma membrane of frog skeletal muscle the first acetylcholine (ACh)-activated single channel (Neher and Sakmann, 1976). For their discoveries concerning the function of single ion channels in cells, Neher and Sackman were awarded the Nobel Prize in 1991. Since then the patch-clamp technique remains the technique of choice for measuring the activity of ion channels.

This technique and its further refinements represent a major advance in the ability to monitor cell membrane function (Hamill et al., 1981). Sealing a small pipette tip to a clean cell membrane allows recording of the ionic currents through single channels contained in small patches of cell membranes. Together with the method of whole-cell recording, patch-clamp techniques permit the investigation of ion channel conductance and kinetic behavior. This information has led to the discovery of new classes of ion channels and their physiological role in cells too small to be amenable to the standard voltage-clamp techniques and to cells that are not electrically excitable.

In this chapter, we describe the well-established techniques of patch-clamp recording with an extension to newly developed high-throughput applications of this technique. This chapter is divided into five parts: the first part focuses

Cell Physiology Sourcebook. DOI: 10.1016/B978-0-12-387738-3.00020-2

on the applications of the patch-clamp technique. The second section focuses on the basis of the patch-clamp technique with an emphasis on the technical aspects of the recording process including equipment and procedural steps. The third part describes the applications of the different recording configurations to measure single-channel activity and whole-cell currents. The fourth section is on data acquisition and analysis of single-channel and whole-cell data. The last part of this chapter presents the automated patch-clamp system, a newly developed multi-well plate format of the patch-clamp technique that allows high-throughput recording of ion-channel activities.

II. APPLICATIONS OF THE PATCH-CLAMP TECHNIQUE

The patch-clamp technique provides the ability to observe, in real time, the changes in the activity of a single channel including changes in conductance (the rate of ions going through the channel) and kinetic properties (the speed with which a channel opens and closes) in response to a pre-set stimulus. Furthermore, it allows determination of the characteristic sensitivities of specific ion channels to voltage, ions and ligands. Patch-clamp studies have led to the *discovery of a variety of ion-channel types and their classification*. In general, ion channels are functionally classified based on their ion selectivity and their modulation by voltage, ligands, second messengers, phosphorylation and mechanical deformations. *Voltage-gated* (or voltage-sensitive) *channels* are activated by changes in membrane potential. To this family belong the well characterized Na^+, K^+ and Ca^{2+} channels of nerve and muscle (Caterall, 2010). The *extracellular ligand-activated channels* are regulated by ligands such as transmitters. These channels are often named according to the ligand to which they bind, e.g. ACh-sensitive channels of the neuromuscular junction and the $GABA_A$ (γ-aminobutyric acid) channels of the inhibitory synapses (Collingridge et al., 2009). The *intracellular ligand-gated ion channels* include channels that are activated indirectly by G-protein-coupled receptors (GPCRs), such as cystic fibrosis transmembrane conductance regulator (CFTR) and other ion channels that are activated by intracellular ligands such as Ca^{2+}, ATP, cyclic AMP and cyclic GMP as well as phosphoinositides (Gadsby et al., 2006). The *mechanosensory and volume-regulated channels* form a rather ubiquitous class of channels that can be activated by mechanical tension of the membrane. To this class belong channels such as transient receptor potential (TRP) and volume-activated Cl^- channels that are important in a variety of key physiological functions ranging from touch sensitivity to regulation of cell volume (Nilius et al., 1996; Sharif-Naeini et al., 2008; Wu et al., 2010). A fifth group includes ion channels that do not have any of the distinct characteristics of the above groups. This group includes the GAP junctions and peptide ion channels like gramicidin (Saez et al., 2003; Kelkar and Chattopadhyay, 2007). There are additional systems of nomenclature which have joined the extracellular- and intracellular-gated channel groups into the "chemically-activated" or just simply "ligand-gated" ion channels. It has been shown by sequence comparison that ion channels within each of the distinct functional groups described above also show the greatest sequence similarity, indicating that they are most likely all descending from a common ancestor. Therefore, within these functional families, ion channels are classified based on the genes encoding their main pore-forming subunits. For the classification of ion channels please refer to the IUPHAR (International Union of Basic and Clinical Pharmacology) database (DB) which provides a cohesive nomenclature and nomenclature guidelines, together with detailed peer-reviewed pharmacological, chemical, genetic, functional and anatomical information on G-protein-coupled receptors, voltage-gated ion channels and ligand-gated ion channels (Harmar et al., 2009). The IUPHAR-DB provides a comprehensive description of the genes encoding these channels and their functions, with information on protein structure and interactions, ligands, expression patterns, signaling mechanisms, functional assays and biologically important channel variants (e.g. single-nucleotide polymorphisms and splice variants). The IUPHAR-DB is freely available at http://www.iuphar-db.org.

Through the patch-clamp technique, the detailed electrical and kinetic properties of a multitude of ion-channel types have been described, giving insight into the physiological modulation of these channels and also their alterations in disease states. Many diseases have been associated with defects in ion channels (Ashcroft, 2000). Ion-channel-associated diseases, i.e. *channelopathies*, often result from a mutation or mutations in the genes encoding the ion channel subunits or associated regulatory subunits. A recent special issue of *Pflügers Archiv European Journal of Physiology* was dedicated to this topic (for relevant websites refer to Nilius, 2010). The patch-clamp technique has been fundamental in discovering the functional implications of mutations in channel protein sequences. Through *structure–function studies*, it is possible to mutate even a single amino acid in a channel protein, express the mutated channel using a heterologous expression system, measure its electrophysiological properties and compare those properties with those of wild-type (native) channels. These studies provide information on how a specific mutation changes the physiological activity of a channel and are thus instrumental in discovering the functional implications of disease-associated mutations. Furthermore, they allow the elucidation of the amino acids associated with specific functional properties of the channels, such as

gating, as well as sensitivity to ligands and second messengers.

Although patch-clamping finds wide application, it still remains a technically challenging method that requires a carefully controlled experimental setting and a skillful experimentalist.

III. PATCH-CLAMP TECHNIQUES

IIIA. Patch-Clamp Set-up

Conventional patch clamping, now also referred to as "manual patch-clamp" to distinguish it from the recently developed "automated patch-clamp" described below (see Section VI), is accomplished by sealing the small tip of a pipette to the surface of the cell membrane in such a way that is possible to isolate a tiny membrane area (patch) from the rest of the membrane and to control its voltage while simultaneously recording the currents through the ion channels in the patch. A typical electrophysiology rig consists of a Faraday cage (which isolates the equipment from electrical noise), a vibration isolation table, a microscope for imaging cells, micromanipulators for moving and positioning the electrodes, low-noise amplifiers, a computer (for generating the stimulus waveform and data acquisition) and a perfusion line. The technique of patch-clamp requires a very steady platform where vibrations are minimized to allow maintaining a stable contact between the pipette and the cell. The first step in reducing vibrations is to find a quiet spot with floors less subject to vibrations. A good anti-vibration table is also used to reduce the problem of vibrations. This table consists of a very heavy tabletop suspended on air cushions. The other main pieces of equipment that are on the table are the microscope and the micromanipulators. The microscope has the optics necessary for the visualization of single cells (ten to one hundred microns in size) and the tip of the patch pipette (a few microns). Usually, phase-contrast and Nomarski (or interference contrast) microscopy allow satisfactory visualization of the membrane. Furthermore, the microscope is an inverted microscope; the objectives are located under the stage. A perfusion (bath) chamber, where the cells are placed for recording, is located on the stage of the microscope. By using an inverted microscope there is sufficient space between the stage and the condenser to place the patch pipette. The schematic of the bath chamber placed on the stage of the microscope is shown in Fig. 20.1. The bath chamber is where the cells are seeded and where the actual patch-clamping procedures occur. The ground electrode in the bath is usually a silver/silver chloride (Ag/AgCl) electrode which has a low junction potential, thus minimizing the development of a solid−liquid junction potential between the electrode and the bath solution (see Section V for description of junction potentials). The patch pipette is usually a borosilicate glass pipette with tip diameter of 1−5 μm and is filled with a salt solution. Quartz glass is instead recommended when patch clamping is combined with fluorescence techniques, such as detection of intracellular Ca^{2+} with a fluorescent ion sensitive dye, as this material has better fluorescence properties. For patch pipettes and their fabrication refer to the publications of Rae and Levis (Levis and Rae, 1998; Rae and Levis, 2001). Patch pipettes, especially for single-channel recordings, may be coated with a hydrophobic material to reduce capacitative currents. The patch pipettes are filled with a conducting salt solution (known as pipette solution) in contact with a recording electrode (Ag/AgCl wire) which feeds the signal to a low-noise amplifier. The amplifier, which contains the appropriate measuring and clamping circuits and controls, processes the experimental commands, such as the voltage imposed to the cell membrane, and receives the data from the membrane. Furthermore, the patch-clamp amplifier is designed to minimize the background electrical noise that obscures very small currents in the single-channel experiments.

Once the appropriate equipment is in place, a series of specific steps are followed to make an actual patch-clamp experiment.

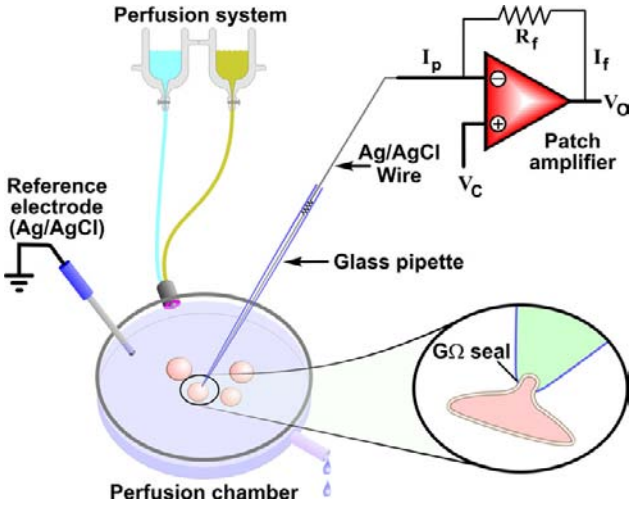

FIGURE 20.1 Schematic of a patch-clamp setting. The cells are plated in the perfusion chamber where solutions of different compositions can be rapidly switched via a perfusion system. The ground (or reference electrode) is made of Ag/AgCl and placed in the perfusion chamber either directly or through an agar bridge (1−3% agar in 0.9% saline) to reduce junction potential. One cell at the time is patched using a glass pipette which comes in contact with the cell membrane and forms the gigaseal (shown in detail in the inset). The glass pipette, filled with a salt solution, is connected to the amplifier via an Ag/AgCl wire. During a voltage-clamp experiment a current is injected through the amplifier so that the recorded voltage (V) (negative junction of the amplifier) is maintained equal to the command V (Vc) in such a way that the output V (Vo) is equal to −Vc. In this condition, $I_f \times R_f = -I_p \times R_f$, where I_f is the feedback current, I_p is the pipette current and R_f is the feedback resistance.

IIIB. Patch-Clamp Experiments

The patch-clamp recording is generally performed to measure the electrical properties of the membrane (or portions of it) attached to the pipette. The sequence of events leading to the patch-clamp recording of channel activity can be described as follows. Isolated cells are placed in the perfusion chamber and bathed in the recording solution (see Fig. 20.1). The patch pipette is then moved towards the cell surface while a low-voltage square pulse is applied to the pipette. The current amplitude of this pulse is monitored to follow the formation of the seal. As soon as the pipette touches the membrane there is an increase in resistance which produces, in accordance with Ohm's law ($I = V/R$ where I = current, V = voltage and R = resistance), a decrease in current. Upon gentle suction, a tight seal is formed, allowing the recording of the current through the channels in the patch with very high resolution. The tight seal that is formed between the membrane and the pipette is called a "gigaseal" because it has a resistance greater than one gigaohm ($10^9\ \Omega$). This high-resistance seal allows the reduction of background noise and makes possible high-resolution recordings of single-channel currents of less than 1 pA. The successful achievement of a gigaseal depends on the enzymatic cleaning of the cell membrane, the pipette configuration and solution composition, among other factors. The tight gigaseal makes the connection between the pipette and the membrane mechanically stable and amenable to manipulations that allow the establishment of different recording configurations. Recording configurations are specific architectures of the membrane patch in relationship to the bath and pipette solutions that allow different degrees of control over the channels under investigation. The recording configuration obtained at this point is the *cell-attached configuration* and, while it is used to measure single channels in their most physiological setting, it is also the starting point to reach other recording configurations (Fig. 20.2).

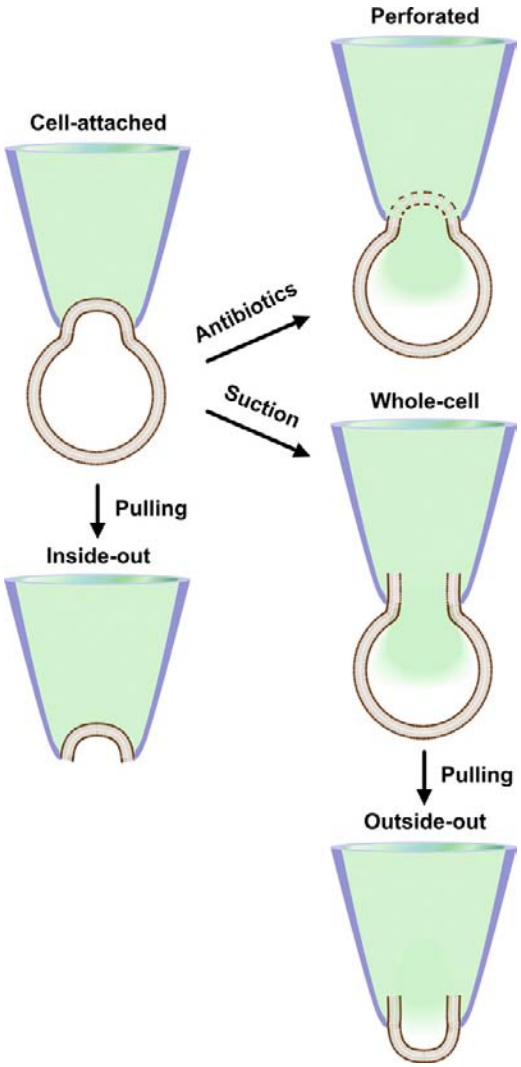

FIGURE 20.2 Patch-clamp recording configurations. The schematic of the recording configurations possible in patch-clamping and the maneuvers necessary to achieve them are shown. Each configuration is described in detail in the text. The patch pipette is labeled in blue and the pipette solution is shown in green.

IIIC. Recording Configurations

Various recording configurations have been used to study ion channels, each with its advantages and disadvantages. These configurations can all be achieved by mechanically manipulating the *cell-attached configuration* described above. The cell-attached configuration itself is ideal to measure the electrophysiological properties of single channels within the patch. The greatest advantage of this configuration is that it is relatively simpler to achieve than other configurations. Moreover, it allows maintaining the most physiological conditions at which to study the channel behavior, as the channel in the patch is in the cell membrane surrounded by the intact membrane microenvironment and intact cytoplasm. Unfortunately, this could be also considered a limitation of this configuration as there is no way to access and control the intracellular environment. Another drawback of this configuration is that the membrane potential is intact, but it is not possible to determine accurately its value. This information is necessary to set the patch potential. Theoretically, it is possible to use another electrode to measure the actual membrane potential, but this is technically quite unpractical. Commonly, it is chosen to use extracellular solutions with high K^+ concentration to "zero" the voltage (the intracellular and extracellular K^+ are made equal so that the equilibrium potential for K^+ (E_K) is set around 0 mV), after which the patch voltage is easily set. These limitations can be overcome by using other recording configurations described below.

When a cell-attached mode is established, the tight seal makes a very strong bond between the membrane and the pipette and the patch of membrane attached to the pipette can be excised from the cell by a variety of methods (see Fig. 20.2). By mechanically pulling the pipette away from the cell, a vesicle is detached. Once exposed to the air the vesicle is destroyed leaving a patch of membrane within the pipette (estimated area of the patch 1−10 μm^2). The patch is detached from the rest of the cell and the intracellular side of the membrane contacts the bath solution. This is known as the *inside-out configuration*. The cytoplasmic side of the membrane is easily accessible because it is immersed in the bath solution, which can be changed to deliver the desired compounds. This is an ideal configuration to study signaling of channels, providing that the lack of the physiological cytoplasmic environment does not modify the activity of the channel and the mechanical breaking of the membrane does not loosen the gigaseal. Other variations of the inside-out configuration are *excised inside-out macro and giant patches* in *Xenopus* oocytes.

The oocytes of the African clawed frog, *Xenopus laevis*, are widely used to study the behavior of ion channels of known molecular identity and have been the expression method of choice for studies of the structure-function relationships of ion channels (Stuhmer, 1998). *Xenopus* oocytes are large cells (ca. 1 mm in diameter) with low expression of endogenous channels. They also have very efficient translation machinery and are easy to use, making them an ideal heterologous expression system. A few days after injection with the messenger RNA of a specific channel, these cells express great quantities of the corresponding channels. Macropatches can be obtained in oocytes using pipettes with an opening 3−8 µm in diameter (Stuhmer et al., 1987). Macropatches allow the recording of macroscopic currents (sum of multiple channels) from a large membrane area, but in an excised configuration that is largely independent of cytosolic factors. Macropatches enable low-noise, fast-clamp patch-recordings of many channels and can be used to study channels with fast kinetics. Furthermore, excised giant membrane patches have also been successfully obtained in *Xenopus* oocytes (Hilgemann, 1995). These giant patches of diameter 12−40 µm allow recordings of transporter currents, charge movements and single-channel recordings of low-density channels. Interestingly, the large size of the oocytes also allows a variation of the inside-out patch that is very useful when studying the regulation of ion channels by cytoplasmic factors. The oocytes offer the unique possibility of reinserting the inside-out patch into the same cell from which the patch was obtained (so-called "*patch cramming*") (Kramer, 1990). It is also possible to introduce the excised patch into another oocyte that has been exposed to different conditions with a technique called "*cross-cramming*" (Parekh et al., 1993).

From the cell-attached configuration it is possible to obtain a second excised patch configuration, *the outside-out configuration* (see Fig. 20.2). First, the gigaseal is broken by applying suction through the glass pipette, reaching the *whole-cell configuration* that will be described in detail below. From this configuration the outside-out configuration is achieved by slowly withdrawing the pipette from the cell. The membrane stretches, eventually breaks and folds back in itself. The electrode thus contains a portion of the membrane with the outside surface facing the bath. This configuration allows making single-channel recordings with easy manipulation of the extracellular milieu while controlling the environment at the intracellular site (with a pipette solution of known composition). Since the external portion of the channel is immersed in the bath solution, it is easily accessible and amenable to manipulations such as exposure to drugs. Still, this remains a difficult configuration to accomplish.

The configurations described so far, with the exception of macro and giant patches in oocytes, allow measurements of the activities of single channels. There are other configurations that are instead used to measure simultaneously the currents through multiple channels on the entire cell membrane: whole-cell and perforated-patch configurations. The *whole-cell configuration* is achieved from a cell-attached configuration by breaking the patch with suction. This allows continuity between the pipette solution and the cytoplasm with dialysis of the cell's content. This can be viewed as an advantage because it provides control over the intracellular ionic concentration and allows delivery of chemicals and peptides to the interior of the cell. However, it is also a disadvantage as it dilutes the cytoplasm. Thus, any response that depends on soluble intracellular second messengers or ionic gradients may be altered. Furthermore, loss of cytoplasmic components essential for maintaining the channel activity can result in progressive decrease or "rundown" of the recorded currents. The *perforated-patch configuration*, like the whole-cell configuration, allows measurement of total currents, but the dialysis of the cytoplasm is reduced. This configuration can be reached from the cell-attached configuration providing that the pipette contains a small amount of an antibiotic, such as amphothericin-B or nystatin (both antifungal drugs) (Horn and Marty, 1988). These compounds form pores in the membrane, providing electrical access to the cell interior. These pores are permeable to ions but do not allow the passage of large molecules, thus reducing the loss of intracellular components. Practically, the pipette tip is filled with antibiotic-free solution and back filled with a solution of the same composition but containing the antibiotic. After the formation of a gigaohm seal, with time, the antibiotic contacts the cell membrane and forms pores. This can take 5 to 15 min, depending on the antibiotic concentration and

the amount of antibiotic-free solution in the pipette. One of the disadvantages of this configuration is that the access resistance (R_{access}) is usually higher (>20 MΩ) than in the whole-cell configuration due to the perforated membrane at the electrode. This decreases voltage-control and current resolution while increasing recording noise. A further disadvantage is that the membrane under the electrode tip is damaged by the perforations and could rupture, in which case the recording will occur in whole-cell mode with antibiotics leaking into the cytoplasm.

Once the desired configuration is achieved, the recording of the activity of a single or multiple channels can begin.

IV. DATA ACQUISITION

Cells express a variety of ion channels, so experimental interventions are made to make sure that recording occurs only from a specific type of channel. The manipulations used are chemical and electrical.

IVA. Chemical Isolation of Specific Channels

When establishing recording configurations, the chemical composition of the bath and the pipette solutions can be controlled. By strategically placing certain ions in the pipette and bath solutions or by replacing certain ions with impermeable ions of equivalent charges, it is possible to isolate specific ionic currents and/or suppress others. Furthermore, it is possible to add drugs that affect the activity of channels such as specific blockers (e.g. intracellular tetraethylammonium to block some potassium channel currents) or drugs that enhance the activity (e.g. Bay K8644 to increase the open probability of L-type calcium channels).

IVB. Voltage-Clamp

The activity of many channels also depends on the membrane voltage and this feature can be used to isolate specific currents from others. The technique used to control the voltage of the membrane is called voltage-clamp and is the most widely used method of recording ion-channel activity associated with the patch-clamp technique. This technique takes advantage of a speedy, low-noise differential patch-clamp amplifier which allows maintaining (clamping), through a feedback circuit, a specified membrane voltage and measuring, at the same time, the current across the membrane. The glass pipette containing a conductive solution is the electrode through which the voltage-clamp is maintained and currents are recorded. In practice, during a voltage-clamp experiment, the electronic feedback system of the amplifier measures the membrane voltage and compares it to a pre-set voltage defined by the experimenter. When a current is activated, the voltage of the membrane changes. To compensate for this change and bring the voltage to the preset value, a current of equivalent magnitude (but opposite direction) is injected through the pipette. In voltage-clamp, different command voltages are applied depending on the channel property under investigation. These command voltages vary in duration and waveform from simple steps to ramps and other complicated waveforms. Most patch-clamp experiments are voltage-clamp experiments. However, it is also possible not to clamp the voltage and to inject a fixed amount of current. This recording technique is called current-clamp.

The concept of voltage-clamp applies to many recording configurations. The electrical parameters involved during a patch-clamp experiment can be described by equivalent electric circuits. These help in understanding the complexity as well as the associated advantages and limitations of each configuration.

IVC. Equivalent Circuits

In every recording mode, the patch pipette and the cell or membrane patch form a complex circuit. The equivalent circuits for the cell-attached, excised-patch and whole-cell configurations are shown in Fig. 20.3.

IVC1. Cell-attached

In this configuration, a patch-pipette is sealed to an intact cell. This configuration allows measuring the current through the channel(s) in the membrane patch within the pipette tip. This is possible because of the high resistance (R) of the patch (R_{patch}). To understand how this technique makes the recording of the patch current possible, we should refer to the associated equivalent circuit. The overall electrical circuit of the cell-attached patch can be viewed as two circuits in series: one at the pipette level and the other at the cell level. The circuit of the intact cell originates from the fact that a cell has a membrane potential (V_m, i.e. the potential difference between the inside and the outside of the cell), a resistance (R_m, the lipid bilayer of the membrane, which acts as a barrier for the movement of charges through the membrane, and any open channels) and a capacitance (C_m, the capacity of the membrane to store charges at a given potential). In the cell-attached configuration, other resistors are present; one at the patch level and another at the pipette level. The latter depends on the opening and length of the pipette and the composition of the pipette solution. Overall, in this recording configuration there are three resistors in series. Since the highest resistance in a series of resistors is the one which dictates the current flow and R_{patch} is higher than R_m and the axial resistance of the pipette (R_p, usually between 1 and 3 MΩ), then, if a voltage (Vp) is applied across the pipette, the circuit effectively monitors current flowing through the ion

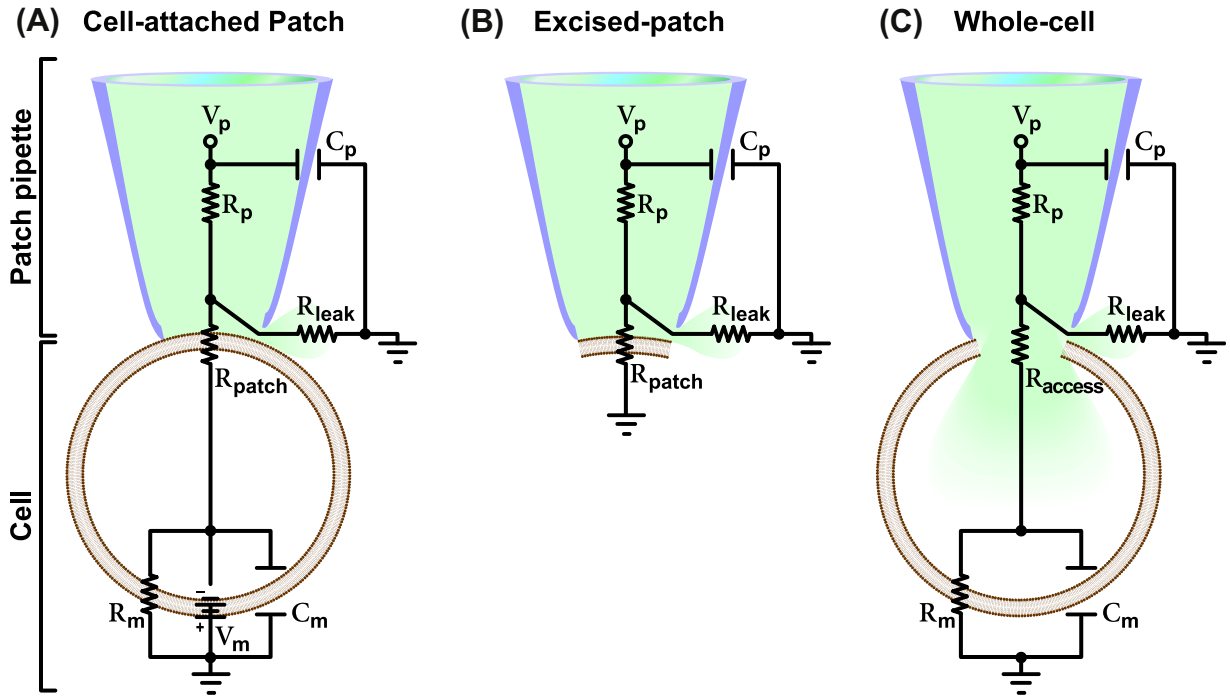

FIGURE 20.3 Recording configuration equivalent circuits. Reported are the equivalent circuitries for the cell-attached patch (A), excised-patch (B) and whole-cell (C) configurations. The patch pipette and cell (or membrane patch) are marked on the left. V_p, R_p and C_p denote the voltage, axial resistance and capacitance of the pipette. V_m, R_m and C_m denote the voltage, resistance and capacitance of the membrane. R_{patch} is the resistance of the patch of membrane which is replaced by the R_{access} in the whole-cell configuration where the patch of membrane is disrupted. R_{leak} denotes the leak resistance which depends on the tightness of the seal between the glass of the pipette and the membrane. Each circuit is described in detail in the text.

channels in the patch. In this circuit there is another resistor in parallel that could drain current away, the leak resistance (R_{leak}), which depends on the quality of the seal between the glass of the pipette and the membrane. A very high R_{leak} means that no significant current will leak away and that the noise is reduced. This explains why the key requirement for a patch-clamp recording is to maintain a high seal resistance, which is the resistance between the pipette solution and the surrounding bath solution. In a low-resistance scenario, there will be a current through the seal that is as high, or higher, than the ionic current to be measured, making the measurement of the actual current impossible. Thus, a gigaohm ($10^9\ \Omega$) seal is necessary for the resolution of ionic currents in the order of picoamperes (10^{-12} A). Three capacitances are present in this circuit: the pipette capacitance (C_p), the whole-cell capacitance (C_m) and the capacitance of the patch of membrane. The latter is very small and thus neglected in the equivalent circuit drawn in Fig. 20.3. The C_p (which depends on the size, shape and material of the patch pipette and also on the height of the bath solution) influences the time-course and the size of the signal, especially when small currents are measured. Patch-clamp amplifiers are equipped with electronics that permit the cancellation of C_p. The whole-cell capacitance C_m is also usually cancelled through the amplifier and/or with the application of a voltage-pulse protocol called positive/negative (P/N) subtraction present in most patch-clamp software. A complication unique to the cell-attached configuration is that the cell is intact; thus the V_m should be factored in unless it is set to 0 mV with a high K^+ extracellular solution as described before (see Section III).

IVC2. Excised-Patch

An excised-patch consists of a small portion of membrane sealed to the patch pipette. This translates into the simplest equivalent circuit (see Fig. 20.3). This circuit is comparable to the one described for the cell-attached configuration without C_m (which is very small for a patch), R_m and V_m. R_{patch} is the dominant resistor and the circuit monitors the current through this resistor. As discussed above for the cell-attached configuration, R_{leak} should be very high to reduce current loss. The R_p is generally very low, but it may vary depending on the size of the pipette tip needed. In some instances, such as when the channels are highly expressed, recording must be done from a small membrane patch. Thus, the pipette has a smaller tip and therefore a higher R_p which must be compensated for. Since the cell is absent in the excised-patch configuration, voltage-clamping is simple. The patch under investigation is clamped at the same voltage as V_p, apart from a very small voltage drop over the R_p. As for cell-attached recordings,

since single-channel currents are very small, on the order of 1 pA or lower, a requisite of this technique is to minimize the background electrical noise that will otherwise obscure the small single-channel current fluctuations. For the detailed analysis of the various components of the equivalent circuits on the minimization of background noise and the features of the patch-clamp amplifiers built in to control for background noise, the reader is referred to other publications (Levis and Rae, 1998).

IVC3. Whole-Cell Recordings

Whole-cell recording allows the measurement of the overall electrical properties of a cell membrane and, specifically, either the total current through all the channels on the membrane or the membrane potential. This configuration is achieved from the cell-attached configuration by breaking the membrane patch within the pipette tip. The equivalent circuit for the whole-cell configuration is simplified compared to that for the cell-attached patch configuration. More importantly, the V_m is disrupted and it can now be controlled by the experimenter. Furthermore, a very small access resistance (R_{access}) replaces the R_{patch} of the cell-attached configuration leaving R_p, R_{access} and R_m as the relevant resistors in series of this circuit. R_m is the largest resistor and thus the one through which the current is monitored. The same considerations described for the other recording configurations should be given to R_{leak}, which must be as high as possible to reduce current loss.

Examples of current measurements through the patch and whole-cell configurations are shown in Fig. 20.4.

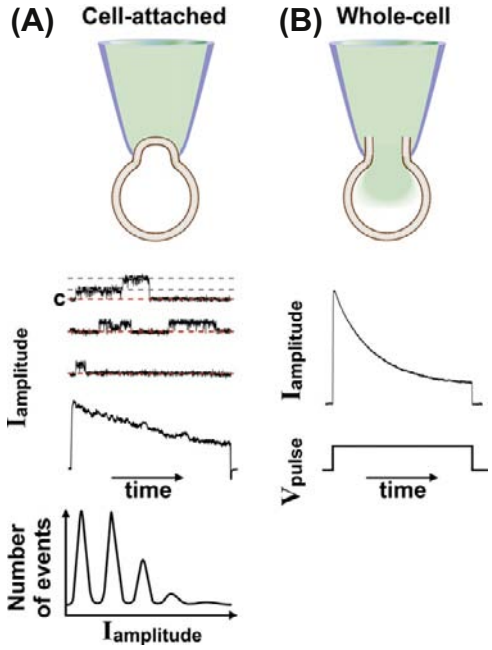

FIGURE 20.4 Current recordings during patch-clamp and whole-cell experiments. (A) Examples of recordings in cell-attached configuration. The cell-attached configuration is reported in the top panel. Middle panel: Single-channel recordings of voltage-dependent outward currents activated by a depolarization step pulse. The voltage pulse is shown in the bottom of panel (B). Three separate recordings of the single-channel fluctuations over time and, below, their corresponding ensemble average current are shown. The closed state (c) and two open states are marked in the upper trace with red and gray dash lines, respectively. Two levels of opening are detectable. Bottom: Amplitude histograms. (B) Example of total current recorded in whole-cell configuration and induced by step depolarization. The whole-cell configuration is reported in the top panel, the outward current in the middle and the pulse protocol in the bottom panel.

V. CURRENT RECORDINGS AND ANALYSIS

VA. Single-Channel Currents

When the appropriate experimental conditions are established, the spontaneous activity of a channel in the patch can be measured. Furthermore, channels can be activated with the appropriate stimulus such as a voltage step/ramp for voltage-gated channels or application of ligands (extracellular or intracellular) for ligand-gated channels. The actual recordings of single-channel activity consist of measurements of the current flowing through an ion channel or a small number of channels over time. Examples of current recordings from a cell-attached patch configuration are shown in Fig. 20.4A. Similar recordings and similar considerations can be applied to excised patches. Basically, recordings of single-channel currents in a patch appear like sudden jumps between current levels and they are generally of small amplitudes (1 pA or less). The jumps correspond to the actual openings and closings of channels which are very rapid stochastic processes due to the protein switching between different conformational states. The small amplitudes and fast kinetics of these events require minimization of the capacitive transients and adequate amplification and filtering to increase the current-to-noise ratio. The noise is reduced using a low-pass filter since the amplitude of noise increases with frequency (Colquhoun and Sigworth, 1995).

Analysis of single-channel data is critical since very little can be concluded from looking at raw recordings due to the random nature of the events. In-depth analyses of single-channel data have been elegantly described elsewhere (Magleby, 1992; Colquhoun and Hawkes, 1995; Colquhoun and Sigworth, 1995). Here we provide a brief description of these methods. The information gained with the analysis of the single-channel recordings are the amplitude(s) of the single-channel currents ($I_{amplitude}$), the durations of the close and open periods (dwell time) and the order in which these events occur. The $I_{amplitude}$ is defined by the difference between two current levels, the close and open states and it is, at least in the simplest cases, nearly constant from one opening to the next. The durations of the open and close events and the order in which they

occur are random. Since the number of channels in a patch can be (and often is) more than one, observation and analysis of the current levels provides information not only of the $I_{amplitude}$ but also of the number and type of channels in the patch. Figure 20.4A shows representative recordings of single currents (middle). Close observation of the uppermost trace indicates that there are at least two channels in the patch. This can be deduced by the two sudden steps from the closed state (C, 0 current) to two open states (indicated by the gray dashed lines) of equal current amplitude. The ensemble average current obtained by averaging a large number of single-channel recordings is shown in the bottom of the traces. A way to display the single-channel data is to report the distribution of amplitudes of each opening separately as *amplitude histograms* (see Fig. 20.4A, bottom). Current levels can be identified by peaks in the histogram: a peak at the closed level and other peaks at each of the open levels. Generally, the number of peaks at the open levels is indicative of the number of channels in the patch (providing that the probability of channel opening allows multiple channel openings to occur within the time of the experiment), but it could also indicate the subconductance states of a channel as some channels undergo multiple conformational changes which are associated with different current levels. In practice, the peaks in the amplitude histograms are fitted by a Gaussian curve using interactive computer algorithms provided in the patch-clamp analysis software. In case of the recording of a single channel in the patch, the area under the open peak is proportional to the fraction of time spent at the open level or *open probability* (Po). Po is one of the parameters that can be measured through the *dwell time analysis* which is applied to study the event transition patterns in single-channel recordings. The Po is the time for which the channel is in the open state relative to the total recording time. The Po is a quick indicator of the activity of the channel and changes in Po are used as measures of the effects of channel activators and blockers. Still, although it can provide such powerful information, the Po does not give any indication of the channel open/closing kinetics. This can be achieved through the analysis of *dwell time distributions*. Ion channels transition through multiple closed and open states. The times a channel dwells (sojourns) in an open or closed state are of different lengths and they can be grouped in dwell time histograms for each current state. This distribution provides information on the stochastic behavior of a channel. Fitting of the distribution of channel open or close dwell times can be done with exponential equations. The exponential terms and the associated time constants are related to the kinetics of the channel transitioning from the open to the closed state and vice versa. Based on these data, it is possible to build mathematical kinetic models that best describe the possible sequence of opening and closing events that lead to the channel behavior observed in response to a certain stimulus (Avdonin and Hoshi, 1998). Because it is very difficult experimentally to determine the behavior of a single channel, even if the single-channel current can be measured with a good degree of resolution, computer modeling is thus an invaluable tool in understanding ion-channel behaviors.

VB. Whole-Cell Currents

While single-channel data can provide a detailed description of the kinetic behavior of a single protein, the sum of the single-channel recordings (the ensemble current) reflects the total current flowing across the channels on the entire membrane surface. The ensemble average current from a series of single-channel recordings is shown in Fig. 20.4A. This current is devoid of contamination of currents from channels other than those in the patch or any current that develops because of the lack of voltage control (described later in this section). The ensemble current is equivalent to the whole-cell currents that can be recorded in whole-cell or perforated-patch configurations (see Fig. 20.4B). Because these configurations measure the currents through all the channels in the membrane, precautions should be taken to isolate the specific channels of interest. This could be achieved through either chemical or electrical interventions as described above in Section IV. Although whole-cell configuration is the configuration of choice for recording macroscopic currents (in the tens to thousands of pA), it presents with a series of limitations that should be considered when establishing and analyzing these types of recordings including rundown, voltage and space control and junction potential.

VB1. Rundown

Rundown is the spontaneous progressive decline of current amplitude over time. In the whole-cell configuration this phenomenon is most likely due to the dilution of regulatory components associated with the channel that occurs with the dialysis of the cytoplasm through the pipette solution. If these factors are known, it is possible to add them to the pipette or bath solution thus maintaining the channel activity. For example, ATP supplementation in the pipette was shown to reduce the rundown rate of Ca^{2+} currents. Similarly, addition of BAYK8644 to the bath prolongs the activity of voltage-dependent Ca^{2+} channels recorded in inside-out patches (Ohya and Sperelakis, 1989). The perforated-patch method, which limits the diffusion of large molecules, is used to minimize rundown (see Section III). This method has been also applied to reduce current rundown in single-channel outside-out recordings. Basically, once the perforated-patch configuration is achieved, the membrane patch is excised with a maneuver similar to that used to

generate outside-out patches (see Fig. 20.2). The only difference is that when the outside-out configuration is achieved the membrane is separated from the pipette via a perforated membrane and contains an intact cytoplasm where the ion composition can be controlled via diffusion of ions through the pores (Levitan and Kramer, 1990).

VB2. Voltage Control and Space-Clamp

The requirement for a successful whole-cell recording under voltage-clamp conditions is that adequate and homogeneous control of the voltage throughout the whole membrane is achieved and maintained. Poor voltage control distorts the kinetics of the current and will give a wrong current-voltage relationship. An inadequate voltage control occurs when the cell membrane is not "space-clamped". According to cable theory, in a linear cable the degree of charge dissipation depends on the electrical properties of the cable. Thus, in the whole-cell circuit (see Fig. 20.3C), when voltage is applied, the actual voltage measured at a point distant from the source (in this case at the membrane) is lower because of the dissipation of charges over the distance. Normally, in round cells the resistance of the cytoplasm is small compared to the R_m. In large cells with long and thin branches, the long volumes of the cytoplasm in the branches can be considered like multiple resistances in series which will add to a significant overall cytoplasmic resistance. Since the voltage is clamped over the dominant resistance in a circuit, poor clamping of the membrane portion far from the pipette will occur. Furthermore, in these large and convoluted cells, the overall C_m is much larger, further delaying the changes in clamp voltage. Inadequate space-clamp is a limitation that should be taken into account when deciding if a cell is suitable for whole-cell experiments. In general, small and electrically tight cells will have a better voltage control than cells with membrane folding and low input R_m, while large cells such as neurons that have formed a dendritic network are unsuitable. Such cells can still be patch-clamped via whole-cell current-clamp recording, which is not subject to space clamping issues. A further consideration to be made regards the type of current recorded: some currents such as voltage-activated Na^+ currents that have a steep voltage-dependent activation and/or inactivation are more prone to space-clamp distortion than others.

VB3. Junction potential

Junction potentials present a problem in voltage-clamp as they can introduce an error in potential, ultimately shifting the actual voltage at which the cell membrane is clamped. Two types of junction potential should be considered during a voltage-clamp experiment. The solid−liquid junction potential is the potential between the surface of the recording electrode and the surface of the ground. Minimization of this potential can be achieved as described in Section III (Neher, 1992). Furthermore, any residual solid−liquid potential can be neutralized after positioning the patch pipette in the bath through the voltage offset compensation of the amplifier. Another source of junction potential for which there is no analog compensation is the liquid−liquid junction potential which occurs when the pipette solution meets the bath solution. Liquid junction potential in general occurs when two solutions of different composition and concentrations are in contact with each other and it is generated by the different mobility of the ions in the two solutions. The rate of diffusion of the ions depends on their size and charge, temperature, hydration, etc. Normally, the pipette and bath solutions include ions with similar mobilities in which case the junction potential is quite small (2−3 mV) and can be ignored. However, when ions are replaced by ions of corresponding charges but of low mobility (such as Na^+ with $Tris^+$ and Cl^- with $aspartate^-$ or $glutamate^-$), the junction potential is fairly large (in the tens of mV) and cannot be ignored. This potential can be assessed experimentally and the actual voltage imposed to the cell should be corrected for this value. Detailed methods for making corrections have been reported (Barry and Lynch, 1991; Neher, 1992).

Overall, manual patch-clamp has been instrumental in understanding the physiology of ion channels. This technique presents with a high degree of flexibility in the recording configuration which provides control over the recording conditions. Furthermore, a highly detailed analysis of channel behavior can be attained. Unfortunately, at the same time, this is a technically challenging method with low throughput. Recently automated high-throughput versions of the patch-clamp technique have been developed.

VI. AUTOMATED PATCH-CLAMP

Conventional patch-clamp has been very effective in measuring, with a great deal of confidence, ionic currents and has supplied invaluable information on ion channels. Unfortunately, this technique is a time-consuming technique of limited throughput. It requires a highly trained patch clamper and, because of the technically challenging steps involved in achieving recording configurations, it only allows recording from a limited number (8−10) of cells during a working day. Multicell-based screening strategies have been developed to increase output. The need for high-throughput is particularly felt in the drug discovery field where screening of a large library of compounds is required. This screening is routinely performed to determine the safety profile of a new compound. It is based on the measurement of its effects on the activity of hERG (human ether-a-go-go-related gene) potassium channels which is indicative of the potential cardiac toxicity of the compound in question (cardiac liability screening). The

hERG channels have been identified as the molecular targets of drugs associated with an increased risk of cardiac arrhythmias (Pollard et al., 2008). Furthermore, it is used to screen libraries of compounds to find new ion-channel blockers/activators. Ion channels are, in fact, arising as attractive targets for new therapeutic agents. Approximately 13% of all marketed drugs have their mechanism of action attributed to modulation of the activity of either ligand- or voltage-gated channels and two out of 18 new compounds approved by the US Food and Drug Administration in 2006 target ion channels (Overington et al., 2006; Dunlop et al., 2008).

Initially, the high-throughput ion-channel assays used were binding, fluorescence and radioactive assays that allowed monitoring ion fluxes and membrane potential simultaneously in a large number of cells. Unfortunately, these assays present with various limitations including a high degree of false-positive and false-negative hits thus requiring verification using conventional patch-clamping. Because of these limitations, several companies have developed automated *patch-clamp systems* that allow testing of hundreds of cells each day. Some of these systems utilize conventional electrodes while others are based on planar arrays (Zhao et al., 2008). The latter have transformed the concept of patch-clamping by switching from the "top-down" access to the cell of conventional patch-clamp technique to a "bottom-up" access in plates or chips (Fig. 20.5). In the manual patch-clamp, the glass electrode approaches cells plated on a dish from above, one cell at the time, and forms a gigaseal with the portion of the membrane that does not make contact with the dish. In the automated system, the cells are suspended on a low-loss dielectric surface partitioning two solutions. This surface is etched with micrometer holes that mimic the conventional glass pipette openings. Application of negative pressure captures the cells on these holes and allows formation of the gigaseals. After this, either through the suction system itself or pore-forming agents, the patch of membrane in the hole is disrupted, allowing access to the interior of the cell and current recording either in whole-cell or in perforated-patch configurations. These new automated systems have integrated features such as fluidic control, suction mechanisms and sophisticated acquisition software that allow the serial execution of the experiment.

The IonWorks platform from Molecular Devices (currently MDS) was the first commercially available automated patch-clamp system, but it used pore-forming agents and did not fully mirror the conventional patch-clamp as it did not form gigaseals (Schroeder et al., 2003). Although this system did not have the low-noise capability of manual patch-clamping and produced lower quality recordings, it was quite effective in reaching high throughput and it has revolutionized the process of screening small compound libraries for ion-channel

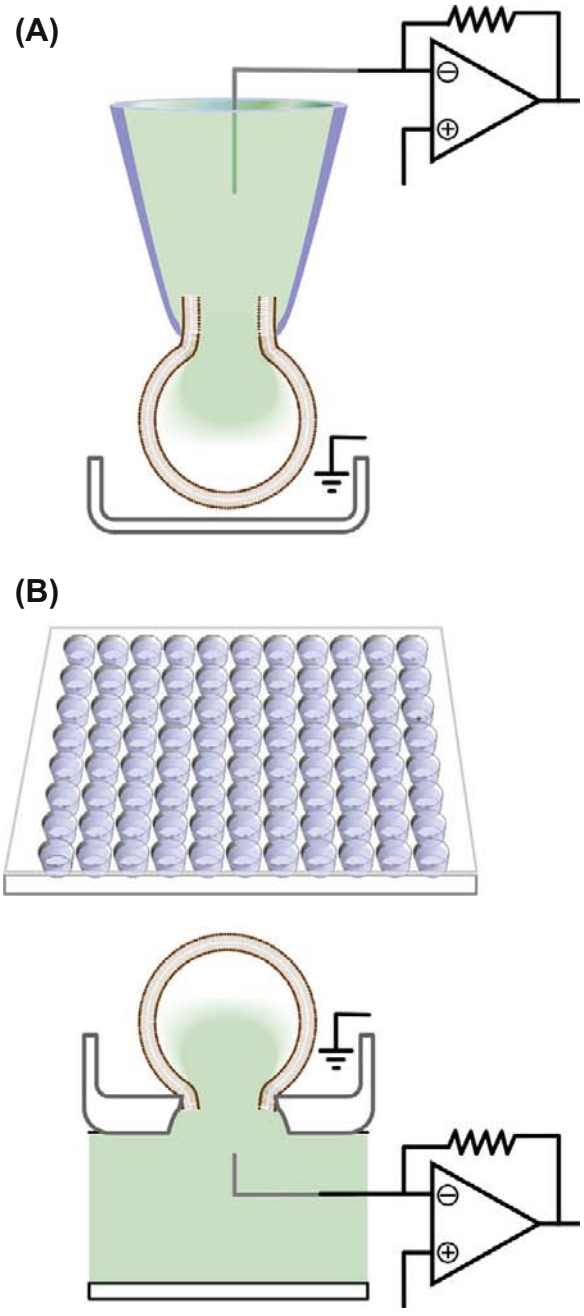

FIGURE 20.5 Comparison of the automated patch and conventional manual patch-clamp settings. (A) Schematic of the "top-down" approach in the conventional patch-clamp. The cell is plated in a dish and contacted by a patch pipette from the top to form the gigaseal and then the whole-cell configuration. (B). Schematic of the automated patch-clamp system performed on a multiwell chip (top). The plates have multiple wells with either single or multiple micrometer holes per well. The cells are seeded in the wells and, upon application of negative pressure, they are sucked in the hole. After this, the portion of the membrane in the hole is disrupted either by further suction or through antibiotics, and the whole-cell configuration is achieved.

targeting (John et al., 2007). After this, a second generation of automated patch-clamp systems followed, including PatchXpress, QPatch, Patchliner and Nanion's Port-a-patch. From single-cell recordings some of these systems have been now optimized for recording from up to 384 cells. A detailed description of these different platforms and their comparison is beside the scope of this chapter (for this please refer to the review of Dunlop et al., 2008) as this field is rapidly changing and new technologies are quickly developing. Our goal here was to introduce the reader to a shift in patch-clamp paradigm that has impacted the way patch-clamping is performed, at least in the pharmaceutical setting. Limitations still exist with these systems that reduce their application in an academic research laboratory.

The major disadvantage of these systems is that they require homogeneous, healthy cells with high expression of the ion channel under investigation which, in reality, only applies to stably transfected cell lines expressing high levels of the ion channels of interest. Primary cell cultures, such as neuronal or cardiac preparations, do not fit these criteria, although robotic multiwell planar patch-clamp has begun to be applied successfully to record native currents from primary cell cultures (Milligan et al., 2009). There are other issues associated with the automated systems that limit their use in an academic research setting where more technically demanding experiments are usually performed. Importantly, since the automated systems only allow limited flexibility, single-channel recordings are still limited to manual patch-clamp and require skilled electrophysiologists. Last, but not least, the costs associated with the platform itself and related consumables such as chips and plates have an impact on the choice of patch-clamp equipment by academic researchers. Future platforms are expected to address these limitations and be useful in both academic and industry settings with a relatively low cost per data point.

Overall, because of these limitations drug screening and cardiac safety profiling are currently the principal applications of these new systems, while conventional patch-clamp still remains the technique of choice for the academic research setting.

ACKNOWLEDGMENTS

My thanks go to Dr Steven Kleene who has critically revised and edited this chapter.

BIBLIOGRAPHY

Ashcroft, F. (2000). *Ion Channels and Disease: Channelopathies*. Boston: Academic Press.

Avdonin, V., & Hoshi, T. (1998). Kinetic models and simulation: practical approaches and implementation notes. In P. M. Conn (Ed.), *Ion Channels part B, Vol. 293* (pp. 724−740). New York: Academic Press.

Barry, P. H., & Lynch, J. W. (1991). Liquid junction potentials and small cell effects in patch-clamp analysis. *J Membr Biol, 121*, 101−117.

Catterall, W. A. (2010). Ion channel voltage sensors: structure, function, and pathophysiology. *Neuron, 67*, 915−928.

Collingridge, G. L., Olsen, R. W., Peters, J., & Spedding, M. (2009). A nomenclature for ligand-gated ion channels. *Neuropharmacology, 56*, 2−5.

Colquhoun, D., & Hawkes, A. G. (1995). The principles of the stochastic interpretation of ion channel mechanisms. In B. Sackman, & E. Neher (Eds.), *Single-channel Recordings* (pp. 397−482). New York: Plenum Press.

Colquhoun, D., & Sigworth, F. J. (1995). Fitting and statistical analysis of single-channel records. In B. Sackman, & E. Neher (Eds.), *Single-channel Recordings* (pp. 483−587). New York: Plenum Press.

Dunlop, J., Bowlby, M., Peri, R., Vasilyev, D., & Arias, R. (2008). High-throughput electrophysiology: an emerging paradigm for ion-channel screening and physiology. *Nat Rev Drug Discov, 7*, 358−368.

Gadsby, D. C., Vergani, P., & Csanady, L. (2006). The ABC protein turned chloride channel whose failure causes cystic fibrosis. *Nature, 440*, 477−483.

Hamill, O. P., Marty, A., Neher, E., Sakmann, B., & Sigworth, F. J. (1981). Improved patch-clamp techniques for high-resolution current recording from cells and cell-free membrane patches. *Pflügers Arch, 391*, 85−100.

Harmar, A. J., Hills, R. A., Rosser, E. M., et al. (2009). IUPHAR-DB: the IUPHAR database of G protein-coupled receptors and ion channels. *Nucl Acids Res, 37*, D680−D685.

Hilgemann, D. W. (1995). The giant membrane patch. In B. Sakmann, & E. Neher (Eds.), *Single-channel Recording* (2nd ed.). (pp. 307−327) New York: Plenum Press.

Hodgkin, A. L., & Huxley, A. F. (1952). A quantitative description of membrane current and its application to conduction and excitation in nerve. *J Physiol, 117*, 500−544.

Horn, R., & Marty, A. (1988). Muscarinic activation of ionic currents measured by a new whole-cell recording method. *J Gen Physiol, 92*, 145−159.

John, V. H., Dale, T. J., Hollands, E. C., et al. (2007). Novel 384-well population patch clamp electrophysiology assays for Ca2+-activated K+ channels. *J Biomolec Screen, 12*, 50−60.

Kelkar, D. A., & Chattopadhyay, A. (2007). The gramicidin ion channel: a model membrane protein. *Biochim Biophys Acta, 1768*, 2011−2025.

Kramer, R. H. (1990). Patch cramming: monitoring intracellular messengers in intact cells with membrane patches containing detector ion channels. *Neuron, 4*, 335−341.

Levis, R. A., & Rae, J. L. (1998). Low-noise patch-clamp techniques. *Meth Enzymol, 293*, 218−266.

Levitan, E. S., & Kramer, R. H. (1990). Neuropeptide modulation of single calcium and potassium channels detected with a new patch clamp configuration. *Nature, 348*, 545−547.

Magleby, K. L. (1992). Preventing artifacts and reducing errors in single-channel analysis. In B. Rudy, & L. E. Iverson (Eds.), *Ion Channels, Vol. 207*. New York: Academic Press.

Milligan, C. J., Li, J., Sukumar, P., et al. (2009). Robotic multiwell planar patch-clamp for native and primary mammalian cells. *Nat. Protocols, 4*, 244−255.

Neher, E. (1992). Correction for liquid junction potentials in patch clamp experiments. *Meth Enzymol, 207*, 123−131.

Neher, E., & Sakmann, B. (1976). Single-channel currents recorded from membrane of denervated frog muscle fibres. *Nature, 260*, 799−802.

Nilius, B. (2010). A special issue on channelopathies. *Pflügers Arch Eur J Physiol, 460*, 221−222.

Nilius, B., Eggermont, J., Voets, T., & Droogmans, G. (1996). Volume-activated Cl- channels. *Gen Pharmacol Vasc Syst, 27*, 1131−1140.

Ohya, Y., & Sperelakis, N. (1989). Modulation of single slow (L-type) calcium channels by intracellular ATP in vascular smooth muscle cells. *Pflügers Arch, 414*, 257−264.

Overington, J. P., Al-Lazikani, B., & Hopkins, A. L. (2006). How many drug targets are there? *Nat Rev Drug Discov, 5*, 993−996.

Parekh, A. B., Terlau, H., & Stuhmer, W. (1993). Depletion of InsP3 stores activates a Ca2+ and K+ current by means of a phosphatase and a diffusible messenger. *Nature, 364*, 814−818.

Pollard, C. E., Valentin, J. P., & Hammond, T. G. (2008). Strategies to reduce the risk of drug-induced QT interval prolongation: a pharmaceutical company perspective. *Br J Pharmacol, 154*, 1538−1543.

Rae, J. L., & Levis, R. A. (2004). Fabrication of patch pipets. *Curr Prot Neurosci, John Wiley & Sons, Inc.*, 6.3.1−6.3.32.

Saez, J. C., Berthoud, V. M., Branes, M. C., Martinez, A. D., & Beyer, E. C. (2003). Plasma membrane channels formed by connexins: their regulation and functions. *Physiol Rev, 83*, 1359−1400.

Sakmann, B., & Neher, E. (1984). Patch clamp techniques for studying ionic channels in excitable membranes. *Annu Rev Physiol, 46*, 455−472.

Schroeder, K., Neagle, B., Trezise, D. J., & Worley, J. (2003). IonWorks™ HT: a new high-throughput electrophysiology measurement platform. *J Biomolec Screen, 8*, 50−64.

Sharif-Naeini, R., Dedman, A., Folgering, J., et al. (2008). TRP channels and mechanosensory transduction: insights into the arterial myogenic response. *Pflügers Arch Eur J Physiol, 456*, 529−540.

Stuhmer, W. (1998). Electrophysiologic recordings from Xenopus oocytes. *Meth Enzymol, 293*, 280−300.

Stuhmer, W., Methfessel, C., Sakmann, B., Noda, M., & Numa, S. (1987). Patch clamp characterization of sodium channels expressed from rat brain cDNA. *Eur Biophys J, 14*, 131−138.

Wu, L.-J., Sweet, T.-B., & Clapham, D. E. (2010). International Union of Basic and Clinical Pharmacology. LXXVI. Current progress in the mammalian TRP ion channel family. *Pharmacol Rev, 62*, 381−404.

Zhao, Y., Inayat, S., Dikin, D. A., Singer, J. H., Ruoff, R. S., & Troy, J. B. (2008). Patch clamp technique: review of the current state of the art and potential contributions from nanoengineering. *Proc Inst Mech Eng J Nanoeng Nanosyst, 222*, 1−11.

This page intentionally left blank

Chapter 21

Structure and Mechanism of Voltage-Gated Ion Channels

Simon Rock Levinson and William A. Sather

Chapter Outline

I. SUMMARY

The structure, mechanism and expression of ion channels are currently intense areas of research interest. The first advances in these areas were made by the application of biochemical techniques to the problems of channel purification. Such studies have told us the size of intact channels and their subunit composition and have yielded clues regarding functionally important domains (such as pores, gates, modulation sites and non-protein modifications). For Na^+ and Ca^{2+} channels, attention has been focused on a large polypeptide (so-called α peptide) found in each purified preparation. These α proteins apparently have all the molecular apparatus required for channel operation, while smaller associated subunits may play other roles in channel modulation, synthesis or cellular localization. Purified material has also been important in the construction of probes to identify clones of channel-encoding DNA fragments.

Cell Physiology Sourcebook. DOI: 10.1016/B978-0-12-387738-3.00021-4

Recent work has applied recombinant DNA technology to determine the primary amino acid sequence of channels through cloning. These sequences have revealed widespread sequence homology among the superfamily of voltage-gated ion channels, e.g. between Na^+ and Ca^{2+} channel α polypeptides. Furthermore, the large α proteins have four domains of homology within their sequences, suggesting that pore formation occurs via a common "staves of a barrel" architecture. K^+ channel sequences, determined via a genetic approach, are relatively shorter and they partially correspond to a single internal repeat of the larger α peptides. Hence, K^+ channels are thought to consist of tetramers with each subunit contributing to the pore wall. Other analyses of amino acid sequences have given clues regarding the mechanistically and structurally important domains of ion channels. One analysis was based on thermodynamic (hydropathy) considerations to identify possible membrane-spanning domains. In addition, the sequences were subjected to an empirical analysis that predicts regions of secondary structure, such as helices and sheets. From such predictions detailed models of channel structure and function have been developed. These models have been tested using immunological and mutagenesis approaches and candidate domains for ion selectivity, pore wall formation, gating and modulation have been identified. However, detailed knowledge of the molecular mechanisms of channel function is still limited.

Finally, molecular studies have revealed an astonishing diversity of ion channels at all levels of organization. In particular, the genome of most organisms can express multiple channel isotypes, sometimes coexisting within the same living cell. Much remains to be learned about channel function and the role of channel isotypes in the biology of both simple and complex organisms.

II. INTRODUCTION: HOW IS ION CHANNEL STRUCTURE STUDIED?

Previous chapters have described how the flow of ions across cell membranes is the basis for electrical excitability and signaling in the nervous system. These flows are controlled by a special class of macromolecules known as *ion channels* that form gated pores in the cell membrane. The structure of ion channels and the current thinking about how these structures form transmembrane pores that gate to open and closed states in response to changes in membrane voltage are discussed in this chapter. Subsequent chapters will describe other important aspects of ion channels, such as interactions with drugs and toxins, modulation by intracellular messengers and specific ion channel types found in intracellular organelles and involved in synaptic transmission.

What are the questions that should be addressed in this chapter? Most fundamentally, we wish to know how these macromolecular structures give rise to the important functional properties of ion channels, namely, the formation of transmembrane pores, the selective transport of specific ions and the ability to open and close the pore; i.e. how do ion channels function as molecular mechanisms? As we will see, these considerations also lead into a brief consideration of the structural diversity among ion channels and the origin and possible purposes of such diversity.

Cellular ion channels are basically proteins. In the earliest structural studies, biochemical methods were employed to purify channel molecules from excitable tissues. This approach has been essential to the current state of knowledge of ion channel structure. However, ion channels have certain physicochemical properties that have limited the amount of information obtained solely through biochemical characterization. This bottleneck has been broken recently through the application of recombinant DNA methodologies, which have uncovered the primary structures of numerous ion channel types, while providing a powerful means to study higher order structure and function. However, this latter approach has its own limitations and, ultimately, we will need to "see" more directly the actual structure of the channels to understand more fully their molecular mechanisms of action. In this regard, it is encouraging that significant progress has been made recently in elucidating the structure of purified channels using x-ray crystallographic techniques.

III. BIOCHEMISTRY OF ION CHANNELS: PURIFICATION AND CHARACTERIZATION OF VOLTAGE-GATED CHANNELS

Before the advent of recombinant DNA methods, ion channels were extensively studied by first purifying channels from an excitable tissue and then characterizing the purified molecules by a combination of chemical and physical techniques. While this biochemical approach has fallen somewhat out of use in favor of DNA cloning techniques, it seems certain to re-emerge as a necessary adjunct to structural studies that now seem feasible (see Section VH). Thus, a brief introduction to channel biochemistry seems appropriate here. The first voltage-gated channel to be purified was the Na^+ channel from the electric eel, *Electrophorus electricus*, and the account of how this was achieved will serve to illustrate the basic rationale for the biochemical approach (see Miller et al., 1983).

The basic procedure for purification of membrane-associated proteins (Fig. 21.1) is as follows. First, an enriched fraction of membranes is usually prepared by disrupting the tissue and its cells mechanically and subsequently separating the insoluble fraction containing membranes and connective tissue components from the soluble fraction consisting of cytoplasmic protein.

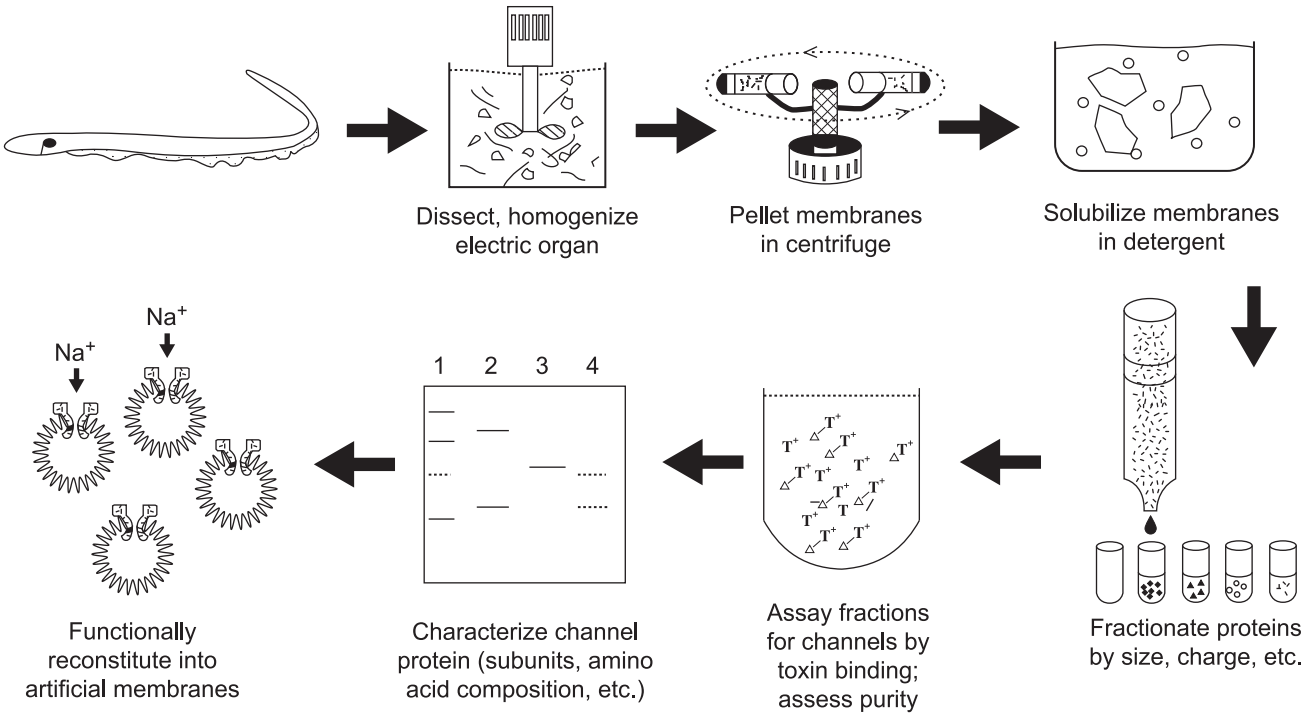

FIGURE 21.1 Scheme used for the biochemical isolation of Na^+ channels from electric tissue of the eel *Electrophorus electricus*. Purification protocols devised for other ion channels utilize similar general principles but differ in details.

Although relatively non-specific, this step also often gives substantial enrichment of ion channel preparations. Next, the membranes are solubilized through the use of detergents. This step disperses the membranes into minute droplets of lipid, protein and detergent known as micelles. This is often the most problematic step of a purification, because the micellar fraction must be dispersed well enough so that no more than one protein molecule is present in each micelle. Too much detergent often results in irreversible denaturation of channels, hence preventing their identification during the purification process. Thus, the solubilization process must be optimized and often many different detergents at various concentrations are tested under a plethora of conditions before the right combination is found. Finally, the dispersed micelles are fractionated based on their physical properties or affinities for certain compounds until a pure sample of channel protein is isolated.

IIIA. Electric Fish Are a Rich Source of Ion Channels

The first requirement for purification of any protein is to have a rich source. Actually, this can be a serious difficulty, since ion channels are present in very small amounts in most excitable tissues. The rarity of channels might at first seem paradoxical in view of the ubiquity of excitability phenomena in nearly all cell membranes. However, the reader should recall that only minute numbers of channels are needed to mediate the flow of ions required to cause the changes in transmembrane voltage during electrical excitation (Table 21.1).

Fortunately, there exist some highly specialized "freaks" of nature that use large ionic currents for purposes other than signaling and stimulus transduction. These are the strongly electric fish, which are capable of generating powerful electrical discharges to stun prey and defend themselves. The electric organs of these animals contain large numbers of ion channels that are present at high density on the surface of the excitable cells of the electric organ (see Chapter 48). As a result, the first two ion channels to be purified were the acetylcholine receptor channel of the electric ray *Torpedo* and the Na^+ channel of the electric eel *Electrophorus*.

IIIB. Toxins and Drugs as Markers for Ion Channels during Purification

Having a rich source of channels does not guarantee a successful isolation of channels. One must also have a very specific and sensitive assay for the presence of solubilized channels to follow the process of fractionation. Unfortunately, unlike enzymes or other chemically

TABLE 21.1 Sodium Channel Densities in Selected Excitable Tissues

Tissue	Surface Density Channels/μm^2	Tissue Density (μg channel/g tissue)
Mammalian		
Vagus nerve (unmyelinated)	110	28
Node of Ranvier	2100	—
Skeletal muscle (various)	2066–557	6–14
Other Animals		
Squid giant axon	166–533	≈1
Frog sartorius muscle	280	6
Electric eel electroplax (excitable surface)	550	38
Garfish olfactory nerve	35	96
Lobster walking leg nerve	90	24

active proteins, the activity of ion channels is to transport ions across membranes. Since this barrier is disrupted during the first stage of purification, the compartments essential to channel function no longer exist and hence the electrically detectable flow of ions through channels no longer occurs. Instead, one may use the binding of powerful neurotoxins to channels to assess the degree of purity attained during fractionation.

For Na^+ channels, there exist highly selective inhibitors of sodium transport known as guanidinium toxins. The most commonly used of these are tetrodotoxin (TTX), obtained from certain species of toxic puffer fish, and saxitoxin (STX), a product of certain dinoflagellates that "bloom" during oceanic "red tides". Either toxin may be radioactively labeled and these substances very specifically interact with Na^+ channels from a wide variety of sources with high affinity. To assess purity, one may thus compare the number of toxin-binding sites in a fraction with the amount of protein present.

IIIC. Isolation of Channel Molecules Based on Fractionation Procedures

With a good source of channels, efficient solubilization procedures and a specific and sensitive assay, one may proceed to attempts at purification. For Na^+ channels, fractionation based on charge, followed by size fractionation of the mixed channel/lipid/detergent micelle, has resulted in highly purified preparations of Na^+ channels. Alternatively, in some protocols, channel proteins have been specifically purified using affinity chromatography, in which channels are selectively retained by a column to which channel-binding substances, such as drugs, toxins or antibodies, are attached.

Skeletal muscle Ca^{2+} channels have also been extensively purified and characterized using much the same approaches as those described for Na^+ channels. In this case, it has been the L-type channels that were isolated, using radiolabeled drugs of the dihydropyridine class to tag channels irreversibly in the intact muscle membrane. This allowed the investigators to isolate the channel protein by following the fractionation of the bound radiolabeled drug (Sharp et al., 1987).

IIID. Information about Channel Structure from Channel Purification

There is much to be learned about channel structure from the physicochemical characteristics of the purified molecule. Some of this information forms the basis for separating the molecule from others in membrane extracts (such as size or charge differences), as described previously, whereas other measurements may be done on the purified material itself. Thus, for Na^+ channels, it was found that the channel is very negatively charged. Furthermore, in detergent solution, the channel appears quite large; in micellar form, its size is on the order of several million molecular weight. Both characteristics are important clues regarding the chemical composition of Na^+ channels.

The subunit composition of a channel is an especially important characteristic to be determined from the purified material. For a number of enzymes, separate functions have been attributed to different subunits; hence breaking down the structural entities represents an important basis for further structure–function correlations. In brief, one usually determines the subunit composition of the purified material by analyzing it using denaturing electrophoresis, in which the intersubunit bonds are broken and each

subunit separated according to size in an electric field. The most commonly used technique is sodium dodecyl sulfate—polyacrylamide gel electrophoresis (SDS-PAGE), in which each polypeptide species appears as a separate band on staining the polyacrylamide sieve used to separate polypeptides. Unfortunately, this is often more difficult than it appears, since (1) one is often not sure whether different bands on a gel are contaminants or true subunits and (2) the stoichiometry of subunits is difficult to establish because of variations in the intrinsic staining intensity among various polypeptides. As a result, considerable effort is expended by various researchers to determine (and argue about!) subunit composition using a wide variety of approaches. For the voltage-gated Na^+ channel, a single large polypeptide apparently accounts for pore formation, ion selectivity and gating. This protein appears on SDS-PAGE as a broad band at high molecular weight.

Given the large size of the eel electric organ, enough protein can be purified to allow study of its chemical composition. Not too surprisingly, Na^+ channels have an elevated proportion of hydrophobic amino acids compared to soluble globular proteins, likely reflecting domains of the channel that insert into the lipid membrane. However, the channel molecule appears to be much more hydrophobic than can be accounted for from its amino acid composition. Thus, further chemical analysis has found that a large number of lipid molecules are bound to the eel protein. Finally, it has been found that Na^+ channels are modified by the presence of extensive domains of carbohydrate. This glycosylation makes up about 30% of the molecule (by weight).

Na^+ channels have also been purified from mammalian brain and muscle tissue. Like the eel channel, they consist primarily of heavily glycosylated large polypeptides. However, unlike the electric organ channel, they are found in association with one or several smaller polypeptides that have been thought to be channel subunits (Table 21.2). The large polypeptide common to Na^+ channels from all sources is referred to as alpha (α) while smaller subunits have been designated as beta (muscle) or $\beta1$ and $\beta2$ (brain). At present, the role of these accessory polypeptides in channel function is not certain, although recent evidence suggests that they may aid in channel expression and modulate channel gating (Isom et al., 1992).

For the skeletal muscle L-type Ca^{2+} channel, it was found that although a single large polypeptide ($\alpha1$) was affinity labeled by the dihydropyridine (DHP) marker, at least four other polypeptides — $\alpha2$, β, gamma (γ), delta (δ)—copurified with the DHP label. As with the Na^+ channel, $\alpha1$ seems to have the mechanisms required for ion channel operation. However, there is evidence that the other subunits are important accessory proteins that may be involved in the key role of this channel as the voltage sensor in excitation—contraction coupling, which is described in Chapter 45.

TABLE 21.2 Subunit Composition of Voltage-Gated Cation Channels

Channel/tissue	Subunit	Molecular Weight[a]
Na^+		
Eel electric organ	α	260 (208)
Rat brain	α	260 (220)
	$\beta1$	36 (23)
	$\beta2$	33
Rat skeletal muscle	α	260 (209)
	β	36
Chick heart	α	235
Ca^{2+}		
L-type, rabbit skeletal muscle	α-1	170 (212)
	α-2	143 (125)[b]
	β	54 (58)
	γ	30 (25)
	δ	24—27 (27)[b]
K^+ Channel		
Drosophila Shaker A	—	65—85 (70)
Rat drk1	—	130 (95)

[a] *First set of values is the apparent molecular weight determined biochemically (SDS-PAGE); weights in parentheses were obtained from cloned DNA sequences.*
[b] *The biochemically observed calcium channel α-2 and δ subunits are derived from proteolysis of a full-length α-2 translation product during biosynthesis.*

Also shown in Table 21.2 are data for voltage-gated K^+ channels. The characterization of K^+ channel subunits was achieved primarily through molecular genetic means, as discussed in Section IVF.

IIIE. Reconstitution of Purified Proteins Confirms their Identity as Channels

An important criterion for purification was the reconstitution of the isolated material into artificial membranes and the demonstration that voltage-gated, sodium-selective, toxin-inhibitable channels were formed (see Miller, 1986). Thus, these experiments showed that purified toxin-binding material could be reinserted into small artificial lipid vesicles (liposomes) or planar lipid films (lipid bilayers) where they retained their ability to transport sodium selectively in response to voltage changes. These reconstituted channels had the same ability to respond to

different pharmacological compounds, such as toxins and anesthetics, as the channels in natural tissue (reviewed in Catterall, 1992). Similar experiments have demonstrated that purified DHP receptors can form functional Ca^{2+} channels in bilayers (Catterall, 1988).

IIIF. Limitations of Biochemical Characterization of Channels

The biochemical approach to channel purification thus gave important information about the size, chemical composition and polypeptide makeup of Na^+ and L-type Ca^{2+} channels. Classically, the next steps would be to sequence the purified material and attempt to obtain a high-resolution structure from crystallographic approaches. However, although these techniques have worked well with a small number of soluble globular proteins, for several reasons they have been relatively unsuccessful with membrane proteins in general and voltage-gated channels in particular. First, sequencing a large polypeptide requires that it be enzymatically or chemically cleaved into overlapping smaller fragments amenable to Edman degradation techniques (which can only sequence from 25 to 50 residues at a time). In such an approach, each small fragment must be separately purified from the fragmented preparation. For the large polypeptides of Na^+ and Ca^{2+} channels, the number of fragments generated by such cleavages is just too great for all of them to be purified separately. Furthermore, many of the interesting membrane-spanning segments do not fragment or isolate well because of their high degree of hydrophobicity ("fears water"). Finally, the amphipathic (i.e. polarized hydrophilic/hydrophobic) nature of membrane proteins prevents their crystallization; instead, in the absence of lipids or detergents, such purified preparations usually form amorphous aggregates or precipitates with little intrinsic order. Hence, the elaboration of detailed structure of biochemically purified channels has been hampered by the unfavorable physical properties of membrane proteins.

IV. CHANNEL STRUCTURE INVESTIGATION THROUGH MANIPULATION OF DNA SEQUENCES ENCODING CHANNEL POLYPEPTIDES

Fortunately, the limitations of classic biochemistry may be partly overcome by the application of techniques that allow one to identify and sequence DNA that encodes channel peptides. The next three subsections describe how the powerful methods of molecular biology are being applied to questions of interest to the cell physiologist. These approaches have given important insights into the structure of channels and how they work. This aspect of channel biology is considered in Sections IVA and IVB. However, molecular biology has also shown us that voltage-gated channels exist in a rich diversity of forms even within a single organism. This aspect of channel biology is described in Section IVC. First, a brief description of how recombinant DNA methods are used in such studies is provided for the novice reader (Fig. 21.2).

IVA. Primary Structure of Ion Channels Determined Using Recombinant DNA Technology

One starts with the same tissues shown to be enriched in channel protein because these are also probably enriched in messenger RNAs (mRNAs) encoding these channels. Using the retroviral enzyme reverse transcriptase, one may then make *complementary DNA copies* (cDNAs) of the mRNAs. Using enzymatic "scissors" (called restriction enzymes), one may then insert each cDNA obtained into a circular DNA *plasmid*. These plasmids have the ability to be replicated along with other genetic material in bacteria and also they encode an enzyme that will destroy certain antibiotics that would otherwise kill their bacterial hosts. The recombinant plasmids are next introduced into a bacterial host so that each bacterium will contain no more than a single plasmid with its unique cDNA insert. The bacteria are then diluted and spread over a plate of agar containing an antibiotic. Thus, bacteria without a plasmid are killed, whereas plasmid-containing bacteria can survive and replicate to form visible colony plaques. Since each such colony arises from a single original plasmid-transformed cell, they are known as *clones*. Each agar plate may contain many thousands of such clones, each clone having many cells with plasmids containing the identical cDNA insert.

The problem is to identify which of the many colonies has a particular cDNA that encodes for the channel protein of interest, among all of the cloned cDNAs that encode the myriad proteins of the original tissue. The severity of this problem can be appreciated from the fact that even highly enriched tissues such as eel electric organ may have at most only one message out of 10 000 or so that encodes a Na^+ channel. Hence, there must be a rapid method for screening the colonies to identify the channel cDNA clones. This is where information from biochemical purification proves to be vital.

Despite the near impossibility of totally sequencing large Na^+ or Ca^{2+} channel polypeptides, from a proteolytic digest one can readily purify a homogeneous preparation of a particular fragment. This fragment may then be partially sequenced using standard Edman degradation techniques. In practice, one only needs a few (perhaps six or so) residues of sequence to be reasonably sure that a unique segment of the protein is encoded. From this short amino acid segment, one can then synthesize (by automated

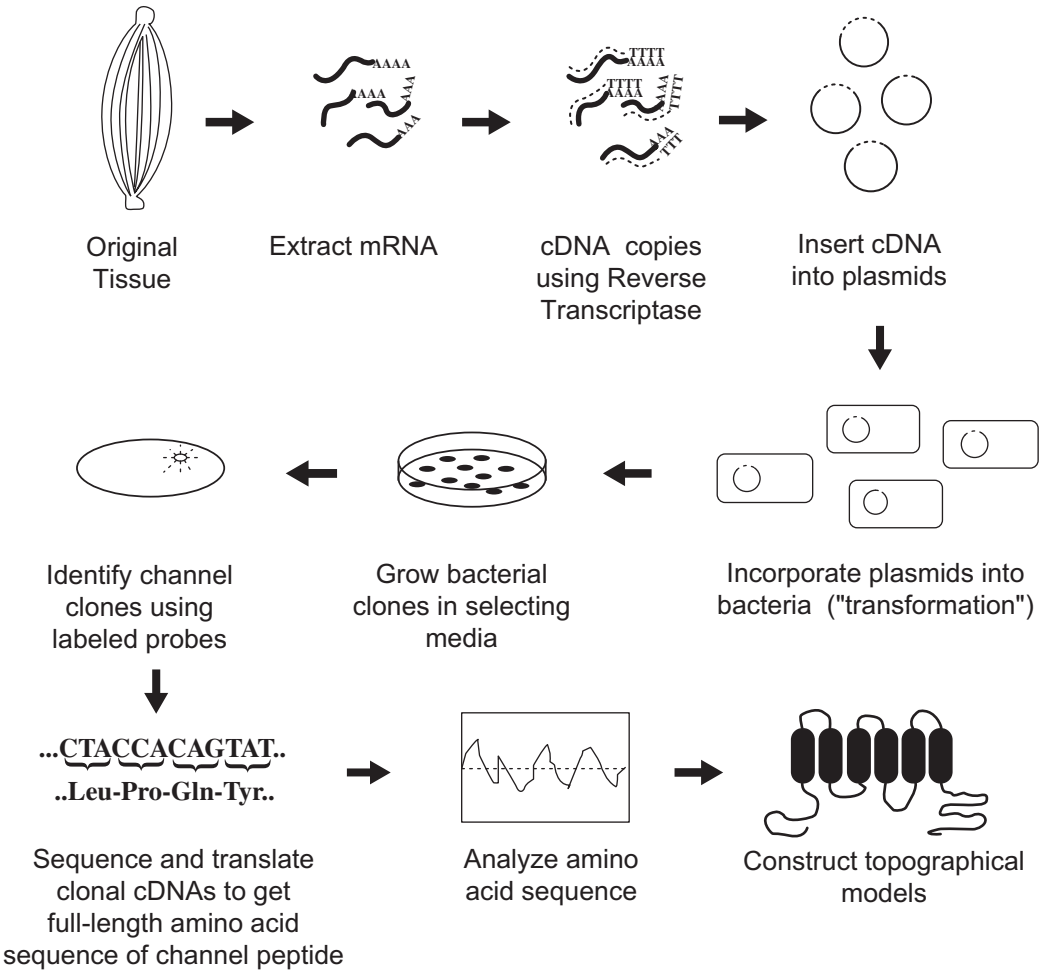

FIGURE 21.2 General strategy used to determine ion channel structure using recombinant DNA approaches.

means) a short DNA fragment, called an *oligonucleotide*, that encodes the segment. Further, this synthetic DNA may be radiolabeled and thus becomes a binding probe to identify cDNA inserts. Identification is done by placing a piece of special paper briefly on top of the agar plate and lifting off a few bacteria from each colony plaque onto the paper. The paper is then placed in a special solution that lyses the bacteria but binds the released DNA immediately on the surface. The radiolabeled synthetic probe may then be washed over the paper; it will bind by complementary interactions to the antisense strand of clonal plasmids encoding the channel protein containing the original sequence. After unbound probe is washed away, the paper is overlaid in the dark with x-ray film. Channel clones are thus identified as dark spots (usually only a few) on the film and may be traced back to the plaque on the original agar plate. This plaque is then lifted from the plate with a toothpick and grown in a nutrient broth to produce many bacteria. This technique provides enough cells from which the plasmids are purified by simple chemical means and the cDNA insert may be readily sequenced. Once the cDNA sequence is known, the genetic code is applied to derive the primary amino acid sequence of the channel protein.

This description of clonal sequencing omits many details. For example, the length of DNA that one may clone or sequence at one time is limited and complex strategies are often required to sequence the entire length of long channel polypeptides. In addition, ion channels that are heteromeric complexes will require that each subunit polypeptide be separately sequenced. Despite these apparent complexities, an organized group of researchers using automated equipment can screen hundreds of thousands of clones and sequence thousands of bases of interesting cDNA inserts in a relatively short time.

IVB. Analysis of the Primary Structure of Large Polypeptide Voltage-Gated Channels

The electroplax Na^+ channel was the first voltage-gated channel to be sequenced (Noda et al., 1984). As

suggested by the biochemistry, it was found to be a long polypeptide of 1820 amino acids (Fig. 21.3). Subsequent cloning of mammalian channels showed them to be similar in size and sequence (see Numa and Noda, 1986). What can one learn about channel structure from such primary sequence data? Typically, one subjects the primary sequence data to several forms of analysis to derive a model of the appearance of the higher order structure. The first striking characteristic revealed in the Na^+ channel sequence was the presence of four repeats (of about 200 amino acids each) that were highly (but not completely) homologous to one another. Furthermore, these internal repeats were found to have great potential for forming membrane-spanning domains of the channel. From such analyses, the model shown later in Fig. 21.6 was obtained.

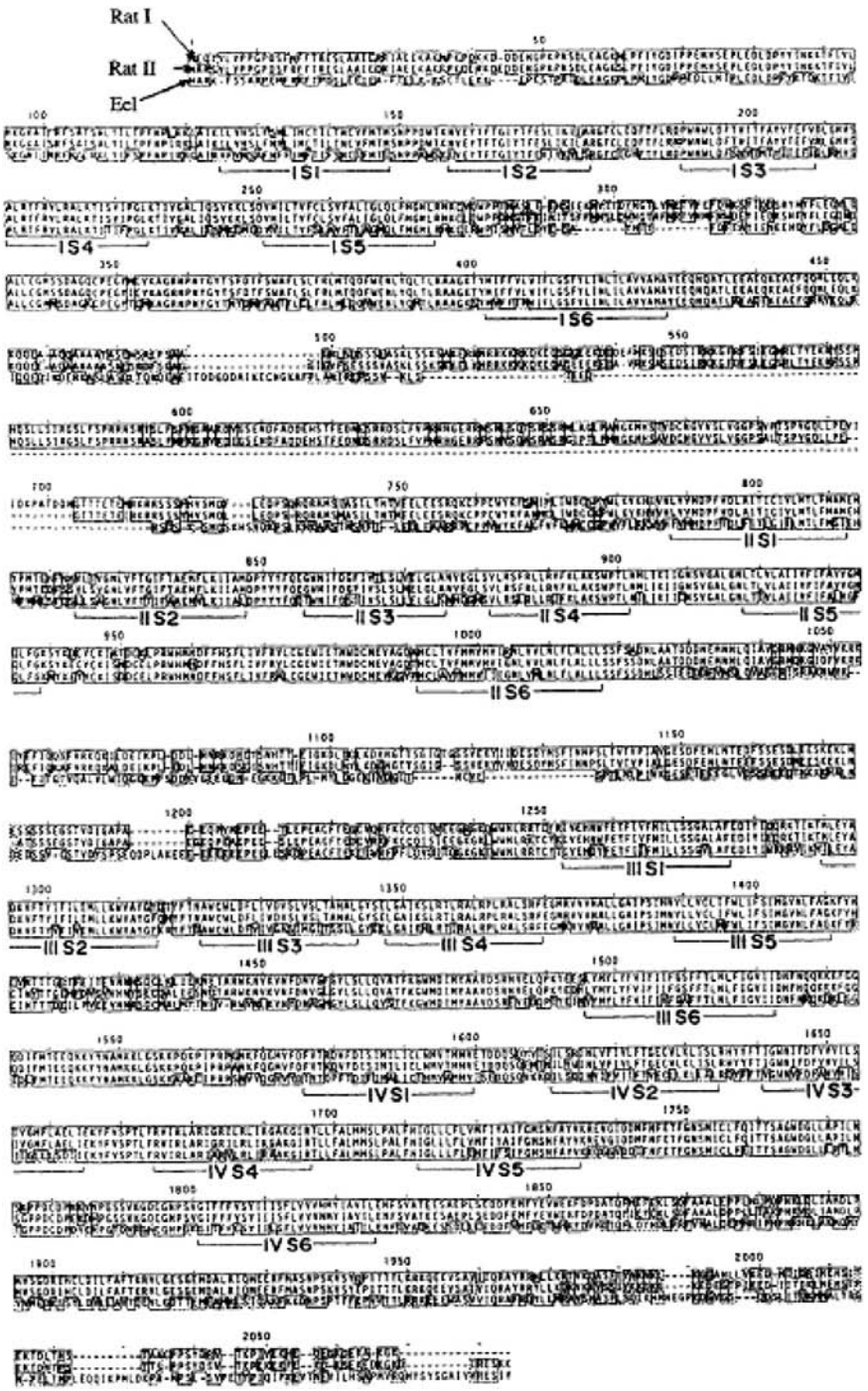

FIGURE 21.3 Amino acid sequences of three Na^+ channels obtained by cDNA cloning techniques. Rat I and II were obtained from rat brain cDNA libraries, while the eel Na^+ channel is that expressed in the electric organ of *Electrophorus electricus*. Boxed residues show homology among the three channels, while dashed lines designate absent segments. Labeled brackets underneath the sequences refer to parts of the highly conserved putative transmembrane repeats (see text and Figs 21.6 and 21.7 for details). *(From Numa and Noda, 1986.)*

How are such analyses performed? Basically, the analyses occur in two or three separate steps. First, one analyzes the sequence of the peptide for regions of high hydrophobicity, on the expectation that membrane-spanning regions should have a high proportion of hydrophobic amino acids. To do this, hydropathy values that reflect its relative hydrophobicity are assigned to each amino acid residue. The assignment of such values is based largely on indirect physical measurements of the hydrophobicity, such as the ability of a given residue to partition from an aqueous solution to an oil phase. Such values may or may not reflect the chemical behavior of a residue in a long polypeptide chain, where chemical properties may be further influenced by neighboring residues. As a result, a number of such hydropathy tables have been developed by various investigators who have significant differences in the way they assign hydropathy weights to a given residue. One of the most popular tables is that of Kyte and Doolittle (1982) shown in Fig. 21.4. In most cases, the assignments are qualitatively obvious, especially for expected hydrophobic groups (e.g. the hydrocarbon chains or leucine or valine) or hydrophilic groups (e.g. the charged residues such as glutamate or lysine).

Figure 21.5 shows hydropathy plots for the Na^+ channel sequences given in Fig. 21.3. The plot is obtained by averaging the hydropathy values of a fixed segment (perhaps 7−15 residues). Starting with the first residues at the N-terminal end, this average is computed and the value is plotted versus the number of the residue in the middle of the segment. This averaging "frame" is then shifted by one residue toward the carboxyl end, the new hydropathy average is recomputed (i.e. the change due to the loss of the

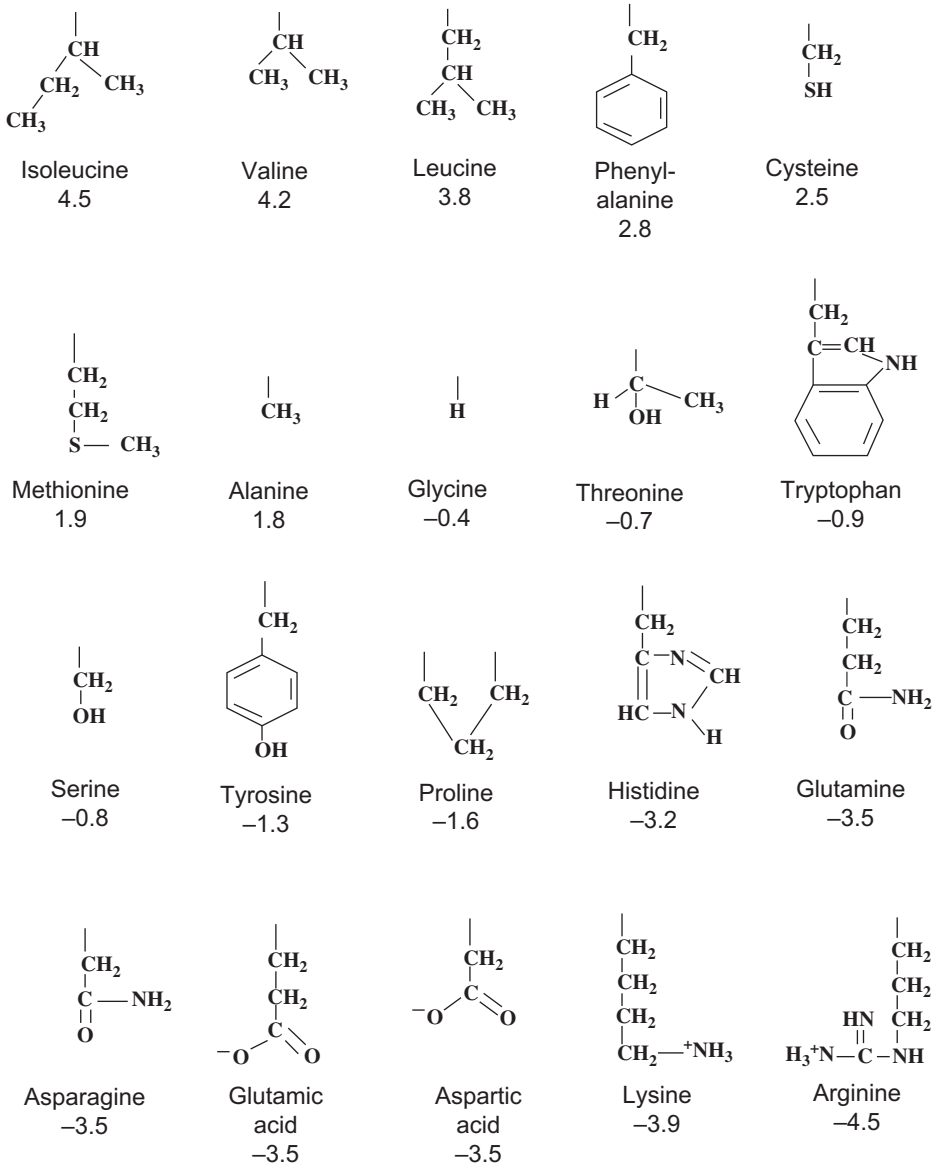

FIGURE 21.4 Structure and hydropathy values of amino acid residues. Arranged from most hydrophobic to most hydrophilic according to relative values assigned by Kyte and Doolittle (1982). Only side groups are shown with hydropathy values underneath.

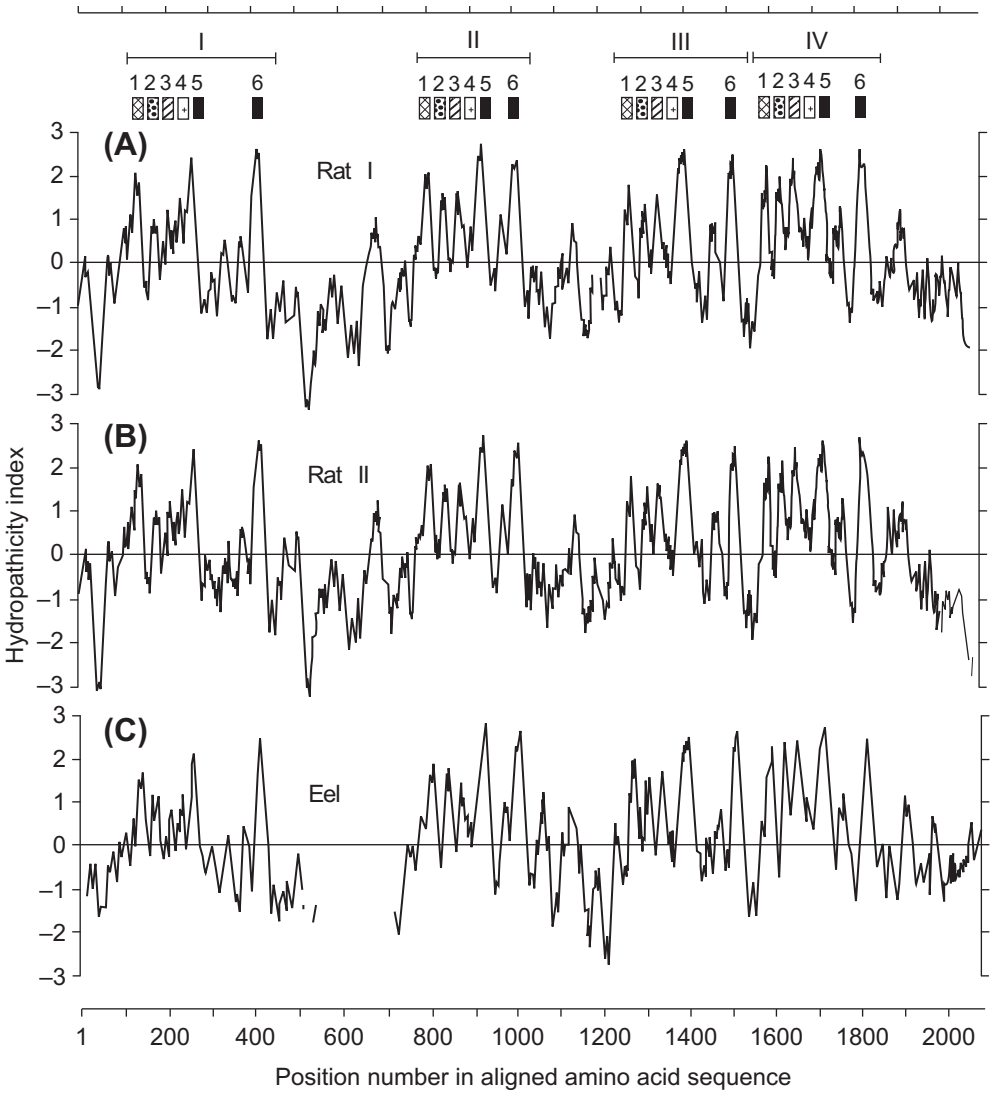

FIGURE 21.5 Hydropathy plots for the three Na^+ channel sequences of Fig. 21.3. Brackets and numbered patterns at top refer to the locations of homologous repeats and transmembrane segments (see text and Fig. 21.7). *(From Numa and Noda, 1986.)*

N-terminal side residue and the gain of the next C-terminal side residue in the sequence) and the value is plotted by incrementing the residue number by one. This *frame-shift* average is thus continued until the end of the protein is reached. The purpose of using the averaging frame is to smooth out sharp variations in hydropathy, so that a pattern may be more readily seen.

As can be seen in Fig. 21.5, there is a repeated pattern of hydropathy for Na^+ channels that reflects the conserved homology of the four internal repeat domains I–IV. Within each domain, there are five or six peaks of hydrophobicity that are each about 20 amino acids long. This is significant because such a length is considered optimal to span the hydrophobic interior of the lipid bilayer. However, hydrophobicity alone is not sufficient to predict a membrane-spanning region; instead, the residues must assume a favorable secondary structure, most commonly assumed to be an α-helix. In the helical conformation, the hydrophobic side chains project radially away from the axis of the helix and presumably into the surrounding lipid. Such a configuration prevents the very hydrophilic peptide backbone of the protein from exposure to the hydrophobic lipid environment and thus represents a favorable low free energy arrangement of the protein–lipid interface.

How are such secondary structures predicted from primary sequence? This too is a highly empirical process (Chou and Fasman, 1978). Basically, investigators have analyzed in detail a number of proteins for which there are high-resolution x-ray structures available at the amino acid level. By cataloging the frequencies with which given amino acids or short combinations of residues are found in helices, β-sheets, or turns, a set of empirical rules has been

developed to predict the secondary structures that a given sequence of amino acids will most probably form (see Fig. 21.5). Although the general accuracy of such predictions has been debated, when combined with hydropathy information the method is apparently rather accurate for the prediction of membrane-spanning domains in membrane proteins. This is probably because of the severe thermodynamic constraints confronting polypeptides needing to cross a boundary of high hydrophobicity while interfacing with a highly hydrophilic aqueous phase on either side of the membrane and in the aqueous channel pore.

IVC. How Is Channel Structure Formed?

In any case, such primary sequence analyses suggest that each internal domain has six α-helical membrane-spanning segments (see Numa and Noda, 1986). The question to consider next is how such an arrangement might form a transmembrane pore for the passage of ions. The answer is that the four transmembrane regions probably contribute equally to the pore walls in a "staves of a barrel" configuration (Fig. 21.6; see Guy and Seetharamulu, 1986). In fact, such a model was comforting to the original investigators, because a similar arrangement had previously been shown to exist among the separate subunits of the synaptic acetylcholine-gated channel, the first ion channel to be purified and sequenced via cDNA cloning.

IVD. Sequence Homology among the Transmembrane Domains of Ion Channels

Analysis of the DHP-sensitive Ca^{2+} channel α-1 peptide revealed that it also has four internal homologous repeats (Fig. 21.7; see Tanabe et al., 1987). Furthermore, these repeats (but not the intervening loops) were found to be highly homologous to the Na^+ channel repeats. The "staves of a barrel" configuration in which either homologous internal repeats (for Na^+ and L-type Ca^{2+} channels) or highly homologous subunits (as in the case of transmitter-gated and K^+ channel—see Section IVG) form a pore seems to be a widespread architecture among ion channels in general.

IVE. How Are Topographical Predictions for Channel Structure Tested?

The modeling approach based on primary structure is highly uncertain and needs to be empirically confirmed for each channel. One of the most popular ways this has been done is through the use of site-directed antibodies raised to synthetic peptides encoding a short stretch (i.e. 10–20 residues) of the channel of which one wishes to know the topographical orientation. These antibodies may be applied to channels in their native membranes or intact cells and the relative sidedness of the epitope may be determined from the side of the membrane to which the antibody is bound. The approach has been used for Na^+ channels in several laboratories and the topographical model shown in Fig. 21.6 has largely been confirmed (see Catterall, 1992). Similar approaches can be used in which impermeant group-reactive chemical reagents are applied to either intact cells or liposomes with oriented channels, followed by some method to identify the site of interaction on the protein (e.g. sequencing of proteolytic fragments). Alternatively, a synthetic, but highly antigenic, short epitope may be recombinantly inserted into the channel sequence and the mutant expressed in cultured cells. In this case, the same antibody may be used in all

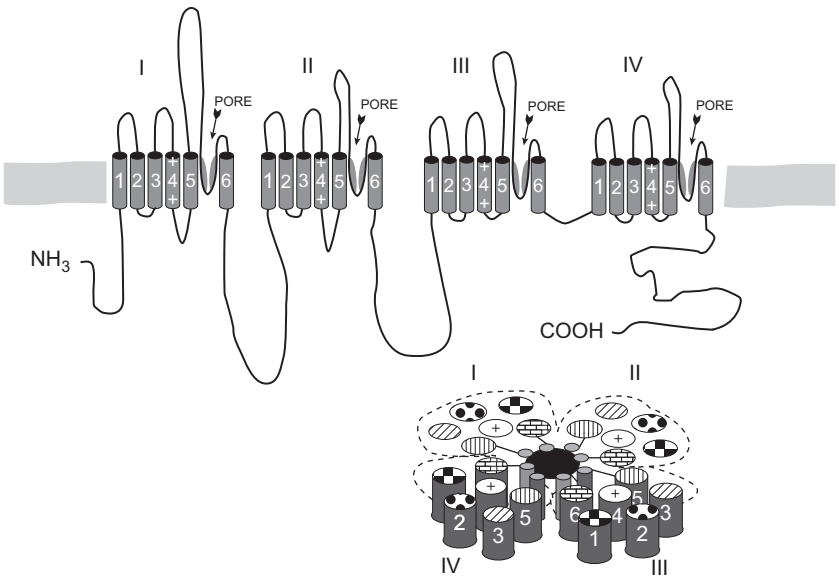

FIGURE 21.6 Model of Na^+ channel structure based on analysis of primary sequence data. The top drawing shows linear placement of four homologous domains, loops and termini (outer surface of membrane is at the top). Possible pore and selectivity regions are labeled and shown as the angled segments between transmembrane segments 5 and 6. The drawing on the bottom right shows a hypothetical arrangement of homology repeats in the "staves of a barrel" configuration to form a pore (placement of transmembrane segments 1–6 is somewhat arbitrary).

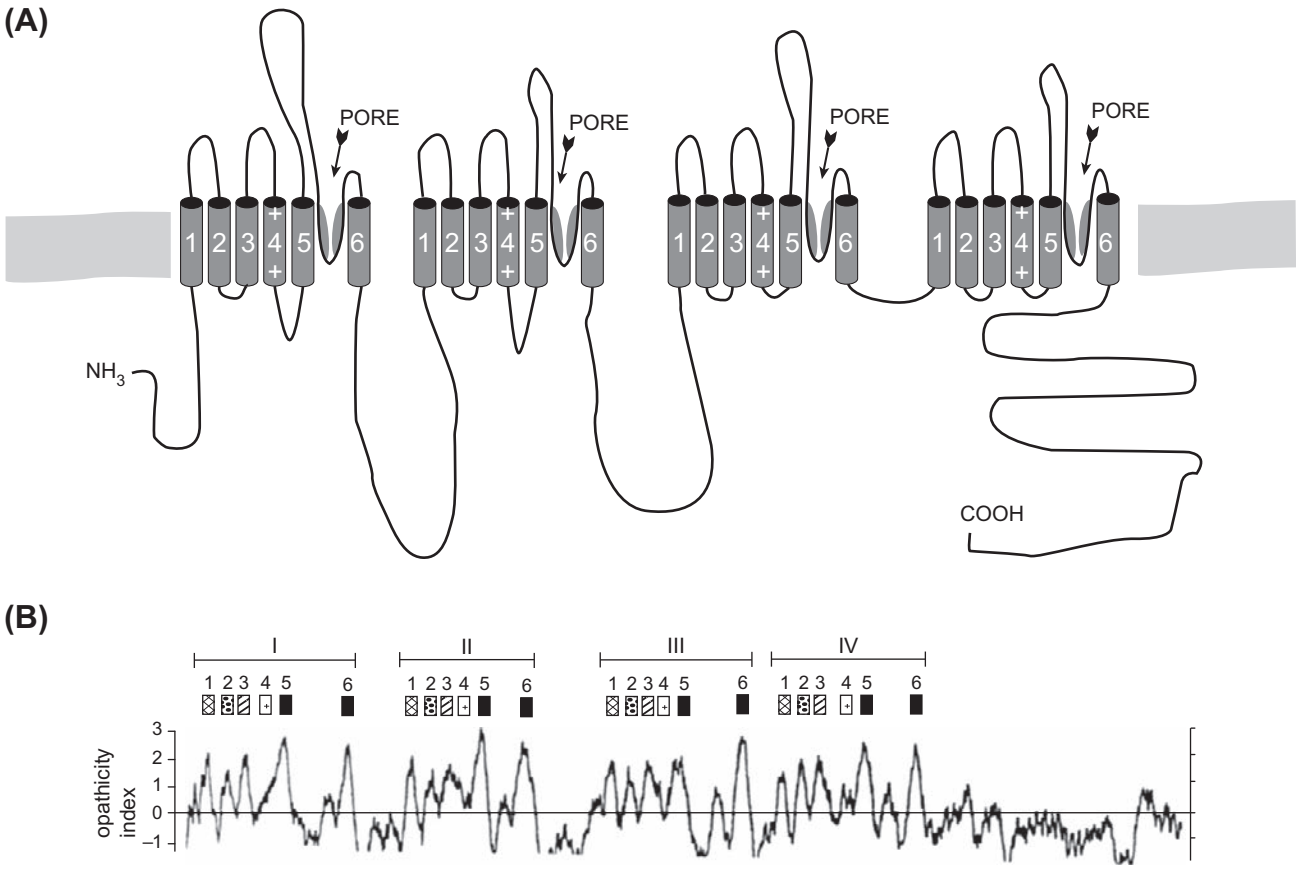

FIGURE 21.7 Model and hydropathy plot (bottom) of L-type skeletal muscle Ca^{2+} channel α-1 subunit. Compare to Figs. 21.5 and 21.6.

experiments to determine on which side of the membrane the epitope tag is located as a function of its position in the native channel sequence.

IVF. The Genetic Approach Used to Identify Nucleic Acid Clones Coding for K^+ Channels

K^+ channels are extremely important in excitation and transduction phenomena. Partly because of the way these channels were cloned and partly because their structure is a simplified version of the long Na^+ and Ca^{2+} channels, they are very valuable systems with which to study the general structures and mechanisms of the voltage-gated ion channel class. Such channels were not originally cloned via the usual biochemical purification—oligonucleotide probe approach described previously because there were few good chemical labels like tetrodotoxin or DHP.

A highly creative, yet complex, approach was taken independently by several laboratories that used behavioral mutants of the fruit fly *Drosophila* (e.g. see Papazian et al., 1987). In brief, mutant strains that had uncontrolled shaking when exposed to ether were identified. Electrophysiology then established that the muscles and certain neurons of such flies had missing or altered K^+ currents of a specific type known as A-type currents that, like sodium currents, inactivate on depolarization. The locus of the genetic defect causing this behavior could be seen as an actual physical defect (translocation) in the polytene salivary chromosomes of these so-called *Shaker* mutants. Since extensive libraries of cloned identified chromosomal DNA fragments of *Drosophila* have long been available (called genomic clones), the investigators were able to obtain the DNA fragment of normal flies on which the mutant defect occurred. This allowed them to sequence such fragments and, by comparison with *Shaker* mutant sequences and by the identification of homologous cDNA fragments (derived as described earlier), the sequence of the A-type K^+ channel could be inferred. Since the *Shaker* mutation allowed a completely genetic elucidation of the channel primary amino acid sequence, the A-current it manifests has become known as the *Shaker*-type K^+ channel.

IVG. K^+ Channels are Homologous to a Single Internal Repeat of Na^+ Channels

An initially surprising finding when the *Shaker* A-type channel sequence was analyzed was that the length of the

sequence was much shorter than that of the other voltage-gated channels, but contained a single domain that was reminiscent of (but strictly speaking not very homologous to) the internal repeat domains of the Na^+ or Ca^{2+} channels (Fig. 21.8; see Pongs, 1992). An obvious hypothesis for channel structure for the *Shaker* channel was that four molecules of this sequence (i.e. subunits) combined to form the "staves of a barrel" structure postulated for the long-channel polypeptides. This tetrameric assembly model has recently received strong support from several elegant experiments (MacKinnon, 1991).

V. MOLECULAR MECHANISMS OF CHANNEL FUNCTION: HOW DOES ONE INVESTIGATE THEM?

We now discuss the methods that can be used to determine which parts of an elucidated channel sequence are involved in the basic channel properties of pore formation, ion selectivity and voltage-dependent gating. Here, too, the methods of recombinant DNA technology have proved to be of great use in that they allow the investigator to change the nucleic acid sequence encoding a channel in the manner desired. Using such mutagenesis techniques, the basic idea is to alter the amino acid sequence via deletion, addition, or change in the primary sequence in specific locations and then to test how such changes affect the function of the mutant channels. The hope is that by obtaining many such structure–function correlations, one might not only infer the part of the sequence that underlies, for example, channel activation, but also infer how this structure works as a mechanism.

VA. Choosing Interesting Sites and Segments as Targets for Mutagenesis

How does one decide which of the many amino acids in a channel polypeptide to change? This is where the modeling approach described previously is so important, for it provides clues or testable hypotheses that focus mutagenesis attempts on reasonable guesses. For example, one might assume that a highly conserved sequence in channels from phylogenetically distant animals might reflect a functionally essential part of the molecule that cannot withstand evolutionary alteration without being deleterious. Another strategy might be to compare the regions of divergence in the sequence of the various voltage-gated channels in the hope of finding candidate regions involved in different functions among channels. For example, the difference in ion selectivity among Na^+, K^+ and Ca^{2+} channels must lie somewhere in the variations in their amino acid sequence. Both approaches have had

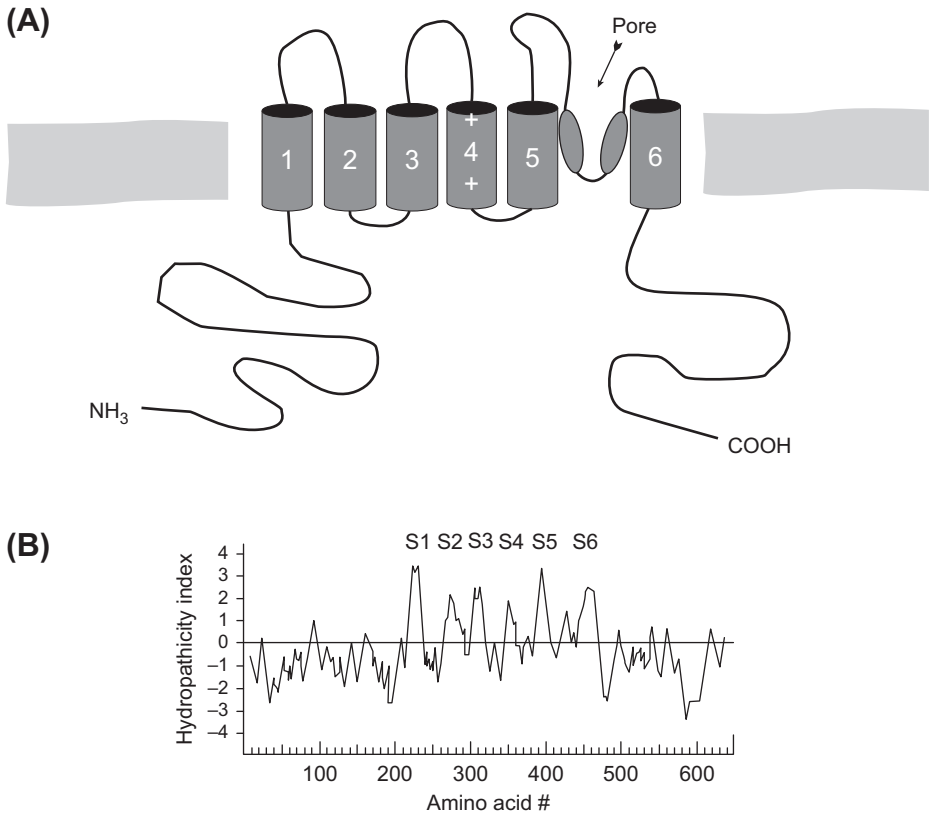

FIGURE 21.8 (A) Model and (B) hydropathy plot of *Shaker* B-type K^+ channel. Compare to Figs. 21.5, 21.6 and 21.7.

a certain degree of success, although "homology" is a relative term and, in reality, large areas of channels are highly variable, even among isotypes of channels from the same organism (see Section VI). This makes it difficult to guess which of these many differences relates to specific functions.

Another approach is to take advantage of certain genetic disorders in which mutations in channel structure occur naturally with functional consequences. A number of human diseases and animal models have been shown to be caused by channel defects. The sequence of such channels can give important clues into structure—function relationships in channels, while directing artificial mutagenesis experiments.

VB. Use of Expression Systems in Mutagenesis Studies

Another essential part of mutagenesis experimentation is the ability to introduce artificially altered genetic material into a cell that is capable of translating it into a protein molecule, processing the molecule appropriately (i.e. folding the polypeptide, assembling subunits, adding sugars or lipids) and inserting the protein into the cell surface. The protein then may be functionally characterized using the biophysical methods described in other chapters. The most popular such *expression system* is the oocyte of the South African frog *Xenopus laevis* (Fig. 21.9; Leonard and Snutch, 1991). In this system, one prepares mRNA from clones of the mutant channel and injects this message into the large (1—2 mm in diameter) oocytes with a micropipette. After waiting a few days for channel synthesis and membrane insertion to occur in sufficient numbers, one observes the expressed ionic currents via voltage-clamp methods, using large microelectrodes to impale the cell. Alternatively, one may also use a very large diameter electrode to patch-clamp a large area of membrane; such macropatch methods give better voltage control than the impaled electrode technique while allowing macroscopic current characterization. Finally, conventional single-channel analysis may be done in all the usual modes using standard patch pipettes. Thus, the oocyte allows the investigator to compare both the macroscopic and single-channel properties of the mutants with the normal wild-type channel.

Although other expression systems in which the altered genetic material may be introduced into cells transiently via

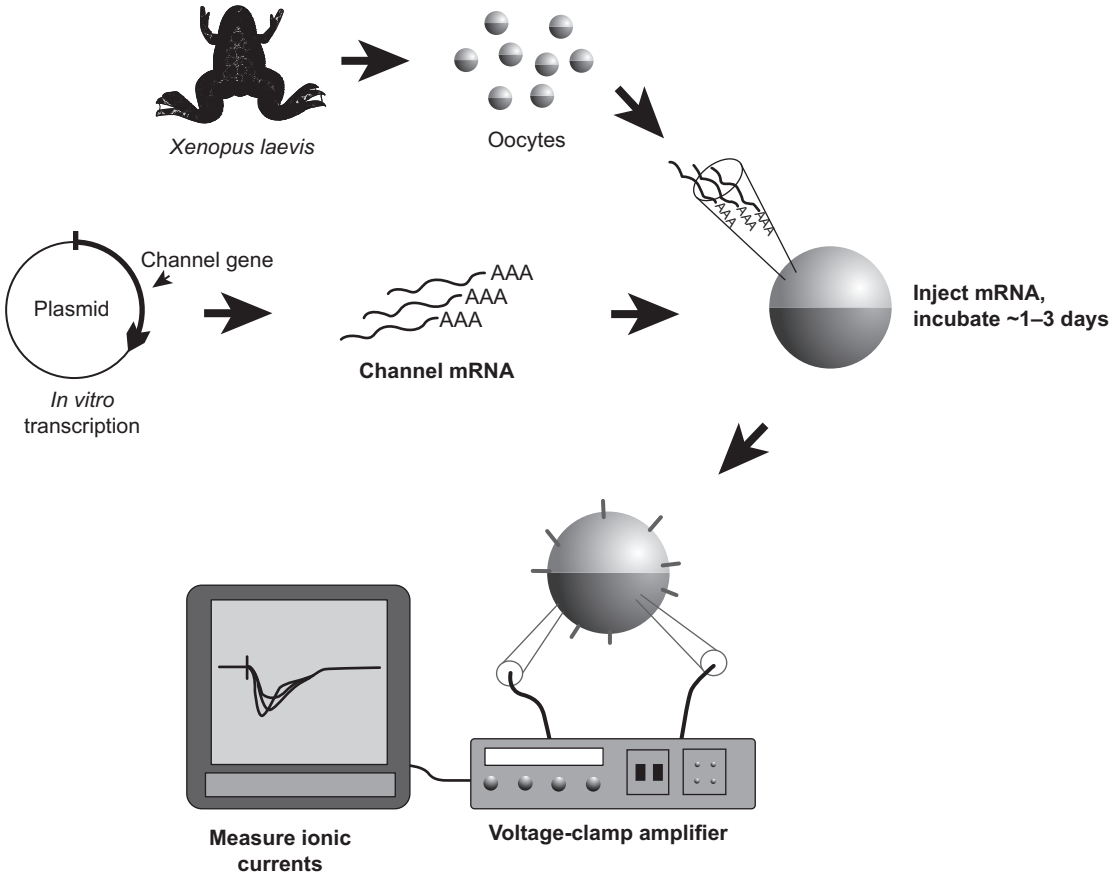

FIGURE 21.9 *Xenopus* oocyte expression system. For details, see text.

viruses or integrated permanently into the host genome (stable transfection) have been developed more recently, the use of such systems is beyond the scope of this chapter. Suffice it to say that the frog oocyte is currently the most popular and productive expression system with which to study structure–function relationships.

Because of its great potential in elucidating channel mechanisms, mutagenesis is being used by a large number of investigators. As a result, both new and altered concepts of channel function appear frequently in the scientific literature. In the brief account that follows, we can only summarize some of the fairly firm basics of gating, pore formation and ion selectivity.

VC. Domains Involved in Voltage-Dependent Activation

The ability to respond to changes in transmembrane potential is a hallmark of voltage-gated channels. Thus investigators looked for common motifs in channel sequences suggestive of voltage sensor domains that might target mutagenesis among the large number of residues in cloned voltage-gated channels. In comparing Na^+, DHP-sensitive Ca^{2+} and *Shaker*-type K^+ channels, the fourth predicted helix in the repeat/subunit motif was seen to display a highly conserved sequence pattern (see Figs. 21.6, 21.7 and 21.8). This segment, known as S4, consists of a repeated triad of a positively charged residue (Arg or Lys), followed by two highly hydrophobic residues (such as Val, Leu, Ile; Fig. 21.10). While the number of such triads in the various S4 segments ranges from three to eight, its structure of both charged and hydrophobic residues suggests an element capable of responding to transmembrane voltage changes (see Catterall, 1992). Accordingly, a number of experiments have now been done in which both the charged and hydrophobic elements have been changed.

In brief, S4 mutagenesis usually causes significant changes in the steady-state activation behavior of the affected channel (Fig. 21.11; Papazian et al., 1991; Lopez et al., 1991). Thus, shifts of the steady-state activation curve along the voltage axis occur with most changes to either charged or hydrophobic residues. In addition, changes in activation slope are frequently seen.

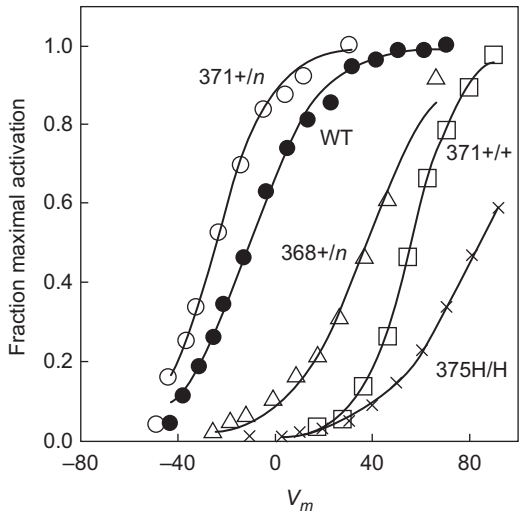

FIGURE 21.11 Effect of S4 mutations on *Shaker* K^+ channel activation expressed in oocytes. Shown are steady-state activation curves for wild-type (WT) and various single amino acid changes. +/*n*, change from a positively charged residue to a neutral one; +/+, a change of positively charged residue for an other charged residue; H/H, replace one hydrophobic residue with another hydrophobic residue. *(Data redrawn from Papazian et al., 1991 and Lopez et al., 1991.)*

The question is whether the observed changes can be explained in terms of a mechanism by which S4 participates in gating (instead of the general hypothesis that S4 is some part of a gating structure). Unfortunately, to date the results obtained from mutagenesis do not discriminate very well among the various possible roles for S4 in gating, for example, as a gating sensor, a part of the transduction linkage to a gating element, or simply an unrelated part of channel structure. Thus, the magnitude or direction of changes in activation behavior does not systematically correlate with changes to S4 charge or sequence. In addition, others have questioned whether the charged groups in the S4 segments can completely account for all the gating charge that moves when channels activate (see Sigworth, 1995). In general, the mutagenesis approach is inherently

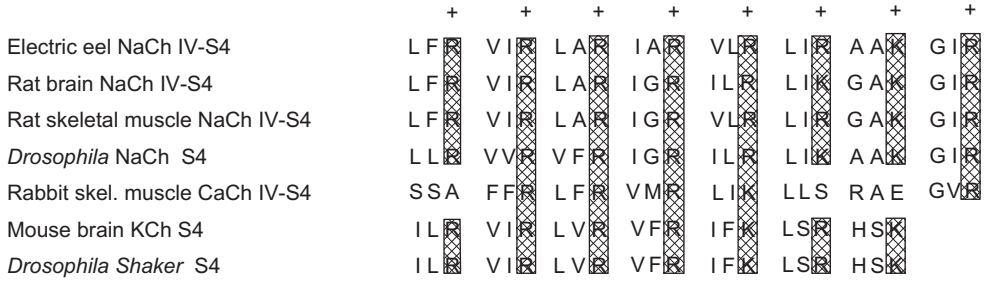

FIGURE 21.10 Comparison of S4 segments from different voltage-gated channels. Note the repeating triadic motif of positive charge (R, Arg; K, Lys) followed by two hydrophobic residues. Hatched areas show conservation of charge among channels; all amino acids designated by single letter codes.

limited in its ability to distinguish between alterations that directly affect a mechanistically important part of the molecule and those that indirectly cause functional effects through structural changes that propagate from mechanistically unrelated domains. This problem arises because protein structures are notoriously sensitive to long-range effects of such alterations, generically known as allosteric ("other site") effects.

VD. Limitations of Mutagenesis in the Study of Channel Mechanisms

The naive reader can understand the problem from a crude analogy in which many of us as children tried to understand the workings of a mechanical watch by a similar approach using simple tools. The child understands the function of the mechanism only by the movement of the hands. However, as we all know, a mechanical watch is quite a delicate machine. Thus, even the act of carelessly opening the case may cause the mechanism to cease working. Are we to conclude that the case is therefore part of the mechanism? Given access to the mechanism itself, the situation is highly complex, since the movement of many parts is required for the ultimate movement of the hands. For example, the result of stopping the second hand by interfering with a given gear tells one very little of the role that gear plays in how the watch operates.

For some time it has been known that the interactions of chemical substances or structural alterations with a site on one side of a protein can dramatically affect the function of another site at some distance, for example, on the other side of the protein. This concern and the potentially complex nature of channel-gating mechanisms should motivate the responsible practitioner of mutagenesis to display caution in interpreting results in mechanistic terms.

How, then, in the face of such limitations does one make progress in elucidating the mechanisms of channel function? In fact, the approach is philosophically identical to the way one attempts to prove any hypothesis, namely, to establish a circumstantial case by as many independent tests as possible. In the example of S4 and mutagenesis, for example, one might wish to demonstrate that mutations to any other part of the molecule have no effect on voltage-dependent activation as a sufficient (but not necessary) test. Unfortunately, mutations to other parts of channel sequence can have equally profound effects as S4 alterations (for example, to the pore-forming region described previously; see Yool and Schwarz, 1991). Thus, while these other mutations do not disprove a role for S4 as a sensor (or any other role), they do suggest, as in the mechanical watch, that a number of segments of the sequence are either directly involved in a complex mechanism of voltage gating or indirectly affect a gating process through allosteric/structural influences.

VE. The Mechanism of Channel Inactivation

Genetic engineering studies of the inactivation process currently provide a better example of what one may learn mechanistically from the mutagenesis approach. Some of the most important such studies have involved the *Shaker* A-type channel. Here early workers found important clues to the segment involved in the inactivation process by comparing naturally occurring variants of the channel (*isotypes*; see Section VI). Thus, Fig. 21.12 shows the pattern of four such isotypes, called A, B, C and D (Timpe et al., 1988). *Shaker* B, C and D were identified from further testing of cDNA clones using probes constructed from the original *Shaker* A sequence as described earlier. When expressed in oocytes, these isotypes displayed very different kinetics of inactivation. Analysis of the regions of homology and differences among the isotypes shown in Fig. 21.12 indicates that fast inactivation properties correlate most strongly with the nature of the N-terminal segment (thought to be cytoplasmic; see Fig. 21.8).

Further evidence for the role of this segment in inactivation was obtained by constructing channel chimeras in which the *Shaker* A clone was modified by replacing its N-terminal segment with those from other isotypes. In each case, the mutant channel assumed the inactivation properties of the isotype donating the N-terminal segment, despite the fact that the rest of the molecule had the sequence of the fast-inactivating *Shaker* isotype (Aldrich et al., 1990).

Finally, investigators mutagenized specific regions of the fast-inactivating *Shaker* B segment to localize those residues involved in the inactivation process (Hoshi et al., 1990). Both by deleting small segments and by replacing others it was found that the crucial part of the molecule was a stretch of residues from the positions 6–83 (i.e. the N-terminal tail of the molecule seen in Fig. 21.8). In this segment there were distant effects of the alterations. Thus, mutations to the residues in the 23–83 residue region tended to produce changes in inactivation kinetics, whereas changes to those in the N-terminal side (6–22) of the segment tended to destroy inactivation completely (see Fig. 21.14).

What might be the mechanism of *Shaker* inactivation? Much earlier, Armstrong and coworkers had reported that internal perfusion of proteases in the squid destroyed the ability of Na^+ channels to inactivate. On the basis of this and other experiments, Armstrong proposed that the inactivation mechanism is a cytoplasmic ball attached to a peptide tether that swings into an open channel to block it from the inside (Fig. 21.13; Armstrong and Bezanilla, 1977). In this hypothesis, the ball blocks the channel by binding to a receptor in the inside of the pore that is accessible only when the channel has opened (activated). The reader may recall the evidence that inactivation is coupled to activation and hence may be intrinsically

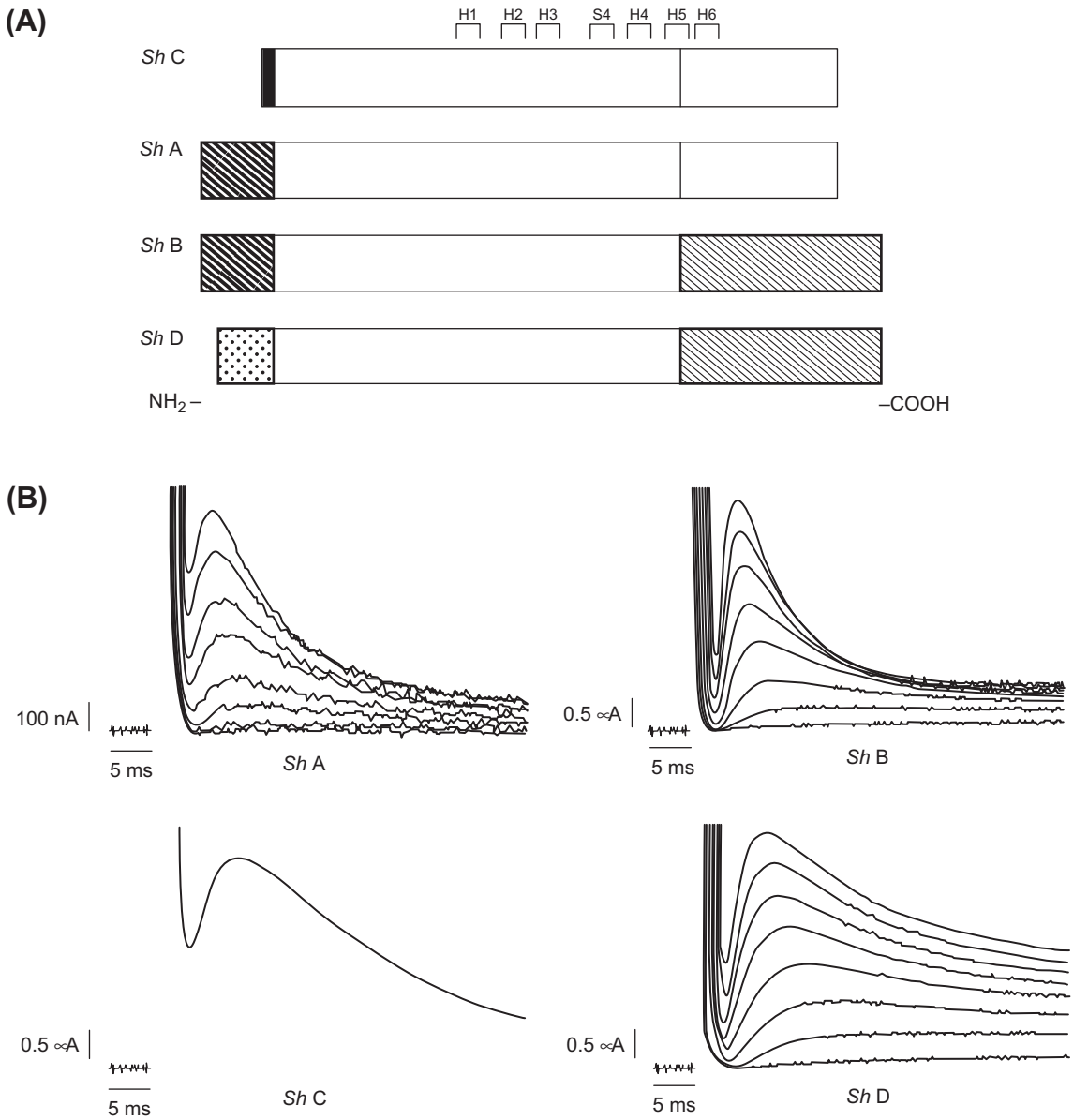

FIGURE 21.12 Gating kinetics of alternatively spliced *Shaker* isoforms expressed in oocytes. (A) Comparison of sequences, with patterned regions representing alternatively spliced domains that are different among isoforms (other unpatterned regions are identical in sequence). (B) Both current traces obtained from oocyte voltage-clamp show currents resulting from each isoform. *(From Timpe et al., 1988. Copyright 1988 by Cell Press.)*

voltage independent. Thus, the ball-and-chain model also explains these properties since the cytoplasmic ball would experience little of the transmembrane field but could swing into the channel only after it had activated and revealed its receptor (hence the coupling properties).

In the case of the *Shaker* channel, Aldrich and colleagues proposed that the N-terminal segment that they identified was just such a mechanism, since changes to the length of the 23–83 segment affected kinetics (as might be expected from changing the length of the chain), while changes to the N-terminal segment (such as alterations of charge) that eliminated inactivation were postulated to prevent the ball from binding to its receptor in the activated channel.

How might such a model be further tested? Here the investigators performed a particularly elegant experiment (Fig. 21.14; Zagotta et al., 1990). First they constructed a mutant *Shaker* channel in which inactivation had been eliminated by a deletion of its own N-terminal segment. Next, a synthetic peptide that had the exact sequence of the deleted region was prepared. The mutant channel was then expressed in oocytes, where both excised macropatch and single-channel observations could be made. The investigators found that when the peptide was applied to the

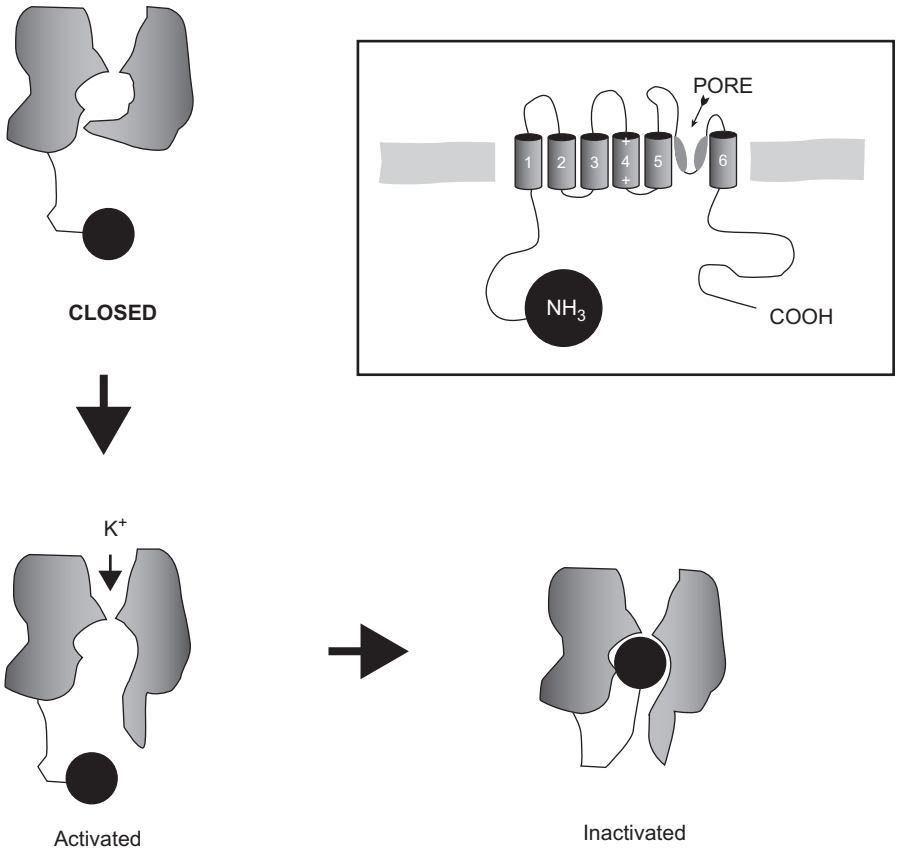

FIGURE 21.13 Ball-and-chain model of inactivation. Not shown are the three other balls that the other subunits of the channel will contribute.

solution bathing the inside surface of the membrane, inactivation was restored to these mutant channels. Furthermore, the kinetics of the restored inactivation depended on the concentration of the peptide in the bath and the inactivation could be reversed by washing away the peptide-containing solution. These observations are thus consistent with a direct blocking interaction of the peptide with a site in the open channel and constitute strong evidence for the ball-and-chain mechanism of inactivation in A-type K^+ channels.

VF. Other Gating-Related Domains in Voltage-Sensitive Channels

Analysis of the homology of the various cloned Na^+ channels revealed that the longest segment of conservation lay in the postulated internal loop between repeats III and IV, even among animals of some phylogenetic distance (see Fig. 21.3). This high degree of conservation suggested a functionally important role for the segment. This idea was initially tested by constructing mutant Na^+ channels in which the channel was expressed in oocytes in two pieces, with the genetic "cut" within this segment (Stuhmer et al., 1989). Interestingly, such artificial dimeric channels were assembled and expressed in the oocyte and displayed relatively normal activation and conductance; however, such channels did not inactivate. Further, site-directed antibodies raised to a synthetic peptide encoding this segment were found to slow or eliminate inactivation when they were applied to the cytoplasmic surface of cells expressing normally inactivating channels (Vassilev et al., 1989). Finally, mutagenesis directed to this segment produced channels with altered inactivation (Catterall, 1992).

However, the sequence of this segment has little resemblance to the N-terminal ball-and-chain *Shaker* domain and it is additionally tethered at both ends. Nonetheless, several lines of evidence now suggest that this domain operates analogously to the *Shaker* ball-and-chain in producing Na^+ channel inactivation. Most notably, via mutagenesis to the III–IV loop, one can produce "inactivationless" sodium channels; in such mutants, inactivation can be restored with the internal application of the same synthetic *Shaker* peptide that restored inactivation to non-inactivating potassium channels in the experiments described above.

For DHP-sensitive Ca^{2+} channels, an isotype of the originally cloned skeletal muscle channel has been cloned from the heart. In the parent tissues, these channels share some characteristics, but differ greatly in the speed by which their calcium currents activate (heart channel currents being much more rapid in responding to voltage).

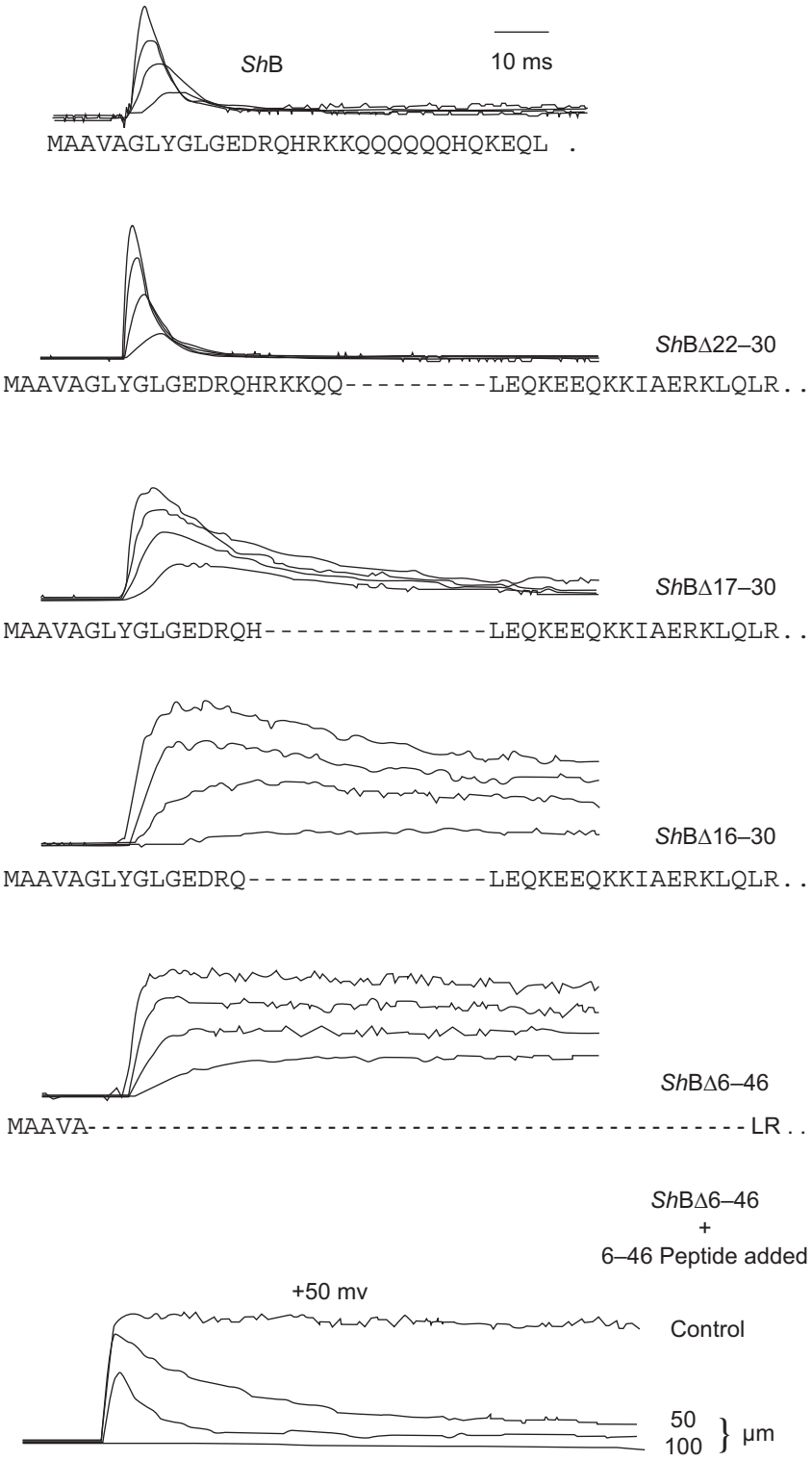

FIGURE 21.14 Identification of a putative ball and chain in *Shaker* B channels expressed in oocytes. Panels 2–5 from the top show the effect of deleting increasing lengths of a segment near the N terminus of the *Shaker* protein. Note that the deletion of residues 6–46 results in a non-inactivating K^+ current. The bottom panel shows that inactivation properties of this latter mutant may be restored by application of the synthetic 6–46 peptide to the inner channel surface in a dose-dependent fashion. *(Reorganized from Hoshi et al., 1990, and Zagotta et al., 1990.)*

Although the isotypes share considerable homology, there is still enough difference in the sequences to make it difficult to guess which residues might be responsible for activation kinetics. This problem was elegantly addressed by Beam, Tanabe and coworkers, who made chimeras of the two channels (Fig. 21.15; Tanabe et al., 1991). To focus the mutagenesis, it was reasoned that only the predicted transmembrane repeats should be involved in voltage-gated activation. Thus, the chimeras swapped the homologous repeats among constructs. As shown in

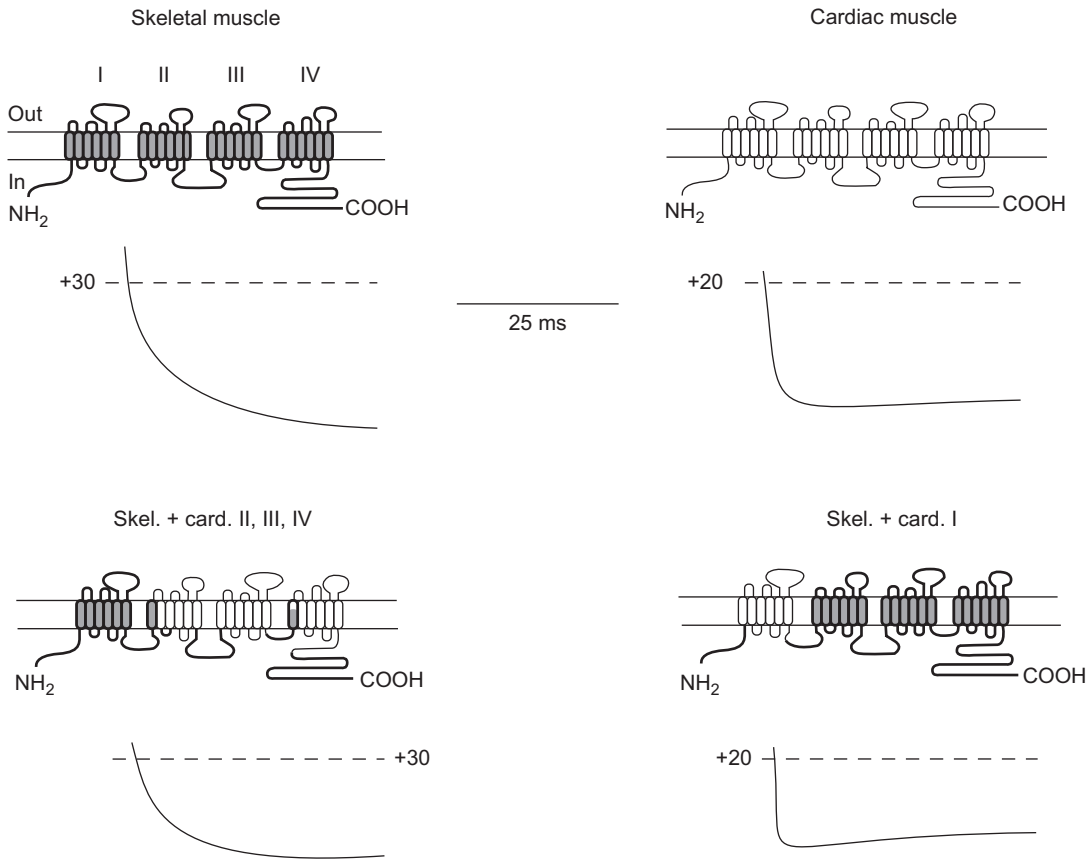

FIGURE 21.15 Identification of regions determining activation kinetics in L-type Ca^{2+} channels from skeletal muscle and heart. In these experiments, hybrids (chimeras) of skeletal muscle and cardiac channels were made in various combinations to localize the domains responsible for the differences in Ca^{2+} current activation kinetics in heart and skeletal muscle. cDNA encoding each construct was injected in cultured muscle cells (myotubes) from mutant mice unable to synthesize active L-type channels. Thus, these mutant cells would express only currents resulting from the genetically engineered DNA introduced into them. The top two panels show the current kinetics resulting from DNA encoding the wild-type skeletal muscle and cardiac channels. The bottom panels show two chimeras in which current kinetics correlate with the donor of repeat domain I. Most of the other possible combinations of channels were also made, with the same correlation of kinetics with domain I. *(Redrawn from Tanabe et al., 1991.)*

Fig. 21.15, the kinetics of activation correlate almost completely with the kinetics of the donor of the first (I) repeat. This finding suggests that despite their approximate homology, the repeats in a given channel contribute differently to gating properties. This is perhaps expected from the observation that the S4 regions among these domains in different channels have somewhat different structures and numbers of charges (e.g. see Fig. 21.10). Having identified the domain responsible, these investigators have been able to narrow their search to shorter segments and, ultimately, will identify the residues involved in this activation phenomenon (Nakai et al., 1994).

VG. Pore Formation and Ion Selectivity

Pores are the defining structures of all ion channels. As such, they provide both an aqueous pathway for ions to traverse the membrane as well as a means for discriminating among ions for access to this path. Studies of the mechanisms of pores provide an especially vivid example of the integration of theoretical modeling, mutagenesis and molecular structural approaches.

Even before the advent of structural studies, Hille hypothesized that ion selectivity and pore formation were performed by the same parts of the channel structure. Experimental evidence also indicated that charged or polar oxygen groups lined the narrowest region of the pore, where cation recognition occurs (see Hille, 1992). This latter finding was a sensible one considering the chemistry of cations in solution. In aqueous solution, metal cations such K^+, Na^+ and Ca^{2+} are stabilized by electrostatic interaction with the electronegative oxygen atoms of water molecules. In the narrowest region of the pore, water molecules must be removed in order for the channel to recognize the preferred cation; lining this narrow region with oxygen-bearing groups provides a chemically favorable *selectivity filter*.

Based on this early work, investigators sought short protein segments that might line the aqueous pore with oxygen atoms. A candidate sequence was initially identified using sophisticated analysis of primary sequence information (Guy and Seetharamulu, 1986). This sequence is 20–25 amino acids long and forms part of the loop connecting the fifth and sixth predicted transmembrane helices in the voltage-gated cation channels (see Figs. 21.6, 21.7 and 21.8). Tests of this putative pore-lining loop's (P-loop) role in pore formation were soon forthcoming.

One type of test was to determine whether site-directed mutations in the P-loop sequence affected the action of known pore-blocking agents on heterologously expressed mutant channels. Among the agents tested in this way were the K^+ channel-blockers tetraethylammonium and charybdotoxin and the Na^+ channel-blocker tetrodotoxin (MacKinnon and Yellen, 1990; MacKinnon et al., 1990; Terlau et al., 1991). Block by the externally effective agents tetrodotoxin or charybdotoxin was specifically affected by mutations at the extracellular end of the P-loop. Tetraethylammonium block of K^+ channels, which occurs by blocker binding at either end of the narrow pore, was altered by mutations at both ends of the P-loop. Results such as these confirmed that the P-loop does indeed form at least part of the pore in voltage-gated ion channels. Does the P-loop also form the ion selectivity filter?

The answer to this question also comes from site-directed mutagenesis studies. In *Shaker*-type K^+ channels, point mutations introduced into the P-loop profoundly altered the channel's preference for K^+ over Rb^+ or NH_4^+ as shown in Fig. 21.16 (Yool and Schwarz, 1991). However, non-conducting channels were produced whenever mutations were introduced into one stretch of eight amino acids in K^+ channel P-loops. This so-called *K^+ channel signature sequence* is highly conserved in K^+ channels found in bacteria to humans and it was therefore suspected of forming the narrow selectivity filter in K^+ channels.

Site-directed mutations in the P-loops of Na^+ channels and Ca^{2+} channels also affect ion selectivity (Heinemann et al., 1992; Yang et al., 1993). In Na^+ channels, a locus of four residues has been identified that confers selectivity for Na^+ over Ca^{2+} (Fig. 21.17). Each of the four P-loops of

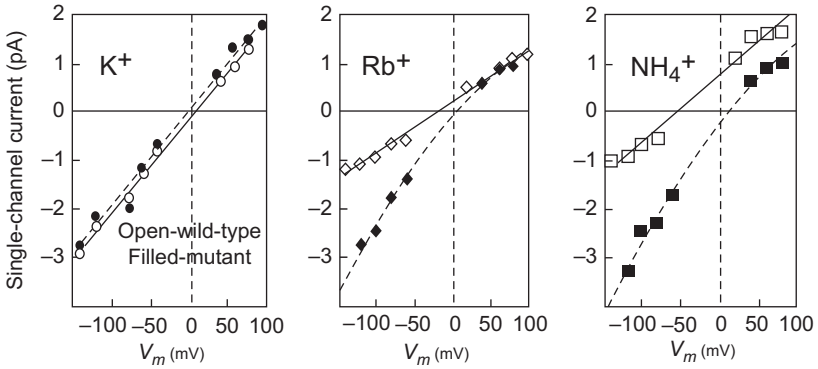

FIGURE 21.16 Alteration of *Shaker* B K^+ channel ion selectivity caused by a mutation in the putative pore-forming region. In these experiments, Phe 433 was mutated to Ser. The oocyte system used to express both wild-type and mutant channels is described in the text. Single-channel currents were measured using patch-clamp methods in which the ion indicated in each panel was applied to the external surface of the channel with K^+ on the inside in all cases. In these bi-ionic conditions, inward (negative) currents will be carried mainly by the test ion, while outward (positive) currents will be mostly K^+ ion fluxes. As can be seen from the increased inward currents, permeability of the channel to Rb and NH_4 ions was greatly enhanced in the mutants, while K^+ was unaffected. *(Data redrawn from Yool and Schwarz, 1991.)*

	Motif I					*Motif II*					*Motif III*					*Motif IV*				
	−2	*−1*	*0*	*1*	*2*	*−2*	*−1*	*0*	*1*	*2*	*−2*	*−1*	*0*	*1*	*2*	*−2*	*−1*	*0*	*1*	*2*
CaCh	T	M	**E**	G	W	T	G	**E**	D	W	T	f	**E**	G	W	T	G	**E**	A	W
NaCh	T	Q	**D**	X	W	C	G	**E**	–	W	T	F	**K**	G	W	T	S	**A**	G	W

FIGURE 21.17 Alignment of Ca^{2+} and Na^+ channel pore sequences. Position 0 in the alignments (shaded) marks the critical residues in the selectivity filter (EEEE locus in Ca^{2+} channels; DEKA locus in Na^+ channels). High-voltage–activated calcium channels are identical to one another in these pore sequences, except at the ñ1 position in motif III: the "f" indicates that this position is occupied by either Phe (F) or Gly (G). In sodium channels, the residue at the +1 position in motif I (x) varies depending on channel isoform. Na^+ channel sensitivity to tetrodotoxin depends partly on the residue present at this position.

a Na^+ channel contributes one residue to the locus, which includes two carboxylate-bearing residues (Asp, Glu) and two non-carboxylate residues (Lys, Ala). Substitution of Glu residues for the Lys and Ala residues dramatically reduces Na^+ selectivity and allows significant amounts of Ca^{2+} to permeate this mutant Na^+ channel. The analogous locus in Ca^{2+} channels is comprised of four Glu residues. Functional analysis of the effects of mutations in this locus has shown that these four Glu residues form the core of the selectivity filter in Ca^{2+} channels (Ellinor et al., 1995).

As described above, oxygen atoms have long been thought to line the selectivity filter in voltage-gated, cation-selective channels. The presence of multiple carboxylate groups in the selectivity filters of Ca^{2+} and Na^+ channels is consonant with the earlier work although, in principle, the carboxylates may either project into the pore or away from it. In fact, Ca^{2+} channel carboxylate groups apparently project into the aqueous pore and thereby provide the electronegative oxygen atoms needed to stabilize Ca^{2+} there. Evidence supporting this picture of selectivity filter structure derives from the fact that protonation of these carboxylate groups blocks current through Ca^{2+} channels; mutational replacement of the carboxylates by non-protonatable groups predictably alters proton block. Orientation of selectivity filter side chains has also been investigated using a technique called the "substituted cysteine accessibility method". In this method, a sulfhydryl-containing Cys residue is substituted for the wild-type residue and a sulfhydryl-modifying agent is bath-applied to the mutant channel. If the side-chain of the substituted Cys projects into the pore, where it may be accessible to the sulfhydryl-modifying agent, then the modifying agent will attach itself to the Cys sulfhydryl and obstruct ion flow. Interruption of channel current thus reports that a particular side chain is oriented into the aqueous pore, whereas absence of block indicates that the side chain faces away from the pore. Application of this method to Na^+ and Ca^{2+} channels indicates that the side chains in the carboxylate-containing loci of these channels all project into the pore (Chiamvimonvat et al., 1996). The extreme narrowness of K^+ channel pores has prevented this technique from being effectively employed with these channels. However, the selectivity filter of K^+ channels may be structurally distinct from that of Ca^{2+} channels and perhaps Na^+ channels.

VH. Crystal Structure of a Bacterial K^+ Channel Pore Region

Results of these site-directed mutagenesis studies have been strikingly confirmed by the first x-ray crystallographic structure obtained for a member of the family of voltage-gated ion channels (Doyle et al., 1998). This structure was solved for a bacterial K^+ channel, which though not in fact voltage-gated, is nevertheless a member of the family of voltage-gated ion channels: most significantly, it possesses the hallmark of all K^+ selective channels, the K^+ channel signature sequence. The crystal structure reveals that the selectivity filter is formed by part of the P-loop, with two K^+ ions stabilized therein, probably by main-chain carbonyl oxygen atoms (Fig. 21.18). That uncharged carbonyl oxygens apparently line the selectivity filter in the bacterial K^+ channel actually agrees with predictions, based on mutagenesis studies, for other K^+ channels.

Why might K^+ channels have evolved a selectivity structure that employs neutral, main-chain carbonyl oxygen atoms, whereas their evolutionary descendants, Ca^{2+} channels, apparently line their selectivity filter with negatively charged, side-chain carboxylate oxygens? Perhaps the negative charge of carboxylate oxygens is necessary in selecting for Ca^{2+}, a charge-dense divalent cation, whereas uncharged carbonyl oxygen atoms are ideal in selecting for certain monovalent cations, such as K^+. How then to account for Na^+ channel selectivity structure? Na^+ channels have evolved from Ca^{2+} channels and the Na^+ channel selectivity filter apparently includes two side-chain carboxylate oxygens. K^+ and Na^+ have the same ionic charge but Na^+ has a higher charge density owing to its smaller ionic radius. As in the case for Ca^{2+}, the relatively high charge density of Na^+ may require carboxylate oxygens for selectivity, though only two rather than the four present in the Ca^{2+} channel selectivity filter.

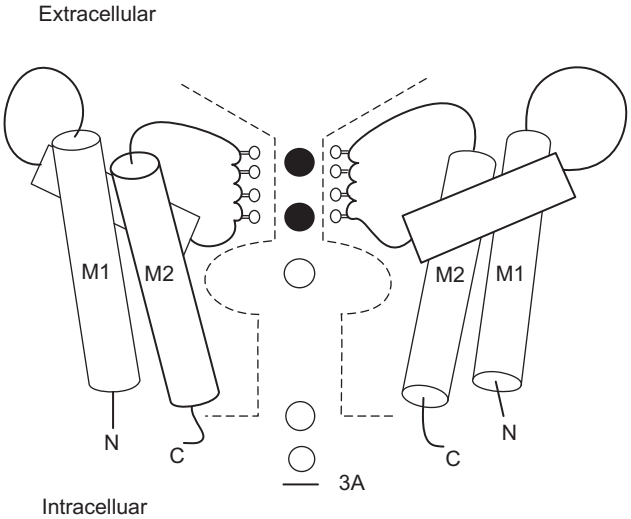

FIGURE 21.18 Cartoon illustration of the bacterial K^+ channel structure. Only two of the four subunits of the channel are shown. Each subunit has a P-loop and two helices (M1, M2), similar to the structure of inwardly rectifying K^+ channels. The segment of the P-loop that lines the ion permeation pathway projects carbonyl oxygen atoms into the pore. A pair of K^+ ions is shown stabilized in the selectivity filter by the rings of carbonyl oxygens. *(Adapted with permission from Choe, S. and Robinson, R. (1998). An ingenious filter: the structural basis for ion channel selectivity. Neuron. 20, 821–823. Copyright 1998 Cell Press.)*

VI. ISOFORMS OF VOLTAGE-GATED CHANNELS AS PART OF A LARGE SUPERFAMILY

One of the most striking results of recombinant DNA analysis of channel clones has been the discovery of numerous channel *isoforms* expressed within the same organism and even within the same cell. Naturally, some degree of homology among channels of different organisms was expected and electrophysiological recordings showed that channels could be functionally diverse at the cellular level. Even a structural similarity among Na^+, Ca^{2+} and K^+ channels had been predicted by some investigators. However, the number and diversity of channels within a single organism revealed by molecular biology were rather unexpected. Channels of a functionally similar class (usually based on ion selectivity) are now called *isotypes* or *isoforms* by analogy to the phenomenon of isoenzymes.

We have previously discussed the *Shaker* isotypes. *Shaker*-derived sequences have also been used to construct probes that have discovered other families of K^+ channels in flies, mammals and other species (Salkoff et al., 1992). These families are so extensive that they challenge investigators to develop appropriate nomenclature for their classification (Table 21.3; Chandy and Gutman, 1995). In any case, although they are all to some degree homologous with the original *Shaker* family, they have much higher degrees of sequence homology among members of their class. Functionally, they run the gamut from inactivating A-type channels to non-inactivating channels of the classic delayed rectifier sort. Interestingly, there is usually a much higher degree of sequence homology among channels of the same class from different animals than there is between channels of separate classes in the same animal. For example, *Shaker* channels from *Drosophila* are much more homologous to *Shaker* channels of mouse brain than they are to the *Drosophila Shab*-type channels.

Recently, several other subfamilies of K^+ channels have been discovered in mammalian and invertebrate genomes. Two of these, the *erg* and KQT subfamilies, are important in mammalian cardiac function. Mutants of these channels have been associated with serious inherited heart and nervous system disorders in humans, in particular the long QT syndrome discussed in other chapters in this book. In any case, in mammals the number of K^+ channel isoforms is already quite large: currently there are 12 known potassium channel subfamilies totaling over 100 isoforms, with more being discovered at frequent intervals (see Coetzee et al., 1999).

Considerable diversity is also found among Na^+ and Ca^{2+} channels (Agnew and Trimmer, 1989; Hofmann et al., 1994). For the main channel-forming α subunits (see Figs. 21.6 and 21.7), there are thought to be at least 10 Na^+ channel and nine Ca^{2+} channel genes in the mammalian genome. Some of these isoforms are expressed very selectively in certain tissues, such as brain, or in only certain cells types or at very specific stages of development.

The term "isoform" is rather non-specific in that it does not convey a sense of relative relatedness among channels. An evolving system of classification refers to the set of voltage-gated channels as a *superfamily*, while the selectivity types (i.e. Na^+, Ca^{2+} or K^+ channels) form families. Because of the impressive degree of diversity found for K^+ channels (see Table 21.3), investigators have formally proposed a uniform system of nomenclature in which the closely related isoforms such as *Shaker* are referred to as subfamilies. A separate nomenclature for isoforms of Ca^{2+} channel subunits has also been developed. Further consideration of channel classification will undoubtedly be useful in understanding the process of channel evolution.

VIA. How Do Isoforms Arise?

In general, two separate mechanisms that create such diversity have been identified. First, there is the expected situation in which distinctly separate genes encode different channels in the same beast. Such is largely the situation for mammalian Na^+ channel and Ca^{2+} channel

TABLE 21.3 Properties of Major Potassium Channel Subfamilies in Fruit Flies and Mammals

Drosophila Gene	Homologous Mammalian Genes (no.)	Properties
Shaker	Kv1.1–1.7 (7)	Extensively spliced in fly; inactivation fast to slow
Shab	Kv2.1, 2.2 (2)	Limited splicing in fly; intermediate inactivation kinetics
Shaw	Kv3.1–3.4 (4)	Limited splicing in fly and mammal; slow inactivation, delayed rectifier characteristics
Shal	Kv4.1–4.3 (3)	Limited splicing in fly; slow inactivation, delayed rectifier characteristics
eag	h-erg (3)	Limited splicing in fly and mammals; slow-activation delayed rectifier

isoforms. However, a second mechanism has been found, called *alternative splicing*, in which a given segment of a channel polypeptide may be encoded in several different stretches of genomic DNA known as *exons*. This is the case for *Shaker* in *Drosophila;* thus, in Fig. 21.12, the various *Shaker* isoforms are generated by mixing and matching the transcripts of different exons. During transcription, some sort of regulatory mechanism exists that decides which one of the alternative coding RNAs for a given segment will be incorporated in the final mRNA. The other undesired homologous segments are then excised from the transcript and the desired RNA segments are spliced together. Currently, there is evidence for the operation of both mechanisms in vertebrates and invertebrates. However, most mammalian systems studied to date appear to rely more heavily on separate genes than alternative splicing whereas, in the fruit fly, both mechanisms appear common.

Finally, for all multisubunit channels there is the possibility of diversification through various combinations of each set of subunit isotypes. The best-studied examples are the heteromeric formation of channels by different K^+ channel subunit isotypes (Salkoff et al., 1992). For example, if the same cell synthesized *Shaker* A and *Shaker* B channel subunits, one might find heteromeric complexes of A and B types as well as the homomeric types. In fact, experiments with the oocyte expression system into which both types of mRNA have been injected show that such heteromeric assembly can occur, yielding functional channels with characteristics different from homomultimers of either channel type. Thus, it is theoretically possible that distinct channel properties may be generated by heteromeric assembly of K^+ channel subunits. Whether this occurs in nature is currently being investigated.

On the other hand, oocyte experiments show that heteromeric association among subunits from different families (e.g. *Shaker* and *Shal*) does not occur. Apparently different families have unique structural domains that allow only homomeric assembly among members of their family. This discovery has led to a recent set of chimeric experiments in which domains among a fly *Shaker* channel and a distantly related mammalian delayed rectifier channel (*drkl*) were exchanged in an attempt to identify the segments specifying assembly specificity (Li et al., 1992). Such a segment was found on the N-terminal part of the peptide. Thus, substitution of the *Shaker* segment into the *drkl* cDNA produced a channel *drkl* subunit that was able to co-assemble with native *Shaker*.

VIB. Why Are Channels So Diverse in a Given Organism?

One obvious reason for the presence of so many channel isotypes in the same animal is that each isotype has different functional properties that are appropriate to the function of its host cell. For example, high-frequency, repetitive firing requires short-duration action potentials that could be created by rapidly gating Na^+ channels and fast-inactivating A-type K^+ channels. In addition, isotypes may be differentially sensitive to intracellular modulators that allow cellular mechanisms to alter the properties of specific channels selectively in response to physiological effectors. On the other hand, many of the discovered isotypes have no significant functional differences among them. In this case, it is possible that it is not the differences in the channels themselves that are important, but rather the way the isotypes are expressed. Thus, in a number of cases it has been shown that expression of one isotype over another occurs developmentally or in response to a physiological stimulus (Ribera and Spitzer, 1992). Such specific expression is thought to be controlled by genetic elements outside the coding region for the channel, known as regulatory elements. These stretches of DNA respond specifically to one of many possible soluble factors by increasing (in the case of promoters and enhancers) or inhibiting (silencers) transcription of the channel gene (see Maue et al., 1990). Separate genes, then, potentially allow the cell to express selectively a given channel in response to a given stimulus or at a specific time during development. Finally, there is the possibility that a given isotype sequence encodes information used by the cellular machinery to localize or cluster it in very discrete locations, such as the nodes of Ranvier in myelinated nerve fibers (Dugandzija-Novakovic et al., 1995), neuronal cell bodies, or dendrites (Maletic-Savatic et al., 1994). The study of the diversity of channels and their biological purpose will continue to be a highly active area of cell biology for some time.

VII. FUTURE DIRECTIONS

The current molecular biological approaches will no doubt be productive for some time. However, it is likely that better understanding of channel mechanism will require more direct and precise resolution of the higher order structure of channel molecules. The problems inherent in a crystallographic approach have been discussed. However, the problem is currently being solved by recombinantly synthesizing smaller segments of channel proteins that may be amenable to crystal formation. To be useful, these small segments must retain a significant part of the structure they have in the original protein (a serious concern). Alternatively, small segments may be structurally studied using advanced spectroscopic techniques, such as magnetic resonance. Finally, some important information has been obtained by direct imaging of purified channels using electron microscopy and modern instruments that promise greatly improved resolution at the molecular level are being developed. Finally, the study of the genetic regulation of channel expression will be expanded through the further

study of regulatory domains in the DNA. This will undoubtedly increase our appreciation of ion channels as important elements in the metabolism of the entire organism.

BIBLIOGRAPHY

Agnew, W. S., & Trimmer, J. (1989). Molecular diversity of voltage-sensitive sodium channels. *Annu Rev Physiol, 51*, 401–418.

Aldrich, R. W., Hoshi, T., & Zagotta, W. N. (1990). Differences in gating among amino terminal variants of Shaker potassium channels. *Cold Spring Harbor Symp Quant Biol, 55*, 19–27.

Armstrong, C. M., & Bezanilla, F. (1977). Inactivation of the sodium channel. II. Gating current experiments. *J Gen Physiol, 70*, 567–590.

Catterall, W. A. (1988). Molecular properties of dihydropyridine sensitive calcium channels in skeletal muscle. *J Biol Chem, 263*, 3535–3538.

Catterall, W. A. (1992). Cellular and molecular biology of voltage-gated sodium channels. *Physiol Rev*, (Suppl. 72), S15–S48.

Chandy, K. G., & Gutman, G. A. (1995). Voltage-gated K^+ channel genes. In R. A. North (Ed.), *CRC Handbook of Receptors and Channels* (pp. 1–71). Boca Raton: CRC Press.

Chiamvimonvat, N., Perez-Garcia, M. T., Ranjan, R., Marban, E., & Tomaselli, G. F. (1996). Depth asymmetries of the pore-lining segments of the Na^+ channel revealed by cysteine mutagenesis. *Neuron, 16*, 1037–1047.

Chou, P. Y., & Fasman, G. D. (1978). Empirical predictions of protein conformation. *Annu Rev Biochem, 47*, 251–276.

Coetzee, W. A., Amarillo, Y., Chiu, J., et al. (1999). Molecular diversity of K^+ channels. *Ann NY Acad Sci., 868*, 233–285.

Doyle, D. A., Cabral, J. M., Pfuetzner, R. A., et al. (1998). The structure of the potassium channel: molecular basis of K^+ conduction and selectivity. *Science, 280*, 69–77.

Dugandzija-Novakovic, S., Koszowski, A. G., Levinson, S. R., & Shrager, P. (1995). Clustering of K^+ channels and node of Ranvier formation in remyelinating axons. *J Neurosci, 15*, 492–503.

Ellinor, P. T., Yang, J., Sather, W. A., Zhang, J.-F., & Tsien, R. (1995). Ca^{2+} channel selectivity at a single locus for high affinity Ca^{2+} interactions. *Neuron, 15*, 1121–1132.

Guy, H. R., & Seetharamulu, P. (1986). Molecular model of the action potential sodium channel. *Proc Natl Acad Sci, USA, 83*, 508–512.

Heinemann, S. H., Terlau, H., Stuhmer, W., Imoto, K., & Numa, S. (1992). Calcium channel characteristics conferred on the sodium channel by single mutations. *Nature, 356*, 441–443.

Hille, B. (1992). *Ionic Channels of Excitable Membranes*. Sunderland: Sinauer Associates.

Hofmann, F., Biel, M., & Flockerzi, V. (1994). Molecular basis for Ca^{2+} channel diversity. *Ann Rev Neurosci, 17*, 399–418.

Hoshi, T., Zagotta, W. N., & Aldrich, R. W. (1990). Biophysical and molecular mechanisms of Shaker potassium channel inactivation. *Science, 250*, 533–538.

Isom, L. L., De Jongh, K. S., Patton, D. E., et al. (1992). Primary structure and functional expression of the β_1 subunit of the rat brain sodium channel. *Science, 256*, 839–842.

Kyte, J., & Doolittle, R. F. (1982). A simple method for displaying the hydropathic character of a protein. *J Mol Biol, 157*, 105–132.

Leonard, J., & Snutch, T. P. (1991). The expression of neurotransmitter receptors and ion channels in Xenopus oocytes. In D. M. Glover, & B. D. Hanes (Eds.), *Molecular Neurobiology: a Practical Approach* (pp. 161–182). New York: Oxford University Press.

Li, M., Jan, Y. N., & Jan, L. Y. (1992). Specification of subunit assembly by the hydrophilic amino-terminal domain of the Shaker potassium channel. *Science, 257*, 1225–1230.

Lopez, G. A., Jan, Y. N., & Jan, L. Y. (1991). Hydrophobic substitution mutations in the S4 sequence alter voltage-dependent gating in Shaker K^+ channels. *Neuron, 7*, 327–336.

MacKinnon, R., Heginbotham, L., & Abramson, T. (1990). Mapping the receptor site for charybdotoxin, a pore-blocking potassium channel inhibitor. *Neuron, 5*, 767–771.

MacKinnon, R., & Yellen, G. (1990). Mutations affecting TEA blockade and ion permeation in voltage-activated K^+ channels. *Science, 250*, 276–279.

MacKinnon, R. (1991). Determination of the subunit stoichiometry of a voltage-activated potassium channel. *Nature, (London), 350*, 232–235.

Maletic-Savatic, M., Lenn, N. J., & Trimmer, J. S. (1994). Differential spatiotemporal expression of K^+ channel polypeptides in rat hippocampal neurons developing in situ and in vitro. *J Neurosci, 15*, 3840–3851.

Maue, R. A., Kraner, S. D., Goodman, R. H., & Mandel, G. (1990). Neuron-specific expression of the rat brain type II sodium channel gene is directed by upstream regulatory elements. *Neuron, 4*, 22–231.

Miller, C. (Ed.), (1986). *Ion Channel Reconstitution*. New York: Plenum.

Miller, J. A., Agnew, W. S., & Levinson, S. R. (1983). Principal glycopeptide of the tetrodotoxin/saxitoxin binding protein from *Electrophorus electricus*: isolation and partial physical and chemical characterization. *Biochemistry, 22*, 462–470.

Nakai, J., Adams, B. A., Imoto, K., & Beam, K. G. (1994). Critical roles of the S3-segment and S3–S4 linker of repeat I in activation of L-type calcium channels. *Proc Natl Acad Sci, USA, 91*, 1014–1018.

Noda, M., Shimizu, S., Tanabe, T., et al. (1984). Primary structure of *Electrophorus electricus* sodium channel deduced from cDNA sequence. *Nature, 312*, 121–127.

Numa, S., & Noda, M. (1986). Molecular structure of sodium channels. *Ann NY Acad Sci, 479*, 338–355.

Papazian, D. M., Timpe, L. C., Jan, Y. N., & Jan, L. Y. (1987). Cloning of genomic and complementary DNA from Shaker, a putative potassium channel gene from Drosophila. *Science, 237*, 749–753.

Papazian, D. M., Timpe, L. C., Jan, Y. N., & Jan, L. Y. (1991). Alteration of voltage- dependence of Shaker potassium channel by mutations in the S4 sequence. *Nature, 349*, 305–310.

Pongs, O. (1992). Molecular biology of voltage-dependent potassium channels. *Physiol Revs,* (Suppl. 72), S69–S88.

Ribera, A. B., & Spitzer, N. C. (1992). Developmental regulation of potassium channels and the impact on neuronal differentiation. In T. Narahashi (Ed.), *Ion Channels, Vol. 3* (pp. 1–38). New York: Plenum Press.

Salkoff, L., Baker, K., Butler, A., Covarrubias, M., Pak, M. D., & Wei, A. (1992). An essential set of K^+ channels conserved in flies, mice, and humans. *TINS, 15*, 161–166.

Sharp, A. H., Imagawa, T., Leung, A. T., & Campbell, K. P. (1987). Identification and characterization of the dihydropyridine-binding subunit of the skeletal muscle dihydropyridine receptor. *J Biol Chem, 262*, 12 309–12 315.

Sigworth, F. J. (1995). Charge movement in the sodium channel. *J Gen Physiol, 106*, 1047–1051.

Stuhmer, W., Conti, F., Suzuki, H., et al. (1989). Structural parts involved in the activation and inactivation of sodium channels. *Nature, 339*, 597−603.

Tanabe, T., Adams, B. A., Numa, S., & Beam, K. G. (1991). Repeat I of the dihydropyridine receptor is critical in determining sodium channel activation kinetics. *Nature, 352*, 800−803.

Tanabe, T., Takeshima, H., Mikami, A., et al. (1987). Primary structure of the receptor for calcium channel blockers from skeletal muscle. *Nature, 328*, 313−318.

Terlau, H., Heinemann, S. H., Stuhmer, W., et al. (1991). Mapping the site of block by tetrodotoxin and saxitoxin of sodium channel II. *FEBS Lett, 293*, 93−96.

Timpe, L. C., Jan, Y. N., & Jan, L. Y. (1988). Four cDNA clones from the Shaker locus of Drosophila induce kinetically distinct A-type potassium currents in Xenopus oocytes. *Neuron, 1*, 659−667.

Vassilev, P., Scheuer, T., & Catterall, W. A. (1989). Inhibition of inactivation of single sodium channels by a site-directed antibody. *Proc Natl Acad Sci, USA, 86*, 8147−8151.

Yang, J., Ellinor, P. T., Sather, W. A., Zhang, J.-F., & Tsien, R. W. (1993). Molecular determinants of Ca^{2+} selectivity and ion permeation in L-type Ca^{2+} channels. *Nature, 366*, 158−161.

Yool, A. J., & Schwarz, T. L. (1991). Alteration of ionic selectivity of a K^+ channel by mutation of the H5 region. *Nature, 349*, 700−704.

Zagotta, W. N., Hoshi, T., & Aldrich, R. W. (1990). Restoration of inactivation in mutants of Shaker potassium channels by a peptide derived from ShB [see comments]. *Science, 250*, 568−571.

Chapter 22

Biology of Gap Junctions

Richard D. Veenstra

Chapter Outline

I. INTRODUCTION

In the late 1950s and early 1960s, physiologists who had been poking fine glass current-injecting and current-recording electrodes into neighboring cells within a variety of tissues made an interesting discovery. They found that while the injection of current into a cell caused a predictable shift in its non-junctional membrane potential, it also caused a similar shift in the non-junctional membrane potential of immediately adjacent cells (Fig. 22.1).

One interpretation of this finding was that the ions emanating from the injection electrode were able to flow freely from the injected cell to the adjacent cell and did so in preference to pathways leading to the extracellular medium or to the intercellular space. Moreover, several studies demonstrated that fluorescent dyes were selectively transferred from cell to cell when injected into the cytoplasm through glass injection pipettes. Many observations such as these led to the hypothesis that some cells were coupled (electrically or with respect to dye transfer) by *permeable cell junctions*.

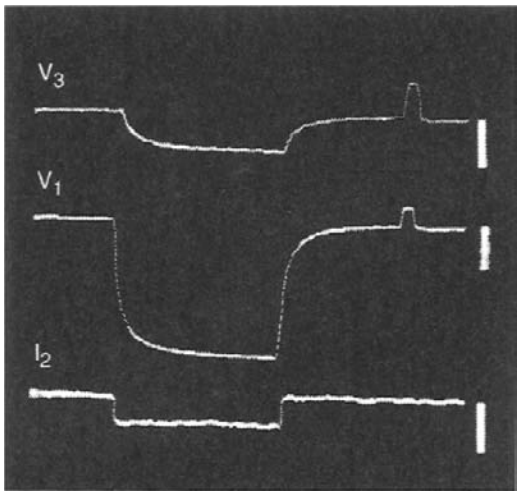

FIGURE 22.1 The injection of current into one cultured WI-26 cell (I2) within a monolayer produces a shift in potential within the injected cell (V1) and in a cell two or three cells removed from the injected cell (V3), indicating that ions may move freely between contacting cells. *(From Furshpan, E.J. and Potter, D D. (1968). Low-resistance junctions between cells in embryos and tissue culture. Curr Top Dev Biol. 3, 95, with permission.)*

Cell Physiology Sourcebook. DOI: 10.1016/B978-0-12-387738-3.00022-6

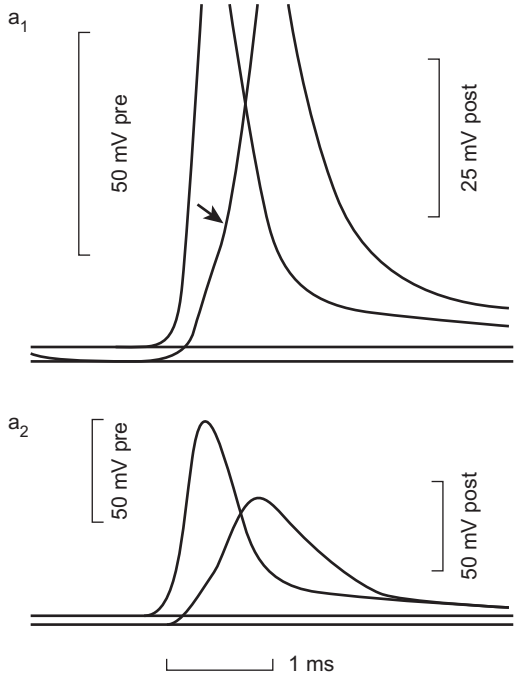

FIGURE 22.2 The upper trace is an AP in the presynaptic element of a crayfish septate axon; the lower trace shows the subsequent AP in the postsynaptic element. The short lag of the latter following the former is typical of electrical synapses. The top and bottom traces were recorded at the same synapse at different amplifications. *(From Furshpan, E.J. and Potter, D.D. (1959). Transmission at the giant motor synapses of the crayfish. J. Physiol. 145, 289, with permission.)*

Additionally, in the neuronal tissues in which this phenomenon had first been witnessed, it was found that action potentials generated in a presynaptic element could be passed to a postsynaptic element much faster than would occur if the presynaptic and postsynaptic elements were connected by chemical synapses (Fig. 22.2). Ironically, this evidence for the presence of permeable cell junctions that could serve as *electrical synapses* in the nervous system came to light soon after the common acceptance of Otto Loewi's findings that supported the idea that neuronal synapses were probably chemical in nature and not electrical as traditionally believed.

II. ADVANTAGES OF ELECTRICAL SYNAPSES IN EXCITABLE CELLS

The utility of electrical synapses in excitable cells is apparent. They may pass action potentials or subthreshold electrical activity more rapidly from one neuronal element to another than can their chemical counterparts. This advantage is especially obvious in neuronal pathways that serve as *escape mechanisms*, such as those in the tail muscles of crayfish and lobsters and those in the pectoral fins of fishes. In these cases, the rapidity of the animal's response to imminent danger has selective value. On the other hand, such permeable junctions connecting smooth muscle cells of the uterus or cardiac muscle cells of the heart wall, provide a mechanism for the systematic cell-to-cell spread of depolarization that is required for *coordinated and effective contractile activity.*

III. UBIQUITOUS MEMBRANE PERMEABLE JUNCTIONS

Numerous studies published in the 1960s and 1970s supported the idea that virtually all cells in normal tissues (even those in inexcitable tissues) were coupled by permeable cell junctions. Based on studies with native biological molecules and with tracers of different sizes, it was also suggested that the pores within vertebrate cell-to-cell junctions were approximately 1.2 nm in diameter and that molecules larger than about 1 kDa were excluded. Thus, it was suggested that the biological molecules capable of freely moving from cell to cell in normal tissues would include a wide range of ions and small metabolites including sugars, nucleotides and nucleosides and possible signaling molecules such as cyclic adenosine monophosphate (cAMP).

Since the pores initially appeared to select molecules only with respect to size, it was suggested that one function of permeable cell junctions was to buffer the concentrations of small metabolites throughout the tissue. Direct evidence for the cell contact-mediated exchange of metabolites, for example, was provided by metabolic cooperation experiments in which it was shown that a normal wild-type cell, able to incorporate thymidine into DNA, could transfer DNA precursor molecules (probably the nucleoside triphosphate form of thymidine) to mutant thymidine kinase-deficient cells only if the wild-type and mutant cell were in contact. In these "kiss-of-life" experiments, the mutant cells were then able to incorporate this nucleoside into DNA required for continued proliferation and survival.

IV. STRUCTURAL CANDIDATES FOR THE PERMEABLE CELL JUNCTION

As electron microscopes first came into common use in the late 1950s, several different kinds of cell–cell junctions were discovered. The *tight junction*, or *occludens-type junction*, was characterized by the fusion of membranes of adjacent cells and so held some appeal as a potential permeable cell junction. *Septate junctions* were also good candidates for the permeable cell junction since they were characterized by cell-to-cell bridges or septa covering a large region of cell–cell apposition in many of the invertebrate tissues shown to be well coupled by

electrophysiological or dye-tracing techniques. The basic argument against their function as permeable cell junctions, however, was that their distribution among tissues and organisms was significantly more limited than was the coupling phenomenon. The septate junction, for example, could not be identified in coupled vertebrate cells. The apparent fusion of plasmalemma between juxtaposed cells in mammalian smooth and cardiac muscle was termed the *nexus* in the early 1960s and was demonstrated to be the site of action potential propagation when hypertonic solutions that separated the nexal membranes also blocked action potential propagation.

V. ULTRASTRUCTURAL CHARACTERIZATION OF GAP JUNCTIONS AND CORRELATIONS WITH CELL COUPLING

In a pioneering study, Revel and Karnovsky (1967) infiltrated the intercellular spaces of heart and liver with an electron opaque dye (lanthanum hydroxide) and then examined these preparations in the electron microscope. They found regions where the membranes of adjacent cells were apposed to one another across a uniform lanthanum-infiltrated intercellular space about 2–4 nm in width (Fig. 22.3B). In addition, in cross-section, they observed small unstained structures bridging the stain-filled gap between adjacent cells in these regions (Fig. 22.3A) and, in en face views, these bridges were packed hexagonally within the intercellular space. Ultimately, freeze-fracture studies provided evidence that these intercellular bridges were in continuity with structures that spanned the lipid bilayers of both cells and thereby could theoretically provide the structural foundation for the cell-to-cell conduit implied by earlier electrophysiological studies.

It was also very important that this cell–cell junction, which Revel and Karnovsky called the *gap junction*, was found in many tissues which were ion- or dye-coupled, including both inexcitable and excitable cells. While well-coupled inexcitable cells, such as liver hepatocytes, possessed large numbers of gap junctions, it was especially satisfying to find that these structures were prominent features of the cell–cell contact regions of excitable cells, such as cardiac myocytes, and were prominent in neuronal systems that had been shown to possess electrical synapses. In addition, in the metabolic cooperation experiments described above, DNA precursor molecules were transferred between test cells only if they were capable of forming gap junctions in regions of cell–cell contact. Moreover, a large body of ultrastructural evidence indicated that gap junctions were components of virtually all tissues in multicellular organisms of the animal kingdom (See Fig. 22.3C–J).

VI. MOLECULAR AND STRUCTURAL STUDIES OF GAP JUNCTION PROTEINS

Application of biochemical and molecular approaches to the study of gap junctions proved to be more perplexing than originally envisioned, but tenacious investigators in a number of laboratories were able to overcome initial obstacles. It is now known that proteins that make up gap junctions in vertebrate tissues are basic and contain significant stretches of hydrophobic sequence. This is not surprising given the fact that these are integral membrane proteins. For these reasons, they proved difficult to isolate and purify. Extraction of tissues with boiling sodium dodecyl sulfate (SDS) proved to be the only reliable method for obtaining morphologically pure fractions of gap junction membranes for many years, but the proteins extracted from these fractions ran at variable molecular weights on polyacrylamide gels. It was controversial as to whether some of these bands were breakdown products or other proteins associated with gap junctions in the cell membrane.

It was not until gentler, non-detergent extraction procedures were developed in the early 1980s that a consistent band on polyacrylamide gels with a predicted molecular weight of 26 kDa could be routinely isolated from rodent livers. Once this native protein was obtained and purified, it was possible to produce a polyclonal antibody. This antibody was used to screen an expression cDNA library to isolate and sequence its gene. This first sequence was published in 1986. Hydropathy analysis of the deduced amino acid sequence of this cDNA revealed a 32-kDa protein which could be interpreted as possessing four potential transmembrane regions, two extracellular loops and an internal loop and amino and carboxyl termini that extended into the cytoplasm (Fig. 22.4). The mapping of these proteins with antibodies directed against specific sequences and their cutting with specific proteases have largely confirmed this initial interpretation of the relationships of gap junction protein segments to the membrane. It was also postulated that six gap junction protein molecules, called *connexins*, constitute each gap junction intramembrane particle (IMP) or *connexon*, thus providing a molecular basis for models of the permeable membrane junction deduced from earlier physiological and structural studies (Figs. 22.4 and 22.5). Indeed, more recent electron cryomicroscopy studies of frozen, rehydrated 2D crystals of a recombinant C-terminal truncated form of Cx43 has revealed even more detail regarding the relationship of connexins to the connexon and the relationship of their specific transmembrane domains to the plasma membrane. These studies show that each connexin subunit contributes a transmembrane α-helix that lines the aqueous pore and an additional α- helix adjacent to the surrounding membrane lipids. In addition, the images

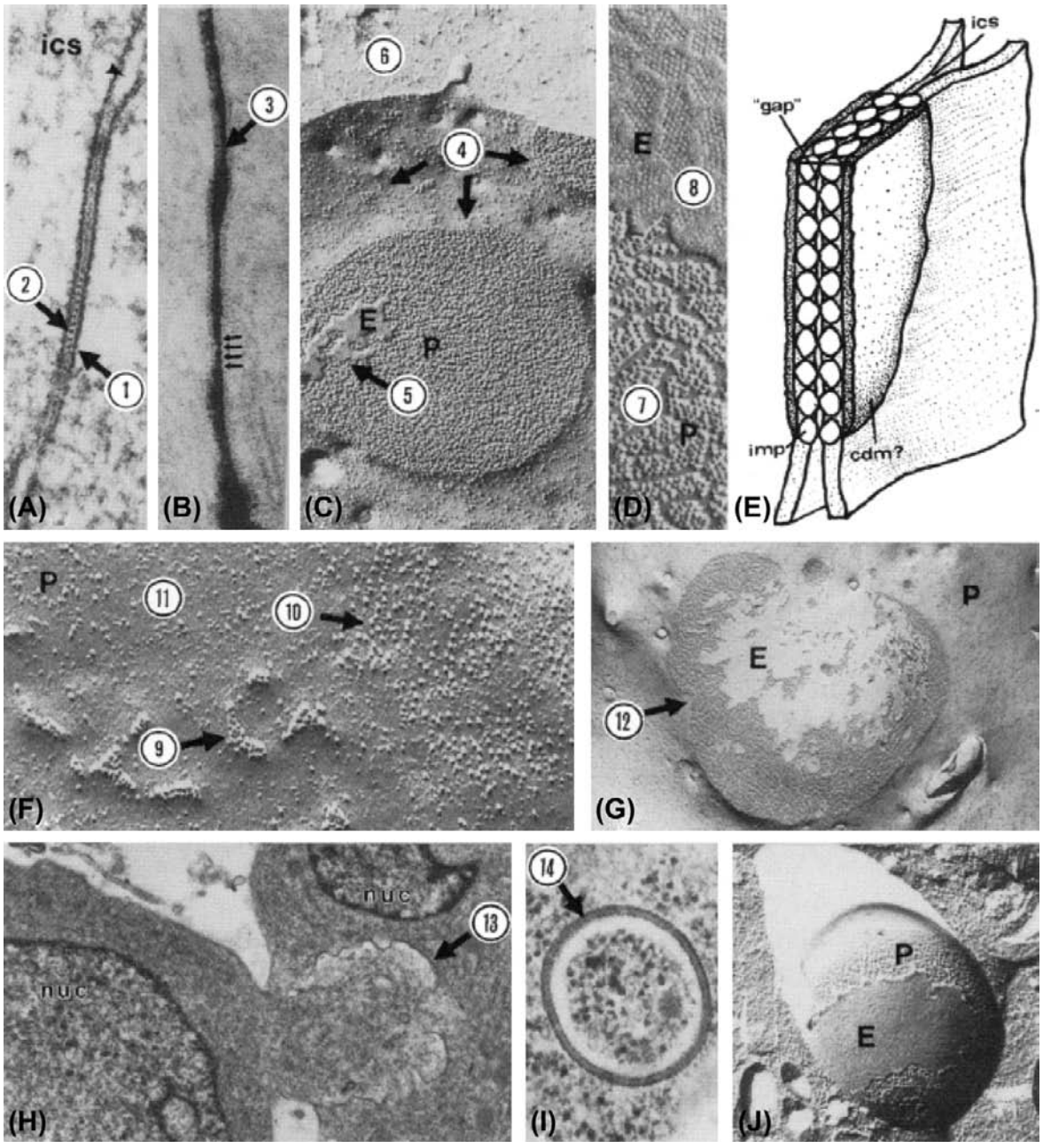

FIGURE 22.3 (A) Thin section of typical gap junction. The entire width of both apposed membranes and the intercellular space is about 18 nm. Dense material is often associated with cytoplasmic surface of gap junction (1). Some gap junctions are characterized by stained periodicites evident at level of "gap" (2). Magnification, 157 500×. *(From Larsen, W.J., Skowron-Lomneth, C. and Carron, C. (1988). Gap junction modulation: possible role in tumor cell behavior. In (H.A. Milman and E. Elmore, eds), Biochemical Mechanisms and Regulation of Intercellular Communication, Vol. 14, p. 151. Princeton Scientific Publ. Co., Princeton, NJ, with permission.)* (B) Lanthanum infiltrated gap junction. The lanthanum infiltrated intercellular "gap" (3) is about 2−4 nm. Magnification, 212 400× *(Reproduced from The Journal of Cell Biology, 1975, vol. 67, p. 801, by copyright permission of the Rockefeller University Press.)* (C) Freeze-fracture image of a gap junction. Each junctional membrane contains a set of particles and a set of pits. In vertebrate tissues, the particles adhere to the protoplasmic leaflet of the lipid bilayer (protoplasmic fracture face, P), whereas the pits remain associated with the extracellular leaflet (extracellular fracture face, E). Gap junction particles aggregate within particle-poor zones (4). The fracture may jump between the two membranes, resulting in adhesion of bits of the E-fracture face from the membrane of the adjacent cell (5) on the P-fracture face or vice versa. Occasionally, the fracture plane leaves the membrane and cuts into the cytoplasm (6). Magnification, 64 800×. *(From Larsen, W.J. (1977). Structural diversity of gap junctions: a review. Tissue Cell, 9, 373, with permission.)* (D) Enlargement of P- and E-fracture faces showing details of gap junction particles (7) and corresponding pits (8). Magnification, 139 000×. *(From Larsen, W.J. (1977). Structural diversity of gap junctions: a review. Tissue Cell, 9, 373, with permission.)* (E) Simple model of gap junction showing particle-particle (imp) contact within the "gap" at the level of the intercellular space (ics). Cytoplasmic dense material (cdm) is particularly apparent in gap junctions in excitable tissues. *(From Larsen, W.J. (1977). Structural diversity of gap*

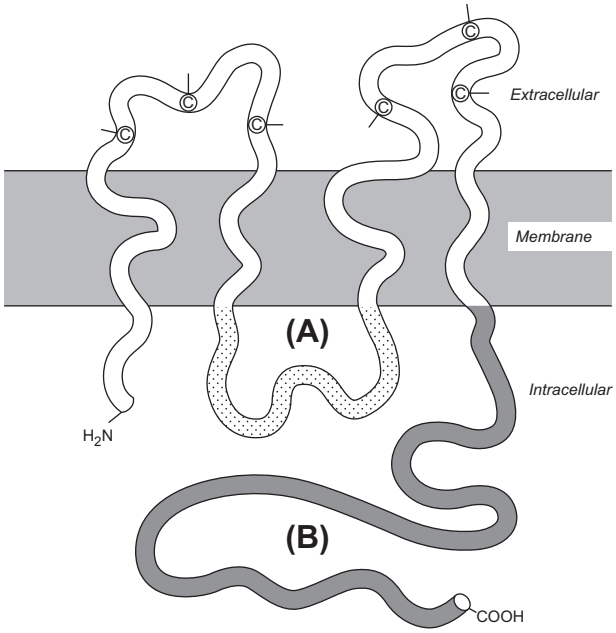

FIGURE 22.4 Structure and topology of a connexin. Both amino and carboxyl termini (B) are located in the cytoplasm along with an intermediate loop (A). Every connexin contains four membrane-spanning regions and two extracellular loops containing highly conserved cyteine residues (C). *(From Beyer, E.C., Paul, D.L. and Goodenough, D.L. (1990). Connexin family of gap junction proteins. J. Membr. Biol., 116, 187, with permission.)*

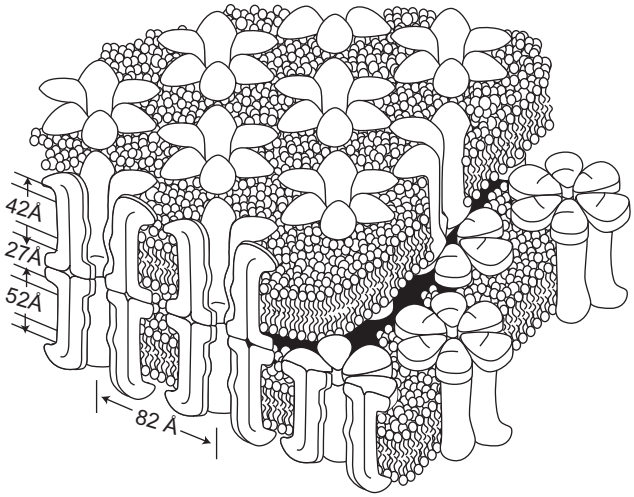

FIGURE 22.5 This diagram of a region of a gap junction isolated from mouse liver is based on electron microscope images and x-ray diffraction data. Each gap junction particle or connexon is composed of six gap junction protein molecules called connexins. Connexons in apposed membranes meet within the intercellular space. *(Reproduced from The Journal of Cell Biology, 1977, 74, p. 449, by copyright permission of the The Rockefeller University Press.)*

reveal that the apposing connexons that form each channel are staggered by about 30°.

VII. TWO LARGE FAMILIES OF GAP JUNCTION PROTEINS

Early structural studies, particularly those utilizing the freeze-fracture technique, demonstrated structural diversity among gap junctions distributed throughout the animal kingdom and within a variety of different tissues. The phylogenetic or species variability in some of these structural features was shown to depend upon the tissue in which the gap junction was identified. This variability in the detailed gap junction structure and composition was not initially understood, although it is now known that gap junctions in different tissues, phyla and species are formed by different protein isoforms within two large families of gap junction proteins. The gap junctions in vertebrate tissues are formed by members of the *connexin family* of gap junction proteins. The gap junctions of invertebrate tissues appear to be formed by members of an analogous *innexin family* of gap junction proteins.

Members of the connexin family of gap junction proteins range in molecular weight from 23 kDa to 62 kDa (Table 22.1). Each connexin is named for its deduced molecular weight in kilodaltons so that the 26-kDa connexin in humans, for example, is called human connexin 26 (human Cx26), while the 30.3-kDa connexin in mice is called mouse connexin 30.3 (mouse Cx30.3). Sequence analysis supports the possibility that at least two major phylogenetic subfamilies of connexins

junctions: a review. Tissue Cell, 9, with permission.) (F) Gap junctions form by the aggregation (9) of single 11-nm particles (10) in particle-poor regions of the membrane (11). Magnification, 222 300×. *(From Larsen, W.J. and Risinger, M.A. (1985). The dynamic life histories of intercellular membrane junctions. In (B. Satir, ed.), Modern Cell Biology, Vol. 4, p. 151. John Wiley & Sons, New York. Copyright 1985 John Wiley & Sons. Reprinted by permission of Wiley-Liss, Inc., a subsidiary of John Wiley & Sons, Inc.)* (G) Very large gap junctions (12) containing thousands of gap junction particles may represent terminal gap junction gaps. Magnification, 21 600×. *(From Larsen, W.J. (1977). Structural diversity of gap junctions: a review. Tissue Cell, 9, 373, with permission.)* (H) The large gap junction caps may invaginate into the cell (13) through an endocytotic mechanism. Magnification, 14 400×. *(From Larsen, W.J. and Tung, H. (1978). Origin and fate of gap junction vesicles in rabbit granulosa cells. Tissue Cell, 10, 585, with permission.)* (I) Bimembranous gap junction vesicles (14) may pinch off from the invaginating junction to fuse with lysosomes before undergoing degradation. Magnification, 52 200×. *(From Larsen, W.J. and Tung, H. (1978). Origin and fate of gap junction vesicles in rabbit granulosa cells. Tissue Cell, 10, 585, with permission.)* (J) Freeze-fracture planes within the cytoplasm may reveal the P-face particles (P) and E-face pits (E) within cytoplasmic gap junction vesicles. Magnification, 38 700×. *(From Larsen, W.J. and Tung, H. (1978). Origin and fate of gap junction vesicles in rabbit granulosa cells. Tissue Cell, 10, 585, with permission.)*

TABLE 22.1 The Connexin Gene and Protein Family[1]

Human Protein Name	Human Gene Name	Mouse Protein Name	Mouse Gene Name
CX43	*GJA1*	Cx43	*Gja1*
CX46	*GJA3*	Cx46	*Gja3*
CX37	*GJA4*	Cx37	*Gja4*
CX40	*GJA5*	Cx40	*Gja5*
—	—	Cx33	*Gja6*
CX50	*GJA8*	Cx50	*Gja8*
CX59	*GJA9*	—	—
CX62	*GJA10*	Cx57	*Gja10*
CX32	*GJB1*	Cx32	*Gjb1*
CX26	*GJB2*	Cx26	*Gjb2*
CX31	*GJB3*	Cx31	*Gjb3*
CX30.3	*GJB4*	Cx30.3	*Gjb4*
CX31.1	*GJB5*	Cx31.1	*Gjb5*
CX30	*GJB6*	Cx30	*Gjb6*
CX25	*GJB7*	—	—
CX45	*GJC1 (GJA7)*	Cx45	*Gjc1*
CX47	*GJC2 (GJA12)*	Cx47	*Gjc2*
CX30.2/CX31.3	*GJC3*	Cx29	*Gjc3*
CX36	*GJD2*	Cx36	*Gjd2*
CX31.9	*GJD3*	Cx30.2	*Gjd3*
CX40.1	*GJD4*	Cx39	*Gjd4*
CX23	*GJE1*	Cx23	*Gje1*

[1]*Adapted from Beyer, E.C. and Berthoud, V.M. (2009). The family of connexin genes. In Connexins: A Guide, p. 8, with permission. Copyright 2009 Humana Press.*

diverged from each other between 1.3 and 1.9 billion years ago; one group ranging in size from about 26 kDa to 32 kDA (β-group), another from about 33 kDa to 62 kDa (α-group) (Fig. 22.6A). Some lesser divergent connexin subfamilies are also indicated (δ/γ/ε). Twenty different connexin genes have been identified in rodents (e.g. mice), 21 in humans, although transcription of the Cx23 gene has not been demonstrated in humans or mice and the functional expression of some connexins have yet to be described (e.g. Cx25, Cx33).

Typically, it appears that two or more connexins comprise the gap junctions within any given tissue. For example, Cx26 and Cx32 constitute gap junctions of mammalian liver and have been shown to coexist within the same gap junction aggregates. On the other hand, the Cx32 and Cx43 documented in thyroid epithelium, appear to be segregated into separate gap junctions formed in different regions of the lateral cell membrane. Likewise, the distribution of three different connexins (Cx40, Cx43 and Cx45) within the human heart appears to be non-random. For example, Cx45 is the first connexin to appear in the embryonic mouse heart. Ultimately, however, its expression is restricted to the region of the sinoatrial (SA) node, while Cx40 is localized in the atrioventricular (AV) node and in myocytes of the atrium and conductive myocardium. In contrast, Cx43 expression occurs within the crista terminalis and other cardiomyocytes of the heart. As many as six different connexin genes (Cx30.1, Cx31, Cx31.1, Cx40, Cx43 and Cx45) are transcribed and translated in mouse embryos as early as the eight-cell stage. These studies imply differential functions for gap junctions composed of different connexins and consequently stimulate the following question: what part of the connexin molecule encodes functional specificity and how do these specificities differ from connexin to connexin?

In general, the amino termini, transmembrane helicies and extracellular loop cysteine-containing regions of the connexins are highly conserved (see Figs. 22.4 and 22.6B). However, the cytoplasmic loops and cytoplasmic carboxyl termini vary significantly in length and amino acid sequence from one connexin to another. The two triple cysteine-containing segments form the two identified connexin signature sequences less Cx23 which contains only two Cys residues within each extracellular loop (see Fig. 22.6C). Heterotypic gap junctions can be formed only with connexons made of particular connexins, suggesting that sequence specificity within the extracellular domains may be relevant to gap junction assembly. Recent studies, therefore, have focused on the potential functional relevance of specific differences in amino acid sequences within the various domains of the connexin proteins (see Sections IX–XIV).

In invertebrates, proteins of the innexin family are able to form gap junctions based on ultrastructural criteria. In addition, studies with a *Xenopus* oocyte expression system have shown that some of the innexin proteins are able to form permeable cell-to-cell channels that may be voltage- or pH-sensitive. As many as 24 innexin genes have been identified in the nematode, *Caenorhabditis elegans*, while six innexin genes have been described in *Drosophila*. While the innexins bear no sequence homology to the connexin family of proteins, the structural similarities of innexins and connexins are dramatically similar. For example, like the connexins, the innexin proteins have four transmembrane domains, two extracellular loops and cytoplasmic N- and C-termini. Moreover, the functions of the innexin proteins in invertebrates parallel functions of the connexins in

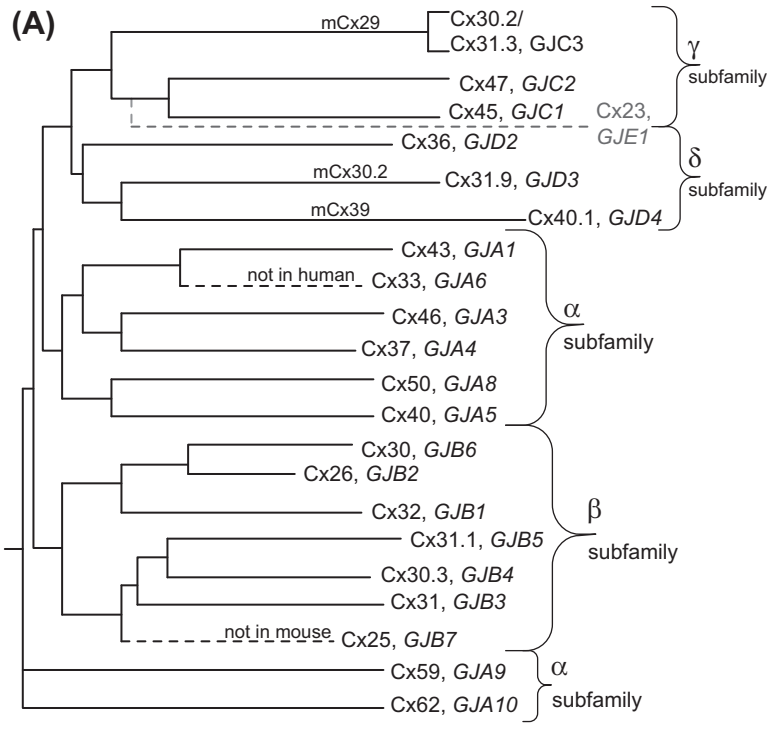

(B)

MXDWXFLXXLLXXXVXX**H**STXXG*KXWLTVLFIFRILVLXVAAEXVWG***DE***Q
S*X***F***X***C***NTX***QPGC***XNV***C***Y***D***XXF***PI******SH***I*RXWVLQIIFVSTPSLLYXGHXXYX*
XXXXEXXXXXXXXXXXXXXXXXXXXXXXXXXXXXXXXXXXXXXXXXXXX
XXXXXXXXXXXXXXXXXXXXXXXXXXXXXXXXXXXXXXXXXXXXXXXXX
XXXXXGXLXXT*YVXSXXXRXXXEXXFLXGQYXLYGX*FXXXPLXX***C***X***R***XX***P***
CPNXVDCFVSR***P***T***EK***TI***F****XXFMXXVSXXCLLLNXX****E****LXHLGXKXXX***R...***

Key: Bold = identical, black ≥ 50% conservation, *italic = transmembrane*

(C)

Connexin signature 1:
C–**[D/N/**H**]**–**[T/L]**–X–**[Q/T]**–P–G–C–X–X–**[**V/A**/I/L]**–C–**[F/Y]**–**D**
Connexin signature 2:
C–X–X–X–X–P–C–X–X–X–**[L/I/**V/M**/T/**A**]**–**[D/E/N/T]**–C–**[F/**Y**/N]**–
[L/I/V/M/Q**]**–**[**S/A**]**–**[K/R/**H**]**–P

FIGURE 22.6 (A) Dendrogram of the mammalian (human, mouse) connexin family tree constructed by aligning the protein sequences for the known connexins using the nomenclature adapted at the 2007 International Gap Junction Conference (see Table 22.1). *(Adapted from Sáez, J.C., Berthoud, V.M., Brañes, M.C., Martínez, A.D. and Beyer, E.C. (2003). Plasma membrane channels formed by connexins: their regulation and functions. Physiol. Rev., 83, 1363, with permission. Copyright 2003 American Physiological Society.)* (B) Consensus sequence for the 20 human connexins (excluding Cx23) illustrating the 50 to 100% conservation of amino acids residues within the amino terminal, first and second extracellular loop and four transmembrane domains with limited sequence homology within the cytoplasmic loop and carboxyl terminal domains. (C) The two connexin signature sequences derived from the consensus sequence underlined in panel B. Cx31 and Cx23 do not match these signature sequences. *(Adapted from Beyer, E.C. and Berthoud, V.M. (2009). The family of connexin genes. In Connexins: a Guide, p. 8, with permission. Copyright 2009 Humana Press.)*

vertebrate tissues. For example, the innexin encoded by the shal-B(neural) locus forms electrical synapses of the *Drosophila* nervous system, while the innexin encoded by the *eat*-5 locus forms permeable junctions responsible for synchronization of pharyngeal musculature in *Drosophila*. There is no signature consensus amino acid sequence common to the Arthropoda, Nematoda, Annelida and other invertebrate phylogeny as there is for the connexins. The innexin extracellular loops contain only two cysteine residues each, in contrast to three for the connexins. Three innexin-related genes are found in the vertebrate genome and these are now referred to as the *pannexins* (*panx1*, *panx2*, *panx3*). Only pannexin1 is capable of forming homologous intercellular channels in *Xenopus* oocytes, suggesting the possibility that pannexins do not form vertebrate gap junctions. Alternatively, it was hypothesized that pannexins form ATP-releasing hemichannels in complex with the purinergic P2X7 receptor. Evidence for functional panx1/P2X7 *hemichannels* in astrocytes and other mammalian cells has received considerable support in recent years, suggesting a more patho/physiological role for pannexins in paracrine signaling pathways than conventional gap junctional communication.

VIII. CHANNELS WITHIN GAP JUNCTIONS

Following the identification of the gap junction as the site of cell-to-cell transfer of ions and small hydrophilic molecules, a hypothesis developed that the pathway for this exchange consisted of an array of parallel aqueous channels. The central aqueous pore resides in each IMP particle in the freeze-fracture images or hexagonal bridge in the negatively stained micrographs of a gap junction plaque. An aqueous pore 16 nm in length with a channel diameter of approximately 14 Å should have a unitary conductance of 10^{-10} Ω (=100 pS). Such a relatively high conductance should produce a detectable electrical signal in support of the channel hypothesis for gap junction permeability. Small stepwise changes in the electrical coupling between paired *Xenopus* embryonic cells provided evidence for the existence of discrete coupling elements, but the low input resistance owing to the large cell size limited the resolution of the electrical signals. Adaptation of the two-cell voltage clamp to cell pairs of high input resistance achieved precise determination of unitary gap junction channel conductance. Concomitant current records from both voltage-clamped cells always appear as mirror images since each cell resides on opposite sides of the junction (Fig. 22.7). This *equal amplitude and opposite polarity* is the criterion used to define junctional current signals in the dual whole cell recording configuration. Channel conductance values of 120 and 160 pS were close to the original predicted value and provided supportive evidence for the existence of relatively large non-selective aqueous channels. Conductance values range from 10 to 300 pS for different gap junction channels under essentially physiological salt conditions. For an aqueous diffusion limited pore, the channel conductance will increase in direct proportion to $2\pi r^2$. For a long pore of 16 nm in length, a 300-pS gap junction channel requires a 26-Å diameter right cylindrical pore. It follows that higher conductance gap junction channels should exhibit less ionic selectivity and a higher molecular permeability than channels with smaller conductance values.

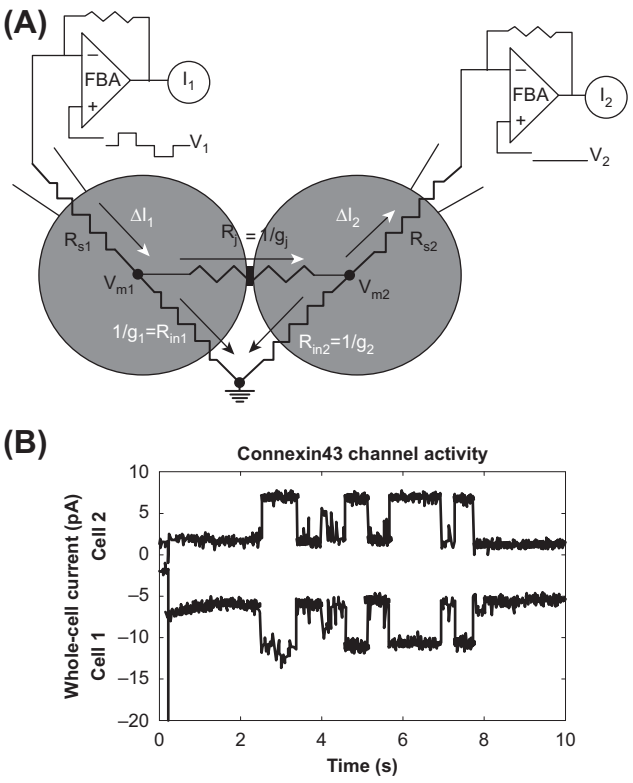

FIGURE 22.7 (A) Dual whole-cell recording configuration. Equivalent resistive circuit for the whole-cell patch-clamp recording configuration from two coupled cells. The voltage command potentials (V_1 and V_2) are applied via each negative feedback patch-clamp amplifier (FBA) through whole-cell patch electrodes. The difference between the command potentials and the cell membrane potentials (V_{m1} and V_{m2}) is minimized by reducing the series resistance (R_{s1} and R_{s2}) to less than 5% of the cell input resistance (R_{in1} and R_{in2}) and junctional resistance (R_j). Accurate junctional current signals are achieved when a majority of the applied current flows across the junction (white arrowheads) instead of the cell membrane (black arrowheads). This condition is readily obtained by using high input resistance cells (R_{in}>1 GΩ). Conductances (g) are the reciprocal of the corresponding resistance element. (B) The whole-cell currents for each amplifier (I_1 and I_2) appear as simultaneous signals of opposite sign. These are unaltered whole-cell currents obtained from a Cx43-transfected N2A cell pair digitized at 1 kHz after low-pass filtering at 100 Hz. The transjunctional voltage was −30 mV.

IX. EVIDENCE FOR CHARGE SELECTIVITY

The apparent permeability to a variety of water-soluble (hydrophilic) molecules (ions, cAMP, sugars, ATP, nucleosides, etc.) suggests the presence of a large-diameter aqueous pore with minimal selectivity based on electrical charge (equivalent valence at physiological pH). Several permeability studies on mammalian cell and invertebrate gap junctions were instrumental in assigning the commonly accepted molecular permeability limit of 1 kDa or diameter <14 Å. However, two of these same studies used tagged fluorescent tracers with different valences and demonstrated that the molecular permeability limit was lower for molecules with higher negativity. Selective permeability of molecules >600 Da and approximately 10 Å in diameter is not surprising since the size of the permeant molecule is approaching the estimated diameter of the pore. Placing any charged surfaces of the pore and the permeable molecule in close proximity to each other would enhance any electrostatic attractive or repulsive forces that might be present. This suggests that the pore of the gap junction channel contains fixed electronegative sites within the pore which reduce the permeability of large negatively charged molecules relative to their neutral or less negative counterparts.

Evidence for selectivity at the ionic level did not exist until the patch-clamp methodology was adapted to the recording of gap junction channel currents. In two cellular preparations, the junctional membranes of the earthworm septate axon and rat lacrimal gland cells were found to be less permeable to Cl^- relative to K^+ by ratios of 0.52 and 0.69, respectively. This modest selectivity among ions with nearly identical aqueous mobilities and diameters of less than 4 Å suggests that there are weak interactions between the permeant ion and the wall of the pore. In a simple diffusion-limited pore, ions interact with water molecules but not with other ions. Observations from four different homotypic connexin hemichannels or gap junction channels reported K^+ to Cl^- permeability ratios of approximately 10:1 with selectivity among monovalent cations in alignment with their relative aqueous mobility sequence. These observations suggest a common theme to the structure of the selectivity filter within the connexin channel pore. This proposed selectivity filter readily permits the passage of hydrated cations while restricting the simultaneous passage of similar aqueous anions by 10-fold. These observations provide direct evidence for cation−anion interactions within the gap junction pore that contradict aqueous diffusion theory. The observed permeability to atomic and large organic cations is consistent with a pore diameter of 10−14 Å for mammalian connexin channels.

The ability to transfer these electrical and chemical signals from cell to cell is important to tissue function. The most direct comparison of connexin-specific molecular permeability differences comes from the use of structurally similar molecules of varying size and valence. Two fluorescein derivatives with varying valences but essentially constant physical dimensions (=10 Å), 2′,7′-dichlorofluorescein (diCl-F) and 6-carboxyfluorescein (6-CF), were readily permeable through rat Cx43 channels. In contrast, both dyes were less permeable through chicken Cx43, human Cx37 and rat Cx40 gap junctions. Chicken Cx45 gap junctions were permeable to diCl-F, but not 6-CF. This indicates that the more anionic 6-CF is restricted in its junctional permeability relative to diCl-F in a connexin-specific manner. Since Cx43 has a lower channel conductance than Cx40 and Cx37, no correlation between the maximum conductance and molecular permeability of the connexin channels exists. This lack of correlation between charge selectivity and channel conductance suggests that pore size and conductance are not directly related. Alternatively, recent channel theory proposes that the pore with the smaller diameter and same electrostatic (fixed structural) charge will exhibit the higher channel conductance due to the increased charge density. This updated charged membrane theory can explain the conductance and selectivity properties of known ion channels, including gap junctions.

X. CHANNEL PROPERTIES OF DIFFERENT CONNEXINS

The functional expression of different connexins, either by mRNA injection into *Xenopus* oocytes or stable expression in communication-deficient cell lines derived from mammalian tumors, has yielded tantalizing results. Single-channel unitary conductance values (the ease with which current flows) are connexin-specific. Channel conductance values vary by 30-fold, from 10 to 300 picosiemens (pS = $1/10^{12}\,\Omega$), while observed ionic selectivities vary by approximately 10-fold. The reporting of channel conductance became more complicated due to the presence of multiple conductance states for several of the connexin channels. The ability of some connexins to form heterotypic (two connexons of different connexin composition) or heteromeric (two different connexins within the same connexon) gap junction channels adds another level of complexity to the function of channel conductance. The physiological relevance of these conductance differences is poorly understood, but several observations now indicate that connexin composition can modulate gap junction channel molecular permeability limits. For example, rat hepatocyte gap junctions contain almost exclusively Cx32 while mouse hepatocyte gap junctions are composed of a mixture of Cx26 and Cx32. Isolated mouse liver gap junctions exhibited a lower size limit to uncharged sugar molecules and cAMP than rat liver gap junctions, consistent with a smaller pore size, and they exhibited possible charge selectivity, contributed by Cx26 to otherwise Cx32-containing gap junctions. Connexin composition and mutations can affect gap junction selectivity in detrimental ways (e.g. disease-causing mutations), although the molecular basis for these permeability alterations remain to be determined.

The regulation of gap junction conductance by intracellular pH, intracellular calcium, protein kinases and transjunctional (cell-to-cell) voltage are also connexin-specific. The most significant differences in the amino acid sequences of the connexins occur within the cytoplasmic loop and carboxyl-terminal domains. These two cytoplasmic domains provide the basis for distinct conductance and regulatory properties upon the assembled multimeric connexin channels. Since a specific gene encodes for each connexin, tissue- and developmental-specific patterns of expression exist. Limited comparisons of the channel conductance and regulatory properties of the connexin channels to gap junctions in native cell types demonstrate the presence of at least two distinct connexin channel types. The presence of multiple connexin channels can explain the properties of the gap junctions found in many cell types. In one study, the expression of three embryonic chicken heart connexins, Cx42, Cx43 and Cx45, demonstrated that each connexin

exhibited unique conductance properties, which coincided with the observance of multiple conductance states in cultured cardiac myocytes. Furthermore, mixing these three connexins in different proportions modeled the response to transjunctional voltage during different stages of cardiac development. Thus, the observed decline in Cx45 expression could significantly explain the decrease in the transjunctional voltage sensitivity of junctional conductance in the developing chicken heart. Developmental and hormonal changes in connexin expression occur in other tissues, suggesting a possible role for this mechanism in the modulation of gap junction communication in a variety of tissues.

XI. GATING BY IONS AND SECOND MESSENGERS

Perhaps of greater physiological relevance than transjunctional voltage is the modulation of junctional communication by highly buffered intracellular cations (protons and calcium) and organic second messengers such as cAMP, diacylglycerol and inositoltrisphosphate. Whether cations directly bind to a regulatory site (or sites) on the connexin or act through intermediate accessory proteins is unknown. This issue remains an important topic for investigation since it has been observed that interventions that lower intracellular pH also increase intracellular free calcium. Conversely, there is direct evidence that several of the connexins are substrates for phosphorylation by protein kinases such as protein kinase A (PKA) and PKC. Protein kinase-dependent phosphorylation often increases or decreases junctional communication, depending on the connexins expressed in each tissue. Physiological correlates at the channel level are rare, owing to the difficulty of observing channel activity under distinct ionic or phosphorylation conditions. Transjunctional voltage (V_j) gating and Cx43 phosphorylation by PKC have both been shown to decrease the channel conductance and increase the ionic/molecular selectivity of gap junctions by inducing the formation of a subconductance state. Generally, cAMP increases junctional conductance and PKC has the opposite effect, at least in Cx43-containing cells. PKA and PKC may both phosphorylate the same serine residue (S233) of Cx32. In contrast, tyrosine phosphorylation by $pp60^{v\text{-}src}$ produces a rapid and reversible uncoupling of Cx43 gap junctions but has no effect on Cx32 gap junctions. Cx43 contains specific v-src SH2- and SH3-binding domains near a tyrosine phosphorylation site (Y265) by $pp60^{v-src}$ (Fig. 22.8A). Cx32 lacks these binding and tyrosine phosphorylation sites. There is increasing evidence that the diversity in the cytoplasmic loop and carboxyl-tail domains of different connexins confers different conductance and regulatory properties on the connexin-specific gap junctions in response to protein kinases and intracellular ions.

XII. REGULATION OF FUNCTIONS OF CONNEXIN-BASED GAP JUNCTIONS AT MULTIPLE LEVELS

As suggested above, a likely reason for differences in the sequence of the carboxyl tail of connexins may be in the regulation of gap junction-mediated tissue-specific or cell-specific biological activities. Indeed, gap junction regulatory mechanisms described so far appear to fall into one of two general categories. On the one hand, rapid changes in cell coupling that occur within seconds or minutes may reflect regulation of gating of pre-existing pores. On the other hand, long-term changes which occur within minutes or a few hours to days are likely to involve the modulation of synthesis, assembly or degradation of connexins (see Fig. 22.8B). Existence of this latter scheme of modulation is supported by studies that show that the half-lives of several different connexins are relatively short, ranging from 1 to 3 hours, and by more recent direct videomicrography of living cells expressing green fluorescent protein tagged connexins. In these latter studies, connexins have been observed as they concentrate within the developing Golgi; as they move to the surface to form plaques in regions of cell—cell contact; and as large fragments of the connexin-positive plaques are internalized as apparent vesicles (see Figs. 22.3H, I and 22.8B). Moreover, a variety of studies supports the idea that gap junctions may be regulated at virtually any stage of their formation, maturation and degradation.

For example, the possible effect of cAMP on transcription of connexin mRNA and its ultimate translation is supported by studies which show that cAMP-mediated increases in coupling or in junction formation in some cells can be blocked by inhibitors of mRNA or protein synthesis. The potential for control at the level of transcription of connexins is also implied by the characterization of their 5′ flanking sequences. For example, the 5′ flanking sequence of the myometrial Cx43 gene has been shown to possess several consensus activator protein-1 (AP-1) binding sites as well as half-palindromic estrogen response elements. Since the AP-1 proteins, Fos and Jun, are expressed in response to increased estrogen, transcription of Cx43 may be indirectly upregulated through its AP-1, *cis*-acting elements. In vascular smooth muscle, the transcription of Cx43 may be upregulated by mechanical load induced by stretch, presumably via an upregulation of *c-fos,* which may act in turn on AP-1 binding sites or upon other sites in the 5′ flanking region of the Cx43 gene. Promoter analysis of other connexin genes has shown that their transcription may also be regulated by

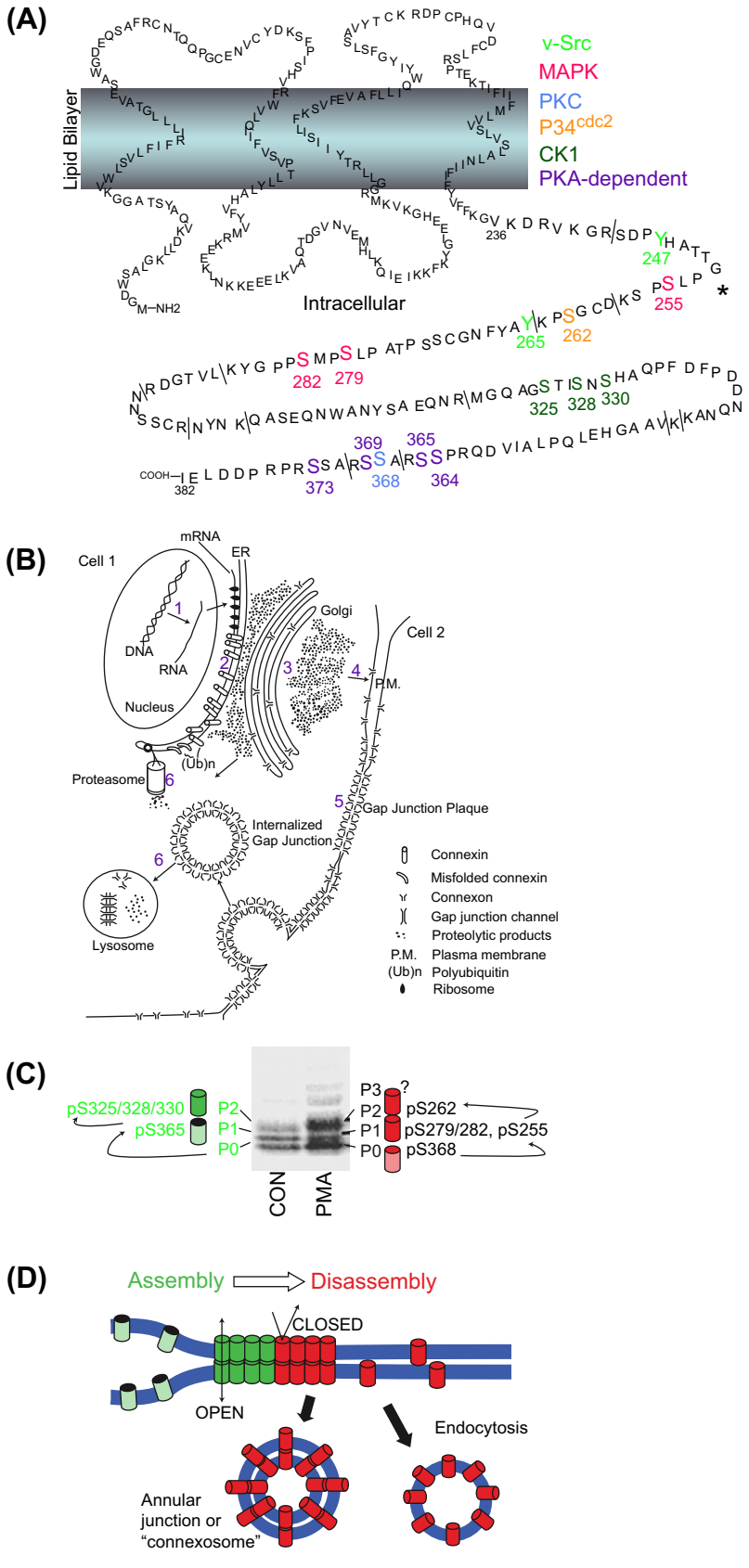

FIGURE 22.8 (A) Graphical illustration of the known protein kinase phosphorylation sites on the carboxyl domain of Cx43 (purple: PKA; blue: PKC; green: CK1; red: MAPK; orange: $p34^{cdc2}$; lime green: v-src, brackets: trypsin cleavage sites). *(Reprinted from Solan, J.L., and Lampe, P.D. (2005). Connexin phosphorylation as a regulatory event linked to gap junction channel assembly. Biochim Biophys Acta, 1711, 155 with permission. Copyright 2005 Elsevier Press.)* (B) Illustration of the life cycle of the connexins beginning with mRNA transcription (*1*), translation and protein folding (*2*), oligomerization and intracellular transport (*3*), hemichannel insertion into the plasmalemma (*4*), hemichannel docking and gap junction formation (*5*), and degradation by the proteasome and lysosome (*6*). *(Reprinted from Beyer, E.C. and Berthoud, V.M. (2009). The family of connexin genes. In Connexins: a Guide, p. 17, with permission. Copyright 2009 Humana Press.)* (C and D) Association of Cx43 phosphorylation-dependent bands on an SDS/PAGE gel with the PO, PI, P2, or P3 isoforms correlated with the protein kinase phosphorylation sites implicated in the assembly (green) or disassembly (red) of gap junctions. Assembled gap junctions are internalized as a double membrane bounded "connexosome" while unassembled hemichannels appear in endocytotic vesicles. *(Reprinted from Solan, J.L. and Lampe, P.D. (2007) Connexin43 phosphorylation: structural changes and biological effects. Biochem. J., 419, 262, with permission. Copyright 2007 Biochemical Society.)*

transcription factor binding sites. For example, two GC boxes, two GT boxes, a TTAAAA box, a YY1-like binding site and a mammary gland factor binding site have been identified in the proximal promoter region of the human Cx26 gene. Likewise AP-1, AP-2, SP-1, TRE and p53 transcription factor binding sites have been identified in the 5′ flanking sequence of the mouse Cx40 gene, while Cx-B2 and P1 and P2 promoters are implicated in the transcriptional regulation of Cx32.

Yet another level of control of gap junction function is revealed by studies that show the upregulation of coupling or gap junction formation in the absence of transcription or translation, perhaps at a post-translational level of control. The direct application of dibutyryl cAMP (dbcAMP) to mammary tumor cells in culture, for example, increases the number of gap junctions as well as cell−cell coupling in the absence of an increase in Cx43 mRNA or protein. Likewise, connexin 43 trafficking within several cultured cell lines appears to be regulated by post-translational mechanisms. Specifically, the trafficking of Cx43 from the cytoplasm to the plasma membrane and its assembly into functional gap junction aggregates may require phosphorylation of two serine phosphorylation consensus sites in the carboxyl tail of this connexin (see Fig. 22.8C, D). For example, two cell lines were studied that could not form gap junctions or become coupled, but were able to synthesize significant amounts of Cx43, which was stored within vesicles in the cytoplasm. The Cx43 in these cells was phosphorylated at only one of its serine residues. When one of these lines was transfected with a gene for a cell adhesion molecule, L-CAM, the Cx43 in the transfected line was phosphorylated again, translocated to the plasma membrane and assembled into gap junctions. Further evidence for the phosphorylation-dependent trafficking and assembly of Cx43 in cardiomyocytes has been obtained in experiments with monensin, a reagent that inhibits translocation of proteins between Golgi cisternae. These studies suggest that phosphorylation of Cx43 to the mature form occurs in a compartment of the cell between the Golgi apparatus and the plasma membrane. Similar results are obtained in studies of effects of brefeldin A, which blocks both Cx43 phosphorylation and trafficking to the plasma membrane in a mammary tumor cell line. Finally, it has also been suggested that the process of connexon clustering that gives rise to functional gap junction plaques may be facilitated by the action of microfilaments. Thus, the increase in Cx43-positive gap junctions and coupling in the absence of Cx43 mRNA synthesis following treatment of cultured prostatic cells with forskolin may be explained by effects of cAMP on post-translational processing of Cx43, namely their assembly into functional plaques and their translocation from the cytoplasm to the membrane.

Numbers of functional gap junctions within the plasma membrane may also be affected by regulation of their removal and degradation. For example, the treatment of some cells with phorbol esters such as 12-*o*-tetradecanoylphorbol-13-acetate (TPA) may stimulate the removal and degradation of gap junctions through phosphorylation of connexins by protein kinase C. Similarly, it is thought that the phosphorylation of mitogen-activated protein (MAP) kinase serine phosphorylation sequences in cultured rat liver cells treated with epidermal growth factor, may mediate the loss of functional gap junctions from the cell membrane. In another example, it has been shown that massive endocytosis of gap junctions in granulosa cells of the ovary is stimulated by high titers of follicle stimulating hormone; that endocytosis is facilitated by clathrin and microfilaments; and that the internalized gap junction vesicles fuse with lysosomes prior to degradation (see Fig. 22.8B). Alternatively, it has been suggested that gap junction plaques and their connexins may be disposed of via a ubiquitin-mediated proteasomal proteolytic pathway. This mechanism is supported by studies showing that connexins accumulate in cells treated with proteasomal inhibitors and by immunogold studies that demonstrate the association of ubiquitin with gap junction plaques (Fig. 22.9).

In summary, it appears that the amount of functional gap junction membrane at the cell surface may be controlled at virtually any point in the gap junction's life history; namely through regulation of (1) transcription of connexin mRNA,

FIGURE 22.9 Image of gap junction in cultured HeLa cell transfected with Cx40 and Cx43. The replica was immunostained with antibodies to Cx40, Cx43, and ubiquitin. The 6-nm gold particles indicate Cx40, the 10-nm gold particles stain for Cx43, and the 15-nm gold particles indicate epitopes for ubiquitin.

(2) translation of connexin protein, and then through post-translational modifications, which affect the (3) assembly of functional plaques, (4) gating of junctional channels, (5) channel conductance and (6) degradation of functional gap junctions.

XIII. SPECIFIC BIOLOGICAL FUNCTIONS OF GAP JUNCTIONS

Early speculations regarding the general functional significance of gap junctions, such as the electrical coupling of some neurons and the buffering of metabolites within a tissue mass, have not been seriously challenged for the past three decades (see Sections I, II and IX). Several recent studies, however, have begun to establish even more specific functional relationships between gap junctions and tissue activities and behaviors, most notably with respect to the regulation of smooth muscle contraction and ligand-mediated secretory activity.

Perhaps one of the best-studied cases is that of the myometrial connexin, Cx43. It is known, for example, that the myometrium of the non-pregnant uterus in a variety of species is virtually devoid of gap junctions and expresses very little, if any myometrial Cx43 mRNA or protein. In contrast, however, Cx43 mRNA is rapidly synthesized and translated and then gap junctions appear coincident with rising estrogen and declining progesterone titers just prior to parturition. Experimental manipulations of these hormones also predictably induce or inhibit the appearance of gap junctions in experimental models of preterm labor or tocolysis respectively (effective labor coincides with their induction while myometrial quiescence parallels their inhibition). For example, removal of the ovaries or the injection of RU-486 during the latter part of pregnancy effectively increases the estrogen:progesterone ratio, the expression of Cx43 mRNA and protein, the assembly of myometrial gap junctions and concomitant preterm labor. Conversely, the injection of progesterone several days prior to term inhibits the formation of gap junctions and onset of labor. Thus, it is likely that transcription and translation of Cx43 are required for gap junction formation and coordinated myometrial contractions in humans. Moreover, the evidence for the presence of AP-1 binding sites in 5′ flanking sequences of the myometrial Cx43 gene and the estrogen-mediated expression of Jun and Fos described above (see Section XII) is consistent with this notion. The function of myometrial gap junctions and contractility may also be regulated at the level of post-translational processing. For example, high levels of myometrial Cx43 appear a full day prior to delivery in rats (Fig. 22.10) but most of the Cx43 in these cells is located within perinuclear vesicles which also stain with an antibody against a Golgi-associated protein (Fig. 22.10B). Six to 12 hours prior to onset of delivery, however, Cx43 immunopositive plaques are observed in the plasma membrane (Fig. 22.10C). Conversely, cessation of delivery is accompanied by the loss of gap junctions from the cell surface by a process of endocytosis (Fig. 22.10E).

Gap junctions have also been implicated in the process of secretion and other ligand-mediated functions in many different kinds of cells. For example, gap junctions are well developed in differentiated endocrine and exocrine cells and are typically sparse or absent in proliferating stem cells. Moreover, the induction of secretory activity itself appears to be correlated with increased numbers of gap junctions in luteal cells, adrenal cortical cells, pancreatic exocrine cells, mammary alveolar cells and thyroid cells. Studies of osteoblasts have demonstrated a close correlation between the effects of hormones on the generation of a second messenger, formation of gap junctions and cell function. In addition, gap junctions appear to be more abundant in cultured confluent osteoblasts than proliferating cells and osteoblast cell coupling in culture and cAMP production are enhanced by the application of parathyroid hormone (PTH). Conversely, an analog of PTH which binds to PTH receptors but attenuates cAMP accumulation, results in a decrease in cell coupling. Finally, transfection of osteoblasts with antisense Cx43 mRNA results in significant concomitant reductions in coupling and in cAMP synthesis in response to PTH.

It has been suggested that the development of gap junctions may enhance the sensitivity of hormonally responsive cells to their specific ligand as a consequence of the transfer of cAMP through gap junctions. Thus, cells not receiving direct stimulation by binding of the secretogogue to its receptor may also respond to the ligand-mediated production of cAMP in neighboring cells which possess the appropriate receptor. Such a hypothesis has been invoked to explain the maintenance of meiotic arrest of mammalian primary oocytes. These germ cells initiate the first meiotic division during embryonic life but are then almost immediately arrested at the first meiotic prophase stage. Typically, a primary oocyte does not resume meiotic maturation until it responds to an ovulatory surge of gonadotropic hormones following puberty. However, since meiosis spontaneously resumes when the oocyte is removed from the follicle and cultured in medium-lacking hormones, it has been postulated that the follicular environment is inhibitory to resumption of meiotic maturation. Meiotic arrest may be maintained by follicle cell-generated cAMP which enters the oocyte through a well-developed network of gap junctions. Conversely, it has been suggested that meiotic resumption may be signaled by the LH-mediated disruption of the gap junction pathway within the cumulus mass (following an ovulatory surge of gonadotropins), thus preventing cAMP manufactured within the follicle cells

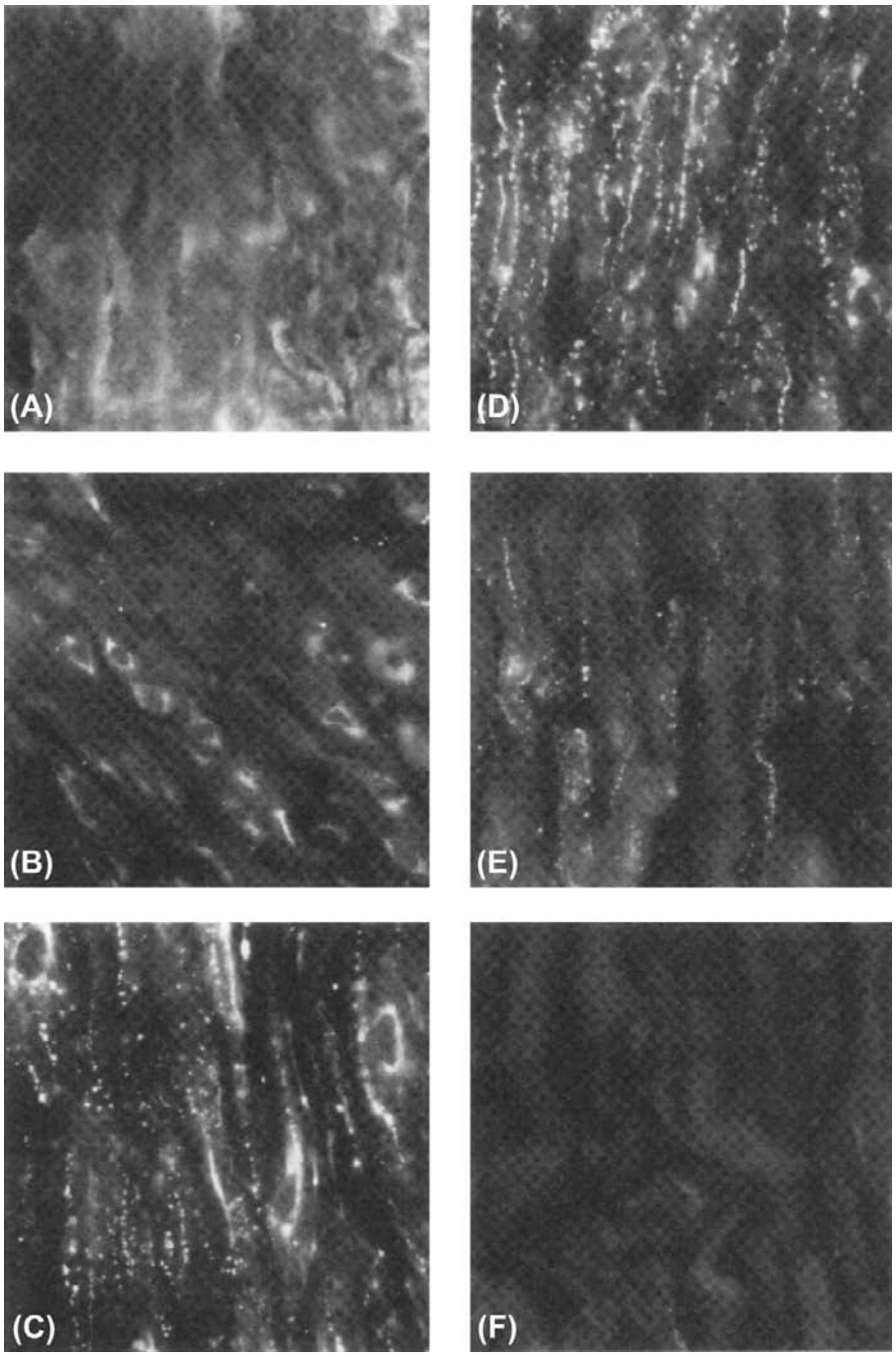

FIGURE 22.10 Immunofluorescent staining of myometrium sections incubated with site-specific antibodies to the carboxyl terminus of Cx43 from pregnant rat sacrificed on day 19 (A) or day 21 (B), at midnight on day 21 (C), during delivery on day 22 (D), 6 h after delivery (E) or 24 h after delivery (F). Magnification, 500×. *(From Hendrix, E.M., Mao, S.J.T., Everson, W. and Larsen, W.J. (1992). Myometrical connexin 43 trafficking and gap junction assembly at term and in preterm labor. Mol. Reprod. Dev., 33, 27, with permission. Copyright 1992 Wiley-Liss, a division of John Wiley & Sons, Inc.)*

from entering the oocyte. Other hypotheses of both negative and positive regulation of meiotic resumption have also been proposed.

It has recently been proposed that gap junction connexins (specifically Cx43) may function in a role somewhat different than those described above; namely in protein trafficking. It has been shown, for example, that the second PDZ domain (of three) of the tight junction-associated protein ZO-1 binds to the extreme C-terminal end of the Cx43 molecule typically resulting in cell membrane colocalization of Cx43 and ZO-1 in cells that co-express these proteins. In support of the possibility that Cx43 is required for shuttling of ZO-1 to the cell membrane, it was found that both ZO-1 and Cx43 fail to accumulate at the cell membrane in Cx43 knockout astrocytes.

XIV. GAP JUNCTIONS IN HUMAN DISEASE AND IN MURINE MODELS OF HUMAN DISEASE

The first hypothesis for a direct link between connexin gap junction function and a human disease was formulated in the 1970s based on the positive correlation between the loss of gap junction function and uncontrolled cell growth as exhibited in carcinogenesis. Over the last two decades, hereditary links to central and peripheral neuropathies, deafness, skin disorders, cataracts, cardiac arrhythmias and multisyndromic craniofacial dysplasias have been identified for 10 different connexins to date. Essentially, all of the known connexin mutations are loss-of-function mutations, either by rendering the resultant gap junction communication-deficient or by preventing the assembly of gap junctions due to connexin misfolding and/or trafficking defects. The precise molecular mechanisms by which a particular connexin mutation produces a communication or trafficking defect are not fully understood but may include alterations in channel permeability, regulatory gating or critical structural components key to correct protein assembly/trafficking and function. A graphical summary of many known connexin-linked human diseases is provided in Fig. 22.11. It should be noted that genetic mutations in *tight junction* and *desmosome* intercellular junction protein constituents are also known to occur.

XIVA. Carcinogenesis

Studies that compared the presence or absence of coupling or gap junctions in normal cells and in several tumors and cancer cell lines initially supported this hypothesis. For example, coupling or gap junctions were found to be deficient in certain hepatoma cells and in L-cell derivatives such as the clone-1D cell line in contrast to their normal counterparts. Indeed, more recent studies support these early observations. For example, an extensive study has examined the role of gap junctions in tumor progression in rat liver following initiation by diethylnitrosamine (DEN) and promotion by either phenobarbitol (PB) or 2,3-dichloro-7,8-dibenzo-*p*-dioxin (TCDD). Transcripts and protein levels of Cx26, Cx32 and Cx43 were measured and reductions in Cx26- and Cx32-positive gap junctions were observed in all resulting neoplasms. However, it was also demonstrated that these decreases were not always associated with reductions in specific m-RNA transcripts for these connexins, suggesting that the loss of junctions could result from the modulation of transcription or translation or from post-translational modification affecting assembly or degradation (see Section XII). Consistent with these observations, the transfection of HeLa cells with cDNA encoding Cx26, but not Cx40 or Cx43, results in inhibition of tumor formation in nude mice, suggesting that Cx26 gap junctions play a pivotal role in growth control. Similarly, the transfection of communication-deficient hepatoma cells (SKHep1) with cDNA encoding Cx32 results in slowing of the growth rate of tumors in nude mice, compared with tumors arising from communication-deficient parental SKHep1 cells.

In conflict with these findings, however, other highly malignant tumor cells have been shown to be well coupled or to possess large numbers of gap junctions. These include Novikoff hepatoma cells, human SW-13 adrenal cortical carcinoma cells and murine B16 melanoma cells.

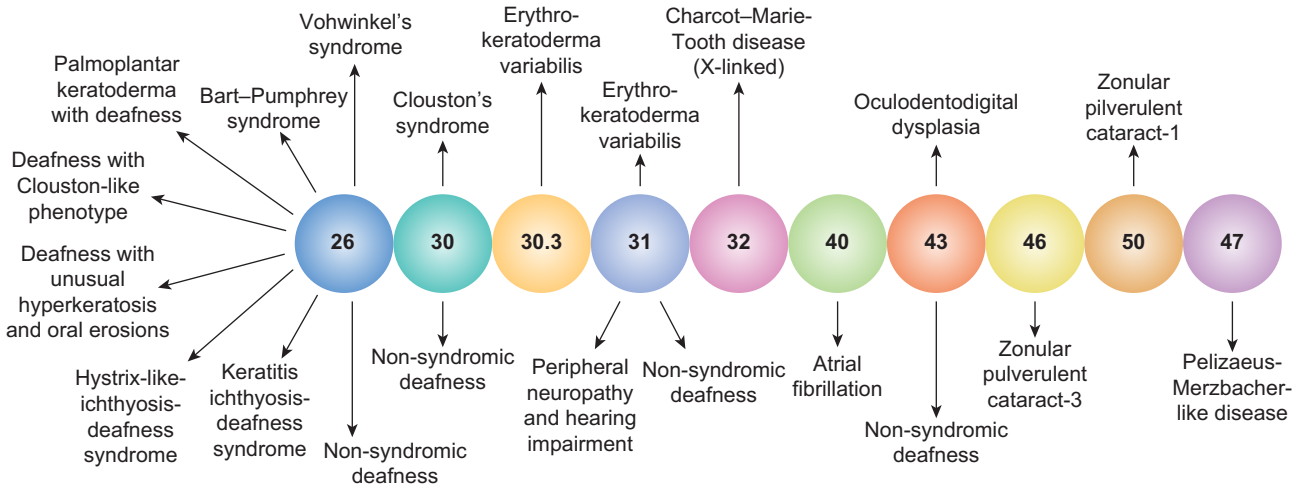

FIGURE 22.11 An illustration of the relationship between inherited connexin mutations and human disease phenotypes. The majority of inherited connexin disorders are autosomal dominant and all involve a loss-of-function due to improper protein folding and trafficking or deficits in gap junction communication. *(Adapted from Lai-Chong, J.E., Arita, K. and McGrath, J.A. (2007). Genetic diseases of junctions. J. Invest. Dermatol., 127, 2715, with permission. Copyright 2007 The Society for Investigative Dermatology.)*

Moreover, other studies have analyzed gap junctions during tumor progression in skin tumors and in hepatocarcinoma and have found that, while gap junctions or coupling may disappear during the transformation of normal cells by cancer-causing agents (such as tumor promoters), their loss seems to follow, rather than lead the changes which transform these normal cells to tumor cells. In response to results such as these, a modified *defective communication* hypothesis was proposed to include cancer cells which might not necessarily exhibit an absence of, or obvious structural defect in the gap junction itself, but which might be defective with respect to some other part of the gap junction communication mechanism, for example, lack of ability of the cell to synthesize the postulated regulatory message or defects in the receptor which translates the cell's activity. Other modifications of the hypothesis have also been advanced, proposing, for example, that some cancer cells (e.g. cultured human SW13 cells and diethylstilbestrol-induced tumors of the proximal tubule in the Syrian hamster) are not able to maintain a steady-state gap junction level through a regulated balance of synthesis or degradation of gap junctions. Under some circumstances, these cells possess normal or even excessive gap junction complements and are mitotically quiescent while, under other conditions, the cells lose most or all of their junctions, resulting in cancerous growth. A temporal relationship between gap junction formation and degradation and the rate of proliferation is also exhibited by normal liver cells in partially hepatectomized rats. Normal rat liver cells remaining after partial hepatectomy initially lose their gap junctions and proliferate rapidly. By 40 hours after partial hepatectomy, the liver cells regain their gap junctions coincident with a reduction in the rate of DNA synthesis and cell division.

Another variation of the hypothesis is based upon a series of experiments that demonstrate that normal cells may have the ability to suppress tumor cell behavior in some normal tumor cell co-cultures as long as the tumor cells can also form gap junctions with the co-cultured normal cells. Other tumor cells may not be able to form gap junctions with normal cells but may be able to form gap junctions between themselves. In these tumor cells, contact with normal cells does not suppress the transformed phenotype of the tumor cell. However, the ability of certain tumor cells to make gap junctions with one another may result in more efficient killing by antitumor agents by allowing the cell-to-cell movement of lethal metabolites formed in some, but not all of the tumor cells within the interconnected network. This phenomenon is called *the bystander effect*. Apoptotic signals may also be propagated by the bystander effect.

In conclusion, despite decades of research, a direct causal link between cancerous growth and deficiencies in gap junction intercellular communication remains elusive. In numerous instances, there is a positive correlation between the development or progression of cancerous tumors and the loss of gap junction communication, but this is not always the case. It is also unlikely that mechanisms of gap junction-mediated growth control will be identical in all cells or tumors where the activity of gap junctions can be demonstrated to play a pivotal role due to the differential expression of connexins.

XIVB. Demyelinating Neuropathies of Cx32 and Cx47 Mutations

Spontaneous mutations of Cx32 result in a common peripheral neuropathy in humans, Charcot-Marie-Tooth disease, which affects one of every 2500 individuals. While this demyelinating disease may arise as a consequence of mutations of a peripheral myelin protein PMP22 (on chromosome 17) or of the myelin constituent Po (on chromosome 1), numerous families have been identified with an X-linked dominant form of the disease characterized by as many as 150 different mutations of Cx32 (CMTX). Mutations may involve single-base substitutions, formation of a premature stop codon, frame-shift or elimination of an amino acid residue. They may occur in amino or carboxyl termini, cytoplasmic or extracellular loops, or in transmembrane regions of the connexin. The causal relationship between these diverse mutations of Cx32 and demyelination of peripheral nerves is obviously varied since the mutations are quite diverse and may or may not affect channel properties. In some cases, it seems possible that mutations may directly affect the function of Cx32 gap junctions in peripheral myelin by interfering with their possible function as ATP-sensitive hemichannels, their function in the exchange of nutrients between the perinuclear region of the Schwann cell and the Schmidt–Lantermann incisures and paranodal processes at the node of Ranvier, or their possible function in signaling between internodes. In other cases, it is thought that the mutations may indirectly affect Cx32 function through effects on Cx32 synthesis and trafficking within the cell. Targeted knockout of connexin 32 in mice also results in changes in liver enzyme activities and in glucose mobilization but, most interestingly, these Cx32-deficient mice have an increased susceptibility to hepatocarcinogenesis. Otherwise, they are vital and fertile. There are >300 *GJB1* mutations thus far identified. A list of these CMTX mutations can be found at http://www.molgen.ua.ac.be/CMTMutations/Mutations/MutByGene.cfm. Oligodendrocytes in the central nervous system also develop a demyelinating neuropathy, Pelizaeus–Merzbacher–like disease (PLMD1) owing to mutations in Cx47 (*GJC2,* formerly *GJA12*). For additional information go to http://www.ncbi.nlm.nih.gov/omim/608804.

XIVC. Cataract Formation and Mutations of Cx50 and Cx46

The maintenance of junctional communication between lens fiber cells is necessary for the homeostatic maintenance of normal transparency of the lens since it is an avascular tissue and the cells are devoid of intracellular organelles. Targeted knockout in mice or mutations in Cx50 lead to development of zonular pulverulent cataracts of the lens but also results in microphthalmia. These results thus implicate Cx50 not only in the maintenance of lens transparency but also in the growth of the eye. Cx46 null mice or mutations in Cx46 produce a more severe form of autosomal dominant zonular pulverulent cataracts, but not microphthalmia. Substituting Cx46 for Cx50 prevents the cataract phenotype but does not rescue the microphthalmia, indicative of differential roles for the two lens connexins in the maintenance of lens homeostasis and crystalline solubility, but not developmental growth control. Additional information can be found at http://www.ncbi.nlm.nih.gov/omim/116200 or /601885.

XIVD. Deafness and Mutations of Cx26, Cx30, Cx31 and Cx43

A variety of mutations of Cx26 including missense mutations and mutations resulting in frameshifts and formation of premature stop codons have been linked to both autosomal recessive and autosomal dominant hearing loss in humans. It is known that deletion of the Cx26 gene leads to the progressive degeneration of the outer hair cells, supporting cells in the outer and middle organ of Corti and spiral ganglion neurons, presumably by disruption of the gap-mediated ion and endolymph circulation in the cochlea. Greater than 100 total *GJB2* mutations have now been identified to cause syndromic (dominant) or non-syndromic (recessive) deafness. Anywhere from two to five non-sydromic deafness mutations have also been identified in the *GJA1* (Cx43), *GJB3* (Cx31) and *GJB6* (Cx30) genes. A database of connexin-linked inherited deafness mutations can be found at http://davinci.crg.es/deafness/index.php?seccion=mut_db&db=synd&synd=cx26synd, or _db&db=nonsynd&nonsynd=cx26mut, …=cx31mut, …=cx30mut, and …=cx43mut. Germline knockout of Cx26 resulted in embryonic lethality as a consequence of placental dysfunction but conditional Cx26 (cCx26) knockout and Cx30 null mice are viable and recapitulate the deafness phenotype.

XIVE. Skin Disorders

Several of the Cx26 mutations associated with syndromic deafness also cause ectodermal skin disorders such as palmoplantar keratoderma, hyperkeratosis, ectodermal dysplasia keratitis-ichthyosis and mutilating keratoderma (Vohwinkel's syndrome). Deafness and non-deafness mutations in Cx31 are known to produce erythrokeratoderma variabilis. Cx30.3 (*GJB4*) also cause erythrokeratoderma variabilis and non-deafness mutations in Cx30 produce autosomal dominant hidrotic ectodermal dysplasia (Clouston syndrome).

XIVF. Oculodentodigital dysplasia (ODDD)

Within the last decade, a multisymptom human disorder including bilateral microphthalmia, microcornea, glaucoma, hypertelorism, narrow nose, microdontia, syndactyly of the fourth and fifth fingers and various neurological and cardiac anomalies were linked to mutations in Cx43. Sixty-two *GJA1* mutations are already known and the vast majority are autosomal dominant but exhibit phenotypic variability for unknown reasons (see http://www.ncbi.nlm.nih.gov/omim/164200). Some mutations result in Cx43 trafficking defects while others form non-communicating or communication-deficient gap junctions, the common theme being a loss-of-function. Already, three murine models of Cx43 ODDD mutations (G60S, I130T, G138R) have been demonstrated to exhibit an increased susceptibility to cardiac arrhythmias, whereas clinically cardiac abnormalities are observed in only 3% of human ODDD patients, 10-fold less than the observed rate for neurological disorders and >20 times less frequent than the observed syndactyly. Perhaps the low incidence of cardiac abnormalities observed with Cx43 mutations is that severe defects likely result in embryonic or neonatal lethality.

XIVG. Heart Function and Mutations of Cx43 and Cx40

While few specific heart defects related to mutations of Cx43 have been observed in humans, a series of studies with animal models of ischemia support a role for Cx43 gap junctions in recovery from injuries to the myocardium. For example, the number of gap junction plaques within the intercalated disk has been shown to decrease in the region of the border of the healing infarct. In addition, the spatial distribution of gap junctions is also abnormal in these areas. These observations, along with studies that show the critical role of Cx43 in conduction (particularly in the ventricle), have led to suggestions that alterations in Cx43 levels and distributions may play an important role in development of infarct-mediated arrhythmias. Targeted knockouts of Cx43 and mice overexpressing Cx43 are characterized by abnormal development of the pulmonary (right ventricular) outflow tract resulting in their death immediately following birth. Enlargement of the right ventricle with thinning of the wall, attenuation of the ductus

arteriosus and formation of one or two abnormal pouches at the base of the pulmonary outflow tract were also observed. It has been suggested that these defects of conotruncal development may result from disruption of the cardiac neural crest. In addition, Cx43 knockout mice of both sexes have small gonads, resulting in part from deficiencies in germ cell development. Since these mice die shortly after birth, the gonads were cultured to determine their capacity for folliculogenesis. It was found that follicles in these ovaries develop only to the primary follicle stage. Targeted knockout of Cx40 results in defects consistent with its localization in the AV node and in conductive myocardium. Electrocardiography of Cx40 knockout animals was characterized by reduced conduction velocities and abnormalities characteristic of first-degree atrioventricular block with associated bundle branch block.

At least half a dozen mutations in Cx40 have been identified in human patients suffering from chronic atrial fibrillation (AF) in recent years and Cx40 polymorphisms have been linked to atrial standstill as well as AF. Conditional Cx43 knockout and Cx43 ODDD mutation mouse models have further revealed that heterogeneous loss of Cx43 from the myocardium increases the susceptibility to atrial or ventricular arrhythmias to a greater extent than uniform reductions in Cx43 expression. Many of these Cx40 or Cx43 mutations again result in a loss-of-function, although the underlying precise molecular mechanisms are poorly understood. Chronic AF and myocardial ischemia or infarction cause cardiac remodeling of gap junctions that sustain AF or increase susceptibility to ventricular arrhythmias due to increased heterogeneity and reductions in the safety margin for conduction disturbances especially during rapid stimulation rates. Our understanding of acute and chronic changes in cardiac gap junction distribution and function will likely evolve through further investigations of Cx40/Cx43 mutations and the molecular mechanisms involved in their redistribution and function.

XIVH. Fertility and Targeted Knockout of Cx37

While no human syndrome resulting from mutations of Cx37 (the human ortholog of *Xenopus* oocyte Cx38 [*GJA2*]) is known, the targeted knockout of Cx37 in mice has been shown to result in the disruption of folliculogenesis. Follicles develop only to early antral stages, the oocytes fail to acquire meiotic competence and ovulation does not occur. Cx43 is essential to (antral) follicular maturation.

IN MEMORIAM

This chapter is dedicated to the memory of William J. Larsen who previously co-authored this chapter before losing his life to cancer soon after publication of the 3rd edition in 2001.

BIBLIOGRAPHY

Alcolea, S., Theveniau-Ruissy, M., Jarry-Gnichard, T., et al. (1999). Downregulation of connexin 45 gene products during mouse heart development. *Circ Res, 84*, 1365−1379.

Bai, S., Schoenfeld, A., Pietrangelo, A., & Burk, R. D. (1995). Basal promoter of the rat connexin 32 gene: identification and characterization of an essential element and its DNA-binding protein. *Mol Cell Biol, 15*, 1439−1445.

Barr, L., Dewey, M. M., & Berger, W. (1965). Propagation of action potentials and the structure of the nexus in cardiac muscle. *J Gen Physiol, 48*, 797−823.

Bevans, C. G., Kordel, M., Rhee, S. K., & Harris, A. L. (1998). Isoform composition of connexin channels determines selectivity among second messengers and uncharged molecules. *J Biol Chem, 272*, 2808−2816.

Beyer, E. C., & Berthoud, V. M. (2009). The family of connexin genes. In *Connexins: A Guide* (pp. 3−26). New York: Humana Press.

Beyer, E. C., Paul, D. L., & Goodenough, D. L. (1990). Connexin family of gap junction proteins. *J Membr Biol, 116*, 187−194.

Brink, P. R., & Dewey, M. M. (1980). Evidence for fixed charge in the nexus. *Nature, 285*, 101−102.

Brink, P. R., & Fan, S.-F. (1989). Patch clamp recordings from membranes which contain gap junction channels. *Biophys J, 56*, 579−593.

Budunova, I. V., Carbajal, S., Viaje, A., & Slaga, T. J. (1996). Connexin expression in epidermal cell lines from SENCAR mouse skin tumors. *Mol Carcinog, 15*, 190−201.

Bukauskas, F. F., Bukauskiene, A., & Verselis, V. K. (2002). Conductance and permeability of the residual state of connexin43 gap junction channels. *J Gen Physiol, 119*, 171−185.

Chiba, H., Sawada, N., Oyamada, M., et al. (1993). Relationship between the expression of the gap junction protein and osteoblast phenotype in a human osteoblastic cell line during cell proliferation. *Cell Struct Func, 19*, 419−426.

Coppen, S. R., Kodama, I., Boyett, M. R., et al. (1999). Connexin45, a major connexin of the rabbit sinoatrial node, is co-expressed with connexin43 in a restricted zone at the nodal-crista terminalis border. *J Histochem Cytochem, 47*, 907−918.

Cowan, D. B., Lye, S. J., & Langille, B. L. (1998). Regulation of vascular connexin43 gene expression by mechanical loads. *Circ Res, 82*, 786−793.

Dahl, G., & Locovei, S. (2006). Pannexin: to gap or not to gap, is that a question? *IUBMB Life, 58*, 409−419.

Darrow, B. J., Laing, J. G., Lampe, P. D., Saffitz, J. E., & Beyer, E. C. (1995). Expression of multiple connexins in cultured neonatal rat ventricular myocytes. *Circ Res, 76*, 381−387.

Donahue, H. J., McLeod, K. J., Rubin, C. T., et al. (1995). Cell-to-cell communication in osteoblastic networks: cell line-dependent hormonal regulation of gap junction function. *J Bone Min Res, 10*, 881−889.

Ek-Vitorin, J. F., King, T. J., Heyman, N. S., Lampe, P. D., & Burt, J. M. (2006). Selectivity of connexin43 gap junction channels is regulated through protein kinase C-dependent phosphorylation. *Circ Res, 98*, 1498−1505.

Ewart, J. L., Cohen, M. F., Meyer, R. A., et al. (1997). Heart and neural tube defects in transgensis mice overexpressing the Cx43 gap junction gene. *Development, 124*, 1281−1292.

Filson, A. J., Azarnia, R., Beyer, E. C., Loewenstein, W. R., & Brugge, J. A. (1990). Tyrosine phosphorylation of a gap junction protein correlated with inhibition of cell-to-cell communication. *Cell Growth Diff, 1*, 661−668.

Flagg-Newton, J., Simpson, I., & Loewenstein, W. R. (1979). Permeability of the cell-to-cell membrane channels in mammalian cell junction. *Science, 205*, 404–407.

Forge, A., Becker, D., Casalotti, S., et al. (1999). Gap junctions and connexin expression in the inner ear. *Novartis Found Symp, 219*, 134–150.

Furshpan, E. J., & Potter, D. D. (1959). Transmission at the giant motor synapses of the crayfish. *J Physiol, 145*, 289–325.

Furshpan, E. J., & Potter, D. D. (1968). Low-resistance junctions between cells in embryos and tissue culture. *Curr Top Dev Biol, 3*, 95–127.

Gerido, D. A., & White, T. W. (2004). Connexin disorders of the ear skin, and lens. *Biochim Biophys Acta, 1662*, 159–170.

Giepmans, B. N., & Moolenaar, W. H. (1998). The gap junction protein connexin43 interacts with the second PDZ domain of the zona occludens-1 protein. *Curr Biol, 8*, 931–934.

Goldberg, G. S., Martyn, K. D., & Lau, A. F. (1994). A connexin 43 antisense vector reduces the ability of normal cells to inhibit the foci formation of transformed cells. *Mol Cytogen, 11*, 106–114.

Gollob, D. A., Jones, D. L., Krahn, A. D., et al. (2006). Somatic mutations in the connexin 40 gene (GJA5). *N Engl J Med, 354*, 2677–2688.

Goodenough, D. A., Simon, A. M., & Paul, D. L. (1999). Gap junctional intercellular communication in the mouse ovarian follicle. *Novartis Found Symp, 219*, 226–235.

Gutstein, D. E., Morley, G. E., Vaidya, D., et al. (2001). Heterogeneous expression of gap junction channels in the heart leads to conduction defects and ventricular dysfunction. *Circulation, 104*, 1194–1199.

Harris, A. L. (2007). Connexin channel permeability to cytoplasmic molecules. *Prog Biophys Molec Biol, 94*, 120–143.

Hauer, R. N. W., Groenewegen, W. A., Firouzi, M., Ramanna, H., & Jongsma, H. J. (2006). Cx40 polymorphisms in human atrial fibrillation. *Adv Cardiol, 42*, 284–291.

Hendrix, E. M., Mao, S. J. T., Everson, W., & Larsen, W. J. (1992). Myometrial connexin 43 trafficking and gap junction assembly at term and in preterm labor. *Mol Reprod Develop, 33*, 27–38.

Hendrix, E. M., Myatt, L., Sellers, S., Russell, P. T., & Larsen, W. J. (1995). Steroid hormone regulation of rat myometrial gap junction formation: effects on Cx43 levels and trafficking. *Biol Reprod, 53*, 547–560.

Hille, B. (1992). *Ionic Channels of Excitable Membranes* (2nd ed.). Sunderland: Sinauer Assoc.

Huelser, D. F., Rehkopf, B., & Traub, O. (1997). Dispersed and aggregated gap junction channels I identified by immunogold labeling of freeze-fractured membranes. *Exp Cell Res, 233*, 240–251.

Iglesias, R., Locovei, S., Roque, A., et al. (2008). P2X7 receptor-Panenxin1 complex: pharmacology and signaling. *Am J Physiol (Cell Physiol), 295*, C752–C760.

Jordan, K., Solan, J. L., Dominguez, M., et al. (1999). Trafficking, assembly, and function of a connexin 43-green fluorescent protein chimera in live mammalian cells. *Mol Biol Cell, 10*, 2033–2050.

Juneja, S. C., Barr, K. J., Enders, G. C., & Kidder, G. M. (1999). Defects in the germ line and gonads of mice lacking connexin43. *Biol Reprod, 60*, 1263–1270.

Kalcheva, N., Qu, J., Sandeep, N., et al. (2007). Gap junction remodeling and cardiac arrhythmogenesis in a murine model of oculodentodigital dysplasia. *Proc Natl Acad Sci USA, 104*, 20512–20516.

Kamibayashi, Y., Oyamada, Y., Mori, M., & Oyamada, M. (1995). Aberrant expression of gap junction proteins (connexins) is associated with tumor progression during multistage mouse skin carcinogenesis. *Carcinogen, 16*, 1287–1297.

Kanemitsu, M. Y., Loo, L. W. M., Simon, S., Lau, A. F., & Eckhart, W. (1997). Tyrosine phosphorylation of connexin 43 by v-src is mediated by SH2 and SH3 domain interactions. *J Biol Chem, 272*, 22824–22831.

Kanter, H. L., Saffitz, J. E., & Beyer, E. C. (1992). Cardiac myocytes express multiple gap junction proteins. *Circ Res, 70*, 438–444.

Kenne, K., Fransson-Steen, R., Honkasalo, S., & Warngard, L. (1994). Two inhibitors of gap junction intercellular communication, TPA and endosulfan: different effects on phosphorylation of connexin 43 in the rat liver epithelial cell line, IAR 20. *Carcinogen, 15*, 1161–1165.

Khan-Dawood, F. S., Yang, J., & Dawood, M. Y. (1996). Expression of gap junction protein connexin-43 in the human and baboon corpus luteum. *J Clin Endocrinol Metab, 81*, 835–842.

Kiang, D. T., Jin, N., Tu, Z. J., & Lin, H. H. (1997). Upstream genomic sequence of the human connexin26 gene. *Gene, 199*, 165–171.

Kirchhoff, S., Nelles, E., Hagendorff, A., Kruger, O., Traub, O., & Willecke, K. (1998). Reduced cardiac conduction velocity and predisposition to arrythmias in connexin40-deficient mice. *Curr Biol, 8*, 299–302.

Lai-Chong, J. E., Arita, K., & McGrath, J. A. (2007). Genetic diseases of junctions. *J Invest Dermatol, 127*, 2713–2725.

Laird, D. W. (2007). Closing the gap on autosomal dominant connexin-26 and connexin-43 mutants linked to human disease. *J.Biol Chem, 283*, 2997–3001.

Laird, D. W., Puranam, K. L., & Revel, J.-P. (1991). Turnover and phosphorylation dynamics of connexin43 gap junction protein in cultured cardiac myocytes. *Biochem J, 273*, 67–72.

Laird, D. W., Castillo, M., & Kasprzak, L. (1995). Gap junction turnover, intracellular trafficking and phosphorylation of connexin 43 in brefeldin A-treated rat mammary tumor cells. *J Cell Biol, 131*, 1193–1203.

Landesman, Y., White, T. W., Starich, T. A., Shaw, J. E., Goodenough, D. A., & Paul, D. L. (1999). Innexin-3 forms connexin-like intercellular channels. *J Cell Sci, 112*, 2391–2396.

Larsen, W. J., Wert, S. E., & Brunner, G. D. (1987). Differential modulation of follicle cell gap junction populations at ovulation. *Dev Biol, 122*, 61–71.

Lo, C. W., Cohen, M. F., Huang, G. Y., et al. (1997). Cx43 gap junction gene expression and gap junctional communication in mouse neural crest cells. *Dev Genet, 20*, 119–132.

Loewenstein, W. R. (1979). Junctional intercellular communication and control of growth. *Biochim Biophys Acta, 560*, 1–65.

Loewenstein, W. R. (1985). Regulation of cell-to-cell communication by phosphorylation. *Biochem Soc Symp, 50*, 43–58.

Loewenstein, W. R., Kanno, Y., & Socolar, S. J. (1978). Quantum leaps of conductance during formation of membrane channels at cell-cell junction. *Nature, 274*, 133–136.

Loo, L. W., Berestecky, J. M., Kanemitsu, M. Y., & Lau, A. F. (1995). pp60src-mediated phosphorylation of connexin 43, a gap junction protein. *J Biol Chem, 270*, 12751–12761.

Maestrini, E., Korge, B. P., Ocana-Sierra, J., et al. (1999). A missense mutation in connexin26, D66H, causes mutiliating keratoderma with sensorineural deafness (Vohwinkel's syndrome) in three unrelated families. *Hum Mol Genet, 8*, 1237–1243.

Makowski, L., Caspar, D. L. D., Phillips, W. C., & Goodenough, D. A. (1977). Gap junction structures. II. Analysis of the x-ray diffraction data. *J Cell Biol, 74*, 629–645.

Mesnil, M., Crespin, S., Avanzo, J. L., & Dagli, M. L. (2005). Defective gap junctional intercelluar communication in the carcinogenic process. *Biochim Biophys Acta, 1719*, 125−145.

Mesnil, M., Krutovskikh, V., Piccoli, C., et al. (1995). Negative growth control of HeLa cells by connexin genes: connexin specificity. *Cancer Res, 55*, 629−639.

Moennikes, O., Buchmann, A., Ott, T., Willecke, K., & Schwarz, M. (1999). The effect of connexin32 null mutation on hepatocarcinogenesis in different mouse strains. *Carcinogenesis, 20*, 1379−1382.

Musil, L. S., & Goodenough, D. A. (1990). Gap junctional intercellular communication and the regulation of connexin expression and function. *Curr Opin Cell Biol, 2*, 875−880.

Neuhaus, I. M., Bone, L., Wang, S., Ionascescu, V., & Werner, R. (1996). The human connexin32 gene is transcribed from two tissue-specific promoters. *Biosci Rep, 16*, 239−248.

Neveu, M. J., Hully, J. R., Babcock, K. L., et al. (1994). Multiple mechanisms are responsible for altered expression of gap junction genes during oncogenesis in rat liver. *J Cell Sci, 107*, 83−95.

Neyton, J., & Trautmann, A. (1985). Single-channel currents of an intercellular junction. *Nature, 317*, 331−335.

Nonner, W., & Eisenberg, B. (1998). Ion permeation and glutamate residues linked by Poisson-Nernst-Planck Theory in L-type calcium channels. *Biophys J, 75*, 1287−1305.

Orsino, A., Taylor, C. V., & Lye, S. J. (1996). Connexin-26 and connexin-43 are differentially expressed and regulated in the rat myometrium throughout late pregnancy and the onset of labor. *Endocrinology, 137*, 1545−1553.

Pal, J. D., Berthoud, V. M., Beyer, E. C., Mackay, D., Shiels, A., & Ebihara, L. (1999). Molecular mechanism underlying a Cx50-linked congenital cataract. *Am J Physiol, 276*, c1443−c1446.

Paznekas, W. A., Karczeski, B., Vermeer, S., et al. (2009). GJA1 mutations, variants, and connexin43 dysfunction as it relates to the oculodentodigital dysplasia phenotype. *Hum Mutat, 30*, 724−733.

Peters, N. S. (1996). New insights into myocardial arrythmogenesis: distribution of gap junctional coupling in normal ischaemic and hypertrophied human hearts. *Clin Sci, 90*, 447−452.

Phelan, P. (2005). Innexins: members of an evolutionarily conserved family of gap junction proteins. *Biochim Biophys Acta, 1711*, 225−245.

Piersanti, M., & Lye, S. J. (1995). Increase in messenger ribonucleic acid encoding the myometrial gap junction protein, connexin-43, requires protein synthesis and is associated with increased expression of the activator protein-1, c-fos. *Endocrinology, 136*, 3571−3578.

Qu, Y., & Dahl, G. (2002). Function of the voltage gate of gap junction channels: selective exclusion of of molecules. *Proc Natl Acad Sci USA, 99*, 697−702.

Reaume, A. G., de Sousa, P. A., Kulkarni, S., et al. (1995). Cardiac malformation in neonatal mice lacking connexin43. *Science, 267*, 1831−1834.

Revel, J.-P., & Karnovsky, M. J. (1967). Hexagonal array of subunits in intercellular junctions in the mouse heart and liver. *J Cell Biol, 38*, C7−C12.

Revel, J.-P., Hoh, J. H., John, S. A., Laird, D. W., Puranam, K., & Yancey, S. B. (1992). Aspects of gap junction structure and assembly. *Sem Cell Biol, 3*, 21−28.

Sáez, J. C., Berthoud, V. M., Brañes, M. C., Martínez, A. D., & Beyer, E. C. (2003). Plasma membrane channels formed by connexins: their regulation and functions. *Physiol Rev, 83*. 13659−1400.

Saez, J., Nairn, A. C., Czernik, A. J., et al. (1990). Phosphorylation of connexin32, a hepatocyte gap junction protein, by cAMP-dependent protein kinase, protein kinase C and Ca^{2+}/calmodulin-dependent protein kinase II. *Eur J Biochem, 192*, 263−273.

Seul, K. H., Tadros, P. N., & Beyer, E. C. (1997). Mouse connexin40: gene structure and promoter analysis. *Genomics, 46*, 120−126.

Simon, A. M., Goodenough, D. A., & Paul, D. L. (1998). Mice lacking connexin40 have cardiac conduction abnormalities characteristic of atriventricular block and bundle branch block. *Curr Biol, 8*, 295−298.

Simpson, I., Rose, B., & Loewenstein, W. R. (1977). Size limit of molecules permeating the junctional membrane channels. *Science, 195*, 294−296.

Solan, J. L., & Lampe, P. D. (2005). Connexin phosphorylation as a regulatory event linked to gap junction channel assembly. *Biochim Biophys Acta, 1711*, 154−163.

Solan, J. L., & Lampe, P. D. (2007). Connexin43 phosphorylation: structural changes and biological effects. *Biochem J, 419*, 261−272.

Spray, D. C., & Dermietzel, R. (1995). X-linked dominant Charcot-Marie-Tooth disease and other potential gap junction diseases of the nervous system. *TINS, 18*, 256−262.

Sun, Y., Tang, W., Chang, Q., Wang, Y., Kong, W., & Lin, X. (2009). Connexin30 null and conditional mice connexin26 null mice display distinct pattern and time course of cellular degeneration in the cochlea. *J Comp Neurol, 516*, 569−579.

Swenson, K. I., Piwnica-Worms, H., McNamee, H., & Paul, D. L. (1990). Tyrosine phosphorylation of the gap junction protein connexin43 is required for the pp60v-src-induced inhibition of communication. *Cell Reg, 1*, 989−1002.

Tu, Z. J., & Kiang, D. T. (1998). Mapping and characterization of the basal promoter of the human connexin26 gene. *Biochim Biophys Acta, 1441*, 169−181.

Unger, V. M., Kumar, N. M., Gilula, N. B., & Yeager, M. (1999). Three-dimensional structure of a recombinant gap junction membrane channel. *Science, 283*, 1176−1180.

Veenstra, R. D. (2000). Ion permeation through connexin gap junction channels: effects on conductance and selectivity. In C. Perrachia (Ed.), *Current Topics in Membranes*, Vol. 49, pp. 95−129.

Veenstra, R. D., & DeHaan, R. L. (1986). Measurement of single channel currents from cardiac gap junctions. *Science, 233*, 972−974.

Veenstra, R. D., Wang, H.-Z., Beblo, D. A., et al. (1995). Selectivity of connexin-specific gap junctions does not correlate with channel conductance. *Circ Res, 77*, 1156−1165.

Veenstra, R. D., Wang, H.-Z., Westphale, E. M., & Beyer, E. C. (1992). Multiple connexins confer distinct regulatory and conductance properties of gap junctions in developing heart. *Circ Res, 71*, 1277−1283.

Waldo, K. L., Lo, C. W., & Kirby, M. L. (1999). Connexin43 expression reflects neural crest patterns during cardiovascular development. *Dev Biol, 208*, 307−323.

Warn-Cramer, B. J., Lampe, P. D., Kurata, W. E., et al. (1996). Characterization of the mitogen-activated protein kinase phosphorylation sites on the connexin-43 gap junction protein. *J Biol Chem, 271*, 3779−3786.

White, T. W., Goodenough, D. A., & Paul, P. L. (1998). Targeted ablation of connexin 50 in mice results in micropthalmia and zonular pulverulent cataracts. *J Cell Biol, 143*, 815−825.

Yamaguchi, D. T., Huang, J. T., & Ma, D. (1995). Regulation of gap junction intercellular communication by pH in MC3T3-E1 osteoblastic cells. *J Bone Min Res, 10*, 1891−1899.

Yamasaki, H. (1991). Aberrant expression and function of gap junctions during carcinogenesis. *Env Health Prosp, 93*, 191−197.

Yang, Y. Q., Liu, X., Zhang, X. L., et al. (2010). Novel connexin40 missense mutations in patients with familial atrial fibrillation. *Europace, 12*, 1421−1427.

Yu, W., Dahl, G., & Werner, R. (1994). The connexin43 gene is responsive to oestrogen. *Proc Roy Soc (London) Series B Biol Sci, 255*, 125−132.

This page intentionally left blank

Chapter 23

Regulation of Cardiac Ion Channels by Cyclic Nucleotide-Dependent Phosphorylation

Gordon M. Wahler and Nicholas Sperelakis

Chapter Outline

I. SUMMARY

Ion channels in the heart are regulated by many physiological mechanisms. One of the most important mechanisms is the regulation by cyclic nucleotide protein kinases. Calcium channels in the heart play a central role in excitation–contraction coupling and the physiological modulation of these channels is crucial to the functioning of the heart under differing conditions. Phosphorylation–dephosphorylation reactions regulate the cardiac calcium channel activity. Activation of the cyclic AMP-dependent protein kinase stimulates the channel activity, whereas activation of the cyclic GMP-dependent protein kinase inhibits the channel activity. Both synthesis and degradation of the cyclic nucleotides are regulated by a large number of physiological and pathophysiological first messengers. There is considerable compartmentalization of the components of the cyclic nucleotide pathways and there are significant interactions between the two cyclic nucleotides. The complexities of these two cyclic nucleotide systems allows for fine control of calcium channel activity in the heart.

II. INTRODUCTION

Phosphorylation of ion channel proteins by various protein kinases is one of the primary mechanisms for physiological modulation of ion channel activity. One of the most widely-studied examples of this regulatory mechanism is cyclic nucleotide-dependent phosphorylation of the calcium channels in the heart.

There exist several different subtypes of voltage (V)-dependent Ca^{2+} channels in excitable cells. In cardiac muscle cells, the primary channels responsible for entry of Ca^{2+} ions into the cell during an action potential (AP) are the V-dependent "L-type" (i.e. "long-lasting") Ca^{2+} channels responsible for the L-type Ca^{2+} current (I_{Ca}). This chapter will focus on the L-type Ca^{2+} channel of cardiac myocytes and modulation of I_{Ca} by the cyclic nucleotide-dependent phosphorylation, in order to illustrate some important principles that are involved in ion channel regulation.

The L-type channels play a central role in excitation–contraction (E-C) coupling. During an AP, Ca^{2+} influx through the L-type channels leads to: (1) direct activation

Cell Physiology Sourcebook. DOI: 10.1016/B978-0-12-387738-3.00023-8

of the myofilaments; (2) Ca^{2+} loading of the sarcoplasmic reticulum (SR); and (3) release of Ca^{2+} from the SR ("calcium-induced calcium release"). Thus, controlling the amount of Ca^{2+} influx through the L-type channels is a key mechanism for regulation of myocardial contractility.

The L-type Ca^{2+} channels have some special properties, including functional dependence on metabolic energy, selective blockade by acidosis and regulation by intracellular second messengers. Because of these special properties of these channels, Ca^{2+} influx into the myocardial cell can be controlled by both extrinsic factors (such as autonomic nerve stimulation or circulating hormones) and intrinsic factors (such as intracellular pH or ATP levels). Thus, there are many sites for physiological and pathophysiological modulation of I_{Ca}.

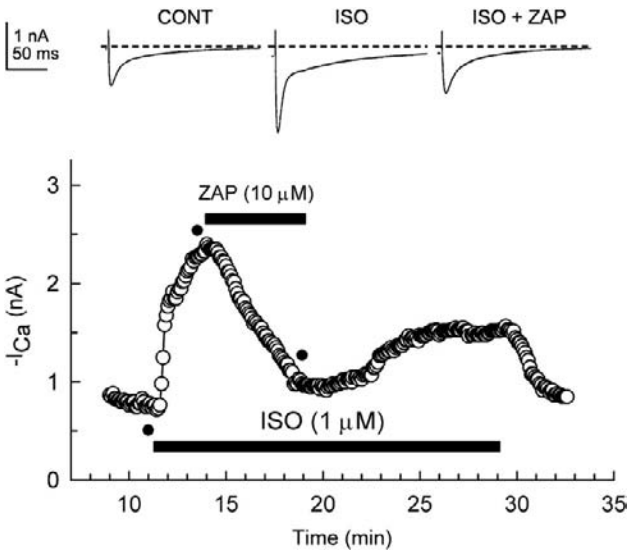

FIGURE 23.1 Zaprinast inhibited the isoproterenol-stimulated I_{Ca}. Shown are the original currents (upper panel) and the amplitude of I_{Ca} at 0 mV over time (lower panel) during superfusion of the cells with control (CONT), 1 μM isoproterenol-containing (ISO), or isoproterenol plus 10 μM zaprinast-containing (ISO + ZAP) solutions. Superfusion of the cell with 1 μM isoproterenol caused a large stimulation of I_{Ca}. Subsequent superfusion of the cell with 10 μM zaprinast caused a substantial inhibition of the isoproterenol-induced stimulation of I_{Ca}. Upon washout of zaprinast there was a partial recovery of the isoproterenol-stimulated I_{Ca}. Standard whole-cell recording (calcium-free pipette solution) was used. Individual current traces were obtained at time points indicated by the filled circles in the lower panel. *(From Ziolo et al., 2003; used with permission).*

III. REGULATION OF THE CARDIAC L-TYPE Ca^{2+} CHANNELS BY CYCLIC AMP

IIIA. Evidence for Cyclic AMP Modulation of L-Type Ca^{2+} Channel Function

A major physiological modulator of ion channels and E-C coupling in the heart is the β-adrenergic pathway. It has long been known that the β-adrenergic-cAMP pathway modulates the functioning of the L-type Ca^{2+} channels (Shigenobu and Sperelakis, 1972; Tsien et al., 1972) (Fig. 23.1). Every step in the pathway has been shown to alter I_{Ca}. Stimulation of cardiac β-adrenergic receptors (e.g. in response to the release of norepinephrine from sympathetic nerves) causes adenylate cyclase activation. This results in increase of intracellular cyclic AMP (cAMP) levels and enhanced activation of the cAMP-dependent protein kinase (PK-A). The activated PK-A phosphorylates a number of proteins, including several involved in E-C coupling (e.g. Stojanovic et al., 2001).

Thus, induction of Ca^{2+}-dependent slow APs, an indirect measure of I_{Ca}, was observed with exposure to direct activators of adenylate cyclase (forskolin, Gpp(NH)p) (Josephson and Sperelakis, 1978; Wahler and Sperelakis, 1986). These effects have been repeatedly confirmed by direct measurement of adenylate cyclase activators on I_{Ca} (e.g. Ziolo et al., 2003; Fig. 23.2). Additionally, direct injection of cAMP into ventricular muscle cells was shown rapidly to (within seconds) induce Ca^{2+}-dependent slow APs (Vogel and Sperelakis, 1981; Li and Sperelakis, 1983; Bkaily and Sperelakis, 1985) and enhance I_{Ca} (Irisawa and Kokubun, 1983). Similarly, rapid enhancement of I_{Ca} was observed with intracellular photochemical activation of cAMP in ventricular myocytes (Nargeot et al., 1983). Other neurotransmitters, hormones and autacoids that stimulate cAMP production (e.g. histamine) also enhance I_{Ca}.

Since PK-A phosphorylation of the L-type Ca^{2+} channels leads to an increase in I_{Ca} and enhanced Ca^{2+} influx during the plateau phase of the AP, this causes a direct increase in the amount of Ca^{2+} available to the contractile proteins. It also indirectly increases the Ca^{2+} available to the contractile proteins due to effects of increased Ca^{2+} influx on Ca^{2+} cycling and release by the SR. The direct and indirect effects of the phosphorylated L-type Ca^{2+} channel, together with the effects of PK-A-phosphorylated SR proteins, mediate the vast majority of the positive inotropic effects of β-adrenergic stimulation on the heart.

Single-channel analysis indicates that β-adrenergic stimulation causes an increase in the mean open time of Ca^{2+} channels and increases the probability of opening (largely by decreasing interval between bursts of openings), whereas the single-channel conductance is unaffected (Reuter et al., 1982; Klein et al., 2000). These effects on the channels lead to an increased I_{Ca} during the AP.

IIIB. The Phosphorylation Hypothesis

Because of the relationship between cAMP and the number of available L-type Ca^{2+} channels and because of the metabolic dependence of the functioning of these

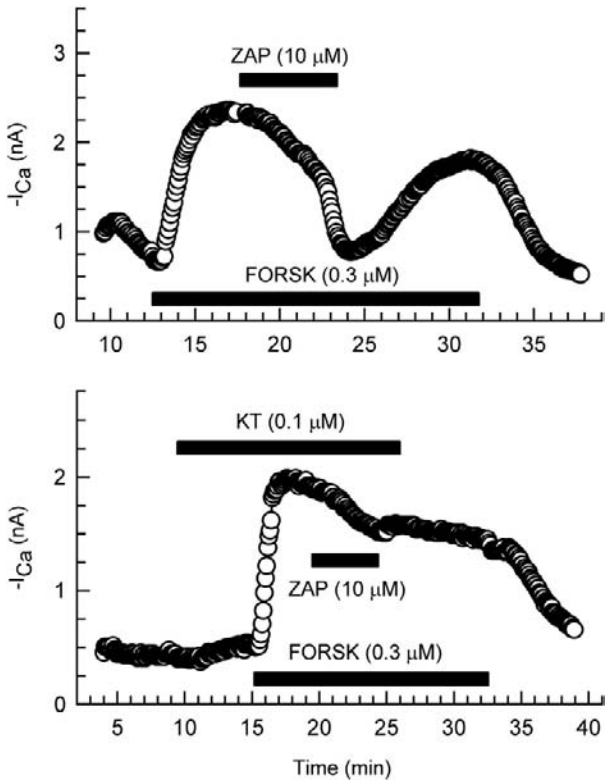

FIGURE 23.2 Zaprinast inhibition of the forskolin-stimulated I_{Ca} in the absence and presence of an inhibitor of PK-G (KT5823). Superfusion of a cell with 0.3 μM forskolin (FORSK), a direct activator of adenylate cyclase, caused a large stimulation of I_{Ca}. Upper panel: under control conditions, subsequent superfusion of the cell with 10 μM zaprinast (ZAP) caused a substantial reversible inhibition of the forskolin-induced stimulation of I_{Ca}. Lower panel: in contrast, in the presence of 0.1 μM KT5823 (KT), the inhibitory effect of zaprinast was greatly attenuated. Standard whole-cell recording was used. *(Modified from Ziolo et al., 2003; used with permission).*

channels, it was hypothesized that one of the proteins that is phosphorylated is the L-type Ca^{2+} channel protein (or a contiguous regulatory protein). That is, the L-type channel must be phosphorylated for it to become available for voltage activation (Shigenobu and Sperelakis, 1972; Tsien et al., 1972). According to the phosphorylation hypothesis (Fig. 23.3), agents that elevate cAMP increase the fraction of the channels that are in the phosphorylated form and hence readily available for voltage activation. Whatever the precise molecular mechanism for the effect phosphorylation has on channel activity, in the phosphorylation model, the phosphorylated form of the L-type channel is the active (operational) form and the dephosphorylated form is the inactive (inoperative) form. The dephosphorylated channels are virtually silent electrically (i.e. their opening probability approaches zero). Phosphorylation increases the probability of channel opening with depolarization. An equilibrium should exist between the phosphorylated and dephosphorylated forms of the channel under a given set of conditions.

IIIC. Protein Kinase-A (PK-A) Activation

Over the years, considerable evidence has accumulated that supports the phosphorylation hypothesis. For example, intracellular injection of the catalytic subunit of PK-A induces and increases the slow Ca^{2+}-dependent APs and potentiates I_{Ca} (Osterreider et al., 1982; Bkaily and Sperelakis, 1984). Injection of a PK-A inhibitor protein into heart cells inhibits slow Ca^{2+}-dependent APs and I_{Ca} (Bkaily and Sperelakis, 1984; Kameyama et al., 1986). These results verify that the regulatory effect of cAMP on I_{Ca} is mediated by PK-A and phosphorylation.

Also consistent with the phosphorylation hypothesis, L-type Ca^{2+} channel activity disappears within 90 s in isolated membrane inside-out patches, but can be restored (in neurons) by applying the catalytic subunit of PK-A together with MgATP (Armstrong and Eckert, 1987). This is consistent with the washing away of regulatory components of the Ca^{2+} channels or of the enzymes necessary to phosphorylate the channel. Even in whole-cell voltage-clamp, there is a progressive run-down of the Ca^{2+} current, which is slowed or partially reversed by conditions that enhance PK-A phosphorylation.

IIID. Phosphatases

While much research has been done on the role of phosphorylation in the regulation of ion channels, much less is known about the reverse reaction, i.e. the role of dephosphorylation of ion channels by phophatases. Based on the rapid decay of the response to microinjected cAMP, the mean life span of a phosphorylated channel is probably only a few seconds at most. Agents that affect or regulate the phosphatase that dephosphorylates the channel would affect the life span of the phosphorylated channel. Thus, channel stimulation can be produced either by increasing the rate of phosphorylation (by PK-A activation) or by decreasing the rate of dephosphorylation (inhibition of the phosphatase).

In ventricular cells, several phosphatases have been shown to inhibit I_{Ca} (e.g. Kameyama et al., 1986; duBell and Rogers, 2004), consistent with the phosphorylation hypothesis. Additionally, phosphatase inhibitors, such as okadaic acid and microcystin, cause large increases in I_{Ca} (Hescheler et al., 1987, 1988; Frace and Hartzell, 1993). There is some disagreement about the relative effectiveness of specific phosphatases (particularly type 1 versus type 2A) in reducing I_{Ca} and whether basal I_{Ca} is significantly inhibited by phosphatases, or if only the cAMP-stimulated I_{Ca} (e.g. by a β-adrenergic agonist) is affected.

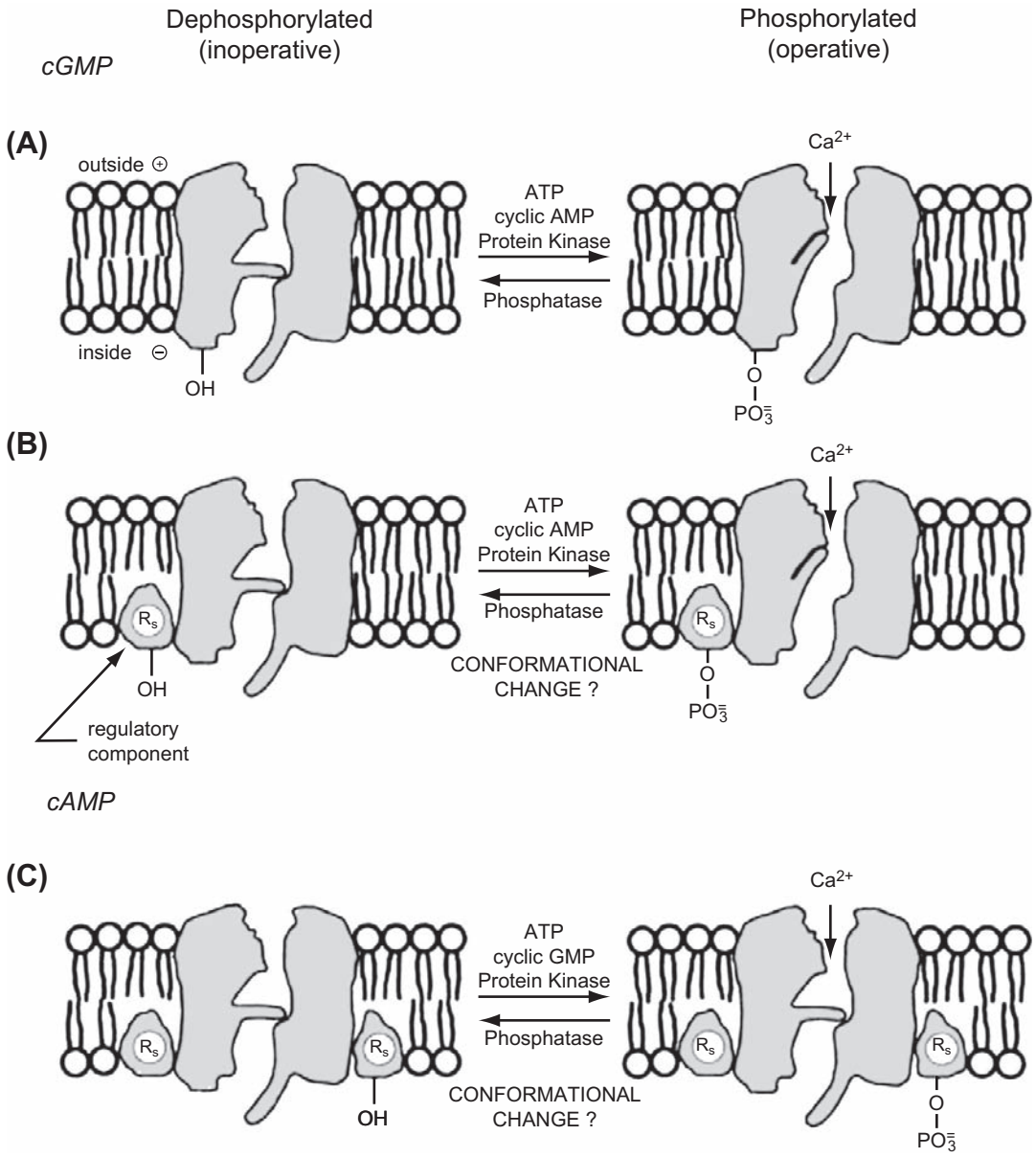

FIGURE 23.3 The phosphorylation hypothesis. Schematic model for an L-type Ca^{2+} channel in myocardial cell membrane in two hypothetical forms: dephosphorylated (or electrically silent) form (left diagrams) and phosphorylated form (right diagrams). The two gates associated with the channel are an activation gate and an inactivation gate. The phosphorylation hypothesis states that a protein constituent of the Ca^{2+} channel itself (A) or a regulatory protein associated with the channel (B) must be phosphorylated for the channel to be in a state available for voltage activation. Phosphorylation of a serine (or threonine) residue occurs by PK-A in the presence of ATP. Phosphorylation may produce a conformational change that effectively allows the channel gates to operate. The L-type channel (or an associated regulatory protein) may also be phosphorylated by PK-G (C), thus mediating the inhibitory effects of cGMP on the Ca^{2+} channel. *(Adapted from Sperelakis and Schneider, 1976).*

Protein phosphatase-type 1 activity is inhibited by (at least) two low-molecular-weight proteins, protein phosphatase inhibitor-1 (PPI-1) and protein phosphatase inhibitor-2 (PPI-2). PPI-1 is present in ventricular myocytes and it may be an important additional component of the modulation of the phosphorylation−dephosphorylation cycle of the L-type channel. The activity of PPI-1 is enhanced by phosphorylation with PK-A (Ahmad et al., 1989; Gupta et al., 1996). Thus, PK-A not only phosphorylates the Ca^{2+} channel, it also decreases the rate of channel dephosphorylation. Both actions stimulate channel activity.

In contrast to the effects of other phosphatases examined to date, calcineurin has been shown to enhance I_{Ca} (Tandan et al., 2009). Calcineurin binds to the L-type Ca^{2+} channel near the site where PP2A binds and

dephosphorylates the channel but, unlike PP2A, calcineurin upregulates channel activity. Additionally, calcineurin inhibitors inhibit I_{Ca}. Thus, while dephosphorylation of the Ca^{2+} channel does not always inhibit I_{Ca}, it does appear that phosphatases are an additional important determinant of the amplitude of I_{Ca}. Alternatively, there may be more than one site on the channel that can be phosporylated.

IV. REGULATION OF THE L-TYPE Ca^{2+} CHANNELS BY CYCLIC GMP

IVA. Cyclic GMP Effects

The physiological role played by cyclic GMP (cGMP) on cardiac function appears to be more complex than that of cAMP. It was originally proposed that cGMP plays a role antagonistic to that of cAMP (Goldberg et al., 1975) and, in most instances, but not all, this appears to be the case. Thus, considerable evidence has accumulated demonstrating cGMP inhibition of I_{Ca}. For example, 8-Br-cGMP, a more permeable and hydrolysis-resistant analog of cGMP, has been shown to shorten the AP duration in rat atria (accompanied by a negative inotropic effect) (Nawrath, 1977) and to inhibit Ca^{2+}-dependent slow APs (Kohlhardt and Haap, 1978; Wahler and Sperelakis, 1985) and accompanying contractions (Wahler and Sperelakis, 1985). Intracellular injection of cGMP into atrial, ventricular and Purkinje fiber preparations was also shown rapidly to depress or abolish slow APs (Mehegan et al., 1985; Wahler and Sperelakis, 1985).

In whole-cell voltage-clamp experiments on single cardiomyocytes from a variety of species, it has been directly shown that cGMP regulates I_{Ca} (e.g. Fischmeister and Hartzell, 1987; Levi et al., 1989, 1994; Wahler et al., 1990; Mery et al., 1991; Wahler and Dollinger, 1995; Sumii and Sperelakis, 1995; Ziolo et al., 2003) (Fig. 23.4). For example, in voltage-clamp experiments on single ventricular cardiomyocytes from embryonic chicks or neonatal rats, stimulation of I_{Ca} produced by 8-Br-cAMP added to the bath could be completely reversed by the addition of 8-Br-cGMP (Masuda and Sperelakis, unpublished observations; Fig. 23.5). The ratio of cAMP/cGMP apparently determines the degree of stimulation of I_{Ca}.

In some instances, the cGMP inhibition of I_{Ca} is dependent on prior stimulation of I_{Ca} by cAMP. However, it has also been directly demonstrated that, under some conditions, 8-Br-cGMP inhibits basal I_{Ca} (i.e. unstimulated by cAMP) in voltage-clamped ventricular myocytes (e.g. Wahler et al., 1990; Haddad et al., 1995) (see Fig 23.4). Inhibition of basal Ca^{2+} channel activity by cGMP has also been demonstrated at the single-channel level in embryonic chick heart (Tohse and Sperelakis, 1991) (Fig. 23.6), under conditions in which the intracellular environment is likely to be more normal than during whole-cell voltage clamp experiments. Addition of 8-Br-cGMP to the bath completely inhibited Ca^{2+} channel activity. Cyclic GMP did not change the conductance of the Ca^{2+} channel, but prolonged the closed times and shortened the open times. In contrast, 8-Br-cGMP had no effect on the basal Ca^{2+} single-channel activity in mouse ventricular myocytes, but did reverse all the stimulatory effects of the β-adrenergic agonist isoproterenol (Klein et al., 2000). However, the debate about whether basal I_{Ca} is inhibited by cGMP is likely more of academic than physiological importance, since in vivo there would consistently be tonic activation of β-adrenergic receptors due to sympathetic nerve activity and adrenal release of catecholamines. Under such conditions, no true "basal" (i.e. unstimulated by cAMP) I_{Ca} would exist.

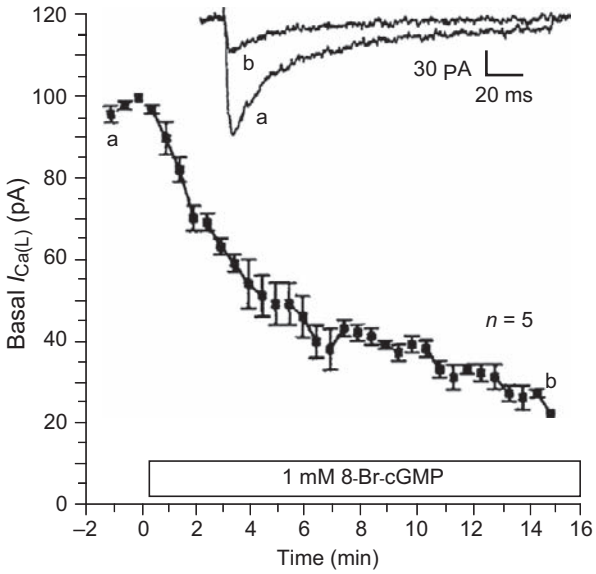

FIGURE 23.4 Time course of the inhibition of the basal I_{Ca} by 8-Br-cGMP (1 mM) in 17-day-old embryonic chick heart cells. Data points plotted are the mean ± standard error. The upper two traces show the original current recordings of I_{Ca} taken at the time points shown by the corresponding letters in the graph. I_{Ca} was elicited by 200 ms depolarizing pulses to +10 mV from a holding potential of −45 mV. Experiments conducted at room temperature. *(From Haddad et al., 1995.)*

IVB. Mechanisms for cGMP Inhibition of I_{Ca}

As noted above, cGMP regulates the functioning of the L-type Ca^{2+} channels in a manner that is antagonistic to that of cAMP. It was hypothesized that the Ca^{2+} channel protein has a second site that can be phosphorylated by the cGMP-dependent protein kinase (PK-G) and that, when phosphorylated, inhibits the Ca^{2+} channel (Wahler and Sperelakis, 1985). Another possibility is that there is a second type of regulatory protein that is inhibitory when phosphorylated (see Fig. 23.3). Subsequently, it was shown that, similar to activated PK-A, activated

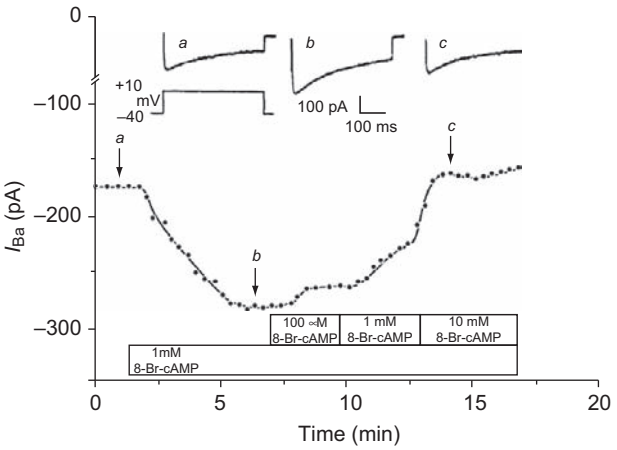

FIGURE 23.5 Antagonism of the stimulating effect of 8-Br-cAMP on I_{Ca} by 8-Br-cGMP in a single 2-day rat ventricular myocyte. Upper tracings show three original current recordings of I_{Ca} corresponding to the three time points labeled in the lower graph. I_{Ca} was elicited by 300 ms depolarizing pulses to +10 mV from a holding potential of −40 mV. Ba^{2+} (20 mM) was used as the charge carrier. Experiments conducted at room temperature of 25°C. *(From Masuda and Sperelakis, unpublished.)*

PK-G phosphorylates a number of proteins involved in E-C coupling (e.g. Stojanovic et al., 2001), including the L-type Ca^{2+} channel (Schröder et al., 2003; Yang et al., 2007).

There is considerable evidence that the PK-G-mediated phosphorylation of the L-type Ca^{2+} channel is functionally significant, i.e. that the reduction of I_{Ca} observed with cGMP is mediated by this phosphorylation (at least in mammalian and avian ventricular myocytes; see below). Observation of inhibition of I_{Ca} by 8-Br-cGMP (see Figs. 23.4–23.6), which is a potent activator of PK-G, supports the view that PK-G is responsible for the inhibitory effect of cGMP on I_{Ca}.

In some preparations (e.g. embryonic chick, neonatal rat), when PK-G is directly added to the patch pipette for diffusion into the cell during whole-cell voltage clamp, basal I_{Ca} is inhibited markedly and rapidly, with maximum inhibition reached in about 3–5 min (Fig. 23.7). Note that inhibition of basal I_{Ca} began about 80 s after breaking into the cell. Similar effects of PK-G infusion were observed in early neonatal rat ventricular myocytes, as illustrated in Fig. 23.8 (Sumii and Sperelakis, 1995). As can be seen, there is a rapid and prominent inhibition of basal I_{Ca} by PK-G. Addition of H-8 (a blocker of both PK-A and PK-G) to the bath often causes a rapid restoration of I_{Ca} to about the original basal level. Addition of 1 mM 8-Br-cAMP can produce only a small stimulation of I_{Ca} in the continued presence of PK-G (see Fig. 23.8). Therefore, these findings indicate that the inhibitory effects of cGMP on I_{Ca} in mammalian and avian ventricular myocytes are mediated by activation of PK-G and resultant phosphorylation. Because 8-Br-cGMP is a potent activator of PK-G and does not stimulate cAMP hydrolysis, cGMP-induced inhibition of the basal activity of the Ca^{2+} channels (not prestimulated by cAMP) is likely also to be mediated by PK-G.

In ventricular muscle from wild-type mice, 8-Br-cGMP inhibited contractility, consistent with observations in other cardiac preparations. In addition, in the same study (Wegener et al., 2002), 8-Br-cGMP had no effect on contractility in PK-G-1 knockout mice, supporting the view that PK-G mediated the inhibition of contractility caused by 8-Br-cGMP. In contrast, muscarinic cholinergic stimulation reduced myocyte contractility, not only in wild-type, but also in the PK-G-1 knockout mouse, suggesting that muscarinic inhibition of contractility may be independent of PK-G-1 activation.

In single-channel recordings in mouse ventricular myocytes, 8-Br-cGMP has no effect on basal single Ca^{2+}

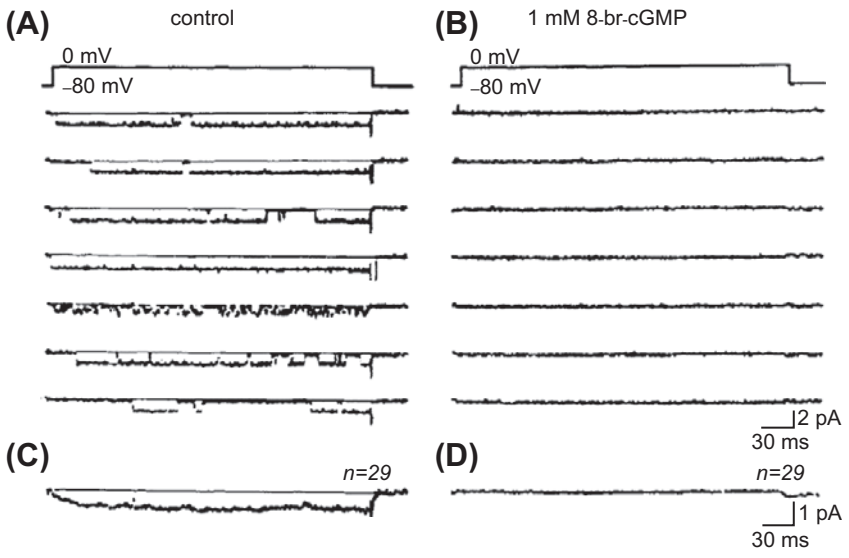

FIGURE 23.6 Current recordings from a cell-attached patch showing the effect of 8-Br-cGMP on the Ca^{2+} channel activity in a single myocardial cell isolated from a 3-day-old embryonic chick heart. Single channel currents were evoked by depolarizing voltage pulses to 0 mV from a holding potential of −80 mV, at a duration of 300 ms and stimulation frequency of 0.5 Hz. (A and B) Examples of original current recordings from the same patch, before (A) and after (B) superfusion with 1.0 mM 8-Br-cGMP. (C and D) Ensemble-averaged currents calculated from the current recordings (n = 29 traces). *(Data from Tohse and Sperelakis, 1991.)*

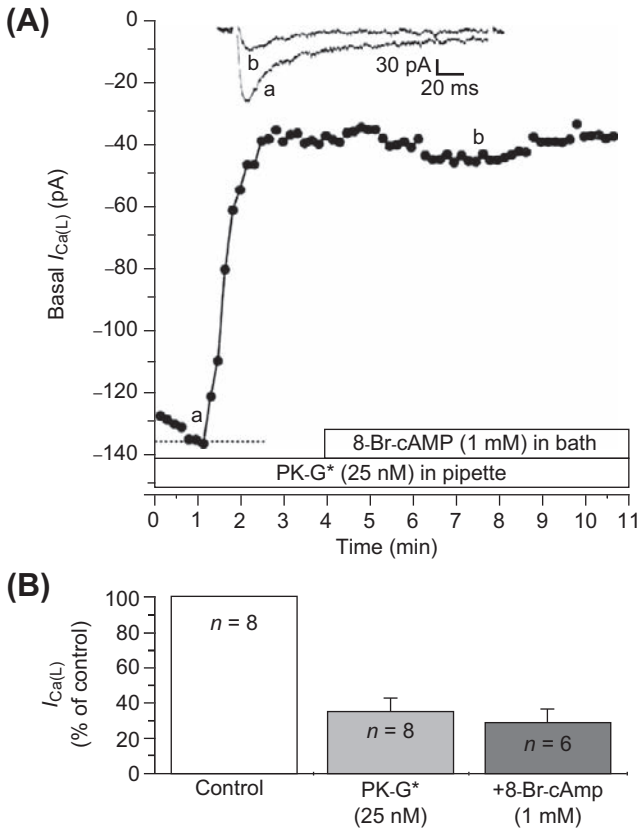

FIGURE 23.7 Inhibition of basal I_{Ca} of 17-day-old embryonic chick cardiomyocytes by PK-G. (A) PK-G (25 nM) was present in the patch pipette for diffusion into the cell during whole-cell voltage clamp. Inhibition of I_{Ca} began within 70 s after breaking into the cell and reached maximum at about 2.5 min. Addition of 1 mM 8-Br-cAMP into the bath failed to reverse the inhibition produced by PK-G. The two current traces illustrated at the top correspond to the time points labeled a and b in the graph. (B) Bar graph summary of the inhibition of basal I_{Ca} by PK-G in eight cells, and the lack of reversal by 8-Br-cAMP in six cells. Experiments were done at room temperature. *(From Haddad et al., 1995.)*

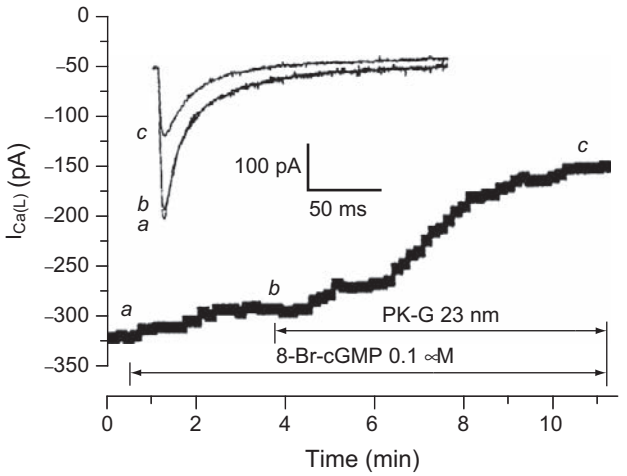

FIGURE 23.8 Inhibition of basal I_{Ca} by PK-G (25 mM) in a ventricular myocyte from an early (4 day) neonatal rat heart. Time course of the effect of low doses of 8-Br-cGMP (0.1 μM) and PK-G (25 nM) on basal (not stimulated) I_{Ca}. 8-Br-cGMP and PK-G were applied using the perfusion patch-pipette technique. As shown, when 8-Br-cGMP was applied in advance of PK-G, it had only a little effect, whereas subsequent addition of PK-G produced rapid inhibition (inset). Selected current traces of I_{Ca} (a, b, and c) at points denoted on the time course curve. *(Reproduced with permission from Sumii and Sperelakis, 1995.)*

channel activity, but reverses all the stimulatory effects of the β-adrenergic agonist isoproterenol (Klein et al., 2000). This inhibitory effect of 8-Br-cGMP is also blocked by a PK-G inhibitor, indicating that the effect is mediated by PK-G.

The effects of cardiac myocyte-selective overexpression of PK-G 1 (the primary isoform of PK-G in cardiac myocytes) on the Ca^{2+}-channel response to cGMP have also been investigated at the single-channel level (Schröder et al., 2003). 8-Br-cGMP, DEA-NO (an NO donor) and carbachol (a muscarinic agonist) all inhibited the β-adrenergic stimulation of L-type Ca^{2+} activity in wild-type mouse ventricular myocytes. This inhibition of channel activity was dramatically enhanced for 8-Br-cGMP and DEA-NO (but not carbachol) in the myocytes from mice that overexpressed PK-G 1. Furthermore, while none of the three agents had any effect on the basal L-type Ca^{2+} channel activity in myocytes from wild-type mice, in myocytes overexpressing PK-G 1, 8-Br-cGMP and DEA-NO (but not carbachol) had a dramatic inhibitory effect on basal L-type channel activity. These data again support the hypothesis that the inhibitory effects of 8-Br-cGMP and NO are mediated by PK-G 1, but not the inhibitory effects of muscarinic agonists.

There is another mechanism for cGMP inhibition of I_{Ca} that has been reported for some preparations. This indirect mechanism involves cGMP stimulation of PDE 2, leading to an anti-adrenergic effect due to a reduction in cAMP levels. Evidence for this mechanism comes primarily from frog ventricular myocytes, in which intracellular application of cGMP inhibited I_{Ca} only after the cAMP levels had been increased and EHNA (a selective PDE 2 inhibitor) blocked the cGMP inhibition (Hartzell and Fischmeister 1986; Fischmeister and Hartzell, 1987). It was concluded that cGMP activates PDE 2 (a cGMP-stimulated isoform of phosphodiesterase), resulting in degradation of cAMP. This cGMP-stimulated PDE mechanism for inhibition of I_{Ca} was also found to occur in human atrial cells (Rivet-Bastide et al., 1997).

However, this mechanism (cGMP stimulation of PDE) for cGMP inhibition of I_{Ca} does not appear to be present in mammalian ventricular myocytes. For example, EHNA has no effect on basal or β-stimulated I_{Ca} in mammalian ventricular myocytes (Rivet-Bastide et al., 1997). In mammalian and avian ventricular myocytes, the inhibition of I_{Ca} by cGMP is not mediated by PDE 2, but rather by

PK-G (Levi et al., 1989; Wahler et al., 1990; Mery et al., 1991; Wahler and Dollinger, 1995). 8-Br-cGMP (which does not stimulate PDE 2), not only inhibits slow APs in mammalian cardiac muscle, but it does so without decreasing cAMP levels (Thakkar et al., 1989). Additionally, the inhibitory effect on I_{Ca} of agents that elevate cGMP is maintained when there is a general inhibition of PDEs, including PDE 2, with a non-specific PDE inhibitor (IBMX) (Fig. 23.9). In contrast, the anti-adrenergic action of cGMP is blocked by KT5823, a selective inhibitor of PK-G (Wahler and Dollinger, 1995; Ziolo et al., 2003; see Figs. 23.2 and 23.9).

IVC. Effects of Nitric Oxide on I_{Ca}

Nitric oxide (NO) is known to be an important regulator of a variety of cellular functions, including contractility of the heart. Many (though not all) of the effects of NO are mediated through stimulation of soluble guanylate cyclase (G-cyclase) activity and the resulting enhanced cGMP production. As numerous studies have shown that cGMP inhibits I_{Ca} in cardiac myocytes, the depression of contractility by NO may be in large part due to a cGMP-mediated inhibition of I_{Ca}.

Due to the highly labile nature of NO, NO donors are often used to examine the effect of NO. The NO donor SIN-1 has been shown to have an anti-adrenergic effect on I_{Ca} in both frog and mammalian ventricular myocytes (Mery et al., 1993; Wahler and Dollinger, 1995), similar to the effects of cGMP. The spontaneous breakdown of SIN-1 in solution, not only generates NO, but also generates superoxide anions which can inactivate NO and lead to formation of peroxynitrite, a strong oxidizing agent. Thus, SIN-1 is also used as a peroxynitrite donor and the effects of SIN-1 observed on I_{Ca} could be caused by peroxynitrite, rather than by NO. The addition of superoxide dismutase and catalase, which should degrade superoxide (thereby protecting NO and minimizing peroxynitrite formation) enhanced the effects of SIN-1 on I_{Ca} (Wahler and Dollinger, 1995). Furthermore, LY83583, which blocks cGMP formation by G-cyclase (Kontos and Wei, 1993), or KT5823, which inhibits PK-G, nearly abolished the I_{Ca} response to SIN-1 (see Fig. 23.9). Together these results strongly suggest that NO, rather than peroxynitrite, mediates the effects of SIN-1 on I_{Ca} and that this occurs through enhanced activity of PK-G.

Although in the virtual absence of intracellular (pipette) Ca^{2+}, SIN-1 was reported to have no effect on ventricular I_{Ca}, when a physiological concentration of Ca^{2+} (pCa = 6.85) was present in the pipette solution, SIN-1 did reduce basal I_{Ca} (Matsumoto, 1997). Thus, it is clear that cGMP can also inhibit basal I_{Ca} at least in some preparations under physiological intracellular conditions.

SIN-1, in addition to producing a prominent inhibitory (anti-adrenergic) effect, can occasionally cause an

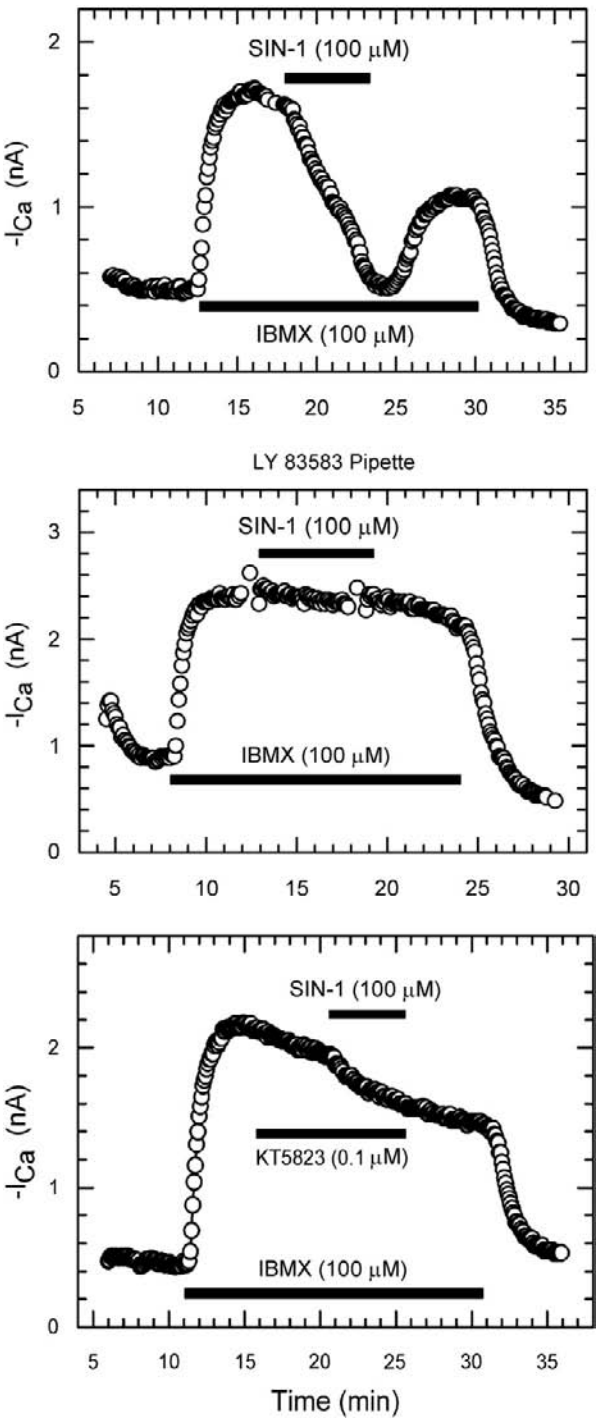

FIGURE 23.9 Blockade of SIN-1 inhibition of I_{Ca} by LY-83583 or KT5823. Top panel: shown is an example of SIN-1 (100 μM) inhibition of IBMX-enhanced I_{Ca} under control conditions. Central panel: inclusion of 10 μM LY-83583 in the pipette solution virtually abolished the response to SIN-1. Bottom panel: superfusion of the cell with 0.1 μM KT5823 had little effect on IBMX-stimulated ICa, but greatly reduced the effect of SIN-1. *(Modified from Wahler and Dollinger, 1995; used with permission.)*

enhancement of I_{Ca} in frog and mammalian ventricular myocytes (Mery et al., 1993; Wahler and Dollinger, 1995). Thus, in cells in which the response to β-agonists was relatively small, low doses of SIN-1 sometimes caused a stimulation of I_{Ca} rather than an inhibition (Fig. 23.10). A similar enhancement of β-stimulated I_{Ca} by low doses of pipette cGMP had been reported previously (Ono and Trautwein, 1991). Thus, while NO and cGMP generally have an inhibitory effect on I_{Ca}, in some instances, they can actually enhance the response to β-stimulation of I_{Ca}. The stimulatory effect of SIN-1 occasionally observed is likely to be mediated by the same mechanism thought to be responsible for cGMP stimulation of cAMP-enhanced I_{Ca} previously described for guinea pig ventricular myocytes, i.e. cGMP inhibition of the cGMP-inhibited PDE (Ono and Trautwein, 1991).

IVD. Pathophysiological Effects of Nitric Oxide/cGMP

Nitric oxide is synthesized by nitric oxide synthase (NOS) from L-arginine. NOS exists in three isoforms, neuronal nitric oxide synthase (NOS-1 or nNOS), inducible nitric oxide synthase (NOS-2 or iNOS), and endothelial nitric oxide synthase (NOS-3 or eNOS) (Alderton et al., 2001). The constitutive isoforms of NOS (NOS-1 and NOS-3) produce relatively small amounts of NO in a Ca^{2+}-dependent fashion (Xie and Nathan, 1994). In cardiac myocytes, constitutive NOS (primarily eNOS) is normally present and functional (Schulz et al., 1992). In contrast, iNOS (which produces much more NO than the constitutive isoform and for longer periods of time) is not normally present in most types of cells, including cardiac myocytes. However, it is expressed in cardiac myocytes under pathological conditions that involve exposure of the cells to cytokines. Thus, it may be that NO produced by constitutive NOS mediates the physiological effects of NO, whereas the much higher levels of NO produced by iNOS may mediate the pathophysiological actions of NO in a number of pathological conditions of the heart. For example, pre-exposure of guinea pig ventricular myocytes to IL-1β for several hours has an anti-adrenergic effect on I_{Ca} that is L-arginine-dependent and NO-mediated (Rozanski and Witt, 1994).

Transplanted hearts are exposed to a variety of cytokines during rejection and have an increased NO production and depressed contractility. Myocytes isolated from rejecting hearts exhibit parallel increases in NO (and cGMP) production (due to the expression of the inducible form of nitric oxide synthase) (Yang et al., 1994; Ziolo et al., 1998) and both a reduced basal contraction and inotropic response to β-adrenergic stimulation (Pyo and Wahler, 1995; Ziolo et al., 1998). The reduced contractile function is due to an NO/cGMP-mediated inhibition of I_{Ca}. Thus, I_{Ca} is reduced in myocytes from rejecting transplanted rat hearts (allografts) compared to myocytes from non-rejecting transplanted control hearts (isografts) (Ziolo et al., 2001). This reduction in I_{Ca} in the allograft myocytes is dependent on L-arginine (the precursor of NO). Additionally, aminoguanidine (a selective inhibitor of the inducible nitric oxide synthase) and KT5823 (a selective inhibitor of PK-G) rapidly reversed the elevated NO and cGMP production, the inhibition of I_{Ca} and the contractile depression in allograft myocytes, but had no effect on I_{Ca} or contraction of isograft myocytes (Ziolo et al., 1998, 2001). In human transplant patients, expression of iNOS in rejecting hearts correlates with increased cGMP levels and

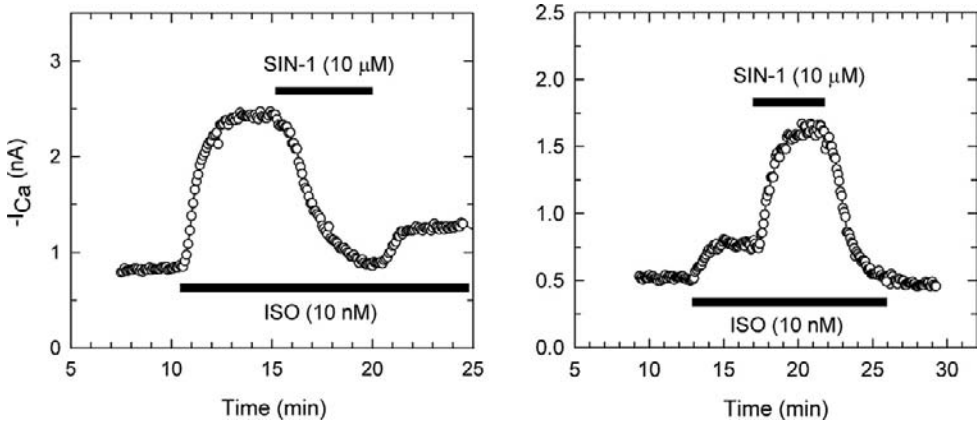

FIGURE 23.10 SIN-1 inhibition and stimulation of isoproterenol (ISO)-enhanced calcium current (I_{Ca}). Shown are time courses of I_{Ca} response during superfusion of cells with control (CONT), 10 nM ISO, and IS0 plus 10 μM SIN-1 (IS0 + SIN-1) bath solutions. Currents were recorded at 0 mV. Left panel: in this cell, 10 nM IS0 had a large effect on I_{Ca}, and subsequent exposure to 10 μM SIN-1 caused a considerable inhibition of ISO-enhanced I_{Ca}. I_{Ca} partially recovered following washout of SIN-1 with IS0 solution. Right panel: in another cell, the response to 10 nM IS0 was quite small, compared with the left panel example, and exposure to 10 μM SIN-1 substantially increased ISO-enhanced I_{Ca}. *(Modified from Wahler and Dollinger, 1995; used with permission.)*

depressed contractility (Lewis et al., 1996; Paulus et al., 1997).

V. PHOSPHODIESTERASES

VA. cAMP PDEs

The hydrolysis of cyclic nucleotides occurs via phosphodiesterases (PDEs). There are 11 isoform families of these enzymes that hydrolyze cAMP and/or cGMP, of which PDEs 2-5 seem to be the most important ones for cyclic nucleotide regulation in cardiac myocytes (for review see Fischmeister et al., 2006). Previous studies have found that inhibitors of PDEs, not only can increase basal I_{Ca}, they can also potentiate the effect of β-adrenergic stimulation on I_{Ca} (e.g. Fischmeister and Hartzell, 1991; Mubagwa et al., 1993; Kawamura and Wahler, 1994; Wahler and Dollinger, 1995; Kajimoto et al., 1997; Verde et al., 1999). Thus, it is clear that both the synthesis and the rate of hydrolysis of cAMP are important in regulating I_{Ca}.

It should be noted that cGMP interacts with several isoforms of PDE that preferentially hydrolyze cAMP. Thus, the activity PDE 2 (the PDE responsible for the anti-adrenergic effects of cGMP in frog ventricular myocytes) is stimulated by cGMP. In addition, PDE 3 is a cGMP-inhibited PDE and it is this PDE which appears to mediate the positive (stimulatory) effect of cGMP on I_{Ca}.

VB. cGMP PDE

Of the multiple isoforms of PDE, some preferentially degrade cAMP, whereas others hydrolyze both cAMP and cGMP equally. One family of isoforms (PDE 5) preferentially hydrolyzes cGMP (for review, see Francis et al., 2010). The inhibitory action of exogenous cGMP on I_{Ca} can be mimicked by reducing cGMP hydrolysis through inhibition of PDE 5. A commonly used inhibitor of PDE 5 is zaprinast, which has been shown to be a specific inhibitor of this PDE isoform in the heart (Prigent et al., 1988; Kotera et al., 1998). Zaprinast has been shown to have an anti-adrenergic effect on I_{Ca} similar to exogenous cGMP (Ziolo et al., 2003). That is, zaprinast inhibited the I_{Ca} of cardiac myocytes following stimulation by isoproterenol or forskolin (see Figs. 23.1 and 23.2). The inhibitory effect of zaprinast was blocked by the PK-G inhibitor, KT5823 (see Fig. 23.2) and it was accompanied by an approximately threefold increase in intracellular cGMP levels and no change in cAMP levels. Since cAMP levels were not altered by zaprinast at the concentrations used in this study, significant non-specific inhibition of other PDE isoforms does not appear to occur with zaprinast at this concentration. These results also suggest that the effects of zaprinast were unlikely to be due to indirect effects of cGMP-induced decreases in cAMP levels caused by stimulation of PDE 2.

In standard whole-cell recording, in which intracellular Ca^{2+} concentration is unphysiologically low, zaprinast did not significantly alter basal (unstimulated) I_{Ca}. In contrast, zaprinast did inhibit basal I_{Ca} when the perforated-patch technique was used (which maintains a more physiological intracellular environment) or when whole-cell recording was used with free Ca^{2+} concentration maintained at a more physiological level (pCa = 7) (Ziolo et al., 2003). These results indicate that, under more physiological intracellular conditions, increases in endogenous cGMP can inhibit both the basal and cAMP-stimulated I_{Ca} via a mechanism that involves PK-G.

Intracellular Ca^{2+} modulates the activity of several isoforms of the enzymes that synthesize and hydrolyze cyclic nucleotides. As a result, the overall effects of the unphysiologically low levels of intracellular Ca^{2+} often used in standard whole-cell voltage clamp recording on modulation of I_{Ca} by different steps in the cAMP and/or cGMP pathways can be unpredictable. For example, perforated-patch recording enhances the I_{Ca} response to β-adrenergic stimulation, but reduces the I_{Ca} response to the non-specific PDE inhibitor IBMX (Kawamura and Wahler, 1994). Perhaps one reason that, with cGMP elevation, the basal response of I_{Ca} is typically small or non-existent while there is a much greater response of the cAMP-enhanced I_{Ca}, is that increased cAMP levels typically lead to an increase in intracellular Ca^{2+} levels, which then may upregulate one or more steps in the cGMP—PK-G pathway. As noted earlier, basal Ca^{2+} channel activity can be inhibited by PK-G under some circumstances (e.g. following overproduction of PK-G 1 in cardiac myocytes; Schröder et al., 2003) in which PK-G levels and/or activity are enhanced.

VI. COMPARTMENTALIZATION OF CYCLIC NUCLEOTIDES

The cyclic nucleotide signaling pathways are known to demonstrate a substantial amount of compartmentation. For example, although both particulate and soluble G-cyclases synthesize cGMP, the two cyclases respond to different agonists (natriuretic peptides for the particulate enzyme and NO for the soluble one) and their responses are mediated by different effectors. Additionally, there are clearly localized microdomains in which synthesizing enzymes, PDEs and effectors are in close proximity and act as a functional unit. What has only recently begun to be appreciated is that the spatial distribution of components of the system is not always fixed (not solely due to physical constraints).

Some of the isoforms of the enzymes involved in synthesizing and degrading cyclic nucleotides are substrates for cyclic nucleotide-dependent kinases. Thus, cAMP exerts a negative feedback control of its own concentration and localization due to PK-A stimulation of

PDE activity (Fischmeister et al., 2006). Similarly, PDE 5 (which is co-localized with soluble G-cyclase) is a substrate for PK-G and its activity is increased by PK-G phosphorylation. PK-G decreases the accumulation of soluble G-cyclase-generated cGMP by enhancing PDE 5 activity. On the other hand, PK-G increases the accumulation of particulate G-cyclase-generated cGMP by stimulating particulate G-cyclase activity. As a result, the distribution of cGMP within the cell is altered in response to PK-G activation. Additionally, when PDE activity is largely eliminated with a non-specific PDE inhibitor (IBMX), cGMP compartmentalization disappears and cGMP diffusion is no longer restricted, suggesting that cGMP diffusion within the cell is restricted primarily by the activity of PDEs, rather than by physical barriers (Castro et al., 2010).

Such regulation of cyclic nucleotide compartmentalization is not limited to feedback regulation of a cyclic nucleotide by its own effectors. That is, there is considerable cross-talk between the cAMP and cGMP systems. For example, the contractile response to β-adrenergic stimulation has been shown to be modulated by the soluble cGMP pool (i.e. the cGMP synthesized by soluble G-cyclase and degraded by PDE 5), but not the particulate cGMP pool, even though stimulation of particulate G-cyclase causes a larger global increase in cGMP levels than stimulation of soluble G-cyclase (Takimoto et al., 2007).

BIBLIOGRAPHY

Ahmad, Z., Green, F. J., Subuhi, H. S., & Watanabe, A. M. (1989). Autonomic regulation of type 1 protein phosphatase in cardiac muscle. *J Biol Chem, 264*, 3859–3863.

Alderton, W. K., Cooper, C. E., & Knowles, R. G. (2001). Nitric oxide synthases: structure, function and inhibition. *Biochem J, 357*, 593–615.

Armstrong, D., & Eckert, R. (1987). Voltage-activated calcium channels that must be phosphorylation to respond to membrane depolarization. *Proc Natl Acad Sci USA, 84*. 2518–1522.

Bkaily, G., & Sperelakis, N. (1984). Injection of protein kinase inhibitor into cultured heart cells blocks calcium slow channels. *Am J Physiol, 248*, H745–H749.

Bkaily, G., & Sperelakis, N. (1985). Injection of cyclic GMP into heart cells blocks the Ca^{2+} slow channels. *Am J Physiol, 248*, H745–H749.

Castro, L. R. V., Schittl, J., & Fischmeister, R. (2010). Feedback control through cGMP-dependent protein kinase contributes to differential regulation and compartmentation of cGMP in rat cardiac myocytes. *Circ Res, 107*, 1232–1240.

duBell, W. H., & Rogers, T. B. (2004). Protein phosphatase 1 and an opposing protein kinase regulate steady-state L-type Ca^{2+} current in mouse cardiac myocytes. *J Physiol, 556*, 79–93.

Fischmeister, R., & Hartzell, H. C. (1987). Cyclic guanosine 3′,5′-monophosphate regulates the calcium current in single cells from frog ventricle. *J Physiol, 387*, 455–472.

Fischmeister, R., & Hartzell, H. C. (1991). Cyclic AMP phosphodiesterases and Ca^{2+} current regulation in cardiac cells. *Life Sci, 48*, 2365–2376.

Fischmeister, R., Castro, L. R. V., Abi-Gerges, A., et al. (2006). Compartmentation of cyclic nucleotide signaling in the heart. The role of cyclic nucleotide phosphodiesterases. *Circ Res, 99*, 816–828.

Frace, A. M., & Hartzell, H. C. (1993). Opposite effects of phosphatase inhibitors on L-type calcium and delayed rectifier currents in frog ventricular myocytes. *J Physiol, 472*, 305–326.

Francis, S. H., Busch, J. L., & Corbin, J. D. (2010). cGMP-dependent protein kinases and cGMP phosphodiesterases in nitric oxide and cGMP action. *Pharmacol Rev, 62*, 525–563.

Goldberg, N. D., Haddox, M. K., Nicol, S. E., et al. (1975). Biological regulation through opposing influences of cyclic GMP and cyclic AMP: the Yin Yang hypothesis. *Adv Cyclic Nucleotides, 5*, 307–330.

Gupta, R. C., Neumann, J., Watanabe, A. M., Lesch, M., & Sabbah, H. N. (1996). Evidence for presence and hormonal regulation of protein phosphatase inhibitor-1 in ventricular cardiomyocytes. *Am J Physiol, 270*, H1159–H1164.

Haddad, G. E., Sperelakis, N., & Bkaily, G. (1995). Regulation of calcium channel by cyclic GMP-dependent protein kinase in chick heart cells. *Mol Cell Biochem, 148*, 89–94.

Hartzell, H. C., & Fischmeister, R. (1986). Opposite effects of cyclic GMP and cyclic AMP on Ca2+ current in single heart cells. *Nature, 323*, 273–275.

Hescheler, J., Kameyama, M., Trautwein, W., Mieskes, G., & Soling, H. D. (1987). Regulation of the cardiac calcium channel by protein phosphatases. *Eur J Biochem, 165*, 261–266.

Hescheler, J., Mieskes, G., Ruegg, J. C., Takai, A., & Trautwein, W. (1988). Effects of a protein phosphatase inhibitor, okadaic acid, on membrane currents of isolated guinea-pig cardiac myocytes. *Pflügers Arch, 412*, 248–252.

Irisawa, H., & Kokubun, S. (1983). Modulation of intracellular ATP and cyclic AMP of the slow inward current in isolated single ventricular cells of the guinea-pig. *J Physiol, 338*, 321–327.

Josephson, I., & Sperelakis, N. (1978). 5′Guanylimidophosphate stimulation of slow Ca^{2+} current in myocardial cells. *J Molec Cell Cardiol, 10*, 1157–1166.

Kajimoto, K., Hagiwara, N., Kasanuki, H., & Hosoda, S. (1997). Contribution of phosphodiesterase isozymes to the regulation of the L-type calcium current in human cardiac myocytes. *Br J Pharmacol, 121*, 1549–1556.

Kameyama, M., Hoffman, F., & Trautwein, W. (1986). On the mechanism of β-adrenergic regulation of the Ca^{2+} channel in the guinea pig heart. *Pflügers Arch, 405*, 285–293.

Kawamura, A., & Wahler, G. M. (1994). Perforated-patch recording does not enhance effect of 3-isobutyl-l-methylxanthine on cardiac calcium current. *Am J Physiol, 266*, C1619–C1627.

Klein, G., Drexler, H., & Schröder, F. (2000). Protein kinase G reverses all isoproterenol induced changes of cardiac L-type calcium channel gating. *Cardiovasc Res, 48*, 367–374.

Kohlhardt, M., & Haap, K. (1978). 8-Bromo-guanosine-3′, 5′-monophosphate mimics the effect of acetylcholine on slow response action potential and contractile force in mammalian atrial myocardium. *J Mol Cell Cardiol, 10*, 573–578.

Kontos, H. A., & Wei, E. P. (1993). Hydroxyl radical-dependent inactivation of guanylate cyclase in cerebral arteries by methylene blue and LY83583. *Stroke, 24*, 427–433.

Kotera, J., Fujishige, K., Akatsuka, H., et al. (1998). Novel alternative splice variants of cGMP-binding cGMP-specifc phosphodiesterase. *J Biol Chem, 273*, 26982–26990.

Levi, R. C., Alloatti, G., & Fischmeister, R. (1989). Cyclic GMP regulates the Ca-channel current in guinea pig ventricular myocytes. *Pflügers Arch, 413*, 685−687.

Levi, R. C., AIloatti, G., Penna, C., & Gallo, M. P. (1994). Guanylate cyclase-mediated inhibition of cardiac I_{Ca}, by carbachol and sodium nitroprusside. *Pflügers Arch, 426*, 419−426.

Lewis, N. P., Tsao, P. S., Rickenbacker, P. R., et al. (1996). Induction of nitric oxide synthase in human cardiac allograft is associated with contractile dysfunction of the left ventricle. *Circulation, 93*, 720−729.

Li, T., & Sperelakis, N. (1983). Stimulation of slow action potentials in guinea pig papillary muscle cells by intracellular injection of cAMP, Gpp(NH)p, and cholera toxin. *Circ Res, 52*, 111−117.

Matsumoto, S. (1997). Effect of molsidomine on basal Ca^{2+} current in rat cardiac cells. *Life Sci, 50*, 383−390.

Mehegan, J. P., Muir, W. W., Unverferth, D. V., Fertel, R. H., & McGuirck, S. M. (1985). Electrophysiological effects of cyclic GMP on canine cardiac Purkinje fibers. *J Cardiovasc Pharmacol, 7*, 30−35.

Mery, P. F., Lohmann, S. M., Walter, U., & Fischmeister, R. (1991). Ca^{2+} current is regulated by cyclic GMP-dependent protein kinase in mammalian cardiac myocytes. *Proc Natl Acad Sci USA, 88*, 1197−1201.

Mery, P. F., Pavoine, C., Belhassen, L., Pecker, F., & Fischmeister, R. (1993). Nitric oxide regulates cardiac Ca^{2+} current. Involvement of cGMP-inhibited and cGMP-stimulated phosphodiesterases through guanylyl cyclase activation. *J Biol Chem, 268*, 26286−26295.

Mubagwa, K., Shirayama, T., Moreau, M., & Pappano, A. J. (1993). Effects of phosphodiesterase inhibitors and carbachol on the L-type calcium current in guinea pig ventricular myocytes. *Am J Physiol, 264*, H1353−H1363.

Nargeot, J., Nerbonne, J. M., Engels, J., & Lester, H. A. (1983). Time course of the increase in myocardial slow inward current after a photochemically generated concentration jump of intracellular cAMP. *Proc Natl Acad Sci USA, 80*, 2395−2399.

Nawrath, H. (1977). Does cyclic GMP mediate the negative inotropic effect of acetylcholine in the heart? *Nature, 267*, 72−74.

Ono, K., & Trautwein, W. (1991). Potentiation by cyclic GMP of β-adrenergic effect on Ca^{2+} current in guinea-pig ventricular cells. *J Physiol, 443*, 387−404.

Osterreider, W., Brum, G., Hescheler, J., et al. (1982). Injection of subunits of cyclic AMP-dependent protein kinase into cardiac myocytes modulates Ca^{2+} current. *Nature, 298*, 576−578.

Paulus, W. J., Kastner, S., Pujadas, P., et al. (1997). Left ventricular contractile effects of inducible nitric oxide synthase in the human allograft. *Circulation, 96*, 3336−3342.

Pyo, R., & Wahler, G. M. (1995). Ventricular myocytes isolated from rejecting cardiac allografts exhibit a reduced β-adrenergic contractile response. *J Molec Cell Cardiol, 27*, 773−776.

Prigent, A. F., Fougier, S., Nemoz, G., et al. (1988). Comparison of cyclic nucleotide phosphodiesterase isozymes from rat heart and bovine aorta. Separation and inhibition by selective reference phosphodiesterase inhibitors. *Biochem Pharmacol, 37*, 3671−3681.

Reuter, H., Stevens, C.-F., Tsien, R. W., & Yellen, G. (1982). Properties of single calcium channels in cardiac cell culture. *Nature, 297*, 501−504.

Rivet-Bastide, M., Vandecasteele, G., Hatem, S., et al. (1997). cGMP-stimulated cyclic nucleotide phosphodiesterase regulates the basal calcium current in human atrial myocytes. *J Clin Invest, 99*, 2710−2718.

Rozanski, G. J., & Witt, R. C. (1994). IL-1 inhibits β-adrenergic control of cardiac calcium current: role of L-arginine/nitric oxide pathway. *Am J Physiol, 267*, H1753−H1758.

Schröder, F., Klein, G., Fiedler, B., et al. (2003). Single L-type Ca^{2+} channel regulation by cGMP-dependent protein kinase type 1 in adult cardiomyocytes from PKG 1 transgenic mice. *Cardiovasc Res, 60*, 268−277.

Schulz, R., Nava, E., & Moncada, S. (1992). Induction and potential biological relevance of a Ca^{2+}-independent nitric oxide synthase in the myocardium. *Br J Pharmacol, 105*, 575−580.

Shigenobu, K., & Sperelakis, N. (1972). Ca^{2+} current channels induced by catecholamines in chick embryonic hearts whose fast Na^{+} channels are blocked by tetrodotoxin or elevated K^{+}. *Circ Res, 31*, 932−952.

Stojanovic, M. O., Ziolo, M. T., Wahler, G. M., & Wolska, B. M. (2001). Anti-adrenergic effects of nitric oxide donor SIN-1 in rat cardiac myocytes. *Am J Physiol, 281*, C342−C349.

Sumii, K., & Sperelakis, N. (1995). Cyclic GMP-dependent protein kinase regulation of the L-type calcium current in neonatal rat ventricular myocytes. *Circ Res, 77*, 803−812.

Takimoto, E., Belardi, D., Tocchetti, C. G., et al. (2007). Compartmentalization of cardiac β-adrenergic inotropy modulation by phosphodiesterase type 5. *Circulation, 115*, 2159−2167.

Tandan, S., Wang, Y., Wang, T. T., et al. (2009). Physical and functional interaction between calcineurin and the cardiac L-type Ca^{2+} channel. *Circ Res, 150*, 51−60.

Thakkar, J., Tang, S. B., Sperelakis, N., & Wahler, G. M. (1989). Inhibition of cardiac slow action potentials by 8-bromo-cyclic GMP occurs independent of changes in cyclic AMP levels. *Can J Physiol Pharmacol, 66*, 1092−1095.

Tohse, N., & Sperelakis, N. (1991). Cyclic GMP inhibits the activity of single calcium channels in embryonic chick heart cells. *Circ Res, 69*, 325−331.

Tsien, R. W., Giles, W., & Greengard, P. (1972). Cyclic AMP mediates the action of adrenaline on the action potential plateau of cardiac Purkinje fibers. *Nature, 240*, 181−183.

Verde, I., Vandecasteele, G., Lezoualc'h, F., & Fischmeister, R. (1999). Characterization of the cyclic nucleotide phosphodiesterase subtypes involved in the regulation of the L-type Ca^{2+} current in rat ventricular myocytes. *Br J Pharmacol, 127*, 65−74.

Vogel, S., & Sperelakis, N. (1981). Induction of slow action potentials by microiontophoresis of cyclic AMP into heart cells. *J Molec Cell Cardiol, 13*, 51−64.

Wahler, G. M., & Dollinger, S. J. (1995). Nitric oxide donor SIN-1 inhibits mammalian cardiac calcium current through cGMP-dependent protein kinase. *Am J Physiol, 268*, C45−C54.

Wahler, G. M., & Sperelakis, N. (1985). Intracellular injection of cyclic GMP depresses cardiac slow action potentials. *J Cyclic Nucleotide Protein Phosphorylation Res, 10*, 83−95.

Wahler, G. M., & Sperelakis, N. (1986). Cholinergic attenuation of the electrophysiological effects of forskolin. *J Cyclic Nucleotide Protein Phosphorylation Res, 11*, 1−10.

Wahler, G. M., Rusch, N. J., & Sperelakis, N. (1990). 8-Bromo-cyclic GMP inhibits the calcium channel current in embryonic chick ventricular myocytes. *Can J Physiol Pharmacol, 68*, 531−534.

Wegener, J. W., Nawrath, H., Wolfsgruber, W., et al. (2002). cGMP-dependent protein kinase I mediates the negative inotropic effect of cGMP in the murine myocardium. *Circ Res, 90*, 18−20.

Xie, Q., & Nathan, C. (1994). The high-output nitric oxide pathway: role and regulation. *J Leukocyte Biol, 56*, 572−582.

Yang, X., Chowdhury, N., Cai, B., et al. (1994). Induction of myocardial nitric oxide synthase by cardiac allograft rejection. *J Clin Invest, 94*, 714−721.

Yang, L., Liu, G., Zakharov, S. I., et al. (2007). Protein kinase G phosphorylates Cav1.2 alpha1c and beta2 subunits. *Circ Res, 101*, 465−474.

Ziolo, M. T., Dollinger, S. J., & Wahler, G. M. (1998). Myocytes isolated from rejecting transplanted hearts exhibit reduced basal shortening which is reversible by aminoguanidine. *J Molec Cell Cardiol, 30*, 1009−1017.

Ziolo, M. T., Harshbarger, C. H., Roycroft, K. E., et al. (2001). Myocytes isolated from rejecting transplanted rat hearts exhibit a nitric oxide-mediated reduction in the calcium current. *J Molec Cell Cardiol, 33*, 1691−1699.

Ziolo, M. T., Lewandowski, S. J., Smith, J. M., Romano, F. D., & Wahler, G. M. (2003). Inhibition of cyclic GMP hydrolysis with zaprinast reduces basal and cyclic AMP-elevated L-type calcium current in guinea pig ventricular myocytes. *Br J Pharmacol, 138*, 986−994.

This page intentionally left blank

Chapter 24

Direct Regulation of Ion Channels by GTP-Binding Proteins

Atsushi Inanobe and Yoshihisa Kurachi

Chapter Outline

I. INTRODUCTION

Various extracellular stimuli can initiate physiological processes by changing membrane potentials. These stimuli regulate ionic flows by controlling the opening and closing of ion channel pores. A cluster of membrane receptors that are coupled to heterotrimeric GTP-binding proteins (G proteins) provide the largest contribution to these signaling pathways. This type of receptor is called a G-protein-coupled receptor (GPCR) and it regulates a relatively small number of different enzymes and ion channels. Because sequential protein interactions mediate GPCR signaling, the signaling pathways cause the temporal range of cellular responses to vary from milliseconds to hours. The responses are obviously slower than those evoked by ionotropic neurotransmitter receptors, which operate within milliseconds. Many ion channels are under direct or indirect control by G proteins. One example of the regulation of an ion channel by the direct action of G proteins is that of activation by acetylcholine (ACh) of the muscarinic K^+ channel in the heart (Kurachi, 1995). This action is responsible for the deceleration of the heartbeat upon stimulation of the vagus nerve (Fig. 24.1A) (Loewi, 1921). This K^+ channel is also responsible for the formation of the slow inhibitory postsynaptic potential in the central nervous system (Fig. 24.1B) (Lüscher and Slesinger, 2010). Furthermore, it is also known that this system is responsible for inhibition of presynaptic Ca^{2+} channels (Dolphin, 1998; Currie, 2010). Direct regulation of ion channels by G proteins is therefore an important cell signaling system.

II. G-PROTEIN-COUPLED RECEPTORS

G-protein-coupled receptors (GPCRs) are encoded by over 900 genes and they constitute the largest family of

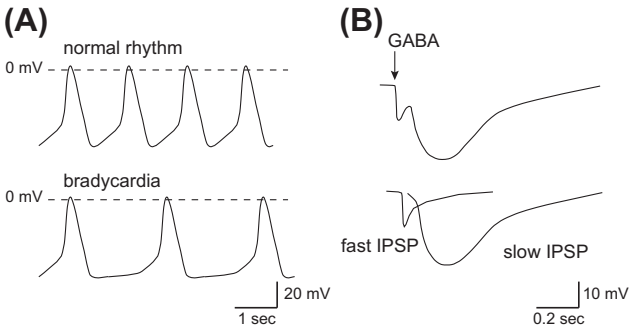

FIGURE 24.1 Physiological implications of the control of cell excitability by K_G channels. (A) Control of cell excitability in the sinoatrial nodal cells. Vagus nerve stimulation augments K^+ conductance at potentials near the equilibrium potential of K^+ and prolongs the interval between action potentials without affecting the action potential configuration. (B) The control of excitability at the inhibitory postsynaptic membranes. γ-Amino butyric acid (GABA) released at the synaptic cleft elicits biphasic changes in the postsynaptic membrane potential of inhibitory synapses (IPSP). While ionotropic $GABA_A$ receptors carrying Cl^- influx mediate the fast response, metabotropic $GABA_B$ receptors increase the K^+ efflux via G proteins.

Cell Physiology Sourcebook. DOI: 10.1016/B978-0-12-387738-3.00023-8

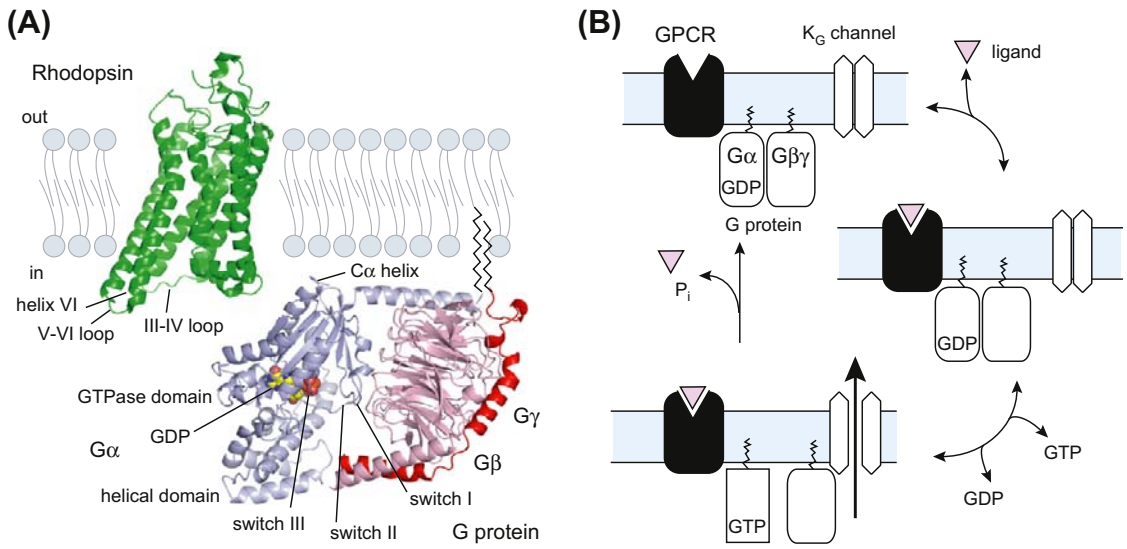

FIGURE 24.2 Molecular architectures of GPCR and G proteins and the G-protein cycle. (A) Molecular architectures of rhodopsin and G protein. The structures of retinal-free rhodopsin (Protein Data Bank identifier 3DQB) is colored in green and the trimeric complexes containing the $G\alpha_t/G\alpha_i$ chimera and the $G\beta\gamma_1$ subunits (1GOT) are colored in blue-gray and pink, respectively. The bound nucleotide on Gα is represented as a sphere. Palmitoylation and myristoylation are common post-transcriptional modifications at the N-terminus of Gα and the C-terminus of Gγ, respectively. (B) Schematic representation of the G-protein cycle. GPCR: G-protein-coupled receptor; Gα and Gβγ: α and βγ subunits of trimeric G protein, respectively; K_G channel: G-protein-gated inwardly rectifying K^+ channel.

membrane-embedded proteins in the mammalian genome (Fredriksson et al., 2003; Bjarnadottir et al., 2006). GPCRs are important targets for drugs in all therapeutic areas, and they form the sites for the effects of 25−30% of existing drugs (Overington et al., 2006). GPCRs possess heptahelical transmembrane segments and their N- and C-termini are exposed to the extracellular and intracellular sides of the membrane, respectively (Fig. 24.2A). The GPCRs in the human genome can be divided into five subfamilies that have diverse N-terminal extracellular architectures at the sites where ligands bind and trigger activation of the receptor (Fredriksson et al., 2003). Although the ligands interact with sites differently positioned within GPCRs, they ultimately evoke conformational changes at the cytoplasmic interface to activate G proteins. The most significant conformational change is probably an outward movement of helix VI and subsequent reorientation of the cytoplasmic end of the helix (Fig. 24.2A). This may be linked with the opening of a crevice within the intracellular surface of the receptor and it could allow Gα proteins to interact at their C-termini (Scheerer et al., 2008).

III. THE G-PROTEIN CYCLIC REACTION MEDIATES RECEPTOR-TO-CHANNEL SIGNAL TRANSMISSION

G proteins consist of Gα, Gβ and Gγ subunits (Gilman, 1987; Sprang, 1997; Oldham and Hamm, 2008). To date, at least 16 Gα, 5 Gβ and 12 Gγ genes have been identified. Gα has been subclassified into four groups ($G\alpha_s$, $G\alpha_i$, $G\alpha_q$ and $G\alpha_{12}$) on the basis of sequence similarity, coupling effectors and sensitivity to toxins. The crystal structures of Gα and Gαβγ have revealed the presence of two preserved domain architectures: the GTPase domain and the helical domain. The former is conserved among all members of G proteins and it hydrolyzes GTP. The latter is specific for Gα, which interacts with the GTPase domain by covering the nucleotide-binding pocket. Under physiological conditions, Gβ and Gγ associate tightly to form a dimer (Gβγ). Gβ is in the form of a seven-bladed propeller, each blade of which is a four-stranded anti-parallel β−sheet. The N-terminus of Gβ possesses an α-helix that forms a coiled-coil with the N-terminus of Gγ. The physiological significance of the possible heterogeneity of Gβγ has been a matter of debate.

In the absence of agonists, Gα exists predominantly in an inactive GDP-bound state (Gα-GDP) (see Fig. 24.2B) (Gilman, 1987; Oldham and Hamm, 2008). Gα-GDP has a high affinity for Gβγ, forming a heterotrimer. Receptor stimulation allows Gα and GDP to dissociate, which results in marked acceleration of the GDP−GTP exchange reaction. Formation of GTP-bound Gα (Gα-GTP) leads to dissociation of Gβγ from Gα-GTP. The separate components of the G protein (Gα-GTP and Gβγ) are subsequently available to transduce signals to the downstream effectors. Gα hydrolyzes the bound GTP to GDP, thereby returning to its GDP-bound state (Gα-GDP), which re-associates with Gβγ. This reaction terminates effector regulation, and

the agonist-occupied receptor triggers the heterotrimeric G protein to restart the cycle.

The C-terminus of Gα probably binds to the open crevice in a ligand-associated GPCR (Sprang, 1997; Scheerer et al., 2008). Multiple contacts mediate the interaction of Gα with GPCR. Furthermore, Gβ and Gγ stabilize the GPCR-G protein complex. Extensive contact is necessary for a change to occur in the conformation of Gα, leading to the GDP—GTP exchange reaction. The partially overlapped areas are thought to be involved in the specificity of GPCR-coupling on G proteins. Although poor sequence conservation prevents the identification of the source of G-protein-coupling specificity on GPCR, cytoplasmic loops III—IV and the C-terminus are believed to be closely involved.

IV. ELECTROPHYSIOLOGICAL EVIDENCE FOR K^+ CHANNEL ACTIVATION BY G PROTEINS

On stimulation of vagus nerves, ACh released from synaptic terminals decelerates the heartbeat and decreases atrioventricular conduction (see Fig. 24.1A) (Loewi, 1921). ACh causes membrane hyperpolarization in the heart (Del Castillo and Katz, 1955), by increasing K^+ efflux across the cell membrane (Hutter and Trautwein, 1956). A specific population of K^+ channels, the muscarinic K^+ (K_{ACh}) channels, is responsible for this efflux (Trautwein and Dudel, 1958; Noma and Trautwein, 1978) and treatment with a toxin from *Bordetella pertussis* prevents activation of the channel by m_2-muscarinic and A_1-adenosine receptors (Kurachi et al., 1986a). In cell-free inside-out membrane patches, internal GTP (in the presence of extracellular agonists) and non-hydrolyzable analog of GTP, GTPγS, activate the K_{ACh} channel (Kurachi et al., 1986b). These observations led to the proposal that the channel is directly activated by G proteins in a membrane-delimited manner. Subsequently, it was found that Gβγ, but not Gα, was the subunit responsible for activating the K_{ACh} channel (Logothetis et al., 1987). Because G-protein-sensitive K^+ (K_G) channels in neurons and endocrine cells are also regulated by Gβγ like cardiac K_{ACh} channels, we refer to these types of channel as "K_G channels" henceforth.

V. ELECTROPHYSIOLOGICAL PROPERTIES OF K_G CHANNELS

The difference between the membrane potential (V_m) and the equilibrium potential of K^+ (E_K) drives K^+ ions through K_G channels (Trautwein and Dudel, 1958; Noma and Trautwein, 1978; Kurachi, 1995; Yamada et al., 1998). The manner of K^+ conduction through K_G channels is unique, involving a large K^+ conductance at potentials negative relative to E_K, but less outward current flow at potentials positive relative to E_K (Fig. 24.3A). Blocking of the outward K^+ flow by intracellular Mg^{2+} and polyamines is responsible for this diode-like conduction and this property is similar to that originally observed as "anomalous" rectifier K^+ currents in skeletal muscles of the frog (Katz, 1949). The unidirectional conduction permits a prolongation of the interval of action potential with little effect on the action potential configuration (see Fig. 24.1A). Therefore, the inward rectification property of K_G channels is fundamental to their physiological function.

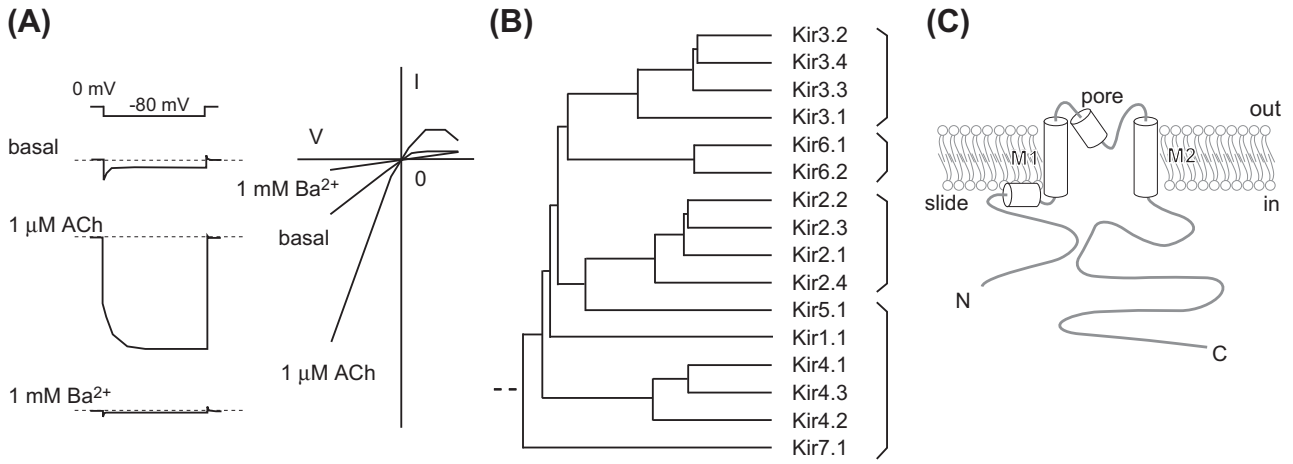

FIGURE 24.3 Kir channel members and their structural description. (A) Representative current response of the K_G channel. The reconstituted K_G channel with Kir3.1, Kir3.4 and m_2-muscarinic receptor shows a rapid change in current followed by a gradual increase on application of hyperpolarizing voltage steps from E_K. External Ba^{2+} practically blocks most Kir channels. (B) Phylogenic tree of Kir channels. The Kir channel members can be classified into four groups: G: protein-gated Kir (K_G) channels, Kir3.x; ATP-sensitive Kir channels, Kir6.x; classical Kir channels, Kir2.x; K^+ transport-Kir channels, Kir1.1, Kir4.x, Kir5.1 and Kir7.1. (C) Simple representation of Kir channels. Each subunit contains a transmembrane domain that flanks cytoplasmic N- and C-termini.

The activity of the K_G channel increases in response to GPCR activation. As discussed below, direct interactions with Gβγ and the K_G channel are responsible for this response. How does Gβγ augment the channel activity? The macroscopic current amplitude (I) of the K_G channels can be defined as follows:

$$I = N \times P_o \times i = N \times P_o \times \gamma \times (V_m - {}_EK) \quad (24.1)$$

where N is the number of channels in the patch membrane, P_o is the probability of the channel being open, i is the single-channel current amplitude and γ is the single-channel conductance. Therefore, the changes in macroscopic current amplitude during continuous recording can be explained in terms of changes in P_o and γ. The single-channel conductance of either a native or a recombinant K_G channel is dependent on the difference between V_m and ${}_EK$ and is independent of receptor stimulation, thereby showing that the increase in current amplitude caused by Gβγ is the result of an increase in the P_o of the channels.

VI. DIRECT COUPLING OF K_G CHANNEL SUBUNITS TO Gβγ

Mammalian K_G channels form a subgroup of inward rectifier K^+ (Kir) channels (see Fig. 24.3B) (Yamada et al., 1998; Hibino et al., 2010). Each channel consists of four Kir3.x subunits: Kir3.1, Kir3.2, Kir3.3 and Kir3.4 (Kubo et al., 2005). Kir3.1/GIRK1 was the first K_G channel subunit to be isolated from rat atrium (Kubo et al., 1993). Subsequently, Kir3.2−Kir3.4 were isolated from brain and atrial cDNA libraries (Krapivinsky et al., 1995). These gene transcripts are translated into several splicing variants. Four individual Kir3.x subunits assemble to form functional channels. The primary combination of subunits for the I_{kach} is Kir3.1 and Kir3.4 (Krapivinsky et al., 1995). In neural tissues, the K_G channels consist mainly of a heteromeric Kir3.1/Kir3.2 channel and a homomeric Kir3.2 channel. Kir3.3 also assembles to form neuronal K_G channels with Kir3.1 and/or Kir3.2. The primary amino acid sequences of Kir channels show that they possess common transmembrane segments (TM1 and TM2), flanked by a pore-forming region that has a signature motif (T-X-G-Y/F-G) for K^+-selective ion channels (see Fig. 24.3C) (Jan and Jan, 1997). Furthermore, it has been speculated that the unique cytoplasmic N- and C-termini to Kir channels play roles in ion conduction and regulation of gating specific to Kir channels.

Proof of the regulation of K_G channel activity by direct interactions of Gβγ has been provided by several experiments. First, the co-expression of m_2-muscarinic receptor with K_G channel subunits in host cells yielded ACh-dependent channel activity (see Fig. 24.3A) (Reuveny et al., 1994). Secondly, further expression of Gβγ resulted in a constitutively active channel, an effect that could be cancelled by additional expression of the Gβγ-binding domain of β-adrenergic receptor kinase 1 (Reuveny et al., 1994). Thirdly, Gβγ directly bound purified cytoplasmic N- and C-termini of K_G channel subunits, as well as purified recombinant and native K_G channels composed of Kir3.1 and Kir3.4 (Yamada et al., 1998; Bichet et al., 2003). The potential sites for Gβγ binding were thus narrowed down to two distinct regions in the N- and C-termini and several amino acids (the corresponding His57, Leu262, Leu333, and Gly336 in Kir3.1) appear to be critically involved in the Gβγ-dependent activation process.

Because all Kir channels require phosphatidylinositol 4,5-bisphosphate [PtdIns(4,5)P_2] for activation, the lipid is a prerequisite for opening of the K_G channel (Logothetis et al., 2007; Hibino et al., 2010). However, Gβγ and PtdIns(4,5)P_2 cannot activate the channel by themselves. How then do Gβγ and PtdIns(4,5)P_2 regulate the activity of the K_G channel? Electrophysiological and biochemical experiments have shown that the association of Gβγ probably strengthens the channel−PtdIns(4,5)P_2 interactions (Hilgemann and Ball, 1996). Differences in the turnover rate of PtdIns(4,5)P_2 or in the membrane property of lateral diffusion of PtdIns(4,5)P_2 may account for differences in the sensitivity of K_G channels to PtdIns(4,5)P_2 in different cell lines.

VII. STRUCTURAL BASIS OF THE REGULATION OF K_G CHANNEL ACTIVITY

The crystal structures of the isolated cytoplasmic domain of Kir3.1 (Nishida and MacKinnon, 2002) and of the entire bacterial Kir channel homolog KirBac1.1 (Kuo et al., 2003) revealed the structural features of Kir channels (Fig. 24.4A). The Kir channel consists of two functionally and structurally distinct domains: the transmembrane domain and cytoplasmic domain (Bichet et al., 2003; Kuo et al., 2003). The former has a significant degree of similarity with those in other K^+ channels and consists primarily of two long helices (TM1 and TM2), two short helices (slide and pore helices) and a selectivity filter (see Figs. 24.3C and 24.4B). The ion-conduction pathway is located at the center of this assembly. The pore starts at the external vestibule and connects to the selectivity filter. In the middle of the membrane, there is a widening in space, called the central cavity. The C-terminal end of the pore helix is oriented toward the midpoint of the cavity and this is presumed to play a role in the positioning of K^+. The TM2 helix from each subunit makes a physical constraint at the area closed to the cytoplasm. The slide helix located at the internal surface of membrane is connected to the cytoplasmic N-terminus through a short portion consisting of about 10 amino acids.

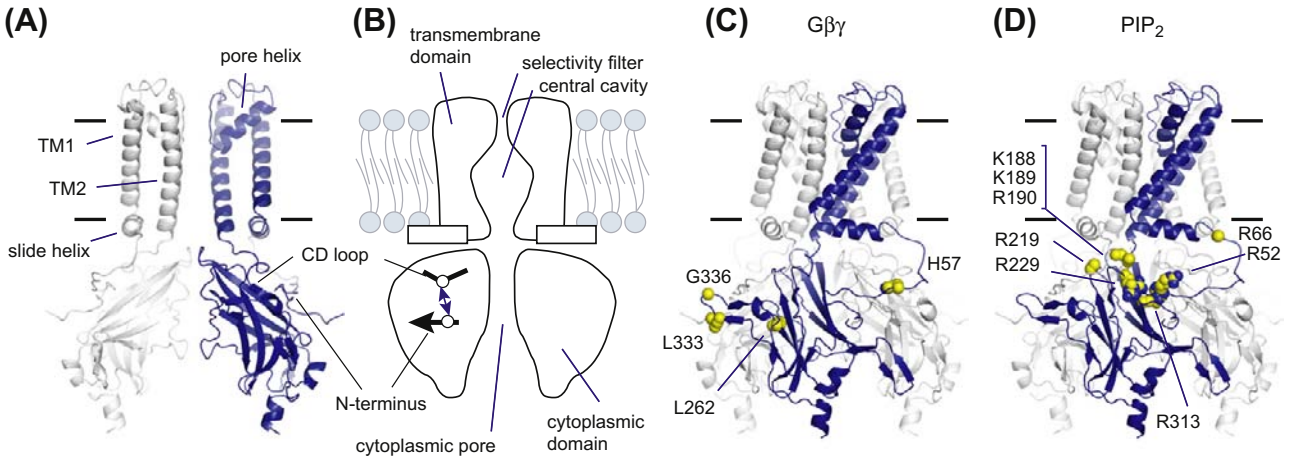

FIGURE 24.4 Structural features of K_G channels. (A) Molecular architecture of K_G channels. The K_G channel has an ion-conduction pathway at the center of a tetrameric assembly. The front and back subunits are omitted for clarity. (B) A schematic representation of K_G channels. The channels consist of two structurally distinct domains: a transmembrane domain and a cytoplasmic domain. The inter-subunit ionic bond between the N-terminus and the CD loop lowers the sensitivity to PtdIns(4,5)P_2 and stabilizes a closed conformation (Inanobe et al., 2010). (C) Residues involved in Gβγ-interaction. Several residues in the K_G channel subunits have been reported to mediate Gβγ-dependent activation. The equivalent residues in Kir3.1 are shown by spheres. (D) Mapping of residues participating in PtdIns(4,5)P_2-dependent activation. Many residues in Kir channels have been identified as being involved in PtdIns(4,5)P_2-dependent activation. The corresponding residues in Kir3.1 are indicated by spheres.

The cytoplasmic N- and C-termini contribute to a domain folding (see Fig. 24.4A). The domain consists of four individual subunits, each of which has an immunoglobulin-like β-sandwich fold. There is a water-filled pore at the fourfold symmetry axis perpendicular to the membrane. Because the residues involved in the inward rectification are distributed on the internal surface of the pore, the cytoplasmic pore extends the distance that K^+ must travel to cross the membrane. The N-terminus of one subunit interacts with the C-terminus of an adjacent subunit.

The residues involved in association with Gβγ and PtdIns(4,5)P_2 can be mapped onto the three-dimensional model (see Figs. 24.4C and D). Among the residues involved in Gβγ-dependent channel activation in Kir3.1, His57 is located on the N-terminus, whereas Leu333 and Gly336 are positioned on a loop between the βL and βM strands (see Fig. 24.4C) (Bichet et al., 2003; Logothetis et al., 2007; Hibino et al., 2010). In addition, the regions involved in the binding to Gβγ are clustered at the outer edge of a tetrameric assembly where the sites permit interaction with Gβγ. PtdIns(4,5)P_2-sensitive residues are widely distributed in the cytoplasmic domain facing the membrane (see Fig. 24.4D) (Logothetis et al., 2007; Hibino et al., 2010). The cytoplasmic end of TM2 accommodates a cluster of positively charged residues and the linker connecting the cytoplasmic N-terminus to a slide helix and a loop between the βC and βD strands (CD loop) also contains basic amino residues.

What is the mechanism underlying the Gβγ-induced increase in the affinity to PtdIns(4,5)P_2? One hypothesis is that the association of Gβγ induces a conformational change that creates a binding pocket for PtdIns(4,5)P_2. Another hypothesis is that Gβγ disrupts the inhibitory mechanism that hinders association with PtdIns(4,5)P_2. It becomes apparent that, to keep the channel insensitive to PtdIns(4,5)P_2, Kir3.2 forms an inter-subunit ionic bond between His69 on the N-terminus and Asp228 on the CD loop (see Fig. 24.4B) (Inanobe et al., 2010); the former residue is equivalent to the residues that are crucial for Gβγ-dependent activation and the latter residue is mandatory for Na^+-dependent activation. The crevice between the N-terminus and the CD loop serves as a high-affinity binding site for Cd^{2+} and the bound Cd^{2+} tethers the N-terminus and CD loop to inhibit Kir3.2 activity. It seems likely therefore that the mode of action of Gβγ is liberation of the channel from the inactive state to allow the channel to have a high affinity for PtdIns(4,5)P_2. These observations also suggest that the cytoplasmic domain of K_G channel changes its conformation during gating. How does such conformational change lead to opening of the channel? At the transmembrane domain, the pivoting movement of TM2 and restructuring of the selectivity filter appear to be involved in the control of ionic flow (Jin et al., 2002; Bichet et al., 2003). The rotational and rigid conformational changes of the transmembrane domain against the cytoplasmic domain are also predicted to be coupled with gating (Riven et al., 2003). Furthermore, the widening of the cytoplasmic pore and the rearrangement of the domain interface have also been proposed as potential conformational changes in the bacterial Kir channel (Clarke et al., 2010).

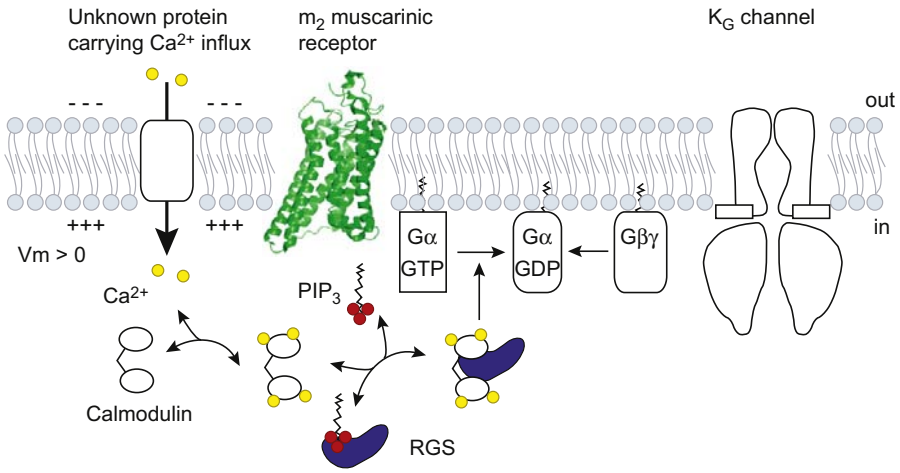

FIGURE 24.5 Regulation of G-protein-mediating channel activation by RGS proteins. Ca^{2+} influx facilitates the formation of Ca^{2+}/CaM, which binds to RGS proteins and competes with PtdIns(3,4,5)P_3. This binding restores the GAP activity and control the G protein cycle negatively.

VIII. RGS PROTEINS CONFER VOLTAGE-DEPENDENT GATING ON K_G CHANNEL

Upon hyperpolarization, the K_G channel current increases progressively after a current jump, whereas the opposite occurs upon depolarization. The slow time-dependent current change is called "relaxation" and is characteristic for the native K_G current (see Fig. 24.3A) (Noma and Trautwein, 1978). The degree of the relaxation varies with the strength of the receptor stimulation, but such relaxation behavior is not observed in cells that express only K_G channels and m_2-muscarinic receptor.

Regulators of G-protein signaling (RGS) proteins function as GTPase-activating proteins (GAP) specific to Gα to terminate G-protein-mediated signaling (Ross and Wilkie, 2000). To date, more than 20 RGS proteins have been identified. They share a conserved structure of 120 amino acids, designated the "RGS domain", which is responsible for their GAP activity. Actually, RGS proteins accelerate the time-course of activation and deactivation of K_G currents induced by agonists (Saitoh et al., 1997). Subsequently, RGS protein has been recognized as the protein that confers depolarization-induced facilitation on the channel by decreasing the K_G channel availability (Fig. 24.5) (Ishii et al., 2001). In the resting state, PtdIns(3,4,5)P_3 binds to the RGS domain and the GAP activity of RGS is inhibited. Depolarization facilitates the influx of Ca^{2+}, resulting in the formation of Ca^{2+}/calmodulin (CaM). This complex binds to the RGS domain, thereby ending the PtdIns(3,4,5)P_3-mediated inhibition and restoring GAP activity. Therefore, at depolarized potentials, the G-protein cycle is negatively regulated by Ca^{2+}/CaM-bound RGS proteins and the number of active K_G channels is decreased by the number of Gβγ moieties available to open the K_G channels. This is the mechanism of the voltage-dependent relaxation behavior of K_G channels.

IX. CONCLUSIONS

Research in the last decade has provided structural insights into the polypeptides that are involved in G-protein signaling at the atomic level. Since available conformations are limited, it is still difficult to address how proteins change their conformation and transduce the signals. Molecular dynamics simulation is a powerful tool to provide statistical mechanics of the proteins. However, restrictions by computational power and its theory hamper the precise corroboration of the ideas about dynamic features of the proteins and signaling. Therefore, multiple structural models for different functional states are necessary to grasp how the molecule operates and transfers signals. Furthermore, a lipid raft, an organization of specialized membrane microdomains in which cholesterol, sphingolipids and membrane proteins are preferentially associated, has the power to modulate this membrane-delimited signal transduction. Such a system may be linked to the idea that GPCR, G proteins, RGS proteins and K_G channels are precoupled, even in the absence of ligands (Lüscher and Slesinger, 2010). In addition, the molecular entity participating in the Ca^{2+} influx should be clarified to permit understanding of the convergence of two different cellular signaling pathways involving the G protein and the membrane potential, respectively (Ishii et al., 2001). We therefore need to achieve greater clarification regarding the regulatory mechanism of ion channels at the molecular level as well as at the cellular level.

BIBLIOGRAPHY

Bichet, D., Haass, F. A., & Jan, L. Y. (2003). Merging functional studies with structures of inward-rectifier K^+ channels. *Nat Rev Neurosci, 4*, 957–967.

Bjarnadottir, T. K., Gloriam, D. E., Hellstrand, S. H., Kristiansson, H., Fredriksson, R., & Schioth, H. B. (2006). Comprehensive repertoire and phylogenetic analysis of the G protein-coupled receptors in human and mouse. *Genomics, 88*, 263–273.

Clarke, O. B., Caputo, A. T., Hill, A. P., Vandenberg, J. I., Smith, B. J., & Gulbis, J. M. (2010). Domain reorientation and rotation of an intracellular assembly regulate conduction in Kir potassium channels. *Cell, 141*, 1018−1029.

Currie, K. P. (2010). G protein modulation of CaV2 voltage-gated calcium channels. *Channels (Austin), 4*, 497−509.

Del Castillo, J., & Katz, B. (1955). Production of membrane potential changes in the frog's heart by inhibitory nerve impulses. *Nature, 175*, 1035.

Dolphin, A. C. (1998). Mechanisms of modulation of voltage-dependent calcium channels by G proteins. *J Physiol, 506*, 3−11.

Fredriksson, R., Lagerstrom, M. C., Lundin, L. G., & Schioth, H. B. (2003). The G-protein-coupled receptors in the human genome form five main families. Phylogenetic analysis, paralogon groups, and fingerprints. *Mol Pharmacol, 63*, 1256−1272.

Gilman, A. G. (1987). G proteins: transducers of receptor-generated signals. *Annu Rev Biochem, 56*, 615−649.

Hibino, H., Inanobe, A., Furutani, K., Murakami, S., Findlay, I., & Kurachi, Y. (2010). Inwardly rectifying potassium channels: their structure, function, and physiological roles. *Physiol Rev, 90*, 291−366.

Hilgemann, D. W., & Ball, R. (1996). Regulation of cardiac Na^+, Ca^{2+} exchange and K_{ATP} potassium channels by PIP_2. *Science, 273*, 956−959.

Hutter, O. F., & Trautwein, W. (1956). Vagal and sympathetic effects on the pacemaker fibers in the sinus venosus of the heart. *J Gen Physiol, 39*, 715−733.

Inanobe, A., Nakagawa, A., Matsuura, T., & Kurachi, Y. (2010). A structural determinant for the control of PIP_2 sensitivity in G protein-gated inward rectifier K^+ channels. *J Biol Chem, 285*, 38517−38523.

Ishii, M., Inanobe, A., Fujita, S., Makino, Y., Hosoya, Y., & Kurachi, Y. (2001). Ca^{2+} elevation evoked by membrane depolarization regulates G protein cycle via RGS proteins in the heart. *Circ Res, 89*, 1045−1050.

Jan, L. Y., & Jan, Y. N. (1997). Cloned potassium channels from eukaryotes and prokaryotes. *Annu Rev Neurosci, 20*, 91−123.

Jin, T., Peng, L., Mirshahi, T., Rohacs, T., et al. (2002). The βγ subunits of G proteins gate a K^+ channel by pivoted bending of a transmembrane segment. *Mol Cell, 10*, 469−481.

Katz, B. (1949). Les constantes electriques de la membrane du muscle. *Arch Sci Physiol, 3*, 285−299.

Krapivinsky, G., Gordon, E. A., Wickman, K., Velimirovic, B., Krapivinsky, L., & Clapham, D. E. (1995). The G-protein-gated atrial K^+ channel I_{KACh} is a heteromultimer of two inwardly rectifying K^+-channel proteins. *Nature, 374*, 135−141.

Kubo, Y., Adelman, J. P., Clapham, D. E., et al. (2005). International Union of Pharmacology. LIV. Nomenclature and molecular relationships of inwardly rectifying potassium channels. *Pharmacol Rev, 57*, 509−526.

Kubo, Y., Reuveny, E., Slesinger, P. A., Jan, Y. N., & Jan, L. Y. (1993). Primary structure and functional expression of a rat G-protein-coupled muscarinic potassium channel. *Nature, 364*, 802−806.

Kuo, A., Gulbis, J. M., Antcliff, J. F., et al. (2003). Crystal structure of the potassium channel KirBac1.1 in the closed state. *Science, 300*, 1922−1926.

Kurachi, Y. (1995). G protein regulation of cardiac muscarinic potassium channel. *Am J Physiol, 269*, C821−C830.

Kurachi, Y., Nakajima, T., & Sugimoto, T. (1986a). Acetylcholine activation of K^+ channels in cell-free membrane of atrial cells. *Am J Physiol, 251*, H681−H684.

Kurachi, Y., Nakajima, T., & Sugimoto, T. (1986b). On the mechanism of activation of muscarinic K^+ channels by adenosine in isolated atrial cells: involvement of GTP-binding proteins. *Pflügers Arch, 407*, 264−274.

Loewi, O. (1921). Über humorale Übertragbarkeit der Herznervenwirkung. *Pflügers Arch, 189*, 239−242.

Logothetis, D. E., Jin, T., Lupyan, D., & Rosenhouse-Dantsker, A. (2007). Phosphoinositide-mediated gating of inwardly rectifying K^+ channels. *Pflügers Arch, 455*, 83−95.

Logothetis, D. E., Kurachi, Y., Galper, J., Neer, E. J., & Clapham, D. E. (1987). The βγ subunits of GTP-binding proteins activate the muscarinic K^+ channel in heart. *Nature, 325*, 321−326.

Lüscher, C., & Slesinger, P. A. (2010). Emerging roles for G protein-gated inwardly rectifying potassium (GIRK) channels in health and disease. *Nat Rev Neurosci, 11*, 301−315.

Nishida, M., & MacKinnon, R. (2002). Structural basis of inward rectification: cytoplasmic pore of the G protein-gated inward rectifier GIRK1 at 1.8 Å resolution. *Cell, 111*, 957−965.

Noma, A., & Trautwein, W. (1978). Relaxation of the ACh-induced potassium current in the rabbit sinoatrial node cell. *Pflügers Arch, 377*, 193−200.

Oldham, W. M., & Hamm, H. E. (2008). Heterotrimeric G protein activation by G-protein-coupled receptors. *Nat Rev Mol Cell Biol, 9*, 60−71.

Overington, J. P., Al-Lazikani, B., & Hopkins, A. L. (2006). How many drug targets are there? *Nat Rev Drug Discov, 5*, 993−996.

Reuveny, E., Slesinger, P. A., Inglese, J., et al. (1994). Activation of the cloned muscarinic potassium channel by G protein βγ subunits. *Nature, 370*, 143−146.

Riven, I., Kalmanzon, E., Segev, L., & Reuveny, E. (2003). Conformational rearrangements associated with the gating of the G protein-coupled potassium channel revealed by FRET microscopy. *Neuron, 38*, 225−235.

Ross, E. M., & Wilkie, T. M. (2000). GTPase-activating proteins for heterotrimeric G proteins: regulators of G protein signaling (RGS) and RGS-like proteins. *Annu Rev Biochem, 69*, 795−827.

Saitoh, O., Kubo, Y., Miyatani, Y., Asano, T., & Nakata, H. (1997). RGS8 accelerates G-protein-mediated modulation of K^+ currents. *Nature, 390*, 525−529.

Scheerer, P., Park, J. H., Hildebrand, P. W., et al. (2008). Crystal structure of opsin in its G-protein-interacting conformation. *Nature, 455*, 497−502.

Sprang, S. R. (1997). G protein mechanisms: insights from structural analysis. *Annu Rev Biochem, 66*, 639−678.

Trautwein, W., & Dudel, J. (1958). [Mechanism of membrane effect of acetylcholine on myocardial fibers]. *Pflügers Arch, 266*, 324−334.

Yamada, M., Inanobe, A., & Kurachi, Y. (1998). G protein regulation of potassium ion channels. *Pharmacol Rev, 50*, 723−760.

This page intentionally left blank

Chapter 25

Developmental Changes in Ion Channels

Takeshi Kobayashi, Noritsugu Tohse, Hisashi Yokoshiki and Nicholas Sperelakis

Chapter Outline

I. SUMMARY

Action potentials (APs) and resting potentials (RPs) in excitable cells, such as cardiomyocytes, skeletal muscle fibers and neurons, are greatly altered during development. In general, the RP increases (becomes more negative), the AP rate of rise increases, overshoot increases and duration decreases. These electrophysiological alterations are mainly produced by developmental changes in the ion channels, i.e. by changes in the types, number and kinetic properties of the ion channels.

In cardiomyocytes, the RP at the early embryonic/fetal period is low and there is a gradual hyperpolarization during development. This increase in the RP during development can be accounted for by the increase in the density of inward-rectifier K^+ current (I_{K1}) and the resultant decrease in the permeability ratio for Na^+ to K^+ (P_{Na}/P_K ratio). In contrast, the hyperpolarization-activated inward current (I_h), which may affect automaticity, is dominant in early embryonic chick and mouse cardiomyocytes and disappears during development.

The Na^+ current of cardiomyocytes increases markedly during development. This increase in number (density) of fast Na^+ channels accounts for the large increase in the maximal rate of depolarization of the AP (max dV/dt) during development. The fast Na^+ current in embryonic/fetal hearts has a significant sustained component. The sustained component decreases during development and this decrease contributes, at least in part, to the abbreviation of the AP duration.

Developmental change of Ca^{2+} channels varies with the species. The density of total Ca^{2+} current in chick cardiomyocytes decreases during the developmental period from fetal to neonate. In rat and mouse, however, it increases from the fetal to the neonatal period, followed by a substantial decrease in the adult. In contrast, the current density in the neonatal period is smaller than that in the adult in rabbit and guinea pig.

In fetal heart cells, the role of the sarcoplasmic reticulum (SR) increases with embryonic development. Therefore, Ca^{2+} influx through the Ca^{2+} channels is especially important for the excitation–contraction (E-C) coupling process of immature cardiomyocytes.

The density of the transient outward current (I_{to}) of cardiomyocytes increases during development. An increase in the density of the delayed-rectifier K^+ current (I_K) also occurs during early development and decreases during the

Cell Physiology Sourcebook. DOI: 10.1016/B978-0-12-387738-3.00025-1

postnatal period. The change of these voltage-gated outward currents acts to abbreviate the AP duration during development.

In skeletal muscle fibers, there is an overall trend toward an increase in the density of I_{K1} during the early developmental period. However, there is a transient period during which the current density actually decreases. This transient period parallels the increased incidence of spontaneous firings, presumably due to a less stable RP. The major voltage-gated inward currents, the Na^+ and Ca^{2+} currents, are already present in the early embryonic skeletal myocytes in culture and they increase in intensity during development. These changes contribute to the increases in the AP rate of rise, overshoot and propagation velocity.

The nicotinic acetylcholine receptor/channel (nAChR), which is essential to transmission at the neuromuscular junction, is converted from fetal-type to adult-type and this conversion may be related to innervation of the muscles that occurs during development.

In neuronal cells, there is an overall trend that the ionic dependence of the AP is altered during development from being Ca^{2+}-dependent (prolonged AP duration) to Na^+-dependent (brief AP duration). The pattern of ion channel development varies among different types of neuronal cells, with faster development of Ca^{2+} channels occurring in some cells. Another important factor that determines the ionic dependence of the AP is the developmental increase in I_K. Therefore, the change in the I_K/I_{Ca} ratio during development is the major determinant of the conversion of the AP configuration and influences Ca^{2+} influx. The activities of ligand-gated Ca^{2+} permeable channels (such as NMDA receptor/channels and AMPA-gated receptor/channels) are also altered during development. Therefore, the Ca^{2+} influx through the voltage-gated and the ligand-gated Ca^{2+} channels, and the subsequent effects on intracellular Ca^{2+}, may affect the structural changes of the developing neurons and help the establishment of the neuronal network.

II. INTRODUCTION

Cellular functions and tissue structures change dramatically during development. Ion channels are responsible for cellular signaling and maintenance of the intracellular environment. For example, the Ca^{2+} channels allow Ca^{2+} influx into the cell, which acts as a second messenger that affects several structures: activation of enzymes; activation of some ion channels; and activation of the contractile proteins. The ion channels change in their types, number and kinetic properties during the embryonic/fetal period and the neonatal period. Particularly in excitable cells (i.e. cardiomyocytes, skeletal muscle fibers, neurons), their resting potential (RP) and action potentials (APs) are progressively altered during the developmental stages. For example, the RP increases in amplitude during development and large changes occur in the AP rate of rise, overshoot and duration. In general, the rate of rise increases markedly, the overshoot increases and the duration decreases during development. This chapter focuses primarily on the ion channels of cardiomyocytes, skeletal muscle fibers and neurons, where most is known about the developmental changes.

III. CARDIOMYOCYTES

IIIA. Resting Potential

In the early embryonic period, the heart primordium (the so-called cardiac crescent) begins to contract before the appearance of a linear heart tube (Kobayashi et al., 2011). In the middle embryonic period, the heart tube twists and then the cardiac loop is constructed. In this period, the ventricular portion becomes distinguished from the atrial portion.

The electrophysiological properties are also altered during development. The RP of the ventricular cells in the early embryonic/fetal period is low (e.g. −40 to −55 mV) and there is a gradual hyperpolarization during development. Finally, in the late embryonic period, the RP becomes nearly equal to that of adult cells (around −80 mV) (Bernard, 1975). During this increase of the RP, a decrease in the permeability ratio for Na^+ to K^+ (P_{Na}/P_K ratio) occurs (Sperelakis and Shigenobu, 1972). The developmental changes in the RP cannot be accounted for by changes in the intracellular ion concentrations because $[K^+]_i$ is already high in the early embryonic period. Although the Na^+-K^+ pump specific activity was found to be low in the early embryonic period (Sperelakis and Lee, 1971), the Na^+-K^+ pump is sufficient to maintain a high $[K^+]_i$ and low $[Na^+]_i$ because of the less leaky membrane (i.e. high in resistance) (Sperelakis and Shigenobu, 1972). Therefore, the developmental change in the RP is due to changes in membrane permeability (conductance) for the ions.

In the early embryonic period, the low RP of the ventricular cells is not stable, but exhibits a spontaneous depolarization, the *pacemaker potential* (phase 4 diastolic depolarization). During embryonic development, the *maximum diastolic potential* increases (hyperpolarized) and the slope of the pacemaker potential progressively decreases. When the RP has attained the adult level in the late embryonic period, the pacemaker potential disappears. Thus, automaticity of the ventricular cells is lost by the late embryonic period. One possible factor in the loss of automaticity is the decrease in the P_{Na}/P_K ratio and the resultant hyperpolarization. This factor is closely related to the increase in the inward-rectifier K^+ current (I_{K1}) and the loss of the hyperpolarization-activated inward current (I_h or I_f) (see Sections IIIE and IIIG).

IIIB. Action Potential

The *action potentials* (APs) get larger and rise faster during embryonic development (Couch et al., 1969; Sperelakis and Shigenobu, 1972; Bernard, 1975; Kojima et al., 1990). These changes are accompanied by the hyperpolarization of the RP and by an increase in overshoot to about +30 mV. The maximal rate of depolarization (max *dV/dt*) progressively increases during development, from about 20 V/s to 200 V/s in the late embryonic stage, which is about the adult level. However, the time course of the increase in max *dV/dt* is not parallel to the increase in RP. The increase in RP precedes the increase in max *dV/dt* by several days. Therefore, this increase in max *dV/dt* is not simply due to the hyperpolarization, but is produced by a much greater number (density) of tetrodotoxin (TTX)-sensitive fast Na^+ channels (see Section IIIC).

The duration of the AP (e.g. at 50% repolarization, APD_{50}) hardly changes in the chick during development (Sperelakis and Shigenobu, 1972). The same is true of the guinea pig heart, as well as in many other mammalian species (Sanchez-Chapula et al., 1994; Kato et al., 1996). However, in human atrial cells, the APD_{50} is significantly shortened with development (Wang et al., 2003). The rat also shows a marked decrease in APD_{50} beginning in the late fetal period and extending through the first 3 weeks of the neonatal period, after which adult-like brief APs are attained (Kojima et al., 1990). Several factors contribute to this marked abbreviation of the AP in the rat, including increase in the transient outward current (I_{to}) and loss of the sustained component of the fast Na^+ current (see Section IIIC).

IIIC. Na^+ Channels

Slow Ca^{2+} channel current makes a major contribution to the upstroke of the AP in the early embryonic period (Bernard, 1975). The fast Na^+ current in ventricular cells increases markedly during development by a factor of about 10-fold in chick, rat and murine hearts (Fujii et al., 1988; Sada et al., 1995; 1988; Conforti et al., 1993; Davies et al., 1996). However, in rabbit and canine sinoatrial node cells, the fast Na^+ current actually decreases during development (Baruscotti et al., 1996; Protas et al., 2010). Tetrodotoxin- (TTX, a specific blocker of the fast Na^+ channels) binding studies indicated that a marked increase in density of the fast Na^+ channel protein occurs during development of embryonic chick heart (Renaud et al., 1981, 1983). This increase in number (density) of fast Na^+ channels accounts for the large increase in max *dV/dt* of the AP that occurs. Therefore, the contribution of fast Na^+ channel current to the AP of ventricular cells progressively increases during development.

The heart greatly enlarges in size during development. Thus, the excitation wave must travel over longer distances in the larger hearts during the late embryonic and adult periods. A fast conduction velocity for excitation is required to allow a synchronized contraction of the ventricle, i.e. to allow the heart to serve as an effective pump. The increase in max *dV/dt* during development would contribute to the required increase in conduction velocity. Another factor involved in conduction velocity is that the cell size (i.e. diameter) becomes much greater. It is well known that conduction velocity is a function of the square root of cell diameter (see Chapter 18).

The TTX sensitivity of the fast Na^+ current in avian cardiomyocytes (in the nanomolar range) is about 1000-fold greater than that for adult mammalian hearts (such as guinea pig), which are in the micromolar range (Sada et al., unpublished observation). It is not known whether the high TTX sensitivity of chick embryonic hearts is due to a different isoform of the channel. This finding is in agreement with previous reports of the high sensitivity of embryonic chick hearts to TTX (Iijima and Pappano, 1979; Marcus and Fozzard, 1981; Fujii et al., 1988).

The fast Na^+ channels are completely blocked by 10 μM TTX in fetal rat cardiomyocytes (Conforti et al., 1993) and by 30 μM TTX in adult rat cardiomyocytes (Brown et al., 1981). Binding studies using TTX and saxitoxin (STX, also a specific blocker of the fast Na^+ channels) revealed that fetal and newborn rat ventricular myocytes have only low-sensitivity Na^+ channels. In contrast, adult rat ventricular myocytes have both high-sensitive and low-sensitive to (TTX/STX) Na^+ channels, leading to the discovery of the low-sensitive "cardiac" isoform of the Na^+ channel ($Na_v1.5$) (Renaud et al., 1983; Rogart et al., 1989). In mouse heart, high TTX-sensitive Na^+ channel isoforms ($Na_v1.1$—$Na_v1.4$) increase with development, although the "cardiac" isoform Na^+ channel is always predominantly expressed during development (Haufe et al., 2005; Dominguez et al., 2008).

The fast Na^+ current has a slow inactivating or sustained component. This component is small, but has a larger contribution in the embryonic period than in adult (Conforti et al., 1993). Sustained Na^+ current, which is blocked by 10 μM TTX, is observed in the early embryonic period of chicks. Reopening of some of the fast Na^+ channels during a long depolarizing clamp step is one explanation for the small sustained component (Josephson and Sperelakis, 1989). The sustained component may reflect the *window current* produced by a balance between the activating (m) gate and the inactivating (h) gate (Sada et al., 1995) (see Chapter 19). In rat heart cells, the fast Na^+ current has a slow inactivating component and its time constant decreases in neonatal cells compared to fetal cells (Conforti et al., 1993). Although the slow component of the Na^+ current is small, inward current produced by the slow component helps to maintain the longer duration of the AP plateau in the fetal period. TTX, which is specific for fast

Na^+ channels, shortens the AP duration in rat fetal cardiomyocytes (Fig. 25.1) (Conforti et al., 1993). A key factor that may contribute to the shortening of the AP duration during development of rat heart is the loss of the slow component of the Na^+ current. However, in adult hearts, it appears that the sustained component of the Na^+ current persists in the Purkinje fiber, because its AP plateau is substantially shortened by TTX (Morikawa et al., 1987). Another factor responsible is an increase in I_{to} carried primarily by K^+ (see Section IIIF).

IIID. Ca^{2+} Channels

Changes in the slow (L-type) Ca^{2+} current also occur during development of the heart. However, the direction of the change is opposite in avian versus mammalian hearts (Fig. 25.2). In rat hearts, the L-type Ca^{2+} current increases during development (Masuda et al., 1995), whereas in chick hearts it actually decreases (Tohse et al., 1992b). In the chick early embryonic period, the current density of the L-type channels is 8 μA/cm^2 which is comparable to that in other adult animals (about 10 μA/cm^2). The current density decreased during development to about 5 μA/cm^2 in the late embryonic period (Fig. 25.2B). However, the current density of the L-type Ca^{2+} channels of rat cardiomyocytes increases through the middle fetal, late fetal and neonatal period (Masuda et al., 1995) (Fig. 25.2A). In mouse, the current density of L-type Ca^{2+} channels increases with development (Davies et al., 1996; Liu et al., 2002; Nguemo et al., 2007). Another investigation demonstrated that the current density in the neonatal period is actually larger than that in adult rat (Cohen and Lederer, 1988). That is, in the development of rat heart, the current density increases, followed by a decrease. In contrast, in rabbit (Osaka and Joyner, 1991; Huang et al., 2006) and guinea pig (Kato et al., 1996) cardiomyocytes, the current density in the neonatal period is smaller than that in adults. Thus, the changes in the L-type Ca^{2+} channel density that occur during development are complex and vary from one species to another.

Other types of Ca^{2+} channels are also observed during development. In chick embryonic heart cells, it has been reported that the T-type channel is dominant in the early embryonic period, but that the L-type current is dominant in the late embryonic period (Kawano and DeHaan, 1991; Kitchens et al., 2003). However, other reports indicate that the L-type current is also dominant in the early chick embryonic period (Tohse and Sperelakis, 1990; Tohse et al., 1992b). In rat and mouse fetal cardiomyocytes, although L-type current is always dominant, T-type current is observed during the embryonic and postnatal periods and decreases with development (Leuranguer et al., 2000; Ferron et al., 2002; Niwa et al., 2004). However, another report shows that embryonic rat ventricle myocytes have a substantial fraction of the total Ca^{2+} current that is resistant to nifedipine (a relatively selective blocker of L-type Ca^{2+} channels) shown in Fig. 25.3 (Tohse et al., 1992a). This nifedipine-resistant current is not blocked by ω-conotoxin (N-type Ca^{2+} channel-blocker), tetramethrine (T-type Ca^{2+}

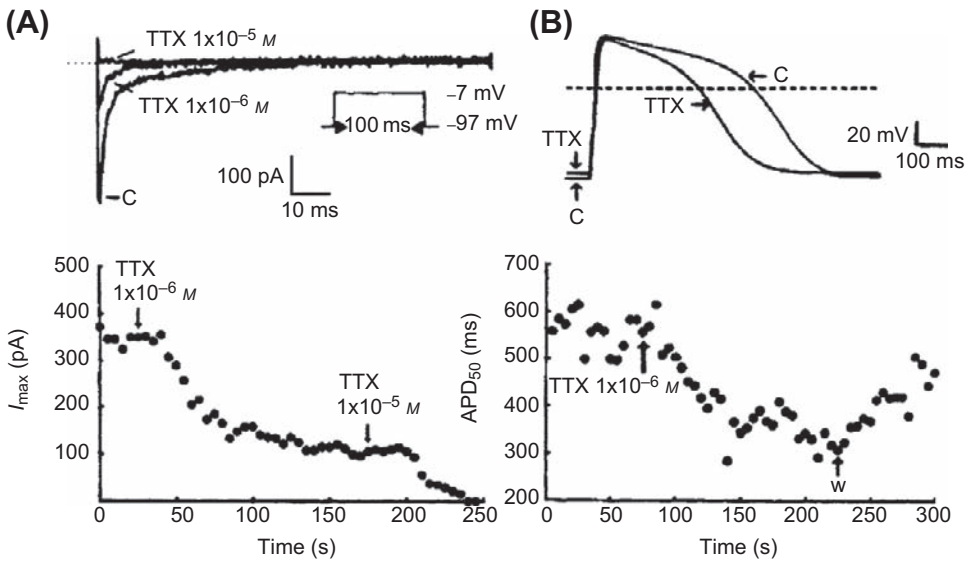

FIGURE 25.1 Effect of TTX on the Na^+ current and the AP configuration recorded from a fetal rat cardiomyocyte. (A) Top panel: superimposed current traces showing the Na^+ current recorded before (C, Control) and after 90-s exposure to 1 and 10 μM TTX. Holding potential (HP) was −97 mV and the test potential was −7 mV. Bottom panel: time course of the TTX effect. Steady-state responses were attained at about 1−2 min. (B) Effect of TTX on the AP configuration of a fetal cell recorded in current-clamp mode. Top panel: superimposed traces (averaged from 10 consecutive records) showing APs before (C, Control) and after a 90-s exposure to 1 μM TTX. Bottom panel: time course of the change in APD_{50} produced by TTX. Arrows indicate points of introduction and washout (w) of TTX. *(Reproduced with permission from Conforti et al., 1993.)*

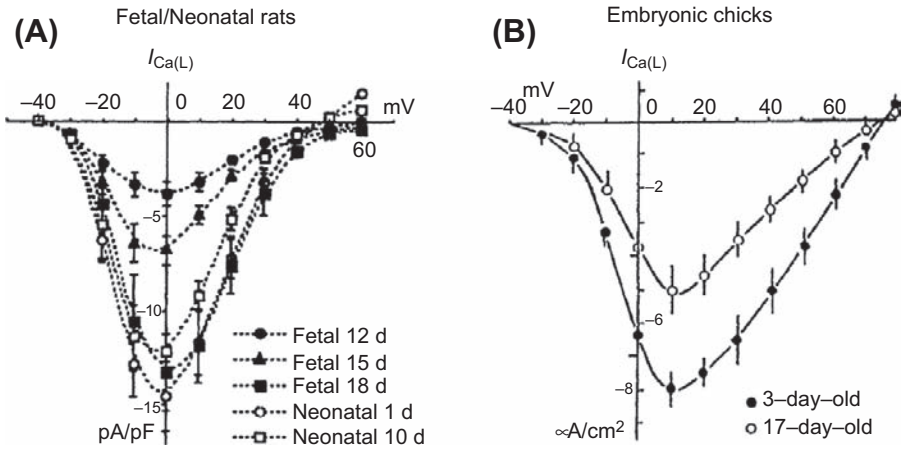

FIGURE 25.2 Developmental changes of $I_{Ca(L)}$ in (A) fetal/neonatal rats and (B) embryonic chicks. (A) Ba^{2+} currents through L-type Ca^{2+} channels ($I_{Ca(L)}$) were elicited by depolarizing steps from an HP of −40 mV (22°C). Current−voltage curves (normalized as current density (in pA/pF)(mean ± SE)) are shown for the different developmental stages (from day 12 fetal to day 10 neonatal). (B) Changes in the density of $I_{Ca(L)}$ in isolated embryonic chick heart cells; 1.8 mM $[Ca^{2+}]_o$, 35°C. *((A) modified with permission from Masuda et al. (1995). Long openings of calcium channels in fetal rat ventricular cardiomyocytes. Pflügers Arch. 429, 595−597, copyright Springer-Verlag. (B) Tohse et al. (1992b). Developmental changes in long-opening behavior of L-type Ca^{2+} channels in embryonic chick heart cell. Circ. Res. 71, 376−384. Reproduced with permission* Circulation Research. *Copyright 1992 American Heart Association.)*

channel-blocker) and is only partially inhibited by 30 μM Ni^{2+}, which is a blocker of T-type Ca^{2+} channels. Therefore, this channel is called a *fetal-type* (F-type) Ca^{2+} channel. The F-type Ca^{2+} current is absent in adult heart cells. That is, in the fetal period, the total Ca^{2+} current has two main components: L-type current, which is blocked by nifedipine and the F-type current, which is not blocked by nifedipine.

In chick embryonic heart, unit conductance of the L-type Ca^{2+} channel is 26 pS (using 50 mM Ba^{2+} in the pipette), which is comparable to that in adult heart cells (Tohse and Sperelakis, 1990). The single-channel activity of the L-type Ca^{2+} channel in the embryonic cells was completely blocked by nifedipine.

The kinetics of opening of the L-type Ca^{2+} channels in embryonic heart cells is different from that in adult heart cells. Long-lasting openings of the channels occur relatively frequently, in addition to the more usual brief bursting openings observed in adult heart cells (Fig. 25.4). These long-lasting openings are similar to the mode 2 openings produced by Ca^{2+} agonists, such as the dihydropyridine Bay-K-8644. For example, Fig. 25.4 shows long openings that persist over the entire duration of the clamp pulse (i.e. 300 ms); the long openings are sometimes punctuated by brief closures. As can be seen, in many sweeps, the open probability (P_0) is close to 1.00. The long-lasting openings gradually disappear during development (Tohse et al., 1992b; Masuda et al., 1995).

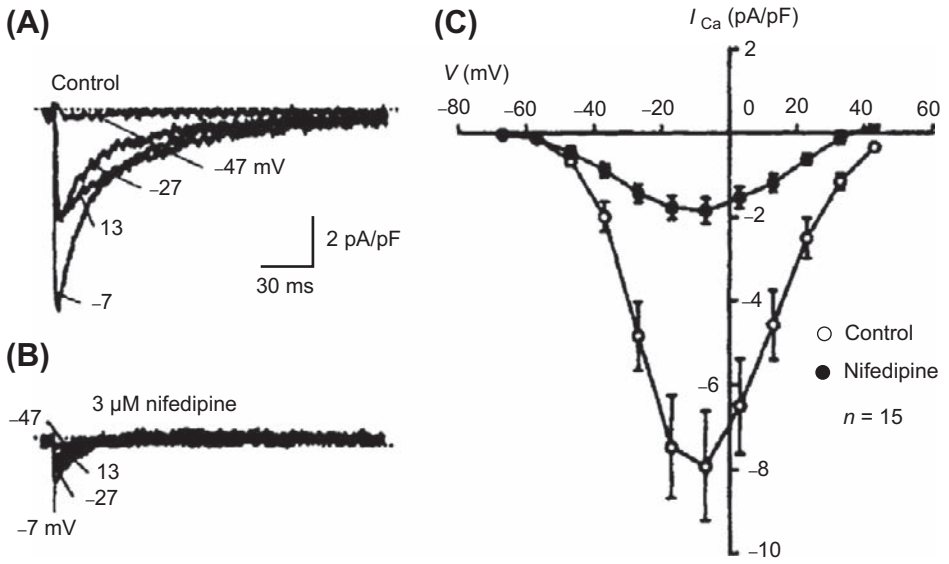

FIGURE 25.3 Presence of fetal-type Ca^{2+} channels in fetal (18-day) rat cardiomyocytes. (A) Currents elicited by 300-ms (only 150 ms shown) depolarizing pulses to −47, −27, −7 and 13 mV from an HP of −87 mV. (B) In the presence of 3 μM nifedipine, a significant inward current remained at each potential. (C) Current-voltage relationship; data points given as mean ± SE. Nifedipine did not completely block the Ca^{2+} current, indicating the presence of a nifedipine-resistant Ca^{2+} current. *(Reproduced with permission from Tohse et al., 1992a.)*

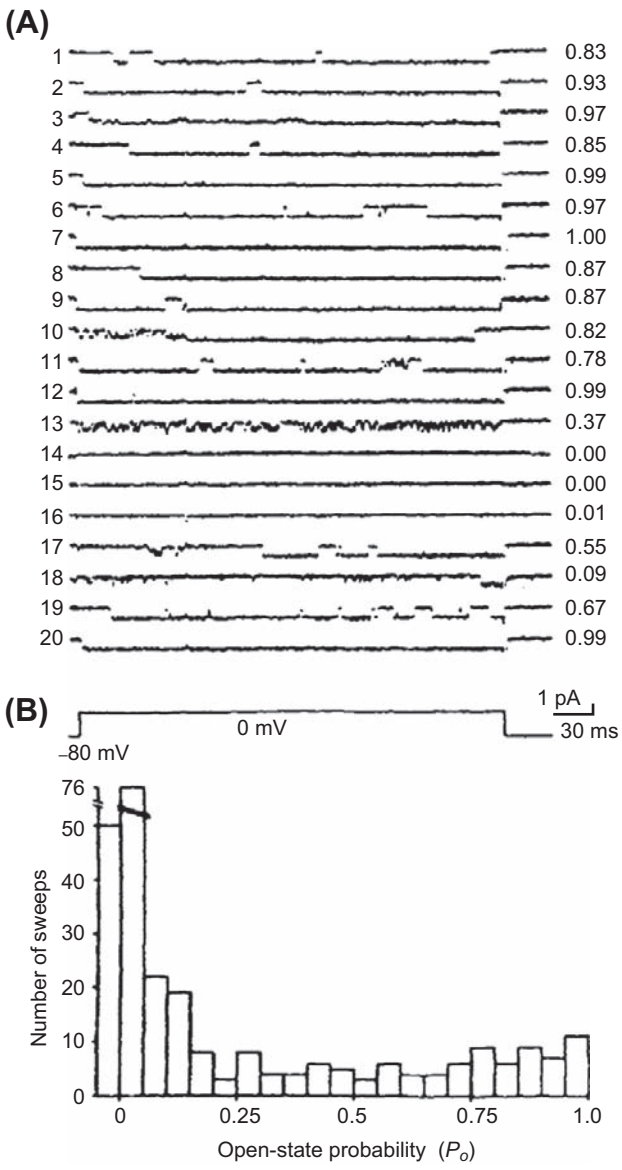

FIGURE 25.4 Presence of long openings of the slow (L-type) Ca^{2+} channels in young embryonic (3-day) chick heart cell. (A) Single-channel activity elicited by consecutive command pulses to 0 mV (from an HP of −80 mV) every 2 s. Sweep-to-sweep variations of the probability of the channel opening (P_0) are given in the right-hand column. (B) A histogram of P_0 data from nine cells (30 sweeps each). Note that many sweeps showed long openings and high P_0. *(Reproduced with permission from Tohse and Sperelakis, 1990.)*

IIIE. Inward-Rectifier K^+ Channels

It has been demonstrated that the inward-rectifier K^+ current (I_{K1} or $I_{K(IR)}$) of ventricular cells increases markedly during development of rabbit (Huynh et al., 1992; Sanchez-Chapula et al., 1994) and embryonic chick heart (Josephson and Sperelakis, 1990). In rat ventricle, I_{K1} increases from the embryonic to neonatal period, whereas some gradual decrease (due to an increase in cell membrane capacitance) is evident in myocytes from neonate to adult period (Kilborn and Fedida, 1990; Masuda and Sperelakis, 1993; Xie et al., 1997; Nagashima et al., 2001). In mouse atrial and ventricular myocytes, I_{K1} substantially increases with development, although it is still controversial whether the current density of I_{K1} increases or not during the embryonic period (Davies et al., 1996; Trepanier-Boulay et al., 2004; Grandy et al., 2007; Liu et al., 2010).

The increase in I_{K1} is likely to be a major factor responsible for the increase in the RP (hyperpolarization) that occurs during development, concomitant with a decrease in membrane resistivity and in the membrane time constant ($\tau_m = R_m C_m$). The increase in I_{K1} channels can also account for the decrease in the P_{Na}/P_K ratio that occurs during development (Sperelakis and Shigenobu, 1972); namely, it results in an increase in the K^+ permeability (P_K). Similar change in the P_{Na}/P_K ratio during development is shown in the skeletal muscle fibers (see Section IVA).

The increase in I_{K1} during development may be due to two factors: (1) an increase in the number of channel molecules and (2) an increase in single-channel conductance (Masuda and Sperelakis, 1993). The single-channel conductance in young fetal rats is much less than that in old fetuses and neonates (Fig. 25.5). However, the mean open time of the channels is longer in young fetal cells than in old fetal and neonatal cells. These observations suggest that the structure (i.e. a different isoform) of the inward-rectifier K^+ channel changes dramatically during development. On the other hand, a later study (Xie et al., 1997) suggests that the small conductance events in young fetal heart are sublevels of the large conductance channels in old fetal hearts. The developmental changes of the molecular correlate of I_{K1} (Kir2.1−2.3) were evaluated in rat and mouse heart. During development of the rat embryonic ventricle, the expression of Kir 2.1 and 2.2 mRNA increases, whereas Kir2.3 is not detected (Nagashima et al., 2001). In mouse atrial and ventricular myocytes, it has been demonstrated that the expression of Kir 2.1 and 2.2 increase during development, whereas Kir2.3 decreases (Nakamura et al., 1999; Trepanier-Boulay et al., 2004; Grandy et al., 2007; Liu et al., 2010).

IIIF. Voltage-Gated K^+ Channels

Transient outward current (I_{to}) density, mainly carried by K^+ ion, has been reported to increase during development. A substantial amount of I_{to} has been observed in early embryonic chick heart cells (Satoh, 1995). In rat ventricular myocytes, the density of I_{to} was reported to increase with development (Kilborn and Fedida, 1990; Wahler et al., 1994; Kobayashi et al., 2003). In mouse (Wang and Duff, 1997), rabbit (Sanchez-Chapula et al., 1994) and canine ventricular cells (Jeck and Boyden, 1992), a postnatal increase of I_{to} was

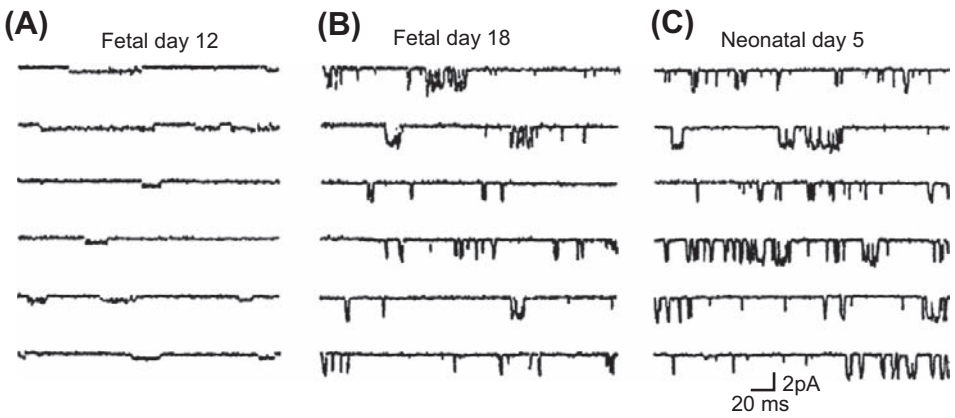

FIGURE 25.5 Developmental increase in I_{K1} in maturing rats. Single-channel activities illustrated for (A) 12-day fetal, (B) 18-day fetal and (C) 5-day neonatal ventricular myocytes. Single-channel activities were recorded at −80 mV. *(Reproduced with permission from Masuda and Sperelakis, 1993.)*

also observed. This increase in I_{to} contributes to the abbreviation of the AP that occurs in the neonatal period.

In the mammalian ventricular myocytes, I_{to} is composed of at least two components; one is characterized by a relatively fast recovery from inactivation ($I_{to,f}$) and another by a slow recovery from inactivation ($I_{to,s}$). The molecular correlate of $I_{to,f}$ is thought to be Kv4.2/4.3 and that of $I_{to,s}$ is Kv1.4. In rat ventricular myocytes, Kv4.2 protein levels increase during postnatal development, whereas Kv1.4 decreases (Matsubara et al., 1993; Xu et al., 1996). Therefore, the developmental increase in I_{to} was thought to be associated with the increase in $I_{to,f}$. However, there is a mismatch in the expression of Kv4.2 and I_{to} between postnatal days 5 and 30 (Xu et al., 1996). Recently, it has been demonstrated that the expression of voltage-gated K^+ channel-interacting proteins 2 (KChIP2) increases from embryonic day 12 to postnatal day 10, whereas Kv4.2 and Kv4.3 do not increase (Kobayashi et al., 2003). Therefore, KChIP2 is thought to be crucial to induce $I_{to,f}$ during development.

Between postnatal days 8 and 20, rat plasma thyroid hormone (T3) level increases (Shimoni et al., 1997). T3 stimulation enhanced Kv4.2 and Kv4.3 expression and decreased Kv1.4 transcription, while KChIP2 remained unaffected (Wickenden et al., 1997; Guo et al., 1998; Gassanov et al., 2009). Therefore, it has been suggested that T3 plays a role in postnatal upregulation of $I_{to,f}$. In addition, basic fibroblast growth factor (bFGF), which has tyrosine kinase activity, may also promote the expression of I_{to} during development (Guo et al., 1995).

As I_{to} in neonatal rat ventricular cells is smaller than that in adult cells, an ultrarapidly activating delayed-rectifier K^+ current (I_{Kur}) predominates I_{to} only during the early neonatal period (Guo et al., 1997b). In cultured neonatal rat ventricular cells, IGF-I promotes the expression of I_{Kur} as well as Kv1.5 protein (Guo et al., 1997a). I_{Kur} in ventricular cells decreases during postnatal development, which is associated with a reduction of the Kv1.5 expression. However, no substantial change in Kv1.5 protein is also reported from neonate to adult in the same preparation (Xu et al., 1996). Recently, it has been demonstrated that co-expression of KChIP2 decreases Kv1.5-encoded K^+ currents (Li et al., 2005). Therefore, KChIP2 is thought to be crucial to the decreased I_{Kur} during development.

In mouse fetal ventricular cells, a rapidly activating delayed-rectifier K^+ current (I_{Kr}) is the dominant component of delayed-rectifier I_K, whereas a slowly activating delayed-rectifier K^+ current (I_{Ks}) becomes dominant in early postnatal period (day one to three). However, both components disappear in adult mouse ventricular cells (Davies et al., 1996; Wang et al., 1996). Similarly, I_{Kr} in rat ventricular cells functions during the fetal period, but is negligible in adults. The main molecular correlates of I_{Kr} are thought to be ERG and MiRP1, whereas those of I_{Ks} are KvLQT1 and minK. ERG expression is observed in mouse ventricle in the embryonic period, whereas MiRP1 expression is not observed (Franco et al., 2001). Evaluating the expression of mRNAs of mouse heart during the embryonic and postnatal periods revealed that KvLQT1 decreases during development, whereas minK increases until late embryonic period and then decreases (Mai et al., 2004).

The density of I_K (the sum of I_{Kr} and I_{Ks}) in guinea pig ventricles is smaller in fetal cells than in neonatal and adult cells, suggesting a developmental increase in I_K (Kato et al., 1996). No substantial changes in the kinetics and voltage dependency of I_K are observed during development.

IIIG. Hyperpolarization-Activated Inward Current

The hyperpolarization-activated inward current (I_h or I_f), which is mainly carried by Na^+ and K^+ ions, is observed in sinoatrial node and early embryonic cardiomyocytes. In the

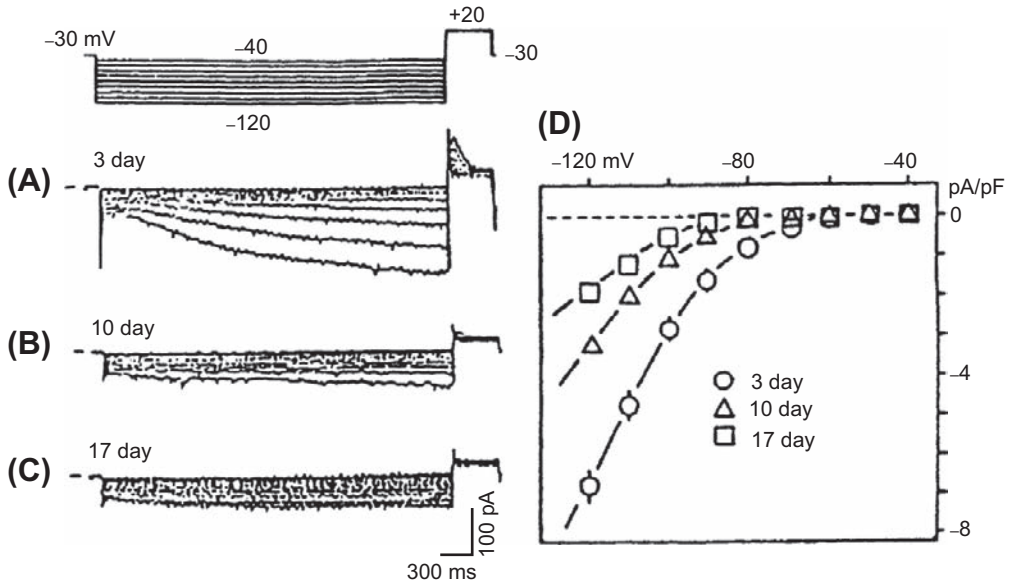

FIGURE 25.6 Developmental changes of the hyperpolarization-activated inward current (I_h) in young embryonic chick ventricular cells. Test pulses were applied between −40 mV and −120 mV, in 10-mV increments, from an HP of −30 mV. (A) A large inward current was slowly activated by hyperpolarization in a 3-day-old cell. (B) Smaller I_h in a 10-day-old cell. (C) Further reduced I_h in a 17-day-old cell. (D) Current-voltage relations for I_h current density at the three developmental stages (mean ± SE). *(Reproduced from Satoh, H. and Sperelakis, N. (1993). Hyperpolarization-activated inward current embryonic chick cardiac myocytes: developmental changes and modulation by isoproterenol and carbachol. Eur J Pharmacol, 240, 283–290, Copyright 1993. With permission from Elsevier Science.)*

chick ventricular myocytes, I_h progressively decreased during development and essentially disappears in the late embryonic period (Fig. 25.6) (Satoh and Sperelakis, 1993). In rabbit sinoatrial node, a slope conductance of I_h in neonatal cells is larger than that in the adult cells (Accili et al., 1997). In the rat ventricular myocytes, it is still controversial whether the current density of I_h decreases or not during the postnatal period (Robinson et al., 1997; Cerbai et al., 1999). In the mouse cardiomyocyte, I_h increases at the early embryonic period (between embryonic day 8.5 to 9.5) and then decreases (between embryonic day 9.5 and 18) (Yasui et al., 2001; Stieber et al., 2003).

The I_h is called the *pacemaker current* in adult cardiomyocytes. In Purkinje fibers, I_h plays a key role in pacemaker depolarization during the diastolic phase. In sinoatrial node cells, the contribution of I_h to pacemaker potential is still controversial for two reasons (Irisawa et al., 1993): the time course of activation of I_h is too slow to account for the high frequency of the pacemaker and the threshold potential for activation of I_h (close to −70 mV) is beyond the maximum diastolic potential (−60 to −70 mV) for the nodal cells. In chick embryonic cardiomyocytes, although the time course of decrease in I_h parallels the disappearance of the pacemaker potential, the contribution of I_h to the pacemaking may still be small (Satoh and Sperelakis, 1993).

Recently, it has been demonstrated that the I_h current is mediated by hyperpolarization-activated and cyclic nucleotide-gated (HCN) channels. In the early embryonic period, HCN4 mRNA is highly expressed in mouse ventricle and then the expression decreases with development (Yasui et al., 2001). Mice with a selective deletion of HCN4 in cardiomyocytes die between embryonic days 9.5 and 11.5 (Stieber et al., 2003). In mouse heart, although small I_h current could be detected in HCN4 knockout mice, it has been suggested that the HCN4 channel plays a key role in pacemaker depolarization during the diastolic phase.

IIIH. Excitation–Contraction Coupling

Changes in the excitation–contraction coupling process also occur during development of the heart. In particular, the source of Ca^{2+} for producing contraction is altered during development (Fig. 25.7) (Nakanishi et al., 1988; Kitchens et al., 2003; Seki et al., 2003; Tohse et al., 2004; Kobayashi et al., 2011). In fetal heart cells, the role of the sarcoplasmic reticulum (SR) is none at first and increases with embryonic development. Therefore, most of the Ca^{2+} required for contraction of embryonic cells is derived from Ca^{2+} influx through the voltage-dependent Ca^{2+} channels (L-type and T-type), i.e. originates from the extracellular space. In neonatal heart cells, the SR matures and plays a main role as the source of Ca^{2+} for contraction. Therefore, the Ca^{2+}-induced Ca^{2+} release from the SR compartment (Fabiato and Fabiato, 1978) becomes the more important system for contraction. That is, in adult heart cells, most of the Ca^{2+} for

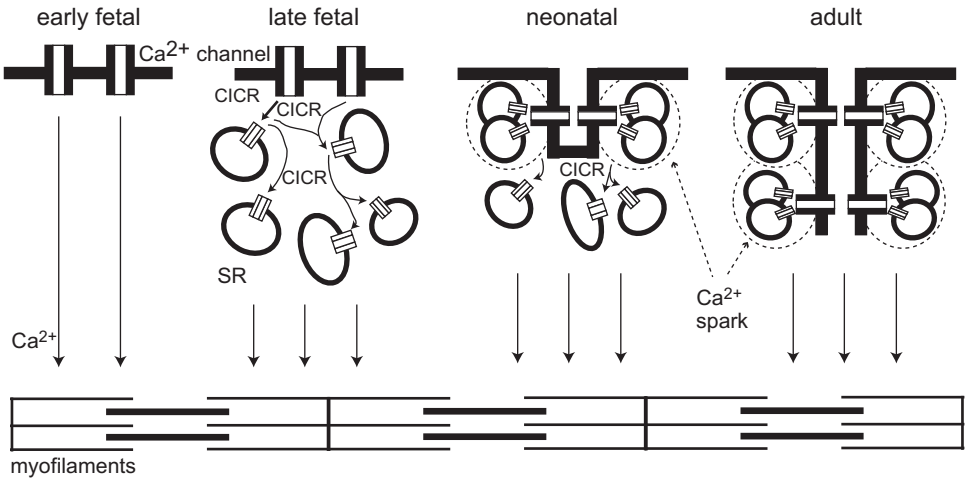

FIGURE 25.7 Schematic model of excitation–contraction (E-C) coupling during heart development. In the early fetal period at which the heart begins to contract, Ca^{2+} entering the cell through the sarcolemmal Ca^{2+} channels directly activates the myofilaments. During embryonic development, Ca^{2+} release from the sarcoplasmic reticulum (SR) through the ryanodine receptor (RyR) increases. This released Ca^{2+} from SR also stimulated another SR, as shown in "late fetal" panel. In the neonatal period, the formation of the T-tube system starts. A few L-type Ca^{2+} channels are close to RyRs and can evoke the Ca^{2+} spark in the periphery of cardiomyocytes. In the center of cardiomyocytes, the slow cascade of CICR still evokes. In the adult period, the T-tube system is established in all areas of cardioymyocytes. Each L-type Ca^{2+} channel is close to RyRs. The Ca^{2+} sparks simultaneously evoke in the periphery and centers of cells, producing fast and large Ca^{2+} transient in adulthood. *(Reproduced in modified form, with permission, from Tohse et al., 2004.)*

contraction comes from the internal SR stores. However, Ca^{2+} influx through the sarcolemma remains the determining factor for contractile force, because the Ca^{2+} influx controls the amount of Ca^{2+} released.

IV. SKELETAL MUSCLE FIBERS

IVA. Resting Potential and Action Potential

In skeletal muscle fibers, the RP also increases during development and differentiation from the individual myoblast stage to the multinucleated myotube stage to the mature fiber. (The myoblasts fuse end to end to form the myotubes which get progressively larger in length and diameter.) For example, the RP of cultured chick embryonic skeletal myocytes is low in the immature stage (short mononucleated myoblasts) and is dramatically hyperpolarized during differentiation (to long myotubes or mature fibers) (Fig. 25.8A) (Fischbach et al., 1971; Spector and Prives, 1977). The mature fibers in older cultures consist of multinucleated myotubes with cross-striations (i.e. aligned myofibrils). In the immature myoblasts, the RP generally is about −40 mV. However, the RP of the maturing myotubes is about −60 mV, which is approximately equal to that of adult skeletal muscles bathed in the same culture medium (Fig. 25.8A). A similar change in the RP occurs in rat skeletal myoblasts/myotubes during development (Ritchie and Fambrough, 1975). A progressive decrease in the P_{Na}/P_K ratio, which sets the RP closer to the equilibrium potential for K^+ (E_K), accounts for the developmental changes in the RP (Fig. 25.8B). The family of curves shown in Fig. 25.8B is similar to that reported in developing chick heart (Sperelakis and Shigenobu, 1972).

In human skeletal muscle (from biopsy), the RP increases (hyperpolarization) during culture. Fetal and postnatal myocytes exhibit RPs of about −8 to −35 mV in the early period of culture and then hyperpolarize to about −50 to −74 mV in later culture (Iannaccone et al., 1987; Liu et al., 1998, 2003). This hyperpolarization, which is due to the sequential expression of I_K and I_{K1}, induces an increase in intracellular Ca^{2+} concentration, which is essential for myoblast differentiation and fusion to occur (Bijlenga et al., 2000; Fischer-Lougheed et al., 2001; Konig et al., 2006).

The AP configuration of skeletal muscle fibers also changes during development and differentiation. For example, in one study of chick embryonic myotubes, prolonged APs that persist for more than 500 ms, with prolonged contraction, were exhibited on day 5 in culture (Spector and Prives, 1977). By culture day 7, the myotubes exhibited primarily brief APs (less than 10 ms) and brief twitch contraction. (On day 5, small regions of the myotubes sometimes displayed brief APs with localized twitches in those regions.) Thus, the brief AP becomes more dominant during development that proceeds in culture.

A second study on cultured chick skeletal myoblast/myotubes is depicted in Fig. 25.9. As can be seen, at the early stage, the AP is small and does not overshoot (the zero membrane potential level) (Fig. 25.9A, upper record). In the myotubes formed by fusion of myoblasts after a few

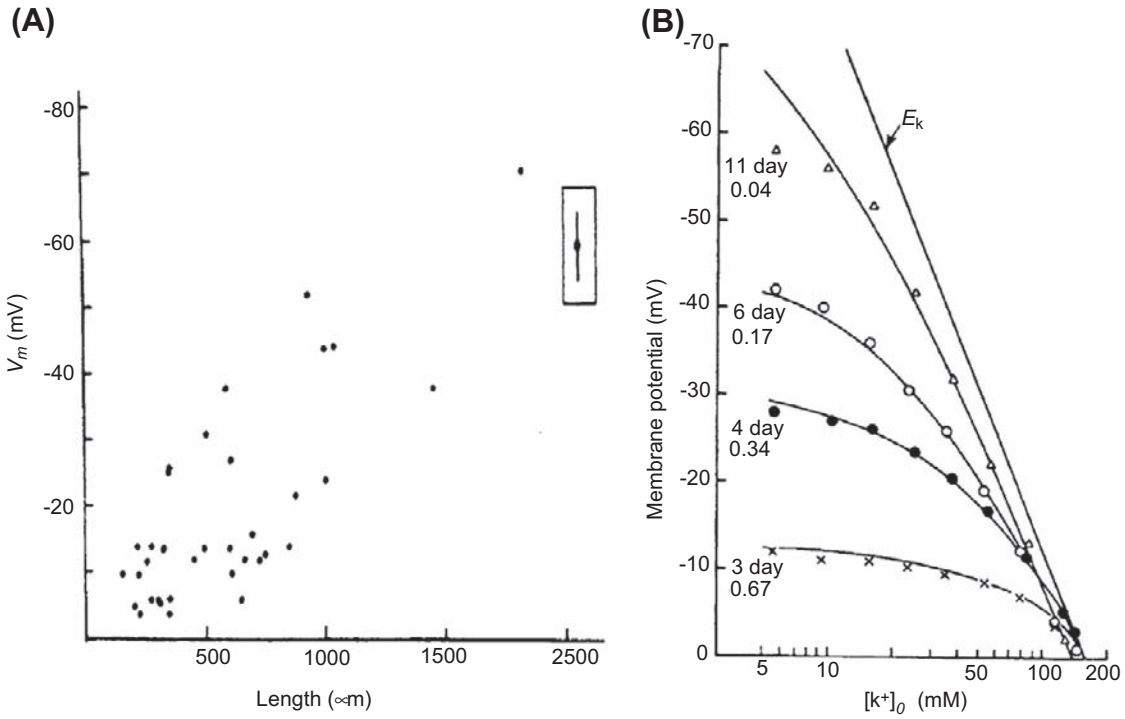

FIGURE 25.8 Developmental changes of resting potential in the skeletal myoblasts/myotubes from (A) embryonic chick and (B) fetal rat. (A) The relation between the RP and length of the chick skeletal myoblasts/myotubes in culture. The filled circle enclosed within the box is the mean (± 2SE) resting potential of 20 myotubes. (B) The relationship between the RP and external K^+ ion concentration ($[K^+]_o$) for rat skeletal myotubes of different periods in culture. The Nernst equilibrium potential for K^+ is indicated by the straight line labeled E_K. The solid line for each myotube is the theoretical curve predicted by the Goldman equation for the P_{Na}/P_K ratios given at the left and the extrapolated $[K^+]_i$ value. *(Reproduced with permission from (A) Fischbach et al. (1971). J. Cell. Physiol. 78, 289–300. Copyright 1971 John Wiley & Sons, Inc. Reprinted by permission of Wiley-Liss, Inc., a subsidiary of John Wiley & Sons, Inc. and (B) Ritchie and Fambrough, 1975. Reproduced from The Journal of General Physiology, by copyright permission of The Rockefeller University Press.)*

more days in culture (day 7 and 11), the amplitude and maximum rate of the spikelike APs increased markedly during development while in culture (Fig. 25.9A, middle and lower records, and Fig. 25.9B). A plot of max *dV/dt* versus the number of days in culture is given in Fig. 25.9B. Since the APs were blocked by TTX in almost all myotubes tested (Fig. 25.9A, right side, and Fig. 25.9B), differentiation of the spike-like APs is due to progressively increased intensity of inward current through fast Na^+ channels (Kano and Yamamoto, 1977). That is, an increase in the number (density) of fast Na^+ channels allows a regenerative AP to be produced, and the maximum rate of rise to become faster and faster.

In myocytes of a marine tunicate (ascidian), AP duration abbreviates during the embryonic period (Greaves et al., 1996). There is a progressive decrease in AP duration from the middle embryonic to the late embryonic period and a corresponding increase in the rate of rise and fall of the AP. Spontaneous firing of APs is observed in most ascidian myocytes in the middle embryonic period. The automaticity progressively disappears during development.

IVB. Inward-Rectifier K^+ Channels

The RP of maturing myotubes gets closer to E_K because the P_{Na}/P_K ratio is gradually decreased during development (see Fig. 25.8B). These characteristics are also observed in chick embryonic cardiomyocytes during development (Sperelakis and Shigenobu, 1972) and are produced by marked expression of the inward-rectifier K^+ channels in the surface membrane of the myocytes (Shin et al., 1997). Therefore, it seems likely that the hyperpolarization of the RP of skeletal myocytes in culture is produced by a similar developmental change of inward-rectifier K^+ channels.

The I_{K1} is present in skeletal muscle cells from early embryonic amphibian (Linsdell and Moody, 1995). Although there is a brief period (approximately 4 h) during which its density decreases, the overall trend is an increase during development.

In ascidian myocytes, I_{K1} exhibited dramatic changes during development (Fig. 25.10C) (Greaves et al., 1996). In the ascidian, the inward-rectifier K^+ current is gained after fertilization of the egg. (The same change also occurs in other species.) When gastrulation ends (at 16 h after

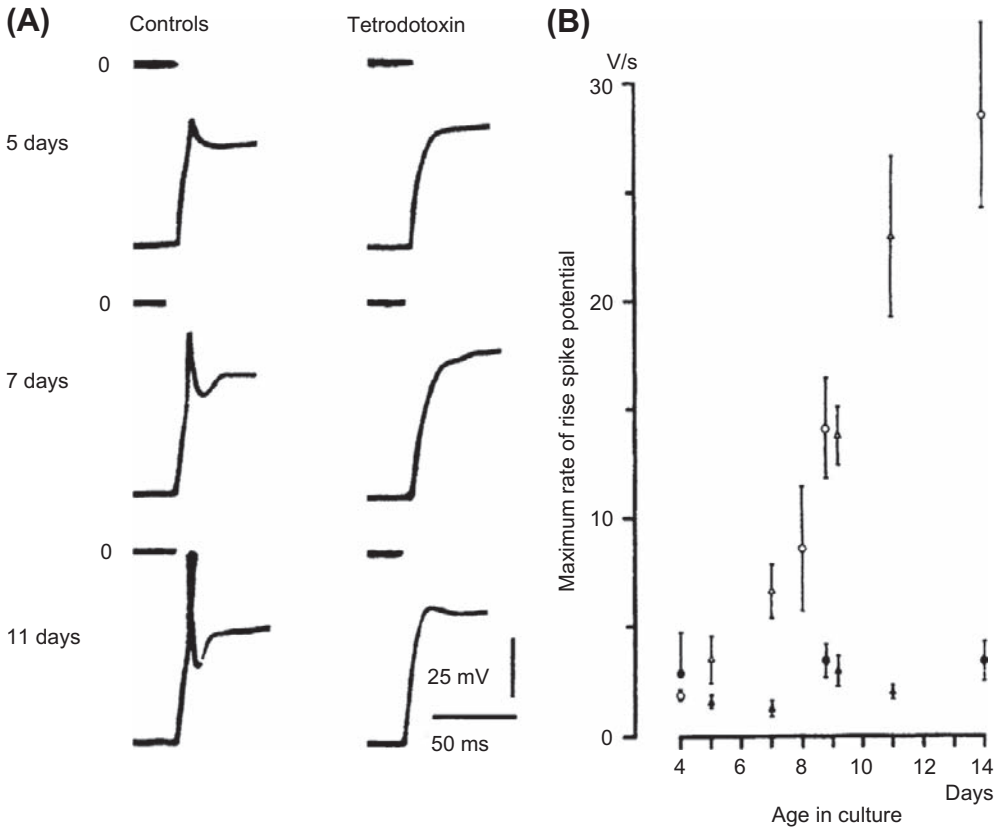

FIGURE 25.9 Spike-like APs and their maximum rate of rise in maturing skeletal myotubes from chick embryo. (A) Responses of three myotubes at different ages in culture: 5 days (upper), 7 days (middle) and 11 days (lower). Each pair of records is taken from the same myotube before (left) and after (right) application of TTX (10^{-7} M). Depolarizing current pulses were applied after the membrane potential was hyperpolarized to a standard level of −80 mV. The zero potential level is indicated. (B) Maximum rate of rise of spike potentials as a function of the age in culture (mean ± SE). Circles and triangles represent two different batches of culture; filled symbol indicates presence of TTX. *(From Kano and Yamamoto (1977). Development of spike potentials in skeletal muscle cells differentiated in vitro from chick embryo. J. Cell. Physiol. 90, 439–444. Copyright © 1977 Journal of Cellular Physiology. Reprinted by permission of Wiley-Liss, Inc., a subsidiary of John Wiley & Sons, Inc.)*

fertilization), the current density suddenly decreases from 4 to 0.5 pA/pF. After the tailbud stage (22 h after fertilization), the current density progressively increases again and reaches a value of 5 pA/pF before hatching. Because I_{K1} is one of the most important resting conductances (which stabilizes and helps to set the RP), this transient decrease and subsequent increase in the current density parallels the generation of spontaneous APs.

Evaluating the human myoblast fusion revealed that the I_{K1} increases during differentiation (Liu et al., 1998). In addition, inhibition of Kir 2.1 expression with an antisense-Kir2.1-RNA reduced the endogenous I_{K1} and blocked fusion (Fischer-Lougheed et al., 2001). Therefore, it seems likely that the increase in I_{K1} is required for human muscle differentiation.

IVC. Delayed-Rectifier K^+ Channels

The delayed-rectifier K^+ current (I_K) in skeletal myocytes of early embryonic amphibian progressively increases during development in culture (Linsdell and Moody, 1995). A similar increase in I_K occurs in ascidian myocytes after the neurula stage (16 h postfertilization) (see Fig. 25.10B) (Greaves et al., 1996). However, $I_{K(Ca)}$ progressively increases after 26 h postfertilization. The increase in $I_{K(Ca)}$ closely parallels the increase in sustained L-type Ca^{2+} current (see Figs. 25.10A,B). These developmental changes in K^+ channels contribute to the abbreviation of AP duration during the late developmental period.

Evaluating the human myoblast fusion revealed that I_K increases during differentiation (Bijlenga et al., 1998; Fischer-Lougheed et al., 2001). It seems likely that I_K contributes to the RP, because the cells were depolarized by 5 μM dofetilide, a class III antiarrhythmic agent known selectively to inhibit ERG channels. However, it remains unknown whether I_K is a prerequisite for myoblast fusion to occur, because the inhibition of I_K accelerates the rate of human myoblast fusion (Liu et al., 2003). Further experiments are necessary to reveal the precise roles of I_K during differentiation.

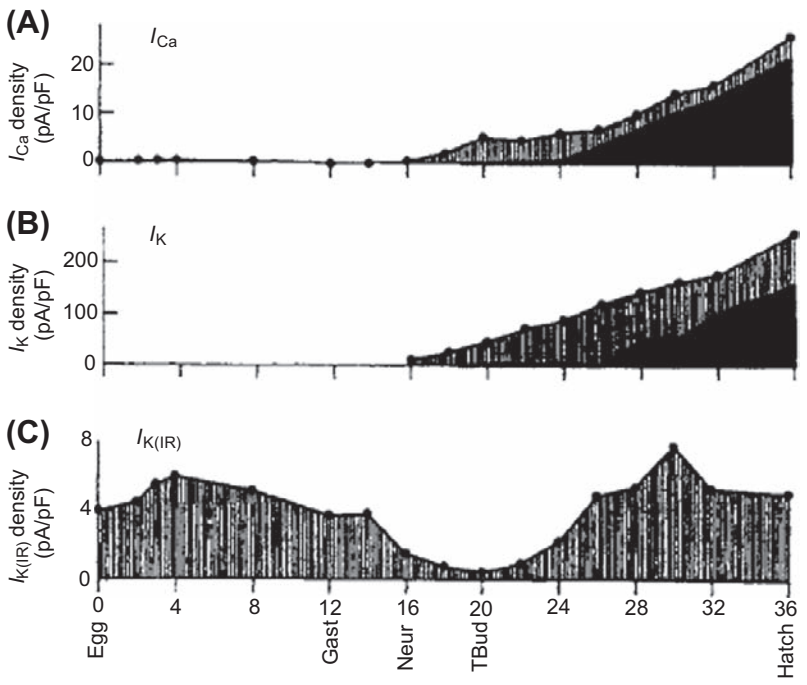

FIGURE 25.10 Development of Ca^{2+} and K^+ currents in skeletal muscle of a marine tunicate (ascidian). The plots start at fertilization (0 h). (A) Total Ca^{2+} current density (filled circles), with inactivating (hatched) and sustained (solid) components. (B) Total K^+ current density (filled circles), with voltage-dependent (hatched) and Ca^{2+}-dependent (solid) components. (C) Inward-rectifier K^+ current (I_{K1} or $I_{K(IR)}$) density. Gast, Neur and Tbud indicate the stages of gastrula, neurula and tailbud, respectively. *(Modified with permission from Greaves et al., 1996.)*

IVD. Ca^{2+} Channels and Na^+ Channels

High-voltage-activated Ca^{2+} channels have also been observed in the ascidian embryo (see Fig. 25.10A) (Greaves et al., 1996). These Ca^{2+} channels exhibit inactivation and may be an N-type Ca^{2+} channel because the current is blocked by conotoxin. The channels increase after the neurula stage (16 h after fertilization). After the tailbud stage, sustained Ca^{2+} channel activity (probably L-type) begins to increase and dominates at the time of hatching. Low voltage-activating, rapidly inactivating Ca^{2+} channels (T-type) are detected in about 50% of the cells at each stage of development. The contribution of the T-type channels to total Ca^{2+} influx is relatively small in comparison with L-type and N-type channels.

In early embryonic amphibian skeletal myocytes, substantial Ca^{2+} current and Na^+ current appeared almost at the same time (after 10–12 h in culture) (Linsdell and Moody, 1995). These channel currents continued to increase steadily over an observation period of 10–28 h in culture.

In mouse skeletal muscle, L-type Ca^{2+} current increases during embryonic development, whereas T-type Ca^{2+} current increases until embryonic day 16 followed by a decrease until birth (Shimahara and Bournaud, 1991; Strube et al., 2000; Berthier et al., 2002). It seems likely that this developmental change of T-type Ca^{2+} current is involved in the early stages of muscle differentiation via the increase in the intracellular Ca^{2+} concentration, because the inhibition of T-type Ca^{2+} current by 100 μM amiloride, 200 μM Ni^{2+} or antisense oligonucleotides directed against the α1H subunit suppresses fusion of myoblasts (Bijlenga et al., 2000).

IVE. Acetylcholine Receptor/Channel

The nicotinic acetylcholine receptor/channel (nAChR) is essential to transmission at the neuromuscular junction (see chapter on synaptic transmission). During development, the nAChR channels in embryonic muscles are converted to adult-type nAChR channels around the time of birth (Mishina et al., 1986). The fetal nAChR channel is composed of α-, β-, γ- and δ-subunits and, in the adult channel, the γ-subunit is substituted by an ε-subunit. In functional characteristics, the fetal channel exhibits a low conductance and long openings compared with those of the adult channel. This conversion of the nAChR channel may be related to innervation of the muscles that occurs during development, because the substitution of the fetal-type nAChR channels with an adult-type nAChR channels substantially alters the innervation pattern of mouse muscle by the motor nerve (Koenen et al., 2005).

In the early embryonic period, nAChR channels are present at a moderate level throughout the myotube surface. In adult muscle, nAChR channels are highly concentrated in the neuromuscular junction (Sanes and Lichtman, 2001). A recent study has revealed the coordinated activities of Wnt3 and agrin, which are both secreted by motoneurons, in clustering nAChR channels at the neuromuscular junction (Henriquez et al., 2008).

IVF. Regulation of Expression of Ion Channels

It has been well analyzed that several humoral factors regulate expression of ion channels during development. Activin, a member of the TGFβ family, has proved to be a particularly potent inducing agent to form different mesodermal cell types from animal cap cells. In vitro induction of animal cap *Xenopus* cells under culturing with activin triggers a whole cascade of developmental events, resulting in the differentiation of skeletal muscle (Currie and Moody, 1999). The developmental pattern of ion channel expression in muscle induced in vitro by activin is close to that of normal muscle. First, the same currents (I_K, I_{K1}, I_{Na}, I_A, I_{Ca}) are expressed over a similar time course during differentiation. The sequence in which the currents are expressed is also maintained, with I_K and I_{K1} being expressed first, followed by I_{Na}, I_A and I_{Ca} at slightly later stages. This study indicates that activin is very important for development of electrical activity in skeletal muscle.

V. NEURONS

VA. Action Potential

The ionic dependence of the neuronal AP is altered during the early stages of embryonic development (Spitzer and Baccaglini, 1976; Spitzer et al., 1994). Initially, the AP exhibits a prominent Ca^{2+} dependence (i.e. Ca^{2+}-dependent AP) and its duration is prolonged. Later in development, the AP duration becomes brief and most of the inward current during the depolarizing phase is carried by Na^+ (i.e. Na^+-dependent AP). The Na^+-dependent APs continue until maturation of the neuron. For example, in embryonic amphibian neurons in vivo, the AP is prolonged and the rate of rise is slow at a relatively early stage (Fig. 25.11A). Removal of Na^+ ion does not affect the AP configuration at this stage, whereas it is almost abolished by Co^{2+} ion, an inorganic blocker of voltage-dependent Ca^{2+} channels. In the late embryonic stage, the AP becomes greatly abbreviated and loses the shoulder on its falling phase (Fig. 25.11B). This AP is completely blocked by removal of Na^+ ion (or by TTX), but is unaffected by Co^{2+} (Spitzer and Baccaglini, 1976).

In rat spinal motoneurons at embryonic day 16, the AP upstroke may be dependent upon Na^+ ion, although maximum rate of rise of the AP is slow (about 20 V/s) (Gao and Ziskind-Conhaim, 1998). Duration of the AP at day 16 is prolonged (about 10 ms). At postnatal day 3, the AP upstroke is very fast (about 70 V/s) and duration of the AP is very short (2–3 ms).

In mouse cortical neurons at embryonic day 14, the AP duration is prolonged. During development, the AP duration becomes brief. This developmental change is mainly due to the increase in Na^+ current density, while outward K^+ current density remains almost unchanged (Picken Bahrey and Moody, 2003).

VB. Ca^{2+} Transient

Spontaneous transient elevation of intracellular Ca^{2+} is observed in developing neurons. The spontaneous Ca^{2+} transient (recorded by use of fluorescent dyes, e.g. FURA-2, fluo-3, indo-1, etc.) is exclusively dependent on Ca^{2+} influx because it is abolished either by removal of extracellular Ca^{2+} or by agents that block Ca^{2+} channels (Holliday and Spitzer, 1990; Spitzer, 1994). Therefore, the observed intracellular Ca^{2+} transient is due to Ca^{2+} influx from the extracellular space.

Two classes of spontaneous Ca^{2+} transients have been detected: rapid events, termed Ca^{2+} *spikes* (Gu et al., 1994) and slow events, termed Ca^{2+} *waves*. The incidence of

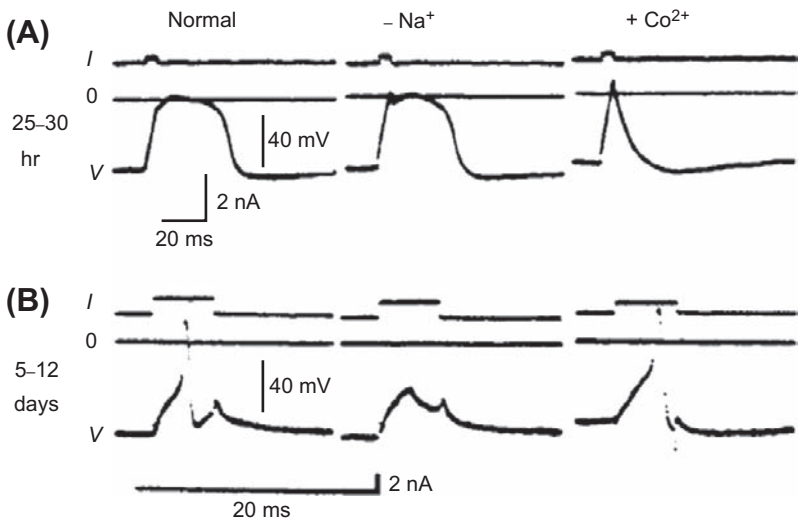

FIGURE 25.11 Developmental changes in APs of embryonic amphibian neurons at two different stages: (A) 25–30 h and (B) 5–12 days after fertilization of the egg. Depolarizing current (*I*) is applied to evoke the AP (*V*). The zero potential is shown by a solid line (0). (A) The AP is of long duration and the rate of rise is slow at this early stage. This AP is little affected by removal of Na^+, but is abolished by Co^{2+}. (B) The AP at this late stage is brief and its amplitude is large. This AP is blocked by removal of Na^+ and is unaffected by Co^{2+}. *(Modified from Spizer, N.C. and Baccaglini, P.I. (1976). Development of the action potential in embryo amphibian neurons in vivo, Brain Res. 107, 610–616, Copyright 1976, with permission from Elsevier Science.)*

these Ca^{2+} transients changes during development in culture. Ca^{2+} spikes in the cell body (soma) are triggered by spontaneous APs and are rapidly propagated to the growth cone. Ca^{2+} spikes also use the intracellular Ca^{2+} store because depletion of the store with caffeine substantially reduces their amplitude. Ca^{2+} spikes may be required for the normal appearance of the transmitter γ-aminobutyric acid (GABA), since blocking of Ca^{2+} spikes by a Ca^{2+} channel-blocker prevents the acquisition of GABA immunoreactivity (Spitzer et al., 1993). The normal developmental increase in the activation kinetics of K^+ currents is also prevented by the blocking of Ca^{2+} spikes.

Ca^{2+} waves occur often (about 10/h) in the growth cone and they are not generally propagated to the soma. The Ca^{2+} waves in the soma occur at a lower frequency (about 2/h). Therefore, the Ca^{2+} waves are local and occur independently in separate growth cones of the same neuron. Because there seems to be some relation between external Ca^{2+} and the length of the neurite, Ca^{2+} waves in growth cones are likely to regulate neurite extension (Gu et al., 1994; Spitzer, 1994; Spitzer et al., 1994).

The recent evaluation of Ca^{2+} signaling in gastrula stage embryos revealed that not only Ca^{2+} transients (Ca^{2+} spikes and Ca^{2+} waves) but also a slow increase in $[Ca^{2+}]_i$ was observed during early gastrulation of *Xenopus* and zebrafish (Gilland et al., 1999; Leclerc et al., 2000; Webb et al., 2005). Inhibition of these Ca^{2+} signalings decreases the expression of neuralising genes, *Zic3* and *geminin*, and proto-oncogene, *c-fos* and FOS-related protein (Leclerc et al., 1999, 2000). Furthermore, the activators of L-type Ca^{2+} channel (ConA and Bay-K-8644) trigger neural induction (Moreau et al., 1994). Although the precise downstream targets of the Ca^{2+} signaling cascades remain to be elucidated, Ca^{2+} might be a key central regulator in the process of neural induction (Webb et al., 2005).

VC. Voltage-Gated Ion Channels

In mature excitable cell membranes, the major inward currents consist of two ions, Na^+ and Ca^{2+}, which are carried through voltage-gated Na^+ channels and Ca^{2+} channels, respectively. Na^+ and Ca^{2+} channels exhibit two patterns of development (Gottmann et al., 1988; O'Dowd et al., 1988). In the first pattern, Ca^{2+} channels appear earlier and develop faster than Na^+ channels. This explains, at least in part, the conversion of the Ca^{2+}-dependent AP to the Na^+-dependent one discussed earlier.

In the second pattern, Ca^{2+} channels and Na^+ channels become expressed almost at the same time. For example, in cultured embryonic amphibian neurons, Ca^{2+} currents are large even at the early stage of development and the peak current density does not change from the early stage to the late stage (Fig. 25.12A). Na^+ currents are also present, but the current density is small at the early stage. The peak

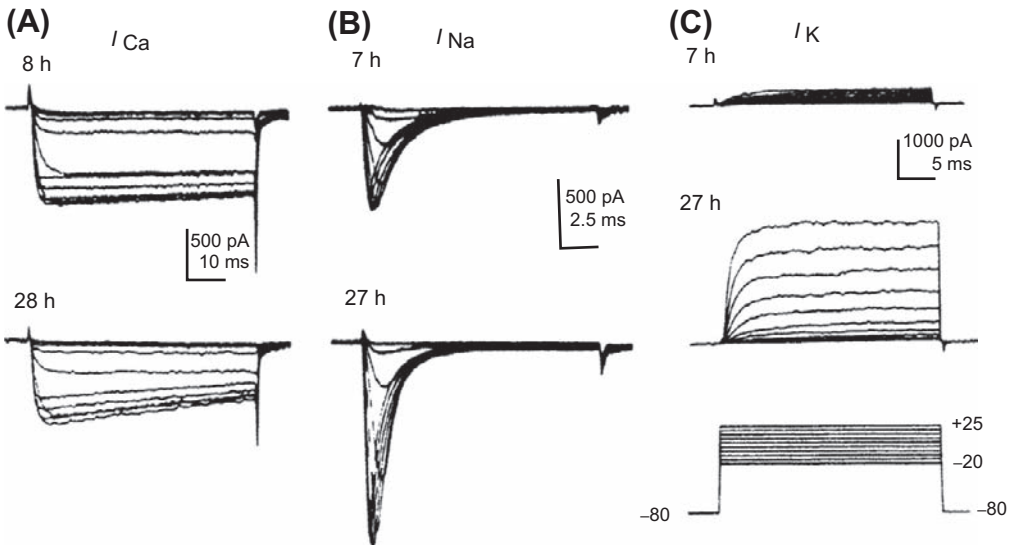

FIGURE 25.12 Developmental changes in ionic currents of cultured maturing neurons of embryonic amphibian. Records from cells in the early stage (7−8 h in culture)(upper traces) and the late stage (27−28 h)(lower traces). Records in (A) and (B) were obtained in presence of Cs^+ (internal solution) and TEA (external solution) to block outward K^+ currents. (A) Ca^{2+} current (I_{Ca}) recorded in Na^+-free solution. The amplitude of I_{Ca} was nearly equal at early and late stages. (B) Na^+ current (I_{Na}) recorded in presence of Co^{2+} to I_{Ca} block. I_{Na} was smaller at the early stage than at the late stage. (C) K^+ current (I_K) recorded in the presence of Co^{2+} and TTX to block the inward currents (I_{Ca} and I_{Na}). I_K is small at the early stage and gets larger in amplitude and faster in rate of activation at the late stage. Pulse protocols for (A), (B) and (C) are given at the bottom of (C). *(Modified with permission from O'Dowd et al. (1988). Development of voltage-dependent calcium, sodium and potassium currents in* Xenopus *spinal neuron. J. Neurosci. 8, 792−805, Copyright 1988 by the Society for Neuroscience.)*

density of the Na^+ current approximately doubles between the early and late stages of development in culture (Fig. 25.12B).

In ascidian embryos, Na^+ channels in neural cells dramatically change during the early developmental stage (Takahashi and Okamura, 1998). In unfertilized eggs, a small amount of Na^+ current (type A) is already observed. However, the type A Na^+ current is almost abolished after fertilization. After fertilization, fast-activating and inactivating Na^+ current (type C) with slow-inactivating Na^+ current (type B) is markedly increased. However, in the blastomere, which develops into neurons, the type B current is abolished in a moment. Finally, the type C current, corresponding to neural-specific *TuNa I* gene, increases further and becomes responsible for the neural Na^+ spike.

Patch-clamp experiments with acute sliced preparation of brain revealed that Na^+ current densities of neurons increase during development of mouse cortical plate of neocortex (Picken Bahrey and Moody, 2003), mouse cerebellum (Fry, 2006) and rat spine (Gao and Ziskind-Conhaim, 1998). On the other hand, Na^+ current densities remain almost unchanged in the intermediate zone of mouse neocortex (Picken Bahrey and Moody, 2003) and layers III−V of rat neocortex (Wang et al., 2009).

As described earlier, the Ca^{2+} channel allows Ca^{2+} influx and is responsible for the spontaneous Ca^{2+} transient in developing neurons. However, regulation of Ca^{2+} influx during development is not always due to change in the density of the Ca^{2+} channels, because some neurons show no increase in the Ca^{2+} current density (Salgado et al., 2005). The ratio of the K^+ current to the Ca^{2+} current (I_K/I_{Ca}) affects the configuration of the APs, because the inward I_{Ca} is deactivated earlier when the outward I_K is augmented, resulting in a decrease in the net inward current. In other words, any outward (K^+) current subtracts from the inward (Ca^{2+}) current to give a lower net inward current. In addition, the change in the amplitude and the kinetics of I_K that occurs during development greatly affects the AP configuration and apparent ionic dependence (Barish, 1986; Lockery and Spitzer, 1992). Therefore, the I_K/I_{Ca} ratio determines whether Ca^{2+}-independent APs are exhibited as well as influences the Ca^{2+} influx.

It is well known that Ca^{2+} channels are classified by their threshold voltage (low-voltage activated, LVA; high-voltage activated, HVA) or specific blockers (T-, L- and N-type). In rat cortical neurons of neocortex and phrenic motoneurons of cervical spine, the major Ca^{2+} channel subtype shifts from the LVA (T-type) Ca^{2+} current to the HVA Ca^{2+} current during development (Tarasenko et al., 1998; Martin-Caraballo and Greer, 2001). In mouse brainstem neurons, the density of LVA Ca^{2+} currents increases during the first postnatal week, while the density of HVA Ca^{2+} currents increases after the first postnatal week (Zhang et al., 1999).

The developmental increase in K^+ currents and change in their activation kinetics have been investigated in amphibian neurons in intact (isolated) spinal cord (Desarmenien et al., 1993) and in dissociated cell culture (see Fig. 25.12C) (Barish, 1986; O'Dowd et al., 1988). The general rule regarding the order of appearance of ionic conductances in developing neurons is that K^+ currents appear first before functional expression of the voltage-dependent inward currents (Spitzer et al., 1994). However, the types of K^+ currents regulating the AP duration and the order of their maturation vary among different neuronal cells at early stages of development. In some neurons, delayed-rectifier K^+ current precedes the appearance of the transient outward K^+ current (I_A or I_{to}). In contrast, in other neurons, the inactivating K^+ current (I_A) precedes expression of the delayed-rectifier K^+ current (Bader et al., 1985; Aguayo, 1989; Beck et al., 1992).

The Ca^{2+}-activated K^+ channels play a pivotal role for afterhyperpolarization and regulation of repetitive firing in neurons. In rat spinal motoneurons, the Ca^{2+}-activated K^+ current is markedly increased from the embryonic period to the postnatal period (Gao and Ziskind-Conhaim, 1998). The increase in this current shortens the duration of the action potential and produces the afterhyperpolarization. In addition, the Ca^{2+}-activated K^+ current reduces the frequency of action potential repetitive firing after birth. In rat Purkinje cells of cerebellum, the large-conductance Ca^{2+}-activated K^+ channels (BK) increase during development, whereas the small-conductance Ca^{2+}-activated K^+ channels (SK) decrease (Muller et al., 1998; Muller and Yool, 1998; Cingolani et al., 2002).

VD. Ligand-Gated Channels

Ionotropic glutamate receptors (iGluRs) are heteromeric ligand-gated ion channels. Based on their pharmacological and electrophysiological properties, iGluRs can be subdivided into three families: AMPA (α-amino-3-hydroxymethyl-4-isoxazolepropionic acid) receptor; NMDA (N-methyl-D-aspartate) receptor and KA (kinate) receptor.

In Purkinje and granule cells of cerebellum, NMDA receptors are expressed transiently during early stages of development, resulting in the increase in intracellular Ca^{2+} which could lead to neuronal differentiation (Garthwaite et al., 1987).

AMPA receptors in immature neurons produce Ca^{2+} influx and elevation of intracellular Ca^{2+}. The Ca^{2+} permeability of iGluRs is governed by their subunit composition as well as by single amino acid substitutions generated by RNA editing; both factors may be developmentally regulated (Hume et al., 1991; Burnashev et al., 1992). It has been reported that AMPA receptors express in

the early stage of differentiation of *Xenopus* spinal neurons. Ca^{2+} influx to regulate the neural differentiation mainly flows through AMPA receptors soon after neurite initiation and before expression of NMDA receptors (Gleason and Spitzer, 1998).

The evaluation of long-term potentiation (LTP) in hippocampus revealed an increase in the ratio of current carried by AMPA receptors relative to NMDA receptors during development (Hsia et al., 1998; Abrahamsson et al., 2008). It may be presumed that such developmental change is due to, not only the developmental change in the expression of iGluRs subunits, but also to the change of molecules that associate/regulate iGluRs subunits (Petralia et al., 2005; Hall and Ghosh, 2008).

VI. CONCLUDING REMARKS

Action potentials (APs) and resting potentials (RPs) in excitable cells, such as cardiomyocytes, skeletal muscle fibers and neurons, are greatly altered during development. In general, the RP increases (becomes more negative), the AP rate of rise increases, overshoot increases and duration decreases. These electrophysiological alterations are mainly produced by developmental changes in the ion channels, i.e. by changes in the types, number and kinetic properties of the ion channels.

In cardiomyocytes, the density of inward-rectifier K^+ currents (I_{K1}) usually increases during development. This increase may result from changes in the single-channel conductance, as well as in the number and open probability of the channel, because the conductance of early fetal myocytes is much smaller than those of neonatal myocytes. The hyperpolarization of the RP during development can be accounted for by the increase in the density of I_{K1} and the resultant decrease in the P_{Na}/P_K ratio. In contrast, the hyperpolarization-activated inward current (I_h), which may affect automaticity, is dominant in early embryonic chick and mouse cardiomyocytes and disappears during development.

The Na^+ current also increases markedly during development. That is, there are few or no functional fast Na^+ channels present at the earliest stages, and the density of these channels increases progressively during development. The fast Na^+ current is responsible for the increase in the AP rate of rise (independent of the hyperpolarization of RP). The max dV/dt increases dramatically during development, e.g. in chick heart, from 20 to 200 V/s.

The fast Na^+ current in embryonic/fetal hearts has a significant sustained (i.e. slow-inactivating or steady-state) component. The sustained component of the embryonic/fetal Na^+ current decreases during development and this decrease contributes, at least in part, to the abbreviation of the AP duration.

Development of Ca^{2+} channels seems more complex. The density of total Ca^{2+} current in chick cardiomyocytes decreases during the developmental period from fetal to neonate. In rat and mouse, however, it increases from the fetal to the neonatal period, followed by a substantial decrease in the adult. In rabbit and guinea pig cardiomyocytes, the current density in the neonatal period is smaller than that in the adult. The total Ca^{2+} current is composed of currents through several different types of channels: L-type, T-type, and F-type. (1) The proportion of the T-type Ca^{2+} channel current in immature cells is generally more than that in mature cells and it may actually disappear in adults. That is, the L-type Ca^{2+} channel current becomes more dominant in mature cells. (2) A nifedipine-resistant F-type Ca^{2+} channel current is also present in early fetal cardiomyocytes of rats. (3) Long-lasting openings of the L-type Ca^{2+} channels are relatively frequently observed in embryonic chick and fetal rat cardiomyocytes, but are quite unusual in adult cells.

Ca^{2+} influx through the Ca^{2+} channels is especially important for the excitation–contraction coupling process of fetal cardiomyocytes. This is because the SR function and/or the essential component for Ca^{2+} release from the SR is immature and so Ca^{2+} influx from the extracellular space is the main source of Ca^{2+} for contraction.

The density of the transient outward current (I_{to}) increases during development. An increase in the density of the delayed-rectifier K^+ current (I_K) also occurs during early development and decreases during the postnatal period. The change of these voltage-gated outward currents (i.e. I_{to} and I_K) helps to abbreviate the AP duration during development.

In skeletal muscle fibers, there is an overall trend toward an increase in the density of I_{K1} during the early developmental period. However, there is a transient period during which the current density decreases. This transient period parallels the increased incidence of spontaneous firings, presumably due to a less stable RP. The major voltage-gated inward currents, the Na^+ and Ca^{2+} currents, are already present in the early embryonic skeletal myocytes in culture and they increase in intensity during development. These changes contribute to the increases in the AP rate of rise, overshoot and propagation velocity. Prolonged APs and brief APs can be elicited in chick embryonic skeletal myotubes, depending on the stage of development. The prolonged APs are associated with long-lasting contractions of the myotubes. The brief APs become more dominant during development in culture and are associated with myotube twitches. The nicotinic acetylcholine receptor/channel, which is essential to transmission at the neuromuscular junction, is converted from fetal-type to adult-type and this conversion may be related to innervation of the muscles that occurs during development. Activin, a member of the TGFβ family, is important for development of ion channels in skeletal muscles. Activin stimulates the expression of the same ion channels (I_K, I_{K1}, I_{Na}, I_A, I_{Ca}) in cultured skeletal

myoblasts. The sequence in which currents are expressed is also maintained (I_K and I_{K1} are expressed first).

In neuronal cells, there is an overall trend that the ionic dependence of the AP is altered from Ca^{2+}-dependent (prolonged AP duration) to Na^+-dependent (brief AP duration) during development. The pattern of ion channel development varies among different types of neuronal cells, with faster development of Ca^{2+} channels in some cells. Another important factor that determines the ionic dependence of the AP is the developmental increase in I_K. Therefore, the I_K/I_{Ca} ratio is the major determinant of the conversion of the AP configuration and influences Ca^{2+} influx during development. Two types of Ca^{2+} transients, Ca^{2+} spikes and Ca^{2+} waves, are present in developing neurons. Ca^{2+} spikes in the cell body (soma) are generated by spontaneous APs and propagate to the growth cone. The incidence of these Ca^{2+} transients changes in developing neurons in culture. In addition to Ca^{2+} transients, a slow increase in $[Ca^{2+}]_i$ is observed during neural induction. The activities of ligand-gated Ca^{2+}-permeable channels (such as NMDA receptor/channels and AMPA-gated receptor channels) are also altered during development. Therefore, the Ca^{2+} influx through the voltage-gated (LVA or HVA channels) and the ligand-gated Ca^{2+} channels, and the subsequent effects on intracellular Ca^{2+}, may affect the structural changes of the developing neurons and help the establishment of the neuronal network.

As described earlier, ion channels exhibit dramatic changes during development in their type, structure, function and distribution. These dynamic alterations are controlled by expression of genes coding ion channels and may be essential to cellular growth and differentiation by affecting intracellular Ca^{2+} concentration and excitability. Thus, molecular biology, combined with electrophysiology, has enabled large advances in our understanding of cell function.

BIBLIOGRAPHY

Abrahamsson, T., Gustafsson, B., & Hanse, E. (2008). AMPA silencing is a prerequisite for developmental long-term potentiation in the hippocampal CA1 region. *J Neurophysiol, 100*, 2605−2614.

Accili, E. A., Robinson, R. B., & DiFrancesco, D. (1997). Properties and modulation of If in newborn versus adult cardiac SA node. *Am J Physiol, 272*, H1549−H1552.

Aguayo, L. G. (1989). Post-natal development of K+ currents studied in isolated rat pineal cells. *J Physiol, 414*, 283−300.

Bader, C. R., Bertrand, D., & Dupin, E. (1985). Voltage-dependent potassium currents in developing neurones from quail mesencephalic neural crest. *J Physiol, 366*, 129−151.

Barish, M. E. (1986). Differentiation of voltage-gated potassium current and modulation of excitability in cultured amphibian spinal neurones. *J Physiol, 375*, 229−250.

Baruscotti, M., DiFrancesco, D., & Robinson, R. B. (1996). A TTX-sensitive inward sodium current contributes to spontaneous activity in newborn rabbit sino-atrial node cells. *J Physiol, 492*, 21−30.

Beck, H., Ficker, E., & Heinemann, U. (1992). Properties of two voltage-activated potassium currents in acutely isolated juvenile rat dentate gyrus granule cells. *J Neurophysiol, 68*, 2086−2099.

Bernard, C. (1975). *Establishment of Ionic Permeabilities of the Myocardial Membrane during Embryonic Development of the Rat. Developmental and Physiological Correlates of Cardiac Muscle*. New York: L.M. and S. T. Raven Press.

Berthier, C., Monteil, A., Lory, P., & Strube, C. (2002). Alpha(1H) mRNA in single skeletal muscle fibres accounts for T-type calcium current transient expression during fetal development in mice. *J Physiol, 539*, 681−691.

Bijlenga, P., Liu, J. H., Espinos, E., et al. (2000). T-type alpha 1H Ca2+ channels are involved in Ca2+ signaling during terminal differentiation (fusion) of human myoblasts. *Proc Natl Acad Sci USA, 97*, 7627−7632.

Bijlenga, P., Occhiodoro, T., Liu, J. H., et al. (1998). An ether -a-go-go K+ current, Ih-eag, contributes to the hyperpolarization of human fusion-competent myoblasts. *J Physiol, 512*, 317−323.

Brown, A. M., Lee, K. S., & Powell, T. (1981). Sodium current in single rat heart muscle cells. *J Physiol, 318*, 479−500.

Burnashev, N., Monyer, H., Seeburg, P. H., & Sakmann, B. (1992). Divalent ion permeability of AMPA receptor channels is dominated by the edited form of a single subunit. *Neuron, 8*, 189−198.

Cerbai, E., Pino, R., Sartiani, L., & Mugelli, A. (1999). Influence of postnatal-development on I(f) occurrence and properties in neonatal rat ventricular myocytes. *Cardiovasc Res, 42*, 416−423.

Cingolani, L. A., Gymnopoulos, M., Boccaccio, A., Stocker, M., & Pedarzani, P. (2002). Developmental regulation of small-conductance Ca2+-activated K+ channel expression and function in rat Purkinje neurons. *J Neurosci, 22*, 4456−4467.

Cohen, N. M., & Lederer, W. J. (1988). Changes in the calcium current of rat heart ventricular myocytes during development. *J Physiol, 406*, 115−146.

Conforti, L., Tohse, N., & Sperelakis, N. (1993). Tetrodotoxin-sensitive sodium current in rat fetal ventricular myocytes − contribution to the plateau phase of action potential. *J Mol Cell Cardiol, 25*, 159−173.

Couch, J. R., West, T. C., & Hoff, H. E. (1969). Development of the action potential of the prenatal rat heart. *Circ Res, 24*, 19−31.

Currie, D. A., & Moody, W. J. (1999). Time course of ion channel development in Xenopus muscle induced in vitro by activin. *Dev Biol, 209*, 40−51.

Davies, M. P., An, R. H., Doevendans, P., et al. (1996). Developmental changes in ionic channel activity in the embryonic murine heart. *Circ Res, 78*, 15−25.

Desarmenien, M. G., Clendening, B., & Spitzer, N. C. (1993). In vivo development of voltage-dependent ionic currents in embryonic Xenopus spinal neurons. *J Neurosci, 13*, 2575−2581.

Dominguez, J. N., de la Rosa, A., Navarro, F., Franco, D., & Aranega, A. E. (2008). Tissue distribution and subcellular localization of the cardiac sodium channel during mouse heart development. *Cardiovasc Res, 78*, 45−52.

Fabiato, A., & Fabiato, F. (1978). Calcium-induced release of calcium from the sarcoplasmic reticulum of skinned cells from adult human, dog, cat, rabbit, rat, and frog hearts and from fetal and new-born rat ventricles. *Ann NY Acad Sci, 307*, 491−522.

Ferron, L., Capuano, V., Deroubaix, E., Coulombe, A., & Renaud, J. F. (2002). Functional and molecular characterization of a T-type Ca(2+) channel during fetal and postnatal rat heart development. *J Mol Cell Cardiol, 34*, 533−546.

Fischbach, G. D., Nameroff, M., & Nelson, P. G. (1971). Electrical properties of chick skeletal muscle fibers developing in cell culture. *J Cell Physiol, 78*, 289–299.

Fischer-Lougheed, J., Liu, J. H., Espinos, E., et al. (2001). Human myoblast fusion requires expression of functional inward rectifier Kir2.1 channels. *J Cell Biol, 153*, 677–686.

Franco, D., Demolombe, S., Kupershmidt, S., et al. (2001). Divergent expression of delayed rectifier K(+) channel subunits during mouse heart development. *Cardiovasc Res, 52*, 65–75.

Fry, M. (2006). Developmental expression of Na+ currents in mouse Purkinje neurons. *Eur J Neurosci, 24*, 2557–2566.

Fujii, S., Ayer, R. K., Jr., & DeHaan, R. L. (1988). Development of the fast sodium current in early embryonic chick heart cells. *J Membr Biol, 101*, 209–223.

Gao, B. X., & Ziskind-Conhaim, L. (1998). Development of ionic currents underlying changes in action potential waveforms in rat spinal motoneurons. *J Neurophysiol, 80*, 3047–3061.

Garthwaite, G., Yamini, B., Jr., & Garthwaite, J. (1987). Selective loss of Purkinje and granule cell responsiveness to N-methyl-D-aspartate in rat cerebellum during development. *Brain Res, 433*, 288–292.

Gassanov, N., Er, F., Michels, G., et al. (2009). Divergent regulation of cardiac KCND3 potassium channel expression by the thyroid hormone receptors alpha1 and beta1. *J Physiol, 587*, 1319–1329.

Gilland, E., Miller, A. L., Karplus, E., Baker, R., & Webb, S. E. (1999). Imaging of multicellular large-scale rhythmic calcium waves during zebrafish gastrulation. *Proc Natl Acad Sci USA, 96*, 157–161.

Gleason, E. L., & Spitzer, N. C. (1998). AMPA and NMDA receptors expressed by differentiating Xenopus spinal neurons. *J Neurophysiol, 79*, 2986–2998.

Gottmann, K., Dietzel, I. D., Lux, H. D., Huck, S., & Rohrer, H. (1988). Development of inward currents in chick sensory and autonomic neuronal precursor cells in culture. *J Neurosci, 8*, 3722–3732.

Grandy, S. A., Trepanier-Boulay, V., & Fiset, C. (2007). Postnatal development has a marked effect on ventricular repolarization in mice. *Am J Physiol Heart Circ Physiol, 293*, H2168–H2177.

Greaves, A. A., Davis, A. K., Dallmanm, J. E., & Moody, W. J. (1996). Co-ordinated modulation of Ca2+ and K+ currents during ascidian muscle development. *J Physiol, 497*, 39–52.

Gu, X., Olson, E. C., & Spitzer, N. C. (1994). Spontaneous neuronal calcium spikes and waves during early differentiation. *J Neurosci, 14*, 6325–6335.

Guo, W., Kada, K., Kamiya, K., & Toyama, J. (1997a). IGF-I regulates K(+)-channel expression of cultured neonatal rat ventricular myocytes. *Am J Physiol, 272*, H2599–H2606.

Guo, W., Kamiya, K., Hojo, M., Kodama, I., & Toyama, J. (1998). Regulation of Kv4.2 and Kv1.4 K+ channel expression by myocardial hypertrophic factors in cultured newborn rat ventricular cells. *J Mol Cell Cardiol, 30*, 1449–1455.

Guo, W., Kamiya, K., Liu, W., & Toyama, J. (1997b). Developmental changes of the ultrarapid delayed rectifier K+ current in rat ventricular myocytes. *Pflügers Arch, 433*, 442–445.

Guo, W., Kamiya, K., & Toyama, J. (1995). bFGF promotes functional expression of transient outward currents in cultured neonatal rat ventricular cells. *Pflügers Arch, 430*, 1015–1017.

Hall, B. J., & Ghosh, A. (2008). Regulation of AMPA receptor recruitment at developing synapses. *Trends Neurosci, 31*, 82–89.

Haufe, V., Camacho, J. A., Dumaine, R., et al. (2005). Expression pattern of neuronal and skeletal muscle voltage-gated Na+ channels in the developing mouse heart. *J Physiol, 564*, 683–696.

Henriquez, J. P., Webb, A., Bence, M., et al. (2008). Wnt signaling promotes AChR aggregation at the neuromuscular synapse in collaboration with agrin. *Proc Natl Acad Sci USA, 105*, 18812–18817.

Holliday, J., & Spitzer, N. C. (1990). Spontaneous calcium influx and its roles in differentiation of spinal neurons in culture. *Dev Biol, 141*, 13–23.

Hsia, A. Y., Malenka, R. C., & Nicoll, R. A. (1998). Development of excitatory circuitry in the hippocampus. *J Neurophysiol, 79*, 2013–2024.

Huang, J., Xu, L., Thomas, M., et al. (2006). L-type Ca2+ channel function and expression in neonatal rabbit ventricular myocytes. *Am J Physiol Heart Circ Physiol, 290*, H2267–H2276.

Hume, R. I., Dingledine, R., & Heinemann, S. F. (1991). Identification of a site in glutamate receptor subunits that controls calcium permeability. *Science, 253*, 1028–1031.

Huynh, T. V., Chen, F., Wetzel, G. T., Friedman, W. F., & Klitzner, T. S. (1992). Developmental changes in membrane Ca2+ and K+ currents in fetal, neonatal, and adult rabbit ventricular myocytes. *Circ Res, 70*, 508–515.

Iannaccone, S. T., Li, K. X., & Sperelakis, N. (1987). Transmembrane electrical characteristics of cultured human skeletal muscle cells. *J Cell Physiol, 133*, 409–413.

Iijima, T., & Pappano, A. J. (1979). Ontogenetic increase of the maximal rate of rise of the chick embryonic heart action potential. Relationship to voltage, time, and tetrodotoxin. *Circ Res, 44*, 358–367.

Irisawa, H., Brown, H. F., & Giles, W. (1993). Cardiac pacemaking in the sinoatrial node. *Physiol Rev, 73*, 197–227.

Jeck, C. D., & Boyden, P. A. (1992). Age-related appearance of outward currents may contribute to developmental differences in ventricular repolarization. *Circ Res, 71*, 1390–1403.

Josephson, I. R., & Sperelakis, N. (1989). Tetrodotoxin differentially blocks peak and steady-state sodium channel currents in early embryonic chick ventricular myocytes. *Pflügers Arch, 414*, 354–359.

Josephson, I. R., & Sperelakis, N. (1990). Developmental increases in the inwardly-rectifying K+ current of embryonic chick ventricular myocytes. *Biochim Biophys Acta, 1052*, 123–127.

Kano, M., & Yamamoto, M. (1977). Development of spike potentials in skeletal muscle cells differentiated in vitro from chick embryo. *J Cell Physiol, 90*, 439–444.

Kato, Y., Masumiya, H., Agata, N., Tanaka, H., & Shigenobu, K. (1996). Developmental changes in action potential and membrane currents in fetal, neonatal and adult guinea-pig ventricular myocytes. *J Mol Cell Cardiol, 28*, 1515–1522.

Kawano, S., & DeHaan, R. L. (1991). Developmental changes in the calcium currents in embryonic chick ventricular myocytes. *J Membr Biol, 120*, 17–28.

Kilborn, M. J., & Fedida, D. (1990). A study of the developmental changes in outward currents of rat ventricular myocytes. *J Physiol, 430*, 37–60.

Kitchens, S. A., Burch, J., & Creazzo, T. L. (2003). T-type Ca2+ current contribution to Ca2+-induced Ca2+ release in developing myocardium. *J Mol Cell Cardiol, 35*, 515–523.

Kobayashi, T., Maeda, S., Ichise, N., et al. (2011). The beginning of the calcium transient in rat embryonic heart. *J Physiol Sci, 61*, 141−149.

Kobayashi, T., Yamada, Y., Nagashima, M., et al. (2003). Contribution of KChIP2 to the developmental increase in transient outward current of rat cardiomyocytes. *J Mol Cell Cardiol, 35*, 1073−1082.

Koenen, M., Peter, C., Villarroel, A., Witzemann, V., & Sakmann, B. (2005). Acetylcholine receptor channel subtype directs the innervation pattern of skeletal muscle. *EMBO Rep, 6*, 570−576.

Kojima, M., Sada, H., & Sperelakis, N. (1990). Developmental changes in beta-adrenergic and cholinergic interactions on calcium-dependent slow action potentials in rat ventricular muscles. *Br J Pharmacol, 99*, 327−333.

Konig, S., Beguet, A., Bader, C. R., & Bernheim, L. (2006). The calcineurin pathway links hyperpolarization (Kir2.1)-induced Ca2+ signals to human myoblast differentiation and fusion. *Development, 133*, 3107−3114.

Leclerc, C., Duprat, A. M., & Moreau, M. (1999). Noggin upregulates Fos expression by a calcium-mediated pathway in amphibian embryos. *Dev Growth Differ, 41*, 227−238.

Leclerc, C., Webb, S. E., Daguzan, C., Moreau, M., & Miller, A. L. (2000). Imaging patterns of calcium transients during neural induction in Xenopus laevis embryos. *J Cell Sci, 113*, 3519−3529.

Leuranguer, V., Monteil, A., Bourinet, E., Dayanithi, G., & Nargeot, J. (2000). T-type calcium currents in rat cardiomyocytes during postnatal development: contribution to hormone secretion. *Am J Physiol Heart Circ Physiol, 279*, H2540−H2548.

Li, H., Guo, W., Mellor, R. L., & Nerbonne, J. M. (2005). KChIP2 modulates the cell surface expression of Kv 1.5-encoded K(+) channels. *J Mol Cell Cardiol, 39*, 121−132.

Linsdell, P., & Moody, W. J. (1995). Electrical activity and calcium influx regulate ion channel development in embryonic Xenopus skeletal muscle. *J Neurosci, 15*, 4507−4514.

Liu, A., Tang, M., Xi, J., et al. (2010). Functional characterization of inward rectifier potassium ion channel in murine fetal ventricular cardiomyocytes. *Cell Physiol Biochem, 26*, 413−420.

Liu, J. H., Bijlenga, P., Fischer-Lougheed, J., et al. (1998). Role of an inward rectifier K+ current and of hyperpolarization in human myoblast fusion. *J Physiol, 510*, 467−476.

Liu, J. H., Konig, S., Michel, M., et al. (2003). Acceleration of human myoblast fusion by depolarization: graded Ca2+ signals involved. *Development, 130*, 3437−3446.

Liu, W., Yasui, K., Opthof, T., et al. (2002). Developmental changes of Ca(2+) handling in mouse ventricular cells from early embryo to adulthood. *Life Sci, 71*, 1279−1292.

Lockery, S. R., & Spitzer, N. C. (1992). Reconstruction of action potential development from whole-cell currents of differentiating spinal neurons. *J Neurosci, 12*, 2268−2287.

Mai, W., Janier, M. F., Allioli, N., et al. (2004). Thyroid hormone receptor alpha is a molecular switch of cardiac function between fetal and postnatal life. *Proc Natl Acad Sci USA, 101*, 10332−10337.

Marcus, N. C., & Fozzard, H. (1981). Tetrodotoxin sensitivity in the developing and adult chick heart. *J Mol Cell Cardiol, 13*, 335−340.

Martin-Caraballo, M., & Greer, J. J. (2001). Voltage-sensitive calcium currents and their role in regulating phrenic motoneuron electrical excitability during the perinatal period. *J Neurobiol, 46*, 231−248.

Masuda, H., & Sperelakis, N. (1993). Inwardly rectifying potassium current in rat fetal and neonatal ventricular cardiomyocytes. *Am J Physiol, 265*, H1107−H1111.

Masuda, H., Sumii, K., & Sperelakis, N. (1995). Long openings of calcium channels in fetal rat ventricular cardiomyocytes. *Pflügers Arch, 429*, 595−597.

Matsubara, H., Suzuki, J., & Inada, M. (1993). Shaker-related potassium channel, Kv1.4, mRNA regulation in cultured rat heart myocytes and differential expression of Kv1.4 and Kv1.5 genes in myocardial development and hypertrophy. *J Clin Invest, 92*, 1659−1666.

Mishina, M., Takai, T., Imoto, K., et al. (1986). Molecular distinction between fetal and adult forms of muscle acetylcholine receptor. *Nature, 321*, 406−411.

Moreau, M., Leclerc, C., Gualandris-Parisot, L., & Duprat, A. M. (1994). Increased internal Ca2+ mediates neural induction in the amphibian embryo. *Proc Natl Acad Sci USA, 91*, 12639−12643.

Morikawa, Y., Rosen, M. R., Meiri, H., & Robinson, R. B. (1987). Developmental changes in the response of cardiac Purkinje fibers to SC-72-14. *Am J Physiol, 252*, H771−H776.

Muller, Y. L., & Yool, A. J. (1998). Increased calcium-dependent K+ channel activity contributes to the maturation of cellular firing patterns in developing cerebellar Purkinje neurons. *Brain Res Dev Brain Res, 108*, 193−203.

Muller, Y. L., Reitstetter, R., & Yool, A. J. (1998). Regulation of Ca2+-dependent K+ channel expression in rat cerebellum during postnatal development. *J Neurosci, 18*, 16−25.

Nagashima, M., Tohse, N., Kimura, K., et al. (2001). Alternation of inwardly rectifying background K+ channel during development of rat fetal cardiomyocytes. *J Mol Cell Cardiol, 33*, 533−543.

Nakamura, T. Y., Lee, K., Artman, M., Rudy, B., & Coetzee, W. A. (1999). The role of Kir2.1 in the genesis of native cardiac inward-rectifier K+ currents during pre- and postnatal development. *Ann NY Acad Sci, 868*, 434−437.

Nakanishi, T., Seguchi, M., & Takao, A. (1988). Development of the myocardial contractile system. *Experientia, 44*, 936−944.

Nguemo, F., Fleischmann, B. K., Schunkert, H., Hescheler, J., & Reppel, M. (2007). Functional expression and inactivation of L-type Ca2+ currents during murine heart development − implications for cardiac Ca2+ homeostasis. *Cell Physiol Biochem, 20*, 809−824.

Niwa, N., Yasui, K., Opthof, T., et al. (2004). Cav3.2 subunit underlies the functional T-type Ca2+ channel in murine hearts during the embryonic period. *Am J Physiol Heart Circ Physiol, 286*, H2257−H2263.

O'Dowd, D. K., Ribera, A. B., & Spitzer, N. C. (1988). Development of voltage-dependent calcium, sodium, and potassium currents in Xenopus spinal neurons. *J Neurosci, 8*, 792−805.

Osaka, T., & Joyner, R. W. (1991). Developmental changes in calcium currents of rabbit ventricular cells. *Circ Res, 68*, 788−796.

Petralia, R. S., Sans, N., Wang, Y. X., & Wenthold, R. J. (2005). Ontogeny of postsynaptic density proteins at glutamatergic synapses. *Mol Cell Neurosci, 29*, 436−452.

Picken Bahrey, H. L., & Moody, W. J. (2003). Early development of voltage-gated ion currents and firing properties in neurons of the mouse cerebral cortex. *J Neurophysiol, 89*, 1761−1773.

Protas, L., Oren, R. V., Clancy, C. E., & Robinson, R. B. (2010). Age-dependent changes in Na current magnitude and TTX-sensitivity in the canine sinoatrial node. *J Mol Cell Cardiol, 48*, 172−180.

Renaud, J. F., Kazazoglou, T., Lombet, A., et al. (1983). The Na+ channel in mammalian cardiac cells. Two kinds of tetrodotoxin receptors in rat heart membranes. *J Biol Chem, 258*, 8799−8805.

Renaud, J. F., Romey, G., Lombet, A., & Lazdunski, M. (1981). Differentiation of the fast Na+ channel in embryonic heart cells: interaction of the channel with neurotoxins. *Proc Natl Acad Sci USA, 78*, 5348−5352.

Ritchie, A. K., & Fambrough, D. M. (1975). Electrophysiological properties of the membrane and acetylcholine receptor in developing rat and chick myotubes. *J Gen Physiol, 66*, 327−355.

Robinson, R. B., Yu, H., Chang, F., & Cohen, I. S. (1997). Developmental change in the voltage-dependence of the pacemaker current, if, in rat ventricle cells. *Pflügers Arch, 433*, 533−535.

Rogart, R. B., Cribbs, L. L., Muglia, L. K., Kephart, D. D., & Kaiser, M. W. (1989). Molecular cloning of a putative tetrodotoxin-resistant rat heart Na+ channel isoform. *Proc Natl Acad Sci USA, 86*, 8170−8174.

Sada, H., Ban, T., Fujita, T., Ebina, Y., & Sperelakis, N. (1995). Developmental change in fast Na channel properties in embryonic chick ventricular heart cells. *Can J Physiol Pharmacol, 73*, 1475−1484.

Sada, H., Kojima, M., & Sperelakis, N. (1988). Fast inward current properties of voltage-clamped ventricular cells of embryonic chick heart. *Am J Physiol, 255*, H540−H553.

Salgado, H., Tecuapetla, F., Perez-Rosello, T., et al. (2005). A reconfiguration of CaV2 Ca2+ channel current and its dopaminergic D2 modulation in developing neostriatal neurons. *J Neurophysiol, 94*, 3771−3787.

Sanchez-Chapula, J., Elizalde, A., Navarro-Polanco, R., & Barajas, H. (1994). Differences in outward currents between neonatal and adult rabbit ventricular cells. *Am J Physiol, 266*, H1184−H1194.

Sanes, J. R., & Lichtman, J. W. (2001). Induction, assembly, maturation and maintenance of a postsynaptic apparatus. *Nat Rev Neurosci, 2*, 791−805.

Satoh, H. (1995). Identification of and developmental changes in transient outward current in embryonic chick cardiomyocytes. *Reprod Fertil Dev, 7*, 1369−1374.

Satoh, H., & Sperelakis, N. (1993). Hyperpolarization-activated inward current in embryonic chick cardiac myocytes: developmental changes and modulation by isoproterenol and carbachol. *Eur J Pharmacol, 240*, 283−290.

Seki, S., Nagashima, M., Yamada, Y., et al. (2003). Fetal and postnatal development of Ca2+ transients and Ca2+ sparks in rat cardiomyocytes. *Cardiovasc Res, 58*, 535−548.

Shimahara, T., & Bournaud, R. (1991). Barium currents in developing skeletal muscle cells of normal and mutant mice foetuses with 'muscular dysgenesis'. *Cell Calcium, 12*, 727−733.

Shimoni, Y., Fiset, C., Clark, R. B., et al. (1997). Thyroid hormone regulates postnatal expression of transient K+ channel isoforms in rat ventricle. *J Physiol, 500*, 65−73.

Shin, K. S., Park, J. Y., Kwon, H., Chung, C. H., & Kang, M. S. (1997). A possible role of inwardly rectifying K+ channels in chick myoblast differentiation. *Am J Physiol, 272*, C894−C900.

Spector, I., & Prives, J. M. (1977). Development of electrophysiological and biochemical membrane properties during differentiation of embryonic skeletal muscle in culture. *Proc Natl Acad Sci USA, 74*, 5166−5170.

Sperelakis, N., & Lee, E. C. (1971). Characterization of (Na+, K+)-ATPase isolated from embryonic chick hearts and cultured chick heart cells. *Biochim Biophys Acta, 233*, 562−579.

Sperelakis, N., & Shigenobu, K. (1972). Changes in membrane properties of chick embryonic hearts during development. *J Gen Physiol, 60*, 430−453.

Spitzer, N. C. (1994). Spontaneous Ca2+ spikes and waves in embryonic neurons: signaling systems for differentiation. *Trends Neurosci, 17*, 115−118.

Spitzer, N. C., & Baccaglini, P. I. (1976). Development of the action potential in embryo amphibian neurons in vivo. *Brain Res, 107*, 610−616.

Spitzer, N. C., Debaca, R. C., Allen, K. A., & Holliday, J. (1993). Calcium dependence of differentiation of GABA immunoreactivity in spinal neurons. *J Comp Neurol, 337*, 168−175.

Spitzer, N. C., Gu, X., & Olson, E. (1994). Action potentials, calcium transients and the control of differentiation of excitable cells. *Curr Opin Neurobiol, 4*, 70−77.

Stieber, J., Herrmann, S., Feil, S., et al. (2003). The hyperpolarization-activated channel HCN4 is required for the generation of pacemaker action potentials in the embryonic heart. *Proc Natl Acad Sci USA, 100*, 15235−15240.

Strube, C., Tourneur, Y., & Ojeda, C. (2000). Functional expression of the L-type calcium channel in mice skeletal muscle during prenatal myogenesis. *Biophys J, 78*, 1282−1292.

Takahashi, K., & Okamura, Y. (1998). Ion channels and early development of neural cells. *Physiol Rev, 78*, 307−337.

Tarasenko, A. N., Isaev, D. S., Eremin, A. V., & Kostyuk, P. G. (1998). Developmental changes in the expression of low-voltage-activated Ca2+ channels in rat visual cortical neurones. *J Physiol, 509*, 385−394.

Tohse, N., Masuda, H., & Sperelakis, N. (1992a). Novel isoform of Ca2+ channel in rat fetal cardiomyocytes. *J Physiol, 451*, 295−306.

Tohse, N., Meszaros, J., & Sperelakis, N. (1992b). Developmental changes in long-opening behavior of L-type Ca2+ channels in embryonic chick heart cells. *Circ Res, 71*, 376−384.

Tohse, N., Seki, S., Kobayashi, T., et al. (2004). Development of excitation-contraction coupling in cardiomyocytes. *Jap J Physiol, 54*, 1−6.

Tohse, N., & Sperelakis, N. (1990). Long-lasting openings of single slow (L-type) Ca2+ channels in chick embryonic heart cells. *Am J Physiol, 259*, H639−H642.

Trepanier-Boulay, V., Lupien, M. A., St-Michel, C., & Fiset, C. (2004). Postnatal development of atrial repolarization in the mouse. *Cardiovasc Res, 64*, 84−93.

Wahler, G. M., Dollinger, S. J., Smith, J. M., & Flemal, K. L. (1994). Time course of postnatal changes in rat heart action potential and in transient outward current is different. *Am J Physiol, 267*, H1157−H1166.

Wang, K., Cui, J., Cai, Y., et al. (2009). Critical roles of voltage-dependent sodium channels in the process of synaptogenesis during the postnatal cortical development of rats. *Cell Mol Neurobiol, 29*, 1131−1142.

Wang, L., & Duff, H. J. (1997). Developmental changes in transient outward current in mouse ventricle. *Circ Res, 81*, 120−127.

Wang, L., Feng, Z. P., Kondo, C. S., Sheldon, R. S., & Duff, H. J. (1996). Developmental changes in the delayed rectifier K+ channels in mouse heart. *Circ Res, 79*, 79−85.

Wang, Y., Xu, H., Kumar, R., et al. (2003). Differences in transient outward current properties between neonatal and adult human atrial myocytes. *J Mol Cell Cardiol, 35*, 1083−1092.

Webb, S. E., Moreau, M., Leclerc, C., & Miller, A. L. (2005). Calcium transients and neural induction in vertebrates. *Cell Calcium, 37*, 375−385.

Wickenden, A. D., Kaprielian, R., Parker, T. G., Jones, O. T., & Backx, P. H. (1997). Effects of development and thyroid hormone on K+ currents and K+ channel gene expression in rat ventricle. *J Physiol, 504*, 271−286.

Xie, L. H., Takano, M., & Noma, A. (1997). Development of inwardly rectifying K+ channel family in rat ventricular myocytes. *Am J Physiol, 272*, H1741−H1750.

Xu, H., Dixon, J. E., Barry, D. M., et al. (1996). Developmental analysis reveals mismatches in the expression of K+ channel alpha subunits and voltage-gated K+ channel currents in rat ventricular myocytes. *J Gen Physiol, 108*, 405−419.

Yasui, K., Liu, W., Opthof, T., et al. (2001). I(f) current and spontaneous activity in mouse embryonic ventricular myocytes. *Circ Res, 88*, 536−542.

Zhang, W., Elsen, F., Barnbrock, A., & Richter, D. W. (1999). Postnatal development of GABAB receptor-mediated modulation of voltage-activated Ca2+ currents in mouse brain-stem neurons. *Eur J Neurosci, 11*, 2332−2342.

This page intentionally left blank

Chapter 26

Regulation of Ion Channel Localization and Activity Through Interactions with the Cytoskeleton

Stephen Lambert

Chapter Outline

I. SUMMARY

The physiological function of a variety of cell types is dependent upon their ability to organize and cluster ion channels into specialized areas of the plasma membrane. Studies over the last 20 years have indicated a role for interactions between ion channels and the cellular cytoskeleton in achieving this complex organization. A variety of adaptor/scaffolding proteins that tether ion channels to the cytoskeleton has been identified. In addition to localizing ion channels, interactions with the cytoskeleton may also regulate channel activity. This could be through direct binding to the channel by actin or scaffolding molecules, or by the co-recruitment of signaling molecules that regulate channel activity into a macromolecular complex by scaffolding proteins.

In this chapter, we will review three examples of specialized membrane domains: the axon initial segment and node of Ranvier; the postsynaptic membrane; and the apical domain of the epithelial cell. We will examine the unique adaptor/scaffolding systems found in each of these domains and how they have evolved in response to their particular physiological requirements.

Cell Physiology Sourcebook. DOI: 10.1016/B978-0-12-387738-3.00026-3

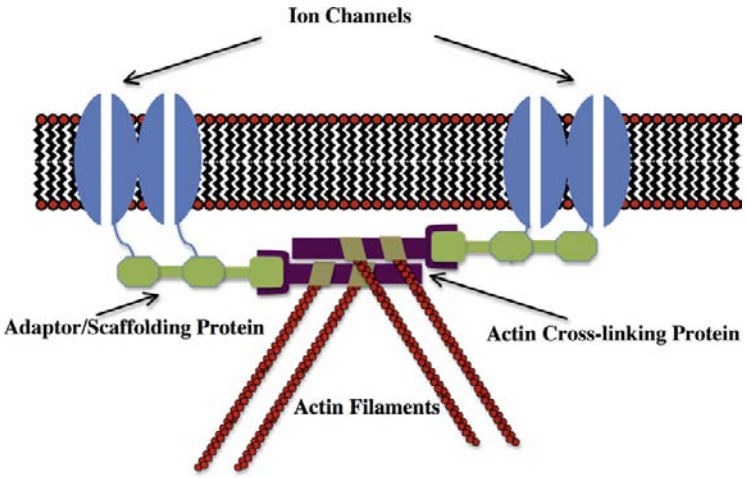

FIGURE 26.1 Conceptual model of a general mechanism for the interaction of ion channels with the cytoskeleton.

II. GENERAL INTRODUCTION

Ion channels are selective "pores" for the passage of ions across the hydrophobic barrier of the plasma membrane. The physiological activity of a number of cell types is dependent upon their ability to organize integral membrane proteins and, in particular, ion channels, into functionally specialized domains of the plasma membrane. This organization underlies a wide range of cellular functions including the propagation and integration of electrical signals in the nervous and muscular system by "excitable" membranes. A general mechanism whereby ion channels become organized into these membrane domains is shown in Fig. 26.1 and reflects an interaction between the ion channel and the cellular cytoskeleton, particularly the actin microfilament system. This mechanism localizes the lateral mobility of ion channels to a membrane domain through direct tethering of the ion channel to the cytoskeleton utilizing adaptor or scaffold proteins.

As well as restricting the localization of ion channels, interactions with the cytoskeleton and adaptor proteins can also regulate their activity. This could result from direct interactions between actin or adaptor proteins with functional domains of the channel and/or the organization of functional microdomains, whereby ion channels through the activity of scaffold proteins, are brought into close proximity with molecules that can regulate their activity. Conversely, several lines of evidence, particularly from the nervous system, have shown that it is possible for ion channel activity to activate signaling pathways that remodel the actin cytoskeleton.

In this chapter, we will examine a number of different examples of ion channel–cytoskeleton interactions illustrating some of the important concepts in this area. The rapid development of knowledge in this field over the last decade makes it impossible to list all of the known examples of these types of interactions. For example, we have not included discussion of the neuromuscular junction, which is a well-characterized example of the role of the cytoskeleton in the immobilization of postsynaptic receptors or the rapidly growing area of mechanosensory transduction. Apologies are therefore offered to all colleagues where space limitations have prevented mention of their work.

III. MECHANISMS FOR INTERACTIONS BETWEEN THE CYTOSKELETON AND ION CHANNELS

IIIA. The Spectrin-Based Membrane Skeleton

IIIA1. Characteristics of the Spectrin-Based Membrane Skeleton

Originally described in the human erythrocyte, where it plays a major role in maintaining cell shape (reviewed in Bennett and Gilligan, 1993), the spectrin-based membrane skeleton is perhaps the best characterized complex of proteins linking ion channels to the actin cytoskeleton. As shown in Fig. 26.2, at the heart of this complex of proteins is the filamentous protein spectrin, which exists as a 200 nm flexible rod composed of a heterotetramer of α and β subunits. Beta subunits are characterized by the possession of an actin-binding domain at their N-terminus. Heterotetramers and other higher ordered structures form through head to head association of the heterodimer to yield a molecule capable of cross-linking actin through binding sites at opposite ends. In the red cell membrane, short actin oligomers (10–14 monomers) are cross-linked in this fashion to yield a series of pentameric or hexameric structures with actin at the junction (termed the junctional complex) and spectrin filaments organized like spokes of a wheel. Stretched

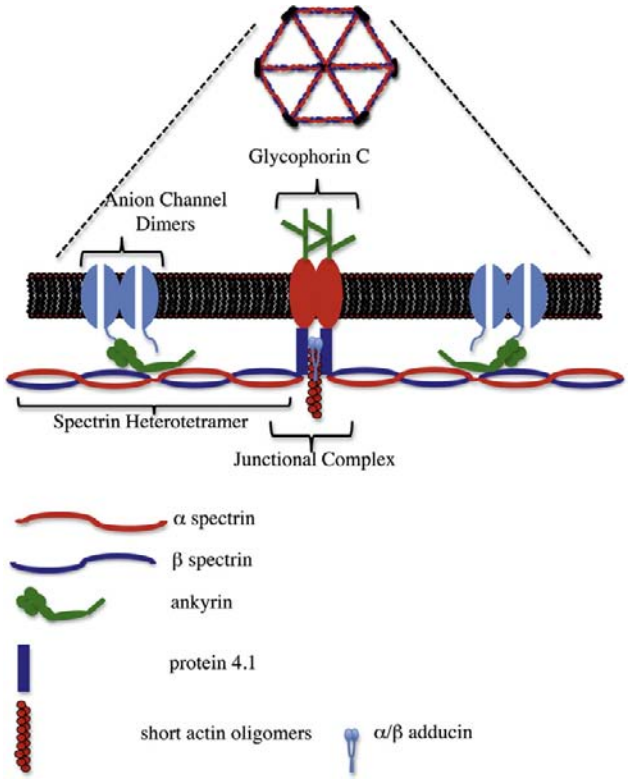

FIGURE 26.2 Cartoon of the major features of the spectrin-based membrane skeleton. Spectrin heterotetramers are arranged around an actin-based junctional complex to generate a hexagonal/pentagonal lattice that can be viewed under the electron microscope when the membrane skeleton is stretched. This lattice is laminated to the bilayer through the interactions of ankyrin with the anion channel and β-spectrin, in addition to interactions between protein 4.1, spectrin and glycophorin C at the junctional complex.

examples of this structure have been visualized by electron microscopy (Byers and Branton, 1985). The molecules protein 4.1 and adducin facilitate the interaction of spectrin with actin at these junctional complexes (Bennett and Gilligan, 1993).

The spectrin-based membrane skeleton forms an electron dense subplasmalemmal undercoating, which can be visualized by electron microscopy and is associated with a number of specialized plasma membrane domains. In red cells, the skeleton is laminated to the bilayer through two major sites of interaction: an association between protein 4.1 which binds both to the β subunit of spectrin and the integral membrane protein glycophorin C and through the molecule ankyrin, which binds both to the β spectrin subunit and to the cytoplasmic domain of the anion channel band 3 (AE1). Mutations that affect the anion channel–ankyrin–spectrin association in red cells result in a loss of membrane lamination, destabilization of the lipid bilayer and a loss of plasma membrane resulting in a shift in cell morphology from discocytes to spherocytes (Palek and Lambert, 1990). In this system, the lateral mobility of the anion channel is restricted in two ways: (1) through the direct interaction of the anion channel with ankyrin and the spectrin bilayer; and (2) through the "corralling" of anion channels within compartments demarcated by the spectrin lattice (Kodippili et al., 2009). However, for the purposes of this review we shall focus on the direct interactions of ankyrins with integral proteins and how this mechanism is used to localize ion channels to specialized plasma membrane domains.

IIIA2. The Ankyrins and their Binding Partners

As shown in Fig. 26.2, the ankyrins are multifunctional adaptors characterized by domains that associate with the β subunit of spectrin and with the cytoplasmic domains of a wide variety of integral membrane proteins, including cell adhesion molecules, transporters and ion channels (Bennett and Healy, 2009). The domain that associates with integral proteins (the membrane-binding domain) consists of 24 copies of the ANK repeat motif now identified in a large number of polypeptides. These repeats are stacked in an array with four basic subdomains such that protein–protein interactions may involve the participation of contact sites from multiple different repeats (Michaely and Bennett, 1993). Binding sites within integral membrane proteins for this domain of ankyrin have arisen independently a number of times during evolution. Hence, it is not easily possible to identify ankyrin-binding sequences within integral proteins from simple analysis of primary sequence. For example, the amino acid sequence associated with ankyrin binding in the family of voltage-gated sodium channels (Garrido et al., 2001; Lemaillet et al., 2003), bears no homology to that identified for members of the L1 family of cell adhesion molecules that also bind ankyrin (Davis and Bennett, 1994). Intriguingly, the same ankyrin-binding sequence that is found in voltage-gated sodium channels is also found in the voltage-gated potassium channels KCNQ2/3 (Pan et al., 2006), responsible for the so-called M-type current. These sequences in KCNQ2/3 appear to have evolved independently and at a later stage in evolution than that of the sodium channels, as one of the first examples of convergent molecular evolution (Hill et al., 2008).

In addition to the membrane and spectrin-binding domains that are highly conserved among different members of the ankyrin family, ankyrins also exhibit an unstructured C-terminal regulatory domain, which is less conserved. The function of this domain is still relatively unclear but it has been implicated in the regulation of the activity of the membrane and spectrin-binding domains (Hall and Bennett, 1997; Abdi et al., 2006). This may well be important as conservation between the various ankyrin membrane-binding domains leads to the question as to how specific ankyrins and their integral

partners are associated within specialized membrane domains.

The vertebrate ankyrin gene family consists of three members, ankyrin$_R$ (encoded by the ANK1 gene), ankyrin$_B$ (ANK2) and ankyrin$_G$ (ANK3) reflecting the distribution of these isoforms within tissues (ankyrin$_R$ being the isoform initially identified in red cells). Many tissues, such as the nervous system, express variants of all three family members. Diversity in ankyrin structure is also achieved through alternative mRNA processing and the use of alternate promotors. The most prominent of these is the insertion of a large sequence between the ankyrin spectrin-binding and C-terminal regulatory domains to produce the "giant" ankyrin molecules, ankyrin$_G$ 480 kDa (Kordeli et al., 1995) and ankyrin$_B$ 440 kDa (Otto et al., 1991). These isoforms are almost twice the size of the originally characterized red cell ankyrin (Lambert et al., 1990). The functions of these large inserted sequences remains unknown, although they appear to be mainly associated with isoforms of ankyrin that are targeted to axonal membrane domains (Chan et al., 1993; Kordeli et al., 1995). As the inserted sequences appear to have an extended conformation, they have the potential to link integral proteins in the axonal membrane with structures deep within the axoplasm. "Giant" isoforms of ankyrin have also been reported in *Drosophila* where the inserted sequences interact with microtubules at the presynaptic neuromuscular junction (Bennett and Healy, 2009).

IIIA3. The Spectrin-Based Membrane Skeleton at the Axon Initial Segment and Nodes of Ranvier

The axon initial segment (AIS) represents a physiologically specialized area of the axon adjacent to the cell body and enriched in cytoplasmic and integral membrane proteins (reviewed in Grubb and Burrone, 2010). It is credited with two major functions in the neuron: (1) the initiation of action potentials; and (2) the formation of a molecular barrier that separates axonal and somatodendritic compartments of the cell to establish and maintain their identity. Key to the organization of this specialized membrane domain is an isoform of ankyrin$_G$ (ankyrin$_G$ 480 kDa) that has been localized to this area of the axon (Kordeli et al., 1995), although other smaller isoforms of ankyrin$_G$ may also be present within this domain. A specialized form of spectrin (β-IV) is also found at the AIS (Grubb and Burrone, 2010). This molecule appears to be important in maintaining or stabilizing integral membrane concentrations at the AIS, as its knockdown does not prevent the initial recruitment of ankyrin$_G$ and its membrane-binding partners to the AIS in cultured neurons. The recruitment of ankyrin$_G$ to the AIS occurs early in development of the axon, although how this molecule is specifically targeted to the AIS is still unknown. This may reflect the nature of the microtubules in this region of the axon which, in some ways, resemble those of dendrites (Gomis-Ruth et al., 2008). Such microtubules could potentially interact with the ankyrin$_G$ 480 kDa inserted region.

Ankyrin$_G$ is thought to establish and maintain the localization of a large number of integral proteins from ion channels to cell adhesion molecules at the AIS and it is thought that this high density of integral proteins forms a diffusion barrier that inhibits the migration of non-ankyrin-associated integral proteins between somatodendritic and axonal compartments of the cell (Winckler et al., 1999). It has also been shown that a barrier exists at the AIS for movement within the axonal cytoplasm (Song et al., 2009) and that this selectivity filter is dependent upon the presence of ankyrin$_G$. Knockdown of ankyrin$_G$ function in cultured hippocampal neurons not only has been found to dismantle the AIS, but also causes the axon to acquire dendritic characteristics including the formation of spine-like protrusions associated with excitatory synapses (Grubb and Burrone, 2010).

The AIS is the main site of action potential initiation. This is achieved through the establishment of high concentrations of both voltage-gated sodium (vgsc) and potassium channels (vgpc) in the AIS membrane, through interactions with ankyrin$_G$. Vgsc consist of an α subunit composed of 24 transmembrane segments divided into four subdomains that generate an ion-selective pore and an auxillary β subunit that regulates channel activity and membrane expression (Goldin, 1999). There are nine different genes that encode α subunits and proteins encoded by these genes all share an ankyrin-binding sequence within the cytoplasmic domain linking domains II and III (Lemaillet et al., 2003). This sequence is also conserved in the KCNQ2/3 (also referred to as Kv7.2 and Kv7.3) subunits of the M-type potassium channel, responsible for stabilizing the resting membrane potential and preventing repetitive action potentials (Pan et al., 2006). The AIS localization of both vgsc and KCNQ2/3 channels is missing in ankyrin$_G$ knockout animals (Zhou et al., 1998; Pan et al., 2006). Consequently, Purkinje neurons from these animals exhibit deficiencies in their ability to initiate action potentials (Zhou et al., 1998).

Ankyrin has also been reported to bind to the accessory β subunits of the voltage-gated sodium channel (Malhotra et al., 2000), although this finding was not supported in alternative studies (Lemaillet et al., 2003). This difference may reflect a requirement for tyrosine phosphorylation within the cytoplasmic domain of the β1 subunit to facilitate ankyrin-binding (Malhotra et al., 2002). Finally, the identification of a di-leucine motif in the C-terminus of the Nav1.2 sodium channel suggests a mechanism whereby

voltage-gated sodium channels not bound to ankyrin at the AIS can be selectively removed from the membrane by endocytosis (Garrido et al., 2003) thereby helping to concentrate molecules retained by ankyrin$_G$ at the AIS.

Physiologically related to the AIS, the nodes of Ranvier are enriched in ion channels (particularly vgsc) necessary for the propagation of the saltatory action potential (Fig. 26.3). Vgsc densities here are typically 25-fold compared to those observed in the internodal area (Salzer et al., 2008). Nodes are small gaps (1 μM) in the myelin sheath between adjacent myelinating glia. Unlike the AIS whose formation is intrinsic to the neuron, node formation in the PNS requires glial cell contact (Ching et al., 1999). Clustering of sodium channels in the CNS is less understood but at the very least requires soluble factors released from the oligodendrocyte (Kaplan et al., 1997).

Key to the formation of the nodes of Ranvier is the binding of ankyrin to members of the L1 family of cell adhesion molecules (CAMs) through a conserved sequence regulated by phosphorylation (Garver et al., 1997; Bennett and Healy, 2009). Both NrCAM and neurofascin 186 kDa from this family are present at both the AIS and nodes of Ranvier and co-localize with ankyrin$_G$ 480 kDa and vgsc (Bennett and Healy, 2009). The function of these CAMs at the AIS is unclear, but may be important for the formation of GABAergic synaptic inputs that target the AIS (Grubb and Burrone, 2010). However, at the nodes of Ranvier these CAMs have a clear role in facilitating contacts between the myelinating Schwann cell and the axolemma. Schwann cell microvilli, identified by the presence of ERM (ezrin, radixin, moesin) proteins (Melendez-Vasquez et al., 2001; Gatto et al., 2003) express a unique extracellular matrix that contains multimers of the soluble protein gliomedin complexed with heparin sulphate proteoglycans (HSPGs) (Salzer et al., 2008). Gliomedin binds to the extracellular domain of neurofascin 186 kDa and NrCAM, hence clustering it at the tips of myelinating Schwann cells (Salzer et al., 2008). This results in the recruitment of ankyrin$_G$ (Lambert et al., 1997) providing a platform for the immobilization of vgsc and KCNQ2/3 molecules in the nodal membrane. Theoretically, ankyrin$_G$ can simultaneously associate with both the CAM and vgsc allowing Schwann cells to regulate directly the clustering of ion channels in the nodal membrane. In addition, the β subunit of the sodium channel has been shown to interact in a *cis*-like fashion with neurofascin 186 kDa to further promote this clustering (Ratcliffe et al., 2001). As myelination progresses, clusters of nodal complexes associated with the adjoining Schwann cells are brought together to form the mature nodal membrane (Lambert et al., 1997).

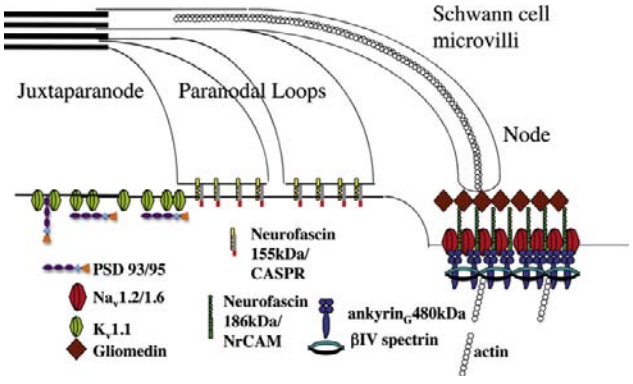

FIGURE 26.3 Mechanisms involved in the localization of ion channels at the nodes of Ranvier. A specialized isoform of ankyrin, ankyrin$_G$ 480 kDa binds to voltage-gated sodium channels Nav1.2/1.6 at the nodal membrane along with the cell adhesion molecule neurofascin 186 kDa. This molecule is associated with a specialized isoform of spectrin, β-IV. The release of gliomedin from the myelinating Schwann cell causes neurofascin 186 kDa to cluster, which leads to the recruitment of the ankyrin$_G$ 480 kDa and associated Nav1.2/1.6 voltage-gated sodium channels into these clusters. The voltage-gated potassium channel Kv1.1 is able to bind to the PDZ domain containing proteins PSD 93/95 and co-localizes with them in the juxtaparanode.

Further maintenance of the nodal membrane comes from the formation of the flanking paranodal junctions that act as diffusion barriers to prevent the movement of proteins between nodal and internodal compartments of the axonal membrane (Salzer et al., 2008). Paranodal junctions composed of glial loops anchored to the axolemma through the interactions of the axonal contactin/caspr complex with Schwann cell neurofascin 155 kDa (Salzer et al., 2008). This results in a very close apposition (3−5 nm) between the Schwann cell and the axonal membrane that limits the diffusion of ions between the nodal and internodal areas. The definitive roles of alternatively spliced neurofascin isoforms in nodal development are clearly demonstrated by specific rescues of these isoforms in neurofascin knockout mice (Zonta et al., 2008). Interestingly, the presence of isoforms of neurofascin in the nodal membrane also prevents the invasion of paranodal loops into the nodal membrane domain (Thaxton et al., 2011).

In the juxtaparanodal region of the axon, insulated from the nodal membrane by the paranodal junctions, lie concentrations of vgpc composed of the Kv1 channel subunits Kv1.1, 1.2 and 1.4 (reviewed in Rasband, 2010). As these channels lie under the myelin sheath where they are electrically insulated, their function is somewhat controversial. However, they are thought to modulate action potential propagation and dampen the repetitive firing properties of early myelinating axons. As with ankyrins at the nodal membrane, these proteins exist in a complex that includes both CAMs and adaptors that link them to the cytoskeleton. In this case, an important *trans* interaction between axon and glial cell is established through an interaction between axonal Caspr2 and glial TAG-1. Caspr2 can also associate with protein 4.1B, a homolog of the molecule characterized in red cells, that

links this complex to the spectrin-based membrane skeleton and actin cytoskeleton. Caspr2 also has the ability to link up with multiple PDZ domain containing proteins through its C-terminus. Two of these proteins, PSD-95 and PSD-93 (to be discussed in more detail in the next section), are able to bind to Kv1.1 and 1.2 and have been localized to the juxtaparanodes. However, current observations suggest their activity is not required for vgpc localization (Rasband et al., 2002). Recently, the metalloprotease ADAM22, originally identified as a Kv1 binding partner, has been observed at the juxtaparanode and has been shown to play a role in the clustering of PSD-95 and PSD-93 (Ogawa et al., 2010).

IIIA4. The Spectrin-Based Membrane Skeleton in Muscle Physiology

The wide variety of integral binding partners for ankyrin facilitates its use in the establishment of a range of specialized membranes within a variety of cell types. Studies from the Bennett laboratory in the last decade have shown a range of functions for ankyrin molecules in muscle physiology. As found in other "excitable" cells, ankyrin$_G$ is crucial to the localization of vgsc to allow the propagation of action potentials. In cardiomyocytes, this involves the localization and surface expression of Nav1.5 to the intercalated disk, to allow propagation of the action potential between adjoining cells (Mohler et al., 2004).

As well as the intercalated disk, Nav1.5 is also found with ankyrin$_G$ in the plasma membrane of the t-tubule (Mohler et al., 2004). T-tubules are extensive invaginations of the plasma membrane that allow it to be brought into close proximity with the sarcoplasmic reticulum at various points along its length. This proximity is crucial for facilitating excitation–contraction coupling in the cardiomyocyte. The t-tubule system consists of a number of specialized microdomains that strictly regulate the movement of calcium between these different membrane compartments to initiate contraction. Key to this activity is a complex between L-type voltage-gated calcium channels in the plasma membrane with ryanodine receptors in the sarcoplasmic reticulum. The localization of Nav1.5 by ankyrin$_G$ in microdomains adjacent to this complex is thought to be responsible for activating the voltage-gated calcium channels in this complex. This allows for the passage of small amounts of calcium which, in turn, mobilize calcium stores from the sarcoplasmic reticulum (Bennett and Healy, 2009; Orchard et al., 2009).

A third specialized microdomain within the t-tubule system is enriched in the Na/Ca exchanger (NCX1), which allows for the passage of calcium back across the t-tubule membrane. NCX1 binds to and co-localizes with ankyrin$_B$ in these microdomains (Bennett and Healy, 2009). In addition, the Na/K ATPase and the IP3 receptor, which are also known to bind ankyrin, co-localize with ankyrin$_B$ in these areas (Mohler et al., 2005). Animals lacking ankyrin$_B$ expression in their cardiomyocytes exhibit aberrant localization of these three integral proteins (Mohler et al., 2005) with deficient cardiomyocytes showing increased contractility and increased calcium transients (Mohler et al., 2003, 2005). This suggests an attractive model whereby ankyrin$_B$ brings together a functional coupling between the NCX1 and Na/K ATPase with sodium ions entering the cell in exchange for calcium ions. The IP3 receptor in this scenario could be coupled to allow the passage of Ca ions directly from the sarcoplasmic reticulum through NCX1 (Mohler et al., 2005). It would be interesting to determine if ankyrin$_B$ is capable of simultaneously associating with both NCX1 and the Na/K ATPase to facilitate formation of a functional macromolecular complex.

Cardimyocytes derived from the ankyrin$_B$ knockout mouse also show defects in sodium channel currents suggesting a role for ankyrin$_B$ in vgsc activity (Chauhan et al., 2000). These defects include changes in sodium current density detected using whole cell voltage clamp techniques. This suggests a role for ankyrin$_B$ in the trafficking and/or stabilization of vgsc on the plasma membrane. Interestingly, changes were also observed in the activation kinetics of the sodium currents suggesting that the binding of ankyrin may also exert functional changes in channel activity.

IIIA5. Mutations Affecting Ankyrin Interactions in Human Cardiac Pathology

Knockout animals have proven invaluable to understanding the role of ankyrins in organizing potentially complex plasma membrane systems such as the t-tubules. Of interest, however, is that some of the same phenotypes can be observed in humans with inherited cardiac disorders and that these phenotypes can be traced to mutations in components of the ankyrin–spectrin based membrane skeleton (reviewed in Ackerman and Mohler, 2010). For example, the E1053K mutation in Nav1.5 is associated with Brugada syndrome, a disorder characterized by cardiac arrhythmia. This mutation falls within the defined ankyrin$_G$ binding site (Lemaillet et al., 2003) and abolishes the ability of Nav1.5 to associate with ankyrin$_G$ which, in vitro, perturbs the surface expression of the molecule and its localization to intercalated disks.

As well as ankyrin$_G$ mutations, mutations within ankyrin$_B$ have been associated with cardiac arrhythmias (Ackerman and Mohler, 2010). LQT4 (type 4 long QT syndrome), a disease characterized by prolonged QTc, catecholaminergic polymorphic ventricular arrhythmia and sudden death, was localized to human chromosome 4q25-27 in a large four generation French kindred. This lies within the same region as the ANK2 gene. Further

examination of the original kindred showed a missense mutation localized to the regulatory domain of ankyrin$_B$ resulting in a loss of function. Subsequent studies have now identified a number of kindreds with similar arrhythmias due to mutations in the ANK2 gene. Phenotypes associated with these individuals range from severe to mild with sinus node dysfunction and atrial fibrillation as hallmarks of this disease. This disease has now been renamed ankyrin-B syndrome (Mohler et al., 2007). These findings illustrate the tip of a potential iceberg in which a number of "channelopathies" might be traced to defects in the adaptor system used to localize them to specific membrane domains or regulate their activity.

IIIA6. Regulation of the Association Between Ankyrin and its Integral Partners

Despite the static nature of the AIS and nodes of Ranvier, evidence has been presented for the dynamic regulation of the ankyrin-integral protein interaction that may be important in the formation or maintenance of these structures. It may also explain one of the conundrums of ankyrin activity. How does a specific ankyrin isoform become targeted to these domains and associate in a non-redundant fashion with its integral partner, given that the ankyrin membrane-binding domains are highly conserved? For example, both ankyrin$_G$ and ankyrin$_B$ are expressed in axons and both can bind with equal affinitity to ank-CAMs vgsc and vgpc. However, within the axon, ankyrin$_G$ is found only at the AIS with neurofascin 186 kDa and vgsc (Bennett and Healy, 2009), whereas ankyrin$_B$ is distributed along the length of the axon (Chan et al., 1993). This problem is yet to be fully answered but may lie in the modulation of ankyrin interactions by the divergent regulatory domain (Bennett and Healy, 2009) or control of ankyrin trafficking by the same domain (Mohler et al., 2002). Another possibility is that ankyrin interactions may be regulated by post-translational modifications such as phosphorylation.

Within the cytoplasmic loop between subdomains II and III of the voltage-gated sodium channel are residues phosphorylated by protein kinase CK2 (CK2) (Brechet et al., 2008). Phosphorylation of these residues enhances ankyrin-binding and CK2 is specifically localized to the AIS in neurons through mechanisms currently unknown. Disruption of CK2 activity results in an aberrant localization for voltage-gated sodium channels within the axon (Brechet et al., 2008). This suggests a mechanism whereby the interaction of ankyrin$_G$ with vgsc is locally regulated at the AIS.

The ankyrin-binding site in the cytoplasmic C-terminus of neurofascin (the FIGQY motif) contains a tyrosine residue, which when phosphorylated abolishes ankyrin binding (Garver et al., 1997). In axons, neurofascin phosphorylated in this position is excluded from the node of Ranvier and localized to the paranodes (Bennett and Healy, 2009). In contrast, this post-translational event is required for the binding of neurofascin to the microtubule associated protein doublecortin (Bennett and Healy, 2009), suggesting a "switch" mechanism whereby neurofascin is able to associate with different cytoskeletal systems when needed.

IIIB. PDZ Proteins and the Postsynaptic Density

IIIB1. The Postsynaptic Density and the Dendritic Spine: Dynamic Interactions Between Ion Channel Receptors and the Actin Cytoskeleton

The postsynaptic compartment of excitatory glutamatergic synapses is localized to small, highly dynamic protruberances that emanate from the dendritic shaft known as dendritic spines. These structures, which are up to a few microns in length, contain all of the signaling molecules and organelles necessary for the receipt, integration and propagation of the synaptic chemical signal. In addition, spines assume a range of dynamic morphologies and mounting evidence has supported the idea that changes in spine morphology alter the propagation of postsynaptic signals. These changes in spine morphology are an important component of synaptic plasticity and hence memory and learning. Dendritic spines themselves are enriched in actin filaments that determine the morphology of the spine and provide a scaffold for the immobilization of postsynaptic receptors and signaling molecules. In turn, these signaling molecules, in response to the activity of synaptic receptors, can regulate the actin cytoskeleton to change the morphology of the spine, thereby regulating synaptic strength. In this section, we will examine the molecules present in the spine, which participate in the immobilization of postsynaptic receptors and signaling molecules regulating dendritic spine morphology.

IIIB2. PDZ Proteins and the Immobilization of Postsynaptic Receptors

The NMDA (N-methyl-D-aspartate) and AMPA (α-amino-3-hydroxy-5-methyl-4-isoaxazole propionic acid) receptors are the major receptors for glutamate in the postsynaptic membrane. Both are ionotrophic receptors which behave as ion channels for the influx of calcium ions to invoke a membrane depolarization in response to glutamate binding. Quantitative analysis of the numbers of such receptors present in the postsynaptic density indicates that the number of NMDA receptors stays largely fixed at ≈ 20 molecules/synapse, whereas the AMPA receptor number can

vary from ≈5 to 200 (reviewed in Sheng and Hoogenraad, 2007). The variety in AMPA receptor number is believed to correlate with the size of the spine head and the dynamic nature of AMPA receptor trafficking to and from the postsynaptic density to be an important feature of synaptic plasticity (Shepherd and Huganir, 2007). Both of these channels form heterotetrameric pores in the membrane to allow for the passage of calcium. The NMDA receptor consists of two NR1 subunits and two NR2 subunits. There are eight variants of the NR1 (NR1-1a/b, 2a/b, 3a/b and 4a/b) subunit produced from a single gene by alternative mRNA processing and four distinct isoforms of the NR2 variant (NR2A-D) (Hollmann et al., 1993). It is the differential expression of the NR2 subunit across cells that determines the particular electrophysiological characteristics of a receptor. A third subunit (NR3) is also found, which has an inhibitory affect on receptor function. AMPA receptors consist of four subunits (GluR1−4). The majority of subunits found in these receptor types have PDZ-domain interacting motifs in their C-termini, which facilitate their interactions with scaffolding and signaling molecules.

Canonical PDZ domains are ≈90 amino acid sequences consisting of six β-strands and two α-helices arranged in a barrel-like conformation (reviewed in Feng and Zhang, 2009). These domains function in protein−protein recognition and typically recognize a short stretch of amino acids (5−7 residues) at the C-termini of target proteins. There are currently thought to be 335 non-redundant PDZ domains present in the human genome. Many PDZ domain-containing proteins contain more than one PDZ domain, which may or may not have different recognition sequences. This then allows for the clustering of proteins or co-clustering of proteins that may have interrelated functions. Interactions of the PDZ domain lend themselves to analysis using the yeast 2-hybrid technique, which has allowed for the elucidation of a complex network of interacting proteins starting with the C-terminal domains of the NMDA and AMPA receptors and traveling deep within the postsynaptic density and head of the dendritic spine. Details of this network of proteins that form the postsynaptic density is shown in Fig. 26.4.

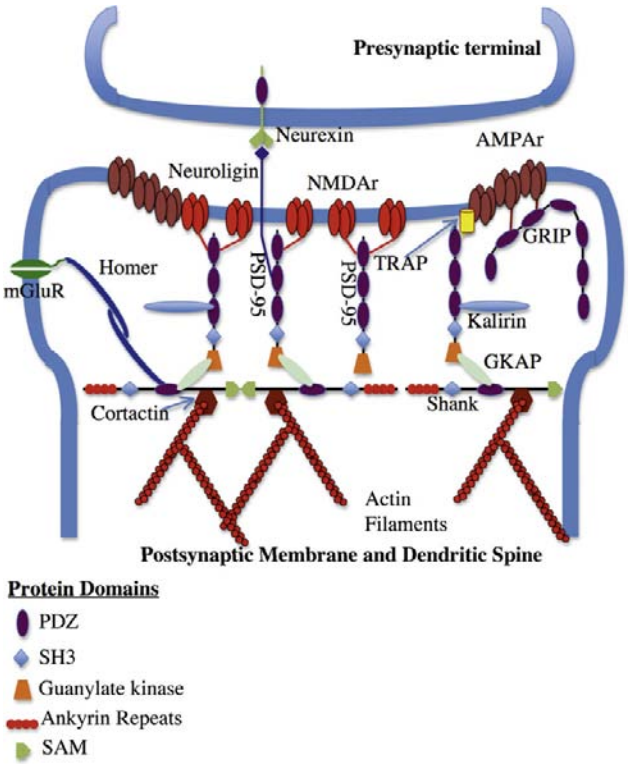

FIGURE 26.4 Interactions of PDZ domain containing proteins at the postsynaptic membrane. NMDA and AMPA receptors at the postsynaptic membrane interact with members of the MAGUK family of scaffolding proteins through their PDZ domains. These scaffolding proteins can also interact with cell adhesion molecules involved in connections with the presynaptic membrane. Interactions with the "higher order" scaffolding proteins (Shanks) link the MAGUKs to the actin cytoskeleton through cortactin. *(Adapted from Feng and Zhang, 2009.)*

IIIB3. MAGUKS

Studies to identify proteins interacting with the cytoplasmic C-termini of NMDA receptors, in particular the NR2 subunit, led to the identification of a new family of proteins referred to as the MAGUKs (membrane associated guanylate kinases) (Kornau et al., 1995; Niethammer et al., 1996). The possession of three PDZ domains, an SH3 domain involved in protein−protein interactions, and an inactive guanylate kinase domain characterize this family of proteins (reviewed in Dimitratos et al., 1999). MAGUKS have now been identified in a number of specialized membrane domains in cell types where they appear to have a role in the targeting and/or immobilization of integral proteins. The protein found to associate with NMDA receptor subunits in the postsynaptic density was termed PSD-95 (also known as DLG4) and has been found to exist as a family of proteins at the excitatory synapse with PSD-93, SAP-102 and SAP-97. The multimodular nature of these proteins means that they can cluster multiple integral proteins through their multiple PDZ domains or bring together different proteins within functional microdomains. For example, PSD-95 is theoretically able to associate simultaneously with the CAM neuroligin (which associates in a *trans* fashion with the presynaptic protein neurexin) and the AMPA receptor allowing the presynaptic area to guide development of the postsynaptic density (Feng and Zhang, 2009). Although these proteins are widely expressed throughout the nervous system, their copy number varies according to the neuronal type and developmental stage. The copy number can also vary in accordance with activity-dependent changes underlying synaptic plasticity. It is thought that a typical postsynaptic density contains

≈300−400 copies of MAGUK family members related to PSD-95 (Sheng and Hoogenraad, 2007).

Since the original identification of MAGUKs at the postsynaptic density, a large number of interacting proteins has been identified (see Fig. 26.4). For example AMPA receptors can bind indirectly to PSD-95 family members using the adaptor protein stargazing (Chen et al., 2000) or, alternatively, to the PDZ domain containing protein GRIP (Dong et al., 1997). The development of specific antibodies to these proteins, combined with advances in EM tomography, has allowed a high-resolution anatomical map of the spine head and postsynaptic density to be constructed (Chen et al., 2008). This map divides the postsynaptic density into three layers, the first being at the plasma membrane which encompasses CAMs involved in contact between pre- and postsynaptic areas, ion channels as well as the NMDA and AMPA receptors. Within the spine head the NMDA receptor is observed in the center, whereas AMPA receptors are distributed around the outside of the spine head (Chenet al., 2008). The second layer is enriched in MAGUKs and other scaffolding proteins, arranged such that the N-termini of these molecules are closely associated with the plasma membrane and the C-termini reach down into the density. Finally, the third layer is enriched in large scaffolding proteins termed Shanks (Sh3 domain and Ank repeat domain containing protein).

Shank proteins are large (120−230 kDa) multidomain proteins characterized by the presence of a series of ankyrin repeats, SH3 and PDZ domains, a long proline-rich region and a C-terminal SAM (*sterile alpha*) domain (reviewed in Kreienkamp, 2008). Three Shank genes have been described which give rise to a diverse range of proteins as a result of alternative mRNA processing and promotor usage. It is estimated that approximately 100 Shank molecules are localized deep within the postsynaptic density (Sheng and Hoogenraad, 2007). Shank proteins are thought to function as higher order scaffolding molecules, organizing the postsynaptic density by connecting different scaffold/receptor complexes through their multiple functional domains. Shank molecules also self-assemble through their C-terminal Sam domain in a head-to-head fashion and connect with the actin cytoskeleton indirectly through an interaction with the actin-binding proteins cortactin and/or fodrin (non-erythroid spectrin) (Kreienkamp, 2008). Receptor scaffolding complexes can anchor to Shank proteins through GKAP (also termed SAP-associated proteins or SAPAP) molecules, which can bind both to the guanylate kinase domain of PSD-95/PSD-93 and with the PDZ domains of Shank (Kreienkamp, 2008). Other ion channels and receptors within the postsynaptic density can also associate with Shank. These include the metabotrophic glutamate receptor (mGluR1), which can associate with the Shank complex through the dimeric linker protein Homer (Tu et al., 1999).

IIIB4. Regulation of Synaptic Strength through Interactions with Scaffolding Proteins

Activity-dependent changes in synaptic strength define synaptic plasticity and hence, memory and learning. At the electrical level, it is possible to regulate synaptic strength either through changing the ionotrophic characteristics of the receptor, or by altering the expression levels of the channel in the plasma membrane. As mentioned previously, the copy number of the NMDA receptor remains fairly fixed in the postsynaptic membrane, whereas that of the AMPA receptor varies widely (Sheng and Hoogenraad, 2007). In the last few years, there has been increasing evidence suggesting that an important component of synaptic strength is the turnover of AMPA receptors in the postsynaptic membrane. At the same time, evidence has accumulated to say that this turnover to some extent is regulated by interactions between the AMPA receptor and scaffolding proteins (reviewed in Elias and Nicoll, 2007).

Evidence of a role for MAGUK proteins in the regulation of AMPA trafficking to the postsynaptic membrane originally came from overexpression studies of PSD-95 in dissociated neurons and slice cultures (Elias and Nicoll, 2007). In these experiments, a large change in AMPA receptor excitatory postsynaptic currents (epscs) was observed when PSD-95 was overexpressed without a concomitant increase in NMDA epscs. This conclusion however, was not supported in studies of knockout animals lacking either PSD-95 or PSD-93, where epscs were unaffected. This finding may reflect functional redundancy between these two similar proteins (Elias and Nicoll, 2007). Indeed, further studies using RNAi to target specific isoforms of MAGUK proteins, when combined with electrophysiology have now shown that the regulation of AMPA receptor surface expression is complex, with multiple MAGUKs within the same neuron playing a role (Elias and Nicoll, 2007).

Perturbing the activity of MAGUKs has also been found to affect the activity of NMDA receptors. The overexpression of PSD-95 has been shown to reduce sensitization of the NMDA receptor in cultured neurons and increases the NMDA receptor opening probability. In heterologous systems, it also results in increased insertion into the plasma membrane (Aoki et al., 2001; Abel et al., 2004). However, these results remain to be reconciled with those of PSD-95 overexpression studies as mentioned above.

IIIB5. Regulation of Dendritic Spine Morphology

Chemical transmission across the glutamergic synapse involving the NMDA and AMPA receptors produces an epsc that is dependent upon the influx of calcium. It is now clear that dendritic spines serve to compartmentalize

calcium changes from the dendritic shaft, where the length and diameter of the spine neck influences the strength and nature of the calcium signal in response to glutamate stimulation (Tada and Sheng, 2006). As increasing lines of evidence indicate that spine morphology can be remodeled by synaptic activity, then spine morphology is closely associated with synaptic plasticity. The morphology of dendritic spines reflects the underlying actin cytoskeleton. Hence, the cytoskeleton not only serves to anchor the ion channels necessary for synaptic activity, but is also remodeled in response to that activity. Not surprisingly then, changes in dendritic spine morphology and numbers has been observed in a number of human neurological disorders ranging from autism (Pickett and London, 2005) to Alzheimer's (Knobloch and Mansuy, 2008).

Although highly varied in their shape, dendritic spines can be roughly classified into three main types: thin, stubby and mushroom, with larger spine heads correlating with increased synaptic strength (Tada and Sheng, 2006). As mentioned earlier, this is thought to reflect increased levels of AMPA receptors in the postsynaptic membrane. Studies using stimuli that induce long-term potentiation (LTP) (Noguchi et al., 2005) and in vivo two-photon microscopy studies of spine turnover (Holtmaat et al., 2005) show that larger spines are more stable and less plastic, whereas smaller spines preferentially undergo LTP. These spines can undergo dramatic changes in their morphology including "splitting" to form two individual postsynaptic areas (Dyson and Jones, 1984). The reason why smaller spines may be susceptible to LTP probably reflects their "neck" geometry, where smaller spines show enhanced elevation of calcium concentrations in the spine head in response to stimuli due to decreased calcium leak through their thinner spine neck (Noguchi et al., 2005).

Dendritic spines are thought to arise from highly dynamic actin-based structures known as filopodia and are induced when these structures contact the nascent presynaptic region (Tada and Sheng, 2006). Finger-like filopodia are associated with a number of motile structures, including the growth cones of neurons and owe their dynamic nature to rapid remodeling of their actin cytoskeleton. Hence, many of the molecules involved in actin remodeling in other cellular structures are also localized in the dendritic spine and play a role in activity-dependent morphological changes. These include molecules that regulate the kinetics of actin polymerization and depolymerization such as profilin, a molecule that associates with actin monomers to limit their availability for the polymerization of actin (Birbach, 2008). Stimulation of NMDA receptors causes the recruitment of profilin to spine heads with the concomitant blocking of actin-related shape changes in the spine (Ackermann and Matus, 2003).

Members of the RhoGTPase family along with proteins that control their activity have also been localized to the spine with their overexpression or inhibition causing major changes in spine morphology (Yoshihara et al., 2009). RhoGTPases act as molecular switches to regulate the actin cytoskeleton (reviewed in Heasman and Ridley, 2008). When associated with GTP, these small G proteins bind to downstream effectors to regulate their activity. A number of proteins are found that cycle RhoGTPases between active (GTP bound) and inactive (GDP bound) states. An example of one of these proteins in dendritic spines is kalirin-7, which is a GEF (guanine-nucleotide exchange factor) that activates the RacGTPase (reviewed in Penzes and Jones, 2008). During synaptogenesis, kalirin-7 activity is induced downstream of signals from the intercellular CAM ephrinB and its receptor. Studies with knockout animals have demonstrated a critical role for kalirin-7 in the regulation of both spine number as well as morphology (Ma, 2010).

Downstream of RacGTPase activity in many cell types is the Lim-kinase cofilin pathway, which is involved in the severing of actin filaments to provide nucleation sites for new actin filament growth. This pathway has also been shown to play a role in synaptic plasticity (Meng et al., 2003). Knockout animals lacking Lim-kinase exhibit dendritic spines with abnormal morphologies and have impaired spatial learning and synaptic plasticity (Meng et al., 2002). As the loss of dendritic spines has been associated with the cognitive defects found in Alzheimer's disease (Tackenberg et al., 2009), it is not surprising to note that changes in this signaling pathway have also been observed in this disorder (Zhao et al., 2006).

Finally, overexpression or knockdown experiments of scaffold proteins such as Shank or PSD-95 have also been shown to alter the morphology of dendritic spines. This may reflect the functions of these proteins in the recruitment of signaling proteins to these structures (Tada and Sheng, 2006). Given the large number of molecules involved in regulating the actin cytoskeleton that have now been localized to the dendritic spine, the challenge is now to elucidate how the function (or localization) of these molecules is regulated in response to synaptic activity.

IIIC. Gephyrin and the Inhibitory Synapse

As described above, the molecules involved in the formation and maintenance of the excitatory synapse, their interactions and localizations have been characterized with a high degree of resolution. Unfortunately, despite its clinical significance, the same cannot be said of the inhibitory synapse. To some extent this may reflect the ease with which the excitatory synapse can be purified compared with its inhibitory counterpart. However, purification of the glycine receptor did yield a binding protein involved in the linkage of these receptor molecules to the microtubule-based cytoskeletal system. This protein has been termed gephyrin (reviewed in Fritschy et al., 2008). Gephyrin has

a predicted molecular mass of 83 kDa and consists of three major structural domains, although multiple isoforms are generated by alternative mRNA processing. Two of these domains are termed G and E. This nomenclature comes about because of sequence homologies between gephyrin and the bacterial Moco (molybdenum co-factor) synthesizing enzymes MogA and MoeA. Indeed, gephyrin is highly conserved between species and mediates Moco biosynthesis in addition to serving as a postsynaptic protein (Feng et al., 1998).

Gephyrin's function in clustering glycine receptors at the inhibitory synapse is based largely on its self-aggregation properties. The protein is thought to form trimers through self-association sites in the G domain and sites in the E domain associate with the large intracellular M3−M4 loops of the pentameric glycine receptor (Fritschy et al., 2008). These trimers are believed to assemble into higher order structures as postulated from aggregation studies of isolated domains in various cell lines (Sola et al., 2001). However, the observation that gephyrin clusters are observed only at the postsynaptic membrane suggests that other factors also regulate this aggregation, including the activation of glycine receptors (Kirsch and Betz, 1998).

As well as binding directly to microtubules, gephyrin associates with the dynein light chain, therefore linking it to motor molecules that utilize the microtubule system for intercellular transport (Fuhrmann et al., 2002). This interaction is supported by live cell imaging studies that show the movement of intracellular complexes of glycine receptor and gephyrin (Maas et al., 2006). In addition, evidence suggests that these complexes may also be able to associate with the actin cytoskeleton as well as providing a second anchorage system for glycine receptor−gephyrin complexes at the inhibitory membrane (Fritschy et al., 2008).

Gephyrin also is found at GABA- (γ-aminobutyric acid) ergic synapses, although interactions between the GABA receptor and gephyrin are currently not well understood (Fritschy et al., 2008). This interaction may be indirect through the protein GABARAP, which has been shown to bind both gephyrin and the GABA receptor (Kanematsu et al., 2007), although it has been shown that this protein is not essential for GABA targeting to the synapse (O'Sullivan et al., 2005). Unlike the glycine receptor, clusters of GABA receptors have been observed independently of gephyrin in neurons. However, gephyrin gene targeting experiments clearly demonstrate a requirement for gephyrin in GABA receptor clustering (Yu et al., 2007), with the recruitment of gephyrin to GABAergic synapses dependent on GABA receptor clustering. This suggests that gephyrin's role may be in the stabilization of GABA receptor clusters at the postsynaptic membrane, rather than in their formation. The role of gephyrin in the recruitment of GABA receptors remains to be elucidated, along with the question of how different GABA receptors with different subunit compositions are targeted to specific synapses and the role gephyrin plays in that selectivity.

IIID. The Interaction of Epithelial Ion Channels with the Cytoskeleton

So far this review has focused on the role of the cytoskeleton in the establishment and maintenance of "excitable" membrane systems such as the AIS and the postsynaptic membrane. In this section, we will now look at how cytoskeleton−ion channel interactions contribute to the polarized nature of epithelial cells. Epithelial cells line cavities and surfaces throughout an organism and form a barrier between the "outside" and the "inside". The use of an array of junctions including adherens and tight junctions on the lateral surface ensures that the passage of solutes between these two compartments occurs through, rather than around the epithelial cell. In this way epithelial cells control processes such as secretion and selective adsorption, as well as play a role in the detection of sensation. In order to achieve this function, epithelial cells become highly polarized during differentiation into two plasma membrane domains associated with the two physiological compartments that they bridge: an apical domain and a basolateral domain that sits on a specialized extracellular matrix (Fig. 26.5). The restriction of ion channels to these two domains is in part due to their interaction with the actin-based cytoskeleton of these cells. In addition, this interaction can help contribute to the function of these ion channels particularly in the area of sensation detection.

Electrophysiology studies of epithelial ion channel activity first suggested a functional link between these molecules and the actin cytoskeleton. Treatment of epithelial cells with cytochalasins, drugs that cause a depolymerization of the actin cytoskeleton, either activated or inactivated epithelial sodium, chloride and potassium channel activity when examined by patch-clamp electrophysiology (reviewed in Mazzochi et al., 2006). However, from these experiments it was impossible to tell whether affects observed were from binding of the channel to the cytoskeleton or the activation of cytoskeleton-associated second messenger systems that affect channel activity. It is now known that a number of channels associate with the actin cytoskeleton using adaptor and scaffolding systems similar to those described for "excitable" membrane domains in the nervous system.

IIID1. CFTR and PDZ Domain Scaffold Proteins in the Apical Membrane

The cystic fibrosis transmembrane conductance regulator (CFTR) is an ion channel of the ABC-transporter class involved in the movement of chloride and thiocyanate ions

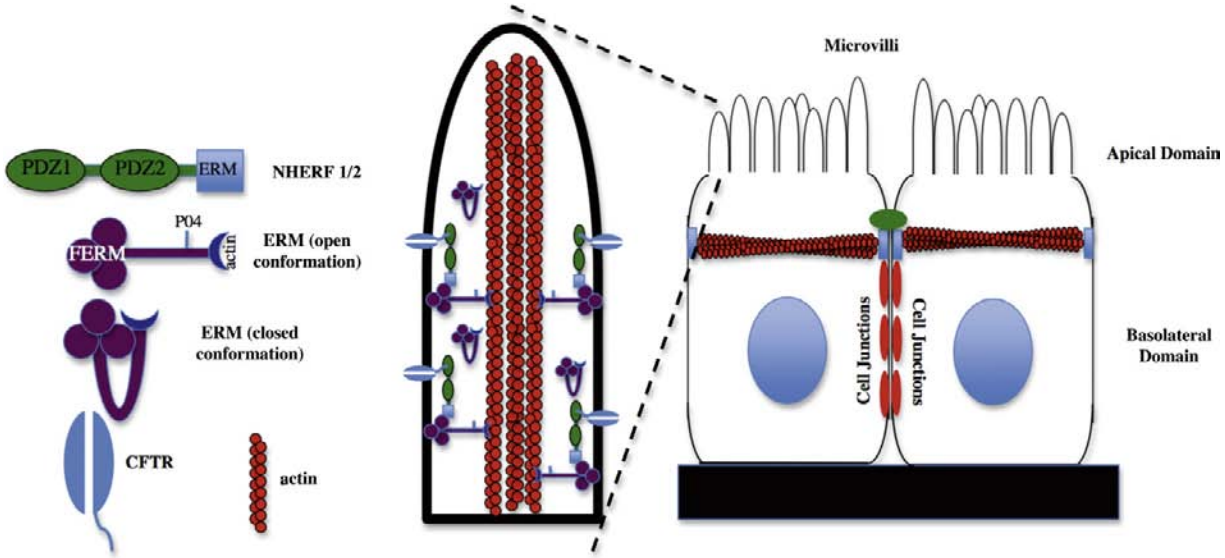

FIGURE 26.5 Interactions that localize CFTR to the apical microvilli of epithelial cells. Epithelial cells are polarized into apical and basolateral domains. The CFTR is localized to the apical compartment of these cells and here is shown localized to apical microvilli. CFTR binds to the PDZ domain of NHERF1/2 which, in turn, binds indirectly to the actin cytoskeleton in the apical domain through an association with ERM (ezrin, radixin, moesin) proteins. As shown, ERM proteins exist in both "open" and "closed" conformations. Binding sites for NHERF1/2 and actin are masked on ERM proteins in the "closed" conformation.

across the apical membrane of epithelial cells (Miller, 2010). Essentially, the channel acts as an ATP-gated anion channel allowing anions such as chloride to flow down their electrochemical gradient in response to cAMP activation. This is in contrast to other ABC transporters where ATP is used to drive the passage of ions against the gradient (Miller, 2010). CFTR is found in a number of epithelia but has been well characterized in the lung where the movement of chloride ions from the epithelial cell to the covering mucus results in the movement of water by osmosis and a more fluid mucus (Kreindler, 2010). The importance of this is clearly seen in mutations of the CFTR that give rise to cystic fibrosis, one of the most common genetic disorders among Caucasians. This disease is characterized by the presence of thick mucus that can block airways and glands and acts as a reservoir for bacterial infections (Kreindler, 2010).

The characterization and identification of C-terminal cytoplasmic sequences in CFTR capable of interacting with PDZ-domain containing proteins led to the idea that CFTR maybe anchored to the apical surface through an interaction with a PDZ-domain scaffolding protein. This protein was found to be a previously identified molecule termed NHERF1 (Na^+/H^+ exchanger regulatory protein) also known as EBP-50 (ezrin-binding protein 50 kDa) (Mazzochi et al., 2006). NHERF proteins are a family of four members that possess either two or four PDZ domains. Family members include the closely related NHERF1 (ebp-50) and NHERF2 (also known as E3KARP) and the four PDZ domain containing proteins NHERF3 (also known as PDZK1, CAP70) and NHERF4 (IKEPP) (Donowitz et al., 2005). As well as their PDZ domains NHERF family members also possess a C-terminal ERM (ezrin-radixin-moesin) binding domain, which therefore indirectly links them to the actin-based cytoskeleton as shown in Fig. 26.5.

NHERF proteins have now been implicated as a major mechanism for the connection of epithelial ion channels to the actin cytoskeleton. These molecules were originally identified as binding partners for the apical membrane Na^+/H^+ exchanger type 3 (NHE3) (Weinman et al., 1995; Yun et al., 1997; Donowitz et al., 2005). They have been shown to be responsible for the localization of the TRPV5/6 epithelial calcium channels (Embark et al., 2004), TRPC4/5 non-selective cation channels (Tang et al., 2000), the β-adrenergic receptor (Hall et al., 1998), CIC-3 chloride channel (Gentzsch et al., 2003) and ROMK potassium channels (Yoo et al., 2004) in addition to their interactions with CFTR. As with other PDZ domain proteins, the possession of multiple PDZ domains allows NHERF proteins to cluster ion channels and/or establish signaling platforms whereby ion channels are brought into close proximity with proteins that regulate their activity. This is clearly illustrated with CFTR, where the molecule has been shown to bind to both PDZ domains of NHERF1 with physiologically relevant affinity (Raghuram et al., 2001). These interactions have been shown to promote dimerization of the CFTR molecule affecting its activity. In addition, CFTR has been localized in a macromolecular complex with the β-adrenergic receptor bound to NHERF2

(Naren et al., 2003). Given that these two molecules are functionally coupled with activation of the receptor stimulating CFTR activity, interactions with NHERF2 represent an important mechanism for regulating CFTR activity in the cell.

Although interactions between CFTR, NHERFs and ERM proteins are necessary for the trafficking and/or stabilization of CFTR in the apical membrane (Mazzochi et al., 2006), these interactions are found to be fairly dynamic and regulated by cell signaling pathways. Interaction of the CFTR with NHERF1 can be regulated by protein kinase C- (PKC-) mediated phosphorylation of a single residue (S162) within PDZ domain 2 of NHERF1 (Raghuram et al., 2001). Phosphorylation of this residue decreases the binding of CFTR to NHERF1. The binding of NHERFs to ERM proteins is also regulated. ERM proteins are characterized by a globular FERM domain and an extended "tail" region that contains an actin-binding site. Within these two domains are sites of self-association that allow the protein to assume a "closed" conformation, where N- and C-termini interact (reviewed in Fehon et al., 2010). Binding sites for actin and NHERF proteins are blocked in this "closed" conformation (see Fig. 26.5). Movement between "closed" and "open" conformations of the ERM proteins is downstream of cell signaling events. These include an interaction between the FERM domain of ERM proteins with PIP2 (phosphatidylinositol 4,5-bisphosphate) synthesized in the membrane in response to G-protein receptor signaling and phosphorylation of ERM proteins in response to activation of RhoGTPases (Fehon et al., 2010). The dynamic nature of the interaction of CFTR with the actin cytoskeleton through NHERF proteins has been demonstrated using a series of FRAP (fluorescence recovery after photobleaching) studies with GFP-labeled CFTR (Haggie et al., 2004). These studies showed that the diffusion of CFTR in the plane of the membrane is dependent on its ability to bind to PDZ-domain-containing proteins, but that this interaction is highly dynamic with these interactions constantly occurring on a time scale of seconds or faster. In support of the dynamic nature of these interactions, it has been reported that NHERF proteins constitute only a small amount ($\approx$2%) of proteins found in CFTR-containing macromolecular complexes (Li et al., 2004).

IIID2. Interactions of Epithelial Ion Channels with Actin-Binding Proteins

The epithelial sodium channel (ENaC, also known as the amiloride sensitive sodium channel) is present in the apical membrane of epithelial cells (particularly the kidney) where it plays a major role in the reabsorption of sodium. These channels are also closely related to the degenerins family of proteins in *Caenorhabditis elegans* that are implicated in mechanosensory transduction (Lumpkin et al., 2010). The channel consists of three subunits termed α, β and γ that form a pore with selective permeability for Li^+ and Na^+ ions (Garty and Palmer, 1997). An interaction between the α subunit of the ENaC and the SH3 domain of α spectrin has been reported (Rotin et al., 1994). This interaction maps to a proline-rich sequence present in the cytoplasmic C-terminal region of the subunit. Microinjection of this domain into rat alveolar epithelial cells causes it to co-localize with α-spectrin in the apical domain. This is in contrast to a domain from the N-terminal region of the ENaC which remains diffuse in the cytoplasm (Rotin et al., 1994).

Other members of the spectrin superfamily of proteins, characterized by the presence of the 106 amino acid spectrin repeat (Hartwig, 1994) are also expressed in epithelial cells. α-Actinin, which consists of four spectrin repeat motifs, is arranged as an anti-parallel homodimer to bind and cross-link actin filaments (Sjoblom et al., 2008). This molecule has been shown to bind to PC2 (polycystin-2 also known as TRPP2) through its spectrin repeat domains (Li et al., 2005), thereby cross-linking PC2 to the actin cytoskeleton. PC2 is a member of the TRP (transient receptor potential) superfamily of ion channels and is a Ca^{2+}-permeable cation channel. Mutations in the PKD2 gene that encodes PC2 are associated with autosomal dominant polycystic kidney disease (ADPKD) (Gonzalez-Perrett et al., 2001). Although PC2 is predominantly localized to the cilia, it is also found in the apical plasma membrane of epithelial cells (Ong and Harris, 2005). Interestingly α-actinin was able to stimulate the activity of PC2 when incorporated into lipid bilayers, suggesting that this interaction may also have a direct regulatory role on PC2 activity as well as regulating its subcellular localization (Li et al., 2005).

IIID3. Direct Interactions Between Epithelial Ion Channels and Actin Filaments

We have so far examined examples of a model in which ion channels couple to the actin cytoskeleton through intermediary adaptor or scaffold proteins. However, increasing lines of evidence support the idea that some ion channels in epithelial cells can directly associate with actin. Actin has been shown to interact directly with the CIC-2 chloride channel using actin overlay and co-sedimentation assays (Ahmed et al., 2000). In addition, treatment of *Xenopus laevis* oocytes expressing CIC-2 with cytochalasin D or latrunculin that disrupt the actin cytoskeleton significantly increased channel activity. Similarly, changes in conductance of ENaC channels incorporated into lipid bilayers were observed in the presence of short actin filaments (Berdiev et al., 1996) and these channels were found to be activated by protein kinase A (PKA) only in the presence of actin. The concept that ion channel activity may be regulated by the presence of short actin filaments is supported

by patch-clamp studies in *X. laevis* cells showing an increase in ENaC activity within 5 minutes of applying cytochalasin D to the cells (Cantiello et al., 1991). Further experiments utilizing gelsolin, which preferentially stabilizes the polymerization of actin into short oligomers, have demonstrated that it is the interaction of ENaC with short actin filaments, rather than just with actin itself, that regulates ENaC activity (Prat et al., 1993). Mapping studies have localized a putative actin-binding site to the region between E631 and F644 of the α-ENaC molecule (Copeland et al., 2001).

IV. GENERAL CONCLUSIONS

The localization of ion channels to physiologically specialized membrane domains is crucial to the function of a wide variety of metazoan cell types. This localization is dependent upon interactions, either direct or indirect, between ion channels and the actin or microtubule-based cytoskeleton. In this review, we have examined some examples of these interactions and how they contribute to the physiological function of these specialized membrane domains. As is observed, the interaction between ion channels and cytoskeletal elements not only facilitates channel localization, but also may regulate their activity. Regulation of ion channel activity can reflect the affects of direct interactions of the cytoskeleton or cytoskeletal adaptor/scaffolding proteins with components of the channel. An area where this concept becomes crucial, but not covered in this review, is in the area of mechanosensitive transduction. There, the interaction of ion channels with the cytoskeleton and the extracellular matrix serves to regulate channel activity in response to mechanical changes (Lumpkin et al., 2010). Alternatively, ion channel activity can be regulated by the formation of functional microdomains brought about by scaffolding proteins that bring the channel into close proximity with signaling molecules that regulate its activity.

As evidenced in the dendritic spine, the activity of ion channels can also serve to regulate the cytoskeleton to achieve changes in cell shape. These changes can themselves affect how epscs are propagated to the dendritic shaft and are an important component of synaptic plasticity, a crucial concept underlying memory and learning. Dendritic spines themselves contain molecules that have been demonstrated to have a regulatory affect on their morphology. The challenge in upcoming years will be to try to understand how synaptic activity, with its accompanying ion channel involvement, regulates the function of these molecules to change spine morphologies.

A number of insights have occurred over the last 10 years into how these specialized membrane domains are localized and assembled. However, a significant number of important questions remain to be answered. Are ion channels and their associated trafficking proteins trafficked together to the plasma membrane as macromolecular complexes or is assembly localized to these sites? In the case of the excitatory postsynaptic density, we know that at least some of these proteins are already preassembled prior to reaching the postsynaptic membrane (Naisbitt et al., 1999). Similarly, a role for various motor proteins in synapse assembly has been noted (reviewed in Hirokawa et al., 2010), although mechanisms underlying the specific targeting of protein complexes to these sites have yet to be elucidated. The discovery that certain scaffold proteins simultaneously bind to both CAMs and ion channels suggests a mechanism whereby *trans* interactions between cells could direct ion channel clustering and formation of specialized membrane domains. For example, at the node of Ranvier, gliomedin released from the myelinating Schwann cell clusters the ankyrin-binding molecule neurofascin (Salzer et al., 2008) to direct ankyrin recruitment (Lambert et al., 1997). As ankyrin also binds the vgsc (Lemaillet et al., 2003), a series of molecular interactions allow the Schwann cell to orchestrate directly early assembly of the nodal membrane. However, this model does not explain how these same players are assembled at the AIS, which is an intrinsic feature of the neuron and can be assembled in the absence of cell contacts. Again, the answer to these question lies in understanding mechanisms undergoing the trafficking of these proteins to their specialized membrane domains.

The use of knockout and transgenic animals has been extremely useful in demonstrating the physiological consequences of aberrant interactions between ion channels and the cytoskeleton. However, we have also seen that mutations in these interactions can also be associated with human disease as is seen with ankyrin in the heart (Ackerman and Mohler, 2010) and CFTR in epithelial cells (Kreindler, 2010). In addition, increasing evidence suggests that proteins that affect the dendritic spine cytoskeleton and, hence, its morphology, may be associated with human neurological disorders such as Alzheimer's disease (Knobloch and Mansuy, 2008; Penzes and Jones, 2008). It may well be that these disorders represent only the tip of the iceberg when it comes to channelopathies that result from aberrant interactions with the cytoskeleton.

BIBLIOGRAPHY

Abdi, K. M., Mohler, P. J., Davis, J. Q., & Bennett, V. (2006). Isoform specificity of ankyrin-B: a site in the divergent C-terminal domain is required for intramolecular association. *J Biol Chem, 281*, 5741–5749.

Abel, H. J., Lee, J. C., Callaway, J. C., & Foehring, R. C. (2004). Relationships between intracellular calcium and after hyperpolarizations in neocortical pyramidal neurons. *J Neurophysiol, 91*, 324–335.

Ackerman, M. J., & Mohler, P. J. (2010). Defining a new paradigm for human arrhythmia syndromes: phenotypic manifestations of gene mutations in ion channel- and transporter-associated proteins. *Circ Res, 107*, 457−465.

Ackermann, M., & Matus, A. (2003). Activity-induced targeting of profilin and stabilization of dendritic spine morphology. *Nat Neurosci, 6*, 1194−1200.

Ahmed, N., Ramjeesingh, M., Wong, S., Varga, A., Garami, E., & Bear, C. E. (2000). Chloride channel activity of ClC-2 is modified by the actin cytoskeleton. *Biochem J, 352*, 789−794.

Aoki, C., Miko, I., Oviedo, H., et al. (2001). Electron microscopic immunocytochemical detection of PSD-95, PSD-93, SAP-102, and SAP-97 at postsynaptic, presynaptic, and nonsynaptic sites of adult and neonatal rat visual cortex. *Synapse, 40*, 239−257.

Bennett, V., & Gilligan, D. M. (1993). The spectrin-based membrane skeleton and micron-scale organization of the plasma membrane. *Annu Rev Cell Biol, 9*, 27−66.

Bennett, V., & Healy, J. (2009). Membrane domains based on ankyrin and spectrin associated with cell-cell interactions. *Cold Spring Harb Perspect Biol, 1*, a003012.

Berdiev, B. K., Prat, A. G., Cantiello, H. F., et al. (1996). Regulation of epithelial sodium channels by short actin filaments. *J Biol Chem, 271*, 17704−17710.

Birbach, A. (2008). Profilin, a multi-modal regulator of neuronal plasticity. *Bioessays, 30*, 994−1002.

Brechet, A., Fache, M. P., Brachet, A., et al. (2008). Protein kinase CK2 contributes to the organization of sodium channels in axonal membranes by regulating their interactions with ankyrin G. *J Cell Biol, 183*, 1101−1114.

Byers, T. J., & Branton, D. (1985). Visualization of the protein associations in the erythrocyte membrane skeleton. *Proc Natl Acad Sci USA, 82*, 6153−6157.

Cantiello, H. F., Stow, J. L., Prat, A. G., & Ausiello, D. A. (1991). Actin filaments regulate epithelial Na+ channel activity. *Am J Physiol, 261*, C882−C888.

Chan, W., Kordeli, E., & Bennett, V. (1993). 440-kD ankyrinB: structure of the major developmentally regulated domain and selective localization in unmyelinated axons. *J Cell Biol, 123*, 1463−1473.

Chauhan, V. S., Tuvia, S., Buhusi, M., Bennett, V., & Grant, A. O. (2000). Abnormal cardiac Na(+) channel properties and QT heart rate adaptation in neonatal ankyrin(B) knockout mice. *Circ Res, 86*, 441−447.

Chen, L., Chetkovich, D. M., Petralia, R. S., et al. (2000). Stargazin regulates synaptic targeting of AMPA receptors by two distinct mechanisms. *Nature, 408*, 936−943.

Chen, X., Winters, C., Azzam, R., et al. (2008). Organization of the core structure of the postsynaptic density. *Proc Natl Acad Sci USA, 105*, 4453−4458.

Ching, W., Zanazzi, G., Levinson, S. R., & Salzer, J. L. (1999). Clustering of neuronal sodium channels requires contact with myelinating Schwann cells. *J Neurocytol, 28*, 295−301.

Copeland, S. J., Berdiev, B. K., Ji, H. L., et al. (2001). Regions in the carboxy terminus of alpha-bENaC involved in gating and functional effects of actin. *Am J Physiol Cell Physiol, 281*, C231−C240.

Davis, J. Q., & Bennett, V. (1994). Ankyrin binding activity shared by the neurofascin/L1/NrCAM family of nervous system cell adhesion molecules. *J Biol Chem, 269*, 27163−27166.

Dimitratos, S. D., Woods, D. F., Stathakis, D. G., & Bryant, P. J. (1999). Signaling pathways are focused at specialized regions of the plasma membrane by scaffolding proteins of the MAGUK family. *Bioessays, 21*, 912−921.

Dong, H., O'Brien, R. J., Fung, E. T., Lanahan, A. A., Worley, P. F., & Huganir, R. L. (1997). GRIP: a synaptic PDZ domain-containing protein that interacts with AMPA receptors. *Nature, 386*, 279−284.

Donowitz, M., Cha, B., Zachos, N. C., et al. (2005). NHERF family and NHE3 regulation. *J Physiol, 567*, 3−11.

Dyson, S. E., & Jones, D. G. (1984). Synaptic remodelling during development and maturation: junction differentiation and splitting as a mechanism for modifying connectivity. *Brain Res, 315*, 125−137.

Elias, G. M., & Nicoll, R. A. (2007). Synaptic trafficking of glutamate receptors by MAGUK scaffolding proteins. *Trends Cell Biol, 17*, 343−352.

Embark, H. M., Setiawan, I., Poppendieck, S., et al. (2004). Regulation of the epithelial Ca2+ channel TRPV5 by the NHE regulating factor NHERF2 and the serum and glucocorticoid inducible kinase isoforms SGK1 and SGK3 expressed in Xenopus oocytes. *Cell Physiol Biochem, 14*, 203−212.

Fehon, R. G., McClatchey, A. I., & Bretscher, A. (2010). Organizing the cell cortex: the role of ERM proteins. *Nat Rev Mol Cell Biol, 11*, 276−287.

Feng, G., Tintrup, H., Kirsch, J., et al. (1998). Dual requirement for gephyrin in glycine receptor clustering and molybdoenzyme activity. *Science, 282*, 1321−1324.

Feng, W., & Zhang, M. (2009). Organization and dynamics of PDZ-domain-related supramodules in the postsynaptic density. *Nat Rev Neurosci, 10*, 87−99.

Fritschy, J. M., Harvey, R. J., & Schwarz, G. (2008). Gephyrin: where do we stand, where do we go? *Trends Neurosci, 31*, 257−264.

Fuhrmann, J. C., Kins, S., Rostaing, P., et al. (2002). Gephyrin interacts with Dynein light chains 1 and 2, components of motor protein complexes. *J Neurosci, 22*, 5393−5402.

Garrido, J. J., Fernandes, F., Giraud, P., Mouret, I., et al. (2001). Identification of an axonal determinant in the C-terminus of the sodium channel Na(v)1.2. *EMBO J, 20*, 5950−5961.

Garrido, J. J., Fernandes, F., Moussif, A., Fache, M. P., Giraud, P., & Dargent, B. (2003). Dynamic compartmentalization of the voltage-gated sodium channels in axons. *Biol Cell, 95*, 437−445.

Garty, H., & Palmer, L. G. (1997). Epithelial sodium channels: function, structure, and regulation. *Physiol Rev, 77*, 359−396.

Garver, T. D., Ren, Q., Tuvia, S., & Bennett, V. (1997). Tyrosine phosphorylation at a site highly conserved in the L1 family of cell adhesion molecules abolishes ankyrin binding and increases lateral mobility of neurofascin. *J Cell Biol, 137*, 703−714.

Gatto, C. L., Walker, B. J., & Lambert, S. (2003). Local ERM activation and dynamic growth cones at Schwann cell tips implicated in efficient formation of nodes of Ranvier. *J Cell Biol, 162*, 489−498.

Gentzsch, M., Cui, L., Mengos, A., Chang, X. B., Chen, J. H., & Riordan, J. R. (2003). The PDZ-binding chloride channel ClC-3B localizes to the Golgi and associates with cystic fibrosis transmembrane conductance regulator-interacting PDZ proteins. *J Biol Chem, 278*, 6440−6449.

Goldin, A. L. (1999). Diversity of mammalian voltage-gated sodium channels. *Ann NY Acad Sci, 868*, 38−50.

Gomis-Ruth, S., Wierenga, C. J., & Bradke, F. (2008). Plasticity of polarization: changing dendrites into axons in neurons integrated in neuronal circuits. *Curr Biol, 18*, 992−1000.

Gonzalez-Perrett, S., Kim, K., Ibarra, C., et al. (2001). Polycystin-2, the protein mutated in autosomal dominant polycystic kidney disease (ADPKD), is a Ca2+-permeable nonselective cation channel. *Proc Natl Acad Sci, USA, 98*, 1182−1187.

Grubb, M. S., & Burrone, J. (2010). Building and maintaining the axon initial segment. *Curr Opin Neurobiol, 20*, 481−488.

Haggie, P. M., Stanton, B. A., & Verkman, A. S. (2004). Increased diffusional mobility of CFTR at the plasma membrane after deletion of its C-terminal PDZ binding motif. *J Biol Chem, 279*, 5494−5500.

Hall, R. A., Ostedgaard, L. S., Premont, R. T., et al. (1998). A C-terminal motif found in the beta2-adrenergic receptor, P2Y1 receptor and cystic fibrosis transmembrane conductance regulator determines binding to the Na+/H+ exchanger regulatory factor family of PDZ proteins. *Proc Natl Acad Sci, USA, 95*, 8496−8501.

Hall, T. G., & Bennett, V. (1987). Regulatory domains of erythrocyte ankyrin. *J Biol Chem, 262*, 10537−10545.

Hartwig, J. H. (1994). Actin-binding proteins 1: spectrin superfamily. *Protein Profile, 1*, 706−778.

Heasman, S. J., & Ridley, A. J. (2008). Mammalian Rho GTPases: new insights into their functions from in vivo studies. *Nat Rev Mol Cell Biol, 9*, 690−701.

Hill, A. S., Nishino, A., Nakajo, K., et al. (2008). Ion channel clustering at the axon initial segment and node of Ranvier evolved sequentially in early chordates. *PLoS Genet, 4*, e1000317.

Hirokawa, N., Niwa, S., & Tanaka, Y. (2010). Molecular motors in neurons: transport mechanisms and roles in brain function, development, and disease. *Neuron, 68*, 610−638.

Hollmann, M., Boulter, J., Maron, C., et al. (1993). Zinc potentiates agonist-induced currents at certain splice variants of the NMDA receptor. *Neuron, 10*, 943−954.

Holtmaat, A. J., Trachtenberg, J. T., Wilbrecht, L., et al. (2005). Transient and persistent dendritic spines in the neocortex in vivo. *Neuron, 45*, 279−291.

Kanematsu, T., Mizokami, A., Watanabe, K., & Hirata, M. (2007). Regulation of GABA(A)-receptor surface expression with special reference to the involvement of GABARAP (GABA(A) receptor-associated protein) and PRIP (phospholipase C-related, but catalytically inactive protein). *J Pharmacol Sci, 104*, 285−292.

Kaplan, M. R., Meyer-Franke, A., Lambert, S., et al. (1997). Induction of sodium channel clustering by oligodendrocytes. *Nature, 386*, 724−728.

Kirsch, J., & Betz, H. (1998). Glycine-receptor activation is required for receptor clustering in spinal neurons. *Nature, 392*, 717−720.

Knobloch, M., & Mansuy, I. M. (2008). Dendritic spine loss and synaptic alterations in Alzheimer's disease. *Mol Neurobiol, 37*, 73−82.

Kodippili, G. C., Spector, J., Sullivan, C., et al. (2009). Imaging of the diffusion of single band 3 molecules on normal and mutant erythrocytes. *Blood, 113*, 6237−6245.

Kordeli, E., Lambert, S., & Bennett, V. (1995). AnkyrinG. A new ankyrin gene with neural-specific isoforms localized at the axonal initial segment and node of Ranvier. *J Biol Chem, 270*, 2352−2359.

Kornau, H. C., Schenker, L. T., Kennedy, M. B., & Seeburg, P. H. (1995). Domain interaction between NMDA receptor subunits and the postsynaptic density protein PSD-95. *Science, 269*, 1737−1740.

Kreienkamp, H. J. (2008). Scaffolding proteins at the postsynaptic density: shank as the architectural framework. *Handb Exp Pharmacol,* 365−380.

Kreindler, J. L. (2010). Cystic fibrosis: exploiting its genetic basis in the hunt for new therapies. *Pharmacol Ther, 125*, 219−229.

Lambert, S., Davis, J. Q., & Bennett, V. (1997). Morphogenesis of the node of Ranvier: co-clusters of ankyrin and ankyrin-binding integral proteins define early developmental intermediates. *J Neurosci, 17*, 7025−7036.

Lambert, S., Yu, H., Prchal, J. T., et al. (1990). cDNA sequence for human erythrocyte ankyrin. *Proc Natl Acad Sci USA, 87*, 1730−1734.

Lemaillet, G., Walker, B., & Lambert, S. (2003). Identification of a conserved ankyrin-binding motif in the family of sodium channel alpha subunits. *J Biol Chem, 278*, 27333−27339.

Li, C., Roy, K., Dandridge, K., & Naren, A. P. (2004). Molecular assembly of cystic fibrosis transmembrane conductance regulator in plasma membrane. *J Biol Chem, 279*, 24673−24684.

Li, Q., Montalbetti, N., Shen, P. Y., et al. (2005). Alpha-actinin associates with polycystin-2 and regulates its channel activity. *Hum Mol Genet, 14*, 1587−1603.

Lumpkin, E. A., Marshall, K. L., & Nelson, A. M. (2010). The cell biology of touch. *J Cell Biol, 191*, 237−248.

Ma, X. M. (2010). Kalirin-7 is a key player in the formation of excitatory synapses in hippocampal neurons. *Sci World J, 10*, 1655−1666.

Maas, C., Tagnaouti, N., Loebrich, S., Behrend, B., Lappe-Siefke, C., & Kneussel, M. (2006). Neuronal cotransport of glycine receptor and the scaffold protein gephyrin. *J Cell Biol, 172*, 441−451.

Malhotra, J. D., Kazen-Gillespie, K., Hortsch, M., & Isom, L. L. (2000). Sodium channel beta subunits mediate homophilic cell adhesion and recruit ankyrin to points of cell-cell contact. *J Biol Chem, 275*, 11383−11388.

Malhotra, J. D., Koopmann, M. C., Kazen-Gillespie, K. A., Fettman, N., Hortsch, M., & Isom, L. L. (2002). Structural requirements for interaction of sodium channel beta 1 subunits with ankyrin. *J Biol Chem, 277*, 26681−26688.

Mazzochi, C., Benos, D. J., & Smith, P. R. (2006). Interaction of epithelial ion channels with the actin-based cytoskeleton. *Am J Physiol Renal Physiol, 291*, F1113−F1122.

Melendez-Vasquez, C. V., Rios, J. C., Zanazzi, G., Lambert, S., Bretscher, A., & Salzer, J. L. (2001). Nodes of Ranvier form in association with ezrin-radixin-moesin (ERM)-positive Schwann cell processes. *Proc Natl Acad Sci, SA, 98*, 1235−1240.

Meng, Y., Zhang, Y., Tregoubov, V., et al. (2002). Abnormal spine morphology and enhanced LTP in LIMK-1 knockout mice. *Neuron, 35*, 121−133.

Meng, Y., Zhang, Y., Tregoubov, V., Falls, D. L., & Jia, Z. (2003). Regulation of spine morphology and synaptic function by LIMK and the actin cytoskeleton. *Rev Neurosci, 14*, 233−240.

Michaely, P., & Bennett, V. (1993). The membrane-binding domain of ankyrin contains four independently folded subdomains, each comprised of six ankyrin repeats. *J Biol Chem, 268*, 22703−22709.

Miller, C. (2010). CFTR: break a pump, make a channel. *Proc Natl Acad Sci USA, 107*, 959−960.

Mohler, P. J., Davis, J. Q., & Bennett, V. (2005). Ankyrin-B coordinates the Na/K ATPase, Na/Ca exchanger, and InsP3 receptor in a cardiac T-tubule/SR microdomain. *PLoS Biol, 3*, e423.

Mohler, P. J., Gramolini, A. O., & Bennett, V. (2002). The ankyrin-B C-terminal domain determines activity of ankyrin-B/G chimeras in rescue of abnormal inositol 1,4,5-trisphosphate and ryanodine receptor distribution in ankyrin-B (−/−) neonatal cardiomyocytes. *J Biol Chem, 277*, 10599−10607.

Mohler, P. J., Healy, J. A., Xue, H., et al. (2007). Ankyrin-B syndrome: enhanced cardiac function balanced by risk of cardiac death and premature senescence. *PLoS One, 2*, e1051.

Mohler, P. J., Rivolta, I., Napolitano, C., et al. (2004). Nav1.5 E1053K mutation causing Brugada syndrome blocks binding to ankyrin-G and expression of Nav1.5 on the surface of cardiomyocytes. *Proc Natl Acad Sci USA, 101*, 17533−17538.

Mohler, P. J., Schott, J. J., Gramolini, A. O., et al. (2003). Ankyrin-B mutation causes type 4 long-QT cardiac arrhythmia and sudden cardiac death. *Nature, 421*, 634−639.

Naisbitt, S., Kim, E., Tu, J. C., et al. (1999). Shank, a novel family of postsynaptic density proteins that binds to the NMDA receptor/PSD-95/GKAP complex and cortactin. *Neuron, 23*, 569−582.

Naren, A. P., Cobb, B., Li, C., et al. (2003). A macromolecular complex of beta 2 adrenergic receptor, CFTR, and ezrin/radixin/moesin-binding phosphoprotein 50 is regulated by PKA. *Proc Natl Acad Sci USA, 100*, 342−346.

Niethammer, M., Kim, E., & Sheng, M. (1996). Interaction between the C terminus of NMDA receptor subunits and multiple members of the PSD-95 family of membrane-associated guanylate kinases. *J Neurosci, 16*, 2157−2163.

Noguchi, J., Matsuzaki, M., Ellis-Davies, G. C., & Kasai, H. (2005). Spine-neck geometry determines NMDA receptor-dependent Ca2+ signaling in dendrites. *Neuron, 46*, 609−622.

Ogawa, Y., Oses-Prieto, J., Kim, M. Y., et al. (2010). ADAM22, a Kv1 channel-interacting protein, recruits membrane-associated guanylate kinases to juxtaparanodes of myelinated axons. *J Neurosci, 30*, 1038−1048.

Ong, A. C., & Harris, P. C. (2005). Molecular pathogenesis of ADPKD: the polycystin complex gets complex. *Kidney Int, 67*, 1234−1247.

Orchard, C. H., Pasek, M., & Brette, F. (2009). The role of mammalian cardiac t-tubules in excitation−contraction coupling: experimental and computational approaches. *Exp Physiol, 94*, 509−519.

O'Sullivan, G. A., Kneussel, M., Elazar, Z., & Betz, H. (2005). GABARAP is not essential for GABA receptor targeting to the synapse. *Eur J Neurosci, 22*, 2644−2648.

Otto, E., Kunimoto, M., McLaughlin, T., & Bennett, V. (1991). Isolation and characterization of cDNAs encoding human brain ankyrins reveal a family of alternatively spliced genes. *J Cell Biol, 114*, 241−253.

Palek, J., & Lambert, S. (1990). Genetics of the red cell membrane skeleton. *Semin Hematol, 27*, 290−332.

Pan, Z., Kao, T., Horvath, Z., et al. (2006). A common ankyrin-G-based mechanism retains KCNQ and NaV channels at electrically active domains of the axon. *J Neurosci, 26*, 2599−2613.

Penzes, P., & Jones, K. A. (2008). Dendritic spine dynamics − a key role for kalirin-7. *Trends Neurosci, 31*, 419−427.

Pickett, J., & London, E. (2005). The neuropathology of autism: a review. *J Neuropathol Exp Neurol, 64*, 925−935.

Prat, A. G., Bertorello, A. M., Ausiello, D. A., & Cantiello, H. F. (1993). Activation of epithelial Na+ channels by protein kinase A requires actin filaments. *Am J Physiol, 265*, C224−C233.

Raghuram, V., Mak, D. O., & Foskett, J. K. (2001). Regulation of cystic fibrosis transmembrane conductance regulator single-channel gating by bivalent PDZ-domain-mediated interaction. *Proc Natl Acad Sci USA, 98*, 1300−1305.

Rasband, M. N. (2010). Clustered K+ channel complexes in axons. *Neurosci Lett, 486*, 101−106.

Rasband, M. N., Park, E. W., Zhen, D., et al. (2002). Clustering of neuronal potassium channels is independent of their interaction with PSD-95. *J Cell Biol, 159*, 663−672.

Ratcliffe, C. F., Westenbroek, R. E., Curtis, R., & Catterall, W. A. (2001). Sodium channel beta1 and beta3 subunits associate with neurofascin through their extracellular immunoglobulin-like domain. *J Cell Biol, 154*, 427−434.

Rotin, D., Bar-Sagi, D., O'Brodovich, H., et al. (1994). An SH3 binding region in the epithelial Na+ channel (alpha rENaC) mediates its localization at the apical membrane. *EMBO J, 13*, 4440−4450.

Salzer, J. L., Brophy, P. J., & Peles, E. (2008). Molecular domains of myelinated axons in the peripheral nervous system. *Glia, 56*, 1532−1540.

Sheng, M., & Hoogenraad, C. C. (2007). The postsynaptic architecture of excitatory synapses: a more quantitative view. *Annu Rev Biochem, 76*, 823−847.

Shepherd, J. D., & Huganir, R. L. (2007). The cell biology of synaptic plasticity: AMPA receptor trafficking. *Annu Rev Cell Dev Biol, 23*, 613−643.

Sjoblom, B., Salmazo, A., & Djinovic-Carugo, K. (2008). Alpha-actinin structure and regulation. *Cell Mol Life Sci, 65*, 2688−2701.

Sola, M., Kneussel, M., Heck, I. S., Betz, H., & Weissenhorn, W. (2001). X-ray crystal structure of the trimeric N-terminal domain of gephyrin. *J Biol Chem, 276*, 25294−25301.

Song, A. H., Wang, D., Chen, G., et al. (2009). A selective filter for cytoplasmic transport at the axon initial segment. *Cell, 136*, 1148−1160.

Tackenberg, C., Ghori, A., & Brandt, R. (2009). Thin, stubby or mushroom: spine pathology in Alzheimer's disease. *Curr Alzheimer Res, 6*, 261−268.

Tada, T., & Sheng, M. (2006). Molecular mechanisms of dendritic spine morphogenesis. *Curr Opin Neurobiol, 16*, 95−101.

Tang, Y., Tang, J., Chen, Z., et al. (2000). Association of mammalian trp4 and phospholipase C isozymes with a PDZ domain-containing protein, NHERF. *J Biol Chem, 275*, 37559−37564.

Thaxton, C., Pillai, A. M., Pribisko, A. L., Dupree, J. L., & Bhat, M. A. (2011). Nodes of Ranvier act as barriers to restrict invasion of flanking paranodal domains in myelinated axons. *Neuron, 69*, 244−257.

Tu, J. C., Xiao, B., Naisbitt, S., et al. (1999). Coupling of mGluR/Homer and PSD-95 complexes by the Shank family of postsynaptic density proteins. *Neuron, 23*, 583−592.

Weinman, E. J., Steplock, D., Wang, Y., & Shenolikar, S. (1995). Characterization of a protein cofactor that mediates protein kinase A regulation of the renal brush border membrane Na(+)-H+ exchanger. *J Clin Invest, 95*, 2143−2149.

Winckler, B., Forscher, P., & Mellman, I. (1999). A diffusion barrier maintains distribution of membrane proteins in polarized neurons. *Nature, 397*, 698−701.

Yoo, D., Flagg, T. P., Olsen, O., Raghuram, V., Foskett, J. K., & Welling, P. A. (2004). Assembly and trafficking of a multiprotein ROMK (Kir 1.1) channel complex by PDZ interactions. *J Biol Chem, 279*, 6863−6873.

Yoshihara, Y., De Roo, M., & Muller, D. (2009). Dendritic spine formation and stabilization. *Curr Opin Neurobiol, 19*, 146−153.

Yu, W., Jiang, M., Miralles, C. P., Li, R. W., Chen, G., & de Blas, A. L. (2007). Gephyrin clustering is required for the stability of GABAergic synapses. *Mol Cell Neurosci, 36*, 484−500.

Yun, C. H., Oh, S., Zizak, M., et al. (1997). cAMP-mediated inhibition of the epithelial brush border Na+/H+ exchanger, NHE3, requires an associated regulatory protein. *Proc Natl Acad Sci USA, 94*, 3010−3015.

Zhao, L., Ma, Q. L., Calon, F., et al. (2006). Role of p21-activated kinase pathway defects in the cognitive deficits of Alzheimer disease. *Nat Neurosci, 9*, 234−242.

Zhou, D., Lambert, S., Malen, P. L., Carpenter, S., Boland, L. M., & Bennett, V. (1998). AnkyrinG is required for clustering of voltage-gated Na channels at axon initial segments and for normal action potential firing. *J Cell Biol, 143*, 1295−1304.

Zonta, B., Tait, S., Melrose, S., et al. (2008). Glial and neuronal isoforms of Neurofascin have distinct roles in the assembly of nodes of Ranvier in the central nervous system. *J Cell Biol, 181*, 1169−1177.

Chapter 27

Why are So Many Ion Channels Mechanosensitive?

Catherine E. Morris

Chapter Outline

I. SUMMARY

Reports of stretch-sensitive channels started appearing in the mid-1980s. Briefly, the unidentified mechanosensitive (MS) channels were seen as representatives of a new subclass of channels. There were speculations that "mechano-gating motifs" would soon be discovered. Gradually, however, it emerged that channels showing no mechanosensitivity are the outliers and it became clear that gating energy is supplied by bilayer deformations. Over the last decade, what has been particularly helpful in clarifying the role of bilayer mechanics in the mechanosensitive responses of diverse eukaryotic channels have been converging advances on three fronts: (1) high resolution structure/function data for voltage-gated channels (VGCs); (2) the demonstration that VGCs are inherently mechanosensitive; and (3) experimental and computational data showing how mechanosensitivity emerges from the energetics at the interface of dynamically structured bilayers and dynamically structured proteins. An ongoing task is to establish if and where the reversible mechanosensitive responses of ion channels are physiologically relevant; do they, for instance, contribute to cardiac mechano-electric feedback? Also enormously important, in my view, is to learn what the irreversible MS behaviors of channel reveal about the pathological membrane phenomena associated with trauma, ischemia, inflammation and, in fact, any condition where channel-bearing membranes undergo irreversible structural changes. One likely payoff: "smarter" drugs designed to target not simply channel-X, but channel-X in bilayer-structure-Y – say, leaky sodium channel in nodes of Ranvier where lipid packing has become disorderly and where leaflet asymmetry has been compromised by traumatic brain injury.

II. INTRODUCTION

Even before "channel" entered the physiology lexicon, mechanosensitive (MS) membrane conductances were studied in eukaryotic organisms (Gray and Sato, 1953). Sixty years on, much evidence points to ion channels as the mechanotransducers in vertebrate and invertebrate mechanosensory cells. Transduction channels absorb mechanical gating energy from cytoarchitectural elements arranged to focus and amplify small stimuli; candidates include Peizo1 and Peizo2, proteins with no known homologies (Coste et al., 2010), "TRPs" (transient receptor potentials), multimodal channels with overwhelmingly diverse homologies (Patel et al., 2010) and proteins homologous to "ENaC" (epithelial Na channel) (Cueva et al., 2007). Prokaryotic walled cells express several molecularly unrelated multimeric proteins that, at near-lytic bilayer strain, open as osmolyte channels (Kung et al., 2010); additionally, expanding closed-closed transitions noted for some might serve as membrane spandex, providing tension-relief in high turgor conditions (Boucher et al., 2009). Together, these mechanosensory specialists – unidentified eukaryote mechanotransducers and identified

Cell Physiology Sourcebook. DOI: 10.1016/B978-0-12-387738-3.00027-5

prokayote osmovalves — operate at opposite ends of the mechanostimulus intensity spectrum.

Here I discuss a different phenomenon, that of the many non-specialist ion channels that respond to mechanical stimuli. Non-specialist MS channels, like the prokaryote osmovalve specialists, derive gating energy from bilayer deformation. Eukaryotic mechanotransduction, however, is thought to require stiff vectorial protein assemblies whose gating springs control displacement of a gate (Hudspeth, 2008; Kung et al., 2010) on to a channel that, in stark contrast to the non-specialist MS channels, might be designed to ignore all bilayer "noise".

III. EUKARYOTIC MS CHANNELS — BILAYER STRUCTURE, BILAYER DEFORMATION

Shortly after gigaohm patch-clamp techniques were adopted, reports of stretch-activated cation channels began appearing, first for skeletal muscle, then oocytes (Fig. 27.1A), then everywhere. Early assumptions (Guharay and Sachs, 1984) (1) that these must be MS specialists and (2) that bilayer deformation could not provide sufficient mechano-gating energy to account for the stretch-sensitive activity were dropped (Morris, 1990; Sachs and Morris 1998; Hamill and Martinac, 2001). Interrogated under cell-attached or excised-patch-clamp conditions, it emerged that most channels exhibit mechanosensitivity due, almost certainly, to bilayer deformation (Tabarean and Morris, 2002; Liu et al., 2008). Two reports in 2010 exemplify these points: (1) 20 years after cytic fibrosis transport regulator (CFTR) unitary current was first reported, CFTR was shown to be a "stretch-channel" (Zhang et al., 2010); and (2) a putative cytoplasmic linker protein was shown to be irrelevant, not mandatory, to MS responses of big calcium-activated K channel (BKCa) channels (Wang et al., 2010).

MS cation channels were soon joined by stretch-activated and stretch-inactivated potassium and anion channels, then NMDA-glutamate channels and L-type Ca current (whole-cell recordings were used as well as patches in some cases). Wherever it is sought — from fibroblasts to fish skin to fungi — MS channel activity is found (Morris, 1990, 2001a; Sachs and Morris, 1998; Hamill and Martinac, 2001; Morris and Juranka, 2007a).

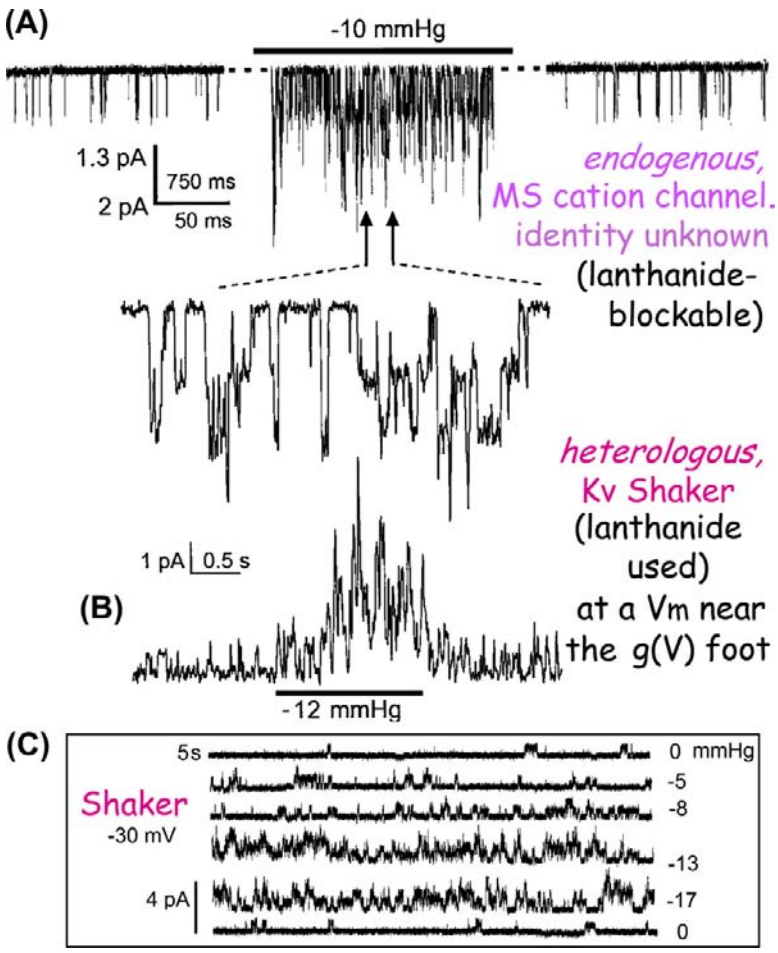

FIGURE 27.1 An unidentified "stretch-activated cation channel" and an equally stretch-sensitive *identified* "stretch-activated" potassium channel (i.e. an archetypical voltage gated K channel, Kv, Shaker WT, inactivation removed) recorded from oocyte patches, before, during and after stretch due to patch suction (A, B) and Shaker current (C) at a fixed voltage near the foot of the Shaker activation Boltzmann, without (0 mmHg), with (−5,−8,−13,−17 mmHg) and again without stretch *(see Gu et al., 2001; Morris and Juranka, 2007a for details).*

Membrane trauma (Fig. 27.2), which implies plastic (irreversible), as opposed to elastic (reversible), changes in membrane structure in response to a mechanical stimulus, can uncover inherent stretch sensitivity in channels normally mechano-protected by a cortical cytoskeleton meshwork (Morris and Horn, 1991; Wan et al., 1999; Hamill and Martinac, 2001; Morris, 2001b; Morris et al., 2006; Liu et al., 2008). Membrane trauma cannot be completely avoided during patch formation and, certainly, patch excision causes plastic changes. Structurally, the plasma membrane becomes a bleb bilayer. During progressive bleb development (Bailey et al., 2009), adhesion to cortical proteins is lost, lateral order in lipids is diminished, lateral mobililty increases and leaflet asymmetry is lost.

In situ, channels could be strongly to weakly mechano-protected, according to the status of the cortical spectrin–actin–myosin membrane skeleton (Morris, 2001b). Local modifications (cellular or subcellular, chronic or transient) might allow for developmentally or physiologically meaningful mechanical signals from channels. To establish convincingly such phenomena, however, identified MS channels with mutant mechano-phenotypes will likely be needed, as will discrete amphiphilic agents that preferentially inhibit (or activate) the identified channels during bilayer deformation (Fig. 27.3).

Disease mutant MS channels in rhythmically active cells (cardiomyocytes, smooth muscle) might provide fertile ground for in situ studies. Consider the contracting, pumping heart. Cardiac rhythm varies with mechanical load and, where causal links exist between mechanical events and cardiac electrophysiology, there is mechano-electric feedback. Voltage-gated channels (VGCs) shape cardiac rhythms and all classes of VGC have proven to be

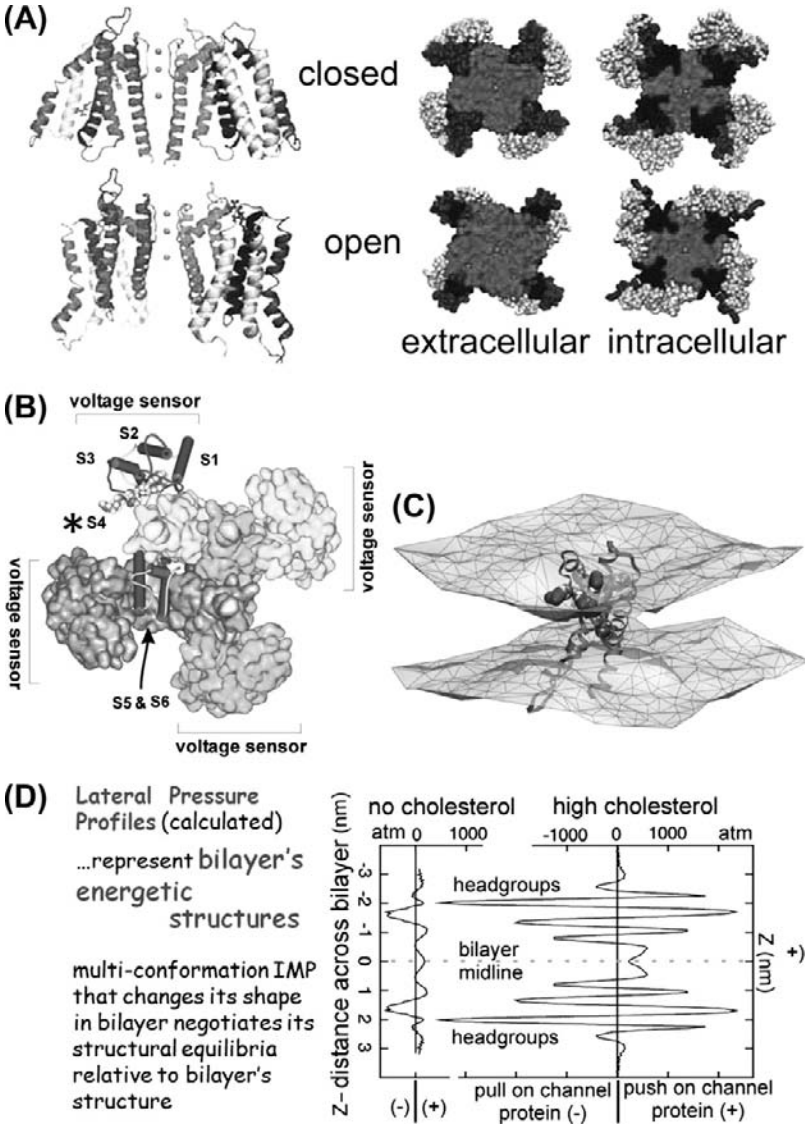

FIGURE 27.2 Protein structure and bilayer structure are interdependent; thence "MS channels". (A) Kv channel, structural models for two conformations. Voltage sensors occupy periphery; note different protein–lipid interfaces and (B) Kv channel indicating peripheral location of S4-based voltage sensors *(A, B modified from Schmidt and MacKinnon, 2008 and references therein).* (C) An activated-state voltage sensor domain locally deforms/thins the bilayer *(modified from Krepkiy et al., 2009).* (D) Different bilayers have composition-dependent structure and energetics. Lateral pressure profiles calculated for symmetric bilayers without/with cholesterol *(see Finol-Urdaneta et al., 2010 for details).*

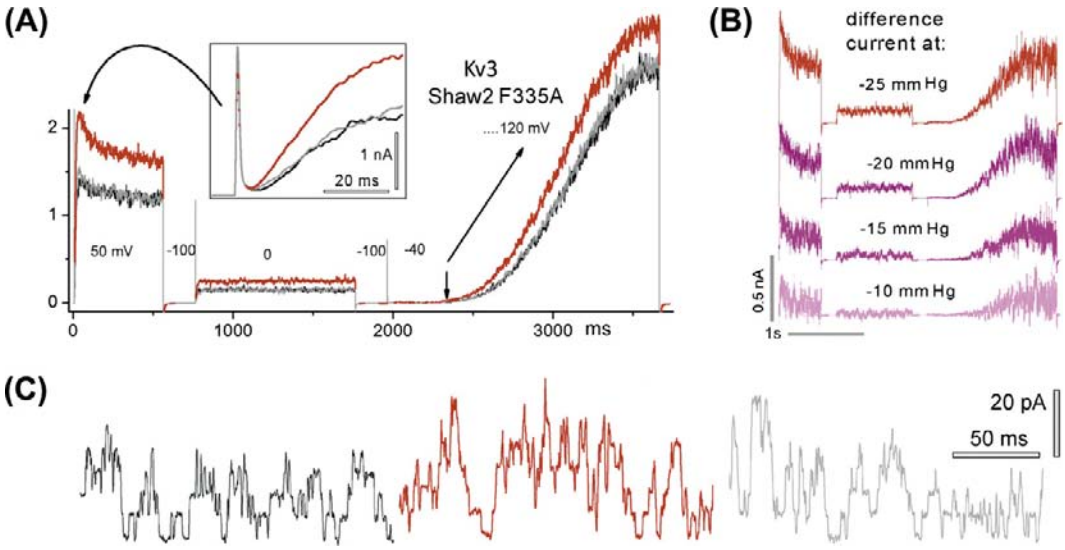

FIGURE 27.3 Kv3 channel activity, before, during and after stretch (black, red and gray traces − same meaning in Figs. 27.6, 27.7, 27.8). (A) Currents during a complex voltage protocol (large then small depolarizing steps followed by a V-ramp); boxed inset, early current); (B) stretch difference currents for different stretch intensities; (C) unitary currents at 0 mV *(see Laitko et al., 2006 for details).*

inherently MS (see Figs. 27.1B,C, 27.4−27.8). To argue a priori that the abundant and ubiquitous VGCs of the myocardium never feel the impacts of shear or stretch forces in the pumping heart would be difficult and yet, evidence showing that any specific MS channel participates in cardiac mechano-electric feedback is lacking. Molecular and genetic tools and modeling approaches now available for VGCs might be usefully exploited to make headway on this question (Morris, 2011a,b).

What can be said, a priori, about ion channel mechanosensitivity? The following: for any structurally dynamic integral membrane protein with >1 bilayer/protein interface conformation, structural deformation of the bilayer will elicit re-equilibration among protein conformations (see Fig. 27.4A). The scope of this simple notion is wide. Consider, for example, voltage-gated sodium channel (Nav) responses in the following circumstances: depletion or addition of membrane cholesterol or fatty acids (Andersen and Koeppe, 2007), traumatic brain injury (Wang et al., 2009), focused ultrasound applied to cortical brain regions (Tufail et al., 2010), stretch of ventricular myocyte sarcolemma (Banderali et al., 2010). Modified

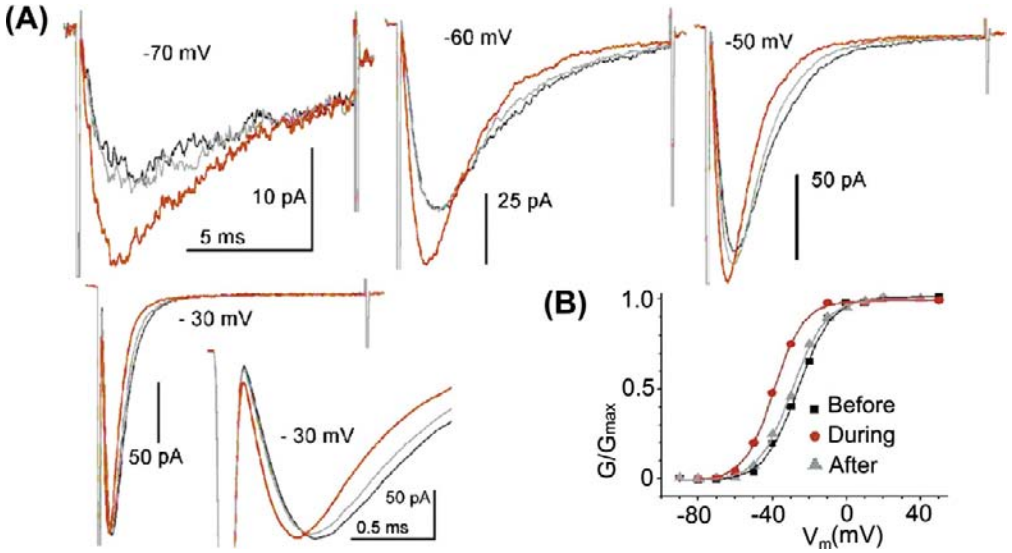

FIGURE 27.4 Nav1.5 currents before during and after stretch. (A) Voltages as labeled; expanded current at −30 mV (which is $\approx g_{max}$) reveals the "purely kinetic" effect of stretch, which is to accelerate current onset and inactivation *(modified from Morris and Juranka, 2007b);* (B) the Nav1.5 g(V) left-shifts reversibly with stretch (due to pipette suction of −30 mmHg) *(modified from Banderali et al., 2010).*

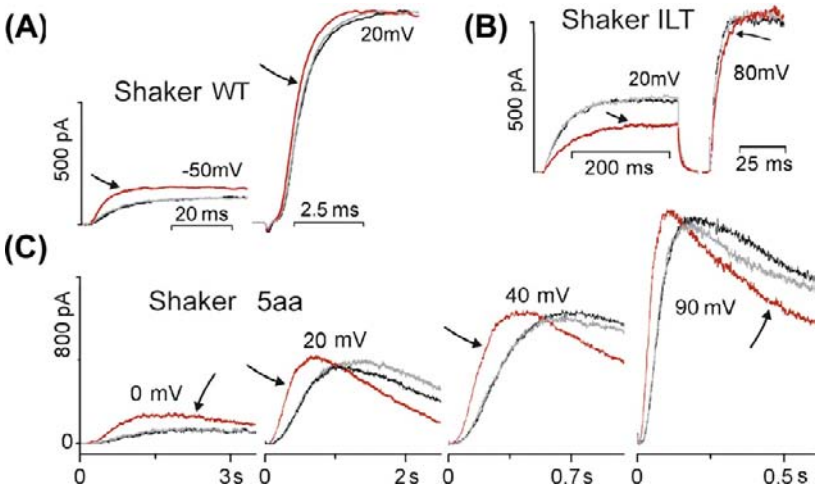

FIGURE 27.5 VGCs are MS channels in which the effects of stretch on particular transitions can be discerned. (A, B, C) Shaker WT and ILT and 5aa as described in the text. Arrows to red traces highlight the during stretch traces. Note that stretch reversibly slows current onset in ILT, while speeding it in WT (as for Nav1.5, the purely kinetic effect is evident at or beyond g_{max}). Not shown, WT g(V) reversibly left-shifts and ILT g(V) reversibly right-shifts with stretch *(see Laitko and Morris, 2004; Laitko et al., 2006 for details).*

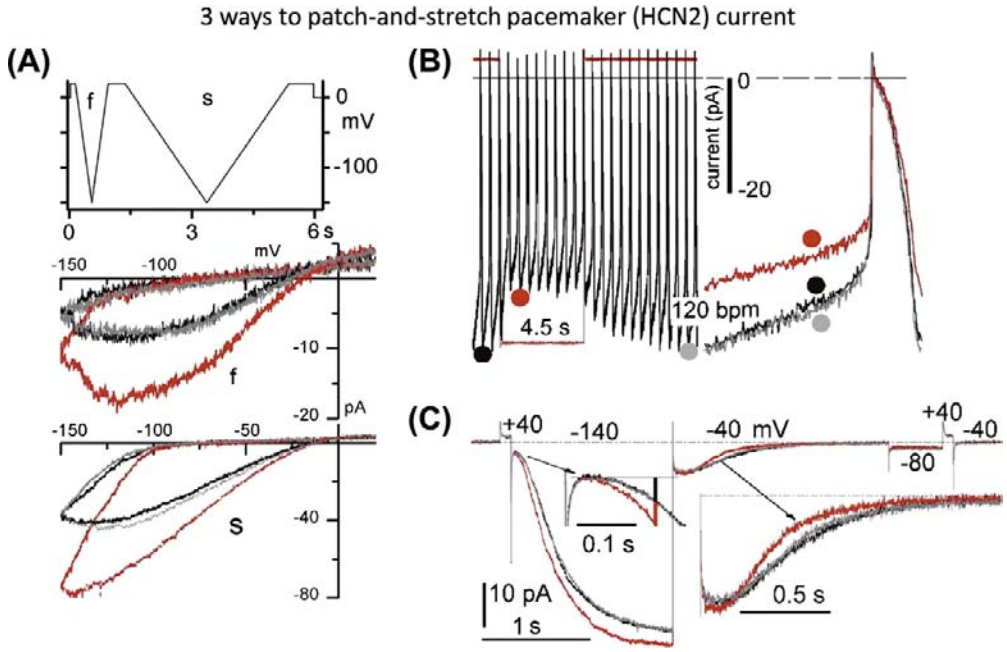

FIGURE 27.6 The pacemaker channel, HCN2, can generate both "SA" and "SI" cation current (*S*tretch-*A*ugmented, *S*tretch-*I*nhibited): (A) V-ramp clamp at two speeds; (B) passive action potential clamp (the net effect under these circumstance: a reversible *stretch-inhibition* of cation current); and (C) V-step clamp reveals stretch acceleration of both HCN2 current onset and turn-off (the turn-off is "equivalent" to Shaker turn-on vis à vis voltage-sensor movements during depolarization). If cells had a background HCN2 conductance, its stretch-accelerated turn-off could be construed as a "SI cation conductance". *(Consult Lin et al., 2007, Morris, 2011a,b, for details.)*

Nav channel activity in each scenario is explained most simply in terms of modified channel/bilayer interactions. This applies generally for VGC channels (Schmidt and MacKinnon, 2008) as well as for Nav channels in particular (Morris and Juranka, 2007a; Wang et al., 2009; Banderali et al., 2010; Morris, 2011b).

"Structure" at the angstroms to tens of nanometers scale encompasses shape, dimensional size and local charge density; together this equates closely to "mechanics". Thus, secondary and tertiary protein structure can be inferred from the set of mechanical forces needed to pull the protein apart from various angles. Applying structure=mechanics thinking to bilayers is fruitful when considering bilayer/membrane protein interfaces (e.g. Butterwick and MacKinnon, 2010). At various depths through the bilayer ("Z"-dimension), bilayer lipids collectively push or pull any embedded protein, with the sign and magnitude of these forces switching dramatically within angstroms (see Fig. 27.4D) and with the Z-dimension integral of push/pull forces in the equilibrated bilayer being zero. For any given

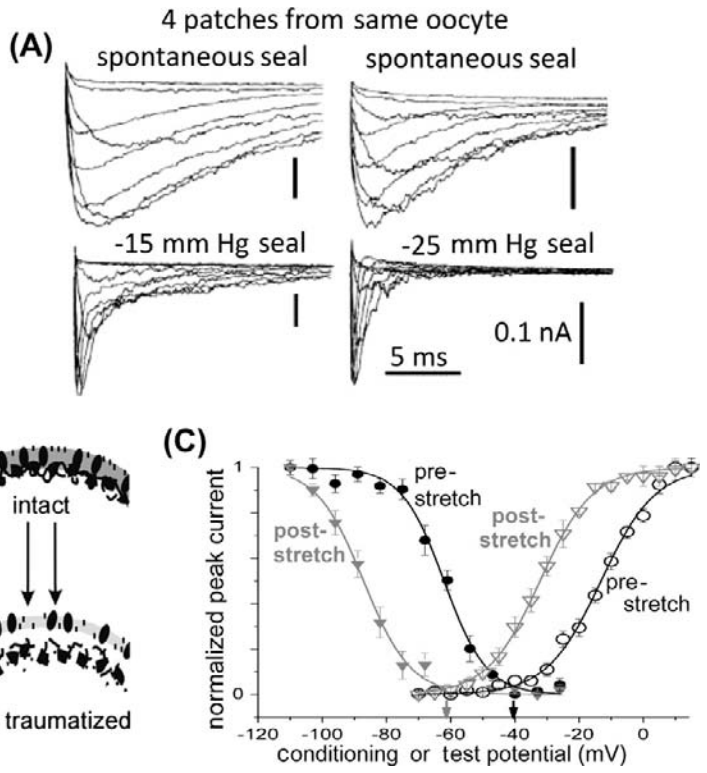

FIGURE 27.7 Membrane trauma can irreversibly alter channel behavior. Trauma here results from gigaohm seal formation accompanied by unintended (A) or intended (C) patch stretch. (A) Four patches, different trauma intensities, same oocyte, Nav1.4 (no beta subunit) current families *(see Morris and Juranka, 2007a; Tabarean et al., 1999)*. (B) Membrane trauma that induces bleb formation irreversibly alters the bilayer environment (△packing order, △thickness, △asymmetry) for channels *(see Wang et al., 2009)*. (C) For several VGCs, gating is irreversibly left-shifted by trauma as in this example for Nav1.6 activation and steady-state inactivation *(Wang et al., 2009)*.

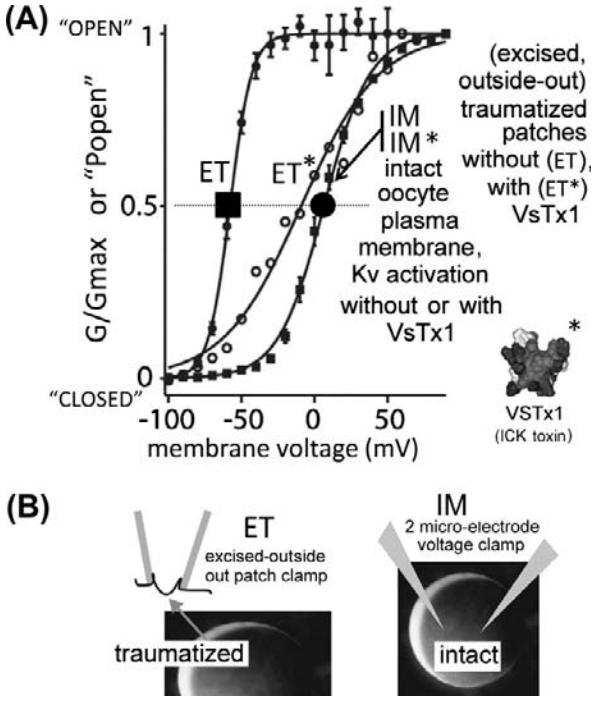

FIGURE 27.8 Bilayer mechanics allows an amphiphilic channel toxin to act like a "silver bullet", targetting only channels in traumatized membrane. A Kv channel that is irreversibly left-shifted by excision trauma (compare g(V) for IM and ET). Kv is unaffected in intact membrane (IM*) by the amphiphilic toxin, VsTx1(*), but is strongly inhibited (right-shifted) by the toxin in traumatized membrane (ET*). *(Modified from Schmidt and MacKinnon, 2008, see further discussion in Morris, 2011a,b).*

bilayer (e.g. Fig. 27.9A,B), this equilibrium "Z-force" summary is its lateral pressure profile (LPP). The prevailing equilibrium (and hence the LPP) can be perturbed by changes in the bilayer's chemical make-up, by applied physical forces (stretch, hydrostatic pressure, enforced curvature) and by temperature changes (Baumgart et al., 2003, 2011; Morris and Juranka, 2007a; Patel et al., 2010; Morris, 2011b).

LPPs are good mnemonics for these ideas, but emerge from calculations, not direct measurements. Channel activity, of course, is exquisitely accessible to measurement. If at least one of a channel's several structural states (i.e. conformations, e.g. open, closed, inactivated, desensitized, partially-open… etc.) differs at the protein/bilayer interface then any bilayer deformation at that interface has the potential to modulate the channel's time-averaged activity and a measurable activity change justifies calling the channel "mechanosensitive".

The first-cloned VGC, Shaker (Kv1), is thus an MS channel based on its response to patch stretch (see Figs. 27.1B,C and 27.7). More generally than just stretch, one can alter bilayer thickness and orderliness by pressure, temperature and by removal/addition of multitudes of different amphiphiles (e.g. fatty acids, cholesterol, sphingomyelin, alkanols, drugs, soluble gases). For "MS-channel-X", each of these bilayer mechanical perturbors could alter the probability of being open (P_{open}) in some fashion. VGCs behave this way (Tilman and Cascio, 2003;

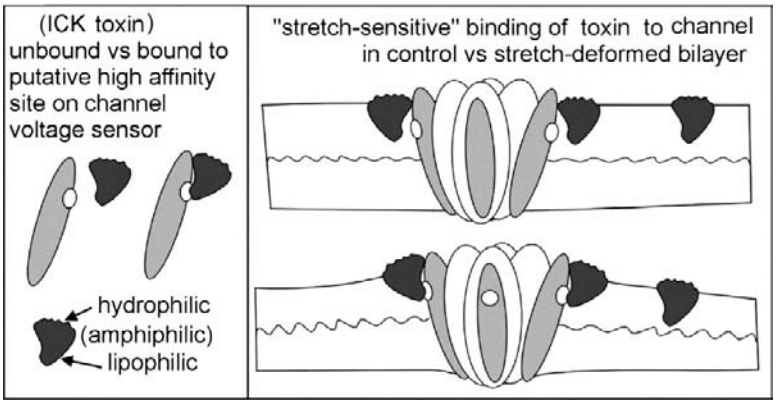

FIGURE 27.9 The efficacy of amphiphilic ICK peptide voltage sensor toxins depends on bilayer mechanics and so some of these toxins might be stretch-sensitive as cartooned here. Other classes of amphiphilic peptide agents with specific binding targets on different classes of channels or non-channel membrane proteins are likely to share this feature *(see Morris, 2011a,b).*

Andersen and Koeppe, 2007; Morris and Juranka, 2007a; Finol-Urdaneta et al., 2010), but "MS-channel-X" encompasses the whole alphabet soup of channel families, from ATP-binding cassettes (ABCs) to ligand-gated ion channels (LICs) to VGCs. Moreover, any multiconformation membrane protein with >1 lipid/bilayer interface structure could be mechanosensitive even though "read-outs" might be trickier in, say, Na/K pumps or Na/Ca exchangers than in Nav, Cav, Kv channels. Thanks to precision readouts from rhodopsin, G-protein coupled receptor bilayer mechanics are rather well understood (Soubias et al., 2010). At the brutal extreme of cytomechanics, gross perturbation of bilayers embedding rhodopsin and axonal Nav channels might explain "seeing stars" and "knock-out punches" (Wang et al., 2009).

IV. CHANNEL MECHANOSENSITIVITY – TUNING OF CHANNEL BEHAVIOR

Fine-tuning of membrane protein function via bilayer structure can have major implications for development, for physiology and for biomedicine (pathology/pharmacology/anesthesiology). Mass spectrometry-based membrane lipidomics is uncovering enormous diversity among bilayer lipids (Shevchenko and Simons, 2010). Understanding their contributions to general bilayer structure and to particular protein/bilayer interfaces will be a task of many years, but already there are big changes. Until recently, the plasma membrane bilayer was seen mostly as a two-dimensional amphiphilic solvent that reliably orients membrane proteins while simultaneously providing an osmotic barrier to define intra- from extracellular. Lipid imaging, biochemistry (Shevchnko and Simons, 2010; Baumgarten et al., 2011) plus high-resolution channel structures (Schmidt et al., 2009) and computational approaches (Marsh, 2008; Krepkiy et al., 2009; Patel et al., 2010; Baumgarten et al., 2011) have helped bilayers garner respect. No longer are VGCs routinely depicted as cylinders with fixed lateral walls or cartooned with their voltage sensors sequestered from bilayer lipids. Structural models of VGCs now depict protein/lipid interfaces regions for different conformations (e.g. open-like and closed-like for Kv channels (see Fig. 27.4A) with different lateral interfaces.

Bilayers at their most basic are established and maintained by thermally-driven processes; they continually self-organize, minimizing the system's free energy (Boal, 2001). Channel activity too is thermally-driven, as is directly evident from unitary currents, whose stochastics, quantified for different conditions, yield "channel kinetics".

e.g. for a one-Nav-channel membrane patch, step 1000X from −100 mV to 0 mV, make a 1000-item histogram of the random-lengthed times-till-first-opening, from plotted histogram obtain the characteristic "first latency" at 0 mV. Repeat for steps to different voltages, plot voltage-dependence of this kinetic parameter. Likewise for open times and closed times (Horn and Vandenberg, 1984).

Taken together, these susceptibilities to thermal energy predict that the rates at which channel conformation changes occur will vary as bilayer structure is varied. Bilayer structure and protein/bilayer interface structure are both subject to the thermal environment; protein and bilayer will therefore accommodate each other structurally (Marsh, 2008). This mutual accommodation has "real-time" consequences – i.e. consequences on the time scales characteristic for activity in any particular channel, whether P_{open} changes re-equilibrate over hundreds of microseconds or hundreds of milliseconds.

To illustrate this last point, consider how stretch affects fast and ultra-slow variants of a particular VGC channel (Tabarean and Morris, 2002). In both, stretch of a given intensity accelerates activation approximately the same-fold. Not, that is, by the absolute amount, but by the same relative amount (say, 1.6-fold). For both channels, stretch tips the relevant energy landscape the same number of kT units. In a Boltzmann equation for $P_{open}(V)$, i.e. for ([open]/[open+closed])(V), the affected term is that for the

conformational energy difference between the two states, which is "the pre-exponential term" in an Arrhenius equation for thermally-activated exponential behavior. Imagine a generic VGC in a membrane whose voltage corresponds to the activation-Boltzmann midpoint for that channel: by definition, the VGC is equally stable open or closed. Single-channel recordings under such conditions directly reveal thermal energy nudging a Kv channel (say) back and forth between open and closed. Now, change the bilayer structure via stretch (see Fig. 27.1C), for example, or via hyperbaric pressure see Morris and Juranka, 2007a) or via amphiphiles (Fig. 27.10) (Andersen and Koeppe, 2007; Finol-Urdaneta et al., 2010; Patel et al., 2010). Voltage is unchanged but the channel has a new P_{open}. These considerations apply for elastic (reversible) change and also for plastic change, like the irreversible bilayer restructuring that occurs when membranes bleb due to trauma, ischemia and inflammatory conditions (see Fig. 27.2).

Bilayer mechanics operate when a bilayer/protein interface structure impacts channel function. Outside the purview of bilayer mechanics is a lipid (e.g. an inositol phosphate) behaving as a ligand at a discrete binding site in a channel. Nevertheless, like ligands or covalent modifications, bilayer-structure-changing amphiphiles extend or "tune" the behavioral repertoire of a membrane protein (Tillman and Cascio, 2003). One gene product in three quite different bilayers is like three slightly different gene products in one bilayer. Auditory hair cells use structural tuning on many fronts to optimize mechano-electrical signaling over the auditory spectrum frequencies. In outer hair cells, electromechanical signaling involves prestin, a charge-transferring membrane protein whose in-plane expand/contract conformation changes generate cellular motion. Since cholesterol and fatty acid levels affect the rates of those transitions (Nilsen et al., 2011), it is inevitable to wonder if prestin "resonances" occur along the cochlea's low-high frequency axis, associated with a gradient of peri-prestin lipid-packing density.

V. VGCs AND THE MECHANOSENSITIVITY OF DISCRETE TRANSITIONS

Voltage sensor proteins in their activated conformations elicit a local (nanometers) thinning of the bilayer (Krepkiy et al., 2009) so, unsurprisingly, membrane stretch favors activated states of VGCs. This cavalier-sounding sentence could not have been written before late 2009 (see Fig. 27.5C) but it is now evident that applied stretch would relieve a voltage sensor of some of the bilayer-thinning work it must do to go from resting to activated. More than for most other classes of membrane protein, structure/function relations of VGCs, especially for voltage-gated K channels (Kv) (Bezanilla, 2008; Schmidt et al., 2009; Hulse et al., 2010) are getting less mysterious. Fortunately, the message of this section, that protein dynamics and

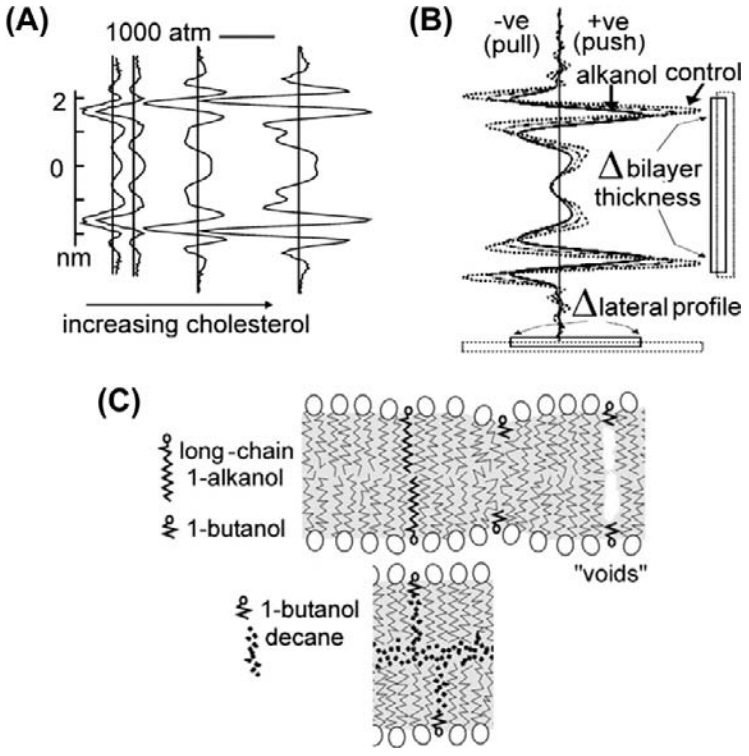

FIGURE 27.10 Calculated LPPs for two different symmetrical bilayers. To each is added increasing abundances of (A) cholesterol and (B) a short chain alkanol. In (C) top, a cartoon depicts impacts of short- and long-chain alkanols in a "bio-bilayer" or any other solvent-free membrane. The planar bilayers from which data in Figure 27.10 were obtained, did have solvent — decane; as cartooned below, a short-chain alkanol can team with decane (which prevents "void collapse") and thus behave like a long-chain alkanol *(see Finol-Urdaneta et al., 2010 for details).*

bilayer structure interdependencies are becoming reasonably explicable, extrapolates to other multiconformation integral membrane proteins (Patel et al., 2010).

Voltage-clamped VGC currents monitored for tens of microseconds to hundreds of seconds allow fast and slow VGC conformation changes to be monitored, yielding gating current, i.e. charge movement associated with voltage sensor motions, and ionic current, i.e. ion flow through a channel's selectivity filter pore or its omega-current pathways. Simultaneously monitored site-directed fluorescence signals provide read-outs about protein movements. Given the resulting database, discrete conformation changes in VGCs can be monitored in conjunction with bilayer mechanical perturbations in cells or artificial bilayers (Schmidt and MacKinnon, 2008; Finol-Urdaneta et al., 2010). Reversible patch stretch is the simplest case to consider. A stretched bilayer will have more disorderly hydrocarbon tails at mid-plane. In a stretched bilayer, the changed propensity for hydrophobic mismatch at any channel/lipid interfaces will have to be compensated.

In Kv1 and in Nav channels, the rate-limiting voltage dependent transition for activation is, it turns out, also a stretch-sensitive transition: in these VGCs, current turn-on accelerates with stretch (Laitko and Morris, 2004; Banderali et al., 2010). In other VGCs, including Cav and Kv3, stretch increases P_{open} without any change in the speed of current turn-on (Calabrese et al., 2002; Morris, 2011a). Since the rate-limiting (*slowest*) transition in the voltage activation pathway of these channels is indifferent to stretch, it probably occurs remote from the bilayer interface.

"ILT" is a mutant Kv1 channel useful because its rate-limiting activation transition happens after the one mentioned above in wild-type (WT) Kv1 channels. In WT-Kv1, each of four identical subunits responds independently to a depolarizing step. Those rate-limiting motions make activation in WT Kv1 current a fourth order process (which, as indicated already, *accelerates* with stretch). In ILT-Kv1, the next step in the activation pathway, a highly cooperative or "concerted" transition (four subunits together) has been rendered so sluggish that it becomes the slowest step. In ILT-Kv1, as a consequence, activation is a first order process and, interestingly, membrane stretch *decelerates* (see Fig. 27.7B) that single-exponential current onset (Laitko et al., 2006; Morris, 2011a).Thus, for Kv1 in a stretch-deformed bilayer, the independent sensor motions become easier to achieve while the concerted transition becomes harder.

These stretch experiments indicate that in Kv1, concerted and independent transitions both "see" the bilayer interface, while the less-understood rate-limiting activation transitions in Kv3 and Cav do not. What of inactivation transitions? In Nav1.5, the cardiac sodium channel, fast inactivation is a "particle-binding" process strongly coupled to activation but not directly affected by stretch either in WT or in disease mutant-Nav1.5 channels with impaired fast inactivation; in both, stretch accelerates fast inactivation only secondarily, via activation (Banderali et al., 2010). By contrast, for Kv1 slow inactivation (a selectivity filter-occlusion process unrelated to Nav inactivation), stretch is a direct accelerator, distinct from its action on activation (Laitko and Morris, 2004).

Short-chain alkanols (e.g. butanol) are excellent chemical agents for reversibly perturbing bilayer mechanics but, over the years, the qualitatively different, albeit comprehensible, behavior of alkanols and cholesterol in solvent-containing (planar) bilayers versus natural membranes has generated confusion (see Fig. 27.9). Recent work shows that, in KvAP channels, gating kinetics and conductance (see Fig. 27.10) respond simultaneously to these surface active agents (Finol-Urdaneta et al., 2010).

VI. BILAYER STRUCTURE IN X, Y AND Z — ONE LPP HERE, ANOTHER LPP THERE

Except in broad biochemical physics terms, plasma membrane bilayer structure in living cells is poorly understood (Shevchenko and Simons, 2010). In the X-Y plane, bilayer structures are non-uniform vis à vis lipid species distribution, leaflet asymmetry, thickness, orderliness and curvature (Baumgart et al., 2010). Sustained high curvature requires protein aggregates, asymmetry requires ATP-flippase activity. Concentrations and arrangements of lipid species of each situation remain to be characterized. Thickness and order differences readily quantified in model systems (Baumgart et al., 2003) are hard to detect in living cells; subdomains in mammalian cells at physiological temperatures are in the 10—200 nm range (Shevchenko and Simons, 2010).

Fluorescent lipid probes like laurdan align parallel to hydrophobic tails of phospholipids in bilayers, emitting at different wavelengths according to nano-environment fluidity/water content. In a fascinating precedent using laurdan, distinctive bilayer heterogeneity is seen in living transparent zebrafish embryos (Owen et al., 2010), poikilotherms for whom lower temperatures are physiological. Gut epithelial cells express transporters and channels differentially along their apical-to-basal axis, so it is fascinating to see, in situ, clear apical-to-basal polarization in the lipid orderliness of living gut cells.

Elevated cholesterol and sphingomyelin typically correlate with thicker more orderly bilayer domains and unsaturated fatty acid with thinner more disorderly bilayers. Large hydrostatic (hyperbaric) pressures increase bilayer thickness by virtue of denser lateral packing (more order), whereas bilayer stretch and elevated temperature both cause thinning and greater disorder. Short-chain

alkanols (e.g. butanol) thin native bilayers and increase mid-plain disorder while reducing surface (interfacial) tension (imposed stretch, by contrast, increases the interfacial tension). Lipid molecules differ in shape, size, internal rigidity, headgroup charge and charge dispersion. These molecular features of lipids collectively determine bilayer structure and hence the energetics (Andersen and Koeppe, 2007; Patel et al., 2010) of bilayer/protein interfaces, collectively, modulating the stability of different membrane protein conformations (Morris and Juranka, 2007a).

Channels have some lipid requirements outside the "bilayer mechanics" repertoire. Kv channel activation, for example, has an absolute requirement for phosphatidylphosphate/S4-arginine interactions (see Schmidt et al., 2009). Stereo-specific binding of amphiphilic voltage sensor toxins occurs at lipid-embedded voltage sensor sites; this, too, is not bilayer mechanics (see Finol-Urdaneta et al., 2010). Nevertheless, the global efficacy of voltage sensor toxins is strikingly sensitive to bilayer mechanics (see Figs. 27.3 and 27.11) (Schmidt and MacKinnon, 2009; see Morris, 2011b).

Specific binding of inner leaflet cholesterol molecules to discrete locations abutting the transmembrane domains of a Kir channel (Rosenhouse-Dannntsker et al., 2011) appears to be an intriguing instance of a channel using its cytoplasmic domains to regulate the LPP at its own bilayer/protein interface. Could "bilayer auto-mechanics" be the appropriate term here? It seems likely that comparable provisions will turn up in other channels.

The idea that healthy plasma membrane bilayer structure represents a controlled disequilibrium has just begun to be contemplated. Bilayers of living cell plasma membranes have asymmetrical leaflets. The exo-leaflet has little phosphatidyl serine or phosphatidyl ethanolamine and abundant phosphatidyl choline. Vice versa for the cyto-leaflet. ATP-dependent lipid flippases generate asymmetry at endomembrane stages. Properly arrayed adherent proteins help maintain the asymmetry. As has long been recognized for apoptotic blebs, the blebbed membrane of cells in traumatized, ischemic and inflamed tissue loses bilayer asymmetry, but the consequences for channel function have received little attention. In mechanically blebbed membrane, some Kv and Nav channels activate at pathologically hyperpolarized potentials (Schmidt and MacKinnon, 2008; Wang et al., 2009) (see Figs. 27.2C and 27.11A). In ischemic tissue, bilayer disorder due to ATP-starved flippases might achieve the same effect.

Having contemplated bilayer asymmetry, we turn back to symmetric spontaneously-formed bilayers and the lateral pressure profile (LPP) summary of Z-dimension energetics. Extensive formation of weak, thermally-labile bonds (van

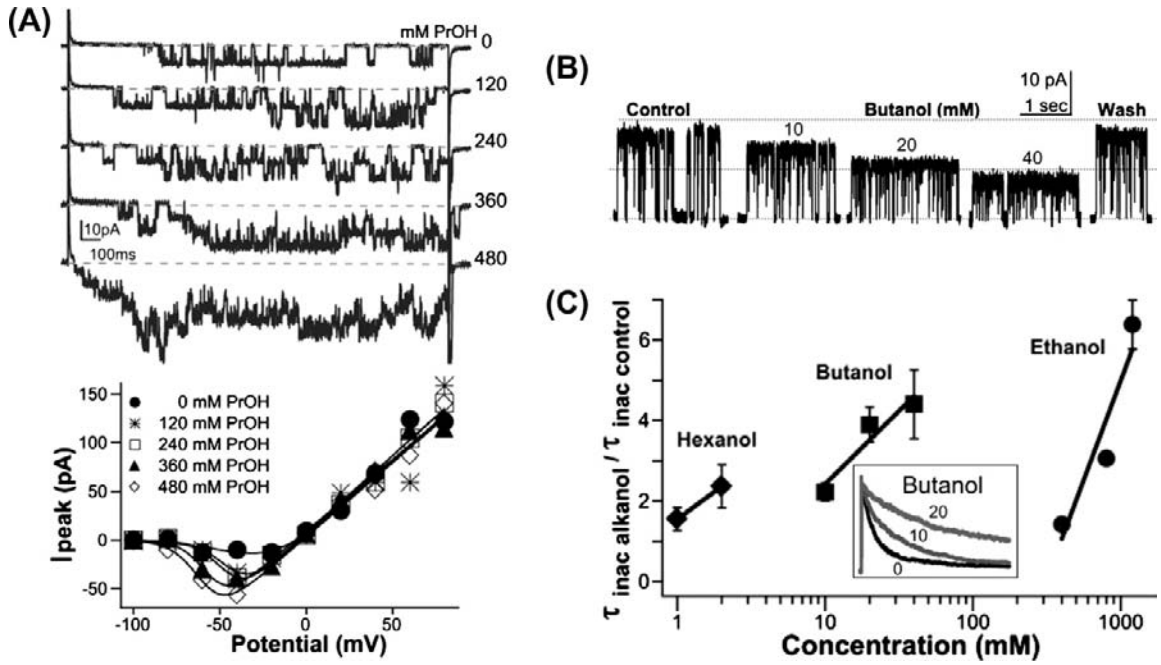

FIGURE 27.11 Surface active agents modulate gating and unitary conductance of a Kv channel in a planar bilayer. (A) KvAP currents traces with increasing abundance of propanol, and below, progressively more left-shifted I/V relations; perhaps short-range bilayer thinning required for voltage sensor activation (see Fig. 27.1C) becomes easier with small alkanols present. (B) Open KvAP in the presence of bilayers of increasing packing order (due to butanol teamed with decane; see Fig. 27.9C) shows a decreasing unitary conductance. (C) Slower entry of KvAP into its slow inactivated state (the state seen in Kv crystal structures) correlates with increased packing order due to alkanols-plus-decane (inset, normalized currents, as labeled) *(see Finol-Urdaneta et al., 2010 for details).*

der Waals, hydrophobic and electrostatic interactions and hydrogen bonds) underlies the free energy minimization that characterizes structural equilibrium. This maximizes the interactions among the lipids' hydrocarbon tails and maximizes water−water interactions. The outcome is minimal contact between water and lipid-"grease", while the lipids' charged-or-polar headgroups are constrained to the two X,Y-plane interfaces separating hydrocarbon from water.

The terms tension, surface tension, interfacial tension, pressure and force are sometimes confusing in bilayer contexts. As in protein structural energetics, forces, in energy units, are what matter. A tension is a force per unit length and pressure is force per unit area. Note that "compression" can take on contradictory context-specific usages. Some speak of a force locally compressing the bilayer where hydrophobic mismatch causes *local thinning*. Others use it for global bilayer compression under hydrostatic pressure, which causes *global bilayer thickening*. In an LPP, "lateral pressures" can be in the ±1000 atm range; these are forces acting over some infinitisimally small "area" encircling an imaginary cylinder in the Z-axis. "Living" bilayers with metabolically forced leaflet asymmetries and/or curvatures (Marsh, 2008), sustained in part by peripheral and integral membrane proteins, will be non-equilibrium structures whose LPPs need not integrate to zero. Since membrane proteins are evolutionarily "designed" for asymmetric cholesterol-rich bilayers but crystallized without them, accommodations (Marsh, 2008) to those absences can be expected in even the most elegant of high-resolution structures.

In the LPPs of Figs. 27.4 and 27.9, bilayer thickness is defined by the distance between the two strongly negative lateral pressure regions at the bilayer−water interfaces. Just exterior to that, repulsions between polar headgroups create a smaller positive pressure; positive pressures tend to compress circumferentially any embedded protein. Interacting lipid tails exclude water where pressures go negative at the two bilayer edges. These narrow zones of intense negative pressure will tend to pull circumferentially on any embedded protein (think "suction" from any embedded protein's point of view) as the lipids fight successfully to stay together. LPPs can be highly structured along Z or flatter. Whereas cholesterol dramatically increases Z-structure in an LLP, addition of short chain alkanols flattens it out. Most eukaryotic membranes are cholesterol-rich in both leaflets, as well as being asymmetrical and so, presumably, most have considerable "Z-structure". The consequence of adding short alkanols to a membrane is colloquially called "lowering the surface tension" (by analogy to the lowering to air−water interfacial [surface] tension upon addition of alcohol), but in reality, the *entire* LPP is "lowered" (i.e. flattened). I mention this to emphasize that any "surface active agent", even if it does not readily cross the bilayer, acts (energetically) *across the entire LPP* of a bilayer.

LPPs for biological (asymmetrical) bilayers would differ among cell types and among subdomains in a given cell. If membrane protein X occurs where there are different LPPs, both its basic behavior and its responses to amphiphiles will vary whenever the LPP varies. Imagine Channel-X (or GCPR-Z) in diverse neurons with different LPPs. Add amphiphile-A (e.g. propofol) or cocktail-Y (e.g. ethanol + resveratrol + tetrahydrocannabinol + dimethyletcetera). Channel-X (or GCPR-Z) will surely show LPP-dependent "side-effects" when confronted with amphiphile-A or cocktail-Y in quantities sufficient to alter LPPs. Membrane proteins whose conformation changes do not occur at bilayer interfaces could avoid amphiphile modulation but, for VGCs and GCPRs, at least, as well as for all the other MS channels, this is not an option.

VII. PHYSIOLOGY? READ WITH CAUTION. PROCEED WITH CAUTION

When it comes to physiology and MS channels, the arena is littered with flawed reports in the highest impact journals and elsewhere. An amazing dynamic range of a few centimeters of water (pipette aspiration pressure) for MS channel activity… surely that indicates exquisitely stretch-sensitive channels? No, it indicates that the so-called "manometer" was corked. Or, readily evident cut-and-paste errors at four points in a report claiming to have cloned an MS calcium-permeant channel − retracted, surely? No, just a "report clarification". The irreproducible "cloning" of ENaC and of TRPC1 as calcium-permeant MS-channels − retracted? No, but at least the latter effort was "revisited". A fundamental problem has been lack of proper controls. In our attempt to clone the stretch-activated cation channel of *Xenopus* oocytes, candidates were tested using blinded stereotyped protocols. After much effort, the dismal conclusion was that none of our clones expressed in mammalian cells yielded more MS current than is seen in controls (Wan et al., 1999; Juranka et al., 2001). Endogenous MS channels tend to activate more readily upon repeated stretch trials; in the absence of blinded stereotyped procedures, this evidently generates the results one expects/wants. Exacerbating problems in this arena have been misuse of gadolinium as a blocker and assertions that GsMTx4 is a specific inhibitor of MS cation channels (see Morris, 2011a,b).

Piezo1 and Piezo2 and CFTR, new entries to the field, and perhaps VGCs, might revitalize the cellular physiology of ion channel mechanosensitivity, though Piezos are probably mechanotransducer specialist proteins. VGCs, the best understood of the identified non-specialist MS channels, generate rhythmic signals in myocardium and smooth muscle. Perhaps arrhythmia-inducing VGC mutants with

distinctive mechano-phenotypes, plus the MS actions of voltage sensor toxins (Morris, 2011a,b) will provide leverage for assessing their possible contributions to mechanophysiology.

BIBLIOGRAPHY

Andersen, O. S., & Koeppe, R. E., 2nd (2007). Bilayer thickness and membrane protein function: an energetic perspective. *Annu Rev Biophys Biomol Struct, 36*, 107–130.

Bailey, R. W., Nguyen, T., Robertson, L., Gibbons, E., Nelson, J., Christensen, R. E., Bell, J. P., Judd, A. M., & Bell, J. D. (2009). Sequence of physical changes to the cell membrane during glucocorticoid-induced apoptosis in S49 lymphoma cells. *Biophys J, 96*, 2709–2718.

Banderali, U., Juranka, P. F., Clark, R. B., Giles, W. R., & Morris, C. E. (2010). Impaired stretch modulation in potentially lethal cardiac sodium channel mutants. *Channels (Austin), 4*, 12–21.

Baumgart, T., Capraro, B. R., Zhu, C., & Das, S. L. (2011). Thermodynamics and mechanics of membrane curvature generation and sensing by proteins and lipids. *Annu Rev Phys Chem, 62*, 483–506.

Baumgart, T., Hess, S. T., & Webb, W. W. (2003). Imaging coexisting fluid domains in biomembrane models coupling curvature and line tension. *Nature, 425*, 821–824.

Bezanilla, F. (2008). Ion channels: from conductance to structure. *Neuron, 60*, 456–468.

Boal, D. (2001). Mechanics of the Cell. Cambridge University Press.

Boucher, P. A., Morris, C. E., & Joós, B. (2009). Mechanosensitive closed-closed transitions in large membrane proteins: osmoprotection and tension damping. *Biophys J, 97*, 2761–2770.

Butterwick, J. A., & MacKinnon, R. (2010). Solution structure and phospholipid interactions of the isolated voltage-sensor domain from KvAP. *J Mol Biol, 403*, 591–606.

Calabrese, B., Tabarean, I. V., Juranka, P., & Morris, C. E. (2002). Mechanosensitivity of N-type calcium channel currents. *Biophys J, 83*, 2560–2574.

Coste, B., Mathur, J., Schmidt, M., Earley, T. J., Ranade, S., Petrus, M. J., Dubin, A. E., & Patapoutian, A. (2010). Piezo1 and Piezo2 are essential components of distinct mechanically activated cation channels. *Science, 330*, 55–60.

Cueva, J. G., Mulholland, A., & Goodman, M. B. (2007). Nanoscale organization of the MEC-4 DEG/ENaC sensory mechanotransduction channel in Caenorhabditis elegans touch receptor neurons. *J Neurosci, 27*, 14089–14098.

Finol-Urdaneta, R. K., McArthur, J. R., Juranka, P. F., French, R. J., & Morris, C. E. (2010). Modulation of KvAP unitary conductance and gating by 1-alkanols and other surface active agents. *Biophys J, 98*, 762–772.

Gray, J. A., & Sato, M. (1953). Properties of the receptor potential in Pacinian corpuscles. *J Physiol, 122*, 610–636.

Gu, C. X., Juranka, P. F., & Morris, C. E. (2001). Stretch-activation and stretch-inactivation of Shaker-IR, a voltage-gated K+ channel. *Biophys J, 80*, 2678–2693.

Guharay, F., & Sachs, F. (1984). Stretch-activated single ion channel currents in tissue-cultured embryonic chick skeletal muscle. *J Physiol, 352*, 685–701.

Hamill, O. P., & Martinac, B. (2001). Molecular basis of mechanotransduction in living cells. *Physiol Rev, 81*, 685–740.

Horn, R., & Vandenberg, C. A. (1984). Statistical properties of single sodium channels. *J Gen Physiol, 84*, 505–534.

Hudspeth, A. J. (2008). Making an effort to listen: mechanical amplification in the ear. *Neuron, 9*, 530–545.

Hulse, R. E., Li, Q., & Perozo, E. (2010). Up a hydrophobic creek with a short paddle. *Cell, 142*, 515–516.

Juranka, P. F., Haghighi, A. P., Gaertner, T., Cooper, E., & Morris, C. E. (2001). Molecular cloning and functional expression of Xenopus laevis oocyte ATP-activated P2X4 channels. *Biochim Biophys Acta, 1512*, 111–124.

Krepkiy, D., Mihailescu, M., Freites, J. A., Schow, T. V., Worcester, D. L., Gawrisch, K., Tobras, D. J., White, S. H., & Swartz, K. J. (2009). Structure and hydration of membranes embedded with voltage-sensing domains. *Nature, 462*, 473–479.

Kung, C., Martinac, B., & Sukharev, S. (2010). Mechanosensitive channels in microbes. *Annu Rev Microbiol, 64*, 313–329.

Laitko, U., & Morris, C. E. (2004). Membrane tension accelerates rate-limiting voltage-dependent activation and slow inactivation steps in a Shaker channel. *J Gen Physiol, 123*, 135–154.

Laitko, U., Juranka, P. F., & Morris, C. E. (2006). Membrane stretch slows the concerted step prior to opening in a Kv channel. *J Gen Physiol, 127*, 687–701.

Lin, W., Laitko, U., Juranka, P. F., & Morris, C. E. (2007). Dual stretch responses of mHCN2 pacemaker channels: accelerated activation, accelerated deactivation. *Biophys J, 92*, 1559–1572.

Liu, X., Huang, H., Wang, W., Wang, J., Sachs, F., & Niu, W. (2008). Stretch-activated potassium channels in hypotonically induced blebs of atrial myocytes. *J Membr Biol, 226*, 17–25.

Lundbaek, J. A., Koeppe, R. E., 2nd, & Andersen, O. S. (2010). Amphiphile regulation of ion channel function by changes in the bilayer spring constant. *Proc Natl Acad Sci USA, 107*, 15427–15430.

Marsh, D. (2008). Protein modulation of lipids, and vice-versa, in membranes. *Biochim Biophys Acta, 1778*, 1545–1575.

Morris, C. E. (1990). Mechanosensitive ion channels. *J Membr Biol, 113*, 93–107.

Morris, C. E. (2001a). Mechanosensitive ion channels in eukaryotic cells. In N. Sperelakis (Ed.), *Cell Physiology Sourcebook* (3rd ed.). (pp. 745–760) Academic Press.

Morris, C. E. (2001b). Mechanoprotection of the plasma membrane in neurons and other non-erythroid cells by the spectrin-based membrane skeleton. *Cell Mol Biol Lett, 6*, 703–720.

Morris, C. E. (2011a). Pacemaker, potassium, calcium, sodium: stretch modulation of the voltage-gated channels. In P. Kohl, F. Sachs, & M. Franz (Eds.), *Cardiac Mechano-Electric Coupling and Arrhythmias: from Pipette to Patient* (2nd ed.). (pp. 43–49) Elsevier Saunders.

Morris, C. E. (2011b). Voltage gated channel mechanosensitivity. Fact or friction? *Front Physiol*. 2:25.

Morris, C. E., & Horn, R. (1991). Failure to elicit neuronal macroscopic mechanosensitive currents anticipated by single-channel studies. *Science, 251*, 1246–1249.

Morris, C. E., & Juranka, P. F. (2007a). Lipid stress at play: mechanosensitivity of voltage-gated channels. In O. Hamill, S. Simon, & D. Benos (Eds.), *Mechanosensitive Ion Channels, Part B. Curr Top Membr, 59* (pp. 297–337).

Morris, C. E., & Juranka, P. F. (2007b). Nav channel mechanosensitivity: activation and inactivation accelerate reversibly with stretch. *Biophys J, 93*, 822–833.

Morris, C. E., Juranka, P. F., Lin, W., Morris, T. J., & Laitko, U. (2006). Studying the mechanosensitivity of voltage-gated channels using oocyte patches. *Methods Mol Biol, 322*, 315−329.

Nilsen, N., Brownell, W. E., Sun, S. X., & Spector, A. A. (2011). Effect of membrane mechanics on charge transfer by the membrane protein prestin. *Biomech Model Mechanobiol,* Mar 2.

Owen, D. M., Magenau, A., Majumdar, A., & Gaus, K. (2010). Imaging membrane lipid order in whole, living vertebrate organisms. *Biophys J, 99*, L7−9.

Patel, A., Sharif-Naeini, R., Folgering, J. R., Bichet, D., Duprat, F., & Honoré, E. (2010). Canonical TRP channels and mechanotransduction: from physiology to disease states. *Pflügers Arch, 460*, 571−581.

Phillips, R., Ursell, T., Wiggins, P., & Sens, P. (2009). Emerging roles for lipids in shaping membrane-protein function. *Nature, 459*, 379−385.

Rosenhouse-Dantsker, A., Logothetis, D. E., & Levitan, I. (2011). Cholesterol sensitivity of KIR2.1 is controlled by a belt of residues around the cytosolic pore. *Biophys J, 100*, 381−389.

Sachs, F., & Morris, C. E. (1998). Mechanosensitive ion channels in nonspecialized cells. *Rev Physiol Biochem Pharmacol, 132*, 1−78.

Schmidt, D., & MacKinnon, R. (2008). Voltage-dependent K+ channel gating and voltage sensor toxin sensitivity depend on the mechanical state of the lipid membrane. *Proc Natl Acad Sci USA, 105*, 19276−19281.

Schmidt, D., Cross, S. R., & MacKinnon, R. (2009). A gating model for the archeal voltage-dependent K(+) channel KvAP in DPhPC and POPE: POPG decane lipid bilayers. *J Mol Biol, 390*, 902−912.

Shevchenko, A., & Simons, K. (2010). Lipidomics: coming to grips with lipid diversity. *Nat Rev Mol Cell Biol, 11*, 593−598.

Soubias, O., Teague, W. E., Jr., Hines, K. G., Mitchell, D. C., & Gawrisch, K. (2010). Contribution of membrane elastic energy to rhodopsin function. *Biophys J, 99*, 817−824.

Tabarean, I. V., & Morris, C. E. (2002). Membrane stretch accelerates activation and slow inactivation in Shaker channels with S3-S4 linker deletions. *Biophys J, 82*, 2982−2994.

Tabarean, I. V., Juranka, P., & Morris, C. E. (1999). Membrane stretch affects gating modes of a skeletal muscle sodium channel. *Biophys J, 77*, 758−774.

Tillman, T. S., & Cascio, M. (2003). Effects of membrane lipids on ion channel structure and function. *Cell Biochem Biophys, 38*, 161−190.

Tufail, Y., Matyushov, A., Baldwin, N., et al. (2010). *Transcranial pulsed ultrasound stimulates intact brain circuits. Neuron, 66*, 681−694.

Wan, X., Juranka, P., & Morris, C. E. (1999). Activation of mechanosensitive currents in traumatized membrane. *Am J Physiol, 276*, C318−C327.

Wang, J. A., Lin, W., Morris, T., Banderali, U., Juranka, P. F., & Morris, C. E. (2009). Membrane trauma and Na+ leak from Nav1.6 channels. *Am J Physiol Cell Physiol, 297*, C823−C834.

Wang, W., Huang, H., Hou, D., Liu, P., Wei, H., Fu, x., & Niu, W. (2010). Mechanosensitivity of STREX-lacking BKCa channels in the colonic smooth muscle of the mouse. *Am J Physiol Gastrointest Liver Physiol, 99*, G1231−G1240.

Zhang, W. K., Wang, D., Duan, Y., Loy, M. M., Chan, H. C., & Huang, P. (2010). Mechanosensitive gating of CFTR. *Nat Cell Biol, 12*, 507−512.

This page intentionally left blank

Section IV

Ion Channels as Targets for Toxins, Drugs, and Genetic Diseases

This page intentionally left blank

Chapter 28

Ion Channels as Targets for Toxins

Kenneth M. Blumenthal

Chapter Outline

I. SUMMARY

Neurotoxins have proven to be invaluable tools in the purification of many of the best-characterized cation channels and, in addition, have contributed significantly to our understanding of how these macromolecules function in excitable tissues. This collection of molecules displays a great deal of diversity in both a chemical and a functional sense. Although many of the compounds are cationic, additional unifying structural themes are conspicuous by their absence. Even within the subgroup of polypeptide toxins, the most well-studied groups (i.e. anemone, scorpion, snail, spider and snake toxins) fail to display any intergroup relatedness at the level of primary structure. Indeed, this is rather surprising in view of the ability of (e.g.) anemone and α-scorpion toxins to compete for a common receptor. While all of the polypeptides do share a cationic character and are rich in disulfide bonds, it remains to be proven that the former property is intimately related to their activity. The latter property is almost certainly a consequence of the necessity for stabilizing small peptides in an extracellular environment. Perhaps the most striking observation is the relatedness between charybdotoxin and the Na^+ channel-directed scorpion toxins at the level of their three-dimensional structures. This clearly raises the possibility of common binding mechanisms having evolved.

Given the vast diversity of the venoms from which each of these toxins is derived and the growing array of ion channels purified and/or channel activities characterized, it is likely that new and interesting toxins will continue to emerge in the future and that their characterization will add significantly to our knowledge of channels and receptors in excitable tissues. Two areas of research that might prove especially fruitful involve using existing (or newly discovered) toxins to probe for specific channel isoforms in different tissues and using behavioral assays to identify new venom components likely to have neuronal activities. This latter approach has already been applied to components of *Conus geographus* venom with very intriguing results, among them being the discovery of the so-called "sleeper" and "King Kong" peptides. It is likely that this surface has as yet only been scratched and that future studies will unveil additional toxins that interact with new, and perhaps presently unknown, target sites.

II. INTRODUCTION

A wide variety of neurotoxins has served as potent tools used by biochemists, biophysicists, physiologists or pharmacologists interested in identifying, purifying and characterizing voltage-sensitive ion channels of excitable membranes and in understanding the molecular details of their structure and function for several decades. This

Cell Physiology Sourcebook. DOI: 10.1016/B978-0-12-387738-3.00028-7

chapter provides brief descriptions of some of these toxins, focusing on their chemical natures, similarities and differences, target macromolecules and effects on transmembrane ionic fluxes. In this chapter, the ion channels are used as an organizational framework and, in those cases where multiple-toxin binding sites have been demonstrated with a single channel, the relationships among these sites are discussed. A number of excellent reviews on this subject have been published in recent years, including a volume of *Toxicon* (49(2), pp. 123-292; Catterall, 2000; Escoubas and Rash, 2004; Olivera, 2006; Catterall et al, 2007; Nicholson, 2007; Swartz, 2007) devoted to gating modifiers.

Toxins are diverse both chemically and functionally. They include an ever-expanding array of polypeptides derived from marine invertebrates and terrestrial arthropods, alkaloids of diverse structures, heterocyclic compounds of the tetrodotoxin family and synthetic insecticides. Functionally, these molecules are equally diverse. Toxins have been characterized that modify the voltage dependence of activation and inactivation gating or block ion fluxes and a growing number have multiple actions. Thus, in addition to being useful probes for purification of channel constituents, they have contributed significantly to our understanding of how these various processes are coupled to one another.

III. VOLTAGE-GATED SODIUM CHANNELS (VGSCS; $Na_V1.x$)

The neuronal sodium channel consists of three polypeptides having molecular masses of 260 (α), 36 (β_1), and 33 kDa (β_2) (Catterall, 2000); whether the smaller subunits are present in all channel isoforms remains unresolved. All of the toxin binding sites characterized to date appear to be associated with the α subunit, reconstitution of which into planar lipid bilayers restores most of the activities of the native channel. Microinjection of mRNA encoding this subunit into *Xenopus* oocytes results in expression of sodium channels which are functionally similar, though not identical, to their natural counterparts and the same is true for mammalian cell lines which stably express the α subunit.

The α subunit is organized into four repeated structurally homologous domains, each containing 300−400 amino acid residues. Each domain includes six transmembrane helices (designated S1−S6) as well as a seventh region (the P-loop), whose length varies among the four domains, that lies at least partially within the membrane. P-loop sequences provide the channel's outer vestibule and selectivity filter and also contribute to the inner lining of the conducting pore. Although no crystal structures have been solved for VGSCs, the MacKinnon laboratory has provided several structures for potassium channels to which they are homologous (Doyle et al, 1998; Jiang et al 2003a; Long et al, 2005), all showing the presence of a non-transmembrane pore helix in this region, followed by a turn and β-strand. Several models of the VGSC pore region which include such a structure have been described (Lipkind and Fozzard, 1994, 2000; Penzotti et al 1998; see below). Several classes of toxin binding sites have been identified on the α subunit by both biochemical and mutagenic analyses, pore blockers interacting with all four channel domains while gating modifiers appear to bind primarily to domains I, II, and IV. Figure 28.1 depicts the putative transmembrane organization of the α subunit of this channel; as described in subsequent sections, this organization is shared by known K^+ channels and the α_1 subunit of the Ca^{2+} channel as well.

A series of elegant analyses, carried out mainly by Catterall, clearly established the presence of four independent classes of neurotoxin binding sites on the rat brain $Na_V1.2$ channel (Catterall, 2000; also, see Summary, Table 28.1). These include sites for: (1) the classic channel inhibitors tetrodotoxin and saxitoxin; (2) activating alkaloids, such as batrachotoxin and veratridine; (3) polypeptide (α) toxins from scorpion and sea anemone venoms, which delay channel inactivation; and (4) a distinct set of scorpion (β-toxins) and tarantula toxins that alter the voltage dependence of channel activation and inactivation. Each class is discussed below.

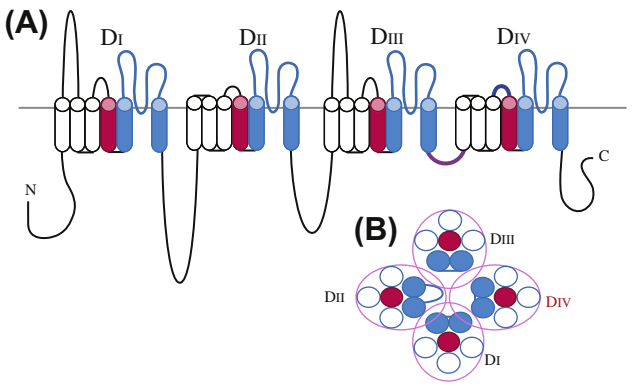

FIGURE 28.1 (A) Transmembrane topology of the voltage-sensitive sodium channel. The channel consists of four homologous domains, each containing six transmembrane segments in addition to a P-loop which contains the channel's outer vestibule. Segments S5 and S6 of each domain, shown in blue, comprise the inner lining of the channel, while S4, shown in red, represents the main voltage sensor. The intracellular linker connecting domains III and IV has been shown to be involved in fast inactivation of the channel. The binding site for tetrodotoxin (site 1) contains elements of all four P-loops; batrachotoxin binding (site 2) determinants are found in the C-terminal portions of the S6 segments of domains I and IV; α-scorpion and anemone toxins bind (site 3) to the S3−S4 loop of domain IV; and β-scorpion toxins (site 4) to the corresponding loop of domain II. (B) Proposed arrangement of the four domains, looking down, with the pore in the center.

TABLE 28.1 Toxin Effectors of Voltage-Sensitive Sodium Channels

Toxin	Binding Affinity	Functional Effect
Tetrodotoxin	1−5 nM (Nerve)	Blockade
	1−10 μM (Heart)	Blockade
Saxitoxin	1 nm (Nerve)	Blockade
	100 nM (Heart)	Blockade
Alkaloids		
Batrachotoxin	0.25 μM	Persistent activation
Grayanotoxin	>1 mM	Persistent activation
Veratridine	50 μM	Persistent activation
Polypeptides		
α-Scorpion toxins	1−2 nM	Delayed inactivation
β-Scorpion toxins	0.5 nM	Modified activation gating
Anemone toxins	10−1000 nM	Delayed inactivation
Tarantula toxins	0.1−100 nM	Multiple
Dinoflagellate Toxins		
Brevetoxin	μM range	Shifts activation
Ciguatoxin	μM range	Depolarization
Goniopora	50 νM	Delayed inactivation

IIIA. Site 1: Tetrodotoxin, Saxitoxin and μ-Conotoxin

The presence of a paralytic toxin in newts, pufferfish and other organisms has been known for well over 50 years and the structure of this compound (Fig. 28.2), called tetrodotoxin, was first described in 1964. Narahashi, Moore and collaborators demonstrated that the toxicity of tetrodotoxin (TTX) was attributable to its ability to block the rapid increase in sodium conductance associated with the rising phase of the action potential in frog muscle. Because TTX and the structurally related dinoflagellate-derived saxitoxin (STX) bind to the channel with high affinity (1−5 nM for the neuronal isoform), a property that is essentially unaltered by detergent solubilization, their discovery provided biochemists with an essential probe for purification of the channel protein. Because of the availability of TTX and STX, purification, biochemical characterization and molecular cloning of voltage-dependent sodium channels from a variety of sources have been accomplished over the past two decades.

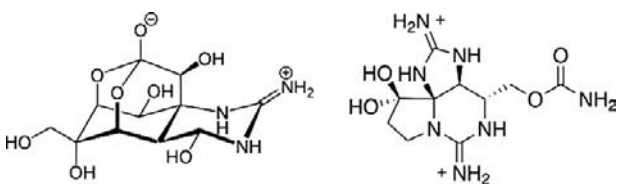

FIGURE 28.2 Structures of the guanidinium channel blockers tetrodotoxin (left) and saxitoxin (right). The guanidinium groups of both compounds are essential for binding to site 1, as are hydrogen bonds contributed by several of the axial hydroxyl groups.

Tetrodotoxin and saxitoxin are heterocyclic guanidinium compounds that bind reversibly and with high affinity ($K_d = 1 - 5$ nM) to a site accessible from the external face of neuronal and muscle Na^+ channels. This K_d agrees well with that obtained from analysis of the effects of these toxins on Na^+ currents in these tissues. Binding of TTX and STX to cardiac Na^+ channels is of much lower affinity, with K_d values on the order of 0.1−1 μM. The cardiac channels are thus defined as being TTX-resistant. Analyses of channels by site-directed mutagenesis (Noda et al., 1989; Satin et al., 1992) have implicated Cys-374 and Arg-377 of the cardiac channel as being important for their decreased TTX sensitivity.

Binding of TTX and STX blocks Na^+ currents and was originally thought to involve interaction of toxin with the ionized form of a channel carboxyl group, which Hille proposed was associated with the channel *selectivity filter*. However, the notion that the carboxylate(s) important in TTX binding was also a part of the selectivity filter was abandoned when it was shown that chemical modification of channel carboxylates, which abolished binding, had no effect on ion selectivity. Subsequent structure−function analysis of TTX and STX, using both natural and synthetic analogs (Mosher, 1986; Shimizu, 1986), clearly delineated the importance of the guanidinium group of TTX (and the corresponding 7, 8, 9 guanidinium of the bifunctional STX) for activity. In addition, the C4, C9 and C10 hydroxyl groups of TTX and the C12 hydroxyl of STX are required. It is assumed that these hydroxyl groups form hydrogen bonds to as yet unknown acceptor sites on the channel. The TTX binding site is located near the external face of the channel and may lie outside of the transmembrane field.

Site-directed mutagenesis of both Na^+ channels and K^+ channels indicates that this region is important both for ion selectivity and binding of channel-specific toxins. Replacement of Arg 377 of the TTX-resistant cardiac ($Na_V1.5$) channel by asparagine results in a small increase in TTX-sensitivity (Noda et al., 1989), whereas the mutation of Cys 374 to tyrosine renders the channel approximately 700-fold more sensitive to TTX (Satin et al., 1992). This latter result raises the possibility that TTX and STX owe their affinity not to ion pairing between their positively charged guanidinium groups and channel carboxylates but rather to interactions with the π-clouds contributed by a cluster of electron-rich aromatic residues located near the

channel mouth. Analogous models have been proposed to account for acetylcholine binding to the nicotinic acetylcholine receptor and tetraethylammonium binding to a variety of potassium channels. However, it is clear that interaction with aromatic residues is not the *sole* binding determinant, since mutagenesis has also identified a carboxyl group, Glu 387, essential for high-affinity TTX binding in the brain $Na_V1.2$ channel. Like Cys 374 and Arg 377, this residue is also located in the SS2 region of the P-loop.

The corresponding S5−S6 linker regions from domains III and IV are also important determinants of ionic selectivity, as shown by the finding that the mutations Lys 1422 to glutamate and Ala 1714 to glutamate give the $Na_V1.2$ channel an ionic selectivity similar to that of a Ca^{2+} channel. Interestingly, mutagenesis has also been used to show that the S5−S6 region of *shaker* K^+ channels is directly involved in both ion transit and interaction of inhibitors such as tetraethylammonium (TEA) and charybdotoxin. Tyr 379 of the K^+ channel RBK-1 has been identified as an important determinant of tetraethylammonium (TEA) binding (MacKinnon and Yellen, 1990), while the introduction of a tyrosine at position 449 of the *shaker* H4 channel greatly increases its sensitivity to TEA. Thus, a leitmotif stressing the importance of aromatic residues in the binding of cationic ligands to ion channels is emerging.

As already noted, the three-dimensional structure of $Na_V1.x$ channels is unknown. However, several modeling studies based on K-channel structures and/or on effects of mutagenesis on toxin binding affinities have predicted elements of the pore structure. Based on the structure of the KcsA channel, Lipkind and Fozzard (2000) have postulated the importance of a hydrophobic core involving residues Leu-396, Gln-399 and Trp-402 ($Na_V1.4$), in addition to the carboxylates and aromatic residues already mentioned, in stabilizing tetrodotoxin binding.

A structurally unrelated peptidic toxin, designated μ-conotoxin or geographutoxin, is a competitive inhibitor of STX binding to muscle, but not nerve, Na^+ channels ($K_d < 100$ nM in muscle versus >1 μM in brain; Cruz et al., 1985; Ohizumi et al., 1986). μ-Conotoxin is a 22-residue, hydroxyproline-containing peptide, tightly cross-linked by three disulfide bonds. Its three-dimensional structure, based on two-dimensional nuclear magnetic resonance (NMR) measurements and simulated annealing protocols, has been described. The overall structure includes a series of tight turns in the N-terminal region and a short stretch of right-handed helix, while the core of the peptide encompasses what the authors refer to as a disulfide cage. A key feature of the structure is that the cationic side chains of arginines 1, 13 and 19, and lysines 8 and 16 all project into solution, away from the core of the molecule as defined by the disulfide bonds. Analysis of synthetic variants of μ-conotoxin has shown that Arg 13 is essential for activity: even conservative replacement by lysine reduces potency by about 10-fold. In contrast, Arg 19 can be replaced by lysine with essentially no change in activity, while substitution at Arg 1 yields an intermediate result (Cruz et al., 1989). It is interesting that binding of both TTX/STX and the μ-conotoxins is at least partially dependent on guanidinium functions, suggestive of a dispersed positive charge being more effective than a point charge in this respect.

Unlike TTX and STX, the binding of μ-conotoxin is dependent on membrane potential, with K_d decreasing *e*-fold for every 34 mV depolarization (Cruz et al., 1989). TTX/STX-resistant (i.e. cardiac) channels are likewise resistant to μ-conotoxins. More recently, a mutated form of μ-conotoxin has been used as a monitor of distance between the voltage sensor and channel pore (French et al., 1996).

IIIB. Site 2: Batrachotoxin, Grayanotoxin, Veratridine and Related Compounds

The existence of low molecular weight hydrophobic compounds having dramatic effects on the gating properties of voltage-sensitive Na^+ channels has been known for over 20 years. The most commonly used of these alkaloids are batrachotoxin, grayanotoxin and veratridine (Fig. 28.3). Despite their differing biological origins (respectively, skin secretions of the frog *P. aurotaenia, Lilaceae* and *Ericaceae* species) and dose−response curves (IC_{50}s are approximately 0.25, 10 and 50 μM for

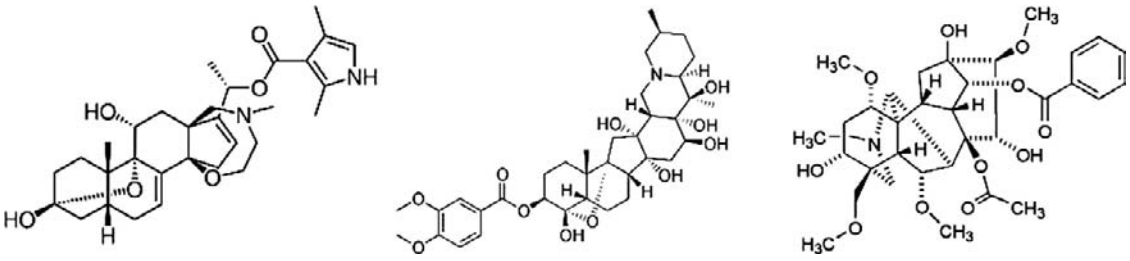

FIGURE 28.3 Structures of some major alkaloid agonists of the voltage-sensitive sodium channel. Left, batrachotoxin; center, veratridine; right, aconitine.

batrachotoxin, grayanotoxin and veratridine), these molecules have very similar effects on channel function. All appear to interact at a common binding site, which is allosterically coupled to both the TTX binding site described in the previous section and the α-scorpion toxin site to be discussed later (Catterall, 1977). Binding of any of the alkaloids to this site causes persistent activation of the channel, leading to membrane depolarization. In addition, alkaloid-treated channels display a more relaxed ionic selectivity than do their naive counterparts. Thus, while the permeability order of untreated Na^+ channels is Na^+: guanidinium:K^+: $Rb^+ = 1{:}0.13{:}0.09{:}0.01$, veratridine increases the relative permeability for guanidinium, K^+ and Rb^+ by factors of 2.7, 4.5, and 10, respectively. Qualitatively similar results are obtained with the other alkaloids of this class and with combinations of alkaloid and polypeptide toxins from scorpion or sea anemone venoms.

The steroidal alkaloid batrachotoxin (BTX) was purified and characterized by Witkop, Daly and their coworkers. In collaboration with Albuquerque, the effects of BTX were measured in a variety of tissues including axons, brain slices and isolated synaptosomes, neuromuscular junctions, heart papillary muscle and cardiac Purkinje fibers. Batrachotoxin binding has been measured directly in rat brain synaptosomes using a tritiated derivative and the measured density of binding sites correlates well with that for TTX and STX. Binding of BTX to this site is competitively inhibited by veratridine with a K_i very similar to the $K_{0.5}$ for veratridine's activation of the channel. Because BTX acts from either side of the membrane, it had been speculated that its binding site might lie within the lipid bilayer and a photoactivatable derivative of batrachotoxin has been demonstrated to specifically label a site within the S6 transmembrane segment of domain I of the rat brain channel (Trainer et al., 1996). Site-directed mutagenesis of $Na_V1.2$ has identified F1764 as an important binding determinant (Linford et al., 1998) and additional mutations in the same domain IV S6 segment have similar effects (Wang and Wang, 1999). Thus, the BTX binding site, which also interacts with local anesthetics, is most likely composed of residues in the C-terminal portions of channel S6 segments.

As discussed later, fluorescent derivatives of BTX have also been important for measuring distances between the various toxin-binding sites by resonance energy transfer experiments. Because the effects of BTX on membrane potential are dependent on the presence of extracellular Na^+ and are blocked by treatment with TTX, they are attributed to the toxin's ability to cause voltage-dependent Na^+ channels to activate at the resting potential and to persist in the activated state. BTX also causes increased permeability to larger cations, consistent with allosteric coupling between the BTX binding site and the selectivity filter of the Na^+ channel.

Other alkaloids that appear to interact with the BTX site with similar functional effects include veratridine, grayanotoxin (GTX) and aconitine. While structurally distinct from one another, these highly hydrophobic compounds do have certain common features, such as the bridged ring systems and esterified aromatic moieties found in BTX, veratridine and aconitine (see Fig. 28.3). In the case of BTX, both the bridge and the esterified group are essential for activity.

For all of these toxins, the available data strongly suggest that interaction of a single toxin molecule per channel is sufficient for activation. The known biological effects of these toxins are ascribed to their ability to interact with the voltage-dependent Na^+ channel, although only BTX binding has been measured directly. Catterall proposed that the alkaloids bind preferentially to the activated conformation of the Na^+ channel, shifting a preexisting equilibrium between active and inactive states toward the former. Thus, toxin action would best be approximated by the allosteric model of Monod, Wyman and Changeaux, in which the binding energy for a given toxin is expressed as a shift in the voltage dependence for channel activation. As will be discussed later, conformational changes in the channel induced by binding of toxins have been directly demonstrated, thus supporting this model.

IIIC. Sites 3 and 4: Scorpion, Sea Anemone and Spider Toxins

An effect of scorpion venom on frog Na^+ channels was first demonstrated about 40 years ago and individual toxins from *Androctonus* venom were purified and sequenced beginning in the mid-1970s. Subsequently, scorpion toxins active on the sodium channel have been purified from the venoms of *Androctonus*, *Leiurus*, *Centruroides*, *Tityus* and *Buthus* species. While these toxins exhibit certain common structural features, the pharmacology of the *Androctonus* and *Leiurus* toxins is quite distinct from that of the corresponding polypeptides from *Centruroides* and *Tityus.* Toxins from the former (α-toxin) group delay or abolish channel inactivation and thus delay repolarization of the membrane via binding to neurotoxin site 3, while the latter (β-toxin) group shifts the voltage dependence of activation to more negative potentials as a result of binding to site 4 (in the Catterall nomenclature), thereby yielding spontaneous activity. α-Toxin binding is dependent on membrane potential, with K_d values in the nanomolar range at the resting potential. In contrast, β-toxin binding is potential-independent and generally of slightly lower affinity. The pharmacologic distinction between the α- and β-toxins is somewhat unexpected in view of the close relationship among these toxins at the level of covalent and tertiary structure. Moreover, recent data raises the possibility that

```
Representative α-toxins
AaH-1       KRDGYIVYPN NCVYHCVPP- -CDGLCKKNG GSSGSSCFLV -PSGLACWC- KDLPDNVPIK
AsH-2       VKDGYIVDDV NCTYFCGRNA YCNEECTKLK GESGY-CQWA SPYGNACYCY K-LPDHVRTK
Lqq-V       LKDGYIVDDK NCTFFCGRNA YCNDECKKKG GESGH-CQWA SPYGNACWCY K-LPDRVSIK
BoT-1       GRDAYIAQPE NCVYECAQNS YCNDLCTKNG ATSGY-CSWL GKYGNACWC- KDLPDNVPIR
BoT-XI      VKDGYIVDDV NCTYFCGRNA YCHEECTKLK GESGY-CQWA SPYGNACYCY K-LPDHVRTK

Consensus   N+DGYIUOXX NCβΦXCXOOO YCOOXCOKXO GOSGO-CXUU OXOGXACΦCY KDLPDOVOβ+

AaH-1       DTSRKCT
AsH-2       GPGP-CH
Lqq-V       EKGR-CN
BoT-1       IPGK-CHF
BoT-XI      GSPGRCH

Consensus   OXOO+CO

Representative β-toxins

CsE1  KEGYLVEKTG CKKTCYKLGE NDFCRECKWK HIGGSYGYCY GFGCYCELGL PDSTQTWPLP -NKCT
TssG  KEGYLMDHEG CKLSCFIRPS -GYCRECGIK K- GSSGYCA WPACYCYGLP NWVKVWDRAT TNKC
```

FIGURE 28.4 Primary structures of representative α- and β-scorpion toxins. Sequences are shown in the single letter code and disulfide bonds link Cys 12 to Cys 63, Cys 16 to Cys 36, Cys 22 to Cys 46 and Cys 26 to Cys 48 in both groups. Numbering is based on the sequence of AaH-II. Highlighted positions are either invariant or occupied by functionally equivalent residues within the α or β subgroup. In the consensus sequence, the coding is: + = Cationic residue; O = Polar residue; X = Character undefined; U = Non-polar residue; Φ = Aromatic residue; β = Branched side chain. AaH, *Androctonus australis* Hector; Lqq, *Leiurus quinquestriatus quinquestriatus*; BoT, *Buthus occitanus Tunetanus*; CsE, *Centruroides sculpturatus* Ewing; TsS, *Tityus serrulatus.*

some site 4 determinants may be found within the membrane (Smith et al., 2005).

The primary structures of representative scorpion toxins are depicted in Fig. 28.4. All scorpion toxins characterized to date are cationic polypeptides of molecular mass approximately 7000 Da and contain four disulfide bonds whose integrity is essential for activity; in addition, they display a significant degree of sequence homology, with approximately 30% of all positions being conserved among the known α-toxins. The β-toxins, exemplified by *Centruroides* toxin 3, are generally similar to those of the α group, but display less extensive homology. It is likely that much of this sequence conservation within a group is essential simply for allowing proper folding of these toxins, similar to results obtained with the conotoxin family, since structure—function analyses of the scorpion toxins have identified relatively few "essential" residues and the three-dimensional structures of representatives of each group show a great deal of similarity in the peptide backbones.

The three-dimensional structures of many scorpion toxins are now known, including members of both the α- and β-classes (Fig. 28.5). As might be anticipated from the highly cross-linked nature of these proteins, both possess a dense core of secondary structure connected by two of the four disulfides; this core contains three strands of antiparallel β-sheet (residues 1—4, 37—41 and 46—50) and a short strand of α-helix (residues 23—32). In addition to several loops that protrude from this core region, a prominent feature of both structures is a relatively non-polar surface

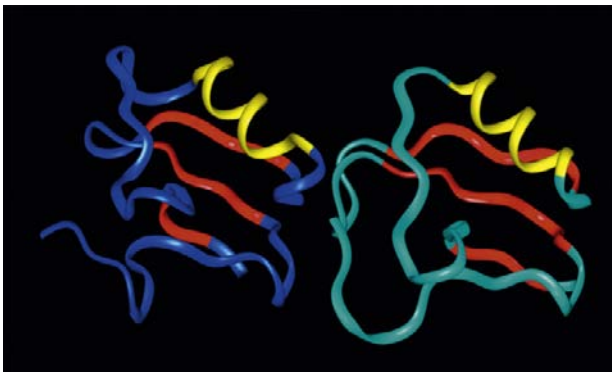

FIGURE 28.5 Comparison of the backbone structures of the site 3 toxin from *Androctonus australis Hector* (right, pdb1PTX) and the site 4 toxin from *Centruroides sculpturatus Ewing* (left, pdb1JZA). The 3-stranded β-sheets of each molecule are colored in red and the single α-helix in yellow. The most divergent portions of these structures are in the loop regions connecting the well-defined core elements.

region, which contains a number of conserved aromatic residues. Because chemical modification of sites external to this surface region is, in general, not deleterious to toxin function and because Lys 56, referred to previously, lies within it, Fontecilla-Camps and coworkers first suggested that this region was essential for receptor binding. Interestingly, this surface is fairly well conserved in both the α- and β-toxins, despite their distinct pharmacologies and non-overlapping binding sites. Indeed, all of the structural features discussed here are common amongst scorpion toxins regardless of binding site or species specificity.

With respect to structure–activity correlations, it has been shown that alkylation of Lys 56 of AaH-I is correlated with its inactivation, suggesting the importance of a cationic group at this position in the α-scorpion toxins and that modification of Arg 2 and Arg 60 likewise results in inactivation. However, chemical modification using group-specific reagents has been relatively uninformative, perhaps owing to the fact that these toxins lack the super reactive residues seen in enzymes, for which this approach has been more successful. Site-directed mutagenesis of cloned α-toxin genes has pointed to an amphiphilic binding site containing a central hydrophobic region surrounded by cationic residues (Zilberberg et al., 1997).

Binding determinants for the α-scorpion toxin LqqV have been mapped to the domain I S5–S6 region of $Na_V1.2$ by photoaffinity labeling, and to the S3–S4 linker of domain IV by mutant cycle analysis (Rogers et al., 1996). The latter site has also been shown to bind site 3 anemone toxins (see below) whose pharmacologic effect is identical to that of LqqV (Benzinger et al., 1998). Interestingly, mutations in the domain IV S3–S4 linker give rise to hyperkalemic periodic paralysis, a condition in which channel inactivation is inhibited. The dominantly heritable disorder paramyotonia congenita, which displays an electrophysiologic phenotype identical to that of an anemone or scorpion toxin-treated, wild-type channel, likewise maps to a set of missense mutations in the S3–S4 linker region of domain IV of the muscle sodium channel (Cannon and Corey, 1993; Chahine et al., 1994; Yang et al., 1994).

In addition to the α-scorpion toxins, site 3 also binds a variety of polypeptide toxins derived from marine invertebrates: the best characterized of these is a diverse family of sea anemone toxins derived from *Anemonia*, *Anthopleura*, *Stichodactyla* and *Radianthus* species. Under appropriate conditions, certain of these polypeptides can function as cardiac stimulants. While also basic and rich in disulfides, the anemone toxins differ from those discussed previously in being somewhat smaller (46–50 residues versus 60–65 residues) and having three, rather than four, disulfides. Moreover, despite the wealth of structural information now available, no sequence homology has been found between neurotoxins from scorpions and anemones. Representative anemone toxin sequences are shown in Fig. 28.6.

The solution structures of several anemone toxins have been solved (Fig. 28.7). Examination of these structures, all having a core of twisted, four-stranded, antiparallel β-pleated sheet (residues 2–4, 18–23, 31–34 and 42–47 in anthopleurin A numbering), demonstrate unequivocally that anemone and scorpion toxins are structurally unrelated. Nonetheless, anemone and α-scorpion toxins have very similar pharmacologies and display mutually competitive binding to Na^+ channel site 3, suggesting that at least a limited degree of relatedness may yet remain to be found. It may be significant that all anemone toxins contain a large loop region (approximately residues 9–20) whose solution structure is very poorly defined and which contains at least two of the amino acid residues known to be important determinants of anemone toxin-binding affinity. In addition, biophysical analyses have provided evidence for the exposure of a number of hydrophobic residues on the surface of homologous anemone toxins. In anthopleurin B, the functional roles played by some of these residues have been analyzed using site-directed mutagenesis of a synthetic gene which encodes the toxin polypeptide. These studies have clearly demonstrated that both Leu 18 and Trp 33 play important roles in regulating high-affinity binding of this toxin to both neuronal and cardiac sodium channels and further show that two other exposed hydrophobic sites, Ile 43 and Trp 45, are external to this binding epitope. Thus, the former pair of residues may act as the functional equivalent of the hydrophobic surface implicated in scorpion toxin binding (Dias-Kadambi et al., 1996a,b). Indeed, charge-neutralizing mutations of all the ionizable groups in this toxin reveal that the contribution to affinity made by hydrophobic contacts is far more

```
AsI         GAPCKCKSDG PNTRGNSMSG TIWV- FGCP SGWNNCEGRA - HGYCCKQ
AsII        GVPCLCDSDG PSVRGNTLSG IIWL- AGCP SGWHNCKKHG PTIGWCCKQ
AsV         GVPCLCDSDG PSVRGNTLSG ILWL- AGCP SGWHNCKKHK PTIGWCCK
ApA         GVSCLCDSDG PSVRGNTLSG TLWLYPSGCP SGWHNCKAHG PTIGWCCKQ
ApB         GVPCLCDSDG PRPRGNTLSG ILWFYPSGCP SGWHNCKAHG PNIGWCCKK
ShI         -AACKCDDEG PDIRTAPLTG - TVDLGSCN AGWEKCASYY TIIADCCRKKK
RpII        -ASCKCDDDG PDVRSATGTG - TVDFWNCN EGWEKCTAVY TPVASCCRKK

Consensus   XUXCUCDODG POXROOOUOG βUXUXXXGCP SGWHCKXXXX PβUGΦCC+
```

FIGURE 28.6 Primary structures of representative sea anemone toxins. Sequences are shown in the single letter code, with the numbering based on the sequence of anthopleurin A. Disulfide bonds link Cys 4 to Cys 46, Cys 6 to Cys 36 and Cys 29 to Cys 47. Highlighted positions are either invariant or contain functionally conservative replacements. In the consensus sequence, the coding is + = Cationic residue; O = Polar residue; X = Character undefined; U = Non-polar residue; Φ = Aromatic residue; β = Branched side chain. As, *Anemonia sulcata*; Ap, *Anthopleura xanthogrammica*; Sh, *Stichodactyla helianthus*; Rp, *Radianthus paumotensis*.

FIGURE 28.7 Solution structure of the site 3 anemone toxin Anthopleurin-B from Protein DataBase file 1APF. Original data from Monks et al. (1995). Structure. 3, 791-803. The backbone ribbon depicts the convergence of 20 NMR models, with individual backbones included to indicate the disorder region (Residues 9−20) in which several residues essential for affinity have been demonstrated. This loop region is conserved in all site 3 anemone toxins of known structure.

significant than any involving electrostatic interactions. Surprisingly, even Arg 14, which is conserved in all known anemone toxins, is revealed by mutagenesis to play at most a minor role in defining binding affinity (Khera and Blumenthal, 1994).

While sea anemone and α-scorpion toxins bind to the channel in a membrane-potential-dependent manner and their binding sites overlap at least in part, β-scorpion toxins bind to a demonstrably distinct site on the same protein and their binding is potential-independent. β-Scorpion toxins are also pharmacologically different from their homologous α-toxin counterparts in that their binding modifies the voltage-dependence of channel activation, rather than inhibiting inactivation. The β-toxin binding site has been mapped by mutagenesis to the S3−S4 linker of domain II, leading to the proposal that these toxins function by trapping the domain II voltage sensor in its deployed conformation (Cestele et al., 1998). Perhaps the most thorough structure−function analysis of the β-toxins has been carried out by alanine scanning mutagenesis of toxin Css4 (Cohen et al., 2005). This work identified a group of aromatic residues (Y24, Y40, Y42, F44 and W58) whose replacement diminishes binding to $Na_V1.2$ by 100−1000 fold without discernible effect on toxin structure. The last four of these residues are located in the second and third β-strands of Css4, forming a surface hydrophobic cluster. In addition to these aromatic sites, mutation of E28 decreases binding affinity by several hundredfold. Both Y24 and E28 are found in the single α-helix of Css4. Somewhat surprisingly, in view of the cationic nature common among scorpion and anemone toxins, no essential positively-charged residues were identified.

Over the past 5−10 years, a number of new polypeptide toxins which modify sodium channel function have been isolated from tarantula venoms and characterized in some detail. These toxins typically contain about 30 amino acid residues and share a three disulfide, cystine-knot (ICK) structural motif and are homologous to other polypeptides which modify K-channel function. Protx-II, the most thoroughly characterized of these toxins, shifts the voltage-dependence of $Na_V1.5$ channel activation in the depolarizing direction and decreases G_{max} at all potentials tested (Edgerton et al., 2008); in the $Na_V1.7$ channel, it appears to delay inactivation as well (Xiao et al., 2010). Mutant cycle analysis of Protx-II binding to $Na_V1.5$ indicates that previously characterized channel sequences required for binding of site 3 or 4 toxins are not important for Protx binding (Smith et al., 2007), although a similar study of $Na_V1.2$ suggests an interaction with the S3−S4 loop of domain II which is known to be essential for binding of site 4 toxins (Sokolov et al., 2008). The interaction of Protx-II with its target channels appears to be dominated by hydrophobic interactions, perhaps suggesting that its binding site lies wholly or partially within the membrane (Smith et al., 2005).

The existence of multiple sodium channel genes that display tissue-specific expression in mammals is well established. It is thus logical to inquire into the isoform selectivity of the toxins discussed above, a question whose answer is of great potential significance in drug design. It is clear, for example, that the cardiac channel $Na_V1.5$ is at least 100 times more sensitive to the sea anemone toxin anthopleurin-B than are the neuronal and muscle channels (Khera et al., 1995) and that the peripheral channel $Na_V1.7$ is two to three orders of magnitude more sensitive than any other Na-channel to the tarantula toxin Protx-II (Smith et al., 2005, 2007). Similarly, μ-conotoxins display a very high selectivity for muscle sodium channels.

IIID. Relationships among Sites 1−4

All of the known polypeptide toxin binding sites are structurally distinct from those for the alkaloid activators

and guanidinium inhibitors. However, it is well-established that these sites communicate with one another. The distances between the various toxin sites have been estimated using resonance energy transfer between fluorescent derivatives of the bound ligands. In addition to confirming that the α- and β-toxin sites are unique and separated by about 22 Å, these studies indicate that the TTX site is some 33 Å removed from that for β-toxins and the BTX site lies about 37 Å distant from that of α-toxins. Both fluorescence resonance energy transfer experiments and direct analyses of binding affinities to the various sites support the existence of allosteric interactions between sites 1 and 2, 1 and 3, and 2 and 3. A very recent study, using mutagenically truncated site 4 toxin, is consistent with allosteric interactions between sites 3 and 4 as well (Cohen et al., 2008).

IIIE. Other Toxins Specific for the Na^+ Channel

A variety of non-proteinaceous substances of diverse (and in some cases, unknown) structure has been shown to interact with the Na^+ channel at sites distinct from those discussed previously. These include lipid-soluble dinoflagellate toxins (brevetoxins, ciguatoxin and maitotoxin), the *Goniopora* toxins and the pyrethroid insecticides. The brevetoxins induce the Na^+ channel to open at membrane potentials of −80 to −160 mV and also abolish rapid inactivation; these effects lead to both generation of repetitive action potentials and ultimately membrane depolarization. Both effects are blocked by TTX. Analyses of brevetoxin binding suggest the existence of a fifth ligand site on the channel, since brevetoxin binding fails to displace toxins bound to sites 1−4. The physiologic effects of ciguatoxin are very similar to those of the brevetoxins, while the mechanism of maitotoxin toxicity is unresolved at this time. *Goniopora* toxins, while not completely characterized, appear to be protein in nature, with molecular weights between 12 000 and 19 000 being reported from different preparations. The mode of action of at least one of these proteins appears to be similar to that of sea anemone toxins, but there is evidence that multiple *Goniopora* toxins with distinct molecular targets exist. Finally, the pyrethroids delay inactivation via interaction with a site distinct from that for polypeptide toxins having the same effect. Physiologic effects of pyrethroids are antagonized by TTX.

IV. VOLTAGE-ACTIVATED AND Ca^{2+}-ACTIVATED POTASSIUM CHANNELS

The use of molecular genetics, electrophysiology and x-ray crystallography has had an enormous impact on our knowledge of the structure, function and diversity of voltage-gated ion channels, and nowhere is this more apparent than in the family of potassium channels ($K_V1.x$−$K_V4.x$). However, despite the enormous power of the genetic approach, the ability of polypeptide toxins specific for this family of channels to distinguish among subtypes is proving an invaluable tool. Both polypeptide and non-proteinaceous blockers, such as tetraethylammonium ions and 4-aminopyridines, were important tools for development of structural models of the K^+ channel pore and the predictions made by these models have been largely borne out by channel crystal structures.

While voltage-dependent Na^+ channels exist in a relatively small number of molecular forms, the diversity seen in K^+ channels is vastly greater: some are ligand-coupled, while others are activated by either Ca^{2+} or depolarization. A large number of channels seem to exist even within this last category. In *Drosophila*, K^+ channels are encoded by genetic loci designated as *shaker*, *shal*, *shab*, *shaw* and *eag* and mammalian counterparts for each of these channel types have been identified. *Shaker* apparently encodes channels of the rapidly inactivating (or A) type and transcripts from this locus display alternative splicing. It seems likely that this gives rise to channel forms that differ with respect to virtually all important properties: pharmacology, voltage-dependence and unit conductance. Multiple transcripts from the *shab* locus have also been observed and the gene products have many of the properties associated with the delayed rectifier channel. The *shal* and *shaw* genes seem to encode A-type and delayed rectifier channels, respectively.

The channels encoded by *shaker* and related genes have many structural features in common with the Na^+ channels discussed above and these proteins display a limited degree of homology at the amino acid level, mostly within their transmembrane regions. In both Na^+ and K^+ channels, the channel "subunit" contains six putative transmembrane helices with the N-terminus being cytoplasmic, and a pore loop located between helices S5 and S6. Helix S4, which contains a series of cationic groups separated by two hydrophobic residues, serves as the main voltage sensor, perhaps with some participation by charged residues in S2 and S3. As with the Na^+ channel, sequences joining the helices designated S5 and S6 are thought to provide the inner lining of the pore and a great deal of evidence that these residues also provide the binding sites for channel-specific toxins has been accumulated over the years. The most obvious structural difference between these channels is that, whereas the Na^+ channel α subunit has a molecular mass of about 260 kDa and contains some 1800 amino acid residues grouped into four homologous domains, the K^+ channel monomer is approximately one-quarter this size. While the monomeric unit of the K^+ channel is thus small relative to its Na^+ and Ca^{2+} counterparts, co-expression of mRNAs encoding distinct channel isoforms in *Xenopus* oocytes results in the appearance of functional channels

having intermediate properties, strongly suggesting that the physiologically relevant form of this channel is a non-covalent tetramer. Crystallographic studies have confirmed this prediction. The possibility of functional diversity arising from both alternative splicing and formation of hetero-oligomeric channels thus arises.

In 1998, MacKinnon's laboratory solved the crystal structure of the *Streptomyces lividans* K^+ channel, KcsA (Doyle et al., 1998) and several other K^+ channel structures, including those from eukaryotes, have since been described (Jiang et al., 2003a; Long et al., 2005). While KcsA is only about 30% as large as the eukaryotic voltage-gated K^+ channels, it displays significant homology within the putative pore-forming regions to (e.g.) the *shaker* and other eukaryotic voltage-gated channels. As a result, the *S. lividans* channel has been useful for modeling the three-dimensional structure of the eukaryotic pore. In the KcsA channel, the pore region contains a 10-residue α-helix (the pore helix) whose C-terminus is oriented toward the center of the pore and is joined to the C-terminal transmembrane helix by a 20-residue linker that lacks regular secondary structure. The helices flanking the pore region are proposed to be analogous to the S5 and S6 helices of eukaryotic K^+ channels. The KcsA-based models of the K^+ channel pore regions were subsequently validated as the structures of archeal and eukaryotic channels were solved.

Most of the known K^+-channel-specific toxins have been purified from scorpion, honeybee, spider and snake venoms (Table 28.2). The first such agent to be characterized was purified by Miller from *Leiurus* venom, and given the colorful, if non-descriptive, name charybdotoxin (Miller et al., 1985). Homologs of this polypeptide have been found in venoms from *Leiurus* (scyllatoxin and agitoxin), *Androctonus* (kaliotoxin), *Buthus* (iberiotoxin) and *Centruroides* (noxiustoxin) species. In addition, the honeybee peptides apamin and mast cell degranulating peptide and a homologous family of snake (*Dendroaspis*) dendrotoxins have been shown to have K^+-channel-blocking activity. Analogous to the case for sodium channels, the potassium channel toxins from scorpion venom comprise a homologous family in which essentially the only *absolutely* conserved residues are involved in disulfide bond formation (Fig. 28.8). Thus, one would reasonably expect these toxins to fold into a generally similar overall structure, but to differ in detail. It is therefore not surprising to realize that at least some of the K^+ channel toxins are able to distinguish among channel subtypes. The honeybee toxins and dendrotoxins display no homology to any of the scorpion polypeptides.

Charybdotoxin (ChTX) was first identified in 1985 as a polypeptide from *Leiurus* venom capable of inhibiting Ca^{2+}-activated K^+ channels from skeletal muscle and is the founding member of a family of structurally homologous peptide blockers of K^+-channels. As such, the following discussion of peptidic K-channel blockers will use ChTX as a paradigm. The three-dimensional structure of ChTX was solved by NMR spectroscopy in 1991 (Fig. 28.9; Bontems et al., 1991a,b; 1992). Its major features include a small, triple-stranded β-sheet encompassing residues 1—2, 25—29 and 32—36 linked by disulfide bonds (Cys 13—Cys 33 and Cys 17—Cys 35) to an α-helix including residues 10—19. Surprisingly, however, this overall fold is quite similar to those of the *Centruroides* and *Androctonus* Na^+-channel-specific toxins for which crystal structures had been obtained during the 1980s. Structural features shared by these toxin families include three disulfide bonds occurring in similar positions and orientations, the triple-stranded β-pleated sheet (residues 1—4, 37—41 and 46—50 of *Centruroides* toxin versus residues 1—2, 25—29 and 32—36 of charybdotoxin), the single strand of α-helix (residues

TABLE 28.2 Polypeptide Blockers of K^+ Channels

Toxin	Channel Type	K_d	Function
Charybdotoxin	Ca^{2+}-activated Voltage-sensitive	Low nM 140 pM	Blocker
Iberiotoxin	Ca^{2+}-activated (BK)	140 pM	Blocker
Kaliotoxin	Ca^{2+}-activated (BK)	250 pM	Blocker
Noxiustoxin	Ca^{2+}-activated (BK)	20 nM	Blocker
Scyllatoxin	Ca^{2+}-activated (SK)	>300 nM	Blocker
Apamin	SK	10—400 pM	Blocker
Dendrotoxins	Voltage-sensitive	100 pM	Blocker
Hanatoxin SgTx1	K_V1.x K_V2.1	High nM 2 μM	Gating modifier Gating modifier

(A) Charybdotxin-like

```
ChTX          QFTNVSCTTS KECWSVCQRL HNTSRGK-CM NKKCRCYS
ScTX             AFCNL- RMCQLSCRSL GLL--GK-CI GDKCECVKH
KaTX        GVEINVKCSGS PQCLKPCKDA GM-RFGK-CM NRKCHCTP
IbTX          QFTDVDCSVS KECWSVCKDL FGVDRGK-CM GKKCRCYQ
NxTX          TIINVKCTSP KQCSKPCKEL YGSSAGAKCM NGKCKCYNN

Consensus     XXβOUOCOXX +XCXXXC+OU XXXOXGO CU OOKCKCΦ
```

(B) ICK Motif Gating Modifiers

```
Hanatoxin          ECRYLFGGCK TTSDCCKHLG ---CKFRDKY CAWDFTFS
Hainatoxin 4       ECLGFGKGCN PSNDQCCKSS NLVCSRKHRW CKYEI
ProTx-1            ECRWLWGGCS AGQT-CCKHL V--CSRRHGW CVWDTGFS
SgTx-1             TCRYLFGGCK TTADCCKHLA ---CRSDGKY CAWDGTF
```

FIGURE 28.8 Primary structures of selected polypeptide toxins specific for K^+ channels. Sequences are depicted in the single letter code, with disulfide bonds linking Cys 7 to Cys 28, Cys 13 to Cys 33 and Cys 17 to Cys 35 in charybdotoxin. Highlighted residues are invariant within a class. In the consensus sequence, the coding is + = Cationic residue; O = Polar residue; X = Character undefined; U = Non-polar residue; Φ = Aromatic residue; β = Branched side chain. ChTX, charybdotoxin; ScTX, scyllatoxin; KaTX, kaliotoxin; IbTX, iberiotoxin; NxTX, noxiustoxin; αDTx, α-dendrotoxin; Dtx_1, dendrotoxin I; kalicludine, K^+ channel blocker from *Anemonia sulcata*. (B) Primary sequences of selected gating modifiers of K_V channels. In the ICK motif to which these toxins conform, disulfide bonds link Cys2—16, Cys9—21 and Cys15—28.

FIGURE 28.9 Solution structure of charybdotoxin. The backbone ribbon depicts the single α-helix (blue) and two strands of the β-sheet (cyan) against which it is docked (pdb2CRD). *(Original data reported in Bontems et al. (1992). Biochemistry. 31, 7756-7764.)*

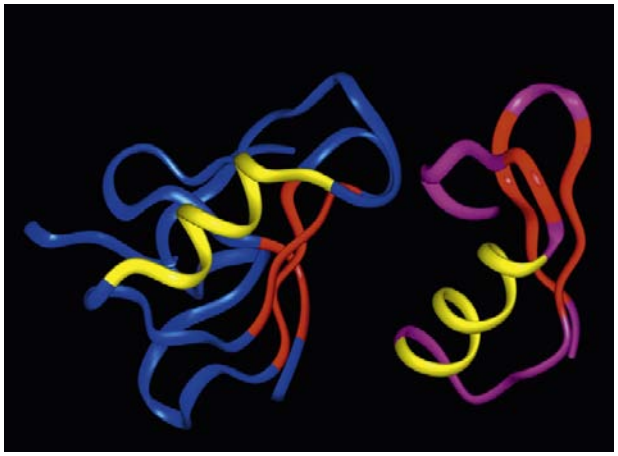

FIGURE 28.10 Comparison of the backbone structures of *Centruroides* toxin (left, pdb2JZA) and charybdotoxin (right, pdb2CRD), color coded to highlight the conservation of a single α-helix (yellow) docked against a three-stranded β-sheet (red).

23—32 versus 10—19) and a significant proportion of extended structure (Fig. 28.10). The differences in comparing the structures of these long and short neurotoxins are most pronounced in loop regions connecting the elements of defined secondary structure. Thus, the scorpion neurotoxins as a group share a common structural motif, apparent only at the level of three-dimensional structure, regardless of the nature of their target channel. The apparent similarities in channel folding thus seem to be mirrored in the structures of their "ligands". Interestingly, this motif appears to be similar to one observed in insect defensins, small peptides produced in response to injury that are thought to play a role in protecting insects against bacterial infections (Bontems et al., 1992). It seems counterintuitive that the scorpion toxins, despite their vastly different pharmacologies, display conservation of tertiary structure, while anemone and scorpion α-toxins, which show very similar pharmacologies, do not. Perhaps this is simply indicative of the fact that our knowledge of the molecular interactions important for productive binding of

these toxins to their target sites remains incomplete (however, see the following). However, it should be noted that the very recently characterized K^+-channel-blockers from anemones (e.g. kalicludines and kaliseptines), which are functional homologs of charybdotoxin and dendrotoxin, appear to share neither this structural motif, sequence homology, nor even disulfide connectivities.

Because ChTX possesses a net charge of +5, it was predicted that ionic interactions with the channel would be important in its binding. This prediction is supported by the observations that: (1) ChTX binding affinity is decreased 100-fold in media of high ionic strength, owing to decreased toxin association; and (2) chemical modification of the channel with the carboxylate-specific reagent trimethyloxonium (TMO) ion greatly reduces ChTX binding. The structure of the *S. lividans* channel reveals that the binding site for cationic toxins like ChTX is rich in acidic amino acid residues. Affinity also depends on membrane potential, with ChTX preferring the open conformation by approximately sevenfold. More recent studies with charybdotoxin mutants are consistent with hydrophobic interactions between channel sites and Met 29 and Tyr 36 of ChTX as also being important for binding.

In addition to BK channels, charybdotoxin also blocks voltage-dependent K^+ channels in frog ganglia and SK channels from *Aplysia*. However, its best known application has been as a molecular ruler useful for mapping the pore of the *shaker* channel in the days before channel crystal structures were available (Goldstein et al., 1994). Mutant cycle analyses using both ChTX and the homologous agitoxin-2 identified both anionic and hydrophobic channel residues whose mutation diminished binding significantly. This work, and that of others, yielded a low-resolution structural map of the channel's outer vestibule. Although these studies are now largely of only historical interest, it is important to realize that the structural models of the pore which arose from these studies has been largely validated by subsequent crystal structures of archaeal and eukaryotic K^+-channels (Doyle et al., 1998).

Other polypeptide K^+-channel blockers may have more restricted specificities than ChTX. For example, iberiotoxin (IbTX), isolated from *Buthus* venom is 70% homologous to ChTX, but significantly less basic. IbTX inhibits ChTX binding to smooth muscle non-competitively, consistent with it having a distinct binding site, and appears to recognize only Ca^{2+}-activated channels in a variety of tissues (Galvez et al., 1990). Studies with chemically-synthesized chimeras of the two toxins suggest that C-terminal sequences of each toxin dictate channel specificity to a large degree: a construct containing the N-terminal 19 residues of ChTX and the C-terminal 18 from IbTX has IbTX-like properties, and vice versa. Two additional scorpion toxins have been shown to target preferentially the BK-type channel. Kaliotoxin, recently purified and characterized from *Androctonus* venom, is approximately 50% homologous to ChTX, IbTX and noxiustoxin and has been shown to suppress the whole-cell Ca^{2+}-activated K^+ current in mollusk and rabbit sympathetic nerve. The affected channel is insensitive to both apamin and dendrotoxins and is blocked by ChTX and TEA. Noxiustoxin (NxTX), purified from *Centruroides* venom, is 50% identical to ChTX, but due to its relatively low affinity in many systems and its apparent interaction with a multiplicity of channel types, it seems unlikely that NxTX will be widely useful for channel purification and/or discrimination studies.

In recent years, several spider toxins, most notably hanatoxin, versustoxin (VsTX) and SgTx, have become important tools in potassium channel research. This family of structurally homologous gating modifiers all shift the voltage dependence of activation upon interaction with the channel's S3−S4 linker (Swartz and MacKinnon, 1997) and as such have been important probes of channel gating mechanisms. In particular, use of VsTX and hanatoxin has helped demonstrate the commonality of the so-called paddle motif in gating of voltage-sensitive channels (Jiang et al., 2003b; Alabi et al., 2007, Bosmans et al., 2008). Their structures, essentially consisting of a series of loops stabilized by three disulfide bonds, all conform to the ICK motif (Fig. 28.11). Another common feature of these toxins

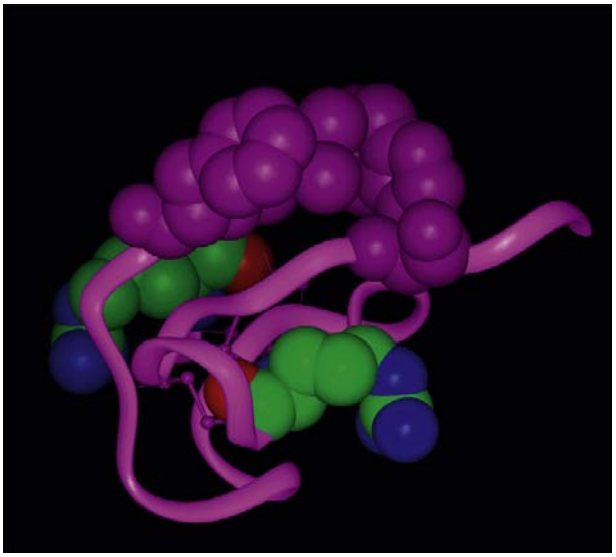

FIGURE 28.11 Solution structure of the ICK-motif K^+-channel gating modifier SgTx-1 (pdb1LA4). The backbone of this polypeptide is largely devoid of regular secondary structure, such that toxin folding is absolutely dependent on the integrity of the three disulfide bonds, shown in ball and stick rendering. Amino acid residues shown in CPK rendering have been shown by Wang et al. (2004) to be essential for binding affinity and include the hydrophobic bulge (Leu5, Phe6 and Trp30) at the top of the molecule plus two cationic residues (Arg3 and Arg22) located on the opposite face. A homologous hydrophobic bulge has been shown to be required for activity in a second ICK toxin, Protx-II. *(Smith et al., 2007)*

is the presence of a hydrophobic bulge protruding from the surface of the molecule (Lee et al., 2004) which contains several residues essential for toxin binding (Wang et al., 2004). These properties have led to the proposal that the spider toxin binding site is at least partially membrane-embedded (Milescu et al., 2007; Lee and MacKinnon, 2004). SgTX-1 is the most thoroughly characterized of these spider toxins in terms of structure−function relationships.

Apamin is an 18-residue polypeptide containing two disulfide bonds; it has an α-helical core comprising residues 9−15 flanked by regions rich in β-turns. Analysis of synthetic analogs of apamin highlights the importance of arginines 13 and 14 for activity. Electrophysiologic analyses and ion flux experiments indicate that apamin is directed against the SK channel in guinea pig hepatocytes, murine neuroblastoma cells and cultured rat muscle cells. Iodinated apamin has been used to demonstrate the existence of high affinity ($K_d = 10 - 400$ pM) receptors in rat brain, with affinity increasing with $[K^+]$. The chemical nature of the apamin-binding protein has been studied by radiation inactivation and chemical cross-linking, but the results have been inconclusive, with multiple polypeptides being labeled.

Dendrotoxins comprise yet another family of toxins which target the K^+ channel and, at present, are the only snake (*Dendroaspis* species) toxins known to do so. Although larger than the scorpion and spider toxins, dendrotoxins (Dtx; four homologs known) are otherwise grossly similar, being highly cationic molecules containing 57−59 amino acid residues cross-linked by three disulfide bonds. Structurally, the Dtxs are clearly related to the small subunit of β-bungarotoxin and to bovine pancreatic trypsin inhibitor (BPTI). Dendrotoxins were first identified by their ability to stimulate neurotransmitter release at both central and peripheral neurons. Available electrophysiologic data now indicate that α-Dtx recognizes a variety of voltage-dependent K^+ channels. The Dtx sensitivity of RCK channels expressed in *Xenopus* oocytes has been analyzed, showing that rapidly inactivating channels are less sensitive than slowly inactivating ones, although all four types were responsive. Based on immunologic cross-reactivity, the α-Dtx receptor in mammalian brain is likely related to proteins encoded by the *shaker* locus and mutations in the S5−S6 linker of RBK1 have been shown to influence strongly Dtx binding to this *shaker* homolog.

V. VOLTAGE-DEPENDENT CALCIUM CHANNELS

Voltage-dependent Ca^{2+} channels are a good deal more complex than the K^+-channels discussed in Section IV, containing five subunits ranging in size from approximately 30 to 170 kDa (Catterall, 1991). Nonetheless, certain structural features of the Ca^{2+} channel are strikingly similar to those of the Na^+ and K^+ channels. Most importantly, the α_1 subunit of the calcium channel is 29% identical to the α subunit of the rat brain $Na_V1.2$ channel and the two proteins have functionally related but chemically distinct residues at about the same frequency. Application of the usual predictive structural algorithms to the α_1 subunit suggest the protein to be organized into four homologous structural domains, each containing the now-familiar six transmembrane helices and P loop. In addition, the sequence of the S4 helix shows that, like its counterparts in Na^+ and K^+ channels, this region functions as the voltage sensor. Heterologous expression experiments in mammalian cells have shown that the α_1 subunit is essential to the properties of dihydropyridine-sensitive Ca^{2+} channels.

Knowledge of the toxinology of Ca^{2+} channels is less extensive than for Na and K channels, at least as regards polypeptide effectors. There are no known scorpion, anemone or snake toxins directed at this channel molecule. Known peptide blockers of the Ca^{2+} channel are the ω−conotoxins and a family of peptides from funnel web spiders that are structurally unrelated to the conotoxins; both groups prevent transmitter release at presynaptic terminals (Venema et al., 1992). In addition, several gating modifier tarantula toxins have recently been described. At least seven ω-conotoxins have been described; their commonalities include their cationic nature, the presence of three disulfide bonds, amidated C-termini and a large number of hydroxylated amino acids, including in some cases hydroxyproline. Two basic classes of these conotoxins are known and homology across these classes amounts to about 40%. However, it should again be emphasized that this value may be misleading in view of the fact that approximately half the identical residues are involved in disulfide bonds.

ω−Conotoxins irreversibly block stimulus-evoked transmitter release in frog neuromuscular preparations; because the muscle retains the ability to respond to a direct stimulus, a presynaptic target for the toxin is indicated. That this target is the Ca^{2+} channel has since been confirmed in chick dorsal root ganglia (DRG). The effect of this toxin seems to be irreversible: in experiments in which DRG was treated with 100 nM toxin, then washed for 2 hours, no recovery of Ca^{2+} activity was observed.

Because many distinct Ca^{2+} channel subtypes have been characterized electrophysiologically, it is natural to ask whether all are equally susceptible to the ω-conotoxins. Clearly, from the experiments described above, muscle channels are unaffected. However, even among neuronal channels, at least three subtypes are distinguishable by a variety of criteria, including gating kinetics, unit conductance and antagonist pharmacology: Nowycky and coworkers, who studied them in chick DRG, designated these channels as T, N, and L-types. The L-type channel is

distinguished by its sensitivity to dihydropyridines (DHPs), whereas T-types are not affected by these agents. ω-Conotoxins block T-type channels only weakly, whereas inhibition of neuronal L-type channels is essentially complete and irreversible in almost all cases; the irreversibility precludes an accurate determination of K_d.

Binding of ω-conotoxins to a variety of tissues has been analyzed, with K_d values in the subnanomolar range commonly reported. However, the validity of these values may fairly be questioned, given the irreversible nature of the toxin's effects. What is most clear is the lack of competition between the conotoxins and any class of organic channel blockers: dihydropyridine, benzothiazepine and phenylalkylamine binding is unaffected in the presence of high concentrations of any of these drugs. In interpreting the literature on ω-conotoxin binding, it must be remembered that distinct forms of this toxin are made by different *Conus* species and these toxins do not invariably have the same specificity.

Two classes of spider toxin blockers, distinguishable by size and amino acid sequences, are now known and have been designated either as agatoxins (not to be confused with agitoxin, discussed previously) or curtatoxins (Adams, 2004). The shorter group (μ-toxins) contains 36−38 residues and is cross-linked by four disulfides; in addition, these μ-toxins are distinguished from the polypeptides discussed previously in being generally less cationic. A second group of spider toxins (ω−agatoxins) contains 65−75 residues and as many as six disulfides and is more cationic than the shorter group. Comparison of representative sequences spider toxin undescores their lack of relatedness to the conotoxins at the level of primary structure.

Type III and IV ω-agatoxins reduce calcium influx by blockade of vertebrate presynaptic L, N and P/Q-type, voltage-gated calcium channels, thereby limiting synaptic neurotransmitter release. ω-Aga-IIA has been shown to inhibit binding of CgTX GVIA to chick brain membranes, while ω-Aga-IA and-IB do not, suggesting that these spider toxins discriminate among channel subtypes. The type III toxins have molecular weights around 8.5 kDa, while a broader range of sizes is seen for type IV agatoxins. Type IV agatoxins appear to be highly selective for P and Q type Ca^{2+}-channels.

In recent years, it has been discovered in several laboratories that toxins previously thought to target a single channel type are actually much less specific. Surprisingly, this promiscuity extends beyond channel isoforms, encompassing channels having different ion specificities. One example of this is the aforementioned tarantula toxin, Protx-II. Originally isolated as an inhibitor of $Na_V1.5$ channels, (Middleton et al., 2002) and characterized most extensively against $Na_V1.2$, 1.5 and 1.8, Protx-II has recently been discovered to inhibit activation of the T-type channel $Ca_V3.1$ (Edgerton et al., 2010). As is true for its actions on the $Na_V1.5$ channel, the toxin both inhibits $Ca_V3.1$-mediated currents and shifts the voltage dependence of activation in the positive direction without altering single channel currents or gating charge. These effects arise from a slowing of channel activation and a destabilization of the open state. In view of its dual specificity for Na/Ca channels, it is surprising that Protx-II displays little or no activity against the T-channel isoforms $Ca_V3.2$ and 3.3.

VI. OTHER TOXINS AND CHANNELS

VIA. α-Conotoxins and the Nicotinic Acetylcholine Receptor-Associated Channel

Although not targeted directly to ion channels, the α-conotoxins will be briefly discussed in the interest of covering all of the conotoxin classes. The α-conotoxins are the smallest of the conotoxin peptides known, comprising 13−15 amino acid residues, of which four are half-cystines involved in disulfide bonds. All of the known α-conotoxins are cationic, with formal charges of +1.5 to +3.5 at neutral pH. Conservative changes are tolerated at most positions without significant loss of activity, so that relatively little information on structure−function relationships can be derived from synthetic analogs. It is clear that the presence of two disulfides in such a short peptide imposes relatively severe constraints upon its three-dimensional structure. The proposed structure for α-conotoxin, based upon NMR measurements, includes β-turns at residues 5−8 and 9−12.

α-Conotoxins are directed at the nicotinic acetylcholine receptor channel and mechanistically act like the snake toxins exemplified by α-bungarotoxin. In fact, the most widely accepted model for α-conotoxin structure places several of its side-chain functional groups into α-conotoxin is consistent with its observed ability to compete with other nAChR antagonists like *d*-tubocurarine and α-BgTX. On this basis, α-conotoxin is, strictly speaking, not truly directed against the ion channel and will not be discussed further.

BIBLIOGRAPHY

Adam, M. E. (2004). Agatoxins: ion channel specific toxins from the American funnel web spider, Agelenopsis aperta. *Toxicon, 43*, 509−525.

Alabi, A. A., Bahamonde, M. I., Jung, H. J., Kim, J. I., & Swartz, K. J. (2007). Portability of paddle motif function and pharmacology in voltage sensors. *Nature, 450*, 370−376.

Benzinger, G. R., Kyle, J. W., Blumenthal, K. M., & Hanck, D. A. (1998). A specific interaction between the cardiac sodium channel and site-3 toxin anthopleurin B. *J Biol Chem, 273*, 80−84.

Bontems, F., Roumestand, C., Boyot, P., et al. (1991a). Three-dimensional structure of natural charybdotoxin in aqueous solution by ^{1}H-NMR. Charybdotoxin possesses a structural motif found in other scorpion toxins. *Eur J Biochem, 196*, 19−28.

Bontems, F., Roumestand, C., Gilquin, B., Menez, A., & Toma, F. (1991). Refined structure of charybdotoxin: common motifs in scorpion toxins and defensins. *Science, 254*, 1521−1523.

Bontems, F., Gilquin, B., Roumestand, C., Menez, J. A., & Toma, F. (1992). Analysis of side-chain organization on a refined model of charybdotoxin: structural and functional implications. *Biochemistry, 31*, 7757−7764.

Bosmans, F., Martin-Eauclaire, M. F., & Swartz, K. J. (2008). Deconstructing voltage-sensor function and pharmacology in sodium channels. *Nature, 456*, 202−208.

Cannon, S. C., & Corey, D. P. (1993). Loss of Na-channel inactivation by anemone toxin mimics the myotonic state in HPP. *J Physiol, 466*, 501.

Catterall, W. A. (1977). Activation of the action potential Na+ ionophore by neurotoxins: an allosteric model. *J Biol Chem, 252*, 8669−8676.

Catterall, W. A. (1991). Functional subunit structure of voltage-gated calcium channels. *Science,* 253.

Catterall, W. A. (2000). From ionic currents to molecular mechanisms: structure and function of voltage-gated sodium channels. *Neuron, 26*, 13−25.

Catterall, W. A., Cestele, S., Yarov-Yarovoy, V., Yu, F. H., Konoki, K., & Scheuer, T. (2007). Voltage-gated ion channels and gating modifier toxins. *Toxicon, 49*, 124−141.

Cestele, S., Qu, Y., Rogers, J. C., Rochat, H., Scheuer, T., & Catterall, W. A. (1998). Voltage sensor-trapping: enhanced activation of sodium channels by β-scorpion toxin bound to the S3−S4 loop in domain II. *Neuron, 21*, 919−931.

Chahine, M., George, A. L., Jr., Zhou, M., et al. (1994). Na channel mutation in paramyotonia congenita uncouple inactivation from activation. *Neuron, 12*, 281.

Cohen, L., Karbat, I., Gilles, N., et al. (2005). Common features in the functional surface of scorpion β-toxins and elements that confer specificity for insect and mammalian voltage-gated sodium channels. *J Biol Chem, 280*, 5045−5053.

Cohen, L., Lipstein, N., Karbat, I., et al. (2008). Miniaturization of scorpion β-toxins uncovers a putative ancestral surface of interaction with voltage-gated sodium channels. *J Biol Chem, 283*, 15169−15176.

Cruz, L. J., Gray, W. R., Olivera, B. M., et al. (1985). Conus geographus toxins that discriminate between neuronal and muscle sodium channels. *J Biol Chem, 260*, 9280−9288.

Cruz, L. J., Kupryszewski, G., LeCheminant, G. W., Gray, W. R., Olivera, B. M., & Rivier, J. (1989). μ-Conotoxin GIIIA, a peptide ligand for muscle sodium channels: chemical synthesis, radiolabeling and receptor characterization. *Biochemistry, 28*, 3437−3442.

Dias-Kadambi, B. L., Combs, K. A., Drum, C. L., Hanck, D. A., & Blumenthal, K. M. (1996a). The role of exposed tryptophan residues in the activity of the cardiotonic polypeptide anthopleurin B. *J Biol Chem, 271*, 23828−23835.

Dias-Kadambi, B. L., Drum, C. L., Hanck, D. A., & Blumenthal, K. M. (1996b). Leucine-18, a hydrophobic residue essential for high affinity binding of anthopleurin-B to the voltage sensitive sodium channel. *J Biol Chem, 271*, 9422−9429.

Doyle, D. A., Cabral, J. M., Pfuetzner, R. A., et al. (1998). The structure of the potassium channel: molecular basis of K-conduction and selectivity. *Science, 280*, 69−77.

Edgerton, G. B., Blumenthal, K. M., & Hanck, D. A. (2008). Evidence for multiple effects of Protx-II on activation gating in $Na_V1.5$. *Toxicon, 52*, 489−500.

Edgerton, G. B., Blumenthal, K. M., & Hanck, D. A. (2010). Inhibition of the activation pathway of the T-type calcium channel $Ca_V3.1$ by Protx-II. *Toxicon, 56*, 624−636.

Escoubas, P., & Rash, L. (2004). Tarantulas: eight-legged pharmacists and combinatorial chemists. *Toxicon, 43*, 555−574.

French, R. J., Sochaczewski, E. P., Zamponi, G. W., Becker, S., Kularatna, A. S., & Horn, R. (1996). Interactions between a pore-blocking peptide and the voltage sensor of the sodium channel: an electrostatic approach to channel geometry. *Neuron, 16*, 407−413.

Galvez, J. A., Gimenez-Gallego, G., Reuben, J. P., et al. (1990). Purification and characterization of a unique, potent, peptidyl probe for the high conductance calcium-activated potassium channel from venom of the scorpion Buthus tamulus. *J Biol Chem, 265*, 11083−11090.

Goldstein, S. A. N. (1996). A structural vignette common to voltage sensors and conduction pores: canaliculi. *Neuron, 16*, 717−722.

Goldstein, S. A. N., Pheasant, D. J., & Miller, C. (1994). The charybdotoxin receptor of a shaker K^+ channel: peptide and channel residues mediating molecular recognition. *Neuron, 12*, 1377−1388.

Jiang, Y., Lee, A., Chen, J., et al. (2003a). X-ray structure of a voltage-dependent K^+ channel. *Nature, 423*, 33−41.

Jiang, Y., Ruta, V., Lee, A., & MacKinnon, R. (2003b). The principle of gating charge movement in a voltage-dependent K^+-channel. *Nature, 423*, 42−48.

Khera, P. K., & Blumenthal, K. M. (1994). Role of the cationic residues Argenine-14 and Lysine-48 in the function of the cardiotonic polypeptide anthopleurin B. *J Biol Chem, 269*, 921−926.

Khera, P. K., Benzinger, G. R., Lipkind, G., Drum, C. L., Hanck, D. A., & Blumenthal, K. M. (1995). Multiple cationic residues of anthopleuruin B that determine high affinity and channel isoform discrimination. *Biochemistry, 34*, 8533−8541.

Lee, C. W., Kim, S., Roh, S. H., et al. (2004). Solution structure and functional characterization of SGTx1, a modifier of Kv2.1 channel gating. *Biochemistry, 43*, 890−897.

Lee, S. Y., & MacKinnon, R. (2004). A membrane access mechanism of ion channel inhibition by voltage sensor toxins from spider venom. *Nature, 430*, 232−235.

Linford, N. J., Cantrell, A. R., Qu, Y., Scheuer, T., & Catterall, W. A. (1998). Interaction of batrachotoxin with the local anesthetic binding site in transmembrane segment IVS6 of the voltage-gated sodium channel. *Proc Natl Acad Sci USA, 95*, 13947−13952.

Lipkind, G. M., & Fozzard, H. A. (1994). A structural model of the tetrodotoxin and saxitoxin binding site of the Na-channel. *Biophys J, 66*, 1−13.

Lipkind, G. M., & Fozzard, H. A. (2000). KcsA crystal structure as a framework for molecular model of the Na-channel pore. *Biochemistry, 39*, 8161−8170.

Long, S. B., Campbell, E. B., & MacKinnon, R. (2005). Crystal structure of a mammalian voltage-dependent shaker K^+ channel. *Science, 309*, 897−903.

MacKinnon, R., & Yellen, G. (1990). Mutations affecting TEA blockade and ion permeation in voltage-activated K+-channels. *Science, 250*, 276−279.

MacKinnon, R., Cohen, S. L., Kuo, A., Lee, A., & Chait, B. T. (1998). Structural conservation in prokaryotic and eukaryotic potassium channels. *Science, 280*, 106−109.

Middleton, R. E., Warren, V. A., Kraus, R. L., et al. (2002). Two tarantula peptides inhibit activation of multiple sodium channels. *Biochemistry, 41*, 14734−14747.

Milescu, M., Vobecky, J., Roh, S., et al. (2007). Tarantula toxins interact with voltage sensors within lipid membranes. *J Gen Physiol, 130*, 497−511.

Miller, C., Moczydlowski, E., Latorre, R., & Phillips, M. (1985). Charybdotoxin, a protein inhibitor of single Ca-activated K channels from mammalian skeletal muscle. *Nature, 313*, 316−318.

Monks, S. A., Pallaghy, P. K., Scanlon, M. J., & Norton, R. S. (1995). Solution structure of the cardiostimulant polypeptide anthopleurin-A. *Structure, 3*, 791−799.

Mosher, H. S. (1986). The chemistry of tetrodotoxin. *Ann N Y Acad Sci, 479*, 32−43.

Nicholson, G. (2007). Insect-selective spider toxins targeting voltage-gated sodium channels. *Toxicon, 49*, 490−512.

Noda, M., Suzuki, H., Numa, S., & Stuhmer, W. (1989). A single point mutation confers tetrodotoxin and saxitoxin insensitivity on the sodium channel II. *FEBS Lett, 259*, 213−216.

Ohizumi, Y., Nakamura, H., Kobayashi, J., & Catterall, W. A. (1986). Specific inhibition of saxitoxin binding to skeletal muscle sodium channels by geographutoxin II, a polypeptide channel blocker. *J Biol Chem, 261*, 6149−6152.

Olivera, B. M. (2006). Conus peptides, biodiversity-based discovery and exogenomics. *J Biol Chem, 281*, 31173−31177.

Penzotti, J. L., Fozzard, H. A., Lipkind, G. M., & Dudley, S. C. (1998). Differences in saxitoxin and tetrodotoxin binding revealed by mutagenesis of the Na-channel outer vestibule. *Biophys J, 75*, 2647−2657.

Rogers, J. C., Qu, Y., Tanada, T. N., Scheuer, T., & Catterall, W. A. (1996). Molecular determinants of high affinity binding of α-scorpion toxin and sea anemone toxin in the S3-S4 extracellular loop in domain IV of the Na-channel α subunit. *J Biol Chem, 271*, 15950−15962.

Satin, J., Kyle, J. W., Chen, M., et al. (1992). A mutant of TTX-resistant cardiac sodium channels with TTX-sensitive properties. *Science, 256*, 1202−1205.

Shimizu, Y. (1986). Chemistry and biochemistry of saxitoxin analogues and tetrodotoxin. *Ann NY Acad Sci, 479*, 24−31.

Smith, J. J., Alphy, S., Seibert, A. L., & Blumenthal, K. M. (2005). Differential phospholipid binding by site 3 and site 4 toxins: implications for structural variability between voltage-sensitive sodium channel domains. *J Biol Chem, 280*, 11127−11133.

Smith, J. J., Cummins, T. R., Alphy, S., & Blumenthal, K. M. (2007). Molecular interactions of the gating modifier toxin Protx-II with $Na_V1.5$: implied existence of a novel toxin binding site coupled to activation. *J Biol Chem, 282*, 12687−12697.

Sokolov, S., Kraus, R. L., Scheuer, T., & Catterall, W. A. (2008). Inhibition of sodium channel gating by trapping the domain II voltage sensor with Protx-II. *Molec Pharmacol, 73*, 1020−1028.

Stuhmer, W., Conti, F., Suzuki, H., et al. (1989). Structural parts involved in activation and inactivation of the sodium channel. *Nature, 339*, 597−603.

Swartz, K. J. (2007). Tarantula toxins interacting with voltage sensors in potassium channels. *Toxicon,* 49.

Swartz, K. J., & MacKinnon, R. (1997). Mapping the receptor site for hanatoxin, a gating modifier of voltage-dependent K+ channels. *Neuron, 18*, 675−682.

Trainer, V. L., Brown, G. B., & Catterall, W. A. (1996). Site of covalent labeling by a photoreactive batrachotoxin derivative near transmembrane segment IS6 of the sodium channel α subunit. *J Biol Chem, 271*, 11261−11267.

Venema, V. J., Swiderek, K. M., Lee, T. D., Hathaway, G. M., & Adams, M. E. (1992). Antagonism of synaptosomal calcium channels by subtypes of omega agatoxins. *J Biol Chem, 267*, 2610−2615.

Wang, J. M., Roh, S. H., Kim, S., Lee, C. W., Kim, J. I., & Swartz, K. J. (2004). Molecular surface of tarantula toxins interacting with voltage sensors in K_V channels. *J Gen Physiol, 123*, 455−467.

Wang, S., & Wang, G. (1999). Batrachotoxin-resistant Na channels derived from point mutations in transmembrane segment D4-S6. *Biophys J, 76*, 3141−3149.

Xiao, Y., Blumenthal, K., Jackson, J. O., Liang, S., & Cummins, T. R. (2010). The tarantula toxins Protx-II and Huwentoxin-IV differentially interact with human $Na_V1.7$ voltage sensors to inhibit channel activation and inactivation. *Molec Pharmacol, 78*, 1124−1134.

Yang, N., Ji, S., Zhou, M., et al. (1994). Na channel mutations in paramyotonia congenita exhibit similar biophysical phenotypes in vitro. *Proc Natl Acad Sci USA, 91*, 12785.

Zilberg, N., Froy, O., Loret, E., et al. (1997). Identification of structural elements of a scorpion α-neurotoxin important for receptor site recognition. *J Biol Chem, 272*, 14810−14817.

Chapter 29

Ion Channels as Targets for Drugs

Seth Robey, Kevin J. Sampson and Robert S. Kass

Chapter Outline

I. SUMMARY

Many drugs exert their therapeutic effects by acting on the ion channels of various tissues. Electrical activity in the heart is generated by the summation of currents through multiple ion channels (Kass, 1995). The ventricular action potential is characterized by a long-lasting plateau period in which a balance is maintained between small inwardly and outwardly directed exchange of ion channel currents and small changes in this balance can have severe functional consequences. During the past 25 years, a wealth of information has evolved characterizing the molecular structures that form the protein pathways for ion conduction in heart and other excitable cells (Nerbonne and Kass, 2005; Caterall 2010). With the emerging molecular and structural information, pharmacological approaches to disease management are evolving to incorporate rational drug intervention based on specific pathological conditions including genetic defects in cardiac ion channels. As illustrations, we will concentrate on only a few of the ion channels of the cardiac muscle. This chapter will focus on recent progress in the development of a molecular pharmacological approach to targeting two types of cardiac ion channels: voltage-gated calcium (Ca^{2+}) and voltage-gated sodium (Na^+) channels.

II. CALCIUM CHANNELS

At least six types of voltage-gated calcium channels (N-, L-, P-, Q-, R- and T-type) have been identified based on their pharmacological and/or biophysical properties (Caterall, 2000b). In the heart, both T- and L-type channels contribute to cardiac electrophysiology. L-type channels, the targets of organic calcium channel modulators and substrates for several cellular signaling cascades, are highly important in the maintenance of calcium homeostasis because they can be under pharmacological and/or neurohormonal control (Catterall et al., 1991; Tsien et al., 1991; Ma et al., 1992; Sculptoreanu et al., 1993a,b; Gutierrez et al., 1994; Zhao et al., 1994). Skeletal and cardiac muscle L-type calcium channels are heteromultimeric proteins consisting of α_1, β_2, and α_2/δ subunits that are part of a large macromolecular complex including a number of other auxiliary proteins that modulate function (Xu and Colecraft, 2009). Figure 29.1 shows a comparison of the primary putative subunit structures of skeletal and cardiac calcium channels as well as proposed phosphorylation sites.

The functional roles of the channel's individual subunits have been studied by several groups (Dolphin, 2003a; Xu and Colecraft, 2009). The α_1 subunit ($Ca_v1.2$ for L-type and $Ca_v3.2$ for T-type) is the pore-forming peptide and, when expressed in heterologous systems, is sufficient to encode channels with most of the biophysical and pharmacological properties of intact native channels (Mikami et al., 1989; Mori et al., 1991; Hofmann et al., 1993; Welling et al., 1993) (see Fig. 29.1). It is structurally remeniscient of the broader class of voltage-gated ion channels (Caterall, 2010), with four homologous domains of six transmembrane helices and a voltage-sensing S4 helix.

While α_1 provides most of the endogenous biophysical properties, several auxiliary proteins are required for the complete reconstitution of native function (Xu and Colecraft, 2009). Co-expression of α and β subunits is essential for both proper trafficking and the functional reconstitution of channel kinetics in heterologous systems (Dolphin, 2003a). Similarly, α_2/δ subunits increase channel number, increase gating charge and increase ionic current in

Cell Physiology Sourcebook. DOI: 10.1016/B978-0-12-387738-3.00029-9

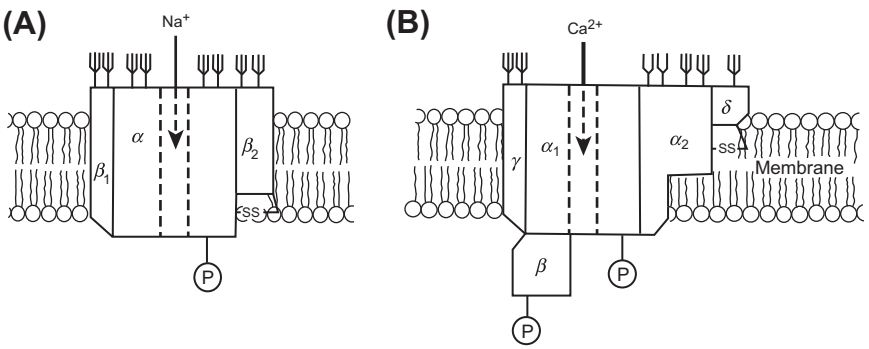

FIGURE 29.1 Block diagram illustrating subunit structures of voltage-gated sodium channels (A) and L-type calcium channels. (B) Sodium channels consist of a central pore-forming subunit (α) and two auxiliary β subunits. L-type calcium channels also contain a pore-forming α subunit and β subunits, but also $\alpha_2\delta$ and γ subunits. *(Catterall, 1988).*

recombinant channels (Bangalore, 1996; Klugbauer et al., 2003). In addition, calmodulin has been shown to associate closely with L-type channels, utilizing its Ca^{2+}-binding capabilities as a feedback regulatory mechanism (Peterson et al., 1999). The γ subunit has been examined less closely than other auxiliary proteins, but appears to have an inhibitory effect on channel function (Xu and Colecraft, 2009). The roles of auxiliary proteins in modulating native channel distribution and function continues to be an area of investigation that will be important in unraveling drug and neurohormonal modulation of L-type calcium channels (Hosey et al., 1996; Dolphin, 2003b).

Functionally, individual L-type calcium channels open, inactivate and close in a voltage- and calcium-dependent manner (Grandi et al., 2010) and their pharmacological and adrenergic modulation has been examined extensively (Triggle, 2007). Perhaps best studied is the marked modulation of L-type calcium channels by the β-adrenergic (β-AR) signaling cascade. Action potentials in the heart are sensitive to catecholamines. Exposure of isolated tissue to norepinephrine increases pacemaker activity (Tsien, 1977), increases the height but decreases the duration of the ventricular action potential plateau and increases the strength of contraction (Reuter and Scholz, 1977). Recent studies have used mass spectometry to identify the precise residues phosphorylated in a protein kinase A (PKA) or CamKII-dependent manner (Emrick et al., 2010).

At a cellular level, calcium entry via L-type channels contributes the localized sparks necessary for initiation of coordinated calcium transients and muscle contraction. Calcium flux across the sarcolemma activates ryanodine receptors (RyR) of the sarcoplasmic reticulum, which are held in close spatial proximity to L-type channels in the plasma membrane. The resulting calcium-dependent calcium release links the excitation of membrane depolarization to the mechanical contraction of the heart (Wier and Balke, 1999; Kushnir and Marks, 2010). In fact, loss of this coupling between sarcolemmal L-type calcium channels and sarcoplasmic RyR has been proposed as a step in the pathogenesis of chronic heart failure (Lyon et al., 2009).

Modulation of L-type Ca^{2+} channel activity by calcium channel antagonists has therefore become a key clinical therapeutic approach to the management of hypertension and certain types of cardiac rhythm disturbances (Triggle, 2007; Viola et al., 2009). Several recent reports, however, have raised questions about the effectiveness and safety of some calcium channel antagonists in the treatment of hypertension (Opie 2001). Of particular concern is the widespread distribution of L-type calcium channels in physiologically diverse systems and the resulting potential for dangerous non-specific drug interactions (Xu and Colecraft, 2009). It is clear that an understanding of the precise molecular targets of this important drug family is crucial to improved therapeutic efficacy.

The drugs that have received the most attention belong to three distinct chemical classes: (1) phenylalkylamines (PAAs), including verapamil and D-600; (2) benzothiazepines ((+) *cis* diltiazem); and the 1,4-dihydropyridines (DHPs), such as nitrendipine, nifedipine and nisoldipine (Xu and Colecraft, 2009) (Fig. 29.2). These drugs bind to distinct but allosterically coupled sites on the α_1 subunit (Hockermann et al., 1997b; Striessnig et al., 1998). Studies of the molecular site(s) and mechanisms of action of calcium channel blockers have focused on the biochemical and biophysical role of the binding site within the α_1 subunit and the relationship of that site to modulation of native L-type channels.

Site-directed mutagenesis studies have revealed specific residues that form the binding domains for all three classes of drugs (Hockerman et al., 1997a; Streissnig et al., 1998). Emerging from these studies is the consensus view that domains III and IV of the α_1 subunit are crucial to modulation of L-type Ca^{2+} channels and it is likely that multiple residues on the α_1 subunit interact in an allosteric manner to cause voltage-dependent modulation of channel gating (Tang et al., 1993; Grabner et al., 1996; Peterson et al., 1996, 1997; Schuster et al., 1996; Ito et al., 1997). The most provocative model for the actions of these drugs has been developed by Catterall and his colleagues, who have proposed that DHPs bind at the domain interface

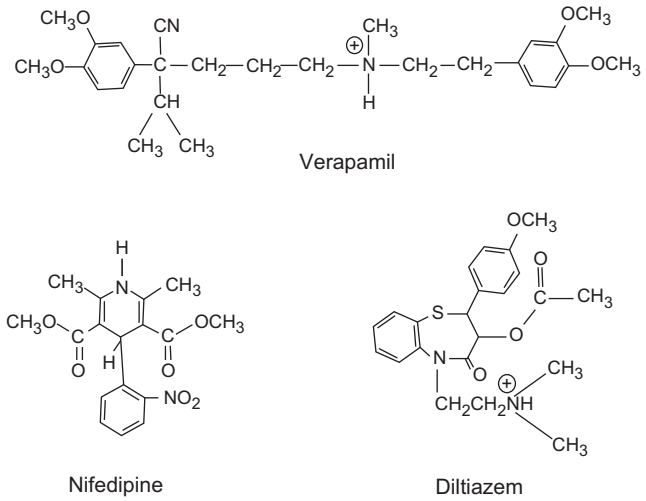

FIGURE 29.2 The major classes of calcium channel blockers: phenylalkylamines (verapamil); dihydropyridines (nifedipine); and benzothiazepines (diltiazem), *(Hille, 1992).*

allosterically to regulate pore dynamics (Fig. 29.3) (Hockerman et al., 1997b; Tikhonov and Zhorov, 2009). Most importantly in this model, allosteric interactions between bound drug and two domains of the α_1 subunit

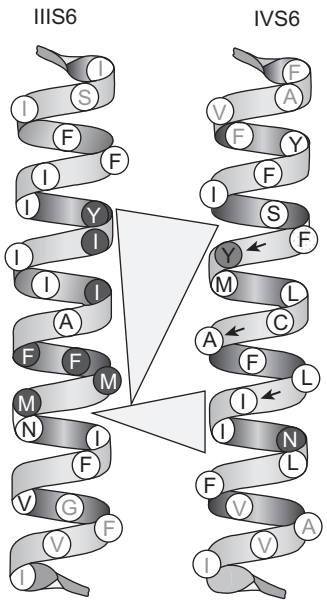

FIGURE 29.3 Domain interface model for dihydropyridine (DHP) binding in the α subunit of the L-type calcium channel. Indicated are key amino acids in domain IIIS6 and domain IVS6 that, when mutated, change dihydropyridine block by factors greater than fivefold. Black letters inside shaded circles represent amino acids that when mutated have significant but less than fivefold reduction in DHP binding. A schematized DHP ligand is illustrated by the triangle contacting the putative key binding residues. It is proposed that channel regulation is a consequence of allosteric interactions between the drug molecule and the two helices IIIS6 and IVS6. *(From Hockermann et al., 1997b.)*

cause conformational changes in the channel, which modify channel gating and control the entry of divalent ions.

Most DHP derivatives previously studied in detail, such as nitrendipine and nisoldipine, are neutral compounds at physiological pH (Rodenkirchen et al., 1982) and inhibit L-type Ca^{2+} channels in a voltage-dependent manner. Repolarization to negative holding potentials readily reverses voltage-enhanced channel inhibition (Sanguinetti and Kass, 1984). The voltage dependence of neutral DHP channel modulation has been interpreted within the general framework of the modulated receptor hypothesis, which accounts for state-dependent allosteric channel block, as in many local anesthetics (see Section III). For DHPs, binding affinity to inactivated channels is high; binding affinity to channels in the resting state is low (Sanguinetti and Kass, 1984; Tikhonov and Zhorov, 2009), consistent with this hypothesis. Interestingly, addition of a charged head-group appears to change this relationship between channel modulation and membrane potential: channel inhibition by charged DHPs is not relieved upon repolarization (Kass, 1994a,b; Lacinova et al., 1999), suggesting the presence of charged salt-bridge partners in the binding pocket.

The interrelationship between the activity of DHPs and divalent ions is also well established (Glossmann et al., 1987). High-affinity DHP labeling of L-type channels in brain, cardiac or smooth muscle membranes depends on the presence of divalent ions (Glossmann and Striessnig, 1990), as does the binding of phenylalkylamines and DHPs to the purified L-type channel (Flockerzi et al., 1986). Ca^{2+} binding to glutamate residues in the putative pore-lining regions (S5−S6) of repeats I−IV in the calcium channel $\alpha_{1C\text{-}a}$ subunit is a critical determinant of ion selectivity and permeation in $\alpha_{1C\text{-}a}$ Ca^{2+} channels (Yang et al., 1993; Tikhonov and Zhorov, 2009). These residues have also been shown to play a significant role in the activity of DHPs and PAAs (Hockerman et al., 1995), suggesting a mechanism by which the drug binding site and ion permeation pathway are allosterically coupled. This notion is supported by the consideration that channel block by charged DHPs is not voltage dependent. Thus, it has been proposed that the binding of Ca^{2+} to the selectivity filter is allosterically coupled to DHP binding via conserved glutamate residues and that stabilization of ions in the permeation pathway makes complete permeation less probable (Peterson and Caterall, 2006).

L-type calcium channels encoded by the smooth muscle splice variant of the α ($\alpha_{1C\text{-}b}$) subunit respond to DHP derivatives differently than channels encoded by the cardiac splice variant ($\alpha_{1C\text{-}a}$) (Zuhlke et al., 1998). In particular, it was found that channels encoded by $\alpha_{1C\text{-}b}$ cDNA were more sensitive to the DHP antagonist nisoldipine than were channels encoded by the $\alpha_{1C\text{-}a}$ splice variant (Fig. 29.4). Subsequent work has shown that this distinct

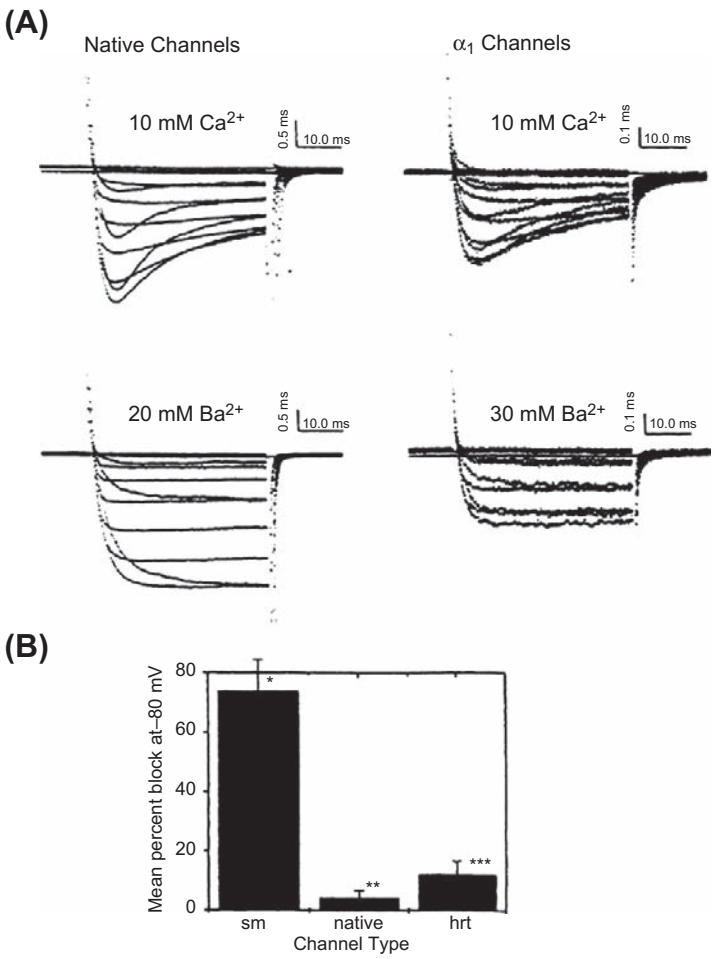

FIGURE 29.4 L-type calcium channels expressed in Chinese hamster ovary (CHO) cells, showing the greater sensitivity of smooth muscle (sm) than heart (hrt) channel variants to dihydropyridine block. (A) Native (left) and recombinant (right) L-type calcium channel activity when calcium (upper row) and barium (lower row) carries the charge. (B) Tonic block of recombinant channel activity by the DHP nisoldipine for $\alpha_{1C\text{-}a}$ (hrt) and $\alpha_{1C\text{-}b}$ (sm) α subunits. *(From Welling et al., 1997.)*

pharmacological profile is due to alternative splicing of the IS6 segments of the 1C gene in cardiac and smooth muscle (Welling et al., 1997). In addition, Welling and colleagues confirmed that $\alpha_{1C\text{-}b}$ is expressed in smooth muscle, but not cardiac, cells, linking the molecular pharmacology to the physiology of the tissues. These experimental results are important because they show that regions of the 1C subunit distinct from the DHP-binding domain influence drug activity, most likely through allosteric interactions. These results for DHP antagonists have been confirmed by others (Hu and Marban, 1998; Zuhlke et al., 1998); however, differences in DHP agonist modulation of smooth muscle versus cardiac muscle L-type calcium channels has not yet been systematically addressed.

T-type calcium channels (Perez-Reyes et al., 2006) have voltage-dependent kinetics, ion permeability and pharmacological properties that distinguish them from L-type calcium channels. They are resistant to block by dihydropyridines, inactivate in a voltage-dependent manner and, most importantly, activate at voltages much more negative than L-type calcium channels (Bean, 1989; Nilius et al., 2006; Xu and Colecraft, 2009). Because of the voltage dependence of T-type channels and the relatively small size of T-channel current in the ventricle (Bean, 1985; Ono and Iijima, 2010), direct activation of contractile proteins and/or calcium-induced release of calcium from the SR is not likely (Balke et al., 1993; Cannell et al., 1995). T-type channel activity has been suggested to contribute to pacemaker activity in nodal cells (Irisawa and Hagiwara, 1991; Vassort et al., 2006), which may be particularly important in the Purkinje fibers in the conduction system of the heart. The cloning of the neuronal T-type channel has opened the possibility of determining the molecular basis for these differences (Perez-Reyes et al., 1998).

III. SODIUM (Na^+) CHANNELS

Voltage-gated Na^+ channels are integral membrane proteins (Catterall, 2000a) that not only control the movement of Na^+ and underlie the spread of excitation in ventricular and atrial muscle cells and in the Purkinje fiber

network throughout the heart, but also can contribute so-called "late" current, which prolongs action potential duration (Attwell et al., 1979). The electrocardiogram can therefore give some insight into channel activity: the QRS interval reflects conduction time through the ventricle and hence the number of available Na^+ channels and the QT interval represents the time to ventricular repolarization. For example, when peak sodium current is diminished in the presence of tetrodotoxin (TTX; an Na^+ channel-blocking toxin) or after sodium removal (Colatsky, 1982; Hiraoka et al., 1986), the rate of action potential initiation is slowed. The consequential slowing of electrical propagation through the myocardium manifests itself as a prolongation of the QRS interval. Conversely, inherited mutation in the cardiac Na^+ channel can impinge upon channel inactivation and cause a substantial non-inactivating, or "late", sodium current. This enhanced depolarizing current prolongs the action potential and can lead to long-QT syndrome (Balser, 1999; Clancy and Rudy, 1999; Zimmer and Surber, 2008). Cardiac sodium channels therefore serve as an important target of antiarrhythmic agents.

In most tissues, the voltage-gated Na^+ channel is a heterotrimeric protein consisting of α (33 kDa), β_1 (36 kDa) and/or β_2 (33 kDa) subunits (Catterall et al., 1992; Catterall, 2000), but only the α subunit (primarily $Na_v1.5$ in the heart) is needed for expression of recombinant channels, particularly for heart channels (Suzuki et al., 1988; Stuhmer et al., 1989a; Noda et al., 1989; Abriel and Kass, 2005). Like the L-type calcium channel α_{1c} subunit, the Na^+ channel α subunit maintains the classical four-domained structure, with S4 serving as a voltage sensor in each domain (Balser, 1999; Abriel and Kass, 2005).

The selective pore of Na^+ channels is responsive to changes in the voltage-sensing domains and, as a first approximation, gating follows the simplified Hodgkin and Huxley model (Hodgkin and Huxley, 1952). At resting membrane potentials, Na^+ channels are in a resting state with the pore closed. Membrane depolarization induces conformational changes in the S4 helix that open the gate (Abriel and Kass, 2005), resulting in conduction of Na^+ ions through the pore and inward Na^+ current. Continued depolarization triggers closure of an inactivation gate, occlusion of the channel pore and termination of the Na^+ current. Membrane repolarization returns the channel to the resting state by allowing S4 to relax, shutting the gate and relieving inhibition.

The molecular determinants of inactivation of the voltage-gated Na^+ channel have been well studied (Caterall, 2000a) and have been shown to be interrelated to the actions of local anesthetics (LAs) in modulating sodium channels (Ragsdale and Avoli, 1998; Kambouris et al., 1998). Multiple groups have provided molecular and biophysical evidence that fast inactivation of this channel occurs by the binding of an intracellular inactivation gate, the loop connecting homologous domains III and IV of the Na^+ channel, to regions around the inner mouth of the Na^+ channel pore through hydrophobic interactions (Vassilev et al., 1988; Stuhmer et al., 1989b; Chahine et al., 1997; Rohl et al., 1999). The docking site of the inactivation gate has been less clearly identified, but the short intracellular loops connecting the S4 and S5 segments in each domain of the channel (McPhee et al., 1998) have been revealed as interaction sites and two residues in the S6 segment of domain IV (F1764 and Y1774 in rat brain IIA channel) have been found to be key in modulating inactivation (McPhee et al., 1995). More recently, it has become evident that the structured proximal segment of the C-terminus is crucial in modulating the docking of the inactivation gate to the pore (Kass, 2006; Zimmer and Surber, 2008).

Our present understanding of LA action relies heavily on the state-dependent hypothesis of Hille and Starmer. Hille (1977) proposed the *modulated receptor hypothesis* in which a single LA receptor lies within the pore, between the selectivity filter and channel gate. Receptor occupation leads to cessation of ion flow and promotion of inactivation. Drugs approach the receptor by an aqueous, hydrophilic pathway through the open cytoplasmic mouth and the pore (see Fig. 29.1) and induce small conformational changes that stabilize drug/channel interactions. Alternatively, Starmer and Courtney (1986) proposed that state-dependent affinity of an intrapore receptor arises from a static receptor that is guarded by the channel gate, a *guarded receptor*. Here, the channel gate regulates access to the receptor, so that open channels provide greater receptor access.

Two drugs, lidocaine and flecainide, differ in their modes of action in that each binds preferentially to a different state of the channel. Lidocaine interacts preferentially with the inactivated state of the channel and drug block is not necessarily dependent on channel openings (Bean et al., 1983; Ragsdale et al., 1996). This is evidenced by the hyperpolarizing shift in the voltage dependence of inactivation and by the voltage range over which the drug is active (Ragsdale et al., 1996). Furthermore, mutation of the hydrophobic IFM motif of the III–IV intracellular loop into QQQ removes fast inactivation of brain IIA (West et al., 1992) and cardiac Na^+ channels (Bennett et al., 1995) and strongly decreases lidocaine efficacy (Fig. 29.5) (Bennett et al., 1995). However, recent data suggest that transitions to the active state may play a more important role in the actions of lidocaine block than previously considered (Vedantham and Cannon, 1999; Scheuer, 1999). Conversely, charged, hydrophilic analogs of LAs, such as the drug flecainide, block sodium channels preferentially in the open state. The activity of flecainide requires channels to open and does not require channels to enter the inactivated state to promote block (Anno and Hondeghem, 1990; Ragsdale et al., 1996). Confirmation of this hypothesis has been illustrated in Markov models of state dependent drug interaction that

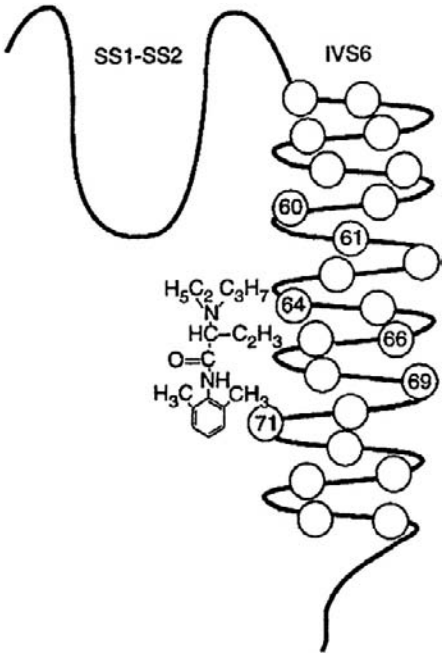

FIGURE 29.5 Schematic diagram of the putative interaction between lidocaine and key residues on domain IV transmembrane segment S6 of the rat brain Na channel. *(Reprinted with permission from Science. Copyright 1994 American Association for the Advancement of Science.)*

reproduce the experimental findings for two different classes of LA (Clancy et al., 2007).

IIIA. Mutation-Specific Drug Actions

Multiple mutations of *SCN5A*, the gene that encodes the human heart Na^+ channel α subunit, have been discovered and linked to two inherited cardiac arrhythmias: the long QT syndrome and the Brugada's syndrome. The fact that these mutations cause functional changes in expressed channel activity has created the unique opportunity to develop specific molecular therapeutic approaches to disease management based on specific functional changes in the channel proteins encoded by mutant genes (Keating and Sanguinetti, 1996).

Pharmacological analysis of mutant channels expressed heterologously has provided evidence that Na^+ channel blockers which preferentially interact with the inactivated state of the channel (Hille, 1977; Hondeghem and Katzung, 1977) block in a targeted manner the maintained current conducted by some mutant LQT (ΔKPQ mutant) channels (An et al., 1996; Compton et al., 1996; Dumaine et al., 1996; Priori et al., 1996; Wang et al., 1997; Dumaine and Kirsch, 1998), shorten action potential duration in cellular studies (Schwartz et al., 1995; Shimizu and Antzelevitch, 1997) and correct QT prolongation in patients (Schwartz et al., 1995; Rosero et al., 1997). Figure 29.6B illustrates the maintained current carried by LQT-3 mutant (ΔKPQ)

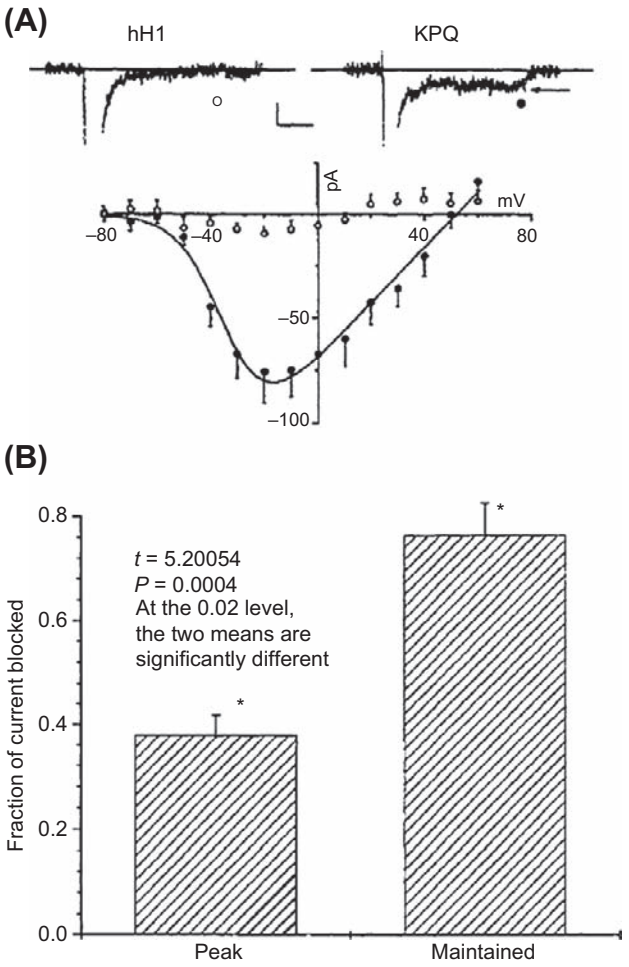

FIGURE 29.6 (A) The ΔKPQ deletion mutation of the cytoplasmic linker between domains III and IV of the human heart Na^+ channel α subunit promotes maintained sodium channel current that is not present in wild-type a (hH1) channels. (B) Summary of experiments in which the fraction of peak inward Na^+ channel current (left bar) was compared with the fraction of late or maintained Na^+ channel current blocked (right bar) by the same concentration of lidocaine (100 μM). The late current is more than twice as sensitive to lidocaine as peak current. *(From An et al., 1996.)*

channels and preferential block of this current by lidocaine. Flecainide, which preferentially blocks open but not inactivated channels (Ragsdale et al., 1996), has also been shown to be effective in inhibiting persistent Na^+ channel current in ΔKPQ mutant channels (Nagatomo et al., 1997) and in shortening and normalizing QT intervals in patients carrying this gene mutation (Windle et al., 2001).

Interestingly, clinical data suggest that flecainide might also be effective in controlling arrhythmias caused by the D1790G mutation located in the C-terminal region of the $Na_v1.5$ channel (Benhorin et al., 1999). This mutation decreases the probability of channel inactivation, allowing for late sodium currents and prolonged action potentials. Flecainide is therefore more active in diseased channels than in WT (wild-type) channels, presumably because

deficiencies in inactivation increase the time over which the drug has access to its intrapore binding site (Liu et al., 2003). Recently, one severe mutation in a newborn, F1473C, had a differential response to flecainide and mexilitine in the patient but not in cellular studies (Bankston et al., 2007). This newborn also harbored a polymorphism in a K^+ channel that may play a role in the unique drug response and highlights the importance in understanding the genetic background in which disease-causing mutations exist.

These studies represent the ongoing effort to target selectively ion channels that have been implicated in both acquired and congenital arrhythmias. Further understanding of the normal and pathological gating and pharmaceutical modulation of these ion channels has led and will continue to lead us to more targeted therapies designed on correcting the defect in an individual ion channel. Ultimately, therapeutic strategies will need to take into account the genetic background of the individual patient in addition to the dysfunction in an ion channel.

BIBLIOGRAPHY

Abriel, H., & Kass, R. S. (2005). Regulation of the voltage-gated cardiac sodium channel Nav1.5 by interacting proteins. *Trends Cardiovasc Med, 15*, 35–40.

An, R. H., Bangalore, R., Rosero, S. Z., & Kass, R. S. (1996). Lidocaine block of LQT-3 mutant human Na^+ channels. *Circ Res, 79*, 103–108.

Anno, T., & Hondeghem, L. M. (1990). Interactions of flecainide with guinea pig cardiac sodium channels. Importance of activation unblocking to the voltage dependence of recovery. *Circ Res, 66*, 789–803.

Attwell, D., Cohen, I., Eisner, D., Ohba, M., & Ojeda, C. (1979). The steady state TTX-sensitive ("window") sodium current in cardiac Purkinje fibres. *Pflügers Arch, 379*, 137–142.

Bankston, J. R., Yue, M., Chung, W., et al. (2007). A novel and lethal de novo LQT-3 mutation in a newborn with distinct molecular pharmacology and therapeutic response. *PLoS One, 2*, 1258.

Balke, C. W., Rose, W. C., O'Rourke, B., Mejia-Alvarez, R., Backx, P., & Marban, E. (1993). Biophysics and physiology of cardiac calcium channels. *Circ, 87*(Suppl. 7), VII49–VII53.

Balser, J. R. (1999). Sodium "channelopathies" and sudden death: must you be so sensitive? *Circ Res, 85*, 872–875.

Bangalore, R., Mehrke, G., Gingrich, K., Hofmann, F., & Kass, R. S. (1996). Influence of the L-type Ca-channel α_2/δ subunit on ionic and gating current in transiently-transfected HEK 293 cells. *Am J Physiol, 270*, H1521–H1528.

Bean, B. P. (1985). Two kinds of calcium channels in canine atrial cells. Differences in kinetics, selectivity, and pharmacology. *J Gen Physiol, 86*, 1–30.

Bean, B. P. (1989). Classes of calcium channels in vertebrate cells. *Ann Rev Physiol, 51*, 367–384.

Bean, B. P., Cohen, C. J., & Tsien, R. W. (1983). Lidocaine block of cardiac sodium channels. *J Gen Physiol, 81*, 613–642.

Benhorin, J., Medina, A., Taub, Y., et al. (2000). Effects of flecainide in patients with a new SCN5A mutation: mutation-specific therapy for Long QT Syndrome? *Circulation, 101*, 1698–1706.

Bennett, P. B., Valenzuela, C., Chen, L. Q., & Kallen, R. G. (1995). On the molecular nature of the lidocaine receptor of cardiac Na^+ channels. Modification of block by alterations in the alpha-subunit III–IV interdomain. *Circ Res, 77*, 584–592.

Cannell, M. B., Cheng, H., & Lederer, W. J. (1995). The control of calcium release in heart muscle. *Science, 268*, 1045–1049.

Catterall, W. A. (1988). Structure and function of voltage-sensitive ion channels. *Science, 242*, 50–61.

Catterall, W. A. (2000a). From ionic currents to molecular mechanisms: the structure and function of voltage-gated sodium channels. *Neuron, 26*, 13–25.

Catterall, W. A. (2000b). Structure and regulation of voltage-gated Ca^{2+} channels. *Annu Rev Cell Dev Biol, 16*, 521–555.

Catterall, W. A. (2010). Ion channel voltage sensors: structure, function, and pathophysiology. *Neuron, 67*, 915–928.

Catterall, W. A., Scheuer, T., Thomsen, W., & Rossie, S. (1991). Structure and modulation of voltage-gated ion channels. [Review]. *Ann NY Acad Sci, 625*, 174–180.

Catterall, W. A., Trainer, V., & Baden, D. G. (1992). Molecular properties of the sodium channel: a receptor for multiple neurotoxins. [Review]. *Bull Soc Pathol Exot, 85*, 481–485.

Chahine, M., Deschenes, I., Trottier, E., Chen, L. Q., & Kallen, R. G. (1997). Restoration of fast inactivation in an inactivation-defective human heart sodium channel by the cysteine modifying reagent benzyl-MTS: analysis of IFM-ICM mutation. *Biochem Biophys Res Commun, 233*, 606–610.

Clancy, C. E., & Rudy, Y. (1999). Linking a genetic defect to its cellular phenotype in a cardiac arrhythmia. *Nature, 400*, 566–569.

Clancy, C. E., Zhu, Z. I., & Rudy, Y. (2007). Pharmacogenetics and anti-arrhythmic drug therapy: a theoretical investigation. *Am J Heart Circ Physiol, 292*, H66–H75.

Colatsky, T. J. (1982). Mechanisms of action of lidocaine and quinidine on action potential duration in rabbit Purkinje fibers, an effect on steady state sodium currents? *Circ Res, 50*, 17–27.

Compton, S. J., Lux, R. L., Ramsey, M. R., et al. (1996). Genetically defined therapy of inherited long-QT syndrome – correction of abnormal repolarization by potassium. *Circulation, 94*, 1018–1022.

Dolphin, A. C. (2003a). Beta subunits of voltage-gated calcium channels. *J Bioenerg Biomembr, 35*, 599–620.

Dolphin, A. C. (2003b). G protein modulation of voltage-gated calcium channels. *Pharmacol Rev, 55*, 607–627.

Dumaine, R., & Kirsch, G. E. (1998). Mechanism of lidocaine block of late current in long Q-T mutant Na^+ channels. *Am J Physiol, 274*, H477–H487.

Dumaine, R., Wang, Q., Keating, M. T., et al. (1996). Multiple mechanisms of Na^+ channel linked long-QT syndrome. *Circ Res, 78*, 916–924.

Emrick, M. A., Sadelik, M., Konoki, K., & Catterall, W. (2010). Beta-adrenergic-regulated phosphorylation of the skeletal muscle Ca(V)1.1 channel in the fight-or-flight response. *Proc Natl Acad Sci USA, 107*, 18712–18717.

Flockerzi, V., et al. (1986). Purification of dihydropyridine-binding site from skeletal muscle t-tubules is a functional calcium channel. *Nature, 323*, 66–86.

Glossmann, H., & Striessnig, J. (1990). Molecular properties of calcium channels. *Rev Physiol Biochem Pharmacol, 114*, 1–105.

Glossmann, H., Striessnig, J., Ferry, D. R., Goll, A., Moosburger, K., & Schirmer, M. (1987). Interaction between calcium channel ligands and calcium channels. *Circ Res, 61*, 130–136.

Grabner, M., Wang, Z., Hering, S., Striessnig, J., & Glossmann, H. (1996). Transfer of 1,4-dihydropyridine sensitivity from L-type to class A (BI) calcium channels. *Neuron, 16*, 207−218.

Grandi, E., Morotti, S., Ginsberg, K. S., Severi, S., & Bers, D. M. (2010). Interplay of voltage and Ca-dependent inactivation of L-type Ca current. *Prog Biophys Mol Biol, 103*, 44−50.

Gutierrez, L. M., Zhao, X. L., & Hosey, M. M. (1994). Protein kinase C−mediated regulation of L-type Ca channels from skeletal muscle requires phosphorylation of the alpha 1 subunit. *Biochem Biophys Res Commun, 202*, 857−865.

Hille, B. (1977). Local anesthetics: hydrophilic and hydrophobic pathways for the drug-receptor reaction. *J Gen Physiol, 69*, 497−515.

Hille, B. (1992). *Ionic Channels of Excitable Membranes* (2nd ed.). Sunderland: Sinauer.

Hiraoka, M., Sawada, K., & Kawano, S. (1986). Effect of quinidine on plateau currents of guinea-pig ventricular myocytes. *J Molec Cell Cardiol, 18*, 1097−1106.

Hockerman, G. H., Johnson, B. D., Scheuer, T., & Catterall, W. A. (1995). *Molecular determinants of high affinity phenylalkylamine block of L-type calcium channels, 270*, 22119−22122.

Hockerman, G. H., Peterson, B. Z., Johnson, B. D., & Catterall, W. A. (1997a). Molecular determinants of drug binding and action on L-type calcium channels. [Review]. *Annu Rev Pharmacol Toxicol, 37*, 361−396.

Hockerman, G. H., Peterson, B. Z., Sharp, E., Tanada, T. N., Scheuer, T., & Catterall, W. A. (1997b). Construction of a high-affinity receptor site for dihydropyridine agonists and antagonists by single amino acid substitutions in a non-L-type Ca2+ channel. *Proc Natl Acad Sci USA, 94*, 14906−14911.

Hodgkin, A. L., & Huxley, A. F. (1952). A quantitative description of membrane current and its application to conduction and excitation in nerve. *J Physiol (London), 117*, 500−544.

Hofmann, F., Biel, M., Bosse, E., Flockerzi, V., Ruth, P., & Welling, A. (1993). Functional expression of cardiac and smooth muscle calcium channels. In A. M. Brown, W. A. Catterrall, G. J. Kaczorowski, P. S. Spooner, & H. C. Strauss (Eds.), *Ion Channels in the Cardiovascular System: Function and Dysfunction*. Washington: AAAS Press.

Hondeghem, L. M., & Katzung, B. G. (1977). Time- and voltage-dependent interactions of antiarrhythmic drugs with cardiac sodium channels. [Review]. *Biochim Biophys Acta, 472*, 373−398.

Hosey, M. M., Chien, A. J., & Puri, T. S. (1996). Structure and regulation of L-type calcium channels − a current assessment of the properties and roles of channel subunits. *Trends Cardiovasc Med, 6*, 265−273.

Hu, H., & Marban, E. (1998). Isoform-specific inhibition of L-type calcium channels by dihydropyridines is independent of isoform-specific gating properties. *Mol Pharmacol, 53*, 902−907.

Irisawa, H., & Hagiwara, N. (1991). Ionic current in sinoatrial node cells. *J Cardiovasc Electrophys, 2*, 531−540.

Ito, H., Klugbauer, N., & Hofmann, F. (1997). Transfer of the high-affinity dihydropyridine sensitivity from L-type to non−L-type calcium channels. *Mol Pharmacol, 52*, 735−740.

Kambouris, N. G., Hastings, L. A., Stepanovic, S., Marban, E., Tomaselli, G. F., & Balser, J. R. (1998). Mechanistic link between lidocaine block and inactivation probed by outer pore mutations in the rat micro1 skeletal muscle sodium channel. *J Physiol (London), 512*, 693−705.

Kass, R. S. (1994a). Dihydropyridine modulation of cardiovascular L-type calcium channels: molecular and cellular pharmacology. In P. M. Spooner, A. M. Brown, W. A. Catterall, G. J. Kaczorowski, & H. C. Strauss (Eds.), *Ion Channels in the Cardiovascular System: Function and Dysfunction* (pp. 425−440). Armonk: Futura Publishing Co.

Kass, R. S. (1994b). Molecular pharmacology of cardiac L-type calcium channels. In C. Peracchia (Ed.), *Handbook of Membrane Channels: Molecular and Cellular Physiology* (pp. 187−198). Orlando: Academic Press.

Kass, R. S. (1995). Ionic basis of electrical activity in the heart. In N. Sperelakis (Ed.), *Physiology and Pathophysiology of the Heart* (pp. 77−90). Norwell: Kluwer Academic.

Kass, R. S. (2006). Sodium channel inactivation in heart: a novel role of the carboxy-terminal domain. *J Cardiovasc Electrophysiol, 17*, S21−S25.

Keating, M. T., & Sanguinetti, M. C. (1996). Pathophysiology of ion channel mutations. Curr Opin Gen. *Devel, 6*, 326−333.

Klugbauer, N., Marais, E., & Hofmann, F. (2003). Calcium channel alpha2delta subunits: differential expression, function, and drug binding. *J Bioenerg Biomembr, 35*, 639−647.

Kushnir, A., & Marks, A. (2010). The ryanodine receptor in cardiac physiology and disease. *Adv Pharmacol, 59*, 1−30.

Lacinová, L., An, R. H., Xia, J., et al. (1999). Distinctions in the molecular determinants of charged and neutral dihydropyridine block of L-type calcium channels. *J Pharmacol Exp Ther, 289*, 1472−1479.

Liu, H., Atkins, J., & Kass, R. S. (2003). Common molecular determinants of flecainide and lidocaine block of heart Na+ channels: evidence from experiments with neutral and quaternary flecainide analogues. *J Gen Physiol, 121*, 199−214.

Lyon, A. R., MacLeod, K. T., Zhang, Y., et al. (2009). Loss of T-tubules and other changes to surface topography in ventricular myocytes from failing human and rat heart. *Proc Natl Acad Sci USA, 106*, 6854−6859.

Ma, J., Gutierrez, L. M., Hosey, M. M., & Rios, E. (1992). Dihydropyridine-sensitive skeletal muscle Ca channels in polarized planar bilayers. 3. Effects of phosphorylation by protein kinase C. *Biophys J, 63*, 639−647.

McPhee, J. C., Ragsdale, D. S., Scheuer, T., & Catterall, W. A. (1995). A critical role for transmembrane segment IVS6 of the sodium channel alpha subunit in fast inactivation. *J Biol Chem, 270*, 12025−12034.

McPhee, J. C., Ragsdale, D. S., Scheuer, T., & Catterall, W. A. (1998). A critical role for the S4−S5 intracellular loop in domain IV of the sodium channel alpha-subunit in fast inactivation. *J Biol Chem, 273*, 1121−1129.

Mikami, A., Imoto, K., Tanabe, T., et al. (1989). Primary structure and functional expression of the cardiac dihydropyridine-sensitive calcium channel. *Nature, 340*, 230−233.

Mori, Y., Friedrich, T., Kim, M.-S., et al. (1991). Primary structure and functional expression from complementary DNA of a brain calcium channel. *Nature, 350*, 398−402.

Nagatomo, T., Fan, Z., Ye, B., January, C. T., & Makielski, J. C. (1997). Effects of flecainide on the long QT sodium channel syndrome. *Circulation, 96*, 677.

Nerbonne, J. M., & Kass, R. S. (2005). Molecular physiology of cardiac repolarization. *Physiol Rev, 85*, 1205−1253.

Nilius, B., Talavera, K., & Verkhratsky, A. (2006). T-type calcium channels: the never ending story. *Cell Calcium, 40*, 81−88.

Noda, M., Suzuki, H., Numa, S., & Stuhmer, W. (1989). A single point mutation confers tetrodotoxin and saxitoxin insensitivity on the sodium channel II. *FEBS Lett, 259*, 213−216.

Ono, K., & Iijima, T. (2010). Cardiac T-type Ca(2+) channels in the heart. *J Mol Cell Cardiol, 48*, 65−70.

Opie, L. H. (2001). Calcium channel blockers in hypertension: reappraisal after new trials and major meta-analyses. *Am J Hypertens, 14*, 1074−1081.

Perez-Reyes, E. (1998). Molecular characterization of a novel family of low voltage-activated, T-type, calcium channels. *J Bioeng Biomembr, 30*, 313−318.

Perez-Reyes, E., & Lory, P. (2006). Molecular biology of T-type calcium channels. *CNS Neurol Disord Drug Targets, 5*, 605−609.

Peterson, B. Z., & Catterall, W. A. (2006). Allosteric interactions required for high-affinity binding of dihydropyridine antagonists to Ca(V)1.1 Channels are modulated by calcium in the pore. *Mol Pharmacol, 70*, 667−675.

Peterson, S. G., DeMaria, C. D., Adelman, J. P., & Yue, D. T. (1999). Calmodulin is the Ca2+ sensor for Ca2+ -dependent inactivation of L-type calcium channels. *Neuron, 22*, 549−558.

Peterson, B. Z., Johnson, B. D., Hockerman, G. H., Acheson, M., Scheuer, T., & Catterall, W. A. (1997). Analysis of the dihydropyridine receptor site of L-type calcium channels by alanine-scanning mutagenesis. *J Biol Chem, 272*, 18 752−18 758.

Peterson, B. Z., Tanada, T. N., & Catterall, W. A. (1996). Molecular determinants of high affinity dihydropyridine binding in L-type calcium channels. *J Biol Chem, 271*, 5293−5296.

Priori, S. G., Napolitano, C., Cantu, F., Brown, A. M., & Schwartz, P. J. (1996). Differential response to Na^+ channel blockade, beta-adrenergic stimulation and rapid pacing in a cellular model mimicking the SCN5A and HERG defects present in the long-QT syndrome. *Circ Res, 78*, 1009−1015.

Ragsdale, D. S., & Avoli, M. (1998). Sodium channels as molecular targets for antiepileptic drugs. *Brain Res Rev, 26*, 16−28.

Ragsdale, D. S., McPhee, J. C., Scheuer, T., & Catterall, W. A. (1996). Common molecular determinants of local anesthetic, antiarrhythmic, and anticonvulsant block of voltage-gated Na^+ channels. *Proc Natl Acad Sci USA, 93*, 9270−9275.

Reuter, H., & Scholz, H. (1977). The regulation of Ca conductance of cardiac muscle by adrenaline. *J Physiol, 264*, 49−62.

Rodenkirchen, R., Bayer, R., & Mannhold, R. (1982). Specific and non-specific Ca antagonists: a structure-activity analysis of cardiodepressive drugs. *Progr Pharmacol, 5*, 9−23.

Rohl, C. A., Boeckman, F. A., Baker, C., Scheuer, T., Catterall, W. A., & Klevit, R. E. (1999). Solution structure of the sodium channel inactivation gate. *Biochemistry, 38*, 855−861.

Rosero, S. Z., Zareba, W., Robinson, J. L., & Moss, A. (1997). Gene-specific therapy for long QT syndrome: QT shortening with lidocaine and tocainide in patients with mutation of the sodium channel gene. *Ann Noninvasive Electrocardiol, 2*, 274−278.

Sanguinetti, M. C., & Kass, R. S. (1984). Voltage-dependent block of calcium channel current in the calf cardiac Purkinje fiber by dihydropyridine calcium channel antagonists. *Circ Res, 55*, 336−348.

Scheuer, T. (1999). Commentary: a revised view of local anesthetic action: what channel state is really stabilized? *J Gen Physiol, 113*, 3−6.

Schuster, A., Lacinova, L., Klugbauer, N., Ito, H., Birnbaumer, L., & Hormann, F. (1996). The IVS6 segment of the L-type calcium channel is critical for the action of dihydropyridines and phenylalkylamines. *EMBO J, 15*, 2365−2370.

Schwartz, P. J., Priori, S. G., Locati, E. H., et al. (1995). Long QT syndrome patients with mutations of the SCN5A and HERG genes have differential responses to Na^+ channel blockade and to increases in heart rate: implications for gene-specific therapy. *Circulation, 92*, 3381−3386.

Sculptoreanu, A., Rotman, E., Takahashi, M., Scheuer, T., & Catterall, W. A. (1993a). Voltage-dependent potentiation of the activity of cardiac L-type calcium channel alpha 1 subunits due to phosphorylation by cAMP-dependent protein kinase. *Proc Natl Acad Sci USA, 90*, 10 135−10 139.

Sculptoreanu, A., Scheuer, T., & Catterall, W. A. (1993b). Voltage-dependent potentiation of L-type Ca^{2+} channels due to phosphorylation by cAMP-dependent protein kinase. *Nature, 364*, 240−243.

Shimizu, W., & Antzelevitch, C. (1997). Sodium channel block with mexiletine is effective in reducing dispersion of repolarization and preventing torsade des pointes in LQT2 and LQT3 models of the long-QT syndrome. *Circulation, 96*, 2038−2047.

Starmer, C. F., & Courtney, K. R. (1986). Modeling ion channel blockade at guarded binding sites: application to tertiary drugs. *Am J Physiol, 251*, H848−H856.

Striessnig, J., Grabner, M., Mitterdorfer, J., Hering, S., Sinnegger, M. J., & Glossmann, H. (1998). Structural basis of drug binding to L Ca2+ channels. *Trends Pharmacol Sci, 19*, 108−115.

Stuhmer, W., Conti, F., Suzuki, H., et al. (1989b). Structural parts involved in activation and inactivation of the sodium channel. *Nature, 339*, 597−603.

Stuhmer, W., Conti, F., Suzuki, H., et al. (1989a). Structural parts involved in activation and inactivation of the sodium channel. *Nature, 339*, 597−603.

Suzuki, H., Beckh, S., Kubo, H., et al. (1988). Functional expression of cloned cDNA encoding sodium channel III. *FEBS Lett, 228*, 195−200.

Tang, S., Yatani, A., Bahinski, A., Mori, Y., & Schwartz, A. (1993). Molecular localization of regions in the L-type calcium channel critical for dihydropyridine action. *Neuron, 11*, 1013−1021.

Tikhonov, D. B., & Zhorov, B. S. (2009). Structural model for dihydropyridine binding to L-type calcium channels. *J Biol Chem, 284*, 19006−19017.

Triggle, D. J. (2007). Calcium channel antagonists: clinical uses − past, present, and future. *Biochem Pharmacol, 74*, 1−9.

Tsien, R. W. (1977). Effects of epinephrine on the pacemaker potassium current of cardiac Purkinje fibers. *J Gen Physiol, 64*, 293−319.

Tsien, R. W., Ellinor, P. T., & Horne, W. A. (1991). Molecular diversity of voltage-dependent Ca^{2+} channels. [Rev.]. *TIPS, 12*, 349−354.

Vassilev, P. M., Scheuer, T., & Catterall, W. A. (1988). Identification of an intracellular peptide segment involved in sodium channel inactivation. *Science, 241*, 1658−1661.

Vassort, G., Talavera, K., & Alvarez, J. L. (2006). Role of T-type Ca2+ channels in the heart. *Cell Calcium, 40*, 205−220.

Vedantham, V., & Cannon, S. C. (1999). The position of the fastinactivation gate during lidocaine block of voltage-gated Na^+ channels. *J Gen Physiol, 113*, 7−16.

Viola, H. M., Macdonald, W. A., Tang, H., & Hool, L. C. (2009). The L-type Ca(2+) channel as a therapeutic target in heart disease. *Curr Med Chem, 16*, 3341−3358.

Wang, D. W., Yazawa, K., Makita, N., George, A. L., & Bennett, P. B. (1997). Pharmacological targeting of long QT mutant sodium channels. *J Clin Invest, 99*, 1714−1720.

Welling, A., Kwan, Y. W., Bosse, E., Flockerzi, V., Hofmann, F., & Kass, R. S. (1993). Subunit-dependent modulation of recombinant L-type calcium channels: molecular basis for dihydropyridine tissue selectivity. *Circ Res, 73*, 974–980.

Welling, A., Ludwig, A., Zimmer, S., Klugbauer, N., Flockerzi, V., & Hofmann, F. (1997). Alternatively spliced IS6 segments of the alpha 1C gene determine the tissue-specific dihydropyridine sensitivity of cardiac and vascular smooth muscle L-type Ca^{2+} channels. *Circ Res, 81*, 526–532.

West, J. W., Patton, D. E., Scheuer, T., Wang, Y., Goldin, A. L., & Catterall, W. A. (1992). A cluster of hydrophobic amino acid residues required for fast Na(+)-channel inactivation. *Proc Natl Acad Sci USA, 89*, 10 910–10 914.

Wier, W. G., & Balke, C. W. (1999). Ca(2+) release mechanisms, Ca(2+) sparks, and local control of excitation-contraction coupling in normal heart muscle. *Circ Res, 85*, 770–776.

Windle, J. R., Geletka, R. C., Moss, A. J., & Atkins, D. L. (2001). Normalization of ventricular repolarization with flecainide in patients with the LQT3 form (SCN5A) of long QT syndrome. *Ann Noninvasive Electrocardial, 6*, 153–158.

Xu, X., & Colecraft, H. (2009). Engineering proteins for custom inhibition of Ca(V) channels. *Physiology, 24*, 210–218.

Yang, J., Ellinor, P. T., Sather, W. A., Zhang, J. F., & Tsien, R. W. (1993). Molecular determinates of Ca^{2+} selectivity and ion permeation in L-type Ca^{2+} channels. *Nature, 366*, 158–161.

Zhao, X. L., Gutierrez, L. M., Chang, C. F., & Hosey, M. M. (1994). The alpha 1-subunit of skeletal muscle L-type Ca channels is the key target for regulation by A-kinase and protein phosphatase-1C. *Biochem Biophys Res Commun, 198*, 166–173.

Zimmer, T., & Surber, R. (2008). SCN5A channelopathies – an update on mutations and mechanisms. *Prog Biophys Mol Biol, 98*, 120–136.

Zuhlke, R. D., Bouron, A., Soldatov, N. M., & Reuter, H. (1998). Ca^{2+} channel sensitivity towards the blocker isradipine is affected by alternative splicing of the human alpha1C subunit gene. *FEBS Lett, 427*, 220–224.

Chapter 30

Inherited Diseases of Ion Transport

Robert A. Farley

Chapter Outline

I. SUMMARY

Diseases caused by mutations in genes that encode ion channels or ion transporters affect nearly every organ in the body. This chapter describes the genetic basis for several of these diseases, including the effect of gene mutations on protein structure and function, the biochemical and physiological consequences of the mutant proteins on organ function, the relationship of altered ion transport to disease symptoms and available treatments for the diseases.

II. INTRODUCTION

In 2010, four of the 20 best-selling drugs in the world targeted ion transporters because inhibition of these transporters is an effective way to alleviate the symptoms of many diseases. This should not be surprising since ion transport is a fundamental physiological activity in all tissues of the body and many diseases and pathological conditions are caused by dysfunctions of ion transport. For many diseases, such as type II diabetes, in which the disease pathology is manifest in several different organs, the abnormal ion transport may not be the primary cause of the disease and correction of the ion transport defect may not relieve the symptoms of the disease or cure the patient. In an increasing number of diseases, however, it is known that disease is caused by a mutation in a single gene that codes for an ion transport protein or for a regulator of an ion transport protein. Diseases of this type are found in many different organs in the body and include cystic fibrosis, familial hemiplegic migraine, long QT syndrome, myotonias and periodic paralyses of skeletal muscle, malignant hyperthermia and several different forms of hypertension. This chapter summarizes current knowledge about the origin of several of these inherited diseases of ion transport, the effects of the gene mutations on protein structure and function, the mechanisms whereby alterations in transport function can explain the symptoms of the disease and therapeutic approaches to relieve the symptoms of the disease or cure the patient. The excellent book by Frances Ashcroft (2000) discusses many diseases associated with altered ion channel function as they were understood prior to the year 2000.

III. IDENTIFYING HERITABLE MUTATIONS UNDERLYING DISEASES OF ION TRANSPORT

The most powerful techniques available to identify genes that contain mutations causing symptoms of common diseases such as diabetes, cardiovascular disease and hypertension are genome-wide association techniques. Very large numbers of samples are needed because the symptoms of these diseases are usually caused by mutations in multiple genes and the contribution of any single mutation to the disease symptoms in the population may be small. For diseases of this sort, the "common disease—common variant" hypothesis, that the genetic variations

Cell Physiology Sourcebook. DOI: 10.1016/B978-0-12-387738-3.00030-5

that underlie a disease should be over-represented in individuals with the disease, is assumed.

For rare diseases that occur in a small number of cases, genome-wide association techniques are not applicable, although these techniques are beginning to be applied to study some rare diseases. Most of the diseases of ion transport that are discussed in this chapter are rare diseases that segregate in a Mendelian pattern and the underlying mutations have been identified in genes using positional cloning and linkage analysis. In this approach, individuals from a large family in which several members suffer from the disease are collected and a pedigree is constructed to show how the disease segregates between generations. DNA from both affected family members and those who are not affected is screened with multiple chromosomal markers in order to identify a region on a chromosome that is associated with the inheritance of the disease. Examples of genetic markers that have been used for this type of analysis are restriction fragment length polymorphisms (RFLPs), microsatellite or short tandem repeat polymorphisms (STRs or STRPs) and single nucleotide polymorphisms (SNPs). Once a region of a chromosome has been identified as a candidate for the location of the mutation, the fine structure of the DNA is analyzed by studying the inheritance pattern of several different genes located in this region of the chromosome to identify those that segregate with the disease symptoms and, finally, DNA sequence analysis to identify mutations in the DNA of affected individuals. Using these methods, the gene encoding the protein whose mutations are responsible for cystic fibrosis was identified in 1989 (Riordan et al., 1989). This was the first gene associated with a disease of ion transport in humans to be identified. It is noteworthy that linkage between cystic fibrosis and the DNA marker DOCRI-917 in humans was reported in 1985 and that it took four years to identify the gene after the linkage was established.

IV. FAMILIAL HEMIPLEGIC MIGRAINE

Migraine is a common episodic headache disorder that can occur either with preceding visual or other sensory discomfort (migraine with aura) or without these symptoms (migraine without aura). Migraine attacks are typically characterized by pulsating headache, nausea, vomiting and photo- and phonophobia and may last between 4 and 72 hours. Migraine occurs approximately twice as often in females as in males, with up to 25% of females reporting two or more occurrences. Family, twin or population-based studies indicate that there are genetic factors involved in the susceptibility to migraine, but the complexity of the symptoms reported by different groups indicates that there are likely to be several different physiological mechanisms that contribute to the occurrence of migraine in different populations. Familial hemiplegic migraine is a rare autosomal dominant form of migraine with aura that is associated with paralysis of one side of the body during the attack (ictal hemiparesis) (Gargus, 2009). Unlike other forms of migraine, permanent cerebellar symptoms such as progressive cerebellar ataxia or nystagmus with cerebellar atrophy are observed in some cases of familial hemiplegic migraine. A gene locus for familial hemiplegic migraine on chromosome 19 was identified by positional cloning and, in 1996, mutations in the CACNA1A gene that encodes a calcium channel $\alpha 1$ subunit were identified as causing both familial hemiplegic migraine (FHM1) and episodic ataxia type-2, which is another autosomal dominant paroxysmal cerebral disorder having migraine-like symptoms (Ophoff et al., 1996). Subsequently, mutations in the ATP1A2 gene (Vanmolkot et al., 2003), encoding the $\alpha 2$ subunit of Na^+/K^+-ATPase, and in the SCN1A gene (Dichgans et al., 2005), encoding the α subunit of a voltage-gated sodium channel, have been identified in subpopulations of patients with familial hemiplegic migraine FHM2 and FHM3, respectively. Patients with FHM2 or FHM3 do not have mutations in the CACNA1A gene.

Migraine headache pain is initiated by activation of nociceptive sensory afferents of the trigeminal nerve (Pietrobon, 2005). These neurons release vasoactive neuropeptides at their nerve terminals that activate second-order neurons in the trigeminal nucleus caudalis, with further activation of additional neuronal pathways that are involved in the processing and perception of pain. The mechanisms whereby the trigeminal nociceptors are activated remain incompletely understood at this time; however, studies in animals and humans implicate cortical spreading depression as a possible cause of migraine headache pain. Cortical spreading depression is an electrophysiological occurrence of a wave of depolarization followed by a short-lasting depression of electrical activity that spreads across the cortex at a rate of 2−6 mm/min, a rate similar to the rate of spread of the aura associated with migraine. Cortical spreading depression is also associated with changes in cerebral blood flow that are due to coupling between neuropeptide release and cerebrovascular tone. The changes in blood flow that have been measured during aura are synchronous with increased release of excitatory amino acids and this suggests that the mechanism of cortical spreading depression may underlie migraine aura and headache.

The CACNA1A gene encodes the pore-forming subunit of $Ca_v2.1$, a voltage-gated P/Q-type Ca^{2+}-channel. P/Q-type Ca^{2+}-channels are found in presynaptic terminals and somatodendritic membranes throughout the mammalian brain and spinal cord where they play a prominent role in initiating action potential-evoked neurotransmitter release. They have been identified in all of the brain structures that have been implicated in the pathogenesis of

migraine pain and they are involved in the mechanism of release of vasoactive neuropeptides from terminals of the trigeminal nerve and the release of excitatory neurotransmitters in several different cortical areas. As of 2010, 21 missense mutations had been identified in CACNA1A that produce amino acid substitutions in conserved regions of the $Ca_v2.1$ Ca^{2+}-channel. Analysis of whole cell or single-channel Ca^{2+}-channel currents from different mutants showed that different effects were produced by different mutations, but all of the mutants seemed to show voltage-activation curves that were shifted to more negative voltages. This shift results in a higher open probability and single channel Ca^{2+} influx through open channels. Despite this single channel gain of function effect, whole cell Ca^{2+} current density was reduced in cells overexpressing mutant channels. Analysis of the number of functional channels overexpressed in either HEK293 cells or in $Ca_v2.1^{-/-}$ cells showed that the number of mutant channels on the cell surface was reduced compared to the number of wild-type channels. In knock-in mice, however, in which the mutant channels are expressed at near physiological levels, the effect of the mutations is seen to be consistent with the gain of function seen in the single channel measurements. Gain-of-function mutations in the $Ca_v2.1$ channels lead to increased evoked Ca^{2+}-dependent neurotransmitter release in individuals with familial hemiplegic migraine. Consistent with this mechanism, the induction and propagation of cortical spreading depression were larger in mice containing mutant $Ca_v2.1$ channels than in wild-type mice.

The multiple mutations in the ATP1A2 gene that encodes the $\alpha2$ subunit of Na^+,K^+-ATPase and that have been identified in patients with familial hemiplegic migraine type 2 (FHM2) have been found to cluster in six regions of the protein: the N-domain, which is involved in ATP binding; the A-domain, called the actuator domain; the P-domain, which the site of the aspartate residue that is phosphoryated by ATP during the catalytic cycle; at the interface between the transmembrane domain and the P-domain, which is involved in coupling ATP hydrolysis to ion transport; near the carboxy-terminus of the α subunit; and in the extracellular loops of the α subunit, which may form a pathway for release of transported ions to the extracellular solution (Morth et al., 2009). Only some of the mutants have been characterized for biochemical effects of the mutations and pumps that are either functionally inactive or pumps that are functionally active but have reduced activity have been identified. The functionally active pumps either have altered affinity for Na^+ or K^+, or have reduced catalytic turnover for other reasons. The decrease in Na^+,K^+-ATPase activity associated with these mutants may lead to the symptoms of familial hemiplegic migraine by causing an increase in extracellular K^+ that would depolarize the cell resting membrane potential and induce spontaneous waves of cortical spreading depression. A correlation between extracellular K^+ concentrations and the frequency of waves of spontaneous spreading depression in chicken retina has been reported (Dahlem et al., 2003). On the other hand, the $\alpha2$ isoform of Na^+,K^+-ATPase constitutes only about 10% of the total Na^+,K^+-ATPase activity in the brain and it might seem surprising that mutations in the $\alpha2$ subunit would have such severe effects. This apparent inconsistency might be resolved, however, if the $\alpha2$ isoform of the sodium pump were confined to microdomains of the cell membrane that are associated with other transporters involved in calcium signaling and homeostasis, such as the Na^+/Ca^{2+} exchanger and Ca^{2+} channels, where they could influence neurotransmitter release (see Chapter 14).

The SCN1A gene encodes the pore-forming subunit of the voltage-gated sodium channel $Na_V1.1$ and at least three missense mutations in this gene have been linked to familial hemiplegic migraine type 3 (FHM3). Each of the mutant sodium channels exhibits a different set of functional consequences. Both loss-of-function and gain-of-function phenotypes have been found, as well as a mutant that is defective in the trafficking to the plasma membrane. It has been suggested that the loss-of-function mutants may affect primarily inhibitory GABAergic (γ-aminobutyric acid) neurons whereas gain-of-function mutants may primarily affect the activity of excitatory neurons. Either of these consequences of mutations in the $Na_V1.1$ channel could reduce the threshold for spontaneous action potentials and the initiation of cortical spreading depression in FHM3 patients.

V. CYSTIC FIBROSIS

Cystic fibrosis, the most common lethal genetic disease in Caucasians, was the first inherited disease of ion transport for which the genetic locus was identified. More than 1000 mutations have been identified in a gene on chromosome 7 that encodes the CFTR protein (cystic fibrosis transmembrane conductance regulator) and lead to symptoms of varying severity that characterize the disease. Cystic fibrosis is an autosomal recessive disease that occurs with a frequency of approximately 1 in 2000 Caucasians and it has been estimated that approximately 1 in 20 people of European descent are carriers with a mutation in one allele. Because of the severity of the disease and the availability of information about many of the mutations in the CF gene that cause cystic fibrosis, screening of newborns for CFTR mutations is nearly universal in the USA.

The clinical symptoms of cystic fibrosis include abnormally high concentrations of Na^+ and Cl^- in sweat, persistent pulmonary infection with *Pseudomonas aeruginosa*, thick and viscous mucus, pancreatic insufficiency, muscle weakness and failure to thrive. CFTR is a cAMP-activated Cl^- channel that is present on the apical surface

of many epithelial cells and is involved in Cl^- absorption or secretion. In secretory epithelia, the symptoms of the disease are caused by reduced NaCl transport out of the cells and an associated reduction in hydration of the lumen of the secretory organs. This leads to thickened and dehydrated mucus that blocks motility in organs such as the pancreas, the trachea and the intestinal tract. Pancreatic and intestinal blockage prevent release of digestive enzymes and the efficient absorption of nutrients and explains the muscle weakness and failure to thrive seen in CF children. Obstruction of pancreatic ducts eventually leads to tissue destruction, with fibrotic tissue and fat depositions replacing normal pancreatic parenchyma. Children with cystic fibrosis are routinely treated with oral enzyme replacements to offset this deficiency of pancreatic enzyme secretion. Tracheal blockage is responsible for the persistent coughing of CF patients and also provides a hospitable environment for *Pseudomonas* growth. Persistent bacterial infection and the associated inflammation lead to progressive pulmonary insufficiency due to damaged lung parenchyma and recurrent pneumothoraces. The major cause of morbidity and mortality in CF patients is progressive pulmonary disease. In absorptive epithelia such as the sweat gland, the reduced absorption of NaCl leads to the elevated concentrations of salt that is the characteristic feature of the disease. The diagnostic criterion for cystic fibrosis is the elevated Na^+ and Cl^- concentrations in the sweat. Normal sweat chloride levels are 10−35 mEq/L, whereas patients with cystic fibrosis usually have sweat chloride concentrations of 60 mEq/L or greater. Intermediate levels of 35−60 mEq/L may be found in some CF patients, as well as in the normal population.

The major anion secreted by the pancreas is bicarbonate and there is some uncertainty about whether CFTR transports bicarbonate as well as Cl^- in the pancreas. Evidence supporting this mechanism has been published, but an alternative explanation for pancreatic insufficiency due to mutations in CFTR is that CFTR is the route of Cl^- efflux from pancreatic acinar cells and this extracellular Cl^- is then recycled back into the cell via the Cl^-/HCO_3^- exchanger, with efflux of bicarbonate. Mutations in CFTR that reduce Cl^- efflux would have the effect of also reducing bicarbonate secretion through this mechanism. The trachea has both absorptive and a secretory functions and, in cystic fibrosis, the balance between these two functions shifts toward increased absorption.

Mutations in the CF gene may reduce chloride absorption and secretion by epithelia by different mechanisms. Some mutations are nonsense, frameshift or splicing mutations that prevent the CFTR protein from being synthesized. The most common mutation in cystic fibrosis patients, a deletion of one amino acid (ΔF508) in CFTR, is found in about 70% of cystic fibrosis patients and causes CFTR to fold incorrectly. The biosynthesis of misfolded CFTR is disrupted, trapping the protein in the endoplasmic reticulum and the channel is not delivered to the plasma membrane. Other mutations, such as the missense mutation G551D, result in CFTR channels that reach the plasma membrane but rarely open. Studies in cell cultures suggest the possibility of reversing some of these abnormalities and many trials have been undertaken to correct different defects in CFTR. Among the most promising at this time are efforts to use small molecules to potentiate the activity of mutants, such as the G551D mutant, by increasing the open lifetime of the channel. The most important target, however, remains the ΔF508 mutation, because of its prevalence in the CF population, and high-throughput screening has identified some candidate molecules that improve the processing of this mutant and increase its abundance in the plasma membrane of cells where it functions as a chloride channel.

VI. LONG QT SYNDROME

Cardiac contraction is the end result of action potentials that are initiated at the sinoatrial node by the spontaneous depolarization of the nodal cells to threshold and the subsequent transmission of triggered action potentials in different cells of the cardiac conduction pathway to the atrial and ventricular muscle fibers. The amount of charge that moves across cell membranes during action potentials in most cells of the conduction system is small; however, because atrial muscle and ventricular muscle are sufficiently massive, charge movement during contraction and relaxation of these tissues can be detected at the surface of the body. It is the movement of charge during cardiac muscle contraction and relaxation that is measured in the electrocardiogram (EKG; ECG). A 12-lead EKG from a heart showing normal sinus rhythm is shown in Fig. 30.1A. The deflections are most easily identified using lead II, shown in Fig. 30.1B.

The deflections or waves in the EKG correspond to atrial muscle depolarization and contraction (P wave), ventricular depolarization and contraction (QRS complex) and ventricular repolarization and relaxation (T wave). Among the parameters that are measured on an EKG are the times between specific events, such as the beginning of the T wave and the end of the R wave (PR interval) and the beginning of the Q wave and the end of the T wave (QT interval). In the normal population, the PR interval is 0.12−0.20 s. The QT interval is most often reported as a "corrected" QT interval, $QT/\sqrt{RR}$, in recognition of the fact that the QT interval changes as heart rate changes. Corrected QT intervals in the normal population are less than 0.44 s. When the QT interval is longer than 0.44 s, individuals are said to have long QT syndrome.

The presence and timing of the different deflections on the EKG reflect the highly coordinated opening and closing

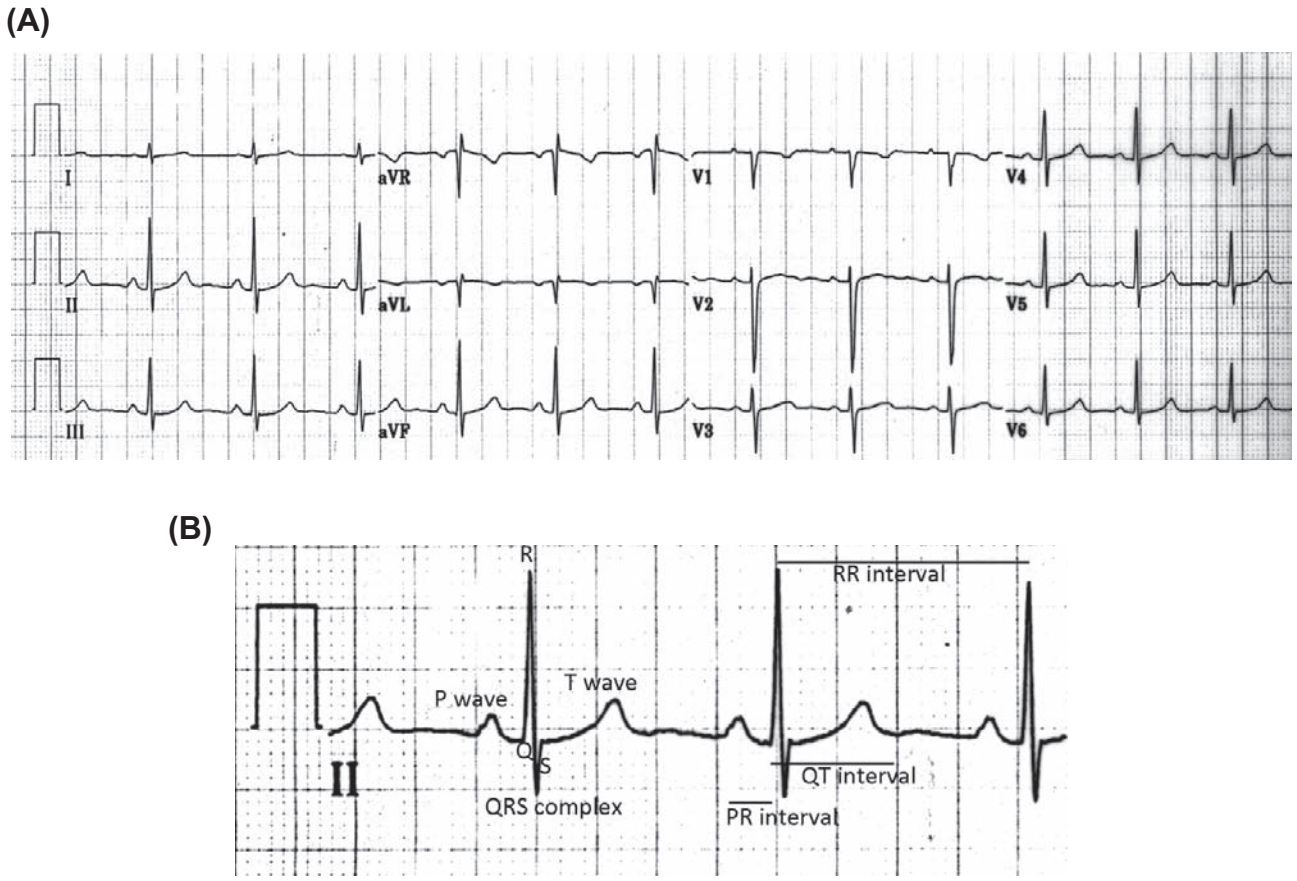

FIGURE 30.1 Electrocardiogram (EKG) showing normal sinus rhythm. (A) 12-lead EKG record. The horizontal axis is time and the vertical axis is voltage. Each lead is identified below the EKG trace that is recorded from that lead. (B) EKG trace from lead II in (A) showing the names of the deflections and intervals. *(See text for details.)*

of ion channels in the cardiac myocytes. A typical action potential in ventricular myocytes is shown in Fig 30.2, with the different phases of the action potential labeled as phases 0–4. In the EKG, the QRS complex corresponds to muscle depolarization and contraction, or phase 0 in the action potential, whereas the T wave corresponds to muscle repolarization and relaxation, or phase 3 of the action potential.

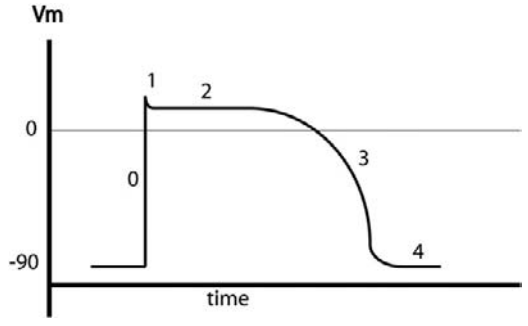

FIGURE 30.2 Drawing of an action potential from a cardiac ventricular myocyte. The phases of the action potential are identified by the numbers 0–4. The value of the membrane potential is shown on the vertical axis as a function of time on the horizontal axis. *(See text for details.)*

The phase 0 depolarization of the action potential is due to the opening of voltage-gated Na^+ channels that are encoded by the SCN5A gene. These channels inactivate toward the end of phase 0 and, in phase 1, the reduction in sodium conductance due to the closure of these channels, together with the delayed opening of transient-open K^+ channels, is responsible for the slight repolarization of the membrane potential that is observed. During phase 2 of the action potential, there is a relative balance between inward current carried primarily by Ca^{2+} and Na^+ ions through voltage-gated L-type Ca^{2+} channels and outward current through delayed rectifier K^+ channels. Toward the end of phase 2, the voltage-gated Ca^{2+} channels close while delayed rectifier K^+ channels continue to activate, shifting the balance of current flow to outward K^+ current. This shift in charge movement repolarizes the membrane potential and triggers muscle relaxation. On the EKG, the QT interval can be understood as a reflection of the balance between the depolarization due to open Na^+ channels and repolarization due to open K^+ channels. Mutations in any

of the channels that affect the action potential duration might be expected to affect the QT interval and at least 10 forms of long QT syndrome have been identified in patients, reflecting underlying mutations in these different channels or other proteins associated with them.

Long QT syndrome type 1 (LQT1) is due to mutations in the KCNQ1 gene that encodes the pore forming α subunit of the slow delayed rectifier K^+ channel. In phase 2 of the action potential, two different delayed rectifier K^+ channels open at different rates, a fast delayed rectifier and a slow delayed rectifier. The slow delayed rectifier channel consists of a pore forming α subunit (K_vLQT1) and a β subunit (MinK) that is encoded by the KCNE1 gene. LQT5 is caused by mutations in the KCNE1 gene. The faster-opening delayed rectifier K^+ channel contains a pore-forming α subunit that is encoded by the HERG gene and a β subunit (MiRP1) encoded by the KCNE2 gene. LQT2 is due to mutations in the HERG gene and LQT6 is caused by mutations in the KCNE2 gene. A different type of K^+ channel, an inward rectifier K^+ channel, plays little or no role during phase 2 of the cardiac action potential, but is important during the phase 3 repolarization phase. The current carried by these channels is called I_{K1} and is due to the inward rectifier Kir2.1 channel that is encoded by the KCNJ2 gene. Reductions in I_{K1} prolong the repolarization phase of the action potential and mutations in KCNJ2 underlie LQT7. As discussed in the next section, Kir2.1 K^+ channels are also expressed in skeletal muscle and mutations in KCNJ2 lead to a form of periodic paralysis in skeletal muscle that is called Andersen's syndrome (Andersen–Tawil syndrome). All of the forms of long QT syndrome that are caused by mutations in genes encoding K^+ channel subunits are loss-of-function mutations that lead to reductions in repolarizing currents. This reduction in repolarization prolongs phase 2 of the action potential, which is manifest as a longer QT interval on the EKG.

In contrast to the loss-of-function mutations in K^+ channels, mutations in the SCN5A gene encoding the voltage-gated Na^+ channel that are associated with LQT5 are gain-of-function mutations. These mutations do not alter the conductance of the channel but rather affect the inactivation of the channel. Electrophysiological measurements and computer simulations of channel activity show that a small fraction of voltage-gated Na^+ channels with LQT5 mutations reopen during phase 2 of the action potential and result in a sustained inward Na^+ current. This inward Na^+ current is depolarizing and opposes the repolarization that is due to opening of K^+ channels.

Other forms of long QT syndrome have been identified in which mutations occur in genes that encode other proteins that influence the action potential, such as voltage-gated Ca^{2+} channels or proteins that affect the subcellular localization of the channels, such as ankyrin. The molecular characterization of the effects of these mutations has not been so well characterized, however, as those described above.

VII. MYOTONIA AND PERIODIC PARALYSIS OF SKELETAL MUSCLE

Mutations in genes that encode voltage-gated sodium channels or potassium channel subunits in the heart are responsible for long QT syndrome and altered myocardial contraction. Inherited mutations in a voltage-gated sodium channel or in any of several potassium channel subunits are also responsible for various forms of paralysis or myotonia in skeletal muscle. Like in the heart, mutations in these channels in skeletal muscle primarily affect the rates of entry into the inactivated state or the recovery from inactivation and have little or no affect on ion selectivity or single channel conductance. The clinical hallmark of periodic paralysis is the episodic occurrence of attacks of flaccid weakness. Periodic paralysis in skeletal muscle is often associated with abnormally high or low serum K^+ concentrations and is called either hyperkalemic periodic paralysis or hypokalemic periodic paralysis, depending on whether ictal serum K^+ concentrations are elevated or depressed compared to normal levels. The changes in serum $[K^+]$ associated with these diseases, however, can be variable. Although mutations in the SCN4A gene encoding the voltage-gated sodium channel in skeletal muscle can lead to either hyperkalemic periodic paralysis or hypokalemic periodic paralysis, most patients who are diagnosed with hypokalemic periodic paralysis have mutations in the CACNA1S gene that encodes an L-type voltage-gated calcium channel. Andersen's syndrome, which is caused by mutations in the KCNJ2 gene that encodes the inward rectifier Kir 2.1 channel and is also called Andersen–Tawil syndrome, is the only form of inherited periodic paralysis in humans that affects tissues other than skeletal muscle. In addition to periodic paralysis of skeletal muscle, patients with Andersen's syndrome often have ventricular arrhythmias and dysmorphic features such as clinodactyly, low-set ears, short stature and hypoplastic mandible.

Myotonia is a state of sustained muscle contraction that is difficult to relax. During myotonic contractions, electrophysiological measurements show that repetitive action potentials fire in muscle cells even in the absence of nervous input. Paramyotonia congenita is a form of myotonia that is caused by mutations in the SCN4A gene. Another form of myotonia, called myotonia congenital, is caused by mutations in the CLCN1 gene that encodes a voltage-gated chloride channel found in the transverse tubules. Myotonia congenita is also called Thomsen's disease for the Danish physician who first described the symptoms in himself. Note that, depending on the nature of

the mutation in SCN4A, amino acid substitutions in the skeletal muscle voltage-gated sodium channel may lead to either paralysis or myotonia. Furthermore, episodes of mytonia may also occur in patients with hyperkalemic periodic paralysis, sometimes within minutes of the paralysis. All of the myotonias and familial periodic paralyses are inherited in an autosomal dominant pattern and are in contrast to a generalized form of myotonia called Becker's type that is inherited in a recessive pattern. Becker's myotonia is also caused by mutations in the CLCN1 gene.

Mutations in SCN4A that lead to hyperkalemic periodic paralysis reduce the rate of inactivation of the voltage-gated Na^+ channels, which are responsible for the initiation of the action potential in the skeletal muscle cells. Furthermore, a small fraction of Na^+ channels (1.5−5%) may remain open after depolarization of the muscle fiber and lead to a persistent inward current and slight depolarization of the skeletal muscle membrane potential (Cannon, 2002). Tonic depolarization of the membrane potential leads to inactivation of sodium channels with the result that there is an insufficient number of channels available to initiate an action potential in response to nervous stimulation. Muscle weakness and paralysis then ensue. The failure of these mutant channels to inactivate normally is exaggerated when serum K^+ concentrations are elevated. In addition, the voltage dependence of opening of the mutant channels is shifted to hyperpolarized potentials, also resulting in a small persistent inward Na^+ current at membrane potentials where wild-type channels are normally closed. Ingestion of a carbohydrate-rich meal can sometimes alleviate the symptoms of hyperkalemic periodic paralysis, because the carbohydrates stimulate insulin release and insulin is an activator of Na^+,K^+-ATPase, which would pump K^+ into cells and reduce plasma K^+ concentrations.

Mutations in SCN4A are responsible for only about 10% of patients with hypokelemic periodic paralysis, whereas about 70% of these patients have been found to have mutations in the CACNA1S gene, which encodes an L-type Ca^{2+} channel that is located in the transverse tubule of the myocyte. The molecular mechanisms responsible for this type of paralysis are not understood and it seems paradoxical that muscle from patients with hypokalemic periodic paralysis will depolarize when serum K^+ concentrations are less than normal. All of the mutations in CACNA1S that are found in patients with hypokelemic periodic paralysis are located in the one of the four S4 segments of the channel, which is part of the voltage-sensor. In vitro studies indicate that the Ca^{2+} current density of muscle fibers from these patients is only about 50% of controls and the channels demonstrate a reduction in the rate of activation in response to a stimulus. Microelectrode recordings from muscle fibers containing sodium channel mutations in SCN4A show a shift in the voltage-dependence of inactivation to hyperpolarized potentials, which would result in an increase in the fraction of inactivated channels at mildly depolarized potentials. There is also some evidence that mutations in the voltage-gated Na^+ channel can lead to a non-selective inward monovalent cation leak through the channel at hyperpolarized potentials, but it has been shown that most cases of hypokalemic periodic paralysis are characterized by mutations in the voltage-sensor segments of either the Na^+ channels or the Ca^{2+} channels. Taken together, the defects in the voltage-gated Na^+ channels and Ca^{2+} channels are consistent with a mechanistic disruption of the coupling between nervous stimulation of the muscle and contraction, and with consequent muscle weakness and paralysis. How hypokalemia induces muscle cell depolarization, however, remains unknown. The reader is referred to Chapter 9 where a roll-over in the RP vs $(K)_o$ curve at low $(K)_o$ levels is shown and discussed.

Patients with paramyotonia congenita are often alerted to the disease by myotonia that is induced by cold weather. Paramyotonia congenita is also aggravated by prolonged exercise and, whereas patients with paramyotonia congenita may also have episodic periods of muscle weakness that is associated with elevated serum $[K^+]$ or prolonged cooling, the aggravation of symptoms with prolonged exercise is not observed in hyperkalemic periodic paralysis. Mutations in SCN4A that are associated with paramyotonia congenita slow inactivation of the sodium channels and increase the rate of recovery from inactivation. Computer simulations (Fig. 30.3) indicate that these effects promote repetitive firing of the muscle fiber followed by decreased excitability due to sustained depolarization of the membrane (Hayward et al., 1996). Like the mutant sodium channels in hyperkalemic periodic paralysis that also show slow inactivation, channels associated with paramyotonia congenita do not inactivate completely and a persistent inward current at the end of depolarization is observed.

Andersen's syndrome is caused by missense or deletion mutations in the KCNJ2 gene that encodes an inward rectifier potassium channel Kir2.1 in humans. Inward rectifier K^+ channels are important for setting the resting membrane potential in many cells. There are multiple inward rectifier channels expressed in skeletal muscle and the contribution of each channel type to the maintenance of resting membrane potential in these cells has not been established. Expression of Kir2.1 channels with any of several missense mutations associated with Andersen's syndrome in *Xenopus* oocytes does not result in measurable K^+ current and it has been shown that this is the result of the failure of the channels to assemble properly and be transported to the cell surface (Bendahhou et al., 2003). Expression of mutant subunits together with wild-type subunits, however, results in assembly of hybrid channels containing both wild-type and mutant subunits. Some of these hybrid channels are transported to the cell surface but

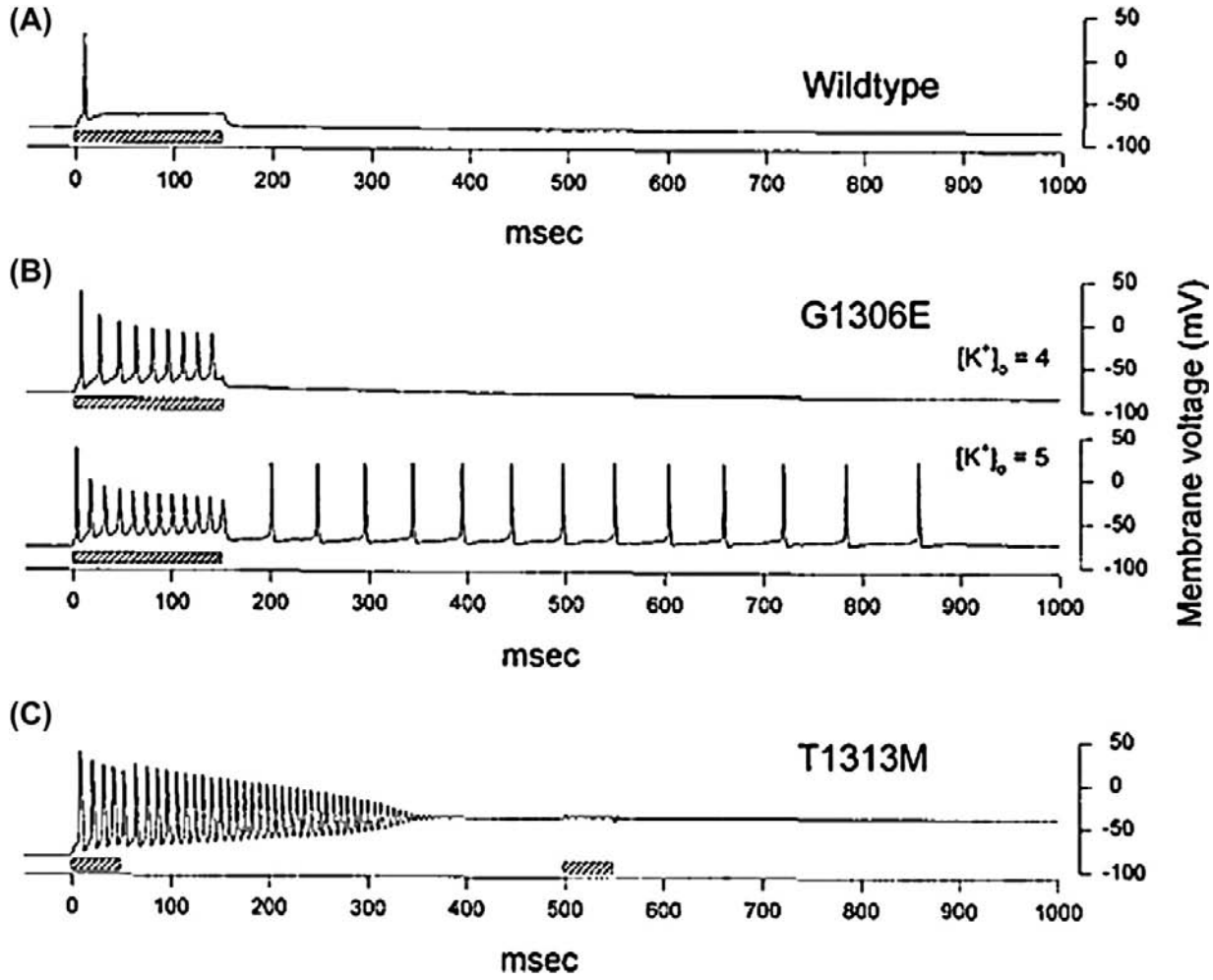

FIGURE 30.3 Simulated membrane potential changes in response to injected current pulses in cells containing G1306E and T1313M mutations in the cardiac voltage gated Na^+ channel gene SCN4A. (A) The wild-type response to a 150 ms stimulus (shaded bar) is a single action potential. (B) The G1306E mutation is found in patients with sodium channel myotonia. The response of cells containing this mutant channel to a 150 ms stimulus is repetitive firing of action potentials (myotonia). At normal $[K^+]$ the action potentials cease once the stimulus is stopped and the membrane potential returns to the baseline. At slightly elevated $[K^+]$, repetitive action potentials continue even after stimulation of the cells has stopped. (C) The T1313M mutation is found in the SCN4A gene of patients with paramyotonia congenita. Repetitive action potentials are observed during and following cessation of a 150 ms stimulus. The membrane potential remains depolarized after cessation of the stimulus, which renders the cell unresponsive to a second stimulus delivered at t = 500 ms. *(Figure reproduced from Hayward et al., 1996 with permission.)*

they are non-functional, indicating that the mutant subunits have a dominant-negative effect on the wild-type subunits. Other mutants fail to assemble with the wild-type subunits or assemble with wild-type subunits but are not transported to the cell surface. In all of these instances, the number of functional inward rectifier channels is reduced and the cell membrane potential will be depolarized. Depolarization will inactivate the sodium channels and make the muscle fiber electrically inexcitable. Because the Kir2.1 channel also contributes to the repolarization of the cardiac action potential, reductions in this component of the K^+ current at the end of the plateau phase will delay repolarization and lead to a long QT interval (LQT7) and increased susceptibility to cardiac arrhythmias. The role of Kir2.1 channels in craniofacial, limb and axial skeletal development has not been completely described, but the K^+ current through these channels must be involved in this process early in development because the targeted disruption of Kir2.1 in knockout mice causes neonatal lethality.

Unlike most mammalian cell membranes, the skeletal muscle plasma membrane is significantly more permeable to Cl^- ions than to K^+ ions. The reader is referred to the Chapter 42 where this is discussed in great detail. During muscle contraction there is a significant increase of $[K^+]$ in the confined space of the transverse tubules and the efflux of Cl^- through voltage-gated ClC-1 Cl^- channels neutralizes this charge buildup, preventing prolonged depolarization of the membrane potential. In myotonia congenita,

mutations in the CLCN1 gene that encodes the ClC-1 channel cause a shift in the voltage-activation of the ClC-1 channel to more positive potentials or result in the reduction of the number of functional channels in the cell membrane (Lossin and George, 2008). Both of these effects on the channel increase the concentration of K^+ in the lumen of the transverse tubules and lead to depolarization of the membrane potential and periods of repetitive action potential initiation. The electrical basis for the myotonia was determined in the laboratory of Shirley Bryant in 1974 from electrophysiological recordings from muscle fibers from myotonic goats (Adrian and Bryant, 1974). Strains of these goats are known to collapse for short periods of time after being startled. Patients with myotonia congenita often find that the muscle stiffness caused by the myotonia is alleviated by periods of mild exercise. This improvement in the symptoms of myotonia congenita, like in hyperkalemic periodic paralysis, may be due to the increased activity of Na^+,K^+-ATPase which will pump K^+ from the tubules into the cells. The reader is referred to the Chapter 42 where myotonia involving a low Cl^- conductance is discussed.

VIII. MALIGNANT HYPERTHERMIA

Malignant hyperthermia is detected as a rapid rise in body temperature in response to volatile anesthetics and depolarizing muscle relaxants, such as succinylcholine, that are administered during surgery. The disease is inherited as an autosomal dominant trait with an incidence in adults undergoing surgery with anesthesia of approximately 1 in 60 000 and 1 in 15 000 in children and adolescents. The increase in body temperature is caused by the uncontrolled release of Ca^{2+} from the sarcoplasmic reticulum, leading to sustained muscle contraction with utilization of ATP and the generation of heat (MacLennan and Zvaritch, 2010). Other symptoms of malignant hyperthermia include hyperkalemia, respiratory and metabolic acidosis and tachycardia. Malignant hyperthermia is potentially fatal and fatalities as high as 80% were reported in the 1960s. Dantrolene sodium is a muscle relaxant that was found to be effective in blocking the progression of a malignant hyperthermia episode and was introduced as a treatment for malignant hyperthermia in 1979. By the 1990s, fatalities had been reduced to less than 10% using this drug. Genetic testing has identified mutations in the RYR1 gene encoding the skeletal muscle ryanodine receptor Ca^{2+} channel in approximately 70% of patients with malignant hyperthermia and dantrolene has been shown to inhibit Ca^{2+} release from the sarcopasmic reticulum by binding to the ryanodine receptor Ca^{2+} release channel and preventing Ca^{2+} release. A small number of patients have mutations in the CACNA1S gene encoding the transverse tubule voltage-gated L-type Ca^{2+} channel. There is a strong correlation between the incidence of malignant hyperthermia and central core disease, another congenital sarcoplasmic myopathy that is characterized by hypotonia and proximal muscle weakness. Linkage between central core disease and mutations in the RYR1 gene has been established and the majority of the mutations in the ryanodine receptor associated with central core disease are located in the carboxy-terminal region of the polypeptide.

Identification of the genetic locus of the malignant hyperthermia mutations was facilitated by the identification of certain lines of pigs that suffered from porcine stress syndrome. Episodes of porcine stress syndrome could be triggered in these animals by exercise, mating, overheating or emotional stress induced during shipping to the slaughterhouse and also by halothane. Breeders of the pigs selecting for large hams and lean muscle mass had identified a single autosomal gene (HAL) that segregated with the porcine stress syndrome/malignant hyperthermia characteristics in these pigs (Fuji et al., 1991). Following the cloning of the large (>15 000 base pairs) cDNAs for human and rabbit ryanodine receptor genes, linkage between the human RYR1 gene on chromosome 19 and malignant hyperthermia susceptibility was shown. The RYR1 gene locus in humans is isologous with the location of the HAL gene on pig chromosome 6 and mutations causing malignant hyperthermia were soon identified in both pigs and humans. Only one mutation in the pig ryanodine receptor has ever been identified in pigs with malignant hyperthermia (R615C), making it possible that all of the affected breeds originate from a single founder animal.

Multiple mutations in the human ryanodine receptor channel have been identified in patients with malignant hyperthermia and there is no simple genetic test to diagnose the disease. Mutations in the RYR1 gene have not been found in all patients with malignant hyperthermia suggesting that other loci must exist. Mutations in the CACNA1S gene encoding the transverse tubule voltage-gated Ca^{2+} channel have been found in some patients with malignant hyperthermia who do not have mutations in the RYR1 gene. This finding is consistent with a disruption in the excitation–contraction coupling mechanism in skeletal muscle as the mechanism for the symptoms of malignant hyperthermia since the Ca^{2+} channel interacts directly with the ryanodine receptor in the sarcoplasmic reticulum membrane to promote Ca^{2+} release through the ryanodine receptor in response to T-tubule depolarization.

The mechanism whereby volatile anesthetics trigger malignant hyperthermia appears to be due to an increase in the sensitivity of the mutant ryanodine receptor channels to activation by the volatile anesthetics, as well as caffeine, and to a decrease in the threshold of the channels to activation by SR luminal [Ca^{2+}] (Jiang et al., 2008). Once the channel is triggered to open by the anesthetic, Ca^{2+} leaves the sarcoplasmic reticulum and activates the contractile

proteins. The SERCA Ca^{2+} pump hydrolyzes ATP as it returns the Ca^{2+} to the SR, but because the channel remains open in the presence of the anesthetic and, because the threshold for activation of the channel by luminal Ca^{2+} is low, the SR [Ca^{2+}] continues to activate the channel and be released into the cytoplasm. Continuous or repetitive cycles of this process contribute to rapid generation of heat and the other symptoms of the disease.

IX. LIDDLE'S SYNDROME

Hypertension is associated with increased susceptibility to stroke, myocardial infarction and renal failure. Evidence from different populations indicates that hypertension can be caused by any of several different physiological disturbances, some of which are genetically determined. Because there are multiple factors that contribute to elevated blood pressure, identification of the underlying causes of inherited hypertension in different individuals must be done in restricted populations. Patients with Liddle's syndrome are an extremely small subset of the hypertensive population, with fewer than 30 pedigrees reported worldwide as of 2008. This restricted population of patients facilitated genetic linkage analysis of these individuals and, in 1994, it was shown that there was complete linkage of the gene encoding the β subunit of the epithelial sodium channel (ENaC) to Liddle's syndrome in Liddle's original kindred (Shimkets et al., 1994). Liddle's syndrome is characterized by elevated blood pressure with serum hypokelemia. Similar symptoms are also seen in pediatric patients with hypertension caused by elevated aldosterone levels (hyperaldosteronism) but, because aldosterone levels are not elevated in Liddle's syndrome patients, this disease is also called pseudoaldosteronism.

ENaC is composed of three homologous subunits (αENaC, βENaC and γENaC), with 30−35% amino acid identity, in a 2α:1β:1γ stoichiometry. Each subunit polypeptide consists of short intracellular amino- and carboxy-terminal sequences, two transmembrane helices and a large extracellular loop connecting the transmembrane helices. The extracellular loop comprises more than 80% of each subunit. Epithelial sodium channels are located in the apical membrane of polarized epithelial cells and Na^+ entry into the epithelial cell through ENaC represents the rate-limiting step in sodium absorption across epithelial barriers. In contrast to the voltage-gated Na^+ channels of excitable membranes, sodium currents through ENaC are not affected by changes in the membrane potential. Despite being insensitive to changes in voltage, ENaC does undergo slow transitions between open and closed states, but the mechanisms underlying these transitions have not been well characterized. Epithelial sodium channels are also more selective for Na^+ over K^+ than are the voltage-gated channels.

Maintenance of fluid and electrolyte balance involves tight regulation of Na^+ absorption via ENaC. Sodium absorption varies widely under conditions of Na^+ excess or depletion and is primarily regulated by the hormones aldosterone and vasopressin, both of which increase renal Na^+ absorption by acting on the principal cells of the kidney. Aldosterone, acting through the mineralocorticoid receptor, increases the transcription of mRNA for several ion transporting proteins including the Na^+,K^+-ATPase and ENaC in target cells in the distal nephron and the collecting duct, with the net effect of increasing the number of these pumps and channels at the cell surface. Hyperaldosteronism resulting from increased aldosterone synthesis and release from adrenal tumors is another rare form of hypertension. Vasopressin promotes the activation of ENaC in the apical membrane of the principal cells in the distal nephron and also insertion of additional channels into this membrane via a cAMP-dependent mechanism. ENaC abundance in the apical membrane of the renal cells is a balance between the insertion of new channels in response to aldosterone or vasopressin release and the degradation of existing channels. In cultured cells, the half-life of ENaC subunits is between 1 and 3 hours, suggesting that the channel is a short-lived protein in cells. The degradation of ENaC at the cell surface is mediated by the E3 ubiquitin-ligase Nedd-4-2, which binds to PY motifs in the carboxy-terminal region of ENaC and catalyzes the ubiquitination of ENaC α, β and γ subunits. Ubiquitinated ENaC subunits are removed from the membrane by endocytosis and degraded in the proteasome and the lysosome.

In patients with Liddle's syndrome, the genes for either the β or the γ subunits of ENaC contain premature termination or frameshift mutations that either truncate the polypeptides and delete the PY motifs or disrupt the PY motifs of these subunits. As a result, Nedd4-2 cannot bind to these ENaC subunits and ubiquitination does not occur (Staub et al., 1996). The result is that there is an increase in the abundance of functional channels at the cell surface that facilitates excess Na^+ uptake and salt and water retention, leading to elevated blood pressure.

X. BARTTER SYNDROME

Approximately two-thirds of the renal reabsorption of Na^+ that is filtered by the glomerulus is done in the proximal tubule and most of the remaining absorption of sodium is done by transporters located in the limb of Henle. In the thick ascending limb of the loop of Henle, mutiple ion channels and transporters cooperate to control salt and water absorption (Fig. 30.4). In the absence of vasopressin, the thick ascending limb and other downstream segments of the kidney are relatively impermeable to water and the combination of NaCl absorption and low water permeability in this region of the nephron enables the kidney to

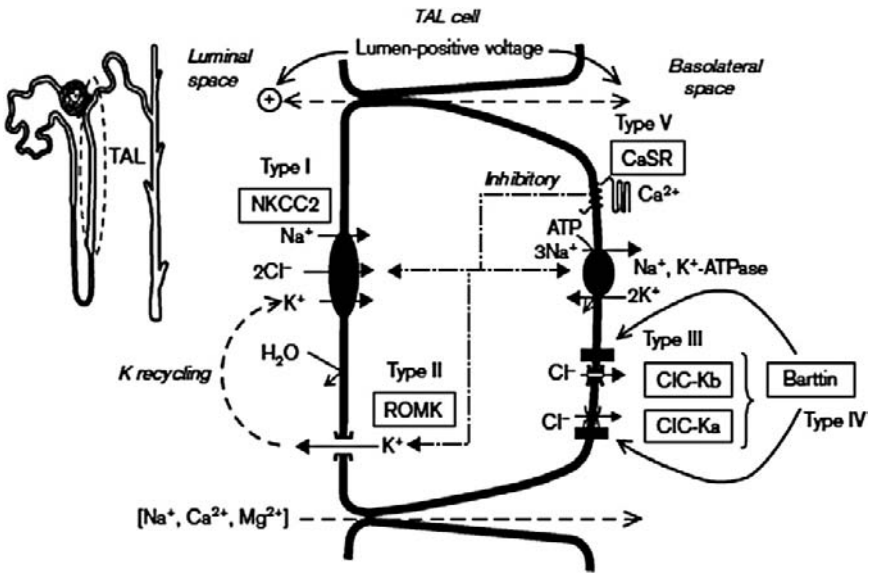

FIGURE 30.4 A model of salt transport by the thick ascending limb of Henle, depicting the five types (I–V) of Bartter syndrome discussed in the text. Each Bartter type is associated with mutations in a specific gene that encodes the protein whose name is indicated in a rectangle. (See text for details.) The insert shows the anatomical organization of the nephron. *(Figure is reproduced with permission from Staub et al., 1996.)*

generate a low luminal [Na^+] and osmolality with respect to the surrounding interstitial fluid. In the thick ascending limb, Na^+ reabsorption occurs both by the transcellular pathway and by the paracellular pathway. In the transcellular pathway, the NKCC2 transporter in the apical membrane of the cells couples the influx of 1 Na^+, 1 K^+ and 2 Cl^- ions in an electroneutral process. NKCC2 is encoded by the SLC12A1 gene in humans and is inhibited by loop diuretics such as furosemide and bumetinide. Sodium also enters the epithelial cells using the NHE3 sodium–proton antiporter. A large fraction of the K^+ that enters the cells through NKCC2 is recycled back to the tubular lumen through apical ROMK potassium channels that are encoded by the KCNJ1 gene. Recycling of K^+ across the luminal membrane is necessary to maintain tubular [K^+] at sufficiently high levels that are necessary for NKCC2 to function. Movement of K^+ into the tubular lumen also creates a lumen-positive potential that serves as the driving force for paracellular Na^+, Ca^{2+} and Mg^{2+} movement from the lumen to the interstium. Na^+ entering cells through NKCC2 is pumped out of the cells at the basolateral membrane by the Na^+,K^+-ATPase. Most of the Cl^- that enters the cells of the thick ascending limb is transported out of the cells through basolateral ClC-Ka and ClC-Kb Cl^- channels. The pore-forming subunit of the ClC-Kb channel is encoded by the CLCNKB gene. The ClC-Ka and ClC-Kb channels also contain a β subunit called barttin, encoded by the BSND gene that is required for translocation of the ClC-Ka and ClC-Kb channels to the plasma membrane from the Golgi.

Bartter syndrome is a group of rare autosomal recessive disorders that are characterized by renal salt loss, chronic hypokalemia and metabolic alkalosis (Herbert, 2003). Renin and aldosterone levels are elevated in patients, but blood pressure is usually normal or low. Many patients with Bartter syndrome also have elevated urinary Ca^{2+} excretion. Mutations in the SLC12A gene (Bartter syndrome type 1), in the KCNJ1 gene (Bartter syndrome type 2), in the CLCNKB gene (Bartter syndrome type 3) and in the BSND gene (Bartter syndrome type 4) have been identified in patients with these symptoms. Patients with Bartter syndrome type 4 also have sensorineural deafness. Bartter syndrome type 5 is associated with mutations in the gene for an extracellular Ca^{2+} sensor (CaSR) that is located on the basolateral membrane of cells of the thick ascending limb. The Ca^{2+} sensor is a G-protein-coupled receptor that is activated by increases in extracellular [Ca^{2+}]. Activation of this receptor inhibits salt uptake and activating gain-of-function mutations in the gene for CaSR are found in individuals with Bartter syndrome type 5. The symptoms of Bartter syndrome types 1–4 can all be understood as arising from loss-of-function mutations in genes encoding the NKCC2 transporter (decreased Na^+, K^+ and Cl^- absorption), ROMK (reduced K^+ recycling that compromises NKCC2 function and transepithelial voltage difference) and ClC-Kb or barttin (reduced number of Cl^- channels in the basolateral membrane that prevents transepithelial Cl^- movement). The symptoms of Bartter syndrome type 4 are typically more severe than those of Bartter syndrome type 3 because mutations in barttin affect all segments of the nephron expressing either ClC-Ka or ClC-Kb, whereas when ClC-Kb function is compromised in Bartter syndrome type 3, Cl^- uptake can still occur through ClC-Ka channels. Furthermore, sensorineural deafness is associated with Bartter syndrome type 4 patients but not type 3 patients because mutations in barttin will similarly reduce the abundance of both types of ClC-K channels in the marginal cells that produce endolymph in the inner ear. The secretion of K^+-rich endolymph by these cells is required for the normal function of the hair cells that mediate transduction of sound

waves into electrical impulses. Cytoplasmic [K^+] is increased in the marginal cells through the activity of the $Na^+/K^+/2Cl^-$-co-transporter NKCC1 located in the basolateral membrane of these cells. K^+ is secreted from the cells through apical K^+ channels and Cl^- is recycled across the basolateral membrane through ClC-K channels. The need for Cl^- recycling across the basolateral membrane of these cells in the inner ear is analogous to the role of K^+ recycling across the apical membrane of epithelial cells in the thick ascending limb of the loop of Henle through ROMK channels. Gain-of-function mutations in the extracellular Ca^{2+} sensor CaSR on the basolateral surface of the cells activate the receptor at concentrations of interstitial Ca^{2+} below those that normally activate the receptor (Riccardi and Brown, 2009). The activated CaSR inhibits salt absorption by inhibiting K^+ recycling through the ROMK channel.

BIBLIOGRAPHY

Adrian, R. H., & Bryant, S. H. (1974). On the repetitive discharge in myotonic muscle fibres. *J Physiol, 240*, 505–515.

Ashcroft, F. M. (2000). *Ion Channels and Disease*. San Diego, CA: Academic Press.

Bendahhou, S., Donaldson, M. R., Plaster, N. M., Tristani-Firouzi, M., Fu, Y.-H., & Ptacek, L. J. (2003). Defective potassium channel Kir2.1 trafficking underlies Andersen-Tawill syndrome. *J Biol Chem, 278*, 51779–51785.

Cannon, S. C. (2002). An expanding view for the molecular basis of familial periodic paralyses. *Neuromusc Disord, 12*, 533–543.

Dahlem, Y. A., Dahlem, M. A., Mair, T., Braun, K., & Müller, S. C. (2003). Extracellular potassium alters frequency and profile of retinal spreading depression waves. *Exp Brain Res, 152*, 221–228.

Dichgans, M., Freilinger, T., Eckstein, G., et al. (2005). Mutation in the neuronal voltage-gated sodium channel SCN1A in familial hemiplegic migraine. *Lancet, 366*, 371–377.

Fuji, J., Otsu, K., Zorzato, F., et al. (1991). Identification of a mutation in porcine ryanodine receptor associated with malignant hyperthermia. *Science, 253*, 448–451.

Gargus, J. J. (2009). Genetic calcium signaling abnormalities in the central nervous system: seizures, migraine, and autism. *Ann NY Acad Sci, 1151*, 133–156.

Hayward, L. J., Brown, R. H., Jr., & Cannon, S. C. (1996). Inactivation defects caused by myotonia-associated mutations in the sodium channel III-IV linker. *J Gen Physiol, 107*, 559–576.

Hebert, S. C. (2003). Bartter syndrome. *Curr Opin Nephrol Hypertens, 12*, 527–532.

Jiang, D., Chen, W., Xiao, J., et al. (2008). Reduced threshold for luminal Ca^{2+} activation of RyR1 underlies a causal mechanism of porcine malignant hyperthermia. *J Biol Chem, 283*, 20813–20820.

Lossin, C., & George, A. L., Jr. (2008). Myotonia congenita. *Adv Genet, 63*, 25–55.

MacLennan, D. H., & Zvaritch, E. (2010). Mechanistic models for muscle diseases and disorders originating in the sarcoplasmic reticulum. *Biochim Biophys Acta*. [Epub ahead of print].

Morth, J. P., Poulsen, H., Toustrup-Jensen, M. S., et al. (2009). The structure of the Na^+, K^+-ATPase and mapping of isoform differences and disease-related mutations. *Phil Trans R Soc B, 364*, 217–227.

Ophoff, R. A., Terwindt, G. M., Vergouwe, M. N., et al. (1996). Familial hemiplegic migraine and episodic ataxia type-2 are caused by mutations in the Ca^{2+} channel gene CACNL1A4. *Cell, 87*, 543–552.

Pietrobon, D. (2005). Migraine: new molecular mechanisms. *Neuroscientist, 11*, 373–386.

Riccardi, D., & Brown, E. M. (2009). Physiology and pathophysiology of the calcium-sensing receptor in the kidney. *Am J Physiol Renal Physiol, 298*, F485–F499.

Riordan, J. R., Rommens, J. M., Kerem, B.-S., et al. (1989). Identification of the cystic fibrosis gene: cloning and characterization of complementary DNA. *Science, 245*, 1066–1073.

Shimkets, R. A., Warnock, D. G., Gositis, C. M., et al. (1994). Liddle's syndrome: heritable human hypertension caused by mutations in the β subunit of the epithelial sodium channel. *Cell, 79*, 407–414.

Staub, O., Dho, S., Henry, P. C., et al. (1996). *EMBO J, 15*, 2371–2380.

Vanmolkot, K. R. J., Kors, E. E., Hottenga, J.-J., et al. (2003). Novel mutations in the Na^+, K^+-ATPase pump gene ATP1A2 associated with familial hemiplegic migraine and benign familial infantile convulsions. *Ann Neurol, 54*, 360–366.

Section V

Synaptic Transmission and Sensory Transduction

This page intentionally left blank

Chapter 31

Ligand-Gated Ion Channels

Kenneth R. Tovar and Gary L. Westbrook

Chapter Outline

I. SUMMARY

Ligand-gated ion channels are membrane proteins that are fundamental signaling molecules in neurons. These molecules are localized in the plasmalemma and on intracellular organelles and can be gated by both intracellular and extracellular ligands. The neurotransmitter-gated ion channels discussed in this chapter mediate fast excitation and inhibition in the nervous system and have now been well characterized by physiological and molecular studies. Studies using the technique of voltage and patch-clamp recording have examined the three basic features of an ion channel: gating, conductance and selective permeability. In general, ligand-gated ion channels can be described by kinetic models involving binding of two or more ligand molecules that induce a conformational change in the protein. As a result, a central, water-filled pore opens and conducts ions at very high rates of up to 10^7 ions per second. Channel activity is terminated when the channel closes or when it enters a nonconducting (desensitized) state. In vertebrates, acetylcholine (Ach) and glutamate receptors are cation channels, whereas γ-aminobutyric acid (GABA) and glycine receptors are anion channels. The ACh, GABA and glycine receptors constitute the Cys-loop receptor superfamily that presumably evolved from a common ancestral gene. Glutamate receptors comprise a separate protein family. The ligand-binding domain of glutamate channels shares homology with bacterial amino acid binding proteins, whereas the pore shares homology with the pore of voltage-dependent ion channels.

Each of the neurotransmitter-gated channels appears to be comprised of a hetero-oligomeric complex of closely related subunits surrounding a central ion pore. For each receptor type there are a number of possible subunit combinations that can form functional channels. AChR subunits have four transmembrane domains with the second transmembrane domain lining the pore. Charged amino acid residues near the mouth of the pore are important in determining the selectivity and conductance of the individual channel types. The glutamate subunits have three transmembrane domains and a reentrant loop domain that forms a portion of the pore. The recent availability of crystal structures of a homomeric Cys-loop receptor and a glutamate receptor will allow atomic level resolution of the conformational movements involved in binding and gating of these channels.

II. INTRODUCTION

Ion channels are fundamental signaling molecules in virtually all cells. Studies of ion channel in the plasmalemma of excitable cells have provided the foundation for our knowledge of these important molecules. In the nervous system, voltage-gated ion channels mediate action potentials (APs) and trigger neurotransmitter release, whereas ligand-gated channels are responsible for chemical signaling mediated by classical fast-acting transmitters. Neurotransmitters also trigger slower synaptic responses that are mediated by G-protein-coupled receptors.

Until the 1980s, the molecular properties of ion channel proteins were largely inferred from physiological and biophysical studies (Hille, 2001). In retrospect, many of the predictions from early biophysical studies have been

Cell Physiology Sourcebook. DOI: 10.1016/B978-0-12-387738-3.00031-7

confirmed and extended following the elucidation of the amino acid sequence of voltage- and ligand-gated ion channels by molecular cloning. However, the increasing knowledge of the three-dimensional molecular structure of ion channels and their homologs in lower organisms now permit sophisticated correlations of protein structure with function (Sine and Engel, 2004; Mayer, 2005). These advances have dramatically increased our understanding of the molecular operation of these prototypic membrane proteins. These molecules have captured the interest of many outstanding scientists whose studies of ion channel function and structure have led to several Nobel Prizes (Neher, 1992; Sakmann, 1992; McKinnon, 2004). Neurological disorders can also be caused by mutations in ion channels, the so-called "channelopathies" (Kullmann, 2010) and by autoimmune mechanisms that target ligand-gated ion channel proteins (Graus et al., 2010).

A biophysical approach to ion channels was pioneered by studies of voltage-gated ion channels in squid axon. These studies established that a conductance change was associated with the AP and that this conductance change could be attributed to selective increases in the membrane permeability to Na^+ and K^+ ions, with the energy for the process derived from the transmembrane ion gradients created by the Na^+, K^+-ATPase. These findings suggested that there were discrete pores in the membrane that accounted for the Na^+ and K^+ conductance. However, it was not until the 1970s that the existence of ion channels as discrete membrane proteins was confirmed, first by measurements of the statistical properties of currents through populations of ion channels, a technique called *fluctuation* or *noise analysis*. Later, this conclusion was refined by the introduction of *patch-clamp recording*, which allowed measurement of the current through single ion channels (Neher, 1992; Sakmann, 1992). Patch-clamp recording revolutionized the study of ion channels because it allowed detailed biophysical studies of the electrical activity of single molecules. Protein purification and molecular cloning revealed that ion channels are a large and diverse group of membrane proteins. Although ligand-gated ion channels vary in structural details, they share a common basic structure in that they are composed of multiple subunits arranged around a central water-filled pore. Each subunit is a polypeptide encoded by a separate gene. Generally, there are a large number of possible subunit combinations; thus, the particular subunits expressed in a certain class of neurons can result in channels with distinct functional characteristics.

This chapter is divided into three topic areas. In the first, the categories of ligand-gated ion channels are briefly reviewed. The basic physiological properties and general molecular structure of ligand-gated channels are then discussed using the muscle nicotinic acetylcholine receptor (AChR) and the N-methyl-D-aspartate (NMDA)-type glutamate receptor as the prototypes. In the third section, the features of neurotransmitter-gated channels that are responsible for fast synaptic transmission are discussed with an emphasis on their distinctive characteristics. Channels gated by acetylcholine (ACh), γ-aminobutyric acid (GABA), glycine and glutamate are included as representative examples. Related topics on ion channels are discussed in other chapters in Sections III through V of this book. The reader is also referred to the excellent monographs and reviews listed in the references for further details.

III. CLASSES OF LIGAND-GATED ION CHANNELS

Ligands that activate ion channels in nerve cell membranes can be roughly divided into two major categories, neurotransmitters and intracellular ligands (Table 31.1). The neurotransmitter-gated ion channels involved in fast chemical synaptic transmission have been extensively studied. These include ACh, which is the transmitter at the vertebrate neuromuscular junction and in autonomic ganglia and the amino acids, L-glutamate and GABA, which mediate the majority of fast excitatory and inhibitory synaptic transmission, respectively, in the vertebrate central nervous system. Each of these ligands also activates receptors that are coupled to second messengers via GTP-binding (G) proteins. G-protein-coupled receptors generally mediate slower and neuromodulatory transmembrane signaling. Other neurotransmitters that activate ligand-gated ion channels in various cell types include serotonin, glycine, histamine and adenosine triphosphate (ATP). For example, the $5HT_3$ receptor activated by serotonin is a ligand-gated ion channel (Julius, 1991). ATP is released from nerve terminals in several pathways and activates the P2X family of channels (Burnstock, 2007; Browne et al., 2010). The transient receptor potential (TRP) channels provide a particularly large and diverse group that are activated not by classical neurotransmitters, but rather by diverse chemical as well as physical stimuli (Wu et al., 2010).

In addition to neurotransmitter-gated ion channels, increasing attention has focused on ligand-gated ion channels that are activated by intracellular ligands. These ligands include Ca^{2+}, cyclic nucleotides, ATP and inositol trisphosphate (IP_3). Intracellular ligands can increase (Ca^{2+}, cAMP, IP_3) or decrease (cGMP, ATP) activity of the associated channel. These channels play important roles in cell function. For example, Ca^{2+}-dependent potassium, chloride and non-specific cation channels modify the excitability of the nerve cell membrane and thus can alter the AP and release of transmitter from nerve terminals. The cyclic nucleotide (cAMP, cGMP)-gated channels mediate sensory transduction in the visual and olfactory system. Light results in the closing of cGMP channels in vertebrate

TABLE 31.1 Ligand-Gated Ion Channels

Ligand	Receptor	Ion Selectivity[a]
Neurotransmitters		
Acetylcholine	Muscle, neuronal AChRs	NS
Glutamate	AMPA, kainate, NMDA	NS
GABA	$GABA_A$	Cl
Glycine	GlyR	Cl
Serotonin	$5HT_3$ receptor	NS
ATP	P2X receptor	NS
Intracellular Ligands		
Calcium	Calcium-dependent channels	K, Cl, NS
Cyclic nucleotides	cGMP and cAMP receptors	NS
ATP	ATP-dependent channel	K
IP_3	Calcium release channel	Ca

[a]*Abbreviations for ion selectivity are: NS: non-selective cation permeability, some with calcium permeability; Cl: permeable to chloride; K: permeable to potassium; and Ca: permeable to calcium.*

photoreceptors whereas odors trigger the opening of cAMP-gated channels in olfactory receptor neurons. (See Chapters 35 and 39 for more discussion of channels gated by cyclic nucleotides.)

IV. BASIC PHYSIOLOGICAL FEATURES

Patch-clamp techniques allow investigators to define the three fundamental properties of any ion channel — *conductance*, *selective permeability* and *gating* — in molecular terms. In addition to these fundamental properties, *modulation*, *channel block* and *desensitization* are processes that alter the activity of ligand-gated ion channels and are important in shaping the impact of channel activity on membrane excitability. The biophysical basis of these properties will be discussed first and then the structural features of ligand-gated channels that control these properties will be considered.

Conductance reflects the flux of charged ions through the channel and is measured in picoSiemens (pS). Most ligand-gated ion channels have a conductance of 5−50 pS, which corresponds to the movement of more than 1×10^6 ions per second through the channel pore. These high flux rates initially suggested that ligand-gated channels must contain a water-filled pore, because this rate is much higher than that predicted for other transport mechanisms, such as pumps or exchangers. The size of the single-channel conductance (γ) is characteristic for a given channel. Several openings of a glutamate-activated channel in a hippocampal neuron are shown in Fig. 31.1. The conductance of the open channel is usually near 50 pS, but drops occasionally to subconductance states of 8, 35, 40 and 45 pS. The conductance of a channel increases as the permeant ion concentration is raised, but eventually saturates at concentrations well above physiological levels. This behavior can be described by Michaelis−Menten kinetics, suggesting that ions bind to sites within the pore rather than simply obeying the laws of free diffusion. Most permeant ions have a low K_m of approximately 100 mM (K_m is the concentration at which the conductance is half-maximal, as defined by the Michaelis−Menten equation); thus the ions bind for only a microsecond or so before continuing through the pore.

The current carried by the opening of a single-channel is measured in picoamperes (pA) with the single-channel current given by:

$$i = \gamma(V - Veq) \qquad (31.1)$$

where V is the membrane potential and Veq is the equilibrium potential, at which no net current is measured. This equation is simply Ohm's law, where (V−Veq) is the electrochemical driving force for ions that can pass through the channel. For example, if the extracellular and cytoplasmic concentrations of permeant ions are equal, then Veq is 0 mV. Thus, as the membrane potential changes, the size of the single-channel current also changes; a plot of this relationship is called a current−voltage or I-V plot. For channels, such as the muscle AChR, that are permeable to

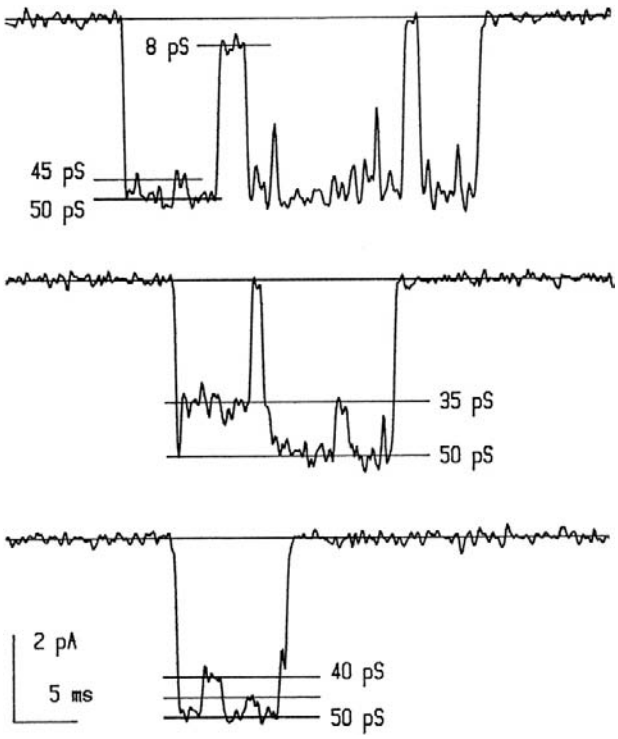

FIGURE 31.1 Activity of single ligand-gated channels as measured by patch-clamp recording. Examples of NMDA-type glutamate channel recording in an outside-out membrane patch obtained from a cultured hippocampal neuron. Downward deflections indicate opening of the channel in the presence of ligand (in this case, 20 μM NMDA). The channel usually opens to the 50 pS level, but may switch to lower levels of 8, 35, 40 or 45 pS before closing to the baseline level. *(Modified with permission from Jahr and Stevens (1987). Nature. 325, 522–525. Copyright 1987 by Macmillan Magazines Limited.)*

Na^+ and K^+, the reversal potential is 0 mV and the I-V curve is nearly linear. However, some channels deviate from linear behavior and show inward or outward rectification (i.e. the channel passes current in one direction better than in the other), analogous to the behavior of some voltage-gated K^+ channels.

Channels are not equally permeable to all ions, i.e. they exhibit selective permeability. As listed in Table 31.1, most ligand-gated ion channels are permeable to either monovalent cations or anions. The selective permeability of channels is partly due to the physical size of the pore. For example, the muscle AChR is permeable to cations with diameters up to about 6.5 Å. In general, cationic ligand-gated ion channels are less selective than voltage-gated ion channels, which are highly selective for Na^+, K^+ or Ca^{2+}, but more selective than gap junction channels, which are permeable to small molecular weight molecules such as cyclic nucleotides as well as to ions. Because anions and cations are approximately the same size, it is obvious that the pore dimensions cannot totally account for selective permeability. As discussed later, positively- and negatively-charged amino acid residues at the entrances to the channel and within the pore provide a means for this discrimination. Selective permeability is extremely important in considering the function of an ion channel. For example, channels that are permeable to Na^+ and K^+ do not significantly alter the ion concentrations on either side of the membrane but, instead, provide an electrical signal that depolarizes the neuron and brings the membrane potential closer to the threshold for AP generation. However, channels with significant Ca^{2+} permeability can transiently increase the cytoplasmic Ca^{2+} concentration and thus act as a biochemical signal. The relative Ca^{2+} permeability of ligand-gated channels, such as the NMDA receptor and some nicotinic receptors, is an important aspect of their role in neuronal function. The reader is referred to the monograph by Hille (2001) for a full discussion of channel permeability and its measurement.

Channel gating refers to the conformational change in the ion channel protein that is triggered by ligand binding. The conformational change results in a rapid switch between conducting (open) and non-conducting (closed) states of the channel. The gating behavior of channels has many parallels with the allosteric behavior of enzymes, with the binding of ligand providing the free energy necessary to maintain the channel in the open conformation. Gating between the open and closed configuration is extremely rapid (approximately 10 μs) and thus is beyond the resolution of standard recording methods. Each channel opening usually lasts a few milliseconds, but can, on some occasions, last up to several hundred milliseconds. Binding of more than one agonist molecule is usually necessary to open a channel. The binding of multiple agonist molecules creates a sigmoidal dose–response relationship, characteristic of the cooperative binding of substrates to enzymes. The steep activation created by sigmoidal kinetics prevents the channel from opening in the presence of a low concentration of agonist, which could be quite important in preventing desensitization of synaptic receptors. In general, the higher the binding affinity of the agonist, the longer the channel will remain open. This is because the channel can remain open (or reopen) until the agonist dissociates.

The gating of ligand-gated ion channels can be described by multistate kinetic diagrams as shown in Fig. 31.2A. Such state diagrams have been developed for many ligand-gated ion channels, based on the analysis of open and closed time distributions obtained in single channel recording. For example, the presence of two exponentials in an open time histogram implies the existence of two open states. The minimal kinetic model for a ligand-gated channel usually has at least four states, including closed and unbound, closed and bound, open and bound and non-conducting (desensitized). For the case shown in Fig. 31.2A and B, note that the channel opens only when two agonist molecules are bound. For fast-acting neurotransmitters, the concentration of transmitter in the

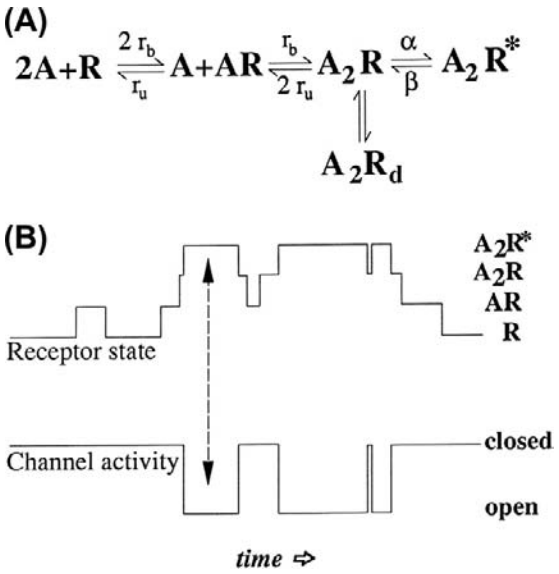

FIGURE 31.2 Kinetics of ligand-gated channels. (A) Example of a four-state kinetic scheme used to describe the behavior of ligand-gated ion channels. In this example, two agonist molecules (A) must bind before the channel can open (A_2R^*) or enter a non-conducting desensitized state (A_2R_d). The rate constants for agonist binding and unbinding are designated r_b and r_u, and the rate constants for channel opening and closing are designated as β and α. (B) Relationship of the state of the receptor to the open and closing of the channel. The channel opens only when the receptor is in the A_2R^* state as indicated by the arrows.

synaptic cleft is typically very high for a brief period. At high concentrations of agonist the receptors quickly reach the fully liganded but closed state because transition to this state is determined by the concentration of agonist as well as the binding rate, r_b. Thus, the rising and falling phase of the synaptic response largely reflects the unbinding rate, r_u, the channel opening and closing rates (β and α) and, in some cases, the rates in and out of the desensitized state, R_d. Classical pharmacological terms can be interpreted in terms of these kinetic schemes (Colquhoun, 1998). Agonists open the channel, whereas antagonists bind, but apparently do not cause a sufficient conformational change in the channel protein to open the channel. The fraction of time the bound channel spends in the open state is called the *open probability* and may differ between agonists — an agonist that activates the channel with higher probability therefore has a higher efficacy in the nomenclature of classical receptor pharmacology.

Earlier studies of the activity of ligand-gated channels were generally limited to equilibrium measurements because of the limits in the speed of application of agonists to cells or cell-free patches. Such equilibrium measurements are difficult to interpret in terms of state diagrams such as that shown in Fig. 31.2. In addition, the duration of fast-acting transmitters such as glutamate is generally brief, suggesting that the synapse itself operates under non-equilibrium conditions. However, the development of rapid solution exchange techniques allowed agonists to be applied within several hundred microseconds to membrane patches, usually in the "outside-out" configuration to allow agonist in the bath to access the extracellular face of the receptor. Such approaches appear to more closely resemble conditions at synapses and are particularly useful in evaluating the role of channel modulation, channel block and desensitization on synaptic responses. An example of the response of a membrane patch from a hippocampal neuron to a brief application of glutamate is shown in Fig. 31.3.

In general, the conductance and selective permeability of ligand-gated channels are not subject to regulation. However, a number of allosteric control mechanisms can profoundly affect gating (Changeux and Edelstein, 1998). These mechanisms can be manifest as *desensitization*, *channel block* and *allosteric modulation*. Desensitization refers to the loss of the response during the continued presence of agonist and was first noted in studies of the muscle AChR. At the single-channel level, desensitization reflects a non-conducting state of the channel. This phenomenon has now been seen for most ligand-gated channels and can be described by including an extra bound, but non-conducting, state in the kinetic scheme (see Fig. 31.2A). Depending on the channel, the non-conducting state may be accessible from either the closed state (A_2R) or the open state (A_2R^*). Desensitization represents a distinct conformation of the receptor as has been demonstrated by structural studies of AMPA receptors (see below). Very rapid desensitization may play a role in terminating the neuronal response to neurotransmitters at some synapses, whereas slower desensitization may actually prolong synaptic responses as channels re-enter open states after transiting through desensitized states (Jones and Westbrook, 1996).

Ligand-gated channels can be plugged by ions or drugs, a phenomenon referred to as *channel block*. If the blocking particle is charged, such as a large ion, the block will be influenced by the voltage across the membrane. Thus, the reduction in channel activity will be more pronounced at some membrane potentials. The voltage-dependent block of NMDA-type glutamate channels by extracellular Mg^{2+} is an example of this phenomenon (Ascher and Nowak, 1987). At the single channel level, channel block is usually seen as rapid interruptions ("flickers") of the open state as illustrated in Fig. 31.4A and B. A characteristic feature of most forms of channel block is that the blocker is only effective when the channel is open. Thus, the binding site for the blocker resides within the pore of the channel, or at least at a site that is only available in the open conformation of the channel. Channel block is the mechanism of action for a number of drugs, such as the local anesthetic lidocaine and psychoactive compounds, such as phencyclidine (PCP).

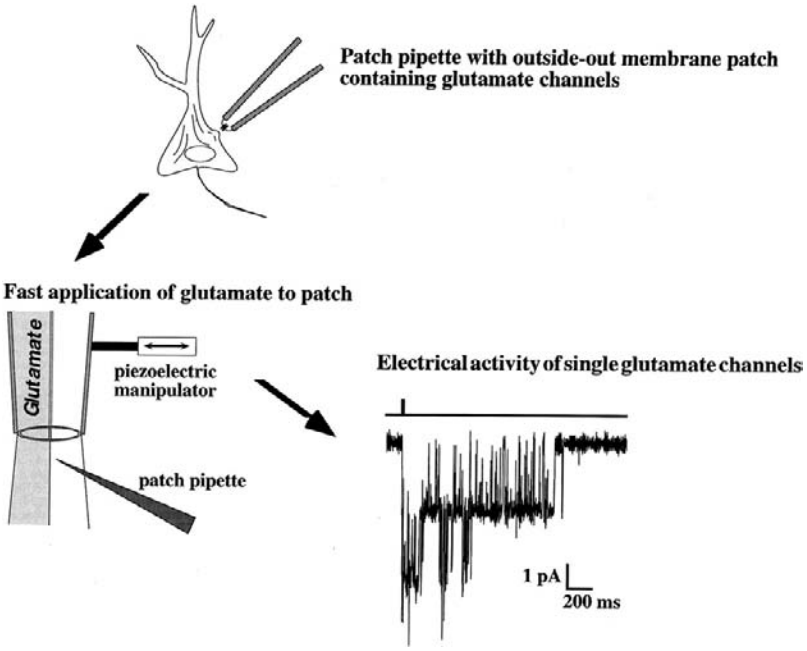

FIGURE 31.3 Use of rapid application methods to study kinetics of ligand-gated channels. The patch-clamp technique allows small membrane patches to be removed from a cell, such as a hippocampal neuron, with the extracellular side of the membrane facing the bath (outside-out configuration). The tip of the pipette is then placed in the interface of two rapidly moving streams of solution. A piezoelectric manipulator moves the solutions to change the solution flow over the patch in less than 1 ms, which mimics what occurs at glutamate release sites. The response, recorded as the opening of glutamate channels of the NMDA type, greatly outlasts the brief application of agonist. The bar above the channel activity indicates the duration of the glutamate application.

Channel gating is also subject to *modulation* by either covalent modification, such as phosphorylation (Swope et al., 1999), or via the non-covalent binding of modulators to the channel. Most ligand-gated channels undergo phosphorylation of intracellular portions of the channel protein; however, the resulting effect on channel function is dependent on the specific channel and the type of kinase involved. Phosphate groups are highly charged and thus can modify interactions in local regions. For example, phosphorylation of the AChR enhances desensitization and may also be important in clustering of AChR molecules at sites of innervation. The list of non-covalent modulators is long and includes Ca^{2+}, toxins, drugs and some endogenous substances such as protons and steroid hormones. These modulators usually act in a non-competitive manner, i.e. they do not directly interfere with ligand binding. Most of these

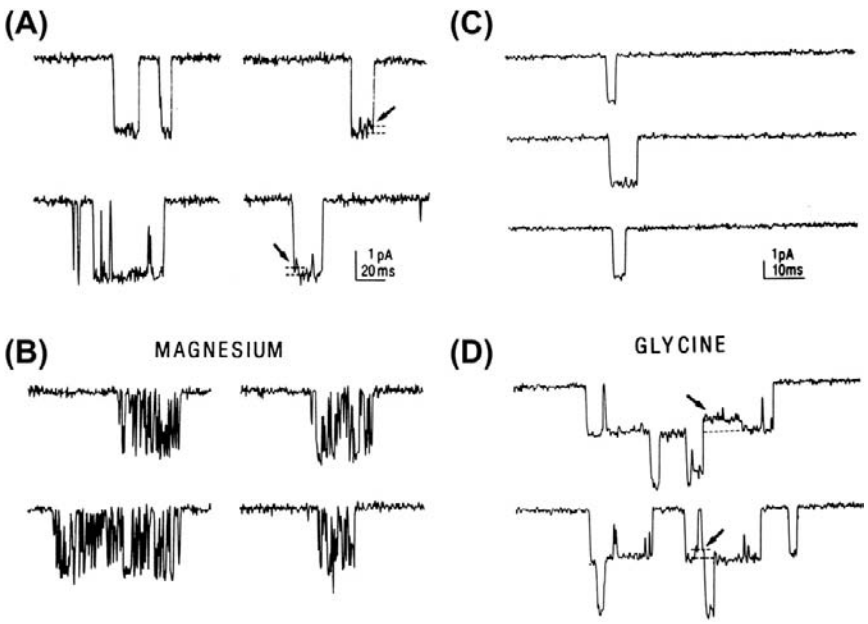

FIGURE 31.4 NMDA-type glutamate receptors illustrate two common mechanisms of channel regulation: channel block and allosteric modulation. (A and B). Channels activated by NMDA in a membrane patch from a hippocampal neuron in the absence of extracellular Mg^{2+} remain open (downward deflection) for several milliseconds before closing (A). However, in the presence of Mg^{2+} (B), the openings are interrupted by brief closures due to plugging of the pore by Mg^{2+} ions. (C and D) The frequency of NMDA channel opening is increased in the presence of extracellular glycine (D) compared to glycine-free solutions (C). The stepwise increase in current in part D indicates that at least two channels were present in the membrane patch. Because glycine is required for NMDA channel opening, the occasional openings in part C probably reflect contamination of the solution with low levels of glycine. *(Modified with permission from Ascher, R. and Nowak, L. (1987). Trends Neurosci. 10, 284–288.)*

reagents affect gating by altering the rate of channel opening or the time spent in the open state. For example, glycine binds to the NMDA channel and results in an increased probability of opening (see Figs. 31.4C and D). This is a dramatic example of allosteric regulation because the channel will not open unless both glycine and the transmitter (glutamate) are bound. A less profound, but equally important, example is the upregulation of $GABA_A$ receptor activity by benzodiazepines (Olsen and Sieghart, 2009).

V. MOLECULAR STRUCTURE

The ligand-gated ion channels can be divided into three main structural classes: the Cys-loop receptors, the glutamate receptors and the P2X receptors. Channels in these three families are formed as combinations 5, 4 and 3 subunits, respectively (Fig. 31.5). We discuss here structural information on the pentameric Cys-loop receptor superfamily that includes the nicotinic, $GABA_A$, glycine and 5-HT3 receptors, and the tetrameric glutamate receptor family that includes the AMPA, kainate and NMDA receptors. For the Cys-loop and glutamate receptor families, structural studies are providing a more and more detailed understanding of the main functional features of

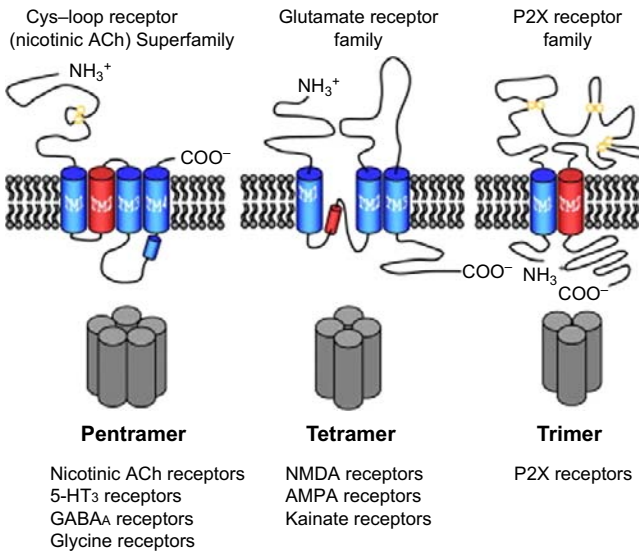

FIGURE 31.5 The topology of the three families of ligand-gated ion channel subunits. The general topologies of ligand-gated receptor subunits for each of the main receptor families are shown in the upper row. The stoichiometry of subunits in an assembled receptor are shown in the lower row. The Cys-loop family of receptors are pentameric, whereas the glutamate receptors are tetrameric and P2X receptors are trimeric. The three protein families also differ in the general structure of extracellular, intramembrane and intracellular domains. The red cylinders indicate the intramembrane pore region through which ions flow, M2 (TM2) in the case of Cys-loop and P2X receptors and the P loop for glutamate receptors. *(Modified with permission from Collingridge, G.L., Olsen, R.W., Peters, J., Spedding, M. (2009). Neuropharmacology. 56, 2–5.)*

ligand-gated ion channels: binding of ligand, the gating and ion selectivity of the channel and the coupling of ligand binding to channel gating. For information on the unique structure of the trimeric P2X receptors activated by ATP, see Browne et al. (2010).

The AChR led the way in determining the molecular structure of ligand-gated channels, beginning with biochemical studies of the muscle-type receptor (Karlin, 1991). This analysis took advantage of the high density of AChRs in the electric organ of the ray (*Torpedo californica*) and the high-affinity snake toxin, α-bungarotoxin, that binds to muscle-type AChRs. Protein purification revealed an approximately 250-kDa complex with two α-bungarotoxin binding sites per complex and separation on denaturing gels revealed polypeptides of 40, 50, 60 and 65 kDa designated as the α, β, γ and δ subunits. Because of the molecular weight of the complex and the binding of toxin molecules, a pentameric structure with two α subunits and single copies of β, γ and δ was proposed. Using the partial amino acid sequence of the purified subunits, the cDNAs encoding AChRs in the *Torpedo* electric organ were cloned and sequenced in the early 1980s. Incorporation of the purified protein complex in lipid bilayers or expression of AChR mRNA in *Xenopus* oocytes demonstrated channels activated by acetylcholine, confirming the identity of the molecule. Consistent with the proposed combination of subunits in intact receptors, the expression of AChRs in oocytes was much greater when all four subunit mRNAs were included. The α subunit was essential in order to obtain responses to acetylcholine.

Based on the hydrophobicity of amino acid residues in the primary sequence, the proposed transmembrane topology included four putative transmembrane domains (M1−M4), large N-terminal domain and short C-terminal extracellular domains and two cytoplasmic loops − a short one between M1 and M2 and a longer loop containing phosphorylation sites between M3 and M4. The early evidence that M2 lines the pore came from amino acid substitutions within that domain. In addition, a 23-amino-acid peptide fragment containing the M2 region of the *Torpedo* δ AChR subunit formed a cation channel when incorporated into lipid bilayers. The analysis of the primary amino acid sequence gives limited information about three-dimensional protein structure. Subsequently, two-dimensional crystals of AChRs from the *Torpedo* electric organ were analyzed with the electron microscope (Miyazawa et al., 1999), providing a good first estimate of the overall shape and structural features of the AChR.

Yet it was identification and high-resolution crystal structure of an acetylcholine-binding protein (AChBP) from the freshwater snail (*Lymnaea stagnalis*) that provided the next level of resolution (Smit et al., 2001; Brejc et al., 2001). Thc AChBP is a pentamer of identical subunits that is homologous to the extracellular ACh-binding

portion of the AChR and thus provided improved molecular resolution of ligand-binding domain. Combining AChBP with two-dimensional arrays of *Torpedo* channels began to reveal the relationship of the extracellular binding domains and the structural movements that lead to opening of the intramembrane channel (Unwin, 2005). Crystal structures of two full length homomeric channels related to the Cys-loop family now allow the first glimpse of the structure of an entire protein of this class. Interestingly, these structures are not those of well-studied members of the Cys-loop family, but rather include a pentameric ligand-gated channel from bacteria (Hilf and Dutzler, 2009) and a glutamate-gated chloride channel from *C. elegans* (Hibbs and Gouaux, 2011).

Each of the two binding pockets in the Cys-loop receptors is composed of hydrophobic and aromatic amino acid residues contributed by discontinuous segments of an α and a non-α subunit. The Cys-loop receptors get their name from an N-terminal 13 amino acid sequence flanked by cysteines that form a disulfide bond and make a closed loop in the extracellular domain. The binding pocket is capped by the "C-loop" contributed by the alpha subunit, which must be open for agonist access and is locked in place when the agonist is bound and thus fully enveloped. The structure also suggests a mechanism by which agonist binding can result in channel opening through linkers that connect to the first transmembrane domain. The new Cys-loop receptor crystal structures promise a much clearer picture of the conformational movements that underlie the open, closed and desensitized states.

As with the Cys-loop receptors, the proposed quarternary structure of glutamate channels involves multisubunit complexes surrounding a central pore (Fig. 31.6). However, cloning of the glutamate channels revealed that they differed substantially from the Cys-loop receptors in their primary amino acid sequence (Nakanishi, 1992; Hollmann and Heinemann, 1994). Notable differences include the much longer N-terminal domain (approximately 500 residues). In addition, the second hydrophobic domain of the glutamate subunits is a re-entrant loop that enters and exits the membrane from the cytoplasmic side without fully traversing the membrane. This "P" loop shows homology to the P loop of voltage-gated channels that lines the channel pore and controls ion selectivity and conductance. A prokaryotic glutamate receptor may provide an evolutionary link between the voltage-gated potassium channels and glutamate receptors (Chen et al., 1999). Secondly, the region between the third and fourth hydrophobic domains is extracellular in glutamate subunits whereas it is cytoplasmic in the AChR subunits. Finally, the C-terminus of the glutamate subunits is cytoplasmic. These unique features provided important clues to the location of the transmitter binding site(s), the behavior of the channel pore and sites of interaction with proteins that anchor and/or localize glutamate receptor subunits at synapses.

The extracellular component of glutamate receptors constitutes two separate domains (see Fig. 31.6). The amino terminal domain (ATD) of approximately 380 amino acids is involved in subunit assembly. The agonist-binding domain is discontinuous, being formed from the first extracellular region (D1) and the extracellular loop between the second and third transmembrane regions (D2). Both of these domains are homologous to bacterial proteins that bind amino acids. This homology led to a proposed model for the

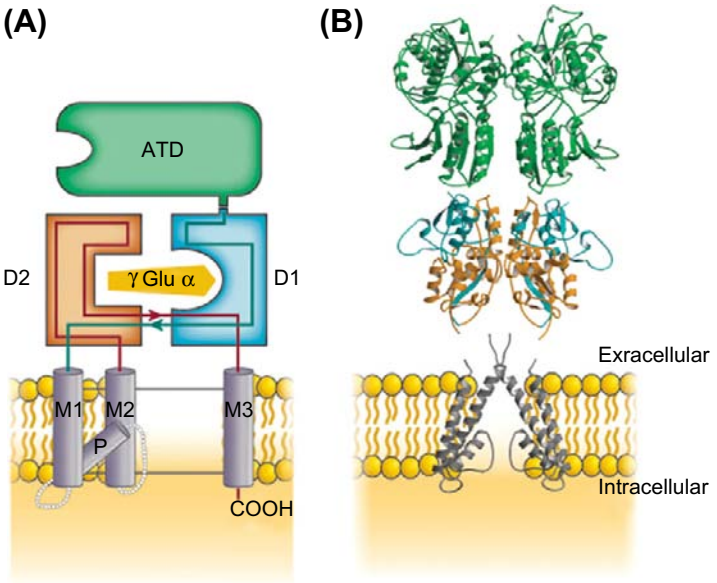

FIGURE 31.6 The domain organization of glutamate receptor subunits. (A) As shown in this schematic diagram, the extracellular region contains two domains, the ATD shown in green and the agonist-binding domain show in orange and blue surrounding an agonist molecule. The hydrophobic transmembrane domains M1, M2 and M3 as well as the P loop of the pore are shown in lavender. The intracellular domain is truncated in this schematic (-COOH). (B) A glutamate receptor assembles as a dimer of dimers. One representative dimer is shown here based on the crystal structures. The color-coded domains illustrate the secondary structure of α-helices and β-sheets that contribute to each domain. *(Modified with permission from Mayer, M.L. (2006). Nature. 440, 456-462.)*

glutamate binding site based on the crystal structure of the bacterial periplasmic binding proteins and subsequently confirmed based on chimeric receptors with domains from two glutamate subunits with distinct pharmacology (Stern-Bach et al., 1994). In GluN1, glycine occupies the agonist-binding domain instead of a glutamate, which binds to the GluN2 subunit. Selectivity for glycine over glutamate is conferred by the volume of the agonist-binding cavity resulting from steric constraints from residues present only in GluN1 (Furukawa and Gouaux, 2003).

Unlike AMPA or kainate receptors, which can form homomeric channels, functional NMDA channels are heteromeric, requiring two GluN1 and two GluN2 subunits. The general tetrameric organization of glutamate receptors was confirmed with the solving of a homomeric AMPA receptor structure (Sobolevsky et al., 2009). Unlike Cys-loop receptors, agonist binding in glutamate receptors occurs in a subunit-autonomous manner, requiring no inter-subunit interactions. The ligand binding regions of NMDA receptors are arranged as dimeric pairs (see Fig. 31.6B). Within a subunit, ligand binding occurs at the D1/D2 interface, which results in the closure of this structure in a clamshell fashion. These domain movements are thought to be associated with channel gating behavior, specifically, opening, closing and desensitization.

VI. NEURONAL ACETYLCHOLINE RECEPTOR CHANNELS

Studies of acetylcholine receptors began with the skeletal muscle isoforms (Steinbach, 1989), but AChRs are also expressed in neurons. The embryonic muscle AChR consists of an $\alpha_2\beta\gamma\delta$ pentamer, but later in development the γ subunit is replaced by an ε subunit. A much greater heterogeneity of receptor subunits is involved in the expression of AChRs at central synapses. (Dani and Bertrand, 2007). Neuronal AChRs mediate excitatory synaptic transmission in autonomic ganglia and at the recurrent collateral synapse of spinal motoneurons onto Renshaw cells (inhibitory interneurons). The functional role of nAChRs in the central nervous system was more difficult to establish despite the well-known action of nicotine (via cigarette smoke) on human behavior. nAChRs differ in several respects from muscle AChRs. First, α-bungarotoxin blocks muscle AChRs, but not most nAChRs. However, α-bungarotoxin binding sites represent a distinct subtype of nAChRs that have faster kinetics and a higher calcium permeability than other nAChR subtypes. The Ca^{2+} permeability of some nAChRs and changes in channel properties during synaptogenesis suggest that various nAChR subtypes play a role in synaptic plasticity and development. The activity of nAChRs are also modulated by phosphorylation. The kinase activation can be due to the actions of neuropeptides, such as vasoactive intestinal peptide and substance P, that are co-released with acetylcholine at some synapses.

Perhaps even more than for other ligand-gated channels, the cloning and characterization of subunit genes greatly accelerated studies of the structure and function of nAChRs (Role, 1992). Unlike the muscle AChRs, the nAChR pentamer is composed of only two classes of subunits, aptly named α and β. Subunits with cysteines at residues 192 and 193 are designated as α; subunits lacking these cysteines are called β. The genes for nine α (α_{2-10}) and three β (β_{2-4}) subunits have been cloned from rat and chick brain cDNA libraries. The stoichiometry of each channel molecule can be either homo-oligomeric (five alpha subunits) or heteromeric (usually with two α and three β subunits). Expression of single subunits and combination of subunits in *Xenopus* oocytes narrowed the possible combinations of subunits in functional channels. For example, α_{2-6} and β_{2-4} form heteromeric channels, whereas α_7, α_8 and α_9 do not. Combinations of subunits differ in their single-channel properties, ligand affinity and sensitivity to antagonists such as α-bungarotoxin. The $\alpha_4\beta_2$ receptor is a common heteromer in the CNS. It has a relatively high affinity for nicotinic agonists and thus is a principal target of the nicotine in tobacco smoke. Homo-oligomeric α_7 channels have a relatively low affinity for ACh and rapidly desensitize. This subunit has the closest homology to the snail AChBP and has been used to probe the structural substrates of channel properties such as desensitization, ion flux and selectivity. Homo-oligomeric α_7, α_8 and α_9 channels are sensitive to α-bungarotoxin, but α_7 is the predominant subunit of these three in brain. Presynaptic homomeric α_7 receptors with their high calcium permeability can enhance the release of glutamate and other transmitters. The α_9 subunit is unique due to its limited expression in the outer hair cells of the cochlea as well as its mixed muscarinic/nicotinic pharmacology.

Many central neurons have responses to exogenous application of nicotinic agonists and there is a wide distribution of nAChR subunit genes as revealed by in situ hybridization. However, there is a reasonable correlation between pathways with functional nAChRs (e.g. the cholinergic input to the hippocampus and medial habenula from the medial septum and diagonal band), the presence of nicotinic binding sites and the expression of nAChR subunits. Studies of nAChRs in different neuronal cell types have revealed a spectrum of channel properties and pharmacological characteristics, suggesting that individual neurons express several combinations of nAChR subunits. For example, *in situ* hybridization studies of neurons in the medial habenular nucleus have revealed two α and three β subunit genes. As for many classes of ligand-gated channels, the role of specific nAChR subunits has been investigated using genetically-engineered knockout and knock-in mice to investigate subunit-specific functions.

Interest in the nAChRs has been further fueled by studies indicating that mutations in α_4 or β_2 subunits cause a genetic form of human epilepsy.

VII. γ-AMINOBUTYRIC ACID AND GLYCINE RECEPTOR CHANNELS

Synaptic inhibition in the central nervous system (CNS) is mediated largely by $GABA_A$ and glycine receptors. These ligand-gated receptor channels are selectively permeable to anions, principally Cl^- under physiological conditions. GABA-gated Cl^- channels are designated $GABA_A$ receptors to distinguish them from the G-protein-coupled $GABA_B$ receptor (Padgett and Slesinger, 2010). $GABA_A$ and glycine receptors are members of the Cys-loop receptor family. Unlike other mammalian Cys-loop receptors that are non-selective cation channels, $GABA_A$ and glycine channels are selectively permeable to anions.

Virtually all CNS neurons have $GABA_A$ receptors, whereas the anatomical distribution of glycine receptors is generally restricted to the brainstem and spinal cord. $GABA_A$ receptors are often localized on proximal dendrites of central neurons, but also are expressed on axon initial segments and distal dendrites. Because the Cl^- equilibrium potential in many neurons is more negative than the resting potential, the opening of $GABA_A$ or glycine channels hyperpolarizes the cell membrane potential and reduces excitability. In addition to hyperpolarizing the membrane potential, the opening of large numbers of these channels lowers the membrane electrical resistance. Thus $GABA_A$ channels at proximal dendrites effectively "shunt" excitation traveling down the dendrite from excitatory synapses on more distal dendritic branches. In some neurons, particularly during early development, the Cl^- equilibrium is more positive than the resting potential, resulting in depolarizing $GABA_A$ or glycine responses. Depolarizing $GABA_A$ responses occurring in axons can increase excitability and neurotransmitter release. Finally, some inhibitory synapses in the spinal cord and brainstem contain both $GABA_A$ and glycine receptors. Analysis of unitary release events at these sites indicates that single synaptic vesicles contain both GABA and glycine and that a subpopulation of postsynaptic sites contains both receptor types (Jonas et al., 1998). As with other ligand-gated neurotransmitter receptors, molecular studies have revealed anchoring and regulatory proteins that interact with glycine and $GABA_A$ receptors, such as gephyrin (Fritschy et al., 2008) and GABA receptor-associated protein (GABARAP; Mohrluder et al., 2009). Gephyrin was identified as a cytoplasmic protein that interacts directly with glycine receptors. Gephyrin also interacts with tubulin and the actin-binding protein profilin and thus acts as a bridge between glycine receptors and the cytoskeleton. Gephyrin is also co-localized with $GABA_A$ receptors at postsynaptic sites but, unlike glycine receptors, has not been shown to bind to $GABA_A$ receptors. GABARAP interacts with many $GABA_A$ receptor subtypes, as well as binding to gephyrin and tubulin. Interaction with these cytoplasmic factors may alter the localization and trafficking of $GABA_A$ and glycine receptors as well as create zones of localized signal transduction.

The behavior of single $GABA_A$ and glycine channels can be described by a kinetic scheme similar to that of the nAChR with the binding of two agonist molecules required for channel opening (Macdonald and Twyman, 1992). Analysis of the openings and closings of single $GABA_A$ channels suggests that the channel may open briefly following the binding of a single $GABA_A$ molecule and into two longer-lived open states from the doubly liganded configuration. Comparison of the total open duration of singly- and doubly-liganded receptors demonstrates that occupancy of both agonist sites results in many more channel openings. Channels may close and re-enter longer-lived open states before the agonist dissociates from the receptor. These so-called *bursts* are composed of short closings interrupting a series of openings and they can last tens of milliseconds. Desensitization of $GABA_A$ channels results in long closed intervals that are grouped with bursts into *clusters* lasting up to several hundred milliseconds. These clusters are important in determining the duration of inhibitory postsynaptic potentials at some synapses (Jones and Westbrook, 1996).

The drugs that act on $GABA_A$ and glycine channels comprise a fascinatingly rich assortment of clinically important compounds (Olsen et al., 1991). Because these channels underlie synaptic inhibition in the CNS, enhancement or reduction in their activity can lead to profound changes in brain function, including amnesia (increased $GABA_A$ activity) or seizures (decreased $GABA_A$ activity). Antagonists for these receptors include strychnine, which inhibits glycine receptors; bicuculline, which inhibits $GABA_A$ receptors; and picrotoxin, which inhibits both receptor types. The $GABA_A$ receptor is also the target of sedative-hypnotic drugs, such as the benzodiazepines and barbiturates. Benzodiazepines (BDZ) increase the probability of channel opening, whereas barbiturates appear to act by prolonging long channel openings (bursts). The pharmacology of benzodiazepine modulation of the $GABA_A$ receptor is particularly interesting, because compounds either can enhance channel opening (BDZ agonists), reduce channel opening (BDZ inverse agonists) or block the effects of BDZ agonists (BDZ antagonists). $GABA_A$ receptor activity is also modulated by alcohol, volatile anesthetics, such as isoflurane, and some steroid anesthetics (or their endogenous equivalents, the neurosteroids).

Using benzodiazepines and strychnine as selective ligands, $GABA_A$ and glycine receptors were purified as

multimeric protein complexes, each with molecular weights of approximately 50−60 kDa. The solubilized receptor complex had a molecular weight of approximately 250 kDa, suggesting that, as for the AChR, five subunits constitute a receptor. Subsequent molecular cloning identified a series of receptor subunits for both receptors. The glycine subunits include the strychnine-binding subunit (α) of which four have been cloned and a single β subunit, with a stoichiometry of $(\alpha)_2(\beta)_3$ for receptors from mature animals. Interestingly, the immature form of the glycine receptor contains only α subunits. Gephyrin binds to the β subunit, thus the interaction between gephyrin and glycine receptors is limited to the adult form. Nineteen $GABA_A$ subunits have been identified and grouped according to sequence similarity. These include six α, three β, three γ, three ρ subunits and single δ, ε, π, and Θ subtypes (Wisden and Seeburg, 1992; Olsen and Sieghart, 2009). In heterologous systems, expression of single $GABA_A$ or glycine receptor subunits can result in functional homomeric receptors. However, given the broad co-expression patterns of many $GABA_A$ and glycine receptor subunits and the functional heterogeneity of native receptors, homomeric receptors probably occur rarely. The large number of $GABA_A$ receptor subunits provides a formidable challenge in determining which combinations form functional receptors in neurons. $GABA_A$ and glycine receptor subunit expression also varies during development and with neuronal cell type. Based on pharmacology, expression, biochemistry and subcellular localization, at least 26 different types of native $GABA_A$ receptors have been identified in CNS neurons (Olsen and Sieghart, 2009).

Subunit composition can have a strong influence on the biophysical and pharmacological properties of $GABA_A$ and glycine receptors. The GABA and benzodiazepine binding sites reside at the interface between an α subunit and a β or γ subunit (usually γ_2), respectively. The γ_2 subunit is broadly and highly expressed in the CNS and genetic deletion greatly reduces BDZ binding sites in the brain. Interestingly, the α_6 subunit has a low affinity for BDZ agonists, but still can bind BDZ inverse agonists or antagonists, which may explain benzodiazepine-insensitive $GABA_A$ receptors in some neurons. Homomeric receptors composed of the $GABA_A$ receptor ρ subunit are bicuculine-insensitive, weakly antagonized by picrotoxin and insensitive to BDZs, barbiturates and neurosteroids. These channels also show distinct gating properties and conductances compared to other $GABA_A$ receptors. They were initially referred to as $GABA_C$ receptors. However, due to their sequence similarity and proposed structure, they are currently thought of as a subtype of $GABA_A$ receptors. The three ρ subunits ($\rho1$, $\rho2$ and $\rho3$) are expressed throughout the CNS but expression is predominantly in several cell types in the retina.

VIII. GLUTAMATE RECEPTOR CHANNELS

Although it was known from the early 1950s that L-glutamate was a neuroexcitant, it was not until the 1980s that the role of glutamate-gated ion channels in central synaptic transmission was widely accepted (Collingridge and Lester, 1989; Westbrook and Jahr, 1989). It is now clear that glutamate receptor channels mediate a substantial portion of fast excitatory transmission in the brain and spinal cord through the simultaneous activation of two types of ion channels co-localized at excitatory synapses. Characterization of this family of ligand-gated ion channels was initially based on selective activation by the exogenous amino acid ligands: NMDA, kainate and quisqualate. AMPA (α-amino-3-hydroxy-5-methyl-4-isoxazole propionic acid) replaced quisqualate as one of the prototypic ligands because quisqualate also activates a G-protein-coupled receptor. It soon became apparent that NMDA receptors were distinct from kainate and AMPA receptors, but for some time it was debated whether kainate and AMPA (i.e. non-NMDA) responses arose from the same or different receptors. It is now clear that AMPA and kainate receptors are distinct molecular entities, although kainate can activate both classes of receptors.

Initial studies of native AMPA/kainate receptor channels demonstrated many of the same features as AChRs. In hippocampal pyramidal neurons, AMPA receptor activation leads to brief openings (1−5 ms) of monovalent cation channels that show little or no voltage dependence. However, in some neurons, particularly interneurons, AMPA receptors have a higher calcium permeability and are inwardly rectifying. AMPA receptors rapidly desensitize when gated by glutamate and agonist dissociation (unbinding) and desensitization (agonist still bound but the channel is non-conducting) can contribute to the decay of the synaptic current. The behavior of AMPA channels seems well suited to the rapid relay of information that characterizes the fast component of excitatory postsynaptic potentials in the brain.

The NMDA channel provides perhaps the best example of the linkage between fundamental properties of ion channels and the electrical activity of single cells and complex behavioral phenomena (Bekkers and Stevens, 1990; McBain and Mayer, 1994). This linkage is primarily based on three features of NMDA channels: (1) voltage-dependent block of the open channel by extracellular Mg^{2+}; (2) a relatively high permeability to Ca^{2+}; and (3) slow channel kinetics resulting in long-lasting channel activity. Because Mg^{2+} ions are positively charged and thus sense the membrane electric field, they are drawn into the open NMDA receptor channel at negative membrane potentials. Mg^{2+} binds in the channel pore and impedes the flow of permeant ions, even though the agonists (glutamate and glycine) remains bound. However, during synaptic

activity as the cell membrane depolarizes, Mg^{2+} falls out of the channel and permeant cations flow through the channel. Thus, ion flux through the channel is voltage dependent. This mechanism differs from other voltage-dependent ion channels, such as the sodium or calcium channel, where voltage dependence results from an intrinsic conformational change in the channel protein. However, the end result is the same; current flows through the NMDA receptor channel more effectively with depolarization and thus acts as a positive feedback on synaptic activation.

Unlike many AMPA channels, Ca^{2+} contributes a substantial fraction of the flux through NMDA channels. However, the rate of flux of Ca^{2+} through the NMDA channel is slower than Na^{+} because Ca^{2+} transiently binds with higher affinity to sites within the channel (*energy wells*). Thus most of the current through open NMDA channels is due to Na^{+}, which is present in 50-fold excess in the extracellular space compared to calcium. Nonetheless, the 5−10% of the current that is carried by Ca^{2+} is sufficient to act as a biochemical signal for such processes as the induction of long-term potentiation in the hippocampus, an experimental model of associative learning. Excessive activation of glutamate receptors may also cause neuronal damage, presumably through elevations of intracellular Ca^{2+} concentration and subsequent activation of proteases and free radical formation. This mechanism, called *excitotoxicity*, has been implicated in brain damage due to prolonged seizures, following strokes and may also contribute to loss of neurons in several degenerative neurological diseases.

Because no high-affinity ligands were available for purification of glutamate receptors, molecular biologists were forced to use the somewhat laborious task of expression cloning to isolate cDNA clones for glutamate receptor subunits. The first AMPA receptor subunit (GluA1) was isolated by this technique in 1989 and the first NMDA receptor clone (GluN1) was also isolated by expression cloning in 1991. Using these initial AMPA and NMDA clones to screen for homologous sequences, 16 related glutamate receptor subunits were isolated from rat and mouse cDNA libraries. On the basis of glutamate receptor sequence homology and the characteristics of the expressed receptors, the subunits can be grouped into three categories: four AMPA subunits (GluA1-4, formerly called GluR1−4 or A−D), five high-affinity kainate subunits (GluK1−5, formerly GluR5−7, KA-1, KA-2) and seven NMDA subunits (GluN1, GluN2A−D, GluN3A−B, formerly NR1, NR2A−D, NR3A−B). GluD1 and GluD2 have significant homology to glutamate receptor subunits yet they do not bind glutamate agonists. They are referred to as orphan subunits and their function remains unclear. The GluD2 subunit is particularly intriguing because a mutation in the gene encoding this protein is responsible for the neurological phenotype of the *Lurcher* mouse. Relatively little is known about GluN3 subunits and it is unclear whether neurons make NMDA receptors that contain NR3 subunits. Curiously, when GluN1 and GluN3A or GluN3B are co-expressed in heterologous cells, they form excitatory channels that are gated by glycine rather than glutamate.

Some AMPA receptor subunits can combine to form functional homo-oligomeric receptors and this has revealed some interesting and curious phenomena. For example, the genes for GluA2, GluK1 and GluK2 code for a glutamine in the P loop region. However, the mRNA undergoes editing such that the expressed protein has an arginine residue at this site. This switch has a profound effect on the behavior of the channel. The current evoked by homo-oligomeric expression of unedited subunits shows marked inward rectification and an increased permeability to Ca^{2+}. The edited versions have a linear current−voltage relationship and are permeable only to monovalent cations (Na^{+} and K^{+}). Because the synaptic response mediated by AMPA receptors in hippocampal pyramidal cells has a linear current−voltage relationship, most AMPA receptors in these neurons contain one or more edited copies of GluA2. However, in interneurons in cortex and hippocampus as well as in dorsal horn neurons of the spinal cord, AMPA receptors lacking edited GluA2 subunits show inward rectification and increased permeability to Ca^{2+}.

Glutamate channels, particularly NMDA channels, are regulated by a variety of allosteric mechanisms and by phosphorylation. The most dramatic are the actions of glycine as a *co-agonist* that is required for the opening of NMDA channels and extracellular Mg^{2+} that blocks NMDA channels. Binding of two molecules of glutamate and two molecules of glycine are required to activate an NMDA channel. Because glutamate channels are tetramers, it is thought that each subunit contributes to agonist binding. The glycine concentration in cerebrospinal fluid exceeds the EC_{50} for the glycine site, thus it is likely that the glycine site is tonically saturated. Recent evidence indicates that endogenous D-serine may also bind to the glycine site, with approximately the same affinity and efficacy as glycine. Although AMPA receptor channels do not require a co-agonist, given their homology with NMDA receptor channels, four molecules of glutamate are probably necessary to activate AMPA channels (Rosenmund et al., 1998). Other regulatory factors that affect NMDA channel activity include extracellular protons, Zn^{2+}, polyamines, redox potential and intracellular Ca^{2+}. The ability of these factors to affect NMDA receptors can depend on subunit composition. For example, the GluN1/GluN2A receptors are almost 100-fold more sensitive to Zn^{2+} than GluN1/GluN2B receptors. There are numerous phosphorylation sites on the C-terminal domains of AMPA and NMDA receptor subunits that can be regulated by protein kinase A and C, tyrosine kinases and Ca^{2+}/calmodulin-dependent

kinase (Chen and Roche, 2007). Kinase activation can alter any of a number of channel properties including gating and membrane trafficking. Phosphorylation of AMPA and NMDA receptors can also affect receptor trafficking that can then govern the ability of synapses to respond to stimuli that trigger long-term changes in synaptic efficacy. Activation of the NMDA receptor itself and the subsequent Ca^{2+} influx can result in PKC activation, which can then alter AMPA receptor trafficking. The impact of these regulatory mechanisms on synaptic function is a continuing area of investigation (Lee, 2006).

As with other neurotransmitter receptors, glutamate receptors are clustered in the postsynaptic membrane at synaptic sites. Recent studies have revealed a number of proteins that are involved in the clustering and localization of glutamate receptor channels. Glutamate channels are imbedded in the postsynaptic density (PSD) that contains receptors, regulatory proteins and cytoskeletal proteins. Biochemical studies suggest that calmodulin and cytoskeletal proteins can interact with C-terminal domains of several NMDA receptor subunits at domains that are involved in the regulation of NMDA receptor desensitization, suggesting an intriguing link between dynamic regulation of channel activity (e.g. by compartmentalized regulatory proteins) and structural features, such as channel anchoring or localization at synapses. A family of proteins with a PDZ domain are involved in interactions with AMPA and NMDA subunits (Ehlers et al., 1996; Sheng and Pak, 2002). TARPs (transmembrane AMPA receptor regulatory proteins) are a family of proteins that share homology with auxiliary subunits of voltage-gated calcium channels. TARPs alter the gating and pharmacological sensitivity of AMPA receptors (Milstein and Nicoll, 2008) and thus are considered auxiliary AMPA receptor subunits (Mayer, 2005). Other recently identified proteins, like CKAMP44, may have similar regulatory actions on AMPA receptors. The interactions between glutamate receptors and their associated proteins is important in receptor lateral mobility and trafficking, synapse development and the dynamic regulation of activity of ligand-gated channels in a broad range of brain functions including learning and memory.

BIBLIOGRAPHY

Ascher, P., & Nowak, L. (1987). Electrophysiological studies of NMDA receptors. *Trends Neurosci, 10*, 284−288.

Bekkers, J. M., & Stevens, C. F. (1990). Computational implications of NMDA receptor channels. *Cold Spring Harbor Symp Quant Biol, 55*, 131−135.

Brejc, K., van Dijk, W. J., Klaassen, R. V., et al. (2001). Crystal structure of Ach-binding protein reveals the ligand-binding domain of nicotinic receptors. *Nature, 411*, 269−276.

Browne, L. E., Jiang, L. H., & North, R. A. (2010). New structure enlivens interest in P2X receptors. *Trends Pharmacol Sci, 31*, 229−237.

Burnstock, G. (2007). Physiology and pathophysiology of purinergic neurotransmission. *Physiol Rev, 87*, 659−797.

Changeux, J.-P., & Edelstein, S. J. (1998). Allosteric receptors after 30 years. *Neuron, 21*, 959−980.

Chen, B. S., & Roche, K. W. (2007). Regulation of NMDA receptors by phosphorylation. *Neuropharmacology, 53*, 362−368.

Chen, G. Q., Cui, C., Mayer, M. L., & Gouaux, E. (1999). Functional characterization of a potassium-selective prokaryotic glutamate receptor. *Nature, 402*, 817−821.

Collingridge, G. L., & Lester, R. A. (1989). Excitatory amino acid receptors in the vertebrate central nervous system. *Pharmacol Rev, 41*, 143−210.

Collingridge, G. L., Olsen, R., Peters, J., & Spedding, M. (2009). A nomenclature for ligand- gated ion channels. *Neuropharmacology, 56*, 2−5.

Colquhoun, D. (1998). Binding, gating, affinity and efficacy: the interpretation of structure-activity relationships for agonists and of the effects of mutating receptors. *Brit J Pharmacol, 125*, 923−947.

Dani, J. A., & Bertrand, D. (2007). Nicotinic acetylcholine receptors and nicotinic cholinergic mechanisms of the central nervous system. *Annu Rev Pharamacol Toxicol, 47*, 699−729.

Ehlers, M. D., Mammen, A. L., Lau, L. F., & Huganir, R. L. (1996). Synaptic targeting of glutamate receptors. *Curr Opin Cell Biol, 8*, 484−489.

Fritschy, J. M., Harvey, R. J., & Schwarz, G. (2008). Gephyrin: where do we stand, where do we go? *Trends Neurosci, 31*, 257−264.

Furukawa, H., & Gouaux, E. (2003). Mechanisms of activation, inhibition and specificity: crystal structures of the NMDA receptor NR1 ligand-binding core. *EMBO J, 22*, 2873−2885.

Graus, F., Saiz, A., & Dalmau, J. (2010). Antibodies and neuronal autoimmune disorders of the CNS. *J Neurol, 257*, 509−517.

Hibbs, R. E., & Gouaux, E. (2011). Principles of activation and permeation in an anion-selective Cys-loop receptor. *Nature*, May 15 [Epub ahead of print].

Hilf, R. J., & Dutzler, R. (2009). A procaryotic perspective on pentameric ligand-gated ion channel structure. *Curr Opin Struct Biol, 19*, 418−424.

Hille, B. (2001). *Ionic Channels of Excitable Membranes* (3rd ed.). Sunderland, MA: Sinauer Associates Inc.

Hollmann, M., & Heinemann, S. (1994). Cloned glutamate receptors. *Annu Rev Neurosci, 17*, 31−108.

Jahr, C. E., & Stevens, C. F. (1987). Glutamate activates multiple single channel conductances in hippocampal neurons. *Nature, 325*, 522−525.

Jonas, P., Bischofberger, J., & Sandkühler, J. (1998). Corelease of two fast neurotransmitter at a central synapse. *Science, 281*, 419−424.

Jones, M. V., & Westbrook, G. L. (1996). The impact of receptor desensitization on fast synaptic transmission. *Trends Neurosci, 19*, 96−101.

Julius, D. (1991). Molecular biology of serotonin receptors. *Annu Rev Neurosci, 14*, 335−360.

Karlin, A. (1991). Explorations of the nicotinic acetylcholine receptor. *Harvey Lectures, 85*, 71−107.

Kullmann, D. M. (2010). Neurological channelopathies. *Annu Rev Neurosci, 33*, 151−172.

Lee, H.-K. (2006). Synaptic plasticity and phosphorylation. *Pharmacol Therapeut, 112*, 810−832.

Macdonald, R. L., & Twyman, R. E. (1992). Kinetic properties and regulation of $GABA_A$ receptor channels. *Ion Channels, 3*, 315−343.

MacKinnon, R. (2004). Nobel lecture. *Potassium channels and the atomic basis of selective ion conduction Biosci Rep, 24*, 75−100.

Mayer, M. L. (2005). Glutamate receptor ion channels. *Curr Opin Neurobiol, 15*, 282–288.

Mayer, M. L. (2006). Glutamate receptors at atomic resolution. *Nature, 440*, 456–462.

McBain, C., & Mayer, M. (1994). N-methyl-D-aspartic acid receptor structure and function. *Physiol Rev, 74*, 723–759.

Milstein, A. D., & Nicoll, R. A. (2008). Regulation of AMPA receptor gating and pharmacology by TARP auxiliary subunits. *Trends Pharmacol Sci, 29*, 333–339.

Miyazawa, A., Fujiyoshi, Y., Stowell, M., & Unwin, N. (1999). Nicotinic acetylcholine receptor at 4.6 A resolution: transverse tunnels in the channel wall. *J Mol Biol, 288*, 765–786.

Mohrluder, J., Schwarten, M., & Willbold, D. (2009). Structure and potential function of gamma-aminobutyrate type A receptor-associated protein. *FEBS J, 279*, 4989–5005.

Nakanishi, S. (1992). Molecular diversity of glutamate receptors and implications for brain function. *Science, 258*, 597–603.

Neher, E. (1992). Ion channels for communication between and within cells. *Science, 256*, 498–502.

Olsen, R. W., Sapp, D. M., Bureau, M. H., Turner, D. M., & Kokka, N. (1991). Allosteric actions of central nervous system depressants including anesthetics on subtypes of the inhibitory gamma-aminobutyric $acid_A$ receptor-chloride channel complex. *Ann NY Acad Sci, 625*, 145–154.

Olsen, R. W., & Sieghart, W. (2009). $GABA_A$ receptors: subtypes provide diversity of function and pharmacology. *Neuropharmacology, 56*, 141–148.

Padgett, C. L., & Slesinger, P. A. (2010). $GABA_B$ receptor coupling to G-proteins and ion channels. *Adv Pharmacol, 58*, 123–147.

Role, L. W. (1992). Diversity in primary structure and function of neuronal nicotinic acetylcholine receptor channels. *Curr Opin Neurobiol, 2*, 254–262.

Rosenmund, C., Stern-Bach, Y., & Stevens, C. F. (1998). The tetrameric structure of a glutamate receptor channel. *Science, 280*, 1596–1599.

Sakmann, B. (1992). Nobel lecture. Elementary steps in synaptic transmission revealed by currents through single ion channels. *Neuron, 8*, 613–629.

Sheng, M., & Pak, D. T. (2002). Ligand-gated ion channel interactions with cytoskeletal and signaling proteins. *Annu Rev Physiol, 62*, 755–778.

Sine, S. M., & Engel, A. G. (2004). Recent advances in Cys-loop receptor structure and function. *Nature, 440*, 448–455.

Smit, A. B., Syed, L. I., Schaap, D., et al. (2001). A glial-derived acetylcholine-binding-protein that modulates synaptic transmission. *Nature, 411*, 261–268.

Sobolevsky, A. I., Rosconi, M. P., & Gouaux, E. (2009). X-ray structure, symmetry and mechanism of an AMPA-subtype glutamate receptor. *Nature, 462*, 745–756.

Steinbach, J. H. (1989). Structural and functional diversity in vertebrate skeletal muscle nicotinic acetylcholine receptors. *Annu Rev Physiol, 51*, 353–365.

Stern-Bach, Y., Bettler, B., Hartley, M., Sheppard, P. O., O'Hara, P. J., & Heineman, S. F. (1994). Agonist selectivity of glutamate receptors is specified by two domains structurally related to bacterial amino acid-binding proteins. *Neuron, 13*, 1345–1357.

Swope, S. L., Moss, S. J., Raymond, L. A., & Huganir, R. L. (1999). Regulation of ligand-gated ion channels by protein phosphorylation. *Adv Second Messenger Phosphoprotein Res, 33*, 49–78.

Unwin, N. (2005). Refined structure of the nicotinic acetylcholine receptor at 4 A resolution. *J Mol Biol, 346*, 967–989.

Westbrook, G. L., & Jahr, C. E. (1989). Glutamate receptors in excitatory neurotransmission. *Sem Neurosci, 1*, 103–114.

Wisden, W., & Seeburg, P. H. (1992). $GABA_A$ receptor channels: from subunits to functional entities. *Curr Opin Neurobiol, 2*, 263–269.

Wu, L. J., Sweet, T. B., & Clapham, D. E. (2010). International Union of Basic and Clinical Pharmacology. LXXVI. Current progress in the mammalian TRP ion channel family. *Pharmacol Rev, 262*, 381–404.

Chapter 32

Synaptic Transmission

Janusz B. Suszkiw

Chapter Outline

I. SUMMARY

The transmission of synaptic signals is mediated by chemical neurotransmitter substances. Neurotransmitters are synthesized in presynaptic terminals and stored in synaptic vesicles. Transmitter release is evoked by presynaptic action potentials (APs), which activate influx of Ca^{2+} into terminals and trigger a Ca^{2+}-dependent exocytosis of transmitter from synaptic vesicles into the synaptic cleft. Once released, neurotransmitters activate specific receptor-gated channels in the postsynaptic cell and elicit a transient change in the membrane permeability to cations or anions. Fast synaptic transmission is mediated by ionophoric receptors. Slow synaptic transmission is mediated by G-protein-coupled receptors. Excitatory postsynaptic potentials (EPSPs) are associated with transmitter-induced increase in Na^+ and K^+ conductance of the synaptic membrane, resulting in net entry of positive charge carried by Na^+ and membrane depolarization. Inhibitory postsynaptic potentials (IPSPs) are associated with transmitter-activated influx of Cl^- and membrane hyperpolarization. The EPSPs at the skeletal neuromuscular junction are called end-plate potentials (EPPs). In a healthy neuromuscular junction, the EPPs are always large enough to depolarize the muscle membrane to threshold and trigger muscle APs. The EPSPs generated at any single neuro-neuronal synapse are usually too small to depolarize the postsynaptic neuron to threshold. Synaptic signals converging onto a neuron are normally integrated through summation of EPSPs and IPSPs and an AP is triggered only when the resultant membrane potential reaches or exceeds the threshold. Chemical synaptic transmission is subject to modulation by intrinsic and extrinsic factors, including frequency and pattern of AP firing, which can either facilitate or depress the transmission across any given synapse.

II. INTRODUCTION

The function of nerve cells is to receive, process and transmit information. Intercellular transfer of signals among neurons or from neurons to effector cells is

Cell Physiology Sourcebook. DOI: 10.1016/B978-0-12-387738-3.00032-9

accomplished at specialized intercellular junctions called *synapses* and is by and large chemically mediated. A characteristic feature of a chemical synapses is the presence of a 20−100 nm wide extracellular space, the *synaptic cleft*, which separates the *presynaptic* (transmitting) and *postsynaptic* (receiving) elements of the synapse. This physical discontinuity prevents efficient transfer of current between the cells and necessitates intervention of a diffusible chemical transmitter substance. The fundamental aspect of chemically-mediated transmission is the transduction of voltage signal into the release of neurotransmitter from the presynaptic neuron and transduction of transmitter binding to a specific receptor into voltage change in the postsynaptic cell.

The basic principles of chemical neurotransmission have been elaborated in a series of seminal experiments conducted on the vertebrate skeletal neuromuscular junction by B. Katz and his collaborators in the 1950s and 1960s (Katz, 1966). At about the same time, the pioneering work by J.C. Eccles and his coworkers on spinal motor neurons showed that the general principles of chemical transmission established at the vertebrate neuromuscular junction also apply to central synapses (Eccles, l964). Since then, new insights into the mechanism of synaptic transmission have been gained on the molecular level through the application of contemporary techniques of molecular biology and electrophysiology.

This chapter focuses on chemical synaptic transmission; however, the reader should be cognizant of another form of signal transfer, referred to as *electrical transmission*. Electrical transmission is mediated by the *gap junctions* (Bennett, 1997). Gap junctions consist of channel aggregates that bridge the closely apposed cell membranes and thus provide electrical continuity between the communicating cells. Unlike the chemical synapses, gap junctions and the electrical coupling they mediate are not unique to the nervous system but are also found in many other tissues. Gap junctions and electrotonic transmission are discussed in greater detail elsewhere in this volume.

III. STRUCTURE AND FUNCTION OF CHEMICAL SYNAPSES: AN OVERVIEW

Based on their morphofunctional characteristics, synaptic junctions may be classified as directed, fast-acting or non-directed, slow-acting synapses. Although the configurations of synaptic junctions can vary considerably, all share common features (Fig. 32.1). The presynaptic element, usually an axon terminal bouton or axon varicosity, is characterized by the presence of membrane-bound spherical organelles, the *synaptic vesicles*, which store the transmitter prior to its release. A subset of synaptic vesicles clusters near the presynaptic *active zone*, a structural specialization of the presynaptic membrane for synaptic vesicle docking and exocytosis. The juxtaposed postsynaptic membrane contains specific receptors for the transmitter released from the presynaptic terminal. A thickening of postsynaptic membrane, the *postsynaptic density*, is frequently observed and thought to play a role in localizing the neurotransmitter receptors at the synaptic membrane. The width of the synaptic cleft at highly directed (point-to-point), fast-acting synapses typically varies from about 20−50 nm but can be considerably wider at non-directed, slow-acting synapses. The synaptic cleft contains proteinaceous material, including various cell adhesion molecules (Hall and Sanes, 1993), thought to serve as an adherent for stabilizing the synapse. The junction is enveloped by glial elements, which insulate the synapse as well as perform other functions such as, for example, transmitter removal from the synaptic cleft. For a detailed discussion of synaptic ultrastructure, the student may wish to consult the articles in Pappas and Purpura (l972) and a more recent review by Burns and Augustine (1995).

Transmission at chemical synapses is *unidirectional* from the presynaptic to postsynaptic element. The presynaptic terminals are specialized for transmitter biosynthesis, packaging of transmitter into the synaptic vesicles and vesicular transmitter exocytosis. The transmitter receptors in the postsynaptic membrane transduce transmitter binding into ionic current which generates the *postsynaptic potential* (PSP). Postsynaptic potentials at fast synapses are generated by activation of *ionophoric*, or channel-forming, receptors. The synaptic potentials are typically fast in onset and last for only a few milliseconds. The generation of the postsynaptic potentials is, however, not instantaneous but rather registers 0.3−0.5 ms after the arrival of the action potential at the presynaptic terminal. This *synaptic delay* is a characteristic feature of chemical synapses and reflects, for the most part, the time required for the molecular events associated with the transmitter release. At non-directed, slow synapses, channels are not directly transmitter-gated but rather are coupled to the receptor via G protein and second messenger systems. These receptors are referred to as *metabotropic*. The synaptic potential generated by activation of the metabotropic receptors is slower in onset and longer lasting.

The process of chemical neurotransmission involves (1) synthesis and vesicular uptake of neurotransmitter in presynaptic terminal, (2) exocytotic release of vesicular transmitter into the synaptic cleft, (3) diffusion and binding of transmitter to postsynaptic receptors and generation of synaptic potential and (4) termination of synaptic activity. As indicated above, transmitters are synthesized in the nerve ending of the presynaptic neuron and are concentrated and stored in synaptic vesicles. The intravesicular packet or *quantum* of transmitter that is stored in the vesicles is released by Ca^{2+}-dependent exocytosis. Exocytosis is triggered when an AP in the presynaptic

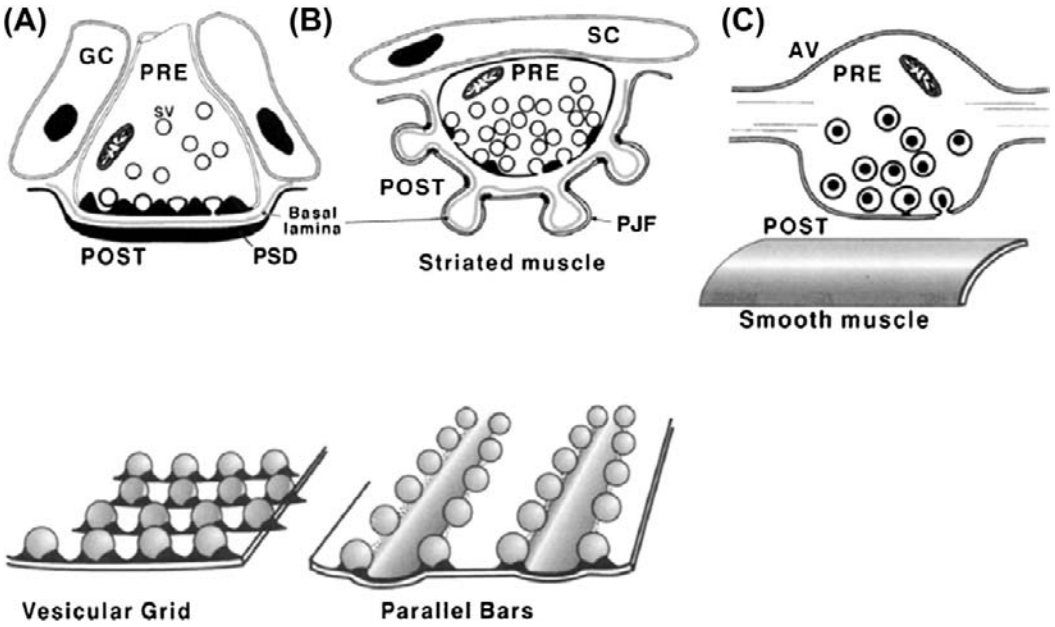

FIGURE 32.1 Schematic representations of neuro-neuronal and neuro-effector synaptic junctions. (A) A directed neuro-neuronal synapse subserving fast synaptic transmission in the CNS. The presynaptic terminal bouton contains mitochondria (M), clear-cored, about 40 nm in diameter, synaptic vesicles (SV), a subset of which is seen docked at the presynaptic vesicular grid. The receptors are localized in the juxtaposed thickening of postsynaptic membrane, the postsynaptic density (PSD). The presynaptic vesicular grid together with the juxtaposed PSD define the active zone of the synapse. The synaptic cleft is typically about 20 nm wide and contains dense material, with filamentous structures seen sometimes to span the cleft from pre-to-postsynaptic membrane. Glial cells (GC) cap and insulate the synapse. (B) The vertebrate skeletal neuromuscular junction (NMJ), a directed synapse subserving fast transmission from motor neuron to striated muscle. These large terminals are filled with many clear-cored, acetylcholine-containing synaptic vesicles. A few dense-cored vesicles can be also seen. A subset of clear-cored synaptic vesicles aggregate at the presynaptic active zone, which is defined by the presence of the presynaptic density. The presynaptic density appears to have the configuration of a bar defined by parallel rows of intramembrane particles, thought to represent the calcium channels, with two rows of vesicles attached on either side of the bar (bottom). The receptors for acetylcholine (AChR) are localized in the crests of the postjunctional folds (PJF) directly opposite the presynaptic active zones. The synaptic cleft at the vertebrate NMJ is typically 50 nm wide. The basal lamina within the synaptic cleft contains AChE, an enzyme that degrades ACh released into the synaptic cleft. The junction is insulated by Schwann cell (SC) processes. (C) A non-directed, slow-acting synapse between a presynaptic axon varicosity (AV) of a sympathetic neuron and smooth muscle. The varicosity contains large (>60 nm) dense-core, norepinephrine-containing vesicles. This synapse is characterized by the absence of distinct active zone structures and a variable but usually wide (>100 nm) separation between the presynaptic and postsynaptic elements of the junction.

neurons invades and depolarizes the nerve terminal, thereby opening the presynaptic voltage-gated Ca^{2+} channels and allowing influx of Ca^{2+} into the terminal. The resulting transient rise in $[Ca^{2+}]_i$ triggers fusion of synaptic vesicles with the plasmalemma and transmitter exocytosis. The requirement for Ca^{2+} influx is absolute. In absence of Ca^{2+}, the presynaptic AP will fail to trigger release.

Following its release into the synaptic cleft, transmitter combines with specific receptors in the postsynaptic membrane, causing a change in its permeability to specific ions. Change in membrane permeability to ions gives rise to synaptic current which, depending on ions involved, depolarizes or hyperpolarizes the postsynaptic membrane (Fig. 32.2). The depolarizing potential is called an *excitatory postsynaptic potential* (EPSP) because it tends to bring the cell membrane potential toward the threshold for an AP. EPSPs are associated with a change in the postsynaptic membrane permeability to Na^+ and K^+ ions and a net influx of positive charges (inward current carried by Na^+). The hyperpolarizing potential is called an *inhibitory postsynaptic potential* (IPSP), because it tends to move or hold the membrane potential away from the threshold, thus decreasing the likelihood of an AP being fired. The IPSPs elicited by activation of ionophoric receptors at fast synapses are associated with an increase in the postsynaptic membrane permeability to Cl^-. PSPs associated with activation of metabotropic receptors usually involve change in membrane permeability to K^+ ions.

Transmitter release normally terminates within less than 1 ms. As the presynaptic AP decays and the terminal repolarizes back toward the resting potential, the depolarization-activated calcium channels reclose, Ca^{2+} influx ceases and $[Ca^{2+}]_i$ is rapidly lowered to the prestimulus level. Transmitter action on the receptors in the postsynaptic membrane is terminated by diffusion and enzymatic degradation into an ineffective substance or clearance from the synaptic cleft by reuptake into the nerve terminals and/or glial cells. Reuptake and subsequent catabolism is the primary route of transmitter inactivation for most transmitters. The exception is acetylcholine, in

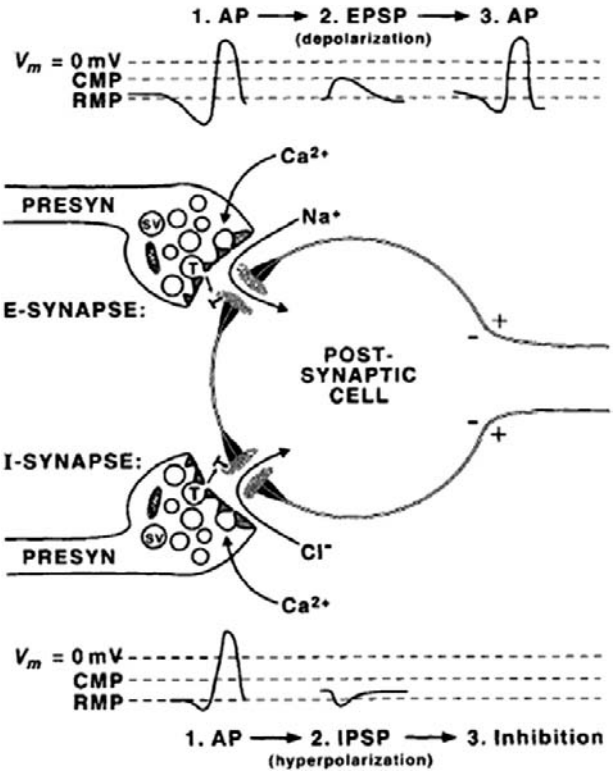

FIGURE 32.2 Fast excitatory versus inhibitory synaptic transmission. At an excitatory (E) synapse, the presynaptic action potential releases transmitters that activate cationic channels, resulting in an inward synaptic current carried by Na^+ ions and depolarizing potential, the excitatory postsynaptic potential (EPSP). EPSPs increase the likelihood of an action potential (AP) being fired by the postsynaptic cell. At an inhibitory (I) synapse, the transmitter activates receptor-gated chloride channels and influx of Cl^- ions, resulting in hyperpolarizing potential, the inhibitory postsynaptic potential (IPSP). The likelihood of an AP is diminished by activation of I-synapses because IPSPs hold or move the membrane potential of the postsynaptic cell away from the threshold. RMP, resting membrane potential; CMP, critical membrane potential (threshold) at which an AP is triggered.

which case inactivation is primarily by means of extracellular degradation of ACh to inactive acetate and choline.

IV. NEUROTRANSMISSION

IVA. Neurotransmitters and Neurotransmitter Receptors

Several criteria define a chemical substance as a neurotransmitter. (1) The biosynthetic enzymes for the synthesis of the substance must be present in the identified presynaptic neuron to catalyze the synthesis of transmitter in the nerve terminals. (2) The substance must be released by stimulation of the presynaptic neuron in a Ca^{2+}-dependent manner. (3) Application of the substance to the postsynaptic cell must mimic the actions of the neurally released substance. (4) A specific mechanism for inactivation of the transmitter substance, such as a selective uptake system in the presynaptic terminals or the presence of degradative enzyme(s), must be demonstrated at the synapse investigated.

Amino acid glutamate is the major excitatory neurotransmitter and γ-aminobutyric acid (GABA) and glycine serve as inhibitory transmitters in the CNS. Acetylcholine (ACh), dopamine (DA), norepinephrine (NE), epinephrine, serotonin (5-HT), histamine and ATP are all recognized as neurotransmitters or neurotransmitter candidates. Acetylcholine and norepinephrine are the established transmitters in the peripheral nervous system. In addition, there is good evidence that in the vascular smooth muscle, ATP is co-released and acts as a co-transmitter with NE. Neurons may also co-store and co-release various peptide hormones. These may act as co-transmitters or modulate the synaptic actions of conventional transmitters. Common low-molecular-weight transmitter substances and their chemical structures are shown in Fig. 32.3.

Neurotransmitter receptors (Table 32.1) are integral membrane proteins containing the transmitter recognition site and the transducer site. Ionophoric or channel-forming receptors include the muscle and neural nicotinic acetylcholine receptors; three pharmacologically distinguishable glutamate receptors that are selectively activated by analogs of glutamate — kainate, α-amino-3-hydroxy-5-methylisoxazole-4-propionic acid (AMPA) or N-methyl-D-aspartic acid (NMDA); the $5HT_3$ serotonin receptor; and

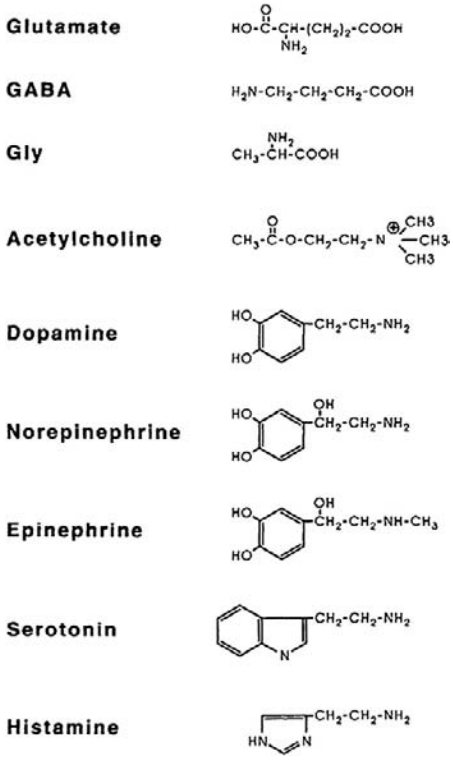

FIGURE 32.3 Structural formulas of common neurotransmitters.

TABLE 32.1 Common Neurotransmitters and Major Receptor Types

Transmission type	Neurotransmitter	Receptor[a]
Amino acidergic	Glutamic acid	**Kainate**, **AMPA**, **NMDA**, mGluR
	Gamma-aminobutyric acid (GABA)	**$GABA_A$**, $GABA_B$, **$GABA_C$**
	Glycine	**Gly-R**
Cholinergic	Acetylcholine	**nAChR**, mAChR
Aminergic	Dopamine	D_1, D_2
	Norepinephrine	α_1, α_2, β_1, β_2
	Serotonin	$5HT_1$, $5HT_2$, **$5HT_3$**
	Histamine	H_1, H_2, H_3
Purinergic	ATP, adenosine	P_1, **P_{2x}**, P_{2y}

[a]*Ionophoric or channel-forming receptors are indicated in bold. Regular lettering indicates metabotropic or G-protein-coupled receptors.*

the P_{2x} purinoceptor for ATP. These relatively non-specific cationic channels permit passage of Na^+, K^+ and, in some cases, Ca^{2+} ions, but exclude anions. The anionic (Cl^-) channel-forming receptors include the $GABA_A$ and $GABA_C$ receptors and the glycine receptors (Gly-R).

Metabotropic receptors transduce the transmitter binding into a physiological response via G-protein/second messenger-coupled mechanisms. The synaptic actions of monoamines, dopamine, norepinephrine, epinephrine, serotonin and histamine are exerted via the G-protein/second messenger-coupled mechanisms systems. The G-protein-coupled receptors also include the muscarinic ACh receptors, metabotropic glutamate receptor (mGluR), $GABA_B$ and several receptors for adenosine and ATP. Ligand-gated and G-protein-coupled channels are discussed elsewhere in this volume.

IVB. Biosynthesis, Storage and Inactivation of Neurotransmitters

Conventional, low-molecular-weight neurotransmitters are synthesized locally in the nerve terminals and packaged into synaptic vesicles (SV) prior to release. The local synthesis of transmitter in the nerve terminals assures that transmitter is available for refilling the vesicles after they have released their contents into the synaptic cleft. The vesicular uptake of transmitters is mediated by specific transporters and is driven by an electrochemical gradient generated by electrogenic proton pump in the vesicular membrane (McMahon and Nicholls, 1991). Following release, the synaptic neurotransmitter action is terminated by diffusion, reuptake into presynaptic terminals or glial cells and degradation. Reuptake of transmitters from the extracellular space is energetically coupled to a transmembrane Na^+ gradient and is mediated by specific high affinity transporters that are distinct from the vesicular transporters. Two families of plasmalemmal transporters have been identified. The carriers for excitatory amino acids require the presence of extracellular Na^+, whereas the carriers for biogenic amines, GABA and glycine require both Na^+ and Cl^- for uptake (Fig. 32.4). (Amara and Arriza, 1993; Sonders and Amara, 1996.)

The key enzyme(s) involved in transmitter synthesis are selectively expressed in the neurons and define their neurotransmitter phenotype. Choline acetyltransferase (ChAT) is the marker enzyme for cholinergic neurons where it catalyzes the synthesis of acetylcholine (ACh) from acetyl coenzyme A (AcCoA) and choline (Ch):

$$\text{AcCoA} + \text{Ch} \xrightarrow{\text{ChAT}} \text{ACh}$$

Acetyl coenzyme A derives from the tricarboxylic acid (TCA) cycle whereas choline is transported into nerve terminals from the extracellular medium by the sodium-dependent, high-affinity carrier system that is localized in the presynaptic terminals. Transport of choline and synthesis of ACh are tightly coupled and both the rate of choline uptake and ACh synthesis increase during activity, ensuring adequate supply of the transmitter. The vesicular

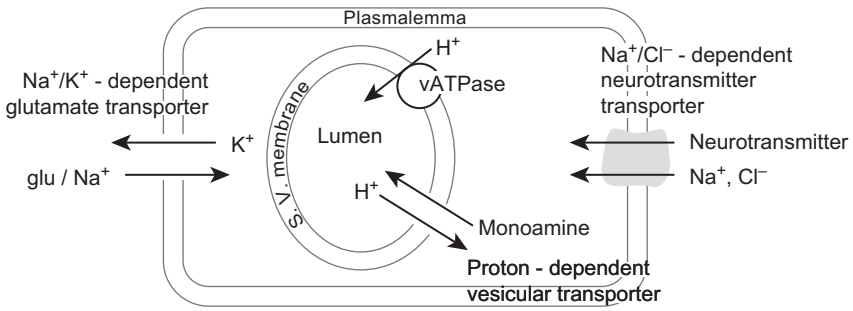

FIGURE 32.4 Neurotransmitter transport systems in vesicular and plasmalemmal membranes. *(Based on Amara and Arriza, 1993.)*

ACh transporter (VAChT) mediates uptake of ACh from the cytosol into synaptic vesicles. The plasmalemmal Ch uptake is selectively inhibited by a chemical hemicholinium-3 (HC-3) whereas vesamicol blocks vesicular uptake of ACh. Either of these drugs will cause depletion of ACh and failure of cholinergic transmission. Following its release, the synaptic action of ACh is terminated by diffusion and acetylcholinesterase (AChE)-catalyzed hydrolysis to inactive acetate and choline. Much of the choline is recaptured by the nerve terminals and reutilized in new ACh synthesis.

Catecholaminergic neurons and their synaptic connections comprise dopaminergic, noradrenergic (norepinephrine) and adrenergic (epinephrine) systems. The rate-limiting step in catecholamine biosynthesis is the tyrosine hydroxylase (TH)-catalyzed hydroxylation of tyrosine to L-dihydroxyphenylalanine (l-DOPA), which is then decarboxylated by a non-specific aromatic l-amino acid decarboxylase (L-AADC) to dopamine. Dopamine is taken up into synaptic vesicles and serves as a transmitter at dopaminergic synapses. In noradrenergic nerve endings, dopamine is further converted to norepinephrine by intravesicularly localized dopamine-β-hydroxylase (DβH). Methylation of norepinephrine to epinephrine at adrenergic synapses is catalyzed in cytosol by phenylethanolamine-N-methyltransferase (PNMT) in a reaction requiring S-adenosylmethionine as methyl donor:

$$\text{tyrosine} \xrightarrow{\text{TH}} \text{L-DOPA}$$

$$\text{L-DOPA} \xrightarrow{\text{L-AADC}} \text{dopamine}$$

$$\text{dopamine} \xrightarrow{\text{D}\beta\text{H}} \text{norepinephrine}$$

$$\text{norepinephrine} \xrightarrow{\text{PNMT}} \text{epinephrine}$$

Vesicular monoamine transporters (VMATs) mediate the uptake of catecholamines into synaptic vesicles. Reserpine inhibits the VMATs and thereby depletes vesicular stores of catecholamines. Synaptic actions of catecholamines are terminated by high-affinity neuronal reuptake followed by intracellular degradation or reuptake into synaptic vesicles. The plasmalemmal catecholamine transporters are distinct from VMATs. Plasmalemmal reuptake is insensitive to reserpine but is blocked by psychoactive drugs, such as cocaine and amphetamine, which thereby increase extracellular levels of catecholamines. The major catabolic pathway for catecholamines involves the mitochondrial monoamine oxidase (MAO)-catalyzed oxidative deamination to aldehydes followed by their rapid conversion by hydrogenases and reductases to corresponding acids and alcohols.

Serotonergic neurons utilize serotonin as the transmitter. Serotonin, an indoleamine, is formed by tryptophan hydroxylase-mediated hydroxylation of tryptophan to 5-hydroxytryptophan (5-HTP), followed by l-AADC-mediated decarboxylation of 5-HTP to 5-hydroxytryptamine (5-HT, serotonin):

$$\text{tryptophan} \xrightarrow{\text{Trp-hydroxylase}} \text{5-HTP} \xrightarrow{\text{L-AADC}} \text{5-HT}$$

Uptake of serotonin into synaptic vesicles appears to be mediated by the same or a closely related VMAT that mediates vesicular transport of catecholamines. The synaptic action of serotonin is terminated primarily by neuronal sodium-dependent reuptake, mediated by a transporter that is homologous to the plasmalemmal transporters for catecholamines. Following reuptake, serotonin is degraded by MAO-catalyzed oxidative deamination to 5-hydroxyindole acid aldehyde and 5-hydroxyindole acetic acid.

Glutamic acid, GABA and glycine are the major amino acid neurotransmitters in the CNS. Because glutamic acid and glycine are common constituents of amino acid pools found in all cells, their use as neurotransmitters at glutamatergic and glycinergic synapses implies subcompartmentation within the respective nerve terminals. This subcompartment in all likelihood corresponds to synaptic vesicles (SV), which presumably selectively accumulate glutamic acid and glycine from the cytosol and release them during synaptic transmission. The amino acid neurotransmitters are synthesized in nerve terminals from intermediates of the tricarboxylic acid (TCA) cycle. Glutamate is formed by transamination of α-ketoglutaric acid (α-KA) and GABA is formed from glutamate in a reaction catalyzed by glutamic acid dehydrogenase (GAD), a marker enzyme for GABAergic neurons. Inactivation of synaptic actions of glutamate and GABA is through reuptake into nerve terminals as well as the glial cells, where both amino acids are converted to glutamine, which is in turn exported to the nerve terminals and reutilized in the formation of glutamate:

$$\alpha\text{ - KA}_{(\text{TCA})} \xleftrightarrow{\text{transaminase}} \text{glutamate} \xleftarrow{\text{glutaminase}} \text{glutamine}$$

$$\text{glutamate} \xrightarrow{\text{GAD}} \text{GABA}$$

IVC. Transmitter Release

Transmitter release is evoked by arrival of an action potential at the presynaptic terminal. Depolarization of the nerve terminal membrane activates (opens) the plasmalemmal voltage-gated Ca^{2+} channels, allowing influx of extracellular Ca^{2+} into the terminal. The resultant transient increase of Ca^{2+} concentration near the plasmalemmal

release sites triggers a cascade of biochemical events that culminate in synaptic vesicle–plasmalemma fusion and exocytosis of transmitter into the synaptic cleft. The process terminates upon nerve terminal repolarization when the Ca^{2+} channels deactivate (close), Ca^{2+} entry ceases and intracellular Ca^{2+} returns to prestimulus levels.

IVC1. Quantal-Vesicular Hypothesis of Transmitter Release

The evolution of the current understanding of the mechanism of transmitter release began with the formulation of the *quantal-vesicular hypothesis* of transmitter release by Bernard Katz and his collaborators (Fatt and Katz, 1952; delCastillo and Katz, 1954). Katz and colleagues observed that, in the resting neuromuscular junction, i.e. in the absence of stimulation, nerve terminals spontaneously release ACh, giving rise to small depolarizations that occur at random intervals and average about 0.5 mV in amplitude (Fig. 32.5A). These small potentials behaved in all respects as miniature replicas of the end-plate potential (EPP) evoked by presynaptic APs (Fig. 32.5B) and therefore were called miniature end-plate potentials (MEPPs). The crucial insight into the relationship between MEPPs and EPPs was provided by the observation that when evoked release was reduced in low-Ca^{2+}/high-Mg^{2+} solutions, the size of EPPs fluctuated in a random manner (Fig. 32.5C) such that the EPP amplitudes appeared to be made up of integral multiples of the average MEPP amplitude and could be described by Poisson distribution (Fig. 32.6). Katz concluded that transmitter release is a stochastic process, consisting of random release of multimolecular packets or quanta of ACh each producing a unit response (MEPPs) and that the EPP is a summation of many quantal units released nearly synchronously by a presynaptic AP.

For detailed discussion of the statistics of transmitter release, the interested reader is referred to Martin (1977). For the present purpose, it suffices to state that transmitter release can be described by a simple statistical expression:

$$m = nP$$

The parameter m is the average number of quanta released per presynaptic impulse when a large number of trials are performed and is called the *quantal content* of the EPP. The parameter n represents the number of quanta immediately available for release and most likely corresponds to either the population of synaptic vesicles associated with the presynaptic active zones or the number of release sites. P is the probability of any single quantum being released and primarily reflects the probability of a productive Ca^{2+}-dependent vesicle fusion with the plasmalemma as a function of Ca^{2+} concentration at the release sites. Reducing the availability of Ca^{2+} to enter terminals would reduce P, thus accounting for a reduction of transmitter release in low-Ca^{2+}/high-Mg^{2+} media. Conversely, increasing the concentration of Ca^{2+} at or near the release sites would tend to enhance the probability of exocytosis, i.e. facilitate transmitter release.

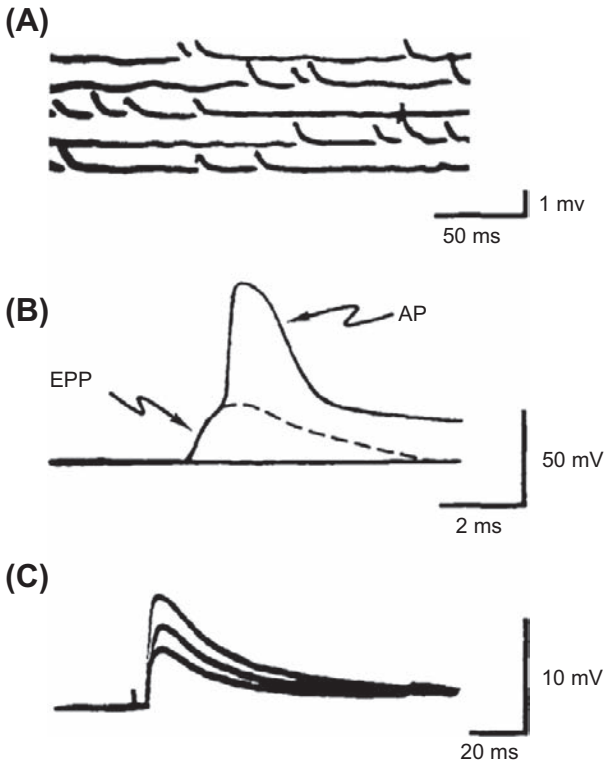

FIGURE 32.5 Intracellular recordings from the frog end-plate. (A) Spontaneous, miniature end-plate potentials (MEPPs) recorded from resting (not stimulated) junction. Note that these small depolarizing potentials are less than 1 mV in amplitude and occur randomly. (B) Postsynaptic response to a presynaptic action potential. The initial hump on the recorded waveform is the end-plate potential (EPP) elicited by ACh released by the presynaptic AP. Note that the EPP is a large depolarization (>40 mV), sufficient to bring the end-plate to threshold and trigger a muscle AP. (C) Fluctuations in EPPs when transmitter output has been reduced by adding 10 mM Mg^{2+} to the bathing medium. *(Adapted from Fatt and Katz, 1952, and delCastillo and Katz, 1954.)*

IVC2. Essential Role of Ca^{2+} in Depolarization-Release Coupling

The voltage-gated calcium channels in the presynaptic plasma membrane couple membrane depolarization to transmitter exocytosis. The essential role of Ca^{2+} influx in transmitter release was demonstrated by Katz and Miledi (1967), who showed that depolarization of presynaptic terminals failed to evoke transmitter release when Ca^{2+} was absent or its entry into nerve terminals was prevented by high Mg^{2+} concentration in the extracellular medium (Fig. 32.7). In subsequent experiments carried out at the squid giant synapse, where it is possible to make intracellular recordings from both pre- and postsynaptic cells simultaneously, Miledi (1973)

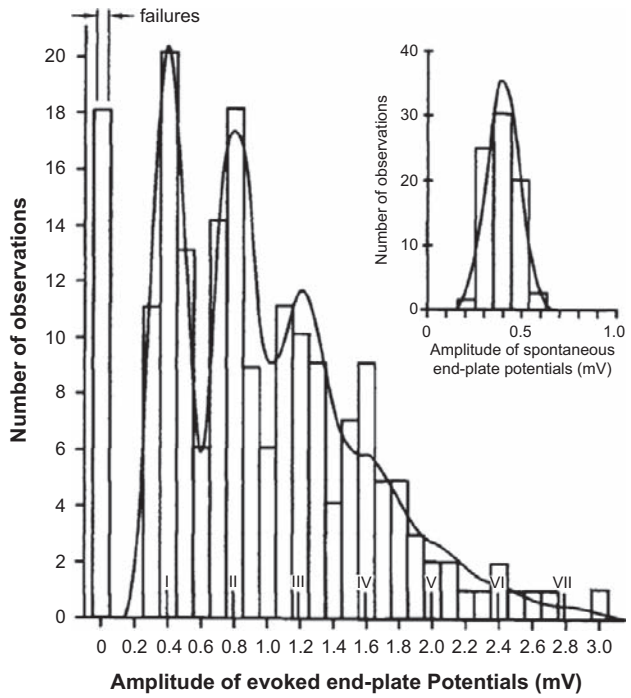

FIGURE 32.6 Distribution of EPP amplitudes recorded from mammalian end-plate under conditions of reduced transmitter release in high (12.5 mM) Mg^{2+}. The inset shows a histogram of spontaneous potentials (MEPPs) recorded from resting junction. Note that EPP amplitudes group around multiples of mean MEPPs amplitude and the number of experimentally observed failures (0 quanta released) and single, double, triple, or more quantal responses, fit the theoretical distribution (solid curve) calculated from the Poisson equation. *(From Boyd and Martin, 1956.)*

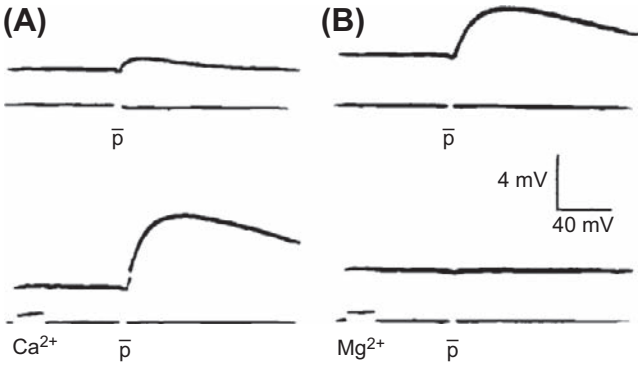

FIGURE 32.7 Calcium is required for transmitter release evoked by depolarization of nerve terminals. In the absence of Ca^{2+}, a depolarizing pulse (p) applied to a presynaptic nerve fails to evoke transmitter release and the postsynaptic response is nearly absent (A, top). Application of a pulse of Ca^{2+} to the neuromuscular junction shortly before applying stimulus (p) to the presynaptic nerve enables transmitter release as shown by the appearance of a postsynaptic response (A, bottom). The normal postsynaptic response in Ca^{2+}-containing media (B, top) is blocked by applying a pulse of high Mg^{2+} prior to the depolarizing pulse (p) (B, bottom). The failure to elicit transmitter release in the presence of high Mg^{2+} is due to block of Ca^{2+} influx into the terminals. *(Adapted from Katz and Miledi, 1967.)*

showed that injection of Ca^{2+} into presynaptic terminals elicited transmitter release, thus providing direct evidence that a rise in intracellular Ca^{2+} alone is sufficient for activation of the release process. Furthermore, using voltage-clamping to control the membrane potential of the presynaptic terminals at the squid giant synapse, Llinas (1977) showed that the quantity of synaptic transmitter released, monitored as the size of the postsynaptic potential, is related to the size of the presynaptic calcium current which, in turn, depends on the extent of nerve terminal depolarization (Fig. 32.8).

The presynaptic calcium channels that couple membrane depolarization to transmitter release at fast synapses appear to be strategically localized near the release sites (Robitaille et al., 1990). Opening of these channels results in domains of calcium entry, giving rise to localized subplasmalemmal calcium concentrations that may reach 0.1 mM or higher very rapidly and for a very brief duration (Smith and Augustine, 1988). These subplasmalemmal calcium transients represent more than a thousand-fold increase of $[Ca^{2+}]$ relative to the resting cytosolic calcium level of about 0.1 μM and provide a powerful trigger for focal synaptic vesicle exocytosis. The relationship between intracellular calcium concentration and the rate of exocytosis investigated in the terminals of goldfish retinal bipolar neurons indicates half-saturation at about 200 μM and cooperative interactions involving at least four calcium ions in activation of synaptic vesicle exocytosis (Heidelberger et al., 1994). Transmitter release occurs within about 60 μs following calcium entry into presynaptic terminals, indicating that Ca^{2+}-triggered exocytosis involves activation of a preassembled vesicle–plasmalemma docking/fusion complex (Bruns and Jahn, 1995; Sabatini and Regehr, 1996).

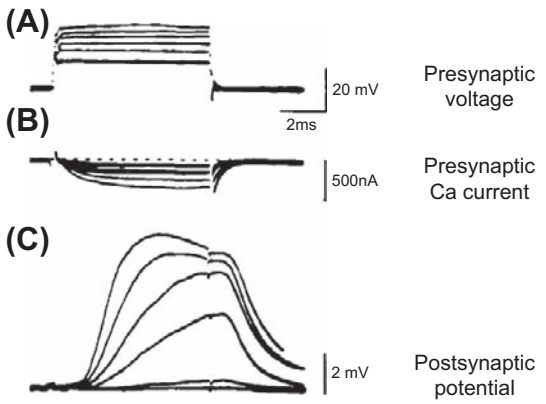

FIGURE 32.8 Experiments in the squid giant synapse illustrating the relationship between magnitude of presynaptic Ca^{2+} current and transmitter release monitored by recording postsynaptic potentials. Graded depolarizations of presynaptic terminals (A) evoke graded inward Ca^{2+}currents (B) that correlate with graded postsynaptic potentials (C), which reflect the amount of transmitter released. *(Adapted from Llinas, 1977.)*

IVC3. Exocytosis and Recycling of Synaptic Vesicles

The active zones in the presynaptic nerve terminals provide plasmalemmal specializations for synaptic vesicle docking and exocytosis. In ingenious experiments, Heuser and coworkers (1979) employed a specially constructed quick-freeze apparatus that enabled them to capture images of vesicle exocytosis at the active zone of the frog neuromuscular junction (Fig. 32.9). The comparison of the number of exocytotic pores captured in the quick-freeze experiment correlated with the estimated number of quanta released under similar conditions of stimulation, providing the most direct, structural evidence that exocytosis of synaptic vesicles at the active zone region is the likely mechanism of quantal transmitter release.

Synaptic vesicles within the terminal are distributed among the so-called readily available and reserve pools. The *readily available pool* is thought to correspond to the vesicles docked at the active zone and immediately available for release, whereas the *reserve pool* comprises the vesicles distributed within the terminal at some distance from the active zone. It is evident that, in order to maintain the availability of quanta for release, exocytosis must be accompanied by mobilization of new vesicles from the reserve pool within the terminal to the plasmalemmal release sites. Mobilization of vesicles is thought to involve alteration in vesicle cytoskeleton interactions that are regulated by phospho-dephosphorylation of synaptic vesicle-associated proteins, synapsins. Dephosphorylated synapsin seems to stabilize vesicle–cytoskeletal interactions and inhibit vesicle mobilization, whereas phosphorylation of synapsin by the Ca^{2+}-calmodulin-dependent protein kinase II is thought to promote vesicle mobilization (Llinas et al., 1991; Greengard et al., 1993).

The mechanism of vesicle docking and initiation of exocytosis by Ca^{2+} has not been yet completely worked out; however, remarkable progress has been made since the early 1990s. Studies initially conducted in model systems such as mast cells or chromaffin cells and then extended to synaptic preparations indicate that secretion is accompanied by a stepwise increase in cell capacitance, consistent with fusion of secretory granules with the cell membrane. Electrical measurements further suggest that the first event in exocytosis may be the formation of a pore that connects vesicle lumen with the extracellular space and may provide a channel for the release of soluble contents into the synaptic cleft and/or promote collapse and complete fusion of vesicle with the plasma membrane (Lindau and Almers, 1995; Matthews, 1996).

Beginning with the identification and cloning of synaptic proteins in the early 1990s (reviewed in Südhof, 1995), extraordinarily rapid progress has been made during the last few years in defining the molecular machinery of exocytosis. Current evidence indicates that the synaptic exocytotic apparatus makes use of constitutive membrane fusion machinery that has been placed under control of

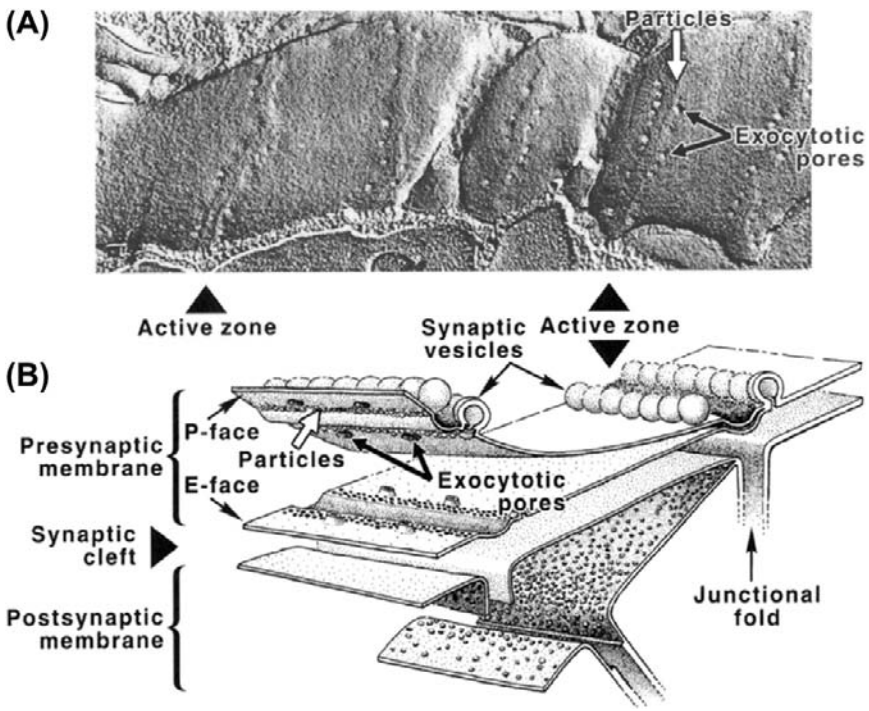

FIGURE 32.9 Synaptic vesicle exocytosis captured by a rapid-freezing technique. (A) P-face of freeze-fractured replica of a stimulated and rapidly frozen nerve terminal showing images of synaptic vesicles caught in the process of exocytosis at the active zones. The junction was activated in presence of 1 mM 4-aminopyridine to enhance the level of transmitter release per single presynaptic impulse. (*Adapted from Heuser et al. (1979). J Cell Biol. 81, 275–300.*) (B) Three-dimensional representation of pre- and postsynaptic membranes in relation to the freeze-fracture image above. The freeze-fracture splits membrane bilayers into protoplasmic (P-face) and extracellular (E-face) leaflets of the bilayer. The rows of intramembrane particles seen in P- and E-faces are thought to be the presynaptic Ca^{2+} channels. The openings in the P-face and their craterlike continuations in the E-face are the exocytotic pores formed when synaptic vesicles fuse with the plasmalemma along the parallel bars of the active zone. *(Adapted from Heuser et al. (1979). J Cell Biol. 81, 275–300.)*

a calcium sensor. The elements of the constitutive docking–fusion apparatus at synapses are the synaptic vesicle membrane-associated protein (VAMP) synaptobrevin and the plasma membrane proteins syntaxin and SNAP-25 (25-kDa, synaptosome-associated protein). The VAMP, syntaxin and SNAP-25 belong to a class of highly conserved membrane-targeting proteins that serve as SNAP (soluble NSF attachment protein) receptors and hence are referred to as SNAREs (Söllner et al., 1993a,b). The SNAREs have been shown to associate into a stable, 7-S core complex that links the apposed vesicle and plasma membranes through formation of parallel bundles of four interacting α-helices, with syntaxin and synaptobrevin each contributing one helix and SNAP-25 contributing two helices (Sutton et al., 1998). The evidence for the crucial role of SNARE complexes in exocytosis has been provided by the observation that selective proteolysis of either VAMP, syntaxin or SNAP-25 by clostridial neurotoxins prevents formation of the complex and inhibits transmitter release (Niemann et al., 1994; Hayashi et al., 1994). Biochemical studies indicate that the core complex is primed by ATP-dependent, SNAP-assisted binding of NSF (N-maleimide-sensitive factor). NSF is an ATPase whose activation is thought to play an important role in fusion by inducing a conformational change in syntaxin and disassembly of the SNARE complex (Whiteheart et al., 1994; Hanson et al., 1997). The synaptic vesicle membrane protein synaptotagmin 1, whose cytosolic domains contain two Ca^{2+}-binding C2 motifs homologous to the C2 regulatory domain of protein kinase C, is believed to serve as the Ca^{2+}-sensor of exocytosis (Brose et al., 1992; Shao et al., 1977). Biochemical experiments indicate that Ca^{2+} activation of synaptotagmin is associated with simultaneous binding of its C2 domains to the membrane phospholipids and the SNARE complex. The kinetics of synaptotagmin–Ca^{2+}–core complex interactions occur on a microsecond time scale consistent with its postulated function as Ca^{2+}-trigger receptor of exocytosis (Davis et al., 1999). Another protein that has been implicated in exocytosis is neurexin (Petrenko et al., 1991), a plasmalemmal protein that provides a target for α-latrotoxin, a component of black widow spider venom that induces massive Ca^{2+}-independent transmitter exocytosis. Through its capacity to associate with synaptotagmin, neurexin could somehow modulate interactions between synaptotagmin and SNAREs. A simplified model of a vesicle docking–fusion complex is illustrated in Fig. 32.10. Several other synaptic vesicle- and plasma membrane-associated proteins have been identified that are likely to have either accessory or regulatory functions in vesicle exocytosis/endocytosis (Südhof, 1995); however, their precise function and mechanism of action still remain by and large unresolved.

Following the release of transmitter, exocytosis may be terminated in at least two ways. One is simply through reclosure of the pore and fission of vesicles at the active zone. These postexocytotic vesicles may then refill with locally synthesized transmitter and, by virtue of being already positioned close to or at the active zone, release the newly formed transmitter in preference to the reserve pool. This could explain the well-documented phenomenon of the preferential release of newly synthesized transmitter. A more generally accepted idea is that, following fusion and exocytosis, vesicle membrane collapses into the

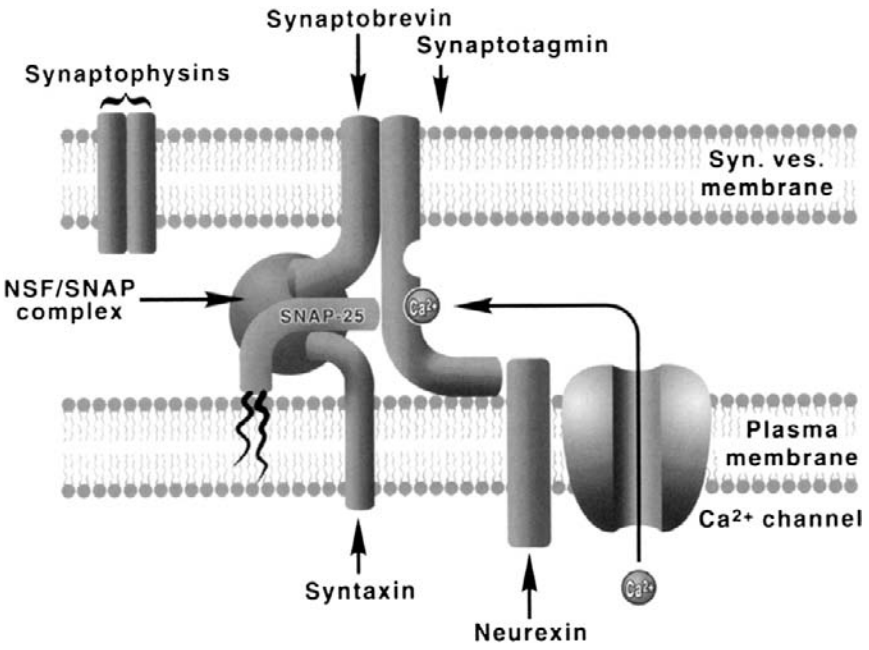

FIGURE 32.10 A simplified model of a vesicle docking–fusion complex. The model incorporates interactions among the proteins of synaptic vesicles (synaptobrevins and synaptotagmins), plasma membrane proteins (syntaxins, SNAP-25, neurexin) and the soluble elements of constitutive fusion machinery (NSF, SNAP). Synaptobrevin, syntaxin and SNAP-25 form a stable, 7-S core complex to which SNAP and NSF (an ATPase) bind to form a 20-S complex. Activation of NSF ATPase leads to disassembly of the complex, perhaps assisting in the final step of membrane fusion. The complex is thought to form in close proximity to the plasmalemmal calcium channels, with synaptotagmin serving as the key Ca^{2+} sensor. The plasma membrane protein neurexin interacts with synaptotagmin and may modulate its interactions with the core complex.

presynaptic plasmalemma to be retrieved in a series of transformations starting with clathrin-mediated endocytosis followed by endosomal fusion-budding and reformation of functional vesicles (Fig. 32.11). It is likely that both types, the rapid exo-endocytosis as well as the slower, clathrin-mediated endocytosis occur, but the extent to which one predominates over the other depends on the rate of presynaptic stimulation and possibly other factors. The evidence for local recycling of synaptic vesicles in the nerve terminals has been provided by the observation that vesicles become labeled with high-molecular-weight markers such as horseradish peroxidase (HRP) or dextrans when motor nerve terminals are stimulated with these markers in the extracellular medium (Ceccarelli et al., l973). More recent evidence for vesicle recycling has been provided by tracking the movement of fluorescent-labeled synaptic vesicles during stimulation of motor nerve terminals at the frog neuromuscular junction (Betz and Bewick, 1992) and in other synaptic preparations (Ryan et al., 1993; Lagnado et al., 1996).

Vesicles undergoing local recycling within the nerve terminals are progressively degraded and replaced by vesicles that are formed de novo in the cell body and transported to the nerve terminals by fast axoplasmic transport. The half-life of vesicles has been estimated at 7−14 days. Evidently, synaptic vesicles can undergo numerous cycles of transmitter release-reloading before being replaced with new ones.

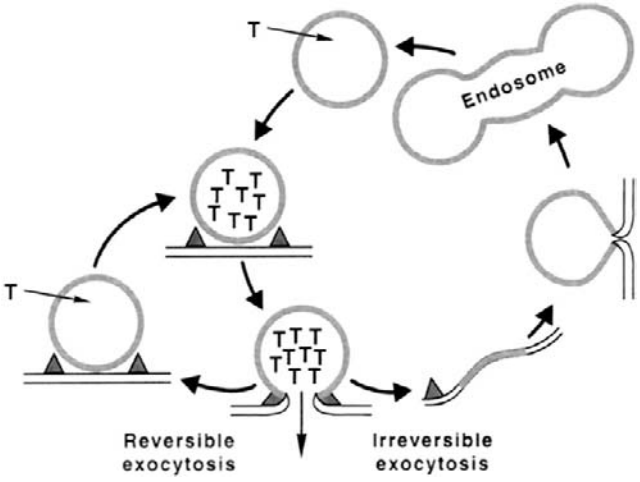

FIGURE 32.11 Synaptic vesicle cycling in nerve endings. Following vesicle docking and fusion, synaptic vesicles can recycle through a short or long pathway. The short pathway (left) involves transient fusion between vesicle and plasma membrane, followed by fission and recharging of the emptied vesicle with new transmitter (T). In the long pathway (right), vesicle membrane collapses into the plasmalemma to be eventually retrieved and reformed via a sequence of steps, then reloaded with new transmitter.

IVD. Generation of Postsynaptic Potentials at Fast Synapses

The nature of postsynaptic responses is determined by the type of receptor-gated ionic conductances that are activated in the postsynaptic membrane. At excitatory synapses, the transmitters activate receptor-gated channels that conduct cations, principally Na^+ and K^+. The net current through the synaptic channels is inward and carried by Na^+ ions, causing a depolarization of the postsynaptic membrane, or EPSP. The EPSPs generated at the skeletal neuromuscular junction are called end-plate potentials (EPPs) and those at other peripheral synapses, e.g. at nerve−smooth muscle junctions, are frequently referred to as excitatory junctional potentials, or EJPs. At inhibitory synapses, transmitters activate receptor-gated channels that conduct Cl^- ions. Influx of chloride ions through the synaptic channels tends to increase the negativity of the cell interior and hyperpolarizes the postsynaptic membrane. The hyperpolarizing postsynaptic potentials are called inhibitory postsynaptic potentials (IPSPs) because they tend to move the membrane potential away from the threshold.

IVD1. Synaptic Current and Synaptic Equilibrium Potential

The synaptic current *(i_S)* flowing through a single transmitter-activated channel is determined by the channel conductance *(γ_S)* and the electrochemical driving force ($V_m - E_s$) acting on the ions moving through the channel:

$$i_S = \gamma_S(V_m - E_S) \tag{32.1}$$

where V_m and E_S are membrane potential and the synaptic equilibrium potential, respectively.

In resting synapse, most of the receptor-gated channels are closed and the conductance of the postsynaptic membrane to ions is very low. When transmitter is released by presynaptic impulse, it binds to its receptors in the postsynaptic membrane and opens the associated channels for a short, 1−2 ms duration. The resultant total synaptic current, I_S, is a sum of currents through all opened channels:

$$I_S = n\gamma_S(V_m - E_S) = g_S(V_m - E_S) \tag{32.2}$$

where n is the number of active channels and g_S is the total synaptic conductance *($n\gamma_S$)*.

At excitatory synapses, the transmitter-activated channels permit the passage of both Na^+ and K^+ ions with about equal ease and the excitatory postsynaptic current $I_{S(E)}$ is the sum of Na^+ and K^+ currents:

$$I_{S(E)} = I_{Na} + I_K = g_{Na}(V_m - E_{Na}) + g_K(V_m - E_K) \tag{32.3}$$

where g_{Na} and g_K are Na^+ and K^+ ion conductances and E_{Na} and E_K are the Na^+ and K^+ equilibrium potentials, respectively. The direction and magnitude of ion flux is determined by the electrochemical driving forces ($V_m - E_i$). Because $g_{Na}(V_m - E_{Na}) > g_K(V_m - E_K)$, i.e. $I_{Na} > I_K$, the net synaptic current is always inward and carried by Na^+ ions, resulting in membrane depolarization. As the membrane potential (V_m) becomes depolarized, the term ($V_m - E_{Na}$) decreases and ($V_m - E_K$) increases until equilibrium is reached, where the inward Na^+ current is exactly equal to the outward K^+ current:

$$I_{Na} = -I_K \tag{32.4}$$

or

$$g_{Na}(V_m - E_{Na}) = -g_K(V_m - E_K) \tag{32.5}$$

The membrane potential V_m at which this occurs is the synaptic equilibrium potential (E_S). By solving for V_m, it is seen that E_S is a weighted average of sodium and potassium equilibrium potentials:

$$E_S = (g_{Na}/(g_{Na} + g_K))E_{Na} + (g_K/(g_K + g_{Na}))E_K \tag{32.6}$$

E_S is the limiting potential to which the postsynaptic membrane can be depolarized during the transmitter action. Any further depolarization beyond this point would result in $I_K > I_{Na}$ and reversal of net synaptic current from inward to outward direction. Therefore, the E_S is also called a *reversal potential* (E_r).

It is evident that activation of receptor-gated Cl^- channels at inhibitory synapses results in the synaptic current given by:

$$I_{S(I)} = g_S(V_m - E_S) \tag{32.7}$$

where the equilibrium potential E_S is the chloride equilibrium potential, E_{Cl}. This is the limiting potential to which a synaptic membrane can be hyperpolarized during the action of transmitter at inhibitory synapse.

IVD2. Relationship Between Synaptic Currents and Postsynaptic Potentials

The relationship between the synaptic current and postsynaptic potential can be analyzed in terms of an equivalent electrical circuit consisting of parallel synaptic and non-synaptic branches, as is illustrated for an excitatory synapse in Fig. 32.12. The synaptic branch represents the synaptic receptor-gated conductance (g_S) in series with the synaptic battery of the synaptic equilibrium potential E_S. The non-synaptic branch consists of membrane capacitance C_m and leakage channels (g_m) in series with the battery of the resting membrane potential, E_m.

During the synaptic action of transmitter at the E-synapses, the synaptic current (I_S) flows inward through the synaptic branch and outward through the parallel capacitive and resistive elements of the non-synaptic branch as I_C and I_m. The direction of current flow at the I-synapses is a mirror image of that at excitatory synapses.

$$I_{S(E)} = -(I_C - I_m) \tag{32.8a}$$

and

$$-I_{S(I)} = -(I_C + I_m) \tag{32.8b}$$

where

$$I_C = C_m dV_m/dt \tag{32.9}$$

and

$$I_m = g_m(V_m - E_m) \tag{32.10}$$

At the onset of synaptic action most of the synaptic current flows through the capacitive branch because the outward driving force ($V_m - E_m$) on current flow through the non-synaptic channels (g_m) is small. Once the membrane capacitance is discharged (depolarization) or charged (hyperpolarization) to its final value, all synaptic current exits through the leakage channels (g_m). Thus, at the peak of synaptic activation, $I_C = 0$ and

$$I_{S(E)} = -I_m \tag{32.11a}$$

$$-I_{S(I)} = I_m \tag{32.11b}$$

at E- and I-synapses, respectively.

Substituting Equations 32.2 and 32.10 into Equation 32.11 and solving for V_m yields the expression for the postsynaptic membrane potential at the peak of synaptic activation:

$$V_m = (g_S/(g_S + g_m))E_S + (g_m/(g_S + g_m))E_m \tag{32.12}$$

Equation 32.12 shows that the value of membrane potential (V_m) at the peak of synaptic activation is a weighted average of E_S and E_m, where the weighting factors are the relative magnitudes of synaptic (g_S) and non-synaptic (g_m) conductances. During peak activation of synaptic channels, $g_S > g_m$ and the membrane potential will tend toward the E_S but the amplitude of PSP (i.e. $V_m - E_m$) will be influenced by g_m of the non-synaptic membrane.

IVD3. Time Course of PSPs

The synaptic potentials are electrotonic potentials: they decay passively as a function of time and distance. The time course of the rising phase of the synaptic potential is determined by both active and passive properties of the membrane. As the synaptic channels spontaneously reclose, the PSP decays in an exponential fashion. The decay of the PSP is purely a passive process whose time course is a function of the membrane time constant, τ. The membrane time constant is the time required for an

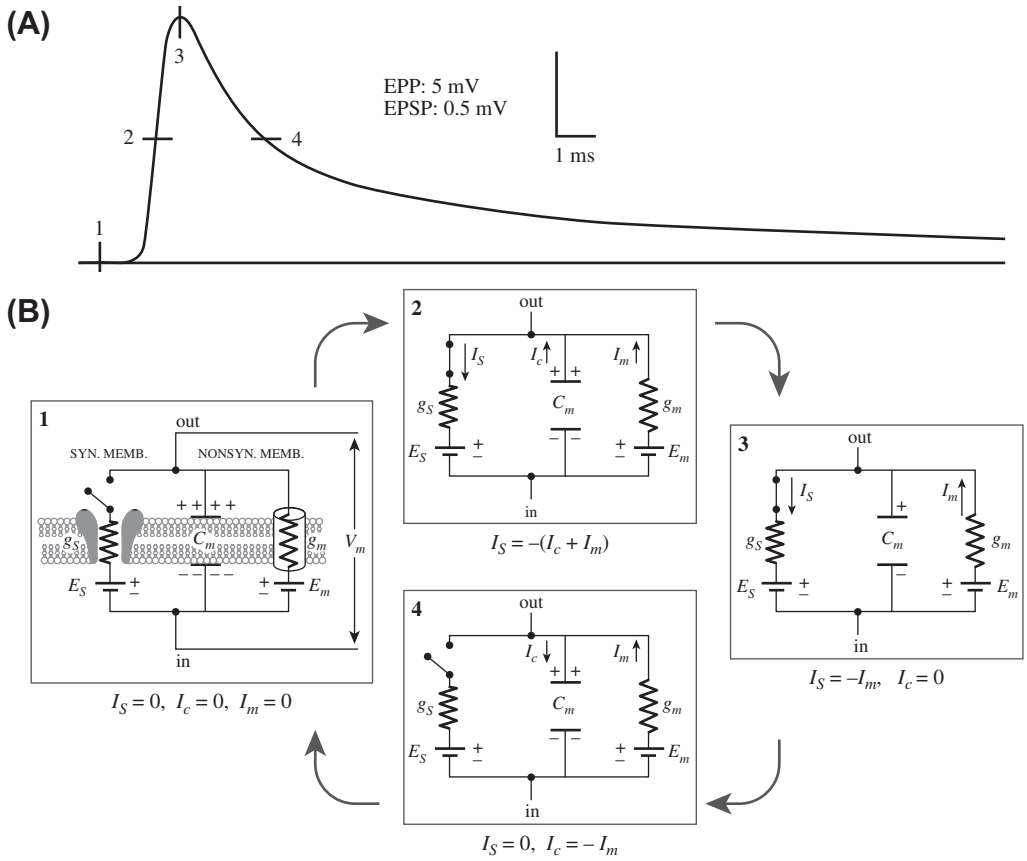

FIGURE 32.12 Equivalent electrical circuit description of excitatory synaptic potential. Four phases of the postsynaptic potential (A) and the corresponding equivalent circuit representations (B) are illustrated. (1) At rest, the transmitter-gated synaptic channels are closed (circuit open; no current flow; $dV/dt = 0$). (2) Onset of synaptic action (active phase). Synaptic channels are opened by transmitter binding to the receptor (the synaptic switch is closed) and I_s flows inward through the synaptic branch (g_s) and outward as I_c and I_m through the non-synaptic branch. (3) At the peak of synaptic action, capacitance C_m has discharged to its final value, $I_c = 0$ and $I_s = -I_m$ ($dV/dt = 0$). (4) Passive decay phase. Synaptic channels have reclosed (synaptic switch open) and $I_s = 0$. The current through the non-synaptic membrane consists of outward I_m and inward I_c, which recharges the membrane capacitance and repolarizes the membrane back to the prestimulus membrane potential. *(Based on Kandel et al. (2000). Principles of Neural Science. McGraw-Hill, New York. Reproduced with permission of The McGraw-Hill Companies.)*

electrotonic potential to decay to 1/e or 37% of its peak value. The time constant of neurons is in the range of 1−20 ms. The amplitude of the synaptic potentials decreases exponentially from the maximum recorded focally at the synapse as a function of the membrane length constant, γ. The length constant is the distance at which electrotonic potentials decay to 1/*e* or 37% of their amplitude at the point of origin. The length constant of dendrites is typically in the range 0.1 to 1 mm.

IVE. Slow Synaptic Transmission Mediated by G-Protein-Coupled Receptors

In contrast to fast synaptic potentials mediated by directly transmitter-gated channels, slow synaptic responses are mediated by a distinct family of proteins that transduce the transmitter binding into cellular responses through activation of GTP-binding regulatory proteins or G proteins. Binding of a transmitter to a specific receptor transforms the associated G protein into an active form that modulates activity of ionic channels at some distance from the receptor either through direct interaction with the channel and/or through second messenger systems. The slow synaptic transmission may involve either increase or decrease in postsynaptic membrane conductance due to a channel opening or channel closure, respectively. For example, activation of muscarinic receptors in heart muscle causes a G-protein-mediated opening of a certain class of voltage-gated K^+ channels and relatively long-lasting (seconds) membrane hyperpolarization. Similar, G-protein modulated potassium channels K(G) are present in central neurons, where they mediate slow IPSPs. In contrast, activation of a muscarinic receptor in sympathetic ganglion neurons and certain neurons in the central nervous system is associated with a second-messenger-mediated closure of K^+ channels and membrane depolarization. The responses

to transmitter activation of G-protein-coupled receptors need not be limited to modulation of ionic channels but also involve modifications of other regulatory proteins resulting in long-term modifications of the postsynaptic cell's physiology. For a more detailed discussion of G proteins and second messengers in slow synaptic actions of neurotransmitters, the reader is referred to Schulman and Hyman (1999).

IVF. Synaptic Integration versus Amplification

Central neurons can receive from several dozens to several thousand excitatory (E) and inhibitory (I) synaptic connections converging on the target neuron from a variety of other neurons in the brain. Whether or not a neuron discharges a propagated AP is determined by the number of E-synapses and I-synapses active at any one time. It should be noted that, even in absence of IPSPs, activation of a single excitatory synapse would be insufficient to discharge an AP, because individual PSPs generated at central synapses are very small, usually in the range of 0.5−2 mV in amplitude. Therefore, summation of several EPSPs is usually necessary to bring the membrane of the postsynaptic neuron to the threshold potential.

The postsynaptic neurons integrate the synaptic potentials by adding the EPSPs and subtracting the IPSPs from the membrane potential at any instant of time. Algebraic summation of two or more topographically separated synapses that are activated nearly simultaneously is called *spatial summation*. The effectiveness of spatial summation depends on the membrane space constant which, it will be recalled, is the distance at which electrotonic potentials decay to 37% of their amplitude at the point of origin. Clearly, synaptic inputs separated by a distance smaller than the space constant can sum together more effectively than those that are separated by distances larger than the space constant. When a presynaptic neuron fires at a rate such that the interval between successive presynaptic APs is less than the duration of the PSP, each succeeding PSP adds to its predecessor. This process is referred to as *temporal summation*. Effectiveness of temporal summation depends on the membrane time constant (i.e. the time required for an electrotonic potential to decay to 37% of its peak value). The larger the time constant, the longer is the duration of the PSP and thus the greater the opportunity for summation of successive PSPs to occur. A propagated action potential will be triggered only if the net current is of sufficient magnitude to depolarize the neuronal membrane to the threshold. An action potential is normally triggered at the initial segment of an axon, the region of the neuron with the lowest threshold. Since summation of synaptic currents at the initial segment is the principal determinant of whether or not an AP will be fired, the initial segment is referred to as the *integrative zone* of the neuron.

In contrast to the integrative activity at central synapses, the function of the neuromuscular junction is to transfer without failure the AP from the presynaptic motor neuron to the postsynaptic muscle fiber. In this case, the excitatory postsynaptic potential referred to as the endplate potential (EPP) is normally always suprathreshold and sufficient to trigger the muscle AP. It may be noted that because the nerve terminal is very small in diameter compared with the muscle fiber it innervates, even if these two membranes were contiguous, the current generated during the invasion of presynaptic terminal by an AP would be insufficient to depolarize the postsynaptic membrane to threshold due to impedance mismatch between the two membranes; i.e. the small nerve terminal cannot provide enough action current to depolarize the large-diameter skeletal muscle fiber much more than about 1 mV. Thus, the function of transmitter at the neuromuscular junction is to amplify the presynaptic signal.

IVG. Modulation of Synaptic Transmission

The efficacy of signal transmission at chemical synapses can be modulated by extrinsic and intrinsic factors, including the pattern of ongoing activity as well as history of previous activity. The efficacy of transmission may be altered by mechanisms that affect the dynamics of presynaptic transmitter release and/or modify the postsynaptic receptor-mediated events. This modification may be short lasting or may persist for some time. Thus, synaptic modulation provides for fine-tuning of ongoing synaptic activity as well as for longer lasting changes that are likely to play an important role in learning processes.

IVG1. Depression

Depression or fatigue of synaptic transmission refers to progressive reduction in the amplitudes of postsynaptic potentials in the course of prolonged, relatively high-frequency activation of presynaptic neurons, reflecting progressive depletion of releasable transmitter stores. Recovery from fatigue may take from minutes to hours.

IVG2. Facilitation

Facilitation is a frequency-dependent increase in the amplitude of postsynaptic potentials evoked by closely spaced presynaptic action potentials. The increase in the amplitudes of succeeding PSPs reflects the progressively larger amount of transmitter released with each nerve impulse in the course of stimulation. The mechanism is thought to involve build-up of ionized Ca^{2+} within the

terminals. That is, when presynaptic neuron is stimulated at certain frequency, the diffusion and clearance of Ca^{2+} from the release sites begins to lag and the residual Ca^{2+} adds to the Ca^{2+} transient evoked by the next arriving impulse. Build-up of Ca^{2+} increases the probability (P) of transmitter quanta being released. Facilitation is a relatively short-lived process that lasts for a few seconds.

IVG3. Post-Tetanic Potentiation

When the nerve is activated with relatively prolonged and/or high-frequency (tetanic) bursts of impulses, the quantity of transmitter is increased upon subsequent stimulation, even after a relatively long intervening rest period. This phenomenon is known as post-tetanic potentiation. In contrast to facilitation, post-tetanic potentiation may last for minutes and sometimes hours, suggesting a long-term modification of presynaptic function secondary to increase in cytosolic Ca^{2+} levels.

IVG4. Long-Term Potentiation

Long-term potentiation (LTP) refers to a long-lasting increase in EPSP following tetanic stimulation in the presynaptic neurons. It is distinguished from post-tetanic potentiation (PTP) in that the latter is a strictly presynaptic phenomenon, whereas induction and expression of LTP involves both postsynaptic and presynaptic elements. LTP was first described (Bliss and Lomo, 1973) and analyzed most extensively in the hippocampus. In the CA1 region, the LTP involves a special glutamate receptor subtype, the NMDA receptor. The NMDA receptor-gated channel is normally blocked by Mg^{2+}, but can be activated by glutamate when the postsynaptic neuron is sufficiently depolarized so that the Mg^{2+} blockade of the channel is relieved. The induction of LTP appears to be associated with influx of Ca^{2+} and activation of Ca^{2+}-dependent protein kinases CaM kinase II and protein kinase C, and possibly other protein kinases in the postsynaptic dendritic spine, which leads to increased efficacy of synaptic transmission that may last for days to weeks. It is thought that while induction of LTP involves the postsynaptic events, the maintenance of LTP may be associated with long-term increase in the probability of transmitter release, a presynaptic event.

IVH. Presynaptic Receptors and Transmitter Release

Receptors for neurotransmitters are not confined to postsynaptic sites, but are also found on presynaptic nerve terminals. The modulation of transmitter release by presynaptic receptors that respond to transmitter released by another neuron is referred to as *heterosynaptic modulation*. Heterosynaptic modulation may involve either inhibition or facilitation of transmitter release. In addition, certain presynaptic autoreceptors recognize the cell's own neurotransmitter. In this case, the neuron's transmitter may modulate its own release by interacting with these receptors. This is called *automodulation*. For example, many cholinergic neuron terminals possess muscarinic autoreceptors and ACh released from these terminals acts on the autoreceptors to inhibit its own release. Although the physiological role of presynaptic receptors has been a subject of debate, it is evident that they provide a potential mechanism for fine-tuning of transmitter release.

BIBLIOGRAPHY

Amara, S. G., & Arriza, J. L. (1993). Neurotransmitter transporters: three distinct gene families. *Curr Opin Neurobiol, 3*, 337–344.

Bennett, M. V. L. (1997). Gap junctions as electrical synapses. *J Neurocyt, 26*, 349–366.

Bennett, M. K., & Scheller, R. H. (1993). The molecular machinery for secretion is conserved from yeast to neurons. *Proc Natl Acad Sci USA, 90*, 2559–2563.

Betz, W. J., & Bewick, G. S. (1992). Optical analysis of synaptic vesicle recycling at the frog neuromuscular junction. *Science, 255*, 200–203.

Bliss, T. V. P., & Lomo, T. (1973). Long-lasting potentiation of synaptic transmission in the dentate area of the anaesthetized rabbit following stimulation of the perforant path. *J Physiol, 232*, 331–356.

Boyd, I. A., & Martin, A. R. (1956). The end-plate potential in mammalian muscle. *J Physiol, 132*, 30–38.

Brose, N., Petrenko, A. G., Südhof, T. C., & Jahn, R. (1992). Synaptotagmin: a calcium sensor on the synaptic vesicle surface. *Science, 256*, 1021–1025.

Bruns, D., & Jahn, R. (1995). Real-time measurement of transmitter release from single synaptic vesicles. *Nature, 377*, 62–65.

Burns, M. E., & Augustine, G. J. (1995). Synaptic structure and function: dynamic organization yields architectural precision. *Cell, 83*, 187–194.

Ceccarelli, B., Hurlbut, W. P., & Mauro, A. (1973). Turnover of transmitter and synaptic vesicles at the frog neuromuscular junction. *J Cell Biol, 54*, 30–38.

Davis, A. F., Bai, J., Fasshauer, D., Wolowick, M. J., Lewis, J. L., & Chapman, E. R. (1999). Kinetics of synaptotagmin responses to $Ca^{2+}$and assembly with the core SNARE complex onto membranes. *Neuron, 24*, 363–376.

delCastillo, J., & Katz, B. (1954). Quantal components of the end-plate potential. *J Physiol, 124*, 560–573.

Dreyer, F., Peper, K., Akert, K., Sandri, C., & Moor, H. (1973). Ultrastructure of the "active zone" in the frog neuromuscular junction. *Brain Res, 62*, 373–380.

Eccles, J. C. (1964). *The Physiology of Synapses*. New York: Academic Press, Inc.

Fatt, P., & Katz, B. (1952). Spontaneous subthreshold activity at motor nerve endings. *J Physiol, 117*, 109–128.

Greengard, P., Valtorta, F., Czernik, A. J., & Benfenati, F. (1993). Synaptic vesicle phosphoproteins and regulation of synaptic function. *Science, 259*, 780–784.

Hall, Z. W., & Sanes, J. R. (1993). Synaptic structure and development: the neuromuscular junction. *Neuron, 72*(suppl.), 99–121.

Hanson, P. I., Roth, R., Morisaki, H., Jahn, R., & Heuser, J. E. (1997). Structure and conformational changes in NSF and its membrane receptor complexes visualized by quick-freeze/deep etch electron microscopy. *Cell, 90*, 523–535.

Hayashi, T., McMahon, H., Yamasaki, S., et al. (1994). Synaptic vesicle fusion complex: action of clostridial neurotoxins on assembly. *EMBO J, 13*, 5051–5061.

Heidelberger, R., Heinemann, C., Neher, E., & Matthews, G. (1994). Calcium dependence of the rate of exocytosis in a synaptic terminal. *Nature, 371*, 513–515.

Heuser, J. E., Reese, T. S., Dennis, M. J., Jan, Y., Jan, L., & Evans, L. (1979). Synaptic vesicle exocytosis captured by quick freezing and correlated with quantal transmitter release. *J Cell Biol, 81*, 275–300.

Kandel, E. R., & Siegelbaum, S. A. (2000). Signalling at the nerve-muscle synapse: directly gated transmission. In E. R. Kandel, J. H. Schware, & T. M. Jessell (Eds.), *Principles of Neural Science* (pp. 187–206). New York: McGraw-Hill.

Katz, B. (1966). *Nerve, Muscle, and Synapse*. New York: McGraw-Hill Book Co., Inc.

Katz, B., & Miledi, R. (1967). The timing of calcium action during neuromuscular transmission. *J Physiol, 189*, 535–544.

Kuffler, S. W., & Nicholls, J. G. (1977). *From Neuron to Brain: a Cellular Approach to the Function of the Nervous System*. Sunderland: Sinauer Associates, Inc.

Lagnado, L., Gomis, A., & Job, C. (1996). Continuous vesicle cycling in the synaptic terminal of retinal bipolar cells. *Neuron, 17*, 957–967.

Lindau, M., & Almers, W. (1995). Structure and function of fusion pores in exocytosis and ectoplasmic membrane fusion. *Curr Opin Cell Biol, 7*, 509–517.

Llinas, R. R. (1977). Calcium and transmitter release in squid synapse. In W. M. Cowan, & J. A. Ferrendelli (Eds.), *Approaches to the Cell Biology of Neurons, Society for Neuroscience Symposia, II* (pp. 139–169). Bethesda: Society for Neuroscience.

Llinas, R. R., Gruner, J. A., Sugimori, M., McGuinness, T. L., & Greengard, P. (1991). Regulation by synapsin I and Ca^{2+}-calmodulin-dependent protein kinase II of transmitter release in squid giant synapse. *J Physiol, 436*, 257–282.

Martin, R. A. (1977). Junctional transmission II. Presynaptic mechanisms. In *Handbook of Physiology. The Nervous System, Vol. 1* (pp. 329–355). Bethesda: American Physiological Society.

Matthews, G. (1996). Synaptic vesicle exocytosis and endocytosis: capacitance measurements. *Curr Opin Neurobiol, 6*, 358–364.

Maycox, P. R., Hell, J. W., & Jahn, R. (1990). Amino acid neurotransmission: spotlight on synaptic vesicles. *Trends Neurosci, 13*, 83–87.

McMahon, H. T., & Nicholls, D. G. (1991). The bioenergetics of neurotransmitter release. *Biochim Biophys Acta, 1059*, 243–264.

Miledi, R. (1973). Transmitter release induced by injection of calcium ions into nerve terminals. *Proc Roy Soc, 183*, 421–425.

Niemann, H., Blasi, J., & Jahn, R. (1994). Clostridial neurotoxins: new tools for dissecting exocytosis. *Trends Cell Biol, 4*, 179–185.

Pappas, G. D., & Purpura, D. P. (Eds.), (1972). *Structure and Function of Synapses*. New York: Raven Press Publishers.

Petrenko, A. G., Perin, M. S., Davletov, B. A., Ushkaryov, Y. A., Geppert, M., & Südhof, T. C. (1991). Binding of synaptotagmin to the a-latrotoxin receptor. *Nature, 353*, 65–68.

Robitaille, R., Adler, E. M., & Charlton, M. P. (1990). Strategic location of calcium channels at transmitter release sites of frog neuromuscular junction. *Neuron, 5*, 773–779.

Ryan, T. A., Reuters, H., Wendland, B., Schweizer, F. E., & Smith, S. J. (1993). The kinetics of synaptic vesicle recycling measured at single presynaptic boutons. *Neuron, 11*, 713–724.

Sabatini, B., & Regehr, W. G. (1996). Timing of neurotransmission at fast synapses in the mammalian brain. *Nature, 384*, 170–172.

Schulman, H., & Hyman, S. E. (1999). Intracellular signaling. In M. J. Zigmond, F. E. Bloom, S. C. Landis, J. L. Roberst, & L. R. Squire (Eds.), *Fundamental Neuroscience* (pp. 269–316). San Diego: Academic Press.

Shao, X., Davletov, B. A., Sutton, R. B., Südhof, T. C., & Rizo, J. (1997). Bipartite Ca binding motif in C2 domains of synaptotagmin and protein kinase C. *Science, 273*, 248–251.

Smith, S. J., & Augustine, G. J. (1988). Calcium ions, active zones and synaptic transmitter release. *Trends Neurosci, 11*, 458–464.

Söllner, T., Bennett, M., Whiteheart, S., Scheller, R., & Rothman, J. (1993a). A protein assembly-disassembly pathway in vitro that may correspond to sequential steps of synaptic vesicle docking, activation and fusion. *Cell, 75*, 409–418.

Söllner, T., Whiteheart, S. W., Brunner, M., et al. (1993b). SNAP receptors implicated in vesicle targeting and fusion. *Nature, 362*, 318–324.

Sonders, M. S., & Amara, S. G. (1996). Channels in transporters. *Curr Opin Neurobiol, 6*, 294–302.

Spray, D. C., Scemes, E., & Rozental, R. (1999). Cell-cell communication via gap junctions. In M. J. Zigmond, F. E. Bloom, S. C. Landis, J. L. Roberts, & L. R. Squire (Eds.), *Fundamental Neuroscience* (pp. 317–343). San Diego: Academic Press.

Südhof, T. C. (1995). The synaptic vesicle cycle: a cascade of protein-protein interactions. *Nature, 375*, 645–653.

Sutton, R. B., Fasshauer, D., Jahn, R., & Brunger, A. T. (1998). Crystal structure of a SNARE complex involved in synaptic exocytosis at 2.4 Å resolution. *Nature, 395*, 347–353.

Whiteheart, S. W., Rossnagel, K., Buhrow, S. A., Brunner, M., Jaenicke, R., & Rothman, J. E. (1994). N-ethylmaleimide-sen-sitive fusion protein: a trimeric ATPase whose hydrolysis of ATP is required for membrane fusion. *J Cell Biol, 126*, 945–954.

Chapter 33

Excitation–Secretion Coupling

Nicole Gallo-Payet and Marcel Daniel Payet

Chapter Outline

I. SUMMARY

The first step in the secretory process for peptide hormones and neurotransmitters involves synthesis, modification and sorting of the molecules to be secreted. These secretory molecules are packaged in secretory granules or vesicles, which are then transported to the cell periphery, where they are released in the extracellular space by fusion with the plasma membrane. This complex process is named *exocytosis*. Exocytosis is an all-or-none phenomenon in which Ca^{2+} plays a pivotal role.

Interaction of cytoskeletal structures with transmembrane signaling is an important feature of excitation–secretion coupling. Actin-binding proteins are in large part responsible for cytoskeleton–receptor interactions. In resting cells, more than 95% of the phosphatidylinositol bisphosphate ($PtdInsP_2$) may be complexed with profilin. This interaction promotes actin polymerization. Following receptor activation, phospholipase C activity increases to a level where profilin protection can be overcome, resulting in $PtdInsP_2$ hydrolysis. In resting cells, the bulk of gelsolin is cytosolic. When the cell is activated, there is a transient rise in $[Ca^{2+}]_i$ due to $InsP_3$ action and/or Ca^{2+} influx, which activates gelsolin, causing a 200-fold increase in its affinity for actin. This results in rapid filament side-binding, followed by severing and capping, inducing a dramatic disruption of existing actin network structure in the vicinity of $[Ca^{2+}]_i$ elevation.

Dynamic changes in the cytoskeletal network are required for exocytosis. The subplasmalemmal area of secretory cells is characterized by the presence of a highly organized cytoskeletal network where F-actin, together with specific actin-binding proteins, forms a dense viscoelastic gel. Some actin-associated proteins, such as fodrin,

Cell Physiology Sourcebook. DOI: 10.1016/B978-0-12-387738-3.00033-0

caldesmon, gelsolin and scinderin, exist on secretory granule membranes, linking actin microfilaments to secretory granules. Caldesmon and synapsin I are other proteins that are associated with synaptic vesicles. Synapsin I binds to spectrin and actin microfilaments and may serve as an anchor between synaptic vesicles and the cytoskeleton. Synapsin I phosphorylation results in the release of synaptic vesicles from their anchoring site on the cytoskeleton, allowing the vesicles to move to the active synaptic zones.

Secretion is a process that requires (1) the movement of secretory vesicles toward the plasma membrane, (2) the fusion of vesicles with the plasma membrane and (3) subsequent release of secretory contents into the cell exterior. The process of secretion is mediated by contractile elements either associated with secretory vesicles or present elsewhere in the cell. As microfilaments (F-actin) are preferentially localized in the cortical surface of the chromaffin cell, F-actin may act as a barrier to the secretory granules, impeding their contact with the plasma membrane. Upon stimulation, fodrin rearranges into patches beneath the plasma membrane. Such a redistribution could be related to the clearing of exocytotic sites at the level of the plasma membrane. Scinderin is a cytosolic protein that shortens actin filament length when Ca^{2+} is present in the medium. Stimulation induces both redistribution of scinderin from the cytosol to the cell cortex and F-actin disassembly, which precedes exocytosis. Docking of granules on the plasma membrane is an important step in exocytosis. Several proteins are involved in this process: synaptobrevin, syntaxin and SNAP-25, which form the SNAP receptor (SNARE). Priming of the granules is also a pivotal step in exocytosis. N-ethylmalimide-sensitive fusion protein (NSF) primes the granule through ATP hydrolysis; once primed, an increase in $[Ca^{2+}]_i$ triggers the release. All these processes require the presence of Ca^{2+} in the extracellular medium. Therefore, only secretagogues that induce Ca^{2+} entry are able to produce these effects.

In regulated exocytosis, fusion of secretory granules with the plasma membrane is triggered by an appropriate signal. Every time a secretory granule fuses with the plasma membrane, the total capacitance of the cell increases by a value proportional to the surface of the new membrane added to the existing cell membrane. Capacitance step values generally range from 1 to 30 fF, corresponding to granule diameters of 0.2 to 1 pm. Freeze-fracture images of exocytosis reveal the presence of narrow pores formed between the granules and the plasma membrane called *fusion pores*. The size of the pore increases as fusion progresses, allowing for the release of vesicle contents.

Control of exocytosis occurs not only in electrically excitable cells, but also in non-excitable systems in response to receptor activation. The regulatory pathways that couple stimulation and secretion vary widely among cell types. In many cells, Ca^{2+} is the key signal for triggering exocytosis. Ca^{2+} influx from the external medium is crucial for secretion, but internal Ca^{2+} release from internal stores also plays a pivotal role, depending on cell type. In some cases, Ca^{2+} alone is not able to trigger secretion, but the presence of a guanine nucleotide together with Ca^{2+} is necessary and sufficient for exocytosis.

II. INTRODUCTION

The process of excitation–secretion coupling is completely different depending on the peptide/amine or lipid nature of the secretory products. The secretory process for peptide and amine molecules begins with the synthesis, modification and sorting of the molecules to be secreted. Synthesis occurs in the rough endoplasmic reticulum (RER) and sorting occurs in the Golgi complex. The secretory molecules are packaged in secretory granules or vesicles, which are then transported to the cell periphery before they are released in the extracellular space by fusion with the plasma membrane. This complex process is named *exocytosis* or *reverse pinocytosis* and can be operated either by a constitutive or a regulated mechanism. Constitutive secretion is unregulated and closely follows the rate of synthesis of the secretory products. This form of secretion occurs in many cell types, including lymphocytes, hepatocytes and pancreatic β cells. In regulated secretion, fusion of the secretory granules with the plasma membrane is initiated by a specific signal (ligand-receptor coupling), triggered by an increase in cytosolic calcium concentration ($[Ca^{2+}]_i$). In steroid-secreting cells (adrenal cortex, ovary, testis), the process of synthesis begins with cholesterol stored in lipid droplets followed by subsequent steps occurring in mitochondria and smooth endoplasmic reticulum. It is generally assumed that steroids are free to diffuse throughout the aqueous cytoplasm and lipid phase of the plasma membrane. Secretory vesicles are not present and secretion and/or release of steroids is tightly coupled to steroid synthesis.

Although the process of synthesis differs, stimulation of secretion of peptide hormones, neurotransmitters and steroids involves similar cascades of molecular events. After binding to their specific receptors, the stimuli activate second messenger production, several cascades of phosphorylation/dephosphorylation of intracellular proteins, cytoskeleton reorganization, synthesis of new products and release of secretory products. Cytoskeleton and Ca^{2+} ion are certainly the most important players involved in this excitation–secretion coupling. However, while disruption of the actin network is necessary to trigger fusion of secretory vesicles with the cell membrane, a well-preserved organization seems important for steroid release.

III. CELLULAR COMPONENTS INVOLVED IN EXCITATION–SECRETION COUPLING

IIIA. Interaction of Cytoskeletal Structures with Transmembrane Signaling Molecules

The cytoskeletal elements are described in Chapter 5. Therefore, the brief descriptions given here on microfilaments and microtubules are aimed at understanding the mechanisms involved in excitation–secretion coupling (Schmidt and Hall, 1998). In the living cell, actin filaments, F-actin (consisting of two staggered, parallel rows of monomers, G-actin, non-covalently bound and twisted into a helix), interact with several proteins, such as vinculin, α-actinin, villin and fodrin, which cross-link and bundle microfilaments into a well-organized three-dimensional network. They can also cross-link myosin, forming a contractile network, or form a very dense network at the cell periphery, the cell cortex (Figs. 33.1A and 33.2A). This dynamic organization of microfilaments depends on a large and diverse group of actin-binding proteins, including profilin and caldesmon (which bind G-actin) and gelsolin and scinderin (which cap and sever F-actin). On the other hand, polymerization, stabilization and modulation of microtubules depend on several microtubule-associated proteins (MAPs) that adorn the tubulin-containing core of the tubules. The complete cell cytoskeletal network includes interaction between microfilaments, microtubules and intermediate filaments (see Figs. 33.1 and 33.2 and Chapter 5).

Association of cell surface molecules with the cytoskeleton is widely believed to be one of the earliest consequences of cellular activation for many systems. These cell surface molecules include not only receptors, but also *integrins*, the receptors of the components of extracellular matrix. Appropriate stimulation of receptors and integrins has immediate and profound effects on the organization and activity of the microfilaments (Aplin et al., 1998). Several studies have shown that microfilament disruption (with cytochalasins) or microtubule disruption (with colchicine or vinblastine) increased exocytosis (i.e. peptide or amine secretion), although steroid hormone secretion is decreased or abolished. In other words, these observations indicate that cytoskeleton is a barrier in the former, but a requirement for the latter. In both cases, microfilaments are active players in the process of excitation–secretion coupling. Several studies indicate that receptors (either G-protein-coupled or tyrosine kinase types), α subunits of heterotrimeric G proteins (α_i, α_s, α_q), monomeric G proteins (Rho, Rac, Cdc42), second-messenger-activating enzymes (adenylyl cyclase, phospholipase C [PLC]), Ca^{2+}, K^+ or Cl^- channels (see Chapter 31) and proteins up or downstream from second messenger production (phosphatases, protein kinase C [PKC], mitogenic associated protein kinase [MAPK]) are associated with microfilaments. For example, anchoring of PKC-e to F-actin is required for glutamate release in nerve endings of neuronal cells (Janmey, 1998). In general, these associations occur mainly via acting-binding proteins, which bind effectors or phosphoinositides through specific domains, called plecktrin homology domains, (PH domains). PH domains are essential for the membrane recruitment of several proteins that contain them and are frequently accompanied by other motifs (Src homology domains SH2 and SH3 and proline-rich, Dbl homology [DH], or GTP exchange domains), indicating that the recruitment of the PH domain protein would nucleate sites on the membrane for protein complex assembly (Inglese et al., 1995; Janmey, 1998; Martin, 1998). In addition, close functional association between G proteins and microtubules has also been extensively described (Popova et al., 1997). Such observations indicate that the cytoskeleton operates as a matrix improving the efficiency of the signal transduction cascade and that actin-binding proteins are in large part responsible for these cytoskeleton–membrane receptor interactions.

IIIB. Actin-Binding Proteins Important in Signaling

The physical properties of actin networks depend on the length of microfilaments and the architecture of the three-dimensional network formed by interaction between actin and several actin-binding proteins. The aim of this section is to point attention to the F-actin cross-linking proteins which may be regulated by Ca^{2+} and thus involved in the process of excitation–secretion coupling (Schmidt and Hall, 1998).

Profilin was the first actin-binding protein described in signaling. Profilin also contains a $PtdInsP_2$ binding site and binding of $PtdInsP_2$ to this site triggers the dissociation of profilin from actin, promoting actin polymerization (see Fig. 33.1A). $PtdInsP_2$ molecules bind to profilin with a stoichiometry of about 8:1. This 8:1 association of $PtdInsP_2$:profilin complexes protects $PtdInsP_2$ from cleavage by phospholipase C_γ (PLC_γ). In a similar fashion, also in resting conditions, PLC_γ may also bind profilin. However, when PLC_γ becomes tyrosine phosphorylated (by appropriate ligand activation), its affinity for $PtdInsP_2$ increases to a level where profilin protection can be overcome, resulting in $PtdInsP_2$ hydrolysis. Hydrolysis of one or two of the eight $PtdInsP_2$ molecules bound to each profilin leads to a rapid decrease in $PtdInsP_2$ affinity and release of the remaining profilin-bound $PtdInsP_2$ molecules (see Fig. 33.1B). Thus, the binding of profilin to $PtdInsP_2$ not only liberates polymerization-competent G-actin, but also affects hydrolysis of $PtdInsP_2$ by PLC_γ (Forscher, 1989; Janmey, 1998).

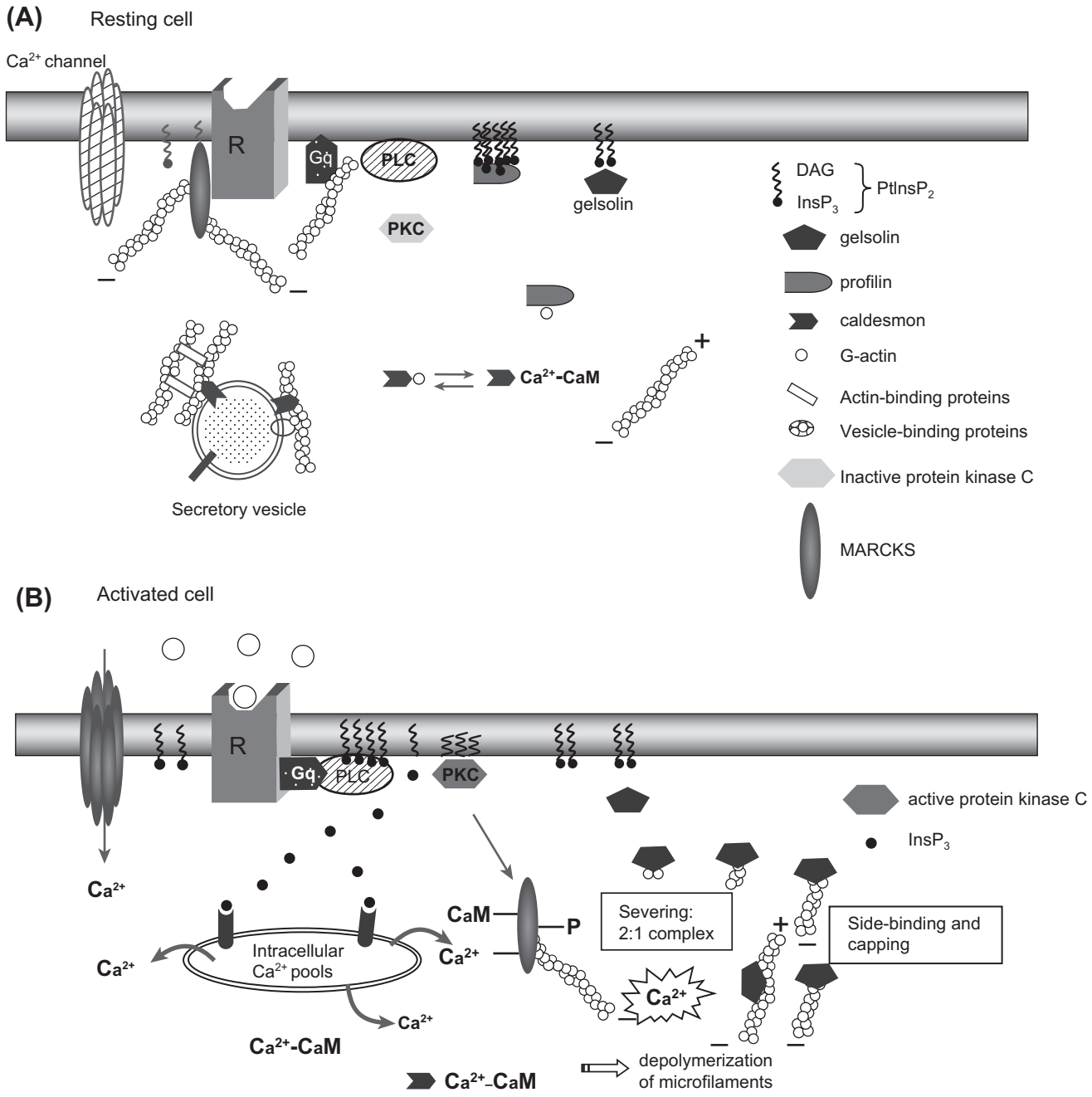

FIGURE 33.1 Interaction of cytoskeletal structures with transmembrane signaling. In resting cells (A), receptors, G proteins, phospholipase C (or adenylyl cyclase) and phosphoinositides are not linked together, but are associated with microfilaments or actin-associated proteins. For example, profilin interacts with high affinity with eight molecules of PtdInsP2, protecting them from hydrolysis by phospholipase C; gelsolin is also associated with $PtInsP_2$; the protein caldesmon is associated with both actin monomers and calmodulin; MARCKS (myristoylated, alanine-rich C kinase substrate) is a specific protein kinase C substrate associated with the cytoplasmic face of the membrane under resting conditions. In its non-phosphorylated form, MARCKS cross-links actin, favoring a rigid actin meshwork at the membrane level. In activated cells (B), ligand binding to its receptor activates phospholipase C, which hydrolyzes $PtdInsP_2$ and leads to $InsP_3$ and diacylglycerol (DAG). The rise in $[Ca^{2+}]$ (due to the $InsP_3$ binding to intracellular pools of Ca^{2+}) induces F-actin depolymerization. Moreover, calmodulin–caldesmon complex binds to Ca^{2+}, gelsolin binds, severs and caps actin filaments into 2:1 complexes to the barbed ends. Activated protein kinase C (now at the membrane) phosphorylates MARCKS, which is released from the membrane. All these modifications decrease cell rigidity, making the actin network more plastic.

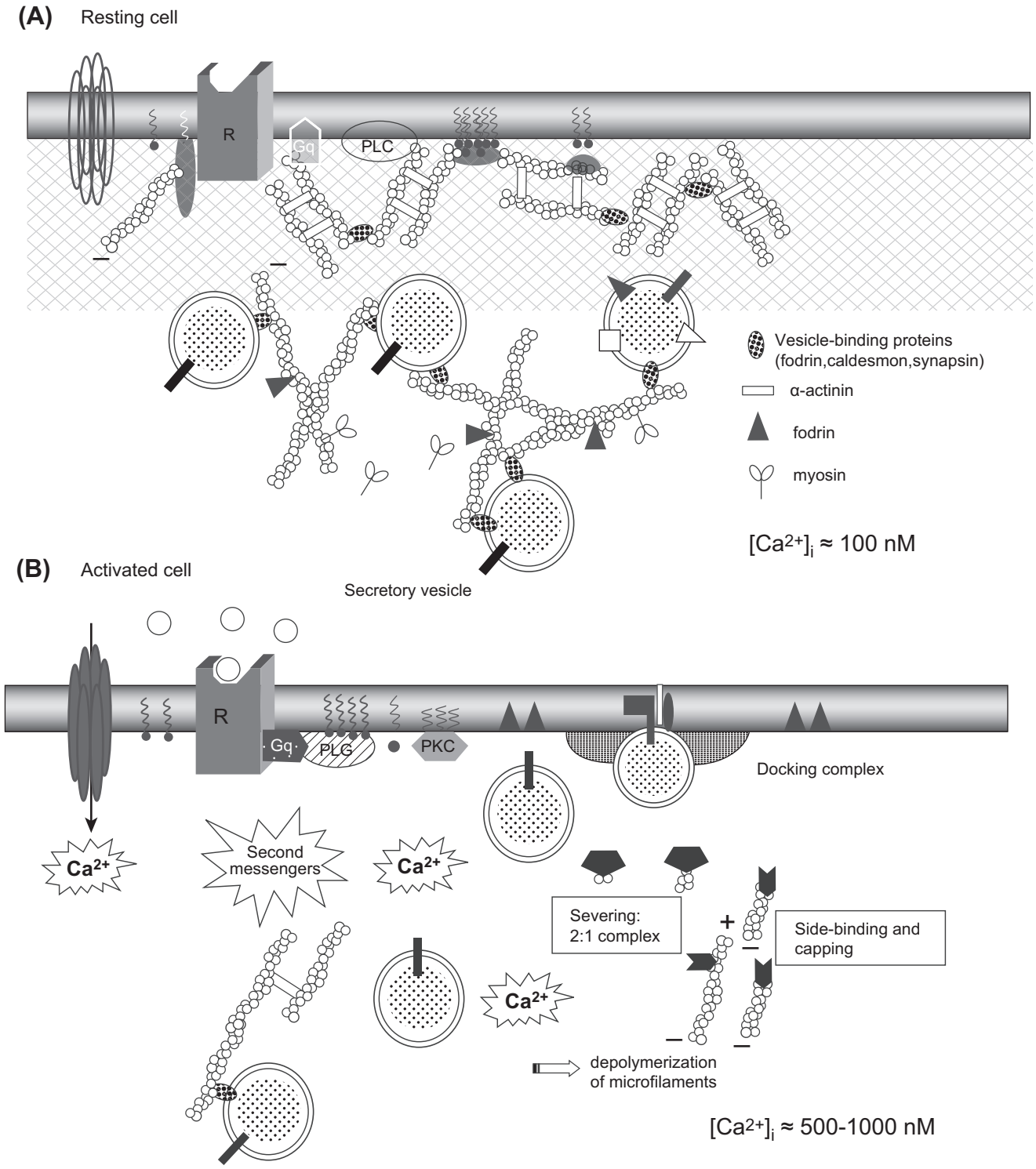

FIGURE 33.2 Dynamic changes in cytoskeleton during exocytosis. In resting cells ($[Ca^{2+}]_i \approx 100$ nM) (A), microfilaments interact with several proteins (including fodrin and α-actinin) that cross-link and bundle microfilaments into a well-organized three-dimensional network. In vesicle-secretory cells, microfilaments can also cross-link myosin, forming a contractile network, or form a very dense network at the cell periphery, the cell cortex. Activation of cells by appropriate stimulation (B) is associated with a reduction in the cell cortex rigidity, due to characteristic changes in cytoskeletal properties from "gel" (solid) to "sol" (liquid) states. These changes are primarily under the control of Ca^{2+}, which cooperates with phospholipid messengers to induce microfilament disruption. An increase in intracellular calcium ($[Ca^{2+}]_i$ (≈0.5–1 μM) induces several cellular modifications. In addition to capping and severing of the actin microfilaments (see Fig. 33.1), there is dissociation of actin from actin-associated proteins, such as fodrin, patching of fodrin along the plane of the plasma membrane (docking site) and dissociation of caldesmon from secretory vesicles. These events result in a decrease in viscosity, which favors movement of granules toward the plasma membrane releasing sites. Actin–myosin interactions could facilitate granule displacement in cytosol.

Gelsolin is a Ca^{2+}-dependent F-actin severing molecule which, along with villin, fragmin, adseverin and scinderin, is able to sever actin filaments. These proteins bind to actin filaments and bend and cleave them in a Ca^{2+}-dependent manner and afterwards cap the barbed filament ends. Severing actin filaments promotes cell cortex transition from a "gel" state to a "sol" state upon addition of Ca^{2+}. Gelsolin contains two spatially separate binding sites: a G-actin Ca^{2+}-sensitive site in the C-terminal domain and a PtdIns-sensitive site closer to the N-terminal portion. In resting cells ($[Ca^{2+}]_i \approx 100$ nM), the bulk of gelsolin is cytoplasmic and a small proportion is $PtdInsP_2$-associated. Gelsolin has little affinity for actin under these conditions and is in an actin-free state (see Fig. 33.1A). When the cell is activated, there is a transient rise in $[Ca^{2+}]$ due to $InsP_3$ action or Ca^{2+} influx that then activates gelsolin, causing a 200-fold increase in its affinity for F-actin. This results in rapid filament side-binding, followed by severing and capping of any free barbed filament ends, inducing a dramatic disruption of existing actin network structure in the vicinity of Ca^{2+} elevation (see Fig. 33.1B). The activities of these severing proteins are inhibited by binding to $PtdInsP_2$.

In the absence of PtdIns turnover, much of the $PtdInsP_2$ is likely to be tightly associated with profilin and thus unavailable to gelsolin. If gelsolin is activated under these conditions (e.g. by an increase in $[Ca^{2+}]_i$, independent of the PtdIns turnover), severing of actin networks is observed, but without subsequent actin reassembly. This leads to two possible modes of gelsolin activation: (1) calcium influx produced by activation of PtdInsP-independent pathways (i.e. voltage- or agonist-gated Ca^{2+} channels) leads to actin severing and capping only; (2) in contrast, activation of these same Ca^{2+} channels concomitant with PtdInsP turnover results in severing and capping followed by actin polymerization, i.e. actin remodeling (Forscher, 1989; Janmey, 1998).

In summary, association of actin-binding proteins with phosphoinositides causes opposite effects to those observed upon association with Ca^{2+}. In the former, such associations (profilin: $PtInsP_2$) promotes actin polymerization, favoring the cortical actin "gel" near the plasma membrane, while increased Ca^{2+} concentration favors association of actin-binding proteins (profilin, gelsolin) with Ca^{2+}, inducing depolymerization and thus "sol" state of actin filaments.

Caldesmon is a calmodulin-dependent actin-binding protein that, at low Ca^{2+} concentrations (100 nM), binds and cross-links actin monomers, inhibiting actin polymerization. Under these conditions, caldesmon interacts reversibly with secretory granules. At greater concentrations of Ca^{2+} (μM ranges), Ca^{2+}-calmodulin complex binds to caldesmon and reverses this inhibition. The flip-flop regulation of caldesmon may be important for secretory vesicle function during the changes in intracellular Ca^{2+} levels observed upon stimulation (see Figs. 33.1 and 33.2).

MARCKS (myristoylated, alanine-rich C kinase substrate) is a specific protein kinase C substrate that is targeted to the membrane by its amino-terminal binding domain. In resting cells, MARCKS associates with the cytoplasmic face of the membrane. In its non-phosphorylated form, MARCKS cross-links actin, favoring a rigid actin meshwork at the membrane level (see Fig. 33.1A). Activated protein kinase C phosphorylates MARCKS, which remains associated with actin filaments, but can no longer cross-link actin fibers, making the actin network more plastic (see Fig. 33.1B). In addition, an increase in intracellular Ca^{2+} concentration promotes binding of calmodulin to MAR-CKS, inhibiting its actin cross-linking activity, again resulting in a less rigid actin meshwork. Thus, PKC induces a local destabilization of the actin skeleton through the phosphorylation of MARCKS. MARCKS is phosphorylated when synaptosomes are depolarized, suggesting a role in secretion (Arbuzova et al., 1998).

Several newly identified proteins, such as the focal adhesion molecule ($p125^{FAK}$), paxillin and the small GTP-binding protein Rho are also closely implicated in actin polymerization after hormonal stimulation. Tyrosine phosphorylation of $p125^{FAK}$ and paxillin and their association with cytoskeleton and $\beta\gamma$ subunits of G proteins have been recently identified as early events in the action of several growth factors and G-protein-coupled receptors (such as angiotensin II and vasopressin). However, to date, their role has been ascribed to regulating cell adhesion, motility or proliferation rather than secretion (Inglese et al., 1995; Tapon and Hall, 1997; Hall, 1998).

IIIC. Interaction between Microtubules and Microtubule-Associated Proteins in Signaling

As mentioned earlier, polymerization, stabilization and plasticity of microtubules depend on several microtubule-associated proteins (MAPs), which differentially cross-link microtubules (Matus, 1988). Recent studies have shown that some MAPs could be implicated in the secretory process (Gundersen and Cook, 1999). MAPs are substrates for several protein kinases, including a Ca^{2+}-calmodulin-dependent kinase, a cAMP-dependent kinase, tyrosine kinases and protein kinase C. Both cAMP (via protein kinase A) and Ca^{2+} (via Ca^{2+}-calmodulin kinase) lead to phosphorylation of MAP-2. Moreover, MAP-1 and MAP-2 are responsible for binding secretory granules to microtubules, either in cells from the anterior pituitary gland, the β cells of the endocrine pancreas or in synaptic vesicles of neurons. These results strengthen the probable role of MAPs in secretory processes.

IIID. Actin-Binding, Docking and Fusion Proteins of the Secretory Granules

Granule vesicles for peptides or amine products not only allow secretory tissues to store large amounts of secretory products in a relatively small volume, but also protect this material from intracellular degradation while providing a very efficient means for transporting and releasing fixed quantities of secretory material.

IIID1. Actin-binding Proteins Associated with Secretory Granules

Induction of exocytosis is associated with a loss in the cell cortex rigidity, due to characteristic changes in cytoskeletal properties from "gel" to "sol" states. These changes are primarily under the control of Ca^{2+}, which cooperates with phospholipid messengers to induce microfilament disruption (see Figs. 33.1B and 33.2B) (Tchakarov et al., 1998). Moreover, several pieces of evidence indicate that microfilaments, rather than microtubules or intermediate filaments, are responsible for the mechanical changes initiated by Ca^{2+}. Chromaffin cells of the adrenal medulla and mast cells from the immune system synthesize and, along with neuronal synaptic vesicles, store and secrete large amounts of neurotransmitters or neuropeptides. These cells contain numerous electron-dense secretory granules which discharge their contents into the extracellular space by exocytosis. The subplasmalemmal area is characterized by the presence of a highly organized cytoskeletal network. F-actin seems to be exclusively localized in this area and, together with specific actin-binding proteins, forms a dense viscoelastic gel.

Fodrin, vinculin, α-actinin and caldesmon, four actin-binding proteins, as well as gelsolin and scinderin, two actin-severing proteins, are found in the plasmalemmal region. Moreover, fodrin, caldesmon and α-actinin binding sites also exist on secretory granule membranes, indicating that actin filaments can also link to secretory granules (see Fig. 33.2A). Chromaffin granules can be entrapped in this subplasmalemmal lattice and thus the cytoskeleton acts as a barrier preventing exocytosis (Burgoyne, 1995; Burgoyne and Morgan, 1998a).

Synapsin I, a phosphoprotein and a substrate for protein kinase A and calmodulin-dependent protein kinase II (CaM kinase II), is associated with synaptic vesicles. Synapsin I also binds to spectrin and actin microfilaments and may serve as an anchor between synaptic vesicles and the cytoskeleton. The affinity of synapsin I for synaptic vesicles is decreased by phosphorylation and neurotransmitter release is preceded by a reversible phosphorylation of synapsin I. Therefore, synapsin I phosphorylation results in the release of synaptic vesicles from their anchorage sites on the cytoskeleton, thus allowing the vesicles to move to the active exocytosis zones.

IIID2. Docking and Fusion Proteins

In addition to the actin-binding proteins, several proteins from the secretory vesicle membrane, the plasma membrane and the bulk cytosol interact together to form the core complex (or a *docking complex*) with docking, priming and fusioning properties (or *budding properties*). The most important of these properties are described next (Südhof, 1995; Fernandez-Chacon and Südhof, 1999).

The vesicular proteins synaptobrevins (or vesicle-associated membrane proteins, VAMPS) and the plasma membrane proteins syntaxin and synaptosome-associated protein (SNAP-25, M_r 25 kDa) form the three complex membrane proteins (called the core complex) essential to the regulated exocytosis machinery in neurons and neuroendocrine and endocrine cell types. Moreover, the potential involvement of the cytosolic proteins, N-ethylmalimide-sensitive fusion protein (NSF) and the soluble NSF attachment proteins (SNAPs) (α, β, γ isoforms), was demonstrated by the discovery that all these proteins interact to form a complex named SNARE (for SNAP receptor) (Fig. 33.3). Based on in vitro studies, a model for neurotransmitter release was proposed in which synaptic vesicles become docked at the plasma membrane by a specific pairing of VAMP (the vesicle membrane, v-SNARE) with syntaxin 1 and SNAP-25 (the target membrane, t-SNARE). The proposed sequence for docking and priming is described hereafter (Südhof, 1995; Aroeti et al., 1998; Burgoyne and Morgan, 1998a). Before and/or during docking, syntaxin is bound to Munc 18 and synaptophysin to synaptobrevin. These two complexes, syntaxin–Munc18 and synaptophysin–synaptobrevin, must dissociate in order for the core complex to be formed. Formation of this complex is considered to be the first step of vesicle priming. Syntaxin and SNAP-25 (t-SNARE) can then bind tightly together to form a high-affinity site for synaptobrevin (v-SNARE) located on the vesicle membrane; the core complex has a stoichiometry of 1:1:1. The trimeric core complex serves as a receptor (SNARE) for the soluble SNAPs (not related to SNAP-25). NSF will only interact with SNAPs (α, β) bounded on the trimeric complex. The NSF-SNAP receptor forms a multisubunit particle that sediments at 20S; it may form the core of a generalized apparatus catalyzing bilayer fusion (Söllner et al., 1993). NSF is a trimeric protein that cross-links multiple core complexes into a network. The core complex is then disrupted by enzymatic activity of NSF under ATP hydrolysis. Botulinum A and tetanus toxins are toxin proteases able to digest synaptobrevin, SNAP-25 and syntaxin. When entering in the nerve terminal, they irreversibly inhibit exocytosis. However, the number of docked granules is not decreased by the toxins, indicating that the primary function of the core complex is fusion and not docking. Hydrolysis of ATP by NSF is followed by

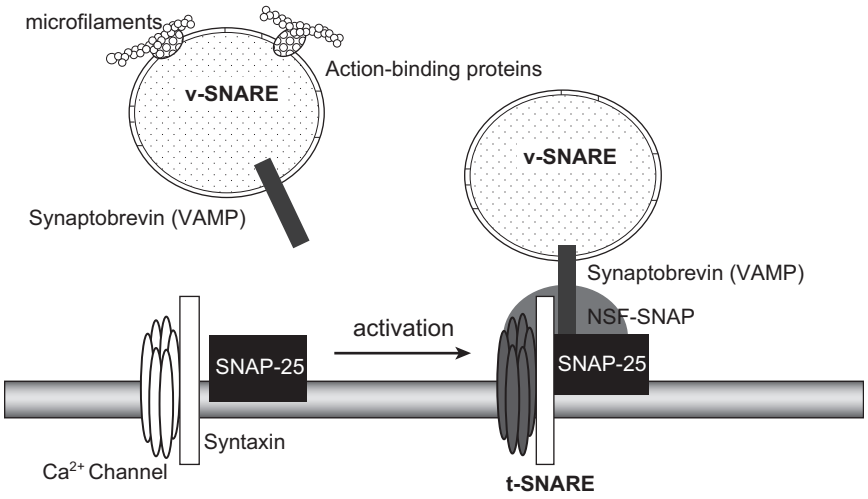

FIGURE 33.3 SNARE, the receptor involved in docking and fusion. The 20S particle that forms the core complex contains several interacting proteins. v-SNARE, related to synaptobrevin (VAMP) and located on the vesicle, binds to t-SNARE, related to syntaxin and SNAP-25 and located on the plasma membrane, to form the SNARE or SNAP receptor. SNAPs and NSF can then bind to the receptor to complete the core complex. Numerous SNARE-related proteins, each specific for a single kind of vesicle or target membrane, ensure vesicle-to-target specificity. Binding of synaptobrevin relies on the inhibition of the Ca^{2+} channel.

ATP-independent steps (see later) sensitive to temperature, H^+ and Ca^{2+}. The last step is Ca^{2+}-sensitive and likely involves a Ca^{2+} sensor at the site of exocytosis.

Synaptotagmins (Syt) are membrane glycoproteins found in brain secretory vesicles of which eight forms have been cloned. One of these, synaptotagmin I (Syt I), plays a pivotal role in the Ca^{2+}-triggered neurotransmitter release as a Ca^{2+} sensor (Südhof and Rizo, 1996; Goda and Südhof, 1997; Burgoyne and Morgan, 1998b). The functional implication of multiple synaptotagmins is unknown. Syt I binds Ca^{2+} cooperatively and undergoes a Ca^{2+}-dependent conformational change; the coefficient of cooperativity (4) is similar to that observed for Ca^{2+}-triggered release. Syt I also binds phospholipids as a function of Ca^{2+} with high affinity (half maximal binding, 5–6 μM). Syntaxin, one of the proteins of the core complex, in addition to its role in the docking and fusion process of the vesicle, controls the entry of Ca^{2+} by the voltage-dependent Ca^{2+} channels (L- and N-type). Indeed, binding of syntaxin to the Ca^{2+} channel prevents the opening of the channel by membrane depolarization. When the vesicle docks to the membrane by binding to syntaxin and SNAP-25, the inhibition of syntaxin on the channel is relieved, allowing voltage-dependent opening of the channel (see Fig. 33.3) (Geppert and Südhof, 1998).

In addition to phospholipids and syntaxin, Syt I binds to neuroxins, a family of neuronal cell surface proteins, and to AP-2, a protein complex involved in synaptic vesicle endocytosis. In addition to a Ca^{2+} sensitivity similar to Ca^{2+}-triggered release, the role of Syt I as a Ca^{2+} sensor has been illustrated in several ways. Knockout mice for Syt I have impaired Ca^{2+}-triggered transmitter release, but release can still be obtained by Ca^{2+}-independent agents, such as hypertonic sucrose or the excitatory neurotoxin α-latrotoxin (the receptor for α-latrotoxin belongs to the neuroxin family). Synaptotagmin *Drosophila* mutants show a severe but incomplete block of neurotransmission with an altered Ca^{2+}-dependence in some mutants. Injection of synaptotagmin peptide in squid nerve terminal inhibits release and vesicles accumulate possibly by competing for a common effector. Synaptotagmins are also able to interact with non-neuronal syntaxin, indicating that they can play a role in a variety of cell types from endocrine and immune systems.

Synaptophysin and the related protein synaptogyrin are major integral membrane proteins of small presynaptic vesicles. The presence of phosphorylation sites for tyrosine kinase of the Src family could indicate that phosphorylation modulates protein activity. The primary structure was deduced from the cDNA sequence, leading to the proposition that synaptophysin and synaptogyrin span the membrane four times with N- and C-terminals located in the cytoplasm. Ubiquitous isoforms of these two proteins are co-expressed in all cells and could represent invariant components of trafficking organelles.

The annexin family includes several Ca^{2+}- and phospholipid-binding proteins with conserved structure. Two of these are thought to be involved in the mechanism of exocytosis. Synexin (annexin VII) is a calcium-binding protein (47 kDa) with four transmembrane domains. This protein demonstrates a voltage-dependent Ca^{2+} channel activity. Synexin is able to induce the aggregation of chromaffin vesicles in the presence of Ca^{2+}. A model for the synexin-driven Ca^{2+}-dependent membrane fusion has been proposed in which synexin monomers polymerize as the concentration of Ca^{2+} increases. The polymerized synexin forms a hydrophobic bridge between the two membranes. Annexin II (calpactin) is located on the cytoplasmic side of the plasma membrane in chromaffin cells. Sites of phosphorylation for protein kinase C and camp- and calmodulin-dependent protein kinases have been localized within the N-terminal domain; phosphorylation

of these sites could inactivate the protein. A possible role for annexin II could be to link the granule with the plasma membrane (docking) and/or to induce fusion (Burgoyne, 1991).

Exocytotic fusion mechanisms also involve PtdIns transfer protein, PtdIns 4-kinase (PI4K), and PI5K to promote formation of PtIns4,5P_2 on the vesicle membrane (Martin, 1998).

IV. CELLULAR AND MOLECULAR EVENTS IN CHROMAFFIN, MAST CELLS AND NEURONAL SYNAPTIC VESICLES

Exocytosis is an all-or-none phenomenon in which Ca^{2+} plays a pivotal role. Ca^{2+} is required for second messenger activity, for the control of cytoskeletal dynamics and for the vesicle–plasma membrane fusion process. In neurons, neuroendocrine cells and some endocrine cells, the electrical activity of the cell, the action potential, leads to the opening of voltage-dependent Ca^{2+} channels with a subsequent increase in cytosolic Ca^{2+}. Neurotransmitter release at synaptic and neuromuscular junctions, peptide hormone secretion and catecholamine release by the adrenal medulla all belong to this class. In non-excitable cells, the triggering Ca^{2+} signal is provided by release of Ca^{2+} from intracellular stores after appropriate stimulation. Depletion in Ca^{2+} from these intracellular pools activates an influx of Ca^{2+}, which is responsible for the sustained increase in $[Ca^{2+}]_i$ observed in many cell types. Moreover, this Ca^{2+} influx provides Ca^{2+} ions for the replenishment of internal stores.

IVA. Dynamic Changes in the Cytoskeletal Networks are Required for Exocytosis

Secretion is a process that requires (1) the movement of secretory vesicles toward the plasma membrane, (2) the fusion of vesicles with the plasma membrane, and (3) subsequent release of secretory contents in the cell exterior.

As explained before, in resting conditions, actin filaments (F-actin) are preferentially localized in the cell surface and act as a barrier to the secretory granules, impeding their contact with the plasma membrane (Trifaró et al., 1992). Stimulation of chromaffin or mast cells as well as neuronal synaptic vesicles produces disassembly of the actin network and removal of the barrier (Tchakarov et al., 1998) (see Fig. 33.2). Several observations support this concept: (1) direct evidence for an actin barrier has come from the use of drugs that affect actin assembly and disassembly. Cytochalasin B and DNase I prevent actin assembly and drive the system toward net disassembly and increased secretion in permeabilized chromaffin cells. (2) Studies using fluorescent rhodamine-labeled phalloidin (a drug that stabilizes actin filaments in vitro and stops actin disassembly on stimulation) and actin antibodies have shown, in resting cells, a strong cortical fluorescent ring of filamentous actin. Cholinergic receptor stimulation produces a fragmentation of the fluorescent ring, leaving cell cortical areas devoid of fluorescence. These changes are accompanied by a decrease in F-actin associated with a concomitant increase in G-actin (Tchakarov et al., 1998) (Fig. 33.4). (3) Results from the use of toxins also support the concept of a cortical actin barrier. Botulinum C2 toxin,

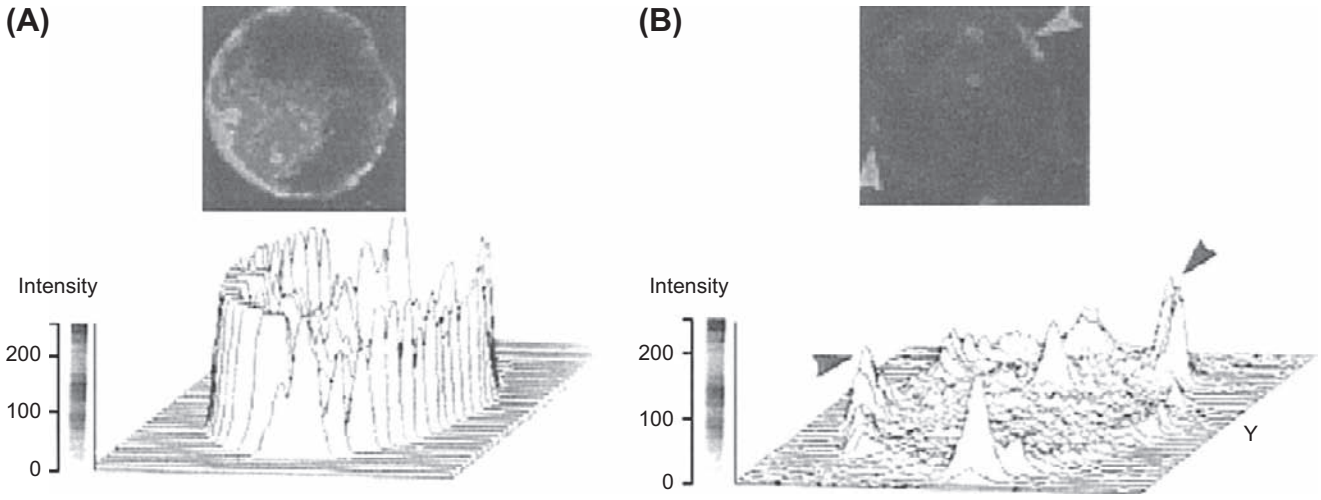

FIGURE 33.4 Rhodamine–phalloidin fluorescence of chromaffin cell cytoskeleton. Cultured chromaffin cells were incubated for 40 s in Locke's solution in the absence (A) or in the presence (B) of 10 μM nicotine. Cells were fixed and processed for fluorescence studies. Resting chromaffin cells showed a bright and continuous cortical fluorescent ring (A), while nicotinic-receptor-stimulated cells showed disruption in the cortical fluorescent ring. Some fluorescent patches are shown by arrowheads (B). Three-dimensional image analysis of the same patterns is shown below each cell. In control cells, there is a uniform cortical fluorescence intensity pattern, whereas in stimulated cells, the cortical fluorescent intensity pattern shows irregularities such as valleys and peaks. These peaks correspond to the patches observed in cells. *(Adapted with permission from Tchakarov et al., 1998.)*

which ADP-ribosylates actin and inhibits actin polymerization, enhances secretion in PC12 cells. In contrast, tetanus and botulinum A toxins, which block actin disassembly, inhibit exocytosis upon cholinergic stimulation.

Several actin-binding proteins present in the cell cortex undergo changes upon stimulation. In a resting cell, fodrin is localized in the cell cortex. On stimulation, it rearranges into patches beneath the plasma membrane. This redistribution could be related to the clearing of exocytotic sites at the plasma membrane. Scinderin is a cytosolic protein that shortens actin filament length when Ca^{2+} is present in the medium. Stimulation induces both redistribution of scinderin from cytosol to cell cortex and F-actin disassembly, which precedes exocytosis. Thus, stimulation-induced redistribution of scinderin and F-actin disassembly produce subplasmalemmal areas of decreased cytoplasmic viscosity and high secretory vesicle mobility. All these processes require the presence of Ca^{2+} in the extracellular medium. Therefore, only secretagogues that induce Ca^{2+} entry are able to produce these effects (see Fig. 33.2B).

In isolated chromaffin cells, stimulation with nicotinic agonists can result in secretion of about 30% of the total catecholamine. Electron microscopic observations show that a small number of granules lie within the exclusion zone of the cell cortex. This demonstrates the importance of changes in cortical actin to allow movement of the bulk of the granules involved in a full secretory response. Nevertheless, low levels of exocytosis, due to these granules in the cortical exclusion zone, could occur without generalized changes in cortical actin. Thus, in a physiological situation, where relatively few exocytotic events occur per stimulus, changes in cortical actin may not be necessary for the initial wave of exocytosis, but are required for the movement, into the cortical exclusion zone, of granules ready for the next stimulus. A similar picture has emerged from studies on the nerve terminal cytoskeletal phosphoprotein, synapsin I, which is believed to cross-link synaptic vesicles and release them following depolarization and phosphorylation of the synapsin I.

IVB. Physical Events Associated with the Fusion of Vesicles to Plasma Membrane

In regulated exocytosis, fusion of the secretory granules with the plasma membrane is triggered by an appropriate signal. The fusion process, following the triggering signal, can be very fast, such as in mammalian nerve terminals, with delays of less than 0.2 ms between the action potential and exocytosis. In some cells, however, delays of 0.2 s (chromaffin cells) to 50 s (mast cells) are observed. This delay is thought to be caused by the time required for production of second messengers possibly involved in exocytosis and removal of the cytoskeletal barrier that immobilizes the vesicles. However, the physical interactions between the granule membrane and the plasma membrane remain similar whether the exocytotic delay is fast or slow. Accordingly, the following fusion events will be described along general lines based on a sequence proposed by Almers (1990).

IVB1. Capacitance Jump

Each time a secretory granule fuses with the plasma membrane, the total capacitance of the cell increases by a value proportional to the surface area of the new membrane added to the existing cell membrane. Assuming that biological membranes have a constant specific capacitance of about 1 $\mu F/cm^2$ allows a simple calculation of the granule size. Upon fusion of a single vesicle, the capacitance value increases abruptly to a new stable value as the membrane of the vesicle and the plasma membrane become continuous and the vesicle lumen opens into the extracellular space. Figure 33.5 illustrates the equivalent circuitry of a resting cell (Fig. 33.5A) and that of a cell undergoing exocytosis (Fig. 33.5B). During degranulation, several granules fuse with the plasma membrane, which produces a typical staircase recording (Fig. 33.5C). Degranulation in three different cell types are presented in Fig. 33.6: human neutrophil (Fig. 33.6A), guinea pig eosinophil (Fig. 33.6B) and horse eosinophil (Fig. 33.6C). Note that the amplitude of the individual step capacitance is lower in human neutrophil than in horse eosinophil, reflecting the different sizes of the vesicles. A capacitance step amplitude histogram is built by measuring the step height of a large number of individual events. An example of this is illustrated in Fig. 33.6D for neutrophils. The capacitance step amplitudes range from 1 to 6 fF (1 to 6×10^{-15} F), with a greater number of events having an amplitude of 2 fF. Assuming a spherical shape, the diameter of the granule can be calculated from the step change in capacitance, δC_m in fF, by the relation:

$$\delta C_m = \pi d^2 \tag{33.1}$$

The frequency distribution of the sizes of the granules obtained from the capacitance step amplitude histogram is represented in Fig. 33.6E for guinea pig eosinophils. The distribution is fitted (smooth line) by the sum of two Gaussian curves with means of 520 and 590 nm (Lindau and Gomperts, 1991). This size distribution fits in well with the morphometric data obtained by direct microscopic observation of the secretory vesicles. Capacitance step measurements have been achieved in a variety of cell types, including adrenal chromaffin cells, mast cells, pancreatic acinar cells, neutrophils, eosinophils, basophils, pituitary lactotrophs and nerve terminals derived from the posterior pituitary. Capacitance step values generally range between 1 and 30 fF, corresponding to granule diameters of 0.2 to 1 μm.

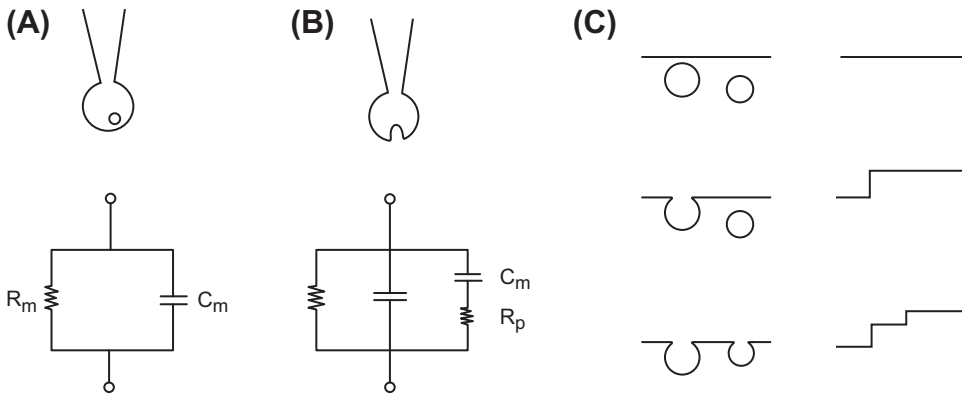

FIGURE 33.5 Capacitance measurement and equivalent electrical circuit. (A) The cell is patch-clamped in the whole-cell configuration. The cell is at rest and an unfused granule is shown near the plasma membrane. The equivalent circuit is represented by membrane resistance R in parallel with membrane capacitance C_m. The series resistance due mainly to the micropipette has been omitted for clarity. (B) Once the granule has fused with the plasma membrane, its capacitance C_v, proportional to the surface of membrane added, is added to the total capacitance of the cell. R_p is the fusion pore resistance, which will rapidly decrease as the pore dilates. (C) The fusion of a granule with the plasma membrane increases the capacitance by step. Granules of identical sizes induce the same increases in capacitance.

Giant vesicles with diameters ranging from 1 to 5 µm are found in mast cells from a strain of genetically defective beige mice (strain C57BL/6J-bg^j/bg^j). In these mice, mast cells and other granulocytes are unable to limit the size of their secretory vesicles; mast cells contain 10 to 40 giant vesicles that can easily be observed under photonic microscopy. These cells thus provide an ideal material for exocytosis studies and, for this reason, have been extensively used. The capacitance method offers the possibility to study degranulation in real time online; time analysis of the secretory process reveals that the granules fuse sequentially, one by one, with the plasma membrane. However, in mast cells, capacitance step analysis demonstrates the presence of step values greater than 60 fF, which could not be produced by the fusion of a single vesicle. A detailed analysis of the capacitance step histogram reveals a multimodal distribution of granule size, which indicates that the larger granules could be formed by the fusion of two to five single granules with each other.

IVB2. Capacitance Flickering

The pattern of the staircase increase in capacitance during degranulation demonstrates that each step builds upon the previous one, indicating that the fusion event is irreversible. However, closer observation of capacitance jumps in

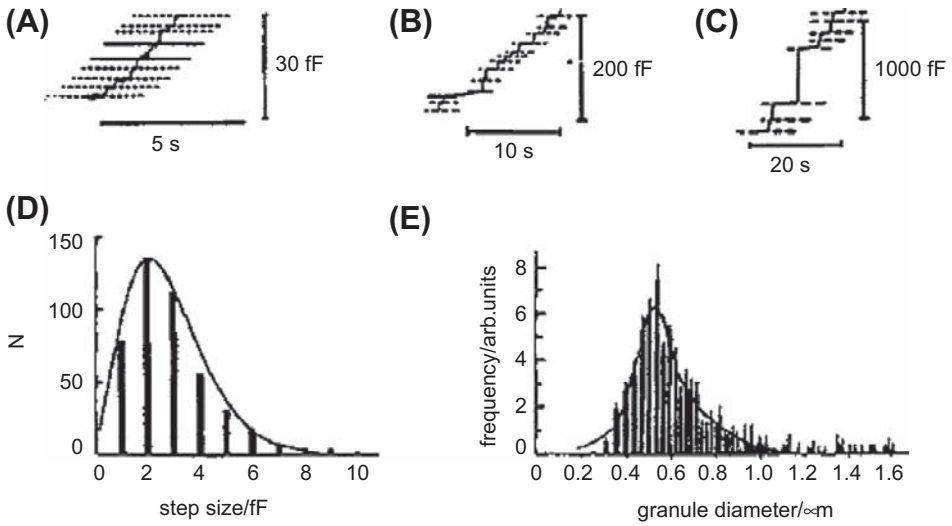

FIGURE 33.6 Analysis of step capacitance. Capacitance recordings obtained from different cells: (A) human neutrophils, (B) guinea pig eosinophils, (C) horse eosinophils. Note the staircase appearance of the recordings, which reflects the sequential fusion of individual granules and the size of the step capacitances, which are proportional to the size of the granules. (D) Frequency distribution of step sizes for human neutrophils. (E) Distribution of granule size for guinea pig eosinophils derived from capacitance measurement. *(Adapted with permission from Lindau and Gomperts, 1991.)*

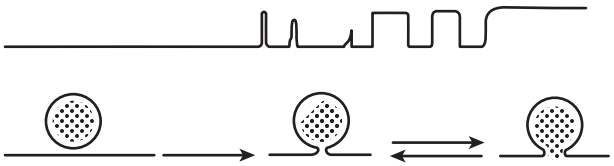

FIGURE 33.7 Flickering of the membrane capacitance. Fusion of the granule is reversible and can oscillate between an unfused state and a fused state. Each time the granule fuses with the plasma membrane, the capacitance of the cell increases by a step. If the fusion pore closes, the capacitance recovers its initial value; incomplete recovery indicates very brief closures exceeding the speed of the recording system. Eventually, a stable fused state can be reached.

mast cells reveals the existence of "on" and "off" steps. The "on" step is produced by the opening of a small-diameter pore, called a *fusion pore*, which adds the surface of the vesicle to that of the cell. Once opened, the fusion pore can close quickly and reopen (Fig. 33.7). Rapid oscillation between open and closed states gives the appearance of a flickering of the capacitance (Almers, 1990). Size distribution of capacitance steps during the flickering period shows that large steps are absent and that all steps remain in the range of values expected for single vesicle fusion events. The size of the fusion pore is proportional to its conductance. An unexpected result is that the reclosing of the pore occurs, not only in small-diameter pores (low conductance), but also in larger-sized pores having a conductance of several nS. Capacitance flickering is rather frequent in mast cells, but very few have been observed in eosinophils. This raises the question of the undetectable presence of flickering during the fusion of all vesicles before the irreversible fused state is attained. Indeed, the initial phase of fusion is a very fast process which cannot be faithfully recorded by the speed of the recording techniques used. The earliest steps as well as short-lived flickering are certainly missed.

IVB3. Fusion Pore

Freeze-fracture images of exocytosis in mast cells and neutrophils reveal the presence of narrow pores formed between the granules and the plasma membrane. The size of the pore increases as fusion progresses, allowing the release of vesicle contents. The presence of pores joining two secretory vesicles is also observed (Lindau and Gompertz, 1991). Electrically, the first opening of the fusion pore generates a brief transient current from which several parameters can be deduced.

Size of Fusion Pore

The conductance of the fusion pore can be calculated from the current transient produced by movement of the charges between two differently charged membranes, i.e. the plasma membrane and vesicle membrane. The initial value of the current, I_0, is related to the initial pore conductance, g_0, by the relationship:

$$g_0 = I_0/(E_c - E_v) \tag{33.2}$$

where E_c is the potential across the plasma membrane and E_v the potential across the vesicle membrane.

The initial conductance of the fusion pore in mast cells was found to be 230 pS. The corresponding pore diameter was calculated assuming a resistivity of 100 Ω-cm and a pore length of 15 nm. The abrupt increase in conductance corresponds to the all-or-none opening of a pore having an inner diameter of less than 2 nm. For comparison purposes, gap junction channels have conductances that vary from 80 to 240 pS and a diameter of approximately 2 nm. It can thus be proposed that the fusion pore is a large protein spanning across two membrane thicknesses and having a structure and function resembling that of a channel. Data obtained from electron microscopic observations reveal that the smallest pores that can be observed have diameters between 30 and 50 nm, values far higher than the values reported from conductance measurements. A rapid dilatation of the pore soon after its formation might explain this discrepancy. Once the pore has been formed, the conductance increases abruptly to a value near 250 pS. Thereafter, the pore begins to dilate, possibly by infiltration of lipid molecules between the subunits of the protein structure, followed by an increase in conductance. The pore conductance increases from 500 pS to 3000 pS in about 25 ms; a plateau is reached after 150 ms, corresponding to a pore diameter of more than 16 nm.

Does the Fusion Pore Leak?

Once established, the diameter of the fusion pore is similar to that of the gap junction, between 1.5 and 2 nm. Since gap junctions allow the intercellular passage of molecules weighing up to 1.9 kDa, the question can be asked as to whether granule contents can leak through the fusion pore. In guinea pig eosinophils, the irreversible fusion of the granule with the plasma membrane is occasionally preceded by a long-lived fusion pore having a conductance of 70−250 pS. When granules were loaded with the fluorescent dye quinacrine, no release of the dye in the extracellular medium could be observed during the life of the fusion pore. Only after the fusion pore had completely dilated and the vesicle had reached its irreversible state of fusion was the dye released. These results indicate that the fusion pore is too narrow for the release of granule contents.

However, computations based on the diffusion of a small molecule such as histamine predict that a granule with a diameter of 0.8 mm should release its contents rapidly through the opening of the fusion pore. Experimental proof was provided by Neher and collaborators

using bovine chromaffin cells (Chow et al., 1992). Secretion was measured by voltametry, while cells were studied by voltage-clamp. The cells were stimulated by depolarizing the membrane from a holding potential of −60 mV to a step potential of +10 mV for 25 ms to activate the Ca^{2+} channels. The amperometric signals, which represent the detection of the released catecholamine molecules by the carbon electrode (potential of 800 mV), were transient with a fast or slow rising phase and variable amplitudes. A histogram of integrals of current transient amplitude obtained on several cells showed that the mean charge transfer had a value of 0.76 pC, which is equivalent to the release of 2.36×10^6 molecules of catecholamine. Sometimes, larger events were detected, presumably corresponding to multigranular exocytosis. One interesting and surprising feature was that the majority of the fast-rising events were preceded by a small "foot" or "pedestal," as illustrated in Fig. 33.8A. The mean duration of the foot was 8.26 ms and the mean charge 34 fC, equivalent to 1.05×10^5 molecules (Fig. 33.8B). The foot was interpreted as reflecting a slow leakage of catecholamine molecules through the fusion pore formed during the early step of the fusion process. A second important result of this study was the discovery and quantification of a long latency period between the end of the stimulus and catecholamine release. The majority of the secretory events occurred 5 to 100 ms after the end of the electrical stimulus, which is rather long when compared to nerve endings, where the delay is about 1 ms. A complex cascade of intracellular events triggered by the increase of cytosolic Ca^{2+} concentration could be responsible for this long latency.

IVB4. Membrane Tension as a Driving Force for Fusion

As previously described, flickering is characterized by the opening and closing of the fusion pore. In some cases, it has been shown that after a period of flickering, the capacitance of the plasma membrane declines to a value lower than its initial value (Monck et al., 1990). Figure 33.9A shows that this decrease in capacitance is paralleled by an increase in the conductance of the fusion pore (Fig. 33.9B), thus establishing a relationship between the dilatation of the pore and decreased plasma membrane capacitance. Once the flickering stops, the conductance recovers its initial value but the whole-cell capacitance remains lower. These results are interpreted as reflecting a decrease of the plasma membrane surface due to a net transfer of material to the granule membrane. The difference between the "on" and "off" steps (found in one-half of the transient fusions with values between −2 to −4 fF) is proportional to the duration of contact between the plasma membrane and the secretory vesicle (Fig. 33.9C). The rate of cell surface area reduction

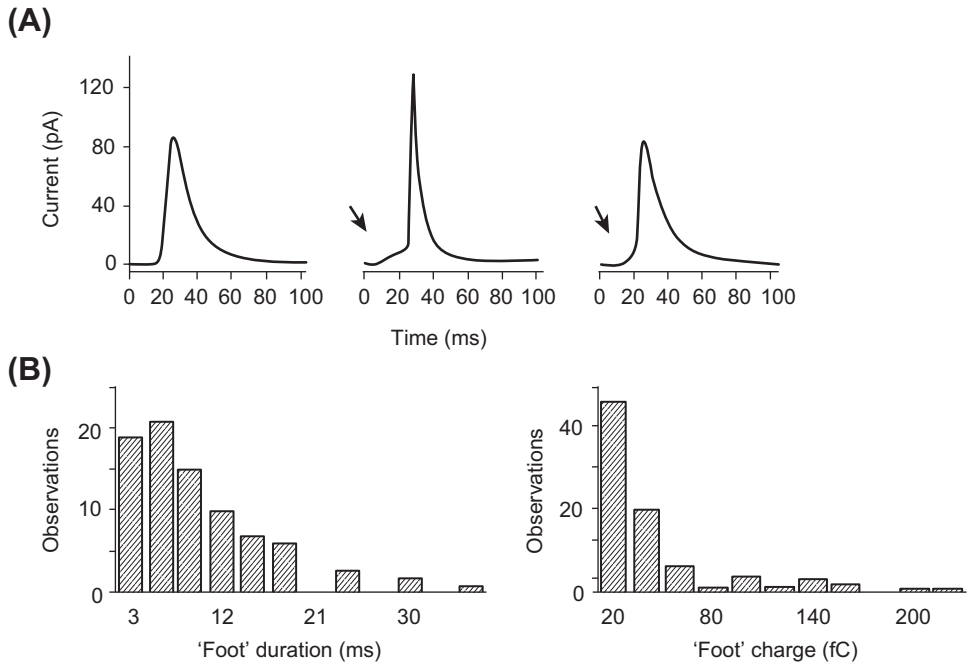

FIGURE 33.8 Amperometric current recorded in chromaffin cells. (A) The amperometric signal recorded with the voltametry method shows a fast rising phase followed by a slower decrease. Occasionally, the rising phase is preceded by a pedestal or foot. The foot signal is thought to be due to the leak of catecholamine by the fusion pore before its complete dilatation. (B) Histogram of the foot signal duration (left panel) and histogram of the charge of the foot signal (right panel), with a mean of 34 fC corresponding to 1.05×10^5 molecules. *(Adapted with permission from Chow et al. (1992). Nature. 356, 60–63. Copyright 1992 Macmillan Magazines Limited.)*

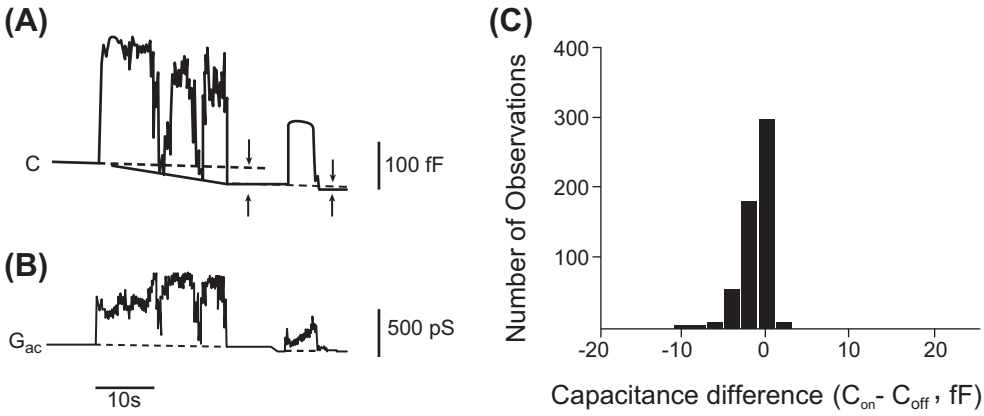

FIGURE 33.9 Decrease of total membrane capacitance after fusion. Capacitance (A) and conductance (B) measurements during transient fusion of a giant secretory granule from beige mouse mast cell. Capacitance and conductance increase on fusion. The fusion pore closes twice with a decrease in conductance and capacitance. Note that the conductance returns to its initial level but that the capacitance of the cell is lower than its initial value. This indicates a reduction of the surface of the plasma membrane due to a leak of lipid molecules toward the granule membrane. (C) Histogram showing the size distribution of the capacitance difference measured after transient fusion in mast cells. *(Reproduced with permission from Monck et al. 1990.)*

is 0.16 $\mu m^2 \cdot s^{-1}$. The transfer of membrane is facilitated by the fact that the membrane of the secretory vesicle is under tension. Upon fusion, a movement of phospholipid molecules occurs from the plasma membrane to the granule membrane. A possible mechanism for generating tension in the granule membrane is osmotic swelling. However, fusion can proceed in isotonic, hypotonic or hypertonic solutions with no change in the kinetics of capacitance increase.

IVB5. Fusion Steps

Several lines of evidence favor the hypothesis that a pore-forming protein could be involved in the fusion process. The abrupt opening of the fusion pore with an initial conductance of 250 pS, similar to the conductance of the gap junction channel and the occurrence of rapid flickering are the strongest arguments. Prior to their fusion, secretory granules are docked to the plasma membrane. In synaptic nerve endings, docking is localized to a restricted region and, upon stimulation, yields localized secretions. Docked granules have been observed in a variety of systems, including chromaffin cells. In these cells, localized secretion was also reported, depending on the applied stimulus.

IVC. Control of Exocytosis

Exocytosis occurs in a variety of electrically excitable and non-excitable systems in response to receptor activation. The regulatory pathways that couple stimulation and secretion vary widely among cell types. In the following section, analysis of the factors controlling exocytosis mainly focuses on two well-studied systems: the chromaffin cell from the adrenal medulla, which belongs to the class of excitable cells, and the mast cell from the immune system, a non-excitable cell.

IVC1. Effectors of Exocytosis

Calcium Signaling and Sources of Calcium

In many cells, Ca^{2+} is the key signal for triggering exocytosis. In chromaffin cells, the resting Ca^{2+} concentration has a value ranging between 50 and 100 nM. Chromaffin cells can be stimulated by two different classes of acetylcholine receptors. The nicotinic receptor has a channel-like structure consisting of five transmembrane subunits. The binding of two acetylcholine molecules opens the channel, which leads to a large net influx of Na^+ ions. This influx causes a membrane depolarization which can activate voltage-dependent Ca^{2+} channels. The nicotinic receptor channel is also permeable to K^+ ions and, to a lesser extent, Ca^{2+} ions. The muscarinic receptor belongs to the family of the seven-span transmembrane domain receptor proteins, which utilizes the G protein cascade pathway as its signal-transducing mechanism. Stimulation of chromaffin cells with the cholinergic agonist nicotine induces a rapid rise in $[Ca^{2+}]_i$ (measured with Ca^{2+}-sensitive fluorescent dye) up to 1 μM; this $[Ca^{2+}]_i$ increase is followed by F-actin disassembly (see Fig. 33.4) and exocytosis. Muscarinic stimulation of chromaffin cells also increases $[Ca^{2+}]_i$ but does not induce secretion.

In a Ca^{2+}-free external medium, secretion is abolished regardless of the stimulus. This observation reinforces the fact that Ca^{2+} influx from the external medium is crucial for secretion in chromaffin cells. Several voltage-dependent Ca^{2+} channels have been described in chromaffin cells, namely: (1) the L-type dihydropyridine-sensitive channels; (2) the N-type ω-conotoxin-sensitive

dihydropyridine-insensitive Ca^{2+} channels; and (3) the dihydropyridine-sensitive facilitation Ca^{2+} channels. Electrical depolarization, K^+ depolarization and nicotinic stimulation open the Ca^{2+} channels, allowing an immediate influx of Ca^{2+} ions from the external medium. The video-imaging technique allows the recording of $[Ca^{2+}]_i$ with good spatial definition. As shown in Fig. 33.10 (right panel), the increase in $[Ca^{2+}]_i$ is restricted to the immediate vicinity of the plasma membrane after activation of Ca^{2+} channels. The requirement of high Ca^{2+} concentration for exocytosis implies that secretory granules are stored near the Ca^{2+} channels. Recent experimental evidence confirms that when Ca^{2+} channels are activated, the concentration of Ca^{2+} at the secretory sites could range from 10 to 100 pM, creating a Ca^{2+} microdomain (Neher, 1998).

In chromaffin cells, internal Ca^{2+} release is provided by two different pools: the $InsP_3$-sensitive pool and the Ca^{2+}-induced Ca^{2+} release pool (CICR). The activation of the PtdIns-specific phospholipase C by the G_q-protein-coupled receptor or by cytosolic Ca^{2+} elevation induces the hydrolysis of $PtdInsP_2$, thus generating two messengers: $InsP_3$ and diacylglycerol (DAG) (see Figs. 33.1 and 33.2). The binding of $InsP_3$ to specific sites on the endoplasmic reticulum induces Ca^{2+} release. $InsP_3$ receptors were also found in secretory granules of endocrine and neuroendocrine cells. Their activation by $InsP_3$ induces the release of Ca^{2+} ions from the granules and provides a localized increase of $[Ca^{2+}]_i$. Ca^{2+} ion alone or caffeine can trigger the release of Ca^{2+} from the second pool (CICR). The muscarinic receptor induces the release of Ca^{2+} from the $InsP_3$-sensitive store without Ca^{2+} channel activation. The observed Ca^{2+} increase is low and sometimes localized to one pole of the cell (Fig. 33.10, left panel). Despite this $[Ca^{2+}]_i$ increase, there is little or no stimulation of secretion at the site where $[Ca^{2+}]_i$ has increased. A more uniform $[Ca^{2+}]_i$ increase can be generated by release from the Ca^{2+}-induced Ca^{2+} release pool by caffeine or from the $InsP_3$ pool by introduction of GTP-γS into the cell. However exocytosis still remains unstimulated. These results conclusively demonstrate that, in chromaffin cells, only a considerable rise in Ca^{2+} concentration in the proximity of the plasma membrane is able to trigger exocytosis. This highly localized $[Ca^{2+}]_i$ increase can only be achieved via the Ca^{2+} channels and not by a small increase due to release from internal stores.

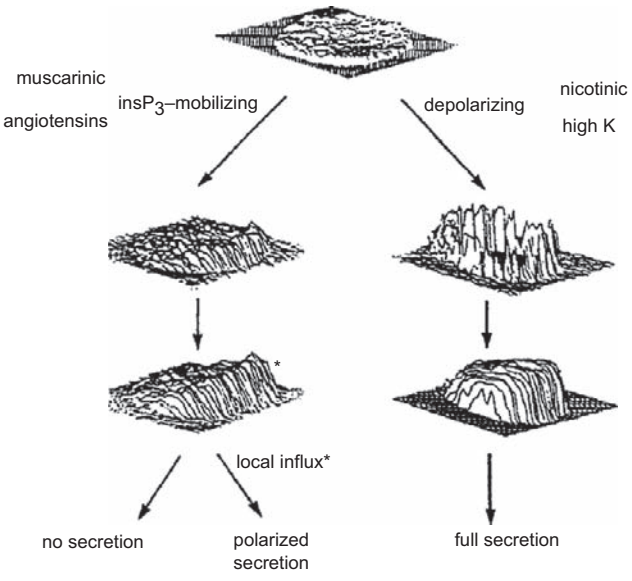

FIGURE 33.10 Ca^{2+} signal in a chromaffin cell in response to various agonists. The distribution of $[Ca^{2+}]_i$ is obtained by video-imaging. The figure illustrates the fact that level and distribution of $[Ca^{2+}]_i$ are important for full secretion. The right portion of the figure shows that a depolarization of the plasma membrane, induced by high $[K^+]_o$ or nicotinic agonist, opens voltage-activated Ca^{2+} channels with an immediate and high $[Ca^{2+}]_i$ increase at the periphery of the cell. Afterwards, $[Ca^{2+}]_i$ increases in the entire cell due to release of Ca^{2+} from internal stores; a full secretion is obtained. The left portion of the figure shows that release of Ca^{2+} from the IP_3-sensitive pool is not sufficient to induce secretion, although some localized secretion can be obtained in the region of the cell where $[Ca^{2+}]_i$ increase was the highest. *(Adapted with permission from Burgoyne, 1991.)*

Mast cells are able to synthesize, store and secrete histamine. However, Ca^{2+} alone is not able to trigger histamine secretion. There is a requirement for a guanine nucleotide together with Ca^{2+} for exocytosis. Mast cells are stimulated by antigenic binding on cell surface IgE receptors or by compound 48/80. A sudden rise in Ca^{2+} concentration (released from $InsP_3$-sensitive pool) is observed, reaching a level of up to several micromolar. The signal is transient and $[Ca^{2+}]_i$ declines within several seconds to its original baseline value. Degranulation begins soon after this transient response. Two important features should be noted concerning $[Ca^{2+}]_i$ and secretion in mast cells: (1) the $[Ca^{2+}]_i$ transient is not dependent on the presence of Ca^{2+} in the external medium; and (2) simultaneous recording of capacitance and membrane conductance reveals that conductance is constant throughout the duration of exocytosis. These results indicate that Ca^{2+} entry through Ca^{2+} channels is not a required signal for exocytosis, but rather its release from internal stores. A Ca^{2+} current, called I_{CRAC} (calcium-release activated calcium), was described in mast cells (Hoth and Penner, 1992); I_{CRAC} is activated by the depletion of intracellular Ca^{2+} pools. The role of I_{CRAC} in non-excitable cells could be to maintain a high $[Ca^{2+}]_i$ and to replenish empty Ca^{2+} stores after stimulation. A possible direct role in exocytosis has not yet been shown.

One conclusion is that Ca^{2+} release from internal stores is sufficient for exocytosis in mast cells. However, intracellular application of $InsP_3$ induces a transient $[Ca^{2+}]_i$ increase but does not trigger secretion, emphasizing that the signal is more complex. Application of the non-hydrolyzable GTP analog GTP-γS (100 μM) inside a mast cell (via a patch pipette) induces a transient

$[Ca^{2+}]_i$ increase, after a delay of 10–20 s, followed by an increase in capacitance. GTP-γS activates G proteins, including the G_q protein coupled to PLC, with a resulting production of $InsP_3$ and DAG. Ca^{2+} is released from the $InsP_3$-sensitive pool by the same mechanism as with the direct application of $InsP_3$ described above. However, in this case, exocytosis is stimulated, leading to the conclusion that GTP-γS activates a G protein that plays a crucial role in exocytosis.

Guanine Nucleotides

As seen earlier, Ca^{2+} and a guanine nucleotide are necessary and sufficient effectors to ensure secretion in mast cells. The stable analog GTP-γS is the commonly used guanine nucleotide, although any ligand that binds to G protein is able to stimulate secretion. In chromaffin cells, two types of observations have been recorded: (1) GTP-γS increases the Ca^{2+} sensitivity of secretion in permeabilized cells; and (2) GTP analogs stimulate secretion in a Ca^{2+}-independent manner (Morgan and Burgoyne, 1990). GTP analogs do not enhance the secretion induced by high Ca^{2+} concentration (10 μM), which indicates that the two stimuli (GTP and Ca^{2+}) act on the same exocytotic pathway.

Evidence for the involvement of a GTP-binding protein in secretion has been obtained from a variety of cells: neutrophils; platelets; parathyroid; pituitary lactotroph, gonadotroph and melanotroph; insulin-secreting cells; and pancreatic acinar cells. Various effects have also been observed in these cells: GTP or GTP analogs behave as effectors able to trigger a Ca^{2+}-independent secretion, or as modulators that increase Ca^{2+} sensitivity, or more surprisingly as inhibitors that block the exocytotic pathway at a late stage. The exact nature of the G proteins is not yet known, although some analogy can be made with GTP proteins involved in vesicular traffic (Rothman and Orci, 1992).

The small Ras-like GTPases are involved in the formation, transport and fusion of vesicles. In yeast, the small Ras-related GTP-binding protein SEC4 is required for targeting and/or fusion of vesicles to the plasma membrane. Rab3A from the rab family of proteins has been located in the membrane of neurosecretory vesicles. More than 30 Rabs have been identified. They have a regulatory role in secretion. In its GTP-bound form, Rab3A inhibits secretion, possibly by stabilizing a fusion-incompatible conformation. Under an appropriate signal, GTP is hydrolyzed to GDP with the help of GAP (a GTPase-activating protein); this exchange of GTP for GDP releases the inhibition. The fusion can then proceed to subsequent steps. Two accessory proteins are involved in the cycle: rabphilin-3A, which binds to the GTP-Rab3A form, and GDI (a GDP-dissociation inhibitor), which binds to the GDP-Rab3A form. Rabphilin is phosphorylated by many kinases and contains binding sites for Ca^{2+} and phospholipids. In endocrine cells, Nac2 binds GTP-Rab3A; this protein has a high similarity to the Rab3A-binding domain of rabphilin, but lacks the Ca^{2+} binding sites and phospholipids. GDI binds to Rab3A in its GDP form and removes it from the membrane. After dissociation of the GDI-GDP-Rab3A complex, GTP-Rab3A can bind again to another vesicle. Thus, rabphilin-3A and GDI control the Rab3A cycle but do not directly participate in the fusion (Südhof, 1995; Geppert and Südhof, 1998).

IVC2. Modulators of Exocytosis

ATP

Permeabilized cells rapidly lose their secretory response to agonists unless ATP is present in the medium. However, the sequence of exocytosis can be separated in an early phase that requires MgATP to proceed and a late phase that is MgATP-independent. ATP could act at various levels of the secretory response, acting as a substrate for protein phosphorylation or modulating various kinases involved in secretion. The last ATP-requiring steps in exocytosis have been identified; they involve ATPase, NSF and the formation of $PtdInsP_2$. NSF forms a large (20S) complex with the attachment proteins (SNAPs) and SNAP receptors (SNAREs), which has been proposed to be the fusion particle (see Fig. 33.3). The hydrolysis of ATP by NSF is thought to produce energy for the fusion (priming step). The formation of $PtdInsP_2$ by phosphatidylinositol 4-phosphatase-5-kinase and a phosphatidylinositol transfer protein requires the presence of ATP. $PtdInsP_2$ is thought to be involved in the interaction between cytoskeleton and secretory granules (docking step). Docking and priming of secretory granules are thus ATP-dependent. During vesicle transport through the Golgi, ATP hydrolysis by NSF occurs after docking, but in granule secretion no such evidence exists.

Cyclic Nucleotides

In chromaffin cells, cAMP concentration increases after cholinergic stimulation, leading to the hypothesis that cAMP could have a role in exocytosis. In pancreatic β cells, the cAMP-dependent protein kinase A enhances secretion. However, contradictory results have been reported on the effects of high and low cAMP concentrations on secretion modulation, i.e. inhibition and potentiation, respectively. Nicotinic-induced secretion in chromaffin cells is inhibited by high cGMP concentration, whereas low concentrations potentiate the secretory response.

Calmodulin

A calmodulin-binding protein of 65 kDa, called 65-CMBP or p65, has been found in several secretory vesicles, such as synaptic, neurohypophyseal, chromaffin, platelets and pancreatic islet granules. This protein also binds to

phospholipids with high affinity. A possible role of calmodulin in exocytosis was investigated by blocking its action. The calmodulin antagonist calmidazolium inhibits secretion from intact chromaffin cells. Antibodies raised against calmodulin inhibit the Ca^{2+}-dependent binding of calmodulin to vesicle membrane by acting on the docking and/or fusion steps of exocytosis. However, some reports indicate that the less specific calmodulin inhibitor trifluoperazine (TFP) has no effect on permeabilized cells. At present, it appears that calmodulin is not essential for Ca^{2+}-dependent exocytosis, although interaction between calmodulin and cytoskeletal proteins should nevertheless be considered.

Protein Kinase C

A role for PKC in secretion could be inferred from the fact that any agonist that stimulates secretion also induces activation of PKC. PKC has a modulating role in Ca^{2+} affinity, by decreasing Ca^{2+} requirements for exocytosis. Inhibition of PKC by staurosporine or through down-regulation partially inhibits secretion. However, in gonadotrophs, PKC-stimulated luteinizing hormone exocytosis is independent of Ca^{2+}. Obviously, the role of PKC in exocytosis is not yet completely understood. It is possible that PKC is not essential for Ca^{2+}-dependent exocytosis (modulator), but that a second Ca^{2+}-independent pathway could coexist in which PKC acts as an effector of secretion. Indeed, it has been recently shown in chromaffin cells that PKC acts at a late stage in exocytosis before the final Ca^{2+}-sensitive step. The role of PKC would be to increase the size of the readily releasable pool (RRP) of secretory granules by speeding their maturation after they dock with the plasma membrane. Moreover, direct stimulation of PKC by the phorbol ester PMA (phorbol 1,2-myristate-1,3-acetate) leads to a disruption of the actin network near the plasma membrane, which increases the number of docked granules. Several proteins involved in the regulation of the cytoskeleton are substrates for PKC: annexin I, annexin II and MARCKS (see Fig. 33.1).

Phospholipase A2 and Arachidonic Acid

A possible fusogen role of arachidonic acid was inferred from the fact that, in vitro, granules aggregated by synexin and Ca^{2+} fuse together if arachidonic acid is added to the medium. As previously mentioned for PKC activation, arachidonic acid is produced each time secretion is stimulated. Inhibition of phospholipase A2 and arachidonic acid metabolism inhibits secretion of chromaffin cells due to a blockage of Ca^{2+} entry.

IVC3. Secretory Granule Pools

In bovine chromaffin cells, increase in $[Ca^{2+}]_i$ triggers secretion at various rates: ultrafast secretion (time constant <0.5 s), fast secretion (time constant 3 s) and slow secretion (time constant 10 to 30 s). Nevertheless there is a weak correlation between the rate of secretion and $[Ca^{2+}]_i$ levels, the three types of responses are mainly observed for 10 to 50 μM, above 80 μM and around 170 μM $[Ca^{2+}]_i$, respectively. The time constant of the increase in membrane capacitance can be considered as a measure of the hormone released from a particular store. This indicates that the secretory granules are in various states of releasability. The ultrafast response comes from vesicles docked to the plasma membrane and immediately available for release by an increase in $[Ca^{2+}]_i$; they belong to the immediately releasable pool (IRP). A second pool of granules are located near the membrane in a nearly releasable pool (NRP) and can be released within seconds of a rise in $[Ca^{2+}]_i$; the fast response originates from this pool. Finally, the slow response originates from vesicles from a depot store in the bulk cytoplasm (Neher and Zucker, 1993). Movement of granules from the NRP to the IRP is Ca^{2+}-dependent and could involve calpactin in the docking process. However, not all the docked granules are available for the last steps, opening of the granule induced by Ca^{2+}. The fastest response, the exocytotic burst, mobilizes only one-tenth of the docked granules, which indicates that, after docking, granules undergo a maturation process in the IRP. Figure 33.11 describes a possible sequence for exocytosis in endocrine cells. PKC and ATP hydrolysis are involved in the docking and priming steps. Thereafter, three steps have been proposed based on their sensitivity to temperature, blockage by acidification and Ca^{2+} ion (three or four ions) triggering; PKC is thought to play a role in this sequence. The pivotal role of ATP in secretion has been outlined, however, a large pool of granules can be released in the absence of ATP by an increase in $[Ca^{2+}]_i$. This indicates first, that ATP hydrolysis by NSF is an early step in the priming process and, second, that if the energy of hydrolysis powers fusion, it remains stored in the core complex until $[Ca^{2+}]_i$ increases (Parsons et al., 1995; Gillis et al., 1996).

V. HORMONE RELEASE IN ENDOCRINE CELLS

VA. Polypeptide and Thyroid Hormones

Most of the events described previously could be applied for most of the endocrine secretory cells.

VA1. Secretion of Insulin

Insulin secretion by the pancreatic β cells provides an excellent example of a cellular activity that requires direction. Insulin is packaged in secretory vesicles which have to migrate to the plasma membrane and fuse with it to release the entrapped insulin. Both microscopic and

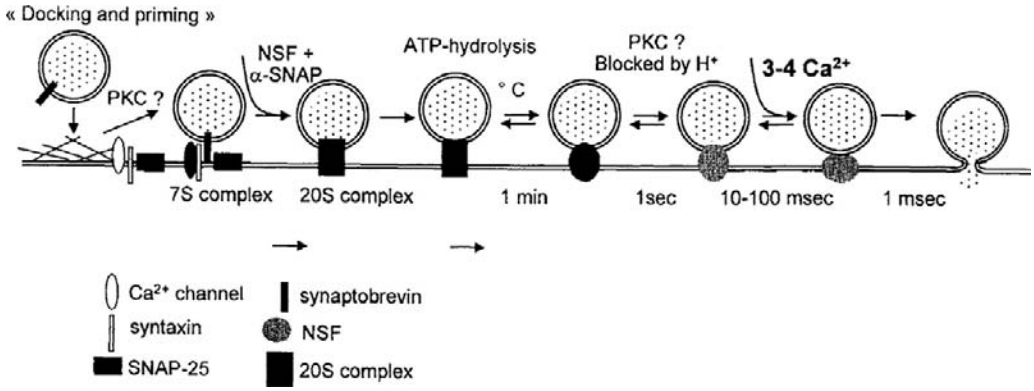

FIGURE 33.11 Docking and fusion of secretory granules in endocrine cells. Docking of vesicles involves the proteins synaptobrevin and syntaxin/SNAP-25. In the first step of docking, protein kinase C (PKC) could have a role in the disruption of the actin barrier. ATP hydrolyzed by NSF is thought to produce energy for fusion. Several steps have been identified after the ATP-dependent step based on their temperature, H^+ and Ca^{2+} dependence. PKC could be involved before the final Ca^{2+}-dependent step. *(Adapted with permission from Parsons et al., 1995 and Gillis et al., 1996.)*

biochemical studies have shown that secretory granules are linked to microtubules which direct attached vesicles to the cell surface. However, a cortical band of fine microfilaments is consistently observed in β cells. Alteration of this cell web by cytochalasin B is associated with an enhancement of glucose-induced secretion of insulin by isolated islets. This microfilamentous web plays an important role in the exocytosis of insulin secretory granules by controlling access to the cell membrane via a mechanism probably similar to that previously described for chromaffin cells. Ca^{2+} appears to initiate the cascade of events by which microtubules facilitate the displacement of granules toward the cell membrane. Glucose metabolism increases intracellular concentration of ATP, which closes the ATP-sensitive K^+ channels, consequently inducing cell depolarization and Ca^{2+} influx, while cAMP modifies the intracellular distribution of Ca^{2+} by increasing the cytosolic pool at the expense of Ca^{2+} bound to intracellular organelles. Protein kinase C also appears to be involved in the secretion of insulin.

VA2. Secretion of Pituitary Hormones

Anterior pituitary cells, in their diversity and heterogeneity, provide a rich source of models for secretory function. Secretion of the pituitary hormones is controlled by both specific hypothalamic-releasing peptides and neurotransmitters. Upon binding to their receptors, these agonists activate both Ca^{2+} influx by different types of Ca^{2+} channels (voltage-activated channels, ligand-activated channels and second messenger-activated channels) and second messenger production, thus resulting in hormone secretion. As a second messenger, cAMP appears to be as potent as $InsP_3$ and PKC in interacting with Ca^{2+} to trigger secretion. As for insulin secretion, cytoskeletal structures are tightly associated with hormone release. Purified secretory granule membranes co-sediment with microtubules, MAPs being involved in this association. This suggests that microtubules facilitate the movement of secretory granules from the Golgi apparatus to the plasma membrane, by providing tracks along which the granules can move. The granule membrane can then dissociate from the microtubules and fuse with the cell membrane, followed by exocytosis and release of the hormone into the circulation. Moreover, actin and microtubules are cross-linked by MAPs, forming three-dimensional networks. This cross-linking activity can be inhibited if MAPs are heavily phosphorylated. These observations suggest that MAPs might play an important role in the binding of secretory granules to tubulin and actin. Binding of actin to secretory granules suggests a role for actin in the final steps of exocytosis, as described previously.

VB. Stimulation of Steroid Synthesis and Secretion

While disruption of the actin network is necessary to trigger fusion of secretory vesicles with the cell membrane, a well-preserved organization seems important for steroid release. Several studies have shown that microfilament disruption (with cytochalasins) or microtubule disruption (with colchicine or vinblastine) decreases or blocks second messenger production and steroid secretion, either from the adrenal cortex or gonads. In contrast with peptide hormones, steroids are not packaged in vesicles. Steroid hormones are synthesized from cholesterol contained in lipid droplets. The process of steroidogenesis begins in the mitochondria, where cholesterol is converted to pregnenolone, from which others steroids are synthesized. Stimuli induce rapid increase in the production and secretion of steroids, without cytoplasmic storage. More recent biochemical analysis and fluorescence studies indicate

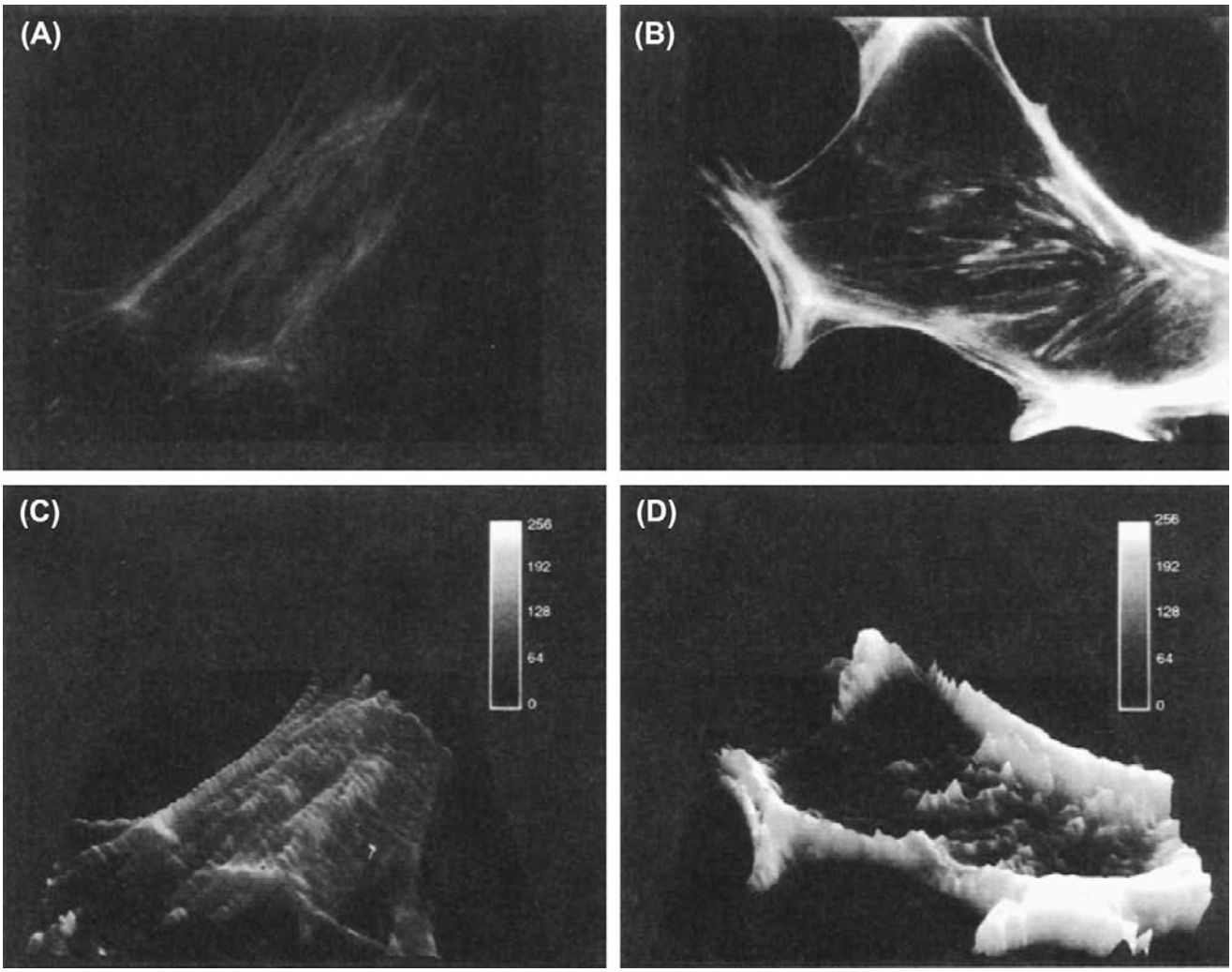

FIGURE 33.12 Effect of Ang II on immunofluorescence labeling of actin in rat glomerulosa cells. Rat glomerulosa cells were cultured for 3 days on plastic coverslips and then incubated without (A) or with (B) 100 nM angiotensin II for 1 min. After formaldehyde fixation and permeabilization with 0.1% Triton X-100, cells were processed for immunofluorescence labeling of actin using rhodamine-phalloidin. (C) and (D) represent the same images as (A) and (B) after computer analysis. Bars represent 13 µm. *(Adapted from Côté et al., 1997.)*

that ligand-receptor interaction induces a rapid polymerization of actin, demonstrated by a rise in the proportion of F-actin over G-actin and by an increased interaction of F-actin with the membrane (Fig. 33.12A and B versus C and D). Moreover, $G_{q/11}$ protein localization overlaps F-actin distribution and cell activation is accompanied by a rapid translocation of $G_q/_{11}$ and F-actin from the cytosol to the membrane, an association essential in promoting phospholipase C activation (Côté et al., 1997).

It has been shown that microfilaments are strictly required for both spontaneous and stimuli-induced corticosteroid secretions, including those utilizing the cAMP-dependent pathways (ACTH, serotonin and vasoactive intestinal peptide), as well as those utilizing the phosphoinositide pathway (angiotensin II and acetylcholine). They are involved in a common and probably late step of steroidogenesis (translocation of the DOC from RER to mitochondria). In contrast, microtubules seem involved in an early step in the mechanism of hormone action, probably at the level of their interaction with the α subunit of the G protein. Microtubules and microfilaments are closely associated with the plasma membrane. That colchicine and vinblastine stimulate basal steroidogenesis may be explained by the fact that most of the tubulin is linked to cholesterol, in lipid droplets. Thus, by acting on tubulin, antimicrotubular drugs could release cholesterol, causing an increase in basal steroid secretion (Feuillolley and Vaudry, 1996). Moreover, in adrenocortical cells, findings suggest that intermediate filaments could facilitate or increase the transport of cholesterol to mitochondria in response to ACTH and cAMP. Figure 33.13 summarizes the role of the three types of

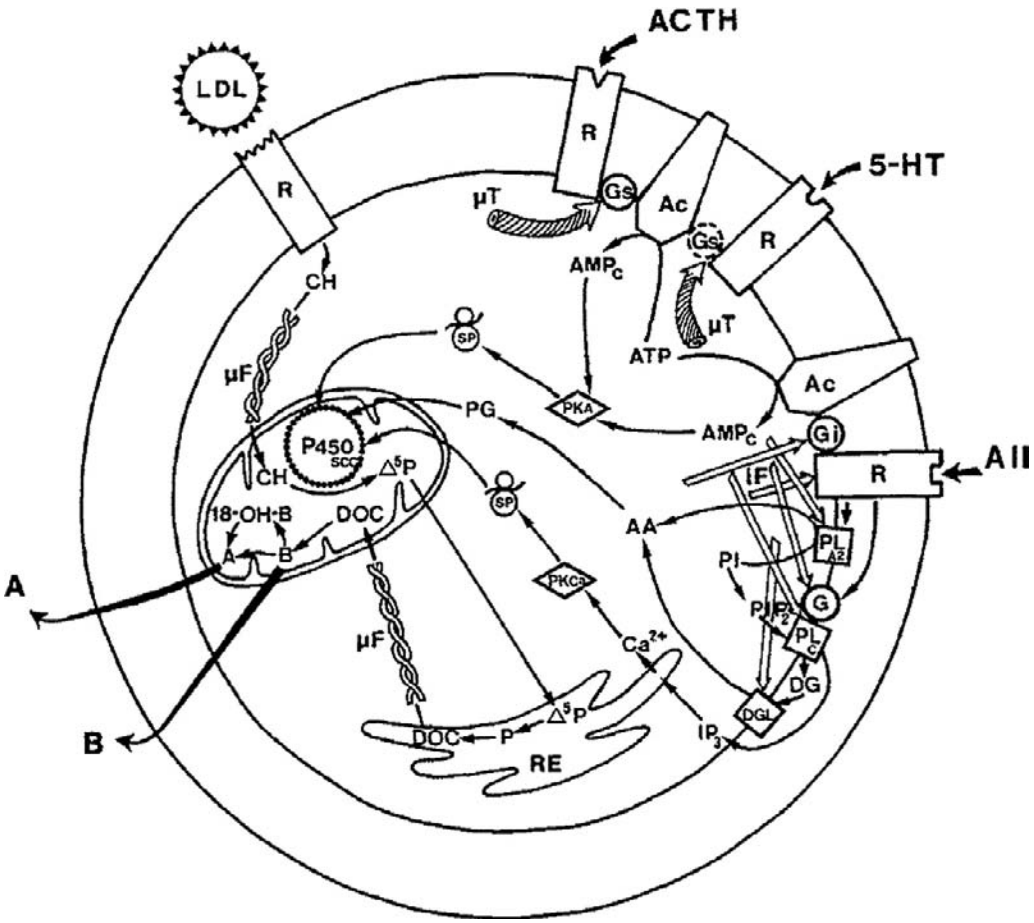

FIGURE 33.13 Cytoskeleton implication in adrenal corticosteroidogenesis. Microtubules (μT) are implicated in the action of ACTH and serotonin (5-HT), probably at a level of G_s protein. Microfilaments (μF) control the transfer of steroid precursors (cholesterol from lipid droplets or membrane low-density lipoproteins to mitochondria and from mitochondria to endoplasmic reticulum). Intermediate filaments (IF) appear to be implicated in the action of angiotensin II (AII), between hormone-receptor coupling and second messenger production. A, aldosterone; AA, arachidonic acid; AC, adenylyl cyclase; cAMP, cyclic adenosine monophosphate; ATP, adenosine triphosphate; B, corticosterone; DAG, diacylglycerol; DOC, 11-deoxycorticosterone; 18-OH-B, 18-hydroxycorticosterone; P, progesterone; P450scc, P450scc cytochrome; Δ^5P, pregnenolone; PG, prostaglandins; PI, PtdIns; PIP_2, $PtdInsP_2$; PKA, protein kinase A; PKCa, protein kinase Ca^{2+}-dependent; PLA_2, phospholipase A_2; PLC, phospholipase C; PS, protein synthesis. *(Reproduced with permission from Feuilloley et al., 1989.)*

cytoskeletal fibers in the steroidogenic effects of the main stimuli of corticosterone and aldosterone secretions (Feuillolley and Vaudry, 1996).

ACKNOWLEDGMENTS

The authors thank Dr Mylène Côté for critical review of the revised version and fruitful discussions and Dusan Chorvat, Jr, from the International Laser Center, Bratislava (Slovakia), for image analysis.

BIBLIOGRAPHY

Almers, W. (1990). Exocytosis. *Annu Rev Physiol, 52*, 607–624.

Aplin, A., Howe, A., Alahari, S., & Juliano, R. (1998). Signal transduction and signal modulation by cell adhesion receptors: the role of integrins, cadherins, immunoglobulin-cell adhesion molecules, and selectins. *Pharmacol Rev, 50*, 197–263.

Arbuzova, A., Murray, D., & McLaughlin, S. (1998). MARCKS, membranes, and calmodulin: kinetics of their interaction. *Biochim Biophys Acta, 1376*, 369–379.

Aroeti, B., Okhrimenko, H., Reich, V., & Orzech, E. (1998). Polarized trafficking of plasma membrane proteins: emerging roles for coats, SNAREs, GTPases and their link to the cytoskeleton. *Biochim Biophys Acta, 1376*, 57–90.

Burgoyne, R. D. (1991). Control of exocytosis in adrenal chromaffin cells. *Biochim Biophys Acta, 1071*, 174–202.

Burgoyne, R. (1995). Mechanisms of catecholamine secretion from adrenal chromaffin cells. *J Physiol Pharmacol, 46*, 273–283.

Burgoyne, R., & Morgan, A. (1998a). Analysis of regulated exocytosis in adrenal chromaffin cells: insights into NSF/SNAP/SNARE function. *Bioessays, 20*, 328–335.

Burgoyne, R., & Morgan, A. (1998b). Calcium sensors in regulated exocytosis. *Cell Calcium, 24*, 367–376.

Chow, R. H., Von Rüden, L., & Neher, E. (1992). Delay in vesicle fusion revealed by electrochemical monitoring of single secretory events in adrenal chromaffin cells. *Nature, 356*, 60–63.

Côté, M., Payet, M.-D., Dufour, M.-N., Guillon, G., & Gallo-Payet, N. (1997). Association of the G protein α_q/α_{11}-subunit with cytoskeleton in adrenal glomerulosa cells: role in receptor-effector coupling. *Endocrinology, 138*, 3299–3307.

Fernandez-Chacon, R., & Südhof, T. (1999). Genetics of synaptic vesicle function: toward the complete functional anatomy of an organelle. *Annu Rev Physiol, 61*, 753–776.

Feuillolley, M., & Vaudry, H. (1996). Role of the cytoskeleton in adrenocortical cells. *Endocr Rev, 17*, 269–288.

Forscher, P. (1989). Calcium and polyphosphoinositide control of cytoskeletal dynamics. *Trends Neurosci, 12*, 468–474.

Geppert, M., & Südhof, T. (1998). RAB3 and synaptotagmin: the yin and yang of synaptic membrane fusion. *Annu Rev Neurosci, 21*, 75–95.

Gillis, K. D., Mössner, R., & Neher, E. (1996). Protein kinase C enhances exocytosis from chromaffin cells by increasing the size of the readily releasable pool of secretory granules. *Neuron, 16*, 1209–1220.

Goda, Y., & Südhof, T. (1997). Calcium regulation of neurotransmitter release: reliably unreliable? *Curr Opin Cell Biol, 9*, 513–518.

Gundersen, G., & Cook, T. (1999). Microtubules and signal transduction. *Curr Opin Cell Biol, 11*, 81–94.

Hall, A. (1998). Rho GTPases and the actin cytoskeleton. *Science, 279*, 509–514.

Hoth, M., & Penner, R. (1992). Depletion of intracellular calcium stores activates a calcium current in mast cells. *Nature, 355*, 353–356.

Inglese, J., Koch, W., Touhara, K., & Lefkowitz, R. (1995). G beta gamma interactions with PH domains and Ras-MAPK signaling pathways. *Trends Biochem Sci, 20*, 151–156.

Janmey, P. (1998). The cytoskeleton and cell signaling: component localization and mechanical coupling. *Physiol Rev, 78*, 763–781.

Lindau, M., & Gomperts, B. D. (1991). Techniques and concepts in exocytosis: focus on mast cells. *Biochim Biophys Acta, 1071*, 429–471.

Martin, T. (1998). Phosphoinositides as signaling molecules. *Annu Rev Cell Dev Biol, 14*, 231–264.

Matus, A. (1988). Microtubule-associated proteins: their potential role in determining neuronal morphology. *Annu Rev Neurosci, 11*, 29–44.

Monck, J. R., Alvarez de Toledo, G., & Fernandez, J. M. (1990). Tension in secretory granule membranes causes extensive membrane transfer through the exocytotic fusion pore. *Proc Natl Acad Sci USA, 87*, 7804–7808.

Morgan, D., & Burgoyne, R. D. (1990). Stimulation of Ca^{2+}-inde-pendent catecholamine secretion from digitonin-permeabilized bovine adrenal chromaffin cells by guanine nucleotide analogues. Relationship to arachidonate release. *Biochem J, 269*, 521–526.

Neher, E. (1998). Vesicle pools and Ca^{2+} microdomains: new tools for understanding their roles in neurotransmitter release. *Neuron, 20*, 389–399.

Neher, E., & Zucker, R. S. (1993). Multiple calcium-dependent processes related to secretion in bovine chromaffin cells. *Neuron, 10*, 21–30.

Parsons, T. D., Coorssen, J. R., Horstmann, H., & Almers, W. (1995). Docked granules, the exocytic burst, and the need for ATP hydrolysis in endocrine cells. *Neuron, 15*, 1085–1096.

Popova, J. S., Garrison, J. C., Rhee, S. G., & Rasenik, M. M. (1997). Tubulin, Gq, and phosphatidylinositol 4,5-bisphosphate interact to regulate phospholipase $C\beta_1$ signalling. *J Biol Chem, 272*, 6760–6765.

Rothman, J. E., & Orci, L. (1992). Molecular dissection of the secretory pathway. *Nature, 355*, 409–415.

Schmidt, A., & Hall, M. (1998). Signaling to the actin cytoskeleton. *Annu Rev Cell Dev Biol, 14*, 305–338.

Söllner, T., Whiteheart, S. W., Brunner, M., et al. (1993). SNAP receptors implicated in vesicle targeting and fusion. *Nature, 362*, 318–323.

Südhof, T. C. (1995). The synaptic vesicle cycle: a cascade of protein-protein interactions. *Nature, 375*, 645–653.

Südhof, T., & Rizo, J. (1996). Synaptotagmins: C2-domain proteins that regulate membrane traffic. *Neuron, 17*, 379–388.

Tapon, N., & Hall, A. (1997). Rho, Rac and Cdc42 GTPases regulate the organization of the actin cytoskeleton. *Curr Opin Cell Biol, 9*, 86–92.

Tchakarov, L., Zhang, L., Rose, S., Tang, R., & Trifaro, J. (1998). Light and electron microscopic study of changes in the organization of the cortical actin cytoskeleton during chromaffin cell secretion. *J Histochem Cytochem, 46*, 193–203.

Trifaró, J.-M., Vitale, M. L., & Rodriguez Del Castillo, A. (1992). Cytoskeleton and molecular mechanisms in neurotransmitter release by neurosecretory cells. *Eur J Pharmacol, 225*, 83–104.

This page intentionally left blank

Chapter 34

Stimulus–Response Coupling in Metabolic Sensor Cells

Stan Misler

Chapter Outline

I. INTRODUCTION

The term *sensory receptor* is usually applied to a limited group of cells, located near the surface of the organism, designed to transduce stimuli from the external environment (e.g. photons of light or air or water-borne molecules or pressure disturbances) into the release of a chemical transmitter, which ultimately signals neurons that project into the central nervous system. However, to maintain a "steady state," organisms must also detect changes in their internal environment. To do this, specialized internal receptors must sense changes (1) in the levels of circulating metabolic fuels (e.g. nutrient metabolites and O_2); (2) in the levels of metabolic wastes (e.g. CO_2); (3) in the ionic composition of the extracellular lymph-like fluid which bathes the cells; and (4) in the internal or lumenal tension in hollow tubular organs (e.g. blood vessels and gut).

Currently, among the internal receptors, those sensitive to metabolic changes are better understood than those responding to changes in ionic composition or lumenal tension. In this chapter, we shall examine, in some detail, sensory transduction by five types of *metabolic sensor cells*.

1. *Pancreatic islet cells:* these cells sense changes in the levels of several circulating metabolites, especially glucose and amino acids, and respond with secretion of the hormone insulin and glucagon. Insulin promotes the uptake of glucose and its storage as glycogen in muscle and liver and maintains fat stores in adipocytes, while glucagon mobilizes fat and glycogen stores.
2. *Cardiac and skeletal myocytes and some neurons:* these cells curtail their excitability during hypoxia and substrate deprivation, thereby saving themselves from severe hypometabolic injury.
3. *Chemoreceptor cells of carotid body:* these cells sense changes in the O_2 and CO_2 content of blood and synapse onto sensory nerve fibers which project into the central nervous system (CNS) and help shape respiratory drive.

Cell Physiology Sourcebook. DOI: 10.1016/B978-0-12-387738-3.00034-2

4. *Vascular smooth muscle cells:* these cells sense local changes in O_2 tension and respond by regulating their tone, thereby locally controlling blood flow.
5. *Hypoxia-secreting renal interstitial cells and liver Ito cells:* in response to hypoxia, these cells secrete erythropoetin, the hormone critical for maturation and release from bone marrow of oxygen-carrying erythrocytes.

The first four types of metabolic sensor cells share a common property; each makes use of K^+ channels specially attuned to metabolic changes to transduce stimuli. Some also use the metabolic intermediates to modulate more distal processes in their scheme of *stimulus–response coupling*. The fifth cell makes use of what might be called *stimulus–synthesis coupling*. Familiarity with different patch-clamp recording configurations and basic concepts of excitation–secretion coupling in nerve cells is assumed (see Chapters 20 and 33).

II. STIMULUS–SECRETION COUPLING IN THE PANCREATIC ISLET CELLS

The pancreas consists of islands of endocrine tissue, islets of Langerhans, that regulate metabolite uptake, storage and release by liver, adipocytes and skeletal muscle, surrounded by a sea of exocrine tissue, acini and their ducts, that secrete alkaline digestive juices into the duodenum. Each islet contains about 1000 cells. Roughly 65% are insulin-producing β cells, triggered by an increase in serum glucose. These are the largest of the islet cells and have distinct crystals in their secretory granules. Roughly 20% are glucagon-producing α cells, largely triggered by a decrease in serum glucose. The remaining 15% are δ or PP cells secreting somatostatin or pancreatic polypeptide. After dispersal of the islet into single cells, α cells can be separated from β cells on the basis of their smaller size and decreased NAD^- autofluorescence. Though isolated islet cells secrete in response to appropriate stimuli, they secrete best when they are in clusters containing representatives of each cell type. Beta cells are electrically coupled. Alpha, beta and delta cells all "talk" to each other via paracrine interactions; glucagon enhances stimulus-induced insulin secretion, whereas somatostatin inhibits it. Insulin, glucagon and somatostatin all inhibit glucagon secretion.

The study of how a rise in plasma glucose leads to rapid secretion of insulin by β cells has provided fertile ground for the interaction of a wide range of disciplines in cell physiology. Since the mid-1970s, it has been widely appreciated that the release of insulin, which is stored in secretory granules, is dependent on extracellular Ca^{2+} concentration $[Ca^{2+}]_o$ (the *calcium hypothesis*), requires oxidative metabolism of glucose or other metabolite fuels (the *fuel hypothesis*) and follows the onset of complex electrical activity in the β cells (the *depolarization–secretion coupling hypothesis*). These features were first established using techniques of islet perifusion and radioimmunoassay of secreted insulin (Fig. 34.1A). In these experiments, islets are mounted on a filter and exposed to a continuous flow of solution able to trap secreted insulin. Timed aliquots of solution are collected and the insulin content is measured by radioimmunoassay, i.e. the ability of the secreted insulin to displace radioactively labeled insulin bound to an anti-insulin antibody. Note that insulin secretion induced by raising glucose from preprandial levels of 2–3 mM to levels above 5 mM occurs in two phases, a transient "first phase" and a sustained "second phase." In vivo, the "first phase" may saturate hepatic insulin receptors, as it is often not readily detected in assays of peripheral insulin levels. Note that the "second phase" of release is reversibly reduced by (1) transient reduction of the Ca^{2+} concentration of the perifusing solution or (2) addition of an inhibitor of glucose metabolism, in this case, sodium azide (NaN_3), an inhibitor of the mitochondrial respiration (see Fig. 34.1A). In parallel experiments, it was found that islets bathed in preprandial levels of glucose rapidly released insulin in response to exposure to high $[K^+]$, provided adequate extracellular Ca^{2+} was present.

When the *fuel hypothesis* was extensively tested, insulin release was found to be (1) stimulated by amino acids, glycolytic intermediates and ketone bodies shown to be metabolized by β cells but (2) inhibited by substances that specifically block uptake and metabolism of these substrates or by general inhibitors of mitochondrial function. The *calcium hypothesis* and the *depolarization–secretion coupling hypothesis* were tested with intracellular recording from islet cells in intact and perifused islets. Beta cells were found to maintain resting potentials of about −60 mV at fasting glucose concentrations. The resting potential varies with $[K^+]_o$ according to the Nernst equation, hence suggesting that it is largely due to K^+ permeability (P_K). Within several minutes of exposure to "secretagogue" concentrations of fuel metabolites, these cells depolarize, coincident with a decline in resting membrane conductance and shortly thereafter exhibit bursts of action potentials whose overshoots are a function of $[Ca^{2+}]_o$. In cells loaded with a Ca^{2+} indicator, "spikes" of cytosolic Ca^{2+} coincide with bursts of action potentials (see Fig. 34.1B).

From these observations emerged an early critical unifying hypothesis: *fuel metabolism → reduced P_K → electrical activity → Ca^{2+} entry → insulin release.* It is worth mentioning that this scheme also accommodates the actions of a class of hypoglycemic agents, called sulfonylureas. Though not related to fuel metabolites, and themselves not metabolized, sulfonylureas potentiate the

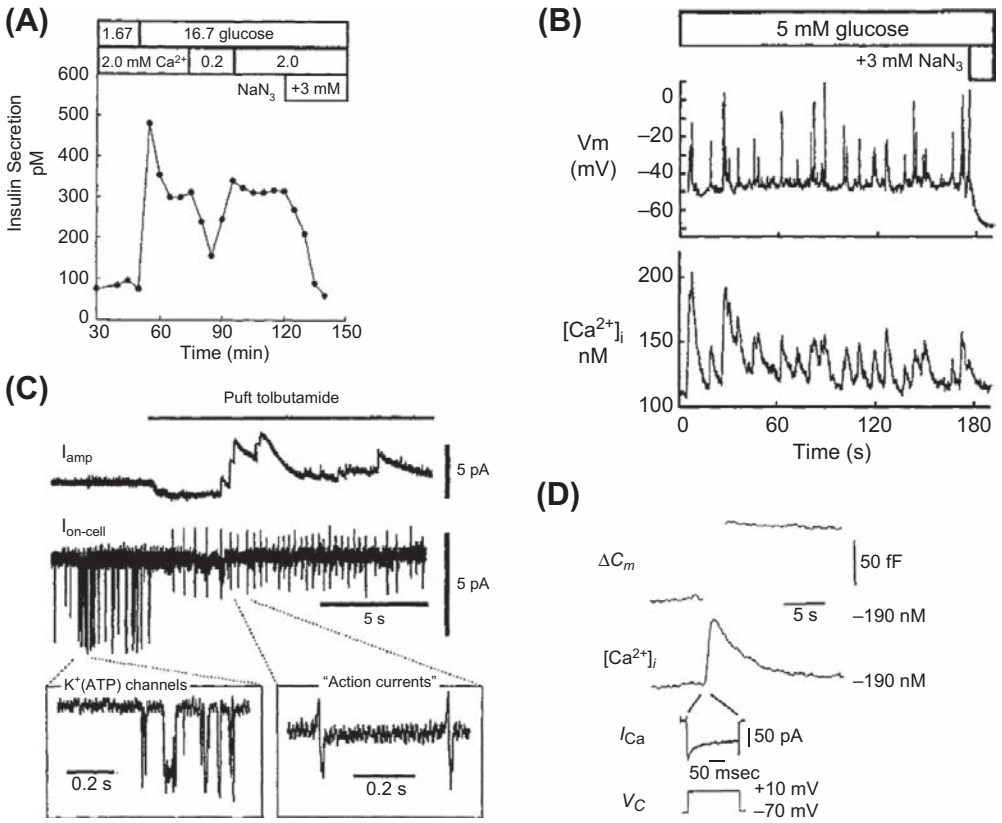

FIGURE 34.1 Overview of basic evidence supporting "fuel hypothesis," "calcium hypothesis" and "depolarization–secretion coupling hypothesis" of glucose-induced insulin release from pancreatic β cells. (A) Insulin secretion, measured by radioimmunoassay, from isolated intact human pancreatic islets of Langerhans. Note the rapid onset of biphasic insulin secretion on increasing glucose from 1.67 to 16.7 mM, the interruption of the plateau phase by reduction in extracellular [Ca^{2+}] from 0.2 to 2.0 mM and the termination of secretion by the addition of sodium azide (NaN_3), an inhibitor of electron transport by mitochondrial cytochromes. Leucine, glyceraldehyde and acetoacetate produce similar patterns of secretion in the presence of Ca^{2+}. (B) Simultaneous recording of electrical activity and cytosolic Ca^{2+} transients from single cryopreserved/thawed human β cells loaded with Ca^{2+} indicator FURA-2. Note that in the presence of 5 mM extracellular glucose, the cell fires individual or short trains of action potentials and that even single action potentials are sufficient to induce a Ca^{2+} transient. Subsequent addition of NaN_3 abruptly hyperpolarizes the cell to ≈ -70 mV and blocks the appearance of Ca^{2+} transients. (Unpublished experiments by D. Barnett and S. Misler.) (C) Single cell exocytosis detected by amperometry and capacitance. Simultaneous cell-attached patch recording and amperometry from small clamp of islet cells preloaded with serotonin. The amperometric electrode was positioned at the confluence of cells. In 2 mM glucose, the $I_{on\text{-}cell}$ trace shows single-channel openings, which will later be identified as those of ATP-sensitive K^+ channels (K^+(ATP)). After addition of tolbutamide, single channels close and "action currents" develop. After several impulses have fired, amperometric events are noted on the I_{amp} trace. Those events, slower than those observed when recording for single isolated cells, probably reflect simultaneous exocytotic discharge at several sites, each distant from the electrode. (D) Simultaneous-monitoring membrane capacitance and cytosolic Ca^{2+} from a voltage-clamped β cell. Note that a 200-ms depolarization from -70 to $+10$ mV increases global cytosolic [Ca^{2+}] by an estimated 100 µm and membrane capacitance by 75 fF. This corresponds to the fusion of 30–60 insulin granules, given that the C_m increase per granule is estimated at 1.25–2.5 fF.

action of glucose even when glucose metabolism is modestly inhibited. They reduce resting P_K, depolarize the cell, set off action potentials and stimulate insulin secretion even at preprandial levels of glucose. As we shall discuss in short order, these substances have been found to block directly the K^+ conductance that is physiologically gated by cell metabolism.

Critical clues to the validity and the molecular details of this hypothesis have been provided by (1) patch-clamp recording plus molecular biology of channels (cloning and site-directed mutagenesis) and (2) single-cell, real-time monitoring of exocytosis (or fusion of the granule membrane with the plasma membrane). In patch-clamped β cells, the workings of ATP-inhibited K^+ channels, whose closure underlies cell depolarization, have been analyzed in great molecular detail, in large part due to the identification of this molecule as the β cell's major sulfonylurea receptor. In patch-clamped β cells, depolarization-induced exocytosis can be measured electrically as an increase in membrane capacitance *(C_m),* while agonist- (e.g. sulfonylurea-) induced release can be monitored electrochemically as release of packets of native insulin or the false transmitter serotonin previously loaded into insulin granules (see Fig. 34.1C). Using either measure, exocytosis

is found to be graded with the amount of Ca^{2+} entry induced by depolarization.

(Here it is worth recalling that exocytosis involves simultaneous fusion of the membrane of the secretory granule with the plasma membrane as well as the release of the granule content into the extracellular space. The membrane fusion event, an increase in plasma membrane surface area, is usually detectable as an increase in plasma membrane capacitance. Membrane capacitance is estimated from the ability of the membrane circuit to "phase shift," or displace in time, a sine wave of voltage excitation. The release of a packet of transmitter [or hormone] can be detected "biologically," by a receptive patch of membrane, or "electrochemically," at the surface of an electrode held at a potential sufficient to oxidize or reduce a component of the granule content. In either case, a brief spike of current is produced. When dealing with cells with large secretory granules, one can be more adequately convinced that exocytosis has occurred when it is possible to demonstrate the following points: (1) the jumps in C_m thought to represent single granule fusion events have amplitudes predictable from the surface area of the granule; (2) the single electrochemical spike [or "amperometric event"] coincides in time with jumps in C_m and represents the release of at least many tens to hundreds of thousands of molecules that are either native to the granule or else preloaded as a marker. In the case of β cells, the preloaded marker is serotonin. It is worth remembering that capacitance and amperometry are complementary techniques; capacitance monitors net increase in total membrane surface area [exocytosis minus endocytosis], whereas amperometry often permits direct counting of quantal release, albeit from a fraction of the cell surface.)

On the basis of these and other experiments, over the past decade a more detailed "consensus hypothesis" has emerged for glucose-induced insulin secretion from β cells (Fig. 34.2, right-hand side). Uptake of glucose (predominantly via a Glut-2 type transporter) provides glucose entry into glycolysis (via glucokinase, a low affinity hexokinase) and the mitochondrial Krebs cycle results in the generation of ATP and consumption of ADP (Step 1). This leads to the closure of ATP-inhibited K^+ channels, here abbreviated as *K^+(ATP)* (Step 2). Against a background of tonic activity of non-selective cation channels that pass Na^+ inward, K^+(ATP) channel closure results in the depolarization of the β-cell membrane (Step 3). When V_m reaches the threshold for activating voltage-dependent Ca^{2+} and Na^+ channels, electrical activity and voltage-dependent Ca^{2+}

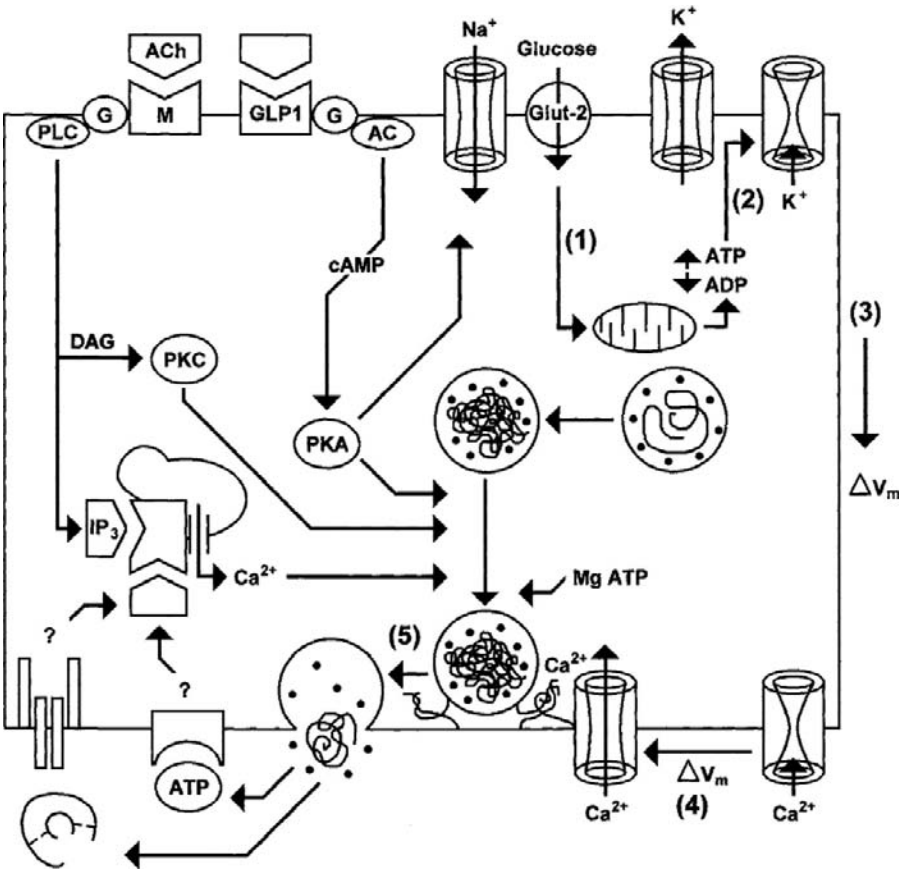

FIGURE 34.2 Overview of stimulus–secretion coupling in the pancreatic β cell. The right-hand side shows (1–5) a "consensus scheme" of stimulus–secretion coupling: glucose transport and phosphorylation (1), → to intermediate metabolism, ATP production/ADP consumption and K^+(ATP) channel closure (2), → membrane depolarization (3), → opening of voltage-dependent Ca^{2+} channels (4) and, finally, Ca^{2+} binding to granule docking complex and granule fusion (5). Non-selective cation channels that form the counterweight to K^+(ATP) channels at rest are shown to the left of the Glut-2 transporter. Further to the left are the G-protein-linked receptor cascades for muscarinic, cholinergic agonists and the incretin GLP-1. The latter two "priming" compounds produce second messengers capable of releasing Ca^{2+} from intracellular stores and/or activating protein kinases to modulate channel activity and granule mobilization. Lastly, the contents of the secretory granule, namely insulin and ATP, may "feed back" on the β cell via cell surface receptors and complex signaling cascades.

entry begins (Step 4). The resultant rise in cytosolic Ca^{2+} triggers Ca^{2+}-dependent fusion of insulin granules with the plasma membrane (Step 5). Steps 4 and 5 are reminiscent of the process of depolarization–secretion coupling, well studied at nerve terminals and other electrically excitable endocrine cells (adrenal chromaffin cells, pituitary lactotropes and melanotropes and terminals of the supraoptic nucleus cells), with subtle differences that shall be discussed later.

However, this scheme does not answer some rather old questions. (1) How do enhancers of cAMP serve to restore stimulus–secretion coupling in metabolically and electrically active but non-secreting β cells? (2) How, aside from possibly depolarizing the β cell, do anticipatory or modulatory factors such as gut hormones and acetylcholine work? The anticipatory–modulatory pathways of receptor-mediated stimulus–secretion coupling, as well as possible autocrine effects of insulin and ATP released by exocytosis, are outlined on the left of Fig. 34.2 and also will be discussed later. In fact, it may be possible that, under very extreme conditions, modulatory pathways may result in some secretion independent of an inciting Ca^{2+} current or a detectable rise in global cytosolic Ca^{2+}. This might occur through the combination of a very localized rise in cytosolic Ca^{2+} with a vastly increased readiness of the secretory apparatus. However, it should never be forgotten that the "sui generis" of the β cell remains metabolic regulation of cell electrical activity via K^+(ATP) channels.

IIA. Role of ATP-Sensitive K^+ Channels in Coupling Metabolism to β-Cell Depolarization

How do fuel metabolites produce β-cell depolarization? Early patch-clamp experiments, using the cell-attached mode of recording, revealed the presence of a very interesting K^+ channel that was open at fasting levels of extracellular glucose (2–3 mM), but rapidly closed on raising ambient glucose concentrations to those encountered after a meal (5–7 mM). Usually, channel closure is followed closely by the onset of electrical activity. This channel is open at the cell's resting potential and its activity is not dependent on membrane voltage. However, the channel is inward rectifying (i.e. single channels pass inward flow of potassium better than outward). These channels have many features predictable from the fuel metabolism hypothesis: addition to the bath of any metabolized fuel closes the channel, yet the channel is reopened subsequently by the addition to the bath of inhibitors of metabolite transport or oxidation. The time course and relative change in channel activity seen in a cell-attached patch during a variety of metabolic maneuvers closely parallels the changes in whole-cell resting conductance (G_m), monitored as the change in membrane potential in response to a given test pulse of current applied (Fig. 34.3A, B). The latter strongly suggested that the activity of this channel, which tends to move V_m to a level near the potassium equilibrium potential, E_K, critically controls the cell's resting potential. Since this channel population is the predominant type open at rest, its closure

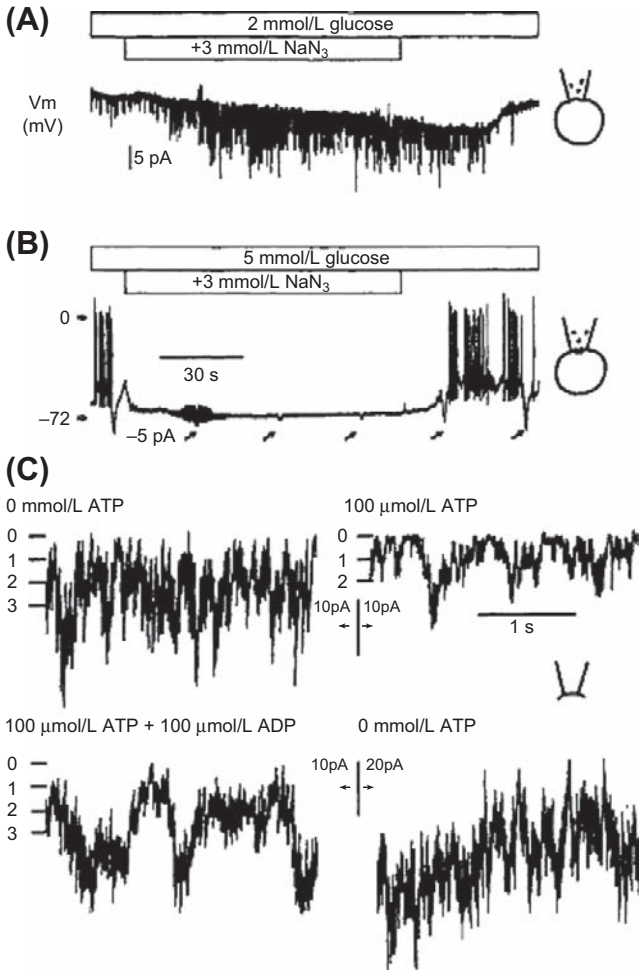

FIGURE 34.3 ATP-sensitive K^+ channels and electrical activity in canine pancreatic islet β cells. (A) A cell-attached patch was formed with the pore-forming antibiotic nystatin in the pipette. Shortly thereafter, ion-channel activity was recorded before, during and after application of sodium azide (NaN_3, 3 mM) to the low-glucose bath. (B) Electrical activity recorded 20 minutes later. By that time, the patch of membrane encompassed by the pipette had been permeabilized by insertion of nystatin channels, thereby permitting recording of membrane current or voltage from the whole cells. Reapplication of NaN_3 results in membrane hyperpolarization, abolition of electrical activity and increased membrane conductance (signified by the reductions in transient hyperpolarizations accompanying −5 pA currents applied at arrows). V_m denotes cell membrane potential. (C) Nucleotide gating of K^+(ATP) channel activity in the excised patch. Addition of 100 micromolar ATP (100 µM) reduces channel activity by threefold (C, upper right panel); further addition of ADP restores channel activity (C, lower left panel), whereas washout of ATP and ADP results in overshoot of channel activity (C, lower right panel) *(D.M. Pressel and S. Misler, unpublished data).*

en masse would be needed to make the K^+ conductance of the cell comparable to that of other conductance pathways operative at rest. The latter are non-selective cation conductance channels and anion conductance channels with estimated equilibrium potentials of 0 or ≈ -30 mV respectively. This would permit V_m to depolarize to the threshold for activating cell electrical activity (≈ -45 mV). Another hint of the importance of this type of channel was that it is closed by oral hypoglycemic agents.

How is this channel gated? In the cell-attached patch-recording configuration, in which the exterior of the channel was isolated from bath glucose by a very tight pipette-to-membrane seal, it is safe to assume that the channel is gated by one or more metabolic intermediates. A priori, cell metabolism might affect a host of metabolic intermediates, ranging from high-energy phosphate compounds (e.g. ATP and ADP), to redox equivalents, to cytosolic H^+ or Ca^{2+}. Early experiments (see Fig. 34.3C) showed that after excision of the patch, in an inside-out excised patch configuration, the metabolite-regulated K^+ channel was avidly gated by ATP at its inner surface, hence the name K^+(ATP) channel. Free concentrations of ATP, or its non-hydrolyzable analogs (e.g. AMP-PNP) as low as 10 μM reduce channel activity by half even in the absence of Mg. This suggests that ATP closes this channel by directly "gating" it rather than "phosphorylating" it. In parallel with this, in whole-cell patch experiments where ATP dialyzes out of the cell (due to the absence of ATP in the pipette), resting G_m increases and the cell hyperpolarizes. Interestingly, ATP inhibition of channel activity in the excised (inside-out) patch can be partially reversed by addition of MgADP to the bath. Hence, changes in the relative concentrations of ATP and ADP, which usually change in a reciprocal fashion as metabolism is altered, should be an important factor in physiological channel gating. In most cells, ATP concentrations change little with metabolism, but percentage-wise, ADP levels change more dramatically. Hence the channel may have been misnamed. To be sure, the activity of the K^+(ATP) channel is also altered by other potential intermediates whose cytosolic concentrations change with metabolic stimulation (e.g. NADH/NAD ratio, H^+ and Ca^{2+}), but these effects are much smaller and require changes beyond the physiological range.

A puzzling question regarding the function of this channel is how its low K_d value (μM) for ATP-induced channel closure in the excised membrane patch can be reconciled with the millimolar-range concentration of ATP in the cytosol. Several factors mitigate this discrepancy:

1. *Complex effects of ADP on channel activity.* ADP competition for an ATP binding site, combined with allosteric action of ADP at an independent binding site, adjusts the half-maximal effective concentration (K_d) of ATP, measured in the presence of ADP, closer to the mM range.
2. *Compartmentation of the ATP and steep ATP gradients from source to sink*. It is likely that the overwhelming majority of ATP is of mitochondrial origin: mitochondrial inhibition totally prevents glucose-induced channel closure, while ketone bodies, amino acids and their deamination products (e.g. leucine and ketoisovalerate), which directly enter mitochondria, stimulate channel closure even in the face of inhibition of glycolysis. In addition, given the random localization of these channels over the surface of cultured cells, it is likely that the channels are interspersed among ATPases. Hence, steep cytoplasmic gradients of ATP and ADP, due to en passant consumption of ATP and concomitant local production of ADP by neighboring plasma membrane ATPases, should make the ATP/ADP available to the channel different from the average cytosolic concentrations actually measured.
3. *Modulation of gating by other metabolic intermediates* such as long chain fatty acids.
4. *Artifactual enhancement of channel sensitivity to ATP in the excised patch by progressive washout of intrinsic channel inhibitors* such as anionic lipids (phosphoinositol phosphates), from the exposed membrane. Polyanionic molecules might specifically compete with ATP for binding to the channel or else contribute to a negative surface charge at the inner surface of the plasma membrane, thereby electrostatically repelling soluble anions.

Two features of the metabolite-regulated K^+(ATP) channel proved critical to its cloning and structure–function analysis. (1) The channel functions as an inward rectifier K^+ channel and hence could be cloned as a member of that family. (2) The channel is the major locus of action of hypoglycemic (glucose-lowering) sulfonylureas and could be cloned as a sulfonylurea receptor (SUR). The sulfonylureas (e.g. *tolbutamide* and *glyburide* [glibenclamide]) enhance glucose-induced insulin release by β cells and are useful in the treatment of non-insulin-dependent diabetes mellitus, in which β cells produce significant quantities of insulin, but release it out of synchrony with the appearance of the glucose load. At concentrations equal to free plasma levels that enhance glucose-induced electrical activity and insulin secretion in intact animals, the *sulfonylureas* close K^+(ATP) channels in cell-attached or excised patches alike, while leaving voltage and calcium gated K^+ channels unaffected. Curiously, though K^+(ATP) channels in myocytes show similar conductance, kinetics and ATP sensitivity, they have greatly reduced sulfonylurea sensitivity.

To reconstitute channel activity in a naive cell (e.g. *Xenopus* oocyte or clonal cell), it was necessary to transfect or inject the cell with cDNA or mRNA coding for

(1) a standard inward rectifier type subunit (Kir6.2), comprised of two membrane-spanning domains separated by an H loop dipping into the bilayer, and (2) the SUR from β cells (SUR1) (Fig. 34.4A, B). SUR 1 is a complex protein with multiple transmembrane domains (hydropathy plot analysis suggests 17!). Structurally, it contains two motifs resembling those of the ATP-binding cassettes of members of the ABC transporter superfamily, the most famous of which are the cystic fibrosis gene product, CFTR, and the multidrug resistance p-glycoprotein. SUR1 has two distinct cytoplasmic loops (or facettes) that bind nucleotide di- and triphosphates in the presence of Mg (NBFs). The channel itself is likely to be an octamer consisting of an inner ring of four Kir6.2 subunits (the confluence of the four H loops forming the ion selective pore) and an outer ring of four SUR1 subunits. The two types of subunits are needed to chaperone each other into the membrane as well as to provide full channel gating; without SUR1, Kir6.2 is not expressed. Clinically, mutations in SUR1 have been identified in persistent hyperinsulinemic, hypoglycemia of infancy, a disease where K^+(ATP) channel activity is not detected even after metabolic inhibition and β cells are persistently depolarized and secreting. Point mutations to NBF result in channels that are closed by ATP in excised patches, but are not reopened by MgADP, while more extensive mutations result in the absence of channel activity under any test circumstance. In contrast, a C-terminal truncated mutant of Kir6.2 (Kir6.2ΔC26) forms K^+ channels gated by ATP in the absence of Mg. These channels have lower affinity for ATP ($K_d \approx 10\,\mu M$ in the absence of Mg) than the native or Kir6.2/SUR1 cloned channel ($K_d \approx 100\,\mu M$) but show similar need for ATP cooperativity in channel gating ($n = 4$). However, these channels lack both inhibition of activity by sulfonylureas and enhancement of activity by MgADP. Hence, while Kir6.2 might be considered the ATP gating subunit, SUR1 with its NBFs is the ATP-hypersensitizing subunit as well as the subunit endowing the channel with special sensitivity to drugs and MgADP. A schematic model of K^+(ATP) channel gating is presented in Fig. 34.4C. SUR might have a natural ligand, a cytoplasmic protein called endosulfine, recently demonstrated to displace sulfonylureas from SUR binding sites.

Analysis of mutant channels has also elucidated the origin of a number of previously puzzling effects. One example is the "refreshment effect" of MgATP. That is, rapid wash-in and wash-out of MgATP, even in concentrations of 10–100 μM, can restore channel activity that otherwise would run down in time in its absence (see Fig. 34.3C). This effect can now be partially explained by the finding that small concentrations of MgATP as well as MgADP activate the channel by binding to a "Walker motif"

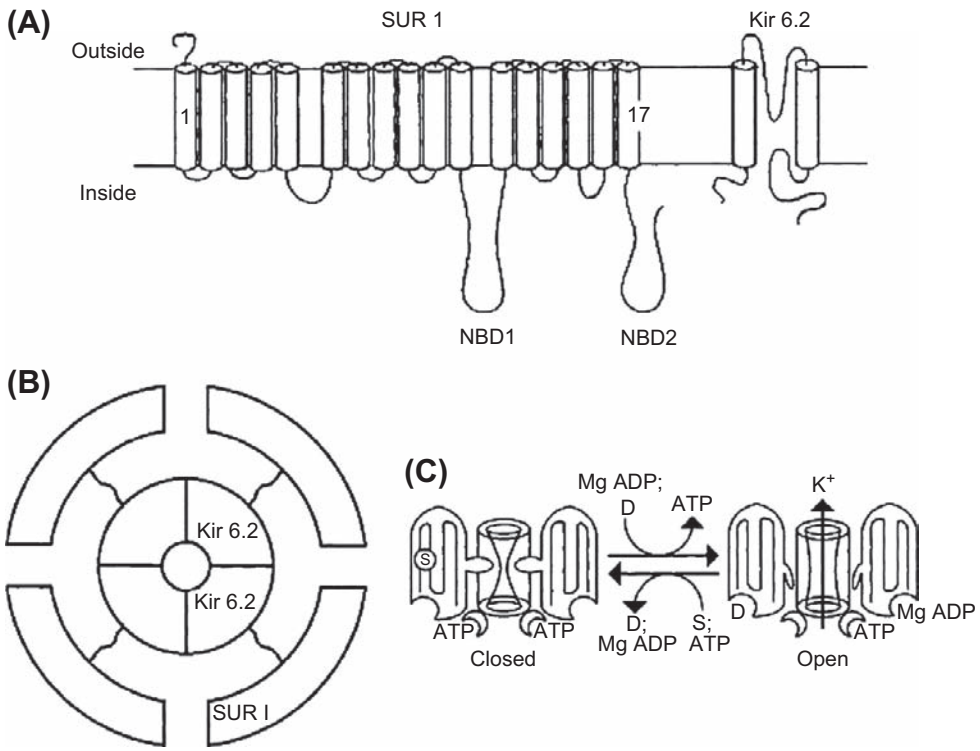

FIGURE 34.4 Illustrations depicting K^+(ATP) channel structure and function. (A) Transmembrane orientations of SUR1 and Kir6.2 subunits based on structural homology, hydropathy and site-directed mutagenesis. (B) Proposed octamer array of SUR1 and Kir6.2 subunits. (C) Simplified reaction scheme in channel gating.

of the NBF in native forms of SUR1 but not in those SURs whose NBFs have been mutated. Likewise, channel modulation by Mg-guanidine nucleotides also occurs at these sites, suggesting that there is no need to invoke G proteins in GTP or GDP modulation of channel gating (though G-protein-coupled receptors may independently modulate channel activity). Both effects require hydrolyzable nucleotides and Mg, suggesting that some phosphorylation reaction may be involved. A second example is the ability of certain vasodilator drugs, such as diazoxide, to open K^+(ATP) channels, hyperpolarize the β cell and inhibit glucose-induced insulin secretion. These drugs also bind to the "Walker motif". A third example is the differential sulfonylurea sensitivity of K^+(ATP) channels in β cells as compared with those in cardiac myocytes. While both channels have similar Kir6.2 subunits, their SURs differ. Replacing transmembrane domains 13−16 of cardiac SUR (SUR2) with the corresponding region of SUR by engineering of a chimeric SUR restores sulfonylurea sensitivity.

Is this finely tuned coupling of cell metabolism to K^+(ATP) channel activity used as a sensory mechanism by the two other major glucose receptor cells of the body, namely the *satiety center* of the hypothalamus and the peripheral sweet *taste receptors*? Recently, K^+(ATP) channels have been sought in glucose-receptive (GR) neurons of the ventromedial nucleus (VMN) whose activity is associated with suppression of food intake. In these neurons, reduction of bath glucose or addition of the glycolytic inhibitor mannoheptulose results in hyperpolarization and cessation of electrical activity accompanied by an increase in resting G_m; oppositely, tolbutamide produces excitation. In cell-attached patch recordings, cessation of electrical activity is associated with increased activity of a K^+-selective channel, which is voltage-insensitive. After excision of the membrane patch, the latter channel is inhibited by cytoplasmic ATP. However, this K^+ channel is quite distinct from the K^+(ATP) channel in β cells: under identical excised patch recording conditions, the K_i for ATP inhibition is 2.3 mM (rather than 20 μM in β cells) and the singlechannel conductance is 135 pS (rather than 55−65 pS in β cells). One very interesting feature of this channel is that it is opened and the cell is hyperpolarized by leptin, a protein released by adipocytes, or fat-storing cells, in proportion to their triglyceride storage. Leptin also opens K^+(ATP) channels in β cells and appears to do this in a manner dependent on activation of PI-3 kinase. Does leptin serve as a negative feedback hormone, that is signaling adequate energy stores by downregulating both appetite-induced caloric intake and insulin-dependent depot storage? One indication of this comes from obese, hyperphagic, hyperinsulinemic and hyperglycemic db/db rats, where leptin has little influence on the firing rate of VMN neurons.

In peripheral taste receptors, glucose chemoreception may occur through G proteins and a second messenger cascade. In these cells, application of sucrose or saccharin reduces the amplitude of a voltage-dependent outward K^+ current. This effect can be mimicked by application of membrane-permeable analogs of cAMP. In excised patches, K^+ channels with similar features are closed by exposure of the patch to ATP and cAMP-dependent protein kinase, but not by exposure to ATP alone, suggesting that this K^+ channel is "gated" by phosphorylation.

IIB. Metabolic Regulation of Depolarization−Secretion Coupling?

Recall that closure of K^+(ATP) channels only depolarizes the cell. Calcium must enter the cells and insulin granules must be ready to be released. Does metabolism alter the "calcium trigger" or maintain the "readily releasable pool" of insulin granules?

IIB1. The "Ca Trigger"

When β cells, exposed to sufficient glucose, a cAMP enhancer and near physiological temperature, are depolarized for many tens to hundreds of milliseconds, they exocytose in a Ca^{2+}-entry-dependent manner. Under these conditions, several studies have shown an approximately 3rd power dependence of exocytosis, as measured by amperometry or capacitance, on the total Ca^{2+} entering the cell (i.e. the integral of the Ca^{2+} current). Though most of the Ca^{2+} current is carried by L-type Ca^{2+} channels, in a subset of human β cells, where they are present in sufficient density, lower threshold T-type Ca^{2+} channels also support exocytosis. We might expect changes in cell metabolism to affect the gating of Ca^{2+} channels via phosphorylation or lipidation. To date, data supporting the hypothesis that enhanced glucose enhances Ca^{2+} channel activation or slows inactivation have been inconsistent. Another paradigm, however, which illustrates other aspects of depolarization−secretion coupling may provide some other clues.

Beta cells in intact islets secrete pulses of insulin that are time-linked to "bursts" of electrical activity. Longer "bursts" evoke larger pulses of insulin. Contrary to the situation at most nerve terminals and despite quite sizeable Ca^{2+} currents, it is very rare to see an isolated action potential, or a brief depolarization (10−50 ms in duration), provoke quantal release (here measured by amperometry). However, when the depolarization is extended out to many tens to several hundreds of milliseconds, release routinely commences in the course of the depolarization and often continues for several seconds after Ca^{2+} entry ceases, while cytosolic Ca^{2+} is falling (Fig. 34.5). These data suggest that Ca^{2+} might have to "jump through a few hoops" before triggering secretion and that it might set up a "chain reaction" that outlasts the peak Ca^{2+} concentration (Fig. 34.6).

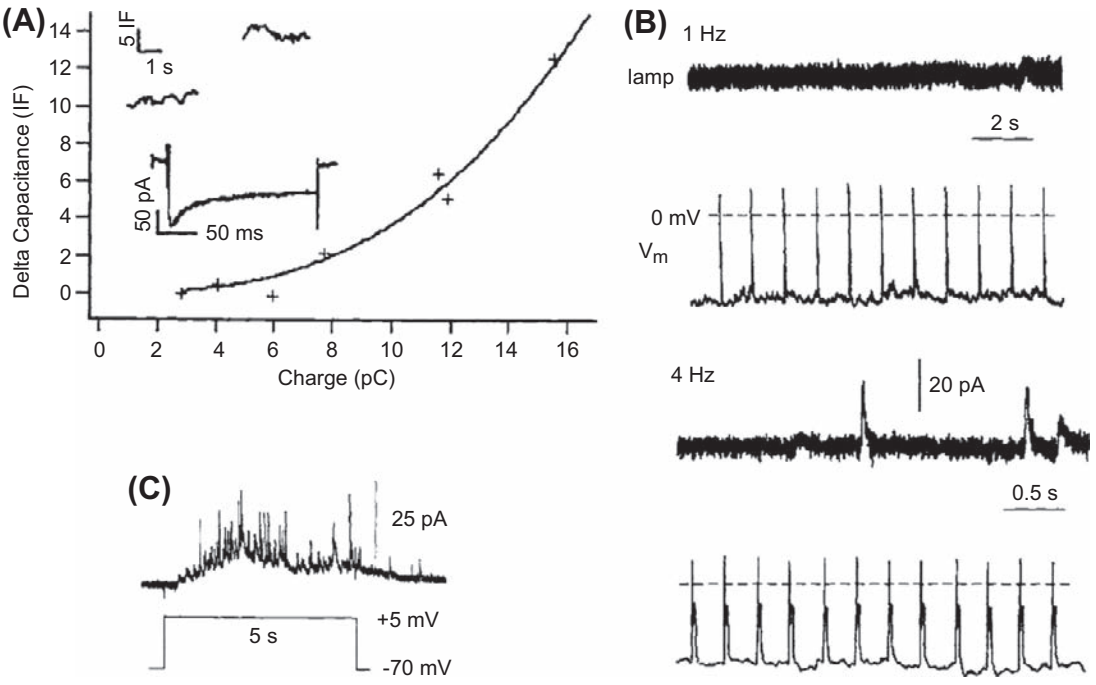

FIGURE 34.5 Aspects of Ca^{2+} dependence of exocytosis in β cells (A) Relationship of capacitance increase to total Ca^{2+} entry (integral of Ca^{2+} current Q_{Ca}) during β-cell depolarization. Ca^{2+} entry was altered by changing the membrane potential to which the cell was voltage-clamped for the 200-ms test stimulus *(unpublished data by D. Barnett and S. Misler)*. (B) Time course of amperometric events during trains of action potentials stimulated at 1 Hz (upper panel) and 4 Hz (lower panel) Note that none of the 11 action potentials occurring at 1 Hz stimulation results in quantal release, while at 4 Hz stimulation quantal release begins after several action potentials. (C) Time course of amperometric events recorded during continuous depolarization to +10 mV, where Ca^{2+} entry is maximal. Note that the first release event is seen ≈120 ms after start of voltage-clamp pulse, while release events continue, albeit at a low frequency, for nearly 3 s after depolarization is completed *(unpublished data by Z. Zhou and S. Misler)*.

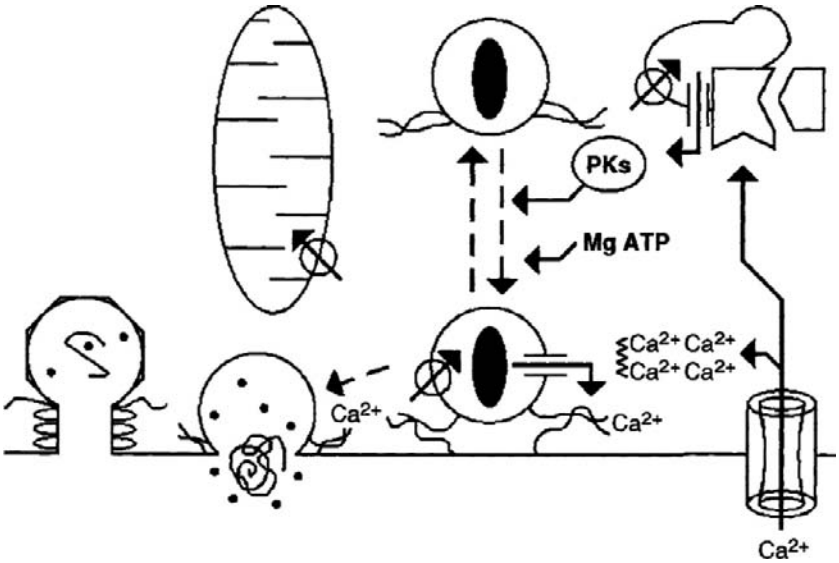

FIGURE 34.6 Calcium metabolism in β cells: potential sites for modulation of depolarization–secretion coupling. After calcium enters the cytoplasm, it is likely that much of it rapidly binds to either fixed or mobile buffers, the latter perhaps resembling the tetra-clawed EGTA. Some of the bound Ca^{2+} unbinds to diffuse further. Diffusing Ca^{2+} may then bind to one of the following: (1) a Ca^{2+}-binding protein (e.g. synaptotagmin) that is part of the docking complex that anchors a granule to the membrane and thereby directly triggers exocytosis, (2) a protein kinase, whose activity enhances the movement of granules along "motorized" tracks, (3) a binding site on Ca^{2+}-gated channels in Ca^{2+} storage organelles, including the secretory granule itself, which thereby triggers Ca^{2+}-induced Ca^{2+} release. Calcium uptake into organelles (granules, mitochondria and ER) is probably slower (on the time scale of hundreds of milliseconds to seconds). After fusion with the plasma membrane, granule membrane may be retrieved piecemeal by a local "pinch off" mechanism, by using dynamin, or as part of a large endocytic "slurp".

Several possibilities for this "slow-to-start, slow-to-stop" pattern of secretion are currently under investigation. First, with large-sized granules that are not clustered in any regular array, Ca^{2+} channels and granule release sites may not be all that closely co-localized. To be sure, the interspersed cytosol has many Ca^{2+}-buffering molecules. Hence, if the site where Ca^{2+} triggers exocytosis were, on average, a distance of 1–2 granule radii

(say 200−300 nm) from the inner mouth of the Ca^{2+} channel site, local cytoplasmic buffers would need to be saturated before Ca^{2+} could appear at the release site. This would cause a slight delay in the onset of exocytosis. At this distance, during continuous Ca^{2+} entry there might be good spatial equilibration of Ca^{2+} so that the Ca^{2+} concentration at the release site might closely follow the average Ca^{2+} concentration of the cell. This is in no way counterintuitive because it is well appreciated that Ca^{2+} and cytosolic Ca^{2+} concentrations as low as 1.5 μM evoke respectable rates of release (Fig. 34.7B). Conversely, once Ca^{2+} no longer enters the cell, the buffer might serve as a continuing source for Ca^{2+} and support a "secretagogue" level of free cytosolic Ca^{2+} for some time. This feature has been examined and modeled extensively in adrenal chromaffin cells but has only been explored in a cursory manner in β cells.

Second, Ca^{2+} entry might be causing regenerative release of Ca^{2+} from some intracellular stores, thus providing a sort of propagating Ca^{2+} wave, while the increase in cytosolic Ca^{2+} might be stimulating Ca^{2+} uptake by other stores for later use. To date, while it is well appreciated that Ca^{2+} can be released from ER stores by the generation of IP_3, blockade of Ca^{2+} release from ER stores has yielded only small changes in depolarization-induced rises in cytosolic Ca^{2+} or exocytosis. However, the picture may be more complex in other situations. For example, when GLP-1 is applied to voltage-clamped β cells in the presence of 20 mM Ca^{2+}, "spontaneous" spikes of cytosolic Ca^{2+} occur between depolarizations. To be sure, there are multiple stores of intracellular Ca^{2+}, aside from the IP_3-releasable ones in ER. For example, mitochondria- and hormone-containing granules might be expected to release as well as "mop-up" Ca^{2+}, but little is known about their release and uptake rates during various patterns of electrical stimulation or exposure to hormones and transmitters. Some recent evidence suggests that depletion of the Ca^{2+} content of the acidic compartment of cytoplasmic organelles, which includes secretory granules, reduces depolarization-induced Ca^{2+} release. In a metabolically stimulated cell where the Krebs cycle intermediates, NAD-derived redox equivalents and local ATP concentrations may be changing, it would not be surprising that changes in cell Ca^{2+} metabolism in response to Ca^{2+} influx might be a very dynamic feature.

Third, entering Ca^{2+} might rapidly recruit granules into a small, "readily releasable pool" waiting to be triggered.

IIB2. The "readily releasable pool" (RRP)

In cells designed for rapid secretion, it is convenient to assume that vesicles are lined up against the plasma membrane and ready to fuse as soon as the appropriate level of second messenger is achieved in the cytoplasm. Morphologically, in β cells, this does not appear to be the case (see Fig. 34.6). When viewed under the electron microscope, very few of the ≈10 000 granules in the β cell are within one granule diameter of the membrane. Physiologically, experiments with single cells reveal that secretion is actually quite "wimpy" unless "revved up" by other maneuvers; with repeated depolarizations, exocytosis "poops out" and may take many tens of seconds to recover. This suggests that the RRP of available granules is actually

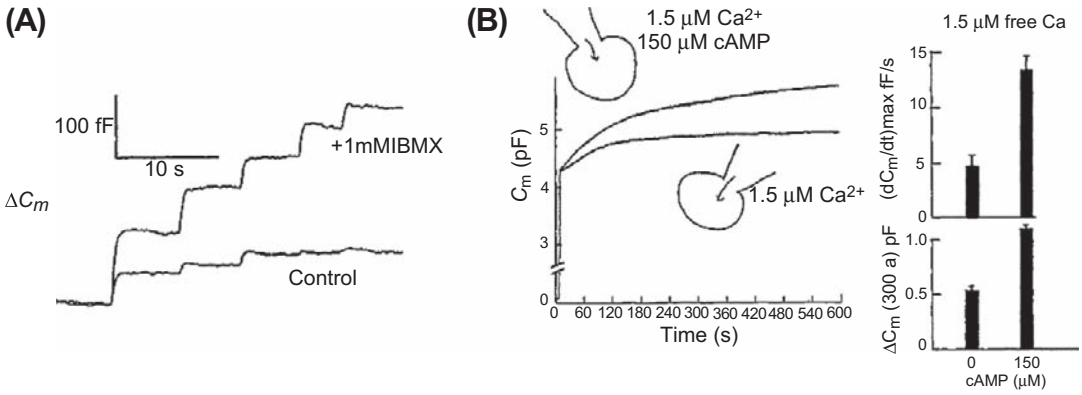

FIGURE 34.7 Enhancement of cytosolic cAMP appears to increase the pool of readily releasable granules. Test by repetitive stimulation. (A) Note that in the "control," repetitive depolarization produces rapid rundown of capacitance response so that by the fourth depolarization there is no evidence of further net exocytosis. In contrast, after addition of membrane permeable cAMP or a phosphodiesterase inhibitor, isobutylmethylxanthine (IBMX), not only is the response to initial depolarization enhanced, but response to 4th depolarization is nearly as large as the response to the 1st depolarization in the "control". In this cell, total Ca^{2+} entry over the entire series of depolarizations differed by less than 15% across the two runs. Perforated patch recording from rat β cell. Test by cell dialysis. (B) Cells with similar baseline capacitance (4−6 pF at break-in to the cell at time 0) were dialyzed against pipette solutions containing 1.5 μM Ca^{2+} versus 1.5 μM Ca^{2+} + 150 μM cAMP. Note that, in the presence of cAMP, not only was the maximum rate of rise of capacitance, abbreviated (dC_m/dt) max, on average nearly 2.5-fold greater, but the total capacitance increase over the entire 6 min of recording was on average nearly twofold greater.

quite small and that maintaining it under high output demand is a non-trivial matter. However, in β cells, two ideal sources of "physiological revving" of secretion are (1) activation of protein kinases (A and C) and (2) the provision of ATP by enhanced substrate metabolism. *Protein kinases* are well known to facilitate the attachment of a variety of granules to tracks (microtubules, actin filaments) that bring them in close proximity to the membrane. In β cells, during feeding, insulin secretion is "primed" even before serum glucose rises, by release of two substance that activate protein kinases, acetylcholine from vagal fibers and incretins (e.g. glucagon-like peptide [GLP-1]) from enterochromaffin cells. Activation of muscarinic ACh receptors results in activation of phospholipase C and production of IP_3 and diacylglycerol. Activation of incretin receptors results in activation of protein kinase A pathway and enhanced cytosolic cAMP levels. These ACh and GLP-1 pathways might enhance distal processes in excitation–secretion coupling, along with increasing the rate of β-cell depolarization in response to glucose, by affecting ATP-sensitive K^+ channels and/or the non-selective cation channels. Hence both background electrical activity and insulin release- and metabolite-induced electrical activity and insulin release could be enhanced. Changes in *cytosolic MgATP* would be expected to alter the fueling of vesicle transport processes as well as the molecular motors (e.g. NSF) that untwine paired attachment proteins (SNAREs) on granules and the target membrane. The latter permits SNAREs subsequently to intertwine with their cohorts on the complementary membrane, thereby accomplishing vesicle docking. In β cells, glucose is known to enhance insulin secretion evoked by elevated $[K^+]_o$ even when K^+(ATP) channels are already closed, while metabolic inhibition can block insulin secretion, even as cytosolic $[Ca^{2+}]$ rises into the micromolar range.

Experiments monitoring exocytosis from single β cells support the motion that the RRP is small, easily depletable and requires constant replenishment by processes that are cAMP, MgATP and temperature dependent. Three approaches have been used. In the first approach, the cell is rapidly depolarized, in the presence versus absence of a modulator, until there is no further increase in capacitance. An estimate of the total number of granules exocytosed provides a measure of RRP, while the time to recovery of full response provides a measure of the refilling rate. Then, a rough estimate of size and dynamics of vesicle pools, in the presence versus absence of a modulatory factor, is obtained by examining the time course of release after introduction of a given concentration of Ca^{2+} into cell. A final approach is to measure the capacitance increase, in the presence versus absence of the modulator, in response to instantaneous "uncaging," by flash photolysis, of Ca^{2+} bound to a chelator introduced into the cytosol, or "uncaging" a fraction of the modulator, now bound to a chelator, in the presence of a fixed level of cytosolic Ca^{2+}. Sample experiments demonstrating that stimulators of cytosolic cAMP enhance initial Ca^{2+}-entry-dependent, depolarization-evoked release, as well as maintain release with repeated depolarization, all with little attendant change in Ca^{2+} entry are shown in Fig. 34.7A. Sample experiments demonstrating that cAMP enhances both the initial maximum rate of exocytosis and the total exocytosis in cells dialyzed against a pipette with fixed concentrations of Ca^{2+} are shown in Fig. 34.7B. More recently, similar experiments using all three approaches have been performed at varying cytosolic levels of MgATP. ATP appears to modulate RRP as well.

Lastly, to be sure, anticipation of future high rates of release requires activity-stimulated, energy-dependent insulin synthesis followed by processing in specialized membrane compartments. With prolonged continuous stimulation, β cells undergo several phases of insulin release; after an initial spurt of release lasting several minutes, insulin secretion wanes and then, beginning 10–15 min later, rises to a plateau that is sustained for hours. Also, islets rechallenged with glucose several hours after an initial brief bout of secretion display greater "peak" insulin release on the second round of stimulation and do this with newly synthesized insulin. Thus islets display a crude but effective form of "memory" for previous stimulation. As activity-stimulated protein synthesis can be triggered by changes in cell Ca^{2+}, cAMP and ATP levels, their relative contributions to synthesis of competent new insulin granules is receiving intense scrutiny.

IIC. The Paradox of Stimulus–Secretion Coupling in the Glucagon-Secreting α Cell

Alpha cells secrete glucagon at preprandial levels of glucose (2–3 mM); secretion is further enhanced by amino acids such as arginine and depressed by higher levels of glucose. Curiously, under some conditions, the glucagon secretion is stimulated by tolbutamide and inhibited by diazoxide, both at concentrations that alter insulin secretion from β cells. So, do α cells have K^+(ATP) channels and, if so, do these channels contribute to α-cell function?

In the presence of 0–3 mM glucose, α cells generate spontaneous Na_o^+- and Ca_o^{2+}-dependent action potentials from their resting potential of ≈ -60 mV. They hyperpolarize on their exposure to increased glucose (5–20 mM); they depolarize and show enhanced spike frequency on exposure to 10 mM arginine. Under voltage-clamp control, depolarization of the α cell results in Ca^{2+}-entry-dependent increases in cytosolic Ca^{2+} and increases in membrane capacitance, the latter enhanced by agents that increase cytosolic cAMP (e.g. β2 adrenergic agonists).

Single-channel and whole-cell patch-clamp recording from α cells reveals inward rectifier K^+ currents that have

similar single-channel conductance and kinetics to those in β cells as well as similar K_d for inhibition by ATP and activation by MgADP and PIP_2. In situ hybridization identifies Kir6.2 and SUR1 subunits of characteristic of β-cell K^+(ATP) channels on glucagon-bearing cells; in fact, the densities of these subunits are even higher than those in β cells.

With apparently functional K^+(ATP) channels in place, the α cell's inability to respond to glucose or metabolic inhibition is probably related to their extraordinarily high cytosolic [ATP] and [ATP]/[ADP] ratio that remains virtually unchanged after increases in extracellular glucose. (α Cells are much less efficient transporters and metabolizers of glucose than are β cells.) In contrast, the α cell's response to arginine may be related to the depolarizing effect of the electrogenic transport of this cationic amino acid coupled to the low threshold for excitability of this cell type (i.e. low resting membrane conductance and abundance of low-voltage-activated [T-type] Ca^{2+} channels). (Arginine also depolarizes β cells without closing K^+(ATP) channels, although it usually does not enhance electrical activity unless suprathreshold concentrations of glucose are also present.) However, the crucial element of physiological regulation of the α cell, the inhibition of its electrical activity and secretion by glucose, remain unexplained on the basis of K^+(ATP) channel activity. It is possible that the inhibitory effect of glucose results largely from a paracrine interaction within the islet. α Cells display a robust γ-aminobutyric acid (GABA) activated Cl^- current which, when stimulated, can abolish arginine-enhanced electrical activity. β Cells are known to secrete GABA along with insulin. Hence secretagogue-induced β-cell exocytosis might be the "suppressor" of α-cell activity.

IID. Implications for Pathophysiology and Therapeutics

Diabetes mellitus, a disease characterized by hyperglycemia and dysregulation of metabolite use and culminating in multiorgan system damage, comes in two general varieties. The insulin-dependent, ketosis-prone variety (IDDM) is usually an autoimmune disease of rapid onset, characterized by destruction of β cells as a result of massive assault by antibodies and cytokines. In contrast, the non-insulin-dependent, non-ketosis-prone variety (NIDDM) is a spectrum of diseases characterized by increasing insulin resistance coupled with poorly timed, inadequate insulin secretion. One of its earliest indicators of this condition is the loss of the transient "first phase" of glucose-induced insulin secretion, thought to be "primed" by acetylcholine released by the vagus nerve and GLP-1 released by enterochrommaffin cells. Accompanying this is a "compensatory" increase in insulin release during the prolonged "second phase." Unfortunately, this contributes to downregulation or "tonic tune out" of insulin receptors. Possible defects in NIDDM have been proposed for every link along the β-cell's stimulus–secretion coupling cascade (i.e. from reduced affinity of glucose transporters to reduced efficiency of intracellular handling of Ca^{2+}). A recently explored model for NIDDM features insulin resistance of the β cell with chronically decreased release of Ca^{2+} from intracellular (ER) stores. No doubt, the single cell approaches outlined above will be increasingly brought to bear to dissect out cellular mechanisms underlying NIDDM.

Those approaches may be expected to spur the development of more "physiologically targeted" pharmacotherapy for NIDDM, including carefully timed, pre-prandial administration of (1) GLP-1 and other gut-secreted incretins and (2) highly selective sulfonylurea-type agents of shorter onset and duration of action than those currently marketed. To be sure, two realizations, (1) that α cells contain sulfonylurea-inhibited K^+(ATP) channels possibly of identical structure, and (2) that constant activation of α cells coupled with waning of β-cell function, may contribute to the progressive sulfonylurea insensitivity, are now promoting synthesis of hypoglycemic drugs more selectively targeted at β-cell function.

It is worth noting that sulfonylureas also modify the gating of some Cl^- conductance channels in β cells as well as the activity of Na^+-K^+ ATPase and the efficacy of depolarization–secretion coupling in a manner similar to the effects of protein kinase C enhancement. As mentioned above, the NBFs of SUR resemble those of CFTR. Spare CFTR subunits appear to interact with a variety of Cl^- channels and even with the epithelial Na^+ channel (EnaC) in epithelial cells. Do spare SUR subunits likewise interact with integral membrane or membrane associated proteins in β cells to modulate a variety of events in stimulus-secretion coupling?

III. METABOLIC SENSING AS PROTECTION FROM HYPOMETABOLIC INJURY

The hyperpolarization and increased K^+(ATP) channel activity displayed by β cells exposed to metabolic inhibitors that reduce cytosolic [ATP]/[ADP] suggests that a safeguard against hypoxic damage of an excitable cell might be hypoxia-induced opening of K^+(ATP) channels. This mechanism appears to apply to skeletal and cardiac myocytes and to some neurons. As in β cells, in these cells metabolically sensitive channels are very often K^+(ATP) channels consisting of Kir and SUR subunits, though often the SUR subunit (SUR2) has much lower affinity for some sulphonylureas than does SUR1. In addition, in skeletal myocytes, which produce lactate under hypoxic conditions, the K^+(ATP) channel displays pH_i sensitivity that is the reverse of K^+(ATP) channels in β cells; in these myocytes,

intracellular acidosis vigorously opens K^+(ATP) channels even at fixed [ATP]/[ADP]. Recent evidence suggests that, in highly active regions of the brain, those cell types with higher density of K^+(ATP) channels show most rapid excitability block in response to hypoxia and survive it best. However, what may be an adaptive feature to individual cells may have disastrous consequences for the entire organism. In skeletal muscle, a drop in tension development by some motor units results, via spinal reflex, in recruitment of other less active motor units. More extended fatigue due to inexcitability may preserve enough ATP to maintain sarcolemmal integrity and avert leak of myoplasmic contents such as myoglobin. (The latter condition, known as rhabdomyolysis, is the chief cause of extended incapacity and systemic illnesses, such as with acute renal failure, seen after intense bouts of exercise.) However, in contrast, in cardiac ventricle, block of excitability or excitation contraction coupling in one part of the electromechanical syncitium may predispose to an arrhythmia or severely dyskinetic contraction, while in neurons, excitability block can result in a depressed level of central consciousness and even coma.

As an example of hypoxia-induced excitation block, let us examine block of excitation–contraction coupling in the cardiac ventricular myocyte. Historically, this phenomenon was key to the original discovery of the K^+(ATP) current. In these cells, deprivation of substrate or oxygen, or inhibition of substrate metabolism, was found to result in shortening of Ca_o^{2+}-dependent plateau phase of the action potential with attendant abbreviation or block of generation of contractile force. This was found to have occurred prior to detectable changes in membrane potential or voltage-dependent Na^+ and Ca^{2+} currents and it was accompanied by major augmentation of resting K^+ conductance. Critically, plateau phase shortening and reduced contraction were reversed by intracellular injection of MgATP. As shown in Fig. 34.8, the key to this phenomenon is very basic. The plateau phase of the ventricular action potential represents a delicate moment-to-moment balance between two opposing tendencies. These are (1) the "depolarizing tendency" of the voltage-dependent, but slowly inactivating Ca^{2+} conductance and (2) the "repolarizing tendency" of the sum of a variety of K^+ currents that are either slowly activating or slowly emerging from "inward rectification" (i.e. polyamine or Mg block). Increases in background K^+ current provided by opening of K^+(ATP) channel tip the balance in favor of repolarization, as soon as the huge inward Na^+ current, underlying the rapid upstroke of the action potential, wanes. However, shortening of the broadly propagating action potential may reduce the refractory period and promote local impulse re-entry or rebound excitation. In addition, the period of reoxygenation may enhance arrhythmogenicity by promoting large transient inward currents (I_{ti}) which result in spontaneous

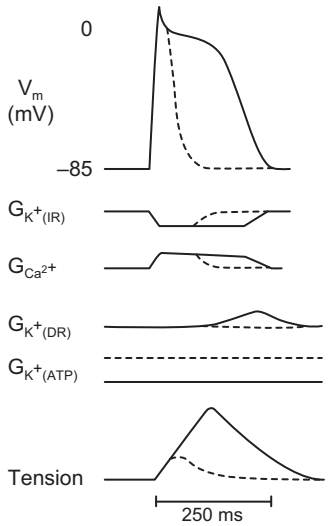

FIGURE 34.8 K^+(ATP) channels and cardiac excitability. A steady-state enhancement of K^+(ATP) conductance ($G_{K^+(ATP)}$), resulting from metabolic inhibition, shortens the time courses of the ventricular action potential and twitch tension and alters the time courses and magnitudes of the underlying ionic conductances. Solid lines indicate control; dashed lines indicate effects of metabolic inhibition.

depolarizations. Hence, it would appear to be better for the ventricle to anticipate rather than react to metabolic deprivation. Physiologically, this is exactly what happens: ventricular hypoxia results in dilation of coronary arterioles leading to greater supply of oxygen and metabolites (see Section VA). However, as often happens in critical physiological processes, there is yet another factor at work. Short bouts of hypoxia, with opening of K^+(ATP) channels, may actually "precondition" myocytes and ameliorate some of the effects of subsequent, more prolonged bouts. In that case, does prevention of hypoxia-induced opening of K^+(ATP) channels, as might occur in the presence of a sulfonylurea, predispose to hypoxia-induced cell injury? Controversy still surrounds this issue.

It is worth mentioning other mechanisms that might contribute to ischemia-induced contractile failure. These include (1) altered $[Ca^{2+}]_i$ "homeostasis," (2) changes in the binding affinity of the contractile apparatus for Ca^{2+} induced by accumulation of acid equivalents and (3) activation of other K^+ channels, such as muscarinic and G-protein gated K^+ channels, by metabolic intermediates generated during hypoxia.

IV. STIMULUS–SECRETION COUPLING IN CAROTID CHEMORECEPTOR CELLS

Neural control of respiratory drive is critical in maintaining physiologic levels of plasma O_2, CO_2 and H^+. In the rhythmic, neuromuscular process of breathing, trains of action potentials, generated by pacemaker cells in the CNS,

trigger motor neurons and activate periodic contractions of the inspiratory muscles (diaphragm and intercostal muscles). This action expands the chest, thereby sucking air of high-O_2, low-CO_2 content into the lungs. Gas exchange consists of net CO_2 diffusion from capillary to adjacent lung air spaces (alveoli) and net O_2 diffusion from alveoli to the capillary. Relaxation of inspiratory muscles, sometimes combined with the contraction of expiratory muscles, expels the air of high CO_2, low O_2 content from the lungs. A major stimulus for altering the pattern of respiratory drive is a drop in the partial pressure of O_2 dissolved in plasma (i.e. plasma pO_2); a secondary stimulus is a rise in plasma pCO_2 or a fall in pH. The carotid body is the organ that senses changes in plasma pO_2, pCO_2 and pH and mediates changes in CNS respiratory drive. Located at the bifurcation of the carotid artery, a branch of the aorta, the carotid body consists of a central core of *chemoreceptor* (or *glomus*) *cells*; these originate from the neural crest. Glomus cells synapse on dendritic endings of sensory nerve fibers that comprise the carotid sinus nerve travelling into the CNS. The glomus cell core is surrounded by more superficial glial, or sustentacular, cells, as well as by a dense network of highly porous capillaries. The glomus cell is the site of transduction of changes in plasma pO_2, pCO_2 and pH into changes in electrical activity of the afferent carotid sinus nerve. Decreases in pO_2, as well increases in pCO_2 or decreases in pH, lead to an increase in release of dopamine and probably to an increase in as-yet-unidentified transmitters from glomus cells, as well as to an increased action potential frequency in the dopamine-sensitive carotid sinus nerve. This contributes to increased respiratory drive.

IVA. Role of O_2-Sensitive K^+ Channels in Transduction of the Hypoxic Stimulus

Two divergent views have emerged concerning chemotransduction of hypoxia by glomus cells (Fig. 34.9A). The first theory proposed that hypoxia induces cell depolarization, followed by opening of voltage-gated Ca^{2+} channels, Ca^{2+} influx and synchronized exocytotic release of dopamine. This might give rise to sufficiently large excitatory postsynaptic potentials in the dendritic regions of single sinus nerve fibers to trigger propagating action potential. An alternative view proposed that hypoxia induces quantal release of transmitter in a Ca^{2+}-dependent manner that is independent of voltage-gated Ca^{2+} entry but dependent on the discharge of Ca^{2+} from intracellular stores. The latter should increase asynchronous quantal release of transmitter, generating a rise in the frequency of miniature excitatory postsynaptic potentials and should enhance ongoing electrical activity in the low-threshold carotid sinus nerve fiber. These contrasting viewpoints have arisen from data generated with different preparations from different species.

There are several lines of evidence supporting the classical scheme for "depolarization–secretion coupling" in glomus cells. First, glomi are electrically excitable sensory cells and contain HVA Ca^{2+} currents, delayed rectifier K^+ currents and, in some cases, voltage-dependent

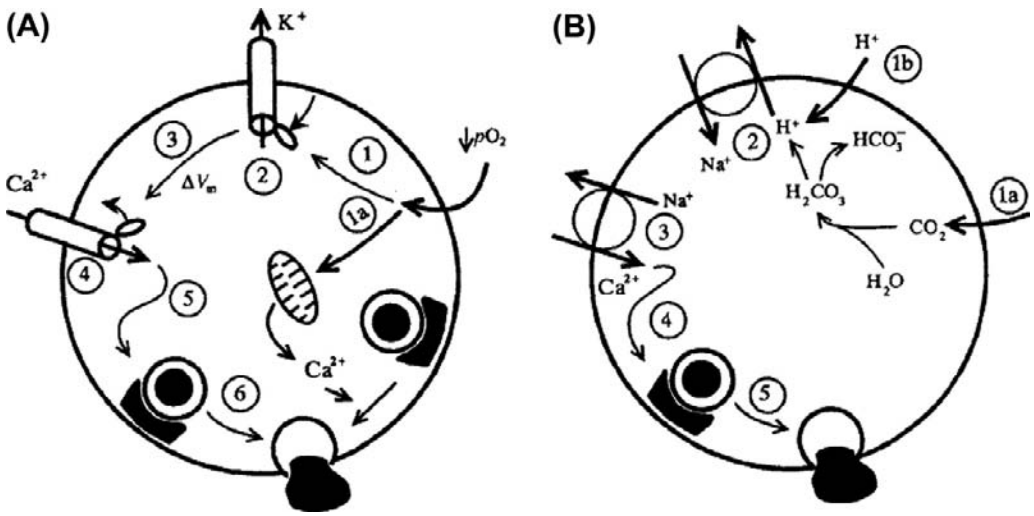

FIGURE 34.9 Stimulus–secretion coupling in carotid chemoreceptor cells. (A) O_2-induced transmitter release. Key steps in classical scheme of depolarization–secretion coupling are outlined. Decreased pO_2 results in decreased O_2 binding to the intracellular receptor coupling to a specific voltage-dependent K^+ channel (1). This results in the closure of the channel (2), cell depolarization (3), increased probability of the opening of HVA Ca^{2+} channels (4), increased calcium entry (5) and the enhanced rate of fusion of dopamine-containing vesicles with the plasma membrane (6). Alternatively (see path beginning with 1a), hypoxia-induced rundown of the mitochondrial proton gradient might result in reduced ATP generation, slow release of Ca^{2+} from mitochondria or other stores and, ultimately, a slow rise in spontaneous quantal release. (B) CO_2 and H-induced transmitter release. Increased pCO_2 or H entry (1b) results in decreased cytosolic pH and stimulation of the Na^+-H exchanger (2). The resultant influx in Na^+ stimulates the Ca^{2+}-Na^+ exchanger (3). This, in turn, increases Ca^{2+} influx (4) and Ca^{2+}-dependent exocytosis (5).

Na^+ currents. Second, in some isolated cell preparations, glomus cells respond to hypoxia by depolarizing and generating action potentials. (However, in other preparations, glomus cells fire action potentials only in response to current injection or release of the cell from sustained hyperpolarization. These cells show no change in passive electrical activity in response to hypoxia.) Third, in glomus cells that fire in response to hypoxia, depolarization increases both cytosolic Ca^{2+}, measured with intracellular dyes, and dopamine release, measured by amperometry. In these cells, depolarization–secretion coupling is reduced by exposure to blockers of the HVA-type Ca^{2+} channels or by reduction in extracellular Ca^{2+}.

A very exciting development in chemoreceptor physiology consistent with the depolarization–secretion coupling scheme outlined above is the discovery that, in whole-cell recordings, lowering ambient pO_2 selectively and reversibly reduces the outward K^+ current flowing through delayed rectifier K^+(DR) channels of the glomus cells. Reducing pO_2 from 160 mmHg to 90 mmHg reduces peak K^+(DR) current by ≈30%. This effect is not dependent on the concentrations of ATP (0–3 mM) or Ca^{2+} (<1 nM–0.5 mM) in the pipette. In outside-out patches of membrane, reduced ambient pO_2 reversibly decreases the probability of opening (P_o) of a 20-pS K^+(DR) type channel (Fig. 34.10). The first reports suggested that in vitro this channel was most responsive to changes in O_2 over the range of pO_2 values between 110 and 150 mmHg, in contrast to the intact carotid sinus nerve that actually fires optimally at pO_2s <70 mmHg. However, the O_2 sensitivity of the channel can be shifted into a more physiological range by the addition of a membrane-permeant analog of cAMP and recent data have shown K^+(DR)-type channel activity pO_2s ranging from 20 to 150 mmHg. In whole-cell, current-clamp recordings, the effect of a reduction in pO_2 is (1) an increase in the rate of cell depolarization on release from maintained hyperpolarization, (2) an increase in the frequency of spike activity in the resultant short train impulses and (3) an increase in AP overshoot. Hence, in glomus cells with some intrinsic spontaneous electrical pacemaker activity, O_2-dependent changes in K^+ current could alter the frequency of action potentials and large Ca^{2+} transients, thereby increasing [Ca^{2+}]-dependent transmitter release onto the afferent nerve. In glomus cells with little automaticity that maintain resting potentials of between −50 and −40 mV, closure of K^+(DR)-type channels could still cause steady-state depolarization "generator potential" and trigger electrical activity de novo. More extensive perforated-patch recordings will be needed to determine the range of electrical activity patterns exhibited by these cells.

These data suggest that O_2 maintains the activity of a delayed rectifier type K^+ channel through a novel gating mechanism. Several possibilities for the molecular mechanism of O_2 transduction and its relationship to channel gating have been suggested, but there is no definitive evidence for any of them. The first is that a heme protein, analogous to a subunit of the O_2-carrying protein hemoglobin, is attached to the channel, or to a functional subunit

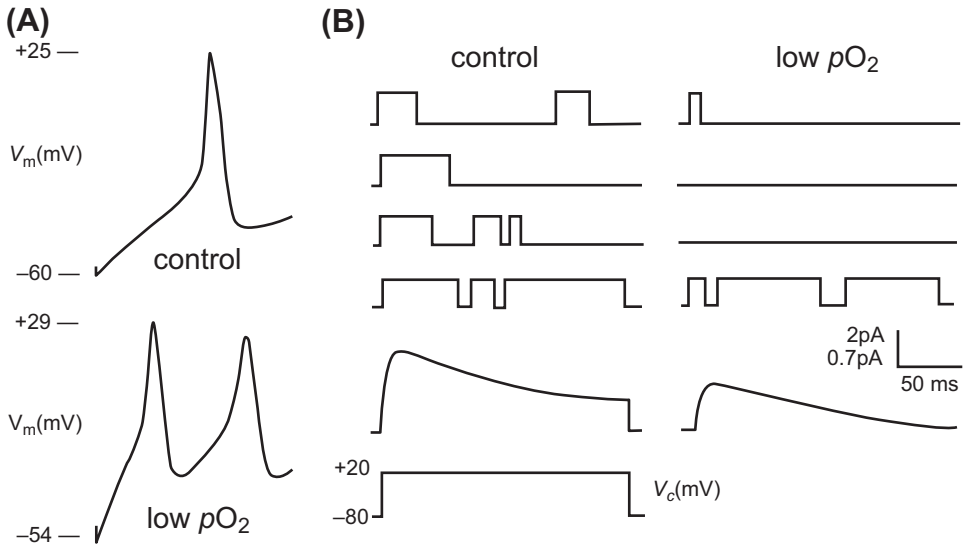

FIGURE 34.10 Origin of low-pO_2-induced enhancement of electrical activity in carotid glomus chemoreceptors. (A) Reduction in ambient pO_2 results in increased frequency of spontaneous AP activity, partly due to reduced rate of repolarization of the AP. Hence, any background depolarizing current might be more effective in raising the membrane potential toward threshold for firing a spike. *(Reproduced from* The Journal of General Physiology, *1989, Vol. 93, p. 979, Fig. 14. By permission of the Rockefeller University Press.)* (B) Reduction in ambient pO_2 reduces the probability (P_o) that a K^+(DR) channel will open on depolarizing the cell from −80 to +20 mV. Lowest traces in each column represent the average of many individual channel current traces. *(Idealized traces adapted from Ganfornina and Lopez Barneo, 1991.)*

of the channel. In this way, a change in configuration of the protein, on losing O_2, would alter channel gating. The second is the presence of an oxidase which, on reduction of cytosolic pO_2, produces less hydrogen peroxide (H_2O_2), consequently altering the concentration of redox intermediates and thereby of channel conformation.

The alternative view of chemotransduction of hypoxia in glomus cells is that the rise in intracellular Ca^{2+} necessary for dopamine secretion is due to Ca^{2+} release from intracellular stores and that voltage-activated currents play only a secondary role, perhaps allowing replenishment of intracellular Ca^{2+} stores. This hypothesis has arisen from data generated from both isolated glomus cells and in situ carotid cell bodies. Mitochondrial poisons, such as cyanide, produce a condition known as *histotoxic hypoxia*, which mimics true hypoxia in stimulating carotid body nerve activity and respiratory drive. These poisons produce increases in intracellular Ca^{2+} that are unaffected by pharmacologic maneuvers designed to abolish or enhance the action potential, hence suggesting that increases in cytosolic Ca^{2+} arise from intracellular stores. Hypoxia and mitochondrial poisons produce a rise of cell NAD(P)H. Additionally, studies from in situ carotid bodies have shown (1) that action potentials induced in carotid sinus nerve by hypoxia are not blocked by drugs that block outward K^+ currents and (2) that whole cell glomus membrane resistance is not changed in response to hypoxia. A proposed mechanism whereby hypoxia induces intracellular Ca^{2+} release is that low O_2 decreases mitochondrial efficiency, perhaps slowing electron transfer in the respiratory chain, and reducing the proton gradient across the mitochondrial inner membrane. A consequence of this could be the release of Ca^{2+} from mitochondria or decreased ATP production, resulting in slow Ca^{2+} release from other intracellular stores (e.g. the ER). For this mitochondrial-based hypothesis to work, it might be necessary that O_2-trapping properties of mitochondrial cytochrome oxidase and Ca^{2+}-storage properties of mitochondria in glomus cells differ significantly from their counterparts in other tissues.

IVB. Transduction of Increased pCO_2 and Decreased Plasma pH

Glomus cells rapidly equilibrate pH_i and pH_o. Hence, it is probable that with acidic stimuli the cell is actually sensing a fall in pH_i. But how does an increase in $[H^+]_i$ result in Ca_o^{2+}-dependent transmitter release, especially as H_i^+-induced release is insensitive to blockers of HVA Ca^{2+} channels and HVA Ca^{2+} channels are often inhibited by reduction in pH_i? The proposed link between increased $[H^+]_i$ and Ca^{2+} entry in promoting dopamine release is that increased $[H^+]_i$ activates an Na_o^+-H_i^+ exchanger which, in turn, elevates Na^+ and recruits a Na^+-Ca^{2+} exchanger. The activity of the latter exchanger is often augmented by cell depolarization; this may, in fact, occur because a drop in pH_i reduces K^+(DR) type K^+ current much as a drop in pO_2 does. An increase in background "spontaneous" quantal release of dopamine, which is not phase-linked to action potential activity, could increase steady-state depolarization of carotid nerve fibers and, perhaps, augment on-going impulse activity (see Fig. 34.9B). In considering this scheme, it should be cautioned that thus far, good evidence exists only for activation of an Na^+-H^+ exchanger.

To be sure, respiratory drive varies significantly according to age and physiologic status. Human fetuses do not exhibit regular respiratory movements in utero, whereas newborn infants often display periodic breathing different from breathing patterns seen in older children and adults. Disease states produce abnormal breathing patterns, such as Cheyne–Stokes breathing, the diamond-shaped changes in respiratory excursions followed by a period of non-breathing (apnea), seen in stroke, congestive heart failure and chronic hypoxia. In infants, prolonged apnea despite persistent hypoxia or hypercarbia can culminate in sudden infant death syndrome (SIDS). Recent data suggest that carotid body glomus cells from animals raised under hypoxic conditions show blunted electrophysiologic responses to hypoxia compared to cells from healthy animals. Disorders of breathing such as apnea and SIDS are seen in higher frequency in infants at increased risk for chronic hypoxia due to conditions such as prematurity or second-hand cigarette smoke exposure. Studies on the mechanism of changes in carotid body chemoreception in normal development and in various disease states should be a fruitful area for further inquiry.

V. STIMULUS–CONTRACTION COUPLING IN VASCULAR SMOOTH MUSCLE CELLS

VA. Hypoxic Vasodilation of Coronary and Mesenteric Vessels

Smooth muscle cells of resistance arterioles are very sophisticated metabolic sensors. In fact, they encompass a complete vasodilator reflex system in a single cell. In response to a drop in ambient pO_2, these cells reduce their tension generation. This results in vessel relaxation and the local redistribution of O_2 supply to O_2-consuming tissue. As in the case of the cardiac myocyte, a key to the explanation of this phenomenon is the increase in K^+ conductance and membrane hyperpolarization, which precedes the fall in tension.

It is well appreciated that resistance vessels in the coronary and mesenteric (gut) circulation display resting tone. Their myocytes maintain a resting potential of −40 to −50 mV and have an abundance of K^+(ATP) and

L-type (HVA) Ca^{2+} channels. In fact, in smooth muscle of mesenteric artery, the K_d value (μM) for ATP-induced closure of K^+(ATP) channels is roughly double that in cardiac myocytes, in principle making K^+(ATP) channels of these myocytes more sensitive to hypoxia than the K^+(ATP) channels in the heart. Under these circumstances, small changes in resting potential would be expected to affect resting tone. A small depolarization (of 5–10 mV) caused by closure of K^+(ATP) channels should result in increased opening of HVA Ca^{2+} channels and subsequent vasoconstriction (Fig. 34.11A). In contrast, a small hyperpolarization of 5–10 mV, affected by addition of a K^+(ATP) channel opener or a dihydropyridine Ca^{2+} channel antagonist, should reduce resting tone and result in vasodilation. These predictions have been borne out experimentally. A modest drop in microenvironment pO_2, insufficient to affect cardiac excitation–contraction coupling, is sufficient to reduce cytosolic ATP in vascular smooth muscle cells, open K^+(ATP) channels and cause vasodilation. (In bulk cardiac muscle in situ, preferential opening of smooth muscle K^+(ATP) channels might be further augmented by the release of adenosine by active cardiac tissue; extracellular adenosine has been shown to activate K^+(ATP) channels via a G-protein-dependent mechanism.) Hence preferential hypoxia-induced arteriolar dilation, with its attendant increases in local O_2 delivery, may spare cardiac myocytes the risk of hypoxia-induced alterations in excitation–contraction coupling. This scheme might work for the regulation of local blood supply to the brain and gut as well as to the heart.

VB. Hypoxia-Induced Vasoconstriction of Pulmonary Vessels

In contrast to coronary, mesenteric and cerebral vessels, pulmonary artery and its smooth muscle constrict in response to a drop in pO_2. This hypoxic pulmonary vasoconstriction (HPV) constitutes an adaptive response in the lung bed because it ensures that areas of the lung that are poorly oxygenated will receive less blood flow; the extra blood flow is "redirected" towards better oxygenated areas to optimize gas exchange. HPV is critical in fetal pulmonary development when the maturing air spaces are filled with secreted fluid rather than inspired air. Under these conditions, HPV maintains the relatively high pulmonary vascular resistance that shunts venous return around the low flow pulmonary bed, through the ductus arteriosus of the cardiac septum and into the left heart. With inflation of the newborn's lungs to air containing substantially higher pO_2, O_2-induced pulmonary vasodilation occurs, thereby promoting blood flow through the pulmonary circulation. In the adult, HPV is useful in maintaining moment-to-moment matching of local ventilation to perfusion; this reduces the risk of hypoxia that can occur when a portion of the lung is poorly inflated. However, when the areas of local poor ventilation are widespread, or with chronic hypoxia (such as at high altitudes), chronic HPV is accompanied by

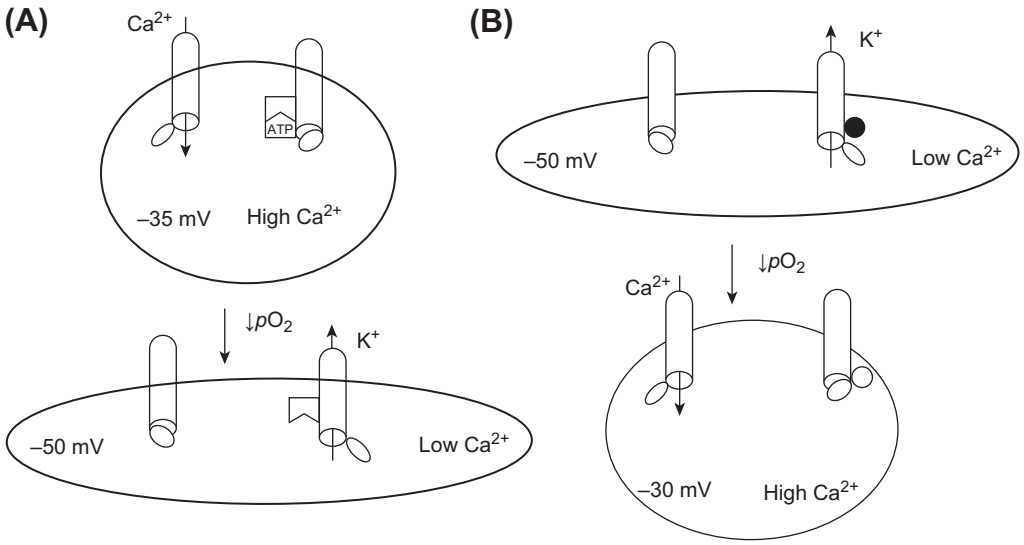

FIGURE 34.11 Hypoxia alters stimulus–contraction coupling in vascular myocytes. (A) Model of hypoxia-induced vasodilation in cardiac, cerebral and mesenteric vessels. In normoxic conditions, K^+(ATP) channels are largely closed, but voltage-dependent Ca^{2+} channels are open, $V_m \approx -35$ mV, and cytosolic Ca^{2+} is low. With a decrease in pO_2, cytosolic ATP levels drop, resulting in the opening of K^+(ATP) channels, repolarization to ≈ -50 mV, closure of Ca^{2+} channels, a drop in cytosolic Ca^{2+} and myocyte relaxation. (B) Model of hypoxia-induced vasoconstriction in pulmonary arteries. In normoxic conditions, $V_m \approx -50$ mV, O_2-sensitive K^+ channels are largely open and voltage-dependent Ca^{2+} channels are largely closed. Hence, cytosolic Ca^{2+} levels are low and there is little resting tension. With a decrease in pO_2, O_2-sensitive K^+ channels close, resulting in depolarization, opening of Ca^{2+} channels, Ca^{2+} entry and myocyte contraction.

smooth muscle proliferation (i.e. "work hypertrophy of muscle"). The end result is the development of increased resistance and pressure in the total pulmonary vascular bed. This "pulmonary artery hypertension" imposes an increased "afterload" on the right ventricle, thus becoming a stimulus for its hypertrophy.

What cellular mechanisms support HPV? Pulmonary artery myocytes maintain a low resting tension, a V_m of ≈ -40 mV and a resting cytosolic $[Ca^{2+}]$ of <100 nM. They respond to progressive hypoxia (e.g. a slow fall in pO_2 from 150 to 15 mmHg) with a 15-mV depolarization, which is not affected by changes in $[Ca^{2+}]_o$, followed by Ca_o^{2+}-dependent increases in both cytosolic Ca^{2+} and tension. Given that V_m in these cells shows a Nernstian relationship to $[K^+]_o$, these results suggest that membrane depolarization is due to a large decrease in Ca_o^{2+}-independent resting membrane conductance (e.g. GK). However, depolarization ultimately results in a small increase in G_{Ca}. This is sufficient to provide entry to trigger contraction. Tension is maintained so long as Ca^{2+} entry through voltage-gated Ca^{2+} channels exceeds Ca^{2+} efflux via the Na^+-Ca^{2+} exchanger. Whole-cell voltage-clamp experiments have provided good evidence that a voltage-activated, delayed rectifier type K^+ current seen at V_m values positive to -50 mV and, hence, open at rest, is significantly inhibited by hypoxia. Depolarization of a few mV would be sufficient to open HVA Ca^{2+} channels and result in vasoconstriction (see Fig. 34.11B). Hence, as in the carotid chemoreceptor, hypoxia-induced reduction in the activity of K^+(DR) type channels in a cell with a very low background G_m, appears to be responsible for depolarization and stimulus–response coupling.

An important paradox, which remains to be explained, is how pulmonary artery myocytes manage to "hide" K^+(ATP) channels, known to be present in the sarcolemma, during hypoxia. In these cells, K^+(ATP) channel openers abort high $[K^+]_o$-induced tension increase, while sulfonylureas enhance tension generation, as they do in resistance vessels, yet hypoxia does not open these channels. Are mechanisms similar to those in pancreatic α cells at play here?

VI. COUPLING OF OXYGEN SENSING TO RED CELL PRODUCTION BY ERYTHROPOIETIN-SECRETING CELLS

The ultimate metabolic sensors are the erythropoietin-(epo-) secreting cells of the renal interstitium and liver. These modified fibroblasts respond slowly to hypoxia by increasing their synthesis and constitutive secretion of epo which, in turn, serves as a maturation factor for erythrocyte precursors in bone marrow. Epo binds to a membrane receptor, which serves as a scaffold for the activation of numerous growth and division signaling pathways including JAK/STAT and ras/MAP kinases; epo also increases the expression of Bcl-Xl, an anti-apoptotic peptide. Mature erythrocytes are virtually cytoplasmic bags of hemoglobin (Hb) which bind O_2. In high pO_2 and pH environs (arterioles), Hb binds O_2, while at lower pO_2 and pH environs, Hb gives off its O_2. In this way Hb ferries O_2. The net effect of this receptor–effector cell pair is that hypoxia can ensure an increase in blood O_2 carriage for up to 120 days, the life span of an erythrocyte. A clue to the mechanism of O_2-reception epo-producing cells is that their exposure to cobalt, nickel and manganese mimics the effects of hypoxia, whereas exposure to metabolic (mitochondrial) inhibitors such as cyanide cannot. This suggests that the O_2 sensor is an Hb-type molecule, which can be locked into a deoxygenated form, rather than a molecule involved in red-ox transfer, which uses O_2 as the final acceptor. The epo gene has been cloned and its *cis*-regulatory element has been found to bind a hypoxically inducible factor (HIF) that can transfer from the cytoplasm into the nucleus (Fig. 34.12A). Epo regulation is

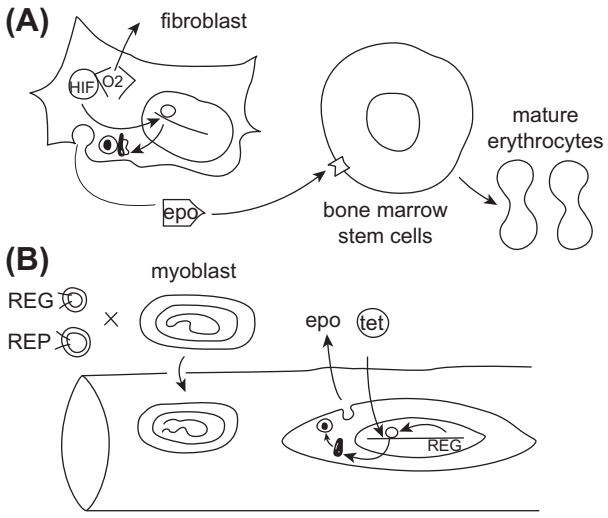

FIGURE 34.12 Native and bioengineered stimulus–synthesis coupling in erythropoietin production. (A) Stimulus–synthesis coupling in renal interstitial fibroblasts and hepatic Ito cells likely consists of triggering of epo gene transcription by a hypoxically induced factor (HIF), which is freed to enter the nucleus after O_2 dissociates from a heme pigment receptor. Newly synthesized epo is packaged and constitutively released. The kidneys are an excellent primary site for an O_2 sensor because under control conditions they are perfused with $\approx 20\%$ of the cardiac output. Circulating epo binds to erythroblasts (erythrocyte stem cells) in bone marrow and triggers their proliferation and maturation to enucleated erythrocytes that circulate as hemoglobin-packed, O_2 carrying sacs for an average of 120 days. (B) Genetically engineered stimulus–synthesis coupling for epo production in skeletal myocytes. Myoblasts are co-transfected with (i) a regulator gene (REG) under the control of mature muscle cells and (ii) a reporter gene (REP) coding for epo and under control of a tetracycline-sensitive product of the regulator gene. These co-transfected myoblasts are injected into muscle where they fuse with multinucleated myocytes. Under the control of exogenously added tetracycline (tet), myocytes are induced to synthesize and secrete epo.

an example of a widespread system for gene induction by O_2; this system includes pathways for induction vascular growth factors and changing isoforms of glycolytic enzymes in metabolically active cells.

Erythropoietin production wanes in chronic renal failure, as scar tissue replaces metabolically active cells. While epo can be replaced by weekly injection, the recombinant molecule is costly. To circumvent this, significant effort has recently been made to engineer cells that might tonically secrete epo on exposure to a simple, gene-activating stimulus. Primary myoblasts are co-transfected with two retroviruses and then injected into muscle where they fuse with mature, multinucleated myocytes. One of the transfecting retroviruses contains a regulator, or reverse transactivation, gene (REG) designed to be under the control of a promoter only activated in mature myocytes. The second retrovirus contains the reporter gene (REP), coding for epo, but under control of both the protein coded by REG and tetracycline (tet). Once in the mature muscle, the REG protein and tet control can tonically activate the epo gene. Significantly, when mice are injected with these engineered myoblasts, epo secretion can be switched on and off over months, depending on the availability of tet in the drinking water.

ACKNOWLEDGMENTS

Original data traces shown here were obtained in our laboratory through the support of NIH grant DK37380. I thank Todd Owyoung for preparing Figures 34.2 and 34.6, David Bryant for preparing Figures 34.9–34.11 and Drs David Pressel and David Barnett for sharing insights and delicate turns of phrase during the preparation of a prior version of this chapter.

This chapter is dedicated to the memory of Golda Hazak, wit and sage of Kiryat Yam.

BIBLIOGRAPHY

Ashcroft, F. M., & Grimble, F. M. (1999). K-ATP channels and insulin secretion; their role in health and disease. *Diabetologia, 42*, 9039–9196.

Ashcroft, F. M., & Rorsman, P. (1989). Electrophysiology of the pancreatic Beta cell. *Prog Biophys Mol Biol, 54*, 87–143.

Bohl, D., Naffakh, N., & Heard, J. M. (1997). Long-term control of erythropoietin secretion by doxycycline in mice transplanted with engineered primary myoblasts. *Nat Med, 3*, 299–304.

Bokvist, K., Olsen, H. L., Hoy, M., et al. (1999). Characterisation of sulphonylurea and ATP-regulated K^+ channels in rat pancreatic A-cells. *Pflügers Arch Eur J Physiol, 438*, 428–436.

Ganfornina, M. D., & Lopez-Barneo, J. (1991). Single K channels in membrane patches of arterial chemoreceptor cells are modulated by O_2 tension. *Proc Natl Acad Sci USA, 88*, 2927–2930.

Gonzalez, C., Almaraz, L., Obeso, A., & Rigual, R. (1992). Oxygen and acid chemoreception in the carotid body chemoreceptors. *TINS, 15*, 146–157.

Gromada, J., Holst, J. J., & Rorsman, P. (1998). Cellular regulation of islet hormone secretion by the incretin hormone glucagon-like pep-tide 1. *Pflügers Arch Eur J Physiol, 435*, 583–594.

Harvey, J., McKay, N. G., Walker, K. S., Van der Kay, J., Downes, C. P., & Ashford, M. L. J. (2000). Essential role of ohosphoinosotide 3-kinase in leptin induced K-ATP channel activation. *J Biol Chem, 275*, 4660–4669.

Inagaki, N., Gonoi, T., Clement I.V, J. P., et al. (1995). Reconstitution of I-K^+(ATP): an inward rectifier subunit plus the sulfonylurea receptor. *Science, 270*, 1166–1169.

Johnson, J. D., & Chang, J. P. (2000). Function– and agonist-specific Ca^{2+} signalling: the requirement for and mechanism of spatial and temporal complexity in Ca^{2+} signals. *Biochem Cell Biol.,* (in press).

Klingauf, J., & Neher, E. (1997). Modeling buffered Ca diffusion near the membrane: implications for secretion in neuroendocrine calls. *Biophys J, 72*, 674–690.

Misler, S., Barnett, D. W., Pressel, D. M., & Gillis, K. D. (1992). Electrophysiology of stimulus-secretion coupling in human betacells. *Diabetes, 42*, 1220–1227.

Nichols, C. G., & Lederer, W. J. (1991). Adenosine triphosphatesensitive potassium channels in the cardiovascular system. *Am J Physiol, 261*, H1675–H1686.

Nichols, C. G., Shyng, S.-L., Nestorowicz, A., et al. (1996). Adenosine diphosphate as an intracellular regulator of insulin secretion. *Science, 272*, 1785–1787.

Ratcliffe, P. J., Ebert, B. L., Ferguson, D. J. P., et al. (1995). Regulation of the erythropoietin gene. *Nephrol Dial Transplant, 10*, 18–27.

Rorsman, P., Ashcroft, F. M., & Berggren, P. O. (1991). Regulation of glucagon release from pancreatic A-cells. *Biochem Pharmacol, 41*, 1783–1790.

Seino, S., Inagaki, N., Namba, N., & Gonoi, T. (1996). Molecular biology of the beta-cell ATP-sensitive K channel. *Diabetes Rev, 4*, 177–190.

Weir, E. K., & Archer, S. L. (1995). The mechanism of acute hypoxic pulmonary vasoconstriction: the tale of two channels. *FASEB J, 9*, 183–189.

Wollheim, C. B., Lang, J., & Regazzi, R. (1996). The exocytotic process of insulin secretion and its regulation by Ca and G-proteins. *Diabetes Rev, 4*, 276–297.

Zawar, C., & Neumcke, B. (2000). Differential activation of ATP-sensitive potassium channels during energy depletion in Ca_1 pyramidal cells and interneurones of rat hippocampus. *Pflügers Arch Eur J Physiol, 439*, 256–262.

Zhou, Z., & Misler, S. (1996). Amperometric detection of quantal secretion from patch-clamped rat pancreatic beta-cells. *J Biol Chem, 271*, 270–277.

This page intentionally left blank

Chapter 35

Cyclic Nucleotide-Gated Ion Channels

Anita L. Zimmerman

Chapter Outline

I. SUMMARY

Cyclic nucleotide-gated (CNG) channels are directly activated by the binding of cGMP and/or cAMP, which are controlled by G-protein enzyme cascades. Their cousins, the hyperpolarization-activated, cyclic nucleotide-gated (HCN) channels, are voltage-gated, but their voltage sensitivity is regulated by the binding of cAMP. Both CNG and HCN channels are members of the superfamily of voltage-gated cation channels. CNG channels have established roles in sensory transduction, but they are also found in many non-sensory tissues. HCN channels are best known for their pacemaking role in the cardiac sinoatrial node. Both CNG and HCN channels are excitatory, since their opening allows Na^+ and Ca^{2+} entry. In the brain, both CNG and HCN channels are implicated in synaptic plasticity and other excitation processes, in addition to their pacemaking role in rhythmic neurons. There continues to be fast-moving research on these channels in the areas of structure/function, physiological roles, modulation, gating, permeation and development of pharmacological tools.

II. INTRODUCTION

Cyclic nucleotides have long been known as intracellular second messengers that regulate cell function by controlling the activity of protein kinases which, in turn, control many other cellular proteins. However, in 1985, Fesenko and his colleagues made a startling discovery that changed our view of the physiological role of cyclic nucleotides. These investigators found that the ion channel mediating the electrical response to light in retinal rod cells was directly opened by the binding of guanosine 3′,5′-cyclic monophosphate (cGMP); no phosphorylation reaction was required. Now the rod channel is considered to be a member of a special class of ion channels — the *c*yclic *n*ucleotide-*g*ated (CNG) channels, which are actually part of the superfamily of voltage-gated cation channels (reviewed in Yu et al., 2005). These channels are discussed in many recent reviews (Kaupp and Seifert, 2002; Barnstable et al., 2004; Broillet and Firestein, 2004; Bradley et al., 2005; Hofmann et al., 2005; Craven and Zagotta, 2006; Pifferi et al., 2006; Biel, 2009; Biel and Michalakis, 2009; Mazzolini et al., 2010; Cukkemane et al., 2011).

Since the discovery of CNG channels, a related class of ion channels has been found to underlie pacemaker currents (usually referred to as I_h or I_f) in the heart and brain (reviewed in Gauss and Seifert, 2000; Kaupp and Seifert, 2001; Craven and Zagotta, 2006; Biel, 2009; Wahl-Schott and Biel, 2009; DiFrancesco, 2010). These channels are called HCN channels, which stands for *h*yperpolarization-activated, *c*yclic *n*ucleotide-regulated channels. Their structure is similar to that of CNG channels, but they are mainly gated by voltage, with their voltage activation regulated by the direct binding of cyclic nucleotides. This chapter will focus mainly on CNG channels, but will make comparisons with HCN channels as well. Finally, although cyclic nucleotide binding domains have been found in Eag-like (ether à-go-go) K^+ channels and plant K^+ channels, the functional role of cyclic nucleotide binding to these channels remains under investigation and these channels will not be discussed here.

Cell Physiology Sourcebook. DOI: 10.1016/B978-0-12-387738-3.00035-4

Why would Nature directly gate or regulate ion channels with cyclic nucleotides? When a cyclic nucleotide regulates a kinase, it is also in effect regulating all the proteins controlled by that kinase and by substrates of the kinase. Regulating ion channels is similar in that, like kinases, ion channels have diverse physiological effects. For example, the opening of non-selective cation channels (such as those opened by cyclic nucleotides) depolarizes the cell membrane (via Na^+ entry) and also allows the entry of Ca^{2+}, another important second messenger. Membrane depolarization opens voltage-gated Ca^{2+} channels, further increasing the entry of Ca^{2+}. Many cell functions are controlled by membrane potential and/or intracellular Ca^{2+}, including nerve impulses, muscle contraction, gene transcription and the secretion of neurotransmitters and hormones. Finally, depolarization and intracellular Ca^{2+} open K^+ channels, which repolarize the membrane and thereby contribute to the termination of the cellular response. Thus, there are numerous possibilities for control of cell function by cyclic nucleotide-gated, and cyclic nucleotide-regulated, ion channels. In addition, ion channel gating and permeation are much faster than phosphorylation reactions. Thus, changes in cyclic nucleotide levels could have fast effects mediated by ion channels, followed by slower, longer lasting effects mediated by protein kinases.

III. PHYSIOLOGICAL ROLES AND LOCATIONS

Since their discovery in retinal rods, and their subsequent purification and cloning, CNG channels have been identified in many other types of cells. They have been implicated generally in sensory transduction, as they also have been found in retinal cones, olfactory cells, invertebrate photoreceptors and pineal gland cells (reviewed in Kaupp and Seifert, 2002). Furthermore, mRNA probes against the rod CNG channel have revealed its expression in cells of the heart, brain, muscle, liver, kidney and testis. In the brain, both CNG and HCN channels have been implicated in synaptic plasticity (reviewed in Barnstaple et al., 2004, Biel, 2009; Wahl-Schott and Biel, 2009). The CNG channels have been studied most thoroughly in vertebrate photoreceptors and olfactory cells and, therefore, the CNG channels from these cells are discussed in the most detail here.

In rods and cones, CNG channels are key players in visual transduction (discussed in Chapter 38). It is these channels that conduct the so-called *dark current* and whose closure generates the hyperpolarizing response to light, which decreases the secretion of glutamate onto bipolar cells at the rod−bipolar synapse. The physiological second messenger in the photoreceptors is cGMP, which is at relatively high cytosolic concentration in the dark and decreases in the light after hydrolysis by a phosphodiesterase (PDE). Activation of PDE occurs when a photon is absorbed by a G-protein-coupled-receptor (a GPCR, which in this case is the photopigment rhodopsin), which then triggers a G-protein cascade. A similar system operates in cone visual transduction. An overview of the enzyme cascade controlling the level of cGMP is given in the next section, with more detail provided in Chapter 38.

Rods and cones are particularly well suited to patch-clamp studies of CNG channels, since the plasma membranes of their light-sensitive outer segments contain no other type of ion channel (although Na^+:Ca^{2+},K^+ exchange carriers are present; see Section V and Chapter 38). Furthermore, the rod outer segment plasma membrane has an extremely high density of CNG channels − hundreds per square micrometer − allowing as much as nanoamperes of current to be recorded from a single excised patch (with blocking divalent cations removed; see Section VB below). Such large currents are especially useful in studying pharmacological agents and modulators. In contrast, cone outer segments have relatively low channel densities, allowing the study of single-channel kinetics in patches containing only one channel. However, rods and cones actually have about the same total number of CNG channels because of the much larger plasma membrane area in cone outer segments (a consequence of the characteristic infolding of this membrane that forms "sacs" rather than the internal "disks" found in rods; see Chapter 38).

Olfactory receptor cells use CNG channels in sensing odorants (reviewed in Chapter 39). In this system, however, there are numerous odorant-activated GPCR types. Furthermore, adenosine 3′,5′-cyclic monophosphate (cAMP) is the physiological second messenger and the stimulus triggers cAMP *production* by adenylate cyclase, rather than its degradation by a PDE. Thus, in response to an odorant, the CNG channels open and the olfactory receptor cell depolarizes, increasing the probability of generation of an action potential. In addition, the Ca^{2+} that enters through the CNG channels activates Ca^{2+}-activated Cl^- channels, whose opening further depolarizes the cell (note that for these cells, unlike most other cells, the Cl^- concentration is higher inside than outside the cell, which is why its flow through the channels depolarizes the cell).

Like rods and cones, the olfactory cell has its CNG channels concentrated in a specialized region: the olfactory cilia and ciliary knob. Although the channels have been studied in excised patches from olfactory cilia (Nakamura and Gold, 1987), such experiments are extremely difficult because of the small diameter of a cilium. Luckily, the knob is larger and some CNG channels are also located (at lower density) in the membrane of the soma. Furthermore,

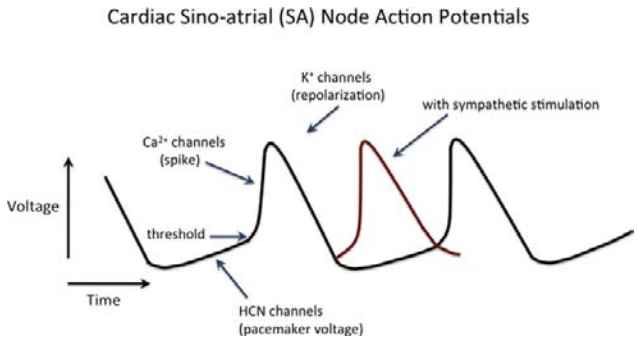

FIGURE 35.1 The role of HCN channels in the cardiac SA node action potential. The HCN channels are activated by hyperpolarization at the end of an action potential and their opening causes a slow depolarization that drives the membrane potential to threshold to trigger the next spike. Voltage-gated Ca^{2+} channels are responsible for the upstroke and voltage-gated K^+ channels repolarize the membrane. The inward pacemaker current through HCN channels is called I_h or I_f and is carried mainly by Na^+ under physiological conditions, despite the relatively high K^+ selectivity of HCN channels. Red trace: sympathetic agonists (e.g. norepinephrine) speed the heart by increasing the concentration of cAMP, which makes the HCN channels open more quickly (increased slope of pacemaker depolarization) and at less negative voltages, so that the next spike occurs sooner.

whole-cell patch-clamp methods have yielded considerable information on the olfactory CNG channels.

HCN channels were first studied in the sinoatrial (SA) node of the heart, where their opening produces the pacemaker current (I_h) that sets the heart rate by giving the initial slow depolarization at the beginning of the SA node action potential (Fig. 35.1; reviewed in DiFrancesco, 2010). Since the initial studies, HCN channels have been found in many other tissues as well, most notably in the brain, where they appear to play a role in synaptic plasticity, dendritic integration and maintenance of resting membrane potential (reviewed in Biel, 2009; Wahl-Schott and Biel, 2009). HCN channels also have been found to play a role in rhythmic activity in the central nervous system, especially in the thalamus (reviewed in Gauss and Seifert, 2000).

IV. CONTROL BY CYCLIC NUCLEOTIDE ENZYME CASCADES

Like cyclic nucleotide-regulated protein kinases, CNG and HCN channels are sensors of the local concentration of cyclic nucleotides. Stimulus-induced changes in cyclic nucleotide levels are mediated by GTP-binding proteins (G proteins). The stimulus-activated receptor interacts with a G protein, causing it to release GDP and bind GTP and to dissociate into two components: an α subunit and a $\beta\gamma$ subunit complex. The α subunit of the G protein, now bound to GTP, stimulates either adenylate cyclase (in olfactory receptors and cardiac SA node cells) or a cGMP-specific phosphodiesterase (in rods and cones). For the photoreceptors, the stimulus that activates the receptor is a photon, whereas for olfactory cells, the stimulus is an odorant molecule that acts as a receptor ligand, and for the SA node cells, the typical stimulus is a sympathetic agonist (e.g. norepinephrine) acting on a β-adrenergic receptor. A cyclic nucleotide enzyme cascade is diagrammed in Fig. 35.2 for a rod photoreceptor and in Fig. 35.3 for an olfactory cell. The cascade in cones is similar to that in rods, except that all the membrane-associated players are located on the plasma membrane, since cones lack internal disks (see Chapter 38). For the cardiac SA node cells, the cascade resembles that of the olfactory cell, however, cAMP does not activate the HCN channel, but rather makes the channel's activation by voltage occur sooner (i.e. at less negative voltages) and more quickly. This gives a speeding of the heart, since the SA node action potentials that set the timing of the heartbeat come more frequently. Activation of a muscarinic receptor by a parasympathetic agonist decreases [cAMP] and thereby slows the heart.

Cyclic nucleotide enzyme cascades are not fixed in their behavior. Instead, they are regulated by feedback systems, some of which involve CNG channels. For example, in rods, the Ca^{2+} that enters through CNG channels has been found to modulate the cGMP cascade. There is evidence that Ca^{2+} (in association with Ca^{2+} binding proteins) inhibits guanylate cyclase and inhibits the shutoff of rhodopsin (see Chapter 38). In olfactory receptors, Ca^{2+} appears to be involved in both excitation and adaptation (reviewed in Pifferi et al., 2006 and Chapter 39).

In addition to such feedback regulatory systems, there are the standard shutoff mechanisms employed in cyclic nucleotide cascades (e.g. see Chapter 38). These include phosphorylation of the receptor (e.g. the phosphorylation of rhodopsin, followed by its binding to arrestin), GTPase activity of the G protein (converting it back to the GDP-bound, inactive form), cessation of the stimulus and competing hydrolysis or synthesis of the cyclic nucleotide. There also are hints that the ability of the channels to respond to the cyclic nucleotide may be modulated (see Section VI).

V. FUNCTIONAL PROPERTIES

VA. Channel Gating

CNG channels are very sensitive detectors of the local concentration of cyclic nucleotides and they appear designed to work in the physiological concentration range of their respective agonists. Dose-response curves (e.g. Fig. 35.4) for activation of rod channels by cGMP give half-saturating concentrations ($K_{1/2}$ values) ranging from about 5 to 100 μM, which is within the expected physiological concentration range. The rather wide range of values of $K_{1/2}$ may reflect functional modulation of the channels by other factors (see Section VI).

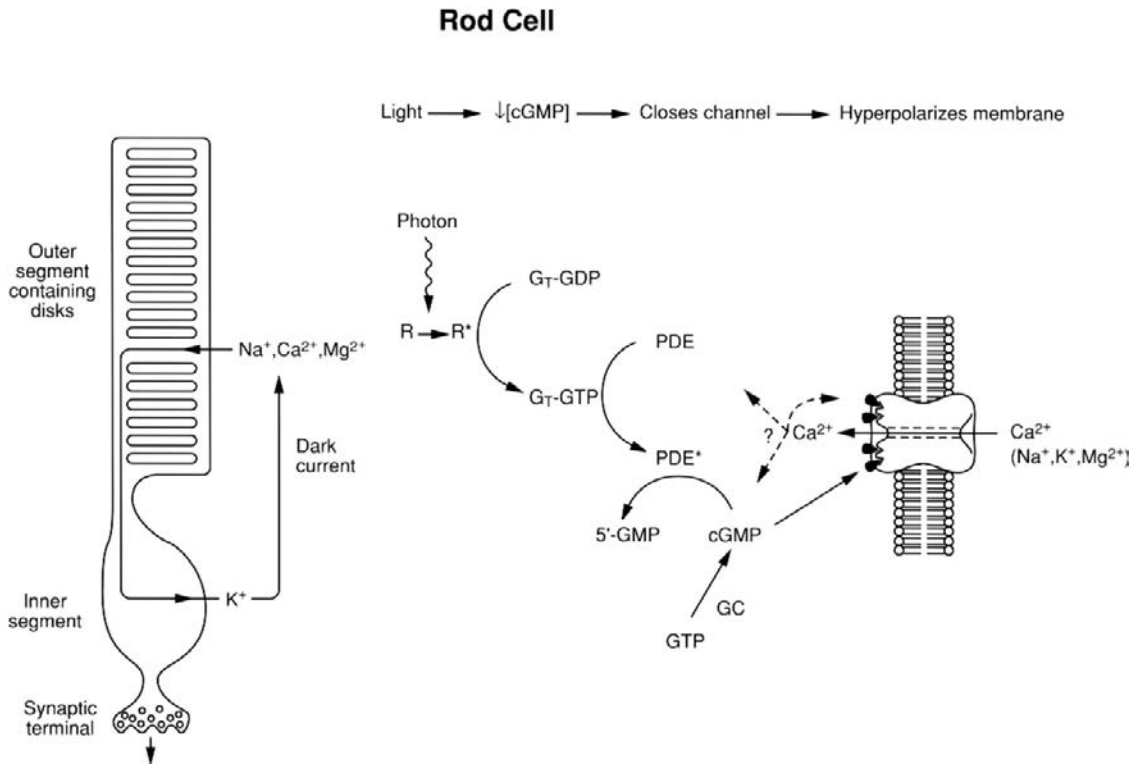

FIGURE 35.2 The cyclic nucleotide cascade controlling CNG channels in rods. R, R*, rhodopsin in its inactive and active forms, respectively. G_T, G protein ("Transducin"), bound to either GDP or GTP. PDE, PDE*, phosphodiesterase in its inactive and active forms, respectively. GC, guanylate cyclase. Calcium ions entering through the CNG channels are thought to modulate the function of several players in the cascade, including the channels themselves. A similar cascade operates in cones.

The form of the dose–response curve is well-described by the Hill equation:

$$\frac{r}{r_{\max}} = \frac{[\text{cGMP}]^n}{K_{1/2}^n + [\text{cGMP}]^n}$$

where r is the response to cGMP (e.g. the cGMP-activated component of the membrane current measured in a patch-clamp experiment), $r_{\max}$ is the maximum response (obtained with a saturating concentration of cGMP to activate all channels in the patch) and n is the Hill coefficient. Reported Hill coefficients have ranged between about 1.5 and 4, suggesting that several molecules of cGMP typically bind to each channel to open it. As discussed later, a channel seems to consist of four subunits, each with a cyclic nucleotide binding site (reviewed in Bradley et al., 2005; Craven and Zagotta, 2006; Biel, 2009). Because the dose–response curve for channel activation is so steep, small changes in the concentration of cAMP or cGMP produce very large changes in channel open probability. Furthermore, unlike most ligand-gated ion channels, CNG channels do not desensitize in the continued presence of agonist (reviewed in Mazzolini et al., 2010).

Activation of olfactory CNG channels is similar to that of rod and cone channels except for relative cyclic nucleotide sensitivities and efficacies. Rod and cone channels are much less sensitive to cAMP than to cGMP, with a $K_{1/2}$ for activation by cAMP of about 1.5 mM. Native olfactory CNG channels are more sensitive to both cyclic nucleotides than are photoreceptor channels, but they are only two to five times more sensitive to cGMP than to cAMP, with most $K_{1/2}$ values for activation by cGMP in the range of 1 to 5 μM (and a few as high as 20 μM; see Nakamura and Gold, 1987). Furthermore, cAMP acts as only a partial agonist for the rod channel: even at saturating concentrations, it gives only a fraction of the open probability obtained with saturating cGMP (see Fig. 35.4). However, both cAMP and cGMP are full agonists for the olfactory channel. This difference in agonist efficacy can be explained by assuming that cGMP is a more effective agonist than cAMP for both channels, and that after agonist binding, the olfactory channel opens more easily than does the rod channel (i.e. the olfactory channel's opening conformational change is more energetically favored) (Gordon and Zagotta, 1995). Interestingly, HCN channels prefer cAMP to cGMP by about a factor of ten (reviewed in Craven and Zagotta, 2006).

Although some voltage-activated channels (e.g. HCN and Eag-like K^+ channels) are regulated by cyclic nucleotides, channels that are primarily activated by cyclic

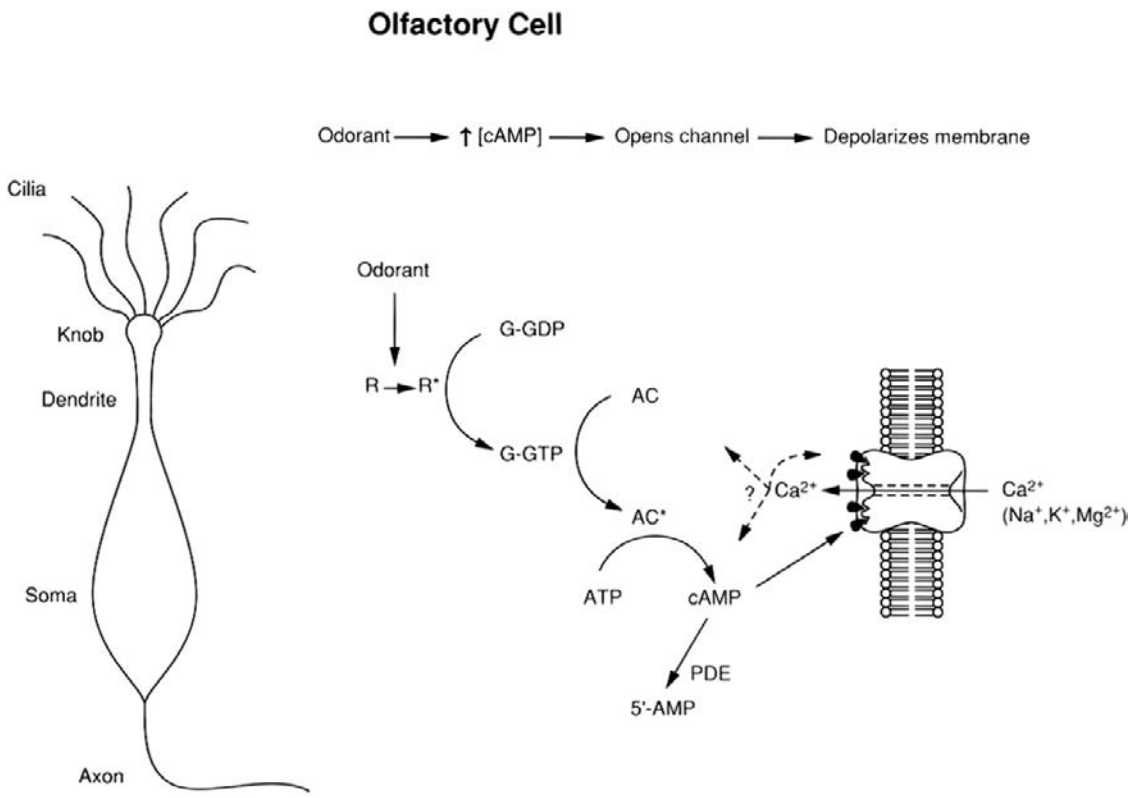

FIGURE 35.3 The cyclic nucleotide cascade controlling CNG channels in olfactory cells. R, R*, odorant receptor in its inactive and active (odorant-bound) forms, respectively. G, G protein, bound to either GDP or GTP. AC, AC*, adenylate cyclase in its inactive and active forms, respectively. PDE, phosphodiesterase. Here, as in photoreceptors, entering Ca^{2+} appears to modulate the cascade, including the CNG channels. The Ca^{2+} that enters through the CNG channels also opens Ca^{2+}-activated Cl^- channels (not shown), which further depolarize the cell.

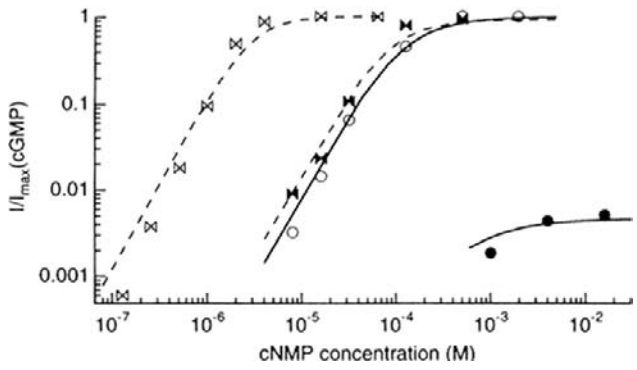

FIGURE 35.4 Dose–response curves for activation of cloned rod (circles) and olfactory (bows) α-homomultimeric channels. Both CNG channels show a higher apparent affinity (lower $K_{1/2}$) for cGMP (open symbols) than for cAMP (filled symbols), but for the rod channel cAMP appears to be a partial agonist, giving only a fraction of the current produced by a saturating concentration of cGMP. The smooth and dashed curves were calculated using a model in which the only difference between the results with cGMP and those with cAMP is that cGMP more effectively triggers the opening conformational change of the channels after it is bound. Currents were measured in response to voltage pulses of +100 mV from a holding potential of 0 mV and normalized to the current obtained in saturating cGMP (I_{max}). *(Reproduced with permission from Gordon and Zagotta, 1995. Copyright 1995 Cell Press.)*

nucleotides (CNG channels) are only weakly voltage dependent, with no voltage-dependent inactivation. In current–voltage (I-V) relations from excised patches, the voltage dependence of CNG channel gating is most obvious at low cyclic nucleotide concentrations, where it introduces significant non-linearity (e.g. see Fig. 35.7D). High concentrations of cyclic nucleotides overcome the voltage dependence of gating, driving the channels (by mass action) toward high open probabilities at all voltages and linearizing the I-V curves. Note, however, that much of the CNG channel rectification seen in intact cells probably results from voltage-dependent channel block by Ca^{2+} and Mg^{2+}, as discussed in Section VB below. The end result of both forms of non-linearity is that current is relatively independent of voltage in the physiological voltage range (for rods and cones, this would be about −40 to −80 mV). Thus, sensory CNG channels are able to transduce their stimulus faithfully in the face of changes in membrane potential that originate at either the transducing region or elsewhere in the cell, where there are many kinds of voltage-dependent ion channels.

Since CNG channels have voltage-sensing S4 segments, it is surprising that they have only very weak voltage

sensitivity. It has been proposed that glutamate residues in the vicinity of S4 contribute negative charges that may neutralize the effects of the positively-charged arginine and lysine residues of S4 that are thought to confer voltage sensitivity to the channel (Wohlfart et al., 1992; Tang and Papazian, 1997). Perhaps even more surprising is the fact that HCN channels, which also have S4 regions, have a voltage dependence that is the opposite of that found in most other voltage-dependent channels − HCN channels are activated by hyperpolarization, rather than by depolarization. Like CNG channels, most HCN channels do not inactivate with voltage. The one known exception is the spHCN channel from sea urchin sperm, which inactivates in the absence of cAMP (reviewed in Kaupp and Seifert, 2002; Hofmann et al., 2005; Craven and Zagotta, 2006; Biel and Michalakis, 2009).

Single-channel studies demonstrate that CNG channels have particularly fast open-shut transitions in the native membrane. This flickery behavior is striking in the cell-attached and excised-patch recordings obtained from toad rods by Matthews and Watanabe (1987) (Fig. 35.5).

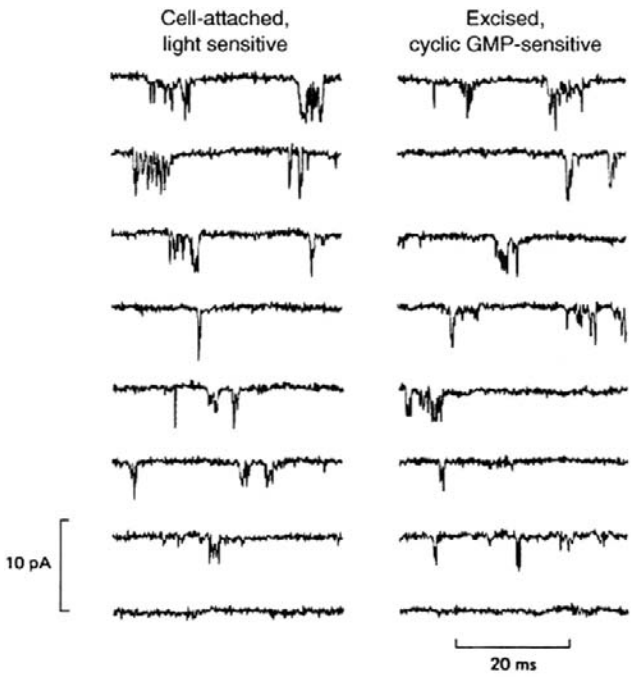

FIGURE 35.5 Single-channel recordings of CNG channels in native rod outer segment membranes demonstrate such rapid gating kinetics that many open-shut transitions are poorly resolved. Channel openings give downward deflections; holding potential −148 mV. Left: cell attached patch from toad rod outer segment; the bottom trace was obtained in a saturating light and all others in darkness. To prevent channel block, the pipette was filled with a solution lacking Ca^{2+} and Mg^{2+}. Right: the same patch after excision, with the intracellular surface bathed in either no cGMP (bottom trace) or 10 μM cGMP (all other traces); both pipette and bathing solutions lacked Ca^{2+} and Mg^{2+}. *(Reproduced with permission from Matthews and Watanabe, 1987.)*

However, when purified and reconstituted, or cloned and heterologously expressed, the channels were initially found to have much slower gating kinetics that are more typical of many other ion channels. Although Ca^{2+} and Mg^{2+} produce flicker block of these channels, the flickery gating behavior persists even in the absence of these ions. Furthermore, the transitions are too fast to reflect the binding and unbinding of cyclic nucleotides and they also apparently do not simply reflect block by protons. Accumulated evidence suggests that the flickery gating pattern of the native rod CNG channel results partly from the presence of a second channel subunit that was missing in the original reconstitution and expression studies, in which only one kind of subunit was identified (see Section VI below). This additional subunit also gives the channel its characteristic sensitivity to L-*cis*-diltiazem. Unlike the α subunit, the β subunit (also called *subunit 2*) does not produce cyclic nucleotide-activated currents when expressed alone.

For the olfactory channel, a second subunit (CNGA4, previously called r0CNC2) not only gives more flickery gating kinetics, but also increases the apparent affinity for cyclic nucleotides, giving more channel activity at low cyclic nucleotide concentrations (Fig. 35.6) (Bradley et al., 1994; Linman and Buck, 1994). Like the rod β subunit, this subunit also does not appear to produce cyclic nucleotide-activated currents when expressed alone. However, it is possible to obtain currents by treating the channel with nitric oxide (reviewed in Broillet and Firestein, 2004). With both rod and olfactory CNG channels, there still seem to be discrepancies between the behavior of the channels in vivo and in expression systems. Some of these differences may result from effects of channel modulators (see Section VI).

Although there remains disagreement over the detailed mechanism of activation (reviewed in Craven and Zagotta, 2006), it is clear that CNG channels can open with fewer than four ligands bound, but have highest open probabilities with all four sites occupied. Some studies suggest that a channel gate resides with the pore, at or near the selectivity filter (Karpen et al., 1993; Contreras et al., 2008). Certain mutations in this region switch the channel from ligand gated to voltage gated (Martinez-Francois et al., 2009). Innovative methods have been very useful in dissecting the molecular mechanism of gating. These include: covalent activation (reviewed in Kaupp and Seifert, 2002), polymer-linked cGMP dimers (reviewed in Brown et al., 2006), chimeras of different channel types (e.g. Gordon and Zagotta, 1995) and the use of modulatory substances, such as Ni^{2+}, to discern subunit interactions (reviewed in Kaupp and Seifert, 2002).

The cyclic nucleotide binding domain (CNBD) in HCN channels is thought to function as an autoinhibitory domain, causing the channel to require relatively large

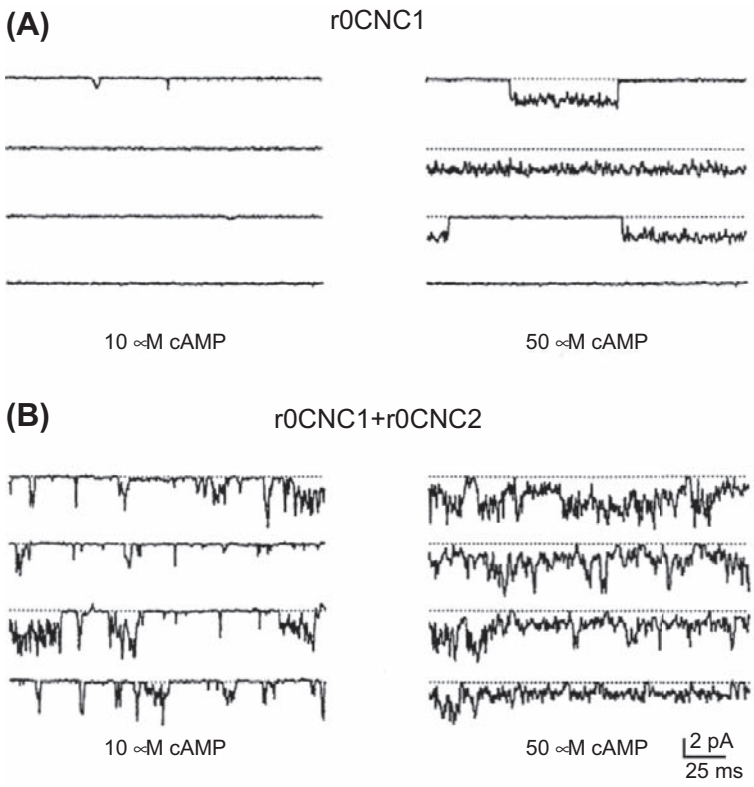

FIGURE 35.6 Increased cAMP sensitivity and flickery gating produced by co-expressing the second olfactory CNG channel subunit (r0CNC2; now called CNGA4) with the first (r0CNC1; now called CNGA2). When the first subunit is expressed alone (A) there are very few channel openings in 10 μM cAMP and the openings with 50 μM cAMP are much less flickery than those seen in (B), where both subunits are expressed in the same cell. Holding potential is −80 mV. *(Reproduced with permission from Liman and Buck, 1994. Copyright 1994 Cell Press.)*

negative voltages to activate (reviewed in Biel, 2009; Wahl-Schott and Biel, 2009). The binding of cAMP to the CNBD relieves that inhibition, allowing the channel to open at less negative voltages. The binding of cAMP also accelerates channel opening, leading to a steeper upstroke in the SA node action potential. Another function of cAMP in the SA node cells is activation of cAMP-dependent protein kinase, which phosphorylates voltage-dependent Ca^{2+} channels, facilitating their opening and further contributing to the increased frequency of SA node action potentials.

VB. Permeation, Selectivity and Block

CNG channels are relatively non-selective cation channels with no significant anion permeability. Thus, reversal potentials for most CNG channels studied under normal ionic conditions are about +5 to +20 mV. The monovalent alkali cation permeability sequence for the rod channel has been reported to be $Li^+ \geq Na^+ \geq K^+ \geq Rb^+ \geq Cs^+$ and Ca^{2+} and Mg^{2+} ions appear to be more permeant than the monovalent cations (reviewed in Kaupp and Seifert, 2002).

Cone and olfactory CNG channels also poorly discriminate among monovalent alkali cations, although their exact permeability sequences and ratios are not identical to those of the rod CNG channel. Strict comparisons are difficult because there is some variability in reported permeability ratios for each channel type. Relative permeabilities obtained may depend on whether the channels are studied in the intact cell, in excised patches, or in reconstitution or expression systems. The permeabilities may also depend on intracellular factors controlling functional modulation of the channels (see Section VI). In intact rods, the relative currents carried by monovalent and divalent cations have been found to depend on the concentration of cGMP (reviewed in Kaupp and Seifert, 2002). This finding, along with the dependence of subconductance states on cGMP (see below), suggests that the functional properties of CNG channels may change with the number of ligand molecules bound. If so, this may reflect a very interesting feature of these channels and one with tremendous potential for modifying physiological responses.

HCN channels differ from CNG channels in being significantly more selective for K^+ over Na^+ and having much lower Ca^{2+} permeability. Consistent with this high K^+ selectivity, the pore of an HCN channel contains the amino acid sequence, GYG (glycine-tyrosine-glycine) that is the hallmark of K^+-selective channels. Nevertheless, under physiological conditions (i.e. physiological concentration gradients and membrane potential), the main ion flowing through these channels is Na^+. Thus, under normal conditions, the opening of HCN channels, like that of CNG channels, produces a membrane depolarization.

Under physiological conditions, the rod CNG channel is occupied by Ca^{2+} or Mg^{2+} most of the time and these ions prevent the passage of Na^+ and K^+, which pass through the pore much more rapidly. Thus, these divalent cations behave as "permeant blockers". As a result of the very slow transport rate of the divalent cations, the mean single-channel conductance is extremely low – only about 0.1 pS in rods studied under physiological conditions. The channels can be blocked from either side but, under physiological conditions, they are mostly blocked by extracellular Ca^{2+} and Mg^{2+}. To resolve single-channel currents, one must reduce the concentration of divalent cations to the micromolar range. In the absence of divalent cations, the single-channel conductance is as high as tens of picosiemens. The extremely low single-channel conductance in physiological solutions gives an excellent signal-to-noise ratio for photon detection by rods, since the random openings and closings of individual channels produce only very tiny fluctuations in the dark current. The absorption of a single photon elicits the closure of hundreds of channels, giving a smooth, stereotypical waveform. If all those channels had single-channel conductances in the range of tens of picosiemens, the rod cell would have to contend with the consequences of a huge influx of Na^+ and Ca^{2+}. Cones and olfactory cells would have a similar problem, since their transducing regions also contain many CNG channels.

In the absence of divalent cations, *I-V* relations for CNG channels (with saturating cyclic nucleotide concentrations) are linear or nearly so (Fig. 35.7A and D, upper curve). Divalent cations introduce extreme non-linearity in the *I-V* relations (Fig. 35.7B and C). When the rod channel is studied in the presence of physiological concentrations of divalent cations, its *I-V* relation is very outwardly rectified.

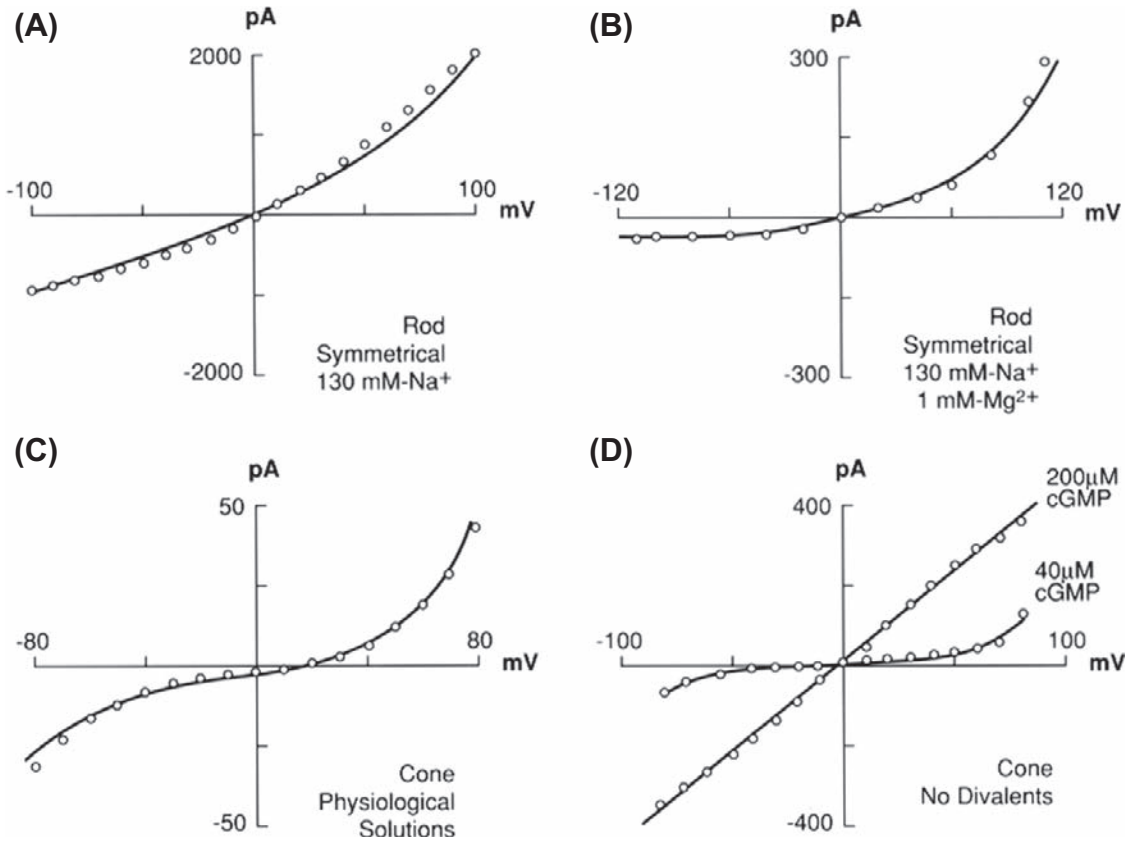

FIGURE 35.7 Current-voltage relations for photoreceptor cyclic GMP-activated currents from multichannel, excised patches. (A) The rod CNG channel relation is almost linear with saturating [cGMP] and no divalent cations. Olfactory CNG channels demonstrate a similar relation (not shown). (B) The addition of millimolar Mg^{2+} to both sides of the membrane gives strong outward rectification. Similar outward rectification has been reported for olfactory CNG channels. (C) Cone CNG channels show both outward and inward rectification in the presences of physiological (millimolar) levels of Mg^{2+} and Ca^{2+}. (D) The *I-V* relation for cone CNG channels is approximately linear with saturating [cGMP] and no divalent cations (top curve). Decreasing [cGMP] produces a non-linear *I-V* relation (bottom curve), because gating is slightly voltage dependent. Voltage-dependent gating of rod CNG channels also produces a very non-linear *I-V* relation [resembling that in (B)] in the absence of divalent cations, at low [cGMP]. *(Redrawn with permission from Zimmerman and Baylor, 1992 (A) and (B); from* Nature*, Haynes and Yau, 1985, Copyright 1985 Macmillan Magazines Limited (C); and Picones and Korenbrot, 1992 (D) Reproduced from The Journal of General Physiology, 1992, 100, 647–673, by copyright permission of The Rockefeller University Press.)*

Although some of this rectification is a consequence of the weak voltage dependence of channel gating described earlier, much of it results from channel block by Ca^{2+} and Mg^{2+}. Thus, at negative membrane potentials in the physiological range (about −40 to −80 mV), external Ca^{2+} and Mg^{2+} are drawn into the pore, reducing Na^{+} entry and giving an approximately flat *I-V* relation over a wide range of voltage. This very low, voltage-independent conductance in the physiological voltage range allows light-triggered outer segment voltage changes to travel relatively unattenuated to the inner segment to regulate synaptic transmission and also prevents the outer segment photon-sensing mechanism from fluctuating with voltage.

I-V relations of the olfactory channel, with and without divalent cations, are essentially indistinguishable from those of the rod channel, but surprisingly, the *I-V* relation for the cone channel is rather different. Whereas cone *I-V* curves from excised patches are linear in the absence of divalent cations, they are almost S-shaped when divalents are present (see Fig. 35.7C). Although the functional significance of this difference between cone CNG channels and those in rod cells and olfactory receptors is not clear, structurally, it may reflect a different location of the dominant ion-binding site within the cone channel. At subsaturating concentrations of cyclic nucleotides (which are closer to the physiological concentrations), the cone channel *I-V* relation is much more flat in the physiological range of membrane potential even in the absence of divalent cations (see Fig. 35.7D, lower curve). Similarly, the rod channel *I-V* curve shows increasing outward rectification as the cGMP concentration is lowered (not shown).

Single-channel recordings of the rod CNG channel in the absence of divalent cations have revealed at least two conductance states: one of about 25 to 30 pS and the other with a conductance about one-third as large. However, it has been suggested that the channel has at least one more, and perhaps many more, conductance levels. Because of the extremely rapid gating kinetics of this channel, numerous open-closed transitions are no doubt unresolved in the single-channel records. Thus, it is difficult to determine the exact number of distinct conductance states. It is also not clear whether these states are characterized by truly different ion transport rates or merely by different (incompletely resolved) open times, giving the appearance of different conductance levels. In the absence of divalent cations, the olfactory and cone CNG channels demonstrate major single-channel conductances around 45 to 50 pS, also with apparent subconductance states. Some results suggest a switching of the rod CNG channel from low to high conductance states with increasing ligand occupancy (reviewed in Kaupp and Seifert, 2002). The single-channel conductance of HCN channels is currently unresolved because there is a wide range of reported values — from 1 to 30 picoseimens. This large variability probably reflects variation in recording methods and types of cellular preparations (reviewed in Wahl-Schott and Biel, 2009).

Many pharmacological agents have been tested on CNG and HCN channels. Since CNG channels have a strong affinity for Ca^{2+}, various calcium channel blockers, such as verapamil and diltiazem, have been tested. Most block only weakly or not at all, but a few (e.g. L-*cis*-diltiazem and an amiloride analogue, 3′,4′-dichlorobenzamil) have been found to block effectively from the cytoplasmic surface of the membrane, with K_i values in the micromolar range. CNG channels also have been found to be blocked by a variety of other pharmacological agents (reviewed in Brown et al., 2006), but none have been found to bind with sufficient affinity and specificity. This also has been true for pharmacological agents against HCN channels, where the focus often has been K^{+} channel blockers.

VI. MOLECULAR STRUCTURE

Although CNG channels are ligand-gated channels, their molecular structures place them in the superfamily of voltage-gated cation channels, along with the HCN channels. The members of this family are characterized by a repeating structural motif, like that shown in Fig. 35.8, containing six putative membrane-spanning segments,

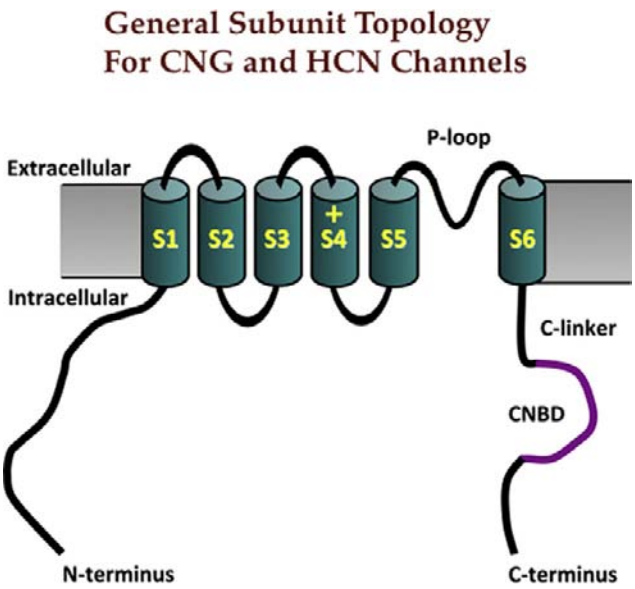

FIGURE 35.8 A model for the general organization of a CNG or HCN channel subunit. The model is based on information from many studies. Like typical voltage-gated K^{+} channel subunits, CNG channels are characterized by intracellular N- and C-termini, six transmembrane segments (S1−S6) and a region called the P-loop that lies between S5 and S6 and forms the selectivity filter through which ions pass. Cyclic nucleotide monophosphates, like cAMP and cGMP, bind in the cyclic nucleotide binding domain (CNBD) of the intracellular C-terminus. The C-linker region is thought to connect cyclic nucleotide binding at the CNBD to the allosteric opening transition involving movement of S6.

located between the hydrophilic N- and C-terminal regions that project into the cytosol. Also characteristic of these channels is a putative pore region (P-region) and an S4 transmembrane segment that contains many basic residues and is thought to be a voltage-sensing region. Of course, the channel region that best distinguishes CNG and HCN channels from a typical voltage-gated cation channel is the C-terminal cyclic nucleotide binding domain (CNBD), which resembles that found in other cyclic nucleotide-regulated proteins (e.g. cGMP-dependent protein kinase). A region often referred to as the C-linker, that connects the CNBD with the last transmembrane segment (S6), has been proposed functionally to link the cyclic nucleotide binding event to the allosteric opening transition of the channel (reviewed in Craven and Zagotta, 2006).

When the first subunit of the bovine rod CNG channel was cloned, the channel was proposed to consist of multiple identical subunits, each with a cGMP-binding site located in the C-terminal region. It now seems clear that the rod channel is a tetramer consisting of α and β subunits (CNGA1 and CNGB1, respectively; reviewed in Hofmann et al., 2005) and that there is a variety of other subunits that can associate to form functional CNG channels. The following subunit types have been identified in vertebrates: CNGA1, CNGA2, CNGA3, CNGA4, CNGA5, CNGB1 and CNGB3. The most recent addition to the list is CNGA5, which so far has only been found in the brain and pituitary of the zebrafish (Tetreault et al., 2006; Kahn et al., 2010). Functional homomeric channels can be made from all α subunits except CNGA4, but not from any β subunits. The subunit stoichiometry that has been proposed for rod, cone and olfactory CNG channels is as follows: in rods, three CNGA1s and one CNGB1; in cones, two CNGA3s and two CNGB3s; and in olfactory receptor cells, two CNGA2s, one CNGA4 and one CNGB1b (an alternatively spliced variant of CNGB1) (reviewed in Zimmerman, 2002; Bradley et al., 2005). Subunit stoichiometry and order remain to be determined for CNG channels in other cell types.

The known vertebrate HCN subunit types are HCN1, HCN2, HCN3 and HCN4. Each type has been found to form functional homomeric channels. Although some combinations have been identified in specific tissues and species (e.g. the rabbit heart SA node contains heteromeric channels that consist of HCN1 and HCN4), the subunit stoichiometries and arrangements have not been determined in any preparation. Outside the vertebrate world, an interesting HCN channel from sea urchin sperm (spHCN) has unusual gating properties that have provided some recent insights into voltage-dependent activation of HCN channels (reviewed in Wahl-Schott and Biel, 2009).

In addition to having two types of subunits, the rod CNG channel is part of a larger molecular complex. The rod β subunit (CNGB1) contains a very long glutamic acid-rich peptide (GARP) near its N-terminus. This GARP region connects with structural molecules on the rod cell's disk rims (see Chapter 38), giving it a potential role not only in channel function, but also in the structural stability and development of the rod cell and its internal disks. Free GARP molecules also have been found to inhibit the rod CNG channel (Michalakis et al., 2011). Furthermore, the rod CNG channel α subunits (CNGA1s) are tightly associated with Na^+:Ca^{2+},K^+ exchange carriers (see Chapter 38). The nature of the interactions of the rod CNG channel with these other molecules, and their functional consequences, are still under investigation.

There are currently no available crystal structures of an entire CNG or HCN channel. However, the CNBD has been crystallized for HCN2 and for a bacterial CNG channel, MloK1 (Zagotta et al., 2003; Schünke et al., 2011; reviewed in Craven and Zagotta, 2006). Although these structures have provided important information, numerous structural questions remain to be answered for both CNG and HCN channels, especially since crystal structures are static and since the CNBDs in those structures were disconnected from other channel regions. For example, despite extensive structure—function research, we still know only a few of the molecular details regarding interactions between subunits and between N- and C-terminal domains. In olfactory CNG channels, the latter interaction seems to be autoexcitatory and is disrupted by Ca^{2+}-calmodulin, which strongly inhibits channel opening (reviewed in Trudeau and Zagotta, 2003). It is also not known why the rod CNG α subunit is post-translationally cleaved *in vivo*, so that before its insertion into the rod membrane its molecular weight is reduced from 78 kilodaltons to 63 kilodaltons, with the loss of the end of its N-terminal tail (reviewed in Kaupp and Seifert, 2002). It also is not known exactly what structural changes occur in converting the binding of cyclic nucleotide at the C-terminus to the opening of the channel, how the selectivity filter is involved in this, or how the action of channel modulators (see following) is structurally linked to changes in channel gating. Finally, the nature of the regulation of HCN channels by cyclic nucleotides remains a mystery: although all HCN subunits have CNBDs, cAMP has a large effect on HCN2 and HCN4, but very little effect on HCN1 and HCN3. Mutational studies suggest this difference may be explained by the presence or absence of some type of "silencing" region outside the CNBD (reviewed in Wahl-Schott and Biel, 2009).

VII. FUNCTIONAL MODULATION

New information suggests that CNG channels may be modulated in ways that are only beginning to be elucidated. As mentioned above, there are hints that the ionic selectivity of the rod CNG channel may vary with the amount of cyclic nucleotide bound. There is also now evidence that the cGMP sensitivity of the rod channel may be tuned up or

down by phosphorylation and reduced by calmodulin in the presence of Ca^{2+} (reviewed in Kaupp and Seifert, 2002). It has not been determined whether other channel properties are also altered by these modulators. Protons modulate the rod CNG channel, increasing its open probability, while reducing its single-channel conductance (Gavazzo et al., 1997). Transition metal divalent cations, such as Ni^{2+}, also modulate CNG channel gating (reviewed in Kaupp and Seifert, 2002); interestingly, 10 μM Ni^{2+} increases the open probability of the rod channel, but decreases the open probability of the olfactory channel. Higher concentrations of Ni^{2+} block the pores of both rod and olfactory channels. Finally, there is mounting evidence that, in rods, the CNG channel interacts with Na^+:Ca^{2+},K^+ exchange carriers (see Chapter 38). The detailed functional significance of this interaction remains to be determined but, at the very least, it would allow the Ca^{2+} that enters through the CNG channels to be expelled more rapidly than if this tight association did not exist. Functional modulation of the rod CNG channel may help explain the large variability in reported cGMP affinity and cooperativity and may play a role in some aspects of visual transduction.

The gating of olfactory CNG channels has been found to be dramatically modulated by intracellular Ca^{2+}. Fig. 35.9 (Zufall et al., 1991) shows single-channel recordings obtained from an excised patch of olfactory dendritic membrane. When the concentration of Ca^{2+} bathing the intracellular surface of the patch was increased from 0.1 to 3 μM, there was a striking increase in channel closed time, giving a decrease in open probability. This modulation also has been found to involve calmodulin and, possibly, an endogenous Ca^{2+} binding protein distinct from calmodulin (reviewed in Pifferi et al., 2006 and Chapter 39). Research on cloned olfactory CNG channels suggests this inhibition results from disruption of an autoexcitatory interaction between the channel's N- and C-termini (reviewed in Trudeau and Zagotta, 2003).

HCN channels have been found to be modulated by a variety of factors, including protons, phosphoinositides, phosphorylation enzymes and Cl^-. These channels also appear to be regulated by interactions with a variety of proteins, including scaffolding proteins and other auxiliary proteins. Evidence suggests that such functional regulation of HCN occurs within elaborate intracellular molecular complexes (reviewed in Wahl-Schott and Biel, 2009).

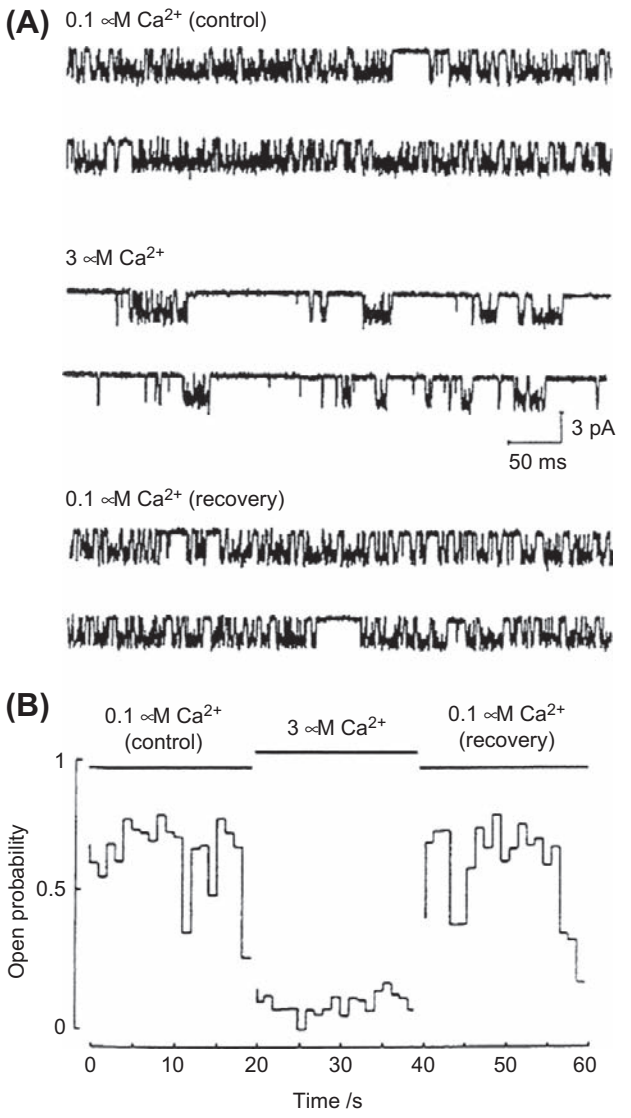

FIGURE 35.9 Modulation of an olfactory CNG channel by Ca^{2+}. Raising the Ca^{2+} concentration from 0.1 to 3 μM at the intracellular surface of an excised patch produced a reversible increase in channel closed time, resulting in a decrease in channel open probability. The cAMP concentration was 100 μM and the holding potential was −60 mV. Channel opening gives a downward deflection in current. *(Reproduced with permission from Zufall et al., 1991.)*

BIBLIOGRAPHY

Barnstable, C. J., Wei, J. Y., & Han, M. H. (2004). Modulation of synaptic function by cGMP and cGMP-gated cation channels. *Neurochem Int, 45*, 875–884.

Biel, M. (2009). Cyclic nucleotide-regulated cation channels. *J Biol Chem, 284*, 9017–9021.

Biel, M., & Michalakis, S. (2009). Cyclic nucleotide-gated channels. *Handb Exp Pharmacol, 191*, 111–136.

Bradley, J., Li, J., Davidson, N., Lester, H. A., & Zinn, K. (1994). Heteromeric olfactory cyclic nucleotide-gated channels: α subunit that confers increased sensitivity to cAMP. *Proc Natl Acad Sci USA, 91*, 8890–8894.

Bradley, J., Reisert, J., & Frings, S. (2005). Regulation of cyclic nucleotide-gated channels. *Curr Opin Neurobiol, 15*, 343–349.

Broillet, M.-C., & Firestein, S. (2004). Cyclic nucleotide-gated channels: multiple isoforms, multiple roles. *Adv Mol Cell Biol, 32*, 251–267.

Brown, R. L., Strassmaier, T., Brady, J. D., & Karpen, J. W. (2006). The pharmacology of cyclic nucleotide-gated channels: emerging from the darkness. *Curr Pharm Des, 12*, 3597–3613.

Contreras, J. E., Srikumar, D., & Holmgren, M. (2008). Gating at the selectivity filter in cyclic nucleotide-gated channels. *Proc Natl Acad Sci USA, 105*, 3310–3314.

Craven, K. B., & Zagotta, W. N. (2006). CNG and HCN channels: two peas, one pod. *Annu Rev Physiol, 68*, 375–401.

Cukkemane, A., Seifert, R., & Kaupp, U. B. (2011). Cooperative and uncooperative cyclic-nucleotide-gated ion channels. *Trends Biochem Sci, 36*, 55–64.

DiFrancesco, D. (2010). The role of the funny current in pacemaker activity. *Circ Res, 106*, 434–446.

Fesenko, E. E., Kolesnikov, S. S., & Lyubarsky, A. L. (1985). Induction by cyclic GMP of cationic conductance in plasma membrane of retinal rod outer segment. *Nature, 313*, 310–313.

Gauss, R., & Seifert, R. (2000). Pacemaker oscillations in heart and brain: a key role for hyperpolarization-activated cation channels. *Chronobiol Int, 17*, 453–469.

Gavazzo, P., Picco, C., & Menini, A. (1997). Mechanisms of modulation by internal protons of cyclic nucleotide-gated channels cloned from sensory receptor cells. *Proc Biol Sci, 264*, 1157–1165.

Gordon, S. E., & Zagotta, W. N. (1995). Localization of regions affecting an allosteric transition in cyclic nucleotide-activated channels. *Neuron, 14*, 857–864.

Haynes, L., & Yau, K.-W. (1985). Cyclic GMP-sensitive conductance in outer segment membrane of catfish cones. *Nature, 317*, 61–64.

Hofmann, F., Biel, M., & Kaupp, U. B. (2005). International Union of Pharmacology. LI. Nomenclature and structure-function relationships of cyclic nucleotide-regulated channels. *Pharm Rev, 57*, 455–462.

Karpen, J. W., Brown, R. L., Stryer, L., & Baylor, D. A. (1993). Interactions between divalent cations and the gating machinery of cyclic GMP-activated channels in salamander retinal rods. *J Gen Physiol, 101*, 1–25.

Kaupp, U. B., & Seifert, R. (2001). Molecular diversity of pacemaker ion channels. *Annu Rev Physiol, 63*, 235–257.

Kaupp, U. B., & Seifert, R. (2002). Cyclic nucleotide-gated ion channels. *Physiol Rev, 82*, 769–824.

Khan, S., Perry, C., Tetreault, M. L., et al. (2010). A novel cyclic nucleotide-gated ion channel enriched in synaptic terminals of isotocin neurons in zebrafish brain and pituitary. *Neuroscience, 165*, 79–89.

Liman, E. R., & Buck, L. B. (1994). A second subunit of the olfactory cyclic nucleotide-gated channel confers high sensitivity to cAMP. *Neuron, 13*, 611–621.

Martínez-François, J. R., Xu, Y., & Lu, Z. (2009). Mutations reveal voltage gating of CNGA1 channels in saturating cGMP. *J Gen Physiol, 134*, 151–164.

Matthews, G., & Watanabe, S.-I. (1987). Properties of ion channels closed by light and opened by guanosine 3′5′-cyclic monophosphate in toad retinal rods. *J Physiol, 389*, 691–715.

Mazzolini, M., Marchesi, A., Giorgetti, A., & Torre, V. (2010). Gating in CNGA1 channels. *Pflügers Arch Eur J Physiol, 459*, 547–555.

Michalakis, S., Zong, X., Becirovic, E., et al. (2011). The glutamic acid-rich protein is a gating inhibitor of cyclic nucleotide-gated channels. *J Neurosci, 31*, 133–141.

Nakamura, T., & Gold, G. H. (1987). A cyclic nuceotide-gated conductance in olfactory receptor cilia. *Nature, 325*, 442–444.

Picones, A., & Korenbrot, J. I. (1992). Permeation and interaction of monovalent cations with the cGMP-gated channel of cone photoreceptors. *J Gen Physiol, 100*, 647–673.

Pifferi, S., Boccaccio, A., & Menini, A. (2006). Cyclic nucleotide-gated ion channels in sensory transducion. *FEBS Lett, 580*, 2853–2859.

Schünke, S., Stoldt, M., Novak, K., Kaupp, U. B., & Willbold, D. (2011). Solution structure of the Mesorhizobium loti K1 channel cyclic nucleotide-binding domain in complex with cAMP. *EMBO Rep, 10*, 729–735.

Tang, C. Y., & Papazian, D. M. (1997). Transfer of voltage independence from a rat olfactory channel to the Drosophila ether-a-go-go K^+ channel. *J Gen Physiol, 109*, 301–311.

Tetreault, M. L., Henry, D., Horrigan, D. M., Matthews, G., & Zimmerman, A. L. (2006). Characterization of a novel cyclic nucleotide-gated channel from zebrafish brain. *Biochem Biophys Res Commun, 348*, 441–449.

Trudeau, M. C., & Zagotta, W. N. (2003). Calcium/calmodulin modulation of olfactory and rod cyclic nucleotide-gated ion channels. *J Biol Chem, 278*, 18705–18708.

Wahl-Schott, C., & Biel, M. (2009). HCN channels: structure, cellular regulation and physiological function. *Cell Mol Life Sci, 66*, 470–494.

Wohlfart, P., Haase, W., Molday, R. S., & Cook, N. J. (1992). Antibodies against synthetic peptides used to determine the topology and site of glycosylation of the cGMP-gated channel from bovine rod photoreceptors. *J Biol Chem, 267*, 644–648.

Yu, F. H., Yarov-Yarovoy, V., Gutman, G. A., & Catterall, W. A. (2005). Overview of molecular relationships in the voltage-gated ion channel superfamily. *Pharmacol Rev, 57*, 387–395.

Zagotta, W. N., Olivier, N. B., Black, K. D., Young, E. C., Olson, R., & Gouaux, E. (2003). Structural basis for modulation and agonist specificity of HCN pacemaker channels. *Nature, 425*, 200–205.

Zimmerman, A. L. (2002). Two B or not two B? Questioning the rotational symmetry of tetrameric ion channels. *Neuron, 36*, 997–999.

Zimmerman, A. L., & Baylor, D. A. (1992). Cation interactions within the cyclic GMP-activated channel of retinal rods from the tiger salamander. *J Physiol, 449*, 759–783.

Zufall, F., Shepherd, G. M., & Firestein, S. (1991). Inhibition of the olfactory cyclic nucleotide gated ion channel by intracellular calcium. *Proc R Soc London Ser B, 246*, 225–230.

Chapter 36

Sensory Receptors and Mechanotransduction

Andrew S. French and Päivi H. Torkkeli

Chapter Outline

I. INTRODUCTION

While most living cells can detect and respond to a variety of changes in their external physical and chemical environments, we usually reserve the term *sensory receptor* for those cells that transmit information about such changes to the animal's nervous system. Even this classification must be qualified. For example, the heart and other hollow organs have localized, mainly autonomous, nervous systems that allow sensory receptors to produce very local functional changes. Moreover, some of the mechanisms that cells use to detect external events seem to be very similar as we move from unicellular animals to the complex sensory organs of humans. With these caveats in mind, this chapter is restricted to those cells (usually neurons) that transmit sensory information into one or more divisions of the central nervous system.

Several general principles can be applied to all sensory receptors. The concept of *modality* means that each sensory cell transmits information about only one type of environmental stimulus. Photoreceptors detect light but are insensitive to touch, while stretch receptors do not respond to odorant molecules. Within the modalities there are further specializations, so that cold temperature receptors do not respond to hot stimuli and sweet taste receptors do not respond to bitter substances. Each type of receptor seems to produce specific molecular machinery for detecting just one type of stimulus. An exception to this rule is provided by the cutaneous polymodal pain receptors (McGlone and Reilly, 2009) which respond to mechanical, thermal or chemical stimuli.

Neurons carrying information into the nervous system form *labeled lines* that signal specific modalities and specific locations. Artificially stimulating a sensory nerve by electrical or mechanical stimulation produces a sensation that reflects the modality and location of the sensory ending, not the artificial stimulus. Another general principle is that the intensity of the stimulus is encoded as the amplitude of the electrical signal passing along the sensory neuron. In most cases, this means the action potentials propagating along the sensory axon, with more action potentials per second representing a stronger stimulus. In some cases, the stimulus produces a decrease in ongoing neuronal activity. However, there are several situations where the primary sensory cell does not produce action potentials at all, but a graded change in membrane potential that is conducted decrementally along the cell. Graded potentials can usually be propagated for only very short distances (a few millimeters at most), so such cells are

Cell Physiology Sourcebook. DOI: 10.1016/B978-0-12-387738-3.00036-6

generally small. Well-known examples are the rods and cones of the retina and the hair cells of the inner ear.

II. SENSORY TRANSDUCTION

Sensory cells respond to an external stimulus by changing their membrane potential, although several processes may occur before and after this *transduction* step. This change in membrane potential is called a *receptor potential* and it is a graded potential, increasing and decreasing with the intensity of the stimulus. Non-sensory neurons are insensitive to external stimuli, such as mechanical stress, temperature or light, unless these reach such intensity as to threaten the cell's normal function or integrity. Therefore, sensory receptors must have specializations to detect external stimuli (Fig. 36.1). Conceptually, the simplest receptors are the electroreceptors, which use an external electrical current to change their own membrane potential by direct current flow. Although the concept is simple, these cells are highly specialized to maximize their electrical sensitivity. Current flows through resting membranes by the passage of ions through ion channels that are open at rest. The salt taste receptors of the tongue and mouth also rely on direct ion flow through ion channels. In this case, the channels are selective for Na^+ and can be blocked by amiloride, so that placing a small amount of amiloride in the mouth removes the ability to taste salt. Na^+ diffuses through these channels to depolarize the taste cell membrane. An additional level of complexity is illustrated by sour taste receptors, where cation channels are believed to be closed by external hydrogen ions, reducing outward K^+ current and depolarizing the cell. However, the sour taste receptor has not yet been identified.

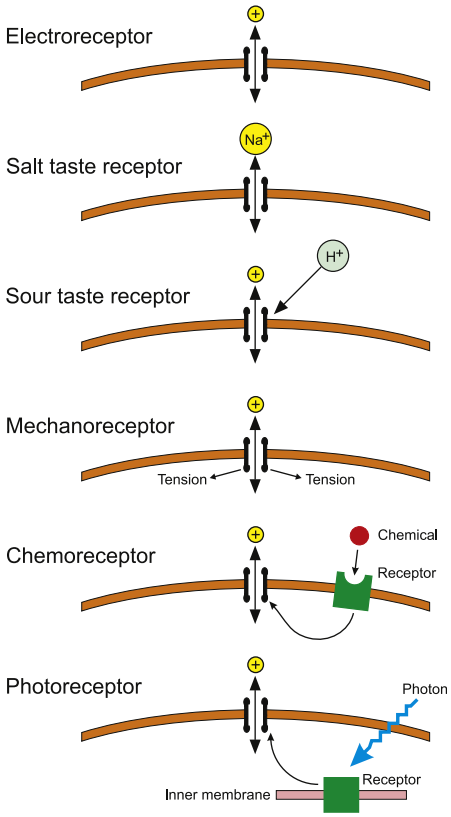

FIGURE 36.1 Mechanisms of sensory transduction organized by level of complexity. In each case the cell has specialized ion channels that produce a receptor current. Modulation of the current is achieved by changing the electrochemical force for the permeant ion in the cases of electroreceptors and salt taste receptors. In other receptors, the external stimulus changes the channel open probability, either by acting directly on the channel protein or via a second messenger cascade. Chemoreceptors have receptor proteins in the cell membrane. In vertebrate rods, the light-sensitive pigments, rhodopsins are in the internal disk membranes, but cones and invertebrate photoreceptors have their photopigments in invaginated cell membranes.

The fundamental transduction step in mechanoreceptors is not well understood, but is assumed to involve mechanically activated ion channels. These channels are believed to be either directly gated by forces acting on the plasma membrane or by tethers that connect the channel to the cytoskeleton or extracellular matrix (Christensen and Corey, 2007). If either model is true, this is another case where the external stimulus acts directly to open or close an ion channel. Finally, there are cases where the external stimulus acts indirectly through intermediate membrane receptors. In many chemoreceptors, specialized receptor proteins in the outer cell membrane activate ion channels through a second messenger cascade when they bind an appropriate stimulus molecule. In the case of rod photoreceptors, light activates specialized light-sensitive pigments in internal cell membranes, producing a second messenger cascade that eventually closes ion channels in the external membrane. Some models of mechanotransduction also suggest that a conformational change in a distant force-sensing component is communicated to the mechanotransduction channel by a second messenger (Christensen and Corey, 2007). It is not known which types of sensory receptor mechanisms evolved first, but it is clear that several, if not all, of these processes have close parallels in other non-sensory tissues, such as the Na^+ channels of epithelia, the mechanically activated channels of muscle and the second messenger cascades of synapses and secretory cells. It seems likely that the evolution of different sense modalities has taken advantage of pre-existing cellular mechanisms.

III. SENSORY ADAPTATION

Sensory receptors often have to deal with wide ranges of stimulus amplitudes. Therefore, they need high sensitivity to detect weak stimuli, plus the ability to reduce their sensitivity if the stimulus is strong. In some cases, the maximum sensitivity approaches the limits imposed by

physics or chemistry. Human rod photoreceptors and some arthropod photoreceptors can detect single photons arriving in the eye, which is clearly the physical limit. The human ear can detect air movements of about 0.01 nm, close to the diameter of a hydrogen atom (Hudspeth, 2005). In such cases, the sensory cells must amplify the initial signal considerably, which at least partly explains the complex morphologies of human rod photoreceptors and the cochlea.

The reduction in sensitivity following an increase in stimulus is called *adaptation*. It may be seen as a decrease in receptor potential with time during a constant stimulus, or as an increase in the strength of stimulus required to produce a constant response. All sensory receptors adapt to some extent, but there is a wide range of adaptation speeds and amounts. At one extreme are receptors such as Pacinian corpuscles (Loewenstein and Mendelson, 1965) and spider slit sensilla (French et al., 2002), which fire only one or two action potentials with even a strong, continuous stimulus. At the other extreme are Ruffini endings (Malinovsky, 1996), which continue to fire steadily for long periods. The type of adaptation is always appropriate to the function of the receptor. Muscle and joint receptors that signal limb position would not be useful if they adapted to silence in a few seconds, because the sense of limb position, or *proprioception*, would vanish if one did not keep moving. On the other hand, photoreceptors must function under a wide range of light intensities and it is essential that they can adjust their sensitivity to the ambient light level. The rapid adaptation of Pacinian corpuscles makes them ideally suited for detecting vibration, since a rapidly changing stimulus will repeatedly excite the receptor, while a steady stimulus will produce little response.

The mechanisms of adaptation vary widely and may occur at different stages of the process. Some involve components outside the sensory cell, such as the mechanical creep of the muscle in muscle spindles or the movements of screening pigments in insect eyes. Others may involve chemical signals within and between cells, as found in photoreceptors and olfactory receptors. Mechanical adaptation by the capsule of the Pacinian corpuscle is very well known from the pioneering work of Loewenstein and Mendelson (1965), who described the dramatic reduction in receptor potential adaptation that can be achieved by removing most of the capsule (Fig. 36.2). Unfortunately, many descriptions stop at this point, leaving the impression that mechanical adaptation dominates Pacinian corpuscle behavior, but Loewenstein and Mendelson showed that, even after decapsulation, the receptor will only fire one or two action potentials in response to a prolonged step stimulus (Fig. 36.2C). They described this as electrical adaptation and it now seems probable that many receptors use voltage- or calcium-activated ion channels in their membranes to produce electrical adaptation by raising the threshold for action potential production. This has been clearly established in several arthropod and vertebrate mechanoreceptors and is likely to occur in other types of receptors that use action potentials to encode the sensory signal (French and Torkkeli, 1994).

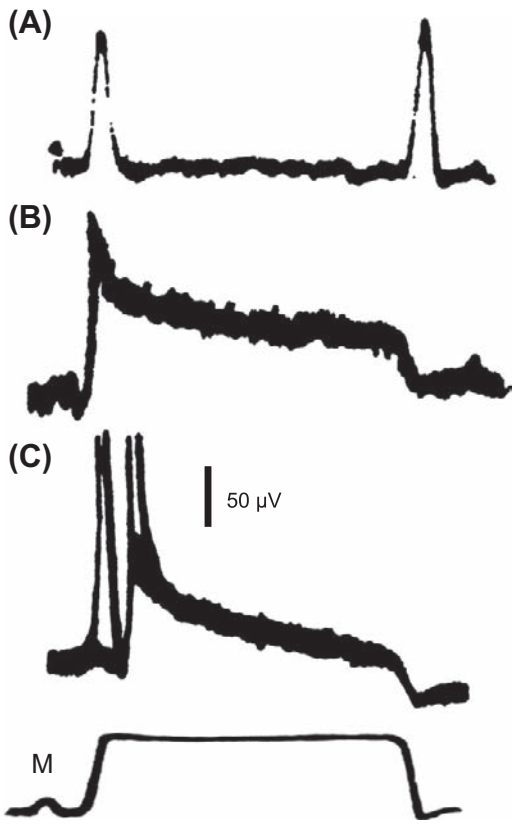

FIGURE 36.2 Adaptation in the mammalian Pacinian corpuscle occurs in two stages. (A) Stimulating a normal receptor with a mechanical step (M: bottom) causes rapidly adapting receptor potential responses at the start and end of the step. (B) Removing most of the lamellae surrounding the sensory ending (decapsulation) eliminates most of the adaptation to reveal a slowly adapting receptor potential. (C) Suprathreshold stimulation of a decapsulated receptor still produces only two action potentials, showing that there is rapid adaptation in the conversion of receptor potential to action potentials. *(Redrawn from Loewenstein and Mendelson, 1965.)*

IV. INFORMATION TRANSMISSION BY SENSORY RECEPTORS

Nervous systems and individual nerve cells deal with information. Cells with long axons transmit information over considerable distances and we assume that all nerve cells process information to some extent. Unfortunately, it is usually difficult to decide what the nature of the information is and how it is being processed, except in general terms. Sensory cells have been particularly important in trying to understand quantitatively how information is encoded and transmitted by nerve cells because it is usually

easier to define the input signal of a receptor neuron than other nerve cells. For example, the intensity and wavelength of light entering a photoreceptor or the length of a muscle spindle receptor can be accurately controlled while the output of the receptor in terms of receptor or action potentials is recorded.

Quantitative investigations of information flowing through sensory neurons have been based on ideas developed by engineers for dealing with artificial communication systems, such as telephone or television signals. Widespread use of digital communications has made the concept of *information transmission rate* (usually in bits per second, or bps) familiar. If we know the nature of the information being transmitted, we can measure the actual rate of transmission, but even if nothing is known about the kind of information being transmitted, it is possible to calculate the theoretical maximum rate that could be achieved by an optimum encoding scheme. This is called the *information capacity* of the system and it is closely related to the inherent noise in the system. The basic idea is that inherent noise limits the amplitudes and bandwidths of the signals that can be received unambiguously and thus the amount of information that can be transmitted and received in a given time. Note that when a noisy neuron fires action potentials the noise appears primarily as variability or randomness in the timing of the action potentials.

If a system behaves linearly, its information capacity can be calculated from the signal-to-noise ratio. This approach has been used in most estimates of receptor cell information capacity. Although relatively few measurements have been made, it is clear that cells using action potentials to transmit information have lower information capacities than those that do not. Spiking mechanoreceptors in cricket cercal mechanoreceptors and spider slit sensilla had capacities of 300 bps and 200 bps respectively, compared to values of 1650 bps for fly photoreceptors and 2240 bps for the receptor potential in spider slit sensilla before encoding (Juusola and French, 1997). However, it was possible to transmit information at rates up to 500 bps for short periods using a defined encoding scheme in a cockroach mechanoreceptor (French and Torkkeli, 1998), so we must be cautious about these estimates until we understand the actual encoding schemes that neurons use.

These findings support the concept that nerve cells use action potentials to transmit information faithfully over long distances, but there is a significant cost in information capacity. This probably explains why some sensory systems have elaborate neural structures located peripherally, close to the primary sensory neurons. A familiar example is the vertebrate retina, with two layers of nonspiking cells and complex synaptic interactions before the spiking ganglion cells. This arrangement presumably allows important information processing to take place on the high capacity input from the photoreceptors before it is encoded into the lower capacity ganglion cell axons.

V. MECHANORECEPTORS

VA. Vertebrate Mechanoreceptors

Vertebrate mechanoreceptors have such a wide variety of shapes and functions that classification is difficult. Many receptors bear the names of their original discoverers or rediscoverers, such as Meissner corpuscles and Ruffini endings. A variety of classification schemes have been used, based on features such as the morphology of the sensory ending and its associated tissues, rates of adaptation and location in the body. The hair cells of the vertebrate auditory and vestibular systems have been studied extensively (Hudspeth, 2005; Fettiplace, 2009), and are described in Chapter 37. Mammalian cutaneous mechanoreceptors have their sensory endings in the skin and their cell bodies in the dorsal root or trigeminal ganglion (Tsunozaki and Bautista, 2009). Figure 36.3 shows a classification of these mechanoreceptors according to the embryonic origin of the tissues associated with the sensory ending and the complexity of the sensory ending itself (Malinovsky, 1996). Type I receptors are associated with tissues of mesodermal origin (connective tissues and muscle) and include the Ruffini endings of the joints and skin, the Golgi tendon organs and the muscle spindles. Type II receptors are transitional between type I and type III and are associated with tissues of endodermal or ectodermal origin. They include the Merkel endings, where each sensory ending is closely apposed to a specialized

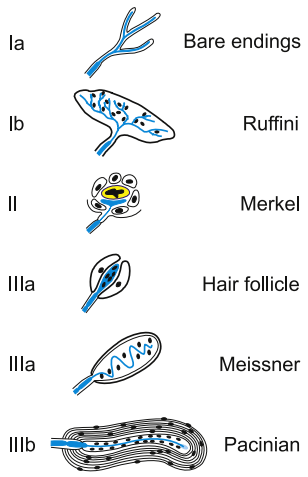

FIGURE 36.3 Classification of vertebrate mechanoreceptors by embryonic origin of associated tissues and complexity of ending; showing major examples. Type I are associated with tissues of mesodermal origin, type II with endodermal or epidermal and type III with epidermal. Subtypes (Ia, Ib, etc.) indicate morphological complexity. *(Redrawn from Malinovsky, 1996.)*

Merkel cell that is derived from epidermal lineage. Type III receptors are clearly associated with tissues of ectodermal origin and comprise a wide range of receptors including the bulbous endings found in hair follicles, the Meissner corpuscles and the Pacinian corpuscles. This classification broadly accompanies a functional shift from slowly adapting receptors (such as Ruffini endings) in the type I group to rapidly adapting receptors in the type III groups (such as Pacinian corpuscles). Phylogenetically, type I and type II receptors are found in all classes of vertebrates from fish to primates, while type III receptors are unknown in fish, start to occur in amphibia and become increasingly common in higher vertebrates (Malinovsky, 1996).

Vertebrate mechanoreceptors and nociceptors can also be classified based on myelination, conduction velocity of the afferent nerve fibers and whether they have low or high threshold as shown in Table 36.1 (Tsunozaki and Bautista, 2009). A further classification is based on the receptive field of the low threshold receptors; Meissner corpuscles and Merkel disks are located close to the skin surface and have small receptive fields while Pacinian corpuscles and Ruffini endings are located deeper in the dermis and have large receptive fields (McGlone and Reilly, 2009). Although most unmyelinated C-fibers originate from nociceptors that respond to one or more types of painful stimuli, one type of C-fiber is purely a touch receptor. These tactile C-fibers are only found in hairy skin and respond to slowly moving mechanical stimuli (McGlone and Reilly, 2009).

VB. Invertebrate Mechanoreceptors

Arthropods, especially insects, spiders and crustaceans, have provided important preparations for the investigation of mechanoreceptor function. Their receptors can be divided into two major groups, cuticular and multipolar, sometimes called type I and type II mechanoreceptors. *Cuticular receptors*, as the name implies, are generally associated with the arthropod cuticle and have their cell bodies in the periphery, close to the sensory ending. This arrangement is very different than most vertebrate and other invertebrate mechanoreceptors, which have their cell bodies in the central nervous system, distant from the sensory ending, and it allows recordings to be made close to the site of mechanotransduction. In addition, many

TABLE 36.1 Mammalian Cutaneous Sensory Fiber Types

	Fiber Group	Diameter (μm)	Fiber Type	Sensory Ending	Sensation	Conduction Velocity (m/s)	Von Frey Threshold (mN)
Myelinated	Aα	20	Proprioceptors from muscles and tendons		Proprioception	120	
	Aβ	5–12	Low threshold, rapidly adapting	Pacinian, Meissner	Touch	>10	1.0
			Low threshold, slowly adapting	Merkel, Ruffini	Touch	>10	1.5
	Aδ	2–5	Low threshold	Hair	Touch	2–10	<0.5
			Aδ mechanoreceptor	Free nerve ending	Mechanonociception	2–10	5
Unmyelinated	C	0.3–1.3	Polymodal	Free nerve ending	Mechano- heat- and chemonociception	<1.5	10
			Uni- or multimodal	Free nerve ending	Mechano- and/or heat- and/or cold-nociception	<1.5	6
			Silent[1]	Free nerve ending	Mechano- and/or heat-nociception	<1.5	N/A
			Low threshold	Free nerve ending	Touch	<1.5	<0.5

Approximate measurements are from cat.
[1]*Silent fibers activate only after sensitization (Kress, M., Koltzenburg, M., Reeh, P.W. and Handwerker, H.O. (1992). Responsiveness and functional attributes of electrically localized terminals of cutaneous C-fibers in vivo and in vitro. J Neurophysiol. 68, 581-595).*
Based on McGlone and Reilly, 2009; Smith, E.S. and Lewin G.R. (2009). Nociceptors: a phylogenetic view. J Comp Physiol A. 195, 1089-1106.

arthropod receptor cells are relatively large, allowing penetration by microelectrodes, which is impossible in most vertebrate receptors.

There are three major groups of cuticular receptors (Fig. 36.4). *Hair-like* receptors are found all over the outer surfaces of most arthropods in a variety of shapes and sizes from long, thin hairs to short pegs. The hair is supported by flexible cuticle within a socket and moves relative to the skin. In insects, a single mechanoreceptor neuron is closely apposed to the base and its sensory ending contains microtubules that end in a dense tubular body. It is assumed that movement of the hair compresses the ending, with the tubular body perhaps adding a rigid structure that the compression can work against. Crustacean and spider hairs are similar, but with two to four mechanosensory neurons in each hair. All arthropod hair types can contain other sensory neurons in addition to the mechanoreceptors, such as chemoreceptors in taste hairs. *Campaniform* (bell-shaped) sensilla are found in insects, where they detect stress in the cuticle. The stress leads to compression of a dendritic tip containing a tubular body by squeezing the bell as it is pushed downwards. Arachnids have analogous stress-detecting receptors called slit sensilla, where the neurons are located in cuticular slits. *Chordotonal* receptors are generally found further beneath the integument, although they can be connected to the integument by attachment structures. They serve a variety of functions,

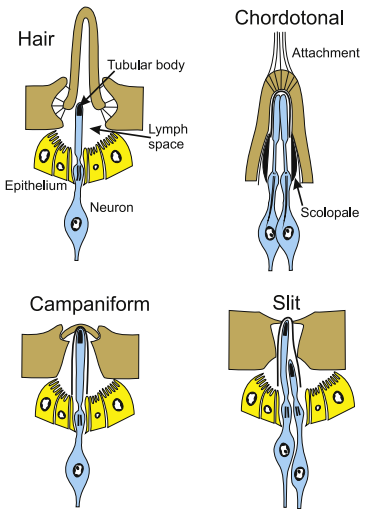

FIGURE 36.4 Four common types of ciliated arthropod cuticular mechanoreceptors. Hair receptors of various shapes are prevalent in many arthropods. Chordotonal receptors are found in insects and crustaceans, campaniform sensilla in insects and slit sensilla in arachnids. Sensory dendrites are usually surrounded by a dense sheath and often contain tubular bodies formed from microtubules embedded in electron-dense material. Epithelial layers connected by tight junctions form a lymph space surrounding the dendrite. Chordotonal sensilla feature dense scolopale rods surrounding sensory dendrites and may have an attachment to another structure, such as a joint.

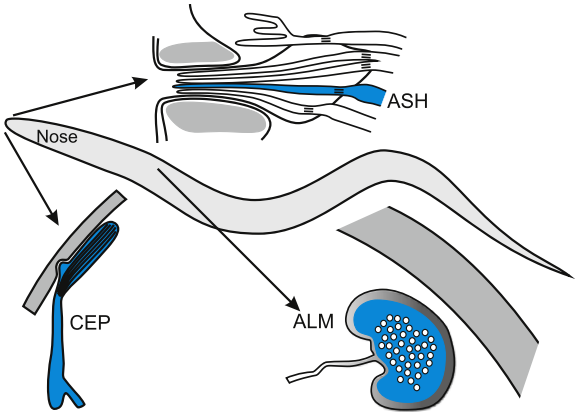

FIGURE 36.5 Mechanoreceptors of the nematode *C. elegans*. Ciliated amphid (ASH) and cephalic (CEP) sensory neurons are found in the nose of the animal; ASH neurons are with a group of chemosensory neurons in the labial region and CEP neurons are closely apposed to cuticle. Gentle touch of the body is detected by anterior lateral microtubule (ALM) neurons, which contain many microtubules and are surrounded by extracellular matrix. *(Based on Chalfie, 2009.)*

including hearing and joint movement detection. They generally lack tubular bodies but have dense scolopale structures surrounding the dendrite and can have multiple mechanosensory neurons.

The nematode *Caenorhabditis elegans* also provides important models of mechanotransduction (Fig. 36.5). Its mechanoreceptors can be divided into three groups based on the specialization of their cytoskeleton. The first group has ciliated sensory endings, some of which abut to the cuticle while others, such as the polymodal sensory neuron in the nose, are located in channels that are open to external environment. Mechanoreceptors in the second group, including the gentle touch receptor neurons, are not ciliated but have large diameter microtubules in their sensory processes that are surrounded by an extracellular matrix, the mantle. The third group, including the harsh touch receptor, do not have specialized cytoskeleton. As the morphological differences suggest, research involving genetic manipulations combined with patch-clamp recordings have shown that several different mechanisms are involved in *C. elegans* mechanotransduction (O'Hagan et al., 2005; Chalfie, 2009; Kang et al., 2010).

VC. Muscle Mechanoreceptors

One of the best-known arthropod mechanoreceptors is the crayfish stretch receptor, which has interesting similarities to vertebrate muscle spindles (Fig. 36.6). These receptors are found on many muscles in crustaceans and are multipolar or type II arthropod mechanoreceptors. The large cell bodies are located in the periphery and the sensory endings consist of finely divided dendrites that cover part of the muscle surface. Unlike muscle spindles, crayfish stretch receptors

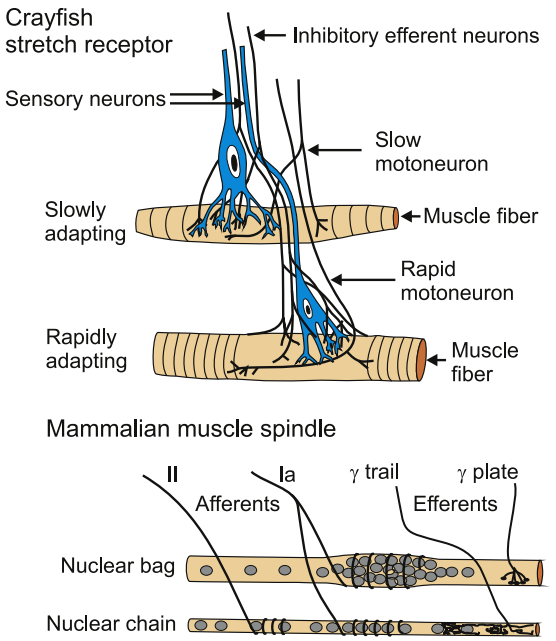

FIGURE 36.6 Invertebrate and vertebrate muscle mechanoreceptors. Crustacean stretch receptors are multipolar mechanoreceptors with many fine dendrites embedded in muscle fibers. There are two types of sensory neurons with different adaptation properties. Efferent GABAergic inhibitory neurons synapse onto the sensory neurons as well as the muscle fibers. *(Partly based on Rydqvist et al., 2007.)* Mammalian muscle spindles are modified muscle cells located within the main muscle and contain two types of fibers (nuclear bag and nuclear chain) with their own efferent innervation via two types of γ-motoneurons (γ-plate and γ-trail) that are activated separately from the main muscle fibers. There are also two types of sensory endings (Ia and II) with different adaptation characteristics. A whole muscle may contain hundreds of the much smaller muscle spindles.

are located on the main, force-producing muscle, and so are directly excited by passive stretch of the muscle or activation of motoneurons. This opens stretch activated ion channels that are permeable to Na^+, K^+ and Ca^{2+}. Crayfish stretch receptors also receive presynaptic γ-aminobutyric acid (GABA) -ergic innervation to the sensory neuron directly, as well as the muscle (Rydqvist et al., 2007).

Vertebrate muscle spindles are prominent and numerous mechanoreceptors that detect muscle stretch and are believed to be crucially involved in the control of muscle activation. However, they also make a major contribution to the senses of body position and movement (proprioception and kinesthesia) because appropriate artificial stimulation of muscle spindles gives sensations that the limbs are moving or in incorrect positions. Mammalian muscle spindles are small, modified muscle fibers located between the main, force-producing muscle fibers. Two types of sensory endings contact the spindle fibers and detect their length using mechanically activated cation channels. Spindle fibers are innervated by separate γ-motoneurons that allow the central nervous system to adjust their length, and hence the sensitivity of the receptors.

Closely associated with muscle spindles are the Golgi tendon organs. Located at the insertion of muscle fibers into the skeletal muscle tendons, these receptors use mechanically activated cation channels to detect muscle tension, rather than length, and contribute to reflex control of muscle activity.

VI. EXPERIMENTAL MECHANORECEPTOR PREPARATIONS

The complicated structures of many mechanoreceptor preparations make it challenging to record the receptor potential or receptor current, particularly while providing mechanical stimulation. Depending on the accessibility of the sensory neurons, various methods have been used (Fig. 36.7). *Decremental conduction* relies on insulating the sensory axon from the extracellular fluid as close as possible to the sensory ending, usually with a non-conducting substance, such as paraffin wax, petroleum jelly or sucrose solution, before leading it to a separate conducting solution. As the receptor is stimulated, some of the receptor current flows decrementally along the axon but cannot follow its normal path to the extracellular solution because of the insulation. It can only return through the second bath, where it is measured. This method has been used to observe the receptor potential in Pacinian corpuscles, muscle spindles and insect cuticular receptors. It allows a relatively stable preparation, because the receptor is not very disturbed and fine positioning is not needed after the initial setup. However, only a relatively small fraction of the total receptor current can usually be observed and the decremental conduction causes a selective loss of high-frequency signals through the membrane capacitance to ground, so that the observed receptor potential is attenuated and filtered. It is generally difficult to estimate accurately the amplitude and waveform of the original receptor potential.

Arthropod cuticular receptors have the sensory neurons so close to the surface that it is possible to observe part of the current flowing through the neuron from the exterior. For a hair receptor, a small pool of conducting solution can be placed in the hair socket and an electrode of some sort (glass, wire, wick) measures the potential in the pool. These *transepithelial* measurements rely on the high-resistance epithelium that surrounds cuticular receptor neurons (see below) and the relatively low resistance of the thin, flexible socket. A similar technique is used for cuticular chemoreceptors, where it is common to cut the hair and place the tip of an electrode over the cut end to obtain even better electrical contact. This is more difficult for mechanoreceptors, where the hair must be moved to stimulate transduction. However, this method has been successfully used to record mechanotransduction currents in *Drosophila* bristle hairs, an experimental preparation that also allowed electrophysiological testing of mechanoreceptive mutant

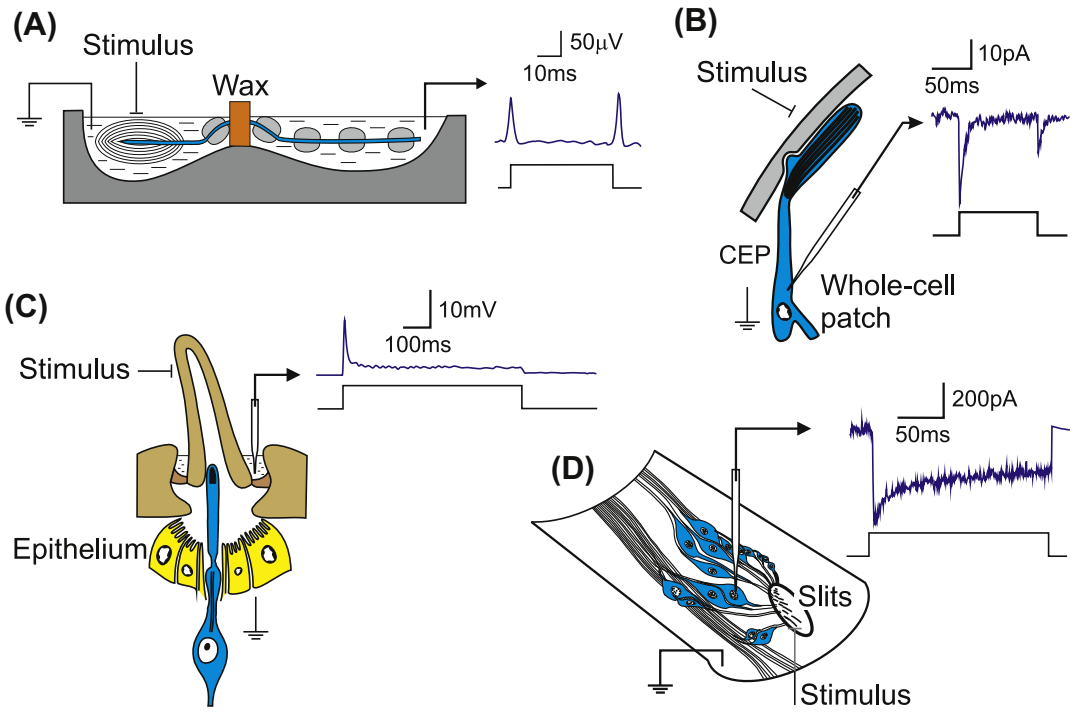

FIGURE 36.7 Examples of four methods that have been used to observe the receptor current and potential in mechanoreceptors. (A) Decremental conduction measures the current flowing along the sensory axon from a Pacinian corpuscle by insulating the axon as close as possible to the receptor. This prevents receptor current from reaching ground, except via the measuring bath. (B) Whole-cell patch-clamp of a CEP mechanosensory neuron beneath the nose cuticle of *C. elegans* while stimulating the external cuticle. (C) Transepithelial measurement of an arthropod hair receptor by sampling the voltage as close as possible to the lymph space surrounding the sensory ending and relying on the high resistance of the epithelium. (D) Intracellular recording from a neuron in the spider slit sensillum during mechanical stimulation of the slits from below. *(Redrawn in part from French et al., 2002; Kang et al., 2010.)*

flies (Walker et al., 2000). Transepithelial measurements allow a relatively stable recording situation, but the high-resistance access pathway attenuates the signal and emphasizes high frequencies, which can pass more easily through the cuticle. Here again, it is difficult to estimate the original receptor potential amplitude and time course with accuracy.

Intracellular recording close to the site of sensory transduction is clearly desirable if it can be accomplished. However, it requires stable penetration of a small neuron while the sensory ending is moved nearby and has only been successfully achieved in a few preparations. Even more useful is *voltage-clamp* of the sensory receptor membrane, since this allows the voltage across the ion channels to be controlled while the current flowing through them is recorded. Crustacean stretch receptors are relatively easy to penetrate, even with two microelectrodes, and have been used for pioneering studies of the mechano-transduction and other currents that contribute to the electrical properties of the neurons during sensory transduction (Rydqvist et al., 2007). However, the transduction currents probably originate in very fine endings embedded in the muscle (see Fig. 36.7) so that accurate voltage-clamp of this current is difficult. Voltage-clamp of arthropod cuticular receptors was first performed in the cockroach tactile spine (Torkkeli and French, 1994). A more successful cuticular preparation is that of spider slit sensilla, where it is possible to clamp the receptor potential close to the sensory ending while stimulating the slits (French et al., 2002).

Whole-cell patch-clamp recordings of *C. elegans* touch receptor neurons during mechanical stimulation have recently become possible (see Figs. 36.5 and 36.7) providing preparations where receptor currents and potentials can be studied in an animal model that also allows genetic screening (O'Hagan et al., 2005; Kang et al., 2010). Patch-clamp recordings from rat dissociated dorsal root ganglion neurons that detect touch and pain are also possible (Hu and Lewin, 2006; McCarter and Levine, 2006). However, dissociated neurons in culture lack the components that normally connect the physical stimulus to the membrane of the sensory neurons (Hu and Lewin, 2006).

VII. STEPS IN MECHANORECEPTION

Mechanoreception can be viewed as a three-stage process comprising *coupling*, *transduction* and *encoding* (Loewenstein and Mendelson, 1965). The stimulus is first mechanically coupled from its origin to the membrane

of the sensory cell where it is transduced into a receptor potential and, in cells with long sensory axons, this is encoded into action potentials that propagate to the central nervous system.

VIIA. Coupling

Living cells are not normally exposed to the outside surface of an animal, so most, if not all, external mechanoreceptors have some kind of tissue between them and the source of the mechanical input. In some cases, these surrounding tissues are elaborate and obviously designed to modify the input signal by affecting its amplitude and possibly its dynamic properties. Internal mechanoreceptors also have a variety of surrounding tissues with presumably similar functions. The morphology of these structures varies so strongly between different mechanoreceptors that it is widely used for classification, as described above (see Figs. 36.3 and 36.4). The Pacinian corpuscle is probably the most illustrated vertebrate mechanoreceptor, with its complex lamellar structure, but it represents only one extreme of a wide range of vertebrate mechanoreceptor endings. Invertebrate mechanoreceptors also display many morphological forms, including the well-known hair receptors that cover the outside surfaces of insects and spiders and the stretch receptors of crayfish and lobsters. Although we generally assume that these elaborate extracellular structures modify the spatial and temporal sensitivities of the receptors, there is relatively little quantitative information about these functions.

In many cases, the external structures attenuate the stimulus, so that the displacement of the receptor cell membrane is much smaller than the original movement. For example, hairs on the human skin can be moved by several millimeters, but the resulting movements of the follicle receptors are only a few micrometers. Estimates of this attenuation have been made in some cases. For the Pacinian corpuscle, it has been suggested that the pressure reaching the inner capsule is attenuated by about two orders of magnitude (100) compared to the pressure on the outer lamellae (Bell et al., 1994), but this force may already be greatly reduced compared to the initial stimulus at the skin. An attenuation of about 100 was also reported for insect hairs, based on the morphology of the sensory structure and the location of the moving elements (French, 1992). Estimates of attenuation during coupling also allow us to estimate the *threshold*, or minimum amplitude of movement at the cell membrane that leads to sensation. For Pacinian corpuscles, movements of 1−10 nm at the capsule are probably adequate to produce action potentials at the optimum vibration frequency of about 250 Hz and sinusoidal movements of about 0.3 nm can stimulate auditory hair cells (Hudspeth, 2005). For insect cuticular hair receptors, threshold estimates of 4 nm and 3 nm were obtained for bee and cockroach (French, 1992). Estimates of the mechanical force required at the surface of the animal for transduction vary more, from about 25 μN in spider slit sensilla to more than 10 mN in mammalian glabrous skin (Goodman and Schwarz, 2003), which probably reflects the wide range of coupling structures involved.

The few attempts that have been made to quantify the mechanical effects of coupling over a range of input movements indicate that it can have significant temporal effects and be substantially non-linear. The mechanical properties of crayfish stretch receptors have been studied thoroughly (Rydqvist et al., 2007) and require non-linear springs plus at least one dashpot (or Voigt element) to account for the passive properties of the receptor without any muscular activity. No mechanical description is available that includes active contraction. Muscle spindles also have strongly time-dependent mechanical properties, with probably more complex dynamic behavior during γ-motoneuron activation. The viscoelastic properties of Pacinian corpuscles are assumed to be responsible for most of the time dependence of the receptor current, but have not yet been quantified.

VIIB. Transduction

Transduction in mechanoreceptors probably involves mechanically activated ion channels in the receptor cell membrane (see Chapter 27 and recent reviews by Christensen and Corey, 2007; Chalfie, 2009; Árnadóttir and Chalfie, 2010; Lumpkin et al., 2010). Identification of these channels has only been made in a small number of mechanosensory neurons. The mechanotransduction channels in *C. elegans* gentle touch receptor neurons belong to the DEG/ENaC/ASIC (degenerin/epithelial sodium/acid sensitive ion channel) family (O'Hagan et al., 2005), while the pore-forming subunit in the ciliated touch receptors in *C. elegans* nose belong to the transient receptor potential (TRP) family (Kang et al., 2010). This TRP-4 protein is a member of the TRPN (or NompC) subfamily, and the NompC protein is also needed for mechanotransduction in *Drosophila* bristle hairs (Walker et al., 2000). Several members of the TRP and DEG/ENaC/ASIC families are expressed in mammalian mechanoreceptors, but it is not known if any of them are directly or indirectly involved in mechanotransduction (Tsunozaki and Bautista, 2009; Árnadóttir and Chalfie, 2010; Lumpkin et al., 2010).

The complex structures of the mechanoreceptor cells and the small numbers of mechanotransduction channels per cell mean that we do not yet have definitive single-channel recordings in intact, normally functioning mechanoreceptors. Single mechanically activated ion channels have been seen in crayfish stretch receptor neurons

(French, 1992) and in tissue-cultured moth antennal mechanoreceptor neurons (Torkkeli and French, 1999), but these channels were not located on the fine sensory endings where transduction is thought to occur. The crayfish channels had maximum conductance to K^+ (≈70 pS) but were also permeable to other cations. The moth channels were also permeable to K^+ with a conductance of ≈40 pS, but their selectivity has not yet been established. Single channel conductance is better characterized in auditory and vestibular hair cells, with a range of at least 100−300 pS and wide cation permeability (Fettiplace, 2009; also see Chapter 37).

Although single-channel data are sparse, we have significant information about some transduction channels, including ionic selectivity, ionic conductance, blocking chemicals and the numbers of transduction channels in each receptor cell (Fig. 36.8). In Pacinian corpuscles, muscle spindles, crayfish stretch receptors, spider slit sensilla and *C. elegans* gentle touch receptors, mechanotransduction current is carried by Na^+ ions. However, a variety of other cations can pass through most of these channels. (French, 1992; Bell et al., 1994; French et al., 2002; O'Hagan et al., 2005; Rydqvist et al., 2007). The mechanotransduction channels in *C. elegans* ciliated mechanoreceptor neurons (Kang et al., 2010) and in cultured rat dorsal root ganglion neurons (McCarter and Levine, 2006) are non-selective cation channels. In mouse dorsal root ganglion cells, the selectivity varied in different cell types so that slowly adapting current was non-selective to cations, while the rapidly adapting current was Na^+ selective (Hu and Lewin, 2006).

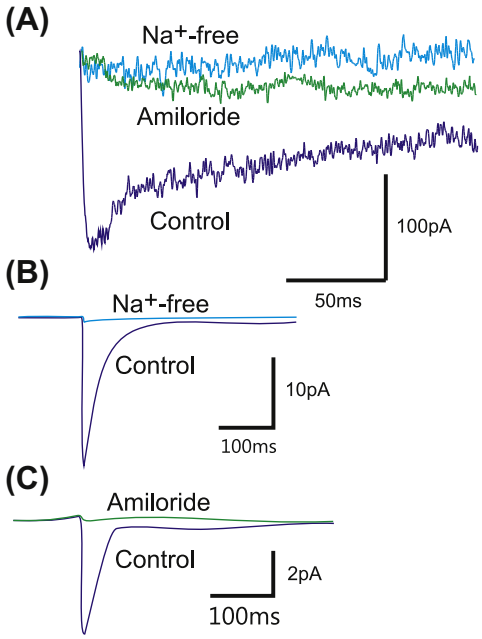

FIGURE 36.8 Sodium selectivity and block of receptor current by amiloride in two mechanoreceptors. (A) Step movements of a spider slit sensillum activate an inward current that is reduced to zero by replacing the Na^+ with impermeable choline or by adding 1 mM amiloride to the bath. (B and C) Sodium removal or application of 200 μM amiloride reduce the receptor current in whole-cell recordings from *C. elegans* PLM neurons. *(Redrawn from French et al., 2002 and O'Hagan et al., 2005.)*

In several of these cells, the sensory ending is surrounded by an elevated Na^+ concentration and Na^+ entry during transduction causes a graded depolarization that leads to action potentials if the stimulus is strong enough. In vertebrate auditory and vestibular hair cells, the mechanotransduction channels are preferably permeant to divalent cations, such as Ca^{2+} and Mg^{2+}. However, in the inner ear, the hair bundles are bathed in endolymph that has high K^+ concentration and the transduction current is mainly carried by K^+ with a minor contribution from Ca^{2+} (Fettiplace, 2009). Similarly, in insect cuticular mechanoreceptors, the sensory ending is surrounded by lymph that is rich in K^+ and has a positive electrical potential relative to the normal hemolymph (French, 1992). The cases where K^+ is used to carry the receptor current generally rely on separating two regions of the sensory neurons by embedding them in an epithelial layer with tight junctions so that a K^+ concentration gradient, usually combined with an electrical gradient, can drive K^+ through the cell, depolarizing the membrane; similar arrangements exist for some of the Na-dependent systems. Cells with non-selective mechanotransduction channels may also receive a significant Ca^{2+} flux during transduction, because the inward Ca^{2+} electrochemical gradient is usually high.

Like many other ion channels, mechanotransduction channels can be blocked or closed by several chemicals. Gadolinium blocks mechanically-activated currents in several preparations including the crayfish stretch receptor (Rydqvist et al., 2007), the spider slit sensilla (French et al., 2002), cultured mouse dorsal root ganglion neurons (Hu and Lewin, 2006) and cochlear hair cells (Fettiplace, 2009). Sensitivity to gadolinium is sometimes used as an indicator that mechanically-activated channels are involved in a physiological process, but Gd^{3+} also blocks many Ca^{2+} channels, as well as some ligand- and voltage-gated cation channels. Amiloride is a well-known blocker of epithelial Na^+ channels and it blocks mechanotransduction current in the *C. elegans* gentle touch receptor neurons that are members of this family (O'Hagan et al., 2005) and in the spider slit sensilla (French et al., 2002) (see Fig. 36.8). The mechanotransduction current in ciliated touch receptor neurons in *C. elegans* nose are insensitive to amiloride, indicating that the TRP-4 channels are not sensitive to this blocker (Kang et al., 2010). Mechanically-activated currents in the cultured mouse dorsal root ganglion neurons (Hu and Lewin, 2006) and crayfish stretch receptors (Rydqvist et al., 2007) are also insensitive to amiloride, but it is not known which gene family these channels belong to. Interestingly, the mechanotransduction current

in vertebrate cochlear hair cells is blocked by amiloride, even though there is no evidence that this channel is a member of the ENaC family (Fettiplace, 2009). Some local anesthetics have also been used to block the receptor current in the crayfish stretch receptor (Rydqvist et al., 2007) and certain antibiotics as well as La^{3+}, ruthenium red, FM1-45 and Ca^{2+} are known to block transduction in auditory hair cells (Fettiplace, 2009).

The acid sensitive ion channel (ASIC) family has been associated with some mechanosensitive neurons and several members of the DEG/ENaC channel family are known to be opened by low pH (Árnadóttir and Chalfie, 2010). Mechanical sensitivity was enhanced by low pH in spider slit sensilla (French et al., 2002) although there was no evidence of direct acid activation.

Whole cell mechanotransduction currents have been recorded in some cells and noise, or fluctuation, analysis has been used to estimate single-channel conductance and the numbers of channels per cell in several cases. *Noise analysis* relies upon the idea that receptor channels opening and closing create variance in the mean receptor current, because all known channels regulate their average conductance by switching rapidly between open and closed states. Therefore, the variance is minimal when all receptor channels are either fully open or fully closed and maximal when the mean open probability is 0.5. Assuming that the noise variance is due to the summation of currents flowing through many independent, identical channels that are randomly opening and closing, it is possible to quantify the relationships between the membrane potential, total cell membrane current variance, total current, number of channels, single-channel conductance and mean channel open probability. In a few cases, noise analysis measurements in non-receptor systems have been confirmed by single-channel experiments. Noise analysis measurements are challenging because of the inherent difficulty of making good recordings of membrane currents in mechanoreceptor cells. However, the cases where they have been made have produced rather consistent results. In statocyst cells of the snail *Hermissenda*, noise analysis gave values of 5 pS for the single-channel conductance and 40 channels per cell (French, 1992). In vertebrate hair cells, the corresponding values were 12 pS and 280 channels per cell (Hudspeth, 2005) and in spider slit sensilla neurons, 7.5 pS and 300 channels per cell (French et al., 2002). In *C. elegans* gentle touch receptor neurons, the single channel conductance was 25 pS and the number of channels per cell was estimated to be 14 to 25 (O'Hagan et al., 2005) while the ciliated touch receptor neurons had 21 channels per cell with a conductance of 16 pS per channel (Kang et al., 2010). These single-channel conductances are all at the low end of the range of known mechanically-activated ion channels and significantly lower than the single-channel measurements described above. The total membrane conductances due to mechanotransduction channels observed during these measurements agree with several estimates made in other mechanosensory neurons, and would provide enough current to depolarize the neurons to produce action potentials. Therefore, it seems likely that the number of channels in each cell is limited to a few hundred at most, raising difficulties for electrophysiological, molecular and histological attempts at localization or characterization.

Another interesting property of mechanotransduction channels is their *temperature sensitivity*. This has been measured in at least six invertebrate and vertebrate preparations with activation energy values in the range of 12−22 kcal/mol (≈50−100 kJ/mol) (French et al., 2002). These energy values are similar to those required to break chemical bonds and significantly more than the energy barriers associated with ionic diffusion or conductance through ion channels. Little is known about the activation energy of mechanically-activated ion channels, but it seems likely that some crucial stage in the link between membrane tension and ion channel opening leads to this relatively high energetic barrier.

VIIC. Encoding

Most mechanoreceptors use action potentials to transmit information to the central nervous system. The action potentials are produced by conventional combinations of voltage-dependent Na^+ and K^+ channels. Accurate characterization of these currents and other currents involved in the control of membrane excitability relies on voltage-clamp recordings, which have only been possible in a few cases. *Tetrodotoxin-sensitive Na^+ channels* are clearly responsible for the action potential upswing in Pacinian corpuscles (Loewenstein and Mendelson, 1965), lobster and crayfish stretch receptors (French, 1992; Rydqvist et al., 2007), the cockroach tactile spine (Torkkeli and French, 1994) and spider slit sensilla (French et al., 2002). The distribution of these channels in the cell membrane determines where the receptor potential is converted to action potentials. Voltage-gated Na^+ channels are present and the action potentials initiated at the first node of Ranvier under the lamellae of the Pacinian corpuscle (Pawson and Bolanowski, 2002). In the slowly adapting crayfish stretch receptor, the channels are located on the axon and the cell body but, in the rapidly adapting receptor, the channels are restricted to the axon itself (Rydqvist et al., 2007). In spider slit sensilla, Na^+ channels are more evenly distributed, with a significant concentration on the sensory dendrite and the soma, with action potentials initiated in the dendrite (French et al., 2002). An additional slow component of Na^+ inactivation was needed to model the firing behavior of lobster stretch receptors and is probably present in the slowly adapting crayfish stretch receptor (Rydqvist et al., 2007) and the cockroach tactile spine (French and

Torkkeli, 1994). *C. elegans* neurons do not have voltage-gated Na^+ channels, but transmit signals as graded or plateau potentials that are believed to be carried by Ca^{2+} (Lockery and Goodman, 2009).

Delayed-rectifier K^+ currents seem to be responsible for action potential repolarization in all of the mechanoreceptors studied, but other types of K^+ currents are found in different receptors. Transient K^+ currents resembling the A-type current have been described in the slowly adapting cockroach tactile spine (Torkkeli and French, 1994) but not in spider slit sensilla that adapt significantly faster (French et al., 2002). The slowly adapting crayfish stretch receptor neuron has two components of delayed rectifier K^+ current and an A-current (Rydqvist et al., 2007). *Ca^{2+}-activated K^+ currents* were found in the cockroach tactile spine (Torkkeli and French, 1995) and vertebrate auditory hair cells (Hudspeth, 2005). An *inwardly rectifying K^+ current* is present in the slowly adapting lobster stretch receptor (French, 1992) but has not been described in other mechanoreceptors.

Ca^{2+} currents are present in vertebrate auditory neurons and negative feedback from depolarization-induced Ca^{2+} entry to hyperpolarization via Ca^{2+}-activated K^+ current has been suggested to cause frequency tuning (Hudspeth, 2005). Ca^{2+} currents are also present in spider slit sensilla (French et al., 2002) and increased intracellular Ca^{2+} modulates both the receptor current and firing rate (Höger et al., 2010). *Electrogenic Na^+ pumping* is well established in crayfish stretch receptors and contributes to adaptation of action potential discharge by repolarizing the cell after Na^+ entry. There is also evidence for its contribution to adaptation in the cockroach tactile spine neuron (French, 1992).

The terms *rapid adaptation* and *slow adaptation* are qualitative and have been used to describe a wide range of time dependence. However, some mechanoreceptors adapt so rapidly that only one or a few action potentials are produced in response to a step stimulus (Fig. 36.9) and so can truly be called "rapidly adapting". Rapid adaptation generally infers a cessation of activity soon after the start of a constant stimulus, but many rapidly adapting mechanoreceptors can fire action potentials as long as the stimulus is moving, which makes them excellent vibration detectors (Fig. 36.9). It has been known for many years that the encoding stage of the Pacinian corpuscle limits its response to one or two action potentials (Loewenstein and Mendelson, 1965), although the ionic basis for the effect is not known. In the cockroach tactile spine, removal of the rapidly deactivating K^+ A-current increased the overall rate of firing, but the receptor continued to adapt, while removal of the Ca^{2+}-activated K^+ current removed most of the adaptation (Torkkeli and French, 1994, 1995). However, blockade of these currents does not affect the shape of individual action potentials because their rapid repolarization is due to the delayed-rectifier current. Rapid adaptation in spider VS-3 neurons seems to be partially due to the slow recovery of voltage activated Na^+ channels from their normal rapid inactivation (French et al., 2002).

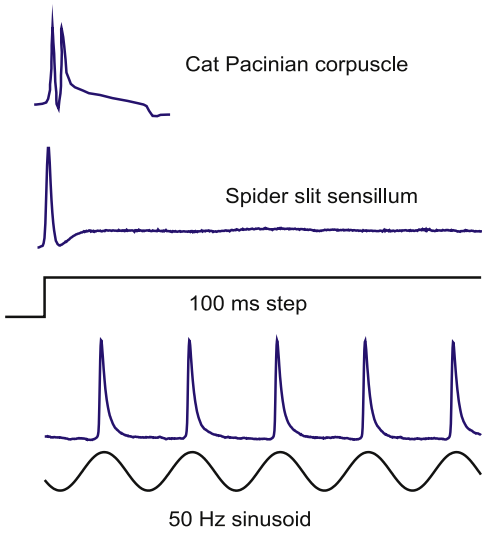

FIGURE 36.9 Rapid adaptation in vertebrate and invertebrate mechanoreceptors. A Pacinian corpuscle and a spider slit sensillum neuron each fire one or two action potentials in response to a step deformation and are then silent. But such receptors usually respond strongly to oscillating stimuli, making them good vibration detectors. Lower traces show a slit sensillum neuron firing 50 action potentials per second with sinusoidal mechanical stimulation. *(Partly redrawn from French and Torkkeli, 1994.)*

Following the encoding stage, action potentials propagate into the central nervous system along nerve axons. In vertebrates, the cell bodies of the neurons are located in the dorsal root ganglia of the spinal cord and the axons enter via the dorsal roots. Cell bodies of the cranial mechanoreceptor nerves are located in the trigeminal ganglion. The major transmitter at the first central synapse is probably the excitatory amino acid glutamate. Arthropod mechanoreceptors have their cell bodies in the periphery and send axons into the central nervous system via nerve roots of the segmental ganglia, which are sometimes fused into larger structures. Conduction velocities are typically 1−5 m/s. The dominant transmitter for arthropod mechanoreceptors is acetylcholine (Burrows, 1996), although several spider mechanosensory neurons also contain histamine (Fabian et al., 2002). Relevant information about crustacean muscle, including the unique innervation, is given in the Appendix to Chapter 47.

VIII. EFFERENT CONTROL OF MECHANORECEPTORS

All mechanoreceptors receive inhibitory efferent innervation close to the output synapses of their centrally located axon terminals. Other well-known examples of efferent control are the gamma innervation of muscle spindles

(see Fig. 36.6) and presynaptic inhibition of peripheral mechanoreceptors and pain receptors (Rudomin, 2009). Presynaptic inhibition of mechanosensory neurons is remarkably similar in all vertebrate and invertebrate species studied so far (Burrows, 1996; Torkkeli and Panek, 2002; Rudomin, 2009). In addition to the GABAergic inhibitory control of axon terminals, most mechanosensory neurons are also regulated by other chemical agents. In many cases, the sensory endings and cell bodies also receive synaptic input from efferent neurons or accessory cells. Transmitter receptors are found in the somata of vertebrate dorsal root ganglion neurons (Robertson, 1989) and in the nerve fibers inside the Pacinian corpuscles (Pawson et al., 2009).

Merkel cells form synaptic contacts with mechanosensory afferents and, although Merkel cells have recently been shown to be necessary for the light touch responses, it is still not clear whether these cells are mainly modulatory or the actual sites of mechanotransduction (Lumpkin et al., 2010). Keratinocytes of the skin epidermis are also believed to perform signaling roles to mechanosensory endings (Tsunozaki and Bautista, 2009; Lumpkin et al., 2010). Modulation of vertebrate cutaneous mechanoreceptors and pain receptors by circulating factors has also been recognized for a long time. For example, sympathetic efferents have modulatory effects on muscle spindles, Pacinian corpuscles, several types of low-threshold skin mechanoreceptors and pain receptors, and these neurons express adrenergic receptors (Birder and Perl, 1999). Rohon–Beard neurons, which are developmentally early amphibian and fish touch receptors, have serotonergic efferent innervation and 5-HT is believed to alter their sensitivity to mechanical stimuli by inhibiting both low- and high-voltage-activated Ca^{2+} currents (Sun and Dale, 1997).

Arthropod mechanosensory neurons are modulated by biogenic amines, especially octopamine, the invertebrate analog of norepinephrine (Burrows, 1996). The dorsal unpaired median neurons of locust, which secrete octopamine, have terminals in the periphery, closely associated with the dendrites of mechanoreceptors that are modulated by octopamine. Similarly, octopamine-containing efferent neurons innervate spider mechanosensory afferents, which have octopamine receptors and are modulated by octopamine (Torkkeli et al., 2011). Although octopaminergic modulation in arthropods is probably the most thoroughly studied neuromodulatory system, there are no clear conclusions about the mechanisms involved. Octopamine may increase or decrease spiking frequency, even in the same mechanosensory neuron and it may act by increasing intracellular Ca^{2+} or cAMP concentration or both (Torkkeli et al., 2011).

The most conclusive evidence that peripheral regions of mechanoreceptors receive efferent innervation comes from immunocytochemical findings in arachnid and crustacean mechanoreceptors (see Figs. 36.6 and 36.10). Both types of receptors have dense efferent innervation, forming several types of synapses on all parts of the sensory neurons, including their somata and dendrites (Fabian-Fine et al., 2002). Spider cuticular mechanoreceptors have at least four different types of synaptic structures on the efferent terminals. In addition to octopamine, the efferent neurons contain GABA, glutamate and acetylcholine and all of these agents modulate the excitability of mechanosensory

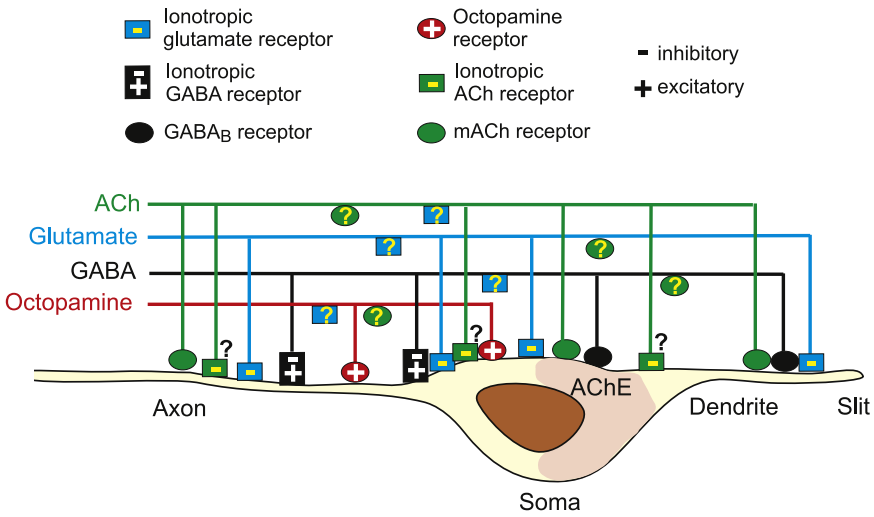

FIGURE 36.10 A schematic diagram showing the transmitter receptors on spider mechanosensory neurons and the efferent fibers innervating these neurons. At least three GABAergic, one glutamatergic and one octopaminergic efferent fiber have been identified by immunocytochemistry. In addition, choline acetyltransferase (ChAT) activity was present in one efferent fiber. Ionotropic inhibitory glutamate receptors (I_{Glu}) are located in all parts of the sensory neurons. Excitatory G-protein coupled octopamine receptors are only found in the axons and proximal parts of the somata. Ionotropic inhibitory-excitatory GABA receptors are probably also only present in the axons and somata. In contrast, the metabotropic $GABA_B$ receptors were found only at the distal parts of the soma and the dendrites. Ionotropic inhibitory ACh receptors are only present in the very rapidly adapting subgroup of VS-3 neurons (type A), but their distribution in these cells has not been determined, therefore these receptors are indicated with question marks. Muscarinic ACh receptors (mAChR) are present on all parts of the sensory neurons. AChE activity was present only in the type A VS-3 neuron and concentrated on the distal parts of the somata. I_{Glu} and mACh receptors are also found on some of the efferent neurons, but these have not been identified and therefore the receptors are indicated by question marks. *(Fabian-Fine et al., 2002; Widmer et al., 2006; Pfeiffer et al., 2009; Torkkeli et al., 2011).*

neurons, which have a variety of receptors to these transmitters (Widmer et al., 2006; Pfeiffer et al., 2009; Torkkeli et al., 2011). It is clear that the central nervous systems can control the sensitivity of mechanosensory neurons, although the full extent of this control is not yet completely understood.

IX. CONCLUSIONS

The large variety of morphological forms of mechanoreceptors indicates that the external components surrounding the sensitive endings play important roles in controlling the receptor behavior. Most of this control is assumed to involve coupling of initial movement into deformation of the membrane containing mechanically-activated channels. However, the mechanism involved has not been thoroughly decoded in any receptor and there may be other schemes involved, such as chemical modulation of excitability. Characterization of mechanically-activated channels is proceeding, but it is important to realize that no single-channel recordings have yet been unequivocally linked to mechanotransduction in any mechanosensory neuron. Therefore, it may yet emerge that an unknown family, or several different families, of channel proteins is responsible for this function in true mechanoreceptors. The encoding of action potentials from receptor current and the general control of receptor excitability involves voltage- and Ca^{2+}-activated ion channels, similar to those in other excitable cells, and complete models of encoding in some receptors are now available. Adaptation and general dynamic properties of mechanoreception involve both the coupling and encoding stages of the process. There may also be significant dynamic behavior of mechanotransduction channels, but this will not become clear until the channels themselves are better known. Efferent control of transduction and adaptation in mechanoreceptors is common but only well described in a small number of preparations.

Mechanoreception is a widespread and crucially important process for many physiological functions. Recent developments in electrophysiological techniques and new experimental preparations have provided important information about each stage of mechanoreception from initial deformation to action potential production, but much remains to be learned. In particular, the lack of vertebrate preparations that would allow voltage-clamp of receptor currents at the intact sensory ending or detailed examination of action potential encoding is a major problem. When the molecules responsible for mechanotransduction are known, it should be possible to discover how they are linked to other cellular components to confer mechanical sensitivity and from there to complete models of mechanoreception in intact sensory cells.

BIBLIOGRAPHY

Árnadóttir, J., & Chalfie, M. (2010). Eukaryotic mechanosensitive channels. *Annu Rev Biophys, 39*, 111–137.

Bell, J., Bolanowski, S., & Holmes, M. H. (1994). The structure and function of Pacinian corpuscles: a review. *Prog Neurobiol, 42*, 79–128.

Birder, L. A., & Perl, E. R. (1999). Expression of α_2-adrenergic receptors in rat primary afferent neurones after peripheral nerve injury or inflammation. *J Physiol, 515*, 533–542.

Burrows, M. (1996). *The Neurobiology of an Insect Brain,* Oxford: Oxford University Press.

Chalfie, M. (2009). Neurosensory mechanotransduction. *Nat Rev Mol Cell Biol, 10*, 44–52.

Christensen, A. P., & Corey, D. P. (2007). TRP channels in mechanosensation: direct or indirect activation? *Nat Rev Neurosci, 8*, 510–521.

Fabian-Fine, R., Seyfarth, E.-A., & Meinertzhagen, I. A. (2002). Peripheral synaptic contacts at mechanoreceptors in arachnids and crustaceans: morphological and immunocytochemical characteristics. *Microsc Res Tech, 58*, 283–298.

Fettiplace, R. (2009). Defining features of the hair cell mechanoelectrical transducer channel. *Pflügers Arch, 458*, 1115–1123.

French, A. S. (1992). Mechanotransduction. *Annu Rev Physiol, 54*, 135–152.

French, A. S., & Torkkeli, P. H. (1998). Information transmission at 500 bits/s by action potentials in a mechanosensory neuron of the cockroach. *Neurosci Lett, 243*, 113–116.

French, A. S., & Torkkeli, P. H. (1994). The basis of rapid adaptation in mechanoreceptors. *News Physiol Sci, 9*, 158–161.

French, A. S., Torkkeli, P. H., & Seyfarth, E.-A. (2002). From stress and strain to spikes: mechanotransduction in spider slit sensilla. *J Comp Physiol A, 188*, 739–752.

Goodman, M. B., & Schwarz, E. M. (2003). Transducing touch in *Caenorhabditis elegans*. *Annu Rev Physiol, 65*, 429–452.

Hu, J., & Lewin, G. R. (2006). Mechanosensitive currents in the neurites of cultured mouse sensory neurones. *J Physiol, 577*, 815–828.

Hudspeth, A. J. (2005). How the ear's works work: mechanoelectrical transduction and amplification by hair cells. *C R Biol, 328*, 155–162.

Höger, U., Torkkeli, P. H., & French, A. S. (2010). Feedback modulation of transduction by calcium in a spider mechanoreceptor. *Eur J Neurosci, 32*, 1473–1479.

Juusola, M., & French, A. S. (1997). The efficiency of sensory information coding by mechanoreceptor neurons. *Neuron, 18*, 959–968.

Kang, L., Gao, J., Schafer, W. R., Xie, Z., & Xu, X. Z. (2010). *C. elegans* TRP family protein TRP-4 is a pore-forming subunit of a native mechanotransduction channel. *Neuron, 67*, 381–391.

Lockery, S. R., & Goodman, M. B. (2009). The quest for action potentials in *C. elegans* neurons hits a plateau. *Nat Neurosci, 12*, 377–378.

Loewenstein, W. R., & Mendelson, M. (1965). Components of receptor adaptation in a Pacinian corpuscle. *J Physiol, 177*, 377–397.

Lumpkin, E. A., Marshall, K. L., & Nelson, A. M. (2010). The cell biology of touch. *J Cell Biol, 191*, 237–248.

Malinovsky, L. (1996). Sensory nerve formations in the skin and their classification. *Microsc Res Tech, 34*, 283–301.

McCarter, G. C., & Levine, J. D. (2006). Ionic basis of a mechanotransduction current in adult rat dorsal root ganglion neurons. *Mol Pain, 2*, 28–40.

McGlone, F., & Reilly, D. (2009). The cutaneous sensory system. *Neurosci Biobehav Rev, 34*, 148–159.

O'Hagan, R., Chalfie, M., & Goodman, M. B. (2005). The MEC-4 DEG/ENaC channel of *Caenorhabditis elegans* touch receptor neurons transduces mechanical signals. *Nat Neurosci, 8*, 43−50.

Pawson, L., & Bolanowski, S. J. (2002). Voltage-gated sodium channels are present on both the neural and capsular structures of Pacinian corpuscles. *Somatosens Mot Res, 19*, 231−237.

Pawson, L., Prestia, L. T., Mahoney, G. K., Guclu, B., Cox, P. J., & Pack, A. K. (2009). GABAergic/glutamatergic-glial/neuronal interaction contributes to rapid adaptation in Pacinian corpuscles. *J Neurosci, 29*, 2695−2705.

Pfeiffer, K., Panek, I., Höger, U., French, A. S., & Torkkeli, P. H. (2009). Random stimulation of spider mechanosensory neurons reveals long-lasting excitation by GABA and muscimol. *J Neurophysiol, 101*, 54−66.

Robertson, B. (1989). Characteristics of GABA-activated chloride channels in mammalian dorsal root ganglion neurones. *J Physiol, 411*, 285−300.

Rudomin, P. (2009). In search of lost presynaptic inhibition. *Exp Brain Res, 196*, 139−151.

Rydqvist, B., Lin, J. H., Sand, P., & Swerup, C. (2007). Mechanotransduction and the crayfish stretch receptor. *Physiol Behav, 92*, 21−28.

Sun, Q. Q., & Dale, N. (1997). Serotonergic inhibition of the T-type and high voltage-activated Ca^{2+} currents in the primary sensory neurons of *Xenopus* larvae. *J Neurosci, 17*, 6639−6649.

Torkkeli, P. H., & French, A. S. (1994). Characterization of a transient outward current in a rapidly adapting insect mechanoreceptor neuron. *Pflügers Arch, 429*, 72−78.

Torkkeli, P. H., & French, A. S. (1995). Slowly inactivating outward currents in a cuticular mechanoreceptor neuron of the cockroach (Periplaneta americana). *J Neurophysiol, 74*, 1200−1211.

Torkkeli, P. H., & French, A. S. (1999). Primary culture of antennal mechanoreceptor neurons of *Manduca sexta*. *Cell Tissue Res, 297*, 301−309.

Torkkeli, P. H., & Panek, I. (2002). Neuromodulation of arthropod mechanosensory neurons. *Microsc Res Tech, 58*, 299−311.

Torkkeli, P. H., Panek, I., & Meisner, S. (2011). Ca^{2+}/calmodulin dependent protein kinase II mediates octopamine-induced increase in sensitivity in spider VS-3 mechanosensory neurons. *Eur J Neurosci.,* (in press).

Tsunozaki, M., & Bautista, D. M. (2009). Mammalian somatosensory mechanotransduction. *Curr Opin Neurobiol, 19*, 362−369.

Walker, R. G., Willingham, A. T., & Zuker, C. S. (2000). A *Drosophila* mechanosensory transduction channel. *Science, 287*, 2229−2234.

Widmer, A., Panek, I., Höger, U., Meisner, S., French, A. S., & Torkkeli, P. H. (2006). Acetylcholine receptors in spider peripheral mechanosensilla. *J Comp Physiol. A, 192*, 85−95.

This page intentionally left blank

Chapter 37

Acoustic Transduction

Daniel C. Marcus

Chapter Outline

I. SUMMARY

The exquisite sensitivity of our sense of hearing results from the concerted action of many subsystems. The auditory peripheral organ, the cochlea, contains specialized cells for amplifying and sensing the mechanical auditory stimulus and other cells to create and maintain the unusual ionic environment in the cochlear lumen that powers and enables the transduction process. Function of these cells depends on specific gene expression patterns. A number of gene mutations are known to underlie specific clinical syndromic and non-syndromic hereditary hearing loss. It is perhaps surprising that most of these clinically important genes are located in the cells that engage in ion transport rather than the auditory sensory and neural cells. Major aspects of hearing and deafness can be understood as an integration of the many cellular processes that comprise the auditory organ.

II. INTRODUCTION

The detection of sound by mammals depends on a series of biological systems beginning with the collection of sound pressure waves by the external ear, followed by the mechanical transmission through the middle ear ossicles to the *cochlea* of the inner ear (Fig. 37.1). The sound pressure waves in the cochlea induce motion of the basilar membrane to which the sensory organ, the *organ of Corti*, is attached. The organ of Corti is comprised of the sensory *inner and outer hair cells* (Fig. 37.2), which are surrounded by Deiters' cells, pillar cells and Hensen's cells. Motion of the organ of Corti with respect to another structure (tectorial membrane) causes movements of the sensory cilia (hairs) on the hair cells and modulation of the flow of current through these hair cells, leading to modulation of the rate of firing of the afferent auditory nerve fibers, which synapse to the base of the hair cells. The nerve fibers carry the auditory information to the brain where the signal undergoes central processing, leading to the perception of sound. Peripheral auditory processing is modulated by efferent signals originating from the brain. This chapter focuses on the cellular aspects of acoustic transduction in the auditory periphery. Much of what we know about the cellular physiology of the mammalian cochlea is derived from experiments performed on

Cell Physiology Sourcebook. DOI: 10.1016/B978-0-12-387738-3.00037-8

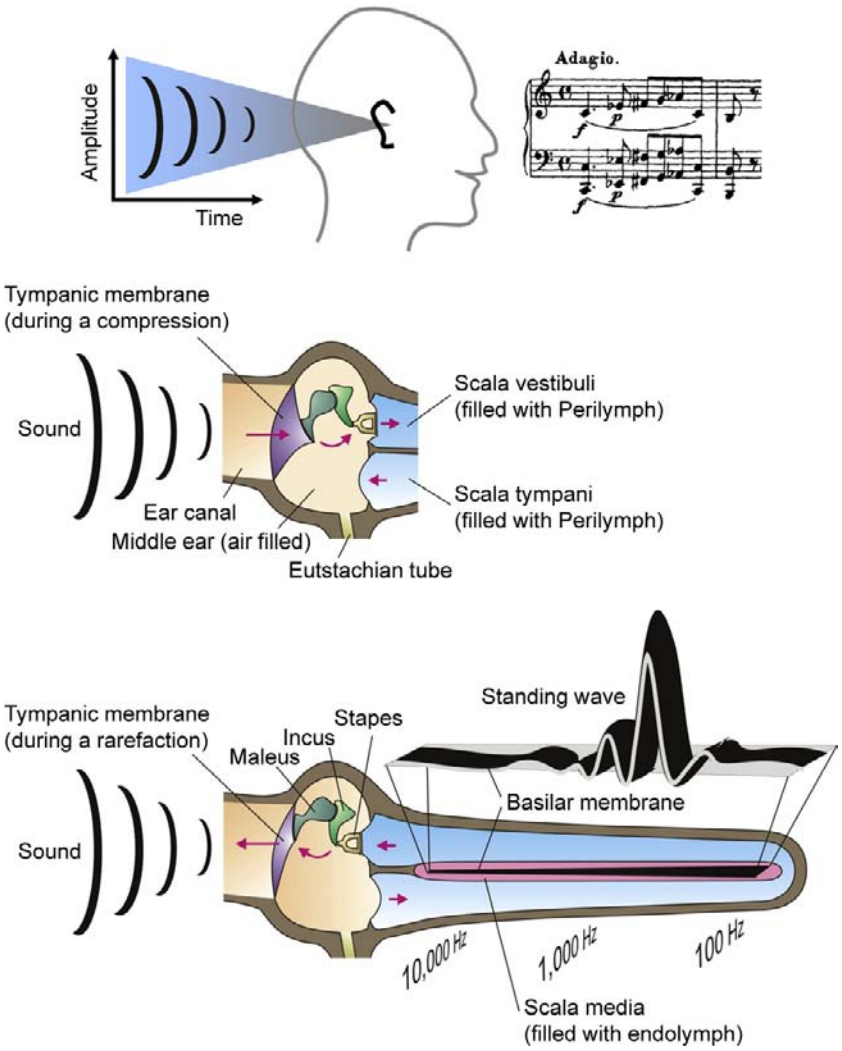

FIGURE 37.1 Diagrams of the physical pathway and effects of sounds from the environment to the cochlea. (Upper panel): Sound waves enter the outer ear and (middle panel) are transmitted by the tympanic membrane to the middle ear bones (ossicles: maleus, incus, stapes). The sound waves are then transmitted to scala vestibuli of the inner ear through the oval window. Acoustic energy enters the cochlea (lower panel; diagrammed uncoiled) where the frequency content of the sound waves is analyzed by the creation of standing waves along the basilar membrane and excites receptors and associated neurons at locations that code for the frequencies comprising the sound. *(Reproduced with permission from Marcus and Wangemann, (2009). In F.J. Alvarez-Leefmans and E. Delpire, eds), Physiology and Pathology of Chloride Transporters and Channels in the Nervous System – From Molecules to Diseases, pp. 425–437. Elsevier, New York.)*

preparations from the vestibular labyrinth of mammals, birds and amphibians, and from the cochlea of birds. There are strong homologies between the cochlea and vestibular labyrinth which are reviewed elsewhere (Lee and Marcus, 2008; Marcus and Wangemann, 2009, 2010; Kim and Marcus, 2011).

III. MAMMALIAN INNER EAR STRUCTURE

The transduction apparatus is part of an *epithelium* forming the *cochlear duct* and separating two distinct cochlear fluids, *endolymph* and *perilymph*. The composition and importance of these fluids is related later. A diagram of a cross-section of the mammalian cochlear duct is shown in Fig. 37.2. A mechanically stiff apical surface of the organ of Corti, the *reticular lamina*, is formed by cuticular plates just under the apical membrane of these cells. The organ of Corti sits on the *basilar membrane*, a fibrous sheet that transmits the acoustic stimulus.

In the medial direction from the organ of Corti, the duct is comprised of inner sulcus cells and interdental cells of the spiral limbus. The *tectorial membrane* is a gelatinous, acellular structure in the cochlear lumen apparently secreted by the interdental cells. Lateral from the organ of Corti, the cochlear duct consists of outer sulcus cells, spiral prominence cells and *marginal cells* of the *stria vascularis*. Reissner's membrane forms the remaining wall of the triangular-shaped cochlear duct and is comprised of a thin, avascular sheet of epithelial cells.

The apical and basolateral membranes of all of these cells are separated by tight junction complexes near the endolymphatic surface, which serve to join each cell to its neighbor and to complete the barrier between endolymph and the fluid bathing the basolateral membranes. The basolateral fluid is perilymph for all cell types except strial marginal cells, as described later. The cochlear duct is closed at the apex of the cochlea and is joined at the base of

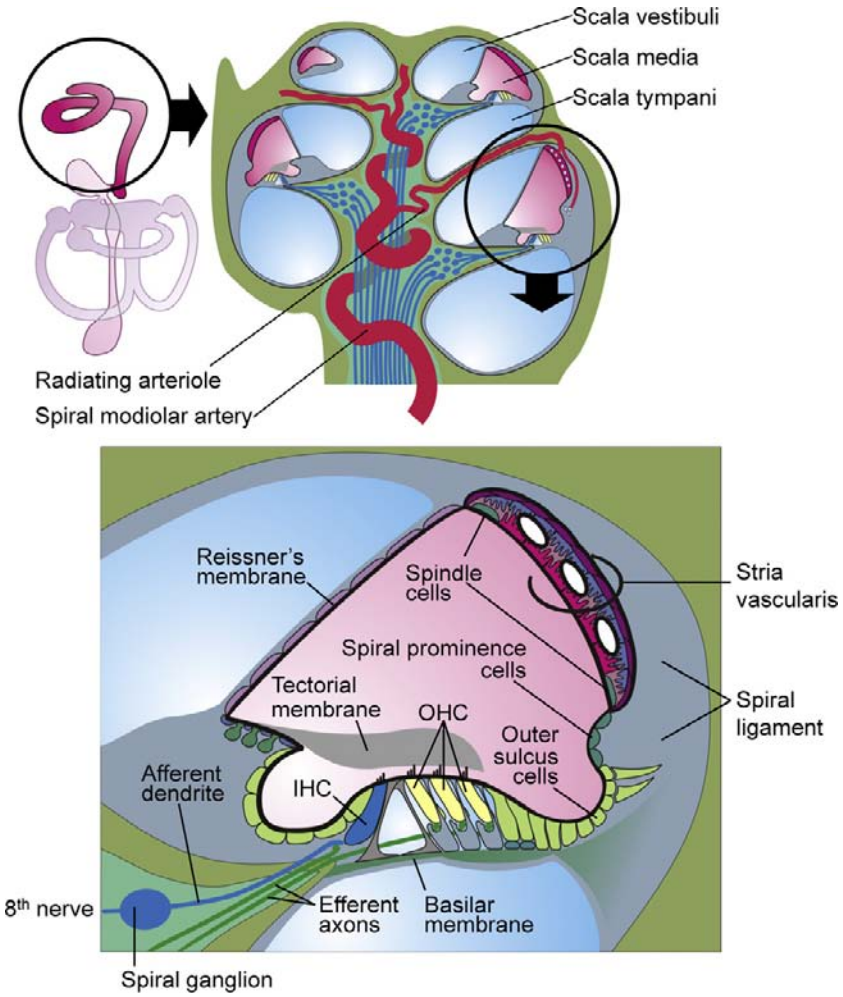

FIGURE 37.2 Diagram of a cross-section of a coiled cochlea. Upper panel shows the membranous structures of the inner ear (left) with the cochlea in the circle and a cross-section of the entire cochlea (right). Lower panel shows a cross-section of one turn of the cochlear lumen, scala media (pink), which is filled with endolymph, an unusual extracellular fluid that is high in K^+ and low in Na^+ and Ca^{2+} content. The composition of this fluid is maintained by the epithelial cells bounding the lumen that include the stria vascularis in the lateral wall, Reissner's membrane and organ of Corti that contains the sensory inner hair cells and the outer hair cells that provide amplification of the sound-induced mechanical vibrations of the basilar membrane. *(Reproduced with permission from Kim, H. M. and Wangemann, P. (2011) Epithelial cell stretching and luminal acidification lead to a retarded development of stria vascularis and deafness in mice lacking pendrin. PLoS.One. 6(3):e17949; Griffith, A. J. and Wangemann P. (2011) Hearing Loss Associated with Enlargement of the Vestibular Aqueduct: Mechanistic Insights from Clinical Phenotypes, Genotypes, and Mouse Models. Hear Res, doi:10.1016/j.heares.2011.05.009; Marcus and Wangemann, (2009). In (F.J. Alvarez-Leefmans and E. Delpire, eds), Physiology and Pathology of Chloride Transporters and Channels in the Nervous System—From Molecules to Diseases, pp. 425—337. Elsevier, New York.)*

the cochlea via a constriction in the epithelial lumen (ductus reuniens) to the vestibular system. Cellular physiologists have focused much of their attention on the strial marginal cells, which provide the energy source for the transduction process, and on the sensory hair cells themselves. In recent years, the contributions of other cell types bordering the cochlear lumen to endolymph ion homeostasis have been determined and are under continuing investigation.

IV. CELL PHYSIOLOGY OF ENDOLYMPH HOMEOSTASIS

IVA. Composition

Even in the absence of an acoustic stimulus, the cochlea is highly active, maintaining the electrolyte composition of endolymph (Table 37.1) and a standing current analogous to the "dark current" of photoreceptors (see Chapter 38) (Marcus and Wangemann, 2010). The transduction current from endolymph through the hair cells is carried predominantly by K^+ and so depends on the high concentration of that ion in endolymph. A low concentration of Ca^{2+} in endolymph is regulated by several cells types; this ion maintains the integrity of tip links between stereocilia of hair cells and enters the transduction channels of hair cells to modulate transduction processes. Gross changes in endolymph composition by a tear in *Reissner's membrane*, by drug action or by genetic interference in K^+ secretion led to degeneration of the hair cells with subsequent degeneration of the synapsing afferent auditory nerve (Vetter et al., 1996). The dimensions of the gelatinous tectorial membrane are sensitive to the levels of K^+, Na^+, H^+ and Ca^{2+} as well as to unknown chemical factors (Shah et al., 1995). Swelling has been associated with substitution of Na^+ for K^+ and with decreases of Ca^{2+}. Maintenance of the tectorial membrane structural properties is needed for normal hearing since it is one of the physical structures coupling the acoustic stimulus to hair cells.

TABLE 37.1 Approximate Ion Composition and Electrical Potential of Cochlear Endolymph and Perilymph[a]

Ion	Endolymph	Perilymph
Potassium (mM)	157	4.2
Sodium (mM)	1.3	148
Calcium (mM)	0.02	1.3
Chloride (mM)	132	119
Bicarbonate (mM)	31	21
Protein (mg/dL)	38	178
pH	7.5	7.3
Potential (mV)	+80	0

[a]*Reproduced by permission from D.C. Marcus and P. Wangemann (2010). Inner ear fluid homeostasis. In P.A. Fuchs, ed.), The Oxford Handbook of Auditory Science: The Ear, pp. 213–230. Oxford University Press, Oxford.*

IVB. Cellular Basis of Endolymphatic Ion Homeostasis

The ion composition of fluid compartments in the body is maintained by epithelial ion transport. The known epithelial domains in the ear responsible for K^+ and Na^+ transport are shown in Fig. 37.3A. Homeostatic imbalance leads to swelling or collapse of the cochlear lumen (Fig. 37.3B), as observed in Pendred syndrome or Scheibe's deformity, respectively.

Transepithelial transport is accomplished through expression of a special constellation of specific ion channels, transporters and pumps in the apical and basolateral membranes. The influx and efflux pathways for Na^+ and K^+ in the cochlea are illustrated in Fig. 37.3A. K^+ is taken up by the *stria vascularis* from the *spiral ligament* in the lateral wall and secreted into endolymph. K^+ enters the hair cells through *mechanosensitive transduction channels* in the apical stereocilia and this entry flux is modulated by the acoustically-gated mechanosensitive channels. K^+ then leaves the hair cells across their basolateral membranes via K^+-selective ion channels. The accumulated K^+ in the extracellular fluid surrounding the hair cells returns to the spiral ligament by diffusion. Three alternate pathways have been proposed and are described in Fig. 37.4. K^+ reaching the spiral ligament is then returned to the endolymph by the stria vascularis. Additional descriptions of K^+ transport by the stria vascularis and of the transduction process are given below.

Endolymphatic $[Na^+]$ is maintained below electrochemical equilibrium with the perilymph; it "leaks" into the cochlear lumen and so must be actively removed. Two types of transport have been identified and described (reviewed in Kim and Marcus, 2011) (see Fig. 37.3B, C). The outer sulcus cells and the hair cells possess nonselective cation (NSC) channels in their apical membranes (small-conductance NSC channels and the large mechanosensitive transduction channels, respectively). Na^+, as well as K^+, enters the cells via these channels and are removed from the cells into perilymph by basolateral Na^+, K^+-ATPase (the Na^+-pump) in parallel with K^+ channels. The outer sulcus cells thereby act as a parasensory K^+ pathway in addition to their function as a Na^+ extrusion mechanism. This parasensory Na^+ and K^+ efflux is modulated by luminal ATP via P2X ionotropic receptors (Chapter 31).

A second, and perhaps more significant, Na^+ efflux pathway is through Reissner's membrane epithelium (reviewed in Kim and Marcus, 2011). These cells utilize apical epithelial Na^+ channels (ENaC) to mediate Na^+ absorption. ENaC activity can be under a variety of intracellular and extracellular control mechanisms. Na^+ absorption by Reissner's membrane is known to be stimulated by glucocorticoids via a genomic pathway and appears to be controlled by luminal ATP. ATP would increase the Na^+ absorption via ligand-gated NSC channels (P2X receptors) and decrease Na^+ absorption via signalling from P2Y4 receptors.

IVC. Stria Vascularis

The stria vascularis has two primary known functions: secretion of K^+ and generation of the lumen-positive *endocochlear potential* (EP; ca. +80 mV). The high endolymphatic K^+ concentration provides the carrier of the transduction current. The driving force for that current consists almost exclusively of the voltage across the transduction channels in the stereocilia (see Section VI) and that voltage is the sum of the intracellular potential of the hair cells and the EP. The large EP therefore heightens the sensitivity of the cochlear transduction process compared to vestibular organs, which do not have this high transepithelial electrical polarization. The cellular transport model by which the stria vascularis secretes potassium and generates the EP is shown in Fig. 37.4 and described next. Recall that all epithelial cells that produce a vectorial transport of substances do so by virtue of different membrane properties of their apical and basolateral membranes.

IVC1. Division of Function between Marginal and Basal Cell Barriers

The stria vascularis consists of two barriers formed by the marginal cells and the basal cells. Each barrier consists of a continuous sheet of cells joined by tight junction

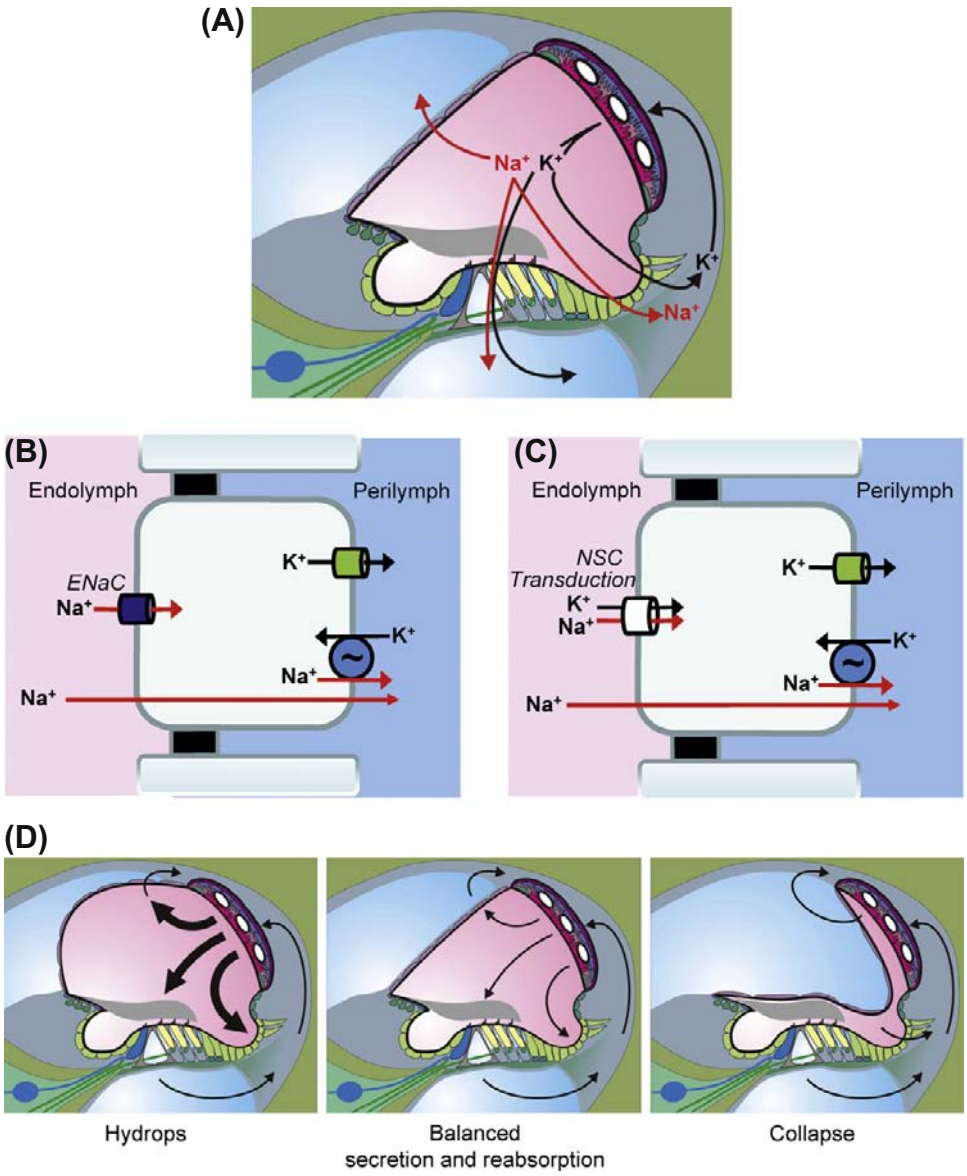

FIGURE 37.3 Schematic cross-sections through one cochlear turn illustrating inner ear ion and water transport. (A) K^+ secretion by stria vascularis (SV) and absorption by sensory cells in the organ of Corti and outer sulcus cells; Na^+ absorption by Reissner's membrane, hair cells and outer sulcus cells. Cell models of transepithelial Na^+ absorption via Na^+-selective epithelial Na^+ channels (ENaC) (B) or non-selective cation channels (C), including the non-selective transduction channels of hair cells. (D) Effects of hypoabsorption and/or hypersecretion (hydrops) of balanced transport (normal cross-section) and of hyperabsorption and/or hyposecretion (collapse). (C). *(Reproduced with permission from Kim, S.H. and Marcus, D.C. (2011). Regulation of sodium transport in the inner ear. Hear Res. 280, 21–29, and Wangemann, P. (2002). Adrenergic and muscarinic control of cochlear endolymph production. Adv Otorhinolaryngol. 59, 42–50, and Marcus and Wangemann, (2009). In (F.J. Alvarez-Leefmans and E. Delpire, eds), Physiology and Pathology of Chloride Transporters and Channels in the Nervous System–From Molecules to Diseases, pp. 425–437. Elsevier, New York).*

complexes (see Fig. 37.4). Between these barriers is the intrastrial space with the capillary bed for which the tissue is named and a discontinuous layer of *intermediate cells*. The basal cells are joined via *gap junctions* (see Chapter 22) to the intermediate cells and to fibrocytes in the adjacent connective tissue, suggesting a level of cooperation among these three cell types (Kikuchi et al., 2000). Unlike most sheets of epithelial cells, strial marginal cells are not coupled to each other nor to other cells by gap junctions (Takeuchi and Ando, 1998; Kikuchi et al., 2000). The physiological significance of this functional independence of marginal cells is not known.

The basal cell/intermédiate cell syncytium produces and supports the endocochlear potential and the strial marginal cells secrete K^+. In spite of the distinct cellular functions, the two processes are closely tied together through the composition of the intrastrial space. For example, inhibition of K^+ secretion by the marginal cells

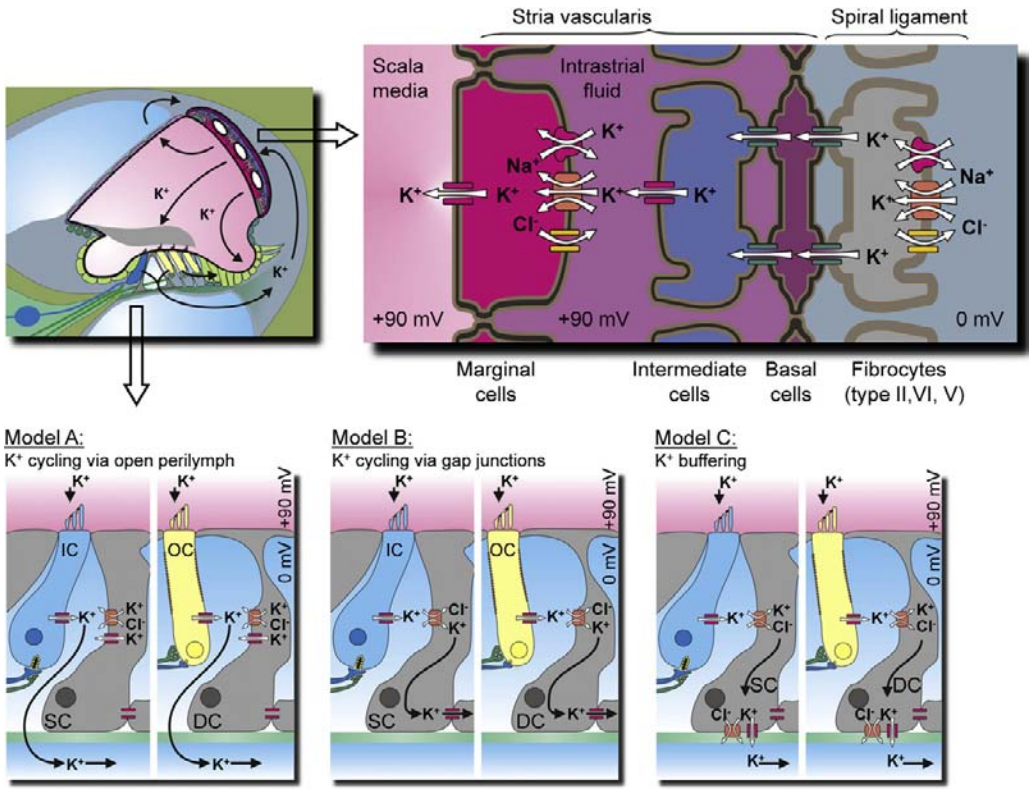

FIGURE 37.4 Overview of the stria vascularis and its K^+ transport mechanisms and three models of K^+ pathways that remove K^+ from the hair cells. (Inset) Cochlear cross-section. (Top panel) The stria vascularis consists of three distinct cell types: marginal, intermediate and basal cells. Intermediate cells are connected via gap junctions to basal cells which, in turn, form gap junctions with underlying fibrocytes. Gap junctions among the fibrocytes are not shown. (Bottom panel) Model A: postulates that K^+ released from hair cells cycles back to the stria vascularis through the open perilymph space; Model B: entails K^+ recycling through inner phalangeal cells, marked as supporting cells (SC) by the inner hair cells (IC) or Deiters' cells (DC) by the outer hair cells (OC); Model C: the supporting cells act as a K^+ buffer. Note that these three models are not mutually exclusive. *(Reproduced with permission from Zdebik, A.A., Wangemann, P. and Jentsch, T.J. (2009). Potassium ion movement in the inner ear: insights from genetic disease and mouse models. Physiology (Bethesda.) 24, 307–316, and Marcus and Wangemann, (2009). In (F.J. Alvarez-Leefmans and E. Delpire, eds), Physiology and Pathology of Chloride Transporters and Channels in the Nervous System–From Molecules to Diseases, pp. 425–437. Elsevier, New York.)*

leads to a decline of the endocochlear potential. This would occur by a rise in intrastrial K^+ concentration upon cessation of K^+ uptake by the marginal cells and the consequent depolarization of the K^+-selective intermediate cell membrane (see below). Several lines of evidence, including histochemical, biochemical, electrophysiological and flux studies, have strongly suggested that the stria vascularis is responsible for secretion of K^+ into the cochlear lumen and for production of the EP (reviewed in Marcus and Wangemann, 2010).

IVC2. K^+ Secretion by Strial Marginal Cell Epithelium

Active K^+ secretion in the cochlear duct has been demonstrated by flux measurements of radiolabeled K^+ introduced in either the perilymphatic or vascular space and its appearance in endolymph (Konishi et al., 1978; Sterkers et al., 1982). These fluxes were inhibited by transport blockers and anoxia. The stria was assumed to be the site of secretion since the flux was nearly the same when the radiotracer was added to either scala vestibuli or scala tympani; possible contributions by the spiral limbus were disregarded.

More recently, the stria was isolated from the cochlear duct, a K^+-selective self-referencing probe was placed near the tissue in vitro and a K^+ gradient was found directed away from the luminal surface (Wangemann et al., 1995) (Fig. 37.5A). The marginal cell layer of the stria vascularis produces this K^+ flux using the constellation of transport processes shown in Fig. 37.4. K^+ is taken up across the *basolateral membrane* from the *intrastrial space* fluid by two transporters: the *Na^+,K^+-ATPase (Na^+ pump)* and the *NKCC1 Na^+-K^+-Cl^- co-transporter*. The first is a primary active process, which uses the energy from cytosolic adenosine triphosphate (ATP) and the second is secondary active and uses the large Na^+ concentration gradient between extracellular and intracellular compartments created by the Na^+,K^+-ATPase. Na^+ and Cl^- taken up by the co-transporter are removed from the cytosol by the

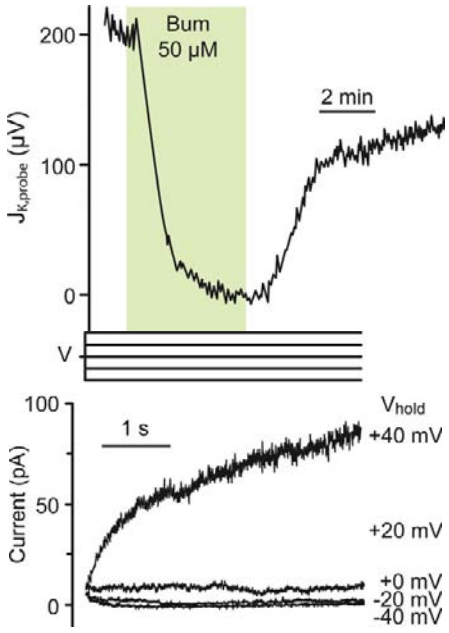

FIGURE 37.5 Transepithelial K^+ flux and apical membrane K^+ currents via KCNQ1/KCNE1 K channels. (A) K^+ secretory flux from stria vascularis measured with a K^+-selective self-referencing probe. The ordinate is the flux expressed as the difference in microvolts measured at the two positions of the probe. Flux was decreased by basolateral perfusion of the inhibitor of Na^+-K^+-Cl^- co-transport, bumetanide (Bum). (*Adapted from Wangemann, P., Liu, J. and Marcus, D.C. (1995). Ion transport mechanisms responsible for K^+ secretion and the transepithelial voltage across marginal cells of stria vascularis in vitro. Hear Res. 84, 19–29, Copyright 1995 with kind permission of Elsevier Science-NL, Sara Burgerhartstraat 25, 1055 KV Amsterdam, The Netherlands.*). (B) Patch-clamp currents from the apical membrane of a strial marginal cell, on-cell configuration. Sustained depolarizations activate the current slowly over several seconds, characteristic of KCNQ1/KCNE1 K^+ channels. *(Reproduced with permission from Shen, Z., Marcus, D.C., Sunose, H., Chiba, T. and Wangemann, P. (1997). I_{sK} channel in strial marginal cells: voltage-dependence, ion-selectivity, inhibition by 293B and sensitivity to clofilium. Auditory Neurosci. 3, 215–230.)*

Na^+,K^+-ATPase and basolateral *ClC-K/barttin (/BSND) Cl^- channels*, respectively (Marcus and Wangemann, 2010).

K^+ secretion occurs passively via channels in the apical membrane (see Figs. 37.4 and 37.5). These channels are products of the genes KCNQ1 and KCNE1, which code for the pore-forming α subunit and the regulatory β subunit of the channel, respectively. The KCNQ1/KCNE1 channels are characterized by slow activation (over seconds) in response to depolarization of the cell membrane and have a single-channel conductance of about 14 pS under in vivo-like conditions (see Fig. 37.5B) (Marcus and Shen, 1994; Shen et al., 1997; Marcus and Wangemann, 2010). The essential contributions to K^+ secretion of the apical K^+ channel and of the basolateral co-transporter have been demonstrated with gene knockout mice. Individual deletion of KCNQ1, KCNE1 or NKCC1 (Slc12a2) resulted in a collapsed lumen in knockout mice.

IVC3. Production of Endocochlear Potential by Strial Intermediate and Basal Cells

Two key genes expressed in the stria vascularis are at the heart of EP generation: those that code for the tight junction protein claudin-11 and the KCNJ10 K^+ channel. Tight junctions are formed from an assemblage of a number of proteins and the family of claudin isoforms provides definition to the permeability characteristics of each junction. The basal cell barrier contains claudin-11 and the connections among these cells are the only location for claudin-11 in the inner ear. An important demonstration of the importance of claudin-11 to EP generation was the observation that the EP collapsed in claudin-11 knockout mice, while K^+ secretion continued since marginal cell function was unimpaired (Gow et al., 2004).

The KCNJ10 K^+ channel (also known as Kir4.1) is expressed in the membrane of intermediate cells (see Fig. 37.4). Intracellular K^+ is maintained high by uptake from perilymph by fibrocytes in the spiral ligament and diffusion via gap junctions into basal cells and intermediate cells (see Fig. 37.4) (Kikuchi et al., 2000). Intrastrial K^+ is maintained at an unusually low level in the intrastrial space by the marginal cells. The membrane potential of the intermediate cells is dominated by the KCNJ10 conductance. Normally, one would then expect the intermediate cells to be highly negative, as observed in symmetrical cells that are dominated by a membrane K^+ conductance. However, the basal cells are highly depolarized, perhaps by non-selective cation channels, and the high density of gap junctions between basal cells and intermediate cells effectively "grounds" the cytosol of the intermediate cells. With the intermediate cells near zero with respect to the extracellular fluid of the spiral ligament (perilymph), the intrastrial space (electrically isolated from the perilymph by the claudin-11-containing tight junctions of the basal cells) is highly positive. That high positive potential appears in the endolymph as the EP. The marginal cell layer generates very little contribution to the EP, similar to the K^+-secreting vestibular dark cell epithelium which is a monolayer without the intermediate cell/basal cell layer. The importance of the KCNJ10 channel to EP generation is supported by the observation that KCNJ10 knockout mice have no EP, but maintain an elevated endolymphatic [K^+].

The general scheme of strial function shown in Fig. 37.4 was first supported by observations of the electrical and K^+ profile of the stria obtained with double-barrel electrodes (Salt et al., 1987). In the spiral ligament, the potential was taken as zero and the K^+ concentration was a few millimolar (Fig. 37.6). As the electrode was advanced, a region was found where the K^+ concentration was also low but the

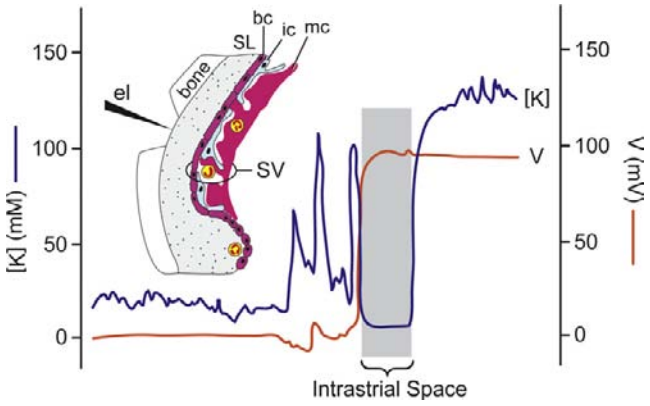

FIGURE 37.6 Recording of profiles for voltage (orange line; right axis) and K^+ concentration (blue line; left axis) during penetration of the stria vascularis (SV). A region was found where the voltage with respect to perilymph was highly positive but the K^+ concentration was low; this region was interpreted to be the intrastrial space. SL, spiral ligament; bc, basal cell; ic, intermediate cell; mc, marginal cell; el, penetrating electrode advanced from left to right. Horizontal axis is time/distance of electrode advancement. *(Adapted with permission from Salt, A.N., Melichar, I. and Thalmann, R. (1987). Mechanisms of endocochlear potential generation by stria vascularis. Laryngoscope. 97, 984-991, and (inset) from Dallos, P. (1996). Overview: Cochlear neurobiology. In (P. Dallos, A.N. Popper, and R.R. Fay, eds), The Cochlea, pp. 1–43. Copyright 1996 by Springer-Verlag.)*

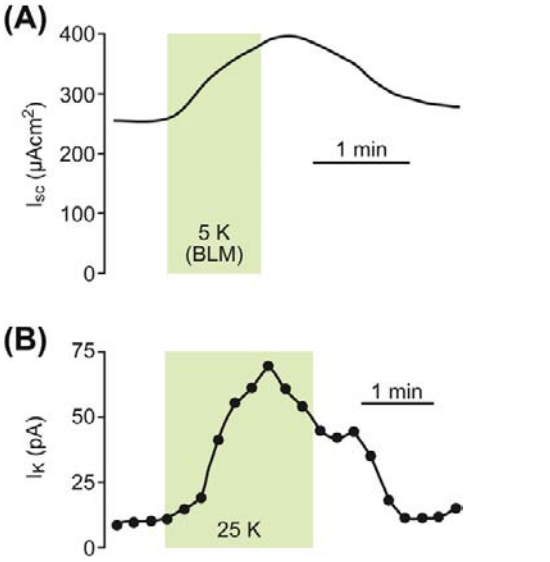

FIGURE 37.7 Stimulation of (A) short circuit current (I_{sc}) and (B) K^+ current through the apical KCNQ1/KCNE1 K^+ channels (I_K) on K^+ concentration in vestibular dark cells, the homologs to strial marginal cells. Basolateral $[K^+]$ was increased from 3.6 mM to 5 mM (A) or 25 mM (B). *(Adapted from Wangemann, P., Shen, Z., and Liu, J. (1996). K^+ induced stimulation of K^+ secretion involves activation of the IKs channel in vestibular dark cells, Hear Res. 100, 201–210. Copyright 1996 with kind permission of Elsevier Science-NL, Sara Burgerhartstraat 25, 1055 KV Amsterdam, The Netherlands.)*

potential had risen to about +80 mV. This was interpreted as being located in the intrastrial space. Further penetration led to a jump of the K^+ concentration to that commonly found in endolymph with no appreciable change in the potential. The voltage gradient was therefore largest across the basal cell layer and the K^+ gradient largest across the marginal cell layer.

IVC4. Regulation of Ion Transport in Strial Marginal Cells

Every cell type encounters perturbations and signals by systemic variables, such as by hormones and/or neurotransmitters, osmotic strength and extracellular $[K^+]$ and pH (pH_o), and by cytosolic variables, such as intracellular Ca^{2+} and pH (pH_i). K^+ secretion in the inner ear is altered in response to many such stimuli.

Basolateral $[K^+]$ and Apical pH

The increase in flow of K^+ through hair cells in response to acoustical stimulation is known to increase the concentration of K^+ in the perilymph surrounding the basolateral membranes of the hair cells and the nerve endings. The rate of basolateral uptake of K^+ in strial marginal cells and of its secretion through the apical K^+ channel has been found to be exquisitely sensitive to the concentration of perilymphatic K^+ (Fig. 37.7). This K^+ sensitivity is believed to play a significant role in regulating the recirculation of K^+ back into endolymph (Wangemann et al., 1996) (see Fig. 37.7). Extracellular pH and $[Ca^{2+}]$ of the lumen is under cellular control in the cochlea (see below). The luminal pH can control key ion transporters in the stria vascularis and other cells. Of particular importance is the stimulation of KCNQ1/KCNE1 K channel activity and the inhibition of TRPV5/6 Ca^{2+} channel activity by extracellular pH (see below).

Hormones

There is no innervation of the stria vascularis, but these cells contain receptors coupled to ion transport for several local or systemic hormones, including catecholamines, ATP and adrenocorticosteroid hormones (Table 37.2). Vasopressin (antidiuretic hormone) affects the EP and longitudinal K^+ concentration gradient (Mori et al., 1989; Julien et al., 1994), but the cells with vasopressin receptors have not yet been identified. Basolateral perfusion in vitro of the β-adrenergic agonist isoproterenol caused maximal increases in I_{sc} of 40–75% in strial marginal cells (Wangemann, 2002).

β-Adrenergic receptors

β-Adrenergic receptors are commonly coupled via G proteins to adenylate cyclase (see Chapter 6). Indeed, an increase of cytosolic cAMP in strial marginal cells by direct stimulation of adenylate cyclase, by perfusion of a membrane-permeable cAMP analog, or by inhibition of phosphodiesterases that catalyze the breakdown of

TABLE 37.2 Hormones and Signal Pathways Regulating KCNQ1/KCNE1 Current

Hormone/Signal	Stimulate	Inhibit
β-Adrenergic agonist		
Basolateral	X	
Purinergic agonist		
Apical	Transient	X
Basolateral		X
cAMP	X	
Phospholipase C		X
Protein kinase C		X
Cytosolic Ca^{2+}	X	
Cytosolic pH	Transient	X
Cell swelling	X	

cAMP, all lead to an increase of I_{sc}. The stimulation of K^+ secretion by adrenergic agonists was found to be mediated by β-adrenergic receptors through determination of the potency order of specific antagonists and by demonstration of the presence of transcripts for this subtype in cochlear tissue.

In isolated strial marginal cell epithelium, both apical and basolateral perfusion of micromolar ATP significantly alter I_{sc} (Fig. 37.8) (Lee and Marcus, 2008). Apical ATP and analogs monotonically downregulate I_{sc}, whereas basolateral ATP and analogs transiently increase I_{sc} followed by downregulation. The data are consistent with the presence of purinergic receptors of the $P2Y_4$ subtype on the apical membrane and $P2Y_2$ subtypes on the basolateral membrane. Additional purinergic receptors may also play a role.

P2Y receptor subtypes are known in other cells to be coupled to G proteins that stimulate phospholipase C (PLC). PLC catalyzes the breakdown of membrane phospholipid to produce both inositol trisphosphate (IP_3) and diacylglycerol (DAG) (see Chapter 6). It is most common that the IP_3 branch of the PLC pathway regulates ion channel activity through the cytosolic level of free Ca^{2+}. However, it was shown that the apical $P2Y_4$ receptor downregulates K^+ secretion primarily via the DAG-protein kinase C (PKC) branch (Lee and Marcus, 2008) even though inositol phosphate production is increased in the cochlear lateral wall in response to P2Y agonists (Ogawa and Schacht, 1995).

Basolateral muscarinic receptors (M_3 and/or M_4) were observed to inhibit K secretion by strial marginal cells, but the lack of direct innervations led to the speculation that

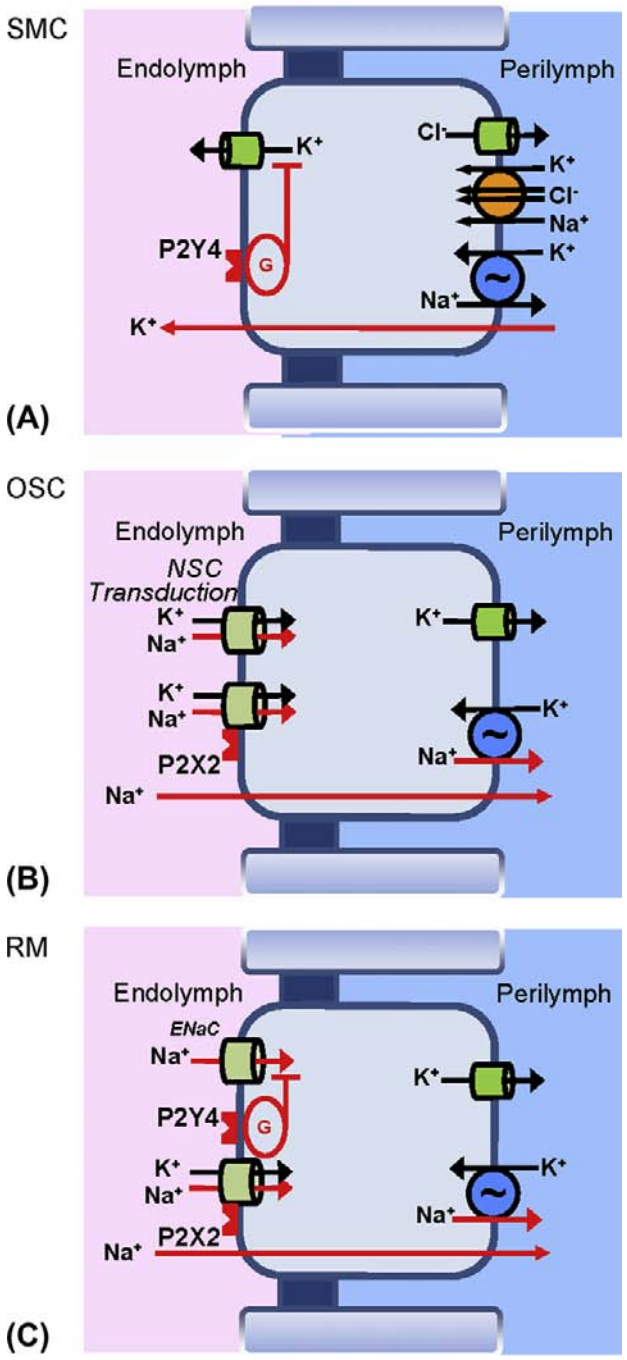

FIGURE 37.8 Purinergic signaling in the cochlear epithelium. (A) stria vascularis marginal cells; activation of P2Y4 receptors in the apical membrane reduce secretory K^+ flux via a G-protein (G) signal cascade (Lee and Marcus, 2008). There are additional purinergic receptors on the basolateral side (Lee and Marcus, 2008). (B) Outer sulcus cells; activation of apical P2X2 receptors open the associated non-selective cation channels (Lee and Marcus, 2008). (C) Reissner's membrane epithelial cells; activation of P2Y4 receptors (membrane location unknown) reduces ENaC-mediated Na^+ absorption, and activation of apical P2X2 receptors open the associated non-selective cation channels. *(Reproduced by permission from Kim, S.H. and Marcus, D.C. (2011). Regulation of sodium transport in the inner ear. Hear Res. 280, 21–29, and Lee, J.H., and Marcus, D.C. (2008). Purinergic signaling in the inner ear. Hear Res 235, 1–7.)*

circulating hormone might conceivably provide the agonist (Wangemann, 2002).

Steroid Hormones

Binding sites for both glucocorticosteroid (ten Cate et al., 1993) and mineralocorticosteroid (Yao and Rarey, 1996) have been demonstrated in the stria vascularis. Both corticoids control the activity of Na^+, K^+-ATPase in the stria vascularis (adrenalectomy reduced activity 60% and systemic administration of either the glucocorticosteroid dexamethasone or the mineralocorticosteroid aldosterone restored activity) (Curtis et al., 1993) and the increase in Na^+, K^+-ATPase with aldosterone was not dependent on major changes in blood plasma cation concentration (ten Cate et al., 1994). However, in spite of the strong dependence of the EP on strial Na^+, K^+-ATPase, a reduction of adrenocorticosteroids by adrenalectomy did not significantly reduce the EP in the presence or absence of strong acoustic stimulation (Ma et al., 1995). In addition, glucocorticoid hormones alone apparently do not stimulate the formation of Na^+, K^+-ATPase in the inner ear since no difference in the level of antibody binding to Na^+, K^+-ATPase was observed in glucocorticoid receptor knockout mice (Erichsen et al., 1998). Acute, non-genomic actions of steroid hormones were observed on currents from stria vascularis (Lee and Marcus, 2001, 2002). Corticosteroids stimulated currents only at therapeutic levels and not at normal circulating levels and estrogen inhibited currents at concentrations only found during the end of pregnancy.

A clear demonstration of steroid regulation of ion transport in the cochlea is on Reissner's membrane. Both Na^+ absorption and the expression of the α subunit of ENaC are markedly increased after 24 h exposure to the synthetic glucocorticoid dexamethasone (Fig. 37.9). This action of dexamethasone was via the glucocorticoid receptor (GR) and not via the mineralocorticoid receptor (MR) since both of the stimulatory actions were blocked by a specific GR inhibitor and not by an MR inhibitor.

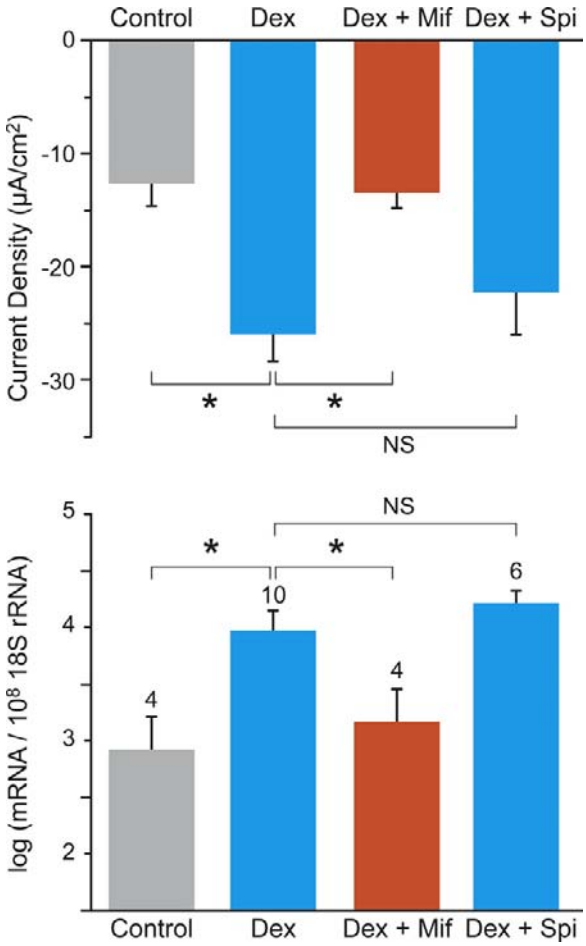

FIGURE 37.9 Stimulation of transepithelial sodium absorption by glucocorticoid, mediated by glucocorticoid receptor. (A) Changes of current density from Reissner's membrane under control conditions (gray bar), dexamethasone (blue bar; 100 nM, 24 h), dexamethasone + the glucocorticoid receptor antagonist mifepristone (orange bar; Mif, 100 nM), and dexamethasone + the mineralocorticoid receptor antagonist spironolactone (2nd blue bar; Spi, 100 nM). (B) qRT-PCR evaluation of transcript expression of the α subunit of ENaC under the same conditions as in (A). *$P < 0.05$; NS, not significant. *(Reproduced with permission from Kim, S.H., Kim, K.X., Raveendran, N.N., Wu, T., Pondugula, S.R. and Marcus, D.C. (2009). Regulation of ENaC-mediated sodium transport by glucocorticoids in Reissner's membrane epithelium. Am J Physiol Cell Physiol. 296, C544–C557.)*

IVD. Calcium and Acid/Base Transport

Endolymphatic [Ca^{2+}] is unusually low for an extracellular fluid (see Table 37.1) and its level is apparently maintained at its set point by a "push-pull" system. Ca^{2+} is secreted ("pushed") into endolymph by the plasma membrane Ca^{2+}-ATPase PMCA2, which is located in the stereocilia of hair cells and likely also in Reissner's membrane (Yamoah et al., 1998; Kim et al., 2009; Marcus et al., 2011). Gene deletion/mutation of PMCA2 leads to a reduced level of endolymphatic [Ca^{2+}] (Wood et al., 2004). An acid-sensitive Ca^{2+} absorptive system ("pull") is expressed in the cochlea and its gate-keeper apical channels, TRPV5 and TRPV6, are located in the inner and outer sulcus cells and have also been observed in marginal cells (Yamauchi et al., 2010).

Endolymphatic acid/base balance is apparently also a "push-pull" system. H^+ secretion from stria vascularis has been observed with self-referencing pH electrodes (Miyazaki, Wangemann and Marcus, unpublished observations). In addition, HCO_3^- secretion occurs via the Cl^-/HCO_3^- exchanger pendrin (*Slc26a4*), which is expressed in the apical membrane of strial spindle cells, spiral prominence and outer sulcus epithelial cells (Wangemann et al., 2004, 2007; Griffith and Wangemann, 2011). Pendrin, and likely other HCO_3^- transporters, maintain endolymph alkaline with respect to perilymph (see Table 37.1). Deletion of *Slc26a4* leads to an acidification of endolymph (Wangemann et al., 2007).

V. GENETIC BASIS OF DEAFNESS

Nearly 50% of profound hearing loss results from hereditary factors (Nance, 2003; Bayazit and Yilmaz, 2006; Morton and Giersch, 2010). Genetic causes of hearing loss are classified and identified in several ways. Clinical manifestations that are solely hearing-related are "non-syndromic" and those with pathologies in the ear plus one or more other organs are "syndromic". The chromosomal loci of non-syndromic hereditary *D*ea*FN*ess are designated with DFN numbers, such as DFNA1 or DFNB 1. The A and B refer to autosomal dominant and autosomal recessive transmission of hearing loss and cases without A or B are X-linked; 80% of cases are of DFNB type (Bayazit and Yilmaz, 2006). Additional forms of deafness occur from mutations of the mitochondrial genome.

Several on-line sources of information on hereditary hearing loss include:

- the American Hearing Loss Foundation (http://www.american-hearing.org/disorders/congenital-deafness/)
- Dr Timothy C. Hain (http://www.dizziness-and-balance.com/disorders/hearing/cong_hearing.html)
- Hereditary Hearing Loss by Dr Guy Van Camp and Dr Richard Smith (http://hereditaryhearingloss.org/)
- Laboratory website of Dr Karen Avraham (http://www.tau.ac.il/~karena/overview-genetics.html).

DFNB1 is the most common DFNB and results from mutations of the gap junction gene coding for connexin-26, GJB2. Gap junctions between epithelial cells and between fibrocytes of the lateral cochlear wall and among fibrocytes, strial basal cells and strial intermediate cells (see Fig. 37.4) are crucial to acoustic transduction. The physical properties of junctions composed of heteromeric connexin-26 and connexin-30 as occur in the cochlea continue to be investigated (Change et al., 2008; Hoang et al., 2009).

Two of the important syndromic hearing losses are Jervell and Lange-Nielsen (JLN) syndrome and Pendred syndrome. JLN results from mutations of the KCNQ1/KCNE1 K channel in either of the subunits. It is "syndromic" because this K channel plays a prominent role in cardiac function as well as providing the sole route of K efflux from strial marginal cells (see above). Pendred syndrome results from mutations of the Cl^-/HCO_3^--exchanger coded by Slc26a4. As mentioned above, deletion of this gene in mice results in an acidic shift of endolymphatic pH, as expected from a HCO_3^--secretory transporter. The effects of pendrin mutation, however, go far beyond this relatively obvious consequence. A series of recent studies (reviewed in Griffith and Wangemann, 2011) has found that hearing loss results from a constellation of events.

Without normal levels of expression of functional pendrin during late embryonic and early postnatal development, there is tremendous expansion of the developing cochlea (10-fold increase in luminal cross-sectional area) that leads to enlargement and acidification of cochlear endolymph, which spread the effect from pendrin-expressing cells to many other cell types. The result is a delayed development of the stria vascularis and a fluctuating local oxidative stress in the stria. This oxidative stress results in downregulation of expression of the KCNJ10 K channel in the intermediate cells (Fig. 37.10). KCNJ10 expression is known to be especially sensitive to oxidative stress and its downregulation compromises the EP, which was proposed to be a factor leading to fluctuating hearing loss (Griffith and Wangemann, 2011).

VI. CELL PHYSIOLOGY OF ACOUSTIC TRANSDUCTION

The mammalian cochlea has an exquisite sensitivity, being able to detect sound pressure fluctuations of less than one millionth atmospheric pressure. At the threshold of hearing, the organ of Corti vibrates less than 1 nm. This sensitivity

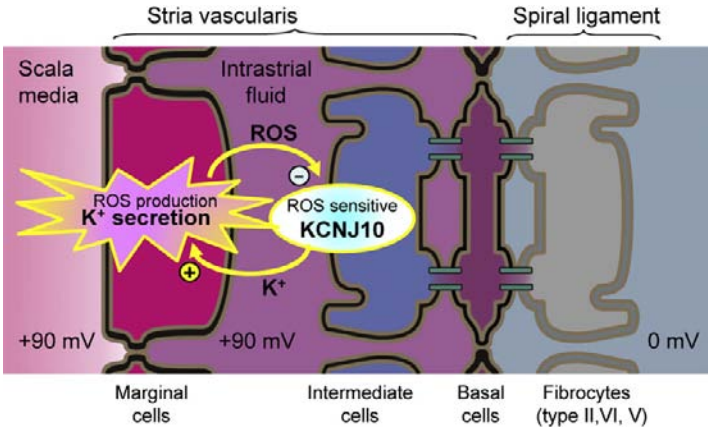

FIGURE 37.10 Proposed mechanism for fluctuating hearing loss. Diagram of the stria vascularis illustrating a feedback mechanism that leads to fluctuating loss of the K^+ channel that generates the endocochlear potential, KCNJ10. An increased rate of K^+ secretion related to the enlarged scala media generates increased levels of reactive oxygen species (ROS) in marginal cells. ROS diffuses to intermediate cells, where they downregulate expression of KCNJ10 channels (−). Reduced KCNJ10 decreases the EP and hearing and also reduces K^+ flux to the intrastrial space, thus limiting K^+ secretion by marginal cells; metabolic activity of marginal cells is reduced and ROS production drops. KCNJ10 expression is restored and the cycle repeats. Fluctuating loss of the endocochlear potential can thereby be expected to lead to fluctuating loss of hearing. *(Reproduced with permission from Griffith, A.J. and Wangemann, P. (2011). Hearing loss associated with enlargement of the vestibular aqueduct: mechanistic insights from clinical phenotypes, genotypes, and mouse models. Hear Res. doi:10.1016/j.hedres.2011.05.009.)*

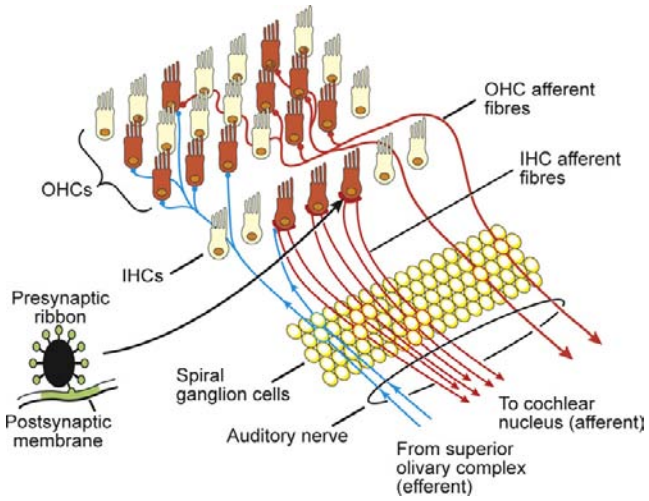

FIGURE 37.11 The organization of the cochlear inner and outer hair cells (IHCs and OHCs) and their (afferent and efferent) innervations. Each inner hair cell is innervated by 5−30 dendrites. The inset shows the schematic profile of the ribbon found at each afferent contact between the hair cells and the postsynaptic afferent terminal. *(Adapted with permission from Hackney, C. (2002). From cochlea to cortex. In D. Roberts, (ed.), Signals and Perception−the Fundamental Human Sensation, p. 31. Palgrave Macmillan Press, New York.)*

includes a gain of 100−1000 due to active mechanical amplification by the outer hair cells of the organ of Corti (but, see Ashmore et al., 2010). In spite of the delicacy of this process, the dynamic range for the amplitude detected by the cochlea is about one million to one due to compression of the response (Patuzzi, 1996).

The organization of the inner and outer hair cells and their innervations is depicted in Fig. 37.11. Afferent synapses to the inner hair cells account for most (95%) of the neural transmission from the cochlea to the brain. Each inner hair cell is innervated by 5−30 dendrites (Meyer and Moser, 2010). The remaining afferent fibers originate from the three rows of outer hair cells. Feedback occurs through an efferent neural supply that synapses with inner hair cell afferent fibers and directly with the body of outer hair cells (Elgoyhen and Fuchs, 2010). A local GABAergic innervation among outer hair cells has also been described (Thiers et al., 2008).

VIA. Transduction Channels

The mechanosensitive organelle of the sensory cells is the hair bundle (Fig. 37.12), which consists of 30−300 *stereocilia* arranged in rows of increasing height. Motion of the hair bundle modulates the fractional open time (open probability P_o) of the *mechanosensitive transduction channels* near the tips of the stereocilia. Modulation of P_o leads to corresponding fluctuations of the current through the apical membrane and to changes in the membrane potential of the hair cell. These changes in the membrane voltage are referred to as the *receptor potential*, the primary event to modulate synaptic transmission.

Bundle movement is believed to be the result of direct interaction of the outer hair cell stereocilia with the tectorial membrane and of the inner hair cell stereocilia with flowing endolymph pumped back and forth in the channel under the tectorial membrane (see Fig. 37.12). The cytoskeleton of the stereocilia is formed by a rigid matrix of actin filaments cross-linked by fimbrin. Deflection of the hair bundle results in a rotation of the individual cilia about a pivotal region at their base, which causes a shearing motion between the ciliary tips. Shear resulting from movement of the hair bundle in the direction of the tallest stereocilia increases P_o of the transduction channels from the resting activity of about 5−15%, whereas movement of the hair bundle in the opposite direction decreases P_o (see Figs. 37.12 and 37.13) (Hudspeth and Gillespie, 1994). Motion in the stimulatory direction is caused by the rarefaction phase of the external acoustic pressure wave. The asymmetric position on the receptor potential-stimulus transfer function of the stereocilia under unstimulated conditions (zero displacement in Fig. 37.13) leads to larger changes in the receptor potential with a given stimulatory displacement than for the same size inhibitory displacement. This asymmetry is a primary cause of distortion, which generates many of the non-linear properties of the auditory system, such as distortion products and otoacoustic emissions (see later section on reverse transduction).

The shear between stereocilia is posited in the *gating-spring model* of hair cell function to transmit a mechanical force through an elastic element (the gating spring) to the mechanosensitive gate of each transduction channel (Hackney and Furness, 2010). Increased tension on the spring increases P_o and decreased tension reduces P_o. The most widely accepted hypothesis is that the fine extracellular links (called tip links) that run between the tips of shorter stereocilia and the sides of taller ones constitute the elastic element of the model. The location of the transduction channels with respect to the attachment of the tip links remains somewhat equivocal, but the channels are apparently near the tips of sterocilia (Hackney and Furness, 2010).

Tip links are thought to be maintained under tension (see next section on adaptation), which is either increased or decreased by motion toward or away from the stimulatory direction. The time constant for response of the receptor current to a step stimulus has been found in saccular hair cells of the bullfrog to be in the range of 100−500 μs at 4°C and to become faster at higher temperatures (Corey and Hudspeth, 1983). This time course is substantially faster than can be accounted for by typical enzymatic or second messenger pathways and points to a direct mechanical coupling between the stimulus and the gate of the transduction channel.

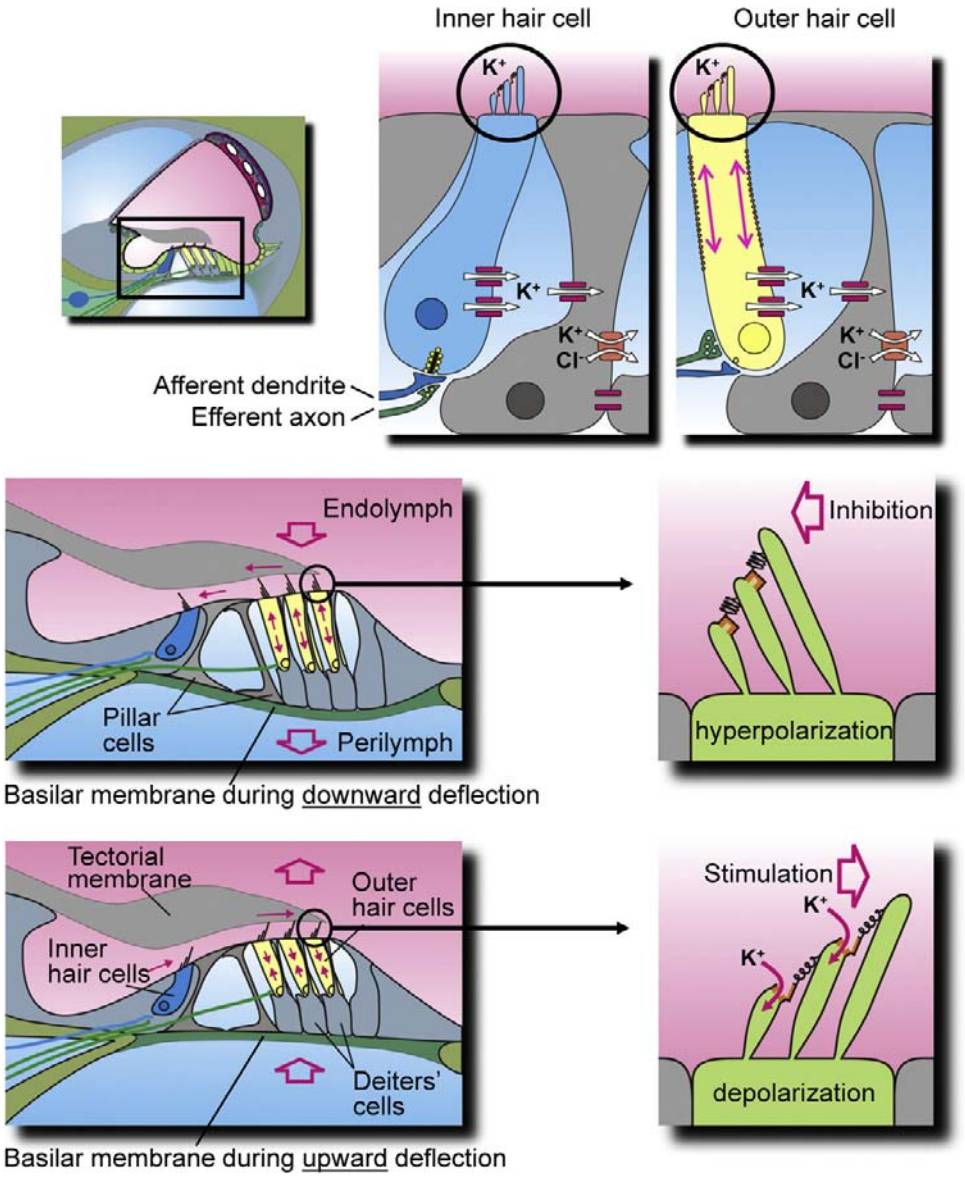

FIGURE 37.12 Diagram of the cochlear sensory structure, the organ of Corti and its inner and outer hair cells. (Top panel) The location of the organ of Corti (rectangle; left) and partial detail of an inner hair cell with supporting cell (middle) and an outer hair cell with supporting Deiters' cell (right). Stereocilia at the apical membrane of the hair cells tip links and transduction channels are circled; channels and transporters involved in putative K^+ buffering are described in the text and Fig. 37.4. (Middle panel) Downward deflection of basilar membrane (left) in response to sound is shown with medial movement of the outer hair cell stereocilia (right), leading to hyperpolarization of the hair cells (reduced afferent nerve transmission and elongation of the outer hair cell). (Bottom panel) Upward deflection of basilar membrane (left) in response to sound is shown with movement of the outer hair cell stereocilia (right), leading to depolarization. Arrows indicate movements of tectorial membrane, subtectorial fluid, basilar membrane (open arrow), K^+ flux through transduction channels at the tips of stereocilia and length changes in outer hair cells. *(Reproduced with permission from Marcus, D.C. and Wangemann, P. (2009). In (F.J. Alvarez-Leefmans and E. Delpire, eds), Physiology and Pathology of Chloride Transporters and Channels in the Nervous System — From Molecules to Diseases, pp. 425–437. Elsevier, New York.)*

The *conductance of the transduction channel* has been estimated from patch-clamp records to be on the order of 300 pS under in vivo conditions (Kros, 1996). The channel is permeable to cations including monovalent, divalent and small organic cations such as tetraethylammonium while selecting against anions (Corey and Hudspeth, 1979). Because potassium and calcium in endolymph are above electrochemical equilibrium with respect to the hair cell cytosol, it is primarily these two cations that flow through the transduction channel. Potassium carries the bulk of the current due to its high concentration, whereas entry of Ca^{2+} through the transduction channel is thought to control adaptation (see below). It was found that Ca^{2+} carries a surprisingly high fraction of the current through the

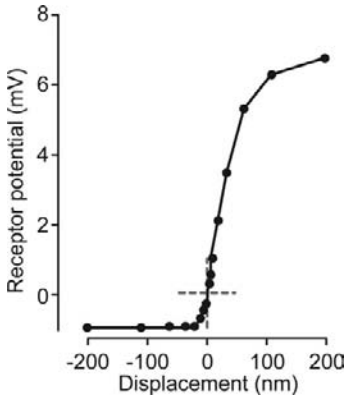

FIGURE 37.13 Response function of the receptor potential of outer hair cells to mechanical displacement of the stereocilia. The asymmetrical position of the quiescent point is indicated by dashed cross-hairs. *(Adapted with permission from Russell, I.J., Koessi, M. and Richardson, G.P. (1992). Nonlinear mechanical responses of mouse cochlear hair bundles. Proc R Soc London Ser B. 250, 217–227.)*

transduction channel (Ricci and Fettiplace, 1998) – about 20% (whereas the concentration of Ca^{2+} in endolymph is only about 0.01% that of K^+; see Table 37.1). This apparent anomaly may be due to the behavior of the transduction channel like a multi-ion pore in which the different ions interact. Sufficient Ca^{2+} enters the stereocilia to drive adaptation despite its low concentration. The channel is known to be blocked by aminoglycoside antibiotics (multivalent cations) and amiloride (a blocker of several Na^+ transport processes).

The non-selective cation permeability of the transduction channel, in concert with the basolateral K conductance and negative basolateral membrane potential, in hair cells is similar to the situation in outer sulcus cells. Therefore, an efflux of Na^+ from endolymph can be expected through hair cells, especially outer hair cells which are greater in number and have a greater basolateral membrane potential than inner hair cells. The molecular identity of the channels is different among the cell types, but the constellation is favorable for Na^+ absorption (Kim and Marcus, 2011).

VIB. Adaptation

When a sustained displacement is applied to hair cells, the transduction current is first stimulated but then relaxes in the continued presence of the stimulus with a complex characteristic time course, processes referred to as fast- and slow-adaptation (Hackney and Furness, 2010). The mechanism underlying slow adaptation is thought to be an active process in which myosin motors in the insertional plaque maintain tension within the tip link through a balance of climbing and slipping (Fig. 37.14). The tip link slackens when there is a deflection in the inhibitory direction but tension is soon re-established as the motor climbs along

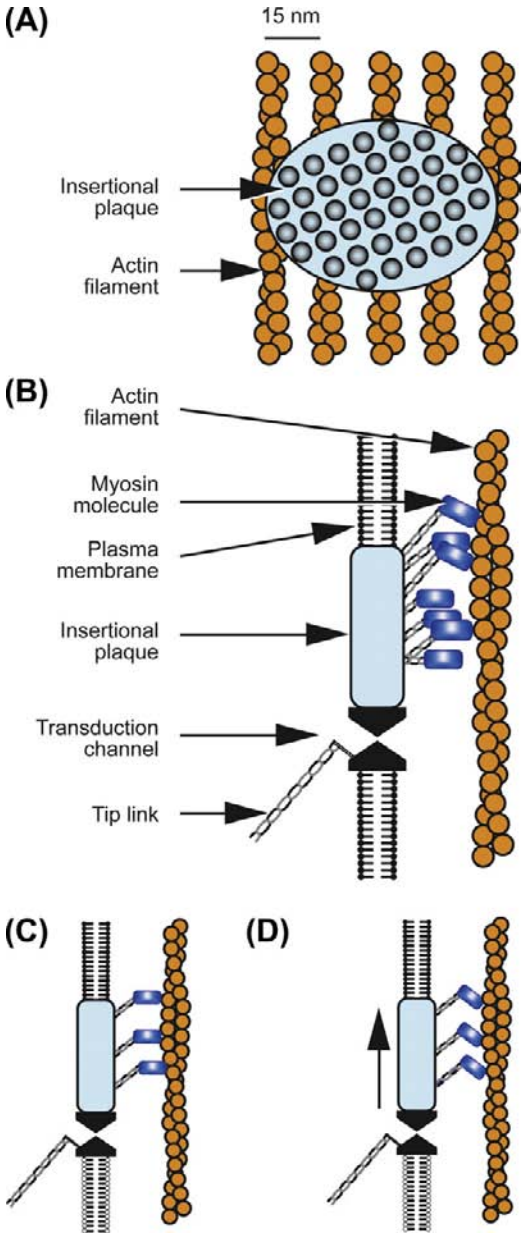

FIGURE 37.14 Proposed mechanism of adaptation: (A) frontal view of insertional plaque on actin filaments; (B) side view of insertional plaque with associated mechanosensitive transduction channel in cell membrane; and (C and D) power stroke of actin–myosin complex. *(Reproduced with permission from Hudspeth and Gillespie, 1994. Copyright 1994 by Cell Press.)*

actin filaments within the taller stereocilium of each pair. Deflection in the stimulatory direction increases tension in the tip links, opening the mechanosensitive transduction channel. Ca^{2+} coming in through the channel is thought to bind to calmodulin, a myosin regulatory protein found to be concentrated in the tips of stereocilia which, in turn, promotes the dissociation of myosin from the actin filaments, allowing the plaque with the motors to slip. Fast

adaptation is thought to be a direct, calcium-dependent effect on the transduction channel.

The physiologic significance of adaptation is clear for vestibular hair cells where prolonged static displacements naturally occur during which sensitivity to transient stimuli must be maintained. However, the function of adaptation in the mammalian cochlea is less obvious (Kros, 1996). The adaptation process has been estimated to have an upper frequency limit of about 160 Hz, limiting its potential usefulness as a response to normal acoustic stimuli. Physiological significance in the cochlea may lie more with homeostasis of the system in the face of small readjustments of the position and/or size of cells during normal changes in systemic osmolarity and local metabolic processes or during development. There may also be a significant importance in controlling the response to infrasound, which gains attention with regard to insults by machinery such as wind turbine generators (Salt and Hullar, 2010).

VIC. Basolateral Membrane Channels

Although there are differences among hair cell types, they all contain a major basolateral K^+ conductance, comprised of voltage-dependent and Ca^{2+}-activated K^+ channels and voltage-gated Ca^{2+} channels (Fuchs, 1992; Kros, 1996). The K^+ channels serve to shape the receptor potential initiated by the acoustically-gated transduction channels and the Ca^{2+} channels to initiate transmitter release at the presynaptic sites, respectively. The presence of voltage-gated Ca^{2+} channels alone would be expected to lead to regenerative depolarization during acoustic stimulation, however, the basolateral voltage-gated K^+ channels provide an active repolarizing influence in the mature cochlea. Interestingly, immature inner hair cells have a different complement of channels including excitable Na^+ channels and a relatively slow K^+ channel, which lead to spontaneous and evoked action potentials. During development (see Chapter 25), a large, fast K^+ channel is expressed that greatly speeds up the membrane time constant, preventing action potentials (Kros et al., 1998).

The Ca^{2+} channels in hair cells appear to be of the L type, which are characterized by activation at depolarized membrane potentials, little or no inactivation, and block by dihydropyridines such as nifedipine. In inner hair cells, the Ca^{2+} currents are activated above −60 mV and peak near −20 to 0 mV, a range that correlates well with that of receptor potentials found in recordings made in vivo and with predictions from in vitro experiments (Kros, 1996). These Ca^{2+} channels are therefore well poised to participate in the graded release of neurotransmitter at the basolateral synapses to type I afferent fibers in the auditory nerve. The kinetics of channel activation have been estimated to be sufficiently fast so as not to limit accurate following of nervous discharge rates to the acoustic stimulus (Kros, 1996). By contrast, the Ca^{2+} currents in outer hair cells are activated only above −30 mV, a range that is far removed from the resting membrane potential near −80 mV found in vivo and never reached by receptor potentials, which apparently saturate at 15 mV (Kros, 1996). There is therefore no evidence at this time for a function of these voltage-gated Ca^{2+} channels in outer hair cells; there are also no measurements of neural activity in the type II afferent fibers in the auditory nerve that synapse exclusively to the outer hair cells.

In inner hair cells, the K^+ currents are activated by depolarization in the range of −60 to −20 mV, a range that correlates well with that of the resting and receptor potentials found in recordings made in vivo and with that of the voltage-gated Ca^{2+} channels described earlier. The resting potential of inner hair cells in vivo is about −40 mV, which reflects a compromise of the highly negative EMF from the basolateral K^+ channels by the depolarized EMF of the non-selective cation conductance in the apical membrane (Dallos, 1986).

VID. Synaptic Release of Vesicles

A comprehensive description of the afferent synapse is given in Ashmore (2010) and a diagram is in Fig. 37.11. Depolarization by acoustic stimulation leads to Ca^{2+}-dependent release of neurotransmitter at the 30–40 synapses with the afferent fibers at the base of each inner hair cell. This process can be monitored in vitro as changes in *membrane capacitance*. Opening of Ca^{2+} channels during depolarization raises the local free Ca^{2+} concentration to tens or hundreds of micromolar (Roberts, 1994), which is thought to trigger synaptic exocytosis of the neurotransmitter glutamate (Ashmore, 2010) (see Chapter 32). Depolarization led to increases in membrane capacitance (up to 5% of the initial value) that continued for up to 2 s. It was estimated that this was sufficient to exhaust more than five times the number of vesicles initially in close apposition to the plasma membrane at active zones, suggesting that hair cells are capable of rapidly replenishing vesicles at release sites (Parsons et al., 1994). Capacitance returned during repolarization toward its prestimulus level with a time constant of about 14 s, but only in perforated-patch recordings (see Chapter 20), suggesting that membrane retrieval depends on a diffusible intracellular factor.

VIE. Reverse Transduction: Cochlear Amplifier

Discrimination of frequency information in acoustic signals is performed broadly at an initial level by mechanical tuning of the basilar membrane as a function of position

along the cochlea. In lower vertebrates, frequency discrimination is accomplished by tuning the electrical properties of the hair cells. The exquisite sensitivity and fine frequency discrimination of mammalian hearing depends on amplification of the incoming sound within the organ of Corti (Ashmore, 2010; Iwasa, 2010). It is widely held that the outer hair cells sense displacements caused by sound and feedback forces that enhance the basilar membrane motion by reducing the inherent damping of the cochlear partition. In support of this hypothesis, outer hair cells show membrane potential-induced length changes at acoustic rates. This process has been termed *reverse transduction* by the *cochlear amplifier*. This property of the organ of Corti leads to an epiphenomenon called *otoacoustic emission* in which mechanical fluctuations are generated by the inner ear, resulting in sounds emanating from the ear (Kemp, 2010).

Reverse transduction occurs by somatic and/or ciliary motility, the former due to a high concentration of the motor molecule prestin (Slc26a5) (Iwasa, 2010) (current opinions: Ashmore et al., 2010). Outer hair cells shorten and lengthen by up to 5% when depolarized and hyperpolarized, respectively. Longitudinal motions of the outer hair cells (see Fig. 37.12) are assumed to be transmitted in vivo to the whole organ of Corti via the tectorial membrane by the rigid reticular lamina at the top and by the Deiters' cell bodies at the base, mechanically coupled to the basilar membrane. Shortening in vivo would cause an upward pull on the basilar membrane and/or a downward pull on the reticular lamina (see Fig. 37.12). The latency is less than 0.1 ms and can be driven to frequencies in excess of 22 kHz (measurement of upper frequency limited by instrumentation) (Dallos and Evans, 1995). This response is driven by membrane potential and is associated with an apparent nonlinear capacitance. The presence of non-linear capacitance suggests that the motors act by conformational changes of the protein rather than by electrostatic repulsion between separate elements within the plane of the lipid bilayer.

Myosin in the stereocilia is estimated to be sufficiently plentiful and powerful to account for ciliary-driven amplification by the organ of Corti. However, if the stereociliary motion were modulated by Ca^{2+} rather than membrane potential, activation of stereociliar myosin by Ca^{2+} would not be restricted by the membrane's time constant. It remains to be determined whether these motors can operate at the highest frequencies detected by the mammalian cochlea (Ashmore, 2010; Iwasa, 2010).

Deiters' cells were previously thought to offer only a passive support to the outer hair cells and a mechanical connection to the acoustic stimulus at the basilar membrane. However, evidence suggests that these cells have a Ca^{2+}-dependent motile response. Increases in cytoplasmic Ca^{2+} caused an extension of the head of the phalangeal process away from the body by 0.5 to 1 μm within a few hundred milliseconds and the stiffness of the phalangeal process increased by 28 to 51% (Dulon, 1995).

VIF. Receptors and Neurotransmitters

A number of receptors for neurotransmitters and neuromodulators have been identified on cochlear hair cells (Ashmore, 2010; Elgoyhen and Fuchs, 2010). Some are known to mediate synaptic transmission while the physiological significance of others has not yet been identified.

VIF1. Outer Hair Cells

Receptors for several neurotransmitters and neuromodulators (Table 37.3) have been identified on outer hair cells by histochemical and electrophysiologic observations (Elgoyhen and Fuchs, 2010). The efferent synapses on the outer hair cells release acetylcholine (ACh) and γ-aminobutyric acid (GABA) as neurotransmitters from two populations of fibers and may co-release ATP with ACh. There is evidence for the presence of both ionotropic and metabotropic receptors for ATP and ACh and for the ionotropic $GABA_A$ receptor (Housley et al., 1995). Ionotropic receptors are coupled directly to ion channels, whereas metabotropic receptors act via G-protein pathways that ultimately regulate ion channel activity and/or other cellular processes (see Chapter 6). Cochlear Ach receptors contain the unusual α_9-receptor isoform subunit. Activation of ACh receptors causes membrane hyperpolarization apparently through an ion channel permeable to cations including Ca^{2+}. The entry of Ca^{2+} activates Ca^{2+}-dependent K^+ channels, likely the SK type (Elgoyhen and Fuchs, 2010), leading to hyperpolarization. Ionotropic ATP receptors depolarize the hair cell by opening associated non-selective cation channels permeable to Ca^{2+} as well as monovalent cations. The channels associated with the ionotropic ATP and ACh receptors admit Ca^{2+} into the cell, leading to a relatively slow elongation (a process referred to

TABLE 37.3 Effects of Outer Hair Cell Receptors on Fast and Slow Motility, Membrane Potential, and Calcium Concentration

	Fast	Slow	*Vc*	$[Ca^{2+}]_i$
ACh	x	x	Hyper.	x
ATP		x	Depol.	x
GABA			Hyper.	No
Substance P			Hyper.	No
CGRP				No, but potentiates ACh response

as slow motility or adaptation; see above). In addition to its effects on slow motility, ACh has been found to control the gain and magnitude of fast motility in outer hair cells (Sziklai et al., 1996). ACh evokes an increase in magnitude and gain of electromotility, which is sensitive to the muscarinic blocker atropine.

Receptors have also been found on outer hair cells for the peptides substance P and calcitonin gene-related peptide (CGRP). Substance P hyperpolarizes these cells by downregulating the non-selective cation conductance in the lateral wall via a pertussis toxin-insensitive G protein (Kakehata et al., 1993). CGRP had no effect on the resting cytoplasmic Ca^{2+} concentration but potentiated by about threefold the increase in Ca^{2+} caused by ACh stimulation in chick hair cells (Shigemoto and Ohmori, 1990).

VIF2. Inner Hair Cells

Inner hair cells have been found to have both metabotropic and ionotropic receptors for extracellular ATP (Sugasawa et al., 1996). At submicromolar ATP concentrations, the metabotropic receptors raise intracellular Ca^{2+} concentration, which hyperpolarizes inner hair cells via Ca^{2+}-sensitive K^+ channels. The ionotropic receptors are non-selective cation channels activated at higher ATP concentrations and which mainly have a depolarizing effect on the inner hair cells. Although the source of agonist for these receptors has not yet been identified, Ca^{2+}-dependent release of ATP from the organ of Corti has been observed (Wangemann, 1996) and ATP release from cochlear cells via connexin/pannexin hemichannels has been reported to reduce outer hair cell motility via purinergic receptors (Zhao et al., 2005).

VIG. Echolocation

Bats can capture flying prey by echolocation (biosonar) even among vegetation and other bats. Sounds are vocalized by the bat at frequencies near 60 kHz (the upper range of human hearing is about 20 kHz) and typically consist of a constant-frequency tone pulse for 10−100 ms followed by a shorter period of dropping frequency. The pulse is reflected from surfaces in front of the bat and is returned and heard before the end of the emitted pulse. Several characteristics of the returned sound pulse are interpreted by the bat as an acoustic image. A Doppler shift of the frequency of the returned sound from that of the emitted sound carries velocity information (the rate of closure on a target). For example, a Doppler shift from 61 to 62 kHz corresponds to 6.3 miles per hour. The delay of the echo gives the distance to the target such that a 1-ms echo delay corresponds to a target distance of 17 cm. Temporal delay acuity has been reported to be as fine as 10 ns (Simmons et al., 1990), a surprisingly short time span for recognition by a biological system. It has been suggested, however, that bats may not respond directly to processing of the time delay but rather to spectral processing, which would require only a resolution of about a few kilohertz (Neuweiler and Schmidt, 1993; Simmons, 1993; Simmons et al., 1996; Fuzessery et al., 2011).

The fine tuning of hearing used in echolocation is mostly achieved by mechanical specializations of the cochlea, which spread out the physical mapping of the biosonar frequencies over a full half turn of the cochlea. There is also an amplifying reverberation of the acoustic wave traveling on the basilar membrane, which is due either to reflections at a discontinuity of the basilar membrane thickness or to different radial oscillation modes of the basilar membrane (Russell and Koessl, 1995). As in other mammalian cochleae, the tuning (and the bat's special reverberation) is thought to depend on active processes in the outer hair cells. Tuning of auditory nerve fibers, and therefore likely tuning of basilar membrane motion, to acoustic stimuli is amazingly high in the bat with Q10 values (center frequency/bandwidth 10 dB from the tip) as high as 610 in comparison to typical values of 1 to 10 for non-echolocating animals (Russell and Koessl, 1995). Processing by central neural pathways of the detected echoes has been reviewed by Fuzessery et al. (2011). An interesting specialization of the bats' prey has been found in the dogbane tiger moth, which apparently emits clicks when a bat approaches in order to interfere with the sonar echoes, thereby jamming the signal and averting becoming a meal (Fullard et al., 1994)!

VII. CONCLUDING REMARKS

The exquisite sensitivity of our sense of hearing results from the concerted action of many subsystems. Sound is conducted from our environment through the outer ear canal at the end of which it is conducted through the middle ear by the three ossicles to the oval window of the inner ear. Sounds can also reach the inner ear by bone conduction. This auditory peripheral organ transduces the mechanical stimulus into nerve impulses that travel to central auditory pathways in the brain where we interpret the impulses as sounds.

This chapter has focused on the cellular processes in the cochlea that support auditory transduction. In particular, several cell types contribute specific ion transport modalities to the creation and maintenance of the ionic composition of the cochlear luminal fluid, endolymph. The potassium, sodium, calcium and pH levels that comprise this unique extracellular environment all serve to power and support the transduction process performed by the sensory inner hair cells and the cochlear amplifier

embodied in several cell types in the organ of Corti and especially the outer hair cells.

All of these cellular processes depend on specific gene expression patterns; a number of gene mutations are known to underlie specific clinical syndromic and non-syndromic hereditary hearing loss. The only "surprise" has been that most of these clinically important genes are located in the cells that engage in ion transport rather than the auditory sensory and neural cells. Current and future areas of investigation include extending our knowledge of ion transport function to early developmental times, development of gene therapy and drug delivery techniques and discovery of cochlear "repair" through new extrinsic nerve stimulation paradigms and/or cochlear cell replacements.

ACKNOWLEDGMENT

This work was supported by NIH grant R01 - DC00212.

BIBLIOGRAPHY

Ashmore, J. (2010). The afferent synapse. In P. A. Fuchs (Ed.), *The Oxford Handbook of Auditory Science: The Ear* (pp. 259−282). Oxford: Oxford University Press.

Ashmore, J., Avan, P., Brownell, W. E., et al. (2010). The remarkable cochlear amplifier. *Hear Res, 266*, 1−17.

Bayazit, Y. A., & Yilmaz, M. (2006). An overview of hereditary hearing loss. *Otorhinolaryngol Relat Spec, 68*, 57−63.

Chang, Q., Tang, W., Ahmad, S., Zhou, B., & Lin, X. (2008). Gap junction mediated intercellular metabolite transfer in the cochlea is compromised in connexin30 null mice. *PLoS One, 3*, e4088.

Corey, D. P., & Hudspeth, A. J. (1979). Ionic basis of the receptor potential in a vertebrate hair cell. *Nature, 281*, 675−677.

Corey, D. P., & Hudspeth, A. J. (1983). Kinetics of the receptor current in bullfrog saccular hair cells. *J Neurosci, 3*, 962−976.

Curtis, L. M., ten Cate, W. J., & Rarey, K. E. (1993). Dynamics of Na, K-ATPase sites in lateral cochlear wall tissues of the rat. *Eur Arch Otorhinolaryngol, 250*, 265−270.

Dallos, P. (1986). Neurobiology of cochlear inner and outer hair cells: intracellular recordings. *Hear Res, 22*, 185−198.

Dallos, P., & Evans, B. N. (1995). High-frequency motility of outer hair cells and the cochlear amplifier. *Science, 267*, 2006−2009.

Dulon, D. (1995). Ca^{2+} signaling in Deiter's cells of the guinea-pig cochlea: active process in supporting cells? In A. Flock, D. Ottoson, & M. Ulfendahl (Eds.), *Active Hearing* (pp. 195−208) New York: Elsevier Science.

Elgoyhen, A. B., & Fuchs, P. A. (2010). Efferent innervation and function. In P. A. Fuchs (Ed.), *The Oxford Handbook of Auditory Science: The Ear* (pp. 283−306). Oxford: Oxford University Press.

Erichsen, S., Stierna, P., Bagger-Sjoback, D., et al. (1998). Distribution of Na, K-ATPase is normal in the inner ear of a mouse with a null mutation of the glucocorticoid receptor. *Hear Res, 124*, 146−154.

Fuchs, P. A. (1992). Ionic currents in cochlear hair cells. *Prog Neurobiol, 39*, 493−505.

Fullard, J. H., Simmons, J. A., & Saillant, P. A. (1994). Jamming bat echolocation: the dogbane tiger moth Cycnia tenera times its clicks to the terminal attack calls of the big brown bat Eptesicus fuscus. *J Exp Biol, 194*, 285−298.

Fuzessery, Z. M., Razak, K. A., & Williams, A. J. (2011). Multiple mechanisms shape selectivity for FM sweep rate and direction in the pallid bat inferior colliculus and auditory cortex. *J Comp Physiol A Neuroethol Sens Neural Behav Physiol, 197*, 615−623.

Gow, A., Davies, C., Southwood, C. M., et al. (2004). Deafness in Claudin 11-null mice reveals the critical contribution of basal cell tight junctions to stria vascularis function. *J Neurosci, 24*, 7051−7062.

Griffith, A. J., & Wangemann, P. (2011). Hearing loss associated with enlargement of the vestibular aqueduct: Mechanistic insights from clinical phenotypes, genotypes, and mouse models. *Hear Res*, doi:10.1016/J.heares.2011.05.009.

Hackney, C. M., & Furness, D. N. (2010). Hair bundle structure and mechanotransduction. In P. A. Fuchs (Ed.), *The Oxford Handbook of Auditory Science: The Ear* (pp. 231−258). Oxford: Oxford University Press.

Hoang, D. E., Ahmad, S., Chang, Q., Tang, W., Stong, B., & Lin, X. (2009). Diverse deafness mechanisms of connexin mutations revealed by studies using in vitro approaches and mouse models. *Brain Res, 1277*, 52−69.

Housley, G. D., Connor, B. J., & Raybould, N. P. (1995). Purinergic modulation of outer hair cell electromotility. In A. Flock, D. Ottoson, & M. Ulfendahl (Eds.), *Active Hearing* (pp. 221−238). New York: Elsevier Science.

Hudspeth, A. J., & Gillespie, P. G. (1994). Pulling springs to tune transduction: adaptation by hair cells. *Neuron, 12*, 1−9.

Iwasa, K. H. (2010). Electromotility of outer hair cells. In P. A. Fuchs (Ed.), *The Oxford Handbook of Auditory Science: The Ear* (pp. 179−212). Oxford: Oxford University Press.

Julien, N., Loiseau, A., Sterkers, O., Amiel, C., & Ferrary, E. (1994). Antidiuretic hormone restores the endolymphatic longitudinal K^+ gradient in the Brattleboro rat cochlea. *Pflügers Arch, 426*, 446−452.

Kakehata, S., Akaike, N., & Takasaka, T. (1993). Substance P decreases the non-selective cation channel conductance in dissociated outer hair cells of guinea pig cochlea. *Ann NY Acad Sci, 707*, 476−479.

Kemp, D. T. (2010). Otoacoustic emissions and evoked potentials. In P. A. Fuchs (Ed.), *The Oxford Handbook of Auditory Science: The Ear* (pp. 93−137). Oxford: Oxford University Press.

Kikuchi, T., Kimura, R. S., Paul, D. L., Takasaka, T., & Adams, J. C. (2000). Gap junction systems in the mammalian cochlea. *Brain Res Brain Res Rev, 32*, 163−166.

Kim, S. H., & Marcus, D. C. (2011). Regulation of sodium transport in the inner ear. *Hear Res, 280*, 21−29.

Kim, S. H., Kim, K. X., Raveendran, N. N., Wu, T., Pondugula, S. R., & Marcus, D. C. (2009). Regulation of ENaC-mediated sodium transport by glucocorticoids in Reissner's membrane epithelium. *Am J Physiol Cell Physiol, 296*, C544−C557.

Konishi, T., Hamrick, P. E., & Walsh, P. J. (1978). Ion transport in guinea pig cochlea. I. Potassium and sodium transport. *Acta Otolaryngol, 86*, 22−34.

Kros, C. J. (1996). Physiology of mammalian cochlear hair cells. In P. Dallos, A. N. Popper, & R. R. Fay (Eds.), *The Cochlea* (pp. 318−385). New York: Springer-Verlag.

Kros, C. J., Ruppersberg, J. P., & Rusch, A. (1998). Expression of a potassium current in inner hair cells during development of hearing in mice. *Nature, 394*, 281−284.

Lee, J. H., & Marcus, D. C. (2001). Estrogen acutely inhibits ion transport by isolated stria vascularis. *Hear Res, 158*, 123−130.

Lee, J. H., & Marcus, D. C. (2002). Nongenomic effects of corticosteroids on ion transport by stria vascularis. *Audiol Neurootol, 7*, 100−106.

Lee, J. H., & Marcus, D. C. (2008). Purinergic signaling in the inner ear. *Hear Res, 235*, 1−7.

Ma, Y. L., Gerhardt, K. J., Curtis, L. M., Rybak, L. P., Whitworth, C., & Rarey, K. E. (1995). Combined effects of adrenalectomy and noise exposure on compound action potentials, endocochlear potentials and endolymphatic potassium concentrations. *Hear Res, 91*, 79−86.

Marcus, D. C., & Shen, Z. (1994). Slowly activating, voltage-dependent K^+ conductance is apical pathway for K^+ secretion in vestibular dark cells. *Am J Physiol, 267*, C857−C864.

Marcus, D. C., & Wangemann, P. (2009). Cochlear and vestibular function and dysfunction. In F. J. Alvarez-Leefmans, & E. Delpire (Eds.), *Physiology and Pathology of Chloride Transporters and Channels in the Nervous System − From Molecules to Diseases* (pp. 425−437). New York: Elsevier.

Marcus, D. C., & Wangemann, P. (2010). Inner ear fluid homeostasis. In P. A. Fuchs (Ed.), *The Oxford Handbook of Auditory Science: The Ear* (pp. 213−230). Oxford: Oxford University Press.

Marcus, D. C., Raveendran, N. N., & Wu, T. (2011). Reissner's membrane, mouse. *GEO* GSE6196.

Meyer, A. C., & Moser, T. (2010). Structure and function of cochlear afferent innervation. *Curr Opin Otolaryngol Head Neck Surg, 18*, 441−446.

Mori, N., Shugyo, A., & Asai, H. (1989). The effect of arginine-vasopressin and its analogues upon the endocochlear potential in the guinea pig. *Acta Otolaryngol, 107*, 80−84.

Morton, C. C., & Giersch, A. B. (2010). Genetics of hearing loss. In P. A. Fuchs (Ed.), *The Oxford Handbook of Auditory Science: The Ear* (pp. 377−408). Oxford: Oxford University Press.

Nance, W. E. (2003). The genetics of deafness. *Ment Retard Dev Disabil Res Rev, 9*, 109−119.

Neuweiler, G., & Schmidt, S. (1993). Audition in echolocating bats. *Curr Opin Neurobiol, 3*, 563−569.

Ogawa, K., & Schacht, J. (1995). P2y purinergic receptors coupled to phosphoinositide hydrolysis in tissues of the cochlear lateral wall. *Neuroreport, 6*, 1538−1540.

Parsons, T. D., Lenzi, D., Almers, W., & Roberts, W. M. (1994). Calcium-triggered exocytosis and endocytosis in an isolated presynaptic cell: capacitance measurements in saccular hair cells. *Neuron, 13*, 875−883.

Patuzzi, R. (1996). Cochlear micromechanics and macromechanics. In P. Dallos, A. N. Popper, & R. R. Fay (Eds.), *The Cochlea* (pp. 186−257). New York: Springer-Verlag.

Ricci, A. J., & Fettiplace, R. (1998). Calcium permeation of the turtle hair cell mechanotransducer channel and its relation to the composition of endolymph. *J Physiol (Lond.), 506*, 159−173.

Roberts, W. M. (1994). Localization of calcium signals by a mobile calcium buffer in frog saccular hair cells. *J Neurosci, 14*, 3246−3262.

Russell, I. J., & Koessl, M. (1995). Measurements of the basilar membrane resonance in the cochlea of the mustached bat. In A. Flock, D. Ottoson, & M. Ulfendahl (Eds.), *Active Hearing* (pp. 295−306). New York: Elsevier Science.

Salt, A. N., & Hullar, T. E. (2010). Responses of the ear to low frequency sounds, infrasound and wind turbines. *Hear Res, 268*, 12−21.

Salt, A. N., Melichar, I., & Thalmann, R. (1987). Mechanisms of endocochlear potential generation by stria vascularis. *Laryngoscope, 97*, 984−991.

Shah, D. M., Freeman, D. M., & Weiss, T. F. (1995). The osmotic response of the isolated, unfixed mouse tectorial membrane to isosmotic solutions: effect of Na^+, K^+, and Ca^{2+} concentration. *Hear Res, 87*, 187−207.

Shen, Z., Marcus, D. C., Sunose, H., Chiba, T., & Wangemann, P. (1997). I_{sK} channel in strial marginal cells: voltage-dependence, ion-selectivity, inhibition by 293B and sensitivity to clofilium. *Auditory Neurosci, 3*, 215−230.

Shigemoto, T., & Ohmori, H. (1990). Muscarinic agonists and ATP increase the intracellular Ca^{2+} concentration in chick cochlear hair cells. *J Physiol (Lond.), 420*, 127−148.

Simmons, J. A. (1993). Evidence for perception of fine echo delay and phase by the FM bat, Eptesicus fuscus. *J Comp Physiol A, 172*, 533−547.

Simmons, J. A., Dear, S. P., Ferragamo, M. J., Haresign, T., & Fritz, J. (1996). Representation of perceptual dimensions of insect prey during terminal pursuit by echolocating bats. *Biol Bull, 191*, 109−121.

Simmons, J. A., Ferragamo, M., Moss, C. F., Stevenson, S. B., & Altes, R. A. (1990). Discrimination of jittered sonar echoes by the echolocating bat, Eptesicus fuscus: the shape of target images in echolocation. *J Comp Physiol A, 167*, 589−616.

Sterkers, O., Saumon, G., Tran Ba, H. P., & Amiel, C. (1982). K, Cl, and H_2O entry in endolymph, perilymph, and cerebrospinal fluid of the rat. *Am J Physiol, 243*, F173−F180.

Sugasawa, M., Erostegui, C., Blanchet, C., & Dulon, D. (1996). ATP activates non-selective cation channels and calcium release in inner hair cells of the guinea-pig cochlea. *J Physiol (Lond.), 491*, 707−718.

Sziklai, I., He, D. Z., & Dallos, P. (1996). Effect of acetylcholine and GABA on the transfer function of electromotility in isolated outer hair cells. *Hear Res, 95*, 87−99.

Takeuchi, S., & Ando, M. (1998). Dye-coupling of melanocytes with endothelial cells and pericytes in the cochlea of gerbils. *Cell Tissue Res, 293*, 271−275.

ten Cate, W. J., Curtis, L. M., & Rarey, K. E. (1994). Effects of low-sodium, high-potassium dietary intake on cochlear lateral wall Na^+, K^+-ATPase. *Eur Arch Otorhinolaryngol, 251*, 6−11.

ten Cate, W. J., Curtis, L. M., Small, G. M., & Rarey, K. E. (1993). Localization of glucocorticoid receptors and glucocorticoid receptor mRNAs in the rat cochlea. *Laryngoscope, 103*, 865−871.

Thiers, F. A., Nadol, J. B., Jr., & Liberman, M. C. (2008). Reciprocal synapses between outer hair cells and their afferent terminals: evidence for a local neural network in the mammalian cochlea. *J Assoc Res Otolaryngol, 9*, 477−489.

Vetter, D. E., Mann, J. R., Wangemann, P., et al. (1996). Inner ear defects induced by null mutation of the isk gene. *Neuron, 17*, 1251−1264.

Wangemann, P. (1996). Ca^{2+}-dependent release of ATP from the organ of Corti measured with a luciferin-luciferase bioluminescence assay. *Auditory Neurosci, 2*, 187−192.

Wangemann, P. (2002). Adrenergic and muscarinic control of cochlear endolymph production. *Adv Otorhinolaryngol, 59*, 42−50.

Wangemann, P., Itza, E. M., Albrecht, B., et al. (2004). Loss of KCNJ10 protein expression abolishes endocochlear potential and causes deafness in Pendred syndrome mouse model. *BMC Med, 2*, 30.

Wangemann, P., Liu, J., & Marcus, D. C. (1995). Ion transport mechanisms responsible for K^+ secretion and the transepithelial voltage across marginal cells of stria vascularis in vitro. *Hear Res, 84*, 19−29.

Wangemann, P., Nakaya, K., Wu, T., et al. (2007). Loss of cochlear HCO_3^- secretion causes deafness via endolymphatic acidification and inhibition of Ca^{2+} reabsorption in a Pendred syndrome mouse model. *Am J Physiol Renal Physiol, 292*, F1345–F1353.

Wangemann, P., Shen, Z., & Liu, J. (1996). K(+)-induced stimulation of K^+ secretion involves activation of the IsK channel in vestibular dark cells. *Hear Res, 100*, 201–210.

Wood, J. D., Muchinsky, S. J., Filoteo, A. G., Penniston, J. T., & Tempel, B. L. (2004). Low endolymph calcium concentrations in deafwaddler2J mice suggest that PMCA2 contributes to endolymph calcium maintenance. *J Assoc Res Otolaryngol, 5*, 99–110.

Yamauchi, D., Nakaya, K., Raveendran, N. N., et al. (2010). Expression of epithelial calcium transport system in rat cochlea and vestibular labyrinth. *BMC Physiol, 10*, 1.

Yamoah, E. N., Lumpkin, E. A., Dumont, R. A., Smith, P. J., Hudspeth, A. J., & Gillespie, P. G. (1998). Plasma membrane Ca^{2+}-ATPase extrudes Ca^{2+} from hair cell stereocilia. *J Neurosci, 18*, 610–624.

Yao, X. F., & Rarey, K. E. (1996). Localization of the mineralocorticoid receptor in rat cochlear tissue. *Acta Otolaryngol (Stockh), 116*, 493–496.

Zhao, H. B., Yu, N., & Fleming, C. R. (2005). Gap junctional hemichannel-mediated ATP release and hearing controls in the inner ear. *Proc Natl Acad Sci USA, 102*, 18724–18729.

Chapter 38

Visual Transduction

Anita L. Zimmerman

Chapter Outline

I. SUMMARY

The process of vertebrate vision begins with photon capture and visual transduction in the rods and cones. The rods are outstanding single photon detectors that are used in dim light, whereas the cones provide excellent visual acuity, movement detection and color vision in bright light. The first step in the response to light is the absorption of a photon by the chromophore, retinal, within a visual pigment molecule. This triggers activation of a G-protein cascade, causing hydrolysis of cyclic guanosine monophosphate (cGMP) and thereby closure of cyclic nucleotide-gated (CNG) cation channels. These channels are normally held open in the dark by cGMP, conducting the inward "dark current". Closure of the channels hyperpolarizes the cell, decreasing neurotransmitter release onto other retinal neurons. There are elaborate mechanisms for shutting off the cascade and for light and dark adaptation. Although many of the fundamental molecular steps in visual transduction have been determined, numerous mysteries still remain.

II. INTRODUCTION

The miracle of vision begins when our photoreceptors absorb light that is reflected by our surroundings. However, the photoreceptor's duty does not end with photon capture. In addition, the photoreceptor must convert the energy of the absorbed photon into an electrochemical signal to be relayed to the visual cortex of the brain. This process of visual transduction involves a G-protein-mediated second messenger system that ultimately controls membrane potential and neurotransmitter release.

This chapter gives an overview of vertebrate visual transduction. Further information can be obtained from many excellent reviews on the subject (e.g. Burns and Baylor, 2001; Fu and Yau, 2007; Kawamura and Tachibanaki, 2008; Gross and Wensel, 2011; Lamb, 2011; MacLeish and Makino, 2011). Details of the cyclic nucleotide-gated ion channels that mediate the light response are covered in Chapter 35. Invertebrate visual transduction is not discussed here, but thorough descriptions and comparisons are available elsewhere, along with discussions of evolutionary links between invertebrate and vertebrate visual transduction (e.g. Katz and Minke, 2009; Lamb, 2009; Yau and Hardie, 2009; Fain et al., 2010). Interestingly, invertebrate photoreceptors use a different light-activated enzyme cascade than that found in rods and cones and their membranes hyperpolarize in response to light, whereas rods and cones depolarize. Finally, this chapter will deal only with image-forming vision. The retina also contains a very interesting pathway for light detection without image formation that is involved in circadian rhythms. This pathway was recently discovered to involve the photopigment melanopsin and a third class of photoreceptors in the retina: intrinsically photosensitive retinal ganglion cells, ipRGCs (reviewed in Do and Yau, 2010; Wong and Berson, 2011).

III. PHOTORECEPTOR CELLS

The two kinds of vertebrate photoreceptors — rods and cones — are specialized for use under different conditions. The rods are employed for vision in dim light, whereas the cones are used in moderate to bright light. Thus, while a rod

Cell Physiology Sourcebook. DOI: 10.1016/B978-0-12-387738-3.00038-X

can reliably detect a single photon in a darkened room, its sensing mechanism shuts down completely when normal room lights are switched on. Cones, on the other hand, are not sensitive enough to detect single photons, but give us color vision and high spatial and temporal resolution when light levels are sufficiently high.

Rods and cones also occupy different parts of the retina. Cones are concentrated in the center of the retina, the fovea, which receives light from the center of our visual field. The rods, however, are almost entirely excluded from the fovea and instead dominate the peripheral retina. However, a few cones are scattered throughout the peripheral retina and a few rods exist at the edge of the fovea. Thus, in daylight, our peripheral vision has much lower spatial resolution than our central vision because of the sparse distribution of peripheral cones. At night, our ability to locate a dim star is enhanced by looking "out of the corners of our eyes", using the abundant rods in the peripheral retina.

As shown in Fig. 38.1, the vertebrate photoreceptor can be divided into three regions: the outer segment, the inner segment and the synaptic terminal. The outer segment is the region of the cell dedicated to photon capture and visual transduction. The inner segment, located closer to the front of the eye, contains the nucleus, abundant mitochondria and other general cell machinery. The synaptic terminal contains vesicles of the neurotransmitter glutamate for release onto the second-order retinal neurons (the bipolar cells).

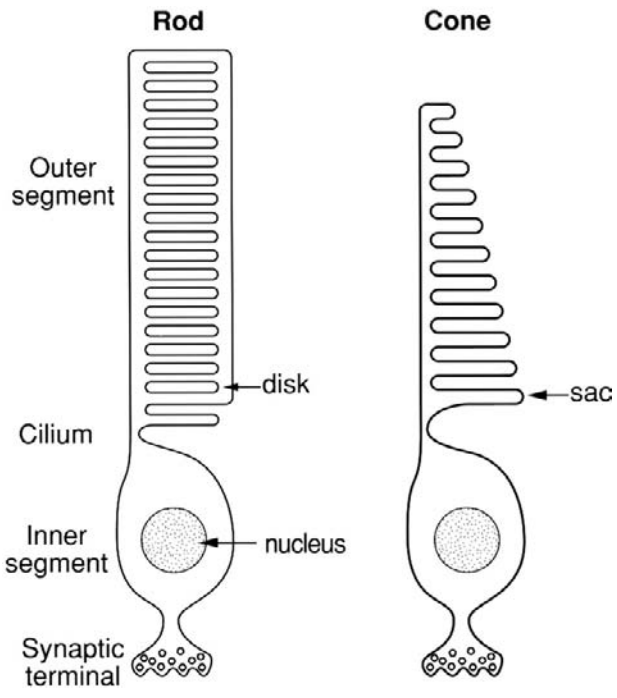

FIGURE 38.1 A simplified view of rod and cone structure. The outer segment is specialized for visual transduction. Cone photopigment molecules are located on infoldings of the plasma membrane, called sacs, rather than in the membranes of intracellular disks as in rods.

The anatomy of rods and cones is very similar, except that cones have a more conical shape and contain infoldings of the plasma membrane, called *sacs* (see Fig. 38.1), rather than the intracellular *disks* found in rods. The membranes of the disks and sacs contain photopigment molecules and various other proteins used in visual transduction. The disks or sacs are packed very tightly together: usually about 1000−2000 in a typical outer segment whose length is about 30−60 μm. This parallel array of membranes serves to align the photopigment molecules in the correct orientation for optimal absorption of light, which normally travels the length of the cell from the synaptic terminal toward the tip of the outer segment. The disks and sacs also serve to concentrate the photopigment molecules (e.g. about a hundred million in a typical rod) and to position the photopigment in close proximity to other important molecules in the visual transduction cascade.

In both rods and cones, the outer and inner segments are connected by a narrow region called the *cilium*. In some way that is not completely understood, the cilium segregates the inner and outer segment membrane proteins. For example, whereas the inner segment plasma membrane contains many types of ion channels (Bader et al., 1982; Barnes and Hille, 1989; reviewed in MacLeish and Makino, 2011), the outer segment plasma membrane contains essentially a pure population of light-regulated cyclic nucleotide-gated (CNG) ion channels (Baylor and Nunn, 1986). It is in the ciliary region that new disks or sacs are inserted during the outer segment regeneration process that occurs constantly. Recent evidence suggests that the formation of disks is accomplished by the repeated fusion of membrane vesicles containing the photopigment rhodopsin (reviewed in Sung and Chuang, 2010). Old disks or sacs are removed from the tip of the outer segment by phagocytosis by the retinal pigment epithelial (RPE) cells. These very opaque cells sit behind the retina, with finger-like cellular processes that hug the photoreceptor outer segments, reducing light scatter, as well as providing some of the molecules essential for visual transduction. Because the cilium is such a narrow structure, outer and inner segments often break apart (and their membranes reseal) during cell isolation from the retina. Thus, many studies of visual transduction are conducted on isolated outer segments, which are somewhat simpler preparations than whole cells.

IV. PHYSIOLOGY OF VISUAL TRANSDUCTION

The physiological trademark of the vertebrate photoreceptor is its light-regulated "dark current" (Fig. 38.2) (reviewed in Burns and Baylor, 2001; Fu and Yau, 2007; MacLeish and Makino, 2011). This current circulates between the outer and inner segments in the dark and is reduced upon light absorption. The dark current is carried

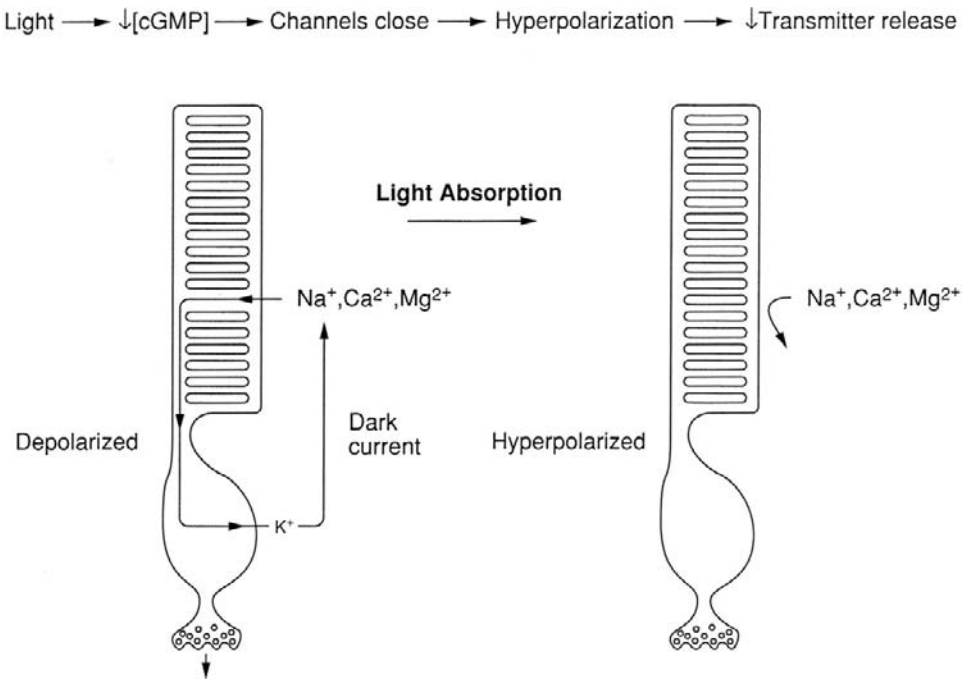

FIGURE 38.2 The absorption of light shuts down the dark current that circulates between the outer and inner segments of the photoreceptor. This reduction in current hyperpolarizes the cell, reducing the release of neurotransmitter.

into the outer segment mainly by Na^+ ions flowing through cyclic nucleotide-gated (CNG), non-selective cation channels (see Chapter 35) and out of the inner segment by K^+ ions flowing through voltage-gated K^+ channels. Because the CNG channels are non-selective cation channels, they allow the entry not only of Na^+, but also of Ca^{2+} and Mg^{2+}. These divalent cations have important consequences for visual transduction. First, Ca^{2+} regulates the light-dependent enzyme cascade (discussed below). Second, both Ca^{2+} and Mg^{2+} pass through CNG channels extremely slowly, reducing the effective single-channel conductance and thereby making the current–voltage relation for the dark current relatively flat in the physiological range of membrane voltages. Thus, under physiological conditions, the divalent cations make the dark current almost independent of voltage and, therefore, a faithful reporter of the light level, rather than of voltage changes induced by channel activity in the inner segment (Zimmerman and Baylor, 1992).

Since the cell has a relatively high Na^+ permeability in the dark, its resting potential is somewhat more positive than that for most cells (about −40 mV, instead of −70 mV). This resting depolarization tends to open voltage-gated Ca^{2+} channels in the synaptic terminal, allowing Ca^{2+} entry and vesicular release of neurotransmitter in the dark. When a photon is absorbed by a rhodopsin molecule in a disk membrane, a series of reactions leads to a reduction in the concentration of guanosine 3′, 5′-cyclic monophosphate (cGMP), which normally binds to, and opens, the outer segment CNG channels in the dark. Since there is less cGMP available to open the channels in the light, they close, decreasing the dark current (i.e. decreasing the Na^+ permeability), causing a membrane hyperpolarization which, in turn, causes closure of the voltage-gated K^+ and Ca^{2+} channels in the inner segment and synaptic terminal and, finally, a decrease in neurotransmitter release. The process is similar in cones.

The dark current and light response can be measured in a variety of ways, including a voltage-clamp method using intracellular microelectrodes, the whole-cell patch-clamp method and the suction electrode method. The relatively non-invasive suction electrode method (Fig. 38.3) works particularly well with mammalian photoreceptors, which are usually quite small and fragile. This method is much gentler than the other techniques, yet is able to measure the dark current without interference from inner segment currents.

Families of light responses recorded with a suction electrode from a monkey rod and cone are shown in Fig. 38.4. Light response amplitudes increase in a graded manner with light intensity until they reach a limiting value obtained with a "saturating light" that shuts off all the inward dark current (i.e. that closes all the CNG channels in the outer segment plasma membrane). Supersaturating light intensities cannot give larger responses, but instead give longer lasting ones. Cones are less sensitive than rods, requiring about a hundred times as many photons to shut down half the dark current; this seems to result at least in

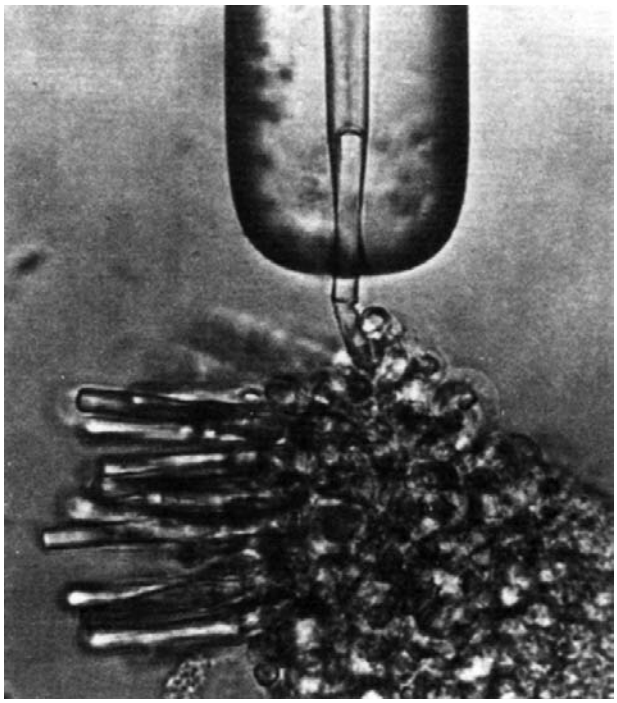

FIGURE 38.3 The use of a suction electrode to record the dark current flowing into the outer segment of a rod attached to a piece of toad retina. The horizontal line just below the suction electrode is the junction between the outer and inner segments. The electrode is filled with a physiological salt solution and connected to a sensitive amplifier. *(Reproduced with permission from Baylor et al., 1979.)*

part from a lower amplification in the G-protein-mediated enzyme cascade described below (reviewed in Gross and Wensel, 2011). However, the cone responses are several times faster than those of rods, as evidenced by the shorter time to peak and faster recovery, and this gives them an advantage over rods in the detection of movement and rapid changes in illumination. The undershoots seen in the cone responses (but not in normal rod responses) are not yet fully understood, but appear to make the cone especially sensitive to changes in illumination (Schnapf et al., 1990).

Although single photon responses are too small to be measured in cones, they are about 1.0 pA in rods, and therefore have been studied in some detail there. Single photon responses are very reliable: they occur at least 80% of the time after absorption of a photon by a rhodopsin molecule and they almost never occur in the absence of photon absorption (reviewed in Baylor, 1987). A single absorbed photon gives a highly amplified response, shutting down 3−5% of the total dark current by closing a few hundred CNG channels in a narrow band (one to a few micrometers in width) of outer segment plasma membrane near the site of absorption. Like the dim flash responses in Fig. 38.4 (bottom traces of each set), the single photon response has a stereotypical waveform, with a slow, S-shaped rise and a very slow decay. These complex, slow kinetics reflect the complex enzyme cascade underlying the response.

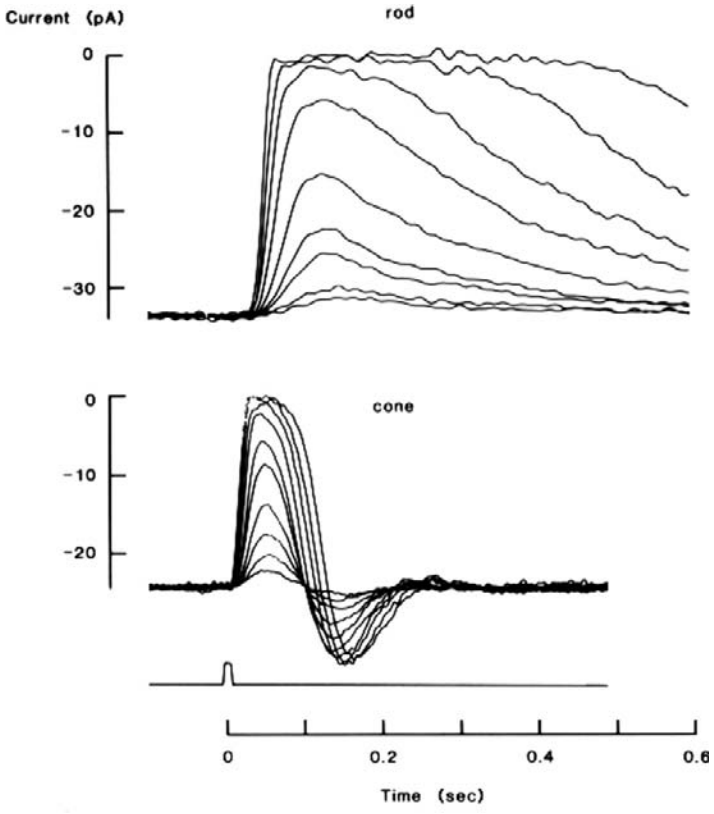

FIGURE 38.4 Families of photocurrents recorded by suction electrode from a rod and a cone of the monkey, *Macaca fascicularis*. Brief light flashes were given at time zero (rectangular pulse below the current recordings). Upward deflections indicate reductions in the inward dark current. From the bottom to the top of each family, flash strengths were increased by factors of 2. Expected numbers of photoisomerizations ranged from 2.9 to 860 for the rod and from 190 to 36 000 for the cone. Saturation of the responses (top traces in each family) occurred when all dark current was shut off. *(Reproduced with permission from Baylor, 1987.)*

When membrane voltage is recorded instead of outer segment current, the waveform resembles an inverted version of the current for dim lights but not for light levels near or beyond saturation. When many photons are absorbed, the voltage recordings (Fig. 38.5) show a characteristic "nose" and "plateau". These features result from a shaping of the response by ion channels in the inner segment. Several types of channels contribute to the waveform (reviewed in MacLeish and Makino, 2011), but the dominant channel giving rise to this more complicated shape appears to be an inner segment, non-selective cation channel that is opened by hyperpolarization (the HCN1 channel). Thus, the closure of outer segment CNG channels gives the initial hyperpolarization (beginning of the nose). This hyperpolarization opens the inner segment HCN1 non-selective cation channels which, in turn, depolarize the membrane, giving the transition from nose to plateau.

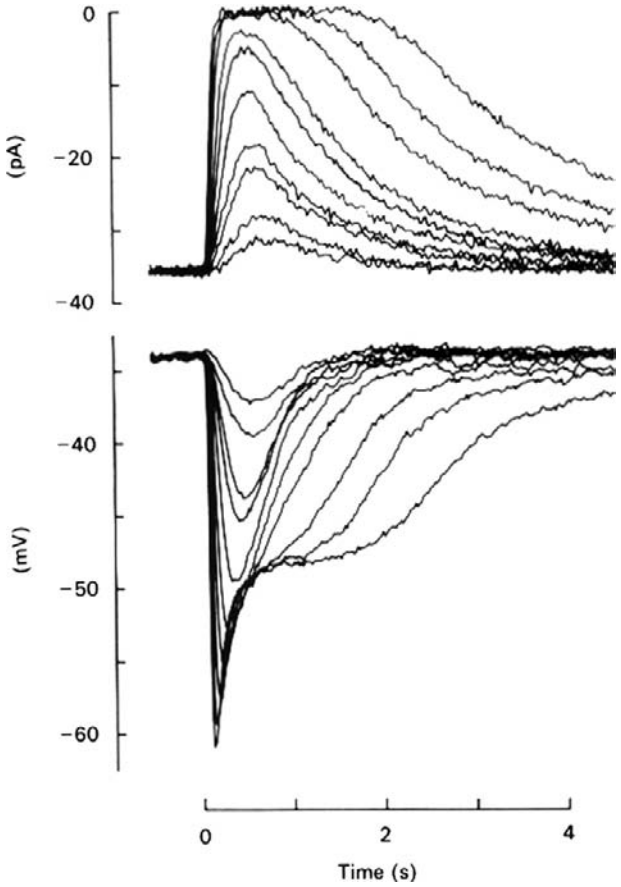

FIGURE 38.5 Comparison of light-evoked changes in outer segment current with those in membrane potential for a salamander rod. The currents were measured by a suction electrode, while the membrane potential was monitored by an intracellular microelectrode. The current and voltage responses to dim flashes have similar form, but a prominent "nose" and "plateau" are seen in the voltage responses to bright flashes. 500-nm, 11-ms flashes were given at $t = 0$ and photon densities increased by factors of about 2 between 1.5 and 430 photons μm^{-2}. *(Reproduced with permission from Baylor and Nunn, 1986.)*

Eventually, these channels close because of the depolarization while, at the same time, the outer segment CNG channels reopen during recovery from the light response and the membrane potential returns to its initial, relatively depolarized, dark value.

Aside from the ion channels described earlier, two other types of ion transport protein are of obvious importance to the vertebrate photoreceptor. First, Na^+-K^+ pumps in the inner segment are responsible for expelling the Na^+ that enters through the CNG channels in the outer segment. Second, Na^+:Ca^{2+},K^+ exchange carriers (NCKX; reviewed in Bauer, 2002; Schnetkamp, 2004) in the outer segment expel the Ca^{2+} that enters through the CNG channels and regulates the enzyme cascade. The Na^+:Ca^{2+},K^+ carriers are particularly important in light adaptation, where intracellular Ca^{2+} plays a large regulatory role.

The ability of the visual system to detect light depends partly on its degree of adaptation to background illumination. Although much of light and dark adaptation involves pupillary responses and processes occurring in the brain and non-photoreceptor layers of the retina, some aspects of adaptation clearly occur in the rods and cones themselves. In continuous light, there is a partial recovery of the dark current after its initial suppression when the light is switched on. This sag in the photoresponse is accompanied by a decrease in light sensitivity and an acceleration of response kinetics (although this acceleration is negligible in monkey cones; Schnapf et al., 1990). Thus, the response to a light flash during continuous background light is smaller and generally briefer than that to an equally bright flash occurring in the dark. To make the amplitude of the flash response equal to that obtained in the dark, one must increase the flash intensity (Fig. 38.6). This light adaptation allows the photoreceptor to respond over a much larger range of light intensities than it otherwise could. In effect, the photoreceptor uses a non-linear gain adjustment partially to overcome the response saturation that occurs as a result of having a finite number of CNG channels to close in the light. Cones light-adapt so well that it is essentially impossible to obtain saturation of their dark current in steady bright light. Saturation is only possible transiently when bright light is applied while the cone is in a very dark-adapted state (reviewed in Lamb, 2011).

Photoreceptor dark adaptation is a rather complicated set of processes that has been most thoroughly studied in rods (reviewed in Lamb and Pugh, 2004). After exposure to a light that is bright enough to bleach all the photopigment, a rod ultimately cannot return to its dark state until non-excited photopigment molecules have been regenerated (including reinsertion of the chromophore, see following). However, when a rod has been exposed to only moderately bright light, which leaves some photopigment unbleached, it is able to respond to light again after a briefer period of adaptation. This period is characterized by a lingering

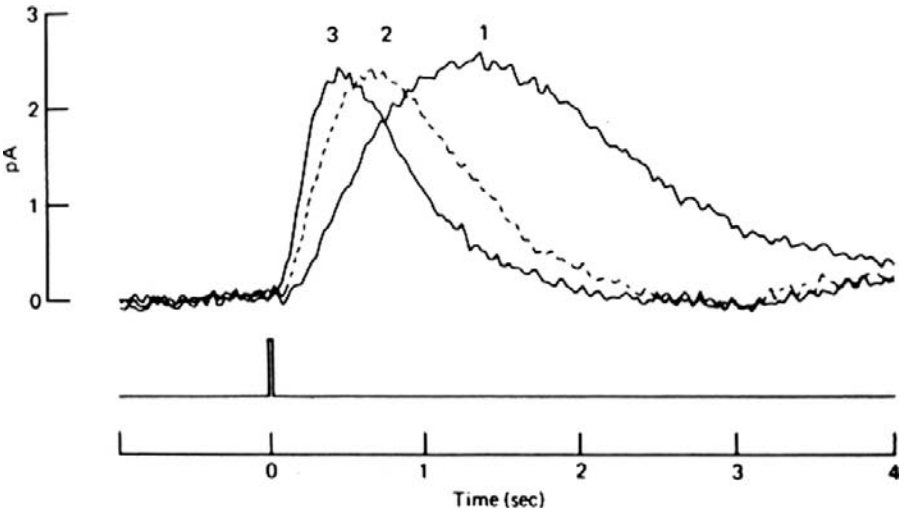

FIGURE 38.6 Decreased sensitivity and accelerated flash response kinetics characteristic of adaptation to background light in a rod. These outer segment currents were obtained by suction electrode recording from a toad rod that was given a test light flash in darkness (curve 1), with a dim background light (curve 2) and with a brighter background light (curve 3). In the presence of background light, the test flash intensity had to be increased to obtain responses of approximately the same amplitude. For example, the flash intensity used to obtain curve 2 was approximately five times the intensity used to obtain curve 1. *(Reproduced with permission from Baylor et al., 1979.)*

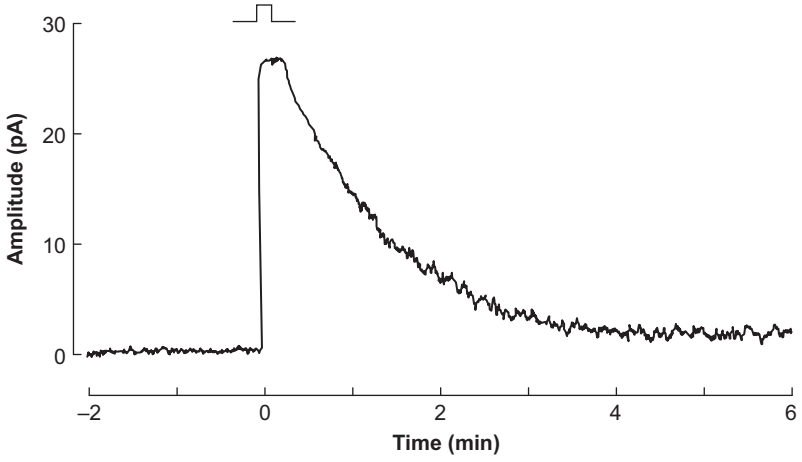

FIGURE 38.7 Prolonged dark current suppression and increased noise following a strong bleach. The rectangular pulse above the response indicates when the dark-adapted rod was given a bright flash of light that bleached about 0.7% of its rhodopsin (72×10^5 photons μm^{-2}, calculated to isomerize 1.8×10^7 rhodopsins). Closer examination of the lingering noise revealed a strong resemblance to that produced by the absorption of single photons. *(Reprinted with permission from Nature, Lamb, 1980. Copyright 1980 Macmillan Magazines Limited.)*

suppression of the dark current for many minutes after the light is switched off, a decrease in light sensitivity similar to that found in the presence of background light and an increase in outer segment current noise (Fig. 38.7). These features limit visual detection and appear to derive from incomplete shutoff of the photopigment after loss of its chromophore. Ultimately, the speed with which the rod recovers from a bright light is limited by the rate at which 11-*cis*-retinal is delivered to opsin. Cones recover from a bright light so rapidly that it has been hypothesized that the shut-off reactions in their transduction enzyme cascade must be extremely fast (reviewed in Lamb, 2011).

V. MOLECULAR MECHANISMS

VA. Photopigment Activation and Shut-off

Visual pigments are integral membrane proteins called *opsins* that consist of *apo-opsin* and a ubiquitous light-absorbing chromophore, *retinal* (Fig. 38.8). Retinal is in a class of molecules called *retinoids* that also includes vitamin A (all-*trans*-retinol). There are many excellent reviews of visual pigments and rhodopsin in particular (e.g. Palczewski, 2006; Nickle and Robinson, 2007; Hofmann et al., 2009; Smith, 2010). Retinal is derived from vitamin A and comes in two forms in vertebrates: $retinal_1$ and dehydroretinal, or $retinal_2$ (reviewed in Nickle and Robinson, 2007). Human photoreceptors use $retinal_1$. Interactions with different opsins change the spectral tuning characteristics of retinal. Thus, each type of photoreceptor has its own type of opsin, which results in a characteristic photopigment absorption spectrum and therefore a characteristic color sensitivity of the cell. Rods contain rhodopsin (Rh) and are therefore most sensitive to blue-green light (peak wavelength around 490 nm), whereas primate cones are of three types, with characteristic peak absorbances in the short-wavelength (peak about 430 nm), middle-wavelength (peak about 530 nm)

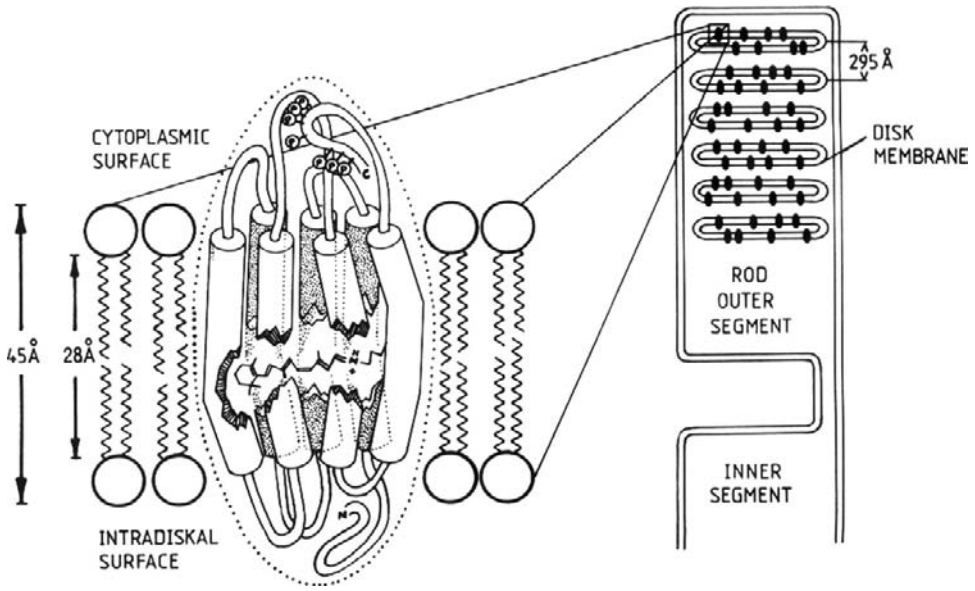

FIGURE 38.8 A model for the structure of rhodopsin in the disk membrane of a rod. The light-absorbing chromophore, retinal, sits in a binding pocket near the middle of the integral membrane protein, opsin. *(Reproduced with permission from Dratz and Hargrave, 1983.)*

and long-wavelength (peak about 560 nm) regions of the visible spectrum (Fig. 38.9). These three types of cone are sometimes referred to as blue-, green- and red-sensitive cones, respectively, although 560 nm actually corresponds to yellow, rather than red, light. The characteristic absorption spectra determine only the probability that a photon will be absorbed by the cell's photopigment. The photoreceptor responds in exactly the same way to any absorbed photon, independent of its wavelength.

Absorption of a photon causes isomerization of retinal from the 11-*cis* to the all-*trans* form (Fig. 38.10), breaking its covalent bond to the protein and destabilizing its position. Eventually all-*trans*-retinal hops out of its binding pocket within opsin, but a chain of conformational intermediates is generated before this dissociation occurs. For the best-studied pigment, rhodopsin, these intermediates are (in the order that follows photon absorption) photorhodopsin, bathorhodopsin, BSI (blue-shifted intermediate), lumirhodopsin, metarhodopsin I, metarhodopsin II and metarhodopsin III (reviewed in Palczewski, 2006; Smith, 2010). Similar transitions are thought to occur in other visual pigments. The metarhodopsin II (meta II) conformational state activates the G protein, transducin, which begins the cellular response to light. As all-*trans*-retinal leaves its binding pocket in opsin, it is released into the interior of the disk. It must then be transferred to the cytosolic side of the disk, apparently via diffusion through the plasma membrane and transport with phosphatidylethanolamine by the ABCA4 lipid carrier (reviewed in Molday and Zhang, 2010). On the cytosolic side, the aldehyde, all-*trans*-retin*al*, is converted by an enzyme (a retinol

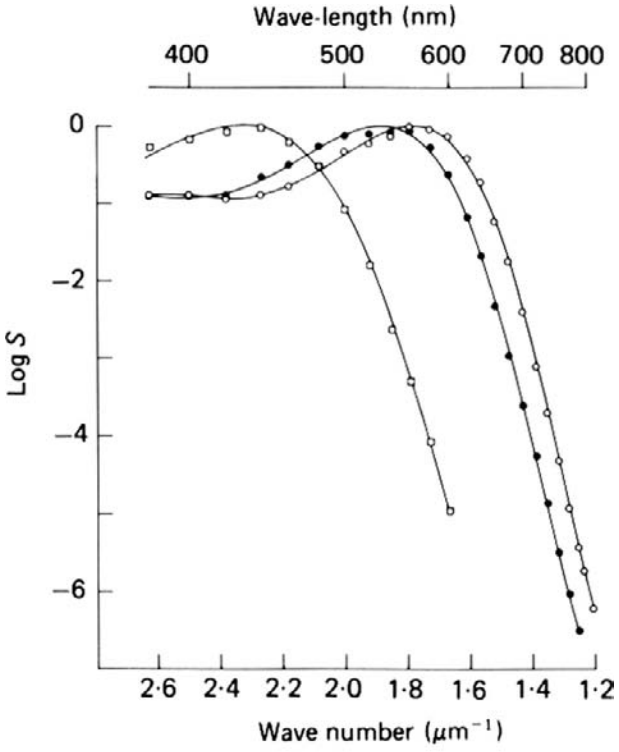

FIGURE 38.9 Cone spectral sensitivities, as measured by the suction electrode method. These spectra were obtained from blue-, green- and red-sensitive monkey cones (squares, filled circles, and open circles, respectively). The spectral sensitivity, S, was derived from the cone's response to flashes of different color and it reflects the probability of absorption of a photon of that color (or wavelength). *(Reproduced with permission from Baylor et al., 1987.)*

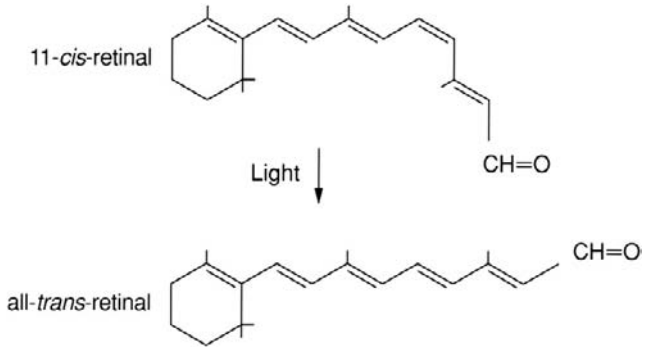

FIGURE 38.10 The light-induced isomerization of retinal$_1$ from the 11-*cis* to the all-*trans* form. This is the first step in vertebrate visual transduction and the only one that is a direct action of light.

dehydrogenase) to the alcohol form, all-*trans*-retin*ol*, which then travels through the plasma membrane into the extracellular space, where it is shuttled via retinoid binding proteins to the RPE and Müller cells. The process by which all-*trans*-retinal is transported and converted back into 11-*cis*-retinal for reloading into opsin is called the *visual cycle* (reviewed in Travis et al., 2007; Wang and Kefalov, 2011).

For the photoreceptor to reset to its dark condition after a light is switched off, the molecular players in the light response also must be switched off. Most of what we know about photopigment shut-off comes from work on rhodopsin (depicted in the top right loop of Fig. 38.11). The shut-off of rhodopsin's ability to activate transducin begins even before all-*trans*-retinal has left the protein. Rhodopsin kinase phosphorylates photoexcited rhodopsin at multiple serine and threonine residues near the C-terminal. A 48-kDa protein called *arrestin* then binds phosphorylated rhodopsin, reducing its interaction with transducin. There are recent hints for still other players in the shut-off process (e.g. RGS9), but all the details have not yet been resolved (reviewed in Gross and Wensel, 2011). Once all-*trans*-retinal has separated from opsin, the photopigment cannot be reset to its photon-receptive dark state until 11-*cis*-retinal has been reinserted, arrestin has been released and a phosphatase (serine/threonine phosphatase type 2A) has removed the phosphates from the C-terminal residues. This process takes several minutes. The new 11-*cis*-retinal that is inserted into opsin is made in the RPE cells and transported into the rods. However, cones obtain new 11-*cis*-retinal by a different mechanism: the surrounding Müller cells make the alcohol form, 11-*cis*-retin*ol*, which is transferred to the cones, where it is converted to the aldehyde, 11-*cis*-retin*al* (Mata et al., 2002; reviewed in Travis et al., 2007; Wang and Kefalov, 2011). Interestingly, in cones, there is much greater activity of the kinase that phosphorylates their pigments and this may partly explain why cones recover from a light response much more quickly than do rods (reviewed in Gross and Wensel, 2011). Furthermore, in cones there is a less stable interaction between 11-*cis*-retinal and the visual pigment, leading to a greater concentration of apo-opsin, which itself stimulates transducin (reviewed in Kawamura and Tachibanaki, 2008).

VB. Cyclic Nucleotide Cascade

A cyclic nucleotide enzyme cascade is used to translate the message of photon absorption into the language of the brain — electrical and chemical signals. The key second

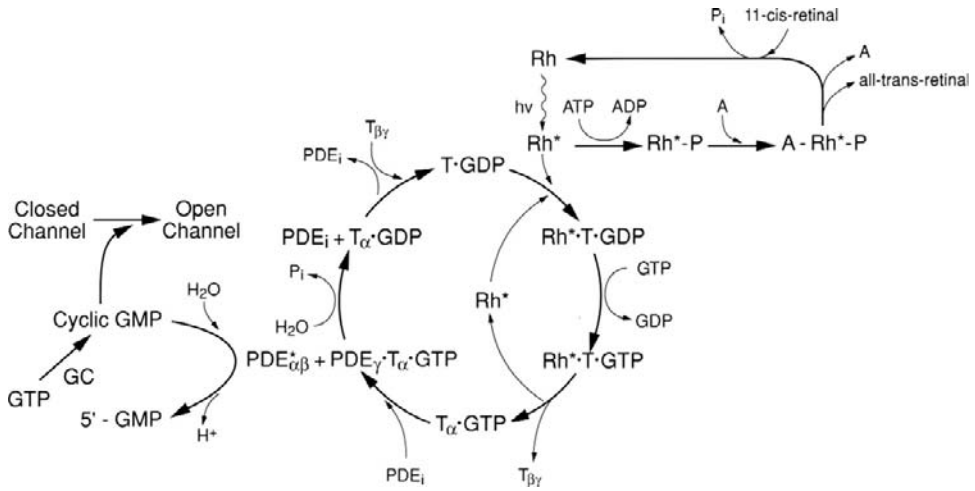

FIGURE 38.11 The enzyme cascade controlling visual transduction in rods. Abbreviations: A: arrestin; channel: cyclic nucleotide-gated (CNG) outer-segment ion channel; GC: guanylate cyclase; PDE: cGMP-specific phosphodiesterase (*, active form); Rh: rhodopsin (*, photoexcited, active form); T: the G protein, transducin. There is increasing evidence that, in spite of its complexity, this diagram is quite incomplete. *(Modified with permission from Stryer, 1991 and drawing on information from Palczewski, 2006; Nickle and Robinson, 2007; Hofmann et al., 2009; Smith, 2010.)*

messenger is cGMP, with another second messenger, Ca^{2+}, involved in more subtle aspects of visual transduction. Most of our information on the molecular mechanism of visual transduction derives from studies on rods, but the process appears to be similar in cones. A large body of biochemical and physiological evidence suggests that absorption of a single photon by rhodopsin initiates the following chain of events (diagrammed in Fig. 38.11):

1. Photoexcited rhodopsin (Rh*) catalyzes the replacement of GDP by GTP on the G protein, transducin (T). Both Rh* and the peripheral membrane protein, T, are able to diffuse laterally in the disk membrane, where they find each other and interact. Before Rh* is shut off, it activates about 500 Ts, representing the first amplification step in the transduction process.
2. The α subunit of T, now with GTP bound, dissociates from the rest of T (the $\beta\gamma$ subunit complex) and binds to and removes the γ inhibitory subunit of another peripheral disk membrane protein, cGMP-specific phosphodiesterase (PDE). Each Tα can activate only one PDE since the catalytic portion of PDE, PDE$\alpha\beta$, is only free to work when PDEγ is bound to Tα (and therefore unable to reassociate with PDE$\alpha\beta$).
3. Once disinhibited, one PDE molecule (PDE$\alpha\beta$) hydrolyzes about a million cGMP molecules, leading to the closure of hundreds of CNG ion channels and thereby halting entry of over a million Na^+ ions during the time course of the single photon response.

The recovery of the dark current after photon absorption is accomplished by many processes, including these:

1. Shut-off of rhodopsin, as discussed above.
2. Inherent GTPase activity of Tα, converting Tα back to the GDP-bound, inactive form that reassociates with T$\beta\gamma$.
3. Reassociation of PDEγ with PDE$\alpha\beta$, returning PDE to its more inhibited, dark state.
4. Synthesis of new cGMP from GTP by guanylate cyclase (GC).
5. Reopening of CNG ion channels, as more cGMP becomes available.

Although these processes are the most established ones, there is recent evidence that other processes and factors may be involved in regulating the cGMP cascade, mostly through feedback mechanisms. Some of the factors that may play a role are: regulatory cGMP-binding sites on PDE; auxiliary retinoid binding sites on opsin (Heck et al., 2003; Makino et al., 2010); calcium-binding proteins and other regulatory proteins that affect guanylate cyclase, PDE, rhodopsin, transducin and/or the CNG channel (e.g. guanylate cyclase activating protein, or GCAP; reviewed in Gross and Wensel, 2011); members of the inositol phosphate system whose function has not yet been established; and various kinases and phosphatases whose functions are also not yet clear. The field of regulation of the photoreceptor cGMP cascade is currently very unsettled and very intriguing.

An interesting set of molecular interactions that seems to regulate visual transduction, and even rod outer segment morphogenesis, occurs at the interface between the rod disks and the plasma membrane. The rod CNG channel is a heterotetramer consisting of three α (CNGA1) subunits and one β (CNGB1) subunit (see Chapter 35). But this channel does not stand alone. Instead, its α subunits are linked to Na^+:Ca^{2+}, K^+ exchange carriers in the plasma membrane and these carriers expel the calcium ions that enter the cell through the CNG channel. Furthermore, the β subunit of the CNG channel is physically linked, via its cytosolic GARP (glutamic acid rich protein) region, to a molecular complex in the disk rim. This disk rim complex consists of an oligomer of Peripherin-2 and Rom-1, which also interacts with other GARPs that associate with the cytosolic side of the disks (reviewed in Sung and Chuang, 2010). Interestingly, a genetic knockout of the CNG channel's β subunit and the GARPs disrupts the orderly array of disks in the rod outer segment, produces shorter outer segments and reduces the light sensitivity of the rod (Zhang et al., 2009). Thus, these molecular complexes are vital to both visual transduction and rod morphogenesis.

One aspect of visual transduction that is controlled by feedback regulation is light adaptation (reviewed in Lamb, 2011) and a large body of evidence supports involvement of Ca^{2+} in this process. Coupled with calcium-binding proteins, Ca^{2+} has been found to inhibit guanylate cyclase (GC), to stimulate PDE via inhibition of Rh phosphorylation and to inhibit the CNG channels (see Chapter 35). All three types of Ca^{2+} feedback appear to occur in both rods and cones, but with different molecular details and rates. For example, inhibition of the CNG channels by Ca^{2+} is much greater in cones than in rods (Rebrik and Korenbrot, 2004). Calcium feedback in rods and cones is thought to involve the following steps. In the dark, when the cGMP concentration is relatively high, Ca^{2+} enters the cell through the CNG channels, raising the intracellular concentration of Ca^{2+} ($[Ca^{2+}]_i$). When the channels close following photon absorption, $[Ca^{2+}]_i$ decreases, because its influx through the channels is decreased while its extrusion by Na^+:Ca^{2+}, K^+ exchangers continues. The decreased $[Ca^{2+}]_i$ would be expected to stimulate guanylate cyclase and to inhibit PDE, leading to a subsequent partial recovery of the cGMP level and a reopening of some of the channels. The feedback mechanisms involving Ca^{2+} are mediated by several calcium binding proteins (reviewed in Gross and Wensel, 2011), but the most significant Ca^{2+} feedback effect on visual transduction appears to be that mediated by guanylate cyclase activating proteins, or GCAPs

(e.g. Burns et al., 2002; reviewed in Gross and Wensel, 2011). GCAPs are Ca^{2+} binding proteins that bind to guanylate cyclase. The GCAPs stimulate guanylate cyclase to make more cGMP but, when Ca^{2+} binds to a GCAP, the GCAP is less stimulatory, so guanylate cyclase makes less cGMP, resulting in closure of CNG channels and thereby reducing Ca^{2+} entry. This same negative feedback system works in reverse in the light: fewer CNG channels are open, so less Ca^{2+} enters; then lower intracellular [Ca^{2+}] produces stimulation of guanylate cyclase by GCAPs, resulting in higher [cGMP], more channel opening and therefore more Ca^{2+} entry. The accumulated knowledge of these feedback processes and the associated enzyme cascade has made vertebrate visual transduction a model system for understanding G-protein-mediated signal transduction in general.

BIBLIOGRAPHY

Bader, C. R., Bertrand, D., & Schwartz, E. A. (1982). Voltage-activated and calcium-activated currents studied in solitary rod inner segments from the salamander retina. *J Physiol, 331*, 253–284.

Barnes, S., & Hille, B. (1989). Ionic channels of the inner segment of tiger salamander cone photoreceptors. *J Gen Physiol, 94*, 718–743.

Bauer, P. J. (2002). Binding of the retinal rod Na^+/Ca^{2+}-K^+ exchanger to the cGMP-gated channel indicates local Ca^{2+}-signaling in vertebrate photoreceptors. *Ann NY Acad Sci, 476*, 325–334.

Baylor, D. A. (1987). Photoreceptor signals and vision. *Invest Ophthalmol Visual Sci, 28*, 34–49.

Baylor, D. A., & Nunn, B. J. (1986). Electrical properties of the light-sensitive conductance of rods of the salamander *Ambystoma tigrinum*. *J Physiol London, 371*, 115–145.

Baylor, D. A., Lamb, T. D., & Yau, K.-W. (1979). The membrane current of single rod outer segments. *J Physiol London, 288*, 589–611.

Baylor, D. A., Nunn, B. J., & Schnapf, J. L. (1987). Spectral sensitivity of cones of the monkey *Macaca fascicularis*. *J Physiol London, 390*, 145–160.

Burns, M. E., & Baylor, D. A. (2001). Activation, deactivation, and adaptation in vertebrate photoreceptor cells. *Annu Rev Neurosci, 24*, 779–805.

Burns, M. E., Mendez, A., Chen, J., & Baylor, D. A. (2002). Dynamics of cyclic GMP synthesis in retinal rods. *Neuron, 36*, 81–91.

Do, M. T. H., & Yau, K.-W. (2010). Intrinsically photosensitive retinal ganglion cells. *Physiol Rev, 90*, 1547–1581.

Dratz, E. A., & Hargrave, P. A. (1983). The structure of rhodopsin and the rod outer segment disk membrane. *Trends Biochem Sci, 8*, 128–131.

Fain, G. L., Hardie, R., & Laughlin, S. B. (2010). Phototransduction and the evolution of photoreceptors. *Curr Biol, 20*, R114–R124.

Fu, Y., & Yau, K.-W. (2007). Phototransduction in mouse rods and cones. *Pflügers Arch, 454*, 805–819.

Gross, A. K., & Wensel, T. G. (2011). Biochemical cascade of phototransduction. In P. L. Kaufman, A. Alm, L. L. Levin, S. F. E. Nilsson, J. N. Ver Hoeve, & S. M. Wu (Eds.), *Adler's Physiology of the Eye* (11th ed.). (pp. 394–410). Elsevier.

Heck, M., Schädel, S. A., Maretzki, D., & Hofmann, K. P. (2003). Secondary binding sites of retinoids in opsin: characterization and role in regeneration. *Vis Res, 43*, 3003–3010.

Hofmann, K. P., Scheerer, P., Hildebrand, P. W., et al. (2009). A G protein-coupled receptor at work: the rhodopsin model. *Trends Biochem Sci, 34*, 540–552.

Katz, B., & Minke, B. (2009). Drosophila photoreceptors and signaling mechanisms. *Front Cell Neurosci, 3*, 1–18.

Kawamura, S., & Tachibanaki, S. (2008). Rod and cone photoreceptors: molecular basis of the difference in their physiology. *Comp Biochem Physiol Part A, 150*, 369–377.

Lamb, T. D. (1980). Spontaneous quantal events induced in toad rods by pigment bleaching. *Nature, 287*, 349–351.

Lamb, T. D. (2009). Evolution of vertebrate retinal photoreception. *Phil Trans R Soc B, 364*, 2911–2924.

Lamb, T. D. (2011). Light adaptation in photoreceptors. In P. L. Kaufman, A. Alm, L. L. Levin, S. F. E. Nilsson, J. N. Ver Hoeve, & S. M. Wu (Eds.), *Adler's Physiology of the Eye* (11th ed.). (pp. 429–442) Elsevier.

Lamb, T. D., & Pugh, E. N., Jr. (2004). Dark adaptation and the retinoid cycle of vision. *Prog Ret Eye Res, 23*, 307–380.

MacLeish, P. R., & Makino, C. L. (2011). Photoresponses of rods and cones. In P. L. Kaufman, A. Alm, L. L. Levin, S. F. E. Nilsson, J. N. Ver Hoeve, & S. M. Wu (Eds.), *Adler's Physiology of the Eye* (11th ed.). (pp. 411–428) Elsevier.

Makino, C. L., Riley, C. K., Looney, J., Crouch, R. K., & Okada, T. (2010). Binding of more than one retinoid to visual opsins. *Biophys J, 99*, 2366–2373.

Mata, N. L., Radu, R. A., Clemmons, R. S., & Travis, G. H. (2002). Isomerization and oxidation of Vitamin A in cone-dominant retinas: a novel pathway for visual-pigment regeneration in daylight. *Neuron, 36*, 69–80.

Molday, R. S., & Zhang, K. (2010). Defective lipid transport and biosynthesis in recessive and dominant Stargardt macular degeneration. *Prog Lipid Res, 49*, 476–492.

Nickle, B., & Robinson, P. R. (2007). The opsins of the vertebrate retina: insights from structural, biochemical, and evolutionary studies. *Cell Molec Life Sci, 64*, 2917–2932.

Palczewski, K. (2006). G protein-coupled receptor rhodopsin. *Annu Rev Biochem, 75*, 743–767.

Rebrik, T. I., & Korenbrot, J. I. (2004). In intact mammalian photoreceptors, Ca^{2+}-dependent modulation of cGMP-gated ion channels is detectable in cones but not in rods. *J Gen Physiol, 123*, 63–75.

Schnapf, J. L., Nunn, B. J., Meister, M., & Baylor, D. A. (1990). Visual transduction in cones of the monkey *Macaca fascicularis*. *J Physiol London, 427*, 681–713.

Schnetkamp, P. P. M. (2004). The SLC24 Na^+/Ca^{2+}-K^+ exchanger family: vision and beyond. *Pflügers Arch Eur J Physiol, 447*, 683–688.

Smith, S. O. (2010). Structure and activation of the visual pigment rhodopsin. *Annu Rev Biochem, 39*, 309–328.

Stryer, L. (1991). Visual excitation and recovery. *J Biol Chem, 266*, 10711–10714.

Sung, C.-H., & Chuang, J.-Z. (2010). The cell biology of vision. *J Cell Biol, 190*, 953–963.

Travis, G. H., Golczak, M., Moise, A. R., & Palczewski, K. (2007). Diseases caused by defects in the visual cycle: retinoids as potential therapeutic agents. *Annu Rev Pharm Toxicol, 47*, 469–512.

Wang, J.-S., & Kefalov, V. J. (2011). The cone-specific visual cycle. *Prog Ret Eye Res, 30*, 115–128.

Wong, K. Y., & Berson, D. M. (2011). Ganglion-cell photoreceptors and non-image-forming vision. In P. L. Kaufman, A. Alm, L. L. Levin, S. F. E. Nilsson, J. N. Ver Hoeve, & S. M. Wu (Eds.), *Adler's Physiology of the Eye* (11th ed.). (pp. 526–544) Elsevier.

Yau, K.-W., & Hardie, R. C. (2009). Phototransduction motifs and variations. *Cell, 139*, 246–264.

Zhang, Y., Molday, L. L., Molday, R. S., et al. (2009). Knock out of GARPs and the β-subunit of the rod cGMP-gated channel disrupts disk morphogenesis and rod outer segment structural integrity. *J Cell Sci, 122*, 1192–1200.

Zimmerman, A. L., & Baylor, D. A. (1992). Cation interactions within the cyclic GMP-activated channel of retinal rods from the tiger salamander. *J Physiol London, 449*, 759–783.

This page intentionally left blank

Chapter 39

Gustatory and Olfactory Sensory Transduction

Stephen D. Roper

Chapter Outline

I. SUMMARY

Taste and olfaction share certain common features. Receptor cells for both senses are epithelial cells and part of a renewing population. Olfactory and taste sensory cells alike lie at the interface between two strikingly different environments — an external environment of volatile odors or water-borne tastants, respectively, versus a relatively constant milieu of interstitial fluid. Moreover, transduction mechanisms in both these chemical senses involves G-protein-coupled receptors, although transduction mechanisms in gustation also include ion channels through which certain taste stimuli pass. Transduction channels and integral membrane receptors appear to be concentrated on the exposed apical tips of both types of chemosensory receptor cells, although the basolateral membranes of taste cells may be additional sites for chemosensory transduction. In some regards, sensory transduction in olfaction is similar to that in photoreception. Photoreceptors and olfactory receptor neurons alike possess cyclic nucleotide-gated ion channels. Nonetheless there are key differences between olfaction and taste. Olfactory receptor neurons are optimized for low concentrations of chemical stimuli; gustatory sensory cells require much higher concentrations of stimuli to become activated. Current topics of intensive research in the peripheral transduction mechanisms for taste and olfaction include, among others, discovering structural details of, and ligand-binding pockets for, the receptor proteins, learning how an olfactory receptor neuron determines which one odorant receptor gene it will express from the several hundred in its genome; identifying transmitters and determining synaptic mechanisms that transmit signals between cells in the taste bud; and understanding how the output signals from the peripheral sensory organs of olfaction and gustation are encoded as patterns of nerve impulses (the sensory code) that are transmitted to the brain and produce odor and taste perceptions.

II. INTRODUCTION

Peripheral sensory cells in olfaction, taste, hearing and vision are modified epithelial cells and share certain properties common to epithelial tissues. These properties

Cell Physiology Sourcebook. DOI: 10.1016/B978-0-12-387738-3.00039-1

include (1) an ongoing renewal of the cell population[1] and (2) cellular polarity, manifest in epithelial cells as two distinctive membrane regions – *apical* versus *basolateral surfaces*, with a barrier of tight junctions to separate the superficial (apical) environment from the tissue spaces surrounding the rest of the cell. Apical and basolateral cell surfaces in epithelial cells and many sensory receptor cells are exposed to two vastly different ionic milieus. This is especially true in *gustatory* and *olfactory* receptor cells. The apical membrane tips in these sensory cells confront external chemical environments in the oral and nasal cavities, respectively, that can change profoundly during stimulation and that can often be quite harsh. In contrast, the cell bodies of gustatory and olfactory sensory cells are bathed in a protected, relatively unchanging medium – interstitial fluid.

Chemical stimuli are initially *transduced* into intracellular electrical signals at the exposed apical tips of taste and olfactory sensory cells. Tight junctions confine most chemical stimuli to the specialized apical membrane and prevent the stimuli from penetrating deeper into the sensory epithelium (although there may be exceptions in gustatory sensory cells, see Section III). This has two implications for gustation and olfaction. First, molecular receptors for signal transduction must reside in the apical membrane of the sensory cells where chemical stimuli contact the cells. Second, because chemosensory stimulation is usually associated with a *receptor* (or *generator*) *current* (flux of ions) across the apical chemosensitive membrane, the ionic environment at the exposed apical region can have a significant impact on transduction. For example, olfactory sensory cells possess a Cl^- conductance that exploits the low external and high intracellular Cl^- concentrations at the apical membrane of these cells to generate an *inward current* during odor stimulation (discussed in detail below). This Cl^- current amplifies the sensory signal.

Olfactory receptor neurons possess axons and transmit their signals directly to the brain and, specifically, the olfactory bulb (Fig. 39.1). Odor signals are decoded and processed in the olfactory bulb and in higher brain centers. In sharp contrast, taste receptor cells transmit their signals via synapses onto primary sensory fibers innervating taste buds. The primary sensory fibers then communicate with the brain. Moreover, cells within a taste bud interact via *chemical* and *electrical synapses* to process gustatory signals via excitatory and inhibitory cell–cell interactions (Roper, 1992; Chaudhari and Roper, 2010). Thus, some degree of cross-talk and information processing occurs in the end organs of taste. The details and significance of these cell–cell interactions are only now emerging.

This chapter describes events taking place in mammalian taste and olfactory sensory cells. Reference to other vertebrate species will occasionally be made, but chemosensory transduction in mammals will be the focus. Distinctly different molecules and mechanisms for taste and olfaction occur in invertebrates and these will not be described.

III. TASTE RECEPTOR CELLS

IIIA. General Comments

Peripheral sensory organs for taste consist of clusters of receptor cells, the taste buds, found throughout the oral cavity. There are 2000–10 000 taste buds in humans. This number varies considerably from individual to individual. Each taste bud consists of 50–100 cells. Taste buds are embedded in the lingual epithelium in specialized protuberances, or papillae (*fungiform*, *foliate* and *circumvallate papillae*). Taste buds are also found on the soft palate, uvula, epiglottis, pharynx, larynx and have even been reported in the upper esophagus. Interestingly, certain cells in the walls of the stomach and intestine express proteins that previously were associated only with taste buds, indicating that chemosensing most likely occurs throughout the length of the digestive tract. However, cells in the stomach and intestines that have taste bud-like proteins are not gustatory sensory cells. They are not organized into collections resembling taste buds; they are not innervated by cranial gustatory nerves; and they are not known to generate taste perceptions.

Taste buds respond to a number of basic taste qualities, including sweet, sour, salty, bitter, *umami* (discussed later) and perhaps others such as fat. Early investigators tested whether particular regions of the tongue were specialized for these different qualities (Hänig, 1901). They found a somewhat greater sensitivity to bitter in the posterior tongue and to sweet at the tip (Fig. 39.2). However, these original findings were overinterpreted in the intervening years, leading to the popular misconception that there is a discrete and well-delineated "taste map" on the tongue. The truth is that all parts of the tongue sense the basic qualities, as shown in Fig. 39.2, and individual taste buds have been shown to respond to several different taste qualities.

Most of the cells in a taste bud are narrow elongate cells, extending nearly the full thickness of the lingual epithelium. The basal processes of taste bud cells reach to the basement membrane below the lingual epithelium and the apical processes extend up into a tiny cavity in the lingual surface at the top of the taste bud, the *taste pore*.

[1] This epithelial property is not shared, however, with inner ear hair cells (auditory and vestibular) or, strictly speaking, with retinal photoreceptors. These sensory cells do not renew and are not replaced if damaged. Admittedly, retinal photoreceptors undergo continuous recycling of their photoreceptive components (opsin-containing disk membranes are shed and renewed), but the somata remain stable.

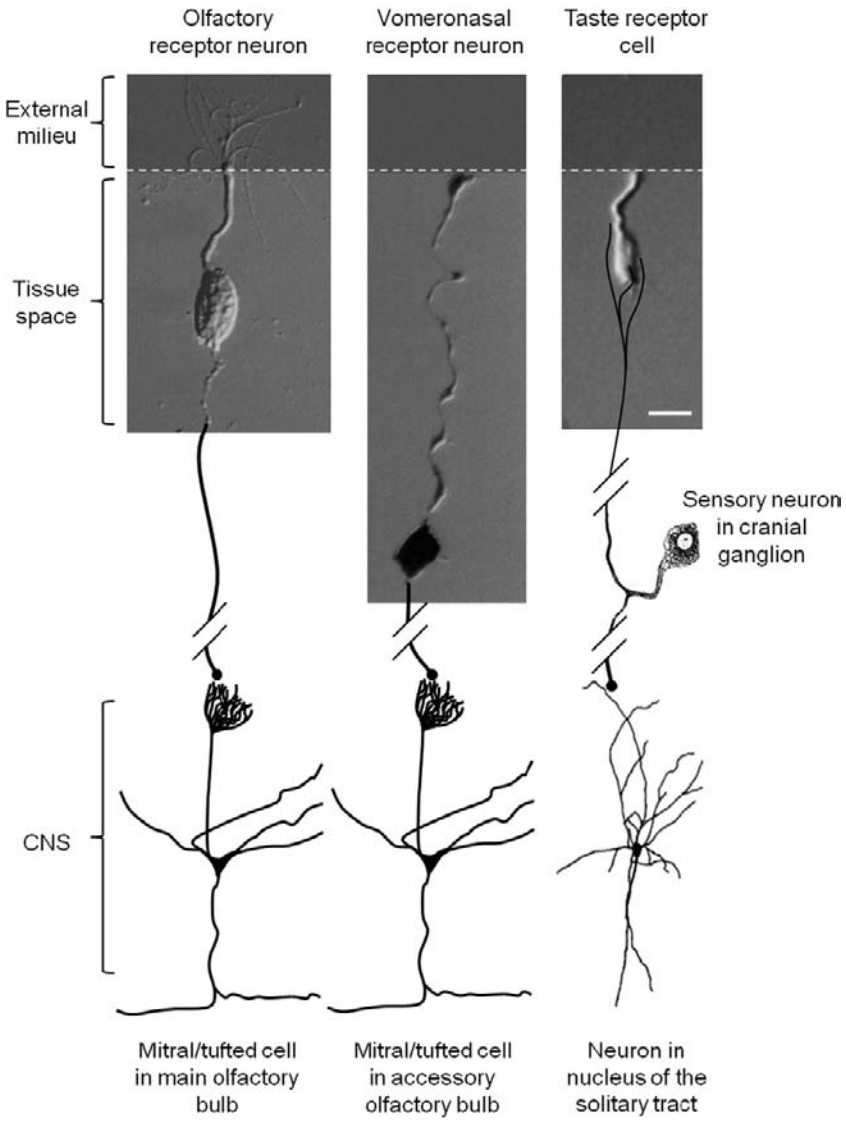

FIGURE 39.1 Schematic drawing comparing sensory cells experimentally isolated from olfactory epithelium, vomeronasal organs and taste buds. The apical tips of these cells are exposed to the external environment (dark shaded) where the initial events in chemosensory transduction occur. The basolateral membrane of the cells lies below the apical junctional complex (white dashed line) and is surrounded by interstitial fluid. Olfactory receptor neurons and vomeronasal sensory cells have axons (drawn in here) that project into the central nervous system (CNS) where they form synapses with mitral/tufted cells in the olfactory bulb. In contrast gustatory receptor cells form synapses in the taste bud with primary sensory fibers from cranial sensory ganglion neurons. Calibrations = 10 µm. *(Olfactory receptor neuron modified from Kleene and Gesteland, 1981; vomeronasal receptor neuron modified from Ghiaroni et al., 2003; taste receptor neuron modified from Bigiani et al., 2002.)*

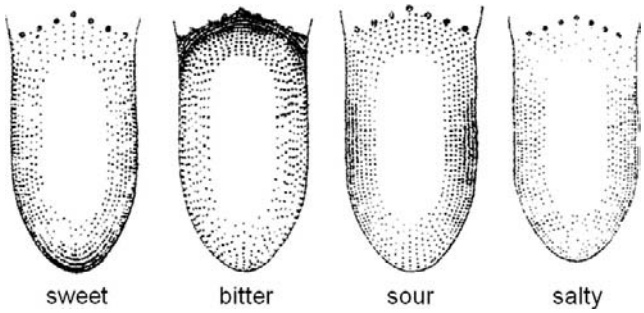

FIGURE 39.2 Regional distribution of sweet, bitter, sour and salty taste on the human tongue, as originally determined by D.P. Hänig (1901). The sensitivity for a particular taste quality is represented by the density of stippling. There is a slight tendency for the anterior tip of the tongue to be more sensitive to sweet, the lateral regions to be more sensitive to sour and the posterior to bitter. However, there is complete overlap for all these taste qualities. Also, see discussion in Lindemann, (1999).

The elongate, columnar morphology of gustatory sensory cells sets taste buds apart from the surrounding laminated ("stratified") epithelium. That is, taste buds form tiny islands of simple columnar epithelium within the larger sheet of stratified squamous lingual epithelium. Such an arrangement positions taste cells directly across the electric field generated by lingual transepithelial ion transport currents. This may have implications for taste transduction.

There are three or more different types of cells in mammalian taste buds. Based on cytological features, histologists categorized taste cells as dark cells and light cells. Later, electron microscopists delineated *types I*, *II* and *III cells* based on ultrastructural features, including that only one of the cell types (type III) possesses synaptic connections. These morphological classifications have

recently been tremendously clarified by combining molecular profiling with functional analyses on isolated taste cells. It is now recognized that type I cells are *glial-like*; type II cells express *G-protein-coupled receptors* for and respond to sweet, bitter and umami tastes; and type III cells express synaptic proteins associated with *vesicular release*, possess synaptic specializations and respond to sour (acid) taste (reviewed in Chaudhari and Roper, 2010). The taste cells responsible for salt (NaCl) taste have not yet been identified unambiguously, though there are suggestions that type I and III cells participate. In recognition of the functional roles of the cells comprising taste buds, type II cells have also been termed receptor cells and type III cells named presynaptic cells.

Taste cells, like the adjacent non-taste stratified epithelium, represent a *renewing population*. Taste bud cells have an estimated average life span of approximately 10 days in the mammal, longer than the surrounding non-sensory epithelium (3−4 days). There are early indications that the type I, II (receptor) and III (presynaptic) taste cells may have different longevities, but the data are only preliminary. Taste cells may be born from stem cells at the base of the taste bud. They may also originate from adjacent epithelial cells immediately surrounding taste buds. The precise origin of taste bud cells and whether the different cell types have a common lineage during development and in the adult are questions currently under investigation.

Recent investigations indicate that there are important cell−cell synaptic interactions in the taste bud, including feed forward and feedback signaling (reviewed in Roper, 2007; Herness and Zhao, 2009; Chaudhari and Roper, 2010). These interactions appear to shape the signals generated within the taste bud during taste excitation and may be critical in establishing a taste code that is transmitted to the brain for further processing. A discussion of signal processing in taste buds and how gustatory information is decoded in the central nervous system are topics beyond the scope of this chapter.

IIIB. Nature of Taste Stimuli

Many, if not most water-soluble chemicals probably elicit a taste. Chemical stimuli have been grouped into five primary taste qualities: sweet, sour, salty, bitter and umami. There is ongoing debate whether there are additional taste qualities such as fatty and astringent, though these categories are blurred by somatosensory contributions (tactile, texture, etc). The existence of primary taste qualities argues there are distinct transduction mechanisms and signaling pathways for each of the basic tastes and this notion has guided taste research.

Chemicals that elicit taste usually do so only at high concentrations (millimolar to molar). However, certain bitter-tasting substances (such as quinine, caffeine, strychnine) and artificial sweeteners are relatively potent stimuli and elicit taste responses at μM concentrations. Nonetheless, it is clear that taste cells are relatively insensitive when compared with the exquisite responsiveness of photoreceptors (i.e. single photons) or olfactory and pheromone chemoreceptors (i.e. picomolar stimulus concentrations, possibly even single molecules). Primary functions of taste organs include regulating the intake of important nutrients and protecting against the ingestion of spoiled food and other harmful substances. Therefore, the generally low sensitivity of gustatory sensory cells to nutrients (carbohydrates, *sweet*; amino acids/protein, *umami*; Na^+, *salty*) and high sensitivity to potentially detrimental compounds (toxins and rancid food, bitter) may represent an optimization for tastant concentrations that are physiologically relevant. That is, low taste sensitivity prevents receptors from becoming saturated and unresponsive to tastants that are required in abundance (nutrients); high bitter sensitivity assures that dangerous compounds will be detected and avoided even at low concentrations. (Many bitter-tasting chemicals are toxic and, conversely, many toxic chemicals elicit bitter taste.) In this light, the biological significance of sour taste (acids) is somewhat enigmatic. Sourness is an aversive taste to non-human animals and human infants but can be an acquired taste in adults. Further, rancid or spoiled food is often acidic.

Taste stimuli are dissolved in saliva to bathe the chemosensitive (apical) surface of gustatory sensory cells. Most chemical stimuli are prevented from gaining access to the basolateral regions of the taste bud by the *tight junctions* of the junctional complex at the taste pore. Notable exceptions are organic acids, such as acetic acid (vinegar) and citric acid, which elicit sour taste, and which rapidly breach the epithelial barrier. In their fully protonated form (i.e. neutral molecules), these acids penetrate into and throughout the epithelium, including into the cellular interior. Inside cells, the protonated molecules dissociate to release H^+. This penetration of organic ("weak") acids into the cytosol is believed to be an important contribution to sour taste stimulation (see below). Also, tight junctions between taste bud cells are somewhat leaky to certain ions, such as Na^+, K^+ and Cl^- (Ye et al., 1993). These ions pass from the lingual surface into the intercellular spaces within the taste bud. It is possible that chemotransduction mechanisms for NaCl, KCl and possibly other stimuli exist on the basolateral membranes of taste receptor cells as well as on their exposed apical tips. Basolateral transduction mechanisms may explain intravascular taste, where blood-borne chemicals elicit gustatory sensations (Bradley, 1973). The bitter taste of some drugs injected intravenously and the sweet taste of intravenously-injected saccharin, once used

to monitor blood circulation, are examples of intravascular taste.

IIIC. Initiation of Taste Receptor Potentials

Taste cells are excitable and generate action potentials when depolarized sufficiently. This was first demonstrated with intracellular recordings from the large taste bud cells found in the amphibian, *Necturus maculosus* (Roper, 1983), but has subsequently been verified with patch-clamp recordings from mammalian taste cells (Fig. 39.3A, B). Specifically, taste bud cells (types II and III) possess inward, voltage-dependent, tetrodotoxin-sensitive Na^+ currents and outward, TEA-sensitive K^+ currents (Fig. 39.3C, D), typical of many neurons. Type III cells, but not type II cells, also have inward, voltage-dependent Ca^{2+} currents.

Gustatory stimuli generate *receptor potentials* and *transient increases of* $[Ca^{2+}]$ inside taste bud cells (Fig. 39.3E–H). The conversion of a gustatory chemical signal into an intracellular receptor potential or Ca^{2+} transient is termed *taste transduction*. The endpoint of taste transduction is the release of neurotransmitter(s) from the sensory cell.

Unlike signal transduction in most other sensory cells, there is no single unifying mechanism underlying taste transduction. The necessity of taste organs to sense a wide

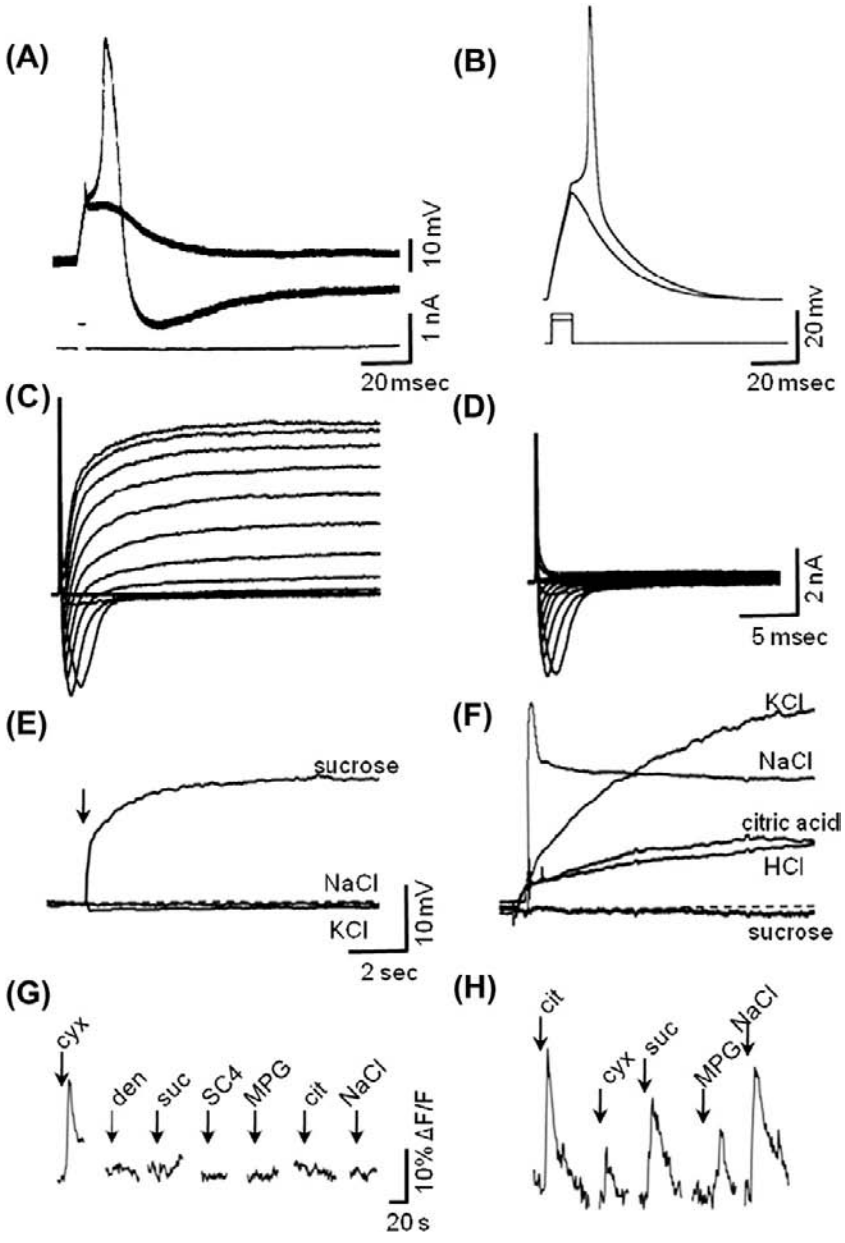

FIGURE 39.3 Taste receptor cells are excitable and respond to taste stimulation with depolarizing generator potentials and intracellular Ca^{2+} increases. (A) Intracellular recording from amphibian taste receptor cell showing responses to threshold current pulses passed through the recording electrode. (B) Patch electrode recording from mouse taste receptor cell, current clamp mode, showing responses to depolarizing current pulses at threshold. (C) Patch-clamp recording from mouse taste receptor cell showing inward and outward currents produced by current steps. (D) As in (C), but in presence of TEA to block outward K current. (E) Patch electrode recording of rat taste receptor cell, current clamp mode, showing a depolarizing response to sucrose applied to the apical, chemosensitive tip, but no responses to similarly applied solutions of NaCl or KCl. (F) As in (E), but showing another taste cell that was broadly sensitive to KCl, NaCl, citric acid and HCl, but not sucrose. (G) Mouse type II taste cell showing Ca^{2+} responses evoked by a series of different chemical stimuli applied to the apical chemosensitive tip. This cell responded only to one stimulus, a bitter taste (cycloheximide, cyx). (H) A mouse type III taste cell showing Ca^{2+} responses to several different stimuli, including sour (citric acid), bitter (cycloheximide, cyx), sweet (sucrose, suc), umami (monopotassium glutamate, MPG) and salty (NaCl). (G, H) were taken from calcium imaging experiments showing changes in fluorescence (ΔF) of an intracellular Ca^{2+}-sensitive dye. *((A) Modified from Roper, 1983, (B, C, D) modified from Bigiani et al., 2002, (E, F) modified from Gilbertson et al., 2001, (G, H) modified from Tomchik et al., 2007.)*

range of chemical substances, from simple ions to complex proteins, has led to the evolution of *multiple taste transduction mechanisms* (reviewed by Smith and Margolskee, 2001; Sugita, 2006; Roper, 2007; Chaudhari and Roper, 2010). Different taste bud cells possess distinct transduction mechanisms and respond to different taste stimuli. For instance, receptor (type II) taste cells respond specifically to sweet, bitter or umami taste compounds. Presynaptic (type III) taste cells respond to sour taste. Moreover, due to excitatory interactions between receptor and presynaptic cells, presynaptic cells also respond (indirectly) to sweet, bitter and umami (Tomchik et al., 2007). Presynaptic cells also are excited by salty stimuli, though whether this is due to direct stimulation or to indirect activation via intercellular communication from other taste bud cells remains unsolved.

Taste transduction can be divided into two primary mechanisms:

1. *Ion permeation through specific channels*. Certain taste stimuli, most notably Na^+, enter taste cells through ion channels in the membrane, thereby generating transmembrane *receptor currents* and receptor potentials. Protons may also pass through ion channels and elicit sour taste responses.
2. *Receptor-ligand binding*. Interactions occur between chemical stimuli (ligands) and specific membrane bound receptors (in particular, G-protein-coupled receptors, GPCRs) that ultimately lead to receptor currents or the release of intracellular Ca^{2+}, or both.

Parenthetically, some researchers believe that amphipathic stimuli, such as saccharin and quinine, may bypass ion channels and receptors and penetrate through the lipid plasma membrane to act directly on intracellular signaling cascades. Whether this occurs at physiologically relevant concentrations of the taste compounds, however, remains to be established.

IIIC1. Ion Permeation Through Specific Channels

ENaC Channels and Salt Taste

Sodium salts ("salty taste") are believed to be transduced in a subset of taste cells by the direct permeation of Na^+ through passive Na^+-selective channels (as opposed to TTX-sensitive, voltage-dependent Na^+ channels that underlie action potentials). Most of salt taste is transduced by a mechanism that is sensitive to the diuretic, amiloride. The most likely candidate Na taste transducer to date is the *amiloride-sensitive epithelial Na^+ channel* (ENaC) found in renal tubules and elsewhere (Heck et al., 1984). Indeed, mRNA isolated from lingual epithelium and immunostaining of taste buds shows that all three ENaC subunits (α, β and γ) are expressed in taste cells (Kretz et al., 1999; Lin et al., 1999). Where it has been measured (in frog taste cells), taste Na^+ channels have small unitary conductance (1−2 pS) and are blocked by low concentrations of amiloride (K_i = 0.2−1 μM), consistent with ENaC channels. Recent findings from mouse taste buds show that certain taste cells manifest ENaC-like ion currents (Vandenbeuch et al., 2008) and taste cells expressing ENaC respond to NaCl stimulation (Chandrashekar et al., 2010).

ENaC channels are open at rest and allow an ongoing influx of Na^+, driven by this cation's electrochemical gradient. The concentration of Na^+ in human saliva varies from about 3 to 63 mM, depending on the rate of salivary secretion. This results in an equilibrium potential for Na^+ (E_{Na}) of about −30 to +50 mV (assuming $[Na^+]_i$ is 10 mM) across the apical membrane of salt-sensitive taste cells. Thus, with a resting potential estimated to be −60 to −80 mV, there is likely to be a small steady-state influx of salivary Na^+. During stimulation with NaCl when $[Na^+]$ in the oral cavity can reach concentrations up to a fraction of a mole (a typical soup, for instance, contains ≈0.25 M NaCl), the electrochemical gradient driving Na^+ into the cells increases and Na^+ influx depolarizes the cell. This current exits across the base of the cell forming a complete current loop via an extracellular (paracellular) pathway that includes the junctional complex near the taste pore. Consequently, any factors that affect the basolateral membrane conductance or the paracellular resistance, especially at the tight junctions near the taste pore, will also affect the magnitude of the receptor currents.

As mentioned previously, Na^+ on the tongue surface may also partly penetrate the apical junctional complex of taste buds and raise $[Na^+]_o$ in the interstitial spaces surrounding taste cells. If Na^+ transduction channels are expressed on the basolateral as well as apical membrane of salt-sensitive taste cells, penetration of Na^+ into the interior of the taste bud would provide another avenue for Na^+ taste stimulation. Immunostaining for ENaC channels has suggested their presence on the basolateral membrane (Lindemann et al., 1998), but Na^+ responses in mouse fungiform taste cells were unaffected when their basolateral surface was exposed to the ENaC antagonist amiloride (Yoshida et al., 2009a). This suggests that if basolateral Na^+ transduction occurs, it is unlikely to be via ENaC channels.

Although the evidence is good in experimental animals, particularly rodents, a role for ENaC channels in human salt taste has been questioned. Amiloride appears to affect only the sourness, not saltiness, of NaCl solutions in psychophysical studies (Ossebaard and Smith, 1996). Furthermore, even in non-human species, not all salt taste can be explained by ENaC channels. A component of salt taste in experimental animals is unaffected by amiloride, especially in the posterior tongue. Mechanisms other

than amiloride-sensitive (presumably ENaC) channels must exist.

Proton (H^+) Channels and Sour Taste

How acids (sour taste) are transduced may differ from species to species and our understanding of sour transduction remains incomplete. In the amphibian, *Necturus*, protons block apical K^+ channels and depolarize the cell. Additionally, protons themselves permeate the apical membrane, providing a depolarizing inward receptor current. Interestingly, protons permeate hamster taste cells via amiloride-sensitive Na^+ channels, believed to be ENaC (Fig. 39.4A). Protons bind to the ion selectivity site in the ENaC channel more strongly than do Na^+ ions. Consequently, H^+ conductance of ENaC is less than that of Na^+. This also means that protons interfere with the flux of Na^+ through the channel. In contrast, protons permeate mouse taste cells via proton-gated channels that are unaffected by amiloride and thus are unlikely to be related to ENaC (Fig. 39.4B). In humans, psychophysical studies implicate a role for amiloride-sensitive Na^+ channels in sour taste (Ossebaard and Smith, 1996). (The interference between Na^+ and H^+ permeation of amiloride-sensitive Na^+ channels may help explain the culinary wisdom that acidifying food, for example by adding vinegar or lemon juice, reduces its salty taste.) In short, our understanding of roles for ion channels and proton influx in sour taste is fragmentary.

However, a major component of sour taste may be unrelated to the influx of protons and generation of a depolarizing H^+ current. Namely, organic acids such as acetic acid (vinegar), citric acid (fruit) and tartaric acid (wine) are potent sour stimuli. In fact, at equal pH values, organic ("weak") acids are more sour than mineral ("strong") acids such as HCl. This cannot easily be explained by H^+ influx through proton channels. At equal pH, the H^+ concentration of an organic and a mineral acid

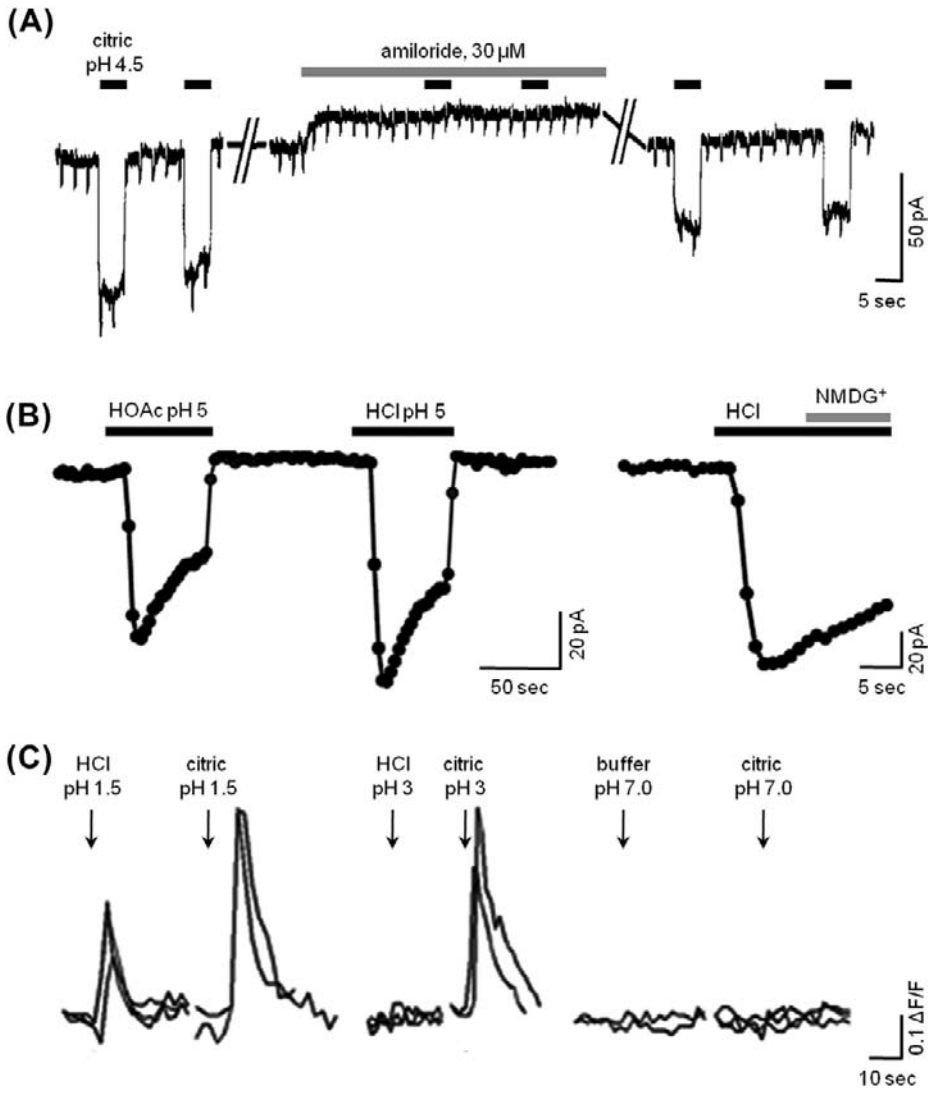

FIGURE 39.4 Sour taste transduction. (A) In hamsters, sour taste stimulation triggers an inward proton flux through amiloride-sensitive (presumably ENaC) channels. These traces are patch-clamp recordings of an isolated fungiform taste cell showing inward current responses evoked by 2.5 mM citric acid (pH 4.5) and their block by 30 µM amiloride (modified from Gilbertson et al., 1993). (B) In sour-sensitive taste cells from mice, acid stimulation also evokes inward proton currents. Unlike those in hamsters (A), these currents are not affected by amiloride (data not shown). Traces show patch-clamp recordings from an isolated mouse fungiform taste cell showing inward current responses evoked by 2 mM acetic acid (HOAc, pH 5) and 10 mM HCl (pH 5). Replacing Na^+ with $NMDG^+$ had no effect on the HCl-evoked response (final trace), consistent with the current being carried by protons, not Na^+ *(modified from Chang et al., 2010)*. (C) Sour stimuli also elicit Ca^{2+} transients in taste cells, recorded with functional imaging. The traces show Ca^{2+} influx in sour-sensitive circumvallate taste cells from a mouse. The responses were triggered by brief applications of acid stimuli applied focally to the taste pore in a lingual slice preparation. Citric acid was much more effective than HCl at equivalent pH values, *(modified from Richter et al., 2003)*.

stimulus, and hence the inward driving force for protons across the taste cell membrane, would be identical. Organic and mineral acids at the same pH would be expected to be equally sour, which is not the case. Psychophysical measurements of sourness, taste nerve responses to acid stimuli and responses of sour-sensitive taste cells consistently indicate that organic acids are more effective than mineral acids at a given pH (e.g. see Fig. 39.4C) (Richter et al., 2003; Huang et al., 2008). The explanation is that the protonated organic acid molecules readily pass through cell membranes and penetrate into the taste cell interior where they dissociate into proton(s) and anion(s) (see Roper, 2007). Permeation of organic acid molecules into the cell results in cytosolic acidification, which is believed to contribute markedly to sour taste transduction. That is, intracellular protons, not extracellular H^+, appear to be a proximate stimulus for sour taste (Lyall et al., 2001). Accordingly, a cytosolic protein or the intracellular face of a membrane transducer likely binds protons and initiates the events leading to a signaling cascade for sour taste. One such candidate that has been shown to transduce acid-evoked nociception and that involves cytosolic acidification is the cation channel TRPA1 (Wang et al., 2011). However, to date, there is no strong evidence for the expression of TRPA1 in taste buds or TRPA1-mediated sour taste transduction. Other candidate intracellular targets that have been hypothesized include 2-pore domain K^+ channels that are blocked by cytosolic acidification (Richter et al., 2004).

In all likelihood, sour taste transduction may eventually be explained by a combination of events – proton-gated channels triggered by extracellular H^+ and cytosolic acidification leading to modification of intracellular proteins. The end result of sour taste transduction is depolarization of the acid-sensitive (presynaptic or type III) taste cells, influx of Ca^{2+} through voltage-gated Ca channels and release of transmitter(s), including serotonin (Huang et al., 2008).

IIIC2. G-Protein-Coupled Receptors for Taste

G-protein-coupled receptors (GPCRs) have been identified for three of the primary tastes – sweet, bitter and umami. These are the *T1Rs* (sweet, umami) and *T2Rs* (bitter) and their corresponding genes, *Tas1Rs* and *Tas2Rs* (Chandrashekar et al., 2000, 2006; Nelson et al., 2001, 2002; Max et al., 2001; Sainz et al., 2001). In humans and many other mammals, there are three members of the small family of T1R GPCRs – T1R*1*, T1R*2* and T1R*3*. These GPCRs form heterodimers to create either a sweet (T1R2+T1R3) or an umami (T1R1+T1R3) receptor. (Interestingly, in frogs, there are no T1Rs, implying that these amphibia do not sense sweet or umami tastes, at least not transduced by T1Rs). The dimeric sweet receptor (T1R2+T1R3) responds to a variety of different sugars (sucrose, fructose, glucose, etc.) as well as to artificial sweeteners (e.g. saccharin, aspartame, acesulfame potassium, cyclamate) and sweet-tasting proteins (monellin, thaumatin, brazzein)[2]. The binding pockets on the dimeric T1R2+T1R3 differ for the different sweet ligands. For example, glucose, sucrose and aspartame bind to the extensive amino termini ("venus fly trap" domain) of T1R2 and T1R3; other artificial sweeteners, such as cyclamate, to a pocket in the transmembrane region of T1R3; and sweet proteins to a cysteine-rich domain that links the large extracellular amino terminus of T1R3 to its seven transmembrane domains. Nonetheless, ligand interactions with T1R2+T1R3, whether at one or more of these different binding sites, activate a common downstream effector pathway, described below.

Taste receptors responding to amino acids, particularly sodium glutamate (monosodium glutamate, MSG) and that elicit "umami" are constructed from the combination of T1R1+T1R3. Thus, T1R3 is common to sweet and umami taste receptors. Glutamate most likely binds to the large amino terminal, *venus fly trap domain*. Other binding sites have not been extensively explored to date. Taste receptors other than T1R1+T1R3 are believed to exist for umami, based on findings that mutant mice lacking T1R3 still detect, albeit less robustly, solutions of umami compounds. Additional candidate umami receptors include variants of G-protein-coupled synaptic glutamate receptors, mGluR4 and mGluR1.

Bitter taste is transduced by the T2R class of receptors. In contrast to the small number of T1Rs, T2R genes (Tas2R) comprise a larger family. The number of T2R genes varies from species to species. In humans, there are 25 functional T2R receptors; in frogs, 47; in zebrafish, 4. It is unclear whether T2Rs exist as monomers or oligomers. T2Rs lack the extensive N termini that characterize T1Rs. Bitter compounds are believed to bind in a single transmembrane pocket of a given T2R, with certain T2Rs being more selective and others more broadly responsive to multiple, related ligands.

Taste GPCRs (i.e. T1Rs and T2Rs) are expressed by the type II (receptor) taste cells. In general, a given receptor (type II) cell expresses only one type of taste receptor – either sweet, umami, or bitter receptors. Consistent with this finding, in physiological studies, receptor cells have been shown mainly to respond (i.e. are "tuned") to single taste qualities, sweet, bitter or umami (Tomchik et al., 2007; Yoshida et al., 2009b). Receptor taste cells that respond to bitter compounds express small, overlapping subsets of four to 11 T2Rs of the full repertoire of 25 human T2Rs (Behrens et al., 2007). Thus, it is understandable that

[2] The human T1R2+T1R3 dimer responds to monellin and thaumatin, but the equivalent rodent sweet receptor dimer does not. This is explained by sequence differences between human and rodent sweet taste receptors.

bitter-sensitive taste receptor cells, each expressing a subset of T2Rs, respond to multiple bitter compounds.

IIIC3. Downstream Effectors

Activating either T1Rs or T2Rs on receptor cells by sweet, umami or bitter compounds initiates a common signaling cascade, consisting of liberating $G_{\beta\gamma}$ proteins (specifically $G_{\beta3}/G_{\gamma13}$) bound to the taste GPCR, triggering a taste-specific phospholipase C (PLCβ2), generating IP_3 and consequently stimulating IP_3 receptors on intracellular Ca^{2+} stores (specifically, IP_3R3), thereby releasing Ca^{2+} into the cytosol (reviewed by Chaudhari and Roper, 2010). Thus, the net effect of taste stimulation is to mobilize intracellular Ca^{2+} (see Fig. 39.3G, H). The increased $[Ca^{2+}]_i$ has a dual effect. Intracellular Ca^{2+} opens taste-specific cation channels in the basolateral membrane of receptor cells, TRPM5, allowing Na^+ influx and thereby producing a depolarizing current. Ca^{2+} also acts on pannexin 1 gap junction hemichannels embedded in the plasma membrane. Pannexin 1 hemichannels are triggered open by the combined action of TRPM5-mediated depolarization and IP3-mediated Ca^{2+} increases. Opening pannexin 1 channels allows the efflux of taste transmitter, ATP, from receptor cells (Huang et al., 2007; Romanov et al., 2007), the end result of taste stimulation for these cells (Fig. 39.5A).

In addition to $G_{\beta\gamma}$ proteins released during taste GPCR activation, a taste-specific G_α protein, G_α gustducin (McLaughlin et al., 1992) is liberated from the receptor. Unlike the $G_{\beta\gamma}$ pathway, G_α signaling in taste transduction is not as well characterized. Gene-knockout mice lacking G_α gustducin show deficits in their ability to sense bitter, sweet and umami tastes, but whether this taste-specific G_α protein is directly intercalated in the taste transduction pathway is disputed. Evidence suggests that G_α gustducin plays an indirect role. G_α gustducin is a type of G_i protein, related to transducin in photoreceptors. By stimulating a phosphodiesterase present in taste cells, G_α gustducin acts to lower cytosolic cAMP. Because cAMP inhibits PLCβ2/IP_3/Ca^{2+} signaling, lowering cytosolic cAMP enhances the receptor cell's sensitivity to taste compounds (Clapp et al., 2008). In mutant mice lacking G_α gustducin, cAMP accumulates in receptor cells and depresses sensitivity to sweet, umami and bitter taste stimuli.

Figure 39.5 summarizes the several transduction pathways for taste stimulation.

IIID. Termination of Taste Signals

Termination of chemostimulation in taste cells is probably due to two factors: diffusion of the stimulus away from the apical chemosensitive tips and receptor cell adaptation.

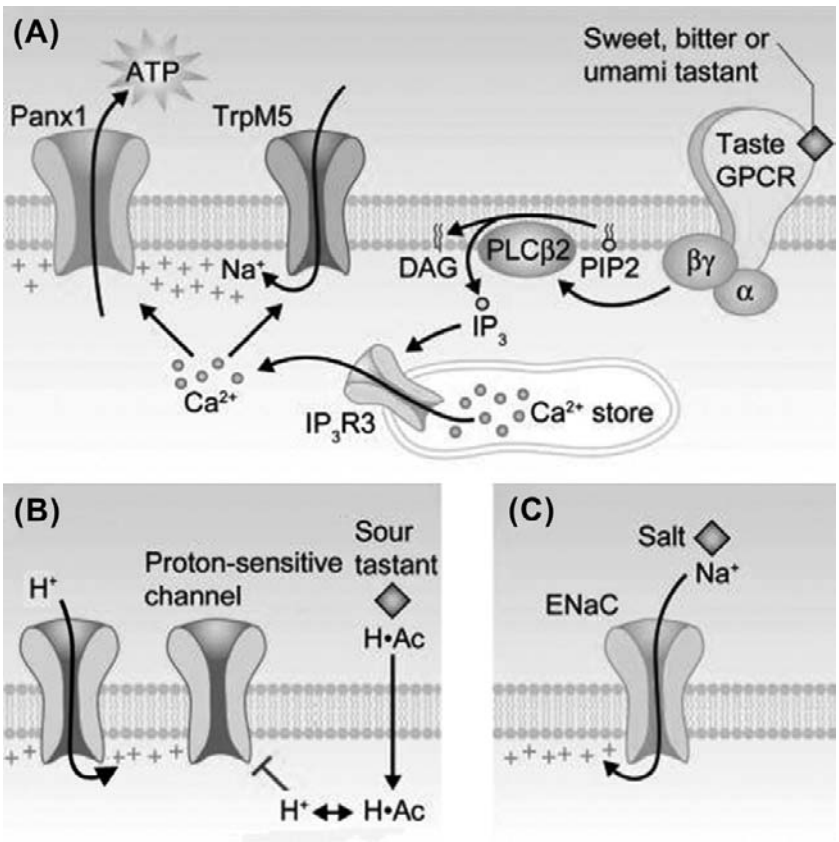

FIGURE 39.5 Taste transduction mechanisms for sweet, bitter, umami, sour and salty. (A) Sweet, bitter and umami compounds bind to G-protein-coupled taste receptors (shown at far right) on taste receptor (type II) cells and initiate a downstream cascade of $G_{\beta\gamma}$ proteins, phospholipase C and intracellular Ca^{2+} release. (G-protein-coupled receptors for sweet and umami exist as heterodimers, not depicted in this cartoon.) Intracellular Ca^{2+} activates a cation channel, TrpM5, and a plasma membrane gap junction hemichannel, pannexin 1 (Panx1). When Panx1 opens, the taste neurotransmitter ATP is released into the interstitial spaces (Huang et al., 2007; Romanov et al., 2007). (B) Sour taste may involve proton influx through channels (left) and penetration of the sour tastant (shown here, acetic acid, H · Ac) across the plasma membrane to acidify the cytosol. Cytosolic acidification may block proton-sensitive K^+ channels, as yet unidentified. (C) Salty taste can be evoked by Na^+ influx through ENaC channels. This mechanism has been demonstrated in rodents but its generalization to humans has been questioned and remains to be established, *(modified from Chaudhari and Roper, 2010).*

Little is known about adaptation in gustatory sensory cells. It is plausible that the Ca^{2+}-dependent Cl^- conductance that exists in taste bud cells contributes to sensory adaptation in taste (Taylor and Roper, 1994; Herness and Sun, 1999). Ca^{2+} mobilization in receptor cells during taste transduction would be expected to activate a basolateral Ca^{2+}-dependent Cl^--conductance, triggering an influx of Cl^- from the interstitial fluid surrounding taste cells and generating an outward, repolarizing current.

IV. OLFACTORY RECEPTOR CELLS

IVA. General Comments

Receptor cells for odorants are distributed in specialized patches of olfactory sensory epithelium embedded within the nasal respiratory epithelium. These patches comprise about 1 cm^2 of surface in each nostril in the human, or approximately 0.5−1% of the total nasal epithelium. The area of olfactory epithelium decreases with age, perhaps contributing to the decline of the sense of smell in the elderly.

Olfactory receptor cells are specialized neurons and are often termed olfactory receptor neurons (ORNs). Olfactory receptor neurons are elongate cells that extend from the base of the epithelium to the surface. Receptor neurons stand side by side with columnar supporting cells in the olfactory epithelium. The apical tips of ORNs consist of a tiny knob from which extend six to 12 long cilia (see Fig. 39.1). At their base, olfactory receptor neurons extend an axon that travels upward through perforations in the region of the cranium that overlies the olfactory epithelium (the cribriform plate) to reach the olfactory bulb of the CNS. Consequently, olfactory receptor neurons bypass any synaptic intervention in the periphery and transmit action potentials directly into the brain[3].

Stem cells (horizontal and globose basal cells) reside at the base of the olfactory epithelium. These cells provide a reservoir of progenitors for the continuous renewal of the olfactory epithelium. Basal stem cells divide and differentiate into olfactory receptor neurons and supporting cells. The lifespan of olfactory receptor neurons was originally thought to be approximately 30 days (Graziadei and Monti Graziadei, 1978), but later findings indicate that ORNs may live for many months (Mackay-Sim and Kittel, 1991a,b).

Closely related to nasal olfactory epithelium is another peripheral chemosensory structure, the vomeronasal organ (VNO). The VNO detects a special category of volatile and non-volatile chemical stimuli which include pheromones. This sensory end organ is an invagination of the nasal epithelium in mammals[4] or, in reptiles such as snakes, an opening in the oral cavity. Pheromones are chemical signals produced by one member of a species to communicate with other members of that same species (conspecific). Pheromones play a key role in endocrine responses and in shaping social and sexual interactions (e.g. territoriality, mating) among conspecifics, at least in non-human animals, and perhaps even in humans (Gelstein et al., 2011). Pheromone stimuli for VNO sensory neurons include airborne molecules (such as dihydro-exo-brevicomin, a volatile constituent of male mouse urine) and non-volatile molecules (such as aphrodisin, a component of vaginal secretions in hamsters). Animals also use their VNO to detect chemical stimuli such as predator odors from different species (heterospecific), as well as to identify food odors. Lastly, VNO sensory neurons may signal the health status of a conspecific (Riviere et al., 2009).

Receptor neurons in the VNO, as in the olfactory epithelium, possess axons that travel to and innervate portions of the olfactory bulb. However, unlike ORNs, sensory neurons of the VNO possess apical microvilli, not cilia. The initial events of transduction are believed to occur on the microvilli. Moreover, VNO sensory neurons send their axons to a separate portion of the olfactory bulb (the accessory olfactory bulb) reserved for processing pheromone stimuli. Sensory mechanisms for transducing pheromones and odorants are believed to be quite dissimilar, as will be discussed next. This chapter will focus mainly on olfactory transduction, which has been studied much more extensively to date (see reviews by Frings, 2001; Ache and Young, 2005; Munger et al., 2009; DeMaria and Ngai, 2010).

IVB. Nature of Olfactory Stimuli

Odorants for land-dwelling animals are volatile compounds, typically diluted in large volumes of air. Odorants are only poorly soluble in aqueous solutions, including the mucus layer overlaying the olfactory epithelium. ORNs and VNO sensory neurons are much more sensitive to chemical stimulation than are taste receptor cells. Odorants and pheromones in the range of subnanomolar to micromolar concentrations can be detected. Many animals have a keen sense of smell; for example, dogs have been reported to detect as few as 5000 to 10 000 molecules/cm^3. Reports of extreme chemosensitivity, such as the ability of certain species (e.g. moths, dogs and

[3] This raises the intriguing possibility that certain agents, such as drugs or toxins, can be taken up by ORNs and transported along their axons directly into the brain. That is, the olfactory epithelium represents a "window" into the brain that might be exploited for pharmaceutical therapies or may be at the root of certain central nervous system disorders that are linked to environmental contaminants.

[4] In humans, the VNO consists of shallow bilateral pits located in the nasal cavity, anterior to the olfactory epithelium. Arguably, the VNO may only be a vestigial structure in humans. If humans sense pheromones, these stimuli may be transduced by sensory cells lying in the olfactory epithelium. Meredith (2001) summarizes evidence for and against the existence of human vomeronasal organs.

sharks) to detect single molecules of pheromones or odorants may be overestimates based on theoretical calculations that assume uniform spread of the odors in air or water. The actual dispersion of odorant and pheromone molecules is more often in the form of irregular plumes rather than uniform diffusion. Within the plume, concentrations are much higher than predicted by simple diffusion. Nonetheless, olfactory and pheromone receptors are notoriously responsive to chemical stimuli. The acute sensitivity of these receptor neurons might be an optimization of the sensory neuron to the low concentrations of biologically important chemical signals that must be detected.

Volatile odoriferous compounds partition into the mucus layer covering the olfactory epithelial surface. A specialized carrier or transport protein has been identified in the mucus layer-odorant binding protein (OBP). It has been hypothesized that OBP facilitates the partitioning of odorants into the mucus. According to this hypothesis, odorants bound to OBP are carried and presented to the chemoreceptive surface on the cilia that protrude up into the mucus layer.

The low concentration of odorants imposes certain constraints on the possible receptor mechanisms for olfaction (pheromone transduction in VNO sensory neurons will be discussed later). Namely, amplifying second messenger cascades are involved in transduction. Additionally, ORNs have a substantial input resistance (up to 30 GΩ). Consequently, tiny receptor currents — some investigators believe even those generated by stimulation by a single odorant molecule — can produce measureable voltage changes in an olfactory receptor neuron. If sufficiently large, these currents depolarize an ORN to threshold and generate action potentials. Intracellular second messenger cascades and a high input resistance combine to increase the sensitivity of olfactory receptor neurons.

IVC. Initiation of Olfactory Receptor Potentials

Olfactory transduction involves ligand (odorant) binding to specific receptors localized in the ciliary membrane of olfactory receptor neurons.

IVC1. Odorant Receptors (ORs)

The transduction pathways that have been characterized for olfaction to date involve GPCRs that are integral proteins of the ciliary membrane. When stimulated by an odor, odorant receptors (ORs) activate an olfactory-specific G_α protein, G_{olf}, and increase cAMP inside the cilia (see below). Volatile compounds, being lipophilic, may also partition into the membrane. However, this is not believed to contribute prominently to olfactory transduction.

GPCRs for odorants have been cloned and sequenced (Buck and Axel, 1991; Reed, 1992; Raming et al., 1993). ORs are members of a huge GPCR superfamily. In rodents there are ≈1400 OR genes located in clusters throughout the genome, ≈1000 of which are functional (Zhang et al., 2004). In humans, there are perhaps 855 OR genes but only ≈400 are functional, the rest being pseudogenes (Hasin-Brumshtein et al., 2009). The total number of OR genes represents a sizeable fraction of the genome (the human genome having ≈30 000 genes). From the large number of possible OR genes, a given olfactory receptor neuron expresses but a single OR throughout its lifespan. How a receptor neuron selects which OR to express is a topic of intense research.

IVC2. G Proteins in Olfactory Receptor Neurons

Odorant binding to receptors triggers second messenger pathways, beginning with activation of G proteins. The canonical odorant transduction pathway involves G_{olf}, a type of G_s protein that is enriched in olfactory epithelium. Ligand binding to ORs liberates G_{olf}, which then activates type III adenylyl cyclase, also expressed selectively in olfactory epithelium, resulting in the formation of cAMP (Pace et al., 1985; Bakalyar & Reed, 1990). It has long been known that exposing isolated olfactory cilia to low concentrations of certain fruity, floral or herbaceous odors results in an increase in intracellular cAMP. These observations were key in establishing adenylyl cyclase in the intracellular pathway for signal transduction in olfaction, especially for what are considered pleasant odors. A less well-established G-protein pathway, believed by some to act as an intermediary for signaling in putrid and unpleasant odors, is discussed later.

IVC3. Cyclic AMP and Cyclic Nucleotide-Gated Channels in Olfactory Receptor Neurons

The ion channels that ultimately are activated by odorant binding and that produce a depolarizing flow of current into olfactory receptor neurons are triggered open by cAMP. Intracellular cAMP binds to and rapidly opens these nonselective cation (Na^+, K^+, Ca^{2+}) channels, named cyclic nucleotide-gated (CNG) channels. CNG channels are distributed along the ciliary membrane of the olfactory receptor neurons. CNG channels were first demonstrated by applying cAMP and cGMP to isolated patches of membrane removed from olfactory cilia (Nakamura and Gold, 1987) or to isolated olfactory receptor neurons (Firestein et al., 1991). CNG channels have little or no voltage dependence and, under physiological conditions (i.e. in the presence of extracellular Ca^{2+} and Mg^{2+}), have a small conductance, ≈100 fS. Inward depolarizing current (Fig. 39.6A) is carried principally by Ca^{2+} and Na^+.

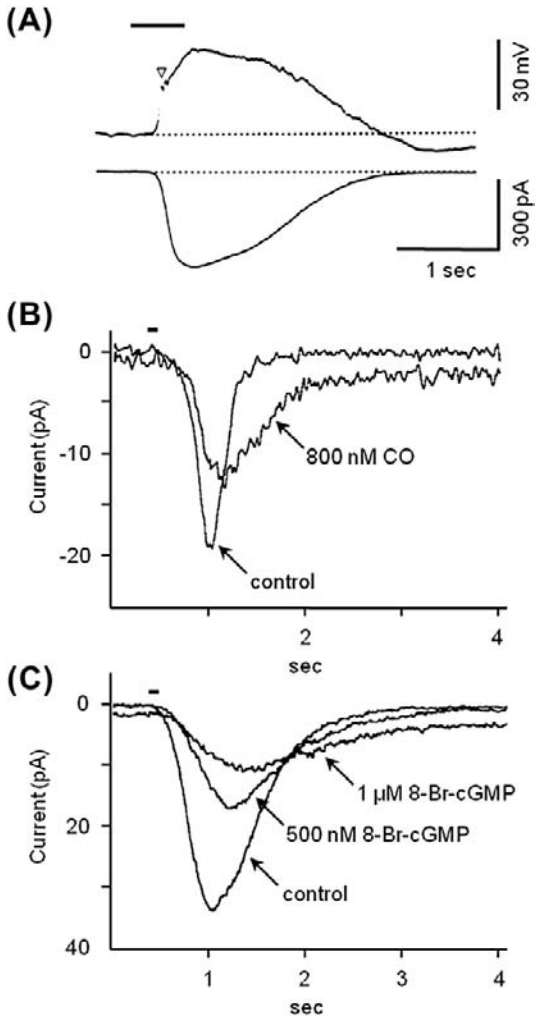

FIGURE 39.6 Patch-clamp recordings from olfactory receptor neurons. (A) Traces show the depolarizing receptor potential (top) and receptor current (bottom) elicited by applying an odorant (10 mM n-amyl acetate) to the olfactory cilia of isolated newt olfactory receptor neurons (bar above trace). Traces are from two different cells *(modified from Kurahashi, 1989)*. (B) Inhibitory effects of carbon monoxide, CO and (C) of 8-Br-cGMP on receptor currents in salamander olfactory receptor neurons after brief applications of an odorant (100 pM cineole, bar above traces). CO stimulates the formation of cGMP during odorant stimulation, which ultimately decreases odor responses and may underlie long-lasting olfactory adaptation, *(modified from Leinders-Zufall et al., 1996)*.

CNG channels from olfactory receptor neurons have been cloned and sequenced (Dhallan et al., 1990). Olfactory CNG channels are quite similar to CNG channels found in photoreceptors, though they differ in their sensitivity to cyclic nucleotides. CNG channels in olfactory receptor neurons respond to cAMP and cGMP alike, with cGMP being somewhat more potent. In contrast, cAMP is far less effective than cGMP in gating open photoreceptor CNG channels. It is an enigma that olfactory CNG channels are more sensitive to cGMP than cAMP because odorant stimulation is believed principally to elevate cAMP. A possible role for an indirect elevation of cGMP in olfactory adaptation (discussed later) may resolve this puzzle. Details of CNG channels are given in Chapter 35.

Calcium ion influx is a key component of the odorant-evoked current through olfactory CNG channels. The influx of Ca^{2+} has several important consequences in addition to supplying inward (depolarizing) current. First, Ca^{2+} influx activates a Ca^{2+}-dependent Cl^- conductance in the olfactory cilia[5]. This results in an outflow of Cl^-, thereby producing an inward (depolarizing) current[6]. Inward current through the Ca^{2+}-activated Cl^- channels (i.e. efflux of Cl^-) amplifies the ongoing inward current (Na^+ and Ca^{2+} influx) through CNG channels. Indeed, in mouse olfactory receptor neurons, the Ca^{2+}-activated Cl^- current is even greater than the initial Na^+ and Ca^{2+} current through CNG channels and can constitute up to 90% of the total inward current generated during odorant stimulation (Boccaccio and Menini, 2007). The combined action of the cAMP-gated cation channels and Ca^{2+}-dependent Cl^--channels may exist to ensure a depolarizing receptor current even in the face of fluctuating extracellular (mucosal) cation concentrations[7]. Figure 39.7 summarizes this olfactory transduction pathway.

Ca^{2+} influx through CNG channels during odorant stimulation also exerts negative feedback onto the CNG channel itself, acting as a brake to retard further activity. Lastly, Ca^{2+} regulates the activity of a number of the enzymes involved in the second messenger cascades in olfactory signal transduction. These actions of Ca^{2+} are particularly important for signal adaptation (discussed later).

[5] Initially, this conductance was believed to be generated by the bestrophin-2 (Best2) channels that are present in olfactory cilia. However, olfactory sensory neurons from mutant mice lacking Best2 channels show normal Ca^{2+}-activated Cl^- current (Pifferi et al., 2009), dispelling the notion that Best2 channels underlie this amplifying inward current.

[6] Olfactory cilia are suspended in a mucus that has a Cl^- concentration of about 55 mM. Cl^- concentration inside the apical tips of olfactory receptor neurons appears to be maintained at a remarkably high level ($\approx$50 mM, Kaneko et al., 2004). This ratio of $[Cl]_o/[Cl]_i$ yields an $\approx$0 mV Cl^--equilibrium potential across the apical tips and explains why opening Cl^- channels produces a Cl^- efflux (i.e. inward, depolarizing current).

[7] Activating the Ca^{2+}-dependent anion conductance in gustatory sensory cells results in the opposite effect than at the cilia of olfactory receptor neurons. Namely, in taste bud cells this conductance produces an influx of Cl^- (i.e. a repolarizing, outward current). This is because the basolateral membrane of taste cells – where the Cl^- conductance channels are situated – is exposed to interstitial fluid. Furthermore, $[Cl^-]_i$ in taste cells is believed to be low. Consequently, in taste cells, the equilibrium potential for Cl^- is likely to be near the resting potential. Opening Cl^- channels when the cell is depolarized will allow Cl^- to enter the taste cell and repolarize the membrane.

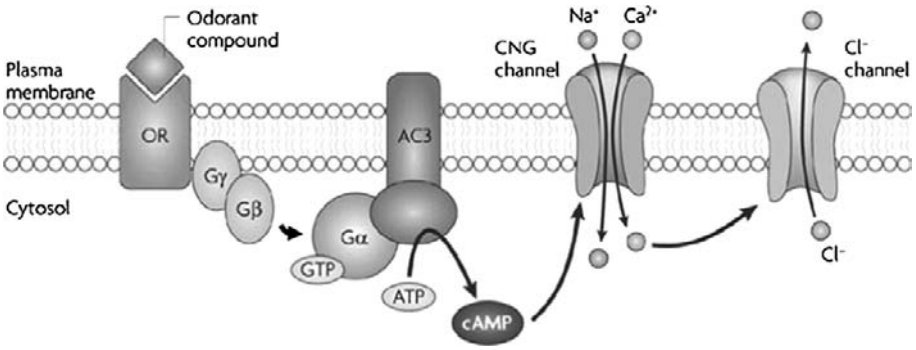

FIGURE 39.7 The canonical odorant transduction pathway. Binding of odorant compounds to an odorant receptor (OR far left) initiates a transduction cascade involving a G protein and activation of adenylate cyclase 3 (AC3) which, in turn, generates the second messenger cyclic AMP. cAMP binds to a cyclic nucleotide-gated (CNG) channel and results in the influx of cations (Na^+ and Ca^{2+}) which depolarize the cell membrane. Ca^{2+} also activates a Ca^{2+}-dependent Cl^- channel. Olfactory sensory neurons (OSNs) maintain a high intracellular Cl^- concentration, such that this channel supports an efflux of negatively charged Cl^-, producing a further depolarization of the cell membrane, *(modified from Zou et al., 2009)*.

IVC4. TAAR Receptors

Another class of receptors found in olfactory sensory neurons and distinct from the OR superfamily was discovered in 2006 – trace amine-associated receptors (TAARs) (Liberles and Buck, 2006). These GPCRs are found in a small population of olfactory epithelial receptor neurons that do not express ORs. TAAR receptors comprise a much smaller family of GPCRs than ORs. Of the 15 TAAR receptor genes (mouse), at least 14 are expressed in ORNs (Liberles, 2009). In humans, there are six TAAR receptor genes (Fleischer et al., 2009). Ligands for TAARs are still being identified. In rodents, where they have been studied best, TAARs are stimulated by volatile amines, many of which are found in urine. This origin for TAAR ligands suggests that TAARs may function to detect social cues, akin to pheromones. Transduction mechanisms for olfactory TAARs are not known, though in rodent olfactory receptor neurons TAARs are co-expressed with G_{olf} and in heterologous expression systems, stimulating TAARs increases cAMP. These data suggest a downstream pathway for TAARs similar to that for ORs.

IVC5. IP_3 in Olfactory Receptor Neurons

There is suggestive evidence that a second messenger cascade other than the canonical pathway discussed above is activated in olfactory epithelial cells (reviewed in Ache, 2010). Albeit existence of this alternative pathway is controversial in mammals, there is little doubt that it exists in invertebrates. This alternative pathway may be triggered by a different set of odorants than those that are transduced by the canonical pathway involving G_{olf}, adenylyl cyclase and cAMP. The main impetus to search for alternative signal transduction pathways stems from observations that certain odorants stimulate the rapid generation of inositol trisphosphate (IP_3) in olfactory epithelium. According to this hypothesis, odorant receptors couple to $G_{\alpha q}/G_{\alpha 11}$-like proteins, quite different from G_{olf}. These G proteins are believed to activate membrane-bound enzyme phospholipase C (PLC). PLC hydrolyzes a phospholipid, phosphatidyl inositol 4,5-bisphosphate, in the plasma membrane. The resultant by-products, IP_3 and diacylglycerol (DAG), are powerful bioactive compounds. IP_3 in particular activates specific IP_3 receptors on internal Ca^{2+} stores and triggers Ca^{2+} release into the cytoplasm. Recently, IP_3 receptors have been localized only to a small population of microvillar cells within the olfactory epithelium (Hegg et al., 2010). These cells lack olfactory cilia and axons. They appear to be innervated and may represent a second, parallel chemosensory cell alongside olfactory receptor neurons. Little is currently understood about their function and the significance of an IP_3 pathway in mammalian olfaction remains unresolved.

IVC6. Transduction in the Vomeronasal Organ (VNO)

Transduction pathways in VNO sensory neurons for pheromones and other chemical stimuli are presently under investigation. It appears that VNO sensory neurons utilize distinctive GPCRs, a different set of G proteins and different downstream effectors than ORNs. For example, VNO sensory neurons express two different families of GPCRs, V1Rs and V2Rs, that are unrelated to odorant receptors (Dulac and Axel, 1995). In the mouse, there are ≈240 functional V1R and 60 functional V2R genes; in humans there are only three to five functional V1R genes and no functional V2R genes (Rodriguez and Mombaerts, 2002; Shi and Zhang, 2007; Young et al., 2010). Parenthetically, because there is only a vestigial, if any, vomeronasal organ in adults, V1R in humans must be expressed elsewhere, such as in the olfactory epithelium. In non-human mammals, the two families of VNO receptors are expressed in anatomically separate regions of the VNO sensory epithelium and they send their axons to different regions of the olfactory bulb. Furthermore, V1Rs versus V2Rs respond to different types of stimuli and may mediate different behavioral responses. For instance, V1Rs are found in the more superficial (apical) layer of VNO sensory cells and respond to volatile compounds. In contrast, V2Rs are expressed in the more

basal layer of the VNO epithelium and bind small water-soluble peptides. The behavioral consequences of activating V1Rs and V2Rs are still being scrutinized. To date, roles for V1Rs and V2Rs in gender discrimination, territoriality, aggression, social dominance and male/female sexual interactions have been implicated in non-human animals and perhaps in humans as well (Gelstein et al., 2011).

V1Rs and V2Rs initiate a downstream signaling pathway that markedly differs from that triggered by ORs in the olfactory epithelium. Instead of cAMP/CNG (or IP_3/Ca^{2+} pathways), V1Rs and V2Rs activate a Ca-permeable ion channel, TRPC2 (*c*anonical *t*ransient *r*eceptor *p*otential channel 2, formerly called TRP2) that is highly expressed in vomeronasal sensory neurons[8] (Liman et al., 1999). The complete signaling pathway for V1Rs/V2Rs and TRPC2 awaits elucidation. Indications to date are that activation of the vomeronasal V1 and V2 GPCRs leads to the formation of diacylglycerol (DAG) which stimulates TRPC2 and allows Ca^{2+} influx, thereby depolarizing the sensory cells and initiating action potentials.

In addition to the V1Rs and V2Rs, another small family of GPCRs was recently identified in vomeronasal sensory neurons − formyl peptide receptors (FPRs) (Riviere et al., 2009; Liberles et al., 2009). Five members of this family of receptors were identified. Interestingly, FPRs are also expressed on immune cells where they bind formyl peptides and lipids from microorganisms and signal the presence of pathogens. Expression of these FPR-like receptors in the vomeronasal organ may explain the ability of animals, especially rodents, to detect stimuli in urine and bodily secretions and recognize diseased conspecifics.

IVD. Termination of Olfactory Signals

Olfactory receptor neuron excitation is terminated by a number of mechanisms. An obvious one is the unbinding and disappearance of the odorant from the chemoreceptive surface of the cilia, perhaps aided by odorant binding protein (OBP). The removal of odorants is complicated by the lipophilic nature of most odoriferous compounds; they will tend to partition into the plasma membrane and thus may linger in the vicinity of the receptors. Although the details are only now unfolding, one proposed mechanism for ridding the chemosensitive surfaces of odorants is the enzymatic modification of odorants by broad-spectrum biotransformation enzymes found in the mucus. These enzymes are similar to the detoxification enzymes found in the liver. Olfactory epithelial supporting cells adjacent to receptor neurons contain high concentrations of the detoxifying enzymes glutathione transferase, cytochrome P-450 and UDP gluconosyl transferase (Lazard et al., 1991). Indeed, the lipophilic nature of many odorants and their absorption into the sensory epithelium may necessitate the existence of such degradative mechanisms. Enzymatic biotransformation of volatiles in the mucosal layer occurs very quickly. In addition to terminating the actions of inhaled odorants, enzymatic biotransformation can yield olfactory stimuli that differ chemically and produce smells distinct from what had initially been present.

Besides disappearance of the odorant, sensory adaptation is also key in terminating olfactory signals. Adaptation in olfactory receptor neurons is explained by multiple mechanisms, many of which involve Ca^{2+}. First, short-term adaptive mechanisms are believed to be set in motion by the Ca^{2+} that enters through CNG channels during odorant stimulation. Ca^{2+}, acting via calmodulin inhibits CNG channels themselves (Chen & Yau, 1994; Kurahashi and Menini, 1997), a direct negative feedback on the olfactory signal. That is, an increase in Ca^{2+} in the ciliary cytosol will depress odorant responses by shutting down effector (CNG) channels.

Second, heightened intracellular Ca^{2+} also depresses the cascade of enzymes that are triggered during olfactory transduction. At high (μM) concentrations, Ca^{2+} inhibits adenylyl cyclase, thereby reducing the continued generation of cAMP during maintained stimulation. In olfactory receptor neurons, this inhibition appears to be mediated by Ca^{2+}-calmodulin-induced phosphorylation via the enzyme Ca^{2+}-calmodulin-dependent protein kinase II (CaMKII). However, at nM to pM concentrations, Ca^{2+} has the opposite effect, namely, it stimulates adenylyl cyclase. Consequently, the net effect of Ca^{2+} influx on adenylyl cyclase activity during odor stimulation is concentration dependent.

Additionally, Ca^{2+} influx stimulates phosphodiesterase (PDE), thereby accelerating the degradation of cAMP and reducing the odorant response.

Finally, Ca^{2+} influx activates Ca^{2+}-dependent K^+ channels that initiate an outward, repolarizing current. Counterbalancing this, Ca^{2+} also activates a Cl^- conductance in the olfactory cilia that produces an inward depolarizing current, as described previously.

Thus, the actions of Ca^{2+} are complex. The net effect of Ca^{2+} entry through CNG channels during olfactory stimulation appears to be to reduce the responsiveness of olfactory receptor neurons perhaps as much as 20-fold, moving the stimulus−response relationship to a higher range of odorant concentrations. Longer-lasting adaption to a maintained odor stimulus involves another mechanism. A prolonged adaptation in olfactory receptor neurons, involving an intriguing role for the novel gaseous neurotransmitter carbon monoxide (CO), has been proposed (Leinders-Zufall et al., 1996) (see Fig. 39.6 B,C). CO, like the related neurotransmitter nitric oxide (NO), is a highly-diffusible substance and is generated during olfactory

[8] In humans, TRPC2 is a pseudogene and thus no functional channels are expressed. This fact, combined with the severely limited number of V1Rs and absence of V2Rs in humans, underscores the lack of definitive evidence for human pheromones (but see Gelstein et al., 2011).

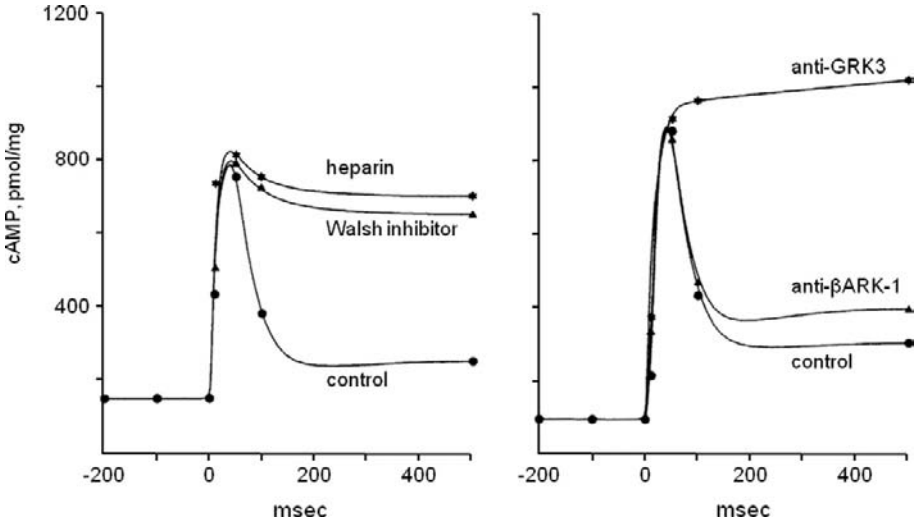

FIGURE 39.8 Desensitization of odorant receptors during prolonged stimulation. Olfactory second messenger signaling is quenched by phosphorylation cascades. Left, inhibiting protein kinase activity with Walsh inhibitor or heparin markedly prolongs increases in olfactory cAMP induced by odorant stimulation in cilia preparations from the rat. (●) odorant alone (1 μM citralva); (▲) odorant stimulation of cilia pretreated with Walsh inhibitor (3.8 μM); (∗) odorant stimulation of cilia pretreated with heparin (1 μM). Right, pretreating the cilia preparation with antibodies to GRK3 specifically prevents desensitization of odorant receptors and prolongs their activation (measured here as an increase in cAMP). (●) odorant alone (1 μM citralva); (▲) odorant stimulation of cilia pretreated with anti-βARK-1 antibodies (diluted 1:5000); (∗) odorant stimulation of cilia pretreated with anti-GRK3 antibodies (diluted 1:5000); abscissae, time in ms, *(modified from Schleicher et al., 1993).*

transduction via a mechanism that is not yet well characterized. CO, in turn, activates soluble guanylyl cyclase (sGC) and leads to the production of cGMP in the stimulated olfactory receptor neuron as well as in surrounding cells. As discussed previously, cGMP is a very effective ligand for olfactory CNG channels. At first glance, generating cGMP might seem contrary to adaptation and represent positive feedback during odorant stimulation. However, activation of olfactory CNG channels via the CO pathway produces only a low-level, subthreshold inward current. This maintains a persistent trickle of Ca^{2+} into the olfactory receptor neurons, chronically reducing CNG channel activity. The rapid transient influx of Ca^{2+} through CNG channels (the immediate effect of odorant stimulation), combined with a sustained low-level influx via cGMP activation of these channels (the CO pathway), overall leads to a long-lasting (minutes) reduction of the sensitivity of olfactory receptor neurons after the initial excitation.[9]

In addition to these sensory adaptation mechanisms, direct desensitization of ORs following odorant stimulation also plays a key role in terminating odorant responses (Schleicher et al., 1993). cAMP produced by odor stimulation opens CNG cation channels and secondarily activates protein kinase A (PKA). PKA and a specialized G-protein-coupled receptor kinase, GRK3[10], phosphorylate odorant-bond receptors (Fig. 39.8). These protein kinases, together with regulatory proteins, such as arrestin, render the odorant receptor inactive and quench the subsequent transduction cascade. Receptors are resensitized by the action of phosphatases. Thus, a cycle of phosphorylation/dephosphorylation controls the active state of odorant receptors and, ultimately, the responsiveness of olfactory receptor neurons.

Collectively, short-term adaptation, long-term adaptation and receptor desensitization act to shape and terminate olfactory responses to prolonged odor stimulation. Sensory adaptation in many sensory systems, including olfaction, serves a dual purpose. First, over time, a steady stimulus ceases to excite responses, i.e. the sensory organ adapts to the stimulus. In this sense, adaptation tends to accentuate signals from stimuli that fluctuate and emphasizes the dynamic aspects of sensory stimuli. Second, adaptation reduces responsivity to increasingly intense stimuli. This prevents the output from the sensory organs from becoming saturated by only moderately intense stimulus intensities while, at the same time, preserving the ability of the organ to respond well to very weak stimuli. That is, adaptation greatly extends the dynamic range of stimulus intensities over which a sensory organ can respond.

[9] Previously, it was believed that NO played this role in olfactory adaptation. However, data utilizing blockers of CO synthesis now implicate CO, not NO, as the diffusible intra- and intercellular controller of CNG channel activity in olfactory receptor neurons.

[10] GRK3 was formerly named β-adrenergic receptor kinase 2, or βARK-2.

BIBLIOGRAPHY

Ache, B. W. (2010). Odorant-specific modes of signaling in mammalian olfaction. *Chem Senses, 35*, 533–539.

Ache, B. W., & Young, J. M. (2005). Olfaction: diverse species, conserved principles. *Neuron, 48*, 417–430.

Bakalyar, H., & Reed, R. R. (1990). Identification of a specialized adenylyl cyclase that may mediate odorant detection. *Science, 250*, 1403–1406.

Behrens, M., Foerster, S., Staehler, F., Raguse, J. D., & Meyerhof, W. (2007). Gustatory expression pattern of the human TAS2R bitter

receptor gene family reveals a heterogenous population of bitter responsive taste receptor cells. *J Neurosci, 27*, 12630–12640.

Bigiani, A., Cristiani, R., Fieni, F., Ghiaroni, V., Bagnoli, P., & Pietra, P. (2002). Postnatal development of membrane excitability in taste cells of the mouse vallate papilla. *J Neurosci, 22*, 493–504.

Boccaccio, A., & Menini, A. (2007). Temporal development of cyclic nucleotide-gated and Ca^{2+} -activated Cl^- currents in isolated mouse olfactory sensory neurons. *J Neurophysiol, 98*, 153–160.

Bradley, R. M. (1973). Electrophysiological investigations of intravascular taste using perfused rat tongue. *Am J Physiol, 224*, 300–304.

Buck, L., & Axel, R. (1991). A novel multigene family may encode odorant receptors: a molecular basis for odor recognition. *Cell, 65*, 175–187.

Chandrashekar, J., Hoon, M. A., Ryba, N. J., & Zuker, C. S. (2006). The receptors and cells for mammalian taste. *Nature, 444*, 288–294.

Chandrashekar, J., Kuhn, C., Oka, Y., et al. (2010). The cells and peripheral representation of sodium taste in mice. *Nature, 464*, 297–301.

Chandrashekar, J., Mueller, K. L., Hoon, M. A., et al. (2000). T2Rs function as bitter taste receptors. *Cell, 100*, 703–711.

Chang, R. B., Waters, H., & Liman, E. R. (2010). A proton current drives action potentials in genetically identified sour taste cells. *Proc Natl Acad Sci USA, 107*, 22320–22325.

Chaudhari, N., & Roper, S. D. (2010). The cell biology of taste. *J Cell Biol, 190*, 285–296.

Chen, T. Y., & Yau, K. W. (1994). Direct modulation by Ca^{2+}-calmodulin of cyclic nucleotide-activated channel of rat olfactory receptor neurons. *Nature, 368*, 545–548.

Clapp, T. R., Trubey, K. R., Vandenbeuch, A., et al. (2008). Tonic activity of Galpha-gustducin regulates taste cell responsivity. *FEBS Lett, 582*, 3783–3787.

DeMaria, S., & Ngai, J. (2010). The cell biology of smell. *J Cell Biol, 191*, 443–452.

Dhallan, R. S., Yau, K. W., Schrader, K. A., & Reed, R. R. (1990). Primary structure and functional expression of a cyclic nucleotide-activated channel from olfactory neurons. *Nature, 347*, 184–187.

Dulac, C., & Axel, R. (1995). A novel family of genes encoding putative pheromone receptors in mammals. *Cell, 83*, 195–206.

Firestein, S., Darrow, B., & Shepherd, G. M. (1991). Activation of the sensory current in salamander olfactory receptor neurons depends on a G protein-mediated cAMP second messenger system. *Neuron, 6*, 825–835.

Fleischer, J., Breer, H., & Strotmann, J. (2009). Mammalian olfactory receptors. *Front Cell Neurosci, 3*, 9.

Frings, S. (2001). Chemoelectrical signal transduction in olfactory sensory neurons of air-breathing vertebrates. *Cell Mol Life Sci, 58*, 510–519.

Gelstein., S., Yeshurun, Y., Rozenkrantz, L., et al. (2011). Human tears contain a chemosignal. *Science, 331*, 226–230.

Ghiaroni, V., Fieni, F., Tirindelli, R., Pietra, P., & Bigiani, A. (2003). Ion conductances in supporting cells isolated from the mouse vomeronasal organ. *J Neurophysiol, 89*, 118–127.

Gilbertson, T. A., Boughter, J. D., Jr., Zhang, H., & Smith, D. V. (2001). Distribution of gustatory sensitivities in rat taste cells: whole-cell responses to apical chemical stimulation. *J Neurosci, 21*, 4931–4941.

Gilbertson, T. A., Roper, S. D., & Kinnamon, S. C. (1993). Proton currents through amiloride-sensitive Na+ channels in isolated hamster taste cells: enhancement by vasopressin and cAMP. *Neuron, 10*, 931–942.

Graziadei, P. P. C., & Monti Graziadei, G. A. (1978). Continuous nerve cell renewal in the olfactory system. In M. Jacobson (Ed.), *Handbook of Sensory Physiology* (pp. 55–82). New York: Springer-Verlag.

Hänig, D. P. (1901). Zur Psychophysik des Geschmackssinnes. *Philosophische Studien, 17*, 576–623.

Hasin-Brumshtein, Y., Lancet, D., & Olender, T. (2009). Human olfaction: from genomic variation to phenotypic diversity. *Trends Genet, 25*, 178–184.

Heck, G. L., Mierson, S., & DeSimone, J. A. (1984). Salt taste transduction occurs through an amiloride-sensitive sodium transport pathway. *Science, 223*, 403–405.

Hegg, C. C., Jia, C., Chick, W. S., Restrepo, D., & Hansen, A. (2010). Microvillous cells expressing IP3 receptor type 3 in the olfactory epithelium of mice. *Eur J Neurosci, 32*, 1632–1645.

Herness, M. S., & Sun, X. D. (1999). Characterization of chloride currents and their noradrenergic modulation in rat taste receptor cells. *J Neurophysiol, 82*, 260–271.

Herness, S., & Zhao, F. L. (2009). The neuropeptides CCK and NPY and the changing view of cell-to-cell communication in the taste bud. *Physiol Behav, 97*, 581–591.

Huang, Y. A., Maruyama, Y., Stimac, R., & Roper, S. D. (2008). Presynaptic (Type III) cells in mouse taste buds sense sour (acid) taste. *J Physiol, 586*, 2903–2912.

Huang, Y. J., Maruyama, Y., Dvoryanchikov, G., Pereira, E., Chaudhari, N., & Roper, S. D. (2007). The role of pannexin 1 hemichannels in ATP release and cell-cell communication in mouse taste buds. *Proc Natl Acad Sci USA, 104*, 6436–6441.

Kaneko, H., Putzier, I., Frings, S., Kaupp, U. B., & Gensch, T. (2004). Chloride accumulation in mammalian olfactory sensory neurons. *J Neurosci, 24*, 7931–7938.

Kleene, S. J., & Gesteland, R. C. (1981). Dissociation of frog olfactory epithelium with N-ethylmaleimide. *Brain Res, 229*, 536–540.

Kretz, O., Barbry, P., Bock, R., & Lindemann, B. (1999). Differential expression of RNA and protein of the three pore-forming subunits of the amiloride-sensitive epithelial sodium channel in taste buds of the rat. *J Histochem Cytochem, 47*, 51–64.

Kurahashi, T. (1989). Activation by odorants of cation-selective conductance in the olfactory receptor cell isolated from the newt. *J Physiol, 419*, 177–192.

Kurahashi, T., & Menini, A. (1997). Mechanism of odorant adaptation in the olfactory receptor cell. *Nature, 385*, 725–729.

Lazard, D., Zupko, K., Poria, Y., et al. (1991). Odorant signal termination by olfactory UDP glucuronosyl transferase. *Nature, 349*, 790–793.

Leinders-Zufall, T., Shepherd, G. M., & Zufall, F. (1996). Modulation by cyclic GMP of the odour sensitivity of vertebrate olfactory receptor cells. *Proc Biol Sci, 263*, 803–811.

Liberles, S. D. (2009). Trace amine-associated receptors are olfactory receptors in vertebrates. *Ann NY Acad Sci, 1170*, 168–172.

Liberles, S. D., & Buck, L. B. (2006). A second class of chemosensory receptors in the olfactory epithelium. *Nature, 442*, 645–650.

Liberles, S. D., Horowitz, L. F., Kuang, D., et al. (2009). Formyl peptide receptors are candidate chemosensory receptors in the vomeronasal organ. *Proc Natl Acad Sci USA, 106*, 9842–9847.

Liman, E. R., Corey, D. P., & Dulac, C. (1999). TRP2: a candidate transduction channel for mammalian pheromone sensory signaling. *Proc Natl Acad Sci USA, 96*, 5791–5796.

Lin, W., Finger, T. E., Rossier, B. C., & Kinnamon, S. C. (1999). Epithelial Na+ channel subunits in rat taste cells: localization and regulation by aldosterone. *J Comp Neurol, 405*, 406–420.

Lindemann, B. (1999). Receptor seeks ligand: on the way to cloning the molecular receptors for sweet and bitter taste. *Nat Med, 5*, 381–382.

Lindemann, B., Barbry, P., Kretz, O., & Bock, R. (1998). Occurrence of ENaC subunit mRNA and immunocytochemistry of the channel subunits in taste buds of the rat vallate papilla. *Ann NY Acad Sci, 855*, 116–127.

Lyall, V., Alam, R. I., Phan, D. Q., et al. (2001). Decrease in rat taste receptor cell intracellular pH is the proximate stimulus in sour taste transduction. *Am J Physiol Cell Physiol, 281*, C1005–C1013.

Mackay-Sim, A., & Kittel, P. (1991a). Cell dynamics in the adult mouse olfactory epithelium: a quantitative autoradiographic study. *J Neurosci, 11*, 979–984.

Mackay-Sim, A., & Kittel, P. W. (1991b). On the life span of olfactory receptor neurons. *Eur J Neurosci, 3*, 209–215.

Max, M., Shanker, Y. G., Huang, L., et al. (2001). Tas1r3, encoding a new candidate taste receptor, is allelic to the sweet responsiveness locus Sac. *Nat Genet, 28*, 58–63.

McLaughlin, S. K., McKinnon, P. J., & Margolskee, R. F. (1992). Gustducin is a taste-cell-specific G protein closely related to the transducins. *Nature, 357*, 563–569.

Meredith, M. (2001). Human vomeronasal organ function: a critical review of best and worst cases. *Chem Senses, 26*, 433–445.

Munger, S. D., Leinders-Zufall, T., & Zufall, F. (2009). Subsystem organization of the mammalian sense of smell. *Annu Rev Physiol, 71*, 115–140.

Nakamura, T., & Gold, G. H. (1987). A cyclic nucleotide-gated conductance in olfactory receptor cilia. *Nature, 325*, 442–444.

Nelson, G., Chandrashekar, J., Hoon, M. A., et al. (2002). An amino-acid taste receptor. *Nature, 416*, 199–202.

Nelson, G., Hoon, M. A., Chandrashekar, J., Zhang, Y., Ryba, N. J., & Zuker, C. S. (2001). Mammalian sweet taste receptors. *Cell, 106*, 381–390.

Ossebaard, C. A., & Smith, D. V. (1996). Amiloride suppresses the sourness of NaCl and LiCl. *Physiol Behav, 60*, 1317–1322.

Pace, U., Hanski, E., Salomon, Y., & Lancet, D. (1985). Odorant-sensitive adenylate cyclase may mediate olfactory reception. *Nature, 316*, 255–258.

Pifferi, S., Dibattista, M., Sagheddu, C., et al. (2009). Calcium-activated chloride currents in olfactory sensory neurons from mice lacking bestrophin-2. *J Physiol, 587*, 4265–4279.

Raming, K., Krieger, J., Strotmann, J., et al. (1993). Cloning and expression of odorant receptors. *Nature, 361*, 353–356.

Reed, R. R. (1992). Signaling pathways in odorant detection. *Neuron, 8*, 205–209.

Richter, T. A., Caicedo, A., & Roper, S. D. (2003). Sour taste stimuli evoke Ca2+ and pH responses in mouse taste cells. *J Physiol, 547*, 475–483.

Richter, T. A., Dvoryanchikov, G. A., Chaudhari, N., & Roper, S. D. (2004). Acid-sensitive two-pore domain potassium (K2P) channels in mouse taste buds. *J Neurophysiol, 92*, 1928–1936.

Riviere, S., Challet, L., Fluegge, D., Spehr, M., & Rodriguez, I. (2009). Formyl peptide receptor-like proteins are a novel family of vomeronasal chemosensors. *Nature, 459*, 574–577.

Rodriguez, I., & Mombaerts, P. (2002). Novel human vomeronasal receptor-like genes reveal species-specific families. *Curr Biol, 12*, R409–R411.

Romanov, R. A., Rogachevskaja, O. A., Bystrova, M. F., Jiang, P., Margolskee, R. F., & Kolesnikov, S. S. (2007). Afferent neurotransmission mediated by hemichannels in mammalian taste cells. *EMBO J, 26*, 657–667.

Roper, S. (1983). Regenerative impulses in taste cells. *Science, 220*, 1311–1312.

Roper, S. D. (1992). The microphysiology of peripheral taste organs. *J Neurosci, 12*, 1127–1134.

Roper, S. D. (2007). Signal transduction and information processing in mammalian taste buds. *Pflügers Arch, 454*, 759–776.

Sainz, E., Korley, J. N., Battey, J. F., & Sullivan, S. L. (2001). Identification of a novel member of the T1R family of putative taste receptors. *J Neurochem, 77*, 896–903.

Schleicher, S., Boekhoff, I., Arriza, J., Lefkowitz, R. J., & Breer, H. (1993). A beta-adrenergic receptor kinase-like enzyme is involved in olfactory signal termination. *Proc Natl Acad Sci USA, 90*, 1420–1424.

Shi, P., & Zhang, J. (2007). Comparative genomic analysis identifies an evolutionary shift of vomeronasal receptor gene repertoires in the vertebrate transition from water to land. *Genome Res, 17*, 166–174.

Smith, D. V., & Margolskee, R. F. (2001). Making sense of taste. *Sci Am, 284*, 32–39.

Sugita, M. (2006). Taste perception and coding in the periphery. *Cell Mol Life Sci, 63*, 2000–2015.

Taylor, R., & Roper, S. (1994). Ca(2+)-dependent Cl conductance in taste cells from Necturus. *J Neurophysiol, 72*, 475–478.

Tomchik, S. M., Berg, S., Kim, J. W., Chaudhari, N., & Roper, S. D. (2007). Breadth of tuning and taste coding in mammalian taste buds. *J Neurosci, 27*, 10840–10848.

Vandenbeuch, A., Clapp, T. R., & Kinnamon, S. C. (2008). Amiloride-sensitive channels in type I fungiform taste cells in mouse. *BMC Neurosci, 9*, 1.

Wang, Y. Y., Chang, R. B., Allgood, S. D., Silver, W. L., & Liman, E. R. (2011). A TRPA1-dependent mechanism for the pungent sensation of weak acids. *J Gen Physiol, 137*, 493–505.

Ye, Q., Heck, G. L., & DeSimone, J. A. (1993). Voltage dependence of the rat chorda tympani response to Na+ salts: implications for the functional organization of taste receptor cells. *J Neurophysiol, 70*, 167–178.

Yoshida, R., Horio, N., Murata, Y., Yasumatsu, K., Shigemura, N., & Ninomiya, Y. (2009a). NaCl responsive taste cells in the mouse fungiform taste buds. *Neuroscience, 159*, 795–803.

Yoshida, R., Miyauchi, A., Yasuo, T., et al. (2009b). Discrimination of taste qualities among mouse fungiform taste bud cells. *J Physiol, 587*, 4425–4439.

Young, J. M., Massa, H. F., Hsu, L., & Trask, B. J. (2010). Extreme variability among mammalian V1R gene families. *Genome Res, 20*, 10–18.

Zhang, X., Rodriguez, I., Mombaerts, P., & Firestein, S. (2004). Odorant and vomeronasal receptor genes in two mouse genome assemblies. *Genomics, 83*, 802–811.

Zou, D. J., Chesler, A., & Firestein, S. (2009). How the olfactory bulb got its glomeruli: a just so story? *Nat Rev Neurosci, 10*, 611–618.

This page intentionally left blank

Chapter 40

Infrared Sensory Organs

Stephen D. Roper and Michael S. Grace

Chapter Outline

I. SUMMARY

Certain snakes, such as pythons and rattlesnakes, utilize infrared radiation as well as visible light to detect prey. Infrared radiation emitted from warm objects is captured mainly by specialized sensory structures in the snake head called pit organs. The anatomy of pit organs is such that a crude image of the infrared-emitting object is cast upon a thin membrane within the organ. This infrared image locally warms the thin tissue which is innervated by heat-sensitive axon terminals of trigeminal sensory ganglion cells. Molecular profiling of snake trigeminal ganglion neurons indicates that a unique variant of the heat-sensitive *t*ransient *r*eceptor *p*otential cation channel, TRPA1, is the heat-transducing protein found in infrared sensory neurons.

II. INTRODUCTION

Infrared radiation is an important and ubiquitous component of the diverse physical environments in which animals live. All warm objects radiate infrared energy. Naturally-occurring infrared sources include terrestrial, atmospheric and astronomical bodies. Animals, especially ectothermic species, use radiant infrared energy to assist in maintaining their body temperature and must avoid excess infrared radiation to avoid overheating. In a few species, infrared radiation is also used in a novel manner – to form spatial images of the environment and to hunt prey. These animals possess specialized infrared-receptive sensory organs, the topic of this chapter.

Infrared-receptive organs occur in both vertebrate and invertebrate animals. Buprestid beetles, including the European fire beetle *Melanophila acuminata*, have specialized infrared receptive organs on the ventral surfaces of their abdomens (Evans, 1964). *Melanophila* and similar beetles congregate in large numbers at forest fire sites to deposit eggs in recently burned wood. They likely use chemoreceptors and mechanoreceptors (to detect wind direction) to guide them to sites of fires, and their infrared detectors to identify potential egg-laying sites of appropriate temperature. The deep-sea shrimp *Rimicaris exoculata* also possesses an elaborate organ capable of detecting 350°C "black smoker" thermal vents in the deep Atlantic Ocean (Pelli and Chamberlain, 1989). Their infrared sensory detection system may help the shrimp maintain close proximity to life-sustaining thermal vents in the deep sea without directly contacting the steep thermocline (350°C to 2°C over a 2–3 cm lateral distance) adjacent to the thermal vent. The common vampire bat (*Desmodus rotundus*) may possess infrared radiation detectors, but its infrared sensory system has been little investigated. Behavioral experiments show that vampire bats can detect infrared radiation as low as 50 $\mu W/cm^2$ and thus should be able to detect mammalian prey at distances of up to 16 cm (also see Campbell et al., 2002). Vampire bats may use their infrared detection system to locate suitable prey.

However, by far the best-studied infrared sensory detectors are those of snakes. As stated previously, ectothermic animals, such as snakes, rely on infrared radiation to regulate their body temperature. In some snakes (Boidae, which include boa constrictors and pythons, and Crotalinae, which include rattlesnakes and water moccasins), infrared radiation is also used for accurate and precise targeting of prey. These

Cell Physiology Sourcebook. DOI: 10.1016/B978-0-12-387738-3.00040-8

snakes preferentially feed on endothermic (warm-blooded) prey. In addition to mediating predatory behavior, the infrared imaging system also mediates defensive behavior (Van Dyke and Grace, 2010). Unlike other infrared-sensing animals, boid and crotaline snakes are the only animals known to form spatial images of their environments using extremely sensitive infrared-receptive organs.

Boid and crotaline snakes are efficient predators. While vision may be useful for some aspects of their predatory behaviors, infrared imaging alone can allow accurate prey targeting. Snakes experimentally blinded by occluding both eyes and snakes born without eyes are capable of accurately placing strikes at mammalian prey (Kardong and Mackessey, 1991). Infrared-imaging snakes can target based upon vision alone but when one eye is occluded, strike-targeting performance is indistinguishable from that of normally sighted snakes (Grace and Woodward, 2001). Moreover, snakes readily strike their prey regardless of visual contrast (black *versus* white mice against a black background) (Grace et al., 2001) and they preferentially target the warm aspect of thermal differentials (Van Dyke and Grace, 2010). Thus, vision and infrared imaging appear to be redundant targeting systems and the infrared imaging system can compensate for loss of visual information.

III. NATURE OF THE STIMULUS: WHAT IS INFRARED (IR) RADIATION?

Radiant infrared energy is a region of the spectrum of electromagnetic radiation that lies between visible light (wavelengths of 400−750 nm) and microwaves (wavelengths of ≈1 mm to 1 cm). The English astronomer Sir William Herschel discovered infrared radiation at the beginning of the 19th century. Herschel was exploring the ability of light passing through a prism to heat a thermometer that he positioned at different points in the color spectrum. Herschel noticed that visible light was capable of heating the thermometer to some extent but that this effect was much more pronounced when the thermometer was placed beyond the red end of the spectrum. Electromagnetic radiation in the infrared region is absorbed as the radiation passes through objects in its pathway. Most of this absorbed infrared energy is dissipated by the resulting increase in molecular collisions (i.e. heat). Infrared radiation penetrates body tissues deeper than does visible light, and thus IR generators produce the so-called deep heat used in physical therapy. Any object above absolute zero radiates electromagnetic waves in the infrared, the more so as it is warmed. With increasing heat, an object radiates increasingly shorter wavelengths. Objects at room temperature radiate entirely in the IR and not at all in the visible light spectrum. At 500°C, objects begin to radiate also in the visible spectrum and they appear dull red. Endothermic (warm-blooded) animals, such as rats and mice, radiate maximally in the infrared region at a wavelength of approximately 10 μm. IR radiation can thus be used to detect objects in the absence of visible light (i.e. in the dark) with an object's detection being enhanced by having a temperature that contrasts with its background temperature.

Water vapor and carbon dioxide in the atmosphere absorb and severely attenuate the transmission of certain wavelengths of the IR spectrum and allow other wavelengths to pass. That is, there are windows for IR transmission in the atmosphere. One of these windows is in a region where certain IR-sensitive photographic emulsions absorb well, thereby allowing IR images of landscapes and cityscapes to be collected by satellite cameras. Another atmospheric transmission window includes the region around 10 μm, i.e. the region of the IR spectrum in which endothermic animals maximally radiate. IR sensory organs in snakes are believed to have a maximum sensitivity in this region (Grace et al., 1999) and thus are well suited to detect endothermic prey.

IV. INFRARED-SENSITIVE PIT ORGANS IN SNAKES

Infrared sensory organs in snakes consist of pit organs. Pit organs are invaginations within or between scales in the head. These invaginations are up to 3−4 mm wide and 3−4 mm deep. In boid snakes (e.g. pythons), the pit organs are arrayed in rows within labial scales of both the upper and lower jaws.[1] In crotaline snakes (e.g. rattlesnakes), there is a single facial pit organ on each side of the face between the nostril and eye (Fig. 40.1). There may be additional infrared-sensitive receptor terminals in the oral cavity (especially the palate) that may be important for guiding the predatory strike when the snake's mouth is open and fangs extended (Dickman et al., 1987) (Fig. 40.2).

A dense plexus of infrared-receptive primary sensory afferent nerve terminals is present in pit organs. In boid snakes, these terminals lie in the epidermis just under the surface of the pit organ. Immediately below the layer of infrared-receptive neuronal terminals is a thick capillary network. In crotaline snakes, a thin (15 μm) membrane stretches across the cavity of the pit (see Fig. 40.1B). Infrared-receptive nerve terminals are embedded within this membrane, also over a thick capillary bed. Infrared receptor terminals and the dense capillary plexus are mainly confined to the pit organs.[2]

The anatomical configuration of the pit organ, namely that the receptive tissue is stretched across the bottom of a cavity that has a narrowed opening to the outside environment, provides the snake with a means to direct its pit

[1] Boid snakes that do not have obvious pit organs possess clusters of infrared-receptive neuronal terminals in these same labial areas.

[2] The oral cavity of rattlesnakes is also sensitive to infrared and possesses dense ramifications of infrared-receptive sensory nerve terminals, similar to those in pit organs (Dickman et al., 1987).

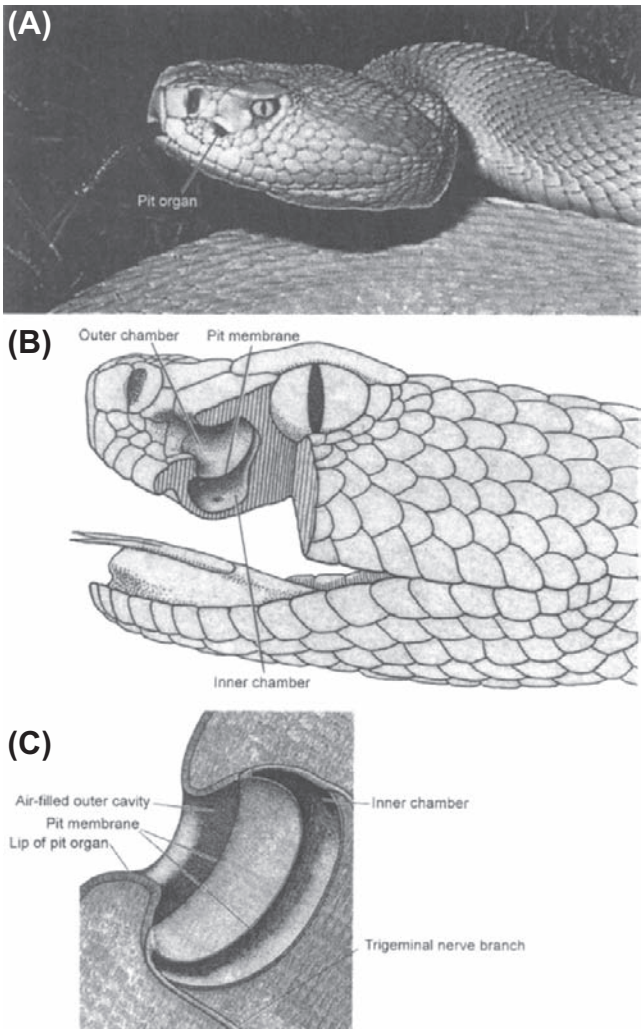

FIGURE 40.1 Infrared pit organ in the rattlesnake. (A) Photograph of the head of a rattlesnake (*Crotalus viridis*) showing the distinctive pit organ between the nostrils and the eye. *(Photograph by Bill Love from The World's Most Spectacular Reptiles and Amphibians, 1997. World Publications, Tampa, FL.)* (B) Schematic drawing of the internal structure of the infrared sensory organ in rattlesnake (*Crotalus viridis*). *(Reproduced from Gamow and Harris, 1973.)* (C) Higher magnification schematic view of the rattlesnake pit organ. *(Reproduced from Newman and Hartline, 1982.)*

FIGURE 40.2 Photograph of a rattlesnake striking at prey, demonstrating how infrared sensing receptors in the oral cavity may play a role in guiding the strike. *(Photograph by Pete Carmichael from Florida's Fabulous Reptiles and Amphibians, 1991. World Publications, Tampa, FL.)*

organs towards prey. Thus, the pit organs can provide information about the location of an infrared-emitting source in front of the snake. A distinct image, per se, such as a pin-hole camera might afford, is not formed in the pit organ, but the shadows cast by the infrared radiation passing through the narrowed opening into the pit project a crude approximation of the infrared source onto the sensory terminals. This "image" is conveyed to the snake's brain, much like visual information, to establish a spatiotopic map on the optic tectum (see Section IVA).

Infrared receptor terminals are embedded within the thin membrane that is stretched across the bottom of the pit organ. These terminals form large, highly-branched, entwined clusters surrounding an aggregate of Schwann cells. Collectively, this structure is called a terminal nerve mass ($\approx$30–100 μm diameter) (Fig. 40.3). Each terminal branch is densely packed with mitochondria. Clusters of electron-lucent vesicles are present just beneath the plasma membrane. These specialized endings are the sites where infrared transduction takes place (see Section IVB). A complex and extensive bed of capillary loops embraces the terminal nerve masses. This capillary bed is believed to have a dual function: (1) to provide a robust oxygen supply for the mitochondria in the receptor terminals; and (2) to act as a thermal exchanger to carry away excess heat and prevent the epithelial tissues from retaining temperature increases produced by infrared radiation (Amemiya et al., 1999). The thermal exchange function of the capillary bed, combined with the low heat capacity of the thin epithelial tissues in the pit organs, may ensure that the sensory receptors are capable of responding to the small transient temperature changes that are expected to occur when an infrared source (e.g. prey) passes in front of the pit organ (discussed in Section IVB).

IVA. Innervation and Central Nervous System Pathways of Pit Organs

Pit organs are innervated by branches of the trigeminal nerve (reviewed by Molenaar, 1992). These same nerve branches also subserve mechanoreception, nociception and thermoreception in the facial region of reptiles, mammals and other vertebrates. Cell bodies for the infrared-sensitive nerve terminals are located in sensory ganglia of the trigeminal nerve.

In infrared-sensitive snakes, sensory neurons in the trigeminal ganglia synapse with neurons in two distinct nuclei located in the hindbrain – the nucleus of the solitary

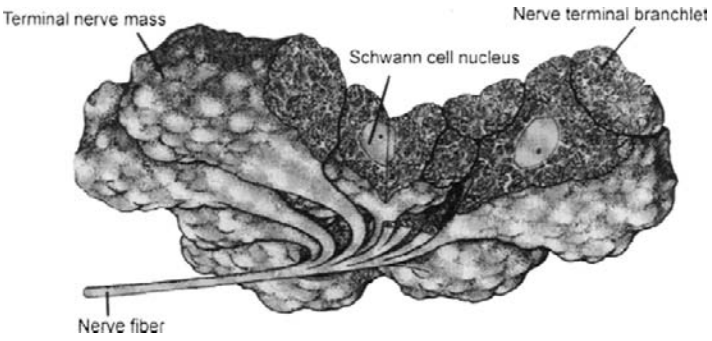

FIGURE 40.3 Reconstruction of the nerve terminals for infrared sensing trigeminal sensory axons. The branches form nerve terminal masses that include Schwann cells and receptor terminals. The nerve terminals are filled with numerous mitochondria. *(Reproduced from Terashima et al., 1970.)*

tract (NST) and a unique group of cells termed the nucleus of the lateral descending trigeminal tract (nLTTD) (see Molenaar, 1992). Neurons in the NST subserve such functions as mechanoreception, thermoreception and nociception, as in other vertebrates. However, the nLTTD is found only in infrared-sensing snakes and is responsible for processing information specifically from the pit organs (Stanford et al., 1981). This nucleus is present in all infrared-sensitive snakes studied thus far, and is absent from animals that are not infrared-sensitive.

Ultimately, infrared information from the nLTTD reaches the optic tectum. Spatial relationships among the axons and synapses of the infrared receptor pathway are preserved such that a systematic topographical map of the receptive membrane in the pit organ is projected onto the tectum, much like the orderly retinotopic mapping of visual information that also occurs in the optic tectum. Indeed, the infrared sensory map overlies and is aligned with the retinotopic map. Individual neurons in the optic tectum may be excited by visual and infrared stimuli arising from approximately the same point in space[3] (Hartline et al., 1978). Thus, snakes possessing infrared-sensitive pit organs view their environments simultaneously using two distinct regions of the electromagnetic spectrum.

IVB. Infrared Sensory Transduction

Infrared-detecting pit organs in snakes are exquisitely sensitive and selective (Bullock and Diecke, 1956; Gamow and Harris, 1973; de Cock Buning et al., 1981a,b; Newman and Hartline, 1982; Hartline, 1999). The adequate stimulus is a sharp thermal gradient, or contrast, in the surrounding environment, such as an endothermic animal (e.g. a mouse) against thermoneutral vegetation, or cool prey (e.g. a frog) against a cooler background (e.g. a pond). The temperature of the snake's body itself is not a significant factor, nor is the average temperature of the surroundings. Air temperature is irrelevant; the pit organ responds only to radiant energy in the infrared, not conductive energy transferred by warm air. Thus, a snake is an effective hunter in the heat of midday as well as in the cool of the night. The sensitivity of pit organs is such that a pit viper can use its infrared detector to orient to and accurately strike a rat at a distance of about 0.5 m. At this distance, a rat with a surface temperature 10°C above background emits infrared radiation (≈10 μm wavelength) that would be expected to warm the pit organ tissues by only 0.001°C (Bullock and Diecke, 1956). This low threshold for temperature detection was also observed experimentally. Researchers infused water of different temperatures into pit organs and measured threshold nerve responses to temperature changes as small as 0.003°C in 0.06 s (Bullock and Diecke, 1956). Rapid temperature increases as small as 0.1°C in the pit organ elicit robust responses (i.e. well above threshold detection) in the receptors (de Cock Buning et al., 1981a,b).[4]

Recent studies at the molecular level have tremendously illuminated how infrared radiation can be transduced into neuronal excitation. Gracheva et al. (2010) reported that rattlesnake trigeminal sensory ganglia express a unique variant of the heat-activated cation channel, TRPA1 (Fig. 40.4). When expressed in heterologous systems, rattlesnake TRPA1 channels are exceptionally sensitive to heat and begin conducting at or above 28°C. In contrast, TRPA1 channels from snakes lacking pit organs are not activated until temperatures reach 37°C.

[3] The two maps — visual and infrared — do not appear to overlap well in the peripheral fields of view. The overlap is more precise in the central field, i.e. directly in front of the snake.

[4] Bullock and Diecke (1956) and de Cock Buning et al. (1981a,b) alike point out that when factors such as the relative thickness of the overlying tissues, the low heat capacity of the thin pit organ membrane and the density of innervation are taken into account, the threshold for snake pit organs is similar to that of other warm receptors, including human cutaneous thermoreceptors. One reason for the apparent higher sensitivity to small temperature increases in snakes is that the density of innervation in pit organs is very high and the epithelial tissue overlying the sensory nerve terminals is extremely thin. Thus, infrared radiation can readily and rapidly increase the temperature around a dense plexus of sensory nerve terminals.

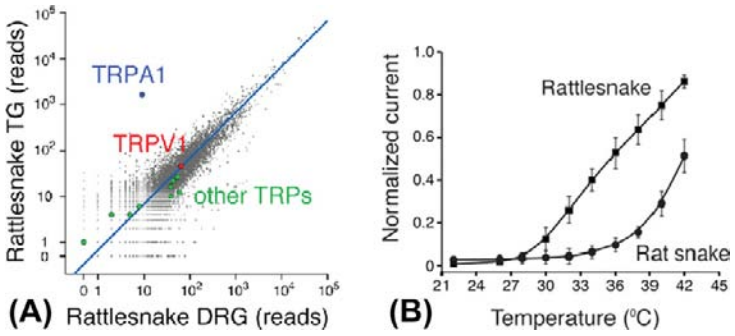

FIGURE 40.4 Rattlesnake TRPA1 channels are highly expressed in sensory neurons innervating the pit organ and are activated by temperatures above 28°C. (A) Quantification of genes expressed in rattlesnake ganglia that innervate the pit organ (trigeminal, TG) relative to rattlesnake dorsal root ganglia (i.e. non-pit organ sensory neurons). Axes show number of mRNA-Seq reads from snake ganglia that align to the chicken proteome. TRPA1 and another heat-sensitive channel, TRPV1, are highlighted, as are other TRP channels. Blue line indicates similar expression levels in the two samples. (B) Functional analysis of snake TRPA1 channels. The graph shows the relative heat response profiles of infrared-sensitive rattlesnake and infrared-sensitive rat snake channels expressed in oocytes (response at each temperature was normalized to maximal response at 45°C). *(Modified from Gracheva et al., 2010.)*

Gracheva et al. (2010) concluded that rattlesnake TRPA1 is the pit organ receptor activated by heat that is generated in the pit membrane during absorption of infrared radiation.[5]

Interestingly, the pit organs in pythons are exquisitely sensitive to gentle touch in addition to infrared radiation (de Cock Buning et al., 1981b). This observation may be explained by the expression of TRPA1 in trigeminal ganglion cells innervating the pit organ. TRPA1 has been identified with mechanotransduction in other species, including mice (Vilceanu and Stucky, 2010).

BIBLIOGRAPHY

Amemiya, E., Nakano, M., Goris, R. C., et al. (1999). Microvasculature of crotaline snake pit organs: possible function as a heat exchange mechanism. *Anat Rec, 254*, 107–115.

Bullock, T. H., & Diecke, E. P. J. (1956). Properties of an infra-red receptor. *J Physiol, 134*, 47–87.

Campbell, A. L., Naik, R. R., Sowards, L., & Stone, M. O. (2002). Biological infrared imaging and sensing. *Micron, 33*, 211–225.

de Cock Buning, T., Terashima, S., & Goris, R. C. (1981a). Crotaline pit organs analyzed as warm receptors. *Cell Mol Neurobiol, 1*, 69–85.

de Cock Buning, T., Terashima, S., & Goris, R. (1981b). Python pit organs analyzed as warm receptors. *Cell Mol Neurobiol, 1*, 271–278.

Dickman, J. D., Colton, J. S., Chiszar, D., & Colton, C. A. (1987). Trigeminal responses to thermal stimulation of the oral cavity in rattlesnakes (*Crotalus viridis*) before and after bilateral anesthetization of the facial pit organs. *Brain Res, 400*, 365–370.

Evans, W. G. (1964). Infra-red receptors in *Melanophila acuminata* DeGeer. *Nature, 202*, 211.

Gamow, R. I., & Harris, J. S. (1973). The infrared receptors of snakes. *Sci Am, 228*, 94–100.

Grace, M. S., Church, D. R., Kelley, C., & Cooper, T. M. (1999a). The python pit organ: immunocytochemical and imaging analysis of a sensitive natural infrared detector. *Biosens Bioelectron, 14*, 53–59.

Grace, M. S., & Woodward, O. M. (2001). Altered visual experience and acute visual deprivation affect predatory targeting by infrared-imaging Boid snakes. *Brain Research, 919*, 250–258.

Grace, M. S., Woodward, O. M., Church, D. R., & Calisch, G. (2001). Prey targeting by the infrared-imaging snake python: effects of experimental and congenital visual deprivation. *Behav Brain Res, 119*, 23–31.

Gracheva, E. O., Ingolia, N. T., Kelly, Y. M., et al. (2010). Molecular basis of infrared detection by snakes. *Nature, 464*, 1006–1011.

Hartline, P. H. (1999). Infrared sense. In G. Adelman, & B. H. Smith (Eds.), *Encyclopedia of Neuroscience* (pp. 957–959). New York: Elsevier.

Hartline, P. H., Kass, L., & Loop, M. S. (1978). Merging of modalities in the optic tectum: infrared and visual integration in rattlesnakes. *Science, 199*, 1225–1229.

Kardong, K., & Mackessey, G. (1991). The strike behavior of a congenitally blind rattlesnake. *J Herpetol, 25*, 208–211.

Molenaar, G. J. (1992). Anatomy and physiology of infrared sensitivity of snakes. In C. Gans, & E. S. Ulinski (Eds.), *Biology of the Reptilia* (pp. 367–453). Chicago: University of Chicago Press.

Newman, E. A., & Hartline, E. H. (1982). The infrared "vision" of snakes. *Sci. Am, 246*, 116–127.

Pelli, D. G., & Chamberlain., S. C. (1989). The visibility of 350°C blackbody radiation by the shrimp *Rimicaris exoculata* and man. *Nature, 337*, 460–461.

[5] Despite these impressive findings, the identification of rattlesnake TRPA1 as the infrared sensor is not entirely without question. There is a discrepancy between the operating range for rattlesnake TRPA1 channels and the temperature response of the pit organ. Rattlesnake TRPA1 channels expressed in HEK293 cells or *Xenopus* oocytes show a monotonic increase in activity with a threshold ≈28° and continuing to respond ≥42°, roughly comparable to the temperature sensitivity of trigeminal ganglion cells isolated from rattlesnakes (Gracheva et al., 2010). In marked contrast, the effective temperature range for the pit organ membrane, measured by the impulse activity of axons innervating the pit organ, is an inverted "U" shape with a threshold of ≈14°C, a peak at ≈25°C and a return to inactivity at ≈33°C (de Cock Buning et al., 1981a). This discrepancy may be explained by technical differences such as properties of TRPA1 in native versus heterologous expression systems, or species differences, or it may indicate that additional molecular mechanisms are involved in infrared detection. In this light, it may be pertinent that a light-sensitive G protein-coupled receptor, rhodopsin, was recently shown to be co-expressed with TRPA1 in temperature-sensitive neurons of *Drosophila* larvae (Shen et al., 2011). Remarkably, the two proteins appear to function in tandem as a temperature sensor, in the vicinity of 18°C.

Shen, W. L., Kwon, Y., Adegbola, A. A., Luo, J., Chess, A., & Montell, C. (2011). Function of rhodopsin in temperature discrimination in Drosophila. *Science, 331*, 1333−1336.

Stanford, L. R., Schroeder, D. M., & Hartline, E. H. (1981). The ascending projection of the nucleus of the lateral descending trigeminal tract: a nucleus in the infrared system of the rattlesnake (*Crotalus viridis*). *J Comp Neurol, 201*, 161−174.

Terashima, S., Goris, R. C., & Katsuki, Y. (1970). Structure of warm fiber terminals in the pit membrane of vipers. *J Ultrastruct Res, 31*, 494−506.

Van Dyke, J. U., & Grace, M. S. (2010). The role of thermal contrast in infrared-based predatory targeting behavior by the copperhead, *Agkistrodon contortrix*. *Anim Behav, 79*, 993−999.

Vilceanu, D., & Stucky, C. L. (2010). TRPA1 mediates mechanical currents in the plasma membrane of mouse sensory neurons. *PLoS One, 5*, e12177.

Chapter 41

Electroreceptors and Magnetoreceptors

Timothy C. Tricas and Bruce A. Carlson

Chapter Outline

I. SUMMARY

Many animals have the ability to detect electric and magnetic fields. Although many species respond and orient to magnetic stimuli, only recently were putative vertebrate receptor systems identified. All organisms generate weak electric fields in water, due to an uneven distribution of ions between the interior of the organism and the external aqueous environment. Ampullary electroreceptors are an ancestral vertebrate trait that allows for the passive detection of these electric fields, which is useful for detecting prey, predators and mates. Although ampullary electroreceptors were lost during vertebrate evolution, they subsequently re-evolved several times independently. In two groups of teleost fishes, both ampullary and tuberous electroreceptors evolved, the latter specialized for the detection of actively generated electric organ discharges, or EODs. These fish generate EODs to communicate in the electrosensory domain, as well as actively to sense their environment by detecting distortions in the self-generated EOD. Many physiological mechanisms involved in electrosensory processing are unique.

II. INTRODUCTION

The production of potent shocks by the electric catfishes (*Malapterurus*), eel (*Electrophorus*) and rays (*Torpedo*) to capture prey were reported in antiquity but it was much later that the shock from these animals, and the imperceptible discharges of others, were found to be electrical in nature (Moller, 1995). Further, the production of weak electrical discharges in the millivolt range indicated that weak electrical signals serve functions other than attack or defense (Lissman, 1958; Lissman and Machin, 1958). Because these weak electrical discharges offered a possible system for sensing the environment and communication among conspecifics, scientists sought the identity of the sensory receptors that detected them. Thus, the study of electroreception arose and has since produced much information on electroreceptors, electrogenic organs and their physiology.

Electroreception is an ancient vertebrate sense that occurred in the predecessors of jawless and jawed vertebrates (Bullock et al., 1983). The electrosense is retained in numerous extant taxa (Fig. 41.1) including lampreys, chondrichthyan fishes, bichirs, sturgeon and paddlefishes, lung-fishes, coelacanths and non-anuran amphibians (salamanders and caecilians). Phylogenetic analysis of character traits indicates that the electrosenses of these animals are homologous, reflecting their common phylogenetic origin (Bullock et al., 1983; Bullock and Heiligenberg, 1986). Electroreception, however, was lost in the vast majority of teleosts, the lineage to which most modern bony fishes belong. Most teleosts, together with their sister groups of gars and bowfin, which collectively comprise the Neopterygii, lack an electrosense. Remarkably, only two distantly related lineages of teleost fishes do possess electroreceptors and it is apparent from character analysis that

Cell Physiology Sourcebook. DOI: 10.1016/B978-0-12-387738-3.00041-X

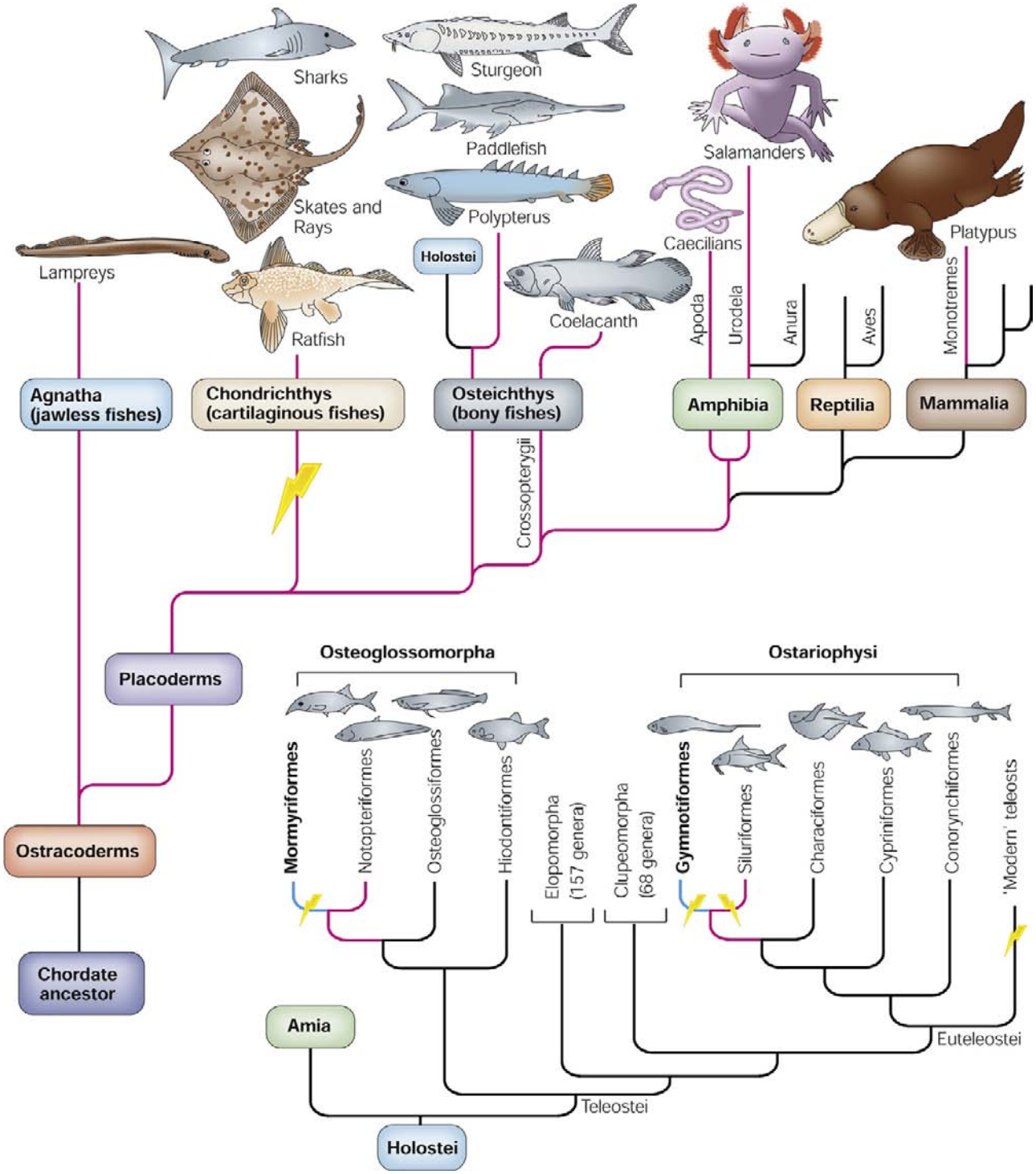

FIGURE 41.1 Cladogram showing the phylogenetic distribution of electroreception and electric organs. Clades with ampullary electroreceptors are indicated by magenta lines, clades with both ampullary and tuberous electroreceptors are indicated by cyan lines (and bold lettering), and clades with electric organs are indicated by lightning bolts. *(Modified from Rose, 2004).*

these have evolved independently (Fig. 41.1). In addition, two species of monotreme mammal, the semiaquatic platypus and the truly terrestrial echidnas, are electroreceptive (Fig. 41.1). Because electrosenses are not present in most other tetrapod lineages, this clearly represents yet another "reinvention" of electroreception.

Electroreceptors of most aquatic vertebrates are classified as either ampullary or tuberous (see Zakon, 1986,

1988). *Ampullary receptors* respond to low-frequency stimuli with best sensitivity to varying electric frequencies between 0.1 and 20 Hz. This range of frequencies includes the detection of standing (DC) bioelectric fields produced by other aquatic organisms that are experienced by a swimming electrosensitive animal as well as those produced by non-living physicochemical sources in aquatic environments. Detection of these extrinsic sources by ampullary receptors is often referred to as electroreception in the *passive mode* (Kalmijn, 1974, 1988). *Tuberous electroreceptors* are tuned to much higher frequencies, with best frequencies in the 0.1−10 kHz range. Tuberous organs are found in fishes possessing weak electric organs of the sort initially described by Lissman (1958) and these receptors have best frequencies that correspond closely to the peak spectral frequency of the discharge of the animal's electric organ. The tuberous organs detect changes in the intensity and temporal pattern of the electric field produced across the body by the electric organ discharge (EOD), whether by the presence of items in the field of objects with different conductances than the water, or by the addition of the electric organ discharges of another individual. Such forms of electrodetection that respond to alterations of the self-generated EOD and the detection of induced electric fields caused by swimming through the Earth's magnetic field are referred to as electroreception in the *active mode* (Kalmijn, 1988). In this chapter, we consider current information on the morphology and physiology of ampullary and tuberous electroreceptors. Space limitations preclude a discussion of the central processing of electrosensory information, which remains one of the most captivating stories in modern neuroethology. The reader is referred to several excellent recent reviews on this topic (Bullock and Heiligenberg, 1986; Bell and Maler, 2005; Kawasaki, 2005).

The ability directly to detect geomagnetic fields is known as *magnetoreception* and the ability to sense and respond to magnetic stimuli is known for a number of animal groups and bacteria (for reviews see Tenforde, 1989; Wiltschko and Wiltschko, 1995). These studies are primarily behavioral, with incomplete information on magnetoreceptor organs and receptors in most taxa. The direct identification of a magnetoreceptor cell has many technical challenges because direct magnetoreception is believed to be associated with localized deposits of magnetite crystals (Fe_3O_4) which are extremely small, easily contaminated, degrade easily in preserved tissues and are difficult to verify. Localized magnetite domains are described in tissues of bees, salmon, tuna, turtles, pigeons, dolphins, humans and many other species (Wiltschko and Wiltschko, 1995). In several birds and one species of fish, candidate magnetoreceptor cells were identified in close association with small rostral branches of the trigeminal nerve. In the homing pigeon, superparamagnetic crystals occur along the surface of afferent nerve terminals of the somatosensory branch that innervates the upper beak (Fleissner et al., 2003) and this arrangement is similar in other migratory and non-migratory species (Falkenberg et al., 2010). Neurophysiology experiments show that fast adapting trigeminal neurons in bobolinks respond to changes in applied magnetic fields as low as 30−50 nT, whereas slow adapting units respond as amplitude detectors (Beason and Semm, 1987; Semm and Beason, 1990). Potential receptor cells that contain single-domain magnetite exist in the lamina propria of the rainbow trout olfactory rosette and are in close association with endings of a rostral branch of the trigeminal nerve that penetrates the olfactory epithelium (Walker et al., 1997; Diebel et al., 2000). Single cell neurophysiology bench experiments show that units respond to rapid changes in applied magnetic fields (Walker et al., 1997). Indirect magnetoreception is also possible in some electroreceptive taxa via the detection of electric fields induced by an animal's movement through a geomagnetic field or drifting in an oceanic current (see discussion later). Evidence for chemical magnetoreception that involves magnetic actions on correlated spin states of radical ions is also proposed for the bird visual system (Ritz et al., 2000) but is not covered here. For recent reviews of the waning magnetoreception controversy, readers are referred to Johnsen and Lohmann (2005) and Walker et al. (2007).

III. AMPULLARY ELECTRORECEPTORS

The wide phylogenetic distribution of ampullary electroreceptors among extant vertebrate taxa indicates that this class of electroreceptor has served important biological functions for hundreds of millions of years and has subsequently "re-evolved" several times (see Fig. 41.1). With the exception of weakly-electric fishes that also possess tuberous electroreceptors, most species with ampullary electroreceptors lack electric organs. Thus, behaviorally relevant ampullary stimuli are thought to originate primarily from extrinsic sources. Ampullary electroreceptors are known to be important for the detection of prey (Kalmijn, 1971; Tricas, 1982; Wilkens et al., 2001), mates (Tricas et al., 1995), potential predators (Sisneros et al., 1998) and orientation to local inanimate electric fields (Kalmijn, 1982; Pals et al., 1982). In addition, the ampullary electroreceptor system is theoretically capable of mediating navigation by detecting electric fields induced by movement of the animal through the Earth's magnetic field (Kalmijn, 1974, 1988; Paulin, 1995), which would represent a form of electroreception in the *active mode*.

IIIA. Development and Morphology

Information on the ontogeny and development of electroreceptors is based largely on descriptive studies and we

refer readers to the excellent recent discussion provided by Northcutt (2005). Ampullary electroreceptor cells in non-teleost aquatic vertebrates develop from ampullary primordia that are derived from the neural crest in the shark (Freitas et al., 2006), associated with the lateral line placodes and sensory ridges (Northcutt et al., 1994, Gibbs and Northcutt, 2004) and possess either a kinocilium, microvilli or both. In teleosts, it remains to be experimentally demonstrated whether tuberous electroreceptors arise from induction in the general ectoderm (Vischer, 1995) or from lateral line placodes (Northcutt, 2003). In contrast, the electrosense of monotreme mammals evolved as a specialization of the trigeminal nerve associated with dermal mucus glands of the snout (Gregory et al., 1989; Pettigrew, 1999).

The lampreys possess an electroreceptor known as an *end bud* that differs considerably in morphology from the ampullary electroreceptors of other fishes (Ronan and Bodznick, 1986). Each end bud consists of numerous support cells and three to 25 sensory cells in the epidermis that are in direct contact with the surrounding water. Individual receptor cells have numerous small microvilli on the apical surface but lack a kinocilium. Small groups or lines of end buds are distributed over the head and body surface with multiple buds being innervated by a single sensory lateral line nerve fiber (Bodznick and Preston, 1983; Ronan, 1986). The excitation of end bud electroreceptors by cathodal (−) stimuli indicates a possibly similar transduction mechanism as the ampullary receptors of more derived non-teleosts (see discussion below). However, it is not known whether end buds represent the ancestral electroreceptor state or whether they are a derived condition unique to the lampreys.

Elasmobranch fishes (rays, skates and sharks) and rat fishes (Fields et al., 1993) possess ampullary electroreceptor organs of a similar morphology. In elasmobranch fishes, the electroreceptive unit is a highly specialized structure known as an *ampulla of Lorenzini* (Fig. 41.2). The ampulla proper in the marine skate is composed of multiple *alveolar sacs* or diverticulae which share a common lumen (Waltman, 1966). The apex of each ampulla chamber is connected by a highly insulated *marginal zone* to a single subdermal *canal*, which is approximately 1 mm in diameter and terminates as a small epidermal pore. The canal wall is 1−2 μm thick and composed of two layers of flattened epithelial cells, which are separated by a basement membrane to which the lumenal layer is also united by tight junctions. Both the canal lumen and the ampullary chambers are filled with a K^+-enriched, mucopolysaccharide, jelly-like matrix that is secreted by the superficial layer. While the resistivity of the gel (25 ohm cm) is similar to that of sea water and has similar responses as seawater to standing DC fields, recent work shows that the electrical properties of the gel exhibit reduced electrical admittance to varying electric stimuli. In combination with long canals

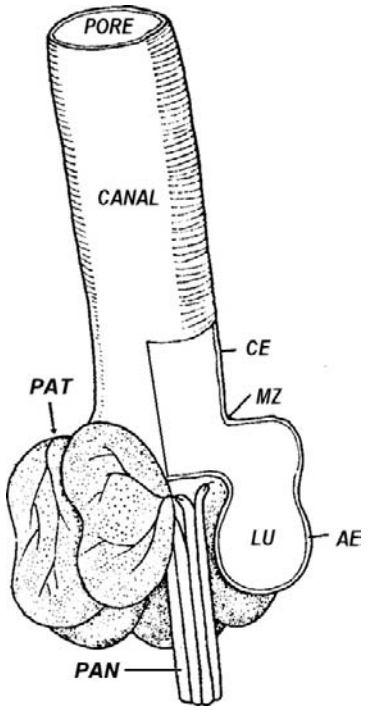

FIGURE 41.2 Ampulla of Lorenzini from the marine skate, *Raja.* The ampulla proper consists of multiple alveoli formed by the alveolar epithelium (AE). A high-resistance marginal zone (MZ) connects the sensory walls of the ampulla to the high-resistance canal epithelium (CE), which projects to the surface of the skin and terminates as a small pore confluent with the surrounding water. The ampulla lumen (LU) and canal are filled with a gel that provides electric conductivity along the length of the canal. Myelinated primary afferent neurons (PANs) innervate the base of the ampullae and their unmyelinated primary afferent terminals (PATs) receive chemical excitation from the basal region of the sensory cells in the epithelial layer. *(Modified from Waltmann, 1966, with permission).*

of narrow 1 mm diameter, the high resistance ampulla−gel−canal complex promotes detection of differences along the length of the canal rather than direct isopotential contact between the ampullary electroreceptors and seawater at the location of the surface pore (Brown et al., 2002, 2005). The sensory epithelium within the alveolus is composed of two cell types, which form a monolayer that is approximately 15 μm thick (Fig. 41.3). The vast majority of the alveolar surface is formed by accessory cells that are highly resistive to transmembrane currents and are bound together by tight junctions that prevent ionic leakage across the lumenal and basal surfaces of the epithelium. Interspersed among the accessory cells are flask-shaped receptor cells (thought to be modified hair cells), which possess a single kinocilium on the apical surface and lack microvilli. This physical arrangement results in only a small fraction of the receptor cell surface being exposed to the ampullary chamber.

The basal membrane surface of the receptor cell forms a ridge seated in a postsynaptic invagination that is separated by a distance of 100−200 Å (Waltmann, 1966).

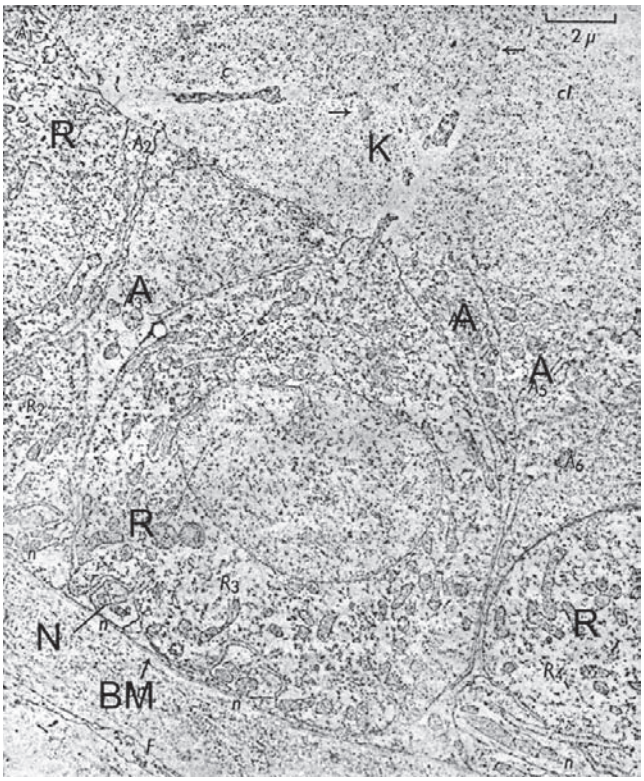

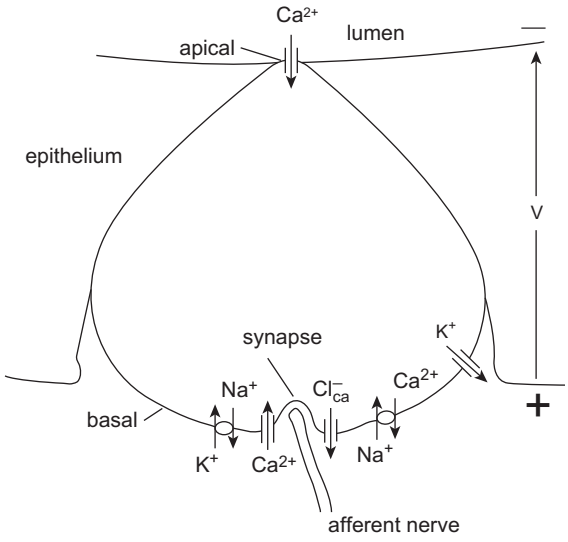

FIGURE 41.3 Receptor cell of the ampulla of Lorenzini in the skate, *Raja*. Top figure is photomicrograph of flask-shaped receptor cells (R) and adjacent accessory cells (A) that are united by tight junctions to form the alveolar epithelium. A single kinocilium (K) projects from each receptor cell into the lumen and, together with a small portion of the apical surface, is exposed to electric stimuli. Primary afferent neurons (N) innervate the basal portion of the receptors. The basement membrane (BM) is located beneath the sensory epithelium (*modified from Waltmann, 1966*.). Bottom figure shows ion channels and transporters involved in steady state conductance and sensory transduction. The excitable region of the cell is the apical membrane that has a partially activated inward bias current. The apical conductance is thought to work with oscillations created by exchangers and channels in the basal membrane that produce regular afferent discharges at the postsynaptic neuron. A weak electric stimulus in the ampulla that is more negative than the potential at the outside basal surface results in excitation of the cell and increased discharge potential in the afferent nerve. *(Top figure from Waltmann, 1966 with permission from Wiley Press and bottom figure modified from Lu and Fishman, 1994 with permission from Elsevier Limited, Kidlington, Oxford.)*

A *synaptic ribbon* about 250 Å wide and 2 μm in length is located within the presynaptic ridge. A single layer of synaptic vesicles covers the ribbon and exocytotic release of chemical neurotransmitter contained within these vesicles depolarizes the postsynaptic membrane of the innervating fibers of the anterior lateral line nerves. Unlike the hair cell receptors of the mechanosensory lateral line and octaval systems, all ampullary electroreceptors, both primitive and derived, lack efferent innervation.

Chondrichthyan fishes typically possess hundreds (or thousands) of ampullae that are associated in specific *ampullary clusters* associated with specific branches of the anterior lateral line nerve and are often closely bound by a dense matrix of connective tissue (Fig. 41.4A). From these clusters the subdermal canals radiate omnidirectionally and terminate in surface pores on the head and on the enlarged pectoral disk of batoids (Rivera-Vicente et al., 2011). The multiple orientations of the receptor canals and the copious distribution of the ampullary pores over the cephalic surface provide an extensive array of receptors with a high degree of spatial resolution. The morphology of the ampullary electroreceptors in freshwater elasmobranchs is thought to reflect sensory adaptations to their highly resistive environment (Kalmijn, 1974; Raschi and Mackanos, 1989). The freshwater rays, *Potamotrygon* and *Dasyatis garouaensis*, have a hypertrophied, thick epidermis that functions to increase transcutaneous electrical resistance. The ampullary electroreceptors are greatly reduced in size and are referred to as *miniampullae* or *microampullae*, which are distributed individually across the skin rather than in clusters and which have very short canals (about 0.3−2.1 mm long) that traverse the integument.

The anatomy and organization of ampullary electroreceptor organs in other non-teleost fishes and amphibians are generally similar to those of elasmobranch fishes, with which they are believed to be homologous. Ampullary electroreceptors in chondrostean (sturgeon and paddlefishes), cladistian (bichirs) and dipnoan fishes (lungfishes) share in most respects a similar morphology among alveoli, canals and ampullary pores. However, the ampullary organs in these freshwater fishes are most commonly arranged as single units or small groups (as opposed to large clusters) and have very short (generally <0.25 mm) and small diameter (generally <0.14 mm) canals. The abundance of receptors are distributed in the head region, with the exception of the lungfishes, in which there are single ampullary electroreceptors on the head and small groups consisting of three to five ampullae scattered widely over the body (Pfeiffer, 1968). Ampullary electroreceptors of the head are innervated by a ramus of the anterior lateral line cranial nerve, while those on the body are innervated by

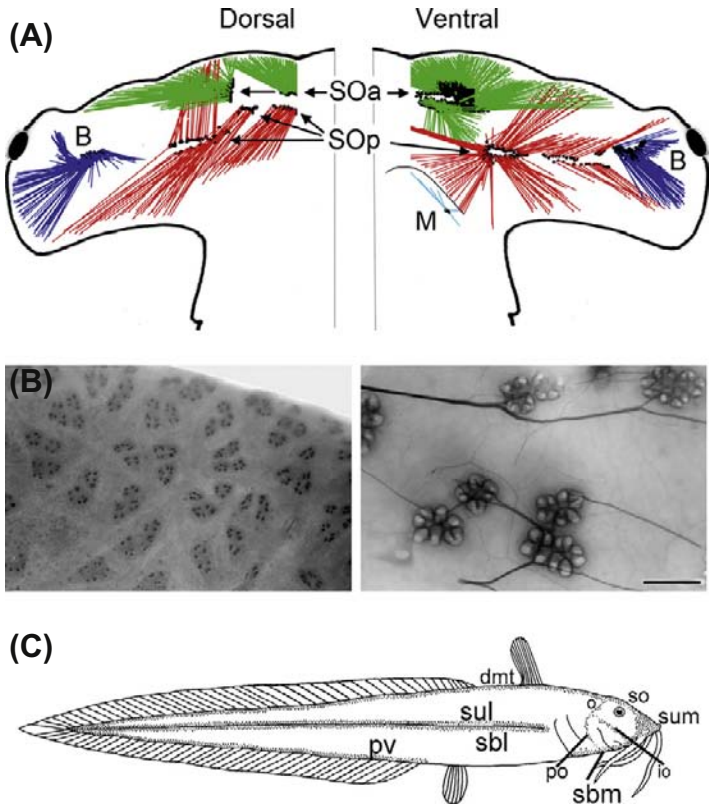

FIGURE 41.4 Distribution of ampullary electroreceptor canal pores in fishes. (A) The scalloped hammerhead shark, *Sphyrna lewini*, has more than 2800 ampullary pores on the dorsal and ventral surfaces of head many of which have long canals that project to the sensory ampullae. Ampullae (small black dots) are grouped into clusters that are associated with branches of the anterior lateral line nerve. Canals and associated clusters are B = buccal (blue), SOa = superficial ophthalmic anterior (green), SOp = superficial ophthalmic posterior (red), M = mandibular nerve (light blue). (*From Rivera-Vicente et al., 2011, with permission from PLoS One.*) (B) Ampullae in the paddlefish, *Polyodon spathula,* have transdermal pores that occur in small clusters. Left photo shows arrangement of pores across the ventral surface of the rostrum. Scale bar = 2 mm. Right photo is a cleared and stained preparation that shows innervation of primary afferent fibers. Scale bar = 1 mm. (*From Wilkens et al., 2002 with permission from Elsevier Limited, Kidlington, Oxford.*) (C) Ampullary pore distributions in the estuarine catfish, *Euristhmus lepturus* (Plotosidae). Each spot represents a single ampullary pore or cluster. Pore distributions are associated with nerve branches: dmt = dorsal midtrunkline, io = infraorbital, o = otic, po = preopercular, pv = posterior ventral, sbl = sublateralis, sbm = submandibular, so = supraorbital, sul = supralateralis and sum = supramandibular. *(From Whitehead et al., 2009, Copyright Springer-Verlag, Inc. Reprinted with permission.)*

a recurrent branch of the anterior lateral line nerve complex. In the bichir, *Polypterus* (Cladistia), there are about 1000 ampullae on the head region (Northcutt, 1986). In sturgeon, the electroreceptor organs are arranged in about 1300 clusters of about 20 ampullae each whereas, in the related paddlefish, *Polyodon*, there are 50 000 to 75 000 ampullae on the elongate rostral "paddle" (see Fig. 41.4B) which are also arranged in small clusters (Wilkens et al., 2001; Jørgensen, 2005). In the marine coelacanth, *Latimeria*, the "rostral organ" located between the eye and olfactory organ represents a complex of three principal canals that end centrally in small sensory crypts (Millot and Anthony, 1956) and is thought to be a homologous structure to the elasmobranch ampullae of Lorenzini (Bemis and Heatherington, 1982).

There is significant variability also in ampullary receptor cell morphology, particularly at the level of the apical membrane (Jørgensen, 2005). Ampullary receptor cells in bichirs and reedfish possess both a single kinocilium and 8–10 microvilli, whereas those of chondrostean sturgeons and paddlefish possess only a kinocilium as in the elasmobranchs. The receptor cells in lungfishes lack a kinocilium, but possess microvilli as in the jawless lampreys. The receptor cells of the urodele amphibians (salamanders) are highly variable in morphology, whereas the tropical subterranean gymnophion have only microvilli. The ancestral condition for non-teleost electroreceptors is generally thought to be one possessing both kinocilium and microvilli (like other hair cells), but the reason for the loss of either kinocilium or microvilli in the various taxa and possible physiological ramifications is not known. These receptors also possess synaptic ribbons in the basal cell region, although some variation in synaptic morphology occurs.

Ampullary canals of marine teleost species are often long as in marine elasmobranchs, although morphological differences associated with habitat may occur within species (Whitehead et al., 2000). Ampullary pores are concentrated on the head and may also occur across the body (see Fig. 41.4C). The fine structure of ampullary electroreceptors in freshwater teleost fishes closely resembles that of the freshwater elasmobranchs (Szabo, 1974) (Fig. 41.5). These receptors, however, are not homologous to non-teleost receptors rather they represent a case of parallel homoplasy, presumably the result of developmental and functional constraints necessary for the detection of extrinsic electric fields and their derivation from the hair cell receptors of the lateral line. The organs are located at the level of the basement membrane of the epidermis with a very short canal (usually about 200 µm)

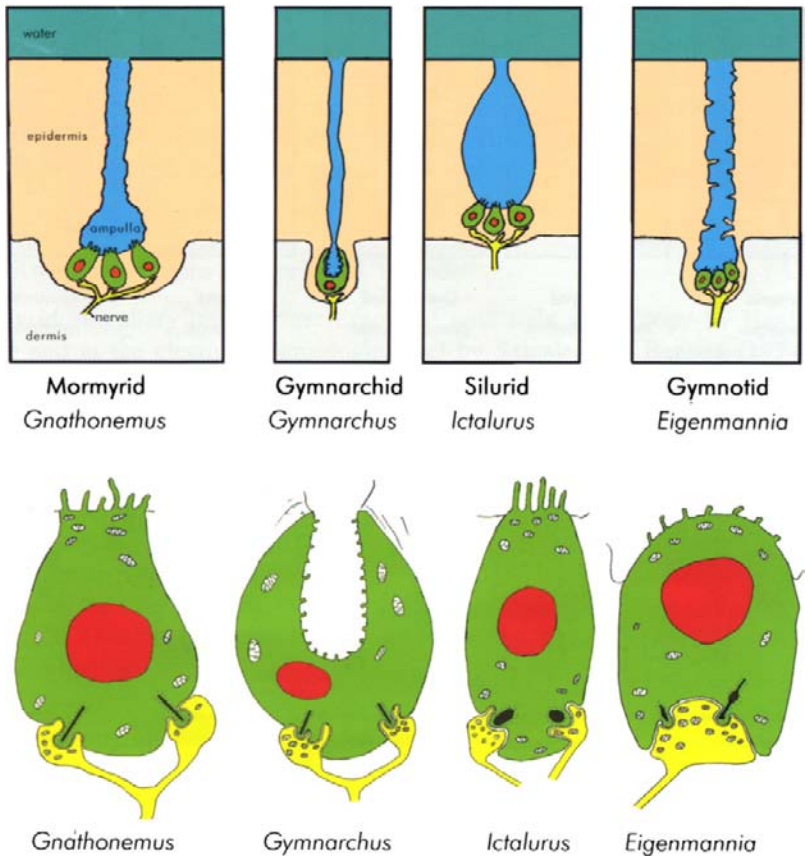

FIGURE 41.5 Diagrammatic representation of ampullary receptor organs in four families of freshwater teleosts. Top row shows cross-section of ampulla pores in contact with water, short canals and the receptor epithelium in the epidermis. Bottom row shows representative differences in receptor morphology and innervation. *(Modified from Jørgensen, 2005.)*

connected to a pore on the skin surface. The cells of the inner walls of the ampulla and canal consist of three to five layers of flattened epithelial cells connected by tight junctions preventing current leakage across the canal wall and the canal is filled with a conductive jelly that provides a low-resistance pathway through the lumen (Pfeiffer, 1968). The parallelism of ampullary electroreceptors among both ancient and derived groups is further demonstrated in the few existing species of electroreceptive marine teleosts. In the marine catfish, *Plotosus*, the ampullary canals are elongated, forming long subdermal tubules terminating centrally in alveolar clusters strikingly similar to the ampullae of Lorenzini in marine elasmobranchs (Obara, 1976). These teleosts can detect electric field stimuli at 80 μV/cm (Kalmijn, 1988), which is much more sensitive than the ampullary system of freshwater species.

The ampullary receptor cells of teleosts are located in the base of the alveolus and are connected to the supporting cells via tight junctions, with only a small portion of their apical face exposed to the lumen. Teleost electroreceptor cells generally possess only microvilli with the exception of the African knifefish *Xenomystus* (Notopteridae) that shows a single short cilium on the electroreceptor (Jørgensen, 2005). The synaptic structure of receptors in more recently derived fishes is similar to those of the more primitive species, in which synaptic ribbons and presynaptic membrane evaginations are surrounded by a prominent postsynaptic "cup" (Szabo, 1974). Unlike most non-teleost ampullary electroreceptor cells, ampullary receptors in teleosts may be innervated by either anterior or posterior lateral line nerves, depending upon location on the body surface. Like most other non-teleost fishes, the ampullae are distributed widely over the head, but differ in that they are usually distributed across the trunk in distinct patterns that are species-specific.

IIIB. Physiology

For marine elasmobranches, such as the thornback ray, *Platyrhinoides*, the resistance of the skin is moderately higher than that of the body tissues (Kalmijn, 1974). When the body encounters a weak external dipole source, such as that produced by small prey, penetration of the electric field into the body is limited and makes the voltage drop across the skin in the region of the pore the effective stimulus. In contrast, external uniform fields, such as those produced by geomagnetic induction in streaming ocean currents, invade the body along the length of the canal and detection may be enhanced by long canal length under these conditions. In freshwater elasmobranches, such as *Potamotrygon*, the resistance of the skin is relatively high compared to marine species and the resistance of the internal tissues is relatively low, presumably as a result of osmoregulatory constraints. In these fishes, the internal environment is essentially at a common reference potential. Individual ampullae detect the transepidermal voltage drop between an applied external field and the internal tissue reference. Hence, most strictly freshwater elasmobranchs, as well as most other ampullary-bearing taxa, have short ampullary canals that cross only the dermis.

Technical challenges make it very difficult to obtain detailed intracellular single-cell recordings from ampullary electroreceptor cells. The membrane biophysics of ampullary receptor excitation for non-teleosts is best described for the skate, *Raja*, in which the voltage stimulus could be clamped or controlled near the sensory epithelium of the ampulla (see Obara and Bennett, 1972; Bennett and Clusin, 1978; Lu and Fishman, 1994, 1995a,b). The excitability of the electroreceptor cell results from voltage-gated Ca^{2+} channels located in the apical membrane (see Fig. 41.4). In unstimulated electroreceptors, there exists a steady-state inward current by L-type Ca^{2+}-channels. The basal membrane has a net outward current that involves K^+ and Ca^{2+}-dependent Cl^- channels that produce an oscillation thought to drive presynaptic neurotransmitter release. In addition, intracellular Ca^{2+} concentrations and the basal membrane voltage are tightly regulated and maintained by Na^+-K^+ and Na^+-Ca^{2+} ion transporters (Lu and Fishman, 1995b). Electric stimuli applied to the ampulla lumen that are more negative than those at the basal outside surface will depolarize the apical membrane and promote additional inward Ca^{2+} conductance. This results in a net outward current across the basal surface of the cell, an influx of Ca^{2+} that promotes presynaptic neurotransmitter release and subsequent depolarization of the postsynaptic afferent fiber. Weak anodal stimuli applied to the lumen decrease apical Ca^{2+} conductance and neurotransmitter release. This model is supported by electric models and empirical measurements (Fig. 41.6A). Voltage clamp experiments provide data on complex admittance (the reciprocal of impedance) at different frequencies and indicate the real part of the admittance at low frequencies is negative and is consistent with inward current at the apical membrane (Lu and Fishman, 1994).

The membrane biophysics of the teleost ampullary electroreceptor also involves several ion channels that also include voltage-sensitive Ca^{2+} channels, but the excitable membrane is at the basal surface of the receptor cell. In the marine catfish (*Plotosus*) and likely in other teleosts, the electroreceptors are excited by anodal potentials in the ampulla chamber near the low resistance and passive apical membrane. Voltage and current clamp experiments on isolated ampullae reveal the existence of an electrogenic Na^+-K^+ pump in the basal receptor membrane (Sugawara, 1989a). This provides a steady outward bias current that activates a sustained non-inactivating inward Ca^{2+} L-type

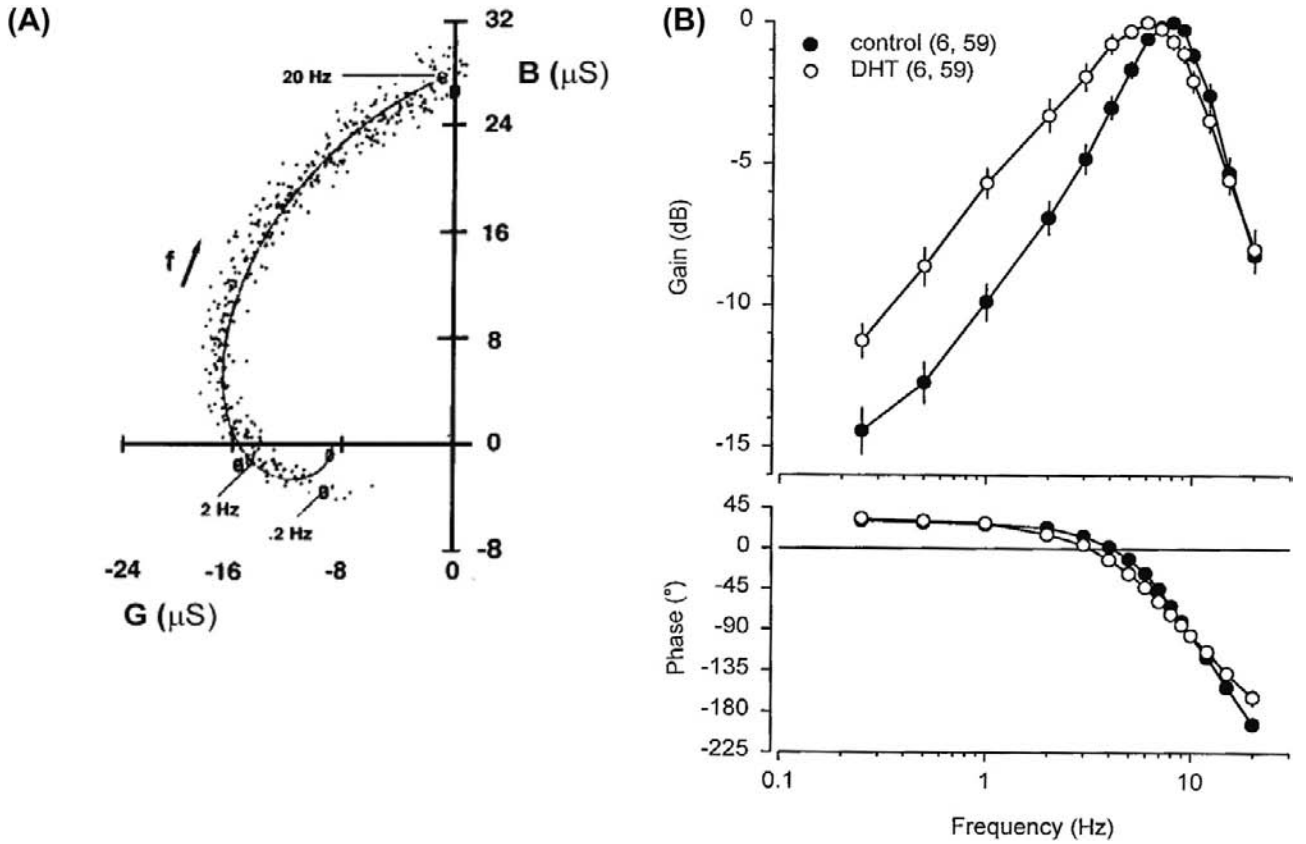

FIGURE 41.6 Frequency response of ampullary receptors and primary afferent neurons in elasmobranch fishes. (A) Locus of the admittance function of complex frequency as determined by voltage clamp experiments on an ampullary organ of the skate, *Raja*. The locus of 400 data point at low frequencies from 0.05 to 20 Hz are plotted in the complex plane [*B(f)* vs *G(f)*] and fall in the left half plane. This describes a negative conductance in this low frequency range. Also, note that the locus plot intercepts the real axis (B(uS) = 0) at 2.1 Hz which indicates solely negative (inward) conductance. (*Reproduced from Lu and Fishman, 1994 with permission from Elsevier Limited, Kidlington, Oxford.*) (B) Bode plot and phase diagram for frequency response of electrosensory primary afferent neurons recorded from adult male Atlantic stingrays, *D. sabina*, after DHT implants. Peak frequency sensitivity decreased from 7−8 Hz to 5−6 Hz for DHT-treated fish and also the low frequency response. The numbers of animals and electrosensory primary afferent neurons tested are indicated in parentheses. Data are plotted as mean and SE. *(Modified from Sisneros and Tricas, 2000.)*

current that maintains the tonic release of neurotransmitter and the regular resting discharge firing rate of afferent neurons (Sugawara, 1989b). This Ca^{2+} conductance is enhanced by an anodal (positive) stimulus in the ampulla to create a superimposed fast Ca^{2+} N-type current that initiates an outward transient Ca^{2+}-gated K current. The conductances are inhibited by phasic cathodal stimuli in the ampullary lumen (Bennett, 1971a; Bennett and Obara, 1986). Primary afferents that innervate ampullary electroreceptors in freshwater fish show regular resting discharges that are excited by anodal stimuli at the lumen and have a dynamic range of ±1 mV in *Gymnotus* (Bennett, 1968) with thresholds that can range from tens to hundreds of microvolts (see Zakon, 1986). The low frequency response of primary afferents in the paddle fish are efficient detectors of bioelectric stimuli from single plankton (Wilkens, 2004) and have proved an intriguing model for detection of signals in noisy environments and sensory oscillators (Neiman and Russell, 2004; Neiman et al., 2007).

The high sensitivity of electrosensory primary afferent neurons was first established for the elasmobranch at a voltage gradient of about 1 μV/cm (Murray, 1962) and has recently been extended to near 20 nV/cm applied to ampullae with long canals by Tricas and New (1998). The neural response to a prolonged, constant current field is sustained for a duration of a few seconds before it begins to adapt back to the resting discharge rate. Prolonged, constant stimulation results in a return to resting levels and accommodation of the receptor, resulting in no change in the overall sensitivity of the receptor (Bodznick et al., 1993). Work on a variety of species with both non-teleost and derived ampullary electrosenses shows a maximum response to sinusoidal electric fields at frequencies of 1−10 Hz (Andrianov et al., 1984; Montgomery, 1984b; Peters and Evers, 1985; New, 1990; Tricas and New, 1998). Sensitivities of primary afferent fibers innervating ampullary electroreceptors to a sinusoidal uniform field are 0.9 spikes per second per μV/cm for the little skate, *Raja*

erinacea (Montgomery and Bodznick, 1993), four spikes per second per μV/cm for the thornback guitarfish, *Platyrhinoidis triserata* (Montgomery, 1984a) and 24 spikes per second per μV/cm average for the round stingray, *Urolophus halleri* (Tricas and New, 1998). The frequency response of primary afferents neurons were shown in the stingray *Dasyatis sabina* to vary across the reproductive season in association with natural surges in serum androgens (Sisneros and Tricas, 2000). In wild males, there was an increased sensitivity to low frequency stimuli from 0.01 to 4 Hz. Experimental implants of dihydrotestosterone induced a similar increased sensitivity in the band of 0.5−2 Hz. These androgen dependent shifts in sensitivity may serve to enhance the detection of potential female mates or other reproductive-related behaviors.

Recordings from the lateral line nerve in behaving elasmobranchs and bench preps show that the regular discharge of primary afferent neurons is modulated in rhythmic bursts that are in phase with the ventilatory movements of the fish. This reafferent neuromodulation is explained by the standing (DC) bioelectric field that arises from the differential distribution of ionic charges in the animal which, in the skate, is a result of both diffusion potentials and osmoregulatory ion pumping at the gills (Bodznick et al., 1992). The modulation of this standing field occurs as the animal opens and closes the mouth, gills or spiracles during the ventilatory cycle, which changes the resistance pathway between the animal's internal tissues and surrounding seawater. The resultant transcutaneous potential is the source of electrosensory self-stimulation or *ventilatory reafference* (Montgomery, 1984b), by which a change in the internal potential of the animal (and basal regions of the ampullary receptor cells) proportionately modulates the regular discharge of all primary afferent neurons. Thus, electrosensory receptors and primary afferents exhibit common mode noise and also a central adaptive filter in the hindbrain circuit, which has important implications for noise rejection and central processing of electrosensory information (see Bodznick and Montgomery, 2005).

IV. TUBEROUS ELECTRORECEPTORS

Tuberous electroreceptors have only been found in teleost fish, though they have evolved multiple times independently (Bullock et al., 1983). They are found only in fish that also have ampullary electroreceptors and the phylogenetic distribution of ampullary and tuberous organs suggest that tuberous organs are evolutionarily derived from ampullary organs (see Fig. 41.1). Within the Osteoglossomorpha, both ampullary and tuberous organs are found within the African Mormyriformes (Zakon, 1986). However, within the closely related Notopteridae, the African subfamily Xenomystinae has only ampullary organs, whereas the Asian subfamily Notopterinae lacks electroreceptors altogether (Braford, 1986). Within the Ostariophysi, the South American Gymnotiformes (knifefishes) possess both ampullary and tuberous organs (Zakon, 1986). The closely related Siluriformes (catfish) generally possess only ampullary organs, although tuberous organs have been described in one species. Despite the independent origins of tuberous electrosensory systems, there are many remarkable similarities in receptor morphology and physiology (Zakon, 1986; Jørgensen, 2005), as well as in the anatomy and physiology of the central sensory systems (Finger et al., 1986).

In general, tuberous electroreceptors are found in fish that have specialized electric organs for actively generating electric fields (see Fig. 41.1), underscoring their functional role in the detection of these fields. However, there is one exceptional case, the blind catfish *Pseudocetopsis* spp., which does not appear actively to generate electric fields and yet has both ampullary and tuberous electroreceptors (Andres et al., 1988). In all other cases, tuberous electroreceptors are tuned to the power spectrum of the species-specific electric organ discharge, or EOD (Carlson, 2006). EODs can be categorized as "wave-type" or "pulse-type": for wave-type EODs, the duration of each pulse is equal to the interval between pulses, resulting in a quasi-sinusoidal, continuous electric field; for pulse-type EODs, the duration of each pulse is much shorter than the intervals between pulses, resulting in discrete pulses of electricity. Both pulse- and wave-type species are found within the African Mormyriformes and South American Gymnotiformes (Fig. 41.7). EODs serve two functions (Fig. 41.8): communication, which is based on detecting the EODs of other individuals (Hopkins, 1986, 2005; Carlson, 2006) and active electrolocation, which is navigation and orientation based on detecting distortions in the self-generated electric field (von der Emde, 1999; Nelson, 2005). Both groups of fish are nocturnal and typically live in tropical rivers, streams and creeks. The electric sense thereby provides an effective sensory modality in conditions under which vision is of limited use. Studies on the neurobiology and behavior of these fish have generated many fundamental insights into neural structure and function (Moller, 1995; Rose, 2004).

IVA. Electric Organs

Strongly electric fish that use electricity as a weapon have electric organs capable of generating hundreds of volts. Weakly electric fish, those that use the EOD for active electrolocation and communication, generate much weaker electric fields (millivolts to a few volts). Electric organs have evolved independently at least six different times (see Fig. 41.1): once in the African Mormyriformes, once in the South American Gymnotiformes, once in the "modern" teleost order Perciformes (the stargazer *Astroscopus*), twice

in cartilaginous fishes (once in the torpedinoids or electric rays and once in the rajoids or skates) and at least once in the Siluriformes (catfish).

In nearly all cases, electric organs are of myogenic origin, i.e. they are derived from muscle (Bass, 1986). The excitable cells, termed electrocytes, are packed densely into the electric organ. They are driven to fire in synchrony by spinal electromotor neurons that receive input from a hindbrain command circuit, such that their individual action potentials (AP) summate to generate an external electric field (Caputi et al., 2005; Carlson, 2006). In wave-type species with a myogenic electric organ, the EOD frequency varies from about 100 to 500 Hz. Pulse-type species typically discharge at a lower rate (<100 Hz). In pulse-type mormyriforms, the EOD rate is highly variable, whereas in pulse-type gymnotiforms, EOD rates are quite regular. In general, the maximum energy in the power

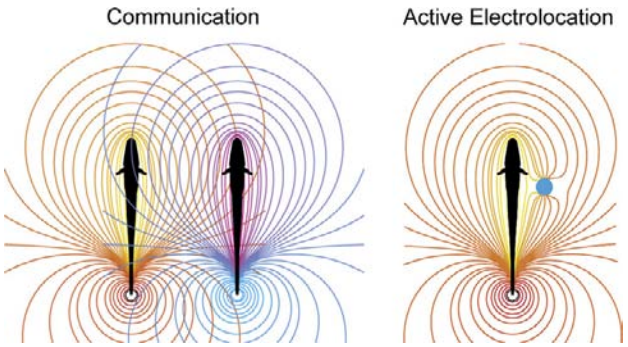

FIGURE 41.8 Electric organ discharges (EODs) serve two distinct functions: electric communication and active electrolocation. The EOD results in an electric field surrounding the fish, shown as isopotential field lines. Electric communication occurs when a fish enters the electric field of a neighboring fish. Active electrolocation occurs when nearby objects cause distortions in the self-generated electric field. The fish can detect these distortions and use them for orientation and navigation purposes. *(From Krahe and Gabbiani, 2004, with permission from Nature Publishing Group.)*

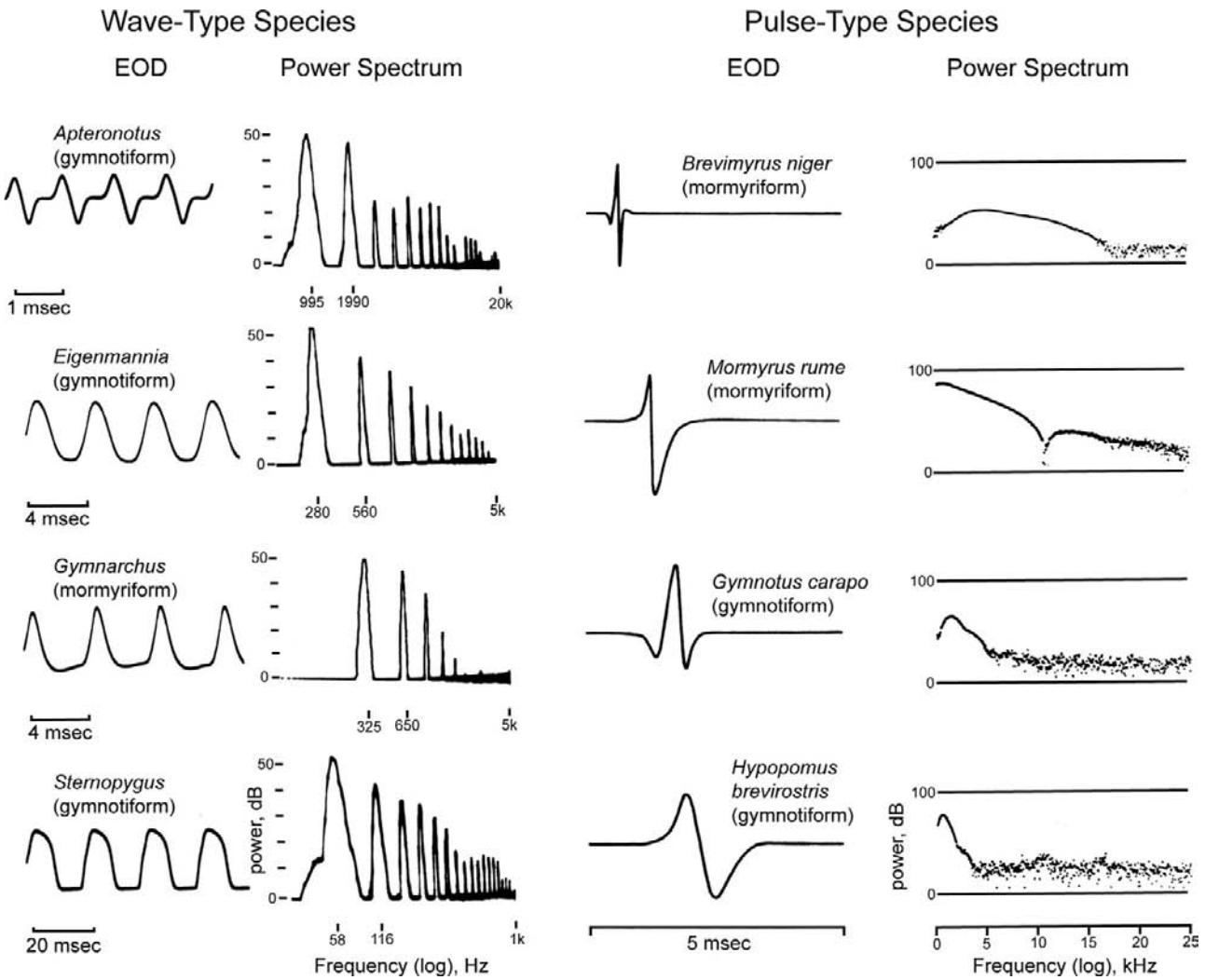

FIGURE 41.7 Electric organ discharges (EODs) and corresponding power spectra produced by several wave-type (left column) and pulse-type (right column) electric fish from the orders Gymnotiformes and Mormyriformes. *(Modified from Heiligenberg, 1991.)*

spectra of pulse-type EODs occurs in the range of about 100 to 10 000 Hz (see Fig. 41.7). Within the Gymnotiformes, one family, the Apteronotidae, possess a neurogenic electric organ that is composed of the axons of spinal electromotor neurons rather than derived from muscle (Bass, 1986). This may represent an adaptation to generating especially high EOD frequencies: the Apteronotidae generate wave-type EODs at frequencies ranging from about 650 to 1500 Hz (see Fig. 41.7). Detailed reviews of electric organ morphology, physiology and central control were published elsewhere (Bennett, 1971b; Bass, 1986; Caputi et al., 2005; Carlson, 2006).

IVB. Tuberous Electroreceptor Anatomy

In general, tuberous electroreceptor organs are distributed across the body surface (Szabo, 1974; Zakon, 1986; Jørgensen, 2005), although the distribution is not always uniform. High densities of tuberous receptors associated with improved electrosensory acuity have been described as electrical fovea, analogous to the visual fovea of the retina (Pusch et al., 2008). In addition, some tuberous organs in some species are organized into discrete clusters, or rosettes, that are localized to specific parts of the body surface (Zakon, 1986; Carlson et al., 2011). The organs themselves consist of a roughly spherical chamber located in the epidermis (Fig. 41.9). This chamber is connected to the external environment by a short canal that perforates the epidermis. Unlike ampullary organs, which have a mucous-filled duct that connects the receptor cells to the surface of the skin, the canals of tuberous organs are composed of a plug of loosely packed epithelial cells. This epithelial plug creates a capacitance in series with the receptor cells, which acts to filter out low stimulus frequencies (Bennett, 1965). Further, the walls of the canal and chamber consist of numerous layers of epithelial cells. These many

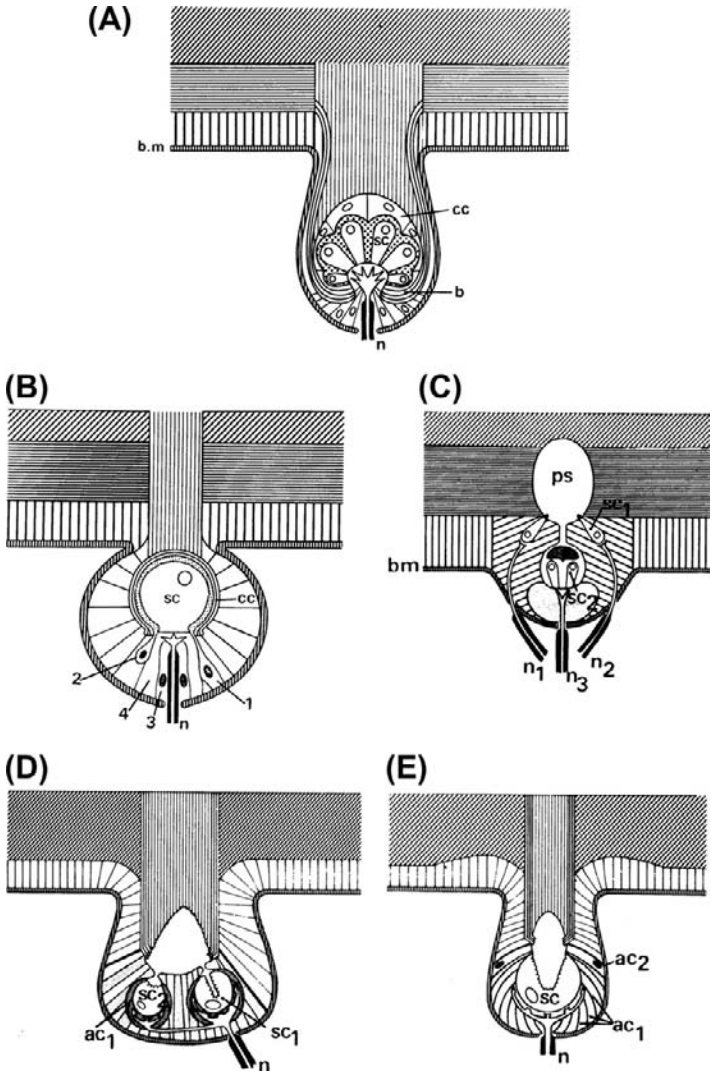

FIGURE 41.9 Schematics illustrating the anatomy of tuberous electroreceptor organs in (A) gymnotiform, (B, C) mormyrid and (D, E) gymnarchid weakly electric fishes. Abbreviations: ac1, ac2: accessory cells; b: capsule wall; bm: basement membrane; cc: covering cells; n#: afferent nerve fibers; ps: perisensory space; sc#: sensory cells. Numbers indicate different cell types within a given organ. *(From Szabo, 1974, with permission from Springer-Verlag, Berlin.)*

epithelial layers cause the wall to have relatively low capacitance, so that there is reduced shunting of high frequencies (Bennett, 1971a). These two distinguishing morphological features partly account for the tuning of tuberous receptors to much higher frequencies than ampullary receptors (Fig. 41.10). Indeed, EOD frequency correlates with the number of epithelial layers in the canal wall: species with low frequency EODs have fewer layers than those with high frequency EODs (Zakon, 1986).

At the base of the canal, the tuberous organ swells into a capsule within the corium. The sensory receptor cells themselves are located on the basal surface of this capsule, with their apical faces exposed to a mucopolysaccharide-filled receptor lumen. These apical faces contain either numerous microvilli or membrane foldings, both of which act to increase surface area, thereby increasing series capacitance while decreasing series resistance (Bennett, 1967, 1971b; Zakon, 1986). The number of receptor cells per organ varies from one to as many as 100, depending on the species and the type of tuberous organ. In all cases, the receptor cells are innervated by branches of the lateral line nerves, with primary afferent fibers that terminate within hindbrain electrosensory regions. In most cases, synaptic vesicles are found near the basal membrane of receptor cells and these mediate chemical synaptic transmission with primary afferent fibers. In one case, however, there may be an electronic junction between receptor cells and primary afferent fibers (see below). Details on the anatomy and physiology of central tuberous electrosensory pathways were reviewed elsewhere (Bell and Maler, 2005; Kawasaki, 2005).

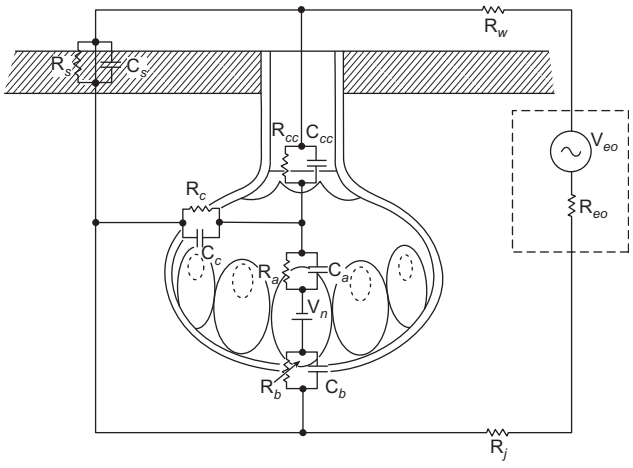

FIGURE 41.10 Electrical equivalent circuits of tuberous electroreceptors. Abbreviations: C_a: capacitance of the receptor cell apical membrane; C_b: capacitance of the receptor cell basal membrane; C_c: capacitance of the canal and capsule wall; C_{cc}: capacitance of the covering cells; C_s: capacitance of the skin; R_a: resistance of the receptor cell apical membrane; R_b: resistance of the receptor cell basal membrane; R_c: resistance of the canal and capsule wall; R_{cc}: resistance of the covering cells; R_{eo}: internal resistance of the electric organ; R_i: internal resistance of the fish; R_s: resistance of the skin; R_w: resistance of the water; V_{eo}: internal voltage of the electric organ; V_n: resting potential of receptor cells. Resistances and capacitances of supporting cells are not indicated and are believed to be passive. The resistance of the receptor cell basal membrane is thought to be voltage-gated. *(Modified from Bennett, 1967.)*

IVC. Tuberous Electroreceptor Physiology

Intracellular recordings from individual tuberous receptor cells have yet to be obtained; therefore, we know little about the underlying transduction mechanisms and much of what we do know about tuberous receptor physiology comes from recordings from their primary afferent fibers. While the apical membrane of receptor cells appears to act solely as a series capacitance that contributes to high-pass filtering, the basal membrane appears to be electrically excitable, generating graded potentials or, in some cases, even spikes (Bennett, 1971a). The receptor cells respond to inward current that creates a voltage drop across the basal membrane of the receptor cell (see Fig. 41.10). Thus, they effectively measure the difference in voltage between the interior of the receptor cell and the internal "reference" potential of the animal (Bennett, 1971a). Tuberous receptors are sensitive to much higher frequencies than ampullary receptors as they are generally tuned to the power spectrum of the species-specific EOD. In wave-type species, this tuning is typically quite sharp, whereas the tuberous receptors of pulse-type species are more broadly-tuned. Although some of this tuning relates to passive electrical filtering due to the morphology of tuberous organs and the apical face of the receptor cells (see above), active mechanisms also contribute substantially to frequency tuning (see Fig. 41.10). Tuberous receptors typically respond to stimulation with potentials that oscillate at a frequency equal to the best frequency of the receptor (Bennett, 1971a) and, in some species at least, this appears to be based on both inward Ca^{2+} and outward K^+ currents (Zakon, 1986). Across taxa, tuberous receptors can be divided into two broad classes based on their responses to electrosensory stimuli: "amplitude-coding" and "time-coding" receptors (Fig. 41.11). As their names suggest, amplitude-coding receptors function primarily in encoding EOD amplitude, whereas time-coding receptors function primarily in encoding the timing of EOD pulses or cycles (Zakon, 1986). Time-coding receptors may generally be distinguished from amplitude-coding receptors as having lower thresholds, greater response probabilities, reduced timing jitter and shorter response latencies.

IVD. Tuberous Electroreceptors in Gymnotiformes

There are currently five recognized families with the order Gymnotiformes, two of which have wave-type EODs (Sternopygidae and Apteronotidae) and three of which

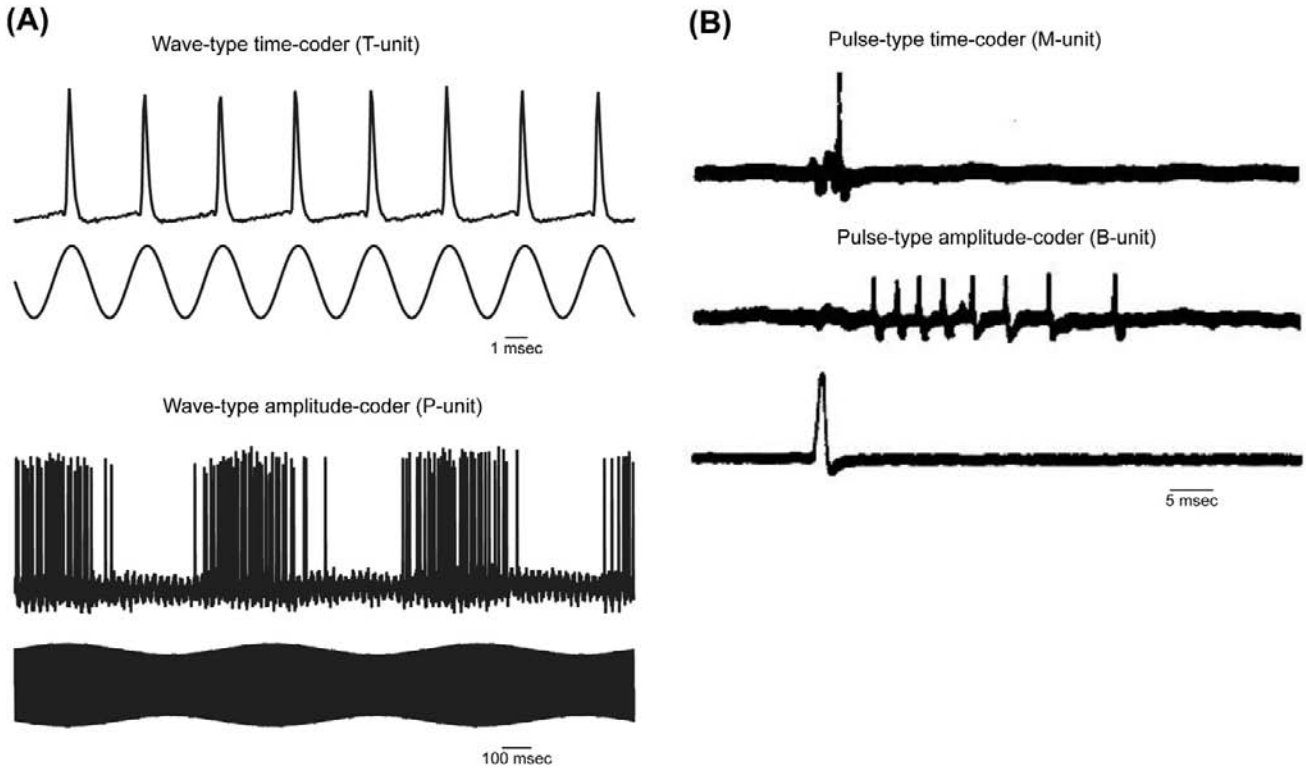

FIGURE 41.11 The primary afferent fibers of tuberous electroreceptors can be classified as either amplitude-coding or time-coding depending on which stimulus feature they respond most strongly to. (A) In the wave-type gymnotiform *Eigenmannia*, T-units fire a single, time-locked action potential (AP) in response to every cycle of an EOD (or a substitute sine wave as shown here), providing a precise marker of EOD timing. P-units do not fire an AP in response to every cycle; instead, their firing probability varies as a function of stimulus amplitude, as can be seen when a stimulus is modulated in amplitude over longer timescales. (*Unpublished recordings from Carlson, 2008a.*) (B) In the pulse-type gymnotiform *Hypopomus*, M-units fire a single, time-locked AP in response to each EOD pulse, whereas B-units fire a burst of spikes in response to each EOD pulse. The number of spikes in a B-unit burst varies as a function of stimulus amplitude. *(From Bastian, 1976.)*

have pulse-type EODs (Gymnotidae, Hypopomidae, and Rhamphichthyidae). The morphology of gymnotiform tuberous organs is essentially similar across all species studied (see Fig. 41.9A) (Szabo, 1974; Zakon, 1986; Jørgensen, 2005). Directly beneath the epithelial plug and above the sensory receptor cells, there is a layer of covering cells that extends across the capsule. These cells are joined to each other and to the walls of the capsule by tight junctions. The layer of covering cells maintains a constant ionic environment within the receptor lumen and also adds an additional series capacitance to the receptor organ.

The number of sensory receptor cells per organ typically varies from 20 to 30, but some tuberous organs can have as many as 100 receptors (Szabo, 1974; Zakon, 1986). The receptor cells are about 20−30 μm long. The apical region of the receptor cell has numerous microvilli exposed to the lumen and large numbers of mitochondria (Szabo, 1974). The receptors are attached to the base of the chamber via tight junctions only at the basal-most portion of the receptor cell's membrane. Thus, 95% of the membrane surface is exposed to the surrounding lumen. The remaining basal portion of the cell membrane is electrically isolated from the lumen via tight junctions with supporting cells (Szabo, 1974; Zakon, 1986). All of the receptor cells within a tuberous organ are innervated by a single afferent fiber, though one fiber may innervate either one or several organs. When an afferent fiber innervates several tuberous organs, those organs form a distinct cluster called a rosette, resulting from the division of a single organ with growth. The receptive field of each primary afferent fiber is centered on the pore of a single tuberous organ (Bennett, 1967; Zakon, 1986).

Two distinct physiological classes of primary afferent fibers have been described in wave-type gymnotiforms: T-units (for *Time-coder*) and P-units (for *Probability-coder*). Within the natural range of stimulus intensities, T-units fire one phase-locked spike per EOD cycle with less than 100 μs of timing jitter (see Fig. 41.11A), thus providing a precise marker of the timing of positive transitions in the EOD (Zakon, 1986; Heiligenberg, 1991; Carlson, 2006, 2008a,b). By contrast, P-units do not fire a spike during each EOD cycle and they have timing jitter greater than 500 μs (Zakon, 1986; Heiligenberg, 1991; Carlson, 2006, 2008a). The probability of P-unit firing

varies with amplitude; thus, the firing rate of P-units codes for EOD amplitude (see Fig. 41.11A). There are a number of additional distinguishing features between the two types of receptors (Zakon, 1986): T-units are more sharply frequency tuned and they are typically tuned to higher frequencies than P-units; P-units readily adapt to changes in steady-state amplitude, whereas T-units do not; although both types of units have dynamic ranges of about 20 dB, the threshold stimulus intensity for T-units is about 15−20 dB lower than that of P-units. Although it remains unclear, P- and T-units may correspond to two distinct anatomical classes of tuberous organs, one which is characterized by one to two receptor organs per axon with thick axon branches and a second which is characterized by four or more receptor organs per axon with thin axon branches (Zakon, 1986).

P- and T-units both play important roles in electrosensory-mediated behaviors (Heiligenberg, 1991). Interference between the EODs of neighboring fish results in modulations in both the amplitude and timing (i.e. phase) of the resulting electric field (Fig. 41.12). Information about the temporal relationship between amplitude and phase modulation is used to determine the EOD frequency of a neighboring fish, a determination that is important for both communication behavior and avoidance of electrosensory jamming (Heiligenberg, 1991; Carlson, 2006, 2008a). Further, wave-type gymnotiforms are able to distinguish purely resistive objects from capacitive objects having complex impedances by comparing the activities of P- and T-units (von der Emde, 1999). Although the two classes of units are clearly specialized for separately encoding the amplitude and timing of stimuli, the distinction is not complete: the spike times of T-units are affected by stimulus amplitude and the firing rate of P-units can be affected by stimulus timing, and this "cross-talk" can ultimately influence electrosensory perception (Carlson, 2008a).

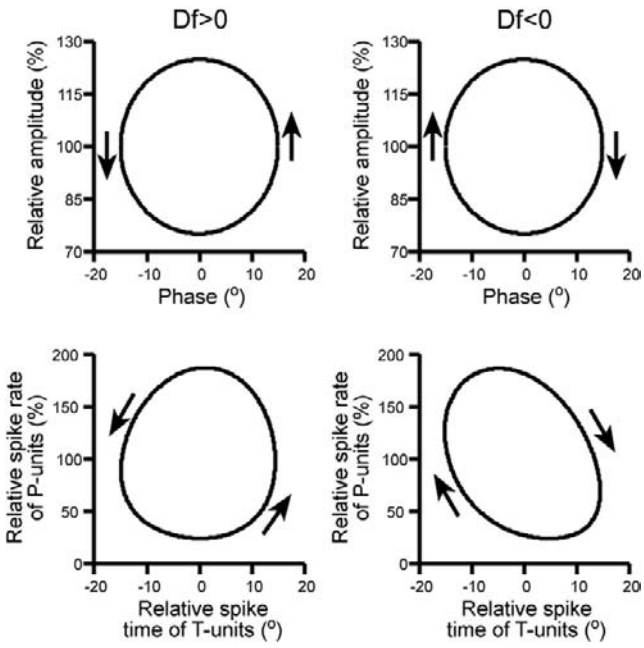

FIGURE 41.12 Neural representations of sinusoidal stimulus modulations caused by interference from a neighboring fish's EOD in the wave-type gymnotiform *Eigenmannia*. The top row shows Lissajous plots that illustrate the temporal relationship between amplitude modulation and phase modulation, with the sense of rotation indicating how these two variables change over time: when the neighboring fish has a higher EOD rate than the focal fish (Df > 0, left), the resulting plot has a counterclockwise sense of rotation. When the neighboring fish has a lower EOD rate than the focal fish (Df < 0, right), the resulting plot has a clockwise sense of rotation. The bottom row shows similar Lissajous plots, except that the average spike rate of P-units is plotted against the average spike time of T-units. Notice how the neural representations of the two different conditions exhibit the same sense of rotation as the stimuli themselves. *(Modified from Carlson, 2008a.)*

Pulse-type gymnotiforms also have two distinct physiological classes of primary afferents (see Fig. 41.11B): M-units (for *pulse Marker*) and B-units (for *Burst duration-coder*). Similar to T-units, M-units fire a single, short latency spike in response to each EOD pulse with little timing jitter; by contrast, B-units respond to each EOD pulse with a longer-latency burst of spikes (Bastian, 1976; Zakon, 1986). The duration of the burst increases with increasing EOD amplitude: at near threshold intensities, B-units may respond to an EOD with a single spike, whereas they respond with 20−40 spikes at higher intensities. Both units are sensitive to the direction of current flow, with greatest responses to stimuli at the best azimuth for transepidermal current flow (Hopkins, 2005).

The physiological distinction between M- and B-units is clearly linked to anatomical differences in the associated receptor organs (Szabo, 1974; Zakon, 1986). M-units have large-diameter axons with large myelinated terminal enlargements within the receptor capsule that give rise to boutons that innervate the receptor cells. By contrast, B-units have smaller-diameter axons that lose their myelination upon entering the capsule and give rise to several thin, unmyelinated terminal branches that innervate the receptor cells.

IVE. Tuberous Electroreceptors in Mormyriformes

The Mormyriformes consist of two distinct sister families, the Mormyridae and the monotypic Gymnarchidae, *Gymnarchus niloticus*. All of the mormyrids have pulse-type EODs, while *Gymnarchus* has a wave-type EOD (see Fig. 41.7). Two distinct physiological classes of receptors have been described in *Gymnarchus*: S- and O-units, which are remarkably similar to the T- and P-units of wave-type gymnotiforms, respectively (Kawasaki, 1997; Carlson, 2008a). S-units have lower thresholds, higher firing probabilities, reduced jitter and less adaptation to steady-state

changes in intensity than O-units. Thus, within the natural range of stimulus intensities, S-units fire 1:1 with each cycle of the EOD and provide a precise marker of the timing of positive transitions, whereas the firing rate of O-units codes for stimulus amplitude. As in the wave-type gymnotiforms, both units provide critical information for determining the EOD frequency of neighboring fish (Kawasaki, 1997). Further, S-units do respond to changes in stimulus amplitude and O-units can respond to changes in stimulus timing, similar to the effects seen in T- and P-units (Carlson, 2008a).

Anatomically, the tuberous organs of *Gymnarchus* are referred to as Gymnarchomasts (Szabo, 1974; Zakon, 1986; Jørgensen, 2005). Type I gymnarchomasts contain two distinct sensory receptor cell types; the organ may contain one or many pairs of these two cell types (see Fig. 41.9D). The larger of the two receptor cell types has a deep invagination filled with numerous microvilli. The microvilli located at the base of the depression are especially long and project upwards into the apical cavity. The smaller receptor cell type has only a slight depression at its apical surface, although it too has densely-packed microvilli. Both sensory cells are surrounded by numerous support cells and only a small portion of receptor cell membrane surface is exposed to the surrounding lumen. All of the receptor cells in an organ are innervated by a single afferent nerve fiber. Physiologically, type I gymnarchomasts have been linked to S-unit primary afferent fibers (Bennett, 1971a; Zakon, 1986). Type II gymnarchomasts consist of several (12−13) sensory receptor cells that are innervated by a single primary afferent fiber. Each individual receptor cell is separated from the surrounding receptor cells by a ring of accessory cells. Thus, the type II organ can be thought of as composed of multiple sensory "units", each with a single receptor cell and multiple accessory cells (see Fig. 41.9E). The receptor cells are similar in morphology to the larger receptor cell of the type I gymnarchomast in having a deeply invaginated apical surface filled with microvilli that project upwards. Type II gymnarchomasts are thought to correspond to O-unit primary afferent fibers (Bennett, 1971a; Zakon, 1986).

The pulse-type mormyrids also have two distinct classes of tuberous receptor organs, amplitude-coding mormyromasts and time-coding knollenorgans (Bennett, 1965, 1971a; Szabo, 1974; Zakon, 1986). Knollenorgans typically have one to 10 sensory receptor cells, although some species have especially large knollenorgans with as many as 60 receptor cells. The receptor cells are large (40−50 μm in diameter) and each is enclosed in its own cavity within the receptor capsule (Szabo, 1974; Zakon, 1986; Jørgensen, 2005). Only the basal-most portion of the receptor cell's membrane is attached to the base of the chamber, similar to the tuberous receptors of gymnotiforms (see Fig. 41.9B). The apical cell membrane is densely packed with microvilli, below which is a dense band of mitochondria. Knollenorgans are unique among tuberous receptors in that the receptor itself generates APs rather than only graded receptor potentials. Further, physiological evidence suggests an electrotonic synapse between the receptor cell and primary afferent fiber (Bennett, 1971a), a conclusion supported by the small numbers of synaptic vesicles and close apposition of pre- and postsynaptic membranes (Zakon, 1986). However, gap junctions have never actually been observed. All of the receptor cells within a knollenorgan are innervated by a single primary afferent fiber that divides to form several terminal boutons onto each individual receptor cell.

Like the pulse marker primary afferents (M-units) of pulse-type gymnotiforms, knollenorgans have a relatively low threshold and fire a single AP in response to an EOD (Bennett, 1965, 1967; Bell, 1990; Carlson, 2008b). The primary afferents of knollenorgans terminate in the hindbrain, where an inhibitory input arising from the electromotor pathway blocks ascending knollenorgan responses whenever the fish generates its own EOD (Carlson, 2008c). Thus, the downstream knollenorgan pathway never "hears" the fish's own EOD, strongly suggesting that knollenorgans function solely in communication behavior (Carlson, 2006). The timing of the knollenorgan AP is tightly phase-locked to the timing of outside-positive positive transitions in the stimulus waveform (Bennett, 1965; Hopkins and Bass, 1981). In response to natural stimuli, different knollenorgans receive EODs with different polarities, resulting in small differences in spike timing across the population of knollenorgans (Fig. 41.13). Behavioral, anatomical and physiological evidence suggests that these spike timing differences mediate the detection of species-specific EOD waveforms (Hopkins and Bass, 1981; Xu-Friedman and Hopkins, 1999; Carlson, 2006), although certain clades of mormyrids appear to lack this ability (Carlson et al., 2011).

Mormyromasts have a distinctive morphology (Jørgensen, 2005). Although the pore and epithelial plug are similar to other tuberous organs, the organ itself consists of two separate chambers, one superficial and one deep, connected to each other by a short duct (see Fig. 41.9C). The two chambers each have their own distinct type of sensory receptor cell: the sensory cells in the upper chamber are referred to as A-type receptor cells, whereas those in the lower chamber are referred to as B-type receptor cells. The number of receptor cells in the two chambers is nearly always equal, varying from two each in the smaller mormyromasts to more than 12 in the larger ones (Jørgensen, 2005). The A-type cells lack microvilli and have only a small portion of their apical surface exposed to the receptor lumen. By contrast, the B-type cells have microvilli and, like knollenorgan receptors, nearly the entire receptor surface area is exposed to the surrounding lumen. The A-cells are contacted by two to three primary

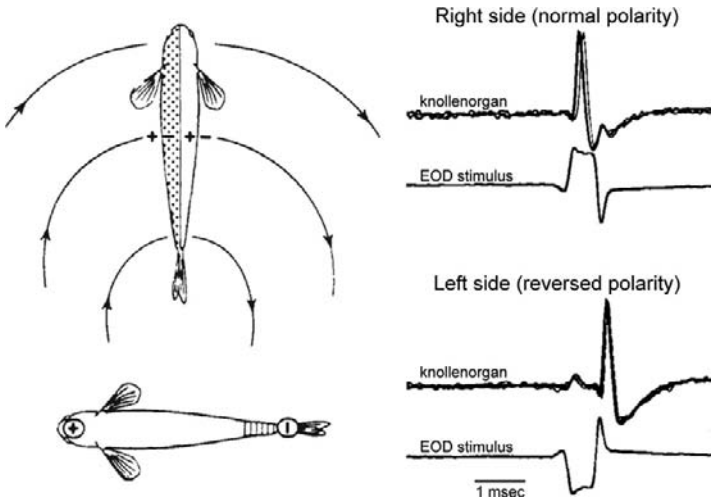

FIGURE 41.13 Knollenorgan electroreceptors in mormyrids mediate species recognition during electric communication. On the left, a signaling fish and receiving fish are viewed from below. The signaling fish is modeled as a simple dipole with "+" and "−" poles at the head and tail, respectively. This causes current to flow into the right side of the receiving fish and out the left side. (*Modified from Hopkins, 1986.*) On the right, the responses of a single knollenorgan to opposite polarity EOD stimuli are shown. Knollenorgans respond to outside-positive changes in voltage. As a result, knollenorgans respond to the start of a normal polarity EOD (simulating the response of a knollenorgan on the right side of the body), but they respond to the end of a reversed polarity EOD (simulating the response of a knollenorgan on the left side of the body). The resulting difference in response latency is used to determine EOD duration. *(Modified from Hopkins and Bass 1981.)*

afferent fibers, whereas all of the B-cells are always contacted by a single primary afferent fiber. The A- and B-cell primary afferents terminate in separate portions of the hindbrain electrosensory lateral line lobe, forming two distinct maps of the body surface (Bell and Maler, 2005). Interestingly, in one genus of mormyrid, *Stomatorhinus*, both the A- and B-cells are present, but only the A-cells receive innervation from primary afferent fibers and this is associated with a complete loss of the associated electrosensory lateral line map (McNamara et al., 2005). This may be related to the extremely short duration (≈250 μs) and high peak power spectral frequencies (≈14−26 kHz) of the EODs in these species, which may preclude the detection of complex impedances based on waveform distortions (see below).

Both A- and B-cell afferents may be classified as amplitude-coding. Like the burst duration coders of pulse-type gymnotiforms, they respond to suprathreshold stimuli by generating a burst of spikes (Bennett, 1965; Bell, 1990). Increases in stimulus amplitude cause both a decrease in first-spike latency, as well as an increase in the number of spikes (Fig. 41.14) (Bennett, 1965; Bell, 1990), although behavioral and physiological evidence suggests that first-spike latency appears to be the critical feature for stimulus coding. In contrast to the knollenorgan sensory pathway, mormyromast input to the hindbrain is gated by an excitatory input arising from the electromotor pathway, rather than inhibited (Carlson, 2008c). As a result, the downstream mormyromast pathway is selectively responsive to the fish's own EOD, indicating that mormyromasts function solely in active electrolocation behavior (von der Emde, 1999).

Compared to knollenorgans, mormyromast primary afferent fibers have higher thresholds and they tend to be

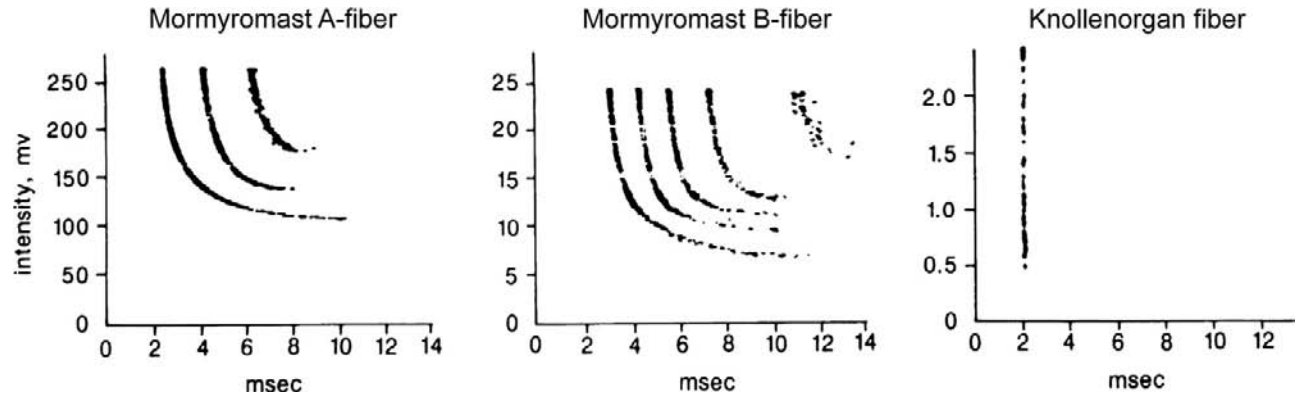

FIGURE 41.14 Differences in the coding of electrosensory stimuli among tuberous electrosensory primary afferent fibers in mormyrids. Stimulus intensity is plotted against the latency of action potentials (Aps) relative to the stimulus. The minimum stimulus intensity required to elicit a response (i.e. threshold) is indicated by the lowest intensity at which any APs occurred. Mormyromast fibers have a much higher threshold than knollenorgan fibers. Further, increases in stimulus intensity cause a decrease in the latency to the first spike, as well as an increase in the number of spikes in mormyromasts, whereas knollenorgans fire only a single spike at a relatively fixed latency. Mormyromast B-fibers tend to have a lower threshold and greater number of spikes per burst compared to A-fibers. *(Modified from Bell, 1990.)*

tuned to frequencies below the peak power frequency of the species-specific EOD (see Fig. 41.14) (Bell, 1990). B-cell afferents tend to have a lower threshold, smaller dynamic range and greater maximum burst number than A-cell afferents. Further, A-cells tend to be tuned to higher frequencies and show more variation in frequency tuning than B-cells. Most importantly, B-cell afferents respond to subtle changes in EOD waveform caused by complex impedances, whereas A-cell afferents do not (von der Emde, 1999). Thus, comparing the responses of the two types of primary afferents may be the mechanism by which mormyrids distinguish simple from complex impedances during active electrolocation (von der Emde, 1999).

IVF. Tuberous Electroreceptors in Siluriformes

Compared to the mormyriforms and gymnotiforms, we know very little about the tuberous receptors found in siluriforms (catfishes). Tuberous organ morphology has been described only in the blind catfish *Pseudocetopsis* spp. (Andres et al., 1988). Compared to tuberous organs in other taxa, this tuberous organ, referred to as a siluromast, is located superficially within the epidermis (Jørgensen, 2005). Each organ has a single sensory receptor cell with a diameter of $\approx$25 μm and an apical surface covered with microvilli. A single primary afferent fiber loses its myelin sheath within the supporting cell layer and then synapses onto the receptor cell with a flattened terminal face. The function of this tuberous organ is unclear, as these fish are not known actively to generate EODs. One intriguing possibility is that these tuberous organs serve a predatory function by allowing the blind catfish passively to electrolocate sympatric gymnotiforms by detecting their EODs (Andres et al., 1988).

BIBLIOGRAPHY

Andres, K. H., von Düring, M., & Petrasch, E. (1988). The fine structure of ampullary and tuberous electroreceptors in the South American blind catfish *Pseudocetopsis* spec. *Anat Embryol, 177*, 523–535.

Andrianov, G. N., Broun, G. R., & Ilyinsky, O. B. (1984). Frequency characteristic of skate electroreceptive central neurons responding to electrical and magnetic stimulation. *Neurophysiology, 16*, 365–376.

Bass, A. H. (1986). Electric organs revisited: evolution of a vertebrate communication and orientation organ. In T. H. Bullock, & W. Heiligenberg (Eds.), *Electroreception* (pp. 13–70). New York: John Wiley and Sons.

Bastian, J. (1976). Frequency-response characteristics of electroreceptors in weakly electric fish (Gymnotoidei) with a pulse discharge. *J Comp Physiol, 112*, 165–180.

Beason, R. C., & Semm, P. (1987). Magnetic responses of the trigeminal nerve system of the Bobolink (*Dolichonyx oryzivorus*). *Neurosci Lett, 80*, 229–234.

Bell, C. C. (1990). Mormyromast electroreceptor organs and their afferent fibers in mormyrid fish. III. Physiological differences between two morphological types of fibers. *J Neurophysiol, 63*, 319–332.

Bell, C., & Maler, L. (2005). Central neuroanatomy of electrosensory systems in fish. In T. H. Bullock, C. D. Hopkins, A. N. Popper, & R. R. Fay (Eds.), *Springer Handbook of Auditory Research: Vol. 21, Electroreception* (pp. 68–111). New York: Springer.

Bemis, W. E., & Hetherington, T. E. (1982). The rostral organ of Latimeria chalumnae: morphological evidence of an electroreceptive function. *Copeia, 1982*, 467–471.

Bennett, M. V. L. (1965). Electroreceptors in mormyrids. *Cold Spring Harbor Symp Quant Biol, 30*, 245–262.

Bennett, M. V. L. (1967). Mechanisms of electroreception. In P. Cahn (Ed.), *Lateral Line Detectors* (pp. 313–393). Bloomington: Indiana University Press.

Bennett, M. V. L. (1968). Similarities between chemically and electrically mediated transmission. In F. D. Carlson (Ed.), *Physiological and Biochemical Aspects of Nervous Integration* (pp. 73–128). Englewood Cliffs: Prentice-Hall.

Bennett, M. V. L. (1971a). Electroreception. In W. S. Hoar, & D. S. Randall (Eds.), *Fish Physiology, Vol. 5* (pp. 493–574). New York: Academic Press.

Bennett, M. V. L. (1971b). Electric organs. In W. S. Hoar, & D. J. Randall (Eds.), *Fish Physiology, Vol. 5* (pp. 347–491). New York: Academic Press.

Bennett, M. V. L., & Clusin, W. T. (1978). Physiology of the ampulla of Lorenzini, the electroreceptor of elasmobranchs. In E. S. Hodgson, & R. F. Mathewson (Eds.), *Sensory Biology of Sharks, Skates, and Rays* (pp. 483–505). Arlington: Office of Naval Research.

Bennett, M. V. L., & Obara, S. (1986). Ionic mechanisms and pharmacology of electroreceptors. In T. H. Bullock, & W. Heiligenberg (Eds.), *Electroreception* (pp. 157–181). New York: John Wiley and Sons.

Bodznick, D., & Montgomery, J. C. (2005). The physiology of low-frequency electrosensory systems. In T. H. Bullock, C. D. Hopkins, A. N. Popper, & R. R. Fay (Eds.), *Springer Handbook of Auditory Research, Vol. 21. Electroreception* (pp. 132–153). New York: Springer.

Bodznick, D., & Preston, D. G. (1983). Physiological characterization of electroreceptors in the lampreys, *Ichthyomyzon unicuspis* and *Petromyzon marinus*. *J Comp Physiol A, 152*, 209–217.

Bodznick, D., Hjelmstad, G., & Bennett, M. V. L. (1993). Accommodation to maintained stimuli in the ampullae of Lorenzini: how an electroreceptive fish achieves sensitivity in a noisy world. *Jap J Physiol, 43*(Suppl. 1), S231–S237.

Bodznick, D., Montgomery, J. C., & Bradley, D. J. (1992). Suppression of common-mode signals within the electrosensory system of the little skate, *Raja erinacea*. *J Exp Biol, 171*, 107–125.

Braford, M. R. (1986). African knifefishes: the Xenomystines. In T. H. Bullock, & W. Heiligenberg (Eds.), *Electroreception* (pp. 453–464). New York: John Wiley and Sons.

Brown, B. R., Hughes, M. E., & Russo, C. (2005). Infrastructure in the electric sense: admittance data from shark hydrogels. *J Comp Physiol A, 191*, 115–123.

Brown, B. R., Hutchison, J. C., Hughes, M. E., Kellogg, D. R., & Murray, R. W. (2002). Electrical characterization of gel collected from shark electrosensors. *Phys Rev E, 65*, 061903.

Bullock, T. H., & Heiligenberg, W. (1986). *Electroreception*. New York: John Wiley and Sons.

Bullock, T. H., Bodznick, D. A., & Northcutt, R. G. (1983). The phylogenetic distribution of electroreception: evidence for convergent evolution of a primitive vertebrate sense modality. *Brain Res Rev, 6*, 25–46.

Caputi, A. A., Carlson, B. A., & Macadar, O. (2005). Electric organs and their control. In T. H. Bullock, C. D. Hopkins, A. N. Popper, & R. R. Fay (Eds.), *Springer Handbook of Auditory Research, Vol. 21, Electroreception* (pp. 410–451). New York: Springer.

Carlson, B. A. (2006). A neuroethology of electrocommunication: senders, receivers, and everything in between. In F. Ladich, S. P. Collin, P. Moller, & B. G. Kapoor (Eds.), *Communication in Fishes, Vol. 2* (pp. 805–848). Enfield: Science Publishers.

Carlson, B. A. (2008a). Phantoms in the brain: ambiguous representations of stimulus amplitude and timing in weakly electric fish. *J Physiol Paris, 102*, 209–222.

Carlson, B. A. (2008b). Temporal coding in electroreception. In M. D. Binder, N. Hirokawa, U. Windhorst, & M. C. Hirsch (Eds.), *Encyclopedia of Neuroscience* (pp. 4039–4044). New York: Springer.

Carlson, B. A. (2008c). Reafferent control in electric communication. In M. D. Binder, N. Hirokawa, U. Windhorst, & M. C. Hirsch (Eds.), *Encyclopedia of Neuroscience* (pp. 3368–3373). New York: Springer.

Carlson, B. A., Hasan, S. M., Hollmann, M., Miller, D. B., Harmon, L. J., & Arnegard, M. E. (2011). Brain evolution triggers increased diversification of electric fishes. *Science, 332*, 583–586.

Diebel, C. E., Proksch, R., Green, C. R., Neilson, P., & Walker, M. M. (2000). Magnetite defines a vertebrate magnetoreceptor. *Nature, 406*, 299–302.

Falkenberg, G., Fleissner, G., Schuchardt, K., et al. (2010). Avian magnetoreception: elaborate iron mineral containing dendrites in the upper beak seem to be a common feature of birds. *PloS one, 5*, e9231.

Fields, R. D., Bullock, T. H., & Lange, O. D. (1993). Ampullary sense organs, peripheral, central and behavioral electroreception in chimeras (Hydrolagus, Holocephali, Chondrichthyes). *Brain Behav Evol, 41*, 269–289.

Finger, T. E., Bell, C. C., & Carr, C. E. (1986). Comparisons among electroreceptive teleosts: why are electrosensory systems so similar? In T. H. Bullock, & W. Heiligenberg (Eds.), *Electroreception* (pp. 465–481) New York: John Wiley and Sons.

Fleissner, G., Holtkamp-Rotzler, E., Hanzlik, M., Winklhofer, M., Petersen, N., & Wiltschko, W. (2003). Ultrastructural analysis of a putative magnetoreceptor in the beak of homing pigeons. *J Comp Neurol, 458*, 350–360.

Freitas, R., Zhang, G., Albert, J. S., Evans, D. H., & Cohn, M. J. (2006). Developmental origin of shark electrosensory organs. *Evol Devel, 8*, 74–80.

Gibbs, M. A., & Northcutt, R. G. (2004). Development of the lateral line system in the shovelnose sturgeon. *Brain Behav Evol, 64*, 70–84.

Gregory, J. E., Iggo, A., McIntyre, A. K., & Proske, U. (1989). Responses of electroreceptors in the snout of the echidna. *J Physiol (London), 414*, 521–538.

Heiligenberg, W. (1991). *Neural Nets in Electric Fish*. Cambridge: MIT Press.

Hopkins, C. D., & Bass, A. H. (1981). Temporal coding of species recognition signals in an electric fish. *Science, 212*, 85–87.

Hopkins, C. D. (1986). Behavior of mormyridae. In T. H. Bullock, & W. Heiligenberg (Eds.), *Electroreception* (pp. 527–576). New York: John Wiley and Sons.

Hopkins, C. D. (2005). Passive electrolocation and the sensory guidance of oriented behavior. In T. H. Bullock, C. D. Hopkins, A. N. Popper, & R. R. Fay (Eds.), *Springer Handbook of Auditory Research, Vol. 21, Electroreception* (pp. 264–289). New York: Springer.

Johnsen, S., & Lohmann, K. J. (2005). The physics and neurobiology of magnetoreception. *Nat Rev Neurosci, 6*, 703–712.

Jørgensen, J. M. (2005). Morphology of electroreceptive sensory organs. In T. H. Bullock, C. D. Hopkins, A. N. Popper, & R. R. Fay (Eds.), *Springer Handbook of Auditory Research, Vol. 21, Electroreception* (pp. 47–67). New York: Springer.

Kalmijn, A. J. (1971). The electric sense of sharks and rays. *J Exp Biol, 55*, 371–383.

Kalmijn, A. J. (1974). The detection of electric fields from inanimate and animate sources other than electric organs. In A. Fessard (Ed.), *Handbook of Sensory Physiology, Vol. III/3* (pp. 147–200). New York: Springer-Verlag.

Kalmijn, A. J. (1982). Electric and magnetic field detection in elasmobranch fishes. *Science, 218*, 915–918.

Kalmijn, A. J. (1988). Detection of weak electric fields. In J. Atema, R. R. Fay, A. N. Popper, & W. N. Tavogla (Eds.), *Sensory Biology of Aquatic Animals* (pp. 151–186). New York: Springer-Verlag.

Kawasaki, M. (1997). Sensory hyperacuity in the jamming avoidance response of weakly electric fish. *Curr Opin Neurobiol, 7*, 473–479.

Kawasaki, M. (2005). Physiology of tuberous electrosensory systems. In T. H. Bullock, C. D. Hopkins, A. N. Popper, & R. R. Fay (Eds.), *Springer Handbook of Auditory Research, Vol. 21, Electroreception* (pp. 154–194). New York: Springer.

Krahe, R., & Gabbiani, F. (2004). Burst firing in sensory systems. *Nat Rev Neurosci, 5*, 13–23.

Lissman, H. W. (1958). On the function and evolution of electric organs in fish. *J Exp Biol, 35*, 156–191.

Lissman, H. W., & Machin, K. E. (1958). The mechanisms of object location in *Gymnarchus niloticus* and similar fish. *J Exp Biol, 35*, 451–486.

Lu, J., & Fishman, H. M. (1994). Interaction of apical and basal membrane ion channels underlies electroreception in ampullary epithelia of skates. *Biophys J, 67*, 1525–1533.

Lu, J., & Fishman, H. M. (1995a). Localization and function of the electrical oscillation in electroreceptive ampullary epithelium from skates. *Biophys J, 69*, 2458–2466.

Lu, J., & Fishman, H. M. (1995b). Ion channels and transporters in the electroreceptive ampullary epithelium from skates. *Biophys J, 69*, 2467–2475.

McNamara, A. M., Denizot, J.-P., & Hopkins, C. D. (2005). Comparative anatomy of the electrosensory lateral line lobe of mormyrids: the mystery of the missing map in the genus Stomatorhinus (Family: Mormyridae). *Brain Behav Evol, 65*, 188–201.

Millot, J., & Anthony, J. (1956). L'organe rostral de Latimeria (Crossoptérygien Coelacanthidé). *Ann Sci Nat Zool 11 Sér, 18*, 381–387.

Moller, P. (1995). Electric fishes: history and behavior. In *Fish and Fisheries Series, 17, pp. xxiv, 584*. London: Chapman & Hall.

Montgomery, J. C. (1984a). Noise cancellation in the electrosensory system of the thornback ray; common mode refection of input produced by the animal's own ventilatory movement. *J Comp Physiol A, 155*, 103–111.

Montgomery, J. C. (1984b). Frequency response characteristics of primary and secondary neurons in the electrosensory system of the thornback ray. *Comp Biochem Physiol, 79A*, 189−195.

Montgomery, J. C., & Bodznick, D. (1993). Hindbrain circuitry mediating common-mode suppression of ventilatory reafference in the electrosensory system of the little skate. *Raja erinacea, J. Exp. Biol., 183*, 203−315.

Murray, R. W. (1962). The response of the ampullae of Lorenzini of elasmobranches to electrical stimulation. *J Exp Biol, 39*, 119−128.

Nelson, M. E. (2005). Target detection, image analysis, and modeling. In T. H. Bullock, C. D. Hopkins, A. N. Popper, & R. R. Fay (Eds.), *Springer Handbook of Auditory Research, Vol. 21, Electroreception* (pp. 290−317). New York: Springer.

New, J. G. (1990). Medullary electrosensory processing in the little skate. I. Response characteristics of neurons in the dorsal octavolateralis nucleus. *J Comp Physiol A, 167*, 285−294.

Neiman, A. B., & Russell, D. F. (2004). Two distinct types of noisy oscillators in electroreceptors of paddlefish. *J Neurophysiol, 92*, 492−509.

Neiman, A. B., Yakusheva, T. A., & Russell, D. F. (2007). Noise-induced transition to bursting in responses of paddlefish electroreceptor afferents. *J Neurophysiol, 98*, 2795−2806.

Northcutt, R. G. (1986). Electroreception in nonteleost bony fishes. In T. H. Bullock, & W. Heiligenberg (Eds.), *Electroreception* (pp. 257−285). New York: John Wiley and Sons.

Northcutt, R. G. (2003). Development of the lateral line system in the channel catfish. In H. I. Browman, & A. B. Skiftesvick (Eds.), *The Big Fish Bang. Proceedings of the 26th Annual Larval Fish Conference* (pp. 137−159). Bergen, Norway: Institute of Marine Research.

Northcutt, R. G. (2005). Ontogeny of electroreceptors and their neural circuitry. In T. H. Bullock, C. D. Hopkins, A. N. Popper, & R. R. Fay (Eds.), *Electroreception* (pp. 112−131). New York: Springer.

Northcutt, R. G., Catania, K. C., & Criley, B. B. (1994). Development of lateral line organs in the axolotl. *J Comp Neurol, 340*, 480−514.

Obara, S. (1976). Mechanisms of electroreception in ampullae of Lorenzini of the marine catfish *Plotosus*. In J. P. Reuben, D. P. Purpura, M. V. L. Bennett, & E. R. Kandel (Eds.), *Electrobiology of Nerve, Synapse and Muscle* (pp. 128−147). New York: Raven Press.

Obara, S., & Bennett, M. V. L. (1972). Mode of operation of ampullae of Lorenzini of the skate, *Raja*. *J Gen Physiol, 60*, 534−557.

Pals, N., Valentijn, P., & Verwey, D. (1982). Orientation reactions of the dogfish, *Scyliorhinus canicula*, to local electric fields. *Netherlands J Zool, 32*, 495−512.

Paulin, M. G. (1995). Electroreception and the compass sense of sharks. *J Theoret Biol, 174*, 325−339.

Peters, R. C., & Evers, H. P. (1985). Frequency selectivity in the ampullary system of an elasmobranch fish (*Scyliorhinus canicula*). *J Expl Biol, 118*, 99−109.

Pettigrew, J. D. (1999). Electroreception in monotremes. *J Exp Biol, 202*, 1447−1454.

Pfeiffer, W. (1968). Die Fahrenholzschen Organe der Dipnoi und Brachiopterygii. *Z Zellforsch, 90*, 127−147.

Pusch, R., von der Emde, G., Hollmann, M., et al. (2008). Active sensing in a mormyrid fish − electric images and peripheral modifications of the signal carrier give evidence of dual foveation. *J Exp Biol, 211*, 921−934.

Raschi, W., & Mackanos, L. A. (1989). The structure of the ampullae of Lorenzini in *Dasyatis garouaensis* and its implications on the evolution of freshwater electroreceptive systems. *J Exp Zool, 2*, 101−111.

Ritz, T., et al. (2000). A model for vision-based magnetoreception in birds. *Biophys J, 78*, 707−718.

Rivera-Vicente, A. C., Sewell, J., & Tricas, T. C. (2011). Electrosensitive spatial vectors in elasmobranch fishes: implications for source localization. *Pub Lib Sci One, 6*, e16008, 1-15.

Ronan, M. C. (1986). Electroreception in cyclostomes. In T. H. Bullock, & W. Heiligenberg (Eds.), *Electroreception* (pp. 209−224). New York: John Wiley and Sons.

Ronan, M. C., & Bodznick, D. (1986). End buds: non-ampullary electroreceptors in adult lampreys. *J Comp Physiol A, 158*, 9−16.

Rose, G. J. (2004). Insights into neural mechanisms and evolution of behaviour from electric fish. *Nat Rev Neurosci, 5*, 943−951.

Semm, P., & Beason, R. C. (1990). Responses to small magnetic variations by the trigeminal system of the bobolink. *Brain Res Bull, 25*, 735−740.

Sisneros, J. A., & Tricas, T. C. (2000). Androgen-induced changes in the response dynamics of ampullary electrosensory primary afferent neurons. *J Neurosci, 20*, 8586−8595.

Sisneros, J. A., Tricas, T. C., & Luer, C. A. (1998). Response properties and biological function of the skate electrosensory system during ontogeny. *J Comp Physiol A, 183*(1), 87−99.

Sugawara, Y. (1989a). Electrogenic NA-K pump at the basal face of the sensory epithelium in the *Plotosus* electroreceptor. *J Comp Physiol A, 164*, 589−596.

Sugawara, Y. (1989b). Two Ca^{++} current components of the receptor current in the electroreceptors of the marine catfish *Plotosus*. *J Gen Physiol, 93*, 365−380.

Szabo, T. (1974). Anatomy of the specialized lateral line organs of electroreception. In A. Fessard (Ed.), *Handbook of Sensory Physiology, Vol. III/3* (pp. 13−58). Berlin: Springer-Verlag.

Tenforde, T. S. (1989). Electroreception and magnetoreception in simple and complex organisms. *Biomagnetics, 10*, 215−221.

Tricas, T. C. (1982). Bioelectric-mediated predation by swell sharks, *Cephaloscyllium ventriosum*. *Copeia, 1982*, 948−952.

Tricas, T. C., & New, J. G. (1998). Sensitivity and response dynamics of elasmobranch electrosensory primary afferent neurons to near threshold fields. *J Comp Physiol A, 182*, 89−101.

Tricas, T. C., Michael, S. W., & Sisneros, J. A. (1995). Electrosensory optimization to conspecific phasic signals for mating. *Neurosci Lett, 202*, 129−132.

Vischer, H. A. (1995). Electroreceptor development in the weakly electric fish *Eigenmannia*: a histological and ultrastructural study. *J Comp Neurol, 360*, 81−100.

Von der Emde, G. (1999). Active electrolocation of objects in weakly electric fish. *J. Exp. Biol., 202*, 1205−1215.

Walker, M. M., Diebel, C. E., Haugh, C. V., Pankhurst, P. M., Montgomery, J. C., & Green, C. R. (1997). Structure and function of the vertebrate magnetic sense. *Nature, 390*, 371−376.

Walker, M. M., Diebel, C. E., & Kirschvink, J. L. (2007). Magnetoreception. In J. H. Toshiaki, & S. Z. Barbara (Eds.), *Fish Physiology, Vol. 25* (pp. 337−376). San Diego: Academic Press.

Waltmann, B. (1966). Electrical properties and fine structure of the ampullary canals of Lorenzini. *Acta Physiol Scand, 66*(Suppl. 264), 1−60.

Whitehead, D., Kwik, J., & Tibbetts, I. (2009). Distribution and morphology of the ampullary organs of the estuarine long-tailed catfish, *Euristhmus lepturus* (Plotosidae, Siluriformes). *Zoomorphology, 128*, 111−117.

Whitehead, D. L., Tibbetts, I. R., & Daddow, L. Y. M. (2000). Ampullary organ morphology of freshwater salmontail catfish, *Arius graeffei*. *J Morphol, 246*, 142−149.

Wilkens, L. A. (2004). Adaptation of the rostral ampullary electrosense for plankton feeding by the paddlefish. In G. von der Emde, J. Mogdans, & B. G. Kapoor (Eds.), *The Senses of Fishes: Adaptations for the Reception of Natural Stimuli* (pp. 288−307). New Dehli: Narosa Publishing House.

Wilkens, L. A., Wettring, B., Wagner, E., Wojtenek, W., & Russell, D. (2001). Prey detection in selective plankton feeding by the paddlefish: is the electric sense sufficient? *J Exp Biol, 204*, 1381−1389.

Wiltschko, R., & Wiltschko, W. (1995). *Magnetic Orientation in Animals*. Berlin: Springer.

Xu-Friedman, M. A., & Hopkins, C. D. (1999). Central mechanisms of temporal analysis in the knollenorgan pathway of mormyrid electric fish. *J Exp Biol, 202*, 1311−1318.

Zakon, H. H. (1986). The electroreceptive periphery. In T. H. Bullock, & W. Heiligenberg (Eds.), *Electroreception* (pp. 103−156). New York: John Wiley and Sons.

Zakon, H. H. (1988). The electroreceptors: diversity in structure and function. In J. Atema, R. R. Fay, A. N. Popper, & W. N. Tavolga (Eds.), *Sensory Biology of Aquatic Animals* (pp. 813−850). New York: Springer.

This page intentionally left blank

Section VI

Muscle and Other Contractile Systems

This page intentionally left blank

Chapter 42

Skeletal Muscle Excitability

Nicholas Sperelakis, Judith Heiny and Hugo Gonzalez-Serratos

Chapter Outline

I. SUMMARY

The resting potential (RP) of skeletal muscle twitch fibers is about −80 mV (mammalian) or −90 mV (amphibian) and the action potential (AP) overshoots to about +40 mV. The maximal rate of rise of the AP is very fast, being about 500−700 V/s and is due to a large inward *fast Na^+ current* (I_{Na}) which brings E_m up close to E_{Na}. The duration of the AP (at 50% repolarization or APD_{50}) is brief, being about 1−3 ms and the falling phase of the AP is produced by several repolarizing factors: (1) increase in the delayed rectifier K^+ conductance; (2) Na^+ channel inactivation and deactivation (due to some repolarization); and (3) Cl^- influx (outward I_{Cl}).

The skeletal muscle fibers are long, being formed by the *fusion of myoblast cells* and thereby producing a multinucleated long myotube or fiber. The fast-rising AP propagates at a velocity of about 5 m/s. Each skeletal muscle twitch fiber is normally closely controlled by the motor innervation, there being one or two *motor end-plates* (neuromuscular junctions) located near the midregion of each fiber. Excitation spreads in both directions from the neuromuscular junction.

The twitch fibers undergo *developmental changes* similar to those in cardiac muscle and neurons. In early development, there are few or no fast Na^+ channels and the AP upstroke is slow and produced by an inward current through slow Ca^{2+} channels. The AP duration is also long because the delayed rectifier K^+ conductance is not fully developed. During subsequent development, fast Na^+ channels are gained, the RP increases (becomes more negative) and the AP shortens to a brief spike.

The skeletal muscle AP spike is immediately followed by a large and prominent early depolarizing afterpotential that slowly decays over 10−20 ms. This *early afterpotential* is caused in part by the persistence and slow decay of the delayed rectifier K^+ conductance (that was turned on by the Na^+ influx-caused depolarization), which has a Na^+:K^+ selectivity or P_{Na}/P_K ratio higher (e.g. 1/30) than that of the resting membrane (e.g. 1/100). This delayed rectifier K^+ conductance holds E_m for a time more depolarized than the normal RP.

After (and during) a tetanic burst (train) of AP spikes, a large prominent *late depolarizing afterpotential* is

Cell Physiology Sourcebook. DOI: 10.1016/B978-0-12-387738-3.00042-1

produced. This late afterpotential is caused by K^+ accumulation in the T-tubules that acts to depolarize them due to the decrease in E_K. Thereby, the surface sarcolemma is depolarized passively. In addition, a slow component of the delayed rectifier K^+ conductance (less selective for K^+ than the resting conductance) may persist during the train.

The *AP invades into the T-tubules* and propagates inward at a slower velocity of about 7−10 cm/s (Gonzalez-Serratos et al., 1978). At this velocity, it would take about 1.0−1.5 ms to propagate to the center of a myofiber having a radius of 30−40 µm. This serves to bring excitation deep into the fiber interior quickly. The depolarization of the T-tubules activates slow (L-type) Ca^{2+} channels located in them and this serves as a critical step in excitation−contraction (EC) coupling. The chapter on EC coupling provides a detailed discussion of a mechanism that involves the Ca^{2+} channels acting as voltage sensors that are coupled to and open the Ca^{2+} release channels in the TC-SR (surface facing the T-tubule).

Some skeletal muscles also contain a fraction of fibers that are non-twitch *slow muscle fibers*, which normally do not fire APs. They are multiply innervated by the motor neuron, with numerous motor end-plates spaced about 1 mm apart along the entire length of the fiber. Graded contraction of each fiber is produced by varying the frequency of axon APs that increase the amplitude of the end-plate potentials (EPPs) by temporal summation. The membrane potential change produced by the summed EPPs is carried passively into the T-tubules to bring about contraction.

II. INTRODUCTION

The normal contraction of vertebrate *twitch-type skeletal muscle fibers* is always preceded by an AP. The AP depolarizes the sarcolemma beyond the membrane potential (E_m) level at which contraction is triggered, i.e. the *mechanical threshold* (see the subsequent chapter on E-C coupling). This is the first step in the chain of events triggered by the initial excitatory process in the sarcolemma, linking it to the final mechanical response. This chain of events is known as *excitation−contraction (E-C) coupling*. In this chapter, we will study the sarcolemmal electrophysiological properties that are the basis of the AP generation. AP generation and excitability in neurons were covered in an earlier chapter. Most of the general electrophysiological principles discussed there also apply to skeletal muscle fibers and so are only briefly reviewed and summarized in this chapter. In most respects, the electrogenesis of the APs in nerve axons and skeletal muscle fibers is quite similar. Both are long fibers and have very brief and fast-rising APs whose inward current is carried by Na^+ ions through fast Na^+ channels. Skeletal muscle fibers, however, have the added complexity of an extensive internal transverse (T) tubular system formed by a periodic invagination of the surface cell membrane (Fig. 42.1), forming an orderly three-dimensional array of tubules that propagate excitation from the cell surface into the deep interior of the fiber for purposes of E-C coupling. In addition, electrogenesis in skeletal muscle fibers differs from nerve fibers in that (1) different types of afterpotentials are produced, (2) propagation is continuous (i.e. saltatory propagation does not occur) and (3) the membrane has a high Cl^- conductance.

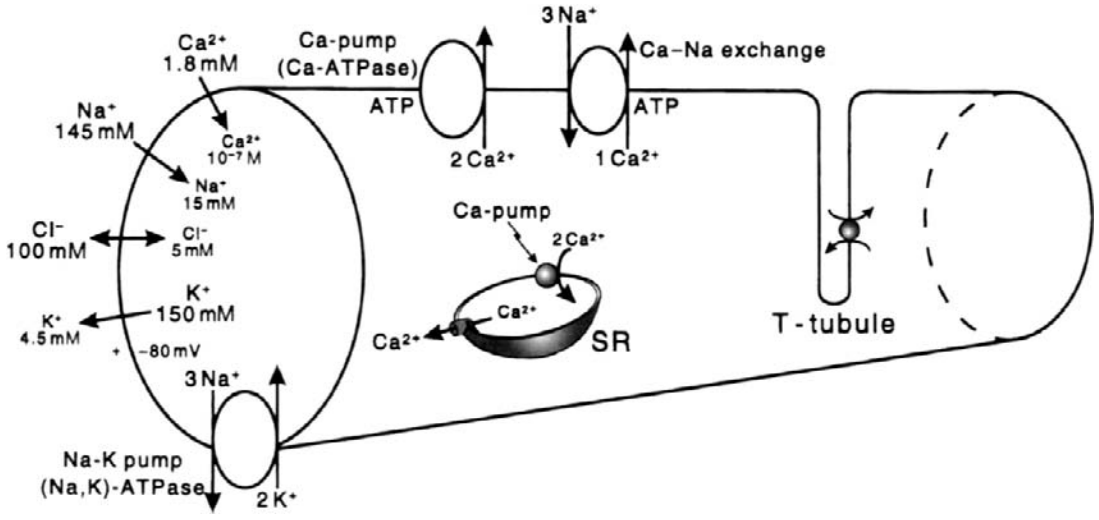

FIGURE 42.1 Intracellular and extracellular ion distributions in vertebrate skeletal muscle fibers. Also shown are the polarity and magnitude of the resting potential (RP). Arrows indicate direction of the net electrochemical gradient. The Na^+-K^+ pump and Ca^{2+}-Na^+ exchange carrier are located in the cell surface and in the T-tubule membranes. A calmodulin-dependent Ca^{2+}-ATPase and Ca^{2+} pump, similar to that in the sarcoplasmic reticulum (SR), is located in the cell surface and T-tubule membranes.

The skeletal muscle AP is considerably different from the AP of *cardiac muscle cells* which have a very long duration with a pronounced plateau and a substantially lower rate of rise and propagation velocity. The myocardial cells are short and there is a slight delay in propagation at each cell-to-cell junction. Like skeletal muscle fibers, myocardial cells have a fast I_{Na} responsible for the rapid upstroke of the AP, but the delayed rectifier K^+ conductance is turned on slowly and there is a substantial inward I_{Ca} during the entire plateau.

The APs of *smooth muscle cells* (SMCs) also are markedly different from those of skeletal muscle fibers, in that the RP (takeoff potential) is lower (more depolarized), the rate of rise of the AP is much slower, the AP overshoot is much less and the AP duration (APD) is considerably longer. Propagation velocity is much slower and the SMCs are short and small in diameter. The inward current for the APs in SMCs is primarily a slow Ca^{2+} current carried through L-type Ca^{2+} channels, but some cells do possess some functioning fast Na^+ channels.

III. GENERAL OVERVIEW OF ELECTROGENESIS OF THE ACTION POTENTIAL

The ion distributions and ion pumps and exchangers found in skeletal muscle fibers are similar to those of other types of cells, as described in the chapters on the RP and nerve APs (see Fig. 42.1). The APs in vertebrate skeletal muscle twitch fibers consist of a *spike* followed by a *depolarizing* ("*negative*") *afterpotential* (Figs. 42.2 and 42.3). A large fast inward Na^+ current, passing through voltage-dependent fast Na^+ channels, is responsible for electrogenesis of the spike depolarization, which rises rapidly (500−700 V/s). Subsequently, a small slow inward Ca^{2+} current, passing through kinetically slow channels, may be involved in E-C coupling. Outward currents passing through K^+ channels and Cl^- channels are responsible for repolarization of the AP.

The skeletal muscle cell membrane has at least two types of voltage-dependent K^+ channels (Fig. 42.4). One type allows K^+ ions to pass more readily inward than outward, the so-called *inward-going rectifier*. This channel is responsible for *anomalous rectification* (i.e. *decrease* in g_K with depolarization). There is a quick decrease in K^+ conductance on depolarization and increase in K^+ conductance with repolarization. The second type of K^+ channel is similar to the usual K^+ channel found in nerve membrane (e.g. squid giant axon), the so-called *delayed rectifier*. Its conductance turns on more slowly than g_{Na} on depolarization. This channel allows K^+ to pass readily outward down the electrochemical gradient for K^+. The activation of this channel produces the large increase in total g_K that helps to terminate the AP (see Fig. 42.3).

The AP amplitude is about 120 mV, from an RP of −80 mV in mammalian myofibers (−90 mV in amphibian)

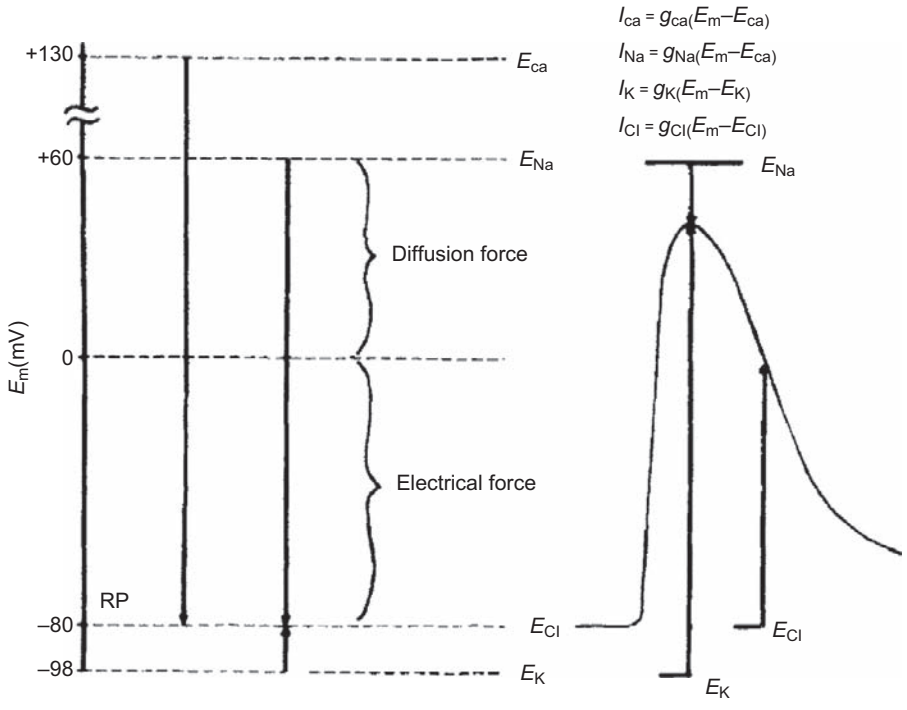

FIGURE 42.2 Representation of the electrochemical driving forces for Na^+, Ca^{2+}, K^+ and Cl^- at rest (left diagram) and during the AP in a skeletal muscle fiber (right diagram). Equilibrium potentials for each ion (e.g. E_{Na}) are positioned vertically according to their magnitude and sign; they were calculated from the Nernst equation for a given set of extracellular and intracellular ion concentrations. Measured RP is assumed to be −80 mV. Electrochemical driving force for an ion is the difference between its equilibrium potential (E_i) and the membrane potential (E_m), i.e. ($E_m - E_i$). Thus, at rest, the driving force for Na^+ is the difference between E_{Na} and the resting E_m; if E_{Na} is +60 mV and resting E_m is −80 mV, the driving force is 140 mV. The driving force is then the algebraic sum of the diffusion force and the electrical force and is represented by the length of the arrows in the diagram. Driving force for Ca^{2+} (about 210 mV) is even greater than that for Na^+, whereas that for K^+ is much less (about 18 mV). Direction of the arrows indicates the direction of the net electrochemical driving force, namely, the direction for K^+ is outward, whereas that for Na^+ and Ca^{2+} is inward. If Cl^- is passively distributed, then for a cell sitting a long time at rest, $E_{Cl} = E_m$ and there is no net driving force. The driving forces change during the AP, as depicted. The equations for the different ionic currents are given in the upper right-hand portion of the figure. *(Adapted from Sperelakis, 1979.)*

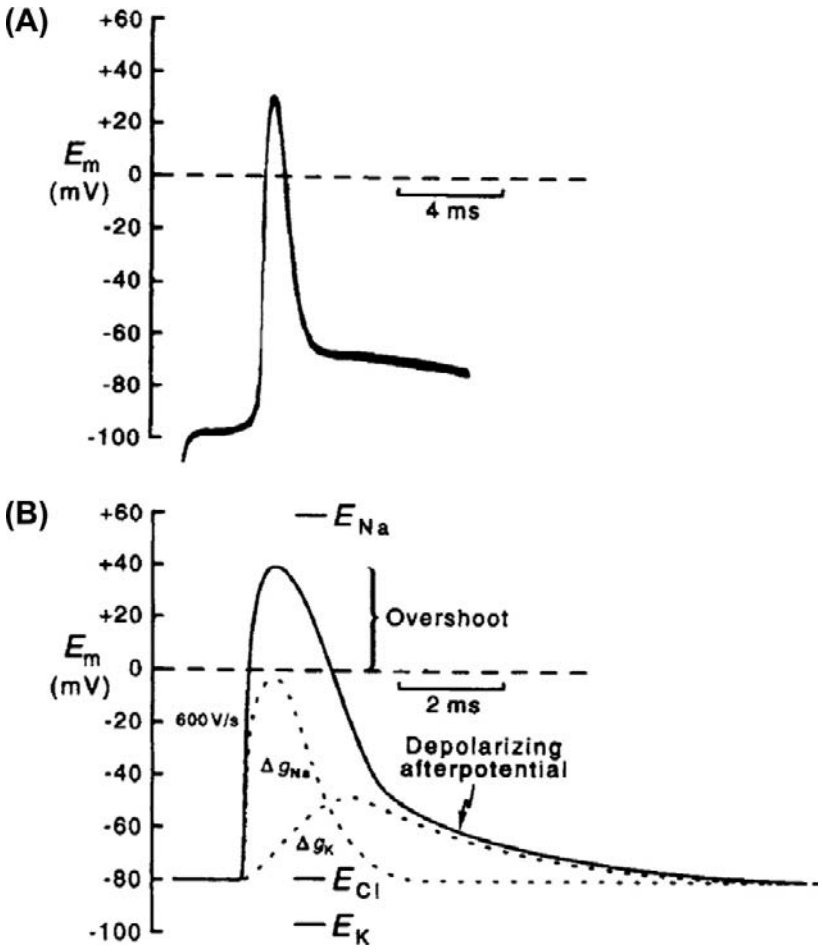

FIGURE 42.3 (A) Action potential (AP) recorded with an intracellular microelectrode in a skeletal muscle fiber of frog semitendinosus muscle bathed in normal frog Ringer's solution. Note the prominent depolarizing afterpotential. Shock artifact is at left of spike. (*Modified from Sperelakis et al., 1973.*) (B) Diagrammatic representation of the relative conductance changes for Na^+ and K^+ during an AP. The rising phase of the AP is caused by an increase in g_{Na}, which brings the E_m toward E_{Na}. The falling phase of the AP is due to the rise in g_K, the decrease in $g_{Na,}$ and to an outward Cl^- current. The depolarizing afterpotential is explained in part by the fact that the delayed rectifier K^+ channel is less selective for K^+ (30:1 over Na^+) than is the resting channel (100:1) and, in part, by the contribution of the AP traveling down the T-tubular network.

to a peak overshoot potential of about +40 mV (see Figs. 42.2 and 42.3). The duration of the AP (at 50% repolarization, or APD_{50}) ranges between 3 and 6 ms, depending on the species and temperature. The *threshold potential* (V_{th}) for triggering of the fast Na^+ channel conductance is about −65 to −55 mV; thus, a *critical depolarization* of about 25 mV is required to reach V_{th}. The turn-on of the fast g_{Na} (fast I_{Na}) is very rapid (within 0.2 ms) and E_m is brought rapidly toward E_{Na} (see Figs. 42.2 and 42.3). There is an explosive (positive exponential initially) increase in g_{Na}, caused by a *positive feedback* relationship between g_{Na} and E_m.

From the current versus voltage (I/V) curves, the maximum inward fast Na^+ current occurs at an E_m of about −20 mV. The current decreases at more depolarized E_m levels because of the diminution in electrochemical driving force as the membrane is further depolarized, even though the conductance remains high. At the reversal potential (E_{rev}) for the current, the current goes to zero; I_{Na} then reverses direction with greater depolarization.

As E_m depolarizes, it crosses V_{th} for slow Ca^{2+} channels (also called *L-type Ca^{2+} channels* or *dihydropyridine receptors*), which is about −35 mV. These Ca^{2+} channels are primarily located in the transverse tubules. Turn-on of the Ca^{2+} conductance (g_{Ca}) and I_{Ca} is relatively slow and the peak I_{Ca} is considerably smaller than the peak I_{Na}. *This Ca^{2+} influx is involved in E-C coupling.*

The molecular rearrangements involved in activation of the slow Ca^{2+} channels are directly coupled to opening of *Ca^{2+}-release channels* (or *ryanodine receptors*) in the sarcoplasmic reticulum (SR) membrane. However, the open probability of these channels is very low. Therefore, the resulting increase in Ca^{2+} conductance (g_{Ca}) and the peak I_{Ca} is relatively slow and considerably smaller than the peak I_{Na}. This Ca^{2+} influx is small during a single AP, but can contribute to E-C coupling during repetitive AP firing.

IV. ION CHANNEL ACTIVATION AND INACTIVATION

As discussed in the chapter on nerve excitability (see Chapter 19), the fast Na^+ channels (and the slow Ca^{2+} channels) have a double gating mechanism; one gate is the *activation gate* (A-gate) and the second gate is the *inactivation gate* (I-gate). For a channel to be conducting, both the A-gate and I-gate must be open; if either one is closed, the channel is non-conducting. The A-gate is closed at the

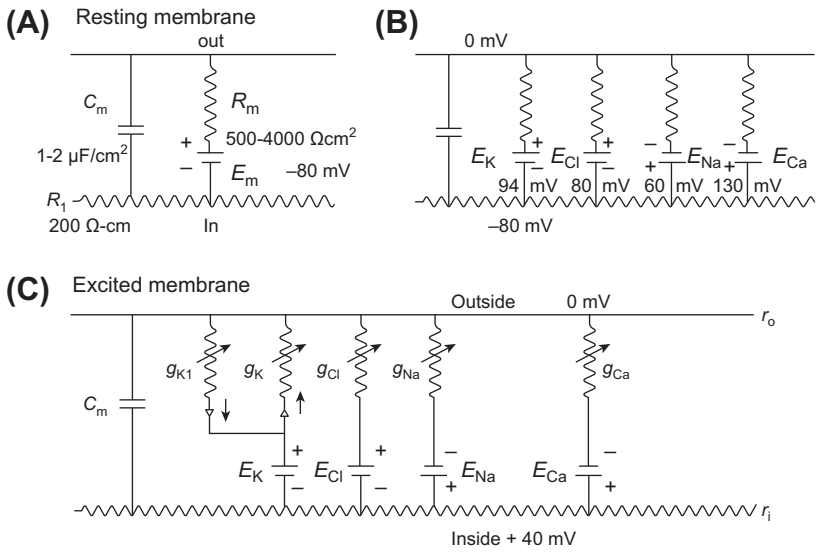

FIGURE 42.4 Electrical equivalent circuits for a skeletal muscle fiber cell membrane at rest (A and B) and during excitation (C). (A) Membrane as a parallel resistance-capacitance circuit, the membrane resistance (R_m) being in parallel with the membrane capacitance (C_m). RP (E_m) is represented by an 80 mV battery in series with the membrane resistance, the negative pole facing inward. (B) Membrane resistance is divided into four component parts, one for each of the four major ions of importance: K^+, Cl^-, Na^+ and Ca^{2+}. Resistances for these ions (R_K, R_{Cl}, R_{Na} and R_{Ca}) are parallel to one another and represent totally separate and independent pathways for permeation of each ion through the resting membrane. These ion resistances are depicted as their reciprocals, namely, ion conductances (g_K, g_{Cl}, g_{Na} and g_{Ca}). Equilibrium potential for each ion (e.g. E_K), determined solely by the ion distribution in the steady-state and calculated from the Nernst equation, is shown in series with the conductance path for that ion. RP of −80 mV is determined by the equilibrium potentials and by the relative conductances. (C) Equivalent circuit is further expanded to illustrate that, for the voltage-dependent conductances, there are at least two separate K^+-conductance pathways (labeled here g_{K1} and g_K). In series with the K^+ conductances are rectifiers pointing in the direction of least resistance to current flow. There is one Na^+ conductance pathway, the kinetically fast Na^+ conductance (g_{Na}). In addition, there is a kinetically slow pathway that allows Ca^{2+} to pass through. Arrows drawn through the resistors indicate that the conductances are variable, depending on membrane potential and time. *(Adapted from Sperelakis, 1979.)*

resting E_m and opens rapidly on depolarization, whereas the I-gate is open at the resting E_m and closes slowly on depolarization. In the Hodgkin–Huxley (1952) analysis, the opening of the A-gate requires simultaneous occupation of three negatively-charged sites by three positively-charged m^+ particles. Therefore:

$$g_{Na} = \overline{g}_{Na} m^3 h \qquad (42.1)$$

where m is the activation variable, h is the inactivation variable and $\overline{g}_{Na}$ is the maximum conductance. A small gating current (I_g) has been measured that corresponds to the movement of the charged m particles (or rotation of an equivalent dipole). The outward I_g leads into the inward I_{Na}.

The fast I_{Na} lasts only for 1–2 ms because of the spontaneous voltage inactivation of the fast Na^+ channels, i.e. they inactivate quickly, even when the membrane remains depolarized. Inactivation is produced by the voltage-dependent closing of the I-gate. The voltage dependence of inactivation is given by the h_∞ versus E_m curve. The Na^+ conductance (g_{Na}) at any time is equal to the maximal value ($\overline{g}_{Na}$) times m^3h. Therefore, when $h = 0$, $g_{Na} = 0$, and when $h = 1.0$, $g_{Na} = \overline{g}_{Na}$ (if $m = 1.0$). At the normal RP, h_∞ is nearly 1.0 and diminishes with depolarization, becoming nearly zero at about −30 mV. The maximal rate of rise of the AP (max *dV/dt*) is directly proportional to the net inward current or I_{Na}, which is directly proportional to g_{Na} and can be expressed as:

$$\max dV/dt \propto \frac{I_{Na}}{C_m} = \frac{\overline{g}_{Na}\, m^3 h\, (E_m - E_{Na})}{C_m} \qquad (42.2)$$

Therefore, a decrease in h_∞ causes decrease in max *dV/dt*. Thus, depolarization by any means (e.g. elevated $[K+]_o$ or applied current pulses) decreases max *dV/dt*, and excitability disappears at about −50 mV.

The slow Ca^{2+} channels behave much the same way as the fast Na^+ channels with respect to activation and inactivation, with one main difference being the voltage range over which the slow channels activate and inactivate. Slow channels inactivate between −45 mV and −10 mV, compared to −70 and −30 mV for the fast Na^+ channels. Another major difference is that the slow Ca^{2+} conductance inactivates much more slowly than the fast Na^+ conductance; i.e. they have a long inactivation time constant (τ_{inact}). (The h variable for the slow channel is sometimes referred to as the f variable and the m variable as the d variable.) Because slow Ca^{2+} channels are located in the T-tubular system, their function is affected by tubular Ca^{2+} depletion caused by the Ca^{2+} ions that flow into the myoplasm. The recovery process for the slow Ca^{2+} channels is slow compared to 1–2 ms for fast Na^+ channels.

The K^+ channel (*delayed rectifier*) may have only an activation gate, because it does not inactivate quickly. In the Hodgkin–Huxley analysis of squid giant axon, the A-gate opens when four positively-charged n^+ particles simultaneously occupy four favorable positions (negatively-charged sites). If n is the probability that one site is occupied, then n^4 is the probability that all four sites are occupied. Therefore,

$$g_K = \overline{g}_K n^4 \qquad (42.3)$$

The fourth power to which n must be raised causes a delay (sigmoidal foot) in turn-on of the K^+ conductance.

V. SLOW DELAYED RECTIFIER K^+ CURRENT

Two types of K^+ delayed rectifier currents occur in skeletal muscle. A slow I_K was first described by Adrian and co-workers (1970a,b) in voltage-clamped frog sartorius fibers. The *slow component* of outward I_K reached a maximum in about 3 s and declined with a time constant of about 0.5 s. In voltage-clamped frog toe muscle, Lynch (1978) observed that most fibers had both a slow component and a *fast component* of the outward I_K (threshold of −55 mV). The voltage dependences of both K^+ currents were shifted equally in the depolarizing direction by elevated $[Ca^{2+}]_o$ or $[H^+]_o$, presumably due to altering the net negative outer surface charge of the membrane, thereby hyperpolarizing. Acidosis also increased the rate of turn-on of the slow delayed rectifier. The fast delayed current was relatively selectively blocked by TEA or by a sulfhydryl reagent, whereas the slow delayed current was selectively depressed by a histidine reagent. It was estimated that about 25% of the delayed rectifier channels are in the T-tubular membrane. The functional significance of the slow I_K is unknown, although it may be partly responsible for the late depolarizing afterpotential (see Section VIII).

VI. MECHANISMS OF REPOLARIZATION

The skeletal muscle AP is terminated by three processes: turn-on of g_K, turn-off of g_{Na} and influx of Cl^- ions. The turn-on of the V-dependent K^+ conductance (g_K) (the *delayed rectifier*) (see Fig. 42.3) acts to bring E_m towards E_K (about −98 mV), since the membrane potential at any time is determined primarily by the ratio of g_{Na}/g_K. This type of g_K channel is activated by depolarization and turned off by repolarization. Therefore, this g_K channel is *self-limiting*, in that it turns itself off as the membrane is repolarized by its action.

In addition to the g_K turn-on, turn-off of g_{Na} occurs (see Fig. 42.3) (contributing to repolarization) for two reasons: (1) spontaneous *inactivation* of fast Na^+ channels that had been activated, i.e. closing of their I-gate (inactivation τ of 1−3 ms) and (2) reversible shifting of activated channels directly back to the resting state (*deactivation*), because of the rapid repolarization that is occurring due to the g_K increase (Fig. 42.5). Theoretically, it would be possible to have an AP that would repolarize (but more slowly) even if there were no g_K mechanism, because the g_{Na} channels would spontaneously inactivate and so the g_{Na}/g_K ratio and E_m would be more slowly restored to their original resting values.

In addition, there is an important third factor involved in repolarization of the AP in skeletal muscle: the *Cl^- current* (see Fig. 42.2). The Cl^- permeability (P_{Cl}) and conductance (g_{Cl}) are very high in skeletal muscle (and are not strongly V-dependent). In fact, P_{Cl} of the surface membrane is much higher than P_K, the P_{Cl}/P_K ratio being about 3−7. As discussed in the chapter on RP (see Chapter 9), the Cl^- ion is passively distributed, or nearly so, and thus cannot determine the RP. However, net Cl^- movements inwards (hyperpolarizing) or outward (depolarizing) do affect E_m transiently until re-equilibration occurs and there is no further net movement. At the RP, there is no net Cl^- current (I_{Cl}), since there is no electrochemical driving force for Cl^- (since $E_m = E_{Cl}$). However, during the AP depolarization, there is a larger and larger driving force for outward I_{Cl} (i.e. Cl^- influx), since $I_{Cl} = g_{Cl}$ ($E_m - E_{Cl}$). In other words, the large electric field that was keeping Cl^- out (i.e. $[Cl^-]_i << [Cl^-]_o$) diminishes during the AP and so Cl^- ion enters the fiber. This Cl^- entry is hyperpolarizing and so tends to repolarize the membrane more quickly than would otherwise occur. That is, AP repolarization is sharpened by the Cl^- mechanism. (Note that influx of the negatively-charged Cl^- ion is an outward Cl^- current, which is repolarizing.)

To illustrate further some of the preceding points on the role of Cl^-, when skeletal muscle fibers are placed into Cl^--free Ringer solution (e.g. methanesulfonate substitution), depolarization and spontaneous APs and twitches occur for a few minutes until most or all of the $[Cl^-]_i$ is washed out. After equilibration, the resting E_m returns to the original value ca. −90 mV for frog skeletal muscle and −80 mV for mammalian, clearly indicating that Cl^- does not determine the RP and that net Cl^- efflux produces depolarization. Re-addition of Cl^- to the bath produces a rapid large hyperpolarization, e.g. to −120 mV, due to net Cl^- influx; the E_m then slowly returns to the original value (e.g. −90 mV) as Cl^- re-equilibrates, i.e. redistributes itself passively. These same effects occur in cardiac muscle, smooth muscle and nerve, but to a lesser extent, because in these tissues P_{Cl} is much lower (e.g. P_{Cl}/P_K ratio is only about 0.5 in vascular smooth muscle).

The importance of the Cl^- current in repolarization in skeletal muscle fibers is illustrated by one type of *myotonia* in which an abnormally low P_{Cl} causes repetitive APs to occur. Because g_{Cl} is abnormally low, total membrane conductance G_m is also low. From the relationship between membrane current (I_m) and G_m ($I_m/G_m = E_m$), it can be deduced that only a smaller outward depolarizing membrane current I_m is necessary to reach threshold E_{th} for an AP. Since g_{Cl} is abnormally low, the membrane resistance R_m will be abnormally high, making the space constant λ larger than normal. Because g_{Cl} is abnormally low, the Cl^- influx during AP repolarization is much less than normal and so the repolarization process is slowed, thus increasing the duration of the AP. As a consequence of the above, when depolarization occurs, the AP threshold is easily and quickly reached and the generated APs spread easily along the sarcolemma. These factors make the whole

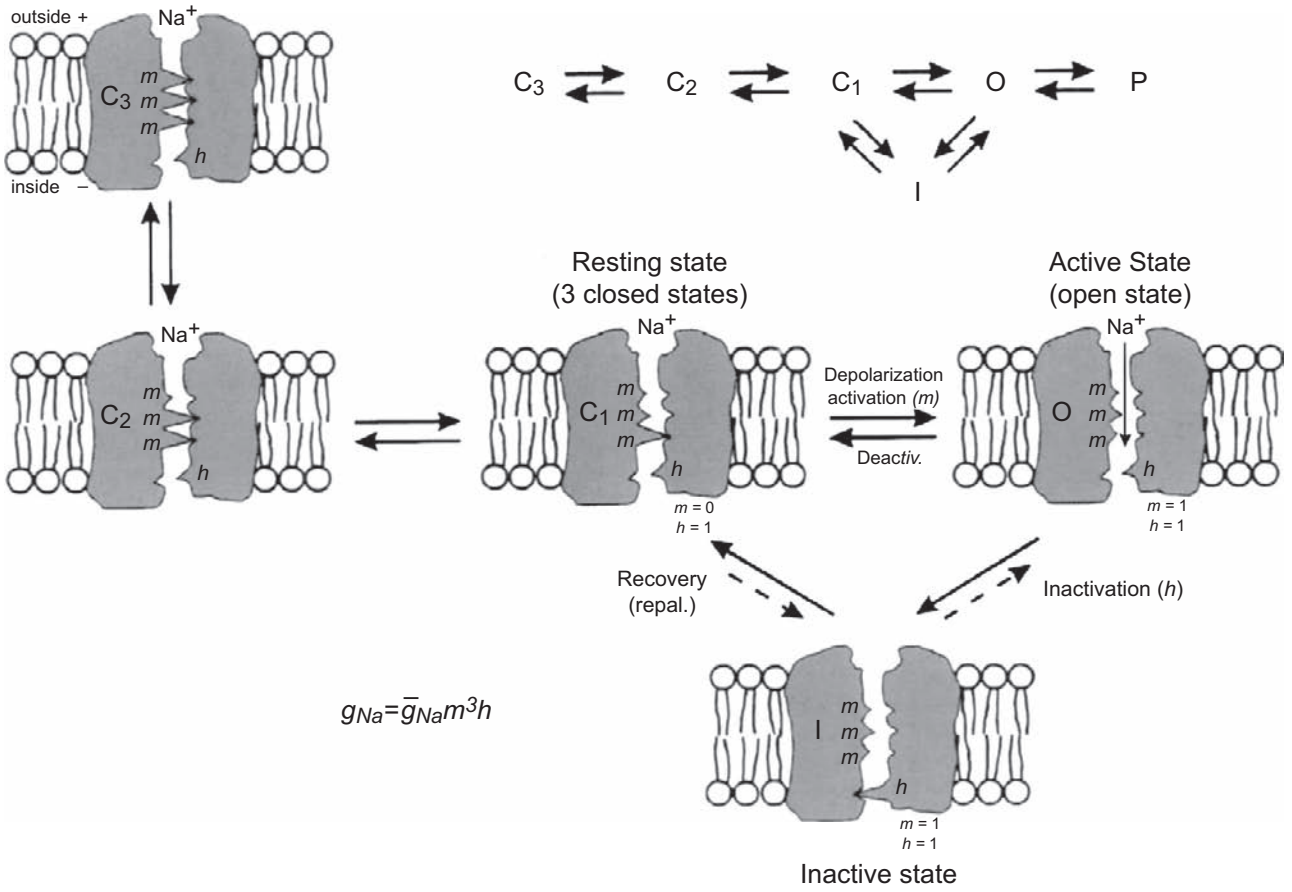

FIGURE 42.5 Illustration of the hypothetical states of the fast Na^+ channel. The three states patterned after the Hodgkin–Huxley view were modified to reflect the fact that there is evidence for three closed states. As depicted, in the most closed state (C_3), all three *m* gates (or particles) are in the closed configuration. In the mid-closed state (C_2), two *m* gates are closed and one is open. In the least closed state (C_1), one gate is closed and two are open. In the resting state, the activation gate (A) is closed and the inactivation gate (I) is open: $m = 0$, $h = 1$. Depolarization to the threshold activates the channel to the active state, the A-gate opening rapidly and the I-gate still being open: $m = 1$, $h = 1$. The activated channel spontaneously inactivates to the inactive state due to closure of the I-gate: $m = I$, $h = 0$. The recovery process on repolarization returns the channel from the inactive state back to the resting state, thus making the channel again available for reactivation. Na^+ ion is depicted as being bound to the outer mouth of the channel and poised for entry down its electrochemical gradient when both gates are open. The reaction between the resting state and the active state is readily reversible and there is some reversibility of the other reactions. The fast Na^+ channel is blocked by tetrotodoxin (TTX) binding to the outer mouth and plugging it.

system unstable and oscillations trigger *repetitive discharge* of APs. That is, the muscle fibers lose their tight control by the motor neurons and so contraction becomes partly involuntary. For example, persons with myotonia find it difficult to release a handshake or to remove their hand from a drinking glass. There are several causes of myotonia, including genetic abnormalities in ion channels, as well as drug-induced conditions. Any agent that greatly lowers P_{Cl} or g_{Cl} will have the same effect. It has been shown that simply decreasing g_{Cl} causes repetitive firing in equivalent circuit models of skeletal muscle fibers. In addition, K^+ ions tend to accumulate in the lumen of the T-tubules under normal conditions (see Section VIII). This accumulation is exaggerated with the prolonged APs and so tends partially to depolarize the fibers and increase their excitability. Some forms of myotonia are produced by *abnormal fast Na^+ channels*; namely, a small fraction of these channels do not inactivate as quickly as usual (i.e. their I-gates do not close normally) and so causes a prolonged small depolarization after the AP and, consequently, a repetitive discharge.

In myotonia, AP repolarization is slowed and the duration of the AP is increased. As AP duration increases, more Na^+ channels have time to return to the resting conformation by deactivation or recovery from inactivation (a process which has a time constant of 2–3 ms). This creates a window of instability during AP repolarization. The membrane potential remains depolarized above threshold, allowing some Na^+ channels to reopen and trigger another AP. The skeletal muscles have a large safety factor with respect to the number of Na^+ channels in the membrane and as few as 3–5% in the open state can trigger an AP. This instability in membrane repolarization is further enhanced by the high membrane resistance. Without

the normal large g_{Cl}, only a smaller than normal outward depolarizing current is required to reach threshold. Because of the high membrane resistance R_m, the space constant λ is longer than normal. Consequently, the APs propagate at a faster velocity. These factors act synergistically to make the whole system unstable. Consequently, when depolarization occurs, the AP threshold is easily and quickly reached, the generated APs spread fast along the sarcolemma and the membrane is more excitable and susceptible to repetitive discharge of APs.

The high g_{Cl} *in skeletal muscle fibers* is due to a large number of voltage-dependent gated Cl^- channels, which are outwardly rectifying. The major Cl^- channel of skeletal muscle is the ClC-1 channel (Steinmeyer et al., 1991), a member of the ClC family of Cl^- channels and Cl^-/H^+ antiporters (Zifarellli and Pusch, 2007). These Cl^- channels are located both on the surface sarcolemma and T-rubule membrane in frogs and mammals. Denervation of mammalian fibers causes g_{Cl} to decrease almost to zero.

VII. ATP-DEPENDENT K^+ CHANNELS

K_{ATP} channels are among the most abundantly expressed K^+ channels in the skeletal muscle sarcolemma, reaching densities of 10 channels per μm^2 of surface membrane (Spruce et al., 1987), comparable to that of K^+ delayed rectifier channels (Standen et al., 1985). K_{ATP} channel currents can be recorded from both surface (Spruce et al., 1985) and transverse tubular membranes (Heiny et al., 1983). However, their physiological role in skeletal muscle is not well understood (reviewed in Flagg et al., 2010). The functional K_{ATP} channel is an octomeric protein composed of four pore-forming Kir subunits (Kir 6.1 and Kir 6.2) and four regulatory SUR (sulfonylurea receptor) subunits assembled in a 4:4 stoichiometry. Functioning of the K_{ATP} channel requires the proper coupling between Kir and SUR subunits. More details on the subunits is given in the Appendix to this chapter.

ATP-dependent K^+ (K_{ATP}) channels are characterized by the inhibition of channel openings by ATP (Yokoshiki et al., 1998). In addition to being ligand sensitive, these K_{ATP} channels are voltage-dependent; the open state probability increases with depolarization. Most studies of K_{ATP} channels have been performed using patch-clamp of isolated inside-out patches of skeletal muscle (Spruce et al., 1987). The unitary conductance of this channel varies with $[K^+]_o$, ranging from 15 pS in 2.5 mM $[K^+]_o$ to 42 pS in 60 mM. K_{ATP} channels are closed when the ATP concentration in the intracellular myoplasm is in the range of 1.0 mM or higher, which is the normal physiological concentration. A decrease in ATP concentration or depolarization activates the channel. The half-maximum inhibition of this channel opening by ATP, measured at a constant $[K^+]_o/[K^+]_i$, is 0.135 mM at pH 7.2 (Fig. 42.6).

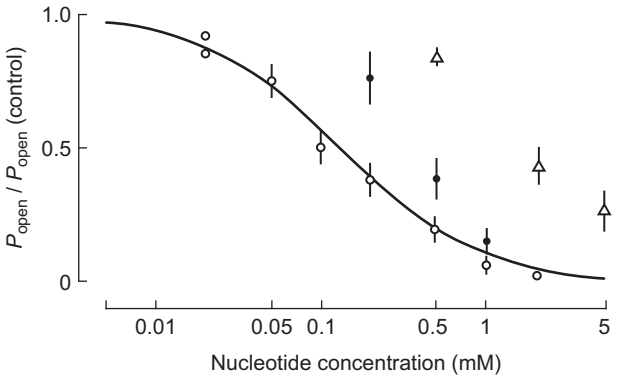

FIGURE 42.6 Effect of ATP (open circles), ADP (filled circles) and AMP (open triangles) on closing the ATP-regulated K^+ channels. Ordinate: open-state probability (P_o) of the channel relative to its value in nucleotide-free solution (P_{open} control). *(Reproduced with permission from Spruce et al., 1987.)*

Hydrolysis of ATP (into ADP + P_i) is not required for ATP to close K_{ATP} channels.

Although ATP is the most specific ligand to close K_{ATP} channels, there are other ligands that modulate these channels. The metabolites produced during contraction, like ADP, Mg^{2+} and H^+ also modulate the channels. The two adenine nucleotides, ADP and AMP (in the absence of ATP), also can block K_{ATP} channels in a dose-dependent manner. However, they are less effective than ATP (see Fig. 42.6). ATP analogs like GTP, ITP, XTP, CTP and UTP also have reduced effectiveness (about tenfold) in closing these channels. ADP shifts the ATP dose—response curve, raising the half-inhibition concentration, consistent with competition between ATP and ADP for the nucleotide binding site on the channel (Spruce et al., 1987; Vivaudou et al., 1991).

A decrease in pH at the cytoplasmic surface (pH_i) reduces the degree of K_{ATP} channel inhibition caused by ATP. The ATP concentration for half-inhibition is 2.5 times and 15 times greater at pH_i 6.8 and 6.3, respectively, as compared to that at pH_i 7.2. Thus, during acidosis, a smaller decrease in ATP concentration will lead to a larger opening of K_{ATP} channels. It was proposed that proton binding to the channel prevents ATP binding (Davies et al., 1992). Mg^{2+} has a similar effect as protons. An increase of cytosolic Mg^{2+} reduces the ability of ATP to close K_{ATP} channels (Vivaudou et al., 1991). Mg^{2+} may bind to the channels and plug them (Woll et al., 1989). In addition, the inhibitory effect may be partly due to the ability of Mg^{2+} to bind to ATP.

K_{ATP} channels have been studied in excised patches of surface membrane blebs from muscles of frogs and mammals. These channels are, therefore, likely to be present in the sarcolemma. It is not known whether they are present in the T-tubular system. As stated earlier, the K_{ATP} channel density has been estimated to be as high as 10 channels per μm^2 of surface membrane (Spruce et al., 1985), a density comparable to that for K^+ delayed rectifier channels.

The physiological role played by K_{ATP} channels in skeletal muscle is not clear. Under physiological conditions, the intracellular ATP concentration is about 5 mM at rest. Therefore, at the resting ATP level, almost all of the K_{ATP} channels should be inactive (Spruce et al., 1987; Davies et al., 1992). Even during repetitive contractions that lead to muscle fatigue, the ATP concentration is maintained at near normal levels by the action of creatine kinase and creatine phosphate (Carlson and Siger, 1960; Nassar-Gentina et al., 1978).

It has been proposed that K_{ATP} channels may be associated with the decrease in force development underlying muscle fatigue. A drug (SR44866) that opens K_{ATP} channels (in frog skeletal muscles) also reduces the AP duration, the early afterpotential and the peak twitch force (without affecting the RP) in intact muscles (Sauviat et al., 1991). The high K^+ permeability found in muscle fibers that have undergone a permanent contracture (rigor) produced by repetitive stimulation when poisoned with cyanide and iodocetate (Fink and Lüttgau, 1976), may be caused by the decreased ATP concentration opening K_{ATP} channels. In metabolically-exhausted frog semitendinosus muscle fibers, the addition of tolbutamide and glyburide, two K_{ATP} channel antagonists, significantly reduces the K^+ efflux rate (Castle and Haylett, 1987). Fatigued muscle fibers can contract when Ca^{2+} is released directly from the intracellular SR stores (Gonzalez-Serratos et al., 1978; Garcia et al., 1991). In intact animals, some of the skeletal muscle fatigue results from synaptic fatigue, including at the neuromuscular junction.

As stated previously, a decrease in pH_i (e.g. from lactic acid production) reduces the inhibitory effect of ATP on K_{ATP} channels. During exercise, with fatigue development, pH_i may decrease by about one unit (Renaud, 1989). A small decrease in ATP concentration is accompanied by an increase in ADP, H^+ and Mg^{2+} concentrations and the overall combination of these chemical changes may then lead to the activation of K_{ATP} channels. As K_{ATP} channels open, they contribute to the increased K^+ efflux found during repetitive muscle contraction. Because of the restricted diffusion out of the T-tubular system and the closeness of the intercellular fiber spacing, extracellular K^+ concentration increases, especially inside the tubular system. This may cause a decrease in cell excitability, which may be reflected as decreased force development. This mechanism may protect skeletal muscle cells from large ATP depletions that would have deleterious effects.

VIII. ELECTROGENESIS OF DEPOLARIZING AFTERPOTENTIALS

As mentioned previously, the AP spike in skeletal muscle fibers is followed by a prominent *depolarizing afterpotential* (also called a *negative afterpotential* based on the old terminology from external recording) (see Fig. 42.3). In addition to this *early depolarizing afterpotential* (i.e. emerging from the spike downstroke), there is a *late depolarizing afterpotential* that follows a tetanic train of spikes (e.g. 10 spikes). The electrogenesis of the early and late afterpotentials is different. The early afterpotential is due to a membrane conductance change, whereas the late afterpotential is due primarily to K^+ accumulation in the T-tubules.

The early depolarizing afterpotential of frog skeletal fibers is about 25 mV in amplitude immediately after the spike component and gradually decays to the RP in 10−20 ms. This afterpotential results from the fact that the delayed rectifier K^+ channel that opens during depolarization to terminate the spike is less selective for K^+ (ca. 30:1, K^+:Na^+) than is the K^+ channel in the resting membrane (ca. 100:1) (Adrian et al.,1970a). Therefore, the constant-field equation predicts that the membrane should be partly depolarized when E_M is dominated by this K^+ conductance that is turned on during the AP. Thus, the early depolarizing afterpotential is partly due to the persistence and slow decay of this less-selective K^+ conductance. Adrian and Peachey (1973) were able to reconstruct the time course of the AP and the early depolarizating afterpotential by giving values to the access resistance of the T-tubular system, presence of Na^+ and K^+ tubular membrane currents and velocity of the tubular AP. The early depolarizing afterpotential reflects, in part, the tubular AP, as evidenced by the disappearance of the early depolarizing afterpotential in muscles in which the T-tubular system has been disrupted and disconnected from the surface membrane by the glycerol osmotic shock method[1] (Eisenberg and Gage, 1969).

The late depolarizing afterpotential of frog skeletal fibers may result from accumulation of K^+ ions in the T-tubules (Adrian and Freygang, 1962). During the AP depolarization and turn-on of g_K (delayed rectifier), there is a large driving force for K^+ efflux from the myoplasm coupled with a large K^+ conductance, resulting in a large outward K^+ current [$I_K = g_K (E_m - E_K)$] across all surfaces of the fiber, namely across the surface sarcolemma and T-tubule walls. The K^+ efflux at the fiber surface membrane can rapidly diffuse away and mix with the relatively large interstitial fluid (ISF) volume, whereas the K^+ efflux into the T-tubules (TT) is trapped in this restricted diffusion space. The resulting high $[K^+]_{TT}$ decreases E_K across the T-tubule membrane and thereby depolarizes this membrane. Because of cable properties, part of this

[1] To produce glycerol osmotic shock, about 300 mOsm glycerol is added to Ringer's solution (Eisenberg and Gage, 1969). The glycerol rapidly permeates into the fiber interior (so the fiber shrinks transiently) and equilibrates. But when the glycerol is washed out, there is a great hypotonic shock produced that disrupts the T-tubules.

depolarization is transmitted to the surface sarcolemma and is recorded by an intracellular microelectrode. The K^+ accumulation in the T-tubules can only be dissipated relatively slowly by diffusion out of the mouth of the T-tubules and by active pumping back into the myoplasm (across the T-tubule wall) by the Na^+-K^+ pump sites located in the T-tubular membrane. Thus, the decay of the late depolarizing afterpotential will be a function of these two processes.

The amplitude and duration of the late depolarizing afterpotential is a function of the number of spikes in the train and their frequency. That is, the greater the spike activity, the greater its amplitude and duration. If the train consists of 20 spikes at a frequency of 50/s, a typical value for the amplitude of the late depolarizing afterpotential in frog fibers is about 20 mV. When the diameter of the T-tubules is increased by placing the fibers in hypertonic solutions[2], the amplitude of the late afterpotential decreases as expected because of the greater dilution of the K^+ ions accumulating in the T-tubule lumen. When the T-tubular system is disrupted and disconnected from the surface membrane by the glycerol osmotic shock method, the late afterpotentials disappear together with the early afterpotentials.

An alternative explanation for the late depolarizing afterpotential is that it may be due to the slow delayed rectifier g_K change described above (Adrian et al., 1970b). The equilibrium potential for the slow I_K is −83 mV and the sign (direction) of the late afterpotential reverses when the fiber is depolarized beyond −80 mV (e.g. to −70 mV). Hence, the late afterpotential could arise from the slow relaxation of a component of the K^+ conductance increase, which is less selective for K^+ than the K^+ channels open in resting membrane. In this view, the electrogenesis of the late afterpotential would be similar to that for the early afterpotential.

All depolarizing afterpotentials, regardless of whether early or late, have physiological importance because they alter excitability and the propagation velocity of the fiber. A depolarizing afterpotential should enhance excitability (lower threshold) to a subsequent AP. This is because the *critical depolarization* required to reach the *threshold potential* would be decreased. A large late depolarizing afterpotential, such as that due to K^+ *accumulation* in the T-tubules, can, under certain pathological conditions, trigger repetitive APs. The effect of depolarizing afterpotentials on velocity of propagation involves two opposing factors: (1) the decrease in critical depolarization required; and (2) the decrease in maximal rate of rise of the AP (max *dV/dt*), which is a function of the takeoff potential (h_∞ versus E_m curve). Therefore, what factor dominates will depend on the degree of depolarization and the shape of the h_∞ curve. When frog skeletal fibers are depolarized slightly by elevating $[K^+]_o$, only a decrease in propagation velocity is observed (Sperelakis et al., 1970).

[2] In hypertonic solutions, skeletal muscle fibers shrink (fiber diameter decreases) like a perfect osmometer (but with an osmotically-inactive volume of about 32%), but their T-tubules swell.

IX. Ca^{2+}-DEPENDENT SLOW ACTION POTENTIALS

Slow APs are recorded under conditions in which the fast Na^+ current is blocked by Na^+-deficient solution, tetrodotoxin (TTX) or voltage inactivation of the fast Na^+ channels in elevated $[K^+]_o$. Under these conditions, the only carrier of inward current available to produce an AP is Ca^{2+} ion. Spontaneously-occurring slow APs were first observed in frog sartorius fibers equilibrated in Cl^--free solution containing TTX (Sperelakis et al., 1967). Upon addition of Ba^{2+} ion (e.g. 0.5 mM), which is a potent blocker of K^+ channels and P_K, the fibers partially depolarize and spontaneously discharge slowly-rising (e.g. 1−10 V/s), overshooting APs of long duration (e.g. several seconds), having a prominent plateau component (resembling a cardiac AP in shape). An abrupt repolarization terminates the slow AP. Ba^{2+} depolarizes rapidly in Cl^--free solution, because the voltage-clamping effect of the Cl^- distribution (E_{Cl}), due to the large P_{Cl}, is circumvented. Cl^--free solution raises the resistance of the cell membrane about sevenfold.

In a frog skeletal muscle fiber, using two intracellular microelectrodes, one for applying current intracellularly and the other for recording voltage a short distance away in the same fiber ($[K^+]_o$ of 25 mM to depolarize the fiber to about −45 mV and thereby inactivate the fast Na^+ channels and $[Na^+]_o$ reduced to zero so that there could be no inward Na^+ current), application of small hyperpolarizing current pulses during the slow AP indicated that membrane resistance increases progressively during the plateau (Kerr and Sperelakis, 1982). The rate of rise, overshoot and duration of the slow APs are a function of $[Ca^{2+}]_o$ (Beaty and Stefani, 1976; Vogel et al., 1978; Kerr and Sperelakis, 1982). For example, the AP duration at 50% amplitude (APD_{50}) was generally 2−8 s. The amplitude of the slow AP plotted against log $[Ca^{2+}]_o$ gave a straight line with a slope of 28 mV/decade, which is close to the theoretical 29 mV/decade (at 21°C) from the Nernst relationship for a situation in which only Ca^{2+} ion carried the inward current. The slow APs were depressed and blocked by the Ca^{2+}-antagonistic and slow-channel-blocking drugs, verapamil and bepridil, with an ED_{50} of about 5×10^{-8} M. The slow AP arises from the T-tubular system of the fiber (Vogel et al., 1978; Kerr and Sperelakis, 1982), based on their disappearance when the T-tubules were disrupted and disconnected from the surface membrane by the glycerol osmotic shock method. The normal fast APs are not affected by the glycerol treatment. These results indicate

that the slow Ca^{2+} channels giving rise to the slow APs are located primarily in the tubular system.

Isotope flux measurements have shown that there is a net Ca^{2+} influx during contractions of phasic skeletal muscle fibers, suggesting that an influx from the extracellular space may initiate the contraction (Bianchi and Shanes 1959). Additionally, voltage-clamped muscle fibers have slow inward Ca^{2+} currents (I_{Ca}) (Stanfield, 1977; Sanchez and Stefani, 1978). Elevation of $[Ca^{2+}]_o$ increased I_{Ca}, and I_{Ca} was depressed by the slow Ca^{2+} channel blockers D-600, nifedipine and Ni^{2+} (Stanfield, 1977; Sanchez and Stefani, 1978; Almers et al., 1981). Detubulation by the glycerol osmotic shock method abolishes I_{Ca} (Nicola-Siri et al., 1980; Potreau and Raymond, 1980). These results support the conclusion that I_{Ca} produces the slow APs. The various conformational states that the Ca^{2+} slow channels undergo during excitation are depicted in Fig. 42.7. These states are similar to those of the fast Na^+ channels (see Fig. 42.5), except there are only two closed states.

Do slow inward calcium currents (I_{CaS}), play a role in E-C coupling? A substantial contraction, of between 20 and 50% of the normal twitch tension, accompanies the slow APs (Vogel et al., 1978), suggesting that the Ca^{2+} channels in the tubular system may play a role during E-C coupling. However, skeletal muscle fibers contract for several minutes after $[Ca^{2+}]_o$ is lowered to 10^{-8} M (Armstrong et al., 1972) and the Ca^{2+}-channel blocker diltiazem did not depress twitch or tetanic force development (Gonzalez-Serratos et al., 1982). These results suggest that I_{Ca} may play no role in E-C coupling in normal amphibian muscles. Nevertheless, in dysgenic mice, in which contraction of skeletal muscles is weak, the Ca^{2+} channels in the T-tubules are few or absent.

Ca^{2+} influx during the slow AP could trigger the release of more Ca^{2+} from the nearby TC-SR via the Ca^{2+}-trigger Ca^{2+}-release mechanism (Fabiato, 1982). Because the time course of the slow AP is much longer than that of a twitch contraction, it was suggested that the inward Ca^{2+} current may play a role in K^+ contracture, in tetanic contraction, or in long-term regulation of contraction, perhaps by increasing the Ca^{2+} concentration in the SR and thereby increasing the amount of internal Ca^{2+} available for release

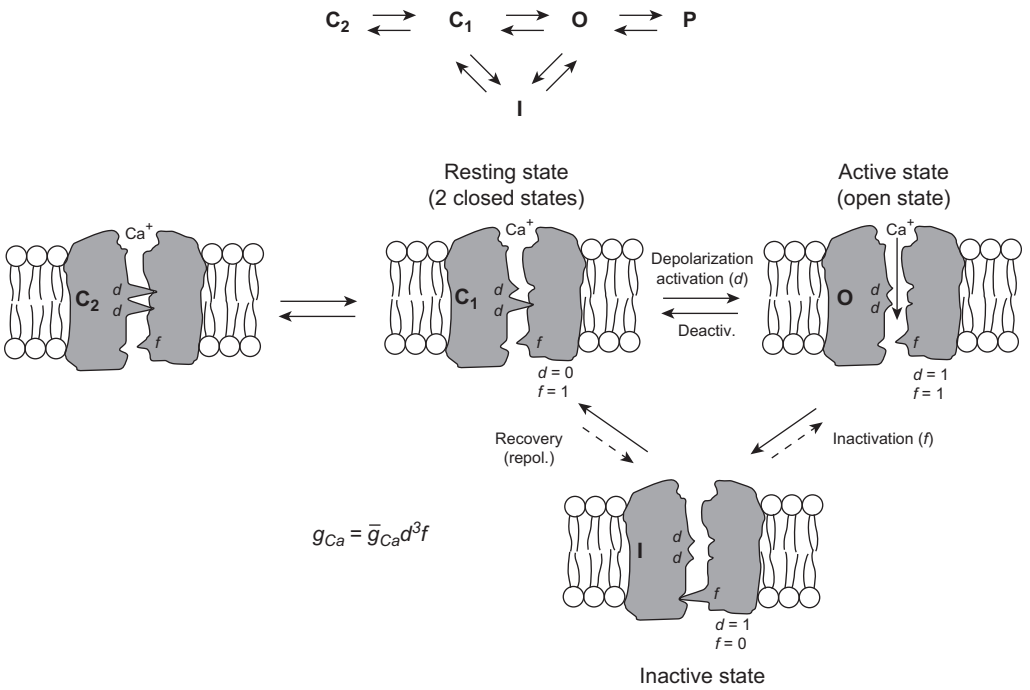

FIGURE 42.7 Illustration of the four hypothetical states of the slow Ca^{2+} channel. There is evidence for two closed states. As depicted, in the most closed state (C_2), both *d* gates (or particles) are in the closed configuration. In the least closed state (C_1), one gate is closed and one is open. In the resting membrane, the activation gate (A) is closed and the inactivation gate (I) is open: $d = 0, f = 1$. Depolarization to the threshold activates the channel to the active state, the A-gate opening rapidly and the I-gate still being open: $d = 1, f = 1$. The activated channel spontaneously inactivates to the inactive state due to closure of the I-gate: $d = 1, f = 0$. The recovery process on repolarization returns the channel from the inactive state back to the resting state, thus making the channel again available for reactivation. Ca^{2+} ion is depicted as being bound to the outer mouth of the channel and poised for entry down its electrochemical gradient when both gates are open. The reaction between the resting state and the active state is readily reversible and there is some reversibility in the other reactions. The slow channels behave similarly to the fast channels, except that their gates appear to move more slowly on a population basis; i.e. the slow channels activate and recover more slowly. (Although the gates of any individual slow channel may move quickly, the stochastic behavior of the population of channels is such that their summed conductance changes slowly.) The slow channel gates operate over a different voltage range than the fast channels (i.e. less negative, more depolarized). TTX does not block the slow channels, but drugs such as nifedipine do block by binding to the channel.

on subsequent activation (Nicola-Siri et al., 1980). $[Ca^{2+}]_{SR}$ does increase following tetanic stimulation (Gonzalez-Serratos et al., 1982).

Slow APs were also recorded from mouse skeletal muscle fibers equilibrated in a solution that was Cl^--free, low Na^+ (10 mM) and high K^+ (20 mM) (Kerr and Sperelakis, 1982). As with frog muscle, the slow APs were abolished after detubulation and blocked by verapamil, bepridil, Mn^{2+} and La^{3+}. Their rate of rise, amplitude and duration increased as a function of $[Ca^{2+}]_o$, with max *dV/dt* being about 0.5 V/s in 8 mM.

During the first 5 days in culture, embryonic skeletal muscle cells from *Xenopus laevis* need extracellular Ca^{2+} to contract when stimulated (in contrast to adult muscles). Thus, an inflow of Ca^{2+} from the extracellular space may be required in embryonic cells as the means to produce contraction. In whole-cell voltage-clamp studies, I_{Ca} currents have been observed in embryonic and neonatal skeletal muscle cells in culture (Moody-Corbett et al., 1989; Cognard et al., 1992; Gonzalez-Serratos et al., 1996; Cordoba-Rodriguez et al., 1997). The current density increased from 1.7 to 3.3 and to 7.9 pA/pF at 1, 5 and 15 days in culture, respectively. These results indicate that the T-tubules and SR are poorly developed or not functional in early stages of muscle development and that, in early development, I_{Ca} may be an important mechanism to trigger contraction.

X. DEVELOPMENTAL CHANGES IN MEMBRANE PROPERTIES

The cell membranes of most excitable cells apparently pass through similar stages of differentiation during development. For example, young (2- to 3-day-old) embryonic chick hearts (tubular) have few or no functional fast Na^+ channels, but have a high density of slow channels (both Na^+ and Ca^{2+}) and fire slowly-rising TTX-insensitive APs. Fast Na^+ channels then appear and progressively increase in number, reaching the maximal (adult) level at late embryonic development (e.g. day 20). The P_{Na}/P_K ratio is high in young hearts, due to a low P_K, and accounts for the low RP and automaticity in nearly all the cells.

Skeletal muscle fibers and neurons also undergo developmental changes in membrane electrical properties (e.g. Spector and Prives, 1977; Spitzer, 1979) (see Chapter 25). In general, fast Na^+ channels are absent in the young, less differentiated cells, but they do possess excitability because of a large number of slow channels. The AP is TTX-insensitive, slowly rising and of long duration (resembling a slow AP in cardiac muscle). Later during development, fast Na^+ channels make their first appearance and the fast Na^+ channels and slow channels coexist. During that period, TTX does not abolish the APs, but reduces max *dV/dt* (i.e. slow APs remain). At a later stage, the slow channels in the sarcolemma are lost (or greatly reduced in number) and the fast Na^+ channels progressively increase in density. The APs become fast rising and of short duration and are completely abolished by TTX. As discussed previously, some functional slow Ca^{2+} channels remain in the T-tubular system.

XI. ELECTROGENIC Na^+-K^+ PUMP STIMULATION

The Na^+, K^+-ATPase pump is *electrogenic* in skeletal muscle fibers (both mammalian and amphibian). The pump produces a net outward current, because three Na^+ ions are pumped out to every two K^+ ions pumped in. The *electrogenic pump potential* contribution to the RP (see Chapter 11 to 9) is very large, about 12−16 mV, in rat skeletal muscle fibers (Sellin and Sperelakis, 1978). The *net pump current* can be stimulated by increasing the number of pump sites per unit area of cell membrane or by increasing the turnover rate of each pump site. β-Adrenergic agonists (e.g. isoproterenol) rapidly hyperpolarize skeletal muscle fibers by 7−9 mV within 5 min. Insulin has a similar effect, but hyperpolarizes more slowly (e.g. peak reached by 10 min) and to a smaller degree (e.g. 5−7 mV) (Iannaccone et al., 1989). Since cAMP also hyperpolarizes, the action of β-agonists is believed to be mediated by elevation of cAMP and phosphorylation of the Na^+-K^+ pump (or an associated regulatory protein) by protein kinase A (PKA). The action of insulin is thought to be mediated by the incorporation of spare membrane from an internal pool, which contains Na^+-K^+ pumps, into the cell membrane.

The pump current (I_p) can be directly measured in single fibers (cultured skeletal myotubes rounded by use of colchicine, a microtubule disrupter) by doing whole-cell voltage clamp under conditions in which all the ionic conductances are blocked. When this is done, the pump current can be measured at different voltages and normalized for unit membrane capacitance (hence membrane area). Values of about 1 pA/pF or 1.0 μA/cm^2 were obtained, with a *reversal potential* (or zero current) of about −140 mV (Li and Sperelakis, 1994).

When $[K^+]_o$ is lowered below the normal physiological level, e.g. from 4.5 mM to about 0.1 mM, a large depolarization occurs in mammalian skeletal muscle fibers (Fig. 42.8). This depolarization is caused, in part, by inhibition of the Na^+-K^+ pump current. The K_m value for $[K^+]_o$ for the Na^+, K^+-ATPase is about 2 mM and the relationship between Na^+, K^+-ATPase activity and $[K^+]_o$ is very steep. Therefore, inhibition of the Na^+-K^+ pump occurs.

XII. SLOW FIBERS

One type of skeletal muscle fibers, known as *slow fibers*, subserves tonic functions, including posture. Slow fibers should not be confused with "*slow twitch fibers*". The true

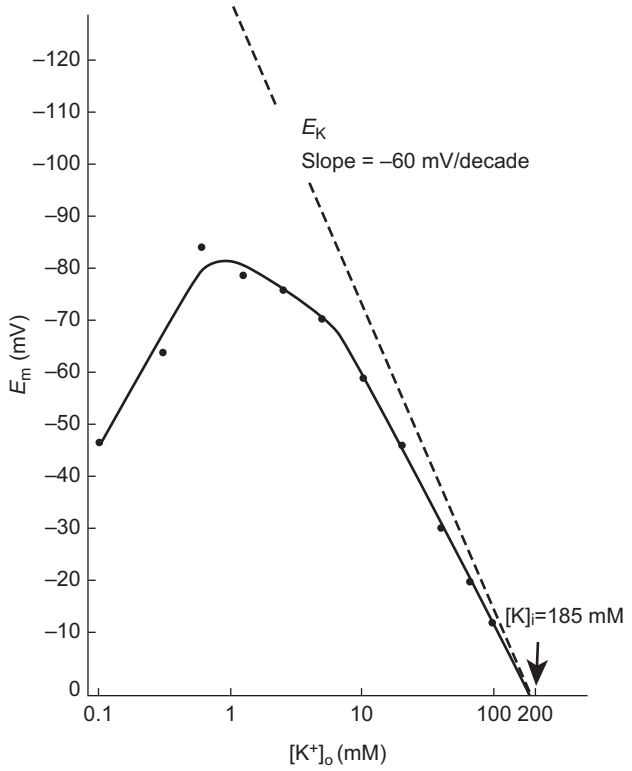

FIGURE 42.8 The mean resting membrane potential (E_m) of normal mouse skeletal muscle plotted as a function of the extracellular K^+ concentration ($[K^+]_o$) on a logarithmic scale. The straight line drawn through the data points for 20 mM $[K^+]_o$ and above has a slope of 50 mV/decade. Extrapolation of this line to zero potential gives the intracellular K^+ concentration ($[K^+]_i$) of 185 mM. The dashed line gives the calculated E_K values (slope of 61 mV/decade). Note the "fold-over" of the E_m curve at $[K^+]_o$, levels below 1 mM, presumably due to inhibition of the electrogenic pump potential (V_p) and to a decrease in P_K and g_K at low $[K^+]_o$ levels. *(Reproduced from Sellin and Sperelakis, 1978.)*

slow fibers do not fire APs, whereas all types of twitch fibers do. The slow fibers are usually smaller in diameter than twitch fibers and they exhibit a less distinct myofibrillar arrangement (so-called "*felden*" *structure*). Slow fibers have been found in a number of vertebrate muscles, e.g. in the frog rectus abdominus muscle, frog ileofibularis muscle and mammalian extraocular muscles. It is probable that careful searching will reveal some slow fibers in other mammalian muscles as well.

The slow fibers have *multiple innervation* by a *series of motor end-plates* (spaced about 1 mm apart), all from a single motor neuron. As with twitch fibers, acetylcholine (ACh) is the synaptic transmitter. The force of contraction of the slow fibers is controlled by graded *end-plate potentials* (EPPs). That is, an increase in frequency of impulses in the motoneuron produces a larger EPP (by *temporal summation*) and this, in turn, produces a greater contraction in the vicinity of the end-plate. Since the end-plates are spaced closely together — at a distance of about one length constant — the entire fiber becomes nearly uniformly depolarized, even though there are no propagated APs. Therefore, the entire length of the slow fiber contracts almost uniformly.

The slow fibers do possess T-tubules which abut at the triadic junctions with the terminal cisternae of the SR (TC-SR). Therefore, the T-tubules may act as *passive conduits* in the slow fibers to bring the depolarization (produced in the surface membrane by the EPP) deep into the fiber interior. Thus, depolarization of the T-tubule occurs by their cable properties. This depolarization, in turn, could bring about the influx of Ca^{2+} by activation of voltage-dependent slow Ca^{2+} channels located in the T-tubules.

APs normally cannot be induced to occur in vertebrate slow fibers under a variety of experimental conditions. However, denervation of frog slow fibers does allow an AP-generating mechanism to appear (Miledi et al., 1971). APs can be induced in slow fibers of invertebrates (e.g. crustacean skeletal muscles) (Fatt and Ginsborg, 1958). Similarly, in the neurogenic horseshoe crab (*Limulus*) heart, which normally is activated by summating excitatory postsynaptic potentials, propagating (ca. 5 cm/s) and overshooting spontaneous APs can be rapidly induced by Ba^{2+} (0.1−10 mM) (Rulon et al., 1971). These slowly-rising (ca. 1.0 V/s) APs are resistant to TTX and these voltage-dependent slow channels can pass Ba^{2+}, Sr^{2+} and Ca^{2+}.

XIII. CONDUCTION OF THE ACTION POTENTIAL

When the EPP, generated at the neuromuscular junction, reaches threshold for eliciting an AP in the vertebrate twitch skeletal muscle fiber, an AP is propagated down the muscle fiber in both directions from the end-plate. (In some muscle fibers, there is a second end-plate innervated by a motoneuron exiting the spinal cord at another level.) The AP is overshooting (to about +40 mV) and propagates at a constant velocity of about 5 m/s over the surface sarcolemma. Propagation occurs by means of the *local-circuit currents* that accompany the impulse, as discussed in Chapter 19. The reader is referred to that chapter for details on the *radial (transmembrane) currents* and the *longitudinal (axial) currents*. The external longitudinal currents can use the entire ISF space (since current takes the path of least resistance), allowing the electromyogram (EMG) to be recorded from the skin overlying an activated skeletal muscle. The amplitude of the EMG potentials becomes larger when more fibers within the muscle are activated (*fiber summation*), because of summation of the IR voltage drops produced by each fiber activated simultaneously. The frequency of the EMG potentials reflects the frequency and asynchrony of activation of the muscle.

The skeletal muscle fibers are formed by *myoblast cells* that have fused end to end to become long multinucleated myotubes and then cylindrical fibers later in development.

They behave as semi-infinite cables. That is, an AP can propagate from one end of the fiber to the other, uniformly and unimpeded. The space constant or *length constant* (λ) of the fiber cable is about 1.5 mm for frog sartorius fibers (Sperelakis et al., 1967) and about 0.76 mm for the rat EDL muscle (Sellin and Sperelakis, 1978). The length constant is the distance over which a voltage applied at one region would decay to 1/e (1/2.717 = 0.368) or 36.8% of the initial value. That is, in a passive cable, voltage decays exponentially with a certain length constant as given by:

$$V_x = V_o\, e^{-x/\lambda} \tag{42.4}$$

where V_x is the voltage at the distance x and V_o is the voltage at the origin ($x = 0$). λ is given by:

$$\lambda = \sqrt{\frac{r_m}{r_i + r_o}}$$
$$\text{cm} = \sqrt{\frac{\Omega.\text{cm}}{\frac{\Omega}{\text{cm}} + \frac{\Omega}{\text{cm}}}} = \sqrt{\text{cm}^2} \tag{42.5}$$

Assuming that r_o (the outside longitudinal resistance) is negligibly small compared to r_i (this would be true for a superficial fiber in a bundle immersed in a large bath):

$$\lambda = \sqrt{\frac{r_m}{r_i}} = \sqrt{\frac{R_m}{R_i}\frac{a}{2}}$$
$$\text{cm} = \sqrt{\frac{\Omega.\text{cm}}{\Omega/\text{cm}}} = \sqrt{\frac{\Omega.\text{cm}^2}{\Omega.\text{cm}}\frac{\text{cm}}{}} = \sqrt{\text{cm}^2} \tag{42.6}$$

where r_m (Ω·cm) and r_i (Ω/cm) are the membrane resistance and the internal longitudinal resistance normalized for unit length of fiber, R_m (Ω·cm^2) is the membrane resistance normalized for both fiber radius and length, R_i (Ω·cm) is the resistivity of the myoplasm (normalized for length and cross-sectional area), and a (cm) is the fiber radius. R_m is often loosely called membrane resistivity, but this is not accurate because for true membrane resistivity (ρ_m) there must be correction for membrane thickness δ:

$$\rho_m = \frac{R_m}{\delta} \tag{42.7}$$

$$\Omega.\text{cm} = \frac{\Omega.\text{cm}^2}{\text{cm}}$$

The factors that determine active velocity of propagation (θ_α) include the intensity of the local-circuit current, threshold potential and the passive cable properties, λ and τ_m. As discussed previously, the greater the rate of rise of the AP, the greater the intensity of the local-circuit current, hence the greater the θ_α. In addition to its dependence on the density of the fast Na^+ channels (determinant of the maximum Na^+ conductance, $\overline{g}_{Na}$), the kinetic properties of

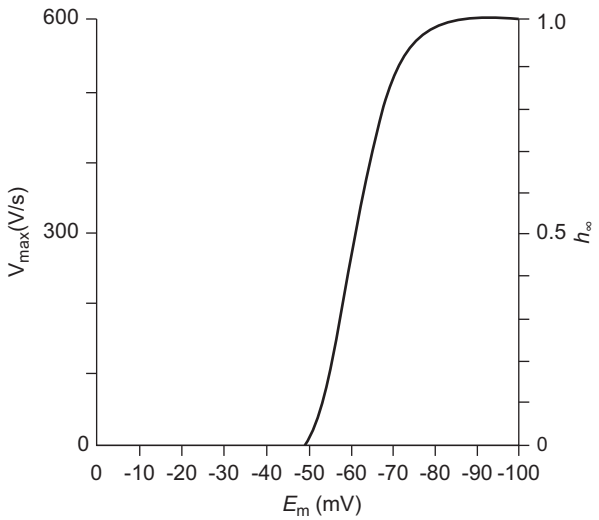

FIGURE 42.9 Graphic representation of the maximal rate of rise of the APl (max *dV/dt*) as a function of resting E_m or takeoff potential. Max *dv/dt* is a measure of the inward current intensity (membrane capacitance being constant), which is dependent on the number of channels available for activation; h is the inactivation factor of Hodgkin–Huxley as $g_{Na} = \overline{g}_{Na} m^3 h$, where g_{Na} is the Na^+ conductance, $\overline{g}_{Na}$ is the maximal conductance and m and h are variables; h_∞ represents h at $t = \infty$ or steady state (practically, after 20 ms). The fast Na^+ channels begin to inactivate at about −75 mV and nearly complete inactivation occurs at about −30 mV (h_∞ low). Therefore, max *dV/dt* decreases because h_∞ decreases.

the channel gating and the threshold potential (V_{th}), max *dV/dt* is determined also by the RP (or takeoff potential) (related to the h_∞ versus E_m curve), as discussed previously (Fig. 42.9). In addition, because cooling decreases Na channel activation ($Q_{10} \simeq 3$), max *dV/dt* and θ_α are slowed accordingly. R_m is increased by cooling, the Q_{10} for R_K in frog sartorius fibers being about 2.8 (ion diffusion in free solution has a Q_{10} of about 1.2) (Sperelakis, 1969). For a description of passive conduction, see Appendix III to this chapter.

XIV. EXCITATION DELIVERY TO FIBER INTERIOR BY CONDUCTION INTO THE T-TUBULAR SYSTEM

The experiments of Huxley and Taylor (1958) were the first to provide evidence that there was some structure, located at the level of the Z-lines in frog skeletal muscle fibers, which is involved in E-C coupling. This structure allows relatively fast conduction of the excitatory process (AP) from the surface membrane to the center of the muscle cells. These investigators applied current pulses at different points along the length of the sarcomeres in isolated fibers and found that when the microelectrode tip was opposite the Z-line, graded contractions of the two half-sarcomeres occurred. The greater the current, the greater was the inward spread of the contraction. In

addition, they discovered that there were sensitive spots located around the perimeter of the fiber at the Z-line level; i.e. the membrane was not uniformly sensitive. At about the same time, it was discovered by electron microscopy that transverse (T-) tubules were located at the level of the Z-lines in amphibian skeletal muscle (and at the level of the A-I junctions of the sarcomere in mammalian skeletal muscle). Thus, the T-tubules probably represent the morphological conduit for the findings of Huxley and Taylor. The morphological arrangements of the sarcotubular system of skeletal muscle fibers are illustrated in Fig. 42.10.

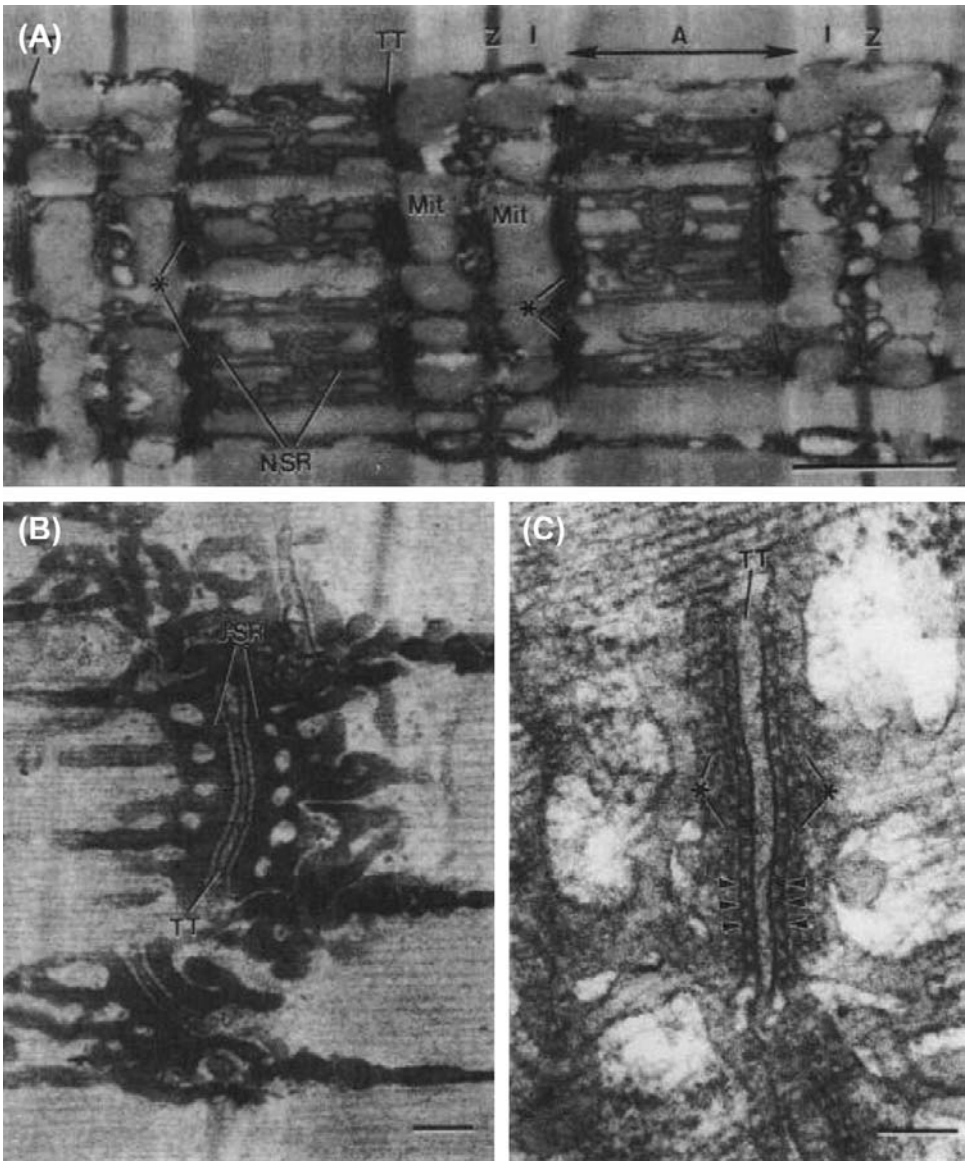

FIGURE 42.10 Sarcotubular system of skeletal muscle fibers from tibialis anterior muscle of mouse (A,C) and iliotibialis muscle of lizard (B). (A) Longitudinal section showing the sarcomere structure of several myofibrils: A-band, I-band, Z-line. The network sarcoplasmic reticulum (N-SR), also known as the longitudinal SR, appears as a torn sleeve surrounding the surface of each myofibril. The N-SR is continuous with the junctional SR (J-SR) that abuts close to the transverse tubules (TT). The TT membranes are invaginations of the cell surface membrane at the level of the A-I junctions in mammalians (or at the level of the Z-line in lizards and amphibians). The J-SR and TT form the complex coupling known as a triad (*). The N-SR is continuous across the I-band, but this is obscured in this section by the presence of paired mitochondria (Mit) over the I-bands. The TT and SR are both selectively filled with osmium tetroxide precipitate, causing their profiles to be more electron opaque than the other structures. Scale bar at lower right represents 1.0 μm. (B) Higher magnification of a triad to show more detail. As shown, the triad consists of a single T-tubule sandwiched between two cisternae of the J-SR. Scale bar = 0.1 μm. (C) High magnification of a triadic junction to illustrate the array of regularly-spaced junctional processes or SR foot processes (several indicated by arrowheads) that project between the TT membrane and the J-SR membrane. There are dense granules within the lumen of the J-SR cisternae (*). Scale bar = 0.1 μm. *(Electron micrographs provided courtesy of Dr Mike Forbes, University of Virginia.)*

Diffusion of some substance from the surface membrane into the skeletal muscle fiber interior is much too slow to account for the relatively short latent period of about 1−3 ms between the beginning of the AP and the beginning of contraction. That is, the diameter of the fibers (mean value of about 70 μm in frog sartorius fibers) is much too large for a diffusion mechanism from the fiber surface to be involved. Diffusion time (for 95% equilibration) increases by the square of the distance and would require about 2.5 s for a small molecule freely diffusing across a cell radius of 50 μm; estimates for Ca^{2+} diffusion time are considerably longer than this (Podolsky and Costantin, 1964). Therefore, the T-tubular system serves as an electrical conduit to bring excitation deep into the fiber interior rapidly and thereby reduces the required diffusion distance to an average value of about 0.7 μm (Sperelakis and Rubio, 1971). It was reported that disruption of the T-tubule system (by a glycerol osmotic-shock method) uncouples contraction from excitation (Eisenberg and Gage, 1969).

Estimates of the length constant of the T-tubules (λ_{TT}), assuming the T-tubule membrane has about the same resistivity (R_m) as the surface membrane $\lambda_{TT} = \sqrt{R_m/R_i}\sqrt{a/2}$ give values of about 50 μm. Because the resistivity of the T-tubule membrane of frog muscle is probably higher than that of the surface sarcolemma because of lower g_{Cl} (Hodgkin and Horowicz, 1959; Adrian and Freygang, 1962; Sperelakis and Schneider, 1968), this would give a longer value. Therefore, it is theoretically possible for the T-tubules to serve as *passive conduits* to bring the depolarization from the surface membrane (during its AP) into the fiber interior. (This mechanism does operate when small depolarizing voltage changes [below the AP threshold] occur on the surface sarcolemma, and conversely any voltage change originating in the T-tubules can be conducted passively to the surface sarcolemma.)

However, direct microscopic observations of the degree of myofibril activation across the width of the fiber caused by raised $[K^+]_o$ depolarization suggested otherwise (Gonzales-Serratos, 1975). Also, during the foot of the AP, only a small outer ring of the tubular network depolarizes beyond the mechanical threshold (Hodgkin and Nakajima, 1972). These results imply that in order for all the myofibrils in the cross-section of a fiber to be activated, which had been demonstrated previously (Gonzalez-Serratos, 1971), there must be a T-tubular AP (TT-AP).

There is evidence that the T-tubules actually do fire APs, i.e. they *actively propagate impulses* inward and so bring large depolarization deep into the fiber interior. The evidence for this includes the observation of a threshold for sudden initiation of localized contraction (Costantin and Podolsky, 1967; Costantin and Taylor, 1973). The TT-AP is sensitive to TTX and is Na^+ dependent and, therefore, is apparently similar in nature to the surface membrane AP. By use of high-speed cinemicrography to measure sequential activation of the myofibrils in a radial direction, Gonzalez-Serratos (1971) estimated the propagation velocity of the TT-AP (θ_{TT}) to be about 10 cm/s, with a Q_{10} of 2.2 (which is similar to the Q_{10} of the surface membrane for AP conduction). This velocity is sufficient to account for the short latent period before contraction begins.

Early evidence for the existence of *active propagation* in the T-tubules came from a number of indirect measurements (reviewed in Caputo, 1978). The speed and Q_{10} (2.2) of the spread of mechanical activation were greater than expected for passive conduction (Gonzalez-serratos 1971). Moreover, twitch tension was reduced by TTX or a Na^+-deficient medium (Costantin, 1970). Depolarization by elevated $[K^+]_o$, which inactivates Na^+ channels, fails to activate contraction in deeper myofibrils (Gonzales-Serratos, 1975). These results suggested that in order for all the myofibrils in the cross-section of a fiber to be activated, there must be fast Na^+ channels in the T-tubules and a T-tubular AP (TT-AP). Subsequently, tubular Na^+ currents have been measured directly (Hille and Campbell, 1976) and direct experimental confirmation of propagating APs in the T-tubules have been demonstrated in amphibian (Nakajima and Gilai, 1980) and mammalian muscle fibers (DiFranco et al., 2005). These direct recordings of the propagating AP in the T-tubules were achieved using potential-sensitive dyes, since the T-tubule membranes are not accessible to conventional microelectrode methods.

In muscles placed in low $[Na^+]_o$ and stimulated briefly at high frequency, the normal tetanic tension rapidly falls, simultaneous with the central myofibrils becoming inactive. These results are due to Na^+ depletion in the T-tubule network, particularly in the deeper parts far from the orifice at the fiber surface (Bezanilla et al., 1972). It is thought that the Na^+ influx (the inward fast Na^+ current) with each AP in the T-tubule produces a progressive decline in $[Na^+]_{TT}$, which slows propagation velocity down the T-tubules and eventually leads to loss of excitability when $[Na]_{TT}$ drops below some critical level (e.g. 30 mM). Na^+ depletion should occur more rapidly deep in the T-tubule network because there would be less diffusion of Na^+ in from the mouth of the T-tubule to replenish the Na^+ loss. Active Na^+-K^+ pumping in the T-tubules may not occur fast enough to keep up with the Na^+ loss into the fiber myoplasm.

There are also voltage-dependent slow Ca^{2+} channels in the T-tubule membrane and slow APs that arise from the T-tubule can be recorded under appropriate conditions (Sperelakis et al., 1967; Vogel et al., 1978). The evidence for the existence of this type of channel and some of its properties was discussed above. The Ca^{2+} influx into the myoplasm through these Ca^{2+} channels could play a role in E-C coupling. For a discussion of the relationship between the T-tubules and the terminal cisternae of the SR, see Appendix IV.

APPENDIX

AI. MORE INFORMATION ON Cl^- CHANNELS

In frog, there are several subtypes of Cl^- channels that have single-channel conductances ranging between 40 and 70 pS and each channel may exhibit several subconductance states. But there is usually a main gate that opens or closes the entire channel. In fetal mammalian fibers, Cl^- channels with conductances of about 40, 60 and 300 pS have been observed. Myoballs cultured from muscle biopsies of patients having one form of myotonia had a reduced (ca. 50%) single-channel conductance for the Cl^- channel, which would contribute to the myotonia (Fahlke et al., 1993). In primary cultures of rat skeletal muscle, the fast Cl^- channel showed a behavior consistent with six closed states and two open states (Weiss and Magleby, 1992). The Cl^- channel in myoblasts and myotubes of the L6 cell line derived from rat skeletal muscle had a high conductance of about 330 pS (Hurnak and Zachar, 1992). Voltage-gated Cl^- channels have also been found in the SR membrane of skeletal muscle.

Some Cl^- channels described for other tissues include: (1) Ca^{2+}-dependent Cl^- channels; (2) stretch-activated Cl^- channels; and (3) cyclic AMP-stimulated Cl^- channels. The receptor-operated Cl^- channels apparently have a G-protein (e.g. G_s or G_i) as intermediate for coupling.

The voltage-dependent Cl^- channels can be blocked relatively selectively by several methods, including acidosis and use of compounds such as the stilbene derivatives (DIDS and SITS) and 9-anthracene carboxylic (9-AC) acid. The Cl^- channels in frog skeletal muscle are relatively insensitive to 9-AC acid, whereas those in adult mammalian muscle are highly sensitive. The anion selectivity sequence for some voltage-dependent Cl^- channels is $I^- > Br^- > Cl^- > F^-$.

AII. MORE INFORMATION ON K_{ATP} CHANNELS

It has been proposed that K_{ATP} channels may be associated with the decrease in force development underlying muscle fatigue. A drug (SR44866) that opens K_{ATP} channels (in sarcolemmal membrane patches from frog skeletal muscles) also reduces the AP duration, the early afterpotential and the peak twitch force (without affecting the RP) in intact frog muscles (Sauviat et al., 1991). The high K^+ permeability found in muscle fibers that have undergone a permanent contracture (rigor) produced by repetitive stimulation while metabolically-poisoned with cyanide and iodocetate (Fink and Lüttgau, 1976), may be caused by the decreased ATP concentration opening K_{ATP} channels. In metabolically-exhausted frog semitendinosus muscle fibers, the addition of tolbutamide and glyburide, two K_{ATP} channel antagonists, significantly reduce the K^+ efflux rate (Castle and Haylett, 1987). As said previously, even under fatigue induced by prolonged repetitive stimulation, the decrease in intracellular ATP is small (Nassar-Gentina et al., 1978) and fatigued muscle fibers can contract when Ca^{2+} is released directly from the intracellular SR stores (Gonzalez-Serratos et al., 1978; Garcia et al., 1991). In intact animals, some of the skeletal muscle fatigue results from synaptic fatigue, including fatigue at the neuromuscular junction.

The Kir6.x channel is a typical inward-rectifier type K^+ channel protein. It has two transmembrane helices that form the pore and K^+ selectivity filter. The cytoplasmic NH_2 and COOH termini interact to form an ATP binding site. A key property of Kir channels is inhibition of channel opening by ATP (Spruce et al., 1987). Each Kir subunit can bind one molecule of ATP. Inhibition by ATP is not a consequence of phosphorylation or ATP hydrolysis, but of direct binding to intracellular domains on the Kir channel (Kakei et al., 1985). That is, ATP is not consumed in this action.

SUR is a regulatory protein that is linked to the C-terminus of Kir. SUR is an ATP-binding cassette (ABC) protein, which itself (unlike other ABC proteins) has no intrinsic transport function, but associates with Kir6.x K^+ channels to form the functional K_{ATP} channel. SUR serves as a regulatory subunit which fine-tunes the activity of Kir6.x in response to changes in cell metabolism. Each SUR subunit contains two nucleotide-binding folds which contain binding sites for Mg^{2+}-adenosine nucleotides. Cytosolic free Mg^{2+} is high in resting skeletal muscles (ca 1 mM). In the absence of Mg^{2+}, nucleotides (such as ADP) act on SUR to inhibit K_{ATP} activity. Therefore, nucleotides can regulate K_{ATP} channels through interactions with both Kir and SUR.

As with other members of the Kir family, the K_{ATP} channel exhibits inward rectification (ir). That is, the open channels pass inward current with increasing hyperpolarization, but outward K^+ current does not flow when the membrane is depolarized by more than about 10 mV above the E_K potential. This property of inward rectification is caused by cytoplasmic ions such as Mg^{2+} and polyamines plugging the pore pathway upon depolarization and thereby obstructing the outward flow of K^+ (Woll et al., 1989).

The half-maximum inhibition of opening of K_{ATP} channels by ATP in skeletal muscle (measured at a constant $[K^+]_o/[K^+]_i$) is 0.135 mM at pH 7.2 (see Fig. 42.6). Intracellular [ATP] is about 5 mM in resting muscle (Dawson et al., 1978, 1980) and it is maintained at near basal levels even during repetitive contractions that lead to muscle fatigue (Carlson and Siger, 1960; Nassar-Gentina et al., 1978). Therefore, the K_{ATP} channels are

largely inactive (or masked) under normal physiological conditions.

In searching for a possible role of the K_{ATP} channel under other conditions, a modest role was demonstrated in maintaining membrane polarization under sustained muscle use and fatigue. Although ATP is the controller of K_{ATP} opening, K_{ATP} activity can be modulated by a number of metabolites through interactions with Kir, SUR or both. These include: K^+, H^+ and phospholipids (such as PIP_2), all of which are known to increase during muscle contraction.

Extracellular K^+ concentration ($[K]_o$) rises dramatically in the muscle extracellular space during repetitive AP activity and can reach 15−50 mM in the transverse tubules (Almers, 1980; Clausen, 2008). The unitary conductance of the K_{ATP} channel increases with $[K^+]_o$, from 15 pS in 2.5 mM to 42 pS in 60 mM. Therefore, at higher $[K_o]$, K_{ATP} channels are more conductive at the same ATP concentration.

Kir channels are also regulated by pH at the cytoplasmic surface (pH_i) (reviewed in Jiang et al., 2002; Qu et al., 2000). Intracellular pH may drop by up to one unit during intense muscle use (Renaud, 1989). A decrease in pH_i reduces the inhibitory effect of ATP on K_{ATP} channels, leading to an increase in the probability of K_{ATP} channel opening (Davies et al., 1992). The ATP concentration required for half-inhibition increases by 2.5 times and 15 times, respectively, at pH_i 6.8 and 6.3, compared to that at pH_i 7.2. That is, a decrease in pH_i increases the ATP concentration required for half-inhibition of channel activity. During acidosis, a small decrease in ATP concentration leads to a greater opening of K_{ATP} channels.

The decrease in pH_i during contraction is matched by an increase in cytosolic free Mg^{2+}. A rise in cytosolic Mg^{2+} reduces the ability of ATP to close K_{ATP} channels (Vivaudou et al., 1991). This is most likely related to the ability of Mg^{2+} to bind to ATP and to the stimulatation of K_{ATP} channels via the SUR regulatory subunit. Although the increases in $[K]_o$, pH_i and $[Mg^{2+}]_i$ may act collectively and synergistically to activate K_{ATP} channels during repetitive muscle contraction, this effect is modest at normal muscle $[ATP]_i$.

On the other hand, K_{ATP} channels may become activated when the muscle is stressed or metabolically compromised (Hussain et al., 1994). Adenosine, which is released from metabolically-compromised muscle, stimulates K_{ATP} (Bartlett-Jolley and Davies, 1997) and, as said previously, intracellular acidosis is a potent activator of K_{ATP} channels. Although the skeletal muscles of genetically-altered mice which lack Kir (Kir6.2 knockout mice) develop fatigue more rapidly than control muscles (Cifelli et al., 2007), the more rapid onset of fatigue is not associated with K_{ATP} channel activation (Boudreault et al., 2010). These findings indicate that K_{ATP} channels are not essential for maintaining force during fatigue.

The activation of K_{ATP} channels after fatigue has developed helps preserve a polarized membrane potential, keeping it near E_K. This function prevents voltage-dependent Ca^{2+} entry that can occur following fatigue and cause fiber injury. Consistent with this idea, both Kir6.2 knockout mice and SUR knockout mice show extensive muscle fiber damage when subjected to exercise training (Thabet et al., 2005; Stoller et al., 2007). Therefore, K_{ATP} channels in muscle serve a myoprotective role to prevent fiber damage following intense fatigue or during metabolic exhaustion. In this respect, the role of K_{ATP} channels in skeletal muscles is similar to that in other cell types, i.e. K_{ATP} channels serve as molecular sensors of cellular metabolism, linking metabolism to membrane excitability.

AIII. FURTHER EVIDENCE THAT THE T-TUBULES FIRE Na^+-DEPENDENT APs

Further evidence of a Na^+-dependent TT-AP came from observations in which muscles placed in low $[Na^+]_o$ and stimulated briefly at high frequency, initially develop normal tetanic tension that rapidly falls and steadily decreases to a lower sustained tension; simultaneously the central myofibrils becoming inactive. These results are due to Na^+ depletion in the T-tubule network, particularly in the deeper parts far from the orifice at the fiber surface. Na^+ depletion occurs because g_{Na} increases during the TT-AP generation, causing an inward Na^+ flow into the myoplasm (Bezanilla et al., 1972). The fatigue occurs more rapidly in fibers pre-equilibrated in low $[Na^+]_o$ (e.g. 60 mM). There is a progressive decline in $[Na^+]_{TT}$, which slows propagation velocity down the T-tubules and eventually leads to loss of excitability when $[Na]_{TT}$ drops below some critical level (e.g. 30 mM). Na^+ depletion should occur more rapidly deep in the T-tubule network because there would be less diffusion of Na^+ in from the mouth of the T-tubule to replenish the Na^+ loss. Active Na^+-K^+ pumping in the T-tubules may not occur fast enough to keep up with the Na^+ loss into the fiber myoplasm.

There is evidence that the T-tubules actually do fire APs, i.e. they actively propagate impulses inward and so bring large depolarization deep into the fiber interior. The evidence for this includes the observation of a threshold for sudden initiation of localized contraction (Costantin and Podolsky, 1967; Costantin and Taylor, 1973). The TT-AP is sensitive to TTX and is Na^+ dependent and, therefore, is apparently similar in nature to the surface membrane AP. By use of high-speed cinemicrography to measure sequential activation of the myofibrils in a radial direction, Gonzalez-Serratos (1971) estimated the propagation velocity of the TT-AP (θ_{TT}) to be about 10 cm/s. The Q_{10} of 2.2 is similar to that of the surface membrane AP. Although this velocity is about 16 times slower than propagation

down the fiber longitudinally (about 1.6 m/s), it is sufficient to account for the short latent period before contraction begins. Additional data supporting the presence of APs in the T-tubules has been obtained more recently using V-sensitive dyes.

AIV. PROPAGATION VELOCITY IN A PASSIVE CABLE

In a passive cable, such as in a resting skeletal muscle fiber, the *passive propagation velocity* (θ_p) is directly proportional to the length constant and inversely proportional to the time constant:

$$\theta_p = \frac{\lambda}{\tau_m} \qquad \frac{\text{cm}}{\text{s}} = \frac{\text{cm}}{\text{s}} \tag{42A.1}$$

$$\theta_p = \frac{\sqrt{\frac{R_m}{R_i}\frac{a}{2}}}{R_m C_m} \qquad \frac{\text{cm}}{\text{s}} = \frac{\sqrt{\frac{\Omega.\text{cm}^2}{\Omega.\text{cm}}\frac{\text{cm}}{}}}{\Omega.\text{cm}^2\frac{\text{F}}{\text{cm}^2}} = \frac{\sqrt{\text{cm}^2}}{\text{s}} \tag{42A.2a}$$

$$\theta_p = \frac{\sqrt{a}}{\sqrt{R_m R_i 2 C_m}} \qquad \frac{\text{cm}}{\text{s}} = \frac{\sqrt{\text{cm}}}{\sqrt{\Omega.\text{cm}^2}\sqrt{\Omega.\text{cm}}\frac{\text{F}}{\text{cm}^2}} = \frac{\sqrt{\text{cm}}}{\text{cm}\sqrt{\text{cm}}\frac{\text{s}}{\text{cm}^2}} = \frac{\text{cm}}{\text{s}} \tag{42A.2b}$$

Therefore, propagation velocity is directly proportional to the square root of the fiber radius (a) and inversely proportional to membrane capacitance (C_m) and to the square root of R_i and the square root of R_m. For example, propagation velocity is greater in large-diameter muscle fibers. The length constant for sinusoidally-varying applied currents (λ_{ac}) is shorter than λ_{dc}, depending on the ac frequency.

The relationship between propagation velocity and membrane current density (I_m) is given by:

$$I_m = \frac{a}{2}\frac{1}{R_i}\frac{1}{\theta^2}\frac{d^2V}{dt^2} \qquad \frac{\text{amp}}{\text{cm}^2} = (\text{cm})\left(\frac{1}{\Omega.\text{cm}}\right)\left(\frac{1}{\text{cm}^2/\text{s}^2}\right)\left(\frac{\text{V}}{\text{s}^2}\right) = \frac{\text{amp}}{\text{cm}^2} \tag{42A.3}$$

where d^2V/dt^2 is the second time derivative of the AP. As indicated, membrane current is proportional to d^2V/dt^2, whereas the longitudinal current (I_l) or the capacitative current (I_c) is proportional to dV/dt:

$$I_c = C_m \frac{dV}{dt} \tag{42A.4}$$

AV. EVIDENCE FOR T-TUBULE COMMUNICATION WITH THE SR ACROSS THE TRIADIC JUNCTION UNDER SOME CONDITIONS

This Appendix section is included to let the student know that there are data that do not fit with currently accepted hypotheses.

Ca^{2+} for contraction in skeletal muscle is primarily released from the TC-SR (Winegrad, 1968) and there is an internal cycling of Ca^{2+} ion. Changes in $[Ca^{2+}]_o$ of the bathing solution take a relatively long time (e.g. 30 min) before exerting a large effect on the force of contraction. In contrast, in cardiac muscle, the effect of lowered $[Ca^{2+}]_o$ is significant within a few seconds, indicating that the primary determinant of the force of contraction is the Ca^{2+} influx across the sarcolemma through the slow Ca^{2+} channels. Therefore, in skeletal muscle, excitation propagates actively down the T-tubules and Ca^{2+} is released from the TC-SR, but it is controversial as to how the signal is transferred from the T-tubule to the TC-SR across the triadic junction.

Electron-opaque tracer molecules, like horseradish peroxidase (HRP) (ca. 60 Å diameter), enter into the T-tubules and from there can enter into some of the TC-SR of frog skeletal muscle (Rubio and Sperelakis, 1972; Kulczycky and Mainwood, 1972) (Fig. 42A.1A,B). Exposure of the fibers to hypertonic solutions facilitates the entry of HRP into the TC-SR, so that nearly 100% of the TC-SR become filled (Fig. 42.A.1C,D). Thus, there may be a functional connection between the SR and the extracellular space (Sperelakis et al., 1973). If so, there may be lumen-to-lumen continuity between the T-tubules and TC-SR during excitation, allowing the AP in the T-tubules to invade directly into the TC-SR to depolarize and bring about the release of Ca^{2+}. The depolarization of the TC-SR could activate voltage-dependent Ca^{2+} channels, allowing Ca^{2+} influx into the myoplasm down an electrochemical gradient.

If the longitudinal SR (L-SR) were electrically isolated from the TC-SR by a substantial resistance (e.g. *zippering* between the two SR compartments, described later), this would account for the fiber capacitance measured being relatively low (Mathias et al., 1980). The effect of this would be to remove the very large membrane surface area of the L-SR and hence greatly reduce the capacitance that would be measured.

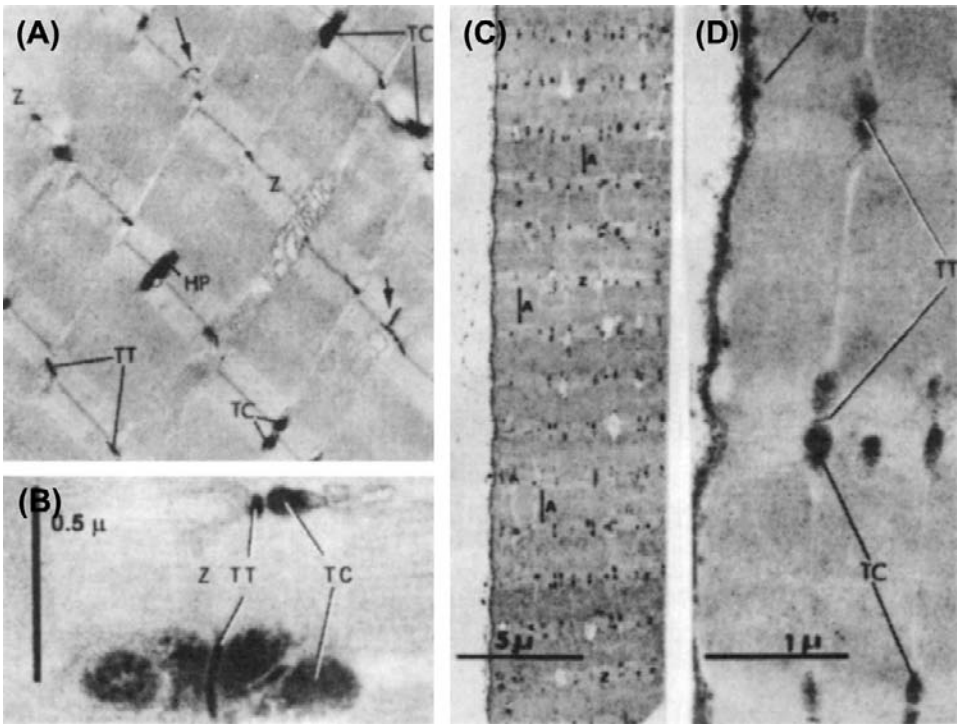

FIGURE 42A.1 Evidence that large molecules of horseradish peroxidase (HP) can enter into the terminal cisternae (TC) of the SR via the transverse tubules (TT) of frog sartorius fibers. Electron micrographs of longitudinal sections. (A,B) Fiber was exposed to HP under isosmotic conditions. (A) Section through several myofibrils showing presence of HP activity (as a dense electron-opaque material) in the TT and in some of the TC at triadic junctions. In amphibian muscle, the TT occur at the level of the Z-lines (Z) of the sarcomeres. Arrows point to two branches of the TT running longitudinally. (B) Higher magnification of two triads, one with both cisternae filled with HP and the other with only one cisterna filled. (C,D) Fiber was exposed to HP under hypertonic condition (3 X isotonic, using NaCl), showing that almost all cisternae were filled with peroxidase. (C) Section at low magnification. (D) Portion of same section as in Part C shown at higher magnification. The surface vesicles (Ves) also became filled with HP. *(Modified from Figs. 2 and 4 of Rubio, R. and Sperelakis, N. (1972). Z. Zellforsch. 124, 57–72.)*

It has been suggested that the SR is depolarized during the release of Ca^{2+} in E-C coupling. For example, optical signals (e.g. birefringence and fluorescence changes) can be recorded from the SR membranes during contraction (e.g. Baylor and Oetliker, 1975; Bezanilla and Horowicz, 1975). In addition, Natori (1965) demonstrated that propagation of contraction (1–3 cm/s) triggered by electrical stimulation can occur in muscle fiber regions that had been denuded (skinned) of their sarcolemma, the propagation of excitation presumably occurring by means of the SR membranes.

It was demonstrated that E-C uncoupling could be produced by exposing frog skeletal muscle fibers to Mn^{2+} (1 mM) or La^{3+} (1 mM) while in hypertonic solution (to facilitate entry of the blockers into the TC-SR) (Sperelakis et al., 1973). After the fibers were returned to normal Ringer solution, normal fast APs could be elicited, but there were no contractions accompanying them; i.e. a "permanent" E-C uncoupling was produced. These results were interpreted as suggesting that Mn^{2+} and La^{3+} entered into the lumen of the TC-SR and blocked the Ca^{2+} channels. A similar exposure of frog sartorius fibers to Mn^{2+}, La^{3+} or to Ca^{2+}-free solution blocked the caffeine-induced contracture as well (Rubio and Sperelakis, 1972). Thus, from these physiological and ultrastructural studies, it was suggested that the lumen of the SR is continuous with that of the T-tubule under conditions of hypertonicity and that substances can enter into the TC-SR to exert an effect on Ca^{2+} release into the myoplasm.

Compartmental analysis of skeletal muscle has also suggested that the SR is open to the ISF. (In contrast, in cardiac muscle, there is no evidence that the SR is open to the ISF [Rubio and Sperelakis, 1972].) For example, Conway (1957), Harris (1963) and Keynes and Steinhardt (1968) concluded that Na^+ inside frog skeletal muscle fibers is distributed in two separate compartments. Harris (1963) suggested that the Na^+, K^+ and Cl^- concentrations in one compartment (presumably the SR) were about equal to those of the ISF. Rogus and Zierler (1973) concluded that the Na^+ concentration in the SR of rat skeletal muscle approximates that of the ISF. The volume of the SR compartment was 14.3% of fiber volume and, in hypertonic solution, the SR volume increased and the washout of the SR compartment was faster. Tasker et al. (1959) also had reported a large sucrose space of 26.5% for frog sartorius fibers.

Other researchers (Birks and Davey, 1969) have demonstrated that the volume changes of the SR of skeletal muscle in hypertonic (sucrose) and hypotonic solutions were always opposite of those occurring within the myoplasmic compartment. They concluded that sucrose must enter into the SR, pulling in water osmotically from the myoplasm, to produce the marked swelling of the SR that occurred in hypertonic solutions. Vinogradova (1968) concluded from the distribution of non-penetrating sugars in frog sartorius muscle that the SR compartment is continuous with the ISF; the inulin space was 19.0% and increased in hypertonic solution and decreased in hypotonic solution and in glycerol-treated fibers (for disruption of the T-tubules).

The total [3H]-sucrose space of frog sartorius muscles was found to be 18.0% in isotonic solution and 22.6% in twofold hypertonic solution (Sperelakis et al., 1978). The relative SR volume (including the small T-tubule volume) was 12.4% and 17.0% of fiber volume, respectively. This value for SR volume of frog skeletal muscle is close to that measured by ultrastructural techniques (Peachey, 1965; Mobley and Eisenberg, 1975). Evidence that the TC-SR and L-SR may not be freely connected to one another under resting conditions comes from the observations that: (1) the L-SR did not fill with HRP, whereas the TC-SR did (Rubio and Sperelakis, 1972); and (2) there is a zippering of the membranes connecting these two components of the SR in mouse and frog skeletal muscle (Howell, 1974; Wallace and Sommer, 1975; Forbes and Sperelakis, 1979).

In ^{45}Ca washout experiments on frog muscles, Kirby et al. (1975) found three compartments, similar to the three sucrose compartments described previously, except the half-times were about two- to threefold shorter. They suggested that the first compartment was the ISF space, the second was the T-tubule plus the TC-SR and the third was the L-SR. Bianchi and Bolton (1974) also found a transient increase in ^{45}Ca efflux and a marked loss of muscle Ca^{2+} from frog sartorius muscles exposed to hypertonic solutions (twice isotonicity) and suggested that hypertonicity produces transient communication between the TC-SR and the T-tubules, thus allowing their Ca^{2+} to be lost to the ISF. In addition, it has been reported in a human muscle disease, polymyositis, that the T-tubules are spatially continuous with the SR, as visualized with lanthanum tracer, and that enzymes leak from the TC-SR into the T-tubules and ISF (Chou et al., 1980).

Frog skeletal muscle fibers have an osmotically inactive volume of about 32% when placed into Ringer solution made hypertonic with sucrose or other non-penetrating solutes; i.e. fiber diameter does not shrink to the theoretical value expected if it were a perfect osmometer (Sperelakis and Schneider, 1968; Sperelakis et al., 1970). For example, in twofold hypertonic solution, there should be a decrease in fiber volume to one-half and fiber radius to 0.707 $(1/\sqrt{2})$ of the original value. The observed change is to only 0.81 of the original diameter. Because the SR volume increases in hypertonic solution (Huxley et al., 1963; Sperelakis and Schneider, 1968; Birks and Davey, 1969), it is likely that the osmotic inactive volume is due to the SR. The swollen SR would prevent the fiber volume from decreasing to one-half in twofold hypertonic solution, even if the volume of the myoplasm proper were to decrease to one-half.

In cardiac muscle, an osmotically-inactive volume is not present (Sperelakis and Rubio, 1971), electron-opaque tracers do not enter the SR (Sperelakis et al., 1974) and the SR volume does not increase with hypertonicity (Sperelakis and Rubio, 1971).

AVI. INVERTEBRATE STRIATED MUSCLE FIBERS

This Appendix was prepared by Hugo Gonzalez-Serratos and Hector Rasgado-Flores and was edited by Nicholas Sperelakis.

Introduction

In 1902, Overton observed that frog skeletal muscle cells lost their excitability when the extracellular Na^+ concentration ($[Na^+]_o$) was decreased below 10% of normal. This was the first indication that excitability of vertebrate skeletal muscle fibers was Na^+-dependent. Using intracellular microelectrodes, Nastuck and Hodgkin demonstrated, in 1950, that skeletal muscle fibers of the frog have a clear relationship between the amplitude of the AP and $[Na^+]_o$. They concluded that vertebrate striated skeletal muscle APs are generated by mechanisms similar to those in squid giant nerve axons. In an attempt to test this Na^+ hypothesis in striated muscle fibers of the crustacean, Fatt and Katz (1953) bathed crayfish muscles with different external Na^+ concentrations. However, against their prediction, they found that there was no effect on the amplitude of the APs. That is, striated invertebrate crayfish muscles were excitable and capable of developing full APs in the absence of external Na^+ ions. Thus, they concluded that invertebrate striated muscle fibers did not have an Na-dependent excitability. Instead, the APs were generated by currents using other ions. The APs of invertebrate striated muscle fibers, compared to vertebrates, are longer in duration and some of them even have a plateau (similar to cardiac muscle) (Fig. 42A.2).

Calcium Hypothesis

What are the ionic currents that generate the APs in invertebrate striated muscle fibers? With zero extracellular Na^+, the invertebrate muscles were capable of generating APs as long as there were Ca^{2+} ions in the bathing solution.

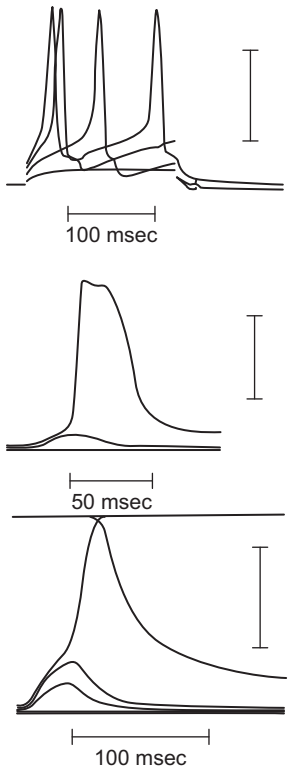

FIGURE 42A.2 Different action potentials in invertebrate striated muscle fibers of different crab species. (A) *Portunus (from Atwood, 1965).* (B) *Carcinus maenas (from Fatt and Katz, 1953).* (C) *Portunus deporatus (from Fatt and Katz, 1953).* Voltage calibration bars:40 mV.

It was concluded that these fibers produced Ca^{2+}-dependent APs (Fatt and Ginsborg, 1958). These APs persisted when Sr^{2+} or Ba^{2+} (which have some physicochemical properties similar to Ca^{2+}) replaced the Ca^{2+}. This led to the *calcium hypothesis*. Hagiwara and Naka (1964) induced APs in the giant barnacle striated muscles fibers (*Balanus nubilus*) in which they changed the intracellular Ca^{2+} concentration by injecting the fibers with Ca^{2+}chelating substances. As the internal free Ca^{2+} concentration was decreased progressively, the AP amplitude increased progressively. At an internal Ca^{2+} concentration of 8×10^{-8} M, the AP became all-or-none (Hagiwara and Nakajima, 1966). Thus, they confirmed the generation of Ca^{2+} APs in invertebrate striated muscle fibers.

Three types of experiments have proven the Ca^{2+} hypothesis for invertebrate striated muscle cells: (1) the Ca^{2+}-dependence of the AP amplitude; (2) the lack of APs in zero Ca^{2+} bathing solution; and (3) the entry of Ca^{2+} ions during the APs.

Ca^{2+} dependence of the APs. Fatt and Ginsborg in 1958 and Pilgrim and Wiersma in 1963 demonstrated that the striated myofibers of the crayfish (*Orconectes virilis*) and lobster (*Homarus americanus*) were capable of generating propagated all-or-none APs. These APs did not disappear when the muscles were immersed in bathing solutions without Na^+, K^+ or Mg^{2+}. However, the amplitude of the APs depended on the extracellular Ca^{2+} concentration $[Ca^{2+}]_o$. The AP amplitude increased with a slope of 25 mV per decade of $[Ca^{2+}]_o$. These results strongly supported the proposal that the APs of invertebrate striated skeletal muscle fibers are generated by inward Ca^{2+} currents. In the crayfish (*Astacus fluvilis*), the potentiating effect of $[Ca^{2+}]_o$ was strongly enhanced in the presence of quaternary ammonium ions like tetraethylammonium (TEA, an inhibitor of outward I_K) (Fig. 42A.3). The maximum rate of depolarization of the APs increased from 8 V/s to 15 V/s when $[Ca^{2+}]_o$ was changed from 4 to 16 mM. In the giant muscle fibers from the barnacle (*Balanus nubilus*), Hoyle and Smith (1963) and Hagiwara and Naka (1964) found that the usual graded responses were converted to all-or-none responses when the gradient between extracellular and intracellular $[Ca^{2+}]$ increased by injecting the cells with Ca^{2+}-chelating substances like EDTA and K_2SO_4. The amplitudes of the APs were a function of the extracellular and intracellular $[Ca^{2+}]$ ratios.

Calcium influx. Hagiwara and Naka (1964) found that, during prolonged stimulations that produced repetitive APs, there was a substantial amount of radioactive Ca^{2+} influx into barnacle giant muscle. They estimated that the intracellular Ca^{2+} concentration increased by an average of 75 pmole/cm^2/impulse and calculated that, during each AP, there was an influx of 6 pmoles of Ca^{2+}/cm^2. This is a very high Ca^{2+} influx compared with the values reported for vertebrate skeletal muscle fibers (Bianchi and Schanes, 1959).

Prolonged depolarization (elicited with high concentrations of extracellular K^+) above the mechanical threshold leads to sustained mechanical activation (contractures). When K^+-contractures were elicited in a bathing solution without Ca^{2+} ions, the K^+-contractures disappeared after a short time**,** even though the membrane remained depolarized. This indicates that, during prolonged depolarization of invertebrate striated muscles, there is a substantial inflow of Ca^{2+} that brings about the mechanical activation.

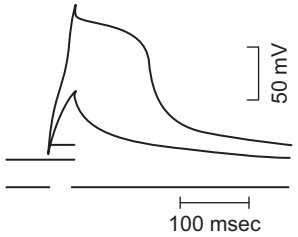

FIGURE 42A.3 Potentiation of invertebrate striated muscle of the crayfish (*Astacus fluvialitis*) with TEA. Upper trace: action potential. Lower trace: applied current. *(From Fatt and Ginsborg, 1958.)*

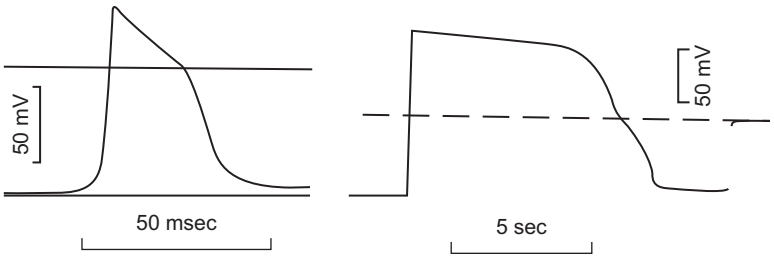

FIGURE 42A.4 Crayfish striated muscles fibers. Action potentials of fibers bathed with strontium (left panel) and barium (right panel). *(From Fatt and Ginsborg, 1958.)*

Potentiation of APs. Fatt and Ginsborg (1958) observed that when all the extracellular Ca^{2+} was removed and substituted with equimolar concentrations of $SrCl_2$ or $BaCl_2$, the crayfish striated muscles not only produced all-or-none APs, but they were of higher amplitude and longer duration (Fig. 42A.4). The RPs were unaffected. These results were confirmed by Werman and Grundfest (1961) in lobster muscle fibers and by Werman et al. (1961) in the muscle of the grasshopper (*Romalea microptera*). Thus, inward $Sr^{2+}$and Ba^{2+} currents are also capable, like Ca^{2+} ions, of generating APs. The increased AP durations were the result of increased durations of the plateau. The control muscle fibers had an average duration of only 3−6 ms. The duration of the Ba^{2+} APs was 15−100 ms, compared with 400−12 000 ms for the Sr^{2+} APs (Fig. 42A.4). The AP overshoot was about 20 mV larger with Ba^{2+} compared with Sr^{2+} in striated muscles from crayfish (*Astacus fluvialis*) and lobster (*Homarus americanus*) (Fatt and Ginsburg, 1958; Werman and Grundfest, 1961). The RP of −90 mV did not change with Sr or Ba ions.

Ionic currents. Hagiwara and Naka (1964), by using a voltage-clamp method, showed that the currents developed during the AP were composed of early inward Ca^{2+} currents, since they varied in amplitude with extracellular Ca^{2+} concentration and were not affected by TTX. It was concluded that, in invertebrate striated muscle fibers, the propagated AP was the consequence of inward Ca^{2+} current. Henĉek et al. (1969) measured Sr^{2+} current in the crayfish (*Astacus fluviaitilis*) using a sucrose-gap voltage-clamp. They found that the currents consisted of early inward current followed by outward current. The Ca^{2+} currents were smaller than the Ba^{2+} currents (Fig. 42A.5). The late outward current was decreased by the K^+-current blocker TEA (Fig. 42A.6).

The AP in invertebrate striated muscles, like in vertebrate striated muscles, fulfills two main roles. One role is to propagate a depolarization wave all along the length of the entire muscle fiber. Another role is to increase the myoplasmic Ca^{2+} to levels that induce the binding of myosin with actin to bring about activation of the contractile proteins (Fig. 42A.7). The mechanical activation develops either shortening, force, or both (producing muscle work).

Regulation of Intracellular Ca^{2+}

Vertebrate skeletal muscle fibers bathed in Ringer's solution containing 1 mM [Ca^{2+}] had an average Ca^{2+} influx at rest of 0.26 pmoles/cm^2/s and, during stimulation, the Ca^{2+} influx increased to 0.73 pmoles/cm^2/impulse (Curtis,1966). Blocking the inward Ca^{2+} current has no effect on the contraction or E-C coupling mechanism (Gonzalez-Serratos et al., 1982). Thus, the main role of inward Ca^{2+} current in vertebrate skeletal muscles fibers is to maintain long-term adequate amounts of intracellular Ca^{2+} (mainly in the SR^{2+}).

In contrast, invertebrate striated muscle fibers have an average Ca^{2+} influx of 75 pmoles/cm^2/impulse (Hagiwara and Naka, 1964). Since the SR is sparse, there must be

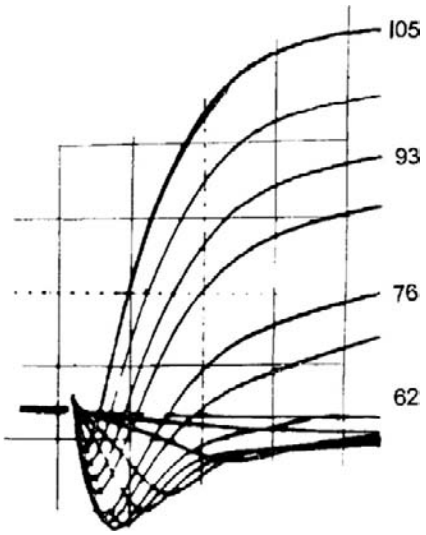

FIGURE 42A.5 Membrane currents under voltage clamp from crayfish striated muscle (*Astacus Fluviatilis*) bathed with extracellular strontium chloride isotonic solution. The clamped membrane potentials are shown in mV. Records below the zero line are inward currents, above are outward currents.

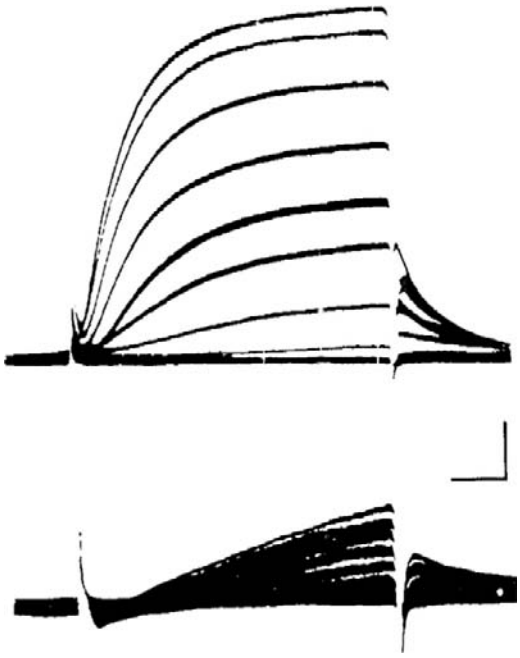

FIGURE 42A.6 Effect of TEA on membrane currents from the crayfish striated muscle (*Astacus Fluviatilis*) under voltage clamp. Top records, bathed with normal extracellular solution. Bottom records, after addition of 50 mM of TEA to the bathing solution. Calibrations: 0.15 mA/cm^2 and 5 ms. *(From Henĉek et al., 1969.)*

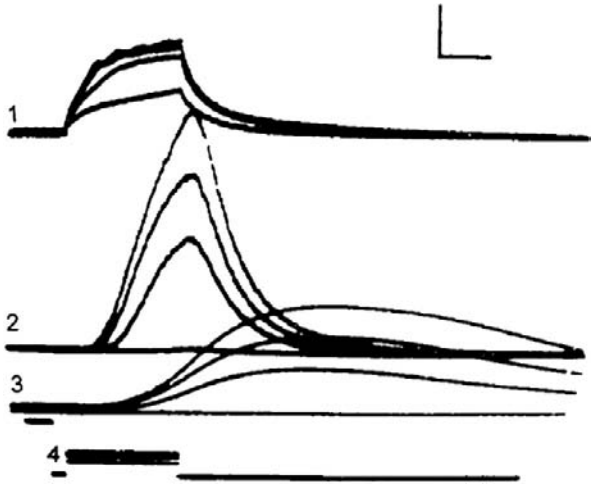

FIGURE 42A.7 Myoplasmic calcium transients recorded with the luminescent ptotein aequorin during stimulations of barnacle (*Balanus nubilis*) striated muscle. Traces: 1: membrane potentials; 2: light output, myoplasma calcium transients; 3: isometric forces; 4: stimulating electrical pulses. On each set of recording traces, the recordings from top to bottom correspond to each other. Vertical calibrations: 20 mV, 3.8×10^{-9} lumens, 5 g. Horizontal calibration: 100 ms. *(From Ashley and Ridgway, 1968.)*

another mechanism to decrease the free myoplasmic Ca^{2+} after activation. Otherwise, these muscles would develop permanent and powerful contractures and suffer deleterious effects. The mechanism by which invertebrate striated muscles decrease and regulate the free intracellular Ca^{2+} concentration is via the sarcolemmal Ca^{2+}/H^+ exchanger mediated by Ca^{2+}-ATPase (DeSantiago et al., 2007) and the Na^+/Ca^{2+} exchanger (Rasgado-Flores et al., 1991). The Na^+/Ca^{2+} exchanger mediates the coupling of the movement of external Na^+ ions down their electrochemical gradient, with the movement of internal Ca^{2+} ions (in the opposite direction) across the sarcolemma. In giant striated muscle of the barnacle (*Balanus nubile*) (like most excitable cells), the Na^+/Ca^{2+} exchanger has a stoichiometry of three Na^+ ions exchanged per each Ca^{2+} ion (Rasgado-Flores et al., 1989).

Innervation of Invertebrate Muscle Fibers

One important characteristic of the innervation of non-vertebrate striated muscle fibers is that the nerve terminals on the muscle fibers form terminal buttons spread all along the muscle fiber. This is in contrast with vertebrate muscle where a motor nerve ends in one button localized near the middle of the fiber. The branching of invertebrate motor nerves leads to multiple nerve terminals that are distributed along the length and around the perimeter of the muscle fibers. There are some differences as a consequence of the differences in the topological distribution of the nerve terminals. The excitatory responses to motor nerve APs can trigger in the muscle fiber either local APs or full-size APs all along the muscle fiber. The transmission of the excitatory process leads to multiple postsynaptic potentials. The regulation of force development during contractions of vertebrate muscles is under central nervous system control. In contrast, in invertebrate muscles, the regulation of the degree of contractions is done peripherally and depends on the number of either excitatory or inhibitory nerve terminals that are activated.

Another feature of invertebrate neuromuscular junctions is that they are structurally simpler than vertebrate motor end-plates. The motor nerves of the crustaceans have short nerve terminals that have periodical swellings in series. The swellings make contact with the surface membrane of the muscle fiber. The nerve terminals are very close together. The response of the invertebrate neuromuscular junction to a nerve AP is called the *junctional potential* (JP). Evoked JPs are due to a large and synchronized release of neurotransmitters triggered by the nerve terminal AP. The JPs of invertebrates are either *excitatory* (EJPs) or *inhibitory* (IJPs). The excitatory neurotransmitter is *glutamate*. The inhibitory neurotransmitter is *GABA* (γ-aminobutyric acid). The release of these transmitters will lead either to excitation and mechanical activation of the muscle fiber or inhibition of the excitation and thus producing relaxation. The RP can be hyperpolarized due to the IJPs. Therefore, the amount of current necessary to

reach the mechanical threshold voltage (for E-C coupling) can also increase as a consequence of the IJPs hyperpolarizing the membrane.

The electrical responses (*postsynaptic potentials*) at the neuromuscular junctions are, in most cases, small and graded. But when the small responses are summated, the muscle membrane reaches threshold that generates a full AP that propagates along the muscle fiber. Another important feature of invertebrate muscle innervations is that a single myofiber can be innervated by more than one motor neuron, i.e. *polyneural innervation*. The polyneural innervation leads to complex electrical and mechanical responses. The topological distribution of nerve junctions and the graded activation permit the existence of fast and slow contractions, as well as excitation and inhibition (often within a single myofiber).

When an EJP reaches the mechanical threshold, a local contraction is produced. When several EJPs are elicited in synchrony, they generate a graded contraction that can show summation. This summation causes a large contraction. IJPs cause hyperpolarization, moving the membrane potential away from the mechanical threshold, thereby causing relaxation. The multiple innervations characteristics of invertebrate muscles cause one muscle fiber to produce EJPs while its neighbor may produce IJPs. The same muscle fiber can show an excitatory response that develops force and an inhibitory response that reduces the force developed (Dudel and Kuffler, 1961). From one to nine excitatory nerves may innervate a single muscle fiber, while the number of inhibitory nerves can be up to three (Kennedy et al., 1966). The size of EJPs (initially of low magnitude) increases progressively during repetitive stimulation and this is called *facilitation* (Hoyle and Wiersma, 1958). In contrast, the large EJPs decrease in size during the repetitive activation due to transmitter depletion or fatigue, a process known as *fatigue* or *anti-facilitation* (Hoyle and Burrows, 1973). Another feature of invertebrate muscle fibers is that the faster fibers display higher E-C thresholds. Therefore, they require EJPs of larger magnitude to reach the E-C threshold. They also develop stronger twitches.

There is relevant information about crayfish muscle stretch receptors given in a previous chapter.

BIBLIOGRAPHY

Adrian, R. H., & Freygang, W. H. (1962). The potassium and chloride conductance of frog muscle membrane. *J Physiol (London), 163*, 61−103.

Adrian, R. H., & Peachey, L. D. (1973). Reconstruction of the action potential of frog sartorius muscle. *J Physiol (London), 235*, 103−131.

Adrian, R. H., Chandler, W. K., & Hodgkin, A. L. (1970a). Voltage clamp experiments in striated muscle fibers. *J Physiol (London), 208*, 607−644.

Adrian, R. H., Chandler, W. K., & Hodgkin, A. L. (1970b). Slow changes in potassium permeability in skeletal muscle. *J Physiol (London), 208*, 645−668.

Almers, W., Fink, R., & Palade, P. T. (1981). Calcium depletion in frog muscle tubules: the decline of calcium depletion in frog muscle tubules: the decline of calcium current under maintained depolarization. *J Physiol (London), 312*, 177−207.

Armstrong, C. M., Bezanilla, F. M., & Horowicz, P. (1972). Twitches in the presence of ethylene glycol bis(β-aminoethyl ether)-N, N′tetraacetic acid. *Biochem Biophys Acta, 267*, 605−608.

Ashley, C. C., & Ridgway, E. B. (1968). Simultaneous recording of membrane potential, calcium transient and tension in single muscle fibers. *Nature, 219*, 1168−1169.

Atwood, H. L. (1965). Characteristics of fibres in the extensor muscle of a crab. *Comp Biochem Physiol, 14*, 205−207.

Baylor, S. M., & Oetliker, H. (1975). Birefingence experiments on isolated skeletal muscle fibres suggest a possible signal from the sarcoplasmic reticulum. *Nature, 253*, 97−101.

Beaty, G. N., & Stefani, I. (1976). Calcium dependent electrical activity in twitch muscle fibers of the frog. *Proc R Soc London (Biol), 194*, 141−150.

Bezanilla, F., & Horowicz, P. (1975). Fluorescence intensity changes associated with contractile activation in frog muscle stained with Nile Blue A. *J Physiol (London), 246*, 709−735.

Bezanilla, F., Caputo, C., Gonzalez-Serratos, H., & Venosa, R. A. (1972). Sodium dependence of the inward spread of activation in isolated twitch muscle fibres of the frog. *J Physiol (London), 223*, 507−523.

Bianchi, C. P., & Bolton, T. C. (1974). Effect of hypertonic solutions and glycerol treatment on calcium and magnesium movements of frog skeletal muscle. *J Pharmacol Exp Ther, 188,* 536−522.

Bianchi, C. P., & Shanes, A. M. (1959). Calcium influx in skeletal muscle at rest, during activity, and during potassium contracture. *J Gen Physiol, 42*, 803−815.

Birks, R. I., & Davey, D. F. (1969). Osmotic responses demonstrating the extracellular character of sarcoplasmic reticulum. *J Physiol (London), 21*, 171−188.

Boudreault, L., Cifelli, C., Bourassa, F., Scott, K., & Renaud, J. M. (2010). Fatigue preconditioning increases fatigue resistance in mouse flexor digitorum brevis muscle with non-functioning K(ATP) channels. *J. Physiol., 588*, 4549−4562.

Caputo, C. (1978). Excitation and contraction processes in muscle. *Annu. Rev. Biophys. Bioeng., 7*, 63−83.

Carlson, E. D., & Siger, A. (1960). The mechanochemistry of muscular contraction. I. The isometric twitch. *J Gen Physiol, 44*, 33−60.

Castle, N. A., & Haylett, D. G. (1987). Effect of channel blockers on potassium efflux from metabolically exhausted frog skeletal muscle. *J Physiol, 383*, 31−43.

Chou, S. M., Nonaka, I., & Voice, G. F. (1980). Anastomoses of transverse tubules with terminal cisternae in polymyositis. *Arch Neurol, 37*, 257−266.

Cifelli, C., Bourassa, F., Gariepy, L., Banas, K., Benkhalti, M., & Renaud, J. M. (2007). KAPT channel deficiency in mouse flexor digitorum brevis causes fiber damage and impairs Ca^{2+} release and force development during fatigue in vitro. *J. Physiol., 582*, 843−857.

Clausen, T. (2008). Clearance of extracellular K^+ during muscle contraction−roles of membrane transport and diffusion. *J. Gen. Physiol., 131*, 473−481.

Cognard, C., Rivet-Bastide, M., Constantin, B., & Raymond, G. (1992). Progressive predominance of 'skeletal' versus 'cardiac' types of excitation-contraction coupling during in vitro skeletal myogenesis. *Pflügers Arch, 422*, 207–209.

Conway, E. J. (1957). Nature and significance of concentration relations of potassium and sodium ions in skeletal muscle. *Physiol Rev, 37*, 84–132.

Cordoba-Rodriguez, R., Gonzalez-Serratos, H., Matteson, D. R., & Rozycka, M. (1997). Ica is important in E-C coupling in developing cultured embryonic amphibian skeletal muscle cells. *Biophys J, 72*, A119, H5.

Cordoba-Rodriguez, R., Matteson, D. R., & Gonzalez-Serratos, H. (1996). Embryonic E-C coupling in cultured skeletal muscle cells. *Biophys J, 70*, A390.

Costantin, L. L. (1970). The role of sodium current in the radial spread of contraction in frog muscle fibers. *J Gen Physiol, 55*, 703–715.

Costantin, L. L., & Podolsky, R. J. (1967). Depolarization of the internal membrane system in the activation of frog skeletal muscle. *J Gen Physiol, 50*, 1101–1124.

Costantin, L. L., & Taylor, S. R. (1973). Graded activation in frog muscle fibers. *J Gen Physiol, 61*, 424–443.

Curtis, R. A. (1966). Ca fluxes in single twitch muscle fibers. *J Gen Physiol, 50*, 225–267.

Davies, N. W., Standen, N. B., & Stanfield, P. R. (1992). The effect of intracellular pH on ATP-dependent potassium channels of frog skeletal muscle. *J Physiol, 445*, 549–568.

Dawson, M. J., Gadian, D. G., & Wilkie, D. R. (1978). Muscular fatigue investigated by phosphorus nuclear magnetic resonance. *Nature, 274*, 861–866.

Dawson, M. J., Gadian, D. G., & Wilkie, D. R. (1980). Mechanical relaxation rate and metabolism studied in fatiguing muscle by phosphorus nuclear magnetic resonance. *J Physiol, 299*, 465–484.

DeSantiago, J., Batlle, D., Khilnani, M., et al. (2007). Ca^{2+}/H^{+} exchange via the plasma membrane Ca^{2+} ATPase in skeletal muscle. *Front Biosci, 12*, 4641–4660.

DiFranco, M., Capote, J., & Vergara, J. L. (2005). Optical imaging and functional characterization of the transverse tubular system of mammalian muscle fibers using the potentiometric indicator di-8-ANEPPS. *J Memb Biol, 208*, 141–153.

Dudel, J., & Kuffler, S. W. (1961). Presynaptic inhibition at the crayfish neuromuscular junction. *J Physiol, 155*, 543–562.

Eisenberg, R. S., & Gage, P. W. (1969). Ionic conductances of the surface and transverse tubular membranes of frog sartorius fibers. *J Gen Physiol, 53*, 279–297.

Fabiato, A. (1982). Mechanism of calcium-induced release of calcium from the sarcoplasmic reticulum of skinned cardiac cells studied with potential-sensitive dyes. In S. T. Ohnishi, & M. Endo (Eds.), *The Mechanism of Gated Calcium Transport Across Biological Membranes* (pp. 237–255). New York: Academic Press.

Fahlke, C., Zachar, E., & Rudel, R. (1993). Chloride channels with reduced single-channel conductance in recessive myotonia congenita. *Neuron, 10*, 225–232.

Fatt, P., & Ginsborg, B. L. (1958). The ionic requirements for the production of action potentials in crustacean muscle fibers. *J Physiol (London), 142*, 156–543.

Fatt, P., & Katz, B. (1953). The electrical properties of crustacean muscle. *J Physiol, 120*, 171–204.

Fink, R., & Lüttgau, H. C. (1976). An evaluation of the membrance constants and the potassium conductance in metabolically exhausted muscle fibers. *J Physiol, 263*, 215–238.

Flagg, T. P., Enkvetchakul, D., Koster, J. C., & Nichols, C. G. (2010). Muscle KATP channels: Recent insights to energy sensing and myoprotection. *Physiol. Rev., 90*, 799–829.

Flucher, B. E., Takekura, H., & Franzini-Armstrong, C. (1993). Development of the excitation-contraction coupling apparatus in skeletal muscle: association of sarcoplasmic reticulum and transverse tubules with myofibrils. *Dev Biol, 160*, 135–147.

Forbes, M. S., & Sperelakis, N. (1979). Ruthenium red staining of skeletal and cardiac muscles. *Z Zellforsch Cell Tissue Res, 200*, 367–382.

Garcia, M.del C., Gonzalez-Serratos, H., Morgan, J. P., Perreault, C. L., & Rozycka, M. (1991). Differential activation of myofibrils during fatigue in phasic skeletal muscle cells. *J Musc Res Cell Motil, 12*, 412–424.

Gonzalez-Serratos, H. (1971). Inward spread of activation in vertebrate muscle fibers. *J Physiol (London), 212*, 777–799.

Gonzalez-Serratos, H. (1975). Graded activation of myofibrils and the effect of diameter on tension development during contractures in isolated skeletal muscle fibers. *J Physiol (London), 253*, 321–339.

Gonzalez-Serratos, H., Cordoba-Rodriguez, R., Matteson, D. R., & Rozycka, M. (1996). Role of calcium currents in excitation-contraction coupling in developing cultured embryonic amphibian skeletal muscle cells. *J Physiol,* 494P.

Gonzalez-Serratos, H., Somlyo, A. V., McClellan, G., Shuman, H., Borrero, L. M., & Somlyo, A. P. (1978). Composition of vacuoles and sarcoplasmic reticulum in fatigued muscle: electron probe analysis. *Proc Natl Acad Sci USA, 75*, 1329–1333.

Gonzalez-Serratos, H., Valle-Aguilera, R., Lathrop, D. A., & Garcia, M.del (1982). Slow inward calcium currents have no obvious role in muscle excitation-contraction coupling. *Nature, 298*, 292–294.

Hagiwara, S., & Naka, K. (1964). The initiation of spike potential in barnacle-muscle fibers under low intracellular Ca^{++}. *J Gen Physiol, 48*, 141–162.

Hagiwara, S., & Nakajima, S. (1966). Difference in Na and Ca spikes as examined by application of tetrodotoxin, procaine, and manganese ions. *J Gen Physiol, 49*, 793–806.

Hagiwara, S., Chichibu, S., & Naka, K. (1964). The effect of various ions on resting and spike potentials of barnacle muscle fibers. *J Gen Physiol, 43*, 163–179.

Harris, E. J. (1963). Distribution and movement of muscle chloride. *J Physiol (London), 166*, 87–109.

Heiny, J. A., Ashcroft, F. M., & Vergara, J. (1983). T-system optical signals associated with inward rectification in skeletal muscle. *Nature, 301*, 164–166.

Henček, M., Nonner, W., & Stämpfli, R. (1969). Voltage clamp of a small muscle membrane area by means of a circular sucrose gap arrangement. *Pflügers Arch, 313*, 71–79.

Hille, B., & Campbell, D. T. (1976). An improved vaseline gap voltage clamp for skeletal muscle fibers. *J Gen Physiol, 67*, 265–293.

Hodgkin, A. L., & Horowicz, P. (1959). The influence of potassium and chloride ions on the membrane potential of single muscle fibers. *J Physiol (London), 148*, 127–160.

Hodgkin, A. L., & Huxley, A. F. (1952). Currents carried by sodium and potassium ions through the membrane of the giant axon of *Loligo*. *J Physiol (London), 116*, 449–472.

Hodgkin, A. L., & Nakajima, S. (1972). Analysis of the membrance capacity in frog muscle. *J Physiol (London), 221*, 121–136.

Howell, J. N. (1974). Intracellular binding of ruthenium red in frog skeletal muscle. *J Cell Biol, 62*, 242–247.

Hoyle, G., & Burrows, M. (1973). Correlated physiological and ultrastructural studies on specialized muscles. 3. neuromuscular physiology of the power-stroke muscle of the swimming leg of portunus sanguinolentus. *J. Exp. Zool., 185*, 83–95.

Hoyle, G., & Smith, T. (1963). Neuromuscular physiology of giant muscle fibres of a barnacle, *Balanus nubilus* Darwin. *Comp Biochem Physiol, 10*, 219–314.

Hoyle, G., & Wiersma, C. A. G. (1958). Excitation at neuromuscular junctions in Crustacea. *J Physiol, 143,* 493–425.

Hurnak, O., & Zachar, J. (1992). Maxi chloride channels in L6 myoblasts. *Gen Physiol Biophys, 11*, 389–400.

Hussain, M., Wareham, A. C., & Head, S. I. (1994). Mechanism of action of a K^+ channel activator BRL 38227 on ATP-sensitive K^+ channels in mouse skeletal muscle fibres. *J. Physiol., 478 Pt 3*, 523–532.

Huxley, A. F., & Taylor, R. E. (1958). Local activation of striated muscle fibres. *J Physiol (London), 144*, 426–441.

Huxley, H. E., Page, S., & Wilkie, D. R. (1963). Appendix. An electron microscopic study of muscle in hypertonic solutions. *J Physiol (London), 169*, 312–329.

Iannaccone, S. T., Li, K.-X., Sperelakis, N., & Lathrop, D. A. (1989). Insulin-induced hyperpolarization in mammalian skeletal muscle. *Am J Physiol, 256*, C368–C374.

Jiang, C., Qu, Z., & Xu, H. (2002). Gating of inward rectifier K(+) channels by proton-mediated interactions of intracellular protein domains. *Trends Cardiovasc. Med., 12*, 5–13.

Kakei, M., Noma, A., & Shibasaki, T. (1985). Properties of adenosine-triphosphate-regulated potassium channels in guinea-pig ventricular cells. *J. Physiol., 363*, 441–462.

Kennedy, D., Evoy, W. H., & Fields., H. L. (1966). The unit bases of some crustacean reflexes. *Symp Soc Exp Biol, 20*, 75–109.

Kerr, L. M., & Sperelakis, N. (1982). Effects of the calcium antagonists verapamil and bepridil (CERM-1978) on Ca^{2+}-dependent slow action potentials in frog skeletal muscle. *J Pharmacol Exp Ther, 222*, 80–86.

Keynes, R. D., & Steinhardt, R. A. (1968). The components of the sodium efflux in frog muscle. *J Physiol (London), 198*, 581–599.

Khan, A. R. (1981). Influence of ethanol and acetaldehyde on electro-mechanical coupling of skeletal muscle fibres. *Acta Physiol Scand, 111*, 425–430.

Kirby, A. C., Lindley, B. D., & Picken, J. R. (1975). Calcium content and exchange in frog skeletal muscle. *J Physiol (London), 253*, 37–52.

Kulczycky, S., & Mainwood, G. W. (1972). Evidence for a functional connection between the sarcoplasmic reticulum and the extracellular space in frog sartorius muscle. *Can J Physiol Pharmacol, 50*, 87–98.

Li, K.-X., & Sperelakis, N. (1994). Electrogenic Na-K pump current in rat skeletal myoballs. *J Cell Physiol, 159*, 181–186.

Lueck, J. D., Rossi, A. E., Thornton, C. A., Campbell, K. P., & Dirksen, R. T. (2010). Sarcolemmal-restricted localization of functional ClC-1 channels in mouse skeletal muscle. *J Gen Physiol, 136*, 597–613.

Lynch, C., III (1978). *Kinetic and biochemical separation of potassium currents in frog striated muscle. PhD. thesis*. New York: University of Rochester.

Mathias, R. T., Levis, R. A., & Eisenberg, R. S. (1980). Electrical models of excitation-contraction coupling and charge movement in skeletal muscle. *J Gen Physiol, 76*, 1–31.

Miledi, R., Parker, R. I., & Schalow, G. (1977). Measurement of calcium transients in frog muscle by the use of arseno III. *Proc R Soc London (Biol), 198*, 201–210.

Miledi, R., Stefani, E., & Steinbach, A. B. (1971). Induction of the action potential mechanism in slow muscle fibres of the frog. *J Physiol (London), 217*, 737–754.

Mobley, B. A., & Eisenberg, B. R. (1975). Sizes of components in frog skeletal muscle measured by methods of stereology. *J Gen Physiol, 66*, 31–45.

Moody-Corbett, F., Gilbert, R., Akbarali, H., & Hall, J. (1989). Calcium current in embryonic Xenopus muscle cells in culture. *Can J Physiol Pharmacol, 67*, 1259–1264.

Nakajima, S., & Gilai, A. (1980). Action potentials of isolated single muscle fibers recorded by potential-sensitive dyes. *J Gen Physiol, 76*, 729–750.

Nassar-Gentina, V., Passonneau, J. V., Vergara, J. L., & Rapoport, S. I. (1978). Metabolic correlates of fatigue and of recovery from fatigue in single frog muscle fibers. *Gen Physiol, 72*, 593–606.

Nastuk, W. L., & Hodgkin, A. L. (1950). The electrical activity of single muscle fibres. *J Cell Comp Physiol, 35*, 39–74.

Natori, R. (1965). Propagated contractions in isolated sarcolemma-free bundle of myofibrils. *Jikeidai Med J, 12*, 214–221.

Nicola-Siri, L., Sanchez, J. A., & Stefani, E. (1980). Effect of glycerol treatment on calcium current of frog skeletal muscle. *J Physiol (London), 305*, 87–96.

Ortega, A., Gonzalez-Serratos, H., & Lepock, J. (1997). Effect of organic calcium channel blocker D-600 on sarcoplasmic reticulum calcium uptake in skeletal muscle. *Am J Physiol, 272*, C310–C317.

Overton, E. (1902). Beitrage zur allgemeinen muskel- und nervenphysiologie I. Abh. I Ueber die osmotischen figenschatten der muskeln. *Pflugers Arch, 92*, 115–280.

Peachey, L. D. (1965). The sarcoplasmic reticulum and transverse tubules of the frog's sartorius. *J Cell Biol, 25*, 209–231.

Peachey, L. D., & Huxley, A. F. (1964). Transverse tubules in crab muscles. *J Cell Biol, 23*, 70A.

Pilgrim, R. I. C., & Wiersma, C. A. G. (1963). Observations on the skeletal and somatic musculature of the abdomen and thorax of *Procambaru clarkii* (Girard) with notes on the thorax of *Panulirus interruptus* and *Astacus*. *J Morphol, 113*, 453–487.

Podolsky, R. J., & Costantin, L. L. (1964). Regulation by calcium of the contraction and relaxation of muscle fibers. *Fed Proc, 23*, 933–939.

Potreau, D., & Raymond, G. (1980). Calcium-dependent electrical activity and contraction of voltage-clamped frog single muscle fibers. *J Physiol (London), 307*, 9–22.

Qu, Z., Yang, Z., Cui, N., Zhu, G., Liu, C., Xu, H., Chanchevalap, S., Shen, W., Wu, J., Li, Y., & Jiang, C. (2000). Gating of inward rectifier K+ channels by proton-mediated interactions of N- and C-terminal domains. *J. Biol. Chem., 275*, 31573–31580.

Rasgado-Flores, H., DeSantiago, J., & Espinosa-Tanguma, R. (1991). Stoichiometry and regulation of the Na-Ca exchanger in barnacle muscle cells. *Ann NY Acad Sci, 639*, 22–33.

Rasgado-Flores, H., Santiago, E. M., & Blaustein, M. P. (1989). Kinetics and stoichiometry of coupled Na efflux and Ca influx (Na/Ca exchange) in barnacle muscle cells. *J Gen Physiol, 93*, 1219–1241.

Renaud, J. M. (1989). The effect of lactate on intracellular pH and force recovery of fatigued sartorius muscles of frog, *Rana pipiens*. *J Physiol, 416*, 31–47.

Rogus, E., & Zierler, K. L. (1973). Sodium and water contents of sarcoplasm and sarcoplasmic reticulum in rat skeletal muscle: Effects

of anisotonic media, ouabain, and external sodium. *J Physiol (London), 233*, 227–270.

Rubio, R., & Sperelakis, N. (1972). Penetration of horseradish peroxidase into the terminal cisternae of frog skeletal muscle fibers and blockade of caffeine contracture by Ca^{++} depletion. *Z Zellforsch, 124*, 57–71.

Rulon, R., Hermsmeyer, K., & Sperelakis, N. (1971). Regenerative action potentials induced in the neurogenic heart of *Limulus polyphemus*. *Comp Biochem Physiol, 39A*, 333–335.

Sanchez, J. A., & Stefani, E. (1978). Inward calcium current in twitch muscle fibers of the frog. *J Physiol (London), 283*, 197–209.

Sauviat, M.-P., Ecault, E., Faivre, J.-F., & Finlay, I. (1991). Activation of ATP-sensitive K channels by a K channel opener (SR 44866) and the effect upon electrical and mechanical activity of frog skeletal muscle. *Pflügers Arch, 418*, 261–265.

Sellin, L. C., & Sperelakis, N. (1978). Decreased potassium permeability in dystrophic mouse skeletal muscle. *Exp Neurol, 62*, 609–617.

Spector, I., & Prives, J. M. (1977). Development of electrophysiological and biochemical membrane properties during differentiation of embryonic skeletal muscle in culture. *Proc Natl Acad Sci USA, 74*, 5166–5170.

Sperelakis, N. (1969). Changes in conductance of frog sartorius fibers produced by CO_2, ReO_4, and temperature. *Am J Physiol, 217*, 1069–1075.

Sperelakis, N. (1979). Origin of the cardiac resting potential. In R. Berne, & N. Sperelakis (Eds.), *Handbook of Physiology, the Cardiovascular System, Vol. 1: the Heart* (pp. 187–267). Bethesda: American Physiological Society.

Sperelakis, N., & Gonzalez-Serratos, H. (2001). Skeletal muscle action potentials. In N. Sperelakis (Ed.), *Cell Physiology Sourcebook* (3rd ed.). (pp. 865–886). San Diego: Academic Press.

Sperelakis, N., Mayer, G., & Macdonald, R. (1970). Velocity of propagation in vertebrate cardiac muscles as functions of tonicity and [K+]. *Am. J. Physiol., 219*, 952–963.

Sperelakis, N., & Rubio, R. (1971). Ultrastructural changes produced by hypertonicity in cat cardiac muscle. *J Mol Cell Cardiol, 3*, 139–156.

Sperelakis, N., & Schneider, M. F. (1968). Membrane ion conductances of frog sartorius fibers as a function of tonicity. *Am J Physiol, 215*, 723–729.

Sperelakis, N., Forbes, M. S., & Rubio, R. (1974). The tubular systems of myocardial cells: ultrastructure and possible function. In N. S. Dhalla, & G. Rona (Eds.), *Recent Advances in Studies on Cardiac Structure and Metabolism, Myocardial Biology, Vol. 4* (pp. 163–194). Baltimore: University Park Press.

Sperelakis, N., Schneider, M. F., & Harris, E. J. (1967). Decreased K^+ conductance produced by Ba^{++} in frog sartorius fibers. *J Gen Physiol, 50*, 1565–1583.

Sperelakis, N., Shigenobu, K., & Rubio, R. (1978). ^{3}H-Sucrose compartments in frog skeletal muscle relative to sarcoplasmic reticulum. *Am J Physiol, 234*, C181–C190.

Sperelakis, N., Valle, R., Orozco, C., Martinez-Palomo, A., & Rubio, R. (1973). Electromechanical uncoupling of frog skeletal muscle by possible change in sarcoplasmic reticular content. *Am J Physiol, 225*, 793–800.

Spitzer, N. C. (1979). Ion channels in development. *Annu Rev Neurosci, 2*, 363–397.

Spruce, A. E., Standen, N. B., & Stanfield, P. R. (1985). Voltage-dependent ATP-sensitive potassium channels of skeletal muscle membrane. *Nature, 316*, 736–738.

Spruce, A. E., Standen, N. B., & Standfield, P. R. (1987). Studies of the unitary properties of adenosine-5′-triphospate-regulated potassium channels of frog skeletal muscle. *J Physiol, 382*, 213–236.

Standen, N. B., Stanfield, P. R., & Ward, T. A. (1985). Properties of single potassium channels in vesicles formed from the sarcolemma of frog skeletal muscle. *J Physiol, 364*, 339–358.

Stanfield, P. R. (1977). A calcium-dependent inward current in frog skeletal muscle fibers. *Pflügers Arch, 368*, 267–270.

Stephenson, E. W. (1981). Activation of fast skeletal muscle: contributions of studies on skinned fibers. *Am J Physiol, 240*, C1–19.

Steinmeyer, K., Ortland, C., & Jentsch, T. J. (1991). Primary structure and functional expression of a developmentally regulated skeletal muscle chloride channel. *Nature, 354*, 301–304.

Stoller, D., Kakkar, R., Smelley, M., Chalupsky, K., Earley, J. U., Shi, N. Q., Makielski, J. C., & McNally, E. M. (2007). Mice lacking sulfonylurea receptor 2 (SUR2) ATP-sensitive potassium channels are resistant to acute cardiovascular stress. *J. Mol. Cell. Cardiol, 43*, 445–454.

Tasker, P., Simon, S. E., Johnstons, B. M., Shankly, K. H., & Shaw, F. H. (1959). The dimensions of the extracellular space in sartorius muscle. *J Gen Physiol, 43*, 39–53.

Thabet, M., Miki, T., Seino, S., & Renaud, J. M. (2005). Treadmill running causes significant fiber damage in skeletal muscle of KATP channel-deficient mice. *Physiol. Genomics, 22*, 204–212.

Vinogradova, N. A. (1968). Distribution of nonpenetrating sugars in the frog's sartorius muscle under hypo- and hypertonic conditions. *Tsitologiya, 10*, 831–838.

Vivaudou, M. B., Arnoult, C., & Villaz, M. (1991). Skeletal muscle ATP-sensitive K^+ channels recorded from sarcolemmal blebs of split fibers: ATP inhibition is reduced by magnesium and ADP. *J Membr Biol, 122*, 165–175.

Vogel, S., Harder, D., & Sperelakis, N. (1978). Ca^{++} dependent electrical and mechanical activities in skeletal muscle. *Fed Proc, 37*, 517.

Wallace, N., & Sommer, J. R. (1975). Fusion of sarcoplasmic reticulum with ruthenium red. *Proc Electron Microsc Soc A, 33*, 500–501.

Weiss, D. S., & Magleby, K. L. (1992). Voltage-dependent gating mechanism for single fast chloride channels from rat skeletal muscle. *J Physiol (London), 453*, 279–306.

Werman, R., & Grundfest, H. (1961). Graded and all-or-none electrogenesis in arthropod muscle. II. The effects of alkali-earth and strontium ions on lobster muscle fibers. *J Gen Physiol, 44*, 997–1027.

Werman, R., McCann, F. V., & Grundfest, H. (1961). Graded and all-or-none electrogenesis in arthropod muscle. I. The effects of alkali-earth cations on the neuromuscular system of *Romalea microptera*. *J Gen Physiol, 44*, 979–995.

Winegrad, S. (1968). Intracellular calcium movements of frog skeletal muscle during recovery from tetanus. *J Gen Physiol, 51*, 65–83.

Woll, K. H., Lonnendonker, U., & Neumcke, B. (1989). ATP-sensitive potassium channels in adult mouse skeletal muscle: different modes of blockage by internal cations, ATP, and tolbutamide. *Pflügers Arch, 414*, 622–628.

Yokoshiki, H., Sunagawa, M., Seki, T., & Sperelakis, N. (1998). ATP-sensitive K^+ channels in pancreatic, cardiac, and vascular smooth muscle cells. Invited Review. *Am J Physiol, 274*, C25–C37.

Zifarelli, G., & Pusch, M. (2007). CLC chloride channels and transporters: A biophysical and physiological perspective. *Rev. Physiol. Biochem. Pharmacol., 158*, 23–76.

Chapter 43

Cardiac Action Potentials

Gordon M. Wahler

Chapter Outline

I. SUMMARY

Action potentials (APs) in the heart are generated by the complex time-dependent interplay of several currents carried primarily by Na^+, K^+ and Ca^{2+} ions. Ventricular APs have very long duration compared to nerve and skeletal muscle APs, due to a plateau phase during which there is an approximate balance between depolarizing and repolarizing currents. Some cardiac cells display automaticity, due to the presence of a cyclical spontaneous depolarization. The cells of the sinoatrial node normally exhibit the fastest spontaneous depolarization of automatic cells in the heart and are therefore the normal pacemaker cells. Automaticity in nodal cells is initiated by several currents, including a hyperpolarization-activated cation current (the "funny current"), a small background Na^+ current, the delayed rectifier K^+ current and Ca^{2+} currents. The sympathetic and parasympathetic nerves play important (and opposite) roles in regulating the force of myocardial contraction and heart rate via their effects on several currents. Mutations in a number of ion channels can lead to arrhythmias.

II. INTRODUCTION

The electrophysiological behavior of heart cells subserves the function of the heart; namely to pump blood to the body. Heart cells are similar to other cell types in that their internal ionic composition is quite different from the extracellular ionic environment. For example, measurement of the intracellular versus extracellular ionic composition shows that the intracellular ionic composition is low in sodium ions (Na^+) and high in potassium ions (K^+), while the reverse is true of the extracellular ionic composition. These concentration differences, together with the selective permeability characteristics of the cell membrane, generate a potential difference of between 80 and 90 mV across the cell membrane of the resting cardiac cell, with the inside being negative with respect to the outside. Additionally, heart cells are excitable cells. That is, they are capable of generating all-or-none electrical responses known as action potentials (APs). The cardiac AP is caused by the complex interaction of a number of different ionic currents. This chapter reviews the characteristics of the cardiac AP, with emphasis on the major

Cell Physiology Sourcebook. DOI: 10.1016/B978-0-12-387738-3.00043-3

currents responsible for the various components or phases of the ventricular APs, as well as the regional differences in cardiac APs. The electrical activity of cardiac cells has been studied for several decades by impaling the cells with high-resistance microelectrodes. The development of methods to isolate viable single adult cardiac cells, together with the development of the patch-clamp technique for recording single-channel (microscopic) currents and whole-cell (macroscopic) currents from single cells, led to an explosion of information on the currents responsible for generation of the cardiac AP. The use of molecular biology techniques to clone and express channel subunits is further revolutionizing our understanding of the precise nature of various currents.

While most of the information on cardiac ion currents has been necessarily obtained from cardiac cells isolated from experimental animals, studies on human cardiac myocytes (e.g. Coraboeuf and Nargeot, 1993) suggest that the currents in the human heart are generally similar to those observed in other animals.

III. RESTING MEMBRANE POTENTIAL

Details on the origin of the resting potential (RP) have been given in a previous chapter. In brief, the cardiac cell membrane is quite permeable to K^+ and relatively impermeable to Na^+ and other ions when at rest. Thus, K^+ flows out of the cell down its concentration gradient, resulting in rapid build up of a negative potential inside the cell. As the electric potential build up increases in magnitude, it becomes sufficient to counterbalance the chemical driving force generated by the concentration gradient. At this potential, called the equilibrium potential, the net ion flux is zero. Note that this does not mean there is no flux of the ion, only that the inward and outward fluxes of the ion are equal and opposite. The Nernst equation describes the relationship between the intracellular and extracellular concentrations of a single ion and its equilibrium potential. The equilibrium potential for ion X (E_X) is calculated by the Nernst equation:

$$E_x = \frac{RT}{ZF} \ln \frac{[X]_i}{[X]_o}$$

where T is the absolute temperature (in degrees Kelvin), z is the valence (or charge) of the ion (for K^+ it is $+1$, for Ca^{2+} it is $+2$, etc.), R is the universal gas constant, F is the Faraday constant, $[X]_i$ is the ion concentration inside the cell, $[X]_o$ is the ion concentration outside the cell and ln is the natural logarithm.

The intracellular and extracellular concentrations of K^+ are such that the equilibrium potential for K^+ (E_K) is approximately -90 mV at 37°C. Since the ventricular cell at rest (i.e. between APs) is very permeable to K^+ and not very permeable to other ions, the RP should be close to the calculated E_K. Indeed, this is the case. For example, in Fig. 43.1, the resting membrane potential is approximately -87 mV. The RP does not quite reach E_K because at rest there is a small, but finite, permeability to Na^+ ions. In addition, there are other ion transport systems (primarily the electrogenic Na^+-K^+-ATPase) which contribute slightly to the RP.

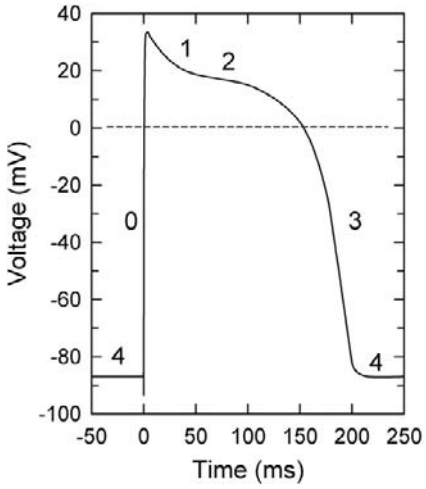

FIGURE 43.1 Ventricular action potential. This is a diagrammatic representation of a typical adult mammalian ventricular AP. The five phases of the ventricular AP are labeled (0–4).

IV. CURRENTS DURING THE ACTION POTENTIAL PHASES

IVA. Overview

Cardiac cells have certain properties in common with other excitable cells, such as nerve and skeletal muscle cells. However, the behavior of cardiac cells also differs from the behavior of nerve and skeletal muscle cells in some important respects. The nerve and skeletal muscle APs are relatively brief, consisting primarily of a rapid depolarization phase (when the inside of the cell becomes more positive) followed immediately by a rapid repolarization phase (when the inside of the cell returns to a more negative potential). The depolarization phase of nerve and skeletal muscle cells is caused by the rapid influx of positive sodium ions into the cell, down the electrochemical gradient for Na^+, which makes the cell interior more positive. The subsequent repolarization is caused by the effiux of positive potassium ions from the cell, down the electrochemical gradient for K^+, which returns the cell interior to its original more negative resting membrane potential. The entire process of the nerve or skeletal muscle APs is largely complete within a few milliseconds. In cardiac cells, the APs are more complex and generally much longer in duration. Thus, for example, a typical cardiac ventricular

AP may be 200 ms or more in duration (see Fig. 43.1). Additionally, unlike for nerve and skeletal muscle cells, APs from different regions of the heart vary substantially in shape.

There are two primary types of cardiac cells. One cell type is found in the working (contractile) cells of the atria and ventricles and also in the specialized conduction cells of the His–Purkinje network. These cells have a high resting K^+ permeability between APs. The APs in these cells are generated by a fast Na^+ current and are known as fast APs. The prolonged duration of the AP in ventricular cells and Purkinje fibers is caused by an approximate balance of inward depolarizing currents (primarily a Ca^{2+} current) and outward repolarizing K^+ currents, which results in a prominent plateau phase. Atrial cells have a less prominent plateau.

The second type of cardiac cell is found in the sinoatrial and atrioventricular nodes. These nodal cells have a low K^+ permeability between APs and are automatic (i.e. they fire APs spontaneously). The upstroke of these nodal APs is generated by a Ca^{2+} current, which is smaller and slower than the fast Na^+ current. Because of this, and the comparatively low density of Ca^{2+} channels when compared to the density of Na^+ channels in fast cells, conduction in nodal cells is much slower than conduction in regions having Na^+-dependent APs. These nodal APs are known as slow APs. Slow APs (a.k.a. slow responses) may sometimes also occur in cells that normally have fast APs when fast Na^+ current (I_{Na}) is blocked pharmacologically or pathophysiologically by tetrodotoxin or voltage inactivation by depolarization with high extracellular K^+.

The shape of the fast cardiac AP is generally divided into phases. The spike and slow wave (plateau) phases were described for isolated cardiac muscle (Hoshiko and Sperelakis, 1962). The following description details all of the five phases found in ventricular cells (phases 0 through 4) and indicates the current or currents that are primarily responsible for each phase. The phases of the ventricle and primary currents responsible are summarized in Table 43.1. Phase 0 is the upstroke of the AP, phase 1 is the early repolarization phase, phase 2 is the plateau phase, phase 3 is the primary repolarization phase and phase 4 is the resting membrane potential phase of the ventricular AP. Additional information about regional differences in the AP phases and currents will be also presented. It should be noted that an isolated single myocardial cell in cell culture exhibits a cardiac AP almost identical to that of a myocardial cell in the intact heart (Sperelakis and Lehmkuhl, 1964).

TABLE 43.1 Phases of the Ventricular Action Potential and Primary Currents Responsible

Phase	Current	Channel Protein
Phase 0	I_{Na}	$Na_v1.5$
Phase 1	I_{to} [I_{to1} ($I_{to,f}$ & $I_{to,s}$)]	$K_v4.2/4.3$ [$I_{to,f}$], $K_v1.4$ [$I_{to,s}$]
Phase 2	$I_{Ca(L)}$ I_{to} I_K I_{Na} "window current"	$Ca_v1.2$ (as in phase 1) (as in phase 3) $Na_v1.5$
Phase 3	I_K [I_{Ks}, I_{Kr}, I_{Kur}] I_{K1}	$K_v7.1$ (a.k.a. K_vLQT1) [I_{Ks}] $K_v11.1$ (a.k.a. HERG1 or ERG1) [I_{Kr}] $K_v1.5$ [I_{Kur}] (as in phase 4)
Phase 4	I_{K1}	Kir2.1/2.2

IVB. Phase 0

Phase 0 is the rapid upstroke of the AP in ventricular cells, as well as in the cells of the atria and His–Purkinje network. This upstroke is dependent on a fast Na^+ current (I_{Na}) quite similar to the current responsible for the upstroke of the nerve or skeletal muscle APs. However, the cardiac channel has a much lower sensitivity to the neurotoxin tetrodotoxin (e.g. Yu and Catterall, 2003). The voltage-gated channel protein ($Na_v1.5$) responsible for this current in cardiac myocytes is encoded by the gene SCN5A. As expected, the $Na_v1.5$ channels are expressed in atrial and ventricular myocytes and the His–Purkinje conduction cells, but not in nodal cells that do not fire fast APs (Nerbonne and Kass, 2005).

This current is designated as fast because it exhibits very rapid activation and inactivation kinetics in comparison to other currents. Thus, in the vast majority of openings, the channel is open for less than 1 ms. Because of the fast upstroke and fast conduction of the ventricular APs, the APs of these cells (and those of atrial and Purkinje fiber cells) are referred to as fast APs, as noted earlier. Figure 43.2 illustrates the kinetics and voltage-dependence of I_{Na}. Following a large depolarization, I_{Na} reaches a peak in less than 1 ms, even at room temperature. Following this peak activation of I_{Na} the amplitude of this current spontaneously decreases. This decay of I_{Na} is due to inactivation of the fast Na^+ channels; thus, I_{Na} is nearly zero after only a few milliseconds. The fast activation and large magnitude of I_{Na} often causes difficulties in accurately recording this current in voltage-clamped cardiac cells. Thus, I_{Na} can generally only be recorded in adult cardiac cells at reduced $[Na^+]_o$ levels and/or at low temperatures. Alternatively, I_{Na} can be studied in very small cells, such as the embryonic chick ventricular cell (e.g. Fig. 43.2) in which I_{Na} (and other currents) are at least an order of magnitude smaller

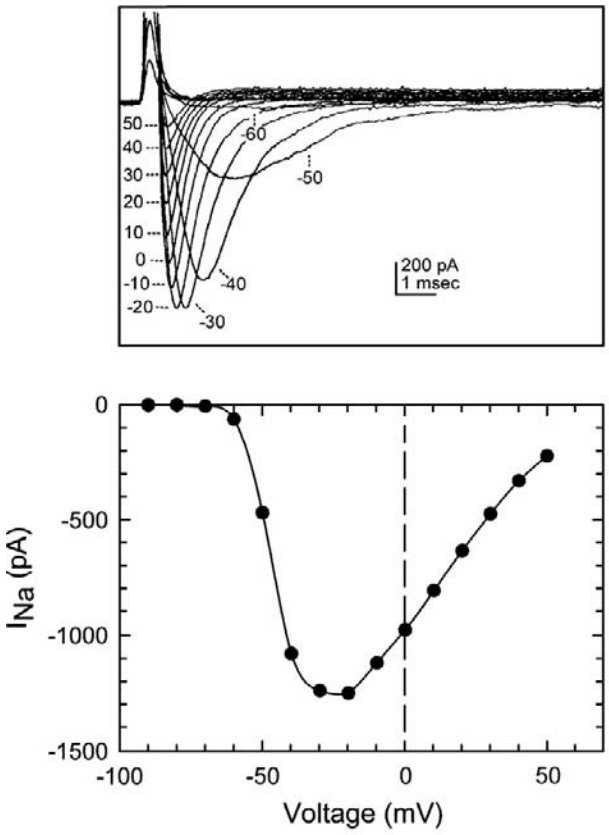

FIGURE 43.2 Sodium current (I_{Na}) recorded from a small embryonic chick ventricular cell. I_{Na} in these cells is much smaller than in adult cells, due to the very small size of these cells. Additionally, the small spherical shape of these cells and lack of t-tubules also contribute to better voltage control. Upper panel: shown are the original I_{Na} currents obtained upon stepwise depolarization from −100 mV to the indicated voltages. The current peaks in less than 1 ms at very depolarized potentials and then rapidly inactivates. Lower panel: the current−voltage curve of the peak current at each voltage. Note that the threshold for I_{Na} is approximately −70 mV and the current peaks at approximately −25 mV.

than in adult cells. For the rapid upstroke of phase 0 to occur, the cell needs to be depolarized to the voltage necessary to open some of the fast Na^+ channels. When the Na^+ channels begin to open, Na^+ flows down its electrochemical gradient into the cell. This causes the cell to depolarize further (i.e. the inside becomes more positive), which opens additional Na^+ channels. Therefore, once sufficient Na^+ channels open, the process becomes self-perpetuating (i.e. a positive-feedback loop), resulting in rapid depolarization (i.e. the membrane potential rapidly moves toward the equilibrium potential for Na^+). The voltage at which a sufficient number of Na^+ channels open to initiate the AP is the threshold for firing of the fast AP (approximately −55 mV). As the cell begins to depolarize further beyond the threshold, I_{Na} increases as more Na^+ channels are activated. Eventually, with even greater depolarization, I_{Na} begins to decline as the membrane potential approaches E_{Na}. Thus, the peak I_{Na} occurs between −30 and −20 mV. The membrane potential never reaches E_{Na} for several reasons: (1) as the membrane potential gets closer to E_{Na}, the driving force for Na^+ influx is diminished; (2) the Na^+ channels close (inactivate) shortly after opening (beginning after about 1 ms), thus, some Na^+ channels are already closing during the latter part of the upstroke; (3) repolarizing currents are beginning to activate during the latter portion of the upstroke. Nevertheless, the upstroke causes a substantial voltage change (110−120 mV) within 1−2 ms in ventricular myocytes and other fast cardiac cells.

IVC. Phase 1

Phase 1 of the cardiac AP is the transient and relatively small repolarization phase which immediately follows the upstroke of the AP. The size of phase 1 repolarization varies greatly between species and also between different regions of the heart within a given species. Thus, APs recorded from the outer (epicardial) layer of ventricular cells display a more prominent phase 1, whereas APs recorded from the inner (endocardial) layer of ventricular cells, display a small phase 1 repolarization (e.g. Antzelevitch and Dumaine, 2002). Phase 1 is also very large in Purkinje fibers and in atrial cells, but is largely absent in nodal cells.

Phase 1 repolarization is primarily due to a transient outward current (I_{to}). I_{to} turns on rapidly with depolarization (i.e. beginning during the final portion of the AP upstroke) and is only active at very depolarized potentials; the threshold for activation is approximately −30 mV (Fig. 43.3). I_{to} has a characteristic transient shape because the rapid activation of this current is followed by inactivation during the AP plateau. I_{to} is actually composed of separate currents (I_{to1} and I_{to2}) which are carried through three physically distinct channels (Tseng and Hoffman, 1989). One of the currents (I_{to1}) is a K^+ current that is independent of the internal Ca^{2+} concentration ($[Ca^{2+}]_i$) and is sensitive to the K^+ channel blocker 4-aminopyridine (4-AP) (Fig. 43.3). This component of I_{to} is very similar to the I_A current recorded in nerve fibers. In cardiac myocytes, I_{to1} consists of fast and slow components ($I_{to,f}$ and $I_{to,s}$) (Xu et al., 1999) which are pharmacologically separable due to the sensitivity of $I_{to,f}$ to Heteropoda spider toxins (Sanguinetti et al., 1997). A heteromultimer made up of channel proteins $K_v4.2$ and $K_v4.3$, and encoded by genes KCND2 and KCND3, corresponds to $I_{to,f}$. $K_v1.4$ is the channel protein for $I_{to,s}$ (for review, see Grunnet, 2010).

In addition to I_{to1}, another component of I_{to} (I_{to2}) is sometimes observed. I_{to2} is a Ca^{2+}-dependent Cl^- current (Zygmunt and Gibbons, 1992) that is less sensitive to 4-AP, but is more sensitive to another K^+ channel blocker,

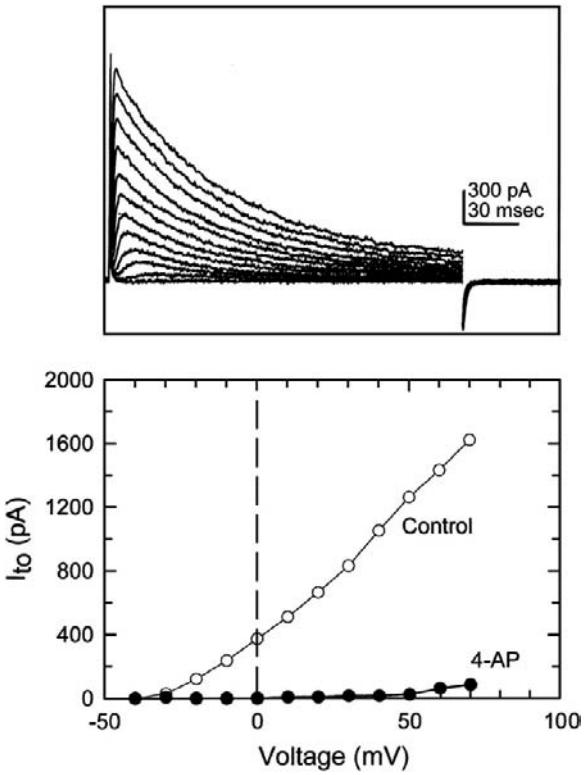

FIGURE 43.3 Transient outward current (I_{to}) recorded from a 21-day-old rat ventricular cell. Upper panel: shown are the original currents obtained upon stepwise depolarization from −80 mV. I_{to} activates rapidly and then inactivates. Currents were recorded in the presence of tetrodotoxin to eliminate I_{Na} and cadmium to eliminate overlapping I_{Ca}. Lower panel: the current-voltage curve shows increasing activation of this current at voltages above approximately −30 mV (indicated by open circles). This current is the Ca^{2+}-independent, 4-aminopyridine-sensitive component of I_{to} (i.e. I_{to1}) and is therefore readily blocked by 4-aminopyridine (4-AP, indicated by closed circles).

tetraethylammonium ion (TEA^+). Under physiological conditions, I_{to1} is much larger than I_{to2}. Thus, efflux of K^+ through the I_{to1} channels is normally responsible for the vast majority of phase 1 repolarization. The second component (I_{to2}) may become more important when intracellular levels of Ca^{2+} become too high. That is, under Ca^{2+}-overload conditions, I_{to2} would be activated and shorten the AP duration, thereby indirectly abbreviating the duration of Ca^{2+} current, resulting in a reduced Ca^{2+} influx. Thus, activation of I_{to2} by intracellular Ca^{2+} likely acts as a protective negative feedback mechanism that reduces calcium overload.

IVD. Phase 2

Phase 2 is commonly called the plateau phase. It follows the early repolarization phase (phase 1) and is a period of time during which the membrane potential remains relatively constant (see Fig. 43.1). The presence of this prominent plateau phase is responsible for the long AP duration in cardiac cells, which is the major difference between cardiac cells and nerve or skeletal muscle fibers. The plateau is caused by an approximate balance of positive inward (depolarizing) and positive outward (repolarizing) currents. The primary inward current during this phase is a Ca^{2+} current. The primary outward current during the plateau phase of ventricular cells, particularly during the latter part of the plateau, is the slowly activating K^+ current known as the delayed rectifier, which is described in greater detail under phase 3 repolarization. The transient outward K^+ current, I_{to}, also contributes to the early plateau phase in those cells that have a substantial I_{to}. As a result of its voltage dependence and time course (see Fig. 43.3), I_{to} significantly overlaps (and opposes) the inward L-type Ca^{2+} current (which is the primary depolarizing current during the plateau phase).

In addition to the Ca^{2+} and K^+ currents, there is a small contribution of the voltage-gated Na^+ current (I_{Na}) to the plateau. Thus, while I_{Na} largely inactivates within a few milliseconds after depolarization, a very small fraction (approximately 1%) of the I_{Na} inactivates slowly (see Fig. 43.2), causing a late Na^+ current known as the sodium window current, which is sufficient to affect the plateau of the AP and, hence, AP duration (Attwell et al., 1979).

The inward Ca^{2+} current (I_{Ca}) exhibits activation and inactivation much like I_{Na} but on a slower time scale (Fig. 43.4). This second inward current peaks within a few ms, but requires a few hundred ms to inactivate completely. I_{Ca} is at least one order of magnitude smaller than I_{Na} in a given cell. The threshold for activation of I_{Ca} is approximately −40 mV, the current is maximal near 0 mV and the E_{Ca} is around +100 mV. Thus, I_{Ca} is active over a more positive (depolarized) potential range than I_{Na}. This classical Ca^{2+} current is commonly referred to as the L-type (for "*L*ong-lasting" or "*L*arge") calcium current ($I_{Ca(L)}$) to distinguish it from the T-type (for "*T*ransient" or "*T*iny") Ca^{2+} current ($I_{Ca(T)}$) described later. The L-type channel is $Ca_v1.2$ encoded by CACNA1C (Catterall, 2000). These channels are located throughout the heart, i.e. they are expressed in the contractile cells of the atria and ventricles, the conduction cells of the His−Purkinje system and the nodal cells (Boyett et al., 2000).

The L-type Ca^{2+} current is central to many aspects of cardiac function. For example, it is the primary link in excitation−contraction coupling in heart muscle. Thus, the influx of Ca^{2+} ions during the plateau of the AP is what links the electrical events of the AP to the mechanical event, namely contraction. Ca^{2+} influx via $I_{Ca(L)}$ stimulates Ca^{2+} release from internal (sarcoplasmic reticular) stores, replenishes the internal Ca^{2+} stores available for subsequent release and also directly activates the contractile proteins. $I_{Ca(L)}$ is also very important in automaticity and conduction, due to the Ca^{2+} dependence of the nodal APs.

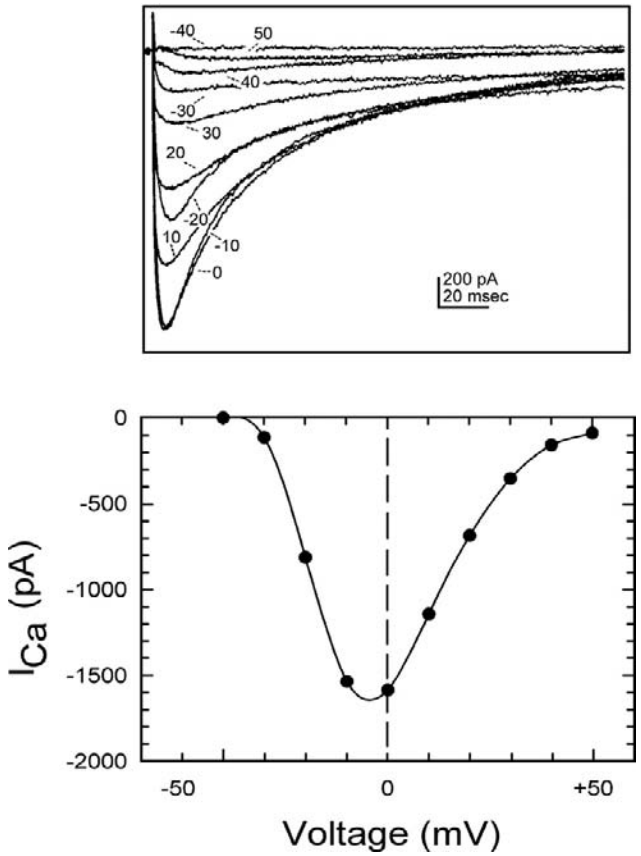

FIGURE 43.4 L-type calcium current ($I_{Ca(L)}$) recorded from an adult guinea pig ventricular cell. Upper panel: shown are the original currents obtained upon stepwise depolarization from −80 mV to the indicated voltages. I_{Na} was inactivated by briefly pulsing to −40 mV prior to applying the indicated test pulse. The Ca^{2+} currents show the same general shape as the Na^+ currents (see Fig. 43.2.), i.e. they activate upon depolarizing steps and inactivate during the voltage pulse. However, both activation and inactivation are much slower than for I_{Na} (note difference in time scale). Lower panel: the current−voltage curve shows a similar shape to the I_{Na} current−voltage relationship; however, both the threshold voltage and peak voltage are shifted approximately 30 mV in the depolarizing direction. $I_{Ca(L)}$ is roughly the same size as the I_{Na} example shown in Fig. 43.2 only because this cell is so much larger than the embryonic chick cell used in Fig. 43.2, I_{Na} in this guinea pig cell would be approximately 20 nA or more and could not be voltage-clamped under these conditions.

The L-type Ca^{2+} channel is also a major regulatory site in control of cardiac electrical activity and contraction by neurotransmitters, hormones, intracellular ions, etc. Perhaps the most important regulator of $I_{Ca(L)}$ in the heart is the autonomic nervous system. Thus, release of norepinephrine from cardiac sympathetic nerves or release of epinephrine from the adrenal gland stimulates the β-adrenergic receptors of the cardiac myocyte. The net result of β-adrenergic stimulation is that $I_{Ca(L)}$, and thereby force of contraction, is augmented. For a detailed review of this process, see Chapter 23. The parasympathetic neurotransmitter, acetylcholine (ACh) has a smaller, inhibitory (anti-adrenergic) effect on $I_{Ca(L)}$. For information about the Ca^{2+} channels in developing hearts, the reader is referred to Chapter 25.

IVE. Phase 3

Phase 3 is the late or final repolarization phase following the AP plateau. It is similar to the repolarization observed in nerve and skeletal muscle cells. Phase 3 repolarization is primarily caused by the unbalance of the currents that were relatively balanced during phase 2. $I_{Ca(L)}$ decreases with time (due to inactivation) and the delayed rectifier current (I_K) increases (due to slow activation). This gradually leads to the outward current, the delayed rectifier (I_K), overwhelming the inward current ($I_{Ca(L)}$). I_K is the primary repolarizing current in most ventricular preparations. The classical delayed rectifier activates slowly, compared to most other currents and does not inactivate significantly with time. Thus, I_K increases gradually during sustained depolarization at voltages around the plateau level. This current is similar to the delayed rectifier in nerve cells, although slower. I_K can be clearly distinguished from I_{to} by slow activation, lack of inactivation and different pharmacology.

The classical delayed rectifier current is divided into a very slowly activating component (I_{Ks}) and a more rapidly activating component (I_{Kr}) (see Grunnet, 2010). The I_{Ks} channel is $K_v7.1$ encoded by KCNQ1 (a.k.a. KVLQT1). The β-adrenergic-cAMP cascade can stimulate I_{Ks}, similar to its ability to stimulate $I_{Ca(L)}$ (e.g. Walsh and Kass, 1988; Sanguinetti and Jurkiewicz, 1990), which would tend to shorten the AP. Thus, β-adrenergic stimulation tends to lengthen the AP duration by enhancing $I_{Ca(L)}$ and, at the same time, tends to shorten AP duration by enhancing I_K. The overall effect of β-adrenergic stimulation on AP duration is thus determined by the relative contribution of the changes in these two currents (and perhaps also a contribution of $I_{Cl,}$ see later discussion). Some ventricular preparations also exhibit a Ca^{2+}-dependent I_K (Tohse, 1990). This component may also help to shorten the AP duration. The other, so-called rapid component of the traditional delayed rectifier (I_{Kr}) opens during phase 3 because the deactivation process is much slower than the rapid recovery from inactivation (following a very transient early opening). This I_{Kr} channel is Kv11.1 (a.k.a. HERG1 or ERG1) encoded by KCNH2 (Grunnet, 2010).

An ultrarapid-activating delayed rectifier K^+ current (I_{Kur}) also contributes to phase 3 repolarization in many preparations. I_{Kur} has slow deactivation and different pharmacology than I_{Ks} and I_{Kf}. It is made up of $K_v1.5/3.1$ encoded by KCNA5 and KCNA1, respectively (Grant, 2009). As the repolarization nears the RP, the inwardly rectifying K^+ current (I_{K1}, which is the primary determinant of the RP; see below) also begins to contribute to phase 3 repolarization. Thus, a number of K^+ currents contribute to phase 3 repolarization of the AP.

IVF. Phase 4

In ventricular cells, and most other cardiac cells, phase 4 is the RP. The RP is defined as the stable negative potential that occurs between APs in non-spontaneous cells. The resulting negative membrane potential is maintained by the Na^+-K^+ pump. The RP is very near E_K due to a relatively high permeability of the resting ventricular cell membrane to K^+ and a very low permeability to other ions (e.g. Na^+). Thus, the RP of non-automatic cardiac cells is similar to the RP in skeletal muscle cells. The RP is largely set by a K^+, current known as the inward rectifier, I_{K1}, made up of Kir2.1/2.2 encoded by KCNJ2/J12 (Grant, 2009). Inward rectification means that, instead of a linear "ohmic" relationship between voltage and current, this channel passes current more readily in the inward direction than in the outward direction. This characteristic is evident in Fig. 43.5. Of course, the outward K^+ current is the only one occurring physiologically, since the membrane potential does not normally hyperpolarize beyond E_K. In most preparations, I_{K1} actually demonstrates a negative slope region in the outward direction. That is, as the cell is depolarized from near its resting membrane potential to progressively more depolarized potentials, the outward current first increases and then decreases with further depolarization, with the outward current dropping to very low levels at voltages positive to −40 mV (Fig. 43.5). Thus, the contribution of I_{K1} to repolarization tends to be less at potentials near the plateau and greater as the membrane potential approaches the resting membrane potential (from approximately −40 mV to the resting membrane potential), at the same time that I_K is declining. Therefore, I_{K1} contributes significantly to late phase 3 repolarization. The inward rectification of the I_{K1} channel current is thought to be due to blockade of the channels by intracellular Mg^{2+} (Matsuda et al., 1987) and polyamines (Lopatin et al., 1994), which is removed late in phase 3 as the interior of the cell becomes quite negative (Lopatin and Nichols, 2001). The large expression of I_{K1} channels in ventricular cells reduces the possibility of ventricular automaticity.

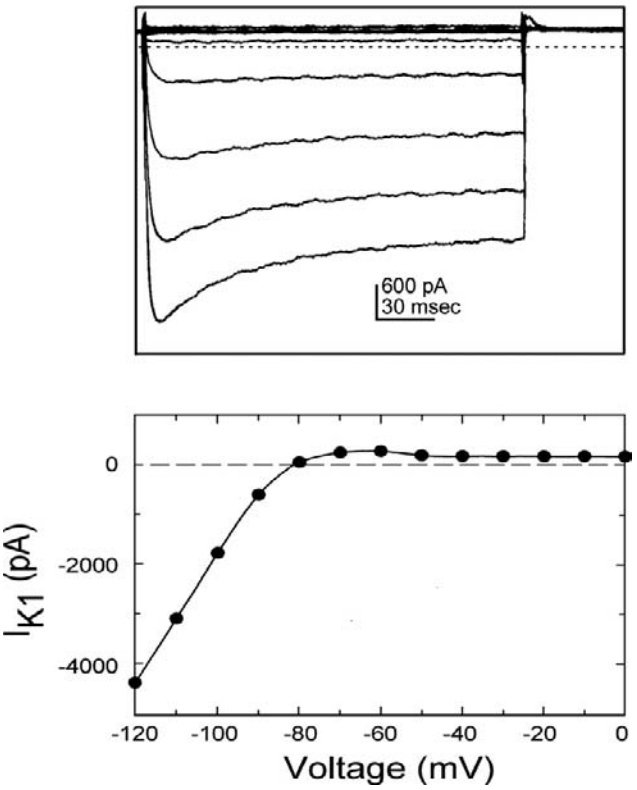

FIGURE 43.5 Inwardly-rectifying K^+ current (I_{K1}) recorded from an adult guinea pig ventricular cell. Upper panel: shown are the original barium-subtracted currents obtained upon stepwise hyperpolarization and depolarization from a holding potential of −40 mV. The current displays the typical inward rectification. That is, the current is smaller in the outward (physiological) direction than the inward direction. Lower panel: the current−voltage curve for I_{K1}. The current also displays a negative slope region between approximately −60 mV and −30 mV. Thus, larger depolarizations actually result in a decrease in outward K^+ flux during this voltage range, such that the current at −30 mV is less than half as large as at −60 mV. The net result is that during repolarization (phase 3) the K^+ current increases as the membrane potential approaches the resting membrane potential.

V. ADDITIONAL CURRENTS CONTRIBUTING TO THE ACTION POTENTIAL

VA. Pump Current

The Na^+,K^+-ATPase, or pump, is the primary transport system that maintains the normal ionic imbalance between the cell exterior and interior. Each pump cycle extrudes three Na^+ ions out of the cell and transports two K^+ ions into the cell, thus building up $[K^+]_i$ and reducing $[Na^+]_i$. Because of the exchange of three positive ions for two positive ions, each pump cycle generates a net loss of one positive charge, which generates a small pump current (I_p). At the RP, I_p is an outward current which may hyperpolarize the membrane potential slightly. In addition, I_p can cause considerable shortening of the AP when $[Na^+]_i$ increases pathologically (Gadsby, 1984). Additionally, blockade of the pump with toxic concentrations of digitalis may lead to a significant increase in intracellular $[Na^+]_i$, which may in turn activate a Na^+-dependent K^+ current ($I_{K(Na)}$) (Luk and Carmeliet, 1990). However, the primary role of the Na^+,K^+-ATPase is to set up and maintain the ionic gradients that generate the electrochemical driving forces for the currents responsible for the AP.

VB. Na^+-Ca^{2+} Exchange Current

An Na^+-Ca^{2+} exchanger (NCX) also exists in the cardiac sarcolemma. Working in the "normal mode" NCX

exchanges intracellular Ca^{2+} for extracellular Na^+; thus, the exchanger is an important mechanism whereby Ca^{2+} is removed from the cytoplasm. The exchanger may also work in the "reverse" mode, exchanging intracellular Na^+ for extracellular Ca^{2+}. Under these conditions, during the initial part of phase 2, NCX contributes a small Ca^{2+} influx for excitation–contraction coupling. The exchanger transports three Na^+ for each Ca^{2+} under most conditions, leading to the net movement of one positive charge. Thus, NCX generates a current which can also contribute to the action potential. The equilibrium potential for this Na^+-Ca^{2+} exchange current (I_{NCX}) is generally slightly negative to 0 mV; therefore, near the resting membrane potential, the exchanger works in the normal mode and I_{NCX} is an inward current. During the initial portion of the plateau, the Na^+-Ca^{2+} exchanger transiently works in the reverse mode and briefly generates an outward current prior to returning to the normal mode. Thus, I_{NCX} may contribute to the shape of the AP (for review, see Janvier and Boyett, 1996).

VC. Chloride Current

Under basal conditions, the Cl^- current (I_{Cl}) in the heart is relatively small and probably does not contribute a great deal to the configuration of the AP. However, when cAMP levels are stimulated (as with sympathetic nerve stimulation), a significant time-independent Cl^- current develops that is separate from the Cl^- current responsible for I_{to2}. Activation of this current by β-adrenergic stimulation can cause a small depolarization of the resting membrane potential and significant shortening of the action potential (Harvey, 1996).

VD. ATP-Sensitive Potassium Current

Many details of this current have been given in the preceding chapter. When the oxygen supply declines, as occurs during ischemia, AP duration shortens. The shortening of the AP duration accelerates inactivation of I_{Ca} thereby reducing contractility. The reduced contractility greatly decreases the energy demands of the cell, thereby sparing ATP. This mechanism contributes to the survival of the myocardial cell during temporary ischemia. However, in addition to this beneficial effect, regional shortening of the AP can also lead to arrhythmias, due to the dispersion of refractory periods.

The shortening of the AP during ischemia is largely caused by activation of a unique outward K^+ current, which is inhibited by intracellular ATP. The decreased oxygen supply reduces ATP levels in the cell and I_{K1} is inhibited. At the same time, the fall in ATP disinhibits the ATP-sensitive K^+ current ($I_{K(ATP)}$) (Noma, 1983), since the current is inhibited by physiological levels of intracellular ATP (Fig. 43.6) and thus appears to contribute little to the AP configuration under conditions of adequate oxygenation. However, during inadequate oxygenation, the AP is shortened as $I_{K(ATP)}$ replaces I_{K1}. This is in large part because $I_{K(ATP)}$ displays less inward rectification than I_{K1} and, thus, has a greater effect on repolarization. This shortening of the AP leads to a shortened phase 2.

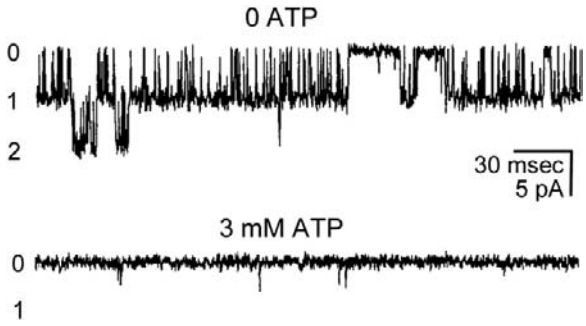

FIGURE 43.6 ATP-sensitive K^+ current $I_{K(ATP)}$ recorded from an inside-out patch from an adult rat ventricular cell. Single-channel currents shown were recorded in the absence of ATP (upper traces) and in the presence of physiological levels of ATP (3 mM, lower traces). Channel openings are downward. In the absence of ATP, channel activity is high. Thus, up to two channels are open simultaneously (number of open channel levels are indicated at the side). In the presence of 3 mM ATP, the channels are rarely open. In the presence of ATP, the openings are extremely brief, such that they do not appear to reach the normal open level (1).

The intracellular ATP levels reached during acute ischemia are generally not sufficiently low to open a substantial number of $I_{K(ATP)}$ channels on its own. However, the decreasing intracellular pH and increasing lactate accumulation that accompany ischemia also enhance $I_{K(ATP)}$ channel opening (Fan and Makielski, 1993) in addition to a fall in intracellular ATP levels. Furthermore, opening of only a small fraction of the large number of $I_{K(ATP)}$ channels may be sufficient to shorten substantially the AP (Faivre and Findlay, 1990).

The physical characteristics of the $I_{K(ATP)}$ channel (e.g. ATP sensitivity and/or degree of rectification) are altered in some pathophysiological states, such as hypertrophy (Cameron et al., 1988) or diabetic cardiomyopathy (Smith and Wahler, 1996; Shimoni et al., 1998). This may be an important factor in the abnormal responses to ischemia in these conditions.

Other channels may also be activated by ischemia, in addition to $I_{K(ATP)}$ channels; e.g. lysophosphatidylcholine and long-chain acylcamitine resulting from membrane phospholipid metabolism rapidly accumulate in early ischemia and may activate the arachidonic acid-activated K^+ channel ($I_{K(AA)}$) and the phosphatidylcholine-activated K^+ channel ($I_{K(PC)}$) (Montsuez, 1997).

VI. REGIONAL DIFFERENCES IN ACTION POTENTIALS

VIA. Overview

The normal pathway for electrical activation of the heart is the following: sinoatrial (SA) node, atria, atrioventricular

(AV) node, bundle of His, Purkinje fibers, ventricles. The APs differ from region to region, reflecting the different roles played by the different cell types. The following description characterizes the APs for each region and indicates how each differs from the ventricular AP.

VIB. Sinoatrial Node

The SA node contains specialized cells that generate APs that are quite different from the ventricular APs described above (Fig. 43.7). Unlike ventricular APs, these cells do not have a true resting membrane potential; i.e. the membrane potential between APs is not stable but rather exhibits a slow spontaneous depolarization known as phase 4 depolarization, or the pacemaker potential. Since there is no resting membrane potential in these cells, the most negative potential the cell reaches between APs is called the maximum diastolic potential. This potential is less negative than the resting membrane potential of ventricular cells, due to a lower K^+ permeability (caused by a lack of I_{K1} in these cells). The maximum diastolic potential ranges from approximately −55 mV for true primary pacemaker cells, to approximately −70 mV for transitional cells on the border between the SA node and atria. The pacemaker potential takes the nodal cell from the maximum diastolic potential to the threshold for generating an AP in these cells (approximately −40 mV). Thus, these cells are spontaneously active and the slope of the phase 4 depolarization is an important determinant of the rate of AP generation and, thereby, heart rate.

VIC. Atria

Atrial cells have APs that are similar in many aspects to the ventricular APs described above. Thus, the resting membrane potential (phase 4) is approximately −85 mV and there is a fast upstroke (phase 0) generated by I_{Na}. The most distinguishing feature of the atrial AP is that it has a more triangular appearance than the ventricular AP. That is, atrial cells do not always have a distinct plateau. This is likely due to the relatively large I_{to} in atrial cells.

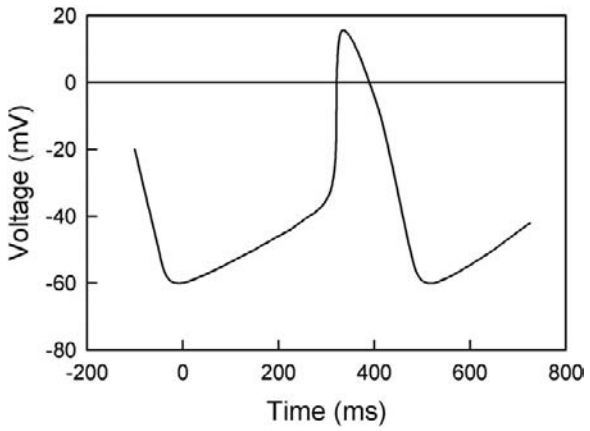

FIGURE 43.7 Sinoatrial node action potential. This is a diagrammatic representation of a typical sinoatrial node AP in the mammalian heart. Note the pacemaker potential and the absence of a resting membrane potential and the slower upstroke compared to the fast AP of the ventricular cell (see Fig. 43.1).

VID. Atrioventricular Node

The cells of the AV node generate APs that are quite similar to the APs of the SA node. Thus, these cells fire Ca^{2+}-dependent APs and also display spontaneous phase 4 depolarization (i.e. automaticity). However, the rate of the phase 4 depolarization in AV nodal cells is much slower than the rate of phase 4 depolarization in SA nodal cells. Thus, the SA node cells fire APs before the AV node cells fire, which is why the SA node cells are the normal pacemaker cells of the heart.

VIE. Purkinje Fibers

Purkinje APs are in most respects similar to the ventricular APs. Thus, these cells have a negative resting membrane potential between APs (phase 4) and a very rapid upstroke (phase 0) generated by I_{Na}. Purkinje fibers do differ from ventricular cells in that they have a more prominent phase 1 repolarization and a longer plateau (phase 2). The plateau is followed by a phase 3 repolarization that is virtually identical to phase 3 in ventricular cells. Cells in the bundle of His appear to have APs similar to those in the Purkinje fibers; however, in general, bundle of His cells have not been studied in detail.

Additionally, Purkinje cells may exhibit automaticity, especially when the extracellular K^+ concentration is low. Thus, under some conditions, they exhibit phase 4 depolarization. Purkinje cells have all the currents found in ventricular cells, described above. However, Purkinje cells also have some additional currents, which are absent or very small in ventricular cells, that are related to the latent pacemaker function of these cells. These additional currents are described in the following section on automaticity.

VII. AUTOMATICITY

VIIA. Overview

Automaticity refers to the ability of some cardiac cells to depolarize and fire repetitive APs spontaneously. Thus, as noted above, automatic cells (e.g. in the SA node) do not have a stable resting membrane potential between APs, but rather have a maximum diastolic potential followed by a spontaneous phase 4 depolarization, known as the pacemaker potential. The spontaneous depolarization to threshold generates the AP in that cell type. Following repolarization of

the AP, the spontaneous phase 4 depolarization occurs again. The slope of the pacemaker potential (i.e. rate of spontaneous phase 4 depolarization) largely determines the rate of AP firing. Because the rate of firing of APs is normally fastest in the primary pacemaker cells of the SA node, this region acts as the normal pacemaker of the heart. Once this region fires an AP, the wave of depolarization is propagated to other regions of the heart, ultimately leading to contraction of the heart. Automatic cells in other regions of the heart (e.g. AV node) normally do not have the opportunity to fire spontaneously before the wave of depolarization arising from the SA node drives them to threshold.

VIIB. Mechanisms of Automaticity

Automaticity is a property of several cell types in the heart under physiological conditions (for review, see Mangoni and Nargeot, 2008). Under pathophysiological conditions, even normally non-spontaneous cells (e.g. ventricular cells) may exhibit automaticity. Physiologically, the most important pacemaker potential is that of the normal pacemaker cells in the SA node. However, technical difficulties have limited our understanding of the pacemaker process in nodal cells and more is known about automaticity in other automatic cell types (e.g. Purkinje fibers).

VIIB1. Automaticity in Purkinje Fibers

Under physiological conditions, Purkinje fibers can have an extremely slow phase 4 pacemaker potential. In contrast to SA node cells, the mechanisms for automaticity in Purkinje cells are fairly well understood. As noted above, the Purkinje cells have all the currents that ventricular cells have, plus some additional currents not found to any significant degree in adult ventricular cells. The large I_{K1} current in Purkinje cells tends to clamp the membrane potential near E_K and, therefore, a large depolarizing current is needed to overcome this clamping effect. The primary current responsible for the pacemaker potential in Purkinje cells has some unusual properties, earning it the designation as the "funny current" (I_f).

I_f is a slowly activating inward depolarizing current which is present in automatic cells. It is a mixed cation current carrying both Na^+ and K^+ ions. In Purkinje cells, I_f is responsible for most of the depolarizing current which generates the pacemaker potential. The molecular basis of I_f will be described in detail below (see Section VIIB2).

In addition to $I_{Ca(L)}$, pacemaker cells have an additional Ca^{2+} current which is activated at more negative potentials and exhibits a much more rapid activation and inactivation than $I_{Ca(L)}$ (Hagiwara et al., 1988). This second Ca^{2+} current (carried by $Ca_v3.1$ and $Ca_v3.2$) has been named the transient T-type Ca^{2+} current ($I_{Ca(T)}$) in contrast to the classical, slowly inactivating long-lasting L-type Ca^{2+} current ($I_{Ca(L)}$). The T-type Ca^{2+} current is small to non-existent in adult ventricular cells, but is present in Purkinje cells. There may be a small contribution of the T-type Ca^{2+} current to the latter stages of the pacemaker potential in Purkinje cells. During pacemaker activity, a small amount of Na^+ through I_{Na} channels may also contribute to the final phase of the pacemaker potential in Purkinje cells, as the membrane potential approaches the threshold for AP generation. Then, as sufficient voltage-gated Na^+ channels are opened, the Purkinje fiber will fire an AP which is generated by essentially the same mechanisms as previously described for ventricular cells.

VIIB2. Automaticity in Nodal Cells

Several factors contribute to the pacemaker potential in nodal cells. Because of the very low density of I_{K1} channels in nodal cells, the resting K^+ permeability is much lower in nodal cells than in ventricular cells. The large resting K^+ permeability in ventricular cells generated by I_{K1} tends to keep the interior of the cells negative, opposing depolarization of the cell toward threshold by "clamping" the membrane potential near E_K. A much smaller current is sufficient to depolarize the nodal cells due to the much lower resting K^+ permeability, leading to a very high input resistance. Thus, currents which may be too small to measure accurately using present electrophysiological techniques (small background currents or currents produced by various electrogenic transport mechanisms) could produce sufficient current to affect the pacemaker potential. Because of this limitation, the analysis of the relative contribution of various currents to the pacemaker potential in nodal cells is much less clear than for Purkinje cells, leading to considerable controversy regarding the precise mechanism of automaticity in SA node cells.

The major depolarizing current during the pacemaker potential of Purkinje cells, I_f, is also present in nodal cells. The hyperpolarization-activated cyclic nucleotide-gated (HCN) channels responsible for I_f are encoded by four gene isoforms (HCN1−4) (for review, see Baruscotti et al., 2010). HCN2 and HCN4 are expressed in the heart, with HCN4 being the predominant isoform in the SA node. As noted earlier, I_f is an unusual depolarizing current in that it is activated by hyperpolarization (DiFrancesco, 1993). As a result, I_f is thought to contribute significantly to the early part of the pacemaker potential in SA node cells.

There is a low density of HCN channels found in ventricular myocytes (see Baruscotti et al., 2010). In contrast to the situation in nodal cells, HCN are normally non-functional in ventricular myocytes because the voltage-dependence of the channels is quite different from HCN channels in nodal cells. That is, the channels can only be activated at unphysiologically negative voltages in ventricular cells (Yu et al., 1993). However, in certain

pathological conditions (e.g. heart failure), the voltage-dependence of the I_f channels in ventricular myocytes shifts to a more positive level (Mangoni and Nargeot, 2008), suggesting that I_f may contribute to ventricular arrhythmias under such conditions.

Other small currents, e.g. the sodium-potassium ATPase pump current (I_p) and the Na^+-Ca^{2+} exchange current (I_{NCX}), also likely contribute to and/or modulate the pacemaker potential in nodal cells. For example, in SA node cells, I_p may help set the maximum diastolic potential (Noma and Irisawa, 1975). A novel involvement of SR calcium release in contributing to the pacemaker potential has also been proposed (see Mangoni and Nargeot, 2008). In this mechanism, local Ca^{2+}-induced-Ca^{2+} release near the sarcolemma leads to a depolarizing current that contributes to the pacemaker potential due to the electrogenic (swapping three Na^+ for one Ca^{2+}) nature of the exchanger.

As noted earlier, the upstroke (phase 0) of nodal cells is generated by an L-type Ca^{2+} current ($I_{Ca(L)}$) rather than a voltage-gated Na^+ current (I_{Na}). The channel responsible appears identical to the classic L-type Ca^{2+} channel ($Ca_v1.2$) for the plateau in ventricular cells. Interestingly, in nodal cells, another $I_{Ca(L)}$ channel isoform ($Ca_v1.3$) has been reported that has a slightly more negative threshold (approximately -50 mV). This component of $I_{Ca(L)}$ is thought to contribute to the late phase of the pacemaker potential and effectively lower the threshold for $I_{Ca(L)}$ (for review, see Mangoni et al., 2003).

The complex interaction of so many different currents leads to the following hypothesis of the generation of the pacemaker potential by sequential activation of several different currents: (1) activation of I_f in late phase 3 repolarization is largely responsible for generating the early part of the pacemaker potential; (2) this early diastolic depolarization depolarizes the cells to the threshold for opening of T-type Ca^{2+} channels, leading to further depolarization; (3) the next threshold to be reached is the threshold for opening of $Ca_v1.3$ channels, causing further depolarization; (4) ultimately, at the very end of the pacemaker potential, $Ca_v1.3$ channels are opened; (5) opening of sufficient number of L-type channels leads to the upstroke of the Ca^{2+}-dependent action potential. Thus, opening of each channel in the sequence depolarizes the cell to the threshold for the opening of the next channel.

An alternative proposal to the sequential activation of I_f and various I_{Ca} components hypothesizes that the interaction between a depolarizing voltage- and time-independent background current (I_b) and the decay of the delayed rectifier (I_K) develops the pacemaker potential in nodal cells. This small, constant depolarizing current (I_b) in nodal cells is a cation current carried primarily by Na^+ ions (Hagiwara et al., 1992). Due to the small size of this current, relatively little is known about its magnitude and characteristics in mammalian SA node cells; however, indirect evidence suggests that it may be a very important component in determining automaticity (Campbell et al., 1992; Dokos et al., 1996). The role of a constant I_b in generating a variable pacemaker potential results from the interaction of I_b with I_K. I_K is the primary current responsible for repolarization in nodal cells, as in other cardiac cells. Similar to ventricular cells, I_K has also been shown to consist of at least two components (I_{Ks} and I_{Kr}) (Dokos et al., 1996). I_K displays essentially no inactivation during a prolonged depolarizing pulse, but displays a slow decay upon repolarization toward E_K. The time course of the I_K decay is very slow at membrane potentials in the voltage range of the pacemaker potential in nodal cells. The depolarizing action of I_b is opposed by I_K. Thus, the depolarization due to a constant background current I_b effectively increases progressively over time due to a gradual loss of opposing repolarizing current (I_K), thereby leading to diastolic depolarization in nodal cells. Since the relative contribution of the various currents to the pacemaker potential in nodal cells cannot be accurately determined experimentally, there has been considerable controversy over which depolarizing current (I_f or I_b) plays the greater role in generating the pacemaker potential in these cells. It is likely that both play a significant role in contributing to automaticity in nodal cells.

VIIC. Modulation of Automaticity by the Autonomic Nervous System

The pacemaker cells of the SA node are richly innervated by sympathetic and parasympathetic nerves. These actions of norepinephrine (NE) and acetylcholine (ACh) on several currents in SA node cells are the basis of the stimulating and inhibiting effect on heart rate of sympathetic or parasympathetic nerve stimulation.

I_f and $I_{Ca(L)}$ are both enhanced by the sympathetic neurotransmitter, norepinephrine and inhibited by the parasympathetic neurotransmitter, acetylcholine. Thus, NE increases the slope of the pacemaker potential, the threshold is reached sooner and heart rate increases. In contrast, ACh decreases the slope of the pacemaker potential. The I_f channel is directly activated by cAMP (DiFrancesco and Mangoni, 1994). Thus, the effects of NE and ACh are mediated by raising and lowering the intracellular cAMP concentration, respectively.

In addition to the cAMP-mediated effects on I_f and $I_{Ca(L)}$, ACh activates a G-protein-coupled inwardly-rectifying K^+ current ($I_{K(ACh)}$) whose structure is similar to I_{K1}. Cardiac $I_{K(ACh)}$ channels are tetramers made up of Kir3.1 and Kir3.4 subunits expressed by KCNJ3 and KCNJ5 and are highly expressed in the SA and AV nodes and atria, but not ventricles (Wickman et al., 1999). Binding of ACh to muscarinic M-2 receptors causes the

release of G-protein $G_{\alpha i}$ and $G_{\beta\gamma}$ subunits. The $G_{\beta\gamma}$ subunit then activates the $I_{K(ACh)}$ channel, causing hyperpolarization (which drives the maximum diastolic potential further from threshold) and a reduction of the slope of the pacemaker potential (for review, see Mangoni and Nargeot, 2008). The end result of activation of $I_{K(ACh)}$ is that it takes SA node cells a longer time to reach threshold and the heart rate is decreased.

VIII. CHANNELOPATHIES

Mutations in the genes encoding I_{Kr}, I_{Ks} and I_{Na} have been reported to be responsible for long QT syndrome, a familial disorder characterized by slowed repolarization, recurrent syncope, increased incidence of torsades de pointes arrhythmias and an increased risk for sudden death (Veldkamp, 1998; Vizgirda, 1999). Interestingly, APs are normally longer in adult females than males, resulting in a greater QT interval. This suggests that the repolarizing currents may be smaller in females than males, which may explain the greater incidence of torsades de pointes arrhythmias in females (Vizgirda, 1999). Gain-of-function mutations in the genes that cause long QT syndrome can cause the opposite effect, namely more rapid repolarization, leading to short QT syndrome (Priori and Cerrone, 2005).

Other mutations in the genes for these ion channels are responsible for a number of other familial arrhythmogenic conditions, such as Brugada syndrome and catecholaminergic polymorphic ventricular tachycardia (Clancy and Kass, 2005; Tester and Ackerman, 2009). It is certain that more electrophysiological abnormalities will be found to have their origins in mutations of genes encoding numerous channel proteins and associated regulatory proteins.

BIBLIOGRAPHY

Antzelevitch, C., & Dumaine, R. (2011). Electrical heterogeneity in the heart: physiological, pharmacological and clinical implications. *Comprehensive Physiology* 654–692.

Attwell, D., Cohen, I., Eisner, D., Ohba, M., & Ojeda, C. (1979). The steady-state TTX-sensitive ("window") sodium current in cardiac Purkinje fibers. *Pflügers Arch, 379*, 137–142.

Baruscotti, M., Bottelli, G., Milanesi, R., DiFrancesco, J. C., & DiFrancesco, D. (2010). HCN-related channelopathies. *Pflügers Arch, 460*, 405–415.

Boyett, M. R., Honjo, H., & Kodama, I. (2000). The sinoatrial node, a heterogenous pacemaker structure. *Cardiovasc Res, 47*, 658–687.

Cameron, J. S., Kimura, S., Jackson-Bums, D. A., Smith, D. B., & Bassett, A. L. (1988). ATP-sensitive K^+ channels are altered in hypertrophied ventricular myocytes. *Am J Physiol, 255*, H1254–H1258.

Campbell, D. L., Rasmussen, R. L., & Strauss, H. C. (1992). Ionic current mechanisms generating vertebrate primary cardiac pacemaker activity at the single cell level: an integrative view. *Annu Rev Physiol, 54*, 279–302.

Catterall, W. A. (2000). Structure and regulation of voltage-gated Ca^{2+} channels. *Annu Rev Cel Dev Biol, 16*, 521–555.

Clancy, C. E., & Kass, R. S. (2005). Inherited and acquired vulnerability to ventricular arrhythmias: cardiac Na^+ and K^+ channels. *Physiol Rev, 85*, 33–47.

Coraboeuf, E., & Nargeot, J. (1993). Electrophysiology of human cardiac cells. *Cardiovasc Res, 27*, 1713–1725.

DiFrancesco, D. (1993). Pacemaker mechanisms in cardiac tissue. *Annu Rev Physiol, 55*, 455–472.

DiFrancesco, D., & Mangoni, M. (1994). Modulation of single hyperpolarization-activated channels [I_f] by cAMP in rabbit sino-atrial node. *J Physiol, 474*, 473–478.

Dokos, S., Celler, B., & Lovell, N. (1996). Ion currents underlying sinoatrial node pacemaker activity: a new single cell mathematical model. *J Theor Biol, 181*, 245–272.

Faivre, J.-E., & Findlay, I. (1990). Action potential duration and activation of ATP-sensitive potassium current in isolated guinea-pig ventricular myocytes. *Biochim Biophys Acta, 1029*, 167–172.

Fan, Z., & Makielski, J. C. (1993). Intracellular H^+ and Ca^{++} modulation of trypsin modified ATP sensitive K^+ channels in rabbit ventricular myocytes. *Circ Res, 72*, 715–722.

Gadsby, D. C. (1984). The Na^+/K^+ pump of cardiac cells. *Annu Rev Biophys Bioeng, 13*, 373–378.

Grant, A. O. (2009). Cardiac ion channels. *Circ Arrhythm Electrophysiol, 2*, 185–194.

Grunnet, M. (2010). Repolarization of the cardiac action potential. Does increase in repolarization capacity constitute a new anti-arrhythmic principle? *Acta Physiol, 198*(Suppl. 676), 1–48.

Hagiwara, N., Irisawa, H., & Kameyama, M. (1988). Contribution of two types of calcium currents to the pacemaker potential of rabbit sino-atrial node cells. *J Physiol, 395*, 233–254.

Hagiwara, N., Irisawa, H., Kasanuki, H., & Hosoda, S. (1992). Background current in sino-atrial node cells of the rabbit heart. *J Physiol, 448*, 53–72.

Harvey, R. D. (1996). Cardiac chloride currents. *NIPS, 11*, 175–181.

Hoshiko, T., & Sperelakis, N. (1962). Components of the cardiac action potential. *Am J Physiol, 203*, 258–260.

Janvier, N. C., & Boyett, M. R. (1996). The role of Na-Ca exchange current in the cardiac action potential. *Cardiovasc Res, 32*, 69–84.

Lopatin, A. N., & Nichols, C. G. (2001). Inward rectifiers in the heart: an update on I(K1). *J Mol Cell Cardiol, 33*, 625–638.

Lopatin, A. N., Makhina, E. N., & Nichols, C. G. (1994). Potassium channel block by cytoplasmic polyamines as the mechanism of intrinsic rectification. *Nature, 372*, 368–369.

Luk, H. N., & Carmeliet, E. (1990). Na^+ activated K^+ current in cardiac cells: rectification, open probability block and role in digitalis toxicity. *Pflügers Arch, 416*, 766–768.

Mangoni, M. E., & Nargeot, J. (2008). Genesis and regulation of the heart automaticity. *Physiol Rev, 88*, 919–982.

Mangoni, M. E., Couette, B., Bourinet, E., Platzer, J., Reimer, D., & Streissnig, J. (2003). Functional role of L-type $Ca_v1.3$ Ca^{2+} channels in cardiac pacemaker activity. *Proc Natl Acad Sci USA, 100*, 5543–5548.

Matsuda, H., Saigusa, A., & Irasawa, H. (1987). Ohmic conductance through the inwardly rectifying K channel and blocking by the integral Mg^{++}. *Nature, 325*, 156–159.

Montsuez, J.-J. (1997). Cardiac potassium currents and channels. Part I: basic science aspects. *Internat J Cardiol, 61*, 209–219.

Nerbonne, J., & Kass, D. (2005). Molecular physiology of cardiac repolarization. *Physiol Rev, 85*, 1205–1253.

Noma, A., & Irisawa, H. (1975). Contribution of an electrogenic sodium pump to the membrane potential in rabbit sinoatrial node cells. *Pflügers Arch, 358*, 289–301.

Noma, A. (1983). ATP-regulated K^+ channels in cardiac muscle. *Nature, 305*, 147–148.

Priori, S. G., & Cerrone, M. (2005). Genetic arrhythmias. *Ital Heart J, 6*, 241–248.

Sanguinetti, M. C., & Jurkiewicz, N. K. (1990). Two components of cardiac delayed rectifier K^+ current. Differential sensitivity to block by class III antiarrhythmic agents. *J Gen Physiol, 96*, 195–215.

Sanguinetti, M. C., Johnson, J. H., Hammerland, L. G., et al. (1997). Heteropodotoxins: peptides isolated from spider venom that block $K_v4.2$ potassium channels. *Molec Pharmacol, 52*, 491–498.

Shimoni, Y., Light, E. E., & French, R. J. (1998). Altered ATP sensitivity of ATP-dependent K^+ channels in diabetic rat hearts. *Am J Physiol, 275*, E568–E576.

Smith, J. M., & Wahler, G. M. (1996). ATP-sensitive potassium channels are altered in ventricular myocytes from diabetic rats. *Mol Cell Biochem, 158*, 43–51.

Sperelakis, N., & Lehmkuhl, D. (1964). Effect of current on transmembrane potentials in cultured chick heart cells. *J Gen Physiol, 47*, 895–927.

Tester, D. J., & Ackerman, M. J. (2009). Cardiomyopathic and channelopathic causes of sudden unexplained death in infants and children. *Annu Rev Med, 60*, 69–84.

Tohse, N. (1990). Calcium-sensitive delayed rectifier potassium current in guinea pig ventricular cells. *Am J Physiol, 258*, H1200–H1207.

Tseng, G. N., & Hoffman, B. E. (1989). Two components of transient outward current in canine ventricular myocytes. *Circ Res, 64*, 633–647.

Veldkamp, M. W. (1998). Is the slowly activating component of the delayed rectifier, I_{Ks}, absent from undiseased human ventricular myocardium? *Cardiovasc Res, 40*, 433–435.

Vizgirda, V. M. (1999). The genetic basics for cardiac dysrhythmias and the long QT syndrome. *J Cardiovasc Nurs, 13*, 34–45.

Walsh, K. B., & Kass, R. S. (1988). Regulation of a heart potassium channel by protein kinase A and C. *Science, 242*, 67–69.

Wickman, K., Krapivinsky, G., Corey, S., et al. (1999). Structure, G protein activation, functional relevance of the cardiac G protein-gated K^+ channel, I_{KACh}. *Ann NY Acad Sci, 868*, 386–398.

Xu, H., Guo, W., & Nerbonne, J. M. (1999). Four kinetically distinct depolarization-activated K^+ currents in adult mouse ventricular myocytes. *J Gen Physiol, 113*, 661–678.

Yu, F. H., & Catterall, W. A. (2003). Overview of the voltage-gated sodium channel family. *Genome Biol, 4*, 207.

Yu, F. H., Chang, E., & Cohen, I. S. (1993). Pacemaker current exists in ventricular myocytes. *Circ Res, 72*, 232–236.

Zygmunt, A. C., & Gibbons, W. R. (1992). Properties of the calcium-activated chloride current in the heart. *Gen Physiol, 99*, 391–414.

This page intentionally left blank

Chapter 44

Smooth Muscle Excitability

Neil D. Detweiler, Anup K. Srivastava, Asif R. Pathan, Sujay V. Kharade and Nancy J. Rusch

Chapter Outline

I. INTRODUCTION

Smooth muscle cells[1] (SMCs) compose many tissues including blood vessels, airways, the gastrointestinal tract, bladder, uterus and vas deferens. These organs have very diverse functions and so, not surprisingly, their SMCs exhibit highly diverse patterns of electrical excitation that have evolved to support the unique physiological roles of the individual organs. For example, the SMCs in blood vessels generally lack spiking action potentials that would drive rhythmic contraction and relaxation of the vasculature and thereby cause profound changes in blood flow and blood pressure. Instead more stable resting membrane potentials (E_m) and slower depolarizing patterns are characteristic of vascular SMCs. This electrical profile enables steady-state Ca^{2+} influx through voltage-gated Ca^{2+} channels to regulate tightly and incrementally vessel diameter. Similarly, the resting SMCs of airways and bladder lack electrical spiking that could trigger rhythmic bronchial constriction or solicit phasic bladder contraction, respectively. In contrast, gastrointestinal (GI) smooth muscle shows spontaneous electrical activity that drives rhythmic contractions and relaxations to enable digestion and peristalsis. The SMCs in the lengthy GI tract that is composed of both circular and longitudinal muscle are further distinguished by their highly site-specific excitability patterns that are tailored to local function. Thus, SMC excitability is highly heterogeneous and characterized by site-specific differences in the resting E_m levels and patterns of excitability in organs with very diverse functions (Fig. 44.1; Table 44.1) (Steedman, 1966; Lee et al., 1990; Lombard et al., 1990; Bercczi et al., 1992; Brayden and Nelson, 1992; Kamei et al., 1994; Gokina and Bevan, 2000; Bramich, 2000; Sanders et al., 2006; Morin et al., 2007; Forrest et al., 2009). Further diversity in patterns of SMC excitation is generated by the wide array of physiological factors (i.e. neurotransmitters, autacoids, circulating factors, stretch) that can quickly modify SMC excitability.

At least several key differences exist between SMCs and the muscle cells that compose skeletal and cardiac tissues. By definition, SMCs lack striations (aligned dark and light bands at the light microscopic level) and, instead, have a less strictly organized arrangement of contractile fibers that mediate graded tone. Another important difference is the very small size of SMCs compared to skeletal or cardiac muscle cells, which requires their dependence on multicellular interactions to coordinate smooth muscle contraction and relaxation even at the local level. Some SMCs exhibit electrical or chemical coupling, whereby a change in the level of E_m or in the concentration of intracellular signaling molecules in individual cells can be propagated to adjacent cells to produce coordinated contraction or relaxation. Finally, SMCs appear to have a mechanism for sustaining contractions for long periods of

[1] Additional information on the basics of excitability of smooth muscles is presented in Appendix I.

Cell Physiology Sourcebook. DOI: 10.1016/B978-0-12-387738-3.00044-5

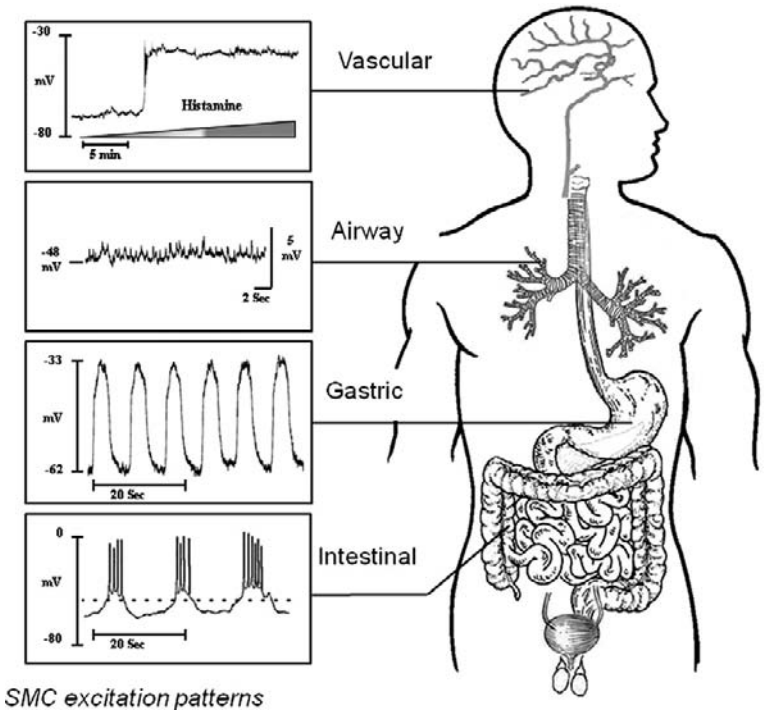

FIGURE 44.1 There are many organs which contain smooth muscle, including the vasculature, airways and gastrointestinal tract. The patterns of excitation are highly heterogeneous, to support the unique functions of each of the organs. *(Reproduced with permission from (A): Gokina et al., Am J Physiol. 2000; (B): Bramich, Am J Physiol. 2000; (C): Forrest et al., Am J Physiol. 2009; (D): Sanders et al., Annu Rev Physiol. 2006.)*

time with relatively low energy cost, a concept referred to as the "latch-state". Physiologically, this is manifested as the ability of SMCs to sustain cross-bridge attachments and contraction while intracellular Ca^{2+} concentration, cross-bridge phosphorylation and ATP consumption rates fall. The mechanisms that enable the "latch-state" are reviewed elsewhere (Hai and Murphy, 1990), but one key concept is that the graded excitation patterns in many types of SMCs combined with their unique ability to sustain contraction at low energy cost permits *smooth muscle tone*, a term that refers to graded, sustained levels of smooth muscle contraction.

II. DETERMINATION OF RESTING MEMBRANE POTENTIAL IN SMCs

The origin of the resting membrane potential (E_m) is detailed elsewhere in this book. However, a short discussion is warranted here, since some determinants of E_m are tissue-specific and unique to SMCs. First, SMCs do not densely express voltage-gated sodium (Na^+) channels in their plasma membrane, which are a hallmark feature of skeletal and cardiac muscle cells. In these striated muscle cells, Na^+ influx, enabled by the opening of voltage-gated Na^+ channels, mediates the rapid depolarization or "upstroke" of the action potential. However, action potentials (if present or induced) in SMCs are primarily mediated by Ca^{2+} influx through voltage-gated Ca^{2+} channels; the Na^+ channels are sparse or absent. Second, the resting E_m in SMCs is generally more positive (−60 mV to −40 mV) than the more negative E_m level (−90 mV to −60 mV) observed in skeletal and cardiac muscle cells. Importantly, the more positive resting E_m of the SMCs is near or even resides within the lower E_m range for opening of voltage-gated Ca^{2+} channels. Thus, even small depolarizations of the SMCs depolarization will result in the opening of voltage-gated Ca^{2+} channels, Ca^{2+} influx and SMC activation. Notably, smooth muscle can contract in either a phasic (short term/rhythmic) or a tonic (long term/sustained) pattern depending on the properties of the particular SMC and its input from external excitatory or inhibitory signals. When smooth muscle initiates phasic contraction, such as during peristalsis of the GI tract, the phasic contractions usually mirror and rely on phasic depolarizations that trigger the voltage-gated Ca^{2+} influx required for SMC activation. Other smooth muscle is characterized by tonic contraction, including the smooth muscle of sphincters, airways and the vasculature. In this case, the level of E_m also is relatively constant. For example, vascular smooth muscle responds to changing needs for oxygen by maintaining tonic states of contraction, which change as a function of arterial oxygen concentration (Fig. 44.2) (Welsh et al., 1998). Thus, the E_m of SMCs can be finely tuned to ensure that the intensity of contraction is placed precisely on the continuum between full relaxation and maximal contraction.

Notably, the control of E_m in all cells is accomplished by a complex system of ion channels, pumps and

TABLE 44.1 Representative Electrical Properties of Different Types of Smooth Muscle

	Smooth Muscle Type Species	Resting E_m (mV)	Slow Wave Amplitude (mV)	Slow Wave Frequency (waves/min)	Ref
Vascular					
Mesenteric artery	Rat	−39	n/a	n/a	Steedman, 1966
Cerebral artery	Rabbit	−37	n/a	n/a	Brayden & Nelson, 1992
Renal artery	Dog	−38	n/a	n/a	Lombard et al., 1990
Saphenous artery	Rat	−39	n/a	n/a	Berczi et al., 1992
Mesenteric artery	Guinea pig	−39	n/a	n/a	Steedman, 1966
Airway					
Trachea	Dog	−60	n/a	n/a	Kamei et al., 1994
Bronchus	Dog	−70	n/a	n/a	Kamei et al., 1994
Bronchus	Human	−52	n/a	n/a	Morin et al., 2007
Trachea	Ferret	−60	n/a	n/a	Lee et al., 1990
Bronchus	Ferret	−70	n/a	n/a	Lee et al., 1990
Gastrointestinal					
Gastric antrum	Mouse	−62	30	8	Forrest et al., 20093
Small intestine	Human	−55	15	8	Sanders et al., 2006
Colon	Human	−55	20	4	Sanders et al., 2006
Small intestine	Canine	−55	25	8	Sanders et al., 2006
Colon	Canine	−75	55	4	Sanders et al., 2006

These values illustrate the adaptation of smooth muscle to the specific needs of each organ. Gastrointestinal smooth muscle exhibits rhythmic and regular depolarizations known as slow waves, which mediate peristalsis. Depolarization in airway and vascular smooth muscle is variable in magnitude and duration. The more depolarized resting E_m in vascular smooth muscle closely couples small reductions in E_m to increases in Ca^{2+} influx.

exchangers, which regulate the movement of ions across the lipid bilayer of the plasma membrane. Active transport systems (ATP-driven ion pumps and exchangers) maintain non-equilibrium concentration gradients across the plasma membrane. There are multiple active transport systems in a single SMC, but the activity of ATP-driven ion pumps still contributes less to resting E_m in SMCs than ion channel flux. The most prominent ATP-driven pump in SMCs is the Na^+,K^+-ATPase enzyme, an electrogenic pump in the plasma membrane that generates a hyperpolarizing current to maintain resting E_m. Traditionally, it is thought that three Na^+ ions are pumped out of the cell in exchange for two K^+ ions that enter during a single pump cycle, which would result in a net intracellular charge of −1. The contribution of Na^+, K^+-ATPase to resting E_m varies between different types of SMCs, but its hyperpolarizing influence may contribute between 5 and 20% of the negative E_m level. Additionally, because the Na^+,K^+-ATPase molecules pump K^+ ions into the cell, they establish a high concentration of intracellular K^+ (135−145 mmol/L), whereas the extracellular K^+ concentration is relatively low (3.5−5 mmol/L). This steep transmembrane K^+ gradient, combined with a dense expression of K^+ channels on the SMC surface, results in basal K^+ efflux and this hyperpolarizing K^+ current is the main determinant of the negative resting E_m in SMCs. Thus, pharmacological block of K^+ channels in SMCs causes a profound depolarization and contraction. In contrast, resting ionic flux through other channels has less influence on resting E_m, but may critically contribute to SMC contraction. For example, voltage-gated, L-type Ca^{2+} channels and cation-permeable *t*ransient *r*eceptor *p*otential (TRP) channels provide activator Ca^{2+} for SMC contraction. Although chloride (Cl^-) channels are expressed in SMCs, their contribution to resting E_m is less clear and the reader is referred to Verkman and Galieta (2009) for

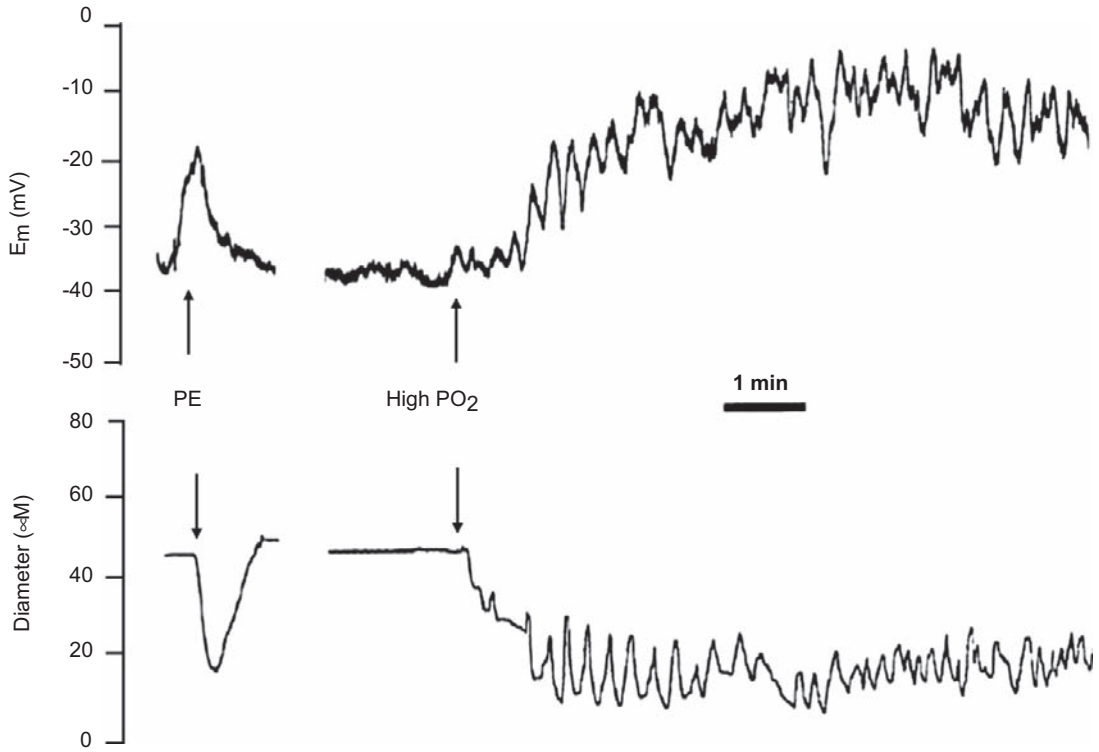

FIGURE 44.2 The vasoconstrictor response of a hamster cheek pouch arteriole to high PO_2 acts as a compensatory mechanism to normalize oxygen delivery to the distal tissues. Membrane potential (E_m) was recorded using an intracellular microelectrode in a vascular SMC (top trace) while recording the corresponding diameter response (lower trace). The arteriole was sequentially exposed to the α-adrenergic receptor agonist, phenylephrine (PE), and then after washout of PE, exposed to high ambient PO_2. High PO_2 elicited a sustained depolarization (top panel) with superimposed oscillations in E_m that was associated with a tonic, vacillating vasoconstriction (lower panel). *(Reproduced with permission from Welsh et al., Am J Physiol. 1998.)*

a review of this topic. For the sake of brevity, this chapter will only focus on the key K^+ and Ca^{2+} -permeable ion channels in SMCs using vascular SMCs as a model (Fig. 44.3). Two final sections will discuss key aspects of excitability in GI and airway smooth muscle.

III. POTASSIUM CHANNELS

The plasma membrane of SMCs expresses diverse populations of K^+ channels and the opening of K^+ channels promotes hyperpolarization and relaxation of SMCs. Distinct types of K^+ channels work in concert to optimize

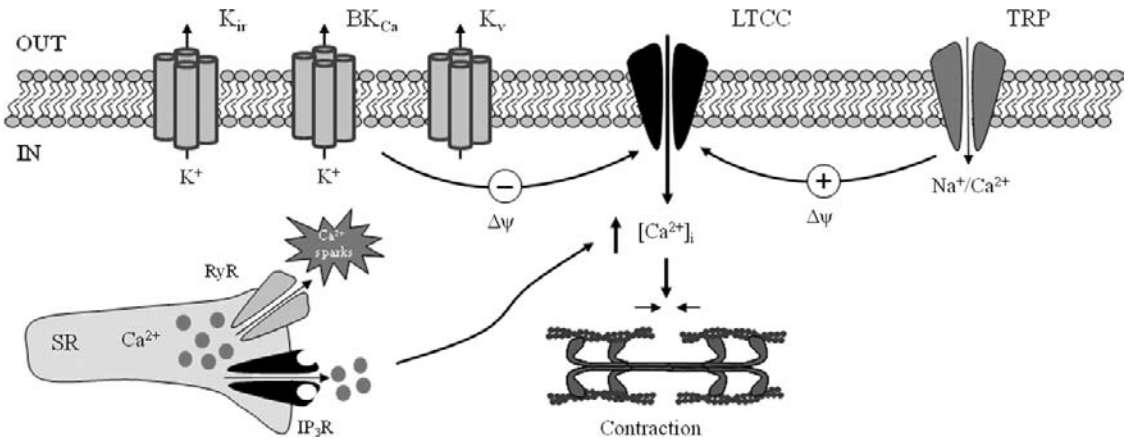

FIGURE 44.3 Some key families of ion channels in vascular SMCs. The K^+ channels include the inwardly rectifying (K_{ir}), voltage-gated (K_v) and high-conductance, Ca^{2+}-sensitive (BK_{Ca}) K^+ channels. The interplay between transient receptor potential (TRP) channels and L-type Ca^{2+} channels (LTCC) provides activator Ca^{2+} for SMC contraction. All of these channels interact with the ryanodine receptors (RyR) and inositol triphosphate receptors (IP_3R) to modulate SMC excitability.

SMC tone in different organs. This section will review three important K^+ channel families: (1) the voltage-gated K^+ (K_V) channels; (2) high-conductance Ca^{2+}-sensitive K^+ (BK_{Ca}) channels; and (3) inwardly rectifying K^+ (K_{ir}) channels. Information on other K^+ channels including the ATP-sensitive K^+ channels and the two pore domain K^+ channels is available elsewhere (Coetzee et al., 1999; Brayden, 2002; Gurney and Manoury, 2009).

IIIA. Voltage-Gated K^+ Channels

The voltage-gated K^+ (K_V) channels are a highly diverse superfamily of K^+ channels that share the common properties of potassium selectivity and voltage-dependent activation. The α subunits are composed of six hydrophobic transmembrane segments (S1−S6) flanked by hydrophilic amino- and carboxyl termini located in the cell interior (Fig. 44.4A) (Epperson et al., 1999). An intrinsic voltage sensor conferred by positively charged amino acids in transmembrane domain S4 is associated with channel gating, while the pore loop (P) confers K^+ selectivity. Four α subunits compose the pore-forming structure of the K_V channel and assemble in the endoplasmic reticulum with four regulatory β subunits that modulate channel expression and function. The K_V channels contribute to the resting E_m of some SMCs. For example, pharmacological block of "*Shaker*-type" K_V channels by correolide (COR) in vascular SMCs of isolated, perfused cerebral arteries (depicted in Fig. 44.4G) causes depolarization and constriction (Fig. 44.4D). Additionally, excitatory stimuli that depolarize and contract SMCs also simultaneously open the voltage-dependent K_V channels. The resulting hyperpolarizing K^+ current limits Ca^{2+} influx through voltage-dependent Ca^{2+} channels (VDCC) to buffer contraction. Thus, the K_V channels have an important role in counteracting SMC excitation (Chen et al., 2006; Albarwani et al., 2003).

IIIB. Large-Conductance, Ca^{2+}-Sensitive K^+ Channels

The large-conductance, Ca^{2+}-sensitive K^+ channels, referred to as "BK_{Ca}" or "maxi-K" channels because of their large single-channel currents, are densely expressed in many SMCs. The α subunit shows partial homology with the K_V channel in six (S1−S6) of its seven (S0−S6) transmembrane domains that include the S4 voltage sensor (see Fig. 44.4B) (Ledoux et al., 2006; Wu and Mark, 2010).

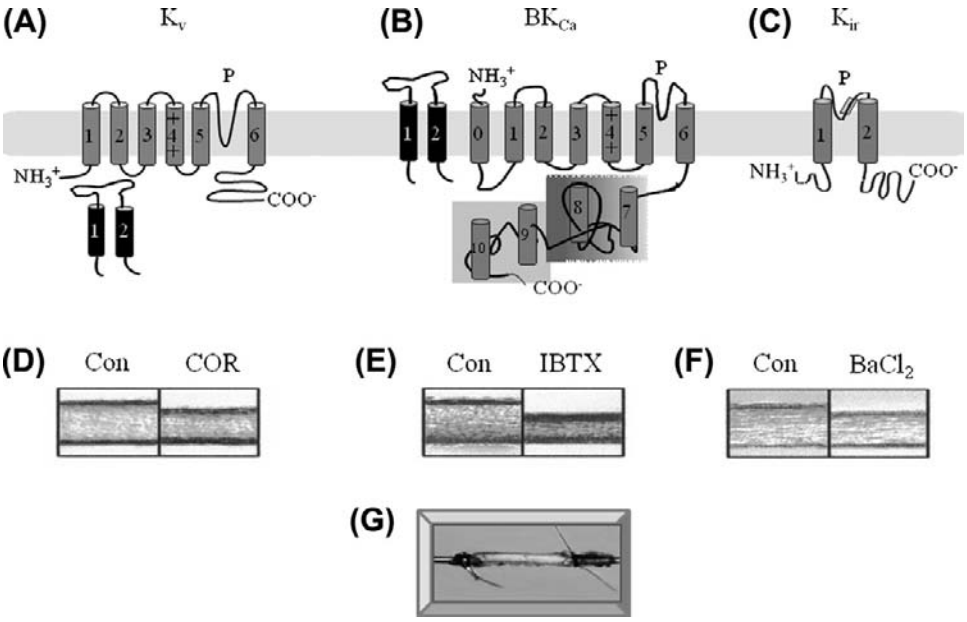

FIGURE 44.4 Proposed topology of K^+ channel α subunits in SMCs and their vasodilator role in cerebral arteries. Details are provided in the text. (A, B) The multiprotein K_V and BK_{Ca} channels are presumed to be composed of pore-forming α subunits and regulatory β subunits. The β subunit is assumed to be intracellular in K_V channels and membrane-delineated in BK_{Ca} channels. (C) The α subunit of the K_{ir} channel is composed of only two transmembrane domains spanning a pore loop. All three K^+ channel types are composed of four α subunits that co-assemble to form a functional tetramer. An additional four β subunits compose the K_V and BK_{Ca} channels. (D, E, F) All three types of K^+ channels contribute to the resting diameter of a rat middle cerebral artery. The artery was cannulated and perfused at an intraluminal pressure of 80 mmHg. In each case, the left panels show the control resting diameter. The right panels show the decrease in vessel diameter after addition of: 10 μmol/L correolide (COR) to block *Shaker*-like K_V channels (D), 100 nmol/L iberiotoxin (IBTX) to block BK_{Ca} channels (E) and 10 μmol/L $BaCl_2$ to block K_{ir} channels (F). Drugs were washed out and the artery returned to resting diameter between drug responses (not shown). (G) A photograph depicting a rat cerebral artery cannulated on glass micropipettes and perfused at 80 mmHg.

Although BK_{Ca} channels are only weakly opened by depolarization in the absence of intracellular calcium ($[Ca]_i$), the voltage-sensitivity of the BK_{Ca} channel increases markedly when $[Ca]_i$ rises. The "Ca^{2+}-sensitivity" of the α subunit is conferred by cytosolic domains S7−S10 and by its β subunit that interacts with the N-terminal S0 domain. Despite their low level of opening at the resting E_m of SMCs, the densely expressed BK_{Ca} channels can mediate a significant hyperpolarizing current. For example, iberiotoxin (IBTX) -induced block of BK_{Ca} channels in cerebral arterial SMCs results in a sustained depolarization (Fig. 44.5A) and elevation of $[Ca]_i$ mediated by Ca^{2+} influx through L-type Ca^{2+} channels (Fig. 44.5B) (Knot et al., 1998). The functional outcome is vasoconstriction (see Fig. 44.4E). Thus, during SMC excitation, the K_V channels and BK_{Ca} channels work in concert as a negative feedback mechanism to buffer excess depolarization and SMC contraction. Not surprisingly, a loss of these K^+ channels has been linked to diseases characterized by abnormal SMC tone.

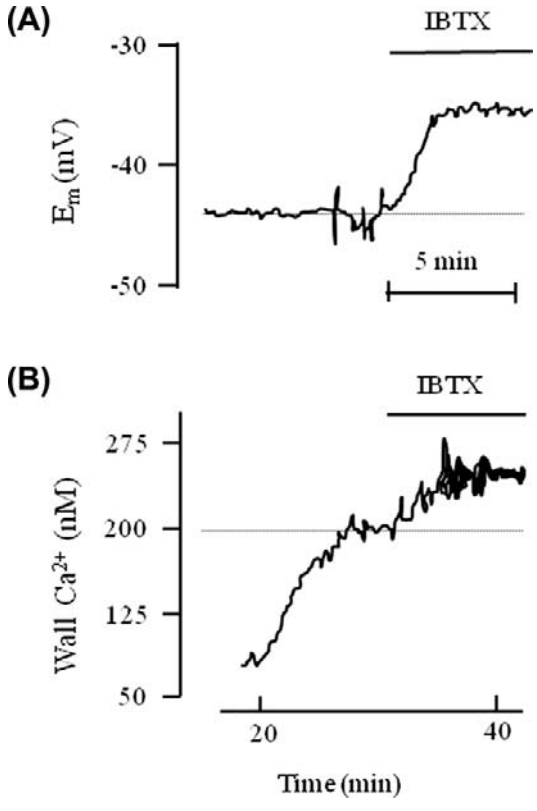

FIGURE 44.5 Measurement of membrane potential (E_m) and arterial wall calcium ($[Ca^{2+}]$) in a rat cerebral artery loaded with the Ca^{2+} indicator, fura-2. Block of BK_{Ca} channels by iberiotoxin (IBTX) resulted in depolarization of the arterial SMCs (A) and a rise in arterial wall $[Ca^{2+}]$ (B). The level of E_m and arterial wall $[Ca^{2+}]$ in the absence of drugs is indicated by the horizontal dotted line. *(Reproduced with permission from Knot et al., J Physiol. 1998.)*

IIIC. Inwardly Rectifying K^+ Channels

Inwardly rectifying K^+ (K_{ir}) channels exhibit the property of "inward rectification", indicating that they readily conduct K^+ into cells at E_m below the K^+ equilibrium potential but show only a limited ability to mediate K^+ efflux at more positive membrane potentials. The property of inward rectification is at least partially conferred by voltage-dependent block of the channel pore by Mg^{2+} and polyamines at the cytoplasmic side (Quayle et al., 1997; Hibino et al., 2010). Similar to the K_v and BK_{Ca} channels, the K_{ir} channels are tetrameric structures composed of four α subunits but no corresponding β subunit has been identified (see Fig. 44.4C). Since the K_{ir} channels are not voltage-dependent they are thought to open readily at negative voltages and contribute to the resting E_m of many cell types including SMCs. Thus, block of K_{ir} channels by barium chloride ($BaCl_2$) results in a loss of hyperpolarizing K^+ current, depolarization and Ca^{2+}-dependent vasoconstriction (see Fig. 44.4F). In contrast, the K_{ir} channels that conduct K^+ poorly at more depolarized potentials may be silenced by vascular activation.

IV. VOLTAGE-DEPENDENT CALCIUM CHANNELS

Calcium influx through voltage-dependent Ca^{2+} channels (VDCCs) is required for normal excitation−contraction coupling in SMCs and at least two gene families of voltage-gated Ca^{2+} channels are expressed. Transient ("T-type") Ca^{2+} channels activate at very negative E_m and then rapidly inactivate to provide a short "burst" of Ca^{2+} influx. The T-type Ca^{2+} channels have been identified in a small subset of SMCs as reviewed by Cribbs (2006). However, T-type Ca^{2+} channels cannot be the prominent Ca^{2+} channel type in most types of SMCs, including those composing blood vessels, airway and bladder, since these tissues require sustained Ca^{2+} influx to maintain tonic contraction and avoid sudden fluctuations of $[Ca^{2+}]_i$ in the SMCs.

In contrast, the long-lasting ("L-type") Ca^{2+} channels open in response to membrane depolarization within the range of resting E_m found in SMCs. The L-type Ca^{2+} channels are thought critically to supply the activator Ca^{2+} that drives contraction in most types of smooth muscle. These channels are multisubunit complexes composed of a large α_{1C} subunit that forms the channel pore and confers most functional properties to the channel including voltage sensing and Ca^{2+} permeability (Dophin, 2009). Smaller regulatory subunits (β, $\alpha_2\delta$) may finely tune Ca^{2+} channel function and promote its expression at the cell surface (Fig. 44.6A).

Voltage-dependent Ca^{2+} channels are the critical link between membrane potential and contraction (electromechanical coupling) in SMCs (Nelson et al., 1990). More

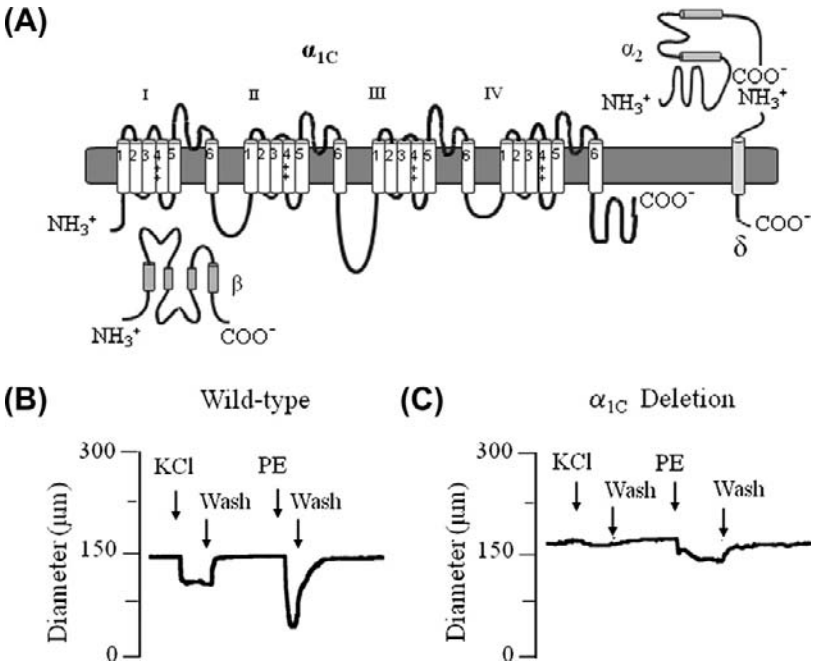

FIGURE 44.6 The α_{1C} subunit (A) is critical for mediating the response to many vasoconstrictor stimuli. Diameter tracings show the different responses of tibialis arteries from wild-type mice (B) and mice lacking the α_{1C} subunit (C). *(Reproduced with permission from Moosmang et al., EMBO J. 2003.)*

positive E_m levels cause more frequent Ca^{2+} channel openings, more Ca^{2+} influx and greater Ca^{2+}-dependent activation of the contractile proteins. Furthermore, since the L-type Ca^{2+} channels inactivate slowly during sustained depolarization, the Ca^{2+} influx permitted by a small fraction of these channels may be sufficient to mediate tonic contraction. For example, direct depolarization of vascular SMCs by high concentrations of potassium chloride (KCl) or activation of excitatory α-adrenergic receptors by phenylephrine (PE) contract small tibialis arteries of normal, wild-type mice (see Fig. 44.6B) (Moosmang et al., 2003). However, similar arteries of genetically modified mice, in which the pore-forming α_{1C} subunit of the L-type Ca^{2+} channel is deleted, only weakly contract to the same stimuli (see Fig. 44.6C). Thus, the L-type Ca^{2+} channel permits many tissues composed of SMCs to perform properly their contractile functions that may involve regulating blood flow (vascular SMCs) or air flow (airway SMCs) or enabling peristalsis and digestion (intestinal SMCs). The SMC tone also provides an excitatory template upon which endogenous substances may act to further modify organ function.

V. TRANSIENT RECEPTOR POTENTIAL (TRP) CHANNELS

Nearly 28 mammalian transient receptor potential (TRP) channels have been identified to date and at least 11 of them are expressed in SMCs (Guibert et al., 2011). Unlike L-type Ca^{2+} channels, TRP channels are non-voltage gated and they are permeable to more than one ion species. The TRP channels conduct cations including Na^+ and Ca^{2+} ions; the preference for a single ion species depends on the channel subtype. The TRP channels are classified into six related protein families on the basis of amino acid sequence homology (Montell, 2005). The "*c*lassical" or "*c*anonical" TRP channels have drawn the most attention in SMCs. Notably, whereas the α subunit of the L-type Ca^{2+} channel is composed of a single large polypeptide, TRP channels are formed by the assembly of four smaller polypeptide subunits as homo- or heterotetramers giving rise to variable channel properties. Each α subunit has six transmembrane spanning domains (S1−6), a pore-forming loop between S5 and S6 and intracellularly located NH_2 and COOH termini (Fig. 44.7A). The S4 segment lacks the positively charged residues necessary for voltage sensing (Gaudet, 2008). Based on their mechanism of activation, TRP channels can be grouped as receptor-operated, store-operated or stretch-activated channels. As examples, store- and receptor-operated TRP channels are activated by muscarinic (M2 and M3) receptor stimulation in visceral SMCs and by α_1-adrenergic receptors in vascular SMCs (Dietrich et al., 2006). Other excitatory native stimuli also can open TRP channels through G-protein coupled receptors in the plasma membrane. A number of signaling molecules generated by receptor occupation can regulate the activity of TRP channels in SMCs (Beech et al., 2004; Albert and Large, 2006).

The functional significance of specific TRP channel subtypes is largely unexplored. Knockout mice with specific TRP channel deletions have been generated

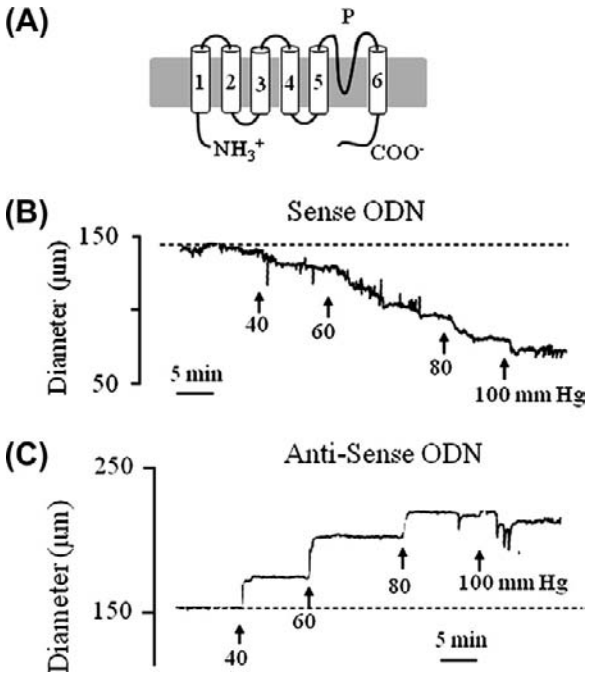

FIGURE 44.7 Structure and function of TRP channels. (A) The α subunit contains six transmembrane spanning domains (S1−S6) with the pore (P) formed between S5 and S6. The S4 domain lacks the positive residues that confer voltage sensitivity. (B) In control vessels treated with sense oligonucleotides (ODNs), step elevations of intraluminal pressure in isolated rat cerebral arteries result in pressure-induced constriction. (C) Arteries treated with TRPC6 antisense ODNs fail to show pressure-induced constriction. The horizontal dotted line represents the arterial diameter before intraluminal pressure was increased. *(Reproduced with permission from Welsh et al., Circ Res. 2002.)*

recently. However, the impact of TRP gene deletion on SMC function often is not straightforward, possibly due to the redundancy generated by this large channel superfamily. This potential dilemma has led to the design of double or triple TRP knockout mice including TRPC4/6 gene-deficient animals. In the intestinal SMCs of these animals, the dual deletion of TRPC4 and TRPC6 impairs muscarinic receptor-induced cationic current and contraction, suggesting the potential importance of the TRP channels in SMC excitability (Tsvilovskyy et al., 2009). Notably, different TRP channel subtypes show highly variable Ca^{2+} permeability and it is unclear if Ca^{2+} influx through TRP channels directly contributes to SMC contraction. However, the combined Na^+ and Ca^{2+} influx corresponding to the inward cationic current through TRP channels is thought to depolarize SMCs leading to the opening of L-type Ca^{2+} channels, Ca^{2+} influx and contractile protein activation. Thus, it appears that one important function of TRP channels is to serve as a triggering mechanism for the activation of L-type Ca^{2+} channels (Gudermann et al., 2004; Dietrich et al., 2006).

Stretch is another important stimulus that regulates visceral and vascular SMC tone. Historically, the existence of stretch-activated cationic channels was recognized. These channels were observed to respond to mechanical stimuli including osmotic stress, membrane stretch and shear force. Now, several TRP channel families are considered to contain member subtypes that are mechanosensitive, but their role in regulating the contractile responses to mechanical stimuli is controversial and not well defined to date (Dietrich and Gudermann, 2011). For example, isolated, perfused rat cerebral arteries respond to step elevations of intraluminal pressure (40, 60, 80 and 100 mmHg) by vasoconstriction (see Fig. 44.7B) (Welsh et al., 2002). However, knockdown of TRPC6 channels using antisense oligonucleotides eliminates the pressure-induced constrictor response in the cerebral arteries, which instead show passive dilation as intraluminal pressure is elevated (see Fig. 44.7C) (Welsh et al., 2002). In contrast to these results, however, another study failed to confirm the mechanosensitivity of TRPC6 channels in arteries of TRPC6 knockout mice (Dietrich et al., 2005). The stimuli that activate TRP channels and the role of specific TRPC subtypes in regulating SMC excitability is an exciting area of discovery that is being intensely investigated.

VI. EXCITATION OF GASTROINTESTINAL SMCs

The excitation patterns of SMCs in the gastrointestinal (GI) tract are designed to provide the contractions required for mixing the ingested food with the digestive enzymes and propulsion of the resulting gastric contents. These two functions are accomplished by highly coordinated movements of circular and longitudinal smooth muscles, which are aligned perpendicular to each other in the wall of the GI tract. Additionally, different organs within the GI tract are required to perform different functions. For example, the stomach and small intestine enable digestion and absorption, whereas the large intestine enables the drying and compaction of waste. Clearly, a complex scheme of excitation is needed to integrate the different functions of the GI tract and electrical mechanisms provide an important source of modulation to regulate organ function. For example, the resting E_m in SMCs varies between −85 mV and −40 mV along the GI tract. The SMCs in the small intestine are more depolarized (≈−55 mV) than those in stomach or colon (≈−75 mV) (Sanders et al., 2006). This electrical heterogeneity is partially achieved by expression of a diverse population of ion channels. The main classes of ion channels expressed in GI smooth muscle mirror those in vascular SMCs and include similar K^+ channel families that set the resting E_m and buffer contraction and the voltage-gated Ca^{2+} channels and cationic TRPC channels that mediate SMC contraction. The tight regulation of resting E_m is vital

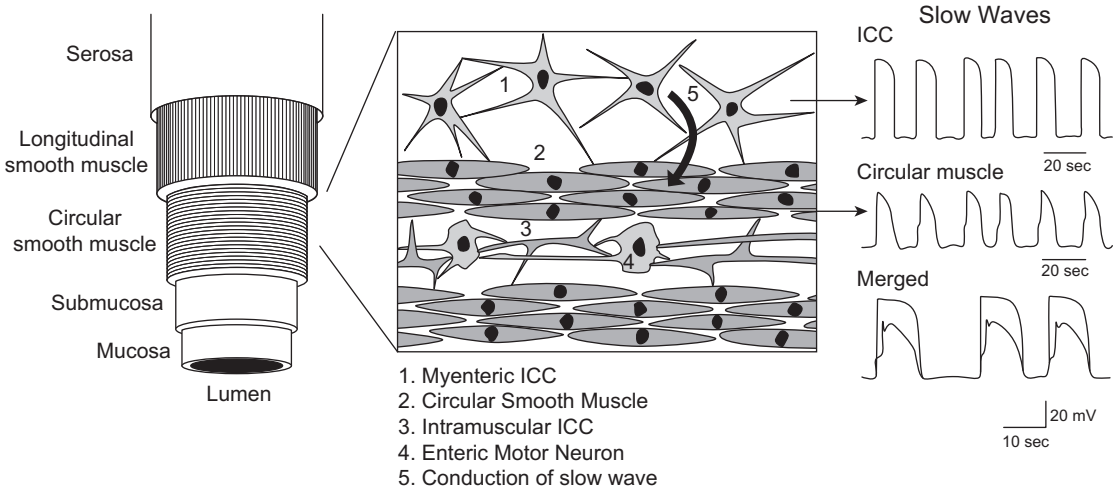

FIGURE 44.8 A cutaway view showing the different layers of the intestinal tract (left). A magnified view of the smooth muscle layers and surrounding layers of ICC (center). Membrane potential recordings of ICC and circular smooth muscle showing the propagation of slow waves from the myenteric ICC to the circular smooth muscle (right). *(Reproduced with permission from Hirst et al., J Physiol. 2001 and Horowitz et al., Annu Rev Physiol. 1999.)*

because it determines if the SMCs can respond to depolarizing stimuli from the interstitial cells of Cajal (explained later) and receptor agonists (Sanders, 2008).

Calcium influx through voltage-gated L-type Ca^{2+} channels is indispensable for GI motility. Slow waves depolarize the SMC membrane to open L-type Ca^{2+} channels and, thus, pharmacological block of L-type Ca^{2+} channels attenuates contraction in GI SMCs (Lyford and Ferrugia, 2003). Additionally, members of the TRPC family are gaining attention for their role in SMC excitability. As mentioned in the previous section, intestinal SMCs of TRPC4/6 knockout mice show defective muscarinic receptor-mediated cationic current and depolarization (Tsvilovskyy et al., 2009).

Although the SMCs ultimately execute force development, a type of interstitial cell in the GI tract called the interstitial cells of Cajal (ICC) plays a vital role in coordinating SMC contraction. The ICC are classified based on morphology: stellate-shaped ICC are found mainly between the muscle layers of the stomach; spindle-shaped ICC largely reside between the smooth muscle fibers of the intestine (Fig. 44.8) (Horowitz et al., 1999; Hirst and Edwards, 2001). They are electrically coupled to each other, the enteric nervous system (ENS) and the SMCs of the GI tract through gap junctions. Networks of ICC generate pacemaker activity and propagate "slow waves" across and down the GI tract. GI motility relies on these rhythmic depolarizations that spread through the GI SMCs at a low frequency (<5/min) and activate voltage-dependent Ca^{2+} channels to cause Ca^{2+}-dependent electrical spiking (Fig. 44.8) and SMC contraction (Sanders, 2008). A key feature of the slow waves is that they propagate faster circumferentially (depolarizing circular SMCs) but slow as they pass down the GI tract (depolarizing longitudinal SMCs) to allow enough time for digestion.

Although the SMCs of the vasculature and GI tract share many ion channels, there are some mechanistic differences in their electrical profiles. Vascular SMCs generally show a stable resting E_m and a tonic level of contraction under resting conditions, whereas the SMCs of the GI tract exhibit tonic and phasic patterns of contractions that reflect stable or fluctuating E_m levels, respectively. The spontaneous excitability of the SMCs in the GI tract emanates from the unique influence of the ICC, which also receive signals from the enteric nervous system (ENS) and paracrine substances. Similarly, the vascular SMCs also are subjected to unique stimuli not found in the GI tract. For example, the intraluminal pressure inside blood vessels can be a powerful force for depolarization and contraction of arterial SMCs (see Fig. 44.7) and this stimulus for cell excitation is unique to the vascular system. In addition to voltage-dependent Ca^{2+} influx mediated by L-type Ca^{2+} channels, the influx of cations through TRP channels may contribute to pressure-induced constriction. Other factors that influence vascular SMC excitability not discussed in this short chapter include neurotransmitters, circulating factors and the release of vasoactive substances from the endothelial cells that line the blood vessel lumen.

VII. AIRWAY SMOOTH MUSCLE

The airway SMCs express a diverse assortment of K^+ channels, voltage-dependent Ca^{2+} channels and TRP channels similar to vascular and GI SMCs. The resting E_m of airway SMCs ranges between −70 mV and −30 mV

(Hirota et al., 2007). It varies slightly between the tracheal and bronchial SMCs with the former value more negative by 10 mV than the latter (Honda and Tomita, 1987; Oonuma et al., 2000). Human airways possess inherent tone which is largely the result of contractile 5-lipoxygenase products (Watson et al., 1997). Although the source of contractile leukotrienes is unclear, airway SMCs or bronchial epithelium and inflammatory cells associated with the SMCs are potential candidates. These electrical characteristics of airway smooth muscle support the function of the respiratory system. The more positive resting E_m in the bronchial compared to tracheal SMCs may reflect the fact that the bronchi play a far more important role in determining resistance to airflow, and the more positive resting E_m may lend susceptibility to excitatory stimuli. Notably, the bronchi also are the locus of inflammation and other functional/structural changes associated with asthma and other conditions of airway hyperexcitability.

The similarities of ion channels and excitation mechanisms between airway smooth muscle and other types of SMCs will not be reiterated here; instead differences will be emphasized. First, the SMCs of airways are uniquely exposed to a broad spectrum of environmental factors that can regulate airway diameter and they also are exposed to autacoids released by mast cell activation. The excitatory ligands may bind to surface receptors on airway SMCs to initiate Ca^{2+} influx through Ca^{2+}-permeable ion channels and/or release Ca^{2+} from the sarcoplasmic reticulum (SR) to elevate $[Ca]_i$. In contrast to the central importance of voltage-dependent Ca^{2+} influx in activation of vascular SMCs, the main trigger for bronchoconstriction may be the release of Ca^{2+} sequestered within the SR. Thus, the two major Ca^{2+} release channels in the SR, the inositol-1, 4, 5-trisphosphate receptor (IP_3R) and the ryanodine receptor (RyR), appear to be prominent features of airway SMCs. The properties of the IP_3R and RyR channels are reviewed elsewhere (Bai and Sanderson, 2006; Tazzeo et al., 2008). Second, agonist activation of SMCs in airways often evokes recurring $[Ca^{2+}]_i$ transients that distinguish airway SMCs from other cell types. This pattern of excitation is characterized by intracellular Ca^{2+} oscillations, whose frequency is inversely dependent on agonist concentration. For example, activation of excitatory cholinergic receptors by methacholine (MCh) on a bronchial SMC triggers Ca^{2+} oscillations in the cell cytosol (Fig. 44.9A) (Bai and Sanderson, 2006). These Ca^{2+} oscillations are associated with SMC contraction (Fig. 44.9B) and a reduction of airway area (Fig. 44.9C). The subsequent addition of isoproterenol (ISO), a β-adrenergic receptor agonist with bronchodilator properties, transiently increases the frequency of Ca^{2+} oscillations, an event that is coupled to a temporary loss of contractile force and increased airway area.

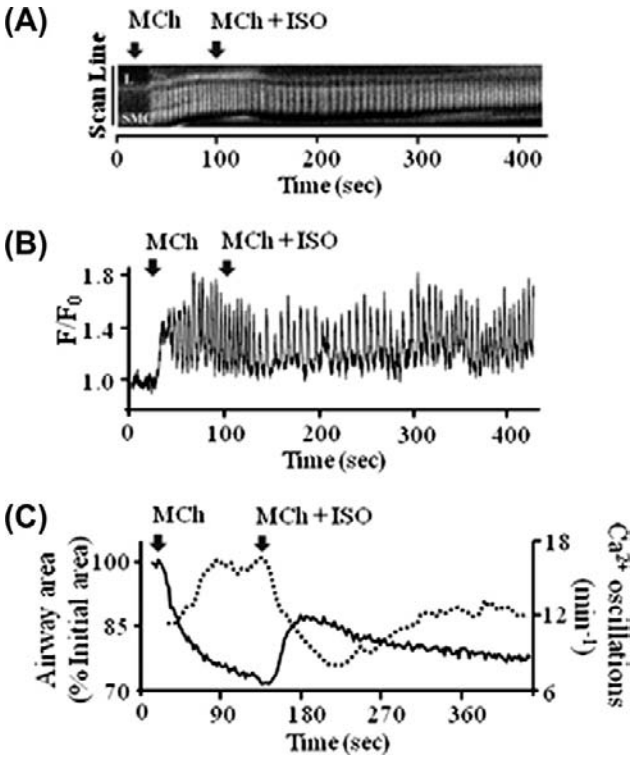

FIGURE 44.9 The effect of methacholine (MCh) and isoproterenol (ISO) on Ca^{2+} signaling of airway SMCs. (A) Line-scan plot constructed from a fluorescent image of an airway SMC loaded with Oregon Green 488 BAPTA-1 AM. Images were obtained by a two-photon microscope and the sequence of recorded images of Ca^{2+} fluorescence in response to MCh (200 nM) and ISO (1 μM) are depicted. (B) Corresponding changes in force generated by the same concentrations of MCh and ISO. (C) The correlation of the Ca^{2+} oscillation frequency (dotted line) and airway area (solid line) in a single cell during contraction induced by MCh (200 nM) and relaxation induced by ISO (10 μM). The frequency of the Ca^{2+} oscillations was inversely coupled to the contraction of the airway. *(Reproduced with permission from Bai et al., Resp Res., 2006.)*

VIII. CONCLUDING REMARKS

This chapter has provided a succinct overview of the basis for SMC excitability with an emphasis on vascular, gastrointestinal and airway smooth muscle. It has outlined the structure and function of key ion channels, including three types of K^+ channels that contribute to the resting E_m of SMCs and counteract cell excitability by mediating a hyperpolarizing K^+ current. Additional sections have reviewed the structure and function of the L-type Ca^{2+} channels and TRP channels, which mediate the influx of Ca^{2+} for excitation–contraction coupling. The cationic TRP channels lack voltage-dependent opening and are activated by receptor-mediated signaling molecules and physical stimuli that include stretch. The ensuing influx of depolarizing cations through the TRP channels is proposed to open the voltage-gated L-type Ca^{2+} channels resulting

in Ca^{2+} influx. Other depolarizing stimuli also open the L-type Ca^{2+} channels that often are vital to SMC contraction. These and other gene families of ion channels and exchangers constitute a large and highly diverse population of proteins that act in concert to regulate the levels of contraction and relaxation in the SMCs of the vasculature, GI tract, airways and other SMC-containing physiological systems. Scrutiny of different types of SMCs has revealed organ and site-specific patterns of cell excitability that are finely tuned to provide unique and localized electrical responses that collectively enable the entire organism to flourish.

ACKNOWLEDGMENTS

The authors were supported by a stipend award from National Center for Research Resources grant UL1RR029884 (N.D.D.), an American Heart Association −South Central Affiliate predoctoral fellowship grant 09PRE2250224 (S.V.K.) and grants R01 HL64806-10 and R01 HL0932526-02 from the National Heart, Lung and Blood Institute of the NIH (N.J.R.).

BIBLIOGRAPHY

Albarwani, S., Nemetz, L. T., Madden, J. A., et al. (2003). Voltage-gated K^+ channels in small rat cerebral arteries: molecular identity of the functional channels. *J Physiol, 551*, 751−763.

Albert, A. P., & Large, W. A. (2006). Signal transduction pathways and gating mechanisms of native TRP-like cation channels in vascular myocytes. *J Physiol, 570*, 45−51.

Bai, Y., & Sanderson, M. J. (2006). Airway smooth muscle relaxation results from a reduction in the frequency of Ca^{2+} oscillations induced by a cAMP-mediated inhibition of the IP_3 receptor. *Resp Res, 7*, 34−53.

Beech, D. J., Muraki, K., & Flemming, R. (2004). Non-selective cationic channels of smooth muscle and the mammalian homologues of Drosophila TRP. *J Physiol, 1559*, 685−706.

Berczi, V., Stekiel, W. J., Contney, S. J., & Rusch, N. J. (1992). Pressure-induced activation of membrane K+ current in rat saphenous artery. *Hypertension, 19*, 725−729.

Bramich, N. J. (2000). Electrical behavior of guinea pig tracheal smooth muscle. *Am J Physiol, 278*, L320−L328.

Brayden, J. E. (2002). Functional roles of K_{ATP} channels in vascular smooth muscle. *Clin Exp Pharmacol Physiol, 29*, 312−316.

Brayden, J. E., & Nelson, M. T. (1992). Regulation of arterial tone by activation of calcium-dependent potassium channels. *Science, 256*, 532−535.

Chen, T. T., Luykenaar, K. D., Walsh, E. J., Walsh, M. P., & Cole, W. C. (2006). Key role of Kv1 channels in vasoregulation. *Circ Res, 99*, 53−60.

Coetzee, W. A., Amarillo, Y., Chiu, J., et al. (1999). Molecular diversity of K^+ channels. *Ann NY Acad Sci, 868*, 233−285.

Cribbs, L. L. (2006). T-type Ca^{2+} channels in vascular smooth muscle: multiple functions. *Cell Calcium, 40*, 221−230.

Dietrich, A., & Gudermann, T. (2011). TRP channels in the cardiopulmonary vasculature. *Adv Exp Med Biol, 704*, 781−810.

Dietrich, A., Chubanov, V., Kalwa, H., Rost, B. R., & Gudermann, T. (2006). Cation channels of the transient receptor potential superfamily: their role in physiological and pathophysiological processes of smooth muscle cells. *Pharmacol Ther, 112*, 744−760.

Dietrich, A., Mederos y Schnitzler, M., Gollasch, M., et al. (2005). Increased vascular smooth muscle contractility in $TRPC6^{-/-}$ mice. *Mol Cell Biol, 25*, 6980−6989.

Dophin, A. C. (2009). Calcium channel diversity: multiple roles of calcium channel subunits. *Curr Opin Neurobiol, 19*, 237−244.

Epperson, A., Bonner, H. P., Ward, S. M., et al. (1999). Molecular diversity of Kv α- and β-subunit expression in canine gastrointestinal smooth muscles. *Am J Physiol, 277*, G127−G136.

Forrest, A. S., Hennig, G. W., Jokela-Willis, S., Park, C. D., & Sanders, K. M. (2009). Prostaglandin regulation of gastric slow waves and peristalsis. *Am J Physiol, 296*, G1180−G1190.

Gaudet, R. (2008). TRP channels entering the structural era. *J Physiol, 586*, 3565−3575.

Gokina, N. I., & Bevan, J. A. (2000). Histamine-induced depolarization: ionic mechanisms and role in sustained contraction of rabbit cerebral arteries. *Am J Physiol, 278*, H2094−H2104.

Gudermann, T., Mederos y Schnitzler, M., & Dietrich, A. (2004). Receptor-operated cation entry−more than esoteric terminology? *Sci Signal, 243*, pe35.

Guibert, C., Ducret, T., & Savineau, J. P. (2011). Expression and physiological roles of TRP channels in smooth muscle cells. *Adv Exp Med Biol, 704*, 687−706.

Gurney, A., & Manoury, B. (2009). Two-pore potassium channels in the cardiovascular system. *Eur Biophys J, 38*, 305−318.

Hai, C. M., & Murphy, R. A. (1990). Crossbridge phosphorylation and regulation of vascular smooth muscle contraction. *Am J Hypertens, 3*, 235−237.

Hibino, H., Inanobe, A., Furutani, K., Murakami, S., Findlay, I., & Kurachi, Y. (2010). Inwardly rectifying potassium channels: their structure, function, and physiological roles. *Physiol Rev, 90*, 291−366.

Hirota, S., Helli, P., & Janssen, L. J. (2007). Ionic mechanisms and Ca^{2+} handling in airway smooth muscle. *Eur Resp J, 30*, 114−133.

Hirst, G. D., & Edwards, F. R. (2001). Generation of slow waves in the antral region of guinea-pig stomach−a stochastic process. *J Physiol, 535*, 165−180.

Honda, K., & Tomita, T. (1987). Electrical activity in isolated human tracheal muscle. *Jap J Physiol, 37*, 333−336.

Horowitz, B., Ward, S. M., & Sanders, K. M. (1999). Cellular and molecular basis for electrical rhythmicity in gastrointestinal muscles. *Annu Rev Physiol, 61*, 19−43.

Kamei, K., Yoshida, S., Imagawa, J., Nabata, H., & Kuriyama, H. (1994). Regional and species differences in glyburide-sensitive K+ channels in airway smooth muscles as estimated from actions of KC 128 and levcromakalim. *Br J Pharmacol, 113*, 889−897.

Knot, H. J., Standen, N. B., & Nelson, M. T. (1998). Ryanodine receptors regulate arterial diameter and wall $[Ca^{2+}]$ in cerebral arteries of rat via Ca^{2+}-dependent K^+ channels. *J Physiol, 508*, 211−221.

Ledoux, J., Werner, M. E., Brayden, J. E., & Nelson, M. T. (2006). Calcium-activated potassium channels and the regulation of vascular tone. *Physiology, 21*, 69−78.

Lee, H. K., Leikauf, G. D., & Sperelakis, N. (1990). Electromechanical effects of endothelin on ferret bronchial and tracheal smooth muscle. *J Appl Physiol, 68*, 417−420.

Lombard, J. H., Eskinder, H., Kauser, K., Osborn, J. L., & Harder, D. R. (1990). Enhanced norepinephrine sensitivity in renal arteries at elevated transmural pressure. *Am J Physiol, 259*, H29−H33.

Lyford, G. L., & Farrugia, G. (2003). Ion channels in gastrointestinal smooth muscle and interstitial cells of Cajal. *Curr Opin Pharmacol, 3*, 583−587.

Montell, C. (2005). The TRP superfamily of cation channels. *Sci Signal, 272*, re3.

Moosmang, S., Schulla, V., Welling, A., et al. (2003). Dominant role of smooth muscle L-type calcium channel Cav1.2 for blood pressure regulation. *EMBO J, 22*, 6027−6034.

Morin, C., Sirois, M., Echave, V., Gomes, M. M., & Rousseau, E. (2007). Functional effects of 20-HETE on human bronchi: hyperpolarization and relaxation due to BK_{Ca} channel activation. *Am J Physiol, 293*, L1037−L1044.

Nelson, M. T., Patlak, J. B., Worley, J. F., & Standen, N. B. (1990). Calcium channels, potassium channels, and voltage dependence of arterial smooth muscle tone. *Am J Physiol, 259*, C3−C18.

Oonuma, H., Nakajima, T., Nagata, T., et al. (2000). Endothelin-1 is a potent activator of non-selective cation currents in human bronchial smooth muscle cells. *Am J Respir Cell Mol Biol, 23*, 213−221.

Quayle, J. M., Nelson, M. T., & Standen, N. B. (1997). ATP-sensitive and inwardly rectifying potassium channels in smooth muscle. *Physiol Rev, 77*, 1165−1232.

Sanders, K. M. (2008). Regulation of smooth muscle excitation and contraction. *Neurogastroenterol Motil, 20*(Suppl. 1), 39−53.

Sanders, K. M., Koh, S. D., & Ward, S. M. (2006). Interstitial cells of cajal as pacemakers in the gastrointestinal tract. *Annu Rev Physiol, 68*, 307−343.

Steedman, W. M. (1966). Micro-electrode studies on mammalian vascular muscle. *J Physiol, 186*, 382−400.

Tazzeo, T., Zhang, Y., Keshavjee, S., & Janssen, L. J. (2008). Ryanodine receptors decant internal Ca^{2+} store in human and bovine airway smooth muscle. *Eur Resp J, 32*, 275−284.

Tsvilovskyy, V. V., Zholos, A. V., Aberle, T., et al. (2009). Deletion of TRPC4 and TRPC6 in mice impairs smooth muscle contraction and intestinal motility in vivo. *Gastroenterology, 137*, 1415−1424.

Verkman, A. S., & Galietta, L. J. (2009). Chloride channels as drug targets. *Nat Rev Drug Discov, 8*, 153−171.

Watson, N., Magnussen, H., & Rabe, K. F. (1997). Inherent tone of human bronchus: role of eicosanoids and the epithelium. *Br J Pharmacol, 121*, 1099−1104.

Welsh, D. G., Jackson, W. F., & Segal, S. S. (1998). Oxygen induces electromechanical coupling in arteriolar smooth muscle cells: a role for L-type Ca^{2+} channels. *Am J Physiol, 274*, H2018−H2024.

Welsh, D. G., Morielli, A. D., Nelson, M. T., & Brayden, J. E. (2002). Transient receptor potential channels regulate myogenic tone of resistance arteries. *Circ Res, 90*, 248−250.

Wu, R. S., & Marx, S. O. (2010). The BK potassium channel in the vascular smooth muscle and kidney: α- and β−subunits. *Kidney Int, 78*, 963−974.

Chapter 45

Excitation–Contraction Coupling in Skeletal Muscle

Judith A. Heiny and Gerhard Meissner

Chapter Outline

I. SUMMARY

Excitation–contraction coupling in skeletal muscle is a fast signal transduction process by which depolarization of the sarcolemmal membranes is coupled to the opening of Ca^{2+} release channels on the sarcoplasmic reticulum (SR). This transduction occurs at specialized triad junctions and is mediated by two key proteins – the t-tubule dihydropyridine receptor (DHPR)/Ca^{2+} channel and the SR ryanodine receptor (RyR) channel. The DHPR and RyR1 associate with other junctional proteins to form a macromolecular complex which spans the triad junction and interacts to control RyR opening. This interaction produces a fast transient rise in $[Ca^{2+}]_i$ which activates the contractile proteins and results in muscle contraction.

II. INTRODUCTION

Skeletal muscle is activated to contract by a sequence of fast, electrically driven events that are collectively termed *excitation–contraction coupling* (EC coupling). EC coupling is a highly organized process of signal transduction that utilizes specialized membranes, membrane junctions and ion channels on both the exterior and interior of the cell. This chapter describes the cellular and molecular processes that mediate electrical excitation of the outer plasma membrane and transduces it into a signal for Ca^{2+} release from the intracellular sarcoplasmic reticulum (SR). The focus is on vertebrate fast-twitch skeletal muscle which is the best characterized.

Skeletal muscle is the fastest contracting of the three major muscle types and is related to cardiac and smooth muscle types evolutionarily and embryonically. The same two key proteins – a voltage-dependent calcium channel on the surface membrane (*dihydropyridine receptor* Ca^{2+} channel, DHPRs) and a Ca^{2+}-release channel (ryanodine receptor, RyR) in the sarcoplasmic reticulum – mediate excitation–contraction in cardiac, smooth and skeletal muscle. These two proteins share a high degree of homology but the different muscle types express different isoforms and combinations of these proteins. Importantly, each muscle type has evolved highly differentiated mechanisms of using these proteins to serve its specialized functions. Cardiac and smooth muscle primarily mediate enteric contractile processes that are under autonomic and humoral control,

Cell Physiology Sourcebook. DOI: 10.1016/B978-0-12-387738-3.00045-7

while skeletal muscle primarily mediates rapid, willed bodily movements that are under the control of the central nervous system. Consequently, the defining features of skeletal muscle activation are speed and voluntary control, as needed for fine control of body movement.

III. OVERVIEW OF EC COUPLING

The sequence of EC coupling in a vertebrate fast-twitch skeletal muscle fiber is shown in Fig. 45.1. Activation begins when an action potential from a *motor neuron* arrives at the *neuromuscular junction* and causes the neurotransmitter *acetylcholine* (ACh) to be released into the postsynaptic clefts (see chapter on synaptic transmission). The opening of AChRs produces a local depolarization, termed the *end-plate potential*, which brings the postsynaptic membrane to threshold potential for exciting an action potential (see chapter on synaptic transmission). The action potential rapidly propagates the depolarization along the outer sarcolemma and into the fiber interior via a specialized system of transversely oriented tubular membranes (*transverse-tubules* or *t-tubules*). The transverse tubules are continuous with and invaginate transversely from the sarcolemma at periodic intervals to form a planar network. The t-tubules provide the conduit for the action potential to reach the fiber interior and also bring the outer membranes into close proximity with the internal *sarcoplasmic reticulum* (SR) at specialized intracellular junctions called *triads*. The triad junctions serve as a platform for assembling sarcolemmal calcium channels (DHPRs), SR Ca^{2+}-release channels (ryanodine receptors) and additional proteins into a macromolecular complex which spans the junctional gap and controls Ca^{2+} release from the SR. The DHPRs serve as the voltage-sensors in this process. DHPRs contain charged, intramembrane domains which move in response to the action potential depolarization; these molecular rearrangements, termed *charge movement*, in turn, drive a conformational change on the RyR1 which causes it to open. These concerted molecular interactions occur between cytoplasmic regions

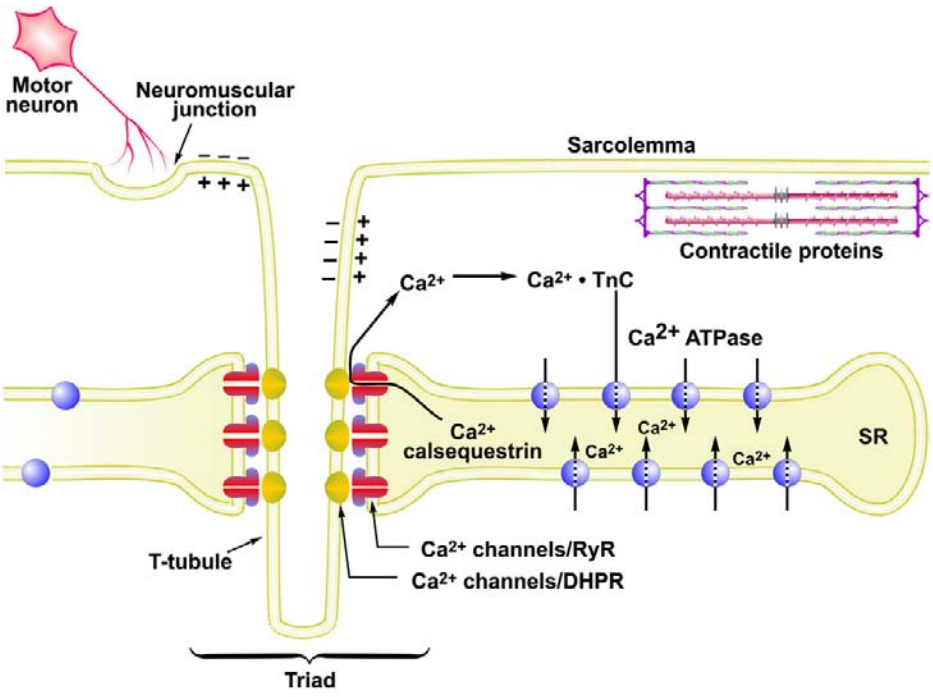

FIGURE 45.1 Sequence of excitation–contraction coupling in skeletal muscle.

of the DHPR and cytoplasmic domains of the RyR1 which face each other at the triad junction. In this way, the opening of an integral SR membrane calcium channel is gated by conformational transitions of a sarcolemmal, voltage-dependent calcium channel. Consequently, Ca^{2+} release in skeletal muscle remains under tight control of the plasma membrane potential.

The SR is a subcellular membrane compartment that is related evolutionarily to the endoplasmic reticulum. In skeletal muscle, it is a highly specialized for controlling cytosolic Ca^{2+}, $[Ca^{2+}]_i$. The SR actively sequesters Ca^{2+} in resting muscle via an ATP-dependent Ca^{2+} pump (SERCA), to maintain the intracellular Ca^{2+} concentration, $[Ca^{2+}]_i$, at submicromolar levels (typically $\approx 0.1\ \mu M$). Ca^{2+} is stored in bound form within the SR, complexed to the Ca^{2+}-binding protein *calsequestrin*. When a muscle is excited to contract, RyRs open and release this Ca^{2+} into the cytosol at rates approaching 100 μM/ms. This rapid Ca^{2+} release transiently raises cytosolic $[Ca^{2+}]_i$ to micromolar levels (typically 1–10 μM). The released Ca^{2+} ions diffuse and bind to *troponin-C* (TnC), the regulatory subunit of troponin, thereby removing troponin's inhibitory effect on the *contractile proteins*, actin and myosin, which shorten to generate force (see Chapter 46). Force output in skeletal muscle is directly proportional to cytosolic Ca^{2+} concentration (Fig. 45.2). Ca^{2+} release from the SR is brief and terminates quickly. As the t-tubule membrane repolarizes, DHPRs return to their inactive conformation and the RyR is itself inactivated by a Ca^{2+}-dependent mechanism. Multiple mechanisms return cytosolic Ca^{2+} to resting levels. The *Ca^{2+}-ATPase* of the SR membrane (SERCA) is stimulated rapidly to pump Ca^{2+} back into the SR. Cytosolic Ca^{2+}-binding proteins with rapid kinetics buffer Ca^{2+} transiently while the SERCA pumps return it to the SR.

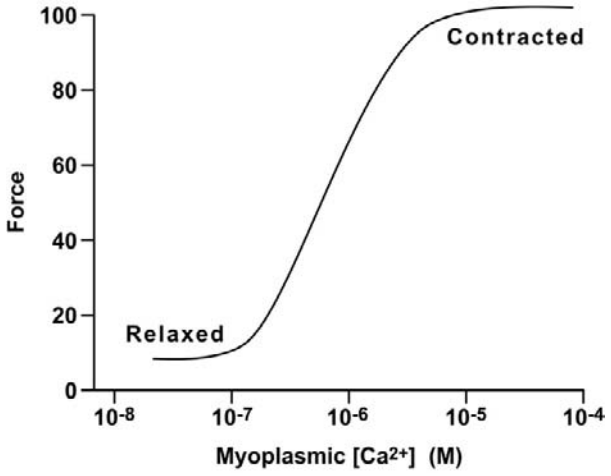

FIGURE 45.2 Relationship between force and myoplasmic Ca^{2+} concentration.

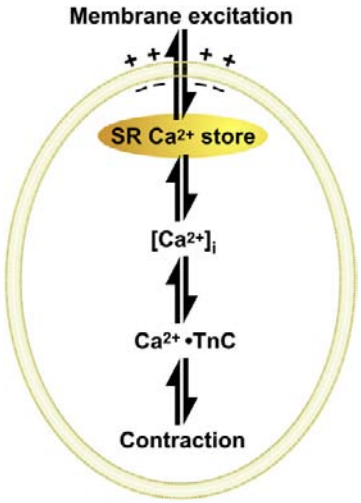

FIGURE 45.3 A rise in cytosolic $[Ca^{2+}]$ links membrane excitation to activation of contractile proteins.

Some Ca^{2+} is also extruded extracellularly by active Ca^{2+} transporters and Ca^{2+} exchangers on the plasma membrane. Force terminates when cytosolic Ca^{2+} returns to resting levels. Thus, cytosolic $[Ca^{2+}]_i$ is the central link between membrane excitation and activation of the contractile proteins (Fig. 45.3). Contraction is inhibited at low resting Ca^{2+} levels, and proceeds when Ca^{2+} is elevated transiently in response to membrane excitation.

IV. SPEED OF SKELETAL MUSCLE ACTIVATION

Activation of skeletal muscle is extremely rapid, occurring in milliseconds. This speed is remarkable given that skeletal muscle fibers are among the largest of mammalian cells. Skeletal muscle fibers are multinucleated cells that form during embryogenesis by fusion of myoblasts. They have a cylindrical shape with diameters from 30 to 150 μM and lengths from millimeters to centimeters. To produce effective mechanical force, the contractile proteins in all regions of a muscle fiber must shorten simultaneously. This synchronous activation is achieved by the propagating action potential which spreads the depolarization along the sarcolemma and into the transverse tubules within milliseconds, and by the anatomical configuration of the triad junctions which directly connect voltage-sensing DHPRs to the RyR Ca^{2+} release channels. Figure 45.4 and Table 45.1 show the relative timing and durations of key events in excitation contraction coupling for amphibian and mammalian muscle. The entire process, from membrane excitation to RyR1 opening, is complete within milliseconds. Overall, it operates largely as an on/off switch, insuring that Ca^{2+} release occurs rapidly and synchronously in response to each excitatory input from the motor nerve.

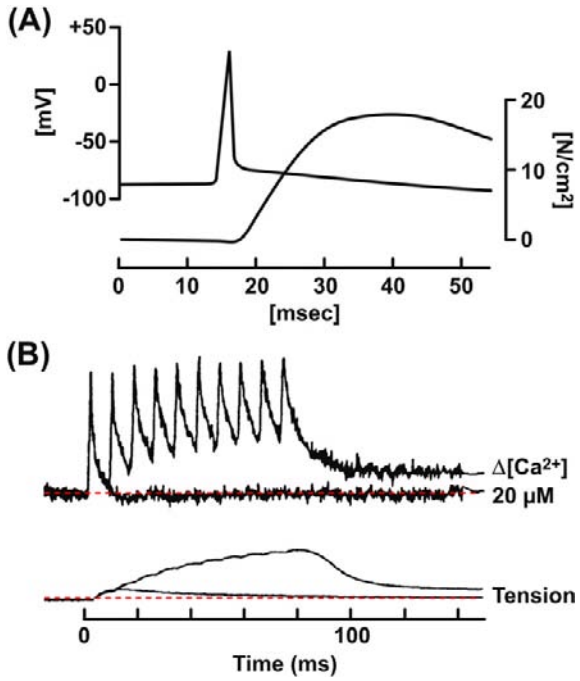

FIGURE 45.4 Speed of EC coupling in amphibian and mammalian skeletal muscles. (A) Time course of the action potential (top trace) and tension development (lower trace) in a fast-twitch frog skeletal muscle fiber at 18°C. *(Modified from Hodgkin and Horowicz, 1957.)* (B) Time course of EC coupling in a mouse skeletal muscle fiber at 37°C. The top traces record the cytosolic $[Ca^{2+}]_i$ change measured with a Ca^{2+} indicator dye. The lower trace shows tension. The fiber was stimulated at time zero with a single action potential and with repetitive action potentials at high frequency, to simulate a muscle tetanus. *(Reproduced from The Journal of General Physiology, 1996, 108, 455–469 by copyright permission of The Rockefeller University Press.)*

V. MEMBRANE ARCHITECTURE OF EC COUPLING

As noted, the outer and intracellular membranes of skeletal muscle are highly organized to achieve rapid communication between the extracellular sarcolemma and the interior SR membrane (Franzini-Armstrong and Jorgensen, 1994; Franzini-Armstrong and Protasi, 1997). Figure 45.5 illustrates the three-dimensional architecture of the sarcolemma, t-tubules, triad junctions and SR membranes of a fast-twitch frog skeletal muscle fiber and their physical relationship to the contractile proteins. The t-tubules comprise the majority of the sarcolemma membrane, representing 50–80% of the plasma membrane area (Peachey, 1965). They invaginate from the sarcolemma in a transverse plane approximately twice every 1–2 μM (or, at two planes per sarcomere in mammalian muscle). Within this plane they branch extensively to form a planar network that covers the entire cross-section of the muscle fiber (Fig. 45.6). This geometry insures that the Ca^{2+} binding sites on TnC are less than a few tenths of a micron diffusion distance from the Ca^{2+} release channels. Up to 80% of the tubular membrane area forms triad junctions with the SR (Peachey, 1965, Dulhunty, 1984). In mammalian skeletal muscles, two planes of transverse tubules form in each sarcomere, at the A-I bands.

The specific positioning of skeletal-type DHPRs in relation to RyR molecules at the triad junction allows the two channels to interact during excitation–contraction coupling (Fig. 45.7). The t-tubule and SR membranes flatten and face each other across a narrow gap of about 15 nm. RyR1s assemble on the junctional surface of the terminal cisternae in an ordered array of two rows with a center-to-center spacing of about 30 nm. Each RyR1 is a tetramer composed of four identical subunits. The RyRs are extremely large molecules (≈5000 amino acids and ≈560 kDa) of approximately 29 × 29 × 12 nm size. An intramembrane region of RyR1 inserts into the SR membrane and a large cytosolic domain extends across the junctional gap and associates with cytosolic domains of the DHPR. Viewed from above, the cytosolic domains of RyR1 roughly resemble a double row of quatrefoil-shaped proteins which interlock with each other in a precisely ordered array. In side view, the RyR1 tetramer assumes

TABLE 45.1 Duration of Key Steps in the Activation of Fast-Twitch Skeletal Muscle

EC Coupling Steps	Duration[a] (ms)
Action potential propagation along sarcolemma	5–10
Action potential propagation to center of fiber along t-tubules	≈0.7
Signal transduction at triad junction, from t-tubule depolarization to activation of RyR on SR	≈0.5
Peak rate of Ca^{2+} release to peak Ca^{2+} binding to TnC (start of tension)	2–3
Peak myoplasmic Ca^{2+} change to peak tension	15–25

[a]*Durations were calculated for a hypothetical frog fiber of 50 μm diameter and 5 cm length, having a central end-plate. Literature values for conduction velocity and duration of intermediate steps (Gonzales-Serratos, 1971; Vergara and Delay, 1986; Jong et al., 1996) were adjusted to 18° C.*

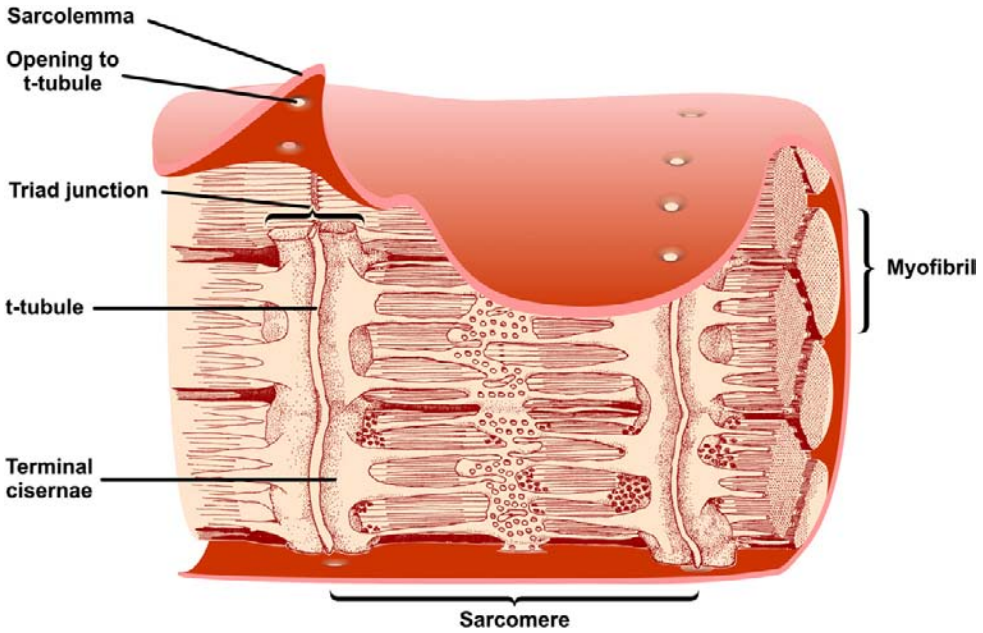

FIGURE 45.5 Three-dimensional reconstruction of a longitudinal section of a skeletal muscle fiber from the frog. The sarcolemma surrounds bundles of contractile proteins called myofibrils. Transverse tubules (t-tubules) invaginate from the sarcolemma in a plane at periodic intervals. The t-tubules form triad junctions with the SR along most of their length. At the triad junctions, the longitudinally oriented SR membranes widen into sacs called terminal cisternae, which closely oppose the t-tubules and contain the Ca^{2+} release channels/RyRs. The terminal cisternae are positioned near the activating Ca^{2+} sites on TnC. The functional unit of force generation is the sarcomere, consisting of overlapping actin and myosin filaments anchored at each end. The longitudinally oriented tubular regions of SR contain the Ca^{2+}-ATPase which takes up released Ca^{2+} all along the sarcomere. *(Reproduced from The Journal of Cell Biology, 1965, 25, 209–232 by copyright permission of The Rockefeller University Press.)*

a mushroom shape with a large extracellular domain and a smaller transmembrane domain that contains the Ca^{2+}-conducting pore (see Section VII below). Every alternate RyR1 associates with a cluster of four DHPRs, termed a *tetrad* (shown here as small blue spheres), i.e. each DHPR in a tetrad interacts with one of the four subunits of RyR1 and every other RyR1 is not directly associated with a tetrad of DHPRs. The DHPR tetrads are arranged in a pattern approximately corresponding to the four outer corners of the cytosolic spheres of the RyR. The outline of the DHPR tetrad is larger than the outline of the RyR1 tetramer and this may explain why tetrads associate only with alternate RyR1s. In non-mammalian muscle, a second ryanodine receptor isoform, RyR3 is present on peripheral regions of the SR junctional membrane. RyR3s do not associate with DHPRs.

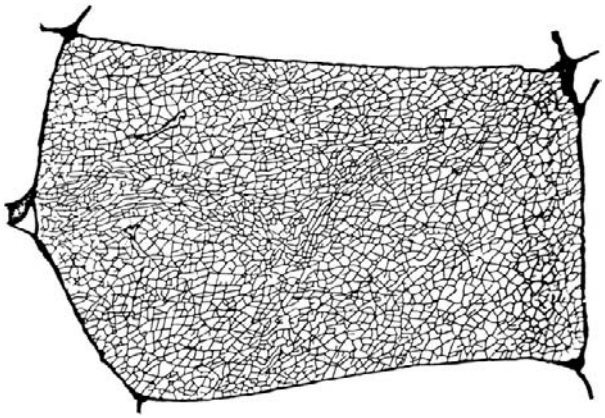

FIGURE 45.6 Reconstruction of the t-tubule network in one cross-sectional plane through a single frog twitch muscle fiber. The reconstruction was made from electron micrographs of transverse serial slices of a muscle fiber perfused with the electron-dense and membrane-impermeant molecule peroxidase, which diffused into the t-tubules. *(From Peachey and Eisenberg, 1978.)*

Figure 45.7 is based on a fish skeletal muscle fiber. A similar arrangement of tetrads is suggested in triads and peripheral couplings of other skeletal muscles from the frog, rat, chicken, mouse and human (Franzini-Armstrong and Jorgensen, 1994). Variations on this structure can occur in different species. These include *dyads*, in which a junctional region of terminal cisterna is opposed to a single short segment of t-tubule, and *peripheral couplings*, in which a junctional region of terminal cisterna is opposed to an approximately circular invagination of the surface membrane. Triads, dyads and peripheral couplings are structurally and functionally equivalent. Each is the intracellular site at which DHPRs and RyR1s interact to control Ca^{2+} release from the SR.

The triad junction has a strong structural integrity. Early studies demonstrated that purified fractions of t-tubule membrane could form junctions with SR membranes and that triad fractions could be isolated intact, despite stringent

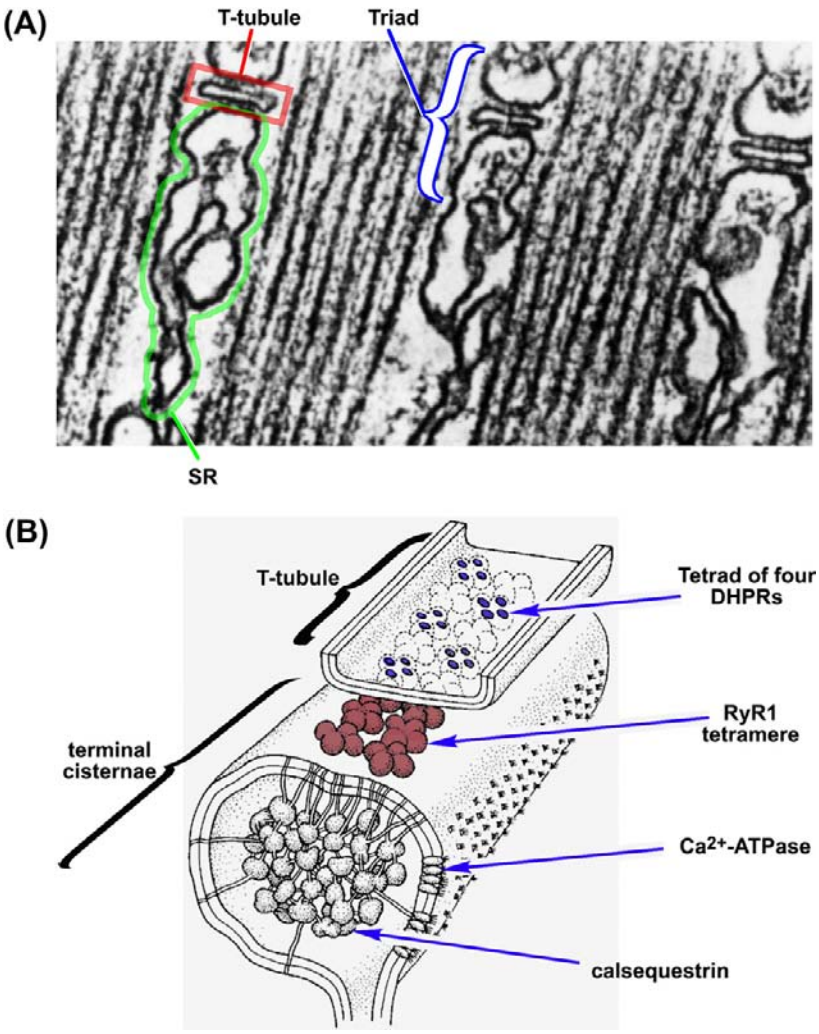

FIGURE 45.7 (A) Electron micrograph showing triad junctions in a longitudinal section through a fish skeletal muscle. Each t-tubule (outlined in red) is flanked on both sides by terminal cisternae of the SR (outlined in green). Contractile proteins are oriented longitudinally. The RyR1s appear as dense electron opaque material between the gap and were initially named "foot proteins" because of this appearance *(From Franzini-Armstrong and Peachey, 1981.)* (B) Three-dimensional reconstruction of a triad showing the spatial organization of the junctional membranes, DHPRs and RyRs. The t-tubule (TT) flattens and apposes a region of SR across a gap of 12–15 nm. RyR1 Ca^{2+} release channels (red) in the SR align in a double row with a skewed spacing such that each RyR1 makes multiple contact points with adjacent RyR1s. A tetrad of four DHPRs (blue) in the TT couples to every *other* RyR1. Non-mammals, such as frog and fish, have a second, RyR3 (green), isoform which is localized at the periphery of the SR membrane at the triad junction. RyR3 isoforms are not associated with TT tetrads (red). *(Reproduced with permission from Felder and Franzini-Armstrong, 2002.)*

fractionation procedures (Caswell et al., 1979). Such strong protein–protein associations at the triad junction are required to preserve the structural integrity of the triad junction as it sustains the strong forces of contraction.

VI. THE DHPR PROTEIN

The skeletal muscle DHPR is a voltage-gated Ca^{2+} channel ($Ca_v1.1$) belonging to the voltage-dependent superfamily of Ca^{2+} channels which share common structural and functional motifs (Yu et al., 2005; see also chapter on structure and mechanisms of voltage-gated ion channels). All Ca_v channels are multisubunit complexes composed of at least three subunits associated in an equimolar ratio: $\alpha 1$, $\alpha 2$-δ and β. The skeletal muscle channel has a fourth γ subunit. Multiple isoforms of the subunits exist and are distributed in a tissue-specific manner. The complete skeletal muscle calcium channel is a heteromultimeric complex consisting of $\alpha 1_s$ (212 kDa), $\alpha 2$-δ_1 (125 kDa), β_{1a} and γ_1 subunits (Fig. 45.8A). The individual subunits have been purified, sequenced, cloned and studied in expression systems. The $\alpha 1_s$ alone can reconstitute a functional Ca^{2+} ion current. However, all four subunits are required to form a functional skeletal muscle DHPR with properties of the native channel (Suh-Kim et al., 1996).

The primary $\alpha 1_s$ subunit contains the major functional domains of the channel. It is an integral membrane protein (212 kDa) that contains the pore-forming and voltage-sensing regions as well as the binding site for dihydropyridines and other calcium channel blockers. It is composed of four hydrophobic repeat domains – I, II, III and IV (see Fig. 45.8B) – which share a high degree of homology. Domains I–IV assemble to form a transmembrane protein with a central pore. Each domain consists of six transmembrane alpha-helical segments, denoted S1–S6, plus two smaller helices between S5 and S6 (pore helices) which fold into the membrane to line the pore. The S4 transmembrane helix within each domain forms the voltage sensor that moves in response to the action potential

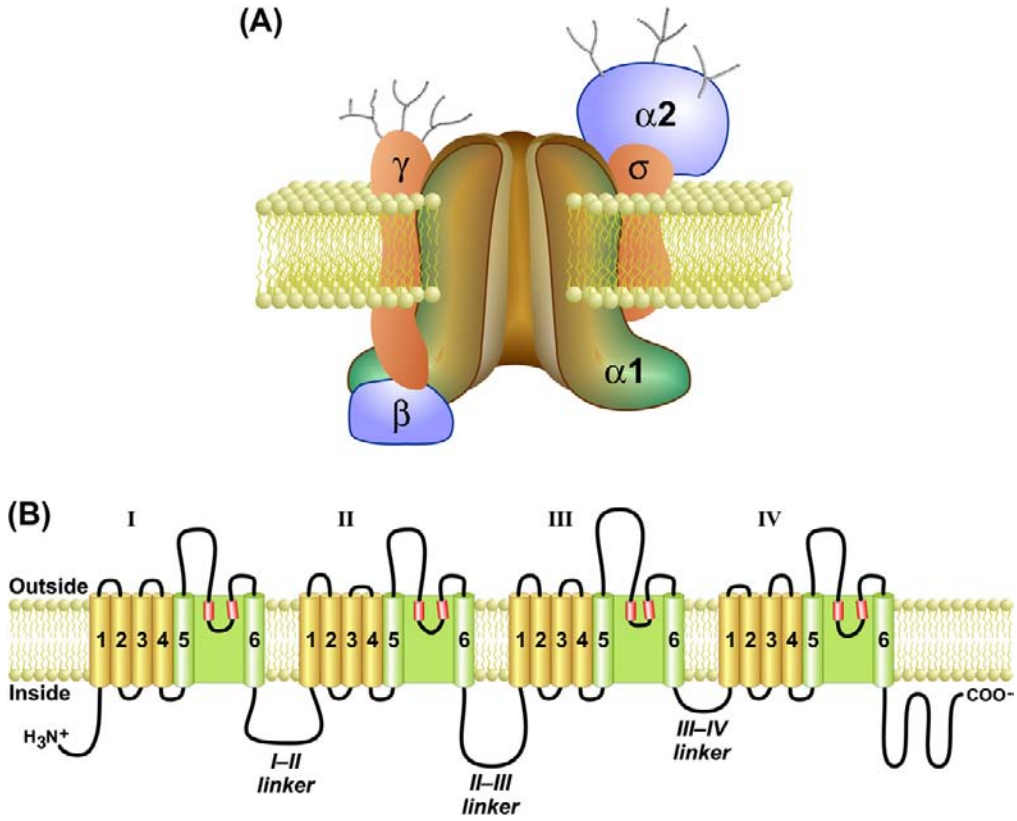

FIGURE 45.8 The skeletal muscle DHPR protein. (A) The skeletal muscle DHPR is composed of four subunits (α_{1s}, α_2-δ, β_{1a}, and γ). The α_{1s} subunit contains the key functional domains of the channel, including the voltage-sensing helices (S4) and the pore (S5–S6 extracellular domains). (B) The primary amino acid sequence of α_{1s} contains four homologous transmembrane domains (I–IV) connected together by cytosolic linker sequences (I–II, II–III and III–IV linkers). Each of the four domains is composed of six transmembrane helices (drawn schematically as cylinders) plus two shorter intramembrane helices that fold into the bilayer (S5–S6 pore helices) to form the ion conducting pore. The cytosolic linker between domains II–III is a key interaction domain with the RyR and is required for skeletal-type EC coupling. The β_{1a} subunit interacts with the I–II linker and with RyR1 and is also required for skeletal muscle type EC coupling.

depolarization. The S4 alpha helix is highly charged, containing a positively-charged residue on every third amino acid. Upon depolarization, all four S4 helices move in a cooperative fashion to activate the DHPR and, in turn, allosterically activate a coupled RyR1. Movement of the intramembrane S4 helices generates the macroscopic charge movement currents that are detected electrically during EC coupling (Schneider and Chandler, 1973). Domains I–IV are connected at the cytosolic face by segments of more hydrophilic amino acids (denoted I–II, II–III and III–IV linkers). The cytosolic region between domains II and III (II–III linker) plays a critical role in interactions with RyR1. The I–II linker also plays an essential role in EC coupling because it is the site for interaction with the β_{1a} subunit which is required for EC coupling (see Section VIIIC; below). The $\beta 1_a$ subunit is a smaller cytoplasmic protein (58 kDa) that associates specifically with the skeletal alpha isoform at an interaction domain on the I–II cytoplasmic linker. The $\alpha 2$-δ_1 subunit (125 kDa) may participate in membrane targeting and anchoring, The γ_1 subunit is a small glycosylated membrane protein (25 kDa) that associates with the skeletal $\alpha 1_s$ isoform but not with heart or brain alpha subunits and may play a regulatory role.

The skeletal muscle Ca^{2+} channel is capable of functioning both as a voltage sensor for EC coupling and as a Ca^{2+} ion channel. However, as a Ca^{2+} channel it has a low probability of opening and is characterized by high-voltage activation, brief openings and small single-channel currents. These features result in a very small, slow Ca^{2+} current through skeletal muscle DHPRs compared to the cardiac isoform (α_{1c}). Therefore, in skeletal muscle, movement of the S4 gating domains may be followed by slower, less steeply voltage-dependent conformational changes that open the pore. It is thought that the early rapid movement of S4 domains, and not the Ca^{2+} current that follows after a delay of several hundred milliseconds, has been exploited evolutionarily by skeletal muscle to control RyR1 activation. This small, slow Ca^{2+} influx through skeletal muscle DHPRs is not significant during a single

action potential. However, it may accumulate to measurable levels during a tetanus, when a skeletal muscle is activated repetitively at rates of 50–100 Hz to elicit a sustained contraction. In this case, Ca^{2+} entry may add to and perhaps modulate intracellular Ca^{2+} release from the SR (Dirksen, 2009).

VII. THE RYANODINE RECEPTOR

VIIA. Distribution, Structure and Isolation of RyRs

The release of Ca^{2+} ions from the endo/sarcoplasmic reticulum via *Ca^{2+}-release channels* is a key step in a wide variety of biological functions. The endo/sarcoplasmic reticulum Ca^{2+}-release channels are commonly referred to as *ryanodine receptors* (RyRs) to distinguish them from other intracellular Ca^{2+} channels. RyRs have been identified in non-vertebrate and vertebrates including flies, crustaceans, birds and amphibians. In mammals, there are three RyR isoforms. RyR1 is the dominant isoform in skeletal muscle. RyR2 is found in high levels in cardiac muscle. RyR3 was initially identified in brain but is expressed in many tissues including diaphragm, smooth muscle and brain.

The RyR/Ca^{2+}-release channels have been extensively studied with rabbit skeletal muscle as the source for RyRs. Fragmentation of the sarcoplasmic reticulum during homogenization and subsequent fractionation by differential and density-gradient centrifugation yields a *heavy SR* vesicle fraction which is enriched in Ca^{2+}-release channels and [^{3}H]ryanodine-binding activity and corresponds to the junctional region of the SR (*junctional SR*) (Meissner, 1984). Another important advance has been the isolation of triads, membrane fractions composed of a t-tubule segment sandwiched between two junctional SR vesicles (Fleischer and Inui, 1989). Microsomal membrane fractions enriched in ryanodine-sensitive Ca^{2+}-release channels have been also isolated from other excitable tissues, including cardiac muscle, smooth muscle and brain. In these cases, however, the membrane fractions are typically of a lower purity than those from skeletal muscle.

The RyRs are 2200 kDa multiprotein complexes that typically span the narrow gap where the SR and t-tubule (and plasmalemma) are within ≈15 nm of each other (Franzini-Armstrong and Protasi, 1997). The mammalian RyRs share ≈70% sequence homology, with the greatest homology in the carboxyl-terminal region. In all isoforms, the C-terminal portion of the protein contains the transmembrane domain. More recent studies suggest that six membrane spanning segments per RyR subunit are sufficient to form a channel. The remaining RyR amino acids form the large catalytic cytoplasmic "*foot*" structure. Experimental information on the structure of the RyRs has been mainly obtained by cryoelectron microscopy. Three-dimensional reconstruction of electron micrographs of frozen-hydrated RyR specimen shows dimensions of $29 \times 29 \times 12$ nm for the large cytoplasmic assembly with a 7 nm length and 8 nm diameter for the transmembrane domain (Fig. 45.9).

The isolation of the RyRs has been greatly facilitated by the identification of ryanodine as a channel-specific ligand. Ryanodine is a neutral plant alkaloid that is obtained from the stems of the South American shrub, *Ryania speciosa*, and is composed of two major compounds: ryanodine and 9,21-didehydroryanodine (Fig. 45.10). Ryanodine is a highly toxic compound. Its pharmacological effects have been most clearly shown in muscle where, depending on muscle type and activity, it can cause either contracture or a decline in contractile force (Sutko and Airey, 1996). Ryanodine activates the channel at low (nanomolar) concentrations, but inhibits the channel at high (micromolar) concentrations (Fig. 45.11). Because the drug binds with high specificity and dissociates slowly from the

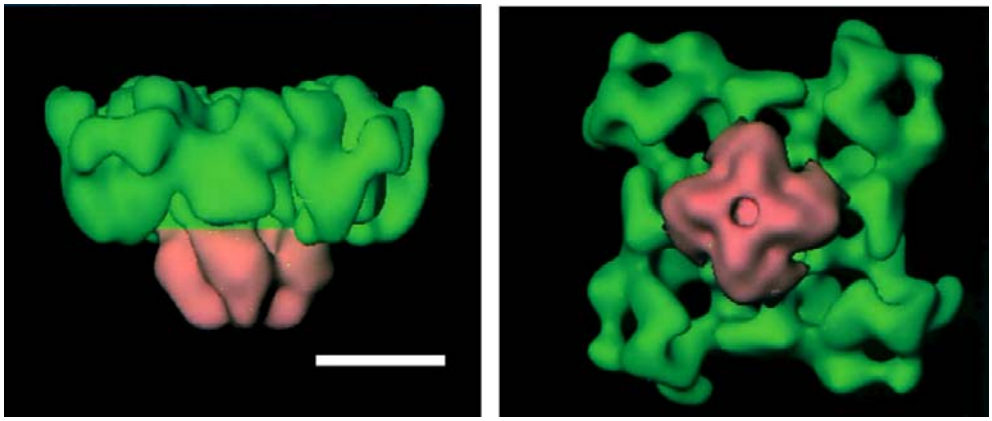

FIGURE 45.9 Dimensional reconstruction of RyR1. The cytoplasmic (green) and transmembrane (pink) domains are shown. Scale bar, 10 nm. *(With permission from M. Samso and T. Wagenknecht (1998) J Struct Biol. 121,172–180.)*

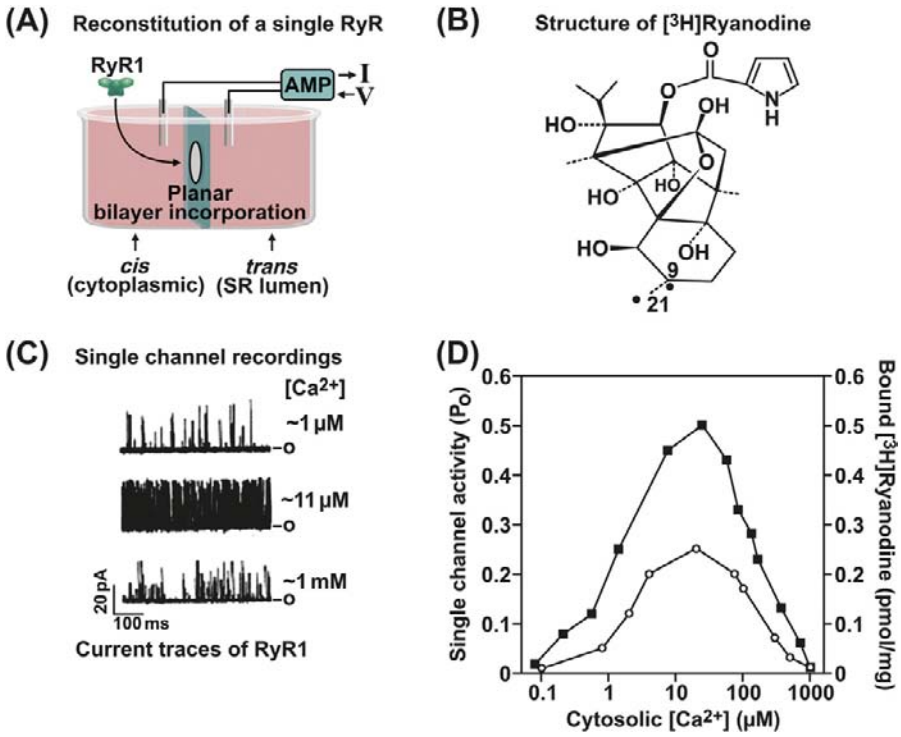

FIGURE 45.10 Measurement of RyR1 activity. (A) Planar lipid bilayer setup. (C) Three current traces of a single RyR1 ion channel recorded in symmetric 250 mM K^+ medium. Bars on right represent the closed (c) channel. The effects of three different *cis* (cytoplasmic) [Ca^{2+}] on channel activity are shown. In the upper trace, the channel is minimally activated by 1 μM Ca^{2+}. Short, often poorly resolved events are seen. Channel activity is increased by increasing cytoplasmic Ca^{2+} from 1 to 11 μM and decreased when further increasing cytoplasmic Ca^{2+} to 1 mM. (D) Bimodal Ca^{2+} dependence of channel activity suggests the presence of high-affinity activating and low-affinity inhibitory Ca^{2+} binding sites. (B) Structure of [^{3}H]ryanodine. (D) [^{3}H]ryanodine binding measurements yield a Ca^{2+} dependence in good agreement with single channel measurements.

high-affinity site of the receptor (either membrane-bound or detergent-solubilized), [^{3}H]ryanodine has been found to be an ideal probe in the isolation of the RyRs from a variety of tissues and species.

The RyR was first isolated from striated muscle because its role in regulating free cytoplasmic Ca^{2+} levels was originally recognized in muscle and relatively large amounts of membranes enriched in [^{3}H]ryanodine-binding activity can be obtained from skeletal muscle and cardiac muscle. The membrane-bound Ca^{2+} release channels were solubilized in the presence of [^{3}H]ryanodine, using the zwitterionic detergent Chaps and high ionic strength (1.0 M NaCl); they can then be purified in essentially one step by density gradient centrifugation through a linear sucrose gradient. Fig. 45.12A shows the [^{3}H]ryanodine pattern on the sucrose gradients and sedimentation profile of the proteins associated with junctional SR vesicles isolated from rabbit skeletal muscle. A single peak of bound radioactivity, co-migrating with a small protein peak possessing an apparent sedimentation coefficient of 30 S, is observed in the lower half of the gradients. Binding to the small protein peak is specific since no radioactivity is present in the lower half of the gradients when the membranes are incubated with an excess of cold ryanodine. A sedimentation coefficient of 30 S revealed that the RyR is a very large protein complex.

The sucrose gradient centrifugation procedure is relatively simple and straightforward. The procedure results in efficient separation of the large 30 S RyR complex from the other solubilized smaller SR proteins because of its faster sedimentation rate. This method has been used to isolate a functional 30 S RyRs from several species and tissues including skeletal muscle, cardiac muscle, smooth muscle and brain.

SDS polyacrylamide gel electrophoresis shows that the 30 S protein complexes of mammalian skeletal and cardiac muscles are composed of a single major high molecular weight RyR polypeptide and isoform-specific low molecular weight immunophilin (FK506 binding protein) which migrate with apparent $M_r > 340\,000$ (see Fig. 45.12B) and $M_r \approx 12\,000$ (not visible on the gels in Fig. 45.12B), respectively. Cloning and sequencing of the complementary DNA of the mammalian skeletal and cardiac muscle RyR isoforms have revealed an open reading frame of about 15 kb and encoding RyR polypeptides of $M_r \approx 560\,000$. In contrast, the presence of two immunologically distinct high molecular weight RyR protein bands (corresponding to the mammalian RyR1 and RyR3) has been described for the main skeletal muscles of chicken, frog and fish (Sutko and Airey, 1996). The two RyR isoforms are present as discrete homo-oligomers in amphibian and avian skeletal muscles. The appearance of the RyR1 isoform alone in some very fast-contracting muscle of fish suggests that this isoform is selectively expressed when rapid contraction is required in non-mammalian vertebrate muscles (O'Brien et al., 1993).

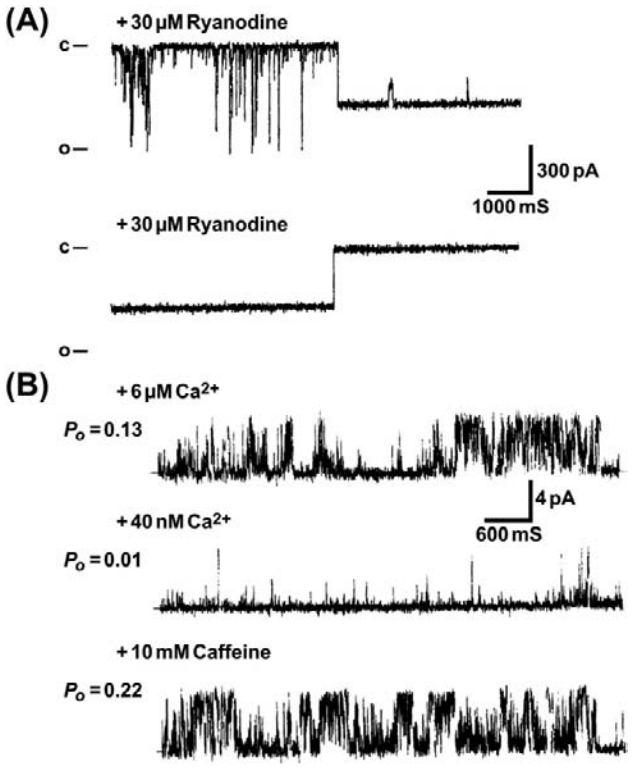

FIGURE 45.11 Effects of ryanodine and caffeine on single skeletal muscle RyRs. 30S purified channel complexes are reconstituted into planar lipid bilayers. (A) Upper trace shows appearance of subconducting channel state with open probability (P_o) of ≈1, following several minutes after the addition of 30 μM *cis* ryanodine. An additional, infrequent substate is also observed. Lower trace illustrates the sudden transition from the subconductance state to a fully closed state 1 min after addition of 2 mM *cis* (cytoplasmic) ryanodine *(from Lai et al., 1989 J Biol Chem. 264, 16776-16785)*. Note, relatively high ryanodine concentrations were used to shorten the time of binding to RyR1. (B) Single channel activity is with 6 μM free cytoplasmic Ca^{2+} (upper trace). Upper free Ca^{2+} is decreased to 40 nM by the addition of a Ca^{2+} buffer (EGTA) (middle trace). After the addition of 10 mM caffeine to the 40 nM free cytoplasmic Ca^{2+} medium (bottom trace). In contrast to ryanodine, caffeine activates the channel without changing its conductance. Bars on left represent the closed (c) channel. Po, channel open probability. *(From Rousseau et al., Arch Biochem Biophys. 267, 75–86, 1988).*

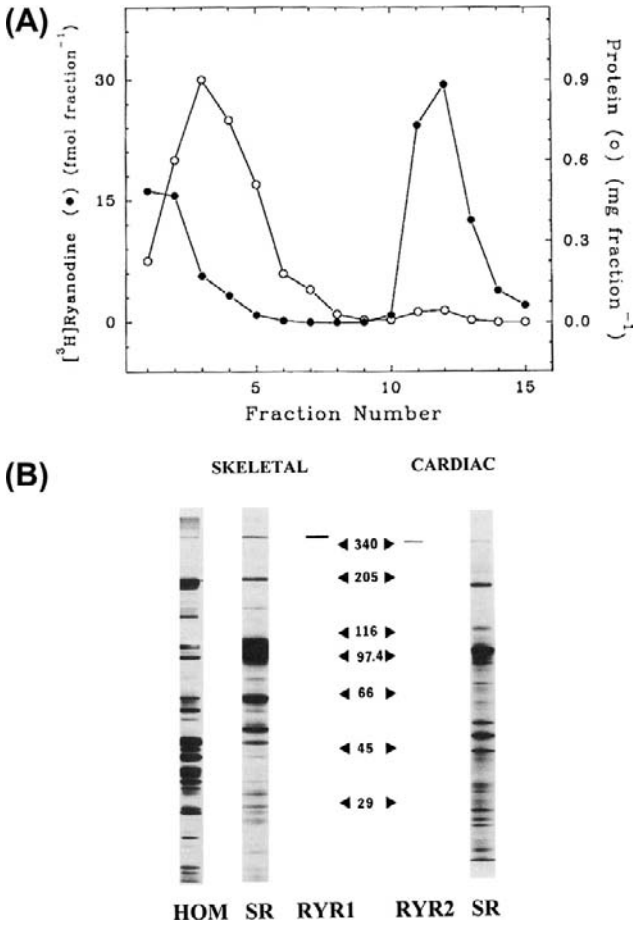

FIGURE 45.12 Sedimentation profile of RyR1 and SDS gel electrophoresis of rabbit skeletal muscle and canine cardiac RyRs. (A) Junctional skeletal muscle SR vesicles were solubilized in Chaps, centrifuged through a linear sucrose gradient and fractionated. Fractions were analyzed for protein and ^{3}H-radioactivity. Unbound [^{3}H]ryanodine and the majority of the solubilized proteins sedimented near the top of the gradient (fractions 1–6), whereas the [^{3}H]ryanodine-labeled RyR comigrated with a small protein peak to the bottom of the gradient (fractions 11–13) *(in modified form from Lai et al., Nature. 331, 315–319, 1988).* (B) Silver stained SDS-polyacrylamide gel of whole rabbit skeletal muscle homogenate (HOM) and rabbit skeletal and canine cardiac muscle heavy SR membranes (SR) and purified RyRs (RYR1 and RYR2). Sizes of molecular weight standards are shown ($\times 10^{-3}$). *(From Meissner et al., 1989 Mol. Cell Biochem. 82, 59–65.)*

VIIB. RyR1 Pore Structure

RyRs have large conductances for both monovalent (≈750 pS with 250 mM K^+) and divalent (≈150 pS with 50 mM Ca^{2+}) cations, while maintaining divalent vs monovalent selectivity (P_{Ca}/P_K ≈7). Sequence comparison, cryoelectron microscopy and extensive mutagenesis and single channel studies indicate that the RyRs have a pore structure similar to that of K^+ channels whose structure is known (Fig. 45.13). In the RyRs, the residues between the two C-terminal membrane-spanning segments are luminally located and have a *pore helix* and an *amino acid motif* (GGGIG) that is similar to the *selectivity filter motif* (TV/IGYG) of K^+ channels whose structure is known. Mutagenesis shows that rings of negative charges in the luminal and cytosolic vestibules maintain the high rates of RyR1 ion fluxes (Xu et al., 2006). Several models of RyR ion permeation based on Eyring rate theory (Tinker et al., 1992), Poisson Nernst Planck-Density Functional Theory (Gillespie et al., 2005) and the solution structure of K^+ channels (Fig. 45.13) have been described.

VIIC. Regulation by Ca^{2+} and Endogenous Effectors

The in vitro function of RyR ion channels has been studied by measurement of *single channels* incorporated in planar

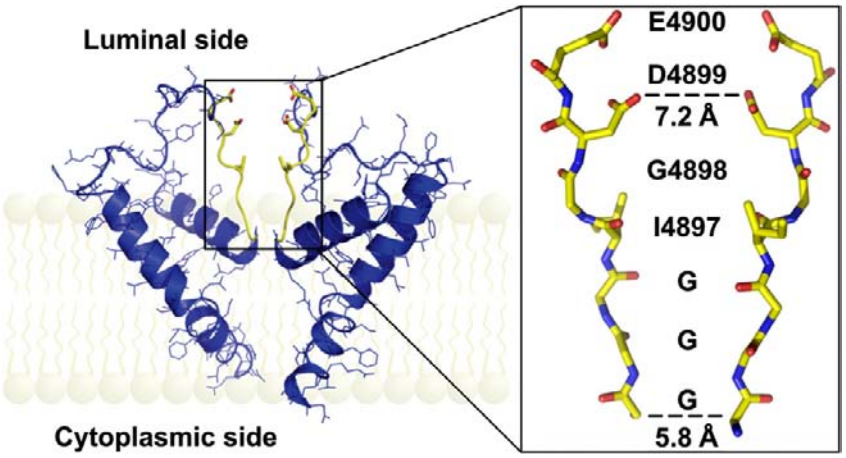

FIGURE 45.13 Pore model of RyR1. (Left panel) Two opposing RyR1 monomers (shown is only one of the six membrane spanning segments per monomer) in cartoon representation. The selectivity filter (4894GGGIGDE) is shown in yellow. (Right panel) Selectivity filter region of two opposing RyR1 monomers in stick representation. The sequence is shown along the path of the ions. *(From Ramachandran et al. PLoS Comput Biol. 5, e1000367, 2009.)*

lipid bilayers and *[^{3}H]ryanodine binding*. These studies have shown that RyRs are *Ca^{2+}-gated channels* that are activated by micromolar Ca^{2+} concentrations and inhibited by millimolar Ca^{2+} concentrations (see Fig. 45.10) (Lanner et al., 2010). Mg^{2+} inhibits RyRs by binding to high-affinity and low-affinity Ca^{2+} binding sites. ATP complexed with Mg^{2+} modifies regulation of RyRs by Ca^{2+} indicating that it is an allosteric modulator of Ca^{2+}-gated RyR activity. In addition to cytosolic Ca^{2+}, SR luminal Ca^{2+} regulates RyRs at several channel sites. Ca^{2+} binds to luminal channel sites and, by passing through the channel, accesses cytosolic Ca^{2+}-activation and inactivation sites.

VIID. RyR-Associated Proteins

A large number of junctional SR membrane proteins and cytosolic and SR luminal proteins have been reported to form a macromolecular complex with the RyRs.

Kinases and phosphatases that are part of the RyR1 and RyR2 multiprotein complexes include protein kinase A (PKA), Ca^{2+}/calmodulin-dependent protein kinase II (CaMKII) and protein phosphatase 1 and protein phosphatase 2A (Zalk et al., 2007). RyR1 has been reported to be phosphorylated at Ser2843. RyR2 is phosphorylated at Ser-2030 by PKA, at Ser-2809 by PKA and CaMKII (corresponding to Ser2843 in RyR1) and at Ser-2815 by CaMKII. Phosphorylation of RyRs by protein kinases has been suggested to result in leaky SR Ca^{2+} channels (see below).

Calmodulin (CaM) is a small, cytoplasmic Ca^{2+}-binding protein that regulates cellular activities including protein kinases and ion channels. RyRs interact with CaM in the absence and presence of Ca^{2+} (Balshaw et al., 2002). The Ca^{2+}-free and Ca^{2+}-bound forms of CaM bind to a highly conserved CaM-binding domain of RyRs. CaM inhibits the three mammalian RyR isoforms at micromolar Ca^{2+} concentrations. At submicromolar Ca^{2+} concentrations, RyR2 is also inhibited by CaM, but RyR1 and RyR3 are activated to different extents by CaM. Mutagenesis, peptide studies and cryoelectron microscopy suggest that Ca^{2+}-free and Ca^{2+}-bound forms of CaM bind to an overlapping region distal to the effector site (ion pore) (Lanner et al., 2010). This suggests that CaM exerts its effects allosterically over relatively long distances within the RyRs. To determine the physiological importance of CaM regulation of RyR2, a mutant mouse was generated with three amino acid substitutions in the CaM-binding site (Yamaguchi et al., 2007). Mice expressing only the mutant form of RyR2 have cardiac hypertrophy as early as 1 day after birth and die around 2 weeks after birth, which suggests that CaM inhibition of RyR2 is required for normal cardiac function in mice.

Other RyR associated proteins include S100A1, triadin, junctin, JP-45, junctate, juncophilin, homer, sorcin, selenoprotein 1 and calseqestrin.

VIIE. Pharmacology of RyRs

A large number of pharmacological reagents modulate the activity of the RyRs. Exogenous effectors found to affect RyR function include ryanodine (see Fig. 45.11A) and other ryanoids, caffeine (see Fig. 45.11B) and other xanthines, toxins, anthraquinones, phenol derivatives, dantrolene, local anesthetics and polycationic and sulfhyryl reacting reagents.

VIIF. RyRs and Muscle Disorders

Mutations in RyR1 give rise to muscle diseases, *malignant hyperthermia* (MH), *central core disease* (CCD) and *multiminicore disease* (MmD) (Lanner et al., 2010). MH is an inherited disease that causes a rapid rise in body temperature and muscle contraction when the affected person receives general anesthesia. MH-linked mutations were

initially mapped to the NH_2 and central domains; however, more recently identified MH mutations appear to be distributed throughout the entire RyR1 coding sequence. CCD is an autosomal dominant congenital myopathy leading to the formation of cores void of mitochondria and oxidative enzymes. In many cases, dominant RyR1 mutations linked to CCD localize to the COOH-terminal domain of the channel. Single channel measurements indicate that CCD mutants lose the ability to conduct Ca^{2+}. MmD is an autosomal recessive congenital myopathy leading to formation of multiple small areas of disorganized sarcomeres. MmD is a genetically heterogeneous disease that is linked to recessive mutations in RyR1 and selenoprotein 1, an RyR1-associated protein that is thought to maintain the receptors normal response to redox active molecules.

RyR2 mutations are associated with catecholaminergic polymorphic ventricular tachycardia and arrhythmogenic right ventricular cardiomyopathy (Lanner et al., 2010). A deficiency in SR lumenal cardiac calsequestrin and missense mutation D307H also result in imbalances of Ca^{2+} handling and catecholaminergic polymorphic ventricular tachycardia. Overexpression of CSQ2 results in severe cardiac hypertrophy in mice. Abnormal Ca^{2+} handling is also observed in mice that lack or overexpress RyR-associated proteins including triadin (Eltit et al., 2010) and junctin (Pritchard and Kranias, 2009).

Loss of the small 12 and 12.6 kDa FK506-binding proteins from RyR1 and RyR2 has been suggested to result in leaky Ca^{2+} channels (Zalk et al., 2007; Kushnir et al., 2010; Lanner et al., 2010). In failing hearts, PKA hyperphosphorylation of RyR2 has been reported to lead to removal of the FKBP12.6 subunit and increased channel activity. In skeletal muscle of animal models with heart failure and patients with heart diseases, exercise is linked to hyperphosphorylation, FKBP12 depletion of the skeletal muscle RyR1, increased RyR1 channel activity and decreased exercise capacity. However, other laboratories have failed to confirm this. In addition to PKA-mediated phosphorylation, mechanisms implicated in generation of "leaky" release channels include increased S-nitrosylation, oxidation and loss of protein phosphatases 1 and 2A and phosphodiesterase 4D from the RyR macromolecular complexes. A 1,4-benzothiazepine derivative, JTV519 (also known as K201), and the more specific derivative S107, have been reported to improve muscle function by stabilizing the RyR−FKBP complexes.

VIII. PHYSIOLOGICAL INTERACTIONS BETWEEN THE DHPR AND RyR1

At the triad junction, a unique intracellular signal transduction occurs whereby a voltage-gated Ca^{2+} channel on an extracellular membrane controls the opening of a separate Ca^{2+} channel on an intracellular membrane. The unique structure of the RyR1, with a Ca^{2+} channel domain embedded in the SR and a large cytosolic domain facing cytosolic regions of the DHPR, suggests that opening and closing of RyR1 could be remotely controlled by the DHPR. The essential steps in this coupling are: detection of the action potential depolarization by voltage-sensing DHPRs in the t-tubules, interactions between the DHPR and RyR1 leading to RyR1 channel opening and Ca^{2+} efflux from the SR.

VIIIA. Voltage Sensing

It was recognized early that EC coupling in fast skeletal muscles of higher vertebrates is directly controlled by membrane potential, without a requirement for extracellular Ca^{2+}. This contrasts with EC coupling in the skeletal muscles of some lower invertebrates and cardiac muscle, in which Ca^{2+} influx through sarcolemmal Ca^{2+} channels is absolutely required for contraction. In cardiac muscle, the Ca^{2+} that enters through the cardiac-specific DHPR ($\alpha 1_c$) functions as a second messenger to activate the cardiac ryanodine receptor isoform, RyR2. This process in cardiac muscle is termed *calcium-induced calcium release*. In a classic experiment, it was demonstrated that a frog skeletal muscle stimulated by action potentials is able to twitch continuously in the complete absence of extracellular Ca^{2+} (Armstrong et al., 1972). Similarly, voltage-clamp experiments demonstrated that a skeletal muscle fiber can develop tension provided only that the membrane is depolarized to a minimum potential and duration, termed the *mechanical threshold*. That is, when the Na^+, K^+ and Cl^- ion channels which mediate the action potential are blocked and/or their permeant ions are removed, all that is required to activate contraction in skeletal muscle is a suprathreshold change in membrane potential. A precise relationship between tension and membrane potential exists in skeletal muscle (Fig. 45.14); development of tension is steeply voltage-dependent in the range from −60 to −40 mV.

Subsequently, Schneider and Chandler (1973) discovered the presence in skeletal muscle membranes of mobile intramembrane charges whose movement could be detected electrically as a voltage-dependent dielectric current, termed *charge movement* (Fig. 45.15). This charge movement was steeply voltage-dependent in the same range of potentials as mechanical activation. Based on the similar kinetics and voltage dependence of charge movement and mechanical activation, they proposed that these gating currents reflected the movement of charged intramembrane domains of a molecule in the t-tubules that functioned as the *voltage sensor* for EC coupling. These measurements suggested that positively-charged regions of the DHPR undergo a net outward movement upon depolarization, away from RyR1. Therefore, they suggested that the voltage sensor might interact directly with a hypothetical Ca^{2+}-release channel on the SR to cause its opening. This mechanical or

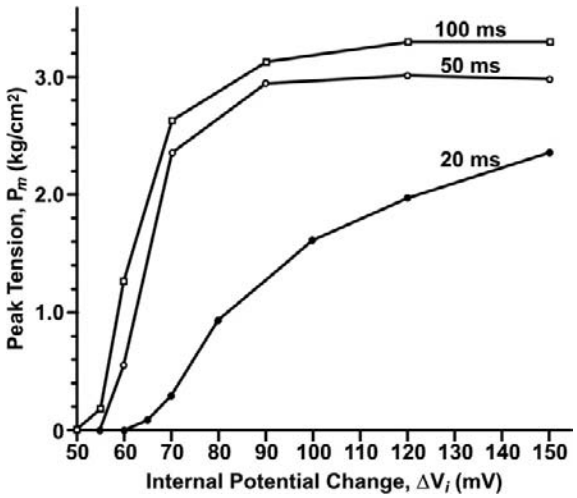

FIGURE 45.14 Voltage-dependence of tension in the absence of an action potential. The fibers were depolarized by holding the membrane potential constant for 20–100 ms with a voltage-clamp. Tension was measured simultaneously with a transducer attached to one tendon. *(Reproduced from The Journal of General Physiology, 1984, 84,133–154, by copyright permission of The Rockefeller University Press.)*

allosteric model of EC coupling, formulated before the proteins of the triad junction had been identified, has formed the framework for subsequent investigations into the nature of the coupling mechanism.

Several lines of evidence led to the identification of the voltage sensor as the DHPR/t-tubule Ca^{2+} channel (Rios and Pizarro, 1991, Schneider, 1994, Melzer et al., 1995). A definitive identification came following the cloning of the skeletal muscle Ca^{2+} channel (Tanabe et al., 1987) and its use in experiments on dysgenic mice (Adams and Beam, 1990). Muscular dysgenesis is a lethal disorder arising from a single point mutation in the gene for the DHPR $\alpha 1_s$; it results in loss of DHPR protein, the absence of slow Ca^{2+} currents and charge movement and failure of EC coupling. Tanabe and colleagues (Tanabe et al., 1988) demonstrated that Ca^{2+} currents, charge movement and EC coupling could be restored in dysgenic muscle fibers by transfecting the cDNA for the $\alpha 1_s$ subunit of the DHPR. This demonstration established the DHPR Ca^{2+} channel as the essential voltage-sensing molecule in EC coupling.

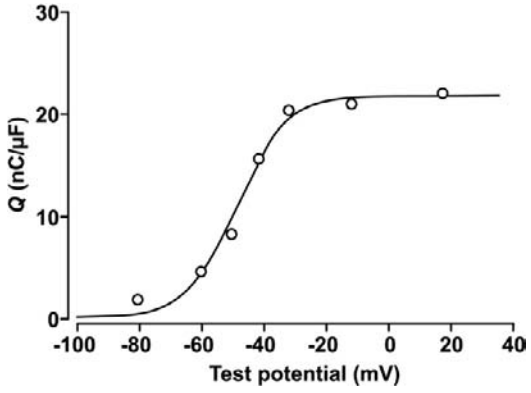

FIGURE 45.15 Voltage-dependence of charge movement (nC/μF vs membrane potential, mV). Charge moved at each potential was obtained by integrating the voltage-dependent capacity current, normalized to the fiber linear capacitance near the resting potential. Symbols represent the mean values of charge moved at the "on" and "off" of the pulse. The continuous curve is a fit of the data to a two-state Boltzmann function, with parameters: $V_{mid} = -47.7$ mV, $k = 8$ mV and $Q_{max} = 21.5$ nC/μF. *(From Chandler et al., 1976.)*

VIIIB. The Myoplasmic Ca^{2+} Release Transient and SR Ca^{2+} Release Flux

In studies using intact skeletal muscle cells, SR Ca^{2+} release is detected by monitoring myoplasmic Ca^{2+} transients using Ca^{2+} indicator dyes introduced into the myoplasm (as shown in Fig. 45.4B). These measurements record the global Ca^{2+} change occurring throughout the myoplasm. Much useful information on the kinetics and voltage-dependence of SR Ca^{2+} release under physiological conditions has come from these studies (Rios and Pizarro, 1991, Melzer et al., 1995). These studies confirmed that a strict relationship exists between the voltage-dependence of Ca^{2+} release and voltage-dependent charge movement, as expected for a coupling mechanism which is controlled by the t-tubule membrane potential. Importantly, it was shown that SR Ca^{2+} release can both be turned on by membrane depolarization and turned off by membrane repolarization. Other studies have also demonstrated that considerable cross-talk exists between t-tubule Ca^{2+} channel functions and SR Ca^{2+} release (Sheridan et al., 2006; Dirksen, 2009). For example, the RyR1 release channel, through its interaction with calsequestrin, is able to respond to surface depolarization in a manner that depends on the Ca^{2+} load within the SR. Changes in SR Ca^{2+} load are reflected in the kinetics of charge movement and the rate of Ca^{2+} release. In addition, although Ca^{2+} entry is not required for skeletal muscle type EC coupling, manipulations that alter the RyR1 or the Ca^{2+} release transient also modify the slow Ca^{2+} current through DHPRs. Such bidirectional cross-talk between the DHPR and RyR, involving both forward and retrograde interactions, is expected for a mechanism that involves protein–protein interactions within a macromolecular complex.

The global myoplasmic Ca^{2+} change (see Fig. 45.4) arises from the summation of thousands of individual Ca^{2+} release events. Discrete, local Ca^{2+} signals, termed Ca^{2+} *sparks*, have been detected in skeletal and cardiac muscle (Fig. 45.16) (Cheng and Lederer, 2008). These discrete Ca^{2+} changes are limited in time and space and can occur spontaneously or in response to membrane depolarization. The Ca^{2+} spark does not reflect the unitary opening of a single RyR1 channel, but is proposed to report an elementary unit of SR Ca^{2+} release arising from

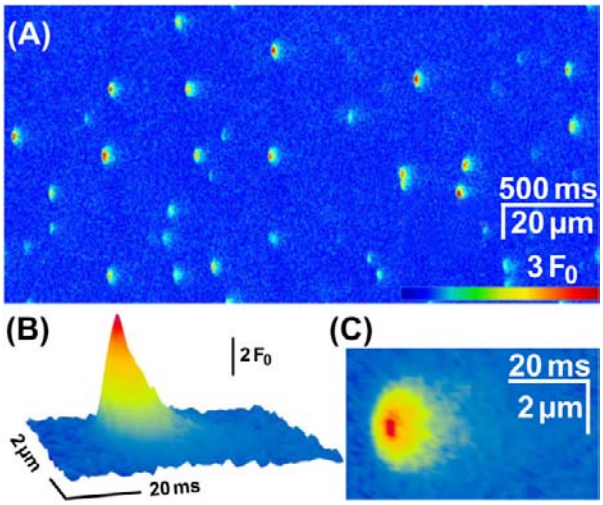

FIGURE 45.16 Spontaneous elementary calcium release events in an amphibian skeletal muscle. (A) A typical line scan image from a permeabilized frog skeletal muscle fiber immersed into a glutamate-based internal solution containing 50 µM fluo-4 as the calcium-sensitive fluorescence indicator. The sparks occur with high frequency and appear relatively homogenous. Time course (B) and spatial distribution (C) of the average spark in amphibian skeletal muscle. *(Reproduced with permission from Csernoch et al., 2004.)*

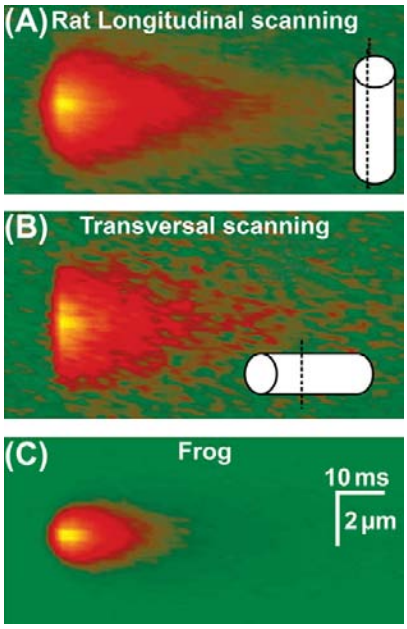

FIGURE 45.17 Elementary Ca^{2+} release events, termed "embers", in a mammalian skeletal muscle of the rat (A, B) compared to frog (C). Averages detected in line scans parallel (A) or perpendicular (B) to the fiber axis. Mammalian embers are wider and longer than the frog sparks. *(Reproduced with permission from Zhou et al., 2003.)*

a Ca^{2+}-release unit. Calcium-release units consist of a cluster of DHPRs, RyR1s and possibly other proteins acting together as a functional unit (see below). Thus, the global depolarization-triggered Ca^{2+} transient represents a summation of discrete unitary events. This mechanism may allow a more graded control of Ca^{2+} release. Some important differences in sparks exist between vertebrate amphibian and mammalian skeletal muscles. Mammalian muscles do not readily show spark activity. Rather, discrete Ca^{2+} release events, termed embers, with longer duration and constant amplitude are observed (Fig. 45.17) (Zhou et al., 2003, Csernoch et al., 2004; Klein and Schneider, 2006). The voltage dependence of embers is manifested in the duration and latency, but not in the amplitude of the individual events. It is possible that these differences in the elementary Ca^{2+} release events may reflect the different protein composition of the unitary Ca^{2+}-release units of amphibian and mammalian muscle. Although both species share the same two key proteins — a skeletal DHPR and RYR1 — amphibian muscle has an addition RyR3 isoform that is positioned peripheral to the double rows of RyR1 which oppose the DHPR tetrads. These parajunctional RyR3 channels in amphibian muscle do not associate with DHPR tetrads and may participate in a secondary Ca^{2+}-induced Ca^{2+} release, to generate sparks with properties similar to those in cardiac muscle. As described above, additional junctional proteins associate with the RyR1 and the molecular composition of the complete, elementary Ca^{2+}-release complex in amphibian and mammalian muscles is not yet defined.

VIIIC. Molecular Interactions Between the DHPR and RyR

The molecular mechanisms by which the pore of RyR1 opens under control of the t-tubule DHPR/Ca^{2+} channel has been the subject of intense research and is still not entirely resolved. Studies using dysgenic and transgenic mice have provided powerful experimental models for identifying the key proteins that are absolutely required for skeletal type EC coupling (Beam and Bannister, 2010). These are the $\alpha 1_s$ and β_{1a} subunits of the DHPR and RyR1. Mice null for either the $\alpha 1_s$ or β_{1a} subunit or the DHPR, or mice lacking the RYR1 protein, show an EC coupling dead phenotype and die perinatally. On the other hand, ablation of the $\alpha 2\text{-}\delta_1$ *or* γ_1 subunits of DHPR has little effect on EC coupling (Obermair et al., 2008).

The muscular dysgenesis mouse (lacking $\alpha 1_s$) has been used to identify further regions of DHPR $\alpha 1_s$ that are critical for interactions with RyR1. The α subunits of the skeletal ($\alpha 1_s$) and cardiac ($\alpha 1_c$) DHPR share a high degree of homology, but only the $\alpha 1_s$ can restore a skeletal-type EC coupling. When the skeletal muscle $\alpha 1_s$ subunit was expressed in dysgenic myotubes, Ca^{2+} release could be elicited in response to electrical depolarization and did not require Ca^{2+} entry; whereas, Ca^{2+} entry was required to elicit Ca^{2+} release when the cardiac $\alpha 1_c$ subunit was expressed. The main sequence differences between $\alpha 1_s$ and $\alpha 1_c$ reside in the large cytosolic regions at the N- and C-termini and the

linker sequences I–II, II–III and III–IV. By constructing chimeric DHPRs with various mixes of cardiac and skeletal sequences, Beam and collaborators (Tanabe et al., 1990) demonstrated that the 138-amino-acid cytoplasmic sequence between domains II and III is a critical determinant of skeletal-type EC coupling. A chimeric DHPR having the cardiac protein backbone but the not critical skeletal II–III linker could elicit skeletal-type EC coupling when expressed in dysgenic myotubes. Further experiments demonstrated that the cytosolic I–II linker, which binds the cytosolic β_{1a} subunit, is also essential for skeletal-type EC coupling. EC coupling is lost in myotubes of transgenic mice when the β subunit gene is knocked out, but is rescued when β_{1a} (but not the cardiac β_{2b}) is expressed. Thus, the interaction of β_{1a} with the I–II linker of the skeletal α_{1s} is also required for skeletal-muscle-type EC coupling.

Other cytosolic regions on the $\alpha 1_s$ subunit have been implicated in interactions with RyR1. A mutation in the III–IV cytosolic linker of the human DHPR (A1086H) is associated with susceptibility to one form of malignant hyperthermia (MH), a hereditary skeletal muscle disorder that is characterized by an uncontrolled, sustained Ca^{2+} release (Monnier et al. 1997). Studies using more complex chimeras between $\alpha 1_s$ and $\alpha 1_c$ have identified specific sites within the II–III linker which interact with RyR1. Biochemical studies have also demonstrated binding of specific fragments of the II–III sequence to RyR1. However, these studies have not yet yielded a consistent picture of the specific sequences which form interaction sites between DHPR and RyR1.

Similarly, regions of RyR1 critical for skeletal-type EC coupling have been studied using mice having a disrupted RyR1 gene (dyspedic mice). Dyspedic mice lack EC coupling, as expected and, in addition, have a 30-fold lower density of calcium channel current (Nakai et al., 1996). Thus, the absence of RyR also alters DHPR function, as expected if the DHPR and RYR1 associate in a macromolecular complex. Expression of the cDNA for RyR1 in dyspedic myotubes restores EC coupling and enhances the DHPR calcium current. This suggests that RyR1, in addition to receiving the EC coupling signal from the DHPR, also transmits a retrograde signal that enhances the function of skeletal DHPRs as calcium channels. These interactions require the skeletal muscle RyR1 isoform and indicate that the identity of the ryanodine receptor isoform also determines the mode of EC coupling. Expression of the predominant cardiac isoform, RyR2, did not restore skeletal-type EC coupling or enhance DHPR calcium channel activity (Nakai et al., 1997). Other studies combining freeze-fracture and pharmacology demonstrate that the spatial orientation of DHPRs and the conformational state of RyR1 are intimately related, further supporting the idea that the DHPR and RyR1 are capable of bidirectional interactions. The average distance between centers of each adjacent DHPR within a tetrad ($\approx 19.5 \approx$ nm) is decreased by ≈ 2 nm upon application of ryanodine at a concentration (500 μM) which locks RyR1 in a subconductance state (Paolini et al., 2004). Thus, the functional state of RyR1 is able to alter the spatial orientation of DHPRs within a tetrad, a phenomenon that could only be a result of physical coupling between RyR1 and the DHPR.

Biochemical studies of isolated triad membranes and proteins in vitro have also provided compelling evidence for protein–protein interactions between the skeletal DHPR and RyR1 (Meissner and Lu, 1995; Leong and MacLennan, 1998) and confirmed that the skeletal muscle isoforms of both DHPR and RyR1 are essential for skeletal type EC coupling. Peptides composed of either the skeletal or cardiac II–III linker sequence can activate isolated RyR1s (Lu et al., 1995), but do not activate the cardiac RyR2 isoform. Binding assays have also been used to identify regions on RyR1 that interact specifically with the skeletal DHPR. However, these studies have not yet led to a consensus on the specific interaction sites. Taken together, the body of biochemical evidence and results of studies using transgenic mice indicate that a minimal complex containing the skeletal muscle DHPR α_{1s} and β_{1a} subunits plus RyR1 is required to initiate Ca^{2+} release by the physiologically relevant (independent of Ca^{2+} entry) mode in fast twitch skeletal muscle. Moreover, the data suggest that the bidirectional interaction between DHPR and RyR1 may involve multiple contact points on both proteins and possibly low affinity interactions (Sheridan et al., 2006; Beam and Bannister, 2010). A more specific identification of the interaction sites will likely become available when detailed structural information becomes available from crystallographic studies.

VIIID. Overall Control and Integration of Ca^{2+}-Release Events

There is general agreement that the initial event leading to calcium release in vertebrate skeletal muscle is a depolarization-driven interaction between a DHPR tetrad and at least one RyR1 tetramer. However, the mechanism by which this signal is communicated to adjacent RyRs which do not underlie a DHPR tetrad is less well understood. The alternate disposition of DHPR tetrads opposite every other RyR1 suggests a dual control of RyR1 activation. One RyR1 may be opened by allosteric movements of the associated DHPR tetrad (a coupled RyR1), while a neighboring RyR1 (non-coupled to a tetrad) may be opened by a different mechanism. One early proposal was that the local Ca^{2+} released through coupled RyR1s binds to and activates adjacent, non-coupled RyR1s (Fig. 45.18), acting as a ligand-gated channel. However, all of the functional evidence indicates that there is little Ca^{2+}-induced-Ca^{2+} release in the mammal. An alternate proposal is that the

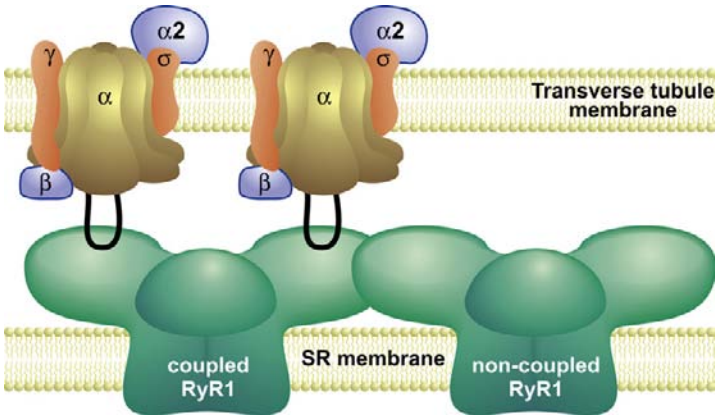

FIGURE 45.18 Integration of Ca^{2+} release from coupled and non-coupled RyR1s. RyR1s associate with each other on the SR surface of the triad junction in an ordered array. Every alternate RyR1 is coupled to a tetrad of four DHPRs in the transverse tubule membrane. This schematic depicts a cross-sectional plane through two subunits of a RyR1 (left) interacting with two DHPRs. Voltage-driven movements of the DHPR initiate molecular interactions between cytosolic regions of the DHPR (II–III loop) and a coupled RyR1, leading to RyR1 channel opening. This initiating event activates non-coupled RyR1s, possibly via coordinated interactions between adjacent RyR1s, to effect a rapid and synchronous efflux of Ca^{2+}.

conformational changes initiated between a coupled RyR1 and a DHPR tetrad is communicated to non-coupled RyR1s through coordinated interactions between physically linked RyR1s. In this model, both populations of RyR1s are activated by depolarization without requiring Ca^{2+} as a ligand. This model is suggested by the tight packing of RyR1s in an ordered, interlocking array. In this model, clusters of RyR1s open simultaneously as a functional Ca^{2+} release unit. Opening of one RyR1 by its coupled DHPR tetrad results in simultaneous opening of all contiguous RyRs in the cluster. The minimal number of RyR1s which constitute an elementary Ca^{2+}-release unit (generating an "ember") is not yet resolved. Such clusters of RyRs operating as a functional unit is expected to generate fast local Ca^{2+} release events and a more synchronous global change in myoplasmic Ca^{2+}. An additional mechanism may operate in amphibian muscle where parajunctional RyR3 channels are also present. The RyR3 channels may be opened by a Ca^{2+}-induced-Ca^{2+}-release mechanism, similar to the cardiac RyR2 channel, and generate the more cardiac-like sparks recorded from frog muscle.

VIIIE. Modulation of EC Coupling

EC coupling can be modulated in response to different demands of muscle use. Potential regulatory sites on both the DHPR and RyR1 have been identified. The DHPR α_{1s} subunit contains consensus phosphorylation sites including a serine residue, Ser 687, within the critical II–III loop that is rapidly phosphorylated by a cAMP-dependent kinase. Phosphorylation of this residue is required for binding of the II–III loop to RyR1 (but not RyR2), but only the dephosphorylated II–III loop can activate the RyR (Lu et al., 1995). Moreover, Ca^{2+} release can be both inhibited and activated by Ca^{2+} acting at specific sites on the RyR1 or α_{1s} (El-Hayek et al., 1995; Meissner, 2004). As noted (see Section VI), RyR1 has both Ca^{2+}-activating and Ca^{2+}-inactivation sites as well as a CaM binding site which can bind either CaM or the soluble protein S100 to modulate Ca^{2+} release. The complete RyR1 complex includes other associated proteins which contribute to EC coupling and to the structural integrity of the triad junction. Finally, long-term regulation of EC coupling may occur at the level of gene expression. It is known that the expression of α_{1s} can be altered during adaptation to physiological demands, including altered patterns of nerve activity, exercise, changes in the load-bearing state and metabolic or endocrine status.

ACKNOWLEDGMENT

Support by National Institutes of Health grants AR018697 and HL073501 and the Physiology Research Fund of the University of Cincinnati is gratefully acknowledged.

BIBLIOGRAPHY

Adams, B. A., & Beam, K. G. (1990). Muscular dysgenesis in mice: a model system for studying excitation-contraction coupling. [Review]. *FASEB J, 4*, 2809–2816.

Armstrong, C. M., Bezanilla, F. M., & Horowicz, P. (1972). Twitches in the presence of ethylene glycol bis(-aminoethyl ether) -N, N'-tetracetic acid. *Biochim Biophys Acta, 267*, 608.

Balshaw, D. M., Yamaguchi, N., & Meissner, G. (2002). Modulation of intracellular calcium-release channels by calmodulin. *J Membr Biol, 185*, 1–8.

Beam, K. G., & Bannister, R. A. (2010). Looking for answers to EC coupling's persistent questions. *J Gen Physiol, 136*, 7–12.

Caswell, A. H., Lau, Y. H., Garcia, M., & Brunschwig, J. P. (1979). Recognition and junction formation by isolated transverse tubules and terminal cisternae of skeletal muscle. *J Biol Chem, 254*, 202–208.

Cheng, H., & Lederer, W. J. (2008). Calcium sparks. *Physiol Rev, 88*, 1491–1545.

Csernoch, L., Zhou., J., Stern, M. D., Brum, G., & Rios, E. (2004). The elementary events of Ca^{2+} release elicited by membrane depolarization in mammalian muscle. *J Physiol, 557*, 43–58.

Dirksen, R. T. (2009). Checking your SOCCs and feet: the molecular mechanisms of Ca^{2+} entry in skeletal muscle. *J Physiol, 587*, 3139–3147.

Dulhunty, A. F. (1984). Heterogeneity of t-tubule geometry in vertebrate skeletal muscle fibres. *J Muscle Res Cell Motil, 5*, 333–347.

El-Hayek, R., Antoniu, B., Wang, J., Hamilton, S. L., & Ikemoto, N. (1995). Identification of calcium release-triggering and blocking regions of the II-III loop of the skeletal muscle dihydropyridine receptor. *J Biol Chem, 270*, 22116–22118.

Eltit, J. M., Feng, W., Lopez, J. R., et al. (2010). Ablation of skeletal muscle triadin impairs FKBP12/RyR1 channel interactions essential for maintaining resting cytoplasmic Ca^{2+}. *J Biol Chem, 285*, 38453–38462.

Felder, E., & Franzini-Armstrong, C. (2002). Type 3 ryanodine receptors of skeletal muscle are segregated in a parajunctional position. *Proc Natl Sci USA, 99*, 1695–1700.

Fleischer, S., & Inui, M. (1989). Biochemistry and biophysics of excitation-contraction coupling. *Annu Rev Biophys Biophys Chem, 18*, 333–364.

Franzini-Armstrong, C., & Jorgensen, A. O. (1994). Structure and development of E-C coupling units in skeletal muscle. *Annu Rev Physiol, 56*, 509–534.

Franzini-Armstrong, C., & Peachey, L. D. (1981). Striated muscle-contractile and control mechanisms. *J Cell Biol, 91*, 166s–186s.

Franzini-Armstrong, C., & Protasi, F. (1997). Ryanodine receptors of striated muscles: a complex channel capable of multiple interactions. *Physiol Rev, 77*, 699–729.

Gillespie, D., Xu, L., Wang, Y., & Meissner, G. (2005). (De)constructing the ryanodine receptor: modeling ion permeation and selectivity of the calcium release channel. *J Phys Chem B, 109*, 15598–15610.

González-Serratos, H. (1971). Inward spread of activation in vertebrate muscle fibres. *J Physiol, 212*, 777–799.

Hodgkin, A. L., & Horowicz, P. (1957). Effects of K and Cl on the membrane potential of isolated muscle fibres. *J Physiol, 137*, 30P.

Jong, D. S., Pape, P. C., Geibel, J., & Chandler, W. K. (1996). Sarcoplasmic reticulum calcium release in frog cut muscle fibres in the presence of a large concentration of EGTA. *Soc Gen Physiol Ser, 51*, 255–268.

Klein, M. G., & Schneider, M. F. (2006). Ca^{2+} sparks in skeletal muscle. *Prog Biophys Mol Biol, 92*, 308–332.

Kushnir, A., Betzenhauser, M. J., & Marks, A. R. (2010). Ryanodine receptor studies using genetically engineered mice. *FEBS Lett, 584*, 1956–1965.

Lanner, J. T., Georgiou, D. K., Joshi, A. D., & Hamilton, S. L. (2010). Ryanodine receptors: structure, expression, molecular details, and function in calcium release. *Cold Spring Harb Perspect Biol,* 2.

Leong, P., & MacLennan, D. H. (1998). Complex interactions between skeletal muscle ryanodine receptor and dihydropyridine receptor proteins. *Biochem Cell Biol, 76*, 681–694.

Lu, X., Xu, L., & Meissner, G. (1995). Phosphorylation of dihydropyridine receptor II-III loop peptide regulates skeletal muscle calcium release channel function. Evidence for an essential role of the beta-OH group of Ser687. *J Biol Chem, 270*, 18459–18464.

Meissner, G. (2004). Molecular regulation of cardiac ryanodine receptor ion channel. *Cell Calcium, 35*, 621–628.

Meissner, G. (1984). Adenine nucleotide stimulation of Ca2+-induced Ca2+ release in sarcoplasmic reticulum. *J Biol Chem, 259*, 2365–2374.

Meissner, G., & Lu, X. (1995). Dihydropyridine receptor-ryanodine receptor interactions in skeletal muscle excitation-contraction coupling. *Biosci Rep, 15*, 399–408.

Melzer, W., Herrmann-Frank, A., & Luttgau, H. C. (1995). The role of Ca2+ ions in excitation-contraction coupling of skeletal muscle fibres. *Biochim Biophys Acta, 1241*, 59–116.

Monnier, N., Procaccio, V., Stieglitz, P., & Lunardi, J. (1997). Malignant-hyperthermia susceptibility is associated with a mutation of the alpha 1-subunit of the human dihydropyridine-sensitive L-type voltage-dependent calcium-channel receptor in skeletal muscle. *Am J Hum Genet, 60*, 1316–1325.

Nakai, J., Dirksen, R. T., Nguyen, H. T., Pessah, I. N., Beam, K. G., & Allen, P. D. (1996). Enhanced dihydropyridine receptor channel activity in the presence of ryanodine receptor. *Nature, 380*, 72–75.

Nakai, J., Ogura, T., Protasi, F., Franzini-Armstrong, C., Allen, P. D., & Beam, K. G. (1997). Functional nonequality of the cardiac and skeletal ryanodine receptors. *Proc Natl Acad Sci USA, 94*, 1019–1022.

Obermair, G. J., Tuluc, P., & Flucher, B. E. (2008). Auxiliary Ca(2+) channel subunits: lessons learned from muscle. *Curr Opin Pharmacol, 8*, 311–318.

O'Brien, J., Meissner, G., & Block, B. A. (1993). The fastest contracting muscles of nonmammalian vertebrates express only one isoform of the ryanodine receptor. *Biophys J, 65*, 2418–2427.

Paolini, C., Fessenden, J. D., Pessah, I. N., & Franzini-Armstrong, C. (2004). Evidence for conformational coupling between two calcium channels. *Proc Natl Acad Sci USA, 101*, 12748–12752.

Peachey, L. D. (1965). The sarcoplasmic reticulum and transverse tubules of the frog's sartorius. *J Cell Biol, 25*(Suppl), 209–231.

Peachey, L. D., & Eisenberg, B. R. (1978). Helicoids in the T system and striations of frog skeletal muscle fibers seen by high voltage electron microscopy. *Biophys J, 22*, 145–154.

Pritchard, T. J., & Kranias, E. G. (2009). Junctin and the histidine-rich Ca2+ binding protein: potential roles in heart failure and arrhythmogenesis. *J Physiol, 587*, 3125–3133.

Rios, E., & Pizarro, G. (1991). Voltage sensor of excitation-contraction coupling in skeletal muscle. *Physiol Rev, 71*, 849–908.

Samsó, M., & Wagenknecht, T. (1998). Contributions of electron microscopy and single-particle techniques to the determination of the ryanodine receptor three-dimensional structure. *J Struct Biol, 121*, 172–180.

Schneider, M. F. (1994). Control of calcium release in functioning skeletal muscle fibers. [Review]. *Annu Rev Physiol, 56*, 463–484.

Schneider, M. F., & Chandler, W. K. (1973). Voltage dependent charge movement of skeletal muscle: a possible step in excitation-contraction coupling. *Nature, 242*, 244–246.

Sheridan, D. C., Takekura, H., Franzini-Armstrong, C., Beam, K. G., Allen, P. D., & Perez, C. F. (2006). Bidirectional signaling between calcium channels of skeletal muscle requires multiple direct and indirect interactions. *Proc Natl Acad Sci USA, 103*, 19760–19765.

Suh-Kim, H., Wei, X., Klos, A., et al. (1996). Reconstitution of the skeletal muscle dihydropyridine receptor. Functional interaction among alpha 1, beta, gamma and alpha 2 delta subunits. *Receptors Channels, 4*, 217–225.

Sutko, J. L., & Airey, J. A. (1996). Ryanodine receptor Ca2+ release channels: does diversity in form equal diversity in function? *Physiol Rev, 76*, 1027–1071.

Tanabe, T., Beam, K. G., Adams, B., Niidome, T., & Numa, S. (1990). Regions of the skeletal muscle dihydropyridine receptor critical for excitation-contraction coupling. *Nature, 346*, 567–569.

Tanabe, T., Beam, K. G., Powell, J., & Numa, S. (1988). Restoration of excitation-contraction coupling and slow calcium current in dysgenic muscle by dihydropyridine receptor complementary DNA. *Nature, 336*, 134–139.

Tanabe, T., Takeshima, H., Mikami, A., et al. (1987). Primary structure of the receptor for calcium channel blockers from skeletal muscle. *Nature, 328*, 313−318.

Tinker, A., Lindsay, A. R., & Williams, A. J. (1992). A model for ionic conduction in the ryanodine receptor channel of sheep cardiac muscle sarcoplasmic reticulum. *J Gen Physiol, 100*, 495−517.

Xu, L., Wang, Y., Gillespie, D., & Meissner, G. (2006). Two rings of negative charges in the cytosolic vestibule of type-1 ryanodine receptor modulate ion fluxes. *Biophys J, 90*, 443−453.

Yamaguchi, N., Takahashi, N., Xu, L., Smithies, O., & Meissner, G. (2007). Early cardiac hypertrophy in mice with impaired calmodulin regulation of cardiac muscle Ca release channel. *J Clin Invest, 117*, 1344−1353.

Yu, F. H., Yarov-Yarovoy, V., Gutman, G. A., & Catterall, W. A. (2005). Overview of molecular relationships in the voltage-gated ion channel superfamily. *Pharmacol Rev, 57*, 387−395.

Vergara, J., & Delay, M. (1986). A transmission delay and the effect of temperature at the triadic junction of skeletal muscle. *Proc R Soc Lond B Biol Sci, 229*, 97−110.

Zalk, R., Lehnart, S. E., & Marks, A. R. (2007). Modulation of the ryanodine receptor and intracellular calcium. *Annu Rev Biochem, 76*, 367−385.

Zhou, J., Brum, G., Gonzalez, A., Launikonis, B. S., Stern, M. D., & Rios, E. (2003). Ca^{2+} sparks and embers of mammalian muscle. Properties of the sources. *J Gen Physiol, 122*, 95−114.

Chapter 46

Contraction of Muscles: Mechanochemistry

Richard J. Paul

Chapter Outline

I. SUMMARY

This chapter focuses largely on muscle structure in relation to muscle mechanics and energetics and relevance to different muscle types. Striated muscle structure is first developed as a paradigm in conjunction with mechanics, leading to the formulation of the sliding-filament theory. Muscle contractility continues with further characterization of the relationships among force, velocity, work and adenosine triphosphate (ATP) utilization. The mechanism at the molecular level, i.e. the cross-bridge cycle, is similarly developed, matching structural and biochemical knowledge with transient mechanical studies. An investigation of the energy requirements in terms of ATP hydrolysis of the cross-bridge cycle is then followed by a discussion of muscle metabolism and the route for synthesis of the ATP necessary for contractile activity. The chapter then shifts from considerations of muscle in general to comparative muscle physiology and behavior of different fiber types. In particular, smooth muscle is treated in detail and its regulation, mechanical properties and energetics are considered and contrasted to those of striated muscle.

II. INTRODUCTION

The generation of force and movement by muscle is an area of physiology and biophysics that has fascinated scientist and layman alike since the dawn of scientific inquiry and reverberates strongly in today's nanomachine quest (Huang and Juluri, 2008). The history of the study of muscle is elegantly chronicled by Dorothy Needham in *Machina Carnis* (1971). Because of its highly organized and repeating structure, skeletal muscle has proven more amenable to structural analysis (such as x-ray diffraction) than most biological tissues. Thus, it has served as a paradigm for unraveling relationships between function and structure. This has become particularly exciting in conjunction with the techniques of molecular biology, which offer the potential for altering particular amino acids and molecular measurements with manipulators, such as laser tweezers. These tools offer the potential for directly testing the links between structure at nanometer resolution and function. The focus of this chapter is on the nature of the muscle mechanics and mechanochemical energy conversion. Muscle is one of the most efficient energy

Cell Physiology Sourcebook. DOI: 10.1016/B978-0-12-387738-3.00046-9

converters known and studies in this area couple classical enzyme kinetics, muscle mechanics and cross-bridge theories (Barclay et al., 2010).

The major focus of this chapter is on the molecular and cellular levels which form the basis understanding muscle contraction for organ and whole organism function, such as sports medicine and kinestheology. Muscle mechanochemistry at the cellular level also has major consequences at the organ and whole-animal levels. Skeletal muscle constitutes approximately 40% of human body mass. If we include cardiac and smooth muscle, the total muscle mass reaches the 50% level. One consequence of this is that approximately 30% of basal metabolism is related to muscle and as much as 90% of a person's total metabolism during strenuous exercise can be related to meeting the energy requirements of muscle. This chemical activity can in turn produce a significant heat load for the organism. Other functions that are associated with the large muscle mass are the storage and mobilization of metabolites (primarily glucose and amino acids). Also, there are significant consequences to alterations in muscle electrolyte metabolism, since it is a major storage site for ions such as H^+, Cl^- and Mg^{2+}. Some of these ramifications are presented as related to molecular processes in muscle.

Our study of the muscle contraction first involves investigation of mechanisms underlying the generation of macroscopic force and shortening. We first consider how force is developed and how the mechanical behavior of muscle is quantitated, a field known collectively as *muscle mechanics*. This is then integrated with the current picture of muscle structure as a first step in constructing theories of muscle function. Next, we consider *muscle energetics*, governed by thermodynamic rules for energy conversion and the constraints they place on models proposed for muscle contraction. We relate energetics and mechanics to the kinetics of the myosin ATPase as a basis for cross-bridge cycling mechanisms. *Muscle metabolism* and the matching of ATP demand with ATP synthesis will complete the picture of mechanochemical energy conversion.

The second major area involves study of the mechanisms underlying the regulation of muscle contraction. The control of intracellular Ca^{2+} concentration, a key intracellular messenger, forms an area of study known as *excitation–contraction coupling*. The intracellular receptors transducing the Ca^{2+} signal reflect the great diversity of types of muscle that have evolved in response to a wide variety of functional needs. These muscles also have much in common. All muscle contains the proteins actin and myosin, which are the locus of the mechanochemical energy conversion. Chemical energy in the form of ATP hydrolysis is the immediate driving reaction for all muscle energy transduction. Another feature common to all muscle types is that calcium ions, at micromolar concentrations, are the primary second messenger in the regulatory mechanisms. We first focus on these common aspects, using a generalized striated muscle as the model. Then with an understanding of these common mechanisms, we consider the different muscle types.

III. THE MECHANISMS OF FORCE PRODUCTION AND SHORTENING: MUSCLE MECHANICS

Studies of the mechanical behavior of muscle have played a central role in our understanding of muscle and have also formed an integral part of the language of muscle physiology (Hill, 1965). These studies before the late 1950s were primarily phenomenological, though they were also important in characterization of muscle performance. Such studies remain important in characterization of muscle myopathies and in current mechanistic studies, e.g. in describing the functional consequences of changing muscle protein isoforms in transgenic animals.

There are two arbitrary but natural divisions in studies of muscle mechanics. The first division involves steady-state relationships in which force and velocity are constant in time. This information was crucial to the development of the three-component model of muscle contraction (see below), a model still valid for whole muscle behavior (Jewell and Wilkie, 1958). Such studies also provided one pillar supporting the sliding-filament theory and were extensively investigated in the 1960s (Gordon et al., 1966).

Studies of mechanical transients form a second division. They assumed a more central importance during the early 1970s (Huxley and Simmons, 1971) with the growing realization that information at the level of individual cross-bridges could be gained from mechanical studies on single fibers. These studies of muscle responses to rapid changes in mechanical constraints are even more valuable to unraveling cross-bridge behavior when coupled with recently improved temporal resolution of x-ray diffraction of muscle (Huxley, 2004; Squire and Knupp, 2005).

IIIA. Steady-State Relations Between Force and Length and the Sliding-Filament Theory

A first step in muscle mechanics involves a description of muscle behavior in terms of relationships between the mechanical variables of force and length. Apparatus for transduction and recording of these variables has evolved considerably over this century, but the historical apparatus is still responsible for much of the language of muscle physiology. Since it was easier to control force than length, by hanging a fixed weight on the muscle, terms such as

preload and afterload entered the vocabulary (see later section on force–velocity relationships). However, in view of what is now known about structure, it is conceptually easier to use length as the independent variable.

Figure 46.1 shows a schematic of an experimental apparatus for measurement of muscle force–length relationships. In this setup, length is the controlled variable and the steady-state force at various lengths is measured. In developing these relationships, we consider the performance of an isolated muscle, or single muscle cell known as a muscle fiber. After mounting in the apparatus, muscle length is adjusted to a specific length then set isometric (fixed total length) and the steady-state force is measured. The relationship between the unstimulated force (often designated as passive force) and muscle length is designated the passive length–tension relationship. This relationship can be characterized as an exponential spring, $F = A_1 + A_2 \exp(A_3 X)$, whose behavior is similar to that of

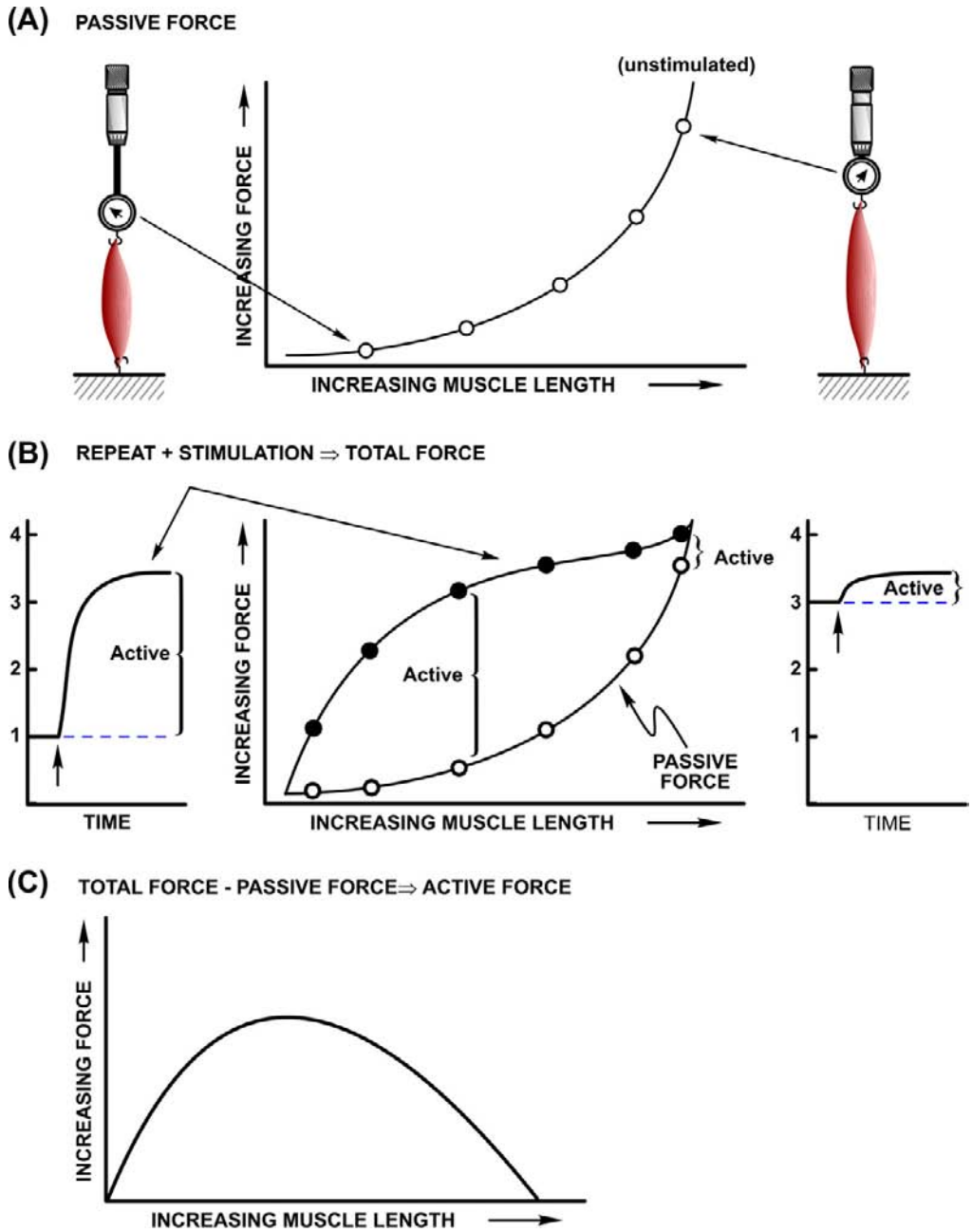

FIGURE 46.1 Measurement and operational definitions of muscle force–length relationships. (A) Relation between isometric force under unstimulated conditions, passive force and muscle length. (B) Relation between isometric force and length under stimulated conditions, total force. (C) Active force operationally defined as the difference between total force and passive force is shown as a function of muscle length.

a rubber band with its stiffness increasing with length. This relationship can also show a dependence on the direction of the imposed length changes, known as hysteresis, but deviations are small in a true steady state. Some form of passive force is common to all muscles, but an exact anatomical assignment of the structures underlying passive force is dependent on both the type of muscle and the preparation studied.

The next stage of this analysis involves a similar protocol but includes stimulation of the muscle to characterize the parameters associated with activated muscle. With active muscle, the language that evolved reflected the state of understanding and the experimental apparatus. The response to a single electrical shock is known as a *twitch* contraction. At one time, this was believed to be some form of elemental or quantal behavior of muscle, hence its historical importance. Increasing the frequency of stimulation leads to a summation in time of the individual twitch responses, known as temporal summation. Beyond a certain frequency (depending on muscle type and temperature), the force response becomes a smooth, fused curve, called an *isometric tetanus*. These responses to stimulation are ultimately related to the Ca^{2+} handling underlying activation of the contractile proteins. For our present purposes, we consider only isometric tetani, so that the mechanical behavior of the fully activated contractile apparatus can be considered, without complications arising from behavior attributable to non-steady-state Ca^{2+} signaling.

Tetanic stimulation adds an additional increment of force to the passive force present at a given length. The passive force plus active (stimulated) force measured as a function of muscle length is shown in Fig. 46.1. This relationship is known as the total force–length curve. The total force–length relationship varies considerably from muscle to muscle, though the component passive and active force–length relationships for skeletal muscles are qualitatively similar. The differences are largely ascribable to the relative amount of passive force developed at the length at which active force is optimal.

For a structure–function mechanism, the relationship between the additional active force generated when a muscle is stimulated and muscle length is paramount. The active force–length relationship is calculated by subtracting the passive force relation from that for *total force*. The active force–length curve is unusual in that it decreases to zero at both long and short muscle lengths. For most materials, including polymers like rubber, force increases as length is increased. This typical behavior is also seen for the passive force as shown in Fig. 46.1. The observation that active force decreased at long muscle lengths was critical to eliminating theories that involved folding of continuous muscle filaments as the basis for the generation of force upon activation. To understand the relationship between active force and muscle length, it is necessary to consider muscle structure.

IIIB. The Structure of Muscle: Interdigitating Filament Systems

Muscle cells are composed of a filament system underlying their mechanical properties and internal membrane systems related to control of contraction. The filament structure repeats on both the transverse and longitudinal directions as shown in Fig. 46.2. A muscle fiber is composed of myofibrils whose fundamental longitudinal repeating unit is the sarcomere. The sarcomere consists of two interdigitating filament systems, thick (14 nm) myosin-containing filaments and thin (7 nm) actin-containing filaments which underlie the banding pattern seen under optical microscopy and the moniker, striated or striped muscle. The optical properties of the sarcomere due to the overlapping filaments gave rise to the nomenclature for the banding regions. The I-band contains only thin filaments and is optically isotropic, whereas the A-band contains both filament types and is anisotropic. The constancy of A-band dimensions, independent of total muscle length (Huxley amd Niedergerke, 1954), was a key experimental finding, leading to the concept that filament length was constant. Constant filament lengths and interdigitating filaments are best observed at the electron microscope level (Fig. 46.3), where interpretation of the changing banding pattern with muscle length was first elucidated (Huxley, 1953).

IIIC. Sliding-Filament Theory

Based on this structure, the sliding-filament theory explains the active–force relationship in terms of active force being proportional to the overlap between thick and thin filaments of constant length, which are free to interdigitate and slide past one another. This mechanical correlate of the proposed sliding-filament structure was tested in the classic work of Gordon et al. (1966) and is summarized in Fig. 46.4. The clearest correlation between the level of active isometric force and extent of filament overlap is in the region of decreasing force between sarcomere lengths of 2.2 and 3.6 μm, i.e. the descending limb of the active force–length curve. The interpretation of the ascending limb of the force–length relation (e.g. 1.2–2.2 μm) is not as straightforward. This is of particular interest for cardiac muscle which normally operates in the ascending limb. Changes in activation, Ca^{2+}-sensitivity and cooperatively of myosin–actin interaction at short lengths have been proposed to explain the ascending limb in cardiac muscle. The loss of force at these lengths can also be attributed to double filament

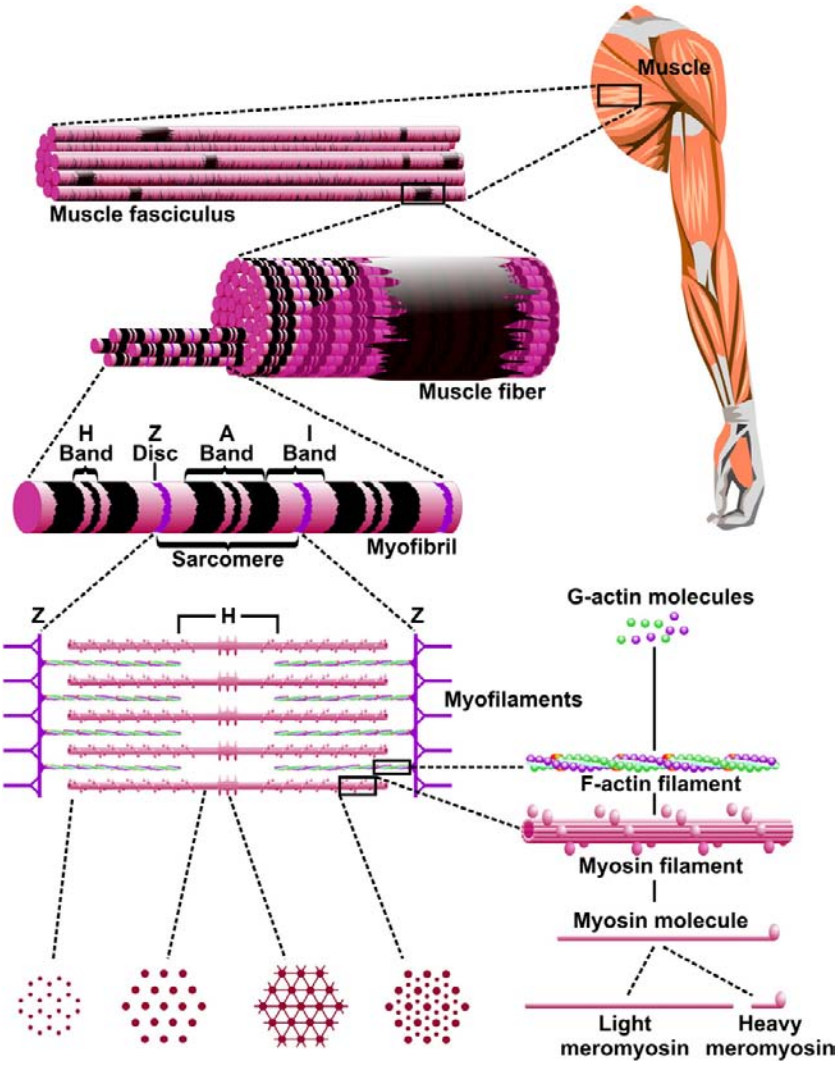

FIGURE 46.2 Skeletal muscle structure. The whole muscle is constructed of fundamental repeating units. A muscle cell or fiber is composed of myofibrils whose fundamental repeating unit is the sarcomere. All views are longitudinal except the cross-sections of the sarcomere (G, H, I).

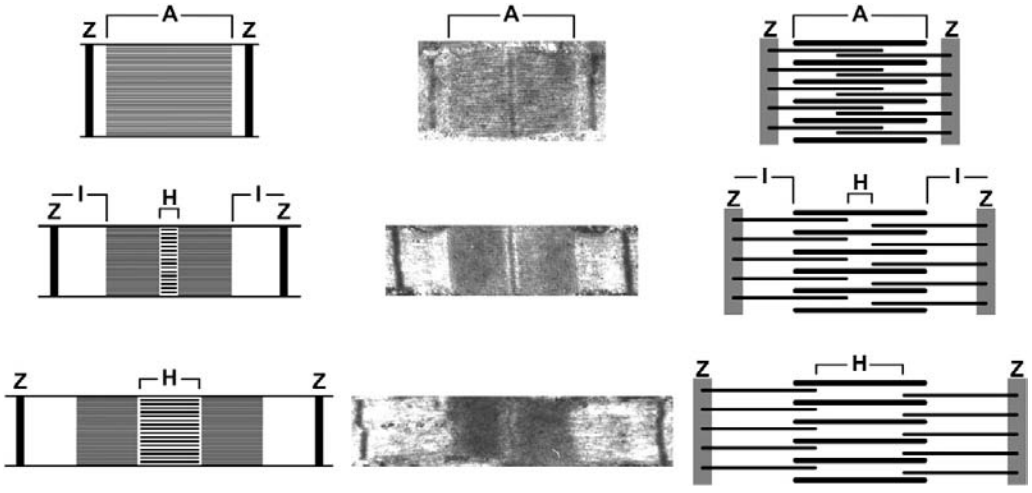

FIGURE 46.3 Electron micrographs and diagrams of sarcomeres at various muscle lengths. The sliding-filament theory is based on the constant length of the thick and thin filaments. Under light microscopy, this leads to the constancy of A-bands (containing both thick and thin filaments, anisotropic, A), while I-bands (containing only thin filaments, isotropic, I). Other designations from light microscopy are the Z-band (Z) and H-zone (H).

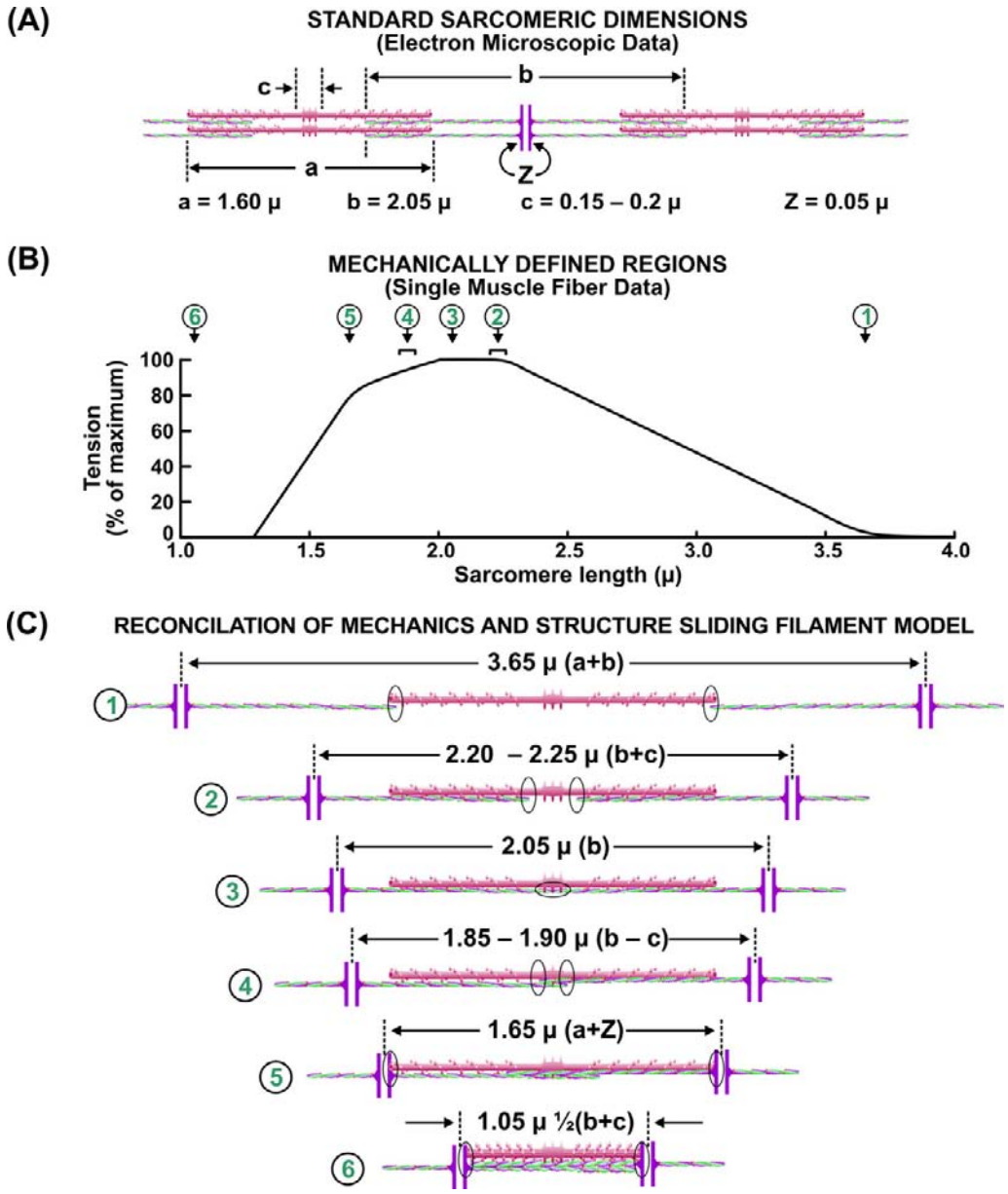

FIGURE 46.4 Structural basis for the active isometric force-length relationship. *(Modified from Gordon et al., 1966.)*

overlap and compression of the contractile elements while interdigitating. Recent interest in structure–function analysis involves the sarcomeric giant protein nebulin (MW 700–900 kDa). Experiments with knockout mice indicate that nebulin plays a critical role in setting the length of the thin filament. One consequence is the length–tension is shifted leftward and maximum force is reduced. This appears to be an important contributor to muscle weakness in patients with nemaline myopathy (Ottenheeeijm and Granzier, 2010). The sliding-filament theory is widely accepted, but the basis of force generation remains an active area of research (see Section IIIE on cross-bridge theory).

IIID. Relationships among Force, Velocity, Work and Energy Utilization

Together with the relationship between force and length, the relationship between force and shortening velocity and the derived work and power are fundamental to characterizing muscle performance. With current technology, one would mechanically impose a constant velocity or force and measure the other as a function of time. Measurements would be carried out under tetanic conditions to eliminate transients during activation and are limited to the plateau region of the force–length relation to avoid any length dependence.

It is of more than just historical interests to consider the apparatus used more than 70 years ago, as the nomenclature prevalent in muscle physiology today, particularly in the language of cardiac physiology, reflects these early measurement protocols.

Figure 46.5A depicts the experimental apparatus used for measurement of force–velocity relations. Using the lever system, a *preload* is placed on the unstimulated muscle. Because the muscle is unconstrained, it stretches to the length at which the preload matches the force on the passive force–length relation. Then a mechanical stop is placed so that no further increases in length can occur. The importance of the preload is that it determines the initial length of the muscle and, consequently, the maximum force possible, in keeping with the active force–length relation. Then a mechanical stop is placed so that no further increases in length can occur. Additional loads now can be placed on the apparatus without changing muscle length. The total load is known as the *afterload*. The name "afterload" derives from the fact that the muscle does not "see" this load, as it is borne by the stop, until "after" it is stimulated. The muscle is then stimulated and when the muscle generates an isometric force just greater than the afterload, the muscle shortens, as indicated in tracing on the drum and shown on the unrolled drum paper in the right panel of Fig. 46.5. During the initial moments after shortening begins, there is a steady rate of shortening (often extrapolated), which subsequently declines and stops as the muscle reaches its final shortened length. This length will correspond to that point in the active force–length curve corresponding to the afterload. Another way of visualizing "why shortening stops" can be seen in Fig. 46.5, in which the route of contraction can be shown against the force–length relation. As the muscle shortens, the afterload becomes isometric at a shorter length where, according to its force–length relation, the muscle can only generate force equal to that of the afterload. This is where shortening stops. Both the distance shortened and the velocity can be seen to be dependent on the afterload. In Fig. 46.5C, the relation between shortening velocity and afterload is plotted. The interesting feature is that this relationship is hyperbolic with the velocity decreases rapidly as the afterload is increased. Several equations have been proposed to fit these data, however, the one most widely used is an equation attributed to A.V. Hill, which is expressed as:

$$(F + a) \times (V + b) = a \times (V_{max} + b) = b \times (F_o + a) \quad (46.1)$$

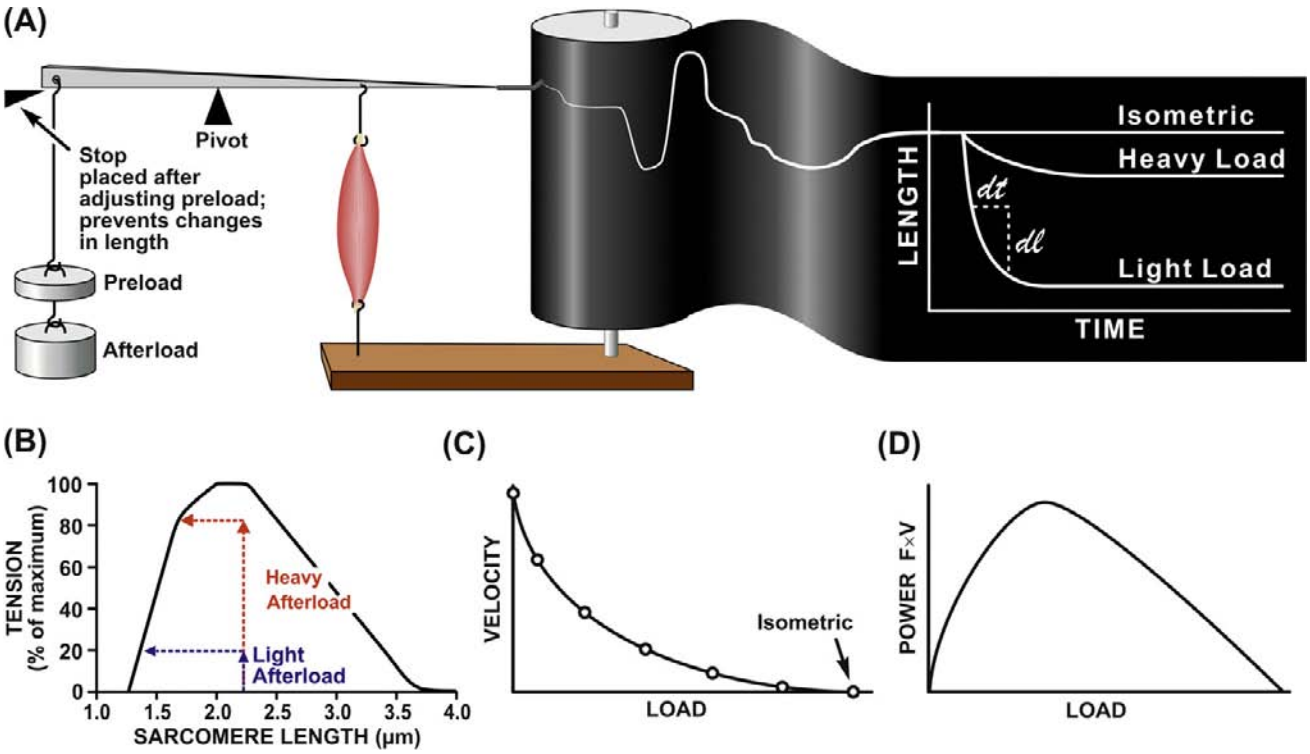

FIGURE 46.5 Relations between afterload and velocity, extent of shortening, and power generated by muscle. (A) Historical "Afterload Contraction" apparatus (left panel) and length tracing vs time (right panel). (B) Afterload contraction trajectory plotted on a length–tension plot. Muscle force–length relation is superimposed, showing its limitation on the extent of muscle shortening. (C) Velocity vs afterload relation. (D) Power (= load×velocity) vs Afterload relation.

where a and b are constants, Fo is the isometric force and Vmax is the unloaded shortening velocity. a/Fo = b· Vmax are dimensionless constants that determine the curvilinearity of the Hill equation and are equal to ≈0.3 for skeletal muscle. The mechanistic origin of this parameter is controversial. Although low values are often associated with efficient muscle performance, a generally accepted theoretical basis remains to be found. The parameter a was initially proposed by Hill to be related to a heat measurement, called the shortening heat, tying energetics to mechanics, but this was shown not to be constant. Although many other equations have been proposed, the scientific stature and an apparent link between heat and mechanical measurements led to the dominance of the Hill equation in the literature.

The power output of muscle, which is the product of afterload times velocity, can be calculated from the relation between afterload and velocity. A consequence of the hyperbolic nature of the Hill equation is that the power output of muscle shows a relatively broad range around a maximum. An advantage of the Hill formulation over others is that it is symmetrical. This can be seen best in its normalized form:

$$(\chi + \theta) \times (\vartheta + \theta) = \theta \times (\theta + 1) \qquad (46.2)$$

where χ is the normalized force (F/Fo), ϑ is normalized velocity (V/Vmax)s and θ = a/Fo = b/Vmax. As power is given by the product of force times velocity, Equation 46.1 or 46.2 can be readily used to derive a relationship between power and load or velocity. The optimal load or velocity for maximum power output can also be derived from these equations and is equal to $\sqrt{\theta^2 + \theta} - \theta$; for skeletal muscle this equals about 0.3 times the maximum load or velocity. These equations are useful in the design of ergonometric devices to optimize performance. The molecular basis for the force−velocity relation is not clear and many hypotheses have been put forth. The widely known of these models is the kinetic scheme of A.F. Huxley (1957). In this model, rate constants for cross-bridge formation/breakage are functions of position. This model (Fig. 46.6) can explain the relationship between force and velocity, but it is not adequate for the transient behavior as those seen (see Fig. 46.10) when rapid step changes are imposed (see Section IIIF on tension transients). While it is relatively easy to envision the "geometric limits" imposed by the sliding-filament model which underlie the force−length relation, especially at long sarcomere lengths (see Fig. 46.4), it is not as easy to visualize the "kinetic constraints" which underlie the force−velocity relation. Simplistically, one possible view is that the probability of making a force generating attachment of a myosin head to an actin is lower when the thick and thin filaments are moving relative to one another.

IIIE. Cross-Bridge Theory

The most prevalent theory for force generation involves the concept of cyclic interactions between the heads of myosin molecules (cross-bridges) projecting from the thick filaments and the actin molecules comprising the thin filaments. Evidence from electron micrographs indicates that these cross-bridges, in various conformations, bridge the gap between thick and thin filaments. Based on both micrographs and x-ray diffraction data, these projections occur at intervals of 14.3 nm. The best evidence (from mass comparisons) is that three myosin molecules are located at each site, with an identical repeat at about 43 nm. The structure of the thick filament is shown in Fig. 46.7.

The evidence for cyclic interaction is partly based on structural considerations. Striated muscle can generate force and shorten over a range of about 50−150% of its rest

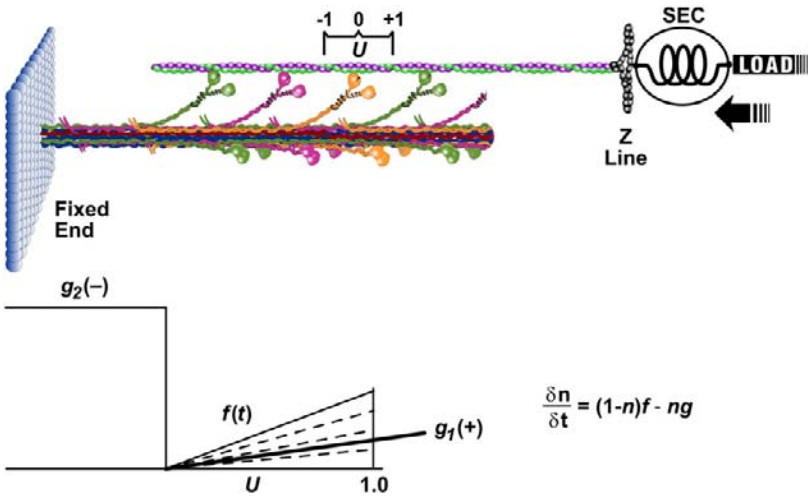

FIGURE 46.6 Schematic representing a two-element model of muscle and Huxley's (1957) mathematical model. Top: Half-sarcomere containing a myosin thick filament and actin-containing thin filament, which constitutes a contractile component, coupled in series with an elastic component (SEC). Bottom left: functional form of rate constants for cross-bridge attachment (f) and detachment (g_1 and g_2) as a function of U, the cross-bridge position coordinate shown at top. Bottom, right: differential equation describing the change in number of cross-bridges. Force generated in this model is equal to the number of attached cross-bridges, n, times the force of an individual cross-bridge.

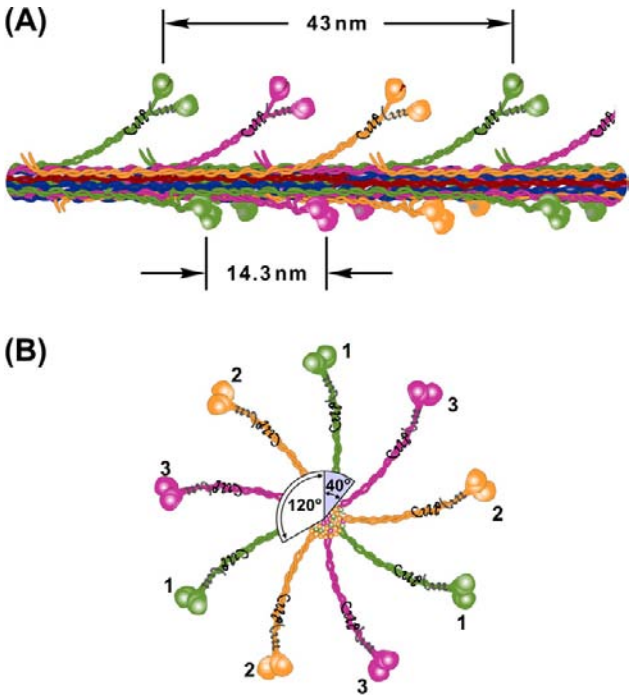

FIGURE 46.7 Rendition of the myosin thick-filament structure based on current evidence. (A) Longitudinal view showing three myosin molecules per site rotated from one another by 120°. Cross-bridge sites occur every 14.3 nm, but are rotated by 40° with respect to the previous site, so that an identical repeat occurs every 43 nm. (B) End view of the filament showing three superimposed color-coded sites.

length. Since a muscle is composed of identical sarcomeres, each sarcomere operates over the same range. For a sarcomere of 2.2 μm, this operating range would be about 1.1−3.3 μm. Since the thin filaments of each half of the sarcomere move toward the center, a sarcomere shortening from 3.3 to 1.1 μm (Δ of 2.2 μm) would require a movement of thin filaments on each side of the sarcomere of one half that distance or 1.1 μm relative to the thick filament. This distance is considerably longer than the cross-bridge spacing (0.014 μm) and is, in fact, longer than a single myosin molecule (0.150 μm). So, it is not possible for a myosin cross-bridge to remain attached to actin in a structure with interdigitating filaments of constant length and relative sliding of more than 1 μm. Hence some form of cyclic interactions between myosin cross-bridges and actin is required to permit the observed relative filament movement. For example, if a cross-bridge can attach over a working range of 10 nm, than 100 repeated cycles of attachment/detachment would be required for a relative filament movement of 1 μm.

A second basis for the cross-bridge theory arises from biochemical studies on isolated muscle proteins. The myosin molecule consists of a long rod-like region important for assembly into thick filaments and a globular head region, which contains the ATPase activity. The globular head, or S1 region (see Fig. 46.7), has dimensions consistent with the projections identified as cross-bridges in electron micrographs. Studies of the kinetics of ATP hydrolysis by myosin, involving stopped-flow apparatus and other techniques for the measurement of rapid time courses, have provided a framework for cyclic interaction of the S1 myosin head with actin. The kinetic scheme is shown in Fig. 46.8. The physiological ATPase activity (known as Mg^{2+}-ATPase activity) of purified myosin is relatively low, but, importantly, it is activated 200-fold by actin, the principal protein of the thin filament. In the absence of ATP, purified actin and myosin bind strongly. In intact muscle, this is the cause for the stiffness of muscle in the absence of nucleotide associated with "rigor". Addition of ATP to a "rigor complex" of actin and myosin dissociates the complex by producing a weak binding state, because the binding of ATP to myosin weakens the binding to actin (see Fig. 46.8, steps 3 to 4). ATP hydrolysis by myosin alters the binding characteristics and cross-bridge orientation (step 4 to 1), leading to a strong binding state (step 1 to 2). The biochemical cycle is completed as the products of ATP hydrolysis, first inorganic phosphate (Pi) and then ADP, dissociate from the myosin head. One ATP molecule is hydrolyzed per cross-bridge cycle. The structural details of this cycle have recently been significantly upgraded due to the high resolution x-ray diffraction data of the myosin head (Rayment et al., 1996) and of single muscle fibers (Lombardi et al., 2004). As shown in the insets in Fig. 46.8, these data suggest that binding of ATP to myosin alters the conformation of the myosin head and consequently its binding to actin. Correlating this cross-bridge cycle based on biochemical data with mechanical steps in force generation is a major focus of muscle

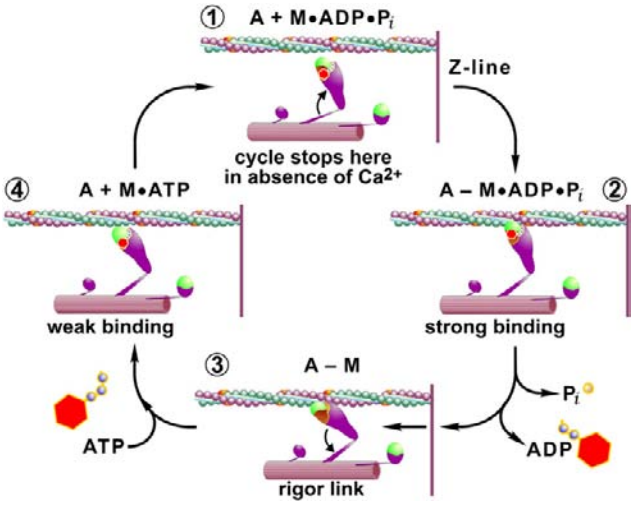

FIGURE 46.8 The cross-bridge cycle. Schematic of the combination of information from muscle mechanics and biochemical kinetics of the actin activated myosin ATPase (see text for details).

physiology. One approach involves the study of rapid mechanical transients.

IIIF. Transient Mechanical Behavior and the Cross-Bridge Cycle

Analysis of the mechanical properties of any material generally involves the imposition of known mechanical perturbations (e.g. step or sinusoidal changes in length or force; called strain) while recording the force (stress) response of the system. When modeling the time course of the response, combination of two types of components (spring-like and viscous elements) can account for the behavior of most materials. The behavior of spring-like material is characterized by an instantaneous relationship between force and length, whereas for a viscous element, a resistive force is proportional to the rate of imposed length change. Combination of these elements can approximate the behavior of many materials (Fig. 46.9).

Using this type of analysis, the steady-state behavior of muscle has long been adequately described by two parallel elements: a spring-like element, representing the passive force–length characteristics and a contractile element representing the characteristics an activated muscle (Hill, 1938). For our generalized skeletal muscle at L_o, a length of optimal filament overlap, little parallel passive force exists. Thus, the behavior we are describing is that of the contractile component alone. Imposition of a rapid step shortening leads to a rapid drop in active force, followed by a redevelopment of tension. This suggests that muscle behavior can be modeled by two elements linked in series (see Fig. 46.9). This model consists of a series elastic spring, which instantaneously responds to the imposed length change and a contractile component, whose behavior is described by the Hill equation, a non-linear, viscous like relationship between force and velocity. For this model, step changes in force yield a rapid, in-phase shortening, attributable to the series elastic spring followed by a slower shortening phase, attributable to the contractile component. This model can explain some aspects of transient mechanical behavior and was the first to be used to associate anatomical elements with model elements. The anatomical site associated with the series elastic component (SEC) has evolved and has considerably altered our view of muscle mechanics.

The SEC can be characterized in terms of the extent of shortening required to discharge the maximal isometric force (F_o). Studies on intact, whole muscle suggested that a change in the length of muscle of 2–3% L_o was sufficient transiently to reduce active force to zero (Jewell and Wilkie, 1958). This elasticity can be attributed to connective elements, such as tendons and similar passive structures, as well as any elasticity in the apparatus used to measure force. A 2–3% change in L_o can be translated to

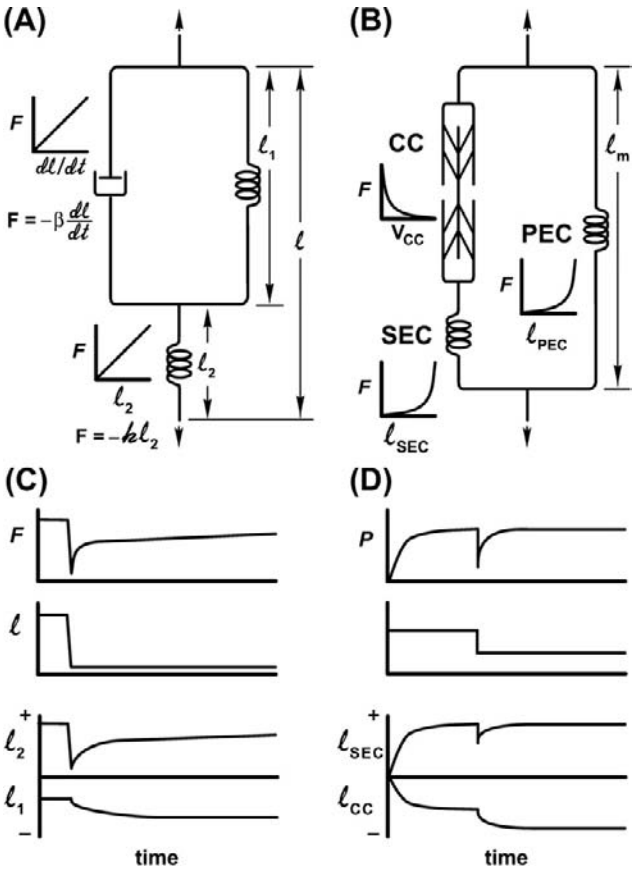

FIGURE 46.9 Models forming the basis of classic analysis of muscle mechanics. (A) Three-element Voight model containing two linear spring elements (l_1 and l_2) combined with a "dashpot", a linear viscous element. (B) Three-element model of muscle containing a contractile component (CC), a parallel elastic component (PEC) and a series elastic component (SEC). Graphs indicate the behavior of each element. (C) Time course of the response of the Voight model and its individual components to imposition of a rapid step change in length. (D) Similar responses of the muscle model to a rapid step change (note that the initial muscle length here is chosen such that the PEC does not play a role in this response).

a relative filament motion of 20–30 nm, i.e. 40–60 nm for a 2.2 μm sarcomere. This is significantly larger than the cross-bridge spacing (14.3 nm), reinforcing the concept that such behavior is external to the contractile component and in series with cross-bridges. The two-component model is phenomenologically useful and it can predict behavior of many whole tissues, particularly those with large intrinsic SEC, such as some smooth muscle. However, as improvements in the temporal resolution of mechanical measurements advanced, this model was found to be inadequate for the behavior of single skeletal muscle fibers.

In the 1970s, techniques for imposition of step changes greatly improved as devices to impose length changes, transducers and recording apparatus achieved millisecond resolution. At the same time, techniques for working with single muscle fibers and "spot follower" devices for control of sarcomere length, rather than overall muscle length,

were developed. These new measurements indicated that the true SEC extent was much smaller than that previously measured in whole muscle. (Previous measurements apparently also included an artifact of the slow response time of the recording system.) Current estimates of the SEC for striated muscle are less than 0.5% L_o, approximately 6 nm per half-sarcomere, clearly in a range to be potentially associated with cross-bridges themselves. Moreover, the time courses of responses (Fig. 46.10) were not consistent with an instantaneous spring connected in series with a contractile element, which also was characterized by an instantaneous force–velocity relationship.

Huxley and Simmons (1971) provided the first evidence that an instantaneous spring-like behavior could be attributed to the cross-bridges themselves. They exploited the fact that the number of cross-bridges could be varied by taking advantage of the force–length relationship. As shown in Fig. 46.10, if the SEC is intrinsic to the cross-bridge, then the magnitude of the shortening step required to discharge the instantaneous elasticity is also intrinsic to the cross-bridge. Thus, the change in length to discharge force would be independent of the number of cross-bridges and, consequently, independent of force. Alternatively, if the instantaneous elasticity were external to the cross-bridges, it would be governed by its own relationship between force and extension. Reduction of force (and number of cross-bridges) by changing the initial muscle length in this case would reduce the step shortening required. They showed that altering active force by changing the initial muscle length did not alter the size of the step shortening required to discharge the maximum isometric force at any initial length. These results supported the concept that the instantaneous spring-like behavior is an intrinsic cross-bridge property and the cross-bridges act as independent force generators. An important corollary of these studies is that the instantaneous stiffness can be used as an index of the number of attached cross-bridges at any moment. This corollary has been used in numerous studies to assess the effects of various interventions on attached cross-bridge number. There is evidence, however, both mechanical (Higuchi et al., 1995) and x-ray

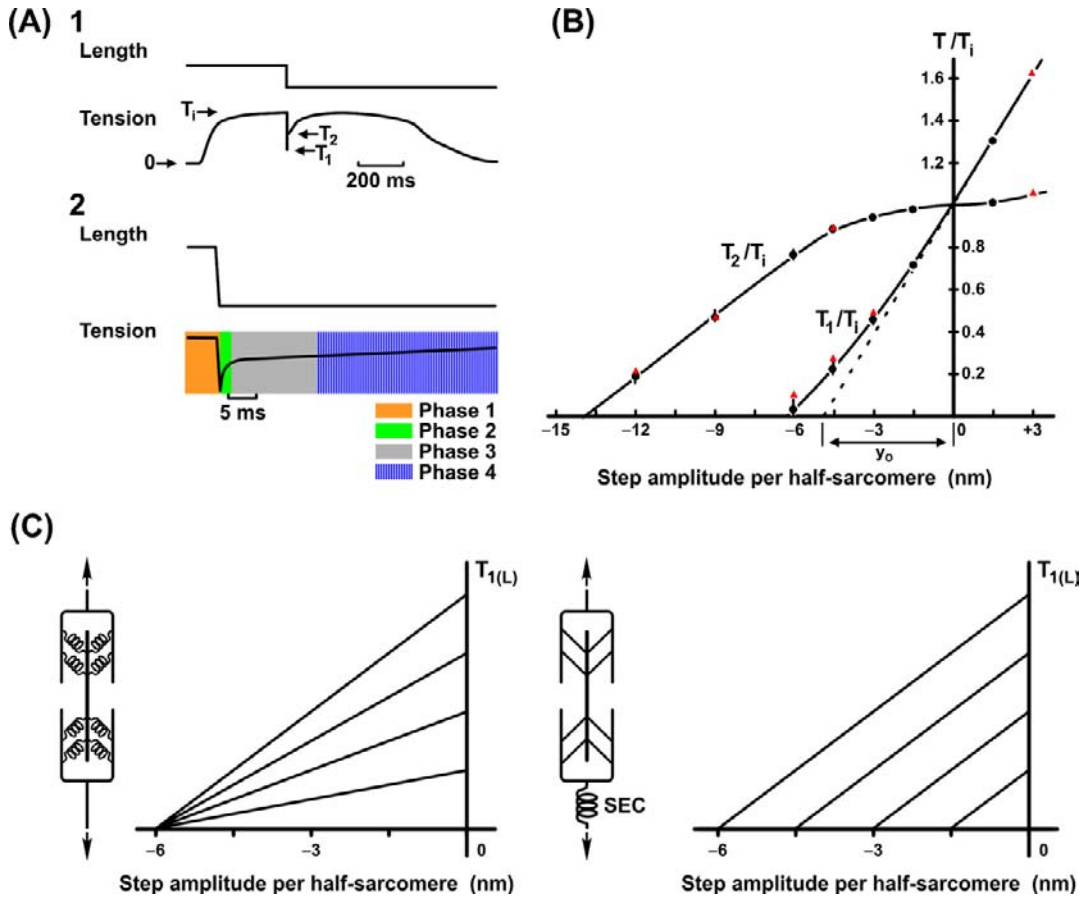

FIGURE 46.10 Huxley–Simmons (1971) experiments. (A) Transient force responses to very rapid (<1 ms) step changes in length, which led to revision of classical muscle mechanics. (B) Dependence of phase 1 and phase 2 force amplitudes on muscle length. (C) Dependence of T_1 if the series elasticity resided within the cross-bridge itself (left) and if the series elasticity was located in a classic SEC (right). Huxley and Simmons data support in the model shown in the left panel of panel of (C).

diffraction (Huxley, 1996), which suggests that a significant fraction of the instantaneous stiffness is attributable to the thin filaments. Thus, one should exercise some caution in the interpretation of stiffness measurements in terms of the number of attached cross-bridges.

To summarize a current consensus understanding of muscle contraction, force generation is due to cyclic interaction of myosin heads projecting from the thick filament with actin of the thin filament. These cross-bridges act as independent sites for force generation. Total active force is proportional to the number of activated cross-bridges whose number is geometrically constrained by the extent of filament overlap. The mechanism of cross-bridge force generation is still the subject of considerable investigation. A current model based on biochemical kinetics and cross-bridge mechanics studies is shown in Fig. 46.8. A shift in orientation of the cross-bridge in the strong binding states (steps 3−4) is associated with the force generating step in this model. Of course, any consensus is just an approximation, likely to be refined in the future. Some of the areas of interest to the understanding cross-bridge mechanisms for the next iteration include (Huxley, 2000, Offer and Ranatunga, 2010): significance, location and accurate measurement of cross-bridge compliance; significance of filament compliance, dependence of rate constants on compliance and the independence of cross-bridges.

IV. MUSCLE ENERGETICS

Studies of muscle energetics parallel those of mechanical and biochemical kinetics and have the same ultimate goal understanding the mechanism of mechanochemical transduction at the cross-bridge level (Barclay et al., 2010). Historically, muscle energetics has been associated with the measurement of muscle heat production. A rise in temperature, the first indication of chemical reactions in muscle, can be measured with a temporal resolution which far exceeds that of direct chemical determinations. Moreover, heat measurements were made long before the chemical reactions driving muscle contraction were known (Hill, 1912). In fact, heat measurements and thermodynamic analysis were essential to ultimately identifying the chemical reactions underlying muscle activity. The essential principle comes from application of the first law of thermodynamics which, under constant pressure, states that the change in enthalpy (ΔH) is equal to the sum of heat (Q) production plus work done (W) by the muscle. The change in enthalpy, in turn, can be related to the sum of the changes in number of moles of each species (Δn_i) multiplied by its specific enthalpy (h_i):

$$\Delta H = \sum (\Delta n_i \times h_i) = Q + W \qquad (46.3)$$

Thus, by measuring muscle heat and work restrictions can be placed on potential underlying chemical reactions. For example, one can test whether the enthalpy change in predicted reaction x sufficient to explain the heat plus work produced during contraction.

One of the first application based on of this type of analysis was carried out by Wallace Fenn (1923), who tested a theory known as the viscoelastic model of muscle contraction:

Thus the view came to be accepted that on stimulation a muscle developed a given amount of heat and a given amount of elastic potential energy, both varying with the length of the fibres of the muscle. The amount of elastic potential energy which could be recovered as work depended merely upon the art of the experimenter in arranging his levers and had no relation to the total energy liberated.

In other words, stimulation elicited a fixed or quantal extent of some unknown reaction(s), whose energy was transduced to a fixed amount of heat plus work. A muscle shortening under a load would produce work and, according to this theory, less heat would be produced than a muscle under isometric conditions not producing work. Fenn's studies showed that the $Q + W$ in a work-producing contraction exceeded the heat produced in an isometric contraction (in which work is minimal). This "Fenn effect" ruled out the viscoelastic model and was important in that theories of muscle energy conversion had to be configured in terms of chemical reactions that were closely coupled to mechanical events. Since that time all models of muscle contraction must pass this stringent energetics test.

The studies of the nature of the chemical reactions coupled to muscle activity, both those immediately coupled mechanical events and those involved in the subsequent recovery by intermediary metabolism, have been closely associated with muscle energetics. The history of the search for the identity of the reactions immediately coupled to muscle mechanical output parallels the history of biochemistry itself. Because of increased understanding of the biochemistry of fermentation and association of lactate with muscle contraction, it was first believed to be a driving reaction, "lactate acid theory". However, Lundsgaard (1938) showed that muscle treated with iodoacetate (which blocks glycolysis via inhibition of G3P dehydrogenase and thus lactate production) could still contract. Fiske and SubbaRow (1927) showed that inorganic phosphate (P_i) is liberated during contraction, arising not from a glycolytic intermediate, but from a new "phosphagen", phosphocreatine (PCr). Myosin was known to be an ATPase, but there was little change in ATP concomitant with contractile activity. The connection was made by Lohmann (1934), who

discovered an enzyme (creatine kinase) which catalyzes the reversible phosphorylation:

$$\mathrm{PCr} + \mathrm{ADP} \leftrightarrow \mathrm{ATP} + \mathrm{Cr} \qquad (46.4)$$

From these observations grew the energetic schema that ATP is the immediate energy source for contraction directly coupled to the myosin ATPase. In intact muscle, PCr rapidly rephosphorylates ADP via the Lohmann reaction (or creatine kinase reaction) and only breakdown of PCr to Cr and P_i can be measured. Tests of whether this was sufficient to account for the change in enthalpy or to account for the free energy change required for the work produced awaited the development of rapid-freezing technology and microchemical analysis of muscle extracts which occurred during the late 1960s. These "energy balance" studies, reviewed in Woledge et al. (1985), tested the validity of Equation 46.3. Under conditions in which metabolic resynthesis was minimized, the measured breakdown of PCr multiplied by its partial molar enthalpy (34 kJ/mol) should be equal to $Q + W$, if this was the only chemical reaction occurring. As shown in Fig. 46.11, this equality was not valid; $Q + W$ was significantly greater than that accounted for by PCr breakdown (Gilbert et al., 1971). The implication was that there was a "missing" reaction associated with an "unexplained" enthalpy production occurring during contraction and, if valid, would overturn the reigning energetic dogma. Moreover, if heat records could not be interpreted in terms of ATP breakdown (coupled to PCr breakdown), then most kinetic models, starting with the classic Huxley (1957) formulation would need to be revised. Thus, energetics studies were focused on identification of the nature of the unexplained enthalpy and a potential missing reaction associated with contraction.

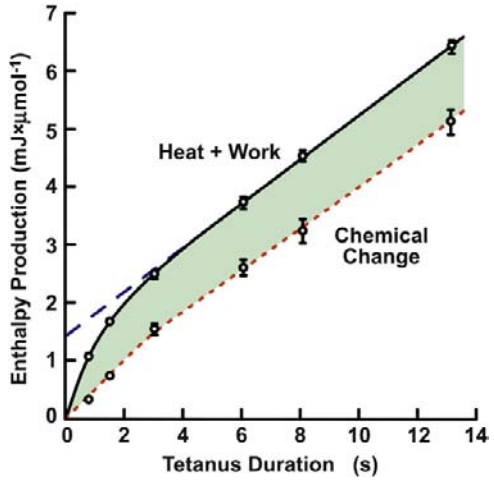

FIGURE 46.11 Skeletal muscle "energy balance". Enthalpy (heat+work) production as a function of tetanus duration is given as the solid line. The expected enthalpy (chemical change times the enthalpy of PCr breakdown, 34 KJ/mol) is plotted as the dotted line. Shaded area represents the unexplained enthalpy. *(Adapted from Woledge et al., 1985.)*

In a parallel fashion, "biochemical" balance studies (Kushmerick, 1983) were also directed at the question of a missing reaction, but with chemical rather than physical techniques. The rationale is that if ATP hydrolysis and its rephosphorylation by PCr are the only reactions occurring during contraction, then the extent of this reaction should be equal to the ATP synthesized during recovery. If resynthesis is governed by theoretical biochemical stoichiometry, then the amount of oxygen consumed during recovery would have been equal to 1/6.5 times the PCr broken down during contraction. The experimental test of this hypothesis is shown in Fig. 46.12. Again an imbalance was observed; the extent of recovery metabolism associated with resynthesis of ATP exceeded that which could be accounted for by PCr breakdown during contraction. Paul (1983), using both physical and biochemical "energy balance" techniques, showed that oxidation of glucose was the only net reaction occurring during a complete contraction/relaxation cycle. Not surprising in today's worldview, this ruled out a number of theories of the time based on a continuous degradation of muscle for each contraction. The combinations of techniques yield data that indicated that the initial chemical imbalance, i.e. less ATP breakdown than predicted during contraction, is accompanied by additional breakdown of ATP after contraction.

A resolution of the "missing" reaction question apparently resided in the discovery of the protein parvalbumin in amphibian muscle and its role as a Ca^{2+}-binding site (Gillis et al., 1982). Parvalbumin binds a significant amount of the Ca^{2+} released by the sarcoplasmic reticulum (SR) during contraction. This binding is associated with a substantial evolution of heat. There is also evidence that Ca^{2+} is returned to the SR after the contraction ceases, which would require activity of the Ca^{2+} pump and concomitant hydrolysis of ATP. This explanation is perhaps the most widely held, but it is not a universal explanation. For example, the biochemical balance studies would suggest that the post-contractile ATP breakdown is proportional to the duration of stimulus, whereas the enthalpy balances apparently indicate that the unexplained enthalpy attains a plateau value. Moreover, some unexplained enthalpy is associated with mammalian striated muscle, which does not contain parvalbumin. Nevertheless, the schema involving ATP as the immediate driving reaction, with PCr as the source of chemical energy for rapid resynthesis in intact muscle appears valid. This is further supported by (1) thermodynamic data indicating that the free energy provided by ATP during contraction is sufficient to account for the work produced (reviewed in Woledge et al., 1985) and (2) many studies using permeabilized muscle indicating that ATP is the only chemical energy source required for contraction.

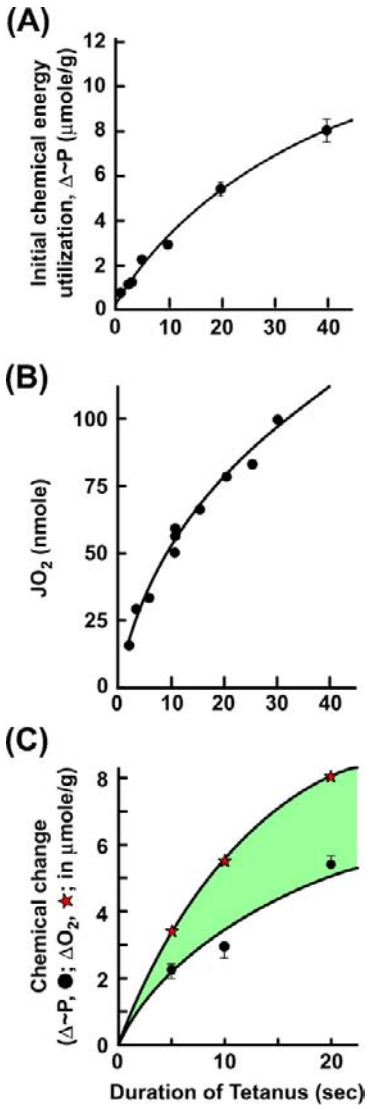

FIGURE 46.12 Skeletal muscle "biochemical energy balance". (A) The initial high-energy phosphagen (PCr + ATP) breakdown during contraction as a function of tetanus duration. (B) Total recovery oxygen consumption elicited by the contraction durations plotted on the ordinate. (C) The total phosphagen resynthesized based on theoretical stoichiometry and the measured O_2 consumption (open stars) and the measured phosphagen breakdown during contraction (filled circles). The shaded area represents the excess of ATP synthesis over the phosphagen breakdown measured during contraction. *(Adapted from Kushmerick, 1983.)*

V. MUSCLE METABOLISM

Mechanochemical energy transformation and the breakdown of high-energy phosphagens under various conditions form one branch of study known as muscle energetics. Energy metabolism and intermediary metabolism are two terms often used to describe the other major branch of energetics, that of the study of the metabolic provision of phosphagen in support of muscle activity and the mechanisms of coordination of metabolism with contractility. Muscle mechanical activity is supported by ATP provided by both oxidative phosphorylation and glycolysis. Historically, the biochemistry of these pathways often mirrors our understanding of muscle, as this tissue was often the major model for biochemical studies. For the historical aspects with respect to muscle contraction, the treatise of Needham is highly recommended (Needham, 1971).

Perhaps of most recent interest in this field is the reexamination of the theories whereby contractile ATP use is coordinated with metabolic resynthesis of ATP. For skeletal muscle, most prevalent theory is that of acceptor- or ADP-limited respiration. In the case of isolated mitochondria in the presence of substrate, their rate of oxidative phosphorylation, state III is limited by the availability of ADP as the substrate for rephosphorylation. Because the hydrolysis of ATP concomitant with contractile activity is increased, one might anticipate that an increase in ADP could naturally couple the increased usage with synthesis. The creatine kinase reaction, coupled with the amount of PCr in striated muscle, buffers the ATP concentration. Under the assumption that this reaction is in equilibrium, the level of free (i.e. not bound) ADP can be calculated to be in the region of 10 μM. This is also in the range for the K_m for ADP for ADP control of mitochondrial oxidative phosphorylation. This mechanism can reasonably well predict PCr breakdown and its resynthesis for a contraction/relaxation cycle in human muscle (Kushmerick, 2005). On the other hand, significant increases in cardiac (Balaban, 2009) and smooth muscle (Hardin et al., 2000) oxidative metabolism occur in the absence of changes in PCr or ATP, indicating that increases in energy metabolism can match the contractile ATP utilization in the absence of changes in ADP. There are a number of hypotheses in this area. The most prominent ones propose regulation of oxidative metabolism by $[Ca^{2+}]_i$ (Liu and O'Rourke, 2009) and mechanisms involving a substrate level "push," e.g. by mobilization of substrate, leading to increased NADH levels.

A second area of growing interest on the metabolism side of muscle energetics is the effect of microcompartmentation of metabolism and its subserved function. Instead of being distributed in a random fashion in solution in the cytosol, many enzymes important in energy metabolism are apparently localized within the cell, often in close apposition to energy-dependent processes. Perhaps the most widely studied system is that of creatine kinase (Ishida et al., 1994) which is localized at the m-line of striated muscle as well as in membrane structures and mitochondria. In permeabilized muscle, endogenous phosphocreatine alone can support contractile activity, suggesting a close relationship between the myosin ATPase and creatine kinase. Similarly, phosphocreatine has been shown to support Ca^{2+} uptake by sarcoplasmic reticulum isolated from skeletal muscle. The enzymes involved with

glycolysis are also localized primarily on the thin filaments and associated with the plasmalemma and sarcoplasmic reticulum. There are increasing numbers of studies for skeletal (James et al., 1996; Levy et al., 2008), cardiac (Weiss and Lamp, 1987) and smooth muscle (Hardin et al., 2000), indicating that ATP provided by glycolysis supports functions different from those dependent on oxidative metabolism. This is particularly striking in smooth muscle, in which the oxidative and glycolytic components of metabolism can be of similar magnitude (Paul et al., 1979). ATP-dependent processes associated with the plasma membrane, such as the Na^+-pump and ATP-dependent potassium channels, are apparently particularly dependent on ATP generated by aerobic glycolysis, whereas the ATP requirements for the force generating actin−myosin ATPase interaction are apparently more strongly correlated with oxidative metabolism. The bases and consequences of this cellular organization are not fully understood, but have been suggested to be related to either greater energy transduction efficiency or the need for independent regulation of different cellular functions.

VI. COMPARATIVE MECHANOCHEMICAL FUNCTION

VIA. Striated Muscle

The general features just described are common to all muscle function, however, there is a great variety of muscle types adapted to specialized conditions. Among skeletal muscle, perhaps the most familiar adaptation is the difference between red and white muscle. The nomenclature has a long history and many different schemes exist. Histologically and functionally three major classifications predominate, termed fast glycolytic (FG), slow oxidative (SO) and fast oxidative−glycolytic (FOG), reflecting their gross properties. Most whole muscle contains various mixtures of these three basic muscle fibers and appears pale compared to red muscle, which is composed primarily of SO fibers. The red color is due to the presence of myoglobin, a protein that facilitates the diffusion of oxygen.

These fiber types are adapted for different power requirements. The FG fibers provide large forces that can be rapidly activated and relaxed, but are susceptible to fatigue. Their metabolism depends heavily on glycolytic production of ATP, which can respond rapidly to large changes in energy requirements associated with muscle contraction but has relatively limited capacity. For low level but continuous muscular activity, such as that required by postural muscles, the SO fibers are adapted with a high oxidative metabolic capacity. A lower actin-activated myosin ATPase of the SO fibers relative to FG fibers facilitates a more economical maintenance of force, however, this is accompanied by a slower velocity of shortening.

In primates, FOG fibers are relatively rare and highly specialized muscles (some ocular muscles appear to be composed primarily of this fiber type). Their twitch duration and shortening speed are intermediate between those of SO and FG fibers and are characterized by high levels of both glycolytic and oxidative metabolism. These differences in adaptation also extend to speed of activation, which is approximately three times faster in FG than SO fibers. Cardiac muscle has its own special adaptations and, in many ways, shares similarities with SO skeletal muscle fibers. A third muscle type, smooth muscle, is significantly different from striated muscle and is discussed in detail in the following section.

These gross differences in muscle fiber type have long been studied. Applying advanced molecular biology techniques, we now know that most muscle proteins exist as isoforms. Thus, recent interest has focused on the isoform−function relationships as well as the regulation of the expression of these various isoforms. What is of particular interest is that the number of expressed isoforms − and the theoretical possible variants − far exceed the three gross skeletal fiber types. Detailed information on isoforms is beyond the scope of this text and is available in specialized treatises (Pette and Staron, 2001; Westerblad et al., 2010).

VIB. Smooth Muscle

Historically, smooth muscle has been of interest because of its specialized function. It lines the hollow organs, such as blood vessels and the gastrointestinal (GI) tract. Its structure is less organized than that of striated muscle and thus somewhat less amenable to biophysical experimentation. For many years, its properties have been simply extrapolated from striated muscle. However, it is now clear that while many similarities exist, there are also significant differences. Studies of smooth muscle have significantly increased over the past decade. This can be attributed largely to its clinical relevance in terms of the diseases of industrialized society such as hypertension, asthma and GI motility disorders. However, much of the current interest has arisen from the discovery that the regulatory mechanisms at the contractile filament level are radically different from those of striated muscle.

Smooth muscle can develop isometric forces per cross-sectional area that are equal to or greater than those generated by striated muscle. This is all the more surprising in that the myosin content of smooth muscle is considerably less (about one-fifth) than that of striated muscle. These large forces can be maintained with a rate of ATP utilization that is 100-to 500-fold lower than the corresponding rate in skeletal muscle. The trade-off for high forces and economy of force maintenance is apparently shortening

velocity, which is much slower (up to 1000-fold) than that in striated muscle. The efficiency, in terms of work per ATP, is also somewhat lower (approximately one-fifth that of skeletal muscle), however, the data here are less extensive. The key question then is how does smooth muscle accomplish these specialized functions given that its contractile apparatus uses basically similar actin and myosin components?

VIB1. Smooth Muscle Structure and Its Relationship to Function

The structure of smooth muscle is shown in Fig. 46.13. Smooth muscle cells are smaller than skeletal muscle, with maximum diameters of the spindle-shaped cells in the range 10−20 μm. Filament structure is less organized, with no distinct sarcomeric or banding structure, hence the name "smooth". There are no Z-bands, but actin filaments are organized through attachment to specialized cytoskeletal regions called dense bodies or patches. These areas contain α-actinin, a Z-band protein, which further strengthens this analogy. It is also likely that these structures mediate transmission of force between cells. The ratio of thin to thick filaments is much higher in smooth muscle (≈15:1) than in striated muscle (2:1).

This latter observation raises the question of whether structural factors could account for these functional differences. The answer clearly depends on the mechanism of contraction in smooth muscle. It is assumed, by analogy to striated muscle, that a sliding-filament mechanism is involved in smooth muscle contraction. There is much less direct evidence than skeletal muscle, but the available data are consistent with this theory. Primarily, the evidence in intact tissue is largely limited to the dependence of active force on length, which is qualitatively similar to that of striated muscle. Smooth muscle appears to shorten to a greater extent, 0.2−0.4 of the optimal length for force generation (Herlihy and Murphy, 1973; Paul and Peterson, 1975), compared to 0.6 for skeletal muscle. On the descending limb of the active force−length curve, the decline may be more rapid, but the large passive forces in this region preclude precise measurements. There is also an element of plasticity in these force−length relations which show a hysteresis, dependent on how the measurements are made (Peterson and Paul, 1974; Seow and Pare, 2007). The loose organization of myofilaments is not readily amenable to direct structural measurements which precludes conclusive evidence based on comparison of the extent of thin−thick filament overlap to force−length behavior. From "motility assays," in which actin filaments are observed to move on a myosin-coated surface, or myosin-coated beads move on actin filament networks (Harris and Warshaw, 1993), one can infer that folding of filaments is not essential to motion, consistent with a sliding-filament model. The only difference between striated and smooth

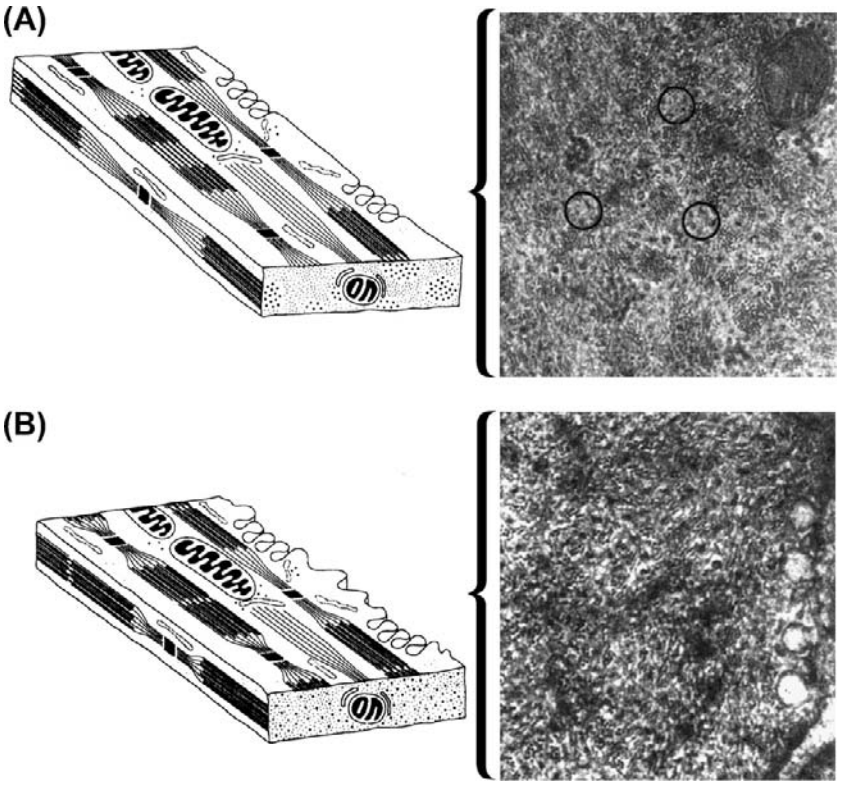

FIGURE 46.13 Morphology of relaxed and contracted smooth muscle. (A) This diagram represents a portion of a relaxed smooth muscle cell, highlighting the arrangement of the actin-containing thin filaments and the myosin-containing thick filaments. This rendering is greatly simplified from the actual arrangement. From the longitudinal orientation, thin filaments arise at dense bodies and project to interact with thick filaments, forming the contractile apparatus. In the cross-section, the filaments are distributed in a non-uniform manner, with thick filaments forming clusters surrounded by groups of thin filaments. This arrangement is shown in the electron micrograph (circled), which is a cross-section of a relaxed visceral smooth muscle cell. (B) A contracted smooth muscle cell. The notable differences from the relaxed cell shown in part (A) are that, in the longitudinal views, the thin filaments overlap considerably more of the thick filaments, drawing the dense bodies closer together and shortening the cell. In cross-section, the thin and thick filaments are randomly distributed to form a uniform pattern. The electron micrograph is a cross-section of a contracted visceral smooth muscle cell which shows more uniform distribution of the thin and thick filaments. *(Diagrams are modified from Heumann, 1973.)*

muscle myosin in these experiments is a slower velocity observed with smooth muscle myosin.

Assuming that an analogous sliding-filament mechanism operates in smooth muscle, what types of structure could account for the differences in function? Force is proportional to the number of cross-bridges in parallel, whereas shortening velocity and the maximal shortened length are related to the number of fundamental units in series. Models of arrangement of cells or sarcomeres yielding an increase in force and holding economy while reducing velocity are shown in Fig. 46.14. While increasing the number of cells in parallel (Fig. 46.14A) works in the appropriate direction (large force, low tension cost), it falls short of true smooth muscle behavior in that the amount of total tissue shortening in this model is very limited. Smooth muscle can shorten to relatively short lengths; some 20−30% of initial tissue length is not uncommon. In the model of Fig. 46.14A, the absolute length change would be that attributable to shortening of only one cell and would not account for the shortening of any macrosize tissue.

In Fig. 46.14B, different mechanical properties are associated with the assembly of the sarcomere. Longer myosin filaments and, consequently, longer sarcomeres are associated with more parallel cross-bridges and higher forces. However, for a given myosin content, this arrangement has fewer sarcomeres in series and hence a slower overall velocity. Moreover, if the individual myosin cross-bridge ATPase is not altered, one would have a similar ATP use for both models and thus the longer sarcomere version would have a greater economy (force maintained per rate of ATP hydrolysis) or a lower tension cost (reciprocal of economy). These changes are in the direction that distinguishes smooth muscle from skeletal

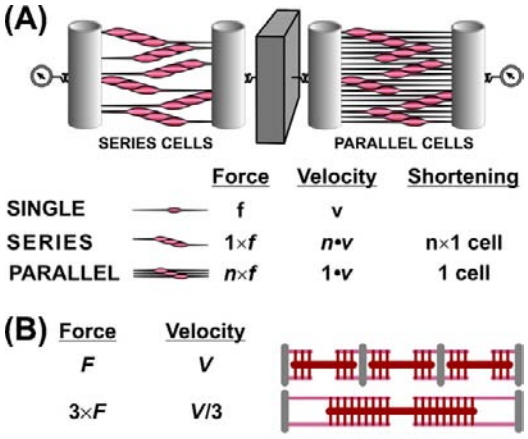

FIGURE 46.14 (A) Parallel and series models of force transmission in a smooth muscle-containing tissue. Parallel arrangement increases total force, but with a decrease in velocity and total shortening compared with cells coupled in series. (B) Parallel and series model at the level of the sarcomere. Both sliding filament models have the same myosin content, but it is arranged in short (top) and long sarcomeres (bottom).

muscle. The question then is how much of the difference between skeletal and smooth muscle can be related to simply the "mechanical advantage" of longer sarcomeres? Although no obvious sarcomeric structure exists for smooth muscle, the length of the myosin filament of smooth muscle relative to striated answers this question. There is evidence that some smooth muscles, particularly in invertebrates, such as the scallop or mussel, whose sarcomere lengths may be up to 10-fold greater than mammalian skeletal muscle, make use of this mechanical advantage. However, for mammalian tissues, myosin filament length has been estimated at approximately 2.2 μm (Somlyo, 1980), a figure not significantly different from that of striated muscle (1.6 μm). The differences in contractile properties between smooth and. skeletal muscles would thus appear to reside largely in the nature of the smooth muscle myosin molecule and its intrinsically lower ATPase.

VIB2. Regulation of Smooth Muscle Contractility

Regulation of contractility can be divided into (1) mechanisms for control of $[Ca^{2+}]_i$ and (2) mechanisms for transduction of the Ca^{2+} signal to activation of the contractile apparatus. Regulation of $[Ca^{2+}]_i$ is considered elsewhere and the focus here is on transduction mechanisms.

Up to the mid-1970s, regulation of mammalian smooth muscle contractility was based largely by analogy to striated muscle and considered to be a "thin-filament" regulated system; i.e. one in which troponin is the Ca^{2+} receptor and tropomyosin is the transducing element. It was quite a surprise when this canonical theory was shown not to be valid for mammalian smooth muscle. Several lines of evidence led to the current, widely accepted view that phosphorylation of the 20 kDa regulatory light chain of myosin (MRLC-P_i) is the primary transduction site for the Ca^{2+} signal (Hartshorne and Siemenkowski, 1981; Kamm and Stull, 1985; Hartshorne, 1987; de Lanerolle and Paul, 1991). Although tropomyosin is known to be a major smooth muscle protein, the Ca^{2+} transducer, troponin, is not present in smooth muscle. Proving that a protein is absent is difficult and that proof came slowly. Smooth muscle actomyosin also proved considerably different from that of striated muscle. One aspect was that as its purity increased, its ATPase activity decreased, the opposite of striated actomyosin. This suggested that purified smooth muscle actomyosin requires activation; in contrast to striated muscle actomyosin which is constitutively active, and requires de-inhibition of the associated troponin−tropomyosin inhibitory proteins. This was rigorously tested by "competition" experiments. In these experiments, the Ca^{2+} sensitivity of the actin-activated, Mg^{2+}-ATPase of myosin was measured using "unregulated" thin filaments (i.e., purified actin without troponin and tropomyosin). Striated muscle myosin showed little Ca^{2+}

sensitivity, whereas mammalian smooth muscle myosin retained Ca^{2+} sensitivity, indicating that the site of its regulation was on the myosin itself. The regulatory site was identified when it was discovered that the ATPase activity of smooth muscle myosin was dependent on phosphorylation of the 20-kDa regulatory light chain (MRLC) of the myosin hexamer. This phosphorylation involves Ca^{2+} binding to calmodulin, the ubiquitous Ca^{2+} binding protein, which in turn binds and thereby activates myosin light chain kinase (MLCK). This kinase is rather remarkable in that MRLC is its only substrate, rare among most kinases which often have multiple targets.

Several lines of evidence supported this thick filament regulatory mechanism. One strategy was to alter MRLC-P_i independent of $[Ca^{2+}]_i$ through manipulation of the kinase or phosphatase. Inhibition of MLCK led to relaxation and dephosphorylation in the presence of Ca^{2+}. Another path involved the proteolysis of MLCK to obtain a constitutively active fragment which, added to permeabilized smooth muscle, generated a contraction in the absence of Ca^{2+} which was indistinguishable from that induced by Ca^{2+}. Another line involved targeting the phosphatase; addition of myosin phosphatase enriched fractions relaxed contracted smooth muscle (Rüegg et al., 1982). Inhibition of myosin phosphatase also leads to smooth muscle contraction. Taken in total, these results suggest that myosin light chain phosphorylation is the major regulatory site and is necessary for activation.

In the past 10 years, the biggest surprise in the regulation of smooth muscle is the importance played by modulation of phosphatase activity (Somlyo and Somlyo, 2000). Myosin phosphatase activity is regulated by it targeting subunit (MYPT1) or myosin binding subunit. MYPT1 binds to the catalytic subunit of type 1 phosphatase and also acts as an interactive platform for many other proteins, in particular, myosin filaments. Phosphorylation of MYPT1 weakens the binding to myosin and, consequently, decreases its apparent phosphatase activity. There are several phosphorylation sites: S696 and S854 are PKA/PKG sites; T697 and T855 are the inhibitory/regulatory sites phosphorylated by several kinases most notably Rho-kinase (ROK) (Matsumura and Hartshorne, 2008).

Activation of smooth muscle contraction by MRLC phosphorylation/dephosphorylation provides multiple points for modulation. Phosphorylation of MLCK by cAMP dependent kinase weakens its binding to calmodulin and leads to Ca^{2+} desensitization of contraction; i.e. less force generated for a given $[Ca^{2+}]_i$ than control. On the other hand, there are two major paths currently known to decrease phosphatase activity, thus leading to an increase in Ca^{2+} sensitivity. In addition to Rho-Kinase, C-kinase phosphorylation of a small inhibitory protein, CPI-17, forms a complex that retards dephosphorylation of MYPT1 decreasing myosin phosphatase activity (Eto et al., 2004). In some smooth muscles, myosin phosphatase can clearly dominate MLCK phosphorylation, such as inhibition of the phosphatase by Rho kinase, a major player in activation. For example, inhibition of Rho kinase can lead to the complete relaxation of receptor-mediated stimulation (Nobe and Paul, 2001). A schematic for the regulation of MRLC phosphorylation/dephosphorylation is shown in Fig. 46.15.

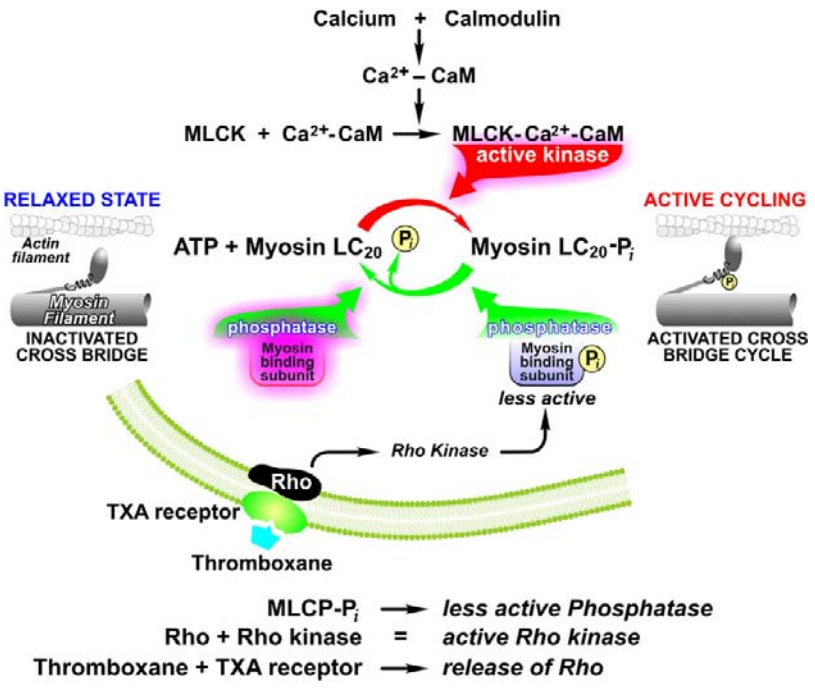

FIGURE 46.15 Schematic showing the mechanisms for phosphorylation/dephosphorylation of myosin regulation light chains and contractile state of smooth muscle.

Whether myosin light chain phosphorylation is sufficient as a regulatory mechanism or indeed has roles in addition to actomyosin activation is open to question. A number of experimental observations suggest that smooth muscle regulation may be more complex than initially envisioned. Figure 46.16 summarizes the time courses of several parameters after stimulation. Isometric force increases monotonically and then maintains a plateau value, whereas MRLC-P_i rapidly increases to a maximum achieved early in the contraction and then decreases. The extent of the decline in the MRLC-P_i is controversial and this is likely attributable to different smooth muscle types, dependence on the nature of the stimulus and measurement technique. Since force is usually assumed to reflect the number of activated cross-bridges, the decline in MRLC-P_i with maintained or increasing force suggests that this is not a simple on-off switch and/or other regulatory factors may play a role. Moreover, near maximal forces are attained with MRLC-P_i levels considerably lower than 100%, often reported to be in the 15–40% range, which further questions its role as a simple switch. The decline in MRLC-P_i also parallels that of $[Ca^{2+}]_i$ and, interestingly, to the decline in shortening velocity and ATPase activity. In view of these observations, Murphy and colleagues (Hai and Murphy, 1988, 1989a) suggested that MRLC-P_i might be a regulator of contractile velocity. They coined the expression "latch" for the state of maintained force with reduced MRLC-P_i and slower contraction speeds. Latch bridges, or cross-bridges, in this state were initially postulated to be non- or slowly cycling and thus they reduced the overall tissue velocity by acting as a type of internal load on the more rapidly cycling bridges. As force retained its dependence on Ca^{2+} in the latch state, it was postulated that latch bridges may be regulated by a system different from MRLC-P_i.

Currently, there are two major classes of theories for latch behavior, which are not necessarily mutually exclusive. Thin-filament regulatory mechanisms based on several actin-binding proteins, namely, leiotonin, caldesmon and calponin, have been suggested. A common feature is that they are all proposed to be inhibitory and, for the latter two, the interaction with actin is sensitive to Ca^{2+}calmodulin. Although all are promising in terms of the ability to inhibit myosin ATPase activity in the test tube, the relevance to intact smooth muscle has yet to be unequivocally demonstrated. As smooth muscle myosin requires activation, these systems could only be ancillary. Based on the ability of MRLC-P_i to activate smooth muscle in the absence of Ca^{2+}, it is difficult to postulate that these systems can be inhibitory in the sense that they regulate activation on an "on-off" basis. However, these systems could regulate cross-bridge cycling and thus velocity (Kim et al., 2008), but more evidence of this is needed.

An alternative hypothesis suggested by Murphy and Rembold (2005) does not require regulatory components beyond myosin light chain phosphorylation–dephosphorylation. A version of their model is shown in Fig. 46.17. They postulate that if a phosphorylated cross-bridge were dephosphorylated while attached, its detachment rate would be significantly slower than if it were to remain phosphorylated. The kinetic scheme of Fig. 46.17 is sufficient to fit the available data on the time courses of force and MRLC-P_i. It can also predict the time course of ATP utilization, which also decreases similarly to velocity, with stimulation duration. This scheme also predicts that the "futile" cycle of myosin light chain phosphorylation–dephosphorylation is the dominant ($\approx$85%) source of ATP utilization, which was challenged based on the

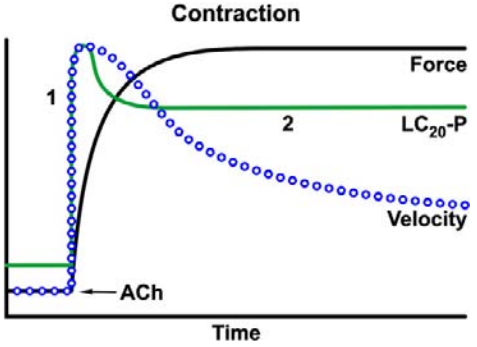

FIGURE 46.16 Relations between isometric force, maximum shortening velocity and myosin regulatory light chain phosphorylation (LC_{20}-P) and the duration of stimulation. Data are for tracheal smooth muscle *(adapted from de Lanerolle and Paul, 1991)*. The decrease in velocity at times when force is maintained is the basis for the latch bridge theories.

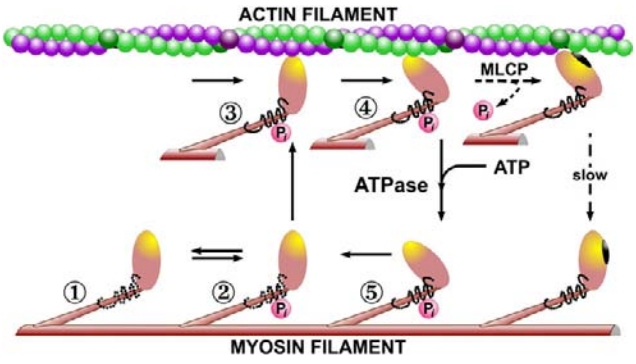

FIGURE 46.17 A schematic model of the interaction of smooth muscle myosin cross-bridges with actin filaments. The transition from state 1 to state 2 represents the Ca^{2+}-calmodulin dependent phosphorylation/dephosphorylation activation mechanism proposed for smooth muscle regulation. The cycle of interaction (states 2–5) hydrolyzes 1 ATP molecule and generates 1 quantum of tension with each pass. Only the angulated attached myosin cross-bridge (state 4) generates isometric force. The inherent speed of the cycle is much slower in smooth muscle than in striated, with the ATP-dependent dissociation step (state 4–5) apparently being slower. The dashed arrows indicate formation of a proposed dephosphorylated actomyosin cross-bridge (Hai and Murphy, 1989b), which dissociates only very slowly and may be responsible for the latch state of vascular smooth muscle.

available smooth muscle energetics data (Paul, 1990). This discrepancy was resolved when it was shown (Wingard et al., 1997) that myosin phosphorylation−dephosphorylation can be an appreciable source of ATP utilization during the initial force development when levels of MRLC-P_i are high, but rapidly drops paralleling Ca^{2+}, MRLC-P_i and velocity. Thus, the high economy of tension maintenance in smooth muscle or lower tension cost in smooth than striated muscle includes a low intrinsic actomyosin ATPase (≈100-fold), longer sarcomeres (≈1.5-fold) and decreasing the cross-bridge cycle rate at constant force (≈3-fold). The role of latch bridges or thin filament proteins in the latter is yet to be fully resolved and universally accepted.

BIBLIOGRAPHY

Balaban, R. S. (2009). Domestication of the cardiac mitochondrion for energy conversion. *J Mol Cell Cardiol, 46*, 832−841.

Barclay, C. J., Woledge, R. C., & Curtin, N. A. (2010). Inferring cross-bridge properties from skeletal muscle energetics. *Prog Biophys Mol Biol, 102*, 53−71.

de Lanerolle, P., & Paul, R. J. (1991). Myosin phosphorylation/dephosphorylation and regulation of airway smooth muscle contractility. *Am J Physiol, 261*, L1−14.

Eto, M., Kitazawa, T., & Brautigan, D. L. (2004). Phosphoprotein inhibitor CPI-17 specificity depends on allosteric regulation of protein phosphatase-1 by regulatory subunits. *Proc Natl Acad Sci USA, 101*, 8888−8893.

Fenn, W. O. (1923). A quantitative comparison between the energy liberated and the work performed by the isolated sartorius muscle of the frog. *J Physiol, 58*, 175−203.

Fiske, C. H., & SubbaRow, Y. (1927). The nature of the "inorganic phosphate" in voluntary muscle. *Science, 65*, 401−403.

Gilbert, C., Kretzschmar, K. M., Wilkie, D. R., & Woledge, R. C. (1971). Chemical change and energy output during muscular contraction. *J Physiol, 218*, 163−193.

Gillis, J. M., Thomason, D., Lefevre, J., & Kretsinger, R. H. (1982). Parvalbumins and muscle relaxation: a computer simulation study. *J Muscle Res Cell Motil, 3*, 377−398.

Gordon, A. M., Huxley, A. F., & Julian, F. J. (1966). The variation in isometric tension with sarcomere length in vertebrate muscle fibres. *J Physiol (Lond), 184*, 170−192.

Hai, C., & Murphy, R. (1989a). Crossbridge phosphorylation and the energetics of contraction in swine carotid media. In R. Paul, G. Elzinga, & K. Yamade (Eds.), *Muscle Energetics* (pp. 253−264). New York: A.R. Liss Publisher.

Hai, C. M., & Murphy, R. A. (1988). Regulation of shortening velocity by cross-bridge phosphorylation in smooth muscle. *Am J Physiol, 255*, C86−C94.

Hai, C. M., & Murphy, R. A. (1989b). Ca2+, crossbridge phosphorylation, and contraction. *Annu Rev Physiol, 51*, 285−298.

Hardin, C. D., Allen, T. J., & Paul, R. J. (Eds.). (2000). *Metabolism and energetics of vascular smooth muscle*. San Diego: Academic Press.

Harris, D. E., & Warshaw, D. M. (1993). Smooth and skeletal muscle actin are mechanically indistinguishable in the in vitro motility assay. *Circ Res, 72*, 219−224.

Hartshorne, D. (1987). Biochemistry of the contractile process in smooth muscle. In L. Johnson (Ed.), *Physiology of the Gastrointestinal Tract* (pp. 423−482). New York: Raven Press.

Hartshorne, D. J., & Siemankowski, R. F. (1981). Regulation of smooth muscle actomyosin. *Annu Rev Physiol, 43*, 519−530.

Herlihy, J. T., & Murphy, R. A. (1973). Length-tension relationship of smooth muscle of the hog carotid artery. *Circ Res, 33*, 275−283.

Heumann, H. G. (1973). Smooth muscle: contraction hypothesis based on the arrangement of actin and myosin filaments in different states of contraction. *Philos Trans R Soc Lond B Biol Sci, 265*, 213−217.

Higuchi, H., Yanagida, T., & Goldman, Y. E. (1995). Compliance of thin filaments in skinned fibers of rabbit skeletal muscle. *Biophys J, 69*, 1000−1010.

Hill, A. V. (1912). The heat-producton of surviving amphibian muscles, during rest, activity, and rigor. *J Physiol, 44*, 466−513.

Hill, A. V. (1938). The heat of shortening and the dynamic constants of muscle. *Proc R Soc Lond B, 126*, 136−195.

Hill, A. V. (1965). *Trails and Trials in Physiology*. London: Arnold.

Huang, T. J., & Juluri, B. K. (2008). Biological and biomimetic molecular machines. *Nanomedicine (Lond), 3*, 107−124.

Huxley, A. F. (1957). Muscle structure and theories of contraction. *Prog Biophys Biophys Chem, 7*, 255−318.

Huxley, A. F. (2000). Mechanics and models of the myosin motor. *Philos Trans R Soc Lond B Biol Sci, 355*, 433−440.

Huxley, A. F., & Niedergerke, R. (1954). Structural changes in muscle during contraction; interference microscopy of living muscle fibres. *Nature, 173*, 971−973.

Huxley, A. F., & Simmons, R. M. (1971). Proposed mechanism of force generation in striated muscle. *Nature, 233*, 533−538.

Huxley, H. E. (1953). Electron microscope studies of the organisation of the filaments in striated muscle. *Biochim Biophys Acta, 12*, 387−394.

Huxley, H. E. (1996). A personal view of muscle and motility mechanisms. *Annu Rev Physiol, 58*, 1−19.

Huxley, H. E. (2004). Recent X-ray diffraction studies of muscle contraction and their implications. *Philos Trans R Soc Lond B Biol Sci, 359*, 1879−1882.

Ishida, Y., Riesinger, I., Wallimann, T., & Paul, R. J. (1994). Compartmentation of ATP synthesis and utilization in smooth muscle: roles of aerobic glycolysis and creatine kinase. *Mol Cell Biochem, 133-134*, 39−50.

James, J. H., Fang, C. H., Schrantz, S. J., Hasselgren, P. O., Paul, R. J., & Fischer, J. E. (1996). Linkage of aerobic glycolysis to sodium-potassium transport in rat skeletal muscle. Implications for increased muscle lactate production in sepsis. *J Clin Invest, 98*, 2388−2397.

Jewell, B. R., & Wilkie, D. R. (1958). An analysis of the mechanical components in frog's striated muscle. *J Physiol, 143*, 515−540.

Kamm, K. E., & Stull, J. T. (1985). The function of myosin and myosin light chain kinase phosphorylation in smooth muscle. *Annu Rev Pharmacol Toxicol, 25*, 593−620.

Kim, H. R., Appel, S., Vetterkind, S., Gangopadhyay, S. S., & Morgan, K. G. (2008). Smooth muscle signalling pathways in health and disease. *J Cell Mol Med, 12*, 2165−2180.

Kushmerick, M. (1983). Energetics of muscle contraction. In L. Peachey (Ed.), *Handbook of Physiology* (pp. 189−236). Bethesda: American Physiological Society.

Kushmerick, M. J. (2005). From crossbridges to metabolism: system biology for energetics. *Adv Exp Med Biol, 565*, 171−180, discussion 180-172, 379-195.

Levy, B., Desebbe, O., Montemont, C., & Gibot, S. (2008). Increased aerobic glycolysis through beta2 stimulation is a common mechanism involved in lactate formation during shock states. *Shock, 30*, 417−421.

Liu, T., & O'Rourke, B. (2009). Regulation of mitochondrial Ca2+ and its effects on energetics and redox balance in normal and failing heart. *J Bioenerg Biomembr, 41*, 127−132.

Lohmann, K. (1934). Ueber die enzymatische Aufspaltung der Kreatinephosphorsauere zugleich ein Beitrag zum Chemismus der Muskelcontraktion. *Biochem Z, 271*, 264−277.

Lombardi, V., Piazzesi, G., Reconditi, M., et al. (2004). X-ray diffraction studies of the contractile mechanism in single muscle fibres. *Philos Trans R Soc Lond B Biol Sci, 359*, 1883−1893.

Lundsgaard, E. (1938). The biochemistry of muscle. *Ann Rev Biochem, 7*, 377−398.

Matsumura, F., & Hartshorne, D. J. (2008). Myosin phosphatase target subunit: many roles in cell function. *Biochem Biophys Res Commun, 369*, 149−156.

Murphy, R. A., & Rembold, C. M. (2005). The latch-bridge hypothesis of smooth muscle contraction. *Can J Physiol Pharmacol, 83*, 857−864.

Needham, D. M. (1971). *Machina carnis*. Cambridge: University Press.

Nobe, K., & Paul, R. J. (2001). Distinct pathways of Ca(2+) sensitization in porcine coronary artery: effects of Rho-related kinase and protein kinase C inhibition on force and intracellular Ca(2+). *Circ Res, 88*, 1283−1290.

Offer, G., & Ranatunga, K. W. (2010). Crossbridge and filament compliance in muscle: implications for tension generation and lever arm swing. *J Muscle Res Cell Motil, 31*, 245−265.

Ottenheijm, C. A., & Granzier, H. (2010). Lifting the nebula: novel insights into skeletal muscle contractility. *Physiology (Bethesda), 25*, 304−310.

Paul, R. J. (1983). Physical and biochemical energy balance during an isometric tetanus and steady state recovery in frog sartorius at 0 degree C. *J Gen Physiol, 81*, 337−354.

Paul, R. J. (1990). Smooth muscle energetics and theories of cross-bridge regulation. *Am J Physiol, 258*, C369−C375.

Paul, R. J., & Peterson, J. W. (1975). Relation between length, isometric force, and O2 consumption rate in vascular smooth muscle. *Am J Physiol, 228*, 915−922.

Paul, R. J., Bauer, M., & Pease, W. (1979). Vascular smooth muscle: aerobic glycolysis linked to sodium and potassium transport processes. *Science, 206*, 1414−1416.

Peterson, J. W., & Paul, R. J. (1974). Effects of initial length and active shortening on vascular smooth muscle contractility. *Am J Physiol, 227*, 1019−1024.

Pette, D., & Staron, R. S. (2001). Transitions of muscle fiber phenotypic profiles. *Histochem Cell Biol, 115*, 359−372.

Rayment, I., Smith, C., & Yount, R. G. (1996). The active site of myosin. *Annu Rev Physiol, 58*, 671−702.

Ruegg, J. C., DiSalvo, J., & Paul, R. J. (1982). Soluble relaxation factor from vascular smooth muscle: a myosin light chain phosphatase? *Biochem Biophys Res Commun, 106*, 1126−1133.

Seow, C. Y., & Pare, P. D. (2007). Ultrastructural basis of airway smooth muscle contraction. *Can J Physiol Pharmacol, 85*, 659−665.

Somlyo, A. P., & Somlyo, A. V. (2000). Signal transduction by G-proteins, rho-kinase and protein phosphatase to smooth muscle and non-muscle myosin II. *J Physiol (Lond), 522* Pt 2, 177−185.

Somlyo, A. V. (1980). Ultrastructure of vascular smooth muscle. In *Handbook of Physiology (Section 2) − The Cardiovascular System (Vol. II) Vascular Smooth Muscle* (pp. 33−67). Bethesda: American Physiological Society.

Squire, J. M., & Knupp, C. (2005). X-ray diffraction studies of muscle and the crossbridge cycle. *Adv Protein Chem, 71*, 195−255.

Weiss, J. N., & Lamp, S. T. (1987). Glycolysis preferentially inhibits ATP-sensitive K+ channels in isolated guinea pig cardiac myocytes. *Science, 238*, 67−69.

Westerblad, H., Bruton, J. D., & Katz, A. (2010). Skeletal muscle: energy metabolism, fiber types, fatigue and adaptability. *Exp Cell Res, 316*, 3093−3099.

Wingard, C. J., Paul, R. J., & Murphy, R. A. (1997). Energetic cost of activation processes during contraction of swine arterial smooth muscle. *J Physiol, 501*(Pt 1), 213−223.

Woledge, R. C., Curtin, N. A., & Homsher, E. (1985). Energetic aspects of muscle contraction. *Monogr Physiol Soc, 41*, 1−357.

This page intentionally left blank

Chapter 47

Flagella, Cilia, Actin- and Centrin-based Movement

Kenneth W. Foster

Chapter Outline

I. INTRODUCTION

To place emphasis on understanding integrated structure and mechanism, I use these pages to discuss just a few examples chosen from a vast literature. A much broader survey of the field with emphasis on the earlier literature is available (Kaneshiro, 2001; Kaneshiro et al., 2001).

Physiology is about the way life works, dynamically. Learning the mechanisms of how something works has

Cell Physiology Sourcebook. DOI: 10.1016/B978-0-12-387738-3.00047-0

often proven to be the most intractable problems in biology. We illustrate this reality with a number of intensely interesting and studied, but incompletely solved problems in the cell physiology of non-muscle motion systems.

Several mechanisms for the generation of force have evolved, including motors driven by ion gradients or ATP, the use of molecular springs driven by calcium regulated conformation change and use of turgor pressure to fire projectiles.

To maintain an easy distinction, bacterial and archaeal flagella are called *flagella* and the completely unrelated eukaryotic flagella and cilia are exclusively called *cilia*. Bacterial and archaeal flagella are quite different structures of separate evolutionary origin but with very similar function as they are both very slender rotating cylinders that enable a cell to move.

IA. Conversion of Free Energy into Work

Basic to movement is the conversion of free energy (the energy in a system that is available to do work) into work. Biology has employed motors with several characteristics atypical compared to most man-made motors. First, the motors are very small with individual force limits of the order of 8 pN. Second, when they are off they keep their position and hence do not require continued energy input unlike electromagnetic continuous and stepping motors. The reason for both characteristics of biomotors is to minimize energy requirements. Recently, with interest in making devices more portable, humans have designed motors with similar characteristics.

It is important to understand how free energy is converted to work and, as a consequence, why making the motors small maximizes their efficiency. While a much more complete discussion is available (Nelson, 2008), let me repeat here the portion of the argument as to why motors need to be small. He considers an analogous system that extracts mechanical work.

Consider the process of lifting a weight with a cylinder of gas with a piston of area A at one end, held down by weights w_1 and w_2 (Fig. 47.1A).

To determine the relationship between free energy and work, let us compare the change in free energy of the gas (equivalently the loss of available energy) that is driving the work with the mechanical work done. Removing w_2 will reduce the weight on the gas causing w_1 to rise. Specifically, removing w_2 will result in L_{initial} increasing by ΔL to L_{final}.

Hence, the work done will be $W = w_1(L_f - L_i)$. From the ideal gas law $p_f\, L_f\, A = N\, k_B\, T$, where k_B is Boltzmann's constant, p_f is the final pressure, L_f is the final length, A is the cross-section of the gas cylinder, N is the number of molecules and T is the absolute temperature. Since $p_f = w_1/A$, then $w_1 = N\, k_B\, T/L_f$ and hence the work $W = N\, k_B\, T\, (L_f - L_i)/L_f$ or $W = N\, k_B\, T\, (\Delta L/L_f)$.

The change in free energy will be due to the change in entropy times the absolute temperature, T. The change in entropy is just $N\, k_B$ times the logarithm of the ratio of the final to initial volumes. Hence, the change in free energy: $\Delta F = N\, k_B\, T \ln(L_f/L_i)$.

Comparing work and free energy:

$$\begin{aligned} &\Delta L/L_f(\text{the work}) < \ln(1/(1-\Delta L/L_f)) \\ &(\text{the change in free energy}) = \\ &-\ln(1-\Delta L/L_f) \approx -\{-\Delta L/L_f - 1/2\cdot(\Delta L/L_f)^2 \\ &\qquad -1/3\cdot(\Delta L/L_f)^3 - \ldots\} \\ &\qquad = \Delta L/L_f + 1/2\cdot(\Delta L/L_f)^2 \\ &\qquad +1/3\cdot(\Delta L/L_f)^3 + \ldots.. \end{aligned} \tag{47.1}$$

By inspection, the first term on the right hand side of the less-than symbol is equal to the term on the left hand side and all other terms on the right are positive. So in general, work is always less than the available free energy to drive it. However, inspection of the positive terms on the right leads one to recognize that they are all small if ΔL is small, so if the steps are sufficiently small almost all the free energy can be converted to work.

Bottom line is that small steps make the most efficient use of available free energy. Of course, chemical energy can be used as the source of free energy.

A few parameters to remember: thermal energy at room temperature is $k_B\, T = 25\,\text{meV} = 4.1\,\text{pN nm}$, a typical membrane potential is $\approx 70\,\text{mV}$, motor forces are a few pN and the energy of ATP hydrolysis is $\approx 25\, k_B\, T$. These parameters apply to all biological motors.

IB. Reynolds Number

Critical to understanding motors and application of molecular devices is appreciating the low Reynolds number regime. Reynolds number is the ratio of inertial forces relative to viscous forces,

$$R = \frac{vL\rho_m}{\eta} \tag{47.2}$$

where v is the velocity, L is the characteristic dimension (length) of the object, typically the diameter for a sphere, ρ_m is the density of the object, and η is the viscosity. When R is small, friction dominates, stirring produces laminar flow and, if an external force stops, fluid flow stops almost immediately. For example, if a swimming cell stops its thrust it comes exponentially to a stop. The time constant of the exponential for coasting is

$$\tau \sim \frac{L^2\rho_m}{18\eta} \tag{47.3}$$

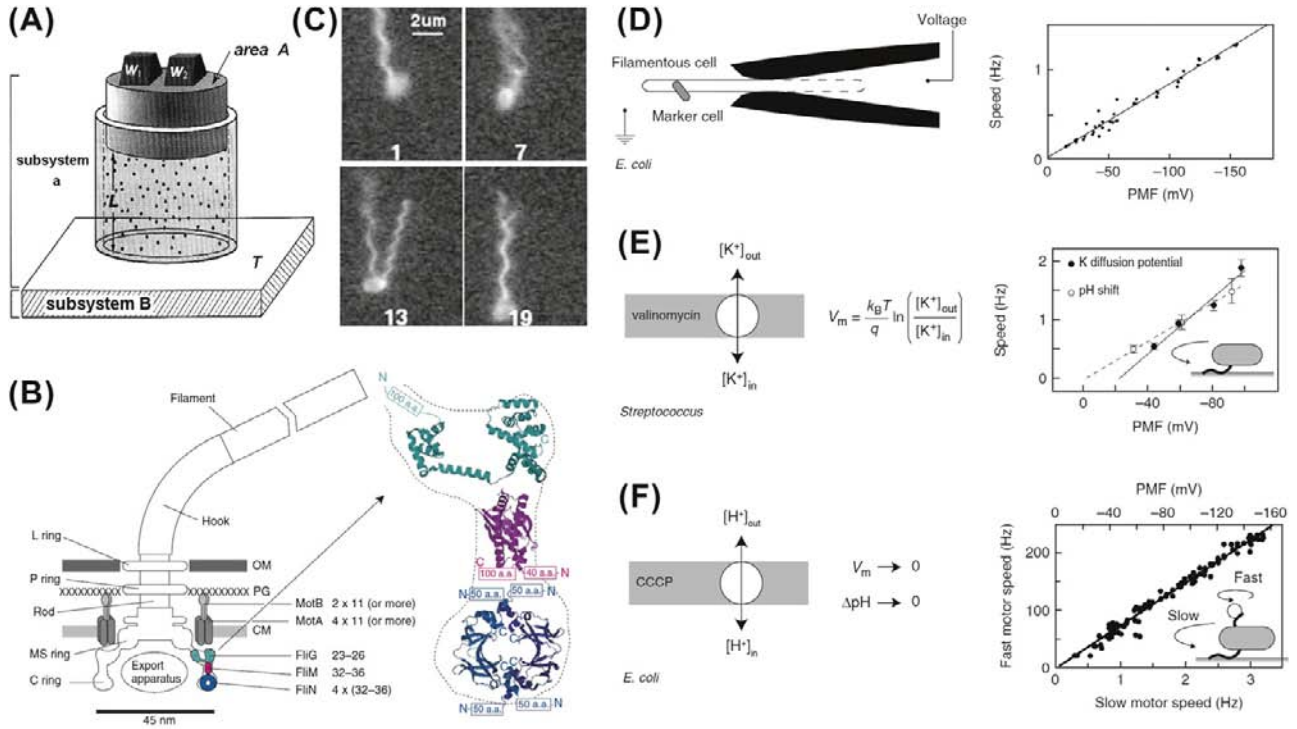

FIGURE 47.1 (A) Obtaining work from available free energy may be illustrated by the mechanical work of lifting a weight extracted by removing a second weight from a gas compressed by this second weight. *(Modified from Nelson, 2008, p. 215, Fig. 6.5.)* (B) Left: Schematic view of an H^+-driven flagellar motor with the proposed locations of proteins involved in torque generation. MotA and MotB form stator complexes with stoichiometry A_4B_2 and FliN forms a tetramer with a 1:1 stoichiometry with FliM. The motor spans the outer membrane (OM), peptidoglycan cell wall (PG) and cytoplasmic membrane (CM). Right: The proposed location and orientation of rotor proteins. X-ray crystal structures of truncated rotor proteins, FliG (cyan), FliM (magenta) and FliN (blue), are shown docked into the rotor structure. N- and C-termini and missing amino acids are indicated (Sowa and Berry, 2008). (C) Stroboscopic images of a fluorescently labeled swimming *E. coli* cell. The numbers are frame numbers, at 1/60 s intervals. Between frames 7 and 13, a single filament leaves the bundle and undergoes polymorphic transitions that cause a change in swimming direction known as a "tumble" (Turner et al., 2000). (D) Torque versus IMF. Left: Schematic of a voltage-clamp method using *E. coli* cells held in micropipettes. The part of the membrane inside the pipette (indicated by the dashed line) is made permeable using the ionophore gramicidin S. Motor speed from observation of a dead cell attached to the motor. Right: Motor speed found proportional to membrane voltage (=PMF) between 0 and −150 mV (Sowa and Berry, 2008). (E) Left: Membrane voltages in *Streptococcus* controlled by a K^+ diffusion potential in the presence of valinomycin. Right: The speed of tethered *Streptococcus* cells found proportional to PMF, and membrane voltage found equivalent to pH gradient (Sowa and Berry, 2008). (F) Left: PMF varied from −150 mV down to 0 by adding small concentrations of carbonyl cyanide, m-chlorophenylhydrazone (CCCP) or sodium azide. Right: Using the result of (D), the speed of a tethered *E. coli* motor (x-lower axis) was used as a proxy for PMF (x-upper axis, absolute value shown). The speed of a second motor on the same cell, attached to a submicron bead, was found proportional to PMF (Sowa and Berry, 2008).

A 2 μm long bacterium, whose motors we will discuss below, swims about 30 μm/s (v_0) with an R of 3×10^{-5} and τ of 0.2 μs and would coast a distance $(\tau \cdot v_0)$ of $d_{coast} \approx 6$ pm if its motors were to stop (of course it will move much more by Brownian motion). Even a much larger (10 μm) eukaryotic swimming cell (140 μm/s) like *Chlamydomonas* has an R of 1.4×10^{-4}, a τ of 20 μs and a $d_{coast} = 2.8$ nm, still very short. The border line between low and modest Reynolds numbers comes with organisms like *Volvox* (1 mm length, 1 mm/s velocity) with an R of ≈1 and a τ of 200 ms and a $d_{coast} = 0.2$ mm. This border can also be crossed slightly by somewhat smaller organisms under special circumstances. *Paramecium* (typically 0.2 mm, 1 mm/s) has an R of ≈0.2, but it can transiently go as fast as 10 mm/s with an R of ≈2 and a d_{coast} of ≈20 μm (Hamel et al., 2011). It might jump most of its length in this burst of motion, but coasting is still a minimal part of it. The low Reynolds number regime is characterized by the uselessness of reciprocal motions as there is nothing to be gained by inertia and hence propulsive systems involve crawling, rotating appendages and wave propagation down appendages (Nelson, 2008).

Study of non-muscle contraction and motility is a work in progress. Substantial changes in understanding of mechanisms are anticipated in the near term with further opportunities for more detailed study likely. Consequently, what is attempted here is emphasis on some basic principles, a coarse description and some suggestions for how to approach future research. If the challenge of researching problems in this area excites you, please appreciate that significant further reading will be necessary.

II. BACTERIAL FLAGELLA

IIA. Introduction

Flagellated bacteria, such as *Escherichia coli*, swim by rotating thin helical filaments; each driven at their base by a reversible 45-nm-diameter rotary motor powered by ion flux (see Fig. 47.1B). The motor develops maximum torque at stall, but can rotate at several hundred Hertz. Its rotation direction is controlled by a sensory system that makes it possible for cells to accumulate in favored regions. A great deal is known about motor structure, genetics, assembly and function, but not precisely how it works (Berg, 2003).

The following sections on the structure, energy supplies and mechanism of motion primarily follows the review by Sowa and Berry (2008), however, it is also further informed by the review of Berg (2003). A brief discussion of the associated behavior follows and the study of fluctuation follows that.

IIB. The Structure

The flagellum is a ≈23-nm-thin, ≈10 000-nm-long helical filament with a rotary motor at its base that turns it like a propeller. The flagellar motor, by bacterial standards, is a large molecular machine made from ≈13 different proteins and a further ≈25 proteins are required for its expression and assembly. The best studied motors are those of the peritrichously flagellated bacterium *Escherichia coli* and the related *Salmonella enterica* Sv *typhimurium* (*S. typhimurium*). These motors switch between rotating counterclockwise (CCW, viewed from the outside) with formation of a bundle of flagella that produces smooth swimming and rotating clockwise (CW) that causes tumbles or rapid rotational diffusion.

The power of bacterial flagella may be estimated from the input and outputs that can be calculated. The input power may be estimated from the measured 1200 protons/revolution at 10 Hz rotation speed with a protonmotive force of −170 mV. Since the proton is a single charge, this corresponds to 2040 eV/s (3.3×10^5 pN nm/s). The output power under the same conditions can be estimated by the torque times the angular velocity, namely 4600 pN nm × 2 π× 10 Hz = 2.9×10^5 pN nm/s (1800 eV/s), essentially the same as the input. There are other flagellated bacteria that swim differently. That bacterial flagella rotate was first observed by the rotation of the cell body tethered to a surface by its flagella. These tethered cells rotated up to ≈20 Hz. They spin faster with lower loads with the maximum recorded speed so far being 1700 Hz in the Na^+-driven motor of *Vibrio alginolyticus* at 37°C.

To measure flagellar rotation, the currently preferred method is to attach submicron polystyrene beads to truncated flagellar filaments of immobilized cells and to record their rotation with either back-focal-plane interferometry or high-speed fluorescence microscopy. The viscous drag coefficient of a 0.5 μm diameter bead on a truncated filament is similar to that of a flagellar filament. The smaller the bead the lower is the load and the higher the speeds that can be recorded.

Single particle image reconstruction from cyroelectron microscopy (EM) has determined the structure of the flagellar motor and their components have been identified by genetic and biochemical studies. Like any rotary motor, the bacterial flagellar motor consists of a rotor, the moving part, and a stator, the stationary part. The rotor spins relative to the cell and is attached to the helical filament by a universal joint called the hook, whereas the stator is anchored to the cell wall. Figure 47.1B shows a schematic diagram of the bacterial flagellum of a Gram-negative bacterium, based on an EM reconstruction of the rotor from *S. typhimurium*. The core of the motor is called the basal body and consists of a set of rings up to ≈45 nm in diameter that spans three layers of the cell envelope. The L and P rings are thought to be embedded in the outer lipopolysaccharide membrane and peptidoglycan cell wall, respectively, and act as a bushing between the rotor and the outer parts of the cell envelope. The rod connects the hook to the MS ring located at the cytoplasmic membrane. The MS ring consists of ≈26 copies of a single protein, FliF. After the MS ring is assembled, the rest of the motor is built from it. The cytoplasmic face of the MS ring is attached to the C ring, which contains the rotor proteins FliG, FliM and FliN and is the site of torque generation. The stators are a complex of two proteins: MotA and MotB in H^+-driven flagellar motors such as those of *E. coli*. The filament grows from its distal end supplied by a channel down its center. To do this an export apparatus inside the C ring pumps down the center of the proteins needed to make the hook and extend the filament.

IIC. Propeller and Universal Joint

The hollow hook and filament are single-protein thin tubular polymers consisting of 11 helical protofilaments. Monomer incorporation is regulated by pentameric cap complexes. Each polymer has a long and short form which creates the helical structures of the hook and filament. During steady rotation, the filament is a rigid propeller. Motor switching in *E. coli* causes a torsionally induced transformation between the alternative filament forms changing the handedness of the filament helix. The transformed filament breaks up the bundle of filaments currently propelling the cell and thus leads to cell reorientation (see Fig. 47.1C). To see this, flagellar filaments have been fluorescent labeled and swimming cells have been recorded with stroboscopic laser illumination and high-speed video microscopy. Response to external forces has been studied with optical tweezers. The hook is much more flexible than

the filament and works as a universal joint to allow several filaments from motors all over the cell to rotate together in a bundle in peritrichiously flagellated species. A great simulation of the assembly process is available at http://www.fbs.osaka-u.ac.jp/labs/namba/npn/index.html.

IID. Energy Transduction

Molecular motors convert chemical or electrical energy to mechanical work and operate close to the level of thermal energy, k_BT. In the bacterial flagellar motor, the free energy input from a single ion passing through the cytoplasmic membrane is a single electric charge times the ion-motive force (IMF; either proton-motive force [PMF] or sodium-motive force [SMF]). The electrochemical potential, IMF = $V_m + k_BT/q \ln (C_i/C_o)$, where V_m is the transmembrane voltage (inside minus outside) and q, C_i and C_o are the charge, inside and outside concentrations of the coupling ion, respectively. With a typical IMF of around −150 mV, the free energy of a single ion transit is $\approx 6\, k_BT$. Torque is defined as the product of force and the perpendicular distance to an axis of rotation and therefore has dimensions of Newton-meters or energy. Because Reynolds number for a spinning flagellar motor is $<<1$, inertia is negligible and torque can be calculated as $M = f\,\omega$, where f is the rotational drag coefficient and ω is the angular velocity.

IIE. Ion Selectivity

Bacterial flagellar motors are driven by ions and not ATP hydrolysis like muscle motors. These can be the driven by the membrane potential and/or by the hydronium or Na^+ gradients.

IIF. Motor Dependence upon IMF

The IMFs drive bacterial flagellar motors oriented in the membrane and ions travel through the motor in a particular direction. Ion drives permit the high stator turnover speeds and high power output. The free energy of $\approx 6\, k_BT$, corresponding to one ion crossing the membrane, is smaller than the free energy of hydrolysis of ATP ($\approx 20\, k_BT$). In addition, the enthalpic contribution is proportional to the continuously variable and reversible membrane voltage. The estimated flux is around 1200 H^+ ions per revolution per motor over a speed range of 20−60 Hz.

By voltage clamping the membrane voltage at the flagellar motor and monitoring motor motion by video microscopy of dead cells attached to the motors, it has been found that their rotation speed is proportional to the applied voltage up to −150 mV (see Fig. 47.1D). By varying the concentration of driving ions and diffusion potential it has also been shown that the electrical and chemical components of the IMF are equivalent at high load in H^+-driven flagellar motors (see Fig. 47.1E). Subsequently, it was found that at low load the faster speed of the motor is also proportional to IMF (see Fig. 47.1F).

IIG. Torque Versus Speed

The torque−speed relationship of the flagellar motor has been measured to clarify the mechanochemical cycle. The speed can be measured over a wide range of viscous load or externally applied torque. With the latter method, the torque of the motor can be measured when forced to rotate backwards or forwards faster than its zero-load speed. The electrorotation method was particularly effective; a rotating electric field (megaHertz) polarizes the cell body and torque is exerted on the cell due to a phase lag between the field and induced dipole moment. Figure 47.2A summarizes the data from spinning the cell body in both directions at speeds up to ≈1 kHz. There is a plateau of nearly constant torque up from backwards speeds of about ≈100 Hz to a "knee" forward speed of several 100 Hz, then the torque falls linearly towards the zero-torque speed at ≈400 Hz (Fig. 47.2A, circles, triangles), at which point the motor resists rotation with a torque of similar magnitude to the plateau torque (Fig. 47.2A, large gray circles). The absolute magnitude of torque generated by the *E. coli* motor was determined to be 1260 ± 190 pN nm using measurements with polystyrene beads of 1 μm diameter. In the torque plateau region, since the output power is proportional to the torque times the angular velocity, the output power increases linearly with speed. Also because the number of protons through the motor per revolution is constant, the input power also increases linearly with the angular velocity, so that a constant efficiency is maintained.

At the torque plateau, transitions linked to ion flux are not rate limiting so speed is only mechanically limited by the load on the motor and depends only on the IMF, a thermodynamic quantity. The continuity of torque on either side of stall indicates that there is no irreversible step in the mechanochemical cycle. Faster than the "knee" transitions in the motor are rate limiting, possibly due to a requirement that ions must be gated across the structure. In this case, motor speed depends on absolute temperature, the hydrogen isotope and which component of the SMF is dominant. High rotation speed decreases the efficiency of ion going across the ion gate through the motor.

IIH. Mechanism of Torque Generation

IIH1. Interactions Between Rotor and Stator

The C ring (containing FliG, FliM and FliN) of the rotor is the key component for torque generation and switching direction from CCW to CW. FliG interacts with MotA to generate torque. Stator complexes anchor to the peptidoglycan cell wall and span the cytoplasmic membrane,

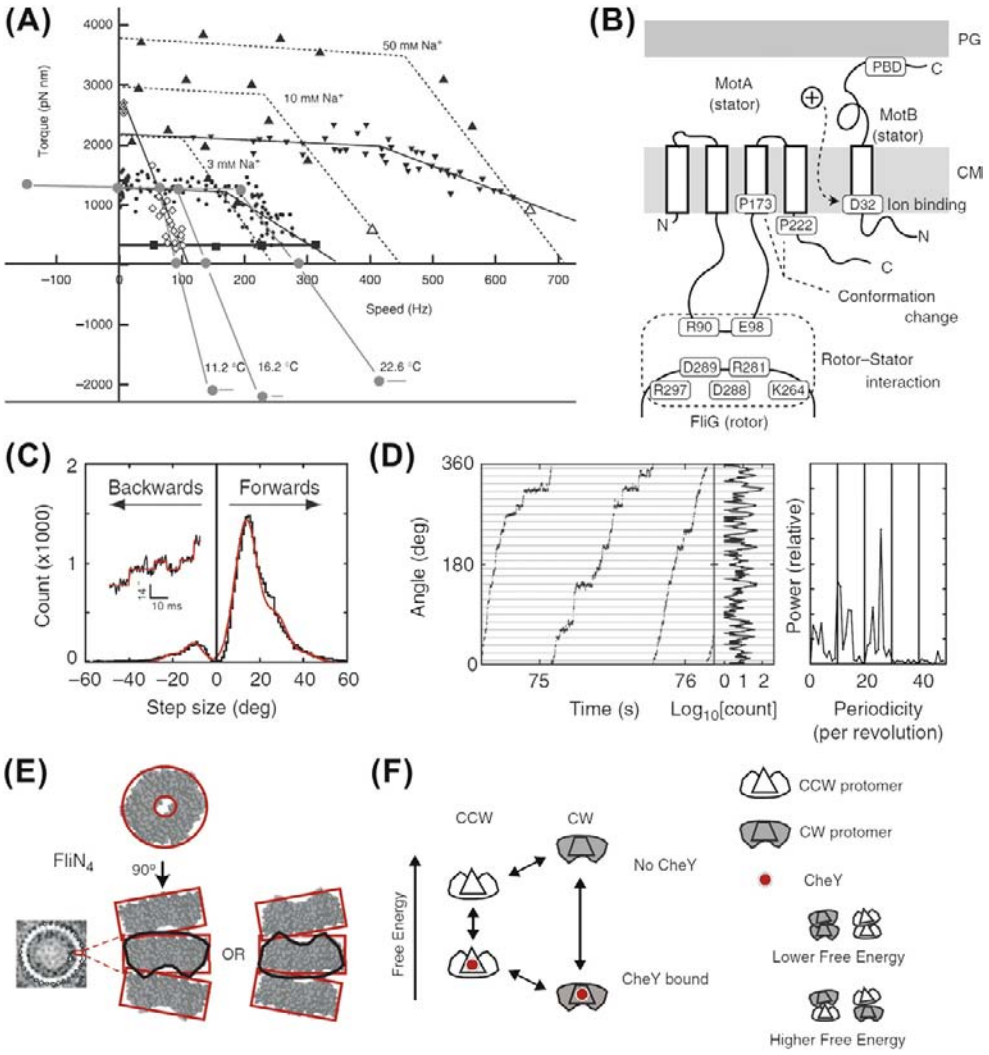

FIGURE 47.2 (A) Torque–speed relationships for flagellar motors of diverse species measured using various methods. All measurements were made at room temperature except where indicated. The *E. coli* experiments using electrorotation (gray circles) and beads (black circles) did not report absolute torques, so these curves are scaled to a stall torque of 1260 pN nm (Sowa and Berry, 2008, where more details may be sought). (B) Stator topology and interaction between rotor and stator in *E. coli*. MotA has four transmembrane α-helices and a cytoplasmic domain between the 2nd and 3rd transmembrane regions. Charged residues of this cytoplasmic domain contains interact with charged residues of FliG. MotB has a periplasmic domain containing a peptidoglycan-binding domain (PBD). PG, peptidoglycan cell wall; CM, cytoplasmic membrane (Sowa and Berry, 2008). (C) Step size distribution (black) with multiple Gaussian fit (red). The peak of forward steps is 13.7°, indicating 26 steps per revolution. An example of steps identified by a step-finding algorithm is shown (inset) (Sowa and Berry, 2008). (D) Plot of angle versus time during three revolutions, a histogram of the corresponding dwell angles and its corresponding power spectrum. The peak at 26 per revolution corresponds to a step size of 13.8° and shows that the motor stops at the same angles on successive revolutions (Sowa and Berry, 2008). (E) X-ray crystal structure of the FliN tetramer showing the puckered ring structure and proposed equivalent stacking configurations of tetramers in the C ring (EM structure of C ring, left) (Sowa and Berry, 2008). (F) Conformational spread model of flagellar switching. Protomers consisting of a FliN tetramer and one molecule of FliM with or without bound CheY can be in either the CW or CCW configurations. CheY binding lowers the free energy of the CW configuration relative to CCW, increasing the probability of CW rotation. Adjacent protomers have a lower free energy of interaction when both are in the same state, which leads to cooperative switching of the whole ring (Sowa and Berry, 2008).

forming ion channels. The cytoplasmic domain of MotA contains two charged residues that interact with five charged residues in the C-terminal domain of FliG to generate torque. An electrostatic interaction at the interface between the two proteins is suggested since no single mutation in these residues completely abolishes torque generation and charge-reversing mutations in both proteins can compensate. The stoichiometry of the stator complexes (of MotA and MotB) appears to be A_4B_2 with the membrane-spanning helices of MotA subunits surrounding a suspected proton-binding site at residue Asp32 (in *E. coli*) of MotB (see Fig. 47.2B).

This charged residue is essential for function. Each stator contains two ion channels with one MotB-Asp32 each. There is evidence that the protonation of Asp32 causes a conformational change in MotA. Proline residues are particularly important as they make possible bends in a helix. This makes particularly interesting that mutations in the conserved proline residues P173 and P222 in *E. coli* MotA severely impair motor function. Thus, a putative mechanism for the motor is that the proton flux coordinates conformational changes in MotA via MotB-Asp32 and that these conformational changes involve motions about the MotA proline residues that lead to a cyclic interaction with FliG that generates torque.

IIH2. Independent Torque Generating Units

When functional Mot proteins are introduced into a mot minus mutant strain, motor speed increases in discrete increments implying independent stator units provide the torque. Up to 11 or 12 speed increments were seen, consistent with the EM images and similarly for the Na^+-driven chimera in *E. coli.* There are also transient speed changes in normally expressed motors, indicating that stators are not permanent, but in constant turnover.

An average of 22 GFP-MotB molecules per cell have been counted consistent with 11 stator complexes each with the A_4B_2 stoichiometry predicted biochemically. Furthermore, a mobile pool of $\approx$200 GFP-MotB molecules was seen in the cell membrane exchanging with GFP-MotB in the motor on a timescale of minutes, confirming that stator units are in dynamic flux.

III. Stepping Rotation

The hook twists when an external torque is applied so that even a single stator generating $\approx$150 pN-nm twists the hook 0.35 radians. In a subsequent step, the motion of an attached bead will be damped with a relaxation time equal to the viscous drag coefficient divided by the spring constant of the hook. To detect steps, the time between steps must be greater than this relaxation time. To overcome these problems, stators were expressed at low levels and the SMF was reduced by lowering external sodium concentration. This achieved $\leq$10 Hz rotation combined with a fast bead response. Rotation was detected by tracking either 0.5-μm beads using back-focal plane interferometry or 0.2-μm fluorescent beads using a high-speed EMCCD camera. The distribution of step sizes was fitted by multiple Gaussians to deal with the possibility that the step-finding algorithm combined two adjacent steps into a double-size step (see Fig. 47.2C). The most probable step size was 13.7° corresponding to 26 steps per revolution (360°/13.7°= 26.3). Histograms of the dwelling angle of beads during several revolutions showed a 26-fold periodicity (see Fig. 47.2D), confirming the step size and showing that the 26 stopping angles are the same in successive revolutions.

Twenty-six steps per revolution is consistent with the periodicity of the ring of FliG, the track on the rotor where rotational torque is believed to be generated.

IIJ. Models of the Mechanism

Most models can be divided into ion turbines, ion turnstiles or binding with conformational change. In an ion turbine model, the path of ions across the membrane is formed by elements in the stator and in the rotor and these elements are arranged in lines that are tilted with respect to each other. The "elements" can be half-binding sites on the rotor and stator that need to be aligned to bind a permeant ion or ion channels in the stator that interact with tilted lines of charge on the rotor by long-range electrostatic interactions. The charged residues on the surface of FliG that are involved in torque generation could, in principle, be arranged in such a way as to provide the electrostatic interactions that are proposed. In a turnstile model, ions are deposited onto the rotor from outside the cell by one type of stator channel and can only complete a transit if the rotor rotates, carrying them to a second type of stator channel that connects to the cell interior as suggested for the F_0-ATPase. In that case, an essential conserved residue on the C subunit provides a probable binding site for ions halfway across the membrane, however, such a binding site is missing in the flagellar motor. In a conformational change model, ion transiting through a stator is proposed to be coupled to a cycle of conformational changes of the stator, which exerts torque on the rotor, either by long-range electrostatic or short-range steric interactions. This type of mechanism is proposed for the ATP-driven molecular motors actin−myosin and F_1-ATPase. Conformational changes in MotA linked to the proposed ion-binding site in MotB provide indirect evidence for this type of model. This model assumes a soft elastic linkage between the motor and the viscous load, tight coupling of motor rotation and ion transport as in the F_0 motor, the power stroke is a conformational transition in the stator triggered by the protons hoping onto and off the stator and the ion channel through the stator is gated by the motor on the rotor.

IIK. Reversibility and Switching

The flagellar motors of *E. coli* are reversible in two ways. Under natural conditions, with an IMF of around −150 mV, motors spontaneously switch direction stochastically about every second. Also, non-switching mutants rotate in the opposite direction when the PMF is reversed. This was achieved using a K^+ diffusion potential in *Streptococcus* and a voltage clamp in *E. coli*. In both cases, only a fraction of motors rotated when the PMF was reversed. In the *E. coli*

experiment, removal of the normal PMF appeared to cause the detachment of stators after a few revolutions. These results indicate that the mechanochemical cycle of the flagellar motor is essentially reversible. As discussed further below, chemotactic switching is induced by binding of the active phosphorylated form of the response regulator CheY (CheY-P) to FliM on the rotor. [CheY-P] is controlled by the chemotactic signaling system with a very steep dependence of motor bias (probability of CW rotation) upon [CheY-P], with a Hill coefficient of ≈ 10.

Currently, the best candidate to explain the switch mechanism is the conformational spread model (see Fig. 47.2E,F) in which the rotor contains ≈ 34 bi-stable protomers (in proportions of 4 of FliN to 1 of FliM to ≈ 1 of FliG). The steep dependence and lack of cooperative binding are predicted if there is a free-energy penalty for adjacent protomers to be in different states, so that the rotor is most stable with all protomers in either the CW or CCW states. A recent atomic structure of the FliN tetramer (lacking 50 amino acids at the C terminal) shows a puckered ring (see Fig. 47.2E) that fits well into the bottom of the C ring from EM reconstructions (see Fig. 47.1B). The pucker breaks the symmetry of the tetramer so they could stack in two equivalent ways, pointing either way around the C ring. Thus, the FliN tetramer is thought to be the bi-stable element in the conformational spread model, with the free-energy penalty coming from adjacent tetramers being puckered in opposite directions.

Sowa and Berry (2008) suggest that the flagellar motor is the first ion-driven molecular machine that can be studied at this level of mechanical detail. The ability to measure the enthalpic (membrane voltage) and entropic (ion concentration gradient) components of the SMF of the chimeric sodium-driven motor in *E. coli* will make it possible to study how molecular motors convert these components of free energy into mechanical work.

IIL. Chemotaxis

These motors enable a cell to swim with an orientation relaxation time constant of about 1 s due to the bacterium's rotational diffusion (Fig. 47.3A). Given they are a very elaborate piece of optimized engineering and must be quite costly to produce, there must be an advantage to swimming. Perhaps then it is not a surprise that their control for chemotaxis is also highly optimized often in surprising ways (Hazelbauer et al., 2007) (Fig. 47.3D,E). From a physiological point of view, understanding how the system works is perhaps best described from a simple linear prospective as represented by a Bode plot and then adding on the additional non-linear modifications that have given it enormously increased dynamic range from what you might anticipate, temperature robustness (Oleksiuk et al., 2011) and extraordinary sensitivity.

The gain-frequency Bode plot (see Fig. 47.3B) (Segall et al., 1986) and temporal plot (see Fig. 47.3C) (Segall et al., 1986) show that, functionally, the linear description is, in no particular order, a differentiator of the input signal (usually most associated with comparison of receptor occupancy and methylation level) and two quadratic-lag second-order low pass filters (≈ 0.2 and ≈ 1.6 Hz). It is left to the reader to assign components and the reactions that are likely responsible. Further optimization is obtained by a so-called trimers-of-dimers-architecture cheA-cheW complex. It would appear that for every receptor molecule activated, 36 kinases are activated, a considerable amplification.

Fluctuation analysis. One might anticipate that, since a responding system cannot distinguish between noise input and signal, then it must respond at low levels of signaling molecules to noise input in the same way as small real signals. The response network is tuned to maximize simultaneously both the random spread of cells in the absence of attractants and the cellular response to gradients of attractant. This advanced topic may be pursued profitably by further reading Emonet and Cluuuzel (2008).

More complex systems. Comparison of the other bacterial chemotactic systems to that of *E. coli*, has shown that most other systems are more complex, even involving cascaded feedback loops which bring greater stability to response. This advanced topic is worth further reading (Hamadeh et al., 2011).

III. CILIA

IIIA. Introduction

Eukaryotic flagella and cilia are alternative names for the slender cylindrical protrusions exclusively of eukaryotic cells that propel a cell or move fluid. Cilia are extraordinarily successful complex organelles found throughout the eukaryotes and perform many tasks in animals. They play a direct or developmental role in the sensors of fluid flow, light, sound, gravity, smells, touch, temperature and taste in mammals. The failure of cilia can lead to hydrocephalus, infertility and blindness. However, in spite of their large role in human function and pathology in terms of their physiology, there is as yet no consensus on how cilia beat or in detail how they are controlled to perform their many functions. Examples of function include moving fluids in brain ventricles and lungs and propelling and steering sperm, larvae and many microorganisms. Hence, there remains a significant opportunity for further research.

Here we are concerned with their role in motility (Foster, 2009). Typically, they are very slender (240 nm to 1200 nm in diameter, but not the 23 nm flagellar thin) and can be quite short (5 μm), most typically 12−50 μm or even amazingly long (>10 000 μm). They can propagate waves

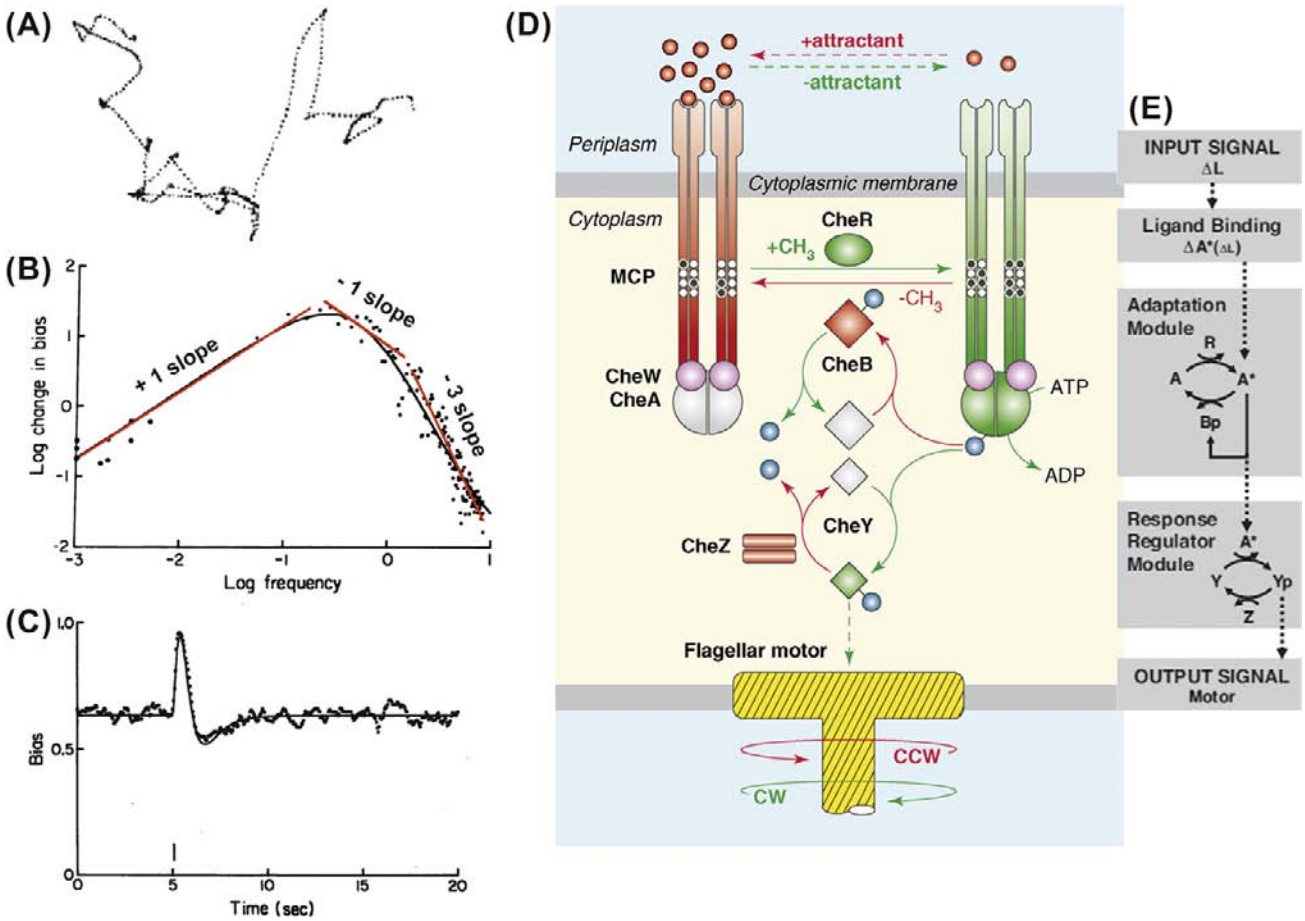

FIGURE 47.3 (A) Swimming track of *E. coli* (Berg and Brown, 1972). (B) Amplitude frequency domain Bode plot of the change in the CW−CCW bias in flagellar rotation of *E. coli* resulting from modulation of attractant, plotted as log (change in bias) versus log (frequency) of temporal modulation of the concentration of α-methylaspartate. The low-frequency data set comes from exponentiated sine-wave stimuli, while the high-frequency data comes from Fourier transforming the impulse response. The red curves show the probable dependences associated with the biochemical pathways (modified from Foster, 2009 and Segall et al., 1986). (C) Impulse response to attractant in wild-type cells. The dotted curve is the probability determined from repetitive stimulation that tethered cells of strain AW405 spin CCW when exposed to pulses of L-aspartate or α-methyl-DL-aspartate beginning at 5.06 s (vertical bar). The smooth curve is a fit to a sum of exponentials. The curve was constructed from 378 records comprising 7566 reversals of 17 cells. Points were determined every 0.05 s (Segall et al., 1986). (D) The chemoreceptor signaling pathway in *E. coli*. Components and reactions in red promote counter clockwise (CCW) flagellar rotation; those in green promote clockwise (CW) flagellar rotation. Components in gray represent inactive forms. Solid lines represent enzymatic reactions; broken lines indicate binding interactions. CheA-derived phosphoryl groups are shown as blue spheres. Receptor modification sites are shown as white (unmethylated) and black (methylated) circles (Hazelbauer et al., 2007). (E) Summary of essentials of chemotaxis pathway. Transmembrane receptors bind the ligand (L) and control the activity of histidine kinases CheA. The kinase CheA phosphorylates the response regulator CheY (Y) into the active form CheY-P (Yp). CheY-P diffuses throughout the cell and interacts with the flagellar motors to induce clockwise rotation (tumble). The phosphatase CheZ (Z) dephosphorylates CheY-P. A sudden increase of ligands L causes the kinase activity to decrease by A*. The chemotaxis system has an adaptation module in which two antagonistic enzymes regulate the activity of the kinase-receptor complexes. Note this is unlike most electronic circuits; here there is a feedback circuit to increase a variable and one to decrease the same variable. The methyltransferase CheR (R) catalyzes the autophosphorylation of CheA by methylating the receptors. The active kinase A* phosphorylates the methylesterase CheB in CheB-P (Bp). CheB-P removes methyl groups from active receptor complexes, which catalyzes kinase deactivation (Emonet amd Cluzel, 2008).

from the base or the tip or, in a few cases, even switch from one to the other. They can have two distinct modes, so-called flagellar or symmetric beating which is whip like and is typically like a sperm, or ciliary or asymmetric beating which is breast-stroke like (see Fig. 47.5C). It is not unusual to be able to switch between the two modes of beating. On a surface, including an air−water interface, they may also crawl.

IIIB. History

It is thought that cilia evolved from a protruding structure with sensory capabilities. Later, some motors invaded the structure from the cytoplasm enabling crawling on a surface much like the cilium of *Peranema* that pulls itself along an air−water interface or harder substrate at 50 μm/s. Later, more motors were inserted and, spontaneously, the

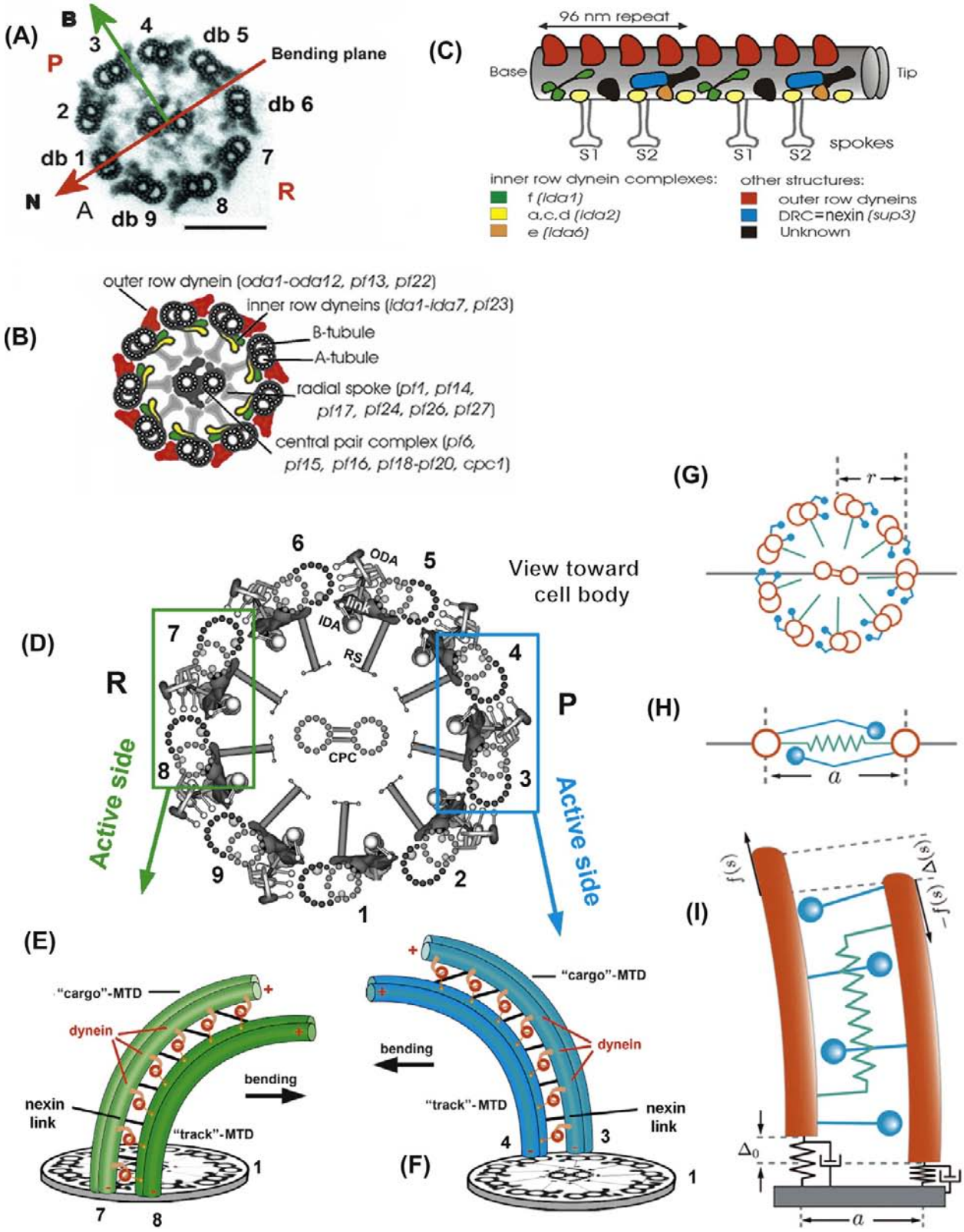
(A)
B
P
N
A
R
db 1
db 5
db 6
db 9
Bending plane
(B)
outer row dynein (oda1-oda12, pf13, pf22)
inner row dyneins (ida1-ida7, pf23)
B-tubule
A-tubule
radial spoke (pf1, pf14, pf17, pf24, pf26, pf27)
central pair complex (pf6, pf15, pf16, pf18-pf20, cpc1)
(C)
96 nm repeat
Base
Tip
spokes
S1
S2
inner row dynein complexes:
f (ida1)
a,c,d (ida2)
e (ida6)
other structures:
outer row dyneins
DRC=nexin (sup3)
Unknown
(D)
View toward cell body
ODA
IDA
link
RS
CPC
R
P
Active side
Active side
(E)
"cargo"-MTD
dynein
bending
nexin link
"track"-MTD
(F)
"cargo"-MTD
dynein
bending
"track"-MTD
nexin link
(G)
r
(H)
a
(I)
f(s)
Δ(s)
−f(s)
Δ0
a

device started to beat in some uncontrolled twirling or nutating fashion with waves propagating from the base toward the tip and the attached cell moved. Later, tip to base waves became possible and, in some species, the ability to do either and hence regulate their direction. Subsequently, the more efficient planar beat was achieved in many species and further optimizations crept into the cilia of different species. One example is that ATP can be supplied consistently at one point in the beating cycle in *Chlamydomonas*. Subsequently, its specializations into sensing and motion established cilia as one of the most useful devices in nature, with most human cells being ciliated at some time in their development. These machines are very complex requiring in humans about 650 genes (representing about 3% of human genome) devoted to their synthesis and control. Consequently, defective cilium has led to ciliary pathologies which has made the study of cilia medically important (Marshall, 2008a).

IIIC. Structure and Beating Cycle

It is very hard to appreciate a cilium without understanding its complex structure.

IIIC1. Basics of Ciliary Geometry and the Beating Cycle

Considerable effort has been aimed at understanding the cilium structure (Foster, 2009). The core structure of each cilium is known as the axoneme (cross-section shown in Fig. 47.4A,B). It consists of nine doublet microtubules (db) arranged around the central pair doublet (the dynein "arms" point to the next higher numbered doublet, if numbers increase clockwise you are looking toward the tip, if counterclockwise you are looking toward the base). Fig. 47.4C shows one of the doublets with its dynein motors, which drive the sliding between the doublets and spokes that connect the doublets to the central pair. The observed bending implies that the motor activity periodically varies from being higher on one side of the axoneme to being higher on the other side. During a P (principal) bend, walking on doublets 1−4 dominates (by attaching/detaching) on the adjacent higher numbered doublet toward the base of the cilium making the cilium bend with doublets 5 and 6 on the inside of the curve (negative curvature according to convention) (Fig. 47.4D,F). Similarly, during an R (recovery) bend, walking on doublets 6−9 dominates on the adjacent higher numbered doublet toward the base making the cilium bend in the opposite direction (positive curvature) (Fig. 47.4D,E). Since the cilium is thin and the distance between the doublets is short, even a short walk can produce a significant bend in the cilium (e.g. 100 nm relative sliding of a doublet may induce a bend as large as 50°). The full sliding of doublets at the end of a cilium measured by in-vitro experiments is no more than ±200 nm. A simplified way of thinking about it is to consider the axoneme as two elastic filaments that slide relative to each other resulting in the bending (Fig. 47.4 G,H,I). The dynein motors provide the shear forces to produce the relative sliding.

The dynein motors are in some ways similar to piezoelectric motors used to focus lenses in cameras and cell phones. As shown in Fig. 47.4C, there are several motors periodically arranged in rows along a doublet. The upper row motors are referred to as the outer dyneins and the lower ones are referred to as the inner dyneins. Fig. 47.5A shows the force−velocity relationship in a limited range for one of the inner dynein motors at two different concentrations of ATP. The force exerted by the motor decreases with the increases in sliding velocity of the driven doublet microtubule and the velocity is approximately linear with ATP concentration.

In addition to causing shear between neighboring doublets, dyneins bind, to variable degrees, the doublet microtubules that together make up the axoneme (interior structure) of a cilium. These doublet attachments remarkably

FIGURE 47.4 (A) EM micrograph through a demembranated ciliary axoneme of *Chlamydomonas* (scale bar = 100 nm). Note the P-side consisting of microtubules doublets (MTD)1−4,which facilitate the principal bend, and the R-side consisting of MTD 6−9,which facilitate the recovery bend *(modified from Foster, 2009)*. (B) Structural components of the axoneme and assembly mutations. Viewed from the cell body looking outward *(modified from Foster, 2009)*. (C) One doublet showing dyneins and related structures along a tubule *(modified from Foster, 2009)*. (D) Simplified cross-sectional view from the ciliary tip of an axoneme with nine outer MTDs surrounding the central pair complex (CPC). Three structures connect neighboring MTDs, the ODAs and IDAs and the nexin link (also called the dynein regulatory complex). The blue and green boxes highlight the most important active doublets from opposite sides of the axoneme. Binding is twelve times higher in the boxed regions *(modified from Heuser et al., 2009)*. (E) and (F) Interdoublet sliding model for ciliary bend formation. Two pairs of MTDs from opposite sides of the axoneme, as highlighted in (D), are shown. The dynein arms are anchored on the cargo MTD in an ATP-independent manner and walk toward the minus end of the track MTD in an ATP-dependent manner, which causes sliding between neighboring MTDs. The links between MTDs are important for transforming MT sliding into bending. Note that the minus end-directed dynein motors (red) have to be active and produce MT sliding on alternate sides of the axoneme (switching between the blue and green side) to generate the principal and reverse bends (with opposite bending directions; black arrows) *(modified from Heuser et al., 2009)*. (G) Cross-section of an axoneme with radius r as seen from the basal end. The microtubule doublets and the central pair are shown in red, the dynein motors in blue and the radial spokes in green. The horizontal gray line indicates the plane of the beat. With this beat plane, the largest sliding displacement occurs between adjacent microtubule doublets at the top and bottom (Riedel-Kruse et al., 2007). (H) Cross-section of a two-dimensional representation of the axoneme in which two flexible filaments slide relative to each other in the beating plane. The shear forces are generated by active elements acting antagonistically between the filaments. Passive elastic elements are represented in green. The separation of the two filaments is a = 2r (Riedel-Kruse et al., 2007). (I) View of the beat plane of this 2D axoneme. Indicated are the local sliding displacement Δ(s) and the internal shear force density f (s) due to the active elements (blue) and the passive cross-linkers (green). The basal connection has a finite stiffness and friction indicated by black springs and dashpots (Riedel-Kruse et al., 2007).

account for most of the bending or flexure rigidity of a cilium. The all dynein attached flexure rigidity, $\kappa = 11\,000$ pN μm^2, is at least 14 times stiffer than when the dyneins are unattached, estimated in the range $\kappa = 150{-}800$ pN μm^2.

Inspired by the motor characteristics of the similar piezoelectric linear motors, these are the hypothesized characteristics of the dynein−tubulin linear motors. The sliding and oscillating mechanism could exploit the dependence of motor characteristics with the distance between the motor and the binding sites as suggested by analogy with ultrasonic motors (see Fig. 47.5B).

IIIC2. Central Pair

The central pair of microtubules carries several complexes of known and unknown function. What is particularly

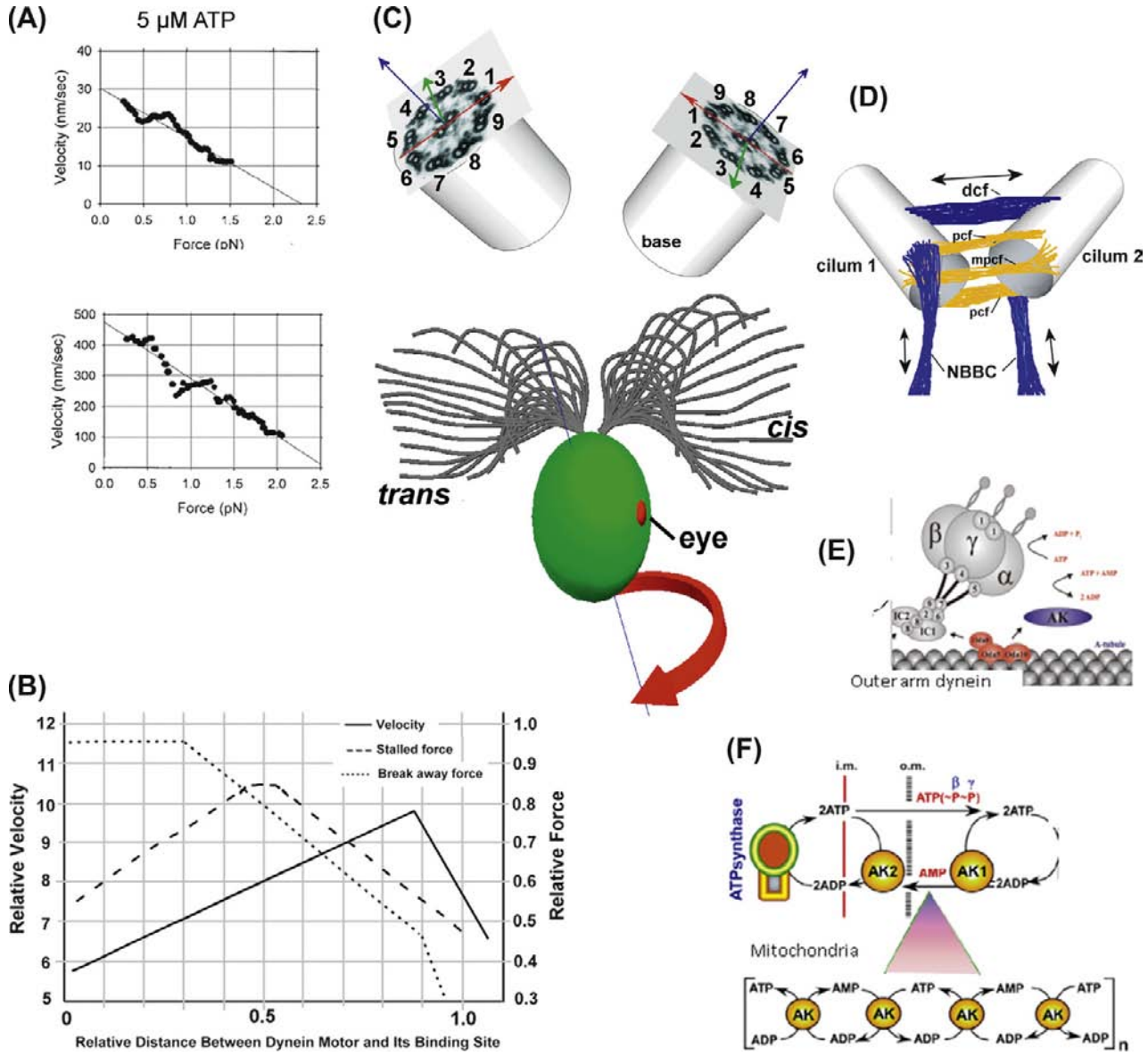

FIGURE 47.5 (A) Velocity-force curve for inner dynein c in the presence of 5 μM ATP and 100 μM ATP. The solid lines are linear fits to the data (Foster, 2009). (B) Inspired by the motor characteristics of the similar piezoelectric linear motors, these are hypothesized characteristics of the dynein−tubulin linear motors (Foster, 2009). (C) Shows attachment of the cilia to the cell body with C2 symmetry (from animation of JyothishVidyadharan and the axoneme cross-section image of Fig. 47.4A). Note the left-hand rotation of the cell, the ciliary beating patterns and the eye (Foster, 2009). (D) An angled view through the basal bodies and the base of the cilia of *C. reinhardtii*. dcf, distal connecting striated fiber joining the two basal bodies; pcf, proximal connecting fiber joining the two basal bodies; medial proximal connecting fibers joining the two basal bodies; NBBC, nucleus-basal body connectors. The NBBC and pcf are contractile. Note the offset of ends of the two cilia at the base (Foster, 2009). (D) Outer dynein arm site for use of ATP from Wirschell et al. (2004). (E) Shows the adenylate kinase (AK) shuttle that facilitates ATP transport from generation site (mitochondria) to utilization site such as outer arm dynein (Dzeja and Terzic, 2009).

noteworthy is that the central pair has chirality and it is not attached directly to any structure, so that for every bending wave that passes it rotates it once, so that the same side is always adjacent to the interior bend. This permits, for example, ATP synthesis to be maintained at the same phase with respect to the bending cycle. Potentially, many ciliary controls could also be positioned at a constant phase with respect to the bending.

IIIC3. Attachment of the Cilia to the Cell Body

The cilia have a very specific orientation with respect to the cell body. Looking down from above near the base, the number-1 doublet microtubule faces the other cilium, in twofold-rotation or C2 symmetry (see Fig. 47.5C), which leads to consistent left-handed cell rotation. According to Riedel-Kruse et al. (2007 and references therein), with respect to bull sperm, the dynamics of the base connecting the cilium to the cell body plays a crucial role in determining the waveform of beating. Thus, cells may control their beating by changing the properties of their basal connection. In the case of *Chlamydomonas*, where much is known about the base, the two cilia (see Fig. 47.5D) are connected to each other through proximal fibers (pcf and mpcf) at the base plate and distal fibers (dcf) at about 250 nm from the base (see Fig. 47.5D). As a result, the dynamics of the two cilia are connected and the cell may use this connection to control or influence the beating pattern. In addition to the distal fibers, which link the dynamics of two cilia, there are other components, such as the nuclear-basal body connectors (NBBC), in the basal body region that may play a significant role in cellular control of the beating. The NBBC and dcf contain centrin (caltractin), which shows calcium-sensitive contractile or elastic behavior. It has been shown that centrin-based flagellar roots are contractile under conditions of elevated calcium in a variety of eukaryotes, including *Chlamydomonas* and *Tetraselmis*. There is also a fine filament that runs between the centers of the proximal ends of each basal body which would be very sensitive to the relative motion of either cilium. However, with very different compliance machinery in a similar organism, the cilia still beat with similar waveforms and the cell still shows phototaxis.

The distal striated fiber (dcf, see Fig. 47.5D) of nominal length 280 nm can contract to as much as 220 nm resulting in the decreased angle between the two cilia from about 65° to 55°. Contraction of the NBBC would also aid this movement and pull the base end inward so that the cilia can more easily exit the fixed holes in the cell wall. This change will induce a force in addition to the force due to sliding caused by dyneins. Now the sum of the forces due to base sliding and connection must be balanced by the component of the total hydrodynamic force parallel to the cilium at the base.

IIID. Energy Supplied to Cilia

A significant part (and in some cases such as mammals, all) of the ATP needed to supply the dynein ATPases (see Fig. 47.5E) is supplied from the base. Mitochondria are typically massed at the base of a cilium. In every case, the ATP has to be transported effectively along the cilium which can be very long. Any time you have long lengths like tens of microns, the idea of diffusion fulfilling requirements seems unlikely. Diffusion of ATP down a centimeter long cilium is utterly unrealistic (at a diffusion rate of 64 $\mu m^2/s$ it would take $\approx 10^6$ s to reach 1 cm or ≈ 9 days). Not surprisingly, there is an adenylate kinase (AK) shuttle (see Fig. 47.5F) that facilitates ATP transport from the ATP synthesis site (mitochondria) to the dynein motors (ATPases) along the cilium. It is reputed to achieve a constant velocity of transport.

In addition, an interior ATP synthesis system exists in some cilia, such as that of *Chlamydomonas*, which is associated with faster beating cilia. Further, it can be rotated with the beating so that it always supplied with the same phase relationship with the motor activity. In *Chlamydomonas*, 3-phosphoglycerate (3PG) (Mitchell et al., 2005), which is central in the glycolytic pathway and is a product of photosynthesis, is processed by the cilium with aid of an enzyme complex containing enolase situated on the C1b arm of the central pair. Since the central pair rotates so that C1 to C2 vector always points toward the inside of the bend, the C1b arm is always to the outside of a bend. However, at the forward traveling edge of a bending wave, the front receives increased ATP. How the 3PG is transported versus diffused or even if it is actively transported is not currently known.

IIIE. Known Effects on Beating and Refinements that Possibly Optimize the Beating Cycle

There are many known effects on ciliary beating. However, their role may not yet be fully appreciated (Woolley, 2010). The list includes, but is not limited to the following:

1. The concentration of ATP affects the beating frequency by changing the sliding velocity (see Fig. 47.5A)
2. Variations in temperature, pressure and the pH have effects consistent with the activity of dynein ATPases
3. External mechanical effects, such as viscosity, lower beating frequency, wavelength and wave velocity while increasing the bend angle
4. The beating behavior is particularly sensitive to the hydrodynamic differences associated with walls
5. Synchronization of beating between adjacent cilia occurs at a higher frequency than either alone, but only occurs where there is mechanical attachment between them

6. Typically, there is beat asymmetry, where the bend in one direction is consistently greater than in the other direction, already referred to as the principal and reverse bends. Even so-called symmetrical beating is not really all that symmetric. The degree of beat asymmetry is calcium concentration dependent
7. Short truncated cilia beat faster than longer ones
8. When the head of a sperm attaches to a surface, there is a decrease in the speed of wave propagation along the cilium.

All these and many other effects must be accounted for in the details of any model.

Refinements that may contribute to improved performance of beating include: (1) splitting the task of moving the cilia into multiple (8) types of dynein motors which can be potentially independently controlled; (2) intricate compliance devices at the attachment site to the cell body; (3) an interior ATP delivery system that rotates with the beating so that it always has the same phase relationship with the motor activity; and (4) geometric changes that accentuate motor activity on the inside of bends.

IIIF. Mechanism of Ciliary Beating

We use the Woolley (2010) review as our starting point.

Each of the many explanations of beating offers some insight into how cilia beat. Woolley optimistically says that what is occurring in molecular terms "has presented an intractable level of difficulty". When the sliding velocity is maximum, the amount of sliding is minimum and vice versa. It is known (most, but not all agree on this) that the dyneins walk unidirectionally and are going in their forward direction when they are progressing toward the base. There is the observed active mode in which the dyneins move forward toward the base. Due to the geometry of the cilia motors, on the opposite side, dyneins must move in the opposite direction, namely backwards. For some authors, this suggests that the dynein motors operate in two modes, active and passive, of motor activity (Brokaw, 2009). Whether there is a controller that switches the motor activity is a basic point which lacks consensus, however, since there is no concrete evidence in its favor, we will assume it does not exist and account for the observations another way. This uncertainty has come about because the action of the relevant dynein motors which are going backwards is not known and, critically, the level of dynein binding on the two sides is not known dynamically.

Many, including this author, believe that ciliary beating is a self-organized beating (SOB) process and that the basic oscillation is not being controlled at the level of every beat, rather the inherent properties of the components is sufficient to get the basic ciliary oscillation. The oscillation is indicated by its phase plot at a particular position along the cilium, rate of sliding versus the amount of sliding (Fig. 47.6A). Potentially confusing researchers are a number of refinements added during evolution that modify the phase and amplitude of beating. If this author is correct there is no per se regulation or switch of the mode of activity of the dynein motors, for example, by some threshold curvature or threshold transverse force or some switch point or basal elastic recoil or by the central pair. However, the forces and sliding these ideas represent may indeed be playing a role in the inherent activity of the dyneins and central pair may (likely) be playing a role in the control of behavior as discussed later. One should note here that the inherent properties of the components will be strongly affected by the degree of sliding, the rate of sliding and the direction of sliding and the forces at that local location.

IIIG. How to Find Out What is Happening

A good start can be made by forming a model and then by analysis of data to determine the relevant parameters (Foster, 2009).

IIIG1. Motor Forces and Sliding

The hydrodynamic force $F_j(s, t)$, together with the cilium position $r_j(s, t)$, s being the distance along the cilium measured from its base, and t the time, may be used to determine the motor forces along the cilium. Since the inertial effects are negligible, the hydrodynamic force is balanced by the elastic forces arising from the bending of the doublets and the internal forces consisting of active forces due to motor activity and passive restraining forces due to nexins (the dynein regulatory complex). The nexins connecting adjacent doublets provide an elastic resistance to longitudinal sliding with a complex non-linear dependence on stretch (estimated to be $16-100\,\text{pN}/\mu\text{m}$ (see Fig. 47.6B) (Lindemann et al., 2005). It is assumed that each doublet is inextensible, but flexible since a single microtubule has been measured to be anisotropic with a shear modulus of $\approx 1.4\,\text{MPa}$ and a Young's modulus of $\approx 100\,\text{MPa}$. The sum of the internal forces at any cross-section of an axoneme must vanish even though some doublets are under tension and others under compression.

For planar beats, it has been shown that the $9+2$ structure of the axoneme can be equivalently replaced by two elastic filaments (groups of doublets) separated by distance a and bending rigidity κ, both of which can be estimated from the known geometry and mechanical properties of the axoneme ($\kappa \approx 1700\,\text{pN}\ \mu\text{m}^2$ for bull sperm) (Riedel-Kruse et al., 2007). Let f be the internal shear force acting along the filament on the inner side of the bend and $-f$ the shear

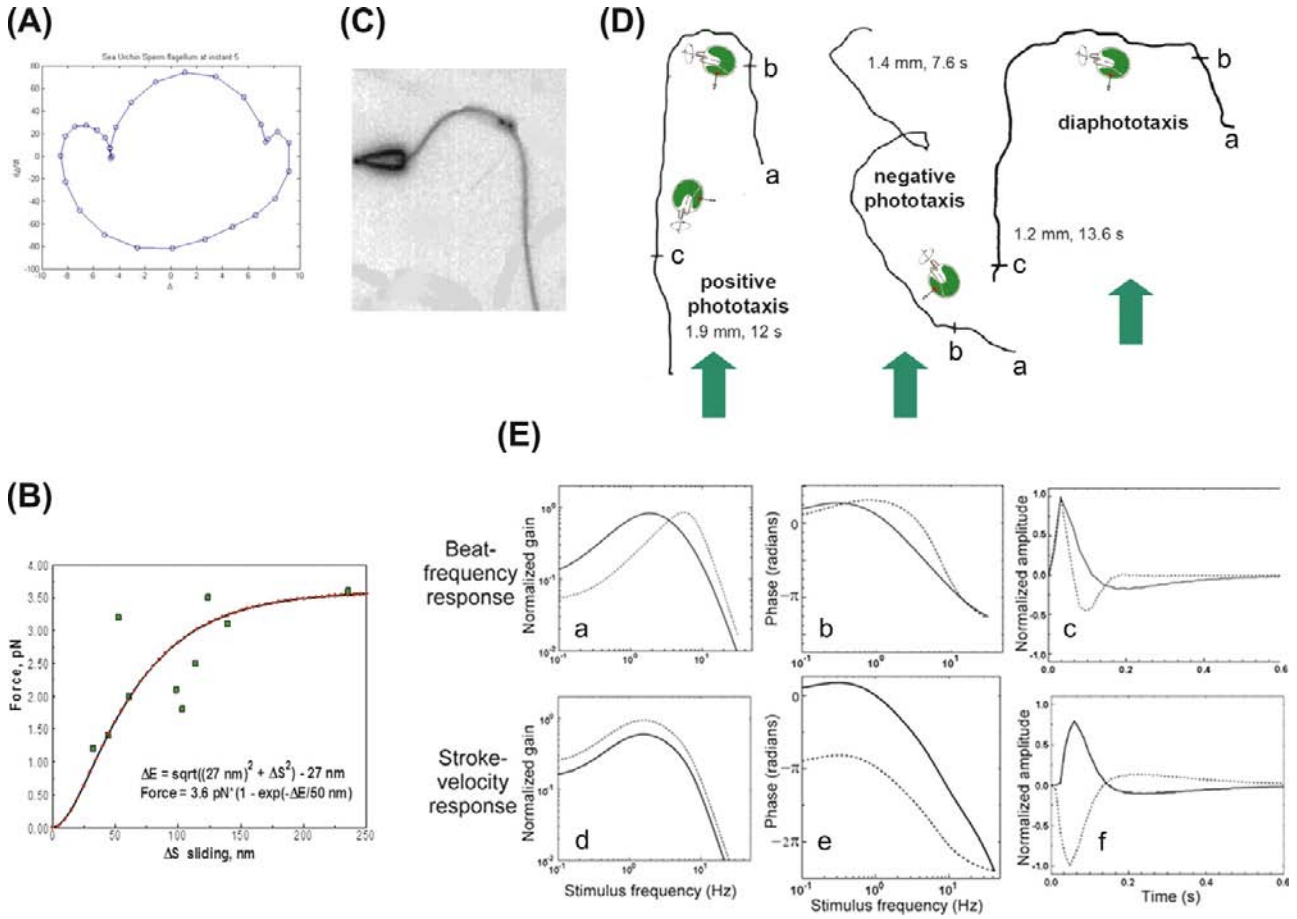

FIGURE 47.6 (A) Shows the dynamic phase plot at a local spot on a sea urchin cilium through one beating cycle. (B) The nexin (dynein regulatory complex) force–extension curve *(data from Lindemann et al., 2005)*. (C) Shows relative sliding of two beads attached to a naked cilium on different microtubules, from which one can estimate the sliding at the base (Brokaw, 1991). (D) Three of the seven types of phototaxis: helical positive, superhelical negative and diaphototaxis *(modified from Foster, 2009)*. (E) Typical ciliary beating frequency (CBF) of the negatively phototactic strain 806 in response to green light (543 nm) modulated by a pseudorandom Gaussian-white-noise (GWN) stimulus. The *cis*- and *trans*-CBF for each record were separately cross-correlated with log10 (stimulus intensities) to produce respective impulse responses (C). The *cis* and *trans* responses were then separately averaged (solid lines for *cis* and dotted lines for *trans*). The Fourier transform of the averaged impulse responses yielded the gains (A) and phases (B). Typical ciliary stroke-velocity response to green light modulated by a GWN stimulus. Stroke velocities for the *cis* and *trans* cilia for each record were independently cross-correlated with log10 (stimulus intensities) to produce impulse responses (F) that were then separately averaged in for *cis* cilium (solid line) and *trans* cilium (dotted line). The Fourier transform of the averaged impulse responses yielded the gains (D) and phases (E). *(Modified from Foster, 2009.)*

force on the outer one. From balancing the forces on a pair of inextensible elastic elements leads to:

$$af(s,t) = \kappa(s,t)\partial_s C(s,t) + n_j(s,t)\int_s^L F_j(s',t)ds' \quad (47.4)$$

where C is the curvature, n_j is the unit normal to the filament in the plane of the beating, δ_s represents the derivative with arc length s, L is the cilium length, and F_j is the hydrodynamic force per unit length. Since all the quantities on the right-hand side of the above equation can be determined from imaging and hydrodynamic analysis, f can be determined along the cilium length.

It is possible that the local bending rigidity or flexure is under control and alterable by internal viscosity, mechanical feedback or cell command. In addition to causing shear between neighboring doublets, dyneins bind, to variable degrees, the doublet microtubules that together make up the axoneme (interior structure) of a cilium. These doublet attachments remarkably account for most of the bending or flexure rigidity of a cilium. The all dynein attached flexure rigidity, $\kappa \approx 11\,000$ pN μm^2, is 14 times stiffer than when the dyneins are unattached, $\kappa \approx 800$ pN μm^2. In our formulation we use the dynein-unattached flexure rigidity, which we find to be about 150 pN μm^2.

All SOB models assume that the motor force is a function of doublet sliding. The relative sliding of the filaments is given by:

$$\Delta(s,t) = \Delta_0(t) + \Delta^c(s,t) \quad (47.5)$$

where

$$\Delta^c(s,t) = \int_0^s aC(s',t)ds' = a(\psi(s) - \psi(0))$$

and $\Delta_0(t)$ is the relative sliding of the two filaments at the base ($s = 0$). Note that since $\Delta^c(s,t)$ can be determined from the ciliary images, the total sliding along the cilium can be determined to within a single parameter $\Delta_0(t)$. This parameter has been assumed to be zero by a number of investigators in the past, an assumption that may not be valid.

IIIG2. Modeling of Basal Connection

According to Riedel-Kruse et al. (2007) and, as previously suggested, $\Delta_0(t)$ the dynamics of the base connecting the cilium to the cell body likely plays a crucial role in determining the waveform of beating in bull sperm. Thus, cells may control their beating by changing the properties of the basal connection. In the case of *Chlamydomonas*, the two cilia (see Fig. 47.5C) are connected to each other through proximal and distal fibers. As a result, the dynamics of the two cilia are connected and the cell may use this connection to control the beating pattern.

In addition to the distal fibers which link the dynamics of two cilia, there are other components in the basal body region that may play significant role in cellular control of the beating. Some of these components contain centrin which shows calcium-sensitive contractile or elastic behavior. It has been shown that centrin-based flagellar roots are contractile under conditions of elevated calcium in a variety of algae, including *Chlamydomonas* and *Tetraselmis*. The contraction of centrin is responsible for changing the base angle in a ciliary to flagellar beating transition in *Chlamydomonas*. The average angle between the cilia decreases with light intensity, the expected result for a calcium dependent contraction. Riedel-Kruse et al. (2007) modeled the component of the base force parallel to the cilium at base as given by:

$$F_B = \gamma_s(d\Delta_0/dt) + k_s\Delta_0 \qquad (47.6)$$

where γ_s and k_s are, respectively, basal friction and stiffness. In the case of bull sperm with a single cilium, the force F_B can be determined by equating it to the component of the total hydrodynamic force parallel to the cilium at the base, thus providing sufficient information for determining γ_s and k_s. In the case of sea urchin sperm experiments (Brokaw, 1991), two beads were attached to the cilium and the relative sliding determined (see Fig. 47.6C). This in principle should give sufficient information to determine the $\Delta_0(t)$ and compared to $F_B(t)$ determine γ_s and k_s.

The base structure in *Chlamydomonas* is different than in bull sperm. The axoneme of each cilium extends to the attached basal bodies connected by a distal striated fiber, which can contract. Any change in the angle θ between the two cilia will therefore induce a force in addition to the force F_B due to sliding. We may assume that this additional connection force is given by $F_C = b\,[\cos(\theta/2 - \cos(\theta_0/2)] \approx -b'(\theta - \theta_0)$ where the (complex) stiffness b is related to the strength of distal fiber and $b' = b\sin(\theta_0/2)/2$. Now, the sum of the forces due to base sliding and connection must be balanced by the component of the total hydrodynamic force parallel to the cilium at the base. We note here that, since these cilia are mechanically linked, it is not surprising they can maintain synchrony.

IIIG3. Hydrodynamic Calculations

The procedure is clear. From rapid images of ciliary motion, one has the local velocities along their length which, with hydrodynamic calculations, can lead to the net forces along their length.

Since the Reynolds number based on the length of the cilium and its stroke velocity is O (10^{-3}; of the order of) or smaller, the flow induced by the cilia beating can be described by the simple Stokes equations of motion. Furthermore, since the diameter of a cilium (≈ 0.24 μm) is much smaller than its length (12−14 μm), slender body theory may be used to determine the force exerted by the fluid along the cilia. The theory is fairly well established and a number of studies show in detail how it may be used to determine the force distribution. The velocity at a point in the fluid is expressed as a line integral (along the cilium) of the force distribution times the velocity induced by the force (Green's function for Stokes equations, also known as the Stokeslet). The Green's function derivative is chosen so that the no-slip boundary condition on the surface of the cell body (approximated as a sphere of diameter about 8 μm) is automatically satisfied. In addition to the Stokeslet distribution along the centerline of the cilium, a source dipole distribution is added that improves the accuracy without significantly increasing the computational effort. Since cells may be held by a micropipette at the posterior end where the flow induced by the cilia is minimal, interference due to the presence of the micropipette may be minimized. All the other boundaries are at least a few millimeters away from the cell so that their effect can be made negligible.

Approximating the velocity by means of a line distribution of Stokeslet is valid in the outer region, away from the surface of the cilium. In the inner region, close to the surface of the cilium, one must construct another approximation that satisfies the no-slip boundary condition at the cilium surface taking into account its cross-section shape. The requirement of matching the inner and outer region

approximations in the overlap region (at large distances from the surface compared to the cilium diameter, but small compared with its length) gives rise to an integral equation for determining the force distribution along the cilium length.

IIIG4. In the Final Analysis

One obtains the net (sum of both sides of the cilium) relationship between the motor forces and doublet sliding along the ciliary length with time in the beating in cycle. In isolation it is likely that the motor force-sliding-velocity curve looks as depicted in Fig. 47.5A, except extended on the right steeply downward at negative velocities and extended to negative forces (the motor is being pushed) at slightly increased velocities. In addition, one must be concerned with the differences in the probability of binding depending on the load, the curvature, the ATP level, the direction of sliding, etc.

After considering Woolley's (2010) review, a tentative consensus maybe made uniting the switching-two-modes view of dynein activity and the SOB model as advocated here. He has suggested the direction of sliding is the primary controlling factor for flagellar oscillation. He adds that "dyneins actively generate force when sliding in one direction is detected and are inhibited from doing so by the detection of sliding in the other direction" (see Fig. 47.4E,F). This is stated in the two-mode view. However, the SOB one-mode view has some similar consequences. In the SOB view, dyneins move according to the force they are pushing against or the force that is pushing them. In other words, they have a single force−velocity curve with force and velocity both vectors relative to their substrate or, in effect, the magnitude and direction of sliding (see Fig. 47.5A and recall above discussion). Quite possibly, when being pushed backward they do not use ATP, as the backward force may be sufficient to disengage dynein motors from attachment sites. Of course, detaching motors causes drag, but it may be minimized if the geometry favors lower binding rates. There are many factors that can also influence the force and movement on each side of the planar beating cilium. These include ATP availability and, likely, calcium which probably influences attaching and detaching of the dyneins. If the opposed force is beyond their stall force they inevitably go backward**.** Due to the nexins and the passive restoring force associated with a bent cilium, dyneins may also be pushed forward.

IIIH. Behavioral Controls

Overlaid on top of the self-organized beating and its optimizations are cellular controls to achieve a rich variety of functions. These include control of cell steering associated with phototaxis and chemotaxis (hypothesized to be at the S2 locus), the stopping of beating to facilitate mating (at the S1 locus, involving a cAMP signal), the temporary turning off of phototaxis when an obstacle is encountered (at the S1 locus, involving calmodulin/Ca^{2+} and not cAMP) and the optimum balance between ballistic and diffusive motion (at the S1 locus, involving cAMP and calmodulin/Ca^{2+}). S1 and S2 refer to the spokes (see Fig. 47.4C). Note that, in the short term, even though S1 and S2 sites are only 48 nm apart, there is enough separation for these controls to be relatively independent in the 18−20 ms of a beat cycle.

By way of an example, it is sufficient here to discuss some of the temporal characteristics of phototaxis control as measured in *Chlamydomonas* (Foster, 2009*).* The correlation of the ciliary responses with stimuli has been measured with a low spatial-resolution quad-photodiode ciliary monitor. Most classical analysis is done in the frequency domain because of the simplicity of its interpretation and its ability to distinguish simply between the beating cycle at 50−60 Hz and response control in the 2−6 Hz range. This approach is represented by Bode plots (see Fig. 47.6E a and b) showing the CBF and stroke-velocity responses (see Fig. 47.6E d and e). The output response was correlated with a 196-s long input light stimulus. The slopes of the gain plot and the phase changes provide directly the nature of the functional processes. For example, the slope at high frequency gives the number of processes involved in the cascade of the processing and the functional modeling is easy. The temporal response (see Fig. 47.6E c and f) is mathematically equivalent and with this representation it is easier to see how the cell would respond as it rotates, but functional modeling is less transparent. The *trans* and *cis* cilia are different. They have their own unique as well as common responses. For example, the CBF and stroke velocity (SV) SRF are quite different. On the other hand, response to changes in availability of ATP (not shown here) appear to be similar. Note, in particular, that the *trans* cilium has a much higher frequency response for CBF than the *cis*. Further, that the phase of the *trans* cilium is about π different from the *cis* and that the delay is markedly, actually reproducibly, longer than for the *trans* cilium.

Such results provide insight into what the signal processing system does to optimize the cell's phototaxis. By averaging over 196 s, high temporal resolution is obtained in spite of the noisiness of individual ciliary responses. Note that the observed delays to response are short relative to a single beating cycle of $\approx$18 ms. Furthermore, these measured responses show significant *cis-trans* differences which contribute to how the cell steers. Note there is an initial delay of the *cis* cilium stroke velocity in Fig. 47.6E f and, further, the *cis* cilium has a slower CBF response than the *trans* in Fig. 47.6E c. The peak times for *cis* and *trans* CBF are approximately 40 and 30 ms, respectively, whereas the peak times for the stroke velocity are 80 and 50 ms. Why the system has *cis* slower than *trans* for both responses is not known. Figure 47.6E f also shows that

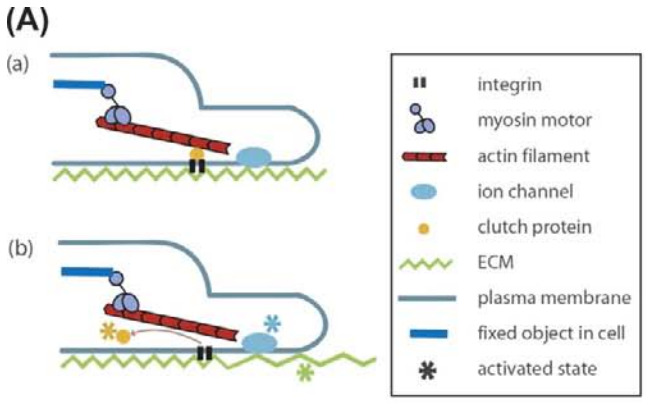
(A)
(a)
(b)
integrin
myosin motor
actin filament
ion channel
clutch protein
ECM
plasma membrane
fixed object in cell
activated state

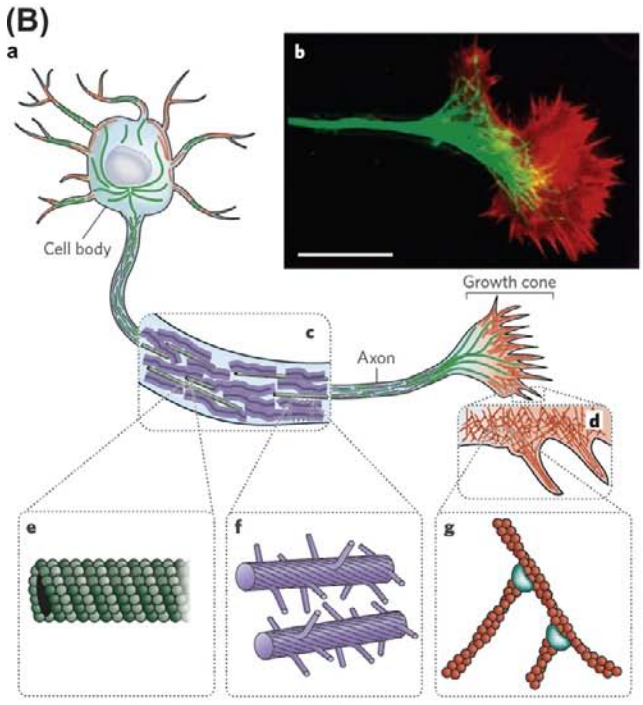
(B)
a
b
Cell body
Growth cone
c
Axon
d
e
f
g

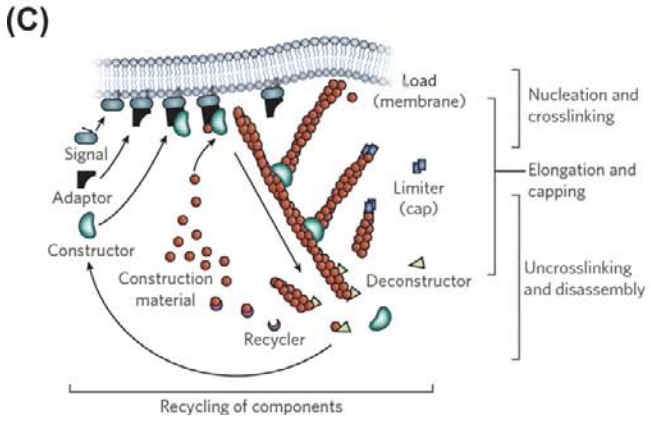
(C)
Load
(membrane)
Signal
Adaptor
Constructor
Construction
material
Limiter
(cap)
Deconstructor
Recycler
Nucleation and
crosslinking
Elongation and
capping
Uncrosslinking
and disassembly
Recycling of components

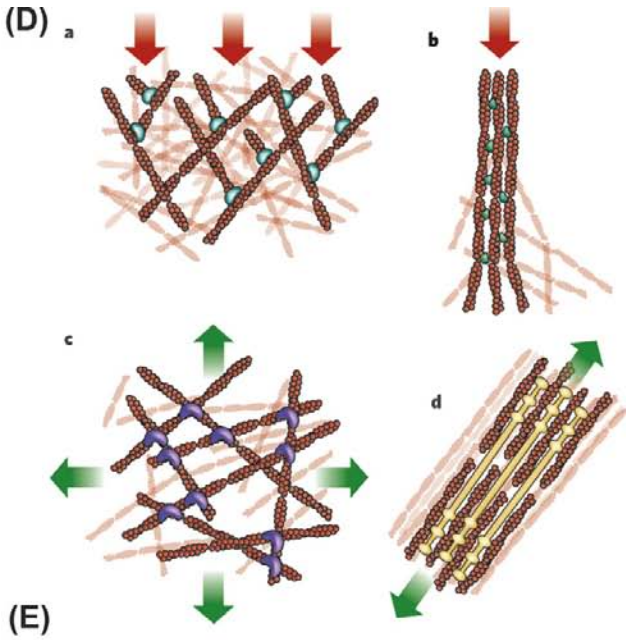
(D)
a
b
c
d

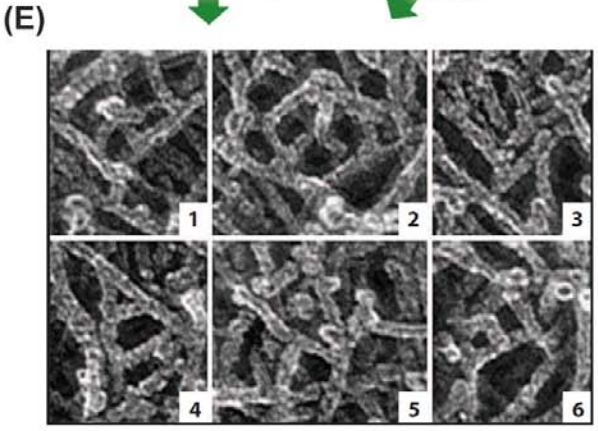
(E)
1
2
3
4
5
6

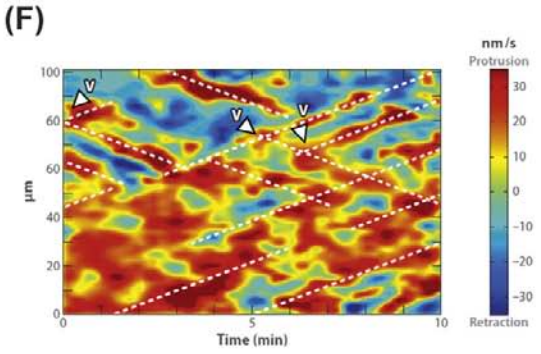
(F)
nm/s
Protrusion
Retraction
μm
Time (min)

steering for phototaxis involves briefly altering the relative effectiveness of the stroke velocity of the *cis* relative to the *trans* cilium. The changes are as if the shape of the *trans* beat exclusively involves the outer dynein arms and the *cis* beat shape is exclusively determined by the inner arms, but with the frequency and power contributed by the outer arms. Eighty percent of the observed variance is captured by a simple linear model (Foster, 2009).

It is anticipated that in future work with the many mutants available, it will be possible to extend into molecular detail the processes involved both in ciliary beating and its behavioral controls.

IV. NON-MUSCLE ACTIN

IVA. Actin-Associated Sensing

IVA1. Mechanical Sensing

Cells appear to be sensitive to information about force, stiffness and adhesiveness. Different cell types respond uniquely to a wide range of forces and stiffness (Fig. 47.7A).

External forces applied to a cell and the resistances that extracellular matrices or surfaces exert on cell-derived forces generate signals that direct cell growth, survival, differentiation and function. Examples of the roles for external forces (Tee et al., 2009) are the promotion of axonal elongation by pN to nN forces to the tips of the neuronal growth cone, the effects of fluid flow on the morphology and signaling of vascular endothelial cells and the loss of bone or muscle mass when gravity or exercise is reduced. Further, mechanical properties of the environment modify a cell's behavior: sarcomeres only form in cultured myocytes when the surface has the approximate stiffness of a muscle and mesenchymal stem cells only differentiate into osteocytes when growing on the appropriately soft surfaces.

IVA2. Force Sensing

A cellular force sensor can passively respond to changes in forces as do the stereocilia of hair cells in the ear when transducing sound waves into neural impulses initiated by changes in membrane ion channel activity or be active as cilia that detect urine flow.

IVA3. Stiffness Sensing

To sense stiffness, a durosensor applies a stress and measures strain or vice versa and then derives the ratio of these variables. To perform this assay, the durosensor uses molecular motors to apply a force to its substrate and measures the resulting movement. From this information, the cell knows

FIGURE 47.7 (A) Cellular components involved in stiffness sensing. (a) A cell in its resting state. Molecular motors such as non-muscle myosin walk on actin filaments exerting forces through focal adhesion proteins, which are connected to transmembrane proteins such as integrins via slip or catch bonds. In this way, traction forces are transmitted to the external substrate via integrin—ligand interactions. Any protein in this pathway from molecular motor to actin to focal adhesion protein to integrin to ligand to extracellular matrix can be stretched and therefore could be activated. Further ligands such as fibronectin and laminin might also be activated. On the plasma membrane, integrins or focal adhesion proteins can also be activated by being stretched; the membrane may be deformed or sheared inducing protein clustering or recruitment. Internally, the tension on the actin filament might affect molecular motor affinity and hence transport of proteins; the nucleus might deform affecting transcription. (b) The response of a cell that applies a stress or a strain will depend on the rigidity of the substrate. In essence, the elasticity of their substrate strongly influences a cell's ability to stretch proteins, generate tension and deform membranes or nuclei (Tee et al., 2009). (B) The cytoskeleton of eukaryotic cells sets the structure and organization, resists and transmits stresses, and drives shape change and movement. (a) Neurons are specialized eukaryotic cells that extend long processes to form connections. Like other eukaryotic cells, neurons have a cytoskeleton that consists of three main polymers: microtubules (green), intermediate filaments (purple) and actin filaments (red). (b) The neuronal growth cone migrates in response to chemical cues during the development of the nervous system (fluorescence micrograph). Microtubules (green) emanate from the axon and actin-filament networks (red) form sheet-like structures and filopodial protrusions at the leading edge. Scale bar, 20 μm. (c) The neuronal axon is a long membrane-bounded extension, in which neurofilaments (a class of intermediate filaments in neurons) form a structural matrix that embeds microtubules, which transport materials from the cell body to the axon terminals at the synapse. (d) The growth cone contains dendritic actin-filament networks and parallel actin-filament filopodia. (e) Microtubules consist of 13 protofilaments of tubulin dimers arranged in a hollow tube. (f) Neurofilaments have flexible polymer arms that repel neighboring neurofilaments and determine the radius of the axon. (g) Actin filaments are arranged into networks. These networks can have various architectures, including branched structures formed by the Arp2/3 complex (blue). The diameters of microtubules, intermediate filaments and actin filaments are similar, but their relative flexibilities differ markedly, as indicated by their persistence lengths [microtubules (5000 μm), actin filaments (13.5 μm) and intermediate filaments (0.5 μm)] (Fletcher and Mullins, 2010). (C) Long-range order of the cytoskeleton network is created by simple rules for assembly and disassembly. The three basic steps in assembly of protrusive, branched actin-filament networks are filament elongation, nucleation and cross-linking of new filaments from filaments close to the membrane and capping of filaments. Disassembly uses a different set of proteins that severs the filaments and recycles the subunits (Fletcher and Mullins, 2010). (D) The cytoskeleton forms structures with a wide variety of architectures associated with different types of cellular force. Shown are four structures generated by actin filaments and the stresses typically encountered by these structures (red arrows, compression; green arrows, tension). (a) Branched actin-filament networks push against the plasma membrane and external barriers generating protrusions, facing an inward compressive force. (b) Filaments bundled into filopodia generate protrusive forces that extend from the cell body and face similar compressive forces. (c) Cortical networks form below the plasma membrane and carry tension loads in multiple directions. (d) Stress fibers form from bundled actin filaments, which are often associated with filaments of myosin, and generate tension against cell adhesions to the extracellular matrix (Fletcher and Mullins, 2010). (E) Branched network structure in keratocyte lamellipodium (Carlsson, 2010). #5 is 0. 17 μm wide. (F) Patterns of protrusion in a PtK1epithelial cell. Color (red for protrusion and blue for retraction) indicates velocity of membrane motion. The y-axis is the distance along the edge of the cell and the x-axis is time. Diagonal lines show the transverse motion of waves (Carlsson, 2010).

the elasticity. Myosin has been suggested as the active stress generator and that the stress is transmitted through actin filaments onto flexible proteins such as talin or filamin which bind transmembrane proteins like integrins.

IVB. Cytoskeleton

The three main functions of the cytoskeleton are spatially to organize the contents of the cell; connect the cell physically and biochemically to the external environment; and coordinate forces to enable the cell to move and change shape (Fletcher and Mullins, 2010). Researchers are motivated by the prospect of understanding the process of self-organization that generates dynamic, robust and elaborate structures that organize and make cells alive. There are three main types of cytoskeletal polymer: actin filaments with at least 150 associated proteins, microtubules and a group of polymers known as intermediate filaments. These polymers control the shape and mechanics of eukaryotic cells (see Fig. 47.7B). The many copies of key pieces fit together to form larger objects that assemble into structures with diverse properties depending on the assembly process, and which can be disassembled and reassembled as needed. The differences among the polymers that distinguish the architecture and function of the networks they form are their mechanical stiffness, the dynamics of their assembly, their polarity and the molecular motors with which they associate.

The stiffest of the three polymers are microtubules and have the most complex assembly and disassembly dynamics. The persistence length of microtubules (≈ 5 mm), a measure of filament flexibility that increases with stiffness, is so large that single microtubules can form straight tracks that span the length of a typical animal cell. Microtubules have two states they switch between: stably growing and rapidly shrinking. This "dynamic instability" enables the microtubule cytoskeleton to reorganize rapidly.

Actin filaments are much less rigid than microtubules, but cross-linkers bind them to assemble organized, stiff structures, including isotropic networks, bundled networks and branched networks. Unlike microtubules, actin filaments do not switch between two discrete states; instead, they elongate steadily in the presence of nucleotide-bound monomers. This steady elongation produces the sustained forces that advance the leading edge of a migrating cell. Also unlike the microtubule cytoskeleton, which is characterized by one or two central organizing centers, the actin cytoskeleton is continually assembled and disassembled in response to signals it receives.

The subunits of both actin filaments and microtubules are structurally asymmetrical at the molecular level making them polarized polymers. Consequently, both polymers function as tracks for molecular motors that move preferentially in one direction. For microtubules, the motors are dyneins or kinesins whereas for actin filaments, they are myosin proteins.

The (de)polymerization of actin filaments and microtubules generates forces that drive changes in cell shape and guide intracellular organization with molecular motors that move along them. The structured networks are controlled by regulatory proteins: nucleation-promoting factors, which initiate filament formation; capping proteins, which terminate growth; polymerases, which promote faster or more sustained growth; depolymerizing factors and severing factors, which disassemble filaments; and cross-linkers and stabilizing proteins, which further organize the networks. External and internal mechanical forces can influence these regulatory factors and hence the network.

The least stiff of the three types of cytoskeletal polymers are the intermediate filaments that resist tensile forces much more effectively than compressive forces. They can be cross-linked to each other, as well as to actin filaments and microtubules, by proteins called plectins. Unlike microtubules and actin filaments, intermediate filaments are not polarized and cannot support directional movement of molecular motors.

One example of how long-range order of an actin-filament network can be created is the formation of branched actin networks (see Fig. 47.7C). Nucleation-promoting factors activate the Arp2/3 complex (including actin-related protein 2 (Arp2) and Arp3) to bind to actin and initiate new actin filaments (typically less than 1 μm, from the sides of pre-existing filaments, forming entangled "dendritic" networks.

In whole cells, the actin cytoskeleton has a wide variety of architectures that are associated with specific functional structures (see Fig.47.7D).

When reconstituted on the end of an atomic-force-microscope cantilever, dendritic networks grow at a constant velocity over a wide range of load forces, suggesting that the network regulates local filament density through a force-sensing element in the network. This same behavior is also observed in lamellipodial protrusions in crawling cells. The observation that growth velocity varies with the force suggests that actin-filament network growth depends on history. Given the cytoskeleton involvement mechanically and biochemically in cellular processes, long-lived cytoskeletal structures could guide variation towards certain phenotypes.

IVC. Actin Dynamics

Actin monomers (G-actin) assemble to form polarized filaments (F-actin) that have a fast-growing barbed end and a slower-growing pointed end (Carlsson, 2010). The actin subunits are arranged in a double helix with a length increment of a = 2.7 nm per added subunit. This

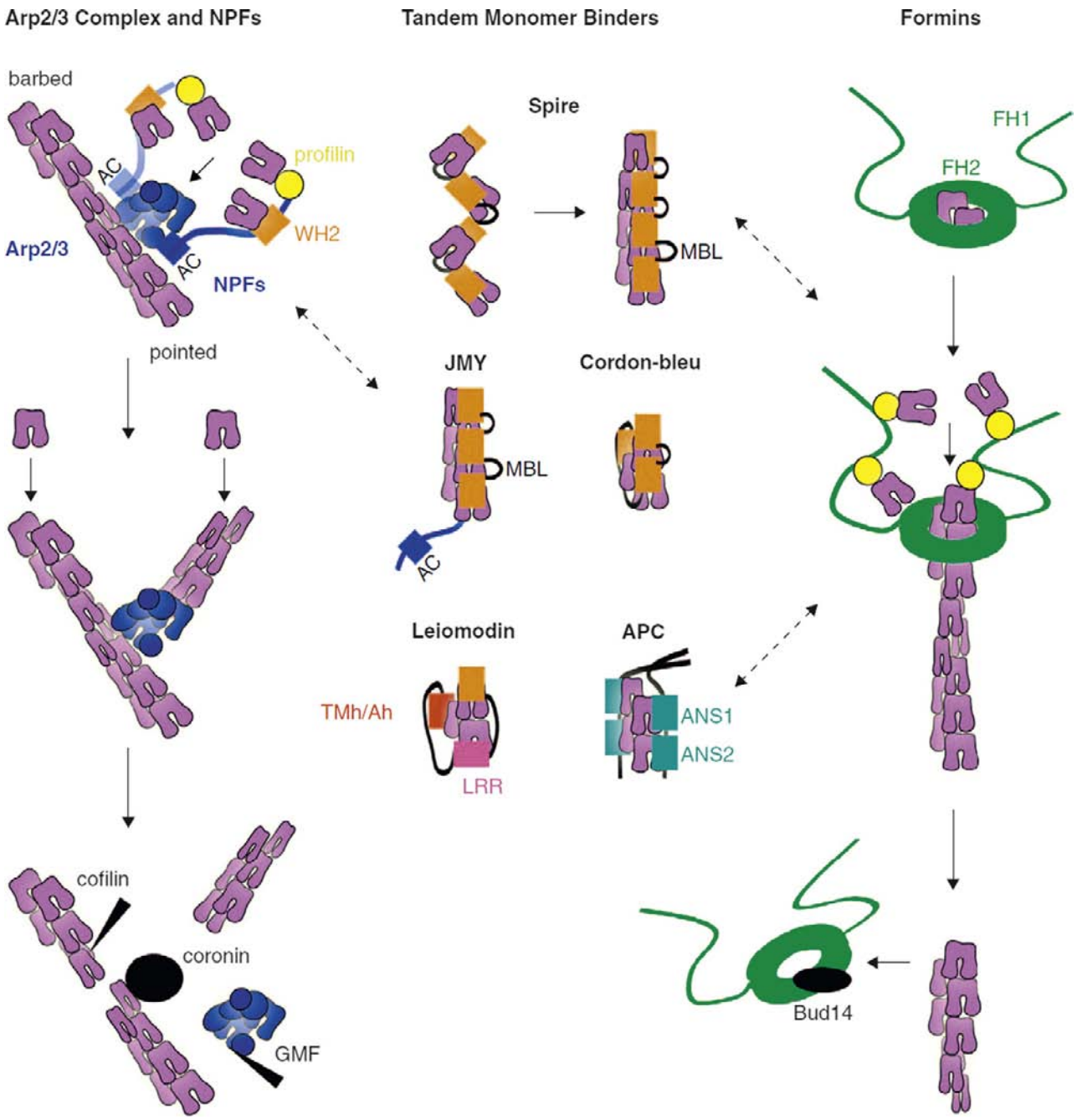

FIGURE 47.8 Models of actin nucleation. Left: Arp2/3 complex is activated by binding to the CA region of NPFs and to the side of actin filaments. In turn, NPFs bind actin monomers via their WH2 domains and profilin–actin monomers via their proline-rich regions and deliver these to a nucleating complex. NPF dimerization enhances their activity, suggesting that dimers may bind to two sites on the Arp2/3 complex. After branch formation, cofilin and GMF stimulate debranching by binding to F-actin and Arp2/3 complex, respectively. Coronin binds both to F-actin and Arp2/3 complex, replaces Arp2/3complex and synergizes with cofilin to promote debranching. Middle: Tandem-monomer-binding nucleators bring together actin monomers through their clustered actin-binding motifs to form a nucleus. Spire and JMY stabilize actin monomers aligned along the long-pitch helix with their WH2domains and monomer-binding linkers (MBL). Cordon-bleu, leiomodin and dimeric APC, with their combination of WH2 domains, leucine-rich repeats (LRR), tropomyosin and actin-binding helices (Tmh/Ah) and actin-nucleating sequences (ANS1-2), stabilize cross-filament interactions along the short pitch helix of an actin filament. Right: Formins generate actin polymerization nuclei by stabilizing actin dimers through their homodimeric FH2 domains. The FH2 dimer stays processively attached to the barbed end of an actin filament as the flanking FH1 domains deliver profilin–actin to the barbed end for continued elongation. In yeast, Bud14p interacts with the FH2 domain and displaces formins from growing barbed ends. Dotted arrows point to the cross-talk between different actin nucleators (Firat-Karalar and Welch, 2011, where additional details may be found).

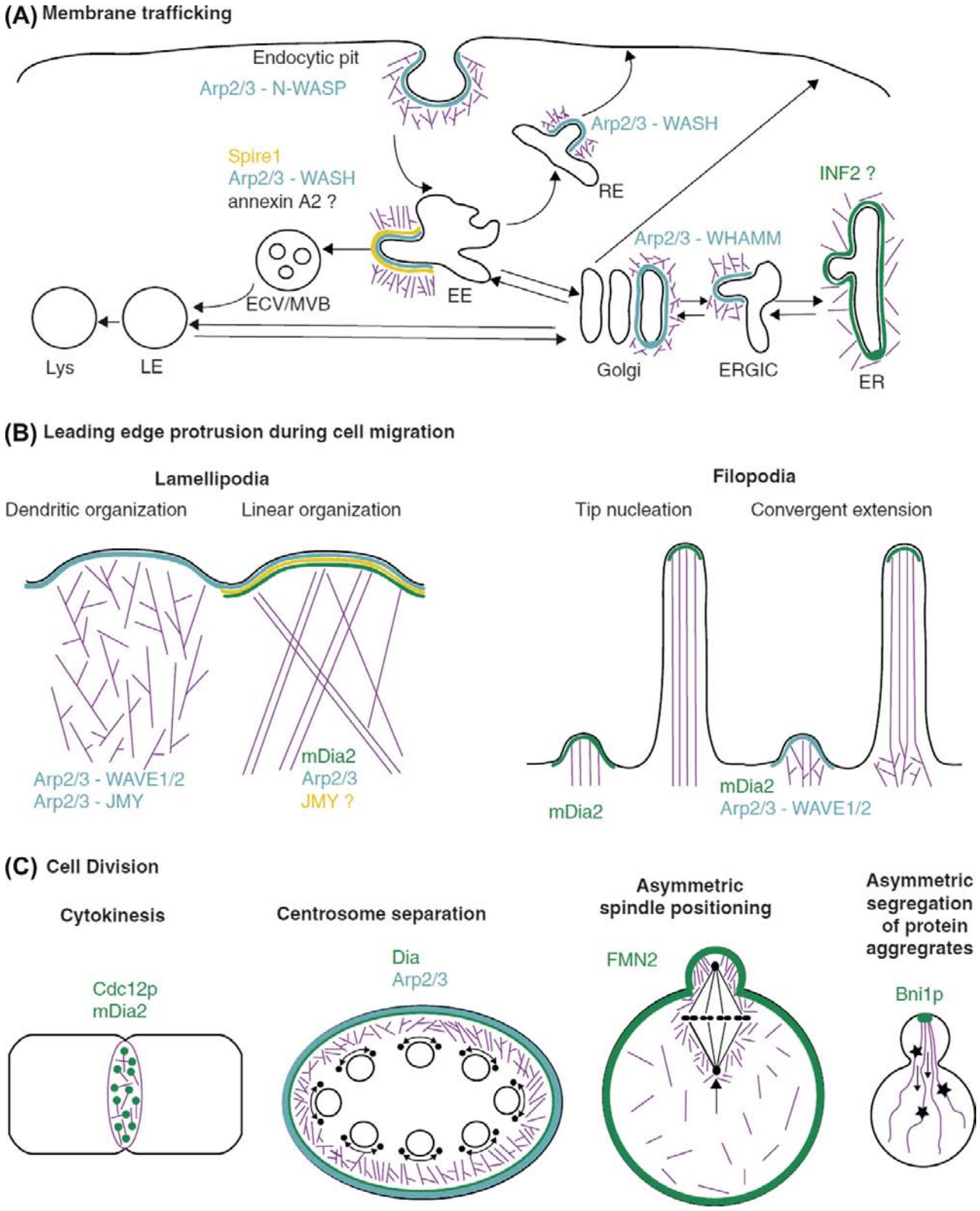
(A) Membrane trafficking
Endocytic pit
Arp2/3 - N-WASP
Arp2/3 - WASH
Spire1
Arp2/3 - WASH
annexin A2 ?
RE
INF2 ?
Arp2/3 - WHAMM
ECV/MVB
EE
Lys
LE
Golgi
ERGIC
ER
(B) Leading edge protrusion during cell migration
Lamellipodia
Dendritic organization
Linear organization
Arp2/3 - WAVE1/2
Arp2/3 - JMY
mDia2
Arp2/3
JMY ?
Filopodia
Tip nucleation
Convergent extension
mDia2
mDia2
Arp2/3 - WAVE1/2
(C) Cell Division
Cytokinesis
Cdc12p
mDia2
Centrosome separation
Dia
Arp2/3
Asymmetric
spindle positioning
FMN2
Asymmetric
segregation
of protein
aggregrates
Bni1p

arrangement allows an incoming subunit to have connections to two subunits in the filament. This double connection means that binding of an incoming subunit can be strongly exothermic, even though a G-actin dimer is unstable. This renders spontaneous *nucleation of actin filaments slow* in comparison to polymerization of existing filaments. Spontaneous nucleation is further slowed by actin-binding proteins.

Because polymerization is exothermic, it can supply the energy to propel a cell through its environment. Actin in cells is dynamic and strongly out of equilibrium. Actin undergoes continuous changes in polymerization fueled by input of chemical energy (ATP) enabling the actin cytoskeleton to respond rapidly to changing external stimuli and to have spontaneous dynamic behaviors. The critical concentrations, the free-actin concentration at which polymerization precisely balances depolymerization, is AcB (barbed) $\approx 0.1\,\mu M$ and AcP (pointed ends) $\approx 0.6\,\mu M$. The difference of the critical concentrations means that the two ends are thermodynamically not equivalent. Actin binds a nucleotide, either ATP, ADP-P_i or ADP, where ADP-Pi is hydrolyzed ATP whose phosphate has not yet been released. In intracellular G-actin, ADP is rapidly exchanged to ATP. In F-actin, ATP spontaneously hydrolyzes to ADP-P_i actin and subsequently becomes ADP. ADP-actin polymerizes less strongly than ATP-actin, and this causes the difference between ABc and APc. Branched networks often occur in broad, thin protrusions extending at the front of a cell or lamellipodia, as shown in Fig. 47.7E. Barbed ends preferentially point toward the membrane. Because the rate of new branch formation is proportional to the number of existing branches, filament nucleation by branching is an autocatalytic process. Additional mechanical stability is provided by cross-linking. Polymerization occurs mainly near the membrane and depolymerization mainly away from the membrane. Their assembly is often signaled by upstream external agents such as growth factors. Disassembly occurs in the absence of active intervention. However, active intervention is a possibility.

Bundles are composed of tightly cross-linked filaments and occur in protrusions such as filopodia. Actin polymerizes near the cell edge and depolymerizes farther way. In response to a stimulus, actin polymerizes and then depolymerizes and actin waves are spatially segregated assembly/disassembly cycles (see Fig. 47.7F).

IVD. Actin Filament Nucleation

IVD1. Introduction

The first assembly step of actin filaments, a stable multimer of actin monomers, is nucleation (Firat-Karaler and Welch, 2011). While slow it is essential for function (Fig. 47.8). This is the rate-limiting step in polymerization due to the instability of actin dimer intermediates and actin monomer-sequestering proteins that suppress spontaneous nucleation in cells. To overcome the kinetic hurdle for nucleation, cells use a diverse set of actin-nucleating proteins, including the actin-related protein 2/3 (Arp2/3) complex, formins and tandem-monomer-binding nucleators.

As these proteins control nucleation they can manipulate the cell structure and its motion and hence nature has found it convenient to involve them in many essential cellular processes (Firat-Karaler and Welch, 2011). A variety of nucleation events is illustrated in Fig. 47.8.

IVD2. Cellular Functions of Actin Nucleators

Membrane Trafficking

Membrane trafficking events include endocytic internalization, endocytic transport and endoplasmic reticulum (ER)- to-Golgi transport (Fig. 47.9). Common to each of these processes is the dynamic shaping and remodeling of membranes. The responsible actin nucleators span all three classes and include the Arp2/3 complex and its NPFs, the

FIGURE 47.9 Models of the cellular localization and function of actin nucleators. (A) A depiction of the role of actin nucleators in membrane-trafficking events including endocytic internalization as well as various stages of endocytic and ER-to-Golgi trafficking. Abbreviations: EE, early endosomes; ECV/MVB, endosomal carrier vesicles/multivesicular bodies; LE, late endosomes; RE, recycling endosomes; Lys, lysosome; ER, Endoplasmic reticulum; ERGIC, endoplasmic reticulum-Golgi intermediate compartment. (B) Diagram of the role of actin nucleators in lamellipodia and filopodia. In the dendritic organization model of actin organization in lamellipodia, branched actin networks are nucleated by the Arp2/3 complex and the NPFsWAVE1/2 and JMY. In the linear organization model, filaments are nucleated by the Arp2/3 complex, but are unbranched, or are nucleated by mDia2 or perhaps JMY. In the tip nucleation model of filopodium formation, bundled arrays of actin filaments are nucleated by mDia2, whereas in the convergent elongation model, filaments are nucleated by the Arp2/3 complex and WAVE1/2, and are elongated by mDia2. (C) Cartoons depicting the role of actin nucleators in cell division. During cytokinesis, formins (Cdc12p in yeast, mDia2 in mammalian cells) nucleate actin filaments from multiple nodes at the division site that then coalesce into the contractile ring in the search, capture, pull and release model. During centrosome separation, dynamic actin reorganization by Dia and Arp2/3 drives centrosome separation in the early syncytial *Drosophila* embryo. For asymmetric spindle positioning in mouse oocytes, FMN2 nucleates a dynamic actin network that moves the spindle to the cell cortex. During the segregation of protein aggregates in *S. cerevisiae*, Bni1p generates actin cables extending from the polarisome that are required for transport of protein aggregates from the daughter to the mother cell. In (A)–(C) nucleators are color-coded as follows: Arp2/3 complex and NPFs (blue), formins (green), tandem-monomer-binding nucleators (yellow). Question marks indicate that the precise role of the nucleating protein is unclear (Firat-Karalar and Welch, 2011).

inverted formin 2 (INF2) and the tandem-monomer-binding nucleator Spire.

Modes of Cell Migration

In migrating cells, actin polymerization in lamellipodia and finger-like protrusions called filopodia provides the driving force for leading edge protrusion. Lamellipodia are proposed to be Y-branched filament networks nucleated by Arp2/3 complex while filopodia are proposed to be linear bundles nucleated by formins, however, the situation may be more complex.

Cell Division

Actin nucleation is also involved in several stages of cell division. The best-studied is the assembly of the contractile ring, essential for cytokinesis, but other proposed roles include centrosome separation and asymmetric positioning of the spindle and chromosomes in oocytes, as well as segregation of protein aggregates in yeast and involvement of cross-participation of diverse actin nucleators.

IVE. Cell Migration

Lämmerman and Sixt (2009) argue that shifting the balance between actin protrusion, actomyosin contraction and adhesion to the extracellular substrate can explain the diversity of amoeboid movement and that blebbing and gliding are just variants of one common migration strategy.

So what do they consider the principles of force generation and force transduction to be that lead to the observed distinct amoeboid phenotypes. Amoeboid migrating cells are heterogeneous and comprise different unicellular eukaryotes and several individually migrating metazoan cell types. Whatever their size, compactness and habitat, during locomotion they constantly change shape by rapidly protruding and retracting cellular extensions. However, different amoeboid cells employ different mechanical strategies like contraction-based blebbing or polymerization-driven gliding.

The different modes of amoeboid migration can be better appreciated by dissecting the components of force generation (protrusion and contraction) and force transduction (adhesiveness). Lämmerman and Sixt (2009) suggest that the relative role of these components creates the observed distinct modes of amoeboid movement (Fig. 47.10), which are driven by the forces of a polarized actomyosin cytoskeleton. Force is generated by network expansion (polymerization) and network shrinkage (contraction). While only contraction can retract the cell, both forces can protrude the plasma membrane: when expanding below the leading plasma membrane, they generate sufficient force to push out lamellipodia (flat, sheet-like) and filopodia (thin, needle-like). Actin-network contraction generates protrusions via hydrostatic pressure gradients. To contract type II myosins, actin filaments slide past one another to create tension in the actin networks. Consequently, there is a local rise in hydrostatic pressure which leads to ruptures in the cortical actin network or to local detachment of the plasma membrane from the cortical cytoskeleton. Along the pressure gradient, a flow of cytosol will protrude the plasma membrane and form a radially expanding membrane bleb. When the pressure equilibrates the bleb will cease to inflate. F-actin and actin binding proteins stabilize the bleb. Eventually myosin II may retract the bleb.

Migrating cells also need adhesion receptors to anchor them to 2D surfaces, consequently, the adhesions need to be disassembled at the trailing edge. Adhesion receptors like integrins can be locally switched off releasing the substrate at the rear of the cell. Myosin II-dependent contraction forces at the trailing edge are also needed mechanically to support de-adhesion and retraction. Imbalances between these forces do not stall protrusion, but result in blebbing or the polymerization driven phenotype.

While surface anchoring is required for 2D-substrates migration, this might not be true for cells in a 3D matrix. Tightly surrounded by fibrils or surfaces, a cell's confinement might sufficiently immobilize it such that anchoring might not be necessary (Fig. 47.10 IV−VI). Traction forces alone might be sufficient to move a cell.

IVF. Focal Adhesions (and Invadopodia and Podosomes)

Focal adhesions are the best-characterized adhesive structures (Fig. 47.11). They contain clusters of transmembrane integrin receptors tethered at one end to the extracellular matrix (ECM) and at the other to actin stress fibers, which are responsible for cell traction and ECM reorganization (Albiges-Rizo et al., 2009). Other adhesive structures are podosomes and invadopodia. Podosomes are found on the ventral side of a wide range of cells, including osteoclasts, macrophages and endothelial cells. In osteoclasts, podosomes are involved in the formation of a sealing zone that establishes an isolated compartment in which bone is degraded. Lymphocytes use podosomes to palpate the surface of, and ultimately form transcellular pores through, the vascular endothelium. Invasive cancer cells and Src-transformed cells have actin-rich membrane protrusions called invadopodia, which are primary sites of rapid actin polymerization and which represent the major sites of matrix degradation in these cells. Invadopodia of tumor cells appear as irregular dots in the vicinity of the nucleus and in proximity to the Golgi complex. Podosomes in osteoclasts and invadopodia in Src-transformed cells self-organize into a ring (the so-called rosette); in the case of osteoclasts, this can expand to a belt called the sealing zone. This self-organization is crucial for efficient matrix degradation and cell invasion.

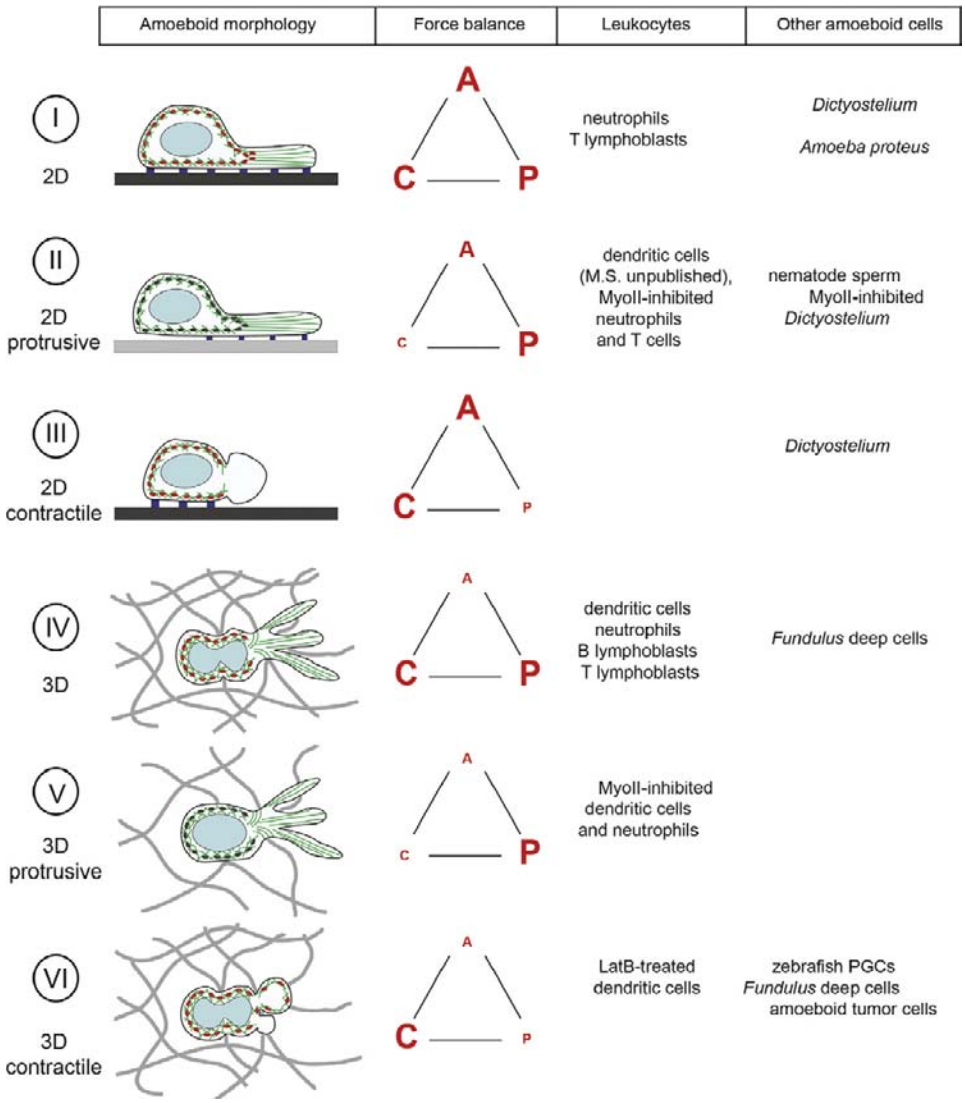

FIGURE 47.10 The force relationship between adhesion, contraction and polymer-network expansion determines the "amoeboid" phenotype. The three major forces in cell migration are adhesion (A), contraction (C) and polymer-network expansion (P). Cell forward locomotion results from their balanced interplay (indicated by the red-lettered triangles). (I–VI) "Amoeboid" crawling shows various migration modes differing in their primary driving forces, however, all are variants of the same scheme. The amoeboid morphology of a specific cell type is determined by its inherent adhesive, contractile and polymerizing equipment. Apart from that, individual cells (e.g. leukocytes) can switch between amoeboid modes after genetic or pharmacological interference with adhesion, contraction or polymer-network expansion. (I–III) Amoeboid cell movement on two-dimensional (2D) surfaces requires adhesion to transduce internal contractile forces onto the substratum. (I) A polymerizing network (green, in most cases actin) "pushes" the membrane forward. Myosin II (MyoII, red ellipses)-based contraction behind the leading edge produces traction underneath the adhesion points (blue). On high adhesive surfaces (black thick line), actomyosin contraction at the back is required to detach the cell from the substrate. Rear end contraction is not necessary when cells migrate on low adhesive substrates (gray thick line) (II). When the contractile function of myosin II is defective (black ellipses), actin polymerization alone can produce traction under adhesion points as has been shown in *Dictyostelium*. Migration without contraction suggests cell retraction can occur either by membrane tension or by polymer-network disassembly. (III) Myosin II-based contraction alone can generate internal hydrostatic pressure to bulge out the plasma membrane. The forming bleb is first cytoplasm-filled and devoid of actin, but fills with actin and myosin II during retraction. Even though blebs are observed during 2D migration, whether they can transduce traction on the surface is still unclear. (IV– VI) Three-dimensional (3D) and confined environments enable migrating cells to exert orthogonal forces between surfaces, which is not possible on 2D substrates. As 3D migration does not require adhesion-mediated traction, orthogonal forces might act as fixation points. (IV) Amoeboid movement in interstitial fibrillar networks (gray) requires contraction only when cells have to squeeze the nucleus (light blue) through narrow pores. (V) In less dense networks, this deforming contraction is not necessary. Here, amoeboid migration is solely driven by polymer-network expansion. Front-to-back gradients of internal stiffness (gel–sol gradients) might facilitate this movement. (VI) Contraction-based increase in internal hydrostatic pressure and directed bleb formation can protrude the leading edge as seen in the migration of zebrafish primordial germ cells (PGCs). How short-lived blebs (first actin-devoid, then actin-filled and myosin II-filled during retraction) generate traction on the environment is unclear. LatB: latrunculin B (actin-depolymerizing agent) (Lämmermann and Sixt, 2009 and references therein).

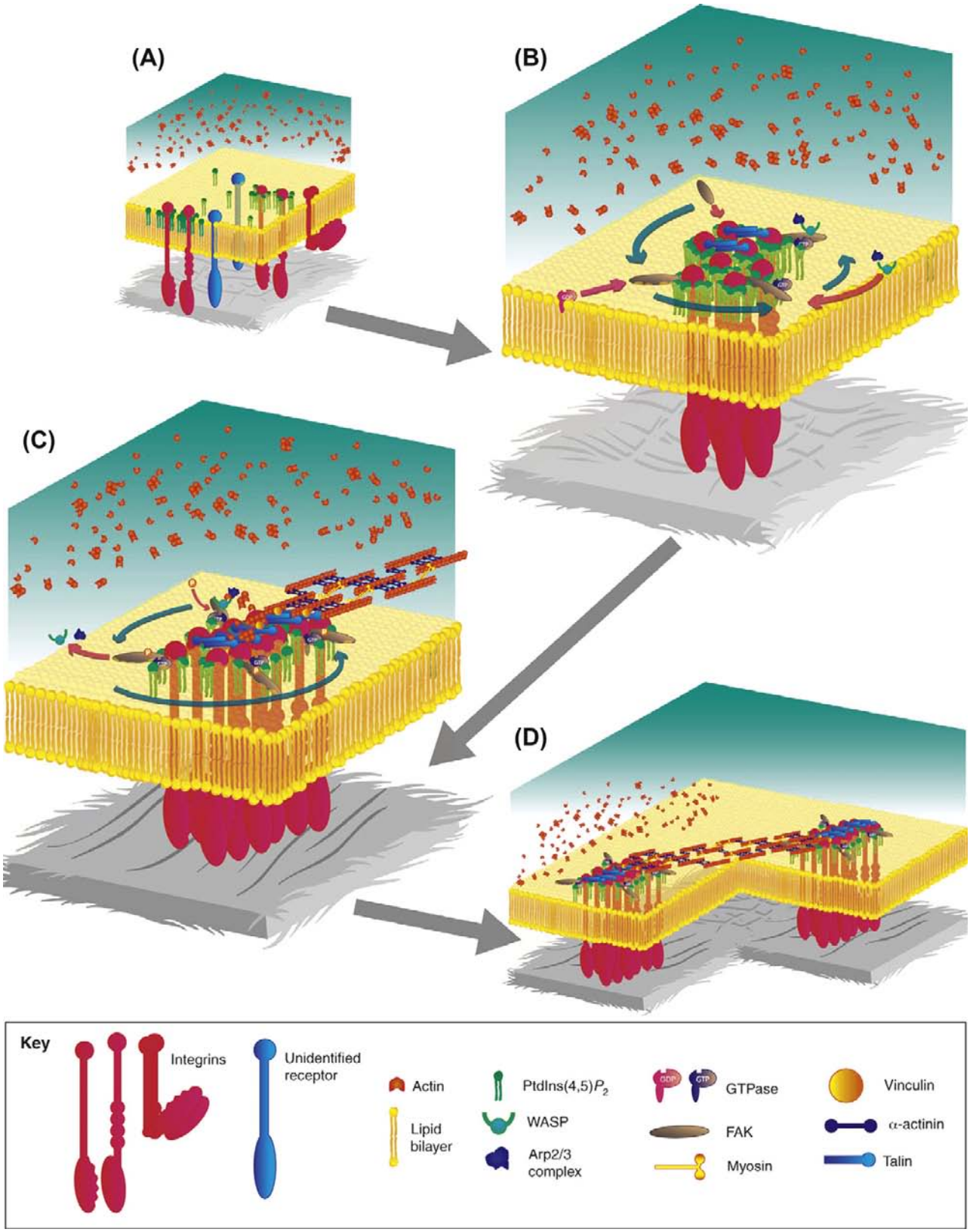
(A)
(B)
(C)
(D)
Key
Integrins
Unidentified receptor
Actin
Lipid bilayer
PtdIns(4,5)P_2
WASP
Arp2/3 complex
GDP
GTP
GTPase
FAK
Myosin
Vinculin
α-actinin
Talin

Invadopodia, podosomes and focal adhesions are all cell-matrix adhesion sites that connect the actin cytoskeleton within the cytosol to the extracellular matrix, but they differ in their architecture and dynamics despite sharing most of the same proteins (such as integrin, talin and paxillin).

IVG. The Model System of Melanophore Transport

The transport of pigment is dependent on an intact cytoskeleton and motor proteins associated with cytoskeletal components (Aspengren et al., 2007). The easily cultured melanophores have proven to be excellent models for organelle transport because the intracellular movements of pigment can be easily visualized and the granules move in response to chemical signals. The ease of morphological and functional transport studies is the advantage of the melanophore system. These studies have the responsible molecular motors, their adapters and transfer of vesicles to other cells. Cellular components are transported by actin and microtubule systems and hence are good models to study such transport in general. Tracking individual melanosomes optically has determined the speed and duration of melanosome movements as a result of different individual motor proteins.

Intracellular transport of melanosomes in fish and amphibian melanophores depends largely on microtubules (MT). Melanosome movements toward the MT plus end result in dispersion, whereas transport toward the minus end results in aggregation of pigment to a central pigment mass that dynein could be involved in aggregation of melanosomes, kinesin-II is the motor responsible for dispersion of melanosomes in *Xenopus* melanophores.

As demonstrated in fish melanophores, actin also plays a role for short-range pigment distribution and in frog melanophores for long-range pigment dispersion.

High levels of the second messenger cAMP are thought to induce dispersion, whereas low levels of cAMP induce aggregation of pigment in melanophores. The subsequent steps in the signaling cascade have been shown to involve protein kinases and phosphatases.

V. BIOLOGICAL SPRINGS

An extended spring may contract when it is triggered or a compressed spring may extend when triggered.

VA. Contractile Springs

The centrin-based family of springs typically contract, sometimes slowly, but sometimes dramatically. Spasmin belongs to this family and is used in the contractile spring spasmoneme.

Centrin molecular springs can be like those used to set and vary the angle between the pair of *Chlamydomonas* cilia (Foster, 2009). The distal fibers connecting the two cilia and the nuclear-basal body connectors respond in a continuous analog fashion to the internal calcium concentration. These fibers contain centrin (also called caltractin). They set the base impedance for the attachment of a cell's cilia to the cell body. Their contraction is much faster than their extension. While the exact purposes of the settings are not understood, this response does facilitate the angle changes needed for flagellar versus ciliary beating. On the other hand, spasmonemes (Marshall, 2008b) are an example of a molecular spring which is designed to release a large amount of stored energy almost all at once and then slowly recover. In this case, calcium triggers further release of calcium in positive feedback so that a dramatic action occurs.

In both cases, energy is required to switch the calcium concentration back and forth between the different levels. Multiple cycles of contraction and extension require multiple switches of calcium concentration. Contraction of isolated spasmonemes is driven by increasing the calcium concentration from 10^{-8} M to 10^{-6} M.

The spasmoneme is triggered when a *Vorticella* cell feels threatened; contracting its tail at a rate of 60−100 mm/s with a tensile force up to 500 nN (Fig. 47.12A,B,C) (Upadhyaya et al., 2008). The speed works out to about 200 lengths per second (L/s). This speed is faster than the fastest muscles, which contract at around 20 L/s. Since the spasmoneme winds helically inside the stalk, the contraction collapses the straight stalk into a helix. The reverse process (recovery) is powered by

FIGURE 47.11 Schematic view of signaling pathways that lead to organization of actin at focal adhesions. (A) In the initial stage of adhesion formation, integrins or other unidentified receptors bind to components of the ECM (gray), leading to clustering of receptors into PtdIns(4,5)P2-enriched areas of plasma membrane. (B) In early spreading adhesions at the cell periphery, the Arp2/3 complex and WASP are targeted to adhesions by FAK. Blue arrows represent the spatiotemporal sequence of structure assembly. Pink arrows indicate protein recruitment. (C) Autophosphorylation of FAK at Tyr397 destabilizes the Arp2/3-WASP-FAK complex. Talin is recruited to adhesions so that integrin-ECM linkages couple to actomyosin; this enables contraction of actomyosin to influence adhesion reinforcement and subsequent maturation. Actin filaments can be cross-linked by α-actinin. Myosin II incorporates into the α-actinin-cross-linked actin-filament bundles. (D) The actin-stress-fiber-mediated connection of focal adhesions describes their collective dynamics. These connections are seen at the front of the cell and with sliding trailing adhesions at the rear of the cell (Albiges-Rizo et al., 2009).

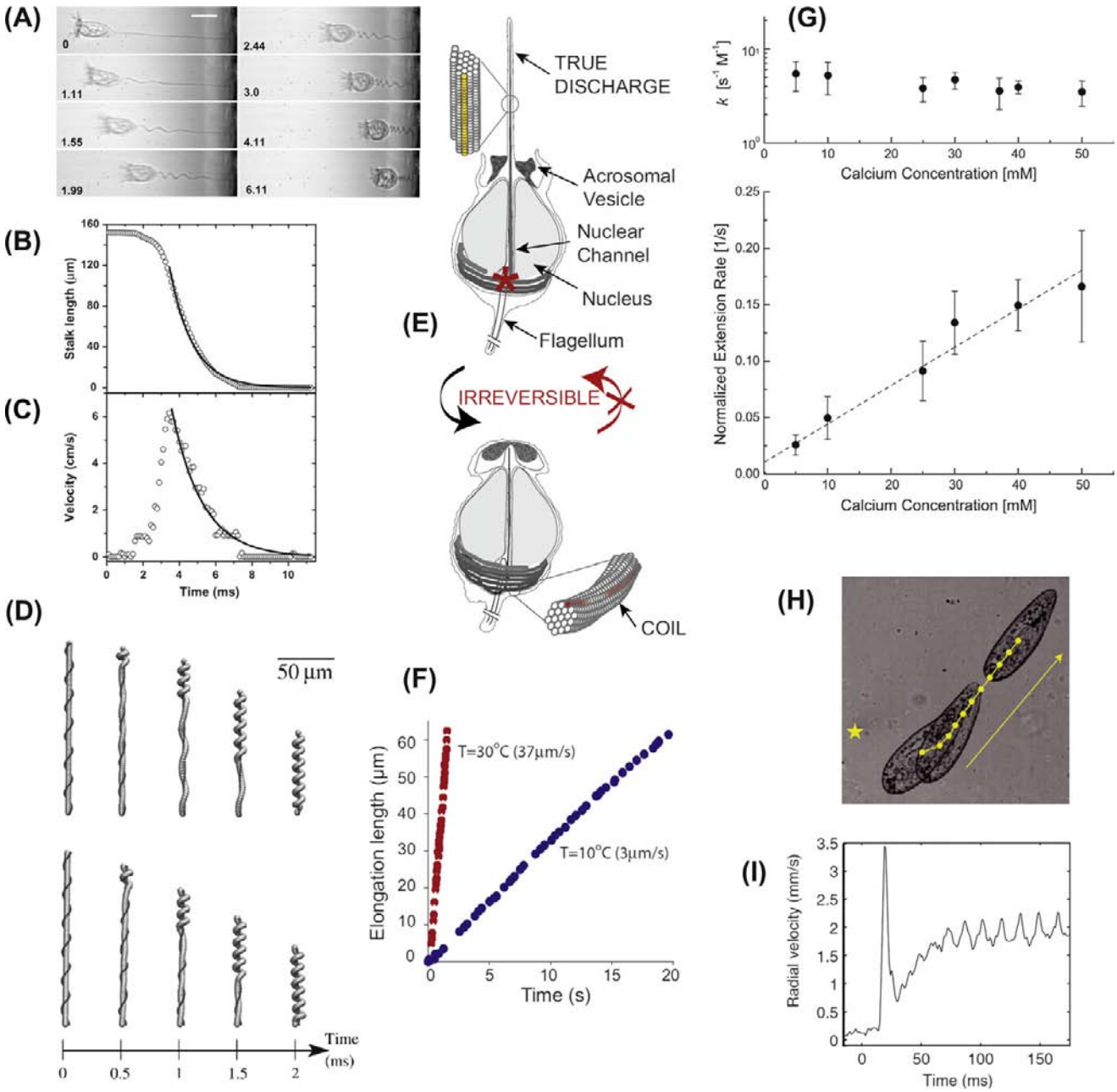

FIGURE 47.12 (A) Dynamics of *Vorticella* contraction. Time series of contraction (time shown in ms). The scale bar is 35 mm (Upadhyaya et al., 2008). (B) *Vorticella* stalk length as a function of time during a contraction. The solid curve is an exponential fit (Upadhyaya et al., 2008). (C) Instantaneous velocity of the cell body as a function of time. The solid curve is an exponential fit to the decaying part of the velocity (Upadhyaya et al., 2008). (D) Time-lapse images of the initial phase of *Vorticella* contraction driven by a propagating calcium signal (for clarity, the head is not shown). (Top) Young's modulus Y = 1 kPa. (Bottom) Y = 4 kPa (Misra et al., 2010). (E) Expansion of actin spring. The geometry and dynamics of the acrosomal reaction. Geometry shows that, in the presence of Ca^{2+}, the bundle switches irreversibly from coil (bottom) to true discharge (top) (Mahadevan et al., 2011). (F) Extrusion occurs at constant speed. The two traces correspond to extrusion at 10°C (3 mm/s) and 30°C (37 mm/s) (Mahadevan et al., 2011). (G) Top: Rate constant *k* calculated using a non-cooperative, constant rate CaM-Ca^{2+} binding mechanism. The slight dependence on $[Ca^{2+}]$ suggests a deviation from the mechanism due to an overestimation of [CaM] participating in the reaction. Bottom: Normalized volume extension rates. Values were calculated from least-squares fitting of volumetric extension profiles as functions of time. The linear behavior (dashed line) suggests a rate mechanism involving calmodulin with one calcium binding site (Tam et al., 2009). (H) Images showing *Paramecium* at different times following a laser pulse in the close neighborhood (Hamel et al., 2011). (I) Radial velocity of the center of mass away from the laser position for the experiments shown above. Time t = 0 corresponds to the moment the laser is switched on (Hamel et al., 2011).

dissociation of Ca^{2+} ions from spasmin and active sequestration back into the calcium storage sites.

Of interest are what molecular mechanisms drive the contraction and how is the contraction coordinated along the length of the entire structure. Using high speed video microscopy, the rate of contraction has been measured as a function of the viscosity of the surrounding media (see Fig. 47.12D) (Misra et al., 2010). From the scaling relation between maximum speed and viscosity, one can conclude that the speed is limited by the power dissipated by dragging the top of the *Vorticella* through the surrounding viscous media. Given that the contraction only takes a few milliseconds, one wonders how the contraction-triggering signal can be transmitted over the whole length of the spasmoneme. The motion of beads stuck onto the *Vorticella* stalk have been tracked to show that contraction initiates near the body of the *Vorticella* and propagates like a wave down the stalk (see Fig. 47.12D). This suggests that the trigger comes from the body and travels down the stalk. Given that contraction is driven by calcium binding, the obvious suggestion would be a calcium wave mediated by calcium-triggered calcium release from the endoplasmic reticulum. In-vivo experiments show that a Ca^{2+} concentration as small as 10^{-7} M is sufficient to trigger the release of stored calcium. However, there is disagreement as to whether such a wave can be as fast as the observed 100 mm/s rate. Perhaps there is an electrical signal or a propagating wave of protein conformational change within the spasmoneme. Its main protein constituent spasmin (40–60% of the spasmoneme dry mass) is closely related to the centrin family of calcium-binding protein found associated with centrioles and basal bodies in many eukaryotes including humans. Centrin assembles into fibers that can contract when calcium is added and, in some organisms, the contraction of centrin fibers is used to steer cell motility by changing the angle at which cilia emerge from the cell surface (Foster, 2009). Presumably the spasmoneme evolved from such structures under selective pressure to contract at high speeds. This suggests that detailed molecular comparisons of centrin and spasmin, together with the behaviors of their corresponding fibers, may shed light on the adaptations that allow spasmin to contract so fast.

VB. Expanding Springs

The acrosomal bundle (cross-linked actin fibers) of the horseshoe crab (*Limulus*) sperm cell is a molecular spring (see Fig. 47.12E) (Tam et al., 2009). The actin bundle is stored at the base of the sperm cell as a twisted coil. Calcium binding to the actin cross-linking protein, scruin, changes its conformation. With further calcium binding along the bundle along its length, the acrosome extends from the sperm cell in order to penetrate and fertilize the horseshoe crab egg. Provided external calcium is continuously available, the 60-μm long bundle extends in 15 s, fast relative to either polymerization or motor protein drive movements. This device illustrates how conformation energy in the form of a twisted bundle can be rapidly released by calcium binding to generate significant cellular movements.

During the acrosome reaction, a 60-μm long coiled and twisted bundle of actin filaments straightens and extends from a sperm cell, penetrating the vitelline layer surrounding the egg. A subtle over twist of 0.2/subunit underlies the mechanochemical basis for the extension of this actin spring. Upon calcium activation, this conformational strain energy is converted to mechanical work, generating the force required to extend the bundle through the vitelline layer. The calcium sequentially binds to calmodulin molecules decorating the actin filaments leading to a collective wave of untwisting of the actin filaments. About a million subunits of actin–scruin–calmodulin achieve a constant expansion of 10 μm/s (3 μm/s at 10°C, 37 μm/s at 30°C (see Fig. 47.12F) with a maximum of force of 1.9 nN and a puncturing pressure of 1.6 MPa (about 15 atmospheres). This force of extension is three times larger than that needed to puncture the vitelline layer.

Mahadevan and collaborators (2011) propose the following model for this mechanochemical engine: (1) Ca^{2+} binds to scruin; (2) the scruin–actin interactions subtly change; (3) a small region of the coil begins to untwist mediated by the scruin which decorates neighboring actin filaments; (4) driven by the potential energy difference between the coil and true states of the bundle, this untwisting deforms the bundle of actin without completely un-cross-linking it in the binding region; and (5) later Ca^{2+} binds to calmodulin releasing the twisted state, leading to the propagation of a front of untwisting that travels along the bundle converting the twisted state irreversibly to the extended state.

This helical arrangement of the bundle is tightly coupled to the conformation of individual actin filaments, each of which has a small overtwist of 0.23°/actin subunit (5 nm in size) relative to the natural chiral structure of an actin filament in the TD. The untwisting produces the extension.

The volumetric rate of expansion is constant at a given concentration of calcium and the volumetric extension rate is proportional to the continuously available calcium concentration (see Fig. 47.12G). These observations (Tam et al., 2009) make sense if the binding of Ca^{2+} to the scruin–CaM complex is according to simple reaction mechanism:

$$CaM + Ca^{2+} \xrightarrow{k} CaM \cdot Ca^{2+} \tag{47.7}$$

where k is an effective rate constant with units of [M^{-1} s^{-1}], which governs the binding of Ca^{2+} to the scruin–CaM complex associated with the twisted filaments.

How strain energy is built in, does not at present appear to be understood.

VI. CANNONS

Another means to achieve motion is to use accentuated turgor pressure Δp and the energy stored in stretched spore cases (Vogel, 2005). At the desired precise time and place (usually at the tip), a weakness is created that fires the spores and fluid out within the case at incredible velocities. The purpose of these "cannons" is to distribute seeds or, for example, spores from coprophilous fungi, like the zygomycete *Pilobolus* (range about 0.8 m, launch velocity 20 m/s), away from the dung they are living on out onto forage plants where they may more probably be eaten.

The energy in a spore case or ascus of the Ascomycetes that can be stored is proportional to the pressure squared and the radius cubed. Given that the biomaterial is basically the same in these organisms, the limit of wall tension is likely to be similar limiting the range of design. The wall tension is due to the pressure difference Δp (inside minus outside) times the radius, so this product is fairly constant among organisms to prevent premature blowout. This means that large asci will have a lower pressure. Hence, a large ascus might have a turgor pressure of 3 atmospheres while a small one up to 15 atmospheres. The energy stored in the stretching of the chamber, which starts out crinkled up, presumably is what leads to its rapid contraction maintaining the pressure during the emptying of the chamber resulting in a complete release of the contents.

The simple consideration that the work, ΔpV, where V is volume available due turgor pressure, should be equal to the consequent kinetic energy of the projectile, $\rho V\frac{v^2}{2}$ where p is the particle density and v is the launch velocity leads to:

$$\text{the launch velocity. } v = \sqrt{\frac{2\Delta p}{\rho}} \qquad (47.8)$$

However, the energy storage capability in the larger chamber more than makes up for the lower pressure. The osmolytes include sugars but probably primarily come from ions pumped into the chamber.

Mechanisms for triggering the breaking of the tip, firing the cannon, do not seem to be described.

There is a helical orientation of wall fibers as is typical for pressurized systems in nature. Also note that the hoop stress is double the longitudinal stress. A further sort of amazing aspect is the incredibly large accelerations seen. This is of course possible due to the small mass of the projectiles, a = F/m (acceleration = force/mass). For example, *Gibberella zeae* exhibits an acceleration of 8.5×10^6 m/s^2 and *Pilobolus* with its relative large 200 µm diameter projectile only has an acceleration of 5×10^5 m/s^2.

Finally, these systems are interesting from the hydrodynamic point of view as they have a big aerodynamic drag problem. The *Pilobolus* sporangium loses 98% of its potential range due to drag (if it could fire into a vacuum it would be really amazing and maybe have a 40 m range). Perhaps not surprisingly spore shapes seem to be optimized to minimize their drag (Roper et al., 2008).

In the above, the cannons fire projectiles, however, for every action there is a reaction and sometimes the reaction is quite important, likely getting oneself out of the way of a predator. *Paramecium* fires trichocysts from its body enabling a transient speed of 10 mm/s, approximately ten times the speed it achieves with its synchronized waves of ciliary beating (see Fig. 47.12H,I) (Hamel et al., 2011).

VII. A FEW LESSONS LEARNED

1. In all instances described, apart from release of turgor pressure, motion is a result of conformation change. Whether it is flagellar motors or dynein, kinesin or myosin or centrin contraction, always it has been found that the key is protein conformation change. This is unlike the mechanical devices that humans have designed where the shape of stators and rotors do not change. The components simply move relative to each other under electromagnetic forces. There are of course biomimetic motors that do depend on repeated conformation change as, for example, ultrasonic motors. An advantage of ultrasonic motors and all the biological motors described here is that they do not have to be energized to hold their place, which is an enormous economy for portable devices.
2. All these motors are actually very efficient and significantly owe their efficiency to the very small steps each motor takes as discussed at the beginning of this chapter.
3. Note continuity of torque or force on each side of stall in each case implying the reversibility of actions, "there is no irreversible step in the mechanochemical cycle" (Sowa and Berry, 2008).

Final comment: with the enlargement of the Web, a search engine will place before you animations and real movies of much of what is described here. Sites have mostly not been given here because they are often transient, but finding them is not hard. Be aware that non-scientific sites exist about flagella and cilia that peddle nonsense.

BIBLIOGRAPHY

Albiges-Rizo, C., Destaing, O., Fourcade, B., Planus, E., & Block, M. R. (2009). Actin machinery and mechanosensitivity in invadopodia, podosomes and focal adhesions. *J Cell Sci, 122*, 3037–3049.

Aspengren, S., Hedberg, D., & Wallin, M. (2007). Melanophores: a model system for neuronal transport and exocytosis? *J Neurosci Res, 85*, 2591–2600.

Berg, H. C. (2003). The rotary motor of bacterial flagella. *Annu Rev Biochem, 7*, 19−54.

Berg, H. C., & Brown, D. A. (1972). Chemotaxis in *Escherichia coli* analyzed by three-dimensional tracking. *Nature, 239*, 500−504.

Brokaw, C. J. (1991). Microtubule sliding in swimming sperm flagella: direct and indirect measurements on sea urchin and tunicate spermatozoa. *J Cell Biol, 114*, 1201−1215, and. http://www.cco.caltech.edu/~brokawc/Demo1/BeadExpt.html.

Brokaw, C. J. (2009). Thinking about flagellar oscillation. *Cell Motil Cytoskeleton, 66*, 425−436.

Carlsson, A. E. (2010). Actin dynamics: from nanoscale to microscale. *Annu Rev Biophys, 39*, 91−110.

Dzeja, P. P., & Terzic, A. (2009). Adenylate kinase and AMP signaling networks: metabolic monitoring, signal communication and body energy sensing. *Int J Mol Sci, 10*, 1729−1772.

Emonet, T., & Cluzel, P. (2008). Relationship between cellular response and behavioral variability in bacterial chemotaxis. *Proc Natl Acad Sci USA, 105*, 3304−3309.

Firat-Karalar, E. N., & Welch, M. D. (2011). New mechanisms and functions of actin nucleation. *Curr Opin Cell Biol, 23*, 4−13.

Fletcher, D. A., & Mullins, R. D. (2010). Cell mechanics and the cytoskeleton. *Nature, 463*, 485−492.

Foster, K. W. (2009). Analysis of the ciliary/flagellar beating of *Chlamydomonas*. In S. M. King, & G. J. Pazour (Eds.), *Cilia: Structure and Motility. Methods in Cell Biology, vol. 91* (pp. 173−239). San Diego: Academic Press.

Hamadeh, A., Roberts, M. A. J., August, E., et al. (2011). Feedback control architecture and the bacterial chemotaxis network. *PloSComputBiol, 7*, e1001130, doi:10.1371/journal.pcbi.1001130.

Hamel, A., Fisch, C., Combettes, L., Dupuis-Williams, P., & Baroud, C. N. (2011). Transitions between three swimming gaits in *Paramecium* escape. *Proc Natl Acad Sci USA, 108*, 7290−7295.

Hazelbauer, G. L., Falke, J. J., & Parkinson, J. S. (2007). Bacterial chemoreceptors: high-performance signaling in networked arrays. *Trends Biochem Sci, 33*, 9−19.

Heuser, T., Raytchev, M., Krell, J., Porter, M. E., & Nicastro, D. (2009). The dynein regulatory complex is the nexin link and a major regulatory node in cilia and flagella. *J Cell Biol, 187*, 921−933.

Kaneshiro, E. S. (2001). Centrin-based contraction and bacterial flagella. In N. Sperelakis (Ed.), *Cell Physiology Source Book* (3rd ed.). (pp. 985−1002) San Diego: Academic Press.

Kaneshiro, E. S., Sanderson, M. J., & Witman, G. B. (2001). Amoeboid movement, cilia, and flagella in cell physiology. In N. Sperelakis (Ed.), *Cell Physiology Source Book* (3rd ed.). (pp. 959−984) San Diego: Academic Press.

Lämmermann, T., & Sixt, M. (2009). Mechanical modes of 'amoeboid' cell migration. *Curr Opin Cell Biol, 21*, 636−644.

Lindemann, C. B., Macauley, L. J., & Lesich, K. A. (2005). The counterbend phenomenon in dynein-disabled rat sperm flagella and what it reveals about the interdoublet elasticity. *Biophys J, 89*, 1165−1174.

Mahadevan, L., Riera, C. S., & Shin, J. H. (2011). Structural dynamics of an actin spring. *Biophys J, 100*, 839−844.

Marshall, W. F. (2008a). .The cell biological basis of ciliary disease. *J Cell Biol, 180*, 17−21.

Marshall, W. F. (2008b). Don't blink: observing the ultra-fast contraction of spasmonemes. *Biophys J, 94*, 4−5.

Misra, G., Dickinson, R. B., & Ladd, A. J. C. (2010). Mechanics of *Vorticella* contraction. *Biophys J, 98*, 2923−2932.

Mitchell, B. F., Pedersen, L. B., Feely, M., Rosenbaum, J. L., & Mitchell, D. R. (2005). ATP production in *Chlamydomonas reinhardtii* flagella by glycolytic enzymes. *Mol Biol Cell, 16*, 4509−4518.

Nelson, P. (2008). *Biological Physics: Energy, Information, Life*. New York: W.H. Freeman.

Oleksiuk, O., Jakovljevic, V., Vladimirov, N., et al. (2011). Thermal robustness of signaling in bacterial chemotaxis. *Cell, 145*, 312−321.

Riedel-Kruse, I. H., Hilfinger, A., Howard, J., & Julicher, F. (2007). How molecular motors shape the flagellar beat. *HFSP J, 1*, 192−208.

Roper, M., Squires, T. M., & Brenner, M. P. (2008). Symmetry unbreaking in the shapes of perfect projectiles. *Phys Fluids, 20*, 093606.

Segall, J. E., Block, S. M., & Berg, H. C. (1986). Temporal comparisons in bacterial chemotaxis. *Proc Natl Acad Sci USA, 83*, 8987−8991.

Sowa, Y., & Berry, R. M. (2008). Bacterial flagellarmotor. *Quart Rev Biophys, 41*, 103−132.

Tam, B. K., Shin, J. H., Pfeiffer, E., Matsudaira, P., & Mahadevan, L. (2009). Calcium regulation of an actin spring. *Biophys J, 97*, 1125−1129.

Tee, S.-Y., Bausch, A., & Janmey, P. A. (2009). The mechanical cell. *Curr Biol, 19*, R745−R748.

Turner, L., Ryu, W. S., & Berg, H. C. (2000). Real-time imaging of fluorescent flagellar filaments. *Journal of Bacteriology, 182*, 2793−2801.

Upadhyaya, A., Baraban, M., Wong, J., Matsudaira, P., van Oudenaarden, A., & Mahadevan, L. (2008). Power-limited contraction dynamics of *Vorticella convallaria*: an ultrafast biological spring. *Biophys J, 94*, 265−272.

Vogel, S. (2005). Living in a physical world II. The bio-ballistics of small projectiles. *J Biosci, 30*, 167−175.

Wirschell, M., Pazour, G., Yoda, A., Hirono, M., Kamiya, R., & Witman, G. B. (2004). Oda5p, a novel axonemal protein required for assembly of the outer dynein arm and an associated adenylate kinase. *Mol Biol Cell, 15*, 2729−2741.

Woolley, D. M. (2010). Flagellar oscillation: a commentary on proposed mechanisms. *Biol Rev Camb Philos Soc, 85*, 453−470.

This page intentionally left blank

Chapter 48

Electrocytes of Electric Fish

Anthony L. Gotter, Marcia A. Kaetzel and John R. Dedman

Chapter Outline

I. SUMMARY

Both the freshwater electric eel and the saltwater electric ray produce extraordinarily powerful electrical discharges with membrane ion channels, receptors and pumps common to other excitable cells. These fish have separately evolved a specialized anatomy and cellular morphology designed for this function. Because of their specialized membrane asymmetry, action potentials and end-plate potentials generated on the innervated membrane are not reproduced on the non-innervated membrane, thereby setting up an asymmetrical flow of current across the cell. The arrangement allows transcellular potentials to be generated, which is essentially the basis for the generation of bioelectricity within the electric organs of these fish. Connective tissue septa that delineate columns of electrocytes prevent transcellular potentials from being short-circuited around the outside of individual electrocytes and also channel the resulting current along the electric organ.

The membrane potentials used by electrocytes to produce transcellular potentials are remarkably similar to those of other excitable cells, such as myocytes and neurons. The electrophysiology, therefore, can be explained by currents conducted through ligand-gated receptors and channels having known characteristics. Currents that give rise to electrocyte membrane potentials can even be represented by equivalent circuits similar to those of other excitable cells. However, two major differences exist between electrocytes and other excitable cells: (1) electrocytes express exaggerated amounts of key excitable membrane proteins, such as the Na^+ channel of *Electrophorus* and the acetylcholine receptor (AChR) of *Torpedo.* These proteins that exist in high density tend to produce greater currents and peak potentials than what is customarily seen on other excitable cells. (2) Membrane proteins are polarized to particular sides of the cell to facilitate the production of transcellular potentials. In the past, however, researchers have taken advantage of these differences to utilize these fish as useful model systems.

Electrophorus electrocytes provide a general model system for excitable cells, such as neurons and myocytes, since they contain common membrane receptors, channels and ATPases. They are also large and easy to dissect in order to perform potential recording, voltage-clamp analysis and patch-clamp measurements. Since it expresses large quantities of proteins, such as the Na^+ channel, the Na^+,K^+-ATPase, AChR and calmodulin, eel electric tissue has been used as a source for the purification of these proteins for molecular and functional analysis.

Torpedo electrocytes, on the other hand, are richly innervated with ACh-releasing electromotor neurons and are electrically inexcitable. Therefore, they provide a very specialized model for the motor end-plate. Because of the

Cell Physiology Sourcebook. DOI: 10.1016/B978-0-12-387738-3.00048-2

exaggerated cholinergic nature of *Torpedo* electric tissue, it has been used as a rich protein and mRNA source for the AChR and AChE. The expression of Cl^- channels on the non-innervated membrane of these cells has led researchers to use this tissue as a source for ClC-0 protein and mRNA as well.

Investigations with electric tissue of both the electric eel and the electric ray have opened wide avenues of study in electrophysiology, protein biochemistry and clinical research. Electrophysiological techniques have been used, refined and, in some cases, developed while using electrocytes as model systems. Like the squid giant axon, these cells have been instrumental in defining and confirming the ionic currents responsible for excitable cell membrane potential changes. Biochemically, *Electrophorus* and *Torpedo* electric tissue has supplied abundant quantities of key excitable membrane proteins that exist in only trace amounts in mammalian tissues. Since electric tissue develops from skeletal muscle, the biochemical properties and three-dimensional structures of these proteins are similar, if not identical, to those of mammalian skeletal muscle and other excitable cells. These discoveries will continue to further our understanding of the mechanisms by which membrane potentials of excitable cells are generated and regulated, as well as the understanding and the treatment of disease.

II. INTRODUCTION

Electric fish such as the marine *electric ray* (genus *Torpedo*) and the freshwater *electric eel* (*Electrophorus electricus*) are capable of generating powerful electrical discharges that can be measured in the water surrounding these animals. These fish use the production of bioelectricity as an effective mechanism to stun prey and ward off predators. Electrical discharges are generated by electric cells, called *electroplax* or *electrocytes*, that produce end-plate potentials and action potentials (APs) that are remarkably similar to the membrane potentials of neurons and myocytes. In fact, the membrane receptors, ion channels and ATPases responsible for electric tissue electrophysiology are biochemically and functionally identical to those of mammalian muscle and nerve. For this reason, electrocytes have been used extensively as a specialized and appropriate model system for the study of excitable cell membrane electrophysiology and biochemistry. Due to the specialized nature of electric tissue, it has also been used as an enriched source of membrane proteins for biochemical studies. Previous chapters have described in detail the generation of acetylcholine (ACh)-mediated muscle end-plate potentials and the propagation of action potentials of nerve and muscle (see Chapters 18, 19, 32, and 42). This chapter examines the anatomy and cellular morphology that electric fish have evolved in order to produce powerful electrical discharges. An electrophysiological and biochemical comparison is made between the electrocytes of the freshwater electric eel and the marine electric ray. The major contributions that electric tissue has made to the understanding of the electrophysiology and biochemistry of excitable membranes are also reviewed.

The shocking sensations produced by electric fish were undoubtedly experienced by mankind long before the recording of scientific phenomena. Some of the first recorded reports of unusual effects produced by electrical discharges of electric fish were of the Nile river catfish, *Malapterus electricus*. Nile river fishermen reported unpleasant sensations when handling live *Malapterus,* or even the water-soaked nets containing the fish. Godigno, a seventeenth century Jesuit father, noted that dead fish could be induced to move when a live *Malapterus* was thrown among them (Grundfest, 1957). At the time when Ben Franklin and other investigators were experimenting with static electricity of the Leyden jar, the electric eel provided insight into the basic conductive properties of electricity. In 1775, John Walsh conducted numerous experiments, one of which involved 10 people holding hands in a circle where the first and last "subjects" touched the opposite ends of a moderate-sized eel. All 10 people received a severe shock. The relative conductivities of various materials, including glass, wood, silk, brass chains and iron rods, were then determined by holding these materials between two of the investigators and noting the severity of the electrical discharge. Although these experiments were likely to be very convincing to Walsh and his assistants, others doubted the electrical nature of the discharge from *Electrophorus* and *Torpedo*. The bioelectric nature of the discharge had not gained widespread acceptance until Du Bois-Raymond demonstrated that nerve and muscle were electrogenic (Grundfest, 1957). Since that time, the usefulness of *Electrophorus*, *Torpedo* and other electric fish as models for excitable membranes has been realized.

III. ANATOMY OF *ELECTROPHORUS* AND MECHANISM OF THE ELECTRICAL DISCHARGE

Powerful electric fish possess a specialized anatomy and cellular morphology devoted to the production of electrical discharges. The electric eel is an excellent example of this specialization. It has been well characterized on the cellular and biochemical level and is used here to describe the production of bioelectricity. Figure 48.1A depicts the location of the electric organs within *Electrophorus*. The viscera are crowded into the rostral 20% of the animal; the remaining 80% is comprised predominantly of electric tissue and swimming muscles. The electric organs are confined to the ventral portion of this caudal region,

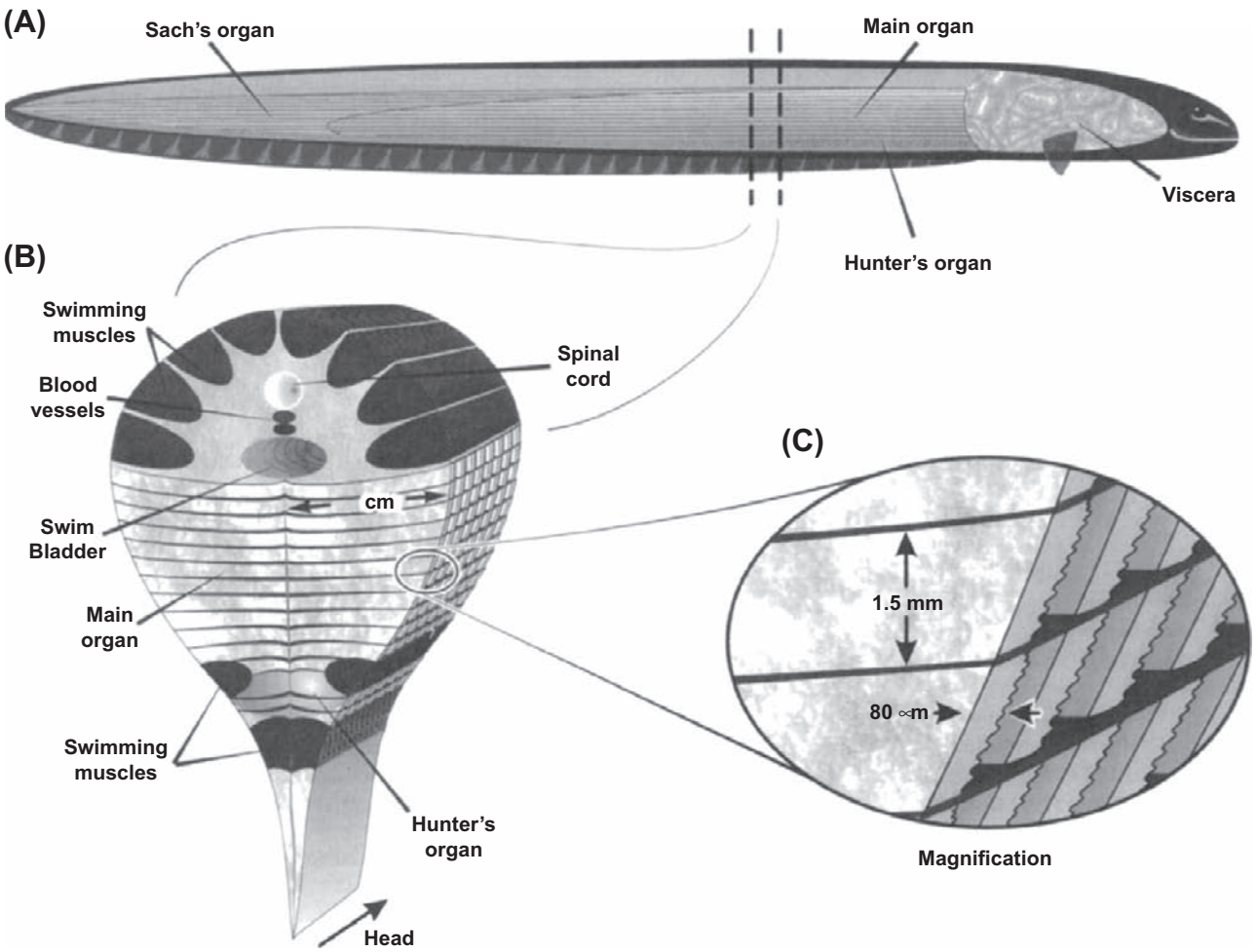

FIGURE 48.1 Anatomy of the electric eel. (A) Diagram illustrating the anatomical orientation of electric organs. (B) A section through the middle portion of the eel, drawn such that the anterior surface is nearest the reader. (C) Columns of electrocytes extend the length of the electric organ. In this panel, the flatter, caudal surface of each electrocyte would be innervated by numerous electromotor neurons (not shown).

whereas most of the swimming muscles, major blood vessels and spinal cord are situated in the dorsal one-third (Fig. 48.1B). The eel also possesses a tubular swim bladder that extends the length of the fish and is positioned dorsal to the main electric organ and ventral to the spinal cord. The central nervous system consists of a small brain typical of teleost fish and a spinal cord that extends down the length of the animal. The electrical discharge is coordinated in the central control nucleus in the medulla. Axons from these neurons of the brain project caudally and synapse on neurons of the electromotor nucleus of the spinal cord. *Electromotor neurons* radiate into the electric organ, innervating individual electrocytes (Bennett and Sandri, 1989). To generate the whole-animal electrical discharge, each electrocyte of the entire electric organ must be stimulated simultaneously. In other words, action potentials reaching proximal electrocytes of the electric organ must be delayed to varying degrees relative to more distal regions. Neurons innervating proximal electrocytes are smaller in diameter and conduct action potentials more slowly. Some of these neurons wind their way to these rostral electrocytes, thereby slowing stimulation of this part of the electric organ, aiding in synchronous activation (Bennett, 1971). The delay may also occur in the electromotor nucleus of the spinal cord where central neurons synapse on electromotor neurons. Presumably, synaptic transmission is slower to electromotor neurons innervating proximal portions of the electric organ, whereas faster signaling occurs between neurons that innervate electrocytes near the tail (Szabo, 1961).

As depicted in Fig. 48.1, *Electrophorus* has three well-defined electric organs. The main organ is the largest and is responsible for voluntarily generating powerful high-voltage discharges. The main organ extends from behind the peritoneal cavity of the viscera down the tail of the eel, where it eventually gives rise to Sach's organ. This organ, along with Hunter's organ, generates repetitive low-voltage discharges and is thought to be involved in electrolocation

of objects in the eel's environment. In the cross-sectional view of Fig. 48.1B, Hunter's organ is seen to be partially delineated from the main organ by two columns of skeletal muscles. Electric tissue develops from these columns of skeletal muscle tissue in immature eels and is thought to arise from embryonic myocyte precursor cells (Keynes, 1961). As shown later, the membranes of electrocytes are biochemically and functionally very similar to skeletal muscle sarcolemma.

Electrocytes of both the main electric organ and Sach's organ are large ribbon-shaped cells. Each electrocyte extends laterally from the midline of the electric organ to the skin, a distance of up to 4 cm. They have a width of up to 1.5 mm and thickness of 80 μm. As seen in Fig. 48.1C, electrocytes are positioned one after another along their flat axis to give rise to long rectangular columns of cells running along the longitudinal axis of the eel. These columns are delineated and electrically insulated from one another by *connective tissue septa*, which help to maintain the physical structure of the electric organ. This stacked arrangement is a common feature of electric organs in electric fish and enables greater voltages to be produced (see later). When viewed under light microscopy, electrocytes are seen as multinucleated syncytia, similar to the skeletal muscle myocytes from which they are derived. Electrocytes are seen in cross-section to have one relatively flat posterior membrane relative to the other more undulated anterior membrane. The flat caudal membrane is innervated by ACh-releasing electromotor neurons that form synapses that are morphologically similar to motor end plates of skeletal muscle cells (Chapter 32).

Immunofluorescent localization microscopy and electrophysiological experiments have led to the understanding of how the electrical discharge is generated at the cellular level. Electrocytes use membrane receptors and ion channels polarized to either the innervated or non-innervated membrane in order to produce *transcellular potentials* that give rise to the discharge of the electric organ (Fig. 48.2A). The caudal innervated membrane contains acetylcholine receptors (AChRs), inward and outward rectifying K^+ channels, a high density of voltage-gated Na^+ channels and only trace amounts of Na^+, K^+-ATPase. This membrane is both chemically and electrically excitable. That is, this surface of the electrocyte produces APs in response to artificial stimulation with AChR agonists or direct electrical stimulation. The non-innervated membrane, on the other hand, does not respond to these manipulations, since it has no AChRs or voltage-gated Na^+ channels. Instead, this membrane contains a high concentration of Na^+, K^+-ATPase and ion channels responsible for maintaining the *resting potential* of −70 to −85 mV. Evidence suggests that the resting current of *Electrophorus* electrocytes is carried predominantly by K^+ channels (Lester, 1978), but the contribution of a Cl^- conductance cannot be excluded (Nakamura et al., 1965). In *Torpedo,* the resting current has been shown to be carried at least partially by Cl^- (Miller and White, 1980). In skeletal muscle myocytes, 30−70% of the resting current is carried by this anion (Chapter 42). Since *Electrophorus* electric tissue is derived from skeletal muscle, it is possible that the resting current of these cells is also carried by Cl^-.

APs arriving at the nerve termini of electromotor neurons cause ACh to be released onto the innervated membrane of electrocytes (see Fig. 48.2A). *End-plate potentials* (EPPs) produced by AChRs surpass the threshold for Na^+ channel activation and trigger the production of APs that propagate very short distances between electromotor junctions and have overshoots of +40 to +65 mV. Meanwhile, the potential of the non-innervated membrane remains at the resting value of up to −85 mV, due to the abundance of resting current channels and the absence of voltage-gated Na^+ channels. When the AP peaks on the innervated membrane, a net *transcellular potential* of up to 150 mV results across the electrocyte (+65 mV of the innervated membrane minus −85 mV of the non-innervated membrane). This transcellular potential difference is accompanied by a net flow of positive current moving in the innervated membrane-to-non-innervated membrane direction (left to right as shown in Fig. 48.2). Insulating septa that form electrocyte columns effectively insulate the extracellular regions on either side of the electrocyte. These connective tissue structures prevent current from flowing around the outside of the electrocyte, which would short-circuit the transcellular potential difference (see Fig. 48.2B). This arrangement allows each electrocyte to act as a simple battery having an electrical potential of up to 150 mV. Since each electrocyte of a column is stimulated simultaneously, the potentials of each electrocyte battery within a column summate to generate a large voltage, as predicted by Ohm's law. In Fig. 48.2B, the potentials of three electrocytes summate to give a potential of 450 mV. In large eels, where the potentials of many thousands of electrocytes summate, the net electric discharge can reach 700 V.[1] Connective tissue septa channel the current down the longitudinal axis of the electric organ toward the head of the eel. The current leaves the eel through low-resistance regions of the skin and is conducted through the water, producing an electric field, the magnitude of which diminishes with the square of the distance from the animal. Objects, like other fish or the human hand, experience a potential difference in this electric field and currents

[1] A discharge of this magnitude requires that at least 4700 electrocytes be stimulated simultaneously. That is, 4700 electrocytes × 0.15 V per electrocyte = 705 V. This situation is analogous to a flashlight, where more batteries aligned in series produce a brighter light source.

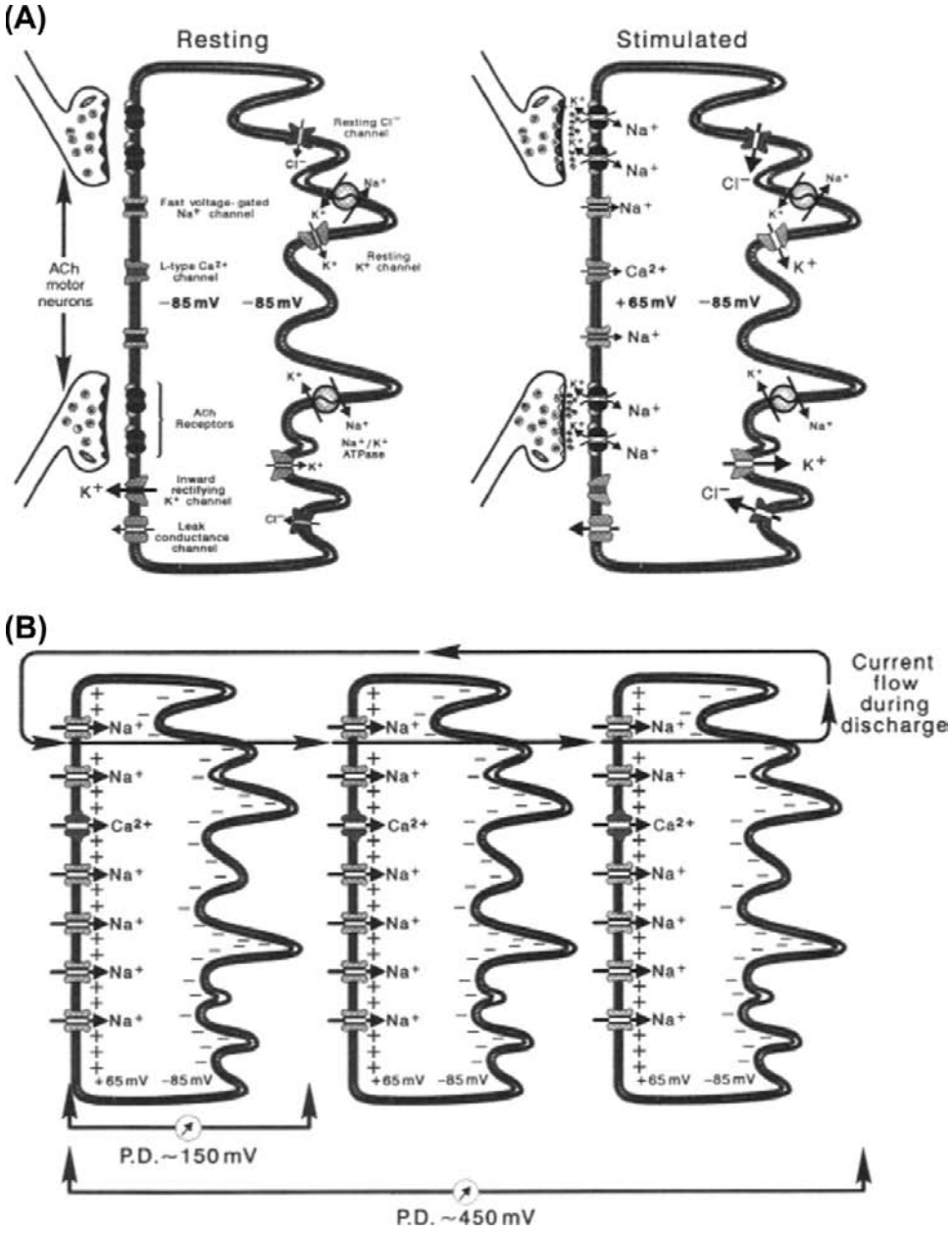

FIGURE 48.2 Diagrammatic representation of electrocytes. The left surface of each cell represents the posterior innervated membrane. (A) At rest, both the innervated and non-innervated membranes exhibit a potential of −85 mV. When stimulated, activated AChRs generate EPPs, triggering Na^+ channel-mediated APs peaking at +55 mV on the innervated membrane. The non-innervated membrane contains no voltage-gated Na^+ channels and maintains the −85-mV resting potential. The result is a transcellular potential difference of approximately 150 mV. (B) Because each cell is stimulated simultaneously, electrocyte transcellular potentials summate. The potentials of three electrocytes culminate to produce 450 mV. Currents generated by stimulated electrocytes flow down electrocyte columns in the posterior-to-anterior direction. The circuit is closed by current flowing out the head of the eel, through the water, and back into the tail region.

sufficient to excite muscles, nerves and sensory endings flow through them, producing a shocking sensation. The circuit of the discharge is closed by current flowing through the skin of the tail region of the eel back into electrocyte columns from which the electromotive force (EMF) originated (Bennett, 1971).

IV. ELECTROCYTE MEMBRANE ELECTROPHYSIOLOGY

IVA. Membrane and Extracellular Potentials

Electrocyte membranes contain many of the same protein elements found in myocytes and neurons. In fact, the

individual APs of the innervated membrane of *Electrophorus* electrocytes are quite similar to those of other excitable cells. However, electric cells are different in that potential changes are polarized to a particular membrane, resulting in the generation of transcellular potentials and an asymmetric flow of current. Also, to produce whole-animal electrical discharges having the maximum possible voltage or current output, electrocytes have evolved to express exaggerated amounts of key excitable membrane proteins.

In electric tissue preparations where the flat innervated electrically excitable surface of electrocytes is exposed, APs can be triggered with extracellular stimulating electrodes situated close to the membrane surface. Membrane potentials and transcellular potentials can then be measured through recording electrodes lowered across the innervated membrane or through the entire cell, respectively (Fig. 48.3). As the recording electrode approaches the innervated membrane and a stimulus is applied, a negative deflection is recorded (Fig. 48.3A). Because the recording electrode measures the potential difference between the region just outside the membrane compared to the reference electrode placed in the bath, the AP here is recorded as a negative deflection. After the electrode is advanced through the innervated membrane, an AP that has propagated from the site of stimulation to the recording electrode is detected. The characteristics of electrocyte membrane potentials vary considerably from cell to cell, but are typically similar to those measured on the myocyte sarcolemma or neuronal axolemma. As seen in Fig. 48.3B, a typical resting potential is about −75 mV and ranges from −65 to −85 mV. The electrocyte AP seen in Fig. 48.3B is typical in its 3.5-ms duration and +50-mV overshoot. Generally, the duration ranges from 2 to 4 ms and the overshoot between +35 and +65 mV. These values for the overshoot are considerably larger than that of other excitable cells and are due to an extraordinarily high density of voltage-gated Na^+ current and a relatively low level of outward rectifying K^+ current (see discussion later). When the recording electrode is lowered even further until it completely penetrates the electrocyte, transcellular APs are recorded. Because the recording electrode is once again in the extracellular space, the resting potential here is measured as 0 mV. However, the interstitium where the recording electrode is positioned is electrically insulated by connective tissue septa from the reference electrode located in the bath solution. When the electrocyte is stimulated, an AP is recorded that is identical to the intracellular AP, except that it initiates at 0 mV. It has a peak equal to the total amplitude of the intracellular AP, in this case about 125 mV. This transcellular AP arises because the non-innervated non-excitable membrane does not fire an AP that would cancel out the spike of the innervated membrane. Insulating connective tissue septa prevent the potential difference from being short-circuited around the outside of the electrocyte. If the stimulus is increased such that the electrocyte beneath the recording electrode is also stimulated, a negative deflection in the extracellular potential is recorded just behind the 125-mV transcellular AP (see Fig. 48.3C, right). This negative deflection corresponds to the resulting AP of the lower electrocyte, which is stimulated later than the electrocyte on the surface. In the intact electric organ, these electrocytes would be stimulated simultaneously by the eel's nervous system such that these APs would be occurring at the same time. In this way, the transcellular potentials summate to yield a powerful electrical discharge.

Ionic currents responsible for *Electrophorus* electrocyte resting potentials, as well as EPPs and APs are similar to other excitable cells and the reader is referred to previous chapters where their mechanisms have been described in detail. However, some differences between electrocyte membranes and those of neurons and myocytes are worthy of mention. The non-innervated membrane of electrocytes has a very low resistance of about 0.1 Ω/cm^2, which is one to two orders of magnitude less than that typically found for nerve or muscle (Nakamura et al., 1965). Physiologically, the eel needs this high K^+ and Cl^- current to clamp the non-innervated membrane at the resting potential in order to set up transcellular potentials like those observed in Fig. 48.3C. On the other hand, the innervated membrane at rest has a resistance of 3−6 Ω/cm^2 (Nakamura et al., 1965). On stimulation, this resistance decreases due to a large voltage-activated Na^+ current. In fact, Shenkel and Sigworth (1991) were able to measure macroscopic Na^+ currents in excised patches of the innervated membrane corresponding to a density of as much as 1300 channels/μm^2. This high density of Na^+ channels is accompanied by relatively few outwardly rectifying K^+ channels. Because of this distribution of channels in the innervated membrane, the electrocyte AP has a large overshoot that nearly reaches the Na^+ equilibrium potential, E_{Na}. The repolarization phase is therefore due primarily to the inactivation of Na^+ channels and secondarily to delayed rectifier K^+ channels and the resting current of the innervated membrane.

Skeletal muscle-like EPPs that trigger APs on the surface of electrocytes are generated by AChR-mediated currents. Basically, macroscopic and single-channel currents conducted by the eel AChR are very similar to those seen on skeletal muscle sarcolemma. The permeability of the eel receptor to both Na^+ and K^+ is nearly equal since the reversal potential is the midpoint between E_{Na} and E_K (Sheridan and Lester, 1977; Pasquale et al., 1986). In other words, the peak of the EPP moves toward a value of approximately −10 mV in order to activate Na^+ channels for an AP. Eel AChRs elicit single-channel opening events that are similar to the receptor from mammalian sources in that their mean open time is dependent on membrane potential, temperature and the

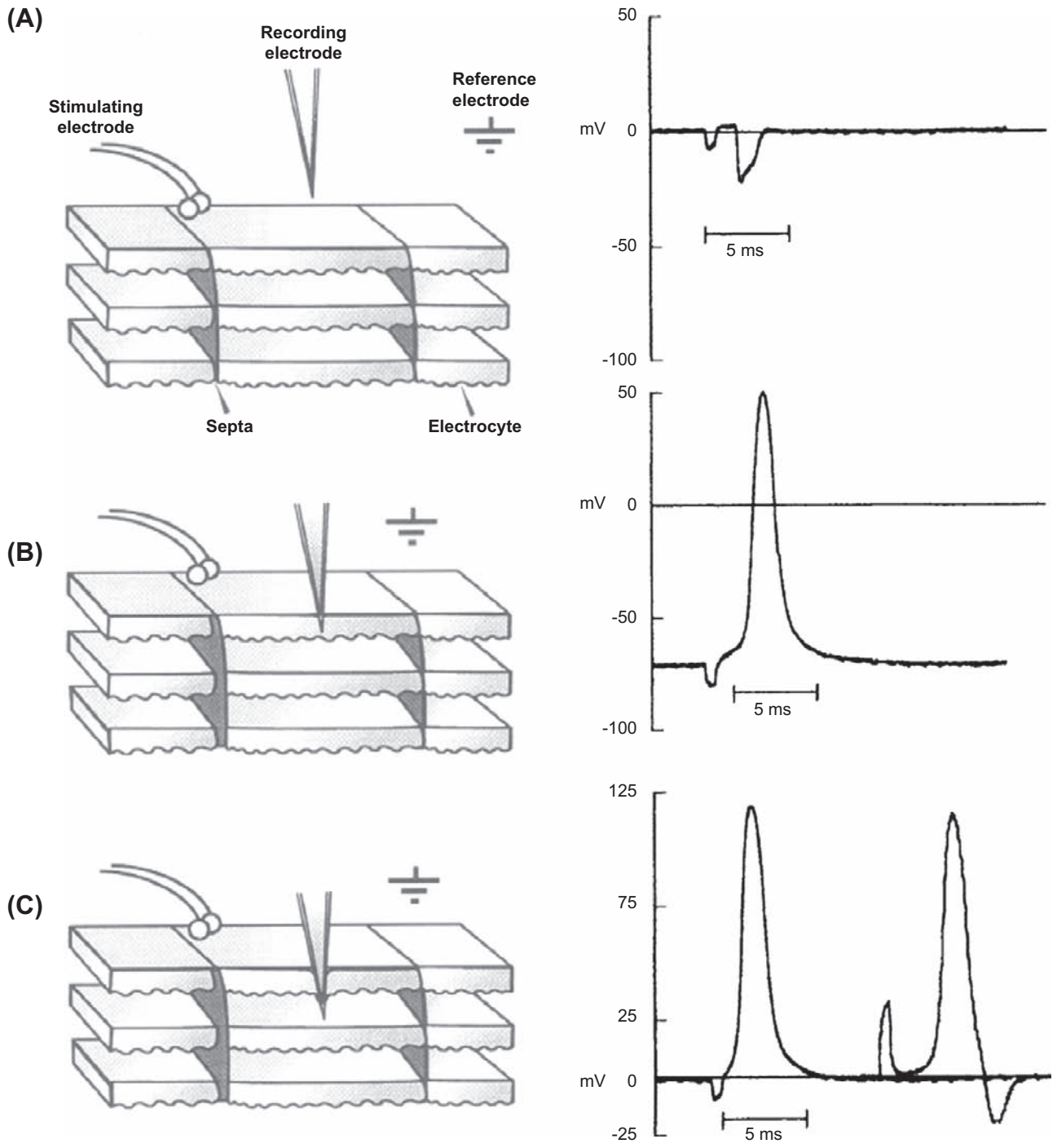

FIGURE 48.3 Extracellular potentials, APs and transcellular potentials of *Electrophorus* electrocytes in an electric tissue slice preparation. Diagrams to the left depict a slice of electric tissue in cross-section where electrocytes are oriented such that the innervated membrane is uppermost. Columns of electrocytes run in the vertical direction and are delineated by insulating connective tissue septa. Potentials recorded by the recording electrode in the indicated positions are shown on the right. (A) The recording electrode near the innervated membrane records a negative deflection in the extracellular potential. (B) The recording electrode penetrating the innervated membrane records an intracellular AP. (C) Transcellular potentials measured after the recording electrode has penetrated the entire electrocyte. The second potential recording on the right shows the negative deflection of the electrocyte beneath the recording electrode when a higher intensity stimulus is applied.

AChR agonist used. Single-channel conductances through individual receptors do not depend on the ligand used. However, these preparations of the eel AChR are different from other excitable cells in that single-channel open times can be fitted to a single exponential compared to the more complex distributions found for other sources of the receptor. This indicates that the eel expresses only one isoform of each of the receptor subunits, yielding a receptor with a single unique conductance.

IVB. Equivalent Circuits

From what is known of electrocyte electrophysiology, equivalent circuits can be derived that explain the production of transcellular potentials that arise during the AP. Because electrocytes are large flat cells comprised of essentially two parallel membranes having a uniform potential across their entire surfaces, whole-cell potentials can be described with two equivalent circuits, pertaining to the innervated and non-innervated membranes, connected by a resistor representing the resistance of the cytoplasm (R_t). At rest, the permeability of both membranes to K^+ and Cl^- is high, so that their equilibrium potentials are expressed more than that of Na^+, resulting in an E_m of about −85 mV (for a detailed description, see Chapter 9). The equivalent circuit for the electrocyte at rest can then be reduced to that seen in Fig. 48.4A (right), where both membranes have composite E_m values that drive an outward flow of positive current. Notice that the equivalent circuits for both membranes are mirror images of one another, both having a symmetrical outward movement of current that cancels to give a transcellular potential of 0 mV. At the peak of the AP, however, the permeability of the innervated membrane to Na^+ increases dramatically, such that the membrane potential is influenced primarily by E_{Na}. The composite E_m of the innervated membrane has now reversed its polarity, so that current across this membrane moves inward (Fig. 48.4B, right). Because the non-innervated membrane has no Na^+ conductance, the polarity of the potential here is the same as at rest and a net outward current continues to flow. Now, the total driving force for both membranes is in the same direction, so that current flows from the innervated membrane to and through the non-innervated membrane. If one considers that R_{cyt} and $R_{m(non)}$ are negligible compared to $R_{m(inn)}$, the equivalent circuit for the electrocyte can be reduced to a resistor and battery in series, where the resistance is equal to $R_{m(inn)}$ and the battery represents the composite potentials of $E_{m(inn)} + E_{m(non)}$. During stimulation, the potential across this unit, then, equals the transcellular potential and has a magnitude equal to that of the amplitude of the innervated membrane's AP, or approximately 150 mV.

In the electric organ of *Electrophorus*, electrocytes are stacked one after another in very long columns. Electrically, this arrangement is represented by many electrocyte resistor-battery units connected in series, as shown in Fig. 48.5A. Each unit contributes an additional 150 mV to the overall electrical discharge. However, Kirchhoff's first law dictates that the current measured at every point along an unbranching leg of a circuit, such as a series of batteries, is constant.[2] In other words, the value of the overall current output of a column of electrocytes does not depend on the number of cells in series, but on the electrocyte that has the greatest resistance to the flow of current. (For a comprehensive description of Ohm's law and Kirchoff's laws applied to biological equivalent circuits, see Sperelakis, 1979.) In order for an electric organ to increase the current of an electrical discharge, it must have additional electrocytes arranged in parallel. This amplification is accomplished in electric fish by having numerous electrocyte columns situated alongside one another. The electric eel, being a long slender animal, has fewer electrocyte columns arranged in parallel relative to some other electric fish. Because of this anatomical arrangement, the eel produces discharges of very high voltage with less current compared to other electric fish, such as *Torpedo*, the electric ray.

The electric ray is a marine elasmobranch with two large electric organs positioned laterally on either side of its flattened head (Fig. 48.6). Hexagonal-shaped columns of electrocytes run in the vertical direction and conduct current up away from the ocean floor, around the edge of the lateral fin and back into the bottom of the electric organ. *Torpedo* has a short but wide electric organ accommodating large numbers of electrocyte columns situated next to one another. As shown in Fig. 48.5B, Kirchoff's law predicts that electrocyte resistor-battery units in parallel will produce electrical discharges of low voltage and high current, proportional to the total number of electrocyte units in parallel. This is indeed the case with the electric ray, in which discharges of up to 16 A and 60 V, totaling up to 1 kW, have been measured (Grundfest, 1960).

V. COMPARATIVE PHYSIOLOGY OF *ELECTROPHORUS* AND *TORPEDO* – MODELS FOR MAMMALIAN EXCITABLE CELLS

VA. *Electrophorus*

VA1. Na^+ Channel

Because electric tissue is specialized for membrane excitability and carries out its function with membrane proteins common to mammalian tissues, electrocytes of electric fish

[2] Specifically, Kirchoff's first law states that the current entering a point along a circuit is equal to the sum of the currents of all the branches leaving that point. Therefore, if the circuit is unbranching, then the current at every point is constant.

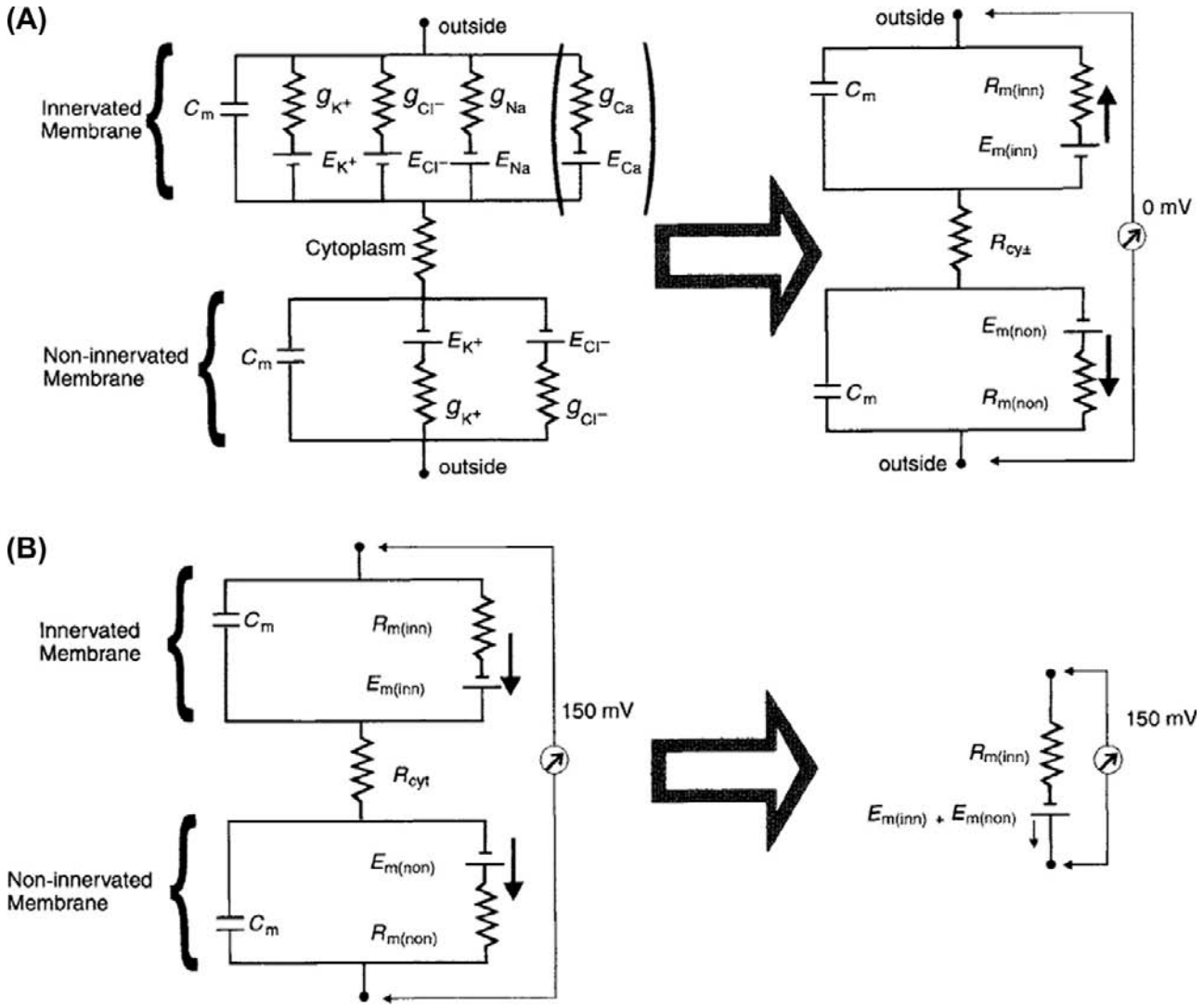

FIGURE 48.4 Electrical equivalent circuit diagrams for both the innervated and non-innervated membranes of an electrocyte. The innervated membrane is uppermost in both A and B. Both membranes are represented by parallel resistance—capacitance circuits and are connected by the cytoplasmic resistance, R_{cyt}. C_m is the membrane's capacitance. The conductances for K^+, Cl^-, Na^+ and Ca^{2+} across the membranes are represented by g_K, g_{Cl}, g_{Na} and g_{Ca}, respectively and are inversely proportional to the resistance of the membrane for these ions. Nernst potentials for each of these ions across the membranes are E_K, E_{Cl}, E_{Na} and E_{Ca}. The Ca^{2+} leg of the circuit is in brackets, since the existence of a selective Ca^{2+} conductance in the electrocyte has not yet been demonstrated. (A) At rest, the innervated membrane reduces to a circuit where $R_{m(inn)}$ represents the total membrane resistance of this face of the cell and is a composite of the resistances of the membrane to each of the ions listed to the left. The $E_{m(inn)}$ and $E_{m(non)}$ are the resting membrane potentials for the innervated membrane and non-innervated membrane, respectively. At rest, E_K and E_{Cl} are expressed the most, since the conductance of the membrane to both these ions is greatest. In this state, the circuit diagrams are mirror images of one another, no net current flows across the cell and the transcellular potential is 0 mV. (B) At the peak of the AP, the conductance of the membrane to Na^+ (and possibly Ca^{2+}) increases dramatically and E_{Na} and E_{Ca} is expressed more than E_K and E_{Cl}. The polarity of the $E_{m(inn)}$ battery is now reversed, such that there is a net flow of positive current in the direction of the non-innervated membrane and a transcellular 150-mV potential results. Given that R_{cyt} and $R_{m(non)}$ are negligible compared to $R_{m(inn)}$, the equivalent circuit can be reduced to the "electrocyte unit" on the right.

provide excellent models for mammalian excitable cell membranes. Compared to electrocytes of *Torpedo* and other electric fish, *Electrophorus* electrocytes express more of the membrane proteins common to mammalian excitable tissues and therefore provide a more general model for excitable membranes. For example, both voltage-gated Na^+ and AChR-mediated currents have been measured from the innervated membranes of these cells. Early preparations took advantage of the large size of these cells by sealing single electrocytes over windows in Lucite chambers (Schoffeniels, 1961). Because the resistance of the non-innervated membrane is negligible relative to the innervated membrane, electrocytes in this configuration are treated as a single membrane without having to thread

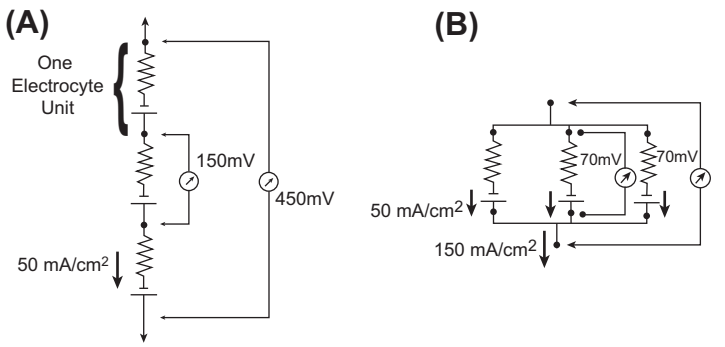

FIGURE 48.5 Electrocyte units in series and in parallel. (A) When connected in series, the potentials of each 150-mV electrocyte unit summate, while the current remains constant. In this case, three electrocyte units are shown to summate their potentials to yield a total of 450 mV. This tends to be the case in the electric organ of *Electrophorus*, where transcellular potentials of 150 mV and currents of 50 mA/cm^2 are measured. (B) The currents of electrocytes in parallel summate while the potential remains constant. Three electrocyte units, each having a current of 50 mA/cm^2, are shown to produce a 150 mA/cm^2 current when arranged in parallel. This is the case in *Torpedo*, where many electrocytes are situated next to one another in parallel. The transcellular potential produced by *Torpedo* electrocytes is 70 mV.

a space-clamping electrode down the middle of the cell. With this method, Nakamura et al. (1965) were able to measure Na^+ currents responsible for the rising phase of eel electrocyte APs and to construct a current–voltage (*I-V*) relation for the *Electrophorus* Na^+ channel. These researchers also described an abundant inward rectifying K^+ current that has an *I-V* relation similar to those seen in myocytes. However, since delayed K^+ currents are not seen in these preparations, the repolarization of the eel electrocyte AP is apparently due to Na^+ channel inactivation. Much of what is known about the electrogenesis of the AP of electrocytes and other excitable cells has come from studies such as this. The innervated membrane of *Electrophorus* electrocytes was also *patch-clamped* to examine macroscopic Na^+ currents in order to determine minute charge movements associated with channel opening, as well as to determine the permeability of the channel to K^+ relative to Na^+. Upon membrane depolarization, the Na^+

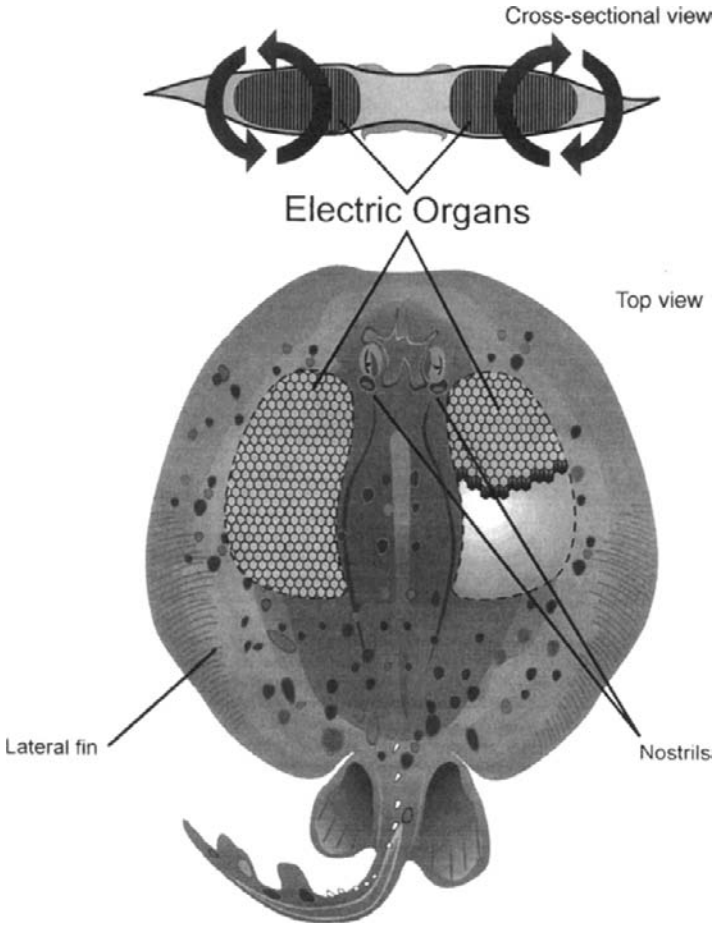

FIGURE 48.6 Drawing of an electric ray (genus *Torpedo*), depicting the location of its two lateral electric organs. The inset shows the direction of the flow of current around the fish while producing an electrical discharge.

channel undergoes a conformational change that is associated with the movement of positively charged amino acids within the protein. This movement of positive charge is thought to be a consequence of the opening of the channel gate and can be measured in a population of Na^+ channels as a small outward current. Opening of the eel Na^+ channel is associated with the movement of approximately 1.5 charges upon channel opening, a value similar to nerve and muscle preparations (Shenkel and Bezanilla, 1991; for a comprehensive description of gating mechanisms, see Hille, 1992). On examining the selective permeability of the eel Na^+ channel for this ion relative to K^+, Shenkel and Sigworth (1991) found P_{Na}/P_K ratios of 8 to 43. This range represents a substantial variation that was even seen in membrane patches taken from the same cell. Given that *Electrophorus* electrocytes are known to express just one isoform of the channel protein, these results suggested that this variability might arise from post-translational modifications such as glycosylation or even *phosphorylation*. This possibility was substantiated by experiments that showed the eel Na^+ channel to be modulated by exogenously applied protein kinase A (Emerick et al., 1993; also see Chapter 23 of this book). These studies contributed to our basic understanding of the electrophysiological function of the Na^+ channel protein.

The first Na^+ channel ever purified, and later sequenced, came from electric tissue of *Electrophorus*. The purified 260-kDa protein is heavily glycosylated and consists of a single functional α subunit (Agnew et al., 1978; Miller et al., 1983). Na^+ channels from mammalian brain and muscle express additional β subunits. Since it has been suggested that these auxiliary subunits may regulate channel gating, preparations of the eel Na^+ channel are advantageous in that they eliminate the possibly complicating influence of β subunits. An *Electrophorus* electric tissue cDNA library was used to clone and sequence the channel for the first time (Noda et al., 1984). Its structure includes four homologous repeats that each contain six membrane-spanning helices. The fourth transmembrane segment contains a cluster of positively charged amino acids thought to be involved in gating of the channel. Movement of these positive amino acids during opening of the channel is thought to be responsible for the minute currents measured in patch-clamp experiments such as those discussed earlier. Compared to sequences of Na^+ channels of mammalian muscle and brain, the eel Na^+ channel shows the greatest homology with the muscle protein, as expected since electrocytes develop ontogenetically from myocytes. Both of these channels, however, lack a 202-amino-acid segment located between the first and second homologous repeat domains of the brain Na^+ channel (for complete discussions of Na^+ channel purification, structure and diversity, see Chapter 21 in this book and Hille, 1992).

VA2. Acetylcholine Receptor

As mentioned in a previous section, the large size of eel electrocytes has facilitated their dissection in order to measure single-channel AChR conductances. Other excitable cells express numerous isoforms of the subunits that make up the receptor and produce single-channel recordings that show complex mean open-time distributions and variable conductance values. The eel AChR yields more homogeneous values owing to its simplified subunit composition (Pasquale et al., 1986). The simple mean open-time distributions for the eel AChR were found for both the main electric organ as well as for Sach's organ, suggesting that AChR diversity evolved in order to meet varying physiological needs of myocytes and neurons. The eel receptor also desensitizes to a lesser extent in the presence of sustained concentrations of agonists (Pallotta and Webb, 1980). Simple subunit composition and lack of agonist-induced desensitization make the eel AchR advantageous for electrophysiological and biochemical studies.

Recognizing the cholinergic nature and the specialization of *Electrophorus* electrocytes, biochemists utilized electric tissue as a source for some of the first purifications of AChRs. Using various separation techniques, including differential centrifugation to separate membrane fractions and affinity chromatography to purify selectively the AChR from other membrane proteins, a 260-kDa macromolecule was isolated (Olsen et al., 1972; Biesecker, 1973). Not knowing a priori that the receptor is a pentameric protein made up of α, β, γ and δ subunits (in a respective ratio of 2:1:1:1), the initial isolation and identification of the peptides that make up the whole receptor were arduous. After some debate, the 44-kDa α subunit was established as the ligand-binding portion of the protein. The 50- to 65-kDa β, γ and δ subunits, along with the α subunit, are arranged symmetrically around a central axis to make up the ion channel pore of the protein (Karlin and Cowburn, 1973; Chang, 1974).

VA3. Na^+, K^+-ATPase

As we have seen, electrocytes express massive quantities of membrane receptors and ion channels in order to carry out their specialized function. To maintain resting potentials in the face of currents associated with EPPs and APs that dissipate Na^+ and K^+ gradients, electrocytes need to express large amounts of *Na^+, K^+-ATPase*. For this reason, *Electrophorus* electric tissue has been used as a source for the purification of this enzyme for structure–function studies. The eel protein, like that from other tissues, consists of a 94-kDa α subunit and a glycosylated 47-kDa β subunit. During purification, the ATPase is solubilized from electrocyte membranes with various detergents. To analyze its functional characteristics, the protein was

reconstituted into liposomes where its ATP-driven translocation of radiolabeled Na^+ and K^+ has been found to be similar to preparations of native electrocyte membranes containing the ATPase (Yoda et al., 1984). These preparations of the eel protein have been invaluable in determining the reaction mechanisms of the ATPase involved in its function. Drugs that target and inhibit different partial reactions of the protein's translocation mechanism have also been investigated and used to examine the pump's function in cell physiology. Drugs, such as the cardiac glycoside digoxin, have also been used clinically specifically to inhibit Na^+, K^+-ATPase function in the heart. This treatment dissipates the membrane Na^+ gradient, which indirectly augments intracellular Ca^{2+} within cardiac myocytes. This results in an increase in the heart's force of contraction, which can alleviate some forms of heart disease (for literature review, see Lingrel and Kuntzweiler, 1994.)

VA4. Calmodulin

Electrophorus electric tissue also expresses large quantities of the calcium-binding protein *calmodulin*. (For a detailed discussion of Ca^{2+}-binding protein function, see Chapter 7.) In fact, calmodulin makes up roughly 2%, by weight, of electrocyte protein (Munjaal et al., 1986). Once again, electric tissue was used as a source for the purification of this 17-kDa soluble protein (Childers and Siegel, 1975). Unlike the membrane proteins discussed earlier, the function of calmodulin within electrocytes remains elusive, even though some of the functions of this Ca^{2+}-mediator protein in intracellular signaling mechanisms is well documented in other electrically excitable cells. Figure 48.7 shows the intracellular location of calmodulin within electrocytes. Calmodulin is present throughout the cytoplasm of electrocytes, but is particularly concentrated near both the innervated and non-innervated membranes. In light of this membrane localization, along with the fact that calmodulin is so abundant in this tissue specialized for membrane excitability, a role for this protein in membrane function is likely. Determining the role of calmodulin in electrocyte function will undoubtedly lend insight into the role of this protein in membrane function of other excitable cells.

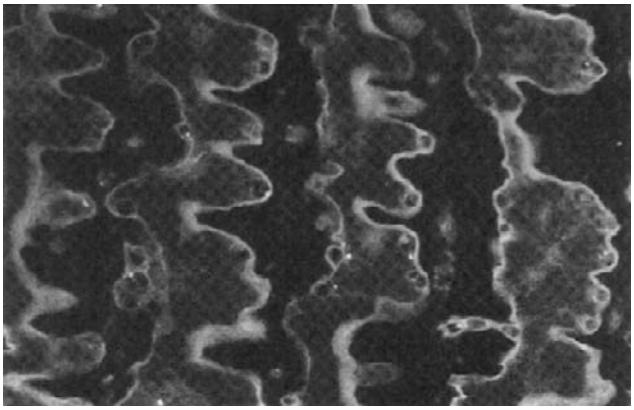

FIGURE 48.7 Immunofluorescent localization of calmodulin within main organ electrocytes. Paraffin-embedded 4-μm sections were probed with anti-calmodulin sheep antibodies. The location of primary antibodies was visualized with fluorescein-labeled rabbit anti-sheep secondary antibodies and photographed using epifluorescence microscopy.

VB. *Torpedo*

VB1. Comparative Electrophysiology

The marine electric ray (genus *Torpedo* and various species: *marmorata*, *californica*, *nobilianae*, *occidentalis*) can produce high-amperage electrical discharges by virtue of numerous electrocyte columns arranged in parallel, as discussed briefly earlier. In this way, it differs from *Electrophorus* which produces high-voltage discharges owing to numerous electrocytes arranged in series. The basic arrangement of *Torpedo* electrocytes within electric organ columns is remarkably similar to that of *Electrophorus*, considering that these two fish belong to different orders and the existence of electric tissue in both orders of fish represents convergent evolution. Although *Torpedo* electrocytes are smaller and pancake shaped (10−30 μm × 5 mm in diameter) relative to wafer-shaped *Electrophorus* electrocytes, they are still stacked one after another in columns delineated by electrically insulating connective tissue septa. *Torpedo* electrocytes also display membrane polarity similar to that depicted in the diagrams of Fig. 48.2.

Some basic differences in the membrane biochemistry and electrophysiology exist between electrocytes of these two fishes, however. Like the eel, *Torpedo* electrocytes can be stimulated to produce EPPs in response to nervous stimulation. That is, these electrocytes are chemically excitable. *Torpedo* electrocytes, however, do not fire APs in response to EPPs or artificially applied electrical stimuli and are therefore electrically non-excitable. This is due to a lack of voltage-dependent Na^+ channels on the innervated membrane that would generate and propagate APs. Instead, these cells are richly innervated by ACh-releasing electromotor neurons and have an abundance of postsynaptic AChRs. These ligand-gated channels conduct EPPs of 5-ms duration that peak just below 0 mV, halfway between E_{Na} and E_K. Like *Electrophorus* electrocytes, the non-innervated membrane of these cells has a large resting current, partially carried by Cl^-. Transcellular potentials measured across *Torpedo* electrocytes then, have an amplitude equal to that of the EPP, or 70 to 85 mV. The equivalent circuits diagrammed in Figs. 48.4A and B also apply to these electrocytes, except that the potential produced by each electrocyte unit equals 70 to 85 mV, instead of 150 mV for *Electrophorus* electrocytes.

VB2. Acetylcholine Receptor

Without voltage-gated Na^+ channels to propagate an AP, EPPs decay exponentially with the distance traveled from the *electromotor end-plate*. However, very little EPP decay is actually measured on the innervated membrane of *Torpedo* electrocytes, because the density of end-plates is so great. In fact, one might describe the innervated membrane of these cells as one large electromotor end-plate. These cells, therefore, provide a very specialized model for the motor end-plate. Like *Electrophorus* electric tissue, *Torpedo* electric tissue has been used for the purification of the AChR, which has supplied a wealth of knowledge about the biochemical properties of the receptor, as described in the previous section. The first sequences ever to be determined for each of the subunits of the receptor were obtained by screening *Torpedo* electric tissue cDNA libraries (Noda et al., 1982, 1983a,b; Claudio et al., 1983). The mRNAs encoding each of the receptor subunits were together injected into *Xenopus* oocytes in order for the functional protein to be expressed on the membrane of these cells. Interestingly, an increase in the ACh-induced conductance could be measured after microinjection (Mishina et al., 1984). By knowing the sequence of the receptor's subunits, a three-dimensional model of the receptor has been constructed and continually amended in light of ongoing biochemical research. (A model of the AChR appears in Chapter 32.) These studies established the basic protein structure of the nicotinic AChR, the findings of which have only been slightly modified to apply to the receptor of mammalian muscle and nerve.

VB3. Acetylcholinesterase

AChE is an important enzyme found in the postsynaptic membrane of cholinergic synapses of neurons, motor end-plates of myocytes and the electromotor end-plates of electrocytes. It catalyzes the hydrolysis of ACh to choline and acetate, thereby terminating ligand-gated activation of the AChR. Some pesticides and chemical warfare agents contain *anti-AChE agents* that cause acute and chronic alterations in central nervous system and neuromuscular function. Anti-AChE drugs have also been developed to alleviate symptoms of glaucoma, Alzheimer's dementia and myesthenia gravis – diseases marked by attenuated postsynaptic AChR density or compromised ACh release (for review, see Millard and Broomfield, 1995). Obviously, great care is needed when administering these drugs because overmedication can cause side effects similar to exposure to harmful anti-AChE agents.

Since the *Torpedo* electrocyte represents an exaggerated cholinergic system, it was used as a source for the purification and subsequent structural analysis of AChE. AChE is an 80-kDa protein that self-associates into tetramers, octamers and dodecamers and is anchored in the postsynaptic membrane through a phospholipid linkage (Parker et al., 1978; Ratman et al., 1986). *Torpedo* electric tissue provided massive enough quantities of AChE for the protein to be crystallized for subsequent x-ray diffraction studies. The resulting diffraction pattern obtained from x-rays shot through these crystals was analyzed to construct a three-dimensional structure of the protein, localizing atoms within the enzyme to within 2.8 Å (Sussman et al., 1991). These experiments with the *Torpedo* enzyme will continue to be invaluable to the development of new drugs aimed at the treatment of cholinergic diseases and for therapies for individuals exposed to toxic anti-AChE agents.

VB4. Cl^- Channel

Perhaps the most dramatic contribution that electric tissue has made to recent membrane biochemistry and physiology has been toward elucidating the structure and function of Cl^- channels. Recall that, in order for electrocytes to produce large transcellular potentials, the non-innervated membrane must have a tremendous resting current. This current clamps the non-innervated membrane potential at highly negative resting potentials even while the innervated membrane depolarizes dramatically. In *Torpedo* electrocytes, the resting current is carried at least partially by Cl^-. Electric tissue of the electric ray, therefore, has been used to isolate the channel protein for physiological studies and as a source for mRNA used in cloning and sequencing of the channel.

In the course of developing the planar lipid bilayer method for measuring ion channel conductances, Miller and White (1980) found that vesicles derived from the non-innervated membrane of *Torpedo* electrocytes contained Cl^- channels having novel "*double-barreled*" *gating kinetics*. With depolarization, individual Cl^- channel complexes acted as two channels with two separate but equal conductances. When one channel of the complex was open, the other was more likely to be subsequently activated as well. Single-channel recordings showed periods of inactivity until one channel of the complex was opened, after which a second equal conductance would superimpose on the first. Purification of the *Torpedo* Cl^- channel confirmed that the protein was a homodimer consisting of two 90-kDa polypeptides. When the purified protein was incorporated into planar lipid bilayers for single-channel recording, the same double-barreled gating kinetics were observed (Middleton et al., 1994).

The first Cl^- channel ever to be sequenced came from *Torpedo* electric tissue and has greatly expanded the field of Cl^- channel molecular biology. Using the expression cloning technique, the mRNA responsible for the *Torpedo* Cl^- conductance was identified and its corresponding cDNA sequenced. The encoded protein was predicted to

consist of 805 amino acids and to have a molecular weight similar to that of the purified protein (Jentsch et al., 1990). When mRNA for this channel, termed ClC-0, was injected into *Xenopus* oocytes, Cl^- conductances having double-barreled gating kinetics were expressed (Bauer et al., 1991). Recognizing that electric tissue is a model for skeletal muscle membranes, Steinmeyer et al. (1991b) screened a rat muscle cDNA library with oligonucleotide sequences derived from the *Torpedo* Cl^- channel. In this way, the sequence for the major Cl^- channel of mammalian skeletal muscle (called ClC-1) was obtained. It was later found that genetic aberrations in the mammalian ClC-1 gene result in symptoms of skeletal muscle myotonia (Steinmeyer et al., 1991a). These findings confirmed the results of Bryant and Morales-Aguilera (1971) that showed this disease to be associated with compromised Cl^- conductance. Once the sequences were known for both ClC-0 and ClC-1, investigators began screening libraries derived from virtually every mammalian tissue. Numerous Cl^- channel sequences have now been determined and have been implicated in various physiological functions from neuronal membrane excitability to epithelial solute transport (for a review, see Fong and Jentsch, 1995). More Cl^- channels having even greater diversity and function will undoubtedly be uncovered in the future.

BIBLIOGRAPHY

Agnew, W. S., Levinson, S. R., Brabson, J. S., & Raftery, M. A. (1978). Purification of the tetrodotoxin-binding component associated with the voltage-sensitive sodium channel from Electrophorus electricus electroplax membranes. *Proc Natl Acad Sci USA, 75*, 2606–2610.

Bauer, C. K., Steinmeyer, K., Schwartz, J. R., & Jentsch, T. J. (1991). Completely functional double-barreled chloride channel expressed from a single Torpedo cDNA. *Proc Natl Acad Sci USA, 88*, 11052–11056.

Bennett, M. V. L. (1971). Electric organs. In W. S. Hoar, & D. J. Randall (Eds.), *Fish Physiology* (pp. 347–491). New York: Academic Press.

Bennett, M. V. L., & Sandri, C. (1989). The electromotor system of the electric eel investigated with horseradish peroxidase as a retrograde tracer. *Brain Res, 488*, 22–30.

Biesecker, G. (1973). Molecular properties of the cholinergic receptor purified from *Electrophorus electricus. Biochemistry, 12*, 4403–4409.

Bryant, S. H., & Morales-Aguilera, A. (1971). Chloride conductance of normal and myotonic goat fibres and the action of monocarboxylic aromatic acids. *J Physiol (London), 219*, 367–382.

Chang, H. W. (1974). Purification and characterization of acetylcho-line receptor-I from *Electrophorus electricus*. *Proc Natl Acad Sci USA, 71*, 2113–2117.

Childers, S. R., & Siegel, F. L. (1975). Isolation and purification of a calcium-binding protein from electroplax of *Electrophorus electricus*. *Biochim Biophys Acta, 455*, 99–108.

Claudio, T., Ballivet, M., Patrick, J., & Heinemann, S. (1983). Nucleotide and deduced amino acid sequences of *Torpedo californica* acetylcholine receptor γ subunit. *Proc Natl Acad Sci USA, 80*, 1111–1115.

Emerick, M. C., Shenkel, S., & Agnew, W. S. (1993). Regulation of the eel electroplax Na channel and phosphorylation of residues on amino- and carboxyl-terminal domains by cAMP-dependent protein kinase. *Biochemistry, 32*, 9435–9444.

Fong, P., & Jentsch, T. J. (1995). Molecular basis of epithelial Cl channels. *J Memb Biol, 144*, 189–197.

Grundfest, H. (1957). The mechanisms of discharge of the electric organs in relation to general and comparative electrophysiology. *Prog Biophys, 7*, 3–74.

Grundfest, H. (1960). Electric organ. *McGraw-Hill Encycl Sci Technol, 8*, 427–433.

Hille, B. (Ed.). (1992). *Ionic Channels of Excitable Membranes*. Sunderland: Sinauer Associates.

Jentsch, T. J., Steinmeyer, K., & Schwarz, G. (1990). Primary structure of *Torpedo marmorata* chloride channel isolated by expression cloning in *Xenopus* oocytes. *Nature, 348*, 510–514.

Karlin, A., & Cowburn, D. (1973). The affinity-labeling of partially purified acetylcholine receptor from electric tissue of *Electrophorus*. *Proc Natl Acad Sci USA, 70*, 3636–3640.

Keynes, R. D. (1961). The development of the electric organ in Electrophorus electricus. In C. Chagas, & A. Paes De Carvalho (Eds.), *Bioelectrogenesis* (pp. 14–19). New York: Elsevier.

Lester, H. (1978). Analysis of sodium and potassium redistribution during sustained permeability increases at the innervated face of *Electrophorus* electroplaques. *J Gen Physiol, 72*, 847–862.

Lingrel, J. B., & Kuntzweiler, T. (1994). Na^+, K^+-ATPase. *J Biol Chem, 269*, 19659–19662.

Middleton, R. E., Pheasant, D. J., & Miller, C. (1994). Purification, reconstitution, and subunit composition of a voltage-gated chloride channel from *Torpedo* electroplax. *Biochemistry, 33*, 13189–13198.

Millard, C. B., & Broomfield, C. A. (1995). Anticholinesterases: medical applications of neurochemical principles. *J Neurochem, 64*, 1909–1918.

Miller, C., & White, M. M. (1980). A voltage-dependent chloride conductance channel from *Torpedo* electroplax membrane. *Ann NY Acad Sci, 80*, 534–551.

Miller, J. A., Agnew, W. S., & Levinson, S. R. (1983). Principal glycopeptide of the tetrodotoxin/saxitoxin binding protein from *Electrophorus electricus*: isolation and partial chemical and physical characterization. *Biochemistry, 22*, 462–470.

Mishina, M., Kurosaki, T., Tobimatsu, T., et al. (1984). Expression of functional acetylcholine receptor from cloned cDNAs. *Nature, 307*, 604–608.

Munjaal, R. P., Conner, C. G., Turner, R., & Dedman, J. R. (1986). Eel electric organ: hyperexpressing calmodulin system. *Molec Cell Biol, 6*, 950–954.

Nakamura, Y., Nakajima, S., & Grundfest, H. (1965). Analysis of spike electrogenesis and depolarizing K inactivation in electroplaques of *Electrophorus electricus*. *L. J Gen Physiol, 49*, 321–349.

Noda, M., Shimizu, S., Tanabe, T., et al. (1984). Primary structure of *Electrophorus electricus* sodium channel deduced from cDNA sequence. *Nature, 312*, 121–127.

Noda, M., Takahashi, H., Tanabe, T., et al. (1982). Primary structure of α-subunit precursor of *Torpedo californica* acetylcholine receptor deduced from cDNA sequence. *Nature, 299*, 793–797.

Noda, M., Takahashi, H., Tanabe, T., et al. (1983a). Structural homology of *Torpedo californica* acetylcholine receptor subunits. *Nature, 302*, 528–532.

Noda, M., Takahashi, H., Tanabe, T., et al. (1983b). Primary structures of β- and δ-subunit precursors of *Torpedo californica* acetylcholine receptor deduced from cDNA sequences. *Nature, 301*, 251−255.

Olsen, R. W., Meunier, J.-C., & Changeux, J.-P. (1972). Progress in the purification of the cholinergic receptor protein from *Electrophorus electricus* by affinity chromatography. *FEBS Lett, 28*, 96−100.

Pallotta, B. S., & Webb, G. D. (1980). The effects of external Ca^{++} and Mg^{++} on the voltage sensitivity of desensitization in *Electrophorus* electroplaques. *J Gen Physiol, 75*, 693−708.

Parker, K. K., Chan, S. L., & Trevor, A. J. (1978). Purification of native forms of eel acetylcholinesterase: active site determination. *Arch Biochem Biophys, 187*, 322−327.

Pasquale, E. B., Udgaonkar, J. B., & Hess, G. P. (1986). Single-channel current recording of acetylcholine receptors in electroplax isolated from the *Electrophorus electricus* main and Sachs' electric organs. *J Memb Biol, 93*, 195−204.

Ratman, M., Sargent, P. B., Sarin, V., et al. (1986). Location of antigenic determinants on primary sequences of subunits of nicotinic acetylcholine receptor by peptide mapping. *Biochemistry, 25*, 2621−2632.

Schoffeniels, E. (1961). The flux of cations in the single isolated electroplax of Electrophorus electricus (L.). In C. Chagas, & A. Paes De Carvalho (Eds.), *Bioelectrogenesis* (pp. 147−165). New York: Elsevier.

Shenkel, S., & Bezanilla, F. (1991). Patch recordings from the electrocytes of *Electrophorus*. Na channel gating currents. *J Gen Physiol, 98*, 465−478.

Shenkel, S., & Sigworth, F. J. (1991). Patch recordings from the electrocytes of *Electrophorus electricus*. Na currents and P_{Na}/P_K variability. *J Gen Physiol, 97*, 1013−1041.

Sheridan, R. E., & Lester, H. A. (1977). Rates and equilibria at the acetylcholine receptor of *Electrophorus* electroplaques. A study of neurally evoked postsynaptic currents and of voltage-jump relaxations. *J Gen Physiol, 70*, 187−219.

Sperelakis, N. (1979). Origin of the cardiac resting potential. In R. M. Berne, & N. Sperelakis (Eds.), *Handbook of Physiology, Vol. 1, The Cardiovascular System* (pp. 187−267). Bethesda: American Physiological Society.

Steinmeyer, K., Klocke, R., Ortland, C., et al. (1991a). Inactivation of muscle chloride channel by transposon insertion in myotonic mice. *Nature, 454*, 304−308.

Steinmeyer, K., Ortland, C., & Jentsch, T. J. (1991b). Primary structure and functional expression of a developmentally regulated skeletal muscle chloride channel. *Nature, 354*, 301−304.

Sussman., J. L., Harel, M., Frolow, F., et al. (1991). Atomic structure of acetylcholinesteras, from *Torpedo californica*: a prototypic acetylcholine-binding protein. *Science, 253*, 872−879.

Szabo, T. H. (1961). Anatomo-physiologie des centres nerveux specifiques de quelques organes electriques. In C. Chagas, & A. Paes De Carvalho (Eds.), *Bioelectrogenesis* (pp. 185−201). New York: Elsevier.

Walsh, J. (1775). Experiments and observations on the *Gymnotus electricus*, or electric eel. *Philos Trans, 65*, 94−101.

Yoda., A., Clark, A. W., & Yoda, S. (1984). Reconstitution of (Na^+ + K^+)-ATPase proteoliposomes having the same turnover rate as the membraneous enzyme. *Biochim Biophys Acta, 778*, 332−340.

This page intentionally left blank

Section VII

Protozoa and Bacteria

This page intentionally left blank

Chapter 49

Physiological Adaptations of Protists

Michael Levandowsky

Chapter Outline

I. INTRODUCTION: TERMINOLOGY AND PHYLOGENY

This chapter introduces the reader to the great diversity to be found in the physiology of the protists. These include many eukaryotic groups, some *autotrophic* or plant-like, some *phagotrophic* or *osmotrophic* and thus animal-like and many with a combination of these traits.

First, a word about terminology and classification. Traditionally, these organisms comprised the *algae* (plant-like) and the *protozoa* (animal-like). Early classifications of protozoa divided them into three groups based mainly on locomotion (*ciliates*, *flagellates*, *amoebae*) and a fourth, parasitic group (*sporozoa*). The algae were classified largely on the basis of pigments (*red algae*, *brown algae*, *golden-brown algae*, *green algae*) and certain distinctive structural features (*cryptophytes*, *dinoflagellates*). Many of the flagellated groups appeared in both classifications and were studied by both botanists and zoologists. All these characteristics are clearly important and the early classifications and terminology tend to persist in informal usage. However, subsequent work with the electron microscope, biochemical advances and, especially, molecular approaches, have

Cell Physiology Sourcebook. DOI: 10.1016/B978-0-12-387738-3.00049-4

changed many of our views on phylogenetic relationships. In this chapter, the term *Protista*, or simply *protists*, will be used to describe all of these groups. Essentially, the protists include all eukaryotic organisms except higher plants, fungi and animals. Most protists are single celled and microscopic, but some, like many of the red algae and the brown algae, are multicellular and macroscopic.

Since the last edition of this Sourcebook, our ideas about classification and phylogeny of the major groups of protists have undergone fundamental changes with the appearance of new molecular data. A decade and a half ago there was a strong general consensus that the earliest eukaryotic cells lacked mitochondria and that this early stage was still represented by certain anaerobic or microaerophilic "amitochondriate" protists, such as the parasites *Entamoeba*, *Trichomonas* and *Giardia*. Since then, however, it has been found that the "amitochondriate" groups retain some mitochondrial genes and the consensus now is that the earliest eukaryotes had mitochondria, derived from a bacterial endosymbiont, and that, in a number of anaerobic or microaerophilic lineages, the mitochondria have evolved to become hydrogenosomes or mitosomes, organelles with very different roles from the typical mirochondrion.

At present, a number of major groups or divisions of protists have been defined by various authors and, in 2005, an attempt at synthesis was made, bringing together a group of 28 experts to define the major groups of protists and other eukaryotes. The result of this was the definition of six major groups of eukaryotes, as follows (Adl et al., 2005):

1. *Amoebozoa.* Amoeboid cells. Includes many free-living and parasitic amoebas, as well as slime molds. Examples: *Acanthamoeba*, *Entamoeba*, *Dictyostelium*.
2. *Opisthokonta.* A large group that includes the fungi, the choanoflagellates and the metazoa.
3. *Rhizaria.* Most of these organisms are also amoeboid. Includes many ecologically important groups, such as the foraminifera and the radiolaria.
4. *Archaeoplastida.* These are photosynthetic, plastid-containing eukaryotes and include the red algae, the green algae and higher plants.
5. *Chromalveolata.* This is a composite group, certainly not monophyletic, and some experts would separate it into four distinct groups. The first of these would be the *alveolates*, which contains ciliates, such as *Paramecium* and *Tetrahymena*, the apicomplexa, such as the malaria parasite *Plasmodium* and the dinoflagellates, prominent in aquatic food chains and responsible for toxic "red tides" in the ocean. The second group would be the *stramenopiles*, which includes a wide variety of subgroups, many of them photosynthetic, such as the diatoms and the brown algae. The third and fourth groups would be the *haptophytes* and the *cryptophytes*, which also contain many photosynthetic species.
6. *Excavata.* This group is also composite, not monophyletic. It includes important parasites, such as the trypanosomes that cause African sleeping sickness, and also many free-living organisms, such as *Euglena*.

It is proposed that these groupings can be considered kingdoms. To explore this higher level classification in more detail on line, an interactive and dynamic Java applet is available (Wolf et al., 2006).

The six major categories give some idea of the great diversity of protists. They should be viewed as provisional, however, reflecting current data and analysis (Cavalier-Smith, 2004, 2009; Simpson and Patterson, 2006; Patterson et al., 2007; Keeling, 2009; Pawlowski and Burki, 2009). There are many protist species classified as *incertae sedis*, meaning that their phylogenetic affinities are unclear. Current studies of DNA extracts from field samples are finding evidence of many uncultured species and, in most cases, we have little or no idea about their morphology, physiology or ecology. Several groups comparable to the six above were proposed on the basis of environmental DNA samples alone (Dawson and Pace, 2003; Stoeck and Epstein, 2003), but these proposals were strongly criticized on technical grounds (Cavalier-Smith, 2004). More recently, an entire new group of uncultured plastid DNA-bearing protists, named the *Rappedomonads* and possibly comparable to the six groups above, has recently been identified solely on the basis of DNA extracts from field samples (*metagenomic data*) (Kim et al., 2011). We don't know what they look like but, since they have plastid DNA, they may be photosynthetic. A useful collection of articles on genomic approaches to the study of protistan evolution is found in a recent volume (Katz and Bhattacharya, 2006).

The phylogenetic diversity of the protists is mirrored by their ecological diversity. While, in general, they are typical eukaryotic cells and follow the principles described elsewhere in this book, a number of evolutionary solutions have appeared in protists that are not present in the cells of multicellular organisms. An example is the *light antenna* or "eyespot" (described below), present in many photoautotrophic flagellates. This structure, which has evolved independently in several protist groups, is not found in the multicellular animals and plants.

A feature of protists just starting to be appreciated is the apparent ease with which many cells "capture" and use physiological units of other cells. A prime example is the sequestration and use of *prey organelles*, such as *chloroplasts*, by phagotrophic protists. Indeed, the incorporation of symbionts is a pervasive feature of protistan physiology, occurring in most if not all groups. There are a variety of endosymbiotic phenomena, ranging from the temporary uptake, endocytosis and use of foreign cells or organelles, to established symbioses in which the endosymbiont has become a permanent, required part of the host cell.

A dramatic example of this was the appearance of an intracellular bacterial infection in a laboratory culture of *Amoeba*. The infecting bacterium, initially deleterious to the host cell, was transformed from an *endoparasite* to an obligate *endosymbiont* over the course of a few years' culture in the laboratory and the host and its endosymbiont are now mutually dependent (Jeon, 1987, 1995). This nearly universal tendency of protists to form temporary or permanent endosymbiotic complexes is a feature that physiologists have come to expect and a major theme of this chapter. Indeed, if one considers plastids and other organelles, it is clear that many of the groups listed above as separate are also linked by past endosymbiotic events. Thus, some (but not all) of the dinoflagellates are photosynthetic and it has become clear that their chloroplasts were obtained endosymbiotically from several other protistan sources. Euglenids, on the other hand, though distantly related to the dinoflagellates, apparently got their chloroplasts endosymbiotically from a different, green algal source. These and other complexities of protistan evolutionary relationships do not appear in simple branching "family tree" diagrams.

Also included in this chapter are descriptions of some striking protistan structures whose functions are not clear, such as the several types of *extrusomes*, microprojectiles that are found in many protistan groups. The functions of these are, in most cases, still a matter of speculation.

A comprehensive review of protistan physiology is not presented, because that would duplicate much of the treatment of basic cell physiology in other chapters. Rather, the focus is on unique or unusual features that have evolved in this group and are not found in the cells of multicellular organisms. These features are adaptations to the various free-living and parasitic niches filled by this very diverse group of organisms. In particular, emphasis is given here to understudied phenomena.

II. BIOPHYSICAL CONSTRAINTS OF SCALE: THE EXAMPLE OF FILTER-FEEDING

The dimensions of most protists and their appendages, the values of relative velocity in water and the viscosity of water all combine to yield *Reynolds numbers*[1] much smaller than one. Thus, inertial forces are generally completely excluded as a factor in protistan biophysics. As an illustration of the practical implications of this, *filter-feeding* in flagellates and ciliates is examined. This has been worked out theoretically and experimentally by Fenchel (1986a,b) for a number of species and his discussion is followed here. Filter-feeding at low Reynolds number has also been studied extensively experimentally and theoretically by Koehl and her colleagues, but mainly in the context of small metazoa, such as copepods (e.g. Cheer and Koehl, 1987; Childress et al., 1987).

Filter-feeding is widespread among protists that consume bacteria, other protists or other particles. Suspended food particles may be "captured" passively by diffusion, where the particle reaches the protist by chance, through Brownian motion or swimming, and sticks to an adhesive surface. This happens with many protistan cells with amoeboid tentacles (e.g. heliozoa). Particles may be caught raptorially by direct interception and ingestion during active swimming (many dinoflagellates, euglenids, ciliates). Finally, they may be obtained by filtering a current of water, which is often produced by the protist. This latter method is examined here.

Following Fenchel, let $U(x)$ be an *uptake function*, where x is the particle concentration. *Clearance*, F, is defined as the volume of water cleared per unit time. The relation between these two quantities is given by $F = U(x)/x$, where U is assumed to be nearly proportional to x at low particle concentrations, but becomes saturated at high concentrations. It is assumed that the rate of retention of particles by the filter is proportional to concentration and that ingestion of retained particles takes a finite time, t, during which no other particles are ingested. These assumptions lead to a hyperbolic equation:

$$U(x) = F_m x(1 - Ut) \tag{49.1}$$

Substituting variables and rearranging yields the equation:

$$U(x) = U_m x/(U_m/F_m + x) \tag{49.2}$$

where $U_m = 1/t$ (the maximum rate of ingestion as $x \rightarrow \infty$), F_m is the maximum clearance realized as $x \rightarrow 0$ and U_m/F_m is a constant (dimension L^{-3}). From Equation 49.2, we can see that the kinetics of filter-feeding is formally identical to the familiar Michaelis–Menten kinetics of enzymology, with the constant U_m/F_m corresponding to the half-saturation constant.

Equation 49.2 has been verified experimentally for protistan uptake of latex particles and of bacterial food and F_m varies greatly with the particle size (Fig. 49.1). When the size for which F_m is maximal is determined experimentally, that size is assumed to be retained with an efficiency approaching 100%; thus, that value of F_m can be taken as a direct measure of the rate of flow of water through the filter. This can then be compared for different flow fields of water and for different species' filter designs.

To understand the biological significance of clearance, it is useful to express it as volume-specific clearance, i.e.:

$$F_m/(\text{cellvolume})$$

[1] Reynolds number is defined as $R = dv/n$, where d is a spatial dimension, v is velocity, and n is the kinematic viscosity. Essentially, it can be thought of as the ratio of inertial to viscous forces acting on a body moving through a fluid. Thus, for a large, fast-moving organism in water, such as a fish, the ratio is much greater than one and inertial forces dominate. For microbes, on the other hand, the ratio is usually much less than one and they live in a world dominated by viscous forces.

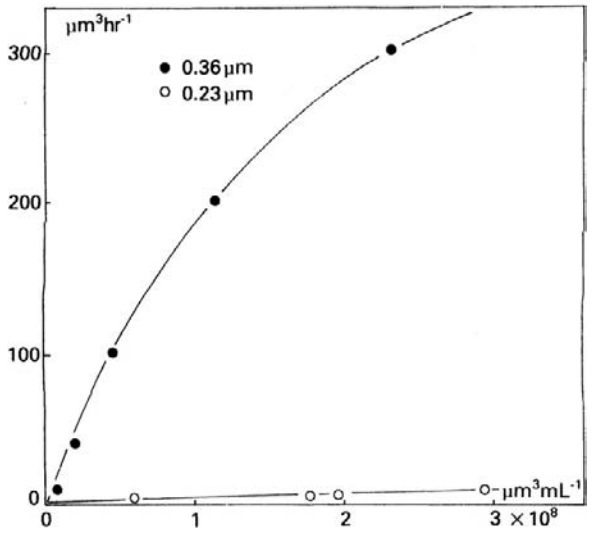

FIGURE 49.1 Volume uptake of two sizes of latex beads as functions of environmental concentration by *Cyclidium* and with the data fitted to Equation 49.2. *(Adapted with permission from Fenchel, 1986a,b.)*

As an example of the application of this theory, consider a situation in which the volume fraction of bacteria in a seawater sample is 10^{-6} (e.g. 2×10^6 cells/mL $\times$ 0.5 µm^3 cell volume). A typical heterotrophic flagellate with a specific clearance of 105/h (it filters 105 times its volume of water per hour) will need 10 h to ingest its own volume of bacteria. With a 50% growth efficiency, it would thus be able to divide every 20 h. Growth efficiency, or yield, of protists is nearly invariant over a large range of growth rates (Fenchel, 1986a, b). For balanced (i.e. log phase) growth:

$$u(x) = U(x)\ Y \tag{49.3}$$

where $u(x)$ is the instantaneous growth rate at a food concentration x and Y is a yield constant. Thus, and as verified experimentally, $u(x)$ and $U(x)$ have similar functional forms, so that growth data can be used to estimate clearance.

Fenchel (1986b) also investigated the flow field generated by various filter-feeding flagellates and ciliates both theoretically and empirically. It is here that the assumption of low Reynolds number is used in calculating the theoretical flow field produced in the medium relative to the cell by ciliary motion. An example is shown in Fig. 49.2, where the predicted theoretical flow field is compared to the observed paths of suspended particles through the filter

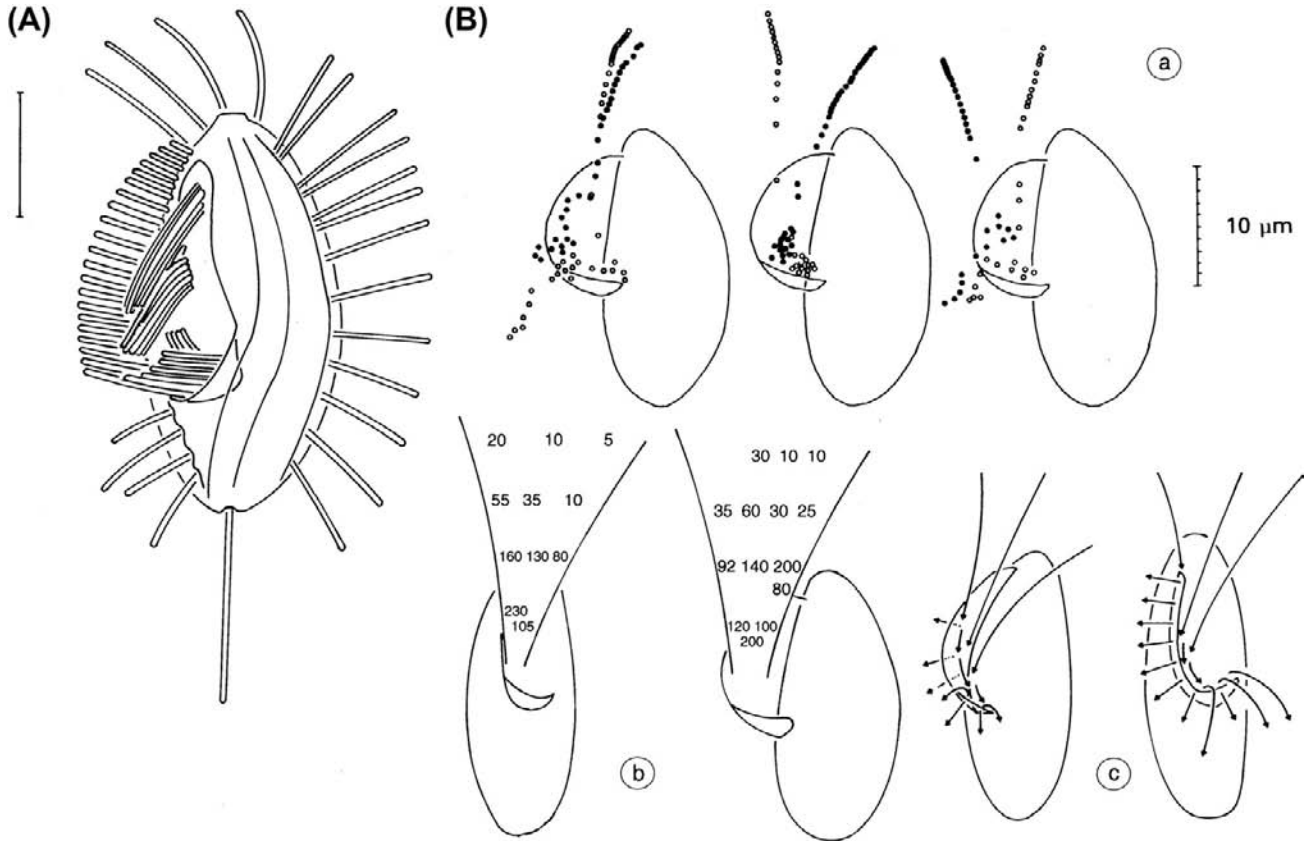

FIGURE 49.2 (A) Diagrammatic rendition of *Cyclidium*, showing filtration apparatus. Bar is 5 µm. (B) a. Position of 1.1-µm latex particles at 0.02-s intervals along six flow lines during fitration by *Cyclidium*. b. Schematic presentation of the critical flow lines and approximate velocities (µm/s). c. Schematic presentation of the flow lines. *(Reprinted with permission from Fenchel, 1986a.)*

apparatus of a ciliate. From these flow lines, one can see that a larger volume is sampled than might be expected simply from the area of the filter itself.

It should be noted that, as Cheer and Koehl (1987) noted in the case of filter feeding copepods and other metazoa, at very small Reynolds numbers the rows of cilia act more as paddles than as rakes. Thus, the picture of flow lines passing through a row of closely spaced cilia, as in Fenchel's picture, as well as the detailed mechanism of prey capture needs to be revisited and modified. Rather than straining the prey from the water, as we would do at high Reynolds number using, say a net, the low Reynolds number filter feeders may instead have to ingest a small blob of fluid that contains the prey.

III. NUTRITION AND EXCRETION

IIIA. Endocytosis, Digestion and Defecation

As with other cells, protists take in nutrients and other materials by a variety of passive and active mechanisms. Of particular interest here are specialized processes of phagocytosis and digestion not found elsewhere. Many ciliates and some flagellates have complex feeding structures. The best known case is *Paramecium*, the subject of many studies by Allen and Fok (Allen, 1984; Fok and Allen, 1990). This cell has a fixed cytopharynx (or buccal cavity), a tube-shaped cavity where food particles are taken in. At the end of this is the cytostome where the food vacuoles (FV) (also phagosomes, or digestive vacuoles) are formed. The cytostomal membrane, which pinches off to form the FV, is distinct from the cell membrane antigenically and in structure. During formation of the FV, it grows by fusion with disk-shaped vesicles, which are transported to it along microtubular ribbons. The movement is thought to be due to cytoplasmic dynein in a microtubule-based motor. The vesicles are essentially recycled membrane from earlier FVs, returning to the cytostome by a defined path.

After forming, the FV follows a defined path through the cytoplasm. As it progresses, vesicles called acidosomes also move along the cytopharyngeal microtubular ribbons and fuse with the vacuole just after it pinches off, lowering the pH of its interior. Whether the acidosomes are filled with acid or simply deliver proton pumps is not resolved yet. The low pH kills the prey and favors the activity of digestive enzymes. The release of the FV from the cytostome and its subsequent movement involve actin. As the acidosomes fuse with it, the original membrane of the FV pinches off to form small vesicles that recycle back to the cytostome, so that the FV is totally reconstituted. Next, lysosomes migrate from the Golgi apparatus and fuse synchronously with the FV, bringing acid hydrolases, including acid phosphatase. The membrane may be completely replaced again at this stage. Digestion takes about 20 m. At the end of this phase, vesicles form and are pinched off from the FV, probably to be used again in lysosomes. The remaining FV membrane binds to microtubules that guide it to the *cytoproct*, or *cytopyge*, where the FV membrane fuses with the cell membrane to form a pore. Its contents (undigested residue) are then egested (*defecation*) and the FV collapses. The cytoproct (cytopyge) is a specific location where the *plasmalemma*, a layer containing infraciliature and other structures, has a gap allowing the food vacuole to reach the cell membrane and fuse with it. After defecation, the membrane is recycled in discoidal vesicles to the cytostome, completing the cycle. This last step appears to involve an actin-based system that may be calcium regulated.

IIIB. The Contractile Vacuole

Protists without cell walls that live in hypotonic media (freshwater species) have *contractile vacuoles* (CV), which periodically excrete fluid. In the best-studied case, the ciliate *Paramecium*, this consists of a central vacuole, a surrounding complex of *ampullae* and a network, or *spongiome*, of tubules (Fig. 49.3). Certain tubules in this complex are decorated with peg-like elements that are vacuolar-type proton pumps. These are found in both the cellular slime mold *Dictyostelium* and the ciliate *Paramecium* (Heuser et al., 1993; Allen, 1997).

Excretion occurs through a cycle. During *diastole*, the vacuole forms and grows by the fusion of smooth-membrane vesicles. During this period, fluid travels from the spongiome to the CV. In *systole*, the vacuole membrane fuses with the cell membrane at one site to form a pore and

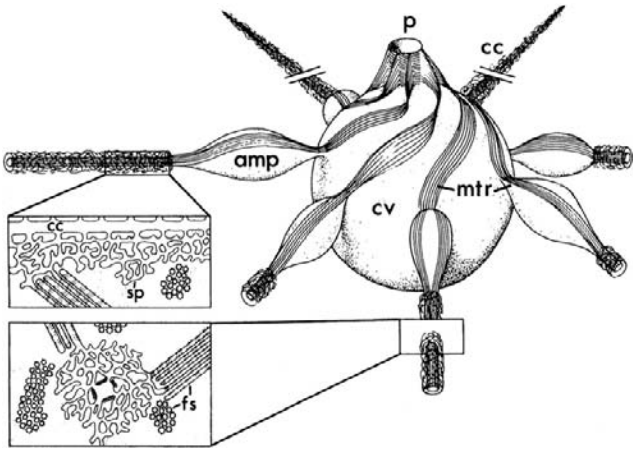

FIGURE 49.3 Contractile vacuole complex in *Paramecium*, showing ampullae (amp), collecting canal (cc), contractile vacuole (cv), pore (pv), spongiomal tubules (sp), fluid segregation organelles (fs) and microtubular ribbons (mtr). *(Adapted with permission from Hausmann and Hülsmann, 1996.)*

the fluid is excreted. As this happens, the vacuole contracts as its membrane fragments and forms vesicles again. Actin has not been detected near the CV and contraction is thought to be due to cellular pressure after the appearance of the pore opening to the exterior. At one time it was thought that the connections of the CV to the spongiome were interrupted during systole, preventing backflow. Recent work, however, indicates that the connections persist throughout the cycle. The narrowness of the tubular connections presents great resistance, so that considerable pressure would be required for a rapid backflow during systole.

A major function of the CV is clearly osmoregulation. The cycle ceases in cells placed in a hypertonic medium, resuming after a time when the cell adapts and increases internal tonicity. Fluid in the CV is high in K^+ and Na^+, relative to the cytoplasm, also suggesting a role in maintenance of ionic balance.

IV. ENERGETIC ADAPTATIONS: MITOCHONDRIA AND THEIR RELATIVES

As noted above in the introduction, evolutionary protistologists now consider the mitochondrion to have entered the eukaryotes at their origin as an endosymbiotic bacterium. Since a major function of the mitochondrion is oxidative metabolism, this suggests that the earliest eukaryotes were aerobes and would appear to have implications regarding conditions on the planet at that time. In any case, today, we find many parasitic and free-living protists inhabiting anaerobic and microaerophilic habitats, where oxidative metabolism is not useful. What appears to have happened, several times independently (convergently), is that the early mitochondrion has evolved into fermentative organelles, hydrogenosomes, which generate ATP anaerobically by metabolizing pyruvate to molecular hydrogen, carbon dioxide and acetate (Müller 1993). The mitosome, also a degenerate mitochondrion, occurs in some anaerobes, but its function is not yet clear (van der Giezen et al., 2005; Tachezy, 2008).

Another fermentative microbody, the glycosome, descended evolutionarily from the peroxisome, appears in trypanosomes and generates ATP by the glycolytic pathway under microaerophilic conditions (Parsons, 2004; Tachezy, 2008).

V. SENSORY ADAPTATIONS, MEMBRANE POTENTIALS AND ION CHANNELS

Like other cells, protists exhibit sensitivity and respond in various ways to environmental stimuli. The basic physiological and biochemical mechanisms, as far as they are known, are similar to those found in metazoan systems. *Paramecium,* for example, has been referred to informally as a "swimming neuron". In this section, several examples of photoreceptors and gravireceptors are examined and then the transduction mechanisms underlying the sensory responses are discussed.

VA. Photoreceptors

Ambient light can be a source of energy to autotrophic protists but, in addition, for motile species, it can serve as a directional signal. Many flagellates, and probably all the motile photosynthetic species, exhibit a positive phototaxis. For this purpose a directional receptor is needed. Directional receptors, or "eyespots", fall into two main categories: (1) receptors with opaque screens, which detect direction by the screen's shadow; and (2) receptors with *antennae* based on interference and diffraction to detect direction, essentially the same optical principle as that seen in a reflection hologram, or in structural color. In addition to these directional detectors, one group of predatory dinoflagellates has developed a system of *ocelloids* with intracellular lenses. In this section, we discuss the antennae and the ocelloids, two unique but understudied systems.

VA1. Receptors with Light Antennae

The interferometric *light antenna* is found in a phylogenetically diverse array of flagellates, including many genera of green algae, dinoflagellates and cryptophytes (Foster and Smyth, 1980; Melkonian and Robenek, 1984; Smyth et al., 1988). In the cases where experiments have been done, these antennae appear to be selective with regard to wavelength and light direction. The presence of essentially similar organelles in a wide array of groups considered on many other grounds, including molecular homology, to be phylogenetically diverse raises a question: are these all cases of convergent evolution? If not, have these organelles spread through endosymbiotic events?

The antennae operate through an interference mechanism similar to that which produces structural color in iridescent objects. The essential structure consists of a number of parallel reflective layers that act as partial mirrors. These are spaced evenly, separated by a distance of a quarter of the wavelength to be selected. Thus, incident light passes through a series of partially reflecting pigment layers spaced at quarter-wavelength intervals. Normally, incident light of the appropriate wavelength is reflected back at each partial mirror. These reflected light rays are in phase with each other and with the incoming radiation, leading to positive reinforcement of this light signal in front of the eyespot, where the receptor pigment is located. Light from other angles, and light of other wavelengths, also passes through this filter, but the reflections are out of phase with each other and the resultant interference minimizes their contribution. The basic principle is the same as that which produces structural color in iridescent feathers of

some birds and the wings of certain tropical butterflies and which is used in reflection (or Denisyuk) holograms.

The most intensive studies of light antennae were done with the green flagellate *Chlamydomonas* (Foster and Smyth, 1980), but the antennae are also found in dinoflagellates, chrysophytes and many other light-responsive flagellates.

VA2. Intracellular Lenses in Dinoflagellates

Perhaps the most complex and surprising photoreceptors are the ocelloids (ocelli), eyespots found in a family of non-photosynthetic dinoflagellates, the Warnowiaceae. A typical ocelloid consists of a lens, a retinoid and an opaque pigment cup (Fig. 49.4). The pigment cup, or *melanosome*, consists of a wall of pigment granules and it surrounds the paracrystalline *retinoid*. In front of this is the lens, or *hyalosome*, consisting of a peripheral corneal zone and a central crystalloid body. The entire organelle is approximately 24 μm long and 15 μm wide (Greuet, 1978, 1987).

Francis (1967) measured the refractive index of the lens in *Nematodinium* by three methods and found it to be approximately 1.52. He determined the focal plane by tracing rays parallel to the optic axis and found that light was focused in the retinoid layer. The field of view in these species was determined to be about 30° but may be wider in other species. From these observations, we conclude that the ocelloids could probably act as directional light receptors.

Given the presence of *nematocysts* (see Section VIC) in these same dinoflagellate species and the fact that they are predators rather than autotrophs, it has been suggested that the ocelloids might act as "range finders", leading to discharge of nematocysts when the contrast of the focused image on the retinoid is maximal. While certainly plausible, such behavior has not been reported yet. Unfortunately, these species have not been cultured and there appear to be no studies of ocelloid function, so that all we have at this time are speculations based on the structure.

VB. Gravity Receptors in Ciliates

Many single-celled organisms orient with respect to the earth's gravitational field while swimming. In some, such as the well-studied ciliate *Paramecium*, this is thought to be a purely hydrodynamic effect due to the shape and the distribution of mass in the cell: as the organism swims, the center of mass pulls the rear of the cell downward, orienting it so that it swims upward (Roberts, 1981). In this case, then, there seems to be no need for a gravity receptor. However, many protists can migrate either up or down, switching between a positive and a negative geotaxis in response to external signals or to a circadian or a tidal rhythm, suggesting a more complex type of response.

In particular, a group of ciliates containing the genera *Loxodes* and *Remanella* has a gravity response that depends on the dissolved oxygen level. In nature, these ciliates collect at the interface between anaerobic and aerobic zones in the water column. In oxygen-containing water they swim downward, while in an anoxic environment they swim upward. They all contain a characteristic organelle, the

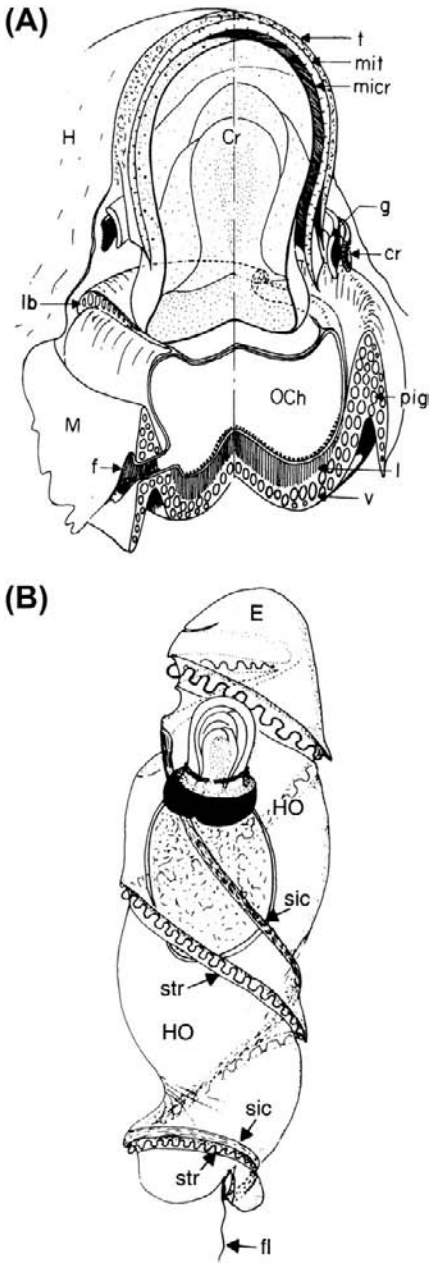

FIGURE 49.4 (A) Diagram of structure of *Nematodinium* ocellus, showing interior structure: crystalline body (Cr), ocelloid channel (f), constricting ring (cr), periocelloid gallery (g), hyalosome (H), lamellae of retinal body (1), microcrystalline layer (micr), mitochondrion (mit), ocelloid chamber (OCh), pigmentary ring (pig), basal plate (lb), micro-tubular layer (t), vesicular layer of the retinal body (v). Magnification: 3900×. (B) Position of ocellus in the *Nematodinium* cell, showing parts of the cell: episome (E), hyposome (HO), intercingular sulcus (sic), cingular sulcus with transverse flagellum (str), posterior flagellum (fl). *(From Greuet, 1978.)*

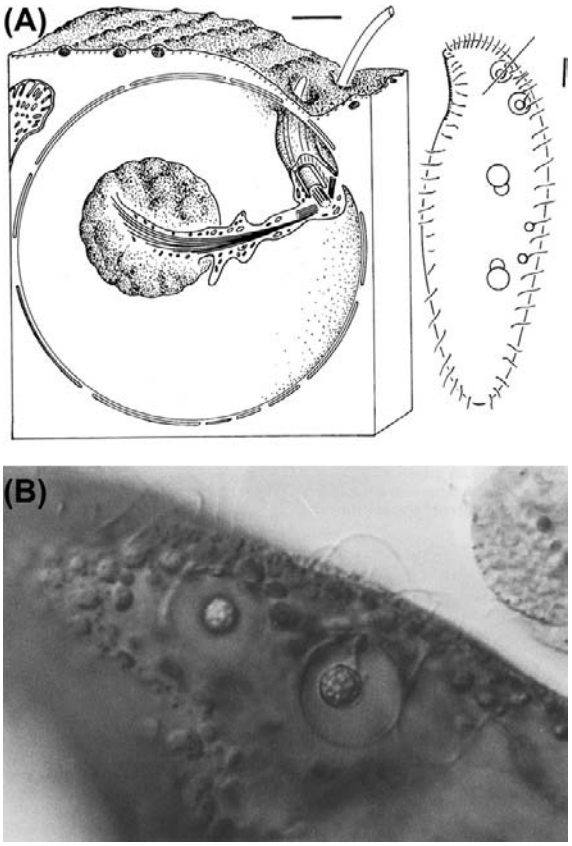

FIGURE 49.5 (A) Müller body, gravity receptor. Drawing showing position in *L. striatus* cell (scale bar: 10 μm) and a three-dimensional reconstruction from serial sections (scale bar: 1 μm). (B) Müller body in living cell of *L. striatus*. *(From Fenchel and Finlay, 1986.)*

Müller body, which acts as a gravity receptor. This is a fluid-filled vesicle in which a membrane-covered mineral body is suspended (Fig. 49.5). The mineral body, consisting of a strontium or barium salt, acts as a statolith, and its position on the interior surface of the vesicle appears to inform the cell of its orientation in the gravitational field (Fenchel and Finlay, 1986). The vesicle is anchored to the system of connected cilia of the cell and it is suggested, by analogy to other mechanoreceptors, that oriented mechanical stress on the cell membrane at this point of connection may lead to a depolarization which, in turn, would affect ciliary beating and determine the orientation of the swimming motion (Fenchel and Findlay, 1986) (see also Section VIII).

VC. Sensory Transduction: Membrane Potentials, Ion Channels and Intracellular Components

VC1. Membrane Potentials, Calcium and Behavior

As with many aspects of protistan physiology, membrane potentials are best known in the large ciliate *Paramecium*. A classic feature of ciliate behavior is the *avoidance reaction*, in which the cell stops, swims backward for a short time, then swims forward again, usually in a somewhat different direction. Early workers observed prolonged backward swimming in cells subjected to various stresses: high temperatures, sudden changes in pH or osmotic pressure, exposure to solvents and other deleterious chemicals. The common denominator in all these proved to be that the cell membrane became "leaky" or permeable to Ca^{2+} and other ions. Using the methods developed by Szent-Gyorgy and others for muscle tissues, *Paramecium* cells were exposed to detergents, such as Triton X-100, to render the cell membrane permeable. Such model extracted-cell preparations would swim forward if provided with ATP and Mg^{2+} in a medium containing $[Ca^{2+}] < 10^{-7}$ M. At higher Ca^{2+} concentrations, the cells swam backward (Naitoh and Kaneko, 1973).

Electrophysiological studies with intracellular electrodes in normal cells have given the following general picture: during forward swimming, a Ca^{2+}-dependent membrane potential is maintained. Appropriate mechanical, chemical or electrical stimuli cause an action potential in which calcium channels open in the membrane, causing depolarization and backward swimming. The membrane potential is restored by a calcium pump after a short time and forward swimming resumes. Cells are depolarized by repellents (stimuli that cause backward swimming) and hyperpolarized by attractants (stimuli that inhibit backward swimming).

VC2. Behavioral Mutants

Kung and his colleagues obtained a number of behavioral mutants in which swimming behavior could be correlated with abnormal electrophysiological properties of the *Paramecium* membrane. Examples include the following:

1. *Pawn* (several types), in which voltage-gated Ca^{2+} channels are affected, depolarization does not occur and the cell cannot swim backward.
2. *Pantophobiac*, where Ca^{2+}-dependent K^+ currents are affected and prolonged responses occur to all stimuli.
3. *Paranoiac* (several types), affecting Ca^{2+}-dependent Na^+ channels. Prolonged responses occur in Na^+ solutions.

Many other behavioral mutants are known (Saimi and Kung, 1987).

VC3. Ion Channel Types and Membrane Excitation

Electrophysiological and behavioral genetic studies have revealed eight distinct types of ion channels in *Paramecium* and at least three types of membrane excitation that govern

behavioral responses, as follows (Hinrichsen and Schultz, 1988):

1. Two mechanically induced currents: a depolarizing, Ca^{2+}-based current in the cell's anterior and a hyperpolarizing, K^+-based current in the posterior.
2. A rectifying K^+ current that can cause regenerating hyperpolarization during the action potential.
3. A second Ca^{2+}-dependent K^+ current, which may play a role in maintaining the resting potential.

VC4. Second Messengers and Transduction Pathways

Second messengers and internal biochemical events following mechanical or chemical stimuli have been the subject of study in various protists. In the case of the *Pantophobiac* mutants of *Paramecium*, for example, it was found that normal behavior could be restored by microinjection of wild-type calmodulin (CaM). This led to the discovery that these mutants were specific point mutations with amino acid substitutions at specific CaM sites. Further studies showed that the Ca^{2+}-CaM complex regulates calcium-dependent Na^+ channels by direct interaction and is also required for the functioning of K^+ channels. Work on responses to acetate and biotin in mutants with different defects in ion conductances, however, indicates that these two stimuli operate via different ion channels (Bell et al., 2007, Valentine et al., 2008).

Progress at this level has been greatest with the cellular slime mold *Dictyostelium discoideum*. In this organism, there appear to be several chemosensory transduction pathways, similar in general to those found in animal cells, such as leukocytes, but differing in some aspects (Van Haastert and Veltman, 2007). In both cases, the presence of multiple pathways introduces a complexity of potential response mechanisms and behavior (Iglesias and Devreotes, 2008).

VI. INCORPORATION OF PHYSIOLOGICAL UNITS FROM OTHER CELLS

Symbiotic relationships, including cellular endosymbiosis, are widespread in biology. In the protists, this tendency appears to be accentuated and many new physiological opportunities have been produced by endosymbiotic combinations. Thus, many protists have prokaryotic or eukaryotic endosymbionts. In some cases, these associations appear to be more or less permanent, as in the green ciliate *Paramecium bursaria*, which always has an algal *Chlorella* endosymbiont. Sometimes the association is more intimate and parts of another cell have been permanently incorporated into the host cell. There are also more transient associations, in which the host "cultures" and uses all or part of an ingested cell in its cytoplasm for a period of time. Examples of all of these possibilities are presented in this section.

VIA. Intracellular Capture and Culture of Foreign Organelles

Early reports of photosynthesis by certain natural populations of chlorophyll-containing ciliates suggested that these supposedly heterotrophic organisms might harbor algal symbionts. Electron microscopy, however, revealed that some ciliates contain isolated fragments of algal cells, which appear to be functional. The photosynthetic marine ciliate *Myrionecta rubrum* (formerly *Mesodinium rubrum*), which sometimes forms "red tides" (massive blooms that color the sea), contains endosymbiotic algal organelles in the form of chloroplast−mitochondrial complexes (Taylor et al., 1971). Other species of planktonic ciliates have been found to contain intact algal chloroplasts, pyrenoids and even eyespots. A significant proportion of the planktonic ciliates in marine habitats has been found to contain "captured" chloroplasts, which remain functional within the ciliate for extended periods, eventually being consumed by the host (Stoecker et al., 1987).

VIB. Xenosomes: Bacterial Endosymbionts

The term *xenosome* was used by Soldo (1987) to describe certain bodies in marine ciliates. These were later identified as endosymbiotic bacteria and Corliss (1985) suggested that the term be defined to include all DNA-containing, membrane-bound intracellular bodies or organisms. By this definition, mitochondria and chloroplasts would be included. In practice, however, the term has been used largely for bacterial endosymbionts of marine ciliates.

VIB1. Bacterial Endosymbionts in Ciliates

Some endosymbiotic bacteria, such as the *Kappa* and *Alpha* particles in *Paramecium* and the *Omicron* particles in Euplotes, are classical objects of study (Görtz 1996). More recently, there have been a number of studies by Soldo and colleagues of the xenosomes from marine ciliates (Soldo, 1987; Soldo et al., 1992). Originally found in the species *Parauronema acutum*, they are infective to 12 strains of this species and also to the phylogenetically distant species *Uronema marinum*, but not to strains from five other marine ciliate genera, or the freshwater genera *Paramecium* and *Tetrahymena*. They are toxic to some marine ciliates, such as *Uronema nigricans*, and the toxic effect is abolished by proteolytic enzymes.

These xenosomes contain DNA, RNA, proteins and lipids in amounts typical of small bacteria and are selectively destroyed by a number of antibiotics, including penicillin, ampicillin, tetracycline and chloramphenicol, but not neomycin or cycloheximide. They are small, Gram-negative

rods, present in numbers ranging from 100 to 200 per host cell and they divide in synchrony with the host. When released by gentle mechanical rupture of the host, they swim with darting motions or spin like propellers. They average two flagella per cell, inserted at random sites in the cell wall. Within the host cytoplasm, they have a fairly typical Gram-negative double outer membrane and single inner membrane, with a layer of peptidoglycan between these. They are not enclosed in vacuoles but contact the host cytoplasm directly.

Xenosome chromosomal DNA is multicopy, consisting of nine to 14 circularly permuted duplex molecules of about 515 kb (kilobase pairs). In addition, there are several plasmids. Analysis of restriction sites revealed that all the adenines of GATC sequences in the plasmids are methylated, whereas those in chromosomal sequences are not, suggesting that there are two replicons, one controlling chromosomal and the other plasmid replication.

Surprisingly, 30% of protein in xenosomes is from the host cell. This is, however, consistent with the relatively small genome. Assuming 1.3 kb of DNA is needed to encode a protein of average M_r 66 000, then the xenosome can encode fewer than 400 proteins, less than one-tenth the number for a typical free-living species such as *Escherichia coli*.

Xenosomes in vitro consume oxygen at a very low rate, comparable to that observed in Rickettsia and *Kappa* symbionts, and preferentially use succinate as an energy source. Symbiont-containing ciliates, on the other hand, consume oxygen at a rate 20−30% higher than symbiont-free ciliates and host glycogen is consumed at a significantly higher rate in the former than in the latter.

The affinities and origins of these organisms present an intriguing problem. Ribosomal RNA analysis of marine ciliate xenosomes indicates some homology to the μ and π xenosomes of *P. aurelia*, but little or no homology to known free-living species, suggesting that these endosymbionts may have a long history of association with ciliates (Soldo et al., 1992).

VIB2. Methanogenic Endosymbionts in Anaerobic Ciliates

Most of the free-living anaerobic ciliates examined have endosymbiotic and/or ectosymbiotic bacteria (Fenchel et al., 1977) and the role of some of the former have been studied in some detail. In particular, a number of species harbor methanogenic bacteria. In the cases where these have been investigated, the bacteria are intimately associated with a series of hydrogenosomes. The arrangement of bacteria and organelles has been compared to a stack of coins, with bacteria and hydrogenosomes alternating and the latter on the ends (Fig. 49.6). This complex is highly organized in some species and possibly a permanent feature of the host cell. In the ciliate *Plagiopyla frontata*, the

FIGURE 49.6 Hydrogenosomes and methanogen symbionts in the ciliate *P. frontata*. The darker bodies are the hydrogenosomes and the lighter bodies are the symbionts. Magnification: 20 000×. *(From Fenchel and Finlay, 1991.)*

bacteria divide synchronously with the host. The number of methanogens per host cell (about 3000) remains constant until a late stage in the host cell cycle, when it doubles. Thus, the ciliate apparently controls reproduction of the symbiont to maintain a stable population density.

When the methanogen inhibitor 2-bromoethanesulfonic acid was used to inactivate the methanogenic symbionts of three ciliate species, *P. frontata*, *Metopus contortus* and *M. palaeoformus*, growth rate and yield were reduced in the first two species, but not in the last. It is suggested that the energetic advantage conferred by the symbiont in the first two species may be due to the secretion of organic material by the bacteria (Fenchel and Finlay, 1991). The advantage to the methanogens of consumption of H_2 and acetate from the adjacent hydrogenosomes seems clear. This could be a significant advantage, especially in marine or other sulfate-rich environments, where free-living methanogenic bacteria would compete with the more efficient sulfate-reducing bacteria for H_2.

VIB3. Bacterial Endosymbionts in Amoeba proteus

Many endosymbionts have been reported in large free-living amoebae, such as *Amoeba proteus* (Jeon, 1995). Particularly dramatic is the case of a bacterial endosymbiont that has been studied from its initial appearance as a contaminant in laboratory culture, through the co-evolution of host and endosymbiont, to a mutually dependent symbiotic

relationship (Jeon, 1987). The bacterium, which first appeared in the culture in 1966, is termed the *X-bacterium*. It infected a culture of the D strain of *A. proteus*, which already contained other symbiont-like particles of unknown origin. The X-bacterium is described as a Gram-negative rod, with an ultrastructure similar to *E. coli*, but is not otherwise identified taxonomically as yet. Initially, most of the infected amoebae died, but a few survived and the X-bacteria gradually lost virulence. The number of bacteria per amoeboid cell, originally greater than 100 000, stabilized at about 42 000. Within a few years, the host cell, now called the xD strain, became dependent on the presence of the endosymbiont. X-bacteria can be transferred into other D strain cells by microinjection or by induced phagocytosis. The bacteria are enclosed in host-generated vesicles, or *symbiosomes*, and when observed in freeze-fracture preparations are found to be embedded in a matrix of fibrous material. The symbiosomes do not fuse with lysosomes and, during infection, the X-bacteria seem to be somewhat resistant to lysozymes, since about 10% of them avoid digestion in the phagolysosomes. Two kinds of plasmids were found in X-bacteria and isolated X-bacteria treated with ethidium bromide or acridine orange for 3 h failed to infect amoebae.

Several molecules produced by the symbiont have been studied. One, the Xd29 protein, appears to be a peripheral membrane protein that is constantly shed into the host cytoplasm, passing readily through the symbiosome membrane. Symbiont-produced lipopolysaccharides (LPS) have also been identified and were shown by immunostaining to be present on the cytoplasmic side of the symbiosomes. Injected antibodies to the LPS abolished the fusion-avoiding properties of symbiosomes, causing them to fuse with lysosomes. A 96-kDa protein from the symbiont is also present on the symbiosome membrane and is suspected of playing a role in preventing lysosomal fusion. X-bacteria contain a large amount of 67-kDa heat-shock protein (HSP, GroEx) but, since there are no free-living X-bacteria cultures for comparison, it is not known whether this is an indication of stress. In other intracellular infective bacteria (e.g. *Legionella*), the GroEx protein in the intracellular bacteria is more than seven times greater than in free-living cells. The complete nucleotide sequence of the *GroEx* operon of the X-bacteria was determined and has a high degree of homology with those of other endoparasitic or symbiotic bacteria, such as *Legionella* and *Coxiella*, and further genomic study indicates that the organism should be considered a new species of *Legionella* (Park et al., 2004).

Some polypeptide bands detected by gel electrophoresis of the amoebae cytosol are no longer present after prolonged endosymbiosis. One protein that disappears after symbiosis is a SAMS (S-adenosyl-L-methionine synthetase). That is, the gene remains in the host genome but becomes inactive, while a gene in the symbiont replaces it and produces bacterial SAMS (Jeon and Jeon, 2003), which may be part of the explanation for the host cell's newly evolved dependance on the symbiont.

Clearly, the analysis of this evolving system is only beginning.

VII. STRUCTURES WITH UNKNOWN FUNCTIONS

Next, emphasizing the opportunities for future research, a number of more or less prominent structures are examined that are not understood at the basic level of function (though some have been the subject of interesting speculations).

VIIA. Rhoptries

A large group of medically important parasitic protists, the *Apicomplexa* (formerly the *Sporozoa*), is defined by a structure called the *apical complex*. This group includes such important parasites as *Plasmodium*, which causes malaria. All the apicomplexa are obligate intracellular parasites at some stage in their life cycle and the apical complex is thought to be an instrument of invasion. A prominent part of this complex are the *rhoptries*, secretory organelles containing lipids and proteins (Fig. 49.7) that

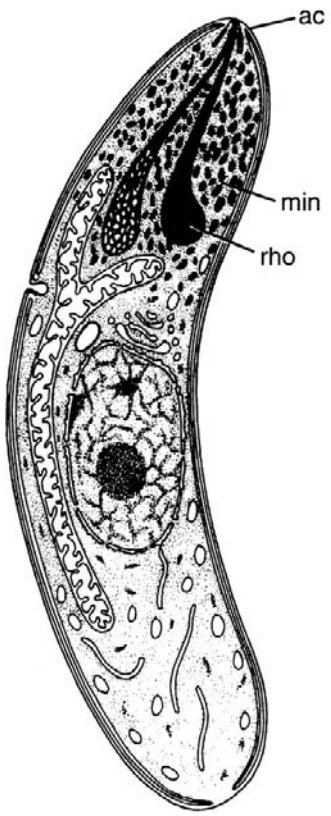

FIGURE 49.7 Diagram of apicomplexid cell, showing rhoptries (rho), micronemes (min), and apical complex (ac). *(Adapted f rom Chobotar and Scholtyseck, 1982.)*

originate in the *Golgi system*, filled with enzymes. For many years, the general assumption has been that rhoptry and microneme secretions must play a role in the invasion of the host cell, but it has proven difficult to identify actual function (Sam-Yellowe, 1996). In some apicomplexid species, the parasite is contained in a *parasitophorous vacuole* after invasion but, in others, the vacuole disappears and the parasite is in direct contact with the host cytoplasm. Rhoptries contain dense protein granules and epitopes corresponding to these have been identified in the host cell membrane, its cytoskeleton and also in the parasitophorous vacuole membrane, where present. Their role, however, is not clear.

VIIB. Apicoplastids

Plasmodium and other parasitic apicocomplexids have a structure that appears to be homologous to the chloroplast of green algae (Köhler et al., 1997). An organelle surrounded by four membranes contains a 35-kb circular fragment of DNA, which is shown by cluster analysis to be most closely related to DNA in green algal chloroplastids. Localization of the fragment was done by an in situ hybridization technique. The organelle divides by binary fission and is introduced into daughter cells early in replication. The genome is transcribed and transcription products have been identified. The presence of four membranes enclosing this organelle suggests that it originated endosymbiotically, following ingestion of an algal protist that contained a plastid (Dzierzinski et al., 1999).

The function of this organelle, which has been named the *apicoplastid*, is not known, but it clearly must have a function. The new organelle has been found in all apicocomplexids examined so far and has generated much excitement as a potential target in the design of new drugs for malaria and other apicocomplexid diseases. Preliminary results with several drugs that inhibit apicoplast replication or metabolism are most promising (Fichera and Roos, 1997; Jomaa et al., 1999).

VIIC. The Paraflagellar Rod

The *paraflagellar rod* (PFR) is found in parasitic kinetoplastids and also in the free-living euglenids and dinoflagellates. The PFR is a complex, lattice-like structure running parallel to the flagellum (Fig. 49.8). In both euglenids and kinetoplastids, there have been many ultrastructural, biochemical and molecular studies of this organelle (Hyams, 1982; Woodward et al., 1994).

Comparison of proteins from flagella of *Euglena* (with PFR) and *Chlamydomonas* (without PFR) indicated a pair of major proteins as PFR components. Subsequently,

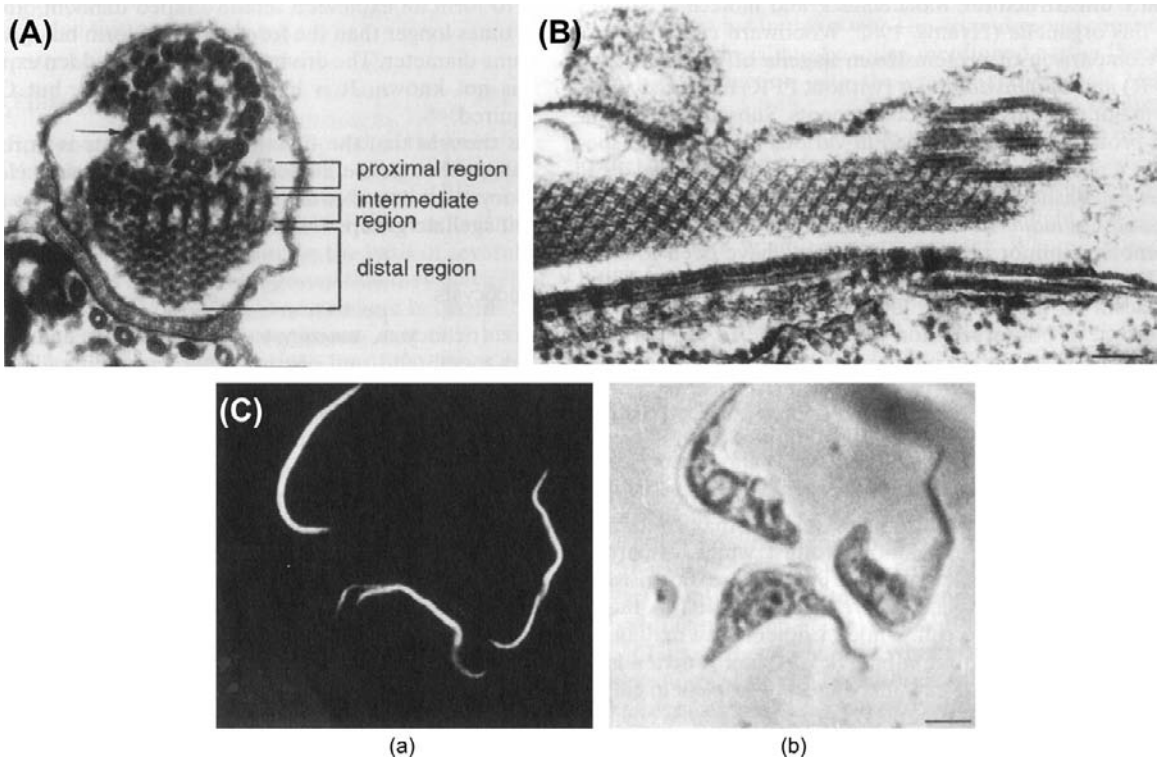

FIGURE 49.8 (A) Cross-section of the flagellum and paraflagellar rod of *Trypanosoma brucei* (scale bar: 74 nm). (B) Longitudinal section (scale bar: 256 nm). (C) Immunofluorescent staging of the PFR with monoclonal antibody ROD-1. Fluorescence picture (a) and phase image (b) (scale bar: 5.5 pm). *(From Sherwin, T. and Gull, K. (1989). Phil Trans Roy Soc Lond Ser B. 323: 575–588.)*

similar protein pairs were found in various kinetoplastid species. Cross-reactivity of kinetoplastid and euglenid PFR was established using antibodies to PFR of the kinetoplastid *Crithidia*. In addition to the two major proteins, a number of minor protein components have been found.

Regarding function, in the euglenids, the PFR is located adjacent to the eyespot and is thought to be the photoreceptor. In the parasitic kinetoplastids, current opinion favors a role in attachment to host cells during infection. Direct evidence for these rather different roles is lacking, however[2] (Bastin et al., 1996).

VIID. Extrusomes

A feature of many protists is the ability to extrude preformed structures. *Extrusomes* are vesicles that contain some organized substance or apparatus, which usually changes its form when released to the exterior in exocytosis. In some cases, these organelles are clearly related to the feeding activities of the cell, while in others, they may be a defensive adaptation but, in many cases, their function is as yet unknown. They are extruded in response to chemical, mechanical or electrical stimuli. While some metazoa eject structures, such as the *cnidocysts* (also called *nematocysts*) of *Hydra* and other coelenterates, such functions are usually performed by differentiated cells. In the unicellular protests, specialized organelles have evolved instead.

The terminology and organization of this section follows that of Hausmann and Hülsmann (1996). The classification is based largely on morphology and it is not clear whether, for example, *trichocysts* in ciliates and flagellates are homologous or represent parallel evolutionary developments. In the case of the *ejectosomes*, a truly remarkable question of homology arises: the *Kappa* particles in the ciliate *Paramecium* (bacterial endosymbionts, see earlier discussion) contain *R-bodies*, which are morphologically indistinguishable from the ejectosomes of certain flagellates (see later section) and these have even been observed to unroll and form tubes, as ejectosomes do. Did the ejectosome originate as part of a bacterial endosymbiont?

VIID1. Spindle Trichocysts

These are probably the best studied of the extrusomes. Spindle trichocysts of *Paramecium*, a favorite demonstration in introductory biology courses, are found in the cortex of the cell, just under the plasma membrane. In the resting state, the trichocyst is a spindle-shaped or rhomboid paracrystalline protein body. In response to various chemical and/or mechanical stimuli, this unfolds in a few milliseconds to form an expanded, thread-shaped filament, about eight times as long as the former resting form but having the same diameter. The driving force for this sudden expansion is not known. It is independent of ATP, but Ca^{2+} is required.

It is thought that the function of trichocysts is to repel predators, though the evidence for this is not very clear. Trichocysts are found in ciliates and in dinoflagellates and other flagellate groups (Hausmann and Hülsmann, 1996).

VIID2. Mucocysts

Like trichocysts, *mucocysts* are found just under the plasma membrane and consist of paracrystalline filamentous bodies. Expansion to the exterior takes place in three dimensions and lasts for several seconds. They are found in various ciliates, flagellates and the ameboid actinopods, where they may be responsible for the sticky surface used in capturing food organisms. Otherwise, they are thought to have a protective function. They resemble the cortical granules of sea urchin eggs, which are involved in the formation of the fertilization membrane.

VIID3. Discobolocysts

Discobolocysts are found in certain flagellates (*chrysophytes* and others). In the intracellular resting state they are almost spherical, with a disk in the part next to the plasma membrane. On ejection, the disk is unaltered, but the remainder is changed into long filamentous material. The function of these organelles is not known.

VIID4. Toxicysts

These are found in ciliates and some phagotrophic flagellates. They function in the capture of prey and perhaps in defense against predators. The toxicyst capsule contains a long tube which, during extrusion, is either telescoped or everted. This enters the prey and is used to inject a toxin, which kills or paralyzes the prey. In the suctorian ciliates, they discharge on contact and serve also to hold the prey until it can be taken in and consumed. The nature of the toxin(s) does not appear to have been investigated.

VIID5. Rhabdocysts

These are rod shaped and occur in one group of ciliates (the *karyorelictids*). As with toxicysts, they discharge telescopically – an event that has been compared to the discharge of an arrow from a blowpipe. Their function is unknown.

VIID6. Ejectosomes

These occur in certain flagellates (*cryptophytes* and *prasinophytes*). In the intracellular resting state, they are like tightly coiled ribbons. Extruded, they unroll and form very long tubes. This is said to be an escape reaction. The remarkable similarity of this organelle with the R-bodies in the *Kappa* particle endosymbionts of *Paramecium* was

[2] Interestingly, the only group of kinetoplastids that lacks a PFR is a group of monogenetic parasites that have bacterial endosymbionts of the genus *Bordetella*.

noted earlier and raises the possibility of an endosymbiotic origin for this organelle.

VIID7. Epixenosomes

Epixenosomes occur tightly bound to the outer surface of the plasma membrane in certain ciliates. They, like the ejectosomes, contain a tightly coiled band that unrolls and forms a tube. They contain DNA, however, and thus are epibionts, not organelles and, on the basis of several structural features, it has been suggested that they may represent a primitive type of organism somewhere between the prokaryotes and the eukaryotes. In any case, they are found in all specimens of different species of the genus *Euplotidinium* from different geographic regions. Thus, this appears to be a tight, ancient symbiotic relation.

VIID8. Nematocysts

These are found in certain dinoflagellates and are thought to function in predation, though this has not been observed. As with toxicysts, they strongly resemble the *cnidocysts* (also known as nematocysts) of multicellular coelenterates such as *Hydra*. They are capsules containing a coiled tube, which evaginates on extrusion.

VIIE. Crystalline Bodies

Many protists contain crystals, usually of calcium and phosphorus salts and with small amounts of magnesium, chloride or organic material, in some cases. Classically, these were considered simply waste products, since they seemed to be somewhat dependent on diet. More recently, it has been suggested that they may be reservoirs of ions needed in metabolism. They are often formed when the cells are grown in optimal conditions and when removed experimentally they tend to be replaced quickly.

VIII. COORDINATED PROTISTAN RESPONSES TO GRAVITY AND TO GRADIENTS OF OXYGEN AND LIGHT: AN EXAMPLE FROM PHYSIOLOGICAL ECOLOGY

In this section, an example is presented of the integration of protists in their environment, based on some of the physiological capacities discussed in earlier sections. The example is taken from a study of a nutrient-rich pond (Berninger et al., 1986). Figure 49.9 shows the distribution

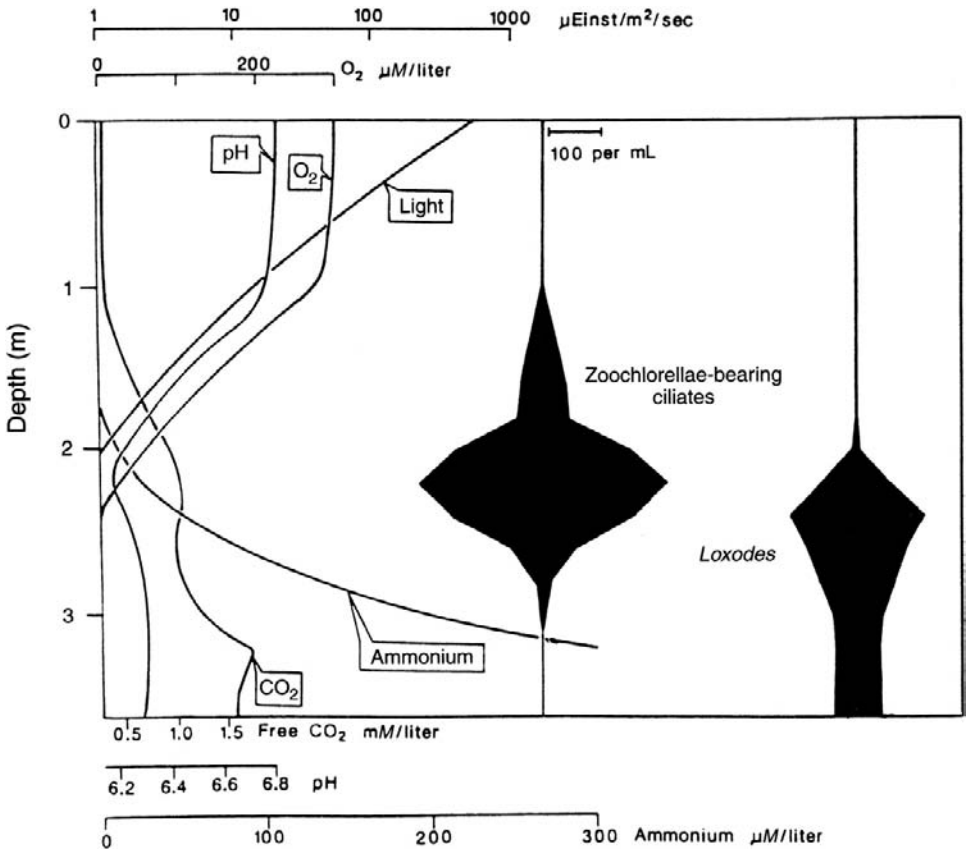

FIGURE 49.9 Vertical distribution of microaerophilic zoochlorellae (algal symbiont)-bearing ciliates and the ciliate *Loxodes* in a small productive pond, with profiles of some relevant physical and chemical factors. *(Adapted from Berninger et al., 1986 and Fenchel and Finlay, 1986.)*

of two kinds of ciliates in relation to several critical physicochemical factors. The situation depicted is typical of summer when temperatures are high and there is not much wind. In these circumstances, bacterial metabolism depletes oxygen in the lower part of the water column and, in the absence of mixing by wind, the pond becomes stratified. The depth profiles of two ciliate populations are shown. The first consists of three species of microaerophilic zoochlorellae-bearing ciliate. These remain in a low-oxygen zone, where major predators have difficulty following them. Their lower limit is set by the light requirement of their symbionts, which produce the oxygen that enables them to survive in this zone. The second group consists of a species of the ciliate *Loxodes*, mentioned earlier (Section VB) in connection with the gravity receptor, or Müller body.

Loxodes responds to three interacting factors: oxygen, blue light and the force of gravity. As noted earlier, in the dark, cells accumulate in regions of low oxygen tension (ca. 5% of saturation). If then exposed to light, they swim into the dark or into anaerobic water. When exposed to high O_2 and light simultaneously, after initial episodes of backward swimming (the *avoiding reaction*), they swim downward (a *positive geotaxis*). If placed in anaerobic water, especially in the dark, they respond by swimming upward (*negative geotaxis*). The end result of all this is that, in the pond, they accumulate by geotaxis in a zone in the *oxycline* (oxygen gradient) that is optimal. Typically this is in the dark, just below the ciliates with zoochlorellae symbionts. The cells are sensitive to very low light levels, so that levels as low as 10 W m^{-2} will cause them to swim down into anaerobic water. *Loxodes* can use nitrate as a terminal electron acceptor, which is unusual in ciliates. Meanwhile, by swimming down into the anaerobic zone, the cells avoid most of their potential predators – zooplankters, planktonic larvae, juvenile fish – which are restricted to the aerobic zone.

Figure 49.10 summarizes what is known or suspected regarding the physiological basis for this adaptive behavior. Obviously, much remains to be done before the physiological basis for some of the arrows in the figure is understood. Photoreception remains to be worked out in detail, but it is clear that a blue light receptor is involved, possibly a flavin, and one product of its excitation in the presence of oxygen is superoxide radical (Finlay and Fenchel, 1986). However, *Loxodes* has only low levels of superoxide dismutase and catalase. Thus, superoxide, or a product of its dismutation, e.g. hydrogen peroxide, might be the internal signal for oxygen perception, binding to cytochrome oxidase or perhaps reducing another component of the electron transport system (ETS), such as cytochrome *c*. A drawback of this speculation is that the ETS is in the mitochondrion, while the pigment granules are in the cell membrane. Thus, a change in the ETS might influence the membrane potential of the mitochondrion, but it is not clear how this signal might be transmitted to the cell membrane to influence ciliary beating and change the swimming behavior (Finlay et al., 1986).

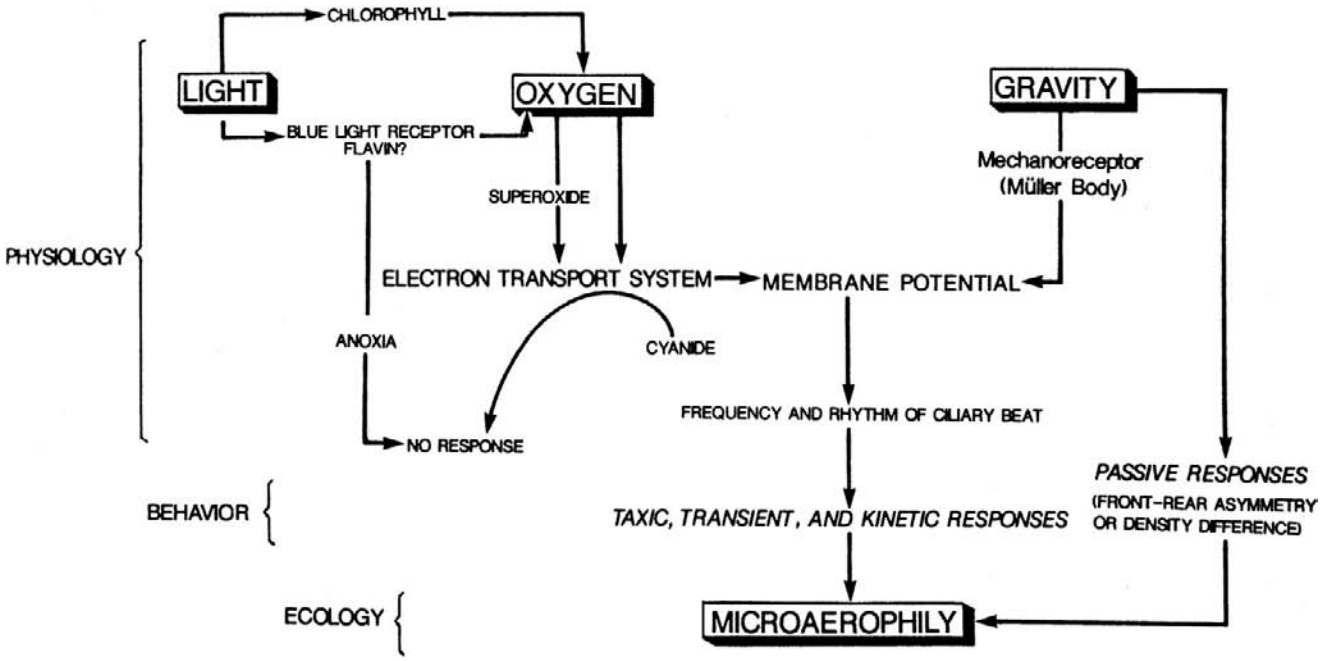

FIGURE 49.10 Model of the probable physiological and behavioral responses to the three cardinal factors (light, oxygen and gravity) controlling microaerophily in ciliated protozoa. *(Adapted with permission from Finlay, 1990.)*

In any case, the linked responses to light, oxygen tension and gravity seem very understandable given the ecology of this organism. What is attractive in this system is the possibility of linking the organism's physiology and its ecology.

IX. SUMMARY: PROTISTAN DIVERSITY

The theme of this chapter has been the physiological diversity that has evolved among the many protistan groups, as seen in some of the better-studied examples. However, even these examples are as yet only poorly understood and many groups remain unstudied or little studied. The diversity of known physiological systems and mechanisms is likely to increase enormously as these groups are explored. Let us consider this at several different levels of organization.

IXA. Molecular Diversity

There is great diversity at the level of molecular genetics, not treated in this chapter. Ciliates, for example, display a slight variation on the otherwise universal genetic code: the universal stop codons, TAA and TGA, instead code for glutamine in some (but not all) ciliates. (It has been suggested that this may serve as a barrier to viruses, which have not been detected in ciliates.) The presence of two nuclei in ciliates is also different: the *micronucleus* serves as the genetic archive, for storage and recombination of the genetic pattern, whereas the *macronucleus* is the regulator of cellular function. In trypanosomes and other kinetoplastids, the *kinetoplast* is a large network of DNA associated with a single giant mitochondrion. This kinetoplast DNA (kDNA) consists of a network of about 50 *maxicircles*, which carry the mitochondrial genes and about 10 000 *minicircles*. It was noticed that many genes in the maxicircles appeared non-functional, since they lacked conventional punctuation and contained frameshifts. However, mRNA with functional coding was produced. It turned out that the minicircle DNA was used to produce "guide RNA", which edited the pre-mRNA from the maxicircles. Since this discovery, similar RNA editing has been found in other organisms, including a mammalian nucleus.

Indeed, protists have been a fruitful source of discovery in fundamental biology. Early in the 20th century, it was noted that some ciliates could divide approximately 50 times asexually and then had to undergo sexual genetic recombination, anticipating Heyflick's epochal discovery of a similar mortality in mammalian cell lines by several decades. The mechanism involved here, change in length of the telomeres with each division, was first discovered in a ciliate, *Tetrahymena* (Blackburn, 1992; Blackburn and Greider, 1995). Studies with this ciliate also revealed for the first time that RNA could be an enzyme (Cech, 1987).

IXB. Organellar Diversity

As seen in this chapter, endosymbiotic events do occur often among protists. Protists are not necessarily prisoners of their phylogenetic past. If a useful invention appears in one evolutionary line, it can cross to another by a symbiotic transfer. Many dinoflagellates are photosynthetic, but ultrastructural evidence indicates that their chloroplasts originated in other evolutionary lines (the cryptophytes and the chrysophytes). The ciliates, distant relatives of the dinoflagellates, also lack chloroplasts but, as noted, planktonic species often "capture" and use chloroplasts from their algal prey and, in some cases, these symbioses appear to have become permanent.

In summary, many authors have constructed "trees" that reflect the phylogeny of sRNA and other nucleic acids in protistan and other eukaryotic cells but, in organellar organization, there has been a great deal of lateral transfer and one evolutionary line can borrow or take from another. At this level, a flowchart is probably more appropriate than a tree.

IXC. Cellular Diversity

Finally, protistan cells can vary in space and time. Some have complex life cycles or can form multicellular structures in which there is specialization and differentiation. Perhaps most well known here are the cellular slime molds. At one stage, these function as individual small amoebae. Under certain conditions, however, the individual cells send chemical signals to each other and come together to form multicellular "slugs". These move about for a time and then metamorphose into a more or less complex multicellular reproductive structure. Curiously, in one group of ciliates, essentially the same thing occurs — presumably a parallel evolution.

This chapter started with the description of filter-feeding by protists — an important ecological process that is illustrative of the problems faced by cells that are also free-living organisms. This was followed by a more detailed discussion of feeding: phagotrophy and digestion in the well-studied case of the ciliate *Paramecium*. Since mitochondria in the protists, though varying somewhat in structure, are essentially similar to those in other cells, their metabolism was not examined here. Instead, the unique glycosomes and hydrogenosomes of anaerobic and microaerophilic protists were discussed.

Returning to the view of protists as organisms, several sensory organelles unique to these cells were examined, followed by a consideration of their sensory transduction. Here, there are some exciting similarities and differences with vertebrate and invertebrate neurons and sensory cells. In particular, a calcium potential dominates in those cells that have been studied and calmodulin-based pathways are prominent aspects of transduction.

The widespread occurrence of endosymbiosis in protists was illustrated with well-documented examples. Next, to emphasize the opportunities for breaking new ground with protistan physiology, a number of striking organelles of unknown function were described. Finally, returning to the original emphasis on the cells as organisms, an example from the physiological ecology of a freshwater ciliate in a high-nutrient freshwater pond was described.

The record suggests that, by studying the diversity of protistan adaptations, cell physiologists can find new answers to old questions and also new questions.

ACKNOWLEDGMENTS

I thank Nigel Yarlett, Miklos Müller, Tom Fenchel, F.J.R. Taylor and Kenneth Foster for helpful discussions.

BIBLIOGRAPHY

Adl, S. M., Simpson, A. G. B., Farmer, M. A., et al. (2005). The next higher level classification of Eukaryotes with emphasis on the taxonomy of Protists. *J Eukaryot Microbiol, 52*, 309−451.

Allen, R. D. (1984). Paramecium phagosome membrane: from oral region to cytoproct and back again. *J Protozool, 31*, 1−6.

Allen, R. D. (1997). Membrane tubulation and proton pumps. New ideas in cell biology. *Protoplasma, 189*, 1−8.

Bastin, P., Matthews, K. R., & Gull, K. (1996). The paraflagellar rod of Kinetoplastida: solved and unsolved questions. *Parasit Today, 12*, 302−307.

Bell, W., Preston, R., Yano, J., & Van Houten, J. (2007). Genetic dissection of chemosensory conductances in Paramecium. *J Exp Biol, 210*, 357−365.

Berninger, U.-G., Finlay, B. J., & Canter, H. M. (1986). The spatial distribution and ecology of zoochlorellae-bearing ciliates in a productive pond. *J Protozool, 33*, 557−563.

Blackburn, E. H. (1992). Telomerases. *Annu Rev Biochem, 61*, 113−129.

Blackburn, E. H., & Greider, C. W. (Eds.). (1995). *Telomeres*. Cold Spring Harbor, New York: Cold Spring Harbor Laboratory Press.

Cavalier-Smith, T. (2004). Only six kingdoms of life. *Proc Roy Soc B, 271*, 1251−1262.

Cavalier-Smith, T. (2009). Megaphylogeny, cell body plans, adaptive zones: causes and timing of eukaryotic basal radiations. *J Eukaryot Microbiol, 56*, 26−33.

Cech, T. (1987). The chemistry of self-splicing RNA and RNA enzymes. *Science, 236*, 1532−1539.

Cheer, A. Y. L., & Koehl, M. (1987). Paddles and rakes. Fluid flow through bristled appendages of small organisms. *J Theoret Biol, 129*, 17−39.

Childress, W. S., Koehl, M., & Miksis, M. (1987). Scanning currents in Stokes flow and the efficient feeding of small organisms. *J Fluid Mech, 177*, 407−436.

Chobotar, W., & Scholtyseck, E. (1982). Ultrastructure. In D. M. Hammond, & P. L. Long (Eds.), *The Biology of the Coccidia* (pp. 10−37). Baltimore: University Park Press.

Corliss, J. O. (1985). Concept, definition, prevalence and host interactions of xenosomes (cytoplasmic and nuclear endosymbionts). *J Protozool, 32*, 373−376.

Dawson, S. C., & Pace, N. R. (2003). Novel kingdom-level eukaryotic diversity in anoxic environments. *Proc Natl Acad Sci USA, 99*, 8324−8329.

Dzierzinski, F., Popescu, O., Toursel, C., Slomianny, C., Yahiaoui, B., & Tomavo, S. (1999). The protozoan parasite *Toxoplasma gondii* expresses two functional plant-like glycolytic enzymes. Implications for evolutionary origin of apicomplexans. *J Biol Chem, 274*, 24888−24895.

Fenchel, T. (1986a). *Ecology of Protozoa*. New York: Springer-Verlag.

Fenchel, T. (1986b). Protozoan filter feeding. *Progr Protistol, 1*, 65−113.

Fenchel, T., & Finlay, B. J. (1986). The structure and function of Müller vesicles in loxodid ciliates. *J Protozool, 33*, 69−76.

Fenchel, T., & Finlay, B. J. (1991). Endosymbiotic methanogenic bacteria in anaerobic ciliates: significance for the growth efficiency of the host. *J Protozool, 38*, 18−22.

Fenchel, T., Perry, T., & Thane, A. (1977). Anaerobiosis and symbiosis with bacteria in free-living ciliates. *J Protozool, 24*, 154−163.

Fichera, M., & Roos, D. (1997). A plastid organelle as a drug target in apicocomplexid parasites. *Nature, 390*, 407−409.

Finlay, B. J. (1990). Ecology of free-living protozoa. *Adv Microb Ecol, 11*, 1−36.

Finlay, B. J., & Fenchel, T. (1986). Physiological ecology of the ciliated protozoon *Loxodes*. *Rep Freshwater Biol Ass, 54*, 73−96.

Finlay, B. J., Fenchel, T., & Gardner, S. (1986). Oxygen perception and O_2 toxicity in the freshwater ciliated protoozoon *Loxodes*. *J Protozool, 33*, 157−165.

Fok, A. K., & Allen, R. D. (1990). The phagosome−lysosome membrane system and its regulation in Paramecium. *Int Rev Cytol, 123*, 61−94.

Foster, K. W., & Smyth, R. D. (1980). Light antennas in phototactic algae. *Microbiol Rev, 44*, 572−630.

Francis, D. (1967). On the eyespot of the dinoflagellate, *Nematodinium*. *J Exp Biol, 47*, 495−501.

Görtz, H. D. (1996). Symbiosis in ciliates. In K. Hausmann, & P. Bradbury (Eds.), *Ciliates* (pp. 441−462). Stuttgart: Gustav Fischer.

Greuet, C. (1978). Organization ultrastructurale de l'ocelloide de Nematodinium. Aspect phylogenetique du photorecepteur de Peridiniens Warnowiidae Lindemann. *Cytobiologie, 17*, 114−136.

Greuet, C. (1987). Complex organelles. In F. J. R. Taylor (Ed.), *The Biology of Dinoflagellates* (pp. 119−142). Oxford: Blackwell.

Hausmann, K., & Hülsmann, N. (1996). *Protozoology*. Stuttgart: Georg Thieme Verlag.

Heuser, J., Zhu, Q., & Clarke, M. (1993). Proton pumps populate the contractile vacuoles of *Dictyostelium amoebae*. *J Cell Biol, 121*, 1311−1327.

Hinrichsen, R. D., & Schultz, J. (1988). Paramecium: a model system for the study of excitable cells. *Trends Neur Sci, 11*, 27−32.

Hyams, J. (1982). The Euglena paraflagellar rod: structure, relationship to other flagellar components and preliminary biochemical characterization. *J Cell Sci, 55*, 199−210.

Iglesias, P. A., & Devreotes, P. N. (2008). Navigating through models of chemotaxis. *Curr Opin Cell Biol, 20*, 35−40.

Jeon, K. W. (1987). Change of cellular pathogens into required cell components. *Ann NY Acad Sci, 503*, 359−371.

Jeon, K. W. (1995). The large, free-living amoebae: wonderful cells for biological studies. *J Eukaryot Microbiol, 42*, 1−7.

Jeon, T. J., & Jeon, K. W. (2003). Characterization of smas genes of *Amoeba proteus* and the endosymbiotic X-bacterium. *J Eukaryot Microbiol, 50*, 61−69.

Jomaa, H., Wiesner, J., Sanderbrand, S., et al. (1999). Inhibitors of the nonmevalonate pathway of isoprenoid biosynthesis as antimalarial drugs. *Science, 285*, 1573−1576.

Katz, L., & Bhattacharya, D. (2006). *Genomics and Evolution of Microbial Eukaryotes*. Oxford: Oxford University Press.

Keeling, P. (2009). Chromalveolates and the evolution of plastids by secondary endosymbiosis. *J Eukaryot Microbiol, 56*, 1−8.

Kim, E., Harrison, J. W., Sudek, S., et al. (2011). Newly identified plastid-bearing branch on the eukaryotic tree of life. *Proc Natl Acad Sci, 108*, 1496−1500.

Köhler, S., Delwiche, C. F., Denny, P., et al. (1997). A plastid of probable green algal origin in Apicomplexan parasites. *Science, 275*, 1485−1489.

Melkonian, M., & Robenek, H. (1984). The eyespot apparatus of flagellated green algae: a critical review. *Progr Phycol Res, 3*, 193−268.

Müller, M. (1993). The hydrogenosome. *J Gen Microbiol, 139*, 2879−2889.

Naitoh, Y., & Kaneko, H. (1973). Control of ciliary activities by adenosine triphosphate and divalent cations in Triton-extracted models of *Paramecium caudatum*. *J Exp Biol, 58*, 657−676.

Park, M., Yun, S. T., Kim, M. S., Chun, J., & Ahn, T. (2004). Legionella-like endosymbiotic X-bacterium in *Amoeba proteus*: a proposal for ' *Candidatus Legionella jeonii* sp. nov.' *Environ Microbiol, 6*, 1252−1263.

Parsons, M. (2004). Glycosomes: parasites and the divergence of peroxisomal purpose. *Mol Microbiol, 53*, 717−724.

Patterson, D. J., Bhattacharya, D., Cole, J., et al. (2006). Classifying protists. *Microbiol Today, Feb 07*, 44−45.

Pawlowski, J., & Burki, F. (2009). Untangling the phylogeny of amoeboid protists. *J Eukaryot Microbiol, 56*, 16−25.

Roberts, A. M. (1981). Hydrodynamics of protozoan swimming. In M. Levandowsky, & S. H. Hutner (Eds.) (2nd ed.). *Biochemistry and Physiology of Protozoa, Vol. 4* (pp. 5−66) New York: Academic Press.

Saimi, Y., & Kung, C. (1987). Behavioral genetics of *Paramecium*. *Annu Rev Genet, 21*, 47−65.

Sam-YelIowe, T. Y. (1996). Rhoptry organelles of the apicomplexa: their role in host cell invasion and intracellular survival. *Parasitol Today, 12*, 308−316.

Sherwin, T., & Gull, K. (1989). The cell cycle of *Trypanosoma brucei brucei*: Timing of event markers and cytoskeletal modifications. *Phil Trans Roy Soc ser B, 323*, 575−588.

Simpson, A. G. B., & Patterson, D. J. (2006). Current perspectives on high-level groupings of protists. In L. Katz, & D. Bhattacharya (Eds.), *Genomics and Evolution of Microbial Eukaryotes*. Oxford: Oxford University Press.

Smyth, R. D., Saranak, J., & Foster, K. W. (1988). Algal visual systems and their photoreceptor pigments. *Progr Phycol Res, 6*, 254−286.

Soldo, A. T. (1987). Parauronema and its xenosomes: a model system. *J Protozool, 34*, 447−451.

Soldo, A. T., Brickson, S. A., & Vazquez, D. (1992). The molecular biology of a bacterial endosymbiont. *J Protozool, 39*, 196−198.

Stoeck, T., & Epstein, S. (2003). Novel eukaryotic lineages inferred from small-subunit rRNA analysis of oxygen-deprived marine environments. *Appl Environ Microbiol, 69*, 2657−2663.

Stoecker, D. K., Michaels, A. E., & Davis, L. H. (1987). Large proportion of marine planktonic ciliates found to contain functional chloroplasts. *Nature, 326*, 790−792.

Tachezy, J. (2008). *Hydrogenosomes and Mitosomes: Mitochondria of Anaerobic Protozoa*. Heidelberg: Springer-Verlag.

Taylor, F. J. R., Blackbourne, D. J., & Blackbourne, J. (1971). The red-water ciliate *Mesodinium rubrum* and its "incomplete symbionts": a review including new ultrastructural observations. *J Fish Res Bd Can, 28*, 391−407.

Valentine, M., Yano, J., & Van Houten, J. (2008). Chemosensory transduction in *Paramecium*. *Jap J Protozool, 41*, 1−7.

Van der Giezen, M., Tovar, J., & Clark, C. G. (2005). Mitochondrion-derived organelles in Protists and fungi. *Int Rev Cytol, 244*, 173−225.

Van Haastert, P. J. M., & Veltman, D. M. (2007). Chemotaxis: navigating by multiple signaling pathways. *Sci STKE,* 40.

Wolf, M., Seibel, P. N., Dandekar, T., & Lynn, D. H. (2006). A java applet for exploring the new higher level classification of eukaryotes with emphasis on the taxonomy of protists. *J Eukaryot Microbiol, 53*, 315.

Woodward, R., Garden, M. J., & Gull, K. (1994). Molecular characterisation of a novel, repetitive protein of the paraflagellar rod in *Trypanosoma brucei*. *Mol Biochem Parasitol, 67*, 31−39.

Chapter 50

Physiology of Prokaryotic Cells

Dennis W. Grogan

Chapter Outline

I. THE DIVERSITY OF PROKARYOTIC ORGANISMS

Prokaryotic cells represent the smallest and simplest form of life that can metabolize, grow and reproduce. They are presumed to resemble the earliest forms of life and they reproduce much more quickly than multicellular organisms do. Taken together, these two properties imply that prokaryotic organisms have had more opportunity to evolve (by orders of magnitude) than plants or animals have had; accordingly, this predicts that prokaryotes should have the most functionally efficient, diverse and specialized of cells, despite their structural simplicity. The key to this paradox is the recognition that genetic variation and natural selection should allow a unicellular organism to improve its performance and acquire new functions without becoming structurally complex. Furthermore, as environments, survival strategies and ecological niches change over time, the criteria of optimal cellular function change which, in turn, sets the stage for new rounds of optimization in various directions. The resulting diversification and specialization can also be expected to make certain features superfluous in certain lineages, leading to cells that may be even simpler than their predecessor.

Functional specialization and optimization of a structurally simple cell seems to account for the observed diversity of modern prokaryotes. Molecular measures of divergence, such as small-subunit ribosomal RNA sequence, indicate that two prokaryotic lineages separated very early and that each encompasses more molecular diversity than multicellular organisms (Fig. 50.1). The two groups distinguished by this early split, *Bacteria* and *Archaea*, each have phylogenetic status equivalent to that of all eukaryotic organisms and the three resulting taxonomic units have been termed *Domains* (Woese et al., 1990). This extensive divergence is also evident in terms of cellular function. Certain bacteria and archaea have metabolic properties not represented among eukaryotes,

Cell Physiology Sourcebook. DOI: 10.1016/B978-0-12-387738-3.00050-0

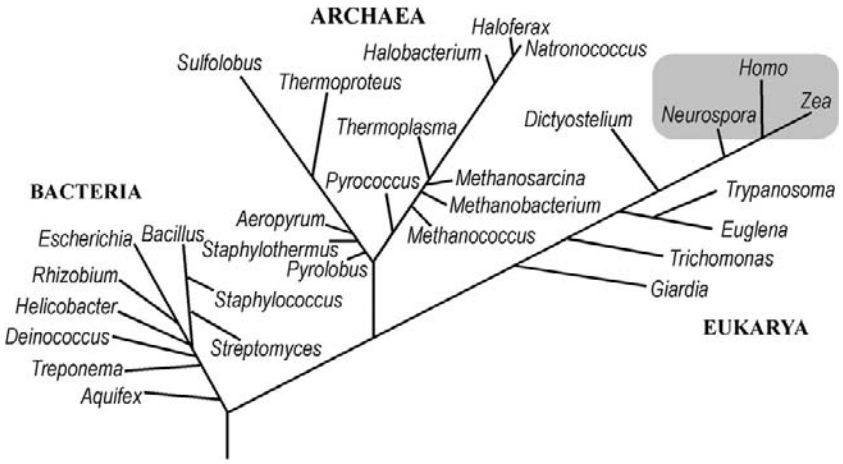

FIGURE 50.1 Phylogenetic relatedness of cellular organisms. Major groups of cellular organisms are indicated by genus names. The lengths of branches connecting two genera indicate the molecular divergence between them, as defined by the sequences of small-subunit ribosomal RNAs (16S rRNAs of bacteria and archaea, 18S rRNAs of eukarya [eukaryotes]). The gray box approximates the molecular diversity of multicellular organisms as measured by small-subunit rRNA.

including N_2 fixation, anoxic photosynthesis, additional routes of CO_2 assimilation and adaptation to extreme environmental conditions. Similarly, archaea (singular: archaeon, or less commonly, archaeum) have cellular features and metabolic pathways not found in bacteria. These uniquely archaeal features include isoprenoid membrane lipids (found in all archaea) and the ability to make methane (found in a number of genera).

One practical consequence of the deep diversity of the bacterial and archaeal lineages is that it precludes any one organism, such as the bacterium *Escherichia coli*, from modeling all aspects of prokaryotic physiology, even though this and several other species can be analyzed in great detail. It should also be noted that some components of eukaryotic cells have bacterial origins. In particular, at least two eukaryotic organelles, the *mitochondrion* and the *chloroplast*, resulted from endosymbiotic acquisitions of bacteria by progenitors of modern eukaryotic cells (Scwartz and Dayhoff, 1978). This relationship provides a context for understanding molecular structure and function of both the eukaryotic organelle and the bacterial cell.

II. PROKARYOTIC CYTOLOGY

IIA. Major Structural Types

Cells of bacteria and archaea generally measure about 1 µm in diameter and thus have about 0.1% or less of the volume and mass of a typical eukaryotic cell. This extremely small size limits the ability of light microscopy to visualize the structural features of these cells (Fig. 50.2). Prokaryotic cells generally have no obvious cytoskeleton, mitotic apparatus or intracellular organelles and span a limited range of structural complexity.

This range is illustrated in Fig. 50.3 as four structural types. Cells of the simplest structural type (Fig. 50.3, panel I) have only a *nucleoid*, a *cytoplasm* and a *cytoplasmic membrane*, each of which is described in more detail below. Examples of this truly minimal cell are relatively rare in nature and include members of the genera *Mycoplasma* and *Thermoplasma*. The former are bacteria, some of which are opportunistic pathogens, while the latter are archaea found in heated acidic soils (Kletzin, 2007). Both genera are osmotically fragile, due to an absence of cell walls (see below).

IIB. Nucleoid

Most prokaryotes have a single chromosome consisting of a single circular DNA of several million base-pairs which is neither confined within a nucleus nor evenly dispersed throughout the cytoplasm. The DNA instead occupies a convoluted region near the center of the cell, called the *nuclear region* or *nucleoid*, which bears a functional analogy to the eukaryotic nucleus (see Fig. 50.3, panel I).

FIGURE 50.2 Live bacteria under the microscope. This is a light micrograph (phase contrast) of *Escherichia coli* cells suspended in growth medium. The average width of the cells is about 0.5 µm; arrowheads show site of constriction (septation) in a cell undergoing division. The micrograph illustrates the limited structural information obtainable by optical methods due to the small size of prokaryotic cells.

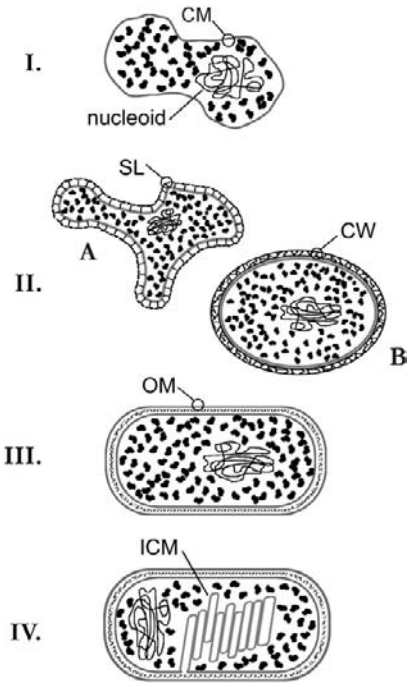

FIGURE 50.3 Examples of prokaryotic cellular structure. The limited range of cellular complexity found among prokaryotic cells has been represented in this diagram by four structural types. I: The minimal cell includes only a nucleoid, cytoplasm and cytyoplasmic membrane (CM). II. Most archaea (A) have an additional S-layer (SL), composed of glycoprotein subunits, providing external structural support for the cell membrane, whereas Gram-positive bacteria (B) have a thick cell wall (CW) composed of peptidoglycan. III. Gram-negative bacteria have a thin cell wall sandwiched between the CM and a second diffusional barrier, the outer membrane (OM). IV. Gram-negative photosynthetic bacteria produce a system of intracytoplasmic membranes (ICM). These contain specialized light-harvesting pigments and may be topologically continuous with each other and the CM.

The nucleoid replicates and partitions itself into daughter cells during growth and cell division and maintains its compacted form despite ongoing replication, transcription and repair. Cations, including Mg^{2+}, spermidine and other polyamines and small "histone-like" proteins contribute to this condensation. In *E. coli*, longer-range organization occurs in the form of 50 to 100 topologically constrained domains or "loops". Lysis of cells under appropriate conditions (non-ionic detergent and high salt concentration) releases nucleoids in a compact, relatively intact form and allows the loops to be visualized by electron microscopy (EM) (Pettijohn, 1996).

IIC. Cytoplasm

All other components of the cell interior are collectively termed the *cytoplasm* or *cytosol*. Although fluid, this mixture is very concentrated and probably reflects a complex and dynamic series of macromolecular associations. The cytosol of an *E. coli* cell adapted to growth in simple glucose medium at 37°C contains about 19 000 ribosomes which, together with transfer RNA and various translation factors, account for nearly half of the total cell mass. This large investment of cellular resources in the machinery of protein synthesis enables the *E. coli* cell to reproduce itself every 40 min under these conditions (Neidhardt et al., 1990). Enriching the simple glucose medium with other nutrients (such as peptides) increases the ribosome content and growth rate even more.

The lack of internal compartmentalization in most prokaryotic cells contributes to their ability to grow quickly and to respond quickly to environmental change. In general, prokaryotic cells have no diffusional barriers segregating the sources of energy, raw material or sequence information needed for DNA, RNA and protein synthesis; this lack of compartmentalization and the small dimensions of the cell ensure that molecular diffusion is extremely rapid throughout the cell interior. Transcription and translation are temporally and spatially coupled, so that ribosomes begin "reading" the mRNA before the mRNA itself has been completed and released from the transcription complex. This coupling not only supports rapid growth, but also provides uniquely prokaryotic modes of genetic regulation, as demonstrated by the phenomenon called *attenuation*. In this regulatory mechanism, adequate levels of particular amino acids lead to disruption of the normally tight coupling between ribosome and RNA polymerase as it begins to transcribe the corresponding amino acid biosynthetic genes. This transient uncoupling, in turn, causes RNA polymerase to terminate transcription before it reaches the biosynthetic genes, thereby avoiding wasteful overproduction of the corresponding enzymes (Yanofsky and Crawford, 1987).

IID. Cytoplasmic Membrane

The third component of the minimal prokaryotic cell structure (see Fig. 50.3 panel I) is a unit membrane called the *cytoplasmic (cell) membrane* (CM) which chemically separates the cytosol and nucleoid from the external environment. A bacterial CM generally conforms to the fluid mosaic model of biological membranes (see Chapter 3). Its matrix is a phospholipid bilayer impermeable to ionic or large polar molecules but intrinsically permeable to gases and water. The selective impermeability is essential for viability, because without it the cell cannot maintain ion potentials or retain metabolites (see below). However, cellular function also requires some chemical exchange with the surroundings, including nutrient uptake and environmental sensing. These functions are provided by a large number of different integral and peripheral proteins which breach the phospholipid bilayer with solute-specific pumps and gates. By means of these proteins, which comprise about 70% of the CM by weight, bacteria maintain

transmembrane gradients and controls transmembrane fluxes of critical solutes. Archaeal membranes appear to have analogous structure and function, although the polar lipids that provide the lamellar barrier differ radically from the phospholipids of other cells. Archaea contain only sn-(2,3 di-O-alkyl)-glycerol membrane lipids, in which the hydrocarbon chains are C_{20} or C_{40} saturated isoprenoids attached to the glycerol backbone via ether linkages (Boucher, 2007).

IIE. Cell Wall

Most archaea and bacteria have some form of *cell wall* immediately outside the cytoplasmic membrane (see Fig. 50.3, IIA, IIB). This structure solves a specific threat to the cell created by hypotonic environments, namely, that the CM cannot block the diffusion of water into the cell interior. Hypotonic environments thus promote cell swelling and rupture, i.e. *lysis*, of cells. Bacterial cell walls prevent lysis by enclosing the cell in a container that, like the cellulosic cell walls of plants, resists expansion. In contrast to plant cell walls, however, the bacterial cell wall is composed of a covalently cross-linked polymer, called *peptidoglycan* or *murein*. The repeating unit (two amino sugars linked via β-1,4 glycosidic bonds) is linked to form linear glycan chains, which are joined at frequent intervals by peptide bridges (Fig. 50.4). This results in one huge, bag-like macromolecule of high tensile strength that completely surrounds the cell membrane. This structural support allows the bacterial cell to maintain an osmotic (turgor) pressure (see Chapter 16), which can be as high as 20 atm. A morphological consequence of constitutive turgor pressure is that the bacterial cell wall determines cell shape and therefore plays a major role in cell division. This can be demonstrated in the effects on cell morphology of antibiotics that specifically disrupt the normal synthesis of peptidoglycan. In rod-shaped bacteria, low concentrations of β-lactam antibiotics, which block cell division but not cell growth, lead to elongated cells of normal diameter. At higher antibiotic concentrations, bulges (rather than constrictions) form at the normal site of bacterial cell division and, at very high antibiotic concentrations, the rod-like cells swell into spheres and lyse (Schwarz et al., 1969).

Some archaea synthesize a polymeric cell wall material similar to peptidoglycan, but most have only a layer of protein or glycoprotein that provides mechanical support for the CM. These archaeal *surface- (S-) layers* (Fig. 50.5) can be very strong structurally, despite the fact that they form by non-covalent association of individual subunits. For example, an experimental procedure used to purify bacterial cell walls as intact sacculi involves hot sodium dodecyl sulfate (SDS) extraction. Application of this method to *Sulfolobus* cells under mildly acidic conditions yields virtually intact S-layer sacculi. The non-covalent nature of the glycoprotein subunit interactions is seen, however, in the ease with which these structures dissociate into monomers at elevated pH (Grogan, 1996). Some archaeal S-layer cell walls appear to be relatively rigid and retain the cell shape, whereas others are flexible and thus not strictly equivalent to bacterial cell walls in all respects.

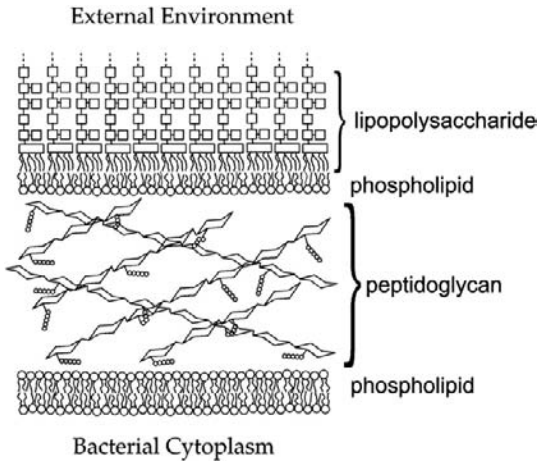

FIGURE 50.4 The cell envelope of Gram-negative bacteria. The bacterial cell wall (CW) is composed of peptidoglycan, whose repeating unit consists of a dimer of two modified amino sugars: N-acetyl muramic acid and N-acetyl glucosamine. Each repeating unit has a short peptide (circles) attached to the N-acetyl muramic acid; the peptides of adjacent glycan chains become joined by enzymes in the periplasm to form the periodic cross-links found in the mature peptidoglycan polymer. The outer membrane (OM) consists of one leaflet of lipopolysaccharide (LPS) and one of phospholipid. Each LPS molecule has a large polysaccharide chain (linked squares) whose precise structure depends on the bacterial species. The cytoplasmic membrane (CM) is composed of phospholipid. In addition to lipid, both the OM and CM contain protein species, which are not depicted in the figure.

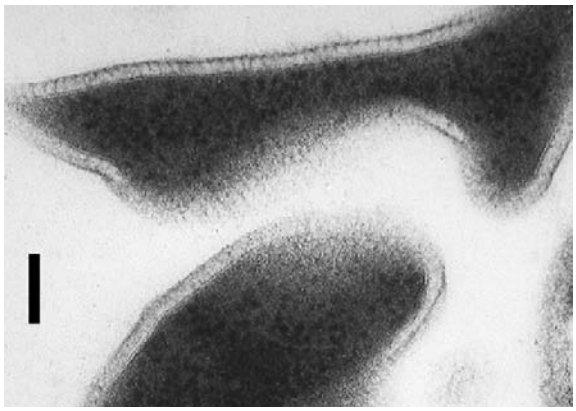

FIGURE 50.5 Cells of *Sulfolobus acidocaldarius*, an archaeon from geothermal environments (Section VII). The ultrathin sections illustrate the irregular cell shape and extracellular location of the glycoprotein S-layer. The S-layer is held at a fixed distance from the cytoplasmic membrane by a spacer (Jaenicke and Böhm, 1998); this results in a "picket fence" appearance for the boundary around cells or cell ghosts at certain points. Bar = 100 nm.

IIF. Outer Membrane

A third, more complex cellular architecture seen in bacteria includes a second lipid bilayer, called the *outer membrane*, which surrounds the cell wall (see Fig. 50.3 panel III). This creates a protected compartment around the cell, bounded by the cytoplasmic and outer membranes, called the *periplasm* (Fig. 50.6). An important bacterial identification technique, the Gram stain, exploits the property of the peptidoglycan cell wall in these bacteria that it is relatively thin and does not retain a complex of crystal violet stain and iodine when rinsed with ethanol or acetone. This staining procedure therefore distinguishes bacteria which have the cell architecture shown in Fig. 50.3 panel IIB (Gram-positive), from those which have the more complex cell envelope illustrated in Fig. 50.3 panel III (Gram-negative). Table 50.1 summarizes the major differences between Gram-positive and Gram-negative bacteria.

The biochemical composition of the outer membrane (OM) differs from that of the bacterial CM with respect to both lipid and protein constituents. With respect to lipid, the OM is a hybrid membrane. Its inner leaflet, which faces the periplasm, incorporates the same phospholipids as the CM does. The outer leaflet, however, consists of much higher molecular weight class of lipid known as *lipopolysaccharide*, or *LPS* (see Fig. 50.4). With respect to protein, the OM has only a few protein species, but these are abundant (Nikaido and Vaara, 1985), which contrasts with the broad heterogeneity of CM proteins.

These two compositional features support the primary physiological function of the OM, which is shielding the Gram-negative cell from toxic, hydrophobic compounds in the environment. An intact LPS leaflet greatly impedes diffusion of soluble hydrophobic (i.e. lipophilic) molecules across the OM. This presumably reflects the permeability properties of the dense array of cooperatively interacting charged and polar sugar residues at the membrane surface, through which non-polar solutes must pass (Fig. 50.4). Experimental evidence of the importance of this screening function can be seen in the sensitivity of Gram-positive bacteria and LPS-depleted Gram-negative cells to toxic dyes, detergents and hydrophobic antibiotics. As in the case of the CM, the OM must nevertheless allow passage of nutrients, which is mediated by relatively non-specific solute channels, or *pores*. These structures form as trimers of corresponding proteins, called *porins*. In *E. coli*, OM pores exclude solutes with molecular weights of about 700 Da and above and tend further to discriminate against anionic solutes (Nikaido and Vaara, 1985).

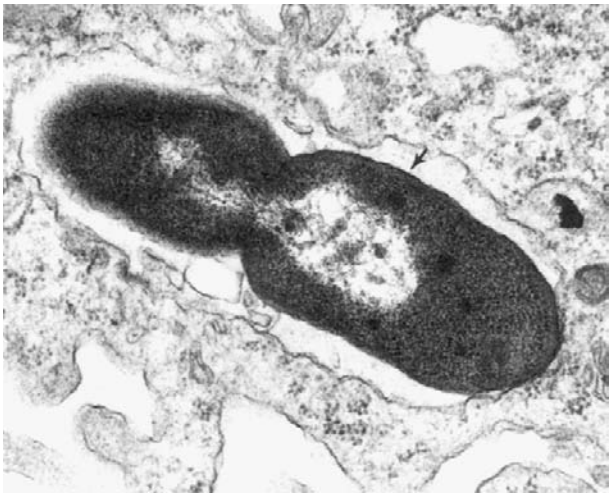

FIGURE 50.6 Electron micrograph (ultrathin section) of a Gram-negative bacterial cell. An *E. coli* cell is shown that has been engulfed by a macrophage and is in the late stages of cell division. The nucleoid is visible as a clear zone in each of the nascent daughter cells. The arrowhead indicates a region in which the three-layer structure of the Gram-negative cell envelope (CM-CW-OM) can be seen. (*Photograph courtesy of A. Mukkada*).

IIG. Intracellular Structures

Still greater complexity can be seen in a few bacterial cells which incorporate additional intracellular structures into the basic bacterial cell architecture described above. Examples of these specialized structures include photosynthetic membranes, internal cytoplasmic compartments and gas vesicles.

Although different groups of photosynthetic bacteria have biochemically diverse forms of photosynthesis, most involve specialized photosynthetic membranes located in the cytoplasm (see Fig. 50.3 panel IV). In the case of cyanobacteria, the intracellular photosynthetic membranes appear to be collapsed and lamellar in form and are called *thylakoids*, in conformity with the corresponding membranes of plant chloroplasts (see Chapter 51). For other types of photosynthetic bacteria, the membranes assume more rounded, vesicular shapes; these *intracytoplasmic membranes* (ICM) appear to be continuous with the CM (Dierstein et al., 1981).

Other membranes have been observed inside several genera of non-photosynthetic bacteria; most of the membranes have no confirmed metabolic function and they divide the cytoplasm into two or more compartments. These bacteria, collectively termed planctomycetes, all lack the peptidoglycan cell wall found in most bacteria and all have at least one large, internal membrane vesicle that divides the cytoplasm into two compartments of comparable volumes. One of these vesicles encloses the nucleoid, which tends to be highly condensed, forming a well-defined structure clearly visible in EM thin sections. In at least one species, a double-membrane structure surrounds the nucleoid, forming an analog of the eukaryotic nuclear membrane. Other species have multiple distinct membranes that create a nested series of cellular compartments (Fuerst, 2005).

TABLE 50.1 Cellular Properties of Gram-Positive and Gram-Negative Bacteria

Property	Gram-Positive Bacteria	Gram-Negative Bacteria
Cell wall		
Chemical constituents	Peptidoglycan	Peptidoglycan
	Teichoic, lipoteichoic and teichuronic acids	
Typical thickness	20–80 nm	2–3 nm
Outer membrane	(Absent)	Composed of LPS and phospholipid
Intrinsic resistance to detergents, dyes, and certain antibiotics	Low	High
Dessication resistance	High	Low
Examples	*Clostridium*	*Escherichia*
	Lactobacillus	*Thiobacillus*

Other bacteria and archaea produce small, regular vesicles in their cytoplasms which form from the self-assembly of protein subunits. The assembly process excludes water, so that the resulting vesicles contain only gas. The function of these *gas vesicles* (or gas vacuoles) appears to be to provide buoyancy, allowing the cell to migrate vertically in natural waters such as ponds. Consistent with this role, their synthesis is often regulated by environmental conditions, such a light intensity and oxygen concentration (Walsby, 1994).

IIH. Extracellular Structures

Bacteria and archaea have several structurally distinct types of external filaments which are anchored in the CM. *Flagella* are helical protein filaments that support rapid swimming motility. Depending on the bacterial species, they may be single or numerous, clustered or dispersed over the cell, or absent altogether. Each flagellum extends several cell lengths (2–20 μm) and is rotated by a protein complex at its base; as a result, it acts like a propeller to push the cell through its liquid medium. Thus, bacterial flagella have a cellular function (i.e. motility) analogous to that of eukaryotic cilia and flagella, but no structural, molecular or mechanistic homology to them (see Chapter 47).

Pili and *fimbriae* are structurally similar to each other and distinct from flagella. Both consist of straight protein fibers that protrude less than about 1 μm from the cell, giving it a bristled or hairy appearance in the electron microscope. Both types of appendages appear to mediate attachment of a bacterium to another cell. In many cases, pili attach a "donor" bacterium to a recipient cell for the subsequent transfer of DNA (conjugation), whereas fimbriae typically attach a pathogenic bacterium to specific cells of its host. In some bacteria, pili mediate a type of slow, surface-dependent motility (Strom and Lory, 1993).

Flagella, pili and fimbriae all form via self-assembly of small protein subunits. Bacterial flagella grow by adding protein subunits to the distal tip, which requires the subunits (monomers) to travel from the cytoplasm to the growing tip of the flagellum, several cell lengths away. This is accomplished by using the hollow core of the flagellum itself as a conduit. In contrast, pili and fimbriae appear to polymerize at the base of the fiber, where it attaches to the CM (Neidhardt et al., 1990).

In addition to these small, discrete structures, many bacteria secrete hydrophilic polymers (usually polysaccharides) that form a gelatinous matrix around the cell. If this matrix remains attached to the cell and forms a defined zone around it, it is called a *capsule*. Capsules inhibit the ingestion of bacteria by human phagocytes or by protozoa and may also help free-living bacteria survive temporary desiccation or starvation. Even if secreted polysaccharide does not form a defined capsule, it aids the non-specific adherence of bacteria to wetted solid surfaces, leading to the formation of "*biofilms*". Bacteria in biofilms tend to survive much higher concentrations of antibiotics than bacteria suspended in fluids and, accordingly, pose serious health risks if they form on surfaces of heart valves or implanted devices (Costerton et al., 1987).

III. ENERGETICS OF BACTERIAL CELLS

With a few notable exceptions, the endergonic cellular processes of bacteria are driven via enzymatic coupling to the hydrolysis of ATP and thus require the cell continuously

to re-supply this energy currency. An *E. coli* cell growing aerobically using glucose regenerates ATP by two fundamentally different strategies: *substrate-level phosphorylation* and *chemiosmotic coupling*. Other prokaryotes may use these two processes in ways that differ from *E. coli* and related bacteria, or may use only one of them.

IIIA. Substrate-Level Phosphorylation

As also occurs in the eukaryotic cytosol, soluble enzymes in the *E. coli* cytoplasm convert one mole of glucose to two moles of pyruvic acid via the Embden–Meyerhof–Parnas pathway ("glycolysis"); this process results in phosphorylation of 2 moles of ADP to form ATP and the reduction of 2 moles NAD^+ to NADH. If the cell has no exogenous electron acceptors available (see below), the two moles of ATP represents the cell's sole energy harvest and the reduced co-factor (NADH) represents unusable electrons. If the electrons are not transferred to some other molecule, the oxidized cofactor (NAD^+) will not be regenerated and additional glucose cannot be metabolized. Bacteria (and eukaryotic cells) solve the latter problem by transferring the electrons to pyruvate or its metabolites, thereby forming various organic compounds which the cell excretes; examples of these end-products include lactic, acetic, propionic or butyric acids and ethanol, butanol or acetone. This metabolic strategy of substrate-level phosphorylation, made possible by reduction of metabolites derived from the growth substrate, constitutes the biochemical definition of *fermentation*.

IIIB. Chemiosmotic Coupling

The general features of chemiosmotic coupling in bacteria and archaea resemble those of mitochondria and chloroplasts, which are described elsewhere in this volume (see Chapters 5 and 51). Also called *oxidative phosphorylation*, the process has two distinct stages, each of which involves vectoral enzymatic processes at the CM (Fig. 50.7). The first (oxidative) stage of chemiosmotic coupling transfers electrons taken from carbon compounds during glycolysis and the tricarboxylic acid cycle to some electron acceptor, such as O_2, via a series of enzymatically catalyzed, strongly exergonic, oxidation–reduction reactions. This respiratory electron transport is coupled at certain points to the extrusion of protons from the cytoplasm, creating a *proton potential* or *protonmotive force* (PMF) across the CM (Fig. 50.7). The second (phosphorylation) stage converts the PMF into ATP, using an *F_1F_0 proton-translocating ATPase* to couple the entry of three protons from outside the cell to phosphorylation of an ADP molecule (Harold and Maloney, 1996). The combination of these two stages yields many times more of ATP per glucose molecule than fermentation does.

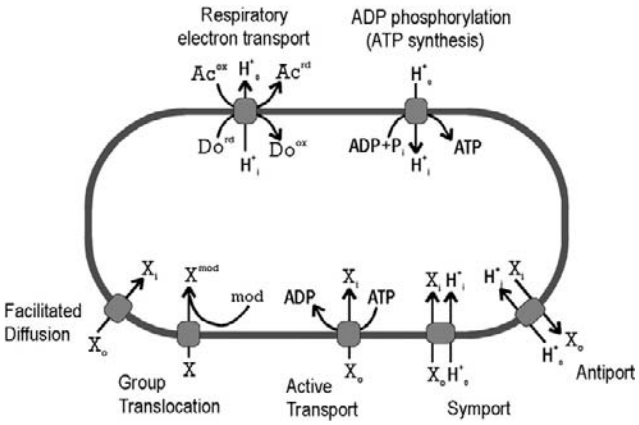

FIGURE 50.7 Energetics of solute transport across the CM. The diagram summarizes the salient features of major classes of energetic coupling to solute transport in prokaryotic cells. For example, the net result of respiratory electron transport is transfer of electrons from a donor (Do) to an acceptor (Ac) coupled to the extrusion of protons. Similarly, controlled entry of a proton through a membrane-bound ATPase drives the phosphorylation of ADP. The remaining processes are those which support growth by promoting the uptake of some necessary solute (X) from the environment. Cellular location is indicated by subscripts (o, outside; i, inside); "mod" indicates a chemical modification.

Oxygen represents only one of several terminal electron acceptors which prokaryotes can use to form a PMF. Accordingly, as summarized in Table 50.2, prokaryotes carry out various types of *anaerobic respiration*, but these may not be used under all conditions. *E. coli*, for example, can use four compounds in addition to oxygen as electron acceptors (Table 50.2), but it restricts the synthesis of the corresponding oxido-reductases according to a complex regulatory hierarchy. This hierarchy ensures that only the energetically most favorable electron acceptor is used, should more than one be available (Gunsalus, 1992).

TABLE 50.2 Respiratory Strategies of Prokaryotes

Electron Acceptor	Reduced Product	Organism
Oxygen	Water	*E. coli*, other aerobes
Nitrate	Nitrite	*E. coli*, other bacteria
Fumarate	Succinate	*E. coli*, other bacteria
Dimethyl sulfoxide	Dimethyl sulfide	*E. coli*, other bacteria
Trimethylamine oxide	Trimethylamine	*E. coli*, other bacteria
Sulfate	Hydrogen sulfide	*Desulfovibrio, Archaeoglobus**
Sulfur	Hydrogen sulfide	*Thermoproteus**
Carbon dioxide	Methane	*Methanobacterium**

**Denotes archaea; all others are bacteria.*

The PMF of a respiring bacterium represents an energetic intermediate in the regeneration of ATP by the oxidation of carbon compounds, yet even bacterial cells that are not respiring, as well as those that cannot respire, maintain a PMF. The *lactic acid bacteria*, for example, have no electron-transport chain and generate ATP only by substrate-level phosphorylation. They nevertheless have an F_1F_0 ATPase and use it in the reverse sense of respiring bacteria, i.e. to maintain a PMF at the expense of ATP hydrolysis. This may reflect the fact that certain basic prokaryotic processes use the PMF directly as their energy source. *E. coli*, for example, uses direct coupling to H^+ influx, rather than ATP hydrolysis, to transport several nutrients (see below) and to drive flagellar rotation.

The PMF consists of two components: the electrical potential ($\Delta\psi$) and the chemical potential (ΔpH). Although the small size of prokaryotic cells precludes direct electrical measurement of these potentials, they can be estimated using chemical probes. The $\Delta\psi$ can be measured by the fluorescence yield of triphenylmethyl- or tetraphenylphosphonium ions, or by the equilibrium distribution of radioactive K^+ across the CM in the presence of valinomycin. The ΔpH can be estimated by the distribution of radioactive weak acids, such as acetic or benzoic acids, across the CM and the overall PMF can be independently estimated by the maximal accumulation of lactose by cells able to transport, but not metabolize, this sugar. According to these methods, which generally agree, a typical *E. coli* cell in medium at pH 6.5 has a $\Delta\psi$ of about 100 mV (inside negative) and a ΔpH that corresponds to an additional 100 mV (Harold and Maloney, 1996).

In those bacteria which live at pH values near 7, both components contribute significantly to the PMF. Extreme acidophiles, however, may maintain an electrical potential which is of opposite polarity as the normal $\Delta\psi$, i.e. inside positive. This helps counteract the very large ΔpH across the cytoplasmic membrane, which can be more than 4 pH units in these organisms. In contrast, extreme alkaliphiles, which grow at external pH values of 10−12, have a negative ΔpH across the CM and, accordingly, a very large $\Delta\psi$ (White, 2000). A number of these organisms, and certain neutrophiles from marine environments, use the more abundant Na^+ ion, rather than protons, to drive ATP synthesis via Na^+-coupled ATP synthases (Skulachev, 1994).

IV. SOLUTE TRANSPORT

While certain membrane proteins generate the ion potentials and ATP needed to drive metabolism, other proteins use related processes to transport a wide range of organic compounds and inorganic ions into the cell as raw material for metabolism and growth. These systems employ different mechanisms and they differ with respect to functional properties, including energetic cost, solute specificity and ability to concentrate the solute inside the cell. These functional properties, in turn, affect biological properties of the organism, including its ability to scavenge critical nutrients from its environment. Fig. 50.7 summarizes the basic transport strategies used by bacterial cells, and the energetic consequences of these processes, as described below.

IVA. Facilitated Diffusion

Although facilitated diffusion (see Fig. 50.7) is mechanistically simple and energetically cheap, it is rare among bacterial transport systems, presumably because it also relatively ineffective. One of the best-studied examples of a facilitated diffusion through a bacterial membrane is glycerol uptake in *E. coli*. In this case, extracellular glycerol diffuses passively through a polyol-specific membrane channel encoded by the *glpF* gene.

IVB. Group Translocation

In an elaboration of facilitated diffusion, the solute becomes chemically modified upon entering the cytoplasm. The chemical modification, or "group translocation" (typically phosphorylation or phosphoribosylation), converts an uncharged solute molecule into an ion that cannot diffuse out through the same membrane-bound carrier. In this way, the uncharged species actually transported by the channel can remain at a lower steady-state concentration inside the cell than outside and the modified solute can be concentrated in the cytoplasm, due to the investment of chemical energy. In most cases, however, the "trapping reaction" doubles as the first step in metabolizing the solute, so the modified form does not necessarily accumulate to high steady-state concentrations.

IVC. Active Transport

Active transport in bacteria is defined by the following features (Neidhardt et al., 1990):

1. specific steric recognition between the solute and a membrane-bound transport protein
2. release of the solute into the cytoplasm in its unmodified form
3. accumulation against a solute concentration gradient, and
4. expenditure of energy.

Two types of active transport are distinguished from each other by the immediate source of energy used (see Fig. 50.7). The first type requires the hydrolysis of ATP or an equivalent high-energy phosphoryl bond. In these

systems, the membrane-bound carriers typically consist of several subunits, one of which contains an ATP-binding site (Furlong, 1987). In Gram-negative bacteria, such a transporter often utilizes a non-membrane (i.e. soluble) protein located in the periplasm. Transport requires these periplasmic solute-binding proteins, as demonstrated by the fact that cold hypotonic shock treatment of bacterial cells, which releases only periplasmic proteins, also destroys transport capability. Studies of bacterial mutants and of cytoplasmic membrane vesicles confirm that the membrane-bound transporter interacts specifically not with external solute in its free form, but with the solute complexed to its cognate binding protein (Furlong, 1987).

The second type of active transport utilizes ionic potentials directly. In some cases, the solute enters via symport with a proton, in other cases, with an Na^+ ion. Alternatively, certain ions, such as Ca^{2+}, are pumped out of the cells by proton-coupled antiport systems (Harold and Maloney, 1996).

V. METABOLIC STRATEGIES

Prokaryotes are metabolically diverse and mediate many different conversions of compounds in their environments as a way to harvest energy and other metabolic resources. These conversions contribute to the global cycling of many ecologically essential elements and several are unique to archaea and bacteria.

VA. Autotrophy

A number of prokaryotes can derive all of their carbonaceous cell material from CO_2. This capability, termed *autotrophy*, requires environmental sources of energy and reducing equivalents (i.e. electrons). For several diverse families of bacteria (collectively called *photoautotrophs*), light provides the energy, whereas various inorganic and organic compounds in the environment provide electrons. Photoautotrophic bacteria exhibit great diversity with regard to the biochemistry of photosynthesis. Among them, only the *cyanobacteria* carry out *oxygenic photosynthesis* like that of plant chloroplasts, which reflects the ability to use water as the electron donor. Cyanobacteria contain *chlorophyll b* and have two connected *photosystems*: photosystem II (PS2) oxidizes water to supply electrons to photosystem I (PS1; see Chapter 51). This is the scheme also used by plant chloroplasts, to which cyanobacteria are evolutionarily related (Schwartz and Dayhoff, 1978).

The remaining groups of photoautotrophic bacteria perform *anaerobic (anoxygenic) photosynthesis*. They have only one photosystem, which can operate in a cyclic manner to produce a proton potential. In these cases, the electron equivalents for the reduction of CO_2 come from H_2S, H_2 or dissolved organic compounds, depending on the type of bacterium and the resources available to it. The photosynthetic pigments of the anoxygenic photoautotrophs, called *bacteriochlorophylls*, differ from cyanobacterial and plant chlorophylls in having intense absorbance maxima in the infra-red region of the spectrum. In many of these organisms, photoautotrophic growth represents only one among several metabolic options and production of photosynthetic pigments occurs only in the absence of oxygen.

Another form of autotrophy, *chemoautotrophy*, is unique to prokaryotes. Analogous to the harvesting of light energy by photoautotrophs, chemoautotrophs derive energy by mediating the oxidation and reduction of inorganic compounds in their environments. Aerobic chemoautotrophs include organisms that oxidize H_2, CO, NH_4^+, NO_2^-, elemental S, H_2S or Fe^{2+} using O_2. Anaerobic chemoautotrophs include organisms that derive energy from the reduction of CO_2 to CH_4, or of SO_4^{--} to H_2S.

Among both photo- and chemoautotrophs, at least three metabolic pathways have been identified by which CO_2 is "fixed" (i.e. reduced and incorporated into some common intermediary metabolite): (1) the *Calvin cycle*; (2) the *acetyl CoA pathway*; and (3) the *reductive tricarboxylic acid cycle* (Caldwell, 1995). Most photoautotrophic bacteria (and all green plants) use the Calvin–Benson cycle: carboxylation of ribulose bis-phosphate to yield two molecules of 3-phosphoglycerate, followed by a complex series of reactions to regenerate ribulose bis-phosphate (see Chapter 51). The acetyl-CoA pathway, used by methanogenic archaea and sulfate-reducing bacteria, involves the differential reduction of two CO_2 molecules. One is reduced to form a methyl group whereas another is reduced to form a carbonyl unit, which is condensed to the methyl group. The resulting acetyl unit is transferred to co-enzyme A for assimilation into cell material. The reductive tricarboxylic acid pathway begins with carboxylation of succinyl CoA to yield 2-oxo-glutarate, which is in turn carboxylated to yield isocitrate. The transformations of the TCA cycle then continue in reverse, leading to the cleavage of citrate by an ATP-dependent citrate lyase to yield acetyl CoA and oxaloacetate. Prokaryotes using this pathway include the "green" photosynthetic bacteria.

VB. Nitrogen Fixation

The only organisms that can fix nitrogen, i.e. convert N_2 into ammonia, are prokaryotes. This capability is relatively rare, however, and widely dispersed phylogenetically. It occurs in various aerobic, anaerobic, facultatively anaerobic bacteria (i.e. those able to grow either aerobically or anaerobically, including both heterotrophs and autotrophs) and in methanogenic archaea. N_2 reduction is carried out by a large enzyme complex, *nitrogenase*. It includes an iron-containing component and a molybdenum- and

iron-containing component and utilizes ATP plus a reduced low-potential ferredoxin or flavoprotein as the source of electrons. Nitrogenases are intrinsically O_2-sensitive and N_2-fixing prokaryotes use a variety of strategies to protect these enzymes from oxidative inactivation. For example, facultative anaerobes such as *Klebsiella* spp. express nitrogenase genes only under anaerobic conditions. Filamentous cyanobacteria, which generate O_2 during photosynthesis, sequester nitrogenase in specialized cells called *heterocysts*, in which the oxygenic photosystem II (PS2) does not operate. *Azotobacter* spp. are obligate aerobes that can fix nitrogen; they appear to scavenge intracellular O_2 by maintaining very high respiration rates.

VI. RESPONDING TO THE ENVIRONMENT

Prokaryotic cells cannot insulate themselves from the chemical and physical properties of their environments. As a result, they must routinely respond to stress and environmental change in order to optimize their growth or simply to survive. The molecular mechanisms underlying these responses are diverse, but all result in changes to the biochemical composition of the cell.

VIA. Osmotic Stress

Some cellular responses to environmental change are mediated directly by activation of existing proteins, as exemplified by the effects of osmotic stress on bacteria. A sharp increase in the extracellular solute concentration triggers a response in which the osmotic strength of the bacterial cytoplasm also increases (Neidhardt et al., 1990). In *E. coli*, the initial increase is primarily due to net K^+ uptake by transporters in the CM, which seem to sense cell turgor directly. At extremely high external ionic strength, however, K^+ accumulation alone does not appear to alleviate the deleterious effects of osmotic stress and the bacterial cells accumulate high concentrations of "*compatible solutes*" in the cytoplasm. Compatible solutes are charged organic molecules of which the two best studied examples are L-proline and glycine betaine. Typically, these compounds are scavenged from the environment and their accumulation in the cytoplasm permits growth at otherwise inhibitory external salt concentrations.

This osmotic stress response, which is typical of bacteria, indicates the physiological importance of water, solutes and turgor pressure for bacterial cells. In particular, the conservation, sophistication and energetic cost of this response suggest that turgor pressure per se is essential. This may reflect the fact that it provides the physical force that expands the bacterial cell, allowing its growth and subsequent division. Second, the importance of compatible solutes in physiological adaptation to high levels of osmotic stress suggests that these compounds perturb enzymatic and other cellular functions less than inorganic salts do, allowing them to accumulate to high intracellular concentrations with less impact on metabolism.

VIB. Acid Stress

Other responses to the environment involve changes in the pattern of gene expression which are often complex and lead to corresponding changes in the protein composition of the prokaryotic cell (Neidhardt et al., 1990). The response of enteric bacteria to pH stress provides an example of this strategy that involves changing the amount of enzymes and other proteins. When the pH of the growth medium decreases sharply, *E. coli* and *Salmonella enterica* increase the synthesis rate of about 50 proteins. These acid-induced proteins include catabolic (degradative) enzymes that decarboxylate basic amino acids (arginine, ornithine and lysine decarboxylases). The action of these enzymes on amino acids taken up from the environment generates CO_2 and diamines; the latter are exported from the cell and act to neutralize the acidic growth medium. Similarly, acid stress during anaerobic growth on a fermentable sugar increases lactate dehydrogenase and formate-hydrogen lyase; both of these enzymes divert the flow of intermediates through fermentative metabolism in ways that decrease the amount of acid produced (Slonczewski and Foster, 1996).

Many other prokaryotic responses to environmental change similarly involve changing the protein composition of the cell by modulating transcription of certain genes. This general strategy takes advantage of the relatively large biosynthetic capacity of the growing prokaryotic cell, its simple organization and a very short half-life of messenger RNA which, in *E. coli* (under standard conditions) averages 1.3 min. Studies of specific responses in bacteria have revealed an array of elegant and diverse molecular mechanisms for controlling gene expression, which lie outside the scope of this chapter. One example will be described, however, which involves transmembrane signaling and appears in many environmental responses in bacteria.

VIC. Phosphate Metabolism and "Two-Component" Regulatory Systems

When Gram-negative bacteria begin to starve for inorganic phosphate, they activate the transcription of several families of genes, whose products help the cell conserve phosphate and take up more of it from the environment (Wanner, 1993). The regulation process, which typifies a mechanism underlying many signal transduction systems in bacteria, involves the specific interaction and phosphorylation of two proteins, PhoR and PhoB, named after their respective genes in *E. coli*.

The phosphorylation state of the PhoB protein determines expression of the various genes of the

phosphate-starvation response. The phosphorylated form of PhoB (here designated "*PhoB") activates transcription of these genes, whereas the unphosphorylated form does not. The relative abundance of *PhoB is in turn determined by the conformational state of a CM protein, PhoR (Fig. 50.8). In its "activated" conformation ("*PhoR"), this protein acts as a PhoB kinase, whereas its "inactive" conformation ("PhoR") acts as a *PhoB phosphatase. Ultimately, the conformational state of PhoR is determined by the availability of inorganic phosphate in the external medium. By a mechanism which is not entirely clear, PhoR can sense the absence of phosphate-periplasmic binding protein complexes in the periplasm and assumes its active conformation under these conditions. The resulting *PhoR phosphorylates PhoB, forming *PhoB which, in turn, stimulates the transcription of *phoA* and other phosphate-scavenging genes (see Fig. 50.6). The result is a rapid increase in certain enzymatic activities which serve to alleviate a particular state of the cell, in this case, phosphate deficiency.

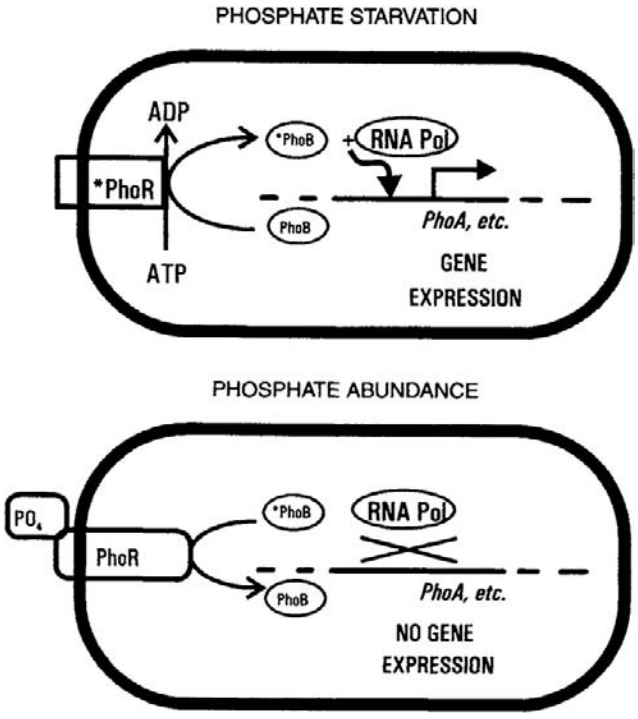

FIGURE 50.8 Essential features of two-component regulatory systems. A simplified version of phosphate-regulated gene expression is shown. The PhoR protein senses the extracellular availability of phosphate, either directly through an externally exposed domain, or indirectly via interaction with the high-affinity phosphate transporter (Neidhardt et al., 1990; Wanner, 1993). When the external phosphate concentration is low, PhoR becomes activated; this activated PhoR phosphorylates itself at the expense of intracellular ATP and then phosphorylates the PhoB protein. When the external phosphate concentration is high, PhoR becomes "de-activated"; in this form it removes phosphate groups from phosphorylated PhoB protein. PhoB is a soluble transcription factor for a specific set of genes, but stimulates transcription only when phosphorylated.

VID. Other Two-Component Regulatory Systems of Bacteria

Protein pairs resembling PhoR/PhoB mediate a wide variety of regulatory responses of bacteria to various types of environmental change (Table 50.3). The PhoR protein, a transmembrane signal transducer, typifies the *component I*, or *sensor-kinase*, of these systems. With a few exceptions, this is a protein of the cytoplasmic membrane that senses the status of some environmental parameter and accordingly adopts either of two conformations. In its "active" conformation, the component I has two characteristic phosphotransferase activities: (1) it phosphorylates one of its own histidine residues, using ATP; (2) it transfers the phosphate to an aspartyl residue on a cognate *component II* or *response regulator*. These two activities result in the net transfer of a phosphate group from ATP to the specific component II, which is usually a transcriptional regulator that activates transcription of a certain set of genes, but only in its phosphorylated form.

The similarities in interactions and biochemical properties of various components I and II (Table 50.4) are underscored by regions of sequence homology. Although they respond to diverse signals, all components I have two highly conserved sequence motifs at their carboxy termini. Similarly, all components II have sequence homology near their amino termini and various subfamilies may share regions of additional homology elsewhere in the amino acid sequence. The conserved regions of components I recognize and interact with the conserved regions of components II as an essential part of the signal-transmission process. The nonconserved regions among the components I and II presumably define their specificity for the external stimulus detected and for the particular cellular response, respectively.

VIE. Other Environmental Responses and their Mechanisms

VIE1. Iron Uptake

In oxidizing environments, iron occurs as the ferric ion and this form is extremely insoluble in neutral or basic solution. Bacteria have a characteristic strategy for scavenging ferric iron, which involves specialized iron chelators called *siderophores*, and transport systems specific for the iron–siderophore complexes (Earhart, 1996).

Nearly 100 distinct siderophores produced by microorganisms have been identified; all are relatively small molecules and they fall into two classes, i.e. those that use catecholate groups to complex the ferric ion vs those that use hydroxamate groups. Bacteria that have been examined intensively, such as *E. coli*, have been found to produce several siderophores of both classes, which they release into the environment under limiting-iron conditions. The siderophores complex ferric iron specifically and

TABLE 50.3 Examples of Two-Component Regulatory Systems

Mnemonic	Environmental Stimulus	Cellular Response	Component I	Component II
Phosphate	Low external [PO_4]	Induction of various PO_4-metabolizing enzymes	PhoR	PhoB
Nitrogen ***r***egulation	Low external [NH_4^+]	Induction of glutamine synthetase	NR_I	NR_{II}
Outer ***m***embrane ***p***rotein	External osmolarity	Regulation of alternate porin synthesis	EnvZ	OmpR
Aerobic ***r***espiratory ***c***ontrol	Oxygen concentration	Regulation of central metabolic enzymes	ArcB	ArcA
Nitr***a***te ***r***eductase	External NO_3^- present, Oxygen absent	Induction of nitrate reductase	NarX	NarL
Chemotaxis	Temporal gradients of attractants and repellants	Change in swimming interval	CheA	CheY

with extremely high affinity (for ferric enterobactin, $K_d = 10^{-52}$ M) and bacteria use specialized, high-affinity transport systems to recover the resulting complexes. In the case of Gram-negative bacteria, transport is complicated by the fact that the complexes, though relatively small, are nevertheless too large to pass through the OM pores formed by porins. Gram-negative bacteria therefore have specialized OM receptors, which appear to function as gated pores that allow the complexes to enter the periplasm. This initial transport step involves a form of energetic coupling whose mechanism is still somewhat unclear, but requires a specific protein (TonB) that energizes transport of a few other solutes across the OM. Transport across the CM involves another siderophore-specific transporter (Earhart, 1996).

TABLE 50.4 General Features of Two-Component Regulators

Feature	Component I	Component II
Cellular location	Membrane	Cytoplasm
Cellular function	Sense and signal an external condition	Control gene expression
Biochemical activities	Autophosphorylation at histidine residue	Binding to regulatory regions of genes
	Phosphorylation of cognate component II	Stimulating transcription of specific genes
	may dephosphorylate cognate component II	May inhibit transcription of other specific genes
Sequence conservation	Two highly conserved regions near carboxyl end	One highly conserved region near amino end (subfamilies have additional regions of homology near carboxyl end)

Once the iron—siderophore complex is inside the bacterial cytoplasm, the cell is faced with two additional challenges. First, the iron must be released from the siderophore; this is made difficult by the extreme affinity of the two components and appears to be solved by chemically modifying one or both of them. In some cases, the siderophore component of the complex appears to be destroyed enzymatically in the bacterial cytoplasm by hydrolases. The alternative strategy, reduction of the complexed ferric ion to ferrous ion, has also been detected, although some question remains as to whether reduction precedes release. Finally, it should be noted that excess (i.e. free) ferrous iron in the cytoplasm presents a serious threat, particularly to aerobic organisms, because it reacts with H_2O_2 to produce the extremely reactive hydroxyl radical. This problem is addressed by close regulation of the iron uptake systems and by synthesis of iron-storage proteins to sequester unused iron intracellularly (Earhart, 1996).

VIE2. Magnetotaxis

Certain motile bacteria have been found that swim along the lines of an externally applied magnet field. Several species of these *magnetotactic bacteria* have been isolated and maintained as pure cultures in the laboratory, but most have resisted cultivation, although they can be observed in samples from natural environments. The difficulty of culturing magnetotactic bacteria stems, in part, from the fact that all known examples are *microaerophiles*, meaning that they require oxygen at low concentrations but are killed by it at atmospheric levels. Accordingly, these organisms typically occur at interfaces between oxic and anoxic layers of natural waters, as occur in marshes or swamps. In these settings, magnetotaxis along the

vertically inclined geomagnetic lines of force, perhaps combined with other environmental cues, may guide the cells to an appropriate position in a vertical oxygen gradient.

The dominant mechanism of magnetotaxis among these bacteria seems to be passive, in the sense that the cell aligns itself with the magnetic field while rotation of the helical flagellum drives it forward (Lefevre et al., 2009). This mechanism requires a strong magnetic dipole that is stably aligned (i.e. fixed) within the cell and parallel to the main axis of the flagellum. In magnetotactic bacteria, the dipole is provided by a short chain of single-domain magnetic crystals, called *magnetosomes*, each of which is enclosed in a phospholipid membrane. Other mechanistic details of magnetosome synthesis, including what determines the magnetic polarity of the chain and how the parallel orientation of internal magnet and flagellum is maintained, remain to be resolved (Jogler and Schüler, 2009).

VII. THE PHYSIOLOGY OF PATHOGENESIS

Bacteria capable of causing disease represent a tiny minority of known species. These *pathogens* are distinguished from the vast majority of bacteria by adaptations that allow them to invade their animal or plant host, elude multiple defense mechanisms (including the immune system), reproduce within host fluids and tissues, and damage host function in some way, thereby causing disease. The host defenses against the pathogens, as well as the mechanisms by which the pathogens damage the host, often involve specialized physiological functions of the host and bacterial cells, respectively.

One of the first host defenses encountered by a bacterium after invading the body is often a *phagocyte*, a specialized motile cell that circulates in the blood and engulfs bacteria. After a bacterial cell has been internalized (see Fig. 50.6), the resulting cytoplasmic vesicle fuses with a lysosome to form a phagolysosome. In addition to the low pH and digestive enzymes typical of lysosomes, phagolysosomes generate high concentrations of nitrous oxide, hypochlorous acid and reactive oxygen species, including hydrogen peroxide, singlet oxygen, superoxide and the hydroxyl radical. Synthesis of these strong oxidants is triggered when a phagocyte is activated and is accompanied by a sudden demand for oxygen, called the *respiratory burst*. The reactive compounds produced in this process, combined with the low pH inside the phagolysosome, normally kill the ingested bacterium.

However, certain pathogenic bacteria can survive in the phagolysosome, escape it and multiply in the cytoplasm of the phagocyte. In some cases, the strategy involves killing the phagocyte by secreting a toxin termed a *leukocidin*. Other bacterial countermeasures against phagocytosis include synthesis of cell-associated carotenoid pigments, which quench singlet oxygen, and synthesis of an external capsule (see Section II), which inhibits the initial engulfment of the bacterial cell.

Various pathogenic bacteria also secrete toxins at other stages of pathogenesis which target specific functions of host cells and tissues in causing disease. Several pathogens, for example, colonize the small intestine and produce an *enterotoxin* that induces diarrhea. *Vibrio cholerae*, which causes cholera, remains one of the most threatening of these bacteria globally, but pathogenic strains of *Bacillus cereus*, *E. coli* and *Salmonella enterica* also cause serious disease. Once established in the host, these bacteria produce enterotoxins that bind to specific gangliosides in the plasma membranes of intestinal epithelial cells. The cholera toxin covalently modifies and inactivates a GTP-binding protein that normally regulates an adenylate cyclase complex in the plasma membrane. Loss of this regulatory function causes overproduction of cAMP in the epithelial cell which, in turn, activates a number of cAMP-stimulated cellular functions, one of which is export of chloride ion. As large amounts of chloride are pumped into the lumen of the intestine, water follows by passive diffusion across the plasma membrane (O'Brien and Holmes, 1996). The massive secretion of salts and water into the lumen of the intestine results in a severe diarrhea, which may be lethal if water and salts are not replaced at an adequate rate.

Another class of damage-inducing proteins from pathogenic bacteria includes the *hemolysins*, named according to the fact that these proteins promote the lysis of erythrocytes (red blood cells). The most common technique for detecting hemolysin production involves incorporating whole blood into the agar plating medium used to grow bacterial colonies. If the bacterium produces a hemolysin, a clear zone, or halo, will form around the colony, caused by lysis of all the red blood cells within a short distance of the colony. Although they differ in some properties, hemolysins are generally small, secreted proteins which bind to the plasma membrane of the blood cells as individual subunits. The membrane-bound subunits then oligomerize to form a large pore in the plasma membrane, through which the cytoplasm escapes.

Bacterial toxins affecting yet a different host function, muscle contraction, are produced by two anaerobic, spore-forming pathogens: *Clostridium tetani* and *Clostridium botulinum*. Both species induce paralysis through disruption of the nervous system, but the two corresponding neurotoxins differ in the form of paralysis and the underlying mechanism. *Cl. tetani* infects host tissue, typically through deep puncture wounds, and produces *tetanus toxin*. This protein accumulates at the ends of inhibitory neurons where it blocks the inhibition of muscle contraction. The resulting uncontrolled contraction leads to a general spastic paralysis which can result in death by asphyxia. In contrast,

the neurotoxin of *Cl. botulinum* is normally produced during growth outside the host, but can be lethal if ingested, even in very small quantities. *Botulism toxin* binds to stimulatory motor neurons and prevents release of acetylcholine at the neuromuscular junction. This blocks muscle contraction, leading to a flaccid paralysis.

VIII. PROKARYOTES LIVING IN EXTREME ENVIRONMENTS

The physiological diversity and specialization of prokaryotes is illustrated dramatically by organisms which not merely tolerate chemical and physical extremes, but actually require them for normal cellular function. This heterogeneous group includes many species of archaea that have been discovered only in recent years as their natural habitats have been subjected to the appropriate sampling and cultivation methods.

Most *extreme halophiles*, organisms that thrive in concentrated brines, such as those that occur in natural salt lakes or artificial evaporation ponds, are archaea. Well-studied species include the rod-shaped *Halobacterium salinarum* (formerly *halobium*) and the irregularly shaped *Haloferax volcanii*. *H. salinarum* grows best in media containing 3−4 M NaCl and will not grow at salt concentrations less than 1.5 M. The cell maintains an internal K^+ concentration of upto 5 M and contains Cl^- as the major counterion. Accordingly, most *H. salinarum* enzymes function best in extremely high salt concentrations and denature at low salt concentrations (Kushner, 1985). The native structure of these halophilic enzymes tends to incorporate an unusually high number of acidic amino acid residues on the protein surface. Other notable features of the *H. salinarum* cell include gas vesicles in the cytoplasm and patches of a special retinal protein, *bacteriorhodopsin*, in the cytoplasmic membrane. The gas vesicles make the cells buoyant and thus help them maintain contact with two sources of energy: O_2 and light. Oxidation of organic compounds in the environment normally supports growth, but if oxygen becomes limiting, extra energy can be supplied by bacteriorhodopsin. This is a membrane-bound retinal protein that functions as a light-driven ion pump. When the cell is illuminated, it pumps protons from the cytoplasm; this contributes to the cell's PMF and thus, to the production of ATP, during O_2 deprivation (Kushner, 1985). Related proteins, collectively termed *proteorhodopsins* have more recently been identified in a number of archaea and also bacteria and some of these rhodopsins may have cellular functions distinct from ATP production (Fuhrman et al., 2008).

Extreme *acidophiles*, organisms which require low pH for optimal cell growth, include both bacteria and archaea. *Thiobacillus* spp. are Gram-negative bacteria that derive energy from the oxidation of reduced sulfur compounds. Since the oxidized end-product is usually H_2SO_4, these bacteria acidify their environment in the normal course of their metabolism. Some *Thiobacillus* cells grow optimally at about pH 2 but maintain a cytoplasmic pH near 6.5. At least one species, *Tb. ferrooxidans,* can also oxidize Fe^{2+}; this metabolic strategy is aided by the fact that autooxidation of Fe^{2+}, which would compete with the biologically mediated process, occurs very slowly at low pH values.

The most extreme acidophile known to date is a moderately thermophilic archaeon, *Picrophilus oshimae*. This organism, isolated from the soil of a Japanese geothermal field, grows optimally in dilute sulfuric acid at about pH 0.9. *P. oshimae* cells can grow at pH 0 but not at pH values above 3.5 and at pH values greater than 5, the cells lyse (Schleper et al., 1995).

Bacteria that require low temperatures are termed *psychrophiles* and typically occur in polar marine environments. Enzymes of these organisms may denature, and the cells may die, at room temperature. In several cases, the minimum temperature for growth has not been determined, but lies below about −10°C. The membrane phospholipids of these bacteria contain unusually high proportions of unsaturated and short-chain fatty acids (Morita, 1975).

At the other extreme, prokaryotes that grow optimally at 80°C or higher temperatures are termed *extreme thermophiles* or *hyperthermophiles* (Stetter et al., 1990). The cultivated species consist primarily of archaea isolated from geothermal habitats such as terrestrial hot springs or submarine thermal vents. Aerobic hyperthermophiles include *Sulfolobus* spp., which require acidic conditions as well as high temperatures. The combination of high temperature and low pH required for optimal growth (about 80°C and pH 3) is extremely effective at denaturing proteins. The *Sulfolobus* cell helps protect its cytoplasmic proteins, which appear to be generally heat-stable but not acid-stable (Grogan, 1996), by maintaining its cytoplasmic pH at about 6 (Schäfer et al., 1990). Physical properties of the unique lipids of *Sulfolobus* spp. probably help maintain the resulting ΔpH. The ether-linked phytanyl chains of these lipids span the entire membrane, forming a stable monolayer. Such membranes exhibit very low rates of proton leakage at high temperature, compared to ester-linked phospholipid bilayers (Van de Vossenberg et al., 1995) and this seems to represent an important prerequisite for efficient function of these cells.

The most thermophilic organisms known are anaerobic archaea isolated from submarine vents, where hydrostatic pressure permits liquid water to be superheated. *Pyrolobus fumarii*, the most thermophilic organism available in culture, grows optimally at about 106°C (Blöchl et al., 1997). The very existence of cells with such growth requirements raises fundamental questions regarding their need to stabilize nucleic acids, proteins and other

molecules necessary for all life. The thermostability of enzymes of most hyperthermophiles appears to be intrinsic, i.e. not due to counter-ions or other solutes. Biophysical analyses indicate that several classes of interactions of the amino acid residues contribute to this intrinsic structural stability (Jaenicke and Böhm, 1998).

IX. CONCLUSIONS

The smallest and simplest living cells are prokaryotic, consist of a nucleoid and cytoplasm enclosed in a cytoplasmic membrane. Most free-living prokaryotes also have a cell wall of some type and many bacteria have a second lipid membrane outside the cell wall, whereas a few have additional, internal structures. Though structurally simple, prokaryotic cells are evolutionarily diverse and include two distinct lineages, the Bacteria and the Archaea, each with a taxonomic status equal to all eukaryotic organisms. The cells of bacteria and archaea are functionally complex, mediating nutrient uptake, energy conversion and conservation, growth, secretion, genome replication, cell division and regulation of gene expression in response to environmental change. Prokaryotes encompass a wide range of metabolic strategies, including many not represented among eukaryotes. Several alternatives of CO_2 fixation and photosynthesis are represented among bacteria and archaea, of which only one, that of the cyanobacteria, has been adopted by green plants. Some prokaryotes grow chemoautotrophically, some can fix N_2 and some can "respire" anaerobically, using electron acceptors other than O_2 in their environments.

Bacteria depend on solute-specific transport proteins located in the CM to accumulate nutrients and to move inorganic ions into and out of the cell. Those proteins involved in active transport display a high affinity for the external solute and expend energy to accumulate it to high intracellular levels. A common type of active transport in Gram-negative bacteria utilizes soluble proteins which bind the solute in the periplasm and deliver it to the corresponding membrane-bound transporter. Some membrane transporters mediate homeostatic responses to environmental stress. Others communicate with "two-component" systems to regulate bacterial gene expression. In most cases, bacteria change their macromolecular compositions in response to changes in external conditions. This form of physiological adaptation can occur quickly, due to the high biosynthetic capacity of prokaryotic cells relative to cell mass.

A few bacteria are specialized to evade the defense systems of multicellular organisms and cause damage to their host. The host defenses of mammals include cells specialized for the destruction of bacteria via controlled generation of reactive chemicals, whereas the damage to the host caused by pathogenic bacteria is, in many cases, mediated by protein toxins which target specific proteins or cell types.

The specialization and functional diversity of prokaryotic cells becomes apparent in extreme environments. Certain bacteria require low external pH or low temperature to survive and grow. Certain archaea require extremely high salt concentration or extremely high temperature for normal cellular function. Because archaea differ radically from *E. coli* and other well-studied microorganisms, pinpointing the physiological and biochemical basis of their adaptation to harsh environments remains a challenging area of research.

BIBLIOGRAPHY

Blöchl, E., Rachel, R., Burggraf, S., Hafenbrandl, D., Jannasch, H., & Stetter, K. O. (1997). *Pyrolobus fumarii*, gen. and sp.nov., represents a novel group of archaea, extending the upper temperature limit for life to 113°C. *Extremophiles, 1*, 14–21.

Boucher, Y. (2007). Lipids: biosynthesis, function, and evolution. In R. Cavicchioli (Ed.), *Archaea: Molecular and Cellular Biology* (pp. 341–353). Washington, DC: American Society for Microbiology.

Caldwell, D. R. (1995). *Microbial Physiology and Metabolism*. Dubuque, IA: William C. Brown Publishers.

Costerton, J. W., Cheng, K.-J., Geesey, G. G., et al. (1987). Bacterial biofilms in nature and disease. *Ann Rev Microbiol, 41*, 435–464.

Dierstein, R., Schumacher, A., & Drews, G. (1981). On insertion of pigment-associated polypeptides during membrane biogenesis in *Rhodopseudomonas capsulata*. *Arch Microbiol, 128*, 376–383.

Earhart, C. F. (1996). Uptake and metabolism of iron and molybdenum. In F. C. Neidhardt (Ed.), *Escherichia coli* and *Salmonella:* Cellular and Molecular Biology (2nd ed.). (pp. 1079–1090) Washington, DC: American Society for Microbiology.

Fuerst, J. A. (2005). Intracellular compartmentation in planctomycetes. *Ann Rev Microbiol, 59*, 299–328.

Fuhrman, J. A., Schwalbach, M. S., & Stingl, U. (2008). Proteorhodopsins: an array of physiological roles? *Nat Rev Microbiol, 6*, 488–494.

Furlong, C. (1987). Osmotic-shock-sensitive transport systems. In F. C. Neidhardt (Ed.), *Escherichia coli* and *Salmonella:* Cellular and Molecular Biology (pp. 768–796). Washington, DC: American Society for Microbiology.

Grogan, D. W. (1996). Organization and interactions of cell envelope proteins of the extreme thermoacidophile *Sulfolobus acidocaldarius*. *Can J Microbiol, 42*, 1163–1171.

Gunsalus, R. P. (1992). Control of electron flow in *Escherichia coli*: coordinated transcription of respiratory pathway genes. *J Bacteriol, 174*, 7069–7074.

Harold, F. M., & Maloney, P. C. (1996). Energy transduction by ion currents. In F. C. Neidhardt (Ed.), *Escherichia coli* and *Salmonella:* Cellular and Molecular Biology (2nd ed.). (pp. 283–306) Washington, DC: American Society for Microbiology.

Jaenicke, R., & Böhm, G. (1998). The stability of proteins in extreme environments. *Curr Opin Struct Biol, 8*, 738–748.

Jogler, C., & Schüler, D. (2009). Genomics, genetics, and cell biology of magnetosome formation. *Annu Rev Microbiol, 63*, 501–521.

Kletzin, A. (2007). General characteristics and important model organisms. In R. Cavicchioli (Ed.), *Archaea: Molecular and Cellular Biology* (pp. 14−92). Washington, DC: American Society for Microbiology.

Kushner, D. J. (1985). The Halobactericeae. In J. R. Socatch, & L. N. Ornston (Eds.), *The Bacteria: vol. VIII Archaebacteria* (pp. 171−214). Orlando: Academic Press, Inc.

Lefevre, C. T., Song, T., Yonnet, J. P., & Wu, L. F. (2009). Characterization of bacterial magnetotactic behaviors by using a magneto-spectrophotometry assay. *Appl Environ Microbiol, 75*, 3835−3841.

Morita, R. Y. (1975). Psychrophilic bacteria. *Bacteriol Rev, 89*, 144−167.

Neidhardt, F. C., Ingraham, J. L., & Schaechter, M. (1990). *Physiology of the Bacterial Cell*. Sunderland, MA: Sinauer Associates, Inc.

Nikaido, H., & Vaara, M. (1985). Molecular basis of bacterial outer membrane permeability. *Microbiol Rev, 49*, 1−32.

O'Brien, A. D., & Holmes, R. K. (1996). Protein toxins of *Escherichia coli* and *Salmonella*. In F. C. Neidhardt (Ed.), *Escherichia coli* and *Salmonella:* Cellular and Molecular Biology (2nd ed.). (pp. 2788−2802) Washington, DC: American Society for Microbiology.

Pettijohn, D. E. (1996). The nucleoid. In F. C. Neidhardt (Ed.), *Escherichia coli* and *Salmonella:* Cellular and Molecular Biology (2nd ed.). (pp. 158−166) Washington, DC: American Society for Microbiology.

Schäfer, G., Anemüller, S., Moll, R., Meyer, W., & Lübben, M. (1990). Electron transport and energy conservation in the archaebacterium *Sulfolobus acidocaldarius*. *FEMS Microbiol Rev, 75*, 335−348.

Schleper, C., Pühler, G., Holz, I., et al. (1995). *Picrophilus* gen. nov., fam. nov: a novel heterotrophic, thermoacidophilic genus and family comprising archaea capable of growth around pH 0. *J Bacteriol, 177*, 7050−7059.

Schwartz, R. M., & Dayhoff, M. O. (1978). Origin of prokaryotes, eukaryotes, mitochondria, and chloroplasts. *Science, 199*, 395−403.

Schwarz, U., Asmus, A., & Frank, H. (1969). Autolytic enzymes and cell division of *Escherichia coli*. *J Mol Biol, 41*, 419−429.

Skulachev, V. P. (1994). The latest news from the sodium world. *Biochim Biophys Acta, 1187*, 216−221.

Slonczewski, J. L., & Foster, J. W. (1996). pH-regulated genes and survival at extreme pH. In F. C. Neidhardt (Ed.), *Escherichia coli* and *Salmonella:* Cellular and Molecular Biology (2nd ed.). (pp. 283−306) Washington, DC: American Society for Microbiology.

Stetter, K. O., Fiala, G., Huber, G., Huber, R., & Segerer, A. (1990). Hyperthermophilic microorganisms. *FEMS Microbiol Rev, 75*, 117−124.

Strom, M., & Lory, S. (1993). Structure−function and biogenesis of the type IV pili. *Ann Rev Microbiol, 47*, 565−596.

Van De Vossenberg, J., Ubbink-Kok, T., Elferink, M., Driessen, A., & Konings, W. N. (1995). Ion permeability of the cytoplasmic membrane limits the maximum growth temperature of bacteria and archaea. *Molec Microbiol, 18*, 925−932.

Walsby, A. E. (1994). Gas vesicles. *Microbiol Rev, 58*, 94−144.

Wanner, B. L. (1993). Gene regulation by phosphate in enteric bacteria. *JCell Biochem, 51*, 47−54.

White, D. (2000). *The Physiology and Biochemistry of Prokaryotes* (2nd ed.). New York: Oxford University Press.

Woese, C. R., Kandler, O., & Wheelis, M. (1990). Towards a natural system of organisms: proposal for the domains Archaea, Bacteria, and Eucarya. *Proc Natl Acad Sci USA, 87*, 4576−4579.

Yanofsky, C., & Crawford, I. P. (1987). The tryptophan operon. In F. C. Neidhardt (Ed.), *Escherichia coli* and *Salmonella typhimurium:* Cellular and Molecular Biology (pp. 1453−1472). Washington, DC: American Society for Microbiology.

Section VIII

Specialized Processes: Photosynthesis and Bioluminescence

This page intentionally left blank

Chapter 51

Photosynthesis

Darrell Fleischman

Chapter Outline

I. SUMMARY

Plants, algae and photosynthetic bacteria capture the energy of sunlight and store it in molecules such as starch and sucrose. Light is absorbed by light-harvesting pigments such as chlorophyll. The energy is transferred to a special pair of chlorophyll molecules in the photosynthetic reaction center. The energy is converted to chemical energy as the special chlorophyll pair transfers an electron to an acceptor. The electron proceeds along an electron transport chain, ultimately reducing $NADP^+$ to NADPH or cycling back to the reaction center. The electron flow creates a proton concentration gradient across the membrane, which drives the formation of ATP. Plants contain chloroplasts. Chloroplasts have two photosystems, connected in series to form an electron transport system known as the Z scheme. In the System 2 reaction center, electrons are extracted from water, releasing O_2. The System 1 reaction center donates electrons to $NADP^+$. The ATP and NADPH are used for the synthesis of carbohydrates in a series of reactions known as the reductive pentose phosphate cycle.

II. INTRODUCTION

IIA. Historical Aspects

It must have been apparent from the earliest times that animals can survive only by eating plants or other animals, whereas plants seem to subsist on nothing but sunshine and a little water and earth. Julius Mayer, who introduced the concept of conservation of energy, suggested in 1845 that green plants can capture the energy of light and store it in a chemical form. His insight was correct. Almost all of the free energy used by living organisms is derived from energy of sunlight, which has been stored in photosynthetically produced molecules.

Clues about how plants might store free energy were obtained early (Loomis, 1960). In 1771, the English philosopher Joseph Priestly began a series of experiments that demonstrated that plants produce a gaseous substance, oxygen, which animals require for respiration. By the end of the 19th century, it was recognized that oxygen is produced only by the green parts of the plant and that its production requires light, carbon dioxide and water. The first visible products of

Cell Physiology Sourcebook. DOI: 10.1016/B978-0-12-387738-3.00051-2

photosynthesis were grains of starch, a polymer of glucose.

We now know that photons are captured by *chlorophyll*, the green pigment found in leaves, as well as by accessory pigments such as carotenoids (Fig. 51.1). Plants use the energy of the photons to extract electrons from water (leaving oxygen as a by-product) and use them to convert inorganic molecules such as carbon dioxide to organic molecules such as glucose:

$$6\ CO_2 + 6\ H_2O \xrightarrow{\text{light}} C_6H_{12}O_6 + 6\ O_2 \qquad (51.1)$$

The products of the above process contain more free energy per mole of glucose formed than do the reactants, that is:

$$\Delta G0 = 686\ \text{kcal/mol} \qquad (51.2)$$

Nitrogen and sulfur also can be fixed, i.e. converted from inorganic to organic form, by the photosynthetic system. Nitrogen and sulfur that are contributed by inorganic starting materials (including dinitrogen (N2), nitrate and sulfate) are incorporated into amino acids and other organic molecules. In this chapter, we discuss in detail only carbon fixation.

A comprehensive discussion of the history of photosynthesis research has been presented by Bacon Ke (2001). A timeline of photosynthesis research by Thomas Brennan (2008) is available on Photobiological Sciences Online. This site, sponsored by the American Society for Photobiology, includes a number of excellent review modules covering various aspects of photosynthesis.

IIB. Bacterial Reaction Centers

Higher plants are not the only organisms that perform photosynthesis. Algae also do, as do many bacteria. In all of them, the energy of light is converted to chemical energy in photosynthetic reaction centers. These are membrane-bound oligomeric protein complexes which contain a chlorophyll or bacteriochlorophyll dimer known as a special pair. The special pair donates an electron to an acceptor molecule following absorption of a photon. The reaction centers of plants, algae and photosynthetic bacteria resemble each other surprisingly closely. It has been suggested that they have evolved from a common ancestor. We will begin by describing bacterial reaction centers. Photosynthetic bacteria are described in more detail by Jones (2009) and Hunter et al. (2008) and reaction centers are discussed by Yocum (2008a).

It has been possible to isolate many of the oligomeric protein complexes involved in photosynthesis by dissolving the membranes in detergent and purifying the complexes through chromatography and other techniques. The reaction centers of purple photosynthetic bacteria are embedded in the cell membrane or in the membranes of

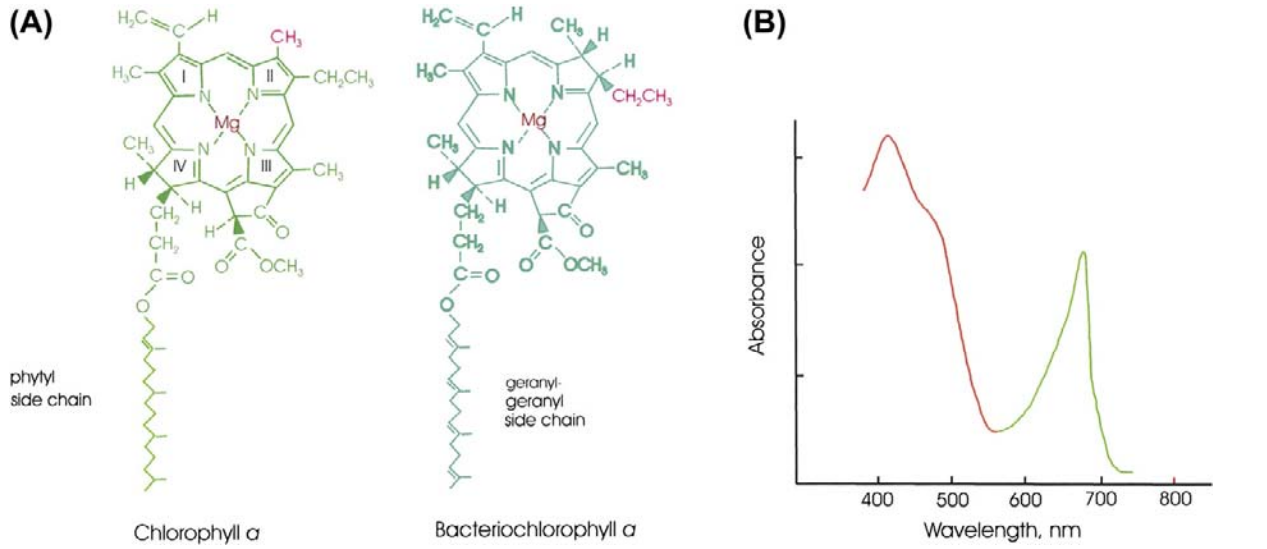

FIGURE 51.1 (A) The structures of chlorophyll *a* (Chl *a*) and bacteriochlorophyll *a* (BChl *a*). Differences between the structures of the various forms of chlorophyll contribute to differences between the absorption spectra of chlorophyll-containing proteins, allowing them to capture light in different regions of the spectrum. The conjugated system in BChl has one fewer double bond (in ring II) than that of Chl *a*. Single resonance forms of the conjugated systems of double bonds are shown. In Chl *b*,-HC=O replaces the red methyl substituent on ring II of Chl *a*. In BChl *b*, =CH-CH_3 replaces the red substituents on ring II of BChl *a*. In some bacteria, phytyl rather than geranylgeranyl serves as the side chain of bacteriochlorophyll *a* or bacteriochlorophyll *b*. Other forms of chlorophyll are found in some organisms. Pheophytins resemble the respective chlorophylls, but the Mg^{2+} is replaced by two protons. (B) Absorption spectrum of a typical plant chloroplast. Both Chl *a* and Chl *b* absorb light between 400 nm and 500 nm and between 600 nm and 700 nm. In addition, β-carotene absorbs light between 400 nm and 500 nm.

intracytoplasmic vesicles which are often called chromatophores. Hartmut Michel, Johann Deisenhofer and Robert Huber isolated reaction centers from the green-colored (!) purple bacterium *Blastochloris viridis* (formerly *Rhodopseudomonas viridis*), devised a way to crystallize them and determined their structure by x-ray diffraction (Diesenhofer and Michel, 1989). This was the first crystallization of a membrane protein and paved the way for determination of the structures of many prokaryotic and eukaryotic membrane proteins. In addition, the reaction center structure provided important insights into the general properties to be expected of integral membrane proteins. The *Blc. viridis* reaction center consists of four subunits. Subunits L and M have similar but not identical amino acid sequences. Each comprises five α-helices that cross the membrane. The co-factors that participate in electron transport are bound to the L and M subunits. Their arrangement is sketched in Fig. 51.2. The primary electron donor (known as P985 because a loss of optical density at 985 nm accompanies its photo-oxidation) is indeed a dimer, in this case of bacteriochlorophyll b. The reaction center also includes two additional molecules of bacteriochlorophyll b, two of bacteriopheophytin b, one molecule each of menaquinone, ubiquinone and carotenoid, and a non-heme ferrous iron ion. Bacteriopheophytin is similar to bacteriochlorophyll, but the Mg^{2+} is replaced by two protons.

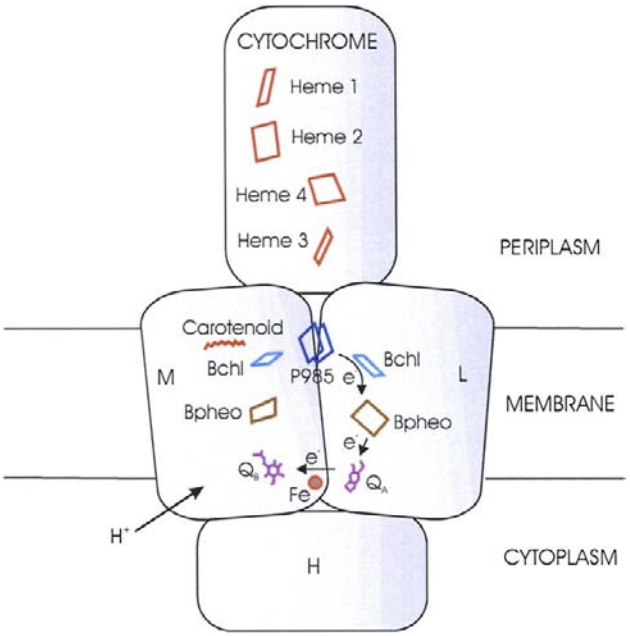

FIGURE 51.2 The arrangement of the co-factors in the *Blastochloris viridis* reaction center. The reaction center has approximate twofold (C_2) symmetry, but electrons move only along the path indicated. After Q_B accepts two electrons, two protons from the cytoplasmic side of the membrane are bound. P985, the photochemically active bacteriochlorophyll *b* dimer; Bchl, bacteriochlorophyll *b;* BPheo, bacteriopheophytin *b;* Q_A, menaquinone; Q_B, ubiquinone; Fe, ferrous iron.

Surprisingly, the reaction center has approximate twofold symmetry. The electrons leaving P985 move down only the L side of the reaction center. The first electron transfer, to the accessory bacteriochlorophyll b, occurs within a few picoseconds (10^{-12} s). The electrons move to the bacteriopheophytin b associated with subunit L, to QA (menaquinone) and, finally, to QB (ubiquinone). Upon receiving two electrons (after two photoacts), the ubiquinone binds two protons from the periplasm as it is reduced to ubihydroquinone. The ubihydroquinone dissociates into the membrane and diffuses to a cytochrome bc_1 complex, where it is re-oxidized. The reaction center also includes a cytochrome subunit containing four hemes, which is located on the periplasmic surface (facing the outside of the cell) of the membrane. The hemes donate electrons to oxidized P985. There is also an H subunit, which forms a sort of cap on the cytoplasmic side of the L and M subunits and is anchored to the membrane by a single membrane-spanning helix. Its function is not known. Purple bacterial reaction centers are embedded in the cytoplasmic membrane or in the membranes of intracellular vesicles which are often termed *chromatophores*.

Photosynthetic electron transport systems are capable of transporting electrons much more rapidly than photons of sunlight arrive at the special pairs. Therefore, reaction centers are accompanied by arrays of *light-harvesting* antenna pigments whose purpose is to capture photons and transfer the excitation energy to the special pairs. Purple bacterial reaction centers are surrounded by a "picket fence" of transmembrane dimers to which are bound bacteriochlorophyll and carotenoid molecules. The monomers, designated α and β, comprise the LH1 (light-harvesting 1) complex (Fig. 51.3). The carotenoids absorb photons in the middle of the visible spectrum and quickly pass the excitation to the bacteriochlorophyll. The bacteriochlorophyll absorbs photons in the blue, red and near-infrared regions of the spectrum. The excitations become delocalized within the circle of bacteriochlorophylls within femtoseconds (10^{-15} s) and are transferred to the special air in tens of picoseconds, faster than many can be lost as heat or fluorescence. Details of these processes are discussed by Blankenship (2002).

Other purple bacterial reaction centers have the same basic structure, but with variations. Most have bacteriochlorophyll α, bacteriopheophytin α and only ubiquinone. Many lack a bound cytochrome subunit. Observation of their topography by atomic force microscopy has revealed a variety of arrangements of LH1, including reaction centers multimers surrounded by continuous LH1 complexes (Sturgis and Niederman, 2008). Many have peripheral light-harvesting complexes, designated LH2, LH3, etc. Like LH1, they are composed of α and β subunits arranged in cylinders. They transfer absorbed excitations to LH1.

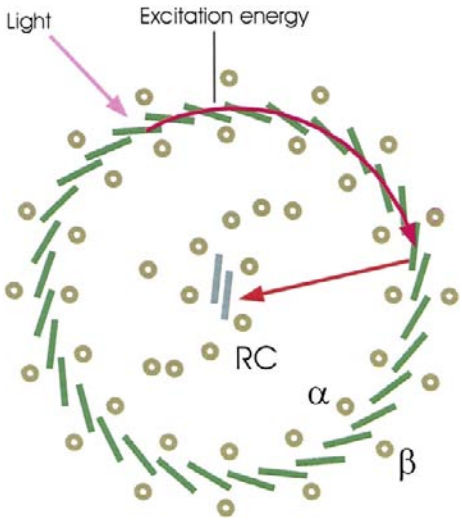

FIGURE 51.3 Light absorption and the transfer and capture of excitation energy. Protein dimers to which BChl and carotenoid molecules are bound form a ring around the reaction center. (Higher plant light harvesting pigments have a quite different structure.) Light is absorbed by any bacteriochlorophyll molecule (dark rectangles). The excitation energy is then delocalized among the bacteriochlorophyll molecules and finally captured by a special bacteriochlorophyll pair in the reaction center (RC). The figure is based on the structure of the bacterial light-harvesting complex reported by Cogdell et al. (1999).

IIC. Photosynthetic Bacteria

Photosynthetic bacteria play many important roles in the environment. As much as a third of the earth's photosynthesis is performed by microorganisms in the oceans. Six bacterial phyla include photosynthetic members (Blankenship, 2002; Jones, 2009; Golbeck, 2010; see Chapter 50). Five of them are termed *anoxygenic* because they are unable to oxidize water and evolve oxygen. Two of these possess *type II reaction centers*, which are basically similar to the *Blc. viridis* reaction center. Their terminal electron acceptors are quinones. Members of two phyla possess *type I reaction centers*. These have quinone acceptors, but rather than becoming doubly reduced and dissociating, the final quinone acceptor donates an electron to a bound iron-sulfur center (Fig. 51.4). Their core proteins are homodimers (identical monomers), rather than heterodimers like the L and M proteins of purple bacteria; they are flanked by two symmetrical light-harvesting domains. Members of the sixth phylum, the cyanobacteria, have both type I and type II reaction centers, connected in series. They are able to oxidize water and evolve oxygen and are termed *oxygenic*.

Purple bacteria belong to the Proteobacteria, along with such bacteria as *E. coli.* They are found in many terrestrial and aquatic environments, sometimes even in symbiotic associations with eukaryotes. Some are obligate anaerobes; others can grow photosynthetically in the absence of oxygen, heterotrophically (using organic compounds as carbon sources) in its presence, or by fermentation. One group, the aerobic anoxygenic phototrophs or aerobic photosynthetic bacteria, form the photosynthetic system only in the presence of oxygen. Most purple bacteria can fix nitrogen. One, related to *Rhodpseudomonas palustris*, may have been the ancestor of *Bradyrhizobum,* which includes the soybean symbiont. The Chloroflexi (green non-sulfur or green filamentous bacteria) have type II reaction centers, although their subunits and co-factors differ somewhat from those of the purple bacteria. They also possess a very large bacteriochlorophyll-containing light-harvesting structure known as a chlorosome (Blankenship, 2002), which allows them to grow in very dim light.

A special issue of *Photosynthesis Research* is devoted to bacteria having type I reaction centers (see Golbeck, 2010). The Chlorobi (green sulfur bacteria) are obligate anaerobes, use reduced sulfur compounds as electron sources and also contain chlorosomes. The Firmicutes (e.g. heliobacteria) are Gram-positive anaerobes that prefer high light environments, use light energy to fix nitrogen and grow on organic compounds. They are often found in rice fields. *Candidatus*, belonging to the Acidobacteria, is thought to be aerobic, contains chlorosomes and does not fix carbon or nitrogen. The Cyanobacteria are oxygenic — they can oxidize water and evolve oxygen and possess both type I and type II reaction centers. They have light-harvesting systems known as phycobilisomes whose chromophores (light-absorbing entities) are linear tetrapyrroles known as phycobilins. They are found in many environments, are active nitrogen fixers and are responsible for the toxic blooms that appear in eutrophic waters. The bacterium *Halobacterium halobium* performs photosynthesis in a quite different way. Rather than chlorophyll, it uses bacteriorhodopsin, a carotenoid-containing protein resembling the visual pigment rhodopsin, to capture the energy of light in a process that does not involve electron transfer (Subramaniam and Henderson, 2000).

IID. Evolution of Photosynthesis

It is believed that the earliest photosynthetic bacterium appeared as early as 3.4 billion years ago at a time when the earth's atmosphere contained almost no oxygen (Blankenship, 2002; Olson and Blankenship, 2004; Blankenship et al., 2007). Its ancestor was presumably a lithotrophic bacterium that used H_2 or sulfide as an electron donor and had an electron transport system that included cytochromes. The chlorophyll biosynthesis pathway probably evolved from the heme biosynthesis pathway; the early steps are identical. Substitution of magnesium for iron would have produced a pigment having a much longer-lived excited state, more able to transfer an electron before it decayed. Reductions of some of the double bonds, perhaps by reductases related to the already

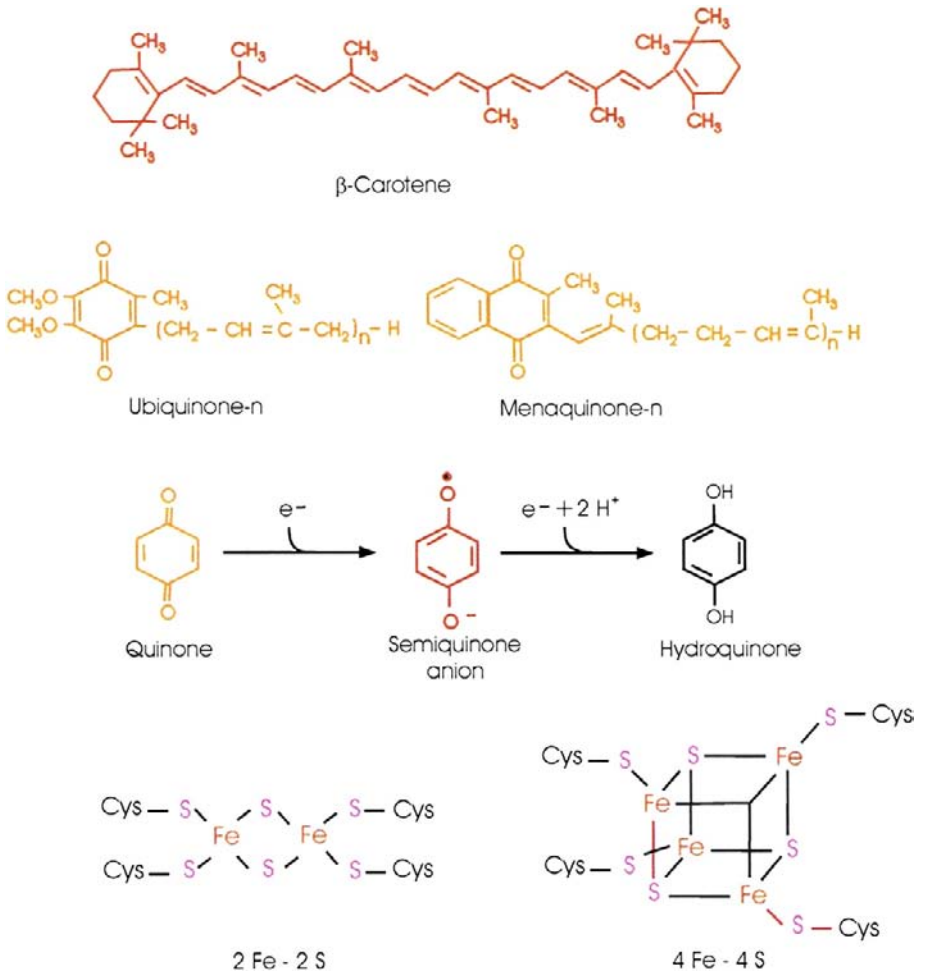

FIGURE 51.4 Structures of some of the molecules and co-factors involved in photosynthesis. Other carotenoids and quinones are found in many photosynthetic organisms. The quinone, semiquinone anion and hydroquinone forms of the quinone six-membered ring are shown.

present nitrogenase, created pigments able to absorb visible or near-infrared light. The first reaction center is thought to have been a monomer. Its structure may have resembled that of cytochrome *b*, which also binds tetrapyrroles and quinones. Gene duplication would have led to a bacterium having a homodimeric reaction center. Further duplications followed by evolutionary changes would have given rise to all of the contemporary reaction center types. Similarities in structure and amino acid sequence have led to the belief that they share a common ancestor. The evolutionary scenario is complicated by extensive lateral gene transfer.

Then, perhaps as early as 2.7 billion years ago, the cyanobacteria appeared. They possessed both type I and type II reaction centers, connected in series, and in the light could generate an oxidant strong enough to oxidize water. The new bacterium had access to a seemingly limitless source of electrons — water. The cyanobacteria may have arisen when genes for type I or type II reaction centers were transferred to a bacterium having the opposite type of reaction center. Alternatively, gene duplication and evolution may have created two reaction centers in the same bacterium. Loss of one or the other might have led to the appearance of each type of photosynthetic bacterium.

The cyanobactria formed oxygen as the byproduct of water oxidation. At first, the oxygen may have been consumed in chemical reactions with reductants such as Fe^{2+} but, by 2.3 billion years ago, it was accumulating in the atmosphere. The oxygen gave rise to the ozone layer and so permitted the development of higher organisms by shielding them from ultraviolet radiation.

Once oxygen was present, respiration and oxidative phosphorylation became possible. Using oxygen as an electron acceptor, bacteria could reoxidize photosynthetically synthesized molecules and regain some of the energy stored in them:

$$C_6H_{12}O_6 + 6\ O_2 \rightarrow O_2 + 6\ H_2O \qquad (51.3)$$

$$\Delta G^0 = -686\ \text{kcal/mol} \qquad (51.4)$$

Many of the proteins photosynthetic bacteria used for photosynthesis could also be used for oxidative

phosphorylation. Several lines of evidence suggest that purple photosynthetic bacteria might have been the ancestors of non-photosynthetic bacteria that perform oxidative phosphorylation and that the mitochondria of eukaryotic cells evolved from such bacteria which had formed symbiotic associations with primitive eukaryotic cells (Woese, 1987). Thus, it is no coincidence that the mechanisms of photosynthesis and respiration are similar in many respects. Much of our understanding of oxidative phosphorylation has come from studies of photosynthesis, which have exploited the experimental advantages of a system that can be driven by light.

In algae and higher plants, photosynthesis takes place in organelles known as *chloroplasts*. There is evidence that chloroplasts evolved from a cyanobacterium or *Prochloron*, which had formed a symbiotic association with a eukaryote about 1.5 million years ago. This eukaryote was the progenitor of the glycophyte, red and green algae (Margulis, 1970; Hackett et al., 2007). The green algae were the ancestors of the land plants. Secondary endosymbioses occurred when some of these algae were incorporated by other eukaryotes, leading to the appearance of still other types of algae.

III. CHLOROPLASTS

In higher plants, most chloroplasts are found in the *mesophyll cells* of leaves (Fig. 51.5). The chloroplast contains a collection of flattened membranous vesicles called *thylakoids* which are enclosed in an *envelope* formed by a double membrane (Fig. 51.6). The outer membrane contains channels formed by the protein *porin* and is freely permeable to substances whose molecular mass is below about 10 kDa. The inner membrane is selectively permeable and contains a number of metabolite transporters which mediate the interaction between metabolism in the plant cytosol and within the chloroplast. The volume surrounding the thylakoids is known as the *stroma*. The thylakoid membranes contain the pigments that capture light and, like the cristae of mitochondria, they contain an electron transport system coupled to an adenosine triphosphate (ATP) synthase. The soluble enzymes responsible for carbon dioxide assimilation are found in the stroma. In many chloroplasts of land plants and green algae, the thylakoid membranes are stacked tightly together in some regions to form structures called *grana*, which look like green grains under the light microscope. The grana are connected by non-stacked thylakoid extensions, the *stroma lamellae*.

Chloroplasts still retain genes, which are located on a chromosome found in the stroma, for many of the proteins involved in photosynthesis and for transfer and ribosomal RNA. Proteins coded by chloroplast genes are synthesized on ribosomes located in the stroma. Genes for other chloroplast proteins are now located on nuclear chromosomes of the plant cell. Remarkably, many multisubunit proteins of the chloroplast thylakoid, including the ATP synthase, contain both subunits coded on nuclear genes and synthesized on cytosolic ribosomes and subunits coded on chloroplast genes and synthesized on stromal ribosomes. Blankenship (2002) summarizes the emerging understanding of how the plant coordinates the synthesis of these subunits. Regulation of the translation of chloroplast-coded mRNA by nucleus-coded proteins that are imported into the chloroplast and degradation of excess subunits that are not incorporated into complexes play major roles. Chloroplast proteins that are synthesized in the plant cytosol are initially formed with amino terminal extensions, termed *transit peptides*, which allow them to bind to receptors on the membranes and then enter the chloroplast. The process requires GTP, ATP and molecular chaperones. After the proteins have entered the chloroplast stroma, the transit peptides are removed by

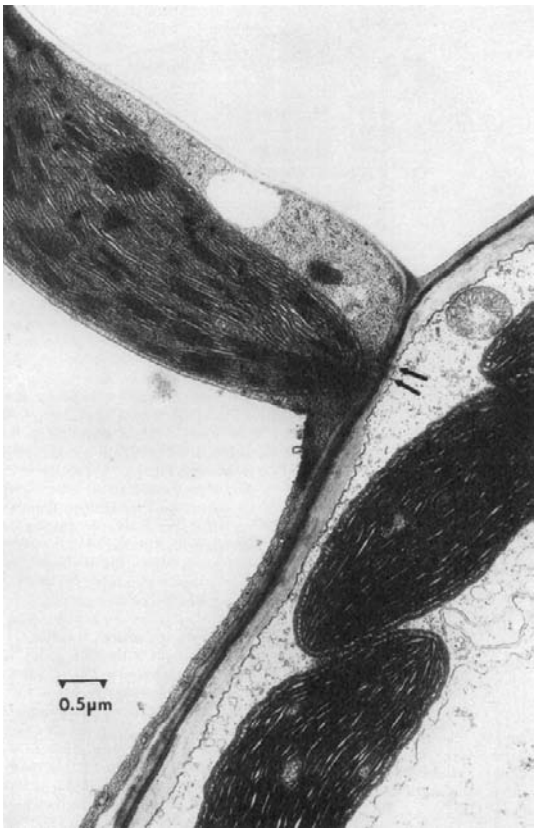

FIGURE 51.5 Transmission electron micrograph of corn (*Zea mays*) chloroplasts. Upper left: chloroplast within mesophyll cell. Lower right: chloroplast within bundle sheath cell. Arrows indicate plasmodesmata through which metabolites are exchanged between the cells. The mesophyll cells lie near the leaf surface. The bundle sheath cells lie near the leaf vascular bundles. Note the grana in the mesophyll chloroplast. *(Micrograph courtesy of Iain M. Miller.)*

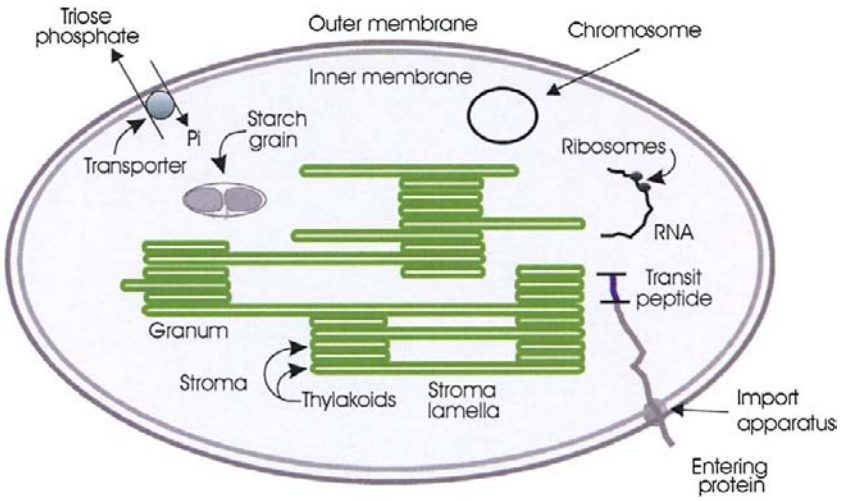

FIGURE 51.6 Diagram of a chloroplast.

a highly specific protease. Proteins destined for the membrane or lumen of the thylakoid are formed with an additional presequence, which is proteolytically cleaved after it has allowed the protein to enter the thylakoid membrane or lumen.

IV. BIOCHEMISTRY OF CARBON ASSIMILATION

IVA. The Reductive Pentose Phosphate Cycle

To determine the sequence of reactions involved in the conversion of carbon dioxide to sugars, in the early 1950s, Melvin Calvin and his associates exposed algae to $^{14}CO_2$ and light for different periods. After treatment with boiling alcohol, the carbon compounds that had been formed were separated by paper chromatography. The manner in which the distribution of ^{14}C among the carbon atoms of the various carbon compounds changed with time revealed the operation of a cyclic process, which has become known as the *reductive pentose phosphate cycle*, or *Calvin cycle* (Fig. 51.7).

In the first step, CO_2 combines with ribulose 1,5-bisphosphate to form two molecules of 3-phosphoglycerate. The reaction is catalyzed by ribulose 1,5-bisphosphate carboxylase/oxygenase, often referred to as *rubisco*. This enzyme has a rather low affinity for CO_2. To compensate, it is present in extremely high concentrations in the chloroplast and is probably the most abundant protein on earth. Next, the 3-phosphoglycerate is phosphorylated to form 1,3-bisphosphoglycerate which, in turn, is reduced to glyceraldehyde 3-phosphate by nicotinamide adenine dinucleotide phosphate (NADPH). In the remaining steps of the cycle, ribulose 1,5-bisphosphate is regenerated by a pathway that includes a complicated series of rearrangements catalyzed by transketolases and aldolases.

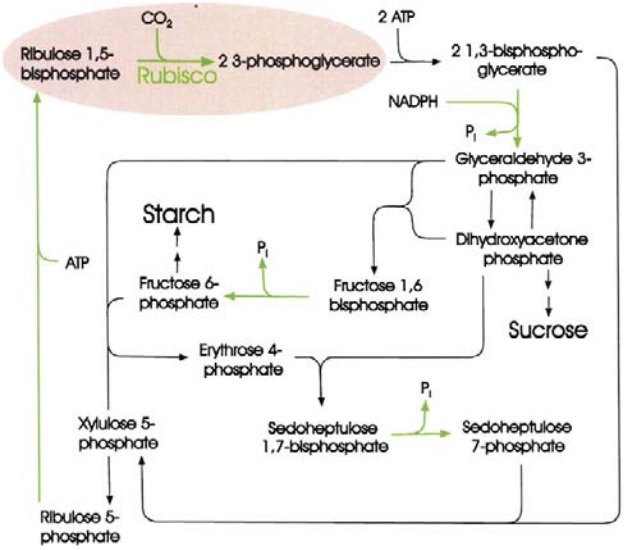

FIGURE 51.7 The reductive pentose phosphate or Calvin cycle. Stoichiometries are shown only for the first two steps. Erythrose, xylulose and sedoheptulose are sugars that contain 4, 5 and 7 carbons, respectively. Green arrows indicate steps catalyzed by light-regulated enzymes (Schurmann and Buchanan, 2008).

Intermediates in the cycle, including fructose 6-phosphate, glyceraldehyde 3-phosphate and dihydroxyacetone phosphate, serve as precursors for the starch, sucrose and amino acids that are the final products of photosynthesis.

ATP is required for the conversion of 3-phosphoglycerate to 1,3-bisphosphoglycerate and for the conversion of ribulose 5-phosphate to ribulose 1,5-bisphosphate. NADPH is required for the reduction of 1,3-bisphosphoglycerate to glyceraldehyde 3-phosphate. For each molecule of CO_2 fixed, three molecules of ATP and two molecules of NADPH are needed. It is the function of the light-driven reactions in the thylakoid membranes to furnish this ATP and NADPH.

IVB. Photorespiration and C_4 Plants

Not only does ribulose 1,5-bisphosphate carboxylase/oxygenase have a low affinity for CO_2, it also catalyzes a competing reaction in which O_2 rather than CO_2, is added to ribulose-1,5-bisphosphate. The products are 3-phosphoglycerate and phosphoglycolate.

$$\text{Ribulose 1,5-bisphosphate} + O_2 \xrightarrow{\text{ribulose } \textit{bis}\text{-phosphate carboxylase/oxygenase}} \times \text{ 3-phospoglycerate} + \text{phosphoglycolate} \quad (51.5)$$

This reaction seems to serve no useful purpose. Many plants grow much faster in a CO_2-enriched atmosphere in which the carboxylation reaction can compete more effectively with the oxygenation reaction. It appears that in the 2 billion years since plants began to fill the atmosphere with oxygen while removing CO_2 from it, they have been unable to modify the enzyme so that its affinity for CO_2 is increased or its affinity for O_2 is decreased significantly. Molecular biologists are now trying to accomplish that task.

Part of the carbon appearing in phosphoglycolate is rescued. In a series of reactions occurring in *peroxisomes* and in mitochondria, two molecules of phosphoglycolate are converted to one molecule of glycerate, which is returned to the chloroplast and re-phosphorylated. But one carbon atom is lost as CO_2 and ATP and O_2 are consumed. This process is known as *photorespiration*. It is not coupled to ATP formation and the net result is waste of ATP and fixed carbon.

A number of plants, including corn, sugarcane and crabgrass, partially avoid photorespiration by concentrating CO_2 in the cells that contain the Calvin cycle enzymes, so that carboxylation can compete more effectively with oxygenation. In these plants, the Calvin cycle enzymes are located in the chloroplasts of the *bundle sheath cells*, which surround the vascular bundles deep within the leaves (see Fig. 51.5). CO_2 is first captured in the mesophyll cells, which lie near the leaf surface, by carboxylation of phospho-enolpyruvate (PEP):

$$\text{PEP} + CO_2 \xrightarrow{\text{PEP carboxylase}} \text{oxaloacetate} + P_i \quad (51.6)$$

The carboxylation is catalyzed by PEP carboxylase, an enzyme that has a high affinity for CO_2 and does not catalyze an oxygenation reaction. Oxaloacetate is next reduced to malate (or transaminated to form aspartate in some plants). The malate or aspartate is transferred to the bundle sheath cells through fibers known as *plasmodesmata*. Some of these can be seen at the arrows in Fig. 51.5. Malate is oxidatively decarboxylated to pyruvate in the bundle sheath cells in a reaction that also generates NADPH. The CO_2 that is released enters the Calvin cycle in the bundle sheath cells (Fig. 51.8). Pyruvate returns to the mesophyll cells where it is again transformed to PEP. The net result is the transfer of CO_2 and NADPH to the bundle sheath cells.

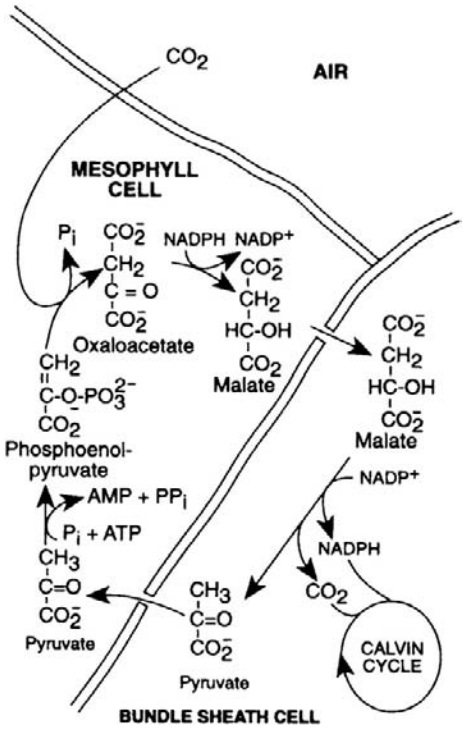

FIGURE 51.8 The mechanism used by C_4 plants to concentrate CO_2 and NADPH in bundle sheath cells. CO_2 is captured in the mesophyll cells by carboxylation of phosphoenolpyruvate. Malate is transferred to the bundle sheath cells where CO_2 is released and NADPH is formed to enter the Calvin cycle. Pyruvate returns to the mesophyll cells.

The CO_2-concentrating mechanism consumes energy, since ATP is converted to adenosine monophosphate (AMP) and phosphate. Nevertheless, plants that use it are often referred to as efficient plants because avoidance of photorespiration more than compensates for this expense. Such plants are usually known as C_4 plants because of the involvement of four-carbon acids. Many C_4 plants are native to tropical areas, where the C_4 pathway is especially advantageous since high temperatures and bright sunlight encourage photorespiration.

V. FORMATION OF ATP

VA. Light-Driven Electron Transport and ATP Synthesis

Carbon dioxide fixation requires ATP and NADPH. It seemed reasonable to suspect that the role of light is to provide the energy necessary for their formation. Photosynthetic membranes contain electron transport chains much like those of mitochondria, and light can drive electron transport along the chains (see Figs. 51.4 and 51.9). As in

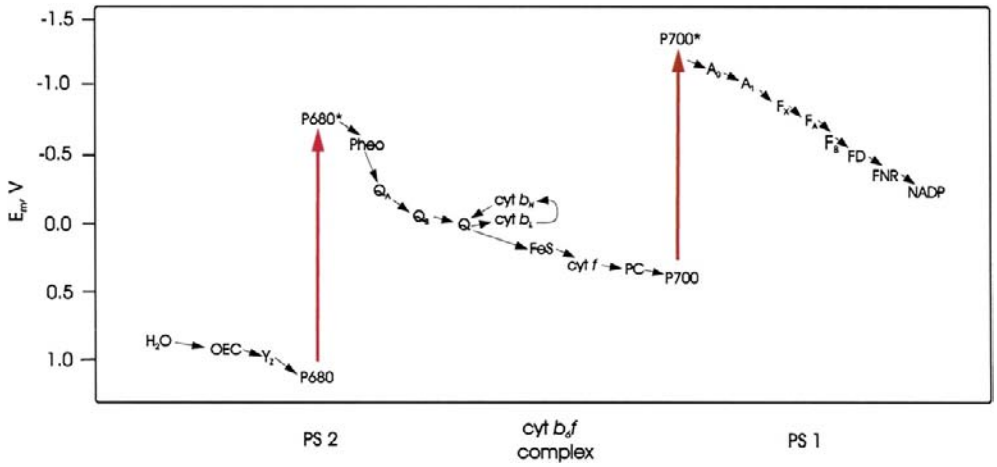

FIGURE 51.9 The electron transport system of higher plant chloroplasts. Midpoint redox potentials (E_m) of the components are indicated. P680 and P700 are chlorophyll *a* dimers which, when excited by light (large arrows), transfer an electron to the acceptors pheophytin *a* (Pheo) and chlorophyll *a* (A_0), respectively. Typical electron transfer times are shown for the electron transfer steps, which are indicated by arrows. ps: picoseconds; μs: microseconds; ms: milliseconds; OEC, a complex containing four manganese nuclei, a calcium ion and a chloride ion that accepts electrons from water; Y_Z, tyrosine; Q_A, Q_B and Q, plastoquinone; cyt b_H and cyt b_L, the high and low potential hemes, respectively, of cytochrome *b;* FeS, the 2Fe−2S center of the Rieske protein; cyt *f,* cytochrome *f;* PC, plastocyanin, a water-soluble copper-containing protein; A_1, phylloquinone; F_X, F_A, F_B, 4 Fe-4 S clusters; FD, ferredoxin, a water-soluble protein containing a 4 Fe−4 S cluster.

mitochondria, ATP formation is coupled to the electron transport.

How can electron flow through the electron carriers shown in Fig. 51.4 cause ATP formation? Mitchell (1979) suggested that electron transport and ATP formation are both coupled to the movement of protons across membranes. His *chemiosmotic hypothesis* helps us understand the reason for the arrangement of the electron carriers within photosynthetic membranes.

VB. The Chemiosmotic Hypothesis

It was known that electron transport in mitochondria and chloroplasts is accompanied by the movement of protons across the cristae or thylakoid membranes. Mitchell suggested that the transmembrane pH difference (often called a proton gradient) that is formed is an intermediate in phosphorylation. Electron transport would drive proton translocation and the proton gradient in turn would drive ATP synthesis.

Two experiments involving photosynthetic material played a critical role in convincing scientists that the chemiosmotic hypothesis must be taken seriously. Chloroplasts will synthesize ATP even if they are illuminated in the absence of ADP and P_i and then left in the dark for several minutes before these substrates are added. A relatively stable "high energy intermediate" has been formed in the light and can later drive ATP formation in the dark. Andre Jagendorf and Ernest Uribe (1966) learned that the illumination step was most efficient when the pH of the medium was about 4, while the ATP synthesis step was most efficient at pH 8. Therefore, they routinely illuminated the chloroplasts in medium buffered at pH 4 with succinate, then increased the pH to 8 before adding ADP and P_i. But ATP was formed by this procedure even if the chloroplasts were not illuminated! The quick increase in pH had created a proton gradient across the thylakoid membranes; the lumen pH had remained near 4 while the external pH had increased to 8. The simplest explanation was that the proton gradient had driven the ATP formation.

Halobacterium halobium is a red bacterium found in lakes that have a high salt content. It can form ATP in the light in a quite unusual way. The membrane of the bacterium contains purple domains in which molecules of the transmembrane protein bacteriorhodopsin are packed together in a hexagonal lattice. Each molecule of bacteriorhodopsin contains a molecule of all-*trans*-retinal attached as a Shiff base to a lysine residue. Upon absorbing light, the retinal is isomerized to the 13-*cis* isomer, initiating a cycle of events resulting in the translocation of a proton from the inside to the outside of the cell and regeneration of all-*trans*-retinal (Subramaniam and Henderson, 2000). The electrochemical proton gradient that is established is used to drive ATP formation.

ATP synthesis in mitochondria is catalyzed by a membrane-associated ATP synthase. Photosynthetic ATP formation is catalyzed by a similar protein. Ephraim Racker and Walter Stoeckenius (1974) incorporated purified bacteriorhodopsin into artificial phospholipid vesicles. When the vesicles were illuminated, protons were pumped into the vesicles. Protons were pumped

inward rather than outward because the bacteriorhodopsin is incorporated into the membranes in an orientation that was opposite to that in the bacterial membrane. When purified mitochondrial ATP synthase was also incorporated into the vesicles, light caused ATP to be formed from ADP and P_i. This experiment showed that the mitochondrial ATP synthase can catalyze ATP formation in the absence of any other mitochondrial protein, including those of the electron transport chain. Only an electrochemical proton gradient is required.

How might the pH gradient be established? Some electron carriers, such as cytochromes and iron–sulfur proteins, cannot cross membranes. Others, such as quinones, are soluble in membranes and, as illustrated in Fig. 51.4, may bind protons after they have accepted electrons.

Mitchell (1979) proposed that the electron carriers are arranged asymmetrically in the membrane. The principle is illustrated in the upper part of Fig. 51.10. Carriers that bind protons would alternate in the electron transport chain with those that do not. Electron transfers that result in H^+ binding (A → B) would occur on one side of the membrane (the stromal side in Fig. 51.10), while electron transfers that result in H^+ release (B → C) would occur on the opposite side (the luminal side). In one direction (from the stromal side to the luminal side), electrons and protons would always move together across the membrane. In Fig. 51.10, BH serves as the carrier of an electron and a proton. Electrons would always move alone across the membrane in the opposite direction (C → D). In this way, the net transfer of protons would accompany electron transport across the membrane. Such electron transport is sometimes described as *vectorial*, since it has a defined direction within the membrane, unlike electron transfer that occurs in solution. As we will see, proton translocation is coupled to electron transport in other ways as well.

Protons would flow back across the membrane through the *ATP synthase*. This proton flow would drive ATP formation. How it does so will be discussed in Section VD.

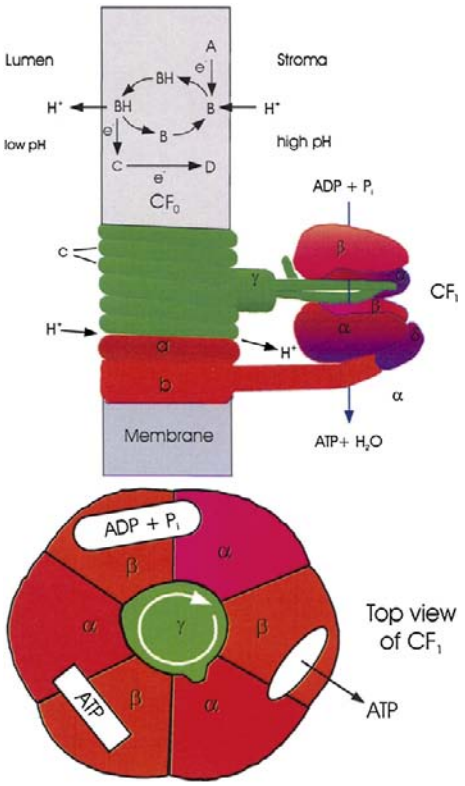

FIGURE 51.10 An illustration of how electron transport and ATP formation might be coupled. Top: Example of how electron and proton transport might be coupled. A, B, C and D are electron carriers that cannot move through the membrane. B is a molecule, such as a quinone, which becomes protonated when it accepts an electron, diffuses across the membrane and releases the proton when it is reoxidized. Center: The ATP synthase, illustrating current conceptions of how proton transport might be coupled to ATP formation. The α and β subunits of CF_1 are held fixed, while H^+ flow through CF_0 causes rotation of the c and γ subunits. As projections of γ contact each $\alpha\beta$ pair in succession, they cause conformational changes that allow binding of ADP and phosphate, ATP formation and ATP release. CF_1 is shown as a section through the γ subunit. Bottom: top view of CF_1, illustrating how rotation of the γ subunit may induce successive steps in ATP formation.

VC. Storage of Free Energy in an Electrochemical Gradient

When an uncharged molecule moves from a region where its concentration is C_1 to a region where its concentration is C_2 there is a free energy change:

$$\Delta G = RT \ln C_2/C_1 \qquad (51.7)$$

per mole transferred. Since:

$$\Delta G = \Delta H - T\Delta S \qquad (51.8)$$

this free energy change is due to the change in entropy, ΔS, that accompanies the change in distribution of the molecules. When a charged particle such as a proton moves between regions whose electrical potentials differ, there is an additional free energy change per mole transferred:

$$\Delta G = z\,F\,\Delta\psi \qquad (51.9)$$

where z is the number of charges on the molecule, F is Faraday's constant (23 kcal/V mol) and $\Delta\psi$ is the electrical potential difference in volts. Such a difference in both concentration and electrical potential is often called an *electrochemical gradient*. There can be an electrochemical proton gradient between the chloroplast stroma and the thylakoid lumen. This gradient is created by the transfer of protons and electrons across the membrane

during electron transport. For the transfer of protons (z = +1) from the stroma to the lumen:

$$\Delta G = RT\,\mathrm{In}([\mathrm{H}^+]_{\mathrm{lumen}}/[\mathrm{H}^+]_{\mathrm{stroma}}) + F\,(\psi_{\mathrm{lumen}} - \psi_{\mathrm{stroma}})$$

$$\Delta G = -2.30\,RT\,\Delta\mathrm{pH} + F\Delta\psi \tag{51.10}$$

This free energy difference is sometimes known as *protonmotive force* and abbreviated Δp, $\Delta\mu_{H+}$, or pmf. Protons can be transported across the thylakoid membrane against their electrochemical gradient because the transfer is coupled to exergonic electron transfer. The proton translocation shown in Fig. 51.10 can occur if the sum of ΔG for proton translocation and ΔG of electron transfer from A to D is less than zero.

VD. ATP Synthase

The chloroplast ATP synthases are found in the stroma lamellae and in the unappressed membranes of the grana, but rarely in appressed granal membranes (see Fig. 51.6). The synthase has a structure similar to that of the mitochondrial ATP synthase (see Fig. 51.10). It consists of a transmembrane domain (CF_0) and a catalytic domain (CF_1) located on the stromal surface of the thylakoid membrane. Each includes several kinds of subunit.

Biochemical (Boyer, 1997) and crystallographic (Abrahams et al., 1994) studies of the ATP synthase have suggested that proton efflux through F_0 may be coupled to ATP formation in the following way. CF_1 includes three α and three β subunits, which form a ring of $\alpha\beta$ dimers (see Fig. 51.10, bottom). Each β subunit contains a catalytic site. At each of the three catalytic sites, the following steps occur. (1) ADP and phosphate bind loosely. (2) After a conformation change, the binding becomes tight and ATP is formed. (3) After a second conformation change, ATP is released. It is this step, rather than ATP formation, that requires the greatest energy input. (4) After a third conformational change, the site is ready to bind ADP and phosphate loosely again. The steps occur at each catalytic site in sequence and cooperatively, e.g. as one site is binding ADP and phosphate, another is converting them to ATP and the third is releasing ATP. What then causes the conformational changes? F_0 includes 9−15 copies of subunit c, a small transmembrane protein. The c subunits form a ring in the membrane. Each subunit may be able to bind a proton from the luminal side of the membrane; the proton may then be released on the stromal side, but only after the c-ring has rotated. Thus, rotation of the c-ring is coupled to proton flow much like rotation of a water wheel is coupled to water flow. The proton translocation is thought to occur at the interface of the c-ring and another transmembrane subunit, the a subunit. The c-ring is attached to the γ subunit, a rod-shaped protein that extends into the hole formed by the $\alpha\beta$ ring. Proton efflux through the c-ring would thus cause the γ subunit to δ subunit). As projections on the γ ring contact each $\alpha\beta$ dimer in turn, they would induce the conformational changes that lead to ATP formation. Translocation of 9−15 protons and formation of three ATPs would accompany each full rotation of the c−γ complex, consistent with the observation that translocation of three to four protons is required for each ATP formed (Feniouk and Junge, 2009). Thus, ATP formation is thermodynamically possible when μ_{H+} is more than one-third or one-fourth of ΔG of ATP formation.

The ATP synthase is intricately regulated, presumably to prevent the reversal of ATP synthesis in the dark. It is activated by the presence of a sufficiently large $\Delta\mu_{H+}$. Until it is activated, it will neither synthesize nor hydrolyze ATP. Reduction of a CF_1 disulfide bridge by reduced thioredoxin, which is formed when chloroplasts are illuminated, enhances the efficiency of the activated ATP synthase when $\Delta\mu_{H+}$ is small.

VI. PHOTOSYNTHETIC ELECTRON TRANSPORT

VIA. The Interaction of Light with Molecules

A light wave consists of an electric field and a magnetic field whose directions are perpendicular to each other. The wave moves through space at a velocity:

$$v = nc \tag{51.11}$$

where n is the refractive index of the medium through which the light is moving and c is the speed of light in a vacuum, 3.0×0^8 m/s. The wavelength of the light, λ, is the distance between the crests of the waves. Visible light has a wavelength between 400 and 700 nm. The frequency of the light, v, is the frequency with which crests of the waves pass a given point in space, and:

$$v = c/\lambda \tag{51.12}$$

According to the principles of quantum theory, light can be absorbed or emitted only in discrete units called *quanta*. The energy, E, of such a quantum depends upon the frequency of the light according to the equation:

$$E = hv \tag{51.13}$$

where h is Planck's constant, 2.86×10^{-37} kcal s.

Just as the electrons of atoms occupy atomic orbitals having discrete energies, the electrons in molecules occupy molecular orbitals having discrete energies. Molecular orbitals may extend over several nuclei. Each molecular orbital can contain two electrons of opposite spin. Absorption of light can promote (excite) an electron to an orbital of higher energy (Fig. 51.11) if the energy difference

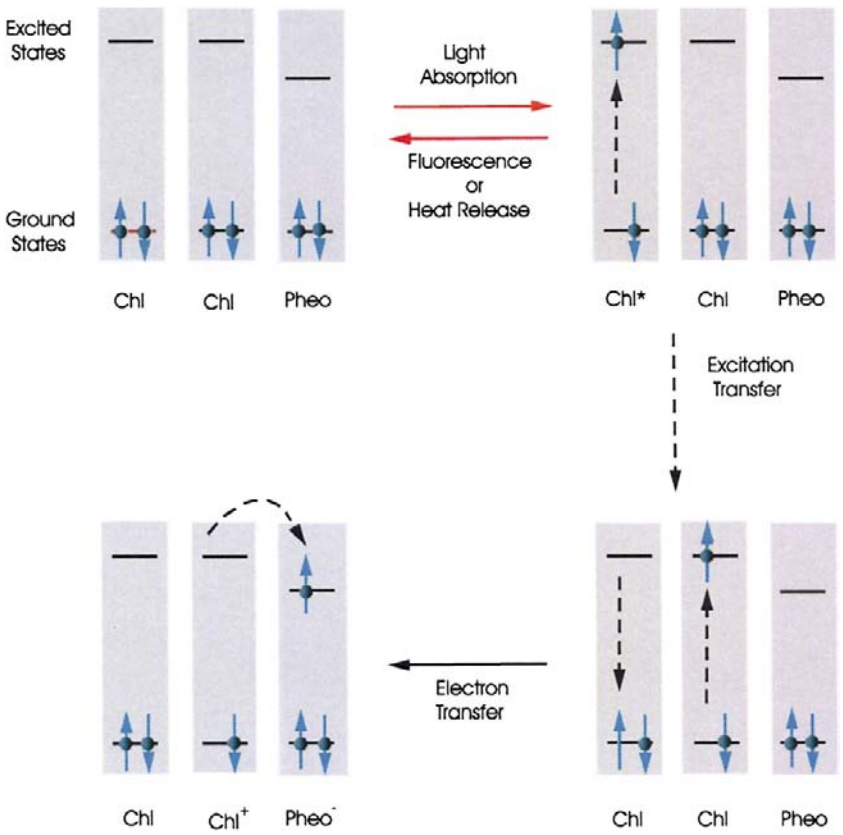

FIGURE 51.11 Light absorption and emission, excitation transfer and photochemical electron transfer. Chlorophyll (Chl) and pheophytin (Pheo) molecules are used as examples. Circles with upward and downward arrows represent electrons having opposite spins. Molecules have many ground and excited orbitals. Only one of each is shown. Chl*, electronically excited Chl; Chl^+, oxidized Chl; $Pheo^-$, reduced Pheo.

between the orbitals is equal to the energy of a quantum of the light. Several competing processes may occur after light is absorbed. The excited electron may drop back to its ground molecular orbital. As it does so, the excitation energy may be re-emitted as light (*fluorescence*), it may be lost as heat, or it may be transferred to a neighboring molecule, causing excitation of one of the neighbor's electrons to a higher orbital. Finally, the excited electron may be transferred to an empty orbital of a neighboring molecule. When this occurs, part of the energy of the absorbed light is conserved as chemical free energy of the electron donor—acceptor pair.

The tendency of a biological molecule to donate electrons is usually expressed as its midpoint redox potential at pH 7, E_{m7}. The *midpoint potential*, E_m, is the electrical potential difference that would exist between the standard hydrogen half cell and a solution in which the oxidized and reduced forms of the molecule are present in equal concentrations. In the standard hydrogen half-cell, the pH is 0 and the partial pressure of H_2 is 1 atm. The E_{m7} values for members of the chloroplast electron transport system are indicated in Fig. 51.9. A molecule in which an electron has been excited to a higher orbital has a more negative E_m than does the molecule in its ground state, by an amount about equal numerically to the energy difference between the ground and excited orbitals (in electron volts). Thus, it is a better electron donor. Note the difference between the E_ms of P680 and P680* (and between P700 and P700*) in Fig. 51.9.

The standard free energy change of an electron transfer is related to the difference between the E_m values of the electron donor and acceptor:

$$\Delta G^o = -n\,F\,\Delta E_m \qquad (51.14)$$

where n is the number of electron equivalents transferred per mole. Thus, excitation of a molecule lowers the free energy change accompanying the transfer of an electron to another molecule. This equation can be used to calculate the free energy changes accompanying the light-induced charge separations and the subsequent electron transfers shown in Fig. 51.9.

Especially lucid explanations of the photochemical processes involved in photosynthesis have been given by Clayton (1970, 1980).

VIB. The Presence of Two Photochemical Reactions in Chloroplasts

The most careful measurements of the *quantum yield* of oxygen evolution indicate that at least eight light quanta must be absorbed for each molecule of oxygen that is

evolved. Because the oxidation of two water molecules to form one O_2 molecule requires the removal of only four electrons,

$$2\ H_2O \rightarrow O_2 + 4\ H^+ + 4\ e^- \qquad (51.15)$$

it appeared that two quanta are necessary for the extraction of each electron from water. Robert Emerson illuminated the green alga *Chlorella* with light of different wavelengths and observed the rates of O_2 evolution. He found that when light of wavelength less than 680 nm and light of wavelength greater than 680 nm were given together, the rate of O_2 evolution was greater than the sum of the rates observed when the algae were illuminated with light of each wavelength separately; i.e. the two wavelengths acted synergistically (Emerson et al., 1957). This phenomenon, which has come to be known as *Emerson enhancement*, suggested that efficient O_2 evolution requires the cooperation of a system which absorbs long-wavelength light and a system which absorbs short-wavelength light. L.N.M. Duysens found that 680-nm light caused the oxidation of cytochrome *f*, whereas 562-nm light caused its re-reduction (Duysens et al., 1961). In 1960, R. Hill and F. Bendall (1960) suggested the *Z scheme*, in which a photosystem driven by short-wavelength light (*photosystem 2, PS 2*) and a photosystem driven by long-wavelength light (*photosystem 1, PS 1*) are connected in series. Light absorbed by PS 2 would cause the transfer of an electron from H_2O to a chain of electron carriers between the photosystems (cytochrome *f* is one of these). Light absorbed by PS 1 would cause the transfer of the electron from this chain to $NADP^+$ to form NADPH:

$$H_2O \rightarrow PS2 \rightarrow \text{cytochrome f(etc.)} \rightarrow PS1 \rightarrow NADP^+ \qquad (51.16)$$

Absorption of two quanta, one by each photosystem, would be required for the transfer of an electron all the way from H_2O to $NADP^+$. Cytochrome *f* would be reduced by PS 2 and oxidized by PS 1. The complete Z-scheme as it is now understood is presented in Fig. 51.9.

The light-absorbing pigments associated with PS 1 and PS 2 have somewhat different absorption spectra. The PS 2 pigments have very little absorption beyond about 680 nm, so light in this wavelength region drives PS 1 almost exclusively.

VIC. Primary Electron Donors and Light-Harvesting Pigments

The absorption spectrum of a typical chloroplast is shown in Fig. 51.1. Bessel Kok noticed that when chloroplasts are illuminated, there is a small decrease in their optical absorbance ("bleaching") at 700 nm. He suggested that the change was due to the light-induced oxidation of a chlorophyll molecule, resulting in the loss of its optical absorbance at that wavelength (Kok and Hoch, 1961). It was suggested that the primary light reaction is the transfer of an electron from a special chlorophyll molecule, named *P700*, to an electron acceptor (see Fig. 51.9). In bacteria, illumination caused cytochrome oxidation (detected as a change in optical absorbance at wavelengths where cytochrome absorbs light) as well as bacteriochlorophyll oxidation. To determine whether bacteriochlorophyll or cytochrome oxidation occurs first, William Parson illuminated bacteria with very short flashes from a Q-switched laser. Immediately after the flash, he observed oxidation of bacteriochlorophyll. The bacteriochlorophyll became reduced again in a few milliseconds and, as it did, the cytochrome became oxidized. The bacteriochlorophyll had been oxidized first; the cytochrome had then donated an electron to the oxidized bacteriochlorophyll (Straley et al., 1973).

The laser flash had been so brief that it ended before the electron lost by the bacteriochlorophyll had been replaced by an electron from the cytochrome, so the flash had caused the transfer of only a single electron from the bacteriochlorophyll. Such *single turnover flashes* have been a powerful tool for the study of photosynthetic electron transport. Lasers capable of producing flashes femtoseconds (10^{-15} s) in duration have made it possible to measure the rates of very early electron transfer steps, some of which occur in picoseconds (10^{-12} s).

P700 is the primary electron donor in PS 1. The primary donor of PS 2 absorbs at 680 nm and is known as *P680*. Oxidized chlorophyll contains an unpaired electron (see Fig. 51.11). Such molecules can be studied by the technique of *electron paramagnetic resonance spectroscopy*, in which the absorption of microwaves by the unpaired electrons is measured. Study of P680 and P700 by this technique, as well as other experiments, suggested that they are *dimers* of chlorophyll *a*. After they have lost an electron, the remaining unpaired electron is shared between the two chlorophyll molecules that comprise the dimers.

The details of many biophysical techniques, including optical spectroscopy and magnetic resonance, which are employed in photosynthesis research are described in Amesz and Hoff (1996).

Most of the chlorophyll in cells serves only to capture light and does not participate in photochemistry. Each photochemically active chlorophyll dimer (P680, P700) is associated with an aggregate of several hundred light-harvesting chlorophyll molecules, known as a *photosynthetic unit*. After any chlorophyll molecule in the unit absorbs a quantum of light, the excitation energy migrates among the chlorophyll molecules in the aggregate (see Fig. 51.11). When the excitation reaches the photochemically active dimer, electron transfer occurs. A typical photosynthetic unit contains about 300 chlorophylls molecules. *Beta-carotene* and other carotenoids also serve as light-harvesting pigments, as do tetrapyrrole pigments known as

phycobilins in cyanobacteria and some algae. The pigments are attached to protein molecules. Such accessory pigments allow the capture of light in regions of the spectrum where chlorophyll does not absorb light strongly.

VID. The Structure and Function of the Chloroplast Electron Transport System

We can now summarize the way the chloroplast electron transport system is believed to operate (see Figs. 51.9 and 51.12). The components have redox potentials that allow electrons to move forward along the chain; they are arranged in the membrane and oriented in such a way that forward electron transfer is fast and electron flow results in translocation of protons across the membrane.

Photosystem 2 particles from a thermophilic cyanobacterium have been isolated and crystallized (Ferreira et al., 2004; Loll et al., 2005). The PS 2 reaction center contains two subunits, D1 and D2, whose amino acid sequences partially resemble those of purple bacterial reaction center subunits L and M. Like the L and M subunits, D1 and D2 bind the electron transport cofactors. PS 2 contains several additional proteins that are not discussed here.

Formation of one O_2 molecule requires the removal of four electrons from two molecules of H_2O. Kok suggested that each photochemical act removes one electron from an *oxygen-evolving complex (OEC)* (Kok et al., 1970). When four electrons have been removed, oxygen molecules are released. The OEC contains four manganese nuclei, a calcium ion and a chloride ion. Its structure and function have been reviewed by Yocum (2008b). The following sequence of events is now believed to occur (see Fig. 51.9). Upon excitation, P680 transfers an electron to a special pheophytin *a* molecule. An electron is then transferred to $P680^+$ from Y_Z, a tyrosine residue, which is part of D1. Next, Y_Z^+ receives an electron from the OEC, leaving a positive charge stored in the OEC. This sequence of events is repeated until four positive charges have been stored in the OEC and O_2 is released. During the process, four protons are released into the chloroplast lumen. The oxidation states of the manganese cluster are known as *S states*. Yocum (2008c) represents the series of events as follows:

$$2\ H_2O + S_0 \Rightarrow S_1{}^{+1} \Rightarrow S_2{}^{+2} \Rightarrow S_3{}^{+3} \Rightarrow S_4{}^{+4} \rightarrow S_0 + O_2 + 4\ H_2O \tag{51.17}$$

where the open arrows represent light-driven electron extractions. All of the S states relax to S_1 in the dark, so in practice O_2 is evolved after the third flash.

The first electron that had been transferred to pheophytin *a* moves to Q_A (plastoquinone) and then to Q_B (also plastoquinone) to form a plastosemiquinone anion. After a second photon is absorbed, a second electron moves down the chain to Q_B, reducing it to $Q_B^{2-}\cdot Q_B^{2-}$ then binds two protons from the stroma to form plastohydroquinone. The structures of quinone, semiquinone anion and hydroquinone are shown in Fig. 51.4. At this point, two protons have been taken up from the stroma and four protons have been released into the lumen.

The herbicides atrazine and diuron act by competing with plastoquinone for binding to the Q_B site on D1.

The plastohydroquinone is released from its binding site on PS 2 and diffuses within the membrane (as QH_2 in Fig. 51.12) until it reaches the cytochrome b_6f complex. Here it binds to a site (Qo) near the luminal surface of the membrane.

At this point, a series of reactions is initiated that will result in the transfer of additional protons across the membrane. A possible mechanism of the proton translocation, which was suggested by Mitchell, is known as a *Q cycle* (Crofts, 2004). The bound QH_2 donates an electron to a 2 Fe−2 S center known as the *Rieske Fe−S center*. The electron moves from there to cytochrome f. The

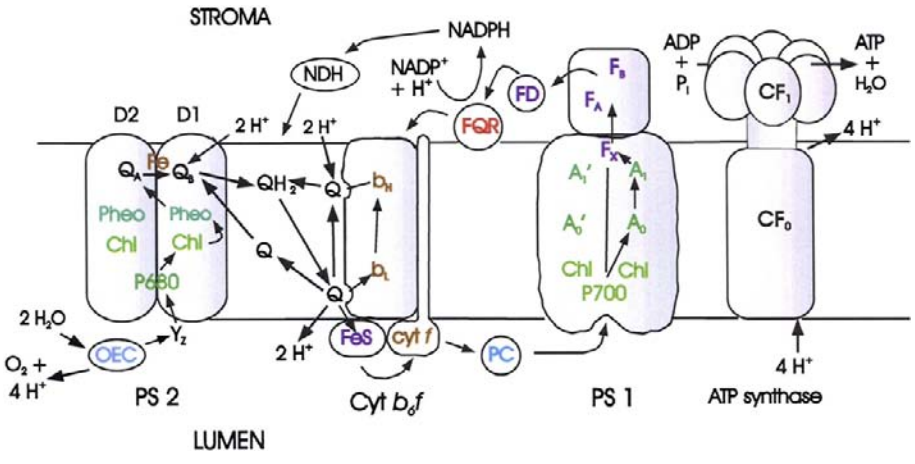

FIGURE 51.12 Electron and proton transport and ATP formation in chloroplasts. FNR, ferredoxin-$NADP^+$ oxidoreductase; NDH, NADPH dehydrogenase; FQR, ferredoxin-plastoquinone oxidoreductase. Other symbols are defined in the legend of Fig. 51.9.

cytochrome b_6f complex also contains two cytochrome *b*-type hemes, b_H and b_L. QH_2 as a reductant is not strong enough to donate an electron to these hemes, but the plastosemiquinone that was formed when QH_2 transferred the electron to the Fe−S center is, and does so. In effect, the transfer of the first electron from QH_2 to the Fe−S center has driven the transfer of the second electron to b_L. QH_2 has been oxidized to Q, releasing two protons into the lumen. A second QH_2 molecule is oxidized by a similar mechanism and a second electron is donated to the hemes. The two heme electrons are then donated to a plastoquinone (Q) molecule, which is bound near the stromal surface. It then binds two protons from the stroma. In the net process occurring at the cytochrome b_6f complex, one QH_2 has been oxidized, two protons have been removed from the stroma and four protons have been released into the lumen.

The electrons that were transferred to cytochrome *f* move to *plastocyanin*, a soluble, copper-containing protein. The plastocyanin diffuses within the lumen until it reaches the PS 1 complex, where it transfers the electron to $P700^+$. P700 is a chlorophyll *a* dimer.

The x-ray structure of PS1 crystals has been determined (Ben-Shem et al., 2003; Nelson and Yocum, 2006). Along with several other proteins, PS 1 contains a protein dimer, the PsaA and PsaB proteins, to which electron transfer cofactors and a large number of light-harvesting chlorophylls are bound. The PsaA-PsaB dimer has approximate twofold rotational symmetry, as does the purple bacterial reaction center dimer. Excited P700 donates an electron to A_0, a chlorophyll *a* monomer (remember that the acceptor in PS 2 is pheophytin *a*. From A_0, the electron moves to A_1, which is phylloquinone, then through the [4Fe−4S] cluster F_X to the [4Fe−4S] clusters F_A and F_B and, finally, to *ferredoxin*, a soluble [4Fe−4S] protein. From ferredoxin the electron is transferred to ($NADP^+$) by way of the flavoprotein *ferredoxin-NADP oxidoreductase, FNR*. On reduction the NADP binds a proton in the stroma. Protons return from the lumen to the stroma through the ATP synthase and ATP is formed.

Some of the ferredoxin molecules may transfer their electrons back to oxidized quinone in the membrane to generate more ATP when cellular metabolism requires a higher ATP/NADH ratio than is provided by linear electron transport. This process is known as *cyclic photophosphorylation*. It may occur by an antimycin A-sensitive pathway from ferredoxin or, as shown in recent studies (Livingston et al., 2010), from NADPH in a process mediate by NADPH dehydrogenase.

VII. REGULATION OF PHOTOSYNTHESIS

Virtually every step in the photosynthetic process is tightly regulated. The precision of this regulation was illustrated in experiments with spinach (Servaites et al., 1989). During illumination of spinach leaves with light whose intensity was varied sinusoidally, the net rate of CO_2 fixation perfectly paralleled the light intensity except between hours 4 and 10, when it was saturated. As the light intensity changed, the rates of the reactions leading to CO_2 uptake changed in such a way that efficiency of the use of the light remained constant. The final output of photosynthesis, export of fixed carbon from the leaves, remained almost perfectly constant throughout the cycle.

If photosynthesis is to work efficiently, PS 1 and PS 2 must transfer electrons at the same rate. Chloroplasts regulate the rates of the photosystems by regulating the transfer of excitation energy to P680 and P700. Both PS 1 and PS 2 contain chlorophyll molecules bound to proteins that are a permanent part of the PS 1 and PS 2 complexes. CP 43 and CP 47 are part of PS 2 and LHC I is part of PS 1. Chlorophyll is also bound to the PsaA and PsaB proteins of PS 1. Such chlorophyll is known as *antenna chlorophyll*. In addition, chloroplasts thylakoids contain a protein, known as *LHC II* (for light-harvesting complex II), to which are typically attached eight molecules of chlorophyll *a,* seven of chlorophyll *b* and one or two of xanthophyll per peptide. Under some conditions, LHC II is tightly attached to PS 2 to which it transfers excitation energy. If PS 2 is working faster than PS 1, the quinone pool between PS 2 and PS 1 becomes overreduced. When this happens, a kinase is activated in response to plastohydroquinone binding to the Qo site of the cytochrome b_6f complex (Lemeille and Rochaix, 2010). The kinase catalyzes the phosphorylation of some of the LHC II. The phosphorylated molecules dissociate from PS 2. As a result, they no longer transfer excitation energy to PS 2 and so its rate slows. Some of the phosphorylated LHC II associates with PS 1, which is found predominantly in the stroma lamellae, and transfer excitation energy to it instead. Once the quinone pool between PS 2 and PS 1 are no longer overreduced, the kinase is inactivated and a phosphatase removes the phosphate from the LHC II. LHC II returns to the grana lamellae and reassociates with PS 2, most of which is located in the grana. These processes, known as *state transitions*, are accompanied by changes in the structures of the grana and stroma lamellae (Chuartzman et al., 2008).

A regulatory mechanism that deserves special mention involves the protein *thioredoxin*, which serves a signal that it is daytime. Thioredoxin contains a disulfide bridge which can be reduced by ferredoxin in a reaction catalyzed by ferredoxin−thioredoxin reductase. In the light, ferredoxin is reduced by PS 1 and, in turn, reduces thioredoxin. Thioredoxin then activates a number of Calvin cycle enzymes and increases the sensitivity of the ATP synthase to $\Delta\mu_{H+}$ by disulfide exchange. As a result, the Calvin cycle and the ATP synthase are active when there is enough light to drive electron transport (Schurmann and Buchanan, 2008).

BIBLIOGRAPHY

Abrahams, J. P., Leslie, A. G. W., Lutter, R., & Walker, J. E. (1994). Crystal structure at 2.8-angstrom resolution of F_1 ATPase from bovine heart mitochondria. *Nature, 370*, 621–628.

Amesz, J., & Hoff, A. J. (Eds.). (1996). *Biophysical Techniques in Photosynthesis*. Dordrecht: Kluwer Academic Publishers.

Ben-Shem., A., Frolow, F., & Nelson, N. (2003). The crystal structure of plant photosystem I. *Nature, 426*, 630–635.

Blankenship, R. E. (2002). *Molecular Mehanisms of Photosynthesis*. Oxford: Blackwell Science Ltd.

Blankenship, R. E., Sadekar, S., & Raymond, J. (2007). The evolutionary transition from anoxygenic to oxygenic photosynthesis. In P. G. Falkowski, & A. H. Knoll (Eds.), *Evolution of Primary Producers in the Sea* (pp. 21–35). San Diego: Elsevier.

Boyer, P. D. (1997). The ATP synthase: a splendid molecular machine. *Annu Rev Biochem, 66*, 717–749.

Brennan, T. (2008). Photosynthesis timelines. In K. C. Smith (Ed.), *Photobiological Sciences Online. American Society for Photobiology.* http://www.photobiology.info/.

Chuartzman, S. G., et al. (2008). Thylakoid membrane remodeling during state transptions in Arabidopsis. *Plant Cell, 20*, 1029–1039.

Clayton, R. K. (1970). *Light and Living Matter, Volume 1: the Physical Part*. New York: McGraw-Hill Book Company.

Clayton, R. K. (1980). *Photosynthesis: Physical Mechanisms and Chemical Patterns*. Cambridge: Cambridge University Press.

Cogdell, R. J., et al. (1999). How photosynthetic bacteria harvest solar energy. *J Bacteriol, 181*, 3869–3879.

Crofts, A. R. (2004). The cytochrome bc1 complex: function in the context of structure. *Ann Rev Physiol, 66*, 689–733.

Deisenhofer, J., & Michel, H. (1989). The photosynthetic reaction centre from the purple bacterium *Rhodopseudomonas viridis*. *EMBO J, 8*, 2149–2169.

Duysens, L. N. M., Amesz, J., & Kamp., B. M. (1961). Two photochemical systems in photosynthesis. *Nature, 190*, 510–511.

Emerson, R., Chalmers, R., & Cederstrand, C. (1957). Some factors influencing the long-wave limit of photosynthesis. *Proc Nat Acad Sci USA, 43*, 133–143.

Feniouk, B. A., & Junge, W. (2009). Proton translocatin and ATP synthesis by the F_0F_1-ATPase of purple bacteria. In C. N. Hunter, F. Daldal, M. C. Thurnauer, & J. T. Beatty (Eds.), *The Purple Photosynthetic Bacteria* (pp. 475–493). Springer Science Business Media BV.

Ferreira, K. N., Iverson, T. M., Maghlaoui, K., Barber, J., & Iwata, S. (2004). Architecture of the photosynthetic oxygen-evolving center. *Science, 303*, 1831–1838.

Golbeck, J. H. (2010). Editorial. *Photosynth Res, 104*, 101–102.

Hackett, J. D., Yoon, H. S., Butterfield, N. J., Anderson, M. J., & Bhattacharya, D. (2007). Plastid endosymbiosis: sources and timing of the major events. In P. G. Falkowski, & A. H. Knoll (Eds.), *Evolution of Primary Producers in the Sea* (pp. 109–132). San Diego: Elsevier.

Hill, R., & Bendall, F. (1960). Function of two cytochrome components in chloroplasts: A working hypothesis. *Nature, 1186*, 136–137.

Hunter, C. N., Daldal, F., Thurnauer, M. C., & Beatty, J. T. (Eds.). (2008). *The Purple Phototrophic Bacteria, Advances in Photosynthesis and Respiration, 28*. Dordrecht, The Netherlands: Springer.

Jagendorf, A. T., & Uribe, E. (1966). ATP formation caused by acid-base transition of spinach chloroplasts. *Proc. Nat. Acad. Sci. USA, 55*, 170–177.

Jones, M. (2009). Photosynthetic bacteria. In K. C. Smith (Ed.), *Photobiological Sciences Online. American Society for Photobiology.* http://www.photobiology.info/.

Ke, B. (2001). *Photosynthesis: Photobiochemistry, and Photobiophysics*. Dordrecht: Kluwer Academic Publishers.

Kok, B., & Hoch, G. (1961). Spectral changes in photosynthesis. In W. D. McElroy, & B. Glass (Eds.), *Light and Life* (pp. 397–416). Johns Hopkins Press.

Kok, B., Forbush, F., & McGloin, M. (1970). Cooperation of charges in photosynthetic O_2 evolution: A linear four step mechanism. *Photochem Photobiol, 11*, 457–475.

Lemeille, S., & Rochaix, J.-D. (2010). State transitions at the crossroad of thylakoid signalling pathways. *Photosynth Res, 106*, 33–46.

Livingston, A. K., Cruz, J. A., Kohzuma, K., Dhingra, A., & Kramer, D. M. (2010). An *Arabidopsis* mutant with high cyclic electron flow around photosystem I (*hcef*) involving the NADPH dehydrogenase complex. *Plant Cell, 22*, 221–233.

Loll, B., Kern, J., Saenger, W., Zouni, A., & Bies, J. (2005). Toward complete cofactor arrangement in the 3.0 A resolution structure of photosystem II. *Nature, 438*, 1040–1044.

Loomis, W. E. (1960). Historical introduction. In W. Ruhland (Ed.), *Encyclopedia of Plant Physiology, Vol. V* (pp. 85–114). Berlin: SpringerVerlag.

Margulis, L. (1970). *Origin of Eukaryotic Cells*. New Haven, Connecticut: Yale University Press.

Mitchell, P. (1979). Keilin's respiratory chain concept and its chemiosmotic consequences. *Science, 206*, 1148–1159.

Nelson, N., & Yocum, D. F. (2006). The structure and function of photosystems I and II. *Ann Rev Plant Biol, 57*, 521–565.

Olson, J. M., & Blankenship, R. E. (2004). Thinking about the evolution of photosynthesis. *Photosynth Res, 80*, 373–386.

Racker, E., & Stockenius, W. (1974). Reconstitution of purple membrane vesicles catalyzing light-driven proton uptake and adenosine triphosphate formation. *J Biol Chem, 249*, 662–663.

Schurmann, P., & Buchanan, B. B. (2008). The ferredoxin/thioredoxin system of oxygenic photosynthesis. *Antioxid Redox Signal, 10*, 1235–1274.

Servaites, J. C., Fondy, B. R., Li, B., & Geiger, D. R. (1989). Source of carbon for export from spinach leaves throughout the day. *Plant Physiol, 90*, 1168–1174.

Straley, S. C., Parson, W. W., Mauzerall, D. C., & Clayton, R. K. (1973). Pigment content and molar extinction coefficients of photosynthetic reaction centers from *Rhodopseudomonas sphaeroides*. *Biochem Biophys Act, 305*, 597–609.

Sturgis, J. N., & Niederman, R. A. (2008). Atomic force microscopy reveals multiple patterns of antenna organization in purple bacteria; implications for energy transduction mechanisms and membrane modeling. *Photosynth Res, 95*, 269–278.

Subramaniam, S., & Henderson, R. (2000). Molecular mechanisms of vectorial proton translocation by bacteriorhodopsin. *Nature, 406*, 653–657.

Woese, C. R. (1987). Bacterial evolution. *Microbiol Rev, 51*, 221–271.

Yocum, C. (2008a). Photosynthetic reaction centers. In K. C. Smith (Ed.), *Photobiological Sciences Online. American Society for Photobiology.* http://www.photobiology.info/.

Yocum, C. F. (2008b). The Ca^{2+} and Cl^- requirements of the O_2-evolving complex. *Coordination Chem Rev, 252*, 296–305.

Yocum, C. F. (2008c). Oxygen evolution. In K. C. Smith (Ed.), *Photobiological Sciences Online. American Society for Photobiology.* http://www.photobiology.info.

Chapter 52

Bioluminescence

J. Woodland Hastings

Chapter Outline

I. SUMMARY

Bioluminescence is an enzymatically-catalyzed chemiluminescence, a chemical reaction that emits light. Though relatively rare, it occurs in a phylogenetically-wide range of species, primarily marine, ranging from bacteria to vertebrates, and has many independent evolutionary origins. Thus, structures of the genes and proteins, as well as the physiological, biochemical and regulatory mechanisms involved, are very different. The principal biochemical components are referred to as luciferin and luciferase, terms that cannot stand alone, being different structurally in different groups. Luminescence provides a selective advantage mediated through its detection and responses by other organisms; its functions may be classed as defensive, offensive or for communication. Physiological control, biochemical mechanisms and functions in four of the major groups, and several less well-known ones, are described. Regulatory mechanisms include autoinduction (quorum sensing; bacteria), action potentials and voltage-gated membrane channels (dinoflagellates, protons; coelenterates, calcium), circadian control (dinoflagellates) and oxygen mobilization (beetles).

II. INTRODUCTION

Unlike most physiological processes, the mechanisms and biochemical components involved in bioluminescence are not the same in different phylogenetic groups, thus indicating that light emission originated many times independently in evolution. For example, fireflies and all beetles use ATP and their flash is triggered by a pulse of oxygen, while flashes of coelenterates are triggered by calcium and ATP is not involved, while bacteria utilize a flavin and dinoflagellates a tetrapyrrole as luciferins. But this is but the tip of the iceberg and, while knowledge of the chemistries and physiological mechanisms of a large fraction of such systems is still below the surface, those that have been elucidated provide important knowledge of physiological mechanisms.

In addition to contributing to fundamental knowledge, some systems have provided unique tools for investigating

Cell Physiology Sourcebook. DOI: 10.1016/B978-0-12-387738-3.00052-4

and understanding other basic physiological processes. Notable, to be sure, was the confirmation in 1976 of the theory that calcium triggers muscle contraction, demonstrated with single barnacle cells injected with the purified intermediate of the coelenterate bioluminescence system (aequorin); upon stimulation, the earliest event recorded was the onset of light emission. Even more familiar and now routinely used at the laboratory bench are genes of luciferases and green fluorescent protein (GFP; the light emitting protein in coelenterates) as reporters. Thereby, a wide variety of molecules and the time course of diverse processes can be visually localized at the cellular level.

Although bioluminescence is rather rare in nature, and in that sense a curiosity, it has several different and fascinating functions. Flashes may be used in several different ways, in fireflies to communicate in courtship or in fish to startle, either to escape predators or capture prey. Its use by many fish and other marine organisms to camouflage the silhouette by emitting a constant ventral glow (intensity adjustable) cries for a study of the physiological mechanism whereby the down-welling light intensity is detected and used to control the intensity of the bioluminescence.

The physiological mechanisms, biochemical systems and genes responsible are similarly very different, *not* evolutionarily conserved, and evidently originated and evolved independently. How many times this may have occurred is difficult to say, but it has been estimated that present day luminous organisms come from as many as thirty or forty different evolutionarily distinct origins (Hastings, 1983; Hastings and Morin, 1991; Haddock et al., 2010).

The four major systems to be described, as well as the lesser well-researched ones, exemplify differences in all aspects, highlighting their independent origins. The luciferases of each of the four have been cloned and sequenced and crystal structures determined. The luciferins and other biochemical components, as well as the identities of the emitting species, are different and known for all. The physiological mechanisms whereby light emission is controlled range from regulation of gene expression and membrane action potentials and channels to osmotically controlled triggering and shutter mechanisms.

III. WHAT IS BIOLUMINESCENCE? PHYSICAL AND CHEMICAL MECHANISMS

Bioluminescence displays, though sometimes obscured by the now-ubiquitous artificial illumination, are bright enough to be seen by other animals and do not include the very dim light emitted by some cells, which is detectable by sensitive instruments now available. This is a chemiluminescence, sometimes attributable to reactions of active oxygen species. And yes, bioluminescence is itself a chemiluminescence (McCapra in Herring, 1978; Wilson, 1985; Campbell, 1988), but distinct in that the reaction is catalyzed by enzymes (generically referred to as luciferases), as well as by the fact it can be seen by eye.

Bioluminescence does not come from or depend on light absorbed by the organism. It derives from a highly exergonic (energy yielding) chemical reaction in which excess energy is transformed into light energy instead of being all lost as heat (Wilson and Hastings, 1998). Thus, in the reaction of substance A with molecular oxygen, one of the reaction products is formed in an electronically *excited state* (B*), which then emits a photon (hν). In all known cases, the reactants remain bound to the luciferase throughout, so that the emission comes from a protein-bound fluorophore (B*, in this example).

$$A + O_2 \xrightarrow{\text{luciferase}} B^* + C$$

$$B^* \rightarrow B + h\nu$$

More generally, the term luminescence refers to any light emission in which energy is specifically channeled to a molecule so that an excited state is produced, not related or due to the temperature. Thus, in addition to chemiluminescence and bioluminescence, these include fluorescence and phosphorescence, in which the excited state is created by the prior absorption of light, as well as triboluminescence and piezoluminescence, involving crystal fracture and electric discharge, respectively. The color is a characteristic of the excited molecule, irrespective of how it was excited. But, as elaborated below, the color may be greatly affected by protein binding, as shown for some bioluminescent systems.

Luminescence is contrasted with incandescence, in which excited states are produced by virtue of the temperature, and the energy is thermal. An example is the light bulb, soon to be phased out for household use, in which a filament is heated, and the color of the light depends on the temperature ("red hot" reflecting a lower temperature than "white hot"). The phasing out is because of its relative inefficiency, due in part to the fact that, unlike luminescence, photons are emitted over a wide range of frequencies, most not in the visible range.

The energy (E) of the photon is related to the color or frequency of the light and is given by the equation $E = h\nu$, where h is Planck's constant and ν the frequency. In the visible-light range, E is quite large in relation to most biochemical reactions. Thus, in visible wavelengths the energy released by a mole of photons (6.02×10^{23}) is about 50 kcal, much more than the energy from the hydrolysis of a mole of ATP, about 7 kcal. In cells, chemical energy from the absorption of a visible photon can power photosynthesis, or it can do damage (mutation; photodynamic action, which can kill). Conversely, it takes a reaction yielding considerable energy to result in an excited state and visible photon.

A question of fundamental importance, then, is what kind of chemical process possesses enough energy, and evidently in a single step (an important point), to populate (create) an excited state? A clue is the fact that both chemi- and bioluminescence in solution require oxygen, which in its reaction with a substrate forms an organic peroxide. The energy from the reaction of such peroxides to form more stable products – which should generate up to 100 kcal per mole – is ample to account for a product in an electronically excited state. Thus, while all known bioluminescent reactions involve peroxide intermediates, their identities differ, because their luciferins (substrates) and also luciferases differ.

The terms luciferin and luciferase are not sufficient for their identification in a given organism. Dubois first showed in 1885 that bioluminescence in beetles could occur in cell-free extracts, with the emission continuing for minutes, or hours in some cases. He demonstrated that the reaction could be characterized as having two components, one heat stable (luciferin) and the other more labile to heat (luciferase). Luciferin was named from the Latin as the component responsible for the light emission (light bearing) and the luciferase as the enzyme. For half a century thereafter, in spite of clear evidence to the contrary, the fact that the luciferins and luciferases from different groups of organisms are different was ignored and the terms were used with abandonment for all species. Today, the persistence of the use of the terms in research publications without naming the organism can be confusing. Luciferin and luciferase are *generic* terms and, to be correct and specific, each must be identified with the organism, thus firefly luciferin or bacterial luciferase, for example.

While luciferases are single proteins, the luciferin fraction may contain more than one substrate, as well as co-factors (Table 52.1). For example, the firefly system involves both ATP and a unique luciferin (a benzothiazole), while the bacterial reaction involves the mixed function oxidation of two substances, reduced flavin mononucleotide and a long chain aliphatic aldehyde. In such cases, there has been some confusion as to which should be called the luciferin, since both contribute to the energy released in the reaction. Sticking to the etymology of the original definition, the benzothiazole and flavin, respectively, are the luciferins in those systems (Hastings, 2011).

IV. LUMINOUS ORGANISMS: ABUNDANCE, DIVERSITY AND DISTRIBUTION

While indeed rare in terms of the total number of luminous species, bioluminescence is phylogenetically diverse, being found in more than 13 phyla (Herring in Herring, 1978). These include bacteria, unicellular algae and fungi, as well as animals ranging from jellyfish, annelids and molluscs to shrimp, fireflies, echinoderms and fishes. Luminescence does not occur in higher plants or in vertebrates above the fishes (Cormier in Herring, 1978). It is also absent in several invertebrate phyla. In some phyla or taxa, a substantial proportion of the genera are luminous (e.g. ctenophores, ≈50%; cephalopods, >50%; echinoderms and annelids, ≈4%). In some cases, all members of a luminous genus emit light, but in others there are both luminous and non-luminous species.

Of the 30 or 40 groups that are believed to be evolutionarily independent, some are found even in different taxa within a phylum or class. Fewer than half of these have been studied in detail and some knowledge of their luciferins and luciferases is available for only about a dozen. Although luminescence is prevalent in the deep sea (Herring, 1985a,b), where there is no sunlight, it is not associated especially with organisms that live in total darkness. There are no known luminous species either in deep fresh water bodies, such as Lake Baikal, Russia, or in the total darkness of terrestrial caves. There are luminous dipteran larvae (*Arachnocampa*) that live near the mouths of caves in New Zealand and Australia, but they also occur in culverts and the undercut banks of streams, where there is considerable daytime illumination. Although insect displays are among the most spectacular, bioluminescence is relatively rare in the terrestrial environment (<0.2% of all genera). Some other terrestrial luminous forms are millipedes,

TABLE 52.1 The Different Luciferases and Luciferins

Luciferases: kDa and E.C.#			Structures of luciferins
Bacterial	~80 (α, 41; β, 39)	1.14.14.3	Reduced flavin mononucleotide long chain aldehyde
Dinoflagellate	~135	NA	Tetrapyrrole
Coelenterate	~35	1.13.12.5	Coelenterazine, Ca^{++}
Firefly	~60	1.13.12.7	Benzthiazole, ATP

centipedes, earthworms and snails, but in none of these is the display especially bright.

For reasons that are still not known, bioluminescence is most prevalent in the marine environment (Haddock et al., 2010), especially at mid-ocean depths (200−1200 m), where daytime illumination fluxes range between $\approx 10^{-1}$ and 10^{-12} $\mu W/cm^2$. In some such locations it may occur in over 95% of the individuals and 75% of the species in fish, and in shrimp and squid about 85% of the individuals and 80% of the species. The mid-water luminous fish *Cyclothone* is considered to be the most abundant vertebrate on the planet. Where high densities of luminous organisms occur, their emissions can exert a significant influence on the communities and may represent an important component in the ecology, behavior and physiology of these organisms. Above and below mid-ocean depths, luminescence decreases to <10% of all individuals and species. At abyssal depths it may be somewhat higher ($\approx$20%), while among coastal species, less than 2% are bioluminescent.

V. FUNCTIONS OF BIOLUMINESCENCE

Bioluminescence is unusual biologically because it is a clear and well-documented example of a function that is not metabolically essential but one that may confer an advantage on the individual. While bioluminescence has evidently arisen independently many times, it may also have been lost many times in different evolutionary lines, not being truly essential. No one can tell.

Bioluminescence may be thought of as a bag of tricks: the light can be used in different ways and for different functions. Most of the perceived functions of bioluminescence may be classed under three main rubrics: defense, offense and communication; a fourth less common one is to enhance propagation (Table 52.2).

Important defensive strategies are to frighten, to serve as a decoy, to provide camouflage**,** or aposematic, serving as a warning to would-be predators (e.g. the animal is distasteful) (Grober, 1988). Organisms may be frightened or diverted by flashes, which are typically bright and brief (0.1 s), too fast to allow a predator to locate motile prey; light is emitted in this way by many organisms, and experimental studies confirm that flashes can indeed frighten (Morin, 1983).

An organism can use a glow defensively by creating a luminous decoy to attract and divert a predator, while it slips off itself under the cover of darkness. This is done by several organisms, such as squid, which squirt luminescence instead of ink; ink would be useless in total darkness. Some organisms sacrifice more than light; in scaleworms and brittle stars, a part of the body may be automized (broken off) and left behind as a luminescent decoy to attract the predator. In these cases, the animal flashes while intact but the detached part glows.

A clever method for evading predation from below is to camouflage the silhouette by emitting light continuously matching the color and intensity of the downwelling background light. By analogy with countershading in reflected light, this is called counterillumination. Consider a plane in the sky during the day. If it could emit light from its belly matching the sky behind, it would be invisible from below. Actually, it is not necessary for the entire surface to emit light; emission by only a part would mean that the object would no longer look like a plane. This can be called disruptive illumination and many luminous marine organisms, including fish and the bobtail squid, use this to help escape detection. Many culture symbiotic

TABLE 52.2 Functions of Bioluminescence

Category	Function	How achieved
Deter, escape predators (defense)	Camouflage	Ventral emission, symbiosis
	Startle, frighten	Brief bright flashes
	Decoy, diversion	Luminous cloud, sacrificial lure
	Predators learn to avoid	Aposematism; danger signal
Aid in predation (offense)	Startle	Brief bright flashes
	Attract prey	Lure
	Aid in vision	See and capture prey
Communication	Courtship, mating	Flash signals
	Species recognition	Photophore patterns
Propagation	Bacterial light emission	Attract feeders, enhance growth

luminous bacteria for use as the light source (McFall-Ngai and Morin, 1991). Another novel defensive strategy has been dubbed the burglar alarm: dinoflagellates flash when grazed upon, which may reveal the grazers and enhance predation on them, thereby reducing grazing on the dinoflagellates (Abrahams and Townsend, 1993).

There are also several ways in which luminescence can aid in predation. Several of these, such as illuminating for vision, may be of value for both offense and defense; offensively, prey may be thereby seen and captured, as flashlight fish do (Fig. 52.1). And flashes, which are more typically used defensively, can be used offensively in order temporarily to startle or blind prey. A glow can also be used offensively: it can serve as a lure. The prey is attracted to the light but is then captured by the organism that produced the light. This is practiced by the deep-sea angler fishes; they also culture symbiotic luminous bacteria for the light source.

Communication involves information exchange between individual members of a species and luminescence is used for this in several groups, including annelids, crustaceans, insects, squid and fishes (Herring, 1990). The most common use of the light is for courtship and mating, as in fireflies (Lloyd, 1977, 1980; Buck, 1988). There are also numerous examples in the ocean (Herring, 1990). In the annelid (syllid) fireworm *Odontosyllis*, a truly extraordinary display occurs as the animals engage in mating, which occurs daily for only a few days after the full moon, timed to start a few minutes after sunset. Readily observed in many parts of the world (e.g. Bermuda), the females come to the surface and swim in a tight luminous circle. A luminous male streaks from below and joins the female; eggs and sperm are shed in the ocean. Another kind of behavior occurs over shallow reefs in the Caribbean: male ostracod crustaceans produce complex species-specific trains of secreted luminous material, ladders of light, which attract females (Fig. 52.2) (Morin and Cohen, 1991, 2010).

FIGURE 52.1 The flashlight fish (Photoblepharon) showing the light organ harboring luminous bacteria just below the eye. *(By permission J.G. Morin.)*

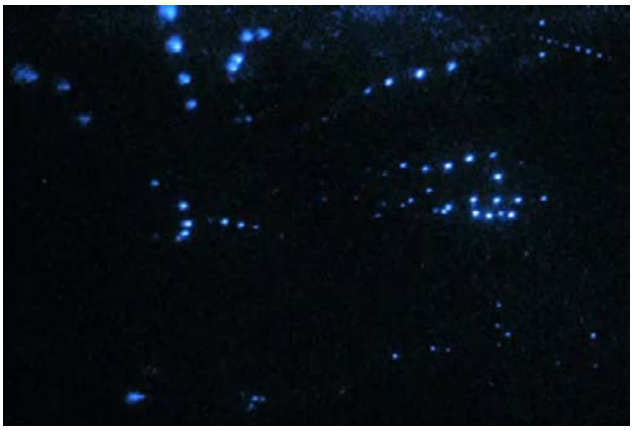

FIGURE 52.2 Video recording of pulses of light secreted sequentially by males of the ostracod crustacean *Vargula* about 1 cm apart in shallow water in the Caribbean as a display in courtship. The several different beads come from different animals active at the same time in the same area. *(By permission J.G. Morin and Martin Dohrn.)*

There remain some cases for which it is difficult to know what the function of the light emission may be. In some cases, it may be an aposematic signal, as coloration is in some animals, but not so recognized. But where the light is not seen, this would not explain it. For example, in the luminous fungi (Fig. 52.3) (Desjardin et al., 2008, 2010), which emit light continuously, the luminous cap is believed to attract insects, which would serve to disperse spores. But, in some, only the mycelium is luminous, and it is essentially never seen, living underground or inside a decaying tree. And no good explanation for luminescence in earthworms, where emission is also underground, has been advanced. The function of luminescence in these and some other cases remains to be understood.

VI. BACTERIAL LUMINESCENCE

VIA. Regulation by "Quorum Sensing" (Autoinduction) and by Shutters or Filters

Bacteria in general had long been regarded as cells that do their own thing, simply dividing and multiplying with no regard for other bacterial cells around them — no "communication". And light emission from luminous bacteria (Fig. 52.4) was well characterized as being continuous and its luminescence not typically subject to a rapid change. The discovery in luminous bacteria of "autoinduction" (Nealson et al., 1970), now referred to as "quorum sensing", revealed massive and environmentally significant regulation at the transcriptional level (Gambello and Iglewski, 1991; Fuqua and Greenberg, 2002).

The basic observation was that in newly inoculated cultures of a luminescent marine bacterium, *Vibrio fischeri*, the onset of exponential growth occurs without a lag but luminescence *does not* increase until mid-logarithmic

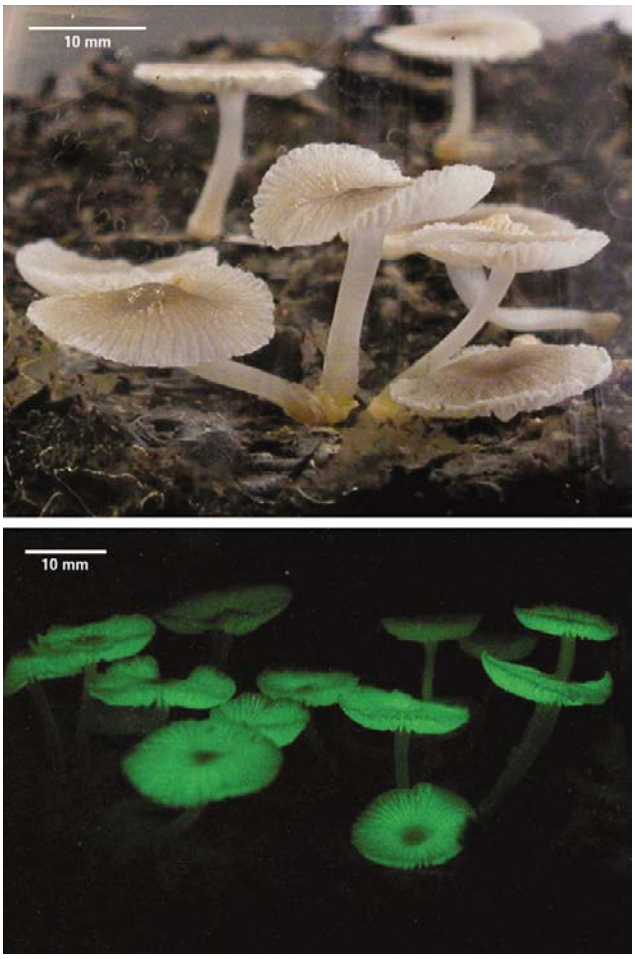

FIGURE 52.3 Photos taken in room light (above) and by their own light of the bioluminescent mushroom *Mycena chlorophos*. Caps but not stipes are luminous; in other species only stipes are luminous, in yet others both emit light, and in one only the underground mycelium emits. *(The specimens were grown and the photo was taken by Dr. Eiji Nagasawa, reproduced by permission).*

FIGURE 52.4 Petri plates inoculated with luminous bacteria, photographed in daylight (left) and by their own light (right) Note non-luminous colony among the cluster of four in the centre of the plate. *(Photograph by author.)*

phase, when transcription of the *lux* operon is triggered and light emission literally shoots up, doubling every four minutes or so (Fig. 52.5). This was shown to be due to an inducer of luciferase synthesis produced by the bacteria themselves, which was therefore dubbed the autoinducer. Its structure was found to be a homoserine lactone (Eberhard et al., 1981); other molecules serve the same role in other species and groups (Schaefer et al., 2008; Ng and Bassler, 2009).

The ecological implications are evident: in planktonic bacteria free-living in the ocean, autoinducer cannot accumulate, so no luciferase synthesis occurs. This makes sense; the open ocean is a habitat where the luminescence of a lone bacterium presumably has no value, whereas it evidently does in a light organ with a trillion others (Parsek and Greenberg, 2005). There, high autoinducer levels are readily reached, so the luminescence genes are transcribed. Many considered this as something special in luminous bacteria until the 1990s, when it was discovered that genes controlling autoinduction occur in many different bacteria, controlling specific genes having similarly evident functional importance (Gambello and Iglewski, 1991; Fuqua and Greenberg, 2002). For example, genes responsible for toxin production are not transcribed until the population is great enough to overwhelm the infected organism. This led to the adoption of the catchy term "quorum sensing" to refer to this mechanism, even though it does not strictly involve an enumeration mechanism as such.

There are a number of other control mechanisms that serve to regulate the transcription of the *lux* operon, including glucose (catabolic repression), nutrient levels, iron and oxygen. Each of these factors represents a different mechanism for the physiological control of gene expression

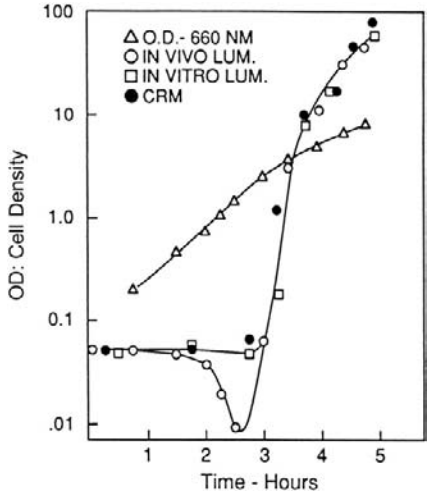

FIGURE 52.5 Autoinduction (quorum sensing) in luminous bacteria. Cells inoculated at a cell density of about 0.1 (660 nm) grow exponentially, but the luciferase remains constant for the first 3 hours, after which it rises steeply, attributable to the accumulation of autoinducer in the medium.

and each has implications concerning the ecology of luminous bacteria and the function of their luminescence. But there is also another control: in some species of bacteria, "dark" (very dim) strains arise spontaneously (see Fig. 52.4). In these, the transcription of the luminescent system scarcely occurs, irrespective of conditions, and this is heritable. However, the genes are evidently not lost, for revertants do occur. Thus, by selection for the dark strain, the organism can compete under conditions where luminescence is not advantageous, yet be able to select for luminous forms and populate the appropriate habitat when and where it is encountered. Indeed, the bacterial *lux* genes may thus occur in many bacterial strains but not be highly expressed. This means that there may be many more potentially luminous bacteria than would be deduced from colonies that are bright on plates.

The possibility that regulation of oxygen supply to bacterial light organs might control light emission has been considered, but there is no strong evidence in support of the idea. However, mechanical shutters, color filters and other optical devices are widespread and important (Morin and Cohen, 1991).

VIB. Occurrence and Functions

Planktonic luminous bacteria occur ubiquitously in the oceans and can be isolated from sea-water samples anywhere in the world, from the surface to depths of 100 m or more. A primary habitat where most species abound is in association with a higher organism or solid substrate, as commensals, parasites or symbionts, where growth and propagation occur. Planktonic forms are ubitquitous, but do not grow significantly, as sea water is a poor medium; their occurrence there is attributed to the overflow from primary habitats (Nealson and Hastings, 1991).

But there are displays in the ocean attributed to bacteria, the so-called "Milky Seas", which have been reported repeatedly over the centuries in logs of merchant ships and accurately described in Verne's "Twenty Thousand Leagues Under the Sea". The phenomenon was recently visualized by satellite imaging (Miller et al., 2005; Nealson and Hastings, 2006), recorded as a continuous night-time luminescence in the ocean off the Horn of Africa covering an area the size of the state of Connecticut, persisting for three nights (Fig. 52.6). It is believed that it is due to bacteria, indicated by the fact that the light is continuous. But this flies in the face of the fact that in all studied luminous bacteria, including "free-living" planktonic forms, regulation has been shown to involve quorum sensing, described above, and sea water should not have the requisite free-living bacterial concentration for autoinducer to accumulate. So, if bacteria are responsible, they may be growing on (possibly decomposing) microfilamentous algae, where autoinducer could accumulate. The isolation of the bacteria responsible and well-designed on-site studies of the phenomenon should be carried out.

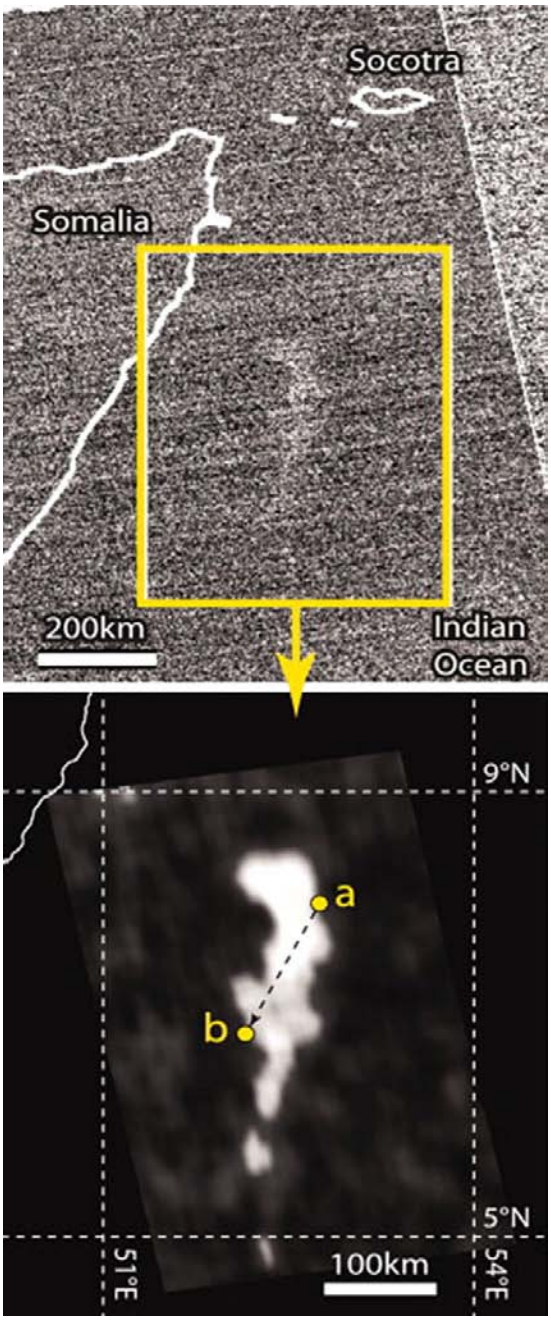

FIGURE 52.6 Raw (top) and digitally enhanced (bottom) images of a "milky sea" on January 25, 1995 detected by satellite-based camera. The land area at the left is the Horn of Africa in Somalia. The points of entry and exit of the ship from the luminous area, as reported in the log of the S.S. Lima, are points a and b in the enhanced image. Scale bars as shown. *(By permission, Steve Miller and Steve Haddock.)*

The most exotic and specific habitats of luminous bacteria are specialized light organs (e.g. in fish and squid) in which a pure culture is maintained at a high density and at high light intensity, as in the flashlight fish. In teleosts,

some 11 different groups carrying such bacteria are known. In such associations, the bacteria receive a niche and nutrients, while the host receives the benefit of the light and may use it for one or more specific purposes, such as for concealing the silhouette. Many aspects of how such symbioses are achieved — the initial infection, exclusion of contaminants, nutrient supply, restriction of growth but bright light emission — are not fully understood (Hastings et al., 1987). But recent studies (Chun et al., 2008) in the bobtail squid have resulted in many new findings over the past decade, including the demonstration that rhodopsin is expressed in the light organ cells, suggesting the presence of extraretinal photoreceptors.

Intestinal bacteria in marine animals, notably fish, are often luminous, and heavy pigmentation of the gut tract is sometimes present, presumably to prevent the light from betraying the location of the fish to predators. Luminous bacteria growing on a substrate, be it a parasitized crustacean, the flesh of a dead fish, or a fecal pellet, can produce a light bright enough to attract other organisms to feed on the material. It has recently been shown by video recording that a fish will selectively feed in total darkness on prey baited with luminous bacteria but completely ignore non-baited prey (M. Zarubin and S. Belkin, personal communication).

The only known terrestrial luminous bacteria are those harbored as symbionts by nematodes, which are parasitic on insects such as caterpillars. The nematode carries the bacteria as symbionts and injects them into the host where they release fertilized eggs. The bacteria grow and the developing nematode larvae feed on them. The dead but now luminous caterpillar (Fig. 52.7) attracts scavengers, which disperse the nematode offspring, along with the bacteria.

VIC. Biochemistry

Luminous bacteria typically emit continuous light peaking at ≈490 nm. When strongly expressed, a single bacterium may emit ≈10^4–10^5 photons/s. The system is biochemically unique and is diagnostic for a bacterial involvement in the luminescence of a higher organism; in some, but not all cases, they can be isolated and grown in the laboratory. (Some symbionts have not been cultured.) The biochemical pathway itself (Fig. 52.8) constitutes a shunt of cellular electron transport at the level of flavin and reduced flavin mononucleotide is the substrate (luciferin) that reacts with oxygen in the presence of bacterial luciferase to produce an intermediate peroxy flavin (Hastings et al., 1985; Baldwin and Ziegler, 1992).

FIGURE 52.7 Caterpillar luminescence due to parasitic luminous bacteria.

This intermediate then reacts with myristic aldehyde to form the acid and the luciferase-bound hydroxy flavin in its excited state. Although there are two substrates in this case, the flavin can claim the name luciferin on etymological grounds, since it forms (bears) the emitter. The bioluminescence quantum yield has been estimated to be about 30%. There are enzyme systems that serve to maintain the supply of aldehyde, and genes coding for these enzymes are part of the lux operon, along with autoinducer and others (Meighen, 1991).

The luciferase and the mechanism of the bacterial reaction have been studied in great detail and its crystal structure is known (Fisher et al., 1996). The enzyme is an external flavin monoxygenase (EC #1.14.14.3), a heterodimeric (α-β) protein (≈80 kDa) in all species, with homology to long chain alkane monooxygenases (Li et al., 2008). Structurally, they appear to be relatively simple: no metals, disulfide bonds, prosthetic groups or non-amino acid residues are involved. The subunits are similar but possess only a single active center per dimer, located on the α subunit. A recent structure crystallized with FMN shows the site of its binding as well as insight concerning the way in the β subunit stabilizes the protein (Fig. 52.9) (Campbell et al., 2009). Curiously, none of other homologous enzymes of this type have been found to emit light, even at very low quantum yields.

An interesting feature of this luciferase reaction is its inherent slowness: at 20°C, the time required for a single catalytic cycle is about 20 s. The luciferase peroxy flavin itself has a long lifetime; at low temperatures (−20°C) it has been isolated, purified and characterized, but not crystallized. It can be further stabilized by aldehyde analogs such as long-chain alcohols and amines, which bind at the aldehyde site.

VII. DINOFLAGELLATE LUMINESCENCE

VIIA. Regulation by pH and a Circadian Clock

Dinoflagellate flashes are brief (≈100 ms), triggered by membrane action potentials, typically initiated mechanically, that sweep around the cell, as determined in the giant heterotrophic species, *Noctiluca* (Eckert, 1965). The active

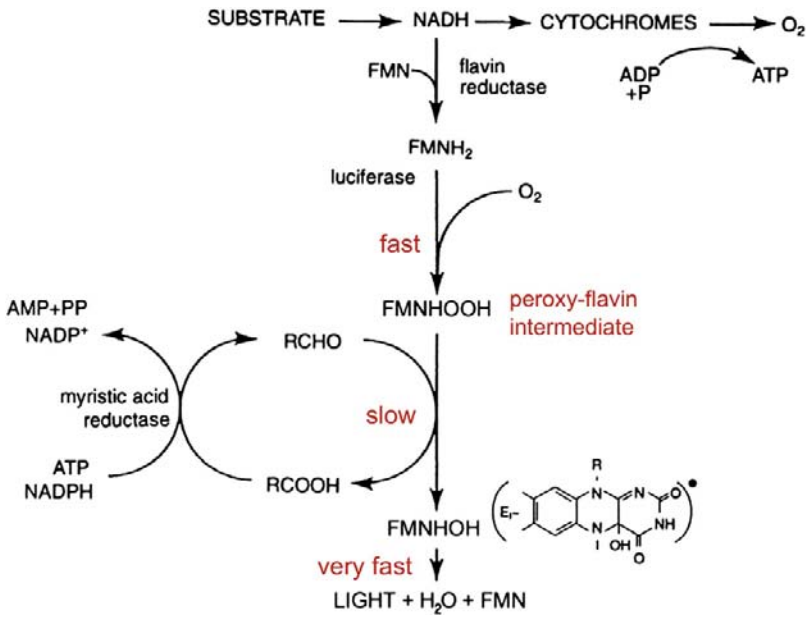

FIGURE 52.8 The luciferase reaction in bacteria. In the electron transport pathway, luciferase shunts electrons at the level of reduced flavin (FMNH2) directly to molecular oxygen. In the next step with long-chain aldehyde, hydroxy FMN is produced in its excited state (*) along with long-chain acid. The FMN product is reduced again and recycles; the aldehyde is also regenerated enzymatically.

membrane surrounding the cell vacuole is the tonoplast and, while the character of the action potential has not been definitely established, it was postulated some years ago (Fogel and Hastings, 1972) that voltage-gated proton channels allow protons from the vacuole to enter the many small membrane-enveloped luminous organelles, called scintillons (Fig. 52.10), initiating the highly pH dependent reaction. The presence of voltage-gated proton channels in a dinoflagellate has recently been demonstrated (Smith et al., 2011).

Neither quorum sensing nor the composition of the medium affect the development and expression of bioluminescence in dinoflagellates. But, on a far different time scale, luminescence in *L. polyedrum* and some other dinoflagellates is regulated by day—night light—dark cycles and an internal circadian biological clock mechanism (Morse et al., 1990; Hastings, 2007). Scintillons are numerous during the night phase but much less so by day (see Fig. 52.10) and both flashes and glow are greater then. The regulation is attributed to an endogenous mechanism; cultures maintained under constant conditions (light, temperature) continue to exhibit rhythmicity for many days, but with a period that is not exactly 24 hours: it is only about one day (=circa-diem).

The basic mechanism of circadian clocks appears to differ in different groups (Loras and Dunlap, 2001; Johnson et al., 2008; Mehra et al., 2009; Qin et al., 2010. Regulation of luminescence in the dinoflagellate *L. polyedrum* has been found to involve a daily de novo synthesis and

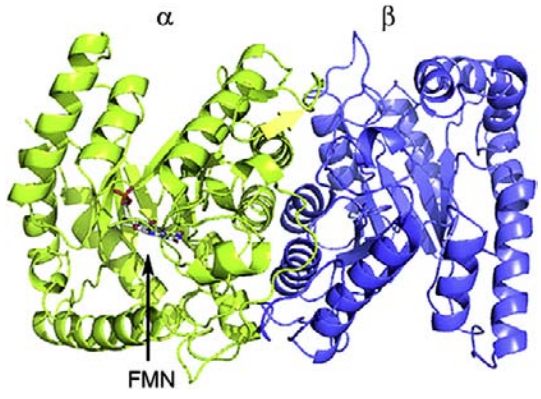

FIGURE 52.9 The crystal structure of FMN-bound bacterial luciferase, showing the α subunit (left, green) and β subunit (right, purple), as well as the site of the bound FMN. *(By permission of authors and publisher, Amer Chem Soc.)*

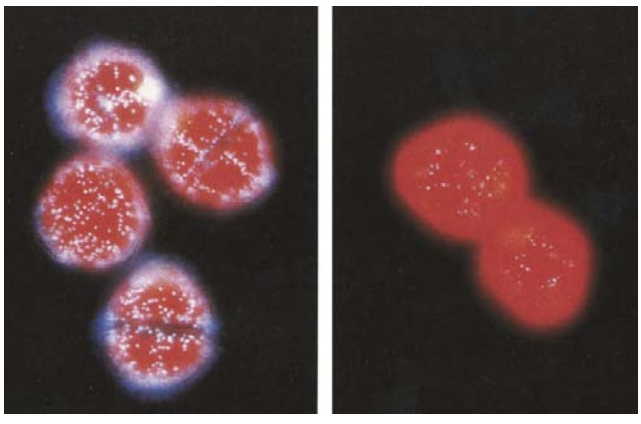

FIGURE 52.10 Fluorescence images of dinoflagellate cells (*Lingulodinium polyedrum*) at night (left) and during day phase (right), showing many luminous organelles (scintillons) at night and very few by day. The red background is fluorescence of the abundant chlorophyll.

destruction of specific proteins, translationally controlled by a still-unknown mechanism. This appears to differ from all other systems, both bacterial and animal, and remains an enigma. In humans and other higher animals, where it regulates the sleep–wake cycle and many other physiological processes, the mechanism involves the nervous system and transcriptional regulation.

VIIB. Occurrence and Function

Dinoflagellates occur ubiquitously in the oceans as planktonic forms and contribute substantially to the so-called "phosphorescence" commonly seen at night in summer when the water is disturbed. They occur abundantly in surface waters and most species are also photosynthetic; some produce neurotoxins (e.g. saxitoxin), which can accumulate in shellfish and constitute a health hazard. In the phosphorescent bays (e.g. in Puerto Rico and Jamaica), high densities of a single species (*Pyrodinium bahamense*) typically occur. The so-called red tides, which occur world-wide and may cause fish kills due to toxins or oxygen deprivation, are blooms of dinoflagellates, sometimes a luminous species. At night during such red tides, one can see waves breaking or the undulating luminescent pattern left behind by fish fleeing as the boat approaches. World War II aviators based on aircraft carriers in the South Pacific tell of the ease with which they relocated their base ship after a night mission – or equally well a target ship: a luminescent wake may extend for many kilometers behind a ship as the persistent turbulence stimulates the cells to emit light.

About 6% of all dinoflagellate genera contain luminous species, all marine. As a group, dinoflagellates are important as symbionts, notably for contributing photosynthesis and carbon fixation in animals but, unlike bacteria, no luminous dinoflagellates are known from symbiotic niches.

VIIC. Biochemistry and Cell Biology

As mentioned above, luminescence in dinoflagellates is emitted from scintillons, many small (≈0.5 µm), novel cortical organelles. They occur as outpocketings of the cytoplasm into the cell vacuole, like a balloon, with the neck remaining connected, as shown in electron micrographs labeled with antiluciferase-labeled gold particles (Fig. 52.11) (Nicolas et al., 1987), diagrammatically represented in Fig. 52.12. They can also be visualized by immunolabeling with fluorescent antibodies raised against the luminescence proteins (Fritz et al., 1990), in vivo by their bioluminescence (Johnson et al., 1985), as well as by the fluorescence of luciferin (see Fig. 52.10). Dinoflagellate luciferin is a novel tetrapyrrole related to chlorophyll (Nakamura et al., 1989). Lase and LBP are the only major proteins in scintillons, other cytoplasmic components being somehow excluded.

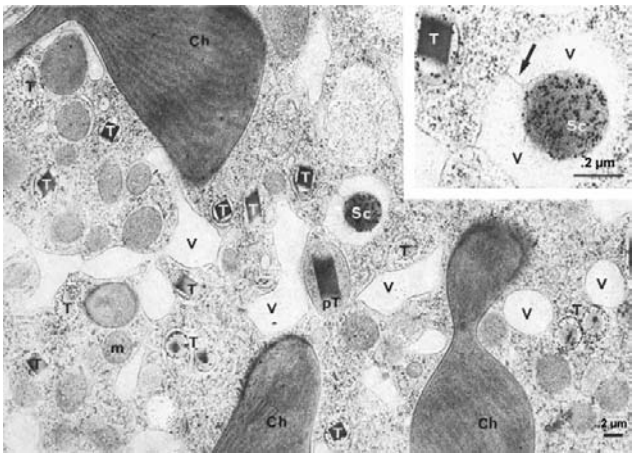

FIGURE 52.11 Immunoelectron microscopy of *Lingulodinium polyedrum*. Gold labeled anti-luciferase marks a scintillon (Sc) hanging in a vacuole (V). Ch, chloroplast; M, mitochondrion; T, trichocyst; pT, pre-trichocyst.

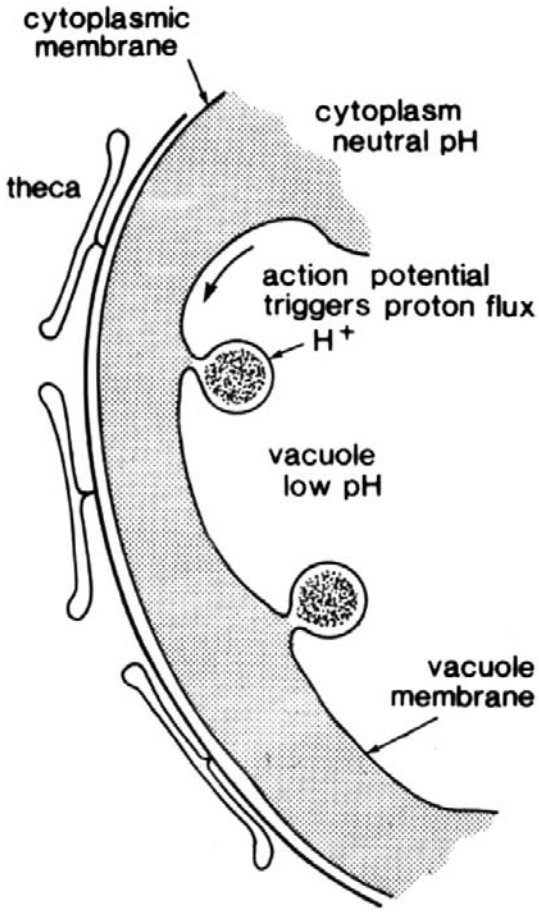

FIGURE 52.12 Scintillons of dinoflagellates represented as organelles formed as cytoplasmic outpocketings hanging in the vacuole.

Activity can be obtained in extracts made at pH 8 simply by shifting the pH from 8 to 6; it occurs in both soluble and particulate fractions; both activities peak at pH 6. The existence of activity in both soluble and particulate (scintillon) fractions indicates that during extraction some scintillons are lysed, while others seal off at the neck and form closed vesicles, which have been purified and characterized. The in vitro activity occurs as a flash (≈200 ms, 10°C), very similar to that of the living cell (Fig. 52.13) and the kinetics are independent of the dilution of the suspension. For the soluble fraction, the kinetics does depend on dilution, as enzyme concentration differs.

The Lase is unique in having three catalytic highly similar sequences, called domains, in a single molecule (Mr, ≈140 kDa). Each domain, when expressed and assayed individually, has activity and the sequences of the central 166 amino acid of the three (>95% identical) constitute the catalytic sites (Fig. 52.14) (Li et al., 1997). The luciferin is bound to LBP (Mr, ≈73 kDa), which also has domains, but four, and less well conserved. Both proteins occur in the genome in many tandem copies and the N-terminal 106 amino acids of the two are ≈50% identical, but the function of that region remain unknown.

In solution, both activities are pH dependent with pKs at 6.7; at pH 8, the LBP binds luciferin and Lase is inactive; at pH 6 luciferin is not bound and Lase is active. As shown by site directed mutagenesis, the pH dependence of Lase is due to four histidines located in the N-terminal region of each domain; if substituted by alanines, the luciferase is fully active at pH 8 (Li et al., 2001).

These Lase features can be visualized in the crystal structure of its domain 3 (Fig. 52.15) (Schultz et al., 2005).

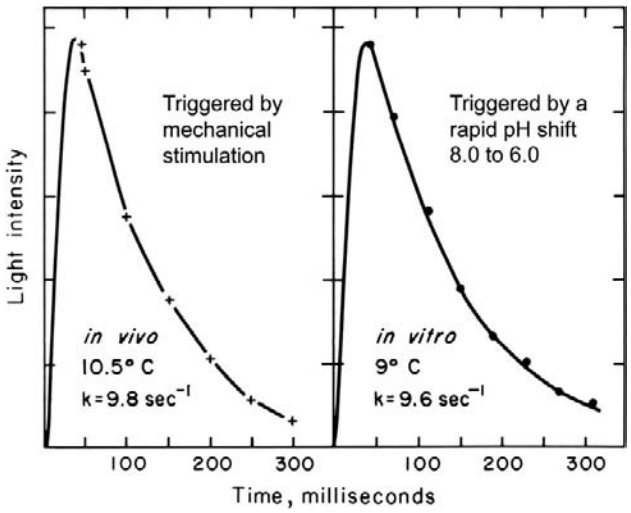

FIGURE 52.13 Kinetics of flashes of a living cell (left) and of isolated scintillons (right).

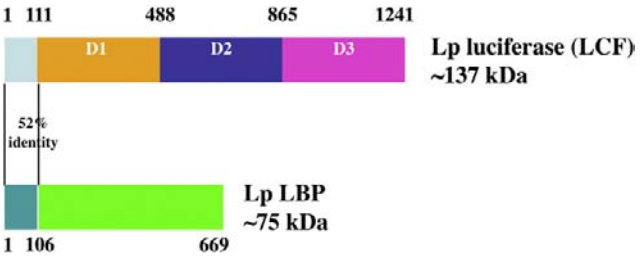

FIGURE 52.14 Organization of the two scintillon proteins in the bioluminescence of *Lingulodinium polyedrum*. The N-terminal regions of the two are similar, but its function is not known. The three domains of luciferase (LCF, upper) are similar and each has catalytic activity alone; the luciferin binding protein (LBP, lower) has four domains with significant but not great similarity.

A major part forms a barrel, inside of which is the luciferin binding site; three alpha helices form a channel but, at pH 8, it is too small for luciferin to enter. The four histidines responsible for the pH-dependent change are located in these sequences; molecular dynamics calculations indicate that when the histidines are protonated or substituted by alanines a conformation change would lead to an opened channel.

The presence of repeated conserved sequences in one enzyme molecule is not unprecedented but, to our knowledge, this is the only case in which each of the sequences has been shown to be separately active. A possible reason for the presence of three active sites on a single molecule is that it allows activity to be greater without an increase in the colloidal osmotic pressure of the scintillon.

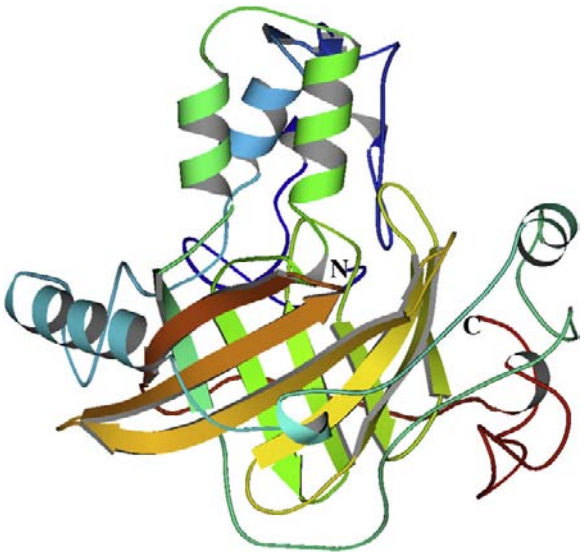

FIGURE 52.15 A ribbon diagram of the crystal structure of *Lingulodinium* luciferase domain 3. The lower barrel structure, where the active site is located, is composed of 10 anti-parallel β-strands. The upper α-helices (green and blue) regulate the opening of a channel for the entry of luciferin.

VIII. COELENTERATES AND CTENOPHORES

VIIIA. Regulation by Ca^{2+}

Early attempts to isolate biochemically and identify active fractions of the luminous jellyfish *Aequorea* were frustrated, even though cell-free extracts exhibited strong light emission lasting an hour or longer. The clue, as once told by Shimomura (personal communication), came when he discarded a still-emitting extract in the sink and noticed that it became much brighter. Tracing this to calcium, he extracted the cells in the presence of EDTA to chelate calcium and discovered that the activity was retained in a single protein, which he named aequorin and dubbed a photoprotein (Shimomura et al., 1962). While at the time he considered photoprotein to be an altogether new type of bioluminescence system, it turned out that it is indeed a luciferin–luciferase type system and that aequorin is a reaction intermediate in which the luciferin bound to the luciferase (apoaequorin) has already reacted with oxygen to form a (very) stable peroxide, as confirmed by crystal structures. While aequorin is analogous in some respects to the bacterial flavin–peroxy intermediate, the latter is far less stable and has not been crystallized or its structure determined.

Aequorin is stored in photocytes; an action potential mobilizes Ca^{2+}, which reacts with aequorin and causes the reaction to go to completion, with the formation of luciferase-bound excited oxidized luciferin and then light emission.

VIIIB. Occurrence and Function

Luminescence is common and widely distributed in ctenophores and coelenterates (Cormier in Herring, 1978; Herring in Herring, 1978), but absent in sea anemones and corals. In the ctenophores (comb jellies), luminous forms comprise over half of all genera, whereas in the coelenterates (cnidaria), it is about 6%. Luminous hydroids, siphonophores, sea pens and jellyfish, among others, are well known. The organisms are mostly sessile or sedentary and, upon stimulation, emit light as flashes. In some groups the luminescence is secreted.

Hydroids occur as plant-like growths, typically adhering to rocks below low tide level in the ocean. Upon touching them there is a sparkling emission conducted along the colony; repetitive waves from the origin may occur. Luminous jellyfish (hydromedusae such as *Aequorea aequorea* and *Pelagia noctiluca*) are well known; the bright flashing comes from photocytes along the edge of the umbrella at the base of the tentacles. *Aequorea* occurs during the summer in the ocean off the northwest USA. The sea pansy, *Renilla*, which occurs near shore on sandy bottoms, has also figured importantly in the elucidation of the biochemistry of coelenterate luminescence (Cormier, 1981).

Photocytes occur as specialized cells located singly or in clusters in the endoderm. They are commonly controlled by epithelial conduction in hydropolyps and siphonophores and by a colonial nerve net in anthozoans. The light may be emitted as one or many flashes per stimulus. The putative neurotransmitter involved in neural control of luminescence in *Renilla* is adrenaline or a related catecholamine.

VIIIC. Biochemistry and Cell Biology

The luciferin of coelenterates, coelenterazine, is notable for its widespread phylogenetic distribution, speculated to serve in non-luminous organisms as an antioxidant. Actually, the jellyfish *Aequorea* obtains coelenterazine from its diet (Haddock et al., 2001), so it is analogous to a vitamin, except for the fact that light emission is not necessary for life. In some cases (e.g. *Renilla*), the sulfated form of luciferin may occur as a precursor or storage form and is convertible to active luciferin by sulfate removal with the co-factor 3′5′-diphosphadenosine. The active form may also be sequestered by a Ca^{2+} sensitive binding protein, analogous to the dinoflagellate binding protein. In this case Ca^{2+} triggers the release of luciferin and then flashing, thus different from the *Aequorea* mechanism.

As described above, in *Aequorea*, *Obelia* and other hydromedusae, the luciferin and luciferase (EC#1.13.12.5) react with oxygen to form a stable peroxide (aequorin or obelin); stored in photocytes, it remains poised for the completion of the reaction (Blinks et al., 1982; Charbonneau et al., 1985; Cormier et al., 1989; Shimomura, 2006). The crystal structure of this intermediate (Fig. 52.16) has been determined for both *Aequorea* and *Obelia* (Head et al., 2000; Liu et al., 2000). An action potential allows Ca^{2+} to enter and bind to the protein, shifting or breaking hydrogen bonds, thus changing its conformational state and allowing the reaction to continue, but without the need for free oxygen at this stage. An enzyme-bound cyclic peroxide, a dioxetanone, is a postulated intermediate; it breaks down with the formation of excited coelenteramide, the emitter, along with a molecule of CO_2. The enzyme itself, called apoaequorin, can react again with coelenterazine and oxygen to form aequorin anew; it is homologous with calmodulin (Lorenz et al., 1991).

It had been reported in the early literature that coelenterates could emit bioluminescence even if fully deprived of oxygen. The explanation is now evident: aequorin is an intermediate in which the substrate has already reacted with oxygen and the cells store it in a stable state; only calcium is needed to emit light.

Remarkably, in vitro, the light emitted from this isolated system is blue, with a broad spectrum peaking at ≈480 nm while, in vivo, the emission is green ($\lambda_{max} = 508$ nm) and its spectrum is narrow. This is due to a different protein with a second chromophore, green fluorescent protein

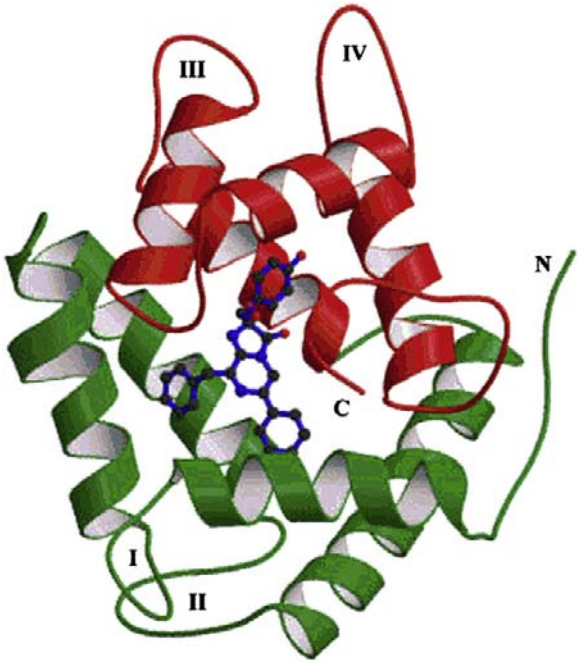

FIGURE 52.16 Structure of the calcium-regulated photoprotein obelin. The N-terminal α-helices are green (lower) and the C-terminal red (upper). The hydroperoxycoelenterazine substrate is the blue stick representation buried between green and red α-helices. *(By permission John Lee.)*

(GFP), which is the emitter. Some years earlier, it had been observed that the photocytes of *Aequorea* exhibited a green fluorescence, corresponding to the color of their bioluminescence. Johnson et al. (1962) observed the blue of the in vitro system along with a green fluorescence in extracts and suggested that it might be responsible by absorption and re-emission. Morin and Hastings (1971) observed that isolated photocytes triggered to emit by Ca^{2+} emitted green light whereas, if lysed before Ca^{2+} addition, the emission was blue, and proposed that this is due to radiationless (Foerster-type) energy transfer to the green fluorescent protein (GFP). This protein, whose chromophore is formed by the slow (≈1 hour, oxygen required) post-translational modification of three centrally located amino acids (Cody et al., 1993), thus covalently attached, is now widely used as a fluorescent marker or reporter gene (see Applications). Its crystal structure (Fig. 52.17) reveals a fascinating lantern-like structure (Ormö et al., 1996; Yang et al., 1996).

The overall reaction is thus:

$$\text{coelenterazine} + \text{apoaequorin} + O_2 \rightarrow \text{aequorin}$$

$$\text{aequorin} + Ca^{2+} \rightarrow \text{apoaequorin} + CO_2 + \text{coelenteramide}^*$$

$$\text{coelenteramide}^* + \text{GFP} \rightarrow \text{coelenteramide} + \text{GFP}^*$$

$$\text{GFP}^* \rightarrow \text{GFP} + \text{hr}$$

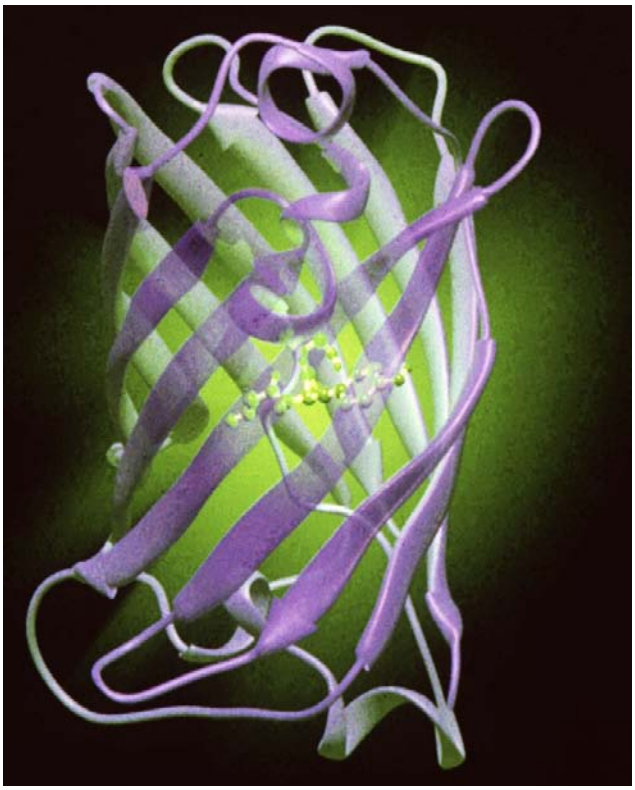

FIGURE 52.17 Crystal structure of GFP showing the chromophore in the center.

More recently, it was discovered that similar proteins occur in a variety of colors in other coelenterates, including corals, not associated with bioluminescence; their use as reporters has been evaluated (Baird et al., 2000) and color mutant GFPs have provided an array of colors that greatly expand the possible applications (Zhang et al., 2002).

Some strains of luminous bacteria also utilize an accessory protein, whereby the color may be either blue- or red-shifted, depending on the fluorophore which, however, is not covalently attached, so not suitable as a label. It has also been determined that the color shift is not attributable to Foerster-type energy transfer in this case; the protein participates in the luciferase reaction itself (Eckstein et al., 1990).

IX. FIREFLY LUMINESCENCE

IXA. Regulation by a Nerve Impulse and Oxygen

The firefly light organ comprises a series of photocytes arranged in a rosette, positioned radially around a central trachea, which supplies oxygen to the organ via tracheoles (Smith, 1963). The organ itself comprises a series of such rosettes, stacked side-by-side in many dorsoventral columns. Photocyte granules or organelles containing

luciferase have been identified with peroxisomes on the basis of immunochemical labeling.

The control of firefly flashing has long intrigued scientists and while there is agreement that it is ultimately controlled by regulating oxygen in the photocytes, the mechanism remains controversial. It is triggered in the first instance by a nerve impulse via the ventral nerve cord (Case and Strause in Herring, 1978); however, the nerves do not terminate on the photocyte, but on adjacent tracheal end cells, which surround the tracheoles entering the photocytes. The transmitter is octopamine and it takes some 50 ms or longer after the arrival of the nerve impulse for the onset of the flash to occur. Thus, the flash is not triggered directly by an action potential. Nor are any of the ions typically gated by membrane potential changes (Na^+, K^+ and Ca^{2+}) likely candidates for controlling luminescence chemistry.

All studies have concluded that the availability of oxygen regulates flashing; there is a strong positive relationship between the extent of the tracheal supply system in the adults of different species and their flashing ability. Also, all assume that photocytes are maintained anaerobic between flashes; the unusually large number of mitochondria buoys the belief. And all, except two recent ones (Trimmer et al., 2001; Ghiradell and Schmidt, 2004), concluded that the onset of the flash is regulated by the entry of oxygen to photocytes and the tracheolar cells were implicated in controlling it. Supporting evidence included the fact that the light organs of larval fireflies, which glow but do not flash, lack the end cells and are directly innervated. Also, firefly lantern tracheoles are reinforced against collapse. Some authors argued that a contractile action of end cells would force air into the photocytes; others proposed that fluid in the tracheoles normally blocks the entry of oxygen and a rapid but transient removal of the fluid, possibly by osmotic means, that allows oxygen to enter and initiate the flash (Timmins et al., 2001). Both were silent on the mechanism responsible for the termination of the flash, but removal of oxygen was tacitly assumed.

A quite different theory was put forward more recently, based on the finding that nitric oxide (NO) can affect the light emission in fireflies (Trimmer et al., 2001). Control of oxygen entry was assumed not to occur; instead it was proposed that oxygen enters continuously and that anaerobiosis is maintained by vigorous and continued mitochondrial respiration, whose inhibition by NO produced in tracheolar cells allows oxygen to enter and react with the luminous organelles. The decline is attributed to its reversal, principally photochemically by the light of the flash itself (Aprille et al., 2004). No follow up or repeats of the studies have appeared.

The second recent proposal is that the cells are indeed maintained anaerobic and that the flash is generated by the release of oxygen from H_2O_2 within the organelles that emit light, which are modified peroxisomes. No studies in support of the idea have appeared.

The rapid onset and decline characteristic of flashes with precision kinetics seem unlikely to be achieved by an inhibitory-type mechanism. Biochemical evidence suggests that the rate constants are determined by the reaction of oxygen with enzyme bound luciferyl adenylate, which accumulates in a slow reaction in the absence of oxygen (McElroy and Hastings, 1956), analogous to the reaction of aequorin with calcium. The firefly species-specific flash duration would be determined by rate constants, not by the enzyme concentration or the removal of oxygen or variable physiological factors. The formation of new luciferyl-adenylate is slow in relation to the flash, so emission terminates even though some oxygen may remain.

IXB. Occurrence, Function

There are only about 100 genera of insects classed as luminous out of a total number of approximately 70 000 (Lloyd in Herring, 1978). But where seen, their luminescence is impressive, most notably in the many species of beetles, the fireflies and their relatives. Fireflies themselves possess ventral light organs on posterior segments, but the South American railroad worm, *Phrixothrix*, has paired green light organs on the abdominal segments and red ones on the head (Fig. 52.18), while the click and fire beetles, Pyrophorini, have both running lights (dorsal) and landing lights (ventral).

The variety of different fireflies, with their different habitats and behaviors, is impressive. The major function of light emission in fireflies is for communication during courtship (Lloyd, 1977, 1980; Case, 1984) and the different flashing kinetics and patterns facilitate species identification. In North American species, a female on the grass or a leaf emits a query flash, while a male responds with a species-specific time delay. Flash flickering occurs in

FIGURE 52.18 The railroad worm, with green emitting photophores on each segment and red ones on the head.

some species, sometimes at frequencies higher than detectable by the human eye (≈40 Hz).

The signal mechanism in the synchronously flashing fireflies in Southeast Asia (*Pteroptyx* spp.) is not so well understood. These form congregations of many thousands in single trees, where the males produce an all-night-long display, with flashes every 1−4 s, dependent on species (Buck, 1988), which may serve to attract females to the tree.

The cave glow worm *Arachnocampa* (a fly) exudes beaded strings of slime from its ceiling perch (Fig. 52.19), which glisten in the reflected light from its caudal light organ and serve to entrap small flying prey that are attracted by the "fishing lines" (Fig. 52.20). While it is similar in some respects to its much less impressive American relative *Orfelia*, the two differ biochemically (Viviani et al., 2002).

FIGURE 52.20 "Fishing lines" produced by *Arachnocampa* as traps for flying insects that wander into the cave.

IXC. Biochemistry and Cell Biology

The firefly system was the first in which the biochemistry was extensively studied. It had been known since before 1900 that cell-free extracts could continue to emit light for several hours or longer, and that after the complete decay of the light, emission could be restored by adding a second extract prepared with hot water (then cooled). The enzyme luciferase was assumed to be in the first, with all the luciferin substrate being used up during the emission, and luciferin in the second, since the enzyme was denatured by the hot-water extraction. This was named the luciferin−luciferase reaction by DuBois in 1885, and it was already known in the first part of the 20th century that luciferins and luciferases from the different major phyla would not cross react, indicative of their independent evolutionary origins (Harvey, 1952).

FIGURE 52.19 Luminous dipteran larvae (*Arachnocampa*) on the ceiling of a cave in New Zealand.

In 1947, it was discovered that the addition of adenosine triphosphate (ATP) alone to an "exhausted" cold water extract, resulted in an enormous bioluminescence response (McElroy, 1947). This response suggested that luciferin had not actually been used up in the cold water extract; but ATP could not be the emitter, since it does not have the appropriate fluorescence. For some time, ATP was thought to be providing the energy for light emission. But, as noted earlier, the energy available from ATP hydrolysis is only about 7 kcal per mole, whereas the energy of a visible photon is ≈50 kcal per mole. It was soon discovered that firefly luciferin, which was shown to be a unique benzothiazole, was still present in large amounts in the "exhausted" cold water extract, and that it was ATP that was used up (by ATPases in crude extracts), but available in the hot water extract. ATP was later shown to be required to form the luciferyl adenylate intermediate which, in a separate step, then reacts with oxygen to form a cyclic luciferyl peroxy species, which breaks down to yield CO_2 and an excited state of the carbonyl product (McElroy and DeLuca in Herring, 1978).

In in vitro reactions in which luminescence has decreased to a low level (emission may continue for days), it was found that emission is greatly increased by coenzyme A, but the reason for this was obscure. The recent discovery

that long-chain acyl-CoA synthetase (EC# 6.2.1.3) has homologies with firefly luciferase (EC# 1.13.12.7) both explains this observation (Fraga, 2008) and indicates the evolutionary origin of the gene.

Firefly luciferase catalyzes both the luciferin activation and the subsequent oxygen reaction leading to the excited product. The crystal structure (Fig. 52.21) revealed the structural basis for the two-step reaction and confirmed that the same protein is responsible for both (Conti et al., 1996). Luciferase has been cloned and expressed in other organisms, including *E. coli* and tobacco. For activity, luciferin must be added exogenously; tobacco "lights up" with the roots dipped in a luciferin solution (Ow et al., 1986). There are some beetles in which the light from different organs is a different color, shown to be due to the luciferase not the luciferin. The same ATP-dependent luciferase reaction with the same luciferin occurs in the different organs, but the luciferases are slightly different, coded by different (but homologous) genes (Wood et al., 1989; Viviani et al., 2006; Branchini et al., 2007; Viviani, 2009). They are presumed to differ with regard to the conformation of the site that binds the excited state, which thereby alters the emission wavelength.

X. OTHER ORGANISMS: OTHER CHEMISTRIES

The four systems described above are known best, but several others have been studied in some detail, revealing interesting differences in both physiological and biochemical aspects.

FIGURE 52.21 Ribbon diagram of the firefly luciferase (*Luc*) structure. The large N-terminal domain (amino acids 1–436) is connected to the smaller C-terminal domain (amino acids 440–550 shown in yellow) through a short hinge peptide. *(Reproduction permission from Nature Publishing Group.)*

XA. Molluscs

Snails (gastropods), clams (bivalves) and cephalopods (squid) all have bioluminescent members (Young and Bennett, 1988). The squid luminous systems are by far the most numerous, and also diverse, both in form and function, rivaling the fishes in these respects, and some produce brilliant displays (Fig. 52.22). As for fish, some squid utilize symbiotic luminous bacteria, but others are self-luminous, indicating that bioluminescence had more than one evolutionary origin within the classes.

Also like some fish, some squid possess photophores, which may be used in spawning and other interspecific displays (communication). Photophores are compound structures with associated optical elements, such as pigment screens, chromatophores, reflectors, lenses and light guides. They may emit different colors of light and are variously located near the eyeball, on tentacles, body integument or associated with the ink sac or other viscera. An octopus with luminescent suckers has been reported (Johnsen et al., 1999). In some species, luminescence intensity has shown to be regulated in response to changes in ambient light, indicative of a camouflage function.

Along the coasts of Europe, there is a clam, *Pholas dactylus*, which inhabits chambers that it makes by boring holes into the soft rock. When irritated, these animals produce a bright cellular luminous secretion, squirted out through the siphon as a blue cloud. This animal and its luminescence has been known since Roman times, and the system was used by DuBois in his discovery and description of the "luciferin–luciferase" reaction in the 1880s (see above). Well ensconced in its rocky enclosure, the animal presumably uses the luminescence somehow to thwart would-be predators.

The *Pholas* reaction has been studied extensively; the luciferin, now called pholasin, has a protein-bound chromophore; it is probably dehydrocoelenterazine. The

FIGURE 52.22 Firefly squid (*Watasenia*) in aquarium tank with onlookers.

luciferase is a copper-containing large (>300 kDa) glycoprotein (Hentry et al., 1975). It can serve as a peroxidase with several alternative substrates, suggesting the involvement of a peroxide in the light emitting pathway; the superoxide ion may be involved in the reaction.

There are luminous species in several families of gastropods; a New Zealand pulmonate limpet, *Latia neritoides*, is notable as the only known luminous organism that can be classed as a truly fresh-water species. It also secretes a bright luminous slime (green emission, $\lambda_{max} = 535$ nm), whose function may be to forewarn predators. Its luciferin is an enol formate of an aldehyde, but the emitter and products in the reaction are unknown; in addition to its luciferase (MW ≈170 kDa; EC#1.14.99.21), a "purple protein" (MW ≈40 KDa) is also required, but only in catalytic quantities, suggesting that it may be somehow involved as a recycling emitter.

XB. Annelids

The annelids also include numerous luminous species, both marine and terrestrial (Herring in Herring 1978). The marine polychaete *Chaetopterus* constructs and lives in buried U-shaped tubes with only the openings at the surface of the sea floor; they pump sea water through the tube and exude luminescence upon stimulation, but the chemistry of the reaction has completely eluded researchers. The function of its emission may be similar to that of *Pholas*. Other marine polychaetes include the Syllidae, such as the Bermuda fireworm, and the polynoid scale worms, which shed their luminous scales as decoys. Both have largely escaped biochemical elucidation, although extracts of the latter have been shown to emit light upon the addition of superoxide ion.

More but still limited knowledge is available concerning the biochemistry of the reaction in terrestrial earthworms, some of which are quite large, over 60 cm in length (Wampler, 1981). Upon stimulation they exude celomic fluid from the mouth, anus and body pores. This exudate contains cells that lyse to produce a luminous mucus, emitting in the blue-green region. In *Diplocardia longa*, the cells responsible for emission have been isolated; luminescence in extracts involves a copper-containing luciferase (MW ≈300 kDa) and the luciferin (N-isovaleryl-3 amino- 1 propanal). The in vitro reaction requires H_2O_2, not free O_2. The exudate from animals deprived of oxygen does not emit, but will do so after the admission of molecular oxygen to the free exudate.

XC. Crustaceans

Many crustaceans are luminescent (Herring, 1985b). The cypridinid ostracods, such as *Vargula* (formerly *Cypridina*) *hilgendorfii*, are small organisms that possess two glands with nozzles from which the luciferin and luciferase (EC#1.13.12.6) are squirted into the sea water, where they react and produce a spot of light that retains its integrity, useful either as a decoy or for communication.

Cypridinid luciferin and its reaction have differences and similarities to the coelenterazine system (Cormier in Herring, 1978). The luciferin in both is a substituted imidazopyrazine nucleus that reacts with oxygen to form an intermediate cyclic peroxide, which then breaks down to yield CO_2 and an excited carbonyl. However, the cypridinid luciferase gene has been cloned and appears to have no homologies with the gene for the corresponding coelenterate proteins and calcium is not involved in the cypridinid reaction. The two different luciferases reacting with similar luciferins have apparently had independent evolutionary origins, indicative of convergent evolution at the molecular level.

Euphausiid shrimp possess compound photophores with accessory optical structures and emit a blue ventrally-directed luminescence. The system is unusual because both luciferase and luciferin cross-react with the dinoflagellate system. This cross-taxon similarity indicates another possible exception to the rule that luminescence in distantly related groups had independent evolutionary origins, thus another case of convergent evolution. The shrimp might obtain luciferin nutritionally, but the explanation for the occurrence of functionally similar proteins is not evident. One possibility is lateral gene transfer; convergent evolution is another. The sequence of the shrimp luciferase has not been determined.

XD. Fishes

Bioluminescence in fishes is highly diverse and occurs in both teleost (bony) and elasmobranch (cartilaginous) fishes. Partly because the animals have not been so readily available, relatively little is known about their physiology and biochemistry, but many have been described from specimens (Herring, 1982).

As already noted, many fish obtain their light emitting ability by culturing luminous bacteria in special organs. Many coastal and deep-sea luminous fishes fall into this category, while others are self-luminous. Those include *Porichthys*, the midshipman fish, so-called because of the array of photophores distributed linearly along the lateral lines, like buttons on a military uniform. It has been the object of considerable study and more is known about the physiological control of luminescence in it than in any other fish. Its luciferin and luciferase cross-react with the ostracod (cypridinid) crustacean system described above. This cross-reactivity was an enigma until it was discovered that Puget Sound fish have photophores but are unable to luminesce, but can do so if the animals are injected with or fed cypridinid luciferin. This observation showed that

luciferin may be obtained nutritionally. Did the luciferase in this fish originate independently making use of the available substrate, or was the ability to synthesize luciferin lost secondarily? If the latter, this would be analogous to the loss of the ability to synthesize vitamins in mammals.

Open sea and mid-water species include sharks, some of which may have several thousand small photophores. The teleosts include the gonostomatids, such as *Cyclothone,* with simple photophores, and the hatchet fishes, having compound photophores with elaborate optical accessories; emission is directed exclusively downwards, indicative of a camouflage function of the light. A number of self-luminous fish eject luminous material; in the searsid fishes this is cellular in nature, but it is not bacterial and its biochemical nature is not known. Such animals may also possess photophores.

Fish often possess different kinds of photophores located on different parts of the body, especially ventrally and around the eyes, evidently with different functions. One interesting arrangement, known in both mid-water squid and myctophids, makes use of a special photophore positioned so as to shine on the eye or on a special photoreceptor. Its intensity parallels that of the other photophores, so it provides information to the animal concerning its own brightness, thus allowing it to match the intensity of its own counterillumination to that of the downwelling ambient light. Another clear case of functional use is in *Neoscopelus*; in addition to the many photophores on the skin, they also occur on the tongue, allowing it to attract prey to just the right location.

Sexual dimorphism is also frequent in luminescent fish. The appropriately named anglerfishes, with their dangling luminous lures, are the most extreme in this respect (Pietsch, 2009). But males and females of the myctophid, *Tarleltonbeania* are also very different and were originally thought to be different species. Only one (now known to be the male) has caudal luminous organs and the occurrence of those fish was only known from stomach contents of predator fishes; what turns out to be the female was captured in nets, but never in the company of the male. A proposed explanation is that when a predator attacks, the males dart off in all directions with their dorsal lights flashing, like a police car, leading the predators on a chase (and sometimes getting caught), leaving the females, who remain in place, safe from the predator in the cover of darkness, but easy to catch in a net.

XI. APPLICATIONS OF BIOLUMINESCENCE

In the recent past, the most frequently asked question about bioluminescence was "What is its function, its survival value for the organism?" Bioluminescence was thus viewed mostly as a fascinating feature of the living world, but the study of its physiological and biochemical basis had seemed a most unlikely area of research to contribute in any practical way. It was put in the category of basic research; knowledge for the sake of knowledge: curiosity driven studies, with no predictable applications. Such interests have not faded but, in more recent years, an equally frequent query has concerned the practical applications of research on bioluminescence, reflecting, to be sure, an awareness of the many ways in which science has enabled new advances over the past decades. Thus, speculative paragraphs in grant applications have turned into reality, largely based on advances in molecular biology. Practical applications, both achieved and in progress, have been mind-boggling, rivaling in that respect many other practical developments in biological sciences, ranging from vaccines and test tube babies to drugs, genetic engineering and stem cells.

Actually, analytical applications of bioluminescence have been in use for 50 years. With the discovery of the ATP requirement for light emission in fireflies and the fact that the amount of light is directly proportional to the amount of ATP, many uses emerged. Somewhat later, the isolation of aequorin opened the way for the detection of calcium. Those, and other such measurements of bioluminescence have at least three major advantages over others: (1) rapidity; only a few seconds or minutes are needed; (2) great sensitivity; amounts of substances a billion or more times less than conventional assays can be readily detected; and (3) proportionality over an enormous concentration range; many such assays can be made over a range of one million or more.

The use of firefly luciferase with luciferin added was quickly adopted for the measurement of the amount of ATP in cell and biochemical research. An application with a wider impact was its use in the slaughterhouse, where undetected fecal contamination of animal carcasses has led to sickness and even death from human consumption of the meat products. Detection of bacteria responsible (usually *E. coli*) was previously done by taking swabs and checking for growth on plates, which takes 24 hours or more; by that time, processing may be complete and the contaminated product on its way to consumers, expensive and hard to track and recall. While the firefly assay is ideal for rapid and sensitive detection of bacteria, such procedures may have a problem; in practice, not all carcasses are sampled so contaminated ones may readily get through, as is known from the fact that contaminated meat continues to be reported from time to time.

The same ATP test is now used for monitoring soft drink production, where mold contamination occurs rarely but unpredictably; all batches are tested, as may be readily done. If discovered only after bottling and distribution to outlets far and wide, it is not only difficult and costly to recall it, the brand may get a poor reputation.

For many years the firefly luciferase used in the ATP tests was purified from fireflies, usually collected by

children paid by the number. With the amounts now used this would be impractical or impossible, so recombinant luciferase is used. Today, the greatest demand may be for a new method for rapid determinations of nucleotide sequences of DNA called "pyro" sequencing (Metzker, 2005). The name is based on the fact that pyrophosphate is released in the nucleotide-determination step which, after being converted to ATP, produces a flash of light. With automation about 500 million base pairs can be determined per 10 hour run on a machine.

Concern with water contamination, especially from industry, led to the passage of the "Clean Rivers Act" and to the development of a test to determine the quality of water in rivers and streams. The problem is different from the earlier examples in that the typical contaminants are chemical substances, not living organisms, and different substances in different cases. The method first adopted was empirical; if a fish survived in the water in question for 5 days, the water was judged satisfactory. So a 5-day-long procedure for such an evaluation was developed, typically by sampling downstream from an industrial facility that discharged its waste water. Mobile laboratories, fully equipped with healthy fish in a tank and scientific personnel carried out the determination, traveled week after week from site to site. A team could check only about 50 sites in a year, and it was not cheap!

A curious scientist noted that the light emission from living luminous bacteria was decreased by many different foreign chemical substances and wondered if the light emission might be a proxy for fish survival. The results were positive and the test is now widely used for the determination of water quality both in the USA and many other countries. The success of the method is astonishing and still viewed with some caution; how can it be that the light emission of living bacteria is affected in the same way as a fish by what must be a wide diversity of (and unknown) chemical substances? But it does work!

As described, one of the features of different bioluminescent systems is that they are biochemically different. This means that many different substances can be determined with one luciferase or another, and many such assays have been established. One of the most significant and widely used in research is the jellyfish system, mentioned in the Introduction, where light emission from aequorin requires calcium ion, a substance of key importance in the physiology and regulation of many different processes in living cells, notably muscle and nerve. With the isolation of the jellyfish luciferase gene, the DNA can be inserted directly into individual cells which, with added coelenterazine, produce aequorin and emit light in the presence of calcium in the cytoplasm.

DNA that codes for a luciferase can be attached to the promoter of some target gene, thus serving as a reporter gene for one responsible for the production of some other substance, so when and where the latter is produced can be determined by light emission, all in a non-invasive way – one has only to observe. The expression of a specific gene can be tracked by time, whether it occurs during the day or the night phase, as in circadian control, or time during development. Similarly, the type of cell and location in the body where a specific gene is expressed can be established. Studies are now being carried out by many scientists to locate cancer cells in the body using such methods, with good preliminary results. Another feature: since different luciferase systems may emit light at different wavelengths, different genes can be tagged by different luciferases and their activities followed concurrently in the same cell.

Green fluorescent protein (GFP) is a remarkable and now widely used fluorescent protein discovered in the course of studies of bioluminescence (Chalfie et al., 2006; Zimmer, 2010); in addition to the fact that it is non-toxic (based on perhaps some 10 000 published studies), it has three other important features. First, like luciferases and some other genes, it can be used as a reporter by attaching the gene coding for its synthesis to a different promoter; second, the fluorophore is part of the primary sequence of the peptide chain, so does not dissociate even at very low concentrations; and mutant GFPs, in which the color of the fluorescence has been altered by virtue of protein conformation changes, have greatly expanded its applications (Baird et al., 2000; Zhang et al., 2002). A drawback is that, like all fluorescent markers, irradiation is required, which itself may have adverse effects on the cell and will always increase the background. But this has not interfered with its widespread use and is now perhaps the most important and widely used of all biological reagents in cell biology; its discovery and application were recognized by the award of a Nobel Prize in 2008 (Chalfie, 2009; Shimomura, 2009; Tsien, 2009).

XII. CONCLUDING REMARKS

Though relatively rare, the emission of visible light by living organisms occurs in a phylogenetically wide range of species, ranging from bacteria to vertebrates, and has many independent evolutionary origins. The structures of the genes and proteins, as well as the physiological, biochemical and regulatory mechanisms involved, are thus very different. Its functions are also many and diverse, and provide a selective advantage mediated by the detection and responses of other organisms to the light.

The functions of the light may be classed under three major headings: offense, defense and communication, and a fourth to enhance propagation. Light may be used defensively to startle or frighten (flashes), to divert predators, as a decoy or to provide camouflage. Offensively, light may be used as a lure to attract prey. Communication occurs in courtship and mating displays.

An unusual and unexplained fact is that bioluminescence is primarily a marine phenomenon. While there are terrestrial forms, it is virtually absent in fresh water; only one such species is known. It is also not confined to or especially prevalent in animals that live in complete darkness (caves, lakes and the deep ocean).

Bioluminescence is an enzymatically-catalyzed chemiluminescence, a chemical reaction that emits light. The enzymes involved are all referred to generically as luciferases, somewhat unfortunately, because they are many that are structurally different. The genes coding for several of the different luciferases have been cloned and sequenced, confirming that they possess no similar regions in common. The substrates, generically called luciferins, react with molecular oxygen to form intermediate luciferase-bound peroxides, which break down to give a product in an excited state, which subsequently emits light. Both terms should be coupled with the name of the organism or group where they occur, thus beetle luciferin or bacterial luciferase.

In the marine environment, luminous bacteria are ubiquitous as planktonic forms in sea water and they are also responsible for the light emission of many species of higher organisms by serving as symbionts. They are not common terrestrially, but do occur as symbionts in soil nematodes, as an agent in the nematode's parasitization of insects. All species utilize the same biochemical system, a shunt of the electron transport pathway, in which reduced flavin and aldehyde are oxidized by molecular oxygen to give a luciferase-bound flavin intermediate in an excited state. Luminous bacteria are versatile with respect to the alternate uses of light emission under different situations, the exploitation of alternate habitats and the capacity to turn the synthesis of the system on and off, regulated by quorum sensing and autoinducers.

Dinoflagellates are unicellular algae; in the ocean these organisms are largely responsible for the sometimes brilliant sparkling "phosphorescence" seen at night when the water is disturbed and also for "red tides". Their luminescent flashing originates from novel cellular organelles called scintillons, formed as spherical outpocketings of the cytoplasm into the vacuole. They contain dinoflagellate luciferase and luciferin (a novel reduced linear tetrapyrrole), the latter bound to a second protein. Flashing is triggered by an action potential in the vacuolar membrane that causes a transient pH change in the scintillon, activating the luciferase and releasing the luciferin from its binding protein. Luminescence in some dinoflagellates is controlled by a cellular circadian biological clock, which causes the synthesis and destruction of the components in some species to occur on a daily cycle.

There are many luminous coelenterates, such as comb jellies, hydroids, siphonophores, sea pens and jellyfish. Upon stimulation, many species emit brief bright flashes, or trains of flashes, triggered by conducted action potentials that facilitate Ca^{2+} entry to specialized photocytes. The reaction of coelenterate luciferase and luciferin (coelenterazine) with oxygen forms a stable enzyme peroxide intermediate called aequorin that requires Ca^{2+} for the completion of the reaction. In many species, an accessory protein, green fluorescent protein (GFP) is the light emitter. The luciferase is homologous with calmodulin.

Fireflies also emit light as flashes, which they use as species-specific signals for communication in courtship. The light organ is a complex structure with photocytes arranged in a rosette pattern, invested with tracheoles that transport the required molecular oxygen directly to the cells. Indeed, while oxygen triggers flashing, a nerve impulse initiates the process. The firefly reaction is unique in having a requirement for ATP, which serves to "activate" the luciferin (a benzothiazole). The luciferyl adenylate is thus the "true" substrate that reacts with oxygen, forming an intermediate luciferase-bound cyclic peroxide whose breakdown results in light emission. Firefly luciferase is homologous with long chain acyl-CoA synthetase.

Other major luminous groups include the molluscs (snails, clams, squid), annelid worms (both marine and terrestrial), crustacea (shrimp and ostracods), echinoderms (brittle stars, starfish, sea cucumbers) and fish, both cartilaginous (sharks) and teleost (bony fishes). Of all the groups, fish and squids have the greatest variety of luminous systems; some make use of symbiotic luminous bacteria as a source of light while others are self-luminous. Luminous organisms are most abundant at mid-water depths (500−1000 m) in the open ocean.

BIBLIOGRAPHY

Abrahams, M. V., & Townsend, L. D. (1993). Bioluminescence in dinoflagellates: a test of the burglar alarm hypothesis. *Ecology, 74*, 258−260.

Aprille, J. R., Lagace, C. J., Modica-Napolitano, J., & Trimmer, B. A. (2004). Role of nitric oxide and mitochondria in control of firefly flash. *Integr Comp Biol, 44*, 213−219.

Baird, G. S., Zacharias, D. A., & Tsien, R. Y. (2000). Biochemistry, mutagenesis, and oligomerization of DsRed, a red fluorescent protein from coral. *Proc Natl Acad Sci USA, 97*, 11984−11989.

Baldwin, T. O., & Ziegler, M. M. (1992). The biochemistry and molecular biology of bacterial luminescence. In F. Müller (Ed.), *Chemistry and Biochemistry of Flavoenzymes, Vol. 3* (pp. 467−530). Boca Raton: CRC Press.

Blinks, J. R., Wier, W. G., Hess, P., & Prendergast, F. G. (1982). Measurement of Ca^{2+} concentrations in living cells. *Prog Biophys Molec Biol, 40*, 1−114.

Branchini, B. R., Ablamsky, D. M., Rosenman, J. M., Uzasci, L., Southworth, T. L., & Zimmer, M. (2007). Synergistic mutations produce blue-shifted bioluminescence in firefly luciferase. *Biochemistry, 46*, 13847−13855.

Buck, J. (1988). Synchronous rhythnic flashing of fireflies II. *Quart Rev Biol, 63*, 265−289.

Campbell, A. K. (1988). *Chemiluminescence: Principles and Applications in Biology and Medicine*. VCH, Chichester and Weinheim.

Campbell, Z. T., Weichsel, A., Montfort, W. R., & Baldwin, T. O. (2009). Crystal structure of the bacterial luciferase/flavin complex provides insight into the function of the beta subunit. *Biochemistry, 48*, 6085−6094.

Case, J. (1984). Firefly behavior and vision. In T. Lewis (Ed.), *Insect Communication* (pp. 195−222). London: Harcourt, Brace, Jovanovich.

Chalfie, M. (2009). GFP: lighting up life (Nobel Lecture). *Angew Chem Int Ed, 48*, 5603−5611.

Chalfie, M., & Kain, S. R. (Eds.), (2006). *Green Fluorescent Protein: Properties, Applications, and Protocols*. Hoboken: Wiley-Interscience.

Charbonneau, H., Walsh, K. A., McCann, R. O., Prendergast, F. G., Cormier, M. J., & Vanaman, T. C. (1985). Amino-acid sequence of the calcium-dependent photoprotein Aequorin. *Biochemistry, 24*, 6762−6771.

Chun, C. K., Troll, J. V., Koroleva, I., et al. (2008). Effects of colonization, luminescence, and autoinducer on host transcription during development of the squid-vibrio association. *Proc Natl Acad Sci USA, 105*, 11323−11328.

Cody, C. W., Prasher, D. C., Westler, W. M., Prendergast, F. G., & Ward, W. W. (1993). Chemical structure of the hexapeptide chromophore of the *Aequorea* green-fluorescent protein. *Biochemistry, 32*, 1212−1218.

Conti, E., Franks, N. P., & Brick, P. (1996). Crystal structure of firefly luciferase throws light on a superfamily of adenylate-forming enzymes. *Structure, 4*, 287−298.

Cormier, M. J. (1981). *Renilla* and *Aequorea* bioluminescence. In M. DeLuca, & W. D. McElroy (Eds.), *Bioluminescence and Chemiluminescence* (pp. 225−233). New York: Academic Press.

Cormier, M. J., Prasher, D. C., Longiaru, M., & McCann, R. O. (1989). The enzymology and molecular biology of the Ca^{2+}-activated photoprotein, aequorin. *Photochem Photobiol, 49*, 509−512.

Desjardin, D. E., Oliveira, A. G., & Stevani, C. V. (2008). Fungi bioluminescence revisited. *Photochem Photobiol Sci, 7*, 170−182.

Desjardin, D. E., Perry, B. A., Lodge, D. J., Stevani, C. V., & Nagasawa, E. (2010). Luminescent Mycena: new and noteworthy species. *Mycologia, 102*, 459−477.

Eberhard, A., Burlingame, A. L., Eberhard, C., Kenyon, G. L., Nealson, K. H., & Oppenheimer, N. J. (1981). Structural identification of autoinducer of *Photobacterium fischeri* luciferase. *Biochemistry, 20*, 2444−2449.

Eckert, R. (1965). Bioelectric control of bioluminescence in the dinoflagellate *Noctiluca*. *Science, 147*, 1140−1145.

Eckstein, J. W., Cho, K. W., Colepicolo, P., Ghisla, S., Hastings, J. W., & Wilson, T. (1990). A time-dependent bacterial bioluminescence emission spectrum in an in vitro single turnover system: energy transfer alone cannot account for the yellow emission of *Vibrio fischeri* Y-1. *Proc Natl Acad Sci USA, 87*, 1466−1470.

Fisher, A. J., Thompson, T. B., Thoden, J. B., Baldwin, T. O., & Rayment, I. (1996). The 1.5-angstrom resolution crystal structure of bacterial luciferase in low salt conditions. *J Biol Chem, 271*, 21956−21968.

Fogel, M., & Hastings, J. W. (1972). Bioluminescence: mechanism and mode of control of scintillon activity. *Proc Natl Acad Sci USA, 69*, 690−693.

Fraga, H. (2008). Firefly luminescence: a historical perspective and recent developments. *Photochem Photobiol Sci, 7*, 146−158.

Fritz, L., Morse, D., & Hastings, J. W. (1990). The circadian bioluminescence rhythm of *Gonyaulax* is related to daily variations in the number of light emitting organelles. *J Cell Sci, 95*, 321−328.

Fuqua, C., & Greenberg, E. P. (2002). Listening in on bacteria: Acyl-homoserine lactone signalling. *Nat Rev Mol Cell Biol, 3*, 685−695.

Gambello, M. J., & Iglewski, B. H. (1991). Cloning and characterization of the *Pseudomonas aeruginosa* lasR gene, a transcriptional activator of elastase expression. *J Bacteriol, 173*, 3000−3009.

Ghiradella, H., & Schmidt, J. T. (2004). Fireflies at one hundred plus: a new look at flash control. *Integr Comp Biol, 44*, 203−212.

Grober, M. S. (1988). Brittle-star bioluminescence functions as an aposematic signal to deter crustacean predators. *Anim Behav, 36*, 493−501.

Haddock, S. H. D., Moline, M. A., & Case, J. F. (2010). Bioluminescence in the sea. *Annu Rev Mar Sci, 2*, 293−343.

Haddock, S. H. D., Rivers, T. J., & Robison, B. H. (2001). Can coelenterates make coelenterazine? Dietary requirement for luciferin in cnidarian bioluminescence. *Proc Natl Acad Sci USA, 98*, 11148−11152.

Harvey, E. N. (1952). *Bioluminescence*. New York: Academic Press.

Hastings, J. W. (1983). Biological diversity, chemical mechanisms and evolutionary origins of bioluminescent systems. *J Mol Evol, 19*, 309−321.

Hastings, J. W. (2007). The Gonyaulax clock at 50: translational control of circadian expression. *Cold Spring Harb Symp Quant Biol, 72*, 141−144.

Hastings, J. W. (2011). Progress and perspectives on bioluminescence: from luminous organisms to molecular mechanisms. In A. Roda (Ed.), *Analytical Chemiluminescence and Bioluminescence: Past, Present, and Future* (pp. 91−112). Cambridge: Royal Society of Chemistry.

Hastings, J. W., & Morin, J. G. (1991). Bioluminescence. In C. L. Prosser (Ed.), *Neural and Integrative Animal Physiology* (pp. 131−170). New York: Wiley Interscience.

Hastings, J. W., Makemson, J., & Dunlap, P. V. (1987). How are growth and luminescence regulated independently in exosymbionts? *Symbiosis, 4*, 3−24.

Hastings, J. W., Potrikus, C. J., Gupta, S., Kurfurst, M., & Makemson, J. C. (1985). Biochemistry and physiology of bioluminescent bacteria. *Adv Microb Physiol, 26*, 235−291.

Head, J. F., Inouye, S., Teranishi, K., & Simomora, O. (2000). The crystal structure of the phosphoprotein aequorin at 2.3 angstrom resolution. *Nature, 405*, 372−376.

Henry, J.-P., Monny, C., & Michelson, A. M. (1975). Characterization and properties of Pholas luciferase as a metalloglycoprotein. *Biochemistry, 14*, 3458−3466.

Herring, P. J. (1982). Luminescence in fishes. *J Oceanogr Mar Biol, 20*, 415−470.

Herring, P. J. (1985a). Review of deep-sea luminescence. In M. S. Laverack (Ed.), *Physiological Adaptations in Marine Animals* (pp. 323−350). Cambridge: Society of Experimental Biology.

Herring, P. J. (1985b). How to survive in the dark: bioluminescence in the deep sea. In M. S. Laverack (Ed.), *Physiological Adaptations in Marine Animals* (pp. 323−350). Cambridge: Society of Experimental Biology.

Herring, P. J. (1987). Systematic distribution of bioluminescence in living organisms. *J Biolum Chemilum, 1*, 147−163.

Herring, P. J. (1990). Bioluminescent communication in the sea. In P. J. Herring, A. K. Campbell, M. Whitfield, & L. Maddock (Eds.), *Light and Life in the Sea* (pp. 245−264). Cambridge: Cambridge University Press.

Herring, P. J. (Ed.), (1978). *Bioluminescence in Action*. New York: Academic Press.

Johnsen, S., Balser, E. J., & Widder, E. A. (1999). Light-emitting suckers in an octopus. *Nature, 398*, 113−114.

Johnson, F. H., Shimomura, O., Saiga, Y., Gershman, G., Reynolds, G. T., & Waters, J. R. (1962). Quantum efficiency of *Cypridina* luminescence with a note on that of *Aequorea*. *J Cell Comp Physiol, 60*, 85−103.

Johnson, C. H., Egli, M., & Stewart, P. L. (2008). Structural insights into a circadian oscillator. *Science, 322*, 697−701.

Johnson, C. H., Inoue, S., Flint, A., & Hastings, J. W. (1985). Compartmentalization of algal bioluminescence: autofluorescence of bioluminescent particles in the dinoflagellate *Gonyaulax* as studied with image-intensified video microscopy and flow cytometry. *J Cell Biol, 100*, 1435−1446.

Li, L., Hong, R., & Hastings, J. W. (1997). Three functional luciferase domains in a single polypeptide chain. *Proc Natl Acad Sci USA, 94*, 8954−8958.

Li, L., Liu, L., Hong, R., Robertson, D., & Hastings, J. W. (2001). N-terminal intramolecularly conserved histidines of three domains in *Gonylaulax* luciferase are responsible for loss of activity in the alkaline region. *Biochemistry, 40*, 1844−1849.

Li, L., Liu, X., Yang, W., Xu, F., et al. (2008). Crystal structure of long-chain alkane monooxygenase (LadA) in complex with coenzyme FMN: unveiling the long-chain alkane hydroxylase. *J Mol Biol, 376*, 453−465.

Liu, Z. J., Vysotski, E. S., Chen, C. J., Rose, J. P., Lee, J., & Wang, B. C. (2000). Structure of the Ca^{2+}-regulated photoprotein obelin at 1.7 angstrom resolution determined directly from its sulfur substructure. *Protein Sci, 9*, 2085−2093.

Lloyd, J. E. (1977). Bioluminescence and communication. In T. A. Sebeok (Ed.), *How Animals Communicate* (pp. 164−183). Bloomington: Indiana University Press.

Lloyd, J. E. (1980). Firefly signal mimicry. *Science, 210*, 669−671.

Lorenz, W. W., McCann, R. O., Longiaru, M., & Cormier, M. J. (1991). Isolation and expression of a cDNA encoding *Renilla reniformis* luciferase. *Proc Natl Acad Sc. USA, 88*, 4438−4442.

Loros, J. J., & Dunlap, J. C. (2001). Genetic and molecular analysis of circadian rhythms in *Neurospora*. *Annu Rev Physiol, 63*, 757−794.

McElroy, W. D. (1947). The energy source for bioluminescence in an isolated system. *Proc Natl Acad Sci USA, 33*, 342−345.

McElroy, W. D., & Hastings, J. W. (1956). Initiation and control of firefly luminescence. In C. L. Prosser (Ed.), *Physiological Triggers* (pp. 80−84). Ronald Press.

McFall-Ngai, M., & Morin, J. G. (1991). Camouflage by disruptive illumination in Leiognathids, a family of shallow-water, bioluminescent fishes. *J Exp Biol, 156*, 119−137.

Mehra, A., Baker, C. L., Loros, J. J., & Dunlap, J. C. (2009). Post-translational modifications in circadian rhythms. *Trends Biochem Sci, 34*, 483−490.

Meighen, E. A. (1991). Molecular biology of bacterial bioluminescence. *Microbiol Rev, 55*, 123−142.

Metzker, M. L. (2005). Emerging technologies in DNA sequencing. *Genome Res, 15*, 1767−1776.

Miller, S. D., Haddock, S. H. D., Elvidge, C. D., & Lee, T. F. (2005). Detection of a bioluminescent milky sea from space. *Proc Natl Acad Sci USA, 102*, 14181−14184.

Morin, J. G., & Hastings, J. W. (1971). Biochemistry of the bioluminescence of colonial hydroids and other coelenterates. *J Cell Physiol, 77*, 303−312.

Morin, J. G. (1983). Coastal bioluminescence: patterns and functions. *Bull Mar Sci, 33*, 787−817.

Morin, J. G., & Cohen, A. C. (1991). Bioluminescent displays, courtship, and reproduction in ostracodes. In R. Bauer, & J. Martin (Eds.), *Crustacean Sexual Biology* (pp. 1−16). New York: Columbia University Press.

Morin, J. G., & Cohen, A. C. (2010). It's all about sex: bioluminescent courtship displays, morphological variation and sexual selection in two new genera of caribbean ostracodes. *J Crustac Biol, 30*, 56−67.

Morse, D., Fritz, L., & Hastings, J. W. (1990). What is the clock? Translational regulation of circadian bioluminescence. *Trends Biochem, 15*, 262−265.

Nakamura, H., Kishi, Y., Shimomura, O., Morse, D., & Hastings, J. W. (1989). Structure of dinoflagellate luciferin and its enzymatic and non-enzymatic air-oxidation products. *J Am Chem Soc, 111*, 7607−7611.

Nealson, K., & Hastings, J. W. (1991). The luminous bacteria. In A. Balows, H. G. Trüper, M. Dworkin, W. Harder, & K. H. Schleifer (Eds.), *The Prokaryotes* (2nd ed.). (pp. 625−639) New York: Springer-Verlag, Vol. I, Part 2, Ch. 25.

Nealson, K. H., & Hastings, J. W. (2006). Quorum sensing on a global scale: massive numbers of bioluminescent bacteria make milky seas. *Appl Environ Microbiol, 72*, 2295−2297.

Nealson, K. H., Platt, T., & Hastings, J. W. (1970). Cellular control of the synthesis and activity of the bacterial luminescent system. *J Bacteriol, 104*, 313−322.

Ng, W. L., & Bassler, B. L. (2009). Bacterial quorum-sensing network architectures. *Annu Rev Genet, 43*, 197−222.

Nicolas, M.-T., Nicolas, G., Johnson, C. H., Bassot, J.-M., & Hastings, J. W. (1987). Characterization of the bioluminescent organelles in *Gonyaulax polyedra* (dinoflagellates) after fast-freeze fixation and antiluciferase immunogold staining. *J Cell Biol, 105*, 723−735.

Ormö, M., Cubitt, A. B., Kallio, K., Gross, L. A., Tsien, R. Y., & Remington, S. J. (1996). Crystal structure of the *Aequorea victoria* green fluorescent protein. *Science, 273*, 1392−1395.

Ow, D. W., Wood, K. V., DeLuca, M., deWet, J. R., Helinski, D. R., & Howell, S. H. (1986). Transient and stable expression of the firefly luciferase gene in plant cells and transgenic plants. *Science, 234*, 856−859.

Parsek, M. R., & Greenberg, E. P. (2005). Sociomicrobiology: the connections between quorum sensing and biofilms. *Trends Microbiol, 13*, 27−33.

Pietsch, T. W. (2009). *Oceanic Anglerfishes*. Berkeley: University of California Press.

Qin, X. M., Byrne, M., & Mori, T. (2010). Intermolecular associations determine the dynamics of the circadian KaiABC oscillator. *Proc Natl Acad Sci USA, 107*, 14805−14810.

Schaefer, A. L., Greenberg, E. P., Oliver, C. M., et al. (2008). A new class of homoserine lactone quorum-sensing signals. *Nature, 454*, 595−599.

Schultz, L. W., Liu, L., Cegielski, M., & Hastings, J. W. (2005). Crystal structure of a pH-regulated luciferase catalyzing the bioluminescent oxidation of an open tetrapyrrole. *Proc Natl Acad Sci USA, 102*, 1378−1383.

Shimomura, O. (2006). *Bioluminescence: Chemical Principles and Methods*. Singapore: World Scientific Publishing Co.

Shimomura, O. (2009). Discovery of green fluorescent protein (GFP) (Nobel Lecture). *Angew Chem Int Ed, 48*, 5590−5602.

Shimomura, O., Johnson, F. H., & Saiga, Y. (1962). Extraction, purification and properties of aequorin, a bioluminescent protein from the luminous hydromedusan, *Aequorea. J Cell Comp Physiol, 59*, 223−240.

Smith, D. S. (1963). Organization and innervation of luminescent organ in a firefly, Photuris Pennsylvanica (Coleoptera). *J Cell Biol, 16*, 323.

Smith, S. M. E., Morgan, D., Musset, B., Cherny, V. V., Place, A. R., Hastings, J. W., & DeCoursey, T. E. (2011). A Voltage-Gated Proton Channel In A Dinoflagellate. *Proc Natl Acad Sci USA, 105,* (in press).

Timmins, G. S., Robb, F. J., Wilmot, C. M., Jackson, S. K., & Swartz, H. M. (2001). Firefly flashing is controlled by gating oxygen to light-emitting cells. *J Exp Biol, 204*, 2795−2801.

Trimmer, B. A., Aprille, J. R., Dudzinski, D. M., et al. (2001). Nitric oxide and the control of firefly flashing. *Science, 292*, 2486−2488.

Tsien, R. Y. (2009). Constructing and exploiting the fluorescent protein paintbox (Nobel Lecture). *Angew Chem Int Ed, 48*, 5612−5626.

Viviani, V. R. (2009). Terrestrial bioluminescence. In K. C. Smith (Ed.), *Photobiological Sciences Online*. Washington, DC: American Society for Photobiology.

Viviani, V. R., Arnoldi, F. G. C., Venkatesh, B., et al. (2006). Active-site properties of Phrixotrix railroad worm green and red bioluminescence-eliciting luciferases. *J Biochem, 140*, 467−474.

Viviani, V. R., Hastings, J. W., & Wilson, T. (2002). Two bioluminescent diptera: the North American *Orfelia fultoni* and the Australian *Arachnocampa flava*. Similar niche, different bioluminescence systems. *Photochem Photobiol, 75*, 22−27.

Wampler, J. E. (1981). Earthworm bioluminescence. In M. A. Deluca, & W. D. McElroy (Eds.), *Bioluminescence and Chemiluminescence* (pp. 249−256). New York: Academic Press.

Wilson, T. (1985). Mechanism of chemiluminescence. In A. Frimer (Ed.), *Singlet Oxygen,* Vol. 2 (pp. 37−57). Boca Raton: CRC.

Wilson, T., & Hastings, J. W. (1998). Bioluminescence. *Annu Rev Cell Dev Biol, 14*, 197−230.

Wood, K. W., Lam, A. Y., Seliger, H. H., & McElroy, W. D. (1989). Complementary DNA coding click beetle luciferases can elicit bioluminescence of different colors. *Science, 244*, 700−702.

Yang, F., Moss, L. G., & Phillips, G. N. (1996). The molecular structure of green fluorescent protein. *Nat Biotechnol, 14*, 1246−1251.

Young, R.E. and Bennett, T.M. (1988). *Cephalopod luminescence*. In M.R. Clarke and E.R. Trueman, (Eds.), The Mollusca, (pp. 241−251). San Diego, CA: Academic Press.

Zhang, J., Campbell, R. E., Ting, A., & Tsien, R. Y. (2002). Creating new fluorescent probes for cell biology. *Nat Rev Mol Biol 3*, 906−918.

Zimmer, M. (2010). Green fluorescent protein: a molecular microscope. In K. C. Smith (Ed.), *Photobiological Sciences Online*. Washington, DC: American Society for Photobiology.

This page intentionally left blank

Appendix

Excitability of Smooth Muscles: Some Basic Facts

Nicholas Sperelakis

This Appendix exclusively covers some of the research on smooth muscles by Sperelakis and his outstanding colleagues. This research began with his MS and PhD theses, with the first publications in 1956 and 1958. There are a large number of publications in high-quality refereed journals, with a large number of postdoctoral trainees over several decades. This Appendix should give the reader a firm grasp of many of the fundamentals of the electrical properties of smooth muscles.

I. FAST NA^+ CHANNELS IN SMOOTH MUSCLE CELLS

Smooth muscle cells are usually thought not to possess *fast Na^+ ion channels*. Instead, the inward depolarizing current for the APs usually is carried by Ca^{2+} ions. However, in some smooth muscle cells, a fast Na^+ current can be demonstrated. In at least one case (pregnant rat uterus), this fast Na^+ current likely plays an important functional role. Three examples of smooth muscle cells in which fast Na^+ current has been demonstrated will be presented here.

The first case is the *pregnant rat uterus*. Inoue and Sperelakis (1991) found that fast Na^+ channels begin to appear in the uterine smooth muscle cells during the *second half of pregnancy* (term is 22 days). The greatest *Na^+ current density*, using whole-cell voltage clamp of isolated single cells, was attained just before delivery (Sperelakis et al., 1992). The Na^+ current density at that time was about equal to, or greater than, the inward Ca^{2+} current. The *Ca^{2+} current density* also increased during the latter part of pregnancy, but the changes were not as pronounced as that for the Na^+ channels (Inoue and Sperelakis, 1991). These investigators concluded that the gain of fast Na^+ channels during pregnancy plays a critical role in insuring *fast propagation* of the APs over the entire uterus to enable simultaneous contraction of the organ to expel the fetus. It was found that protein kinase C stimulates the Ca^{2+} current in the rat myometrial cells during pregnancy (Shimamura et al., 1994).

The second case is the *leiomyosarcoma cell*. This cultured cell line, which is commercially available, was derived from a single fibroid tumor cell in the human uterus. Thus, these cells are derived from uterine smooth muscle cells. Kusaka and Sperelakis (1994a,b), using whole-cell voltage clamp of isolated single cells, found that most of the cells had a substantial fast Na^+ current that was tetrodotoxin (TTX)-sensitive. By varying the amount of serum used in the culture medium, they showed that the current density observed was a function of the amount of serum (Kusaka and Sperelakis, 1994b). Hence, they concluded that some unknown substance in the serum induced fast Na^+ channels. One relevant question is whether these channels play a role in the metastasis of the leiomyosarcoma cells to other sites.

The third case is the *intestinal smooth muscle* cells of the rat colon. Xiong and Sperelakis (1995), using whole-cell voltage clamp of single smooth muscle cells isolated from the ascending colon, found that a substantial fraction of the cells examined had a fast Na^+ current that was TTX-sensitive (Xiong et al., 1993). The amplitude of this inward current was dependent on Na^+ ion concentration of the bathing solution and was not affected by the Ca^{2+} ion concentration. Other portions of the colon had a lower incidence of such cells. It seems likely that the fast current plays a role in non-decremental propagation of the APs and increases the velocity of propagation. Their paper appears to be the first report of fast Na^+ current in intestinal smooth muscle cells.

II. PROPAGATION OF OVERSHOOTING ACTION POTENTIALS IN INTESTINAL SMOOTH MUSCLE

It was observed many years ago that the circular muscle layer of the cat small intestine (ileum) propagates action potentials (APs) at a velocity of about 3−5 cm/s (Prosser and Sperelakis, 1956). These studies were done on isolated rings of circular muscle mounted on a glass rod and suspended in

a warm (37°C), moist chamber and using several pairs of recording electrodes and one pair of stimulating electrodes. The propagating APs in the stimulated ring were demonstrated to excite a quiescent adjacent ring when the two rings were pushed into contact for only a few millimeters. This means that the action currents accompanying the propagating APs were of sufficient intensity to stimulate the quiescent ring. Subsequently, intracellular microelectrode recordings were made (Sperelakis and Prosser, 1958). The average *resting potential* (in good impalements) was about −55 mV and the *maximum rate of rise* of the AP (max *dV/dt*) was usually about 5−6 V/s. The *overshoot* of the AP was to about +5 mV. The *duration of the AP*, measured at 50% amplitude (APD_{50}), was about 30 ms.

However, in many smooth muscle cells, the APs were *undershooting* and small in amplitude. The undershoot is to various degrees. To explain these findings, it was suggested that the *delayed rectifier K^+ conductance* (see Chapter 19) turned on unusually fast in those cells, thus terminating the AP very quickly and causing the undershoot. Evidence for this hypothesis was based on the fact that any agent that slowed and depressed the delayed rectifier K^+ conductance caused the undershooting APs to become overshooting. Such agents include Ba^{2+} ions (ca 0.5 mM), TEA^+ (tetraethylammonium ion) (ca 5 mM) and 5-aminopyridine. Since the usual carrier of the inward current for the AP is Ca^{2+} ion (Xiong et al., 1995a), *elevating the external Ca^{2+}* concentration also increased the amplitude of the APs. See previous section above for evidence that, in some cells, Na^+ ion is also involved in carrying the inward current. Changes in the current densities of the Ca^{2+} and K^+ channels occur during development and aging (Xiong et al., 1995b).

Because, under physiological conditions, many cells fire undershooting APs, the APs tend to *decrement in amplitude and velocity*, and hence die out after a certain distance travelled. This is called *decremental conduction*. Evidence for this could be observed in the ring experiments described in the first paragraph above. If decrement did not occur, then it would be expected that a given ring would continue firing APs once the ring was stimulated a single time. This would be true because the ring circumference was ca 3 cm and, at a propagation velocity of 3 cm/s, it would take ca 1.0 s for excitation to traverse the entire ring once. One second is much beyond the APD_{50} value of ca 30 ms and so the cells should be completely out of their refractory periods.

Intestinal smooth muscle cells, like cardiac muscle and skeletal muscle, possess *K_{ATP} ion channels* (Pluja et al., 1998). These K^+ channels are silent when intracellular ATP concentration is normal, but become active when the ATP concentration is reduced, as during ischemia. In the case of myocardial cells, these channels have been demonstrated to help protect the cells during a period of ischemia (by abbreviating the AP and thereby reducing the Ca^{2+} influx, thus conserving ATP).

III. VASCULAR SMOOTH MUSCLE: PART 1

Vascular smooth muscle (VSM) cells are present in the walls of arteries and veins and they regulate the diameter of the blood vessels by changes in their degree of sustained contraction and hence the peripheral resistance of the vasculature. The latter, in turn, determines the blood pressure, if cardiac output is constant. The degree of *sustained contraction* of the smooth muscle cells (SMCs), or *tonus*, is determined by the *Ca^{2+} influx* through the *slow, L-type Ca^{2+} ion channels*. The greater the Ca^{2+} influx, the greater the tonus, hence the smaller the diameter of the blood vessel. The autonomic innervations to the VSM cells affect their tonus.

In the heart musculature, *cyclic AMP* (cAMP) elevation intracellularly stimulates Ca^{2+} influx through the Ca^{2+} channels and *cGMP* elevation depresses the Ca^{2+} channels, hence influx (Sperelakis et al., 1993). In contrast, in VSM, both *cyclic nucleotides* act in the same direction, namely to depress the activity of the Ca^{2+} channels and hence Ca^{2+} influx (Ousterhout and Sperelakis, 1987; Sperelakis et al., 1993, 1994; Xiong et al., 1994; Xiong and Sperelakis, 1995; Liu et al., 1997a; Sunagawa et al., 1998). One example of inhibition by cAMP is given in Fig. A1. Thus, agents that inhibit the *phosphodiesterase-type 5* (PDE-5) enzyme present in VSM, such as Viagra, result in elevation of cGMP in the cells. This activates the *G-kinase* to a greater extent, which *phosphorylates* various proteins, one of which is the Ca^{2+} channel protein(s). This phosphorylation *inhibits* the channel activity, resulting in vasodilation (Sperelakis and Ohya, 1995). *Tyrosine kinase* is also involved in the regulation of the Ca_L channels of VSM (Liu et al, 1997b).

A number of agents, including some hormones, act via the Ca^{2+} channels to affect the degree of vasoconstriction. For, example, *angiotensin-II* (ang-II) stimulates the Ca^{2+} channels and thereby produces a potent vasoconstriction (Seki et al., 1999). More information about ang-II stimulation is presented in Part 2 below. Attachment to the *cytoskeleton via actin filaments* seems to be required for maximal

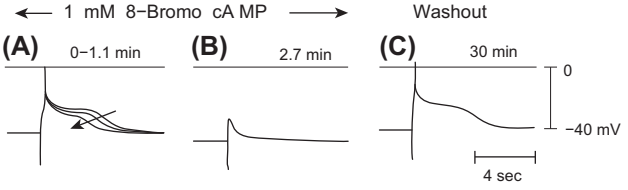

FIGURE A1 Depression and abolition of TEA-induced action potentials (APs) in cultured rat aortic cells by 8-bromo-cAMP (A−C). (A) Superimposed traces of a control AP (in 15 mM TEA) and depression of the AP within 1.1 min after addition of 1.0 mM 8-bromo-cAMP. (B) Abolition of the AP after 2.7 min. (C) Recovery of the AP upon washout for 30 min. (Records A−C were from the same cell.) The stimulation frequency was 0.04 Hz in both experiments. The time and voltage calibrations apply to all records. *(Adapted from Ousterhout and Sperelakis, 1987, with permission.)*

activity of the Ca_L channels, because disruption of the actin filaments inhibits the Ca^{2+} current (Nakamura et al., 2000).

There are a number of types of ion channels in VSM. For example, as in intestinal SMCs stated above, the *K_{ATP} channel* has been demonstrated to be present in VSM cells (Yokoshiki et al., 1997a). The Ca^{2+} channels of VSM cells, as previously shown for myocardial cells, *require ATP to be bound* to them for activity, because it was shown that raising intracellular ATP concentration stimulates the Ca^{2+} current (Ohya and Sperelakis, 1989a,b; Yokoshiki et al., 1997b).

IV. VASCULAR SMOOTH MUSCLE: PART 2

Resting Potential vs $(K)_o$

When the RP was measured, in VSM cells of guinea pig superior mesenteric artery, as a function of the external K^+ concentration and plotted on a log scale, it was found that the average slope of the curve was 32 mV/decade and not the ca 60 mV/decade observed in myocardial cells or skeletal muscle fibers (Harder and Sperelakis, 1987) (Fig. A2). This means that the *P_{Na}/P_K ratio* (see Chapter 9), is relatively high, e.g. 0.1−0.2 (compared to values of about 0.01−0.05 observed in cardiac muscle and skeletal muscle). For example, a P_{Na}/P_K ratio of 0.17 was obtained for guinea pig superior mesenteric artery under control conditions (Table A1). As shown, in the presence of 1.0 mM Ba^{2+}, which depresses P_K, the P_{Na}/P_k ratio became 0.42.

When the curve was extrapolated to zero potential, it gave an estimated *intracellular K^+ concentration* $(K^+)_o$ of 160 mM, a value similar to that obtained for cardiac and skeletal muscles (Fig. A2). When $(K^+)_o$ was lowered below 2 mM, the curve exhibited "fall over", i.e. the RP actually decreased rather than increased. The RP decreased to −32 mV at 0.1 mM K^+. The maximum RP of −54 mV occurred at 2.0 mM. The *fallover of the curve* probably represents the contribution of an *electrogenic pump potential* to the RP (ca 22 mV), because the Na-K pump requires K^+ binding to the outer surface, hence the pump is inhibited at low K_o. (The K_m for K^+ is usually about 2.0 mM). The RPs and input resistances (R_{in}) of several different types of VSM cells is given in Table A1 (Sperelakis and Ohya, 1995).

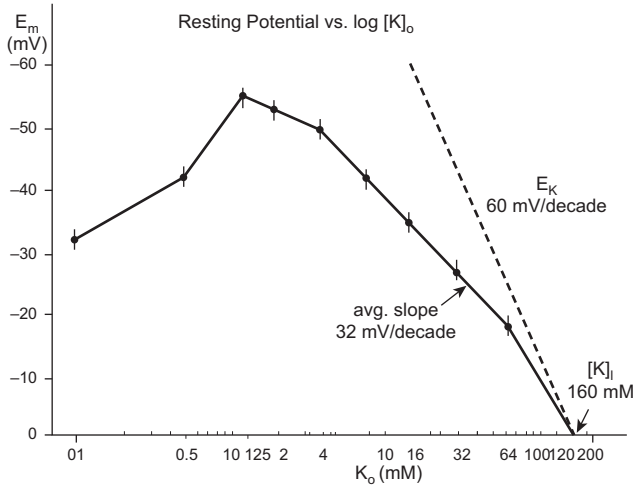

FIGURE A2 Resting potential (E_m) as a function of external K^+ concentration, $[K]_o$ on a log scale, for vascular smooth muscle of guinea pig superior mesenteric artery. The vertical bars represent the mean ±1 SEM for 10−23 impalements in 4−6 muscles. The curve extrapolated to zero potential gives an estimated internal K^+ concentration, $[K]_i$, of 160 mM. The broken line gives the K^+ equilibrium potential (EK), as calculated from the Nernst equation, and has a slope of 60 mV/10-fold change in $[K]_o$. *(From Harder and Sperelakis, 1979, with permission.)*

TABLE A1 Summary of Resting Potentials and Input Resistances of Various Vascular Smooth Muscles

Condition	Resting E_m (mV)	Input Resistance R_{in} (MΩ)	P_{Na}/P_K Ratio
Guinea Pig Superior Mesenteric Artery			
Control	−54 ± 0.6	8.5 ± 0.3	
Ouabain (10^{-5} M)[1]	−46 ± 1.0[a]		0.17
Cl^--free solution	−55 ± 0.6	8.5 ± 0.4	
Ba^{2+} (1.0 mM)	−24 ± 0.8[a]	24.0 ± 1.8*	0.42
Low Na^+ solution	−66 ± 1.3[a]		
Dog Coronary Arteries			
Dog coronary arteries	−56 ± 2	9.0 ± 0.4	
Large diameter	−53 ± 2	10.0 ± 1.0	
Small diameter	−55 ± 1.0		
Small diameter	−54 ± 1.3		

The small coronary arteries were intramural and less than 0.5 mm in diameter; the large coronary arteries were extramural and more than 1.0 mm. Measurements of E_m were made after only 1−5 min exposure to ouabain so that depolarization due to ion shifts would not occur. Data compiled from Harder et al. (1979), Belardinelli et al. (1979), Harder and Sperelakis (1979).

V. HIGH INPUT RESISTANCE AND SHORT LENGTH CONSTANT

As indicated in Table A1, the average input resistance (R_{in}) was 8.5 MOhms in the VSM of guinea pig superior mesenteric artery and 9.0 MOhms in canine coronary artery. This means that current injected intracellularly into one cell does not travel a long distance. Contrary to some reports in the literature, the length constant of intestinal smooth muscle (circular layer), when measured properly, is very short, about the length of one cell (ca 200 μm) (Barr, 1961; Sperelakis and Tarr, 1965). This indicates that there

are either no or very few functioning gap-junction channels between contiguous cells. It was proposed that the intense electric field (EF) that develops in the cell junction when the prejunctional cell fires an AP is the mechanism for the transfer of excitation from cell to cell (Sperelakis and Mann, 1977; Mann and Sperelakis, 1979; Sperelakis et al., 1989; Sperelakis and Ramasamy, 2002).

The **membrane specific resistance R_m** may be calculated from the measured parameters of input resistance (R_{in}), length constant (λ), and fiber radius (α). This was done for smooth muscle, cardiac muscle and skeletal muscle, and the results are summarized in **Table A2.** In those cases in which λ cannot be accurately measured, namely smooth muscle and cardiac muscle [because the cells are short and the end (junctional) membranes have substantial resistance], **equation 1** can be used to calculate R_m, namely the product of R_{in} and fiber membrane surface area (A_s). In the case in which λ can be accurately determined, namely in skeletal muscle (because the multinucleated fibers are very long), **equation 2** may be used to calculate R_m, namely the product of R_{in}, λ, and fiber circumference ($2\pi\alpha$ or πd, where d is the fiber diameter). There is a factor of 2 in equation 2 because the injected current (near the middle of the fiber) spreads in two directions in a long cable. r_m(in Ω-cm) is the membrane resistance of the fiber corrected for unit length (in cm), but not for unit diameter. R_m(in Ω-cm^2) is the membrane resistance corrected for both unit length and unit diameter (to give a fiber circumference of 1.0 cm ($\pi d = 1.0$ cm). The R_M value for squid giant axon is near 1,000 Ω-cm^2.

R_m is sometimes erroneously called the membrane "resistivity". However, the unit of resistivity is always in Ω-cm:

$$\rho_m = R_M/\delta$$

where ρ_m is the true membrane resistivity and δ is the membrane thickness or approximately 0.70×10^{-6} cm. Thus, membrane resistivity would be the resistance of over 10^6 cell membranes stacked in series. A preferred term for R_M is membrane specific resistance.

$$\begin{aligned} R_m &= R_{in\times}A_s \\ &= R_{in} \times \text{circ} \times L \\ &= R_{in} \times n\,d\,L \\ \Omega\text{-cm}^2 &= \Omega \times \text{cm} \times \text{cm} \end{aligned} \qquad \text{eq.1}$$

where d is the cell diameter and L is the cell length. If the membrane surface area is adjusted for the two cell ends (junctional membranes), assuming a corrugation factor of 2.0, then equation 1 becomes:

$$R_m = R_{in} \times (\pi dL + 2(\pi\alpha^2 \times 2.0))$$

However since adding the area of the two end membranes raises the total membrane area by less than 1% (in the case of smooth muscle), the values listed in Table A2 are without the end membranes (namely, A_s).

$$\begin{aligned} R_m &= r_m \times \pi d = (2R_{in}\lambda)\pi d \\ \Omega\text{-cm}^2 &= \Omega\text{-cm} \times \text{cm} \end{aligned} \qquad \text{eq.2}$$

R_M of skeletal muscle was also calculated using equation 1 (see Table A2). In this case, the value of A_s was approximated using the λ value, specifically $2\times\lambda$ or $3\times\lambda$. As can be seen in the table, the value of R_M obtained using $2 \times L$ was almost identical to that obtained from equation 2.

TABLE A2 Summary of Measured Parameters Used to Calculate the Membrane Specific Resistance (R_m)

	Smooth Muscle	Cardiac Muscle	Skeletal Muscle
RP (mV)	–55	–80	–79
R_{in} (M Ω)	8.5	10	0.27
λ (mm)	—	—	0.65
α (μm)	3.0	8.0	28.9
r_m (Ω-cm)	—	—	35.5×10^5
R_m (Ω-cm^2)	320	754	637 (eq 2)
			637 ($2\times\lambda$, eq 1)
			956 ($3\times\lambda$, eq 1)
Dimensions (μm)	6.0×200	16.0×150	57.8×10^4
A_s (cm^2)	3.14×10^{-5}	7.54×10^{-5}	23.6×10^{-4} (for $2 \times \lambda$)
			35.4×10^{-4} (for $3 \times \lambda$)

Smooth muscle: generalized smooth muscles
Cardiac muscle: guinea pig ventricular muscles
Skeletal muscle: mouse EDL muscle (extensor digitorum longus). Values listed were taken from Kerr & Sperelakis, 1983, listed below. The R_n value for frog sartorious muscle is considerably higher.

VI. INDUCTION OF APs BY Ba^{2+} AND TEA^+

Guinea pig superior mesenteric artery VSM cells had large RPs, e.g. −54 mV, but usually were inexcitable to electric stimulation. However, addition of agents that depress the *delayed rectifier K^+ conductance*, such as 4-aminopyridine (4-AP), 0.5 mM Ba^{2+} or 5.0 mM TEA^+ (tetraethylammonium ion) rapidly (usually within 5 min) induced APs, undershooting (Ba^{2+}) or overshooting (TEA^+) to ca +5 mV (Fig. A3). The degree of overshoot could be increased by *elevating the external Ca^{2+}* concentration from the standard 1.8 mM to 4.8 mM

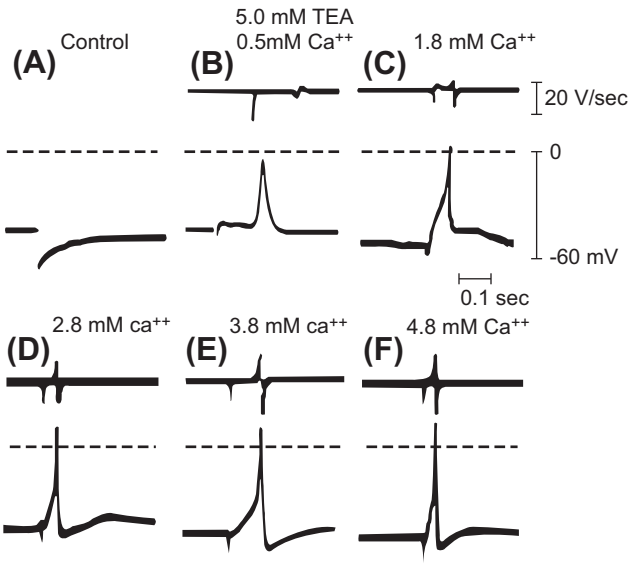

FIGURE A3 Ca^{2+}-dependency of stimulated action potentials (APs) in the presence of TEA^+ in normally inexcitable vascular smooth muscle from guinea pig superior mesenteric artery. All records were taken from one impalement. (A) Control record showing a large RP of −58 mV and lack of spontaneous APs or responses to intense external electrical stimulation (one shock artifact depicted). (B–F) Production of APs (in response to electrical stimulation) after addition of 5 mM TEA, illustrating an increase in amplitude and maximal rate of rise (*dV/dt* max) of APs as $[Ca]_o$ is increased from 0.5 mM (B) to 1.8 mM (C), 2.8 mM (D), 3.8 mM (E) and 4.8 mM (F). The upper trace in (B–F) gives *dV/dt*, the maximal deflection of which is proportional to *dV/dt* max. The horizontal broken line gives the zero potential level. *(Taken from Harder and Sperelakis, 1979, with permission.)*

(Fig. A3). Thus, the inward current for these TEA-induced APs is carried by Ca^{2+} ions through the voltage-dependent slow L-type Ca^{2+} channels (Ca_L channels). A plot of AP amplitude as a function of the Ca^{2+} concentration (on a log scale), gave a slope of about 30 mV/decade (Table A3) (Sperelakis and Ohya, 1995). A slope of ca 30 mV/decade is what is predicted from the Nernst equation if the divalent cation Ca^{2+} were the sole carrier of the inward current during the rising phase of the AP. These Ca^{2+}-dependent APs could be blocked by Ca channel blockers, such as Mn^{2+} ions and verapamil.

VII. ENHANCEMENT OF THE TEA-INDUCED APs

As stated previously above, many VSM cells do not produce APs in response to electrical stimulation. It appeared that the kinetics of the delayed rectifier K^+ channel conductance is too fast to allow an AP to be elicited. Therefore, an agent, such as TEA^+, is added partially to inhibit and slow this K^+ conductance. The following two studies were carried out in the presence of 10 mM or 5 mM TEA^+, respectively.

TABLE A3 Summary of Resting Potentials and Action Potentials of Several Vascular Smooth Muscles

Parameter	Canine Coronary Artery small diam	Canine Coronary Artery large diam	Guinea Pig Superior Mesenteric Artery
Resting E_m (mV)	−53 ± 2	−56 ± 2	−54 ± 1.3
Amplitude of TEA-induced action potentials (mV)	54 ± 1	56 ± 1	59 ± 1
Max *dV/dt* (V/s)	6 ± 1	5 ± 1	6 ± 0.7
Ca^{2+} dependency (mV/decade)	31	30	29

The data are given as the mean ± SE. The duration (at 50% repolarization) of the spikes in the guinea pig was 50–75 ms. From Harder and Speralakis (1979) and Harder and Speralakis (1978), with permission.

The 10 mM TEA-induced APs in cultured VSM cells isolated from rat aorta had overshooting spikes with a pronounced plateau that lasted ca 5 s (Johns and Sperelakis, 1982). Addition of 1.0×10^{-9} M angiotensin-II, a very potent vasoconstrictor, progressively prolonged the plateau component, beginning at ca 5 min and lasting more than 60 min (Fig. A4). At 60 min, the plateau duration was ca 20 s. The spike component did not appear to be affected.

The effect of the cardiac glycoside digoxin was examined on the 5 mM TEA-induced APs of isolated small (ca 0.5 mm) canine coronary arteries (Belardinelli et al., 1979) (Fig. A5). It was found that the amplitude and maximum rate of rise (max *dV/dt*) was greatly enhanced very quickly (ca 2 min). The effects were first noted at 4.0×10^{-9} M and were very prominent at 1.0×10^{-8} M and more-so at 1.0×10^{-7} M. But

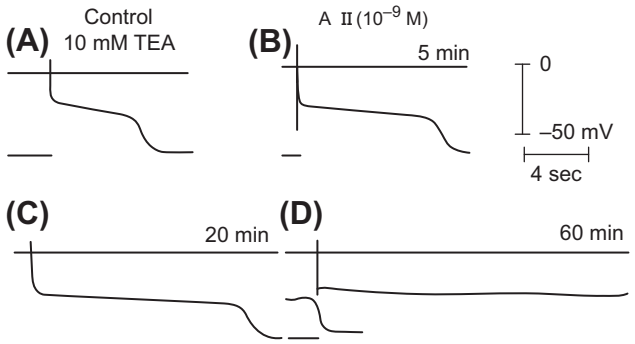

FIGURE A4 Effect of angiotensin (A-II) on the TEA-induced action potential (AP) in a cultured smooth muscle cell from rat aorta. (A) Control AP induced by electrical stimulation in the presence of 10 mM TEA. (B–D) Addition of 10^{-9} M A-II progressively increased the AP duration at 5 min (B), 20 min (C) and 60 min (D). All records were from the same impalement. *(Taken from Johns and Sperelakis, 1982, with permission.)*

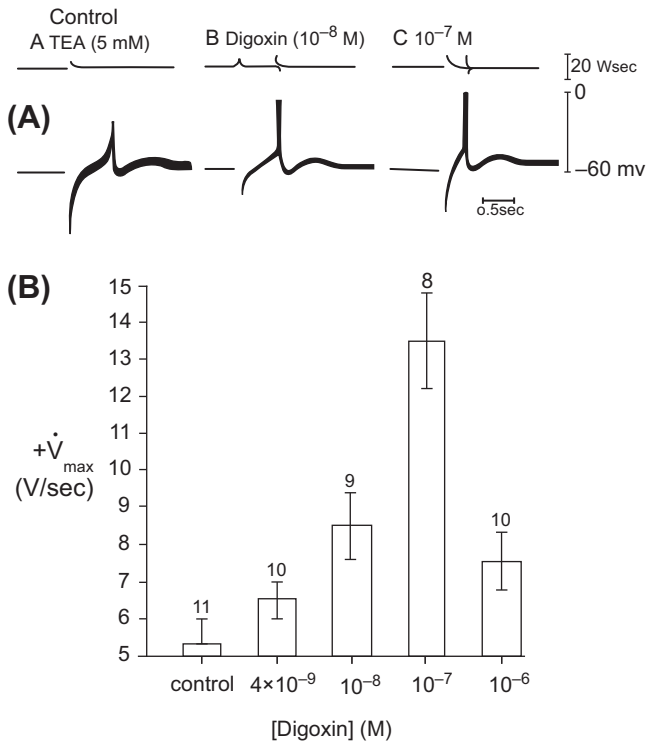

FIGURE A5 (A) Illustration of potentiating effect of digoxin on the amplitude and maximal rate of rise of the action potential (AP). (A) Elicitation of an undershooting AP by electrical stimulation in the presence of TEA (5 mM). (B,C) Records from same cell as in (A) taken within 2 min after the addition of 10^{-8} M (B) and 10^{-7} M (C) digoxin, showing a marked increase in the amplitude and maximal rate of rise of the APs. Upper trace gives *dV/dt*. (B) Summary of data demonstrating the dose-dependency of digoxin on the maximal rate of rise of the AP. The tissue was bathed in 5 mM TEA to allow the elicitation of APs. Each bar gives the mean ± SE for the number of cells impaled (indicated by the number over the bars) in 3–6 coronary arteries. Significant increases in both maximal rate of rise and amplitude occurred at 10^{-8} M and the peak effect occurred at 10^{-7} M. At higher doses of digoxin (10^{-6} M), there was a significant decrease in the maximal rate of rise and amplitude. *(Taken from Belardinelli et al., 1979, with permission.)*

at higher concentrations, the effects became diminished. This very peculiar action may be involved in some of the toxic side effects of cardiac glycosides.

VIII. EXCITATORY JUNCTION POTENTIALS SOMETIMES GIVE RISE TO APs: ANALOGY WITH SLOW FIBERS OF SKELETAL MUSCLE

The ability of *excitatory junction potentials* (EJPs) to trigger APs in the VSM cells of isolated guinea pig superior mesenteric artery was examined (Ishikawa and Sperelakis, 1987). Repetitive nerve stimulation (rectangular pulses 30 μs in duration and 30 V in amplitude) was applied at a frequency of 1.0 Hz for a total of 11 pulses. Each elicited EJP was about 0.5 s in duration (total) and the amplitude of the EJPs varied between ca 3 mV (first one) and ca 8 mV (last one of train of 11) (Fig. A6). That is, the EJPs exhibited *facilitation*. These EJPs, considered "fast", are produced by ATP, the co-transmitter released with norepinephrine (NE) from the nerve terminals. The ion channel that opens up to produce the fast EJP is a *non-selective cation channel* that allows *both Na^+ and Ca^{++} to enter*, thus producing the depolarizing EJP (Zelcer and Sperelakis, 1982).

In some VSMs, e.g. rabbit ear artery, there are *"slow" EJPS* in addition to the fast EJPs. A slow EJP builds up in amplitude during a short train of stimulations. The slow EJPs are *blocked by NE receptor blockers*, such as phentolamine (an α-adrenergic receptor antagonist). In some cases, the slow EJP emerges out of the declining phase of the fast EJP, but is less than half the amplitude of the fast EJP.

As stated above, a fast EJP often triggers an AP. But even if an AP is not elicited, the small depolarization (e.g. ca 8 mV) produced by the EJP itself is sufficient to bring about some Ca^{2+} influx to raise the *level of tone* of the VSM cell. This would be somewhat analogous to the *slow skeletal muscle fibers*, in which a series of motor end-plates, each producing a localized *end-plate potential* (EPP), brings about a slow contraction of the entire fiber (see Chapter 42). That is, the slow fibers do not normally produce APs.

IX. ELECTRICAL EQUIVALENT CIRCUIT FOR VSM CELLS

The electrical equivalent circuit for arterial VSM cells is given in Fig. A7. Only some of the types of ion channels are depicted. For example, the *fast Na^+ channels* that are found in only some SMCs (see above) are not depicted. Likewise, the *K_{ATP} channels*, discussed above, are not presented. Also not depicted are the *T-type* (or fast transient type) Ca^{2+} channels that have been reported to be present in some VSM cells and in some myocardial cells. Finally, there are several types of *receptor-operated channels* (ROCs) that are not shown. One of these is an ROC that is *non-selective for cations*, allowing Na^+, K^+ and Ca^{2+} to pass through. This channel is activated by *norepinephrine* (NE) and is responsible for the genesis of the depolarizing *excitatory junction potential* (EJP) or *excitatory postsynaptic potential* (EPSP) when the sympathetic nerves are active (see above). There is also an NE-activated ROC, specific for Ca^{2+} ions, that is an important source of Ca^{2+} for contraction. Another NE-activated ROC stimulates *phospholipase C*, via a G-protein, to generate *inositol trisphosphate* (IP_3) and diacylglycerol (DG). The IP_3 acts on the SR to release Ca^{2+}. For more details, please refer to Sperelakis and Ohya (1995).

In Fig. A7, the *conductance pathways* are depicted for both the *resting membrane* (g_K, g_{Na}, g_{Ca} and g_{Cl}) and the *excited membrane* (g'_{Ca}, g'_K, $g_{K(Ca)}$). The arrow through any resistance (excited membrane) means that the *resistance*

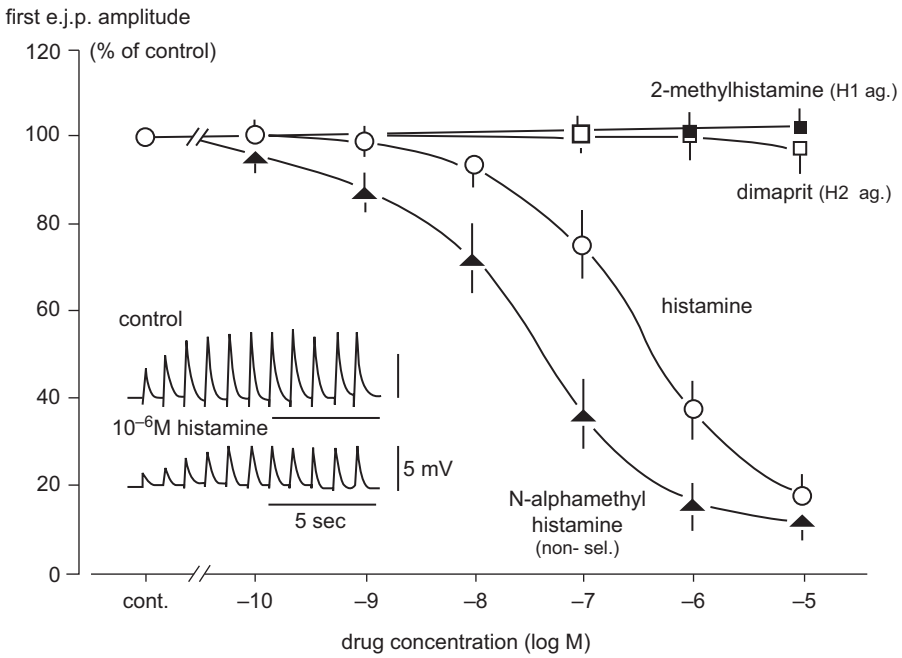

FIGURE A6 Concentration–response curves for the effects of four histamine receptor agonists on neurotransmission in the guinea pig mesenteric artery. The amplitude of the first EJP in a train of stimuli was expressed as a percentage of that in the control. The EJPs were recorded 5–10 min after application of each agonist. The inset shows the inhibitory effect of histamine on the EJPs. The histamine-induced depression of EJP amplitude was not mimicked by 2-methylhistamine (H1 agonist) or dimaprit (H2 agonist). Therefore, it appears that histamine is acting on the H3 receptor. A non-selective histamine derivative, N-α-methyl histamine mimicked the histamine depression with about a 10-fold higher potency than histamine itself. *(Taken from Ishikawa and Sperelakis, 1987, with permission.)*

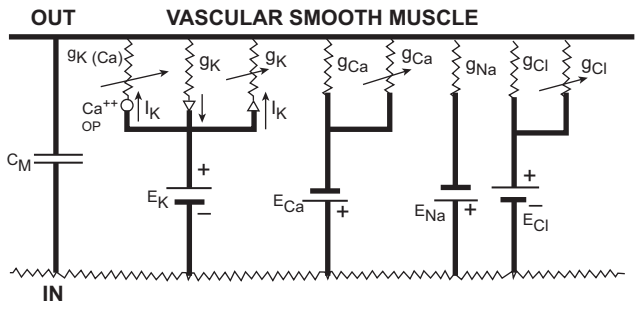

FIGURE A7 Electrical equivalent circuit for the cell membrane of arterial vascular smooth muscle cells. The conductance pathways (channels) are shown both for the resting membrane (g_K, g_{Na}, g_{Ca} and g_{Cl}) and for the excited membrane (g'_{Ca}, g'_K, $g_{K(Ca)}$). The arrow through the resistances (for the excited membrane) represents the fact that the conductance varies with the membrane potential and time, i.e. these are voltage-dependent conductances. $g_{K(Ca)}$ is intracellular Ca^{2+} dependent and voltage dependent, but not time dependent. The equilibrium potentials for the four major ions of concern (E_K, E_{Na}, E_{Ca} and E_{Cl}), as calculated from the Nernst equation for the known ion distributions, are depicted as batteries of differing polarities and magnitudes, as indicated. Ca^{2+} antagonists block the Ca^{2+} channels, whereas TEA^+ and Ba^{2+} block the resting K^+ channels (depress g_K) and depress the kinetics of activation of g_K. One type of voltage-dependent K^+ channel (Ca^{2+} insensitive) allows K^+ to pass more readily outward (outwardly directed rectification or delayed rectification). The AP rising velocity and overshoot is determined by the inward Ca^{2+} current carried through the Ca^{2+} channels. The repolarization of the AP is brought about by a sharp, large increase in g_K and $g_{K(Ca)}$, which are activated by the depolarization and intracellular Ca^{2+}. Inexcitability may be produced when $g_K + g_{K(Ca)}$ is too high. *(Taken from Sperelakis and Ohya, 1995, with permission.)*

varies with voltage and time. The $g_{K(Ca)}$ conductance varies with intracellular *free* Ca^{2+} concentration and voltage. The *equilibrium potentials* for the four major ions, as calculated from the Nernst equation, are depicted as batteries, and are in the *polarity* determined by the direction of the concentration gradients. Please refer to the chapters on electrogenesis of the RP and APs for additional information.

The APs, either natural or induced by TEA^+ (partially to suppress the g_K activation), are generally produced by an inward Ca^{2+} current through V-dependent *slow (L-type)* Ca^{2+} *channels* (Ca_L channels). *Repolarization* of the AP is brought about by two major mechanisms. The first is by a sharp, large *increase in* K^+ *conductance* activated by the depolarization, i.e. the V-dependent K^+ channels (Kv) are activated. The second mechanism is by the increase in Ca^{2+} concentration (produced by the large Ca^{2+} influx through the Ca_L channels) that activates the K_{Ca} channel (or $g_{K(Ca)}$ channel).

BIBLIOGRAPHY

Barr, L. (1961). Transmembrane resistance of smooth muscle cells. *Am J Physiol, 200*, 1251–1255.

Belardinelli, L., Harder, D., Sperelakis, N., Rubio, R., & Berne, R. M. (1979). Cardiac glycoside stimulation of inward Ca^{2+} current in vascular smooth muscle of canine coronary artery. *J Pharmacol Exp Ther, 209*, 62–66.

Harder, D. R., & Sperelakis, N. (1978). Membrane electrical properties of vascular smooth muscle from guinea pig superior mesenteric artery. *Pflügers Arch, 378*, 111–119.

Harder, D. R., & Sperelakis, N. (1979). Action potentials in guinea pig arterial smooth muscle by tetraethylammonium. *Am J Physiol/Cell Physiol, 237*, C75−C80.

Inoue, Y., & Sperelakis, N. (1991). Gestational change in Na+ and Ca2+ channel current densities in rat myometrial smooth muscle cells. *Am J Physiol, 260*, C658−C663.

Ishikawa, S., & Sperelakis, N. (1987). A novel class (H3) of histamine receptors on perivascular nerve terminals. *Nature, 327*, 158−160.

Johns, D. W., & Sperelakis, N. (1982). Angiotensin-II depolarization of cultured vascular smooth muscle cells (abstr). *Circulation, 66*, 204.

Kerr L. M. and N. Sperelakis, Membrane alterations in skeletal muscle fibers of the dystrophic mice. *Muscle &* Nerve, 1983, pages 3−13.

Kusaka, M., & Sperelakis, N. (1994a). Fast sodium currents induced by serum in human uterine leiomyosarcoma cells. *Am J Physiol, 267*, C1288−C1294.

Kusaka, M., & Sperelakis, N. (1994b). Veratridine actions on two types of fast Na+ channels in human uterine leiomyosarcoma cells. *Eur J Pharmacol, 271*, 387−393.

Liu, H., Xiong, Z., & Sperelakis, N. (1997a). Cyclic nucleotides regulate the activity of L-type calcium channels in smooth muscle cells from rat portal vein. *J Mol Cell Cardiol, 29*, 1411−1421.

Liu, H., Li, K., & Sperelakis, N. (1997b). Tyrosine kinase inhibitor, genistein, inhibits macroscopic L-type calcium current in rat portal vein smooth muscle cells. *Can J Physiol Pharmacol, 75*, 1058−1062.

Mann, J. E., Jr., & Sperelakis, N. (1979). Further development of a model for electrical transmission between myocardial cells not connected by low-resistance pathways. *J Electrocardiol, 12*, 23−33.

Nakamura, M., Sunagawa, M., Kosugi, T., & Sperelakis, N. (2000). Actin filament disruption inhibits L-type Ca(2+) channel current in cultured vascular smooth muscle cells. *Am J Physiol Cell Physiol, 279*, C480−C487.

Ohya, Y., & Sperelakis, N. (1989a). Modulation of single slow (L-type) calcium channels by intracellular ATP in vascular smooth muscle cells. *Pflügers Arch, 414*, 257−264.

Ohya, Y., & Sperelakis, N. (1989b). ATP regulation of the slow calcium channels in vascular smooth muscle cells of guinea pig mesenteric artery. *Circ Res, 64*, 145−154.

Ousterhout, J. M., & Sperelakis, N. (1987). Cyclic nucleotides depress action potentials in cultured aortic smooth muscle cells. *Eur J Pharmacol, 144*, 7−14.

Pluja, L., Yokoshiki, H., & Sperelakis, N. (1998). Evidence for presence of ATP-sensitive K+ channels in rat colonic smooth muscle cells. *Can J Physiol Pharmacol, 76*, 1166−1170.

Prosser, C. L., & Sperelakis, N. (1956). Transmission in ganglion-free circular muscle from the cat intestine. *Am J Physiol, 187*, 536−545.

Seki, T., Yokoshiki, H., Sunagawa, M., Nakamura, M., & Sperelakis, N. (1999). Angiotensin II stimulation of Ca2+-channel current in vascular smooth muscle cells is inhibited by lavendustin-A and LY-294002. *Pflügers Arch, 437*, 317−323.

Shimamura, K., Kusaka, M., & Sperelakis, N. (1994). Protein kinase C stimulates Ca2+ current in pregnant rat myometrial cells. *Can J Physiol Pharmacol, 72*, 1304−1307.

Sperelakis, N., & Mann, J. E., Jr. (1977). Evaluation of electric field changes in the cleft between excitable cells. *J Theor Biol, 64*, 71−96.

Sperelakis, N., & Ohya, Y. (1995). Electrophysiology of vascular smooth muscle. In N. Sperelakis (Ed.), *Physiology and Pathophysiology of the Heart* (pp. 859−893). Norwell: Kluwer Academic Publishers.

Sperelakis, N., & Prosser, C. L. (1958). Mechanical and electrical activity in intestinal smooth muscle. *Am J Physiol, 196*, 850−856.

Sperelakis, N., & Ramasamy, L. (2002). Modeling electric field transfer of excitation at cell junctions. *IEEE Eng Med Biol Mag, 21*, 130−143.

Sperelakis, N., & Tarr, M. (1965). Weak electronic interaction between neighboring visceral smooth muscle cells. *Am J Physiol, 208*, 737−747.

Sperelakis, N., Inoue, Y., Nozaki, M., & Ishikawa, S. (1989). Neuromuscular transmission at adrenergic nerve terminals with vascular smooth muscle in guinea-pig mesenteric artery. In N. Sperelakis, & H. Kuriyama (Eds.), *Electrophysiology and Ion Channels of Vascular Smooth Muscle and Endothelial Cells* (pp. 3−15). New York: Elsevier.

Sperelakis, N., Inoue, Y., & Ohya, Y. (1992). Fast Na+ channels in smooth muscle from pregnant rat uterus. *Can J Physiol Pharmacol, 70*, 491−500.

Sperelakis, N., Xiong, Z., Haddad, G., & Masuda, H. (1993). Regulation of slow calcium channels of myocardial cells and vascular smooth muscle cells by cyclic nucleotides and phosphorylation. *Review. Mol Cell Biochem, 140*, 103−117.

Sperelakis, N., Tohse, N., Ohya, Y., & Masuda, H. (1994). Cyclic GMP regulation of calcium slow channels in cardiac muscle and vascular smooth muscle cells. *Review. Adv Pharmacol, 26*, 217−252.

Sunagawa, M., Yokoshiki, H., Seki, T., & Sperelakis, N. (1998). Intracellular application of calmidazolium increases Ca2+ current through activation of protein kinase A in cultured vascular smooth muscle cells. *J Vasc Res, 35*, 303−309.

Xiong, Z., & Sperelakis, N. (1995). Regulation of L-type calcium channels of vascular smooth muscle cells. *Review. J Mol Cell Cardiol, 27*, 75−91.

Xiong, Z., Sperelakis, N., & Fenoglio-Preiser, C. (1994). Regulation of L-type calcium channels by cyclic nucleotides and phosphorylation in smooth muscle cells from rabbit portal vein. *J Vasc Res, 31*, 271−279.

Xiong, Z., Sperelakis, N., Noffsinger, A., & Fenoglio-Preiser, C. (1993). Fast Na+ current in circular smooth muscle cells of the large intestine. *Pflügers Arch, 423*, 485−491.

Xiong, Z., Sperelakis, N., Noffsinger, A., & Fenoglio-Preiser, C. (1995a). Ca2+ currents in human colonic smooth muscle cells. *Am J Physiol, 269*, G378−G385.

Xiong, Z., Sperelakis, N., Noffsinger, A., & Fenoglio-Preiser, C. (1995b). Potassium currents in rat colonic smooth muscle cells and changes during development and aging. *Pflügers Arch, 430*, 563−572.

Yokoshiki, H., Katsube, Y., Sunagawa, M., & Sperelakis, N. (1997a). Levosimendan, a novel Ca2+ sensitizer, activates the glibenclamide-sensitive K+ channel in rat arterial myocytes. *Eur J Pharmacol, 333*, 249−259.

Yokoshiki, H., Katsube, Y., & Sperelakis, N. (1997b). Regulation of Ca2+ channel currents by intracellular ATP in smooth muscle cells of rat mesenteric artery. *Am J Physiol, 272*, H814−H819.

Zelcer, E., & Sperelakis, N. (1982). Spontaneous electrical activity in pressurized small mesenteric arteries in hypertensive rats. *Blood Vessels, 19*, 301−310.

Index

B

C

D

E

F

G

M

N

O

P

T

U

V

W

X

Z